THRALL

VETERINARY DIAGNOSTIC RADIOLOGY

Sixth Edition

ELSEVIER

THRALL

Textbook of

VETERINARY DIAGNOSTIC RADIOLOGY

Sixth Edition



ELSEVIER

http://evolve.elsevier.com

Textbook of
VETERINARY DIAGNOSTIC RADIOLOGY

This page intentionally left blank

Textbook of

VETERINARY DIAGNOSTIC RADIOLOGY

Sixth Edition



DONALD E. THRALL, DVM, PhD

Professor of Radiology
College of Veterinary Medicine
North Carolina State University
Raleigh, North Carolina

ELSEVIER

ELSEVIER
SAUNDERS

3251 Riverport Lane
St. Louis, Missouri 63043

TEXTBOOK OF VETERINARY DIAGNOSTIC RADIOLOGY, SIXTH EDITION 978-1-4557-0364-7

Copyright 2013, 2007, 2002, 1998, 1994, 1986 by Saunders, an imprint of Elsevier Inc.

No part of this publication may be reproduced or transmitted in any form or by any means, electronic or mechanical, including photocopying, recording, or any information storage and retrieval system, without permission in writing from the publisher. Details on how to seek permission, further information about the Publisher's permissions policies and our arrangements with organizations such as the Copyright Clearance Center and the Copyright Licensing Agency, can be found at our website: www.elsevier.com/permissions.

This book and the individual contributions contained in it are protected under copyright by the Publisher (other than as may be noted herein).

Notices

Knowledge and best practice in this field are constantly changing. As new research and experience broaden our understanding, changes in research methods, professional practices, or medical treatment may become necessary.

Practitioners and researchers must always rely on their own experience and knowledge in evaluating and using any information, methods, compounds, or experiments described herein. In using such information or methods they should be mindful of their own safety and the safety of others, including parties for whom they have a professional responsibility.

With respect to any drug or pharmaceutical products identified, readers are advised to check the most current information provided (i) on procedures featured or (ii) by the manufacturer of each product to be administered, to verify the recommended dose or formula, the method and duration of administration, and contraindications. It is the responsibility of practitioners, relying on their own experience and knowledge of their patients, to make diagnoses, to determine dosages and the best treatment for each individual patient, and to take all appropriate safety precautions.

To the fullest extent of the law, neither the Publisher nor the authors, contributors, or editors, assume any liability for any injury and/or damage to persons or property as a matter of products liability, negligence or otherwise, or from any use or operation of any methods, products, instructions, or ideas contained in the material herein.

978-1-4557-0364-7

Vice President and Publisher: Linda Duncan
Content Strategy Director: Penny Rudolph
Content Manager: Shelly Stringer
Publishing Services Manager: Julie Eddy
Senior Project Manager: Andrea Campbell
Design Manager: Teresa McBryan

Working together to grow libraries in developing countries
www.elsevier.com | www.bookaid.org | www.sabre.org
ELSEVIER BOOK AID International Sabre Foundation

Printed in the United States of America

Last digit is the print number: 9 8 7 6 5 4 3 2 1

Contributors

Kate Alexander, DMV, MS, DACVR
Associate Professor, Diagnostic Imaging
Department of Clinical Sciences
Faculty of Veterinary Medicine
University of Montreal
Saint-Hyacinthe, Québec, Canada

Graeme Allan, DVSc, MVSc, FACVSc, DACVR
Radiology and Ultrasound Specialist
Veterinary Imaging Associates
Newtown, New South Wales, Australia
Adjunct Professor
Faculty of Veterinary Science
University of Sydney
Sydney, New South Wales, Australia

Fabrice Audigié, DVM, PhD
Professor in Equine Imaging and Locomotor Pathology
CIRALE
USC Biomécanique et Pathologie Locomotrice du Cheval
Ecole Nationale Vétérinaire d'Alfort
France

Robert J. Bahr, DVM, DACVR
Associate Professor
Veterinary Radiology
Department of Veterinary Clinical Sciences
Center for Veterinary Health Sciences
Oklahoma State University
Stillwater, Oklahoma

Marianna Biggi, DVM, PhD, MRCVS
Radiographer
Centre for Equine Studies
Animal Health Trust
Newmarket, Suffolk, United Kingdom

Lisa G. Britt, DVM, MS, DACVR
Clinical Assistant Professor in Radiology
Department of Veterinary Medicine and Surgery
College of Veterinary Medicine
University of Missouri
Columbia, Missouri

James W. Brown Jr., DVM, MS, DACVR
Clinical Assistant Professor
Department of Molecular and Biomedical Sciences
College of Agriculture & Life Sciences
North Carolina State University
Raleigh, North Carolina

Valeria Busoni, DVM, PhD, DECVDI
Service D'Imagerie Meidcale
Clinique Veterinaire Universitaire—Pôle Equin
Departement Clinique DesAnimaux De Compagnie Et Des Equides
Faculte De Medecine Veterinaire
Universite De Liege
Belgium

Marc-André d'Anjou, DMV, DACVR
Associate Professor in Diagnostic Imaging
Clinical Sciences
Faculté de médecine vétérinaire de l'Université de Montréal
Saint-Hyacinthe, Québec, Canada

William Tod Drost, DVM, DACVR
Associate Professor
Department of Veterinary Clinical Sciences
The Ohio State University
Columbus, Ohio

Sue J. Dyson, MA, VetMB, DEO, PhD, FRCVS
Head of Clinical Orthopaedics
Centre for Equine Studies
Animal Health Trust
Newmarket, Suffolk, United Kingdom

Stephanie C. Essman, DVM, BS, MS, DACVR
Assistant Professor
Department of Veterinary Medicine and Surgery
Veterinary Medical Teaching Hospital
College of Veterinary Medicine
University of Missouri
Columbia, Missouri

Lisa J. Forrest, VMD, DACVR
Professor
Department of Surgical Sciences
School of Veterinary Medicine, University of Wisconsin-Madison
Madison, Wisconsin

Paul M. Frank, DVM, DACVR
Radiologist
Antech Imaging Services
Hillsborough, North Carolina

Lorrie Gaschen, PhD, DVM, Dr. Med. Vet.
Professor
Department of Veterinary Clinical Sciences
Louisiana State University
Baton Rouge, Louisiana

George A. Henry, DVM, DACVR
Clinical Associate
Professor of Radiology
Department of Small Animal Clinical Sciences
College of Veterinary Medicine
University of Tennessee
Knoxville, Tennessee

Jennifer Kinns, BSc, VetMB, MRCVS, DACVR, DECVDI
Assistant Professor;
Residency Program Director
Diagnostic Imaging/Radiology
Departments of Small and Large Animal Clinical Sciences
College of Veterinary Medicine
Michigan State University
East Lansing, Michigan

Martha Moon Larson, DVM, MS, DACVR
Professor of Radiology
Department of Small Animal Clinical Sciences
Virginia-Maryland Regional College of Veterinary Medicine
Virginia Tech
Blacksburg, Virginia

Jimmy C. Lattimer, DVM, BS, MS, DACVR
Associate Professor of Radiology
Department of Veterinary Medicine and Surgery
Veterinary Medical Teaching Hospital
College of Veterinary Medicine
University of Missouri
Columbia, Missouri

Wilfried Mai, Dr. Med. Vet., MS, PhD, DECVDI, DACVR
Assistant Professor of Radiology
Department of Clinical Studies
School of Veterinary Medicine
University of Pennsylvania
Philadelphia, Pennsylvania

Angela J. Marolf, DVM, DACVR
Assistant Professor
Department of Environmental and Radiological Health Sciences
Veterinary Medical Center
College of Veterinary Medicine and Biomedical Sciences
Colorado State University
Fort Collins, Colorado

Federica Morandi, DVM, MS, DECVDI, DACVR
Associate Professor and Director of Radiological Services
Department of Small Animal Clinical Sciences
College of Veterinary Medicine
The University of Tennessee
Knoxville, Tennessee

Rachel Murray, MA, VetMB, MS, PhD, DACVS
Senior Orthopaedic Advisor
Centre for Equine Studies
Animal Health Trust
Newmarket, Suffolk, United Kingdom

Stephanie Nykamp, DVM, DACVR
Associate Professor
Department of Clinical Studies
Ontario Veterinary College
University of Guelph
Guelph, Ontario, Canada

Richard D. Park, DVM, PhD, DACVR
Professor
Department of Environmental and Radiological Health Sciences
Veterinary Teaching Hospital
College of Veterinary Medicine and Biomedical Sciences
Colorado State University
Fort Collins, Colorado

Anthony Pease, DVM, MS, DACVR
Section Chief, Diagnostic Imaging
Department of Small Animal Clinical Sciences
College of Veterinary Medicine
Michigan State University
East Lansing, Michigan

Rachel E. Pollard, DVM, PhD
Assistant Professor
Department of Surgical and Radiological Sciences
School of Veterinary Medicine
University of California
Davis, California

Elissa K. Randall, DVM, MS, DACVR
Assistant Professor
Department of Environmental and Radiological Health Sciences
Colorado State University
Fort Collins, Colorado

Elizabeth Riedesel, DVM, DACVR
Associate Professor
Department of Veterinary Clinical Sciences
College of Veterinary Medicine
Iowa State University
Ames, Iowa

Ian D. Robertson, BVSc, DACVR
Clinical Assistant Professor
Department of Molecular Biomedical Sciences
College of Veterinary Medicine
North Carolina State University
Raleigh, North Carolina

Valerie F. Samii, DVM, DACVR
Adjunct Professor
Department of Veterinary Clinical Sciences
College of Veterinary Medicine
The Ohio State University
Columbus, Ohio

Tobias Schwarz, MA, Dr. Med. Vet., DVR, DECVDI, DACVR
Royal (Dick) School of Veterinary Studies
The University of Edinburgh
Easter Bush Veterinary Centre
Roslin, Scotland, United Kingdom

Gabriela S. Seiler, Dr. Med. Vet., DECVDI, DACVR
Associate Professor Radiology
Department of Molecular Biomedical Sciences
College of Veterinary Medicine
North Carolina State University
Raleigh, North Carolina

James Edgar Smallwood, DVM, MS
Professor of Gross Anatomy
Department of Molecular Biomedical Sciences
College of Veterinary Medicine
North Carolina State University
Raleigh, North Carolina

Kathy Ann Spaulding, DVM, DACVR
Clinical Professor Radiology
Department of Large Animal Clinical Sciences
College of Veterinary Medicine
Texas A&M University
College Station, Texas

Donald E. Thrall, DVM, PhD, MS, DAVCR
Professor
Department of Molecular Biomedical Sciences
College of Veterinary Medicine
North Carolina State University
Raleigh, North Carolina

Russell L. Tucker, DVM, DACVR
Associate Professor
Chief of Radiology
Department of Veterinary Clinical Sciences
College of Veterinary Medicine
Washington State University
Pullman, Washington

William R. Widmer, DVM, MS, DAVCR
Professor Emeritus, Radiology
Department of Veterinary Clinical Sciences
School of Veterinary Medicine
Purdue University
West Lafayette, Indiana

Erik R. Wisner, DVM, DACVR
Professor and Chair
Department of Surgical and Radiological Sciences
School of Veterinary Medicine
University of California
Davis, California

This page intentionally left blank

Preface

As with all previous editions, the primary objective of this book is an instructional aid for students of imaging. It is directed principally at the veterinary student, but we have also provided useful information for those pursuing advanced training in imaging and also those in private veterinary practice. Students at all levels should be able to find material in the 6th edition that helps in the interpretation of basic and challenging images. Valuable features of prior editions such as the self-assessment questions and the atlas of normal anatomy have been retained and widespread revision in content has been undertaken. The normal anatomy material remains dispersed throughout the text so that it can be consulted conveniently and it is also available on the Elsevier website.

The interface between the book and the world-wide web has also been retained. A web portal hosts self-assessment exercises that can be completed online and grading obtained immediately. For some chapters, movies are available online that will assist in the explanation of complex subjects, such as computed tomography (CT) or magnetic resonance (MR) imaging physics, or dynamic disease processes, such as tracheal collapse and esophageal disorders.

As in the second through fifth editions, all chapters have been reviewed carefully, making for an extensive, substantive revision. No chapter has escaped in-depth scrutiny, ensuring that the latest and most accurate information is included. Basic chapters covering the basic aspects of interpretation, applicable when assessing radiographic images of the axial and appendicular skeleton in small and large animals, and the thorax and abdomen in small animals have been rewritten completely. Details of positioning, and specific anatomic features of the body part in question are some of the topics covered in these introductory chapters. These basic chapters offer a framework to increase the understanding of the more detailed chapters dealing with specific anatomic areas.

Veterinary imaging is becoming increasing complex and digital imaging continues to be adopted. As a result, chapters on the basic principles of digital imaging and the MR imaging features of brain disease in small animals have been expanded. Also, the breadth of the CT and MR imaging features of diseases outside of the brain has been broadened, and chapters covering the physical principles of ultrasonography and CT and MR imaging updated significantly. Details regarding techniques that were once a mainstay of veterinary imaging, such as the upper gastrointestinal examination and myelography, have been removed from the book but retained on the Elsevier website for reference when needed.

The basis of interpretation used in this textbook remains centered upon description of radiographic abnormalities in terms of Roentgen signs—changes in size, shape, location, number, margination and opacity. I believe that students who have a firm understanding of Roentgen sign description will be less inclined to make errors by jumping immediately to a diagnosis rather than thoroughly considering radiographic changes in an orderly and efficient manner.

Donald E. Thrall

Acknowledgments

Thanks are extended to all who have used prior editions of this work and to those who have pointed out errors or omissions, thereby allowing this edition to be what I believe is the best yet. As it is impossible for one person to prepare a meaningful, comprehensive textbook of veterinary imaging, I am fortunate to have so many talented authors take time from their busy schedules to prepare material for this book. Many new authors have contributed to this sixth edition and many familiar names are again found as contributors. The expertise of this team heightens the quality of the information contained on these pages and I am honored by their participation.

Donald E. Thrall

Contents

SECTION I
Physics and Principles of Interpretation

1 **Radiation Protection and Physics of Diagnostic Radiology,** 2
Donald E. Thrall • William R. Widmer

2 **Digital Radiographic Imaging,** 22
Ian D. Robertson • Donald E. Thrall

3 **Physics of Ultrasound Imaging,** 38
William Tod Drost

4 **Principles of Computed Tomography and Magnetic Resonance Imaging,** 50
Marc-André d'Anjou

5 **Introduction to Radiographic Interpretation,** 74
Donald E. Thrall

SECTION II
The Axial Skeleton: Canine, Feline, and Equine

6 **Radiographic Anatomy of the Axial Skeleton,** 88
James E. Smallwood • Kathy A. Spaulding

7 **Principles of Radiographic Interpretation of the Axial Skeleton,** 101
Donald E. Thrall

8 **The Cranial and Nasal Cavities: Canine and Feline,** 114
Lisa J. Forrest

9 **Magnetic Resonance Imaging Features of Brain Disease in Small Animals,** 135
Ian D. Robertson

10 **The Equine Head,** 153
Anthony P. Pease

11 **The Canine and Feline Vertebrae,** 172
William R. Widmer • Donald E. Thrall

12 **Magnetic Resonance Imaging and Computed Tomography Features of Canine and Feline Spinal Cord Disease,** 194
Wilfried Mai

SECTION III
The Appendicular Skeleton: Canine, Feline, and Equine

13 **Radiographic Anatomy of the Appendicular Skeleton,** 224
James E. Smallwood • Kathy A. Spaulding

14 **Principles of Radiographic Interpretation of the Appendicular Skeleton,** 252
Donald E. Thrall

15 **Orthopedic Diseases of Young and Growing Dogs and Cats,** 267
Rachel E. Pollard • Erik R. Wisner

16 **Fracture Healing and Complications,** 283
George A. Henry

17 **Radiographic Features of Bone Tumors and Bone Infection,** 307
Donald E. Thrall

18 **Radiographic Signs of Joint Disease in Dogs and Cats,** 319
Graeme Allan

19 **The Equine Stifle and Tarsus,** 349
Valeria Busoni • Fabrice Audigié

20 **The Equine Carpus,** 374
Rachel C. Murray • Sue J. Dyson

21 **The Equine Metacarpal and Metatarsal Regions,** 394
Sue J. Dyson • Marianna Biggi

22 **The Equine Metacarpophalangeal and Metatarsophalangeal Articulation,** 414
Lisa G. Britt • Russell L. Tucker

23 **The Equine Phalanges,** 429
Elizabeth A. Riedesel

24 **The Equine Navicular Bone,** 457
Federica Morandi

SECTION IV
The Thoracic Cavity: Canine, Feline, and Equine

25 **Principles of Radiographic Interpretation of the Thorax,** 474
Donald E. Thrall

26 **The Pharynx, Larynx, and Trachea,** 489
Kate Alexander

27 **The Canine and Feline Esophagus,** 500
Lorrie Gaschen

28 **The Thoracic Wall,** 522
Valerie F. Samii

29 **The Diaphragm,** 535
Elissa K. Randall • Richard D. Park

30 **The Mediastinum,** 550
Donald E. Thrall

31 **The Pleural Space,** 571
Donald E. Thrall

32 **The Heart and Pulmonary Vessels,** 585
Robert Bahr

33 **The Canine and Feline Lung,** 608
Donald E. Thrall

34 **The Equine Thorax,** 632
Stephanie G. Nykamp

SECTION V
The Abdominal Cavity: Canine and Feline

35 **Principles of Radiographic Interpretation of the Abdomen,** 650
Donald E. Thrall

36 **The Peritoneal Space,** 659
Paul M. Frank

37 **The Liver and Spleen,** 679
Martha Moon Larson

38 **The Kidneys and Ureters,** 705
Gabriela S. Seiler

39 **The Urinary Bladder,** 726
Angela J. Marolf • Richard D. Park

40 **The Urethra,** 744
James C. Brown, Jr.

41 **The Prostate Gland,** 749
Jimmy C. Lattimer • Stephanie C. Essman

42 **The Uterus, Ovaries, and Testes,** 757
Jennifer Kinns • Nathan Nelson

43 **The Stomach,** 769
Paul M. Frank

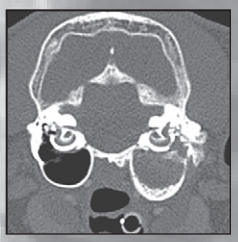
44 **The Small Bowel,** 789
Elizabeth A. Riedesel

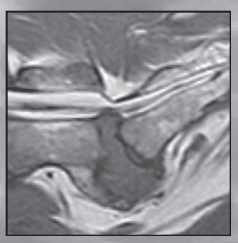
45 **The Large Bowel,** 812
Tobias Schwarz

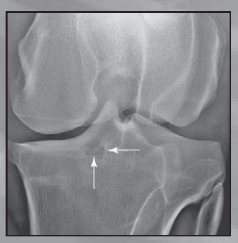
Index, 825

SECTION I

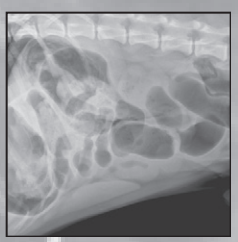
Physics and Principles of Interpretation











1 **Radiation Protection and Physics of Diagnostic Radiology**
Donald E. Thrall
William R. Widmer

2 **Digital Radiographic Imaging**
Ian D. Robertson
Donald E. Thrall

3 **Physics of Ultrasound Imaging**
William Tod Drost

4 **Principles of Computed Tomography and Magnetic Resonance Imaging**
Marc-André d'Anjou

5 **Introduction to Radiographic Interpretation**
Donald E. Thrall

CHAPTER • 1

Radiation Protection and Physics of Diagnostic Radiology

Donald E. Thrall
William R. Widmer

X-rays were discovered on November 8, 1895, by Wilhelm Conrad Roentgen, a German physicist.[1] This new modality was put to use quickly for medical purposes, and many sophisticated medical applications were soon devised. For example, angiography was described in 1896, only 1 year after the initial discovery of x-rays. Roentgen's finding revolutionized the diagnosis and treatment of disease, and in recognition he was awarded the first Nobel Prize for Physics in 1901. More than 110 years after their discovery, x-rays remain in widespread use for radiography and computed tomography in people and animals.

BASIC PROPERTIES OF X-RAYS

X-rays and gamma rays are part of the spectrum of electromagnetic radiation. The only distinction between x-rays and gamma rays is their source; x-rays are produced by electron interactions outside the nucleus, and gamma rays are released from unstable nuclei having excess energy. There is a tendency to believe that gamma rays are more energetic than x-rays, but this is not true universally. The energy of a gamma ray depends on the amount of energy released by an unstable nucleus, and the energy of an x-ray depends on the energy of the electron that interacts with an atom. Familiar types of electromagnetic radiation other than x-rays and gamma rays include radio waves, radar, microwaves, and visible light (Table 1-1).

Electromagnetic radiation is a combination of electric and magnetic fields that travel together, oscillating in orthogonal planes in sine-wave fashion (Fig. 1-1). Sine waves are characterized by two related parameters—frequency and wavelength. The velocity of electromagnetic radiation is constant, at the speed of light, and is the product of the frequency and wavelength:

$$\text{Velocity (m/sec)} = \text{frequency (per sec)} \times \text{wavelength (m)}$$

Because the velocity of electromagnetic radiation is constant, the frequency and wavelength are inversely related; therefore, as frequency increases, wavelength must decrease, and vice versa.

Some physical properties of electromagnetic radiation cannot be explained adequately by the theories of wave propagation illustrated in Figure 1-1. Therefore the *photon* concept was developed to explain the apparent particulate behavior of x-rays and gamma rays. A photon can be considered as a discrete bundle of electromagnetic radiation as opposed to a wave. This makes it easier to understand how x-rays create an image or cause radiation damage. In this book, the terms *x-ray* and *photon* are used interchangeably. Properties of x-rays and gamma rays are given in Box 1-1.

The energy of electromagnetic radiation is described according to the formula:

$$\text{Energy} = \text{Planck's constant} \times \frac{\text{speed of light}}{\text{wavelength}}$$

Planck's constant is a proportionality constant between the energy of a photon and the wavelength of its associated wave, and the speed of light is also a constant. Therefore the energy of electromagnetic radiation is inversely proportional to wavelength. The biologic effects of electromagnetic radiation are linked closely to energy.

The unit of energy for electromagnetic radiation is the *electron volt* (eV). One electron volt is the energy gained by one electron as it is accelerated through a potential difference of 1 V. On an absolute scale, this is a very small amount of energy. However x-rays with energy of only 15 eV* can produce ionization of atoms or molecules. Ionization occurs when an electron is ejected from the atom, in this case by an x-ray. This creates an ion pair consisting of the negatively charged electron and the positively charged atom (Fig. 1-2). The ejected electrons can damage DNA, leading to (1) mutations, (2) abortion or fetal abnormalities, (3) susceptibility to disease and shortened life span, (4) carcinogenesis, and (5) cataracts.[2] Radiation damage to DNA can be thought of as being amplified biologically because DNA controls cellular processes that extend into subsequent generations of daughter cells. Although only 15 eV of energy is required for ionization of biologic molecules, the energy of x-rays used for medical imaging is much higher, and each photon can lead to multiple ionizations as its energy is dissipated in the tissue.

It is important to appreciate the relative risk of biologic injury produced by x-rays or gamma rays compared to other types of electromagnetic radiation. For example, the wavelength of visible light is 10,000 times longer than the wavelength of x-rays, and the wavelength of radio waves is even longer (see Table 1-1). Because the energy of electromagnetic radiation is inversely proportional to wavelength, the energy of light waves and radio waves is many orders of magnitude lower than the energy of x-rays. Thus light and radio waves do not produce tissue ionization or DNA damage. This is not to say that other forms of electromagnetic radiation cannot

*The electron volt (eV) should not be confused with the concept of kilovoltage peak (kVp) applied in an x-ray tube during an exposure; kVp will be discussed later under the topic of x-ray production.

Table • **1-1**

Wavelength of Common Types of Electromagnetic Radiation

TYPE OF ELECTROMAGNETIC RADIATION	WAVELENGTH (CM)
Radio waves	30,000
Microwaves	10
Visible light	0.0001
X-rays	0.00000001

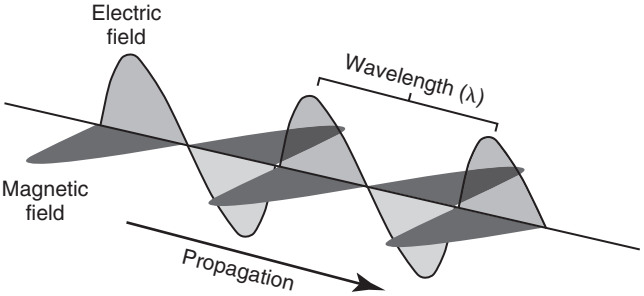


Fig. 1-1 All forms of electromagnetic radiation are characterized by oscillating electric and magnetic fields that move in orthogonal planes. The distance between crests, λ, is the wavelength. Another descriptor of electromagnetic radiation is the frequency, f, or the number of crests per unit time. The velocity (c) of electromagnetic is a constant—the speed of light. Velocity is related to the product of wavelength and frequency; $c = f \times \lambda$. Thus, because velocity is constant, as frequency increases the wavelength must decrease, and vice versa.

Box • **1-1**

Properties of X-Rays and Gamma Rays

Have no charge
Have no mass
Travel at the speed of light
Are invisible
Cannot be felt
Travel in a straight line
Cannot be deflected by magnetic fields
Penetrate all matter to some degree
Cause certain substances to fluoresce
Can expose photographic emulsions
Can ionize atoms

create injury, such as tissue heating from microwaves, just that they do not lead to molecular ionization.

RADIATION PROTECTION

A goal in diagnostic radiology is to obtain maximum diagnostic information with minimal radiation exposure of the patient, radiology personnel, and general public. This is achievable readily in light of the guidelines for safe practice that have been developed, and the technology available to reduce exposure to personnel. However, because x-rays cannot be

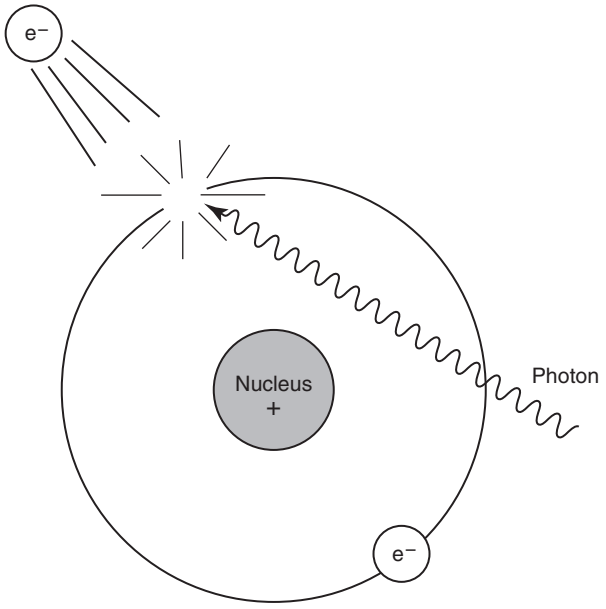


Fig. 1-2 The principle of ionization. A photon ejects an electron from an atom, causing ionization, forming an ion pair. The ion pair consists of the negatively charged electron and the atom; the atom is positively charged after losing the negatively charged electron. After this ionization event, the photon, depending on its energy, may be completely absorbed, or it may interact with other atoms to produce more ionization. The ejected electron can also interact with biologic molecules, such as DNA, and produce damage. The relative size of the nucleus, electrons, and orbital shells is not to scale. The "+" symbol in the nucleus designates the normal nuclear positivity created by the presence of positively charged protons. In a neutral atom, this positive charge in the nucleus is balanced by the negative charge of the orbital electrons.

seen or felt, the idiom "out of sight out of mind" has never been more applicable, and it is easy to disregard the potential danger associated with occupational x-ray exposure (Fig. 1-3). As a result, many veterinarians have developed a cavalier attitude regarding the hazards associated with ionizing radiation and put themselves and their employees at risk, from both medical and financial perspectives. General principles of radiation protection that can form the basis of a safe workplace are discussed later. Any specific recommendations made in this chapter are subject to overrule by local, state, and/or federal regulations.

Radiation Units

Two related concepts are important to understand before radiation units are considered. First, radiation *exposure* and radiation *absorption* are not the same. Some tissues absorb radiation more effectively than others, meaning that the same exposure dose can result in different absorbed doses. Second, the biologic effect of the same absorbed dose can also be different, being a function of both radiation type and energy. A numeric *weighting factor* or *quality factor* has been derived to estimate the difference in biologic effectiveness of various types of radiation (Table 1-2).

Radiation exposure, radiation absorption, and dose equivalent, because of differences in radiation quality, each have their own unit of measure that was defined originally in the centimeter-gram-second (CGS) system of measures. In 1977 the International System of Units (SI units) was developed in keeping with the trend toward universal adoption of the metric system[3] (Table 1-3). In general, the system of SI units has been ignored in the United States,[4,5] and CGS radiation units are still used widely, which can be a source of confusion.

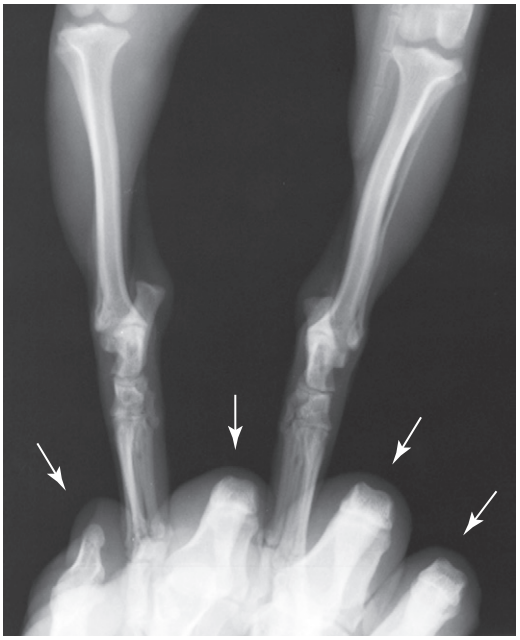


Fig. 1-3 Careless approach to radiography. The radiographer has neglected to wear protective gloves, leading to unshielded fingers (*arrows*) being exposed to the primary x-ray beam. These careless habits are perpetuated because of the stealthy properties of x-rays and lead to unnecessary personnel exposure that could become biologically significant.

Table • **1-2**

Radiation Weighting Factor (Quality Factor) for Various Radiation Types

TYPE OF RADIATION	WEIGHTING FACTOR
X-rays	1
Gamma rays	1
Beta particle (electron)	1
Neutrons	
<10 keV	5
10—100 keV	10
100 keV—2 MeV	20
Alpha particles	20

Exposure

Radiation exposure is quantified by the amount of electrical charge resulting from the ionization of air produced by the radiation flux. Radiation exposure is expressed in the SI system as coulombs* per kilogram of air (C/kg) (see Table 1-3). This SI unit of exposure is cumbersome; thus the previous term of exposure, the roentgen, is still used. One roentgen equals a charge of 2.58 C/kg in air.

Absorbed Dose

The efficiency of x-ray absorption in different materials can vary widely. Therefore the absorbed radiation dose in tissues with different absorption efficiencies will be different when the tissues are exposed to the same amount of radiation (Fig. 1-4). The SI unit for absorbed dose is the *gray* (Gy). The gray is the amount of radiation leading to absorption of 1 joule*/kg of tissue. Before SI units were accepted, the unit of absorbed dose was the rad, which is equal to 100 ergs†/g (see Table 1-3). The term *rad* is obsolete, but it is so engrained in the radiology lexicon that it has not been replaced universally by the Gy, its SI counterpart. By using appropriate conversion factors, it can be shown that 1 Gy = 100 rad.

It is a fact that in soft tissue, exposure to 1 roentgen amounts to an absorbed dose of approximately 0.9 centigray (cGy) or 0.9 rad. However, bone is a more efficient absorber of x-rays than soft tissue, and exposure to bone of 1 roentgen results in a bone-absorbed dose of more than 0.9 cGy. This difference between exposure and absorbed dose in soft tissue versus bone may be as great as a factor of 4 or 5 with low-energy radiation. Differential x-ray absorption between various tissues is the basis of radiographic image formation. As discussed later, the magnitude of the difference between exposure and absorbed dose is inversely proportional to photon energy.

Dose Equivalent

As noted earlier, the same absorbed dose, in Gy, from different types of radiation may not produce the same biologic effect. For example, damage from particulate radiation, such as an alpha particle‡ is greater on a Gy-for-Gy basis than damage from the same dose of x-rays (see Table 1-2). This is related to differences in *ionization density* for different types of radiation. A large charged particle, such as an alpha particle, creates many ionizations that are close together compared to a small lightly charged particle, such as an electron, or an x-ray that has no charge or mass (Fig. 1-5). Neutrons have no charge, but they have a large mass, and they too have a greater ionization density than x-rays. This greater ionization density leads to more biologic damage. Therefore deposition of 1 Gy from an alpha particle or a neutron does more biologic damage than deposition of 1 Gy from an x-ray. The difference in biologic damage from the same absorbed dose of various radiation types is estimated by the weighting factor, as described above (see Table 1-2).

In the SI system, the unit of dose equivalency is the sievert (Sv); the Sv is derived from the product of the absorbed dose in Gy and the weighting factor. Before SI units were accepted, the unit of dose equivalency was the *radiation equivalent in man* (rem; see Table 1-3). The rem was derived from the product of the absorbed dose in rads and the weighting factor. Because 1 Gy = 100 rads, 1 Sv = 100 rem.

Radiation Safety

Principles of radiation safety are based on establishment of guidelines to prevent undesirable and unnecessary exposure to ionizing radiation. The premise of radiation protection is that some low level of radiation exposure to radiation workers is permissible and will not lead to observable abnormalities or disease. Adverse effects can be classified as either *deterministic* or *stochastic*. Deterministic effects have a threshold. In other words, below some dose there is no effect, but above the threshold dose the severity of the effect is dose related.

*A coulomb is the unit of electric charge in the International System of Units. It is the charge transferred by a constant current of 1 ampere in 1 second.

*The joule is the unit of energy in the International System of Units. It is the energy exerted by the force of one newton acting to move an object through a distance of one meter.

†The erg is the unit of energy in the centimeter-gram-second (CGS) system of units. It is the energy exerted by the force of one dyne acting to move an object through a distance of one centimeter.

‡An alpha particle is a helium nucleus, containing two protons and two neutrons, without orbital electrons. An alpha particle has an electrical charge of 2+ and a mass more than 7000 times larger than that of an electron.

Table • **1-3**

Radiation Units

QUANTITY	CGS* UNIT	VALUE	SI† UNIT	VALUE
Exposure dose	roentgen	One electrostatic unit of electricity in 1 cubic centimeter of dry air at 0° C and standard atmospheric pressure	roentgen‡	2.58 × 10–4 C/kg
Absorbed dose	rad	100 ergs/g of tissue	gray (Gy)	1 Gy = 1 joule/kg (1 Gy = 100 rads)
Equivalent biologic dose	rem	Dose in rads times weighting factor§	sievert (Sv)	Dose in Gy times weighting factor (1 rem = 10 mSv)

*CGS, centimeter-gram-second system of units.
†International System of Units.
‡Although the use of roentgen is allowable under the SI system, it is not itself an SI unit, and continued use is strongly discouraged by the National Institute of Standards and Technology.
§Weighting factor is a radiation type-specific quantity that compares the ionization density of various types of radiation; see Table 1-2.

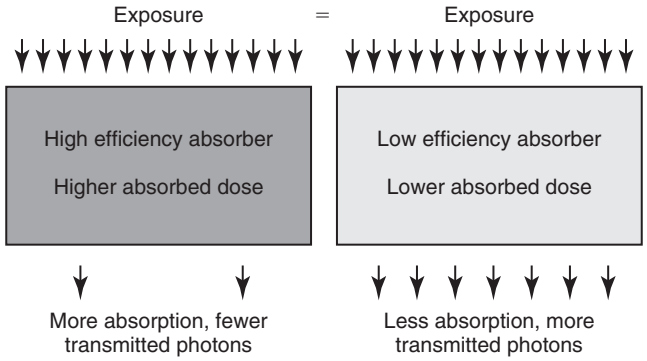


Fig. 1-4 Two materials are exposed to the same number of x-ray photons, represented by the *arrows*. Thus the exposure dose, in roentgens, or in coulombs per kilogram, is the same for both materials. However, the efficiency of x-ray absorption for the two materials is not the same. The material on the left absorbs more oncoming photons than the material on the right. Therefore the absorbed dose will be higher in the material on the left even though the exposure dose is the same. One real-life example of this phenomenon is a limb, where bone would be the high-efficiency absorber and fat or muscle the low-efficiency absorber.

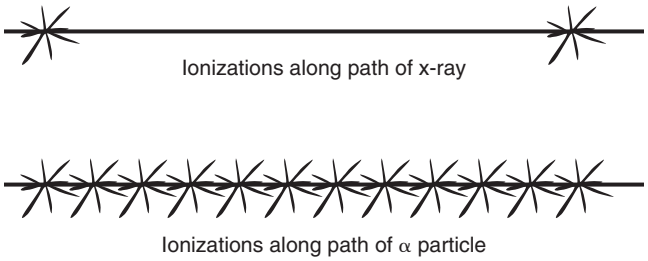


Fig. 1-5 Representation of the ionization density along the paths of an x-ray and an alpha particle. The ionization density along the path of the alpha particle is much higher because of its large mass and 2+ charge. This will lead to greater biologic damage on a Gy-per-Gy basis, and a correction factor will be needed to compare the damage resulting from equal absorbed doses of x-rays versus alpha particles.

Radiation-induced cataracts are an example of a deterministic effect. Conversely, stochastic (random) effects have no dose threshold, and the severity of the effect is independent of dose. Radiation-induced cancer is an example of a stochastic effect.[6]

Maximum permissible dose (MPD) is the maximal amount of absorbed radiation that can be delivered to an individual as a whole-body dose or a dose to a specific organ and still be considered safe. The term *safe* in this context means that there is no conclusive evidence that individuals receiving the MPD will suffer harmful immediate or long-term effects to the body as a whole or to any individual structure or organ. Although the effect of very low doses of radiation is not known with certainty, it is safe to assume that any amount of radiation will have some effect on the subject, and taking steps to minimize one's dose below the MPD is important. An analogy could be made to smoking a cigarette once a month. There is no evidence that physical damage results from this frequency of smoking, but with increasing frequency the probability of physical damage escalates by virtue of a cumulative effect. Unfortunately, no absolute threshold below which damage will not occur or above which damage will definitely result has not been established for either cigarette smoking or radiation exposure.

There are multiple levels of bureaucracy regarding the establishment of guidelines for radiation exposure levels aimed at avoiding deterministic and stochastic effects. Understanding the mission of all involved organizations can be confusing. Furthermore, different exposure limits are defined for workers whose employment results in some level of radiation exposure versus the general public. These exposure limits vary according to risk versus benefit. For example, the small risk to a member of the general public from a thoracic radiograph is outweighed by the benefit of a diagnosis. Likewise, the slightly higher exposure limits allowed for radiation workers are considered acceptable with respect to the missions of the occupation.

The International Commission on Radiological Protection (ICRP) is the primary international body focusing on protection against ionizing radiation. The ICRP is a registered charity and thus not a governmental organization. The ICRP provides recommendations and guidance on protection against the risks associated with ionizing radiation. Their recommendations are published four times each year as the journal *Annals of the ICRP*. The whole-body limit set by the ICRP for avoiding stochastic effects is 20 millisievert (mSv) per year, averaged over 5 years, with the provision that any annual dose should not exceed 50 mSv.[7]

In the United States, the National Council on Radiation Protection (NCRP) was chartered by Congress in 1964. Some of the objectives of the NCRP are to develop recommendations about radiation protection and to cooperate with the ICRP. The whole-body limit set by the NCRP for avoiding stochastic effects is 50 mSv per year with a lifetime

accumulation not to exceed 10 mSv × age in years.[8] The NCRP also recommends that no occupational exposure occur until the age of 18 years. Interestingly, neither the ICRP nor the NCRP has any jurisdiction to enforce its recommendations.

In the United States, the Nuclear Regulatory Commission (NRC) is the agency officially responsible for defining federal exposure standards. The NRC has adopted the annual occupational radiation dose to individual adults as recommended by the NCRP, a maximum of 50 mSv (5 rem) per year.[9] However, the NRC has not established an upper limit for cumulative exposure. Previously, the NRC recommended that cumulative exposure be less than 5 rem (50 mSv)/year x (n –18), where n is the age of the individual. This recommendation has been overruled in favor of the *a*s *l*ow *a*s *r*easonably *a*chievable (ALARA) principle, which is discussed later.

The allowable limit for radiation workers who become pregnant is lower than for nonpregnant radiation workers. Contrary to popular belief, some occupational radiation exposure of pregnant workers is allowed, but this should be minimized. Guidelines state that the monthly exposure limit for the embryo or fetus should not exceed 0.5 mSv (0.05 rem). It is the responsibility of the pregnant radiation worker to notify the supervisor so that any change in work habits needed to stay within the recommended dose limit can be implemented.

For the general public, radiation exposure, excluding that related to medical use, such as diagnostic imaging and radiation therapy, should not exceed 1 mSv (0.1 rem) per year.

The difference in opinion between the NRC and the NCRP regarding the limits for cumulative exposure can be confusing. Although the NRC is the agency officially responsible for identifying federal exposure standards, it has eliminated recommendations regarding cumulative exposure limits, probably because of the uncertainty of such predictions. The NCRP, however, has elected to establish an estimate for acceptable cumulative exposure, which is more conservative than that recommended previously by the NRC (the NRC recommendation was 50 mSv/year versus the NCRP recommendation of 10 mSv/year). Rather than focusing on a specific number for cumulative or annual exposure, the goal should be to minimize any exposure. This is the basis of the ALARA approach, discussed later.

In addition to occupational exposure of radiation workers, the entire population is exposed continually to very low levels of radiation, both natural and manmade. A breakdown of relative exposure of the U.S. public to radiation by various sources was published by the NCRP in 1987 (Fig. 1-6).[10] The average U.S. citizen receives 3.6 mSv (360 millirem [mrem]) annually. Of this, more than 80% is attributable to inhalation of radon gas. The relative levels of different sources of exposure vary on the basis of geographic location. For example, because of the greater altitude, exposure to cosmic radiation is higher in Colorado than in North Carolina, and household radon exposure is greater in eastern Pennsylvania than in most other areas of the United States.

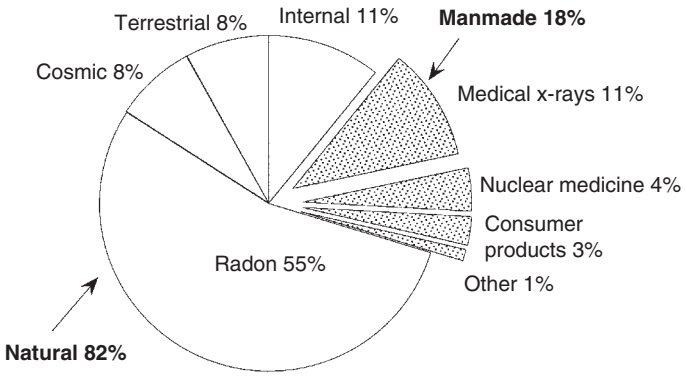


Fig. 1-6 An estimate of sources of exposure dose from ionizing radiation in the United States.

Practical Considerations

Radiation workers in veterinary practices must be aware of the risks of radiation. They should be skilled in patient positioning for radiography, machine operation, and image processing so that repeat studies are minimized. Workers should be instructed on the proper use and care of radiation protection equipment, such as protective aprons and gloves, and in the concepts of the ALARA principle.[11] As noted earlier, rather than focusing on any particular dose limit, the ALARA principle is aimed at limiting one's radiation exposure as much as possible. The major variables used in adhering to ALARA are distance, time, and shielding.

Distance

The distance between the employee and the x-ray tube should be maximized because distance is one of the most effective ways of reducing dose. Doubling the distance reduces exposure, not by a factor of 2 but by a factor of 4. Holding cassettes by hand for equine radiography should be discouraged because this can place the employee in the direct line of fire. Handholding of companion animals for radiography is permissible, but having parts of the body near the primary x-ray beam should be avoided. With the use of chemical restraint and tape and sandbags for positioning, it may be possible for the employee to exit the room during exposure acquisition. Some state veterinary practice acts stipulate that the operator cannot be in the room during the exposure.

Time

Time is directly related to the number of retake views needed. Time can be minimized by using sedation for uncooperative patients. Time can also be minimized by making sure that personnel are familiar with equipment operation. Rotation of the technical staff through the radiology service area will also dilute any exposure over a larger pool, leading to reduction in individual exposure levels.

Shielding

State building codes typically require structural shielding to protect personnel from unnecessary radiation exposure. The specific details regarding requisite structural shielding can be obtained from the state radiation protection office.

The most effective personal shielding for radiation workers is lead-impregnated aprons, gloves, thyroid shields, and eyeglasses. Protective aprons and gloves designed for use in the x-ray room are usually 0.5 mm Pb equivalent. These devices are only effective if used routinely. Wanton disregard for routine use of lead aprons and gloves leads to massive and unnecessary personnel overexposure. When rushing to acquire images, especially of an unruly patient, staff may be tempted to forgo the use of protective aprons and gloves completely to position the patient and to intentionally place the unshielded hands in the primary x-ray beam. This is, of course, unacceptable and exemplifies the ultimate in poor radiation safety practice (Fig. 1-7, *A*; see Fig. 1-3). More commonly, when lead gloves are not used, the radiographer attempts to keep the unshielded hands outside of the primary beam, thinking that the collimator eliminates radiation exposure in this area. This is not true. There is always adequate radiation outside the primary beam to capture an image of parts of the patient or radiographer in that area, and this also leads to unnecessary

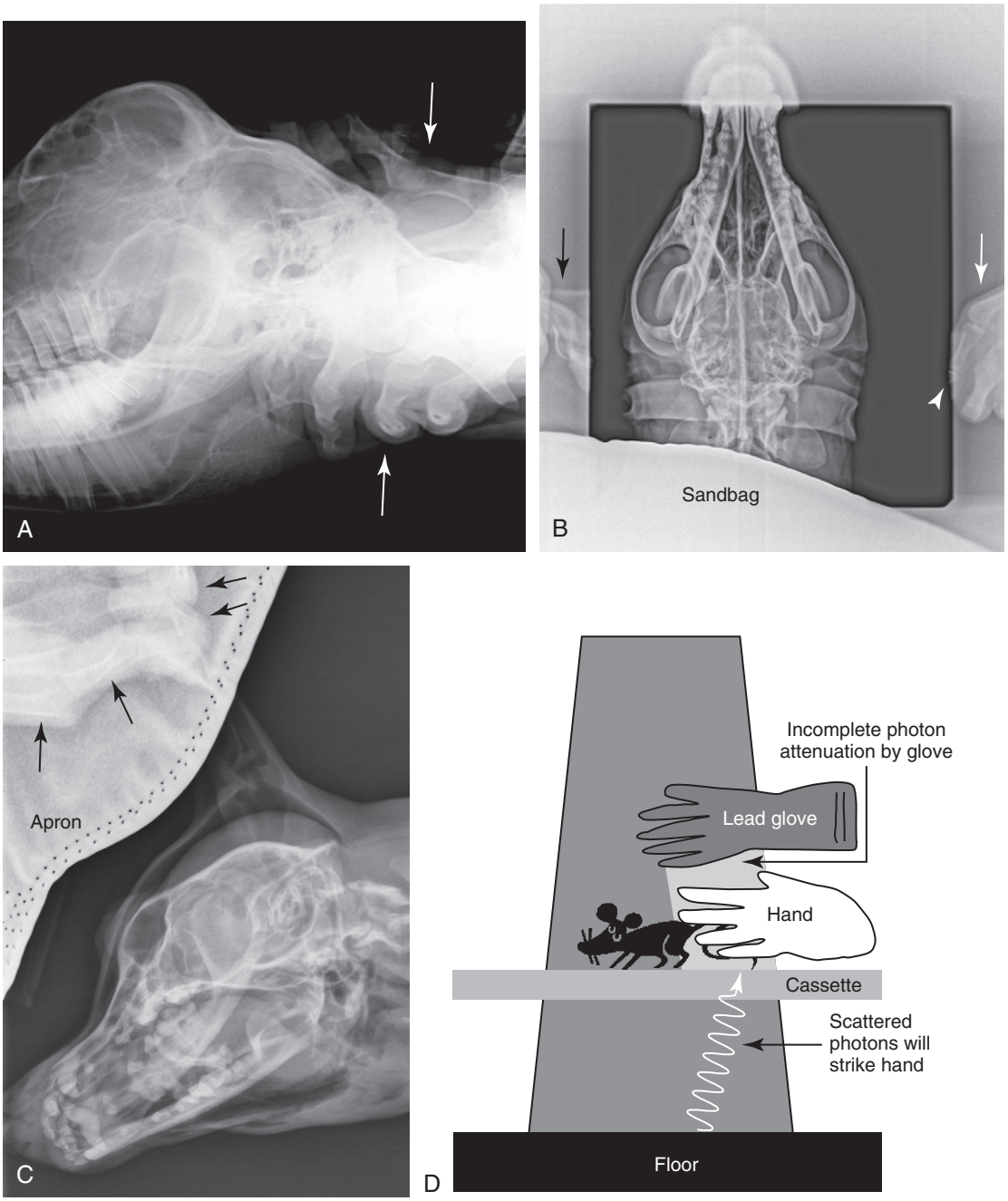


Fig. 1-7 Examples of poor radiation safety practice. **A,** Gloves were not used and the unshielded hand (*arrows*) is in the primary beam to facilitate subject positioning. **B,** Dorsoventral skull radiograph of a dog. A sandbag is being used to secure the neck. The radiographer has decided not to use gloves and has grasped the ears of the dog, which are outside of the primary beam, to keep the head in the proper position. The dog's right ear can be seen (*black arrow*). On the left side, the radiographer's fingers can also be seen (*white arrow*), because of exposure from radiation outside of the primary beam. A tip of a finger is also in the primary beam (*white arrowhead*). A portion of the radiographer's hand can also be seen on the dog's right side, peripheral to the dog's ear but not to the extent that it is identifiable as a hand. The most rostral portion of the dog's nose is also visible outside of the primary beam. **C,** A lateral radiograph of a canine skull was being made. The radiographer held the ears in the primary beam with an unprotected hand and then covered the hand with an apron, thinking the apron would attenuate the x-rays. It did not. The bones in the radiographer's hand are clearly visible (*black arrows*) because of x-rays penetrating the apron. **D,** A small patient is being restrained by an unprotected hand but a lead glove is placed on top of the hand, similar to the situation illustrated in part **C** of this figure. As already stated, this is ineffective because many of the oncoming high energy photons will penetrate the glove and strike the hand. Also, photons penetrating the cassette and table will strike the floor and be scattered back, also striking the hand. This radiation backscatter is also a reason that one should not sit on the edge of the x-ray table while restraining a patient for radiography. In that instance the scattered photons are going to strike a body part or parts that are more revered than a hand.

and excessive personnel exposure (Fig. 1-7, *B*). Additionally, the hand will frequently end up in the periphery of the primary beam, leading to even higher exposure. In fact, in Figure 1-7, *B* the tip of a finger of the hand (white arrowhead) is in the edge of the primary beam, but the fingertip is not visible because of overexposure.

Another common mistake is the belief that because lead aprons and gloves are very heavy, they must provide considerable protection and can be used to shield body parts within the primary beam. This is also not true. Lead aprons and gloves are designed solely for protecting against scattered radiation and must never be placed in the primary beam because they do not attenuate high energy primary photons. It is commonplace for radiographers to hold a body part in the primary beam without gloves and then cover the hand with a lead glove or apron. This is not adequate protection, and the hand will receive unnecessary and excessive radiation dose (Fig. 1-7, C). The effects of scattered photons from the floor of the x-ray room are also usually ignored, but these are an important source of scattered radiation (Fig. 1-7, *D*). Lastly, radiation protection gloves with a slit in the palm are available. Extending the fingers through the slit facilitates positioning but reduces the amount of overlying protective lead material and leads to excessive extremity exposure whether the hand receives primary or secondary radiation.

Improper care of lead aprons and gloves results in cracking or separation of the protective layering that reduces their effectiveness. Aprons and gloves should be placed on racks when not in use. This decreases the risk of creasing and folding that lead to cracking or separation of the protective layering. Use of a glove rack also facilitates the evaporation of perspiration that reduces odor.

Radiation Supervisor

Identifying a member of the staff as a radiation protection supervisor will optimize the quality of images produced and reduce the chances of radiation overexposure. The radiation supervisor can assume the responsibilities defined later and be in charge of establishing safe working conditions that comply with all pertinent federal, state, and local regulations. Having a dedicated radiation protection supervisor provides the employee with ownership in the process, which will increase quality. The continuity of supervision will contribute to a steady stream of high-quality images and low personnel exposure readings.

The following are some reasonable responsibilities of the radiation supervisor:

1. Establish and supervise the implementation of written operating procedures for all employees involved with radiography.
2. Periodically review procedures to ensure conformity with local regulations.
3. Instruct personnel in proper radiation protection practices.
4. Oversee conduction of required radiation surveys and keep records of such surveys and tests, including summaries of corrective measures recommended or instituted.
5. Routinely observe and periodically test interlock switches and warning signals.
6. Ensure that warning signs and signals are properly located.
7. Ensure that all equipment is maintained in top-notch working order.
8. Determine the cause of each known or suspected case of excessive abnormal exposure and take steps to prevent its recurrence.
9. Train staff in proper radiographic positioning and restraint procedures.

Personnel Monitoring

Personnel monitoring is used to check the adequacy of the radiation safety program, disclose improper radiation protection practices, and detect potentially serious radiation exposure situations. A radiation badge is the most commonly used personnel monitoring device. A radiation badge consists of a plastic holder, measuring approximately 2 to 3 cm on a side, which has a clip allowing it to be secured to clothing. The radiation badge may contain a paper-wrapped piece of film that becomes exposed when struck by ionizing radiation; the radiation dose can be extrapolated from the degree of film blackness. Alternatively, radiation badges may contain thermoluminescent dosimeters rather than film. These dosimeters trap electrons energized by oncoming radiation, and the number of trapped electrons can be quantified and related to the amount of exposure. Radiation badges should be analyzed at least quarterly, but a monthly analysis is preferable so that any overexposure problems are detected sooner after occurrence.

Personnel monitoring should be performed in controlled areas for each occupationally exposed individual who has a reasonable possibility of receiving a dose exceeding one fourth the applicable MPD. A qualified expert should be consulted on establishment and evaluation of the personnel monitoring system. The radiation badge must be worn only in the workplace and never when the person is exposed to ionizing radiation as part of his or her own medical or dental examinations. Wearing the radiation badge outside of the workplace can also lead to erroneous readings from temperature exposure if left inside a closed car in warm weather. The radiation badge should be worn on the upper or lower torso. When a protective apron is worn, the radiation badge should be on the outside of the apron for monitoring the radiation environment, but a radiation badge may also be worn inside the apron when an estimate of body exposure is desired.

Basic Radiation Safety Rules for Diagnostic Radiology

1. Only personnel necessary to complete the procedure should be in the x-ray room at the time of exposure.
2. Persons younger than 18 years and pregnant women must not be in the x-ray room during the examination.
3. Personnel who assist with radiographic examinations should have a rotating duty roster to minimize exposure to any one person.
4. Sandbags, sponges, tape, or other restraining devices should be used for positioning the patient rather than manual restraint.
5. Anesthesia or tranquilization should be used when possible to facilitate patient restraint.
6. No part of the technologist should be in the primary beam, whether or not protected by gloves or aprons.
7. Protective aprons should always be worn when positioning an animal.
8. Protective gloves should be worn if hands are placed near the primary beam.
9. Protective glasses should be worn if the work level is heavy or when radiographing large animals. These glasses provide 0.25 mm Pb equivalent protection to the lens.
10. Thyroid shields should be considered. These are "mini-aprons" that are worn around the neck to protect the thyroid gland.
11. The primary beam should be collimated so each film has an unexposed border, proving that the primary beam does not exceed the size of the cassette.
12. All personnel involved with patient radiography should wear a radiation badge during working hours.
13. The radiographic procedure should be planned carefully and the machine settings double-checked.

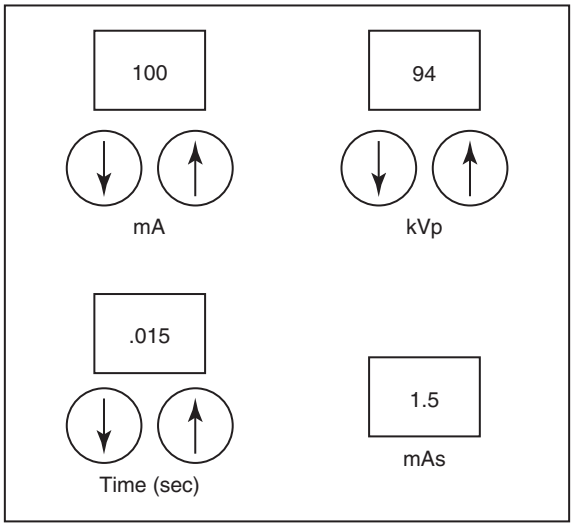


Fig. 1-8 Typical x-ray machine control panel. The time (in seconds), the mA (milliamperes), and the kVp (in kilovolts) are indicated by digital displays and are adjustable individually. As mA and/or time change, the resulting mAs is calculated and displayed automatically.

PRODUCTION OF X-RAYS

X-rays are produced when high-speed electrons strike metal; for radiography, this occurs in an x-ray tube. An x-ray tube contains a positively charged target, the anode, and a negatively charged filament, the cathode, within a glass envelope. X-ray tubes provide for acceleration of electrons from their source at the filament to the metal target where x-rays are produced. To create a source of electrons, electric current is passed through the x-ray tube filament in much the same way that an electric current is used to heat the filament of a lightbulb. The heat allows electrons to "boil" off the surface of the filament into an electron cloud. The number of electrons in the cloud is directly related to the amount of electric current passing through the filament, which is regulated by the milliamperage (mA) control on the x-ray machine control panel (Fig. 1-8). Increasing the mA is analogous to increasing the wattage of a lightbulb. A 100 W bulb has a hotter filament and emits more light rays per unit time than does a 60 W bulb because more current flows through the filament of a 100 W bulb than through a 60 W bulb.

Electrons produced at the filament are accelerated into the metallic target by applying a voltage differential between the filament and target. Because electrons are negatively charged, the electrons will be attracted to the target when the target is positively charged with respect to the filament (opposite charges attract). The energy of x-rays produced is a function of the energy of the electrons striking the target. The potential voltage difference between the filament and target is adjusted with the kilovoltage peak (kVp) control on the x-ray machine control panel (see Fig. 1-8). Increasing kVp increases the voltage difference between the filament and target, and electrons are then accelerated to higher velocities and have more energy when striking the target. This enables the production of high-energy x-rays (Fig. 1-9).

When electrons strike the target, x-rays are produced by both collisional and radiative interactions. Collisional interactions occur when the oncoming electron ejects an orbital electron from the target atom with subsequent release of energy as an x-ray (Fig. 1-10). The energy required to eject an orbital electron is specific to the atom and the shell and is called the *binding energy*. Because the binding energy is specific, the x-rays produced by collisional interactions also have specific energies and are termed *characteristic x-rays*—characteristic of the atom, shell from which they are ejected, and source of electron that fills the shell vacancy. X-rays created by collisional interactions account for only a small fraction of the total number of x-rays produced in a diagnostic x-ray tube.

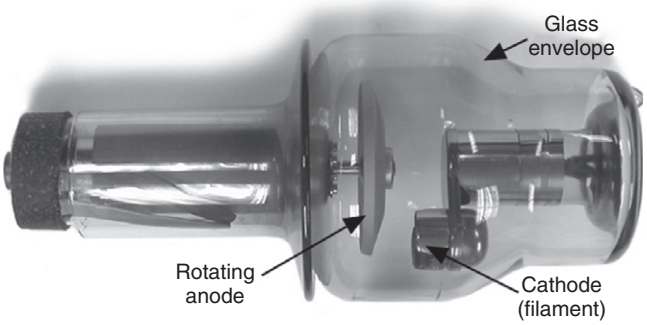


Fig. 1-9 Photograph of an x-ray tube with a rotating anode. The target (anode) rotates at high speed, dissipating heat over a large surface area. Electrons emanate from the filament (cathode). The x-ray tube is encased in a glass envelope from which air has been evacuated; this vacuum prevents electrons from interacting with air molecules as the electrons are accelerated to the target. In the x-ray machine, the x-ray tube is encased in a steel cylinder for protection. (Courtesy of Oak Ridge Associated Universities.)

In a radiative interaction (Fig. 1-11), the oncoming electron passes close to the nucleus of the tungsten target atom, attracted by the opposite charge. The oncoming electron does not eject another electron, but instead the oncoming electron slows (brakes) as it bends around the nucleus and releases energy in the form of an x-ray. The nucleus of the tungsten atom is charged positively to a great extent by the presence of 74 positively charged protons. The much smaller electron, with a charge of only −1, is therefore attracted strongly to the nucleus causing the electron to "brake." X-rays generated by a radiative interaction are called *bremsstrahlung* (from the German, translated as *braking radiation*). Bremsstrahlung radiation has a broad spectrum of energy, depending on the energy of the oncoming electron and how much it slows as it bends around the nucleus. The closer to the nucleus the electron travels, the more it curves, the slower it goes, the more energy it loses, and the more energetic the x-ray produced. Most oncoming electrons undergo multiple braking interactions with the target, and thus a single electron can lead to the production of multiple bremsstrahlung x-rays. The electron can also undergo a collisional interaction after it has braked.

Both collisional and braking processes contribute to the overall energy spectrum of an x-ray beam produced for any given mA-to-kVp combination (Fig. 1-12), but most x-rays arise from radiative interactions. The most energetic x-ray possible in the spectrum will have an energy, in kiloelectron volts (keV), equal to the kVp that was set at the control panel. For a photon to have this maximal energy, an electron must be accelerated from the filament at maximal velocity. This occurs when the voltage between the target and filament is at its maximum (the pattern of voltage fluctuation in the x-ray tube is discussed in the next paragraph). This electron must then lose all of its energy in one radiative interaction. The number of x-ray photons in the spectrum with energy equal to the kVp is very small (see Fig. 1-8). The additional x-rays coming from collisional interactions have specific energies and therefore create peaks on the curve rather than contribute to the overall distribution (see Fig. 1-12).

It is important to understand the difference between kVp and keV.* The kVp is the maximum voltage applied across

*An electron volt (eV) is the amount of energy an electron gains as it is accelerated by a potential difference of 1 V. 1 keV = 1000 eV.

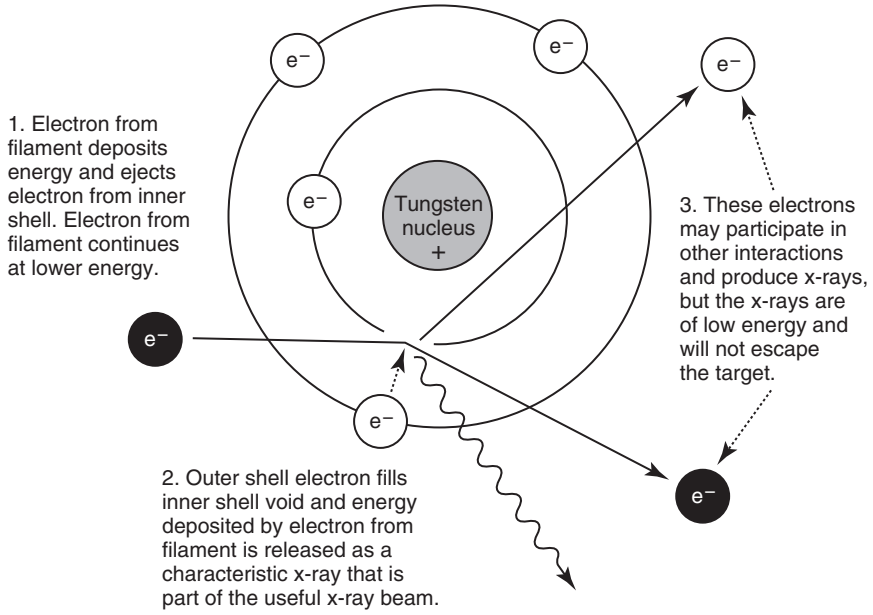


Fig. 1-10 The collisional model of x-ray production. An electron from the filament (shown here in black for illustrative purposes) is accelerated to high speed through a voltage difference and strikes a tungsten atom in the target. The oncoming electron deposits energy and ejects an inner shell electron from the target atom. The electron from the filament continues at a different angle, with reduced energy. Atoms with vacancies in electron shells are unstable, and the vacancy is quickly filled by a more peripheral electron. When the electron shell vacancy is filled, the energy deposited by the electron from the filament to eject the target electron, equal to the binding energy, is released in the form of a *characteristic* x-ray. The electron ejected from the inner shell and the electron from the filament may continue on and be involved in other interactions and produce additional x-rays, but these x-rays are of low energy and usually do not escape the target. The relative size of the nucleus, electrons, and orbital shells is not to scale. The "+" symbol in the nucleus designates the normal nuclear positivity created by the presence of positively charged protons.

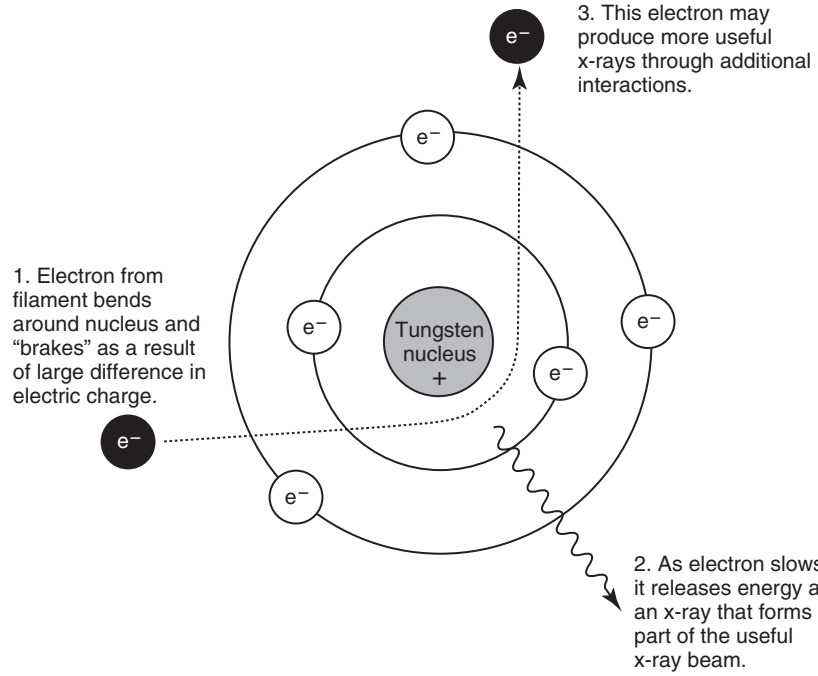


Fig. 1-11 The radiative, or braking, model of x-ray production. An electron from the filament, (shown here in black for illustrative purposes) is deflected as it nears the nucleus because of their different charges. The deflected electron decelerates (brakes) and releases energy in the form of an x-ray. As the deflected electron may pass within various distances of the nucleus, braking radiation has a spectrum of energies. The deflected electron may be involved with additional interactions and produce additional x-rays that contribute to the useful x-ray beam. The relative size of the nucleus, electrons, and orbital shells is not to scale. The "+" symbol in the nucleus designates the normal nuclear positivity created by the presence of positively charged protons.

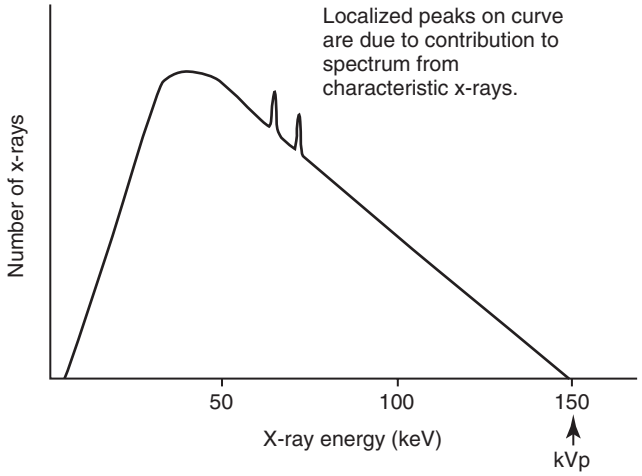


Fig. 1-12 The spectrum of x-ray energies produced by braking and characteristic radiation. The maximum x-ray energy achievable is equal to the kVp (kVp = 150 in this example). For this to occur, an electron must be accelerated at the time when the voltage differential between the filament and target is at the maximum value and then the electron must lose all of its energy in one interaction. As illustrated, the number of x-rays with energy equal to the kVp is very small.

the target-filament gap. In the United States, electric current is alternating at 60 Hz (60 cycles per second). Current coming into the x-ray machine is either at 120 V or 240 V, but this is stepped up to the selected kVp by a transformer. Therefore, because of the alternating nature of incoming current, the voltage difference between the filament and target fluctuates between +kVp and –kVp every 1/60 seconds unless the waveform of the current is modified (Fig. 1-13). The kiloelectron volt (keV) is a unit of energy that describes the energy of either electrons or photons. If the kVp is 100 (100,000 V maximum differential between the target and filament), electrons traveling from filament to the target have energies equal to or less than 100 keV (100,000 eV). There are few electrons with an energy of 100 keV because of the fluctuating nature of the voltage differential as shown in Figure 1-13; the voltage differential is at 100,000 volts for only an instant in each cycle. So, if an electron is accelerated exactly when the voltage difference between the filament and target is 100,000 volts, the electron will have, by definition, an energy of 100 keV. If this electron loses its energy in one single radiative (bremsstrahlung) event, the x-ray created will also have an energy of 100 keV, the same energy as the kVp in the x-ray tube. However, this is very uncommon. Most electrons are accelerated at a voltage lower than the kVp, and most also do not lose all of their energy in one braking reaction. This leads to a spectrum of energies of x-rays in beam (see Fig. 1-12).

If alternating current (see Fig. 1-13, *top panel*) is used for x-ray production, the filament would be positive with respect to the target 50% of the time. During this time, any free electrons at the surface of the target that are present because of the high temperature of the target would be attracted to the filament and damage it. To avoid this, the negative phase of the alternating current is eliminated by a process called *rectification* (see Fig. 1-13, *second* and *third panels*). An in-depth discussion of rectification is beyond the scope of this text. What must be understood here is that rectification results in the target always being positive with respect to the filament, despite alternating current being used. Thus, electrons travel only from the filament to the target.

More than 90% of the energy of the electrons striking the target is converted to heat, not x-rays. Therefore, the target becomes quite hot and must be constructed of material with a high melting point. Tungsten has a melting point of

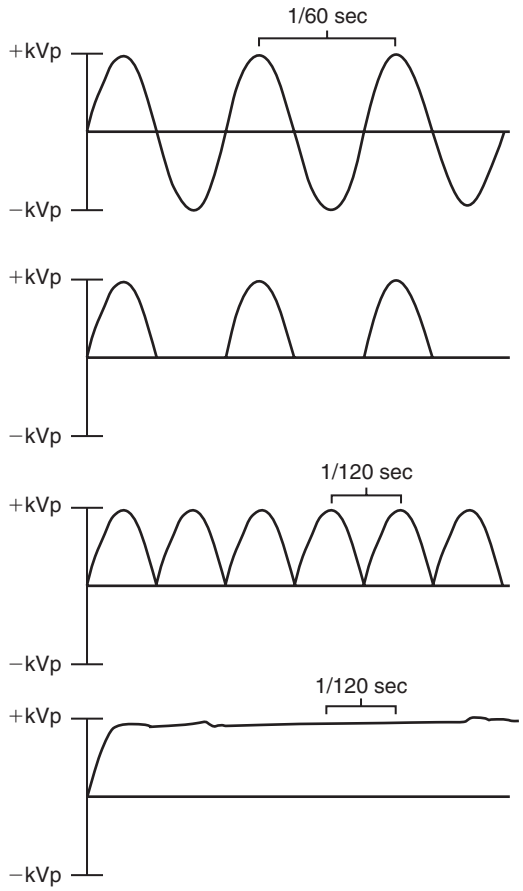


Fig. 1-13 The concept of rectification and the ripple factor. The *upper panel* shows the typical waveform of alternating current in the United States. One complete cycle occurs each 1/60 sec. If this current were used to apply voltage in the x-ray tube, the target would be positive with respect to the filament, which is intended, only 50% of the time. The other 50% of the time, the filament would be positive with respect to the target. This is a waste of time because x-rays cannot be produced when the filament is positive, and any free electrons at the target created by heat buildup would travel to the filament, causing damage. The *second panel* illustrates the waveform obtained when current is not allowed to flow during the negative phase of the cycle; this is termed *half-wave rectification*. In this instance, the filament is never positive with respect to the target, but half of each cycle is wasted. Fortunately, there are electronic methods to reverse the polarity of current flow in the negative portion of the cycle leading to the waveform shown in the *third panel*. This is called *full-wave rectification* and results in one useful pulse of current every 1/120 sec. This increases the efficiency of x-ray production by 100%. This waveform was the standard used in most veterinary x-ray machines until recently. Now, with what is termed a *high-frequency generator*, electronic circuitry is used to convert alternating current to nearly direct current with little voltage fluctuation during the cycle. The waveform of this current is shown in the *bottom panel*. The target is always positive with respect to the filament and the voltage is always high, approximating the kVp at all times. Thus, the voltage fluctuation, or the ripple factor, is the lowest with current from a high-frequency generator, and this increases the efficiency of x-ray production significantly.

3422° C (–6192° F) and is used commonly as a target. Even with this high melting point, the target in high-output x-ray tubes is designed to rotate to increase the surface area struck by the oncoming electrons. Rotation of the target prevents the target from melting or becoming "pitted," as would happen if electrons struck the same region of a stationary target continually. Tungsten also has a high atomic number (74), which increases the efficiency of x-ray production; the higher positively charged nucleus of target atoms leads to more effective braking of electrons from the filament that pass nearby.

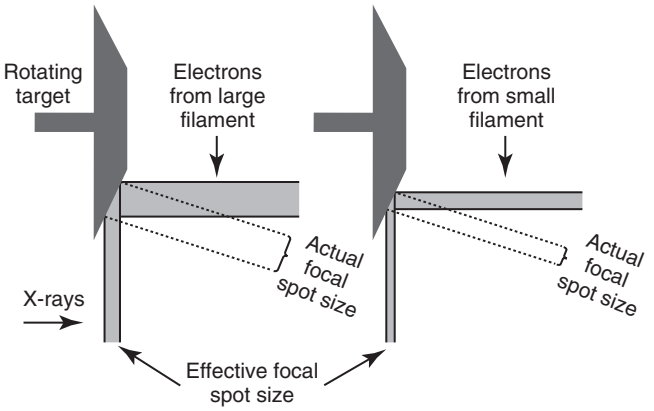


Fig. 1-14 Illustration of the effective focal spot size principle in an x-ray tube with operator-selectable filament size. By angling the rotating anode, the size of the effective focal spot is decreased, whereas the area on the anode that is struck by electrons is larger, facilitating heat distribution. On the *left*, the electrons have emanated from the large filament in the x-ray tube. Although the size of the effective focal spot is reduced compared to the size of the electron stream, the effective focal spot can be reduced even further to improve radiographic detail, as shown on the *right*, by having the electrons emanate from a smaller filament.

The focal spot is the region of the target struck by electrons and is the site of x-ray production. The smaller the focal spot, the better the detail on the radiograph. A practical example of this principle is the sharpness of a shadow cast by a large versus a small light source. A shadow of an object cast by a small light source will be sharper than the shadow cast by a large light source. Therefore, radiographs produced using a small focal spot will have more detail than radiographs produced with a large focal spot. Angling the anode is one way to make the focal spot appear smaller than it really is, creating an effective focal spot, while at the same time maintaining a larger area being struck by electrons to facilitate heat distribution (Fig. 1-14).

Some x-ray machines allow the operator to select the size of the filament from which the electrons emanate. Use of the smaller filament will lead to a smaller effective focal spot. This is illustrated in the right side of Figure 1-14, where the width of the electron path from the filament has been reduced by 50% by using a smaller filament. As a result, the size of the effective focal spot would also be reduced. Reducing focal spot size is useful theoretically when enhanced image detail is necessary, as for radiographing a small bird or reptile, but most of the time only the large focal spot (large filament) is used. A disadvantage of using the small filament is that lower mA values must be used to prevent the filament from overheating and burning out.

As already stated, the number of electrons, and thus the number of x-rays, produced is directly related to the mA setting on the x-ray machine control panel. The number of x-rays produced can also be controlled by the length of time that current is allowed to pass through the filament. The timer on the x-ray machine panel (see Fig. 1-8) controls the length of time current is applied to the filament and is also the time that voltage is applied across the filament-target gap. X-rays are produced only when a source of electrons and a voltage differential are present across the filament-target gap.

The milliampere second (mAs) is used to quantify the amount of radiation produced and is analogous to leaving a 60 W lightbulb burning twice as long as a 120 W lightbulb. In both instances, the total number of light rays emitted would be roughly the same, although the intensity at any one time would be twice as great for the 120 W bulb. mAs is the product of mA and time in seconds. A variety of combinations of milliamperage and time can be used to produce the same mAs value and thus the same number of x-rays (see Table 1-4).

Table • **1-4**

Sample of mA and Time Combinations That Result in 5 mAs

mA	TIME (sec)	mAs
50	0.1	5
100	0.05	5
500	0.01	5
1000	0.005	5

The x-ray tube is one of the two major components of the x-ray machine. The x-ray generator is the other. The generator has a high-voltage circuit that provides the large potential voltage difference between the filament and target and a low-voltage circuit to heat up the filament. The generator also controls the time that the filament is hot and the time that the voltage difference is applied between the filament and the target; that is, the exposure time. Finally, the generator configures the nature of the cyclic current used in the high voltage circuit. As already mentioned, one manipulation that is done to increase the efficiency of x-ray production is to reverse the polarity of the negative phase of the 60 Hz alternating current so that the target is always positive with respect to the filament—that is, full-wave rectification (see Fig. 1-13, *third panel*). This increases the efficiency of x-ray production, but there is still a large amount of time during each phase of the cycle when the voltage is relatively low; in fact, the voltage is at zero every 1/120 second (see Fig. 1-13, *third panel*). Therefore, if the cyclic nature of each cycle could be minimized, there is great opportunity to increase the efficiency of x-ray production. Such an improvement has been made possible by the technology of high-frequency generators.

High-frequency generators are the current state-of-the-art power source for x-ray tubes. These generators produce extremely high-frequency output that leads to nearly constant voltage output (see Fig. 1-13, *bottom panel*). The elimination of the troughs of the voltage waveform increases the efficiency of x-ray output significantly. In a direct comparison of a conventional generator with a high-frequency generator, the high-frequency generator was approximately two times more efficient with a better reproducibility.[12] High-frequency generators are compact, relatively inexpensive, and easily maintained. Therefore, they are the most desired type of x-ray generator and are commonly used in x-ray machines that are manufactured for permanent installation in veterinary practices. Portable units used in the field have voltage waveforms more typical of that shown in the second or third panels of Figure 1-13.

INTERACTION OF RADIATION WITH MATTER

Understanding how photons interact with matter is necessary to understand how radiographs are produced. There are five possible mechanisms of interaction of a photon with matter: (1) coherent scattering, (2) photoelectric effect, (3) Compton scattering, (4) pair production, and (5) photodisintegration. Pair production and photodisintegration have no relevance to diagnostic radiology and are not discussed. A basic description of the coherent, photoelectric, and Compton processes is given herein; sources for more detailed reading are available.[13]

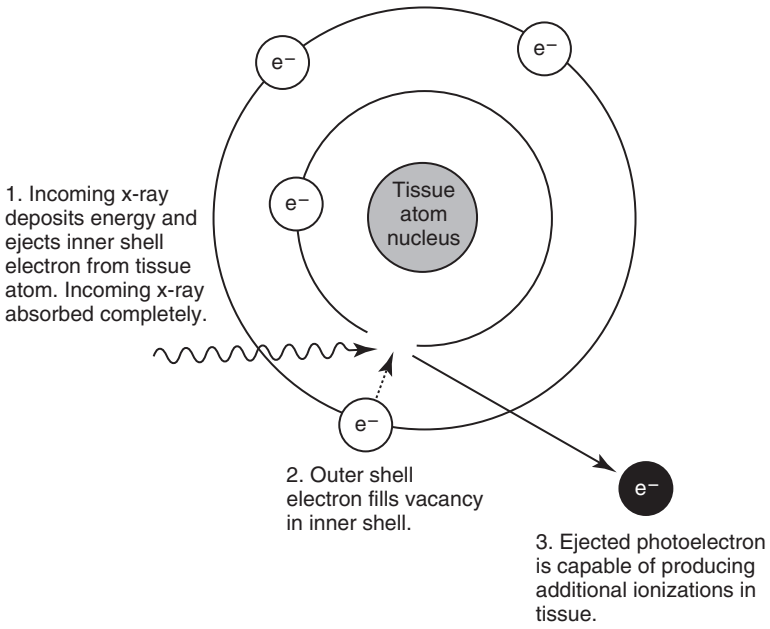


Fig. 1-15 The photoelectric effect. An x-ray from the x-ray tube ejects an electron, usually from an inner shell (K shell) of a tissue atom. The incoming x-ray is absorbed completely. The ejected electron, the photoelectron, has sufficient energy to create additional ionizations in tissue.

Coherent Scattering

A photon interacts with an object and the direction of the photon is changed, but the object does not absorb the photon, and the energy of the photon does not change. The fraction of x-rays striking a patient that undergoes coherent scattering is small, approximately 5%. Not only is coherent scattering not useful in the production of the radiograph; it is, in fact, disadvantageous because the scattered photons may strike the x-ray film and degrade image quality, or they may strike the radiographer and increase personnel exposure.

Photoelectric Effect

The photoelectric effect is the most important type of interaction with reference to producing a radiograph. The photoelectric effect is what results in an image being formed. The x-ray striking the patient is absorbed completely (Fig. 1-15), and therefore there is no scattered radiation to contend with. The complete absorption of the x-ray results in reduced exposure of the film or imaging plate under that part of the patient. The absorbed x-ray photon ejects an electron, called a *photoelectron*, from an inner shell of a tissue atom. The photoelectron may then go on to produce multiple ionizations in the tissue but will be absorbed eventually in the patient.

When the vacancy created by ejection of the photoelectron is filled by a peripheral shell electron, a characteristic x-ray is given off.* The energy of characteristic radiation is a function of the atomic number of the atom from which it arises. Because tissue atoms have a relatively low effective atomic number, the energy of characteristic x-rays produced in tissue is very low, and they are absorbed locally where they contribute to the absorbed dose in the patient being radiographed, but not to production of the radiographic image. This low-energy characteristic x-ray production is not shown in Figure 1-15.

The probability of a photoelectric interaction is directly proportional to the third power of the atomic number (proportional to Z^3) and inversely proportional to the third power of the photon energy (proportional to $1/E^3$). The third-power relationship between the photoelectric process and atomic number is very important because it amplifies differences in absorption between various tissues, such as bone versus soft tissue and soft tissue versus fat. If it were not for the third-power atomic number dependence of the photoelectric effect, there would be insufficient differential absorption of x-rays between tissues for the resultant image to have any contrast. That is, all tissues would be of similar radiographic opacity and the radiograph would be useless. The complete absorption of the x-ray in the photoelectric effect, rather than having a scattered photon, is also advantageous because scattered photons result in fogging of the x-ray film and increased personnel exposure.

The photoelectric effect occurring in the patient should not be confused with collisional x-ray production in the x-ray tube. A characteristic x-ray is produced in both instances because an electron is ejected from an atom in each process, and the void created by the ejected electron is filled by another electron leading to characteristic x-ray production. However, in the photoelectric effect a photon ejects an electron from an atom in tissue, while in collisional x-ray production it is a high-energy electron that ejects the electron from an atom in the target of the x-ray tube. When the vacancy filled by the electron ejection is filled, a characteristic x-ray is emitted in both processes. In the case of the photoelectric effect this x-ray has very low energy because of the low binding energy of inner shell electrons in tissue versus collisional x-ray production where the characteristic x-ray is of much higher energy because of the much higher inner shell binding energy of elections in tungsten, the target material in an x-ray tube.

Compton Scattering

Almost all scattered radiation encountered in diagnostic radiology results from Compton scattering. In the Compton reaction, an incoming x-ray photon interacts with a peripheral shell electron of a tissue atom. The electron is ejected, and the original photon is scattered at a different angle and at a reduced energy (Fig. 1-16). The scattered electron is called either a *Compton electron* or a *recoil electron*. The probability of a Compton reaction is independent of atomic number and depends mainly on physical density (grams per cubic centimeter). The probability of a Compton interaction increases

*This is similar in principle to the characteristic x-ray given off in the target of an x-ray tube when the oncoming electron from the filament creates a vacancy in a target atom.

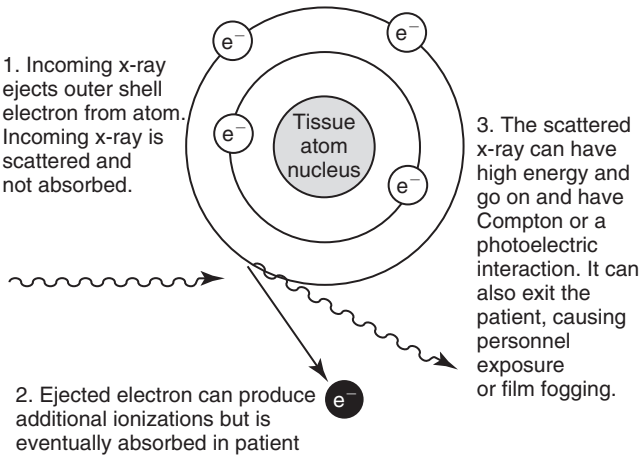


Fig. 1-16 The Compton absorption process. An x-ray produced in the x-ray tube ejects an electron, usually from an outer shell, of a tissue atom. The incoming photon is scattered, not absorbed as in the photoelectric process. The energy of the scattered photon is always lower than that of the original photon. The ejected electron and scattered photon may produce additional ionizations and the scattered photon may exit the patient and fog the film or strike personnel.

up to a point as photon energy increases and then begins to decrease at photon energies over 1.02 MeV. The independence of a Compton event on atomic number is disadvantageous with reference to producing a radiograph. For example, the atomic number dependence of photoelectric absorption results in great differences in absorption, and thus good tissue contrast, between tissues such as bone and muscle. With Compton absorption being independent of atomic number, this differential absorption is diminished, and image contrast is reduced. Thus, if the Compton absorption predominates, the image will have very poor contrast. In good radiographic technique, x-ray beams have an energy in which the photoelectric absorption reaction predominates; this maximizes differential absorption between tissues. The photon scattering that occurs with Compton interactions is also disadvantageous because the scattered photons are radiation safety considerations for bystanders, and they also degrade the image by producing fog.

BASIC CONCEPT OF MAKING A RADIOGRAPH

To make a radiograph, the patient is placed between the x-ray tube and the recorder (Fig. 1-17). As noted earlier, x-rays produced by a diagnostic x-ray tube have a broad spectrum of energies. Very low-energy x-rays serve no useful purpose because they are absorbed by the patient and make no useful contribution to the image. Therefore, filters are placed in the x-ray tube housing to remove these very low-energy x-rays from the x-ray beam. The geometric shape of the x-ray beam passing through the filter is configured to the size needed for the part being radiographed by the beam-shaping collimator. In Figure 1-17, three x-rays pass through the collimator opening. The left x-ray penetrates the patient and will be recorded on the x-ray film. Some fraction of the oncoming x-rays must penetrate the patient or no information would be recorded on the receiver. The middle x-ray hits a structure within the patient and is absorbed. Absorption is also necessary and emphasizes an important point: Radiographs are possible only because of differential absorption of x-rays by the patient. The x-ray on the right hits the patient and is scattered. At this direction of scatter, the x-ray may strike a bystander. If bystanders are not wearing a lead apron, lead gloves, or a thyroid shield, they will receive unnecessary radiation dose. If

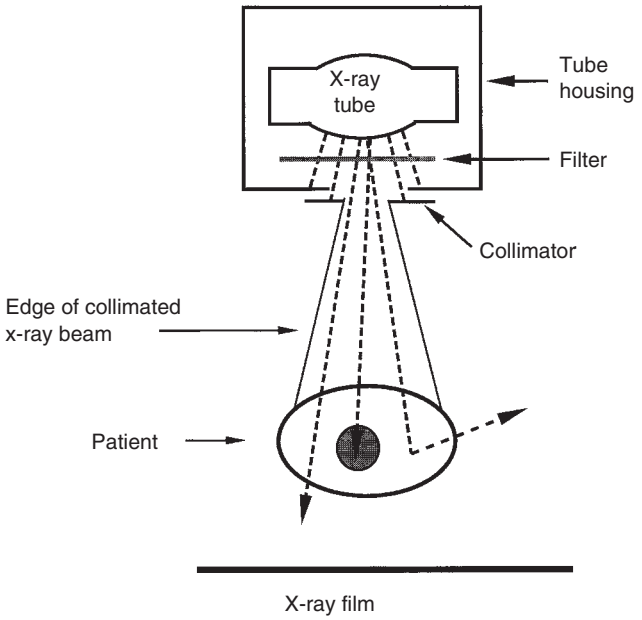


Fig. 1-17 The schematic relation between the x-ray tube, patient, and cassette. A filter in the tube housing removes low-energy x-rays that serve only to increase patient dose. The shape of the beam is configured with a collimator. The fate of three x-rays that pass through the collimator opening and strike the patient is shown. The x-ray on the *left* penetrates the patient and strikes the cassette. The x-ray in the *center* is absorbed by the patient. The x-ray on the *right* is scattered by the patient and could fog the film or contribute to personnel exposure dose.

the angle of scatter had been different, the scattered x-ray may have struck the receiver, causing image fog.

A radiograph is an image of the internal makeup of an object based on the spatial distribution of x-rays transmitted through the patient. Some method of recording the image of the transmitted x-rays must be available. For decades, radiographs were produced on film by taking advantage of the ability of x-rays to expose photographic emulsions. Alternatively, technology has been developed that records the pattern of x-rays being transmitted through a patient in a digital format where the image can be viewed and manipulated on a computer monitor. The basis of film-based (analog) imaging is discussed in this chapter, and digital radiographic imaging is discussed in Chapter 2.

Film Blackness and Opacity

X-ray film is photographic film with a light-sensitive emulsion containing silver halide. After exposure to x-rays or visible light, silver halide crystals become sensitized and precipitate during development, forming neutral silver deposits. These neutral silver deposits appear black on processed film. Unexposed crystals are removed during fixation, leaving clear areas on the film. Thus, the amount of precipitated silver on any particular part of the film determines how black, gray, or clear that part of the film appears. The degree of film blackness is affected by the number of x-rays striking the film, which is related directly to the x-ray machine output (mAs) (Fig. 1-18).

Film blackness is also affected by the energy of the x-ray beam, which is controlled by the kVp setting. As discussed, the kVp determines the magnitude of the voltage difference between the filament and the target. The higher kVp, the higher the potential voltage difference between the filament and the target, the faster the electrons travel from the filament to the target, and the greater the energy of the x-rays produced. As x-ray energy increases, a greater proportion of the x-rays will penetrate the patient, increasing film blackness

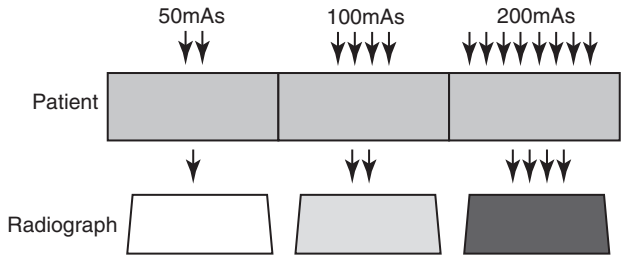


Fig. 1-18 The number of x-rays reaching the film, and thus the film blackness, is a function of the mAs setting. Increasing mAs while keeping the kVp constant will result in more x-rays striking the patient, and then proportionally more will pass through the patient, increasing the blackness of the radiograph. Thus, as mAs is increased, film blackness also increases.

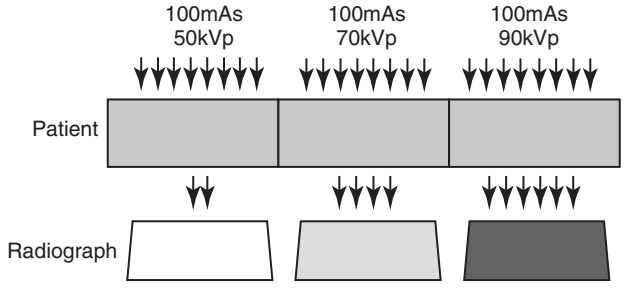


Fig. 1-19 The number of x-rays reaching the film, and thus the film blackness, is a function of the kVp setting. Increasing kVp while keeping mAs constant results in essentially the same number of x-rays being produced, but at higher kVp the x-rays have more energy, and a larger fraction will penetrate the patient. This will result in more x-rays hitting the film and an increase in film blackness.

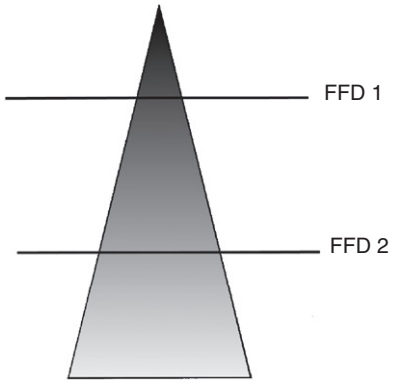


Fig. 1-20 As distance from the focal spot increases, the x-ray intensity in the beam (x-rays/unit area) decreases because of beam divergence. Thus, as FFD increases, film blackness decreases. To obtain film blackness at FFD 2 that is similar to film blackness at FFD 1, the mAs would have to be increased.

(Fig. 1-19). In reality, increasing the kVp also increases the number of x-rays produced slightly, but that effect is of less importance than the effect of kVp on x-ray energy and is not considered in this discussion.

The distance from the x-ray tube to the film also affects film blackness. This distance is referred to as the focal spot—film distance (FFD). As the FFD increases, film blackness decreases because the intensity of x-rays in the x-ray beam (x-rays/unit area) decreases (Fig. 1-20). In the type of x-ray machines used in most small animal practices, the distance from the x-ray tube to the film is relatively fixed. However, in many large animal radiographic settings, the x-ray machine is portable, and the distance between the x-ray tube and

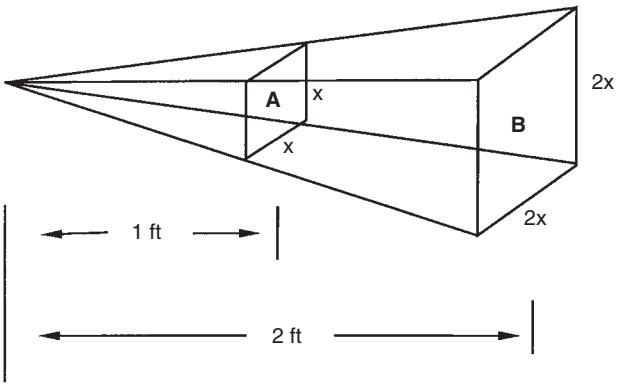


Fig. 1-21 The intensity of an x-ray beam in terms of x-rays/unit area changes with the square of the distance. At a distance of 1 foot, the diverging x-ray beam covers an area represented by square A with each side of dimension x, or an area of (x) times (x) = x^2. At 2 feet, the diverging beam covers an area represented by square B in which each side is now twice as long as it was at 1 foot. The area covered by the beam at 2 feet is therefore (2x) times (2x) = $4x^2$, which is four times the area at 1 foot. The intensity falling on the square at one foot distance must spread out over an area that is four times as large by the time it reaches the large square at a distance of two feet.

cassette is variable. Use of an incorrect FFD is a common source of overexposure or underexposure in equine radiography. One might think that a few inches difference in distance would not lead to detectable differences in film blackness, but that is not true because of the inverse square law, which is described by the equation:

$$\frac{I_1}{I_2} = \frac{(d_2)^2}{(d_1)^2}$$

where I is intensity in terms of number of x-rays/unit area, and d is distance. In the equation, I_1 is the intensity at d_1, and I_2 is the intensity at d_2. Therefore, as FFD increases, intensity and film blackness decrease; this decrease is a function of the square of the distance, not simply the distance (Fig. 1-21).

As an example, assume that when an equine limb is radiographed the FFD should be 40 inches, but instead the machine is held too close, at a distance of 32 inches. If we arbitrarily define the desired x-ray intensity at 40 inches as 100, what change in intensity will result from the error of having the x-ray machine at 32 inches rather than at 40? Thus, in the equation $I_1 = 100$, $d_1 = 40$ inches, $I_2 = ?$, $d_2 = 32$ inches. Substituting, the equation becomes:

$$100/I_2 = (32)^2/(40)^2$$
$$100/I_2 = 1024/2500$$
$$100/I_2 = 0.64$$
$$I_2 = 1.56$$

Therefore, by being 8 inches too close, the exposure to the film is increased by 56%, which will lead to observable overexposure.

The inverse square relationship can also be used to compute a new mAs value if the FFD is changed intentionally. Suppose an exposure of 100 mAs is needed to make a radiograph of the abdomen with a 40-inch FFD. When another x-ray machine is used, the maximum FFD that can be obtained is 30 inches. What milliamperage must be used to maintain the same x-ray intensity as at a 40-inch FFD? Common sense indicates that because the distance is shorter, lower mAs must be used. The required mAs can be calculated from the inverse square principle. The inverse square law equation noted previously cannot be used for this calculation because it relates the *change* in x-ray intensity as a function of distance. In this

example, the same x-ray intensity should be maintained at the film, which is now 10 inches closer to the x-ray tube. The question is, how much does mAs have to decrease to maintain the same x-ray intensity? In this situation, a direct relationship exists between the milliamperage needed to maintain the same x-ray intensity and distance, so the equation is as follows:

$$\frac{mAs_1}{mAs_2} = \frac{(d_1)^2}{(d_2)^2}$$

and from the above, $mAs_1 = 100$, $mAs_2 = ?$, $d_1 = 40$ inches, $d_2 = 30$ inches. Therefore:

$$\frac{100}{mAs_2} = \frac{(40)^2}{(30)^2};$$

$$\frac{100}{mAs_2} = \frac{1600}{900};$$

$$\frac{100}{mAs_2} = 1.77;$$

$$mAs_2 = \frac{100}{1.77};$$

$$mAs_2 = 56.25 \text{ mAs}$$

Thus, the mAs needed at a 30-inch FFD is 56.25, which is lower than the original value of 100 mAs needed at a 40-inch FFD. In this example, the x-ray intensity (x-rays/unit area) at the film will be the same under either circumstance—that is, 100 mAs at 40 inches, or 56.25 mAs at 30 inches.

FACTORS AFFECTING IMAGE DETAIL

Motion

Motion, leading to image unsharpness, is the biggest enemy of detail in veterinary radiology. Short exposure times are used to minimize the effect of motion. In some x-ray machines, the timer is capable of millisecond exposures. When exposure time becomes very short, the mA must be large; otherwise, the mAs will be too low to produce the necessary film blackness. Milliampere values up to 1500 can be obtained in some x-ray machines. In private practice, however, the choice of mA values is usually more limited, with most machines having a maximum capacity of 300 mA. This means that the exposure time must be longer to obtain suitable film blackness, and motion can become more of a problem. Fast intensifying screens, discussed later, are one way to overcome motion artifacts.

Focal Spot Size

Some x-ray tubes have an operator selectable focal spot size (see Fig. 1-14). Use of the small focal spot results in improved detail (Fig. 1-22). The disadvantage of the small focal spot is that lower mAs values must be used to prevent the filament from overheating. With a large focal spot, edges of anatomic structures are projected more unsharply than with the small focal spot. This edge unsharpness is called *penumbra* (see Fig. 1-22). In practice, small focal spots are used rarely because of the associated mAs limitations, as mentioned earlier.

Intensifying Screens

In reality, the sensitivity of the x-ray film emulsion to x-rays is very low. The emulsion is much more sensitive to visible light. Therefore, converting the x-ray energy into visible light and then using the visible light to expose the film is a convenient way to increase the efficiency of radiographic production. Intensifying screens are used for this purpose. Much lower mAs values are needed to create a radiograph when intensifying screens are used compared with using the x-rays to expose the film directly. For example, it may require 100 mAs to obtain a suitable radiograph when using x-rays to expose the film directly, but 1 to 2 mAs can often be used when an intensifying screen intermediary is used.

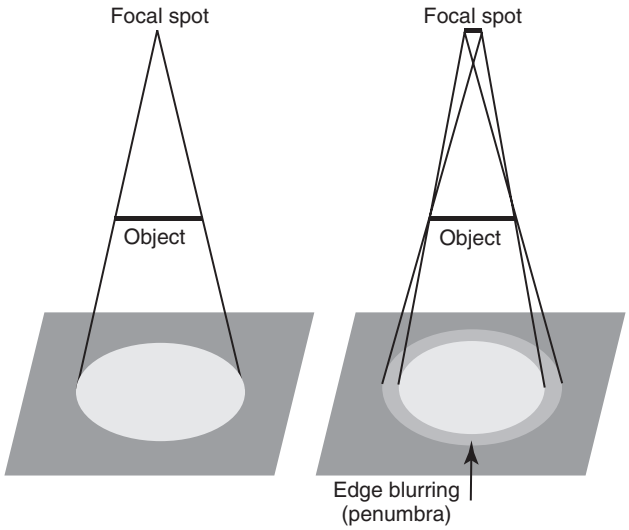


Fig. 1-22 The effect of focal spot size on detail. With a large focal spot, the edge unsharpness, or the penumbra, is larger. This contributes to image unsharpness.



Fig. 1-23 The anatomy of an intensifying screen. Intensifying screens are covered with a protective layer. Beneath this is the fluorescent layer, which emits visible light when struck by x-rays. A reflective layer, which lies deep beneath the fluorescent layer, reflects light back in the direction of the x-ray film. The plastic base provides support for the intensifying screen. In the cassette, the x-ray film is in contact with the protective layer, and the protective base is glued to the cassette.

Producing visible light from x-ray energy is possible because of the property of x-rays to cause certain compounds to fluoresce (see Box 1-1). Intensifying screens contain a fluorescent layer containing phosphorescent crystals that emit light when struck by x-rays (Fig. 1-23). In the cassette, the x-ray film is sandwiched between two intensifying screens (Fig. 1-24). The front of the cassette is composed of a low atomic number, low physical density material that absorbs very little of the incident x-ray beam. The cassette compresses the film between a pair of intensifying screens in the front and back of the cassette to ensure good film-to-screen contact. If there is not good contact between the film and the screens, light from the screens would diffuse before striking the film, and detail would be degraded.

Intensifying screens are characterized by *speed* and *detail* parameters that are inversely related. The thicker the fluorescent layer, the greater the chance of an x-ray being absorbed in the screen and thus more light is produced at any given mAs. But with a thicker fluorescent layer, there is more light diffusion before hitting the film and a degradation in image quality. Thus, as speed increases, detail decreases (Fig. 1-25). In some intensifying screens, particularly those with a thick fluorescent layer, a light-absorbing dye is added to the fluorescent layer to reduce the amount of diffused light reaching the

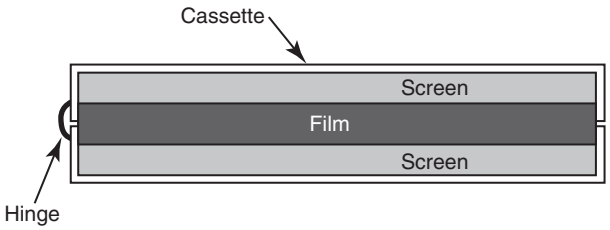


Fig. 1-24 The anatomy of a cassette. X-ray film is placed in a cassette, sandwiched between two intensifying screens. The use of two intensifying screens increases the efficiency of image production compared to using only one screen. The tradeoff of using two intensifying screens rather than one is a slight loss of detail compared with only one screen. The relative thickness of the film versus intensifying screen is not to scale in this image; in reality the film is much thinner than shown here.

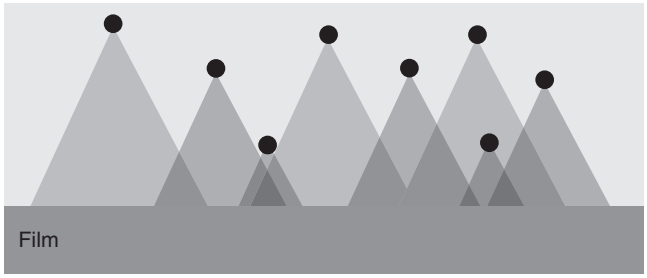




Fig. 1-25 Effect of thickness of fluorescent layer on light diffusion. The fluorescent layer in the top intensifying screen is thicker than in the intensifying screen at the bottom. Phosphorescent crystals are shown in each screen; there are many more crystals in the thicker fluorescent layer than in the thin layer. In the thicker fluorescent layer, there is more light diffusion before striking the film. This will lead to some slight blurring of the image compared with the thinner fluorescent layer at the bottom where there is less light diffusion before striking the film. There is also more overlapping of the light emitted from each crystal in the thicker fluorescent layer, which will also contribute to degradation in detail. The thicker fluorescent layer will require less radiation (lower mAs) to produce the radiograph than the thinner fluorescent layer, but the detail of the radiograph made using the thicker fluorescent layer will be reduced.

x-ray film; this leads to increased radiographic detail. However, these light-reducing dyes also result in more radiation required to produce a satisfactory radiographic image.

Intensifying screens originally incorporated calcium tungstate ($CaWO_4$) as the phosphor, but new phosphors have replaced $CaWO_4$. These new phosphors are called *rare-earth phosphors*, not because the components are uncommon but because some of the components come from the rare-earth series of elements, which includes elements of atomic numbers 57 through 71. The x-ray-to-light conversion factors of these rare-earth intensifying screens are greater than that of $CaWO_4$. For example, one x-ray absorbed in $CaWO_4$ produces approximately 1000 light rays versus approximately 2000 to 4000 produced by a rare-earth phosphor. Thus, lower mAs settings can be used with rare-earth intensifying screens than with calcium tungstate screens.

Grids

If scattered photons originating from Compton scattering reach the film, they will produce a generalized exposure, called *fog*, that reduces detail and contrast. Photon scattering

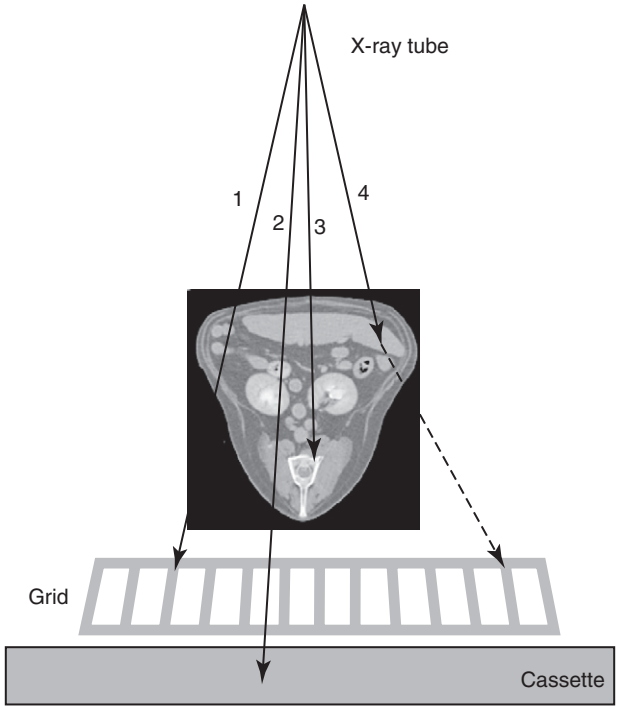


Fig. 1-26 A grid is composed of alternating lead and aluminum strips. The grid is positioned between the patient and the film, usually fixed in the x-ray table. Its purpose is to absorb scattered radiation, preventing fogging of the film. The lead strips in this illustration are shown as gray regions, and the interposed aluminum strips are shown as the interposed clear regions; the size of these strips is exaggerated greatly in this drawing. The aluminum absorbs very little radiation, but the lead strips absorb nearly all of the x-rays that strike them. Photon 1 penetrates the patient, carrying useful information, but does not reach the cassette because it is absorbed by a lead strip. That the grid removes useful information means that the mAs must be increased when a grid is used to ensure that adequate numbers of x-rays reach the cassette. Usually the mAs must be increased by a factor of 2-3. Photon 2 penetrates the patient, carrying useful information, and reaches the cassette. Photon 3 is absorbed in the patient. Differential x-ray absorption, with some x-rays being absorbed and others penetrating the patient, is necessary to create an image. Photon 4 is scattered but strikes a lead strip and is removed by the grid. If the grid were not present, this photon would have degraded the image by fogging.

is increased as the following factors increase: the physical density of the patient, the total volume of tissue irradiated, and beam energy (kVp). Most of the scattered radiation can be removed by a grid before it fogs the film. A grid is a flat, rectangular plate with alternating lead and aluminum strips (Fig. 1-26). Some x-rays passing through the patient will be aligned with the aluminum strips and reach the film (see Fig. 1-26, *photon 2*). Some x-rays interacting with the patient will be scattered and absorbed in the grid, preventing them from reaching the film (see Fig. 1-26, *photon 4*). These scattered x-rays represent useless information, serving only to fog the film. Some primary x-rays also are absorbed in the grid (see Fig. 1-26, *photon 1*). Therefore, the mAs must be increased when grids are used to compensate for the portion of the primary x-ray beam absorbed by the grid. In general, the mAs must be increased by a factor of 2 to 3 when a grid is used. Because small patients do not scatter many x-rays, grids are used only for patients with a thickness greater than approximately 10 cm.

The size of each lead strip in Figure 1-26 has been exaggerated greatly. Typically each linear inch of grid contains approximately 80 to 160 lead lines; thus the lead strips are very thin. Grids with more lead strips per linear inch are preferable because if the lead strips become too thick they will be visible in the radiograph. However, as the number of

lead strips per linear inch increases, so does the cost of the grid. The radiolucent lines created by the lead strips in a grid can be obscured by causing the grid to oscillate during the radiographic exposure. This blurs the radiolucent lines, rendering them invisible. One disadvantage of an oscillating grid is that it may make noise or vibrate during a radiographic exposure, startling the patient and causing unexpected movement. The device in the x-ray table that causes the grid to oscillate is called the *Bucky*, after its inventor.

The grid ratio is another parameter used to describe a grid. The grid ratio describes the relationship of the height of the lead strips to the distance between them; that is, if lead strips are five times as high as the space between them, the grid ratio is 5:1 (Fig. 1-27). The higher the grid ratio, the more effective the grid is in absorbing scatter, but the more difficult it will be for primary x-rays to pass through it. This should be apparent by comparing the 5:1 and 8:1 grids in Figure 1-27. Thus, the higher the grid ratio, the more mAs needed to produce acceptable film blackness. The grid ratio is independent of the number of grid lines per inch. For example, in a 5:1 grid having the same number of lines per inch as an 8:1 grid, the height of the lead strips would have to be lower. In Figure 1-27 there are more grid lines per inch for the 8:1 grid than for the 5:1 grid. The number of lines per inch determines how conspicuous the lead grid lines will be in a radiograph, assuming that the Bucky is not used. The grid ratio determines the effectiveness of scatter removal. A summary of the relationship of grid lines per inch versus grid ratio is given in Table 1-5.

Note that in Figure 1-26 the lead strips are angled more steeply toward the periphery of the grid. This is necessary because of the divergence of the primary x-ray beam from center to periphery. The angle of the lead strips in the grid must match the angle of beam divergence so that the grid does not *cut off* excessive x-rays from the primary beam (Fig. 1-28). Grids constructed with peripheral angulation of the lead strips are called *focused grids*. Focused grids must be used within a defined range of FFDs to maintain a parallel relationship between the oncoming x-ray beam and the radiolucent strips.

When a grid is installed into the x-ray table, the grid is oriented such that the lead strips run parallel with the long axis of the x-ray table (Fig. 1-29). The center of the primary x-ray beam must always be aligned with the centerline of the grid or cutoff will occur (Fig. 1-30; see Fig. 1-29). The excessive loss of the primary beam caused by positioning the center of the primary x-ray beam peripheral to the center line is called *lateral decentering*.

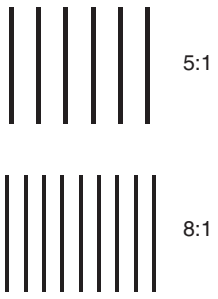


Fig. 1-27 The grid ratio is the ratio of the height of the lead strips, shown here in black, to the distance between them. Two grids are shown here. One has a ratio of 5:1 and the other a ratio of 8:1. It is easy to see that more oncoming radiation will be absorbed in the 8:1 grid because the space between the lead strips is thinner. This increases the chance that an incident x-ray will hit a lead strip.

DISTORTION

Distortion is caused by unequal magnification of the part being radiographed. This results from one part of the object being closer to the x-ray tube than the rest of the object (Figs. 1-31, 1-32). As a result of the three-dimensional nature of patients, there will always be some anatomic distortion. Minimizing the effect of this distortion results from positioning different patients in a standard manner. One learns to recognize the normal pattern of distortion. If patient positioning is not standardized, or is limited by disease, the unfamiliar distortion that results can be confusing and interfere with making an accurate interpretation.

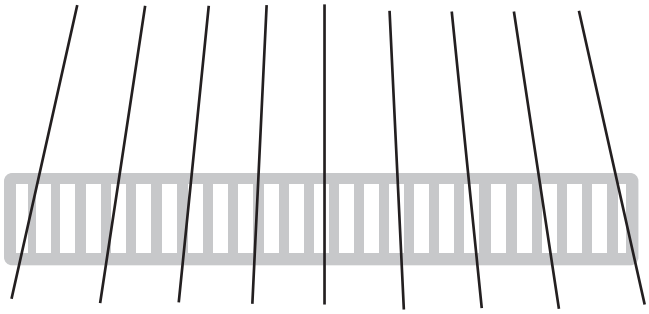


Fig. 1-28 Cutoff of useful radiation because of malalignment of the grid lines and the pattern of x-ray beam divergence. In this example, the lead strips in the grid are all vertical. This would be called an *unfocused grid*. The diverging nature of the primary x-ray beam does not match the verticality of the lead strips, and many oncoming primary photons are absorbed in the grid. An unfocused grid would be functional if the oncoming primary x-ray beam had little or no divergence. This example illustrates the importance of having the properties of the x-ray beam match the properties of the grid.

Table • **1-5**

Criteria Characterizing Grid Efficacy

CRITERION	DEFINITION	TYPICAL VALUES	INFLUENCE ON RADIOGRAPHIC TECHNIQUE
Lines per Inch	Number of lead strips per linear inch of grid	80 lines per inch 100 lines per inch 140 lines per inch	Has no effect on mAs required
Grid Ratio	Ratio of height of lead strips to distance between them	5:1 8:1 10:1	Higher grid ratio requires more mAs for comparable film blackness

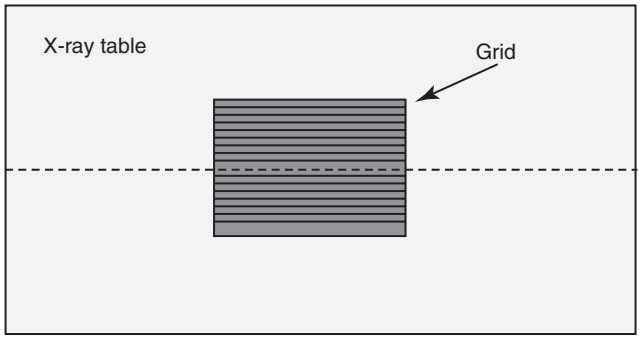


Fig. 1-29 Illustration of proper orientation of the grid with the x-ray table. The grid is centered in the table, and the lead strips run parallel with the long axis of the table. If the grid is a focused grid, with angled lead strips, the center of the primary x-ray beam can be positioned anywhere along the dotted line. But if the center of the primary x-ray beam is peripheral to the dotted line, there will be grid cutoff because the divergence of the x-ray beam no longer matches the divergence of the lead strips.

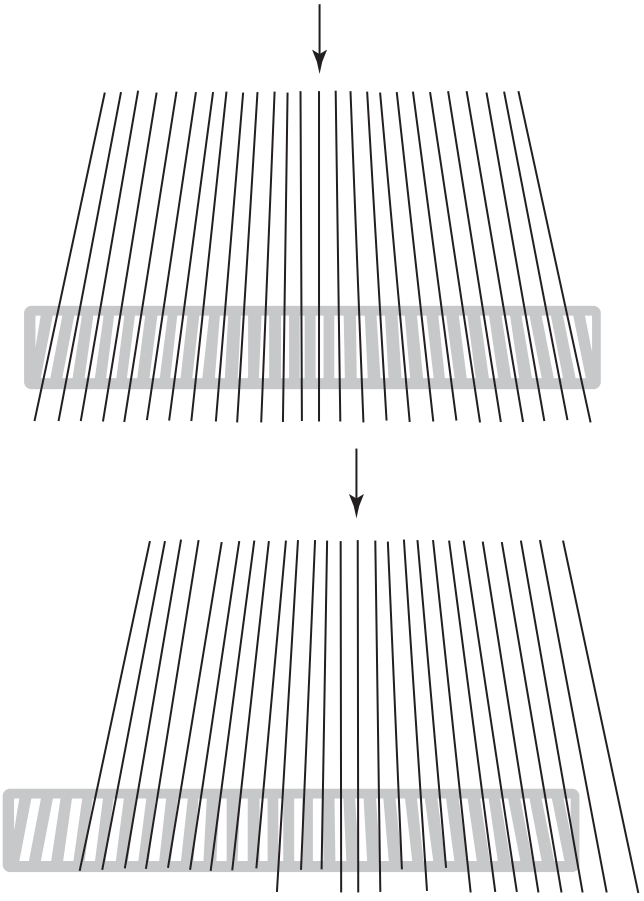


Fig. 1-30 Lateral decentering. When the central ray is centered over a focused grid, the divergence of the x-ray beam matches the divergence of the lead strips and a high percentage of the oncoming primary photons pass through the grid. When the central ray is laterally decentered, the divergence of the beam no longer matches the divergence of the lead strips in the grid, and the lead strips will absorb more of the primary beam, reducing film blackness. Lateral decentering is the most common grid-induced artifact.

FACTORS AFFECTING CONTRAST

Radiographic contrast refers to the difference in film blackness between areas in the image. If no contrast were present, all parts of the patient would be of the same opacity, and no individual structures would be visible. Radiographic contrast depends mainly on radiographic technique and the amount of film fogging.

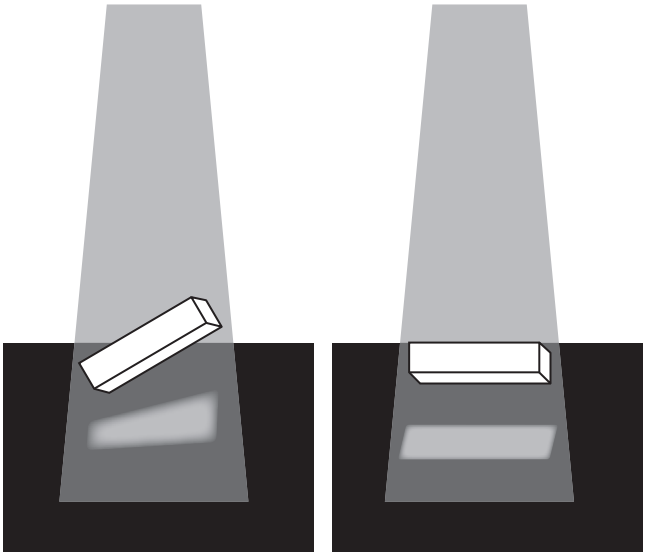


Fig. 1-31 Distortion is caused by unequal magnification of an object. The object on the *right* will be magnified slightly as it is not directly against the cassette. However, the magnification will be uniform because the object is perpendicular to the x-ray beam. On the *left*, the object is angled, and one end is further from the cassette than the other. The image of this object will be distorted because of unequal magnification and will not represent the actual shape accurately.

Radiographic Technique

Radiographic contrast refers to the shades of gray present in the image and is caused by differential x-ray absorption in various body parts. Radiographic contrast is affected by differences in thickness, physical density, atomic number, and x-ray beam energy. The effect of thickness, physical density, and atomic number on x-ray absorption were covered earlier. The effect of x-ray beam energy (kVp) on contrast is covered in this section.

The ability of an x-ray to penetrate tissue depends on its energy (see Fig. 1-19). X-rays generated at higher kVp values have higher energy. Selecting the kVp setting is one of the most important factors to consider in choosing the exposure factors.* For a constant mAs, if the kVp is too low, too few x-rays penetrate the patient, and the radiograph is underexposed (too white), whereas if the kVp is too high, too many x-rays penetrate the patient, and the radiograph is overexposed (too black). The kVp also has an effect on subject contrast. To understand how kVp affects contrast, it is important to realize that there are innumerable combinations of mAs and kVp that will result in an acceptable radiograph in relation to film blackness (Fig. 1-33). If high mAs values are used (many x-rays generated), then low kVp values must be used to prevent too many of the x-rays from penetrating the patient and reaching the film. If low mAs values are used, then high kVp values must be used so that more of the x-rays penetrate the patient and reach the film.

Even though multiple combinations of mAs and kVp can result in a satisfactory radiograph in terms of film blackness, the contrast of the image will depend on the specific kVp-to-mAs combination selected. In a high-contrast radiograph,

*The selection of exposure factors is not as critical if one is using a digital radiographic system compared with a film-screen system; this is discussed in detail in Chapter 2.

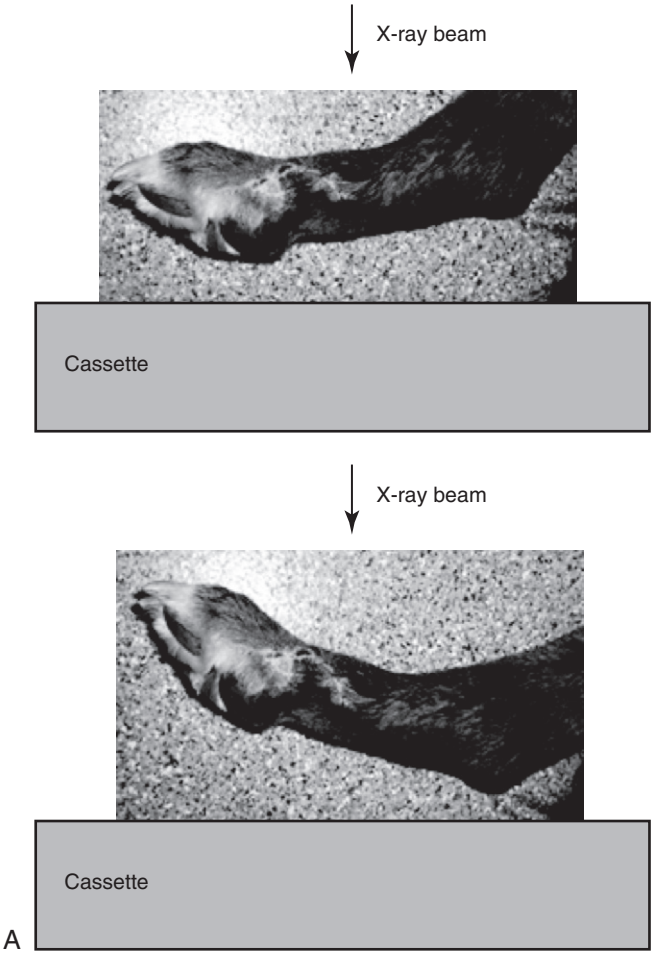


Fig. 1-32 **A,** The pes at the top is positioned properly for radiography with the metatarsus parallel to the surface of the cassette. The pes at the bottom is angled, and the metatarsal bones are not parallel with the cassette. **B,** Radiographs of the canine pes positioned as illustrated in part **A.** The pes on the left was not parallel to the cassette, and it appears shorter. The pes on the right was positioned with the metatarsal bones parallel to the cassette, and the anatomy is not distorted. In the image on the *left*, the phalanges appear larger than normal because of magnification as they were further from the cassette than when the pes was positioned perfectly. Distortion adds another level of complexity to radiographic interpretation, an already difficult art.

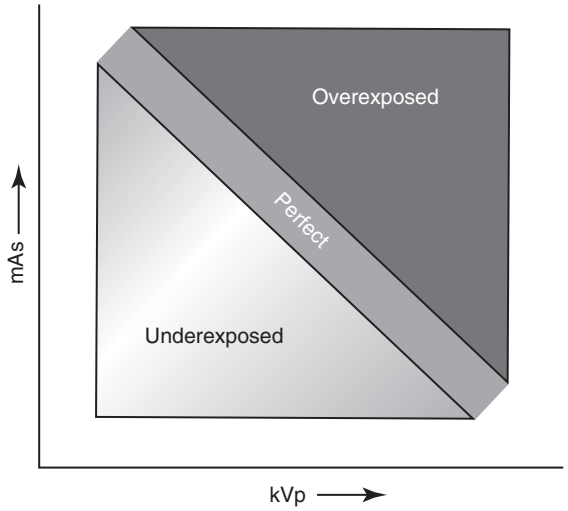


Fig. 1-33 A range of mAs and kVp combinations will produce a satisfactory radiograph. When low numbers of x-rays are generated (low mAs), their energy must be high (high kVp) so that sufficient numbers reach the film. When many x-rays are generated (high mAs), their energy must be lower (low kVp) or too many will reach the film.

mostly black and white opacities and very few shades of gray are present. High-contrast radiographs are also referred to as having a *short scale* of contrast because everything is either black or white. Low-contrast radiographs have few blacks and whites but many shades of gray; low-contrast radiographs are referred to as having a *long scale* of contrast because many shades of gray are present between the lightest and darkest portions of the image (Fig. 1-34).

In general terms, the reason that low kVp–high mAs techniques result in greater radiographic contrast than high kVP–low mAs techniques relates to the relative energies of the x-ray beams produced using these techniques. With the low kVp–high mAs technique, the energy of the x-ray beam is relatively low, and this predisposes to x-rays either being absorbed or not. Using a low kVp also means that the photoelectric absorption predominates, which is highly dependent on atomic number. Thus, bone will absorb many x-rays striking it whereas soft tissue will absorb fewer, and there will be high contrast between these tissues. Conversely, with the high kVP–low mAs technique, the energy of the x-ray beam is higher, and all tissues become less efficient absorbers of x-rays. More photons are absorbed by the Compton process, which is independent of atomic number. Therefore, the differential absorption between bone and soft tissue is minimized, and their radiographic opacity becomes more similar; that is, the radiograph has less contrast.

Film Fogging

The effect of fog is to reduce radiographic contrast. As discussed previously, fog produced by scattered radiation can be prevented by a grid, and radiographs made with a grid have higher contrast than those made without a grid. Film can also become fogged by exposure to pressure or high temperature, or by accidental exposure to light, such as results from a defective darkroom safelight or a faulty light seal around the darkroom door. Taking care to store and handle x-ray film safely will reduce fogging.

FILM PROCESSING

Many technical errors that degrade image quality are related to the processing of radiographic film. If using manual processing, the darkroom should be clean, dry, lightproof, and

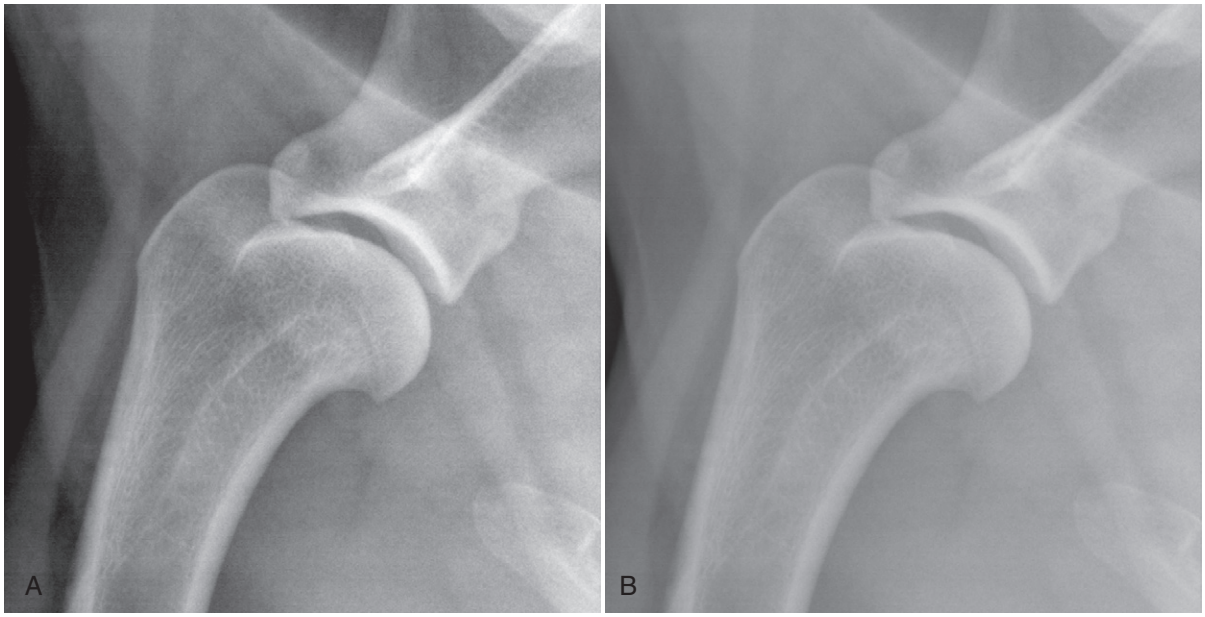


Fig. 1-34 A high-contrast **(A)** and low-contrast **(B)** radiograph of the same canine shoulder. The high-contrast radiograph would be made using a low kVp and high mAs technique, whereas the low-contrast radiograph would be made with a high kVp and low mAs technique. Both radiographs are of acceptable overall film blackness, but the high-contrast image is more useful for assessment of bone architecture. In areas of the body with high inherent contrast, such as the thorax, it would be desirable to use a high kVp–low mAs technique to prevent the radiograph from having too much contrast. Conversely, in areas of the body with low inherent contrast, such as the abdomen, where only fat provides contrast, it would be desirable to use a low kVp–high mAs technique to maximize contrast, and therefore organ discrimination, in the radiograph.

uncluttered. It is difficult to encourage a technician to perform a radiographic examination carefully if the quality of the study is diminished by poor darkroom facilities. Processing radiographic film manually is time consuming and inefficient. In most private practices the radiographic volume justifies a transition to automatic film processing, or in some instances the acquisition of a digital radiographic system.

Automatic film processors can increase the quality of radiographic production significantly. The self-contained nature of these devices eliminates the need for chemical mixing, temperature control, and replenishment. However, automatic film processors cannot be left on autopilot for long durations. They require periodic maintenance, and this is critical to keeping them performing optimally and from producing radiographic artifacts.[14]

REFERENCES

1. Roentgen W: On a new kind of rays, *Vet Radiol Ultrasound* 36:371–374, 1995.
2. Hall E, Giaccia A: *Radiobiology for the radiologist*, ed 6, Philadelphia, 2006, Lippincott Williams & Wilkins.
3. NCRP: *National Council on Radiation Protection and Measurements: NCRP report no. 82—SI units in radiation protection and measurements*, Bethesda, 1985, NCRP Publications.
4. Campion EW: A retreat from SI units, *N Engl J Med* 327(1):49–49, 1992.
5. Clark DE, Laeseke PF: Systeme International in the ICU in the United States, *Chest* 137(4):932–937, 2010.
6. Hall E, Giaccia A: Radiation carcinogenesis. In Hall E, Giaccia A, editors: *Radiobiology for the radiologist*, Philadelphia, 2006, Lippincott Williams & Wilkins.
7. ICRP: Chapters 5 and 6, *Ann ICRP* 37(2-4):81–123, 2007.
8. NCRP: *National Council on Radiation Protection and Measurements: NCRP report no. 116—limitation of exposure to ionizing radiation*, Bethesda, 1993, NCRP Publications.
9. NRC: Title 10, Chapter 1, Code of federal regulations—energy. Part 20, standards for protection against radiation. In *United States Nuclear Regulatory Commission rules and regulations*, Washington, 1995, U.S. Government Printing Office, pp 20–27.
10. NCRP: *National Council on Radiation Protection and Measurements: NCRP report no. 93—ionizing radiation exposure of the population of the United States*, Bethesda, 1987, NCRP Publications.
11. NCRP: *National Council on Radiation Protection and Measurements: NCRP report no. 107—implementation of the principle of as low as reasonably achievable (ALARA) for medical and dental personnel*, Bethesda, 1990, NCRP Publications.
12. Barthez PY et al: Comparison of single-phase and high-frequency generators for x-ray units, *Vet Radiol Ultrasound* 43(2):118–122, 2002.
13. Bushberg JT: The AAPM/RSNA physics tutorial for residents. X-ray interactions, *Radiographics* 18(2):457–468, 1998.
14. Legg LM: Quality control of the automatic processor, *Compend Contin Educ Dent* 22(2):135–138, 140–142; quiz 144, 2001.

ELECTRONIC RESOURCES

evolve

Additional information related to the content in Chapter 1 can be found on the companion Evolve website at http://evolve.elsevier.com/Thrall/vetrad/

- Chapter Quiz

CHAPTER • 2
Digital Radiographic Imaging

Ian D. Robertson
Donald E. Thrall

WHAT IS DIGITAL RADIOGRAPHIC IMAGING?

Digital radiographic imaging is (1) electronic measurement of the pattern of x-ray transmission through the patient, (2) conversion of the electronic measurement into a digital computer file, and (3) viewing the digital file on a computer monitor. This process is much like that of acquiring a photograph with a digital camera where the camera records the pattern of colors and intensities irradiating from an object and converts that information to a picture. Digital radiographic imaging is *not* photographing a radiographic film image with a digital camera, nor is it running a radiographic film image through a film scanner to convert the hard copy image into a digital file.

Conventional x-ray machines are used for digital radiography. Thus, to make the transition from analog to digital imaging, purchase of a new x-ray machine is typically not necessary. A new x-ray machine purchase could be considered if the existing unit is substandard, or if the hardware associated with the new digital-imaging system is actually housed in the x-ray table. This latter situation will be discussed in more detail later when charge-coupled device (CCD) digital radiography systems are described. In veterinary medicine, the transition from analog (film-to-screen) radiographic imaging to digital radiographic imaging has occurred more quickly than most would have anticipated.

There can be substantial capital outlay required to transition from analog to digital radiography, and selecting the correct system requires significant time, energy, and planning. All digital systems are not equal, and low-end, less expensive systems may not deliver optimal quality, and in the end, the full range of advantages of the digital radiographic environment will not be realized; the old saying "you get what you pay for" is relevant. Unless one is thoroughly versed in digital technology, it is worth hiring a consultant to assist with equipment purchasing.

Radiation protection and patient positioning are as much of an issue in digital radiography as they are in the analog world. Overall, however, the digital transition has improved the quality of radiographic studies acquired in veterinary medicine appreciably. It is critical that those working with or considering the purchase of a digital radiographic system have a thorough understanding of all aspects of this exciting new modality.

THE DIGITAL IMAGE FILE

The basis of a digital image is a computer file that contains information relating to a signal that has been measured. In diagnostic medical imaging, the signal can be the pattern of x-ray emission from a patient (radiography), quantification of fan-beam x-ray attenuation by the patient (computed tomography), the pattern of sound waves reflected by the patient (ultrasound), or the pattern of radiofrequency emission from the patient (magnetic resonance imaging, MRI). In digital photography, the signal is the color and intensity of light emitted by a medium and focused by a lens onto a receptor.

In diagnostic medical imaging, the computer file is a DICOM format; DICOM is an acronym for Digital Imaging and Communications in Medicine. A DICOM file is a computer file format of the same basic type as JPEG and TIFF files.[1] In addition to the actual image information, however, each DICOM file has a header that contains other related information about the image, including the manufacturer of the device that generated the image; the date and time of image acquisition; patient demographic information; acquisition parameters; referrer, practitioner, and operator identifiers; and various other image parameters.[1]

The DICOM file format was derived mainly for consistency to ensure interconnectivity between imaging devices.[2] Without interconnectivity, such as would occur if every vendor encoded the digital radiographic image into a proprietary file format, the convenience of having images in a digital format is reduced greatly. For example, without a standard DICOM file format, images acquired on a digital plate from vendor "A" could be viewed only on software provided by vendor "A." This is a disadvantage because the purchaser might like the features of the hardware but not the features of the software. With the DICOM standard, images created on equipment from vendor "A" can be viewed on a variety of platforms, not only on those from vendor "A." Compliance with formatting digital image files in DICOM format is voluntary. Most reputable vendors realize the advantages of total DICOM compliance, and the DICOM format has become the universal standard in medical imaging, across vendors, modalities, and computer operating systems. It is important that vendor adherence to the DICOM standard be verified before hardware is purchased, otherwise this tremendous flexibility in viewing and file transmission is lost. The DICOM standard provides for the transmission of medical images from one device to another, such as modality to server or server to workstation, using a network protocol that runs on top of the existing Internet standard protocol. DICOM images can also be transferred using browser-based technology, and this enhances image portability, particularly when accessing images beyond the local area network.

THE COMPONENTS OF A DIGITAL IMAGE

When the digital file is viewed using appropriate software, discussed later, the digital image comprises *pi*cture *el*ements termed *pixels*. The pixels are arranged in a row by column matrix. In radiographic, ultrasound, computed tomography, and magnetic resonance images, each pixel has a specified shade of gray. In color photographic images, the pixel will have an assigned color and intensity, not a shade of gray. The more pixels in a digital file, the greater the matrix size and the larger the file size. Uncompressed digital radiographic image DICOM files are typically in the order of 4 to 12 MB per image, compared to approximately 0.1 MB for a 30-page document (.doc) file and 0.5 MB to 2.0 MB for a high-resolution, color, digital photographic (.jpg) file.

The size of each pixel in a digital image determines the *spatial resolution* of the image; that is, how small of an object can be detected (Fig. 2-1). The hardware provided by the vendor determines the size of the pixel array in a digital radiographic image. In general, more pixels are better, but for any imaging system there is a point, at which more pixels do not result in a superior image. Although pixel size is important, there are many other hardware and technical factors that ultimately affect the "clinically useful" spatial resolution. Also, detailed later, software manipulation of the raw image file so as to optimize the displayed image is, within limits, more important than pixel density.

As noted before, in medical digital images each pixel is assigned a shade of gray. The number of available gray shades for each pixel will influence the contrast of the image. If a pixel can have only a few gray shades, the image can only have a very short scale of contrast (high contrast) because there will be only black pixels, white pixels, and pixels of a few gray shades. If, conversely, there are many gray shade options for each pixel, the scale of contrast can be long. Computer files use binary notation to assign a gray shade to a pixel. In binary notation, the only digits used are 0 and 1. For grayscale assignment, a zero is assigned black, and a one is assigned white; combinations of zeros and ones can be used for various intermediate gray shades. If n equals the number of allowable number of zeroes and ones per pixel, then 2^n is the number of combinations of zeroes and ones, and consequently the number of gray shades that are possible. The more combinations of zeroes and ones, the more gray shades there are possible in each pixel. The number of possible gray shades is referred to as the *bit depth* of the image (Fig. 2-2). Image file size and bit depth are directly related. Without the ability to assign multiple gray shades to each pixel, the image would have no diagnostic value (Fig. 2-3).

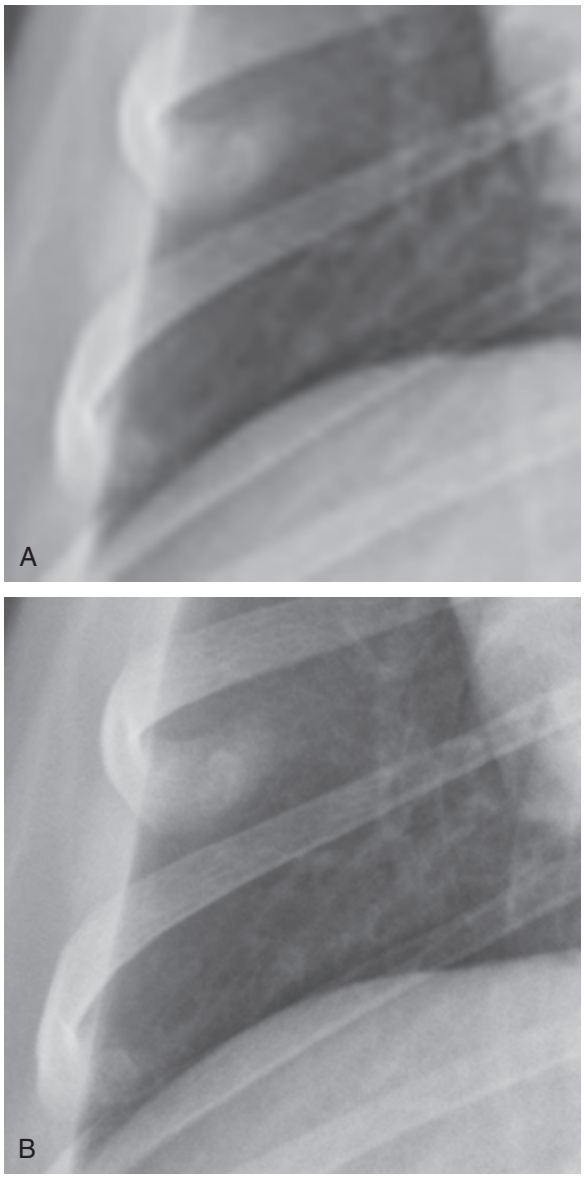


Fig. 2-1 Close-up view of the caudal thorax of a dog. **A,** The resolution of the image file is 72 pixels per inch. **B**, The resolution is 300 pixels per inch. The effect of pixel size on image detail is clear. The requirement for a small pixel size is one reason that digital radiographic image files are very large.

DIGITAL RADIOGRAPHY ACQUISITION HARDWARE

In general, there are two main types of digital radiography acquisition hardware, computed radiography (CR) and direct digital radiography (DDR).[3] As noted earlier, the conventional x-ray tube, x-ray table, and grid are used for both CR and

Bit depth	Possible pixel values	Number of shades of gray
1	0,1	2
2	00,01,10,11	4
4	0000,0001,0010, 0011,0100,0101 0110,0111,1000, 1001,1010,1011, 1100,1101,1110, 1111	16
8	00000000, 00000001, etc. to 11111111	256
12	000000000000, 000000000001, etc. to 111111111111	4096

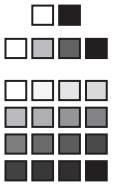


Fig. 2-2 The concept of bit depth. The number of gray shades possible in an image, depends on bit depth, which is the range of binary values that can be assigned to a pixel. If only 0 and 1 are possible (bit depth = 1), the pixel can be only black or white. If both 0 and 1 are possible (bit depth = 2), the possible pixel values are 00, 01, 10, and 11, and the pixel can have one of four gray shades. Other possible pixel values can be seen in this figure, along with a representation of the possible grayscale values for bit depths of 1, 2, and 4. The sheer number of possibilities prevents illustrating all grayscale shades for a bit depth greater than 4.

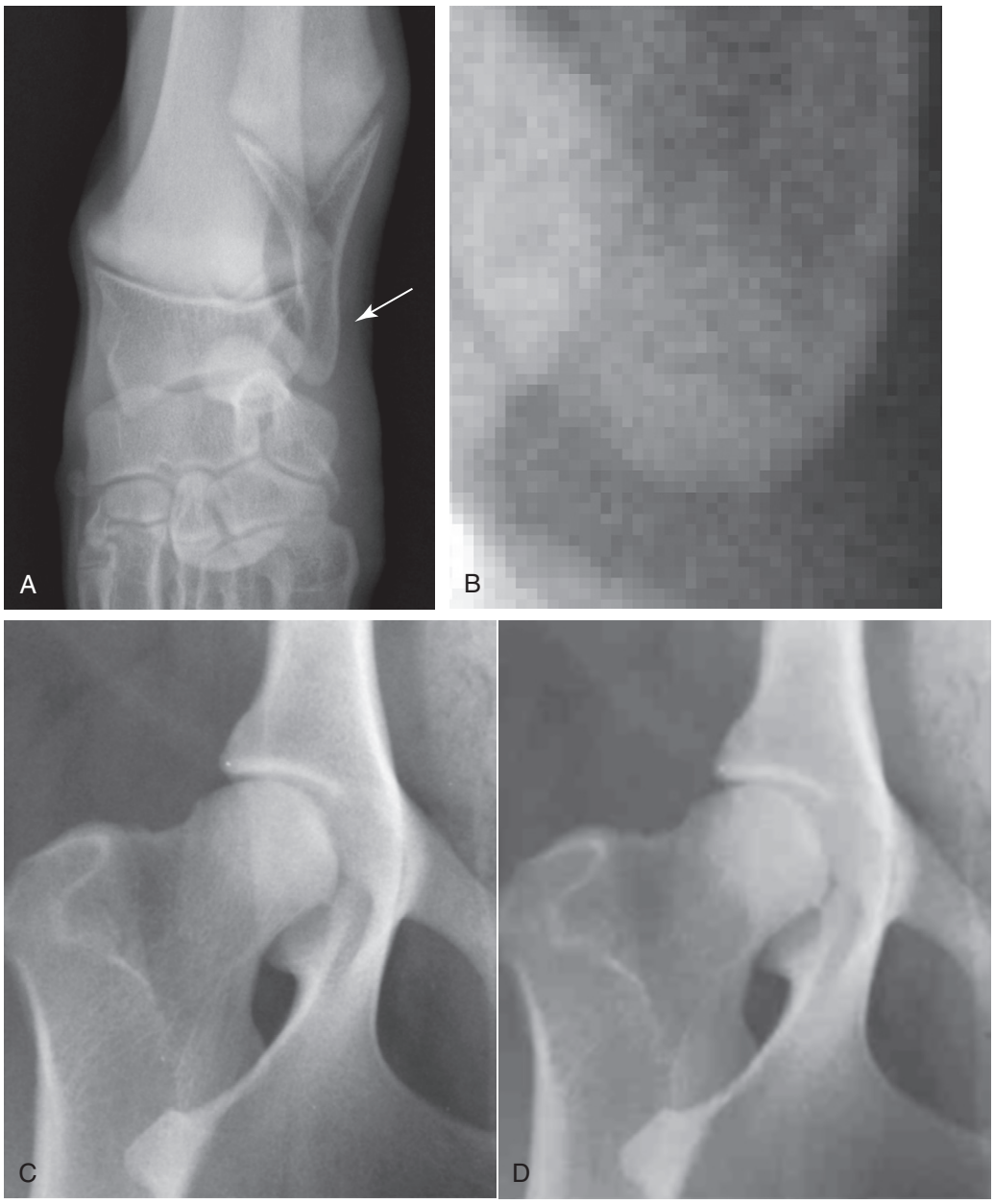


Fig. 2-3 **A,** Craniocaudal radiograph of the distal antebrachium of a dog with a bit depth of 12, meaning that 4096 shades of gray are available for pixel assignment. **B,** is a close-up of the styloid process of the ulna (region of *arrow* in **A**). At this magnification, individual pixels are visible, and the range of gray shades used to create the image can be appreciated. It is easy to see how if the number of gray shades was reduced the contrast in the image would have a very short scale with many blacks and whites but few intermediate gray tones. **C,** The image was acquired at a bit depth of 10. The image **D** was acquired at a bit depth of 8. The inadequate range of gray tones is readily apparent in the 8-bit image.

DDR applications. The difference between analog and digital imaging is that the film cassette, used for analog imaging, is replaced with a digital recording device to record the distribution of x-rays transmitted through the patient. In CR systems the digital recording device is a cassette that contains a flexible imaging plate, and in DDR systems the digital recording device is a rigid imaging plate or imaging chip (no cassette). Charge-coupled device (CCD) systems, which are a special type of DDR, may require purchase of a new x-ray table because the hardware components are housed in the x-ray table, and it may not be possible to retrofit the new equipment into an existing x-ray table adequately.

Computed Radiography

CR was the first digital radiographic system to come on the market. In CR, a cassette that appears outwardly similar to a film cassette is used. The CR cassette does not contain an intensifying screen or x-ray film but instead contains a flexible CR imaging plate coated with a photostimulable phosphor (PSP). In CR, the x-ray attenuation pattern of the patient is temporarily stored as a latent image within the PSP. The latent image is created by changes in electron energy bands that result from x-rays striking the PSP. The latent image is read out optically as photostimulated luminescence when the PSP plate is subsequently stimulated using a scanning laser

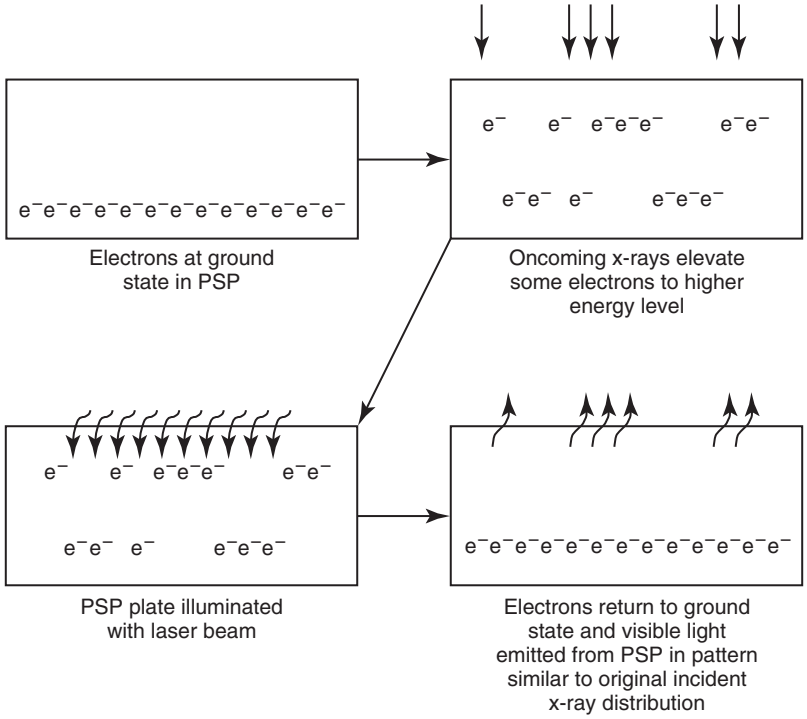


Fig. 2-4 Photostimulable phosphor plate. Prior to exposure, all electrons reside at a low energy state. X-rays that exit the patient elevate electrons to a higher energy state in a pattern that represents the distribution of incident x-rays having been transmitted through the patient. When the photostimuable phosphor (PSP) plate is processed, it is illuminated with a laser that causes the electrons trapped at the higher energy level to return to the ground state; their excess energy is emitted as visible light. The visible light strikes a photomultiplier tube housed in the reader (not shown here) where the light is converted to an electronic signal. The signal is then processed by a computer, and a digital image file is created. The pattern of visible light emission is identical to the pattern of original incident x-ray distribution.

(Fig. 2-4).[4] Therefore, the CR plate must be processed in a plate reader following radiographic exposure. The processing steps in the CR radiography process are summarized as follows:[5]

- After exposure, the CR cassette is removed from the x-ray table and inserted into the reader.
- The PSP plate is removed automatically from the CR cassette by the reader.
- The PSP plate is illuminated in the reader by a laser.
- Visible light is emitted from the PSP plate.
- Emitted light strikes the photomultiplier tube where it is converted into electronic signal.
- The electronic signal is digitized and stored as a digital file.
- The PSP plate is exposed to bright white light to make sure all electrons are at ground state in preparation for the next exposure.
- The PSP plate is returned to the cassette.
- The cassette is ejected from the reader for use on the next patient.

CR remains in widespread use in human imaging but is not as popular in veterinary imaging. There is nothing inherently wrong with CR imaging, and the reason for this relative lack of market penetration is multifactorial. Because the CR plate is handled and manipulated much the same way as an analog film cassette, it may take 1 to 2 minutes for the digital plate to be processed completely in the plate reader, whereas with DDR systems the image is available almost immediately. Because of this, CR does not increase workflow compared with analog imaging. For example, a CR plate reader that can read only one plate at a time is actually slower than a modern automatic x-ray film processor. When throughput is not an issue, a good-quality CR system can function perfectly adequately as a replacement for an analog system. One advantage of a CR system is that damaged cassettes can be replaced relatively inexpensively, whereas the cost of replacing a damaged DDR plate, discussed in the next section, is considerably more expensive. Another advantage of CR is that the cassette is not tethered to a computer by a cable as most digital-imaging plates are; this provides more flexibility and reduces constraints in obtaining nonstandard views, such as images made with an horizontally directed x-ray beam, because the geometric relationship between the x-ray tube and CR plate can be highly variable.

Direct Digital Radiography

There are three distinct types of DDR: (1) indirect flat-panel detector system, (2) direct flat-panel detector system, and (3) CCD system. In DDR, the detector replaces the imaging cassette, and within a few seconds after the radiographic exposure, the digital radiographic image is ready for quality-control evaluation. Direct and indirect flat-panel detectors are commonly tethered to a processing computer by an electric cable, although some wireless systems are available.

Indirect Flat-Panel Detectors

Indirect flat-panel detectors are termed *indirect* because they produce light as an intermediate step in image formation. An x-ray intensifying screen, identical in principle to those discussed in Chapter 1, is used to convert x-ray energy emerging from the patient into visible light.[5,6] The intensifying screen is layered onto a panel containing an array of tiny photodiodes. Much as with the photostimulable phosphor found in the CR plate, the photodiodes convert light emitted from the intensifying screen into an electronic signal that is then read out by a thin-film transistor array and transformed

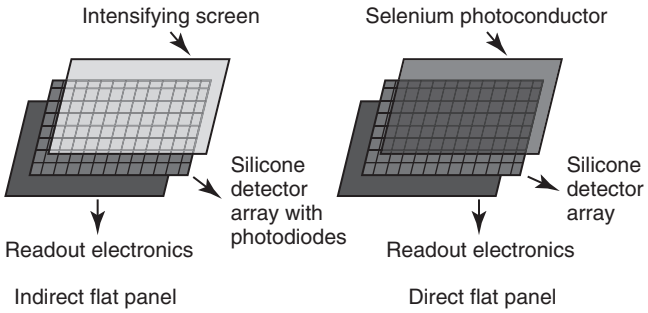


Fig. 2-5 Comparison of the makeup of indirect versus direct flat-panel detectors. With the indirect detector, an x-ray intensifying screen converts oncoming x-ray energy to visible light. The light interacts with the detector array, which is composed of small elements that each contains a photodiode and an amorphous selenium detector. The light from the intensifying screen is converted to an electronic signal by the photodiode and then readout by the amorphous selenium detector. Readout electronics maintain spatial resolution and transmit the information to the computer, where it is converted to an electronic file. With the direct detector, there is no light intermediary. The oncoming x-rays strike a selenium photodetector, where the energy is converted to an electronic signal that is collected by the amorphous silicone detector array directly, with subsequent processing by the readout electronics and formation of an electronic file.

into an electronic file (Fig. 2-5). To have good spatial resolution, the size of each detector element is very small, and a full-size imaging plate measuring approximately 43 cm × 43 cm may have a photodiode matrix of at least 2600 × 2600. Thus, an indirect flat-panel detector can have on the order of 6 to 7 million photodiodes or more. As can be imagined, the electronics needed to record and spatially localize the signal from each photodiode, or pixel, and to also incorporate the photodiode into each detector element is quite complicated. This contributes to the relatively high cost of flat-panel detectors compared with a film-screen cassette system. Indirect flat-panel detectors are commonly capable of a bit depth of 14, meaning there is a grayscale resolution of 16,384 gray shades per pixel.[6] Most digital radiographic systems range in bit depth from 10 to 16 (1024 to 65,536 shades of gray). As the human eye can register only 50 to 100 simultaneous shades of gray, even with extreme manipulation of image contrast (postprocessing—see later), there is probably little benefit in generating images with more than 14- to 16-bit depth.

Direct Flat-Panel Detectors

In a direct flat-panel detector there is no light intermediary. Oncoming x-rays strike a photoconductor, typically composed of amorphous selenium, which has high efficiency x-ray absorption. Electrons liberated in the selenium layer by the oncoming x-ray beam are collected to form a charge. This charge is then read out directly by the thin-film transistor array, processed by the readout electronics and converted to an electronic file (see Fig. 2-5).[5,6] As with indirect flat-panel detectors, there are millions of detectors in the array, and the pixel matrix is of comparable size, also with a bit depth of 14. Thus, the main difference between indirect and direct flat-panel detectors is the intermediate step of light production from the intensifying screen in indirect systems.

As discussed in Chapter 1, there is some light diffusion within an x-ray intensifying screen. This light diffusion, which can potentially lead to blurring, is a purported disadvantage of indirect flat-panel detectors versus direct flat-panel detectors. However, with modern engineering techniques, and the structure of the crystals in the intensifying screen, the amount of light diffusion that actually occurs in the intensifying screen of the indirect flat-panel detector is minimal and not clinically significant. For all practical purposes, the functionality of modern-day indirect and direct flat-panel detectors is comparable.

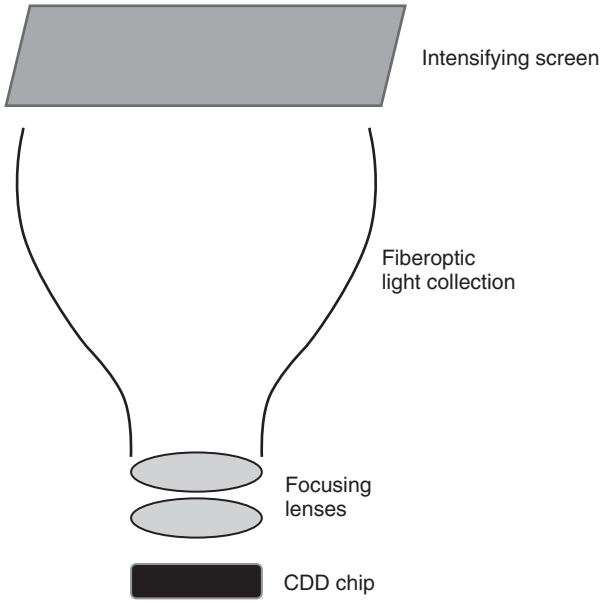


Fig. 2-6 A charge-coupled device (CCD) radiography system. X-rays from the patient strike a conventional intensifying screen where the spatial distribution of x-rays is converted to a comparable spatial distribution of visible light. The light is collected using fiberoptics and strikes focusing lenses that direct it onto the light-sensitive CCD chip. Overall image quality is determined mainly by the efficiency of light collection and the quality of the focusing lenses. All of these components are encased in a housing that must be incorporated into the x-ray table. The housing is fixed, which means that the x-ray tube must always be perpendicular to the face of the housing.

Charged-Coupled Device

CCD chips are used routinely in video camcorders and digital cameras, but their use in radiographic imaging is less common than either CR or flat-panel DDR radiography. However, some vendors are marketing veterinary radiography systems based on the CCD chip. CCD systems are included in the discussion of DDR because no equipment manipulation is needed between radiographic exposure and image visualization, such as is required in processing a CR cassette.

CCD chips are relatively small compared with a flat-panel detector, being only a few centimeters on each side, compared with up to 43 cm for flat-panel detectors. Although small, there may be millions of pixel elements on the surface of a CCD chip. The CCD chip is sensitive to visible light, not x-rays; this is the basis for their use in camcorders and digital cameras. Thus, for radiography based on CCD technology, a light intermediary is necessary, and this, as in indirect flat-panel detectors, is accomplished by integration of a relatively standard x-ray intensifying screen between the patient and CCD chip. When the CCD chip is exposed to light that has been focused from the intensifying screen, the pixels in the CCD chip accumulate electronic charge, which is read out and converted to an electronic file.[5]

The geometry of the CCD system deserves special consideration. Given the small size of the CCD chip, the light output from the intensifying screen needs to be focused onto the chip, whereas in an indirect flat-panel detector the intensifying screen is layered directly onto the detector. Focusing of light from the intensifying screen onto the CCD chip is usually accomplished by integration of fiberoptic light collection and a focusing lens between the intensifying screen and CCD chip (Fig. 2-6). Thus, the quality of the image depends more on the quality of the light collection and focusing than on the quality

of the CCD chip. Also, there is some loss of light and potentially much light distortion between the intensifying screen and CCD chip, leading to image degradation.

CCD chips are becoming more and more elaborate. An important component of this is pixel density. It is important to realize that the pixel density of a CCD chip cannot be compared directly to the pixel density of a flat-panel DDR detector. This is because it is not CCD chip pixel density but rather light capture, image minification, and subsequent light loss and distortion that control the spatial resolution of a CCD system. Multiple CCD chips and focusing devices are a way to increase the efficiency of light collection and focusing, but as yet the technology is not clinically reliable.

In general, CCD radiography in humans has been reserved for situations where the part being imaged is relatively small (e.g., dental radiography and mammography) and there is less need for light focusing. In veterinary medicine, the parts being radiographed are larger and requirements for focusing more stringent; this can lead to poorer images than obtained with flat-panel detectors, and image quality from CCD systems is considered by many to be inferior to both flat-panel and CR systems. Also, the distance required for collecting and focusing the light from the intensifying screen means that the physical device is quite large compared with a flat-panel detector. Because a result, CCD detectors are housed within the x-ray table. As this cannot be done easily in a retrofit manner, purchase of a new x-ray machine may be necessary if CCD technology is chosen. The size of the device also limits portability, and there is a requirement for a constant vertical relationship between the x-ray tube and CCD camera; both of these factors eliminate the possibility of using CCD technology for portable imaging. CCD systems are typically less expensive than flat-panel imaging systems or high-quality CR systems, but image quality is usually inferior. A summary of the various hardware options is shown in Figure 2-7.

IMAGE PROCESSING AND VIEWING

Regardless of which type of digital radiographic hardware is selected, the electronic data are processed by a computer before the final image file is created and displayed. Image file processing and modification occur at a number of points and can be broken down into preprocessing, processing, and postprocessing steps.[7]

Preprocessing of the image is usually beyond the control of the user. Manufacturers apply various corrections to the raw image data to accommodate such things as inhomogeneity in light collection, image distortion by focusing lenses in CCD systems, nonfunctional or dead pixels in the detector, and variation in efficiency between individual detector elements. These preprocessing steps are aimed at eliminating artifacts created by the imaging system itself[7] and are critical to image quality optimization.

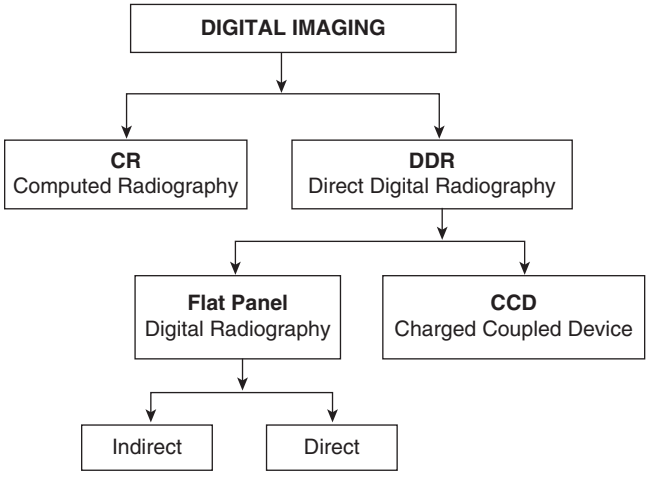


Fig. 2-7 Chart showing the image capture hardware options available in digital imaging.

The *processing* step is aimed at converting the corrected raw image data to a useable radiographic image. These manipulations, also done on the raw image data, can be controlled to some extent by the user and are aimed at optimizing image contrast, edge enhancement, minimizing image noise, and optimizing other aspects of image presentation.[5,7] These settings are usually configured by the vendor as "presets" or factory default settings; however, most systems allow customization by the user. Most commonly, the raw data file is not permanently overwritten, and additional image processing can be performed at a later time if necessary, provided the raw data files have not been deleted from the modality. Assessing image quality at the x-ray machine, and making adjustments to optimize image presentation is part of the "processing" step. Preprocessing and, most importantly, effective image processing are critical, and this functionality is often what sets good vendors and products apart.

Once the preprocessing and processing adjustments have been completed, the image is ready for viewing and interpretation. The processed image file (which may or may not be in DICOM format) is converted to DICOM format, appropriate header information inserted, and the study is distributed through the local network to the viewing computer(s) and an appropriate archive. DICOM files, although a graphics file, cannot be viewed directly in programs such as Adobe Photoshop or Microsoft Paint. Rather, they must be viewed with dedicated DICOM file-viewing software. Licenses for this software are typically sold by the hardware vendor, but free DICOM viewers are available. Examples of free viewers are K-PACS,* ClearCanvas† for Microsoft Windows, and OsiriX‡ for Apple computers. eFilm Workstation§ is a popular medical image viewer in both veterinary and medical imaging. Which viewing software will be adequate for any particular practice should be considered carefully, and consultation with an expert may be needed to make the best selection.

The functionality of DICOM viewing software represents one of the major advantages of making the transition from analog to digital radiography. This is the *postprocessing* step of image manipulation, and this is 100% user-controlled. DICOM viewers allow images to be magnified and rotated, and the image blackness and contrast can be adjusted independently. Other features are also available, such as viewing multiple images simultaneously and obtaining quantitative measures of area and length (Fig. 2-8). The myriad image adjustments that can be accomplished is a tremendous advancement over viewing film-based radiographs, which cannot be manipulated at all following their creation. It should be noted that postprocessing image manipulation does not permanently alter the original image in any way.

Ambient lighting and monitor quality are two important considerations when optimizing image viewing. As ambient light increases, the perceived difference between light and dark on a monitor decreases, and this can affect image interpretation negatively.[8] Interestingly, viewing of digital radiographs in a completely dark room with no light other than the monitor light also reduces accuracy.[9] For this reason, computers used for primary image interpretation should be in a room

*http://www.k-pacs.net
†http://www.clearcanvas.ca
‡http://www.osirix-viewer.com
§http://www.merge.com

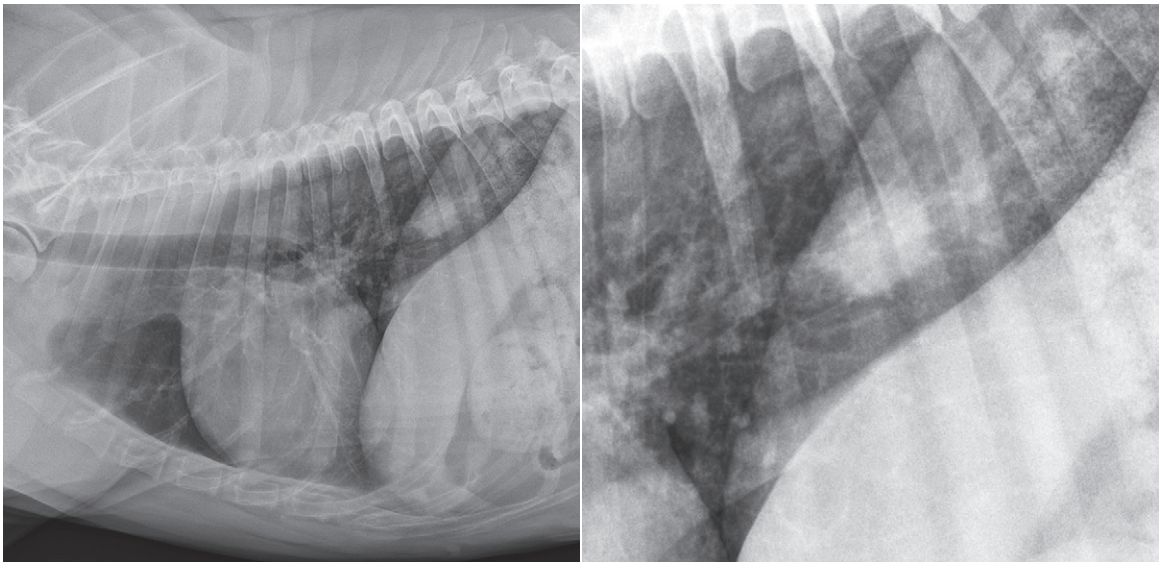


Fig. 2-8 Screen capture from a DICOM viewing program. A left lateral thoracic radiograph is displayed in the *left* panel. In the *right* panel, the same radiograph has been enlarged and the contrast adjusted to increase the conspicuity of a nodule in the caudal lung field.

with adjustable, or permanently dimmed, lighting but not in total darkness.

Monitor quality is another factor that influences the accuracy of interpretation of digital radiographic images. The two basic monitor types are cathode-ray tube (CRT) and liquid crystal display (LCD). There are big differences between CRT and LCD monitors. CRTs are bigger and bulkier than LCD monitors; they consume more power and are prone to screen flicker. LCD monitors introduce the problem of viewing angle and generally have less accurate color replication.* There have been numerous assessments of viewing accuracy using LCD versus CRT monitors, and variable outcomes have been found;[10-13] this is not surprising considering the variety of endpoints and monitor technical specifications. Regardless, for many reasons, CRT monitors have been largely replaced by LCD monitors for all computer applications, and CRT monitors will not be discussed further here.

Both monochrome (black and white) and color LCD monitors are available, and their technical specifications are highly variable, leading to a wide range of image display quality. Ideally, radiographic images are best viewed on a dedicated medical-grade monochrome LCD monitor.[14] Such monitors are characterized by superior brightness, contrast ratio, and resolution. Monitor brightness relates to how bright a white screen is, and a brighter display enables the user to resolve more shades of gray. Contrast ratio is a measure of the monitor's ability to display true black as black and true white as white. Because LCD technology relies on backlighting, displaying true black is technically challenging, and as a result, LCD monitors with a high-contrast ratio are more expensive. Monitor resolution also affects how well digitally captured images appear on the screen. Medical-grade monochrome LCD monitors typically have 3 megapixel resolution or higher. For example, a typical display for such a monitor is 2048 pixels × 1536 pixels, yielding a 3.1 megapixel display. This level of resolution approximates the average resolution of most digital radiographs, which means there is no image downsizing by the graphics card during initial image display. For the user, this means there is no need to routinely magnify images to ensure all the digital information available is evaluated. Viewing angle is also important with LCD monitors, where loss of information occurs as the viewing angle becomes less perpendicular.[15]

Unfortunately, medical-grade monochrome LCD monitors are expensive, and their routine use throughout the veterinary imaging environment cannot be justified financially. Consumer-grade color LCD monitors are improving continuously, and the diagnostic advantage of the more expensive monochrome monitors is becoming less clear. As a result, consumer-grade color LCD monitors are commonly used in many digital-imaging environments,* for both veterinary and human imaging. Even in specialty hospitals, there is no need for expensive monochrome LCD monitors in examination rooms or in the surgery suite. However, given the substantial investment in image acquisition that occurs when transitioning from an analog to a digital radiography system, an additional investment to acquire at least one medical-grade monochrome monitor for viewing digital radiographic images is justifiable.

Whatever viewing system is chosen, it is important to ensure that monitors are calibrated correctly. Test patterns to assist in monitor calibration are available through the Internet.† Medical-grade monochrome LCD monitors should be calibrated using the DICOM grayscale display function standard.

DIGITAL IMAGING IN THE CONTEXT OF THE MEDICAL PRACTICE

The full advantages of the transition to digital imaging are best realized when digital imaging is incorporated into the global practice environment. This means integrating image acquisition and management with the hospital's electronic medical record. In a fully integrated system, radiographic studies are ordered in the electronic medical record. The order subsequently appears seamlessly at the x-ray machine computer

*http://www.webopedia.com/DidYouKnow/Hardware_Software/2005/all_about_monitors.asp. Posted August 28, 2009; updated August 30, 2010; accessed September 30, 2010.

*http://rsna2006.rsna.org/rsna2006/V2006/conference/event_display.cfm?em_id=4434169. Accessed September 30, 2010.

†http://www.duke.edu/~samei/tg18.html. Updated January 10, 2006; accessed September 30, 2010.

monitor using functionality known as *DICOM modality worklist*. Selecting the study to be performed from a list of the examinations requested for the day eliminates data entry errors that might result from having to reenter all patient information de novo as the study is performed. Not having to reenter this information also improves workflow. When the study has been acquired, appropriate charges are posted automatically in the medical record, and the images are sent to a local server for distribution and archiving. Distribution might include transmission of the images to an off-site radiologist for interpretation, with the radiographic report being entered seamlessly into the patient record after it is completed. The images are viewable through the electronic medical record using either DICOM viewing software, as described previously, or through an Internet browser program.

PACS is an acronym for Picture Archiving and Communication System and refers to the host of technologies that contribute to the creation, distribution, and archiving of digital images. The basic components of a PACS that might be found in a private veterinary practice are (1) the device, that is the CR or DDR radiography system; (2) a server that acts as the local image archive; (3) workstations that can retrieve images from the server for remote viewing, in the examination room or surgery for example; (4) a local area network for data transfer; (5) an image communication protocol (the DICOM standard); and (6) off-site secure image storage (Fig. 2-9). When purchasing a digital-imaging system, there is often little attention paid to integration of the radiographic hardware and software into the overall hospital environment. This is a mistake and can result in functionality problems that compromise the advantages of transitioning to digital imaging.

DIGITAL VERSUS ANALOG IMAGING

The advantages of digital imaging are quite far reaching and some have been alluded to in prior sections. It is noteworthy to outline specifically what these advantages are and to expand on those that have not been covered in adequate detail. Advantages of transitioning to digital radiography are (1) reduced expendable supply cost and elimination of darkroom maintenance; (2) exposure latitude and contrast optimization; (3) image postprocessing, ability to adjust image blackness and contrast after exposure; (4) consolidated image storage; (5) enhanced image portability for consultation; and (6) enhanced professionalism in the eyes of the consumer.

Reduced Expendable Supply Cost and Elimination of Darkroom

With the transition to digital imaging, the requirement for purchasing x-ray film, film-filing envelopes, darkroom chemistry, and other related supplies is eliminated. Although these items are not inherently expensive, their use over time can amount to a considerable sum, and this expense is eliminated in the digital world. Also, and perhaps more important, the time and effort required for darkroom maintenance will also be eliminated. Darkroom errors, such as outdated chemicals, incorrect temperature settings, chemical spills and splashes, and safelight fog or other light leaks, make up a substantial fraction of errors that compromise analog image quality. The elimination of darkroom errors is a major factor that contributes to the overall higher quality of a digital versus film-based radiographic system.

Contrast Optimization and Exposure Latitude

When one begins to evaluate digital radiographic images compared with analog film radiographic images, the initial impression may be that of improved detail in the digital radiograph. This is a misconception created by the extreme contrast optimization that characterizes digital radiographs. The detail of an image relates to how small of a structure can actually be discriminated in the image; this is termed *spatial resolution*. The spatial resolution in a digital or analog radiographic image depends on many factors, some of which apply equally to both analog and digital imaging, but there are a few differences

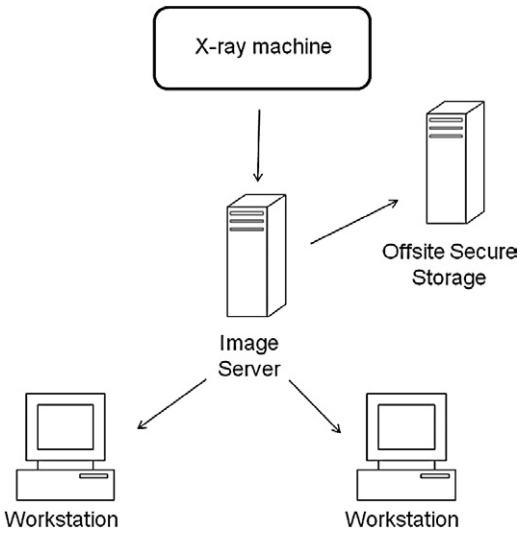


Fig. 2-9 Components of a rudimentary PACS system. Images in DICOM format are transferred from the acquisition device, an x-ray machine in this example, to the central server. Images have been assessed by the technical staff for quality prior to being transmitted to the server. The central server must not be relied on as the sole image storage device. Secure off-site image archiving is needed. Clinicians at remote locations, such as the examination room, the intensive care unit (ICU), or surgery, can retrieve images from the server for interpretation and consultation. Images can also be sent from the server to remote locations for additional consultation.

(Box 2-1). In the end, it is the collective effect of these factors that determines the final spatial resolution. The relative inherent spatial resolution from various medical-imaging techniques is provided in Table 2-1.[16] From Table 2-1 it can be seen that the inherent spatial resolution of digital radiographs is roughly half that of analog radiographs; this is the end result of all factors listed in Box 2-1. Although there is a factor of two difference in spatial resolution between analog and digital radiography, this difference is not relevant clinically because the spatial resolution of both analog and digital radiography is very good. Thus it is not spatial resolution that makes digital radiographs superior to analog film radiographs. The major factors contributing to the superior image quality of digital radiographs are contrast optimization and exposure latitude.

Because the use of an antiscatter grid can have a major effect on both spatial resolution and image contrast, it is worth commenting specifically on their use in digital radiography. Antiscatter grids should be used routinely in analog radiography when patients are thicker than approximately 10 cm to remove unwanted scatter from the x-ray beam before it strikes the cassette; this was described in detail in Chapter 1. Although antiscatter grids can be used in digital radiography, some manufacturers have incorporated a scatter-correction algorithm into the image-processing software that makes grid use unnecessary (Fig. 2-10). When a grid is not used, these scatter-correction algorithms can manipulate the raw image dataset and effectively remove much of the unwanted image plate

Box • 2-1

Factors Contributing to Inherent Spatial Resolution in Digital Versus Analog Radiographs

Digital Radiograph
Focal spot size
Patient scatter
Grid efficiency, if used
Size of crystals in intensifying screen*
Size of detector element in digital plate

Analog Radiograph
Focal spot size
Patient scatter
Grid efficiency, if used
Size of crystals in intensifying screen
Size of light-sensitive crystal in x-ray film emulsion

*For digital radiography, an intensifying screen is used only in indirect flat panels and in CCD systems

Table • 2-1

Inherent Spatial Resolution of Various Imaging Modalities*

MODALITY	RESOLUTION (mm)
Screen film radiography	0.08
Digital radiography	0.17
Ultrasound imaging (5 MHz)	0.30
Computed tomography	0.40
Magnetic resonance imaging	1.00

*Modified from Bushberg JT, Seibert JA, Leidholdt Jr. EM, et al: Introduction to medical imaging. In Bushberg JT et al, editors: *The essential physics of medical imaging*, 2e, Philadelphia, 2002, Lippincott Williams & Wilkins, p 1.

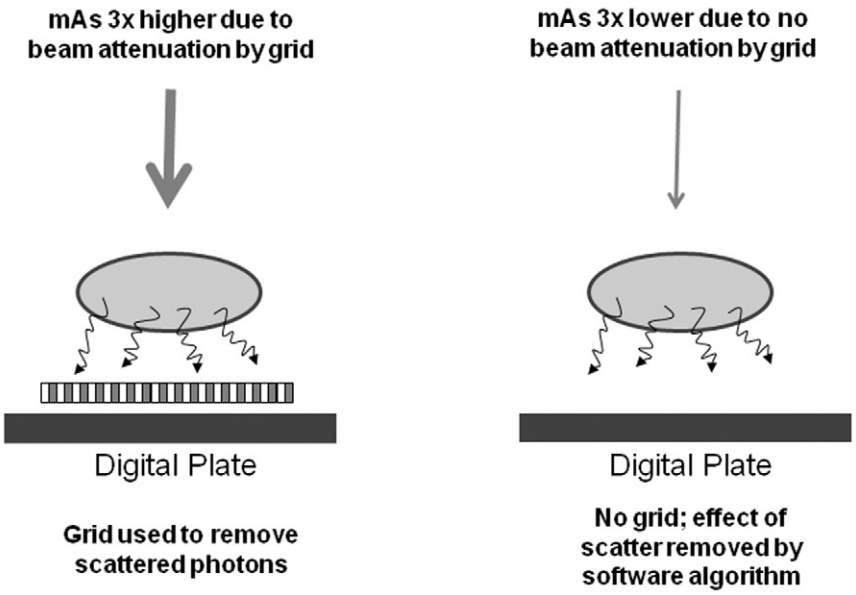


Fig. 2-10 Diagram illustrating the principle of scatter removal by a grid versus a scatter-correction software algorithm. On the *left*, the scattered photons are removed by a grid. This is standard practice in analog radiography and can also be used with computed radiography (CR), direct digital radiography (DDR), and charge-coupled device (CCD) systems. On the *right*, there is no grid, and the effect of the scattered photons has been corrected by a software scatter correction algorithm. The mAs can be lower on the right because there is no attenuation of the primary beam by the grid. Whether the efficacy of any scatter-correction software will be adequate is subjective and should be field-tested prior to purchase.

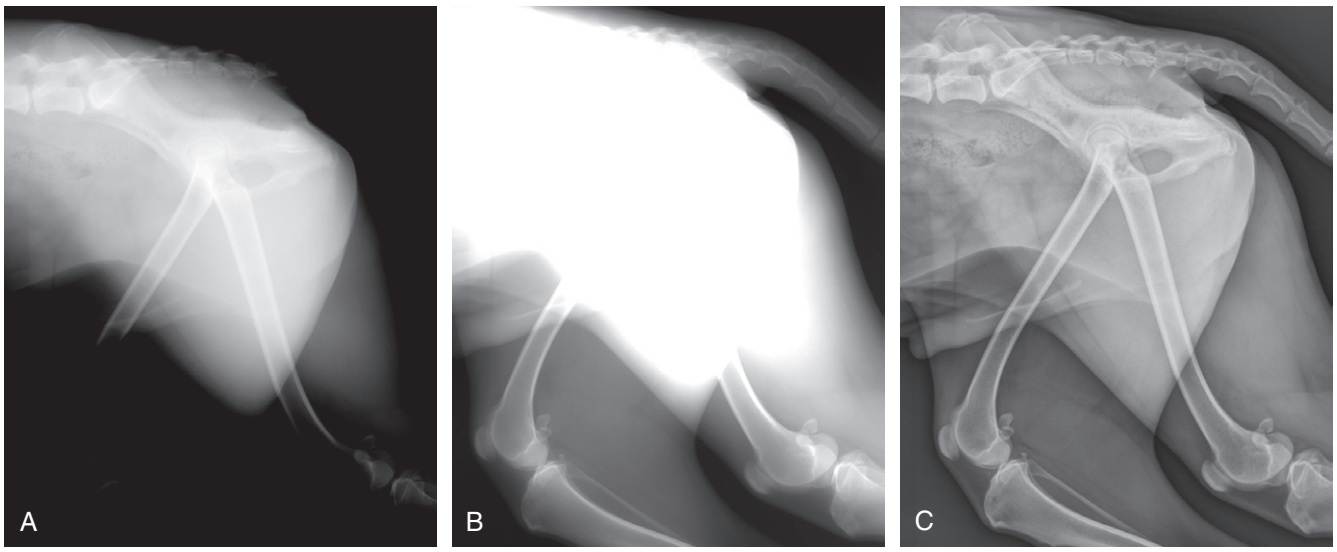


Fig. 2-11 Radiographs illustrating the wide contrast resolution of digital radiographs versus analog radiographs. **A,** Film radiograph made with exposure factors appropriate for the lumbar spine; the distal aspect of the femurs; the stifles are overexposed because they are thinner and cannot be adequately evaluated. **B,** Film radiograph made with exposure factors appropriate for the stifles. The spine and pelvis are underexposed because they are thicker. **C,** Digital radiograph where both the thick and thin aspects of the patient can be assessed. This wide range of gray shades characterizes the wide contrast resolution of digital radiographs. The ability to assign a gray shade to a pixel is the basis of this appearance wide range of gray shades; this is a feature of the processing software provided by the hardware vendor.

exposure that results from scattered photons.[17] Thus the end result of the scatter-correction algorithm is an image that has less degradation resulting from scatter, but without actually using a grid. Implementation of an antiscatter algorithm avoids the higher milliampere second (mAs) values that are needed to compensate for the presence of an actual grid in the x-ray beam (see Fig. 2-10). The possibility of a grid artifact, as described in Chapter 1, is also eliminated when grids are not used. Whether or not the end user will be satisfied with the quality of the antiscatter image-processing algorithm will be a matter of individual preference, and the functionality of this feature should be evaluated in any digital system prior to purchase.

Contrast Optimization

Contrast optimization is a feature of digital radiography that is related to the bit depth of each pixel and the processing software that accompanies the digital-imaging system. The processing software can assign a gray shade to a pixel in a digital image that would have been either black or white in an analog image. This results in more of the image having interpretable gray shades and not appearing overexposed (black) or underexposed (white).

With radiographic film, radiographic contrast is associated rigidly with the relationship between kilovoltage peak (kVp) and mAs, as discussed in detail in Chapter 1. Consider film radiography of a patient where the thickness of various parts of the patient within the primary x-ray beam varies considerably; one example of this would be a lateral radiograph encompassing the caudal abdomen, pelvis, and femurs and stifle joints of a dog. The lumbosacral region of the pelvis is very thick and primarily bone. The caudal abdomen is somewhat thinner and primarily soft tissue. The distal femur and stifle joints are much thinner. When a radiographic technique is used (remember, this is an analog example) that is suitable for the average thickness and physical density (e.g., caudal abdomen), the lumbosacral region will be too white (underexposed because of excessive x-ray absorption) and the thinner parts (stifle) too black (overexposed because of excessive x-ray transmission). One can think of this result as being caused by the film having a bit depth that is too low to capture all the needed gray shades. The region of the film in the lumbosacral region can only be white, and the region of film in the stifle region can only be black.

With digital radiography, however, the wide range of thickness of the patient can be compensated for by the computer assigning a suitable gray shade to pixels in the thick lumbosacral and thin stifle regions, as well as in the caudal abdomen. What this means in practical terms is that opacity differences associated with differences in thickness are much less obvious in digital radiographs than in analog radiographs (Fig. 2-11). This same principle applies to structures of similar thickness but containing parts that have markedly different physical density, such as massive bones (Fig. 2-12) or air-filled lung (Fig. 2-13). The result is a more pleasing image with more gray shades, and there are no parts that cannot be assessed because of being too white or too black. It should be noted that some vendors have superior software in this regard, with not all digital systems being equal. The lateral view of the pelvis of a medium-to-large dog with the pelvic limbs displaced cranially and caudally, as illustrated in Figure 2-11, is a good field test for contrast optimization software.

The terminology used to describe this contrast optimization feature of digital radiographic systems can be confusing. Some have used the term *dynamic range* to mean the same thing as contrast resolution, but there are, in fact, many differing definitions of dynamic range, depending on the system being discussed.* The term *dynamic range* has also been used to describe the low dependence of digital-imaging plates on absolute x-ray exposure (kVp and mAs), which in this chapter we call *exposure latitude*.[18] To avoid this confusion, we recommend use of *contrast resolution* or *contrast optimization* to

*http://www.google.com/search?hl=en&defl=en&q=define:Dynamic+range&ei=IDHcS9jLG5Gu9gTMieGlBw&sa=X&oi=glossary_definition&ct=title&ved=0CAgQkAE. Accessed May 1, 2010.

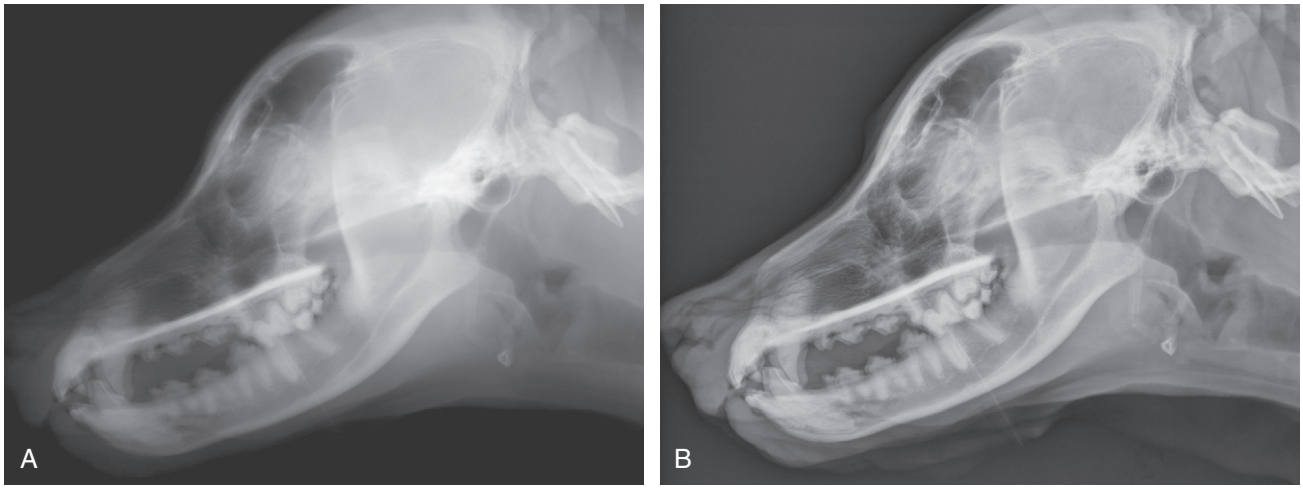


Fig. 2-12 Lateral views of a canine skull made with analog **(A)** and digital **(B)** systems. In **A,** the nasal planum and maxillary structures are overexposed while the temporomandibular joint region is underexposed. Bone underexposure is primarily the result of its increased physical density leading to increased x-ray absorption. In **B,** the image-processing algorithm can compensate for these differences in absorption and assign a more useful gray shade to pixels in soft tissue and bone, leading to an image where thick and thin regions of both bone and soft tissue can be assessed.

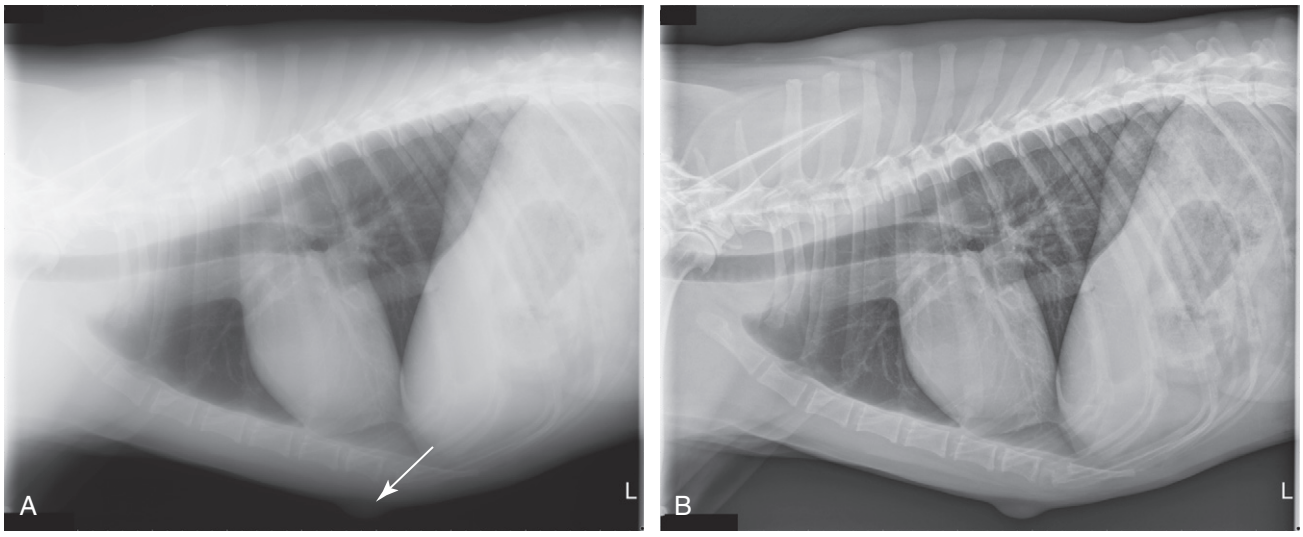


Fig. 2-13 Lateral canine thoracic radiographs of the same patient made with analog **(A)** and digital **(B)** systems. In **A,** the lungs are exposed reasonably and can be interpreted, but the bones, cranial aspect of the abdomen, and paraspinal soft tissues are underexposed, and the periphery of the patient is overexposed; note the poor visibility of the ventral lipoma because of overexposure (*white arrow* in A). The lungs, being of low physical density, absorb few x-rays, and the exposure factors were adjusted for this. The film is incapable of displaying meaningful information in other underexposed or overexposed areas. In **B,** the image-processing algorithm can compensate for the differences in physical density and assign a more useful gray shade to pixels in soft tissue and lung, leading to an image where both can be assessed. Note the increased conspicuity of the small ventral lipoma that was overexposed in the analog image.

define the ability of an imaging system to display thick and thin regions, and regions of low and high atomic number, suitably in one image, and the term *exposure latitude* to define the ability of digital plates to compensate for either high or low kVp-to-mAs combinations that would result in overexposure or underexposure, respectively, in an analog system.

Exposure Latitude

As alluded to before, *exposure latitude* refers to the relative independence of digital radiographic image quality on the magnitude of incident x-ray exposure, for example, radiographic technique. With analog radiography, there is only a narrow range of kVp-to-mAs combinations that will result in satisfactory film blackness, and even then there will usually be regions of the film image that are too white or too black (see Figs. 2-11, 2-12, 2-13). Any combination of kVp-to-mAs outside of the suitable range will result in overall film underexposure or overexposure (Fig. 2-14, Fig. 2-15). With digital plates, however, the ability of the processing software to create an image of suitable blackness is relatively independent of the kVp and mAs values that are used (Fig. 2-16; see Fig. 2-15). The magnitude of the range of radiographic exposures that can be used to create a diagnostic radiographic image is called *exposure latitude*.

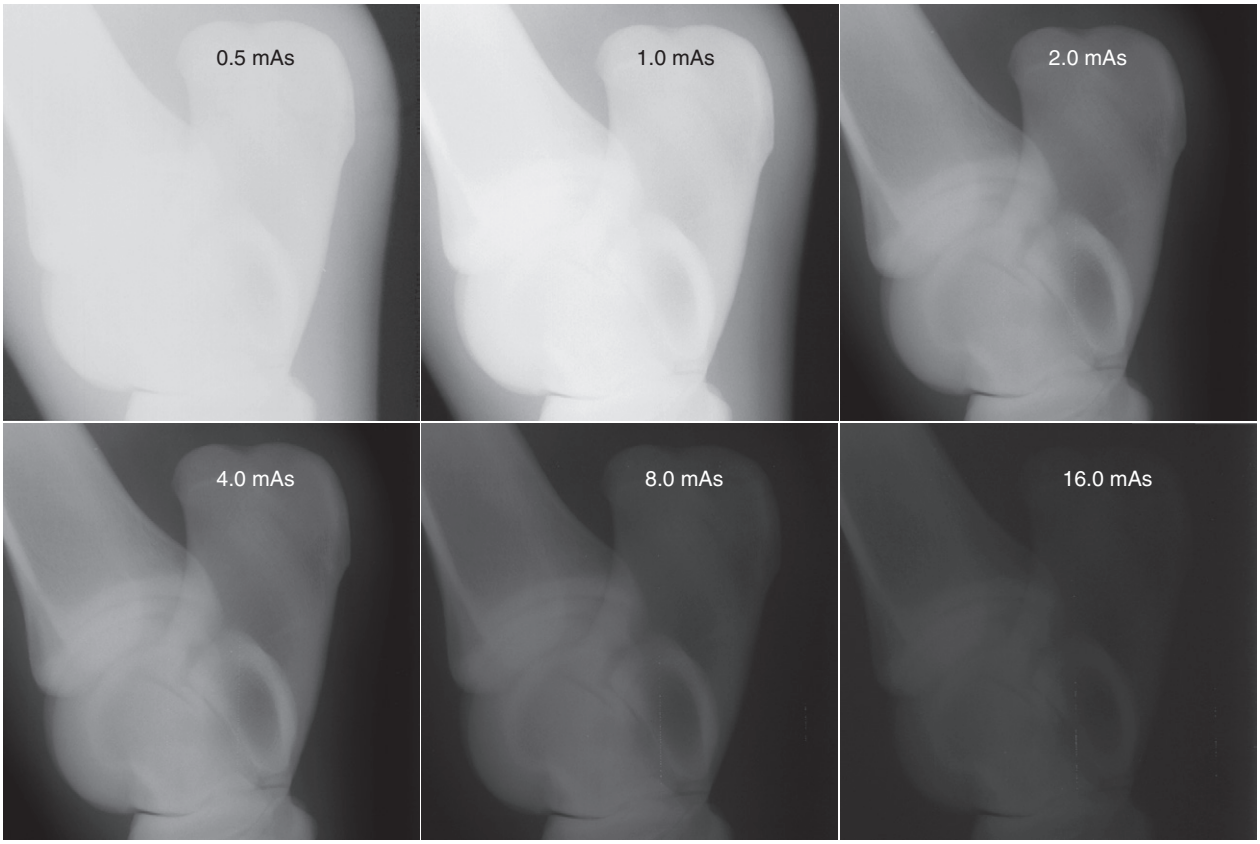


Fig. 2-14 Lateral analog radiographs of an equine tarsus exposed at the same kVp value but at a wide range of mAs values, from 0.5 to 16. At low mAs values, the entire image is underexposed, whereas at high mAs values the entire image is overexposed. At 2 mAs and 4 mAs the soft tissues can be evaluated, and at 8 mAs the bones can be evaluated. This is an example of the narrow exposure latitude of analog radiography. In everyday life, many poor radiographs are produced because of the selection of incorrect exposure factors.

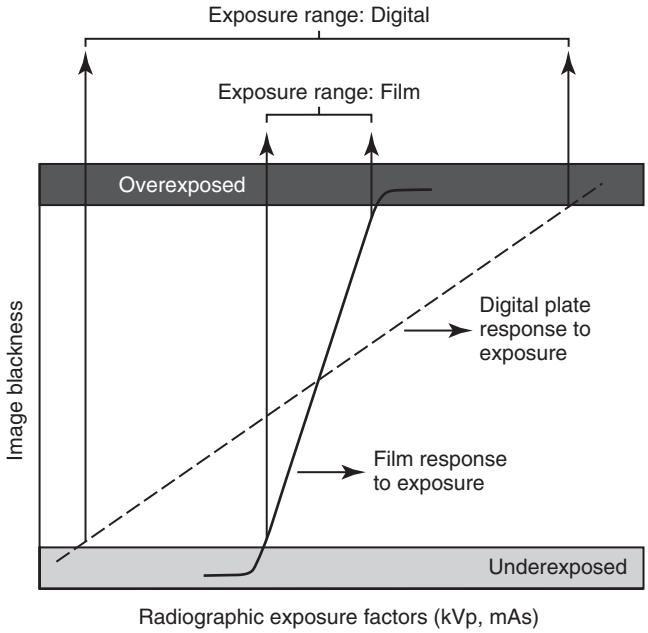


Fig. 2-15 Diagram illustrating the principle of exposure latitude. In this figure, image blackness is plotted as a function of radiographic exposure; that is, kVp and mAs. For film, small changes in kVp and mAs cause dramatic changes in image blackness—the slope of the curve is very steep. There is only a narrow range of exposure that leads to suitable image blackness in an analog system. For digital systems, the slope of the curve is much shallower. This results in many more combinations of kVp and mAs that will result in adequate film blackness. This wide exposure latitude reduces retakes and is a feature of both the hardware and the processing software of the digital-imaging system.

One potential disadvantage of the wide exposure latitude that characterizes digital-imaging plates is *exposure creep*, where unnecessarily high exposure factors are not recognized as they would be in the analog world.[19,20] In analog radiographs, high exposure factors result in excessive film blackening that is recognized easily. This is not true in digital radiography, where overexposure is corrected for by the image-processing software. The disadvantage of exposure creep is unnecessary patient and personnel exposure to ionizing radiation and increased wear and tear on the x-ray tube. Most digital radiography manufacturers have incorporated an exposure index (EI) metric that enables the user to evaluate the amount of incident plate exposure (i.e., the exposure factors) and this EI can be used to judge whether radiographic techniques are too high or too low. However, the EI is only as useful as the frequency with which it is assessed. Routine checking of the EI should be part of the quality assurance process used to evaluate the digital-imaging process for every patient.

The transition to digital radiography has led to a dramatic reduction in the number of retakes, especially those related to errors in radiographic exposure.[21] However, the wide exposure latitude that characterizes digital radiography does not mean that underexposure or overexposure is not a problem; these problems still occur, but only at the extremes of exposure factors. With underexposure, the overall image quality may appear satisfactory from a global perspective, but on close inspection, the underexposed image will appear grainy. This grainy appearance is caused by image noise, created by statistical uncertainty in computer assignment of a gray shade to underexposed regions of the image.[22] This grainy appearance will be obvious on close inspection and could interfere with

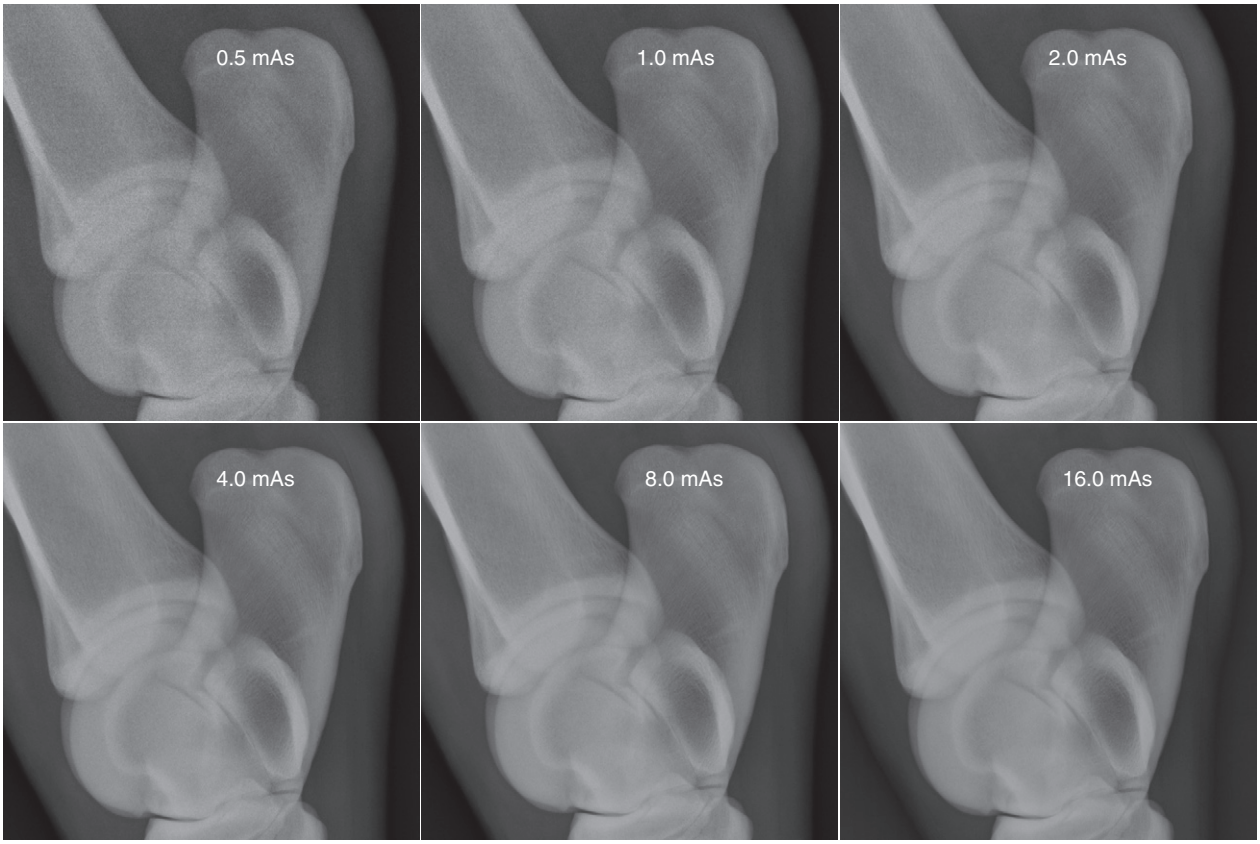


Fig. 2-16 Lateral digital radiographs of the same equine tarsus as in Figure 2-13, acquired with an indirect flat-panel detector. Note the acceptable film blackness and contrast at all mAs values. This illustrates the reduced dependence of the image blackness and contrast of digital radiographs as a function of radiographic exposure. This wide exposure latitude reduces the number of retakes needed because of the selection of incorrect exposure factors.

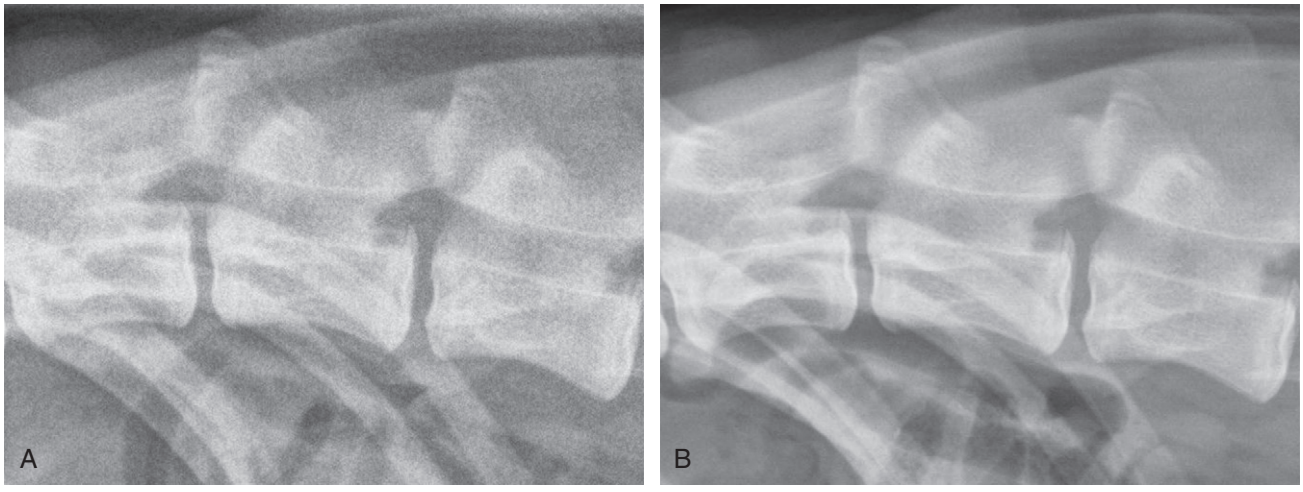


Fig. 2-17 Underexposed **(A)** and properly exposed **(B)** digital radiographs of a portion of the lumbar spine of a dog. In **A,** there is a noticeable grainy appearance to the radiograph because of the underexposure. This represents image noise and is created by uncertainty in grayscale assignment to unexposed pixels. In **B,** the grainy appearance has been eliminated by increasing the exposure factors.

detection of a subtle lesion, especially those affecting the trabecular pattern of bone (Fig. 2-17).

Overexposure of digital radiographs does not result in overall film blackening, as in the analog world. The detector elements and processing software are able to compensate electronically for overexposure, up to a point at which the detector becomes saturated and cannot respond to additional exposure. At saturation, the computer assigns the maximum pixel value, black, to the pixels that are saturated.[22] This results in some parts of the image being interpretable with other parts of the image being absent or having an abnormal gray shade assignment (Fig. 2-18). Because only portions of

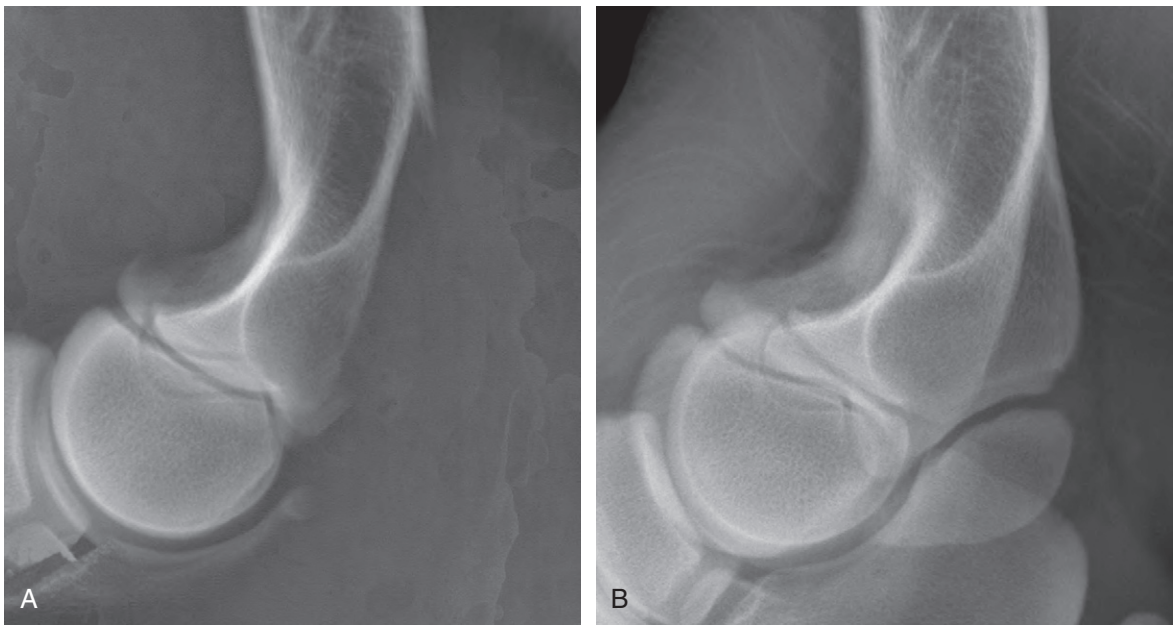


Fig. 2-18 Overexposed **(A)** and properly exposed **(B)** radiograph of the distal humerus of a foal. In **A,** the distocaudal aspect of the humerus, the center of ossification for the medial epicondyle, and the proximal aspect of the ulna are all absent because of plate saturation in this region created by massive overexposure. In **B,** the missing structures are clearly visible. Missing anatomy caused by plate saturation could easily be interpreted as a pathologic lesion, such as bone lysis in **A.**

the image are overexposed, as compared to the entire image, the overexposed region can be misinterpreted easily as a lesion.

Image Postprocessing

Despite the tremendous contrast resolution of digital radiographs, there is sometimes a desire to make some regions of the final processed image blacker or whiter to facilitate interpretation. For example, when thoracic radiographic images are produced by the image-processing software, they may have a long scale of contrast that may not be optimal for evaluating the bones that are visible in the image. Modifying the image blackness and contrast is accomplished easily with DICOM viewing software described earlier in this chapter, and magnification of regions of the image can also be very useful in detecting small lesions that would be overlooked easily in an unmagnified digital image or in an analog film image not viewed with a magnifying glass (Fig. 2-19). The flexibility provided by postprocessing maximizes viewing options for the clinician. As discussed in Chapter 1, most inexperienced interpreters fail to take advantage of the full range of manipulations provided by DICOM viewing software.

Analog film images cannot be postprocessed. Bright spotlights, as described in Chapter 1, can heighten the information gleaned from dark regions in an analog image. Unfortunately, there is absolutely no way to interpret regions of underexposure in an analog film image because the film emulsion is essentially clear. A magnifying glass can help in identifying small lesions that are present in analog images, similar to computer magnification of the image as noted before, and in Figure 2-19. In reality, adjusting the intensity of the light used to view an analog film image, or use of a magnifying glass, is rarely done in practice settings.

Consolidated Image Storage

With digital radiography, the need for storage of many years worth of analog film images, creating of a filing system, and the purchasing of filing envelopes and file cabinets is eliminated. Also eliminated is the problem of lost or destroyed analog film radiographs. Digital radiographs are stored as digital files on an image server, an integral part of the PACS. A common mistake, however, is relying on only one primary storage device to archive the collection of digital radiographic files. Storing digital files on a single archive, typically on a single hard disk drive on one server, is not adequate because the hard drive can fail. Also, any other component of the server can also fail and lead to corrupt data, or the server can be destroyed during a physical disaster such as fire or flood. Storage using a redundant array of independent disks (RAID),* where data are distributed over multiple disks such that if one disk fails, data integrity is preserved, is an absolute minimum for hardware redundancy. Data storage using RAID is much safer than relying on a single hard disk drive. However, although a RAID configuration does protect against individual hard drive failure, it does not protect against other hardware failures, including RAID controllers and other critical components of a server. Additionally, the data are still subject to loss through server damage during a physical disaster, an unprotected power surge, or corruption through a computer virus. The best solution is redundant off-site duplication and storage where digital radiographic data are duplicated and transferred to an off-site computer on a regular basis, preferably daily, for safe storage.

Enhanced Portability for Consultation

It is difficult for most practicing veterinarians to become totally competent in radiographic interpretation. The volume of information and the nearly endless variation in how disease is manifest radiographically is simply too much. Getting a second opinion on radiographic studies has been employed for decades. Analog film images were either hand-carried to a specialist, if one was lucky enough to be sufficiently close, or sent to the expert by mail or courier. The expert would interpret these images, usually telephone the veterinarian with the results, and prepare a written report that would be returned to the veterinarian along with the radiographs. This worked

*http://en.wikipedia.org/wiki/RAID. Accessed May 2, 1010.

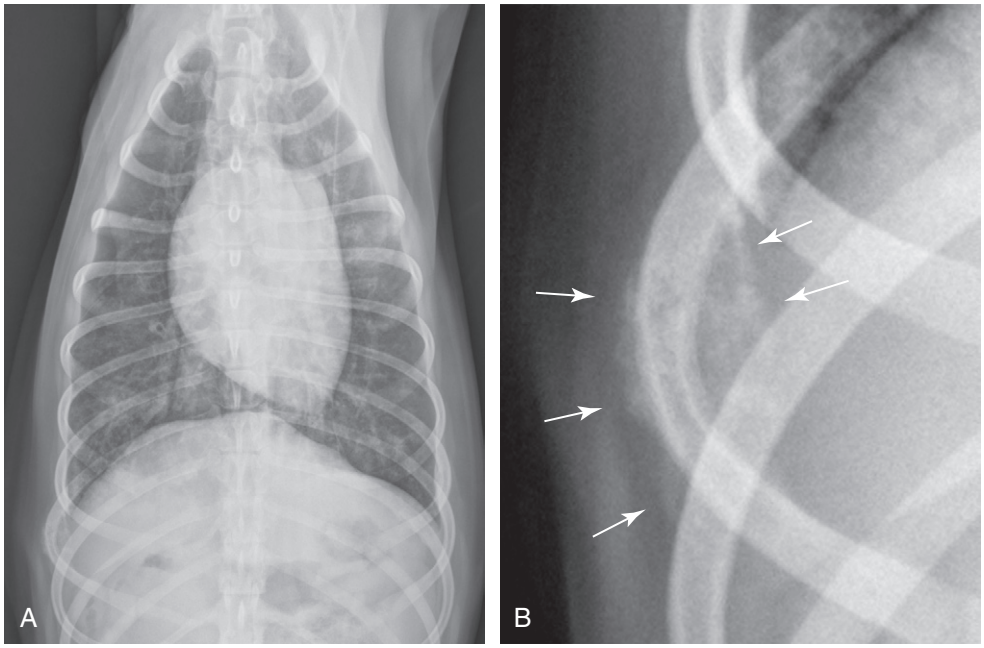


Fig. 2-19 Ventrodorsal thoracic radiograph of a dog with a scapular tumor **(A)**. The right forelimb has been removed. This radiograph was part of a series acquired to examine for pulmonary metastasis and, as such, has been processed by the software with a long scale of contrast. There is an aggressive lesion of the right ninth rib. Had the image only been viewed at this magnification, and at this long scale of contrast, this lesion would have likely been overlooked. With digital radiography, the image can be magnified and every rib examined in detail. Magnification, and making the scale of contrast shorter, greatly increases the conspicuity of the rib lesion, as in **B.**

relatively well, given the constraints of the delivery service and the time required for transportation. With the explosion of digital radiography in veterinary medicine, veterinary teleradiology was born. Teleradiology is the electronic transmission of radiological images from one location to another for the purposes of interpretation and/or consultation.* Veterinary teleradiology was first introduced commercially in the early 1990s with limited success, mostly influenced by slow Internet speeds and large file sizes.[23] DICOM files are large, and transmission as an e-mail attachment can be problematic. Likewise, conversion of DICOM images to small JPEG files for e-mailing is also not suitable, because excessive information is lost from the images. For teleradiology consultation to work smoothly, a method of direct DICOM transfer needs to be established; this is why it is so important to ensure that the vendor of the digital radiography equipment has configured its DICOM file format appropriately. Many veterinarians have been unhappy with their digital radiology purchase for the simple fact that the DICOM file format was not 100% compatible and could not be transferred easily for expert consultation—you get what you pay for. Currently the practice of teleradiology in veterinary medicine is widespread because of the availability of broadband Internet connections, image compression, and economically priced PACS and DICOM software.[23] Also, there are many teleradiology service providers throughout the world who have teleradiographic interpretation as their primary mission. These advancements have made turnaround time very short and stat interpretations possible.

Enhanced Professionalism in Eye of Consumer

Veterinary medicine can be a competitive enterprise, especially in times of economic downturn. Also, pet owners are highly educated and have a wealth of information at their fingertips that they use to help make decisions regarding medical care for their pet. Being perceived as having a modern contemporary practice environment can help maintain and increase a healthy client base regardless of economic and client-education factors. Having digital radiography is one way that practices are viewed as being progressive, and being able to provide high-quality radiographic services can bolster one's professional persona.

It is unfortunate, but true, that for decades many clients did not receive radiographic examinations of their pets that met minimum standards. Based on our own experience of providing radiographic consultations for more than 50 collective years, film radiographic studies were often plagued with problems. These included overexposure, underexposure, darkroom errors, poor positioning, and inadequate views. All of these problems could be solved easily, but many practices failed to do so. The transition to digital radiography can help alleviate problems with radiographic exposure, and darkroom errors are also eliminated. Positioning and selecting the correct radiographic views will not be solved automatically by the transition to digital radiography, but in the digital world, the economic cost of making these modifications is insignificant. For example, in the analog world, many veterinarians were reluctant to obtain all needed views routinely, three projections of the thorax for example, because of the increased cost of expendable supplies required to do so. We have also encountered veterinarians whose policy was not to repeat radiographs that were technically inadequate unless the owner paid an additional fee. These charging policies were not reasonable, even in the analog world. Radiographic studies should be priced on an examination basis, not on a per-image or per-view basis. The fee should be set such that the practice makes a profit, all necessary views are included, and the quality standards are acceptable. Repeats should be the fiscal responsibility of the practice and not the pet owner. Having a digital system where the specific cost of any single view is minuscule should lead to elimination of archaic charging policies that

*http://en.wikipedia.org/wiki/Teleradiology. Accessed May 2, 2010.

were too commonplace in the analog world. This too will enhance the pet owner's perception of the professionalism of the practice.

ARTIFACTS

As with all medical-imaging modalities, there is potential for digital radiographic imaging artifacts. An artifact is an unwanted, usually nonpatient-related anomaly in the image that may or may not compromise image interpretation. These occur in both CR and DDR systems and are unique from those encountered in analog film radiography. Overexposure and underexposure and how these differ in appearance from exposure errors in analog radiography were described previously. The discussion of other imaging artifacts that are observed in digital radiography is beyond the scope of this chapter, but excellent references are available.[22,24]

REFERENCES

1. Graham RN, Perriss RW, Scarsbrook AF: DICOM demystified: a review of digital file formats and their use in radiological practice, *Clin Radiol* 60:1133, 2005.
2. Wright MA, Ballance D, Robertson ID, et al: Introduction to DICOM for the practicing veterinarian, *Vet Radiol Ultrasound* 49:S14, 2008.
3. Widmer WR: Acquisition hardware for digital imaging, *Vet Radiol Ultrasound* 49:S2, 2008.
4. Watt KN, Yan K, DeCrescenzo G, et al: The physics of computed radiography: measurements of pulse height spectra of photostimulable phosphor screens using prompt luminescence, *Med Phys*, 32:3589, 2005.
5. Bushberg JT, Seibert JA, Leidholdt EM Jr, et al: Digital radiography. In Bushberg JT, et al, editors: *The essential physics of medical imaging*, ed 2, Philadelphia, 2002, Lippincott Williams & Wilkins, p 293.
6. Cowen AR, Kengyelics SM, Davies AG: Solid-state, flat-panel, digital radiography detectors and their physical imaging characteristics, *Clin Radiol* 63:487, 2008.
7. Lo WY, Puchalski SM: Digital image processing, *Vet Radiol Ultrasound* 49:S42, 2008.
8. Goo JM, Choi JY, Im JG, et al: Effect of monitor luminance and ambient light on observer performance in soft-copy reading of digital chest radiographs, *Radiology* 232:762, 2004.
9. Brennan PC, McEntee M, Evanoff M, et al: Ambient lighting: effect of illumination on soft-copy viewing of radiographs of the wrist, *AJR Am J Roentgenol* 188:W177, 2007.
10. Cha JH, Moon WK, Cho N, et al: LCD versus CRT monitors for digital mammography: a comparison of observer performance for the detection of clustered microcalcifications and masses, *Acta Radiol* 50:1104, 2009.
11. Uematsu T, Kasami M, Uchida Y: Soft-copy reading in digital mammography of microcalcifications: diagnostic performance of a 5-megapixel cathode ray tube monitor versus a 3-megapixel liquid crystal display monitor in a clinical setting, *Acta Radiol* 48:714, 2007.
12. Buls N, Shabana W, Verbeek P, et al: Influence of display quality on radiologists' performance in the detection of lung nodules on radiographs, *Br J Radiol* 80:738, 2007.
13. Ludewig E, Boeltzig C, Gabler K, et al: Display quality of different monitors in feline digital radiography, *Vet Radiol Ultrasound* 52(1):1–9, 2011.
14. Krupinski EA, Kallergi M: Choosing a radiology workstation: technical and clinical considerations, *Radiology* 242:671, 2007.
15. Hatanaka S, Morishita J, Hiwasa T, et al: Comparison of viewing angle and observer performances in different types of liquid-crystal display monitors, *Radiol Phys Technol* 2:166, 2009.
16. Bushberg JT, Seibert JA, Leidholdt EM Jr, et al: Introduction to medical imaging. In Bushberg JT, et al, editors: *The essential physics of medical imaging*, ed 2, Philadelphia, 2002, Lippincott Williams & Wilkins, p 1.
17. Lo WY, Hornof WJ, Zwingenberger AL, et al: Multiscale image processing and antiscatter grids in digital radiography, *Vet Radiol Ultrasound* 50:569, 2009.
18. Korner M, Weber CH, Wirth S, et al: Advances in digital radiography: physical principles and system overview, *Radiographics* 27:675, 2007.
19. Shepard SJ, Wang J, Flynn M, et al: An exposure indicator for digital radiography: AAPM task group 116 (executive summary), *Med Phys* 36:2898, 2009.
20. Butler ML, Rainford L, Last J, et al: Are exposure index values consistent in clinical practice? A multi-manufacturer investigation, *Radiat Prot Dosimetry* 139(1-3):371–374, 2010.
21. Akhtar W, Aslam M, Ali A, et al: Film retakes in digital and conventional radiography, *J Coll Physicians Surg Pak* 18:151, 2008.
22. Drost WT, Reese DJ, Hornof WJ: Digital radiography artifacts, *Vet Radiol Ultrasound* 49:S48, 2008.
23. Poteet BA: Veterinary teleradiology, *Vet Radiol Ultrasound* 49:S33, 2008.
24. Jimenez DA, Armbrust LJ, O'Brien RT, et al: Artifacts in digital radiography, *Vet Radiol Ultrasound* 49:321, 2008.

ELECTRONIC RESOURCES

evolve

Additional information related to the content in Chapter 2 can be found on the companion Evolve website at http://evolve.elsevier.com/Thrall/vetrad/

- Chapter Quiz

CHAPTER • 3

Physics of Ultrasound Imaging

William Tod Drost

Ultrasound examinations are a widely used, indispensable diagnostic imaging test. It is a highly user-dependant interaction among the sonographer, patient, and machine. An understanding of the physics of ultrasound is important because it helps explain some of the limitations of the modality and artifacts encountered. This is the only diagnostic imaging modality that does not use electromagnetic radiation. In this chapter, the physical principles of ultrasound waves, the interactions of ultrasound waves with matter, transducers, Doppler techniques, and ultrasound artifacts are discussed.

PHYSICAL PRINCIPLES OF ULTRASOUND WAVES

Sound travels in waves and carries information from one location to another. It transmits energy by alternating regions of low pressure (rarefaction) and high pressure (compression).[1-4] Unlike light and radio waves, sound waves require a medium through which to travel.[5] Frequency, wavelength, and velocity are parameters used to describe sound waves; these terms are also used in reference to electromagnetic radiation (see Chapter 1).

Frequency is the number of times a wave is repeated per second. One wave or cycle occurs when pressure starts at a normal value, increases to a high value, decreases (passing the normal value) to a low value, and then returns to normal (Fig. 3-1). A cycle may also be defined as the combination of compression and successive rarefaction.[1] Frequency is expressed in hertz (Hz), where 1 Hz equals one cycle per second. In diagnostic ultrasound, the frequencies are typically between 2 megahertz (MHz) and 15 MHz (1 MHz = 1,000,000 Hz). The audible range of sound frequencies for human beings is 20 Hz to 20,000 Hz; sound less than 20 Hz is infrasound, and sound greater than 20,000 Hz (0.02 MHz) is ultrasound.[1,4,5]

Wavelength is the distance traveled by a sound wave in one cycle. In ultrasonography, wavelength is expressed in millimeters (mm). Wavelength is important for image resolution and is discussed later.

Velocity is the rate at which sound travels through an acoustic medium; it is determined by the physical density (mass per unit volume) and stiffness (hardness) of the transmitting medium.[1,2] The velocity of sound in some commonly encountered tissues is listed in Table 3-1. If physical density remains constant, velocity increases as stiffness increases. If the stiffness remains constant, velocity decreases as physical density increases. As a general rule, velocity is highest in solids, lower in liquids, and the lowest in gases. In solids, molecules are closer together, so sound waves are transmitted faster; in gases, the molecules are far apart, and sound waves travel more slowly. Medically, sound waves travel the fastest in bone and the slowest in gas-filled lungs. Velocity is related to frequency and wavelength of a sound wave in the following equation:

$$\text{Velocity (mm/μs)} = \text{Frequency (MHz)} \times \text{Wavelength (mm)} \quad \text{(Eq 1)}$$

For a constant velocity, frequency and wavelength have an inverse relationship so that as frequency increases, wavelength decreases, and vice versa. Within soft tissue, the average velocity of sound is 1.54 mm/μs (1540 m/s).[1-5] The velocity of sound in soft tissue is important because ultrasound machines use this constant velocity for all calculations.

ULTRASOUND WAVE INTERACTION WITH MATTER

The principle of echo formation is important because echoes contain the diagnostic information about the structures being imaged. The interface that causes the echo reflection and the angle at which the sound wave strikes the reflector, or the angle of incidence, should both be considered.

Acoustic impedance of a tissue is the product of the tissue's physical density and sound velocity within the tissue.[1,4]

$$\text{Acoustic impedance (Z)} = \text{Velocity (υ)} \times \text{Tissue density (p)} \quad \text{(Eq 2)}$$

Changes in acoustic impedance from one tissue to another determine how much of the sound wave is reflected and how much is transmitted into the second tissue. The amplitude of the returning echo is proportional to the difference in acoustic impedance. If two tissues have no difference in acoustic impedance, then no echo is created. If a large difference in acoustic impedance exists between two tissues, then almost all the sound is reflected in an echo.[1,2] The following formulas are used to calculate the percentage of the sound wave that is reflected and transmitted:[1,3,5]

$$\%\ \text{reflected} = (Z_2 - Z_1)/(Z_2 + Z_1) \times 100 \quad \text{(Eq 3)}$$

$$\%\ \text{transmitted} = 100 - \%\ \text{reflected} \quad \text{(Eq 4)}$$

In Equation 3, Z_2 is the acoustic impedance of the second tissue, and Z_1 is the acoustic impedance of the first tissue. The approximate acoustic impedance of tissues encountered commonly is listed in Table 3-2 and the percentage of sound reflected at various tissue interfaces is listed in Table 3-3. By the values in Table 3-2, the largest difference in acoustic impedance occurs at interfaces with bone and gas. Almost all sound is reflected at soft tissue/gas and soft tissue/bone

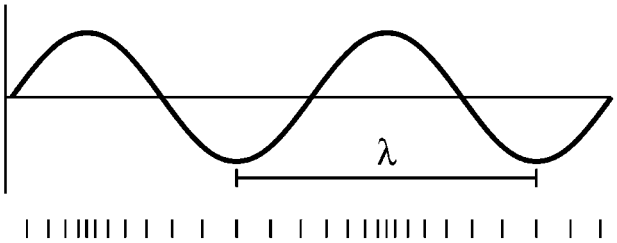


Fig. 3-1 An ultrasound wave depicted as a sine wave (*top*) and as a series of compressions and rarefactions (*bottom*). One wavelength (l) is the distance between two successive peaks or valleys of the sine wave or between two successive compression or rarefaction events.

Table • 3-1

Velocity of Sound in Commonly Encountered Tissues[2]

TISSUE	VELOCITY (MM/μS)
Air	0.331
Fat	1.450
Water (50° C)	1.540
Soft tissue	1.540
Brain	1.541
Liver	1.549
Kidney	1.561
Blood	1.570
Muscle	1.585
Lens of eye	1.620
Bone (skull)	4.080

Table • 3-2

Approximate Acoustic Impedance in Commonly Encountered Tissues[2]

TISSUE	ACOUSTIC IMPEDANCE (IN RAYLS)
Air	0.0004
Fat	1.38
Water (50° C)	1.54
Brain	1.58
Blood	1.61
Kidney	1.62
Liver	1.65
Muscle	1.70
Lens of eye	1.84
Bone (skull)	7.80

Table • 3-3

Percentage of Sound Reflected at Interfaces[5]

BOUNDARY	REFLECTED (%)
Soft tissue/gas	99
Bone/fat	49
Fat/muscle	1.08
Fat/kidney	0.6
Soft tissue/water	0.2

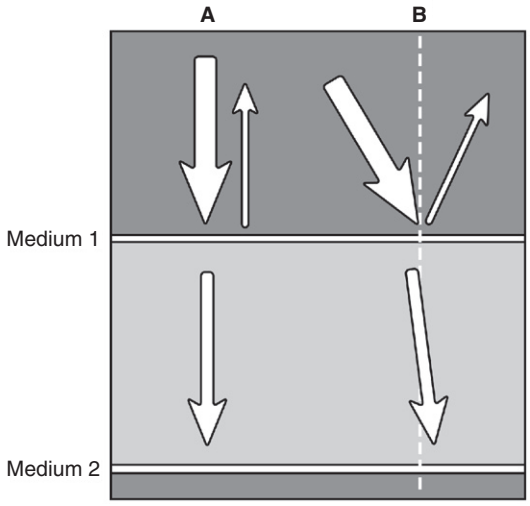


Fig. 3-2 The angle of incidence is the angle at which a sound wave encounters a medium. If the angle of incidence is perpendicular to the reflector **(A)**, the reflected portion of the sound wave travels 180 degrees opposite to the direction of the initial sound wave, and the transmitted portion of the sound wave continues in the same direction as the initial sound wave. If the angle of incidence is not perpendicular **(B)**, then the angle of reflectance equals the angle of incidence; the angle of transmittance depends on the difference in acoustic impedance of *medium 1* versus *medium 2*.

interfaces. Thus little or no sound passes these boundaries. Hence the speed of sound in bone and gas-filled lung is not important clinically. This nearly total sound reflection creates an acoustic void, or *shadow*, deep to the tissue interface. Without placement of acoustic coupling gel between the patient and transducer, the soft tissue/gas interface created by gas trapped between the skin and transducer would prevent imaging because of reflection of all oncoming sound.

Angle of incidence is the angle at which a sound wave encounters a medium. If the angle of incidence is perpendicular (90 degrees) to the reflector, the reflected portion of the sound wave travels 180 degrees opposite to the direction of the initial sound wave, and the transmitted portion of the sound wave continues in the same direction as the initial sound wave (Fig. 3-2, *A*). If the angle of incidence is not perpendicular, then the angle of reflectance equals the angle of incidence (Fig. 3-2, *B*). If a sound wave strikes a reflector more than 3 degrees from perpendicular, then the reflected sound will likely not reach the transducer.[2] The angle of transmission of a nonperpendicular sound wave depends on the relative acoustic impedance of the two media. Any sound wave that is not reflected toward the transducer will not be recorded. A key fact is that the amount of reflected and transmitted sound depends on the *difference in acoustic impedance* of the two media.

An ultrasound beam is attenuated, or loses strength, as it travels through a medium. The amount of attenuation is determined by the distance traveled and the frequency of the sound wave. The amount of attenuation approximates 0.5 decibels (dB)/cm per MHz over a round-trip distance.[4] If a reflector is 3 cm from the transducer, the round trip distance is 6 cm, and the attenuation of the sound beam is 3 dB/MHz. High-frequency sound waves are attenuated more than are lower-frequency sound waves. Attenuation of the sound wave involves three components: absorption, reflection, and scattering.[1-3]

Absorption is the conversion of the mechanical energy of a sound waves to heat.[1,3] Absorption is the dominant component of attenuation of sound in soft tissue.[1,3] The conversion of sound waves to heat occurs primarily by frictional forces.[3,4]

With diagnostic ultrasound machines, the relative amount of sound absorbed is quite low, and the temperature change is insignificant and imperceptible.

Reflection of the sound beam contributes to attenuation. As the sound wave encounters tissue interfaces of different acoustic impedance, a reflection is generated. Only reflections that return to the transducer are used for image formation. The scanning of structures from different angles may enhance image quality if more echoes are returned to the transducer from different angles.

Scattering occurs when sound waves encounter small, irregular surfaces. This occurs mainly within the parenchyma of organs and is responsible for the echotexture of internal organs.[1,3] As the frequency of a sound beam increases, the incidence of scattering increases.

TRANSDUCERS

A transducer is a device that converts one form of energy to another.[3,6] In ultrasound imaging, transducers convert electric current into sound waves, and vice versa.[7] This conversion is accomplished in a piezoelectric crystal. As an electric charge is applied to a piezoelectric crystal, the material deforms and creates a sound wave.[6] Conversely, when sound waves are applied to piezoelectric crystals, they produce an electric signal. Therefore the same crystal is used to send and receive sound waves, but these two processes cannot occur at the same time.[1] For typical ultrasound imaging, the transducer emits sound waves less than 1% of the time and receives sound waves more than 99% of the time.[4]

Ultrasound transducers come in many shapes and sizes. The selection of a transducer depends on the physical properties of the transducer and the characteristics of the anatomic region to be imaged.

Electronic transducers, also called *array transducers*, are composed of several small elements in various arrangements. The elements may be arranged in a line or rectangle (linear array), in a curved line (convex array), or in concentric ring fashion (annular array).[8] The elements that compose these transducers are electronically fired in various sequences to create different-shaped images or to focus the sound beam at specific depths.[7]

Two basic shapes of ultrasound images are commonly encountered. Images made in sector fashion are pie shaped (Fig. 3-3, *A*), and images made in linear fashion are rectangular (Fig. 3-3, *B*). The *footprint* of a transducer is the amount of the transducer that makes contact with the patient. Sector images are often produced from transducers with a small footprint whereas linear transducers usually have larger footprints. For thoracic imaging, sector-shaped transducers are preferable because images must be acquired intercostally. For abdominal imaging, the use of sector or linear transducers is often dictated by the personal preference of the sonographer. In most instances, more than one transducer is used during a single examination.

Diagnostic ultrasound machines operate in pulsed mode for imaging. This means that the ultrasound machine sends only a few cycles of sound into tissue and then spends the rest of the time listening for returning echoes. The pulse repetition frequency (PRF) is the number of times this pattern of sending and listening is repeated within 1 second.[1] The length of space in one pulse of ultrasound is called the spatial pulse length (SPL). If a sound wave has a wavelength of 0.5 mm and three pulses are sent each time, the SPL is 1.5 mm. Spatial pulse length is important for axial resolution.

Resolution is the ability of an ultrasound machine to distinguish echoes on the basis of space, time, and strength.[6] The better the resolution, the more likely an abnormality can be identified. As the frequency of an ultrasound wave increases, the resolution increases. A transducer of the highest possible frequency should be used to get the best possible resolution.

Axial resolution is the resolution of two separate reflectors along the direction in which the sound wave is traveling.[6] It is equal to half the SPL. As previously mentioned, SPL is the length of space over which the pulse of a sound wave travels. When two reflectors are separated by a distance that is greater than half the SPL, the echoes from these two reflectors do not overlap as they return to the transducer and are interpreted

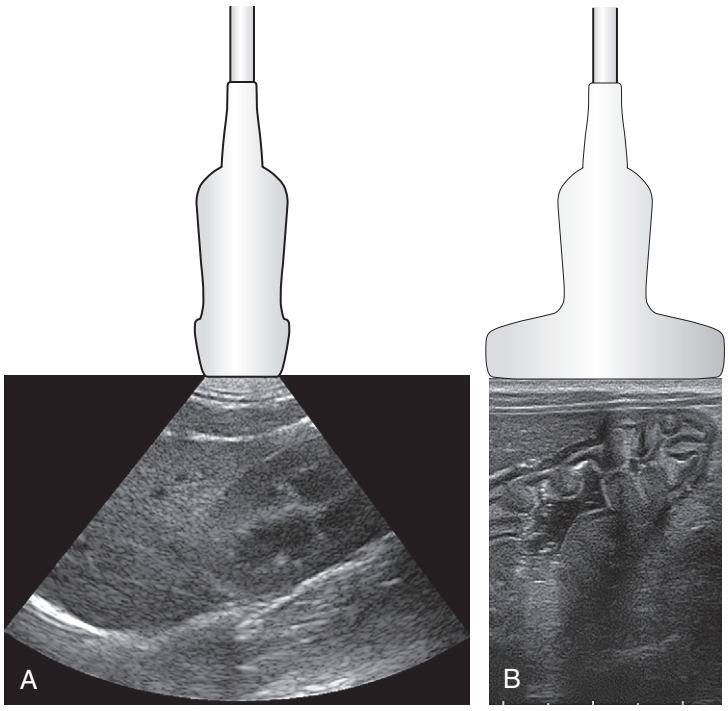


Fig. 3-3 **A,** Image of a canine liver and right kidney made using a curved array transducer. Note the pie-shaped image produced by this type of transducer. **B,** Image of a feline stomach made using a linear array transducer. Note the rectangular image.

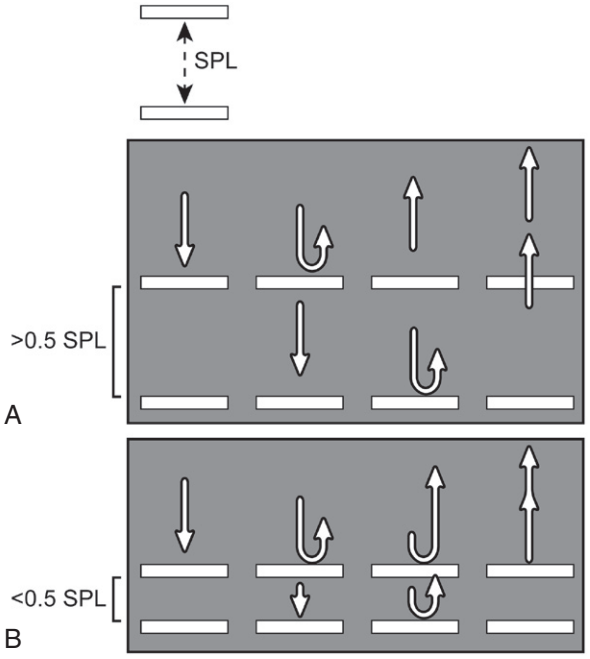


Fig. 3-4 Axial resolution depends on the spatial pulse length (SPL) of the sound wave and the amount of separation of the reflectors. If the reflectors are greater than 0.5 times the SPL **(A)**, the structures return two discrete echoes, as shown by the two *separate arrows*. If the reflectors are less than 0.5 times the SPL **(B)**, the structures return only one echo, as illustrated by the *overlapping arrows*.

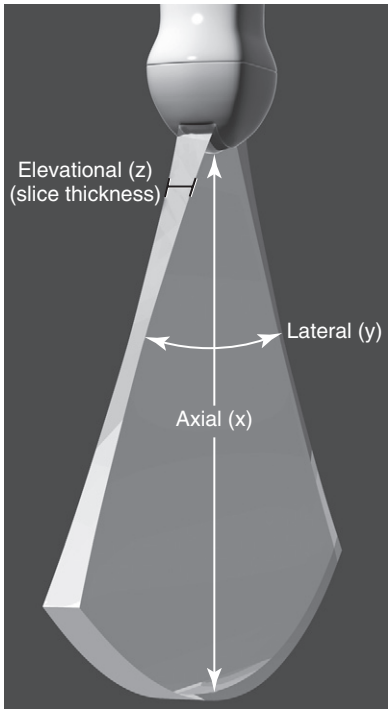


Fig. 3-5 An illustration of the three dimensions of an ultrasound beam emanating from an ultrasound transducer. Axial resolution is along the *x*-axis. Lateral resolution is best where the ultrasound is narrowest in the *y*- and *z*-axes. The *y*- and *z*-axes are narrowest at the focal zone of the ultrasound beam.

as separate echoes (Fig. 3-4). If the distance between the reflectors is less than half the SPL, the returning echoes overlap and are interpreted as a single echo. Because transducers with higher frequency have a shorter SPL, axial resolution is improved.

Lateral resolution is the resolution of two separate reflectors perpendicular to the direction in which the sound wave is traveling (Fig. 3-5).[6] This is determined by the width of the ultrasound beam.[6] To recognize the objects discretely, the ultrasound beam must be narrower than the distance between the objects. The width of an ultrasound beam decreases with increasing frequency. In a focused ultrasound beam, where the width of the beam is restricted, the lateral resolution is best at the focal point of the ultrasound beam because this is the narrowest part of the beam.[6]

Depth of sound-wave penetration varies inversely with frequency. Higher-frequency transducers are best for structures that are close to the surface; lower-frequency transducers are best for deeper structures. The choice of ultrasound transducer varies with the experience of the sonographer. As a guide, one can begin with a higher-frequency transducer because it has better resolution and then switch to a lower-frequency transducer if deeper structures are not imaged well.

Broad bandwidth technology allows for transducers to emit a wide range of frequencies. This allows the user to select various frequencies from the same transducer.[6,7] With older narrow bandwidth transducers, a 4 MHz transducer might emit frequencies between 3.8 and 4.2 MHz, whereas a modern broadband 4MHz transducer can emit frequencies between 1 and 7 MHz.[9] The broadband frequency transducers improve near-field resolution by using the higher frequency of the spectrum and far-field resolution by using the lower frequency of the spectrum. Additionally, axial resolution is improved because these transducers use shorter SPLs.[9]

Harmonic imaging improves normal organ and lesion conspicuity.[9] Harmonics are interval multiples of the frequency of the transmitted ultrasound pulse. If the transmitted frequency (the fundamental frequency or first harmonic) is 4 MHz (F), then the second harmonic is 8 MHz (2F), and the third harmonic is 12 MHz (3F), and so forth.[1,3,9] During the interaction of sound waves and tissue, weak echoes are generated at harmonic frequencies.[5] Usually, only the second harmonic frequency is useful because higher harmonic frequencies are absorbed by tissue.[5] When the echoes return to the ultrasound machine operating in harmonic mode, bandpass filters are applied to reject frequencies that are outside of the specific range.[5,10] For harmonic imaging, the bandpass filter can remove the fundamental frequency allowing the second harmonic frequencies to pass. This results in improved image quality because of three fundamental factors.[10] First, the primary beam is much narrower, improving lateral resolution. Second, grating lobe artifacts (discussed later) are eliminated because the extra beams are not sufficiently strong to generate harmonics. Third, the harmonic beam is generated at a depth beyond where some of the artifactual problems occur thus reducing image degradation.

Spatial compounding is a composite image generated by combining multiple frames from ultrasound beams that are angled in different directions.[3,5,10-12] The sound waves from electronic transducers can be steered in multiple directions without moving the transducer. The multiple angles increase the probability of the sound wave encountering a reflector at a 90-degree angle.[5,10] This improves spatial resolution by improving contrast and margin definition.[3] More time is required for data acquisition, thereby decreasing image and temporal resolution.[5] Acoustic enhancement and shadowing artifacts (discussed later) may be reduced, and this is a potential drawback.[3,5] Using spatial compounding in canine and feline ultrasound imaging, compound images were perceived to have improved contrast resolution, border definition, and/or increased signal-to-noise ratio compared with noncompounded images.[12]

DISPLAY

Image formation is based on the pulse echo principle.[3,13] A small burst of sound waves is sent into a structure by a transducer, and the transducer becomes an echo receiver. In between, the transducer is dampened to stop the piezoelectric crystal from vibrating. The electric signals generated from the returning echoes are amplified to form the final image. When the initial burst of sound is sent into the tissue, a timer is started to determine the amount of time it takes to receive echoes. The elapsed time from sending to receiving is directly related to the distance traveled by the sound wave.[13]

$$\text{Rate (mm/μs)} \times \text{Time (μs)} = \text{Distance (mm)} \quad \text{(Eq 5)}$$

The ultrasound machine assumes a constant rate for the velocity of sound (1.54 mm/μs), and because time is recorded, distance can easily be calculated. Remember that the trip from the transducer to the reflector and back is twice the actual distance from the reflector to the transducer.[1] This assumes that the sound wave travels in a straight line with no side trips along the way.

Two modes of echo display are used commonly in ultrasonography: brightness mode (B-mode, B scan, or gray scale) and motion mode (M-mode). B-mode is used commonly in both abdominal and cardiac imaging. M-mode is used only for echocardiography.[1]

B-mode images are composed of a collection of dots that correspond to the amplitude or strength of the returning echo (see Fig. 3-3).[10] These dots are displayed on a black background, and the brightness or gray scale of the dot is highest (whitest) for the strongest returning echoes. The depth of the structure returning the echoes determines the position of the dots relative to the position of the transducer. Multiple thin scan lines make up a complete image so that B-mode images look like a slice of tissue.[2]

M-mode records a thin section of an ultrasound image over time (Fig. 3-6). The region for M-mode imaging is chosen on a B-mode image; this is usually represented on the screen as a line. Once the M-mode cursor is in the desired location, M-mode is activated. On an M-mode image, the depth of the image is displayed on the vertical axis, and time is displayed on the horizontal axis. The brightness of the dots is proportional to the strength of the returning echoes, as in B-mode. When holding the transducer stationary, the examiner can evaluate how structures move over time. M-mode imaging is used most commonly in echocardiography to evaluate the function of the ventricles and heart valves quantitatively.

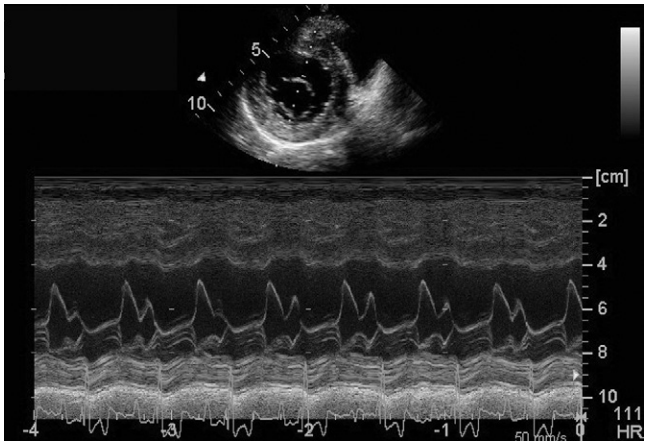


Fig. 3-6 M-mode image depicting movement of the mitral valve. At the top of the image is a B-mode, short-axis image of the left ventricle at the level of the mitral valve. The *dotted line* in the middle of the B-mode image marks the location of the M-mode tracing on the bottom of the image. The M-mode tracing depicts the movement of the mitral valve and left ventricle over time. An electrocardiograph tracing is superimposed in the bottom of the image.

Orientation of the B-mode image varies with the structure being imaged. The left side of the screen is cranial, and the top of the screen is dorsal (toward the patient's spine) for longitudinal images. For transverse images, the left side of the screen is dorsal. For cardiac imaging, the right side of the screen is cranial (toward the patient's head) with long-axis images. The portion of the image closest to the transducer, usually the top of the screen, is called the *near field* and the opposite side is called the *far field*.

BASIC SCANNER CONTROLS

The power control modifies the intensity of sound output by the transducer.[4] This is accomplished by adjusting the voltage applied to the piezoelectric crystal. Increasing the power leads to a uniform increase in the amplitude of returning echoes and thereby increases overall image echogenicity (brightness). Keeping the power level low helps improve image resolution and helps prevent artifacts.[4]

Gain affects the amplification of the returning echoes within the receiver. Increasing or decreasing the gain increases or decreases the brightness of the image displayed on the screen. If the gain is too low, the subtle parenchymal detail of tissue is lost. If the gain is too high, the image is too bright, and contrast resolution is lost.[10] A common analogy is to compare the gain knob on the ultrasound machine with the volume control on an MP3 player. At low settings, subtle music cannot be heard, and at high settings, the music is too offensive to be enjoyed.

Because sound waves lose intensity (attenuation) as they travel in tissue, echoes returning from deeper tissues are weaker than echoes returning from tissues closer to the transducer. To make an image uniform in brightness, amplification of the echoes from deeper tissues to a greater degree than echoes from shallow tissues is helpful. Time gain compensation controls allow the user to adjust the gain in selected regions of the image based on the arrival time of echoes to the transducer.[10] Echoes from deeper structures take longer to reach the transducer. Typically, an ultrasound machine has a series of slider-bars that control gain to echoes that emanate from various depths. The top sliders control gain for structures in the near field and bottom sliders for gain in the far field. Overall gain should be adjusted first, then specific regions of the image using the time gain compensation.[10]

The reject function of an ultrasound machine is a method of reducing unwanted, low-amplitude noise. This noise, electronic or acoustic, is not useful and can subtly degrade the image. Many machines allow the user to select how much of the low-level noise is filtered from the image. If the reject is set too high, some of the subtle parenchymal echotexture is also removed.

PRINCIPLES OF INTERPRETATION

Echogenicity relates to the relative brightness of a structure. Anechoic structures have no echoes and appear black. When the echogenicity of two structures is compared, the darker structure is hypoechoic, and the brighter structure is hyperechoic. If the structures have the same degree of brightness, they are isoechoic to each another. Because tissue derangements result in changes in echogenicity, it is important to know the relative echogenicity of each abdominal organ. Box 3-1 lists abdominal organs in order of relative echogenicity.[14,15] Detecting diffuse changes in echogenicity of a whole organ is

Box • 3-1

Relative Echogenicity of Commonly Encountered Structures in Order of Decreasing Echogenicity[14,15]

Bone, gas, organ boundaries
Structural fat, vessel walls
Renal sinus
Prostate
Spleen
Storage fat
Liver
Renal cortex
Muscle
Renal medulla
Bile, urine

difficult, and accurate detection is related to the experience of the sonographer. Multiple abdominal organs should be compared to determine which are truly abnormal. Additional complexity results from the fact that machine settings may alter the echogenicity of an organ. Focal changes in echogenicity are easier to detect because the adjacent, normal parenchyma can be compared.

ARTIFACTS

Misrepresentation of structures caused by some characteristic of the imaging technique is an artifact. In diagnostic radiology, artifacts hinder evaluation of the image and are undesirable. In ultrasound imaging, artifacts are not always undesirable and may actually enhance evaluation of structures by providing insight regarding the composition of structures. For example, sonographic imaging of a fluid-filled structure is characterized by enhancement of soft tissues distal to the fluid-filled structure, whereas with a hypoechoic tissue mass, which may appear similar to a fluid-filled structure, there is no distal enhancement.

Before discussing specific artifacts, it is important to remember assumptions that are made when using ultrasound.[16,17] These assumptions are as follows:

- Sound waves travel in a straight line.
- Echoes originate only from objects located on the beam axis.
- Echoes return to the transducer after a single reflection.
- The speed of sound in tissue is constant.
- The amplitude of returning echoes is related directly to the reflecting or scattering properties of distant objects.
- The distance and/or depth to the reflecting or scattering object is proportional to the round trip travel time of the sound wave.
- The energy of a sound wave is attenuated uniformly.

Acoustic shadows are regions of decreased echogenicity distal to structures of high reflectivity (Fig. 3-7).[15-19] In these situations, the primary sound beam is almost completely reflected or absorbed. An insufficient quantity of echoes returned from the location distal to the strong reflector makes these regions appear anechoic (black). The shadowing is a useful artifact because it gives information about the composition of the structure causing the shadowing. Naturally occurring acoustic shadows are found at soft-tissue/bone and soft tissue/gas, such as in bowel and lung, interfaces. Pathologic acoustic shadows occur most commonly with renal, cystic, or cholecystic calculi. Acoustic shadowing artifacts are minimized with spatial compounding.[16,20] This may allow a lesion hidden by a shadowing artifact to be identified. Conversely, the composition of a structure may be misinterpreted because it is not shadowing.[3]

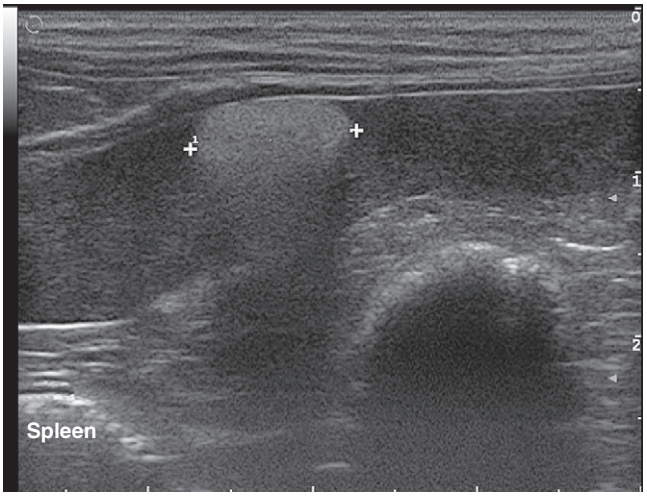


Fig. 3-7 Longitudinal image of a feline spleen made using a linear transducer. A hyperechoic nodule (between the "+" marks) causes distal acoustic shadowing (*black area* beneath the nodule). Additionally, a transverse section of large intestine (*curved hyperechoic line*) in the far field from the spleen also has distal acoustic shadowing (hypoechoic region distal to curved line).

Acoustic enhancement is a region of increased echogenicity behind structures of low attenuation (Fig. 3-8).[16,18,19] This results in areas of increased echogenicity distal to areas of low attenuation. The two most common sites for acoustic enhancement are distal to the gallbladder and distal to the urinary bladder. To better understand this artifact, the acoustic shadowing caused by the gallbladder is considered. Sound wave 1 travels through the liver, then through bile within the gallbladder, then through liver again. Sound wave 2 travels only through liver. As sound wave 1 passes through the bile, it is attenuated less than sound wave 2 as it passes only through liver. Thus, at a distance distal to the gallbladder, sound wave 1 has a higher intensity and returns stronger echoes to the transducer (see Fig. 3-8).

Reverberation artifacts occur when the sound waves reflect multiple times between two strong reflectors.[15-17] This violates the assumption that echoes return to the transducer after a single reflection.[17] Reverberation artifacts appear as multiple hyperechoic foci that occur at regular intervals. The first echo is recorded at the actual depth of the object, and subsequent echoes are at increased distance from the transducer. One of the highly reflective surfaces can be the ultrasound transducer. Reverberation occurs when the sound wave encounters an area of high reflectivity, such as bowel gas, and the sound wave is reflected back toward the transducer. When the reflected sound wave encounters the transducer, most of it is reflected back into the tissue, where it again encounters the area of high reflectivity. This cycle of bouncing between the transducer and the patient continues many times, resulting in the regularly spaced hyperechoic foci (Fig. 3-9). The distance between the transducer and the highly reflective surface determines the spacing of the hyperechoic foci.

Comet tail and *ring-down* artifacts are a variation of a reverberation artifact.[17] For comet tail artifacts, the reverberation is caused by two closely spaced, discrete highly reflective surfaces.[16,17] Comet tail artifacts can be created by the front and back of a gas bubble or small metallic object such as a pellet. On the display, comet tail artifacts are typically thin, hyperechoic bands with a triangular, tapered shape in which the sequential echoes are so close together that they are not

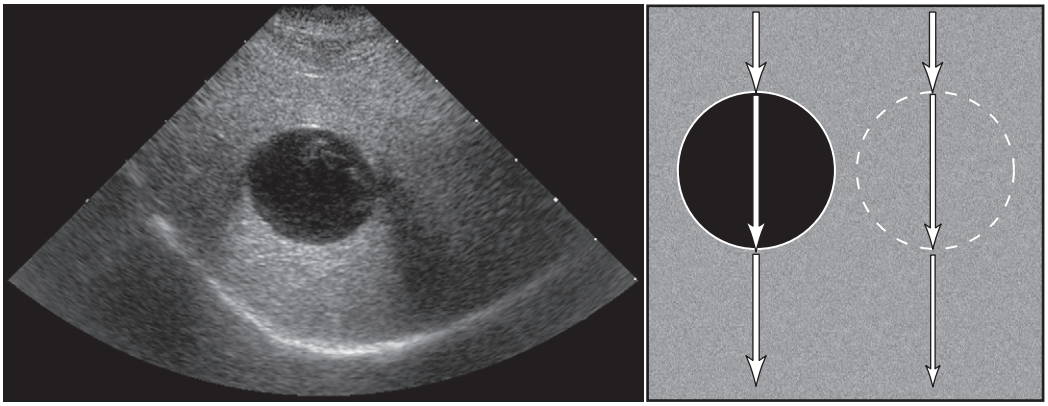


Fig. 3-8 Acoustic enhancement is a region of increased echogenicity beyond structures of low attenuation. In the sonographic image on the *left*, bile in the gallbladder (*black circular structure*) does not attenuate the sound waves as much as the equivalent amount of liver tissue would. This creates acoustic enhancement (*bright area* distal to the gallbladder). The *black triangular area* on the right aspect of the region of acoustic enhancement is an edge-shadowing artifact. In the schematic on the *right*, the left sound wave travels through the liver, then through bile within the gallbladder (*white circle*) and then continues through the liver. The right sound wave travels only through liver. As the left sound wave passes through bile, it is attenuated less than the right sound wave as it travels through liver. Thus when the left sound wave exits the gallbladder, it has a higher intensity, leading to the return of stronger echoes to the transducer, which creates the distal acoustic enhancement.

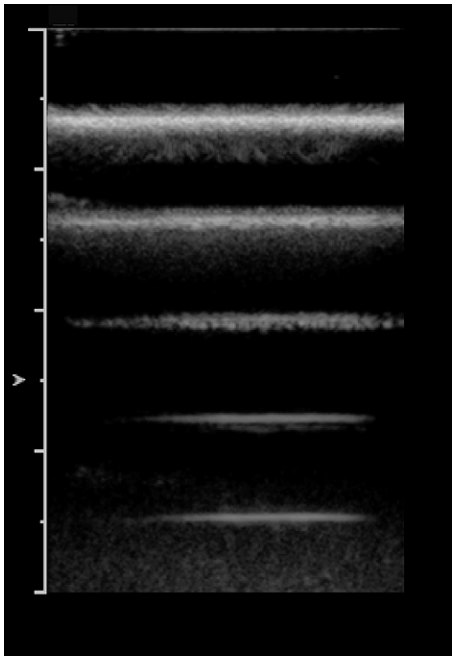


Fig. 3-9 A reverberation artifact was created by submerging a tongue depressor in a water bath. The actual tongue depressor is the strongest hyperechoic line, closest to the transducer, and the four other hyperechoic lines are reverberation artifacts. Some of the sound waves reflected by the tongue depressor are reflected by the transducer instead of being recorded and then are reflected again by the tongue depressor. The ultrasound machine interprets the twice-reflected signal at a depth of twice the actual distance between the transducer and tongue depressor because the echoes took twice as long to return. The deeper three reverberation artifacts took three, four, and five times as long, respectively, to be recorded by the ultrasound machine and are recorded sequentially farther from the transducer as overall time between recording increases.

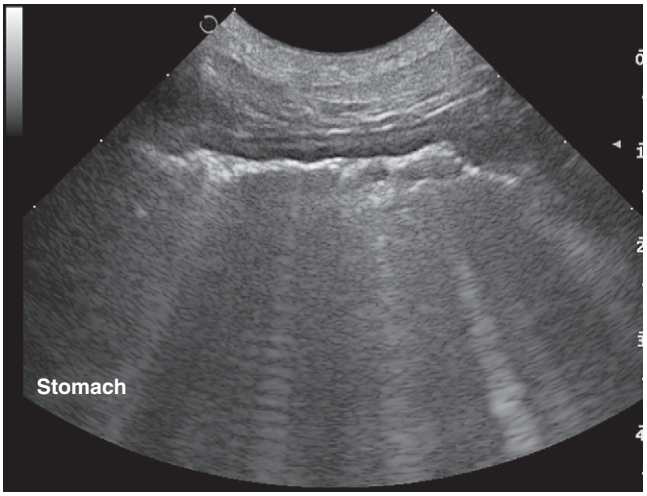


Fig. 3-10 Image of a feline stomach made using a curved array transducer. Multiple hyperechoic comet tail artifacts originate in the near field from the gas/stomach wall interface. Note how the comet tails thin and become progressively wider in the far field.

seen as separate echoes (Fig. 3-10).[17] Ring-down artifacts are created when ultrasound reverberates within fluid trapped between a tetrahedron of air bubbles.[17,18]

Mirror-image artifacts appear as duplication of a normal structure on the opposite side of a strong reflector (Fig. 3-11).[16] This violates the assumption that echoes return to the transducer after a single reflection and that sound waves travel in a straight line.[17] This is most commonly encountered when the liver is imaged with the diaphragm/lung interface acting as a highly reflective structure. Apparent duplication of the gallbladder can be used to explain the artifact. Normally the sound wave sent toward the gallbladder is reflected back to the transducer and recorded on the screen according to how long it took the sound to return to the transducer. For the artifactual gallbladder, the sound from the transducer bounces off the diaphragm/lung interface toward the gallbladder, then instead of reaching the transducer, some sound is reflected off the gallbladder back toward the diaphragm/lung interface where it is reflected again toward the transducer. The sound reflected from the diaphragm/lung interface took longer to return to the transducer; thus an artificial gallbladder is created at an incorrect location within the patient.

Side lobes and *grating lobes* are secondary sound beams that emanate in a different direction than the primary sound beam.[17,18,21] Side lobes are associated with all transducers and originate from additional mode vibrations of the piezoelectric

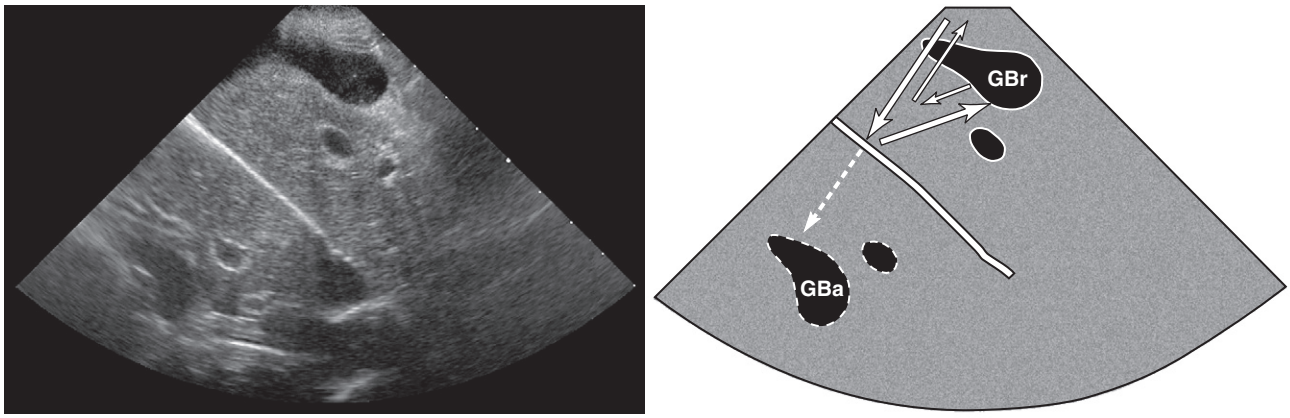


Fig. 3-11 A mirror image artifact of a canine gallbladder occurred at the lung/diaphragm interface. The real gallbladder (GBr) is in the near field, and the artifactual gallbladder is in the far field (GBa). The lung/diaphragm interface is the *curved, thin white line* separating the actual gallbladder from the artifactual gallbladder. The schematic shows the route that the sound wave travels (*white arrows*) to create the image of the artifactual gallbladder. Because the ultrasound machine cannot detect that the sound wave changed direction during its travel, the ultrasound machine assumes another gallbladder (GBa) is present below the lung/diaphragm interface.

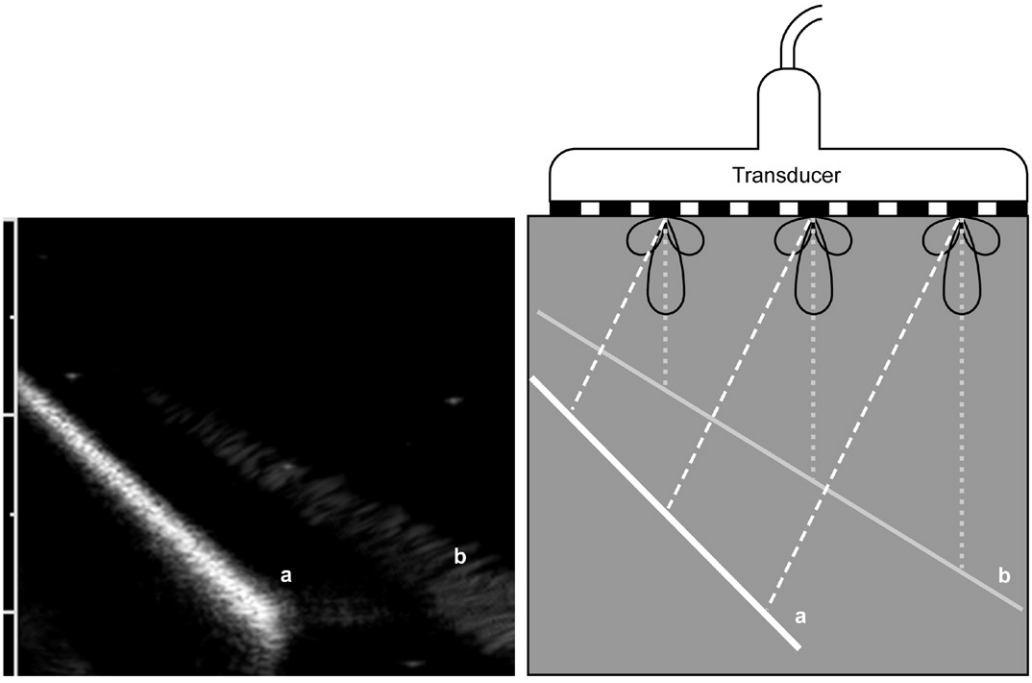


Fig. 3-12 The image on the left was created in a water bath by using a linear array transducer and a tongue depressor. The tongue depressor is the *bright linear structure* closer to the *bottom left* of the image (*a*). The grating lobe artifacts (*b*) are between the transducer (*top right*) and the tongue depressor. The schematic on the right shows the grating lobes emitted from selected elements of a linear transducer and how they interact with the tongue depressor (*a*) and create the artifact (*b*). The *angled dotted lines* show the actual path of the grating lobes, and the *vertical dotted lines* illustrate where the ultrasound machine places the image. (Modified from Barthez PY, Leveille R, Scrivani PV: Side lobes and grating lobes artifacts in ultrasound imaging, *Vet Radiol Ultrasound* 38:387, 1997.)

crystal. Grating lobes emanate from array transducers. In each instance these lobes result in an error in positioning of the returning echo (Fig. 3-12). The side or grating lobes are weaker than the primary sound beam. These lobes must encounter a highly reflective surface and be of sufficient intensity to be noticed.

Slice thickness artifacts are noticed most commonly in association with the urinary bladder and gallbladder. In these structures, slice thickness artifacts mimic the presence of sludge or sediment (Fig. 3-13). A primary sound beam, which is three-dimensional, has thickness. When the periphery of the urinary bladder is imaged, part of the thickness of the primary sound beam strikes the bladder wall while the other part strikes anechoic urine. The computer averages these two parts to create the pseudo-sludge artifact. The surface of the pseudo-sludge is usually curved, but the surface of real sludge is flat.[19] Imaging the bladder from a slightly different angle usually eliminates the artifact (Fig. 3-13, *B*).

Refraction occurs as the sound wave traverses tissues of different acoustic impedance. As the sound wave moves to the

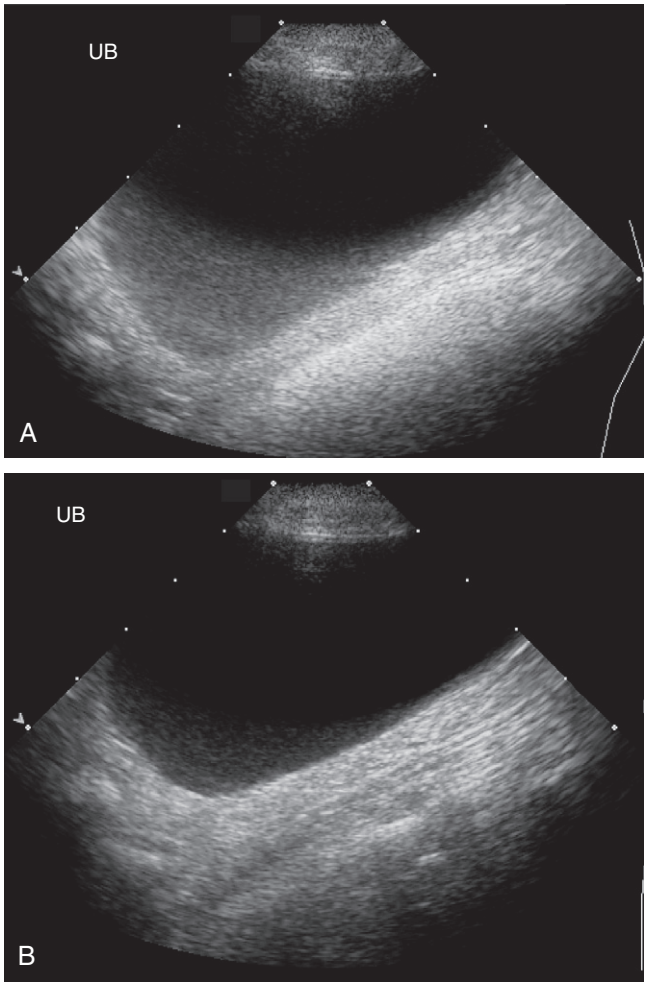


Fig. 3-13 **A,** An ultrasound image of a canine urinary bladder illustrating slice thickness artifacts. The hypoechoic region in the urinary bladder (left ventral aspect) is created when part of the ultrasound beam images the anechoic urine and part images the isoechoic urinary bladder wall. (Remember that the ultrasound beam has thickness, as seen in Fig. 3-5). The two parts of the beam are averaged together to create the hypoechoic region that could be confused with sediment. **B,** An ultrasound image of the same urinary bladder after altering the angle of insonation slightly. The artifact was eliminated.

new medium, it is bent. The bending of the sound wave may result in the display of organs in incorrect locations, usually to the side of their actual location.[16,17] Refraction artifacts may lead to measurement errors because organs may appear wider than normal.[17]

Edge-shadowing artifacts are refraction artifacts that are created when sound waves are bent as they encounter a curved surface tangentially (Fig. 3-14; see Fig. 3-8).[18] Anechoic regions are present distal to the curved surfaces because of absence of sound waves that have been bent by the curved surface. The edge-shadowing artifact occurs commonly when the kidneys, urinary bladder, or gallbladder is imaged. Edge-shadowing artifact can be eliminated with spatial compounding.[20]

DOPPLER TECHNIQUES

The pitch of a train whistle or a siren changes as the source approaches or moves away from the listener. The change in pitch, or sound-wave frequency, is called the *Doppler shift*. This principle has been applied to medical sonography,

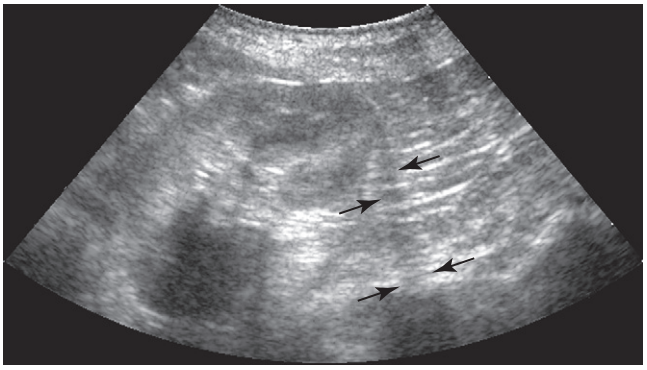


Fig. 3-14 Ultrasound image of a canine kidney illustrating an edge-shadowing artifact caused by sound wave refraction. As sound waves encounter curved surfaces tangentially, they are bent so that no sound wave is transmitted distal to the curved surface. The triangular black areas (*arrows*) distal to the caudal aspect of the kidney are edge-shadowing artifacts.

allowing imaging of the direction and velocity of blood flow. The Doppler effect is named for Johann Christian Andreas Doppler, an Austrian mathematician and physicist, who first proposed the effect in 1842.

A moving object that is emitting sound is enveloped by a ring of sound. Sound waves are compressed in the direction of the source movement toward a reference point, such as the listener, causing increased frequency of the sound wave and a higher pitch.[22] As the source moves away from the listener, the sound waves are expanded, the frequency of the sound wave decreases, and the pitch becomes lower.[22] Therefore, at a train crossing, the pitch of the whistle gets higher as the train approaches and the pitch of the whistle gets lower as the train moves away.

In ultrasonography, the change in sound frequency is caused by a moving reflector, most commonly red blood cells. The Doppler shift is the frequency difference between the incident sound waves and the reflected sound waves and is described by the following formula:[22]

$$f_D = (2 \times f_O \times \upsilon_{RBC})/c \qquad \text{(Eq 6)}$$

where f_D is the frequency of Doppler shift, f_O is the original frequency; υ_{RBC} is the velocity of red blood cells; and c is the speed of sound in soft tissue. The frequency of Doppler shift, recorded in Hz (versus MHz used for sonographic imaging) is in the audible range. Hence ultrasound machines emit sound related to the Doppler shift.

It is assumed in Equation 6 that the sound waves are parallel to the direction of blood flow. Realistically, when sound waves strike blood vessels, the sound waves are rarely parallel to the direction of flow. The Doppler angle is the angle between the blood-flow direction and the sound wave direction.[22] Without accounting for the Doppler angle, the Doppler shift is underestimated.[22] This is very important for quantification of blood flow. Accounting for the Doppler angle, the velocity of blood flow is calculated by the following formula:[22]

$$\upsilon_{RBC} = (f_D \times c)/(2 \times f_O \times \cos\theta) \qquad \text{(Eq 7)}$$

where υ_{RBC} is the velocity of red blood cells, f_D is the frequency of Doppler shift, c is the speed of sound in soft tissue, f_O is the original frequency, cos is cosine, and θ is the Doppler angle.

Doppler shift cannot be measured if the Doppler angle is 90 degrees because the cosine of a 90-degree angle is 0, and division by 0 is not possible. The Doppler angle (q) should be less than 60 degrees for the velocity to be considered accurate[23] with angles between 30 and 60 degrees being easiest to image.[22]

DOPPLER MODES

Four Doppler modes are discussed: (1) continuous-wave Doppler, (2) pulsed-wave Doppler, (3) color Doppler, and (4) power Doppler.

Continuous-wave Doppler is performed by using two separate crystals housed in one transducer.[22] One crystal emits sound continuously, and the second receives echoes continuously. Continuous-wave Doppler is highly accurate for measuring the Doppler shift. Compared with pulsed-wave Doppler, much higher velocities can be recorded with continuous-wave Doppler because of the continuous signal sampling. The crystal emitting the sound does not have to wait to receive echoes because the second crystal handles the echo-receiving task. However, with continuous-wave Doppler, all Doppler shifts along the path of the sound wave are measured, making differentiation of blood-flow velocity from two blood vessels in the path of the sound wave impossible.

Pulsed-wave Doppler is performed by using the same crystal for sending and receiving sound.[22] Pulsed-wave Doppler is used in combination with B-mode imaging; this is termed *duplex Doppler* (Fig 3-15, *A*).[4,22] A blood vessel is selected in the B-mode image for Doppler interrogation, and an electronic region of frequency sampling, called the *gate*, is positioned in the blood vessel. In Figure 3-15, *A*, the gate, two parallel lines, is in the aorta. The electronic gate is the only

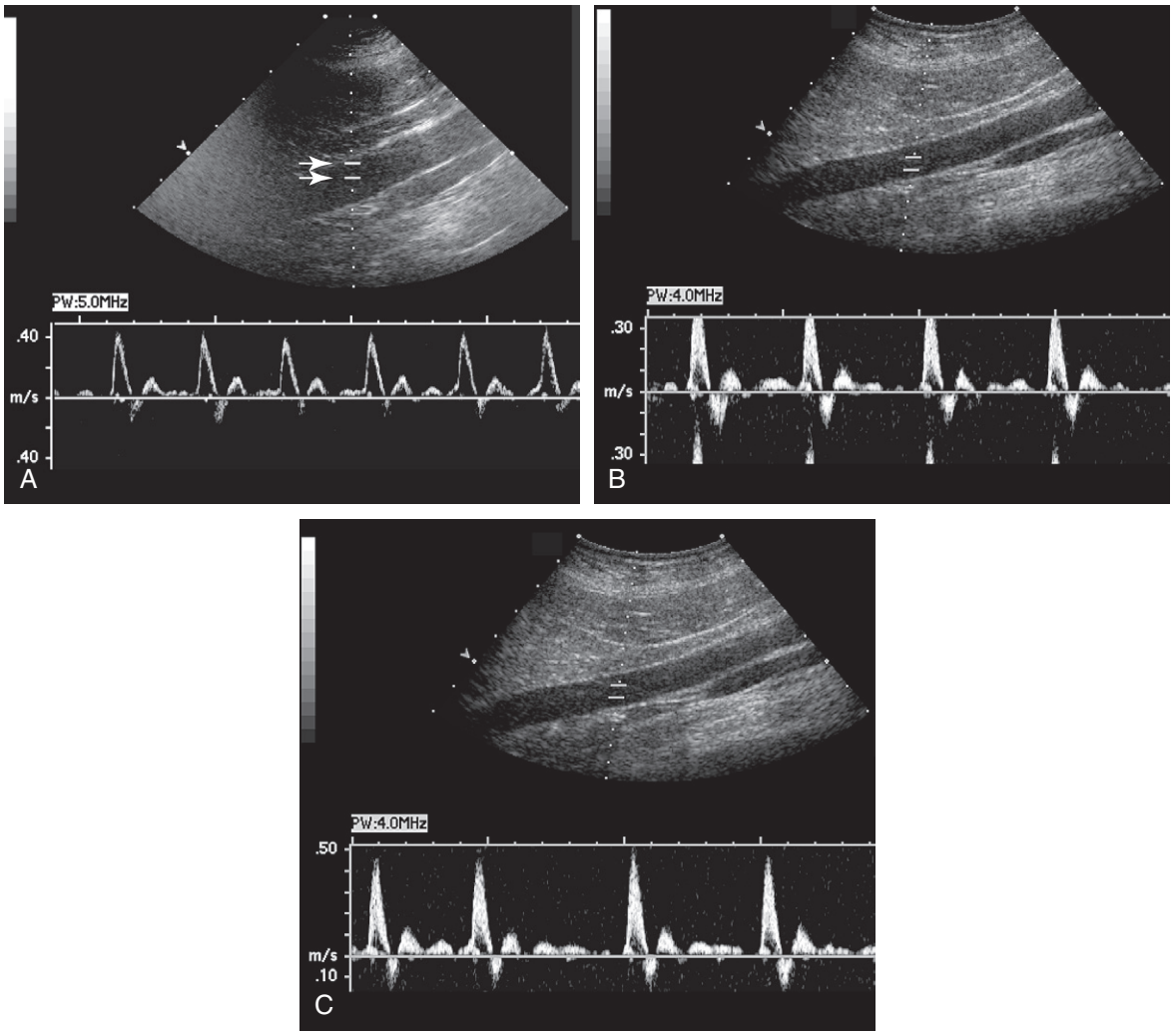


Fig. 3-15 **A,** Duplex Doppler image illustrating pulsed-wave Doppler interrogation of a canine aorta. The B-mode image, in the near field, shows placement of the pulsed-wave Doppler gate (*parallel lines, white arrows*) in the central aspect of the aorta. This is the region in which blood-flow velocity is measured. The pulsed-wave Doppler spectral tracing is in the far field. The *solid white line* in the center of the spectral tracing represents the baseline where blood flow = 0 m/s. Signal above baseline represents flow toward the transducer, whereas signal below the baseline represents flow away from the transducer. The velocity scale on the left ranges from 0 to 0.50 m/s toward the transducer and 0 to 0.50 m/s away from the transducer. The pulsatile velocity tracing is typical of an artery. **B,** Aliasing of the spectral tracing is noted by the peaks of the "tall spike" being displayed on the bottom of the spectral tracing. The scale indicates that the highest velocity is 0.30 m/s. Because the peak velocity of blood flow within the aorta is greater than 0.30 m/s, the computer displays the tracing on the other end of the scale. Aliasing is corrected **(see A)** by increasing the scale, which increases the pulse repetition frequency (PRF). Note that the width of the spectral tracing in **B** is wider than in **A.** This is caused by more homogenous velocity of blood flow within the pulsed-wave Doppler gate in part A. **C,** Aliasing is corrected by changing the range of velocities displayed; this is also called adjusting the baseline. The velocity range displayed is now from 0.20 m/s away from the transducer to 0.50 m/s toward the transducer compared with part **B,** and aliasing has been eliminated.

area from which echoes are accepted for flow quantification. Being able to select a blood vessel for interrogation visually is a benefit of pulsed-wave Doppler.

A spectral tracing is produced with both continuous- and pulsed-wave Doppler. The tracing records the velocity and direction of blood flow as a function of time (see Fig. 3-15, *A*). Tracing above the baseline represents blood flow toward the transducer, and tracing below the baseline represents blood flow away from the transducer.[23] Spectral broadening refers to the thickness of the spectral tracing.[22] If a large range of blood-flow velocity is present within the sample area, the spectral tracing will be broad. Alternatively, spectral broadening can occur if the transducer is close to the blood vessel, resulting in multiple ultrasound beam angles between the transducer and blood vessel.[22] If the blood-flow velocity within the sample area is homogenous, the spectral tracing will be thin (see Fig. 3-15, *A*).

Color Doppler is a variation of pulsed-wave Doppler.[4,22] Blood-flow velocity is recorded in multiple regions within an image, and the velocities are color-coded. The user determines the size and location of the color Doppler region of interest, which can be much larger than the sample gate used for pulsed-wave Doppler. Color-coded information is superimposed on the grayscale B-mode image within the region of interest (Fig. 3-16). Red and blue hues are used commonly for color Doppler, but other color combinations exist depending on the manufacturer of the machine. One color indicates net blood flow toward the transducer, and the other color in the reference scale indicates net blood flow away from the transducer. Velocity of flow is indicated by the intensity or hue of the color. Limitations of color Doppler include that only mean velocity is displayed and that the maximum velocity that can be displayed is limited.[4] Color Doppler is angle dependent so that no Doppler shift is recorded when blood flow is 90 degrees to the transducer. In this instance, no color is recorded at this location, and care should be taken not to interpret this as lack of blood flow. Color Doppler is useful to determine the presence or absence, direction, speed, and/or character of blood flow.[24]

Power Doppler is a signal-processing method that analyzes the total strength of the Doppler signal while ignoring direction.[16,22,25] This is determined by the concentration of the moving red blood cells. With power Doppler, a color map of the Doppler shift will be created, where the hue and brightness of the color represent the power of the Doppler signal. Power Doppler information is superimposed on the grayscale B-mode image, and a color-coded reference scale is displayed on the ultrasound machine monitor when the machine is in power Doppler mode. Orange hues are commonly used for power Doppler, but other variations exist depending on the manufacturer of the machine. Compared with color Doppler,

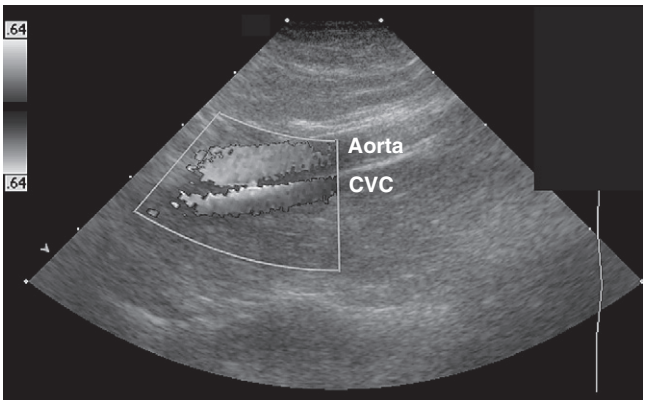


Fig. 3-16 Doppler image of the distal aorta and caudal vena in a dog (see Evolve website for color version). The aorta is in the near field and is red, and the caudal vena cava is in the far field and is blue. According to the color scale, red represents blood flowing toward the transducer, and blue represents blood flowing away from the transducer. The colors are assigned by the ultrasound machine and are related to the direction of blood flow. In other words, arteries will not always be red, and veins will not always be blue. Blood-flow velocity ranges from 0.64 m/s toward the transducer (red/yellow) to 0.64 m/s away from the transducer (blues). The *black bar* in the middle of the scale represents zero flow. Yellow and light blue represent faster velocities in their respective directions.

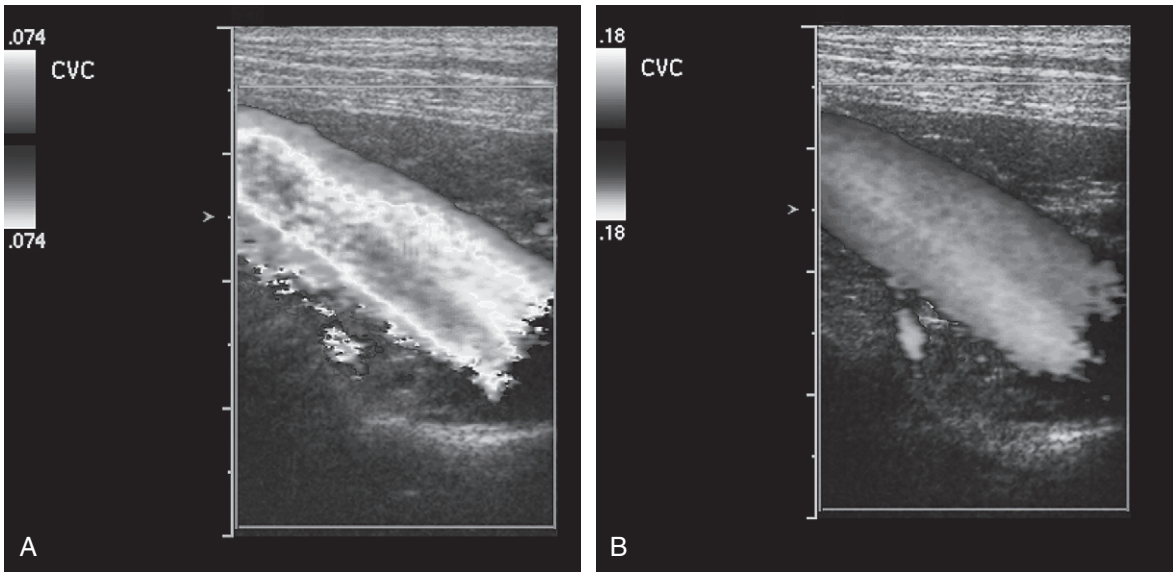


Fig. 3-17 Color Doppler image of the caudal vena cava (CVC) in a dog (see Evolve website for color version). **A,** Color Doppler aliasing appears as a mixture of red and blue hues (shades of gray). As the blood-flow velocity exceeds 0.074 m/s toward the transducer, the computer changes the color coding from yellow to light blue (light gray to dark gray). **B,** The aliasing was corrected by increasing the velocity scale to 0.18 m/s. Increasing the velocity scale increased the pulse repetition frequency (PRF). Note: The red and blue hues in **A** were assigned light and dark gray hues using a graphics program.

power Doppler detects very-low-velocity blood flow and small blood vessels; it is essentially angle independent and not prone to aliasing artifact.[16,22]

DOPPLER ARTIFACTS

Aliasing occurs with pulsed-wave Doppler when the PRF is too low. A portion of the tracing wraps around on the spectral tracing of the Doppler signal (Fig. 3-15, *B*), to the opposite direction and is therefore displayed on the wrong side of baseline.[4,16] On a color Doppler image (Fig. 3-17), aliasing is seen as the addition of color from the opposite end of the color scale. The sampling rate of the ultrasound machine needs to be twice the highest Doppler shift frequency of the blood flow.[4,22] Methods to resolve aliasing including increasing the PRF, decreasing the depth of the Doppler sampling gate, reducing the frequency of the transmitted ultrasound wave, and decreasing the Doppler shift angle (θ).[22]

Typically, the velocity scale may be widened because many ultrasound machines have the PRF of the Doppler unit linked to the scale setting. When using pulsed-wave Doppler, if most of the spectral tracing is on one side of baseline, the baseline can be adjusted to eliminate the aliasing (seec Fig. 3-15, C). However, increasing the PRF may lead to another artifact called *range ambiguity*.

Range ambiguity occurs when the PRF is high enough that not all the returning echoes are received before the next sound-wave pulse is sent.[26] As a result, the lagging echoes are misinterpreted as being closer to the transducer than they actually are. This creates ghost images between the structure of interest and the skin surface. These ghost images may not interfere with image interpretation, especially if the user is aware they exist.

Stationary objects with rough, highly reflective surfaces may produce an artifactual color Doppler signal.[27,28] This is called a twinkling artifact that appears as a quickly fluctuating mixture of Doppler signals. The presence of this artifact is highly dependent on ultrasound machine settings.[27] This artifact occurs with urinary calculi, including crystaluria.[28]

REFERENCES

1. Kremkau FW: Ultrasound. In Kremkau FW, editor: *Sonography: principles and instruments*, ed 8, St. Louis, 2011, Elsevier Saunders, p 13.
2. Curry TS III, Dowdy JE, Murry RC Jr: Ultrasound. In Curry TS III, Dowdy JE, Murry RC Jr, editors: *Christensen's physics of diagnostic radiology*, ed 4, Philadelphia, 1990, Lea & Febiger, p 323.
3. Hangiandreou NJ: AAPM/RSNA physics tutorial for residents. Topics in US: B-mode US: basic concepts and new technology, *Radiographics* 23:1019, 2003.
4. Nyland TG, Mattoon JS, Herrgesell EJ, et al: Physical principles, instrumentation, and safety of diagnostic ultrasound. In Nyland TG, Mattoon JS, editors: *Small animal diagnostic ultrasound*, ed 2, Philadelphia, 2002, Saunders, p 1.
5. Lieu D: Ultrasound physics and instrumentation for pathologists, *Arch Pathol Lab Med* 134:1541, 2010.
6. Kremkau FW: Transducers. In Kremkau FW, editor: *Sonography: principles and instruments*, ed 8, St. Louis, 2011, Elsevier Saunders, p 40.
7. Fischetti AJ, Scott RC: Basic ultrasound beam formation and instrumentation, *Clin Tech Small Anim Pract* 22:90, 2007.
8. Kremkau FW: Transducers. In Kremkau FW, editor: *Diagnostic ultrasound—principles and instrumentation*, ed 5, Philadelphia, 1998, Saunders, p 79.
9. Ziegler L, O'Brien RT: Harmonic ultrasound: a review, *Vet Radiol Ultrasound* 43:501, 2002.
10. Kremkau FW: Instruments. In Kremkau FW, editor: *Sonography: principles and instruments*, ed 8, St. Louis, 2011, Elsevier Saunders, p 69.
11. O'Brien RT, Holmes SP: Recent advances in ultrasound technology, *Clin Tech Small Anim Pract* 22:93, 2007.
12. Whatmough C, Guitian J, Baines E, et al: Ultrasound image compounding: effect on perceived image quality, *Vet Radiol Ultrasound* 48:141, 2007.
13. Kremkau FW: Introduction. In Kremkau FW, editor: *Sonography: principles and instruments*, ed 8, St. Louis, 2011, Elsevier Saunders, p 1.
14. Nyland TG, Park RD, Lattimer JC, et al: Gray-scale ultrasonography of the canine abdomen, *Vet Radiol* 22:220, 1981.
15. Park RD, Nyland TG, Lattimer JC, et al: B-mode gray-scale ultrasound: imaging artifacts and interpretation principles, *Vet Radiol* 22:204, 1981.
16. Kremkau FW: Artifacts. In Kremkau FW, editor: *Sonography: principles and instruments*, ed 8, St. Louis, 2011, Elsevier Saunders, p 176.
17. Feldman MK, Katyal S, Blackwood MS: US artifacts, *Radiographics* 29:1179, 2009.
18. Kirberger RM: Imaging artifacts in diagnostic ultrasound—a review, *Vet Radiol Ultrasound* 36:297, 1995.
19. Penninck DG: Artifacts. In Nyland TG, Mattoon JS, editors: *Small animal diagnostic ultrasound*, ed 2, Philadelphia, 2002, Saunders, p 19.
20. Heng HG, Widmer WR: Appearance of common ultrasound artifacts in conventional vs. spatial compound imaging, *Vet Radiol Ultrasound* 51:621, 2010.
21. Barthez PY, Leveille R, Scrivani PV: Side lobes and grating lobes artifacts in ultrasound imaging, *Vet Radiol Ultrasound* 38:387, 1997.
22. Boote EJ: AAPM/RSNA physics tutorial for residents: topics in US: Doppler US techniques: concepts of blood flow detection and flow dynamics, *Radiographics* 23:1315, 2003.
23. Wood MM, Romine LE, Lee YK, et al: Spectral Doppler signature waveforms in ultrasonography: a review of normal and abnormal waveforms, *Ultrasound Q*, 26:83, 2010.
24. Kremkau FW: Doppler principles. In Kremkau FW, editor: *Sonography: principles and instruments*, ed 8, St. Louis, 2011, Elsevier Saunders, p 125.
25. Bude RO, Rubin JM: Power Doppler sonography, *Radiology* 200:21, 1996.
26. O'Brien RT, Zagzebski JA, Delaney FA: Ultrasound corner: range ambiguity artifact, *Vet Radiol Ultrasound* 42:542, 2001.
27. Kamaya A, Tuthill T, Rubin JM: Twinkling artifact on color Doppler sonography: dependence on machine parameters and underlying cause, *AJR* 180:215, 2003.
28. Louvet A: Twinkling artifact in small animal color-Doppler sonography. *Vet Radiol Ultrasound* 47:384, 2006.

ELECTRONIC RESOURCES

evolve

Additional information related to the content in Chapter 3 can be found on the companion Evolve website at http://evolve.elsevier.com/Thrall/vetrad/

- Videos
- Audio Clips
- Chapter Quiz

CHAPTER • 4

Principles of Computed Tomography and Magnetic Resonance Imaging

Marc-André d'Anjou

Computed tomography (CT) and magnetic resonance (MR) imaging are significant assets to veterinarians in the pursuit of a diagnosis. Yet a general understanding of the physical principles inherent to both modalities is important not only to optimize their use in practice but also to recognize their limitations. Although most diseases result in some level of tissue alteration that can be depicted with these tools, these changes are not specific to a particular process, at least not when considered individually. Nonetheless, technologic advances in CT such as multirow detector imaging and the ongoing development of MR sequences and improved hardware and software components have contributed to increasing the accuracy of both modalities in veterinary medicine.

THE ROLE OF COMPUTED TOMOGRAPHY AND MAGNETIC RESONANCE IMAGING IN VETERINARY PRACTICE

CT and MR imaging offer superior diagnostic possibilities over conventional radiography because of two primary advantages, which are their *tomographic nature* and *increased contrast resolution*. Indeed, as opposed to radiographs that represent two-dimensional, or flat, projections of three-dimensional structures, tissues are examined with CT and MR in thin sections, or slices, thereby eliminating superimposition. Organs and other structures can then be identified more easily and differentiated (Figs. 4-1 and 4-2). Moreover, CT and MR volume datasets can be reformatted in any imaging plane, or as three-dimensional (3-D) projections, allowing better representations of structural anatomic relationships.

Contrast resolution is the capacity of a system to accurately represent differences in tissue, physical, and/or biochemical characteristics, which are intrinsically linked to x-ray attenuation (CT) or signal intensity (MR). The better the contrast resolution, the more likely subtle variations in tissue components will be displayed as pixels of different shades of gray, whether these components are normal or pathologic (Fig. 4-3, *A*). For example, differences in x-ray attenuation as little as 0.5% can be identified with CT, as opposed to approximately 5% on a radiograph.[1] This difference is mainly explained by the virtual elimination of scatter that reduces contrast on radiographs.[2] As with ultrasonography, pure liquids can be differentiated from soft tissues with CT, which cannot be done with radiographs. MR imaging is recognized even more for its great contrast resolution (Fig. 4-3, *B*), which can be enhanced by the combined use of different imaging sequences.

Conversely, *spatial resolution*, which corresponds to the minimum resolvable separation between high-contrast objects (see Fig. 4-3, *A*), is relatively limited with CT and MR imaging, as opposed to radiography. The spatial resolution of CT and MR imaging, which is typically linked to the slice thickness, is approximately 0.4 and 1.0 mm,[3] respectively, although technical advances and increased magnetic field strength have contributed to reducing this value for MR imaging. In comparison, screen-film and digital radiography are associated with a spatial resolution of approximately 0.08 to 0.17 mm,[3] which allows smaller details to be depicted. However, the elimination of superimposition and superior contrast resolutions inherent to CT and MR imaging more than compensate for this limitation.

IMAGE FORMATION: GENERAL CONCEPTS

CT and MR imaging share several characteristics regarding image formation. Each generated image represents a thin section, or slice, of the body, composed of a matrix filled with small cubical sections, known as *voxels*, or *vo*lume *el*ements, which is displayed on a flat monitor as a matrix of *pixels*, or *p*icture *el*ements (Fig. 4-4). For both CT and MR imaging, each voxel of the matrix is associated with an electronic current that is spatially localized in the body and processed by a specialized computer system. Variations in electronic current intensity are expressed as variable pixel brightness on a monitor. Thus, a voxel associated with greater tissue signal intensity on MR or x-ray attenuation on CT will be displayed as a brighter, or whiter, pixel, whereas lack of signal or x-ray attenuation, such as with air, will appear dark. Although several different values can coexist in each voxel, especially if the voxel is large and if composed of heterogeneous tissue components, only the mean value is expressed and converted to pixel brightness (Fig. 4-5). The image grayscale is then determined by the range of brightness values filling each matrix.

This concept of *voxel-to-pixel translation* is intimately related to spatial and contrast resolution, which were discussed earlier. Indeed, a large voxel can contain tissue composed of smaller elements of different morphologic and biochemical characteristics. Hence, both normal and abnormal tissue elements may be combined in a voxel, limiting the resolving capabilities of the modality. Generally, the limiting factor with CT and MR imaging is the slice thickness, which is typically the largest dimension of each voxel. Much of the technical advances aim to reach isotropic resolution, that is, to image sections of tissue with perfectly cubical voxels— the *x*, *y*, and *z* dimensions are the same.[2] Figure 4-6 illustrates the impact of voxel dimension on image detail.

Among the differences between CT and MR imaging, an important aspect is that image sections can be acquired in any

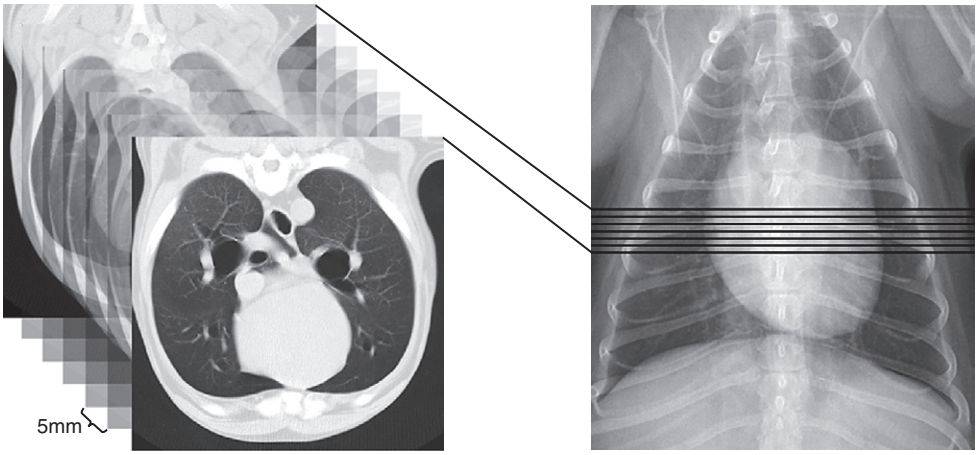


Fig. 4-1 Computed tomography (CT) generates sections, or images, of the body, allowing visualization of structures without superimposition. This fundamental characteristic of tomographic imaging is evident on these contiguous 5-mm-thick images of the thorax of this dog.

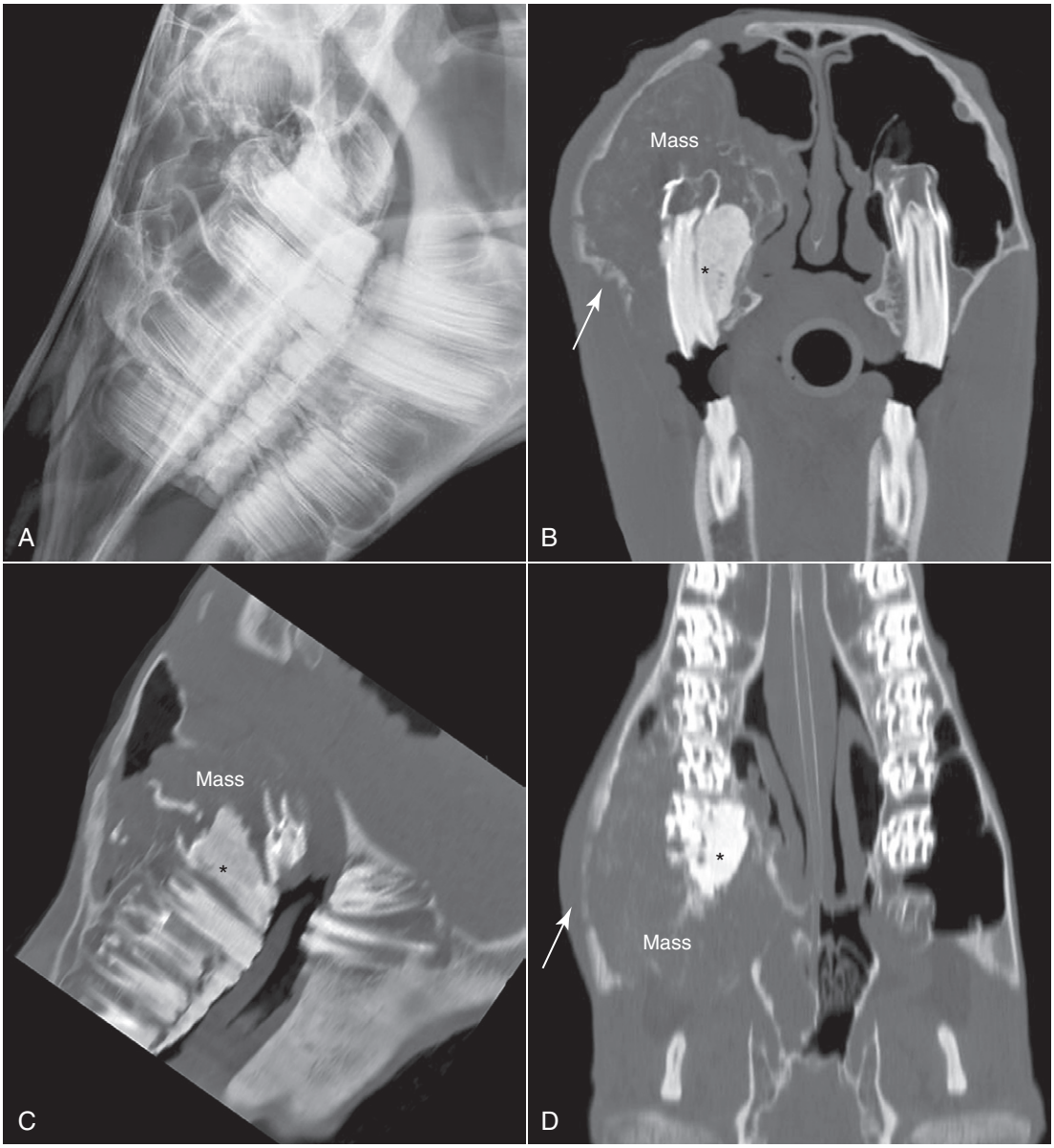


Fig. 4-2 The equine head is anatomically complex with several superimposed structures of variable opacity, making radiographic **(A)** interpretation challenging. In this horse, a large mass associated with maxillary sinus enlargement and bone lysis (*arrows*) is more easily evaluated on transverse **(B)** and reformatted sagittal **(C)** and dorsal **(D)** CT images. The mass is mainly formed of soft tissue with a well-defined mineral component attached to the last molar alveolar bone. An odontoma was confirmed histologically.

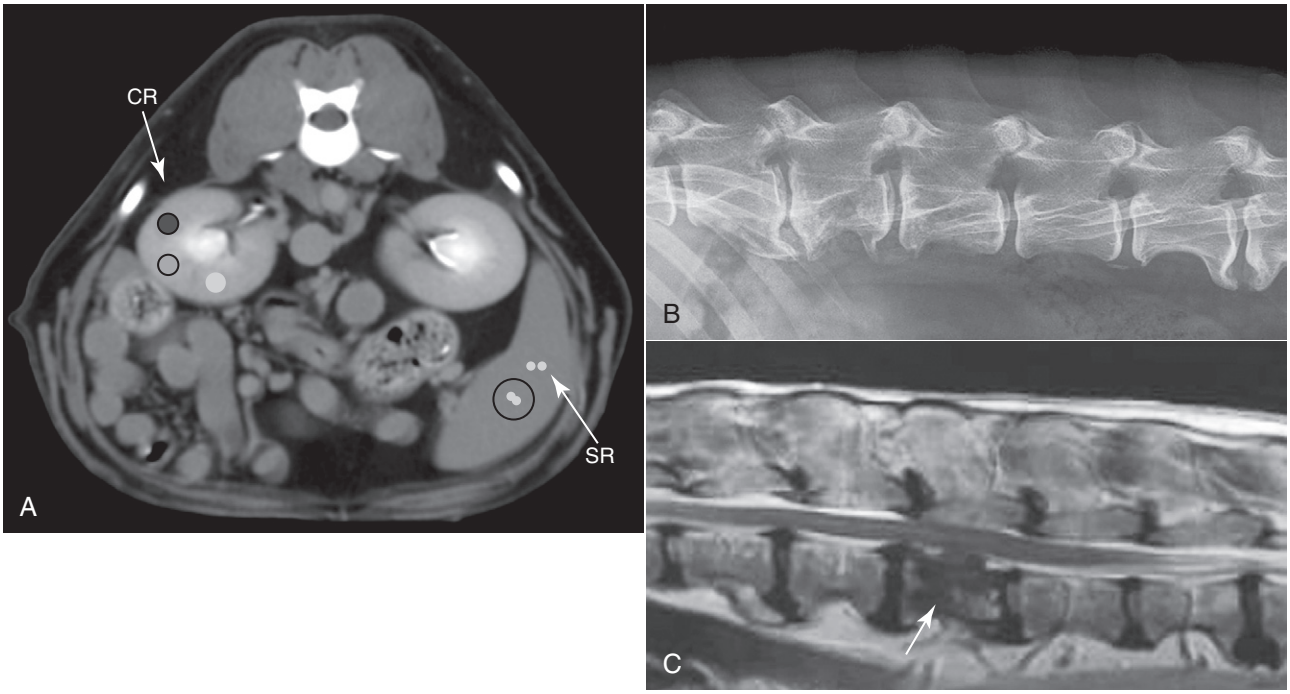


Fig. 4-3 **A,** Schematization of contrast resolution (CR) and spatial resolution (SR) using CT. Simulated nodules in the right kidney are more easily detected; their attenuation value (physical density) differs from the rest of the parenchyma. CT offers superior contrast resolution over radiography. In the spleen, the two most dorsal simulated nodules (*arrow*) are well differentiated, whereas the more ventral simulated nodules (*circle*) are confused for one single lesion, highlighting the limit of spatial resolution in this image. **B** and **C,** MR imaging is recognized for its great contrast resolution. In this dog with back pain, a malignant neoplasm involving the third lumbar vertebra (*arrow*) is clearly detected with MR imaging **(B)** but was not conspicuous radiographically **(C)**.

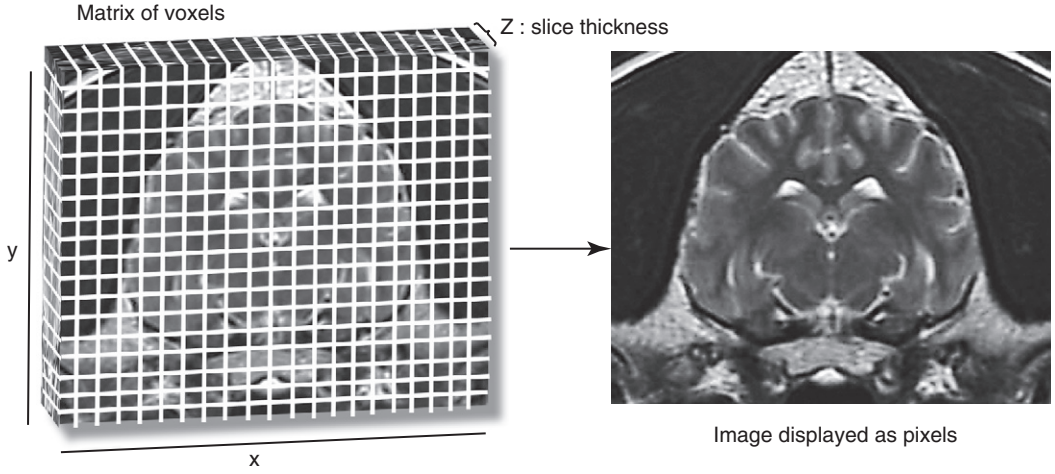


Fig. 4-4 Concept of "voxel-to-pixel" translation in tomographic imaging. The information contained in individual cubes (voxels) of the imaged matrix is displayed as pixels on the computer monitor. Hence, the two-dimensional image is a representation a three-dimensional slab of tissue.

plane with MR imaging (Fig. 4-7). That is, images can be obtained in transverse, sagittal, dorsal, or any oblique plane. Conversely, with CT, images can be acquired only parallel to the system gantry. Thus, images are typically transverse to body parts lying on the CT table. Fortunately, sections are scanned contiguously, forming a volume dataset of millions of tiny cubes, each associated with an attenuation value. It is therefore possible to rearrange, or *reformat*, images so that voxels along a plane different than the transverse plane are now displayed as a new matrix of pixels (Fig. 4-8, Video 1). This process is known as *multiplanar reformatting*. These new images can assist in structure recognition, especially when tubular or tortuous, and allow more complete assessment (measurements, etc.) of normal and abnormal tissues. Moreover, imaging software can be used to generate 3-D representations through volume or surface rendering methods, helping clinicians, especially those less familiar with tomographic imaging, better understand morphologic changes and plan surgery. Although these manipulations can be performed with any CT dataset, the quality of reformatted or 3-D images is influenced by the initial image spatial resolution, and mainly its slice thickness. For example, transverse images obtained from 5- to 7-mm-thick sections, once reformatted along the sagittal or dorsal planes, will be associated with steplike contour artifacts (Fig. 4-9). Conversely, image reformatting using 0.62 mm-thick sections (i.e., nearly isotropic resolution) will generate images of structures with smoother contours. This represents an important benefit of multirow detector technologies. Although this level of resolution may not always be necessary, it can exert an impact on diagnostic accuracy, especially when very small structures (e.g., bone fragments, lung nodules) are imaged.

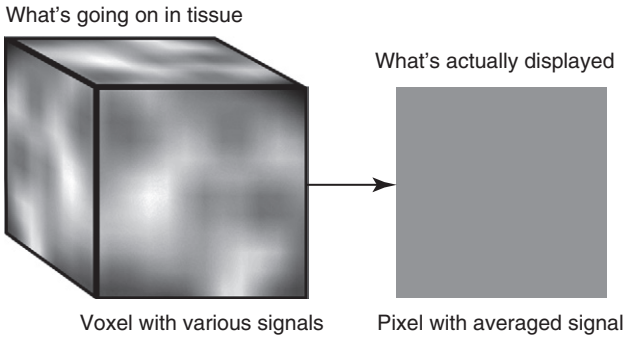


Fig. 4-5 Signal averaging. Although a single voxel may contain tissue of heterogeneous signal intensity, only the average is displayed as a pixel of uniform brightness. More signal would translate to brighter pixel, whereas lack of signal would be displayed as a dark pixel.

COMPUTED TOMOGRAPHY

In 1979, G. N. Hounsfield and A. M. Cormack were awarded the Nobel Prize in medicine for the invention of CT,[1] which was considered by many to be the greatest advance in medicine since the invention of radiography. Individual images that took several minutes to acquire and reconstruct with sophisticated computers back then can now be generated in fractions of a second, significantly expanding the range of diagnostic

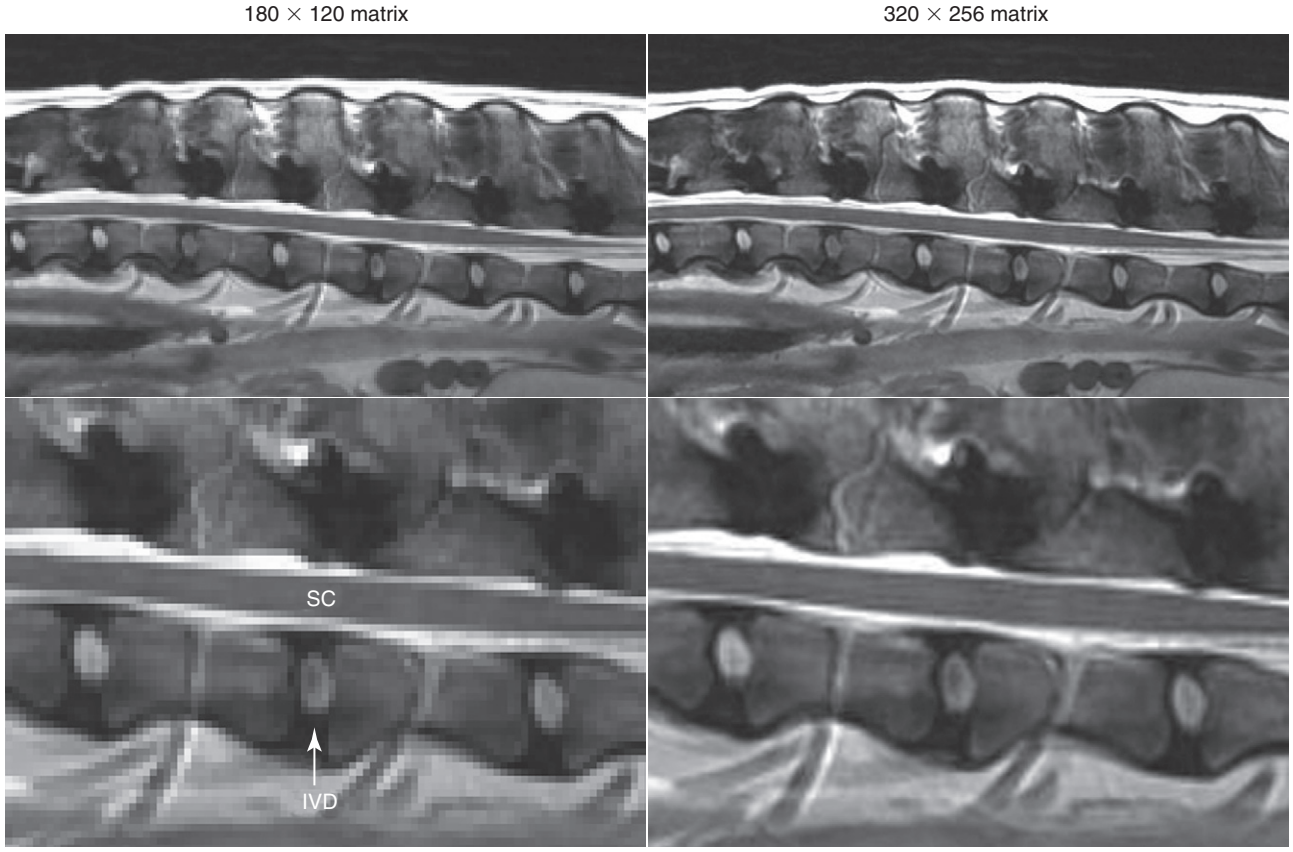


Fig. 4-6 Image matrix and spatial resolution. With a given field-of-view, a small matrix (180 × 120) contains larger pixels that result in steplike contours. The spinal cord (SC) in this dog is smoother in contour when a larger matrix (320 × 256) (i.e., smaller pixels) is used. This superior spatial resolution increases diagnostic accuracy. IVD, intervertebral disc.

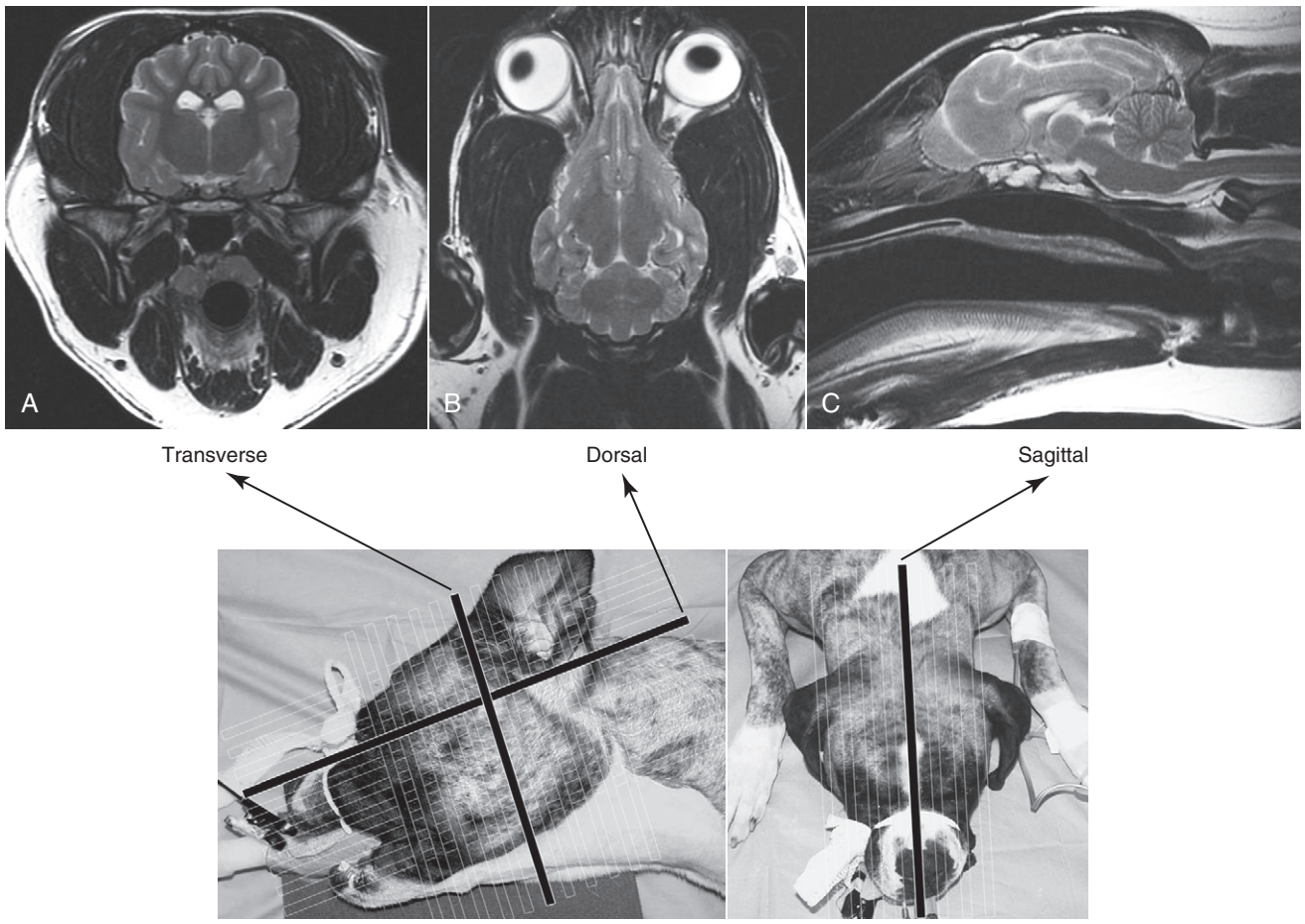


Fig. 4-7 MR images can be obtained in any plane. Transverse **(A),** dorsal **(B),** and sagittal **(C)** planes are typically obtained in most patients, allowing better three-dimensional representation. Image localization is illustrated in the bottom images. Note that all planes can be obtained without having to move the patient.

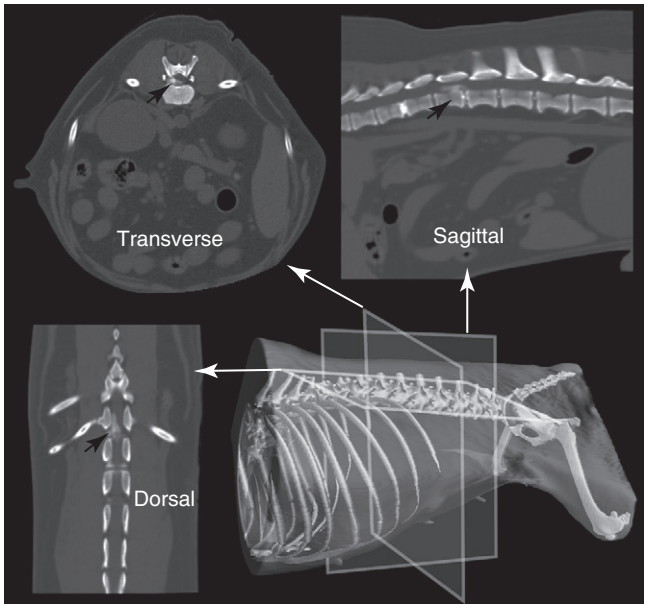


Fig. 4-8 Multiplanar reformatting with CT. Transverse images are obtained initially, but can be reformatted in any plane to help better understand the anatomy. With multi-row detector CT, thinner sections can be acquired more rapidly, resulting in smoother images with reduced steplike artifacts (see also Fig. 4-9). The three-dimensional extent of the extruded mineralized disc material is well depicted in all planes (*arrows*).

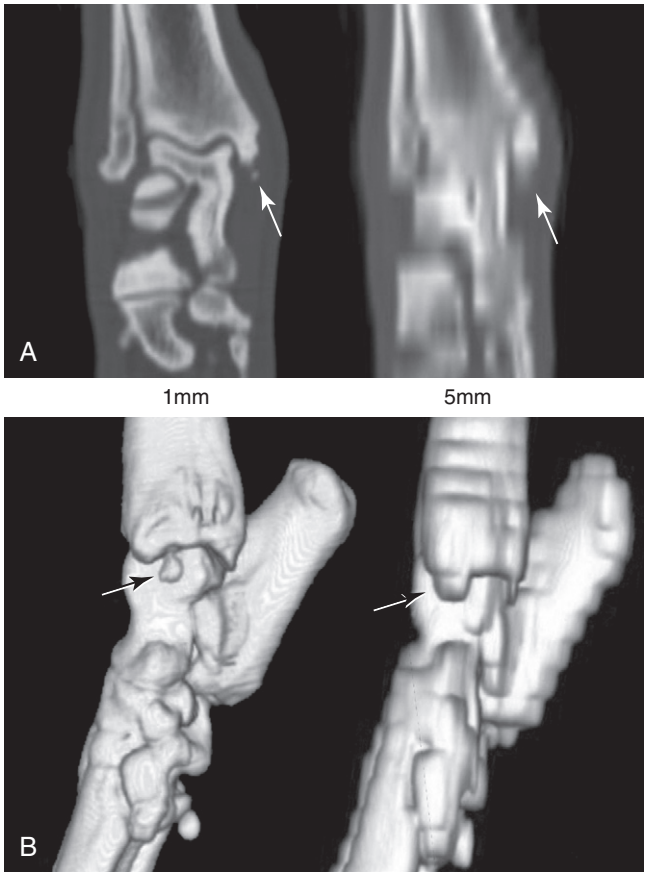


Fig. 4-9 Impact of slice thickness on quality of reformatted images. With 1 mm-thick CT transverse sections reformatted in the dorsal plane **(A)** or visualized as three-dimensional surface rendering **(B),** bone contours are smoother, and smaller structures, such as bone fragments, are depicted more clearly. Reformatted images obtained with thicker (5 mm) slices are associated with steplike contours. The bone fragment distal to the medial tibial malleolus (*arrows*) is easily confused for an osteophyte in images acquired using thicker slices.

applications while improving patient comfort and reducing motion artifact.

CT technology was based on Radon's mathematic principles developed in 1917, which proved that an image of an object could be produced by the use of an infinite number of projections through that object.[1] With conventional radiographs, orthogonal projections are used to mentally reconstruct anatomic structures in 3-D based on the visualization of their shape on perpendicular projections. This process is reliable for simple shapes, but to represent structures with irregular contours accurately, many more projections are necessary. Now, if thousands of projections could be performed at precise angles, and if x-ray transmission through tissues could be quantified for each of these projections, a sophisticated computer would be able to geometrically *reconstruct* these data and assign specific x-ray transmission values to individual regions of the body. By using a thinly collimated x-ray beam rotating around a patient, slices of tissues can then be computerized, each with its own matrix of voxels associated with definite attenuation values. This is the fundamental concept of CT.

Computed Tomography System Geometry

A CT system is mainly composed of a scanning unit (i.e., the *gantry*) with a rotating x-ray emitting tube and a detector system, a patient table, and a console equipped with a sophisticated computer that allows adjusting acquisition parameters and image reconstruction (Fig. 4-10). The rotating x-ray tube is powerful enough to operate for long periods of time without overheating, thus permitting acquisition of large volumes of data. Initially, information could be obtained only one slice at a time because of the wire joining the rotating tube to the stationary electric circuitry in the gantry. Thus, the tube was rotated back to its original position after each scan, introducing an additional delay between each image acquisition. Slip-ring electromechanical devices, consisting of circular electrical conductive rings and brushes allowing the transmission of power from the stationary circuitry to the rotating tube, were then developed to allow uninterrupted tube rotation. Along with the concurrent development of high-capacity x-ray tubes, the introduction of slip-rings opened the door to *helical* (or *spiral*) *scanning*, a revolutionary advancement in CT imaging (Fig. 4-11, *A*). With the traditional *sequential, or slice-by-slice mode*, a cross-sectional image is produced by scanning a flat, transverse slice of the body of a patient lying on a stationary table. Because of body motion that may be difficult to control (e.g., respiration or peristalsis), images may not be consistent with the patient anatomy, leading to tissue misregistration. For example, a small lung nodule may not be detected if it moves because of respiration during sequential scanning (Fig. 4-11, *B*). With helical scanning, however, an entire body region, or the whole body, can be imaged without interruption and at greater speed, eliminating such acquisition gaps. Helical scanning is possible because of concurrent table advancement into the gantry as the tube rotates around the patient, which then traces a helical path around the body and produces a data volume rather than a single slice. Using interpolation methods, flat slices of cubical voxels can be reconstructed from any part of the dataset. Additionally, helical scans are performed much faster, reducing motion artifact and allowing angiographic procedures that require precise contrast-medium bolus tracking. Moreover, because of the geometry of helical scans, multiplanar and 3-D reformatting are less prone to steplike artifacts, resulting in smoother images. For these reasons, helical scanning is the standard in veterinary medicine, although sequential scans are also performed when motion is less an issue (e.g., scanning the head) and to prevent tube heat overload.

The *detector system* also plays an important role in image quality. It converts the incident x-rays that traverse tissue into electronic signals. Ceramic, solid-state detectors have better x-ray absorption and are used in current systems.[1,4] Each detector is composed of a scintillation crystal that reacts with the incident x-ray, and through an amplification process, generates light that is converted into digital pulses (Fig. 4-12). Detectors are aligned over a semicircular (generally 60 degrees) or annular (360 degrees) array, depending on the system geometry. Annular arrays are stationary, whereas semicircular arrays move synchronously with the opposing x-ray tube (see Fig. 4-10, *B*). Although most CT scanners used currently in veterinary practices are of single-row configuration, multi-row detectors are increasingly available (Fig. 4-13). The use of very thin slices with single-row scanners is limited by the fact that only one slice is imaged at a time. For example, 5 mm-thick slices of a 30 cm-long thorax, imaged helically at a pitch of 1 and with a tube rotation of 1 second, would require 60 seconds to image, which is far better than conventional section-by-section scanning, but still difficult to achieve without respiratory motion. Multi-row detectors use radiation delivered from x-ray tube more efficiently than single-row detectors. By simultaneously scanning several slices, scan times can be reduced significantly, or the smallest details can be scanned within practical scan times.[2] This improves the quality of angiographic procedures such as those used for portosystemic shunt detection.

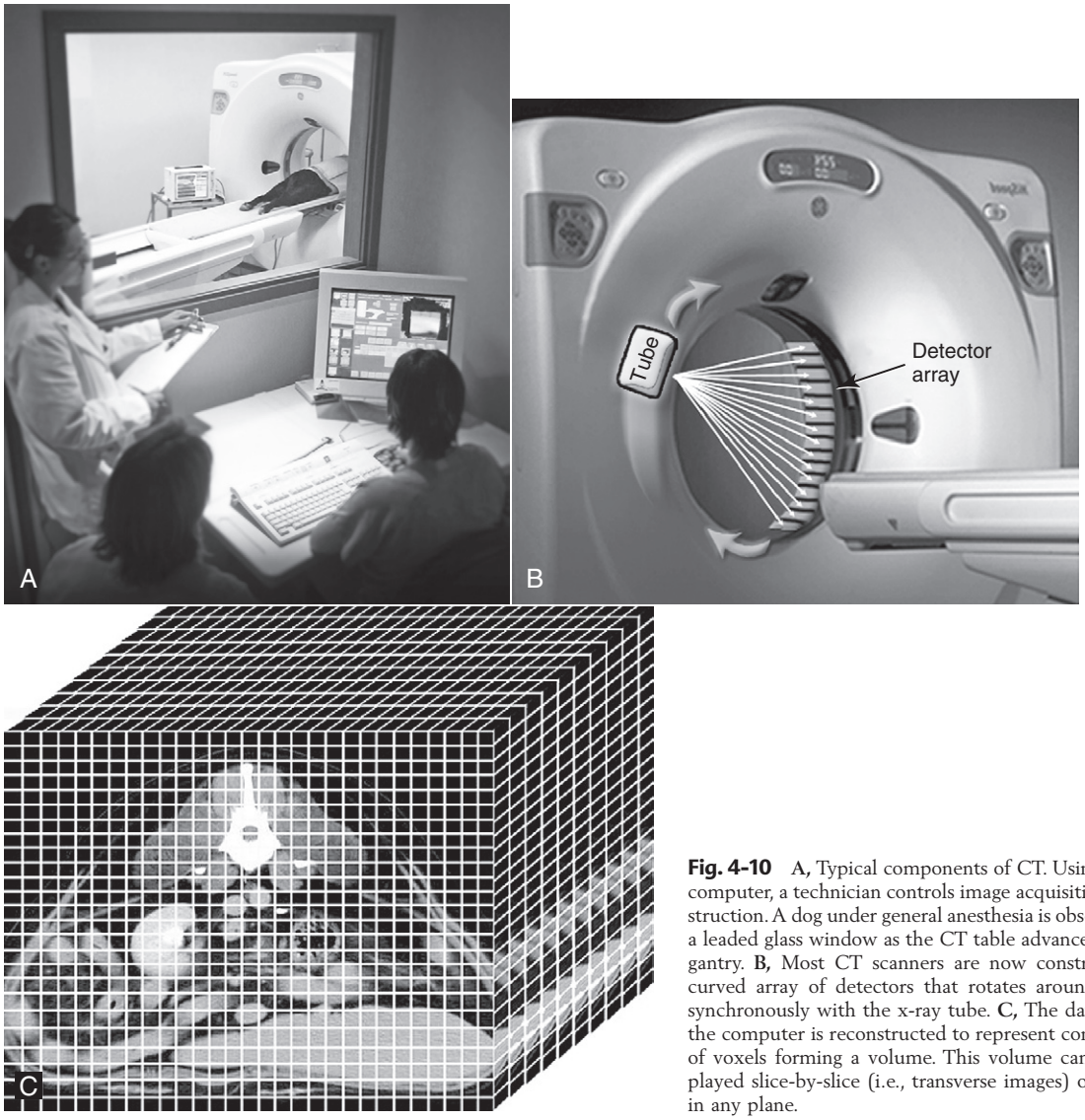


Fig. 4-10 **A,** Typical components of CT. Using a dedicated computer, a technician controls image acquisition and reconstruction. A dog under general anesthesia is observed through a leaded glass window as the CT table advances into the CT gantry. **B,** Most CT scanners are now constructed with a curved array of detectors that rotates around the patient synchronously with the x-ray tube. **C,** The dataset reaching the computer is reconstructed to represent contiguous slices of voxels forming a volume. This volume can then be displayed slice-by-slice (i.e., transverse images) or reformatted in any plane.

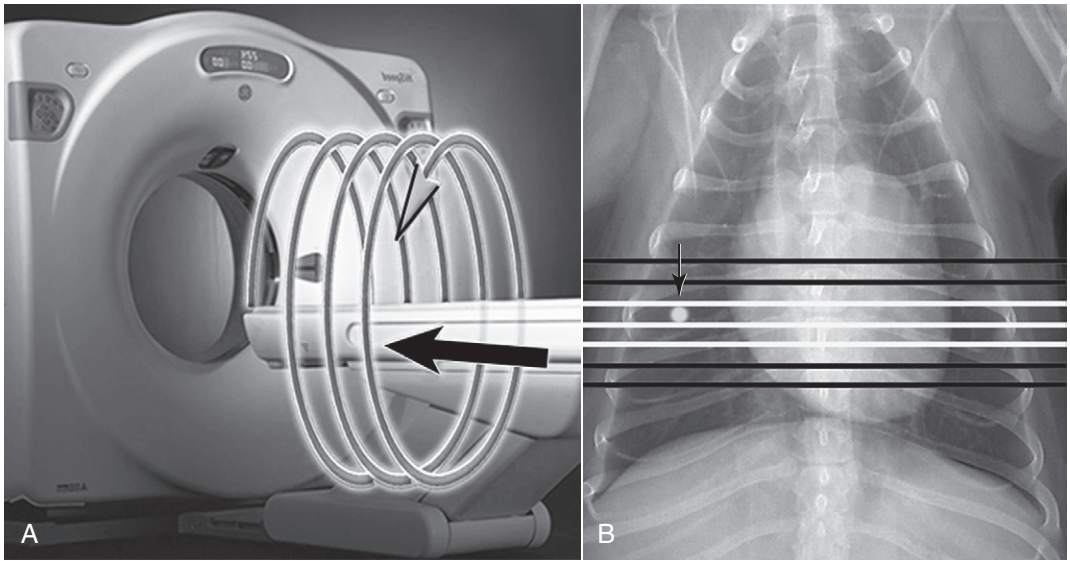


Fig. 4-11 Helical CT scanning. **A,** The table incursion into the gantry as the tube rotates around it results in helicoidal, or spiral, body scanning. This type of acquisition allows images of contiguous sections of tissue, preventing gaps. With sequential scanning **(B),** tissues slices (area between horizontal black and white lines) are imaged one after the other. Because of respiration motion, some sections can be scanned multiple times, whereas other sections can move out of the collimation and not be scanned at all. Thus, there is a possibility for a focal lesion, such as a lung nodule (*arrow*), to be undetected with sequential scanning.

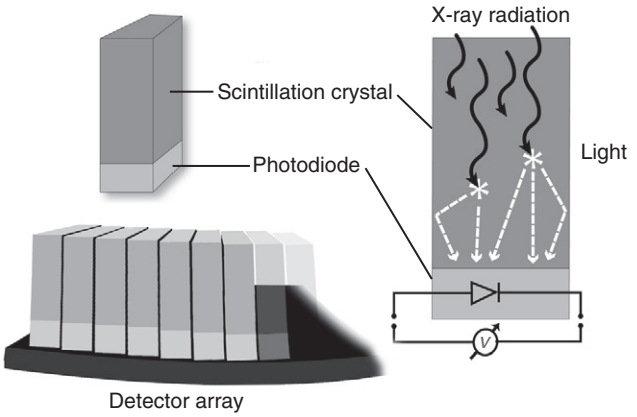


Fig. 4-12 Solid state CT detectors. X-rays reaching the scintillation crystal generate light photons that are converted to electric current in the photodiode, which is then converted to attenuation values, forming the image.

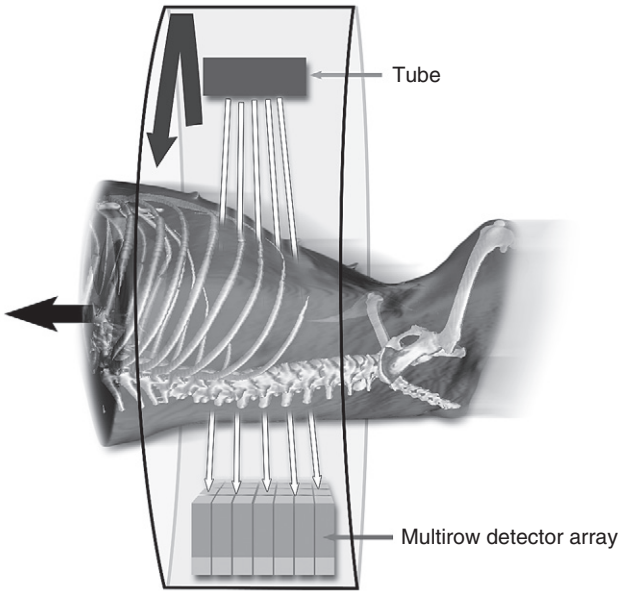


Fig. 4-13 Multi-row (or multislice) CT scanning. When using more than one row of detectors, larger areas of the body can be imaged during a single tube rotation, allowing faster table advancement, and thus faster scanning.

Image Formation

CT images are composed of pixels that, as discussed earlier, represent the mean attenuation values attributed to the corresponding boxlike tissue elements (i.e., voxels). The mechanism by which the system reconstructs the data measured by each detector as the tube rotates around the patient is sophisticated, yet relatively simple. It starts with the concept of x-ray attenuation, which mainly depends on the electron density of the medium. X-ray attenuation is quantified by measuring the fraction of radiation removed in passing through a given thickness of a specific material. The absorption probability is described by the *linear attenuation coefficient* (μ). Attenuation results in removal of x-ray photons according to equation (1)[5]:

$$N_t = N_0\, e^{-\mu x} \qquad (1)$$

where N_0 is the number of initial photons (detected at the tube exit), N_t is the number of transmitted photons measured by the detector, e is the base of the natural logarithm (2.718), x is the thickness of the absorber, and μ is the total linear coefficient of all tissues present along the x-ray path (called *ray*). After rearranging this formula, μ can be derived because N_0 and N_t are measured in the system, and e and x are known. This mathematic process is complicated by the fact that, for a single CT image, approximately 800 transmission measurements are obtained at 1000 different projection angles (*fan-beam geometry*), for a total of approximately 800,000 transmission measurements. Once μ is measured for a signal ray, the μ of each individual voxel composing the image matrix can be determined, generally using another mathematic process called *filtered backprojection*. Practically, for a single image with a 512 × 512 pixel matrix, this represents 262,144 different μ values. For display purposes, these values are transformed into Hounsfield units (HU) or CT numbers, normalized to voxel values containing water (μ_w). HU for other tissues are then calculated from Equation (2):[1]

$$\text{HU of a tissue} = [(\mu_{\text{tissue}} - \mu_w)/\mu_w] \times 1000 \qquad (2)$$

Based on this formula, the HU of pure water is zero, and any structure causing more x-ray attenuation than water will have a HU value above zero, whereas hypoattenuating media will have a HU value less than zero (negative). Figure 4-14 illustrates the range of HU among normal and abnormal tissues. The fact that liquids and soft tissues can be discriminated based on their HU values confirms the greater contrast resolution of CT over radiography.

Other important parameters that are set before image reconstruction include *slice reconstruction interval*, which adjusts the proportion of overlap between adjacent slices of tissues used for image reconstruction, and *reconstruction filter*, which determines the level of edge reinforcement applied while processing raw data. These parameters must be set carefully according to the region of interest. For example, a low-pass filter, commonly known as "standard or soft tissue filter" is recommended when soft tissue contrast must be emphasized, such as in brain imaging, with the downside of creating blurry images (Fig. 4-15). "Bone filters," conversely, maximize spatial resolution, but introduce more noise, thus reducing contrast resolution. Such images are sharper but grainier

Image Display

HU values that can be measured with typical scanners range from approximately −1000 to +3095 HU, for a total of 4096 shades of gray (12 bits of grayscale*). This range of values cannot be resolved by the human eye, which cannot differentiate more than 90 shades of gray.[1] To visualize and appreciate all tissues composed of variable HU, the *window width* (W) and *level* (L) of the image grayscale must be adjusted, according to the median and range of HU composing the area of interest. The DICOM viewing software allows adjustment of the extent (maximum-to-minimum) of gray shades (W) displayed (i.e., the image *contrast*) and the HU at the center of the window (L) (Fig. 4-16, Video 2). W/L must be adapted to the tissues evaluated and usually requires several adjustments during an examination for all tissues to be evaluated completely.

Interpretation of CT images requires an appropriate understanding of radiographic opacities and anatomy. The attenuation characteristics of tissues can be assessed qualitatively. However, another important benefit of CT over conventional radiography comes from the fact that HU values are quantified. With the DICOM viewing software, CT numbers are determined precisely after defining a region of interest (ROI) over a definite number of pixels (Fig. 4-17). This can help in distinguishing subtle differences in HU that might not be initially perceived, thus increasing contrast resolution.

*See Chapter 2 for a discussion of bit depth.

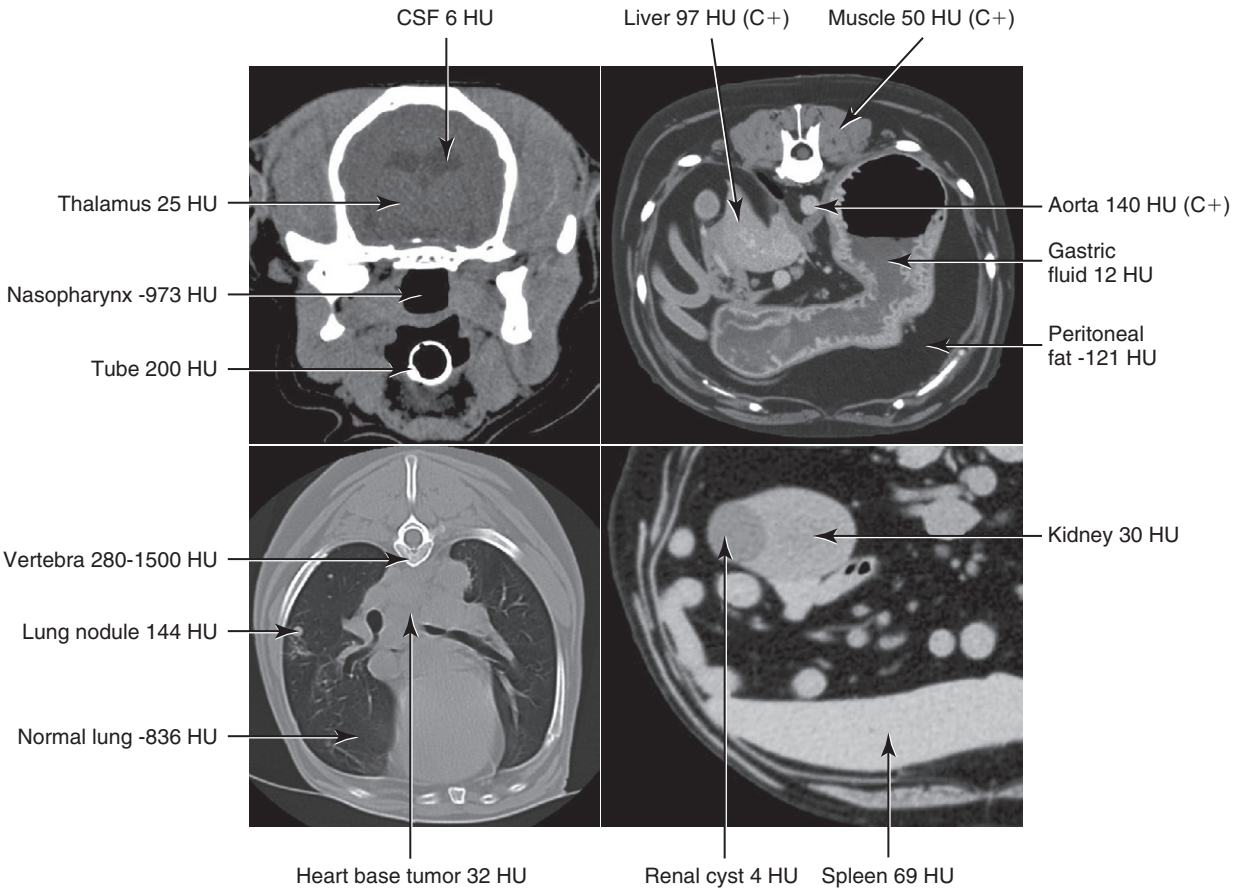


Fig. 4-14 Tissue attenuation (determined as Hounsfield units [HU]) can be quantified precisely based on values measured by the CT computer. More subtle differences in attenuation (HU values) are perceived with CT than radiography, leading to the increasing contrast resolution of CT. For example, the fluid contained in a renal cyst or in the cerebral ventricles can be differentiated from soft tissues; this is not possible radiographically. Intravenous injection of iodinated contrast medium (C+) increases the HU of vascularized tissues, further increasing the contrast resolution of CT. *CSF,* cerebrospinal fluid.

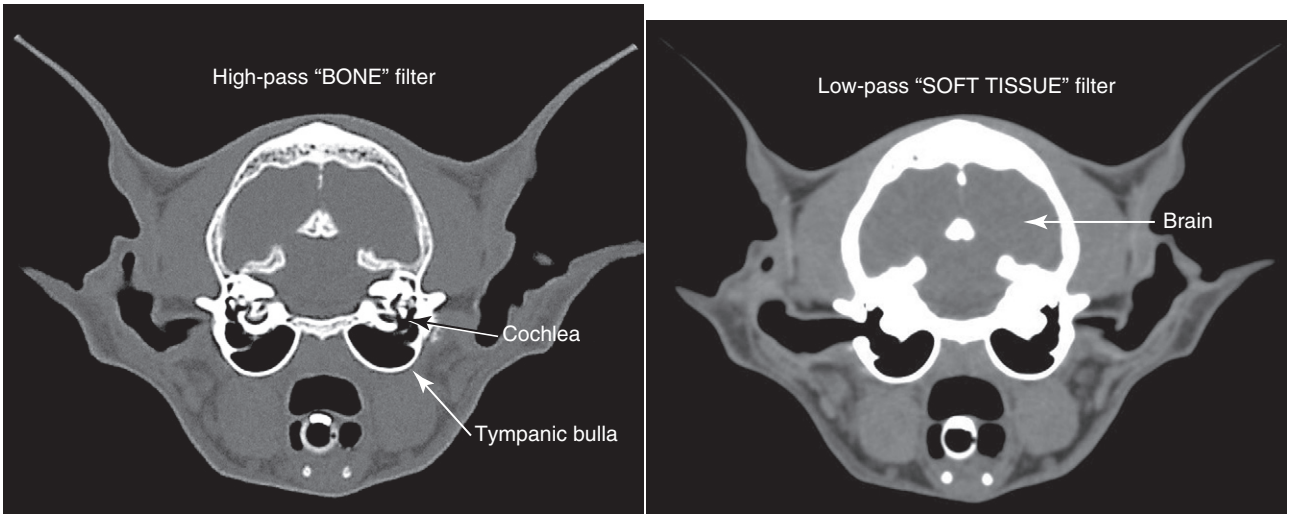


Fig. 4-15 Image reconstruction algorithm. High-pass filtering, also known as "bone filtering," results in sharper images, whereas images reconstructed with low-pass "soft tissue" filter are smoother (or blurrier). The inner ear cochlea is better defined, and the tympanic bulla is thinner with bone filtering, but the brain and other soft tissues of the head are grainier (i.e., noisier) with the same filter. Such filtering is an important part of the image reconstruction steps and requires raw data.

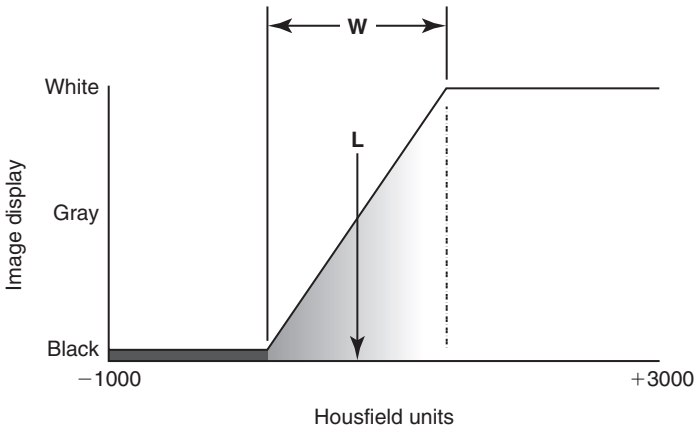


Fig. 4-16 Window width and level adjustments. Because of the limited capacity of the human eye to distinguish different shades of gray, the range of CT numbers (or Hounsfield units) composing the image—from approximately –1000 to +3000—cannot be displayed at once. With the DICOM viewing software, the window level (*L*) is set at the mean HU of the region of interest, and the window width (*W*) is set to include the range of values to be represented. Practically, L controls the image brightness and W, the image contrast. A small W, such as 400, will result in increased image contrast. Setting the L to 40 allows better distinction of cardiac chambers filled with diluted contrast medium. Conversely, with these settings, lungs and bone exceed the lower and upper limits of the grayscale and are thus represented with totally black or white pixels, respectively. To assess lung tissue, the W must be widened (1600) and the L must be centered on its mean HU of lung (–600 to –800), whereas bone assessment requires even larger W (2000) and higher L (300). These values must be adapted to the patient. *Ao,* aorta; *Br,* bronchus; *LV,* left ventricle; *M,* muscle; *PV,* pulmonary vein; *RV,* right ventricle.

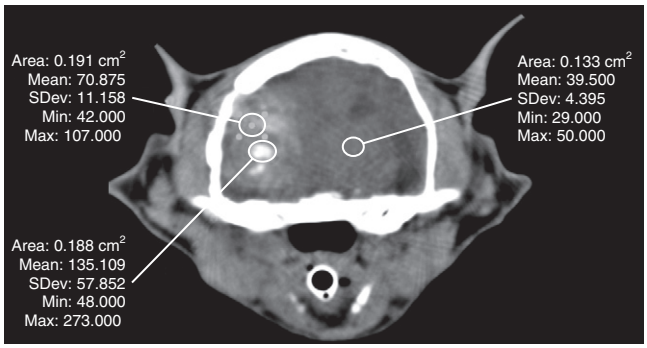


Fig. 4-17 HU measurements. Differences in HU among normal and pathologic tissues can be determined with the CT viewing software in specific regions of interest (ROI). Information such as ROI surface area and mean, maximal, and minimal HU is provided. Such method allows detection of more subtle differences in HU than what the eye can perceive. In this cat, a mineralized meningioma was identified.

Contrast-Enhanced Procedures

The use of iodinated contrast medium has become standard for several CT procedures in veterinary medicine.[6] After intravenous bolus injection, the distribution of this hyperattenuating substance can be tracked throughout the body, providing information on the perfusion of tissues and integrity of natural barriers, such as the blood-brain barrier. Typically, for nonangiographic procedures, postcontrast scans are performed a few minutes following bolus injection, to allow contrast medium to pass from its original intravascular space into the extravascular space. Hence, the HU of a tissue will increase in proportion to the concentration of the contrast medium, the volume of its blood space, and the permeability of its capillary bed.[7] When comparing postcontrast to precontrast CT images, the degree of enhancement can be assessed qualitatively (Fig. 4-18) and quantitatively (see Fig. 4-14). Enhancement characteristics can be used to complement other morphologic observations and increase both sensitivity and specificity of CT examinations.

Angiography represents another important application of CT in veterinary medicine. Such a procedure requires helical scanning and is optimized with multi-row detector configurations and with the use of automated contrast-medium injectors. Scans are performed rapidly after the injection of a contrast-medium bolus and timed according to the vascular phase examined and its enhancement peak. For example, when injecting into a cephalic vein, contrast medium reaches sequentially the cranial vena cava, the right atrium and right ventricle, the pulmonary arteries and veins, the left atrium and ventricle, the aorta and peripheral arteries, before returning to the heart through the vena cava, and to the liver through the portal vein. Precise acquisition timing is required to isolate a group of vessels, which is important when, for example, looking for portosystemic shunts (Fig. 4-19).

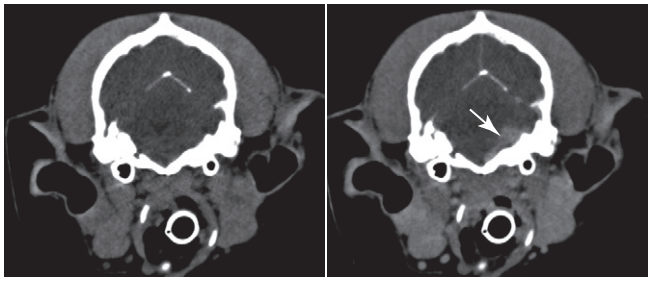


Fig. 4-18 Intravenous injection of iodinated contrast medium increases contrast resolution of CT. In this dog, a contrast-enhancing meningioma (*arrow*), with a broad base along the left temporal bone, was detected only after contrast-medium injection.

Because of the fact that iodinated contrast medium is eliminated essentially by glomerular filtration, contrast-enhanced CT can also be used to estimate the rate at which this occurs, as well as to assess the renal collecting system.[8] *Intravenous urography* is superior when done using CT rather than with radiography because of the elimination of superimposition, allowing, for example, more accurate identification of ureteral ectopia.[9]

The impact of radiation exposure with CT has not yet been documented in companion animals. However, the potential side effects associated with intravenous injection of contrast medium are known in animals, and the risk of a reaction to the contrast medium must be weighed against the potential benefit of the procedure.

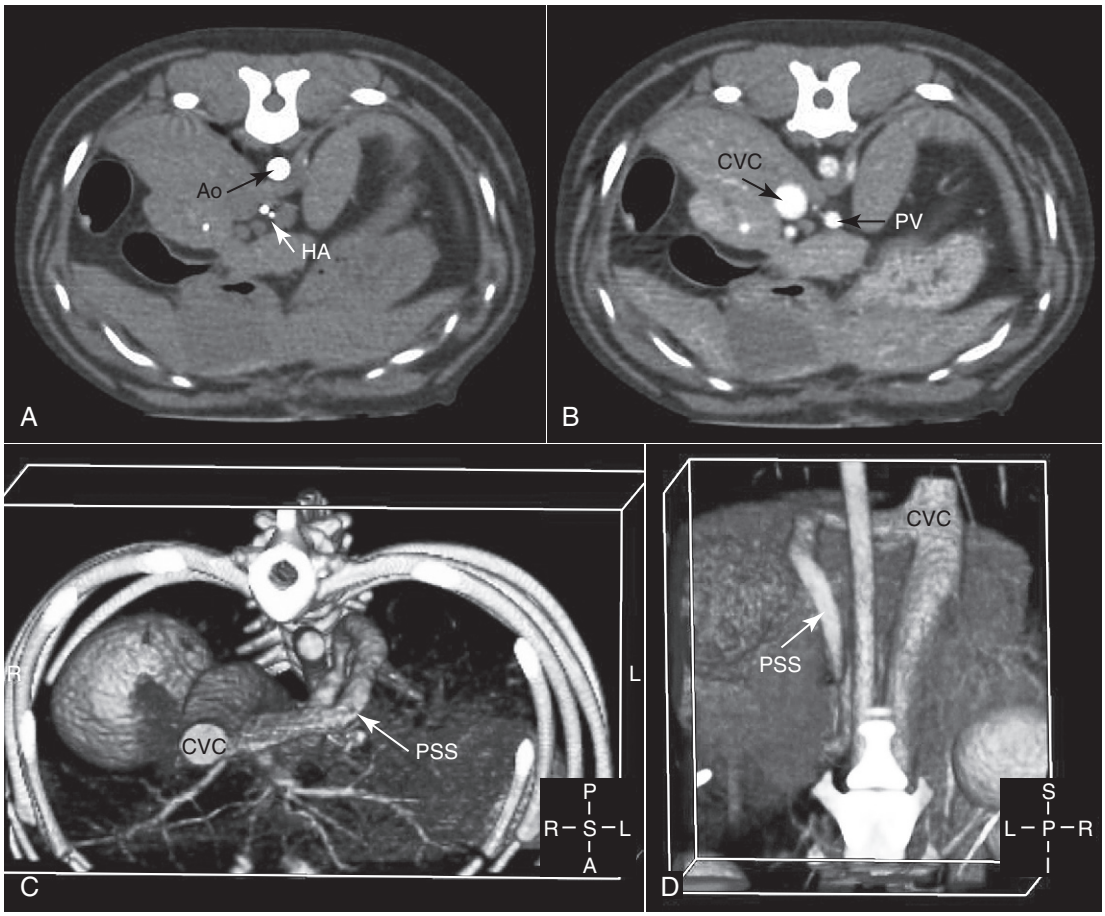


Fig. 4-19 Multiphase CT angiography for portosystemic shunt *(PSS)* detection. **A,** A few seconds after intravenous injection of a bolus of contrast medium, initial scanning highlights the arterial phase of contrast medium distribution. The aorta *(Ao)* and hepatic artery *(HA)* are very bright. **B,** Shortly thereafter, contrast medium returns through the caudal vena cava *(CVC)* and portal vein *(PV)*, while it gradually diminished in concentration in the aorta. At this point, vascularized tissues also contrast-enhance. **C** and **D,** 3-D volume rendering allows a more comprehensive representation of the PSS location and termination. The 3-D image can be moved on the display in any direction and clipped to include only a specific region. Here, cranial **(C)** and dorsal **(D)** views are represented.

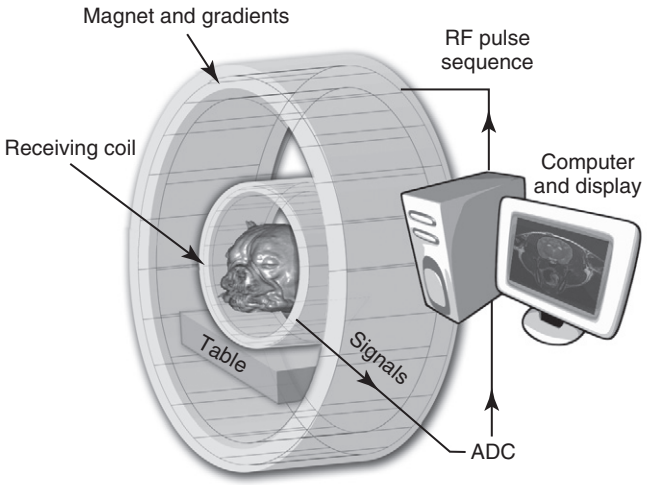


Fig. 4-20 Components of the MR unit. The region of the patient to be imaged is placed in the center of the gantry (i.e., maximal magnetic field) and a coil (of variable shape) is placed around or very close to this region. The computer is manipulated to prepare RF pulse sequences that cause tissue magnetization before signals can be detected as echoes. Different gradients inside the gantry allow localization of individual echoes and are used for gradient-recalled pulse sequences. Analog signals are converted into digital pulses that are transformed into interpretable images. *ADC*, analog-to-digital converter.

MAGNETIC RESONANCE IMAGING

MR imaging has become a significant diagnostic tool in veterinary medicine, mainly because of its inherent high-contrast resolution that allows soft tissues to be characterized sensitively. This characterization fundamentally revolves around the electromagnetic properties of hydrogen nuclei (protons), which are abundant in body tissues. Energy transfer to and from these protons can be localized spatially (i.e., in individual voxels) and is the source of image formation. Equipment sophistication and pulse-sequence development are responsible for the growing applicability and accuracy of this modality. Although MR imaging is used mainly to investigate neurologic conditions, several other body parts of small and large animals—especially equine—can be imaged favorably with MR.

Instrumentation

MR systems constitute the most sophisticated equipment in diagnostic imaging, combining electronics, radiofrequency (RF) generators, coils, and gradients that interact with a computer. This combination is necessary for proper tissue excitation and reception and localization of tissue signals. The magnet provides the external magnetic field in which the patient is placed, and its performance is influenced by its field strength, stability, and uniformity. Several types of systems are available, and some of their characteristics will be discussed later. Figure 4-20 illustrates the main components of the typical MR system.

Main Magnetic Field and Radiofrequency Energy

Accordingly to Faraday's law of induction, when an electronic current travels along a loop of wire, a magnetic field is generated perpendicularly in proportion to the strength of the current (Fig. 4-21).[10] Fundamentally, this is how most MR scanners work, particularly those of higher fields (>1 tesla [T]). To generate and maintain such high magnetic fields, superconducting wires are immersed in liquid helium, which serves as cooling agent.

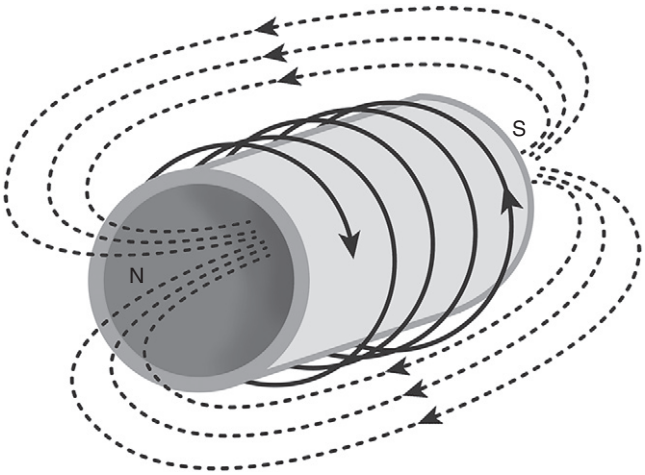


Fig. 4-21 According to Faraday's law of induction, when an electronic current travels through a loop of wire, a magnetic field is generated perpendicularly in proportion to the strength of the current. The magnetic field—illustrated here as *curved dashed lines*—is oriented from north *(N)* to south *(S)*.

Spins, Excitation, and Relaxation

Each hydrogen proton is positively charged (H^+) and rotates about its axis, like a spinning top, or the earth rotating about its own axis. These spinning protons, or *spins*, act like tiny magnets whose individual magnetization vectors are oriented randomly in the body and cancel out under normal circumstances (Fig. 4-22). Molecular motions and collisions result in spin-spin magnetic interactions that fluctuate constantly, affecting the behavior of these spins—thus signals generated—during the scanning process.[5]

When placed in a strong external magnetic field, spins are forced to align along the axis of this field (B_0), either in the same direction (parallel) or opposite (anti-parallel). The magnetic fields of most of these spins cancel out, but a slight excess of these spins, which is proportional to the strength of the magnetic field, will be parallel to B_0, producing a *net magnetization* along that axis (see Fig. 4-22). The size of this equilibrium magnetization also depends on the proton density of tissues present in the field.[10,11]

Influenced by the external B_0 in which they are placed, spins wobble about its axis, a behavior called *precession* (Fig. 4-23).[10,11] This wobbling motion occurs because of the external force applied to the spins magnetization vectors. The frequency of this precession, also called resonance or *Larmor frequency* (ω_0), is proportional to the main magnetic field strength: $\omega_0 = \gamma B_0$. The constant γ, or *gyromagnetic ratio*, is characteristic of each type of nuclei. For hydrogen protons, this constant equals 42.6 MHz/T (megahertz per tesla). Hence, in a 1.5 T magnet, the frequency of spin precession will equal 42.6 MHz/T × 1.5 T or approximately 64 MHz (64 million times per second).[12]

The phenomenon of precession implies that the magnetization moment of each spinning proton can be broken down into two orthogonal, vectorial components: one aligned or longitudinal to B_0—the *z*-axis—and one transverse to it, lying on the *xy*-plane (see Fig. 4-23). Although a positive net magnetization is present along the *z*-axis in the equilibrium state, *xy* vectorial components of spins that precess out of phase cancel out.

By applying a RF pulse that matches the Larmor frequency of these spins, energy can be transferred through a process known as *resonance*. The absorption of this energy by the spins, called *excitation*, causes a state of imbalance. The excited protons jump to a higher energy state during excitation (from parallel to anti-parallel), and the macroscopic net

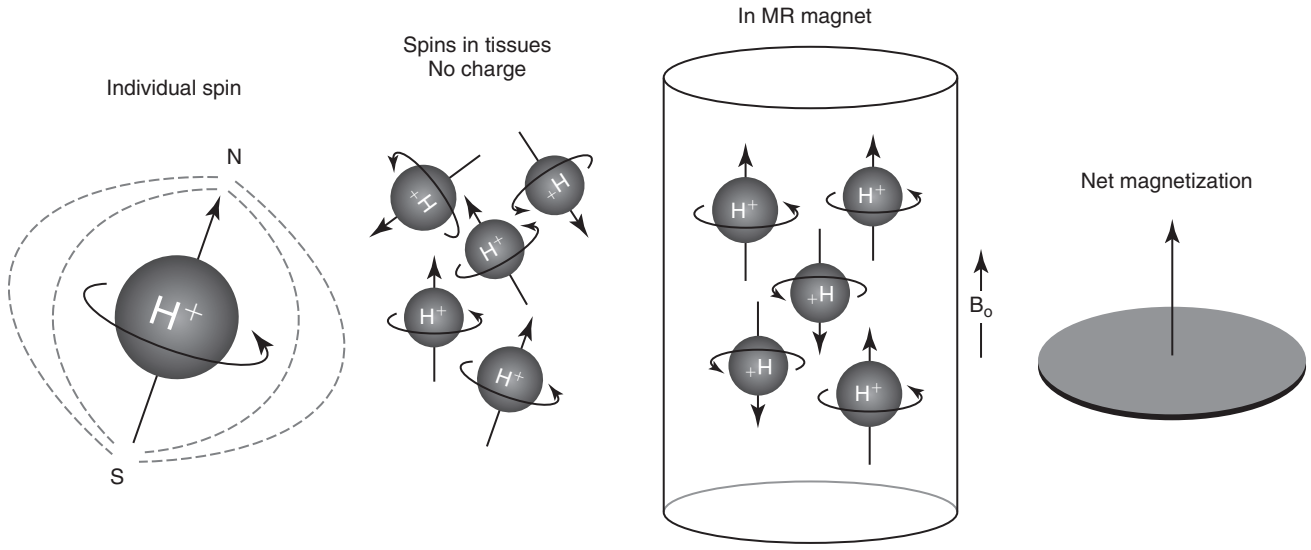


Fig. 4-22 Hydrogen protons (H+) are used for MR imaging because of their abundance in soft tissues and their magnetic characteristics. The positively charged nucleus spins about its axis, generating a very small, local magnetic field, and thus acting as tiny magnet. These protons, or spins, are oriented randomly in tissues under normal conditions so that their magnetic fields cancel out. When placed inside a strong, external magnetic field with linear orientation (B_0), these spins are flipped and orient themselves either parallel or anti-parallel to this field. A small excess of these spins (proportional to the strength of B_0) are parallel, thus generating a net magnetization of tissues. This net magnetization, which at equilibrium is oriented longitudinally, is targeted during imaging sequences.

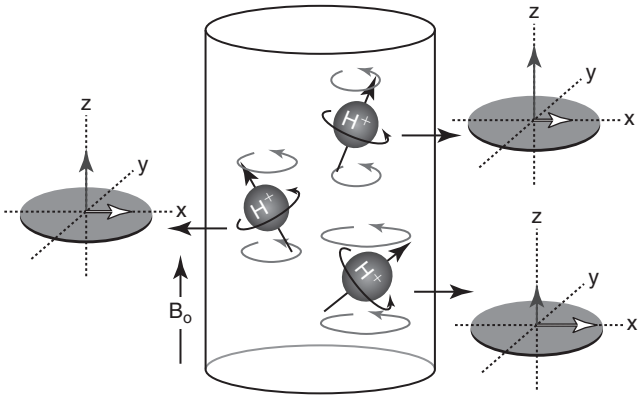


Fig. 4-23 Spin precession. Influenced by the strong external magnetic field, spinning protons wobble about its linear axis, a process called *precession*. This phenomenon implies that the magnetization moment of each spin can be broken down into two vectorial components: one aligned or longitudinal to B_0—the *z*-axis—and one transverse to it, lying on the *xy*-plane. The magnitude of each of these vectors depends on the orientation of these spins in regard to B_0 during the MR imaging sequence process. Notice that as the proton becomes progressively out of alignment with the main magnetic field (B_0), the size of the magnetization vector in the *z*-axis decreases and the size of the magnetization vector in the *xy*-axis increases.

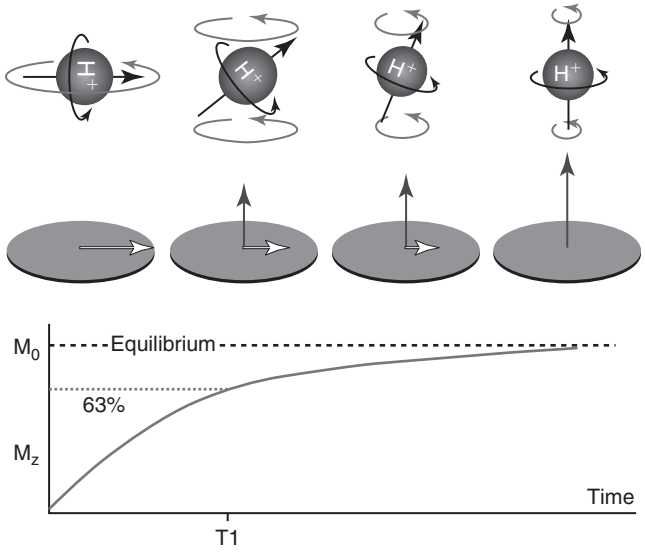


Fig. 4-24 Once the radiofrequency pulse is stopped, spins immediately start to realign with the main MR magnetic field in the *z*-axis direction transferring their absorbed energy to their molecular environment (the lattice). This is T1 relaxation. During this process, the transverse vectorial component of magnetization (M_z) decreases in magnitude while the longitudinal component increases to reach the equilibrium (i.e., low-energy state). The T1 of a tissue represents the time required for the longitudinal magnetization to recover approximately 63% of its original value. M_0, Longitudinal magnetization at equilibrium state.

magnetization vector flips away from the *z*-axis, toward the *xy*-plane, following a spiral path caused by the precession phenomenon.[11] The angle that the net magnetization vector flips away from the *z*-axis is called the *flip angle*, which depends on the strength and duration of the RF pulse. As soon as the RF pulse is stopped, spins return to their original state of equilibrium in a recovery process called *relaxation* and transmit their excess energy to the lattice.

Whereas the change in longitudinal magnetization is caused by a difference in the number of spins in parallel as opposed to anti-parallel states, the transverse magnetization vector growth is caused by spins getting into phase coherence.[11] That is, these tiny magnets become globally aligned and precess synchronously. Once relaxation begins, two distinct processes occur simultaneously: longitudinal, *T1*, and transverse, *T2*, relaxations. The release of energy from spins into their molecular environment, the *lattice*, results in more spins getting back to the low-energy state; that is, realigned with B_0 (T1 relaxation; Fig. 4-24). At the same time, in-phase

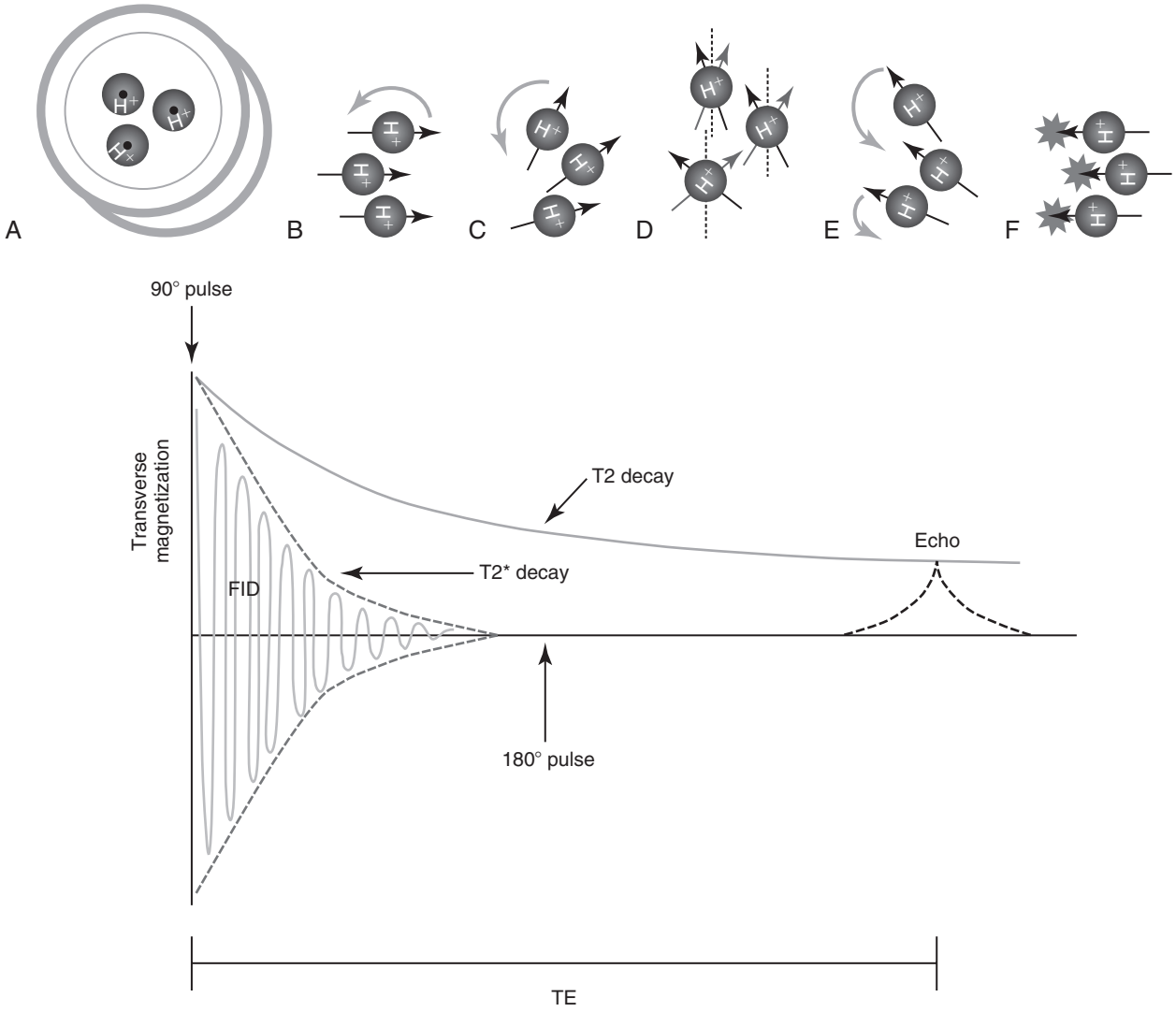


Fig. 4-25 T2 and T2* relaxation. **A,** When placed in the MR magnet (cylindrical in this case), protons align longitudinally along the axis of its magnetic field. **B,** The first step of the spin echo sequence consists of a radiofrequency (RF) 90-degree pulse that flips the magnetization moment of protons toward the transverse plane. At this point, protons precess in coherence (i.e., synchronously), which causes strong transverse magnetization in the *xy*-axis. **C,** As soon as this pulse is ended, protons start to dephase because of imperfections in the magnetic field that is not completely uniform. Indeed, the slight changes in field strength cause protons to precess more or less rapidly. This process results in rapid loss of transverse net magnetization—called T2* decay, or relaxation. **D,** To counteract this process, another RF pulse is applied to flip back these spins 180 degrees. **E,** Spins rotating more rapidly are then behind slower spins, and once all protons become coherent again, transverse magnetization regrows **(F),** peaking at a time called time between excitation and echo (TE). In all spin-echo sequences, a 180-degree RF pulse is applied so that transverse magnetization decays more slowly—a process called T2 relaxation—allowing echoes to be perceived. *FID,* free induction decay.

spins start interacting with each other, rapidly causing dephasing, and thus eliminating the transverse magnetization (T2 relaxation; Fig. 4-25). The rate at which T1 and T2 relaxation phenomena occur varies among tissues, and the exploitation of these differences is the fundamental source of tissue contrast in MR imaging (discussed later).

Spin Echo Sequences

MR images are created once signals arising from excited tissues are detected as echoes by receiving coils, localized spatially, and processed. Because of the differences in relaxation characteristics among tissues, several technical methods, or *sequences*, can be used to excite and receive signals using RF and gradient pulses, with variable timing and duration. Sequences are divided into two main groups—*spin echo* and *gradient recalled* sequences. Image interpretation is then based on the evaluation of all sequences obtained in a single examination.

As previously discussed, RF pulses energize tissue protons, which then start to process synchronously, leading to strong transverse magnetization. This process of "flipping" the magnetization away from the *z*-axis is essential to measure its strength. By placing one or several loops of wire (i.e., *receiving coil*) around the patient, in a plane perpendicular to the transverse axis, the strength of this transverse magnetic field is proportional to the electronic current induced in the coil (Fig. 4-26).

Once the RF pulse is stopped, spins dephase rapidly because of their molecular interactions (i.e., T2 relaxation). In reality, this process is accelerated further by the fact that the

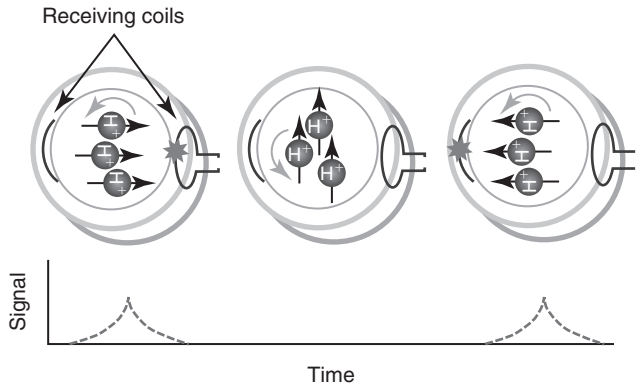


Fig. 4-26 Signal reception. When spins are flipped 90 degrees and precess in phase, they generate a strong transverse magnetization, which in turn induces an electric current in loops of wire placed perpendicularly around the body part being imaged. Signals peak when spins are fully perpendicular to each of the wire loops and decrease when rotating away from them. Using more loops around the patient increases signal intensity.

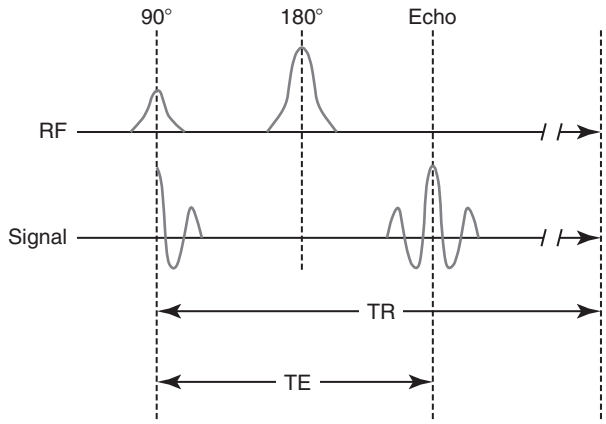


Fig. 4-27 Configuration of a standard spin-echo pulse sequence. Radiofrequency *(RF)* pulses consist of an initial 90-degree pulse followed by a 180-degree pulse. Signals associated with magnetized tissues echo exactly at a time twice the one of the 180-degree pulse. The time it takes for this sequence to be run one time is called the *time to repetition (TR)*.

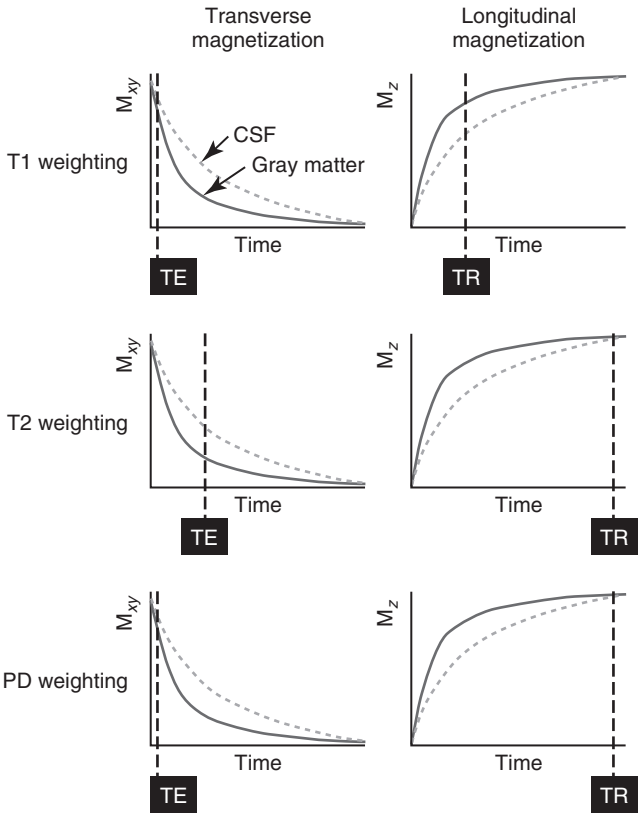


Fig. 4-28 Impact of time of echo *(TE)* and time to repetition *(TR)* on tissue contrast. By adjusting TE and TR, differences in T1 and T2 relaxation characteristics among tissues can be highlighted. By using short TE and short TR, signal echoes from cerebrospinal fluid *(CSF)* and gray matter mainly depend on their differences in longitudinal magnetization *(T1)*, as differences in transverse magnetization *(T2)* are negligible. This type of sequence is T1-weighted. If, however, differences in T2 need to be highlighted and differences in T1 inhibited—i.e., T2-weighting—both TE and TR must be prolonged. Finally, using short TE and long TR inhibits both T1 and T2 effects. In that case, T1 and T2 contrast is reduced between CSF and gray matter, and signal intensity is predominantly associated with the density of protons in these tissues. These images have proton-density *(PD)* weighting.

magnetic field is not perfectly uniform in tissues. Indeed, the magnetic field is slightly stronger in some areas because of the presence of metallic objects, air, or calcium or because of the imperfections of the MR system—for example, 1.505 T for a 1.5 T magnet—and weaker in other parts—for example, 1.495 T.[13] Such inhomogeneities cause protons to rotate at different speeds once the RF pulse is stopped (i.e., some slower than the average and some faster), leading to very rapid dephasing. Thus, instead of decaying according to specific T2 relaxation times, tissue transverse magnetization decays at a very rapid *T2** rate (see Fig. 4-25).

Spin-echo sequences have been developed specifically to address this T2* phenomenon. The rationale is simple: By adding a 180-degree RF pulse after the initial 90-degree pulse, protons start rotating effectively in the opposite direction. This effective change in direction allows slow protons—still affected by the same environment inhomogeneities—to become "in front of" faster protons. Shortly after, all protons become coherent again, exponentially increasing transverse magnetization, which peaks at a time called *time of echo* or *TE* (Fig. 4-27; see Fig. 4-25). TE then represents the time between this peak of echo and the initial 90-degree RF pulse. The time it takes for this sequence to be run one time is called the *time to repetition* or *TR* (see Fig. 4-27). For basic pulse sequences, one row of image data is acquired during each TR. Thus, the acquisition of an MR image with a matrix of 256 by 256 pixels (i.e., voxels) takes 256 times TR. With such matrix, a T1-weighted spin-echo image (at 1.5 T) with a TR of 500 msec would take 128 seconds to acquire.

Tissue Contrast

The great diagnostic potential of MR imaging comes from the fact that tissue contrast can be manipulated to enhance anatomy and/or lesion conspicuity. Indeed, by adjusting TE and TR, differences in T1 and T2 relaxation characteristics among tissues can be highlighted (Fig. 4-28).[10,11,13-15]

Recall that the MR signal that is measured is at its maximum when the transverse magnetization of tissues is completely in phase. When it begins to dephase, the measured MR signal also begins to decrease and becomes null when the magnetization is completely dephased. To detect T2 differences between tissues, time must be allowed for short-T2 tissues to decay enough so that long-T2 tissues are highlighted—that is, high signal at the time of the echo (i.e., at TE). Conversely, maximizing T1 differences requires that the time between subsequent 90-degree RF pulses (i.e., TR) is adjusted so that longitudinal recovery of tissues of short and long T1 is

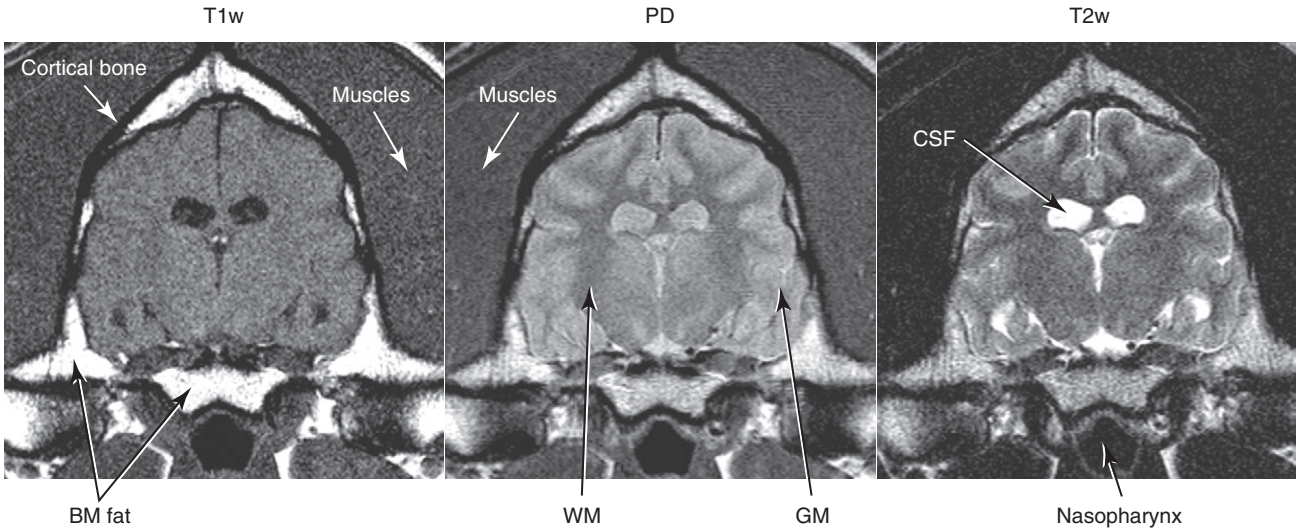


Fig. 4-29 Tissues are associated with variable signal intensity according to the type of weighting. Indeed, cerebrospinal fluid *(CSF)* appears hypointense (dark) in T1-weighting *(T1w)*, moderately intense (mid-gray) in proton-density *(PD)* weighting, and hyperintense (bright) in T2-weighting *(T2w)*. Other soft tissues structures also vary in signal intensity between sequences. Normal cortical bone and air are not magnetized enough to generate a signal on any sequence. *BM*, bone marrow; *WM*, white matter; *GM*, gray matter.

separated. Finally, because T1 and T2 effects occur at the same time, optimizing one necessitates that the other one is inhibited. Hence, *T1-weighting* requires short TR (and short TE), and *T2-weighting* requires long TE (and long TR). If both T1 and T2 effects are inhibited by using long TR and short TE, signal intensities mainly depend on tissue proton density, called *proton-density (PD) weighting*. These manipulations result in varying intensity (or pixel brightness) levels for the same tissue (Fig. 4-29). Although some tissues may appear similar in a given sequence, they may become distinct in another. Standard sequence protocols include multiple sequences to highlight these tissue differences, but new sequences are developed every day to improve the capacity to identify even more subtle differences

Magnetic Resonance Signal Localization

Now that the processes of tissue magnetization and echo detection have been discussed, one important feature of MR imaging relates to the ability to determine the anatomic origin of the signals coming out of tissues. This process is performed by intermittently using three orthogonal linear gradients that generate short-term variations in the magnetic field across the patient (and therefore the Larmor frequencies of protons).[15] These gradients are produced by additional coiled wires placed in the bore of the magnet, linked to electronic circuitry that is adjusted constantly and precisely through additional *pulses* in the imaging sequence. These gradients are responsible for the tapping or clicking sounds heard during scanning, and the gradient strength influences the anatomic details (i.e., spatial resolution) that can be achieved as well as the speed of image acquisition.

The *slice selection gradient* (G_{SS}) causes linear variation of magnetic field strength along B_0, targeting a specific slice of tissue that can be magnetized by adjusting the RF pulse frequency to the Larmor frequency of its protons.[15] Only the protons in this plane will be flipped into the transverse (i.e., emitting) position. Once an individual slice is excited, the next step is to determine the voxel origin of each signal detected. This is accomplished by using *phase-encoding* and *frequency-encoding gradients*. The phase-encoding gradient (G_{PE}) is turned on soon after the 90-degree RF pulse, causing each row of protons in the slice to have a different phase. Then, the frequency-encoding gradient (G_{FE}) is turned on during the echo to alter the Larmor frequencies for each column within the slice. As a consequence, protons in each of the individual voxels forming the matrix of the slice being imaged now precess at a specific frequency and phase, allowing them to be distinguished.

Selection of Spin Echo Sequences

Several types of spin echo sequences are available, some used more consistently and others used in more specific circumstances (Fig. 4-30). T1-weighted and T2-weighted sequences are acquired in most patients, either with the conventional method, or with the application of additional 180-degree rephasing pulses after the single 90-degree RF pulse during the same TR. This allows more signals to be localized at the same time and thus speeds up the acquisition process.[13] Such *fast spin echo* or *turbo spin echo* sequences (name varying among brands) have replaced conventional spin-echo sequences in most systems.

Inversion recovery sequences are used to null the signal from specific tissues or substances, which can help confirm the presence of such components, or improve the conspicuity of nearby tissues with similar signal characteristics. Inversion recovery sequences start with a 180-degree preparatory pulse to flip the magnetization vector of all tissues opposite to B_0—that is, $-z$.[11] Immediately after the end of this pulse, protons begin to relax, and tissue magnetization vectors start to regrow longitudinally along B_0—that is, from $-z$ to $+z$. During this process of recovery, magnetization vectors cross the null point ($z = 0$) at different times, according to the T1 relaxation rates of these tissues. If a standard spin echo sequence is started (i.e., with a 90-degree flip) when the tissue to be suppressed crosses the zero-axis, this tissue will not generate a signal at the time of echo. Hence, the delay between the inversion pulse and the 90-degree RF pulse, or *time of inversion* (*TI*), depends on the T1 relaxation time of the tissue to be nulled. For fat, which has a very short T1 relaxation time, the TI must be short. A short TI recovery (*STIR*) sequence is used in several circumstances to suppress the signal from fat, and because this sequence has T2-weighting, it increases the conspicuity of soft tissue lesions, most of which have prolonged T2 (Fig. 4-31). Unlike chemical fat-signal suppression (discussed below), STIR sequences are not affected by

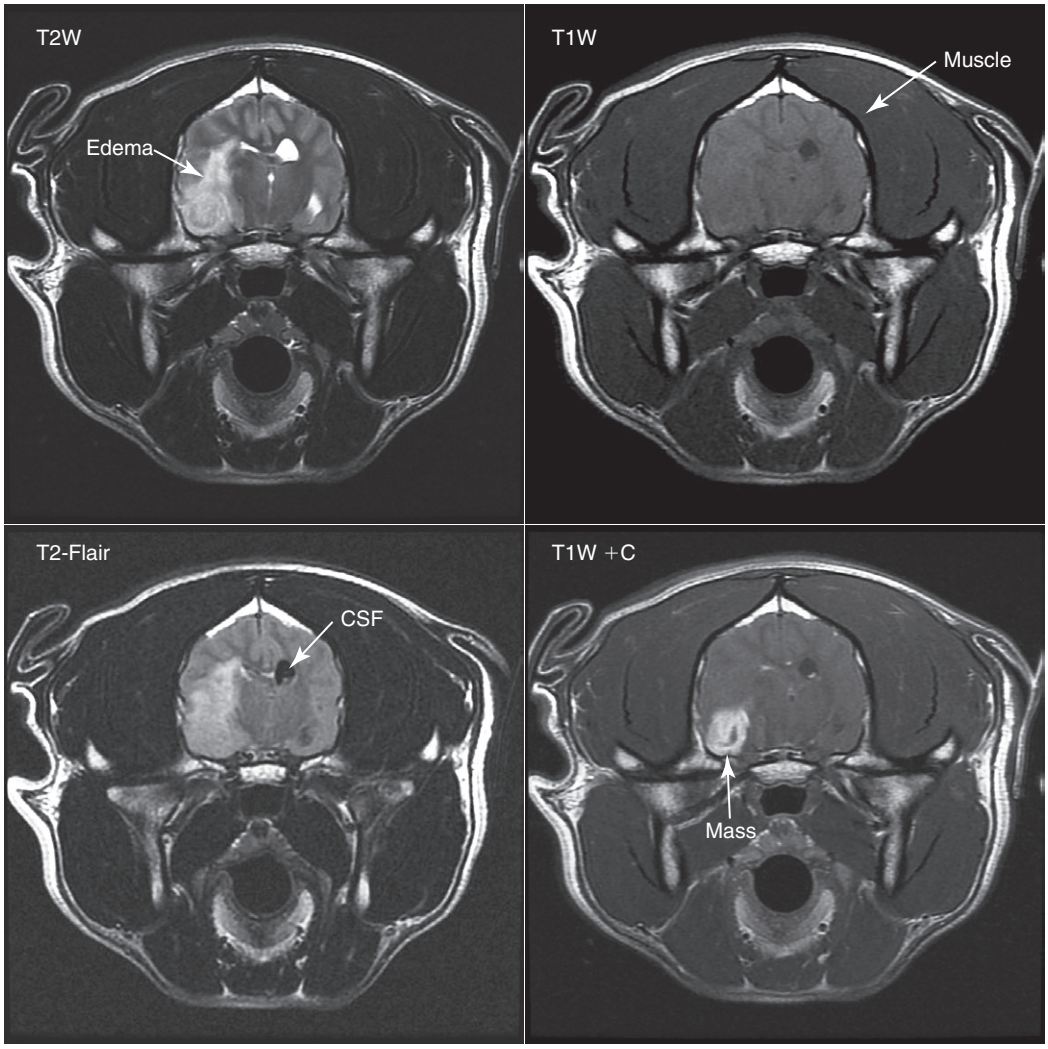


Fig. 4-30 Meningioma in the piriform lobe of a dog. In T2-weighted *(T2w)* images, the mass is confluent with regional vasogenic edema that appears hyperintense, whereas both of these abnormalities are isointense to the rest of the brain in precontrast T1-weighted *(T1w)* images. Following contrast-medium (gadolinium) injection *(T1w+C)*, the mass enhances intensely, except for a central fusiform area. In a T2-weighted fluid-attenuated inversion recovery *(T2-FLAIR)* sequence (designed to decrease signal coming from pure fluid), the signal from the pure cerebrospinal fluid *(CSF)* is attenuated.

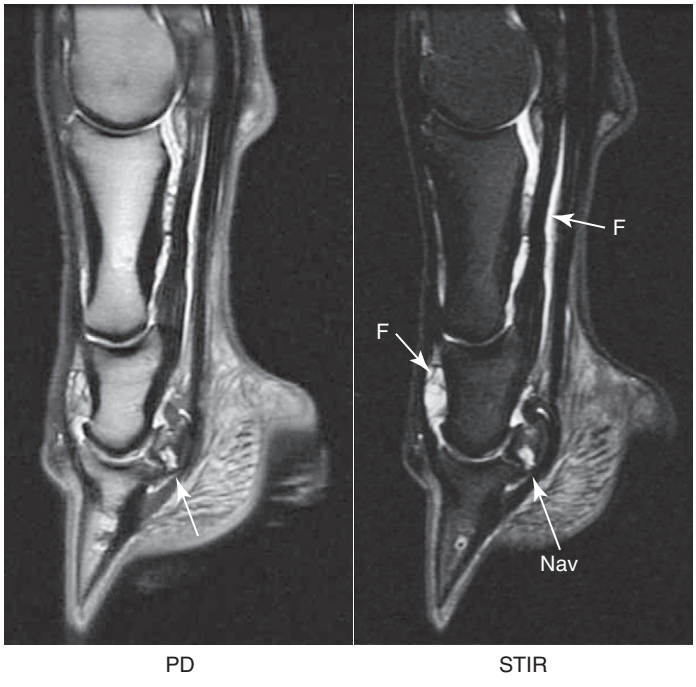


Fig. 4-31 Short TI inversion recovery (STIR) sequence increases the conspicuity of lesions with prolonged T2, particularly when embedded in fat. The attenuation of signal coming from fat (in bone marrow) allows this navicular cyst (*arrow*) to be better depicted. Other fluid-filled structures such as synovial fluid *(F)* are also better outlined. [Sagittal proton density (PD) and STIR images of this equine extremity are compared. Note the low signal coming from marrow fat in the STIR image compared to the high marrow signal in the PD image.]

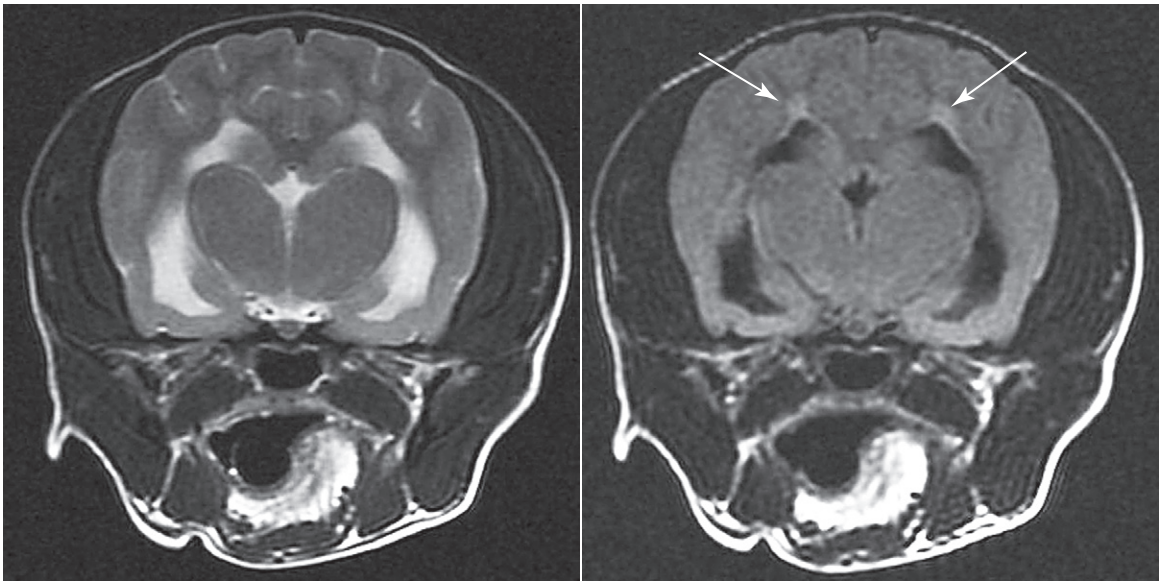


Fig. 4-32 A T2-weighted fluid-attenuated inversion recovery (T2-FLAIR) sequence can allow periventricular hyperintensities to be depicted better than with regular spin-echo T2-weighting. Here, periventricular edema is more evident on T2-FLAIR in this dog with necrotizing encephalitis.

magnetic-field inhomogeneities and therefore result in more uniform fat suppression.[10,11]

Inversion recovery can also be used to null the signal of fluids, such as cerebrospinal fluid (CSF). Such a fluid-attenuated inversion recovery (FLAIR) sequence helps differentiate brain parenchymal lesions from CSF (Fig. 4-32; see Fig. 4-30).[16] For example, a region of increased signal adjacent to a lateral ventricle may not be seen in the T2-weighted spin-echo sequence because of the similar signal characteristics of fluid and tissue water. However, in the FLAIR image, the periventricular lesion may be much more conspicuous because the signal from the free fluid in the ventricle has been nulled (see Fig. 4-32). The FLAIR sequence also aids in confirming a cystic component and the nature of the fluid present. FLAIR sequences are typically used for the brain and can be T2-weighted or T1-weighted.[17]

Gradient Recalled Sequences

As opposed to spin echo sequences, gradient echo sequences use smaller flip angles* (i.e., less than 90 degrees) to start and lack 180-degree refocusing RF pulses. Instead, gradients are used to diphase (negative gradient) and rephase (positive gradient) transverse magnetization to generate echoes from tissues. Gradient echo sequences use shorter TR along with smaller flip angles (i.e., shorter RF pulses), allowing rapid studies with reduced motion artifact to be performed, which can be convenient for procedures such as angiography. Gradient echo sequences are also used typically for initial anatomic orientation at the beginning of an examination, so called localizer images.

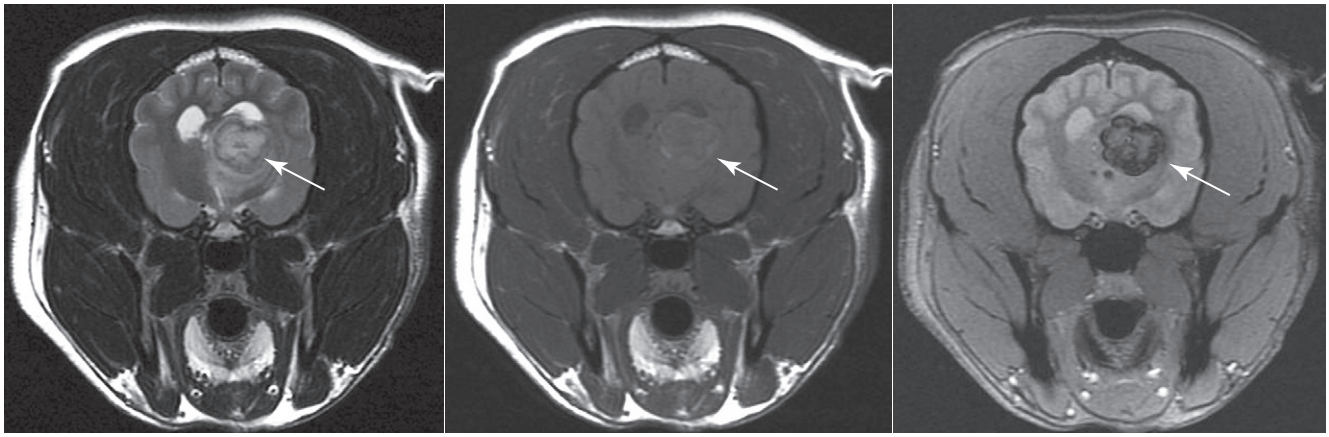
Although changing the orientation of the gradient allows spinning protons to rephase, field inhomogeneities are not compensated for. Thus, gradient sequences with long TEs are T2*-weighted rather than T2-weighted like spin-echo sequences. This also implies that gradient echo sequences are more sensitive to magnetic-field inhomogeneity secondary to magnetic susceptibility differences between tissues. Magnetic susceptibility is the property that describes the degree to which these tissues are magnetized when exposed to a magnetic field.[18] Substances can increase (paramagnetic, ferromagnetic) or decrease (diamagnetic) local magnetic field strength and thus exert an effect on nearby spinning protons. Tissues protons affected by local field inhomogeneity diphase more rapidly, causing signal loss and/or signal misregistration. This phenomenon is even more evident when using a high-field magnet and long TE (e.g., T2*-weighted gradient echo sequence). This concept is exploited for the detection of hemorrhage. Indeed, the iron contained in the hemoglobin increases the local magnetic field substantially, leading to local signal loss and misregistration.[13] T2*-weighted sequences are thus sensitive for detecting hemorrhage (Fig. 4-33).

Several other gradient echo sequences exist, some with more specific application. For example, a spoiled gradient recalled (SPGR) echo sequence highlights articular cartilage (Fig. 4-34),[19] whereas steady state free precession techniques can help depict cranial nerves.[20] It must be pointed out that gradient sequences have specific names that vary among MR imaging system vendors, which can lead to some confusion.[13,21]

Contrast Media

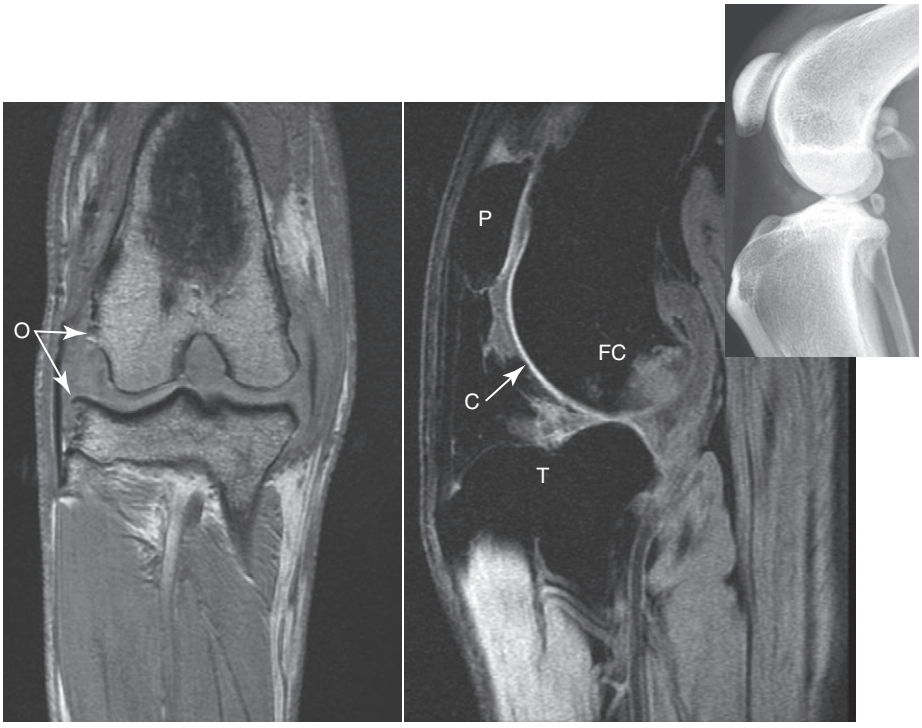
As with CT, contrast media can be injected intravenously for MR imaging to assess the vascular network and tissue perfusion, helping to better detect and characterize pathologic tissues. As opposed to iodinated contrast medium used in CT that is hyperattenuating, leading to an increase in tissue HU in proportion to its concentration, contrast media commonly used in MR imaging exert a paramagnetic effect. This effect is strong and decreases the T2 and T1 relaxation times of protons in vicinity of the contrast medium molecule. At low concentration, such as used in clinical practice, the predominant effect is T1 shortening.[10] Thus, tissues accumulating this substance generate greater signal—*contrast-enhance*—on a T1-weighted pulse sequence (Fig. 4-35; see Fig. 4-30). Gadolinium-based agents chelated to protective ligands are typically used.

*Remember, the flip angle quantifies the amount of deviation of the resting net magnetic vector from the *z*-axis by the first RF pulse.



T2w-FSE T1w-FSE T2*-GRE

Fig. 4-33 T2* gradient echo (GRE) sequences are sensitive to magnetic susceptibility. In this dog with spontaneous brain hemorrhage, the mass lesion (*arrow*) with annular signal void on T2*-GRE in the thalamus corresponds with a susceptibility artifact. The peripheral portion of this lesion appears hyperintense on precontrast T1-weighted fast-spin echo (T1w-FSE) and hypointense on T2-weighted FSE, further confirming the presence of subacute hemorrhage.



Dorsal T1w-GRE Sagittal SPGR +FS

Fig. 4-34 Although spin echo sequences are predominantly used in MR imaging, gradient echo (GRE) sequences are also useful. Osteophytes *(O)* are well demarcated in this dorsal T1-weighted GRE image. In the sagittal spoiled gradient recalled (SPGR) echo sequence acquired with fat saturation (FS), the articular cartilage *(C)* is well depicted. Joint effusion is also present cranial to the cartilage in this dog with ruptured cranial cruciate ligament and osteoarthritis. *FC,* Femoral condyle; *P,* patella; *T,* tibia.

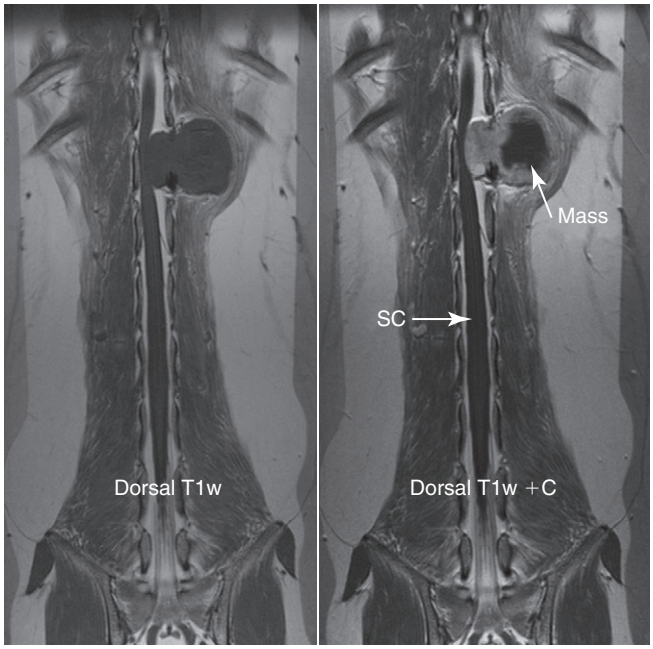


Fig. 4-35 As for CT imaging, the addition of contrast medium in MR imaging (e.g., gadolinium) increases the contrast resolution of this modality. In this ataxic dog, a large mass is seen in dorsal T1-weighted *(T1w)* images to the left of the spine, markedly compressing the spinal cord *(SC)*. The periphery of this mass enhances intensity after gadolinium injection *(+C)*, as opposed to its central part. An undifferentiated sarcoma with a large cavitary component was diagnosed.

Other Magnetic Resonance Sequences

The high signal intensity of adipose tissue on several sequences can limit the visibility of nearby tissues or substances with prolonged T2 relaxation (on T2-weighted sequences) or short T1 relaxation (on T1-weighted sequences). As seen previously, an inversion recovery sequence (i.e., STIR) can be used to attenuate fat signal intensity. Alternatively, fat can be selectively attenuated by exploiting the difference of precessional frequency (i.e., 220 Hz at 1.5 T) that exists between fat and water protons (in or outside tissues). *Chemical fat saturation* uses a frequency-specific preparation pulse to excite lipid protons selectively, followed by a spoiling gradient pulse that dephases the fat signal. Once the initial fat-specific pulse is produced, the signal generated by the subsequent pulse sequence (spin echo or gradient echo) arises only from non-fatty tissues. If a T2-weighted sequence is employed, tissues with prolonged T2—typically pathologic tissues—become more conspicuous (Fig. 4-36). In combination with gadolinium injection, fat-suppressed T1-weighted sequences maximize the visibility of contrast-enhancing lesions. This can be beneficial for detecting lesions embedded in fat, such as within the epidural or retro-orbital spaces, and in bone marrow, for example.[22] Spinal lesions and abnormal nerves are better recognized (Fig. 4-37).

Diffusion-weighted imaging is very sensitive to cytotoxic edema in the early hours of ischemia. Tissue contrast on diffusion-weighted imaging reflects Brownian motion or microscopic movement of water, which is restricted in ischemic tissue.[23] Such technique helps in discriminating early stroke events from structural lesions, such as neoplasia, which can be difficult to differentiate on conventional sequences (Fig. 4-38). *Perfusion-weighted* imaging is another technique that can support a diagnosis of brain infarct.[23] It uses a

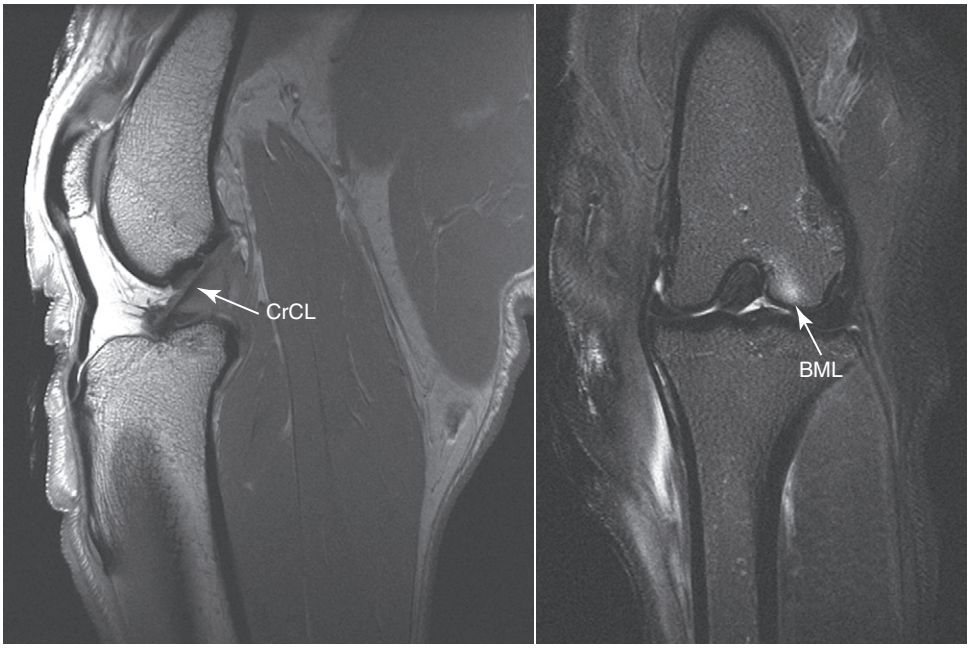


Fig. 4-36 Similar to short TI inversion recovery (STIR) sequences, chemical fat saturation (FS) used with T2-weighting *(T2w)* increases the conspicuity of lesions with prolonged T2 relaxation. A hyperintense bone marrow lesion *(BML)* is identified in the lateral femoral condyle of this dog with intact cranial cruciate ligament *(CrCL)*. *PD,* Proton density.

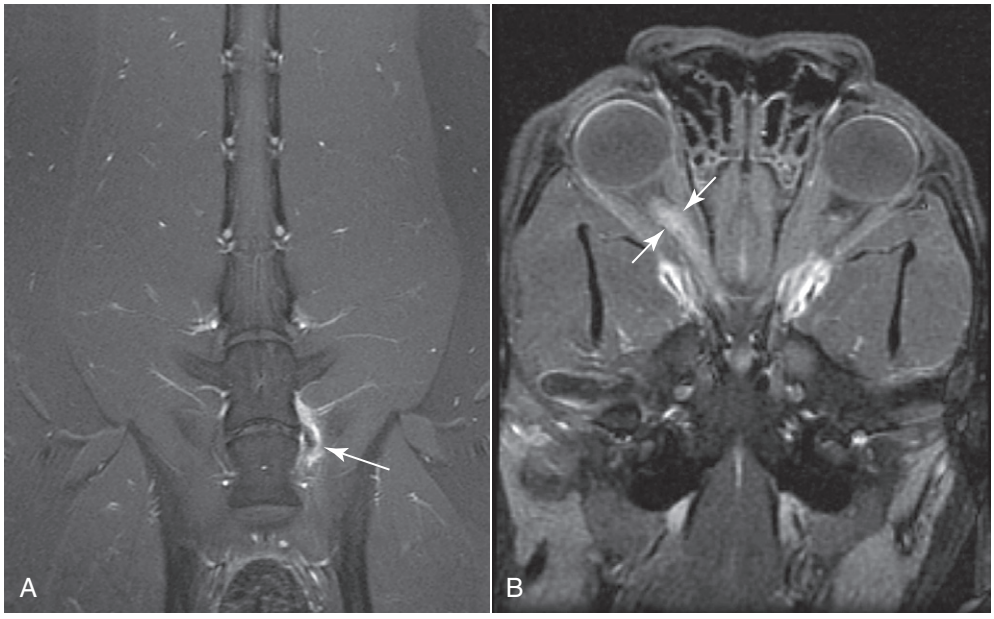


Fig. 4-37 Contrast enhancement is more conspicuous when surrounding fat tissue signal is suppressed in T1-weighted images. **A,** Dorsal image of the lumbar spine of a dog with left pelvic lameness on which a contrast-enhancing tissue reaction is seen around a hypointense lateralized disc extrusion (*arrow*). **B,** Dorsal image of the head of another dog with optic neuritis (*between arrows*).

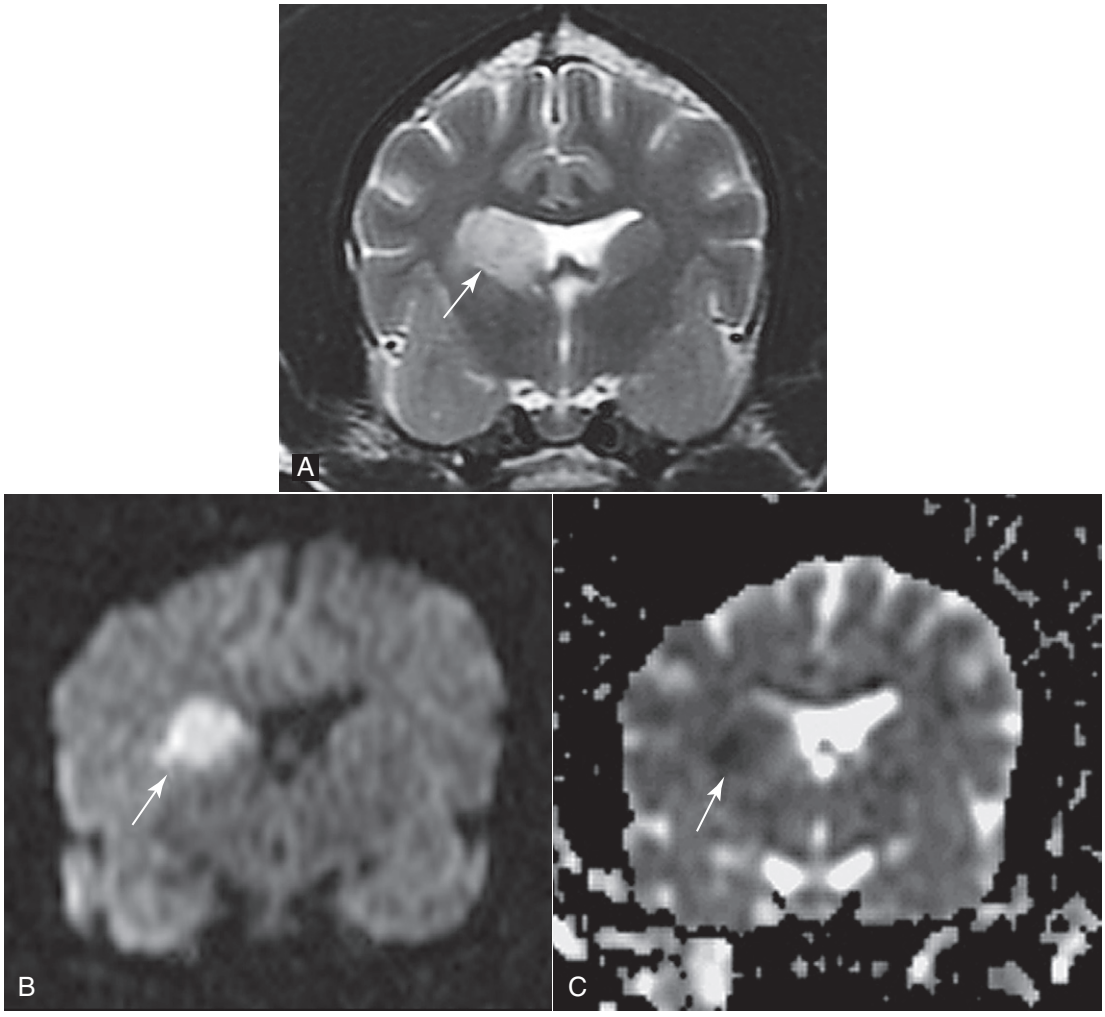


Fig. 4-38 Diffusion-weighted imaging (DWI) is used increasingly to confirm the presence of early ischemic stroke in animals. The right caudate nucleus is enlarged and hyperintense in transverse T2-weighted fast-spin echo **(A)** and in a diffusion-weighted image **(B).** Apparent diffusion coefficient (ADC) mapping reveals a hypointense focus in the same area, indicating restricted water diffusion.

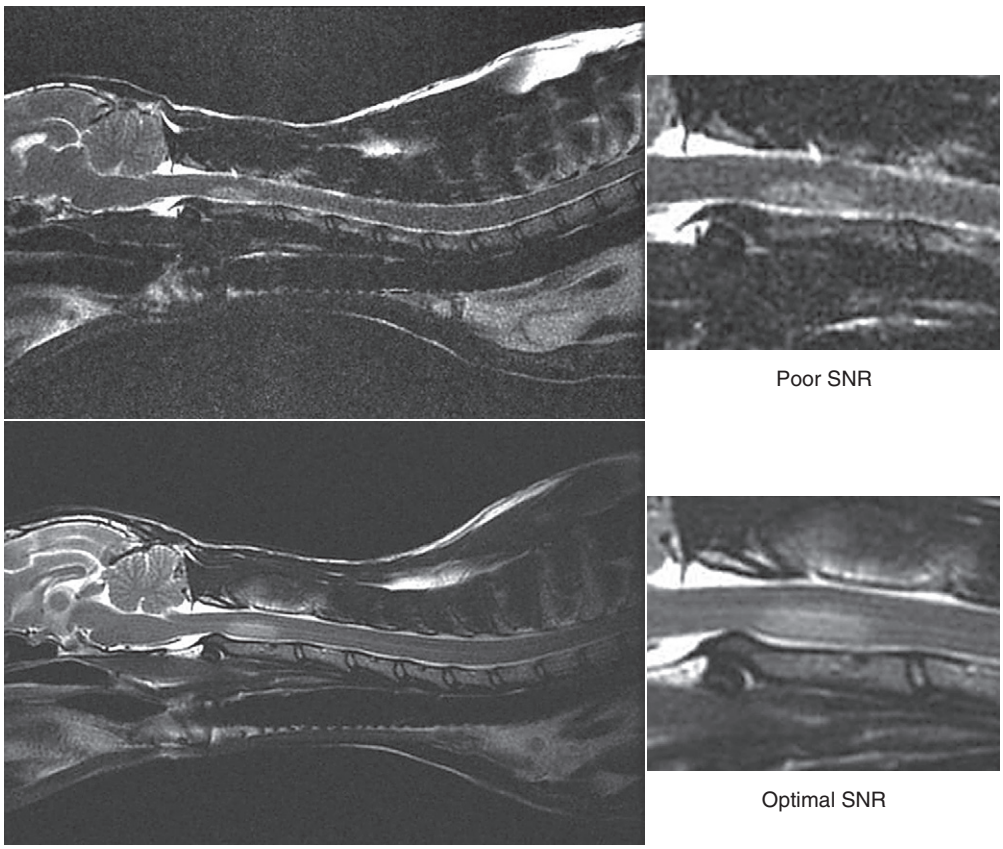


Fig. 4-39 Several factors can influence signal-to-noise (SNR) ratio in MR imaging. In this dog, optimal SNR of the cervical spine was obtained after replacing the receiving coil with a more sensitive one (*bottom* images). The initial image with poor SNR is grainier. The ventral spinal cord hyperintensity is better delineated in the bottom image.

particular T2*-weighted pulse sequence following a bolus injection of contrast medium such as gadolinium. Images are obtained during the first pass of contrast medium through the capillary beds, which results in susceptibility-induced signal loss that resolves over time. Relative blood flow can then be semiquantified.

Vascular networks can also be assessed with MR imaging using different techniques, with or without contrast medium. *Contrast-enhanced MR angiography* is used increasingly to detect shunts and other portal vascular anomalies.[24,25] Time-of-flight and phase-contrast MR angiography represent other techniques that can be used without contrast medium.

Image Quality and Imaging Time

The challenge of imaging animals under anesthesia is to balance image quality and acquisition time. That is, to achieve the most diagnostic examination as quickly as possible. Several parameters are interconnected, making this balance very complex.[26] As discussed earlier, *spatial resolution* dictates the amount of image detail, which influences the ability to clearly see and distinguish anatomic and pathologic structures. Spatial resolution is set by adjusting slice thickness (voxel depth), field of view (FOV), and matrix size (number of voxels). The height and width of each voxel is determined by the number of rows and columns in the matrix, respectively, divided by the image FOV. The smaller the voxels, the better the spatial resolution. Conversely, image quality also greatly depends on the amount of signal arising from protons forming each voxel, often described as the signal-to-noise ratio (SNR) of an image. High spatial resolution images, those with small voxels, are then subject to poor SNR. Although it can be tempting to reduce slice thickness or increase matrix size to improve tissue definition, image quality can suffer greatly. SNR can be improved by averaging signal from sequential excitations, which unfortunately increases acquisition time. Technical improvements in software and hardware (high-field magnets, stronger gradients, more sensitive receiving coils, etc.) have allowed an increase in SNR and spatial resolution at the same time, which is beneficial in small patients (Fig. 4-39).[17]

Artifacts

As with any modality, artifacts can degrade image quality or lead to misdiagnosis. Acknowledgment and comprehension of these artifacts are essential for interpreters.

Besides those that can be controlled to a certain degree (e.g., ghosting and aliasing artifacts),[27] artifacts are often related to magnetic susceptibility and are predominant with gradient echo sequences, as discussed previously. Magnetic susceptibility artifacts occur because of local magnetic field inhomogeneity. Structures that substantially affect this homogeneity, such as metallic objects, whether ferrous or not, have strong magnetic susceptibility effects that lead to field distortion.[28] These artifacts appear as geometric image distortion with progressive or abrupt signal void and sharply defined hyperintense boundaries (Fig. 4-40). In veterinary practice, microchips (Fig. 4-41) and orthopedic devices are most often the source of these artifacts, hampering assessment of nearby structures. It may also occur when microscopic metal fragments are left in place when some devices are used during surgery (e.g., drill bits).[18] Other ballistic or gastrointestinal foreign bodies may cause magnetic susceptibility artifacts that can limit the use of MR imaging in these patients significantly,



Fig. 4-40 Susceptibility artifact in gradient recalled echo (GRE) sequences. In this equine foot imaged with T1-weighted GRE sequences in the sagittal **(A)** and transverse **(B)** planes, there is a sharply demarcated round signal void (*white arrow*), which was presumably the result of a microscopic metallic fragment left in place after a street nail was removed. Note also the damage to the medial lobe of the deep digital flexor tendon (*black arrow*).

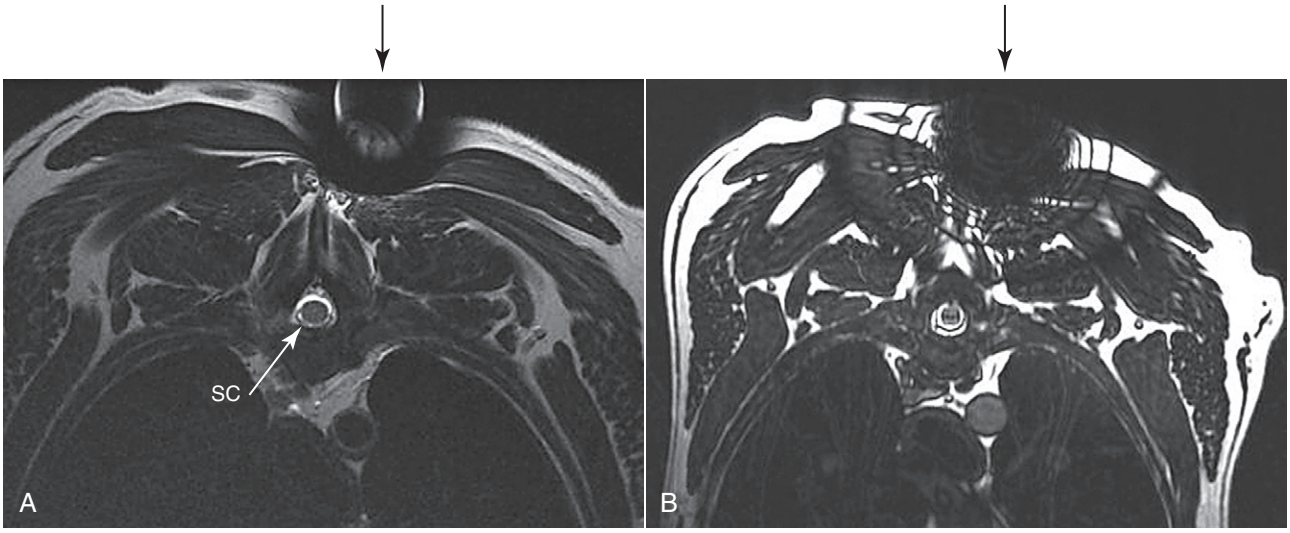


Fig. 4-41 Identification microchips, which are typically placed in the dorsal subcutaneous fat of the neck in dogs, cause magnetic field distortion and signal voids. The appearance of the susceptibility artifact (*arrow*) varies between sequences. Rings of varying intensity are present in the transverse fast-spin echo T2-weighted image **(A),** whereas several concentric hypointense rings are present in the FIESTA (fast imaging employing steady state acquisition) sequence **(B).** Depending on the magnitude of the artifacts and the size of the neck, the interpretation of a spinal cord *(SC)* abnormality may be hampered.

particularly if these objects are ferromagnetic and can therefore migrate as a result of magnetic attraction. Magnetic susceptibility can also occur at soft tissue/air interfaces. This is typically observed on T2* transverse images obtained at the junction of the frontal sinuses and rostral brain.[27]

Impact of Magnetic Field Strength

Although high-field (>1.0 T) MR systems are associated with superior SNR, low-field (0.2–0.4 T) units are installed increasingly in veterinary practices, mainly because of lower purchase and maintenance costs.[21] Units can be dedicated veterinary units or produced originally for human use. The limited SNR with these low-field systems is associated with longer scan times and reduced spatial resolution. Also, FOV is generally reduced, which may necessitate moving the patient in the magnet for complete anatomic coverage. Low-field MR imaging is, however, associated with reduced susceptibility artifact, and its open design allows easy access to patients. Also, because of the lower magnetic field strength, accidents associated with the attraction or migration of ferromagnetic objects, located outside or inside the patient, can be prevented more easily. Moreover, hyperthermia, which can become a

significant issue in smaller patients in high fields, is less probable at lower field strength. Extremities of horses can also be imaged while the animal is standing using dedicated MR units, which is beneficial.

REFERENCES

1. Bushberg J, Seibert J, Leidholdt E Jr, et al: Computed tomography. In Bushberg J, Seibert J, Leidholdt E Jr, Boone J, editors: *The essential physics of medical imaging*, ed 2, Philadelphia, 2002, Lippincott Williams & Wilkins, p 327.
2. Mahesh M: Search for isotropic resolution in CT from conventional through multiple-row detector, *Radiographics* 22:949–962, 2002.
3. Bushberg J, Seibert J, Leidholdt E Jr, et al: Introduction to medical imaging. In Bushberg J, Seibert J, Leidholdt E Jr, Boone J, editors: *The essential physics of medical imaging*, ed 2, Philadelphia, 2002, Lippincott Williams & Wilkins, pp 3–13.
4. Saunders J, Ohlerth S: CT physics and instrumentation. In Schwarz T, Saunders J, editors: *Veterinary computed tomography*, ed 1, Oxford, 2011, Wiley-Blackwell.
5. Tidwell A: Principes of computed tomography and magnetic resonance imaging. In Thrall D, editor: *Textbook of veterinary diagnostic radiology*, ed 4, Philadelphia, 2002, Elsevier Saunders, pp 50–77.
6. Pollard R, Puchalski S: CT contrast media and applications. In Schwarz T, Saunders J, editors: *Veterinary computed tomography*, ed 1, Oxford, 2011, Wiley-Blackwell.
7. Miles KA: Tumour angiogenesis and its relation to contrast enhancement on computed tomography: a review, *Eur J Radiol* 30:198–205, 1999.
8. Alexander K, Dunn M, Carmel EN, et al: Clinical application of Patlak plot CT-GFR in animals with upper urinary tract disease, *Vet Radiol Ultrasound* 51:421–427, 2010.
9. Samii VF, McLoughlin MA, Mattoon JS, et al: Digital fluoroscopic excretory urography, digital fluoroscopic urethrography, helical computed tomography, and cystoscopy in 24 dogs with suspected ureteral ectopia, *J Vet Intern Med* 18:271–281, 2004.
10. McRobbie DW, Moore EA, Graves MJ, et al: *MRI from pictures to protons*, ed 1, Cambridge, 2003, Cambridge University Press.
11. Mitchell DG, Cohen MS: *MRI Principles*, ed 2, Philadelphia, 2004, Saunders.
12. Pooley RA: AAPM/RSNA physics tutorial for residents: fundamental physics of MR imaging, *Radiographics* 25:1087–1099, 2005.
13. Bitar R, Leung G, Perng R, et al: MR pulse sequences: what every radiologist wants to know but is afraid to ask, *Radiographics* 26:513–537, 2006.
14. Plewes DB: The AAPM/RSNA physics tutorial for residents. Contrast mechanisms in spin-echo MR imaging, *Radiographics* 14:1389–1404, 1994.
15. Balter S: An introduction to the physics of magnetic resonance imaging, *Radiographics* 7:371–383, 1987.
16. Benigni L, Lamb CR: Comparison of fluid-attenuated inversion recovery and T2-weighted magnetic resonance images in dogs and cats with suspected brain disease, *Vet Radiol Ultrasound* 46:287–292, 2005.
17. Roberston ID: Optimal magnetic resonance imaging of the brain, *Vet Radiol Ultrasound* 52:S15–S22, 2011.
18. Freer SR, Scrivani PV: Postoperative susceptibility artifact during magnetic resonance imaging of the vertebral column in two dogs and a cat, *Vet Radiol Ultrasound* 49:30–34, 2008.
19. Olive J, d'Anjou MA, Girard C, et al: Fat-suppressed spoiled gradient-recalled imaging of equine metacarpophalangeal articular cartilage, *Vet Radiol Ultrasound* 51:107–115, 2010.
20. Parry AT, Volk HA: Imaging the cranial nerves, *Vet Radiol Ultrasound* 52:S32–S41, 2011.
21. Konar M, Lang J: Pros and cons of low-field magnetic resonance imaging in veterinary medicine, *Vet Radiol Ultrasound* 52:S5-S14, 2011.
22. d'Anjou MA, Carmel EN, Tidwell AS: Value of fat suppression in gadolinium-enhanced magnetic resonance neuroimaging, *Vet Radiol Ultrasound* 52:S85–S90, 2011.
23. Tidwell AS, Roberston ID: Magnetic resonance imaging of normal and abnormal brain perfusion, *Vet Radiol Ultrasound* 52:S62–S71, 2011.
24. Bruehschwein A, Foltin I, Flatz K, et al: Contrast-enhanced magnetic resonance angiography for diagnosis of portosystemic shunts in 10 dogs, *Vet Radiol Ultrasound* 51:116–121, 2010.
25. Mai W, Weisse C: Contrast-enhanced portal magnetic resonance angiography in dogs with suspected congenital portal vascular anomalies, *Vet Radiol Ultrasound* 52(3): 284–288, 2011. Epub December 13, 2010.
26. Gavin P, Bagley RS: *Practical small animal MRI*, ed 1, Ames, IA, 2009, Wiley-Blackwell.
27. Cooper JJ, Young BD, Hoffman A, et al: Intracranial magnetic resonance imaging artifacts and pseudolesions in dogs and cats, *Vet Radiol Ultrasound* 51:587–595, 2010.
28. Hecht S, Adams WH, Narak JN, et al: Magnetic resonance imaging susceptibility artifacts due to metallic foreign bodies, *Vet Radiol Ultrasound* 52(4):409–414. Epub March 7, 2011.

ELECTRONIC RESOURCES

evolve

Additional information related to the content in Chapter 4 can be found on the companion Evolve website at http://evolve.elsevier.com/Thrall/vetrad/.

- Videos
- Chapter Quiz

CHAPTER • 5

Introduction to Radiographic Interpretation

Donald E. Thrall

IMAGE FORMATION AND DIFFERENTIAL ABSORPTION

Radiographic imaging is possible because (1) x-rays penetrate matter, (2) x-ray absorption is a function of tissue type and thickness, and (3) an image of the pattern of x-ray emergence from a patient can be created. Therefore a radiograph is the image of the number and distribution of x-rays that pass through the patient. This principle applies to both analog (film-screen) and digital radiographic systems. Sometimes the term *x-ray* is used as a substitute term for radiograph, but this is incorrect; the term x-ray describes the type of energy used to create the image, not the image itself.

In analog radiography, image blackness depends on the amount of light emitted by the intensifying screen; this was discussed in Chapter 1. This light, which is related to the number of oncoming x-rays, is the major cause of film blackening. In digital radiography, image blackness is also dependent on the number of oncoming x-rays, but in digital radiography the x-rays interact with the imaging plate to produce the image. Digital imaging plates were described in Chapter 2. In digital radiography, computer manipulation of the image after it is produced is also a big factor that controls the amount of image blackness. The analog cassette that contains the film and intensifying screen and the digital imaging plate can each be referred to as a *receiver*.

Regardless of the type of imaging system, the following generalizations apply. First, areas of the image that are black represent regions where many x-rays passed through the patient and struck the receiver. Second, areas of the image that are white represent regions where many x-rays were absorbed in the patient, and few or none struck the receiver. Between these two extremes of black and white are many gray image tones, the opacity of which is directly related to the number of x-rays that penetrate the patient and reach the receiver (Fig. 5-1).

Of particular importance is the fact that x-rays are absorbed heterogeneously by the body, depending on the makeup of the tissue. This differential absorption is caused by the dependence of absorption on the effective atomic number and physical density of the body part, as also discussed in Chapter 1. If x-ray absorption was uniform, the resulting radiographic image would be homogeneously gray or white. If no absorption occurred, the resulting radiographic image would be homogeneously black. The effect of differential absorption is apparent in Figure 5-1, in which areas peripheral to the dog are black because no x-rays were absorbed before reaching the receiver. Soft tissues of the dog are visible because they have absorbed some x-rays from the primary beam. Bones of the dog are more radiopaque than soft tissues; the bones have absorbed more x-rays, and thus the part of the receiver under the bones was struck by fewer x-rays than areas adjacent to the bones. The nail and microchip are nearly totally radiopaque because essentially no x-rays were able to pass through them.

The term *density* is used occasionally to describe the degree to which a patient or object absorbs incident x-rays. For example, in Figure 5-1, the nail and microchip could be described as being denser than adjacent soft tissue. Use of density in this context is confusing because the optical density* of the nail and microchip is low, whereas the radiographic density is high. Further confusion arises when the added variable of physical density (grams per cubic centimeter) of the patient or object is considered. As physical density increases, optical density decreases, and radiographic density increases. This confusing terminology can be eliminated completely by avoiding use of the term *density* to describe radiographic changes. The degree of blackness or whiteness of the patient should be referred to in terms of radiolucency or radiopacity (Fig. 5-2). For example, in Figure 5-1, soft tissues of the abdomen are less radiopaque than the bones; both are more radiolucent than the nail and microchip. It may also be said that the nail and microchip are more radiopaque than the remainder of the dog.

RADIOGRAPHIC OPACITIES

The ability of a radiograph, whether analog or digital, to display subtle differences in x-ray absorption is limited. This concept, termed *contrast resolution*, is what allows adjacent structures to be discriminated from each other in the radiographic image. Unfortunately, the relatively poor contrast resolution of radiographs, compared to computed tomography or magnetic resonance imaging, means that many pathologic alterations will not be visible radiographically. The relatively poor contrast resolution of radiographs also means that the range of opacities visible radiographically can be described, in general terms, according to one of five radiographic terms—*air* (or *gas*) *opacity*, *fat opacity*, *water* (or *soft tissue*) *opacity*, *bone* (or *mineral*) *opacity*, and *metal opacity*. These five radiographic opacities are convenient because they are visually distinct and are created by tissues found commonly in patients being radiographed. Figure 5-3 is the lateral view of the dog in

*Optical *density* is a holdover term from the days when all radiographic images were film-based. It refers to the inherent blackness of the film, quantified by measuring light transmission through the film. Although optical density is not directly applicable to digital images, the concept is still valid for the context in which the term is used here.

Figure 5-1; all five radiographic opacities are present (consult the figure legend). It is important to realize that a radiographic opacity is not specific for the tissue type of origin, but only to groups of substances that have similar attenuation properties (Table 5-1).

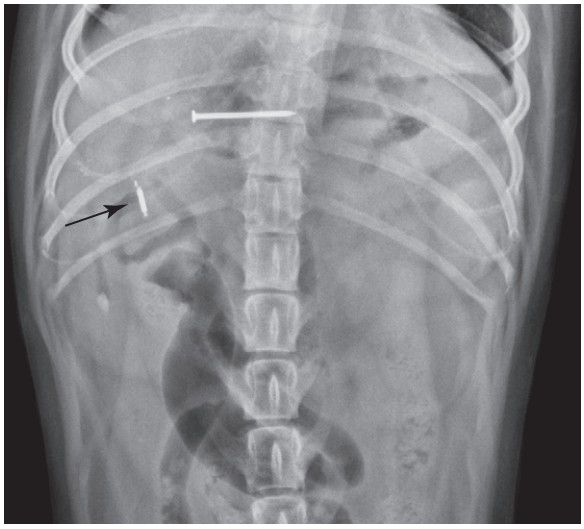


Fig. 5-1 Ventrodorsal radiograph of the cranial aspect of the abdomen of a dog that ingested a nail. The metal nail has absorbed essentially all x-rays striking it, leaving none to strike the receiver. This lack of exposure will appear white (radiopaque) in the radiograph. This dog also has an identification microchip *(black arrow)* in the dorsal subcutaneous tissue that becomes superimposed on the abdomen in this ventrodorsal image. As with the nail, the metallic components of the microchip absorb all x-rays striking it, creating an intense focal radiopacity. The bones are less efficient than metal in absorbing x-rays and thus they create an opacity that is not as intense, or as white, as the metallic objects because some x-rays striking bone penetrate them and reach the receiver. The black radiolucent area peripheral to the abdomen is where no x-rays were absorbed, and all oncoming x-rays struck the receiver. The gas-containing bowel is also relatively radiolucent because of poor x-ray absorption. Between the radiopaque bones and metal and radiolucent bowel gas are many shades of gray that result from intermediate levels of x-ray absorption in soft tissues.

Thickness must also be considered in any discussion of relative inherent radiopacities because as thickness increases, radiopacity increases (Fig. 5-4). Thus the five basic inherent radiopacities (air, fat, soft tissue, bone, and metal) are relative, assuming that the object's thickness is approximately the same. For example, although fat is inherently more radiolucent than bone, if a large thickness of fat is radiographed next to a small thickness of bone, the fat could appear to be more radiopaque (i.e., its total radiopacity would be greater) (Fig. 5-5). An extreme thickness difference that results in a reversal of inherent radiographic opacity is encountered rarely in real life and is used here only to emphasize the importance of thickness in the makeup of the visible radiographic opacity of an object or body part, along with physical density and atomic number.

RADIOGRAPHIC GEOMETRY AND THINKING IN THREE DIMENSIONS

A major limitation of radiographic imaging is that the images are two-dimensional although the patient is three-dimensional. This means that the radiographic appearance of structures and/or lesions will depend on their orientation with respect to the primary x-ray beam and receiver. Consequences of radiographs being two-dimensional are (1) magnification and distortion, (2) image of a familiar part appearing unfamiliar, (3) loss of depth perception, and (4) superimposition.

Magnification and Distortion

Magnification refers to the enlargement of a structure in the image relative to its actual size. Magnification depends mainly on the distance between the object and the receiver; as this distance increases, magnification increases. There will always be some parts of the patient that are farther from the receiver than others, thus some parts of every patient are magnified in the resultant radiograph. Magnification reduces detail because each bit of visual information is spread over a larger area of the image (Fig. 5-6). Based on the decreased detail that characterizes magnified parts, the area of primary interest should always be placed closest to the receiver to minimize the effect of magnification. The only exception to this guideline is in

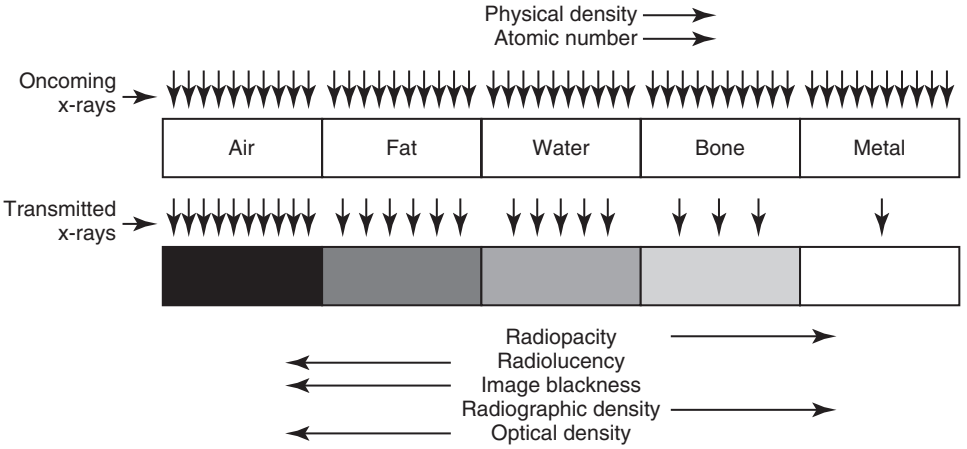


Fig. 5-2 Identical thicknesses of air, fat, water, bone, and metal are struck by an equal number of x-rays. Not all substances absorb x-rays with the same efficiency. In this example, the physical density and effective atomic number of the substances *increase* from left to right. As a result, the number of x-rays penetrating each equal thickness *decreases* from left to right. This *differential absorption* of x-rays as a function of physical density and effective atomic number is what allows x-rays to be useful for producing radiographs. As the number of x-rays passing through the object changes, the blackness of the image also changes; the more x-rays passing through, the blacker the image. The terms used to describe blackness and whiteness in a radiographic image, and their relationship with each other, are listed below the image. The least confusing terminology is to limit the description of a radiographic image to radiopacity and radiolucency and avoid use of density.

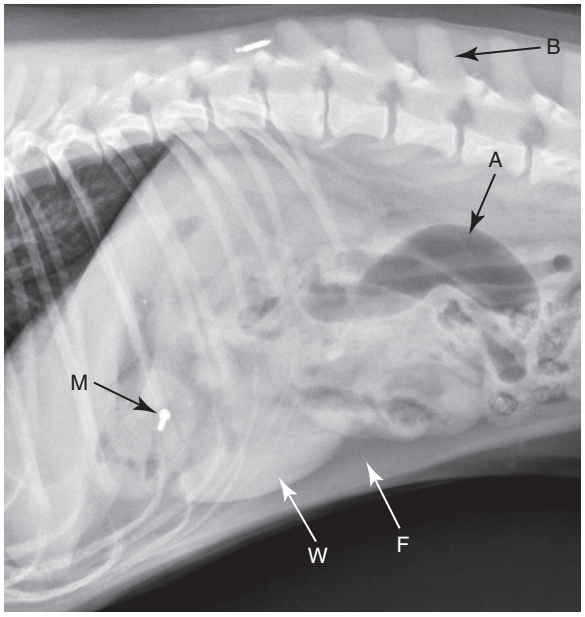


Fig. 5-3 Lateral radiograph of the cranial aspect of the abdomen of the dog in Figure 5-1. The ingested nail in the stomach is an example of metal *(M)* opacity. The microchip dorsal to the thoracolumbar junction is also a metal opacity. Osseous structures are obviously examples of bone *(B)* opacity. Water opacity is equivalent to soft tissue opacity, as all soft tissues are composed mainly of water. In this example, the spleen is labeled as an example of water *(W)* opacity, but the liver and bowel wall are other examples. Fat is slightly more radiolucent than water, and fat intervening between soft tissue organs provides contrast that enables individual soft tissue structures to be discriminated radiographically. In this radiograph, the fat *(F)* opacity that has been identified is omental fat in the ventral aspect of the abdomen. Lastly, air is the most radiolucent of the opacities, and in this radiograph the example that has been identified *(A)* is gas in the bowel.

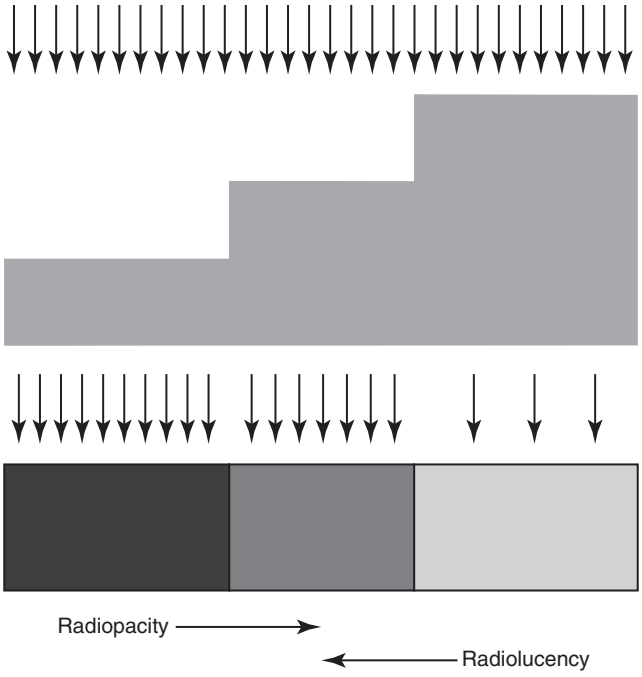


Fig. 5-4 The effect of thickness on radiographic opacity. Increasing the thickness of the object in the path of the x-ray beam will reduce the number of incident x-rays that penetrate the object and reach the receiver. The image will be more radiopaque under thicker parts of the object or patient.

Table • **5-1**

Examples of Various Tissues and Substances According to the Radiographic Opacity Produced

RADIOGRAPHIC OPACITY	SUBSTANCES HAVING THAT OPACITY
Air (gas)	Any gas collection present in the body • Air in lung or bowel • Carbon dioxide used for negative-contrast cystography • Nitrogen in a joint from the vacuum phenomenon • Gas from putrefaction
Fat	Any tissue composed mainly of fat • Omentum • Mediastinal fat • Intrafascial fat • Falciform fat • Retroperitoneal fat • A lipoma
Water (soft tissue)	Any fluid or soft tissue • Parenchymal organs • Fibrous connective tissue • Muscle • Ligaments • Tendons • Cartilage • Blood • Bile • Cerebrospinal fluid • Urine • Transudate • Exudate • Hematoma • A soft tissue tumor
Bone (mineral)	Any mineralized region • Normal skeletal components • Ingested bone (before digestion) • Periosteal reaction • Dystrophic calcification, as from a calcifying hematoma • Metastatic calcification, as from renal failure
Metal	Anything containing metal • Metallic internal fixation devices • Identification microchip • Bullets or bullet fragments • Ingested foreign material • Horseshoe nails

radiography of the small animal thorax in which lesions in the dependent lung are often not visible because the border of the lesion is effaced by the atelectatic dependent lung. In the lung, lesions in the nondependent lung are more conspicuous despite the effect of magnification; this is discussed in Chapter 25.

The confounding effect of magnification is reduced as long as patients are positioned in a standard manner for radiography because any magnification that occurs just becomes part of the normal radiographic appearance. *Distortion*, however, is a more serious problem. Distortion is *unequal magnification*

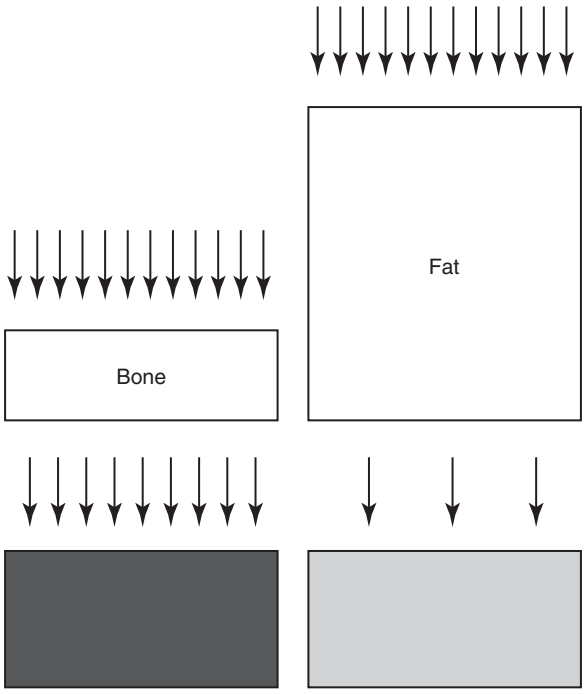


Fig. 5-5 Bone has greater inherent radiopacity than fat (see Figs. 5-2 and 5-3). However, inherent radiopacities are relative, and thickness can cause substances with higher inherent radiopacity to appear less opaque. In this example, the same number of x-rays strike a thin piece of bone and a thick piece of fat. More x-rays are absorbed in the fat because of its greater thickness, and in the resulting radiograph, the fat will appear more opaque than bone even though its inherent radiopacity is less.

that occurs when the object and receiver planes are not parallel. Distortion leads to the image misrepresenting the true shape or position of the object. Just as with magnification, some distortion occurs in every radiograph because there are always some parts of the patient that are not parallel to the plane of the receiver. Distortion caused by deranged anatomy or nonstandard patient positioning, however, can limit the diagnostic quality of the radiograph (Fig. 5-7).

Unfamiliar Image

The appearance of a patient in a radiographic image depends on the orientation of the patient with respect to the primary x-ray beam and receiver. In distortion, a part of the patient is not parallel to the receiver. In the unfamiliar image concept, the entire patient is not oriented in a standard manner with respect to the receiver. As a result, the image will not represent the patient accurately and may not even be recognizable. In other words, the two-dimensional image results in a very poor depiction of the shape of the patient. As with distortion, standardizing patient positioning leads to a familiar image. Repetitive standardization allows one to develop a mental database of how various anatomic regions appear normally and facilitates identification of abnormalities. Should patient positioning deviate from the standard, the unfamiliarity of the image can result in a missed lesion or an incorrect diagnosis (Fig. 5-8).

Loss of Depth Perception

Correct assessment of depth is important in localizing lesions and/or disease spatially within the body. To evaluate depth radiographically, two radiographs of the object are necessary, with one acquired at a 90-degree angle to the other. Depth can then be reconstructed mentally. For example, when looking at Figure 5-1, it is impossible to be sure where the nail and identification microchip are in relation to each other,

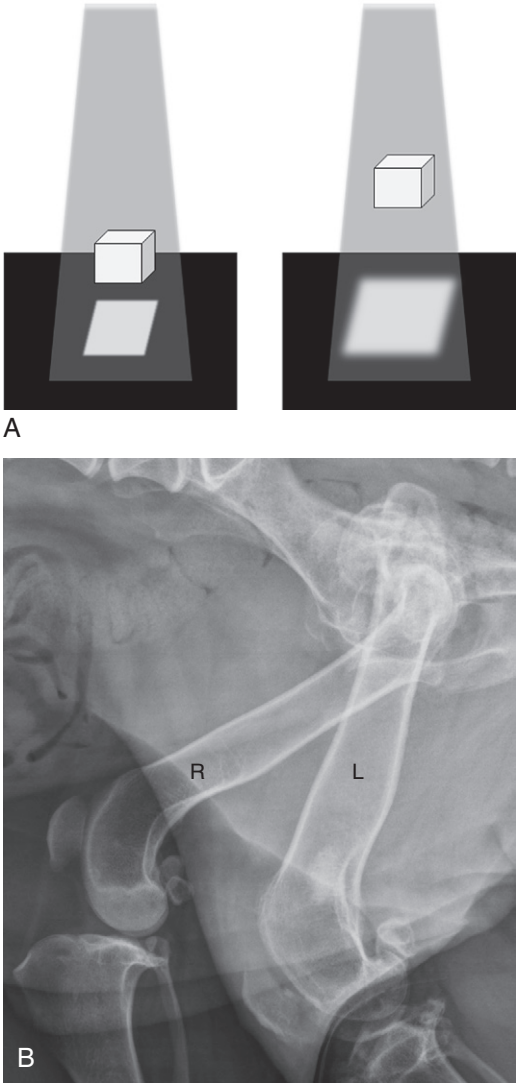


Fig. 5-6 **A,** Geometry of magnification. As the distance between the object and the receiver increases, the image of the object will be larger and less distinct. **B,** Lateral view of the pelvis of a dog in right lateral recumbency. The dependent right pelvic limb *(R)* was pulled cranially, the nondependent left pelvic limb *(L)* caudally. Notice the increased diameter of the nondependent left femur compared with the dependent right femur because of *magnification*—the left femur is farther from the receiver. Margins of the magnified left femur also have poorer detail than those of the right.

or to the dog. One cannot even be sure that these objects are within the dog; they could be lying on the x-ray table between the dog and receiver. Only with the orthogonal radiograph, seen in Figure 5-3, can the correct location of each of these objects be deduced. Also important is the fact that, in some patients, some lesions are apparent in only one radiographic projection and if only one view is made of such patients, the lesion can be missed completely (Fig. 5-9). Thus for each radiographic examination, a minimum of two views should be obtained 90 degrees to each other. Views made 90 degrees to each other are called *orthogonal projections*.

Superimposition

The superimposition of one structure on another can create a very obvious opacity, and some of these superimposition opacities are misinterpreted commonly as disease. Of course, there is extensive superimposition of structures in

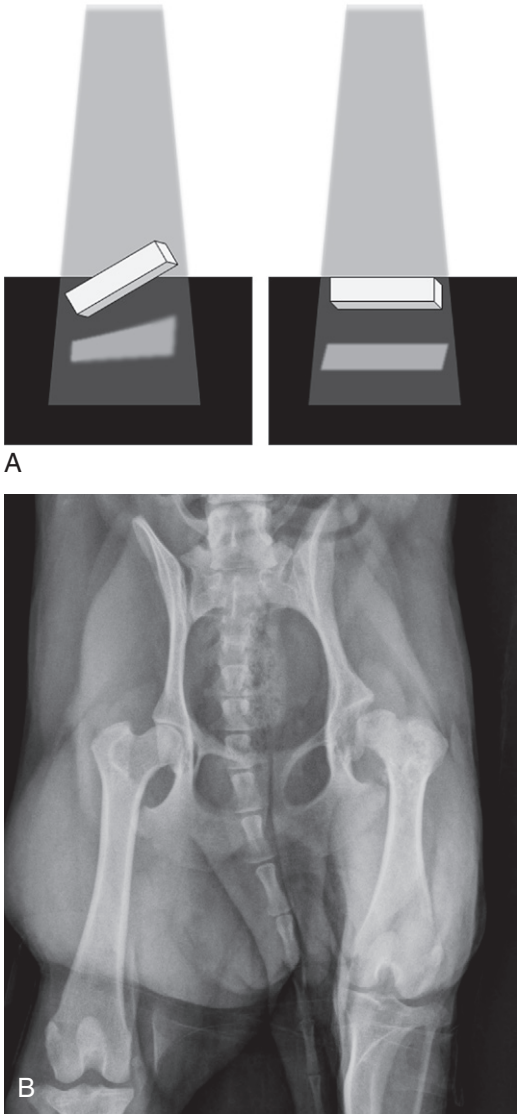


Fig. 5-7 **A,** Geometry of distortion. In the *left panel*, the object is not perpendicular to the x-ray beam. In the image, parts of the object further from the receiver will be magnified to a greater extent and will also be less sharp. The resulting distortion can complicate interpretation because the shape of the image no longer represents the shape of the object. In the *right panel*, the object is perpendicular to the x-ray beam and parallel to the receiver. The image is sharper and represents the shape of the object more accurately. **B,** Ventrodorsal view of the pelvis of a dog with a painful left hip. The right pelvic limb could be extended such that the right femur was parallel to receiver. The left pelvic limb could not be extended because of hip pain, resulting in the left femur being at an angle with respect to the receiver. In the resultant image, the left femur appears shorter than the right and is asymmetrically magnified because of *distortion*.

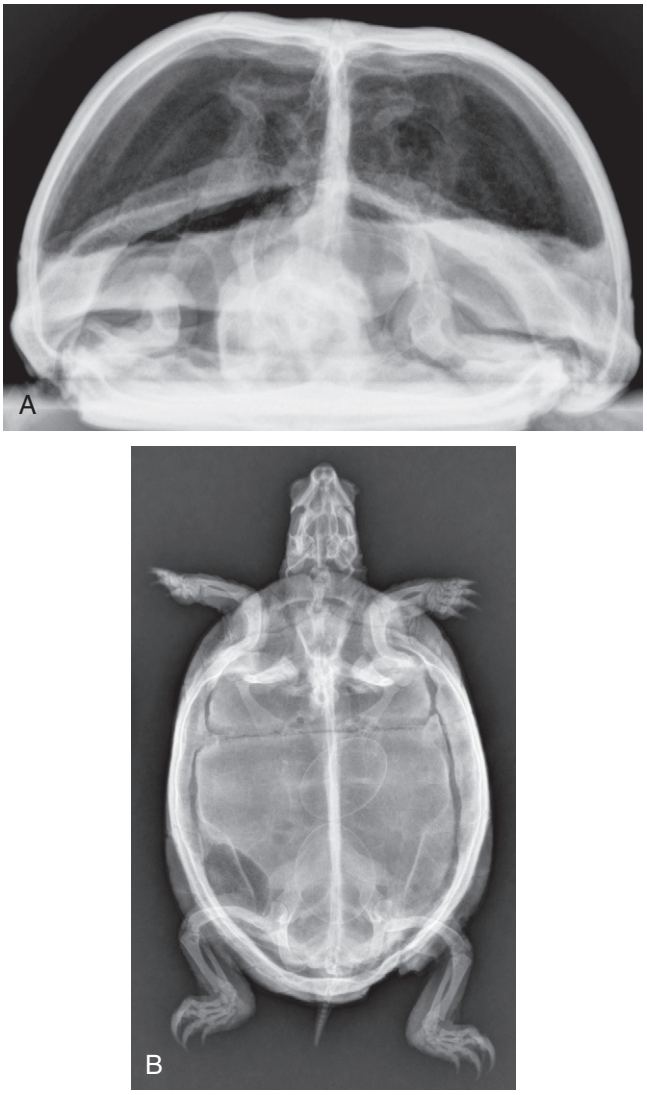


Fig. 5-8 How recognizable an object or a body part is from its radiograph depends on its relation to the x-ray beam and receiver. The object in **A** was oriented in a nonstandard position with respect to the x-ray beam and is less recognizable without the counterpart image in **B,** which was created by placing the object in a standard position. As a result, in **B,** the patient orientation creates a more familiar rendering of the object. Even if the object was identified correctly in **A,** it is unlikely that the gender could be determined as easily as in **B.**

every radiographic image, and superimposition opacities are relatively common. However, as a result of repetitive viewing of radiographs in a standard fashion and using standard patient positioning, most of this superimposition becomes recognized as normal (Figs. 5-10 and 5-11).

Importantly, the intense opacity of many superimposition opacities seems out of proportion to the small absolute size of causative structure, such as with a nipple or the prepuce, as illustrated previously. These small structures cast disproportionately opaque superimposition opacities because they are surrounded by air, and their margins are parallel to the central x-ray beam, thus providing optimal geometry for visualization (Fig. 5-12).

Although many common superimposition opacities are recognized as part of the normal spectrum, there are also many situations where an opacity created by superimposition is not routine, caused by uncommon radiographic positioning (Figs. 5-13 and 5-14) or by the presence of a nonpathologic structure that is usually not present (Fig. 5-15).

The *summation sign* is a special case of superimposition where an opacity is created that does not represent a structure present within the patient. For example, consider a block of Swiss cheese. When looking at this block, the holes on the exterior are caused by the cheese being sliced through gas cavities that formed as the cheese fermented. However, there are more gas cavities inside the block, some of which overlap when viewed from the perspective of the x-ray tube. If the block of Swiss cheese was radiographed, fewer x-rays are absorbed in areas where gas cavities overlap. The more overlapping cavities that are present, the greater the number of x-rays that penetrate the cheese and reach the receiver (Figs. 5-16 and 5-17).

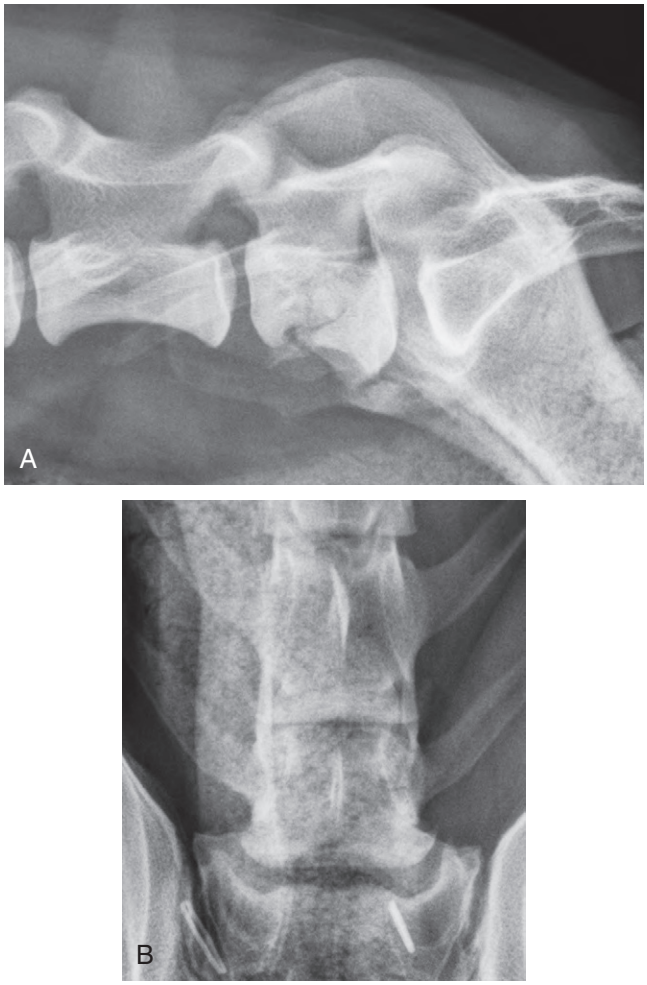


Fig. 5-9 Lateral **(A)** and ventrodorsal **(B)** radiographs of the caudal aspect of a canine lumbar spine. **A,** A comminuted displaced fracture of L7 is visible. **B,** The fracture is not visible because there is no fragment displacement medially or laterally. The difference in the conspicuity of this fracture in these two views illustrates the importance of obtaining at least two orthogonal projections of a body part for every radiographic study. In **B** the linear metallic objects superimposed on the sacrum are surgical clips used to clamp the spermatic cord following orchiectomy.

In the example of Swiss cheese, the resulting summation is radiolucent, or *negative*, because it represents summation of multiple superimposed air spaces. Summation shadows can also be radiopaque, or *positive*. A commonly encountered radiopaque summation shadow is created by the overlapping of the kidneys in a lateral abdominal radiograph, creating a notable opacity at the intersection of the caudal pole of the right kidney with the cranial pole of the left kidney that could be misinterpreted as a mass (Fig. 5-18). Another radiopaque summation shadow encountered commonly results from a pulmonary vessel overlapping with a rib. This nodular summation opacity should not be mistaken for a true pulmonary nodule (Fig. 5-19). Whenever a suspicious radiopacity or radiolucency is identified, the interpretation process must include the consideration that it represents a summation shadow produced by overlapping structures.

Border Effacement (Silhouette Sign)

Border effacement occurs when two structures of the same radiopacity are in contact, leading to the inability to distinguish their margin. Another term for this phenomenon is *silhouette sign*.[1] Conversely, if two structures of the same radiopacity are separated by a substance of a differing

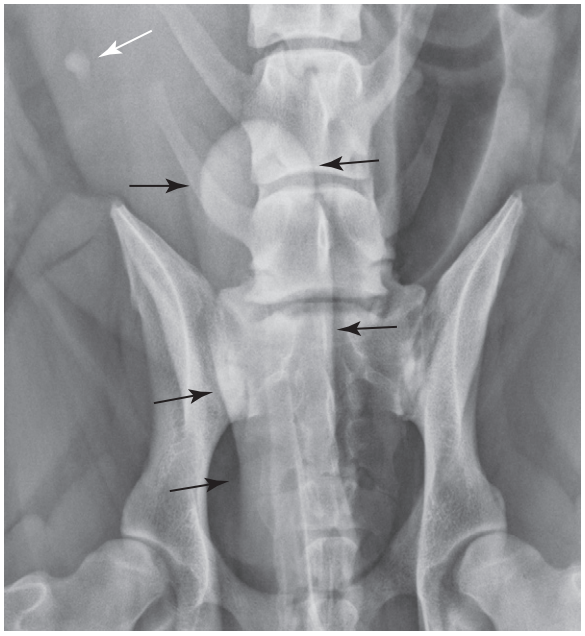


Fig. 5-10 Ventrodorsal radiograph of the pelvic region of a male dog. Superimposition of an abdominal nipple *(white arrow)* and the prepuce *(black arrows)* have created conspicuous superimposition opacities. These structures are seen commonly and have become a recognized variation of normal radiographic anatomy.

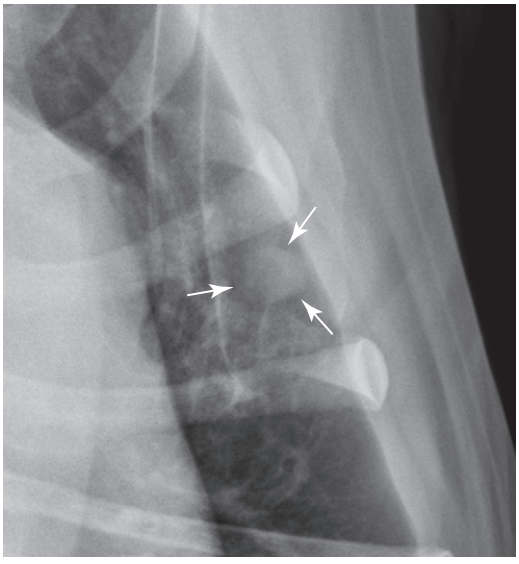


Fig. 5-11 Close-up of a portion of a ventrodorsal thoracic radiograph of a dog. A nipple creates an opacity *(arrows)* that could be confused with a pulmonary nodule. The opacity of the nipple seems out of proportion to its real thickness. This phenomenon results from air providing contrast against a superficial nodule, or structure, which has sides that are relatively perpendicular to the surface of the body

radiopacity, their borders can be distinguished radiographically. For example, consider Figure 5-20, *A*. The drawing represents a thoracic cavity containing the heart, a lung, a coronary artery, and two pulmonary arteries. The coronary artery will not be visible radiographically because it has the same radiographic opacity as the heart, and no intervening tissue of a different radiographic opacity is present; in other words, the border of the coronary vessel is effaced by the myocardium. Both pulmonary arteries will be visible radiographically even though they are of the same radiographic opacity as the heart because they do not touch the heart, and an intervening tissue

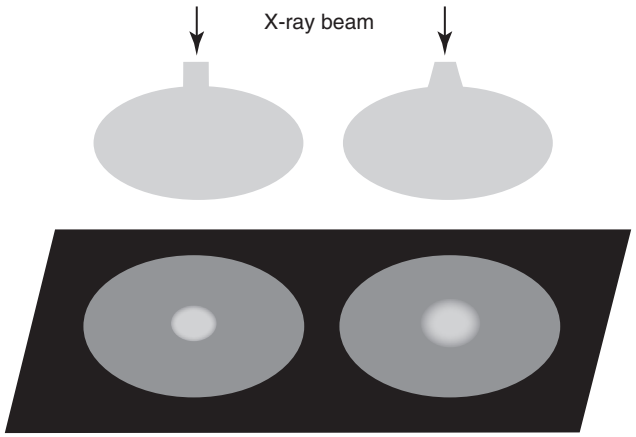


Fig. 5-12 Diagram illustrating why small superficial masses cast conspicuous superimposition opacities. On the *left*, the mass has perpendicular sides and is surrounded on all sides by air. This creates a situation in which the x-ray beam strikes the mass/air interface in a parallel fashion, optimizing contrast. On the *right*, a comparably sized mass has sloping sides that are not in a parallel relation to the primary beam. This mass will be more difficult to identify, even though its inherent opacity may be identical, because the borders are less defined.

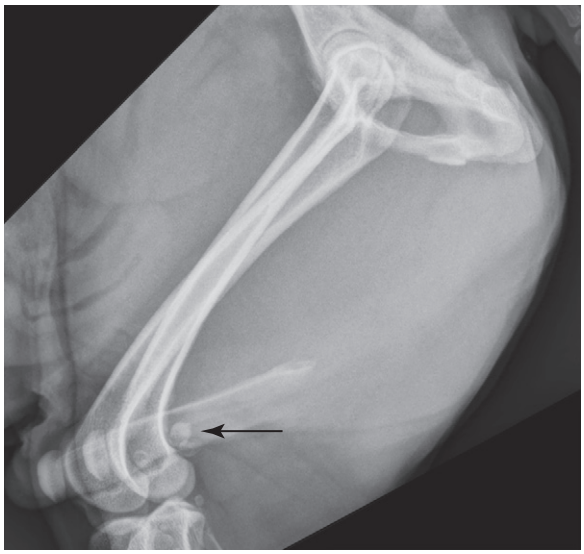


Fig. 5-13 Lateral view of the caudal aspect of the trunk of a dog. The femurs have been pulled cranially slightly, and this has resulted in superimposition of a gastrocnemius fabella on the urethra *(black arrow)*. This could be misinterpreted as a urethral calculus. (Image from Thrall DE, Robertson ID: *Atlas of normal radiographic anatomy and anatomic variants in the dog and cat*, St. Louis, 2011, Elsevier-Saunders.)

(lung) of a different opacity (gas) is present. One practical implication of this phenomenon is the common misinterpretation of a pulmonary vessel superimposed on the heart in lateral radiograph as a coronary artery rather than correctly as a pulmonary artery (see Fig. 5-20, *B*).

It is common for disease to cause border effacement of neighboring structures, such as border effacement of the right aspect of the cardiac silhouette in patients with right middle lobe pneumonia (Fig. 5-21). Other commonly encountered examples of the silhouette sign are in patients with pleural effusion where pooling of fluid around the heart when the patient is radiographed in sternal recumbency (dorsoventral radiograph) renders the heart margin invisible (see Chapter 31), and in patients with peritoneal fluid that leads to diminished organ and bowel serosal margin conspicuity (see Chapter 36).

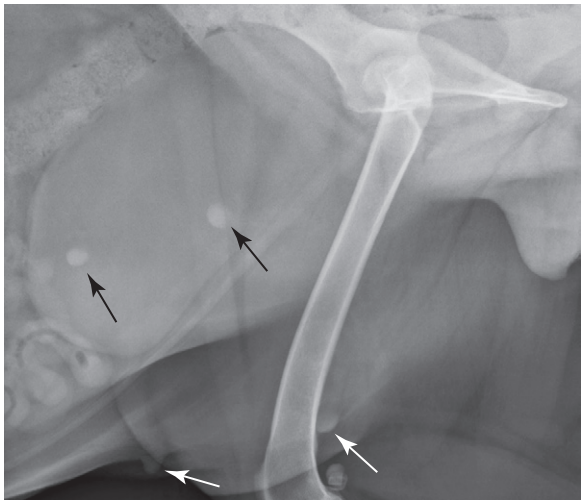


Fig. 5-14 Open-leg lateral view of the right femur of a dog. The left femur has been abducted and is dorsal to the trunk. As a result, ventral abdominal soft tissues are also pulled dorsally and now two nipples are superimposed on the urinary bladder *(black arrows)*, where they could be misinterpreted as cystic calculi. The contralateral nipples can be seen ventrally *(white arrows)*.

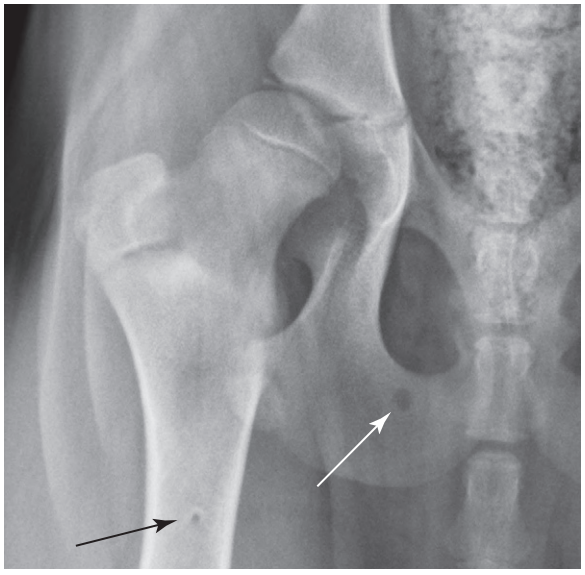


Fig. 5-15 Close-up view of the right ischial region of a young dog. There is a focal radiolucency superimposed on the right ischium *(white arrow)* because of a small gas collection in the anal sac. This superimposition opacity could be misinterpreted at a lytic region in the bone. The focal lucency in the proximal femoral diaphysis *(black arrow)* is the nutrient foramen and not a superimposition opacity.

ROLE OF PERCEPTION IN INTERPRETATION

The eyes are used, obviously, when interpreting radiographs. Unfortunately, the eyes and brain do not always perceive appearances accurately. For example, examine Figure 5-22. The two vertical lines appear curved, but when a straight edge is placed next to each vertical line they are obviously straight and parallel. The curving nature of these lines is an optical illusion created by the radiating lines on which they are superimposed. Therefore what appears as concrete visual evidence is not always such. Perception is an important part of radiographic interpretation. What appears as an obvious finding to beginning radiologists may be incorrect because of a perception error. Only by viewing many radiographs, with the

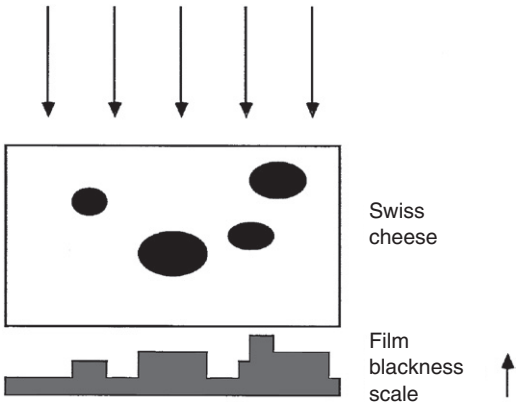


Fig. 5-16 The summation shadow effect. In this diagram, the *white rectangle* represents a block of Swiss cheese and the *black ovals* represent gas cavities. The distribution of the gas cavities influences whether they will overlap from the perspective of the x-ray beam, which is represented by the *vertical arrows*. The two gas cavities on the left will not be superimposed, and the radiolucency beneath the cavities is caused by the individual absorption characteristics of each cavity. The thicker cavity will create a more radiolucent region. The two cavities on the right, however, overlap partially from the perspective of the x-ray beam. In the region of overlap, the radiolucency is increased over that produced from either cavity alone as a result of decreased x-ray absorption in the region of cavity overlap.

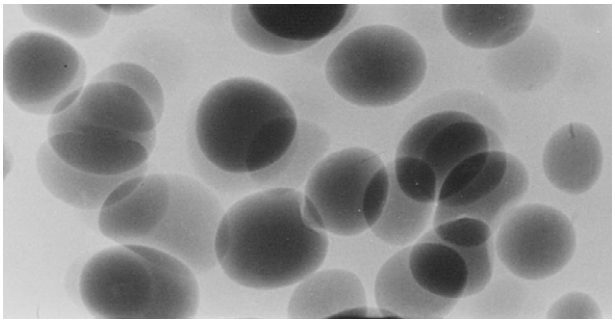


Fig. 5-17 Radiograph of an actual block of Swiss cheese. There are numerous gas-filled cavities in the cheese. Areas in which cavities overlap are more radiolucent than are areas in which no overlapping has occurred. Increased radiolucency is caused by decreased x-ray absorption in areas where cavities overlap. Areas where zero, two, three, and four cavities overlap can be identified. These summation shadows are termed *negative* because they result in increased radiolucency.

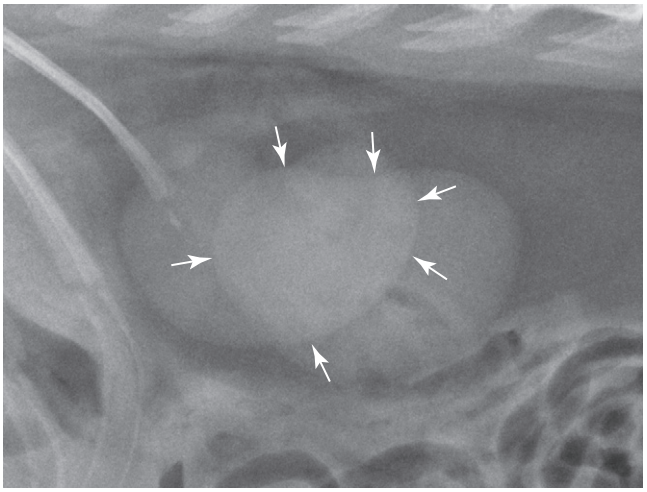


Fig. 5-18 Close-up of the renal region in a lateral abdominal radiograph of a cat. The kidneys are superimposed partially, resulting in creation of a positive summation shadow *(white arrows)*. This opacity could easily be confused with a mass, or with a misshapen kidney. The outline of each kidney can be traced, but these outlines are not as obvious as the positive summation shadow.

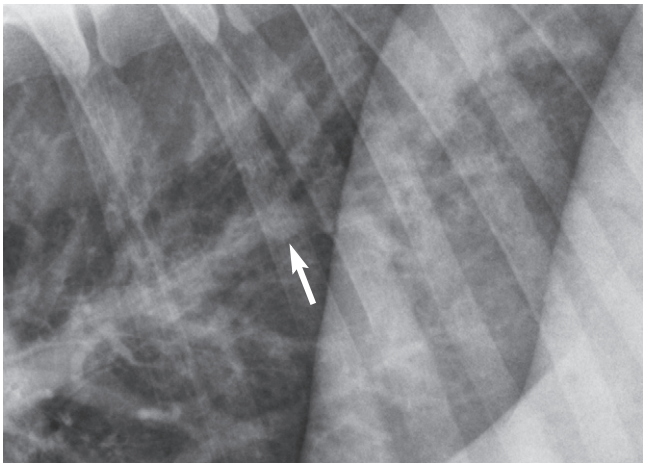


Fig. 5-19 Close-up of the dorsocaudal aspect of the thorax from a dog. There is a focal nodular opacity *(white arrow)* created by overlap of a caudal lobe vessel with a rib. Summation shadows caused by this phenomenon are misinterpreted commonly as lung nodules.

continual feedback of experienced interpreters, can perceptual inaccuracies be minimized. An excellent discussion of how perception influences radiographic interpretation has been prepared by M. Papageorges, DVM, and is available on the Evolve website (http://evolve.elsevier.com/Thrall/vetrad).

Naming Radiographic Projections

Radiographic projections are named according to the direction in which the central ray of the primary x-ray beam penetrates the body part of interest, from *point-of-entrance* to *point-of-exit*.[2] Directional terms listed in the *Nomina Anatomica Veterinaria*[3] should be used to describe radiographic views. For example, an abdominal radiograph made with the dog in dorsal recumbency and an overhead, vertically directed x-ray beam is a ventrodorsal view; with the dog in ventral recumbency, it is a dorsoventral view. The same method is used for other body parts, with the appropriate directional term applied (Fig. 5-23).

Oblique projections should be named by using the same method as standard view, by anatomically designating the points of entrance and exit (Fig. 5-24). Angles of obliquity can also be designated by inserting the number of degrees of obliquity between the directional terms involved. If the dorsolateral palmaromedial oblique (DLPaMO) projection in Figure 5-24 were made by positioning the x-ray tube 60 degrees laterally with respect to dorsal, the designation would be D60LPaMO. This term implies that, beginning dorsally, one proceeds 60 degrees to the lateral side to locate the point of entrance of the x-ray beam.

Names of lateral radiographs of the abdomen and thorax are abbreviated relative to the recumbency of the patient lying on the x-ray table. For example, the radiograph of a canine abdomen made with the dog lying on the left side is referred to as a *left lateral* rather than the more correct *right-left lateral*.

Viewing Radiographs

To assist in developing a consistent mental picture of normal radiographic anatomy, and also to facilitate the detection of abnormalities, radiographic images should always be oriented in a standard manner for viewing.

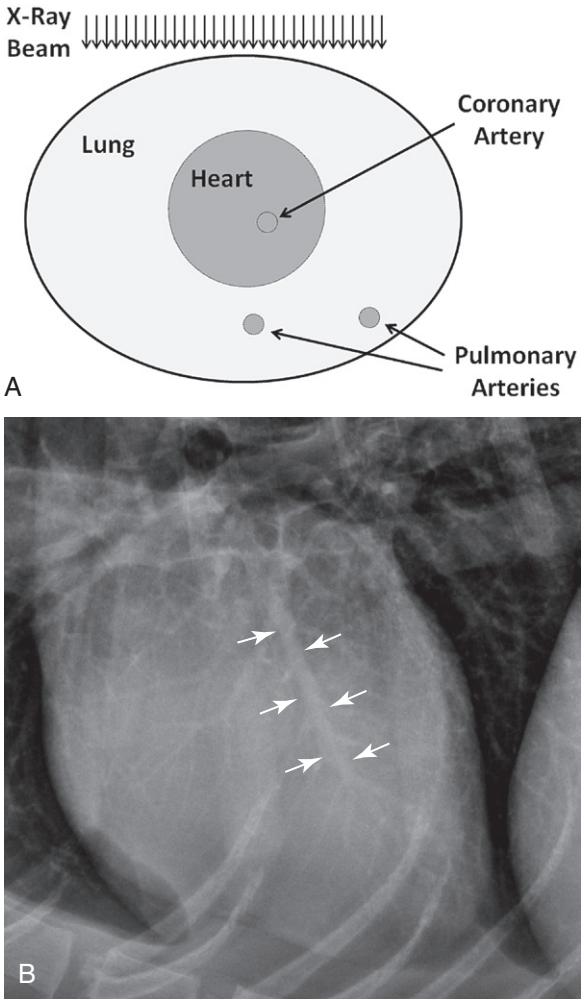


Fig. 5-20 Border effacement, or the silhouette sign. **A,** Illustration of a lung with two pulmonary arteries and the heart with one coronary artery. In a radiograph of this specimen, the coronary artery will not be visible because its border is effaced by the myocardium. The two pulmonary arteries will be seen clearly because they are surrounded by air, which provides contrast. **B,** Lateral thoracic radiograph. The vessel superimposed on the heart *(arrow)* is occasionally mistaken for a coronary artery, but this is not possible; it must be a pulmonary vessel. See text for details.

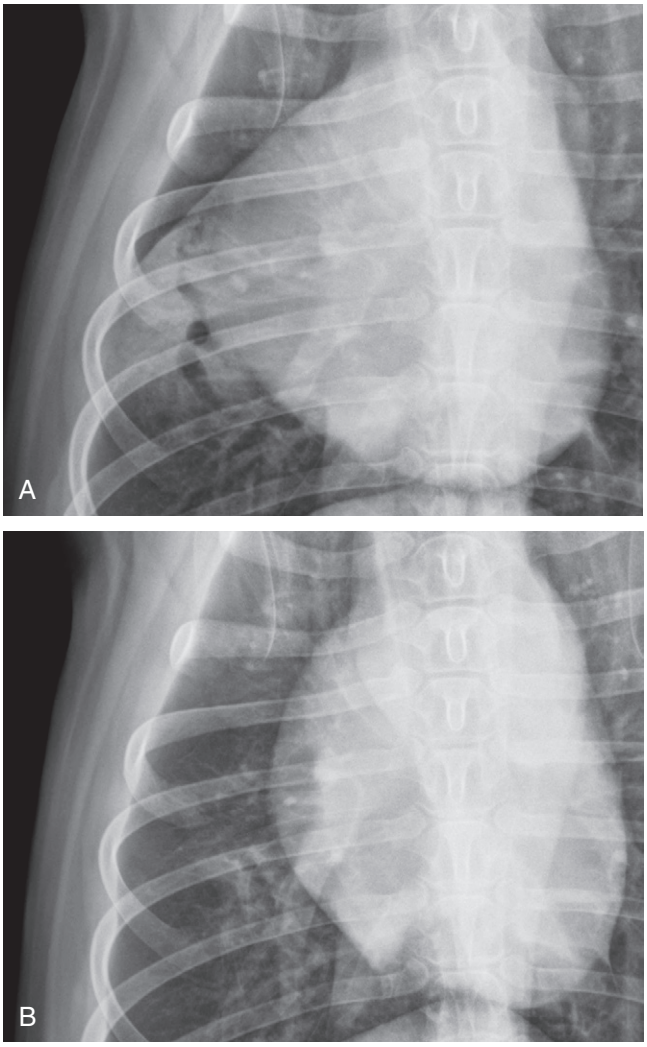


Fig. 5-21 **A,** Ventrodorsal radiograph of a dog with right middle-lobe pneumonia. As the abnormal lung lobe and the cardiac silhouette are both of soft tissue opacity, the border of each is obliterated in the region where they are in contact, and the true edge of the heart cannot be discerned. **B,** After resolution of the pneumonia, the true shape and size of the heart can be determined.

- Lateral views of any part should be oriented with the cranial (rostral) aspect of the animal to the viewer's left.
- Ventrodorsal or dorsoventral radiographs of the head, neck, or trunk should be oriented with the cranial (rostral) part of the animal pointing up and with the left side of the animal to the viewer's right.
- When viewing lateromedial or mediolateral radiographs of the extremities, including oblique projections, the radiograph should be oriented with the proximal aspect of the limb pointing up and the cranial or dorsal aspect of the limb to the viewer's left.
- Caudocranial (plantarodorsal, palmarodorsal) or craniocaudal (dorsopalmar, dorsoplantar) radiographs of the extremities should be oriented with the proximal end of the extremity at the top. No convention exists regarding whether the medial or lateral side of the extremity is oriented to the viewer's right or left. However, consistency is important, so a suggested format is that the lateral aspect of the limb (craniocaudal or dorsopalmar or dorsoplantar radiograph) be on the viewer's left.

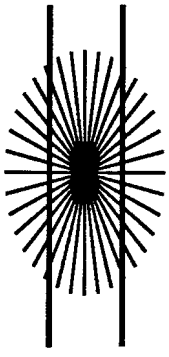


Fig. 5-22 *Perception* artifact. The two *vertical lines* appear curved. By placing a ruler next to each line it will be obvious that they are straight and parallel. This optical illusion is created by the radiating lines upon which the *curved lines* are superimposed. Perception is a common source of error in assessing radiographic abnormalities.

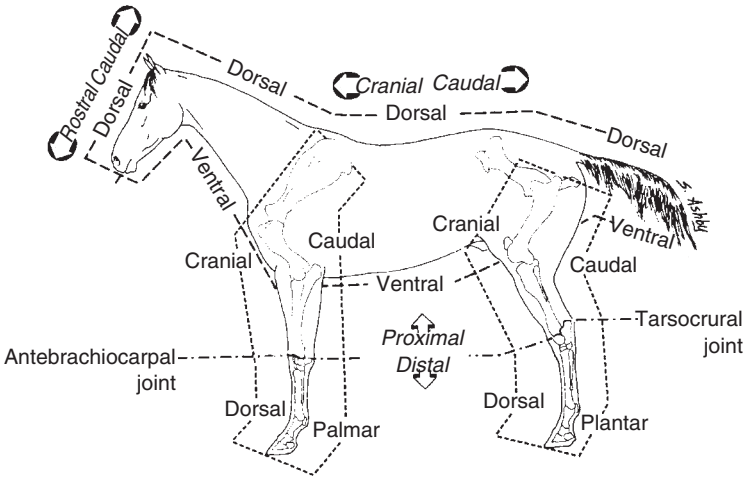


Fig. 5-23 Proper anatomic directional terms as they apply to various parts of the body. (Courtesy of Dr. J. E. Smallwood.)

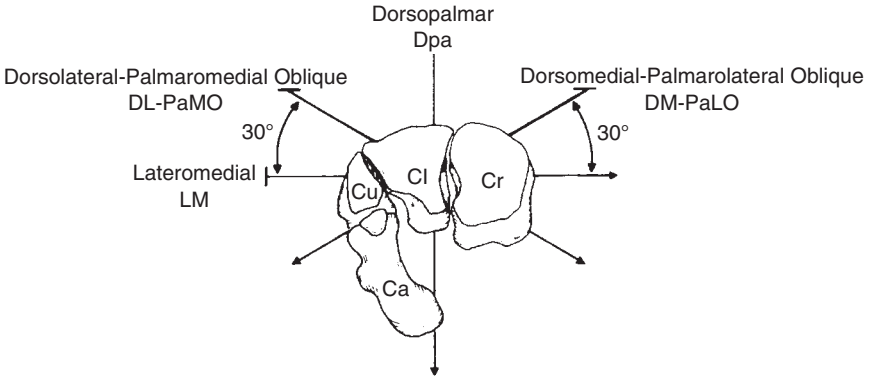


Fig. 5-24 Description of radiographic projections by the direction of the primary x-ray beam from the point of entrance to the point of exit (proximal view of the equine carpal bones). (Courtesy of Dr. J. E. Smallwood.)

Radiographic Interpretation

Radiographs cannot be interpreted accurately in a vacuum. The interpreter must have access to clinical information pertaining to the patient for accuracy to be optimized.[4] As such, the interpreter should be aware of the patient's signalment and medical history and have an understanding of the physical abnormalities present. Most practicing veterinarians will be very familiar with the pertinent clinical information, but this information may not be passed along in adequate detail if consultation from a specialist is requested. Particular attention should be paid to relaying the pertinent clinical information to any outside specialist who is consulting on the patient.

With regard to the signalment, species is always known, but unless the dog is purebred, any breed influence on assessing the significance of the radiographic abnormalities may be impossible to determine. Age may also not be known with certainty, and an estimate may have to be used.

The history provided by the owner or agent may be very helpful in guiding the radiographic interpretation, or it may be misleading. Recognizing that the radiographic findings may not always agree with the historical information is a critical step in formulating a correct radiographic assessment (Fig. 5-25).

Obviously, the physical findings are going to be very important with regard to interpreting the radiographs correctly and also in deciding which regions of the patient should be radiographed. Radiographs should never be used as a substitute for a thorough physical examination; on the contrary, the physical examination should help identify the region to be radiographed. Beginning interpreters may also believe that radiographs are going to provide a diagnosis. Most of the time, reaching the diagnosis is not done radiographically. Radiographs provide mainly an assessment of morphology, although some types of physiologic function can be assessed with highly specialized imaging. The changes in morphology are then used to decide how the diagnosis is going to be reached. This may involve additional imaging using another modality, endoscopy, aspiration cytology, percutaneous biopsy, open biopsy, or surgery.

When it is finally time to radiograph the patient, it is critical that accurate positioning and proper radiographic technique be used. Dr. Peter Suter, a famous veterinary radiologist, had been heard to say ". . . At best, poor radiographs are totally useless and at worst they are totally misleading." It is the responsibility of the attending veterinarian to ensure that adequate views are acquired and that proper radiographic technique is used (Fig. 5-26). If technically inadequate radiographs are produced, it is not the responsibility of the owner to pay an additional fee for additional higher-quality images. The fee for obtaining the radiographic study includes obtaining images of adequate quality and all standard patient positions, regardless of the number of radiographic exposures required to meet these requirements. It is not the purpose of this book to review patient positioning and radiographic technique, although some chapters touch on aspects of these concepts. Other sources are available to provide information on technique and positioning.[5]

Once suitable radiographs of the patient have been produced, the interpretation process begins. Interpreting the images should be done in a quiet, relatively isolated, environment. Distractions should be minimized. This seems obvious, but taking the time to make sure the viewing environment is suitable will pay off with increased accuracy. The actual viewing conditions for assessing film-based images may not be



Fig. 5-25 Lateral view of the distal aspect of the tibia of a cat. The owner reported a lameness of 2 days' duration. The smooth periosteal reaction with a focal lucency has obviously been present for more than 2 days. Here is an example of a history that does not match the radiographic abnormalities. In these instances it will be more difficult to assess the overall significance of the radiographic changes with respect to the patient's health.

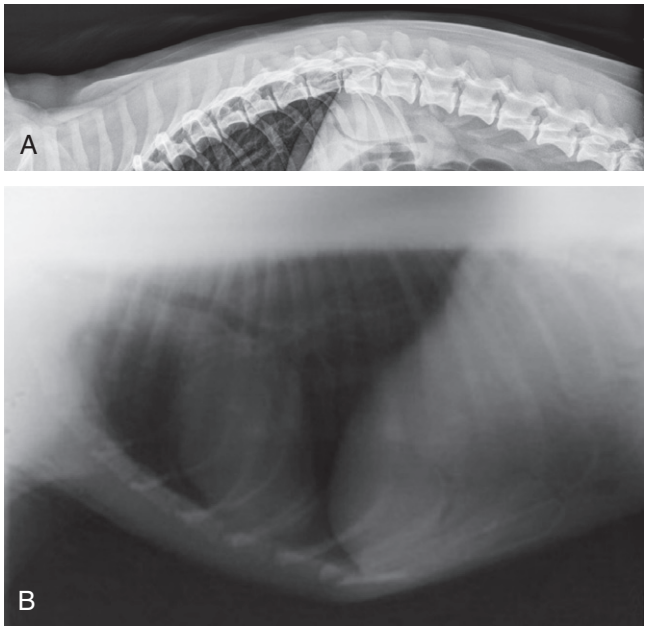


Fig. 5-26 **A,** Poorly positioned lateral spine radiograph. **B,** Overexposed thoracic radiograph. These radiographs are totally worthless.



Fig. 5-27 A hot light, sometimes called a *bright light*, or a *spotlight*, is valuable to view more heavily exposed regions of a film radiograph. This ancillary equipment is indispensable for ensuring that the image is assessed completely.

as important as once thought,[6] and concentration is likely the major determinant of accuracy. For film viewing, the images should be oriented on the viewbox as described previously in this chapter. However, radiographic film cannot be evaluated completely using only the illumination from the viewbox. Certain regions of the image are going to be dark, and an intense *hot light* is required for assessing the more heavily exposed film regions (Fig. 5-27). Under no circumstances should a film radiograph be evaluated by holding it up for illumination from a ceiling-mounted light fixture. Manipulating the blackness and contrast of a digital image electronically has eliminated the need for a hot light if a transition from analog to digital radiography has been made.

The viewing conditions for digital radiographs are also important, but these are quite different than for analog images. The monitor used to view digital images can have a dramatic impact on lesion conspicuity; this is discussed in detail in Chapter 2. DICOM viewing software, also described in Chapter 2, allows the reader to manipulate the orientation, size, blackness, and contrast of digital radiographic images. These manipulations facilitate the image interpretation process and provide obvious advantages over interpreting an analog film. However, manipulating these functions suboptimally can actually impede interpretation. For example, immediately magnifying a part (Fig. 5-28, *A*) or viewing images at too small a size (Fig. 5-28, *B*) will usually result in lesions being fabricated (when image is too big) or missed (when image is too small).

In the days of analog interpretation, reviewers were cautioned to examine the film from a distance of 6 feet and then at 6 inches, in addition to the more typical viewing distance of arms-length. These close and distant inspections were valuable for detecting small and global changes, respectively, and can be incorporated easily into digital image viewing by adjusting the size of the image displayed on the monitor. However, using these close and/or distant perspectives exclusively, without also using more normal magnification, will lead to errors.

When interpretation of the image actually begins, the first question to answer is whether the radiographic image is

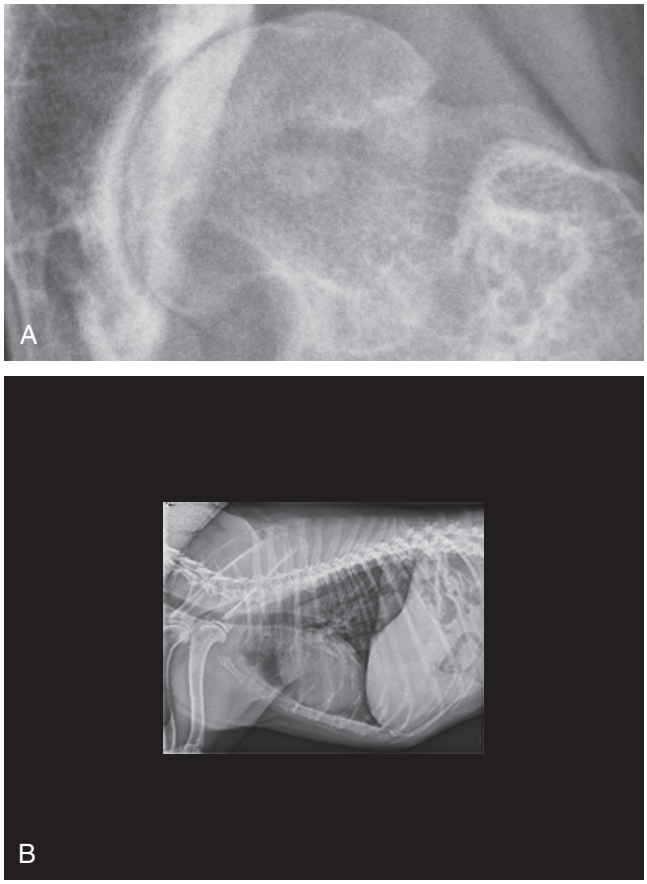


Fig. 5-28 Screen capture images from a DICOM viewing program. In **A,** the coxofemoral joint has been enlarged excessively. This degree of enlargement may be beneficial for characterizing some very small lesions but typically is not needed because there will be a tendency to fabricate abnormalities. Zooming images before assessing the entire part at a lower magnification will invariably lead to incorrect or missed diagnoses. In **B,** the image has not been enlarged to fill the viewing frame, and lesions will be overlooked using this method.



Fig. 5-29 Lateral radiograph of the stifle of a 5-month-old Labrador retriever. The tibial crest has not yet fused to the tibia. This normal appearance is commonly misdiagnosed as an avulsion of the tibial crest.

normal or not; this is absolutely the most difficult of all questions to be answered from the radiograph. The patient has been radiographed for a reason, and there is a tendency to want to find something to address that reason. Also, it is very difficult for beginning interpreters to fully grasp the scale of normal variation that is within acceptable limits. As a result, in many patients normal structures, appearances, and variations are misinterpreted as abnormal (Fig. 5-29). There are numerous options that can increase one's confidence in distinguishing normal from abnormal. These include consultation of normal reference sources. A normal radiographic anatomy resource accompanies this book on the Evolve website at http://evolve.elsevier.com/Thrall/vetrad. This resource does not address normal variants or technical issues that can affect radiographic appearance, but other independent resources are available that discuss these issues in detail.[7] Finally, with the advent of digital imaging, there are many teleradiology consultation sources that can be used to obtain a second opinion.

Once it has been determined that the radiograph is abnormal, it is time to identify and categorize the radiographic abnormalities. Experienced radiologists usually use a random visual search pattern for evaluating the radiograph. This is not recommended for beginning interpreters. Beginners should have a standardized method of image interpretation, either working from the outside in, or the reverse. The best solution may be for beginners to work from a structured checklist. Having a structure for interpretation will help beginners avoid missing lesions; there is even evidence that experienced interpreters benefit from a structured interpretation environment.[8]

Any abnormality should be characterized, and even in a private practice setting the compilation of an interpretation report is advisable. This report does not have to be formal but should be more than a few words hastily scratched into the patient's medical record. The abnormalities should be described, and the possibilities that are considered should be recorded. This exercise will assist in refinement and improvement of the image evaluation method.

The roentgen sign approach has withstood the test of time as a method for describing radiographic abnormalities. Basically, the roentgen sign approach involves describing abnormal radiographic morphology in terms of a change in *size, shape, location, number, margination, or opacity*. Any radiographic abnormality can be described using one or more of these terms. The definition and examples of specific uses of each roentgen sign follow:

- *Size*—a change in size of a structure with the overall shape remaining as expected, such as:
  - Generalized liver enlargement
  - Generalized splenomegaly
  - Generalized cardiomegaly
  - Symmetric prostate gland enlargement
  - Renal atrophy
- *Shape*—a change in shape of a structure such that the overall expected shape has been altered, such as:
  - Isolated right atrial enlargement in a dog with tricuspid dysplasia
  - Left atrial dilation in cats with hypertrophic cardiomyopathy
  - A liver tumor in the left lateral lobe
  - A hemangiosarcoma on the distal extremity of the spleen
  - Gastric compartmentalization in gastric volvulus

In structures that have undergone a shape change, the overall size may be altered as well.

- *Location*—a change in the expected location of a structure, such as:
  - Displacement of the femur as a consequence of coxofemoral luxation
  - Displacement of jejunum into the pleural cavity following diaphragmatic hernia
  - Displacement of the right kidney caudally by an enlarged liver
- *Number*—a change in the expected number of structures, such as:
  - Absent distal phalanges in a cat having undergone an onychectomy
  - Lysis of a distal phalanx as a result of a subungual tumor
  - Polydactyly
- *Margination*—a change in the expected outline of a structure, such as:
  - A periosteal reaction on a bone
  - A liver mass protruding from the surface
  - Renal infarction causing an indentation in the cortex
- *Opacity*—a change in the expected opacity of a structure, such as:
  - Replacement of air in the lung by an exudate
  - Endosteal osteogenesis in response to stress remodeling
  - Cortical destruction from a tumor
  - Disuse bone atrophy

Once the roentgen signs have been compiled, they are considered in concert with the clinical information to arrive at a list of possibilities. This list of possibilities has been referred to as a *gamut*, and there are books that enumerate gamuts for various findings in human beings.[9] As discussed earlier, it is unusual for a diagnosis to be made at the radiographic stage; usually some interventional procedure must be done to finalize the diagnosis. Rare exceptions are purely morphologic derangements such as fracture, gastric volvulus, or diaphragmatic hernia. Formulation of the list of possibilities once roentgen signs have been compiled should not be taken lightly. The mnemonic DAMNITV, standing for *d*egenerative, *a*nomalous, *m*etabolic, *n*eoplastic, *i*nfectious (*i*nflammatory, immune), *t*raumatic, and *v*ascular is a convenient method to help consider all possibilities. The interpreter should mentally consider the possibility that diseases falling into each of these categories has resulted in the radiographic changes observed.

Everyone who interprets radiographic images makes errors, regardless of their level of expertise. Two specific errors in interpretation that all interpreters make deserve consideration—these are *bias* and *satisfaction of search*. Bias results from expecting to find something and then making the radiographic signs fit that expectation. For example, in a dog with acute vomiting, a gas-filled jejunum will be more likely to be interpreted as an obstructive pattern than this same pattern in a normal dog. Satisfaction of search pertains to finding an obvious radiographic abnormality and then stopping the search for more lesions, regardless of whether the finding explains the clinical signs. Avoiding these errors is a gradual transition that comes with experience.

REFERENCES

1. Evans T: AANA Journal course: update for nurse anesthetists—fundamentals of chest radiography: techniques and interpretation for the anesthetist, *AANA J*, 60:45, 1992.
2. Smallwood JE, Shively MJ, Rendano VT, et al: A standardized nomenclature for radiographic projections used in veterinary medicine, *Vet Radiol* 26:2, 1985.
3. International Committee on Veterinary Gross Anatomical Nomenclature (ICVGAN): *Nomina anatomica veterinaria*, ed 5, Hannover, Columbia, Gent, Sapporo, 2005, World Association of Veterinary Anatomists.
4. Loy CT, Irwig L: Accuracy of diagnostic tests read with and without clinical information: a systematic review, *JAMA* 292:1602, 2004.
5. Lavin LM: *Radiography in veterinary technology*, ed 4, St. Louis, 2007, Elsevier-Saunders.
6. Robson KJ: An investigation into the effects of suboptimal viewing conditions in screen-film mammography, *Br J Radiol* 81:219, 2008.
7. Thrall DE, Robertson ID: *Atlas of normal radiographic anatomy and anatomic variants in the dog and cat*, St. Louis, 2011, Elsevier-Saunders.
8. Getty DJ, Pickett RM, D'Orsi CJ, et al: Enhanced interpretation of diagnostic images, *Invest Radiol* 23:240, 1988.
9. Reeder MM, Bradley WG Jr, Merritt CR: *Reeder and Felson's gamuts in radiology: comprehensive lists of roentgen differential diagnosis*, ed 4, New York, 2003, Springer-Verlag.

ELECTRONIC RESOURCES

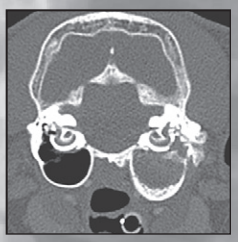
evolve

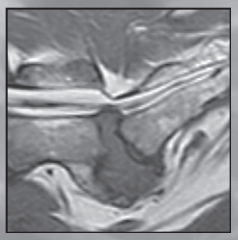
Additional information related to the content in Chapter 5 can be found on the companion website at http://evolve.elsevier.com/Thrall/vetrad/

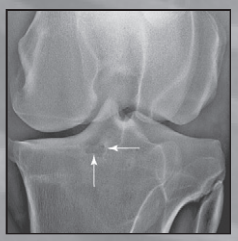
- Chapter Quiz

SECTION II

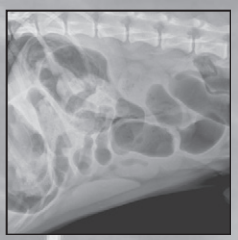
The Axial Skeleton: Canine, Feline, and Equine











6 **Radiographic Anatomy of the Axial Skeleton**
James E. Smallwood
Kathy A. Spaulding

7 **Principles of Radiographic Interpretation of the Axial Skeleton**
Donald E. Thrall

8 **The Cranial and Nasal Cavities: Canine and Feline**
Lisa J. Forrest

9 **Magnetic Resonance Imaging Features of Brain Disease in Small Animals**
Ian D. Robertson

10 **The Equine Head**
Anthony P. Pease

11 **The Canine and Feline Vertebrae**
William R. Widmer
Donald E. Thrall

12 **Magnetic Resonance Imaging and Computed Tomography Features of Canine and Feline Spinal Cord Disease**
Wilfried Mai

CHAPTER • 6

Radiographic Anatomy of the Axial Skeleton

James E. Smallwood
Kathy A. Spaulding

To use the roentgen sign method of recognizing abnormal radiographic findings effectively, an understanding of normal radiographic anatomy for the specific area of interest is necessary. Within the space constraints of a comprehensive veterinary radiology text, this chapter provides a limited reference for the radiographic anatomy of the axial skeleton. For more detailed information, readers are referred to comprehensive texts on radiographic anatomy.[1,2,3] The radiographic nomenclature used in this chapter was approved by the American College of Veterinary Radiology in 1983.[4]

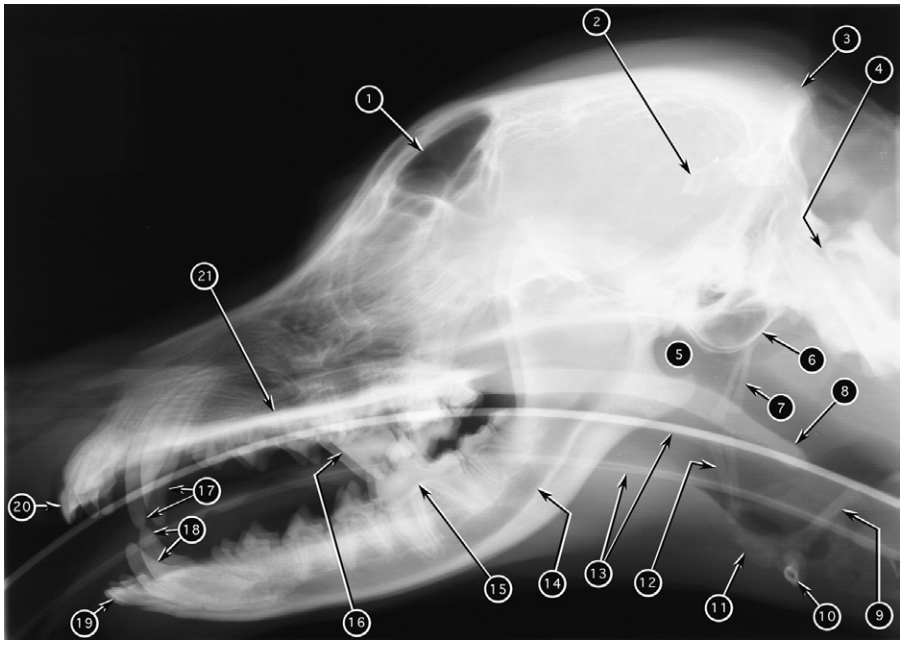


Fig. 6-1 **Left-Right Lateral Radiograph of Canine Head.**

1. Frontal sinuses
2. Tentorium osseum cerebelli
3. External occipital protuberance
4. Atlantooccipital joints
5. Air in nasopharynx
6. Tympanic bullae
7. Stylohyoid bones
8. Soft palate
9. Thyrohyoid bones
10. Basihyoid bone
11. Ceratohyoid bones
12. Epihyoid bones
13. Endotracheal tube
14. Inferior alveolar canals of mandibles
15. Inferior first molar teeth
16. Superior fourth premolar teeth
17. Superior canine teeth
18. Inferior canine teeth
19. Inferior incisor teeth
20. Superior incisor teeth
21. Hard palate

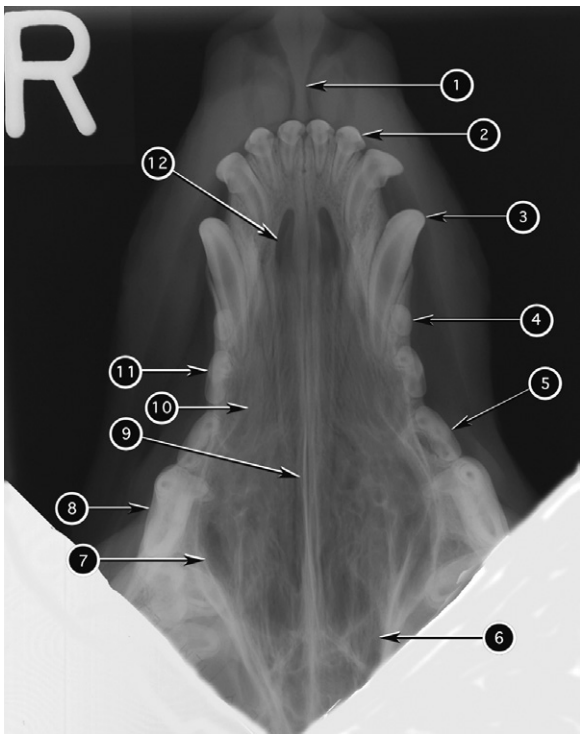


Fig. 6-2 **Intraoral Dorsoventral Radiograph of Canine Nasal Cavity.**
1. Cartilaginous nasal septum
2. Superior incisor 2
3. Superior canine tooth
4. Superior premolar 1
5. Superior premolar 3
6. Ethmoidal conchae
7. Maxillary recess
8. Superior premolar 4
9. Nasal septum
10. Dorsal and ventral nasal conchae
11. Superior premolar 2
12. Palatine fissure

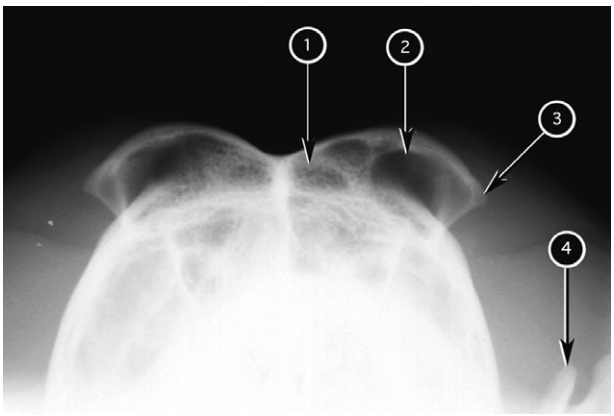


Fig. 6-3 **Rostrodorsal-Caudodorsal Oblique Radiograph of Canine Frontal Sinuses.**
1. Medial frontal sinus
2. Lateral frontal sinus
3. Zygomatic process of frontal bone
4. Coronoid process of mandible

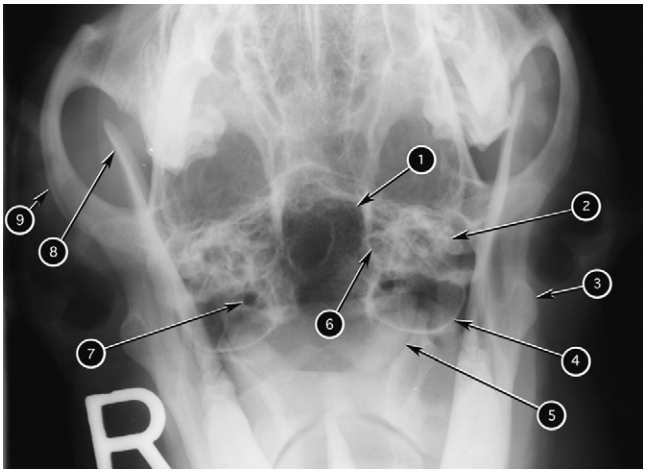


Fig. 6-4 **Rostroventral-Caudodorsal Oblique (Open-Mouth) Radiograph of Canine Tympanic Bullae.**
1. Nasopharynx
2. Petrous temporal bone
3. Angular process of mandible
4. Tympanic bulla
5. Atlantooccipital joint
6. Foramen lacerum
7. Jugular foramen
8. Coronoid process of mandible
9. Zygomatic arch

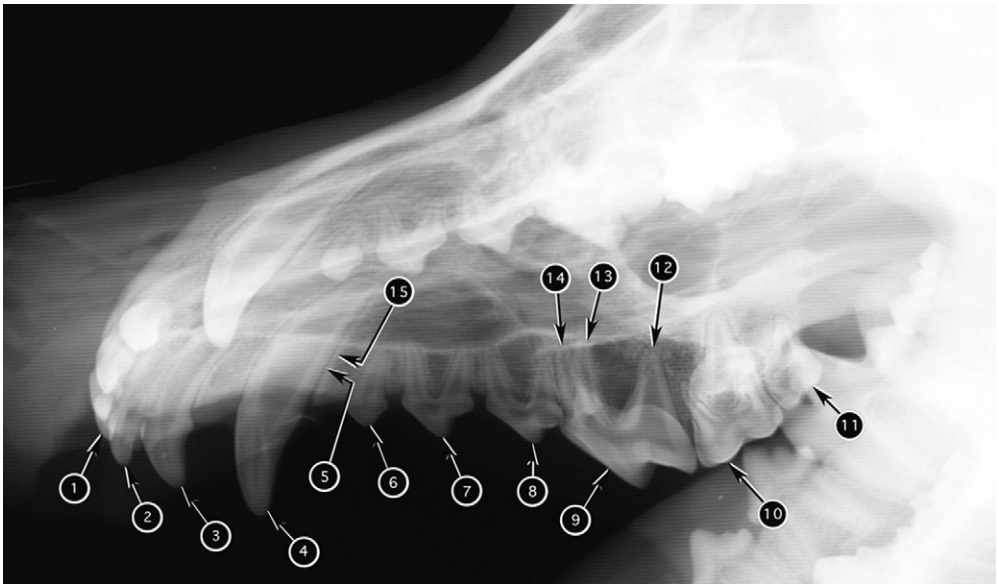


Fig. 6-5 **Left Ventral/Right Dorsal Oblique Radiograph of Canine Superior Teeth.**

1. Superior incisor 1
2. Superior incisor 2
3. Superior incisor 3
4. Superior canine tooth
5. Periodontal ligament
6. Superior premolar 1
7. Superior premolar 2
8. Superior premolar 3
9. Superior premolar 4
10. Superior molar 1
11. Superior molar 2
12. Caudal root of premolar 4
13. Rostromedial root of premolar 4
14. Rostrolateral root of premolar 4
15. Cortical bone forming wall of alveolus

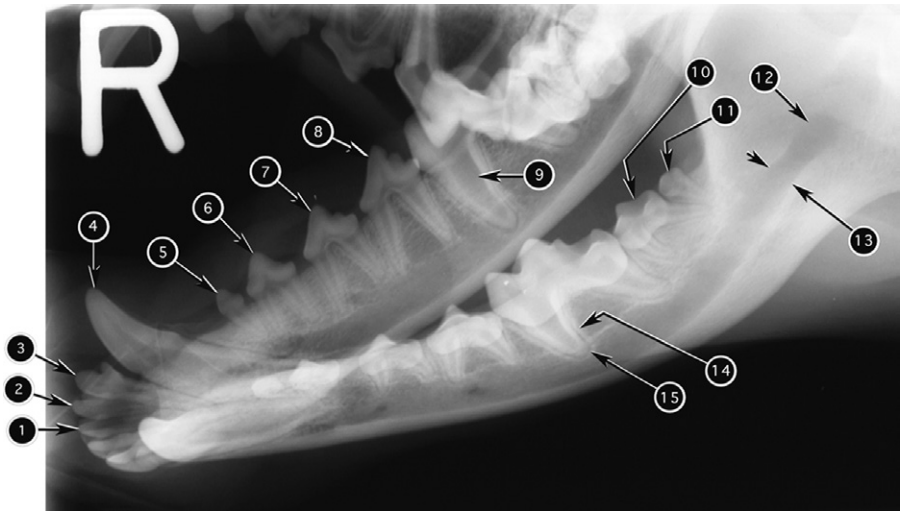


Fig. 6-6 **Left Ventral/Right Dorsal Oblique Radiograph of Canine Superior Teeth.**

1. Inferior incisor 1
2. Inferior incisor 2
3. Inferior incisor 3
4. Inferior canine tooth
5. Inferior premolar 1
6. Inferior premolar 2
7. Inferior premolar 3
8. Inferior premolar 4
9. Dental cavity of inferior molar 1
10. Inferior molar 2
11. Inferior molar 3
12. Mandibular foramen
13. Mandibular canal
14. Cortical bone forming wall of alveolus
15. Periodontal ligament

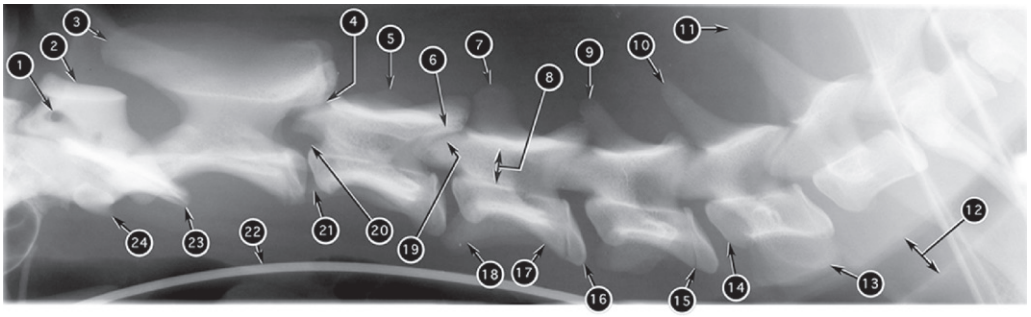


Fig. 6-7 **Left-Right Lateral Radiograph of Canine Cervical Vertebrae.**

1. Lateral vertebral foramina (left and right) of atlas; emergence of cervical nerve 1
2. Dorsal arch of atlas (C1)
3. Spinous process of axis (C2)
4. Synovial joints between articular processes of C2 and C3
5. Spinous process of C3
6. Caudal articular processes of C3
7. Spinous process of C4
8. Vertebral canal of C4
9. Spinous process of C5
10. Spinous process of C6
11. Spinous process of C7
12. Trachea
13. Expanded ventral laminae of transverse processes of C6
14. Cranial extremity (head) of C6
15. Caudal physis of C5
16. Caudal extremity (fossa) of C4
17. Body of C4
18. Transverse processes of C4
19. Cranial articular processes of C4
20. Intervertebral foramina between C2 and C3
21. Intervertebral space (disk) between C2 and C3
22. Endotracheal tube
23. Wings (transverse processes) of atlas
24. Ventral tubercle of atlas

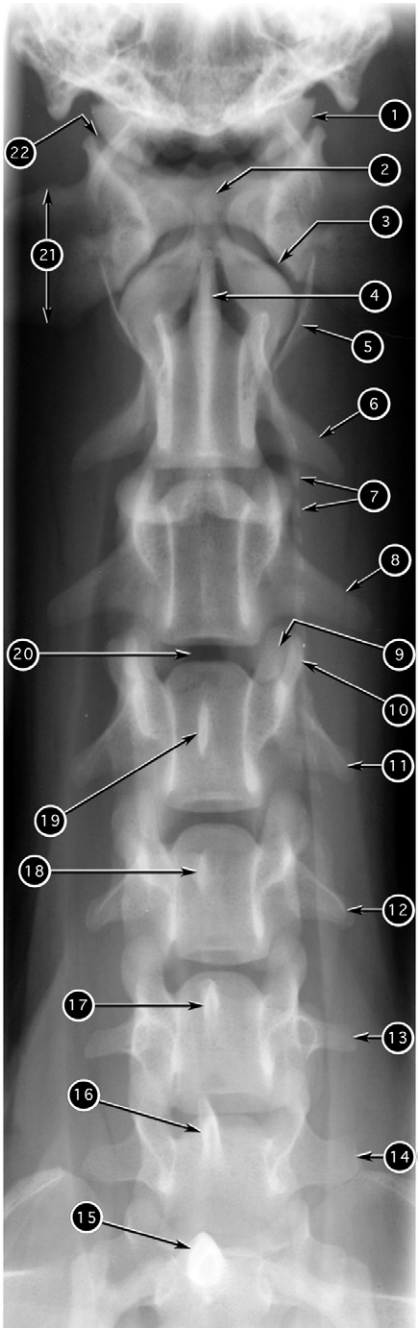


Fig. 6-8 **Ventrodorsal Radiograph of Canine Cervical Vertebrae.**
1. Left occipital condyle
2. Dens of axis
3. Atlantoaxial joint
4. Spinous process of axis
5. Left thyrohyoid bone
6. Left transverse process of axis
7. Tracheal cartilages
8. Left transverse process of C3
9. Left caudal articular process of C3
10. Left cranial articular process of C4
11. Left transverse process of C4
12. Left transverse process of C5
13. Left transverse process of C6
14. Left transverse process of C7
15. Spinous process of T1
16. Spinous process of C7
17. Spinous process of C6
18. Spinous process of C5
19. Spinous process of C4
20. Intervertebral space (disk) between C3 and C4
21. Right wing of atlas
22. Right atlantooccipital joint

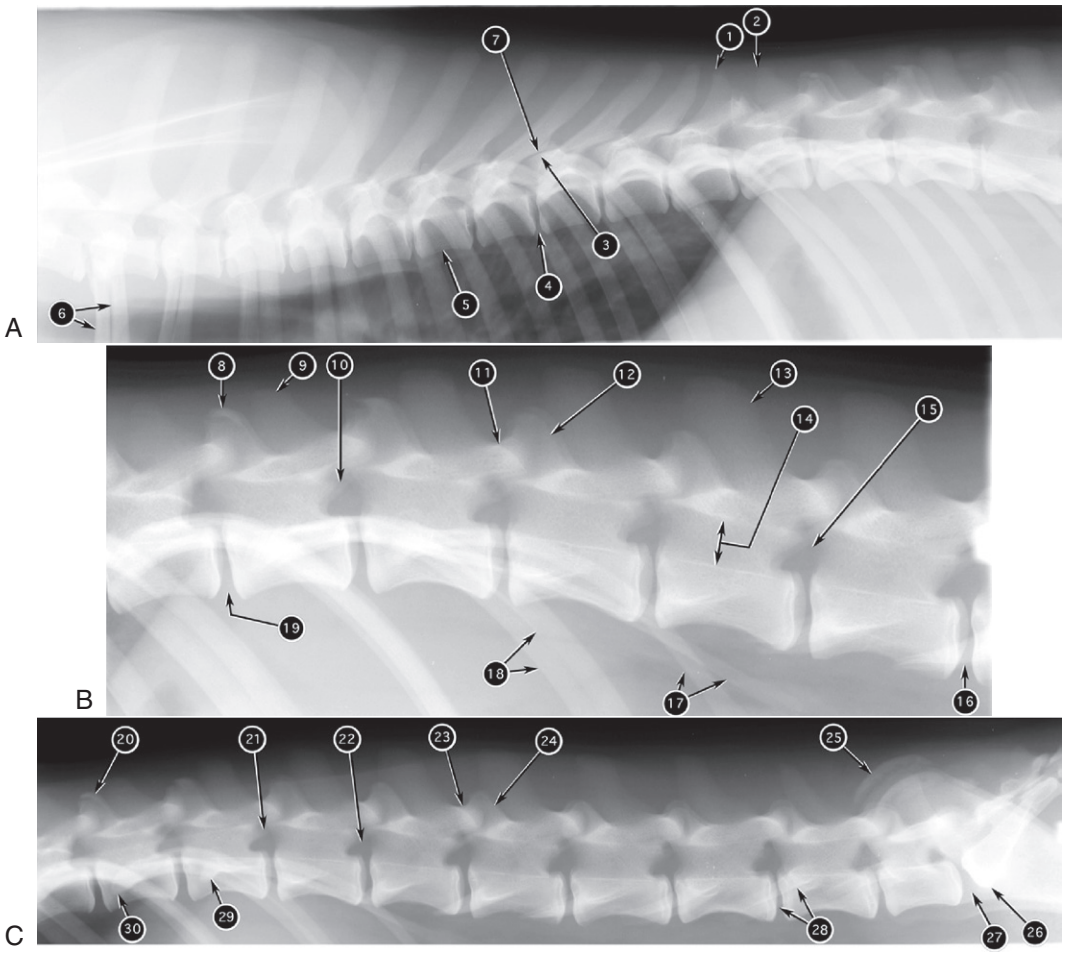


Fig. 6-9 **Left-Right Lateral Radiographs of Canine Thoracic and Lumbar Vertebrae.**

A, Left-right *(Le-Rt)* lateral radiograph of thoracic spine.

1. Spinous process of T10
2. Spinous process of T11 (anticlinal vertebra)
3. Cranial articular processes of T8
4. Intervertebral space (disk) between T7 and T8
5. Body of T6
6. First pair of ribs
7. Caudal articular processes of T7

B, Left-right *(Le-Rt)* lateral radiograph of thoracolumbar spine.

8. Mamillary processes atop cranial articular processes of T12
9. Spinous process of T12
10. Accessory processes of T12
11. Caudal articular processes of T13
12. Cranial articular processes of L1
13. Spinous process of L2
14. Vertebral canal of L2
15. Intervertebral foramina between L2 and L3
16. Transverse processes of L4
17. Thirteenth pair of ribs
18. Twelfth pair of ribs
19. Intervertebral space (disk) between T11 and T12

C, Left-right *(Le-Rt)* lateral radiograph of lumbar spine.

20. Mamillary processes atop cranial articular processes of T12
21. Accessory processes of T13
22. Intervertebral foramina between L1 and L2
23. Caudal articular processes of L2
24. Cranial articular processes of L3
25. Secondary ossification center for crest of ilium
26. Promontory of sacrum
27. Intervertebral space (disk) between L7 and S1
28. Transverse processes of L6
29. Heads of thirteenth ribs superimposed on body of T13
30. Heads of twelfth ribs superimposed on body of T12

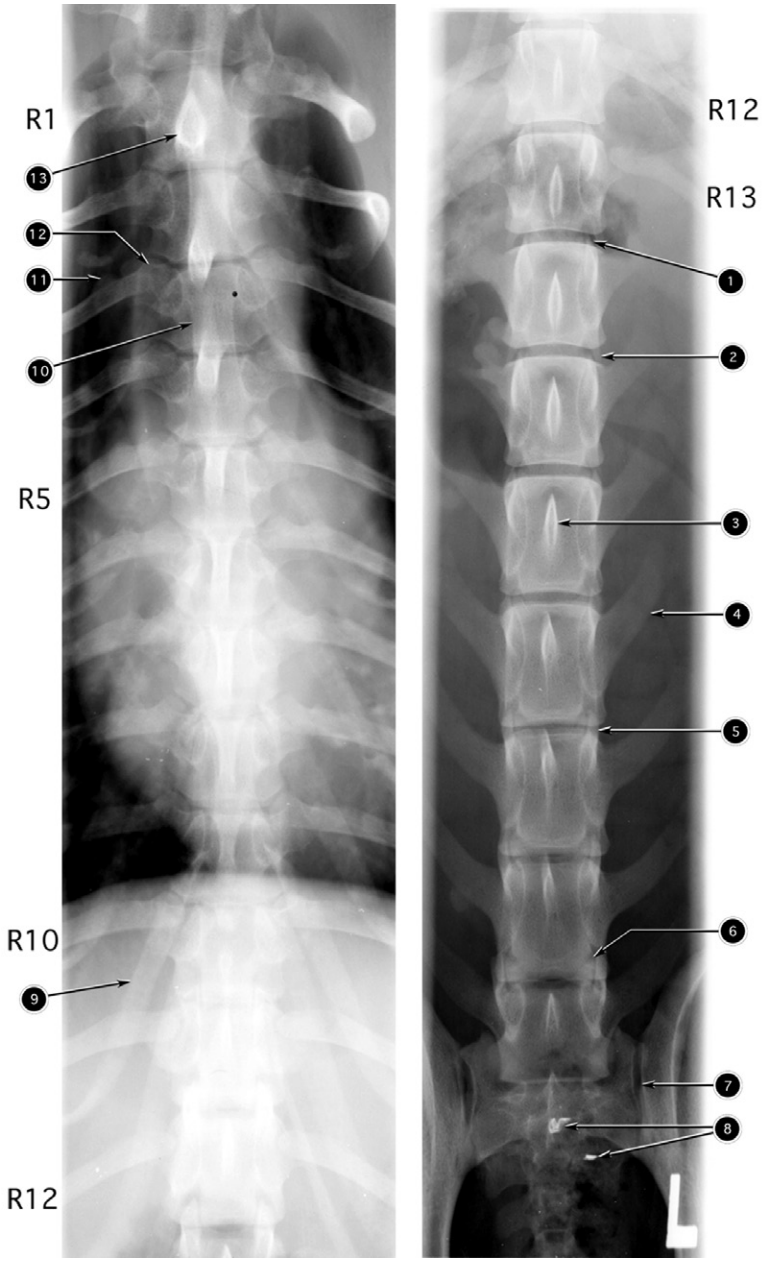


Fig. 6-10 **Ventrodorsal Radiographs of Canine Thoracic and Lumbar Vertebrae (*R* = rib).**

1. Intervertebral space (disk) between T13 and L1
2. Left accessory process of L2
3. Spinous process of L3
4. Left transverse process of L4
5. Left cranial articular process of L5
6. Left caudal articular process of L6
7. Left sacroiliac joint
8. Metallic foreign bodies in descending colon
9. Costal cartilage of right rib 11
10. Sternum superimposed over vertebrae
11. Tubercle of right rib 3
12. Head of right rib 3, articulating with bodies of vertebrae T2 and T3
13. Spinous process of T1

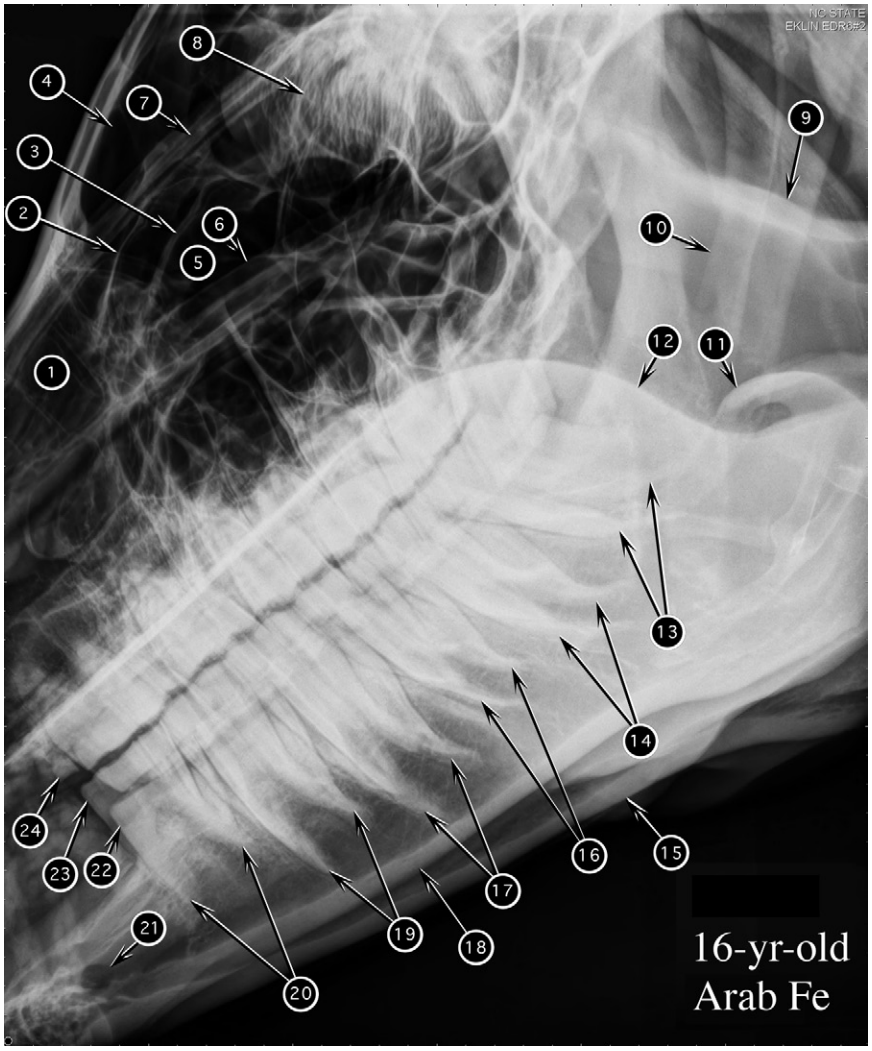


Fig. 6-11 **Right-Left Lateral Radiograph of Middle Region of Equine Head (16 Years Old).**

1. Dorsal conchal sinuses;
2. Septum between left rostral and caudal maxillary sinuses
3. Septum between right rostral and caudal maxillary sinuses;
4. Frontal sinuses (communicate with 1)
5. Caudal maxillary sinuses
6. Left infraorbital canal
7. Nasolacrimal ducts
8. Ethmoidal labyrinth
9. Dorsal wall of nasopharynx
10. Left stylohyoid bone
11. Epiglottic cartilage
12. Soft palate resting on root of tongue
13. Roots of right inferior molar 3 (tooth 411)
14. Roots of right inferior molar 2 (tooth 410)
15. Ventral border of right mandible
16. Roots of right inferior molar 1 (tooth 409)
17. Roots of right inferior premolar 4 (tooth 408)
18. Ventral border of left mandible
19. Roots of right inferior premolar 3 (tooth 407)
20. Roots of right inferior premolar 2 (tooth 406)
21. Left mental foramen
22. Right inferior premolar 2 (tooth 406)
23. Left inferior premolar 2 (tooth 306)
24. Left superior premolar 1 (tooth 205)

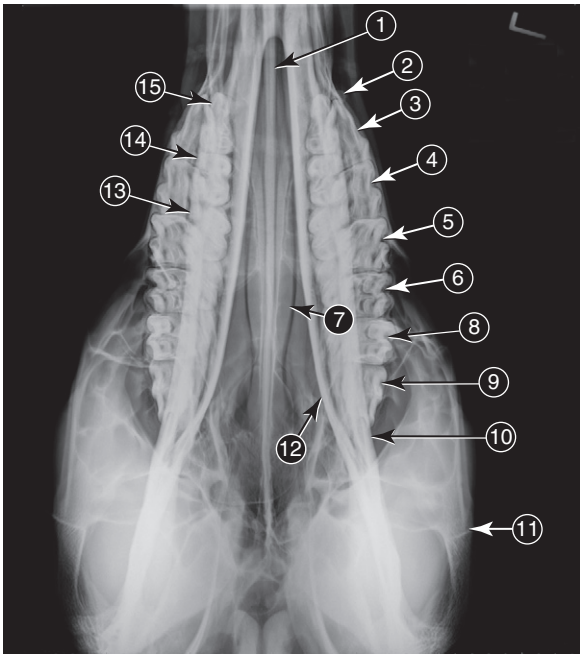


Fig. 6-12 **Dorsoventral Radiograph of Middle Region of Equine Head (16 Years Old).**

1. Cartilaginous nasal septum superimposed on vomer
2. Left superior premolar 1 (tooth 205)
3. Left superior premolar 2 (tooth 206)
4. Left superior premolar 3 (tooth 207)
5. Left superior premolar 4 (tooth 208)
6. Left superior molar 1 (tooth 209)
7. Vascular mucosa covering side of nasal septum
8. Left superior molar 2 (tooth 210)
9. Left superior molar 3 (tooth 211)
10. Lateral surface of left mandible
11. Zygomatic arch
12. Medial surface of left mandible
13. Right inferior premolar 4 (tooth 408)
14. Right inferior premolar 3 (tooth 407)
15. Right inferior premolar 2 (tooth 406)

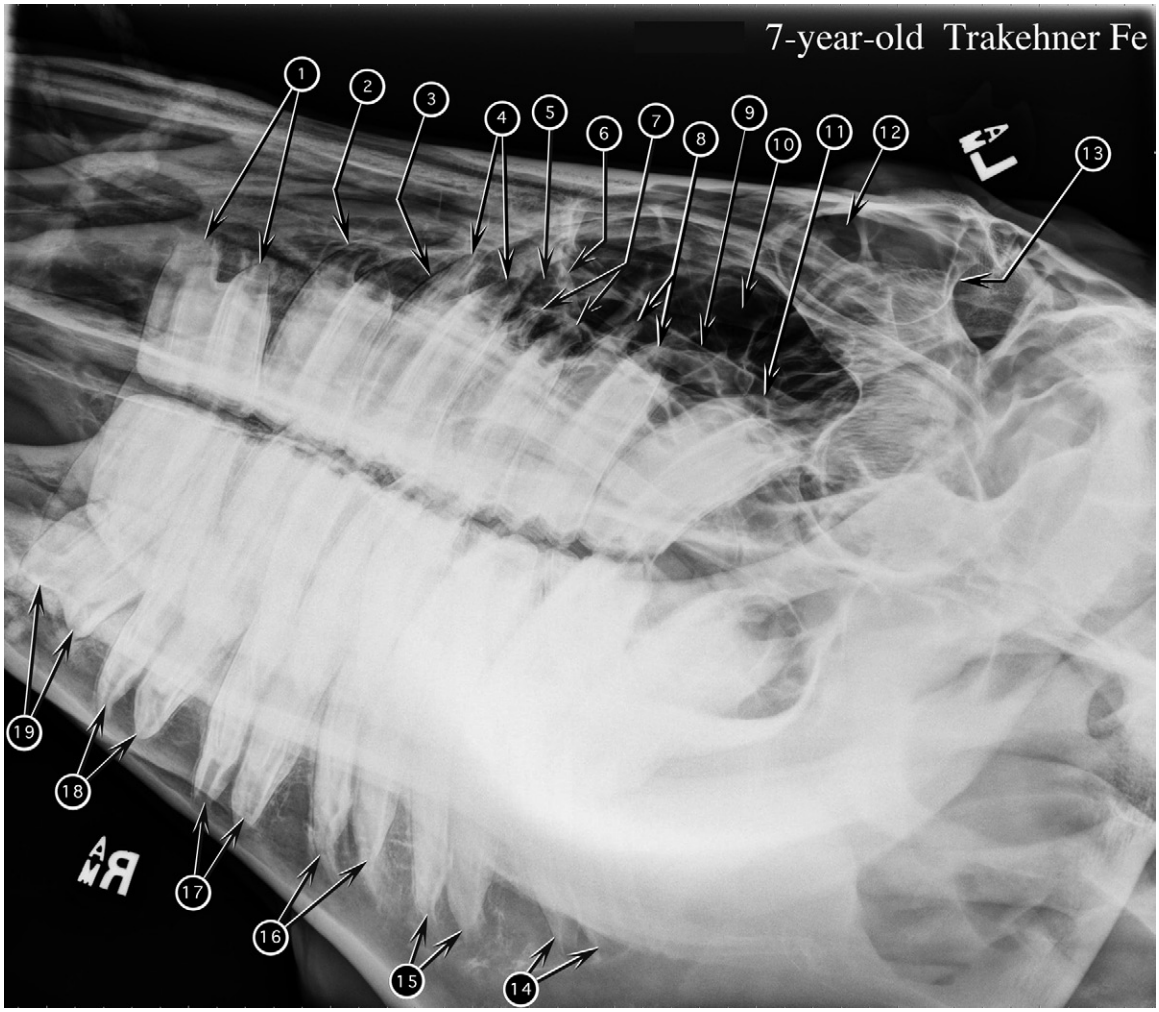


Fig. 6-13 **Left Ventral-Right Dorsal Oblique (LeV-RtDO) Radiograph of Middle Region of Equine Head (7 Years Old).**

1. Roots of left superior premolar 2 (tooth 206)
2. Roots of left superior premolar 3 (tooth 207)
3. Wall of alveolus (*lamina dura dentes*)
4. Roots of left superior premolar 4 (tooth 208)
5. Left rostral maxillary sinus
6. Osseous septum separating 5 from 10
7. Roots of left superior molar 1 (tooth 209)
8. Roots of left superior molar 2 (tooth 210)
9. Left infraorbital canal
10. Left caudal maxillary sinus
11. Roots of left superior molar 3 (tooth 211)
12. Left conchofrontal sinus
13. Zygomatic process of left frontal bone
14. Roots of right inferior molar 3 (tooth 411)
15. Roots of right inferior molar 2 (tooth 410)
16. Roots of inferior molar 1 (tooth 409)
17. Roots of right inferior premolar 4 (tooth 408)
18. Roots of right inferior premolar 3 (tooth 407)
19. Roots of right inferior premolar 2 (tooth 406)

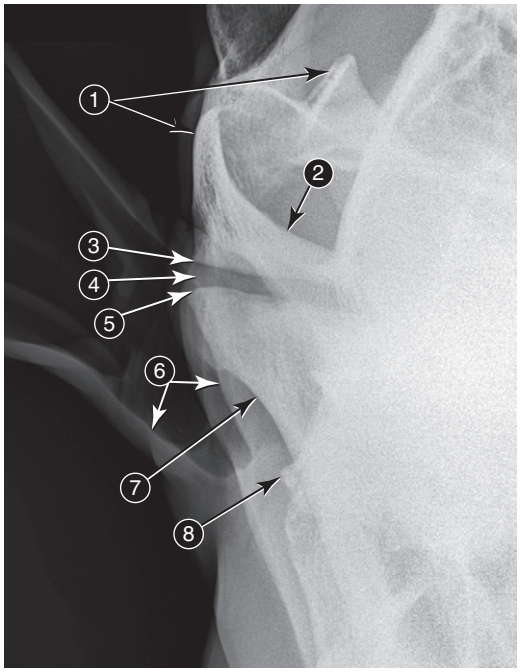


Fig. 6-14 **Rostrodorsal-Caudoventral Oblique (RD-CdVO) Radiograph of Right Equine Temporomandibular Joint (11 Years Old).**
1. Zygomatic arch
2. Zygomatic process of frontal bone
3. Articular surface of squamous temporal bone
4. Articular disc, which completely divides temporomandibular joint into upper (temporal) and lower (mandibular) compartments
5. Head of mandible
6. Air in cartilaginous part of external acoustic meatus
7. Neck of mandible
8. Caudal lacrimal process projecting from rostromedial edge of orbit

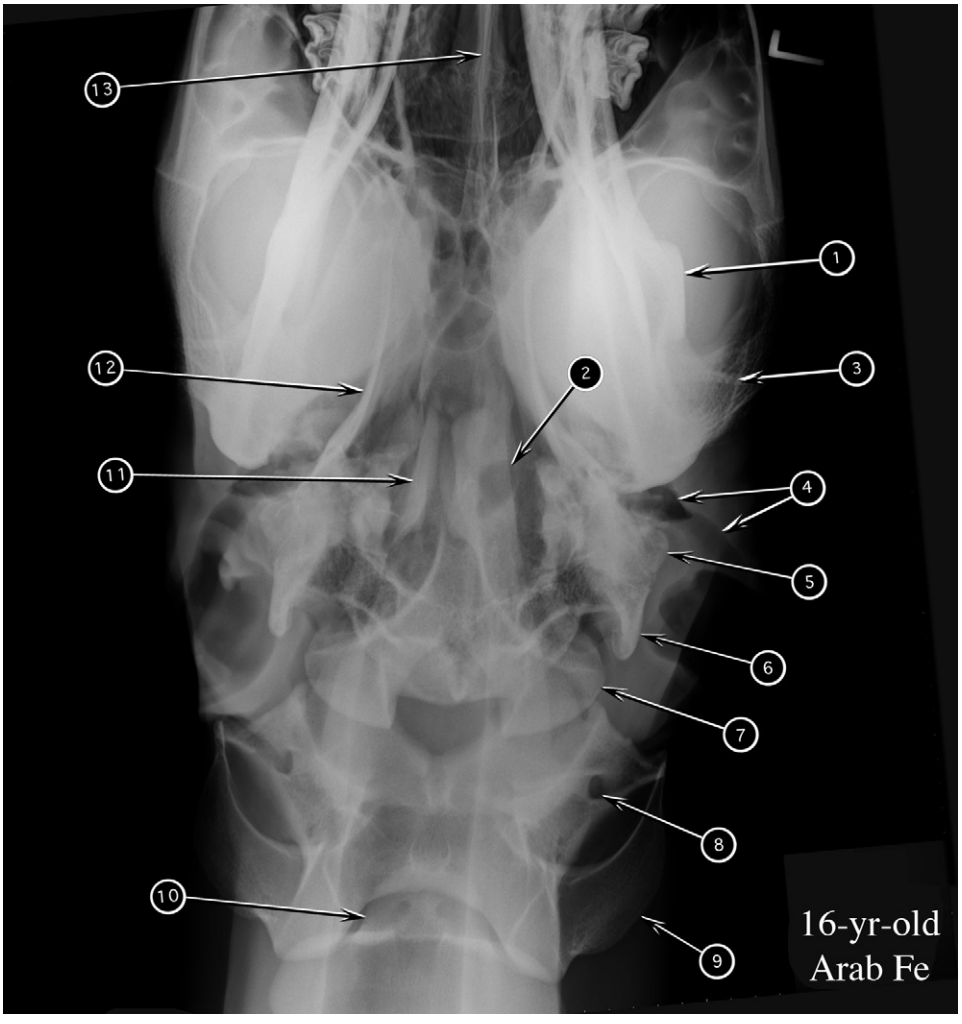


Fig. 6-15 **Dorsoventral Radiograph of Caudal Region of Equine Head (16 Years Old).**
1. Coronoid process of left mandible
2. Left laryngeal ventricle
3. Left temporomandibular joint
4. External ear canal
5. Mastoid process of temporal bone
6. Paracondylar process of occipital bone
7. Occipital condyle
8. Alar foramen of atlas
9. Wing of atlas
10. Dens of axis
11. Right arytenoid cartilage of larynx
12. Right stylohyoid bone
13. Nasal septum

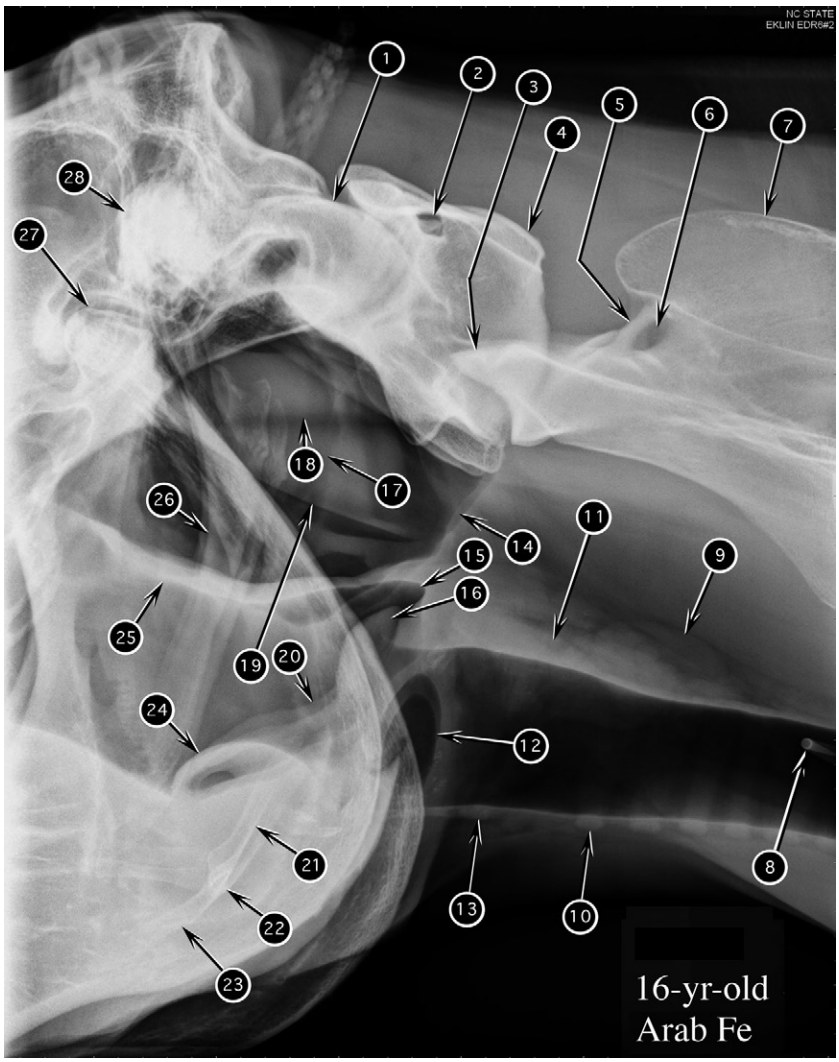


Fig. 6-16 **Left-Right Lateral Radiograph of Occipital Region of Equine Head (16 Years Old).**

1. Occipital condyles
2. Lateral vertebral foramina of atlas
3. Dens of axis
4. Dorsal arch of atlas
5. Ossified ligaments forming cranial boundary of 6 (not ossified in foals)
6. Lateral vertebral foramina of axis
7. Spinous process of axis
8. Catheter in external jugular vein
9. Thyroid gland
10. Tracheal cartilage
11. Lamina of cricoid cartilage
12. Laryngeal ventricles
13. Arch of cricoid cartilage
14. Caudal extent of medial compartments of guttural pouches
15. Laryngopharynx
16. Corniculate processes of arytenoid cartilages
17. Caudal extent of lateral compartments of guttural pouches
18. Rectus capitis ventralis muscle
19. Longus capitis muscles
20. Aryepiglottic folds
21. Thyrohyoid bones
22. Basihyoid bone
23. Lingual process of 22
24. Epiglottic cartilage
25. Dorsal wall of nasopharynx
26. Stylohyoid bones
27. Temporomandibular joints
28. Petrous temporal bones

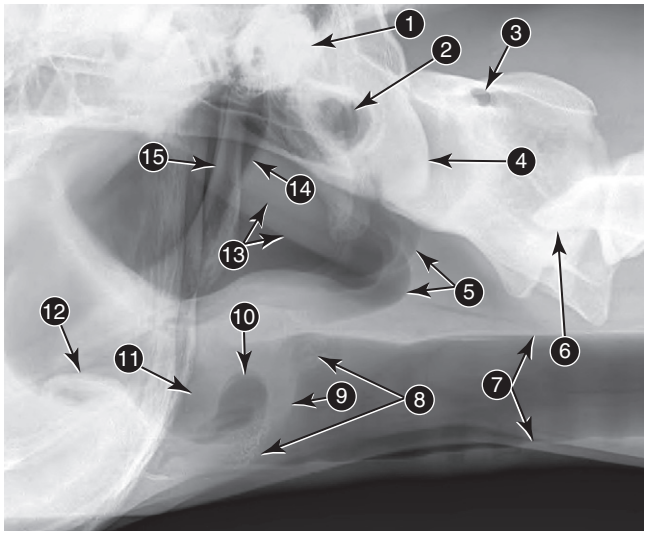


Fig. 6-17 **Left-Right Lateral (Le-RtL) Radiograph of Equine Guttural Pouches and Laryngeal Area (11 Years Old).**

1. Petrous temporal bones
2. Hypoglossal canals
3. Lateral vertebral foramina of atlas
4. Occipital condyles
5. Dens of axis
6. Caudal extent of medial compartments of guttural pouches
7. Air in trachea
8. Early mineralization within thyroid cartilage of larynx*
9. Vocal folds
10. Laryngeal ventricles
11. Vestibular folds
12. Epiglottis
13. Longus capitis muscles
14. Caudal extent of lateral compartments of guttural pouches
15. Stylohyoid bones

*In this horse, the mineralization involves the thyroid cartilage. Mineralization of the laryngeal cartilages in older horses is commonly observed radiographically as an incidental finding, which is not thought to be associated with any clinical problem. However, advanced mineralization of the cricoid or especially arytenoid cartilages may be of clinical concern. (See Tatarniuk, DM, Carmalt, JL, Allen, AL: Induration of the cricoid cartilage complicates prosthetic laryngoplasty in a horse, *Vet Surg* 39:128–130, 2010.)

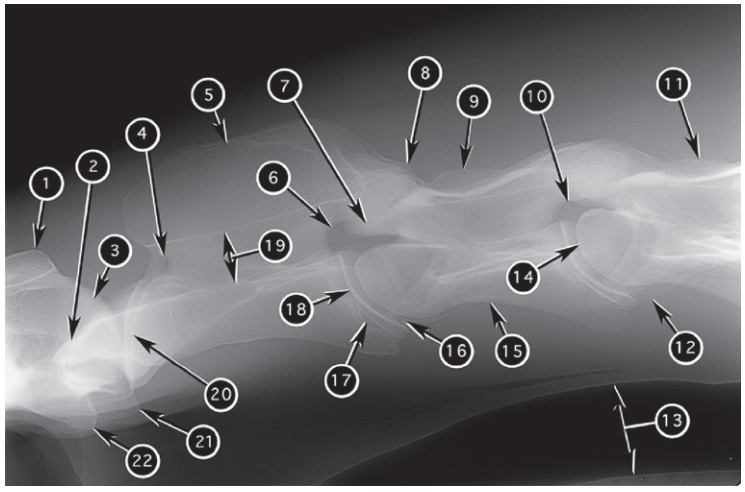


Fig. 6-18 **Left-Right Lateral Radiograph of Equine Cranial Cervical Vertebrae.**

1. Dorsal arch of atlas
2. Dens of axis
3. Caudal articular fovea of atlas
4. Lateral vertebral foramina of axis
5. Spinous process of axis
6. Intervertebral foramina between C2 and C3
7. Cranial articular processes of C3
8. Caudal articular processes of C2
9. Spinous process of C3
10. Intervertebral foramina between C3 and C4
11. Spinous process of C4
12. Transverse processes of C4
13. Trachea
14. Cranial extremity (head) of C4
15. Body of C3
16. Intervertebral space (disk) between C2 and C3
17. Caudal physis of C2
18. Caudal extremity (fossa) of C2
19. Vertebral canal of C2
20. Cranial articular processes of axis
21. Wings of atlas
22. Ventral tubercle of atlas

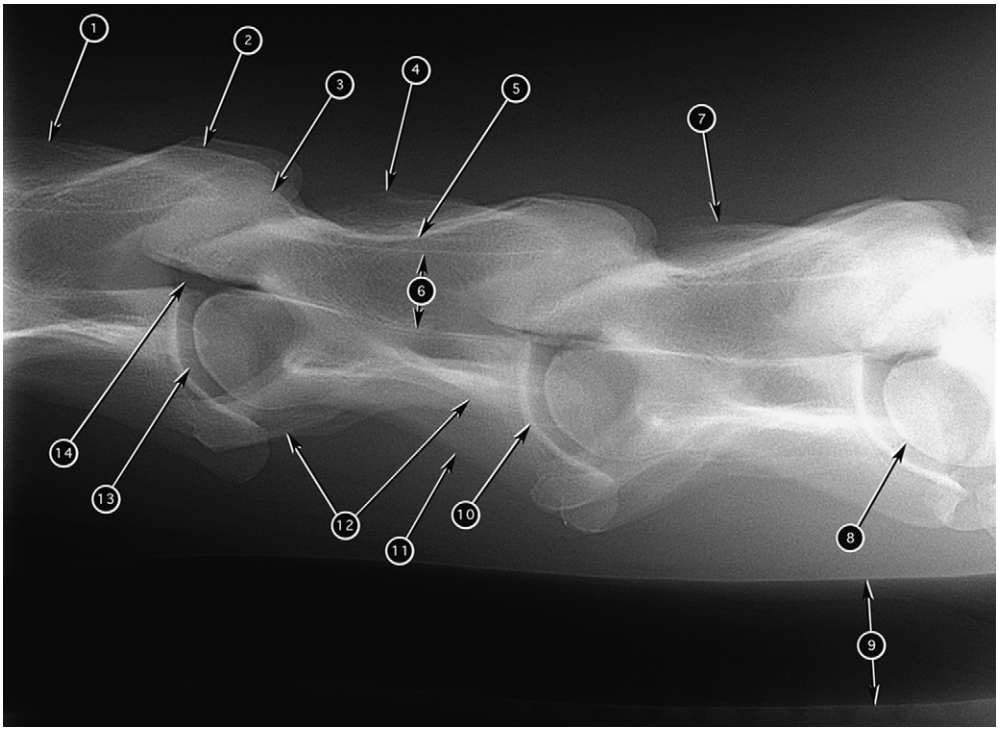


Fig. 6-19 **Left-Right Lateral Radiograph of Equine Middle Cervical Vertebrae.**

1. Spinous process of C3
2. Caudal articular processes of C3
3. Cranial articular processes of C4
4. Spinous process of C4
5. Vertebral arch laminae of C4
6. Vertebral canal of C4
7. Spinous process of C5
8. Cranial extremity (head) of C6
9. Trachea
10. Caudal extremity (fossa) of C4
11. Body of C4
12. Transverse processes of C4
13. Intervertebral space (disk) between C3 and C4
14. Intervertebral foramina between C3 and C4

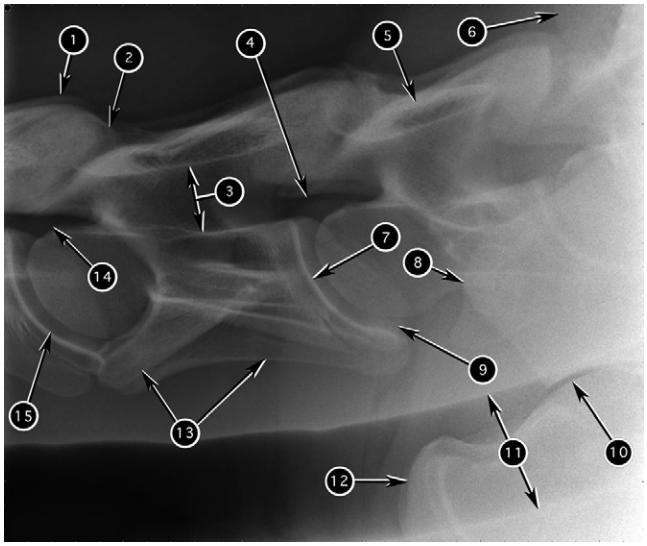


Fig. 6-20 **Left-Right Lateral Radiograph of Equine Caudal Cervical Vertebrae.**

1. Caudal articular processes of C5
2. Cranial articular processes of C6
3. Vertebral canal of C6
4. Intervertebral foramina between C6 and C7
5. Vertebral arch laminae of C7
6. Spinous process of T1
7. Caudal extremity (fossa) of C6
8. Supraglenoid tubercle of scapula
9. Intervertebral space (disk) between C6 and C7
10. Shoulder joint
11. Trachea
12. Intermediate tubercle of humerus
13. Transverse processes of C6
14. Intervertebral foramina between C5 and C6
15. Intervertebral space (disk) between C5 and C

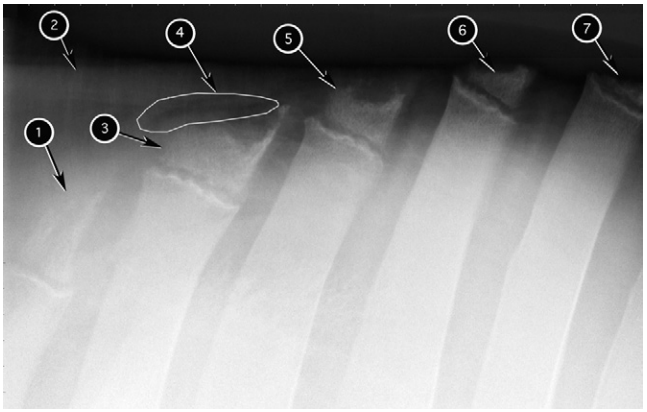


Fig. 6-21 **Left-Right Lateral Radiograph of Equine Withers Region.**

1. Spinous tuberosity of T2
2. Funiculus nuchae
3. Spinous tuberosity of T3
4. Approximate location of supraspinous bursa
5. Spinous tuberosity of T4
6. Spinous tuberosity of T5
7. Spinous tuberosity of T6

REFERENCES

1. Schebitz HCH: *Atlas of radiographic anatomy of the dog*, Stuttgart, Germany, 2005, Parey Verlag.
2. Schebitz H, Wilkens H: *Atlas of radiographic anatomy of the horse*, ed 3, Philadelphia, 1978, Saunders.
3. Thrall D, Robertson ID: *Atlas of normal radiographic anatomy and anatomic variants in the dog and cat*, St. Louis, 2011, Elsevier-Saunders.
4. Smallwood JE, Shively MJ, Rendano VT, et al: A standardized nomenclature for radiographic projections used in veterinary medicine, *Vet Radiol* 26:2, 1985.

ELECTRONIC RESOURCES

evolve

Additional information related to the content in Chapter 6 can be found on the companion Evolve website at http://evolve.elsevier.com/Thrall/vetrad/

CHAPTER • 7

Principles of Radiographic Interpretation of the Axial Skeleton

Donald E. Thrall

SKULL

Skull radiography in dogs and cats has been replaced in specialty practices by computed tomography (CT) and magnetic resonance imaging (MRI), and very few skull radiographs are made currently in that setting. There is more of a need for skull radiography in general practice, but skull radiography will still be one of the more infrequent radiographic examinations performed. Thus, because of the low demand, radiology personnel may become out of practice with regard to acquiring diagnostic canine and feline skull radiographs. Given the complexity of the skull and the number of possible special views that can be acquired, it is easy to understand how this might occur. The framework provided here will assist radiographers in acquiring a skull radiographic study of adequate quality.

Although CT and MRI of the skull are feasible in the horse, skull radiography is still performed commonly in that species because of the need for general anesthesia for CT and MRI and for economic reasons.

Positioning: Dog and Cat

The anatomic complexity of the skull makes it imperative that radiographic positioning be standardized and repeatable; this removes a source of variation that can complicate radiographic interpretation. At a minimum, this standardization necessitates sedation, but general anesthesia is preferable. Making skull radiographs without sedating or anesthetizing the patient leads to the production of poor-quality images that cannot be interpreted intelligently and is a waste of time, effort, and money.

Lateral and dorsoventral (DV) views are the minimum radiographic projections of the canine and feline skull to acquire. The DV view is preferred over the ventrodorsal (VD) view, because for the DV view the mandibles can be compressed mildly against the x-ray table, which facilitates obtaining a symmetrically positioned radiograph (Fig. 7-1). This assumes that there is not mandibular asymmetry, as from a fracture or a mass for example, which would make it impossible to position the head symmetrically using the mandibles as a guide. As the dorsal surface of the head is rarely flat, extreme care must be taken to position the head symmetrically if a VD view is attempted.

For the lateral view, the dog or cat cannot be allowed to rest naturally on the x-ray table. Radiolucent sponges will be needed to elevate the nose in most patients. Sponges may also be needed to elevate the mandibles. The goal is to have left-sided and right-sided structures superimposed perfectly in the resultant radiograph (Fig. 7-2). Care must be taken to keep the positioning devices free of dirt and debris that can introduce artifacts into the image (see Fig. 7-2). The mouth can be either left closed or held open with a speculum. If the disease affects the mandible or maxilla, then there is value in having the mouth open to reduce superimposition.

Because of the complexity of the skull, many ancillary projections have been devised to increase the conspicuity of certain regions. These are listed in Table 7-1, and a few selected examples are included here (Figs. 7-3 through 7-9). Space does not permit a thorough discussion of each of the ancillary views that are available for use in the skull, but other sources are available.[1,2] These ancillary views are not used routinely but are selected based on the purpose of the radiographic examination. Many ancillary views of the skull involve having the skull at an angle with respect to the primary x-ray beam; this requires changing the position of the patient. Some other ancillary views actually require that the x-ray beam be angled from its normal perpendicular perspective with respect to the x-ray table; this requires having an x-ray machine with an x-ray tube head that can be (1) moved longitudinally along the top of the x-ray table and (2) rotated clockwise or counterclockwise to angle the primary x-ray beam.

An important aspect regarding oblique radiographs of the skull is making sure that a reliable external marking system has been used so that left can be distinguished from right in the image. It is helpful to use both "L" *and* "R" markers on the same image to designate which structures are being projected (Fig. 7-10). Taking the time to define a suitable marking system for your practice and explaining it thoroughly to personnel will save confusion in the long run. This is a situation where identification of a radiology supervisor, discussed in Chapter 1, is valuable because he or she can become familiar with the marking system and ensure that it is used correctly and routinely.

Positioning: Horse

Sedation is not required for equine skull radiography, but sedation will facilitate radiographic acquisition, especially for the DV view, where the dropped position of the head will make it easier to position the x-ray tube dorsally. Skull radiographs of most horses are acquired with the horse standing. It may be possible to position a sedated or anesthetized foal on the x-ray table for skull radiography, as for a dog or cat, but this is not done commonly.

For the lateral view, the cassette is positioned against the side of the head and the x-ray beam directed from the opposite side (Fig. 7-11, *A*). The position of the cassette and x-ray beam can be adjusted for acquiring radiographs of different regions of the skull, such as the nasal cavity versus the brain case versus the guttural pouches. Another thing to keep in mind for the lateral view is the effect of magnification. Because



Fig. 7-1 A perfectly positioned DV skull radiograph. Note the perfect symmetry of left and right sides and superimposition of the mandibular symphysis on the vomer bone. Slight downward pressure on the skull during radiography will facilitate obtaining perfect positioning if the mandibles are symmetric because the mandibles provide a flat, stable surface as a supporting base for the head.

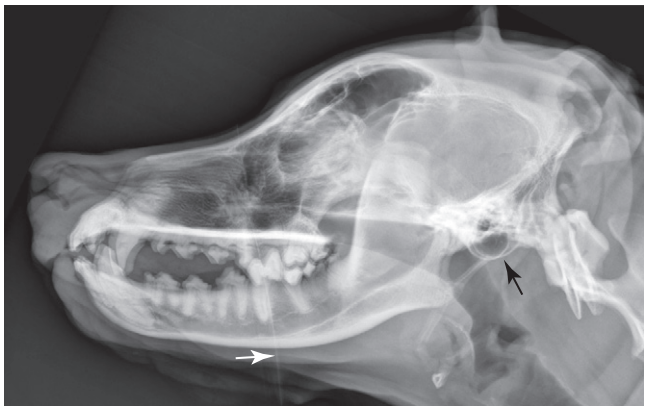


Fig. 7-2 Perfectly positioned lateral skull radiograph. The mandibles have been elevated from the x-ray table using a radiolucent sponge. These positioning devices can become soiled and introduce artifacts into the image, as seen here *(white arrow)*. Care should be taken to keep positioning devices free from debris, which can interfere with interpretation. Despite this artifact, note the perfect superimposition of the tympanic bullae *(black arrow)*. Sedation or anesthesia is necessary to achieve this excellent positioning.



Fig. 7-3 Rostrocaudal frontal sinus view (see Table 7-1, View No. 1). The patient is in dorsal recumbency with the nose pointing directly at the x-ray tube. This view, which provides an unobstructed view of each frontal sinus, is useful only in subjects with developed frontal sinuses. Brachycephalic breeds of dogs and some cats have incompletely developed, and/or nonpneumatized, frontal sinuses. In those patients, this projection has no value to assess the sinus cavity but may be useful for assessing the frontal bone itself. If the sinus cavity contents are of interest, the frontal sinuses should be examined in the lateral view to make sure they are present and pneumatized before going to the trouble of acquiring this rostrocaudal view. *L*, left side; *R*, right side.

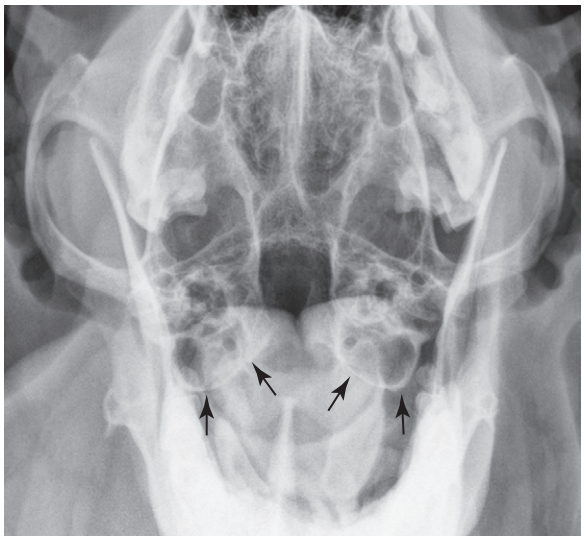


Fig. 7-4 Open-mouth rostrocaudal view of tympanic bullae (see Table 7-1, View No. 8). The patient is in dorsal recumbency with the nose pointing at the x-ray tube. The mouth is then opened by retracting the mandible and maxilla with gauze. Centering the x-ray beam in the back of the open mouth provides a relatively unobstructed view of the tympanic bullae *(black arrows)*.

of the thickness of the equine skull, a lesion on the x-ray tube side of the skull will be magnified considerably and may not be conspicuous because of blurring. Thus if the location of the lesion is known, the cassette should be held against that side of the head and the x-ray beam directed from the opposite side. If the location of the lesion is not known, it is good practice to obtain both the left-right and right-left radiographs of the skull to make sure that a lesion is not overlooked because of magnification.

For the DV view, the cassette is held ventral to the mandibles and the x-ray beam directed onto the dorsal aspect of the head (Fig. 7-11, *B*). It is important to keep the x-ray beam perpendicular to the cassette. As noted before, sedation is very helpful for obtaining the DV view because as the horse lowers its head in response to the sedative, the positioning of the x-ray tube dorsally is facilitated. Without sedation one might be able to acquire a DV view of the nasal passage, but a DV view of the calvaria or brain case will not be possible. VD views of the skull are not made in the standing horse.

Radiation safety becomes paramount when radiographing the equine skull. Placing the cassette in a cassette holder with an extension handle is impractical because the force needed to keep the large cassette in the proper position increases as the hands move further distant on the handle; this leads to cassette motion and blurring of the image. In many instances, the only way to acquire an equine DV skull radiograph is to hold the cassette by hand. If this is done, the hands should be

Table • **7-1**

Ancillary Radiographic Projections of the Canine or Feline Skull

VIEW NO.	PART OF INTEREST	NAME OF PROJECTION	BRIEF DESCRIPTION
1	Frontal sinuses	Rostrocaudal projection of frontal sinuses	Subject in dorsal recumbency. Head flexed 90 degrees to spine such that nose points directly at x-ray tube. Center x-ray beam on frontal sinuses.
2	Right maxillary dental arcade or right tympanic bulla.	Open mouth left 20-degree ventral—right dorsal*	Subject in right recumbency. Secure mouth open with speculum. Elevate mandibles 20 degrees with sponge wedge. Center x-ray beam on right maxillary arcade or tympanic bulla.
3	Left maxillary dental arcade or left tympanic bulla.	Open mouth right 20-degree ventral—left dorsal	Subject in left recumbency. Secure mouth open with speculum. Elevate mandibles 20 degrees with sponge wedge. Center x-ray beam on left maxillary arcade or tympanic bulla.
4	Right mandibular dental arcade	Open mouth left 20-degree dorsal—right ventral	Subject in right recumbency. Secure mouth open with speculum. Elevate maxilla 20 degrees with sponge wedge. Center x-ray beam on right mandibular arcade.
5	Left mandibular dental arcade	Open mouth right 20-degree dorsal—left ventral	Subject in left recumbency. Secure mouth open with speculum. Elevate maxilla 20 degrees with sponge wedge. Center x-ray beam on left mandibular arcade.
6	Nasal cavity	Open mouth ventral 20-degree rostral—dorsocaudal	Subject in dorsal recumbency. Secure maxilla against x-ray table such that hard palate is parallel to tabletop. Open mouth widely with speculum or gauze traction on mandible. Angle x-ray beam 20 degrees rostrally and center x-ray beam on hard palate.
7	Nasal cavity	Intraoral dorsoventral	Subject in ventral recumbency. Slide cassette into mouth. Center x-ray beam on dorsal aspect of maxilla.
8	Tympanic bullae	Open mouth rostrocaudal	Subject in dorsal recumbency. Head flexed 90 degrees to spine such that nose points directly at x-ray tube. Open mouth by retracting maxilla and mandible equally with gauze or tape. Center x-ray beam in back of mouth.
9	Tympanic bullae (cats and brachycephalic dogs)	Rostral 10 degrees ventral—caudodorsal	Subject in dorsal recumbency. Head flexed 90 degrees to spine such that nose points directly at x-ray tube. Angle head/neck 10 degrees caudally, keeping mouth closed. Center x-ray beam at base of skull.
10	Right tympanic bulla/right temporomandibular joint.	Left 20 degrees rostral—right caudal	Subject in right recumbency. Elevate nose 20—30 degrees with sponge. Center x-ray beam on region of temporomandibular joint.
11	Left tympanic bulla/left temporomandibular joint.	Right 20 degrees rostral—left caudal	Subject in left recumbency. Elevate nose 20—30 degrees with sponge. Center x-ray beam on region of temporomandibular joint.

*Any angle specified in this table for this or any other ancillary skull radiograph is an estimate. This will vary among dogs and should be selected based on visual determination of the angle that results in optimal isolation of the area of interest.

shielded with lead gloves, the body with a lead apron, and a thyroid shield and protective glasses should be worn. The x-ray beam must also be collimated such that the gloved hands are never in the primary x-ray beam. Protective lead gloves are adequate for protection only against scattered photons. For the lateral view, these same precautions apply, but care must also be taken to make sure that no part of the body is directly behind the cassette, where it will be in the direct line of fire of photons passing through the patient and then through the cassette.



Fig. 7-5 Intraoral DV radiograph of maxilla (see Table 7-1, View No. 7). The patient is in ventral recumbency with the cassette inserted into the mouth and the x-ray beam directed onto the dorsal surface of the maxilla. Using a thin paper cassette allows the film to be inserted further caudally than when using a conventional film cassette or a computed radiography cassette. Some paper cassettes have no intensifying screen, meaning that x-rays are being used to expose the film rather than visible light from the intensifying screen. This will require considerably higher mAs values than when an intensifying screen is used, but the detail in the image will be exquisite, as seen here. This projection provides an unobstructed view of the nasal cavity.

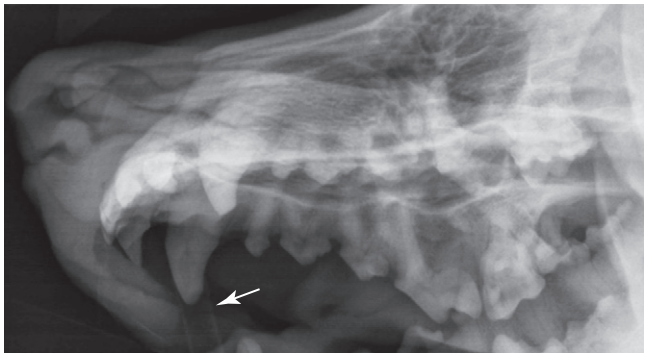


Fig. 7-6 Open mouth, left 20-degree ventral–right dorsal projection of the right maxillary dental arcade (see Table 7-1, View No. 2). The patient is in right recumbency and the mouth secured open with a speculum. A portion of the speculum is visible *(white arrow)*. The mandibles are elevated 20 degrees from the tabletop with a radiolucent sponge. This positions the left maxillary arcade dorsal to the right. The x-ray beam, which is vertical to the tabletop, is centered on the right maxillary arcade.

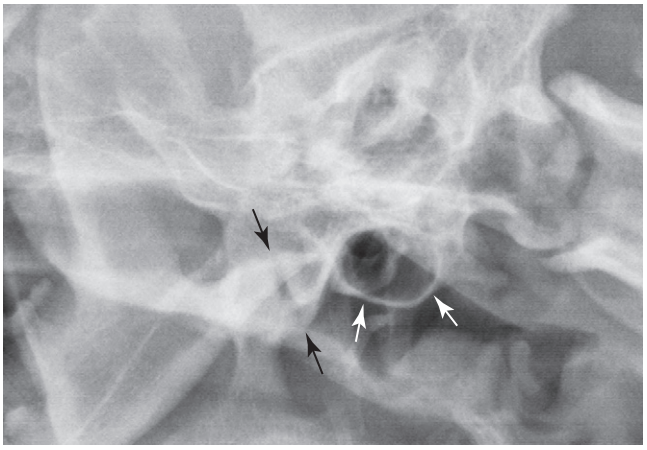


Fig. 7-7 Open-mouth, left 20-degree ventral–right dorsal projection of the right tympanic bulla and temporomandibular joint (see Table 7-1, View No. 2). The patient is positioned exactly as described in the legend for Figure 7-6, except the x-ray beam has been centered on the middle ear. This allows assessment of the right (dependent) tympanic bulla *(white arrows)* and right temporomandibular joint *(black arrows)*. The left (nondependent) tympanic bulla and left temporomandibular joint are located dorsal to the right tympanic bulla and right temporomandibular joint and are superimposed on the skull. Only the right tympanic bulla and temporomandibular joint can be assessed using this positioning. If the left-sided structures are of interest, then the view described in Table 7-1, View No. 3, should be used.

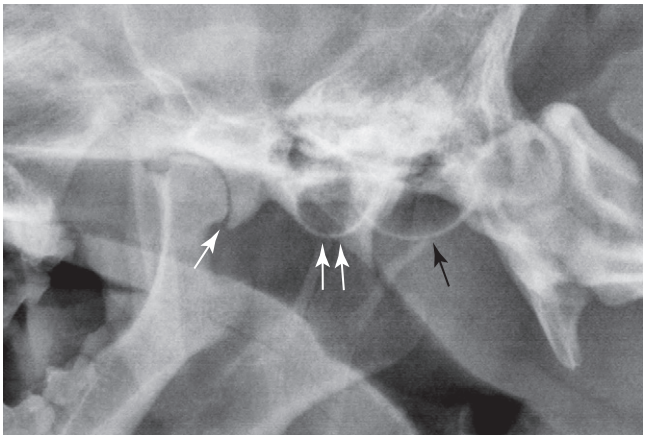


Fig. 7-8 Left 20-degree rostral–right caudal projection of the right temporomandibular joint *(single white arrow)* and right tympanic bulla *(double white arrows)* (see Table 7-1, View No. 10). The patient is in right recumbency, and the tip of the nose is elevated 20 degrees from the tabletop. The x-ray beam is perpendicular to the tabletop and centered on the tympanic bulla region. Elevating the nose positions the upper, left, nondependent tympanic bulla *(single black arrow)*, caudal to the lower, right, dependent tympanic bulla *(double white arrows)*. Compared with Figure 7-7, the contralateral, nondependent, left tympanic bulla *(black arrow)* is positioned caudal to the one of interest rather than being dorsal. Note that the nondependent, left tympanic bulla is larger because of radiographic magnification. In this view, the nondependent, left temporomandibular joint is superimposed on the region where the tympanic bullae overlap.

As in the dog and cat, ancillary oblique views of the equine skull are often needed because of the anatomic complexity. Oblique views commonly used in the horse are those designed to evaluate a nasal passage or a dental arcade (Fig. 7-12). As for oblique views in the dog and cat, development and routine implementation of a standard anatomic marking system is critical to ensure that the structures being projected are identified accurately (Fig. 7-13).

Radiographic Technique: Dog and Cat

When radiographing the canine or feline skull using a film-screen system, there are indications for both low kilovoltage peak (kVp)–high milliampere second (mAs) and high kVp–low mAs techniques. With the low kVp–high mAs technique, contrast will be increased, and assessing bone changes will be enhanced, but soft tissue changes may not be conspicuous. Using a high kVp–low mAs technique will allow the soft

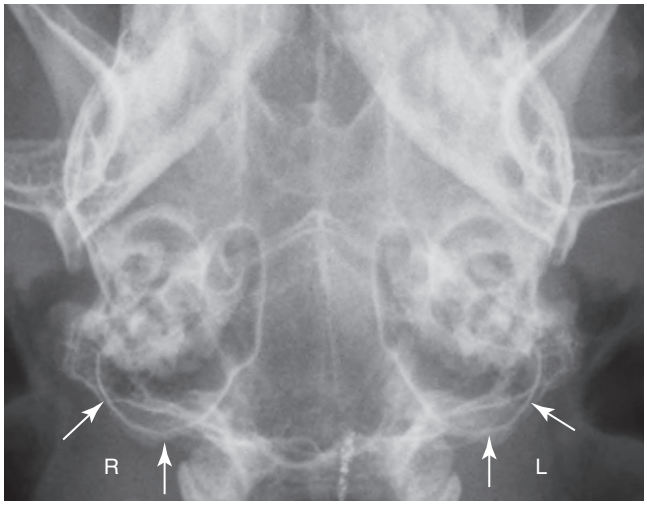


Fig. 7-9 Rostral 10-degree ventral–caudodorsal view of the tympanic bullae *(white arrows)* in a cat (see Table 7-1, View No. 9). The patient is in dorsal recumbency with the nose pointing directly at the x-ray tube. The head and neck are extended 10 degrees, and the x-ray beam, which is perpendicular to the tabletop, is centered at the base of the skull. *L*, left; *R*, right.

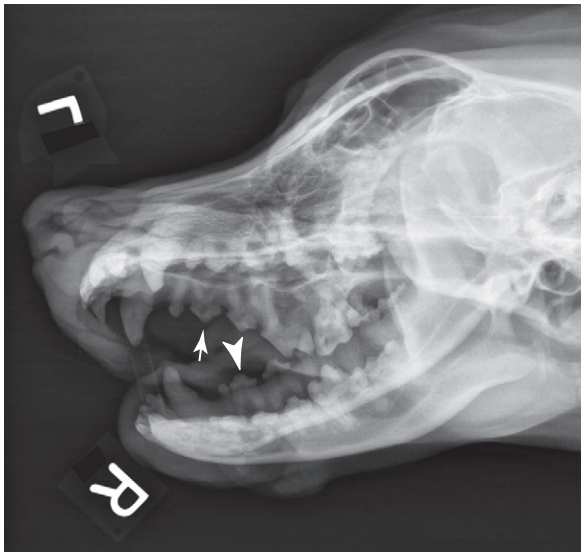


Fig. 7-10 Example of an external marking system for oblique skull radiographs. This is the same projection as described for Figure 7-6. In this system, the *(L)* at the top of the image and the *(R)* at the bottom of the image means that with bilaterally symmetric structures, such as maxilla and mandibles, the left side will be dorsal and the right side ventral. Thus, the positioning used in this dog is such that the right maxillary dental arcade *(arrow)* and the left mandibular dental arcade *(arrowhead)* are projected for unobstructed viewing.

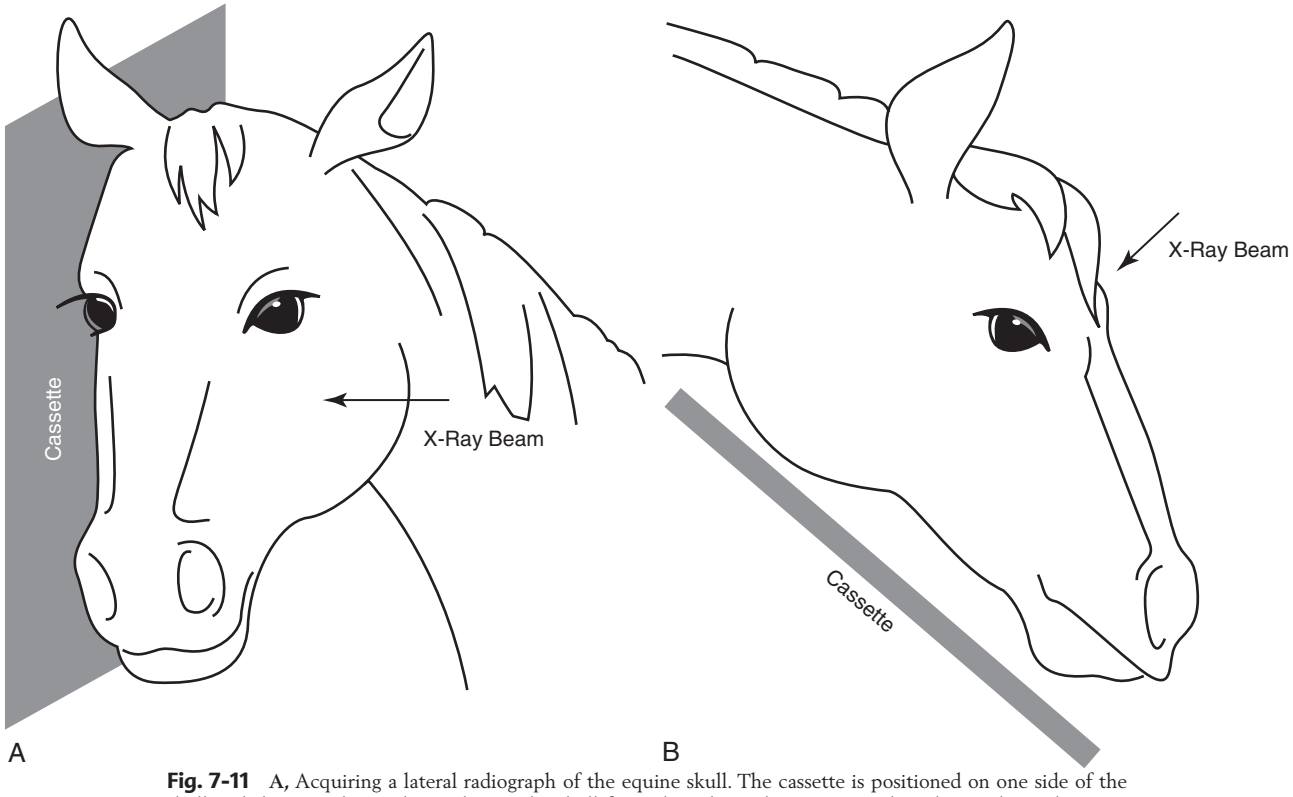


Fig. 7-11 **A,** Acquiring a lateral radiograph of the equine skull. The cassette is positioned on one side of the skull and the x-ray beam directed onto the skull from the other side. Care must be taken to keep the x-ray beam perpendicular to the cassette. **B,** Acquiring a DV radiograph of the equine skull. The cassette is positioned below the mandibles and the x-ray beam directed onto the skull from the dorsal aspect. As with the lateral view, care must be taken to keep the x-ray beam perpendicular to the cassette.

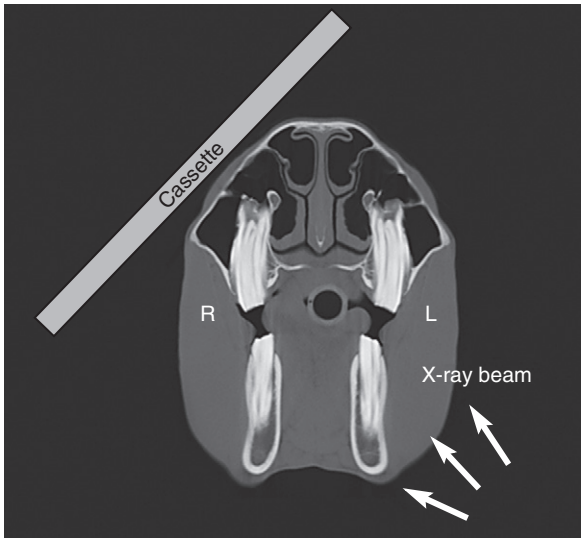


Fig. 7-12 Geometry of a commonly used oblique view of the equine head. A transverse-CT image of the skull at the level of the mid-maxilla is shown, along with the relative positions of the cassette and x-ray beam, represented by the *white arrows*. In this view, termed a *left 45-degree ventral–right dorsal oblique*, the cassette is positioned on the right side at a 45-degree angle to the ground, and the x-ray beam *(white arrows)* is opposed perpendicularly from the left side. This geometry will result in an unobstructed view of the roots of the left maxillary dental arcade and the right mandibular dental arcade. The roots of the left mandibular and right maxillary dental arcades will be superimposed. By keeping this same cassette-beam configuration but moving the center of the beam more caudal, one can project other structures, such as the left supraorbital process or the left ethmoid region.

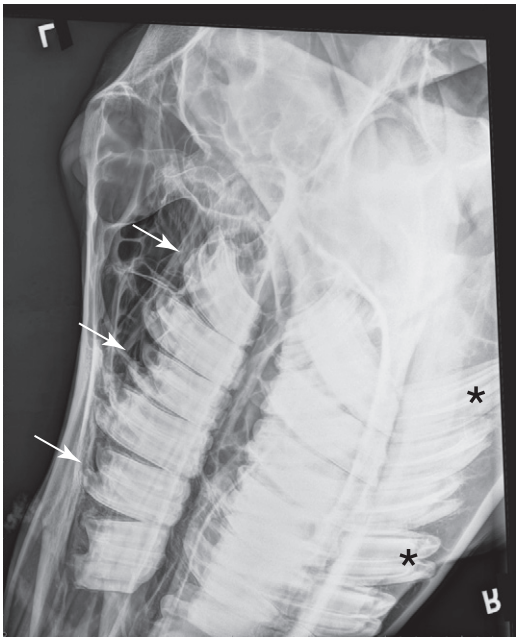


Fig. 7-13 Radiograph acquired using the geometry illustrated in Figure 7-12. Note the use of *(L)* and *(R)* markers to reduce confusion. These markers indicate that the left maxillary and right mandibular arcades are projected unobstructed. The obliquity used resulted in visualization of the entire left maxillary arcade *(white arrows)*. In the right mandible, only the roots *(black asterisk)* are projected unobstructed, and the crowns cannot be seen clearly. The right maxillary and left mandibular arcades are superimposed. Refer to Figure 7-12 if these points are not clear.

tissues to be evaluated more thoroughly. Thus, the radiographic technique is related somewhat to the reason for making the radiographs. If using a digital system, exposure factors are less critical because of the enhanced contrast resolution of digital-imaging systems and the ability to manipulate blackness and contrast after the image is acquired, as discussed in Chapter 2. For patients thicker than 10 cm, a grid should be used to remove scattered x-rays from the beam.

Exposure time is less critical when radiographing the canine or feline skull because the patient will be sedated or anesthetized, and there is no inherent movement of this region. If an endotracheal tube is in place for general anesthesia, care should be taken to ensure that the tube does not end up superimposed on the part of interest, especially in oblique radiographs.

Radiographic Technique: Horse

When radiographing the equine skull using a film-screen system, a relatively high technique will be necessary because of the massive nature of the structure. With a film-screen system, it may be preferable to use a high kVp–low mAs technique. The relatively low mAs values will allow a shorter exposure time and are less stressful on the x-ray tube. Long exposure times that lead to motion artifact are a concern with regard to skull radiography in the horse because of the fact that the patient is standing, and head movement will not be eliminated completely by sedation. If one is using a digital system, the relative kVp versus mAs settings are less critical because of the enhanced contrast resolution of digital-imaging systems, and the ability to adjust blackness and contrast after image acquisition, as discussed in Chapter 2.

Although a grid would be useful in the equine skull to improve image quality by reducing fogging from scattered radiation, the higher mAs needed to compensate for the grid may not be justified. High mAs values are already needed because of the mass of the skull, and increasing the mAs even further to compensate for the grid will introduce more x-ray tube wear and increase personnel exposure. Also, a cassette that contains a grid is extremely heavy and difficult to hold steadily by hand. Finally, maintaining a perpendicular relationship between the primary x-ray beam and a handheld cassette is nearly impossible, leading to grid-line artifacts.

A wall-mounted cassette holder, discussed subsequently for equine cervical radiographs, is one method to incorporate the use of a grid for skull radiography without increasing the risk of motion artifact or occupational exposure to personnel.

Ancillary Factors

In the cat and horse, there is little effect of breed variation, but this is not true in the dog where there will be major variation in the appearance of the skull according to breed. In general, there are three cranial morphologic configurations that describe the skull shape in the dog: brachycephalic, mesaticephalic, and dolichocephalic. These are discussed in more detail in Chapter 8. In general, the usefulness of skull radiographs is greater in mesaticephalic and dolichocephalic dogs than in brachycephalic dogs because brachycephalic dogs are more difficult to position accurately, and the nasal cavity and paranasal sinuses are disproportionally small.

Interpretation Paradigm

As mentioned, there are relatively few things, other than canine breed, that influence the normal radiographic appearance of the skull. But because of the complex morphology of the skull, an organized approach is still needed. Assessing whether there is an abnormality in the skull radiographs of a patient should be the *last* step in the interpretive process. The following questions should always be considered first:

- Are the radiographic views adequate, and are all of the views that are needed present? If all of the necessary views are not present, what is likely to be missed and what additional views would help?
- Is the positioning adequate, or are there positioning problems that will interfere with interpretation?
- Is the radiographic technique adequate, or are the images overexposed or underexposed?
- Were the images acquired with the use of an antiscatter grid? How has this affected the image quality?
- Has sedation or anesthesia been used? If not, how did this affect the usefulness of the radiographs?
- What is the species or breed of the patient, and how did this affect the appearance of the images?
- Were the images acquired with a vertically directed x-ray beam with the cassette in an x-ray table, or on the floor for an anesthetized horse? Was a horizontally directed x-ray beam used with handholding of the cassette or a wall-mounted cassette holder?
- Are the images film-based or digital? If the images are film-based, was the radiographic technique a high-contrast or a low-contrast technique.
- Has an external marking system been used such that the distinction between left and right can be made?

Only after all of these things have been considered should one's attention be directed at the identification of abnormalities. In many patients, the answer to the clinical question will not be found in the skull radiographs. It is well known that the staging of disease involving the skull is more accurate when based on tomographic imaging modalities, such as CT or MRI, than on radiographs.[3-5] If the question that was the basis of skull radiography is not answered adequately from the radiographs, CT or MRI should be considered as a next step.

Experienced radiologists may have a random search pattern, but it is recommended that beginning radiologists develop an organized approach to searching radiographs for abnormalities. [6] The following regions can be searched in order: (1) calvaria, (2) tympanic bullae, (3) temporomandibular joints, (4) stylohyoid bone and guttural pouches (horse only), (5) maxillary and mandibular bone, (6) maxillary and mandibular teeth, (7) nasal passage, (8) pharynx, and finally (9) the frontal/conchal/maxillary sinuses. If the same procedure is followed for every patient, the order of searching will become second nature, and as experience is gained the search pattern will become random without a loss of effectiveness. Until then, it may be beneficial for a checklist to be developed to make sure that every anatomic region of the radiograph is examined.

SPINE

As with the canine and feline skull, tomographic imaging, such as CT and MRI, has replaced the use of radiography for assessing many diseases of the canine and feline vertebral column. However, in most small animal practices there are still many indications for survey spinal radiography because of the relatively high incidence of back pain and paresis. Therefore, survey radiographs of the canine and feline spine are indicated commonly, and it is important that these be acquired correctly if their value is to be maximized.

The equine spine does not lend itself well to imaging with CT or MRI. This relates to the fact that positioning the equine spine deeply enough within the gantry aperture is hindered by the girth of the horse. Foals and small horses can often undergo CT or MRI of any segment of the spine, but in an adult horse the cranial aspect of the cervical spine is the only region that can be imaged adequately with CT or MRI. Thus, most spinal imaging in the horse is radiograph based.

There are some unique features of the spine that should be kept in mind when evaluating spinal radiographs. These are discussed in more detail elsewhere.[1]

- The vertebral formula for the dog and cat is C7 T13 L7 S3 $Cd_{variable}$.
- The vertebral formula for the horse is C7 T18 L6 S5 Cd15-21.
- The number of caudal vertebrae is more variable in dogs and cats than in horses. Some of these variations are breed related (e.g. screw-tail dogs, Manx cats).
- There is no intervertebral disc between C1 and C2.
- C6 has proportionally larger transverse processes in the dog and horse that can serve as an anatomic landmark (Fig. 7-14).
- Thoracic spinous processes in the horse are longer, on a relative basis, than in the dog or cat.
- In the horse, the dorsal tip of spinous processes in the cranial aspect of the thoracic spine may appear highly irregular, and this is often confused with an aggressive process or fracture (Fig. 7-15).
- In the dog and cat, the thoracic vertebra with a vertical spinous process is called the *anticlinal vertebrae*; this can be either T10 or T11 (Fig. 7-16).[7]
- Cranial to the anticlinal vertebra, the spinous processes angle caudally, whereas caudal to the anticlinal vertebra, the spinous processes angle cranially.
- The ventral aspect of L3 and L4 vertebral bodies in the dog may be relatively indistinct compared with other lumbar vertebrae and this can be consufed with effacement from an aggressive process (Fig. 7-17).

Positioning: Dog and Cat

As with the canine and feline skull, sedation or general anesthesia is indicated if radiographs of the canine or feline spine are going to be acquired. It may seem that chemical restraint is not as pertinent for spinal radiography in the dog and cat as for skull radiography, but this is not true. The spine is also complex anatomically, and it is critical that the patient be positioned symmetrically. Positioning of a dog or cat for spinal radiography is more involved than just laying the patient on the x-ray table (Fig. 7-18).

For most canine and feline patients, lateral and ventrodorsal radiographs will be sufficient for assessing the spine. When acquiring lateral views, the goal is to have the sternum and spine in the same plane; that is, a plane through the sternum and spine is parallel to the tabletop. This cannot be accomplished by allowing the subject to lie unrestrained on the x-ray table (Fig. 7-19). In most dogs and cats the sternum will have to be elevated slightly to position the sternum and spine in the same plane. In a minority of subjects, especially those with a round thorax, it may be necessary to actually displace the sternum ventrally slightly to position the sternum and spine in the same plane. The patient should be inspected visually and palpated to determine in which direction, and by how much, the position of the sternum needs to be adjusted.

Once the sternum and spine are in the same plane, there is another adjustment that may be necessary. In some dogs or cats the spine undulates in the plane parallel to the tabletop, and placing pads under sagging regions will assist in getting a less distorted image of the spine (Fig. 7-20). The goal is to have the radiograph represent the vertebral alignment and character of the intervertebral disk spaces accurately, and this will not be possible unless the patient is positioned symmetrically.

The diverging nature of the primary x-ray beam creates a problem when interpreting vertebrae and intervertebral disk spaces. As beam divergence increases peripheral to the central axis of the primary x-ray beam, the photons will be oriented

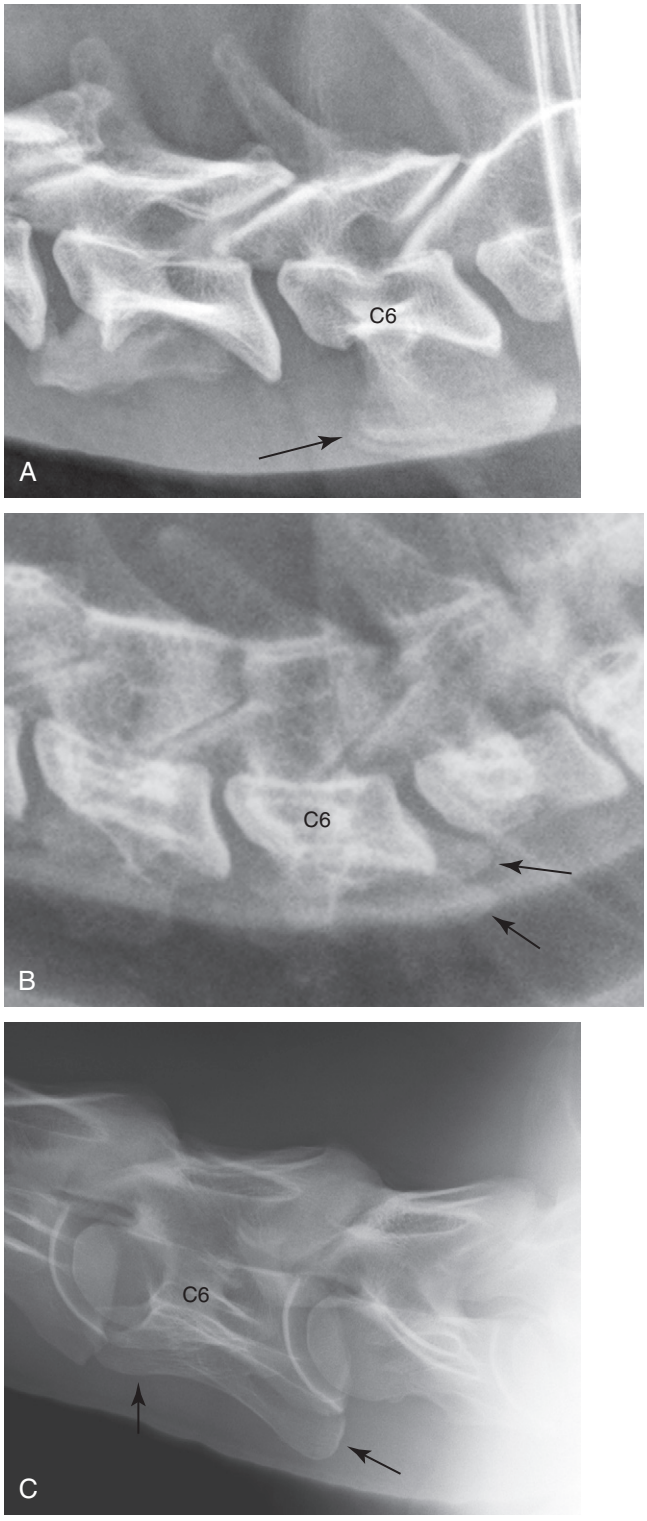


Fig. 7-14 Lateral radiograph of the caudal aspect of the cervical spine in a dog **(A),** cat **(B),** and horse **(C).** In the dog and horse, the transverse processes of C6 *(black arrows)* are larger than on other cervical vertebrae and serve as useful anatomic landmarks. In the cat **(B),** the transverse processes on C6 are only minimally larger *(black arrows)* and not as conspicuous and therefore not as useful as an anatomic landmark.

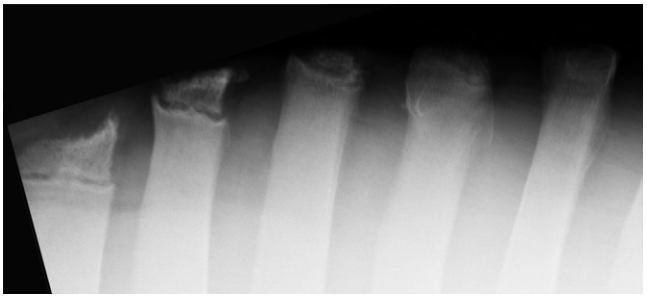


Fig. 7-15 Lateral radiograph of the dorsal aspect of the first few thoracic spinous processes of a horse. The mineralized cartilage cap is often misinterpreted as a fracture. Not all horses have spinous processes with mineralized caps. Some of the spinous processes also have a smooth periosteal reaction; this is also normal.

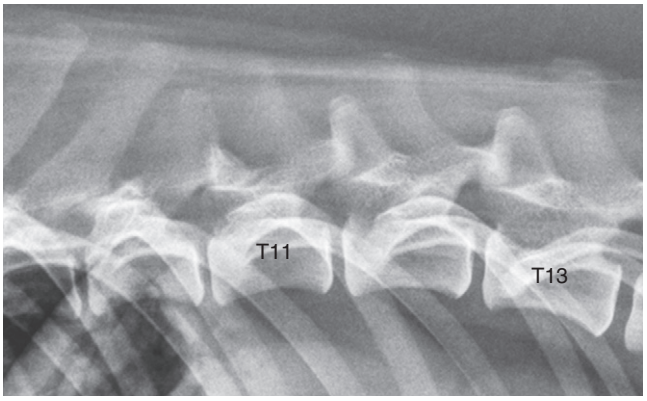


Fig. 7-16 Lateral radiograph of the caudal aspect of the thoracic spine in a dog. The spinous process on T11 is vertical, making it the anticlinal vertebra. Cranial to T11 the spinous processes angle caudally, while caudal to T11 the spinous processes angle cranially. (Reprinted with permission from Thrall DE, Robertson ID: *Atlas of normal radiographic anatomy and anatomic variants in the dog and cat*, St Louis, 2011, Elsevier-Saunders.)

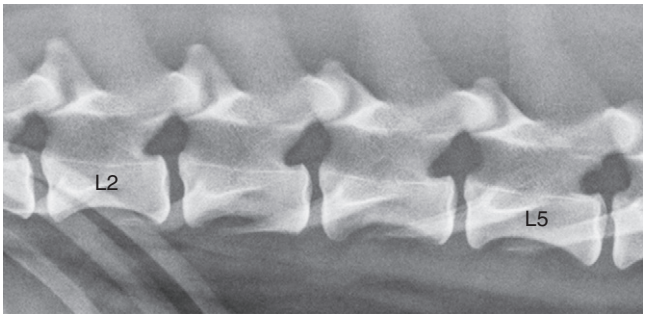


Fig. 7-17 Lateral view of the midlumbar spine of a dog. The ventral aspect of the vertebral bodies of L3 and L4 are less distinct than the ventral aspect of the vertebral bodies on L2 or L5. This loss of distinctness is normal and has been misinterpreted as cortical effacement from an aggressive lesion, such as a tumor.

at a steeper angle with respect to the vertebrae and disk spaces, causing them to be distorted in the image (Fig. 7-21). To accommodate for the beam divergence, multiple centering points (Fig. 7-22) will be needed for a survey radiographic study of the entire spine. These multiple centering points provide for a more vertical relationship between the x-ray beam and vertebrae throughout the spine, and overall a less distorted view of the spine. Obtaining a lateral view of the entire thoracic spine or the entire lumbar spine in one image is not acceptable because of the distortion that occurs at the periphery of the image.

The principles described for obtaining a lateral survey radiographic study of the spine in dogs and cats also apply to obtaining ventrodorsal survey views. Multiple centering points

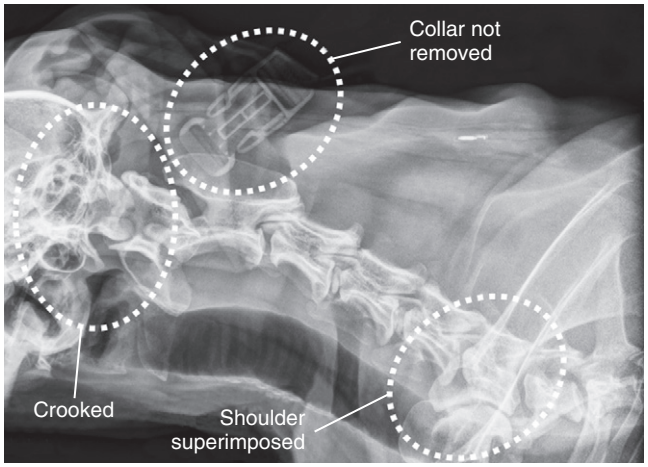


Fig. 7-18 A poorly positioned cervical radiograph that is totally useless. The patient is crooked, the collar has not been removed, and a shoulder is superimposed on the caudal aspect of the cervical spine. This is a careless approach that wastes time and needlessly increases personnel radiation exposure. The patient and owner deserve higher-quality work.

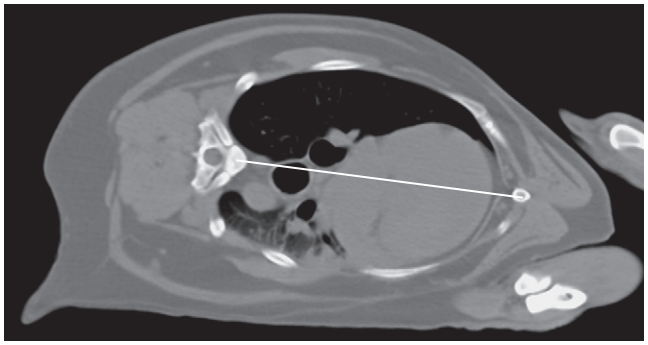


Fig. 7-19 Transverse-CT image of a canine thorax at the level of the heart. This dog was allowed to lie on the CT table while the images were acquired without any other adjustment in the position of the trunk. A line connecting a vertebra and a sternebra *(white line)* is not parallel to the tabletop. If a spinal radiograph were going to be acquired of this dog, the sternum would have to be elevated to prevent the vertebrae from appearing oblique in the image.

will also be needed for ventrodorsal views. Thus, a complete spinal survey study will result in the generation of a large number of images.

Spinal radiographs should always be planned in concert with the results from a neurologic examination, where the anatomic location of the lesion has been determined based on neurologic responses and other clinical signs. Thus, in some patients, the radiographic study may be truncated to the cervical spine, T2-L3 spinal cord segments, or lumbosacral region, depending on the results of the neuroanatomic localization.

It may be tempting to obtain only lateral survey radiographs of the spine, but this should be avoided. It is unquestionable that cutting corners by not acquiring VD radiographs routinely will result in disease being overlooked or missed. The only situation where the radiographic examination should be limited to lateral projections is where a spinal fracture or instability, such as atlantoaxial subluxation, is suspected. In that instance, lateral radiographs should be acquired first and evaluated. If no abnormality is detected, then VD views should be obtained. If an abnormality is detected initially in the lateral views, then the decision can be made to (1) terminate the examination, (2) acquire conventional VD views, or (3) use a horizontal beam to obtain the VD radiograph (Figs. 7-23 and 7-24).

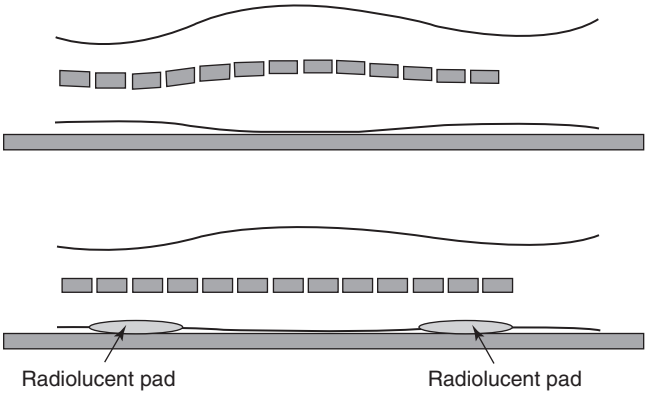


Fig. 7-20 Diagram illustrating the use of nonradiopaque pads for lateral spinal radiographs. Elevation of dependent portions of the vertebral column leads to improved vertebral alignment. The perspective of the image is as if the viewer is looking at the dorsal aspect of a dog while it is lying on the x-ray table. In the *top panel*, the dog is allowed to lie unrestrained on the table. The natural curve of the body will result in the vertebrae not being aligned in one plane. In this instance, the varying relation of the vertebrae with the primary x-ray beam will lead to distortion. In the *bottom panel*, dependent (sagging) portions of the vertebrae are elevated with nonradiopaque pads, which results in all vertebrae being more aligned in a plane parallel with the top of the x-ray table. This maneuver will lead to a less distorted lateral projection of the vertebrae. (Reprinted with permission from Thrall DE, Robertson ID: *Atlas of normal radiographic anatomy and anatomic variants in the dog and cat*, St Louis, 2011, Elsevier-Saunders.)

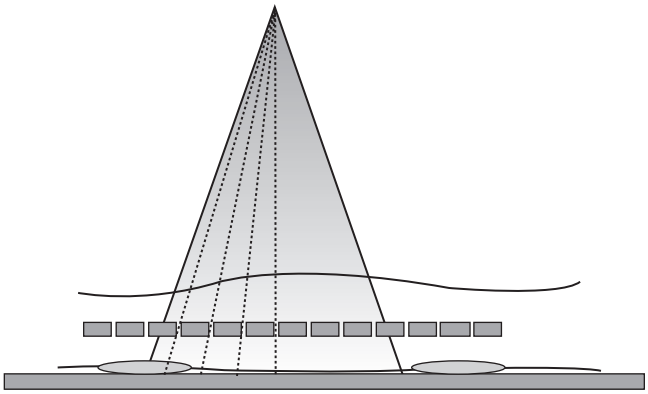


Fig. 7-21 Diagram illustrating the effect of divergence of the x-ray beam on disk-space width. The *gray triangle* represents the diverging x-ray beam. The *dotted lines* represent x-ray photons that will strike four adjacent intervertebral disk spaces. The vertical photon will pass through the central disk space, and the image will be representative of the actual size of the disk space. As one proceeds further peripherally from this central photon to the reader's left, the relationship of the photon with the disk space becomes less aligned, and this will lead to an image of the disk space that is narrower than its actual width and not representative of the true size of the disk space. (Reprinted with permission from Thrall DE, Robertson ID: *Atlas of normal radiographic anatomy and anatomic variants in the dog and cat*, St Louis, 2011, Elsevier-Saunders.)

In dogs with suspected atlantoaxial or lumbosacral instability, it may be desirable to evaluate the extent of mobility by using a flexed lateral view (for atlantoaxial instability) or by comparing flexed versus extended views (for lumbosacral instability). In atlantoaxial instability, the use of flexed lateral radiographs should be undertaken with extreme care because flexion will exacerbate any spinal cord compression, especially if the odontoid process of C2 is present. This is especially true if the patient is anesthetized and supporting soft tissues are relaxed.

Flexed and extended views are safer in patients with lumbosacral instability than in patients with atlantoaxial

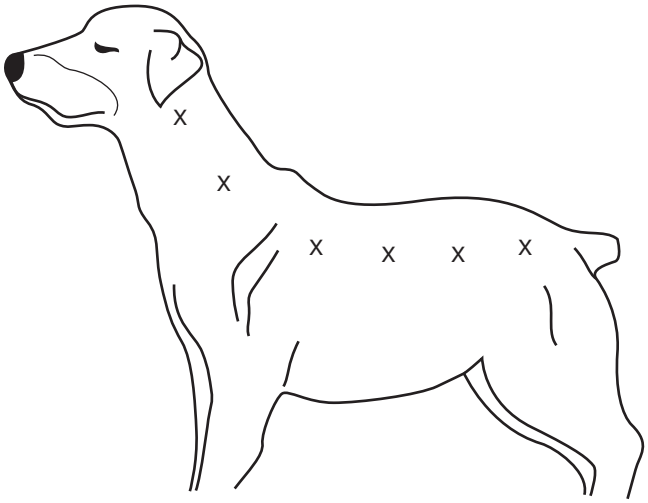


Fig. 7-22 Illustration of the centering points, designated by *X*, needed to obtain a lateral survey radiographic study of the entire spine. Lateral views centered approximately at C2, C7, T4, T13, L3, and L7 will be needed to obtain radiographs that depict spinal anatomy throughout the length of the spine without distortion. In very small subjects this number of projections may be reduced proportionally, but in medium or large subjects this number of views will be needed. The same centering points should be used for VD survey radiographs.

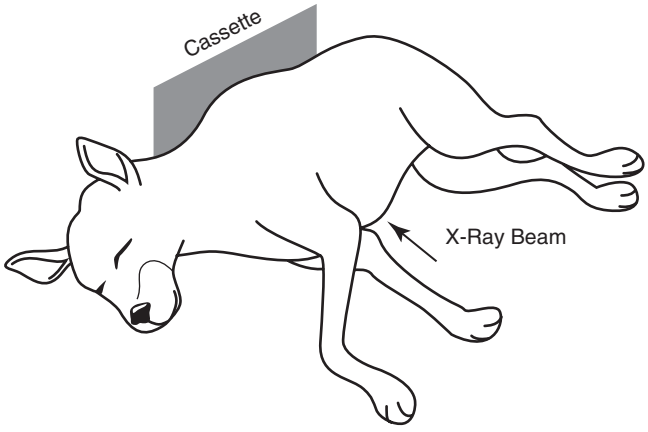


Fig. 7-23 Geometry of a horizontal-beam ventrodorsal radiograph of the spine. The subject is in right recumbency in this example. The cassette is positioned dorsal to the spine, perpendicular to the x-ray table. The x-ray beam is directed horizontally, parallel to the tabletop. It may not be possible to use a grid in this configuration, and this will lead to some reduction in detail. However, the main question is whether there is lateral malalignment at a fracture site, which can usually be answered in spite of the reduced detail created by lack of a grid.

subluxation. *Lumbosacral instability* in this instance refers to inherent instability caused by faulty connective tissue and not to patients with instability caused by an injury. In spite of the increased safety, however, the diagnostic value of comparing flexed versus extended lumbosacral radiographs is questionable. Neural compression resulting from lumbosacral instability is better assessed with either CT or MRI than with survey radiographs or epidurography.

Positioning: Horse

Because of the large body mass, the extent of the spine that can be examined radiographically in the horse is more limited than in the dog or cat; and unless a myelogram is going to be performed, the horse will be imaged standing, not recumbent. Sedation is indicated to reduce motion, and as

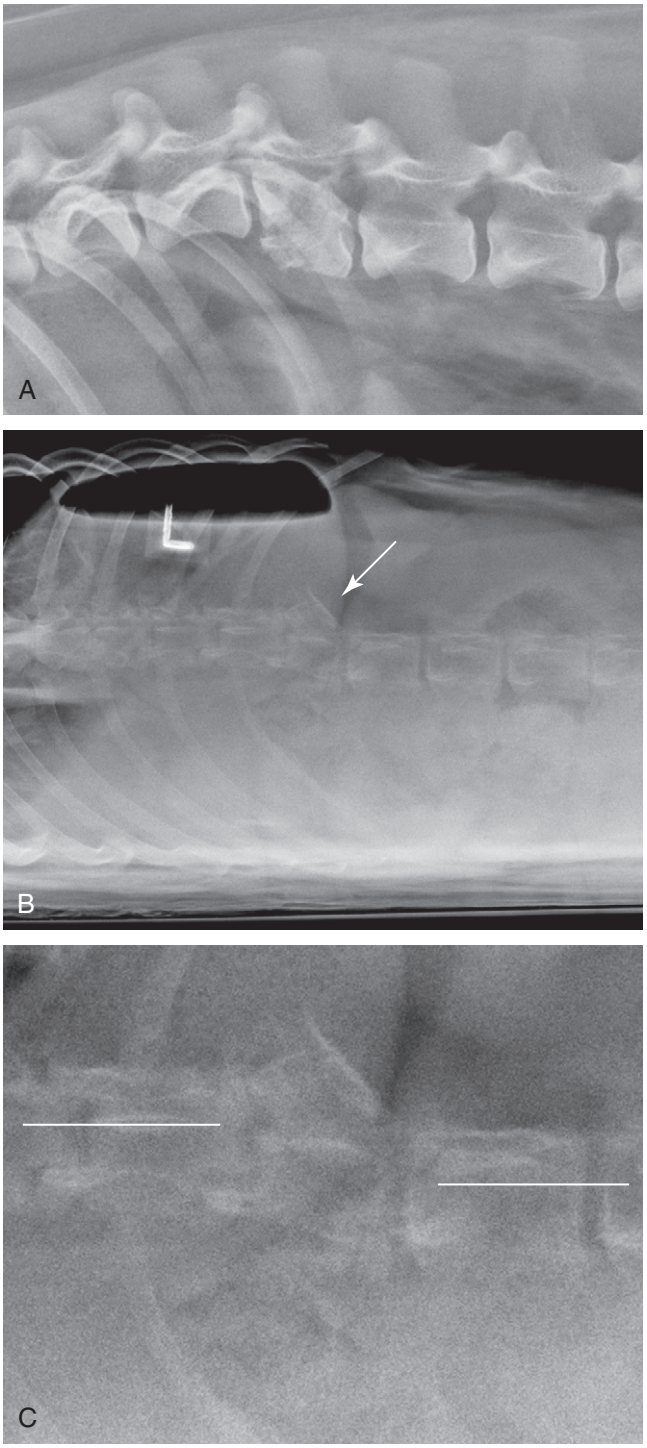


Fig. 7-24 **A,** Lateral radiograph of the thoracolumbar region of a dog that sustained trauma. There is a comminuted fracture of L1 with craniocaudal overriding of the caudal aspect of the body. This patient should not be rolled into dorsal recumbency for a conventional VD radiograph because of instability at the fracture site that may lead to spinal cord damage as the dog is moved. **B,** Horizontal-beam radiograph of the dog using the geometry illustrated in Figure 7-23. The dog was in right recumbency, thus the *(L)* marker at the top of the image. The large gas bubble is in the gastric fundus. The fracture is visible *(arrow)*, and there is lateral malalignment. **C,** Close-up of the horizontal-beam image. The *horizontal lines* mark the midsagittal plane of vertebrae cranial and caudal to the fracture to illustrate the extent of lateral malalignment. This lateral malalignment could not be detected in the lateral view, and the horizontal-beam view provided important additional information.

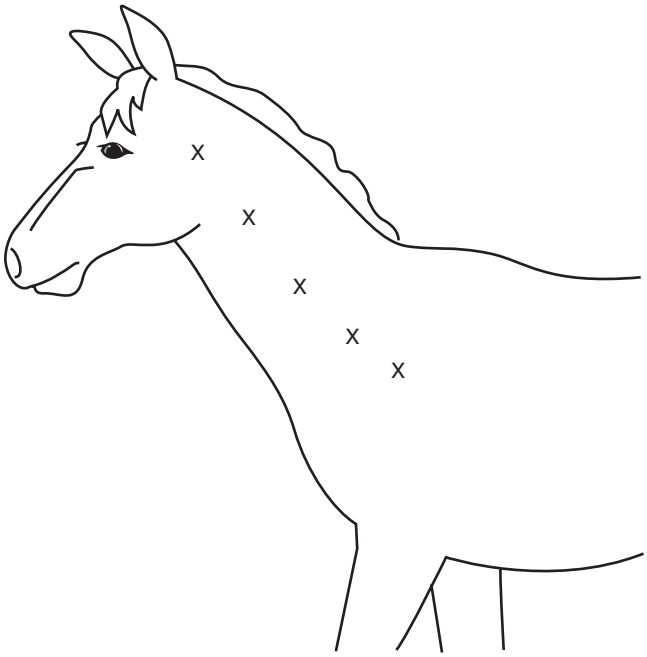


Fig. 7-25 Illustration of the centering points, designated by *X*, needed to obtain a lateral survey radiographic study of the equine spine. Lateral views centered approximately at C1, C3, C5, C6, and T1 will be needed to obtain radiographs that depict spinal anatomy accurately throughout the length of the spine.

mentioned pertaining to skull radiography, the head will drop, making it easier to radiograph the cervical spine.

For the cervical spine, only lateral views are obtained routinely. Standing DV or VD radiographs of adequate quality of the cervical spine, other than a DV view of the atlantooccipital junction, cannot be obtained easily. General anesthesia will have to be used to acquire diagnostic-quality VD or DV radiographs of the cervical spine. Fortunately, the need for VD or DV radiographs of the equine cervical spine is very limited. One example might be to assess the extent of an aggressive lesion. As in the dog and cat, multiple centering points will be needed for lateral spinal radiographs, but for a different reason. The neck of the horse is simply too long to be imaged with one cassette, and four to five centering points will usually be needed to image the entire cervical spine (Fig. 7-25).

The equine thoracic spine is more difficult to assess radiographically than the cervical spine. The thoracic spinous processes can be imaged satisfactorily, but whether the vertebral bodies can be imaged depends on the mass of the horse and which thoracic vertebral bodies are of interest. The cranial thoracic vertebral bodies can often be evaluated, but the caudal thoracic vertebral bodies are more difficult to assess because of superimposed soft tissue (Fig. 7-26).

The equine lumbar spine cannot be evaluated in lateral radiographs, except in very small horses. The body mass is simply too great. The lumbar spine can be assessed in a VD radiograph in small horses, but this requires general anesthesia. Superimposed fecal material will reduce lumbar vertebral detail in VD radiographs, even in small horses.

The cranial aspect of the sacrum cannot be assessed in a lateral radiograph, except in very small horses. The sacrocaudal junction can be seen in most horses in a lateral view. The sacrum can be assessed more thoroughly in a VD radiograph, but this requires general anesthesia. As with the lumbar spine, overlying fecal material will reduce sacral detail in VD radiographs.

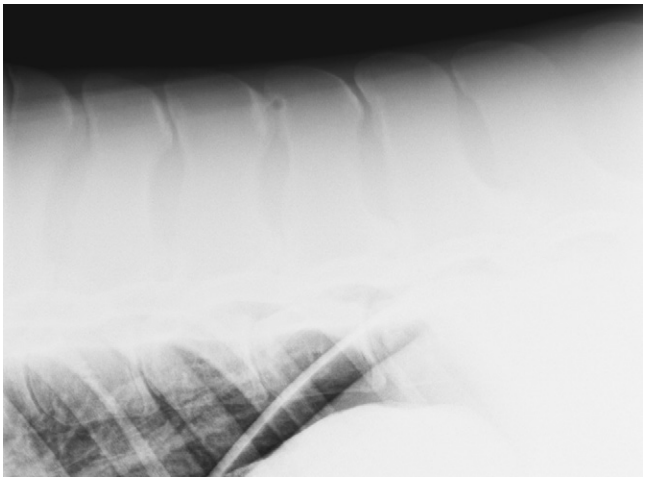


Fig. 7-26 Lateral radiograph of the caudal aspect of an equine thoracic spine. The spinous processes can be assessed, but the vertebral bodies in the caudal aspect of the image cannot because of soft tissue superimposition. These spinous processes are remodeled secondary to interference.

Radiographic Technique: Dog and Cat

When radiographing the canine or feline spine using a film-screen system, a high kVp–low mAs technique is recommended as contrast, and therefore assessing bone changes will be optimized. If one is using a digital system, exposure factors are less critical because of the enhanced contrast resolution of digital-imaging systems and the ability to adjust image blackness and contrast after image acquisition, as discussed in Chapter 2. For patients thicker than 10 cm, a grid should be used to remove scattered x-rays from the beam.

Exposure time is less critical when radiographing the spine because the patient will be sedated or anesthetized, and there is no inherent movement of this region, other than that created by respiration. Acquiring the radiographs at peak exhalation will minimize any blurring from respiratory motion.

Radiographic Technique: Horse

Because of the large size of the horse compared to a dog or cat, high kVp and low mAs techniques are recommended. This reduces the exposure time, making motion artifact less of a problem, and is less stressful to the x-ray tube. Theoretically, a grid should be used for all segments of the equine spine. However, if the cassette is to be held by hand, the same problems arise that were discussed relative to use of a grid for skull radiography, that is (1) the need for even higher mAs settings to compensate for the grid, (2) cassettes that contain a grid are heavy and difficult to hold steady by hand, and (3) maintaining a perpendicular relationship between the primary x-ray beam and a handheld cassette is nearly impossible, leading to grid-line artifacts.

Some facilities have a wall-mounted cassette holder assembly that incorporates a grid. These assemblies are similar to a Bucky tray in an x-ray machine table and secure the cassette parallel to the wall and perpendicular to the floor (Fig. 7-27). If the x-ray machine is designed to generate high mAs techniques and a wall-mounted cassette holder is available, then a grid should be used for all spinal radiographs in the horse. The sedated horse is simply positioned against the wall-mounted cassette holder, which can be raised or lowered to the desired height above the floor of the room, and the radiographic exposure made. These assemblies also avoid the need for handholding of the cassette, leading to a reduction in occupational exposure to personnel.

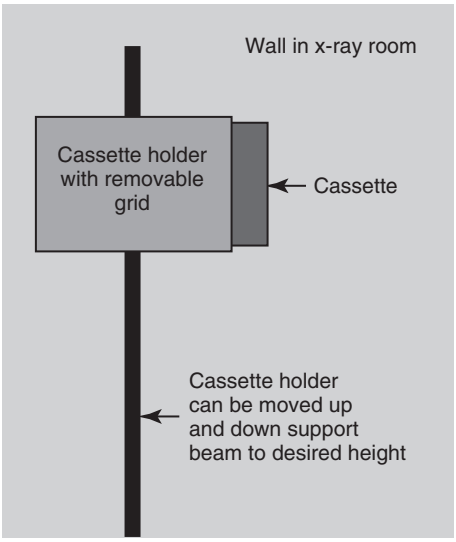


Fig. 7-27 Schematic of the configuration of a wall-mounted cassette holder. The cassette holder is designed such that a grid can be inserted if needed. The cassette holder can be raised or lowered on the support pole to position it at the desired height for the part being radiographed.

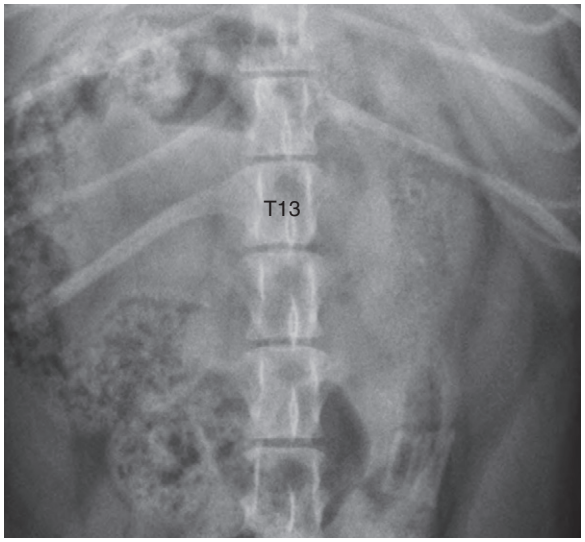


Fig. 7-29 Ventrodorsal radiograph of the thoracolumbar junction of a dog with a transitional anomaly. The right thirteenth rib developed as a malformed transverse process. The left thirteenth rib is absent. If ribs were used to locate the site for spinal surgery, it is imperative that the existence of this anomaly be known or the wrong site could be selected.

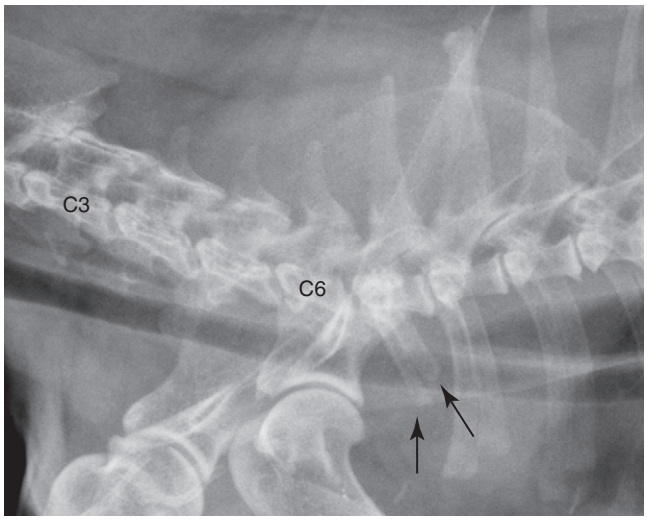


Fig. 7-28 Lateral radiograph of the cervicothoracic region in a cat. There are ribs on C7. This is a type of transitional anomaly. This cat had the normal allotment of 13 thoracic ribs.

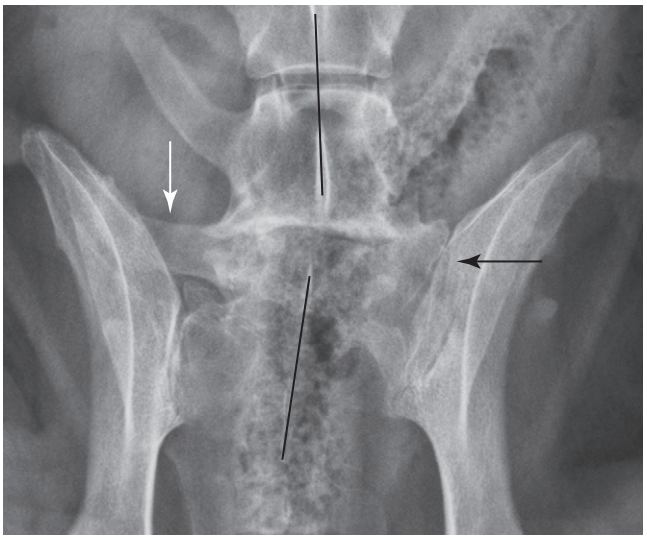


Fig. 7-30 Ventrodorsal radiograph of the lumbosacral region of a dog with sacralization of L7. The right side of L7 has a transverse process *(white arrow)* while the left side is fused with the ilium *(black arrow)*. Note also the malalignment of the sagittal plane of the lumbar vertebral spinous processes and the sacral spinous processes, indicated by the *black lines*. This malalignment will clearly alter the loading of the lumbosacral articulation

Incidental Factors

The most influential incidental factors associated with spinal radiography in the dog and cat are breed variation and some congenital anomalies. One commonly encountered anomaly is that of transitional vertebrae. Transitional vertebral anomalies occur at the cervicothoracic, thoracolumbar, and lumbosacral junctions and are characterized by a vertebra at the junction having anatomic characteristics of each adjoining region. The most common congenital anomaly at the cervicothoracic junction is the presence of vestigial ribs on C7 (Fig. 7-28). Cervical ribs are not clinically significant in dogs or cats, but in human beings they are sometimes associated with development of Horner syndrome. The most common transitional anomaly occurring at the thoracolumbar junction involves asymmetric development of the thirteenth rib. There are multiple variations to this anomaly,[1] but the most clinically significant one is having a unilateral rib on T13. This anomaly is not significant itself, but can lead to spinal surgery being performed at the wrong location if rib morphology is used to locate the surgical site (Fig. 7-29). The most common transitional anomaly at the lumbosacral junction is sacralization of L7, where one side of L7 has the form of a vertebra with a transverse process while the opposite side has the form of a sacrum and articulates with the pelvis (Fig. 7-30). The presence of a lumbosacral transitional anomaly predisposes dogs to the development of lumbosacral disk herniation and nerve root compression,[8,9] likely caused by altered loading.

Interpretation Paradigm

As mentioned, there are relatively few things other than breed variation and congenital anomalies that influence the radiographic appearance of the spine. But because of the complex morphology of the spine, an organized approach is

still needed. Assessing whether there is an abnormality in the spinal radiographs of a patient should be the *last* step in the interpretive process. The following questions should always be considered first:

- Are the radiographic views adequate and are all of the views that are needed present? If all of the necessary views are not present, what is likely to be missed, and what additional views would help?
- Do the views available correspond to the neuroanatomic localization of the lesion?
- Is the positioning adequate, or are there positioning problems that will interfere with interpretation?
- Is the radiographic technique adequate, or are the images overexposed or underexposed?
- Has a grid been used, and how does this affect the quality of the image? Is there excessive scattered radiation? Are there grid lines?
- Has sedation or anesthesia been used? If not, how will this affect the usefulness of the radiographs?
- Has the radiograph been made with a horizontally or vertically directed x-ray beam?
- What is the species and breed of the patient, and how did this affect the appearance of the images?
- Were the images acquired with a vertically directed x-ray beam with the cassette in an x-ray table, or on the floor for an anesthetized horse? Was a horizontally directed x-ray beam used with handholding of the cassette or a wall-mounted cassette holder?
- Was the cassette held by hand? Is there motion artifact?
- Are the images film-based or digital? If the images are film-based, was the radiographic technique a high-contrast or a low-contrast technique?
- If dealing with film images, is a hot light needed to assess the soft tissues and the edge of the bones?
- What congenital anomalies are present that alter the normal appearance of the spine but may not be clinically significant?

Only after all of these things have been considered should one's attention be directed at the identification of abnormalities. In many patients, the answer to the clinical question will not be found in the spinal radiographs. It is well known that the staging of disease involving the spine is much more accurate when based on tomographic imaging modalities, such as CT or MRI, than on radiographs. If the question that was the basis of acquiring spine radiographs is not answered adequately from the radiographs, CT or MRI should be considered as a next step in dogs or cats. In the horse, imaging the spine with CT or MRI is usually not feasible, except in small patients or in the cranial aspect of the cervical spine.

Experienced radiologists may have a random search pattern, but it is recommended that beginning radiologists develop an organized approach to searching radiographs[6] for abnormalities. In the spine it is important to compare each vertebra individually with the adjacent vertebrae. The following parameters can be evaluated in order: (1) the number of vertebral bony segments in each anatomic region; (2) in dogs and cats, the number of ribs in the thoracic spine; (3) presence of transitional anomalies or other congenital malformations; (4) alignment of individual vertebral elements; (5) the symmetry of the vertebral canal throughout the spine; (6) the integrity of the neural arch of individual vertebrae; (7) changes in shape, opacity, or margination of vertebral bodies; (8) changes in shape, opacity, or margination of articular processes; and finally, (9) character of paraspinal soft tissues. If the same procedure is followed for every patient, the order of searching will become second-nature, and as experience is gained the search pattern will become random without a loss of effectiveness. Until then, it may be beneficial for a checklist to be developed to make sure that every anatomic region of the radiograph is examined.

REFERENCES

1. Thrall D, Robertson I, editors: *Atlas of radiographic anatomy and normal anatomic variants in the dog and cat*, St. Louis, 2011, Elsevier-Saunders.
2. Han C, Hurd C: *Practical guide to diagnostic imaging: radiography and ultrasonography*, ed 3, Philadelphia, 1994, Elsevier-Mosby.
3. Thrall D, Robertson I, McLeod D, et al: A comparison of radiographic and computed tomographic findings in 31 dogs with malignant nasal cavity tumors, *Vet Radiol Ultrasound* 30:59, 1989.
4. Petite AF, Dennis R: Comparison of radiography and magnetic resonance imaging for evaluating the extent of nasal neoplasia in dogs, *J Small Anim Pract* 47:529, 2006.
5. Rohleder JJ, Jones JC, Duncan RB, et al: Comparative performance of radiography and computed tomography in the diagnosis of middle ear disease in 31 dogs, *Vet Radiol Ultrasound* 47:45, 2006.
6. Halvorsen JG, Swanson D: Interpreting office radiographs. A guide to systematic evaluation, *J Fam Pract* 31:602, 1990.
7. Baines E, Grandage J, Herrtage M, et al: Radiographic definition of the anticlinal vertebra in the dog, *Vet Radiol Ultrasound* 50:69, 2009.
8. Morgan JP, Bahr A, Franti CE, et al: Lumbosacral transitional vertebrae as a predisposing cause of cauda equina syndrome in German shepherd dogs: 161 cases (1987–1990), *J Am Vet Med Assoc* 202:1877, 1993.
9. Fluckiger M, Damur-Djuric N, Hassig M, et al: A lumbosacral transitional vertebra in the dog predisposes to cauda equine syndrome, *Vet Radiol Ultrasound* 47:39, 2006.

ELECTRONIC RESOURCES

evolve

Additional information related to the content in Chapter 7 can be found on the companion Evolve website at http://evolve.elsevier.com/Thrall/vetrad/

- Chapter Quiz

CHAPTER • 8

The Cranial and Nasal Cavities: Canine and Feline

Lisa J. Forrest

NORMAL ANATOMY

The skull encompasses the brain and houses the sense organs for hearing, equilibrium, sight, smell, and taste. The skull provides attachment sites for teeth, tongue, larynx, and muscles.[1] There is pronounced variation in the shape of the skull in the dog. Three terms are used to designate the different shapes. *Dolichocephalic* breeds, such as collie and Russian wolfhound, have long, narrow heads with an extensive nasal cavity from rostral to caudal. *Mesaticephalic* breeds, such as German shepherd and beagle, have heads of medium proportion (Fig. 8-1). *Brachycephalic* breeds, such as Boston terrier and Pekingese, have short, wide heads. Cats are more uniform in their skull conformation. However, Siamese tend to have longer heads as compared with Himalayan and Persian breeds.

Calvaria and Associated Structures

The calvaria comprises the bones of the brain case, with the occipital bone forming the base of the skull. The occipital crest is the most dorsocaudal aspect of the skull (see Fig. 8-1), and the occipital condyles are caudoventral as seen on lateral radiographs. The foramen magnum, centered between the occipital condyles, forms an orifice for passage of the spinal cord.

Nasal Passages and Paranasal Sinuses

The nasal passage extends caudally from the external nares to the cribriform plate and nasopharynx. The cribriform plate is a sievelike partition between the olfactory bulb and nasal passage. The nasal passage is divided in half by the nasal septum and is filled with thinly scrolled conchae. Caudally, the nasal septum is osseous and fuses with the cribriform plate; it becomes cartilaginous as it extends rostrally.[1] The vomer bone is unpaired and forms the caudoventral bony part of the nasal septum; it is visible radiographically.[2] The cartilaginous nasal septum cannot be seen in radiographs, although it can be distinguished in computed tomography (CT) and magnetic resonance (MR) images. Both dogs and cats have frontal sinuses (see Fig. 8-1), lateral maxillary recesses, and small sphenoidal sinuses. These are named for the bones in which they are located.

Tympanic Bullae and Temporomandibular Joint

The tympanic bullae (see Fig. 8-1) form the ventral part of the temporal bone. These air-filled cavities of the middle ear communicate with the nasopharynx via the auditory tube. The temporal bone consists of the petrosal, tympanic, and squamous sections that are fused in the adult. The petrosal portion is medial and dorsal to the tympanic bulla and is composed of dense bone in the mature animal. The squamous portion of the temporal bone extends rostrally and laterally to form the zygomatic arch.

The temporomandibular joint is a condylar joint. The temporal portion consists of the zygomatic process of the squamous temporal bone, which forms the mandibular fossa and the retroarticular process. The retroarticular process is the ventral extension of the squamous temporal bone. The mandibular aspect of the joint includes the condyloid process, which articulates with the mandibular fossa.

Teeth

The teeth are anchored in alveoli within the mandible and maxilla. The dental formulas for the dog and cat are provided in Box 8-1. Components of the tooth include the root (embedded in bone) and the crown (within the oral cavity); the bone between teeth is referred to as the *alveolar crest*. The dentin, enamel, and lamina dura of the tooth are radiopaque. The pulp cavity and periodontal membrane are of soft-tissue opacity (Fig. 8-2). The size of the pulp cavity becomes smaller with age.[3] Specifics on radiographic technique and positioning for tooth evaluation can be found elsewhere.[4-7]

Cross-Sectional Imaging

Cross-sectional imaging techniques, CT, and MR imaging are being used more commonly for imaging of the head. CT and MR technology provides images without superimposition of structures and better soft tissue delineation compared with radiography (Fig. 8-3).[8-12] There are several references describing the normal CT and MR image anatomy of the dog and cat head.[9,13-22]

CONGENITAL ANOMALIES

Hydrocephalus

Hydrocephalus is excessive accumulation of cerebrospinal fluid within the ventricular system of the brain. Congenital hydrocephalus occurs secondary to structural defects that obstruct cerebrospinal fluid outflow or impede its absorption.[23,24] Canine breeds affected with congenital hydrocephalus include the Maltese, Yorkshire terrier, English bulldog, Chihuahua, Lhasa apso, Chinese pug, toy poodle, Pomeranian, Pekingese, Cairn terrier, and Boston terrier.[23] Hydrocephalus is less common in cats.[23,25,26]

Radiographic signs associated with hydrocephalus include doming of the calvaria and cortical thinning, persistent fontanelles, and a homogeneous appearance to the brain, resulting from the loss of normal convolutional skull markings (Fig. 8-4). Radiographs are very insensitive for detection and characterization of hydrocephalus, and that information is

Box • 8-1

Dental Formulas for the Dog and Cat

Dental Formula—Cat
Deciduous Teeth
2 × (I 3/3, C 1/1, P 3/2) = 26
Permanent Teeth
2 × (I 3/3, C 1/1, P 3/2, M 1/1) = 30

Dental Formula—Dog
Deciduous Teeth
2 × (I 3/3, C 1/1, P 3/3) = 28
Permanent Teeth
2 × (I 3/3, C 1/1, P 4/4, M 2/3) = 42

C, canine teeth; *I*, incisor teeth; *M*, molar teeth; *P*, premolar teeth.

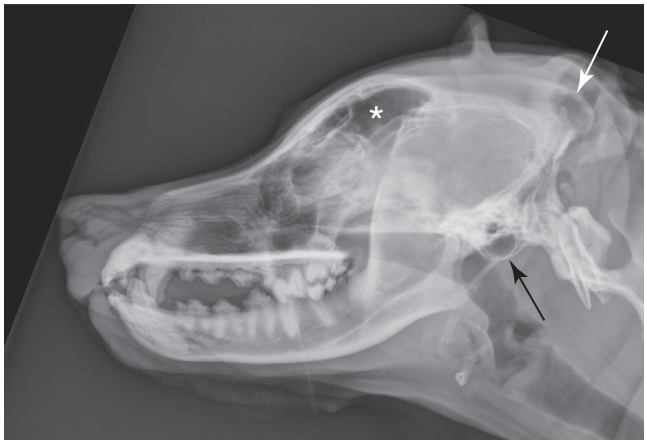


Fig. 8-1 Lateral skull radiograph of a Labrador retriever, which is a mesaticephalic breed. Note the occipital crest *(white arrow)*, superimposed frontal sinuses *(asterisk)*, and tympanic bullae *(black arrow)*.

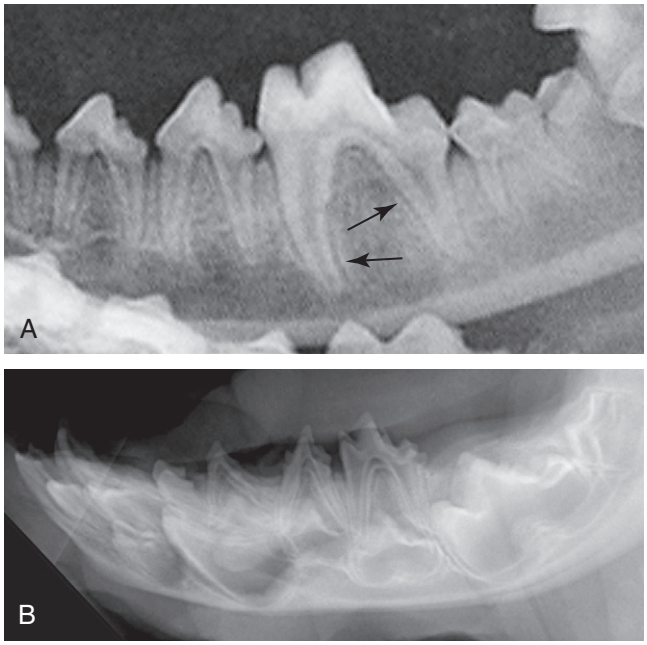


Fig. 8-2 **A,** Lateral radiograph of the mandible of a mature dog. Note the well-defined lamina dura *(arrows)*, which mark the dental alveolus. **B,** Lateral radiograph of the mandible of a 3-month-old dog. Note the open apical foramina of the teeth, the large pulp cavity, and the location of permanent premolars ventral to the deciduous precursors.

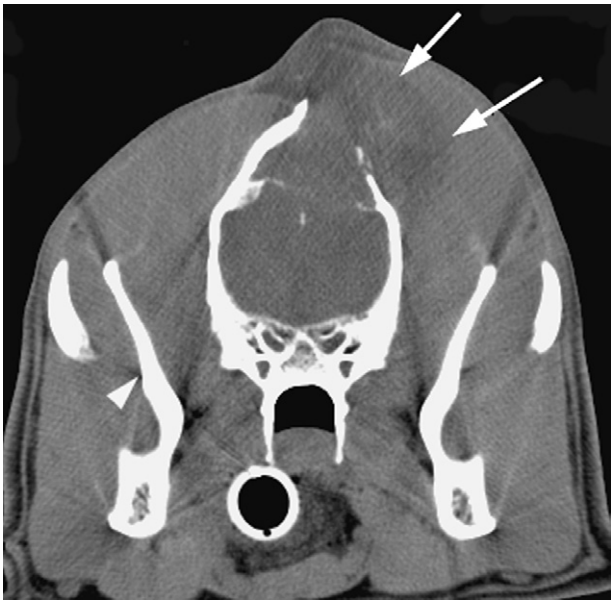


Fig. 8-3 Transverse CT image at the level of the brain and frontal sinus of a dog with an osteosarcoma of the frontal bone. The *white arrows* delineate the soft tissue component of the tumor, which is destroying the right frontal bone and compressing the brain. This accuracy in tumor staging is impossible from radiographs. The *white arrowhead* marks the normal left ramus of the mandible.

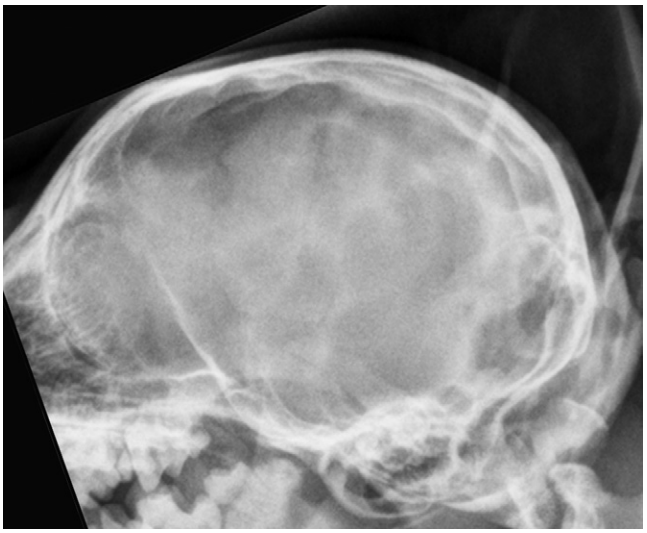


Fig. 8-4 Lateral radiograph of a 19-month-old Papillon with severe hydrocephalus. Note the homogeneous appearance of the calvaria caused by a loss of the normal convolutional skull markings.

now acquired using CT or MR imaging.[23] With persistent fontanelles, ultrasound can also be used to assess ventricular size,[27-34] and normal ventricular appearance and size have been quantified in the dog.[27,28,35,36] The advantage of CT and MR imaging for evaluating ventricular size is the ability to assess the entire brain for causes of hydrocephalus (Fig. 8-5). Asymmetry in ventricular size is often normal in dogs, and correlation between ventricular size and clinical signs is poor.[27,28,30,33,34]

Occipital Dysplasia

Occipital dysplasia is the dorsal extension of the foramen magnum, secondary to a developmental defect in the occipital bone;[37] it has been related to clinical signs of neurologic disease and is usually found in miniature and toy breeds.[38-40]

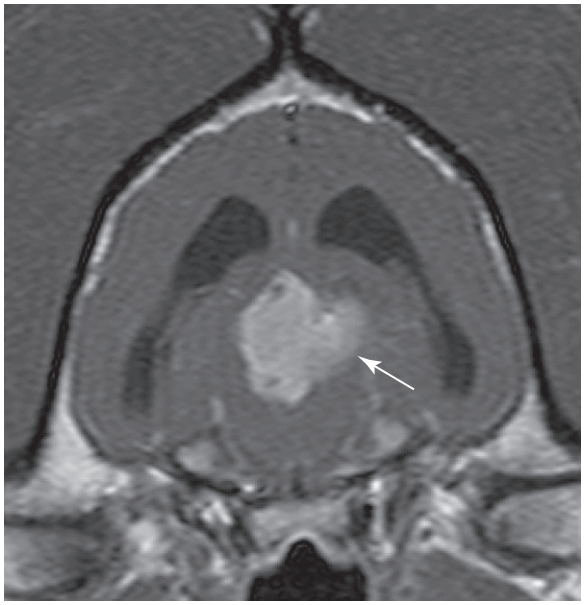


Fig. 8-5 Transverse postcontrast T1-weighted MR image of the brain of a dog with a large mass in the third ventricle *(arrow)*. This mass has resulted in obstruction to CSF flow and secondary obstructive hydrocephalus. The lateral ventricles (black in this MR sequence) are dilated.

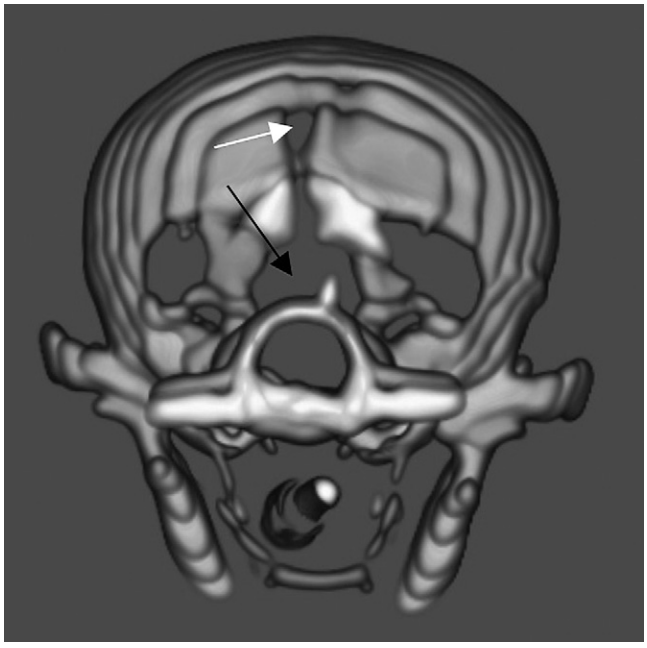


Fig. 8-6 Caudal view of a three-dimensional volume rendering obtained from transverse CT images of the skull. The foramen magnum should be the approximate size of the vertebral canal of C1. Note the extension of the foramen magnum dorsal to C1 *(black arrow)* and a vertical cleft extending even further dorsally *(white arrow)*. Two large dysplastic areas are also visible in the occipital bone to either side of the foramen magnum.

Foramen magnum size and shape can be evaluated in a rostrodorsal-caudoventral skull radiograph,[41] but this projection is generally not used now that CT and MR imaging are more available. The characteristics of the foramen magnum can be assessed more accurately using CT rather than radiographs (Fig. 8-6). Occipital dysplasia may be a normal morphologic variation in brachycephalic dogs.[42-44]

Occipital Bone Malformation and Syringomyelia (Chiari-Like Malformation)

Occipital bone malformation may result in overcrowding of the caudal fossa, leading to obstruction of cerebral spinal fluid (CSF) flow, hydrocephalus, and secondary syringomyelia. This hereditary defect, termed *Chiari-like malformation*, is common in the Cavalier King Charles spaniel[45-49] but is also found in other brachycephalic breeds. CSF flow is obstructed by the malformation, and the cerebellum may be herniated through the foramen magnum with dorsal deviation of the brainstem.[47] Clinical signs vary in severity and usually are seen between the age of 6 months and 2 years; however, neurologic signs may not appear until later in life.[47] Neurologic signs are consistent with a central spinal cord lesion, and dogs with clinical signs generally have a significantly larger syrinx than asymptomatic dogs.[49] Clinically, dogs often present with persistent scratching of the shoulder region, with no dermatologic cause and thought to be a paraesthesia secondary to syringomyelia.[45]

Radiographs are not useful for diagnosis of Chiari-like malformation. Definitive diagnosis is made with MR imaging,[47] whereby the crowding of the cerebellum in the caudal fossa can be detected. There may be herniation of a portion of the vermis of the cerebellum (see Fig. 12-46. A positive correlation has been found between foramen magnum size and length of cerebellar herniation.[49]

Temporomandibular Joint Dysplasia

Open-mouth jaw locking can be caused by temporomandibular joint (TMJ) dysplasia. This congenital condition is uncommon; it is reported most frequently in the basset hound, but has also been seen in Irish setters.[50] The open-mouth jaw locking occurs after hyperextension of the jaw, excessive lateral movement of the condyloid process, and subsequent entrapment lateral to the zygomatic arch. Physical entrapment usually occurs on the side opposite from the joint with the most severe dysplastic changes. Yawning often precipitates jaw locking when it results in extreme opening of the mouth.[50] In spaniels, Pekingese, and dachshunds, TMJ dysplasia is an asymptomatic anatomic anomaly.[20,51,52] Open-mouth jaw locking has also been seen in cats,[53,54] and CT is routinely used to diagnose TMJ dysplasia, with three-dimensional reconstructions aiding in surgical planning.[55]

Mucopolysaccharidosis

Mucopolysaccharidoses are a group of hereditary disorders of lysosomal storage, which occur in humans, dogs, cattle, and cats.[56] Mucopolysaccharidosis VI (MPS-VI) is an autosomal recessive lysosomal storage disease recognized in Siamese cats.[57-60] Radiographic skeletal changes in cats with MPS-VI include epiphyseal dysplasia, generalized osteoporosis, pectus excavatum, and vertebral and skull changes.[61] Specific skull changes seen on radiographs include shortened nasal conchae, aplasia and hypoplasia of the frontal and sphenoid sinuses, and shortened dimensions to the incisive and maxillary bones.[61] Another form of mucopolysaccharidosis, MPS-I, has been documented in the domestic shorthaired cat[62] with radiographic skeletal changes that are similar to those in MPS-VI; however, the facial dysmorphia may not be as pronounced as it is in the Siamese.[59,63] Mucopolysaccharidosis in animals has clinical and pathologic manifestations similar to people and therefore represents an excellent model for studying approaches to therapy and care.[58,60,64,65]

METABOLIC ANOMALIES

Primary or secondary hyperparathyroidism can result in overall decreased bone opacity, often noted easily in the skull.

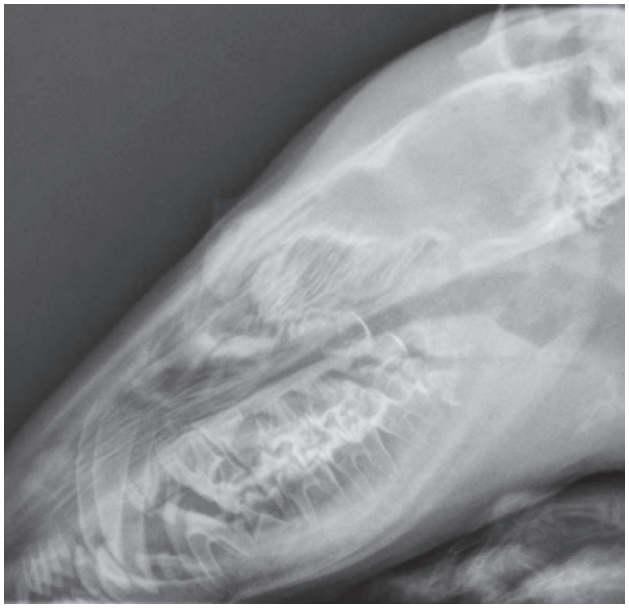


Fig. 8-7 Lateral radiograph of an opossum with nutritional secondary hyperthyroidism. Note the decreased opacity and poor delineation of the skull. This is especially noticeable in the caudal mandibular region, where it is difficult to differentiate the mandible from adjacent soft tissue. Note the lack of visualization of the lamina dura.



Fig. 8-8 Lateral skull radiograph of a 6-year-old dog with chronic renal failure and secondary hyperparathyroidism. The teeth appear very opaque because of the reduction in bone mineral. The lamina dura have been resorbed.

A solitary parathyroid adenoma or carcinoma, or adenomatous hyperplasia of one or both parathyroid glands, causes primary hyperparathyroidism. This results in excessive synthesis and secretion of parathyroid hormone, which leads to hypercalcemia and subsequent bone resorption.[66-68] Secondary hyperparathyroidism, which includes renal and nutritional secondary hyperparathyroidism, is subsequent to nonendocrine alterations in calcium and phosphorus homeostasis that lead to increased levels of parathyroid hormone and ultimate bone resorption.[68]

An early radiographic sign of hyperparathyroidism (primary and secondary) is loss of the lamina dura (Fig. 8-7). This will be followed by overall demineralization of the skull bones as the disease progresses (Fig. 8-8). In fact, it is uncommon to see loss of the lamina dura without some concurrent generalized skeletal demineralization. The level of cortical thinning and degree of overall osteolysis and osteomalacia depend on duration and severity of the hyperparathyroidism. Also, because young animals are growing and have rapid skeletal turnover, they are affected more severely than older animals. In extreme hyperparathyroidism, demineralization is followed by fibrous tissue hyperplasia, termed *fibrous osteodystrophy*. This uncommon development leads to skull thickening caused by fibrous tissue proliferation.

Ultrasound evaluation of the cervical region can be used to evaluate dogs with hypercalcemia to search for a parathyroid mass.[69,70] In 210 dogs with primary hyperparathyroidism, a parathyroid mass with a range of 3 to 23 mm in diameter was identified in 129 of 130 dogs that were imaged sonographically.[67] Thirty-one percent of the dogs had cystic calculi, and all were either calcium phosphate or calcium oxalate (radiopaque).[67]

NEOPLASTIC ABNORMALITIES

Nasal Tumors

Tumors of the nasal cavity in dogs and cats account for approximately 1% to 2% of all neoplasms.[71-73] These tumors occur in older dogs and cats; approximately two thirds of nasal tumors are epithelial (adenocarcinoma, squamous cell carcinoma, undifferentiated carcinoma), and the other one third are mesenchymal (fibrosarcoma, chondrosarcoma, osteosarcoma, undifferentiated sarcoma).[74-77] Intranasal lymphoma can also occur, with a higher prevalence in cats.[75,76,78-80] Tumors of the nasal cavity are locally invasive but have a relatively low metastatic potential. External beam radiotherapy is the current treatment of choice,[79,81-84] with many centers using advanced radiotherapy techniques such as intensity-modulated radiation therapy and image guidance.[85-87] Unfortunately, diagnosis of these tumors often occurs late in the course of disease, resulting in a poor prognosis for outcome in many patients.

Nasal cavity tumors have an aggressive radiographic appearance, with bony invasion and loss of conchal detail being common radiographic features.[12,80,88-90] Tumors may be unilateral or bilateral and cause increased soft-tissue opacity in the nasal cavity with underlying conchal destruction. Destruction of bones adjacent to the nasal cavity is also common in advanced tumors. Nasal tumors may result in increased opacity within the frontal sinus;[80,89-91] it is usually impossible to determine on radiographs whether frontal sinus opacification is caused by tumor extension or by occlusion of the nasofrontal communication with subsequent mucus accumulation in the sinus. Making this distinction can be important for treatment planning. MR imaging, which is based on the chemical composition of the tissue rather than the electron density, is helpful in distinguishing tumor from mucus in the frontal sinus (Fig. 8-9), but contrast-enhanced CT provides similar information.[92]

The most useful radiographic views for evaluating nasal disease include the intraoral dorsoventral and/or the open-mouth ventrodorsal view for detailed evaluation of the nasal cavity without superimposition of the mandible (Fig. 8-10). The open-mouth ventrodorsal view is better for cribriform plate assessment because radiographic film cannot be positioned physically to include the cribriform plate in the intraoral view. The cribriform plate is represented by a V-shaped to C-shaped bony opacity on radiographs, varying according to skull shape (dolichocephalic vs. mesaticephalic and brachycephalic).[93] Evaluation of the cribriform plate is important because nasal tumors often originate from the ethmoid conchae and cribriform plate,[74] and bony lysis detected on radiographs indicates potential tumor extension into the cranial cavity (see Fig. 8-10), which signifies a poorer prognosis. The rostrocaudal frontal sinus projection is

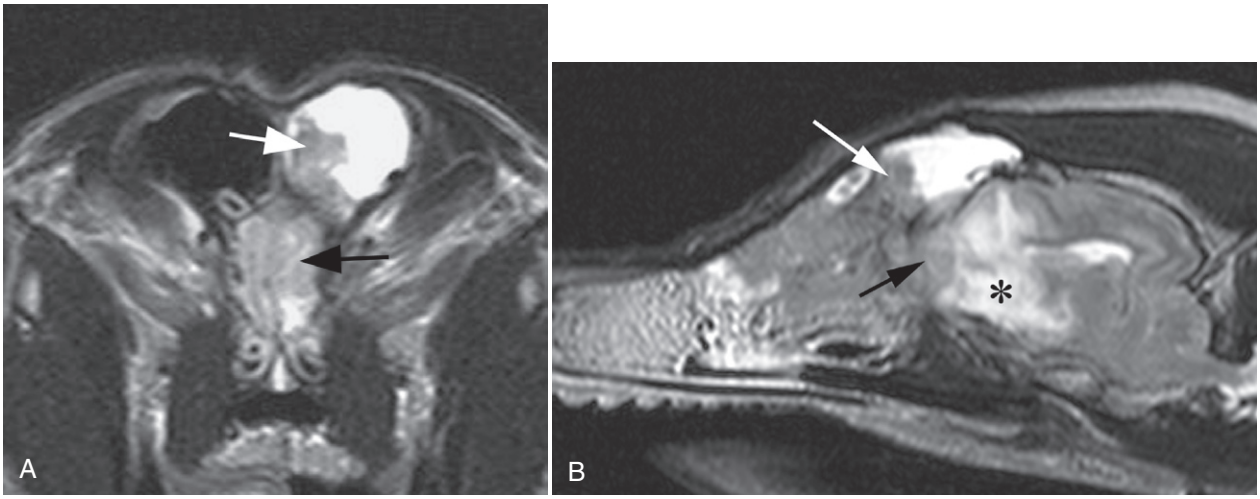


Fig. 8-9 Transverse **(A)** and parasagittal **(B)** fast spin-echo T2-weighted MR images of a dog with a malignant nasal tumor. In **B,** the amorphous tumor mass can be seen in the caudal aspect of the nasal cavity. The tumor has invaded the frontal sinus *(white arrows)*, causing obstruction of the nasofrontal communication and resulting in mucus collection in the sinus dorsal and caudal to the tumor. In these T2-weighted images, this mucus has high signal intensity (appears white), and the tumor has less signal intensity. In radiographs, the frontal sinus, the tumor, and the mucus would have the same opacity, making distinction impossible. This tumor has also invaded the cranial cavity *(black arrows)*, leading to extensive white matter edema (streaky white signal, *asterisk*) caudal to the tumor in the sagittal view.

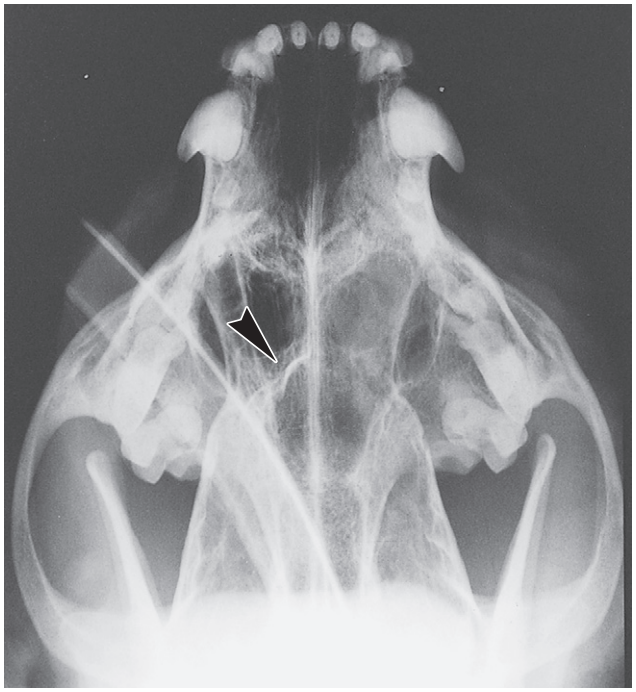


Fig. 8-10 Open-mouth, ventrodorsal radiograph of the nasal cavity of a dog with a 1-week history of left-sided facial swelling and nasal discharge. On the left, note the increased opacity, loss of conchal detail, and bony destruction of the cribriform plate. The right side of the cribriform plate is intact *(black arrowhead)*. Unilateral involvement and bony destruction are suggestive of a nasal cavity tumor. The diagnosis of adenocarcinoma was made histologically.

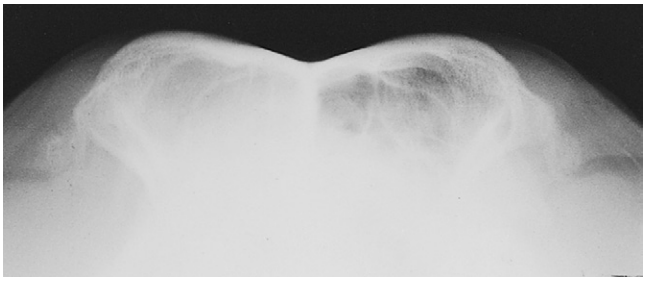


Fig. 8-11 Rostrocaudal frontal sinus radiograph of a 7-year-old German shepherd with a history of epistaxis. Note the increased opacity to the right frontal sinus compared with the left. The increased opacity is nonspecific and could be caused by fluid accumulation or tissue proliferation, or both.

necessary for evaluation of individual frontal sinuses (Fig. 8-11) and is useful especially if CT or MR imaging are not available.[94]

General anesthesia is an absolute requirement for achieving accurate radiographic positioning, and it facilitates evaluation and comparison of the complex nasal passages. Techniques for obtaining radiographic views of the nasal cavity and paranasal sinuses can be found elsewhere[95] and were discussed briefly in Chapter 7.

Aggressive nasal tumors and those with a prolonged duration are more destructive and less confined radiographically, often exhibiting an external soft-tissue mass that represents tumor extension through overlying bone. Conchae destruction and deviation and destruction of the bony nasal septum are apparent on radiographs. Radiographic evidence of bony destruction is an important prognostic sign because it is associated with a poor outcome.[75,90,91,96] Less aggressive tumors and ones that are detected early are difficult to differentiate from rhinitis on radiographs.[90] Radiographic detection of bony lysis of the cribriform plate and naso-orbital wall is difficult radiographically,[93] and better suited to CT or MR imaging.

CT of the nasal passage is superior to routine radiography for accurate tumor staging (Figs. 8-12 and 8-13)[97] and is useful for attempting to differentiate infection from neoplasia.[8,10,12,98-103] It is impossible to determine the stage of a nasal mass adequately from radiographs, and CT is the preferred screening modality for nasal disease. The presence of a mass effect (increased soft tissue in the nasal cavity) along with bone destruction is a hallmark sign of nasal neoplasia (see Fig. 8-13). A destructive pattern without a marked mass effect is more typical of aspergillus infection (discussed later), whereas

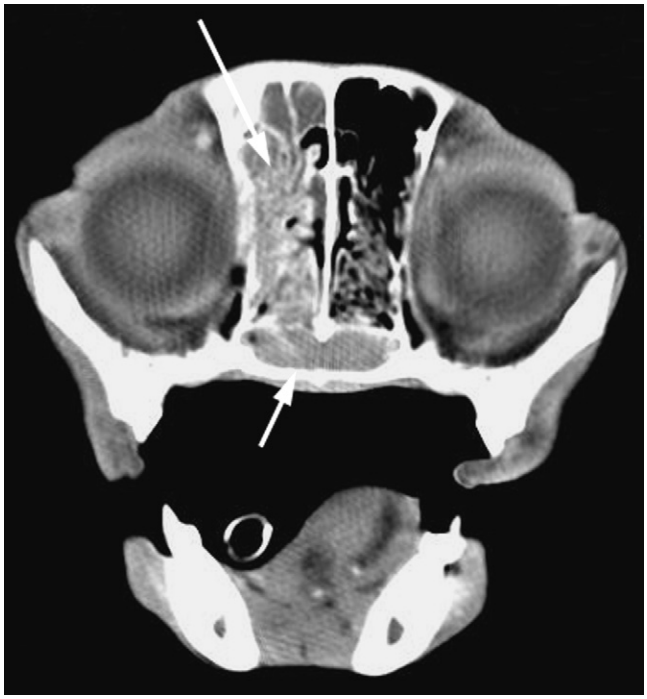


Fig. 8-12 Transverse CT image of the nasal cavity of a cat with nasal lymphoma at the level of the eyes. Tumor is visible within the nasopharynx *(short white arrow)* and the left nasal cavity *(long white arrow)*.

a mass effect without turbinate destruction is also more typical of infection, although usually not aspergillus. CT images of patients with nasal cancer are also used in computerized radiation therapy planning systems. Use of this anatomic information allows optimization of dose distribution across the tumor volume[104] and probable improved survival and decreased normal tissue side effects.[82,87] MR imaging of the nasal passage provides excellent, true three-dimensional images of nasal tumors. Differences in MR signal intensity between sarcomas and carcinomas have been found.[105]

Mandibular and Maxillary Tumors

Tumors of the oral cavity account for approximately 6% of all canine cancers and 3% of feline cancers.[106,107] Squamous cell carcinoma commonly affects the mandible or maxilla in the dog and cat. Fibrosarcoma, malignant melanoma, and tumors of the periodontal ligament (epulis) are common in the dog but occur rarely in cats.[108,109]

In the dog, the rostral mandible is a common site for oral squamous cell carcinoma. This tumor has variable bony lysis, and regional or distant metastasis is rare.[110] Oral fibrosarcoma in dogs can affect the maxilla or mandible with a predilection for the palate.[110] In dogs, 82% of squamous cell carcinomas and 78% of fibrosarcomas were characterized radiographically by bone involvement.[96] Often, oral fibrosarcoma appears benign histologically, but biologic activity is aggressive. These tumors, often found in the maxilla and mandible of large-breed dogs and commonly in golden retrievers, are histologically low-grade yet biologically high-grade aggressive tumors. Bone lysis is a common feature.[111] Dogs with oral fibrosarcoma have a lower median survival as compared with those with soft-tissue sarcomas at other sites[112] (Fig. 8-14). In contrast, malignant melanoma tends to occur in small-breed dogs, commonly metastasizes to regional lymph nodes and lungs, and has variable bony lysis radiographically.[113] Squamous cell carcinoma in cats affects the mandible or maxilla, causing sclerotic and/or lytic changes to bone (Fig. 8-15); common CT features include sublingual and maxillary locations with

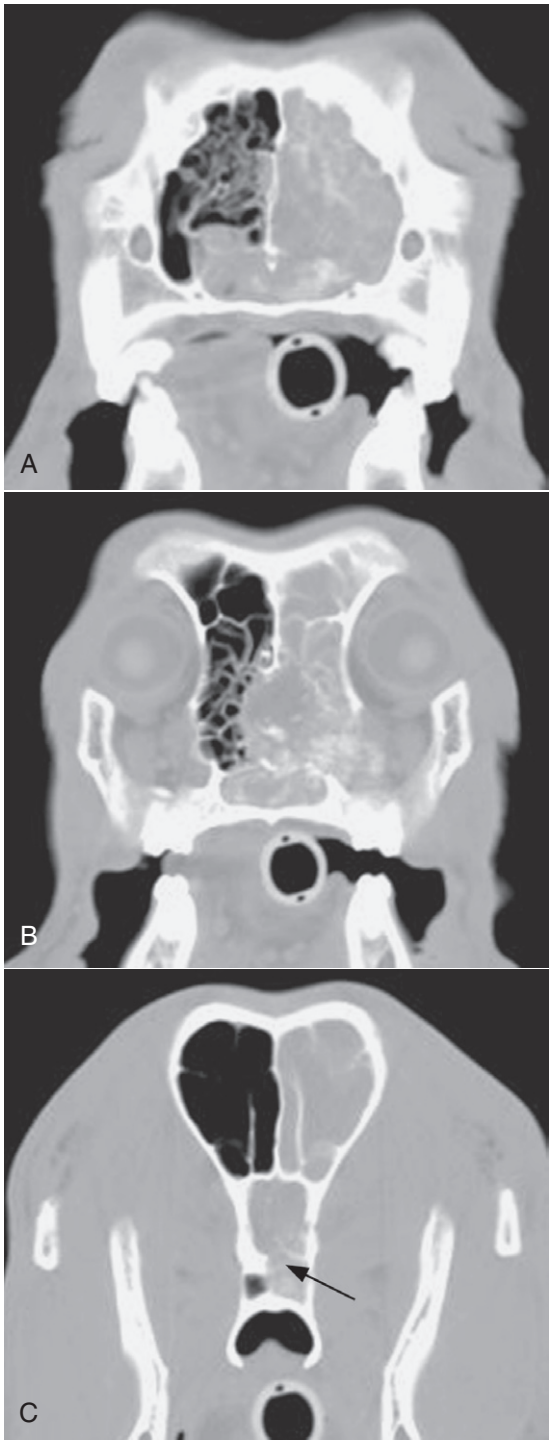


Fig. 8-13 Three transverse CT images from a dog with a malignant nasal tumor. **A,** Erosion of the vomer with extension of the tumor to the right nasal cavity. **B,** Extension into the left pterygopalatine fossa, across the midline to the right nasal cavity and into the nasopharynx. **C,** Erosion of the cranial vault with intracranial extension *(arrow)*. Hyperattenuating material is also present in the left frontal sinus; CT images cannot distinguish tumor extension into the sinus from fluid or mucus collection caused by obstruction of the nasofrontal communication, unless contrast enhancement of tumor extension is seen. This combination of CT abnormalities is characteristic of a malignant nasal tumor. The tumor extensions visible in these CT images would not have been detected in radiographs.



Fig. 8-14 Intraoral dorsoventral radiograph of the maxilla of a dog with a left maxillary gingival mass. In radiographs the mass is visible and contains foci of mineralization. Distortion of the left incisors and marked bone lysis are also present in this area. Lysis extends caudally and blends into normal-appearing conchae. Accurately determining the caudal extent of this tumor with radiographs is impossible; if treatment is undertaken, a CT study of the maxilla should be acquired to stage the extent of involvement more accurately. Determination of the tumor type from radiographs is also impossible, and a biopsy is needed; however, the appearance of this lesion is most consistent with a malignant gingival tumor. The histologic diagnosis was fibrosarcoma.



Fig. 8-15 Intraoral ventrodorsal radiograph of a cat with a swelling of the left mandible. Note the aggressive mottled appearance of the left rostral mandible. The diagnosis of squamous cell carcinoma was made histologically.

marked heterogeneous contrast enhancement (Fig. 8-16).[114] Flea control products and diet may play a role in development of squamous cell carcinoma in cats.[115] Unlike squamous cell carcinoma in the dog, these tumors have a poor prognosis and are less responsive to radiotherapy in cats.[110,116]

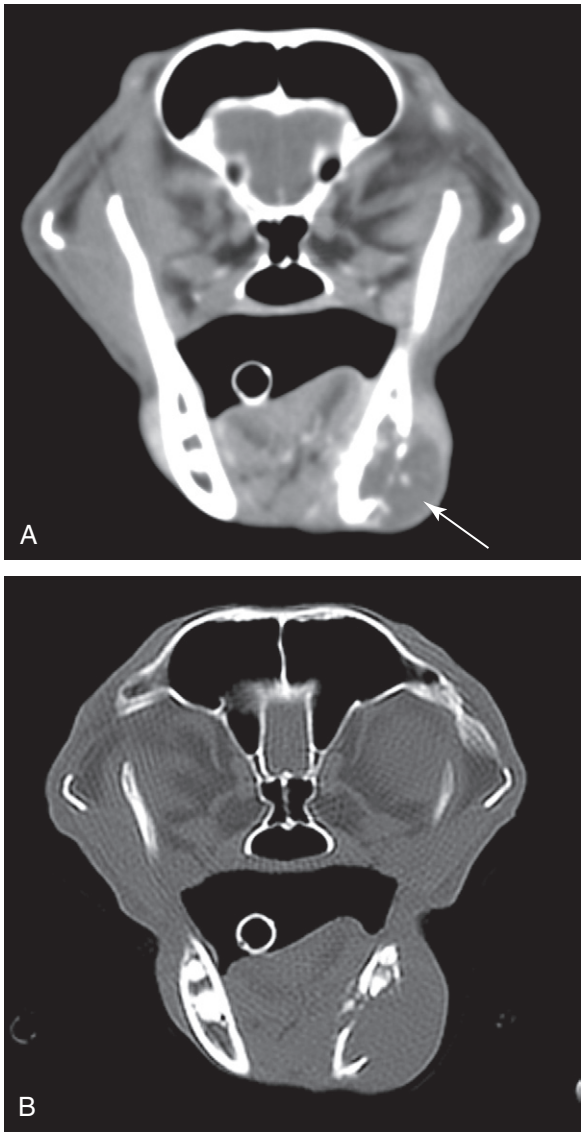


Fig. 8-16 CT images of a cat with a left mandibular squamous cell carcinoma. In the soft tissue window, post contrast administration **(A),** note the heterogeneous enhancement of the soft tissues *(white arrow)*. In the bone window **(B)**, note the lysis of the left mandible and loss of teeth.

The epulides of periodontal origin have been divided into three categories: fibromatous epulis, ossifying epulis, and acanthomatous epulis.[117] Fibromatous and ossifying epulides are similar benign growths cured by surgical excision; the distinctive feature of ossifying epulis is the histologically large segments of osteoid matrix.[108] The predominant feature of acanthomatous epulis, now termed *acanthomatous ameloblastoma*,[118,119] is the sheets of acanthomatous epithelial tissue noted histologically[108] and the local invasion, which often causes bony destruction on radiographs. Although rare, multiple epulides in cats have been reported, tend to recur after surgical excision, yet do not exhibit metastatic behavior.[109] Canine epulides are radiosensitive[120,121] with few complications.[122]

Tumors originating from dental laminar epithelium in dogs and cats include ameloblastoma, odontoma, and inductive fibroameloblastoma. Although rare, ameloblastoma is the most common tumor of dental origin in the dog and presents as a slowly growing, expansile mass.[108] Inductive fibroameloblastoma (feline inductive odontogenic tumor) is a rare tumor

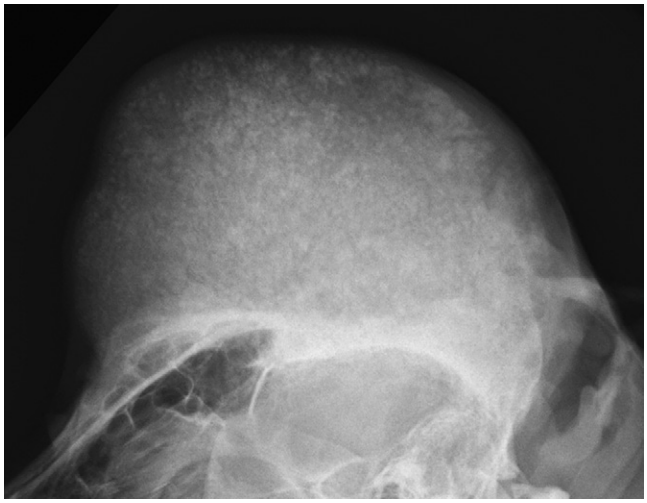


Fig. 8-17 Lateral radiograph of a dog with a dorsal calvarial multilobular osteochondrosarcoma. The granular appearance is typical of this tumor.

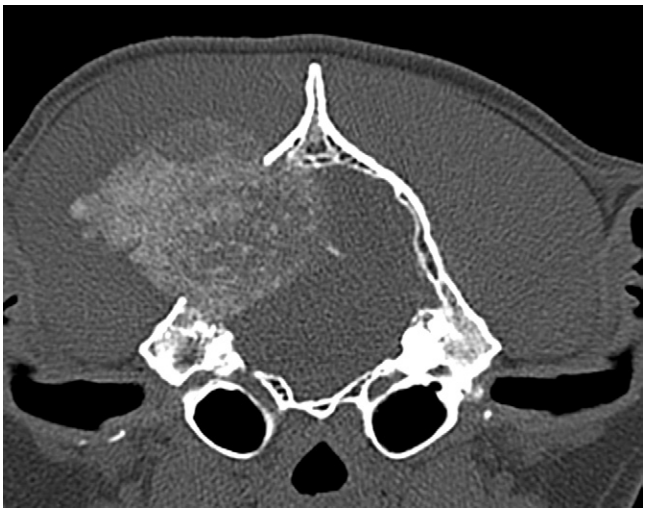


Fig. 8-18 CT image of a dog with a temporal multilobular osteochondrosarcoma. The granular appearance seen in radiographs is also a feature of the CT appearance of this tumor. The tumor has effaced the temporal bone and extends into the cranial cavity.

of the rostral maxilla found in young cats.[108,123,124] It is impossible to determine the histologic type of an oral tumor from radiographs. Radiographic changes are not dependent on tumor type; some tumors will be lytic, some osteoproductive, and some characterized by a combination of these changes. A sense of biologic aggressiveness can be obtained based on the radiographic changes, but a biopsy is necessary for definitive diagnosis. It is also impossible to determine the extent of normal tissue involvement of a tumor from radiographs. If therapy is being considered, either CT or MR imaging should be considered to more accurately determine the extent of tumor involvement.[125]

Treatment options for oral tumors consist of surgical excision alone, radiotherapy alone, a combination of surgery and radiotherapy,[111,120,121,126-128] photodynamic therapy,[129] and in the case of oral melanoma, vaccine and radiotherapy.[113,130] Of 100 dogs with oral tumors treated by mandibulectomy or maxillectomy, excellent survival rates were achieved for carcinoma, acanthomatous ameloblastoma, and squamous cell carcinoma, with poorer outcomes noted for sarcomas (fibrosarcoma, osteosarcoma, and malignant melanoma).[126] Adjuvant chemotherapy in addition to surgery and/or radiotherapy should be considered for oral tumors with the propensity to metastasize.[131]

Multilobular Osteochondrosarcoma

Multilobular osteochondrosarcoma (MLO) is a rare tumor that arises from the skull of dogs. These tumors often arise from the temporo-occipital area, although involvement of the orbit, maxilla, mandible, tympanic bulla, zygomatic arch, and hard palate has been reported.[132-139] An MLO typically has characteristic radiographic features. The margins are well defined, and there is limited lysis of adjacent bone.[140] The central core of the tumor comprises a coarse, granular mineral opacity throughout (Fig. 8-17). The granular appearance is also a feature of the CT appearance of MLO (Fig. 8-18). Dogs with MLO are typically older, large-breed dogs.[133,140] Approximately 50% of dogs experience local recurrence after treatment (surgical excision alone or surgery and radiotherapy), and approximately half develop metastatic disease.[133,136,140] CT is superior for the detection of cranial vault invasion (see Fig. 8-18), which was a common feature in patients described recently.[141] The features of MLO in MR images have been described in three dogs, all of which had a similar appearance of heterogeneous signal intensity with large regions of contrast enhancement; tumor invasion of soft tissues and brain was well delineated.[142]

Other Tumors of the Cranium

Other primary tumors of the cranium include osteosarcoma, osteoma, and osteochondroma. Osteosarcoma is the most common primary bone tumor, with 10% to 15% arising from the skull (see Fig. 8-3). Distribution of canine skull osteosarcoma in one report included cranial vault in 37%, facial bone in 36%, and mandible in 27% of patients.[143] Osteosarcomas arising from the cranial vault do not resemble those from the appendicular skeleton or other skull sites as they tend to be osteoblastic, have well-defined borders, and contain granular areas of calcification.[144] Osteoma is a slow-growing, benign tumor that has a smooth, well-defined border on radiographs These tumors can arise from the mandible, cranial vault, or sinuses.[18]

Most brain tumors do not have associated survey radiographic findings and are best identified with MR imaging.[145-147] Occasionally, sclerosis of the adjacent calvaria may be noted on routine skull radiographs in cats with meningioma (see Fig. 8-18). These tumors may calcify and cause sclerosis and/or lysis of the adjacent bony calvaria.[148] Imaging of brain tumors is covered in Chapter 9.

INFECTIOUS DISORDERS

Nasal Aspergillosis

Nasal aspergillosis is a destructive rhinitis involving the nasal cavity and paranasal sinuses of the dog; it affects younger (less than 4 years of age), nonbrachycephalic dogs more frequently than other types.[149,150] *Aspergillus* species (primarily *Aspergillus fumigatus*) are common environmental saprophytic fungal organisms.[149] Destructive rhinitis caused by other fungal agents, such as *Penicillium* species, is less common.[149,151] Nasal blastomycosis can occur in endemic areas. The most common radiographic appearance of nasal aspergillosis includes lysis of conchae with punctate lucencies of bone (Fig. 8-19).[89,150,152] Increased localized soft-tissue opacity of the nasal cavity is also seen, but frontal sinus involvement is variable and consists of sinus opacity with or without mottled bony thickening.[89,150,152] Bony nasal septum erosion or deviation is uncommon except in advanced disease. *Cryptococcus neoformans*,

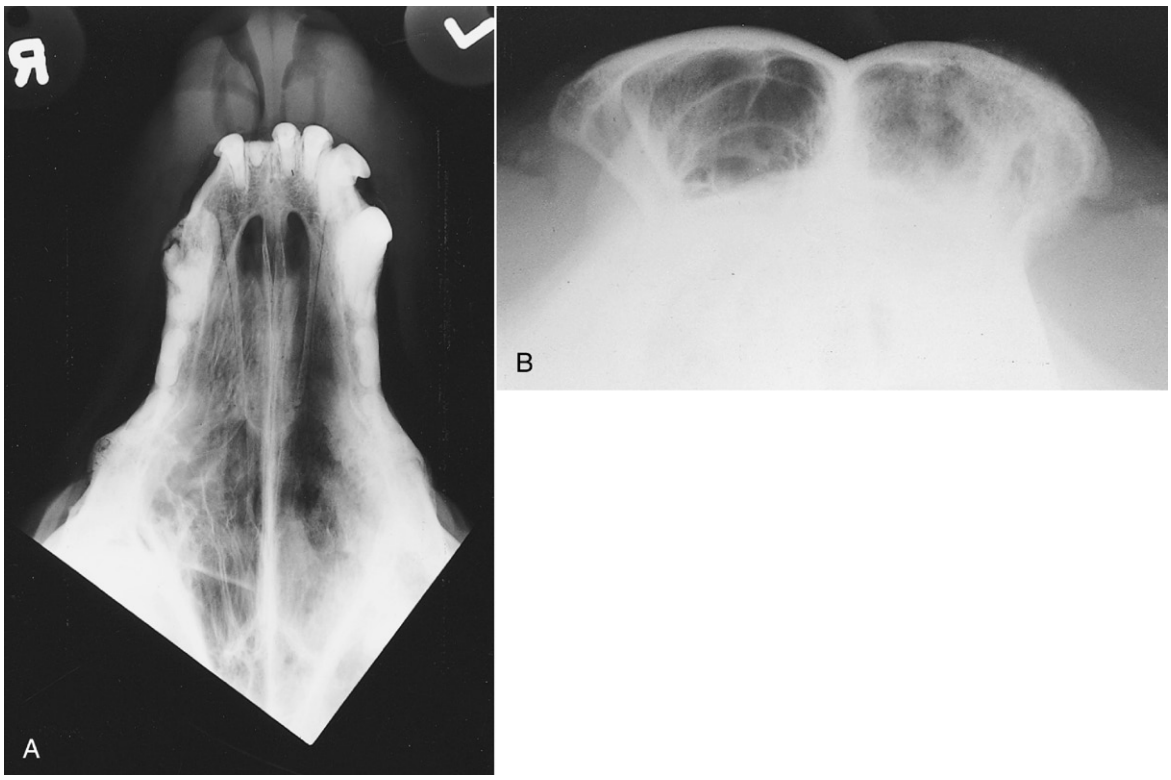


Fig. 8-19 Intraoral dorsoventral maxillary **(A)** and rostrocaudal–frontal sinus **(B)** radiographs of a dog with a 3-month history of nasal discharge. Note the destruction of the nasal conchae in the midportion of the left nasal cavity **(A)** and the increased opacity to the left frontal sinus **(B).** Evidence of frontal-bone irregularity is also present **(B)**, indicating destructive sinusitis. Destructive rhinitis secondary to *Aspergillus fumigatus* was diagnosed by culture.



Fig. 8-20 Intraoral, dorsoventral radiograph of a cat with a history of nasal discharge. Note the increased opacity to the right nasal cavity without loss of conchal detail. *Cryptococcus neoformans* was diagnosed by culture.

a fungal infection more commonly seen in cats, can infect the nasal passages, but generally causes a nondestructive hyperplastic rhinitis (Fig. 8-20).[153,154] Sinonasal fungal disease reported in cats include aspergillosis, cryptococcosis, and hyalohyphomycosis, and clinical signs, age, and CT features can overlap with those found with sinonasal neoplasia.[155]

Destructive rhinitis secondary to fungal disease can be difficult to differentiate radiographically from neoplasia. Both diseases cause loss of conchal detail, but a nasal cavity mass effect and invasion of bones surrounding the nasal cavity are more common features of nasal cavity neoplasia.[89,152] CT and MR imaging have been used for evaluating nasal aspergillosis, with the cross-sectional imaging modalities superior to radiography because of the greater contrast resolution and also because of their cross-sectional nature (Fig. 8-21).[11,99-101] However, diagnoses of fungal disease requires direct visualization of fungal plaques by endoscopy or fungal elements found by cytology or histopathology.[156]

Nasal Rhinitis and Foreign Bodies

Rhinitis secondary to bacterial infection, or corticosteroid-responsive rhinitis with lymphoplasmacytic infiltrates, can have a variable radiographic appearance in dogs and cats. Depending on the chronicity and severity of rhinitis, there may be evidence of destruction of conchae and of bony erosion.[80,100] Chronic rhinitis and sinusitis in cats are common sequelae to viral upper respiratory tract disease (Fig. 8-22). Radiographic changes can range from none in mild infections to an increased opacity of the nasal cavity and frontal sinuses with conchae and vomer bone destruction in severe infections.[80,157]

In five dogs with lymphoplasmacytic rhinitis, the radiographic appearance varied from increased opacity without bony destruction to nasal conchae and vomer bone lysis.[158] Destruction of conchae will be observed more frequently in destructive rhinitis secondary to aspergillosis or neoplasia but can also occur in other forms of rhinitis.[80,158,159] CT and MR imaging provide better delineation of disease and can help differentiate between neoplasia and rhinitis.[102,160,161]

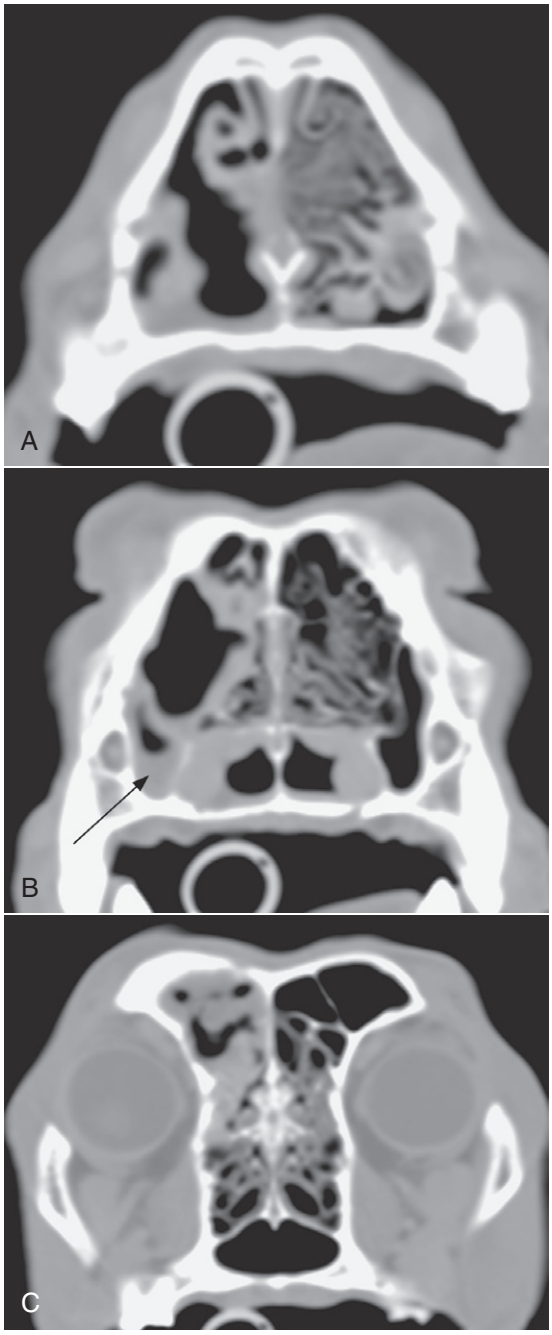


Fig. 8-21 Computed tomographic images of the nasal cavity from a dog with nasal aspergillosis. **A** and **B,** Destruction of conchae on the right side. Note the normal-appearing left conchae. Residual conchae on the right appear thickened and irregular. **B,** A small amount of fluid (note the meniscus effect, *arrow)* is present in the ventral aspect of the nasal cavity. **C,** There are irregular masses in the right frontal sinus without fluid accumulation, hyperostosis of the lateral aspect of the right frontal sinus, and erosion of the dorsomedial aspect of the right frontal sinus. The finding of conchal destruction and irregular frontal sinus mass effect is much more consistent with nasal aspergillosis than a tumor.

Intranasal foreign bodies[162] can occur in dogs, and foreign plant matter is common in certain environments, for example, grass awns in California. Affected dogs have an acute onset of sneezing and pawing at the nose, and they often have a unilateral nasal discharge.[159,163] Radiopaque foreign bodies are obvious in radiographs. Localization of nonopaque foreign bodies may be suspected in radiographs based on the presence of inflammation and mucopurulent material, which appear as increased soft-tissue opacity. CT is more sensitive for identification of foreign bodies than radiography, but not all foreign objects will be hyperattenuating in CT images.

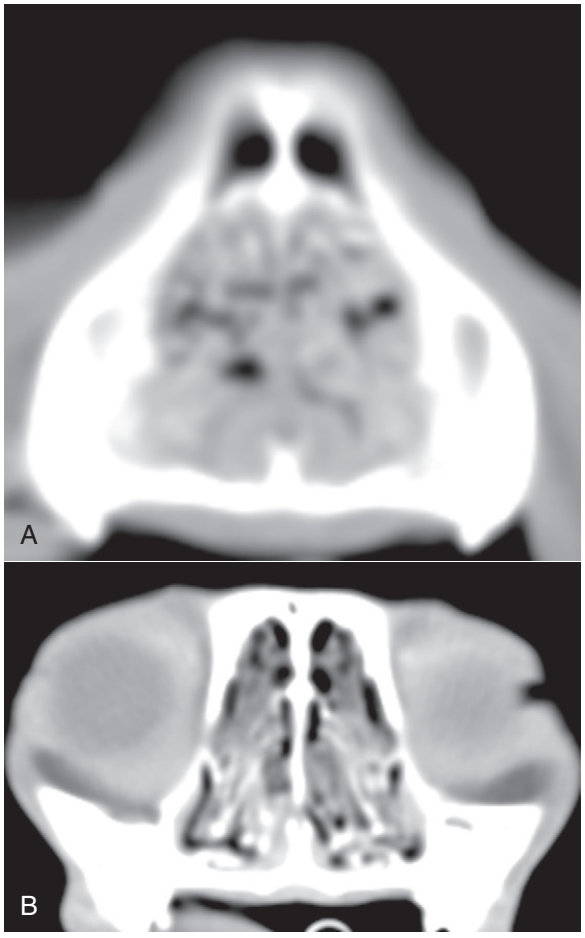


Fig. 8-22 CT images of the nasal cavity from a cat with chronic nasal discharge and presumed lower respiratory infection. Amorphous increased opacity in the nasal cavity is visible with indistinct conchal detail **(A** and **B)** likely caused by edema. This change, without a defined mass effect, and lack of turbinate destruction **(B)** is much more typical of an inflammatory process than a tumor. In radiographs, this change may not have been detected because of its minor nature.

Otitis

Radiographs are an integral part of the diagnostic workup of a dog or cat presenting with ear disease for evaluation of otitis media. Diagnosis of otitis interna is based on clinical signs because it does not reliably produce radiographic changes.[164] However, in ventrodorsal radiographs, external ear canal stenosis and/or mineralization can often be identified.

Otitis media is often secondary to chronic otitis externa. Evaluation of tympanic bullae for the presence of increased opacity or thickening of the osseous bulla, indicating otitis media, is best seen on lateral oblique and open-mouth radiographic projections (Fig. 8-23). Otitis media can be unilateral; when this occurs, the diagnosis is simplified by a comparison between the two tympanic bullae (see Fig. 8-23). In advanced disease, exuberant bony proliferation may involve the petrous temporal bone or the temporomandibular joint. Positioning is crucial when radiography of the bullae is performed; general anesthesia facilitates proper positioning and allows personnel to vacate the room during radiographic exposure. A review of imaging techniques for middle ear disease can be found elsewhere.[165-168]

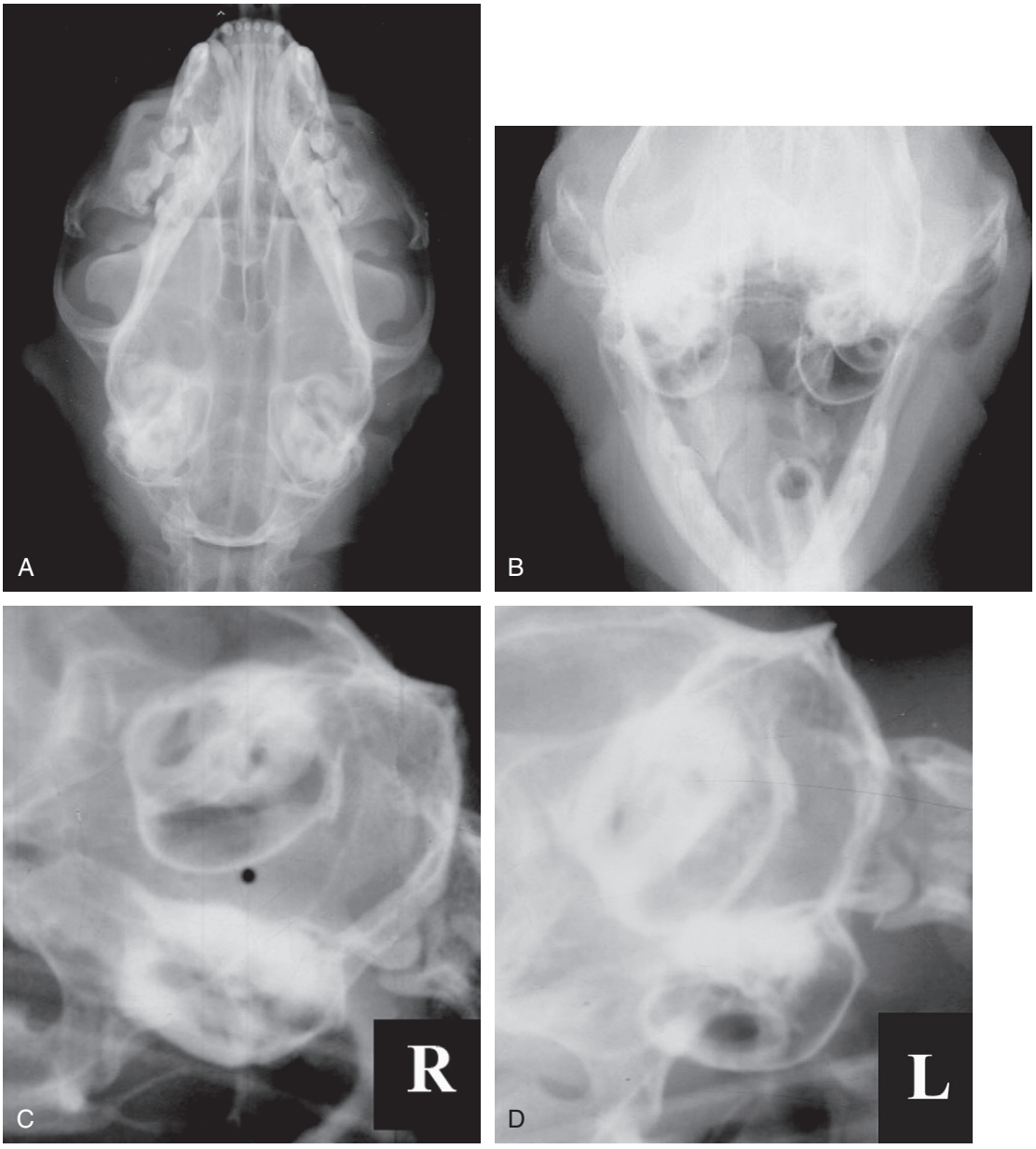


Fig. 8-23 Dorsoventral **(A)**, rostrocaudal open mouth **(B)**, left 20-degree ventral–right dorsal **(C),** and right 20-degree ventral–left dorsal **(D)** tympanic bulla radiographs of a cat with right chronic otitis media. Compare the normal left tympanic bulla (air-filled, thin, bony rim) with the more opaque, thickened right bulla. The open-mouth radiograph must be interpreted with care, as displacement of the tongue will cause one tympanic bulla to have increased opacity. Here the right tympanic bulla is more opaque in **B,** but there is also more soft tissue on the right side superimposed on the tympanic bulla. The oblique radiographs are of great value in this instance to assess the opacity of the tympanic bulla further.

When radiographic and surgical findings of otitis media were compared, all patients with abnormal radiographic findings were confirmed surgically. However, 25% of patients with normal radiographs of the middle ear were abnormal at surgery.[169] CT is a more sensitive test for evaluation of otitis media,[160,170] but proper technique is necessary to avoid artifactual wall thickening of the bulla on CT images (Fig. 8-24).[171] Middle ear changes are commonly identified in MR images of dogs with neurologic disease, and there was no correlation with the signal intensity of material within the middle ear and final diagnosis.[172] Evidence of material within the middle ear in MR images of dogs without clinical signs of otitis media was thought to represent subclinical otitis media or fluid accumulation without inflammation.[172] Whereas in cats, it is thought that obstruction of the auditory tube by sinonasal disease results in effusive tympanic bulla disease seen on CT images.[173]

Feline nasopharyngeal polyps are nonneoplastic growths originating from the mucous membrane of the auditory tube or middle ear.[174] Nasopharyngeal polyps generally occur in younger cats and can extend into the external ear canal, the osseous bulla, or the nasopharynx. Although rare, cats can have multiple polyps.[175] Cats may have signs of middle ear disease, rhinitis, or upper airway disease secondary to the space-occupying polyp. Signs of otitis media (increased soft-tissue opacity of the affected bulla) or nasopharyngeal obstruction (Fig. 8-25) may be noted on radiographs. In 31 cats with nasopharyngeal polyps, a radiographic diagnosis of otitis media

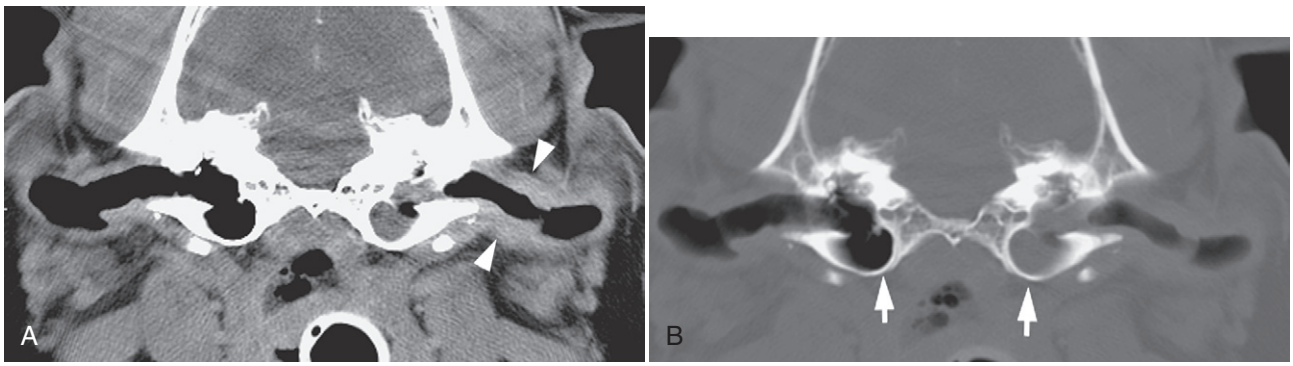


Fig. 8-24 Transverse CT image **(A)** at the level of the ears using a soft tissue window (W 350, L 90) of a dog with a slight head tilt to the right. Note the thickened external ear canal *(white arrowheads)* and the soft tissue attenuating material in the right tympanic bulla. With a bone window (W 2500, L 480) for the same image **(B),** the bone thickness is more accurate. Note the tympanic bullae are the same thickness *(white arrows)*.

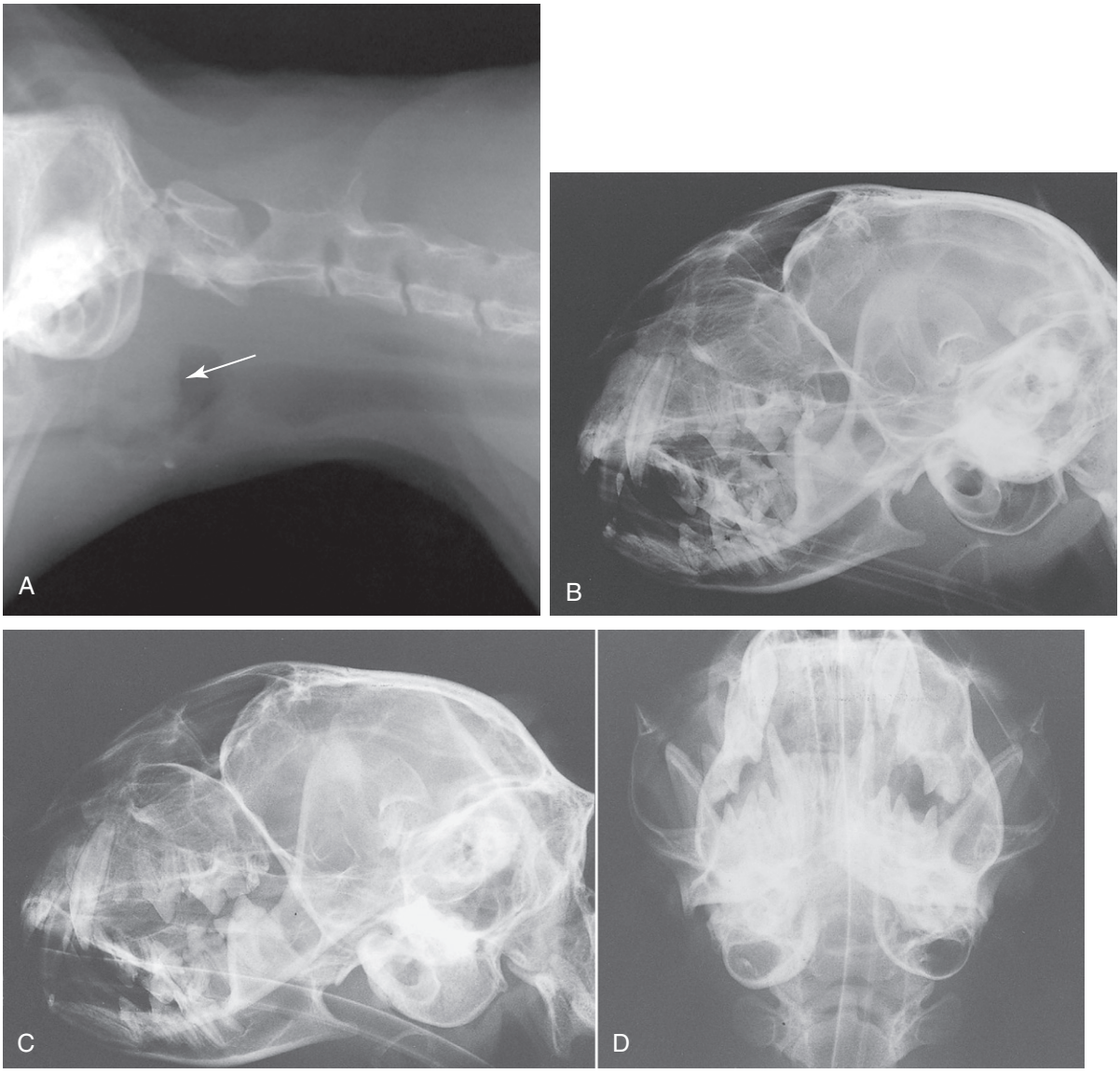


Fig. 8-25 Lateral **(A),** right dorsal–left ventral oblique **(B),** left dorsal–right ventral oblique **(C),** and rostral 10-degree ventral–caudodorsal **(D)** radiographs of a cat with inspiratory dyspnea caused by a nasopharyngeal polyp. Note the soft tissue nodule in the pharyngeal region on the lateral projection (**A,** *arrows*). Increased opacity and bony thickening of the right tympanic bulla is present in **B, C,** and **D** due to otitis media, likely secondary to auditory tube obstruction by the polyp.

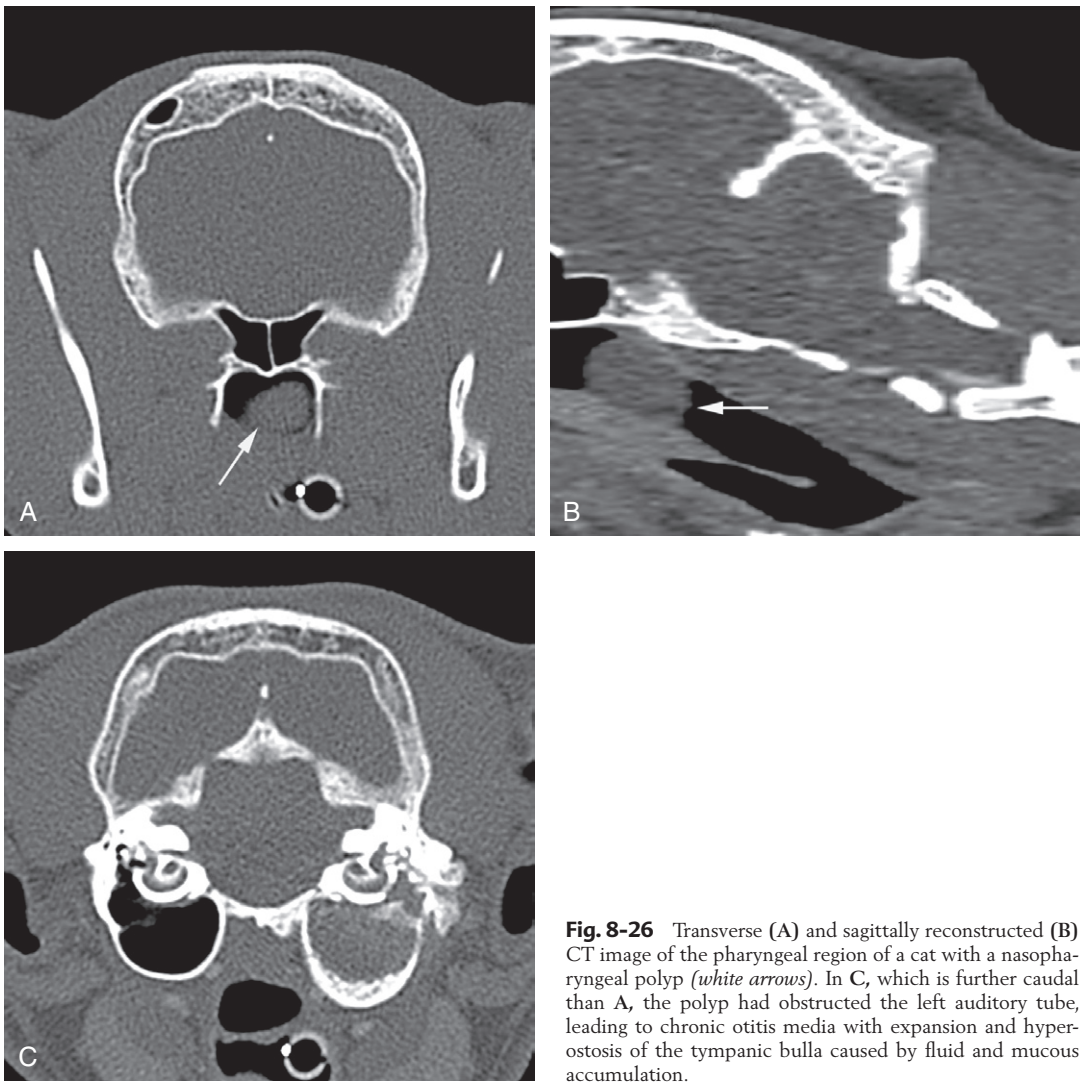


Fig. 8-26 Transverse **(A)** and sagittally reconstructed **(B)** CT image of the pharyngeal region of a cat with a nasopharyngeal polyp *(white arrows)*. In **C,** which is further caudal than **A,** the polyp had obstructed the left auditory tube, leading to chronic otitis media with expansion and hyperostosis of the tympanic bulla caused by fluid and mucous accumulation.

was made in 26 cats, and nasopharyngeal masses were detected in 30 cats.[176] CT and MR imaging can also be used to identify inflammatory polyps in cats (Fig. 8-26).[174,177]

Ear canal tumors occur in dogs and cats. Most often, these tumors are squamous cell carcinoma or mucinous gland adenocarcinoma.[178] These masses obliterate the external ear canal and can cause bony lysis of the adjacent calvaria and osseous bulla (Fig. 8-27). Middle ear cholesteatoma, a benign, slowly growing skin growth in the middle ear has a distinct CT appearance, being characterized by severe bone changes at the contour of the tympanic bulla, including osteolysis, osteoproliferation and osteosclerosis, expansion of the tympanic cavity, and sclerosis or osteoproliferation of the ipsilateral temporomandibular joint and paracondylar process. Cholesteatoma can cause lysis of the petrosal part of the temporal bone, leading to intracranial complications. There is usually no appreciable contrast enhancement of the tympanic bulla contents, but ring enhancement may be present (Fig. 8-28).[179]

Periapical (Tooth Root) Abscess

Periapical infection has a typical radiographic appearance of a radiolucent halo around the affected tooth root with destruction of alveolar bone (Fig. 8-29). Other signs seen include widening of the periodontal space surrounding the apex, bone lysis or sclerosis adjacent to the apex, loss of the lamina dura, and resorption of the tooth root. Periapical infections are common in older animals and may be secondary to periodontal disease or fracture of the affected tooth. In dogs, infections of the fourth maxillary premolar (carnassial tooth) (see Fig. 8-29) often result in a draining fistula below the eye on the affected side.

Dental radiographs can be obtained using conventional x-ray equipment and film-screen combinations, which consist of open-mouth oblique views of the dental arcades. A dental x-ray machine provides enhanced flexibility in adjustment of focal film distance, angulation, and collimation, and it enables the use, with improved accuracy, of small, intraoral dental film.[4] Additional descriptions of technical aspects and interpretation of dental radiographs using dental equipment can be found elsewhere.[180,181] Since the recognition of the American Veterinary Dental College by the American Veterinary Medical Association in 1988, there has been an increase in the number of specialists in veterinary dentistry. It is common practice for these dentists to perform endodontal and periodontal procedures to treat dental disease in dogs and cats.[4]

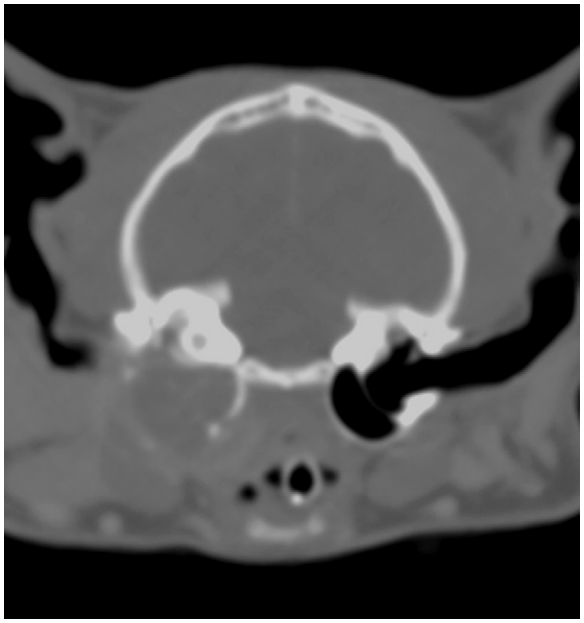


Fig. 8-27 CT image of the tympanic bulla region of a cat with a malignant tumor of the left middle ear. Increased tissue or fluid is present in the left tympanic bulla, and there has been expansion of the lateral and ventral aspects of the left tympanic bulla along with bony lysis. This aggressive appearance is typical of a malignant process and should not occur as a result of infection.

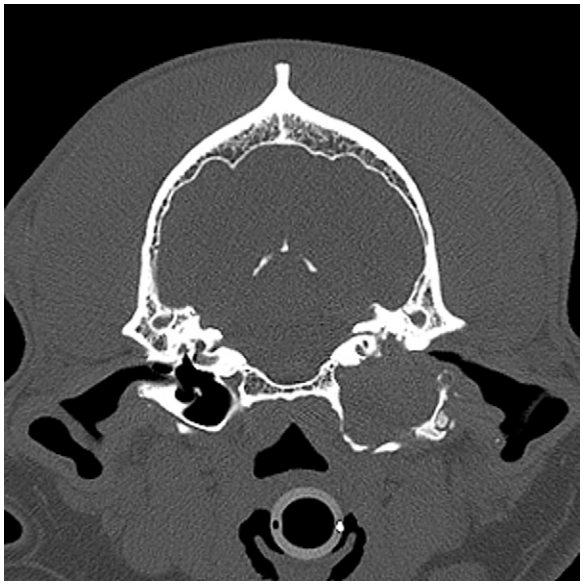


Fig. 8-28 CT image of a dog with a left tympanic bulla cholesteatoma. The lesion causes expansion and pressure necrosis of the tympanic bulla.

TRAUMATIC INJURIES

TMJ luxation can occur in both dogs and cats after external trauma. In the cat, TMJ luxation often occurs after the cat has jumped from a height, and in both dogs and cats, dislocation can occur secondary to being hit by a car.[182] The TMJ is capable of luxation without fracture because it has considerable lateral sliding movement, and the synchondrosis of the mandibular symphysis allows independent movement of the mandibular rami.[52] Dislocation of the TMJ tends to be in the rostrodorsal direction (Fig. 8-30), because ventrocaudal luxation is prevented by the retroarticular process of the temporal bone.[52] Dogs and cats with TMJ dislocation are unable to close the mouth completely, have dental malocclusion with the mandible displaced to one side, and display excessive salivation.[52,182] Luxation is most often unilateral; it may occur alone or with concomitant fractures of the retroarticular process, mandibular fossa, and zygomatic process of the squamous temporal bone or with the condyloid process of the mandible.[182]

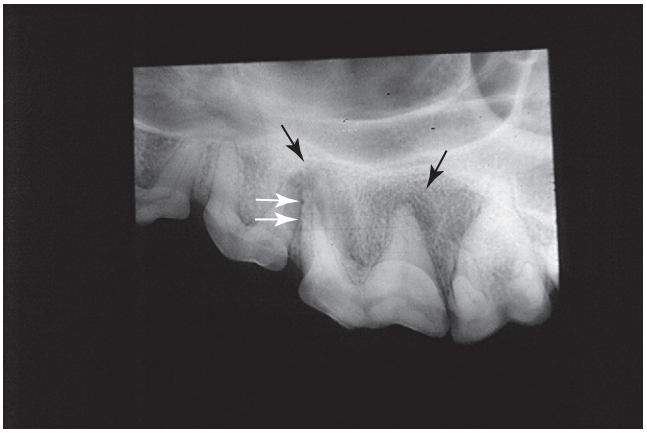


Fig. 8-29 Oblique radiograph of a caudal maxillary arcade in a dog with an abscess of the roots of the fourth maxillary premolar. Note the lysis of alveolar bone *(black arrows)*, loss of lamina dura, and irregularity of the rostral tooth root *(white arrows)*.

Radiographic views necessary for evaluating the TMJ include ventrodorsal and 20-degree lateral oblique views in the cat.[20,182] These views are useful in the dog, but the angle of rotation will vary depending on head conformation.[20,183] A sagittal oblique radiograph, in which the nose is elevated with a foam wedge so that the head is at a 20-degree angle to the cassette from a lateral position, is advocated in dogs as an alternative to lateral oblique views.[20,95,183] CT imaging provides for more accurate assessment of the TMJ.[20]

Skull trauma can occur after vehicular collision in dogs and cats. Currently, CT is used most often to image these patients for surgical planning. The ability to perform three-dimensional reconstructions of the region enhances this planning (Fig. 8-31).

MISCELLANEOUS DISEASES

Craniomandibular Osteopathy

Craniomandibular osteopathy (CMO) is a proliferative bone disease that occurs mainly in young West Highland white, Scottish, Cairn, Boston, and other terriers; it is occasionally seen in nonterrier breeds such as the Labrador retriever, Doberman pinscher, and bullmastiff.[184] There is a known autosomal recessive inheritance in West Highland white terriers.[185] CMO is usually seen in young dogs aged 3 to 8 months; affected dogs have mandibular swelling, prehension difficulties, pain on opening the mouth or with mastication, pyrexia, or combinations of these clinical signs.[63,186]

Radiographically, there is irregular new bone formation in affected areas, primarily the mandible, the tympanic bulla, and the petrous temporal bone (Fig. 8-32). Bony proliferation is often bilateral and may be asymmetric, although unilateral disease can occur. Bony proliferation can involve the temporomandibular joint and can affect jaw movement. Diagnosis is based on signalment and on radiographic findings. Bone biopsy is helpful in nonterrier breeds with unilateral involvement. Concurrent metaphyseal long-bone changes similar to

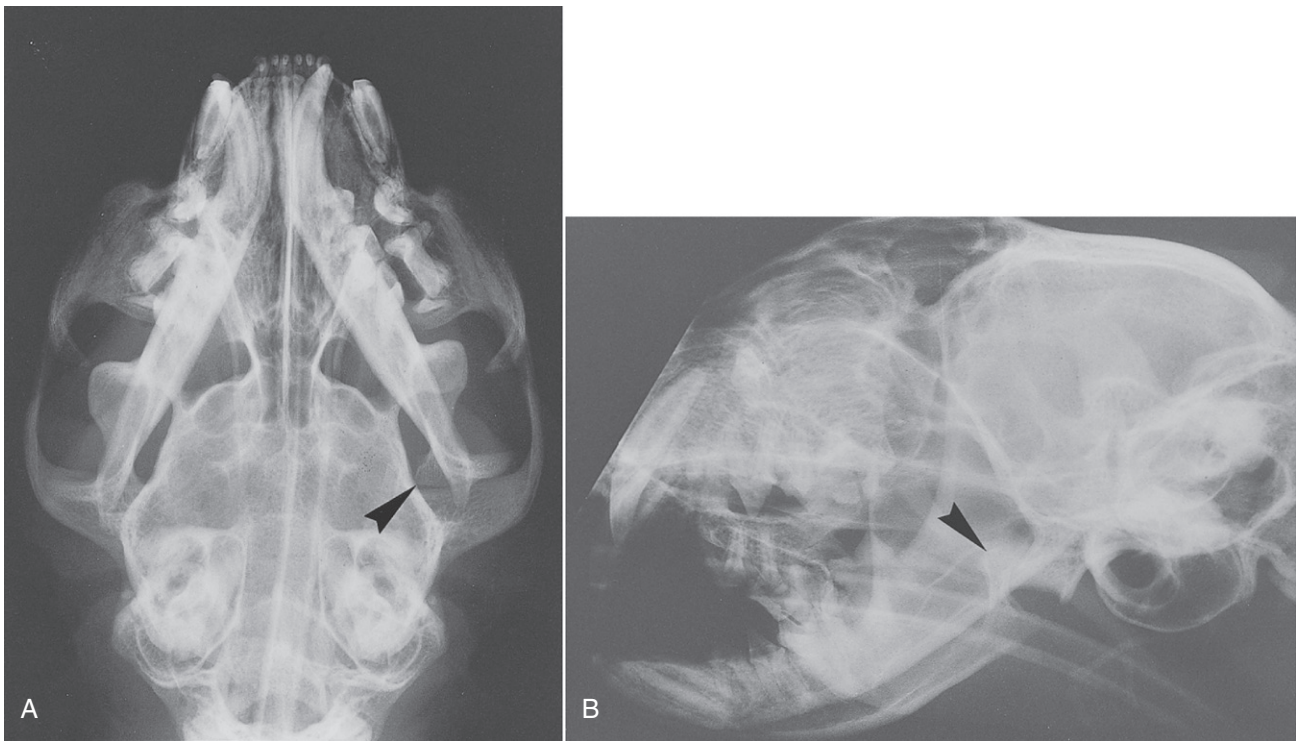


Fig. 8-30 Ventrodorsal **(A)** and right dorsal–left ventral oblique **(B)** radiographs of a 1-year-old domestic shorthair cat with a left temporomandibular luxation. Note the rostral location of the left mandibular condylar process *(arrowhead)* in the ventrodorsal radiograph **(A).** In the lateral oblique radiograph **(B),** note the rostral and dorsal luxation of the mandibular condylar process *(arrowhead)*.

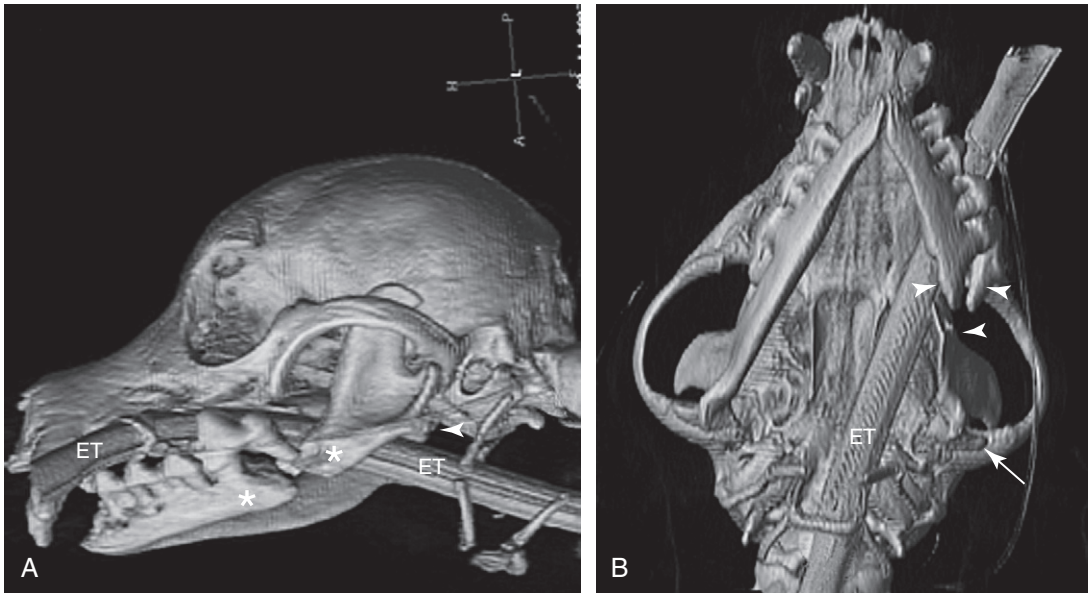


Fig. 8-31 Three-dimensional reconstructed volume rendering of the skull of a dog that sustained a left mandibular fracture. **A,** Left view. Note the obvious fracture fragments of the left mandible *(asterisks)* and that the caudal root of mandibular first molar is no longer embedded in bone. The angular and articular processes of the ramus are ill defined and displaced *(white arrowheads)*, indicating probable TMJ subluxation and possible fracture. **B,** Ventral view. Note three fragments of the fractured left mandible *(white arrowheads)*, deviation of the rostral mandible to the left, and caudal displacement of the left mandibular articular process *(white arrow)* indicating TMJ subluxation. *ET,* Endotracheal tube.

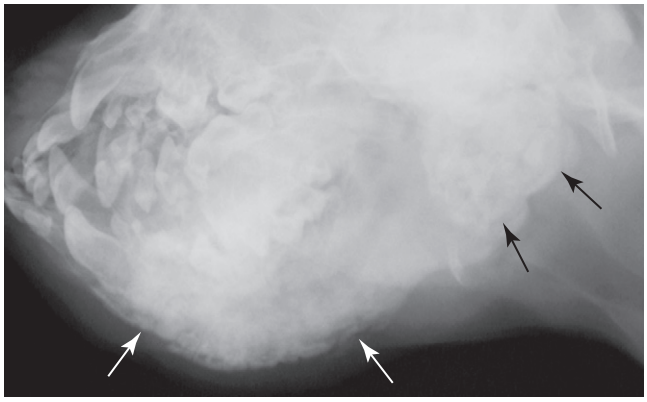


Fig. 8-32 Oblique skull radiograph of a Boston terrier with craniomandibular osteopathy. **A,** There is extensive bone proliferation on the mandibular ramus *(white arrows)* as well as the tympanic bulla *(black arrows)*.



Fig. 8-33 Lateral radiograph of a 6-month-old mastiff. There is smooth thickening of the mandibular, dorsal nasal, and calvarial cortices. Note the small size of the frontal sinuses caused by the peripheral hyperostosis.

hypertrophic osteodystrophy have been seen in dogs with CMO, but this is uncommon.[63] CMO is a self-limiting disease with unknown etiology. Bony proliferation generally ceases with skeletal maturation.

Calvarial Hyperostosis

Calvarial hyperostotic syndrome resembles canine craniomandibular osteopathy but is characterized mainly by progressive and often asymmetric skull-bone involvement. The disease affects young male and female bullmastiff dogs.[187,188] Radiographic findings are smooth thickening of various bones of the calvaria, to various degrees (Fig. 8-33). The smooth bone thickening is dissimilar from the irregular thickening seen in CMO. The etiology of calvarial hyperostosis is unknown.

Periodontal Disease

Periodontal disease is common in the dog and cat.[189,190] The structures that support the teeth include the cementum, the periodontal ligament, the alveolar bone, and the gingiva. Periodontal disease involves both hard tissue (cementum, alveolar bone) and soft tissue (periodontal ligament, gingiva) that surrounds the teeth. Periodontal disease affects dogs and cats commonly.[4,190,191] Gingival recession or hyperplasia and bony resorption in periodontal disease lead to ultimate loss of tooth support. Although radiography provides little information about gingival tissues, it is an important part of the evaluation of bony structures in periodontal disease.



Fig. 8-34 Oblique radiograph of the rostral mandible of a 14-year-old dog with severe dental disease. Note the irregularity of the alveolar crest between the second and third premolar teeth. Also note the lysis of the caudal root of the first premolar and the rostral root of the third premolar, which are changes consistent with dental root caries.

Early radiographic signs of periodontal disease include an irregular surface and bone loss in the alveolar crest. The lamina dura may be ill defined or may lack continuity.[4] As the disease progresses, horizontal bone loss occurs so that alveolar bone resorption develops away from the tooth crown, thus exposing tooth roots. Widening of the periodontal space is also seen. Alveolar bone recession exposes root surfaces, which can lead to root caries and root resorption, seen radiographically as radiolucent defects (Fig. 8-34).[192]

REFERENCES

1. Miller ME, Evans HE: *Miller's anatomy of the dog,* ed 4 St Louis, 2013, Saunders.
2. Harvey CE: The nasal septum of the dog: is it visible radiographically? *Vet Radiol* 20:88–90, 1979.
3. Morgan JP, Miyabayashi T: Dental radiology: ageing changes in permanent teeth of beagle dogs, *J Small Anim Pract* 32:11–18, 1991.
4. Mulligan TW, Aller MS, Williams CA: *Atlas of canine and feline dental radiography*, Trenton, NJ, 1998, Veterinary Learning Systems.
5. San Roman F, Llorens MP, Pena MT, Garcia FA, Prandi D: Dental radiography in the dog with a conventional x-ray device, *Vet Radiol* 31:235–238, 1990.
6. Zontine WJ: Dental radiographic technique and interpretation, *Vet Clin North Am* 4:741–762, 1974.
7. Zontine WJ: Canine dental radiology: Radiographic technique, development, and anatomy of the teeth, *J Am Vet Rad Soc* 16:75–82, 1975.
8. Codner EC, Lurus AG, Miller JB, Gavin PR, Gallina A, Barbee DD: Comparison of computed tomography with radiography as a noninvasive diagnostic technique for chronic nasal disease in dogs, *J Am Vet Med Assoc* 202:1106–1110, 1993.
9. De Rycke LM, Saunders JH, Gielen IM, van Bree HJ, Simoens PJ: Magnetic resonance imaging, computed tomography, and cross-sectional views of the anatomy of normal nasal cavities and paranasal sinuses in mesaticephalic dogs, *Am J Vet Res* 64:1093–1098, 2003.
10. Park RD, Beck ER, LeCouteur RA: Comparison of computed tomography and radiography for detecting changes induced by malignant nasal neoplasia in dogs, *J Am Vet Med Assoc* 201:1720–1724, 1992.

11. Saunders JH, Clercx C, Snaps FR, et al: Radiographic, magnetic resonance imaging, computed tomographic, and rhinoscopic features of nasal aspergillosis in dogs, *J Am Vet Med Assoc* 225:1703–1712, 2004.
12. Thrall DE, Robertson ID, McLeod DA, Heidner GL, Hoopes J, Page RL: A comparison of radiographic and computed tomographic findings in 31 dogs with malignant nasal cavity tumors, *Vet Radiol* 30:59–66, 1989.
13. Burk RL: Computed tomographic anatomy of the canine nasal passages, *Vet Radiol Ultrasound* 33:170–176, 1992.
14. Assheuer J, Sager M: Head. In Assheuer J, Sager M editors: *MRI and CT atlas of the dog*, Berlin, 1997, Blackwell Science, pp 50–57.
15. Feeney D, Fletcher T, Hardy R: *Atlas of correlative imaging anatomy of the normal dog, ultrasound and computed tomography*, Philadelphia, 1991, Saunders.
16. George F, Smallwood J: Anatomic atlas for computed tomography in the mesaticephalic dog: head and neck, *Vet Radiol Ultrasound* 33:217–240, 1992.
17. Lasonsky JH, Abbott LC, Kuriashkin IV: Computed tomography of the normal feline nasal cavity and paranasal sinuses, *Vet Radiol Ultrasound* 38:251–258, 1997.
18. Myer W: Cranial vault and associated structures. In Thrall DE, editor: *Textbook of veterinary diagnostic radiology*, Philadelphia, 1998, Saunders, pp 45–59.
19. Kneissl S, Probst S, Konar M: Low-field magnetic resonance imaging of the canine middle and inner ear, *Vet Radiol Ultrasound* 45:520–522, 2004.
20. Schwarz T, Weller R, Dickie AM, Konar M, Sullivan M: Imaging of the canine and feline temporomandibular joint: a review, *Vet Radiol Ultrasound* 43:85–97, 2002.
21. Couturier L, Degueurce C, Ruel Y, Dennis R, Begon D: Anatomical study of cranial nerve emergence and skull foramina in the dog using magnetic resonance imaging and computed tomography, *Vet Radiol Ultrasound* 46: 375–383, 2005.
22. Mayer MN, Waldner CL, Elliot KM, Sidhu N: Comparison of interfractional variation in canine head position using palpation and a head-repositioning device, *Vet Radiol Ultrasound* 51:472–476, 2010.
23. Thomas WB: Hydrocephalus in dogs and cats, *Vet Clin North Am Small Anim Pract* 40:143–159, 2010.
24. Hecht S, Adams WH: MRI of brain disease in veterinary patients part 1: basic principles and congenital brain disorders, *Vet Clin North Am Small Anim Pract* 40:21–38, 2010.
25. Burt JK, Bhargava AK, Prynn RB: Unilateral hydrocephalus with cranial distortion in a cat, *Vet Med Clin North Am (Small Anim Pract)* 65:745, 1970.
26. Krum S, Johnson K, Wilson J: Hydrocephalus associated with the noneffusive form of feline infectious peritonitis, *J Am Vet Med Assoc* 167:745, 1975.
27. Spaulding KA, Sharp NJH: Ultrasonographic imaging of the lateral cerebral ventricles in the dog, *Vet Radiol* 31:59–64, 1990.
28. Hudson JA, Simpson ST, Buxton DF, Cartee RE, Steiss JE: Ultrasonographic diagnosis of canine hydrocephalus, *Vet Radiol* 31:50–58, 1990.
29. Vite CH, Insko EK, Schotland HM, Panckeri K, Hendricks JC: Quantification of cerebral ventricular volume in English bulldogs, *Vet Radiol Ultrasound* 38:437–443, 1997.
30. Vullo T, Korenman E, Manzo RP, Gomez DG, Deck MD, Cahill PT: Diagnosis of cerebral ventriculomegaly in normal adult beagles using quantitative MRI, *Vet Radiol Ultrasound* 38:277–281, 1997.
31. Kuwamura M, Hattori R, Yamate J, Kotani T, Sasai K: Neuronal ceroid-lipofuscinosis and hydrocephalus in a chihuahua, *J Small Anim Pract* 44:227–230, 2003.
32. Thomas WB: Nonneoplastic disorders of the brain, *Clin Techniques Small Anim Pract* 14:125–147, 1999.
33. Kii S, Uzuka Y, Taura Y, Nakaichi M, Inokuma H, Onishi T: Developmental change of lateral ventricular volume and ratio in beagle-type dogs up to 7 months of age, *Vet Radiol Ultrasound* 39:185–189, 1998.
34. De Hann CE, Kraft SL, Gavin PR, Wendling LR, Griebenow ML: Normal variation in size of the lateral ventricles of the Labrador retriever dog as assessed by magnetic resonance imaging, *Vet Radiol Ultrasound* 35:83–86, 1994.
35. Hudson JA, Cartee RE, Simpson ST, Buxton DF: Ultrasonographic anatomy of the canine brain, *Vet Radiol* 30:13–21, 1989.
36. Hudson JA, Simpson ST, Cox NR, Buxton DF: Ultrasonographic examination of the normal canine neonatal brain, *Vet Radiol* 32:50–59, 1991.
37. Watson AG, de Lahunta A, Evans HE: Dorsal notch of foramen magnum due to incomplete ossification of supraoccipital bone in dogs, *J Small Anim Pract* 30:666–673, 1986.
38. Bardens JW: Congenital malformation of the foramen magnum in dogs, *Southwest Vet* 18:295, 1965.
39. Kelly JH: Occipital dysplasia and hydrocephalus in a toy poodle, *Vet Med Small Anim Clin* 70:940, 1975.
40. Parker AJ, Park RD: Occipital dysplasia in the dog, *J Am Anim Hosp Assoc* 10:520, 1974.
41. Ticer JW: *Radiographic technique in veterinary practice*, Philadelphia, 1984, Saunders.
42. Watson AG: The phylogeny and development of the occipito-atlas-axis complex in the dog, doctoral dissertation, Cornell University, Ithaca, 1981.
43. Wright JA: A study of the radiographic anatomy of the foramen magnum in dogs, *J Small Anim Pract* 20:501, 1979.
44. Simoens P, Poels P, Lauwers H: Morphometric analysis of the foramen magnum in Pekingese dogs, *Am J Vet Res* 55:34–39, 1994.
45. Rusbridge C, MacSweeny JE, Davies JV, et al: Syringohydromyelia in Cavalier King Charles spaniels, *J Am Anim Hosp Assoc* 36:34–41, 2000.
46. Rusbridge C, Knowler SP: Hereditary aspects of occipital bone hypoplasia and syringomyelia (Chiari type I malformation) in Cavalier King Charles spaniels, *Vet Record* 153:107–112, 2003.
47. Rusbridge C: Neurological diseases of the Cavalier King Charles spaniel, *J Small Anim Pract* 46:265–272, 2005.
48. Rusbridge C, Knowler SP: Inheritance of occipital bone hypoplasia (Chiari type I malformation) in Cavalier King Charles spaniels, *J Vet Intern Med* 18:673–678, 2004.
49. Cerda-Gonzalez S, Olby NJ, McCullough S, Pease AP, Broadstone R, Osborne JA: Morphology of the caudal fossa in Cavalier King Charles spaniels, *Vet Radiol Ultrasound* 50:37–46, 2009.
50. Robbins G, Grandage J: Temporomandibular joint dysplasia and open-mouth jaw locking in the dog, *J Am Vet Med Assoc* 171:1072–1076, 1977.
51. Dickie AM, Schwarz T, Sullivan M: Temporomandibular joint morphology in Cavalier King Charles spaniels, *Vet Radiol Ultrasound* 43:260–266, 2002.
52. Lane JG: Disorders of the canine temporomandibular joint, *Vet Annu* 21:175–186, 1982.
53. Reiter AM: Symphysiotomy, symphysiectomy, and intermandibular arthrodesis in a cat with open-mouth jaw locking—case report and literature review, *J Vet Dent* 21:147–158, 2004.

54. Soukup JW, Snyder CJ, Gengler WR: Computed tomography and partial coronoidectomy for open-mouth jaw locking in two cats, *J Vet Dent* 26:226–233, 2009.
55. Beam RC, Kunz DA, Cook CR, Carson RL, Briscoe P, Cook JL: Use of three-dimensional computed tomography for diagnosis and treatment planning for open-mouth jaw locking in a cat, *J Am Vet Med Assoc* 230: 59–63, 2007.
56. Cowell KR, Jezyk PF, Haskins ME, Patterson DF: Mucopolysaccharidosis in a cat, *J Am Vet Med Assoc* 169:334–339, 1976.
57. Haskins ME, Gustavo DA, Jezyk PF, Patterson DF: The pathology of the feline model of mucopolysaccharidosis VI, *Am J Pathol* 101:657–674, 1980.
58. Haskins ME, Casal M, Ellinwood NM, Melniczek J, Mazrier H, Giger U: Animal models for mucopolysaccharidoses and their clinical relevance, *Acta Paediatr Suppl* 91:88–97, 2002.
59. Crawley AC, Muntz FH, Haskins ME, Jones BR, Hopwood JJ: Prevalence of mucopolysaccharidosis type VI mutations in Siamese cats, *J Vet Intern Med* 17:495–498, 2003.
60. Haskins ME: Animal models for mucopolysaccharidosis disorders and their clinical relevance, *Acta Paediatr Suppl* 96:56–62, 2007.
61. Konde LJ, Thrall MA, Gasper P, et al: Radiographically visualized skeletal changes associated with mucopolysaccharidosis VI in cats, *Vet Radiol* 28:223–228, 1987.
62. Haskins ME, Aguirre GD, Jezyk PF, Desnick RJ, Patterson DF: The pathology of the feline model of mucopolysaccharidosis I, *Am J Pathol* 112:27–36, 1983.
63. Johnson KA, Watson ADJ: Skeletal diseases. In Ettinger SJ, Feldman EC, editors: *Textbook of veterinary internal medicine*, St. Louis, 2005, Elsevier Saunders, pp 1965–1992.
64. Crawley A, Ramsay SL, Byers S, Hopwood JJ, Meikle PJ: Monitoring dose response of enzyme replacement therapy in feline mucopolysaccharidosis type VI by tandem mass spectrometry, *Ped Research* 55:585–591, 2004.
65. Cotugno G, Annunziata P, Tessitore A, et al: Long-term amelioration of feline mucopolysaccharidosis VI after AAV-mediated liver gene transfer, *Mol Ther* 19:461–469, 2011.
66. Bonczynski J: Primary hyperparathyroidism in dogs and cats, *Clin Tech Small Anim Pract* 22:70–74, 2007.
67. Feldman EC, Hoar B, Pollard R, Nelson RW: Pretreatment clinical and laboratory findings in dogs with primary hyperparathyroidism: 210 cases (1987–2004), *J Am Vet Med Assoc* 227:756–761, 2005.
68. Kumar R, Thompson JR: The regulation of parathyroid hormone secretion and synthesis, *J Am Soc Nephrol* 22: 216–224, 2011.
69. Feldman EC, Wisner ER, Nelson RW, Feldman MS, Kennedy PC: Comparison of results of hormonal analysis of samples obtained from selected venous sites versus cervical ultrasonography for localizing parathyroid masses in dogs, *J Am Vet Med Assoc* 211:54–56, 1997.
70. Wisner ER, Nyland TG: Ultrasonography of the thyroid and parathyroid glands, *Vet Clin North Am Small Anim Pract* 28:973–991, 1998.
71. Brodey RS: Canine and feline neoplasia, *Adv Vet Sci Comp Med* 14:309–354, 1970.
72. Engle GC, Brodey RS: A retrospective study of 395 feline neoplasms, *J Am Anim Hosp Assoc* 5:21–31, 1969.
73. Madewell BR, Priester WA, Gillette EL, Snyder SP: Neoplasms of the nasal passages and paranasal sinuses in domesticated animals as reported by 13 veterinary colleges, *Am J Vet Res* 37:851–856, 1976.
74. Bright RM, Bojrab MJ: Intranasal neoplasia in the dog and cat, *J Am Anim Hosp Assoc* 12:806, 1976.
75. Cox NR, Brawner WR, Powers RD, Wright JC: Tumors of the nose and paranasal sinuses in cats: 32 cases with comparison to a national database (1977–1987), *J Am Anim Hosp Assoc* 27:339–347, 1991.
76. Legendre AM, Krahwinkel DJ, Spaulding KA: Feline nasal and paranasal sinus tumors, *J Am Anim Hosp Assoc* 17:1038–1039, 1981.
77. Malinowski C: Canine and feline nasal neoplasia, *Clin Tech Small Anim Pract* 21:89–94, 2006.
78. Allen HS, Broussard J, Noone K: Nasopharyngeal diseases in cats: a retrospective study of 53 cases (1991–1998), *J Am Anim Hosp Assoc* 35:457–461, 1999.
79. Evans SM, Hendrick MJ: Radiotherapy of feline nasal tumors: a retrospective study of nine cases, *Vet Radiol* 30:128–132, 1989.
80. O'Brien RT, Evans SM, Wortman JA, Hendrick MJ: Radiographic findings in cats with intranasal neoplasia or chronic rhinitis: 29 cases (1982–1988), *J Am Vet Med Assoc* 208:385–389, 1996.
81. LaDue TA, Dodge R, Page RL, Price GS, Hauck ML, Thrall DE: Factors influencing survival after radiotherapy of nasal tumors in 130 dogs, *Vet Radiol Ultrasound* 40:312–317, 1999.
82. McEntee MC, Page RL, Heidner GL, Cline JM, Thrall DE: A retrospective study of 27 dogs with intranasal neoplasms treated with cobalt radiation, *Vet Radiol* 32:135–139, 1991.
83. Adams WM, Withrow SJ, Walshaw R, et al: Radiotherapy of malignant nasal tumors in 67 dogs, *J Am Vet Med Assoc* 191:311–315, 1987.
84. Adams WM, Miller PE, Vail DM, Forrest LJ, MacEwen EG: An accelerated technique for irradiation of malignant canine nasal and paranasal sinus tumors, *Vet Radiol Ultrasound* 39:475–481, 1998.
85. Buchholz J, Hagen R, Leo C, Ebling A, Roos M, Kaser-Hotz B, et al: 3D conformal radiation therapy for palliative treatment of canine nasal tumors, *Vet Radiol Ultrasound* 50:679–683, 2009.
86. Hunley DW, Mauldin GN, Shiomitsu K, Mauldin GE: Clinical outcome in dogs with nasal tumors treated with intensity-modulated radiation therapy, *Can Vet J* 51:293–300, 2010.
87. Lawrence JA, Forrest LJ, Turek MM, et al: Proof of principle of ocular sparing in dogs with sinonasal tumors treated with intensity-modulated radiation therapy, *Vet Radiol Ultrasound* 51:561–570, 2010.
88. Harvey CE, Biery DN, Morello J, O'Brien JA: Chronic nasal disease in the dog: its radiographic diagnosis, *Vet Radiol* 20:91–98, 1979.
89. Russo M, Lamb MA, Jakovljevic S: Distinguishing rhinitis and nasal neoplasia by radiography, *Vet Radiol Ultrasound* 41:118–124, 2000.
90. Morgan JP, Suter PF, O'Brien TR, Park RD: Tumors in the nasal cavity of the dog: a radiographic study, *J Am Vet Radiol Soc* 13:18–26, 1972.
91. Morris JS, Dunn KJ, Dobson JM, White RAS: Radiological assessment of severity of canine nasal tumours and relationship with survival, *J Small Anim Pract* 37:1–6, 1996.
92. Drees R, Forrest LJ, Chappell R: Comparison of computed tomography and magnetic resonance imaging for the evaluation of canine intranasal neoplasia, *J Small Anim Pract* 50:334–340, 2009.
93. Schwarz T, Sullivan M, Hartung K: Radiographic anatomy of the cribriform plate (lamina cribrosa), *Vet Radiol Ultrasound* 41:220–225, 2000.

94. Kirberger RM, Fourie SL: An investigation into the usefulness of a rostrocaudal nasal radiographic view in the dog, *J S Afr Vet Assoc* 73:171–176, 2002.
95. Morgan JP, Silverman S: *Techniques of veterinary radiography*, Davis, Calif, 1984, Veterinary Radiology Associates.
96. Frew DG, Dobson JM: Radiological assessment of 50 cases of incisive or maxillary neoplasia in the dog, *J Small Anim Pract* 33:11–18, 1992.
97. Adams WM, Kleiter MM, Thrall DE, et al: Prognostic significance of tumor histology and computed tomographic staging for radiation treatment response of canine nasal tumors, *Vet Radiol Ultrasound* 50:330–335, 2009.
98. Burk RL: Computed tomographic imaging of nasal disease in 100 dogs, *Vet Radiol Ultrasound* 33:177–180, 1992.
99. Saunders JH, van Bree H: Comparison of radiography and computed tomography for the diagnosis of canine nasal aspergillosis, *Vet Radiol Ultrasound* 44:414–419, 2003.
100. Saunders JH, van Bree H, Gielen I, de Rooster H: Diagnostic value of computed tomography in dogs with chronic nasal disease, *Vet Radiol Ultrasound* 44:409–413, 2003.
101. Saunders JH, Zonderland JL, Clerex C, et al: Computed tomographic findings in 35 dogs with nasal aspergillosis, *Vet Radiol Ultrasound* 43:5–9, 2002.
102. Lefebvre J, Kuehn NF, Wortinger A: Computed tomography as an aid in the diagnosis of chronic nasal disease in dogs, *J Small Anim Pract* 46:280–285, 2005.
103. Tromblee TC, Jones JC, Etue AE, Forrester SD: Association between clinical characteristics, computed tomography characteristics, and histologic diagnosis for cats with sinonasal disease, *Vet Radiol Ultrasound* 47:241–248, 2006.
104. Pruitt AF, Thrall DE: Use of photon fields with noncoincident isocenters to improve homogeneity of dose distribution, *Vet Radiol Ultrasound* 45:471–475, 2004.
105. Avner A, Dobson JM, Sales JI, Herrtage ME: Retrospective review of 50 canine nasal tumours evaluated by low-field magnetic resonance imaging, *J Small Anim Pract* 49:233–239, 2008.
106. Hoyt RF, Withrow SJ: Oral malignancy in the dog, *J Am Anim Hosp Assoc* 20:83–92, 1984.
107. Stebbins KE, Morse CC, Goldschmidt MH: Feline oral neoplasia: a ten-year survey, *Vet Pathol* 26:121–128, 1989.
108. Dubielzig RR: Proliferative dental and gingival diseases of dogs and cats, *J Am Anim Hosp Assoc* 18:577–584, 1982.
109. Colgin LMA, Schulman FY, Dubielzig RR: Multiple epulides in 13 cats, *Vet Pathol* 38:227–229, 2001.
110. Withrow SJ: Cancer of the gastrointestinal system: cancer of the oral cavity. In MacEwen EG, Withrow SJ, editors: *Small animal clinical oncology*, Philadelphia, 2001, Saunders, pp 305–318.
111. Ciekot PA, Powers BE, Withrow SJ, Straw RC, Ogilvie GK, LaRue SM: Histologically low-grade, yet biologically high-grade, fibrosarcomas of the mandible and maxilla in dogs: 25 cases (1982–1991), *J Am Vet Med Assoc* 204:610–615, 1994.
112. Forrest LJ, Chun R, Adams WM, Cooley AJ, Vail DM: Postoperative radiotherapy for canine soft tissue sarcoma, *J Vet Intern Med* 14:578–582, 2000.
113. Bergman PJ: Canine oral melanoma, *Clin Tech Small Anim Pract* 22:55–60, 2007.
114. Gendler A, Lewis JR, Reetz JA, Schwarz T: Computed tomographic features of oral squamous cell carcinoma in cats: 18 cases (2002–2008), *J Am Vet Med Assoc* 236:319–325, 2010.
115. Bertone ER, Snyder LA, Moore AS: Environmental and lifestyle risk factors for oral squamous cell carcinoma in domestic cats, *J Vet Intern Med* 17:557–562, 2003.
116. Bregazzi VS, LaRue SM, Powers BE, Fettman MJ, Ogilvie GK, Withrow SJ: Response of feline oral squamous cell carcinoma to palliative radiation therapy, *Vet Radiol Ultrasound* 42:77–79, 2001.
117. Dubielzig RR, Goldschmidt MH, Brodey RS: The nomenclature of periodontal epulides in dogs, *Vet Pathol* 16:209–214, 1979.
118. Fiani N, Verstraete FJ, Kass PH, Cox DP: Clinicopathologic characterization of odontogenic tumors and focal fibrous hyperplasia in dogs: 152 cases (1995–2005), *J Am Vet Med Assoc* 238:495–500, 2011.
119. Gardner DG, Baker DC: The relationship of the canine acanthomatous epulis to ameloblastoma, *J Comp Pathol* 108:47–55, 1993.
120. Langham RF, Mostosky UV, Schirmer RG: X-ray therapy of selected odontogenic neoplasms in the dog, *J Am Vet Med Assoc* 170:820–822, 1977.
121. Thrall DE: Orthovoltage radiotherapy of acanthomatous epulides in 39 dogs, *J Am Vet Med Assoc* 184:826–829, 1984.
122. McEntee MC, Page RL, Theon A, Erb HN, Thrall DE: Malignant tumor formation in dogs previously irradiated for acanthomatous epulis, *Vet Radiol Ultrasound* 45:357–361, 2004.
123. Dubielzig RR, Adams WM, Brodey RS: Inductive fibroameloblastoma, an unusual dental tumor of young cats, *J Am Vet Med Assoc* 174:720–722, 1979.
124. Gardner DG, Dubielzig RR: Feline inductive odontogenic tumor (inductive fibroameloblastoma)—a tumor unique to cats, *J Oral Pathol Med* 24:185–190, 1995.
125. Kafka UC, Carstens A, Steenkamp G, Symington H: Diagnostic value of magnetic resonance imaging and computed tomography for oral masses in dogs, *J S Afr Vet Assoc* 75:163–168, 2004.
126. White RAS: Mandibulectomy and maxillectomy in the dog: long term survival in 100 cases, *J Small Anim Pract* 32:69–74, 1991.
127. Bateman KE, Catton PA, Pennock PW, Kruth SA: 0-7-21 Radiation therapy for the treatment of canine oral melanoma, *J Vet Intern Med* 8:267–272, 1994.
128. Blackwood L, Dobson JM: Radiotherapy of oral malignant melanomas in dogs, *J Am Vet Med Assoc* 209:98–102, 1996.
129. McCaw DL, Pope ER, Payne JT, West MK, Tompson RV, Tate D: Treatment of canine oral squamous cell carcinomas with photodynamic therapy, *Br J Cancer* 82:1297–1299, 2000.
130. Proulx DR, Ruslander DM, Dodge RK, et al: A retrospective analysis of 140 dogs with oral melanoma treated with external beam radiation, *Vet Radiol Ultrasound* 44:352–359, 2003.
131. Klein MK: Multimodality therapy for head and neck cancer, *Vet Clin North Am Small Anim Pract* 33:615–628, 2003.
132. Pletcher JM, Koch SA, Stedhem MA: Orbital chondroma rodens in a dog, *J Am Vet Med Assoc* 175:187–190, 1979.
133. Dernell WS, Straw RC, Cooper MF, Powers BE, LaRue SM, Withrow SJ: Multilobular osteochondrosarcoma in 39 dogs: 1979–1993, *J Am Anim Hosp Assoc* 34:11–18, 1998.
134. Zaki FA, Liu S-K, Kay WJ: Calcifying aponeurotic fibroma in a dog, *J Am Vet Med Assoc* 166:384–387, 1975.

135. Selcer BA, McCracken MD: Chondroma rodens in dogs: a report of two case histories and a review of the veterinary literature, *J Vet Orthop* 2:7–11, 1981.
136. McLain DL, Hill JR, Pulley LT: Multilobular osteoma and chondroma (chondroma rodens) with pulmonary metastasis in a dog, *J Am Anim Hosp Assoc* 19:359–362, 1983.
137. Groff JM, Murphy CJ, Pool RR, Koblik P, Bellhorn R: Orbital multilobular tumour of bone in a dog, *J Small Anim Pract* 33:597–600, 1992.
138. McCalla TL, Moore CP, Turk J, Collier LL, Pope ER: Multilobular osteosarcoma of mandible and orbit in a dog, *Vet Pathol* 26:92–94, 1989.
139. Banks TA, Straw RC: Multilobular osteochondrosarcoma of the hard palate in a dog, *Aust Vet J* 82:409–412, 2004.
140. Straw RC, LeCouteur RA, Powers BE, Withrow SJ: Multilobular osteochondrosarcoma of the canine skull: 16 cases (1978–1988), *J Am Vet Med Assoc* 195:1764–1769, 1989.
141. Hathcock JT, Newton JC: Computed tomographic characteristics of multilobular tumor of bone involving the cranium in 7 dogs and zygomatic arch in 2 dogs, *Vet Radiol Ultrasound* 41:214–217, 2000.
142. Lipsitz D, Levitski RE, Berry WL: Magnetic resonance imaging features of multilobular osteochondrosarcoma in 3 dogs, *Vet Radiol Ultrasound* 42:14–19, 2001.
143. Hardy WD, Brodey RS, Riser WH: Osteosarcoma of the canine skull, *J Am Vet Radiol Soc* 8:5, 1967.
144. Chun R, de Lorimier LP: Update on the biology and management of canine osteosarcoma, *Vet Clin North Am Small Anim Pract* 33:491–516, vi, 2003.
145. LeCouteur RA: Current concepts in the diagnosis and treatment of brain tumours in dogs and cats, *J Small Anim Pract* 40:411–416, 1999.
146. Polizopoulou ZS, Koutinas AF, Souftas VD, Kaldrymidou E, Kazakos G, Papadoupoulos G: Diagnostic correlation of CT-MRI and histopathology in 10 dogs with brain neoplasms, *J Vet Med* 51:226–231, 2004.
147. Kraft SL, Gavin PR: Intracranial neoplasia, *Clin Techniques Small Anim Pract* 14:112–123, 1999.
148. Lawson C, Burk RL, Prata RG: Cerebral meningioma in the cat: diagnosis and surgical treatment of 10 cases, *J Am Anim Hosp Assoc* 20:333–342, 1984.
149. Sharp NJH, Harvey CE, Sullivan M: Canine nasal aspergillosis and penicilliosis, *Comp Contin Ed Pract Vet* 13:41–48, 1991.
150. Sullivan M, Lee R, Jakovljevic S, Sharp NJH: The radiological features of aspergillosis of the nasal cavity and frontal sinuses in the dog, *J Small Anim Pract* 27:167–180, 1986.
151. Harvey CE, O'Brien JA, Felsburg PJ, Izenberg HL, Goldschmidt MH: Nasal penicilliosis in six dogs, *J Am Vet Med Assoc* 178:1084–1087, 1981.
152. Gibbs C, Lane JG, Denny HR: Radiological features of intra-nasal lesions in the dog: a review of 100 cases, *J Small Anim Pract* 20:515–535, 1979.
153. Malik R, Martin P, Wigney DI, et al: Nasopharyngeal cryptococcosis, *Aust Vet* 75:483–488, 1997.
154. Wilkinson GT: Feline cryptococcosis: a review and seven case reports, *J Small Anim Pract* 20:749–768, 1979.
155. Karnik K, Reichle JK, Fischetti AJ, Goggin JM: Computed tomographic findings of fungal rhinitis and sinusitis in cats, *Vet Radiol Ultrasound* 50:65–68, 2009.
156. Peeters D, Clercx C: Update on canine sinonasal aspergillosis, *Vet Clin North Am Small Anim Pract* 37:901–916, vi, 2007.
157. Hawkins EC: Chronic viral upper respiratory disease in cats: differential diagnosis and management, *Comp Contin Ed Pract Vet* 10:1003–1012, 1988.
158. Burgener DC, Slocombe RF, Zerbe CA: Lymphoplasmacytic rhinitis in five dogs, *J Am Anim Hosp Assoc* 23:565–568, 1986.
159. Tasker S, Knottenbelt CM, Munro EAC, Stonehewer J, Simpson JW, Mackin AJ: Aetiology and diagnosis of persistent nasal disease in the dog: a retrospective study of 42 cases, *J Small Anim Pract* 40:473–478, 1999.
160. Rohleder JJ, Jones JC, Duncan RB, Larson MM, Waldron DL, Tromblee T: Comparative performance of radiography and computed tomography in the diagnosis of middle ear disease in 31 dogs, *Vet Radiol Ultrasound* 47:45–52, 2006.
161. Miles MS, Dhaliwal RS, Moore MP, Reed AL: Association of magnetic resonance imaging findings and histologic diagnosis in dogs with nasal disease: 78 cases (2001–2004), *J Am Vet Med Assoc* 232:1844–1849, 2008.
162. Lobetti RG: A retrospective study of chronic nasal disease in 75 dogs, *J S Afr Vet Assoc* 80:224–228, 2009.
163. Gartrell CL, O'Handley PA, Perry RL: Canine nasal disease: part II, *Comp Contin Ed Pract Vet* 17:539–546, 1995.
164. Gibbs C: The head—part III: ear disease, *J Small Anim Pract* 19:539–545, 1978.
165. Hoskinson JJ: Imaging techniques in the diagnosis of middle ear disease, *Sem Vet Med Surg* 8:10–16, 1993.
166. Hofer P, Meisen N, Bartholdi S, Kaser-Hotz B: Radiology corner: a new radiographic view of the feline tympanic bullae, *Vet Radiol Ultrasound* 36:14–15, 1995.
167. Bischoff MG, Kneller SK: Diagnostic imaging of the canine and feline ear, *Vet Clin Small Anim* 34:437–438, 2004.
168. Garosi LS, Dennis R, Schwarz T: Review of diagnostic imaging of ear diseases in the dog and cat, *Vet Radiol Ultrasound* 44:137–146, 2003.
169. Remedios AM, Fowler JD, Pharr JW: A comparison of radiographic versus surgical diagnosis of otitis media, *J Am Anim Hosp Assoc* 27:183, 1991.
170. Love NE, Kramer RW, Spodnick GJ, Thrall DE: Radiographic and computed tomographic evaluation of otitis media in the dog, *Vet Radiol Ultrasound* 36:375–379, 1995.
171. Barthez PY, Koblik PD, Hornof WJ, Wisner ER, Seibert JA: Apparent wall thickening in fluid filled versus air filled tympanic bulla in computed tomography, *Vet Radiol Ultrasound* 37:95–98, 1996.
172. Owen MC, Lamb CR, Lu D, Targett MP: Material in the middle ear of dogs having magnetic resonance imaging for investigation of neurologic signs, *Vet Radiol Ultrasound* 45:149–155, 2004.
173. Detweiler DA, Johnson LR, Kass PH, Wisner ER: Computed tomographic evidence of bulla effusion in cats with sinonasal disease: 2001–2004, *J Vet Intern Med* 20:1080–1084, 2006.
174. Kudnig ST: Nasopharyngeal polyps in cats, *Clin Tech Small Anim Pract* 17:174–177, 2002.
175. MacPhail CM, Innocenti CM, Kudnig ST, Veir JK, Lappin MR: Atypical manifestations of feline inflammatory polyps in three cats, *J Feline Med Surg* 9:219–225, 2007.
176. Kapatkin AS, Matthiesen DT, Noone KE, Church EM, Scavelli TE, Patnaik AK: Results of surgery and long-term follow-up in 31 cats with nasopharyngeal polyps, *J Am Anim Hosp Assoc* 26:387–392, 1990.
177. Seitz SE, Lasonsky JM, Marretta SM: Computed tomographic appearance of inflammatory polyps in three cats, *Vet Radiol Ultrasound* 37:99–104, 1996.
178. London CA, Dubilzeig RR, Vail DM, et al: Evaluation of dogs and cats with tumors of the ear canal: 145 cases

(1978–1992), *J Am Vet Med Assoc* 208:1413–1418, 1996.
179. Travetti O, Giudice C, Greci V, Lombardo R, Mortellaro CM, Di Giancamillo M: Computed tomography features of middle ear cholesteatoma in dogs, *Vet Radiol Ultrasound* 51:374–379, 2010.
180. Woodward TM: Interpretation of dental radiographs, *Top Companion Anim Med* 24:37–43, 2009.
181. Woodward TM: Dental radiology, *Top Companion Anim Med* 24:20–36, 2009.
182. Ticer JW, Spencer CP: Injury of the feline temporomandibular joint: radiographic signs, *J Am Vet Radiol Soc* 19:146–156, 1978.
183. Dickie AM, Sullivan M: The effect of obliquity on the radiographic appearance of the temporomandibular joint in dogs, *Vet Radiol Ultrasound* 42:205–217, 2001.
184. Huchkowsky SL: Craniomandibular osteopathy in a bullmastiff, *Can Vet J* 43:883–885, 2002.
185. Padgett GA, Mostosky UV: The mode of inheritance of craniomandibular osteopathy in West Highland White terrier dogs, *Am J Med Genet* 25:9–13, 1986.
186. Riser WH, Parkes LJ, Shirer JF: Canine craniomandibular osteopathy, *J Am Vet Radiol Soc* 8:23–31, 1967.
187. McConnell JF, Hayes A, Platt SR, Smith KC: Calvarial hyperostosis syndrome in two bullmastiffs, *Vet Radiol Ultrasound* 47:72–77, 2006.
188. Pastor KF, Boulay JP, Schelling SH, Carpenter JL: Idiopathic hyperostosis of the calvaria in five young bullmastiffs, *J Am Anim Hosp Assoc* 36:439–445, 2000.
189. Girard N, Servet E, Biourge V, Hennet P: Periodontal health status in a colony of 109 cats, *J Vet Dent* 26:147–155, 2009.
190. Harvey CE. Management of periodontal disease: understanding the options, *Vet Clin North Am Small Anim Pract* 35:819–836, vi, 2005.
191. Roudebush P, Logan E, Hale FA: Evidence-based veterinary dentistry: a systematic review of homecare for prevention of periodontal disease in dogs and cats, *J Vet Dent* 22:6–15, 2005.
192. Grove TK: Periodontal disease. In Harvey CE, editor: *Veterinary dentistry*, Philadelphia, 1985, Saunders, pp 59–77.

ELECTRONIC RESOURCES

evolve

Additional information related to the content in Chapter 8 can be found on the companion Evolve website at http://evolve.elsevier.com/Thrall/vetrad/

- Chapter Quiz

CHAPTER • 9

Magnetic Resonance Imaging Features of Brain Disease in Small Animals

Ian D. Robertson

Magnetic resonance (MR) imaging is the imaging modality of choice for evaluation of brain morphology. The superior soft tissue contrast resolution afforded by MR makes it the superior modality for imaging almost all aspects of intracranial disease. This chapter is a basic overview of the MR imaging characteristics of the most common small animal intracranial disorders. A review of the technical details associated with brain imaging in small animals is available elsewhere.[1]

BASIC MAGNETIC RESONANCE EXAMINATION OF THE BRAIN

A standard MR examination of the canine or feline brain involves the acquisition of multiple sequences in different anatomic planes. A pulse sequence is a set of MR imaging parameters that culminate in images having contrast controlled by particular tissue properties. Pulse sequences are selected to accentuate different tissue properties, so as to maximize lesion conspicuity. Images are usually acquired in transverse, sagittal, and dorsal planes (Fig. 9-1).

Tissues emitting a high signal in a pulse sequence will appear white in the image. This is often referred to as being "bright." Areas of high signal can also be described as being hyperintense relative to either normal tissue or other tissue within the same image, or as having sequence-specific hyperintensity (e.g., a focal region of T2 hyperintensity within the medulla oblongata). Tissues not emitting signal in a given pulse sequence will appear dark or black, and these tissues are described as being hypointense relative to either normal tissue or other tissue within the same image, or as having sequence-specific hypointensity (e.g., a focal region of T1 hypointensity within the medulla oblongata).

Rationale for Sequence Selection

In T2-weighted images, high signal arises from tissues with longer T2 relaxation (see Chapter 4 for a discussion of T1 and T2 relaxation). Conventional fast (turbo) spin-echo T2-weighted sequences are useful for detecting regions of increased fluid within tissues. In T2-weighted images, free fluid (e.g., cerebrospinal spinal fluid [CSF]) is extremely bright. Most common pathologic processes, whether neoplastic or inflammatory, result in increased fluid within tissues, and this is manifested as an increase in brightness of the abnormal tissue relative to the surrounding tissue; the term *increased T2-signal intensity* is used commonly to describe this.

Sometimes it is difficult to identify a T2-hyperintense lesion when it is adjacent to a normal region of high signal, such as adjacent to CSF within the ventricles. A pulse sequence containing an inversion pulse can be used to null the signal from a particular tissue. With respect to a T2-weighted sequence, free fluid can be nulled using a fluid-attenuated inversion recovery (FLAIR) sequence. In T2-weighted FLAIR images, free fluid has very low signal while other hydrated lesions remain white (Fig. 9-2).[2] This makes the detection of subtle lesions adjacent to regions of fluid accumulation easier. A FLAIR sequence may also provide additional information about T2-hyperintense lesions that must be distinguished from CSF, such as cystic meningioma, dermoid and epidermoid cysts, and arachnoid cysts.[3] A cavity containing pure fluid will have markedly reduced signal in a FLAIR image, whereas a cavity with proteinaceous fluid or blood will have less or no signal reduction.

In T1-weighted spin-echo sequences, high signal arises from tissues having rapid T1 relaxation, such as fat and methemoglobin. Conversely, fluid and hydrated lesions have reduced signal intensity in T1-weighted images, appearing dark. A T1-weighted image is excellent for evaluation of extracranial anatomy, but on its own has poor sensitivity for detection of most intracranial lesions, because of their hydrated nature, which leads to low T1 signal. However, regions of disruption of the blood-brain barrier and regions of altered perfusion can be detected on T1-weighted images made after the administration of an MR contrast medium. The most common MR contrast medium is a chelated form of gadolinium, a transitional compound with paramagnetic properties that shorten the T1 relaxation time of tissue in which the material accumulates.[4] In regions of higher gadolinium concentration, therefore, signal will be increased in T1-weighted images.

Many pathologic processes in the brain result in some disruption to the blood-brain barrier, often resulting in an accumulation of contrast medium and thereby increased signal intensity on postcontrast T1-weighted images. After gadolinium administration, T1-weighted images are usually obtained in transverse, dorsal, and sagittal planes. Contrast medium should be administered after all other imaging sequences have been acquired because contrast medium can sometimes affect the appearance of images in other sequences. Although MR contrast media are extremely safe, patients with preexisting renal disease may be at increased risk of developing nephrogenic systemic fibrosis,[5] and caution in the use of gadolinium-based contrast media is warranted in these patients.

Certain abnormalities are easier to detect in a specific scan plane, and ensuring these scan planes are part of the routine examination is imperative. For example, a T2-weighted sagittal sequence should be performed routinely. This allows better evaluation of the morphology of the cerebellum and brainstem and is important in the assessment of

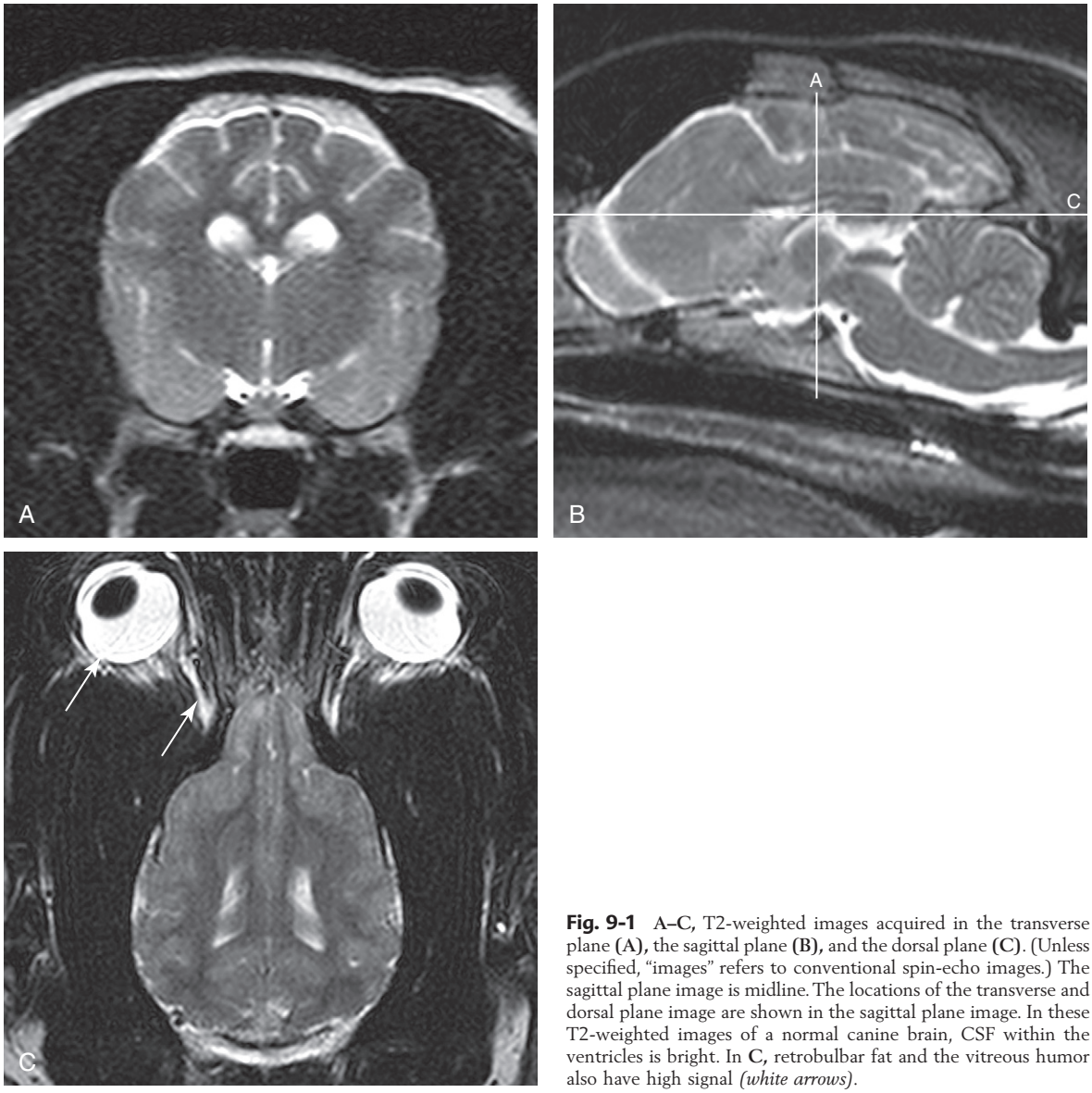


Fig. 9-1 **A–C,** T2-weighted images acquired in the transverse plane **(A),** the sagittal plane **(B),** and the dorsal plane **(C)**. (Unless specified, "images" refers to conventional spin-echo images.) The sagittal plane image is midline. The locations of the transverse and dorsal plane image are shown in the sagittal plane image. In these T2-weighted images of a normal canine brain, CSF within the ventricles is bright. In **C,** retrobulbar fat and the vitreous humor also have high signal *(white arrows)*.

increased intracranial pressure, based on the position of the cerebellum.[6]

Proton density (PD) weighted spin-echo images have excellent anatomic detail and have signal characteristics intermediate between T1- and T2-weighted images. PD-weighted images can be acquired during the acquisition of a T2-weighted sequence (dual echo) and are particularly useful in differentiating white and gray matter.

As discussed in Chapter 4, images can be acquired using spin-echo or gradient recall echo (GRE) pulse sequences. GRE images are more susceptible to magnetic field inhomogeneity, and this is exploited when assessing the brain for evidence of chronic hemorrhage (longer than 2 to 3 days). As the hemorrhage is broken down, the magnetic properties of the ferric/ferrous ions in hemoglobin metabolites cause a local field distortion that destroys the MR signal. This appears as a signal void (a black, so-called susceptibility artifact), which is an extremely sensitive indicator of chronic hemorrhage as might occur in patients with hemorrhagic infarcts, coagulopathies, or hemorrhagic metastasis. The image void is typically much larger than the actual lesion because of blooming (see "Hemorrhagic Infarction" section).

Putting It All Together

At a minimum, a standard MR brain study should comprise T2-weighted spin echo, T2-FLAIR, and T1-weighted spin-echo sequences in at least one plane, typically transverse, a T2-weighted spin-echo sequence in the sagittal plane, a T2-weighted GRE sequence to assess for hemorrhage, and at least one T1-weighted spin-echo sequence acquired after the administration of intravenous-contrast medium. The postcontrast images should be acquired using the same parameters and same imaging plane as the precontrast T1-weighted spin-echo sequence so as to allow direct comparison between the two sequences.

By evaluating the imaging characteristics of a lesion on various sequences, a more accurate assessment of the underlying disease process can be established than with computed tomography (CT), where the image appearance is based solely on the x-ray attenuation characteristics of the tissue. In MR imaging, it is the chemical characteristics of the tissue that determine the signal intensity on the various sequences. For example, consider the following two scenarios.

First, consider a patient with a region of T2 hyperintensity in the right temporal lobe, extending into the white matter

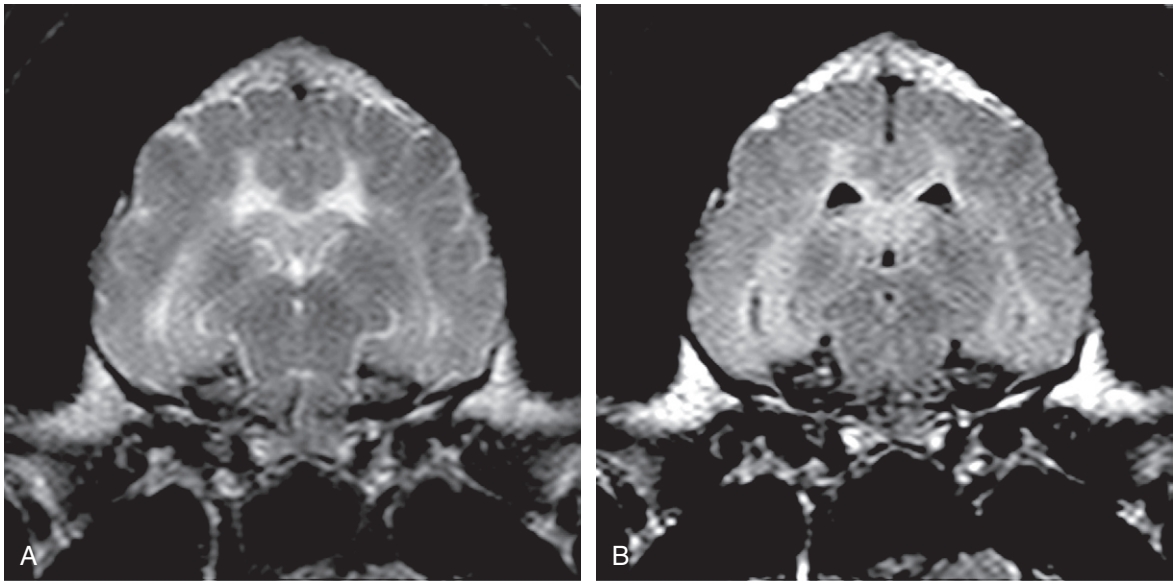


Fig. 9-2 Comparison of T2-weighted spin-echo **(A)** and T2-weighted FLAIR **(B)** images in a dog with leukoencephalitis. In the T2-weighted spin-echo image **(A)** there is considerable T2-hyperintensity in the ventricular region, but it is impossible to determine whether this is caused by signal from CSF or brain edema. Obvious periventricular T2 signal is more conspicuous on the FLAIR image **(B)** as a result of nulling of the high signal from the CSF. Note the lack of signal from CSF in the lateral ventricles in the T2-weighted FLAIR image, as expected.

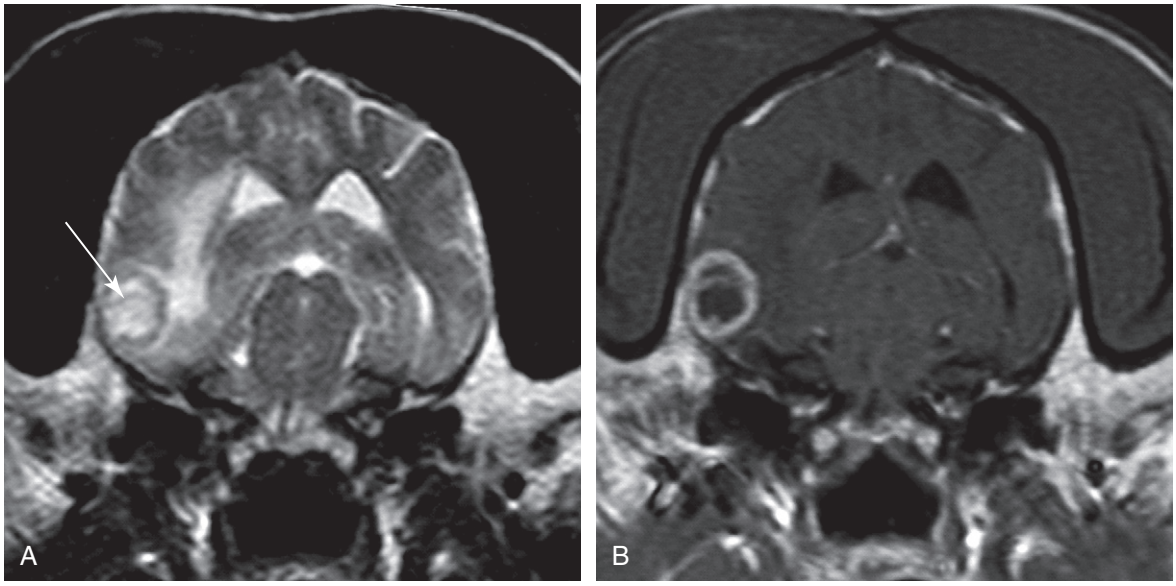


Fig. 9-3 **A,** T2-weighted image. There is a focal T2-hyperintense mass *(white arrow)* with a T2-hypointense border surrounded by adjacent wispy regions of T2-hyperintensity consistent with perilesional white matter edema. **B,** Postcontrast T1-weighted image. The T2-hypointense border is now characterized by marked contrast enhancement, often called *ring enhancement*. The center of the mass does not enhance. In both images there is a contralateral midline shift as a result of the mass and perilesional edema. Final diagnosis was metastatic hemangiosarcoma, but the signs are not specific for this.

lateral to the right lateral ventricle (Fig. 9-3, *A*). After administration of contrast medium, the same region is characterized by a peripherally enhancing lesion with a T1-hypointense center (Fig. 9-3, *B*). The peripheral enhancement was not apparent on T1-weighted images made before the administration of contrast medium. The center of the mass does not enhance, indicating a lack of blood supply to deliver the contrast medium. Additionally the tissue adjacent to the mass does not enhance. The most likely explanation is that the center of the mass is avascular, and the T2 hyperintensity in the adjacent white matter is edema secondary to the presence of the mass.

Second, sometimes it cannot be determined whether the signal coming from the brain is caused by normal fluid, such as CSF, or is caused by periventricular brain edema. In Fig. 9-2, *A*, there is a large amount of high signal, which may just be caused by CSF. In the T2-weighted FLAIR image in Fig. 9-2, *B*, however, the signal from CSF has been removed, and

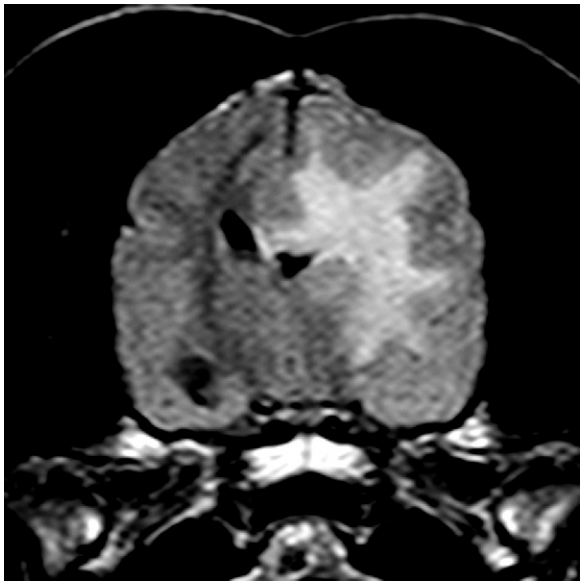


Fig. 9-4 Transverse T2-FLAIR image of a 12-year-old border collie with a meningioma. In this image, caudal to the mass, there is extensive white-matter edema resulting in compression of the ventricular system and a rightward shift of midline structures. The secondary effects of intracranial masses can be severe and the cause of profound clinical signs.

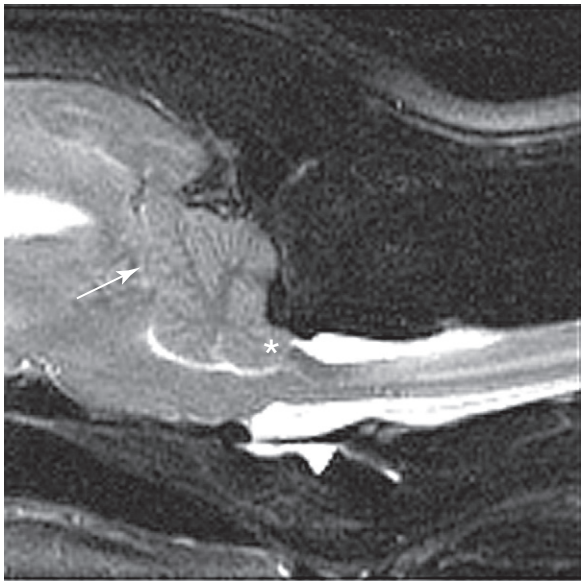


Fig. 9-5 Sagittal T2-weighted image of the occipital-cervical junction of a dog with a large forebrain mass. There is compression of the rostral aspect of the cerebellum *(white arrow)* and herniation of the cerebellar vermis *(asterisk)* into the foramen magnum as a result of increased intracranial pressure. The wispy T2 hyperintensity in the spinal cord is syringohydromyelia, the result of altered CSF flow secondary to brainstem compression. The cranial aspect of the spinal cord is bounded dorsally and ventrally by the highly conspicuous subarachnoid space.

considerable periventricular T2 hyperintensity remains. The conclusion is an abnormal amount of fluid in the neuropil surrounding the lateral ventricles.

These two examples emphasize the ability of tissue type to be predicted from the signal characteristics in a specific pulse sequence, and also how all pulse sequences must be interpreted together to reach the correct conclusion.

Secondary Effects of Focal Intracranial Disease

In addition to altering local signal intensity, brain masses and swelling can also cause major changes to brain morphology. Many masses and the secondary perilesional edema will result in brain compression, with a contralateral midline shift, ventricular obstruction, and ultimately either transtentorial and/or foramen magnum cerebellar herniation (Fig. 9-4). It is critical not to overlook the signs of cerebellar herniation (Fig. 9-5).

Know Normal Anatomy

A working knowledge of normal MR brain anatomy and neuropathophysiologic correlations are prerequisites to characterizing any lesion accurately and correlating it to the clinical signs. Many electronic and hard-copy references for these subjects are available.[7-10]

COMMON INTRACRANIAL CONDITIONS IN SMALL ANIMALS AND THEIR MAGNETIC RESONANCE IMAGING CHARACTERISTICS

Developmental Conditions of the Brain: Hydrocephalus

Hydrocephalus, the most common developmental anomaly, is the excessive accumulation of CSF within the ventricular system. Hydrocephalus occurs when normal flow is obstructed, when there is overproduction compared to absorption, or when there is brain atrophy. The most common form of hydrocephalus is congenital hydrocephalus, where excessive CSF accumulates before or soon after birth. An inherited malformation of the fluid pathway may be present, or perinatal infection or injury leads to scarring that affects CSF reabsorption. Less commonly, hydrocephalus occurs in adult patients, usually the result of tumor or infection, which obstructs CSF flow (Fig. 9-6).

The lateral ventricles are usually relatively symmetric, but there is considerable variation in what is considered normal ventricular size, particularly in small-breed dogs.[11]

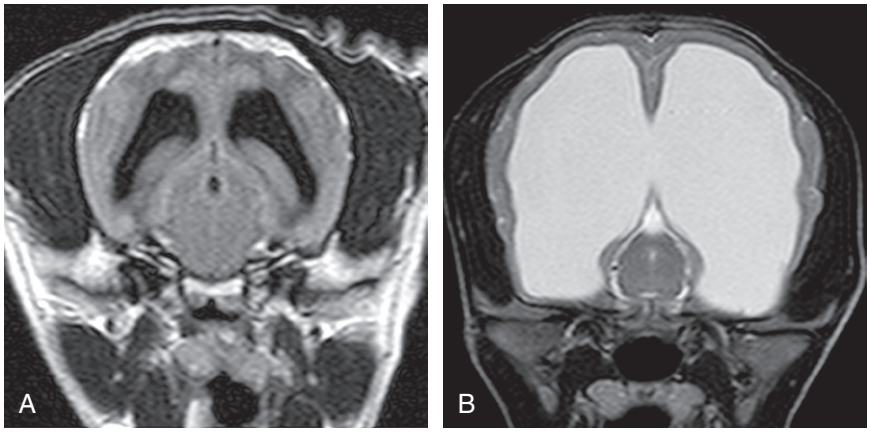


Fig. 9-6 Transverse T2-weighted FLAIR **(A)** and T2-weighted **(B)** images from two dogs with congenital hydrocephalus. The ventricles are much more severely dilated in the dog in **(B).**

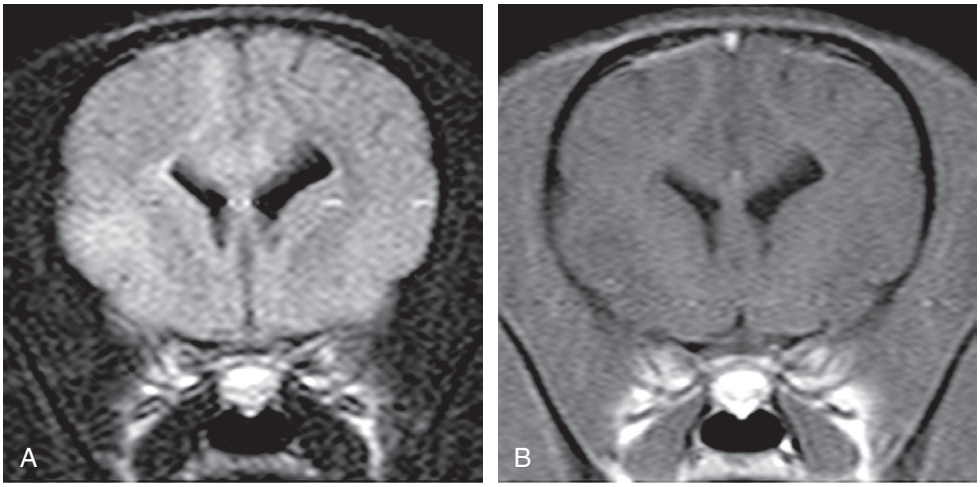


Fig. 9-7 A T2-FLAIR **(A)** and postcontrast T1-weighted image **(B)** of a 4-year-old pug with a history of seizures of progressing severity over a 4-day period. Patchy, ill-defined regions of T2 hyperintensity are present in the right cerebral cortex, most severe in the temporal and parietal lobes. There is minimal mass effect. These regions are mildly T1 hypointense and do not enhance. The most common considerations for these findings are encephalitis, necrotizing encephalitis, and cerebral infarct. On the basis of breed, progressive clinical signs, multifocal distribution of lesions, CSF analysis, and MR findings, necrotizing encephalitis is the most likely diagnosis.

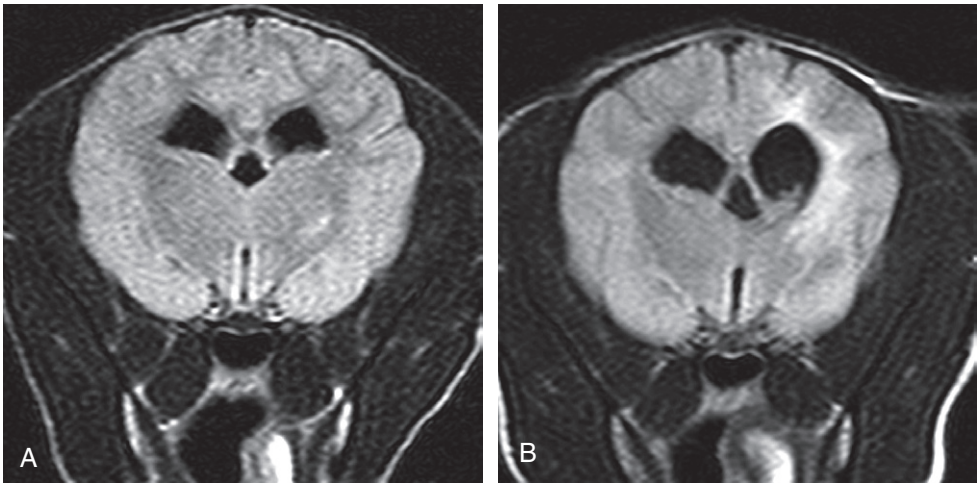


Fig. 9-8 Transverse T2-FLAIR image **(A)** of a 2-year-old Yorkshire terrier and a follow-up image **(B)** at the same level acquired 18 months later. At presentation **(A),** a diagnosis of necrotizing encephalitis was made based on signalment, clinical findings, MR findings, and CSF analysis. In **A,** the ventricular system is mildly enlarged but symmetric. In the later study **B,** the lateral ventricles are larger, asymmetric, and there is a midline shift to the left, toward the side of the larger ventricle. T2 hyperintensity is present in the white matter lateral to the left lateral ventricle. It is likely the ventricular enlargement and midline shift are secondary to parenchymal necrosis; this is often referred to as *compensatory hydrocephalus*. The T2 hyperintensity in **B** did not enhance and, in this patient, reflects unresolved neuropil inflammation.

Inflammatory Conditions of the Brain

Encephalitis can often be detected using MR imaging. Most commonly, an analysis of CSF, including cytologic and immunologic testing is required to help establish a definitive diagnosis. Encephalitis is commonly characterized by a patchy increase in parenchymal T2-signal intensity, often more apparent on FLAIR images. These regions are usually isointense or hypointense on T1-weighted images and have variably increased signal intensity on postcontrast T1-weighted images.

Necrotizing encephalitis, common in the Yorkshire terrier and pug and suspected to be an immune-mediated brain disease, is characterized by regions of T2 hyperintensity that do not suppress on a FLAIR sequence. These regions are usually T1 isointense or mildly T1 hypointense to adjacent neuropil and have minimal contrast enhancement (Fig. 9-7). In chronic cases, regions of brain necrosis may be present, sometimes manifesting as compensatory hydrocephalus, depending on the maturity of the lesion (Fig. 9-8). These lesions usually have no or minimal mass effect.

Encephalitis is often accompanied by meningitis, where there is increased meningeal enhancement following contrast-medium administration[12] (Fig. 9-9). This is best detected when one compares T1-weighted images acquired before and after contrast medium administration. Bypassing the precontrast study will invalidate objective assessment of meningeal enhancement.

Granulomatous meningoencephalitis (GME), a common inflammatory condition of undetermined etiology that most commonly affects young and middle-aged small-breed dogs, can appear as ill-defined focal regions of T2 hyperintensity with minimal or variable patchy contrast enhancement (Fig. 9-10). Some GME lesions have minimal contrast enhancement and, as a result, can appear similar to infarction.

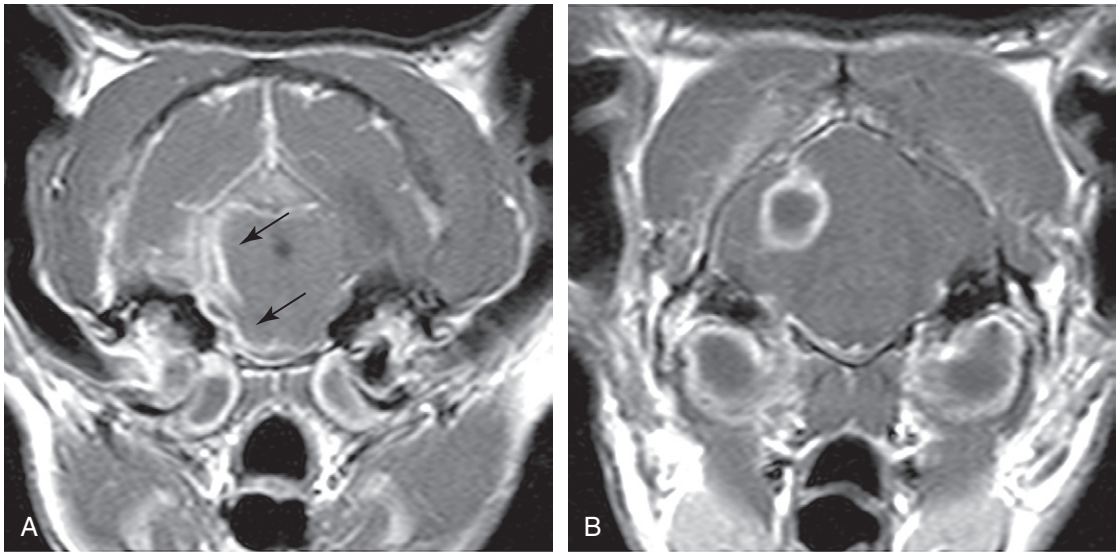


Fig. 9-9 Adjacent transverse T1-weighted postcontrast images in a 5-year-old cat with a head tilt and otitis externa. Increased signal intensity in both tympanic bullae is visible. The lining of the bullae is enhanced, but material within either bulla does not enhance. This is consistent with inflammation (exudate in bullae). The meninges adjacent to the right tympanic bulla are characterized by marked contrast enhancement (*arrows* in **A),** and a ring-enhancing mass is present in the right aspect of the cerebellum. The imaging findings are attributable to otitis media and otitis interna that has progressed to meningoencephalitis and cerebellar abscess.

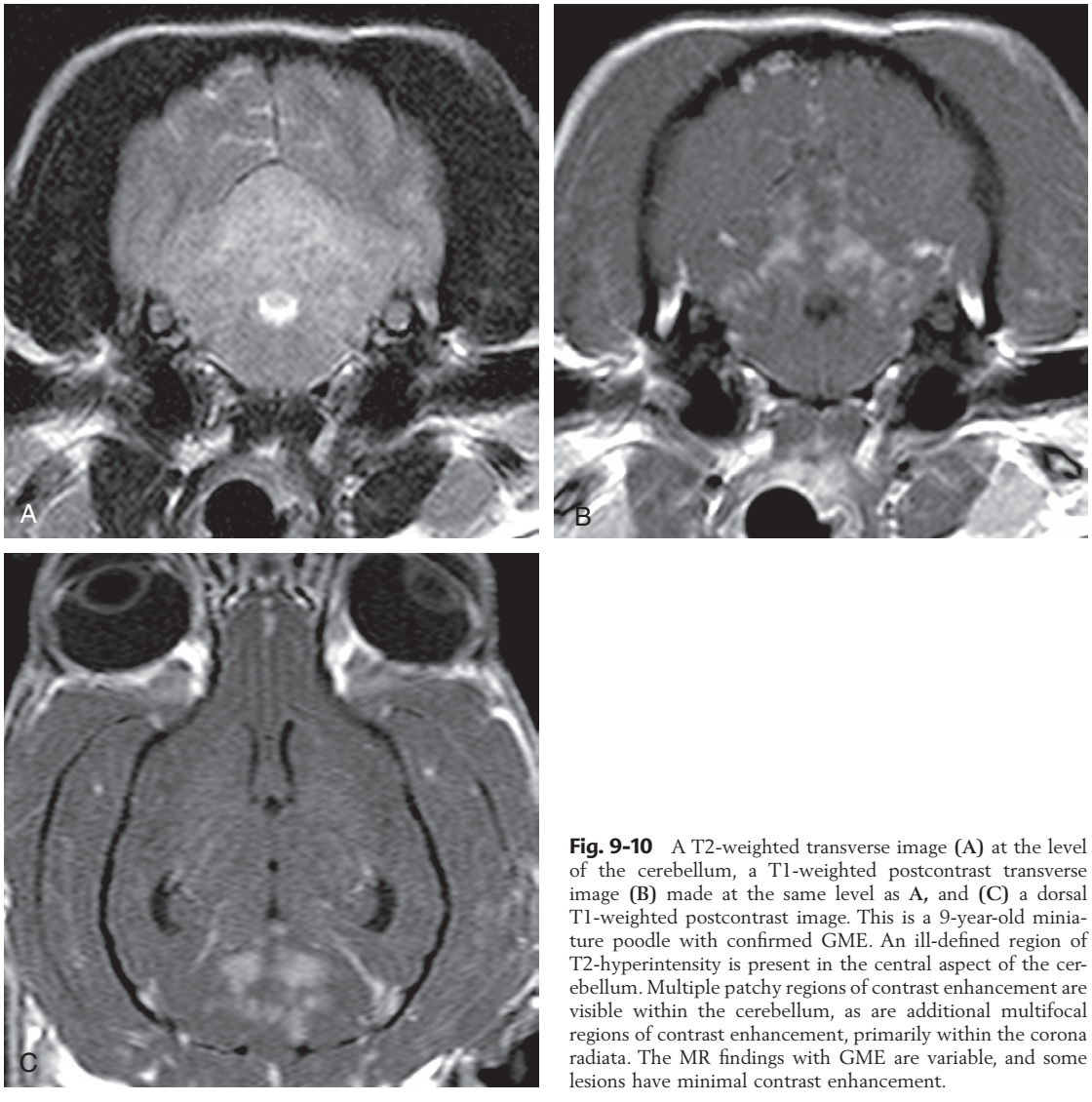


Fig. 9-10 A T2-weighted transverse image **(A)** at the level of the cerebellum, a T1-weighted postcontrast transverse image **(B)** made at the same level as **A,** and **(C)** a dorsal T1-weighted postcontrast image. This is a 9-year-old miniature poodle with confirmed GME. An ill-defined region of T2-hyperintensity is present in the central aspect of the cerebellum. Multiple patchy regions of contrast enhancement are visible within the cerebellum, as are additional multifocal regions of contrast enhancement, primarily within the corona radiata. The MR findings with GME are variable, and some lesions have minimal contrast enhancement.

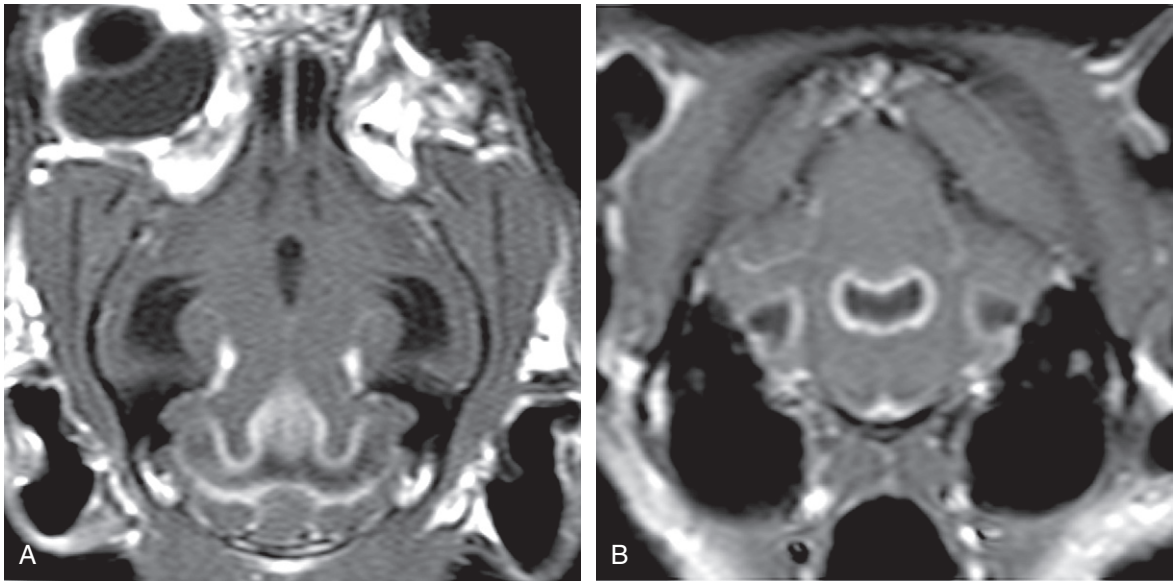


Fig. 9-11 Dorsal **(A)** and transverse **(B)** T1-weighted postcontrast images of a cat with feline infectious peritonitis. Intense contrast enhancement of the lining of the ventricular system is present. This is consistent with ependymitis, a common finding in feline infectious peritonitis. The left eye is absent, removed previously as a result of trauma.

Intracranial feline infectious peritonitis usually causes ependymitis, resulting in marked contrast enhancement of the lining of the ventricular system (Fig. 9-11).

A normal MR study does not rule out the possibility of inflammatory disease, and a CSF tap is required. In one study of 25 patients with CSF alterations consistent with inflammatory brain disease, 24% of the MR studies were considered normal.[12]

BRAIN NEOPLASIA

Extraaxial Tumors

Meningiomas are extraaxial tumors that arise from dural elements. They are the most common intracranial tumor in cats and one of the most common in dogs. Meningiomas are usually benign and grow slowly. They are variable in size and shape and may be irregular, nodular, ovoid, lobulated, or plaquelike (Fig. 9-12), ranging from a few millimeters to several centimeters in diameter. Meningiomas are often firm and encapsulated, are usually discrete, and may contain mineralization or pockets of fluid (Fig. 9-13). Basal and plaquelike meningiomas are common in the floor of the cranial cavity, especially in the optic chiasm and suprasellar regions. They also occur commonly over the cerebral hemispheres, less commonly in the cerebello-pontomedullary region, and rarely in the retrobulbar space, arising from the optic nerve. Multiple meningiomas can occur; this is more common in cats than in dogs. Thickening of bone adjacent to meningiomas, termed *hyperostosis*, may occur, especially in cats (Fig. 9-14). Meningiomas can usually be distinguished from intraaxial tumors because of meningiomas being broad-based, peripherally located, or falx-associated masses that enhance following contrast-medium administration (see Fig. 9-13). Meningiomas are often associated with a dural tail, which is a linear enhancement of thickened dura mater adjacent to an extraaxial mass seen on postcontrast T1-weighted images. In one study the predictive value of the dural tail sign for meningioma was 94%.[6] It is uncertain whether the dural tail represents neoplastic infiltration beyond the margins of the meningioma or a manifestation of associated inflammation. The amount of disruption to adjacent parenchyma is variable, depending on tumor size and location. Some meningiomas have minimal peripheral edema, although others may have extensive peripheral edema that can result in ventricular compression and brain herniation.

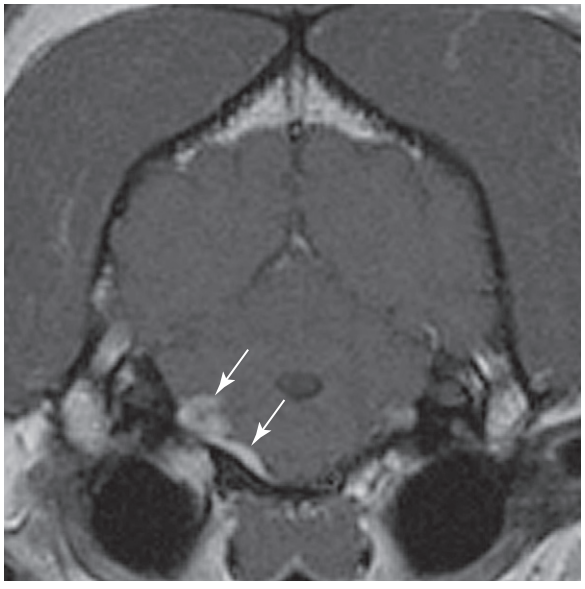


Fig. 9-12 Transverse T1-weighted postcontrast image of an 11-year-old golden retriever. The linear meningeal enhancement *(white arrows)* is a plaque meningioma. Mild ipsilateral temporal muscle atrophy is present, caused by disruption to the adjacent trigeminal nerve nucleus.

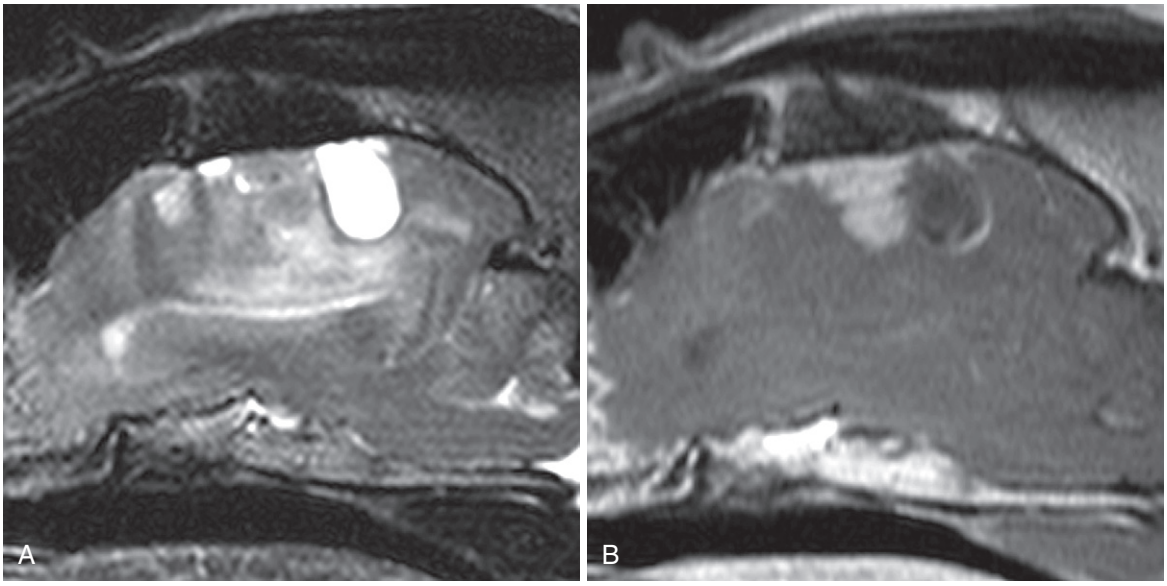


Fig. 9-13 Sagittal T2-weighted **(A)** and T-weighted postcontrast image **(B)** of an 11-year-old Labrador retriever with a cystic meningioma. The focal T2 hyperintensities in **(A)** are T1 hypointense in **(B)** and were suppressed on T2-FLAIR images (not shown) indicating free fluid. In **B,** there is a broad-based intensely contrast-enhancing tumor mass associated with the fluid collections. In **A,** marked perilesional edema is present (diffuse T2 hyperintensity), which is compressing the corpus callosum and ventricular system ventrally.

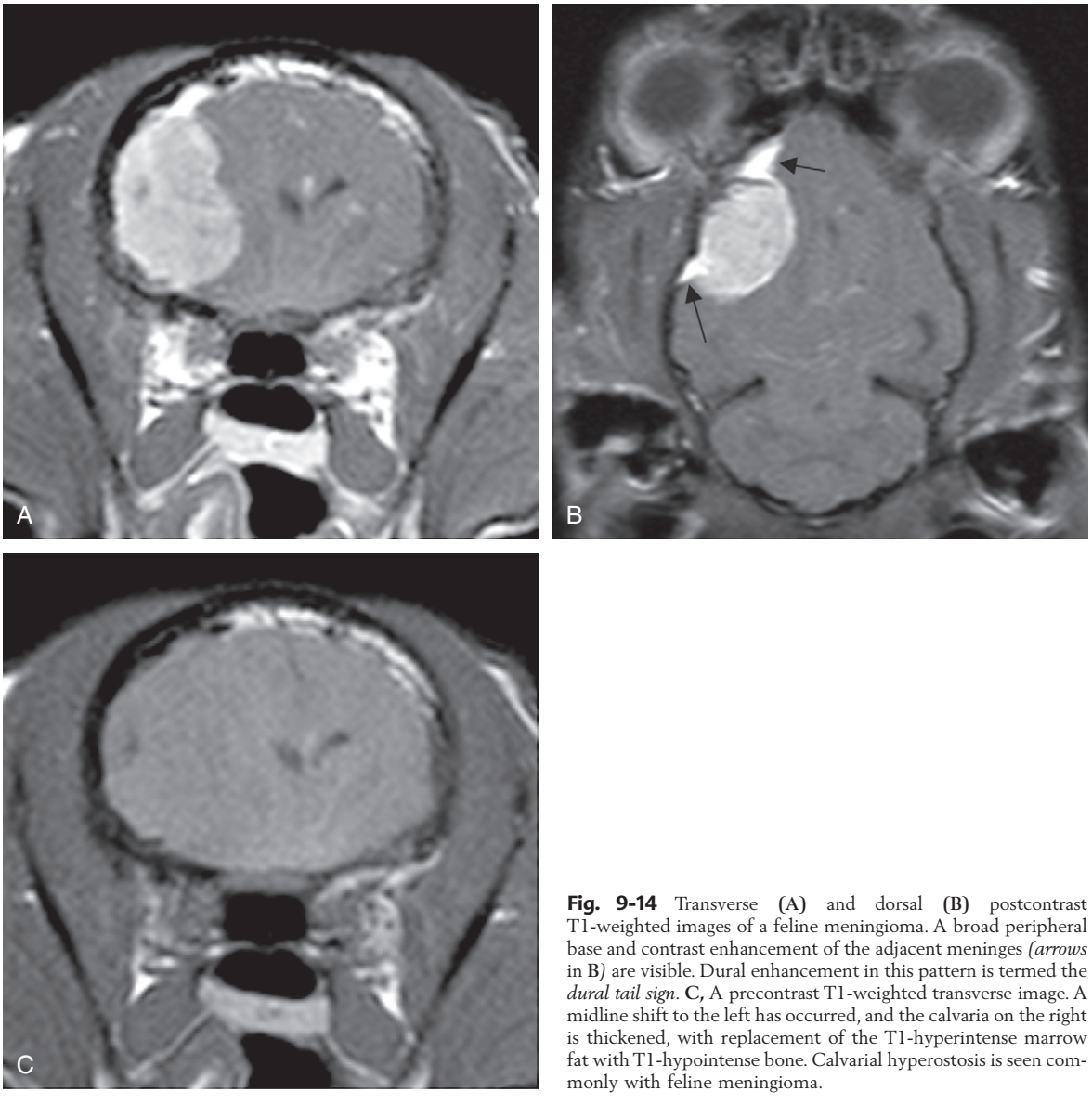


Fig. 9-14 Transverse **(A)** and dorsal **(B)** postcontrast T1-weighted images of a feline meningioma. A broad peripheral base and contrast enhancement of the adjacent meninges *(arrows* in **B***)* are visible. Dural enhancement in this pattern is termed the *dural tail sign*. **C,** A precontrast T1-weighted transverse image. A midline shift to the left has occurred, and the calvaria on the right is thickened, with replacement of the T1-hyperintense marrow fat with T1-hypointense bone. Calvarial hyperostosis is seen commonly with feline meningioma.

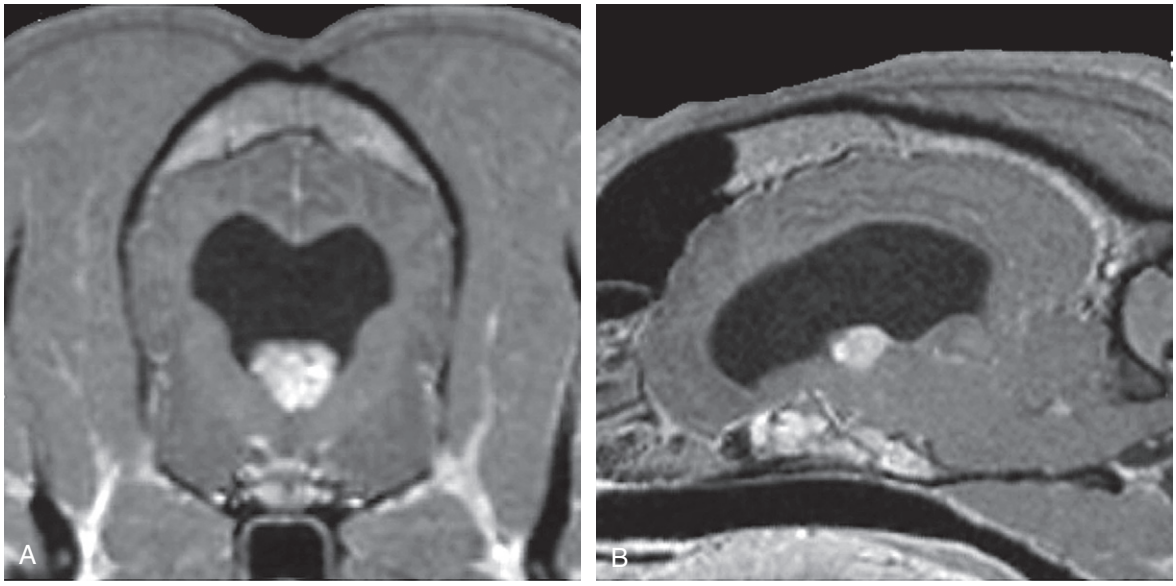


Fig. 9-15 An 8-year-old boxer with depression and head pressing because of a choroid plexus tumor. In T1-weighted postcontrast images (transverse **[A],** and sagittal **[B]**), there is a contrast-enhancing mass in the third ventricle, resulting in obstructive hydrocephalus. The lateral ventricles are enlarged, causing an increase in intracranial pressure and the associated clinical signs.

Choroid Plexus Tumors and Ependymomas

Choroid plexus tumors are common in dogs, occurring most commonly in the third ventricle and in the lateral recess of the fourth ventricle. The choroid plexus epithelium originates from differentiation of the primitive medullary epithelium and is embryologically related to ependymal cells. Choroid plexus tumors have a tendency to bleed, and exfoliation of choroid plexus cells, from both benign and malignant variants, may occur with subsequent tumor seeding to other areas of the brain or spinal cord through the CSF.[13] Because of the intraventricular location of choroid plexus tumors, obstructive hydrocephalus is common and may be life threatening. Additionally, some choroid plexus tumors will cause an overproduction of CSF, which exacerbates any obstructive process. An important distinguishing feature of choroid plexus tumors is that they are located within a ventricle (Fig. 9-15). Like meningiomas, choroid plexus tumors usually have marked contrast enhancement and sometimes have evidence of hemorrhage and/or dystrophic mineralization. The MR imaging characteristics of intraventricular ependymomas are similar to choroid plexus tumors, but ependymomas are much less common.

Pituitary Tumors

Pituitary tumors are common in dogs but uncommon in cats. They may be nonfunctional or functional. Functional pituitary tumors are typically characterized by pituitary-dependent hyperadrenocorticism (PDH). Up to 60% of dogs with PDH but without neurologic signs have a pituitary tumor 4 to 12 mm in diameter at greatest vertical height.[13] Most pituitary tumors tend to grow dorsocaudally, leading to compression and obliteration of the infundibulum, ventral aspect of the third ventricle, hypothalamus, and thalamus. They eventually impinge on the internal capsule and optic tracts. MR imaging is useful for visualizing the presence of both microtumors (3 to 10 mm in diameter) and macrotumors (>10 mm) in dogs with PDH, with or without neurologic signs, especially when endocrine test results are equivocal. Pituitary tumors are always better visualized after contrast-medium administration. Usually these tumors have minimal peritumoral edema, uniform contrast enhancement, and well-defined margins (Fig. 9-16). Cystic regions, or evidence of chronic or recent hemorrhage, sometimes extensive, may be present. Pituitary tumors less than 3 mm in diameter may not be visible with MR imaging.

Intraaxial Tumors: Glioma

The term *glioma* is used to describe tumors that arise from the neuropil. Gliomas include astrocytomas, oligodendrogliomas, and glioblastoma multiforme and are particularly common in brachycephalic breeds such as the boxer, Boston terrier, and bulldog. Gliomas range in malignancy from low grade and slow growing, to high grade, poorly differentiated highly malignant tumors.

Gliomas vary widely in their MR features. They are often difficult to detect using contrast-enhanced CT imaging of the brain because, unlike meningiomas, many gliomas do not enhance, or enhance only minimally, after contrast-medium administration. These tumors are more easily detected with MR imaging, and this is one of the many reasons that MR imaging is so clinically superior to CT imaging when evaluating the brain. Gliomas are often ill-defined, have variable degrees of perilesional edema, and variable contrast enhancement (Fig. 9-17). Occasionally no contrast enhancement is present. A glioma can be difficult to differentiate from a brain abscess and other focal inflammatory conditions of the brain parenchyma,[6] or even from massive infarction.

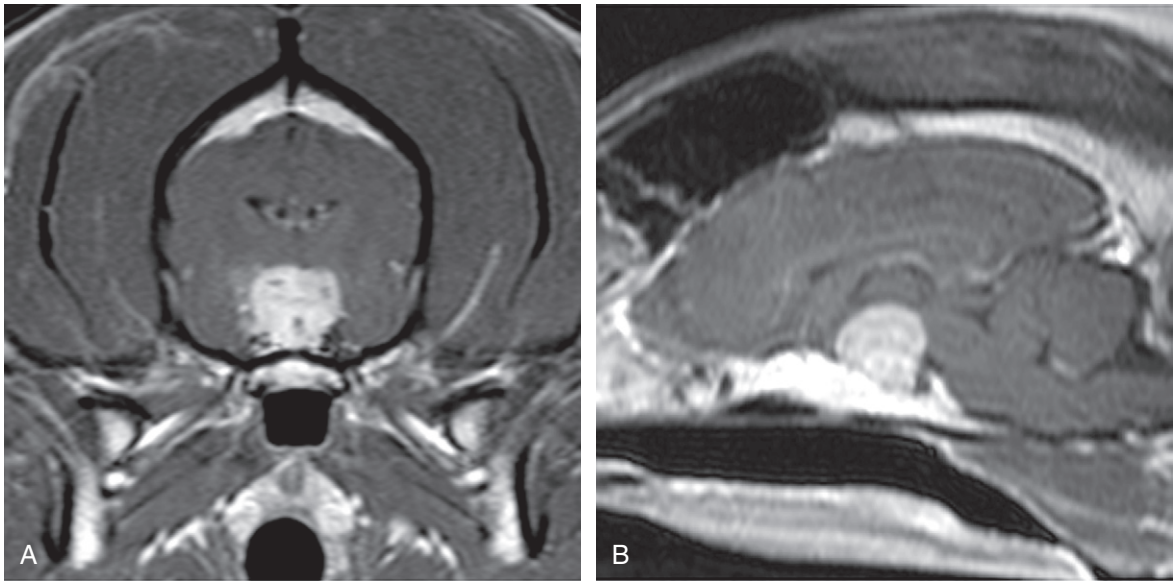


Fig. 9-16 Transverse **(A)** and sagittal **(B)** T1-weighted postcontrast images. A large, relatively homogeneous, contrast-enhancing mass is visible on the floor of the calvaria at the level of the sella turcica. This is typical of a pituitary tumor.

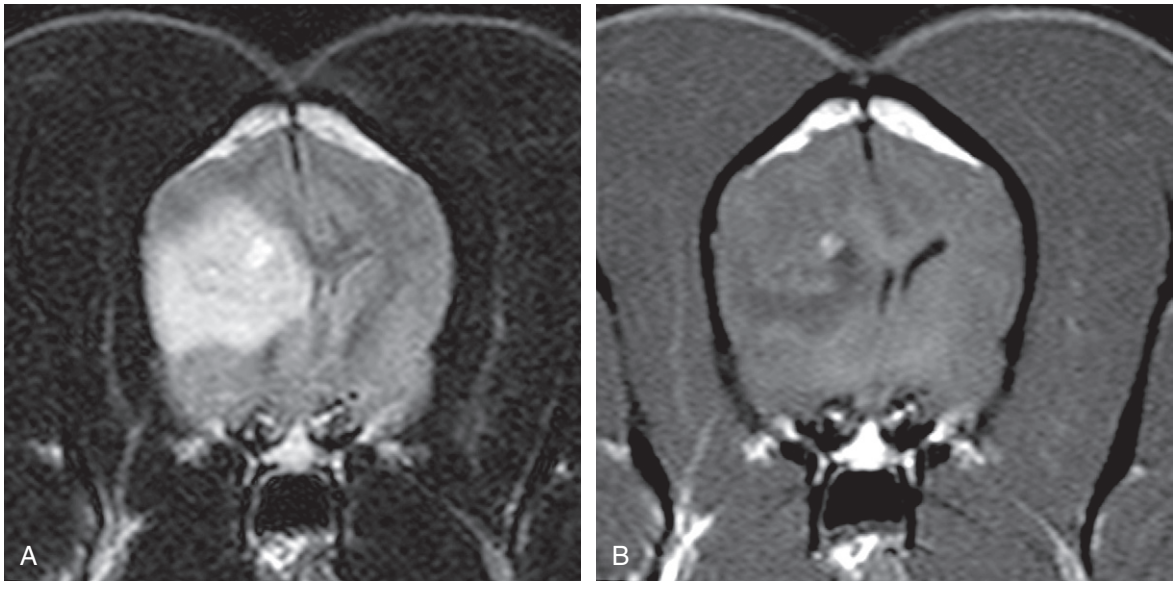




Fig. 9-17 T2-weighted transverse **(A)** and T1-weighted images made before **(B)** and after **(C)** contrast-medium administration in a 7-year-old boxer with seizures and behavioral changes. These images are at the level of the center of a large mass effect, which is causing a leftward midline shift and compression of the ventricular system. The T2 hyperintensity is caused by the increased brain water content associated with this tumor. The precontrast T1-hyperintense focus **(B)** is likely caused by recent hemorrhage; methemoglobin developing approximately 3 days after a hemorrhagic event is highly paramagnetic and acts like gadolinium in shortening T1 relaxation. The wispy contrast-medium enhancement, ill-defined margin, and perilesional edema, most apparent on the T2-weighted image **(A),** are consistent with a glioma.

INVASIVE EXTRACRANIAL TUMORS

Nasal Tumors

Aggressive nasal tumors can extend through the cribriform plate, caudal nasal region, or frontal sinus into the cranial vault, and it is important to include the caudal aspect of the nasal cavity when imaging the brain. Extension of primary nasal cavity tumors into the cranial vault may lead to seizures, behavior changes, paresis, circling, and visual deficits, but sometimes extension can be present without detectable clinical signs. Respiratory signs such as sneezing, nasal discharge, epistaxis, stridor, dyspnea, and mouth breathing are often present but may not be apparent clinically in a patient with caudal nasal or frontal sinus neoplasia (Fig. 9-18). Brain tumors do not commonly extend rostrally through the cribriform plate into the nasal cavity.

Cranial Nerve Tumors

Tumors of cranial and spinal nerves and nerve roots are common in dogs. The terminology given to these tumors is confusing because of differing opinions regarding their cell of origin. Although schwannoma, neurilemmoma, and neurofibroma are used interchangeably, the designation *malignant (peripheral or cranial) nerve sheath tumor* is recommended, because many of these tumors are malignant and determining the cell of origin (Schwann cell, perineurial cell, fibroblast, etc.) is not possible. Of the cranial nerves, malignant nerve sheath tumors commonly involve the trigeminal nerve (cranial nerve V), leading to signs of unilateral trigeminal nerve dysfunction, for example, unilateral temporalis and masseter muscle atrophy. Cranial nerve sheath tumors are usually either T2 isointense or T2 hyperintense and enhance intensely.[14]

The trigeminal nerve arises at the level of the pons and caudal part of the mesencephalon. The nerve courses rostrally and branches to three divisions (mandibular, maxillary, ophthalmic) that continue to course rostrally to exit their respective foramen. Depending on the location of the tumor, foraminal enlargement as a result of pressure remodeling from the expanding tumor can sometimes be seen, and this is an important secondary sign associated with cranial nerve-sheath tumors (Fig. 9-19). Some cranial nerve sheath tumors are primarily outside the cranial vault and are more easily characterized when fat suppression sequences are used. As discussed in Chapter 4, fat suppression[15] removes the high T1 signal inherent to fat, making normal fat dark. Abnormally contrast-enhancing tissue is more conspicuous when



Fig. 9-18 T1-weighted sagittal **(A)**, dorsal **(B)**, and a T2-weighted sagittal image **(C)** of an elderly dog with intermittent epistaxis. A mass is present in the caudal aspect of the left nasal cavity, which extends into the right nasal cavity and also into the rostral fossa. The material in the left frontal sinus is T2 hyperintense **(C)** and T1 isointense **(A)** and does not enhance. On the basis of these signal characteristics, the frontal sinus lesion is more likely to be trapped fluid rather than tumor. Distinguishing mass from trapped fluid cannot be made as easily with contrast-enhanced CT. In the T2-weighted image, extensive white-matter edema is visible as a result of the intracranial extension. The histologic diagnosis was carcinoma.

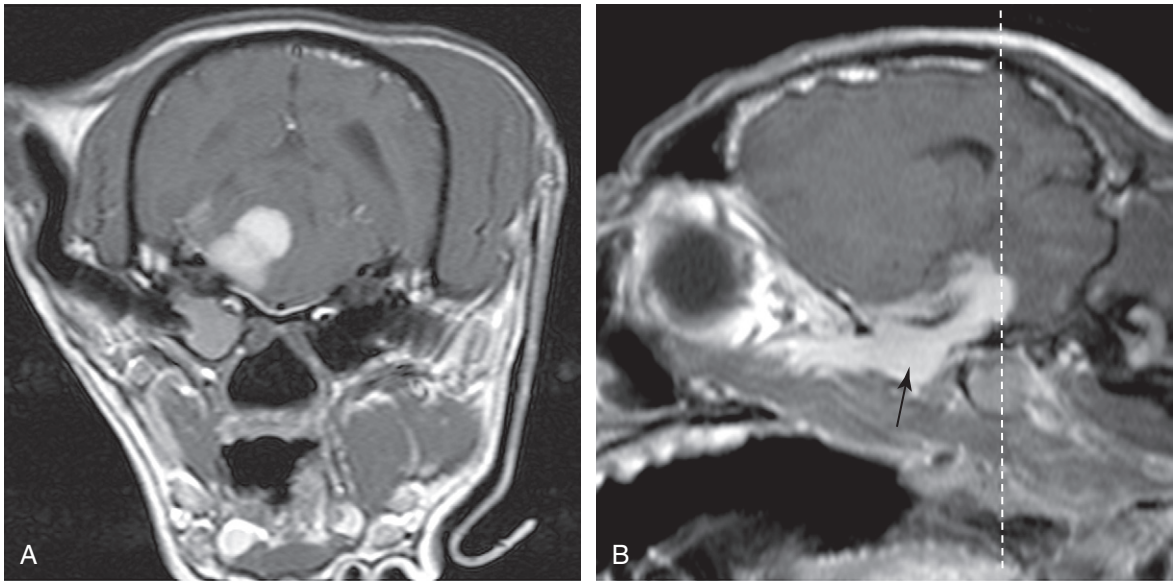


Fig. 9-19 Transverse **(A),** sagittal **(B),** T1-weighted postcontrast images. There is marked atrophy of the temporal musculature on the right side and an intensely contrast-enhancing tubular mass emanates from the right ventral aspect of the pons and courses rostrally through an enlarged orbital fissure (*arrow* in **B**) to the retrobulbar region. The *vertical dashed line* in **B** designates the location of the transverse image seen in **A.** Final diagnosis was trigeminal nerve sheath tumor. Incidentally, fluid is present in the right tympanic cavity.



Fig. 9-20 Transverse T1-weighted postcontrast image of a 10- year-old mixed-breed dog with left temporal muscle atrophy. In this image, the inherent bright signal from fat has been suppressed, and this increases the conspicuity of the extracranial trigeminal nerve tumor *(arrow)* in this patient. There is increased enhancement of the atrophic left temporal muscles compared to the right. This is commonly seen in muscles affected by neurogenic atrophy and thought to be associated with alterations in autonomic control of vascular and capillary bed secondary to denervation.

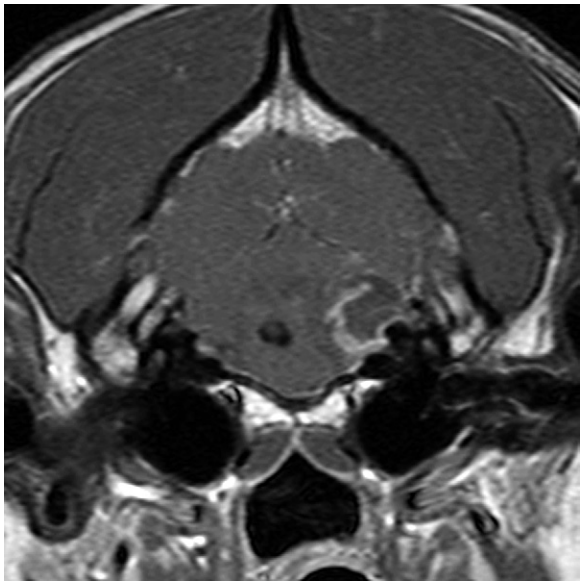


Fig. 9-21 Transverse T1-weighted postcontrast image of a 7-year-old golden retriever. There is a peripherally contrast-enhancing mass at the cerebellopontine angle that appears similar to a cystic meningioma. Extensive peripheral edema and brainstem compression was evident on other sequences. The final diagnosis was histiocytic sarcoma.

contrasted against a background of dark fat. Fat suppression is possible only on high (1 tesla or greater) field magnets (Fig. 9-20).

Other Primary Tumors and Metastatic Tumors

A complete review of brain tumors reported in dogs and cats is beyond the scope of this text, and excellent reviews are available.[13,16] Histiocytic sarcoma is an uncommon extraaxial tumor that has imaging characteristics similar to meningioma, including a dural tail[17] (Fig. 9-21); histiocytic sarcoma can also be intraaxial.[18]

In one study,[19] brain metastases were as common as primary intracranial tumors, with hemangiosarcoma being the most common metastatic lesion (Fig. 9-22). Lymphoma is a common tumor both in dogs and cats, manifesting in many ways. With respect to intracranial lymphoma, it can be solitary or

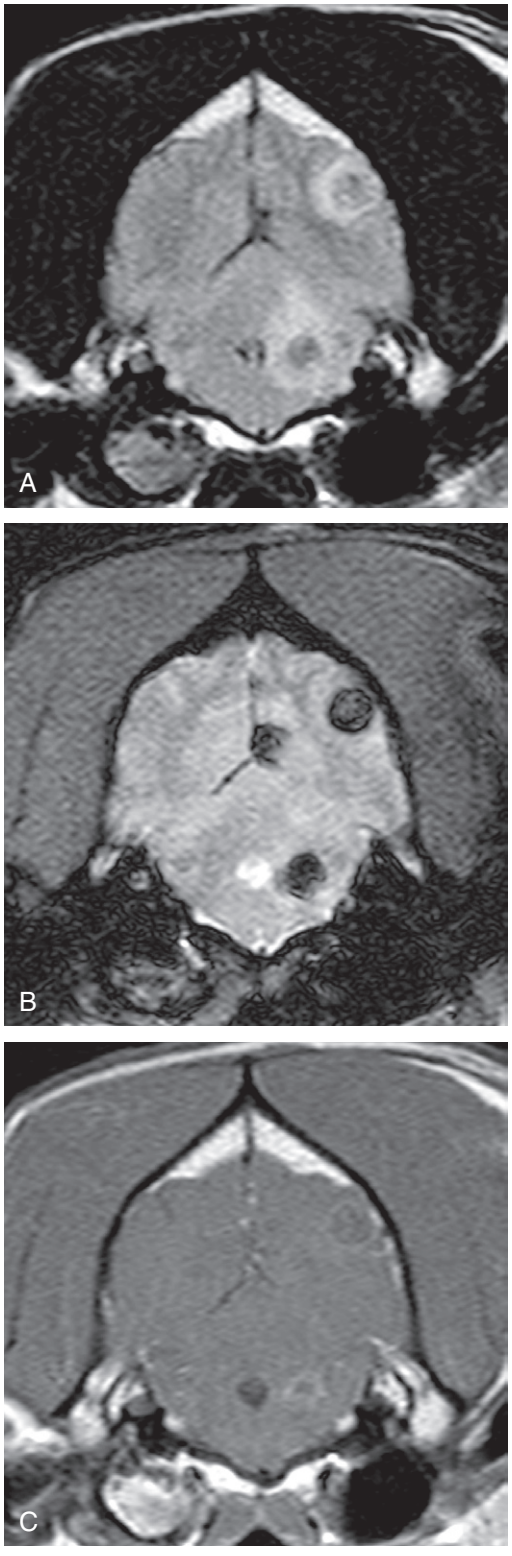


Fig. 9-22 Transverse T2-FLAIR **(A),** GRE **(B),** and T1-weighted postcontrast **(C)** images of a 9-year-old golden retriever with metastatic hemangiosarcoma. In **A** there are two focal hypointense regions with surrounding T2-hyperintensity, presumably edema, in the left occipital lobe and left ventral cerebellum. Minimal mass effect is present. Both lesions have mild peripheral contrast enhancement **(C)** and a susceptibility artifact **(B)** indicating hemorrhage. In **B,** a susceptibility artifact is also present adjacent to the osseous tentorium. This is the border of a similar "out of plane" lesion. The imaging characteristics are consistent with both hemorrhagic infarction of some days' duration (approximately >3) and hemorrhagic tumor foci but in this dog were proven to be metastasis. Incidentally, there is right otitis media.



Fig. 9-23 Dorsal T1-weighted postcontrast image of a 4-year-old Labrador retriever with lymphoma. There is a lobulated intensely contrasting mass in the occipital lobe that is causing ventricular compression and a leftward shift of midline structures. There is thickening of both the peripheral meninges (particularly on the left, *arrow*) and the falx (rostrally). Mass lesions and meningeal infiltration are common manifestations of intracranial lymphoma in both cats and dogs.

associated with multiple organ involvement (Fig. 9-23). The brain is not immune to metastases, and secondary intracranial neoplasia is common.

VASCULAR DISRUPTIONS

Occlusive Brain Infarction

Occlusive brain infarction, long thought not to be a clinical entity in dogs, is being diagnosed with increasing frequency with MR imaging.[20-22] Infarcts occur most commonly in the cerebellum but also occur in the brainstem and forebrain.

Patients with brain infarction are older and typically have acute nonprogressive focal neurologic signs. When the brainstem or cerebellum is involved, an important clinical differential is idiopathic peripheral vestibular disease, in which no abnormal MR findings are present. The typical MR characteristics of cerebellar infarction include a triangular or segmental region of T2 hyperintensity that is often most apparent on FLAIR images. The shape of the signal change usually closely reflects the territory of the affected artery (Fig. 9-24).

With cerebral infarction, the MR findings may overlap with those of a glioma or focal encephalitis. With cerebral infarction there is usually ill-defined T2 hyperintensity, T1 hypointensity, no mass effect, and little to no initial contrast enhancement (Fig. 9-25). As the infarct matures, typically after 3 days, regional vascularity increases, particularly at the periphery of the lesion.[23] One differentiating feature between infarction and glioma is the initial lack of a mass effect with an infarct. Later, however, a mass effect may develop 3 to 5 days postinfarction because of vasogenic edema. A definitive MR imaging distinction between cerebral infarction and glioma may not be possible in some patients, and diffusion-weighted MR imaging or a biopsy may be necessary. Diffusion imaging quantifies the rate of Brownian motion of water molecules in brain tissue. *Brownian motion* refers to the random movement of molecules. Water molecules are in constant motion, and the rate of movement or diffusion depends on

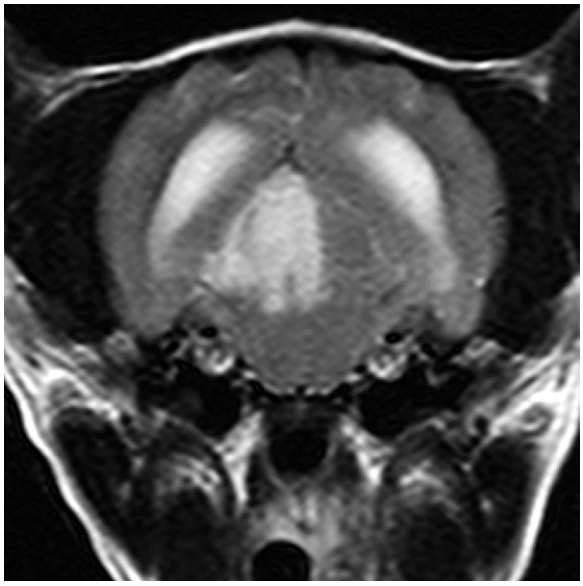


Fig. 9-24 Transverse T2-weighted image at the level of the rostral aspect of the cerebellum of an 8-year-old papillon that developed acute tetraplegia, a right head tilt, and positional vertical nystagmus less than 24 hours previously. The large triangular region of T2 hyperintensity in the right rostral aspect of the cerebellum was mildly T1 hypointense and had no discernible contrast enhancement. The clinical presentation, lesion location, shape, and imaging characteristics are typical of an infarct. This is a particularly large lesion. Diffusion-weighted imaging confirmed restricted water movement, also supporting acute infarction.

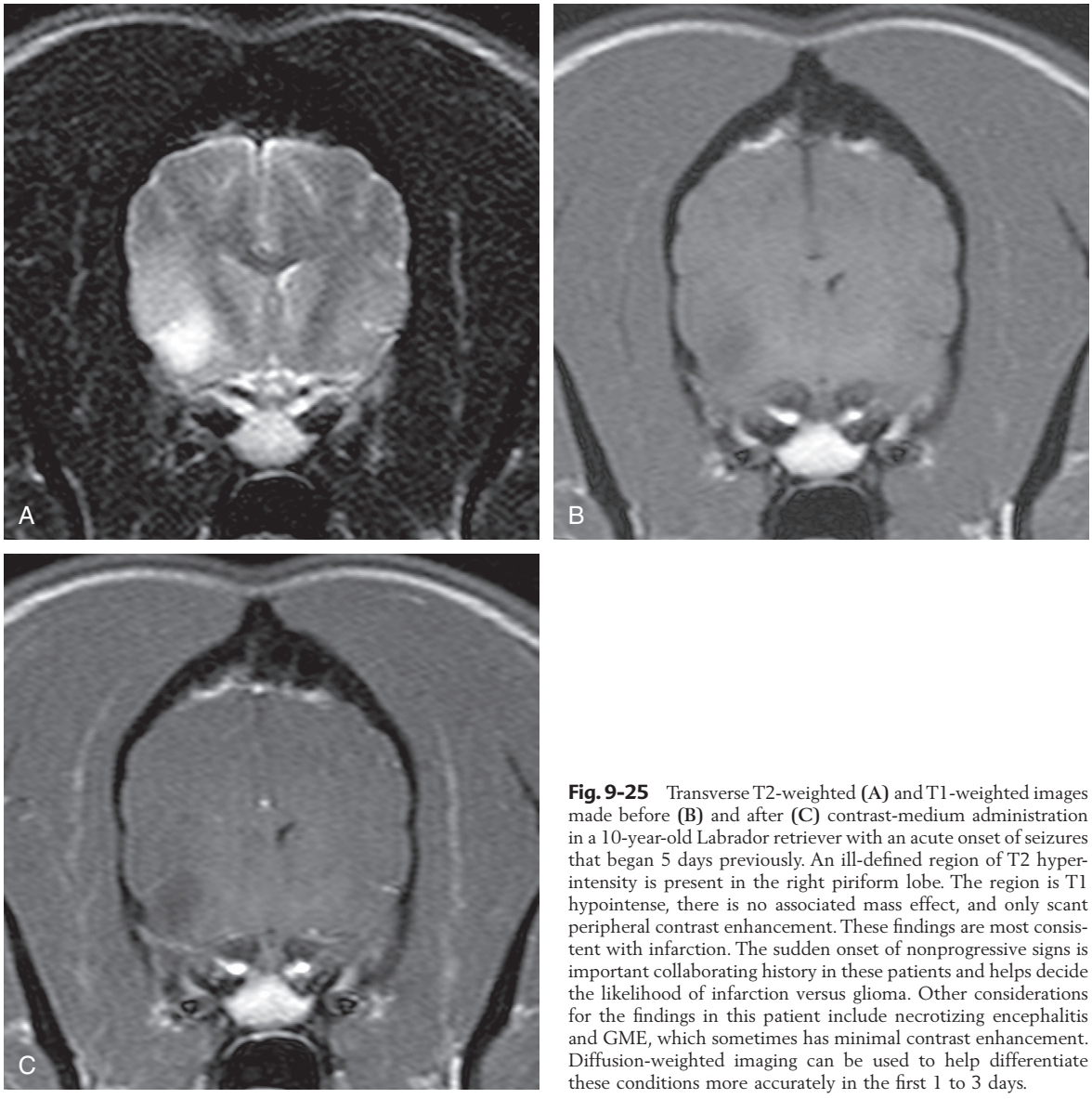


Fig. 9-25 Transverse T2-weighted **(A)** and T1-weighted images made before **(B)** and after **(C)** contrast-medium administration in a 10-year-old Labrador retriever with an acute onset of seizures that began 5 days previously. An ill-defined region of T2 hyperintensity is present in the right piriform lobe. The region is T1 hypointense, there is no associated mass effect, and only scant peripheral contrast enhancement. These findings are most consistent with infarction. The sudden onset of nonprogressive signs is important collaborating history in these patients and helps decide the likelihood of infarction versus glioma. Other considerations for the findings in this patient include necrotizing encephalitis and GME, which sometimes has minimal contrast enhancement. Diffusion-weighted imaging can be used to help differentiate these conditions more accurately in the first 1 to 3 days.

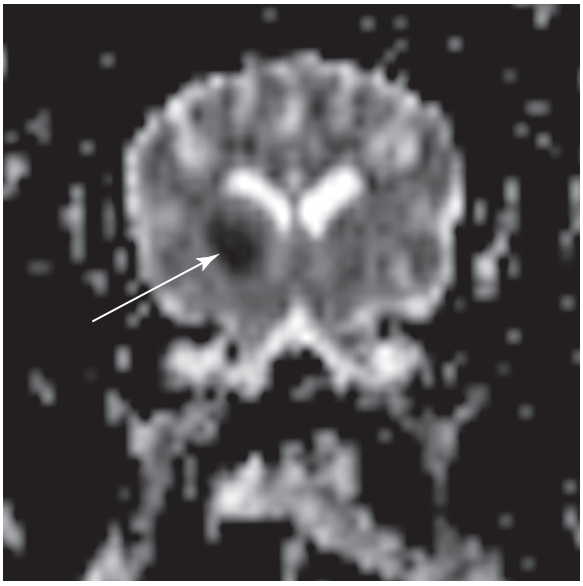


Fig. 9-26 A 4-year-old beagle imaged 2 days after presenting with an acute onset of seizures and pacing to the right. This image is a computer-generated image of the apparent diffusion coefficient of water. Regions of unrestricted water diffusion appear bright while areas of restricted water diffusion appear dark. Note the high signal in the lateral ventricles caused by the completely unrestricted diffusion of water in the CSF. Restricted water diffusion is usually caused by cellular swelling as a result of hypoxia-induced failure of the adenosine triphosphate pump. In this patient, a region of restricted water diffusion causes a focal region of low signal in the right thalamus *(arrow)*. When interpreted in light of the T2 hyperintensity of this lesion and lack of both mass effect and contrast enhancement (not shown), this is compelling evidence for acute infarction.

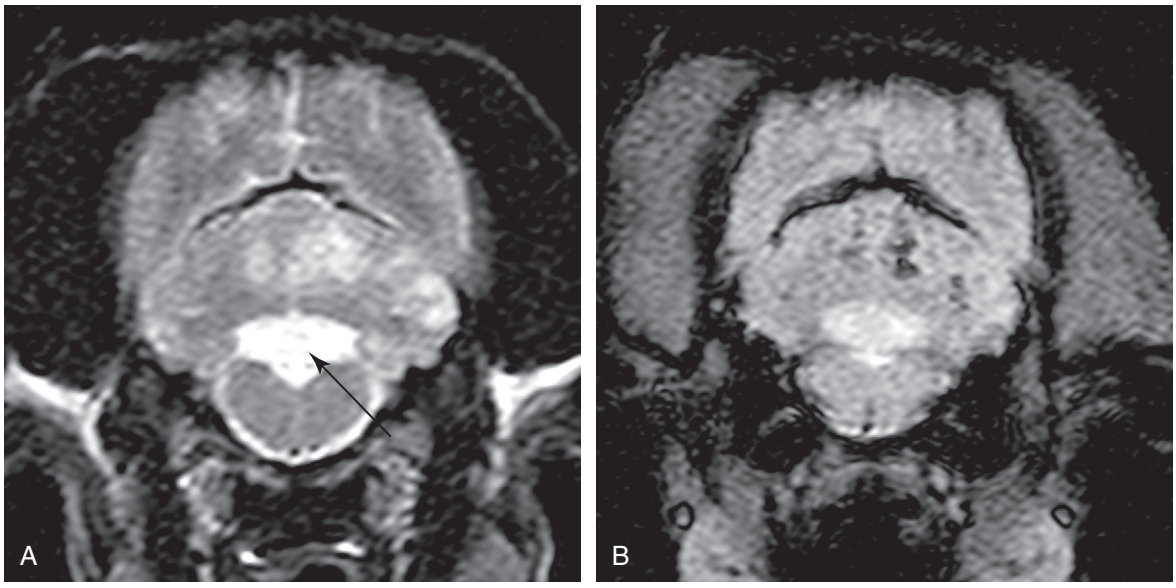


Fig. 9-27 T2-weighted transverse image **(A)** at the level of the cerebellum. The well-defined region of T2 hyperintensity dorsal to the brainstem (*arrow* in **A**) is the fourth ventricle. A region of T2 hyperintensity is present in the central and left aspects of the cerebellum. **B,** T2-weighted GRE (T2*) image at the same level. Hemorrhage is best detected on a GRE sequence because of the magnetic susceptibility effect of hemoglobin breakdown products. The focal regions of signal void are the result of local disruption to the magnetic field because of the magnetic properties of chronic hemorrhage. The size of the signal void does not reflect the size of the hematoma accurately because of blooming artifact.

the kinetic energy of the molecules and temperature. In acute infarction, brain cells become overhydrated from failure of the adenosine triphosphate pump, resulting in restricted movement of water (Fig. 9-26). In tumors, water movement is usually less restricted, and tumors will have less evidence of restricted water diffusion. However, restricted water diffusion in an infarct typically lasts only up to 3 to 5 days postinfarction, so after this time the ability of diffusion-weighted imaging to distinguish infarction from glioma is lost.

Patients wherein occlusive infarction is suspected should be evaluated for conditions resulting in a hypercoagulable state (e.g., Cushing's disease) and loss of antithrombin III.

Hemorrhagic Infarction

Hemorrhagic infarction is most commonly associated with hypertension, thrombocytopenia, or other coagulopathies. The MR imaging characteristics may be similar to those for occlusive infarction (Fig. 9-27). However, the appearance of

Table • **9-1**

Classic Magnetic Resonance Appearance of a Maturing Hematoma* in Human Central Nervous System Tissue

PHASE	TIME	HEMOGLOBIN	T1	T2
Hyperacute	<24 hours	Oxyhemoglobin (intracellular)	Isointense or hypointense	Hyperintense
Acute	1—3 days	Deoxyhemoglobin (intracellular)	Isointense or hypointense	Hypointense
Early subacute	>3 days	Methemoglobin (intracellular)	Hyperintense	Hypointense
Late subacute	>7 days	Methemoglobin (extracellular)	Hyperintense	Hyperintense
Chronic	>14 days	Hemosiderin (extracellular)	Isointense or hypointense	Hypointense

*There is considerable variation in the appearance of hematomas, and these observations have not been clinically validated fully in dogs. This table should act as guide only.
Modified from Bradley WG Jr: MR appearance of hemorrhage in the brain, *Radiology* 189:15–26,1993.

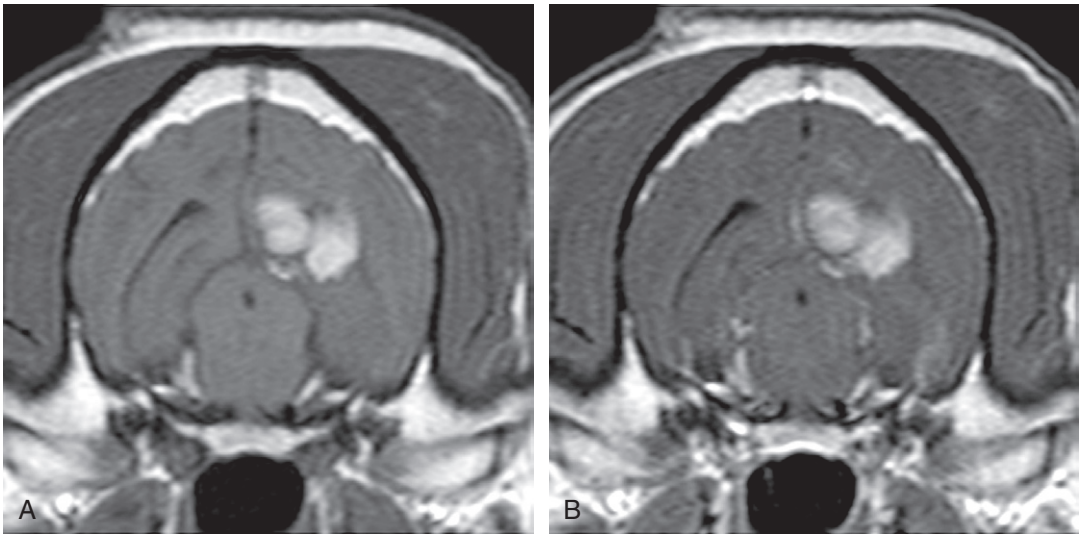


Fig. 9-28 Precontrast **(A)** and postcontrast **(B)** T1-weighted images of a 10-year-old spaniel with acute seizures. The precontrast T1-hyperintense region in **(A)** is hemorrhage of at least 3 days' duration. Both intracellular and extracellular methemoglobin are inherently T1 hyperintense. Other substances that are T1 hyperintense are the normal neurosecretory granules within the pituitary gland, fat, melanin, proteinaceous fluids, and some plasma cell tumors. There is no enhancement of the lesion **(B),** but normal vascular enhancement is apparent adjacent to the lesion.

cerebral hemorrhage changes as the hematoma matures (Table 9-1). The use of standard spin-echo sequences sometimes allows one to estimate the age of a hemorrhagic lesion, based roughly on the signal characteristics of the lesion. The change in appearance of a hematoma on different sequences over time is related to the magnetic properties of iron within hemoglobin as it transitions through intracellular deoxyhemoglobin to methemoglobin and finally extracellular hemosiderin (Fig. 9-28).

As discussed previously, in comparison to fast (turbo) spin-echo sequences, GRE sequences are more susceptible to magnetic field inhomogeneity created by hemoglobin degradation. Chronic hemorrhage acts like ferromagnetic material, causing pronounced local distortion of the local magnetic field and resulting in a signal void (Fig. 9-29; see Figs. 9-22 and 9-27), and for this reason, GRE sequences should be acquired routinely, even though hemorrhage may not be suspected. Low signal on T2-weighted spin-echo and GRE images is, however, not specific for hemorrhage and may also be seen with mineralization, gas, fibrous tissue, or iron deposits.[23] One must interpret susceptibility artifacts in GRE images in light of information gained from all other sequences in the study and the available clinical information.

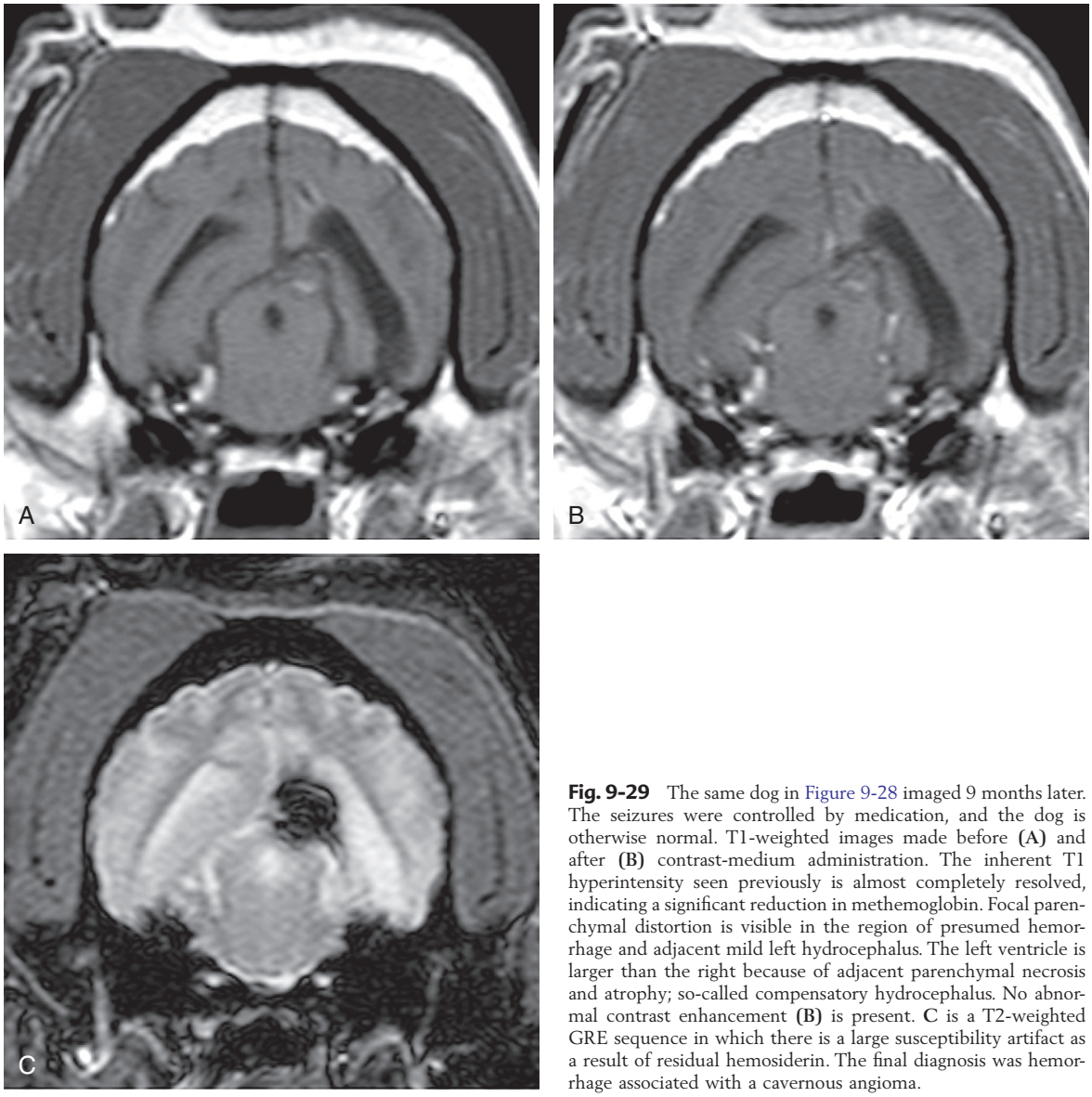


Fig. 9-29 The same dog in Figure 9-28 imaged 9 months later. The seizures were controlled by medication, and the dog is otherwise normal. T1-weighted images made before **(A)** and after **(B)** contrast-medium administration. The inherent T1 hyperintensity seen previously is almost completely resolved, indicating a significant reduction in methemoglobin. Focal parenchymal distortion is visible in the region of presumed hemorrhage and adjacent mild left hydrocephalus. The left ventricle is larger than the right because of adjacent parenchymal necrosis and atrophy; so-called compensatory hydrocephalus. No abnormal contrast enhancement **(B)** is present. **C** is a T2-weighted GRE sequence in which there is a large susceptibility artifact as a result of residual hemosiderin. The final diagnosis was hemorrhage associated with a cavernous angioma.

REFERENCES

1. Robertson ID: Optimal magnetic resonance imaging of the brain, *Vet Radiol Ultrasound* 52(Suppl 1):S15–S22, 2011.
2. Westbrook C, Kaut Roth C, Talbot J: Pulse sequences. In Westbrook C, Kaut Roth C, Talbot J, editors: *MRI in practice*, ed 4, Oxford, 2011, Blackwell.
3. Benigni L, Lamb CR: Comparison of fluid-attenuated inversion recovery and T2-weighted magnetic resonance images in dogs and cats with suspected brain disease, *Vet Radiol Ultrasound* 46:287, 2005.
4. Westbrook C, Kaut Roth C, Talbot J: Contrast agents in MRI. In Westbrook C, Kaut Roth C, Talbot J, editors: *MRI in practice*, ed 3, Oxford, 2005, Blackwell, p 352.
5. Marckmann P: Nephrogenic systemic fibrosis: epidemiology update, *Curr Opin Nephrol Hypertens* 17:315, 2008.
6. Cherubini GB, Mantis P, Martinez TA, et al: Utility of magnetic resonance imaging for distinguishing neoplastic from non-neoplastic brain lesions in dogs and cats, *Vet Radiol Ultrasound* 46:384, 2005.
7. Leigh EJ, Mackillop E, Robertson ID, et al: Clinical anatomy of the canine brain using magnetic resonance imaging, *Vet Radiol Ultrasound* 49:113, 2008.
8. Couturier L, Degueurce C, Ruel Y, et al: Anatomical study of cranial nerve emergence and skull foramina in the dog using magnetic resonance imaging and computed tomography, *Vet Radiol Ultrasound* 46:375, 2005.
9. Gomes E, Degueurce C, Ruel Y, et al: Anatomic study of cranial nerve emergence and associated skull foramina in cats using CT and MRI, *Vet Radiol Ultrasound* 50:398, 2009.
10. Fletcher TF, Saveraid TC, University of Minnesota College of Veterinary Medicine: Canine brain MRI atlas (website). http://vanat.cvm.umn.edu/mriBrainAtlas. Updated April 2009. Accessed October 30, 2011.
11. Esteve-Ratsch B, Kneissl S, Gabler C: Comparative evaluation of the ventricles in the Yorkshire terrier and the German shepherd dog using low-field MRI, *Vet Radiol Ultrasound* 42:410, 2001.
12. Lamb CR, Croson PJ, Cappello R, et al: Magnetic resonance imaging findings in 25 dogs with inflammatory cerebrospinal fluid, *Vet Radiol Ultrasound* 46:17, 2005.

13. Long S, Vite CH, editors: *Braund's clinical neurology in small animals: localization, diagnosis and treatment*, Ithaca, NY, 2006, International Veterinary Information Service.
14. Bagley RS, Wheeler SJ, Klopp L, et al: Clinical features of trigeminal nerve-sheath tumor in 10 dogs, *J Am Anim Hosp Assoc* 34:19, 1998.
15. D'Anjou MA, Carmel EN, Tidwell AS: Value of fat suppression in gadolinium-enhanced magnetic resonance neuroimaging, *Vet Radiol Ultrasound* 52(1 Suppl 1):S85–S90, 2011.
16. Wisner ER, Dickinson PJ, Higgins RJ: Magnetic resonance imaging features of canine intracranial neoplasia, *Vet Radiol Ultrasound* 52(Suppl 1):S52–S61, 2011.
17. Tamura S, Tamura Y, Nakamoto Y, et al: MR imaging of histiocytic sarcoma of the canine brain, *Vet Radiol Ultrasound* 50:178, 2009.
18. Snyder JM, Shofer FS, Van Winkle TJ, et al: Canine intracranial primary neoplasia: 173 cases (1986–2003), *J Vet Intern Med* 20:669, 2006.
19. Snyder JM, Lipitz L, Skorupski KA, et al: Secondary intracranial neoplasia in the dog: 177 cases (1986–2003), *J Vet Intern Med* 22:172, 2008.
20. Garosi L, McConnell JF, Platt SR, et al: Clinical and topographic magnetic resonance characteristics of suspected brain infarction in 40 dogs, *J Vet Intern Med* 20:311, 2006.
21. Rossmeisl JH Jr, Rohleder JJ, Pickett JP, et al: Presumed and confirmed striatocapsular brain infarctions in six dogs, *Vet Ophthalmol* 10:23, 2007.
22. Tidwell AS, Robertson ID: Brain infarcts, *Vet Radiol Ultrasound*, 52(Suppl 1):S62–S71, 2011.
23. Mulkern RV: Fast imaging techniques. In Atlas SW, editor: *Magnetic resonance imaging of the brain and spine*, vol. 1, ed 3, Philadelphia, 2002, Lippincott Williams & Wilkins, p 178.

ELECTRONIC RESOURCES

evolve

Additional information related to the content in Chapter 9 can be found on the companion Evolve website at http://evolve.elsevier.com/Thrall/vetrad/

- Chapter Quiz

CHAPTER • 10
The Equine Head

Anthony P. Pease

RADIOGRAPHY VERSUS OTHER IMAGING MODALITIES

Until recently, the primary imaging modalities available to assess the equine head were radiography and scintigraphy. The equine head is difficult to evaluate completely with radiographs because of the numerous overlying structures, thick bone, and relatively complex anatomy. Radiographic detection of small areas of lysis or soft tissue lesions is sometimes impossible in the equine head. Scintigraphy provides information on osteogenesis and possibly blood flow but has poor spatial resolution.

In the last several years, there has been increased use of cross-sectional imaging modalities such as computed tomography (CT), magnetic resonance (MR) imaging, and ultrasound for imaging the equine head. This has simplified identification of morphologic abnormalities. In addition, postprocessing programs allowing multiplanar and three-dimensional reconstruction of CT and MR images have augmented surgical planning.[1,2] Despite the enhanced capabilities provided by CT, MR imaging, and ultrasound, conventional radiography is still the main modality used to evaluate the equine head.[3-6]

The large gas-filled structures of the equine head, such as the guttural pouches, larynx, pharynx, nasal cavity, and paranasal sinuses, enable diagnostic-quality radiographs to be obtained with portable radiographic units. The main limitation of radiography is the superimposition of multiple complex structures. Despite the difficulties associated with interpretation of conventional equine skull radiographs, they are helpful in providing diagnostic information in a majority of diseases that occur in the head, although the true extent of the disease may be underestimated.[7] Subsequently, other techniques can be used to provide more detailed or specific information after identification with radiography.

Scintigraphy has been applied primarily to localize sites of bone remodeling. Bone-seeking radiopharmaceuticals, such as technetium-99 m methylene diphosphonate, bind to hydroxyapatite crystals in regions of osteoblastic activity. In the head, the main use for nuclear medicine is evaluating dental disease and differentiating sinusitis of dental origin from other causes.[8] This can be particularly difficult radiographically because lesions of the teeth may not be detected as a result of superimposition of normal structures or disease or the presence of only minimal bone lysis. In addition, scintigraphy is also useful for identifying regions of bone remodeling caused by degenerative joint disease within the temporomandibular and temporohyoid joints, which may not be evident on radiographs (Fig. 10-1).

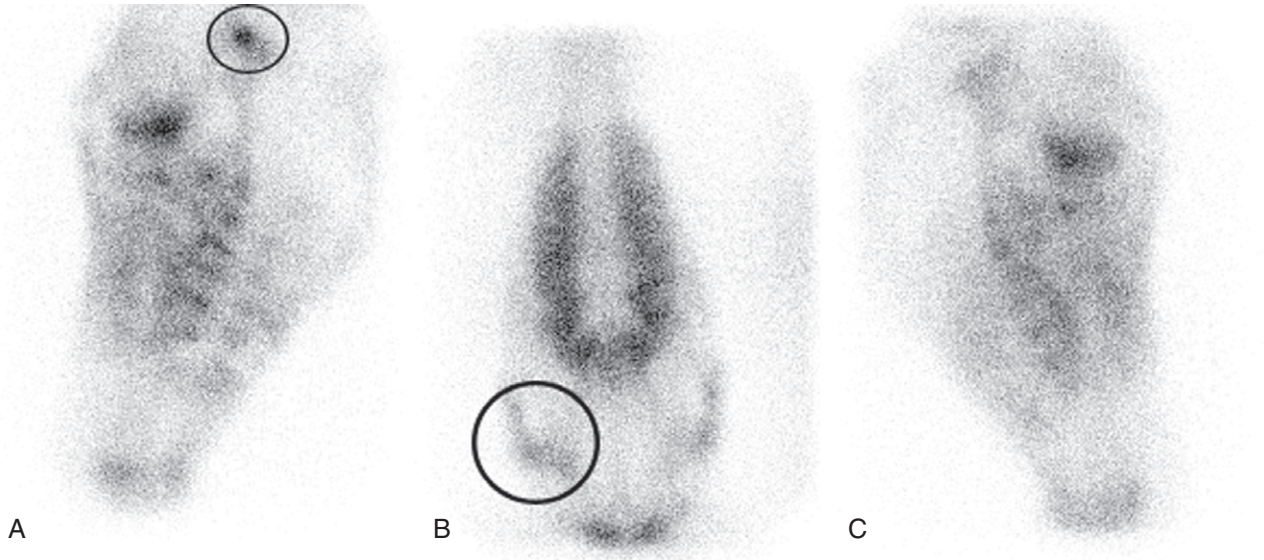


Fig. 10-1 Bone phase scintigrams of an equine head with technetium-99 m methylene diphosphonate. The left lateral **(A)** and dorsal projections **(B)** are characterized by a focal increased activity in the region of the temporomandibular joint *(circles)*. The same area of activity is not visible in the right lateral projection **(C)**.

Radioactive labeling of white blood cells has also been used in the evaluation of tooth abnormalities. However, the overall low level of radioactivity in sites of abnormal white cell accumulation causes poor resolution and does not provide adequate landmarks, making this technique inaccurate.[9]

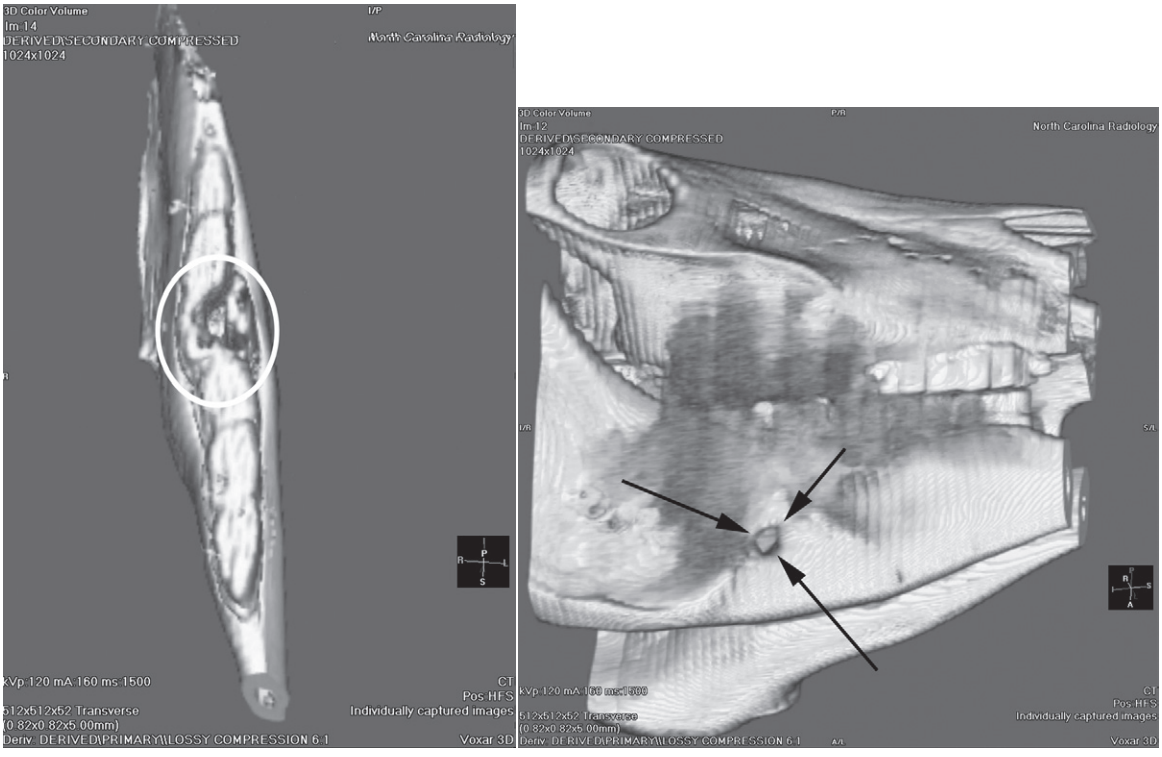
Overall, the primary limitation of scintigraphy is poor spatial resolution. Thus, nuclear medicine has a high sensitivity for detection of bone destruction and remodeling, although scintigraphy is not as specific in detecting the cause of remodeling compared with radiography.[9] The sensitivity of conventional radiography for equine dental disease is only approximately 50%,[9-11] but when used in combination with scintigraphy the sensitivity increases to 97.7% and the specificity to 100%.[9]

The use of cross-sectional imaging eliminates the problem of overlying structures. CT and MR imaging allow the evaluation of transverse slices of the head that are generally 0.5 mm to 1 cm thick. These images provide good anatomic localization (Fig. 10-2). In addition, three-dimensional reconstructions of CT images can be generated that can aid in surgical planning and visualizing lesions not easily identified on transverse images (Fig. 10-3).

CT and MR imaging require specialized equipment, including custom tables and hoists (Fig. 10-4) and a purpose-built room to accommodate the size of the horse. Standing CT units are available in Europe but to date are not present in the United States. These standing units are divided into mobile CT or fixed CT units. With a mobile CT unit, the CT scanner is placed on rails, and the horse is sedated and stands with its head in the CT scanner. Instead of the table moving through the gantry, the gantry moves while the table remains still. The fixed CT unit is a standard CT unit, and the horse is sedated and the head placed on the CT table. The horse is standing in



Fig. 10-2 A transverse CT image at the level of the first maxillary molar. Note the tract extending out of the lateral aspect of the mandible from an apical tooth root abscess (*arrow*).



A B

Fig. 10-3 Three-dimensional reformatted images of the apical tooth root abscess in Figure 10-2. Note the fracture of the first molar along the sagittal plane (**A,** *circle*) as well as the defect in the mandible (**B,** *black arrows*).

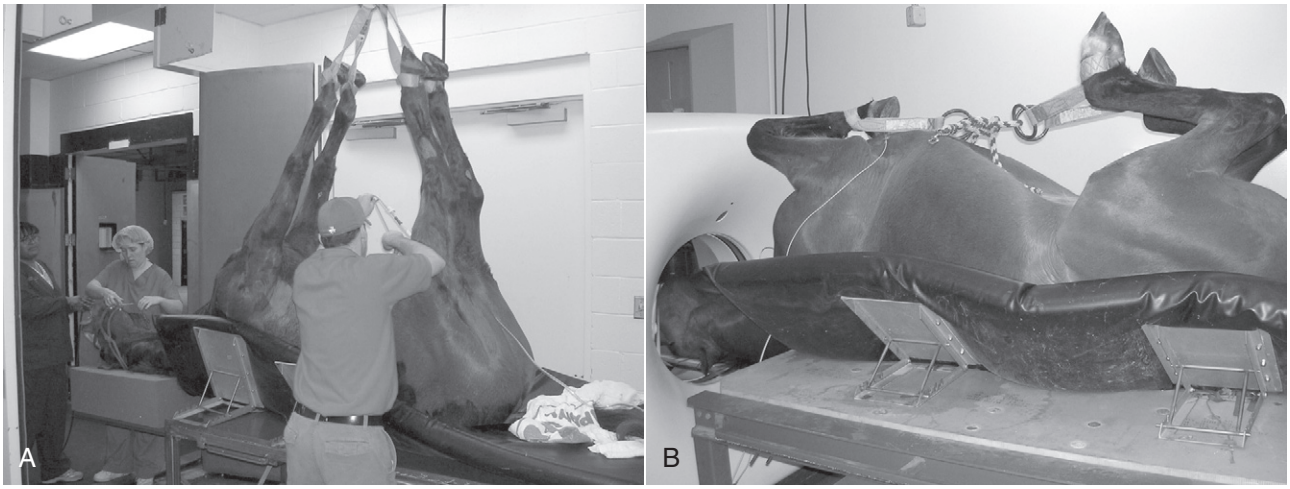


Fig. 10-4 **A,** The hoist required to place a horse on the specialized table for CT or MR imaging. **B,** A horse positioned for a CT examination of the head.

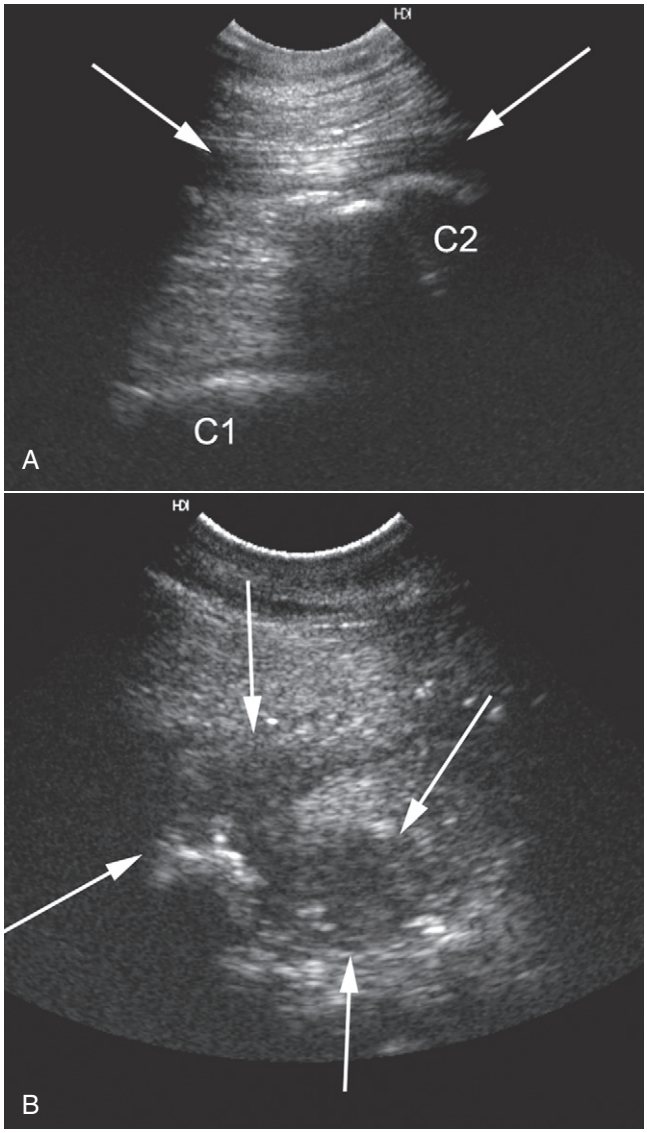


Fig. 10-5 **A,** Longitudinal sonogram of the region of the poll at the level of C1. No abnormalities are seen, and the *white arrows* indicate the normal fiber pattern of the nuchal ligament. **B,** Longitudinal sonogram of the left craniodorsal aspect of the neck at the level of C1 in the same horse. Note the large hypoechoic cavity *(white arrows)* near the bone from an abscess in the nuchal bursa. (Courtesy of Cornell University, Ithaca, NY.)

a specially made stock, and the floor has numerous air jets that allow the stocks and horse to float above the floor. This allows the table to move through the gantry with minimal resistance. Many sources provide CT and MR imaging of normal anatomy.[12-14]

Ultrasonography has been used to evaluate skull fractures as well as temporomandibular joints, retrobulbar masses, and jugular vein thrombosis.[15] Ultrasonography is also useful for evaluation of the superficial soft tissue structures of the head, with the major limitations being the contour of the head, which prevents adequate transducer-skin contact, and the inability of sound to penetrate bone. The most useful application of ultrasound is evaluating soft tissue structures where the bone is not obstructing the region of interest, such as in the guttural pouches to look for fluid, and allowing the evaluation of draining tracts associated with atlantoaxial septic bursitis (Fig. 10-5). Ultrasound can also help evaluate the size and appearance of lymph nodes in horses afflicted with *Streptococcus equi*. In addition, the use of ultrasound has been suggested as an aid in the evaluation of the larynx.[16]

With all these modalities being available, the main consideration when selecting one is the level of invasiveness, the speed of acquisition, and the type of lesion being evaluated. If general anesthesia is possible, CT should be used to evaluate lesions of the skull that involve bone, such as tooth root abscesses, fractures from trauma, or temporohyoid osteoarthropathy. MR imaging is extremely useful for evaluating the equine brain, sinuses, or the surrounding soft tissue structures of the head. Ultrasound can be used to evaluate superficial soft tissue structures in the standing horse, whereas radiography remains the mainstay for rapid evaluation of the equine head, with only minimal sedation needed. Scintigraphy has generally been replaced by the other modalities described previously; however, when appropriate, scintigraphic evaluation can aid in the diagnosis of disease involving the paranasal sinuses as well as the teeth, especially when used in combination with radiography.

ABNORMALITIES OF THE EQUINE HEAD

One approach for beginning a radiographic assessment of the equine head is to divide the head into general locations and then address the diseases that occur at these sites. Although overlap will undoubtedly occur, this method is appropriate, and image acquisition and special views should be focused on when appropriate.



Fig. 10-6 The position for an intraoral, dorsoventral radiograph to evaluate the rostral aspect of the incisive bone.

Rostral Head (Incisive Region and Rostral Mandible)

The rostral aspect of the head is the area rostral to the premolar teeth. The standard radiographic projections to evaluate this region include a lateral and a dorsoventral projection. Intraoral radiographs are useful to eliminate superimposition of structures and are accomplished by placing a plastic bag over a radiographic cassette and then inserting the cassette into the mouth (Fig. 10-6). A dorsoventral projection is used to evaluate the incisive bone, and a ventrodorsal projection allows assessment of the rostral aspect of the mandible.

Diseases that involve the rostral equine head include fractures, neoplasia, and cyst formation.[3,4,6] Fractures generally occur in young, inquisitive animals that become startled while chewing or playing with a fixed object.[6] This causes a displaced fracture involving the incisive teeth with extension into the diastema, which is the portion of the body of the mandible or maxilla without teeth. These fractures are usually moderately displaced and identified easily. However, radiographs tend to underestimate the extent of incomplete fracture lines that may extend into the mandible or involve premolar tooth roots. Involvement of tooth roots by the fracture increases the complications of surgical repair because of the increased likelihood of tooth root infection and abscess formation.

Tumors that occur on the rostral head are rare and generally benign. Osteoma is a benign tumor that can affect the mandible, maxilla, paranasal sinuses, and nasal cavity. The main feature of an osteoma is that it has an intense, well-demarcated mineral opacity and is usually midline in the rostral mandible.[4] Adamantinomas, also known as epidermoid cysts, cause a unilateral enlargement of the rostral mandible or ventral aspect of the body of the mandible in young animals.[3,4,6] This lesion is an expansile mass that can look clinically similar to osteosarcoma.[3] Another cause of cystlike enlargement and septation in the mandible of a young horse is nutritional hyperparathyroidism.[3] Large aneurismal bone cysts are also possible in the rostral mandible of a young horse (Fig. 10-7). Soft tissue tumors have also been described as expansile lesions that cause bone lysis and displace the incisor teeth but generally consist of a large soft tissue mass with secondary bone involvement.[17]

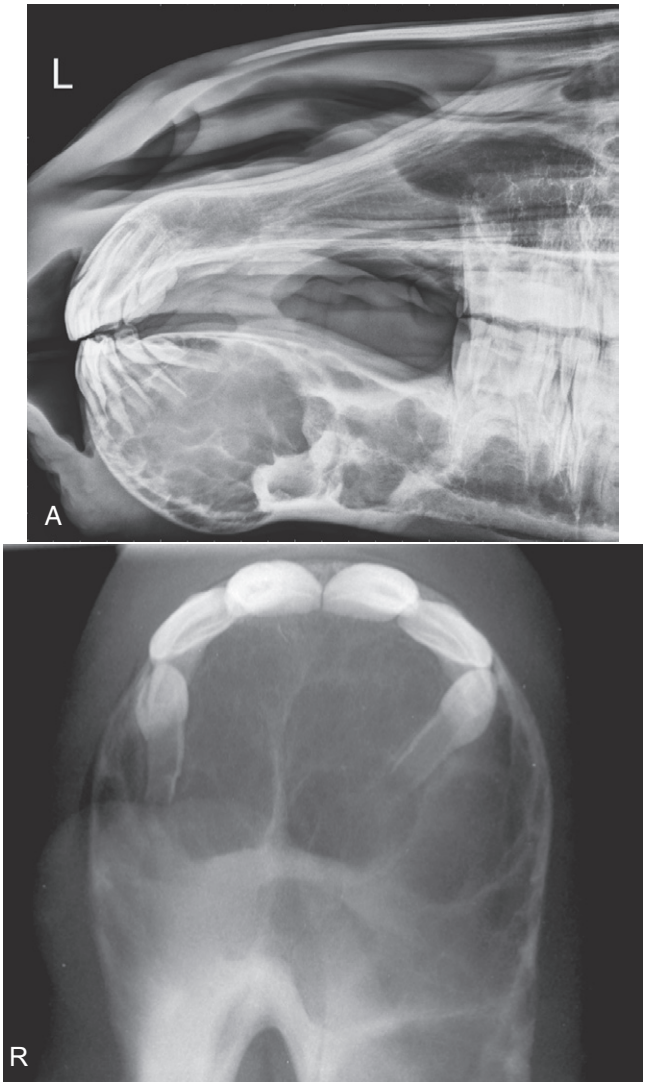


Fig. 10-7 Lateral **(A)** and ventrodorsal intraoral **(B)** radiographs of the rostral aspect of the mandible in a 7-month-old Thoroughbred with an expansile, relatively nonaggressive appearing lesion caused by an aneurismal bone cyst.

Mandible

Either mandible is difficult to examine in its entirety because of superimposition of the contralateral mandible and parts of the skull. Evaluation of the temporomandibular joints and the rami of the mandible requires oblique radiographs, CT imaging, or MR imaging. Standard radiographic views for the mandible include lateral, dorsoventral, and two oblique projections. The goal of an oblique radiograph is to allow the ramus or body of each mandible to be evaluated individually.[4,6] Thus right 45-degree dorsal-left ventral oblique (RDLVO) and left 45-degree dorsal-right ventral oblique (LDRVO) radiographs should be obtained. When obtaining oblique radiographs, care should be taken to place the appropriate radiographic marker to identify the image; this is discussed in detail in Chapter 7.

Radiographs of the mandible are usually performed to evaluate the mandibular tooth roots or the mandibular body for fractures. Mandibular tooth root infections are suspected when swelling is present in the mandibular region that frequently manifests itself as a sinus tract draining from the ventral aspect of the ramus.[6] Evaluation of the extent of this

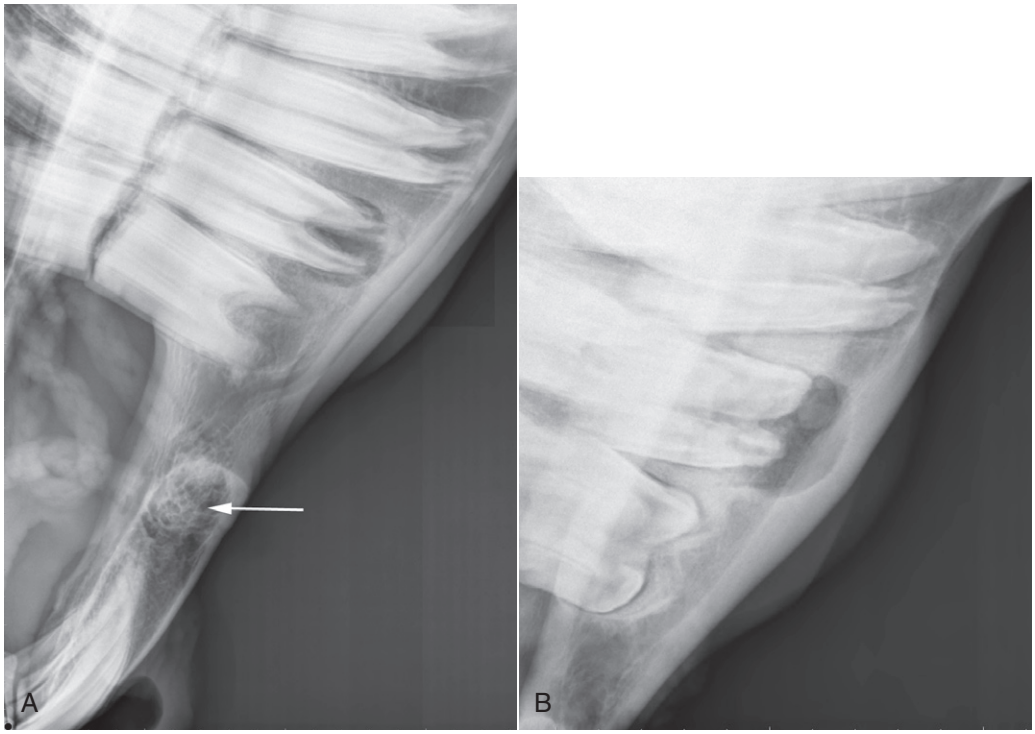


Fig. 10-8 Lateral **(A)** and RDLVO **(B)** radiographs of the rostral aspect of the head of a horse with a tooth root abscess. **A,** A region of lysis is present around the roots of one of the third mandibular premolars. Determining whether the affected tooth is on the left or the right is impossible from a lateral view. The rope halter *(white arrow)* can be seen superimposed over the symphyseal region; care must be taken to avoid misinterpretation of a halter as a lesion. **B,** The lysis is clearly localized to the right arcade. Note the irregularity of the rostral root of the right third mandibular premolar.

tract can be performed by a metallic probe or injection of contrast medium. This contrast-medium procedure is performed while obtaining an oblique radiograph to isolate the involved area of the mandible further while eliminating superimposition. The goal of adding the contrast medium or metallic probe is to trace the sinus tract to the source of the infection, which often centers on the apical aspect of the infected tooth root. The radiographic findings of apical tooth root abscesses include indistinct margins of the lamina dura, loss of the normal outline of the tooth root, blunting of the tooth root, widening of the periodontal membrane, and frequently an associated lytic tract extending out of the ventral cortex of the mandible (Figs. 10-8 and 10-9).[4,6] In chronic infections, the mandible may have a periosteal reaction associated with the defect and extension of the infection into the soft tissues. Bone formation can extend on the medial and lateral borders of the mandible, obscuring the mandible and causing a loss of detail on the radiographs because of superimposition.[6]

Fractures of the caudal aspect of the mandible may be unilateral or bilateral. Because of the superimposition of the teeth, mandibular fractures are difficult to evaluate without the use of oblique radiographic projections.[4,6] Caudal mandibular fractures are usually incomplete and have a worse prognosis if the fracture line involves a tooth root that may lead to a tooth root infection.[4]

Subluxation and osteoarthropathy of the temporomandibular joint are also difficult to assess on conventional radiographs because of the superimposition of the petrous temporal bone. One technique is to acquire a right 30-degree caudal-left rostral oblique radiograph to examine the left temporomandibular joint and a left 30-degree caudal-right rostral oblique radiograph to examine the right temporomandibular joint. Moving the x-ray tube rostral or caudal to the temporomandibular joint will separate the joints without projecting them on the petrous temporal bone. Because the petrous temporal bone is superimposed on the temporomandibular joint, sometimes the projection is also obliqued ventrodorsally. However, when multiple planes are obliqued, interpretation of the image is difficult because distortion of normal structures will occur.

Dorsoventral radiographs can be acquired in the standing horse, but care needs to be used because the x-ray tube is difficult to move out of the way rapidly if the horse becomes startled; this could cause injury to personnel, equipment, and the patient.[18] Recently, more emphasis has been placed on the ultrasonographic appearance of the temporomandibular joint, including the normal appearance.[19] After comparing radiography, scintigraphy, and ultrasound to diagnose temporomandibular arthropathy in a horse, ultrasound was considered the least expensive, technically easiest, and most informative.[20] However, sonography is useful for this purpose only if applied by trained sonographers.

CT and MR imaging are useful to assess the mandible and temporomandibular joint. In terms of assessing tooth root abscesses, the same changes described with radiography can be identified with CT; however, CT is also able to assess whether fragmentation or lucencies within the tooth are present (see Fig. 10-2).[1] In addition, CT can better evaluate mandibular fractures and allow detection of subtle fracture lines obscured by superimposition on conventional radiographs. For the temporomandibular joint, both CT and MR imaging allow evaluation of the surrounding soft tissues for evidence of infection or swelling, determine if the joint is misaligned, and identify bone lysis associated with the mandibular condyle or mandibular fossa.

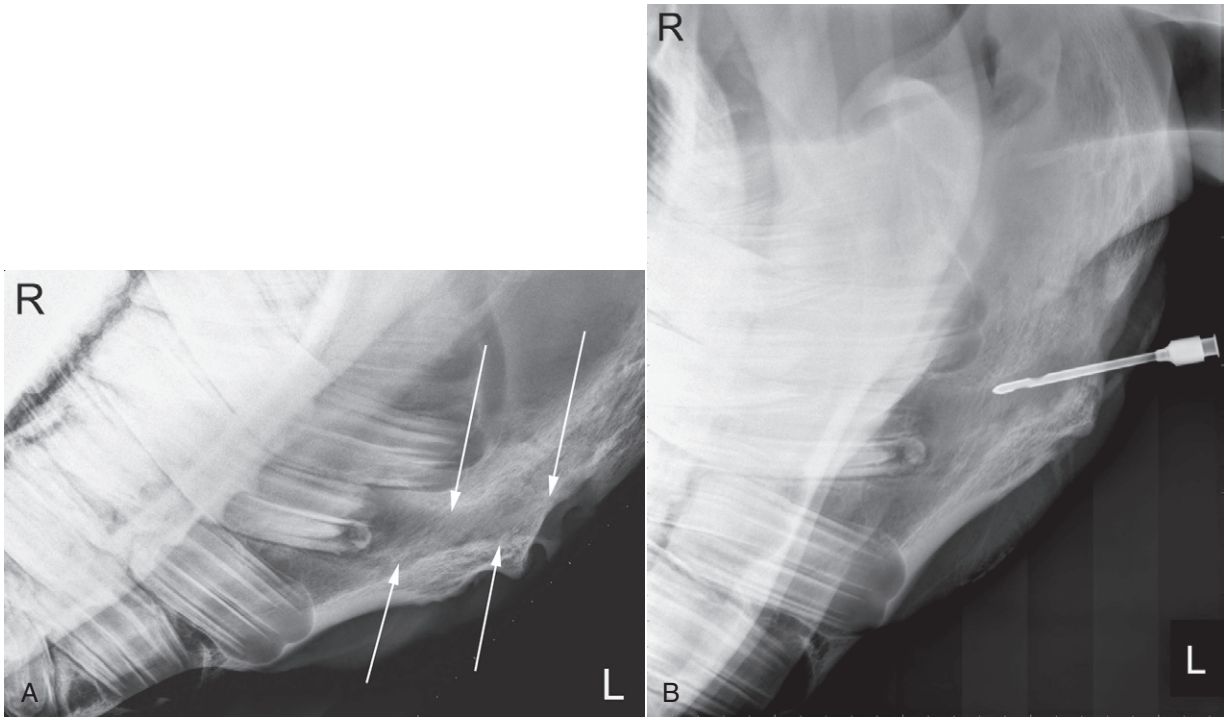


Fig. 10-9 RDLVO projection without **(A)** and with **(B)** a cannula present in a draining tract from the ventral aspect of the mandible. The caudal tooth root of the left mandibular first molar is radiolucent, and a well-margined radiolucent tract is visible in the body of the mandible *(white arrows)*. This is an example of a mandibular apical tooth root abscess with an associated draining tract.

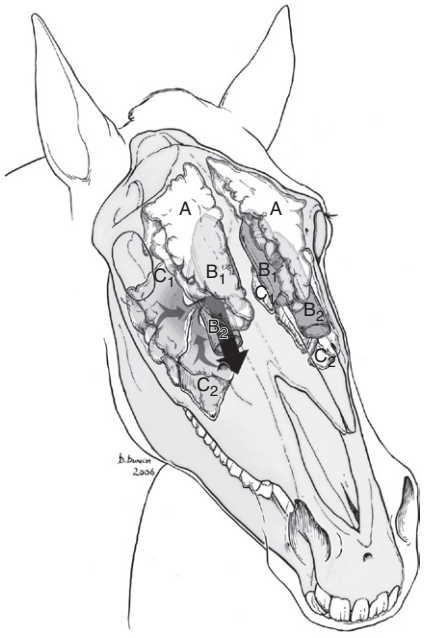


Fig. 10-10 A schematic representation of the equine nasal sinuses and their communications. *A*, Conchofrontal sinus; B_1, dorsal nasal meatus; B_2, middle nasal meatus; C_1, caudal maxillary sinus; C_2, rostral maxillary sinus.

Nasal Cavity, Paranasal Sinuses

Because horses are obligate nasal breathers, the nasal cavity and paranasal sinuses are very large to provide adequate airflow during exercise. The extensive sinus system occupies the majority of the head and has an intricate communication system within the sinuses as well as in the nasal cavity (Fig. 10-10). On each side of the horse are frontal, caudal maxillary, rostral maxillary, and sphenopalatine sinuses. The unique characteristics of this sinus system is that among domestic species the horse is the only species in which the frontal sinus communicates indirectly with the nasal cavity through the caudal maxillary sinus; in other species the communication is direct.[21]

The frontal sinus, more correctly the conchofrontal sinus, is in the caudodorsal aspect of the head and overlies the rostral portion of the calvaria, medial to the orbits and extending rostrally as the closed portion of the dorsal concha. The frontomaxillary opening on the rostrolateral aspect of the conchofrontal sinus allows communication between the conchofrontal and caudal maxillary sinuses. The caudal maxillary sinus and the rostral maxillary sinus are in the lateral aspect of the caudal head and overlie the maxillary cheek teeth. These two sinuses are divided by an oblique septum that varies in position. Both sinuses communicate with the nasal cavity by a small, shared communication nasomaxillary opening that extends to the middle nasal meatus.[21] This opening bifurcates to allow communication with the rostral and caudal maxillary sinuses while preventing direct communication between the two maxillary sinuses.[22]

The sphenopalatine sinus communicates rostrally with the caudal maxillary sinus and infrequently has direct communication with the ventral nasal meatus.[22] This sinus is located ventral to the cranial vault within the sphenoid bone, and the lateral wall is associated with the pterygoid fossa. The septum between the right and left sides of the sphenoid varies in position, and the two sides are never equal size.[22] The sphenopalatine sinus is associated closely with the ethmoid labyrinth and optic canal; therefore disease such as infection or ethmoid hematomas can result in vision loss.

Because of the large network of sinuses and meatuses within the nasal cavity, assessing the location of lesions with conventional radiography can be difficult. Because all the structures are superimposed, determining whether a soft tissue structure is present within a sinus, the nasal cavity, or

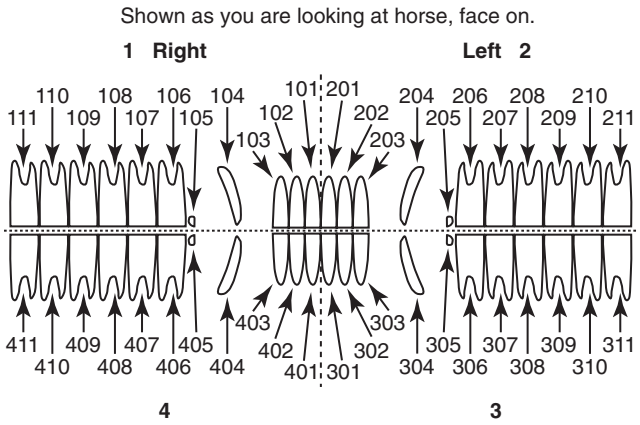


Fig. 10-11 The Triadan numbering system in the horse. The first digit indicates the arcade, the last two digits the specific tooth. From Baker GJ, Easley J, editors. *Equine dentistry*, ed 2, Philadelphia, 2005, Elsevier.

both is sometimes impossible. In addition, the primary limitation of both CT and conventional radiography is that soft tissue and fluid have the same relative attenuation and opacity. Some have suggested the use of intravenous contrast medium–enhanced CT to help differentiate soft tissue from fluid because the soft tissue of a mass or nasal mucosa should enhance with contrast medium, whereas fluid would not. This problem of differentiation is negated with MR imaging where fluid-attenuating inversion recovery (FLAIR) sequences can be used to create signal differences between fluid and soft tissue. This fundamental principle of MR imaging makes it the modality of choice when evaluating soft tissue structures of the head.

For radiography of the nasal cavity and paranasal sinuses, the acquisition of left to right and right to left lateral radiographs is important, as well as dorsoventral, left ventral, right dorsal oblique (LVRDO) and LDRVO radiographs, to maximize the chance of detecting abnormalities such as fluid lines and determine if bilateral disease is present.[23] When performing oblique radiographic projections, the angle should be approximately 60 degrees in the dorsal or ventral direction to try to minimize the superimposition of the contralateral sinus.[4] The oblique radiographs can also be acquired with a speculum placed within the horse's mouth so that the occlusive surface of the teeth can be better evaluated.[24]

The dental nomenclature is divided into two methods, naming the tooth based on location and type, such as right maxillary first premolar, or by a Triadan numeric system. In the Triadan system, teeth are numbered from the central incisor caudally starting with 101 to indicate the right first maxillary incisor and 111 to indicate the right third maxillary molar. The left maxillary teeth begin with 201, the left mandibular teeth begin with 301, and the right mandibular teeth begin with 401 (Fig. 10-11).

To understand the development and association of disease processes in the sinuses and teeth, an understanding of the normal anatomy of the equine head is important. The main point to note is that the maxillary cheek teeth are embedded within a thin rim of alveolar bone that separates the teeth from the surrounding paranasal sinuses. This close association changes throughout the life of the horse. In young foals, the last premolar (08) and first molar (09) project into the rostral and caudal maxillary sinuses, respectively. As the horse grows, the teeth migrate forward so that the rostral maxillary sinus makes contact with the last premolar and first molar, and the caudal maxillary sinus makes contact with the second (10) and third (11) molar. As the horse continues to age, the tooth roots regress, and by 20 years of age, a limited amount of the tooth root is embedded in the maxillary sinus cavity.[21] This constant

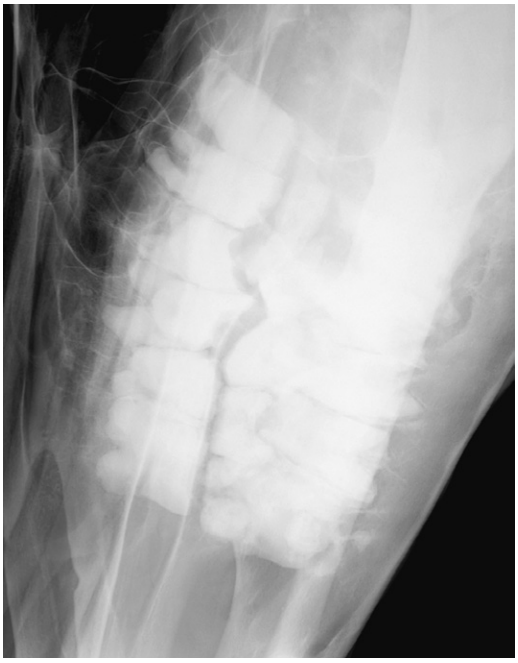


Fig. 10-12 LDRVO radiograph of the head of a 41-year-old pony. Note the irregular occlusive surface of the teeth, termed *wave mouth*. This is usually seen in older animals as a result of improper dental care.

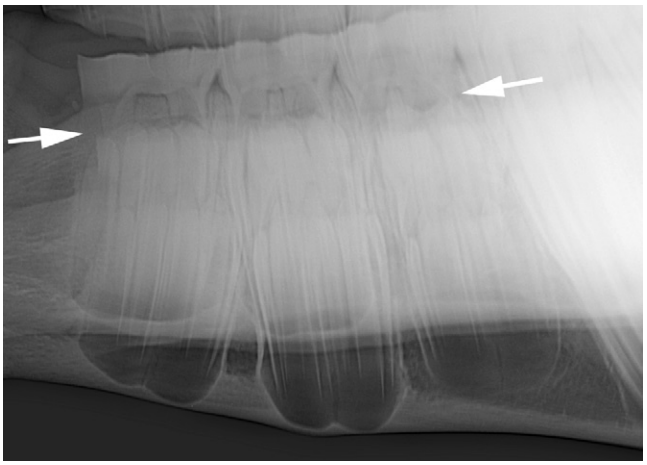


Fig. 10-13 Left 10-degree dorsal–right ventral radiograph of the rostral premolar area of a 2-year-old Oldenburg. The deciduous premolars have not yet been shed. The *arrows* indicate the plane between the deciduous and permanent premolars, and the deciduous premolars, the caps, are present dorsal to this plane. Note the expansile, radiolucent region around the roots of the permanent premolar teeth. This is a normal appearance. These regions are termed *eruption bumps* and may be palpable along the ventral aspect of the mandible. They will remodel as the caps are shed and the permanent premolars erupt. Eruption bumps are often misinterpreted as an abscess but are normal.

growth can cause abnormal wear to occur to some teeth compared with others. Without proper dental care, an undulating pattern to the teeth can occur, usually in older horses. These will cause a malocclusion, or wave mouth (Fig. 10-12) that results in dropping feed during mastication.

Another variation in normal dental anatomy is seen in horses aged approximately 2 to 4 years. At this time, the alveolus surrounding the mandibular tooth roots expands and distorts the ventral margin of the mandible. These eruption bumps are transient and occur because of remnants of the deciduous tooth that prevent normal eruption of the permanent teeth (Fig. 10-13). These deciduous remnants, referred to as *caps*, are usually shed, allowing the permanent tooth to



Fig. 10-14 Right lateral skull radiograph. The maxillary and mandibular wolf teeth are present *(black arrows)*.

erupt, which is followed by mandibular remodeling to the extent that the swellings are no longer detected.[21] Occasionally the tooth root continues to grow ventrally, and this distortion can lead to a tooth root infection.

A final note is that the first premolar (05) teeth are usually absent. However, in the rare instance in which they are present, these so-called wolf teeth can generally be detected only with radiography or palpation because they rarely erupt through the mucosa (Fig. 10-14).[25] The first premolar (05) teeth can be a cause for horses resisting a bit or tossing their heads under the saddle and may require extraction.

The most common diseases of the nasal cavity and paranasal sinuses are fractures, primary sinusitis, sinusitis from dental disease, dentigerous cysts, maxillary sinus cysts, ethmoid hematomas, and neoplasia.[4,25] These can usually be detected with conventional radiography; however, they are difficult to differentiate because of superimposition of structures and the similar opacity between soft tissue and fluid.

Fractures of the nasal cavity and sinuses are frequently the result of direct trauma that causes displacement of bone into the air-filled spaces.[4] These depression fractures can be difficult to assess radiographically because the radiographic projection needs to be tangential to the fracture to see the defect (Fig. 10-15).[4,5] Care must be taken to evaluate fracture fragments for sequestrum formation from a loss of blood supply and infection of the bone fragment.[4,25]

Sinusitis is characterized by the accumulation of fluid in one of the many nasal sinuses. Although sinusitis can occur from a respiratory tract disease, it is also almost equally associated with tooth root abscesses.[4,10,23,25-27] Tooth root abscesses cause sinusitis because the rostral and caudal maxillary sinuses surround certain caudal maxillary cheek teeth with only a narrow portion of bone separating the two structures. In the standing horse, fluid within the sinuses will be in the dependent portion of the involved sinus cavity and will form an air/fluid interface (Fig. 10-16). If the horse is recumbent, a gas/fluid interface will not be seen in the sinus because the x-ray beam will not strike the gas/fluid interface in a parallel orientation. Fluid is generally uniform in opacity and, if heterogeneous, inspissation of the purulent material or mineralization should be considered likely.[25] Care should also be used to determine if multiple fluid lines are present. The location of fluid lines within specific sinuses can help with the differential

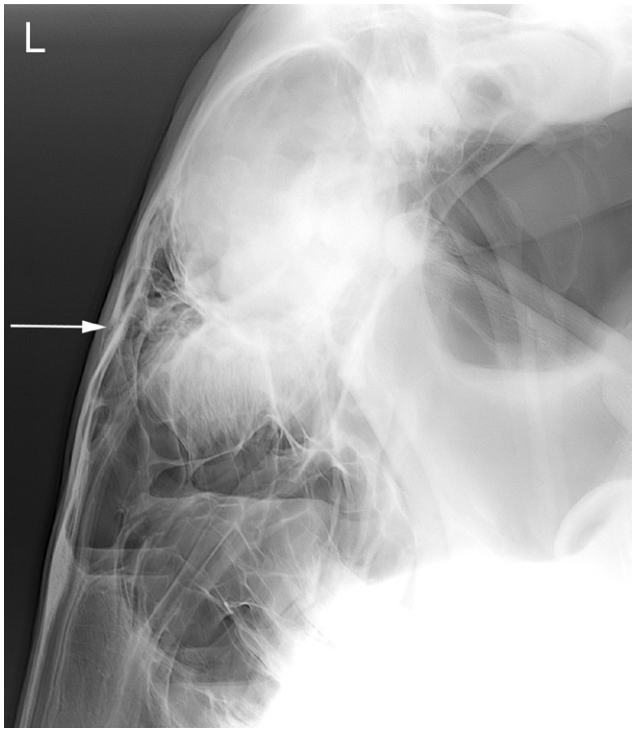


Fig. 10-15 Right-left radiograph of a depression fracture of the frontal bone (*white arrow*). Also note the fluid lines in the conchofrontal, caudal maxillary, and rostral maxillary sinuses because of hemorrhage.

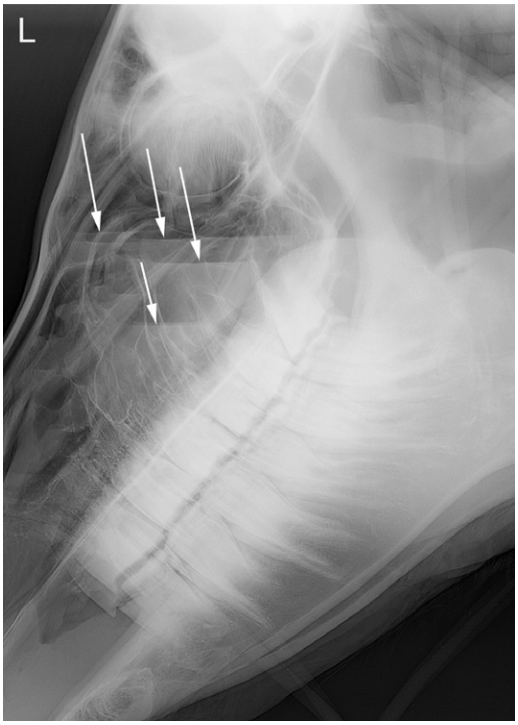


Fig. 10-16 Right-left standing radiograph of the head of a 20-year-old Arabian with sinusitis. There are fluid lines in the conchofrontal, caudal maxillary, and rostral maxillary sinuses *(white arrows)*.

diagnosis. In addition, removing fluid from the sinuses and then repeating radiographs may aid in identifying a tooth root abscesses, cyst, or tumor that was previously masked by the fluid.[4,25]

A dentigerous cyst, also called temporal teratoma or ear tooth, can vary in shape but generally has the appearance of

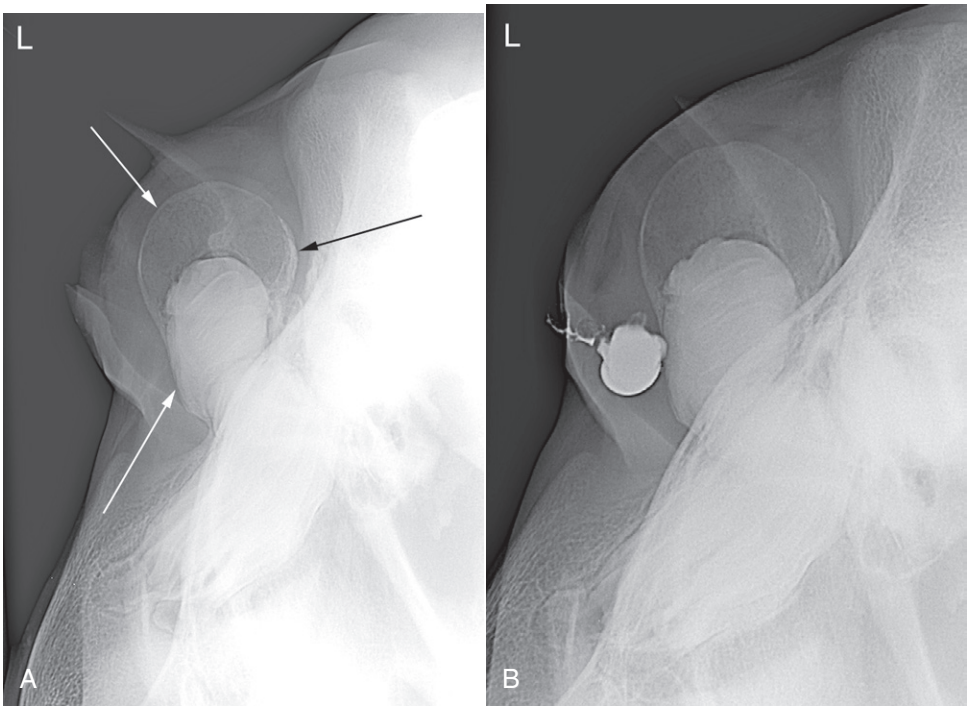


Fig. 10-17 Oblique radiographs of the left temporal region in a 3-year-old quarter horse with swelling and a draining tract caused by a dentigerous cyst. Note that the mineral opacity in the region of the temporal bone on the survey radiograph **(A)** has the appearance of a tooth *(white and black arrows)*. Contrast medium was placed into the draining tract and makes contact with this mineral opacity **(B).**

a tooth near the region of the external acoustic meatus. An associated draining tract usually is present.[4,25,28] The cyst is considered secondary to the failure of the first branchial cleft to close during development.[29] Radiographs tangential to the lesion are helpful to confirm the diagnosis (Fig. 10-17).[4]

Maxillary sinus cysts and progressive ethmoid hematomas appear similar on radiographs and may have a common origin.[27,30] They are both well-margined, round, soft tissue opacities that are within the equine sinuses. Maxillary sinus cysts generally occur rostral to the ethmoid turbinates and are superimposed on the rostral or caudal maxillary sinus. These cysts are usually found in young horses less than 1 year of age or horses older than 9 years (Fig. 10-18).[27]

Ethmoid hematomas usually involve horses older than 7 years, and Arabians and Thoroughbreds are overrepresented.[30,31] A progressive ethmoid hematoma is generally in contact with the ethmoid region; however, they have been reported in the frontal, maxillary, and sphenopalatine sinuses.[30,32,33] Progressive ethmoid hematomas are usually unilateral,[25,30,34] although they may grow large enough to cross the ethmoidal septum (Fig. 10-19).[30] A sinus cyst or an ethmoid hematoma may result in secondary fluid accumulation within the sinus because of physical obstruction of normal sinus drainage. In addition, sinus cysts and neoplasia are the sinonasal disorders that most frequently cause deformation of the skull.[26]

Although neoplasia occurs in the equine nasal passage, it is rare, being reported in 7.6% of 277 horses in one study.[26] Tumors are generally advanced at the time of diagnosis; however, metastasis of nasal tumors is uncommon.[30] The most common nasal tumor is squamous cell carcinoma, and whether it originates from the nasal or oral cavity is unclear.[30,34,35] Other tumors reported include adenocarcinoma,[36,37] fibrosarcoma, osteoma, lymphosarcoma, hemangiosarcoma, myxoma, osteosarcoma, ameloblastic odontoma, and dentigerous cysts, but generally these are single-patient reports.[30,34,38] The two tumors most distinct on radiographs are the osteoma[25,39] and dentigerous cyst.[25] Osteomas are mineral opacities that are smoothly margined and protrude from the bone surface.[30,39] Osteomas are believed to be hamartomas, which are malformations characterized by increased production of normal tissue that stops growing when the animal reaches adulthood.[30] Osteomas are generally monostotic and cause adjacent bones to undergo pressure necrosis.[30]

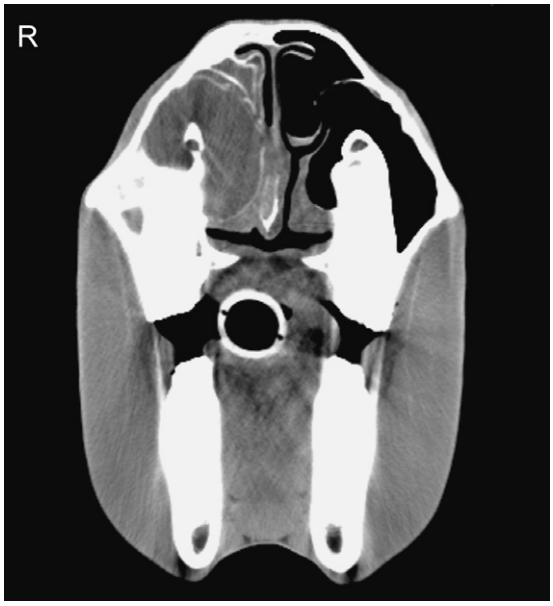


Fig. 10-18 Transverse CT image of the caudal aspect of the nasal cavity displayed in a soft tissue window. A region of soft tissue/fluid surrounds the infraorbital canal and creates a mass effect. There was no enhancement after contrast-medium administration, which supported the abnormality being a fluid-filled cyst.

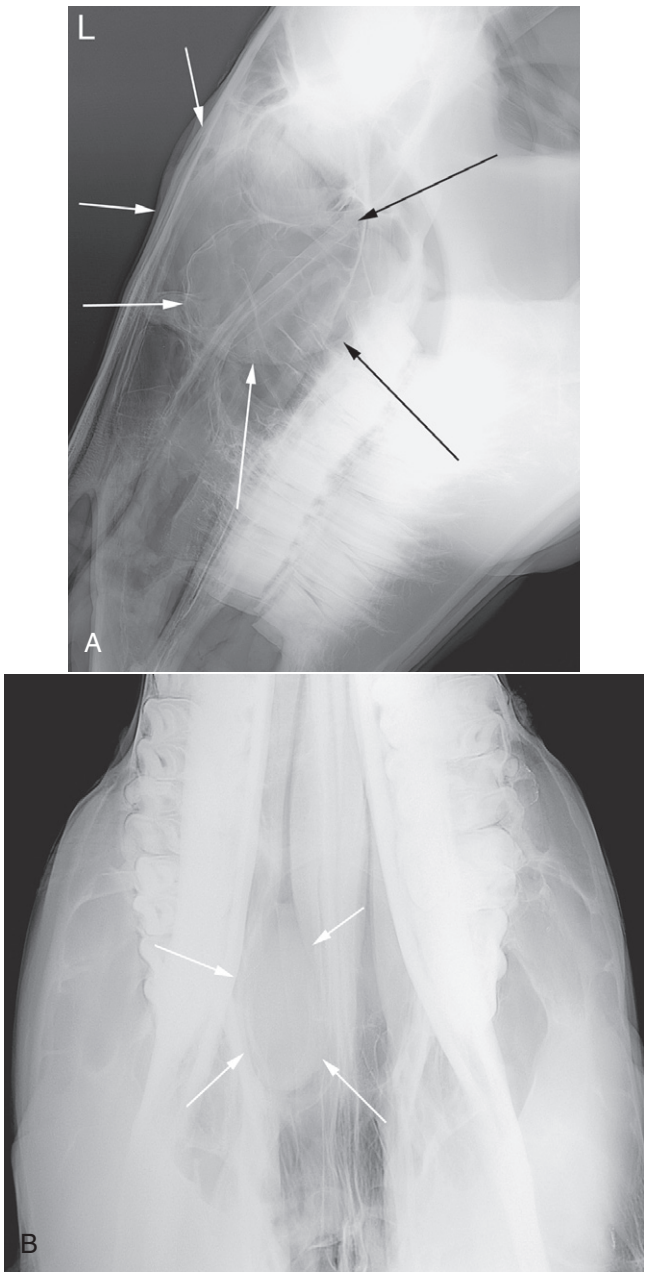


Fig. 10-19 **A,** Right-left radiograph of the head. A soft tissue opacity caused by an ethmoid hematoma *(white and black arrows)* is visible in the region of the ethmoid labyrinth. **B,** Dorsoventral radiograph. The lateralized mass *(white arrows)* is in a typical location of an ethmoid hematoma.

Although determining the difference between a neoplasm and a cyst may not be possible with CT, the location of the mass can be identified accurately, which may guide the most advantageous approach to remove the lesion (Fig. 10-20). MR imaging, or administration of contrast medium during CT evaluation, should help differentiate between a fluid-filled cyst and a neoplastic mass and generally provides more information than conventional radiography alone (Fig. 10-21).[40,41]

Skull and Hyoid Apparatus

Examination of the skull requires a dorsoventral view and right and left lateral radiographs. Further evaluation depends on what portion of the skull is being examined. If an orbital fracture is suspected, then oblique projections are highly recommended. Unlike the oblique radiographs for sinus

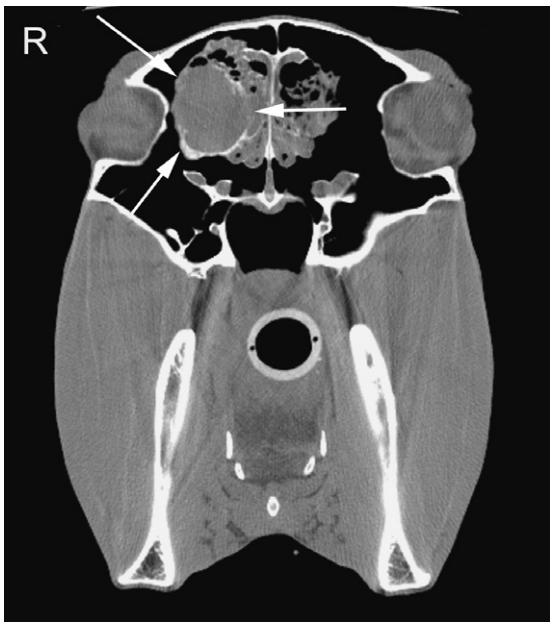


Fig. 10-20 Transverse CT image of the region of the ethmoid labyrinth displayed in a soft tissue window. Note the ethmoid hematoma *(white arrows)*, which has attenuation consistent with either soft tissue or fluid, extending into the right frontal sinus.

evaluation, the oblique radiographs for the orbit require a steeper angle. If a right orbital fracture is suspected, then a right 70-degree ventral-left dorsal oblique radiograph allows the rim of the frontal bone to be visible with minimal superimposition of other structures (Fig. 10-22).

Other fractures involving the skull include nasofrontal suture separation, occipitosphenoid suture separation, and fractures of the stylohyoid and petrous temporal bone caused by temporomandibular osteoarthropathy.[7,25] Nasofrontal suture separation is a periostitis and is usually not associated with trauma. Nasofrontal suture separation has been called *horns* because it generally causes firm bumps to appear where the frontal bone contacts the nasal bone. On lateral or oblique radiographs, nasofrontal suture separation appears as a periostitis with smoothly margined new bone formation causing a raised area. A suture line can usually be seen, and this should not be mistaken for a fracture line. Nasofrontal suture separation is usually not important clinically, although it often leaves permanent disfigurement (Fig. 10-23, see page 164).[25]

Occipitosphenoid suture separation generally occurs when a horse falls backward. When the nuchal crest hits the ground it acts as a pivot point, causing the head to hyperextend.[7] This extension stretches the rectus capitis ventralis minor and the longus capitis muscles and can cause a fracture of the basisphenoid bone or avulsion of the muscular attachment site.[7,42] Because the dorsal aspect of the guttural pouch is adjacent to these muscles, damage to the muscles can lead to hemorrhage within the guttural pouch or the retropharyngeal space (Fig. 10-24, see page 164).[7,42] Older horses are less prone to separation of the occipitosphenoid bones because the suture of the basisphenoid bone fuses between 2 and 5 years of age.[7,42,43]

Temporohyoid osteoarthropathy is characterized by fusion of the stylohyoid bone to the temporal bone at the level of the tympanic bulla. The hyoid apparatus consists of paired stylohyoid bones, paired ceratohyoid bones, a single basihyoid bone, a lingual process, and paired thyrohyoid bones. This apparatus serves to support the tongue, pharynx, and larynx.[44-46] Temporohyoid osteoarthropathy causes ankylosis of the temporohyoid joint, which puts abnormal force on the

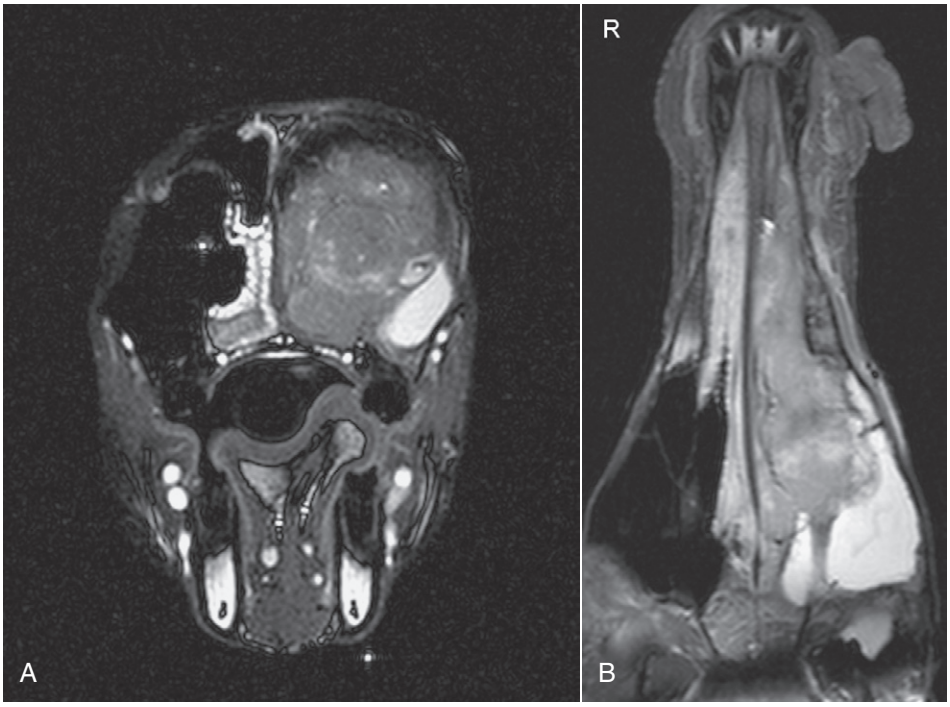


Fig. 10-21 T2-weighted MR images in transverse **(A)** and dorsal **(B)** planes. The regions of very high signal (white) signify collections of fluid adjacent to a lymphoid nasal neoplasm.

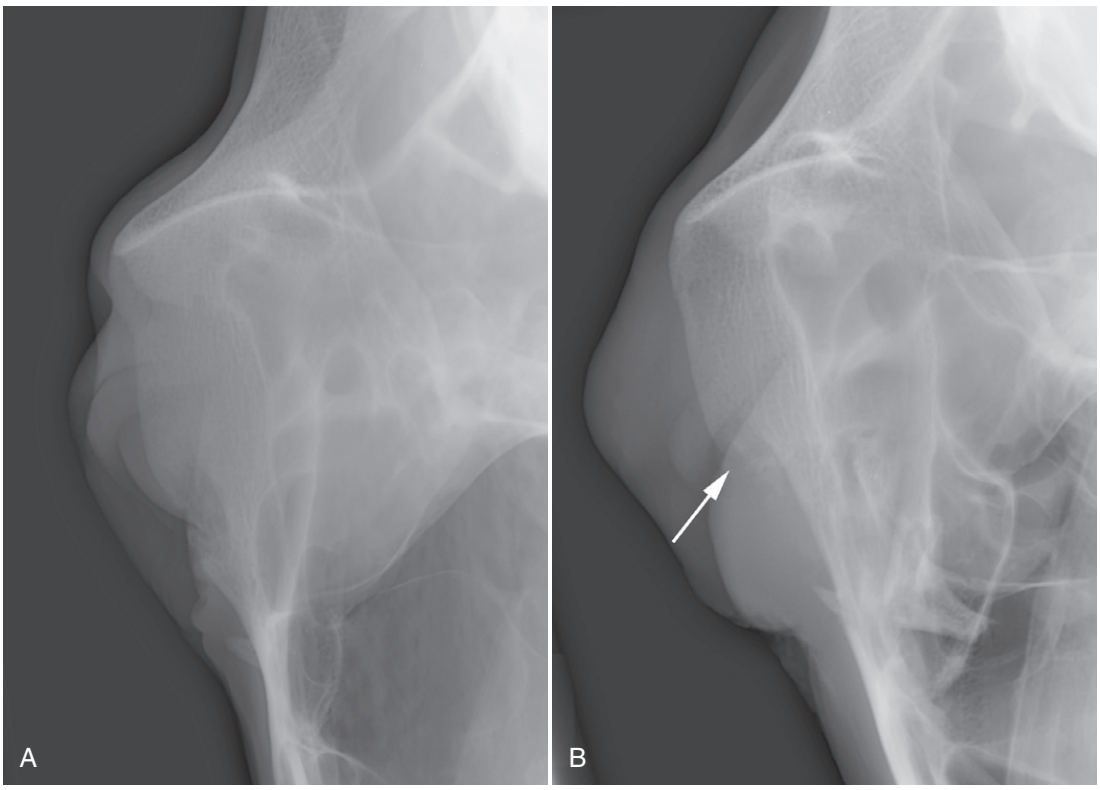


Fig. 10-22 Oblique radiographs of a normal left supraorbital process **(A)** and a right **(B)** supraorbital process that has sustained fractures *(white arrow)*. These images are from the same horse.

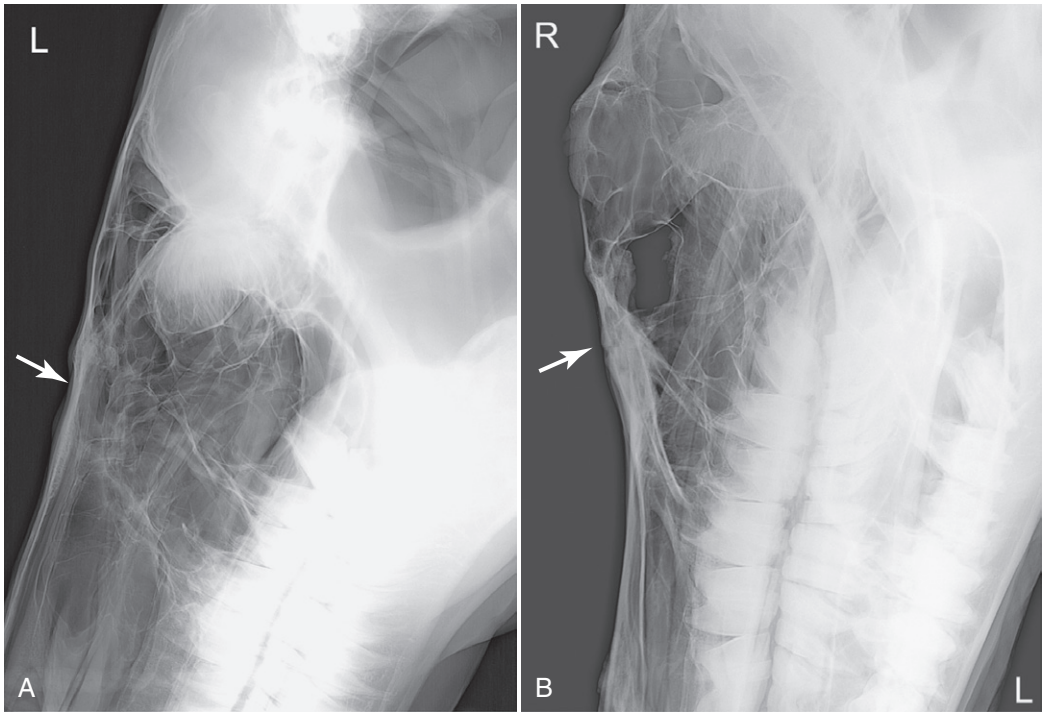


Fig. 10-23 These are right-left **(A)** and left rostrodorsal–right **(B)** caudoventral oblique radiographs of the head. Note the area of increased bone opacity at the rostral aspect of the frontal bone *(white arrows)*. This is an example of nasofrontal suture separation, also known as *horns*.

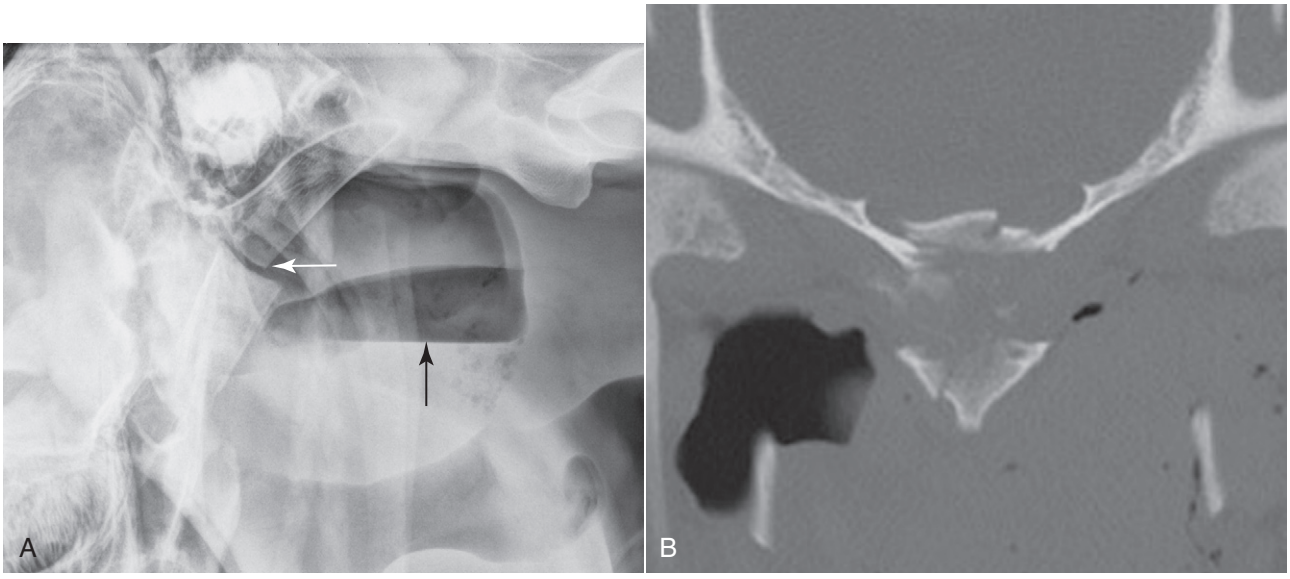


Fig. 10-24 Left-right radiograph of the head **(A)** in an 8-month-old Hanoverian that sustained a fall. The basioccipital bone *(white arrow)* is displaced dorsally in relation to the basisphenoid bone. The guttural pouch is filled partially with a soft tissue–fluid opacity that displaces and compresses the nasopharynx ventrally; a gas/fluid interface is present *(black arrow)*. This is caused by hemorrhage and hematoma formation, likely a result of avulsion of the longus capitis and/or rectus capitis ventralis muscles and fracture of the basisphenoid and basioccipital bones. Small gas bubbles are visible just caudal to the *black arrow*; this suggests an avulsion of the ventral aspect of the sphenoid sinus with release of air. **B** is a CT examination thorough the basisphenoid region in another horse with a basisphenoid-basioccipital fracture. Note the severely displaced and comminuted fracture of the basisphenoid bone.

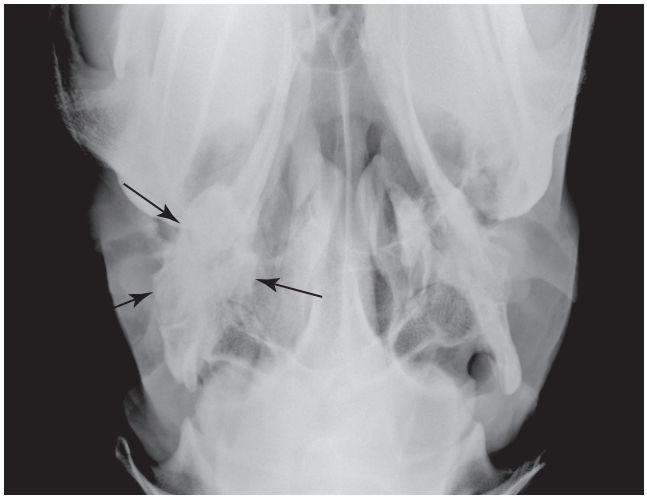


Fig. 10-25 Dorsoventral radiograph of the skull of a horse with temporohyoid osteopathy. The right stylohyoid bone is thickened compared with the left, and there is marked hyperostosis in the region of the petrous temporal bone *(black arrows)*.

petrous temporal bone as well as the stylohyoid bone when the horse swallows or moves the tongue.[44-47] Temporohyoid osteoarthropathy can cause clinical signs of vestibular disease and/or facial paresis as well as behavioral changes; however, it has also been diagnosed in clinically normal horses at postmortem examination.[44,45,47,48] Varying causes have been suggested, ranging from extension of otitis media, otitis externa or guttural pouch infection to a nonseptic osteoarthritis.[44,46-48] To diagnose temporohyoid osteoarthropathy, endoscopy,[46] radiography,[44,48] and CT examination[45] have been used. Although all these modalities are useful, fluid within the tympanic cavity can be detected only with CT.[45] Radiographically there is thickening of the affected stylohyoid bone and hyperostosis in the region of the petrous temporal bone (Fig. 10-25). In severe afflictions, fracture of the stylohyoid bone can occur, which can be detected with conventional radiography or CT examination (Fig. 10-26). With temporal fractures, the main clinical signs are related to damage to the facial (CN VII) and vestibulocochlear (CN VIII) cranial nerves.[49]

Brain

Cholesterol granulomas, pituitary tumors, hydrocephalus, brain tumors, and brain abscess have all been reported in horses. CT and/or MR imaging can be used to determine the diagnosis, extent of disease, and surgical treatment plan.

Brain tumors are uncommon, with the most recognized disorder centered on the accumulation of cholesterol crystals, which are breakdown products of red blood cells, within the ventricular system.[50] On CT, these lesions appear as high attenuating, roughly circular lesions within the lateral ventricles that create a mass effect (Fig. 10-27). Other tumors, such as nasal adenocarcinoma, may arise from the nasal cavity and extend into the brain, but this is rare. These soft tissue tumors generally arise from or involve the cribriform plate and then extend into the cranial vault.[36]

Brain abscesses are also rare but can be seen after severe head trauma and open fractures of the calvaria. Abscess lends itself well to evaluation with CT or MR imaging, but these modalities require general anesthesia, which is complicated in head trauma patients. On CT images, brain abscesses appear as low attenuating regions that create a mass effect and have ring enhancement after contrast-medium administration (Fig. 10-28). With MR imaging, the lesion will have low signal intensity on T1-weighted images but high signal

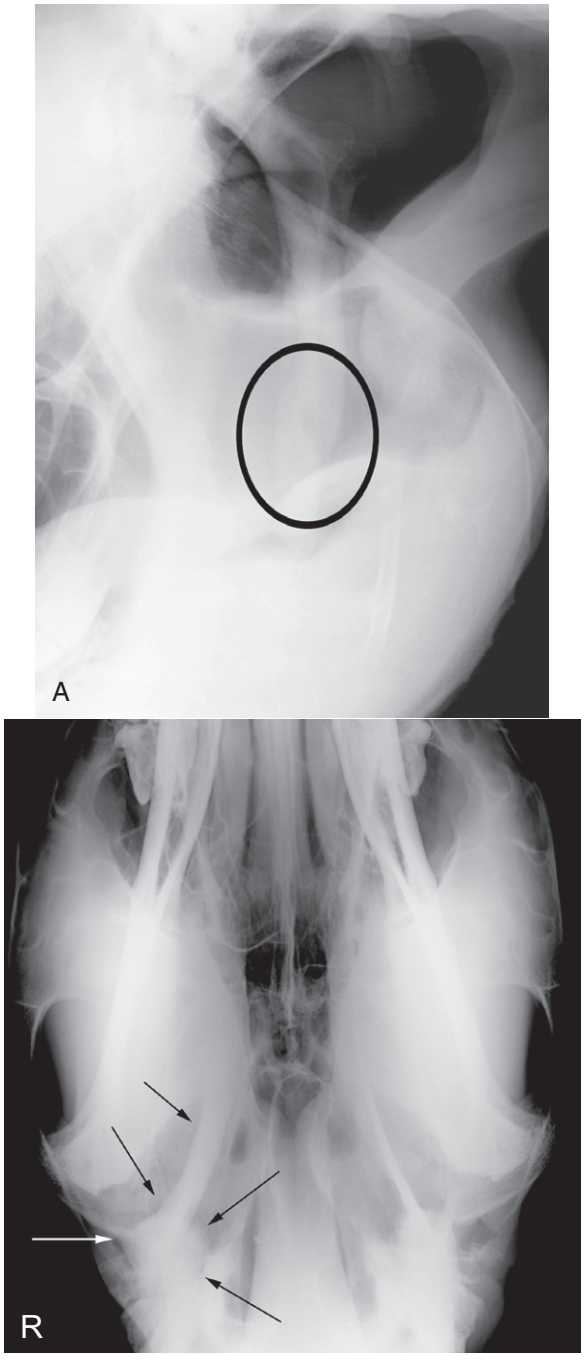


Fig. 10-26 Lateral **(A)** and dorsoventral **(B)** radiographs of the head of a horse with temporohyoid osteopathy. The right stylohyoid bone is fractured *(circle)* and thick *(white and black arrows)* compared with the left.

on T2-weighted images, including FLAIR. The contrast-medium enhancement pattern seen is similar to CT, with a low signal region surrounded by a ring of contrast-medium enhancement.

Pituitary gland macroadenomas have also been described in horses. These tumors can be seen using CT, primarily with contrast medium, and MR imaging. In horses, the normal pituitary gland is approximately 1.6 cm × 1.5 cm × 0.6 cm (length × width × height), whereas horses with hyperadrenocorticism have a pituitary gland that approximates 2 cm × 2.3 cm × 1.6 cm. This difference is statistically significant in width and height but not length (Fig. 10-29).[51]

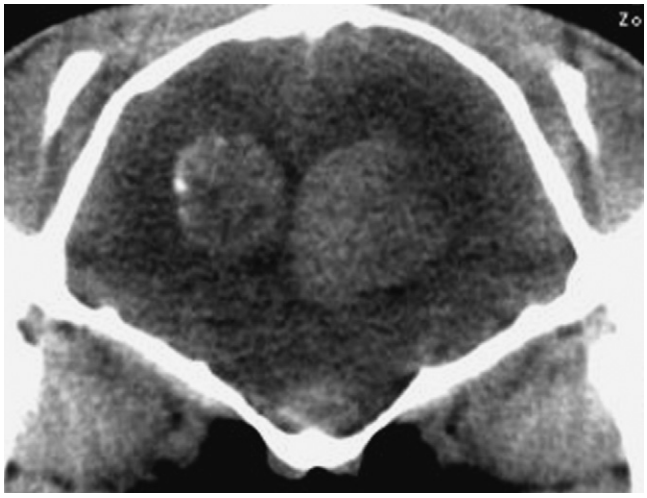


Fig. 10-27 Transverse CT image of the brain in a soft tissue window. Note the two large, circular, mineral-attenuating structures in the region of the lateral ventricles, which are cholesterol granulomas. (Courtesy of Cornell University, Ithaca, NY.)



Fig. 10-28 Transverse CT image of the brain after contrast-medium administration. A depression fracture of the right parietal bone *(white arrowhead)* and a ring-enhancing lesion within the brain *(white arrows)* are present. This ring-enhancing lesion is the vascular capsule of a brain abscess caused by penetrating trauma. (Courtesy of Dr. Nathan Dykes, Cornell University, Ithaca, NY.)

Using MR imaging, the enlarged pituitary gland of horses with hyperadrenocorticism has a central region that has low signal intensity on T1 and T2 images as well as a susceptibility artifact seen with gradient recall echo sequences (Fig. 10-30).

Guttural Pouch and Larynx

The large air-filled spaces of the larynx and guttural pouch make examination of these regions amenable to radiography. In fact, radiography should be considered a complement to endoscopic evaluation of the equine head.[52] Evaluation of the guttural pouches and larynx generally consists of a lateral radiograph. Dorsoventral projections can be accomplished with the patient standing, but obtaining an image sufficiently far caudally without motion artifact is difficult. For this reason, a ventrodorsal radiograph under general anesthesia is better to produce an image of the caudal aspect of the skull and the cranial cervical region of a horse.[52,53] Acquiring both right-left and left-right lateral radiographs has been suggested if the ventrodorsal view cannot be acquired.[18] Another method involves acquiring a right 30-degree caudal-left rostral oblique radiograph and a left 30-degree caudal-right rostral oblique radiograph to separate the guttural pouches.[18] Although this

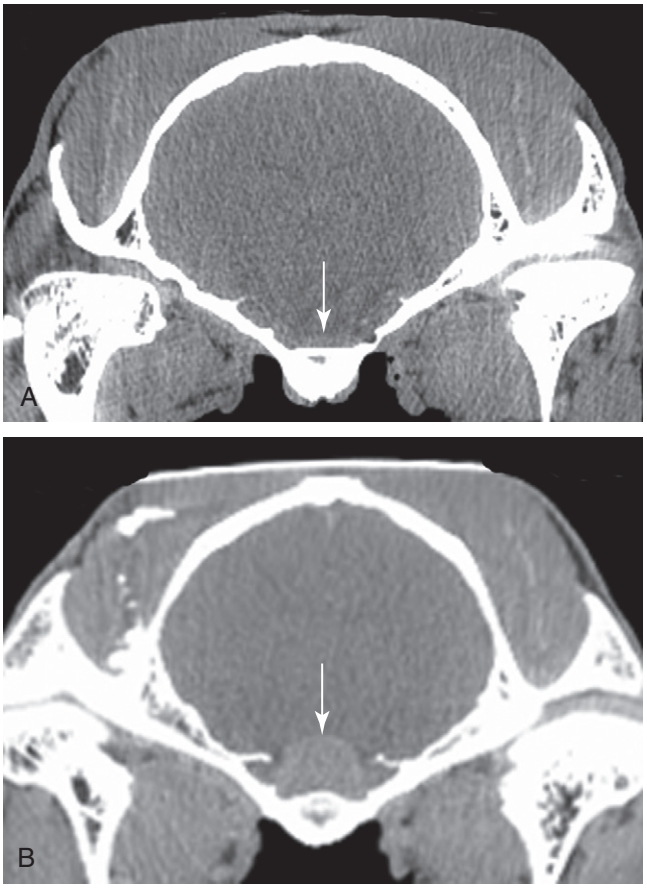


Fig. 10-29 Transverse postcontrast CT images of a normal pituitary gland *(white arrow)* **(A)** and a pituitary gland *(white arrow)* in a horse with hyperadrenocorticism **(B).**



Fig. 10-30 Sagittal T2-weighted image of the pituitary gland in a horse with hyperadrenocorticism. The pituitary gland is enlarged and hypointense *(white arrow)*. The low-signal area is likely secondary to increased dopamine, which is paramagnetic and causes a susceptibility artifact on gradient recalled echo sequences. No evidence of hemorrhage was found histopathologically.



Fig. 10-31 Left caudoventral–right rostrodorsal oblique radiograph of the temporomandibular and guttural pouch regions in a normal horse. Note that right and left guttural pouches can be seen individually, and the right temporomandibular joint is clearly visible. The left temporomandibular joint is superimposed on the petrous temporal bone. An artifact on the guttural pouches results from superimposition of a rope halter.



Fig. 10-32 Right-left radiograph of the laryngeal region of an 11-year-old Arabian with bilateral purulent nasal discharge caused by guttural pouch empyema and retropharyngeal lymph node enlargement. There is a large, heterogeneous soft tissue mass in the region of the guttural pouch and extending caudally into the retropharyngeal region that displaces the larynx and trachea ventrally.

would not result in an orthogonal projection of the larynx or guttural pouches, it would help separate the guttural pouches enough to establish whether unilateral or bilateral disease is present (Fig. 10-31).

The goal of radiography of the guttural pouch is generally to identify the presence of soft tissue opacity in the normally gas-filled structure (Fig. 10-32). The appearance of this opacity



Fig. 10-33 Left-right radiograph of the head. There is a solitary, smoothly margined soft tissue opacity in the guttural pouch. This focus inflammatory debris is a chondroid.

varies depending on the disease, such as multiple smoothly margined, irregularly shaped masses caused by chronic guttural pouch mycosis and chondroids (Fig. 10-33). In addition, fluid lines in the guttural pouch that indicate an air/fluid interface do not provide any information regarding the nature of the fluid (hemorrhage, empyema, or diverticulitis) but may be used to determine whether the disease is unilateral or bilateral.[52,53] Areas that surround the guttural pouch, such as the dorsal wall of the pharynx (the ventral border of the guttural pouch), may appear thick or irregular when pharyngeal lymphoid hyperplasia is present. In addition, in foals the guttural pouch can be diffusely gas filled, or tympanic, and extend beyond the level of the first cervical vertebrae (Fig. 10-34).[25,53]

Tumors or cervical masses in, or encroaching on, the guttural pouch are rare; however, structures displacing the guttural pouch include masses of the parotid salivary gland or retropharyngeal lymph nodes, or a primary tumor of the guttural pouch, usually squamous cell carcinoma.[52] Differentiating masses from fluid, and whether the mass is within or adjacent to the guttural pouch, is difficult and usually requires endoscopy or ultrasonography.[18] Because the parotid salivary gland can sometimes cause guttural pouch lesions, contrast medium can be placed into the salivary gland to produce a sialogram. However, sialography is performed rarely because of the risk of damaging the salivary gland with the hyperosmolar contrast medium.[52] Scintigraphy can also be used to assess salivary gland function. By administering technetium-99 m pertechnetate, which accumulates in salivary glands, documentation of the approximate size of the parotid salivary gland and the function and patency of the parotid salivary duct is possible. After adequate activity is detected in the salivary gland, the duct can be reimaged after offering a piece of food, such as a mint or a carrot, and obtaining a static acquisition of the head in both lateral and ventral planes (Fig. 10-35).

CT has not been reported as an aid to diagnosing guttural pouch disease in the horse, but it has been used to determine

the anatomy of the guttural pouch.[14,54] CT may help identify bone lesions, such as avulsion fractures, or petrous temporal bone fractures that may cause hemorrhage into the guttural pouches.[7] Blood has been reported to accumulate in the guttural pouch as a result of avulsion of the longus capitis muscle[42] and with fracture of the stylohyoid bone.

The primary diseases of the larynx identified by conventional radiography include dorsal displacement of the soft palate, aryepiglottic fold entrapment, subepiglottic cyst, and arytenoiditis. All these diseases can be identified readily on a lateral radiograph if the normal appearance of the equine epiglottis is understood (Fig. 10-36). Because horses are obligate nasal breathers, no gas should be identified in the oral cavity of a horse except if it is heavily sedated. The epiglottis should be located dorsal to the soft palate. If the epiglottis is ventral to the soft palate, then the soft palate is considered dorsally displaced and abnormal (Fig. 10-37). The epiglottis contains a thin piece of cartilage covered by a mucosal surface. This surface is thin and smooth and comes to a definitive point rostrally. If the rostral aspect of the epiglottis appears blunted, then the primary differential diagnosis is an aryepiglottic fold entrapment (Fig. 10-38). A subepiglottic cyst is suspected when the epiglottis is dorsally displaced by a well-margined soft tissue/fluid opacity centered just rostroventral from the larynx (Fig. 10-39). All these lesions can be confirmed by endoscopy; however, care should be taken when evaluating for dorsal displacement of the soft palate because this is a transient condition that can correct itself spontaneously.

Arytenoiditis is more difficult to identify radiographically because it generally causes a subtle irregularity in the margin of the arytenoid cartilage. Ultrasound can be used to identify arytenoiditis in the horse (Fig. 10-40); however, laryngoscopy remains the gold standard.[16]



Fig. 10-34 Right-left radiograph of the cranial cervical region in a 2-month-old quarter horse with guttural pouch tympany. Note the elongated appearance of the guttural pouch. Also observe how the guttural pouch extends beyond its normal anatomic limit of the caudal margin of the first cervical vertebra.

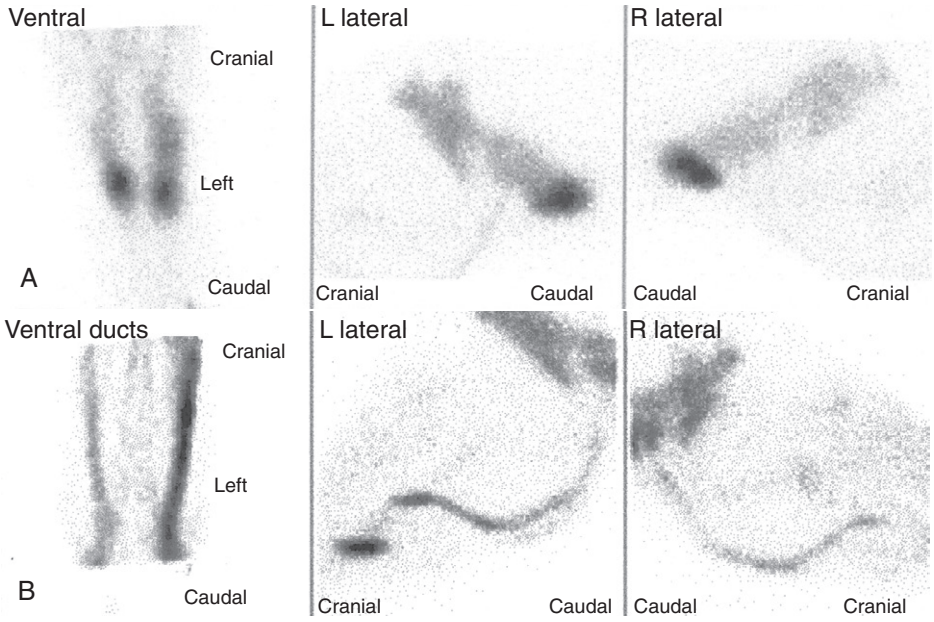


Fig. 10-35 **A,** Scintigraphic images acquired 20 minutes after 50 mCi of technetium-99 m pertechnetate was administered intravenously. The parotid salivary glands are shown, with the right having slightly less activity then the left. **B,** The same horse after being fed a peppermint. Activity is detected within the left parotid salivary duct to a greater degree than the right parotid salivary duct. (Images courtesy of Dr. Nathan Dykes, Cornell University, Ithaca, NY.)



Fig. 10-36 Right-left radiograph of the laryngeal region in a normal horse. Note the sharp, thin appearance of the epiglottis and its position dorsal to the soft palate.



Fig. 10-37 Left-right radiograph of the laryngeal region. The epiglottis is ventral to the soft palate *(black arrows)*, indicating a dorsally displaced soft palate.

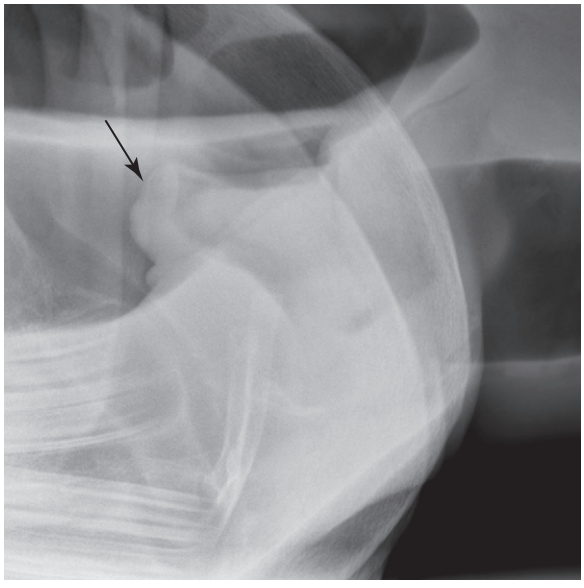


Fig. 10-38 Left-right radiograph of the laryngeal region of a horse. Note the blunt appearance of the epiglottis *(black arrow)* and the conspicuous aryepiglottic fold. This is an example of aryepiglottic entrapment.

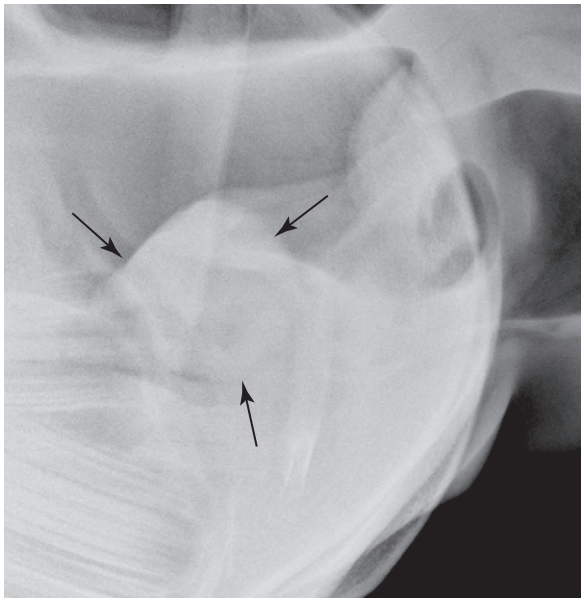


Fig. 10-39 Left-right radiograph of the laryngeal region. There is a large subepiglottic mass *(black arrows)* displacing the epiglottis dorsally that was determined to be a cyst.

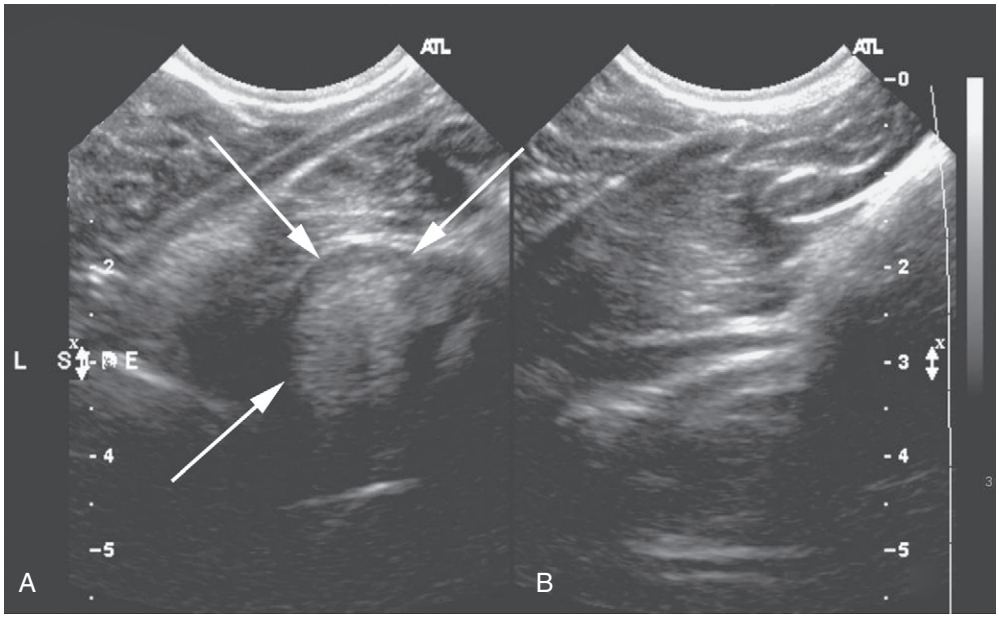


Fig. 10-40 Ultrasound images acquired from the left **(A)** and right **(B)** lateral windows of the laryngeal region of a 4-year-old female Thoroughbred. An endoscopic diagnosis of left arytenoid chondritis was made characterized by incomplete abduction of the left arytenoid cartilage and enlargement of the arytenoid body and corniculate process. The ultrasound image **(A)** depicts that the left arytenoid cartilage is thick and has a smoothly margined 1.7 cm bulge *(white arrows)* on the lateral surface. The right arytenoid cartilage **(B)** is normal and shown for comparison. (Images courtesy of Dr. Heather Chalmers, Cornell University, Ithaca, NY.)

REFERENCES

1. Henninger W, Frame EM, Willmann M, et al: CT features of alveolitis and sinusitis in horses, *Vet Radiol Ultrasound* 44:269, 2003.
2. Tietje S, Becker M, Bockenhoff G: Computed tomographic evaluation of head diseases in the horse: 15 cases, *Equine Vet J* 28:98, 1996.
3. Cook W: Skeletal radiology of the equine head, *J Am Vet Radiol Soc* 11:35, 1970.
4. Park RD: Radiographic examination of the equine head, *Vet Clin North Am Equine Pract* 9:49, 1993.
5. Wyn-Jones G: Interpreting radiographs 6: the head, *Equine Vet J* 17:274, 1985.
6. Wyn-Jones G: Interpreting radiographs 6: radiology of the equine head (part 2), *Equine Vet J* 17:417, 1985.
7. MacKay RJ: Brain injury after head trauma: pathophysiology, diagnosis, and treatment, *Vet Clin North Am Equine Pract* 20:199, 2004.
8. Barakzai S, Tremaine H, Dixon P: Use of scintigraphy for diagnosis of equine paranasal sinus disorders, *Vet Surg* 35:94, 2006.
9. Weller R, Livesey L, Maierl J, et al: Comparison of radiography and scintigraphy in the diagnosis of dental disorders in the horse, *Equine Vet J* 33:49, 2001.
10. Gibbs C, Lane JG: Radiographic examination of the facial, nasal and paranasal sinus regions of the horse. II. Radiological findings, *Equine Vet J* 19:474, 1987.
11. Tremaine WH, Dixon PM: A long-term study of 277 cases of equine sinonasal disease. Part 1: details of horses, historical, clinical and ancillary diagnostic findings, *Equine Vet J* 33:274, 2001.
12. Arencibia A, Vazquez JM, Jaber R, et al: Magnetic resonance imaging and cross sectional anatomy of the normal equine sinuses and nasal passages, *Vet Radiol Ultrasound* 41:313, 2000.
13. Barbee DD, Allen JR, Gavin PR: Computed tomography in horses. Technique, *Vet Radiol Ultrasound* 28:144, 1987.
14. Morrow KL, Park RD, Spurgeon TL, et al: Computed tomographic imaging of the equine head, *Vet Radiol Ultrasound* 41:491, 2000.
15. MacDonald MH: Clinical examination of the equine head, *Vet Clin North Am Equine Pract* 9:25, 1993.
16. Chalmers H, Cheetham J, Yeager A, et al: *Ultrasonography of the equine laryngeal region: technique, normal appearance, and clinical applications*, American College of Veterinary Radiology Annual Scientific Conference Proceedings, Chicago, IL, 2005, p 36.
17. Barber SM, Clark EG, Fretz PB: Fibroblastic tumor of the premaxilla in two horses, *J Am Vet Med Assoc* 182:700, 1983.
18. Perkins G, Pease A, Fubini S: Part I: diagnosis and medical management of guttural pouch disease, *Compend Contin Educ* 25:966, 2003.
19. Weller R, Taylor S, Maierl J, et al: Ultrasonographic anatomy of the equine temporomandibular joint, *Equine Vet J* 31:529, 1999.
20. Weller R, Cauvin ER, Bowen IM, et al: Comparison of radiography, scintigraphy and ultrasonography in the diagnosis of a case of temporomandibular joint arthropathy in a horse, *Vet Rec* 144:377, 1999.
21. Dyce K, Sack W, Wensing C: The head and ventral neck of the horse. In Dyce K, Sack W, Wensing C, editors: *Veterinary anatomy*, Philadelphia, 2002, Saunders, p 488.
22. Schummer A, Nickel R, Sack W: Respiratory organs of the horse. In Schummer A, Nickel R, Sack W, editors: *The viscera of the domestic mammals*, ed 2, Berlin, 1979, Verlag Paul Parey, p 274.
23. Lane JG, Gibbs C, Meynink SE, et al: Radiographic examination of the facial, nasal and paranasal sinus regions of the horse: I. Indications and procedures in 235 cases, *Equine Vet J* 19:466, 1987.
24. Barakzai S, Dixon P: A study of open-mouthed oblique radiographic projections for evaluating lesions of the erupted (clinical) crown, *Equine Vet Educ* AE:183, 2003.

25. Butler JA, Colles CM, Dyson SJ, et al: The head. In Butler JA, Colles CM, Dyson SJ, et al, editors: *Clinical radiology of the horse*, ed 2, London, 2000, Blackwell Science, pp 327–401.
26. Allen JR, Barbee DD, Boulton CR, et al: Brain abscess in a horse: diagnosis by computed tomography and successful surgical treatment, *Equine Vet J* 19:552, 1987.
27. Lane JG, Longstaffe JA, Gibbs C: Equine paranasal sinus cysts: a report of 15 cases, *Equine Vet J* 19:537, 1987.
28. Provost P: Skin conditions amenable to surgery. In Auer J, Stick J, editors: *Equine surgery*, Philadelphia, 1999, Saunders, pp 174–175.
29. DeBowes RM, Gaughan EM: Congenital dental disease of horses, *Vet Clin North Am Equine Pract* 14:273, 1998.
30. Head KW, Dixon PM: Equine nasal and paranasal sinus tumours. Part 1: review of the literature and tumour classification, *Vet J* 157:261, 1999.
31. Specht TE, Colahan PT, Nixon AJ, et al: Ethmoidal hematoma in nine horses, *J Am Vet Med Assoc* 197:613, 1990.
32. Freeman DE, Orsini PG, Ross MW, et al: A large frontonasal bone flap for sinus surgery in the horse, *Vet Surg* 19:122, 1990.
33. Sullivan M, Burrell MH, McCandlish IA: Progressive haematoma of the maxillary sinus in a horse, *Vet Rec* 114:191, 1984.
34. Nickels F: Nasal passages. In Auer J, Stick J, editors: *Equine surgery*, ed 2, Philadelphia, 1999, Saunders, pp 334–335.
35. Walker MA, Schumacher J, Schmitz DG, et al: Cobalt 60 radiotherapy for treatment of squamous cell carcinoma of the nasal cavity and paranasal sinuses in three horses, *J Am Vet Med Assoc* 212:848, 1998.
36. Davis JL, Gilger BC, Spaulding K, et al: Nasal adenocarcinoma with diffuse metastases involving the orbit, cerebrum, and multiple cranial nerves in a horse, *J Am Vet Med Assoc* 221:1460, 2002.
37. Hepburn RJ, Furr MO: Sinonasal adenocarcinoma causing central nervous system disease in a horse, *J Vet Intern Med* 18:125, 2004.
38. Dixon PM, Head KW: Equine nasal and paranasal sinus tumours. Part 2: a contribution of 28 case reports, *Vet J* 157:279, 1999.
39. Schumacher J, Smith BL, Morgan SJ: Osteoma of paranasal sinuses of a horse, *J Am Vet Med Assoc* 192:1449, 1988.
40. Saunders JH, Van Bree H: Comparison of radiography and computed tomography for the diagnosis of canine aspergillosis, *Vet Radiol Ultrasound* 44:414, 2003.
41. Tucker R, Farrell E: Computed tomography and magnetic resonance imaging of the equine head, *Vet Clin North Am Equine Pract* 17:131, 2001.
42. Sweeney CR, Freeman DE, Sweeney RW et al: Hemorrhage into the guttural pouch (auditory tube diverticulum) associated with rupture of the longus capitis muscle in three horses, *J Am Vet Med Assoc* 202:1129, 1993.
43. Ramirez O 3rd, Jorgensen JS, Thrall DE: Imaging basilar skull fractures in the horse: a review, *Vet Radiol Ultrasound* 39:391, 1998.
44. Blythe LL, Watrous BJ: Temporohyoid osteoarthropathy. In Robinson NE, editor: *Current therapy in equine medicine IV*, Philadelphia, 1997, Saunders, pp 323–325.
45. Pease AP, van Biervliet J, Dykes NL, et al: Complication of partial stylohyoidectomy for treatment of temporohyoid osteoarthropathy and an alternative surgical technique in three cases, *Equine Vet J* 36:546–550, 2004.
46. Walker AM, Sellon DC, Cornelisse CJ, et al: Temporohyoid osteoarthropathy in 33 horses (1993–2000), *J Vet Intern Med* 16:697, 2002.
47. Blythe LL, Watrous BJ, Shires GMH, et al: Prophylactic partial stylohyoidostectomy for horses with osteoarthropathy of the temporohyoid joint, *J Equine Vet Sci* 14:32, 1994.
48. Power HT, Watrous BJ, deLahunta A: Facial and vestibulocochlear nerve disease in six horses, *J Am Vet Med Assoc* 183:1076, 1983.
49. Pownder S, Scrivani PV, Bezuidenhout A, et al: Computed tomography of temporal bone fractures and temporal region anatomy in horses, *J Vet Intern Med* 24:398, 2010.
50. Jackson CA, deLahunta A, Dykes NL, et al: Neurological manifestation of cholesterinic granulomas in three horses, *Vet Rec* 135:228, 1994.
51. Pease AP, Schott HC, Howey EB, et al: Computed tomographic findings in the pituitary gland and brain of horses with pituitary pars intermedia dysfunction, *JVIM* 25: 1144–1151, 2011.
52. Cook WR: The auditory tube diverticulum (guttural pouch) in the horse: its radiographic examination, *J Am Radiol Soc* 14:41, 1973.
53. Butler JA, Colles CM, Dyson SJ, et al: Pharynx, larynx and eustachian tube diverticulum. In Butler JA, Colles CM, Dyson SJ, et al, editors: *Clinical radiology of the horse*, ed 2, London, 2000, Blackwell Science, pp 384–393.
54. Sasaki M, Hayashi Y, Koie H, et al: CT examination of the guttural pouch (auditory tube diverticulum) in Przewalski's horse (*Equus przewalskii*), *J Vet Med Sci* 61:1019, 1999.

ELECTRONIC RESOURCES

evolve

Additional information related to the content in Chapter 10 can be found on the companion website at http://evolve.elsevier.com/Thrall/vetrad/

- Chapter Quiz

CHAPTER • 11

The Canine and Feline Vertebrae

William R. Widmer
Donald E. Thrall

Spinal pain and spinal neuropathy are common problems in small animal practice. This leads to the vertebral column being one of the more frequently imaged anatomic regions. Computed tomography (CT) and magnetic resonance (MR) imaging are the modalities of choice for full characterization of abnormalities of the vertebrae and spinal cord in small animals. Many conditions including intervertebral disc disease; various myelopathies; and tumors of the spinal cord, meninges, and vertebral column cannot be characterized completely using radiography. However, judicious use of conventional radiography can provide valuable, cost-effective information regarding numerous diseases of the vertebral column, and survey radiographs should always be made before advanced imaging. Survey radiographs may or may not lead to identification of the cause of the pain or neuropathy, but, especially in older patients, they are rarely normal. Therefore, it is important to have not only an appreciation for the types of spinal abnormalities that can be diagnosed radiographically but also the significance of commonly encountered changes that may not be related directly to the clinical problem. Therefore, the concept that radiography is no longer useful for vertebral imaging is inaccurate. The focus of this chapter is on vertebral diseases that can be imaged effectively with conventional radiography and the significance of commonly encountered incidental findings. Radiographic abnormalities will be supplemented with CT and/or MR images where appropriate. Advanced imaging related specifically to the spinal cord is covered in Chapter 12.

Radiographic technique plays a vital role in radiography of the vertebral column.[1] Suboptimal information is obtained frequently when positioning is inaccurate, multiple centered images are not made, and images do not have adequate spatial resolution. Chemical restraint is necessary for accurate positioning and should be employed unless prohibited by the patient's condition. Technical information relating to spinal radiography is discussed in detail in Chapter 7.

ANATOMIC CONSIDERATIONS

A vertebra consists of the body, also referred to as a *centrum*, and the vertebral arch (Fig. 11-1).[1,2] The vertebral arch is composed of paired right and left pedicles and laminae and the unpaired spinous process. The vertebral arch bounds the vertebral canal, which houses the spinal cord. The articular processes of the lamina form the synovial joints along the dorsum of the vertebral column (Fig. 11-2). The articular process joints are diarthrodial (synovial) joints, being composed of articular processes covered with articular cartilage, a synovial membrane, and synovial fluid. They provide dorsal mechanical stabilization of the vertebral column.

Other than the first cervical vertebra, each vertebral body is narrowed centrally and has cranial and caudal endplates that unite with an interposed intervertebral disc. The anatomic structure of C1 (atlas) and C2 (axis) is complex and differs widely from the remainder of the vertebra (Fig. 11-3).[1-5] C1 has a well-developed vertebral arch, but the body is rudimentary with no distinct vertebral body endplates or spinous process, and the cranial and caudal articular processes are convex. C1 articulates cranially with the occipital condyles, forming the atlantooccipital joint, and caudally with C2, forming the atlantoaxial joint. The wings of C1 are extensive transverse processes that project laterally and serve as attachments for numerous cervical muscles. The lateral and transverse foramina contain the paired vertebral arteries. C2 has an elongated vertebral body and a massive spinous process. The dens is a projection extending cranially from the vertebral body of C2 into the cranioventral aspect of the vertebral canal. The dens originates from the intercentrum of C1, but during development it attaches to C2 and lies within the vertebral foramen of C1. C2 has a small transverse process, two cranial articular processes that articulate with the fovea of the atlas and a caudal endplate.

The sacrum is also much different morphologically than a prototypical vertebra. It is broad in the transverse plane, consists of three fused vertebrae and articulates cranially with the seventh lumbar vertebra, caudally with the first caudal vertebra, and laterally with the ilium, forming the sacroiliac joint.[1,2] The spinous processes of the sacrum are fused, making up the median sacral crest, and the sacral wing has a large facet for the sacroiliac articulation. Multiple foramina are present dorsally and along the pelvic surface, allowing for passage of spinal nerves and blood vessels. There are 6 to 23 caudal vertebrae in the dog.[6] Cranially, the caudal vertebrae are similar to the lumbar elements; caudal to Cd6, they become elongated and lack a vertebral arch. Y-Shaped hemal arches are present ventrally on Cd4-Cd6 and protect the median coccygeal artery, which lies ventral to the vertebral centra.

Important soft tissue structures of the vertebral column include various ligaments, intervertebral discs, and the retinaculum of the articular process joints.[7] Maintaining stability of the atlantoaxial joint is particularly important given the potential for the dens to damage the spinal cord if displaced dorsally. This stabilization is provided by the short, dorsal

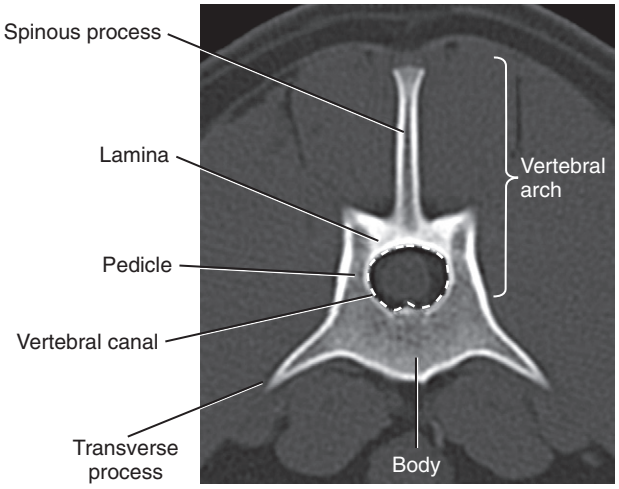


Fig. 11-1 Transverse CT image of a lumbar vertebra. The core components common to all vertebrae are identified. (Reprinted from Thrall DE, Robertson ID: *Textbook of normal radiographic anatomy and normal anatomic variants in the dog and cat*, St. Louis, 2011, Saunders.)

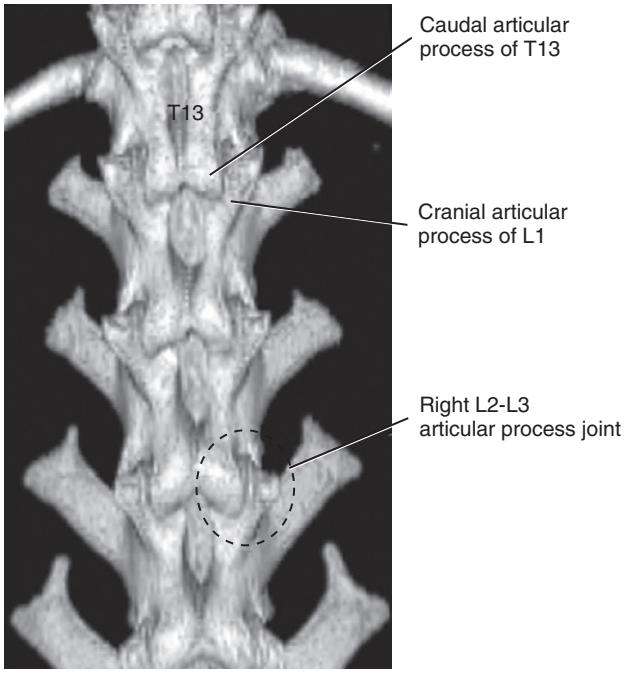
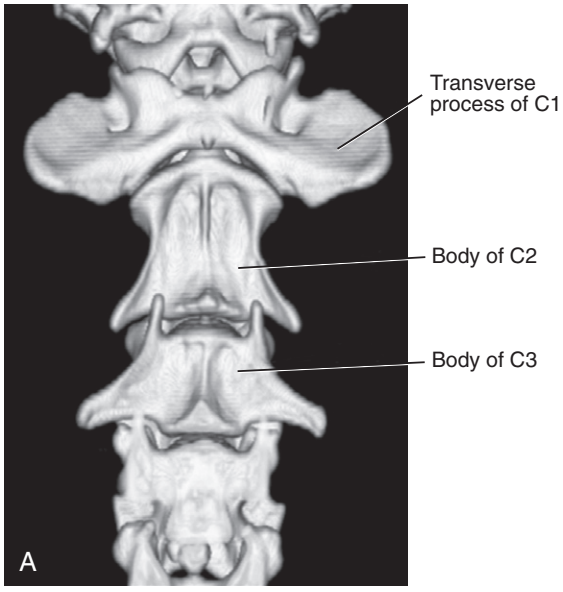
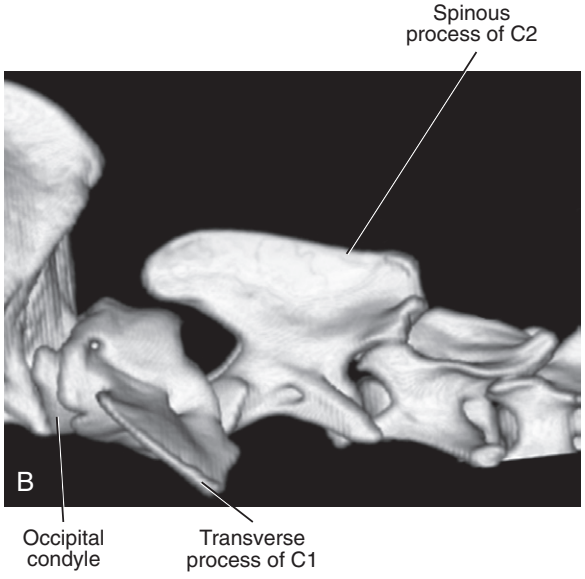


Fig. 11-2 Dorsal view of a three-dimensional rendering of the cranial aspect of the lumbar spine of a dog. The morphology of the articular processes and how they form the dorsal articular process joint can be seen in this rendering. *T13*, Thirteenth vertebral body.





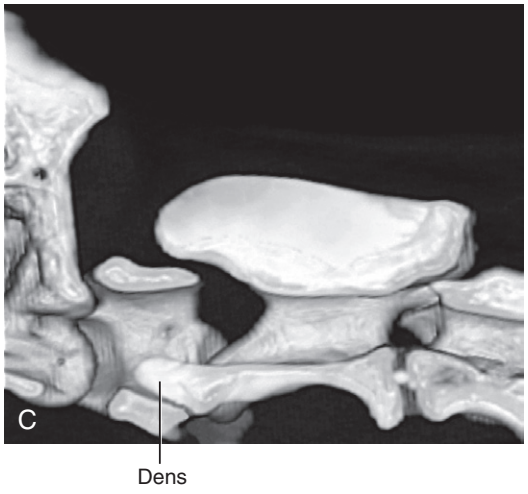


Fig. 11-3 **A,** Ventral view of a three-dimensional rendering of the cranial aspect of the cervical spine of a dog. Note the large transverse processes, called the wings, of C1. **B,** Lateral view of a three-dimensional rendering of the cranial aspect of the cervical spine of a dog. The distinctive shape of C1 and C2 versus other cervical vertebrae is obvious. Note the articulation of C1 with the occipital condyles and the large spinous process of C2. **C,** Midsagittal plane through a three-dimensional rendering of the cranial aspect of the cervical spine of a dog. Note the extension of the dens into the ventral aspect of the vertebral canal of C1. Note also the relationship of the cranial aspect of C1 with the occipital condyle.

atlantoaxial ligament, the apical ligament of the dens with its alar branches, and the transverse ligament of the atlas (Fig. 11-4).

In the dog, the nuchal ligament extends from the spinous process of the axis to the spinous processes of the first three thoracic vertebrae and is continued caudally as the supraspinous ligament. It prevents abnormal separation of the spinous processes during flexion. Short interspinous ligaments join each spinous process, adding additional support to the column. There are also short interarcuate ligaments that bridge each vertebral arch, which contain yellow elastic fibers. Collectively these short ligaments have been referred to as the *ligamentum flavum*. There is no nuchal ligament in the cat.

The dorsal longitudinal ligament lies on the floor of the vertebral canal and extends from the dens to the sacrum (Fig. 11-5). The intercapital ligaments are short, transverse fibrous bands that lie ventral to the dorsal longitudinal ligament, joining contralateral rib heads between T2 and T11. These ligaments buttress the dorsal part of the annulus cranial to T11 and lead to a reduced incidence of disc herniation between T1 and T11.[7,8]

The ventral longitudinal ligament is smaller than the dorsal longitudinal ligament and spans the ventral surface of the vertebral column (see Fig. 11-5). The annulus fibrosus of each intervertebral disc has oblique fibers that course from one endplate to the next, serving as ligaments. A detailed description of the intervertebral disc can be found in the online fifth edition version of this chapter (http://evolve.elsevier.com/Thrall/vetrad). A summary of the most important anatomic considerations of the vertebrae relative to radiographic interpretation is provided in Box 11-1.[9-10]

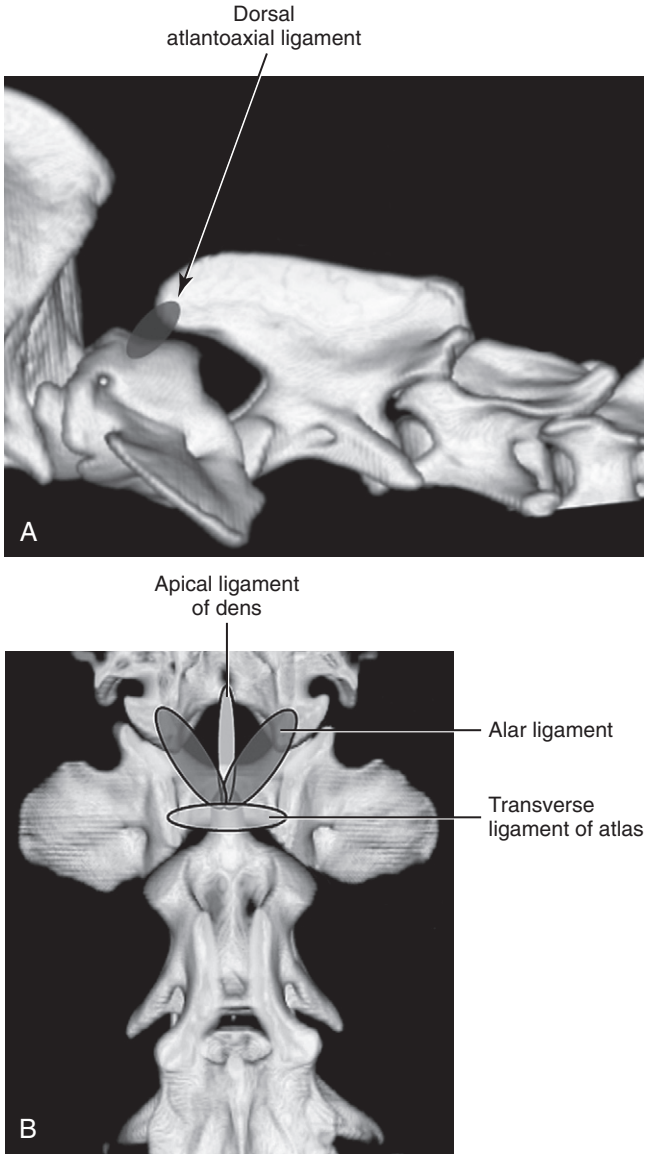


Fig. 11-4 **A,** Lateral view of a three-dimensional rendering of the cranial aspect of the cervical spine in a dog. Note the position of the dorsal atlantoaxial ligament. **B,** Dorsal view of a three-dimensional rendering of the cranial aspect of the cervical spine in a dog. The dorsal lamina of C1 and C2 have been removed to allow visualization of the ligaments on the floor of the vertebral canal. Note how the apical ligament of the dens along with its alar branches and the transverse ligament of the atlas provide stabilization of the atlantoaxial joint.

Box • 11-1

Summary of Important Anatomic Features of the Vertebral Column in Small Animals[9,10]

- Vertebral formulae
  - Dog C7 T13 L7 S3 Cd6-Cd23
  - Cat C7 T13 L7 S3 Cd18-Cd21
- Compared to the dog, the feline vertebral bodies (centra) are longer, the intervertebral disc spaces are narrower, and the transverse processes of the lumbar elements are longer.
- The articular processes of adjacent vertebrae overlap, with the cranial articular process lying ventral to the caudal articular process of an adjacent vertebra.
  - In the cervical region, the articular processes are oriented in an oblique plane, summating the intervertebral foramina and vertebral canal.
  - In the lumbar region, the articular processes lie in a dorsal plane and do not summate the foramina and canal.
- C1-C2 does not have an intervertebral disc.
- The dens is usually masked on a true lateral projection but is easily recognized on a lateral view made with slight axial rotation (obliquity).
- The spinous processes of C1 and C2 normally are in close proximity, and the dorsal laminae are nearly parallel, on the lateral projection. This normal relationship is important in recognizing atlantoaxial subluxation.
- C6 is distinguished by large transverse process.
- The intervertebral disc spaces of the cervical vertebrae become progressively wider between C2-C3 and C6-C7.
- T1 has a pronounced spinous process compared with C7.
- T11 is the anticlinal vertebra in most dogs; however, T10 may also be designated the anticlinal vertebra.
- The T10-T11 intervertebral disc space is narrower than adjacent disc spaces in most dogs.
- The ventral aspect of the bodies of L3 and L4 are entheses for the diaphragmatic crura and may be indistinct, especially in large dogs.

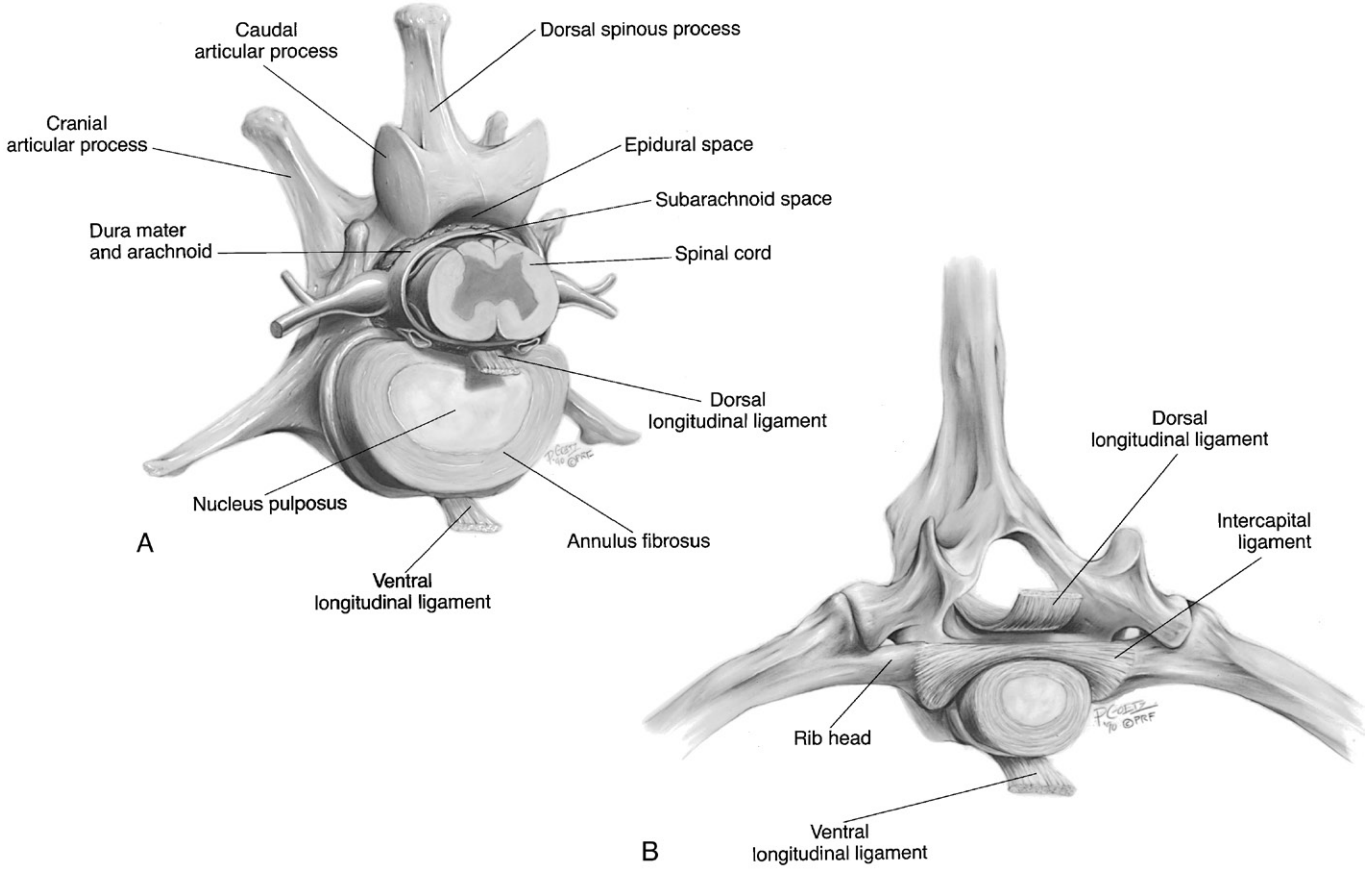


Fig. 11-5 Anatomic components of a typical lumbar vertebra **(A)** and a typical thoracic vertebra and articulation with ribs **(B)**. Modified from Evans HE, Christensen, JC: *Miller's anatomy of the dog*, ed 2, Philadelphia, 1979, Saunders.

ANOMALIES OF THE VERTEBRAL COLUMN

Anomalies of the vertebral column are common and include congenital and developmental malformations.[11-12] Many of these abnormalities are normal variants and have no clinical importance.

Block Vertebrae

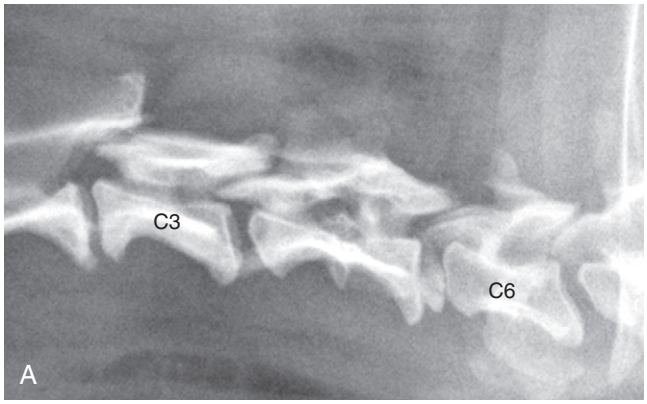
A block vertebra is the result of fusion of two or more vertebral bodies; the vertebral arches may also be fused, or they may be unaffected (Figs. 11-6 and 11-7).[1] The disc space between a block vertebra is often seen radiographically as a thin radiolucent line but may not be visible at all if the fusion is complete. Block vertebrae are most common in the cervical region, but they also occur in the lumbar spine. Biomechanically, block vertebrae may act as a fulcrum, leading to altered loading immediately adjacent to the fusion. This has been hypothesized to increase the risk of disc disease at adjacent sites (see Fig. 11-6) and has also been implicated in leading to atlantoaxial subluxation.[13] The fused sacral vertebrae are a normal type of block vertebra.

Hemivertebrae

Hemivertebrae are the result of failure of the development and eventual ossification of part of a vertebra, usually the body.[1,11,14] The shape of a hemivertebra depends on the area that fails to develop. A wedge-shaped vertebra is seen on the lateral projection when the ventral aspect of the vertebral body is developed incompletely (Fig. 11-8). When this occurs, the vertebral column often develops a kyphotic configuration that can lead to compression of the spinal cord. Not all hemivertebrae are significant clinically, and MR imaging is required to determine if hemivertebrae are the cause of a spinal neuropathy. A butterfly-shaped vertebra occurs when the mid-aspect of the body fails to develop.[15] A butterfly vertebra is best seen on the ventrodorsal (VD) projection (Fig. 11-9). Decreased rib spacing on the VD projection is an important clue that hemivertebrae are present (Fig. 11-10). A hemivertebra should not be confused with a compression fracture; their multiplicity and occurrence in a brachycephalic breed are helpful in this distinction. Also, hemivertebrae have a smoothly marginated cortex, whereas vertebrae affected with a compression fracture have a disrupted margin. The bulldog, French bulldog, Boston terrier, and other screw-tail breeds are most affected with hemivertebrae.[11,12]

Transitional Vertebrae

Vertebrae that have characteristics of two different anatomic divisions are known as *transitional vertebrae*.[1,11,16] These anomalies usually involve the vertebral arch rather than the body and occur at cervicothoracic, thoracolumbar, and lumbosacral junctions. The main clinical significance of transitional vertebral anomalies relates to the use of the most caudal ribs as a landmark to identify a site of spinal decompressive surgery. If the most caudal ribs are asymmetric, then surgery can be performed at the incorrect site unless the asymmetry is recognized. Another significant feature of transitional anomalies is the increased incidence of lumbosacral disc disease and



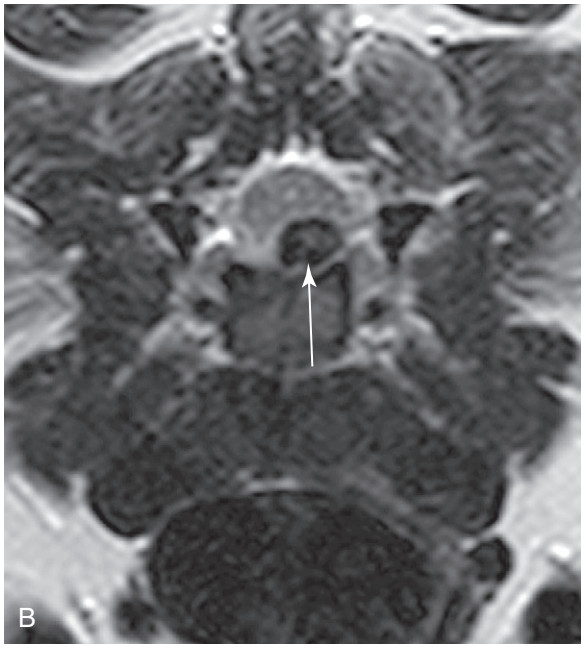


Fig. 11-6 **A,** Lateral cervical radiograph of a dog with a block vertebra affecting C4-C5. The vertebral bodies and arches are fused. The disc space is not visible between the fused vertebrae. Note the mineralized disc at C5-C6. The biomechanics of normal neck function are altered by the block vertebra, often leading to degeneration of the intervertebral disc at adjacent interspaced. C3, Third cervical vertebra; C6, Sixth cervical vertebra. **B,** Transverse T2-weighted MR image acquired at the level of the cranial aspect of C6. There is a large amount of hypointense disc material *(arrow)* in the left ventral aspect of the vertebral canal that is causing moderate spinal cord compression.

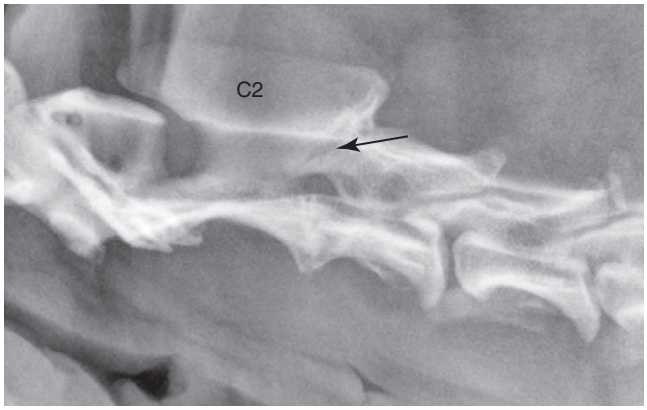
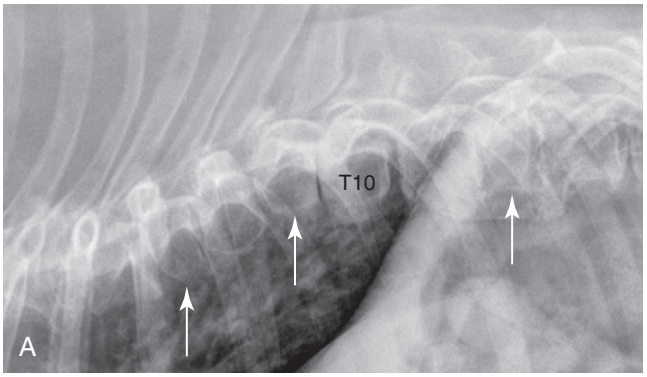


Fig. 11-7 Lateral radiograph of a dog with a block vertebra affecting C2-C3. The intervertebral disc space appears as a thin vertical radiolucent line. A radiolucent line is also visible dorsally at the dorsal articular process joint *(black arrow)*. These lines signify that complete fusion has not occurred in this dog although there is still increased risk of altered loading of the intervertebral disc at C3-C4, immediately caudal to the fusion.



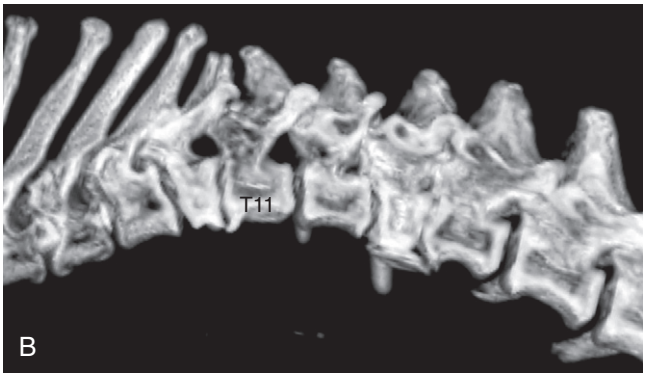


Fig. 11-8 **A,** Lateral thoracic radiograph of a bulldog with multiple hemivertebrae *(white arrows)*. *T10,* Tenth thoracic vertebral body. **B,** Lateral view of a three-dimensional rendering of the spine of another bulldog. There are hemivertebrae at T10 and T13. *T11*, eleventh thoracic vertebral body.

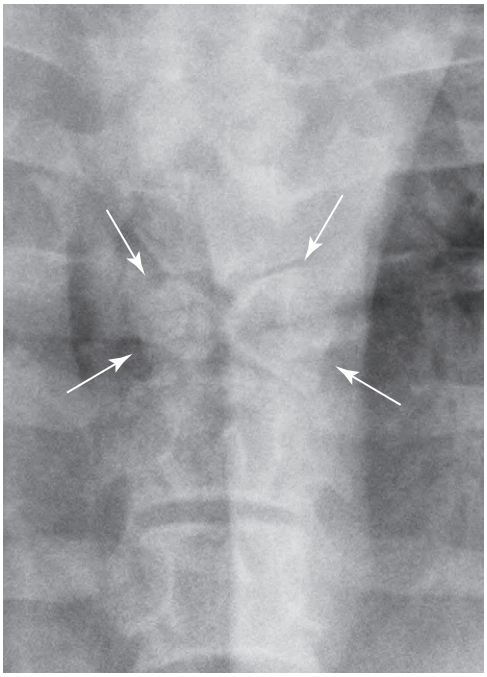


Fig. 11-9 Ventrodorsal radiograph of the caudal aspect for the thoracic spine in a bulldog. A butterfly anomaly is present *(white arrows)*.

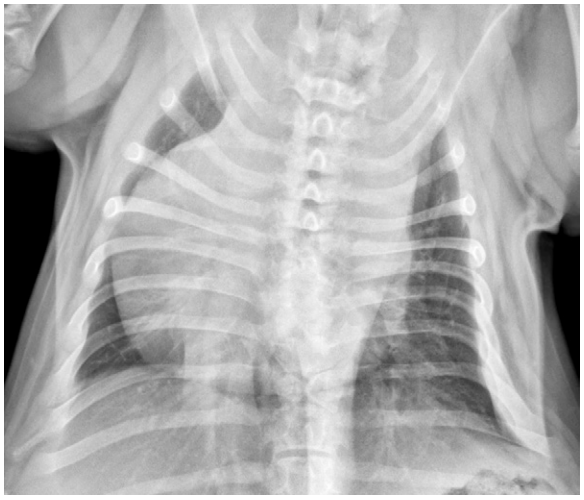


Fig. 11-10 Ventrodorsal radiograph of a bulldog with multiple thoracic hemivertebrae. The abnormal vertebrae lead to thoracic spine foreshortening with secondary crowding of the ribs. This is most noticeable in the left hemithorax.

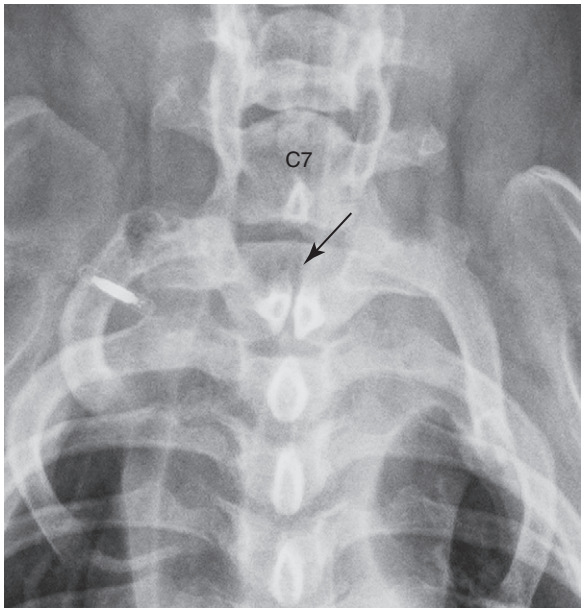


Fig. 11-11 Ventrodorsal thoracic radiograph of a dog wherein T1 is characterized by a split spinous process *(arrow)*. *C7*, Seventh cervical vertebral body.

nerve root compression that occurs in dogs with a lumbosacral transitional malformation.[17] This relates to the altered lumbosacral loading that leads to disc degeneration, instability, spondylosis, and nerve root compression. Transitional vertebral anomalies are also discussed and illustrated in Chapter 7.

Spina Bifida

Spina bifida results from the lack of development of the vertebral arch and may be associated with neural tube defects—that is, meningocele or meningomyelocele.[1] Typically, there is a cleft in the dorsal part of the vertebral arch and absence or splitting of the spinous process. If the defect in the arch is large, a meningocele or meningomyelocele may develop. The most common radiographic manifestation of spina bifida is a split spinous process (Fig. 11-11). There is rarely a neural tube defect in dogs with spina bifida occurring in the thoracic spine.

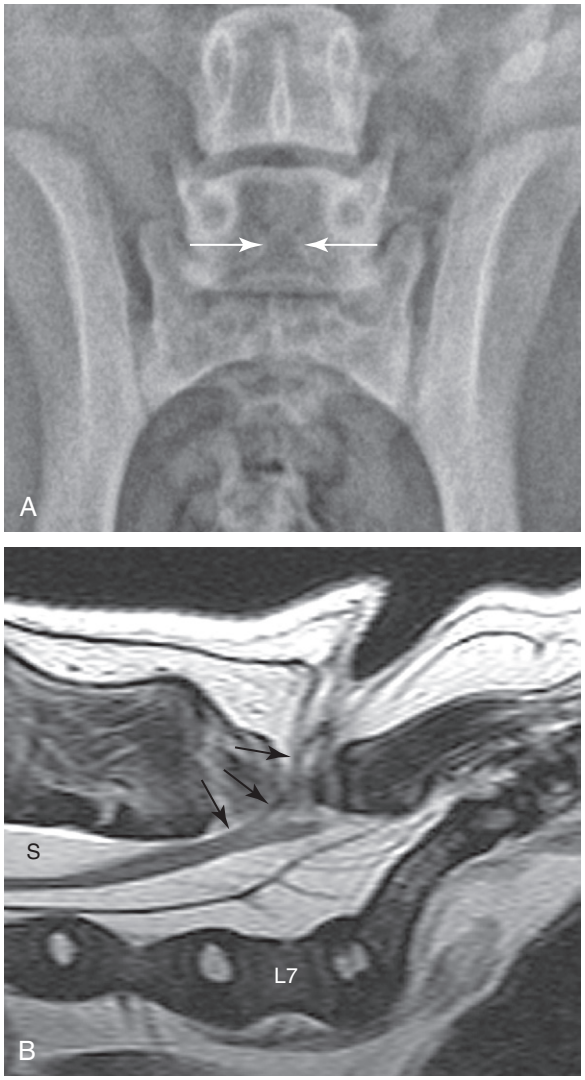


Fig. 11-12 **A,** Ventrodorsal radiograph of a dog with spina bifida. There is no spinous process on L7, and the lamina has a dorsal defect *(white arrows)*. **B,** Sagittal T2-weighted MR image of the dog in **A.** Nerve roots *(black arrows)* are visible tracking dorsally through the laminar defect. There is a large syrinx *(S)* in the caudal aspect of the lumbar spinal cord. *L7*, Seventh lumbar vertebral body.

At the lumbosacral junction, however, the morphologic derangements are often more severe with absent spinous process, laminar defect, and neural tube defect (Fig. 11-12). MR imaging is preferred for characterizing the presence and extent of any neural tube defect (see Fig. 11-12, *B*). Spina bifida is most common in bulldogs and Manx cats.[12,18]

Atlantoaxial Subluxation

In atlantoaxial subluxation, the axis (C2) is displaced dorsally with respect to the atlas (C1), causing compression of the spinal cord. Atlantoaxial subluxation can be a result of either congenital malformation or trauma.[12,18,19] With congenital malformation, the dens is often absent,[20] and there may be deficiencies in the ligaments that support the atlantoaxial joint and prevent flexion (see Fig. 11-4). The clinical signs may be acute with trauma or chronic with congenital malformation and can be characterized mainly by pain and cervical neuropathy.

A variety of lesions may occur in association with atlantoaxial subluxation, and a working knowledge of the

components of the atlantoaxial region is needed for radiographic interpretation.[1,2] Atlantoaxial subluxation occurs frequently with malformation or rupture of the transverse ligament of the atlas. This ligament bridges the ventral aspect of the vertebral arch and stabilizes the dens, preventing the rostral aspect of the axis from impinging on the spinal cord (see Fig. 11-4, *B*). A short apical ligament connects the tip of the dens with the occiput along with the alar ligaments (see Fig. 11-4, *B*). A short, dorsal atlantoaxial ligament is also present dorsally (see Fig. 11-4, *A*). Atlantoaxial subluxation caused by congenital predisposition is most common in toy breed dogs, such as the Yorkshire terrier, but acquired atlantoaxial subluxation can occur in any breed.

Atlantoaxial subluxation is best diagnosed radiographically on a lateral projection of the cranial aspect of the cervical spine. When subluxation is suspected, the patient should be handled carefully, especially when tetraparetic, and the head and neck should not be flexed because this could exacerbate spinal cord damage, especially if the dens is present. On a routine lateral radiograph, the dens is masked by the sheer mass of the atlas. Making a left 15- to 30-degree ventral–right dorsal radiograph will unmask the dens and help identify fractures and malformations of the dens. Even then small fractures may not be apparent. VD projections can also be made, but there is the risk of exacerbating the spinal cord compression, especially in anesthetized patients. The VD projection is not necessary to confirm a diagnosis of atlantoaxial subluxation. Radiographically, the lateral view is the most helpful. If subluxation is present, the axis is displaced dorsally, widening the distance between the vertebral arch of the atlas and the spinous process of the axis. More important, the normal linear relationship between the dorsal lamina of the atlas and the dorsal lamina of the axis becomes angular (Fig. 11-13). This angular relationship between the lamina of C1 and C2 is the most reliable radiographic sign of atlantoaxial subluxation. CT is useful for assessing the morphology of the atlantoaxial junction if surgical stabilization is going to be performed. The additional morphologic information provided in CT images by eliminating the effects of superimposition will be useful when stabilizing such small parts (see Fig. 11-13).

Cervical Spondylomyelopathy

Cervical spondylomyelopathy is included under anomalies because anomalous development of vertebrae or anomalous stabilization is likely to play a role in manifestation of clinical signs. Cervical spondylomyelopathy is also best considered a syndrome rather than a specific entity because it encompasses a constellation of pathologic changes that are not seen in every affected animal.[18,21-25] Abnormalities include malformation of the vertebral body and articular processes, malarticulation, instability and malalignment, and stenosis of the vertebral canal. Secondary changes involving dorsal longitudinal ligament and ligamentum flavum hypertrophy and disc protrusion and/or herniation are also common. The end result and cause of clinical signs is static or dynamic cervical spinal cord compression.

The pathophysiology of canine spondylopathy is complex and understood incompletely.[21-23,26] There is debate as to whether vertebral changes are caused by strict malformation of the vertebrae or result from remodeling with underlying instability of the vertebral column being the primary lesion. In the latter theory, the soft tissues of the vertebral column are insufficient to maintain proper vertebral stability and alignment during postnatal development. Because of the uncertain etiology, there are multiple synonyms for this condition, including cervical spondylomyelopathy, cervical spondylopathy, cervical vertebral malformation-malarticulation, cervical vertebral stenotic myelopathy, and wobbler syndrome, with the latter arising from the fact that affected animals are

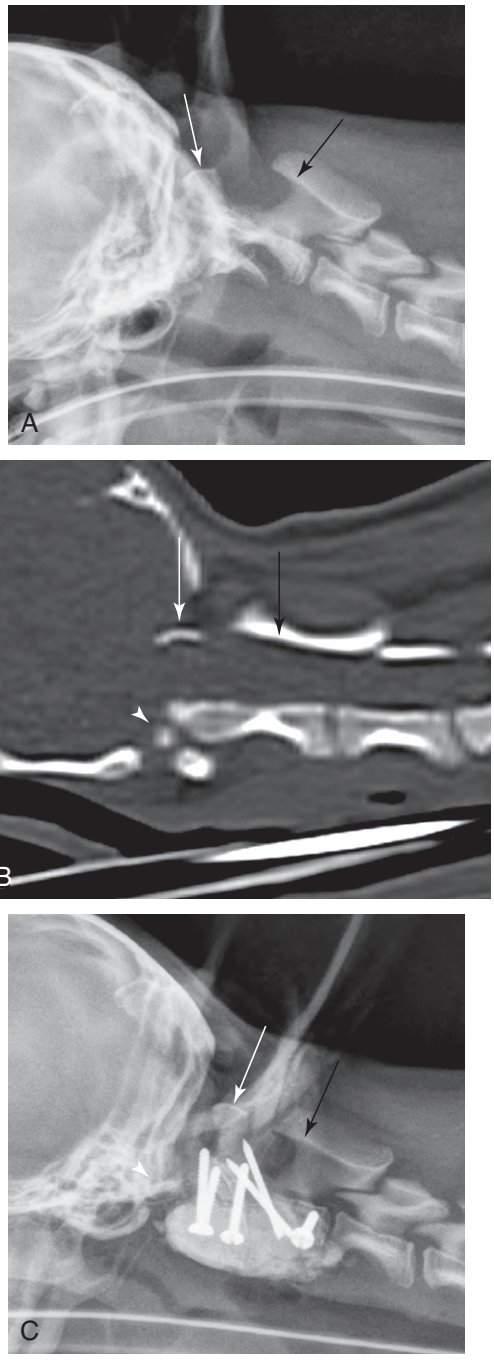


Fig. 11-13 **A,** Lateral radiograph of the cranial aspect of the cervical spine of a dog with an atlantoaxial subluxation. The key to diagnosing atlantoaxial subluxation radiographically is not to assess the space between C1 and C2 but the angular relationship between the lamina of these two vertebrae. Clearly in this dog the lamina of the atlas *(white arrow)* is not parallel with the lamina of the axis *(black arrow)*. A parallel, or nearly parallel, relationship between these structures is normal, whereas a nonparallel relationship indicates malalignment. **B,** Sagittally reformatted CT image of the cranial aspect of the cervical spine of the dog in **A.** The atlantoaxial subluxation has been reduced spontaneously as the dog was positioned for the CT study; the dorsal lamina of the atlas *(white arrow)* and dorsal lamina of the axis *(black arrow)* are parallel. There is a small avulsion fracture of the apical aspect of the dens *(white arrowhead)* that likely contributed to the instability and subluxation. **C,** Postoperative radiograph of the dog in **A.** Screws and pins have been inserted into the body and transverse processes of C1 and the body of C2 and embedded in methylmethacrylate. The dorsal laminae of the atlas *(white arrow)* and axis *(black arrow)* are nearly parallel; this is a normal appearance with regard to the angular relationship of these laminae.

often ataxic with a wobbling or swaying gait. No term is accepted universally.[18,23] Cervical spondylomyelopathy will be used in this discussion.

Cervical spondylomyelopathy is common in young Great Danes and mature Doberman pinschers, but there are many other large breeds that may be affected.[21-23] There are often dissimilarities in the manifestation of cervical spondylomyelopathy in Doberman pinschers versus Great Danes. In the Doberman pinscher, vertebral canal stenosis, disc protrusion and/or herniation, and dorsal longitudinal ligament hypertrophy are common. Affected vertebrae sometimes have craniocaudal flattening because of abnormal formation or remodeling. There can also be stenosis of the vertebral canal that results from underdevelopment of the pedicles (Fig. 11-14). This can result in the vertebral canal appearing cone shaped over the length of a vertebra, with it being narrower at the cranial aspect of the vertebra.[21,23] Disc degeneration with protrusion and/or expulsion with concurrent and hypertrophy of the dorsal annulus fibrosis and the dorsal longitudinal ligament is also common in the Doberman pinscher.[22-25]

Cervical spondylomyelopathy in the Great Dane is often characterized primarily by articular process malformation and hyperostosis. As mentioned earlier, it is not clear whether this is a primary osseous malformation or whether these changes are secondary to cervical instability. Regardless, the hyperostotic articular processes commonly extend medially into the vertebral canal and cause spinal cord compression. Articular malformation and hyperostosis are usually visible radiographically, but MR imaging is preferred to assess the secondary changes, such as synovial cyst formation and spinal cord compression, more accurately (Fig. 11-15).

Although the differences in the manifestation of cervical spondylomyelopathy in the Doberman pinscher versus the Great Dane have been described,[22-25] it is important to realize that any individual dog of these breeds or others can have any combination of the changes described.

As should be apparent from the examination of Figures 11-14 and 11-15, survey radiographic changes of cervical spondylomyelopathy may be sufficient to suggest the diagnosis, but myelography, CT, CT myelography, and MR imaging are necessary to evaluate the location and severity of compressive extradural lesions. MR imaging is the modality of choice as it allows assessment of the integrity of the spinal cord in addition to providing for identification of the osseous changes, disc herniation or protrusion, ligamentous hypertrophy, and synovial cyst formation (see Figs. 11-14 and 11-15).[27,28] Although controversial, obtaining myelographic projections with linear traction, flexion and extension of the cervical spine, in addition to conventional projections, has been advocated to identify the presence of dynamic compression.[21,25] Although these maneuvers might provide insight for surgical decision making, flexion and extension place the anesthetized patient at risk for exacerbation of spinal cord damage. Linear traction, as illustrated in Figure 11-14, is not likely to be harmful, but its clinical value is not characterized completely. Table 11-1 provides a summary of imaging signs of cervical spondylomyelopathy.

FRACTURE AND LUXATION

Vertebral fracture is usually a result of being hit by a motor vehicle, falling, or gunshot injury.[29] Many vertebral fractures and luxations occur at regional junctions, for example, atlantooccipital, atlantoaxial, cervicothoracic, thoracolumbar, and so forth.[30-32] These junctions may be more subject to flexion-extension and torsion and axial loading compared with the vertebrae within a region. Radiographic features of vertebral fractures include asymmetry, specifically of the articular processes and endplates; displacement of a vertebra with respect to adjoining vertebrae (malalignment); and comminution of the endplate or body. Any fracture has the potential to cause narrowing of the vertebral canal and spinal cord contusion and/or compression. Shortening of the vertebral body is often seen with compression fractures of the thoracic vertebrae and L7 (Fig. 11-16).[33]

An incomplete vertebral fracture is difficult to detect radiographically, and malalignment may be the only abnormality found. Radiographic evaluation of patients with suspected vertebral fractures is limited by summation and failure to obtain accurate positioning or an adequate number of projections. Patients with vertebral column trauma are frequently unstable and cannot withstand chemical restraint. In addition, maneuvers to obtain correct positioning may be detrimental to existing spinal trauma, especially VD projections. Flexion, extension, and traction should never be used in animals with spinal trauma. One approach is first to obtain only lateral views of the spine of patients with a suspected vertebral fracture. If a suspected fracture is seen, a horizontally directed x-ray beam can be used to obtain VD views. This principle was discussed and illustrated in Chapter 7.

Table • **11-1**

Summary of Salient Imaging Signs of Cervical Spondylomyelopathy

ABNORMALITY	RADIOGRAPHY	MYELOGRAPHY	CT*	MR†
Vertebral body malformation	✓	✓	✓	✓
Stenosis	✓	✓	✓	✓
Malalignment	✓	✓	✓	✓
Vertebral tipping	✓	✓	✓	✓
Articular process remodeling	✓	✓	✓	✓
Disc degeneration/prolapse		✓	✓	✓
Spinal cord compression		✓	✓	✓
Ligamentum flavum, interarcuate ligament, or joint capsule hypertrophy				✓

*Identifying vertebral malformation, tipping and malignant, is dependent on obtaining high-quality reformatted images in the sagittal plane. Stenosis is apparent on transverse images.
†MR is true multiplanar imaging and it is assumed that dorsal and sagittal, as well as transverse, images are aquired.

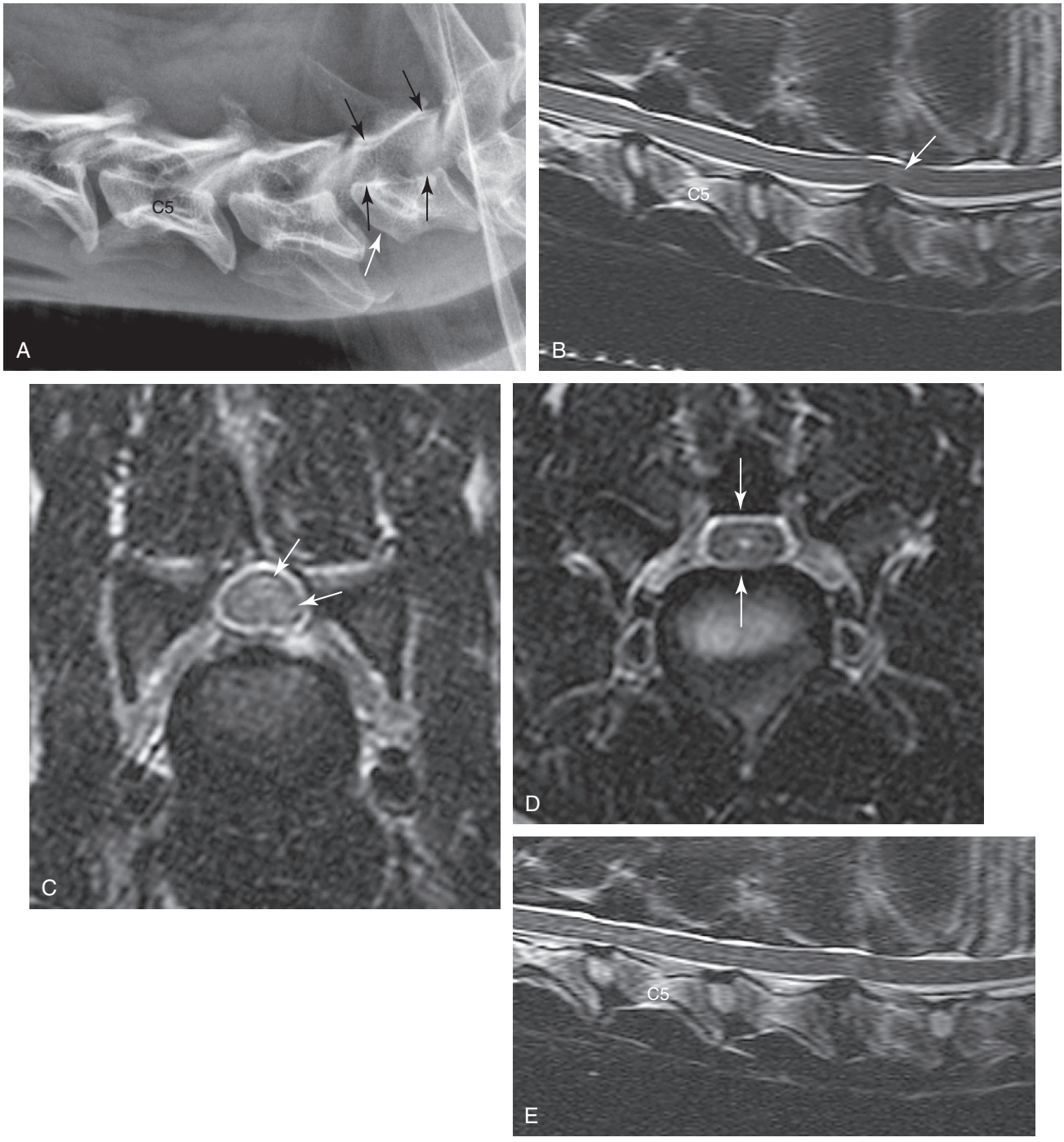


Fig. 11-14 Images from a 6-year-old Doberman pinscher with clinical signs of cervical spondylomyelopathy. **A,** Lateral cervical radiograph. The cranioventral aspect of C7 is flat *(white arrow)*. On inspection of the relationship of the dorsal aspect of the C7 vertebral body and the dorsal lamina *(black arrows)*, it is apparent that the diameter of the vertebral canal is narrower at the cranial aspect of C7 than at the caudal aspect of C7 (cone shaped). **B,** Sagittal T2-weighted image. There is hypointense mass in the ventral aspect of the vertebral canal at C6-C7 that is causing spinal cord compression; this is consistent with disc protrusion and/or hypertrophy of the dorsal longitudinal ligament as a result of chronic instability. The spinal cord has a faint area of T2 hyperintensity *(white arrow)* consistent with bruising from the chronic compression. There also is narrowing of the spinal cord at C4-C5. **C,** Transverse T2-weighted image of the spinal cord at C6-C7. There is only mild spinal cord compression, but the intramedullary T2 hyperintensity caused by chronic compression is obvious *(white arrows)*. For comparison, the signal of the spinal cord in part **D** is normal. **D,** Transverse T2-weighted images of the spinal cord at C4-C5. There is compression of the spinal cord *(white arrows)* because of laminar malformation with secondary vertebral canal stenosis. The signal of the spinal cord is normal; compare this spinal cord signal to the bruised spinal cord in part **C.** This compression at C4-C5 was not detected radiographically. **E,** T2-weighted sagittal image acquired with traction placed on the head. The amount of spinal cord compression at C6-C7 is reduced compared with that present in **A,** which was made without traction. In cervical spondylomyelopathy, traction-responsive compression is attributed to hypertrophy of the dorsal longitudinal ligament rather than disc herniation. This has implications for the type of corrective surgery to be done. *C5,* Fifth cervical vertebral body.

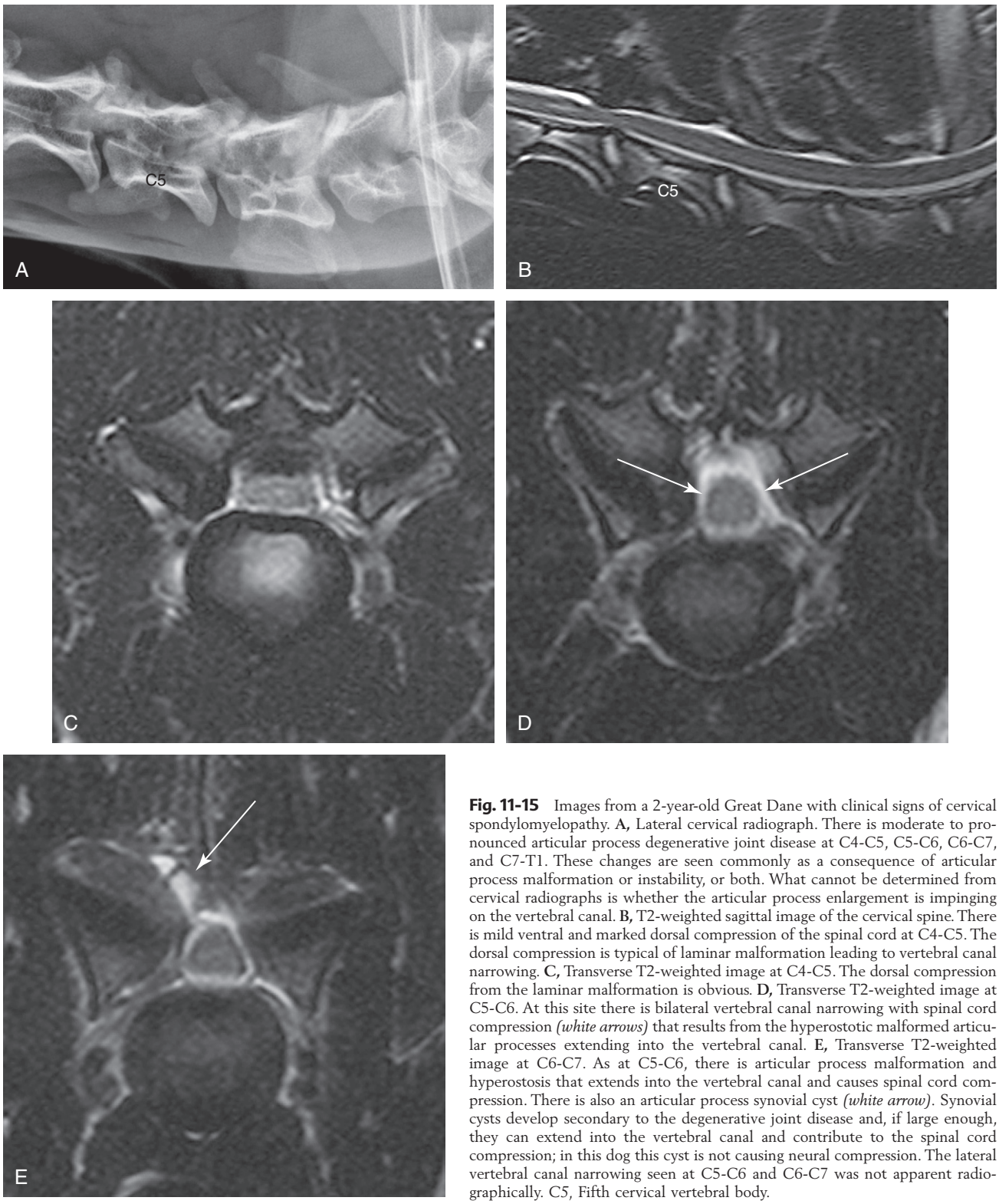


Fig. 11-15 Images from a 2-year-old Great Dane with clinical signs of cervical spondylomyelopathy. **A,** Lateral cervical radiograph. There is moderate to pronounced articular process degenerative joint disease at C4-C5, C5-C6, C6-C7, and C7-T1. These changes are seen commonly as a consequence of articular process malformation or instability, or both. What cannot be determined from cervical radiographs is whether the articular process enlargement is impinging on the vertebral canal. **B,** T2-weighted sagittal image of the cervical spine. There is mild ventral and marked dorsal compression of the spinal cord at C4-C5. The dorsal compression is typical of laminar malformation leading to vertebral canal narrowing. **C,** Transverse T2-weighted image at C4-C5. The dorsal compression from the laminar malformation is obvious. **D,** Transverse T2-weighted image at C5-C6. At this site there is bilateral vertebral canal narrowing with spinal cord compression *(white arrows)* that results from the hyperostotic malformed articular processes extending into the vertebral canal. **E,** Transverse T2-weighted image at C6-C7. As at C5-C6, there is articular process malformation and hyperostosis that extends into the vertebral canal and causes spinal cord compression. There is also an articular process synovial cyst *(white arrow)*. Synovial cysts develop secondary to the degenerative joint disease and, if large enough, they can extend into the vertebral canal and contribute to the spinal cord compression; in this dog this cyst is not causing neural compression. The lateral vertebral canal narrowing seen at C5-C6 and C6-C7 was not apparent radiographically. C5, Fifth cervical vertebral body.

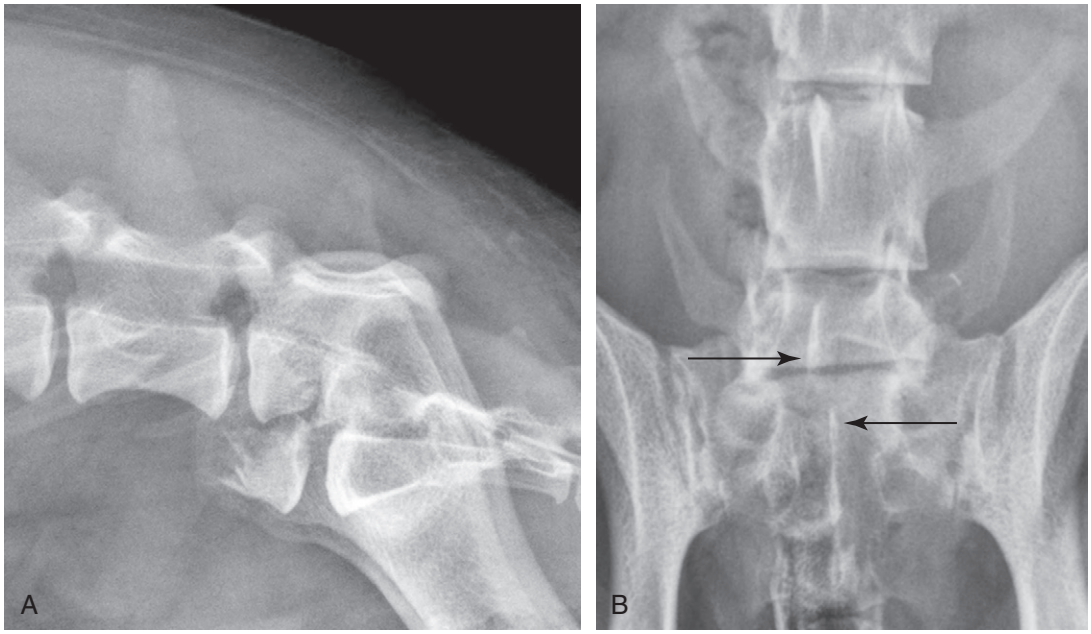


Fig. 11-16 Lateral **(A)** and VD **(B)** radiographs of a dog with a comminuted L7 fracture. In **A,** the caudal fragment is displaced ventrally and cranially because of contraction of the hypaxial muscles of the spine. The fracture is obvious in the lateral view. In **B,** L7 is foreshortened, and unless this is recognized, the fracture would be missed. There is slight sagittal malalignment of the spinous processes of L7 and S1 *(black arrows)* because of axial rotation of the caudal fragment, but this is a subtle finding.

Because of its tomographic nature, CT is superior to radiography for identifying and characterizing vertebral fractures (Fig. 11-17). In 30 dogs with acute spinal trauma, radiographic sensitivity for fractures and luxations was only 72% and 77%, respectively, and fracture fragments within the vertebral canal and narrowing of the vertebral canal were often unrecognized.[34]

A three-compartment approach has been advocated for evaluating the severity and instability of vertebral fractures and luxations.[29,34] The vertebra is divided into three areas: dorsal, middle, and ventral. The dorsal compartment contains the vertebral arch, articular processes, and supportive ligaments; the middle compartment contains spinal cord, dorsal longitudinal ligament, annulus fibrosus, and the dorsal margin of the body; and the ventral compartment includes the remainder of the vertebral body, the annulus, and the ventral longitudinal ligament. If two or more compartments are involved, the fracture-luxation is likely unstable and requires stabilization.[29]

With vertebral fractures and luxations, soft tissue injury is invariably present and may involve the spinal cord, intervertebral discs, and connective tissue. Disc protrusion may be present. Therefore, CT or MR imaging should be considered in all animals with vertebral injury.

INTERVERTEBRAL DISC DISEASE

Clinical signs of intervertebral disc disease result from extension of the intact intervertebral disc or of nuclear disc material into the vertebral canal, compressing the spinal cord or spinal nerve roots.[35,36] Descriptive terms used relative to disc lesions are both confusing and overlapping and include *protrusion*, *hernia*, *extrusion*, *expulsion*, and *prolapse*. The distinction among these lesions cannot be made with conventional radiography and can be difficult even with CT and MR imaging or at surgery. *Protrusion* has been used for any discal mass that is impinging on the spinal cord or spinal nerve roots and will be used here. Chondrodystrophic breeds, including dachshund, Pekingese, beagle, Welsh corgi, Lhasa apso, and Shih Tzu are most commonly affected,[37] but intervertebral disc disease can occur in any breed, including Doberman pinschers with cervical spondylomyelopathy and German shepherds with caudal equina syndrome. Common sites of disc prolapse are C2-C3, C3-C4, T12-T13, and T13-L1. Although clinical signs of intervertebral disc disease are uncommon in cats, cervical disc degeneration frequently occurs in cats older than 6 years of age.[35,36]

Classic type I protrusion follows chondroid degeneration of the nucleus pulposus with eventual expulsion of dehydrated nuclear material into the vertebral canal. Type I lesions usually produce acute neurologic signs because of rapid, forceful expulsion of disc material. Type II protrusion is typified by fibroid degeneration of the nucleus and fibrous metaplasia of the nucleus pulposus. The annulus fibrosus may stretch, hypertrophy, or rupture partially, resulting in chronic, progressive neurologic signs, compared with the acute signs that typically accompany type I disc lesions. A *traumatic* or *missile* disc lesion is variant of a type I protrusion and occurs when a healthy nondegenerative disc is subjected to supraphysiologic pressure.[38] The result is explosive expulsion of normal nuclear material between intact annular fibers into the vertebral canal. This can cause a concussive injury to the spinal cord, and there is usually a secondary inflammatory response within the vertebral canal.

Although survey radiographic evaluation is used commonly to assess animals with signs of intervertebral disc disease, it should be kept in mind sensitivity and specificity are poor compared with CT and MR imaging. Thus, survey radiographic findings should not be used to determine the site and severity of disc lesions before surgical decompression. The most important use of survey radiography in animals with signs of intervertebral disc disease is for ruling out other

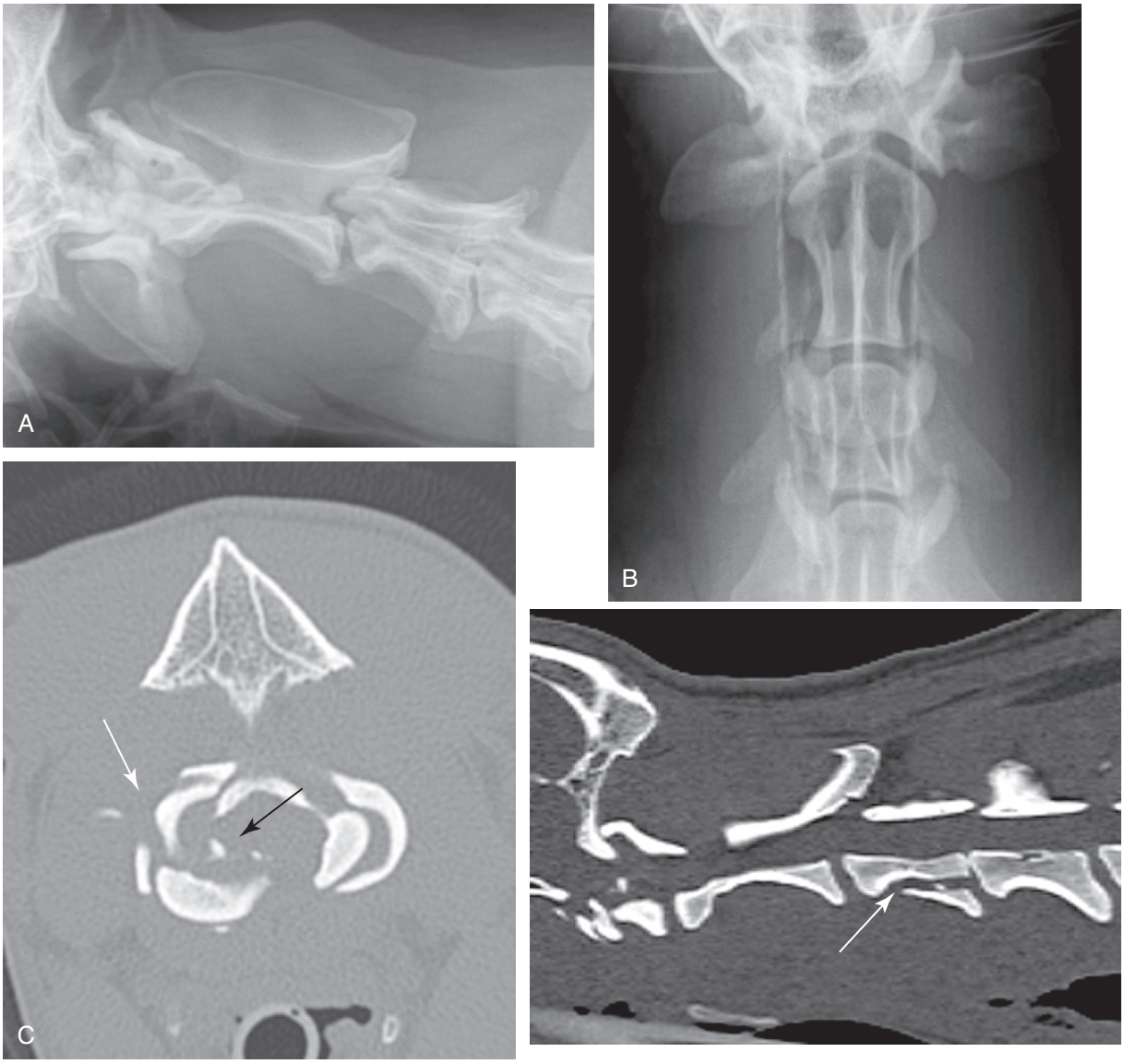


Fig. 11-17 Lateral **(A)** and VD **(B)** radiographs of a patient that was hit by a car. There are severe neurologic signs pointing to a cervical spinal cord injury. In the lateral view there is narrowing of the C3-C4 disc space and mild subluxation with mild dorsal displacement of the cranial aspect of C4 with respect to C3. The atlas looks very abnormal, but this region is rotated and cannot be assessed. Misdiagnosis of a C1 fracture is common in malpositioned cervical radiographs. In the VD view, there is angulation at the atlanto-occipital articulation, but specific injuries cannot be identified. In a transverse CT image of the atlanto-occipital junction **(C),** there are obvious fractures of the occipital bone *(black arrow)* and C1 *(white arrow)*. In a sagittally reconstructed image of the cervical spine, there is also an obvious fracture of C3 *(white arrow)*. CT was needed in this dog to identify the traumatic bone injuries accurately.

conditions, such as a fracture, luxation, or aggressive bone lesions.

Radiographic signs consistent with intervertebral disc protrusion include (1) narrowing of the intervertebral disc space, (2) narrowing of the intervertebral articular process joint space, (3) a small intervertebral foramen, (4) increased opacity within the intervertebral foramen, and (5) mineralized disc material within the vertebral canal (Fig. 11-18). Careful radiographic technique is critical for interpretation of these changes. Oblique positioning and failure to use multipoint centering can lead to erroneous conclusions; these principles were discussed in Chapter 7. Narrowing of disc spaces is not always indicative of significant disc disease and must be interpreted in the context of clinical signs. For example, in normalcy, disc spaces at T10-T11 and L5-L6 are usually narrower than adjacent disc spaces. Following hemilaminectomy or fenestration and resolution of discospondylitis, disc spaces may be narrow in asymptomatic animals. Mid-size to large-breed dogs with chronic intervertebral disc disease may have multiple narrowed disc spaces that do not correlate with the neurologic examination. This may also be complicated by chronic enthesopathy associated with spondylosis deformans, which may be associated with narrowed intervertebral disc spaces without protrusion (see following section). Small intervertebral

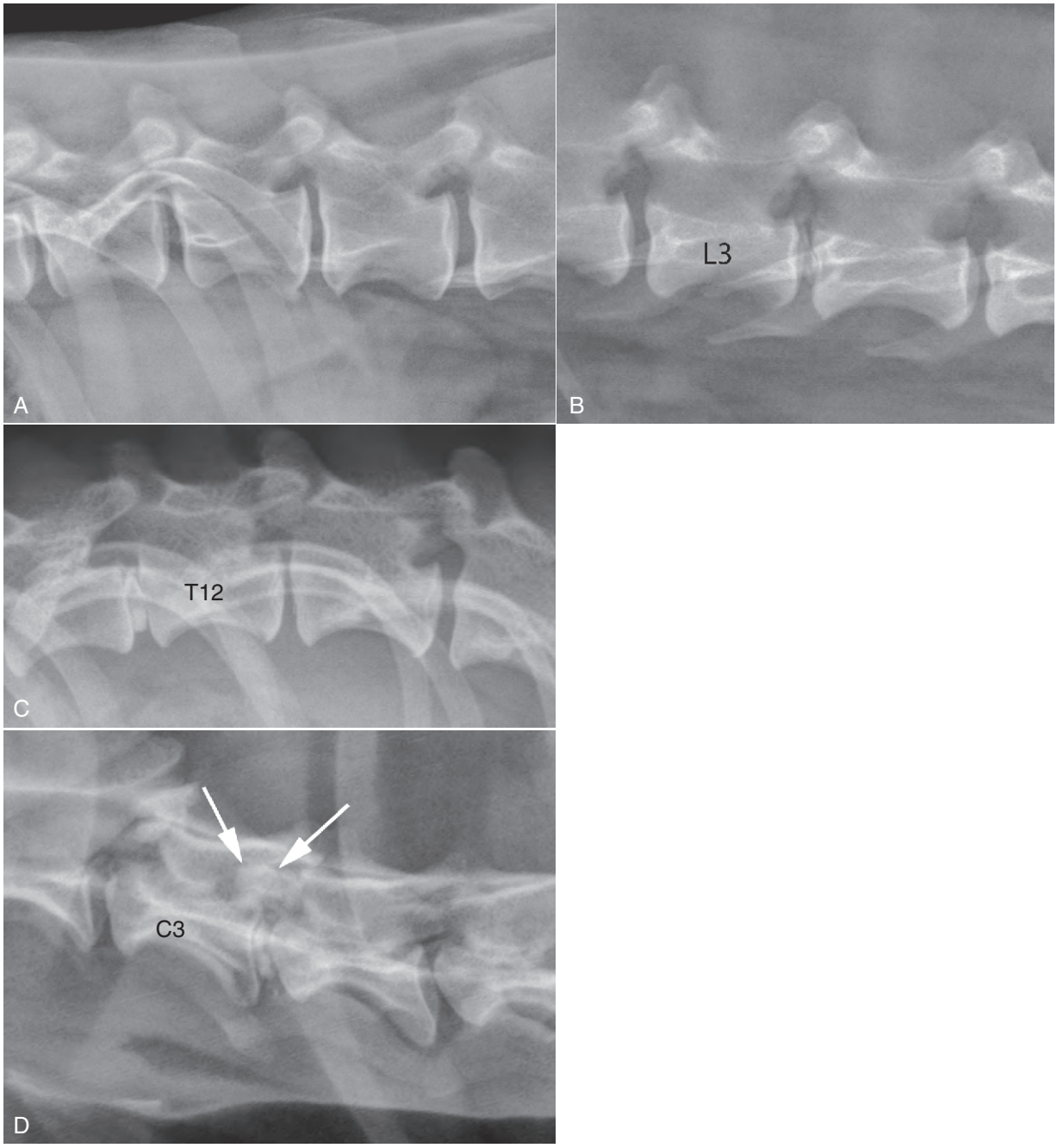


Fig. 11-18 Survey radiographic signs of intervertebral disc disease. **A,** The intervertebral disc space, intervertebral foramen, and dorsal articular process joint space at L1-L2 are all decreased in size compared with adjacent vertebrae. These signs result from vertebrae adjacent to the disc protrusion moving closer together. Mild spondylosis deformans is present at L1-L2. **B,** Mineralization of the disc at L3-L4 and mineralized material superimposed over the intervertebral foramen, consistent with mineralized disc material in the vertebral canal. The disc at L3-L4 has not herniated completely; some residual disc material remains between the vertebral endplates. The intervertebral foramen at L3-L4 is slightly smaller than the foramen at L4-L5. *L3*, Third lumbar vertebral body. **C,** The intervertebral disc space, intervertebral foramen, and dorsal articular process joint space at T12-T13 are all decreased in size compared with adjacent vertebrae. As in **(A)** these signs are caused by vertebrae adjacent to the affected disc moving closer together. There is in situ mineralization of the disc at T11-T12. This is not important clinically and signifies only degeneration of the disc. *T12*, Twelfth thoracic vertebral body. **D,** Mineralization of the disc at C3-C4, with a narrow disc space. The cervical articular processes are larger than in the thoracic or lumbar region and are typically superimposed on the intervertebral foramina, making assessment of the foramina more difficult in the cervical spine. However, a large mineralized opacity is visible in a position consistent with it being in the vertebral canal *(white arrows)*. Confirmation that this opacity is within the vertebral canal requires additional images or modalities. *C3*, Third cervical vertebral body.

foramina and narrowed articular process joint spaces are merely a result of partial collapse of the space between two vertebrae. Increased opacity of the intervertebral foramen is caused by either extruded disc material in the vertebral canal or local inflammation of epidural fat at the site of extrusion. This change is evident only on a true lateral projection with exact superimposition of both lateral margins of both intervertebral foramina. Discal mineralization is indicative of intervertebral disc degeneration but does not mean that this particular disc is causing a clinical problem. In addition, prolapsed disc material is frequently nonmineralized or has insufficient mineral content to be detected on survey radiographs. However, the superior contrast resolution of CT allows detection of both nonmineralized and low-mineral-content prolapsed disc material.

Myelography is valuable for identifying the site of intervertebral disc protrusion and the degree of spinal cord compression but rarely provides meaningful information about the condition of the spinal cord. Overall, myelography remains useful for assessing intervertebral disc disease when CT or MR imaging are not available.[39] Additional information on myelographic technique and interpretation can be found in the online version of this chapter from the fifth edition of this textbook (http://evolve.elsevier.com/Thrall/vetrad).

Imaging features of intervertebral disc disease found in CT and MR images are discussed in detail in Chapter 12.

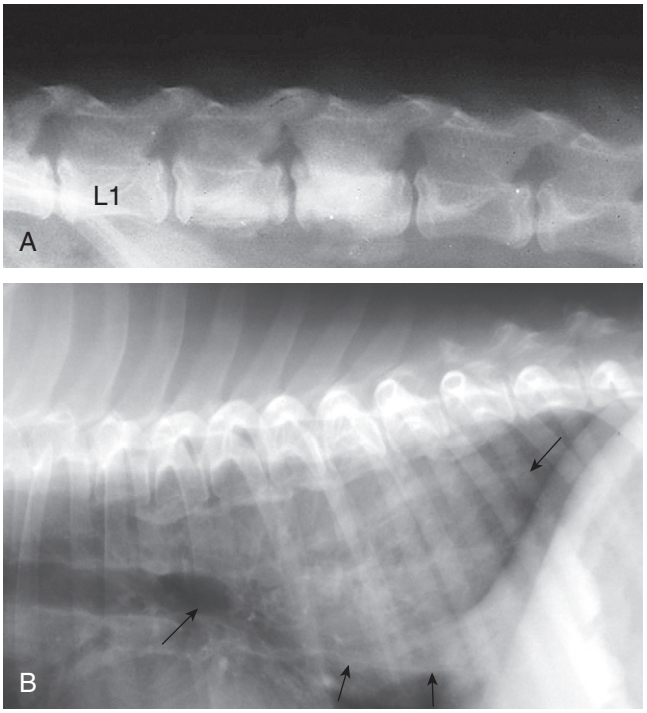


Fig. 11-19 Radiographic signs of spondylitis. **A,** Radiograph of patient with plant awn-induced spondylitis; note increased opacity of the vertebral bodies of L2 and L3 and periosteal reaction. *L1*, First lumbar vertebral body. **B,** Lateral radiograph of a dog with *S. lupi* infection. There is an irregular periosteal response along ventral borders of the thoracic vertebra. Note that the new bone is not centered at the ventral aspect of the disc space, as would be expected in spondylosis. An indistinct soft tissue esophageal mass is present ventral to this area *(white arrows)*. (Fig. 11-19, *B* courtesy of Dr. R. M. Kirberger, University of Pretoria, South Africa.)

INFLAMMATORY CONDITIONS

Spondylitis, Vertebral Osteomyelitis, and Vertebral Physitis

Spondylitis is a nonspecific term referring to inflammation of the vertebrae. *Vertebral osteomyelitis* has also been used synonymously with spondylitis when osteomyelitis of the vertebral body is present. Spondylitis should not be confused with *spondylosis*, or *spondylosis deformans*, a degenerative condition of the vertebral column. Common causes of spondylitis include microbial infection, plant awn migration, and infection with *Spirocerca lupi*.[40-48] Paraspinal abscesses may extend to the spine and cause spondylitis.[49] Radiographic changes are mainly those of increased opacity of the vertebral body and periosteal response of the vertebral body. With osteomyelitis, radiographic features include an aggressive bone response with patchy lysis of the vertebral bodies and an irregular periosteal response[41-43] (Fig. 11-19). Parasite- induced spondylitis caused by *Spirocerca lupi* infection results in osseous proliferation of the ventral aspect of the vertebral bodies of T8-T11.[46] Metastatic neoplasia can cause similar periosteal lesions.[40]

Vertebral physitis occurs in young dogs, and initial radiographic signs include osteolysis of the physeal zone of the affected vertebrae with sparing of the endplates.[50] With progression, there is collapse of the cranial or caudal aspect of the vertebral body and endplate sclerosis. Sepsis is the proposed cause, because of hematogenous localization in the slow-flowing capillaries of the vertebral physis. *Acinetobacter* and *Enterococci* species have been isolated from vertebral biopsy material.[50]

Discospondylitis

Discospondylitis is inflammation of an intervertebral disc and its adjacent vertebral endplates.[47-48,52-53] There is also paraspinal soft tissue infection, but this is not detected radiographically. The etiology involves hematogenous spread of microorganism from distant sites, frequently associated with genitourinary infections and occasionally paraspinal abscess or foreign body migration.[47,51,53] Middle-aged, large-breed dogs are affected commonly, and single or multiple intervertebral discs and adjacent endplates may be involved. Common isolates include *Staphylococcus*, *Streptococcus*, and *Brucella* species and *Escherichia coli*, although numerous other bacterial species and yeasts have been isolated.[47,48,51,53] Discospondylitis is less common in cats but has a similar etiopathogenesis.[52] Initial radiographic features include irregular endplate lysis with extension into the vertebral body (Fig. 11-20). Later, there is collapse of the intervertebral disc space, sclerosis peripheral to the endplate lysis, ventral enthesophyte production, and in some instances subluxation (see Fig. 11-20, *B*). Resolved discospondylitis may have the same appearance as spondylosis deformans (discussed later). Clinical features of discospondylitis can include fever, leukocytosis, paresthesia, paresis, and rarely paralysis.[47-49,51,53] Meningitis is possible if the inflammatory process extends into the vertebral canal and enters the subarachnoid space.[53] Diagnosis is based on clinical signs and the radiographic changes in the vertebral endplates. Radiographic changes of discospondylitis lag behind changes that are apparent in MR images; thus negative radiographs do not rule out a diagnosis of discospondylitis.[53,54]

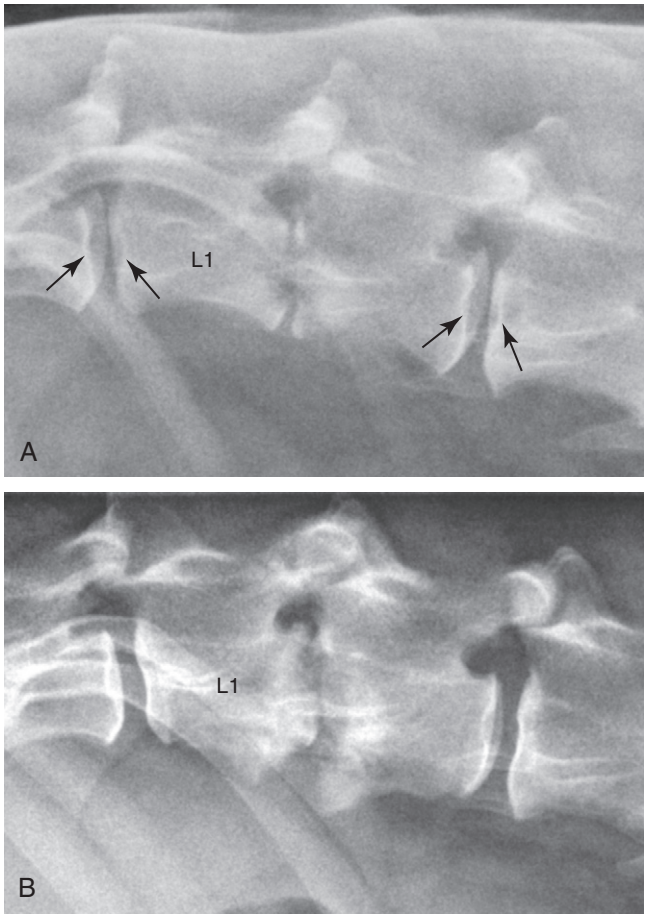


Fig. 11-20 **A,** Lateral radiograph of a dog with acute discospondylitis at L1-L2. There is endplate lysis, but no evidence of new bone formation. The disc space at L1-L2 is also narrow, signifying that the disc is herniated, although the location of the disc material cannot be determined. The disc material may be in the vertebral canal, lateral to the disc, or even within the vertebral body as a result of herniation through the endplate. Note the discrete linear opacity associated with a normal endplate *(black arrows)*. These discrete opacities are absent at L1-L2, and this absence is a clue that the endplates at this site have been effaced. **B,** Lateral radiograph of the same patient made 6 weeks later is characterized by more extensive lysis of the vertebral endplates and sclerosis of the vertebral body adjacent to the endplates. Early changes of spondylosis deformans are also present, and ventral enthesophytes are developing. There is mild subluxation at L1-L2, with L2 being displaced slightly ventrally. The intervertebral foramen at L1-L2 is small because of the disc being herniated and the vertebrae moving closer together.

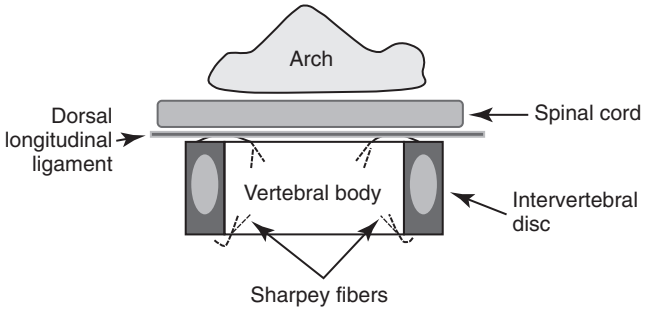


Fig. 11-21 Graphic of the lateral aspect of a typical vertebra and attachments (entheses) of the annulus fibrosis to the vertebral endplate and dorsal longitudinal ligament. Sharpey fibers are a continuation of annular collagen fibers originating in the annulus and are firmly anchored in the cortical bone of the vertebral endplate. Stimuli of these attachments have been postulated to initiate radiographically evident osseous proliferation at the ventral and lateral margins of endplates in animals with spondylosis deformans.

DEGENERATIVE CONDITIONS

Spondylosis Deformans

Spondylosis is defined as ankylosis of a vertebral joint.[55] The term *spondylosis deformans* is preferred because it addresses the spectrum of changes associated with this degenerative condition more completely. Spondylosis deformans is common in dogs, especially boxers and large-breed dogs, and tends to be most prevalent in the thoracolumbar region and the lumbosacrum.[56-59] Most dogs will eventually develop radiographic criteria of spondylosis deformans. Clinicians should be aware that spondylosis deformans is not an inflammatory process but rather a disease of the attachments of the vertebral joints, which involves the fibers joining the intervertebral discs to the vertebral endplates.[59,60] The outer rim of the annulus fibrosus has strong circumferential attachments to the vertebral endplate with Sharpey fibers, which are enmeshed in cortical bone (Fig. 11-21). The annulus fibrosus is also anchored to the dorsal longitudinal ligaments by short fibers, adding stability to the vertebral column. The intervertebral disc acts as a thick-walled pressure vessel that is subject to dynamic loading and deformation during locomotion.[61] Collagen fibers within the annulus provide reinforcement during compression, bending, and torsion of the disc. The exact cause of spondylosis deformans is unknown, but etiopathogenesis might include repetitive trauma, instability, normal aging and wear and tear, and hereditary predisposition.[58,59] However, convincing evidence of a hereditary component was not found in studies of boxer dogs.[62,63] Presently accepted theory states that disruption of Sharpey's fibers is the initiator, leading to radiographically evident osseous proliferation or *enthesopathy* of the margins of the endplate (see Fig. 11-21).[60,61] These enthesophytes are variably sized ventrolateral spurs that have been referred to mistakenly as *osteophytes*. This is incorrect because osteophytes occur at osteochondral junctions of synovial joints, not the retinacular attachments. Eventually ventral vertebral enthesophytes can bridge the intervertebral disc space at single or multiple sites, leading to fusion. When this occurs in the thoracolumbar column, adjacent vertebral junctions are at risk for disc degeneration because they are subject to increased stress and strain. Radiographic findings may also include endplate thickening and narrowing of the intervertebral disc space, which is also possibly related to concurrent disc degeneration and loss of compressibility of the disc[58,59] (Fig. 11-22).

Whether or not disc degeneration is a factor in the development of spondylosis deformans is unclear. In dogs, type II intervertebral disc disease may be part of the pathogenesis of spondylosis deformans (Fig. 11-23).[64] Although type II intervertebral disc disease is often seen in dogs at sites of spondylosis deformans, cause and effect are not clearly established. Tears of the annulus may occur in dogs with spondylosis deformans, predisposing to type II disc protrusion. Most agree that spondylosis deformans is insignificant clinically, unless a concurrent prolapsed disc is present, or if there is bony impingement on the spinal cord or spinal nerve roots. Nerve root compression from spondylosis is rare except in lumbosacral instability where foraminal impingement results from dorsal extension of the enthesophytes.

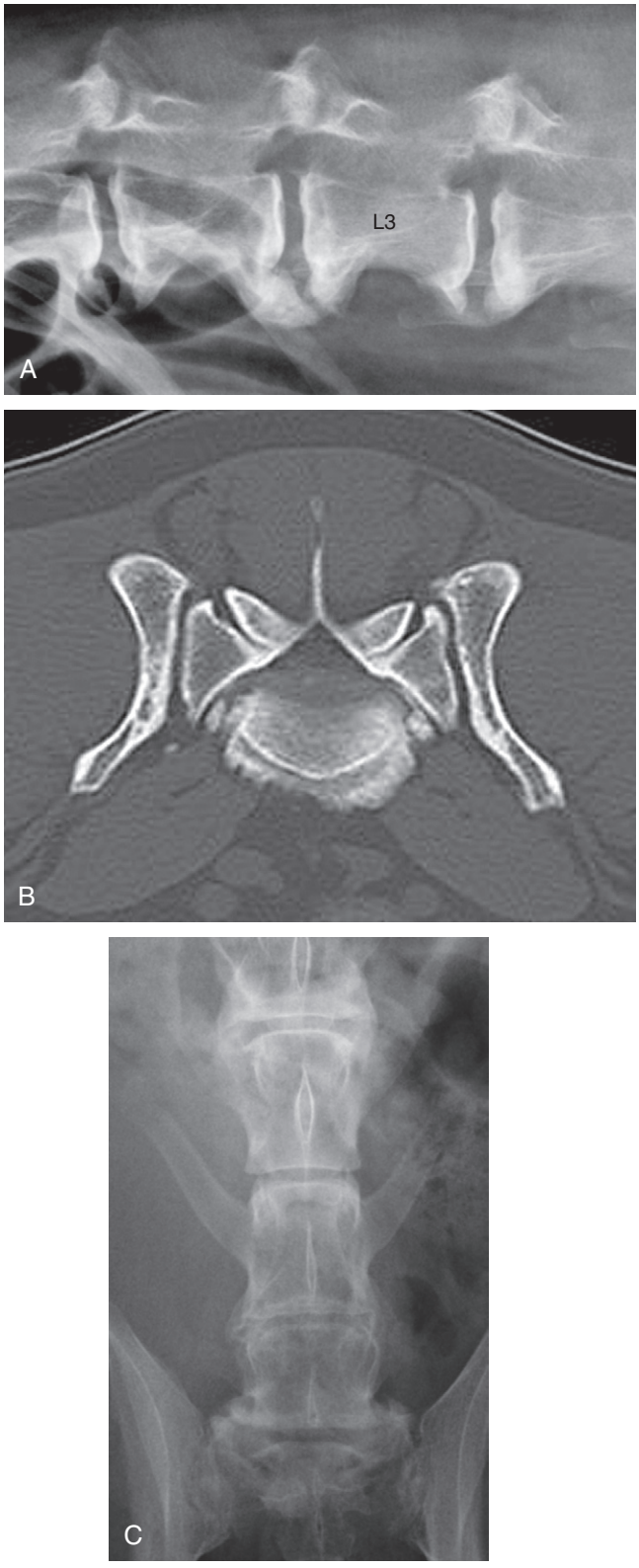


Fig. 11-22 **A,** Lateral radiograph of the lumbar spine. There are ventral enthesophytes at L1-L2, L2-L3, and L3-L4. There is endplate sclerosis of the cranial aspect of L4. The radiolucent region between the ventral enthesophytes at L2-L3 is often confused with a fracture, but this is only a region where the enthesophytes are approaching each other. This gap may eventually fuse completely. *L3*, Third lumbar vertebral body. **B,** Transverse CT image of a dog with spondylosis. There is ventral osseous proliferation without impingement of the vertebral canal. Note that the dorsal intervertebral process joints are unaffected. **C,** Ventrodorsal radiograph of a dog with spondylosis that has resulted in lateral enthesophytes at L4-L5, L6-L7, and L7-S1. Lateral enthesophytes are rarely of clinical importance because their location is ventral to the spinal cord and nerve roots.

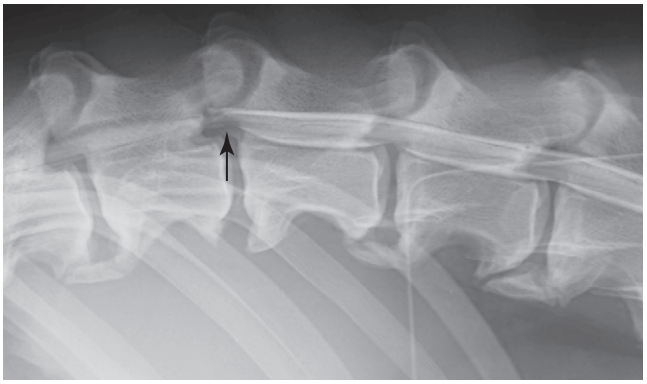


Fig. 11-23 Lateral myelogram of a dog with ataxia and loss of conscious proprioception of the pelvic limbs. There is extensive ventral enthesophyte formation at multiple sites. There is dorsal displacement of the ventral aspect of the subarachnoid space, containing contrast medium *(black arrow)* at T13-L1, and spinal cord compression secondary to a type II intervertebral disc protrusion. Whether or not spondylosis predisposed to disc prolapse is unknown, but the disc prolapse and not the advanced spondylosis deformans was responsible for clinical signs.

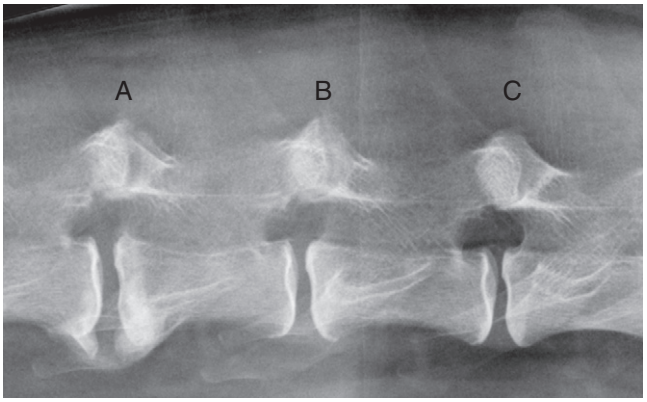


Fig. 11-24 Lateral radiograph of a dog with articular process degenerative joint disease. The joint C is normal. The joint *A* has subchondral sclerosis and mild osteophyte formation. The joint *B* is narrow with large osteophytes. Because of the limited motion of these joints, clinical signs of degenerative joint disease are rarely present; however, in some instances, enlarged articular processes may impinge the spinal cord dorsally, causing neurologic signs.

Osteoarthritis of the Dorsal Intervertebral Articular Process Joints

The synovial joints of the vertebral column are composed of the articular processes of adjoining vertebrae and are subject to degeneration or osteoarthritis as is any other synovial joint.[1] Typical radiographic changes include remodeling of the articular processes, osteophytosis, and thinning of the joint space. These changes are best seen on lateral radiographs (Fig. 11-24). Although osteoarthritis of the articular process joints can be seen concomitantly with spondylosis deformans, these are separate entities. No specific clinical signs have been attributed to articular process degenerative joint disease in dogs, with the exception of instances where there is articular process hypertrophy in dogs with cervical spondylomyelopathy. Osteoarthritis of the articular processes is seen rarely in cats.

Caudal Equina Syndrome

The lumbosacral junction is unique because of its structure, relatively wide range of mobility, and the fact that it houses nerve roots of the caudal aspect of the spinal cord. The terminal part of the spinal cord is the conus medullaris and

contains sacral and caudal segments.[65] In dogs, the spinal cord terminates near the level of L6 or L7, depending on breed,[66] and at L7 in cats.[67] The *cauda equina* refers specifically to the collection of nerve roots that lie within the vertebral canal caudal to the termination of the spinal cord.[68] These nerve roots stream caudally from their respective sacrocaudal cord segment, exiting the vertebral canal through intervertebral foramina, caudal to their origin in the spinal cord. This is because the spinal cord is shorter than the vertebral column insofar as they have differential fetal growth rates. Thus the spinal nerves descending from the L7 spinal cord segment exit the vertebral canal at the L7-S1 intervertebral foramina and are lateral to the remainder of the cauda equina.

Numerous degenerative, inflammatory, traumatic, and neoplastic conditions can affect the lumbosacrum of dogs and cats and result in result in pain, neural dysfunction, and exercise restriction.[69,70] Because most of these conditions involve the cauda equina, the term *cauda equina syndrome* has been applied. Numerous other terms are used in conjunction with cauda equina syndrome and include lumbosacral disease, lumbosacral stenosis and degenerative lumbosacral stenosis, lumbosacral malarticulation malformation, lumbosacral instability, and others.[9,69,71] In most instances, there is compression, inflammation, ischemia, and/or disruption of the cauda equina.[71] Specific conditions causing cauda equina syndrome are also numerous.[9,69-74] In the dog, degenerative lesions are common and include intervertebral disc disease, instability of the lumbosacrum, stenosis from remodeling changes associated with spondylosis deformans, and impingement from capsulitis because of osteoarthritis of the articular process joints[69] (Fig. 11-25).

Lumbosacral fractures, discospondylitis, and neoplasms including nerve sheath tumors and bone and soft tissue sarcomas have the potential to cause cauda equina signs (Fig. 11-26). An osteochondrosis-like lesion of the sacral endplate causing intervertebral disc prolapse and compression of the cauda equina has been reported in German shepherd dogs.[73] Cauda equina syndrome is uncommon in cats, but sacrocaudal trauma or a tail pull injury with avulsion of the cauda equina may be confused with typical signs of cauda equina syndrome.[69]

The various techniques for imaging cauda equina syndrome have been reviewed extensively.[71] MR imaging and CT are the modalities of choice for imaging the lumbosacral region because of their lack of summation, superior contrast resolution, and multiplanar capability. MR imaging allows direct visualization of the spinal cord and the cauda equina.[74] However, conventional radiography can be useful for an initial evaluation of dogs and cats with signs of cauda equina syndrome. Conditions that produce osseous lesions (e.g., discospondylitis, subluxation, stenosis of the vertebral canal, osseous neoplasia, etc.) may be identified on lateral and VD radiographs. Soft tissue lesions of the lumbosacrum, such as prolapse of the intervertebral disc, soft tissue neoplasia, or nerve root entrapment, are not identified; thus conventional radiographic evaluation is subject to a false-negative result.[71] Positional radiography,[75] myelography,[76,77] epidurography,[77] and discography[78] are helpful for diagnosis of lumbosacral disease; however, these invasive modalities are rarely used since the availability of MR imaging and CT. Before employing myelography, it should be noted that the dural sac has a variable termination and may not extend to the lumbosacral junction; therefore a soft tissue lesion, such as a prolapsed disc, may not be detected.

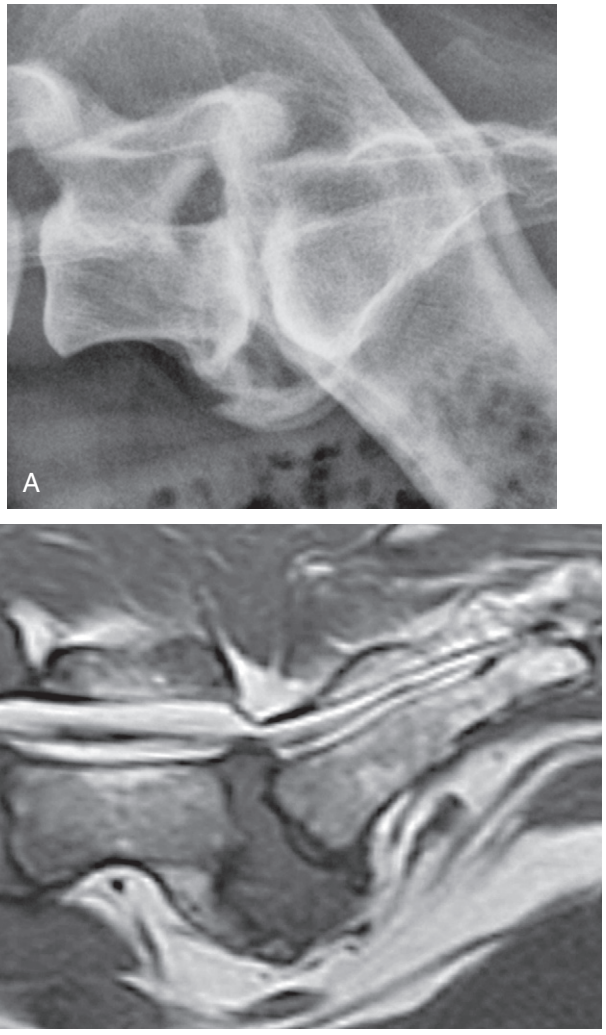


Fig. 11-25 **A,** Lateral radiograph of the lumbosacrum of a dog with chronic lumbosacral pain. There is narrowing of the intervertebral disc space, malalignment of L7-S1 and sclerosis, and remodeling of the endplates. The malalignment leads to entrapment of spinal nerves (cauda equina), and there is often concurrent disc herniation that adds to the compression. Conformation of this change is best accomplished with either MR or CT imaging rather than myelography or epidurography. **B,** MR image, T1-weighted sagittal plane, of a different animal with similar signs. There is protrusion of the intervertebral disc at L7-S1 and compression of the nerve roots in the vertebral canal.

NEOPLASIA

The vertebrae are affected commonly by primary or metastatic neoplasia.[79,80] Pain and/or neuropathy can result, depending on the location and extent of the tumor. Large to medium breeds are overrepresented, and most animals are 7 years old or older. Sarcomas, including osteosarcoma, chondrosarcoma, hemangiosarcoma, and fibrosarcoma are the most common primary vertebral neoplasms in dogs and cats. Multiple myeloma and lymphoma also affect vertebrae. In 61 canine vertebral tumors, the most common site for primary neoplasia was the thoracic area, whereas most metastatic neoplasms were found in the lumbar area.[79] Metastatic neoplasia is more common than primary vertebral neoplasia, and carcinomas and sarcomas are the most common cell type.[79,80] The preceding classification does not include tumors originating from the meninges or spinal cord, although some neoplasms cause local invasion of the vertebra and/or osseous remodeling of the vertebral foramen. Radiographic signs of vertebral neoplasia are nonspecific and typical of an aggressive bone response and include bone lysis, new bone production, and pathologic fracture (Fig. 11-27). Metastatic neoplasms cannot be differentiated reliably from primary neoplasms based on

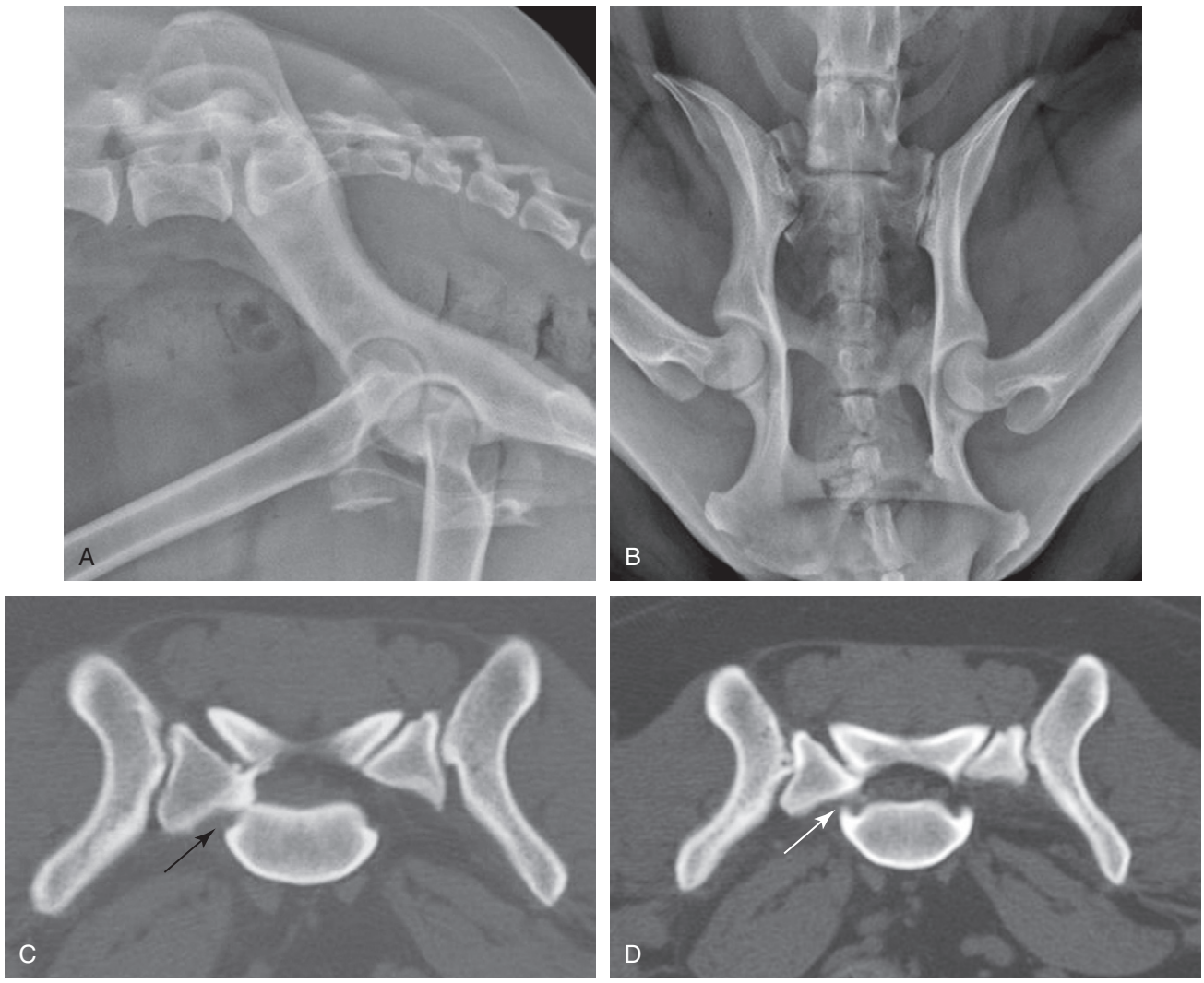


Fig. 11-26 Images of a dog that was hit by a car and presented with right pelvic limb paresis and pain. **A,** Lateral radiograph. There are pubic and ischial fractures. **B,** Ventrodorsal radiograph. There is an oblique fracture of the right sacral wing with mild displacement; pubic and ischial fractures are also present. Although these changes are not striking. Transverse plane CT images **C,** and **D,** of the same animal confirm that the right sacral fracture is segmental and has narrowed the right intervertebral foramen of the lumbosacrum *(black arrow)*, compressing the nerve roots as they exit the vertebral canal. This illustrates the value of cross-sectional imaging in evaluating patients with cauda equina syndrome.

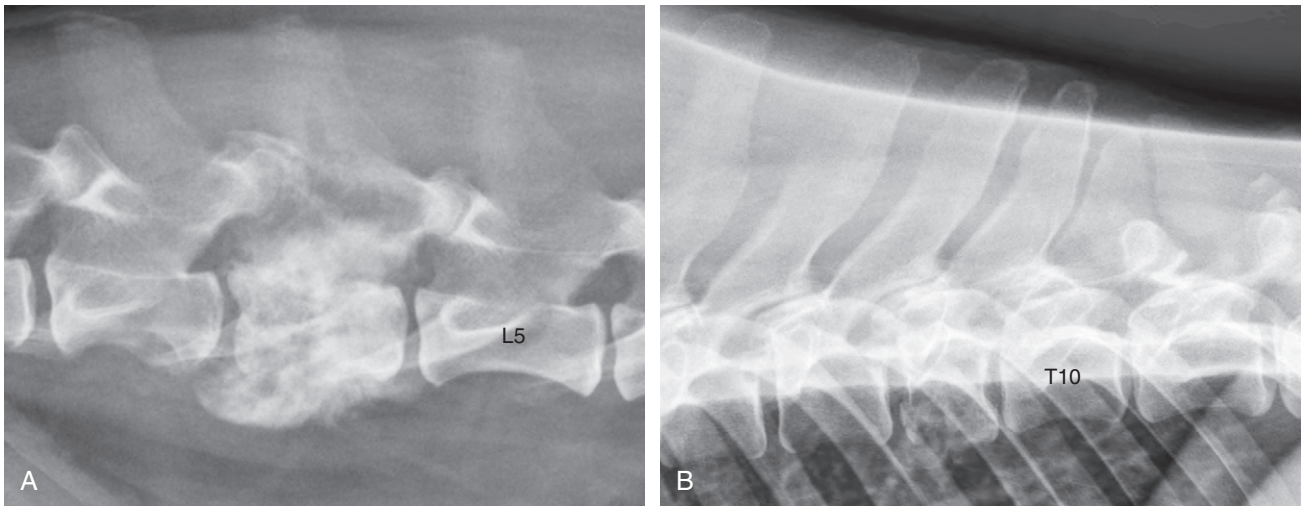


Fig. 11-27 **A,** Lateral radiograph of a dog with a tumor of L4. There are regions of lysis in the vertebral arch and the body, and there is also active new bone formation on the ventral aspect of the body. *L4,* Fourth lumbar vertebral body. **B,** Lateral radiograph of a dog with a compression fracture of T9 caused by metastatic cancer. The body is heterogeneously lytic and foreshortened with multiple areas of cortical effacement. *T10,* Tenth thoracic vertebral body. Each of these lesions is characterized as aggressive radiographically.

radiographic findings; however, primary neoplasms frequently involve only one vertebra, whereas many metastatic neoplasms are polyostotic.

Multiple myeloma and lymphoma frequently cause multiple focal osteolytic lesions in the vertebral processes that are easily recognized on conventional radiographs (Fig. 11-28). However, these changes are not pathognomonic. Additionally, normal old dogs and cats may have a coarse trabecular pattern, especially in C2, that should not be confused with a neoplastic lesion.

It is vital to remember that significant loss of calcified osseous matrix must be present before a destructive lesion is evident radiographically. In people, metastatic lesions within the trabecular bone must be at least 1.5 cm in diameter and have 50% to 75% loss of local calcium before being detected on survey radiographs.[81] CT and MR imaging are superior for determining the extent and soft tissue changes associated with vertebral neoplasms and essential for decision making and staging before therapy. CT in particular is more sensitive for identifying bone loss than conventional radiography. Table 11-2 summarizes salient features of inflammatory and degenerative conditions of the vertebrae.

METABOLIC AND UNCLASSIFIED CONDITIONS

Disseminated Idiopathic Skeletal Hyperostosis

Disseminated idiopathic skeletal hyperostosis (DISH) is recognized infrequently in dogs. Principal radiographic features include extensive linear new bone formation along the ventrolateral aspect of the vertebral column and ankylosis (Fig. 11-29). Although these changes appear similar to advanced spondylosis deformans, DISH is likely a separate entity; the predominant excessive ventral distribution supports this contention. In the dog, seven criteria have been proposed to help distinguish DISH from spondylosis deformans:[82] (1) bridging ossification along ventral and lateral aspects of three contiguous vertebral bodies; (2) relative preservation of disc-space width within involved areas and absence of changes of degenerative disc disease, such as endplate sclerosis, nuclear calcification, or localized spondylosis deformans; (3) osteoarthritis of the dorsal intervertebral process joints; (4) pseudoarthrosis of the spinous processes; (5) enthesopathy of soft tissue attachments in both axial and appendicular skeleton; (6) osteophytes, sclerosis, and ankylosis of the sacroiliac joints; and (7) bony ankylosis of the symphysis pubis. It is suggested that at least four of the seven criteria be present for confirmation of DISH in the dog.[82]

Mucopolysaccharidosis

Radiographic changes of mucopolysaccharidosis type VI in cats include multiple skeletal abnormalities.[83] In the vertebral column, principal changes are remodeling and shape change of the vertebra, spondylosis deformans, and abnormal development of the dens. These changes are primarily a manifestation of vertebral epiphyseal dysplasia (Fig. 11-30). Changes in the appendicular skeleton include epiphyseal dysplasia of long bones, abnormal nasal choncal development, and coxofemoral subluxation.

Table • **11-2**

Salient Radiographic Features of Inflammatory Conditions of the Vertebral Column

CONDITION	OSSEOUS PRODUCTION	OSTEOLYSIS	NARROWED DISC SPACE
Spondylitis	+; vertebral body	—	—
Vertebral Osteomyelitis	+; vertebral body	+; vertebral body	—
Vertebral physitis	+; vertebral endplate	+; vertebral physis	—
Discospondylitis	+; vertebral body and endplate	+; endplate erosion	+



Fig. 11-28 Lateral cervical radiograph of a dog with multiple myeloma. There are numerous regions of bone lysis in the cervical spine, affecting C2-C5.

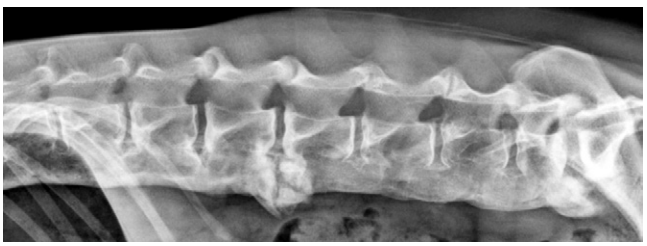


Fig. 11-29 Lateral radiograph of a dog with extensive bridging ventral spondylosis that is consistent with disseminated idiopathic skeletal hyperostosis.



Fig. 11-30 Lateral radiograph of a cat with mucopolysaccharidosis. There is extensive remodeling and shape change of the cervical and thoracic vertebrae. Note the small and irregularly mineralized vertebral epiphyses, typical of this condition.

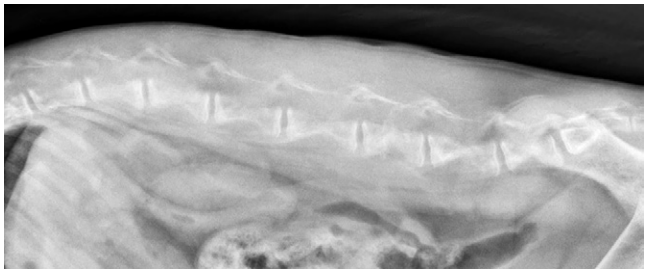


Fig. 11-31 Lateral radiograph of a cat with nutritional secondary hyperparathyroidism. There is marked generalized osteopenia with reduction in bone opacity. The normal high contrast between bone and soft tissue has been lost.

Osteopenia

Nutritional secondary hyperparathyroidism can result in generalized bone loss with cortical and trabecular thinning of the vertebra and pathologic fracture (Fig. 11-31). As mentioned previously, significant calcium loss must occur before radiographic confirmation of vertebral osteolysis is possible. Although senile osteopenia and osteopenia secondary to other endocrinopathies have been described,[9] the degree of bone loss is usually insufficient for detection on survey radiographs of the vertebral column.

REFERENCES

1. Thrall DE, Robertson ID: The spine. *Atlas of normal radiographic anatomy and anatomic variants of the dog and cat*, St. Louis, 2010, Saunders.
2. Evans HE: *Miller's anatomy of the dog*, ed 3, Philadelphia, 1993, Saunders, pp 166–180.
3. Watson AG: *Phylogeny and development of the atlas-axis complex in the dog*, Master's thesis, Ithaca, NY, 1981, Cornell University.
4. Watson AG: Prenatal development of the composite occipito-atlanto-axial synovial joint cavity in the dog, *Anat Rec* 216:423–433, 1986.
5. Watson AG, Evans HE, DeLahunta A: Ossification of the atlas-axis complex in the dog, *Anat Histol Embryo* 15:122–138, 1986.
6. Evans HE: *Miller's anatomy of the dog*, ed 3, Philadelphia, 1993, Saunders, p 178.
7. Evans HE: *Miller's anatomy of the dog*, ed 3, Philadelphia, 1993, Saunders, pp 225–231.
8. Shores A: Intervertebral disc syndrome in the dog. Part I. Pathophysiology and management, *Compend Contin Edu Prac Vet* 7:639, 1981.
9. Walker MA: The vertebrae—canine and feline In Thrall DE: *Textbook of veterinary diagnostic radiology*, ed 4, St. Louis, 2002, Saunders, pp 98–109.
10. Baines, EQ, Grandage J, Herritage, ME, et al: Radiographic definition of the anticlinal vertebra in the dog, *Vet Radiol Ultrasound* 50:69–73, 2009.
11. Morgan JP: Congenital anomalies of the vertebral column of the dog: a study of the incidence and significance based on a radiographic and morphologic study, *J Am Vet Radiol Soc* 9:21–29, 1968.
12. Bailey CS, Morgan JP: Congenital spinal malformations, *Vet Clin North Am Small Anim Pract* 72:985–1015, 1992.
13. Lin J-L, Coolman BR: Atlantoaxial subluxation in two dogs with cervical block vertebrae, *J Am Anim Hosp Assoc* 45:305–310, 2009.
14. Done SH, Drew RA, Robins GM, et al: Hemivertebra in the dog: clinical and pathological observations, *Vet Rec* 14:313–317, 1975.
15. Muller F, O'Rahilly R, Benson DR: The early origin of vertebral anomalies, as illustrated by a "butterfly" vertebra, *J Anat* 149:157–169, 1986.
16. Damur-Djuric N, Steffen F, Hassig M, et al: Lumbosacral transitional vertebrae in dogs: classification, prevalence and association with sacroiliac morphology, *Vet Radiol Ultrasound* 47:32–38, 2006.
17. Fluckiger M, Damur-Djuric N, Hassig M, et al: A lumbosacral transitional vertebra in the dog predisposes to caudal equina syndrome, *Vet Radiol Ultrasound* 47:39–44, 2006.
18. Lorenz, MD, Kornegay JN: *Handbook of veterinary neurology*, ed 4, St. Louis, 2004, Saunders, pp 164–189.
19. Cook JR, Oliver JE: Atlantoaxial luxation in the dog, *Compend Contin Educ Pract Vet* 3:242–252, 1981.
20. Watson AG, DeLahunta A: Atlantoaxial subluxation and absence of a transverse ligament of the atlas in dog, *J Am Vet Med Assoc* 195:235–237, 1989.
21. Lincoln JD: Cervical vertebral malformation/malarticulation syndrome in large dogs, *Vet Clin North Am Small Anim Pract* 22:923–935, 1992.
22. Seim HB, Withrow SJ: Pathophysiology and diagnosis of caudal cervical spondylo-myelopathy with emphasis on the Doberman pinscher, *J Am Anim Hosp Assoc* 18:241, 1982.
23. Van Gundy T: Canine wobbler syndrome. Part I: pathophysiology and diagnosis, *Compend Contin Educ Pract Vet* 11:269, 1989.
24. Selcer B, Oliver J: Cervical spondylopathy: wobbler syndrome in dogs, *J Am Anim Hosp Assoc* 11:175–179, 1975.
25. Seim H: Diagnosis and treatment of cervical vertebral instability-malformation syndromes. In Bonagura JD, editor: *Kirk's current veterinary therapy XIII: small animal practice*, Philadelphia, 2000, Saunders, pp 992–1000.
26. Headhammer A, Wu F, Krook L, et al: Over nutrition and skeletal disease. An experimental study in growing Great Dane dogs, *Cornell Vet* 64(Suppl 5):58, 1974.
27. Lipsitz D, Levitski RE, Chauvet AE, et al: Magnetic resonance features of cervical stenotic myelopathy in 21 dogs, *Vet Radiol Ultrasound* 42:20–27, 2001.
28. Da Costa RC, Parent J, Dobson H: Comparison of magnetic resonance imaging and myelography in 18 Doberman pinscher dogs with cervical spondylo-myelopathy, *Vet Radiol Ultrasound* 47:523–531, 2006.
29. Shores A: Spinal trauma. Pathophysiology and management of traumatic spinal injuries, *Vet Clin North Am Small Anim Pract* 22:859–867, 1992.
30. Matthiesen DT: Thoracolumbar spinal fractures and luxations: surgical management, *Compend Cont Educ Pract Vet* 5:867, 1983.

31. Walker TL, Tomlinson J, Sorjonen DC, et al: Diseases of the spinal column. In Slatter DH, editor: *Textbook of small animal surgery*, Philadelphia, 1985, Saunders, p 1367.
32. Watters DH, Blevins WE, Wallace LJ: Cervical vertebral fractures in 56 dogs: a retrospective study, *J Am Anim Hosp Assoc* 35:135–146, 1999.
33. Slocum B, Rudy RL: Fractures of the seventh lumbar vertebra in the dog, *J Am Anim Hosp Assoc* 11:67, 1975.
34. Kinns J, Mai W, Seiler G, et al: Radiographic sensitivity and negative predictive value for acute canine spinal trauma, *Vet Radiol Ultrasound* 47:563–570, 2006.
35. Hoerlein BF: C*anine neurology: diagnosis and treatment*, ed 3, Philadelphia, 1978, Saunders, pp 470–560.
36. DeLahunta A: *Veterinary neuroanatomy and clinical neurology*, ed 2, Philadelphia, 1983, Saunders, pp 186–188.
37. Priester W: Canine intervertebral disc disease—occurrence by age, breed, and sex among 8,117 cases, *Theriogenology*, 6:93–303, 1976.
38. Chang Y, Dennis R, Platt, et al: Magnetic resonance imaging of traumatic intervertebral disc extension in dogs, *Vet Record* 160:795–799, 2007.
39. Robertson ID, Thrall DE: Imaging dogs with suspected disc herniation: pros and cons of myelography, computed tomography and magnetic resonance, *Vet Radiol Ultrasound* 52(Suppl 1):S81–S84, 2011.
40. Owens JM, Biery DN: Spine. In Owens JM, Biery DN, editors: *Radiographic interpretation for the small animal clinician*, ed 2, Philadelphia, 1999, Williams & Wilkins, pp 143–144.
41. Hugnet C, Marrou B, Dally C, et al: Osteomyelitis and discospondylitis due to *Scedosporium apiospermum* in a dog, *J Vet Diagn Invest* 21:120–123, 2009.
42. Csébi P, Jakab C, Jánoski K: Vertebral osteomyelitis and meningitis caused by *Pasteurella canis* in a dog—clinicopathological case report, *Acta Vet Hung* 58:13–21, 2010.
43. La Croix JA: Vertebral body osteomyelitis: case report, *J Am Vet Rad Soc* 14:17–21, 1973.
44. Kuwamura M, Ide M, Yamate J, et al: Systemic candidiasis in a dog, developing spondylitis, *J Vet Med Sci* 68:1117–1119, 2006.
45. Johnston DE, Summers BA: Osteomyelitis of the lumbar vertebrae in dogs caused by grass-seed-foreign bodies, *Aust Vet J* 47:289, 1971.
46. van der Merwe L, Kirberger RM, Clift S, et al: *Spirocerca lupi* infection in the dog: a review, *Vet J* 176:294–309, 2008.
47. Thomas WB: Discospondylitis and other vertebral infections, *Vet Clin North Am Small Anim Pract* 30:169–182,2000.
48. DeLahunta A: Small animal spinal cord disease. In DeLahunta A, editor: *Veterinary neuroanatomy and clinical neurology*, ed 2, Philadelphia, 1983, Saunders, p 190.
49. Naughton JF, Tucker R, Bagley RS: Radiographic diagnosis-paraspinal abscess in a dog, *Vet Radiol Ultrasound* 46:23–26, 2005.
50. Jimenez MM, O'Callaghan MW: Vertebral physitis: a radiographic diagnosis to be separated from discospondylitis, a preliminary report, *Vet Radiol Ultrasound* 36:188–195, 1995.
51. Moore MP: Discospondylitis, *Vet Clin North Am Small Anim Pract* 22:1027–1033, 1992.
52. Packer RA, Coates JR, Cook CR, et al: Sublumbar abscess and discospondylitis in a cat, *Vet Radiol Ultrasound* 46:396–399, 2005.
53. Tipold A, Stein VM: Inflammatory diseases of the small animal spine, *Vet Clin North Am Small Anim Pract* 40:871–879, 2010.
54. Carrera I, Sullivan M, McConnell F, et al: Magnetic resonance features of discospondylitis in dogs, *Vet Radiol Ultrasound* 52:125–131, 2011.
55. *Dorland's illustrated medical dictionary*, ed 28, Philadelphia, 1996, Saunders, p 1564.
56. Morgan JP: Spondylosis deformans in the dog, *Acta Orthop Scand Suppl* 96, 1967.
57. Morgan JP, Biery DN: Spondylosis deformans. In Newton CD, editor: *Textbook of small animal orthopaedics*, Philadelphia, 1985, Lippincott Williams & Wilkins, pp 733–738.
58. Morgan JP: Spondylosis deformans in the dog: its radiographic appearance, *J Am Vet Radiol Soc* 8:17, 1967.
59. Morgan JP, Miyabayashi T: Degenerative changes in the vertebral column of the dog: common radiographic findings, *Vet Radiol Ultrasound* 29:72–77, 1988.
60. Resnick D: Degenerative disease of the spine. In Resnick D, editor: *Bone and joint imaging*, ed 2, Philadelphia, 1996, Saunders, p 355.
61. Hulkins DW, Meakin, JR: Relationship between structure and mechanical function of the tissues of the intervertebral joint, *Am Zool* 40:42–52, 2000.
62. Carnier P, Gallo L, Sturaro E, et al: Prevalence of spondylosis deformans and estimates of genetic parameters for the degree of osteophytes development in Italian boxer dogs, *J Anim Sci* 82:85–92, 2004.
63. Langeland M, Lingaas F: Spondylosis deformans in the boxer: estimates of heritability, *J Small Anim Pract* 36:166–169, 1995.
64. Levine GJ, Levine JM, Walker MA, et al: Evaluation of the association between spondylosis deformans and clinical signs of intervertebral disc disease in dogs: 172 cases (1999–2000), *J Am Vet Med Assoc* 228:96–100, 2006.
65. Evans HE: *Miller's anatomy of the dog*, ed 3, Philadelphia, 1993, Saunders, pp 804–806.
66. Morgan JP, Atilola M, Bailey CS: Vertebral canal and spinal cord mensuration. A comparative study and its effect on lumbosacral myelography in the dachshund and German shepherd dog, *J Am Vet Med Assoc* 191:951–957, 1987.
67. Pardo AD, Morgan JP: Myelography in the cat: a comparison of cisternal versus lumbar puncture, using metrizamide, *Vet Radiol* 29:89–95, 1988.
68. *Dorland's illustrated medical dictionary*, ed 28, Philadelphia, 1994, Saunders, p 280.
69. Wheeler SJ: Lumbosacral disease, *Vet Clin North Am Small Anim Pract* 22:937–950,1992.
70. Lenehan TM: Canine caudal equina syndrome, C*omp Cont Educ Pract Vet* 5:941–950,1983.
71. Ramirez O, Thrall DE: A review of imaging techniques for canine cauda equina syndrome, *Vet Radiol Ultrasound* 39:283–296, 1998.
72. Jones JC, Sorjonen DC, Simpson ST, et al: Comparison between computed tomographic and surgical finding in 9 large breed dogs with lumbosacral stenosis, *Vet Radiol Ultrasound* 37:247–256, 1996.
73. Lang J, Hani H, Schwalder P: A sacral lesion resembling osteochondrosis in the German shepherd dog, *Vet Radiol Ultrasound* 33:69–76, 1992.
74. Adams WH, Daniel GB, Pardo AD, et al: Magnetic resonance imaging of the caudal lumbar and lumbosacral spine in 13 dogs (1990–1993), *Vet Radiol Ultrasound* 36:3–13, 1995.
75. Lang J: Flexion-extension myelography canine caudal equina, *Vet Radiol Ultrasound* 29:242–257, 1988.
76. Widmer WR, Thrall DE: Canine and feline intervertebral disc disease, myelography, and spinal cord disease. In Thrall DE, editor: *Textbook of veterinary diagnostic radiology*, ed 5, St. Louis, 2007, Saunders, pp 194–219.

77. Roberts RE, Selcer BA: Myelography and epidurography, *Vet Clin North Am Small Anim Pract* 23:307–329, 1993.
78. Barthez PY, Morgan JP, Lipstiz D: Discography and epidurography for evaluation of the lumbosacral junction in dogs with cauda equina syndrome, *Vet Radiol Ultrasound* 35:152–157, 1994.
79. Morgan JP, Ackerman N, Bailey, CS: Vertebral tumors in the dog: a clinical radiologic and pathologic study of 61 primary and secondary lesions, *Vet Radiol Ultrasound* 21:197–212, 1980.
80. Luttgen PL: Neoplasms of the spine, *Vet Clin North Am Small Anim Pract* 22:973–984, 1992.
81. Edelstyn GA, Gillespie PJ, Grebbel FS: The radiological demonstration of osseous metastasis: experimental observations, *Clin Radiol* 18:158, 1967
82. Morgan JP, Stavenborn M: Disseminated idiopathic skeletal hyperostosis (DISH) in a dog, *Vet Radiol Ultrasound* 32: 65–70, 1991.
83. Konde LJ, Thrall MA, Gasper P, et al: Radiographically visualized skeletal changes associated with mucopolysaccharidosis VI in cats, *Vet Radiol Ultrasound* 28:223–228, 1987.

ELECTRONIC RESOURCES

Evolve

Additional information related to the content in Chapter 11 can be found on the companion website at http://evolve.elsevier.com/Thrall/vetrad/

- Chapter Quiz

CHAPTER • 12

Magnetic Resonance Imaging and Computed Tomography Features of Canine and Feline Spinal Cord Disease

Wilfried Mai

Computed tomography (CT) and magnetic resonance (MR) imaging are used routinely in the investigation of spinal diseases in the dog and cat.[1-2] They are both superior to radiography in the diagnosis of many spinal conditions. MR imaging has a better overall diagnostic sensitivity than CT and can be used to diagnose virtually all conditions of the spine. However, there are patients in which CT is still the preferred method, such as for safety reasons, for example, vertebral trauma caused by a gunshot wherein metallic foreign material is present or for the diagnosis of subtle vertebral subluxation or fractures. Although a number of spinal conditions can be diagnosed with radiographs (e.g., discospondylitis), CT and MR imaging may still be warranted to better assess the extent of the condition, which may be important for diagnostic or therapeutic purposes. Earlier diagnosis of some conditions may also be permitted by CT or MR imaging.

NORMAL APPEARANCE OF THE SPINE ON COMPUTED TOMOGRAPHY AND MAGNETIC RESONANCE IMAGING

Normal Anatomy

A schematic representation of the components of the vertebrae and main ligaments of the spine is shown in Figures 12-1 and 12-2. The longitudinal ligaments of the vertebral column provide dorsal and ventral support for the intervertebral discs.[3] The dorsal longitudinal ligament lies on the floor of the vertebral canal. In the cervical region, it is wide and thick, which explains why lateral disc extrusion leading to radiculopathy, or root signature, is more common in the cervical region than other spinal regions. In the thoracolumbar area, the dorsal longitudinal ligament is thinner and centered on the midline allowing dorsal protrusion of disc material leading to spinal cord compression. The intercapital ligaments are short, transverse fibrous bands that lie ventral to the dorsal longitudinal ligament, joining left-to-right rib heads between T2 and T11[3]; they therefore buttress the dorsal part of the annulus fibrosus cranial to T11, reducing the probability of dorsal disc protrusion in this region. The ventral longitudinal ligament spans the ventral surface of the vertebral column.[3] The yellow ligaments *(ligamentum flavum)*, also called *interarcuate ligaments*, are loose, thin, elastic sheets that bridge the space between the arches of adjacent vertebrae.[3]

The spinal cord and spinal nerve roots lie in the vertebral canal, which is formed by the juxtaposition of all the individual vertebral foramina of the spine. The spinal cord begins at the foramen magnum and terminates caudally at the *conus medullaris*, around L6. The actual termination is caudal to L6 in smaller breeds of dogs and cats, whereas it is cranial to L6 in larger canine breeds.[4] Normal segmental widening of the spinal cord is present at the cervical and lumbar intumescences, and this should not be mistaken for pathologic cord swelling.[3] Spinal cord segments and vertebrae have the same numeric designation, with the exception of spinal cord segment C8, but the location of each spinal cord segment is usually cranial to the corresponding vertebral segment.[3] The ratio between the diameter of the spinal cord and the diameter of the vertebral canal varies between dog breeds, being higher in dachshunds and in other chondrodystrophic breeds in general versus nonchondrodystrophic breeds.[5]

The spinal cord is surrounded by the meninges. The pia mater is the innermost meningeal layer; it is firmly attached to the spinal cord and highly vascular.[6] The arachnoid membrane is next, and the dura mater is the outermost meningeal layer. The arachnoid and dura are attached closely to each other by a layer of dural border cells.[6] The subarachnoid space lies between the arachnoid and pia mater and contains cerebrospinal fluid (CSF) and arachnoid trabeculae that attach the arachnoid to the pia mater. The epidural space is peripheral to the dura mater and contains fat and the internal vertebral venous plexus.[6] The nerve roots exit through the intervertebral foramina. The collection of spinal nerve roots in the lumbosacral area is known as the *cauda equina*. CSF is found in the spinal subarachnoid space, which begins at the foramen magnum, where it communicates with the intracranial subarachnoid space, and ends caudally at the *filum terminale* near the lumbosacral junction. CSF is also found in the central canal of the spinal cord, which communicates with the fourth ventricle cranially and terminates caudally blindly at the *conus medullaris* or in some subjects is continuous with the lumbar subarachnoid space (see Figs. 12-1 and 12-2).[3]

Computed Tomography

On CT, cortical bone is thin and of uniformly high attenuation with smooth margins. Cancellous bone has a lacy or honeycomb appearance (Fig. 12-3). All components of the vertebra (laminae, pedicles, body, foramina, basivertebral venous canal, bony processes) are well visualized with CT. At the midportion of the body, the basivertebral venous canal is visible as a Y-shaped lucency, and a small dorsally projecting ridge of bone is seen within the ventral floor of the vertebral foramen at this site (see Fig. 12-3; see also Fig. 12-10).[7] The dorsal articular process diarthrodial joints have thin, smooth subchondral bone, and the articular processes are separated by a hypoattenuating space corresponding to synovial fluid and articular cartilage. On transverse images centered at the disc spaces, the combined margins of the dorsal aspect of the annulus of the

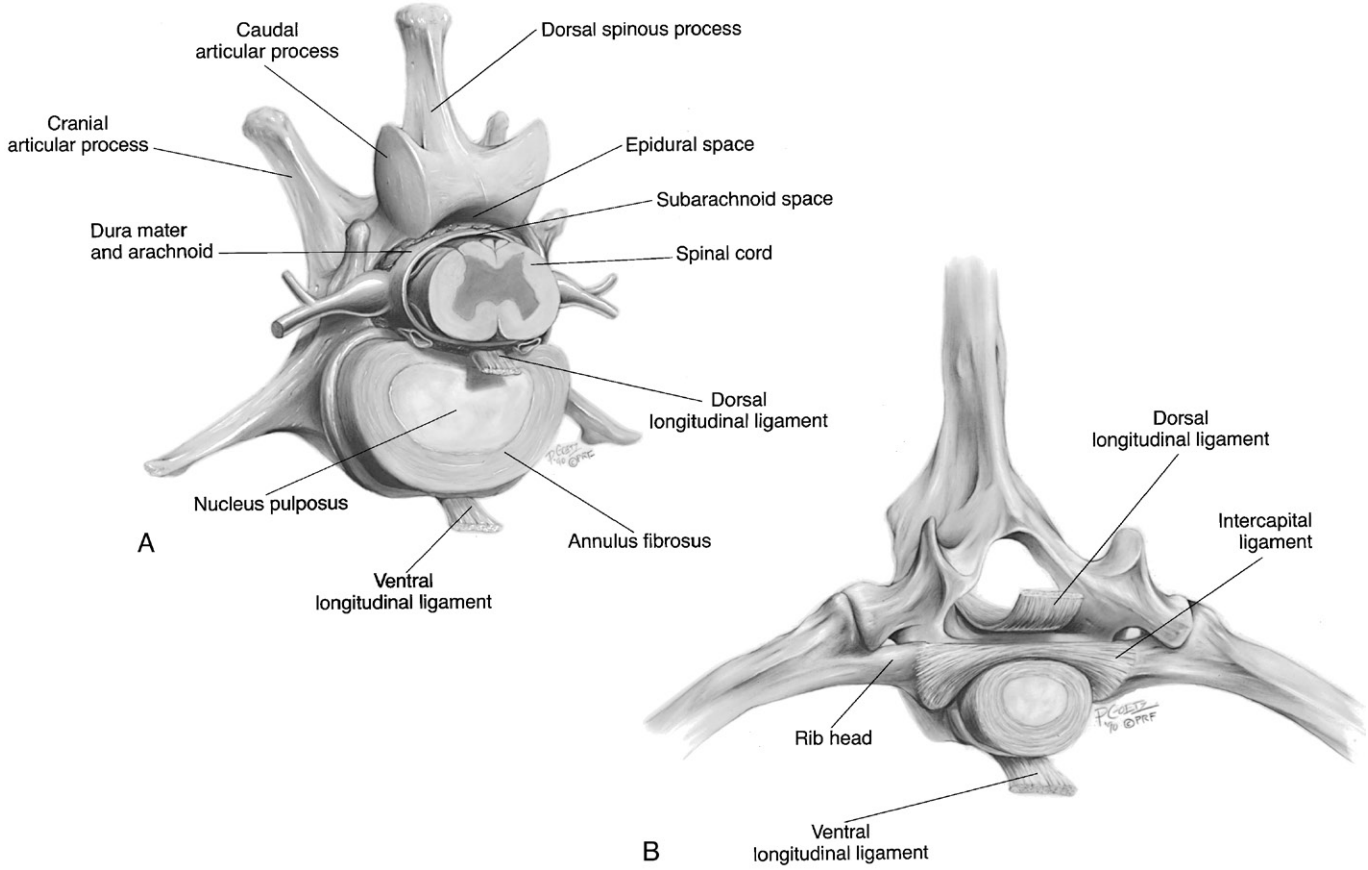


Fig. 12-1 Anatomic components of a typical lumbar vertebra **(A)** and a typical thoracic vertebra and articulation with ribs **(B).** (Modified from Evans HE, Christensen JC: *Miller's anatomy of the dog*, ed 2, Philadelphia, 1979, Saunders.)

intervertebral disc and dorsal longitudinal ligament and ventral aspect of the annulus and ventral longitudinal ligament appear as elliptical soft tissue attenuating structures. Occasionally the interarcuate ligament (ligamentum flavum) is seen as a curvilinear opacity spanning the dorsal laminae and blending with the joint capsule of the articular process joints. The ventral, dorsal, interspinous, and intertransverse ligaments are not resolved from surrounding structures. Epidural fat is hypoattenuating with respect to the soft tissue structures of the vertebral canal. The combination of the spinal cord, blood vessels, subarachnoid space with CSF, and meninges form a round to oval soft tissue attenuating structure in the middle of the vertebral canal that is surrounded by a rim of hypoattenuating epidural fat (see Fig. 12-3). Nerve roots can be seen as circular or linear soft tissue attenuating structures depending on their orientation in the scan plane.

When CT is performed after myelography, the thecal sac is hyperattenuating, allowing for more accurate differentiation among intramedullary, intradural, and extradural conditions. CT myelography can be achieved by injecting iodinated contrast medium in the subarachnoid space, at 25% of the regular myelographic dose.[8] This allows excellent delineation of the spinal cord and is useful in characterizing compressive lesions or spinal cord atrophy. The normal cross section of the cervical spinal cord is kidney shaped and slightly larger at C6-C7. In the thoracic area, there is a dramatic reduction of the spinal cord diameter, and it is also more round.[8]

Magnetic Resonance Imaging

On MR imaging, cortical bone appears as a black shell around the vertebra.[9]

On T1-weighted images, epidural and paraspinal fat are hyperintense to the spinal cord, whereas the intervertebral discs have medium signal intensity (Fig. 12-4).[9] The hyperintense epidural fat provides contrast for other spinal structures. The spinal cord, nerve roots, and bone marrow are isointense or slightly hypointense to the intervertebral discs. A low-signal shell around the cord represents a combination of CSF in the subarachnoid space, chemical shift artifact, and meningeal structures.[9] The dorsal and ventral longitudinal ligaments, as well as the ligamentum flavum, are visible only in the intervertebral areas where they are separated from the bone; they are of low signal intensity.[9] The joint capsule and synovial fluid of the articular process joints are not visible. The internal vertebral venous plexus consists of two symmetric hypointense oval structures, sharply marginated, located ventral to the spinal cord in the mid-body regions and diverging slightly from the ventral location at the level of the intervertebral disc spaces.

On T2-weighted images, normal intervertebral discs have high signal because of high water content in the nucleus pulposus and inner portion of the annulus fibrosus (see Fig. 12-4).[9-10] The epidural and paraspinal fat are still hyperintense, and the spinal cord and nerve roots are hypointense (Fig. 12-5). The bone marrow is hypointense compared with fat and is isointense or hypointense to the spinal cord. Depending on the amount of T2 weighting, the CSF in the subarachnoid space forms a thin hyperintense shell around the cord.[9] Sequences with a very heavy T2 weighting, such as single-shot fast spin echo (SSFSE), enhance the signal from CSF while suppressing the signal from background tissue, giving a natural myelographic effect.[11]

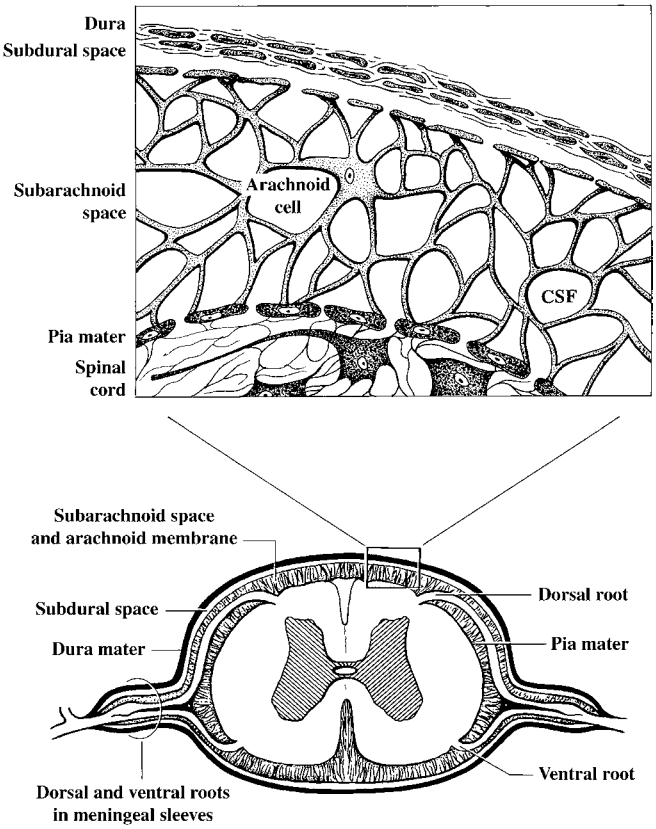


Fig. 12-2 Anatomic relation (transverse plane) of spinal cord, meningeal layers, and subarachnoid space. *Inset* shows microscopic structure of a segment of the meninges and spinal cord. (Modified from Hoerlein BF: *Canine neurology: diagnosis and treatment*, ed 3, Philadelphia, 1978, Saunders.)

INTERVERTEBRAL DISC DISEASE

The Normal Intervertebral Disc

Intervertebral discs are made of a peripheral annulus fibrosus and a central nucleus pulposus.[10] The disc lies in close contact with the cartilaginous vertebral end plates with fibers from the nucleus pulposus and annulus fibrosus being interwoven with the collagen fibers of the cartilaginous end plates and bony trabeculae.[9]

Both the annulus and the nucleus are made of fibrocartilage but differ in the amount of collagen and ground substance.[12] There is more collagen and less ground substance in the annulus than in the nucleus. The ground substance is composed of hyaluronic acid and glycosaminoglycans that hold water because of their strong negative charge.[12] A normal nucleus pulposus has a gelatinous consistency. Water, bound to large proteoglycan molecules, is the principal component of the nucleus pulposus (80% to 88%).[13] The normally very bright signal of the nucleus pulposus on T2-weighted images is caused by the long T2 relaxation time of water in the nucleus (see Fig. 12-4).[10]

Classification of Intervertebral Disc Disease

Apart from trauma causing extrusion of nondegenerated disc material (see specific paragraph later), degeneration of the intervertebral disc occurs before clinically significant intervertebral disc disease (IVDD).[10] Degenerative IVDD was first classified by Hansen.[14] Hansen type I IVDD is herniation of the nucleus pulposus through annular fibers with subsequent extrusion of nuclear material into the vertebral canal. Type I IVDD is more common in chondrodystrophic dogs. The degenerative process leading to type I herniation involves shifting concentrations of glycosaminoglycan, loss of water and proteoglycan content, and increased collagen content. The disc becomes more cartilaginous, and its nucleus becomes

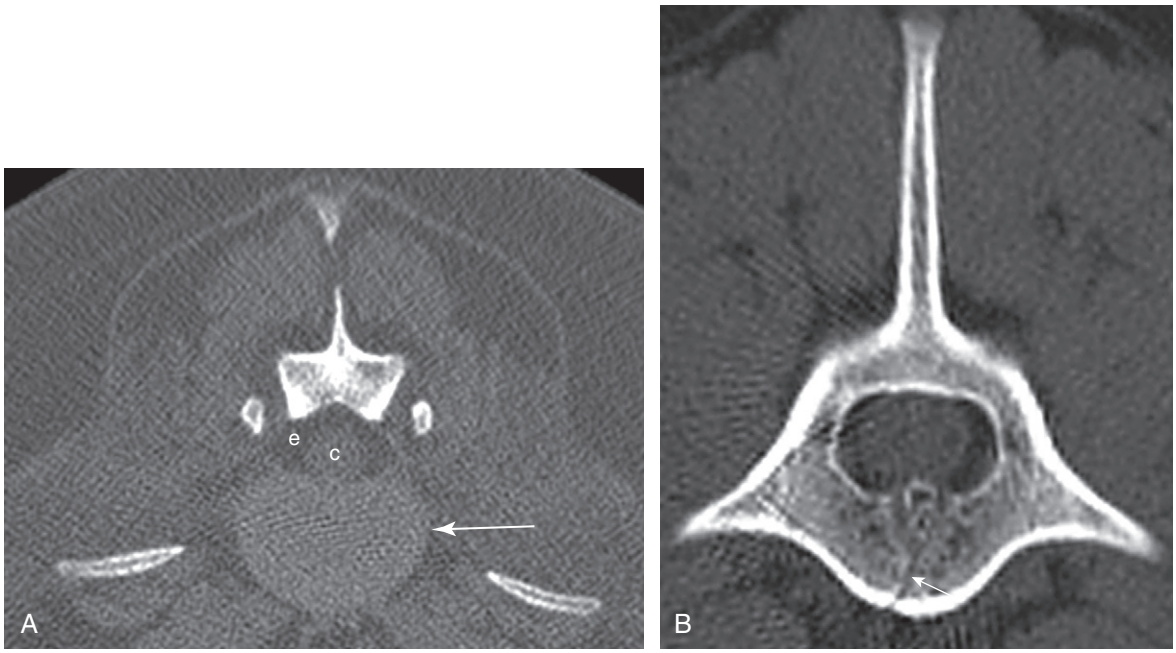


Fig. 12-3 **A,** Transverse CT image at the level of a lumbar intervertebral disc space: The intervertebral disc is indicated by the *white arrow*. The spinal cord together with the meninges and subarachnoid space form an oval soft tissue attenuating structure in the middle of the vertebral canal *(c)*. The epidural fat *(e)* is hypoattenuating and surrounds the spinal cord and meninges. **B,** Transverse CT image in the midportion of the vertebral body. Note the basivertebral venous canal *(white arrow)*. The cortical bone forms a homogeneous hyperattenuating boundary around the vertebra, whereas the cancellous bone has a lacy appearance.

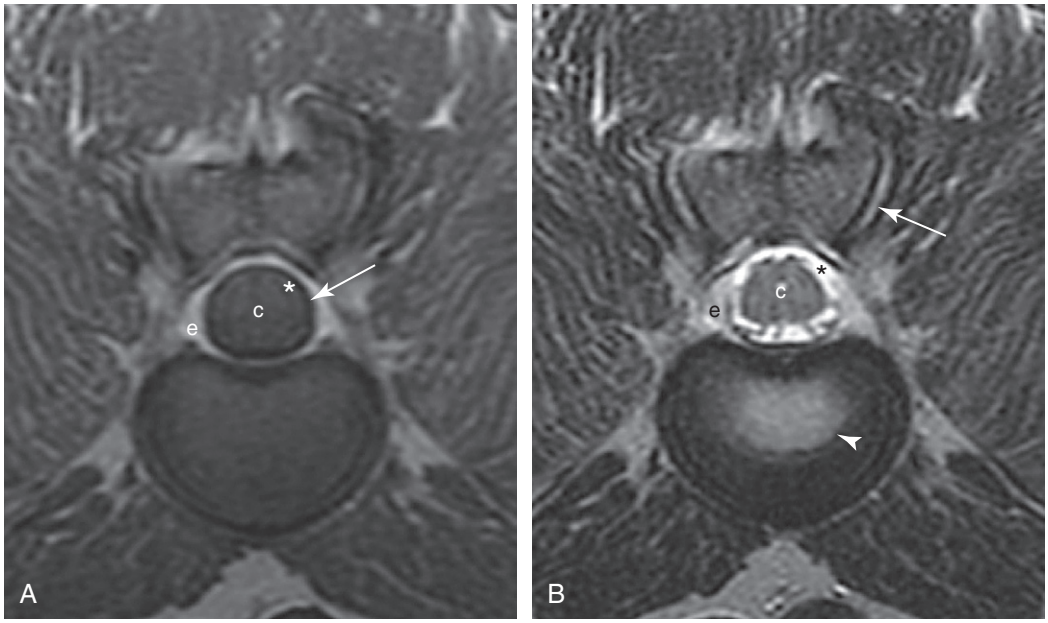


Fig. 12-4 Transverse T1-weighted **(A)** and T2-weighted image **(B)** centered at the L3-L4 intervertebral disc space in a normal dog. The spinal cord *(c)* is in the middle of the vertebral canal. The epidural fat *(e)* is hyperintense on both images. In the T1-weighted image **(A),** the CSF signal *(*)* is barely distinguished from the spinal cord. A hypointense rim around the spinal cord and CSF represents a combination of the meninges and chemical shift artifact *(white arrow)*. In the T2-weighted image **(B),** the hyperintense CSF forms a bright ring around the spinal cord *(*)*. Synovial fluid in the articular process joints forms a thin linear hyperintense signal between the articular processes *(white arrow)*. The cortical bone of the articular processes forms a black linear curved structure. The nucleus pulposus is the hyperintense signal in the middle of the disc *(white arrowhead)*.

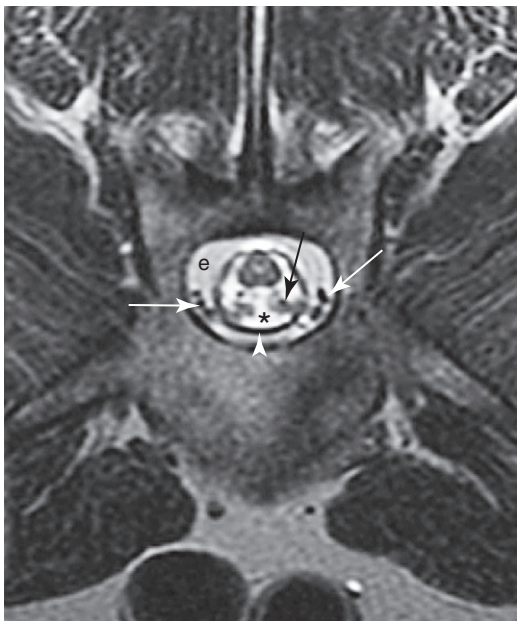


Fig. 12-5 T2-weighted image centered at L5 in a normal dog. The hyperintense CSF within the dural sac is indicated by *(*)*. The extremity of the spinal cord and intradural nerve roots are visible *(black arrow)* in the dural sac, which forms a hypointense rim around the CSF *(white arrowhead)*. The epidural fat around the dural sac is less hyperintense than CSF. Extradural nerve roots are visible as focal hypointensities *(white arrows)* in the epidural space.

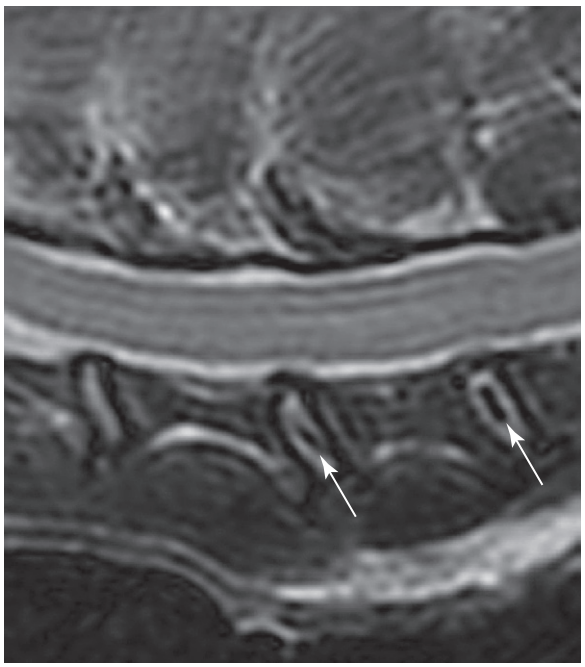


Fig. 12-6 Sagittal T2-weighted image of the caudal aspect of the cervical spine in a dog. Formation of hypointense clefts in the nucleus pulposus *(white arrows)* are signs of intervertebral disc degeneration.

more granular, often mineralizes, and loses its hydroelastic shock-absorbing qualities (Fig. 12-6). The degenerative process starts early in life, and herniation is observed in younger animals (2 to 7 years, with a peak incidence at 4 to 5 years).

Hansen type II IVDD is annular protrusion caused by shifting of the central nuclear material and is commonly associated with fibroid degeneration. Type II herniation is usually observed in nonchondrodystrophic dogs, and the degenerative process starts later in life, with herniation usually observed at approximately 8 to 10 years of age.

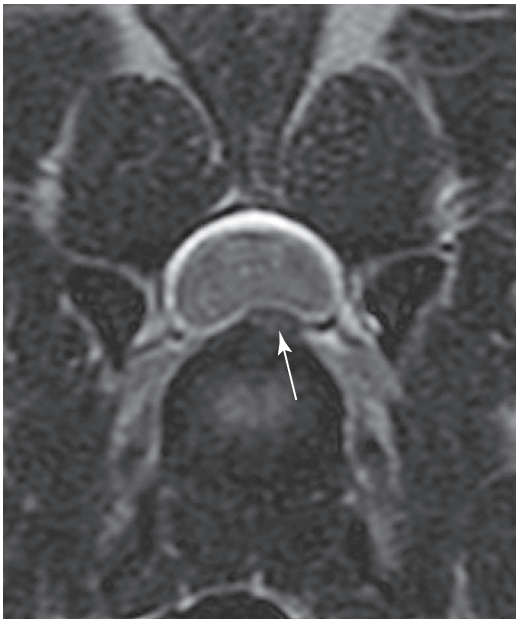


Fig. 12-7 Transverse T2-weighted image of a cervical intervertebral disc space in a dog. There is a Hansen type II disc herniation with protruding hypointense disc material *(white arrow)* causing mild left ventral spinal cord compression.

With more detailed imaging of the patterns of disc herniation that resulted from MR imaging, IVDD can be divided into several categories based on appearance more than physiopathology:[15]

- A bulging disc corresponds to circumferential extension of the disc beyond the margins of the vertebral end plates.
- A protruding disc is the partial extension of the nucleus and inner annulus through disrupted fibers of the outer annulus but without complete rupture of the outer annulus (Hansen type II) (Fig. 12-7).
- An extruded disc represents true herniation (Hansen type I), where portions of the nucleus and inner annulus traverse through all the layers of the outer annulus and form a focal extradural mass deviating epidural fat and, depending on the size of the herniation, the subarachnoid space and spinal cord (Fig. 12-8). This herniated disc material can detach completely from the disc where it originates and form a free extradural mass, with various degrees of dispersion.[15]
- Nondegenerative traumatic disc herniation: If a disc with a normally hydrated nucleus pulposus is placed under extreme stress, the dorsal annulus fibrosus may rupture, and some of the normal jellylike nucleus pulposus may explode into the vertebral canal and cause spinal cord contusion. Because the nucleus material has no degenerative changes and is normally hydrated, it diffuses in the peridural fat, leaving only the secondary changes attributable to acute spinal cord contusion with little or no spinal cord compression.[13] Several terms have been used to describe this syndrome, including *traumatic disc prolapse*, *traumatic disc herniation*, *disc explosion*, *noncompressive nucleus pulposus extrusion*, *Hansen type III disc disease*, *high-velocity-low-volume disc disease*, *traumatic intervertebral disc extrusion*, *missile disc*, and *acute noncompressive nucleus pulposus extrusion*.[13,16] Such herniations are associated most commonly with trauma such as a road traffic accident or running into an obstacle but can also be associated with vigorous exercise.[17]

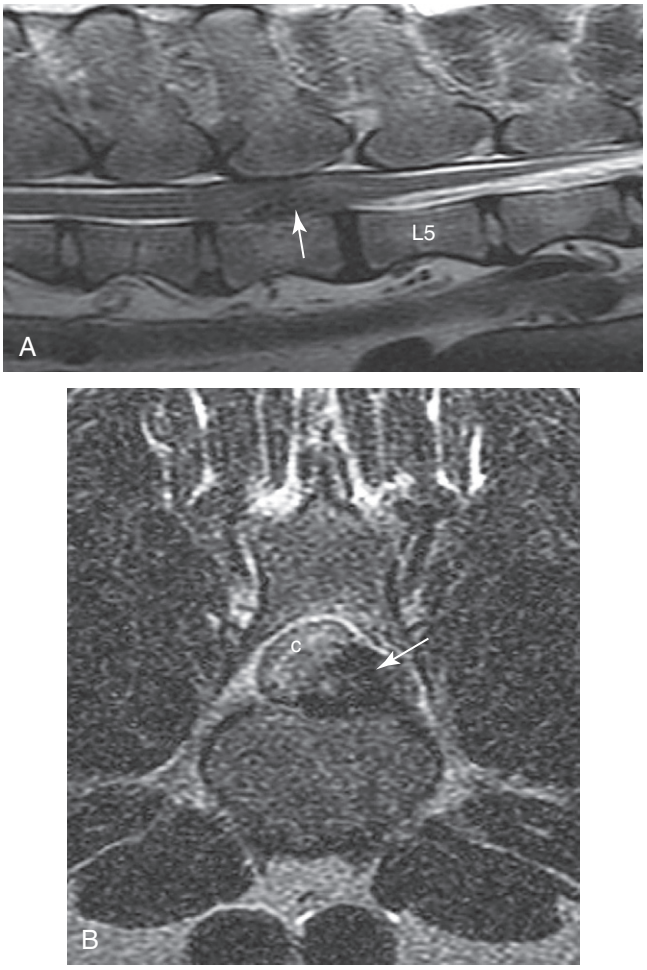


Fig. 12-8 Sagittal **(A)** and transverse **(B)** T2-weighted images in a dog with Hansen type I disc herniation at L4-L5. The longitudinal extent of the hypointense extruded disc material *(white arrow)* is apparent on the sagittal image. The L4-L5 disc is markedly hypointense, consistent with degeneration. On the transverse image **(B),** the hypointense extruded disc material *(white arrow)* causes marked left ventral compression of the spinal cord *(c)*.

Computed Tomography of Intervertebral Disc Disease

CT of the spine for assessing the intervertebral disc should be obtained using thin slices (1 to 2 mm), low pitch (<2), and a medium-frequency image-reconstruction algorithm.[18] When CT is used in the assessment of the spinal cord, subarachnoid injection of iodinated contrast medium is often performed concurrently because the spinal cord is often not clearly visible on CT images. Obviously, the use of CT with subarachnoid contrast medium invalidates the potential advantage of diagnosing disc herniation without the side effects associated with myelography, although the dose of contrast medium for CT myelography is less than that for myelography.

CT without intrathecal injection of iodinated contrast medium for detection of IVDD has been evaluated in chondrodystrophic dogs, which are likely to have some degree of mineralization of the herniated material.[19] On CT, vertebrae can be identified as thoracic or lumbar without difficulty based on the presence of ribs or transverse processes. The location of any particular image can therefore be identified by

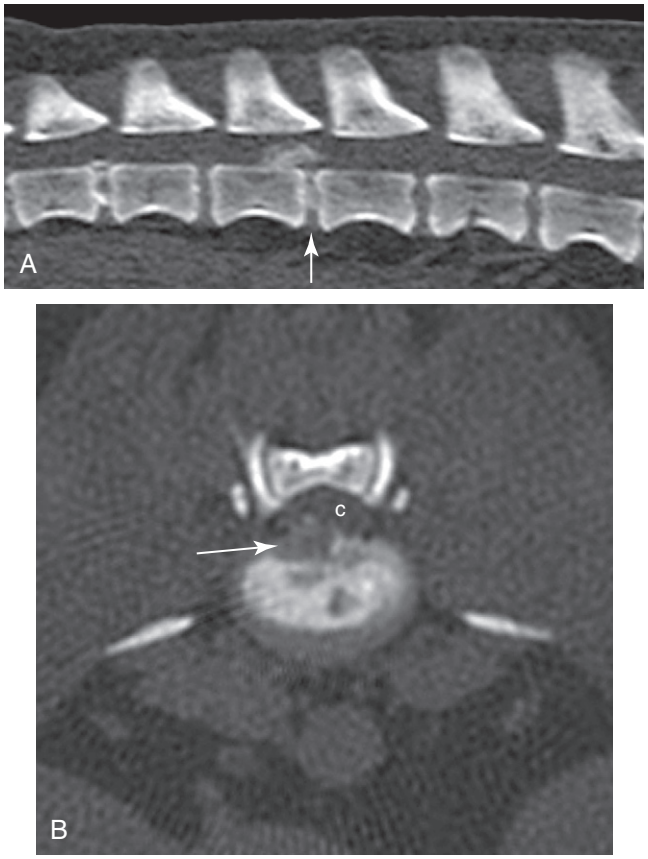


Fig. 12-9 CT without intrathecal contrast medium in a dachshund with acute intervertebral disc herniation. **A,** Sagittal reformatted image. Note the hyperattenuating disc material dorsal to the affected narrowed disc space *(white arrow)*. Extruded disc material extends cranial to the affected disc space. Mineralized disc material is seen in this space and at two intervertebral disc spaces cranial to this. **B,** Transverse image centered on the affected disc space. There is hyperattenuating material *(white arrow)* in the vertebral canal that causes ventral right-sided spinal cord *(c)* compression.

counting sequential vertebrae or by using scout images depicting slice location. Acquiring lateral and ventrodorsal scout images will reduce the risk of missing a vertebral malformation that could affect accurate localization of individual disc spaces at surgery. This is important, because 10% of dachshunds have transitional anomalies that lead to deranged vertebral anatomy.[20] If the scout images are not of sufficient quality to identify vertebral abnormalities, it may be useful to obtain a routine survey radiograph before performing the CT scan. In chondrodystrophic breeds, CT is excellent at identifying herniated disc material and provides accurate information as far as location, laterality, and extent of spinal cord compression (Fig. 12-9). In chondrodystrophic dogs, acute herniation leads to either a large focal amount of markedly hyperattenuating material (approximately 200 HU) compressing the spinal cord or to more diffuse and less hyperattenuating material (approximately 60 HU) causing less severe spinal cord compression. In the latter instance, the material in the vertebral canal corresponds to areas of epidural hemorrhage. In chronic disc herniation, the attenuation of the herniated material is higher than that of acutely herniated disc material (approximately 700 HU) because the herniated material continues to mineralize after acute herniation.[19] Some pitfalls exist when interpreting CT images. For example, a round focus of mineralization is seen occasionally on transverse images dorsal to the vertebral bodies. This focus has been thought to represent mineralization of the dorsal longitudinal

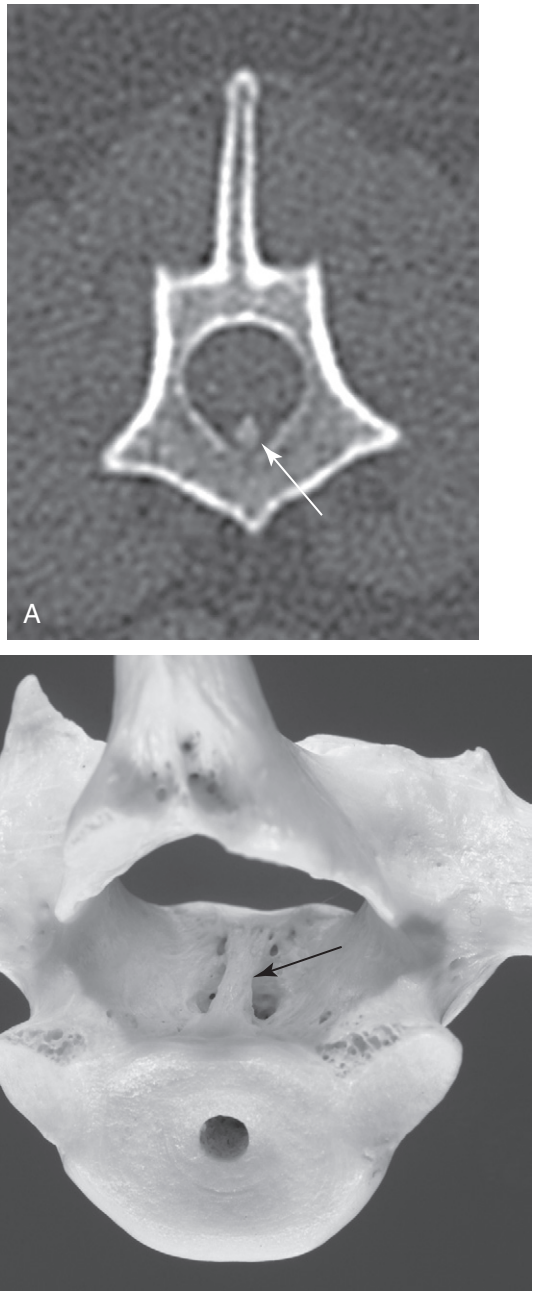


Fig. 12-10 Transverse CT image **(A)** and photograph of a canine vertebra. There is a focal hyperattenuation dorsal to the vertebral body (*white arrow* in **A**) that is created by the bony bridge covering a portion of the dorsal foramina (*black arrow* in **B**). This hyperattenuation is confused with mineralization of the dorsal longitudinal ligament and herniated disc material but is a normal finding. The hole in the end plate in **B** is a drill hole; this drilling did not disturb the normal appearance of the dorsal foramina.

ligament,[19] which fans out to a thin sheet over the intervertebral disc space but narrows to a circular midline structure over the vertebral body. However, this focal hyperattenuation is more likely a transverse image of the small bony ridge between the dorsal vertebral foramina (Fig. 12-10). This hyperattenuation can be mistaken for disc material.

Although conventional CT is adequate for the diagnosis and localization of mineralized Hansen type I disc extrusions in chondrodystrophic breeds, CT myelography is often necessary for diagnosis if no lesion is identified in a chondrodystrophic dog, if plegia is present because of concurrent

extradural compression and spinal cord swelling, or if the dog is nonchondrodystrophic.[21]

Magnetic Resonance Imaging of Intervertebral Disc Disease

Although there may be no improvement in patient outcome when using MR imaging for diagnosis of IVDD,[22] it is the method of choice for presurgical diagnosis because it is noninvasive and provides superior anatomic detail as well as potential prognostic indicators (e.g., myelomalacia).

Diagnosis of IVDD is made from MR images when the following signs are seen:

- Extradural compression of the spinal cord centered at the level of an intervertebral disc (Fig. 12-11; see Fig. 12-8): This is recognized by a loss of signal from the epidural fat and a change in the shape of the spinal cord, as well as a change in the normal ovoid shape of the disc, and is best appreciated on transverse images (see Fig. 12-7).
- Degeneration of the disc (loss of T2-hyperintense signal from the disc).
- Narrowing of the intervertebral disc space: This is usually best evaluated on sagittal T1-weighted images.[23]

MR imaging is accurate in determining the location and craniocaudal length of extruded intervertebral disc material. T2-weighted images are more reliable in determining the extent of the compressive material.[24] Heavily T2-weighted sequences, such as SSFSE, provide a myelographic effect by enhancing the signal of the CSF and suppressing the signal from other structures and can be used to quickly spot areas of cord compression based on identification of interruption and/or deviation of the CSF column (see Fig. 12-11).[11]

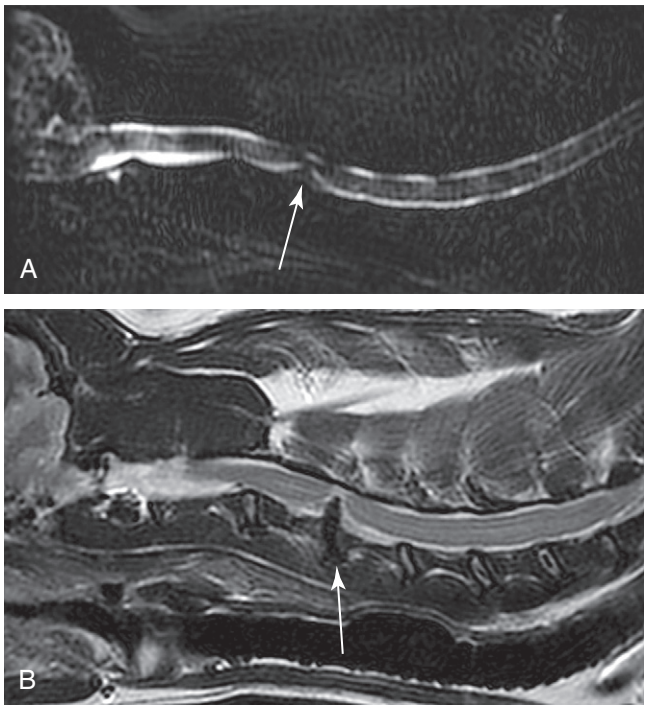


Fig. 12-11 Sagittal SSFSE slab (T2 myelogram) **(A)** and sagittal T2-weighted image **(B)** in a dog with disc herniation at C3-C4. The area of spinal cord compression is obvious on the T2 myelogram *(white arrow)*. On the sagittal T2-weighted image, hypointense material is seen extruded from the disc at C3-C4 causing marked ventral spinal cord compression. The disc has lost its normal hyperintense signal *(white arrow)*.

Epidural hemorrhage and inflammation associated with disc extrusion can be detected with MR imaging.[25] In dogs with thoracolumbar or lumbosacral herniation, the incidence of such epidural changes is approximately 5%.[25] These changes are more common in the caudal aspect of the lumbar spine and observed more commonly when there has been migration of disc material. The signal intensity of these epidural lesions is variable, appearing hyperintense to the spinal cord or heterogeneous on T2-weighted images, and hyper-, hypo-, or isointense to the spinal cord on T1-weighted images.[25] This variation likely reflects changes in magnetic properties depending on the age of the hemorrhage and amount of disc-associated inflammation. Gradient recalled echo T2-weighted pulse sequences are sensitive to the paramagnetic properties of deoxyhemoglobin and methemoglobin, and hemorrhage or hematomas in the epidural space create hypointensities as a result of susceptibility artifact (Fig. 12-12).[26] Contrast enhancement of epidural hemorrhage is common, although it is not associated histopathologically with actual inflammation. In some dogs these secondary epidural changes can mask the extruded disc material. Altogether, these features can cause erroneous diagnosis of a tumor, and this variability needs to be taken into account when interpreting MR images in dogs with acute neurologic presentation. There does not appear to be a difference in clinical outcome in dogs with epidural hemorrhage or inflammation compared with dogs without these changes.[25]

Regardless of whether epidural hemorrhage or inflammation is present, contrast enhancement of the compressive extradural disc material occurs in approximately 50% of dogs with disc extrusion (Fig. 12-13).[25,27] Meningeal contrast enhancement adjacent to extruded extradural disc material also occurs in up to 40% of patients (Fig. 12-14, see page 202).[27]

Regional Characteristics of Intervertebral Disc Disease

Cervical IVDD

Cervical IVDD accounts for 14% to 16% of intervertebral disc disease in dogs.[28] Type I cervical IVDD is common in small-breed dogs, especially dachshunds and beagles, but is also seen in large-breed dogs, especially Labrador retrievers, German shepherd dogs, Rottweilers, and Dalmatians.[29-30] In small-breed dogs, the most common sites of herniation are C2-C3, C3-C4, and C4-C5, whereas in large-breed dogs the most common sites are C4-C5 and C6-C7.[29-30] The amount of compressive myelopathy occurring with cervical IVDD is typically less than with thoracolumbar disc herniation because the dorsal longitudinal ligament is wider in the cervical area than the thoracolumbar region. Cervical disc herniation also occurs most commonly in the dorsolateral direction, between the dorsal longitudinal ligament and vertebral venous sinus, thereby causing nerve root compression with root signature and cervical pain (Fig. 12-15, see page 202). Also, the cervical spinal cord occupies a smaller proportion of the vertebral canal so that the degree of compression caused by an equal volume of herniated disc material is less than in the thoracolumbar area.[28] In the cervical area there is a correlation between the degree of spinal cord compression caused by disc herniation and the neurologic grade at time of imaging; however, there is no correlation with outcome after surgery.[28]

Thoracolumbar IVDD

The most commonly affected discs in the thoracolumbar region are T12-T13 and T13-L1.[31] In dogs with neurologic deficit caused by thoracolumbar disc extrusion (Hansen type I), there is no definitive association between the degree of spinal cord compression as defined on T2-weighted transverse images and the neurologic grade at presentation or outcome after surgery.[31-32] However, the length over which the spinal

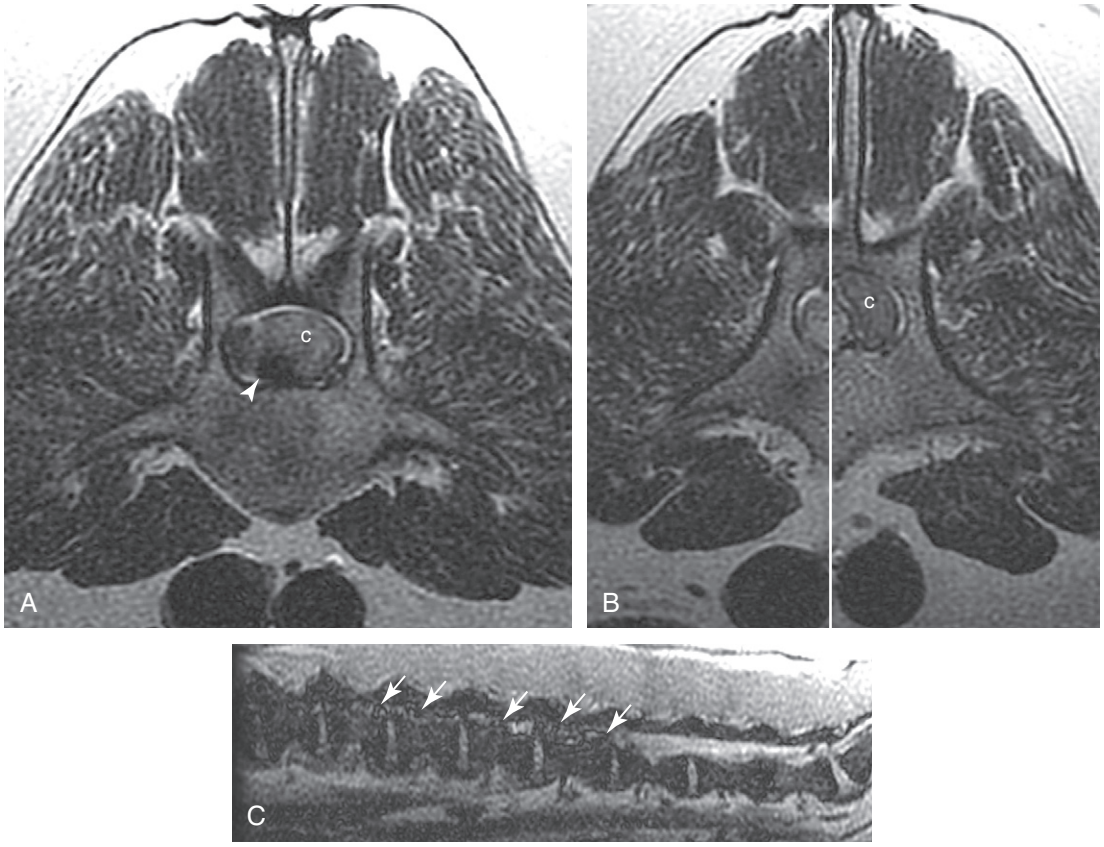


Fig. 12-12 Acute disc herniation at L4-L5 in a dog. Transverse spin echo T2-weighted image at L4-L5 **(A)** and a few millimeters cranial to this **(B)** and a parasagittal T2-weighted gradient recalled echo image **(C).** The imaging plane in **C** is indicated by the vertical line in **B.** Extruded disc material *(white arrowhead)* compresses the spinal cord *(c)* in **A.** Cranial to this, there is a long strand of tissue that is hyperintense to the spinal cord and compressing it, as seen in **B.** There are multiple susceptibility artifacts in the gradient recalled echo image centered on this tissue (*white arrows*, **C**) consistent with hemorrhage extending over several vertebral bodies. Extensive epidural hemorrhage was present surgically.

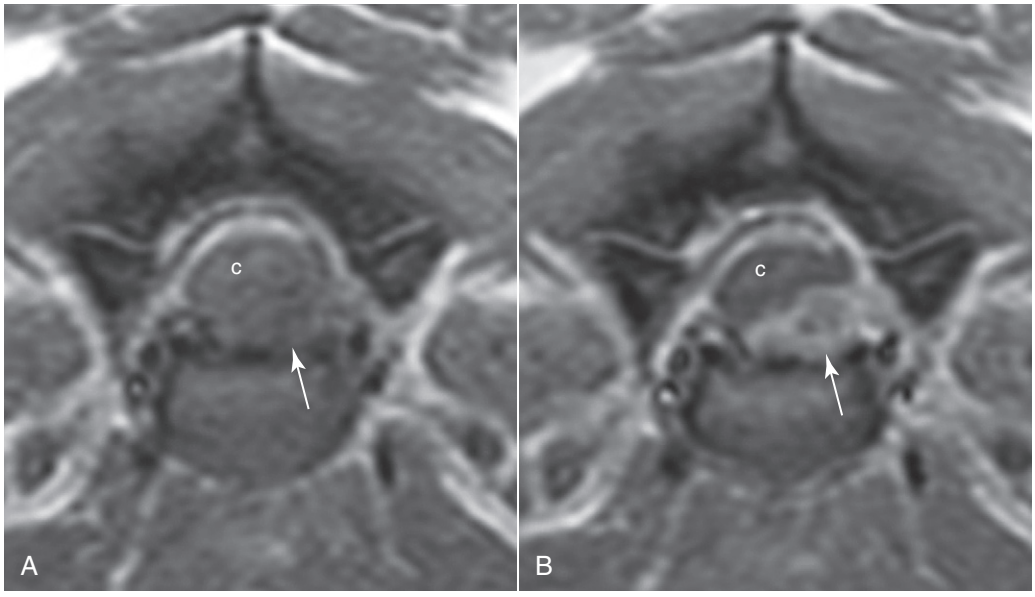


Fig. 12-13 Transverse pre- **(A)** and postcontrast **(B)** T1-weighted images in a dog with disc herniation. The spinal cord *(c)* is compressed by left ventral extradural disc material, and this material is enhancing after contrast-medium injection *(white arrows)*. This is common and should not be misinterpreted as evidence of an extradural tumor. (Reproduced with permission from Suran JN, Durham A, Mai W, et al: Contrast enhancement of extradural compressive material on magnetic resonance imaging, *Vet Radiol Ultrasound* 52:10–16, 2011.)

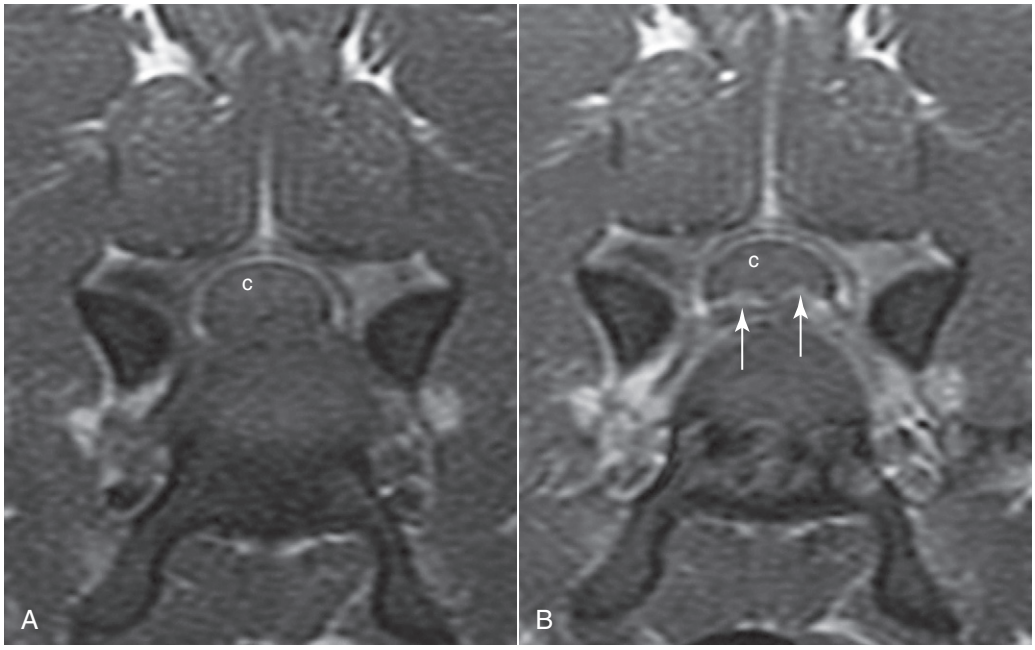


Fig. 12-14 Transverse pre- **(A)** and postcontrast **(B)** T1-weighted images in a dog with disc herniation. The spinal cord *(c)* is compressed by ventral extradural disc material. Ventral meningeal enhancement is present after contrast-medium injection *(white arrows)*. (Reproduced with permission from Suran JN, Durham A, Mai W, et al: Contrast enhancement of extradural compressive material on magnetic resonance imaging, *Vet Radiol Ultrasound* 52:10–16, 2011.)

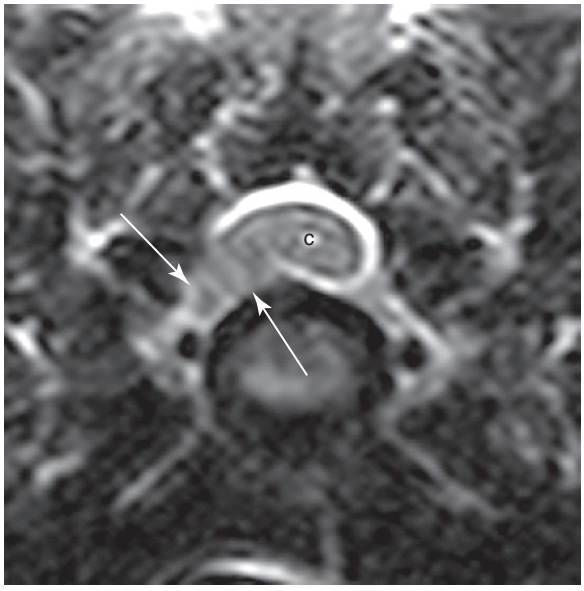


Fig. 12-15 Transverse T2-weighted image of a dog with a foraminal disc herniation at C5-C6. There is disc material in the right ventral aspect of the vertebral canal and in the right foramen *(white arrows)*. The disc material is also compressing the spinal cord *(c)*.

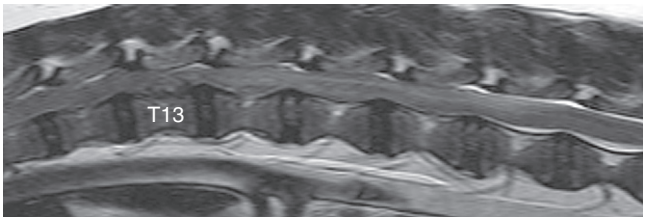


Fig. 12-16 Sagittal T2-weighted image of a dog with disc herniation at T12-T13. There is a heterogeneous mass dorsal to T13 that represents migrated disc material and hemorrhage. Caudal to this lesion there is diffuse intramedullary T2 hyperintensity consistent with edema and inflammation.

cord is compressed is associated with the neurologic grade at presentation, but not with outcome.[32] In dogs with paraplegia because of acute thoracolumbar disc extrusion, areas of spinal cord hyperintensity on T2-weighted series are often present (Fig. 12-16). The development of intramedullary T2 hyperintensity following disc herniation is associated with more severe neurologic deficits at presentation.[25,27,32] Areas of intramedullary T2 hyperintensity that exceed the length of L2 on sagittal images have been associated with a poor outcome in approximately 50% of patients.[33] This feature appears to be a better predictor of poor outcome than loss of deep pain perception[33,34] and is independent from the severity of neurologic signs at presentation.[32]

Sacrococcygeal Disc Herniation

There has been an anecdotal report of sacrocaudal disc extrusion causing tail pain and problems with defecation, with resolution of these clinical signs after surgical correction. MR imaging and CT can be useful in confirming the presence of extruded disc material in the sacrocaudal canal.[35]

Lumbosacral Stenosis

Degenerative lumbosacral stenosis is an abnormal narrowing of the L5-S3 vertebral canal or intervertebral foramina, with compression of the cauda equina and/or its blood supply.[36] Degenerative lumbosacral stenosis is characterized by intervertebral disc degeneration, intervertebral disc protrusion, bone proliferation on the vertebral end plates and articular processes, vertebral subluxation, and hypertrophy of the articular process joint capsule and interarcuate ligament (ligamentum flavum).[36] CT and MR imaging are both excellent for characterizing degenerative lumbosacral stenosis in dogs.[7,9,36-42] In dogs with clinical signs of cauda equina syndrome, CT changes include loss of epidural fat, increased soft tissue opacity in the intervertebral foramen, bulging of the

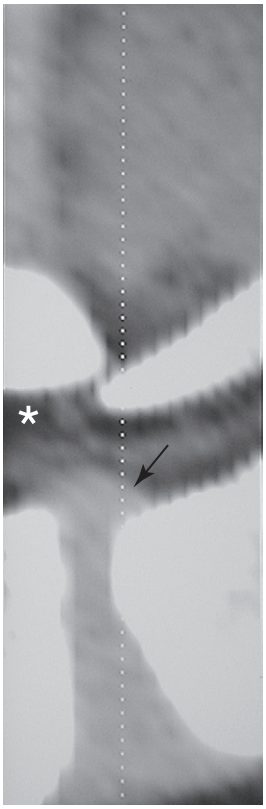


Fig. 12-17 Sagittal reformatted CT image of the L7-S1 junction in a dog with clinical signs of lumbosacral disease. There is bulging of the intervertebral disc *(black arrow)* causing mild nerve root compression. Peridural fat is still present in the area indicated by the hypoattenuating material *(*)* around the nerves. There is a slight step between the floor of the vertebral canal of L7 and that of S1, indicating lumbosacral subluxation and/or instability.

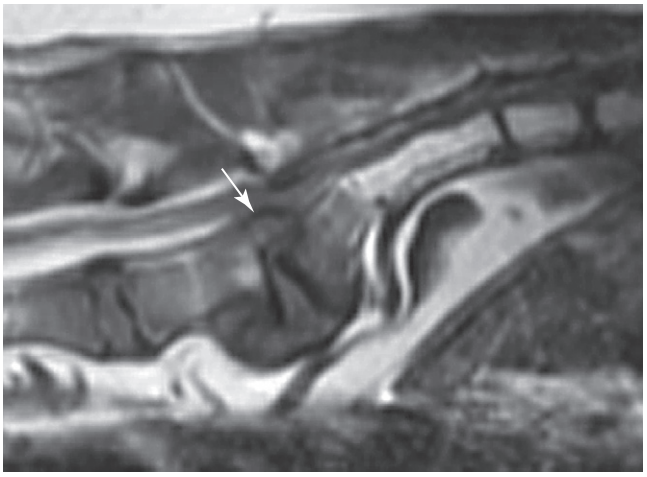


Fig. 12-18 Sagittal T1-weighted image of the caudal lumbar area in a German shepherd with clinical signs of lumbosacral disease. There is a step between the floor of the vertebral canal of L7 and that of S1 indicating lumbosacral subluxation and/or instability. Bulging disc material *(white arrow)* is present dorsal to the lumbosacral disc space causing attenuation of the hyperintense epidural fat. The combined effects of the subluxation and bulging disc are causing stenosis of the vertebral canal with nerve root compression. Ventral spondylosis is present at L7-S1.

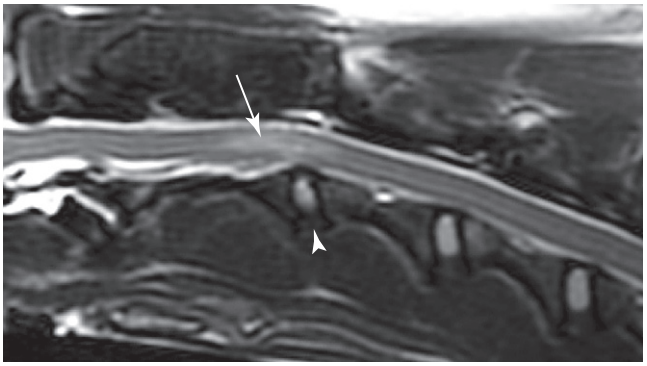


Fig. 12-19 Sagittal T2-weighted image of a dog that ran into a tree and sustained acute noncompressive intervertebral disc extrusion. There is mild loss of volume of the nucleus pulposus at C2-C3 *(white arrowhead)* and ill-defined intramedullary T2 hyperintensity *(white arrow)* overlying this space consistent with edema caused by spinal cord contusion. There is no spinal cord compression.

intervertebral disc, spondylosis, thecal sac displacement, narrowed intervertebral foramen, narrowed vertebral canal, thickened articular processes, articular process subluxation, and articular process osteophytosis. On sagittal images, a step between the floor of the vertebral foramen of L7 and the floor of the vertebral foramen of S1 is often seen (Figs. 12-17 and 12-18).[42] Enhancement of the soft tissue compressive material is often observed after injection of contrast medium, and this feature should not be interpreted as evidence of a tumor.[36] Compression should be suspected in sites where there is increased perineural soft tissue material with absence of epidural fat.[37,41] Interpretation of CT changes in the lumbosacral area must be made with caution, as some changes can be present in dogs free of clinical signs and therefore insignificant clinically. In particular, idiopathic lumbosacral stenosis and loss of perineural fat have been reported in dogs with no clinical signs.[38] In addition, only slight to fair agreement was found when comparing results of CT or MR imaging of the lumbosacral spine to surgery.[42]

For both CT and MR imaging there does not appear to be an association between imaging findings and clinical outcome after surgery in working dogs with clinical signs of degenerative lumbosacral stenosis.[36]

Acute Noncompressive Intervertebral Disc Extrusion

Occasionally, disc extrusion occurs without preexisting degenerative disc disease when an otherwise healthy disc is subjected to a brief excessive force. Such extrusions occur typically during performance of strenuous exercise or following trauma. Names applied to this syndrome were outlined previously in the section "Classification of Intervertebral Disc Disease."[13,16-17,43-48] Typically, the condition is characterized by an acute, often asymmetric myelopathy that is nonprogressive after the first 24 hours.[16] The clinical presentation is similar to primary ischemic myelopathy.[16]

On MR imaging, acute noncompressive intervertebral disc extrusion is characterized by the following:[13,16,48]

- Focal intramedullary T2 hyperintensity overlying an intervertebral disc. The area of maximal hyperintensity is usually just dorsal to the affected intervertebral disc but can sometimes be seen just cranial or caudal to the disc space. The longitudinal extension of the intramedullary hyperintensity is usually more focal than with ischemic myelopathy, which has a similar clinical presentation (Fig. 12-19).[13,16]
- This intramedullary lesion is usually isointense on T1-weighted images and does not enhance after gadolinium injection, although occasional focal precontrast T1-weighted hyper- or hypointensity and mild postcontrast enhancement may be present.[13]

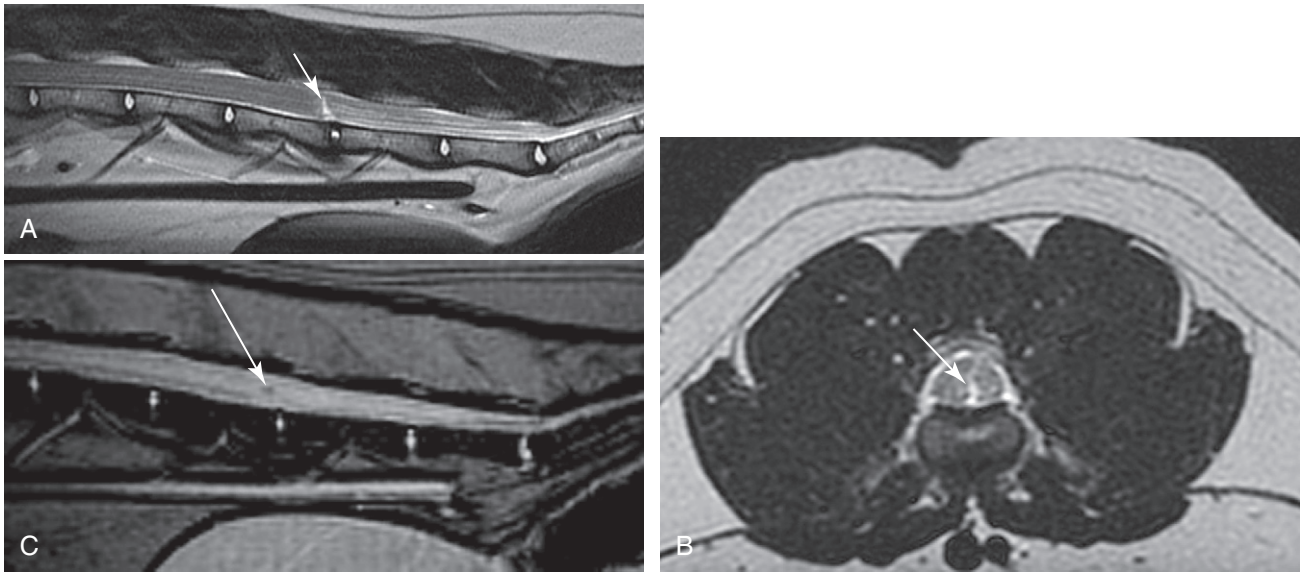


Fig. 12-20 Acute noncompressive intervertebral disc extrusion at L5-L6 in a cat. **A,** T2-weighted sagittal image; **B,** Transverse T2-weighted image centered at L5-L6; **C,** Sagittal gradient recalled echo image matching the location in **A.** A hyperintense intramedullary linear tract extends from the disc space in **A** and **B** *(white arrows)* consistent with intramedullary extrusion of disc material after perforation of the dura mater. Note the loss of volume of the nucleus pulposus at L5-L6. A hypointense intramedullary lesion consistent with hemorrhage *(white arrow)* is present in the gradient recalled echo image.

- There is reduction in volume and signal intensity of the nucleus pulposus of the corresponding disc on T2-weighted images (Fig. 12-20; see Fig. 12-19).
- A narrowed intervertebral disc space is seen on sagittal images.
- There is extraneous material or signal changes within the epidural space dorsal to the affected disc space with absence of or minimal spinal cord compression.
- A communicating T2-hyperintense tract can occasionally be seen traversing the dorsal annulus between the residual nucleus pulposus and the vertebral canal.[13]

The acutely extruded disc material most commonly damages the spinal cord through contusion without penetrating the dura, but occasionally it can cause a dural tear and penetrate the spinal cord.[43,44,46-48] In these instances, a vertical intramedullary linear T2-hyperintense lesion crosses the spinal cord and is contiguous ventrally with the intervertebral disc space. Areas of hypointensity can be seen associated with that tract in gradient recalled echo images because of hemorrhage (see Fig. 12-20).[46,48]

Up to 33% of affected patients have an unsuccessful outcome.[16] Prognostic factors of unsuccessful outcome include severity of neurologic signs at presentation, percentage of cross-sectional area of the intramedullary lesion on transverse T2-weighted images, and presence of intramedullary hemorrhage. An intramedullary cross-sectional area of the T2-hyperintense lesion exceeding 90% of the spinal cord area is associated with a 92% chance of an unsuccessful outcome.[16]

On CT myelography, acute traumatic or exercise-induced disc extrusion can be associated with narrowing of the affected disc space, seen on sagittal or dorsal reformatted images, with evidence of a small amount of minimally compressive extradural material at the level of the disc with spinal cord swelling adjacent to these areas. When the extruded disc material causes rupture of the dura, small leaks of iodinated contrast medium can be seen extending from the subarachnoid space into the epidural space.[49] Leakage of contrast medium into the intervertebral disc in patients with disc-associated dural rupture can be seen with application of spinal traction during conventional myelography.[47] On CT performed after myelography, presence of intramedullary contrast medium can also be seen.[50]

CERVICAL SPONDYLOMYELOPATHY

Cervical spondylomyelopathy refers to a collection of disorders of the caudal cervical spine in large-breed dogs resulting in progressive and chronic spinal cord compression. Other terminology used for this condition includes *wobbler disease, cervical vertebral instability, cervical spondylopathy, cervical spondylolisthesis,* and *cervical vertebral malformation-malarticulation*.[51] The clinical signs range from cervical hyperesthesia to tetraplegia, with the most common being a gait disturbance.

Pathologic changes observed with cervical spondylomyelopathy include the following:[51]

- Stenosis of the vertebral canal because of malaligned or misshapen vertebral bodies and/or abnormal, hypertrophied articular processes
- Hansen type II disc protrusion alone or in combination with hypertrophy of the dorsal longitudinal ligament resulting in ventral compression of the spinal cord
- Hypertrophy of the interarcuate ligament (ligamentum flavum) and the joint capsule of the articular process joints resulting in dorsal and dorsolateral spinal cord compression
- Osteoarthrosis of the articular processes with excessive soft tissue proliferation and synovial cyst formation also potentially causing dorsolateral spinal cord compression

Cervical spondylomyelopathy is seen most commonly in Great Danes and Doberman pinschers but also occurs in other large breeds. In middle-aged to older Doberman pinschers, the most common lesion is Hansen type II disc protrusion and hypertrophy of the ligamentum flavum (interarcuate ligament). In young Doberman pinschers, Great Danes, and other large-breed dogs, the disease is more of the stenotic type

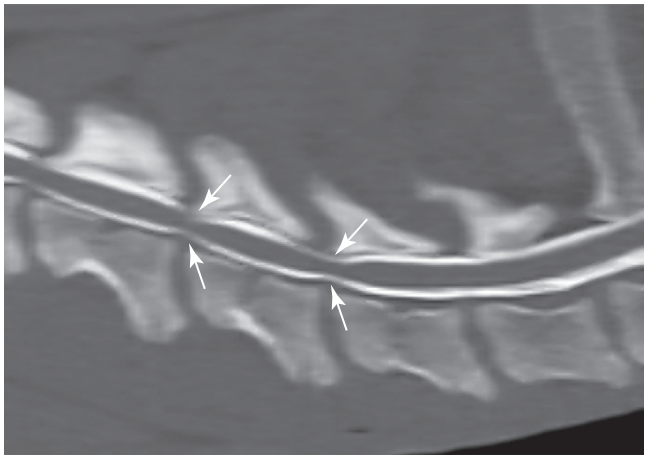


Fig. 12-21 Sagittal reformatted CT myelogram in a dog with caudal cervical spondylomyelopathy. Note the dorsal and ventral spinal cord compression at C4-C5 and C5-C6 *(white arrows)* because of a combination of ligamentum flavum hypertrophy and dorsal longitudinal ligament hypertrophy with disc bulging. (Image courtesy of Dr. Paul Barthez, Clinique Vétérinaire des Halles, Strasbourg, France.)

myelopathy, caused by hypertrophy and degenerative changes of the articular processes and ligamentum flavum hypertrophy, which combined, cause reduction in the size of the vertebral canal.[51]

Computed Tomography of Cervical Spondylomyelopathy

Noncontrast CT is not very useful in the diagnosis of cervical spondylomyelopathy. It allows assessment of the bony abnormalities, such as articular process hypertrophy, malalignment, and spondylosis, but performs poorly in identifying and grade the location of spinal cord compression correctly and does not allow identification of spinal cord atrophy that may be of prognostic value. With CT myelography, conversely, there is excellent delineation of the spinal cord and characterization of the areas of compression (Figs. 12-21 and 12-22). CT myelography provides more information than conventional myelography on the exact location and degree of spinal cord compression. In particular, spinal cord atrophy can be distinguished with CT from reversible spinal cord compression. A further advantage of CT myelography is the superior contrast resolution, which can provide diagnostic images with very little contrast medium in the subarachnoid space.[8] In the Doberman pinscher, several patterns of spinal cord compression have been described on CT.[8]

- Central spinal cord deformity occurs, which most of the time is caused by bulging of the annulus fibrosus and occasionally by nucleus pulposus extrusion.
- Asymmetric spinal cord compression with intervertebral foramen impingement is caused by unilateral disc protrusion.
- Spinal cord atrophy is characterized by reduction in the cross-sectional area of the spinal cord together with relative widening of the subarachnoid space. The atrophic spinal cord can assume an abnormal shape, from a flattened appearance to triangular. It is unclear if spinal cord atrophy is a prognostic indicator of poor outcome, although there are reports of histologic damage, which is likely irreversible, in spinal cords with such a pattern on CT myelography.[8]

The use of traction can provide information on the dynamic nature of spinal cord compression when comparing images in neutral versus stressed positions; sagittal reformatted images are especially useful for this purpose (Fig. 12-23).

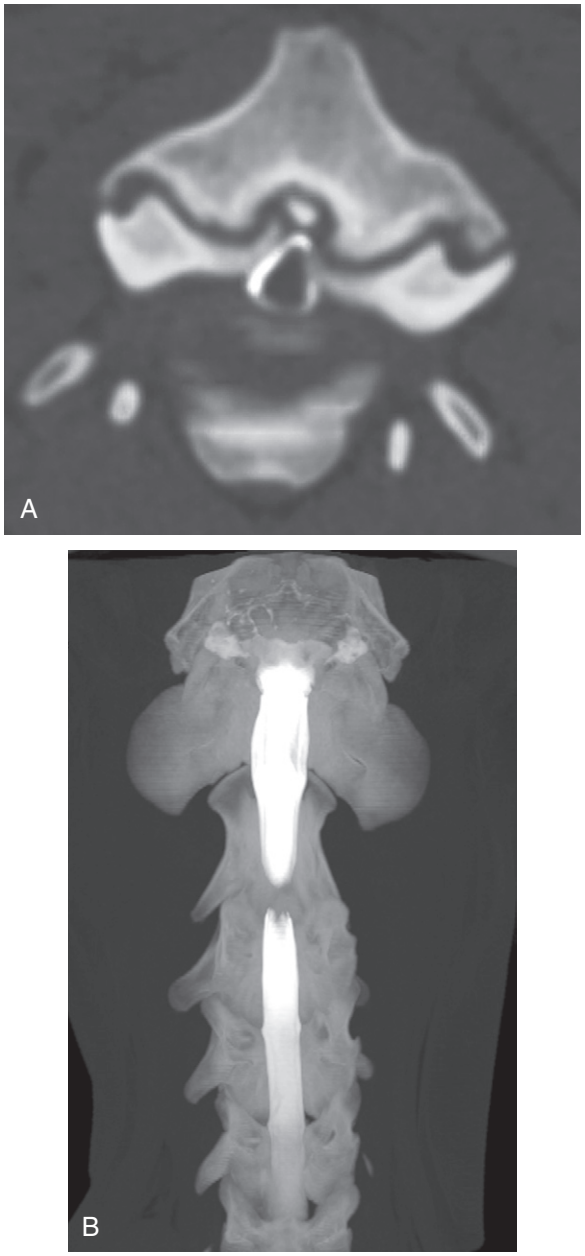


Fig. 12-22 CT myelography in a 7-month-old Great Dane. **A,** Transverse image centered at C2-C3. **B,** Dorsal subvolume maximum intensity projection. There is severe hypertrophy of the articular processes causing marked dorsolateral spinal cord compression at C2-C3. (Image courtesy of Dr. Paul Barthez, Dierenkliniek Causus, Oudenburg, Belgium.)

Magnetic Resonance Imaging of Cervical Spondylomyelopathy

MR imaging is very accurate in imaging the changes associated with cervical spondylomyelopathy. Compared with conventional myelography, MR imaging is more accurate in predicting the site, severity, and nature of the spinal cord compression. Using myelography can lead to an underestimate in the severity of spinal cord compression.[52] MR imaging is also better than myelography in locating the sites of compressive lesions.[52]

In middle-aged or older Doberman pinschers, the disease tends to be disc associated, characterized by disc degeneration, disc bulging and/or herniation causing spinal cord compression, ligamentum flavum hypertrophy causing dorsal spinal cord compression, alterations in spinal cord signal

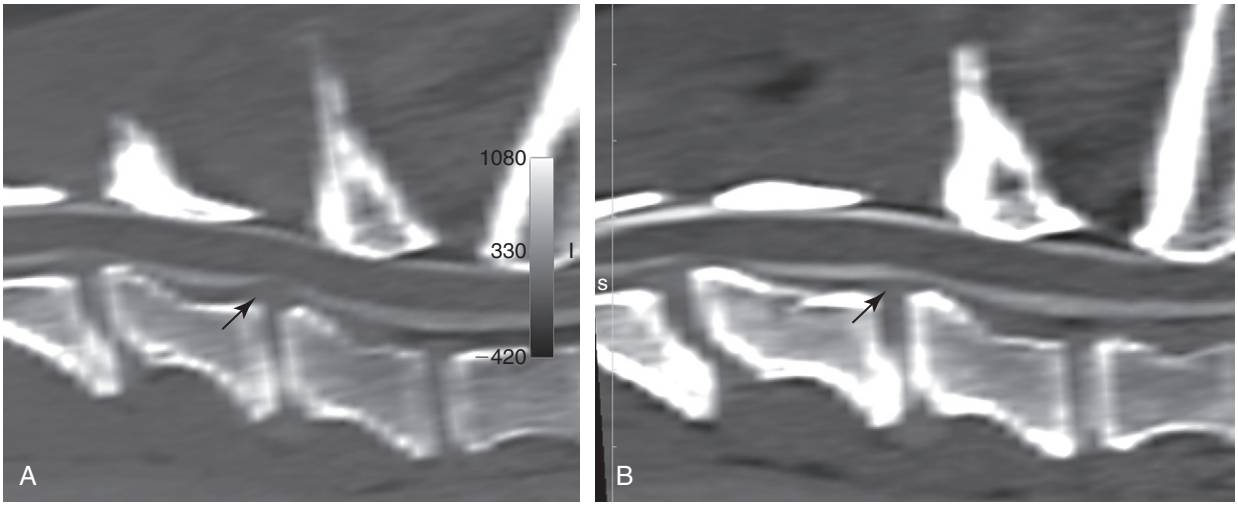


Fig. 12-23 Sagittal reformatted CT-myelographic images of the caudal cervical spine of a middle-aged Doberman pinscher with cervical spondylomyelopathy. **A** is neutral position, and there is ventral spinal cord compression caused by a bulging disc and/or dorsal longitudinal ligament hypertrophy *(black arrow)*. **B** was obtained during cervical traction, and there is reduction in spinal cord compression *(black arrow)*, thereby characterizing the dynamic nature of the compression *(arrow)*. (Image courtesy of Dr. Laurent Couturier, Azur Vet, Cagnes sur Mer, France.)

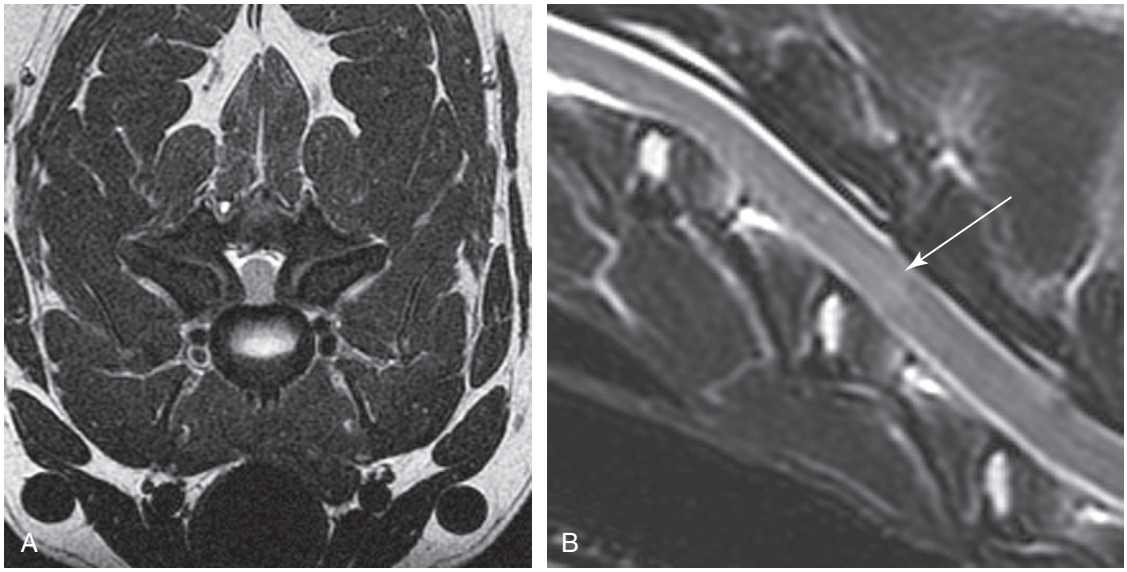


Fig. 12-24 Transverse **(A)** and sagittal **(B)** T2-weighted images in a Great Dane with cervical spondylomyelopathy at C3-C4. There is marked hypertrophy of the articular processes causing lateral spinal cord compression. There is intramedullary T2-hyperintensity in the sagittal image *(white arrow)*. This hyperintensity can help determine the clinical significance of the cervical anomalies.

intensity, and vertebral body abnormalities and spondylosis. The presence of alterations in spinal cord signal intensity is a reliable indicator of clinically relevant spinal cord compression,[52-53] although this has occasionally been reported in the caudal cervical spine of clinically normal dogs.[54] However, such T2-hyperintensities do not seem to correlate to prognosis.[55] What is causing the T2-hyperintensity of the gray matter in the spinal cord of affected dogs is not clearly established, but possible reasons include loss of nerve cells, gliosis, and edema. White matter T2-hyperintensity can be caused by demyelination, edema, and Wallerian degeneration. When areas of corresponding T1 hypointensity are present, more severe changes such as necrosis, myelomalacia, and spongiform changes may be suspected.[55] Dynamic studies with traction MR imaging have questionable accuracy in identifying the static or dynamic nature of the compression.[52,56]

In younger Doberman pinschers and other large-breed dogs such as Great Danes, the MR imaging abnormalities include the following:[51]

- Degenerative changes of the intervertebral discs are seen as decreased signal intensity on T2-weighted images, especially at C6-7 and C5-6.
- Hypertrophy of the dorsal longitudinal ligament and osteoarthrosis of the articular process from C3-4 to C7-T1 is seen, with the most common sites being C4-5, C5-6, and C6-7. These compressive structures appear T1 and T2 hypointense, and spinal cord deformity can be seen on sagittal/parasagittal and transverse images. These abnormalities can cause unilateral or bilateral dorsolateral spinal cord compression, best identified on transverse images (Fig. 12-24).

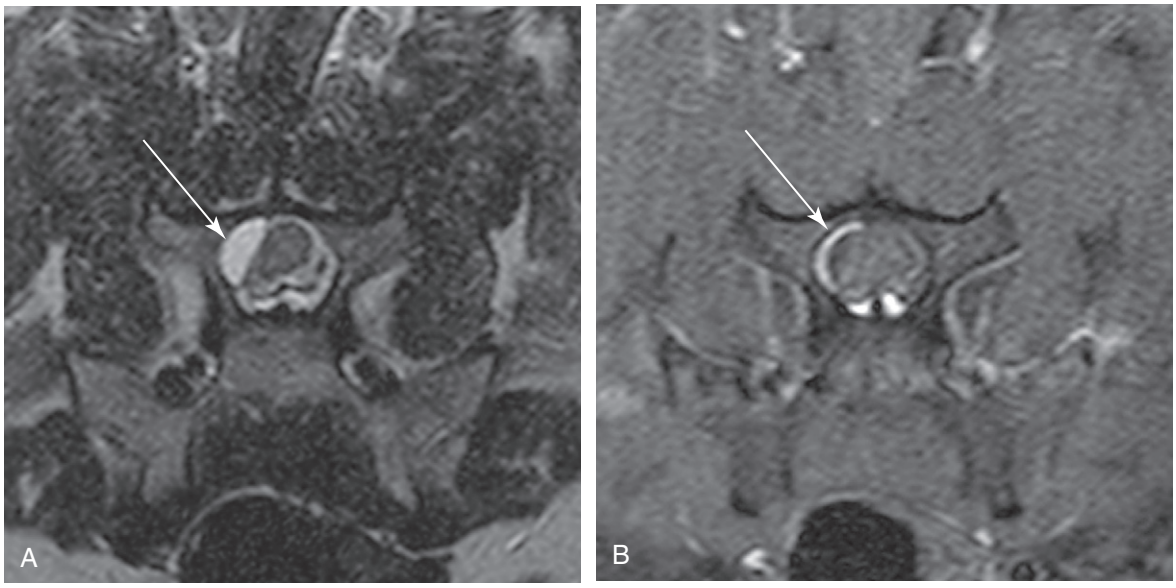


Fig. 12-25 T2-weighted **(A)** and postcontrast, fat-suppressed, T1-weighted **(B)** transverse images of a dog with cervical spondylomyelopathy. There is a large synovial cyst (*white arrow* in **A**) arising from a degenerate articular process joint that is causing moderate spinal cord compression. The joint itself is caudal to this image plane because the cyst has bulged cranially. Following contrast-medium administration, there is enhancement of the wall of the cyst (*white arrow* in **B**).

- Intramedullary T2 hyperintensity is associated with areas of spinal cord compression (see Fig. 12-24).
- Synovial cysts are identified as T1-hypointense, T2-hyperintense structures associated with the articular processes and sometimes contributing to dorsolateral spinal cord compression (Fig. 12-25). The wall of these cysts occasionally enhances after gadolinium injection.
- Occasional disc protrusion (Hansen type II) contributes to ventral spinal cord compression, especially at C6-7.

There is a high incidence of MR imaging abnormalities of the cervical vertebral column in clinically normal large-breed dogs; these have been documented in Doberman pinschers and foxhounds and include complete disc degeneration, spinal cord compression, vertebral body abnormalities, and even intramedullary T2 hyperintensity. Therefore, caution should be exercised when attributing clinical signs to structural abnormalities seen on MR images.[54] Also, there can be significant variability in the assessment and interpretation of MR imaging abnormalities across observers in dogs with disc-associated wobbler syndrome so that interpretation of imaging results must be made with caution.[54]

CYSTIC CHANGES OF THE SPINE

Several types of intraspinal cysts occur in dogs: arachnoid diverticula, epidermoid/dermoid cysts, articular process synovial and ganglion cysts, and discal cysts.

Spinal Arachnoid Diverticula

Spinal arachnoid diverticula are a rare cause of spinal cord compression in dogs and rarely reported in cats.[57-61] In dogs they are located in the subarachnoid space, lined by arachnoid and pia mater, and communicate freely with CSF in the subarachnoid space. Because no true epithelial lining is present, the term *arachnoid diverticula* is used here. These lesions are often congenital but can be associated with spinal cord trauma, intervertebral disc disease, or previous arachnoiditis.

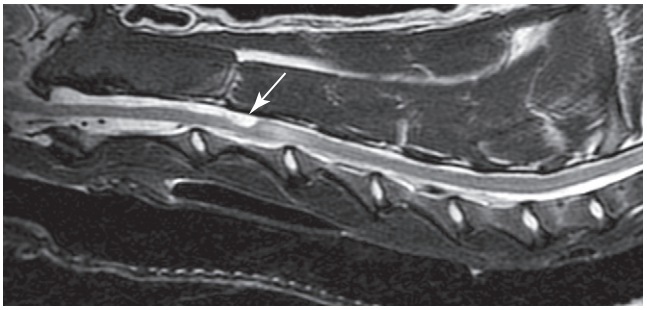


Fig. 12-26 T2-weighted sagittal image in a dog several months after diagnosis of meningitis caused by *Cryptococcus* infection. There is a spinal arachnoid diverticulum *(white arrow)* dorsal to C3 forming a typical teardrop-shaped hyperintense structure dorsal to the spinal cord.

The most common location is in the cranial cervical or caudal thoracic region. These lesions are usually single, but can be multiple. They are most commonly dorsal or dorsolateral to the spinal cord but can be ventral occasionally. Rottweilers are likely to be predisposed for cervical arachnoid diverticula, and pug dogs seem to have a high incidence of thoracolumbar arachnoid diverticula.

In CT without contrast medium, there is a hypoattenuating lesion causing spinal cord compression. Diagnosis is established after subarachnoid injection of contrast medium leads to pooling of contrast medium in the diverticulum. Sagittal reformatted images allow recognition of the typical teardrop shape of the lesion.

On MR imaging, a discrete T1-hypointense region contiguous with the subarachnoid space is present dorsal to the spinal cord. This lesion is T2 hyperintense and suppressed with fluid-attenuated inversion recovery (FLAIR) techniques. The diagnosis is usually most obvious on sagittal images where the typical teardrop shape of these lesions is apparent (Fig. 12-26). The spinal cord is compressed to various degrees at the level of the diverticulum. Pulsation of the diverticulum can lead to spinal cord edema from the repetitive concussion, or there may be syrinx formation because of altered CSF flow in the

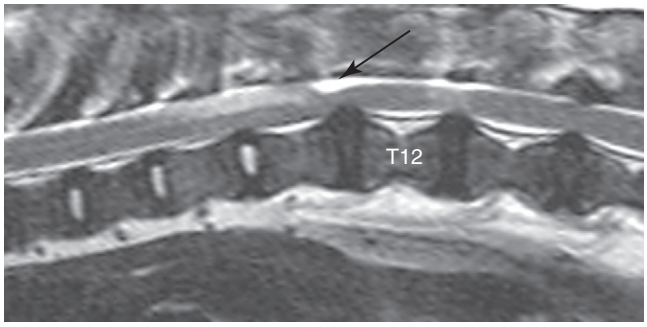


Fig. 12-27 Sagittal T2-weighted image of a dog with a dorsal arachnoid diverticulum *(white arrow)* at T11-T12. There is a region of intramedullary T2 hyperintensity just cranial to the diverticulum that may be edema secondary to pulsation of the diverticulum or a syrinx because of altered CSF flow.

region of the diverticulum (Fig. 12-27). MR imaging is superior to CT myelography for the diagnosis of spinal arachnoid diverticula in the rare instance where the diverticulum does not communicate with the subarachnoid space.

Epidermoid and Dermoid Cysts

Epidermoid and dermoid cysts and sinuses have a complex cyst wall and contain both epidermoid tissue and adnexa. They can be associated with the dermal, ocular, and central nervous system, and the most common central nervous system manifestation is of a sinus connection with the skin surface and extending into the vertebral canal to affect the spinal cord.[62] As opposed to sinuses, epidermoid and dermoid cysts do not have an opening onto the midline surface of the skin.[63]

With epidermoid cysts or sinuses, the wall of the lesion consists of stratified squamous epithelium, supported by connective tissue stroma. Keratin squames are found within the lesion along with a few inflammatory cells. Dermoid cysts and sinuses differ from epidermoid cysts because the dermoid cyst contains other features of skin, such as sweat glands, hair follicles, and sebaceous glands.

Epidermoid and dermoid cysts confined strictly to the central nervous system without a cutaneous or subcutaneous tract develop from skin-determining ectoderm, which remains attached to mesoderm and as the neural tube closes becomes surrounded by the meninges.[64] In such instances, no tract or sinus is present in the dorsal paraspinal soft tissue or skin.[64]

There are only a few reports on the use of CT and MR imaging in the diagnosis and presurgical assessment of epidermoid and dermoid cysts in dogs.[63,65] In one instance, CT imaging allowed detection of a communication with the vertebral canal through a defect in the vertebral arch, with subsequent spinal cord compression and displacement.[65] In humans, dural involvement of cutaneous epidermoid and dermoid cysts appears as tenting of the posterior margin of the dura on MR images.[63] The MR or CT appearance of strictly intramedullary epidermoid and dermoid cysts has not been reported in dogs or cats, although there is a report of a dermoid cyst in the medulla oblongata of a dog. That lesion was heterogeneous but predominantly hyperintense on both T1- and T2-weighted images with no contrast enhancement.[62]

Articular Process Cysts

Cysts associated with the articular process are extradural fluid-filled round or oval well-defined structures that develop as a result of degeneration of the articular process joint.[66-68] They are divided histologically into (1) synovial cysts lined by synovium-like epithelial cells resulting from outpouching of synovial membrane through weakened capsular tissue and (2) ganglion cysts, which are the result of mucinous degeneration of periarticular connective tissue and which do not have a synovial lining. From clinical and imaging perspectives, the two entities are indistinguishable and can therefore be grouped under the terminology *articular process cyst*.[67]

Clinical signs associated with articular process cysts vary from pain to ataxia and tetra- or paraparesis, although in a number of instances, the clinical signs are not attributable to the cyst, but to other causes of spinal cord compression, such as disc herniation, articular process hypertrophy, and vertebral instability. These articular process cysts appear to be more common in large- to giant-breed dogs.[66-68] In giant-breed dogs, the cysts tend to be multiple and located in the cervical spine and more common in young dogs.[66] In large-breed dogs, cysts are more commonly found in the thoracolumbar or lumbosacral area in young adults and older dogs.[66-68] The cysts can be single or multiple and present at one or several locations.

On MR imaging, these lesions have the characteristic signal of a fluid-filled lesion appearing as well-defined round lesions associated with the articular processes and are T1 hypointense and T2 hyperintense (Fig. 12-28).[67-68]

Discal Cysts

Discal cysts are ventral intraspinal cysts associated with the intervertebral disc. They appear as ventral extradural lesions in the vertebral canal immediately adjacent to the intervertebral disc. They are more common in the caudal aspect of the cervical spine.[69] Discal cysts are usually positioned dorsal to the intervertebral disc, are T2-hyperintense and T1-hypointense, and remain hyperintense on T2-weighted FLAIR images, which differentiates them from the surrounding CSF (Fig. 12-29). There is often contrast enhancement of the cyst wall. Variable degrees of disc degeneration can be present immediately ventral to the cyst, and the cyst can cause variable degrees of spinal cord compression.[69] Histopathologically, one cyst had a wall composed of irregular fibrous tissue consistent with fragments of annulus fibrosus and small adjacent parts of nucleus pulposus, hence the name *discal cyst*.

SPINAL TUMORS

Spinal tumors can be classified on the basis of their location relative to the dura mater and can be described as intramedullary, intradural-extramedullary, or extradural.[70] Most extradural tumors are malignant tumors of constituents of the vertebral column, such as the vertebrae or the soft tissues within or surrounding the vertebral column. Intradural-extramedullary tumors are mostly nerve sheath tumors and meningiomas. Intramedullary neoplasms are usually of glial cell origin, such as astrocytomas or ependymomas, but multicentric nonneural neoplasia, such as lymphoma, or metastatic lesions, such as hemangiosarcoma, also occur.

Extradural Tumors

The most common extradural spinal cord tumors in dogs include osteosarcoma and chondrosarcoma.[71] In cats, extradural lymphosarcoma is also frequent.[72] Solitary or disseminated histiocytic sarcoma can also affect the vertebrae and cause spinal cord compression.[73] Other disseminated canine tumors with possible vertebral involvement include lymphosarcoma and multiple myeloma.[71] Metastatic vertebral tumors are also common, in particular prostatic carcinoma or transitional cell carcinoma of the bladder and urethra in dogs.[71] Tumors of the paravertebral soft tissues or extradural soft tissue components of the vertebral canal are also possible, and local invasion can cause spinal cord compression. Examples include soft tissue sarcoma, extradural lymphosarcoma, and infiltrative lipoma.[74]

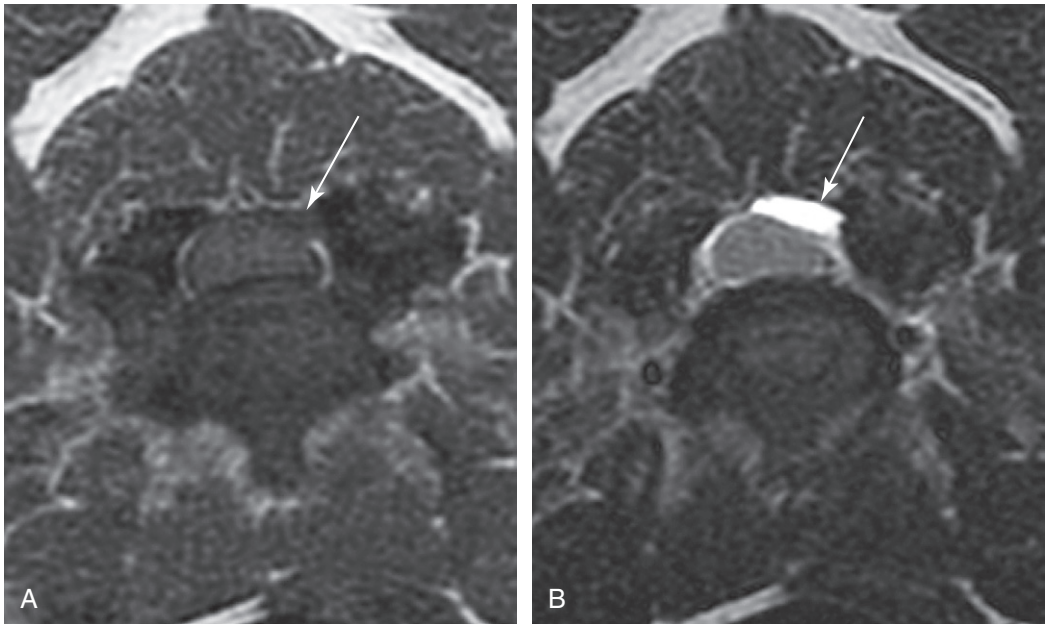


Fig. 12-28 Transverse T1-weighted **(A)** and T2-weighted **(B)** images at C3-C4 in a dog with a left-sided left articular process cyst. The cyst *(white arrows)* is T1 hypointense and markedly T2 hyperintense because of its fluid content. In this dog the cyst caused mild left dorsolateral spinal cord compression.

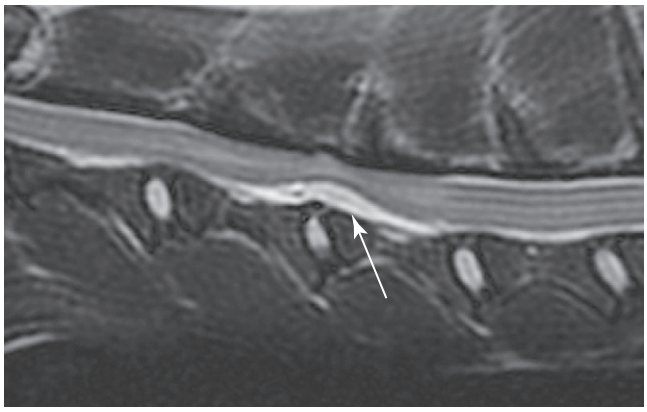


Fig. 12-29 Sagittal T2-weighted image in a dog with a discal cyst at C4-C5. Note the mild degenerative changes in the disc at C4-C5 with reduced size and signal of the nucleus pulposus. The discal cyst appears as a broad-based T2-hyperintense structure *(white arrow)* present dorsal to the C4-C5 space that causes ventral spinal cord compression. Intramedullary T2 hyperintensity at that level is consistent with edema. A fluid-filled cystic structure was found at surgery in the ventral epidural space associated with the C4-C5 disc.



Fig. 12-30 Transverse CT-myelographic image of the thoracic spine in a dog with a vertebral osteochondroma. There is a large proliferative lesion arising from the vertebral arch that causes marked stenosis of the vertebral canal and left dorsolateral compression of the spinal cord *(c)*. The subarachnoid space filled with iodinated contrast medium is indicated by the *white arrow*.

Both MR imaging and CT are more sensitive than radiography in detecting vertebral lesions, and in particular bone lysis that is not apparent radiographically can be demonstrated readily using CT. Vertebral canal tumors can be difficult to localize to the intradural, extradural, or intramedullary compartments on noncontrast CT images.[75] Injection of intravenous contrast medium and, more important, CT myelography are more precise for determining the location of masses in the vertebral canal with respect to the dura. MR imaging is also good for localizing these lesions; however, with MR imaging it is more difficult to localize vertebral canal masses with respect to the dura because of lower spatial resolution.[76] There are no specific CT or MR imaging features that are associated with a specific tumor type.[75-76]

Vertebral tumors produce variable degrees of bone lysis or proliferation, which is detected easily on CT images (Fig. 12-30). On MR images, alteration of the shape of the affected vertebra can be seen as well as disruption of the normally hypointense vertebral cortex (Fig. 12-31). In MR images, periosteal reaction appears as hypointense material surrounding the lesion in the affected vertebra. The signal intensity of the lesion itself varies between patients and depends on tumor type. Relevant conclusions cannot be drawn as to what the signal intensity of a specific tumor type would be. Fat-suppression images are useful for differentiating bone

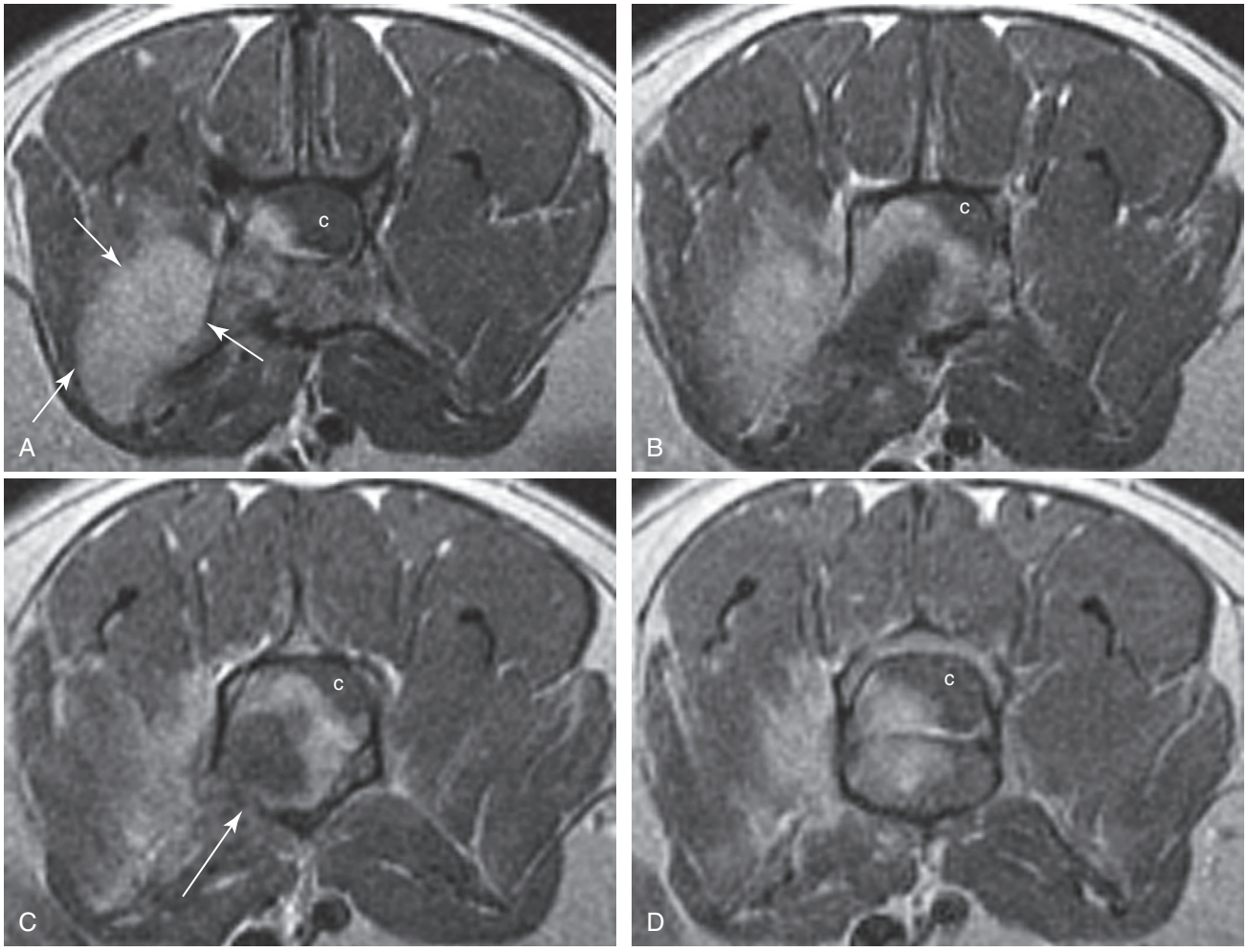


Fig. 12-31 Invasive paravertebral fibrosarcoma in a cat. Successive transverse T1-weighted postcontrast images in the lumbar spine. There is a hyperintense mass (**A,** *arrows*) in the right paraspinal muscles that invades the vertebra **(B),** destroying the normally hypointense cortex (**C,** *white arrow*) and entering the vertebral canal to cause spinal cord *(c)* compression **(B, C, D).**

marrow fat accumulation from true lesions: Both appear hyperintense on T1-weighted and T2-weighted images, but with fat suppression, fat signal will decrease but tumor will remain bright (Fig. 12-32).[77,78]

Paravertebral soft tissue tumors can also be imaged well with CT and MR imaging and can be recognized before they become visible radiographically. MR imaging and CT also allow assessment of surgical resectability and can be used for radiation-therapy planning.

Infiltrative lipomas have specific imaging characteristics. When in a paravertebral location, an infiltrative lipoma can invade the vertebral canal and cause neurologic signs. On CT imaging, infiltrative lipomas are characteristically hypoattenuating, similar to normal fat.[79] On MR imaging, infiltrating lipomas are T1- and T2-hyperintense, and fat suppression techniques are useful to confirm their fatty composition (Fig. 12-33).[77]

Intradural-Extramedullary Tumors

One third of spinal tumors are intradural-extramedullary, and in dogs these are mainly meningiomas and nerve sheath tumors.[80] Other rare intradural tumors, such as nephroblastoma, are reported in dogs.[81-83] In cats the most common intradural-extramedullary tumor is lymphosarcoma, although most of these also have an extradural component.[72]

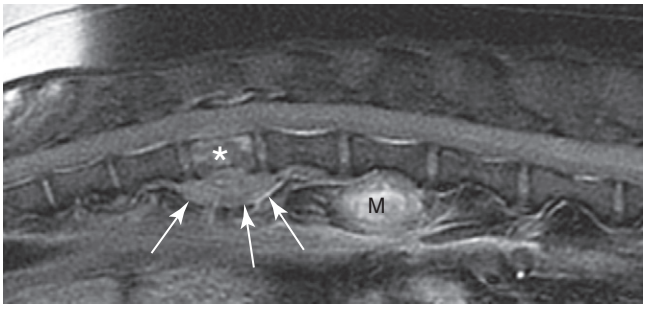


Fig. 12-32 Sagittal postcontrast fat-saturated T1-weighted image of the spine in a dog with metastatic hepatic carcinoma. A hyperintense signal is noted in the vertebral body *(*)*, suggesting metastatic tumor. Hyperintense neoplastic proliferation is present ventral to this vertebra *(white arrows)*. A metastatic sublumbar periaortic lymph node *(M)* is also present. Fat-suppressed pulse sequences optimize vertebral lesion detection by suppressing the hyperintense signal from fat that may obscure mildly enhancing lesions.

Peripheral Nerve Sheath Tumors

Peripheral nerve sheath tumors can be intradural/extramedullary or extradural. Most are found in the brachial plexus and as such are located in the axilla. If involving the vertebral column, they can have an intradural component and

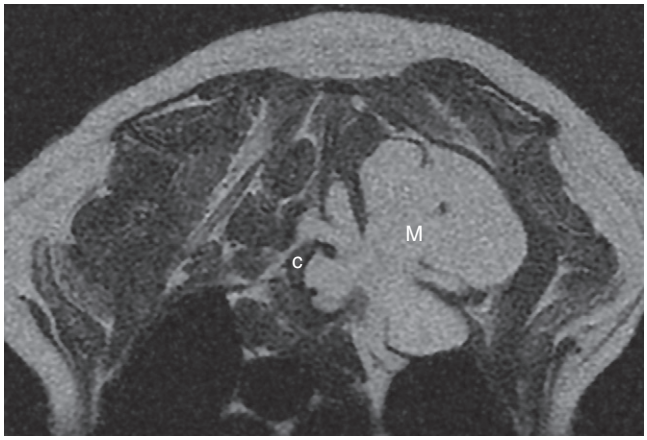


Fig. 12-33 Transverse T1-weighted images of a dog with an infiltrative lipoma in the left paraspinal area. There is a lobulated hyperintense mass *(M)* in the left paraspinal area that is causing vertebral effacement and spinal cord *(c)* compression. Note that the signal of the tumor is identical to the signal of the dorsal subcutaneous fat.

can be difficult to differentiate from intradural lesions such as meningiomas.

Detection of peripheral nerve sheath tumors with CT can be difficult and depends on detecting soft tissue asymmetry because they often have attenuating properties similar to muscle. Small or diffuse peripheral nerve sheath tumors may be subtle and hard to detect, and it can also be difficult to assess nerve structures that are oriented obliquely to the transverse CT imaging plane. CT changes associated with peripheral nerve sheath tumors include unilateral muscle atrophy, presence of a soft tissue mass that is isoattenuating to surrounding muscles, and contrast enhancement that is either uniform, patchy, or rimlike.[84] The mass occasionally tracks in a linear fashion into a neighboring intervertebral foramen and can invade the vertebral canal (Fig. 12-34). Invasion into the thoracic cavity can also be seen. Masses as small as 1 cm can be identified on CT.[84]

With MR imaging, multiple sequences in various planes are necessary to identify and stage peripheral nerve sheath tumors and depict their relationship to the surrounding structures, especially the intervertebral foramen and spinal cord.[85] Imaging should be performed with perfect positioning of the patient usually in dorsal recumbency with perfect symmetric positioning of the limbs.[85] Peripheral nerve sheath tumors can be focal masses or diffuse thickening of affected nerves (Figs. 12-35 and 12-36).[85] Whether the tumor is masslike or diffuse, proximal extension of the lesion into the intervertebral foramen and vertebral canal is possible, and this feature is important to detect as it affects whether the tumor can be excised completely. Compared to surrounding skeletal muscles, the tumor is usually T2-hyperintense, although mixed signal intensity is possible (see Fig. 12-35).[23,85] T2-weighted short T1 inversion recovery pulse sequences, which reduce the signal from fat, are useful in increasing the conspicuity of the tumor.[77,85] Fat saturation on postcontrast images helps identify the tumor by increasing the contrast of enhancing tumor against the background (see Fig. 12-35). The tumor is most commonly T1 isointense on precontrast images but can be hyperintense or of mixed signal intensity. Most tumors have mild to strong contrast enhancement.[23,85] Additional changes seen include ipsilateral muscle atrophy. The atrophic muscles often have abnormal signal, including T2- and T1-hyperintensity, and possible mild contrast enhancement; these changes are consistent with neurogenic atrophy, edema, fat infiltration, and fibrosis.[85]

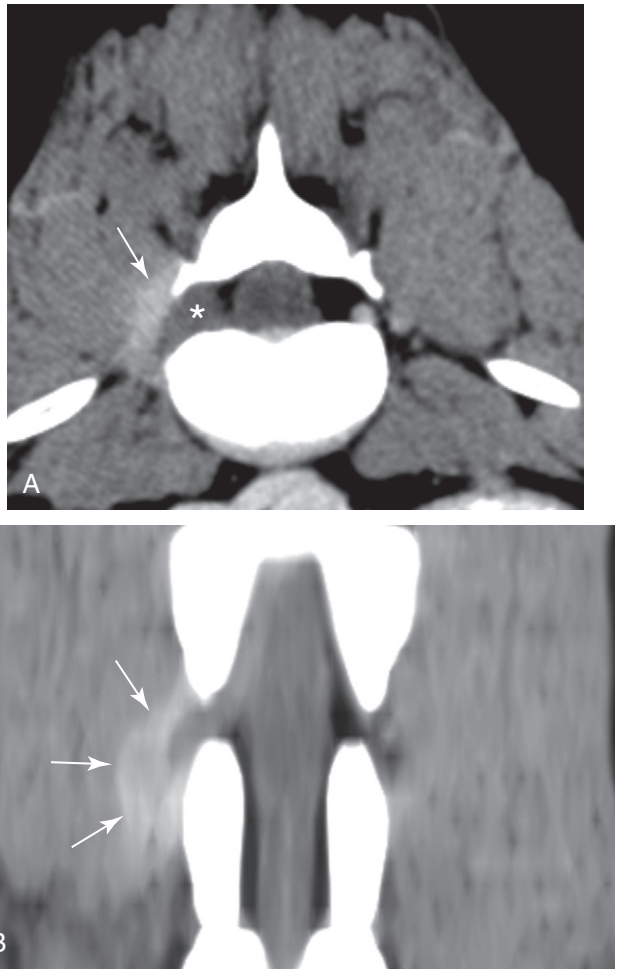


Fig. 12-34 Transverse **(A)** and dorsal **(B)** reformatted postcontrast CT images at the level of the L5-L6 intervertebral disc space in a dog with a nerve root tumor at L5-L6. Note that the right intervertebral foramen is wide compared with the left. There is a soft tissue mass obliterating the right intervertebral foramen at L5-L6 *(*)* and extending outside in the form of an elongated mass that has contrast enhancement *(white arrows)*.

Meningioma

Meningiomas are slowly growing tumors of the meninges that cause neurologic deficits primarily by compression of the spinal cord. Although they can occasionally grow in the epidural space, most meningiomas in dogs and cats are intradural-extramedullary lesions.[86-87] The most common locations are cranial cervical and lumbar regions.[88] Meningiomas are usually single, but multifocal meningiomas are seen occasionally.[88]

On CT myelography, meningiomas appear as an intradural-extramedullary mass, causing a filling defect in the column of contrast medium. A golf-tee sign, similar to the one observed on conventional myelography, appears when the contrast medium diverges to encompass the mass in the subarachnoid space. The golf-tee sign is the hallmark of an intradural-extramedullary lesion and is appreciated best on CT when reformatted sagittal and dorsal images are obtained. If iodinated contrast medium is injected intravenously, there may be enhancement of the mass.[88]

On MR imaging, meningiomas appear as focal masses that are usually hyperintense to the spinal cord on T2-weighted images, and isointense to hypointense to the spinal cord on precontrast T1-weighted images. However, T2-hypointensity and T1-hyperintensity have also been reported.[76,87,88] After gadolinium injection, meningiomas usually have moderate to strong well-defined contrast enhancement.[87,88] Features that

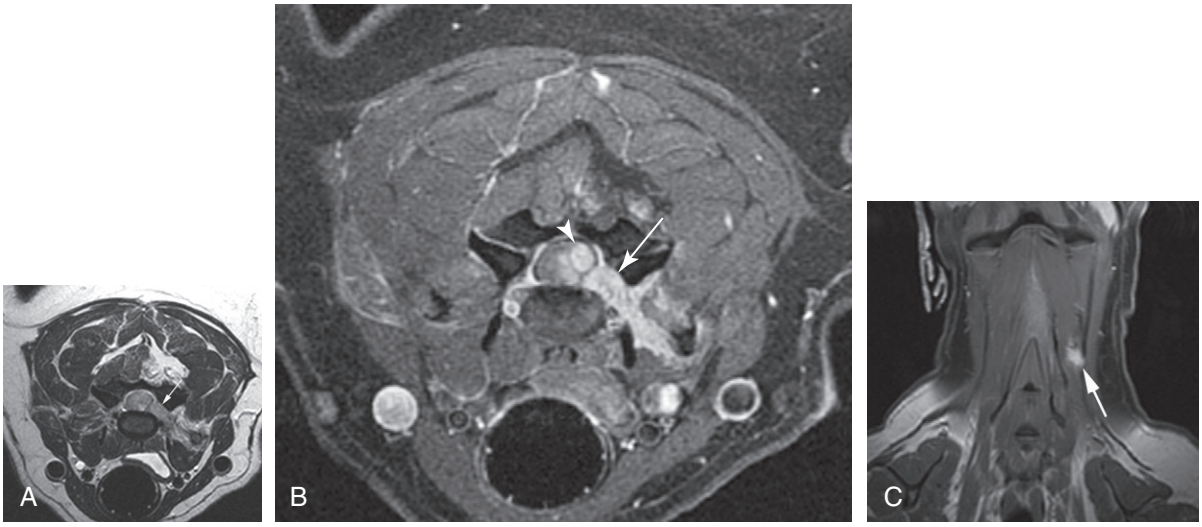


Fig. 12-35 Transverse T2-weighted **(A),** transverse fat-saturated postcontrast T1-weighted **(B)**, and dorsal fat-saturated postcontrast T1-weighted **(C)** images in a dog with a nerve sheath tumor in the left C3-C4 intervertebral foramen. There is a soft tissue tumor obliterating the left intervertebral foramen at C3-C4 (**A,** *white arrow*). The tumor is nearly isointense to spinal cord and extends peripheral to the foramen in the form of an elongated mass. There is marked diffuse contrast enhancement of the tumor (**B,** *white arrow*). The tumor tracks along the nerve path in the paraspinal muscles (**C,** *white arrow*). An intradural component was apparent on the postcontrast images (*white arrowhead,* **B**).

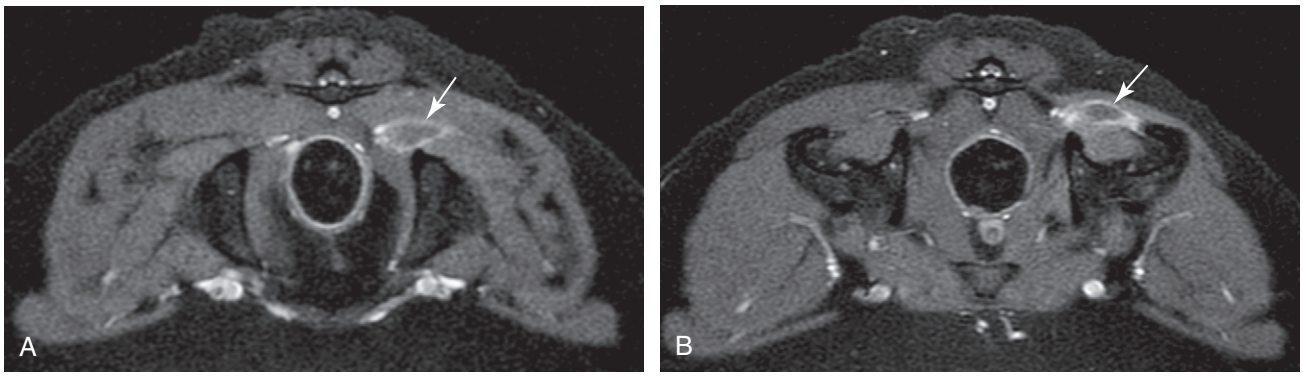


Fig. 12-36 Transverse fat-saturated postcontrast T1-weighted images in a cat with a large extradural sciatic nerve tumor. There is muscle atrophy on the left side. The tumor is slightly hypointense with strong peripheral contrast enhancement *(white arrow)* and follows the path of the sciatic nerve. Fat saturation facilitates the recognition of the abnormal enhancing tissue on postcontrast series.

help in determining the intradural-extramedullary location include the following:[87]

- The broad-based dural margin is seen on at least one of the imaging planes (Fig. 12-37).
- The gradual expansion of the subarachnoid space cranial and caudal to the mass that can be detected on T2-weighted images, especially in the dorsal plane, creates a golf-tee sign similar to that observed with conventional myelography or CT-myelography. Heavily T2-weighted MR pulse sequences (T2-myelograms) can be useful in recognizing this sign.[11,76]

MR-imaging features associated with spinal meningiomas are the dural tail sign, seen as strong linear enhancement of the border of the tumor confluent with the adjacent meninges (see Fig. 12-37).[87] Confusion with a nerve sheath tumor is possible when the meningioma is located within or exits the intervertebral foramen.[87]

Nephroblastoma

This is a rare tumor typically occurring in young (less than 3 years old) dogs, with German shepherd dogs possibly predisposed.[82] The tumor is intradural-extramedullary and located consistently between T10 and L2. It is thought that the tumor arises from ectopic embryonic remnants of renal tissue. A single mass is usually present, although there are rare reports of intraspinal metastases.[89]

On noncontrast CT, swelling of the spinal cord with obliteration of the epidural fat is observed in the affected area; however, the intradural nature of the lesion can only be determined with CT-myelography. Even then it can be difficult to tell if the tumor is intradural-extramedullary or intramedullary, especially because the tumor can invade the spinal cord.

On MR imaging, the tumor is isointense to the spinal cord in T2-weighted images, but it may have heterogeneous signal.[82,83] The mass is also usually isointense to the spinal cord on T1-weighted images, but there is moderate to strong contrast enhancement.[82,83] Transverse and dorsal images allow the peripheral location of the mass in the dural sac to be detected, often with a broad base toward the meninges. Widening of the subarachnoid space cranial or caudal to the mass can be present and help determine its intradural location. However, this sign is not present consistently, and, as with CT, it can be difficult to determine the intradural-extramedullary origin of

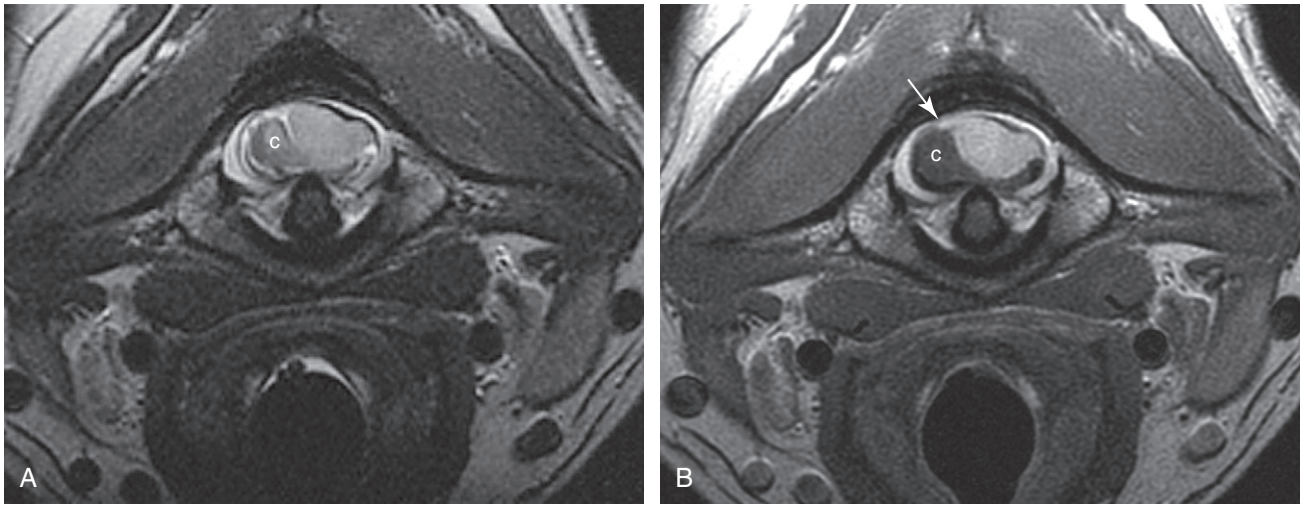


Fig. 12-37 Transverse T2-weighted **(A)** and postcontrast T1-weighted **(B)** images at the level of C1 in a dog with a meningioma. There is an intradural mass in the left dorsal aspect of the subarachnoid space that is broad-based toward the dura and is causing severe spinal cord *(c)* compression. After contrast-medium injection **(B),** the mass is markedly and homogeneously contrast-enhancing, and a dural tail *(white arrow)* is present on the dorsal right margin of the mass.

the mass, especially when the tumor invades the spinal cord (Fig. 12-38).[83]

Intramedullary Tumors

Intramedullary tumors are rare in dogs and cats.[70] Most are primary glial tumors, including astrocytomas, oligodendrogliomas, and ependymomas.[90] Metastatic intramedullary tumors are also possible, such as hemangiosarcoma. In cats intramedullary lymphoma is also common.[91] Usually, intramedullary tumors are T1-isointense and T2-hyperintense because of edema and gliosis. They have variable degrees of contrast enhancement.

MYELOMALACIA

Myelomalacia corresponds to gross softening of the spinal cord resulting from hemorrhagic necrosis.[92,93] It can occur following acute spinal cord injury and is caused by extensive damage to intramedullary vasculature. A core of necrosis may extend cranially and caudally from the level of the spinal cord injury, typically in the base of the dorsal funiculi. A small proportion of dogs with acute disc extrusion will have diffuse myelomalacia, often called ascending or descending myelomalacia.[93] Myelomalacia can affect up to 10% of dogs with acute disc extrusion that exhibit paraplegia and loss of deep pain perception.[93] The prognosis for patients with myelomalacia is usually poor, but improvement is possible in focal disease. Therefore MR imaging is useful in determining prognosis by providing information about the extent of involvement.

On MR imaging, myelomalacia is characterized by diffuse swelling of the spinal cord that is recognized by loss of visualization of the hyperintense signal from CSF and fat around the spinal cord on T2-weighted images. There is diffuse patchy T2-hyperintensity of the spinal cord (Fig. 12-39) that extends over the length of several vertebral bodies. The affected spinal cord parenchyma is isointense to normal spinal cord on T1-weighted images.[92] Areas of hypointensity associated with spinal cord hemorrhage may be visible in T2-weighted gradient recalled echo images.[93] In addition to the areas of T2 hyperintensity, areas of T2 hypointensity may be detected at high field strengths because of deoxyhemoglobin in hemorrhagic spinal cord foci.[92,93]

ISCHEMIC MYELOPATHY

The most common cause of spinal cord ischemia and infarction in dogs and cats is fibrocartilaginous embolism from the nucleus pulposus of the intervertebral disc.[94] In dogs other causes include thromboembolism; a hypercoagulable state; vasculopathy; and parasitic, septic, or neoplastic embolization,[94] whereas in cats only fibrocartilaginous embolism has been identified as a cause of ischemic myelopathy.[95]

The typical clinical presentation is a sudden, frequently asymmetric, mono-, hemi-, or tetraparesis or tetraplegia.[95] Spinal cord thromboembolism is usually nonpainful and nonprogressive after the first 24 hours.[94] MR imaging is useful in recognizing changes associated with ischemic myelopathy and differentiating it from other conditions with similar clinical presentations, such as spinal trauma or intervertebral disc herniation.

Typically there is a focal T2-hyperintense intramedullary lesion that is either T1 hypointense or T1 isointense. On transverse images, the lesion is usually asymmetric (Fig. 12-40). The infarct can sometimes have variable contrast enhancement during the first week.[94,96] The lesion involves mostly gray matter, although a large number of dogs also have some white matter involvement. Focal areas of hypointensity suggestive of hemorrhage are identified occasionally on gradient recalled echo images.

No abnormalities are seen on MR images in approximately 20% of patients. This usually happens when dogs are imaged less than 72 hours after onset of clinical signs.[96] The incidence of abnormal MR imaging findings is higher in nonambulatory dogs with higher neurologic scores than mildly affected dogs.[96] Dogs with clinically suspected ischemic myelopathy and no MR imaging changes have a good clinical outcome.[96]

On average, the length of the spinal cord T2 hyperintensity observed on sagittal MR images in dogs with ischemic myelopathy is approximately 1.8 times the length of C6 for cervical or cervicothoracic lesions and 2.2 times the length of L2 for thoracolumbar and lumbosacral lesions. There is an association between the length of spinal cord affected and severity of clinical signs.[96] A lesion-length-to-vertebral-length ratio greater than 2.0 has a sensitivity of 100% in predicting a poor clinical outcome.[96] The percent cross-sectional area of the spinal cord with T2 hyperintensity is also associated with the

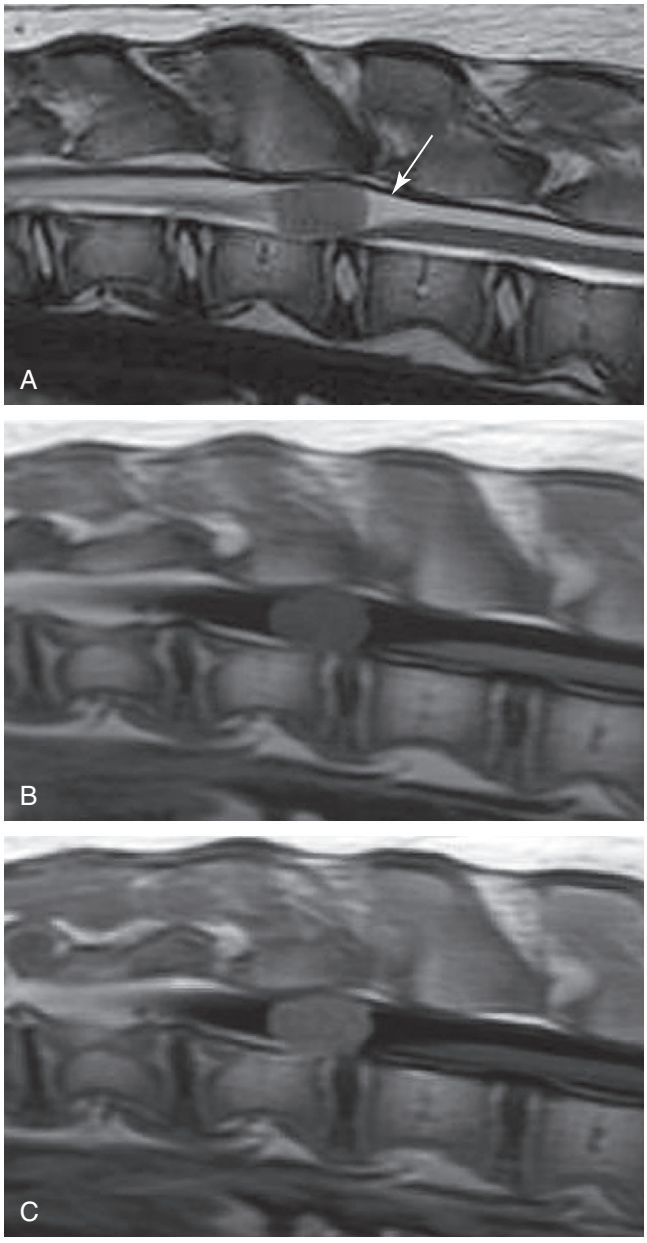


Fig. 12-38 Sagittal T2-weighted **(A),** T1-weighted with fluid-attenuated inversion recovery (FLAIR) **(B),** and postcontrast T1-weighted FLAIR **(C)** images of a young dog with a nephroblastoma. There is an ovoid intradural mass at the level of L1. It is isointense to the spinal cord on precontrast images, and there is strong contrast enhancement. Focal widening of the subarachnoid space is present caudal and cranial to the mass, forming a golf tee sign (*white arrow* in **A**); the CSF in the subarachnoid space is T2 hyperintense and T1 hypointense. (Images courtesy of Dr. Shannon Holmes, University of Georgia.)

severity of the clinical signs.[96] A percentage cross-sectional area of the lesion of more than 67% has a sensitivity of 100% in predicting poor clinical outcome.[96]

SPINAL TRAUMA

Acute spinal trauma can cause unstable spinal injuries that have the potential to lead to failure of the vertebral column to protect the spinal cord and nerve roots from severe insult. Resultant myelopathy and radiculopathy can lead to

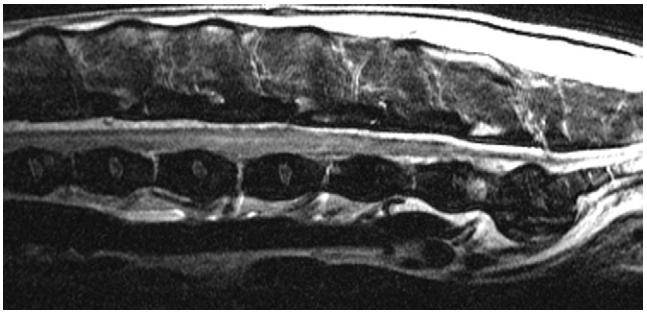


Fig. 12-39 Sagittal T2-weighted image of the lumbar spine in a dog with acute disc herniation at L5-L6 and secondary ascending myelomalacia. There is an ill-defined patchy intramedullary T2 hyperintensity in visible segments of the lumbar spinal cord.

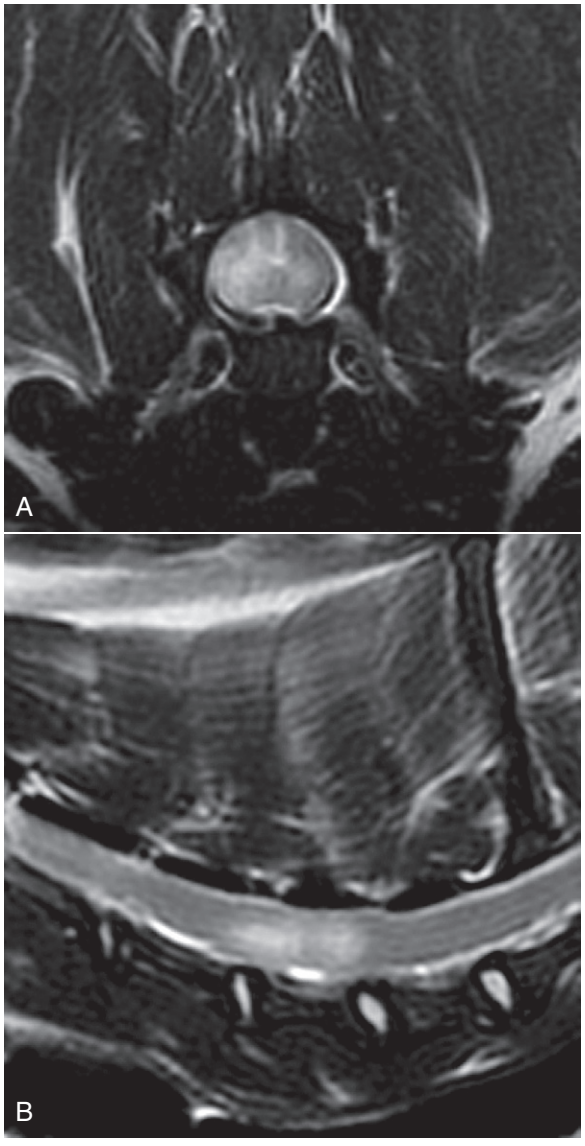


Fig. 12-40 Presumed fibrocartilaginous embolism in a dog. Transverse **(A)** and sagittal **(B)** T2-weighted images. There is a hazy focal hyperintense signal in the spinal cord that is asymmetric on the transverse image, involving both gray and white matter on the right and the ventral gray matter on the left. The intervertebral discs in the vicinity were normal, and there is no compression of the spinal cord. Clinical signs were acute and nonprogressive.

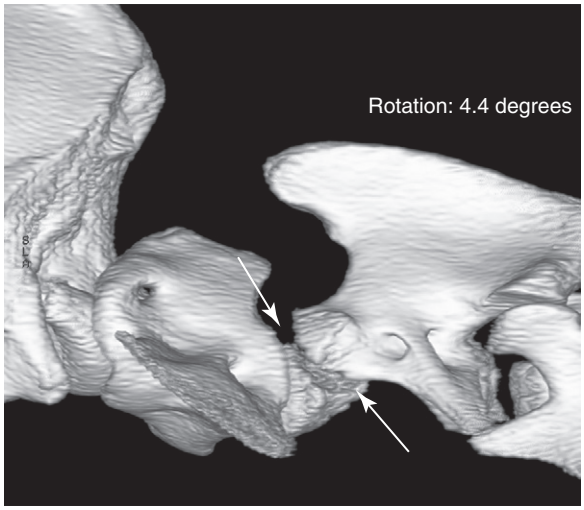


Fig. 12-41 Fracture of the cranial extremity of C2 in a dog. Three-dimensional volume rendering of the cranial cervical spine where the mildly displaced complete transverse fracture of the cranial apex of C2 *(white arrows)* can be seen.

temporary or permanent paralysis. Rapid and accurate evaluation of the vertebral column and the status of the spinal cord facilitate appropriate treatment and a better informed prognosis. Radiography is inadequate to rule out acute vertebral fractures and subluxations and is a poor diagnostic tool to assess the stability of spinal fractures. Survey radiography also cannot be used reliably to detect compressive lesions. CT is recommended in patients with a high clinical suspicion of acute fracture and is superior to radiography in the traumatized patient.[97] Multidetector scanners now provide the ability to obtain 1 mm or submillimeter CT images in a short time, and to perform high-quality multiplanar reformatted images with surface and volume rendering (Fig. 12-41). This enables depiction of complex fractures in a three-dimensional format that can assist in surgical planning.[2] The short acquisition time makes it possible to perform a CT study with the anesthetized or sedated patient strapped to a spinal board, thus protecting against further damage.[97] Although it has not been evaluated in veterinary medicine, MR imaging is more sensitive to assess the spinal cord and integrity of supporting soft tissues, but it is likely that a significant number of spinal fractures can be missed with MR imaging.

INFLAMMATORY/INFECTIOUS CONDITIONS

Discospondylitis

Discospondylitis is infection of two adjacent vertebral end plates and the associated intervertebral disc. Traditionally, discospondylitis was diagnosed based on characteristic radiographic changes together with laboratory findings. A limitation of radiography is the delay of up to a few weeks between the onset of clinical signs and detection of radiographic changes. There is also a discrepancy between clinical and radiographic signs during recovery.[98]

CT and MR imaging can be used to confirm a tentative diagnosis of discospondylitis.[99-102] Compared with survey radiography, MR imaging can assess the soft tissue components of the vertebral canal including the epidural structures and spinal cord, and thereby provide additional information on degree of involvement of these structures and presence and degree of spinal cord compression. MR imaging can reveal changes suggestive of discospondylitis in dogs that have normal radiographs, thereby allowing an earlier diagnosis in dogs with supportive clinical signs but equivocal radiographs (Fig. 12-42).[99]

Typical MR imaging changes seen with discospondylitis include (see Fig. 12-42) the following:[99]

- Abnormal T1-hypointensity and T2-hypointensity of adjacent end plates and bone marrow: These lesions are hyperintense on T2-weighted short T1 inversion recovery images.
- Hyperintense disc on T2-weighted images
- Contrast enhancement of the intervertebral disc, vertebral end plates, and paravertebral soft tissues
- End plate erosion is usually present, but in early stages where end plate erosion is absent, the only change may be T2 hyperintensity of bone marrow adjacent to the end plates.
- Spinal cord compression caused by extension of the infection to the epidural space
- Vertebral subluxation on sagittal images

Spinal Epidural Empyema

Spinal epidural empyema is presence of a suppurative lesion in the epidural space. The clinical signs include fever, pain, and progressive neurologic dysfunction. Spinal empyema is relatively rare in dogs. Causes include extension of adjacent osteomyelitis or discospondylitis or hematogenous spread.

On noncontrast CT, an epidural mass is suspected based on lack of visualization of hypoattenuating epidural fat around the spinal cord, but the epidural mass is best identified with CT myelography.[103] Intrathecal contrast-medium injection can facilitate spread of the infection in the subarachnoid space because of iatrogenic contamination.

MR imaging is better for diagnosing spinal empyema, because it does not require subarachnoid injection of contrast medium.[104] Spinal empyema appears as a well-defined epidural mass in the dorsal or ventral aspect of the vertebral canal. The lesion forms a high or mixed signal mass on T2-weighted images but is usually T1-hypointense. A peripheral, rimlike pattern of contrast enhancement or a diffuse pattern of enhancement can be noted (Fig. 12-43). If gradient recalled echo images are acquired, focal hypointense areas consistent with hemorrhage may be present. Hyperintense lesions in the gray matter of the spinal cord adjacent to the epidural mass can be seen, which may be caused by compression of the spinal cord by the mass or by vascular compromise.[104]

Meningomyelitis

Meningitis and myelitis can have an infectious or noninfectious origin.[105,106] Infectious agents in dogs include viruses (e.g., canine distemper), bacteria (e.g., *Staphylococcus*, *Pasteurella*, *Actinomyces*, and *Nocardia* spp.), fungi (e.g., *Cryptococcus*, *Blastomyces*, *Histoplasma*, and *Coccidioides* spp.), Rickettsiae (e.g., *Ehrlichia* spp., *Rickettsia rickettsii*), protozoa (e.g., *Toxoplasma gondii*, *Neospora caninum*), parasites (e.g., *Dirofilaria immitis*, *Angiostrongylus* spp.), and rarely algae (e.g., *Prototheca wickerhamii*, *Prototheca zopfii*).[107] In cats, feline infectious peritonitis and toxoplasmosis have been reported.[91]

Noninfectious causes of canine meningomyelitis include granulomatous meningoencephalomyelitis,[108] pyogranulomatous meningoencephalomyelitis, and steroid-responsive meningitis arteritis.[107]

CT changes in dogs with meningomyelitis include spinal cord swelling, spinal cord hypoattenuation, and occasionally intramedullary or meningeal contrast enhancement.[105]

On MR imaging, abnormalities include irregular areas of intramedullary T2-hyperintensity (Fig. 12-44). On precontrast T1-weighted images, these areas are either isointense or hypointense to the spinal cord and have various amounts of contrast enhancement.[107-109] The pattern is not specific for

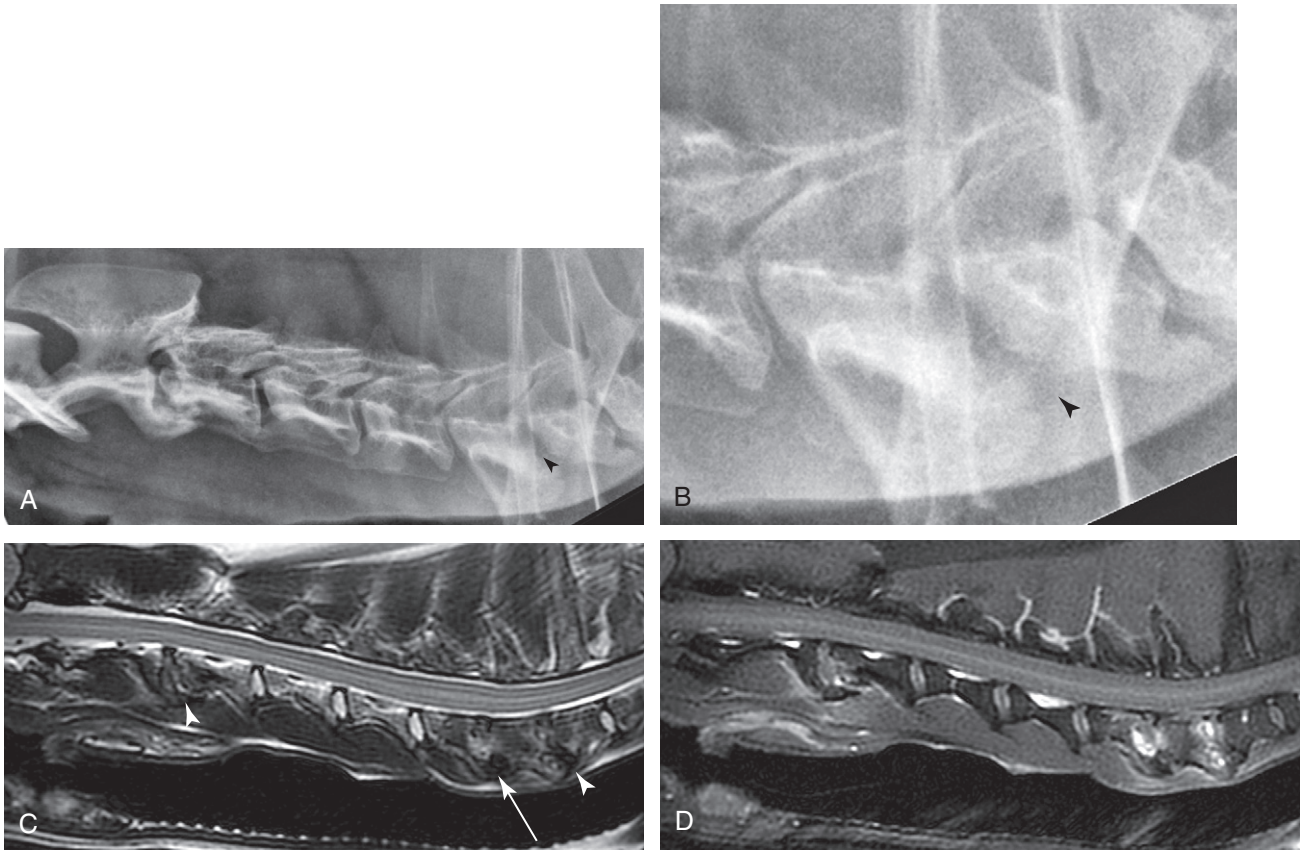


Fig. 12-42 Lateral radiograph of the cervical spine **(A),** close-up radiograph of C5-C6 **(B),** and sagittal T2-weighted **(C),** and postcontrast fat saturated T1-weighted **(D)** images in a dog with fever and cervical pain. Characteristic radiographic changes consistent with discospondylitis were present at C6-C7 (*black arrowhead* in **A and B**). On the MR images, there was irregularity and lysis of the cortical bone around that space (*white arrow* in **C**), and the bone marrow of C6 and C7 has a mixture of increased and decreased intensity on T2-weighted images **(C).** However, additional lesions are present at C2-C3 and C7-T1 that are also characterized by loss of integrity of the end plates and abnormal bone marrow signal in the vertebral bodies with loss of the normal structure of the intervertebral disc spaces (*white arrowheads* in **C**). On the postcontrast fat-saturated T1-weighted images **(D),** there is enhancement of the vertebral bodies around the end plates of these three spaces, as well as of the paravertebral soft tissues ventral to the disc spaces, indicative of inflammation. These changes are consistent with discospondylitis, not only at C6-C7 but also at C2-C3 and C7-T1. Lesions of discospondylitis can be detected earlier with MR images than with radiography.

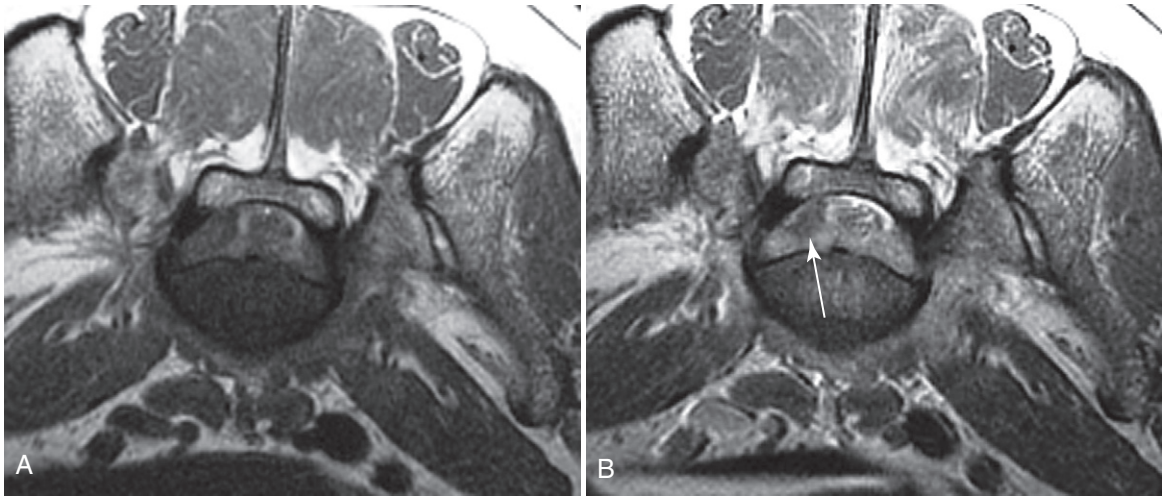


Fig. 12-43 Precontrast **(A)** and postcontrast **(B)** transverse T1-weighted images in the lumbosacral area in a dog with lumbosacral discospondylitis and spinal empyema. The vertebral canal is filled with heterogeneous material that enhances irregularly, with a hypointense nonenhancing area on the right consistent with fluid collection *(white arrow)*. Epidural empyema caused by extension of the infectious process from the disc space into the caudal lumbar vertebral canal was confirmed at surgery.

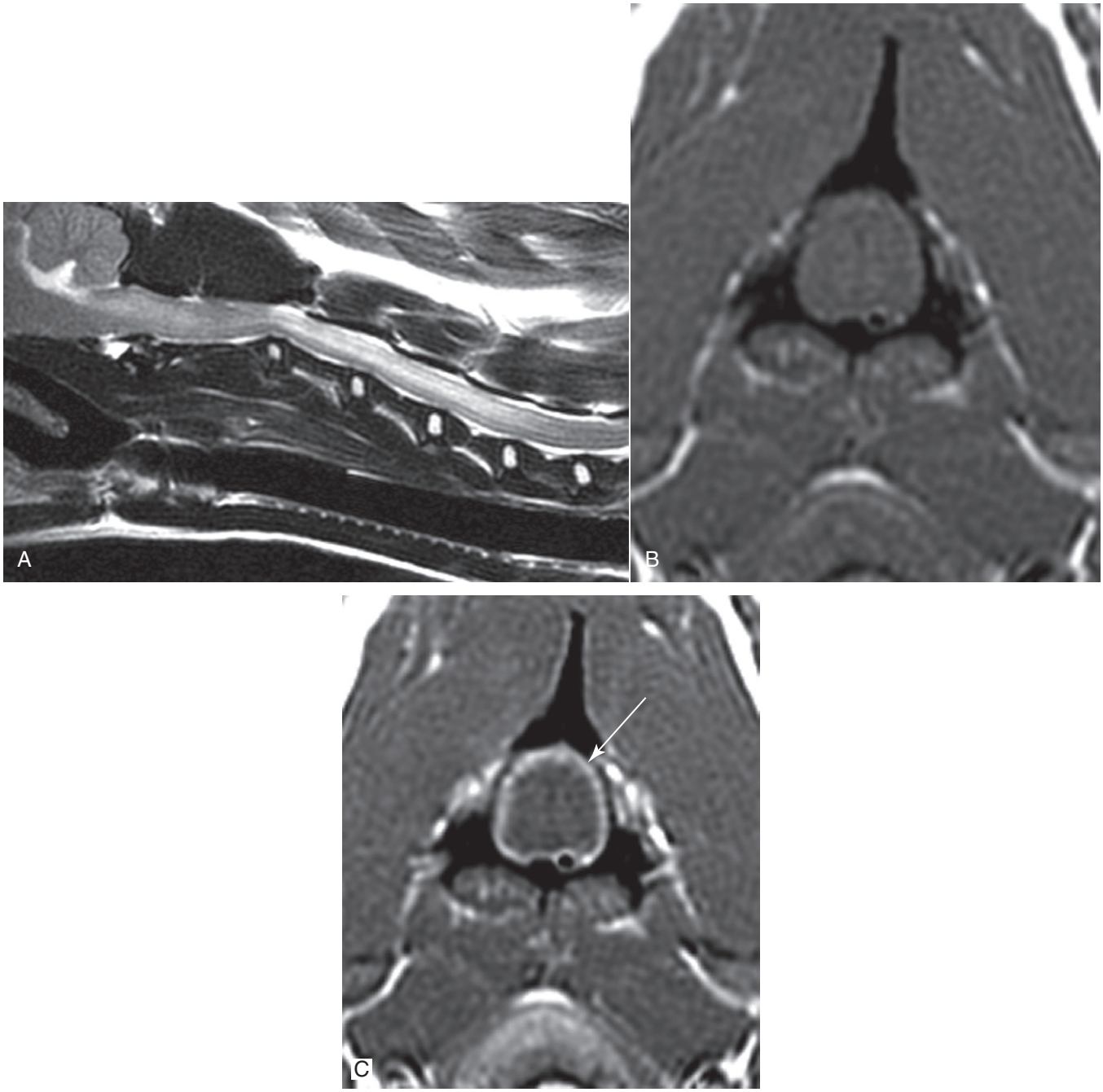


Fig. 12-44 Sagittal T2-weighted **(A),** transverse precontrast T1-weighted **(B),** and transverse postcontrast T1-weighted **(C)** images at the level of C2 in a dog with meningomyelitis caused by *Cryptococcus* infection. On the T2-weighted image, extensive ill-defined areas of T2 hyperintensity are present **(A).** On the postcontrast T1-weighted image, there is strong contrast enhancement (**C,** *white arrow*) of the meninges compared with the precontrast image at the same level **(B).**

meningomyelitis, and other conditions such as myelomalacia or ischemic myelopathy can produce similar changes. Therefore correlation with clinical signs and laboratory test results is necessary. In cats, lymphosarcoma can produce similar MR imaging changes.[91,109]

VERTEBRAL ANOMALIES

Congenital anomalies of the spine that can be assessed with CT or MR imaging include atlantoaxial malformation, hemivertebrae, block vertebrae, butterfly vertebrae, transitional vertebrae, and spina bifida. Most of these anomalies are diagnosed radiographically; however, CT and MR imaging can provide important additional information. CT provides a better understanding of the bony abnormality and spatial relationship between the abnormal and adjacent vertebrae and effect of the anomaly on the vertebral canal and intervertebral foramina (Fig. 12-45). MR imaging is indicated when assessment of the spinal cord and associated nerve roots is desired, especially when the consequences of the vertebral anomalies need to be assessed. For example, spinal bifida can be associated with focal anomalies of the spinal cord and meninges in the form of a myelomeningocele.[110]

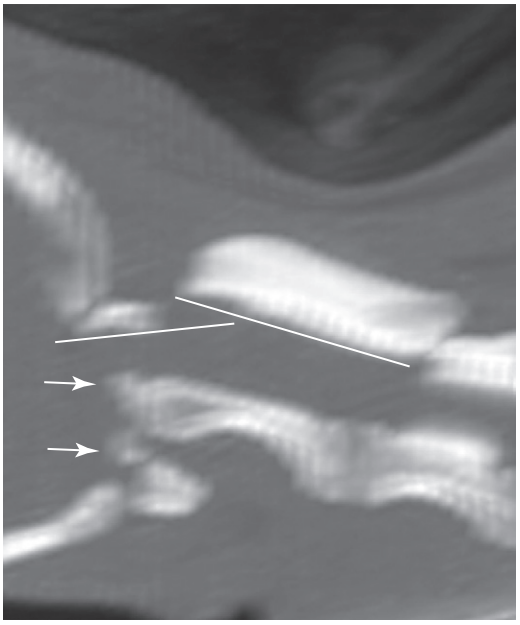


Fig. 12-45 Reformatted sagittal CT image of the cranial aspect of the cervical spine, in a dog with atlantoaxial instability. The dorsal lamina of C1 is not aligned with the dorsal aspect of the vertebral canal of C2 *(lines)* indicating subluxation. Small bone fragments are associated with the dens *(white arrows)*.

SYRINGOMYELIA

Syringomyelia is the development of fluid-filled cavities in the spinal cord. It can be caused by various primary problems including abnormalities of the caudal fossa (Chiari-like malformations), but also other conditions such as a quadrigeminal cistern cyst, tethered spinal cord, trauma, arachnoiditis, and neoplasia.[111,112] Any condition that results in altered CSF flow in the caudal fossa of the skull or in the vertebral column can result in the development of a syrinx.

Chiari-like malformation is common in the Cavalier King Charles spaniel but is reported in other breeds as well.[113] The basioccipital bone is presumed to be short, resulting in a reduced caudal fossa volume. This causes the caudal aspect of the cerebellar vermis and medulla to extend into or through the foramen magnum causing obstruction of CSF flow. CSF displaced by each systolic cycle through the compressed subarachnoid space results in a high-velocity jet, and this causes an abnormal pressure differential between the spinal cord and subarachnoid space in the cervical area.[112,114-117] There is a relative increase in intramedullary pressure and decrease in subarachnoid pressure, the consequence of which is repeated mechanical distention of the spinal cord. This in turn results in fluid accumulation in the spinal cord, with cavitation and accumulation of extracellular fluid that coalesces eventually into elongated cavities and syrinx formation; these cavities are commonly separate from the central canal.[112]

MR imaging is a good modality to assess the presence and extent of the syrinx.[118] The syrinx may take the form of a cavity or be complex with septations. A portion of the central canal is usually involved at some level. The longitudinal extent of the syrinx can be evaluated on sagittal images, appearing T2-hyperintense and T1-hypointense (Fig. 12-46). In Chiari malformation, the cerebellar vermis and medulla extend into or through the foramen magnum, which is occluded with little or no CSF around neural structures. The magnitude of cerebellar herniation is not correlated with severity. There is typically ventricular dilatation. The cranial cervical and cranial thoracic segments of the spinal cord are typically the most severely affected by the syrinx. Maximum syrinx width is the strongest predictor of pain, scratching behavior, and scoliosis; 95% of Cavalier King Charles spaniels with a maximum syrinx width of 0.64 cm or more will have associated clinical signs.[119]

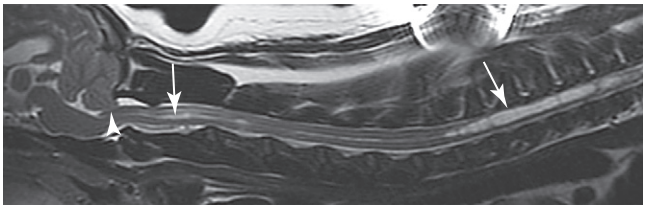


Fig. 12-46 Sagittal T2-weighted image of the caudal brain and cervical spine in a Cavalier King Charles spaniel with Chiari-like malformation and syringomyelia. The caudal fossa is small, causing overcrowding and caudal herniation of the cerebellum into the foramen magnum *(white arrowhead)*. There are multiple areas of elongated irregular dilation of the central canal *(white arrows)* in the cervical and cranial thoracic aspects of the spinal cord that form a long syrinx, more pronounced in the thoracic spine.

REFERENCES

1. Gavin PR: Growth of clinical veterinary magnetic resonance imaging, *Vet Radiol Ultrasound* 52:S2, 2011.
2. Robertson I, Thrall DE: Imaging dogs with suspected disc herniation: pros and cons of myelography, computed tomography, and magnetic resonance, *Vet Radiol Ultrasound* 52:S81, 2011.
3. Evans H: *Miller's anatomy of the dog*, ed 3, Philadelphia, 1993, Saunders.
4. Pardo A, Morgan J: Myelography in the cat: a comparison of cisternal versus lumbar puncture, using metrizamide, *Vet Radiol* 29:89, 1988.
5. Morgan JP, Atilola M, Bailey CS: Vertebral canal and spinal cord mensuration: a comparative study of its effect on lumbosacral myelography in the dachshund and German shepherd dog, *J Am Vet Med Assoc* 191:951, 1987.
6. Scrivani PV, Barthez PY, Leveille R, et al: Subdural injection of contrast medium during cervical myelography, *Vet Radiol Ultrasound* 38:267, 1997.
7. Jones JC, Cartee RE, Bartels JE: Computed tomographic anatomy of the canine lumbosacral spine, *Vet Radiol Ultrasound* 36:91, 1995.
8. Sharp NJH, Med BV, Cofone M, et al: Computed tomography in the evaluation of caudal cervical spondylomyelopathy of the Doberman pinscher, *Vet Radiol Ultrasound* 36:100, 1995.
9. Adams WH, Daniel GB, Pardo AD, et al: Magnetic resonance imaging of the caudal lumbar and lumbosacral spine in 13 dogs (1990–1993), *Vet Radiol Ultrasound* 36:3, 1995.
10. Seiler G, Hani H, Scheidegger J, et al: Staging of lumbar intervertebral disc degeneration in nonchondrodystrophic dogs using low-field magnetic resonance imaging, *Vet Radiol Ultrasound* 44:179, 2003.
11. Pease A, Sullivan S, Olby N, et al: Value of a single-shot turbo spin-echo pulse sequence for assessing the architecture of the subarachnoid space and the constitutive nature of cerebrospinal fluid, *Vet Radiol Ultrasound* 47:254, 2006.
12. Adams WH: The spine, *Clin Tech Small Anim Pract* 14:148, 1999.
13. Chang Y, Dennis R, Platt SR, et al: Magnetic resonance imaging of traumatic intervertebral disc extension in dogs, *Vet Rec* 160:795, 2007.

14. Hansen H: A pathologic-anatomical study on disc degeneration in the dog, *Acta Orthop Scand Suppl*, 1952.
15. Besalti O, Pekcan Z, Sirin YS, et al: Magnetic resonance imaging findings in dogs with thoracolumbar intervertebral disk disease: 69 cases (1997–2005), *J Am Vet Med Assoc* 228:902, 2006.
16. De Risio L, Adams V, Dennis R, et al: Association of clinical and magnetic resonance imaging findings with outcome in dogs with presumptive acute noncompressive nucleus pulposus extrusion: 42 cases (2000–2007), *J Am Vet Med Assoc* 234:495, 2009.
17. McKee WM, Downes CJ, Pink JJ, et al: Presumptive exercise-associated peracute thoracolumbar disc extrusion in 48 dogs, *Vet Rec* 166:523, 2010.
18. Drees R, Dennison SE, Keuler NS, et al: Computed tomographic imaging protocol for the canine cervical and lumbar spine, *Vet Radiol Ultrasound* 50:74, 2009.
19. Olby NJ, Munana KR, Sharp NJ, et al: The computed tomographic appearance of acute thoracolumbar intervertebral disc herniations in dogs, *Vet Radiol Ultrasound* 41:396, 2000.
20. Olby NJ, Dyce J, Houlton JEF: Correlation of plain radiographic and lumbar myelographic findings with surgical findings in thoracolumbar disc disease, *J Small Anim Pract* 35:345, 1994.
21. Dennison SE, Drees R, Rylander H, et al: Evaluation of different computed tomography techniques and myelography for the diagnosis of acute canine myelopathy, *Vet Radiol Ultrasound* 51:254, 2010.
22. Parry AT, Harris A, Upjohn MM, et al: Does choice of imaging modality affect outcome in dogs with thoracolumbar spinal conditions? *J Small Anim Pract* 51:312, 2010.
23. Levitski RE, Lipsitz D, Chauvet AE: Magnetic resonance imaging of the cervical spine in 27 dogs, *Vet Radiol Ultrasound* 40:332, 1999.
24. Naude SH, Lambrechts NE, Wagner WM, et al: Association of preoperative magnetic resonance imaging findings with surgical features in dachshunds with thoracolumbar intervertebral disk extrusion, *J Am Vet Med Assoc* 232:702, 2008.
25. Mateo I, Lorenzo V, Foradada L, et al: Clinical, pathologic, and magnetic resonance imaging characteristics of canine disc extrusion accompanied by epidural hemorrhage or inflammation, *Vet Radiol Ultrasound* 52:17, 2011.
26. Tidwell AS, Specht A, Blaeser L, et al: Magnetic resonance imaging features of extradural hematomas associated with intervertebral disc herniation in a dog, *Vet Radiol Ultrasound* 43:319, 2002.
27. Suran JN, Durham A, Mai W, et al: Contrast enhancement of extradural compressive material on magnetic resonance imaging, *Vet Radiol Ultrasound* 52:10, 2011.
28. Ryan TM, Platt SR, Llabres-Diaz FJ, et al: Detection of spinal cord compression in dogs with cervical intervertebral disc disease by magnetic resonance imaging, *Vet Rec* 163:11, 2008.
29. Cherrone KL, Dewey CW, Coates JR, et al: A retrospective comparison of cervical intervertebral disk disease in nonchondrodystrophic large dogs versus small dogs, *J Am Anim Hosp Assoc* 40:316, 2004.
30. Hillman RB, Kengeri SS, Waters DJ: Reevaluation of predictive factors for complete recovery in dogs with nonambulatory tetraparesis secondary to cervical disk herniation, *J Am Anim Hosp Assoc* 45:155, 2009.
31. Penning V, Platt SR, Dennis R, et al: Association of spinal cord compression seen on magnetic resonance imaging with clinical outcome in 67 dogs with thoracolumbar intervertebral disc extrusion, *J Small Anim Pract* 47:644, 2006.
32. Levine JM, Fosgate GT, Chen AV, et al: Magnetic resonance imaging in dogs with neurologic impairment due to acute thoracic and lumbar intervertebral disk herniation, *J Vet Intern Med* 23:1220, 2009.
33. Ito D, Matsunaga S, Jeffery ND, et al: Prognostic value of magnetic resonance imaging in dogs with paraplegia caused by thoracolumbar intervertebral disk extrusion: 77 cases (2000–2003), *J Am Vet Med Assoc* 227:1454, 2005.
34. Ruddle TL, Allen DA, Schertel ER, et al: Outcome and prognostic factors in non-ambulatory Hansen type I intervertebral disc extrusions: 308 cases, *Vet Comp Orthop Traumatol* 19:29, 2006.
35. Freeman P: Sacrococcygeal intervertebral disc extrusion in a dachshund, *Vet Rec* 167:618, 2010.
36. Jones JC, Banfield CM, Ward DL: Association between postoperative outcome and results of magnetic resonance imaging and computed tomography in working dogs with degenerative lumbosacral stenosis, *J Am Vet Med Assoc* 216:1769, 2000.
37. Jones EC, Sorjonen DC, Simpson ST, et al: Comparison between computed tomographic and surgical findings in nine large-breed dogs with lumbosacral stenosis, *Vet Radiol Ultrasound* 37:247, 1996.
38. Jones JC, Inzana KD: Subclinical CT abnormalities in the lumbosacral spine of older large-breed dogs, *Vet Radiol Ultrasound* 41:19, 2000.
39. Jones JC, Wilson ME, Bartels JE: A review of high resolution computed tomography and a proposed technique for regional examination of the canine lumbosacral spine, *Vet Radiol Ultrasound* 35:339, 1994.
40. Jones JC, Wright JC, Bartels JE: Computed tomographic morphometry of the lumbosacral spine of dogs, *Am J Vet Res* 56:1125, 1995.
41. Ramirez O, 3rd, Thrall DE: A review of imaging techniques for canine cauda equina syndrome, *Vet Radiol Ultrasound* 39:283, 1998.
42. Suwankong N, Voorhout G, Hazewinkel HA, et al: Agreement between computed tomography, magnetic resonance imaging, and surgical findings in dogs with degenerative lumbosacral stenosis, *J Am Vet Med Assoc* 229:1924, 2006.
43. Hay CW, Muir P: Tearing of the dura mater in three dogs, *Vet Rec* 146:279, 2000.
44. Liptak JM, Allan GS, Krockenberger MB, et al: Radiographic diagnosis: intramedullary extrusion of an intervertebral disc, *Vet Radiol Ultrasound* 43:272, 2002.
45. Lu D, Lamb CR, Wesselingh K, et al: Acute intervertebral disc extrusion in a cat: clinical and MRI findings, *J Feline Med Surg* 4:65, 2002.
46. McConnell JF, Garosi LS: Intramedullary intervertebral disk extrusion in a cat, *Vet Radiol Ultrasound* 45:327, 2004.
47. McKee WM, Downes CJ: Rupture of the dura mater in two dogs caused by the peracute extrusion of a cervical disc, *Vet Rec* 162:479, 2008.
48. Sanders SG, Bagley RS, Gavin PR: Intramedullary spinal cord damage associated with intervertebral disk material in a dog, *J Am Vet Med Assoc* 221:1594, 2002.
49. Packer RA, Frank PM, Chambers JN: Traumatic subarachnoid-pleural fistula in a dog, *Vet Radiol Ultrasound* 45:523, 2004.
50. Kent M, Holmes S, Cohen ELI, et al: CT myelography in a dog with intramedullary intervertebral disc herniation, *Vet Radiol Ultrasound* 52:185, 2011.

51. Lipsitz D, Levitski RE, Chauvet AE, et al: Magnetic resonance imaging features of cervical stenotic myelopathy in 21 dogs, *Vet Radiol Ultrasound* 42:20, 2001.
52. da Costa RC, Parent J, Dobson H, et al: Comparison of magnetic resonance imaging and myelography in 18 Doberman pinscher dogs with cervical spondylomyelopathy, *Vet Radiol Ultrasound* 47:523, 2006.
53. da Costa RC, Parent JM, Partlow G, et al: Morphologic and morphometric magnetic resonance imaging features of Doberman Pinschers with and without clinical signs of cervical spondylomyelopathy, *Am J Vet Res* 67:1601, 2006.
54. De Decker S, Gielen IM, Duchateau L, et al: Low-field magnetic resonance imaging findings of the caudal portion of the cervical region in clinically normal Doberman pinschers and foxhounds, *Am J Vet Res* 71:428, 2010.
55. da Costa RC, Parent JM: One-year clinical and magnetic resonance imaging follow-up of Doberman pinschers with cervical spondylomyelopathy treated medically or surgically, *J Am Vet Med Assoc* 231:243, 2007.
56. Penderis J, Dennis R: Use of traction during magnetic resonance imaging of caudal cervical spondylomyelopathy ("wobbler syndrome") in the dog, *Vet Radiol Ultrasound* 45:216, 2004.
57. Galloway AM, Curtis NC, Sommerlad SF, et al: Correlative imaging findings in seven dogs and one cat with spinal arachnoid cysts, *Vet Radiol Ultrasound* 40:445, 1999.
58. Gnirs K, Ruel Y, Blot S, et al: Spinal subarachnoid cysts in 13 dogs, *Vet Radiol Ultrasound* 44:402, 2003.
59. Shamir MH, Shahar R, Aizenberg I: Subarachnoid cyst in a cat, *J Am Anim Hosp Assoc* 33:123, 1997.
60. Skeen TM, Olby NJ, Munana KR, et al: Spinal arachnoid cysts in 17 dogs, *J Am Anim Hosp Assoc* 39:271, 2003.
61. Vignoli M, Rossi F, Sarli G: Spinal subarachnoid cyst in a cat, *Vet Radiol Ultrasound* 40:116, 1999.
62. Targett MP, McInnes E, Dennis R: Magnetic resonance imaging of a medullary dermoid cyst with secondary hydrocephalus in a dog, *Vet Radiol Ultrasound* 40:23, 1999.
63. Davies ESS, Fransson BA, Gavin PR: A confusing magnetic resonance imaging observation complicating surgery for a dermoid cyst in a Rhodesian ridgeback, *Vet Radiol Ultrasound* 45:307, 2004.
64. Shamir MH, Lichovsky D, Aizenberg I, et al: Partial surgical removal of an intramedullary epidermoid cyst from the spinal cord of a dog, *J Small Anim Pract* 40:439, 1999.
65. Fatone G, Brunetti A, Lamagna F, et al: Dermoid sinus and spinal malformations in a Yorkshire terrier: diagnosis and follow-up, *J Small Anim Pract* 36:178, 1995.
66. Dickinson PJ, Sturges BK, Berry WL, et al: Extradural spinal synovial cysts in nine dogs, *J Small Anim Pract* 42:502, 2001.
67. Sale CS, Smith KC: Extradural spinal juxtafacet (synovial) cysts in three dogs, *J Small Anim Pract* 48:116, 2007.
68. Webb AA, Pharr JW, Lew LJ, et al: MR imaging findings in a dog with lumbar ganglion cysts, *Vet Radiol Ultrasound* 42:9, 2001.
69. Konar M, Lang J, Fluhmann G, et al: Ventral intraspinal cysts associated with the intervertebral disc: magnetic resonance imaging observations in seven dogs, *Vet Surg* 37:94, 2008.
70. Bagley RS: Spinal neoplasms in small animals, *Vet Clin North Am Small Anim Pract* 40:915, 2010.
71. Morgan JP, Med V, Ackerman N, et al: Vertebral tumors in the dog: a clinical, radiologic, and pathologic study of 61 primary and secondary lesions, *Vet Radiol* 21:197, 1980.
72. Marioni-Henry K, Van Winkle TJ, Smith SH, et al: Tumors affecting the spinal cord of cats: 85 cases (1980–2005), *J Am Vet Med Assoc* 232:237, 2008.
73. Schultz RM, Puchalski SM, Kent M, et al: Skeletal lesions of histiocytic sarcoma in nineteen dogs, *Vet Radiol Ultrasound* 48:539, 2007.
74. Morgan LW, Toal R, Siemering G, et al: Imaging diagnosis—infiltrative lipoma causing spinal cord compression in a dog, *Vet Radiol Ultrasound* 48:35, 2007.
75. Drost WT, Love NE, Berry CR: Comparison of radiography, myelography, and computed tomography for the evaluation of canine vertebral and spinal cord tumors in sixteen dogs, *Vet Radiol Ultrasound* 37:28, 1996.
76. Kippenes H, Gavin PR, Bagley RS, et al: Magnetic resonance imaging features of tumors of the spine and spinal cord in dogs, *Vet Radiol Ultrasound* 40:627, 1999.
77. D'Anjou M-A, Carmel ÉN, Tidwell AS: Value of fat suppression in gadolinium-enhanced magnetic resonance neuroimaging, *Vet Radiol Ultrasound* 52:S85, 2011.
78. Dennis R: Optimal magnetic resonance imaging of the spine, *Vet Radiol Ultrasound* 52:S72, 2011.
79. McEntee MC, Thrall DE: Computed tomographic imaging of infiltrative lipoma in 22 dogs, *Vet Radiol Ultrasound* 42:221, 2001.
80. Wheeler SJ, Sharp NJH: Neurological deficits in multiple limbs: spinal disorders. In Wheeler SJ, editor: *Manual of small animal neurology*, ed 2, Cheltenham, UK, 1995, British Small Animal Veterinary Association, p 143.
81. Liebel FX, Rossmeisl JH Jr, Lanz OI, et al: Canine spinal nephroblastoma: long-term outcomes associated with treatment of 10 cases (1996–2009), *Vet Surg* 40:244, 2011.
82. McConnell JF, Garosi LS, Dennis R, et al: Imaging of a spinal nephroblastoma in a dog, *Vet Radiol Ultrasound* 44:537, 2003.
83. Sale CS, Skerritt GC, Smith KC: Spinal nephroblastoma in a crossbreed dog, *J Small Anim Pract* 45:267, 2004.
84. Rudich SR, Feeney DA, Anderson KL, et al: Computed tomography of masses of the brachial plexus and contributing nerve roots in dogs, *Vet Radiol Ultrasound* 45:46, 2004.
85. Kraft S, Ehrhart EJ, Gall D, et al: Magnetic resonance imaging characteristics of peripheral nerve sheath tumors of the canine brachial plexus in 18 dogs, *Vet Radiol Ultrasound* 48:1, 2007.
86. McDonnell JJ, Kalbko K, Keating JH, et al: Multiple meningiomas in three dogs, *J Am Anim Hosp Assoc* 43:201, 2007.
87. McDonnell JJ, Tidwell AS, Faissler D, et al: Magnetic resonance imaging features of cervical spinal cord meningiomas, *Vet Radiol Ultrasound* 46:368, 2005.
88. Petersen SA, Sturges BK, Dickinson PJ, et al: Canine intraspinal meningiomas: imaging features, histopathologic classification, and long-term outcome in 34 dogs, *J Vet Intern Med* 22:946, 2008.
89. Terrell SP, Platt SR, Chrisman CL, et al: Possible intraspinal metastasis of a canine spinal cord nephroblastoma, *Vet Pathol* 37:94, 2000.
90. Jeffery ND, Phillips SM: Surgical treatment of intramedullary spinal cord neoplasia in two dogs, *J Small Anim Pract* 36:553, 1995.
91. Goncalves R, Platt SR, Llabres-Diaz FJ, et al: Clinical and magnetic resonance imaging findings in 92 cats with clinical signs of spinal cord disease, *J Feline Med Surg* 11:53, 2009.
92. Okada M, Kitagawa M, Ito D, et al: Magnetic resonance imaging features and clinical signs associated with

presumptive and confirmed progressive myelomalacia in dogs: 12 cases (1997–2008), *J Am Vet Med Assoc* 237:1160, 2010.
93. Platt SR, McConnell JF, Bestbier M: Magnetic resonance imaging characteristics of ascending hemorrhagic myelomalacia in a dog, *Vet Radiol Ultrasound* 47:78, 2006.
94. Abramson CJ, Garosi L, Platt SR, et al: Magnetic resonance imaging appearance of suspected ischemic myelopathy in dogs, *Vet Radiol Ultrasound* 46:225, 2005.
95. MacKay AD, Rusbridge C, Sparkes AH, et al: MRI characteristics of suspected acute spinal cord infarction in two cats, and a review of the literature, *J Feline Med Surg* 7:101, 2005.
96. De Risio L, Adams V, Dennis R, et al: Magnetic resonance imaging findings and clinical associations in 52 dogs with suspected ischemic myelopathy, *J Vet Intern Med* 21:1290, 2007.
97. Kinns J, Mai W, Seiler G, et al: Radiographic sensitivity and negative predictive value for acute canine spinal trauma, *Vet Radiol Ultrasound* 47:563, 2006.
98. Shamir MH, Tavor N, Aizenberg T: Radiographic findings during recovery from discospondylitis, *Vet Radiol Ultrasound* 42:496, 2001.
99. Carrera I, Sullivan M, McConnell F, et al: Magnetic resonance imaging features of discospondylitis in dogs, *Vet Radiol Ultrasound* 52:125, 2011.
100. Gonzalo-Orden JM, Altonaga JR, Orden MA, et al: Magnetic resonance, computed tomographic and radiologic findings in a dog with discospondylitis, *Vet Radiol Ultrasound* 41:142, 2000.
101. Kraft SL, Mussman JM, Smith T, et al: Magnetic resonance imaging of presumptive lumbosacral discospondylitis in a dog, *Vet Radiol Ultrasound* 39:9, 1998.
102. Lipscomb VJ, Muir P: Magnetic resonance imaging of a dog with sciatic nerve root signature, *Vet Rec* 147:393, 2000.
103. Nykamp SG, Steffey MA, Scrivani PV, et al: Computed tomographic appearance of epidural empyema in a dog, *Can Vet J* 44:729, 2003.
104. De Stefani A, Garosi LS, McConnell FJ, et al: Magnetic resonance imaging features of spinal epidural empyema in five dogs, *Vet Radiol Ultrasound* 49:135, 2008.
105. Griffin JF, Levine JM, Levine GJ, et al: Meningomyelitis in dogs: a retrospective review of 28 cases (1999 to 2007), *J Small Anim Pract* 49:509, 2008.
106. Tipold A, Stein VM: Inflammatory diseases of the spine in small animals, *Vet Clin North Am Small Anim Pract* 40:871, 2010.
107. Parry AT, Penning VA, Smith KC, et al: Imaging diagnosis—necrotizing meningomyelitis and polyarthritis, *Vet Radiol Ultrasound* 50:412, 2009.
108. Cherubini GB, Platt SR, Anderson TJ, et al: Characteristics of magnetic resonance images of granulomatous meningoencephalomyelitis in 11 dogs, *Vet Rec* 159:110, 2006.
109. Alves L, Gorgas D, Vandevelde M, et al: Segmental meningomyelitis in 2 cats caused by *Toxoplasma gondii*, *J Vet Intern Med* 25:148, 2011.
110. Fingeroth JM, Johnson GC, Burt JK, et al: Neuroradiographic diagnosis and surgical repair of tethered cord syndrome in an English bulldog with spina bifida and myeloschisis, *J Am Vet Med Assoc* 194:1300, 1989.
111. Kirberger RM, Jacobson LS, Davies JV, et al: Hydromyelia in the dog, *Vet Radiol Ultrasound* 38:30, 1997.
112. Rusbridge C, Greitz D, Iskandar BJ: Syringomyelia: current concepts in pathogenesis, diagnosis, and treatment, *J Vet Intern Med* 20:469, 2006.
113. Rusbridge C, Knowler SP, Pieterse L, et al: Chiari-like malformation in the Griffon Bruxellois, *J Small Anim Pract* 50:386, 2009.
114. Bagley RS, Harrington ML, Tucker RL, et al: Occipital dysplasia and associated cranial spinal cord abnormalities in two dogs, *Vet Radiol Ultrasound* 37:359, 1996.
115. Cerda-Gonzalez S, Dewey CW, Scrivani PV, et al: Imaging features of atlanto-occipital overlapping in dogs, *Vet Radiol Ultrasound* 50:264, 2009.
116. Cerda-Gonzalez S, Olby NJ, McCullough S, et al: Morphology of the caudal fossa in Cavalier King Charles spaniels, *Vet Radiol Ultrasound* 50:37, 2009.
117. Wolfe KC, Poma R: Syringomyelia in the Cavalier King Charles spaniel (CKCS) dog, *Can Vet J* 51:95, 2010.
118. Couturier J, Rault D, Cauzinille L: Chiari-like malformation and syringomyelia in normal cavalier King Charles spaniels: a multiple diagnostic imaging approach, *J Small Anim Pract* 49:438, 2008.
119. Rusbridge C, Carruthers H, Dube MP, et al: Syringomyelia in cavalier King Charles spaniels: the relationship between syrinx dimensions and pain, *J Small Anim Pract* 48:432, 2007.

ELECTRONIC RESOURCES

Evolve

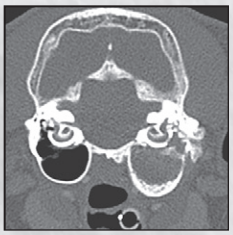
Additional information related to the content in Chapter 12 can be found on the companion Evolve website at http://evolve.elsevier.com/Thrall/vetrad/

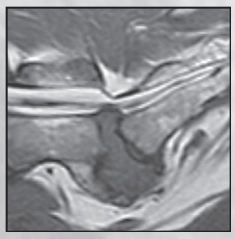
- Chapter Quiz

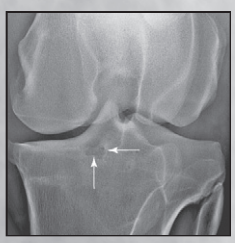
This page intentionally left blank

SECTION III

The Appendicular Skeleton: Canine, Feline, and Equine











13 **Radiographic Anatomy of the Appendicular Skeleton**
James E. Smallwood
Kathy A. Spaulding

14 **Principles of Radiographic Interpretation of the Appendicular Skeleton**
Donald E. Thrall

15 **Orthopedic Diseases of Young and Growing Dogs and Cats**
Rachel E. Pollard
Erik R. Wisner

16 **Fracture Healing and Complications**
George A. Henry

17 **Radiographic Features of Bone Tumors and Bone Infection**
Donald E. Thrall

18 **Radiographic Signs of Joint Disease in Dogs and Cats**
Graeme Allan

19 **The Equine Stifle and Tarsus**
Valeria Busoni
Fabrice Audigié

20 **The Equine Carpus**
Rachel C. Murray
Sue J. Dyson

21 **The Equine Metacarpal and Metatarsal Regions**
Sue J. Dyson
Marianna Biggi

22 **The Equine Metacarpophalangeal and Metatarsophalangeal Articulation**
Lisa G. Britt
Russell L. Tucker

23 **The Equine Phalanges**
Elizabeth A. Riedesel

24 **The Equine Navicular Bone**
Federica Morandi

CHAPTER • 13

Radiographic Anatomy of the Appendicular Skeleton

James E. Smallwood
Kathy A. Spaulding

To use the roentgen sign method of recognizing abnormal radiographic findings effectively, an understanding of normal radiographic anatomy for the specific area of interest is necessary. The purpose of this chapter is to provide a limited reference for the radiographic anatomy of the appendicular skeleton. Refer to comprehensive textbooks on radiographic anatomy for more detailed information.[1-3]

The radiographic nomenclature used in this chapter was approved by the American College of Veterinary Radiology in 1983.[4] Some equine images in this chapter (Figs. 13-30 through 13-49 and 13-54 through 13-57) have been taken from previous publications and are reproduced here with permission of the journals and author.[5-7]

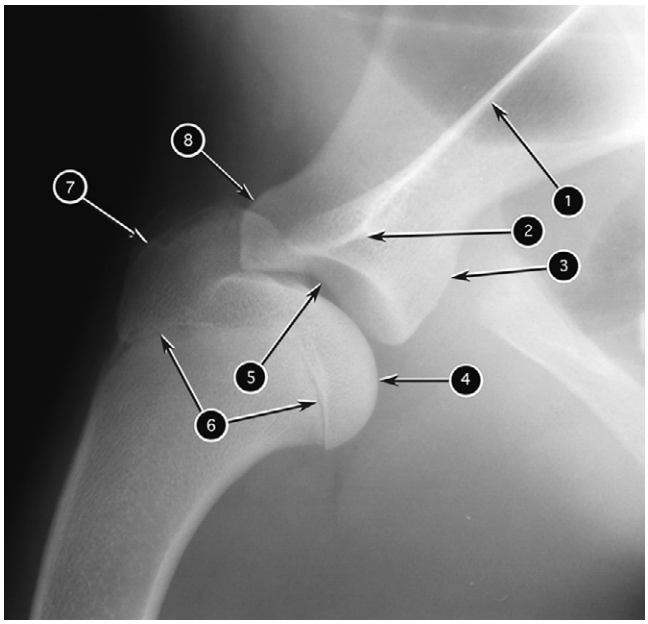


Fig. 13-1 **Mediolateral Radiograph of Canine Shoulder Joint.**
1. Spine of scapula
2. Acromion of scapula
3. Infraglenoid tubercle of scapula
4. Head of humerus
5. Glenoid cavity of scapula
6. Proximal physis of humerus
7. Greater tubercle of humerus
8. Supraglenoid tubercle of scapula

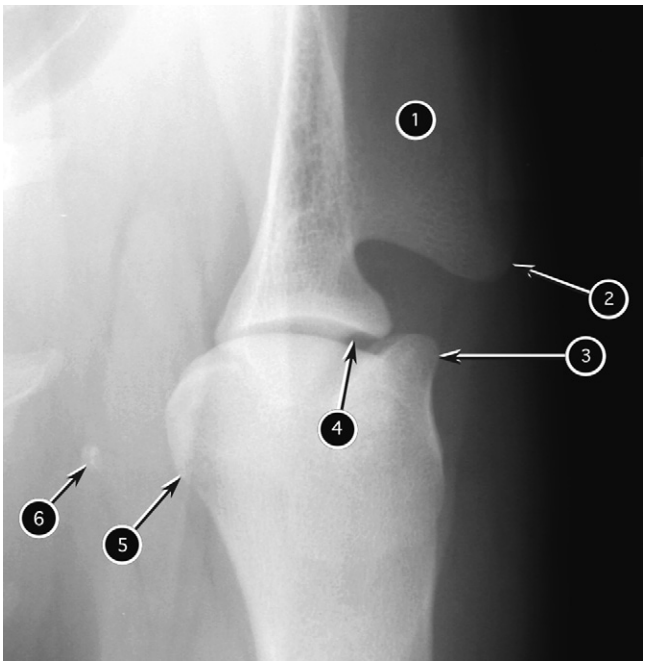


Fig. 13-2 **Caudocranial Radiograph of Canine Shoulder Joint.**
1. Spine of scapula
2. Acromion of scapula
3. Greater tubercle of humerus
4. Humeral (scapulohumeral) joint
5. Lesser tubercle of humerus
6. Clavicle

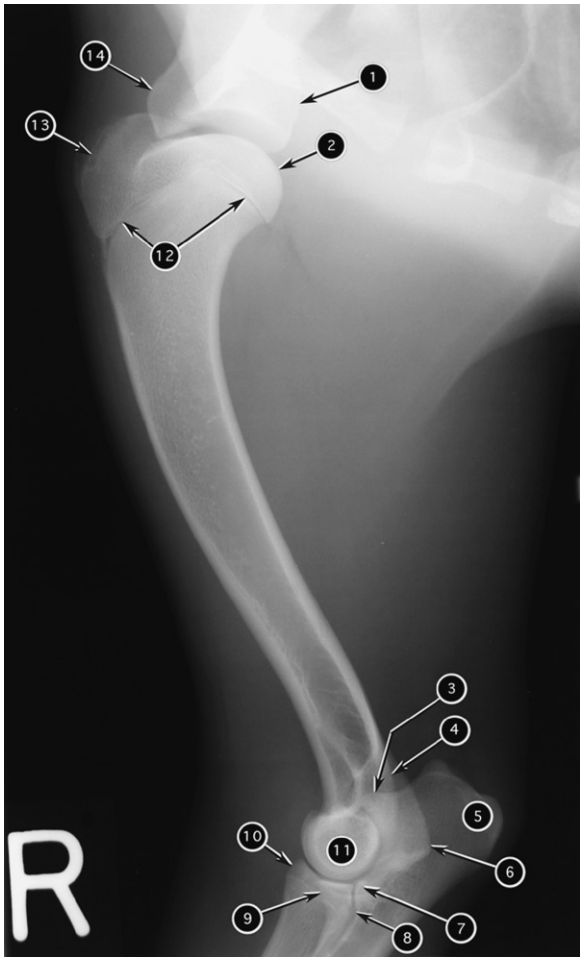


Fig. 13-3 **Mediolateral Radiograph of Canine Humerus.**
1. Infraglenoid tubercle of scapula
2. Head of humerus
3. Anconeal process of ulna
4. Lateral epicondyle of humerus
5. Tuber olecrani
6. Medial epicondyle of humerus
7. Lateral coronoid process of ulna
8. Proximal radioulnar joint
9. Medial coronoid process of ulna
10. Head of radius
11. Condyle of humerus
12. Proximal physis of humerus
13. Greater tubercle of humerus
14. Supraglenoid tubercle of scapula

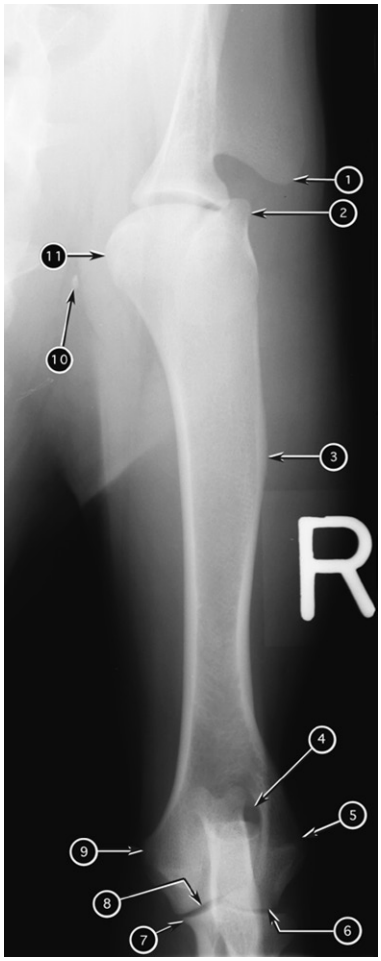


Fig. 13-4 **Caudocranial Radiograph of Canine Humerus.**
1. Acromion of scapula
2. Greater tubercle of humerus
3. Deltoid tuberosity
4. Supratrochlear foramen of humerus
5. Lateral epicondyle of humerus
6. Capitulum of humeral condyle
7. Medial coronoid process of ulna
8. Trochlea of humeral condyle
9. Medial epicondyle of humerus
10. Clavicle
11. Lesser tubercle of humerus

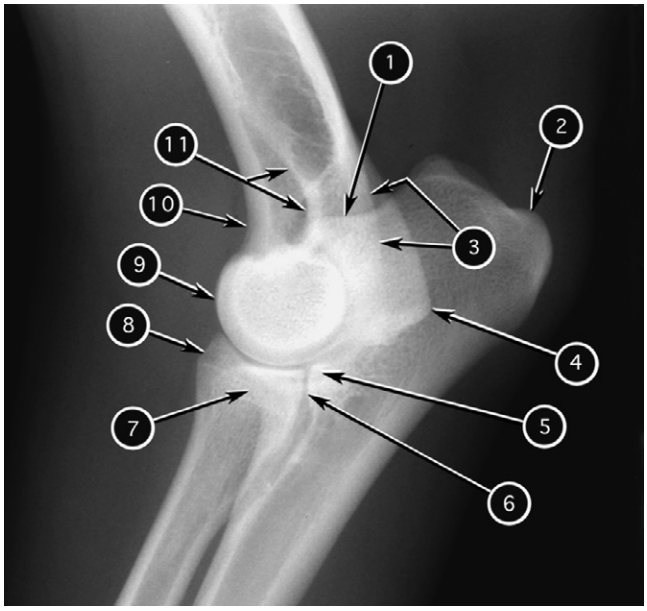


Fig. 13-5 **Mediolateral Radiograph of Canine Elbow Joint.**
1. Anconeal process of ulna
2. Tuber olecrani of ulna
3. Caudal border of lateral epicondyle of humerus
4. Caudal border of medial epicondyle of humerus
5. Lateral coronoid process of ulna
6. Proximal radioulnar joint
7. Medial coronoid process of ulna
8. Head of radius
9. Condyle of humerus
10. Cranial border of medial epicondyle of humerus
11. Cranial border of lateral epicondyle of humerus

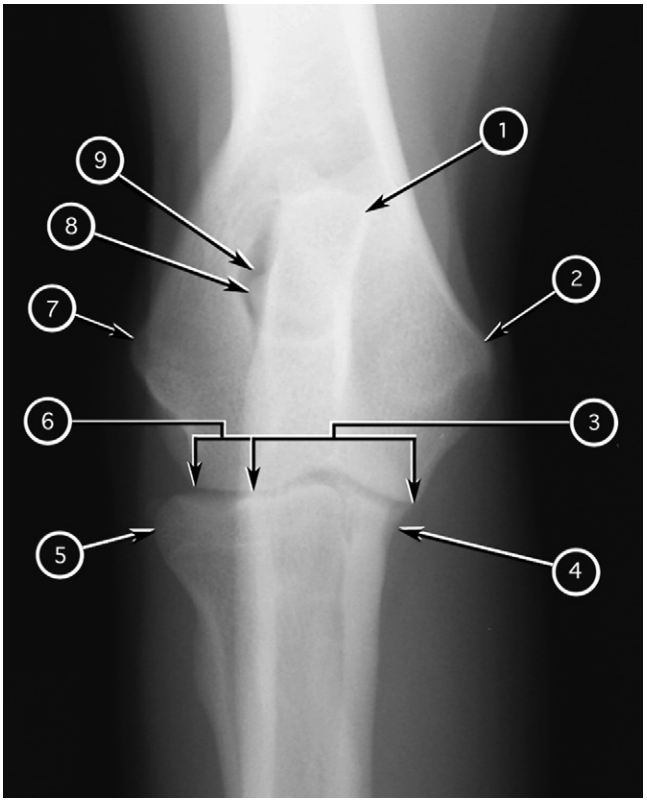


Fig. 13-7 **Craniocaudal Radiograph of Canine Elbow Joint.**
1. Tuber olecrani of ulna
2. Medial epicondyle of humerus
3. Trochlea of humeral condyle
4. Medial coronoid process of ulna
5. Head of radius
6. Capitulum of humeral condyle
7. Lateral epicondyle of humerus
8. Anconeal process of ulna
9. Supratrochlear foramen of humerus

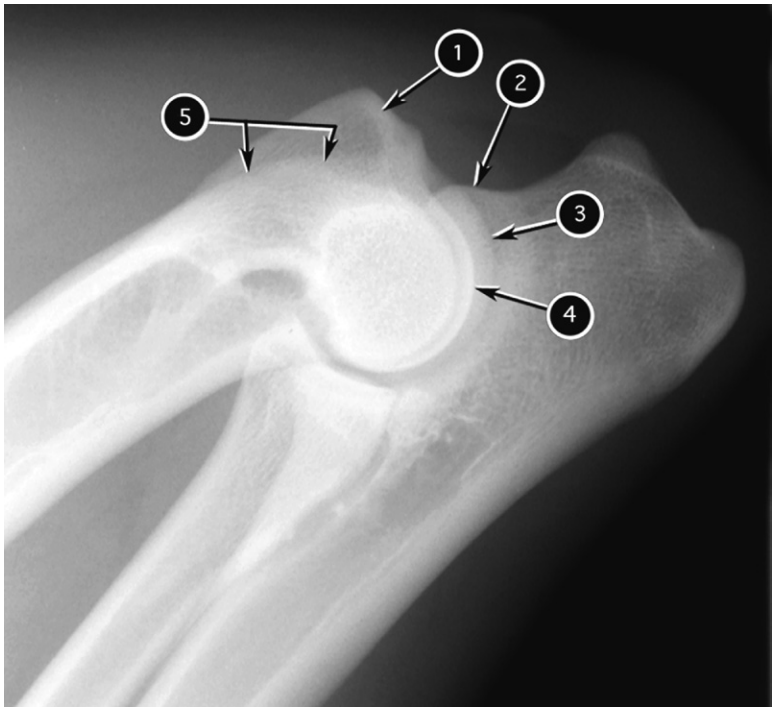


Fig. 13-6 **Mediolateral Radiograph of Flexed Canine Elbow Joint.**
1. Medial epicondyle of humerus
2. Anconeal process of ulna
3. Medial part of humeral condyle
4. Lateral part of humeral condyle
5. Caudal border of lateral epicondyle of humerus

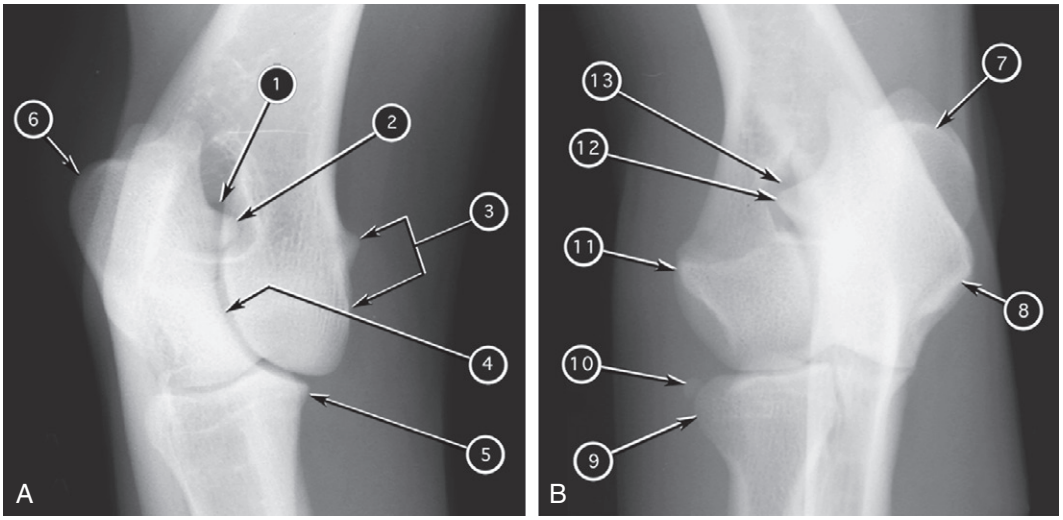


Fig. 13-8 **Craniolateral-Caudomedial Oblique (A) and Craniomedial-Caudolateral Oblique (B) Radiographs of Canine Elbow Joint.**

1. Supratrochlear foramen of humerus
2. Anconeal process of ulna
3. Medial epicondyle of humerus
4. Trochlear notch of ulna
5. Medial coronoid process of ulna
6. Tuber olecrani of ulna
7. Tuber olecrani of ulna
8. Medial epicondyle of humerus
9. Head of radius
10. Sesamoid bone of supinator muscle (inconstant)
11. Lateral epicondyle of humerus
12. Anconeal process of ulna
13. Supratrochlear foramen of humerus

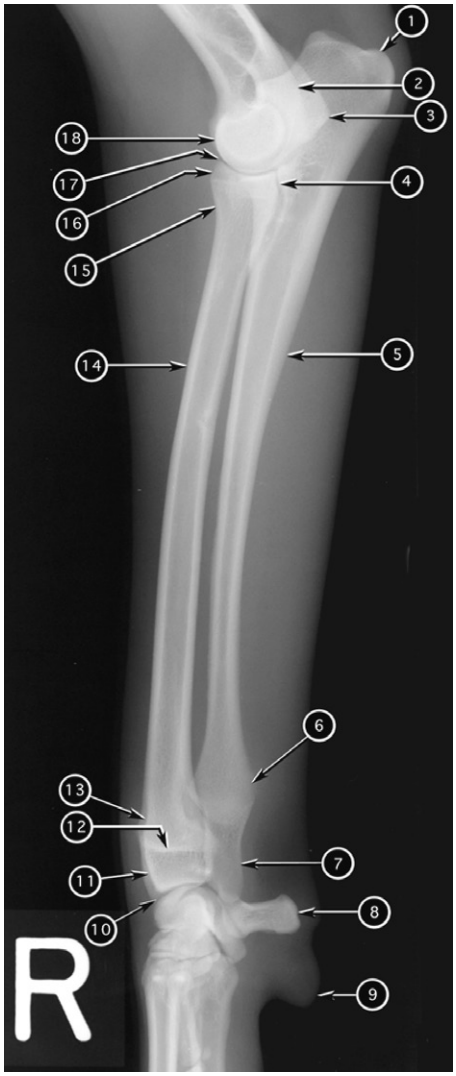


Fig. 13-9 **Mediolateral Radiograph of Canine Antebrachium.**
1. Tuber olecrani of ulna
2. Lateral epicondyle of humerus
3. Medial epicondyle of humerus
4. Proximal radioulnar joint
5. Body of ulna
6. Distal metaphysis of ulna
7. Distal epiphysis of ulna
8. Accessory carpal bone
9. Carpal pad
10. Antebrachiocarpal joint
11. Distal epiphysis of radius
12. Distal physis of radius
13. Distal metaphysis of radius
14. Body of radius
15. Neck of radius
16. Head of radius
17. Elbow (cubital) joint
18. Condyle of humerus

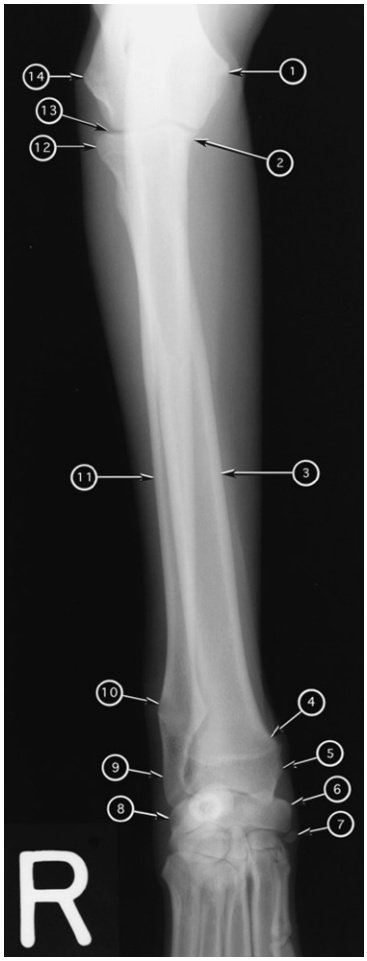


Fig. 13-10 **Craniocaudal Radiograph of Canine Antebrachium.**
1. Medial epicondyle of humerus
2. Medial coronoid process of ulna
3. Body of radius
4. Distal metaphysis of radius
5. Distal epiphysis of radius
6. Intermedioradial carpal bone
7. Sesamoid bone of abductor pollicis longus
8. Ulnar carpal bone
9. Distal epiphysis (styloid process) of ulna
10. Distal metaphysis of ulna
11. Body of ulna
12. Head of radius
13. Elbow (cubital) joint
14. Lateral epicondyle of humerus

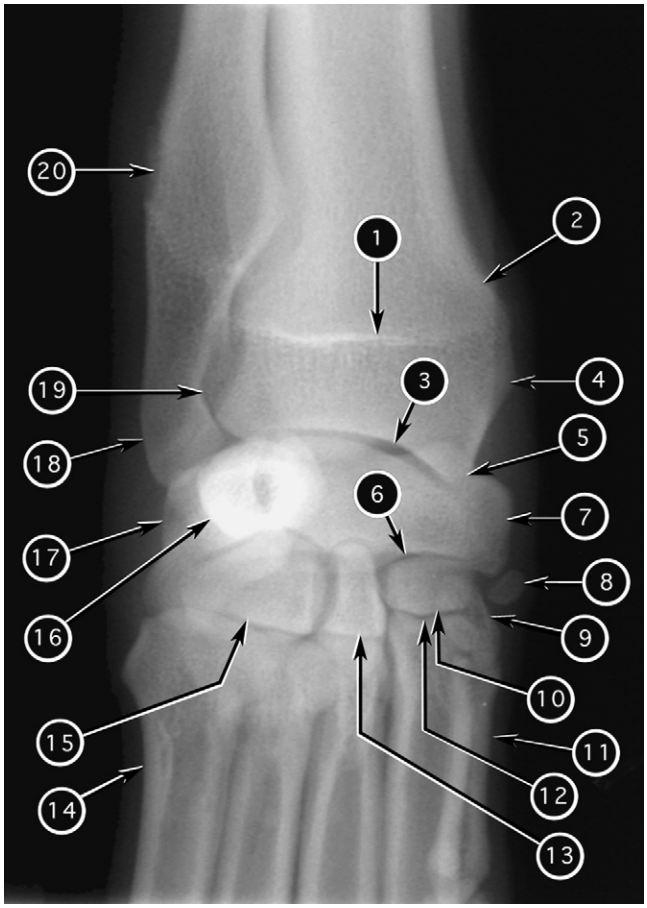


Fig. 13-11 **Dorsopalmar Radiograph of Canine Carpus.**
1. Distal physis of radius
2. Distal metaphysis of radius
3. Antebrachiocarpal joint
4. Distal epiphysis of radius
5. Styloid process (medial) of radius
6. Middle carpal joint
7. Intermedioradial carpal bone
8. Sesamoid bone of abductor pollicis longus
9. First carpal bone
10. Second carpal bone
11. First metacarpal bone
12. Carpometacarpal joint
13. Third carpal bone
14. Fifth metacarpal bone
15. Fourth carpal bone
16. Accessory carpal bone
17. Ulnar carpal bone
18. Distal epiphysis (styloid process) of ulna
19. Distal radioulnar joint
20. Distal metaphysis of ulna

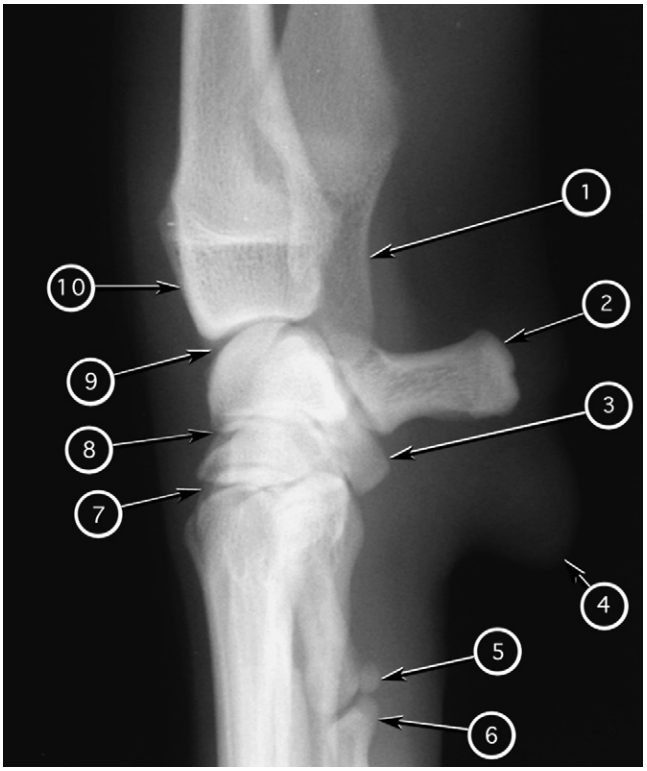


Fig. 13-12 **Mediolateral Radiograph of Canine Carpus.**
1. Distal epiphysis (styloid process) of ulna
2. Accessory carpal bone
3. Ulnar carpal bone
4. Carpal pad
5. Proximal sesamoid bone of first digit
6. Proximal phalanx of first digit
7. Carpometacarpal joint
8. Middle carpal joint
9. Antebrachiocarpal joint
10. Distal epiphysis of radius

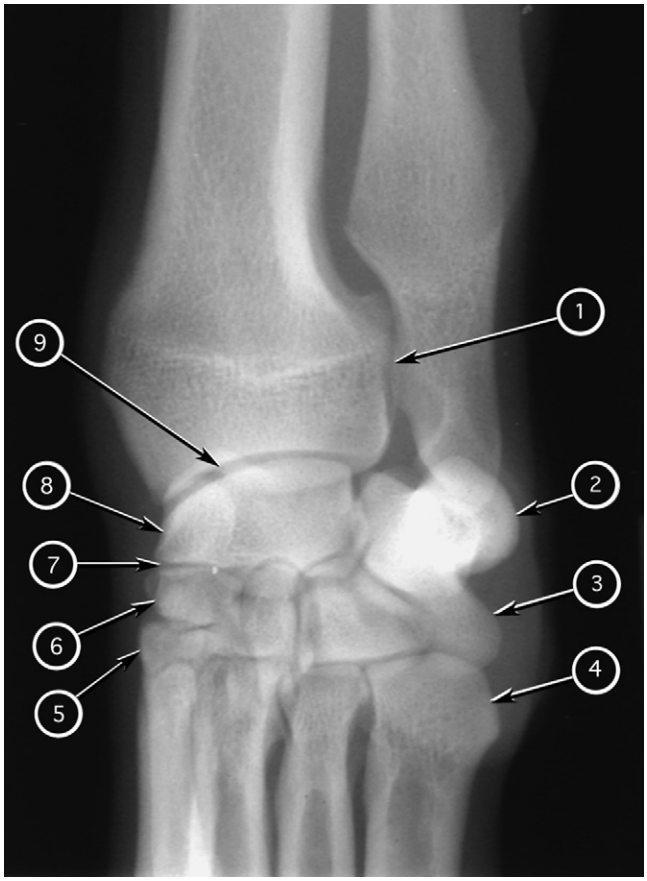


Fig. 13-13 **Dorsolateral-Palmaromedial Oblique Radiograph of Canine Manus.**
1. Distal radioulnar joint
2. Accessory carpal bone
3. Ulnar carpal bone
4. Base of metacarpal bone 5
5. First carpal bone
6. Second carpal bone
7. Middle carpal joint
8. Intermedioradial carpal bone
9. Antebrachiocarpal joint

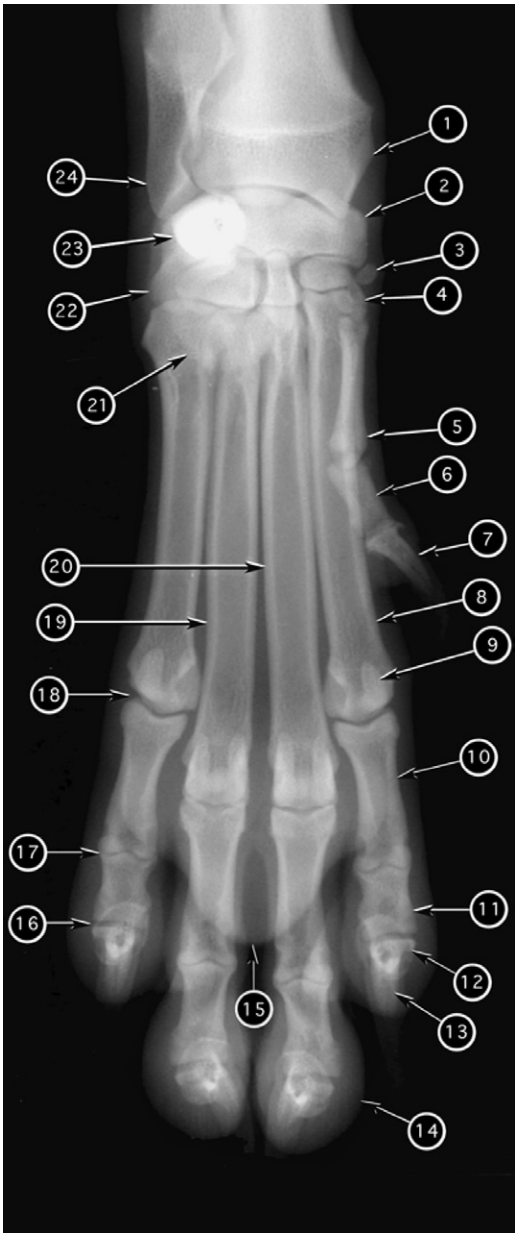


Fig. 13-14 **Dorsopalmar Radiograph of Canine Manus.**
1. Distal epiphysis of radius
2. Intermedioradial carpal bone
3. Sesamoid bone of abductor pollicis longus
4. First carpal bone
5. Metacarpal bone 1
6. Proximal phalanx of digit 1
7. Distal phalanx of digit 1
8. Second metacarpal bone
9. Abaxial proximal sesamoid bone of digit 2
10. Pp of digit 2
11. Middle phalanx of digit 2
12. Unguicular crest of distal phalanx of digit 2
13. Unguicular process of distal phalanx of digit 2
14. Digital pad of digit 3
15. Metacarpal pad
16. Distal interphalangeal joint of digit 5
17. Proximal interphalangeal joint of digit 5
18. Metacarpophalangeal joint of digit 5
19. Fourth metacarpal bone
20. Third metacarpal bone
21. Carpal pad
22. Ulnar carpal bone
23. Accessory carpal bone
24. Distal epiphysis (styloid process) of ulna



Fig. 13-15 **Mediolateral Radiograph of Canine Manus.**
1. Distal epiphysis (styloid process) of ulna
2. Accessory carpal bone
3. Ulnar carpal bone
4. Carpal pad
5. Proximal sesamoid bone of digit 1
6. Distal phalanx of digit 1
7. Dorsal sesamoid bone
8. Antebrachiocarpal joint
9. Distal epiphysis of radius



Fig. 13-16 **Palmaromedial-Dorsolateral Oblique Radiograph of Canine Manus.**
1. Distal epiphysis (styloid process) of ulna
2. Accessory carpal bone
3. Ulnar carpal bone
4. Body of metacarpal bone 5
5. Abaxial proximal sesamoid bone of digit 5
6. Middle phalanx of digit 5
7. Metacarpal pad
8. Digital pad of digit 4
9. Flexor tubercle of distal phalanx of digit 4
10. Unguicular crest of distal phalanx of digit 4
11. Unguicular process of distal phalanx digit 3
12. Proximal phalanx of digit 2
13. Dorsal sesamoid bone of digit 2
14. Middle carpal joint

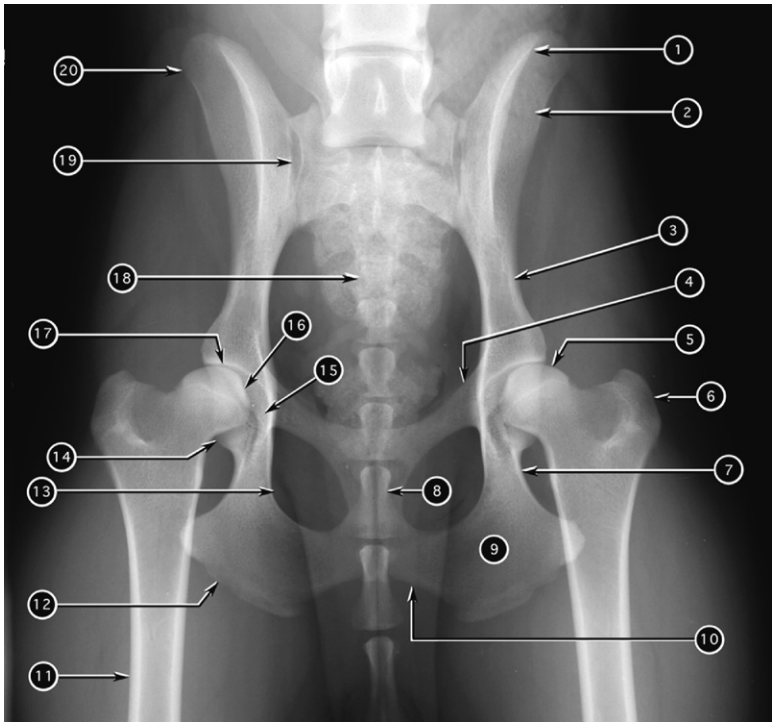


Fig. 13-17 **Ventrodorsal Radiographs of Canine Pelvis.**
1. Crest of left ilium
2. Wing of left ilium
3. Body of left ilium
4. Body of left pubis
5. Head of left femur
6. Greater trochanter of left femur
7. Body of left ischium
8. Caudal vertebra 4
9. Table of left ischium
10. Ischial arch
11. Body of right femur
12. Right tuber ischiadicum (ischiatic tuberosity)
13. Right obturator foramen
14. Caudodorsal aspect of lunate surface of acetabulum
15. Acetabular fossa
16. Fovea capitis of right femur
17. Cranioventral aspect of lunate surface of acetabulum
18. Sacral vertebra 3
19. Right sacroiliac joint
20. Right tuber coxae (cranioventral iliac spine)

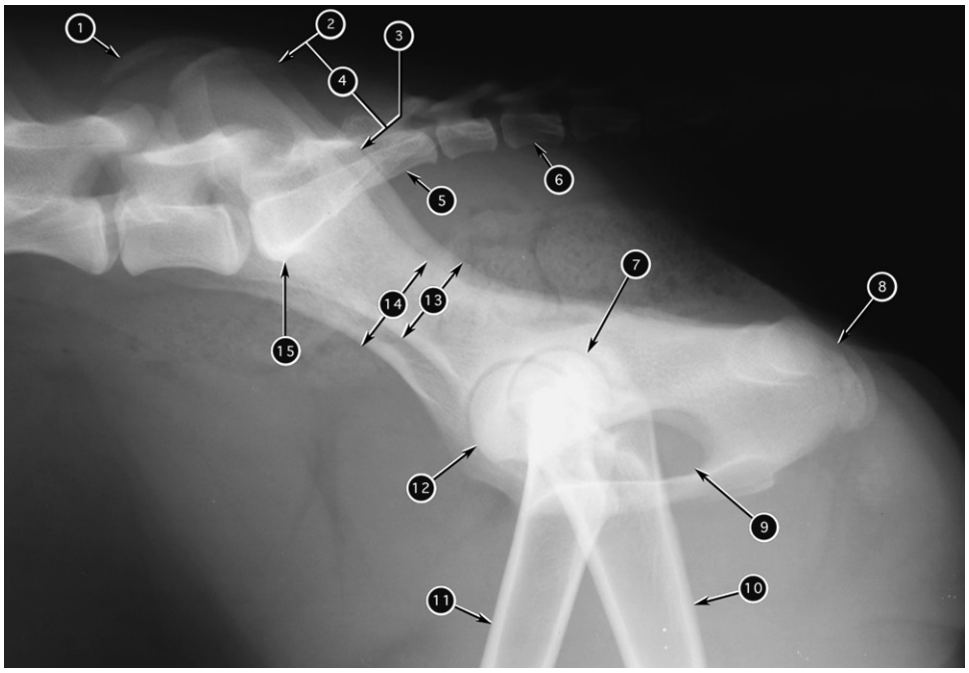


Fig. 13-18 **Right-Left Lateral Radiograph of Canine Pelvis.**
1. Crest of right ilium (more magnified)
2. Craniodorsal iliac spine
3. Caudodorsal iliac spine
4. Left tuber sacrale (less magnified)
5. Sacral vertebra 3
6. Caudal vertebra 2
7. Left coxal joint (less magnified)
8. Superimposed right and left tubera ischiadica
9. Superimposed right and left obturator foramina
10. Body of right femur (more magnified)
11. Body of left femur (less magnified)
12. Head of right femur (more magnified)
13. Body of left ilium (less magnified)
14. Body of right ilium (more magnified)
15. Promontory of sacrum

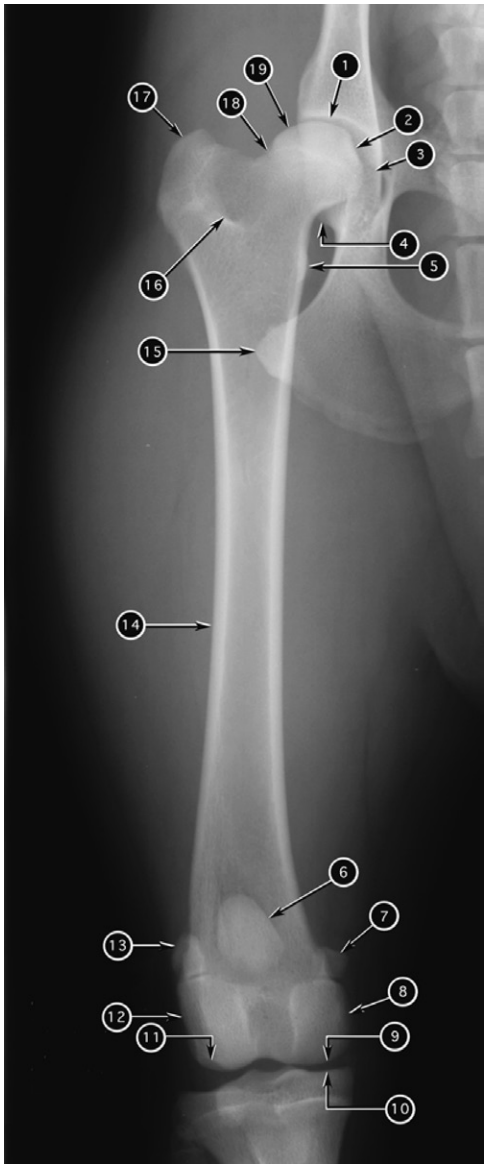


Fig. 13-19 **Craniocaudal Radiograph of Canine Femur.**
1. Cranioventral aspect of lunate surface of acetabulum
2. Fovea capitis of femur
3. Acetabular fossa
4. Caudodorsal aspect of lunate surface of acetabulum
5. Lesser trochanter of femur
6. Patella
7. Medial sesamoid of gastrocnemius muscle
8. Medial epicondyle of femur
9. Medial condyle of femur
10. Medial condyle of tibia
11. Extensor fossa of femur
12. Lateral epicondyle of femur
13. Lateral sesamoid of gastrocnemius muscle
14. Body of femur
15. Tuber ischiadicum
16. Trochanteric fossa of femur
17. Greater trochanter of femur
18. Neck of femur
19. Head of femur

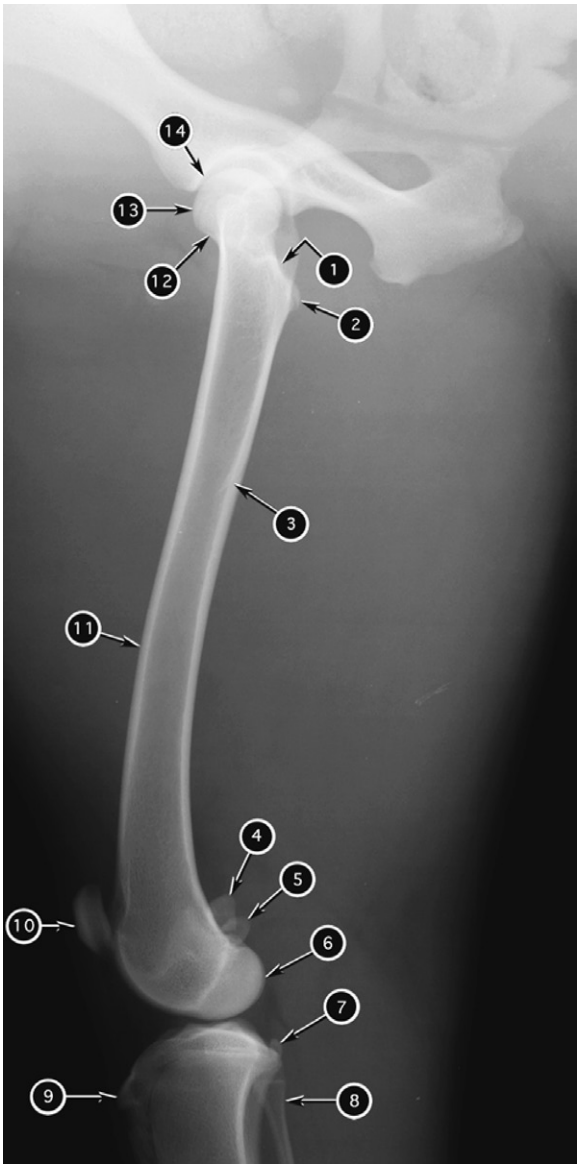


Fig. 13-20 **Mediolateral Radiograph of Canine Femur.**
1. Trochanteric fossa of femur
2. Lesser trochanter of femur
3. Nutrient canal of femur
4. Lateral sesamoid of gastrocnemius muscle
5. Medial sesamoid of gastrocnemius muscle
6. Medial and lateral condyle of femur
7. Sesamoid bone of popliteus muscle
8. Fibula
9. Tibial tuberosity
10. Patella
11. Body of femur
12. Neck of femur
13. Head of femur
14. Craniodorsal aspect of lunate surface of acetabulum

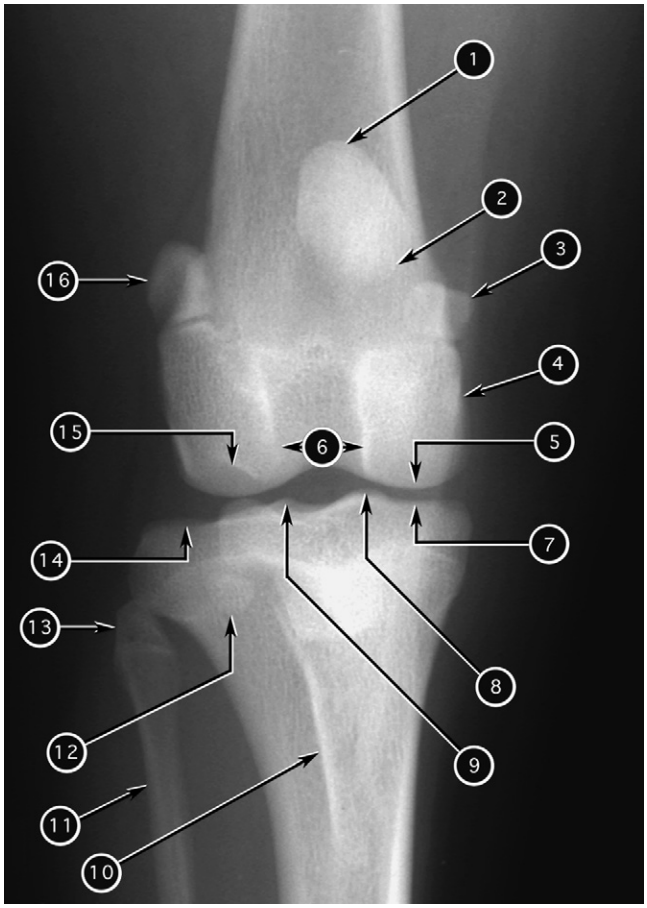


Fig. 13-21 **Craniocaudal Radiograph of Canine Stifle Joint.**

1. Base of patella
2. Apex of patella
3. Medial sesamoid of gastrocnemius muscle
4. Medial epicondyle of femur
5. Medial condyle of femur
6. Intercondylar fossa of femur
7. Medial condyle of tibia
8. Medial tubercle of intercondylar eminence
9. Lateral tubercle of intercondylar eminence
10. Cranial border of tibia
11. Body of fibula
12. Sesamoid bone of popliteus muscle
13. Head of fibula
14. Lateral condyle of tibia
15. Extensor fossa of femur
16. Lateral sesamoid of gastrocnemius

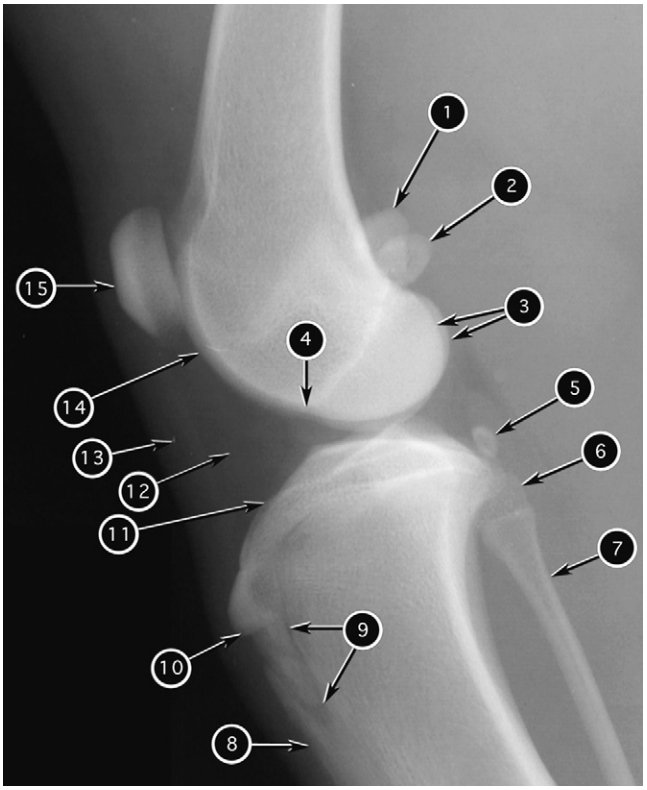


Fig. 13-22 **Mediolateral Radiograph of Canine Stifle Joint.**

1. Lateral sesamoid of gastrocnemius muscle
2. Medial sesamoid of gastrocnemius muscle
3. Medial and lateral condyles of femur
4. Extensor fossa of femur
5. Sesamoid bone of popliteus muscle
6. Head of fibula
7. Body of fibula
8. Cranial border of tibia
9. Cartilage between tibial tuberosity and body of tibia
10. Tibial tuberosity
11. Cranial intercondylar area of tibia
12. Infrapatellar fat body
13. Patellar ligament
14. Superimposed ridges of femoral trochlea
15. Patella

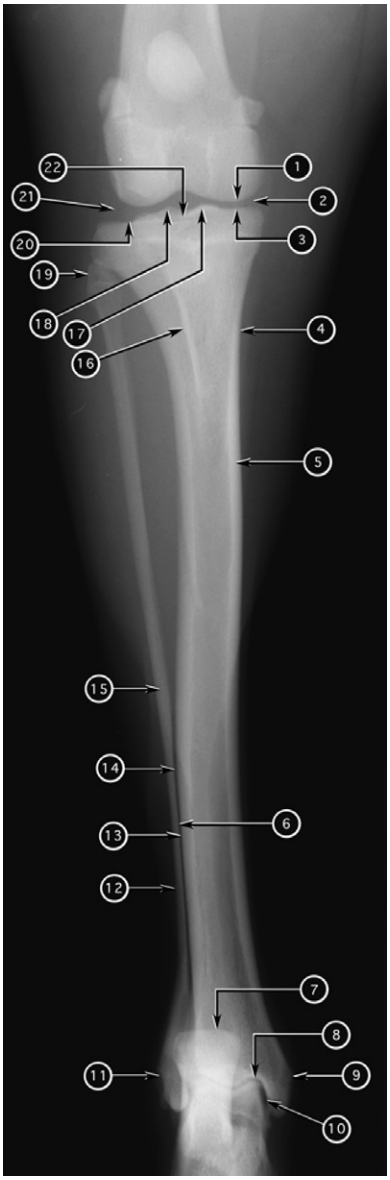


Fig. 13-23 **Craniocaudal Radiograph of Canine Crus.**
1. Medial condyle of femur
2. Medial meniscus
3. Medial condyle of tibia
4. Medial border of tibia
5. Body of tibia
6. Medial surface of fibula (faces tibia)
7. Tuber calcanei
8. Medial groove of tibial cochlea
9. Medial malleolus of tibia
10. Medial aspect of tarsocrural joint
11. Latera malleolus of fibula
12. Lateral surface of fibula
13. Lateral border of tibia (faces fibula)
14. Interosseous membrane
15. Body of fibula
16. Cranial border of tibia
17. Medial tubercle of intercondylar eminence
18. Lateral tubercle of intercondylar eminence
19. Head of fibula
20. Lateral condyle of tibia
21. Lateral meniscus
22. Central intercondylar area of tibia

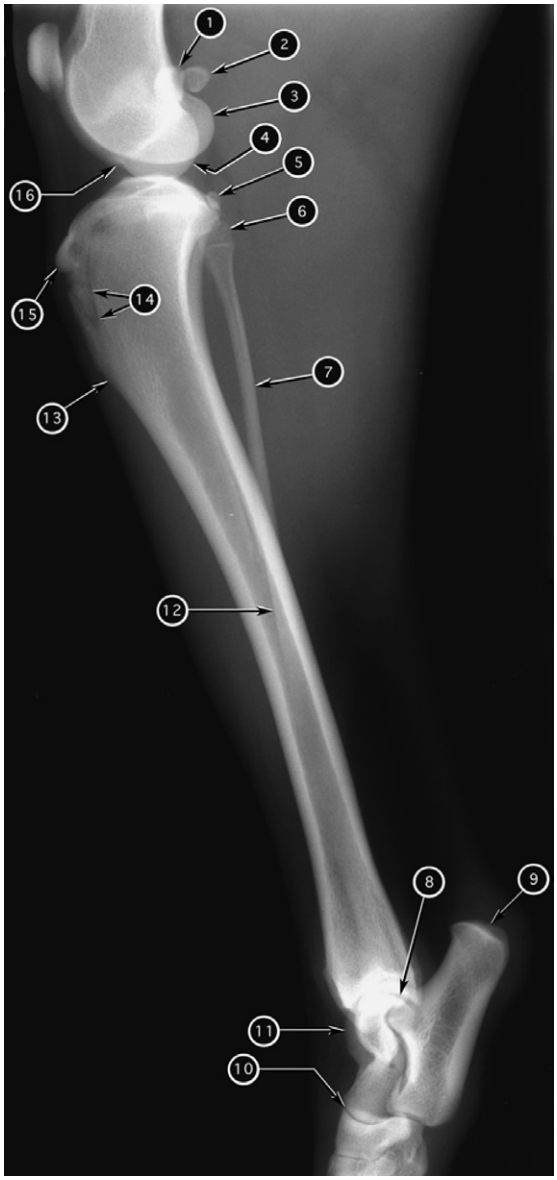


Fig. 13-24 **Mediolateral Radiograph of Canine Crus.**
1. Lateral sesamoid of gastrocnemius muscle
2. Medial sesamoid of gastrocnemius muscle
3. Medial condyle of femur
4. Lateral condyle of femur
5. Sesamoid bone of popliteus muscle
6. Head of fibula
7. Body of fibula
8. Tarsocrural joint
9. Tuber calcanei
10. Proximal intertarsal joint
11. Trochlea of talus
12. Body of fibula superimposed on tibia
13. Cranial border of tibia
14. Cartilage between tibial tuberosity and body of tibia
15. Tibial tuberosity
16. Extensor fossa of femur

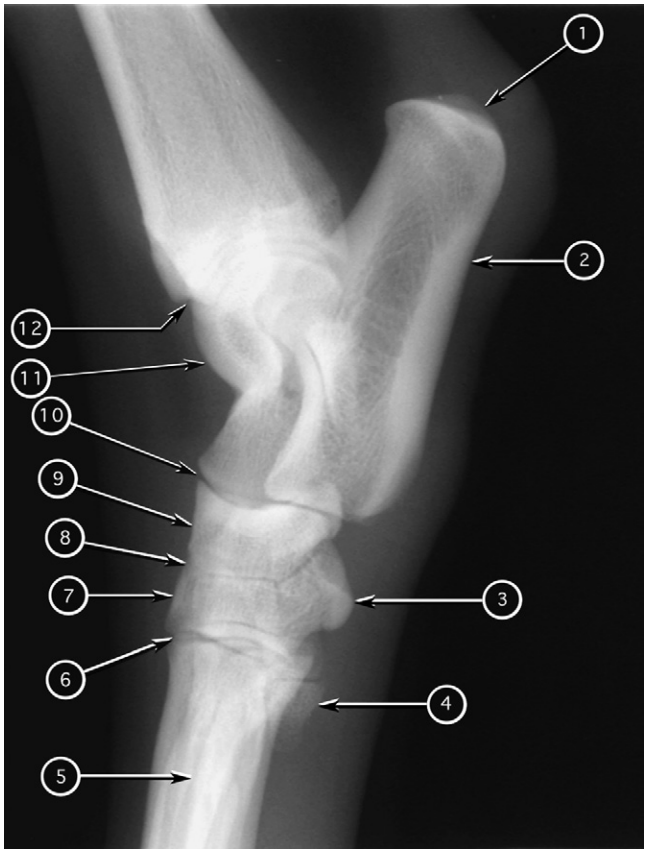


Fig. 13-25 **Mediolateral Radiograph of Canine Tarsus.**
1. Tuber calcanei
2. Body of calcaneus
3. Fourth tarsal bone
4. Metatarsal bone 1
5. Superimposed metatarsal bone 2 through metatarsal bone 5
6. Tarsometatarsal joints
7. Third tarsal bone
8. Distal intertarsal joint
9. Central tarsal bone
10. Proximal intertarsal joint
11. Trochlea tali
12. Tarsocrural joint

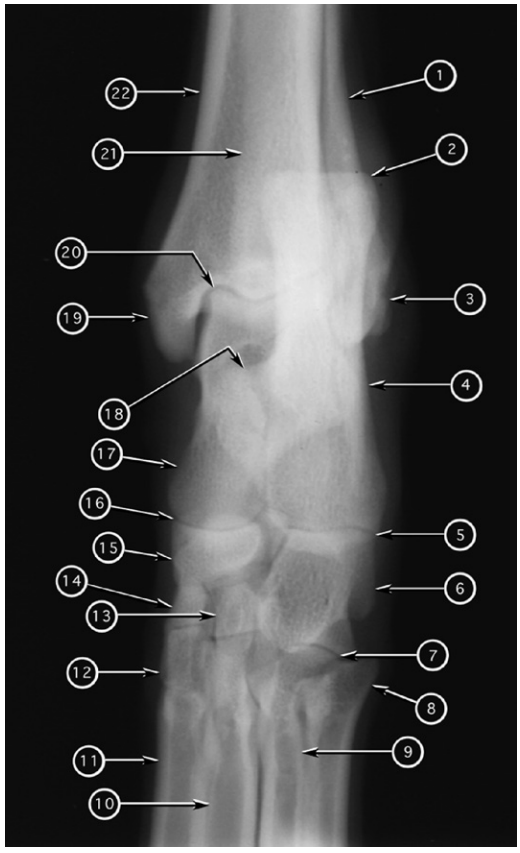


Fig. 13-26 **Dorsoplantar Radiograph of Canine Tarsus.**
1. Body of fibula
2. Tuber calcanei
3. Lateral malleolus of fibula
4. Body of calcaneus
5. Proximal intertarsal (calcaneoquartal) joint
6. Fourth tarsal bone
7. Tarsometatarsal joints
8. Base of metatarsal bone 5
9. Metatarsal bone 4
10. Metatarsal bone 3
11. Metatarsal bone 2
12. Metatarsal bone 1
13. Third tarsal bone
14. Superimposed first tarsal bone and second tarsal bone
15. Central tarsal bone
16. Proximal intertarsal (talocalcaneocentral) joint
17. Talus
18. Sustentaculum tali of calcaneus
19. Medial malleolus of tibia
20. Tarsocrural joint
21. Common calcanean tendon superimposed on tibia
22. Body of tibia

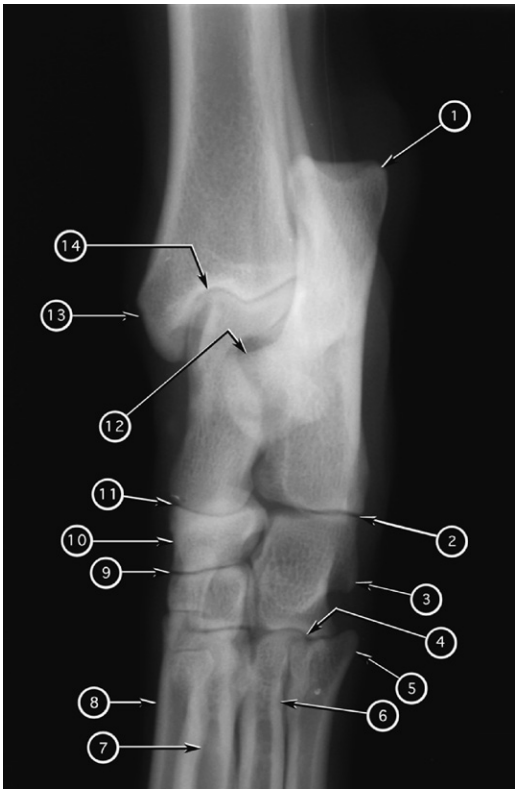


Fig. 13-27 **Dorsolateral-Plantaromedial Oblique Radiograph of Canine Tarsus.**

1. Tuber calcanei
2. Proximal intertarsal (calcaneoquartal) joint
3. Fourth tarsal bone
4. Tarsometatarsal joints
5. Base of metatarsal bone 5
6. Metatarsal bone 4
7. Metatarsal bone 3
8. Metatarsal bone 2
9. Distal intertarsal joint
10. Central tarsal bone
11. Proximal intertarsal (talocalcaneocentral) joint
12. Sustentaculum tali of calcaneus
13. Medial malleolus of tibia
14. Tarsocrural joint

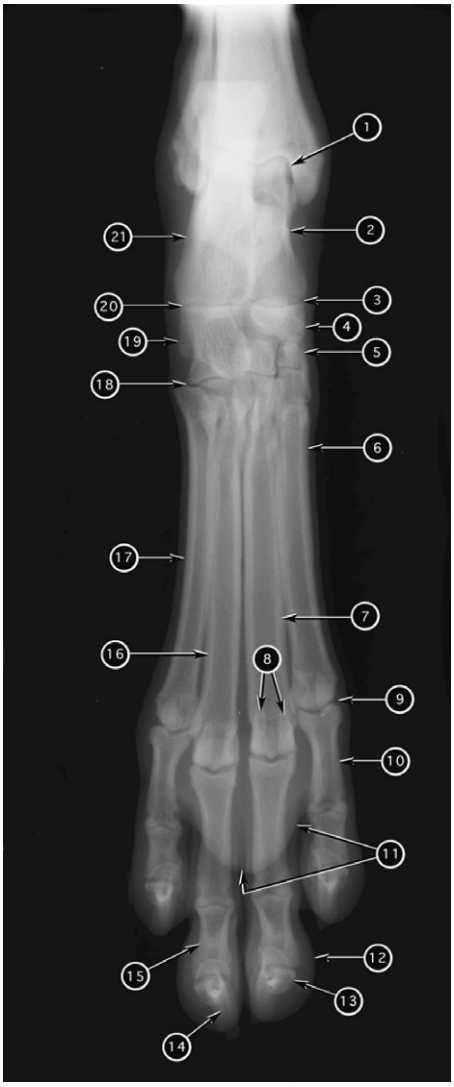


Fig. 13-28 **Dorsoplantar Radiograph of Canine Pes.**

1. Tarsocrural joint
2. Talus
3. Proximal intertarsal (talocalcaneocentral) joint
4. Central tarsal bone
5. Superimposed tarsal bones 1 and 2
6. Metatarsal bone 2
7. Metatarsal bone 3
8. Proximal sesamoid bones of digit 3
9. Metatarsophalangeal joint of digit 2
10. Proximal phalanx of digit 2
11. Metatarsal pad
12. Digital pad of digit 3
13. Distal phalanx of digit 3
14. Unguicular process of distal phalanx of digit 4
15. Middle phalanx of digit 4
16. Metatarsal bone 4
17. Metatarsal bone 5
18. Tarsometatarsal joints
19. Fourth tarsal bone
20. Proximal intertarsal (calcaneoquartal) joint
21. Calcaneus

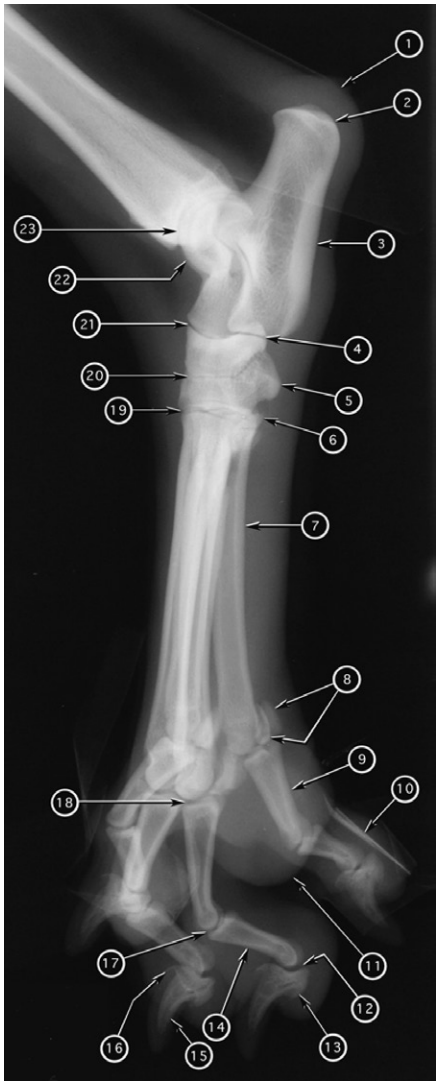


Fig. 13-29 **Mediolateral Radiograph of Canine Pes with Digits Spread.**

1. Superficial digital flexor (SDF) tendon
2. Tuber calcanei
3. Calcaneus
4. Proximal intertarsal (calcaneoquartal) joint
5. Tarsal bone 4
6. Base of metatarsal bone 5
7. Body of metatarsal bone 5
8. Proximal sesamoid bones of digit 5
9. Proximal phalanx of digit 5
10. Tape used in positioning
11. Metatarsal pad
12. Distal interphalangeal joint of digit 4
13. Flexor tubercle of distal phalanx of digit 4
14. Middle phalanx of digit 4
15. Unguicular process of distal phalanx of digit 3
16. Unguicular crest of distal phalanx of digit 3
17. Proximal interphalangeal joint of digit 4
18. Metatarsophalangeal joint of digit 4
19. Tarsometatarsal joints
20. Distal intertarsal joint
21. Proximal intertarsal (talocalcaneocentral) joint
22. Trochlea of talus
23. Tarsocrural joint

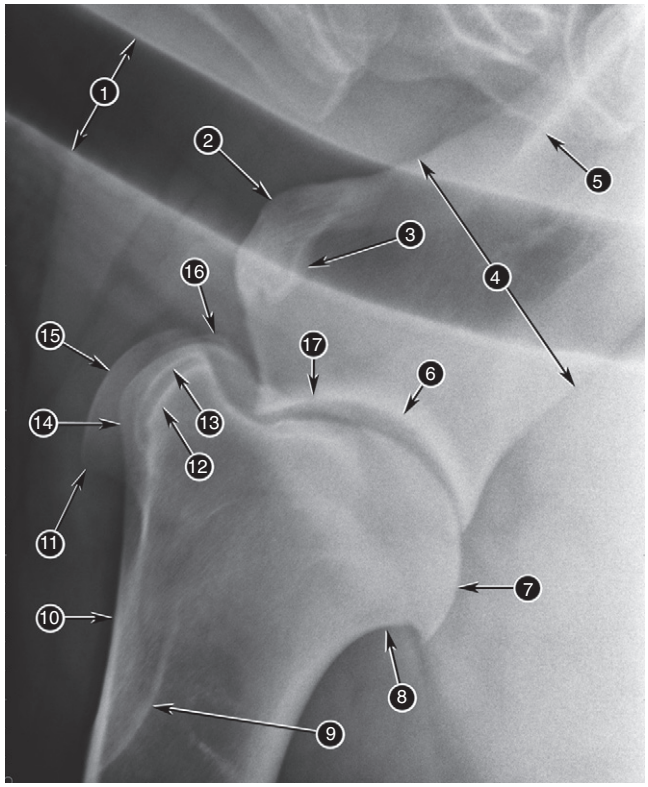


Fig. 13-30 **Mediolateral Radiograph of Equine Shoulder Joint.**

1. Air in trachea
2. Supraglenoid tubercle of scapula
3. Coracoid process of scapula
4. Neck of scapula
5. Spine of scapula
6. Medial edge of glenoid fossa
7. Head of humerus
8. Neck of humerus
9. Deltoid tuberosity of humerus
10. Cranial surface of humerus
11. Pointed distal end of intermediate tubercle
12. Floor of lateral part of intertubercular groove
13. Floor of medial part of intertubercular groove
14. Cranial part of lesser tubercle
15. Intermediate tubercle of humerus
16. Cranial part of greater tubercle
17. Glenoid notch in medial edge of glenoid fossa

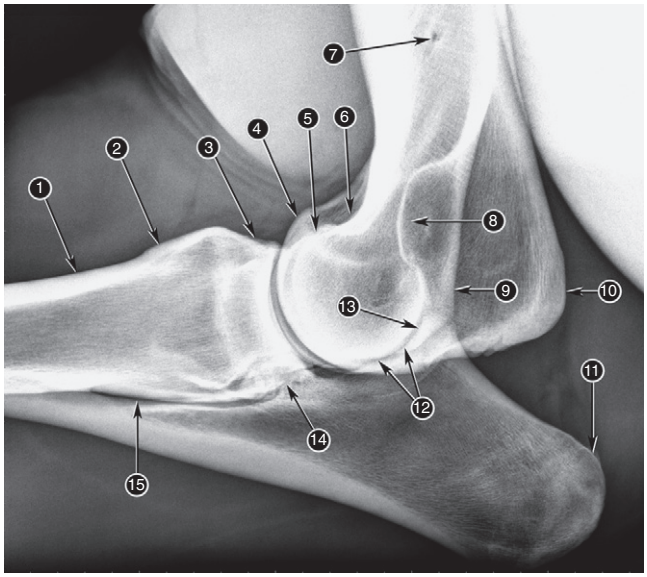


Fig. 13-31 **Mediolateral Radiograph of Equine Elbow Joint.**
1. Body of radius
2. Radial tuberosity
3. Head of radius
4. Trochlea of humeral condyle (medial)
5. Capitulum of humeral condyle (lateral)
6. Radial fossa of humerus
7. Nutrient canal of humerus (medial)
8. Olecranon fossa of humerus
9. Lateral epicondyle of humerus
10. Medial epicondyle of humerus
11. Tuber olecrani
12. Trochlear notch of ulna
13. Anconeal process of ulna
14. Proximal radioulnar joint
15. Proximal interosseous space

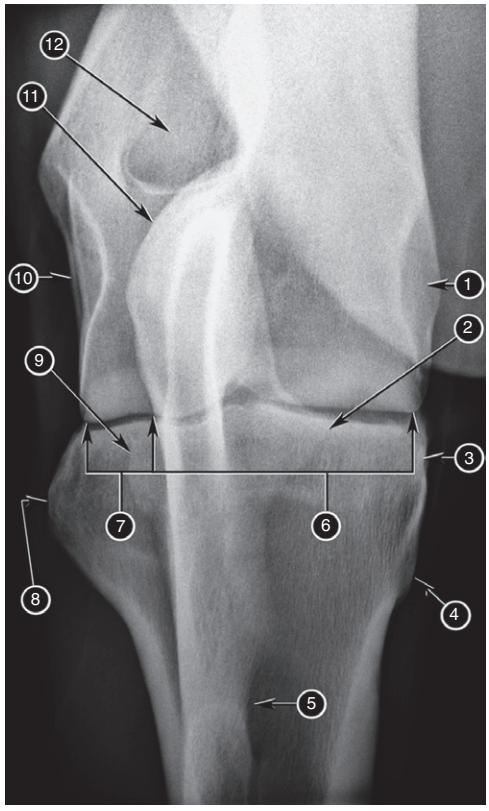


Fig. 13-32 **Craniocaudal Radiograph of Equine Elbow Joint.**
1. Medial epicondyle of humerus
2. Medial coronoid process of ulna
3. Head of radius
4. Radial tuberosity
5. Proximal interosseous space
6. Trochlea of humeral condyle
7. Capitulum of humeral condyle
8. Eminence for lateral collateral ligament
9. Lateral coronoid process of ulna
10. Lateral epicondyle of humerus
11. Tuber olecrani
12. Olecranon fossa of humerus

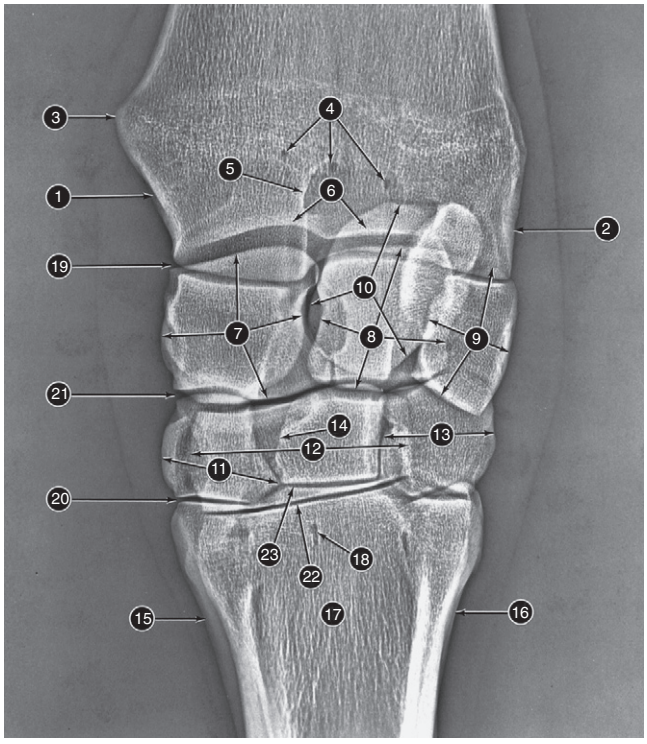


Fig. 13-33 **Dorsopalmar Radiograph of Left Equine Carpus.**

1. Medial styloid process of radius
2. Lateral styloid process of ulna
3. Projection at proximomedial aspect of medial styloid process of radius
4. Vascular channels
5. Caudolateral border of medial styloid process of radius
6. Junction of carpal articular surface with cranial surface of radius
7. Radial carpal bone
8. Intermediate carpal bone
9. Ulnar carpal bone
10. Accessory carpal bone
11. Second carpal bone
12. Third carpal bone
13. Fourth carpal bone
14. Medial border of palmar process of carpal bone 3
15. Metacarpal bone 2
16. Metacarpal bone 4
17. Metacarpal bone 3
18. Vascular channel
19. Antebrachiocarpal joint
20. Carpometacarpal joints
21. Middle carpal joint
22. Shadow cast by dorsal aspects of carpometacarpal joints
23. Shadow cast by palmar aspects of carpometacarpal joints

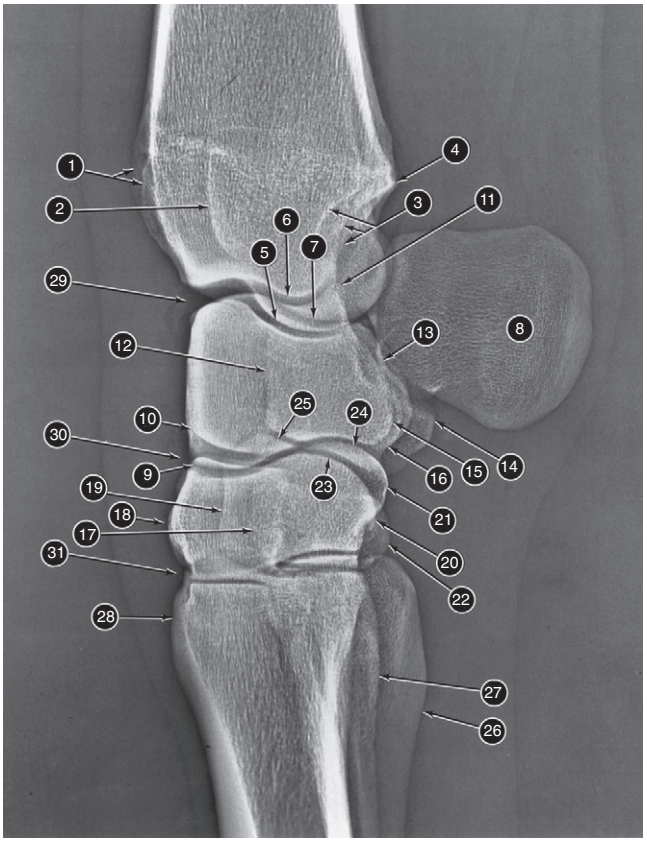


Fig. 13-34 **Lateromedial Radiograph of Left Equine Carpus.**

1. Ridges on cranial surface of radius
2. Ridge adjacent to lateral border of common digital extensor tendon
3. Caudal border of radial trochlea
4. Transverse crest of radius
5. Medial part of carpal articular surface
6. Intermediate part of carpal articular surface
7. Lateral part of carpal articular surface
8. Accessory carpal bone
9. Dorsodistal border of radial carpal bone
10. Dorsodistal border of intermediate carpal bone
11. Proximal process of intermediate carpal bone
12. Dorsal surface of ulnar carpal bone
13. Articulation of accessory carpal bone with ulnar carpal bone
14. Palmar border of ulnar carpal bone
15. Palmar border of intermediate carpal bone
16. Palmar border of radial carpal bone
17. Dorsal border of second carpal bone
18. Dorsal border of third carpal bone
19. Dorsal border of fourth carpal bone
20. Palmar border of second carpal bone
21. Palmar border of third carpal bone
22. Palmar border of fourth carpal bone
23. Proximal border of second carpal bone
24. Proximal border of third carpal bone
25. Proximal border of fourth carpal bone
26. Metacarpal bone 4
27. Metacarpal bone 2
28. Metacarpal tuberosity
29. Antebrachiocarpal joint
30. Middle carpal joint
31. Carpometacarpal joints

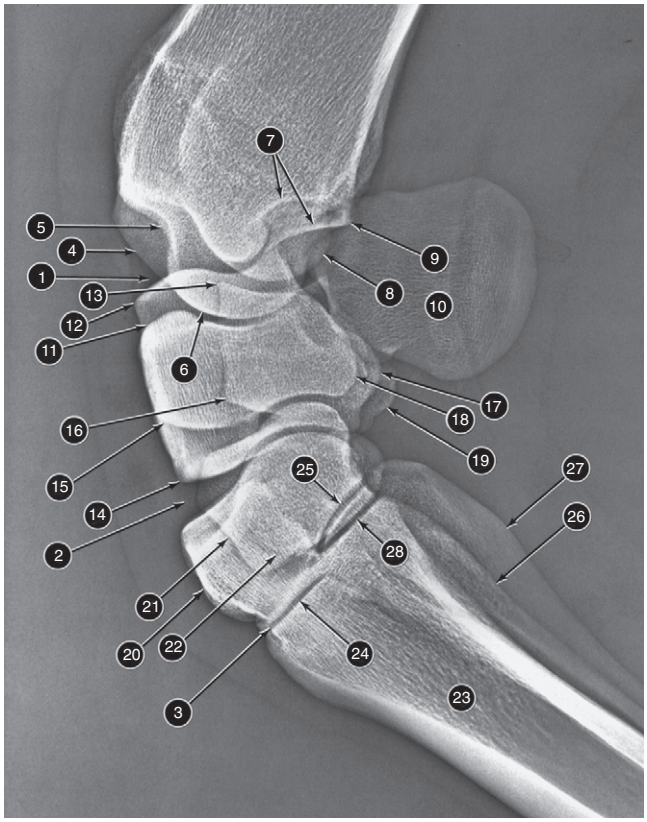


Fig. 13-35 **Lateromedial Radiograph of Flexed Left Equine Carpus.**

1. Antebrachiocarpal joint
2. Middle carpal joint
3. Carpometacarpal joints
4. Medial border of medial part of carpal articular surface
5. Lateral border of medial part of carpal articular surface
6. Medial styloid process
7. Shadows from caudal aspect of intermediate part of radial trochlea
8. Lateral styloid process
9. Transverse crest of radius
10. Accessory carpal bone
11. Dorsoproximal border of radial carpal bone
12. Dorsoproximal border of intermediate carpal bone
13. Dorsoproximal border of ulnar carpal bone
14. Dorsodistal border of radial carpal bone (isolated)
15. Dorsodistal border of intermediate carpal bone
16. Dorsodistal border of ulnar carpal bone
17. Palmar border of radial carpal bone
18. Palmar border of intermediate carpal bone
19. Palmar border of ulnar carpal bone
20. Dorsal border of third carpal bone
21. Dorsal border of fourth carpal bone
22. Dorsal border of second carpal bone
23. Metacarpal bone 3
24. Third carpometacarpal joint
25. Second carpometacarpal joint
26. Metacarpal bone 2
27. Metacarpal bone 4
28. Fourth carpometacarpal joint

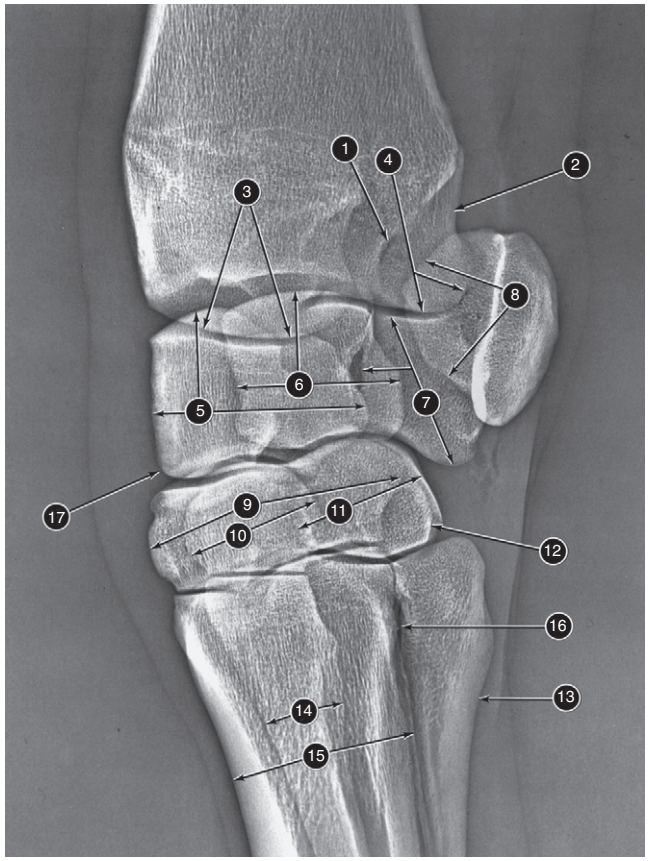


Fig. 13-36 **Dorsolateral-Palmaromedial Oblique Radiograph of Left Equine Carpus.**

1. Radiolucent area at line of fusion between lateral styloid process and radius
2. Lateral styloid process
3. Medial part of radial trochlea
4. Lateral styloid process
5. Radial carpal bone
6. Intermediate carpal bone
7. Ulnar carpal bone
8. Articulations of accessory carpal bone with lateral styloid process and ulnar carpal bone
9. Third carpal bone
10. Second carpal bone
11. Fourth carpal bone
12. Palmar projection of fourth carpal bone
13. Metacarpal bone 4
14. Metacarpal bone 2
15. Metacarpal bone 3
16. Location of metacarpal interosseous ligaments
17. Distal aspect of dorsomedial border of radial carpal bone (isolated)

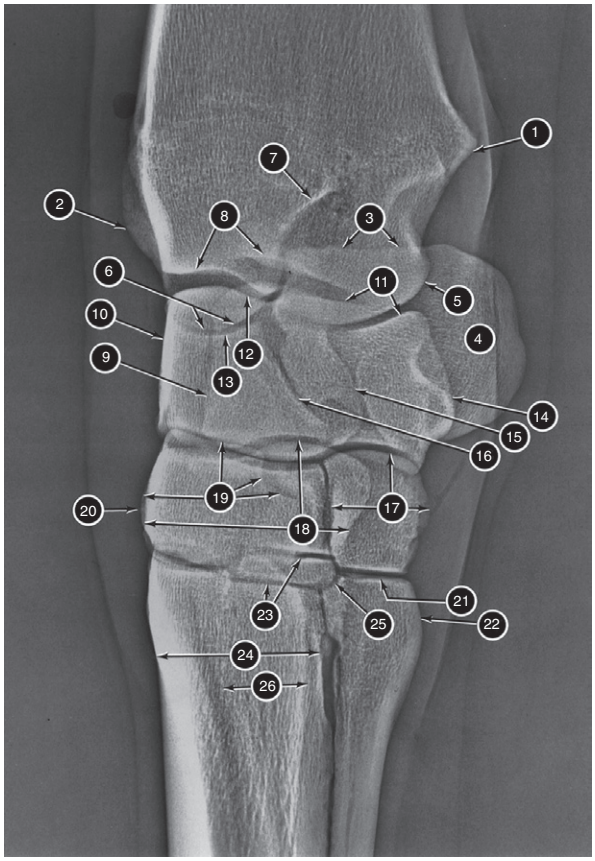


Fig. 13-37 **Dorsomedial-Palmarolateral Oblique Radiograph of Left Equine Carpus.**

1. Projection of radius for attachment of medial collateral ligament
2. Ridge that forms lateral border of groove for common digital extensor tendon
3. Proximal border of accessory carpal bone
4. Accessory carpal bone
5. Medial styloid process of radius
6. Lateral styloid process
7. Ridge on caudal aspect of radius
8. Ridge at junction of cranial surface of radius with carpal articular surface
9. Dorsolateral border of radial carpal bone
10. Dorsolateral borders of ulnar and intermediate carpal bones
11. Proximal surface of radial carpal bone
12. Proximal surface of intermediate carpal bone
13. Proximal surface of ulnar carpal bone
14. Palmaromedial border of radial carpal bone
15. Palmaromedial border of intermediate carpal bone
16. Palmaromedial border of ulnar carpal bone
17. Second carpal bone
18. Third carpal bone
19. Fourth carpal bone
20. Dorsolateral borders of third and fourth carpal bones
21. Articulation between second carpal bone and metacarpal bone 2
22. Metacarpal bone 2
23. Articulation between third carpal bone and metacarpal bone 3
24. Metacarpal bone 3
25. Inconstant articulation between third carpal bone and metacarpal bone 2
26. Metacarpal bone 4

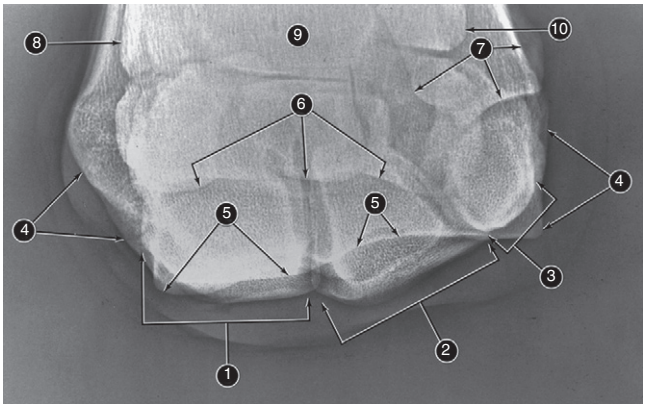


Fig. 13-38 **Dorsoproximal-Dorsodistal Oblique Radiograph of Proximal Row of Equine Carpal Bones.**

1. Dorsal surface of radial carpal bone
2. Dorsal surface of intermediate carpal bone
3. Dorsal surface of ulnar carpal bone
4. Radius
5. Carpal articular surface of radial trochlea
6. Dorsal surfaces of distal carpal bones
7. Accessory carpal bone
8. Metacarpal bone 2
9. Metacarpal bone 3
10. Metacarpal bone 4

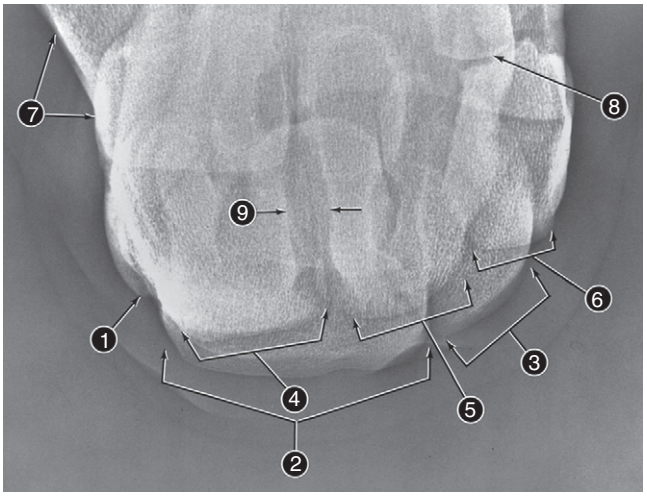


Fig. 13-39 **Dorsoproximal-Dorsodistal Oblique Radiograph of Distal Row of Equine Carpal Bones.**

1. Dorsal surface of second carpal bone
2. Dorsal surface of third carpal bone
3. Dorsal surface of fourth carpal bone
4. Dorsal surface of radial carpal bone
5. Dorsal surface of intermediate carpal bone
6. Dorsal surface of ulnar carpal bone
7. Radius
8. Accessory carpal bone
9. Interosseous space between radial and intermediate carpal bones

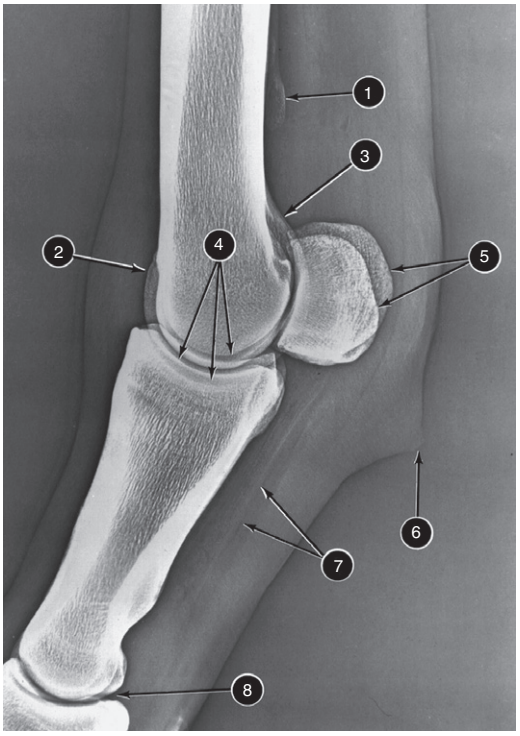


Fig. 13-40 **Lateromedial Radiograph of Left Equine Metacarpophalangeal Joint.**
1. Distal end (head) of small metacarpal bone
2. Dorsal part of sagittal ridge of metacarpal bone 3
3. Palmar part of sagittal ridge of metacarpal bone 3
4. Metacarpophalangeal joint
5. Proximal sesamoid bones
6. Ergot
7. Straight sesamoid ligament
8. Proximal interphalangeal joint

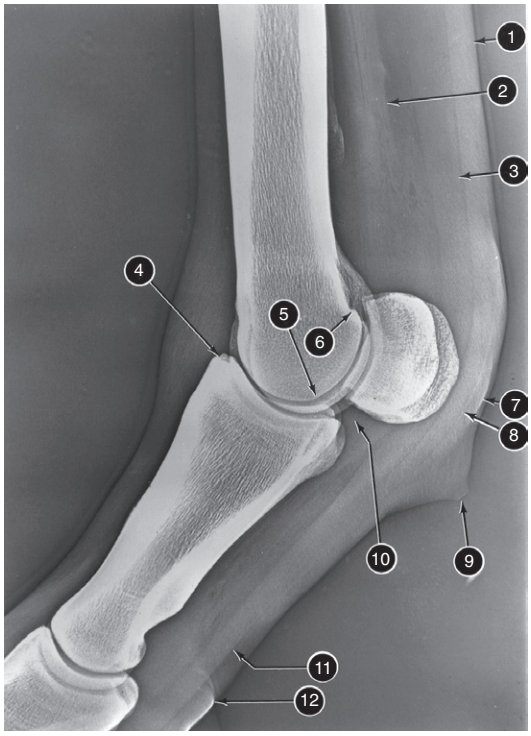


Fig. 13-41 **Lateromedial Radiograph of Left Equine Metacarpophalangeal Joint with Right Limb Lifted to Increase Weight on Left Limb.**
1. Superficial digital flexor tendon
2. Interosseus
3. Deep digital flexor tendon
4. Dorsoproximal aspect of proximal phalanx
5. Subtle transverse ridge on head of metacarpal bone 3
6. Distinct transverse ridge at palmar edge of articular surface
7. Palmar annular ligament of metacarpophalangeal joint
8. Superficial digital flexor tendon
9. Ergot
10. Increased distance between proximal sesamoid bones and proximal phalanx (see Fig. 13-40)
11. Deep distal flexor tendon
12. Distal digital annular ligament

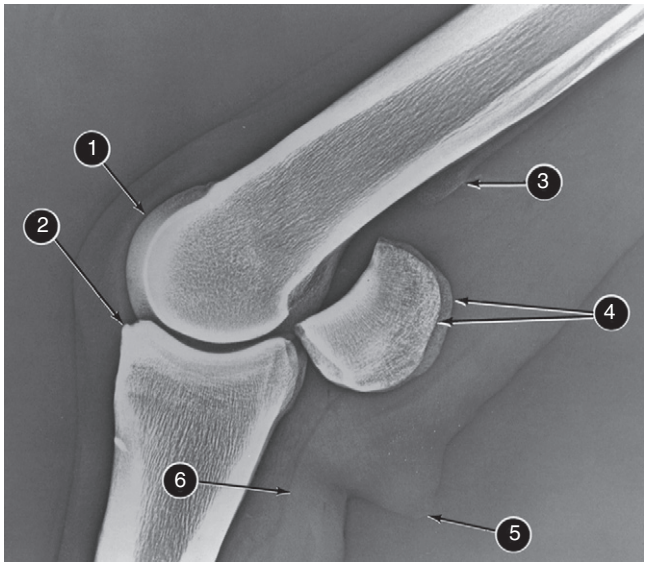


Fig. 13-42 **Lateromedial Radiograph of Flexed Left Equine Metacarpophalangeal Joint.**
1. Sagittal ridge on head of metacarpal bone 3
2. Dorsoproximal aspect of proximal phalanx
3. Distal end of small metacarpal bone
4. Proximal sesamoid bones
5. Ergot
6. Deep digital flexor tendon

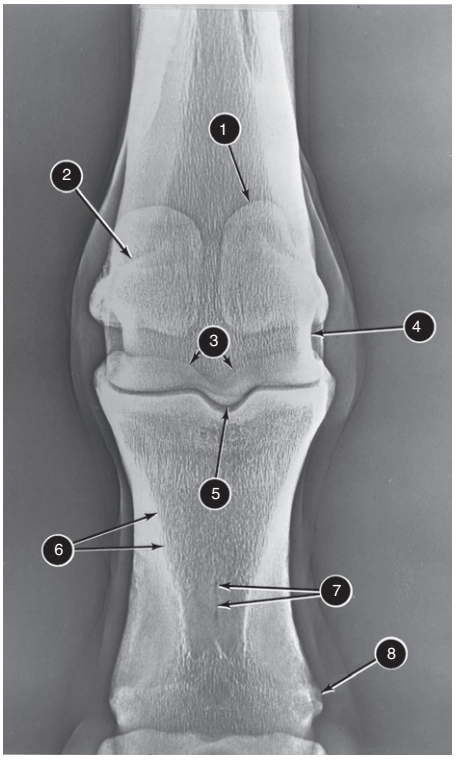


Fig. 13-43 **Dorsoproximal-Palmarodistal Oblique Radiograph of Left Equine Metacarpophalangeal Joint.**
1. Lateral proximal sesamoid bone
2. Depression in interosseus (abaxial) surface of medial proximal sesamoid bone for attachment of interosseus tendon
3. Palmaroproximal edge of proximal phalanx
4. Depression in metacarpal bone 3 for attachment of lateral collateral ligament of metacarpophalangeal joint
5. Sagittal ridge on head of metacarpal bone 3
6. Area of oblique ridge on palmar surface of proximal phalanx for attachment oblique sesamoid ligament
7. Nutrient canal through dorsal cortex of proximal phalanx
8. Lateral distal collateral tubercle of proximal phalanx

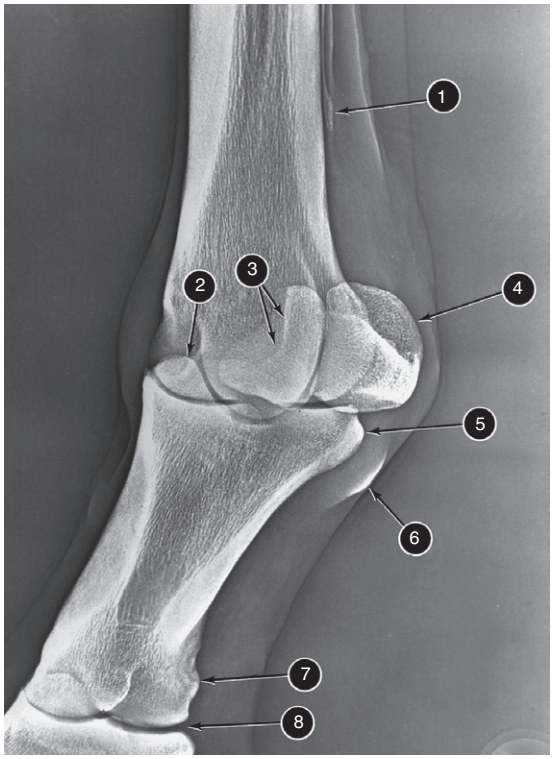


Fig. 13-44 **Dorsolateral-Palmaromedial Oblique Radiograph of Left Equine Metacarpophalangeal Joint.**

1. Distal end of metacarpal bone 4
2. Dorsoproximal aspect of proximal phalanx
3. Depression in interosseus surface of medial proximal sesamoid bone for attachment of interosseus tendon
4. Palmaroabaxial border of lateral proximal sesamoid bone
5. Lateral proximal collateral tubercle of proximal phalanx
6. Ergot
7. Lateral distal collateral tubercle of proximal phalanx
8. Proximal interphalangeal joint

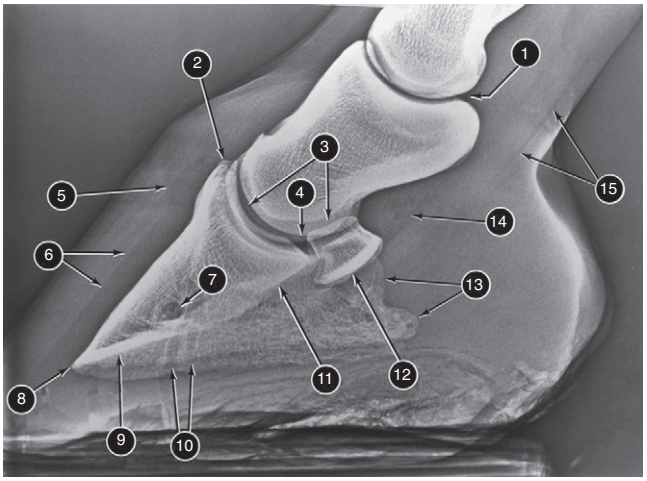


Fig. 13-45 **Lateromedial Radiograph of Left Equine Foredigit.**

1. Proximal interphalangeal joint
2. Extensor process of distal phalanx
3. Distal interphalangeal joint
4. Part of distal interphalangeal joint that extends between distal phalanx and the distal sesamoid (navicular) bone
5. Proximal extent of tubular horn forming stratum medium of hoof wall
6. Junction of stratum medium and laminar horn of stratum internum
7. Transverse part of sole canal of distal phalanx; accommodates terminal arch of digital vessels
8. Sole border of distal phalanx
9. Planum cuneatum (sole surface) of distal phalanx
10. Vascular channels extending from sole canal to sole border of distal phalanx
11. Flexor surface of distal phalanx
12. Flexor surface of navicular bone
13. Superimposed medial and lateral palmar processes of distal phalanx
14. Radiolucent areas created by fat within synovial folds
15. Borders of deep digital flexor tendon; defined by fat within synovial folds of digital sheath

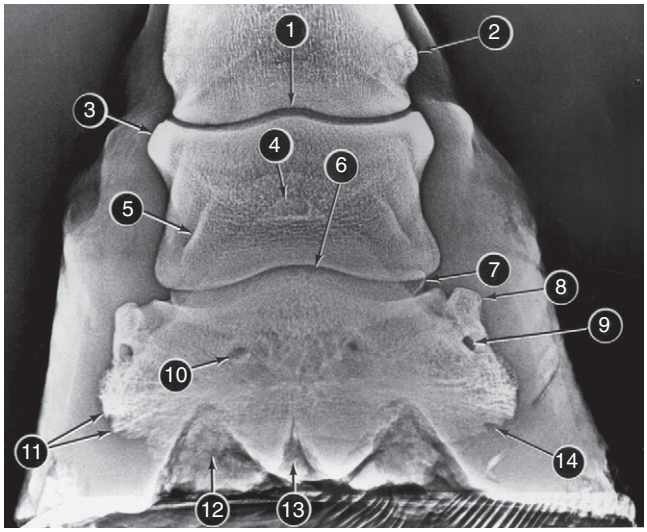


Fig. 13-46 **Dorsopalmar Radiograph of Left Equine Foredigit.**

1. Proximal interphalangeal joint
2. Lateral distal collateral tubercle of proximal phalanx
3. Medial proximal collateral tubercle of middle phalanx
4. Extensor process of distal phalanx
5. Wall of depression in Pm for attachment of medial collateral ligament of distal interphalangeal joint
6. Distal interphalangeal joint
7. Lateral extremity of navicular bone
8. Lateral palmar process of distal phalanx
9. Foramen in lateral palmar process of distal phalanx that accommodates dorsal branches of digital vessels
10. Medial sole foramen of distal phalanx; receives digital vessels as they enter sole canal
11. Sole border of distal phalanx; typically irregular because of notches for vascular channels
12. Medial collateral groove of frog
13. Central groove of frog
14. Notch in sole border associated with vascular channel from sole canal of distal phalanx

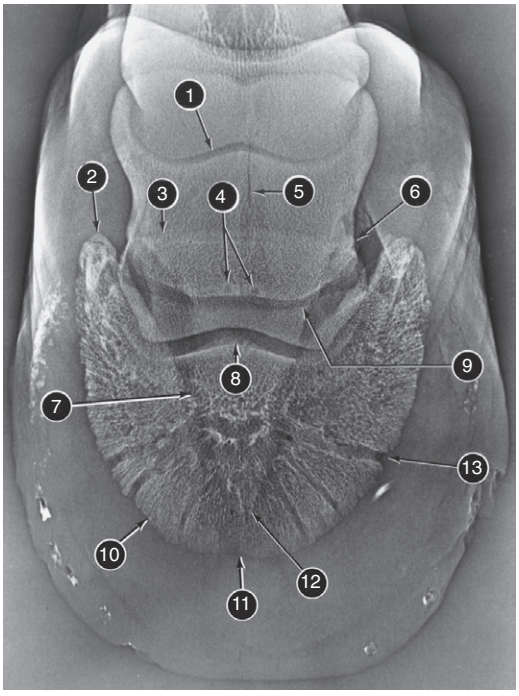


Fig. 13-47 **Dorsal 65-Degree Proximal-Palmarodistal Oblique Radiograph of Left Equine Foredigit.**

1. Proximal interphalangeal joint
2. Medial palmar process of distal phalanx
3. Proximal border of navicular bone
4. Vascular foramina and synovial fossae along distal border of navicular bone
5. Air within central groove of frog
6. Lateral extremity of navicular bone
7. Sole canal of distal phalanx
8. Distal interphalangeal joint
9. Articulation of distal phalanx with navicular bone; part of distal interphalangeal joint
10. Sole border of distal phalanx
11. Crena marginis solaris
12. Apex of frog
13. Vascular channel from sole canal to sole border of distal phalanx

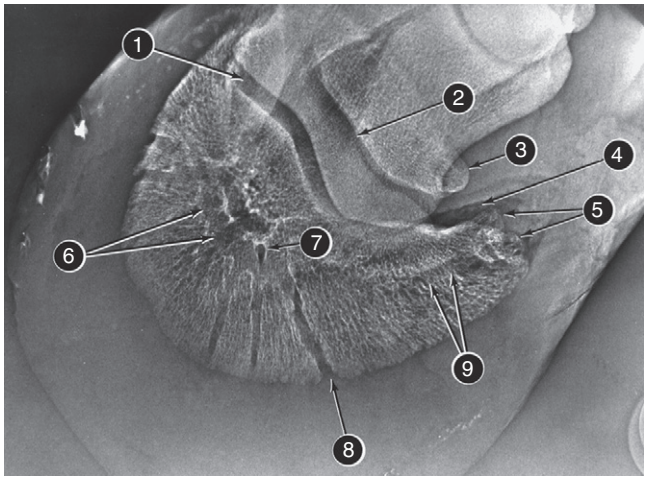


Fig. 13-48 **Dorsoproximolateral-Palmarodistomedial Oblique Radiograph of Left Equine Foredigit.**

1. Distal interphalangeal joint
2. Articulation of Pd with navicular bone; part of distal interphalangeal joint
3. Lateral extremity of navicular bone
4. Air within lateral collateral groove of frog
5. Lateral palmar process of distal phalanx
6. Sole canal of distal phalanx
7. End-on perspective of vascular channel from sole canal to parietal surface of distal phalanx
8. Vascular channel from sole canal to sole border of distal phalanx
9. Lateral parietal groove of distal phalanx; accommodates dorsal branches of digital vessel

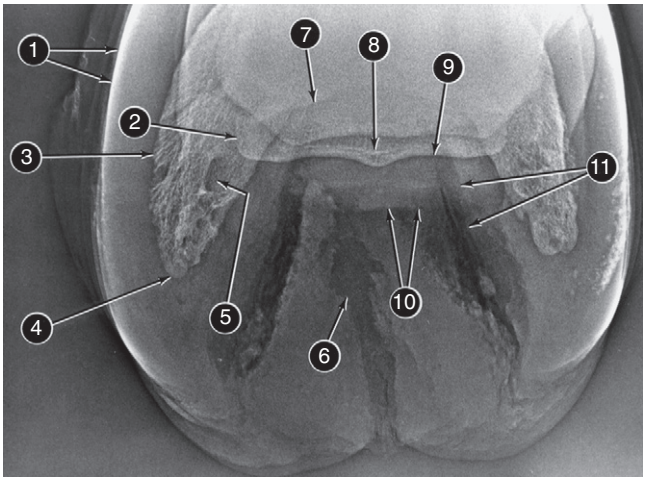


Fig. 13-49 **Palmaroproximal-Palmarodistal Oblique Radiograph of Left Equine Foredigit.**

1. Proximal border of hoof wall
2. Lateral extremity of navicular bone
3. Sole border of distal phalanx
4. Lateral palmar process of distal phalanx
5. Foramen of lateral palmar process
6. Air within central groove of frog
7. Articulation of Pm with navicular bone; part of distal interphalangeal joint
8. Sagittal ridge of navicular bone
9. Flexor surface of navicular bone
10. Deep digital flexor tendon
11. Air within medial collateral groove of frog

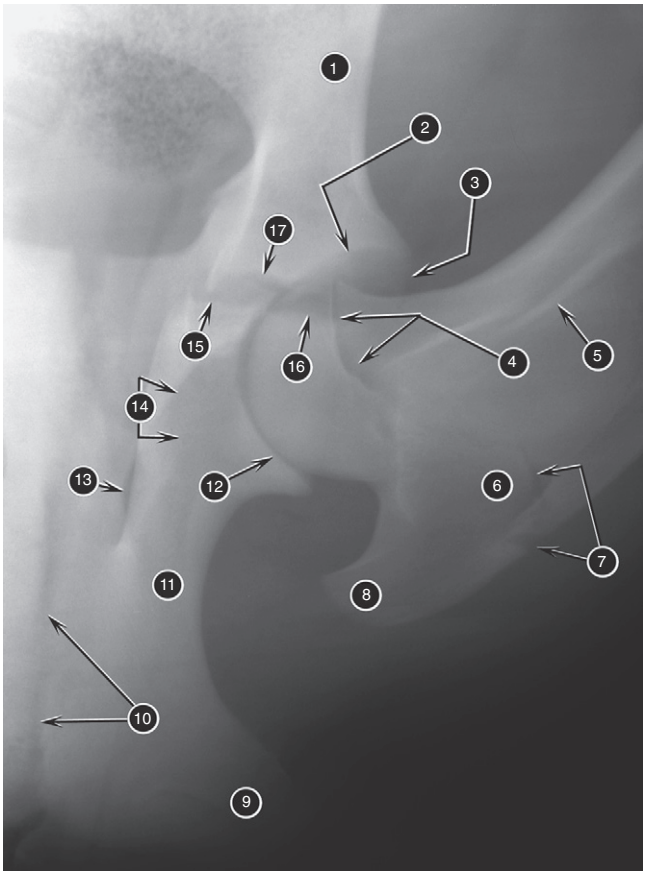


Fig. 13-50 **Ventromedial-Dorsolateral Oblique Radiograph of Equine Hip Joint (8 Months Old).**

1. Body of ilium
2. Cranioventral border of acetabulum
3. Craniodorsal border of acetabulum
4. Proximal physis (epiphyseal cartilage) of femur
5. Shadow created by caudal edge of lesser trochanter
6. Radiolucent area created by trochanteric fossa of femur
7. Cartilaginous junction between greater trochanter and femoral body
8. Greater trochanter of femur, caudal part
9. Tuber ischiadicum
10. Cartilaginous pelvic symphysis
11. Body of ischium
12. Caudoventral border of acetabulum
13. Obturator foramen
14. Radiolucent area created by acetabular fossa
15. Radiolucent area created by groove on ventral surface of pubis for accessory ligament of femoral head
16. Radiolucent area created by fovea capitis of femoral head
17. Cranial edge of acetabular notch

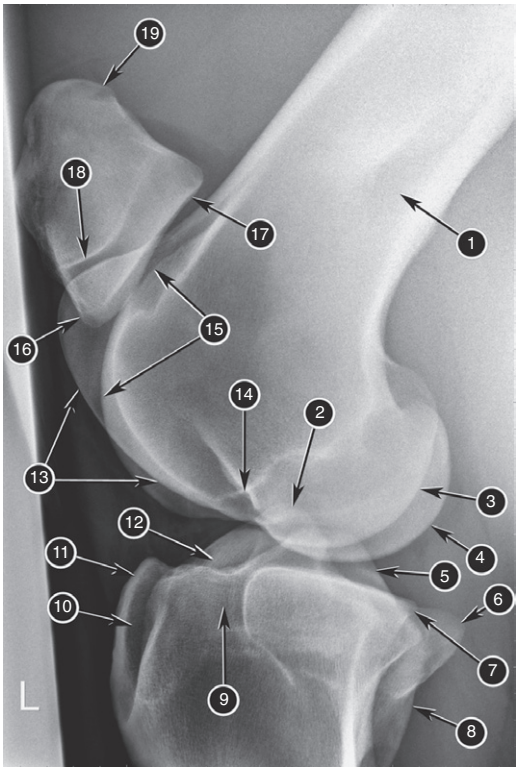


Fig. 13-51 **Lateromedial Radiograph of Equine Stifle Joint.**
1. Supracondylar fossa of femur for SDF
2. Medial tubercle of intercondylar eminence
3. Lateral condyle of femur
4. Medial condyle of femur
5. Lateral tubercle of intercondylar eminence
6. Lateral condyle of tibia
7. Medial condyle of tibia
8. Fibula
9. Extensor groove of tibia
10. Groove for intermediate patellar ligament
11. Lateral part of tibial tuberosity
12. Cranial intercondylar area of tibia
13. Medial ridge of femoral trochlea
14. Extensor fossa of femur
15. Lateral ridge of femoral trochlea
16. Apex of patella
17. Articular surface of patella, gliding part
18. Articular surface of patella, resting part
19. Base of patella

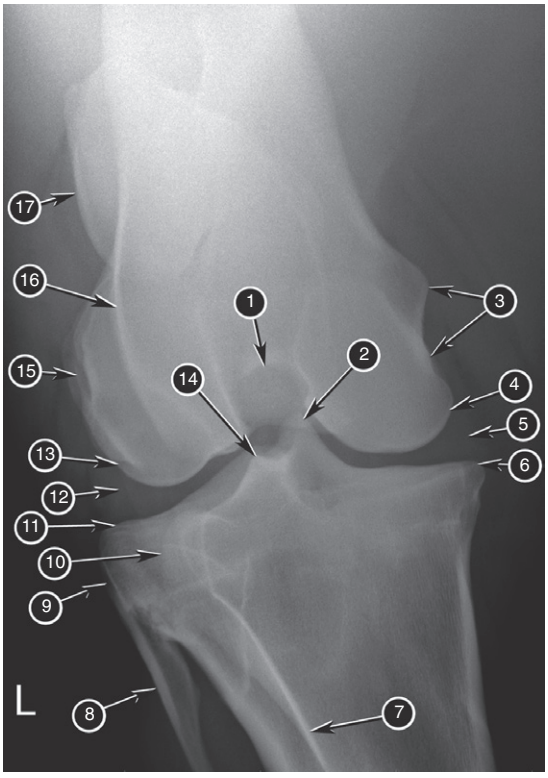


Fig. 13-52 **Caudocranial Radiograph of Equine Stifle Joint.**
1. Intercondylar fossa of femur
2. Medial tubercle of intercondylar eminence
3. Medial epicondyle of femur
4. Medial condyle of femur
5. Medial meniscus and femorotibial joint
6. Medial condyle of tibia
7. Cranial margin of tibia
8. Body of fibula
9. Head of fibula
10. Lateral part of tibial tuberosity
11. Lateral condyle of tibia
12. Lateral meniscus and femorotibial joint
13. Depression for origin of popliteus muscle
14. Lateral tubercle of intercondylar eminence
15. Lateral epicondyle of femur
16. Lateral ridge of femoral trochlea
17. Patella

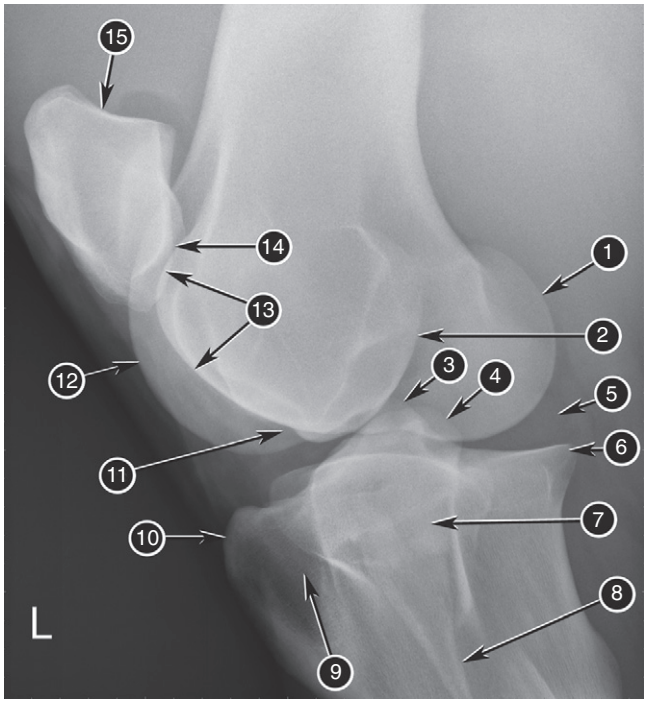


Fig. 13-53 **Caudolateral-Craniomedial Oblique Radiograph of Equine Stifle Joint.**

1. Medial condyle of femur
2. Lateral condyle of femur
3. Medial tubercle of intercondylar eminence
4. Lateral tubercle of intercondylar eminence
5. Medial meniscus and femorotibial joint
6. Medial condyle of tibia
7. Head of fibula
8. Body of fibula
9. Extensor groove of tibia
10. Tibial tuberosity
11. Extensor fossa of femur
12. Lateral ridge of femoral trochlea
13. Groove of femoral trochlea
14. Femoropatellar joint
15. Patella

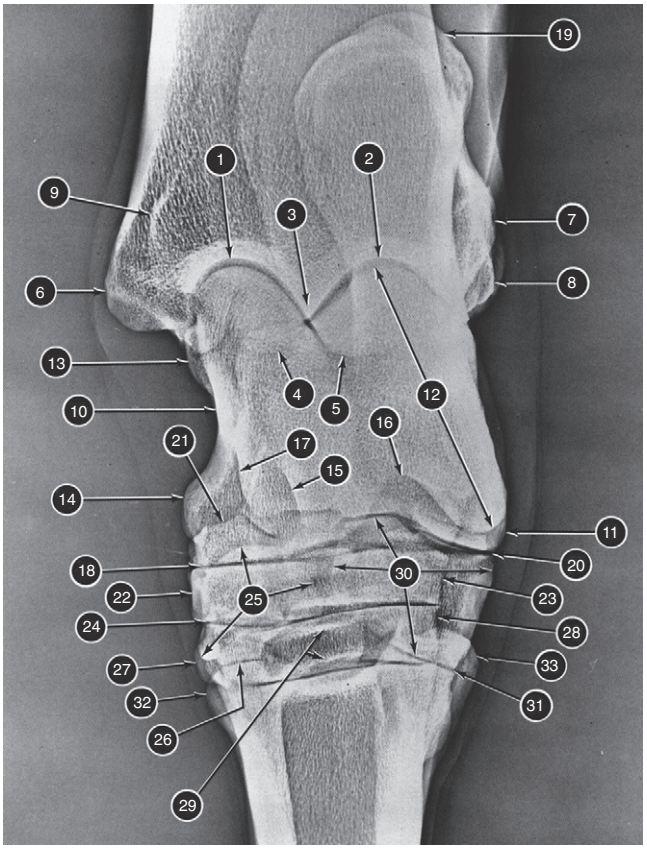


Fig. 13-54 **Dorsoplantar Radiograph of Left Equine Tarsus.**

1. Medial groove of tibial cochlea
2. Lateral groove of tibial cochlea
3. Oblique ridge separating medial and lateral grooves of tibial cochlea
4. Pointed caudal end of oblique ridge
5. Rounded cranial end of oblique ridge
6. Medial malleolus
7. Caudal part of lateral malleolus
8. Cranial part of lateral malleolus
9. Radiopaque shadow
10. Talus
11. Calcaneus
12. Lateral ridge of trochlea tali
13. Proximal tubercle of talus
14. Distal tubercle of talus
15. Medial ridge of trochlea tali
16. Groove between lateral and medial ridges of trochlea tali
17. Medial edge of sustentaculum tali
18. Proximal intertarsal (talocalcaneocentral) joint
19. Tuber calcanei
20. Proximal intertarsal (calcaneoquartal) joint
21. Proximoplantar aspect of central tarsal bone
22. Medial aspect of central tarsal bone
23. Lateral aspect of central tarsal bone
24. Distal intertarsal (centrodistal) joint
25. Fused first and second tarsal bones
26. Articulation between first and second tarsal bones and metatarsal bone 2
27. Medial aspect of third tarsal bone
28. Lateral aspect of third tarsal bone
29. Radiopaque lines produced by walls of nonarticular depressions on third tarsal bone
30. Fourth tarsal bone
31. Tarsometatarsal joints (also articulation between first and second tarsal bones and metatarsal bone 2)
32. Base of metatarsal bone 2
33. Base of metatarsal bone 4

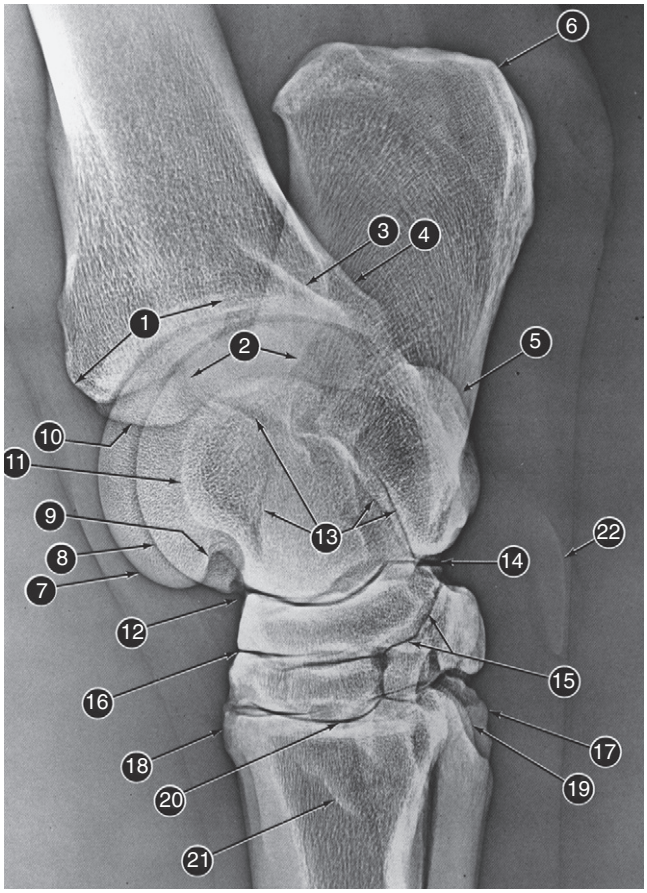


Fig. 13-55 **Lateromedial Radiograph of Left Equine Tarsus.**

1. Lateral malleolus
2. Medial malleolus
3. Radiopaque line produced by ridge on caudal surface of tibia
4. Medial part of caudal surface of tibia
5. Sustentaculum tali
6. Tuber calcanei
7. Lateral ridge of trochlea tali
8. Medial ridge of trochlea tali
9. Larger notch associated with lateral ridge of trochlea tali
10. Intermediate part of tibial cochlea
11. Groove of trochlea tali
12. Proximal intertarsal joint
13. Articular facets between talus and calcaneus
14. Plantar aspect of proximal intertarsal joint
15. Articulation between central tarsal bone and fused first and second tarsal bones
16. Distal intertarsal joint
17. Base of metatarsal bone 2
18. Base of metatarsal bone 3
19. Base of metatarsal bone 4
20. Tarsometatarsal joint
21. Groove on metatarsal bone 3 for dorsal metatarsal artery 3
22. Chestnut (torus tarseus)

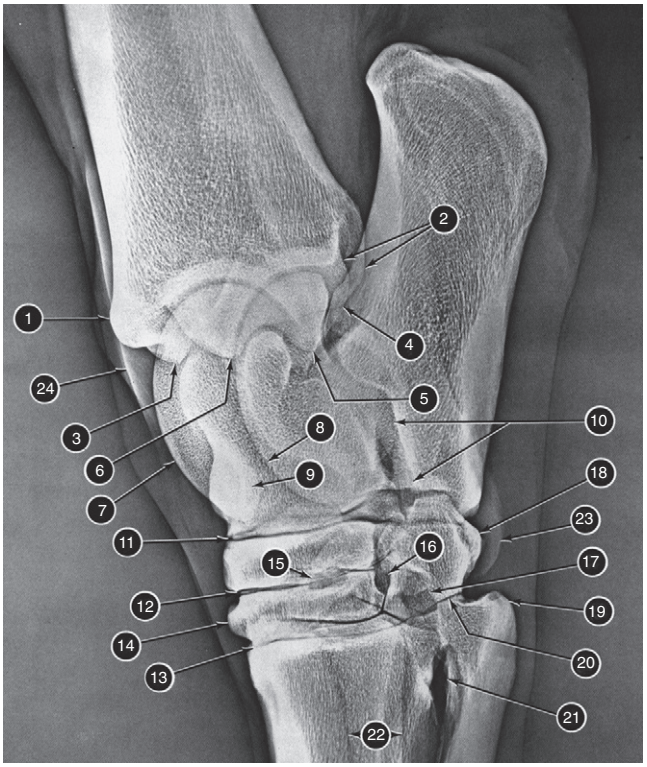


Fig. 13-56 **Dorsolateral-Plantaromedial Oblique Radiograph of Left Equine Tarsus.**

1. Cranial aspect of medial malleolus
2. Shadows produced by borders of groove in lateral malleolus
3. Distal projection of medial malleolus
4. Distal projection of lateral malleolus
5. Caudal aspect of intermediate ridge of tibial cochlea
6. Cranial aspect of intermediate ridge of tibial cochlea
7. Medial ridge of trochlea tali
8. Lateral ridge of trochlea tali
9. Radiopaque area produced by distal tubercle of talus
10. Sinus tarsi
11. Dorsomedial aspect of proximal intertarsal joint
12. Dorsomedial aspect of distal intertarsal joint
13. Dorsomedial aspect of third tarsometatarsal joint
14. Ridge on dorsomedial aspect of third tarsal bone
15. Nonarticular area between central tarsal bone and third tarsal bone
16. Dorsal opening of tarsal canal
17. Plantar opening of tarsal canal
18. Plantar tuberosity on fourth tarsal bone
19. Base of metatarsal bone 4
20. Articulation between fourth tarsal bone and metatarsal bone 4
21. Interosseous space between metatarsal bones 3 and 4
22. Metatarsal bone 2
23. Chestnut
24. Tendons crossing flexor surface of tarsus

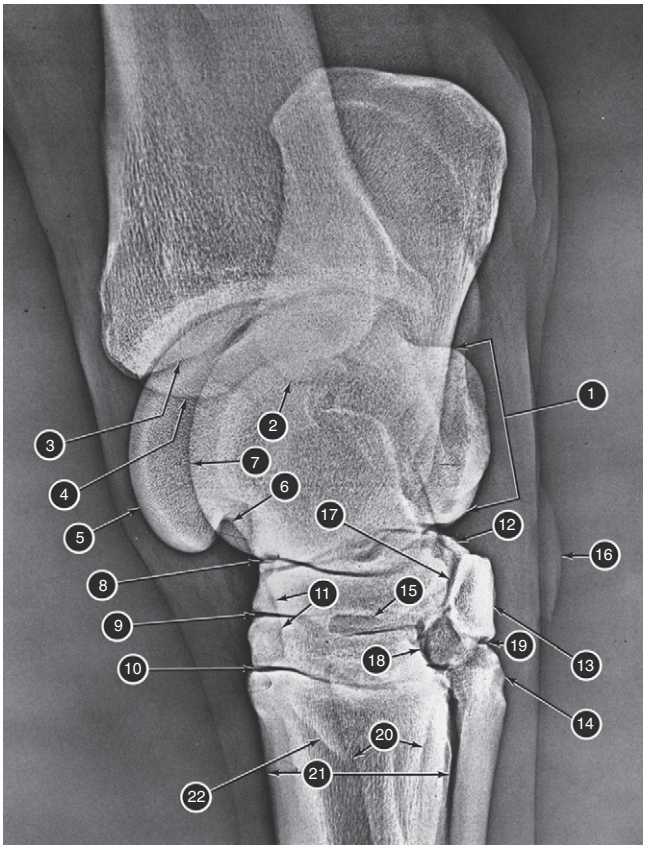


Fig. 13-57 **Dorsomedial-Plantarolateral Oblique Radiograph of Left Equine Tarsus.**

1. Sustentaculum tali
2. Distal extremity of medial malleolus
3. Distal extremity of lateral malleolus
4. Intermediate ridge of tibial cochlea
5. Lateral ridge of trochlea tali
6. Notch distal to lateral ridge of trochlea tali
7. Medial ridge of trochlea tali
8. Dorsolateral aspect of proximal intertarsal joint
9. Dorsolateral aspect of distal intertarsal joint
10. Dorsolateral aspect of third tarsometatarsal joint
11. Dorsal aspect of fourth tarsal bone
12. Plantaromedial aspect of central tarsal bone
13. Plantaromedial aspect of fused first and second tarsal bones
14. Plantaromedial aspect of metatarsal bone 2
15. Nonarticular depression between central tarsal bone and third tarsal bone
16. Chestnut
17. Articulation between fused first and second tarsal bones and central tarsal bone
18. Articulation between fused first and second tarsal bones and third tarsal bone
19. Articulation between fused first and second tarsal bones and metacarpal bone 2
20. Metacarpal bone 4
21. Metacarpal bone 3
22. Radiopaque line produced by border of groove for dorsal metatarsal artery 3

REFERENCES

1. Waibl H, Mayrhofer E, Matis U, et al: *Atlas of radiographic anatomy of the dog*, Stuttgart, 2005, Parey Verlag.
2. Schebitz H, Wilkens H: *Atlas of radiographic anatomy of the horse*, ed 3, Philadelphia, 1978, Saunders.
3. Thrall D, Robertson ID: *Atlas of normal radiographic anatomy and anatomic variants in the dog and cat*, St. Louis, 2011, Elsevier-Saunders.
4. Smallwood JE, Shively MJ, Rendano VT, et al: A standardized nomenclature for radiographic projections used in veterinary medicine, *Vet Radiol* 26:2, 1985.
5. Smallwood JE, Shively MJ: Radiographic and xeroradiographic anatomy of the equine carpus, *Equine Pract* 1:22, 1979.
6. Smallwood JE, Holladay SD: Xeroradiographic anatomy of the equine digit and metacarpophalangeal region, *Vet Radiol* 28:166, 1987.
7. Shively MJ, Smallwood JE: Radiographic and xeroradiographic anatomy of the equine tarsus, *Equine Pract* 2:19, 1980.

CHAPTER • 14

Principles of Radiographic Interpretation of the Appendicular Skeleton

Donald E. Thrall

The acquisition of extremity radiographs is one of the most common radiographic examinations performed in veterinary practice, especially in the horse. Although computed tomography (CT) and magnetic resonance imaging (MRI) can provide valuable information about skeletal disease, radiographs are the mainstay of assessing the skeleton. Obtaining good-quality radiographs of extremities is easier than obtaining good-quality radiographs of the spine, thorax, or abdomen because the parts are thinner and can be positioned more easily. However, there are some important principles that must be adhered to so that quality is maximized.

POSITIONING: DOG AND CAT

Following the general principles of radiographic geometry that were discussed in Chapter 5, radiographic examination of structures in the appendicular skeleton in dogs and cats should consist of a minimum of two orthogonal projections, a lateral view and a craniocaudal (dorsopalmar, dorsoplantar) view. If a bone lesion is suspected, it is important that the field of view include the joint proximal and distal to the bone of interest. If a joint is being investigated, the primary x-ray beam should be centered on the joint.

Also discussed in Chapter 5, the terminology used for radiographs of an extremity made with the x-ray beam striking the front or back of a limb depends on whether it is a front limb or hind limb and whether the center of the x-ray beam strikes the limb proximal or distal to the antebrachiocarpal or tarsocrural joint. In spite of being named differently, whether the x-ray beam strikes the front or back of a limb for any given projection, dorsoplantar versus plantarodorsal for example, does not affect the appearance of the radiograph in most instances because the radiograph is a two-dimensional representation of a three-dimensional object.

For certain regions of the appendicular skeleton of dogs and cats, there are ancillary projections in addition to the standard orthogonal views that can add important information by allowing evaluation of the edge of surfaces that cannot be assessed in the conventional lateral and craniocaudal (dorsopalmar, dorsoplantar) projections. Examples of such ancillary views would be the following:

1. Cranioproximal-craniodistal view of canine proximal humerus for evaluation of bicipital groove for changes associated with biceps or supraspinatus tendinopathy (Fig. 14-1, *A*)
2. Flexed dorsoplantar view of canine tarsus for evaluation of trochlea of talus for changes associated with osteochondrosis, without superimposition of calcaneus (Fig. 14-1, *B*)
3. Dorsal acetabular rim view of canine pelvis for evaluation of lateral aspect of acetabulum for remodeling (Fig. 14-1, *C*)

The views in Figure 14-1 do not encompass all ancillary views that have value in appendicular radiography and are provided only as examples of how changing the orientation of the x-ray beam and skeleton can lead to projection of clinically important surfaces that cannot be assessed adequately in the standard projections. These ancillary views, and others, are discussed throughout the textbook where appropriate, and examples of representative abnormalities are provided.

POSITIONING: HORSE

The principles described for radiographic terminology, the minimum number of projections, and field of view described for the appendicular skeleton in dogs and cats also apply to the horse. In equine long bones, it may not be possible to include the proximal and distal joint in the same image because of the length of the bone. If this is the case, the proximal and distal end of the bone, and the respective joints, should be examined in different images.

There are very few instances in the horse where lateral and craniocaudal (dorsopalmar, dorsoplantar) views of a limb will suffice. These two views might be adequate for examining the radius or tibia, but even in those sites oblique views are often needed to assess all aspects of the surface of these large bones. These oblique views are obtained from a point of entrance different from that used for lateral or craniocaudal (dorsopalmar, dorsoplantar) projections. The principles of obtaining oblique projections and the associated terminology are discussed in detail later. In addition to oblique views, many other ancillary projections have been developed for equine skeletal radiography, and these vary according to the site being radiographed. These ancillary views will be covered in other chapters where specific equine joints and regions are discussed.

One aspect of equine radiography that deserves special mention is the common practice of holding the cassette by hand. Equine-extremity radiographs are almost always acquired with the horse in a standing position, and handholding the cassette is convenient. However, handholding of cassettes increases the chance that occupational radiation exposure limits will be exceeded or radiation safety practices will be compromised. Individuals handholding a cassette for equine radiography should wear protective lead aprons and lead gloves, as well as a thyroid shield and protective lead glasses. It must be remembered that this equipment protects only against scattered photons, and the gloved hand must

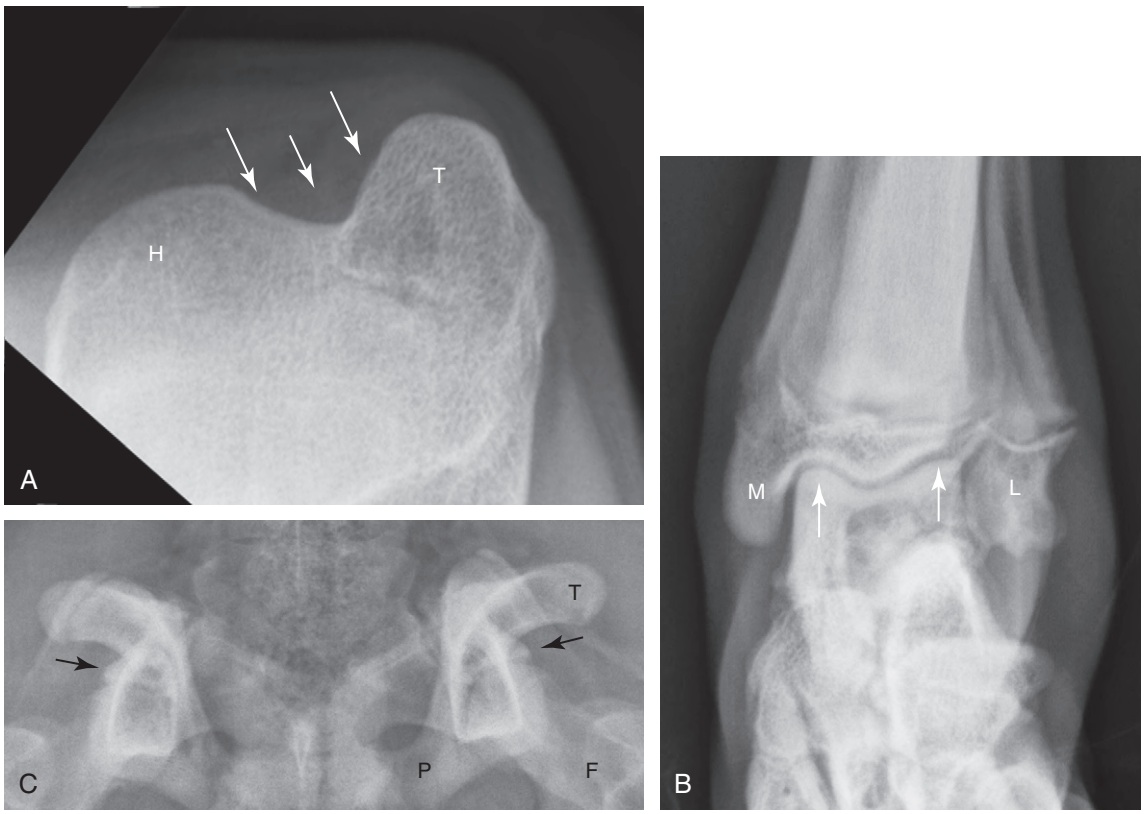


Fig. 14-1 **A,** Cranioproximal-craniodistal view of proximal humerus to project the bicipital groove *(white arrows)*. *H,* Humeral head; *T,* greater tubercle. **B,** Flexed dorsoplantar view of canine tarsus to project the trochlea of the talus *(white arrows)*. *L,* Lateral malleolus; *M,* Medial malleolus. **C,** Dorsal acetabular rim view to project the dorsolateral aspect of the acetabulum *(black arrows)*. *F,* Proximal aspect of femur; *P,* body of pubis; *T,* tuber ischii.

never be placed in the primary x-ray beam; this was addressed in detail in Chapter 1. Also noted in Chapter 1, rotation of technical personnel in and out of the equine radiology service will distribute the occupational radiation dose over a larger number of people and minimize individual exposure doses.

The use of a cassette holder device for equine extremity radiography is encouraged because it will minimize occupational radiation exposure. A cassette holder secures the cassette and has an extension handle so that the hands are distant from the primary x-ray beam. A disadvantage of a cassette holder is that as the distance from the hands to the cassette increases, the force needed to hold the cassette in position also increases, making motion artifact more likely than when holding the cassette directly. However, this is not an excuse to abandon cassette holders. With practice, the technique can be mastered.

OBLIQUE PROJECTIONS

For many anatomic regions in dogs, cats, and horses, especially complex regions such as the carpal and tarsal joints, the occasional ancillary projection is not adequate, and oblique projections should be obtained routinely. Oblique views are generally intended to project different *edges* of a joint or region. More than the edge of a structure can be assessed in any radiograph, but important edge lesions can be overlooked unless they are projected tangentially where they will be visible at the periphery of the part. Oblique views maximize the chances of projecting an edge lesion tangentially in a complex joint. In oblique views of complex joints, the point of entrance of the primary x-ray beam is typically moved 30 to 45 degrees medial and lateral to the point of entrance used for a craniocaudal (dorsopalmar, dorsoplantar) view.

It is important to understand the geometry of oblique projections so that the location of abnormalities can be understood. The concept of oblique projections will be illustrated using the equine carpus as an example, but the principles apply to other regions and other joints. The principles of oblique projections based on radiography of a canine carpus are also available.[1] Labeled oblique radiographs of equine and canine joints are included in Chapter 13.

The edges projected in an oblique radiograph of a limb can be deduced by understanding the geometry of these projections, which is reviewed in Table 14-1 (page 258) and in Figures 14-2 through 14-5 (pages 254-257). In Figures 14-2 through 14-5, the imaging plate or cassette is oriented perpendicular to the primary x-ray beam, but the imaging plate is not shown for the sake of clarity.

In a dorsopalmar view of the carpus, the x-ray beam strikes the dorsal surface, and the medial and lateral edges are projected in an unobstructed fashion (see Fig. 14-2). The x-ray beam could also strike the palmar surface with the same results because the two-dimensional nature of radiographs makes it impossible to distinguish between a dorsopalmar and palmarodorsal radiograph of a joint.

In a lateromedial view of the carpus, the x-ray beam strikes the lateral surface, and the dorsal and palmar edges are projected in an unobstructed fashion (see Fig. 14-3). The x-ray beam could also strike the medial surface with the same results.

In a dorsolateral-palmaromedial view of the carpus, the x-ray beam strikes the dorsolateral surface with the

Text continued on page 258

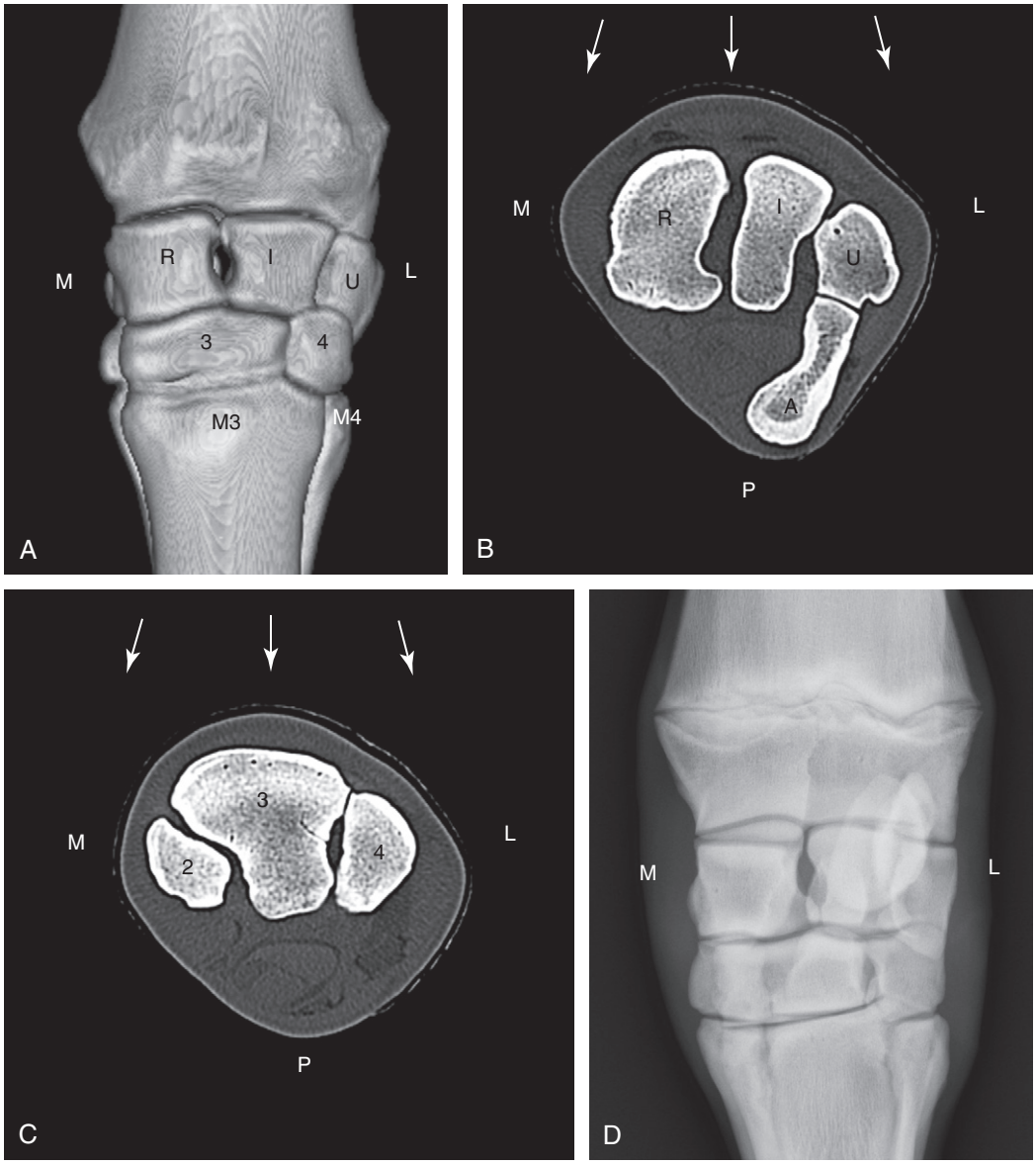


Fig. 14-2 Configuration for a dorsopalmar radiograph of the equine carpus. **A,** Volume-rendered CT image of an equine carpus from a dorsal perspective. **B,** Transverse CT image of an equine carpus through the proximal row of carpal bones. **C,** Transverse CT image of an equine carpus through the distal row of carpal bones. **D,** Dorsopalmar equine carpal radiograph. In **B** and **C,** the *white arrows* indicate the direction of the primary x-ray beam. For a dorsopalmar projection, the x-ray beam strikes the dorsal surface of the carpus. In a dorsopalmar radiograph, the medial and lateral edges of the carpus will be projected. *A*, Accessory carpal bone; *2*, second carpal bone; *3*, third carpal bone; *4*, fourth carpal bone; *I*, intermediate carpal bone; *L*, lateral; *M*, medial; *M3*, third metatarsal bone; *M4*, fourth metatarsal bone; *P*, palmar; *R*, radial carpal bone; *U*, ulnar carpal bone.

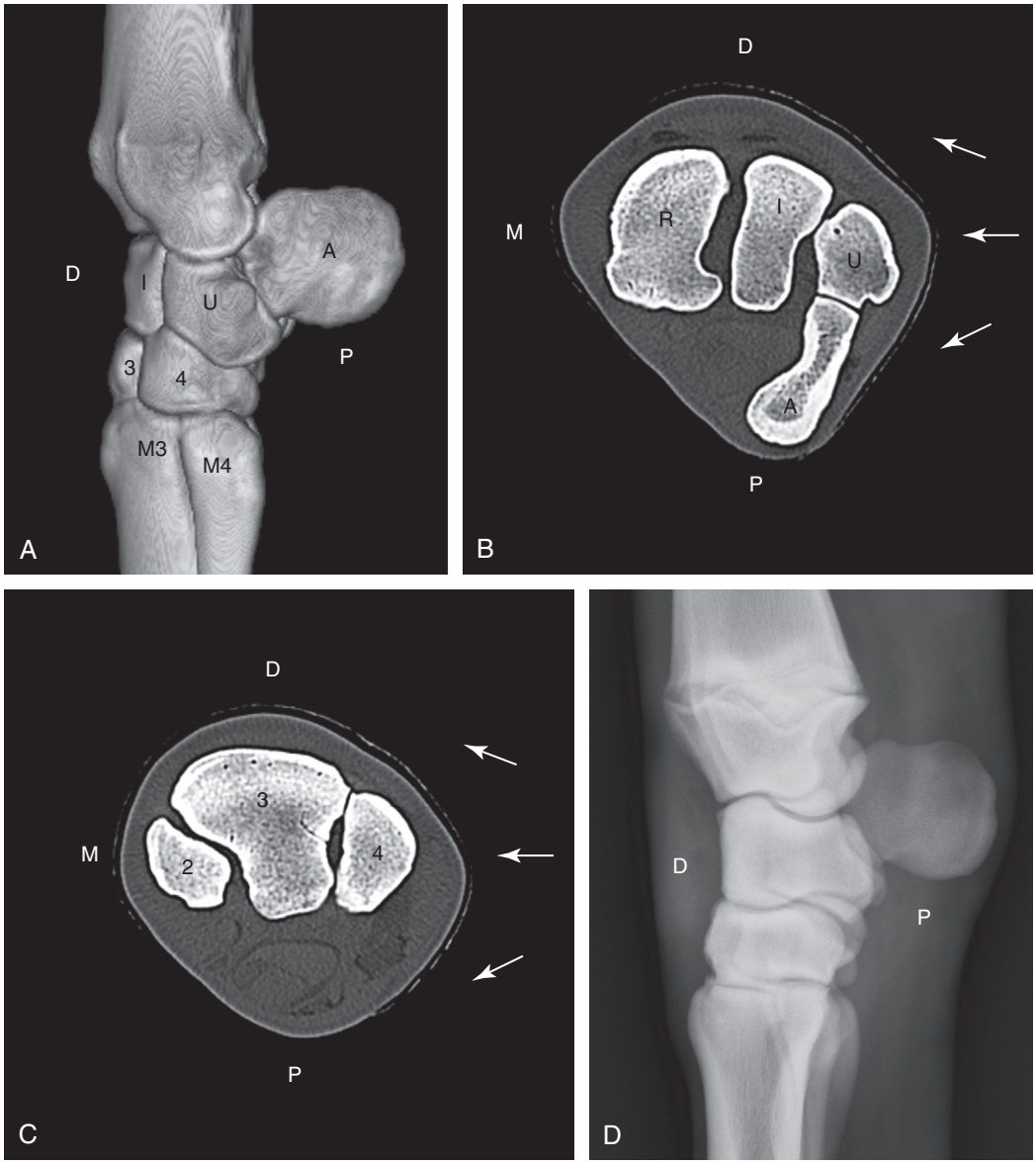


Fig. 14-3 Configuration for a lateromedial radiograph of the equine carpus. **A,** Volume-rendered CT image of an equine carpus from a lateral perspective. **B,** Transverse CT image of an equine carpus through the proximal row of carpal bones. **C,** Transverse CT image of an equine carpus through the distal row of carpal bones. **D,** Lateromedial equine carpal radiograph. In **B** and **C,** the *white arrows* indicate the direction of the primary x-ray beam. For a lateromedial projection, the x-ray beam strikes the lateral surface of the carpus. In a lateromedial radiograph, the dorsal and palmar edges of the carpus will be projected. *A*, Accessory carpal bone; *2*, second carpal bone; *3*, third carpal bone; *4*, fourth carpal bone; *D*, dorsal; *I*, intermediate carpal bone; *M*, medial; *M3*, third metatarsal bone; *M4*, fourth metatarsal bone; *P*, palmar; *R*, radial carpal bone; *U*, ulnar carpal bone.

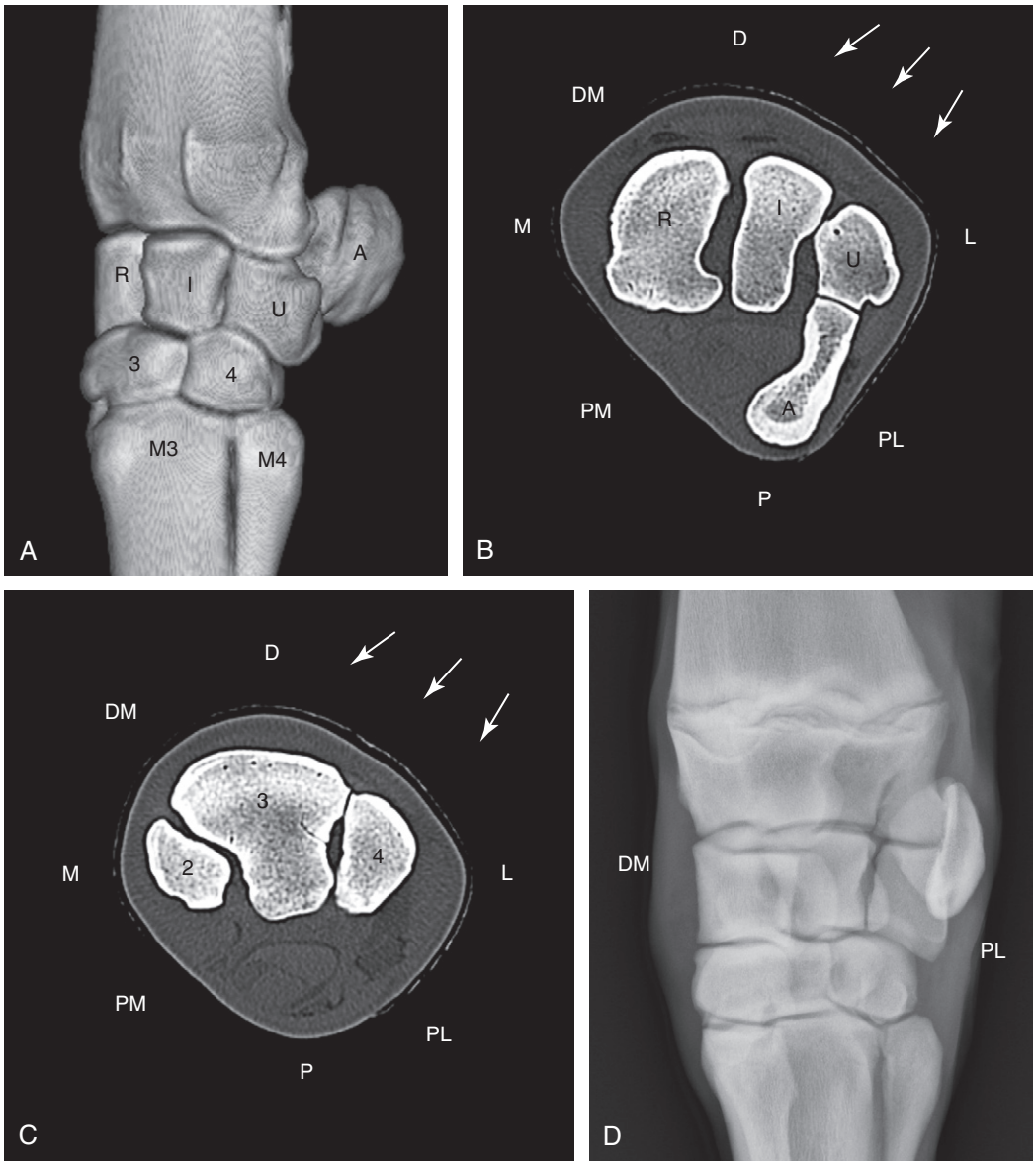


Fig. 14-4 Configuration for a dorsolateral-palmaromedial radiograph of the equine carpus. **A,** Volume-rendered CT image of an equine carpus from a dorsolateral perspective. **B,** Transverse CT image of an equine carpus through the proximal row of carpal bones. **C,** Transverse CT image of an equine carpus through the distal row of carpal bones. **D,** Dorsolateral-palmaromedial equine carpal radiograph. In **B** and **C,** the *white arrows* indicate the direction of the primary x-ray beam. For a dorsolateral-palmaromedial radiograph, the x-ray beam strikes the dorsolateral surface of the carpus, and the dorsomedial and palmarolateral edges of the carpus will be projected. *A*, Accessory carpal bone; *2*, second carpal bone; *3*, third carpal bone; *4*, fourth carpal bone; *D*, dorsal; *DM*, dorsomedial; *I*, intermediate carpal bone; *L*, lateral; *M*, medial; *M3*, third metatarsal bone; *M4*, fourth metatarsal bone; *P*, palmar; *PL*, palmarolateral; *PM*, palmaromedial; *R*, radial carpal bone; *U*, ulnar carpal bone.

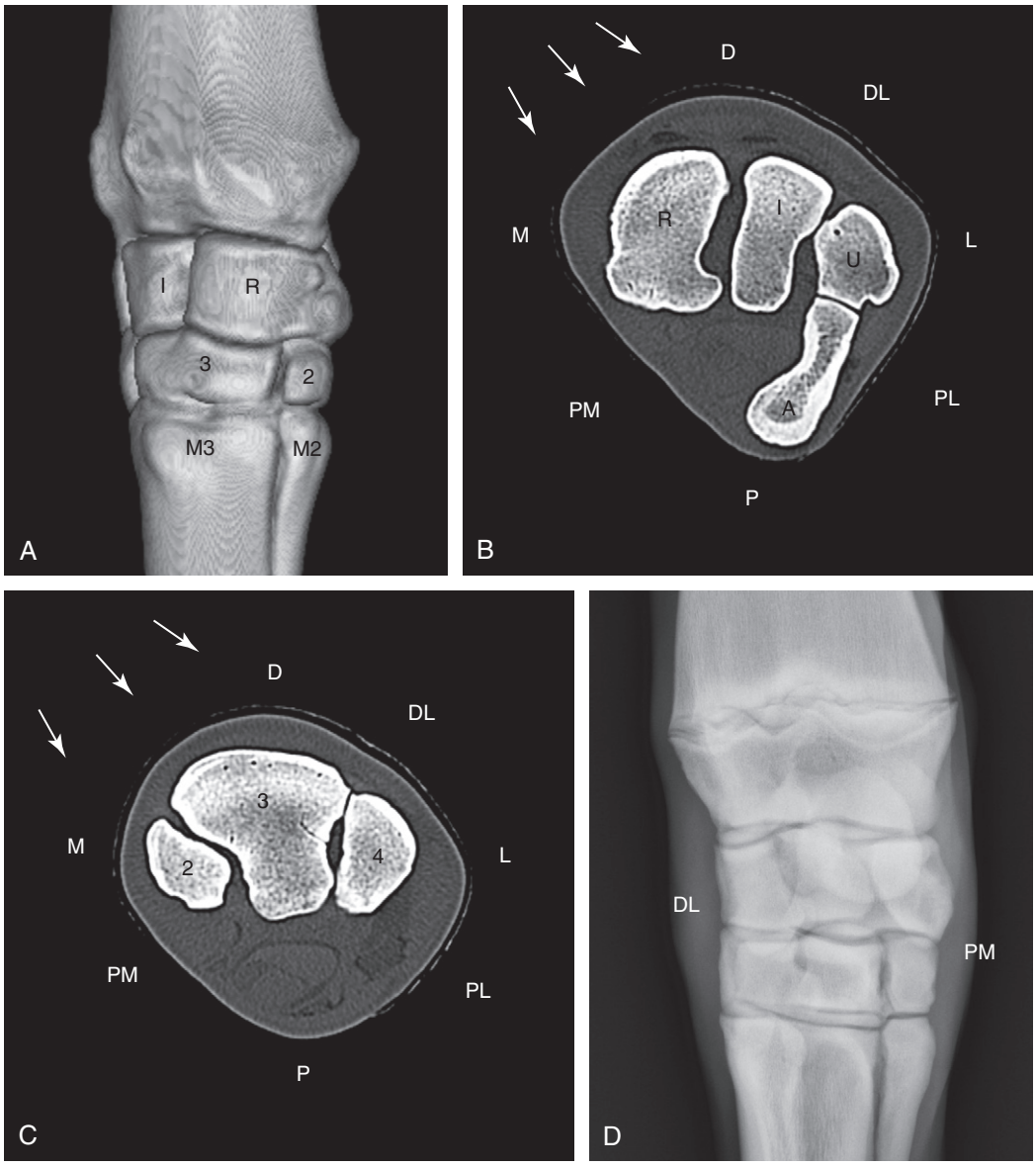


Fig. 14-5 Configuration for a dorsomedial-palmarolateral radiograph of the equine carpus. **A,** Volume-rendered CT image of an equine carpus from a dorsomedial perspective. **B,** Transverse CT image of an equine carpus through the proximal row of carpal bones. **C,** Transverse CT image of an equine carpus through the distal row of carpal bones. **D,** Dorsomedial-palmarolateral equine carpal radiograph. In **B** and **C,** the *white arrows* indicate the direction of the primary x-ray beam. For a dorsomedial-palmarolateral projection, the x-ray beam strikes the dorsomedial surface of the carpus, and the dorsolateral and palmaromedial edges of the carpus will be projected. *A,* Accessory carpal bone; *2,* second carpal bone; *3,* third carpal bone; *4,* fourth carpal bone; *D,* dorsal; *DL,* dorsolateral; *DM,* dorsomedial; *I,* intermediate carpal bone; *L,* lateral; *M,* medial; *M2,* second metatarsal bone; *M3,* third metatarsal bone; *P,* palmar; *PL,* palmarolateral; *PM,* palmaromedial; *R,* radial carpal bone; *U,* ulnar carpal bone.

Table • **14-1**

Summary of Edges Projected in Oblique Radiographs

PROJECTION	STRIKE POINT OF PRIMARY X-RAY BEAM	EDGES PROJECTED
Dorsopalmar	Dorsal	Lateral and Medial
Dorsoplantar	Dorsal	Lateral and Medial
Craniocaudal	Cranial	Lateral and Medial
Palmarodorsal	Palmar	Lateral and Medial
Plantarodorsal	Plantar	Lateral and Medial
Caudocranial	Caudal	Lateral and Medial
Lateromedial	Lateral	Dorsal and Palmar, or Dorsal and Plantar, or Cranial and Caudal
Mediolateral	Medial	Dorsal and Palmar, or Dorsal and Plantar, or Cranial and Caudal
Dorsolateral-Palmaromedial	Dorsolateral	Dorsomedial and Palmarolateral
Palmaromedial-Dorsolateral	Palmaromedial	Dorsomedial and Palmarolateral
Dorsolateral-Plantaromedial	Dorsolateral	Dorsomedial and Plantarolateral
Plantaromedial-Dorsolateral	Plantaromedial	Dorsomedial and Plantarolateral
Craniolateral-Caudomedial	Craniolateral	Craniomedial and Caudolateral
Caudomedial-Craniolateral	Caudomedial	Craniomedial and Caudolateral
Dorsomedial-Palmarolateral	Dorsomedial	Dorsolateral and Palmaromedial
Palmaromedial-Dorsomedial	Palmaromedial	Dorsolateral and Palmaromedial
Dorsomedial-Plantarolateral	Dorsomedial	Dorsolateral and Palmaromedial
Plantarolateral-Dorsomedial	Plantarolateral	Dorsolateral and Palmaromedial

dorsomedial and palmarolateral edges projected in an unobstructed fashion (see Fig. 14-4). The x-ray beam could also strike the palmaromedial surface with the same results.

In a dorsomedial-palmarolateral view of the carpus, the x-ray beam strikes the dorsomedial surface with the dorsolateral and palmaromedial edges projected in an unobstructed fashion (see Fig. 14-5). The x-ray beam could also strike the palmarolateral surface with the same results.

AGGRESSIVE VERSUS NONAGGRESSIVE BONE LESIONS

The principle of using roentgen signs to describe radiographic abnormalities was introduced in Chapter 5, and the roentgen sign method is applicable to describing radiographic lesions of the appendicular skeleton. However, in addition to describing a bone lesion according to changes in roentgen signs an important distinction is whether the bone lesion is caused by an aggressive process, such as a tumor or infection, or by a nonaggressive process such as a bone cyst. Making this distinction between an aggressive and nonaggressive bone lesion involves the consideration of factors other than the basic roentgen signs.

Assessing the aggressiveness of a bone lesion is important because, as already noted, the considerations are different for aggressive versus nonaggressive bone lesions. Also, determining that a bone lesion is aggressive assists in deciding the next diagnostic step to take with the patient. The aggressiveness of a bone lesion is related to three criteria: (1) whether or not there is destruction of the cortex, (2) the character of any periosteal reaction, and (3) the distinctness of the boundary between the bone lesion and the normal bone, called the *transition zone* (Table 14-2). Note that whether a lesion is primarily radiolucent (loss of bone) or sclerotic (production of bone) has no bearing on whether the lesion is aggressive.

Table • **14-2**

Features of Aggressive and Nonaggressive Bone Lesions*

LESION CLASS	CORTICAL DESTRUCTION	PERIOSTEAL REACTION	TRANSITION ZONE
Aggressive	Yes	Active (irregular)	Not distinct
Nonaggressive	None or expansion of cortex without destruction	None or smooth	Distinct

*The presence of any one feature of aggressiveness is sufficient to classify the lesion as such; it is not necessary for all three criteria of aggressiveness to be fulfilled.

Destruction of the Cortex

Many aggressive bone diseases are characterized by destruction of the cortex. For example, malignant bone tumors are often associated with destruction of the cortex, through mechanisms such as increased matrix metalloproteinase activity[2,3] or increased osteoclast activity.[4] Bone infections also can result in destruction of cortical bone, for example by an alteration in the inflammatory response that disrupts the homeostatic balance of bone matrix deposition and resorption, thereby mediating bone destruction.[5] For cortex destruction to be apparent radiographically, the region of destruction must be hit tangentially by the primary x-ray beam; in other words, the *edge* of the cortex destruction must be visible

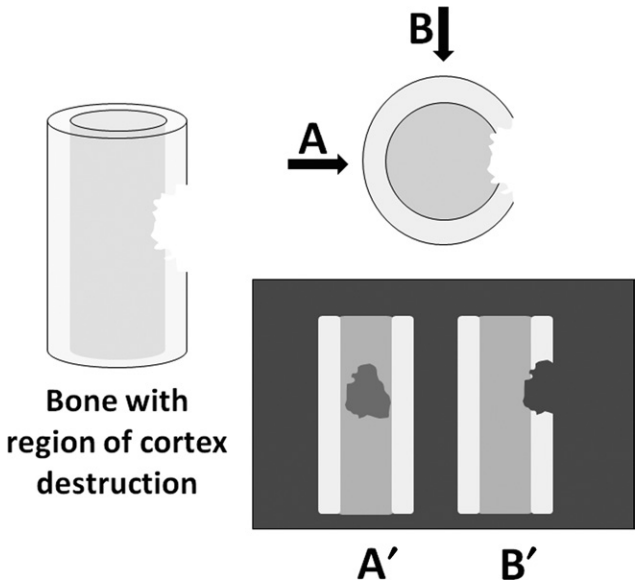


Fig. 14-6 Diagram illustrating the effect of x-ray beam orientation on conspicuity of cortical destruction. The drawing on the left shows a bone that has a region of cortical destruction. At the top right, the drawing is a transverse section of the bone through the region of cortical destruction. Two orientations of the primary x-ray beam are shown. In orientation **(A),** the x-ray beam strikes the region of cortical destruction *en face*. In orientation **(B),** the x-ray beam strikes the region of cortical destruction *tangentially*. At the bottom right is a diagram of the radiograph resulting from each orientation. In radiograph **A′,** the region of cortical destruction will appear as a region of decreased opacity in the medullary cavity, and the diagnosis of cortical destruction cannot be made. This same radiographic appearance would also be produced from a region of bone loss in the medullary cavity that was not characterized by cortex destruction. In radiograph **B′,** the region of cortex destruction is apparent because the affected edge of the bone has been struck tangentially by the primary x-ray beam.

radiographically (Figs. 14-6 through 14-8). If the cortex destruction is not projected tangentially, an important feature of aggressive bone lesions may not be detected. Whether the cortex destruction is projected tangentially depends on its position with respect to the primary x-ray beam (see Fig. 14-6).

An important distinction is that not all bone destruction leads to loss of cortex. Bone loss can be totally within the medullary cavity with preservation of the cortex. Purely medullary bone loss does not mean that the lesion is not aggressive; it means only that one feature of lesion aggressiveness (i.e., cortical destruction) is not present. As discussed later, finding only one of the three criteria of an aggressive lesion is all that is required to place the lesion into the aggressive category.

Some have suggested that an even more detailed classification of bone destruction into *geographic*, *moth-eaten*, and *permeative* patterns can aid in the characterization of lesion aggressiveness.[6] Geographic bone lysis is a large, relatively well-defined region of bone loss (Fig. 14-9). Moth-eaten bone lysis gets its name from the appearance of moth damage in cloth, and is characterized radiographically as multiple small regions of lysis that are less well defined than geographic lysis but more defined than permeative lysis (Fig. 14-10, see page 261). Permeative lysis is the least well-defined lytic pattern, where the bone lysis is confluent and not demarcated clearly from adjacent normal bone. (Fig. 14-11, see page 261). Permeative lysis could result from progression of a lesion that was originally characterized by moth-eaten lysis. Permeative lysis is the most common pattern of bone lysis that accompanies an aggressive bone lesion.

It has been suggested that geographic bone lysis is a less aggressive feature of bone disease than either moth-eaten or permeative lysis.[6] This sentiment is likely because of the common finding of large well-defined regions of bone loss with benign conditions such as an osseous cystlike lesion (Fig. 14-12, see page 262). However, geographic bone lysis is also a common feature of some malignant bone tumors, such as telangiectatic osteosarcoma in humans,[7] for example.

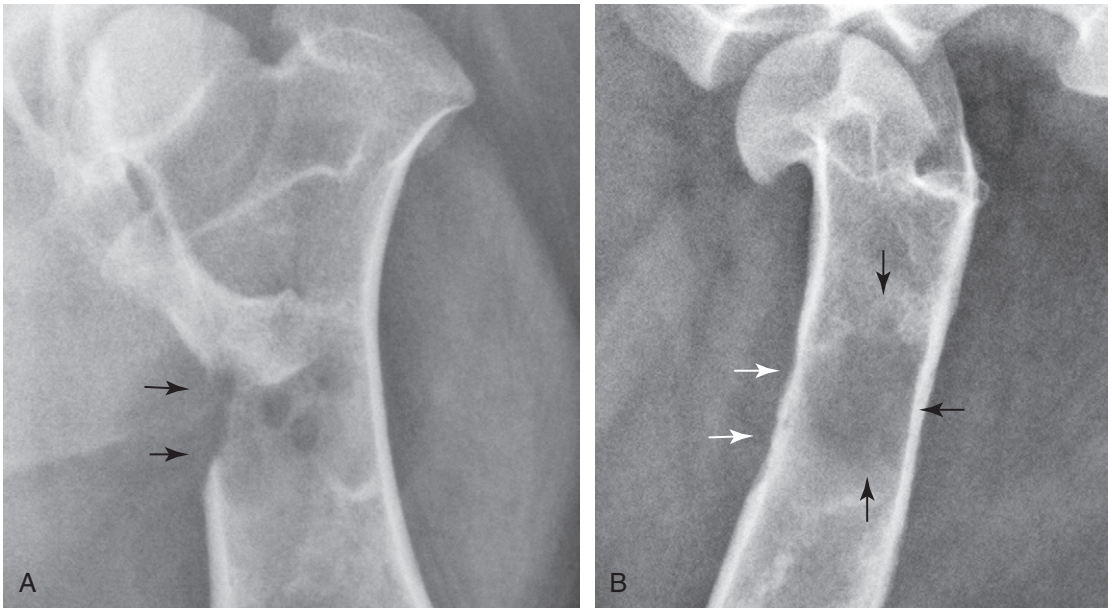


Fig. 14-7 Craniocaudal **(A)** and lateral **(B)** radiographs of the femur of a dog with metastatic carcinoma. In **A,** there is an obvious region of cortical destruction involving the proximal-medial aspect of the femur *(black arrows)*. In **B,** this region is superimposed on the medullary cavity *(black arrows)*, and the extent of cortex destruction is underestimated because the destruction is not projected in tangent. Some cortical irregularity is present in **B** *(white arrows)*, but without the craniocaudal view the extent of destruction would be underestimated.

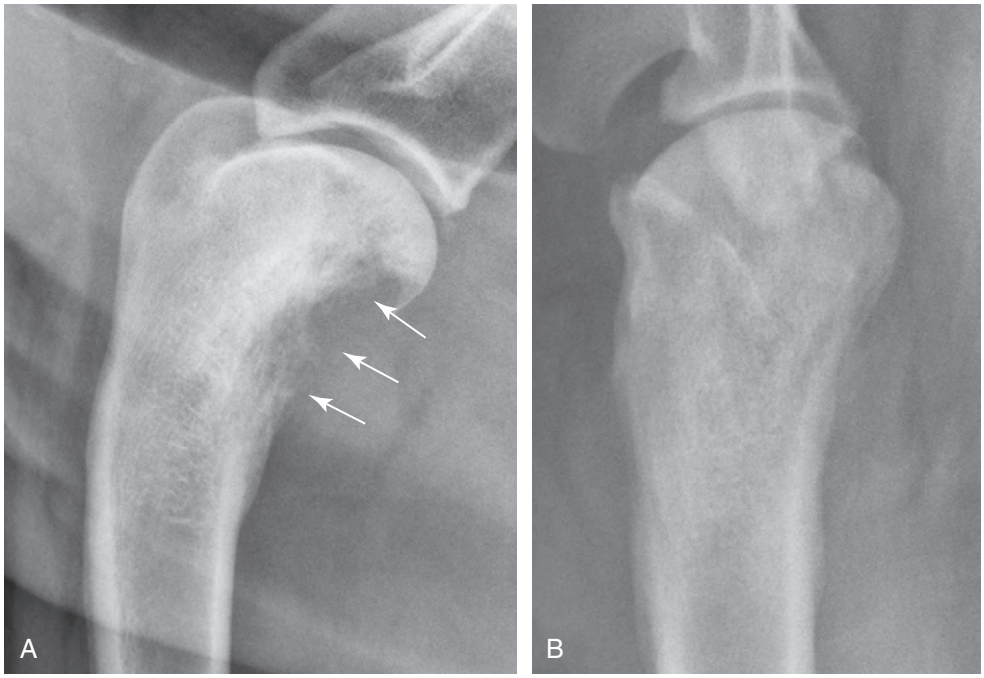


Fig. 14-8 Lateral **(A)** and caudocranial **(B)** views of the proximal aspect of the humerus of a dog with an osteosarcoma. In **A,** there is obvious destruction of the caudal aspect of the cortex in the proximal portion of the bone. In **B,** the bone does not appear normal, with there being periosteal reaction and a heterogeneous appearance to the medullary cavity, but the extent of cortical destruction is not evident, as when it was projected in tangent.

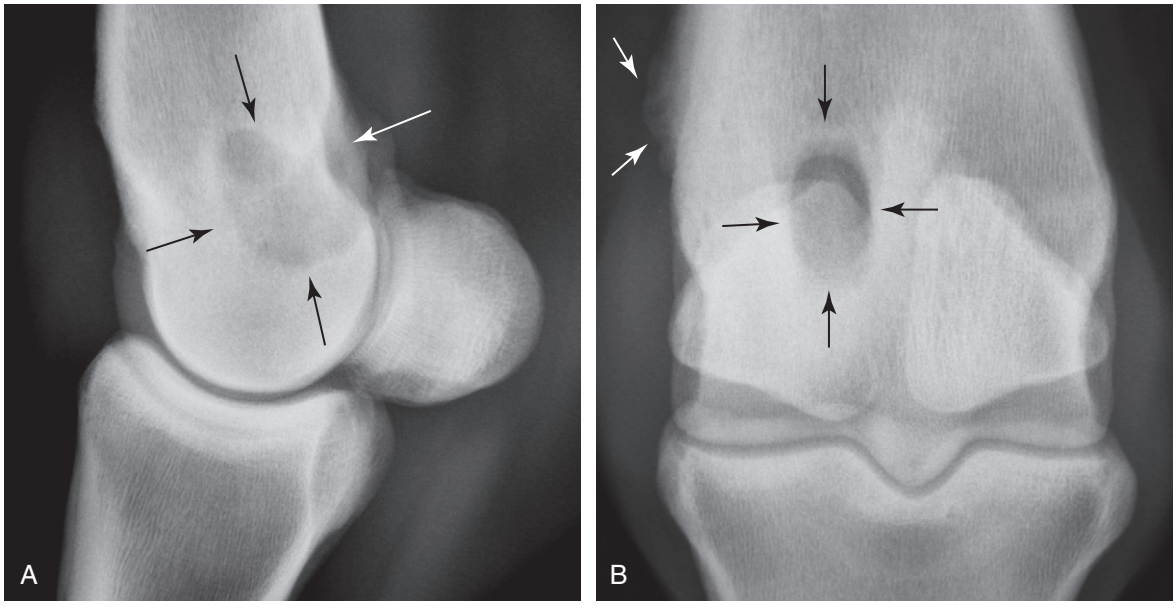


Fig. 14-9 Lateral **(A)** and dorsopalmar **(B)** radiographs of the distal metacarpus of a horse. There is a large region of decreased opacity in the palmarodistal aspect of the third metacarpal bone *(black arrows)*. This can be described as a large region of geographic bone lysis. The margins of this lesion are distinct (i.e., a well-defined transition zone), and the periosteal response on the edge of the bone (*white arrows* in **B**) is smooth. These are features of a nonaggressive bone lesion, and benign processes, such as a benign cartilage tumor or a bone cyst, could lead to this appearance. There is a tendency to associate geographic bone lysis with nonaggressive processes. However, the cortex in the palmarodistal aspect of the third metacarpal bone is absent (*white arrow* in **A**), meaning that an aggressive process cannot be ruled out. Thus, geographic lysis is not always an indicator of a nonaggressive process.

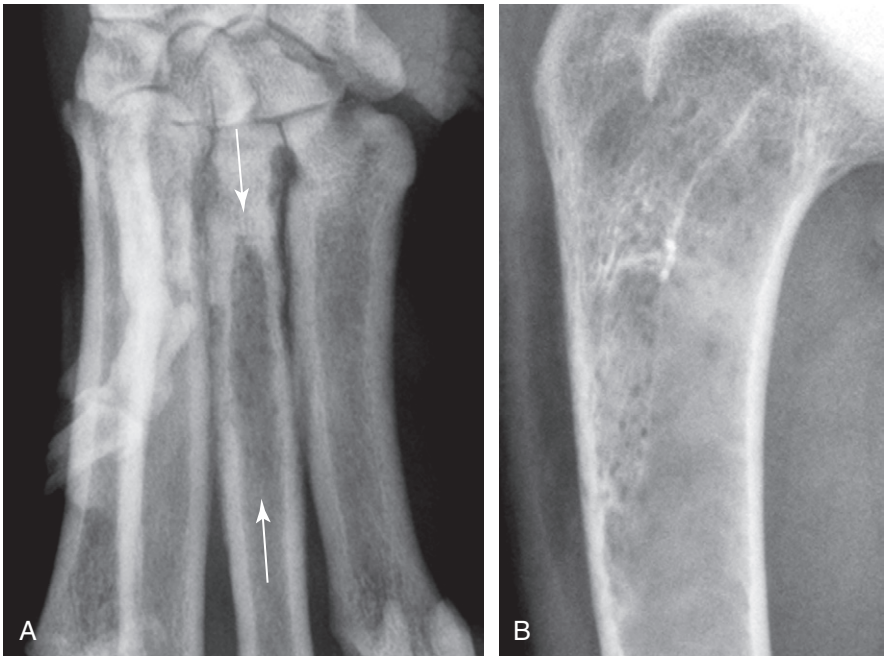


Fig. 14-10 Dorsolateral-palmaromedial radiograph of the metacarpus in a dog **(A)** and lateral radiograph of the proximal humerus in a dog **(B),** with each characterized by regions of moth-eaten lysis. In **A,** the moth-eaten lysis is the region between the two *white arrows* and is characterized by multiple punctate regions of lucency.

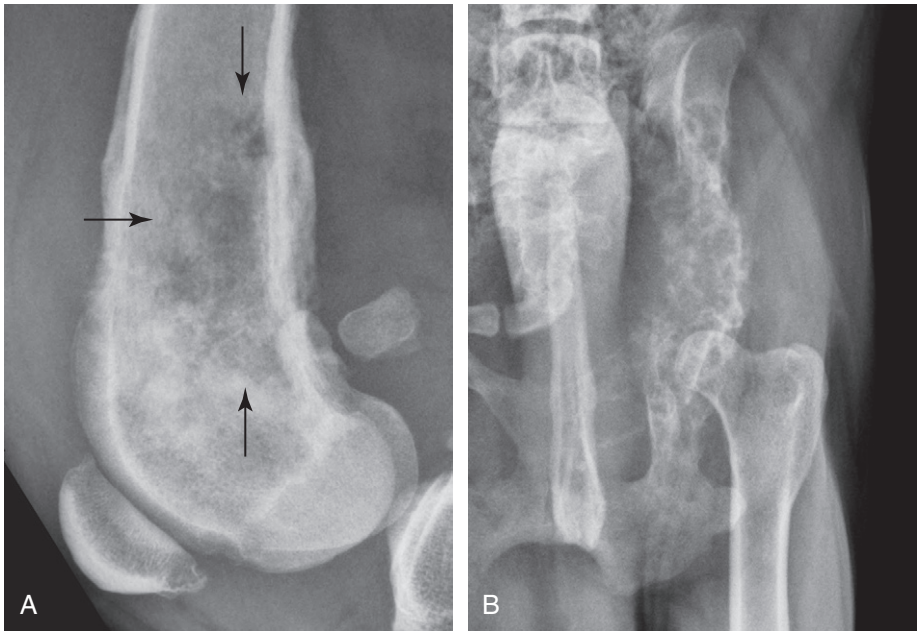


Fig. 14-11 Lateral radiograph of the distal femur in a dog **(A)** and ventrodorsal radiograph of the left hemipelvis of a dog **(B)** with each characterized by a large area of permeative lysis. In **A,** the region of permeative lysis is poorly defined *(black arrows)*. There is also a sclerotic component and a periosteal response. In **B,** the medial cortex of the ilium is also effaced (i.e., cortical destruction). Permeative lysis is characterized by coalescing regions of ill-defined bone destruction. Bone lesions characterized by permeative lysis are very likely to be the result of an aggressive process.

Therefore, if cortical destruction accompanies geographic lysis or if there are other signs of lesion aggressiveness, the lesion should be considered aggressive and potentially malignant or infected until proven otherwise. Rather than relying on the characterization of geographic versus permeative versus moth-eaten lysis, it is preferable to follow the basic guidelines for distinguishing nonaggressive from aggressive bone lesions based on cortical integrity and the character of the periosteal reaction and transition zone.

In a nonaggressive process, the cortex may be completely uninvolved, or it may be expanded without evidence of destruction. Lesions can appear serious in a radiograph, but without a sign of biologic aggressiveness they can be considered to be benign (Fig. 14-13). It is important not to jump to a conclusion about a bone lesion until it has been scrutinized carefully for radiographic signs of aggressiveness.

Periosteal Reaction

Many aggressive bone lesions are characterized by an active periosteal reaction. An active periosteal reaction is one where the margin of the periosteal reaction is *irregular* and not smooth. There are various degrees of periosteal reactivity and almost innumerable specific appearances of an active periosteal reaction. The presence of an irregular margin is the clue that the periosteal reaction is active. The finding of an irregular periosteal margin is more important than whether the periosteal reaction is speculated versus columnar, for example, because periosteal irregularity is the basic change that dictates the lesion is aggressive. Any evidence of periosteal irregularity is consistent with an aggressive bone lesion (Figs. 14-14 through 14-16). As might be expected, a nonaggressive periosteal reaction is characterized by a smooth edge to the periosteal new bone growth (Figs. 14-17 and 14-18, page 263).

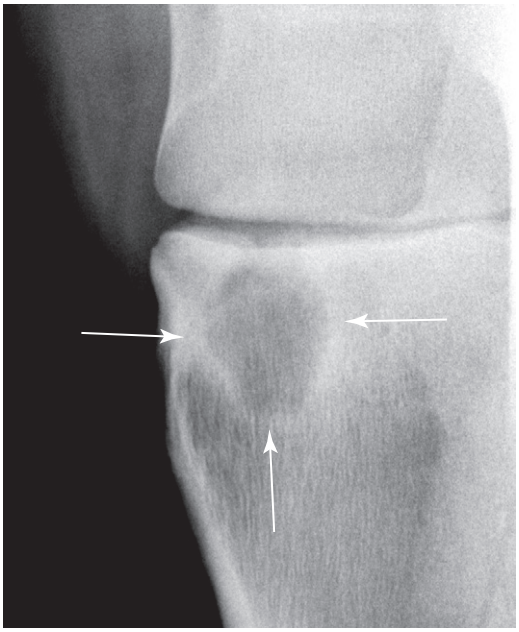


Fig. 14-12 Caudocranial radiograph of an equine elbow. There is a large region of geographic lysis in the proximal-medial aspect of the radius *(white arrows)*. In this patient, the geographic lysis was caused by an osseous cystlike lesion. Because of the common finding of geographic lysis in benign bone lesions, there may be a tendency to think that all lesions with geographic lysis are benign, but this is not true.

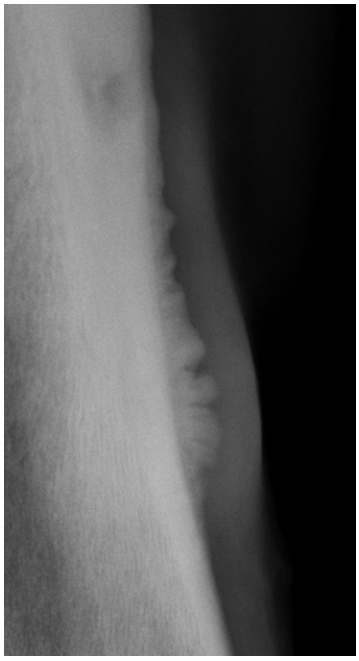


Fig. 14-14 An active periosteal reaction on the palmarodistomedial aspect of the radius of a horse with a nondisplaced fracture; the fracture line is not visible in this image. It would be easy to make the incorrect assessment that this is callus associated with the fracture. However, this periosteal new bone margin is irregular and thus active. It also has a columnar appearance. The significance of a columnar-appearing periosteal reaction is discussed in Chapter 17. Osteomyelitis was confirmed in this patient.



Fig. 14-13 Craniocaudal radiograph of the antebrachium of a dog with a nonaggressive lesion in the ulna. This lesion has caused expansion of the cortex, but there is no evidence of cortex destruction, and the edges of the bone are smooth; that is, there is no active periosteal reaction. Also, the demarcation between abnormal and normal bone, the transition zone, is distinct in this dog *(black arrows)*. The chance of this lesion being caused by a malignant tumor or by an infection is extremely low.

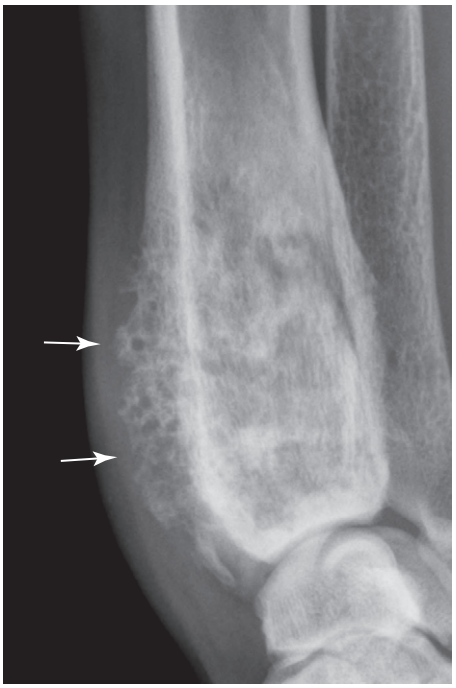


Fig. 14-15 Lateral radiograph of the distal antebrachium of a dog with a distal radial osteosarcoma. There is an active periosteal reaction on the craniodistal aspect of the radius *(white arrows)*. The periosteal reaction is active because the margin is irregular. The transition zone between the proximal end of the lesion and normal bone in the radius is poorly defined. These are features of an aggressive bone lesion.

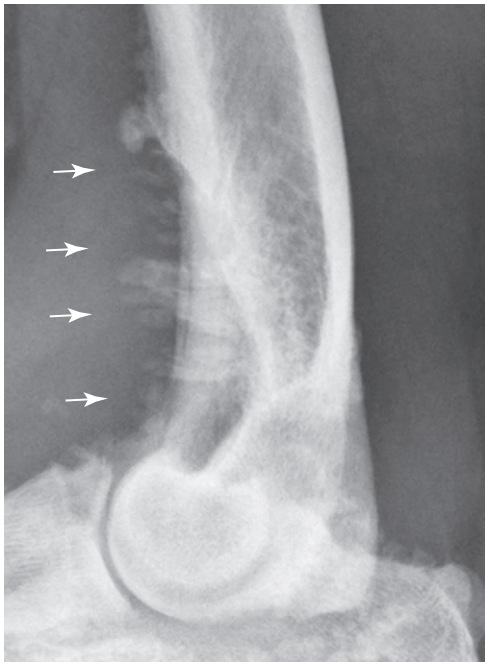


Fig. 14-16 Lateral radiograph of the distal humerus of a dog with an osteosarcoma. There is a speculated to columnar periosteal reaction on the cranial surface of the bone *(white arrows)*.

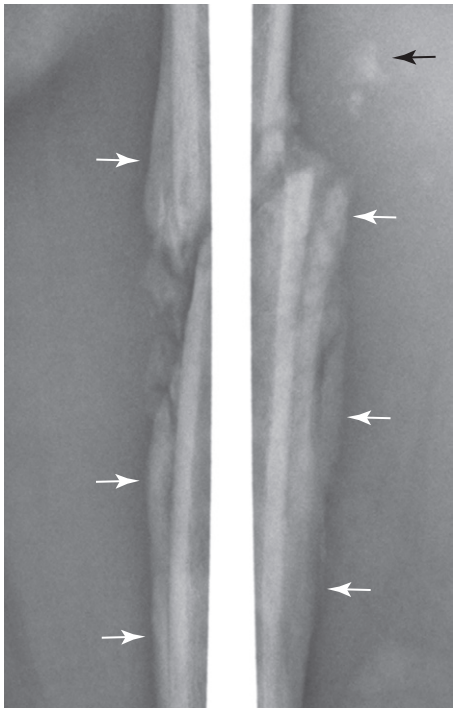


Fig. 14-17 Lateral radiograph of the mid-diaphysis of the femur of a dog with internal fixation of a midshaft fracture using an intramedullary pin. There is extensive periosteal reaction *(white arrows)* because of the fracture and also likely because of subperiosteal hemorrhage, but the margin of the periosteal reaction is smooth, and there is no indication of an aggressive process in this bone. The focus of soft tissue calcification *(black arrow)* is caused by mineralization of a hematoma and is not part of the periosteal reaction.



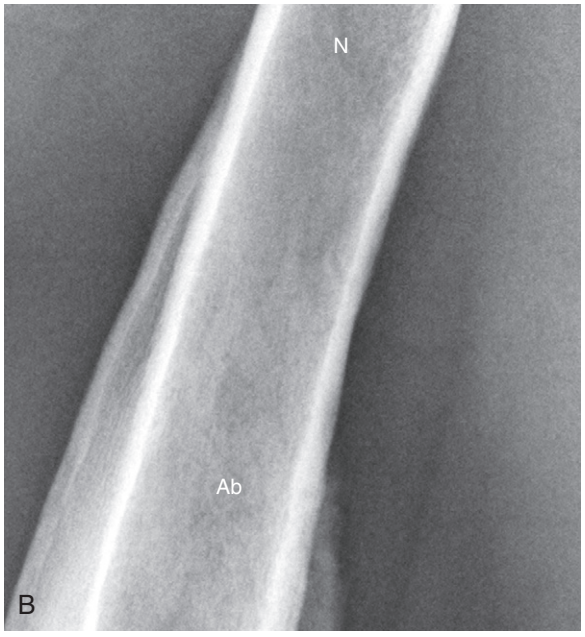


Fig. 14-18 **A,** Lateral radiograph of the femur of a dog with a femoral osteosarcoma. The periosteal reaction associated with this tumor is very smooth. The lesion is characterized as aggressive because of the lack of a defined transition zone in the medullary cavity between the normal and the abnormal bone. **B,** is a close-up view of the transition region. At *Ab* the medullary cavity is clearly abnormal, with a moth-eaten to permeative pattern of lysis, and at *N* the medullary cavity is clearly normal. However, the transition point between *Ab* and *N* is not distinct.

The finding of a smooth periosteal reaction does not mean that the lesion is not aggressive because there may be another sign of aggressiveness and that would place the lesion into the aggressive category. Thus, a lesion with a smooth periosteal reaction but an indistinct transition zone will still be considered aggressive (see Fig. 14-18).

Transition Zone

The character of the junction of the bone lesion with the adjacent normal bone is termed the *transition zone*. The transition zone is typically evaluated in the medullary cavity of the bone, and its character is a clue as to the aggressiveness of the

lesion. The host bone is more able to contain a less aggressive bone lesion, and in this instance the transition zone between the lesion and the host bone will be easy to define radiographically (Fig. 14-19; see Fig. 14-13). In aggressive bone lesions, the host bone is usually unable to contain the lesion, and there is no demarcation, or incomplete poorly defined demarcation, between the lesion and the host bone (Fig. 14-20; see Fig. 14-18). There are some bone lesions where the transition zone concept does not apply. One example would be an infected fracture. The medullary cavity has been disrupted by the original fracture, and singling out the effect of the infection versus the fracture on the appearance of the medulla is usually not possible.

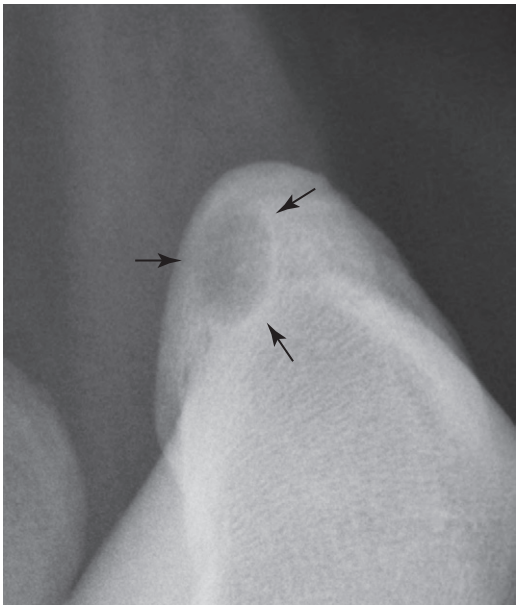


Fig. 14-19 Close-up view of an equine calcaneus from a dorsolateral-plantaromedial radiograph. There is a well-defined region of bone loss in the calcaneus. The edge of the lesion is sharply defined *(black arrows)*. This signifies sharp demarcation of the transition zone. There are no other signs of aggressiveness—that is, no evidence of cortex destruction and no evidence of a periosteal reaction.



Fig. 14-20 Lateral radiograph of the distal femur of a dog with an osteosarcoma. As one evaluates the proximal extent of the lesion, it is impossible to identify the point at which the abnormal bone ends and the normal bone begins. This is an indistinct transition zone because the host bone is incapable of containing the primary lesion.

Consequences of an Aggressive Lesion

As mentioned earlier, it is not necessary for a lesion to have all three features of radiographic aggressiveness (cortical destruction, active periosteal reaction, and an indistinct transition zone) to be characterized as aggressive. Any single criterion is sufficient. Moreover, the combined radiographic features of the aggressiveness of a bone lesion are a continuum from a minor alteration in cortex integrity, periosteal response, or transition zone appearance, to major alterations in all three parameters. Importantly, there is not a clinically applicable correlation between the number of aggressive features of a lesion or the extent of their aggressiveness and the biologic behavior of the lesion. In other words, low radiographic aggressiveness does not mean low biologic aggressiveness. But, importantly, the absence of radiographic evidence of aggressiveness usually means no biologic aggressiveness. Finally, as already mentioned, the categorization of aggressiveness does not take into account whether the lesion is primarily productive or primarily destructive, only the integrity of the cortex and the character of the periosteal response and transition zone.

Determining whether a bone lesion is aggressive will be helpful in directing patient management. It is reasonable to observe nonaggressive bone lesions over time to determine their course. Conversely, if a feature of aggressiveness is found, the main considerations are neoplastic and septic etiologies. In this instance, observing the lesion can jeopardize the patient. Identification of an aggressive bone lesion should prompt consideration of thoracic radiography and biologic sampling of the lesion for histopathologic and possibly microbiologic examinations.

Incidental Factors

As in the axial skeleton, the most influential incidental factors associated with appendicular radiography in the dog and cat are breed variation and common congenital anomalies. There are fewer incidental factors that influence the appearance of equine appendicular radiographs. The extent of the normal variation and anomalies that may be encountered in the appendicular skeleton of dogs and cats is great, and they cannot be covered adequately here. Comprehensive references are available.[1] The concept of radiographing the contralateral limb for comparative purposes when a questionable finding is encountered is valuable (Fig. 14-21).

Interpretation Paradigm

An organized approach to radiographic interpretation of the appendicular skeleton is needed, as is the case for all body systems. Also similar to other body regions, assessing whether there is an abnormality in the appendicular radiographs should be the *last* step in the interpretive process. The following questions should always be considered first.

- Are the radiographic views adequate, and are all of the views that are needed present? If all of the necessary views are not present, what is likely to be missed, and what additional views would help? Are oblique or other ancillary views needed?
- Do the views available correspond to the clinical localization of the lesion?
- Is the positioning adequate, or are there positioning problems that will interfere with interpretation?
- Is the radiographic technique adequate, or are the images overexposed or underexposed?

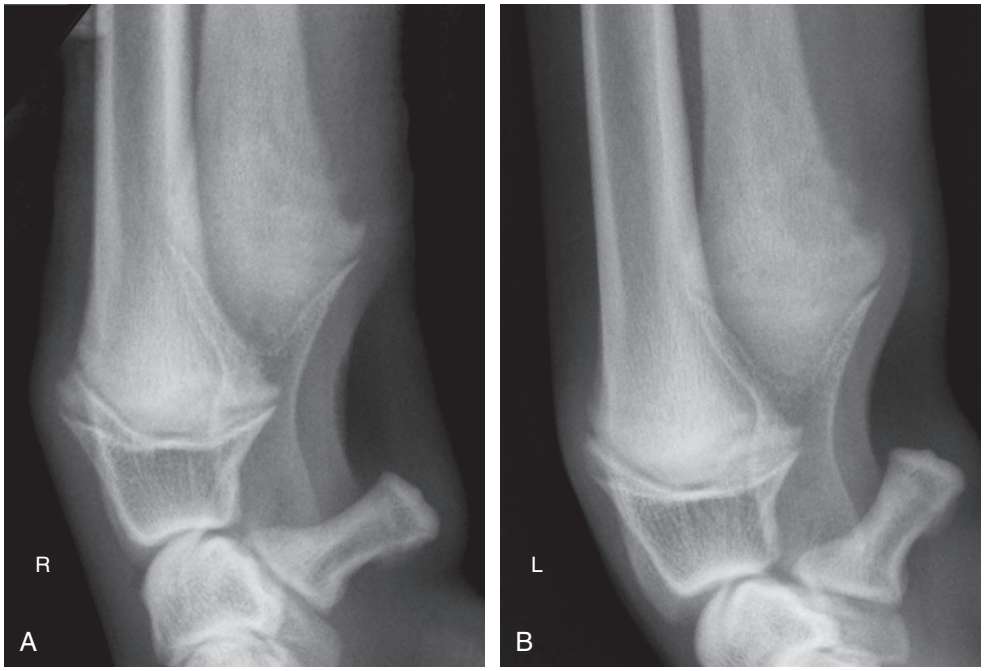


Fig. 14-21 Lateral radiograph **(A)** of the right distal antebrachium of a 5-month-old Irish setter with a right forelimb lameness and pain on carpal palpation. There is an irregular permeative appearance to the distal ulna, especially caudally. It would be easy to misinterpret this as an aggressive lesion, but this is the normal cutback zone because of remodeling of the distal ulna as it elongates. If one does not remember that this is a normal finding in young, rapidly growing dogs, radiographing the contralateral left carpal region **(B)** and finding the same appearance lessens the chance that this is a significant lesion.

- Has a grid been used, and how does this affect the quality of the image? Is there excessive scattered radiation? Are there grid lines?
- Has sedation or anesthesia been used? If not, how will this affect the utility of the radiographs?
- What is the species and breed of the patient, and how is this going to affect the appearance of the images?
- Were the images acquired with a vertically directed x-ray beam with the cassette in an x-ray table, or on the floor for an anesthetized horse? Was a horizontally directed x-ray beam used with handholding of the cassette or a wall-mounted cassette holder?
- Was the cassette held by hand? Is there motion artifact?
- Are the images film-based or digital? If the images are film-based, was the radiographic technique a high-contrast or a low-contrast technique?
- Has the joint above and below the location of a suspected bone lesion been included in the imaging study?
- Will radiographs of the contralateral limb be helpful?
- If dealing with film images, is a hot light needed to assess the soft tissues and the edge of the bones?
- What congenital anomalies are present that alter the normal appearance of the bone but may not be clinically significant?

Only after all of these things have been considered should one's attention be directed at the identification of abnormalities. As mentioned before, in addition to characterizing a bone lesion according to roentgen signs, considering whether it is aggressive or nonaggressive is necessary, and this step must not be overlooked for any bone lesion.

Unfortunately, bone is very limited in its response to injury. There will be either more or less bone than normal, a periosteal response will be either present or not, and the soft tissues will be either involved or not. Thus, the distribution within the skeleton and the assessment of the patient signalment become extremely important factors in formulating a reasonable differential diagnosis and for formulating a plan (Table 14-3). Regardless, especially for aggressive bone lesions, cytologic and/or microbiologic testing of a tissue sample, from bone or other involved tissue, will be needed for definitive diagnosis.

In many patients, the answer to the clinical question will not be found in the appendicular radiographs. As in the axial skeleton, the staging of disease involving the appendicular skeleton is more accurate when based on CT or MRI than on radiographs. This relates to the tomographic nature of CT and MRI and also to the superior soft tissue contrast resolution of MRI. Enhanced contrast resolution can be highly informative with regard to the detection of bone, cartilage, and soft tissue lesions that are not apparent radiographically. This is especially applicable in the horse, where MRI has revolutionized the characterization of lesions involving the deep digital flexor tendon within the hoof capsule.[8] Other than the equine digit, areas where musculoskeletal MRI has proven value are the equine metacarpo(tarso)phalangeal joint, equine proximal metacarpal(tarsal) region, canine stifle for assessment of cruciate ligament and meniscal lesions, and canine shoulder for assessment of lesions of the biceps and supraspinatus tendons.

Experienced radiologists may have a random search pattern, but it is recommended that beginning radiologists develop an organized approach to searching radiographs for abnormalities.[9] Each bone should be scrutinized in its entirety, and the image evaluated with a hot light (analog image) or contrast and brightness adjusted to the extremes (digital image) so that small changes in contour, periosteal response, and soft tissue involvement will not be overlooked. The following parameters can be evaluated in order: (1) number of bones involved; (2) the region of bones involved, for example, diaphysis versus metaphysis versus epiphysis, or a combination; (3) whether or not long bones or joints alone are involved or if bones *and*

Table • **14-3**

Summary of Selected Orthopedic Diseases in Small Animals by Skeletal Distribution and Patient Demographics*

DISEASE	MONOSTOTIC OR POLYOSTOTIC	LOCATION IN BONE	DEMOGRAPHICS
Primary bone cancer	Monostotic	Metaphyseal	Older patients
Metastatic bone cancer	Polyostotic	Metaphyseal or diaphyseal	Older patients
Mycotic osteomyelitis	Polyostotic	Metaphyseal	Middle-aged patients
Bacterial osteomyelitis—hematogenous	Polyostotic	Metaphyseal or diaphyseal	Young patients
Bacterial osteomyelitis—traumatic	Monostotic	Anywhere	Variable
Metabolic bone disease	Polyostotic	Metaphyseal or epiphyseal	Young patients
Panosteitis	Polyostotic	Diaphyseal	Young patients
Hypertrophic osteodystrophy (HOD)	Polyostotic	Metaphyseal	Young patients
Osteochondrosis	Polyostotic	Epiphyseal	Young patients
Hypertrophic osteopathy (HO, HPO, HPOA)	Polyostotic	Epiphyseal and metaphyseal then diaphyseal	Older patients

*These data are generalizations and will not apply to all patients.

joints are involved; (4) the overall opacity of the skeleton; (5) the relative appearance of the cortical bone versus medullary bone; (6) the presence or absence of a periosteal reaction, and whether it is irregular or not; (7) integrity of the cortex; (8) the shape of the bones compared with what would be expected in a comparable normal animal; (9) the character of the transition zone; and finally, (10) character of adjacent soft tissues. If the same procedure is followed for every patient, the order of searching will become second nature, and as experience is gained, the search pattern will become random without a loss of effectiveness. Until then, it may be beneficial for a checklist to be developed to make sure that every anatomic region of the radiograph is examined.

In addition to having an organized search pattern, it is also helpful to scrutinize appendicular radiographs with a preconception of what disease might be found in a particular region in a particular patient. This is particularly true in young canine and feline patients, where developmental and juvenile bone diseases are often characterized by very specific findings. Examples are close examination of the (1) proximal margin of the anconeal process in dogs at risk of having fragmented medial coronoid process, (2) proximal margin of the lateral ridge of the talus in dogs at risk for tarsal osteochondrosis, and (3) distal radial and ulnar physes in young dogs at risk for hypertrophic osteodystrophy. It is critical that this focused approach be used only as an ancillary method; it is a way of double checking, so to speak, that all possibilities have been addressed. Assessing radiographs with only a preconceived idea of what will be present will certainly lead to overlooked lesions and missed diagnoses.

REFERENCES

1. Thrall D, Robertson I: *Atlas of normal radiographic anatomy and anatomic variants in the dog and cat*, St. Louis, 2011, Saunders.
2. Ferrari C, Benassi S, Ponticelli F, et al: Role of MMP-9 and its tissue inhibitor TIMP-1 in human osteosarcoma: findings in 42 patients followed for 1–16 years, *Acta Orthop Scand* 75:487, 2004.
3. Uchibori M, Nishida Y, Nagasaka T, et al: Increased expression of membrane-type matrix metalloproteinase-1 is correlated with poor prognosis in patients with osteosarcoma, *Int J Oncol* 28:33, 2006.
4. Avnet S, Longhi A, Salerno M, et al: Increased osteoclast activity is associated with aggressiveness of osteosarcoma, *Int J Oncol* 33:1231, 2008.
5. Wright JA, Nair SP: Interaction of staphylococci with bone, *Int J Med Microbiol* 300:193, 2010.
6. O'Donnell P: Evaluation of focal bone lesions: basic principles and clinical scenarios, *Imaging* 15:298, 2003.
7. Murphey MD, wan Jaovisidha S, Temple HT, et al: Telangiectatic osteosarcoma: radiologic-pathologic comparison, *Radiology* 229:545, 2003.
8. Blunden A, Murray R, Dyson S: Lesions of the deep digital flexor tendon in the digit: a correlative MRI and post mortem study in control and lame horses, *Equine Vet J* 41:25, 2009.
9. Halvorsen JG, Swanson D: Interpreting office radiographs. A guide to systematic evaluation, *J Fam Pract* 31:602, 1990.

ELECTRONIC RESOURCES

evolve

Additional information related to the content in Chapter 14 can be found on the companion Evolve website at http://evolve.elsevier.com/Thrall/vetrad/

- Chapter Quiz

CHAPTER • 15

Orthopedic Diseases of Young and Growing Dogs and Cats

Rachel E. Pollard
Erik R. Wisner

The radiographic aspects of developmental skeletal disease are as varied as the causes of the disorders themselves. Box 15-1 lists some common and uncommon disorders of the immature skeleton. It is intended to provide some structure to this chapter and should not be considered a definitive classification scheme.

Developmental lesions may be solitary and localized but are often multifocal or generalized. Localized lesions, such as those seen with osteochondrosis, are often bilateral. Lesion location can be predicted on the basis of the characteristic anatomic distribution of many of these diseases. Although radiographic features of the various developmental skeletal diseases vary widely, they generally appear nonaggressive.

Degenerative joint disease is a common sequel to developmental disorders of the immature skeleton, particularly when the primary lesion involves joints or produces limb deformity. Often the most pronounced radiographic findings are those of the degenerative changes, which can mask the original developmental lesion. To reach an accurate radiographic diagnosis, differentiation of the cause (developmental lesion) from the effect (degenerative lesion) is important whenever possible.

DISORDERS PRIMARILY AFFECTING JOINTS

Osteochondrosis and Osteochondritis Dissecans

Osteochondrosis is a common cause of lameness in young, rapidly growing, large-breed dogs. Clinical signs usually develop between 6 and 9 months of age. Osteochondrosis occurs from epiphyseal cartilage necrosis, resulting in a failure of normal endochondral ossification.[1] If the vascular bed of the adjacent subchondral bone can envelop and bypass the region of cartilage necrosis, endochondral ossification may resume without development of a clinical lesion. Otherwise, progressive chondromalacia leads to development of clefts or fissures extending from the surface of the cartilage to the subchondral bone. When a chondral or osteochondral fragment separates from adjacent subchondral bone, the disorder should technically be referred to as *osteochondritis dissecans*.[1] However, in most patients, determination of whether a cartilage fragment exists is impossible from survey radiographs; thus *osteochondrosis* is an acceptable term.

In dogs, osteochondrosis occurs in specific anatomic locations and often involves weight-bearing articular surfaces. It occurs most frequently in the caudal aspect of the proximal humeral head (Fig. 15-1) but also occurs in the distomedial aspect of the humeral trochlea (Fig. 15-2, p. 270), the lateral and medial femoral condyles (Fig. 15-3, see page 270), the femoral trochlea, and the medial and lateral trochlear ridges of the talus (Fig. 15-4, see page 270).[2-9] Osteochondrosis is frequently bilateral, but affected animals may have clinical signs in one limb only. Large subchondral defects are frequently associated with the presence of separate osteochondral fragments, which tend to increase the severity of clinical signs.[10]

Radiographic Signs

Typical radiographic findings of osteochondrosis include flattening or concavity of the affected subchondral bone surface with surrounding subchondral bone sclerosis. This may result in nonuniformity and apparent widening of the joint space. When mineralized, a cartilage flap is sometimes seen within the subchondral defect, and separate osteochondral fragments (joint mice) may migrate within the joint space. Fragments that have migrated often adhere to the synovial lining and may become vascularized and continue to mineralize and enlarge over time. Joint effusion, or joint-capsule thickening, may appear as a localized region of soft tissue swelling centered on the affected joint. A subchondral bone defect is occasionally seen involving the articular surface opposite the primary lesion. These defects are called *kissing lesions*. Degenerative joint disease is a common sequel to osteochondrosis.

Gas is occasionally present within the joint space of dogs with shoulder osteochondrosis. This finding is referred to as the *vacuum phenomenon* and is caused by the intraarticular accumulation of nitrogen gas from negative pressure induced by traction on the joint during positioning (see Fig. 18-10).

With osteochondrosis of the lateral trochlea of the talus, the superimposed calcaneus may obscure the lesion in the dorsoplantar view. In this instance, a dorsolateral-plantaromedial oblique, or a flexed dorsoplantar, view can be acquired to provide an unobstructed view of the lesion. Similarly, supinated projections of the shoulder may help with visualization of lesions on the caudal aspect of the humeral head. In the stifle, the fossa for the origin of the long digital extensor muscle is sometimes mistaken for a lateral femoral condyle osteochondrosis lesion because it is superimposed on the dorsolateral aspect of the condyle on both the lateromedial and the caudocranial views.

Cartilage flaps are not visible on survey radiographs unless calcification or ossification of the fragment has occurred. When a nonmineralized cartilage fragment is present, an arthrogram can be used to outline the flap if contrast medium dissects between the fragment and the underlying

Box • 15-1

Disorders of the Immature Appendicular Skeleton

Disorders Primarily Affecting Joints
- Osteochondrosis, osteochondritis dissecans
- Elbow dysplasia
  - Ununited coronoid process
  - Fragmented medial coronoid process
  - Osteochondrosis of the medial humeral condyle
- Hip dysplasia
  - Aseptic necrosis of the femoral head (Legg-Calvé-Perthes disease)

Disorders Primarily Affecting Bone
- Malformation or agenesis of single or multiple bones
  - Amelia, hemimelia
  - Ectrodactyly, polydactyly
  - Syndactyly
- Skeletal disorders of unknown cause
  - Panosteitis
  - Hypertrophic osteodystrophy
- Metabolic and other generalized disorders
  - Nutritional secondary hyperparathyroidism
  - Congenital hypothyroidism
  - Pituitary dwarfism
  - Mucopolysaccharidosis
  - Osteogenesis imperfecta
  - Osteopetrosis
- Metaphyseal and epiphyseal dysplasias
  - Osteochondrodysplasias
  - Chondrodysplasia: Alaskan malamute, Norwegian elkhound, cocker spaniel, English pointer, Great Pyrenees
  - Oculoskeletal dysplasia: Labrador retriever, Samoyed
  - Osteochondral dysplasia: Scottish Fold cats, Scottish deerhounds, bull terriers
  - Hypochondroplasia: Irish setters
  - Multiple epiphyseal dysplasia: beagles
  - Multiple cartilaginous exostoses
  - Retained cartilage cores
  - Incomplete ossification of the humeral condyle: spaniels, other breeds

subchondral bone. Arthrography may also define migrating intraarticular cartilage fragments (see Fig. 15-1, C).[11,12] Newer nonionic and low-osmolar contrast media provide significantly better arthrographic quality than hyperosmolar, ionic contrast media because the contrast medium is not diluted as quickly from fluid flux into the joint space.[13] However, because arthroscopy has gained acceptance for the diagnosis and definitive treatment of osteochondrosis, arthrography is now used less commonly.[14,15]

Elbow Dysplasia

Elbow dysplasia is a nonspecific term referring to a triad of developmental lesions that include ununited anconeal process, fragmented medial coronoid process of the ulna, and osteochondrosis of the distomedial aspect of the humeral trochlea. Although osteochondrosis has previously been implicated as the cause of all three disorders, asynchronous growth of the radius and ulna and proximal ulnar dysplasia resulting in an elliptically shaped ulnar notch have more recently been suggested as implicating factors.[3,16-20] Elbow joint incongruity may result in nonuniform contact of articulating surfaces, leading to nonunion of the anconeal process or separation or fragmentation of the medial coronoid process.[19,21] Although severe incongruity can be seen radiographically, computed tomography of the elbow seems to be more sensitive.[22,23] One, two, or all three of the primary lesions may be present in the same animal, and both elbow joints are commonly affected.

Ununited Anconeal Process

A number of breeds including German shepherd dogs, greyhounds, pit bull terriers, golden retrievers, and Labrador retrievers, are known to have a separate center of ossification at the anconeal process.[24] This is typically small and poorly defined with incomplete and irregular separation from the olecranon process. Dogs with a separate center of ossification do not always develop an ununited anconeal process, and the two should not be confused with each other. The anconeal process should be fused normally to the olecranon of the ulna by 150 days of age. Breeds at greatest risk for being diagnosed with ununited anconeal process include Bernese mountain dogs, mastiffs, Rottweilers, and Saint Bernards,[25] although other large-breed dogs are also at risk. A flexed lateral radiograph in addition to routine lateral and craniocaudal views of the elbow should be included in the radiographic examination. The flexed lateral view displaces the medial epicondylar physis away from the anconeus, thereby decreasing the possibility that an overlying epicondylar physeal line may be confused with an ununited anconeal process margin.

Radiographic Signs

The primary radiographic finding is best seen on the lateral view and consists of a radiolucent line separating the anconeal process from the olecranon in dogs older than 150 days (Fig. 15-5, see page 271). This lucent line can be sharply defined, or it may appear irregular and of variable width. Degenerative joint disease of the elbow is a common sequel, and periarticular new bone production from osteoarthrosis may partially obscure the lucency between the ulna and the anconeal process.[26-28]

Fragmented Medial Coronoid Process

Fragmented medial coronoid process is the most common developmental disorder involving the elbow joint. It affects medium- and large-breed dogs primarily and has a significantly higher incidence in males. Breeds at greatest risk for fragmented medial coronoid process include Bernese mountain dogs, bullmastiffs, German shepherd dogs, Irish wolfhounds, mastiffs, Rottweilers, and Saint Bernards,[25] although other large-breed dogs are predisposed. Clinical signs may be apparent as early as 4 to 6 months of age. Radiographic visualization of the coronoid fragment is usually not possible because of superimposition of the medial coronoid process on the radius, superimposition of proliferative new bone from degenerative joint disease on the coronoid fragment, or failure of the x-ray beam to strike the fragment plane in a parallel fashion (Fig. 15-6, see page 272). In addition, coronoid fragments that consist mostly of cartilage or that are still partially attached cannot be seen radiographically. In most instances, the radiographic diagnosis of fragmented medial coronoid process is made indirectly through recognition of degenerative changes that accompany the primary lesion.

A neutral lateral and a craniocaudal radiograph of both elbow joints should be made. In addition, a flexed lateral radiograph facilitates visualization of new bone formation on the proximal margin of the anconeal process. Flexing the elbow, however, induces a mild degree of rotation that can partially obscure the medial coronoid margin. A cranial

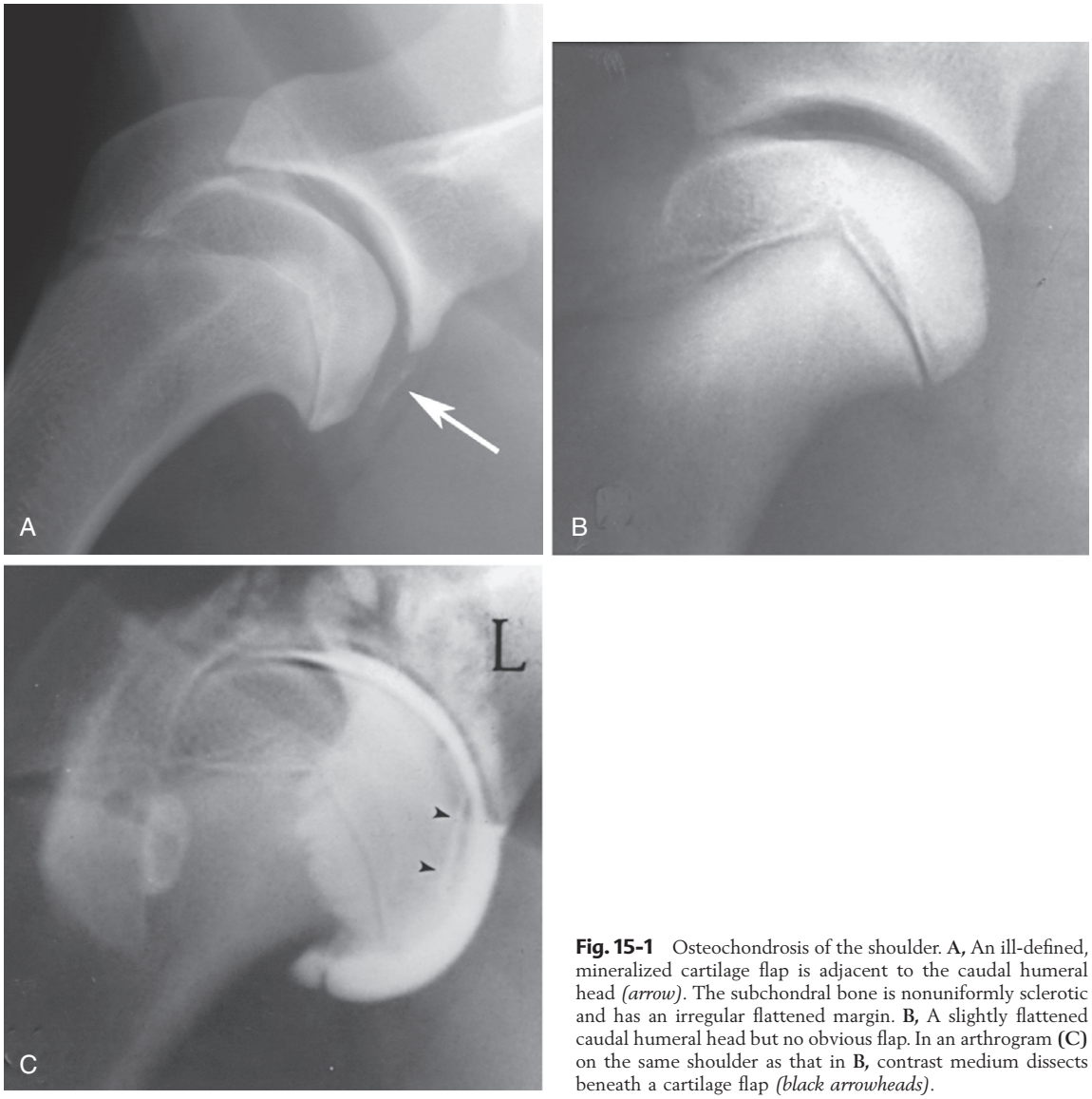


Fig. 15-1 Osteochondrosis of the shoulder. **A,** An ill-defined, mineralized cartilage flap is adjacent to the caudal humeral head *(arrow)*. The subchondral bone is nonuniformly sclerotic and has an irregular flattened margin. **B,** A slightly flattened caudal humeral head but no obvious flap. In an arthrogram **(C)** on the same shoulder as that in **B,** contrast medium dissects beneath a cartilage flap *(black arrowheads)*.

25-degree lateral-caudomedial view can also be obtained to highlight the medial coronoid region and fragmented coronoid process.[29] Although joint incongruity can be seen in association with fragmented coronoid process, caution should be used to prevent overinterpretation of this finding. On the lateral view, the normal overlapping lucent lines representing the complex elbow joint margins can be confused with joint incongruity when even mild positioning obliquity is present. Computed tomography is now used routinely to diagnose fragmented medial coronoid process and is more sensitive than survey radiography for detecting the coronoid fragment.[30-32]

Radiographic Signs

Primary radiographic signs include an abnormal contour, or poor definition, of the cranial margin of the medial coronoid process on the lateral view. Often the margin, which is radiographically distinct in normal dogs, cannot be followed proximally to the articular surface in affected animals. On the craniocaudal view, the medial margin of the medial coronoid process may appear blunted or rounded. A separate osseous body, representing the fractured coronoid process, is seen rarely. Joint incongruity or subluxation may also be present and appears as a stair-step lesion between the ulna and the radial head on the lateral view. Secondary radiographic signs include osteophyte formation on the proximal margin of the anconeal process as one of the earliest signs of degenerative joint disease. Similar new bone is often present on the caudal surface of the lateral epicondyle. Subchondral bone sclerosis also develops adjacent to the trochlear notch and the proximal radioulnar articulation near the lateral coronoid process. These secondary findings are best appreciated on the lateral view. A large osteophyte may arise from the medial coronoid margin on the craniocaudal view in addition to the more generalized degenerative periarticular osteophyte production.[21,28,31,33,34]

Aseptic Necrosis of the Femoral Head (Legg-Calvé-Perthes Disease)

Aseptic necrosis of the femoral head occurs in adolescent toy and small-breed dogs (Fig. 15-7, see page 273). Compromised blood supply to the femoral capital epiphysis causes necrosis of subchondral bone while overlying articular cartilage continues to grow. Revascularization occurs in an attempt to repair the defect, and removal of necrotic bone causes decreased opacity in the affected femoral head. Incomplete removal of necrotic bone and invasion of granulation tissue interferes with healing, resulting in a misshapen femoral head of nonuniform opacity.[35,36]



Fig. 15-2 Osteochondrosis of the medial humeral condyle. A well-defined lucent concavity is present in the subchondral bone of the medial humeral condyle *(arrow)*.



Fig. 15-3 Osteochondrosis of the lateral femoral condyle. The subchondral bone of the lateral femoral condyle is flattened. An irregular lucent area in the condyle is surrounded by sclerosis.

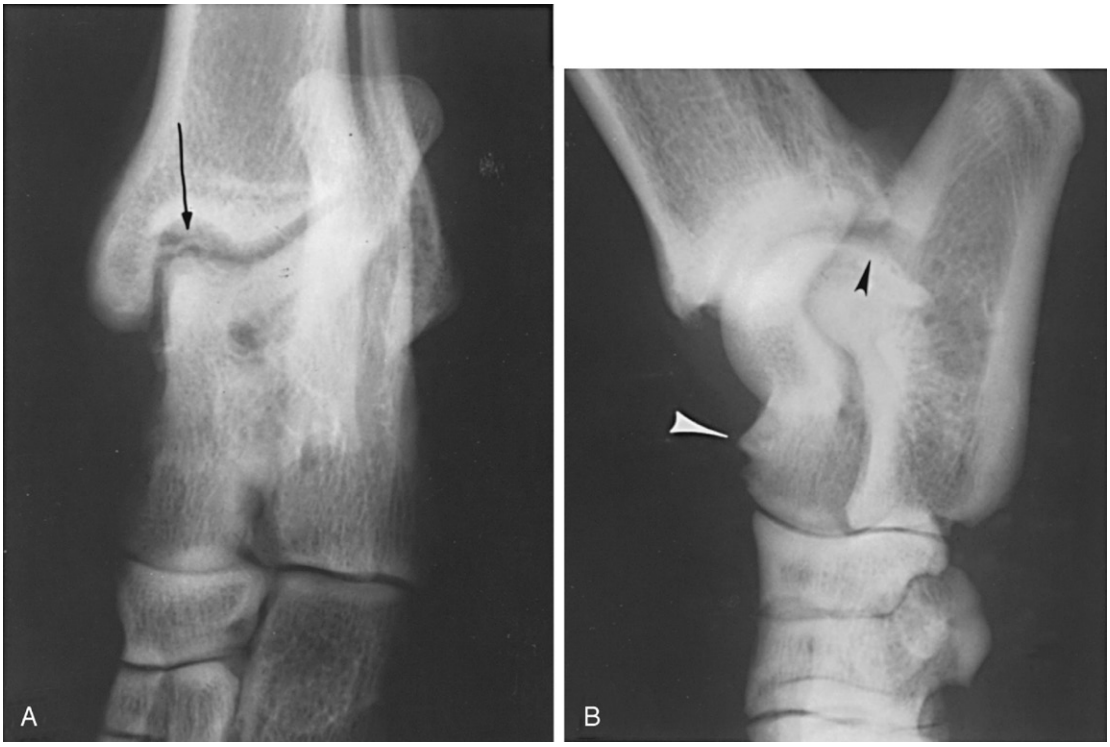


Fig. 15-4 Osteochondrosis of the medial trochlea of the talus. On the dorsoplantar view **(A),** a small bone flap is present proximal to the medial trochlear ridge of the talus *(black arrow)*. Adjacent to the flap the bone is irregular in contour, with lucency surrounded by sclerosis. Flattening of the trochlear ridge and concurrent widening of the tarsocrural joint *(black arrowhead)* are seen on the lateral view **(B).** Osteophyte formation is present on the cranial and caudal margins of the distal tibia and on the dorsal surface of the talus *(white arrowhead)*.



Fig. 15-5 Ununited anconeal process. *Arrowheads* outline the anconeal process, which is separate from the proximal ulna. The bone margins at the site of separation are smooth and sclerotic, indicating chronicity.

Radiographic Signs

As with many of the other developmental skeletal disorders, the radiographic findings of aseptic necrosis of the femoral head vary with the duration of the lesion. Radiographs of the hip joints may appear normal early in the course of the disease. As the disease progresses, linear lucencies can be detected within the subchondral bone deep within the femoral head. Areas of decreased opacity may also appear in both the femoral epiphysis and the metaphysis. Flattening and irregularity of the femoral head and neck become apparent as the affected bone remodels and collapses on itself. Remodeling of the femoral head may cause coxofemoral joint space widening and subluxation. Fragmentation of the femoral head may eventually occur from pathologic fracture. Muscle atrophy and radiographic findings associated with degenerative joint disease usually develop. Radiographic evaluation of both hips is indicated because this disease may be bilateral.

DISORDERS PRIMARILY AFFECTING BONE

Agenesis or Malformation of Single or Multiple Bones

Agenesis and Hypoplasia

Complete agenesis, partial agenesis, or hypoplasia of a long bone may occur. The radius, tibia, and ulna are most often involved, although the metacarpal, metatarsal, and phalangeal bones can also be affected (Fig. 15-8, see page 273). These anomalies, which can usually be detected at or shortly after birth, may be inherited but are more often a result of in utero environmental factors.

Radiographic signs. The affected bone or bones are conspicuously absent, and the limb is usually malformed and shorter than normal. Limb curvature and joint malformation may also be present.

Polymelia

This general term denotes supernumerary limbs or parts of a limb. Polydactyly, the presence of an excess number of digits, is the most common form of polymelia and is seen most often in cats. A few breeds of dogs, such as the Great Pyrenees, have also been bred to retain this trait. The anomaly is generally insignificant clinically.

Radiographic signs. Radiographic signs of polymelia vary according to the bone or bones involved. Findings of polydactyly include a greater-than-normal number of digits, usually arising on the medial side of the limb. Supernumerary digits may include complete or partial metacarpal and metatarsal bones and variable numbers of phalanges.

DISORDERS OF UNKNOWN ETIOLOGY

Panosteitis

Panosteitis is a self-limiting disease that affects the long bones of primarily young, large-breed dogs (Fig. 15-9, see page 273). Males are affected four times more often than are females. Breeds at greatest risk for panosteitis include basset hounds, Chinese Shar-Peis, giant schnauzers, German shepherd dogs, Great Pyrenees, and mastiffs,[25] although other large-breed dogs are also at risk. Dogs between the ages of 5 and 12 months are affected most often; however, German shepherd dogs as young as 2 months and as old as 7 years have been reported. Panosteitis lesions may be solitary, affect multiple sites in a single bone, or be multifocal in multiple bones. Although the lesions can affect any part of the diaphysis of a long bone, they often originate and are most pronounced near the nutrient foramen. Bone involvement is often sequential, and the disease may be protracted over several months, with lesions resolving in some bones while developing in others. Severity and location of radiographic lesions do not necessarily correlate with the severity of clinical signs, and the most clinically affected limb may not have the most pronounced radiographic lesions.[37,38] The term *panosteitis* is a misnomer in that histologically no evidence of an inflammatory response is present. Microscopically, medullary, endosteal, and periosteal osteoblastic and fibroblastic activity is increased.

Radiographic Signs

Early in the course of the disease, blurring and accentuation of trabeculae of the affected long bone are noted. Circumscribed nodular opacities similar in opacity to cortical bone form within the medullary cavity of the diaphysis of long bones, often near nutrient foramina. As the lesion progresses, medullary opacities become more diffuse and homogeneous. Smooth, continuous periosteal new bone formation develops in the diaphysis of affected bones in one third to one half of dogs. Late in the disease, opacities resolve, leaving coarse, thickened trabecular bone that eventually assumes a normal appearance. Cortical thickening may persist as periosteal new bone remodels. These findings should not be confused with the metaphyseal irregularities recently reported as a common incidental lesion in young Newfoundlands. Radiolucent zones surrounded by radiopaque osseous trabeculae have been described in the distal radius and ulna of 46% of asymptomatic Newfoundlands.[39]

Hypertrophic Osteodystrophy

Hypertrophic osteodystrophy is a systemic illness that usually affects large- and giant-breed dogs between the ages of 2 and 7 months. Breeds at greatest risk for hypertrophic osteodystrophy include boxers, Great Danes, Irish setters, and Weimaraners[25] although other large-breed dogs are also at risk. The cause is unknown, but oversupplementation of minerals and vitamins, hypovitaminosis C, and suppurative inflammation without isolation of infectious agents have all been proposed.[40-46] More recently, canine distemper virus has been isolated from metaphyseal bone cells in affected animals and has been suggested as a causative factor.[47-49] Clinical signs, including marked pyrexia, diarrhea, footpad hyperkeratosis, leukocytosis, anemia, and pneumonia, are occasionally seen with hypertrophic osteopathy, lending credibility to

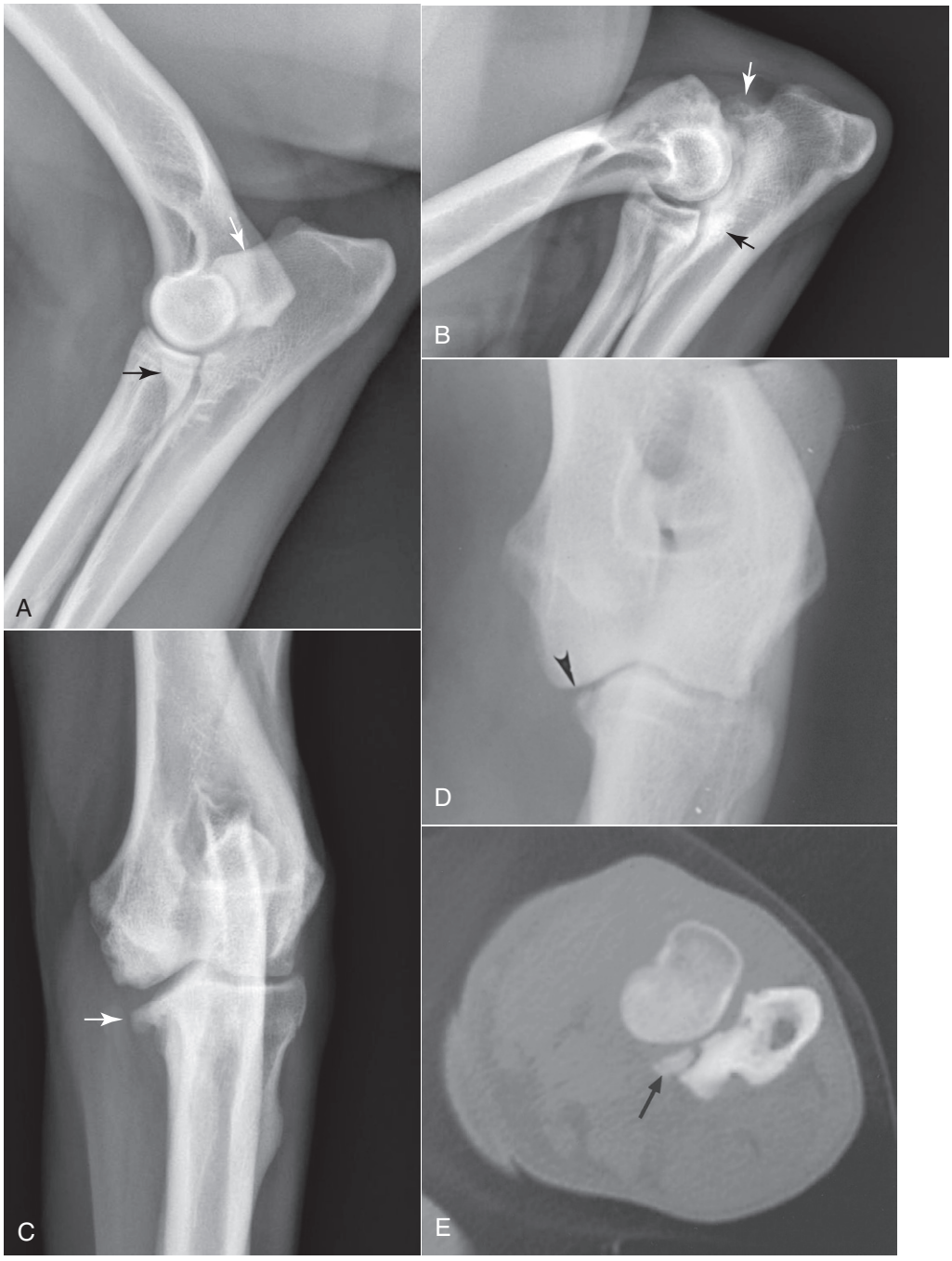


Fig. 15-6 Fragmented medial coronoid process. **A,** Lateral view of a normal elbow. The cranial edge of the medial coronoid process *(black arrow)* has a distinct margin that is superimposed on the head of the radius. The proximal margin of the anconeal process *(white arrow)* is also distinct despite being superimposed on the medial and lateral epicondyles of the humerus. **B,** Fragmented medial coronoid process with degenerative joint disease. The margins of the medial coronoid and anconeal processes are indistinct compared with those in **A.** Subchondral bone sclerosis is also present adjacent to the ulnar notch *(black arrow)*. Visualization of periosteal new bone on the proximal margin of the anconeal process *(white arrow)* is facilitated by flexing the elbow joint. **C,** A large osteophyte arises from the medial margin of the ulna on a craniocaudal view *(white arrow)*. This osteophyte should not be misinterpreted as the coronoid fragment. **D,** Fragmentation of the coronoid process can occasionally be seen on a craniolateral-caudomedial view *(arrow)*. **E,** Computed tomography image of the elbow from a dog with a fragmented medial coronoid process and degenerative joint disease. The fragmented coronoid process *(black arrow)* is easily seen. In addition, the basilar part of the coronoid process is sclerotic and remodeled.

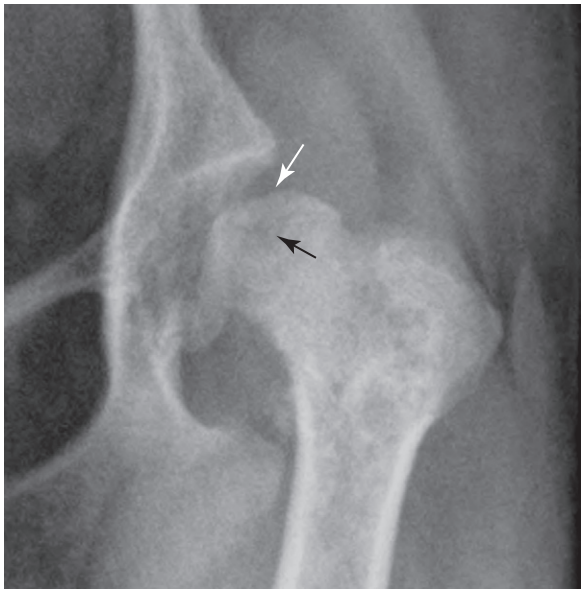


Fig. 15-7 Aseptic necrosis of the left femoral head. The femoral head contains a radiolucent area *(black arrow)*. There is also flattening of the weight-bearing surface of the femoral head *(white arrow)* and thickening of the femoral neck, and the joint space is widened.



Fig. 15-8 Tibial agenesis in a young dog. The tibia is not formed, and the fibula is misshapen. The proximal fibular epiphysis is hypoplastic and poorly mineralized. Tibial agenesis has led to stifle and tarsocrural malformation as well as limb shortening and angular deformity.

the possibility of a systemic infection as a cause for this disease.[46]

Resulting bone lesions are generally bilaterally symmetric and involve the metaphyses of long bones, particularly the distal radius, ulna, and tibia (Fig. 15-10). The costochondral

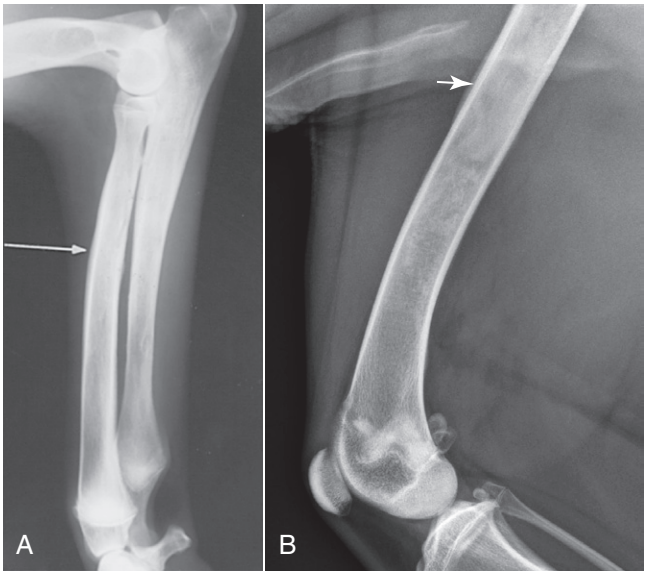


Fig. 15-9 Panosteitis. **A,** Panosteitis of the mid-radial diaphysis. Circumscribed increased opacity is visible in the mid-diaphysis with associated smooth periosteal reaction cranially and caudally *(white arrow)*. **B,** Panosteitis of the proximal femoral diaphysis. Patchy increased medullary opacity is visible with mild periosteal new bone formation present on the cranial femur *(white arrow)*.

junctions, metacarpal and metatarsal bones, proximal humerus,[50] and craniomandibular region may also be involved. Craniomandibular osteopathy may, in fact, be a different clinical manifestation of hypertrophic osteodystrophy.

Although hypertrophic osteodystrophy is usually self-limiting and resolves after a few weeks, more severe involvement can ultimately result in abnormal/premature physeal closure and subsequent skeletal deformity. Histologically, lesions in the metaphyses consist of a neutrophilic inflammatory response associated with necrosis, hemorrhage, and increased osteoclast numbers. Collapse of necrotic metaphyseal trabecular bone and subperiosteal hemorrhage are also seen.[46]

Radiographic Signs

Early radiographic signs include transversely oriented lucent zones within the metaphysis that are parallel and adjacent to the physes (see Fig. 15-10, *A, B*). These are usually best seen in the distal radius and ulna, and this appearance is sometimes referred to as the *double physis sign*, although the second radiolucent zone is not actually a physis. A thin margin of subchondral bone sclerosis may parallel the lucent zone and is caused by collapse of necrotic trabecular bone. Irregular periosteal new bone forms around the metaphysis and is usually distinct and separate from the underlying cortex in the earlier stages of the disease. The extent of new metaphyseal bone formation depends on the severity and duration of the disorder, and such formation may extend to the diaphysis in severely affected dogs (see Fig. 15-10, C). Diffuse soft tissue swelling can be seen centered on the metaphyseal regions. Widening, concavity, and increased opacity of the distal rib ends may be present in some dogs.

METABOLIC AND GENERALIZED BONE DISORDERS

Nutritional Secondary Hyperparathyroidism

Nutritional secondary hyperparathyroidism is caused by a diet that is either calcium deficient or calcium and phosphorus imbalanced. Inadequate dietary calcium intake causes an

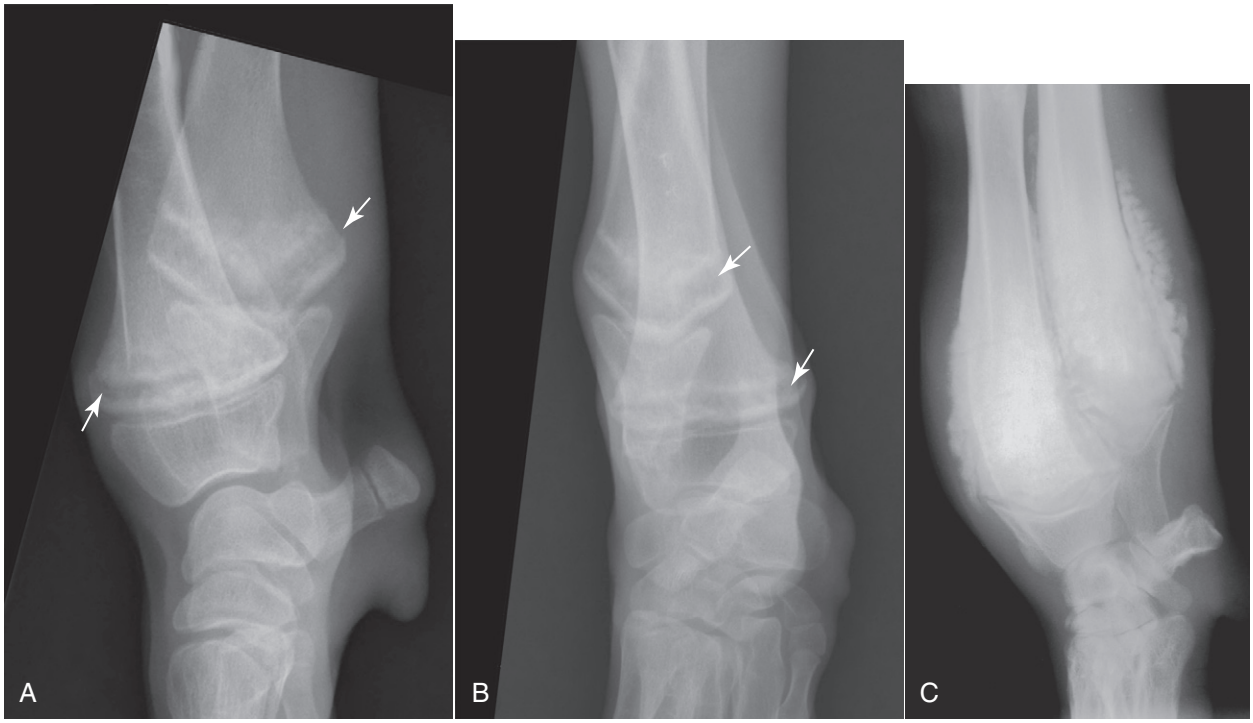


Fig. 15-10 Hypertrophic osteodystrophy. **A** and **B,** Acute phase. Irregular radiolucent regions are evident in the distal radial and ulnar metaphyses, proximal to the physis *(white arrows)*. **C,** Chronic phase. An irregular, palisading periosteal productive response surrounds the radial and ulnar metaphyses. The physes are relatively unaffected.

increase in parathyroid hormone. This, in turn, results in bone calcium resorption and generalized osteomalacia (Fig. 15-11). The skeletal changes are diffuse and generalized.[40,51,52]

Radiographic Signs

Bone opacity is decreased, and cortices may appear abnormally thin. In severely affected animals, bone opacity may be similar to that of soft tissue. A loss of definition of the normally dense dental lamina that surrounds the teeth may also occur (see Fig. 8-8). Spinal deformity and pathologic folding fractures of the appendicular and the axial skeleton are common.

Congenital Hypothyroidism

Congenital hypothyroidism is an uncommon developmental disorder that has been reported in cats, boxers, Scottish deerhounds, giant schnauzers, affenpinschers, and Great Danes and is caused by thyroid aplasia or hypoplasia (Fig. 15-12).[53-57] Clinically, the animals are disproportionate, short-limbed dwarves with bowed limbs and long necks and trunks.

Radiographic Signs

Radiographic findings consist of epiphyseal dysplasia that appears as reduced or delayed ossification of the epiphyseal cartilage model. This is seen most easily in the proximal tibia and the humeral and femoral condyles. Cuboid bone ossification in the carpus and tarsus is also delayed. Vertebral bodies are shorter than normal as a result of endplate dysplasia. The skull may appear shorter and broader than normal. Degenerative joint disease may be seen as a sequel.

Mucopolysaccharidosis

Mucopolysaccharidosis represents a loosely related group of uncommon autosomal recessive inherited disorders that result

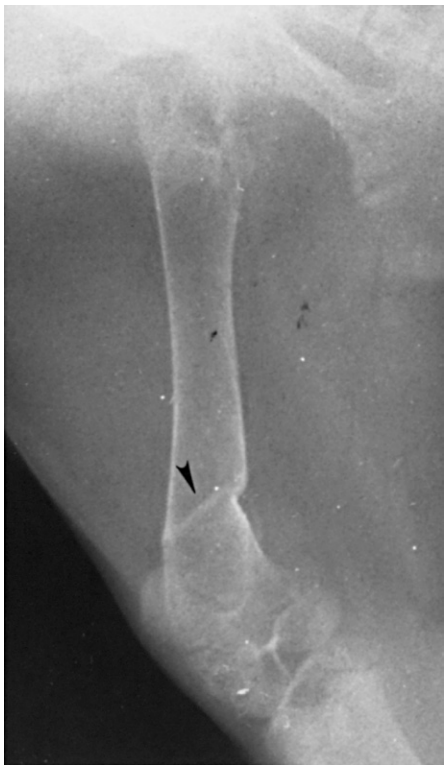


Fig. 15-11 Nutritional secondary hyperparathyroidism. Overall bone opacity of the femur and tibia are decreased, and cortices are thin. A fracture line is visible in the proximal tibial diaphysis with regional sclerosis and callus formation *(black arrowhead)*. Angulation of the limb originates from the pathologic folding fracture.



Fig. 15-12 Congenital hypothyroidism in a skeletally immature dog. Mineralization of the long bone epiphyses and cuboid bones of the carpus is markedly reduced. (From Saunders H: The radiographic appearance of canine congenital hypothyroidism: skeletal changes with delayed treatment, *Vet Radiol* 32:171, 1991.)

in a reduction or absence of glycosaminoglycan catabolism. Lysosomal degradation of these mucopolysaccharides is necessary for normal growth in developing animals, and the abnormal metabolism leads to chronic, progressive, multisystemic disease. More than 10 forms are recognized in human beings, each produced by a different enzyme defect. Many of these have also been identified in dogs and cats.[58-65] The most pronounced clinical manifestations involve the musculoskeletal, ocular, neurologic, hepatic, and cardiovascular systems. Affected animals are often stunted and lame with visual deficits. Clinical manifestations include disproportionate dwarfism and facial dysmorphia, which includes a broad maxilla, widespread eyes, a flat nose, and short ears. Hyperextension of the distal extremity joints occurs as a result of joint laxity.

Radiographic Signs

Radiographic changes of mucopolysaccharidosis involve both the axial and the appendicular skeleton. Generalized epiphyseal dysplasia is present, involving long bones and vertebral end plates. Findings include delayed and incomplete mineralization of the epiphyseal cartilage model. Ossified regions of the epiphyses are smaller than normal and have a nonuniform opacity with a granular appearance. Vertebral bodies appear cuboid and shorter than normal (see Fig. 11-30). The maxilla is short and flattened; the frontal sinuses may be small or absent. Progressive degenerative joint disease occurs as a result of the epiphyseal malformations. Coxofemoral subluxation or luxation may result from femoral head epiphysis remodeling. Ventral, bridging spondylosis is seen in older animals.[62]



Fig. 15-13 Osteopetrosis in a dog. A generalized increase in bone opacity is visible involving the appendicular and the axial skeleton. A loss of corticomedullary junction definition is attributable to increased medullary opacity. In this example, a small distal diaphyseal region of the humeral medullary cavity is not yet affected and appears less opaque than surrounding bone *(white arrow)*.

Osteogenesis Imperfecta

Osteogenesis imperfecta is a rare, generalized multisystemic heritable disease caused by a structural defect in type 1 collagen, which constitutes the majority of the nonmineral bone matrix.[66-68] Affected animals have stunted growth, generalized muscle atrophy, and weakness and are at risk for pathologic fractures. Teeth may also appear pink. Affected animals may have a recurring history of fractures.

Radiographic Signs

A generalized decrease in bone opacity is present, and long bone cortices are thin. Pathologic fractures are common and may be associated with excessively opaque callus formation and medullary sclerosis. Findings are similar to and can be confused with generalized bone mineral loss from secondary hyperparathyroidism.

Osteopetrosis

Osteopetrosis is a rare, inherited metabolic bone disease that is presumed to be caused by abnormal osteoclast function (Fig. 15-13).[69] Affected animals have a generalized increase in bone opacity specifically affecting medullary cavities. A resulting decrease in the number of normal hematopoietic cells subsequently occurs, leading to myelophthisic anemia.

In cats, varying degrees of osteosclerosis with nonregenerative anemia induced by feline leukemia virus have also been reported, and the radiographic appearance is identical to

that described for osteopetrosis.[70,71] Other reports describe generalized osteosclerosis as possibly being a paraneoplastic phenomenon.[72]

Until more information is obtained, the finding of generalized osteosclerosis in cats should be considered nonspecific, but the fact that the bone changes may be attributable to a more serious condition should be considered.

Radiographic Signs

Bone opacity is generally increased, particularly in medullary cavities. The normal trabecular pattern is diminished as a result of the uniform increase in bone opacity, and the internal cortical margins become indistinct. In some animals, the medullary cavity retains normal opacity in the central diaphyseal region.

METAPHYSEAL AND EPIPHYSEAL DYSPLASIAS

Osteochondral Dysplasias

Osteochondral dysplasias include chondrodysplasia, osteochondrodysplasia, enchondrodystrophy, multiple enchondromatosis, oculoskeletal dysplasia, hypochondroplasia, multiple epiphyseal dysplasia, and pseudoachondroplasia. Chondrodysplasia and osteochondrodysplasia result in disproportionate dwarfism and have been reported in a number of breeds, including Alaskan malamutes, Norwegian elkhounds, Great Pyrenees, Scottish deerhounds, bull terriers, and Scottish Fold cats.[73-80] Similar disorders have been described in Irish setters (hypochondroplasia), English pointers (enchondrodystrophy), and miniature poodles (multiple enchondromatosis). Chondrodysplasia associated with ocular defects has been described in Labrador retrievers, Samoyeds, and German shepherd dogs. Although these disorders may sometimes appear clinically and radiographically similar, they represent a histologically and biochemically heterogeneous group of diseases. Characterization is further complicated by the variety of classification systems that were used to describe these lesions when they were reported originally.

In almost all instances in which microscopic findings have been described, marked alterations in chondrocyte morphologic characteristics and cartilage architecture are present. Although many of these disorders are inherited and known to be single autosomal recessive defects, others have not been adequately characterized. In some instances, the genetic defect can also be expressed variably, resulting in a wide variation in severity of clinical signs. Distinguishing between chondrodystrophoid dogs, those that have been bred for many generations to establish a defect as a breed characteristic, and chondrodysplastic dwarves that arise sporadically from normal parents is important. Following are representative descriptions of some of these latter disorders.

Chondrodysplasia of Alaskan Malamutes

This disorder is transmitted by an autosomal recessive gene, and skeletal abnormalities are accompanied by a macrocytic hemolytic anemia (Fig. 15-14). Limb shortening with cranial and lateral deviation of the forelimbs and enlarged carpi are common clinical signs. Abnormalities appear to be limited to the long bones and the cuboidal bones. The skull and spine are unaffected radiographically.

Radiographic Signs

All appendicular growth plates can be affected, but lesions are best seen in the distal ulnar physis and the metaphysis. The distal metaphysis of the radius is flared, and the border is irregular. Trabecular bone is coarse and disorganized, and cortices appear thin. Asynchronous growth of the radius and ulna produces angular limb deformities. Radiographic changes may be detected in dogs as early as 7 to 10 days of age but can be more definitively diagnosed between 5 and 12 weeks of age.[74,76,80,81]



Fig. 15-14 Chondrodysplasia in an Alaskan malamute. The distal ulnar metaphysis is flattened, and the physis is wider than normal *(white arrow)*. The carpal bones are smaller in size than those in normal littermates.

Chondrodysplasia of Norwegian Elkhounds

This is an autosomal recessive disorder of variable expressivity that appears to be fairly widespread.[75,76,78] As with other forms of chondrodysplasia, this disorder produces disproportionate dwarfism, but the front limbs may be more affected than the hindlimbs. Unlike the disorder affecting Alaskan malamutes, this disease also affects the axial skeleton.

Radiographic Signs

Long-bone abnormalities may appear similar to those of Alaskan malamute chondrodysplasia. Forelimb curvature may be evident by 5 weeks of age. Spinal changes include lipping and pleating of the ventral vertebral body margins and delayed union of vertebral end plates. Costochondral junctions may be prominently flared and cupped. The skull appears unaffected radiographically.

Osteochondrodysplasia of Scottish Fold Cats

This disorder is probably caused by a simple autosomal dominant trait that is expressed to some degree in cats displaying the characteristic folding of the pinna. Affected animals are shorter than normal and have difficulty supporting their weight; gait abnormalities and a thick, inflexible tail base. Lesions are radiographically evident by 7 weeks of age.

Radiographic Signs

Metaphyses of the metatarsals and metacarpals are distorted, and physes are widened. Similar but less pronounced abnormalities are seen involving the phalanges. Shortening of the metacarpi, metatarsi, and phalanges results in decreased limb



Fig. 15-15 Scottish Fold osteochondral dysplasia. Metatarsal bones are short and misshapen. Phalanges are also affected. Marked secondary degenerative changes are present at all levels from the tarsocrural joint distally. The large mass of new bone in the plantarolateral aspect of the limb contributes to cuboidal bone fusion and tarsal ankylosis.

length. Punctate lucencies within the carpal and tarsal bones may also be seen. Caudal vertebrae are reduced in length and have widened end plates. Secondary degenerative joint disease invariably develops and leads to carpal or tarsal ankylosis in severely affected cats (Fig. 15-15).[82,83]

Ocular Chondrodysplasia of Labrador Retrievers

Ocular chondrodysplasia also appears to be an uncommon autosomal recessive inherited chondrodysplasia.[73,76,79] In addition to typical skeletal changes, ocular manifestations include cataracts, retinal dysplasia, and retinal detachment.

Radiographic Signs

Long-bone shortening is seen, specifically involving the radius and ulna, and is associated with delayed growth of the anconeal and coronoid processes of the ulna and the medial epicondyle of the humerus. Cortical opacity and thickness are reduced, and a retained cartilage core is sometimes present in the distal ulna. Flaring of the ulnar metaphysis and widening of the adjacent growth plate occur. The opacity of the primary spongiosa is increased in all metaphyses. Retarded and asynchronous radial and ulnar elongation leads to the development of radius curvus. The cuboid bones and the epiphyses are misshapen and larger than normal. Ribs are wider than normal, with prominent flaring at the costochondral junction. Hip dysplasia is a common sequel of this disorder. The skull and spine appear to be spared.

Multiple Epiphyseal Dysplasia of Beagles

Multiple epiphyseal dysplasia is a rare hereditary disorder of variable expression that is characterized by a failure of normal epiphyseal ossification (Fig. 15-16). *Pseudoachondroplasia*, reported in young miniature poodles, is also considered by some to be a form of multiple epiphyseal dysplasia.[84] Affected individuals have delayed growth and never reach normal size.



Fig. 15-16 Epiphyseal dysplasia in a 2-month-old beagle. The distal humeral epiphysis consists of rounded, sclerotic centers of bone formation. The proximal radial and olecranon physes have a normal appearance.

Radiographic Signs

Stippling of the epiphyses and irregular epiphyseal margins are evident by 3 weeks of age, with the most pronounced changes in the humeral condyles at 1 to 3 months of age. Epiphyseal alterations are identified in the humerus, femur, metacarpal and metatarsal bones, and occasionally the vertebrae. Similar stippling may also be seen in the carpal and tarsal bones in some dogs. Affected epiphyses eventually mineralize but are moderately deformed. Aberrant separate

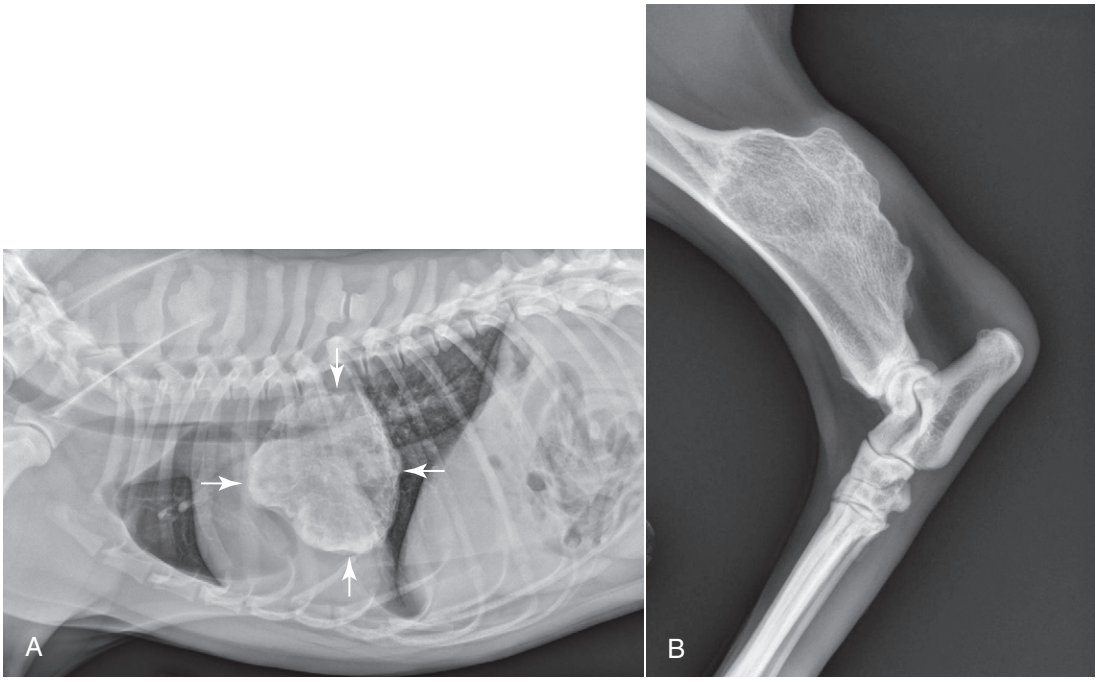


Fig. 15-17 Multiple cartilaginous exostosis. **A,** A large, expansile lesion is present involving the ribs *(white arrows)*. The opacity is mixed bone and soft tissue. Multiple nodular bone masses deform the shape of the thoracic spinous processes. **B,** A large, expansile lesion is present within the distal tibial diaphysis of the same dog as in 15-17, *A*.

centers of ossification that eventually fuse with the normal ossification centers have also been described. Hip dysplasia appears to develop in most affected dogs, and degenerative joint disease of other joints is a typical sequel to the primary disease.[85-87]

Multiple Cartilaginous Exostosis

Multiple cartilaginous exostosis is a benign proliferative disease of bone and cartilage (Fig. 15-17). Hereditary transmission of the disease is suspected in dogs.[88] Any bone that develops by endochondral ossification may be affected, and simultaneous involvement in multiple bones is common. Chondrocytes are pushed into the metaphyses and do not differentiate into osteoblasts. Instead, these cartilage islands continue to proliferate as cartilaginous masses that eventually ossify. Growth usually ceases once the animal has reached maturity, resulting in nonpainful bony protuberances throughout the skeleton. The bone lesions are of no clinical significance unless they arise in an area in which function could be compromised, such as the vertebral canal and the trachea. Most exostoses remain inert once the dog has matured, but malignant transformation has been reported.[89,90] Several atypical examples of multiple cartilaginous exostoses have been reported.[91] One was a 2-year-old Great Dane that developed multiple cartilaginous exostoses after reaching skeletal maturity. The exostoses continued to grow, with some bridging of physeal regions and irregular margins. Another was a 4-month-old border collie that had tumors with a stippled appearance that were not contiguous with adjacent bone. The microscopic appearance in both dogs was consistent with multiple cartilaginous exostoses. More recently, three mixed-breed dogs from the same litter developed symmetric, semiannular, and annular osteochondromas that accompanied limb shortening and angular deformity.[92] A similar disorder is seen in mature cats, and a viral etiology has been proposed.[83,93] In cats, however, the disorder tends to be progressive, resulting in clinical signs related to pain and loss of function.

Radiographic Signs

Rib masses are an amorphous mixture of radiolucency and bone opacity with irregular contours. Long-bone and vertebral masses tend to be more organized in appearance, with radiolucent cartilage and trabecular bone. Cortical bone in the area of the lesion may be present or absent; the bone may be deformed or the exostosis may project externally. The size and shape of exostoses vary.

Retained Cartilage Core

Retained cartilage cores are primarily seen in the distal ulnar metaphysis of large-breed dogs, although they are occasionally seen in the lateral femoral condyle.[94,95] The lesion is caused by a disruption of the normal progression of endochondral ossification with retention of hypertrophied cartilage cells in the central metaphysis. Cartilage retention may cause angular limb deformity from retardation of distal ulnar growth and a resulting mismatch in radial and ulnar elongation, but the lesion is sometimes an incidental finding in otherwise normal dogs.

Radiographic Signs

Primary radiographic findings include the presence of a cone-shaped radiolucent area in the distal ulnar metaphysis or lateral femoral condyle (Fig. 15-18). A narrow zone of sclerosis may surround the radiolucent area. Additional radiographic findings may include angular limb deformity and degenerative joint disease of the elbow and carpal joints.

Incomplete Ossification of the Humeral Condyle

Incomplete ossification of the humeral condyle is a heritable condition of pure-bred and cross-bred spaniels, resulting in a higher-than-normal incidence of humeral condylar fractures associated with normal physical activity (Fig. 15-19).[96] The incidence of the disorder appears to be higher in males. Sporadic reports have been made of other medium- and large-breed dogs affected by this disorder.[97,98] Two separate centers



Fig. 15-18 Retained cartilage core in the distal ulna. A triangular radiolucent region is present in the distal ulnar metaphysis *(white arrows)*. A thin rim of bone sclerosis is present next to the radiolucency.

of ossification in the humeral condyle appear typically by approximately 22 days after birth. The medial and lateral centers of the condyle should fuse by approximately 84 days after birth. Incomplete ossification leads to the presence of a thin fissure separating the medial and lateral halves of the humeral condyle in skeletally mature dogs. When pathologic fractures occur, approximately half are Y- or T-type fractures affecting the entire epicondylar region; the remainder are limited to fractures of the lateral (35%) or medial (15%) condyle.[96] The incidence of incomplete humeral condylar ossification is high enough that bilateral elbow radiographs should be obtained in any spaniel with a unilateral condylar fracture. An increased incidence of fragmented coronoid processes appears to be associated with this disorder.

Radiographic Signs

The primary radiographic finding in dogs with incomplete humeral condylar ossification is a vertically oriented radiolucent line in the central region of the condyle that may extend from the subchondral bone margin of the trochlea to the distal margin of the supratrochlear foramen. This lucency is evident only on the craniocaudal view and may be better seen when the view is obliqued approximately 15 degrees craniomedial to caudolateral, which positions the fissure parallel to the x-ray beam angle. Secondary radiographic signs include smooth periosteal new bone formation along the lateral and caudal aspect of the humeral epicondylar region. This finding may be a response to chronic instability or incomplete, nondisplaced fracture through the nonossified region. Overt,

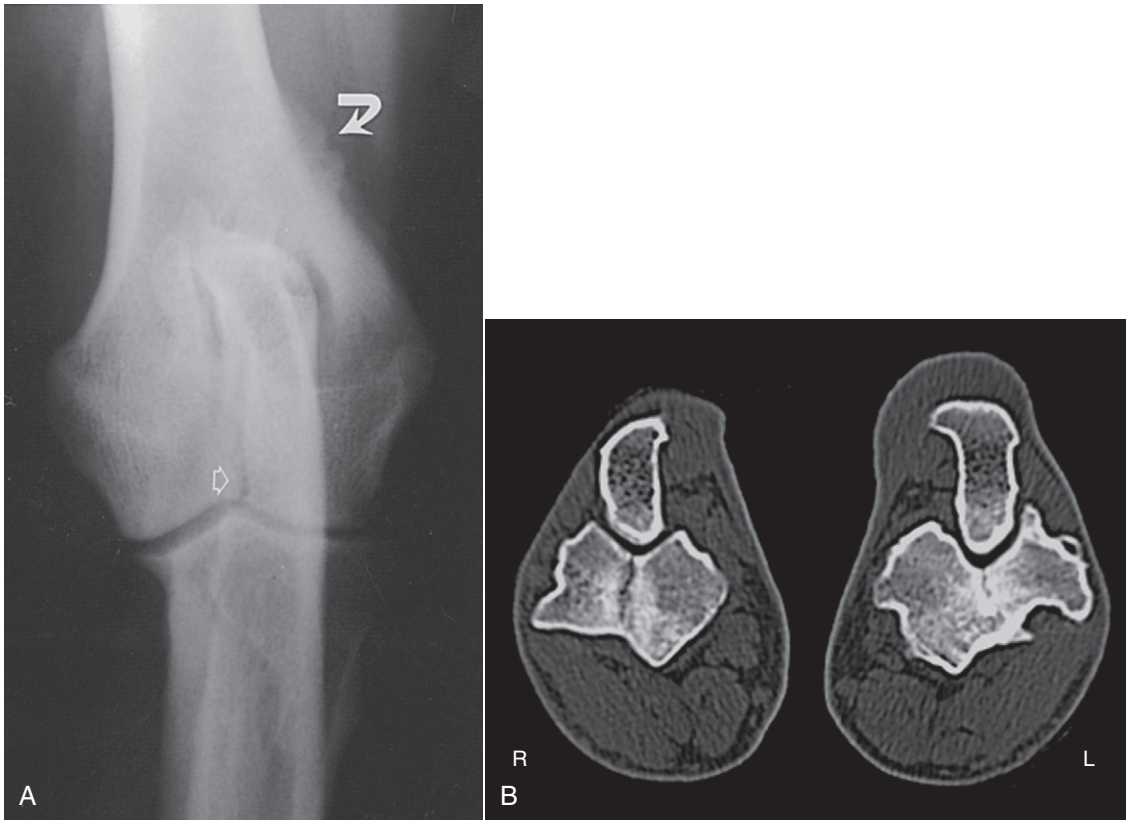


Fig. 15-19 **A,** Incomplete ossification of the humeral condyle. A vertical radiolucent line is present in the distal humeral condyle *(open white arrow)*. Periosteal new bone formation is present on the distal lateral humerus *(curved white arrow)*, probably as a result of motion from an incomplete fracture extending laterally from the supracondylar foramen. **B,** Computed tomography image of the left and right distal humerus of a dog with incomplete humeral condylar ossification. A sagittally oriented lucent line is evident in each condyle, surrounded by sclerosis of adjacent bone. The ossification deficit is more pronounced in the right humerus.

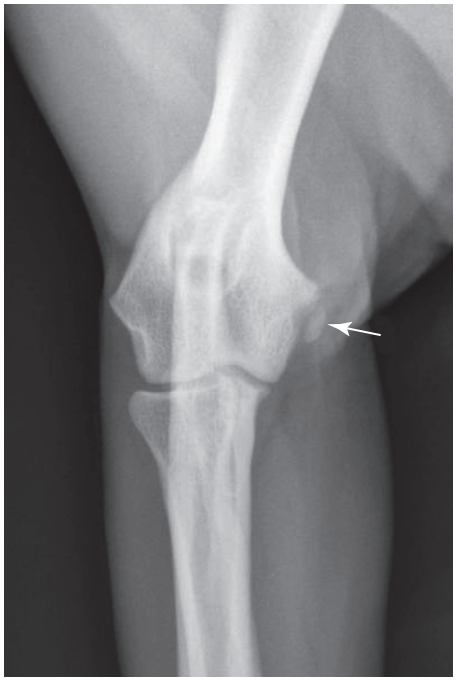


Fig. 15-20 Ununited medial epicondyle of the humerus. A rounded separate osseous structure is present in the soft tissues medial to the medial epicondyle of the humerus *(white arrow)*. The medial epicondyle is irregular with a concave surface.

displaced, pathologic condylar fractures may be present in one or both limbs.

Radiographic evidence of concurrent fragmented medial coronoid process may be present.

Ununited Medial Epicondyle

The presence of a mineralized body medial to the medial epicondyle of the humerus (Fig. 15-20) has been described in the Labrador retriever, German shepherd dog, and English setter with a suspected genetic cause.[99] Although the exact etiology is unknown, this finding is either a result of failed fusion of the medial epicondyle ossification center to the humerus or dystrophic mineralization of the flexor tendons.[100] Dogs with an ununited medial epicondyle may present with evidence of elbow pain or be asymptomatic. There does not appear to be an association between ununited medial epicondyle and the development of degenerative joint disease of the elbow. This disorder can be unilateral or bilateral and often occurs in association with elbow dysplasia, although it can occur as the only lesion.

Radiographic Signs

The primary radiographic finding in dogs with ununited medial epicondyle is a rounded mineral opacity located in the soft tissues along the medial aspect of the medial humeral epicondyle. The bone opacity is best seen on the craniocaudal projection and may not be visible on the lateral projection. A corresponding concavity of the medial humeral epicondyle may also be present.

Radiographic evidence of concurrent fragmented medial coronoid process and/or degenerative joint disease may be present.

REFERENCES

1. Ekman S, Carlson CS: The pathophysiology of osteochondrosis, *Vet Clin North Am Small Anim Pract* 28:17, 1998.
2. Smitach L, Stowater T: Osteochondritis dissecans of the shoulder joint: a review of 35 cases, *J Am Anim Hosp Assoc* 11:658, 1975.
3. Olsson S-E: The early diagnosis of fragmented coronoid process and osteochondritis dissecans of the canine elbow joint, *J Am Anim Hosp Assoc* 19:616, 1983.
4. Alexander J, Richardson D, Selcer B: Osteochondritis dissecans of the elbow, stifle and hock—a review, *J Am Anim Hosp Assoc* 17:51, 1981.
5. Denny H, Gibbs C: Osteochondritis dissecans of the canine stifle joint, *J Small Anim Pract* 21:317, 1980.
6. Fitch RB, Beale BS: Osteochondrosis of the canine tibiotarsal joint, *Vet Clin North Am Small Anim Pract* 28:95, 1998.
7. Harari J: Osteochondrosis of the femur, *Vet Clin North Am Small Anim Pract* 28:87, 1998.
8. Poulos PW Jr: Canine osteochondrosis, *Vet Clin North Am Small Anim Pract* 12:313,1982.
9. Wisner ER, Berry CR, Morgan JP, et al: Osteochondrosis of the lateral trochlear ridge of the talus in seven Rottweiler dogs, *Vet Surg* 19:435, 1990.
10. van Bree H: Evaluation of subchondral lesion size in osteochondrosis of the scapulohumeral joint in dogs, *J Am Vet Med Assoc* 204:1472, 1994.
11. van Bree H: Evaluation of the prognostic value of positive-contrast shoulder arthrography for bilateral osteochondrosis lesions in dogs, *Am J Vet Res* 51:1121, 1990.
12. van Bree H: Comparison of the diagnostic accuracy of positive-contrast arthrography and arthrotomy in evaluation of osteochondrosis lesions in the scapulohumeral joint in dogs, *J Am Vet Med Assoc* 203:84, 1993.
13. van Bree H, Van Rijssen B, Tshamala M, et al: Comparison of the nonionic contrast agents, iopromide and iotrolan, for positive-contrast arthrography of the scapulohumeral joint in dogs, *Am J Vet Res* 53:1622, 1992.
14. Bertrand SG, Lewis DD, Madison JB, et al: Arthroscopic examination and treatment of osteochondritis dissecans of the femoral condyle of six dogs, *J Am Anim Hosp Assoc* 33:451, 1997.
15. van Bree HJ, Van Ryssen B: Diagnostic and surgical arthroscopy in osteochondrosis lesions, *Vet Clin North Am Small Anim Pract* 28:161, 1998.
16. Boudrieau R, Hohn R, Bardet J: Osteochondritis dissecans of the elbow in the dog, *J Am Anim Hosp Assoc* 19:627, 1983.
17. Goring R, Bloomberg M: Selected developmental abnormalities of the canine elbow: radiographic evaluation and surgical management, *Compend Cont Ed Pract Vet* 5:178, 1983.
18. Mason T, Lavelle S, Skipper S, et al: Osteochondrosis of the elbow joint in young dogs, *J Small Anim Pract* 21:641, 1980.
19. Wind A: Elbow incongruity and developmental elbow diseases in the dog: I, *J Am Anim Hosp Assoc* 22:711, 1986.
20. Wind A: Elbow incongruity and developmental elbow diseases in the dog: II, *J Am Anim Hosp Assoc* 22:725, 1986.
21. Boulay J: Fragmented medial coronoid process of the ulna in the dog, *Vet Clin North Am Small Anim Pract* 28:51, 1998.
22. Blond L, Dupuis J, Beauregard G, et al: Sensitivity and specificity of radiographic detection of canine elbow incongruence in an in vitro model, *Vet Radiol Ultrasound* 46:210, 2005.
23. Holsworth IG, Wisner ER, Scherrer WE, et al: Accuracy of computerized tomographic evaluation of canine radio-ulnar incongruence in vitro, *Vet Surg* 34:108, 2005.

24. Frazho JK, Graham J, Peck JN, et al: Radiographic evaluation of the anconeal process in skeletally immature dogs, *Vet Surg* 39:829, 2010.
25. LaFond E, Breur GJ, Austin CC: Breed susceptibility for developmental orthopedic diseases in dogs, *J Am Anim Hosp Assoc* 38:467, 2002.
26. Battershell D: Ununited anconeal process, *J Am Vet Med Assoc* 155:35, 1969.
27. Sjostrom L: Ununited anconeal process in the dog, *Vet Clin North Am Small Anim Pract* 28:75, 1998.
28. Tirgari M: Clinical, radiographical and pathological aspects of ununited medial coronoid process of the elbow joint in dogs, *J Small Anim Pract* 21:595, 1980.
29. Berzon J, Quick C: Fragmented coronoid process: anatomical, clinical, and radiographic considerations with case analyses, *J Am Anim Hosp Assoc* 16:241, 1980.
30. Braden T, Stickle R, Dejardin L, et al: The use of computed tomography in fragmented coronoid disease: a case report, *Vet Comp Orthop Trauma* 7:40, 1994.
31. Hornof WJ, Wind AP, Wallack ST, et al: Canine elbow dysplasia. The early radiographic detection of fragmentation of the coronoid process, *Vet Clin North Am Small Anim Pract* 30:257, 2000.
32. Reichle JK, Park RD, Bahr AM: Computed tomographic findings of dogs with cubital joint lameness, *Vet Radiol Ultrasound* 41:125, 2000.
33. Berry C: Evaluation of the canine elbow for fragmented medial coronoid process, *Vet Radiol Ultrasound* 33:273, 1992.
34. Read R, Wind A, Morgan J, et al: Fragmentation of the medial coronoid process of the ulna in dogs: a study of 109 cases, *J Small Anim Pract* 31:330, 1990.
35. Lee R: A study of the radiographic and histological changes occurring in Legg-Calvé-Perthes disease (LCP) in the dog, *J Small Anim Pract* 11:621, 1970.
36. Lee R: Legg-Perthes disease in the dog: The histological and associated radiological changes, *J Am Vet Radiol Assoc* 15:24, 1974.
37. Burt JK, Wilson GP: A study of eosinophilic panosteitis (enostosis) in German shepherd dogs, *Acta Radiol Suppl* 319:7, 1972.
38. Bohning RH Jr, Suter PF, Hohn RB, et al: Clinical and radiologic survey of canine panosteitis, *J Am Vet Med Assoc* 156:870, 1970.
39. Trangerud C, Sande RD, Rorvik AM, et al: A new type of radiographic bone remodeling in the distal radial and ulnar metaphysis in 54 Newfoundland dogs, *Vet Radiol Ultrasound* 46:108, 2005.
40. Grundalen J: Metaphyseal osteopathy (hypertrophic osteodystrophy) in growing dogs. A clinical study, *J Small Anim Pract* 17:721, 1976.
41. Bennett D: Nutrition and bone disease in the dog and cat, *Vet Rec* 98:313, 1976.
42. Alexander JW: Selected skeletal dysplasias: craniomandibular osteopathy, multiple cartilaginous exostoses, and hypertrophic osteodystrophy, *Vet Clin North Am Small Anim Pract* 13:55, 1983.
43. Woodard JC: Canine hypertrophic osteodystrophy: a study of the spontaneous disease in littermates, *Vet Pathol* 19:337, 1982.
44. Watson AD, Blair RC, Farrow BR, et al: Hypertrophic osteodystrophy in the dog, *Aust Vet J* 49:433, 1973.
45. Olsson S-E: Radiology in veterinary pathology. A review with special reference to hypertrophic osteodystrophy and secondary hyperparathyroidism in the dog, *Acta Radiol Suppl* 319:255, 1972.
46. Muir P, Dubielzig R, Johnson K, et al: Hypertrophic osteodystrophy and calvarial hyperostosis, *Compendium* 18:143, 1996.
47. Baumgartner W, Boyce RW, Weisbrode SE, et al: Histologic and immunocytochemical characterization of canine distemper-associated metaphyseal bone lesions in young dogs following experimental infection, *Vet Pathol* 32:702, 1995.
48. Abeles V, Harrus S, Angles JM, et al: Hypertrophic osteodystrophy in six Weimaraner puppies associated with systemic signs, *Vet Rec* 145:130, 1999.
49. Mee AP, Gordon MT, May C, et al: Canine distemper virus transcripts detected in the bone cells of dogs with metaphyseal osteopathy, *Bone* 14:59, 1993.
50. Franklin MA, Rochat MC, Broaddus KD: Hypertrophic osteodystrophy of the proximal humerus in two dogs, *J Am Anim Hosp Assoc* 44:342, 2008.
51. Riser W: Radiographic differential diagnosis of skeletal diseases of young dogs, *J Am Vet Radiol Soc* 145:5, 1964.
52. Voorhout G: Radiographic features of nutritional secondary hyperparathyroidism in the growing dog and cat [in German], *Tijdschr Diergeneeskd* 106:317, 1981.
53. Crowe A: Congenital hypothyroidism in a cat, *Can Vet J* 45:168, 2004.
54. Greco DS, Feldman EC, Peterson ME, et al: Congenital hypothyroid dwarfism in a family of giant schnauzers, *J Vet Intern Med* 5:57, 1991.
55. Lieb AS, Grooters AM, Tyler JW, et al: Tetraparesis due to vertebral physeal fracture in an adult dog with congenital hypothyroidism, *J Small Anim Pract* 38:364, 1997.
56. Robinson WF, Shaw SE, Stanley B, et al: Congenital hypothyroidism in Scottish deerhound puppies, *Aust Vet J* 65:386, 1988.
57. Saunders H: The radiographic appearance of canine congenital hypothyroidism: skeletal changes with delayed treatment, *Vet Radiol* 32:171, 1991.
58. Haskins M, Jezyk P, Desnick R, et al: Alpha-L-iduronidase deficiency in a cat: a model of mucopolysaccharidosis: I, *Pediatr Res* 13:1294, 1979.
59. Haskins ME, Aguirre GD, Jezyk PF, et al: Mucopolysaccharidosis type VII (sly syndrome). Beta-glucuronidase-deficient mucopolysaccharidosis in the dog, *Am J Pathol* 138:1553, 1991.
60. Haskins ME, Jezyk PF, Desnick RJ, et al: Animal models of mucopolysaccharidosis, *Prog Clin Biol Res* 94:177, 1982.
61. Haskins ME, Otis EJ, Hayden JE, et al: Hepatic storage of glycosaminoglycans in feline and canine models of mucopolysaccharidoses I, VI, and VII, *Vet Pathol* 29:112, 1992.
62. Konde L, Thrall M, Gasper P, et al: Radiographic changes associated with mucopolysaccharidosis in the cat, *Vet Radiol* 28:223, 1987.
63. Shull RM, Helman RG, Spellacy E, et al: Morphologic and biochemical studies of canine mucopolysaccharidosis: I, *Am J Pathol* 114:487, 1984.
64. Shull RM, Munger RJ, Spellacy E, et al: Canine alpha-L-iduronidase deficiency. A model of mucopolysaccharidosis: I, *Am J Pathol* 109:244, 1982.
65. Wilkerson MJ, Lewis DC, Marks SL, et al: Clinical and morphologic features of mucopolysaccharidosis type II in a dog: naturally occurring model of hunter syndrome, *Vet Pathol* 35:230, 1998.
66. Campbell BG, Wootton JA, Krook L, et al: Clinical signs and diagnosis of osteogenesis imperfecta in three dogs, *J Am Vet Med Assoc* 211:183, 1997.
67. Potena A: On osteogenesis imperfecta. Studies of some cases observed in dogs [in Italian], *Acta Med Vet (Napoli)* 14:79, 1968.

68. Schmidt V: Osteogenesis imperfecta in 2 collie litter siblings [in German], *Wien Tierarztl Monatsschr* 54:92, 1967.
69. Lees GE, Sautter JH: Anemia and osteopetrosis in a dog, *J Am Vet Med Assoc* 175:820, 1979.
70. Hoover EA, Kociba GJ: Bone lesions in cats with anemia induced by feline leukemia virus, *J Natl Cancer Inst* 53:1277, 1974.
71. Onions D, Jarrett O, Testa N, et al: Selective effect of feline leukaemia virus on early erythroid precursors, *Nature* 296:156, 1982.
72. Hanel RM, Graham JP, Levy JK, et al: Generalized osteosclerosis in a cat, *Vet Radiol Ultrasound* 45:318, 2004.
73. Carrig CB, MacMillan A, Brundage S, et al: Retinal dysplasia associated with skeletal abnormalities in Labrador retrievers, *J Am Vet Med Assoc* 170:49, 1977.
74. Terpin T, Roach MR: Chondrodysplasia in the Alaskan malamute: involvement of arteries, as well as bone and blood, *Am J Vet Res* 42:1865, 1981.
75. Bingel SA, Sande RD: Chondrodysplasia in the Norwegian elkhound, *Am J Pathol* 107:219, 1982.
76. Sande RD, Bingel SA: Animal models of dwarfism, *Vet Clin North Am Small Anim Pract* 13:71, 1983.
77. Bingel SA, Sande RD, Wight TN: Chondrodysplasia in the Alaskan malamute. Characterization of proteoglycans dissociatively extracted from dwarf growth plates, *Lab Invest* 53:479, 1985.
78. Minor RR, Farnum CE: Animal models with chondrodysplasia/osteochondrodysplasia, *Pathol Immunopathol Res* 7:62, 1988.
79. Carrig CB, Sponenberg DP, Schmidt GM, et al: Inheritance of associated ocular and skeletal dysplasia in Labrador retrievers, *J Am Vet Med Assoc* 193:1269, 1988.
80. Breur GJ, Zerbe CA, Slocombe RF, et al: Clinical, radiographic, pathologic, and genetic features of osteochondrodysplasia in Scottish deerhounds, *J Am Vet Med Assoc* 195:606, 1989.
81. Sande RD, Alexander JE, Padgett GA: Dwarfism in the Alaskan malamute: its radiographic pathogenesis, *J Am Vet Radiol Soc* 15:10, 1974.
82. Malik R, Allan GS, Howlett CR, et al: Osteochondrodysplasia in Scottish Fold cats, *Aust Vet J* 77:85, 1999.
83. Allan GS: Radiographic features of feline joint diseases, *Vet Clin North Am Small Anim Pract* 30:281, 2000.
84. Riser WH, Haskins ME, Jezyk PF, et al: Pseudoachondroplastic dysplasia in miniature Poodles: clinical, radiologic, and pathologic features, *J Am Vet Med Assoc* 176:335, 1980.
85. Rasmussen PG: Multiple epiphyseal dysplasia in a litter of beagle puppies, *J Small Anim Pract* 12:91, 1971.
86. Rasmussen PG: Multiple epiphyseal dysplasia in beagle puppies, *Acta Radiol Suppl* 319:251, 1972.
87. Rasmussen PG, Reimann I: Multiple epiphyseal dysplasia, with special reference to histological findings, *Acta Pathol Microbiol Scand (A)* 81:381, 1973.
88. Gambardella PC, Osborne CA, Stevens JB: Multiple cartilaginous exostoses in the dog, *J Am Vet Med Assoc* 166:761, 1975.
89. Doige C, Pharr J, Withrow S: Chondrosarcoma arising in multiple cartilaginous exostoses in a dog, *J Am Anim Hosp Assoc* 14:605, 1978.
90. Owen L: Multiple cartilaginous exostoses with development of a metastasizing osteosarcoma in a Shetland sheepdog, *J Small Anim Pract* 12:507, 1971.
91. Jacobson LS, Kirberger RM: Canine multiple cartilaginous exostoses: unusual manifestations and a review of the literature, *J Am Anim Hosp Assoc* 32:45, 1996.
92. Mozos E, Novales M, Ginel PJ, et al: A newly recognized pattern of canine osteochondromatosis, *Vet Radiol Ultrasound* 43:132, 2002.
93. Pool R, Harris J: Feline osteochondromatosis, *Feline Pract* 5:24, 1975.
94. Johnson KA: Retardation of endochondral ossification at the distal ulnar growth plate in dogs, *Aust Vet J* 57:474, 1981.
95. Riser W, Lincoln J, Rhodes W, et al: Genu valgum: a stifle deformity of giant dogs, *J Am Vet Radiol Assoc* 10:28, 1969.
96. Marcellin-Little DJ, DeYoung DJ, Ferris KK, et al: Incomplete ossification of the humeral condyle in spaniels, *Vet Surg* 23:475, 1994.
97. Rovesti GL, Fluckiger M, Margini A, et al: Fragmented coronoid process and incomplete ossification of the humeral condyle in a Rottweiler, *Vet Surg* 27:354, 1998.
98. Gabriel P, Pfeil A, Ludewig E, et al: Magnetic resonance imagine diagnosis: incomplete ossification of the humeral condyle in a German Shepherd dog, *J Small Anim Pract* 50:92, 2009.
99. Zontine WJ, Weitkamp RA, Lippincott CL: Redefined type of elbow dysplasia involving calcified tendons attached to the medial humeral epicondyle in three dogs, *J Am Vet Med Assoc* 194:1082, 1989.
100. Paster ER, Biery DN, Lawler DF, et al: Un-united medial epicondyle of the humerus: radiographic prevalence and association with elbow osteoarthritis in a cohort of Labrador retrievers, *Vet Surg* 38:169, 2009.

ELECTRONIC RESOURCES

Evolve

Additional information related to the content in Chapter 15 can be found on the companion Evolve website at http://evolve.elsevier.com/Thrall/vetrad/

- Chapter Quiz

CHAPTER • 16

Fracture Healing and Complications

George A. Henry

BONE TISSUE

Bone is a specialized form of connective tissue that functions as an integral part of the locomotor system. Bones act as lever arms during motion, provide resistance to the effects of gravitational force on the body, and provide protection and support to adjacent structures. Bone also serves as a reservoir of mineral for systemic mineral homeostasis.[1,2]

Bones differ in shape and function and include long, flat, intramembranous, woven, and compact bones. Specialized connective tissue called *periosteum* surrounds the outside surface of the bones and provides protection and nutrition. Long bones are divided into epiphyseal, physeal, metaphyseal, and diaphyseal regions. Woven, cancellous, and lamellar bone is found adjacent to the physis in the epiphyseal and metaphyseal regions; compact or cortical bone surrounds the marrow cavity in the diaphyseal region.[1,2]

Bones contain three principle cell types: osteoblasts, osteocytes, and osteoclasts. Osteoblasts synthesize the osteoid bone matrix. Following mineralization of the osteoid, the osteoblasts become osteocytes. Osteoclasts are larger cells that reside on the surface of the mineralized matrix and remove both mineral and matrix by secretion of acids and enzymes. In normal bone the activities of osteoblasts and osteoclasts are coordinated and occur in response to stress on the bone. The bone pattern and shape of the bone adapt to withstand the stresses placed on it.

The regulation of mineral ions in the serum is controlled mainly by parathyroid hormone, calcitonin, and vitamin D. Parathyroid hormone increases resorption of bone by stimulating osteoclastic activity to increase serum calcium. Calcitonin inhibits the activity of osteoclasts and inhibits intestinal and renal calcium absorption. Vitamin D acts on the intestine to increase absorption of calcium and phosphorous and directly on bone by both mobilization of calcium and phosphorous from previously formed bone and promotion of maturation and mineralization of bone matrix. Bone is an active living tissue that is able to adapt and react, although somewhat slowly, to forces applied to the musculoskeletal system. Although bone can react to external stimuli or forces, it has limited methods of reaction: bone production, bone resorption, or a combination of production and resorption.[1-3]

Bone is formed and grows by means of intramembranous ossification, endochondral ossification, or both. *Intramembranous* bone formation begins with proliferation of mesenchymal cells that transform into osteoblasts that form matrix, which is then calcified. A fibrovascular layer develops on the internal and external surfaces of the bone to provide nutrition and osteogenic cells to allow the continued production and resorption of the bone. Intramembranous bone formation occurs primarily in the bones of the calvarium and mandible. The bones of the extremities, spine, and pelvis form by both intramembranous and endochondral ossification, with endochondral ossification predominant in the long bones. *Endochondral* (intracartilaginous) ossification progresses by the formation of a cartilage model derived from the mesenchyma that is then replaced with bone. Long (tubular) bones begin by a primary center of ossification in the center of the cartilaginous model and grow with intramembranous ossification, with secondary centers appearing later at the ends within the epiphyses and apophyses that continue the growth by endochondral ossification. The physis is organized into five clearly demarcated histologic zones: (1) resting zone containing immature cells on the epiphyseal side of the physis, (2) cell growth or proliferation, (3) cell hypertrophy, (4) provisional calcification, and (5) ossification. The weakest zone is in the area of the hypertrophied cartilage cells; this is the most common area of physeal fracture following trauma.[1-3] Bone healing is similar to the endochondral growth process.[2,3]

BONE HEALING

Bone healing is a normal ongoing process throughout all bones as a result of aging of the bone that requires replacement of bone over time and healing of microfractures, which if not repaired could result in structural failure of the bone and clinical fracture. Processes that interfere with normal bone metabolism or physical trauma that stresses the bone beyond its structural capacity can result in fractures. Bone differs from most other organs in that it retains the potential to regenerate and restore preinjury properties rather than heal by scar tissue of poorer quality than the original tissue. Fracture repair involves a large number of complex coordinated biologic and mechanical interactions that can be conceptualized as involving four major elements, including: (1) mechanical environment, (2) osteoconductive scaffolds, (3) osteogenic cells, and (4) growth factors.[2,4] Fracture healing may occur by two basic methods: *direct* and *indirect* bone healing. *Distraction osteogenesis* is a third type of bone healing that is associated with bone lengthening techniques, which are being used more frequently.[2,3,5,6]

Indirect (secondary) bone healing is the most common type of healing observed in animals and occurs in fractures in which some movement is possible between fracture fragments because of a lack of rigid fixation. Secondary bone healing involves callus formation involving both intramembranous and endochondral ossification. Intramembranous ossification forms bone directly from osteoprogenitor cells and undifferentiated mesenchymal cells in the periosteum away from

the fracture site without a cartilage precursor. Endochondral ossification occurs by ossification of cartilage produced by recruitment, proliferation, and differentiation of undifferentiated mesenchymal cells from the periosteum and external soft tissues adjacent to the fracture site.[7] The initial stage of healing is characterized by hematoma formation and subsequent inflammation. Although callus formation mimics embryonic bone formation, the presence of inflammation is a major difference, and the interaction between the immune system and the skeletal system is an area of emerging understanding in fracture repair.[4,8,9]

Motion between fragments produces strain on the tissues attempting to heal the fracture and causes tissue disruption if the strain is excessive. Initially the fracture gap is bridged by tissues that are more stress tolerant, with replacement of each tissue type by a more rigid type of tissue until a rigid bridge is formed between the fragments. Granulation tissue can withstand 100% stretching before failure, whereas fibrous tissue can withstand only 10% and bone only 2% deformation before failure.[2] The initial hematoma at a fracture site is replaced by granulation tissue followed by fibrous connective tissue that is replaced by fibrocartilage and then endochondral ossification to produce a bony union. The initial bony bridging callus is woven bone that is remodeled over time to produce compact cortical bone (see Fig. 16-11).[2,6]

Direct (primary) bone healing is healing that occurs directly between fracture fragments without a cartilaginous stage and no observable callus. Excellent anatomic reduction and alignment of the fracture fragments with rigid fixation are required. The fracture gap must be very small—no more than 150 to 300 µm. The gap is filled initially with fibrous bone followed by remodeling and reconstruction of the haversian systems across the fracture to provide a stronger union. [3,5,6]

Distraction osteogenesis results from gradual distraction of the bone segments, often after osteotomy. The gradual widening of the osteotomy gap, ideally 1 mm per day, allows deposition of parallel columns of osteoid leading to formation of lamellar bone within these columns if sufficient stability is present (Fig. 16-1). The goal is to lengthen a bone that is too short as a result of premature growth cessation or to correct a misshapen bone.[3,10]

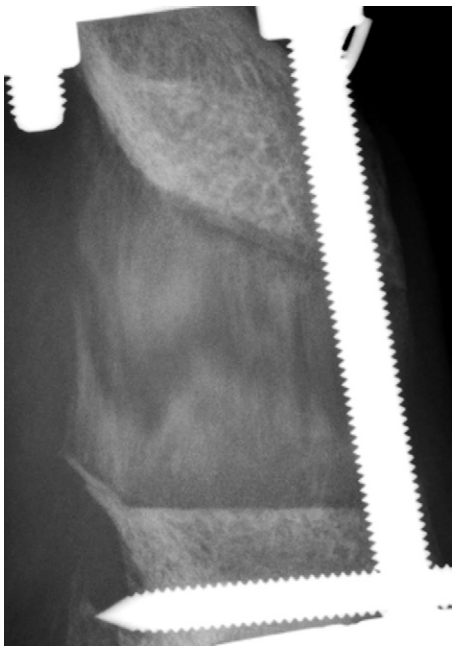


Fig. 16-1 Radial osteotomy performed to correct angular limb deformity and lengthen the limb. Note the vertically oriented lamellar bone formation in the osteotomy site typical of distraction osteogenesis.

FACTORS AFFECTING BONE HEALING

Many factors individually or in combination can have a marked effect on the success or failure of fracture healing. The time required to achieve a clinical union adequate to change or remove orthopedic fixation devices varies significantly depending on these factors. Many variables are known to influence facture healing adversely. These include age and weight of the patient, quality of anatomic reduction, stability of fracture, extent of local blood supply, type of fracture, bone involved, presence of infection, iatrogenic interference, systemic diseases such as metabolic and endocrine diseases, pathologic fracture, corticosteroids, and use of nonsteroidal antiinflammatory drugs.[2,3,5,11-14]

Anatomic reduction with a narrow facture gap will improve the chance of direct or rapid indirect healing. Large fracture gaps or missing bone fragments require more and larger callus formation and a longer time for bridging of the fracture. In addition, anatomic reduction allows the apposition of the bone fragments to enhance the stability of the fracture. Positioning of fracture ends should have at least 50% contact to expect healing of the fracture. However, fracture healing is more likely with anatomic reduction. Anatomic reduction is critical with articular fractures to prevent long-term cartilage damage and degenerative changes from abnormal pressure distribution.[2]

Stability is a key factor in successful healing of a fracture; motion at the fracture site is the most common cause of poor fracture healing in animals. Motion caused by poor fixation or excessive patient activity is a significant contributing factor. Strain produced by movement in the fracture gap can disrupt the tissues, including new blood vessels required for proper healing. Less rigid fixation results in a larger callus with a prolonged chondral phase and continued new bone formation with later initiation of callus remodeling.[15] The effect of mechanical factors on bone healing is well known; however, the detailed mechanisms of mechanotransduction in fracture healing continue to be identified.[16] Lack of stability delays healing until more stable tissues can form in the fracture gap and produce sufficient stability for osteogenesis (Fig. 16-2).[4,17,18]

Viability of the surrounding soft tissues has a significant effect on the ability of bone to heal.[3,19,20] Viable adjacent soft tissue provides protection for bone fragments and a source of extraosseous blood supply that is vital in the healing process. Disruption of the normal blood supply to the fracture zone inhibits the repair process. Blood vessels from surrounding tissues are recruited to provide adequate oxygen and nutrients for fracture repair. When the fracture is healed, these extraosseous vessels become dormant as the normal blood supply to the bone is revitalized. Severe damage or loss of surrounding soft tissue decreases the rate of fracture repair and may prevent healing. Fracture fragments that are denuded of soft tissue and bone grafts require adequate stabilization to allow early revascularization of the bone and healing of the fracture. Without revascularization of these bone fragments, healing will not occur. There is increasing emphasis on minimally invasive fracture stabilization techniques that preserve the biologic environment. The technique of minimally invasive plate osteosynthesis shows evidence of more rapid fracture healing compared with more open stabilization techniques in both humans and animals.[20-22]

The *specific bone involved* in the fracture can affect the outcome of fracture healing. Some bones have less adjacent soft tissue to supply temporary vasculature for healing. Some small canine breeds have delayed healing of antebrachial fractures with a higher complication rate than larger breeds (Fig. 16-3).[23,24] Stabilization of the calcaneus is more difficult because of the normally higher stress on this bone.

Infection of bone or surrounding tissue can have a profound effect on healing. Infection can disrupt healing in the fracture

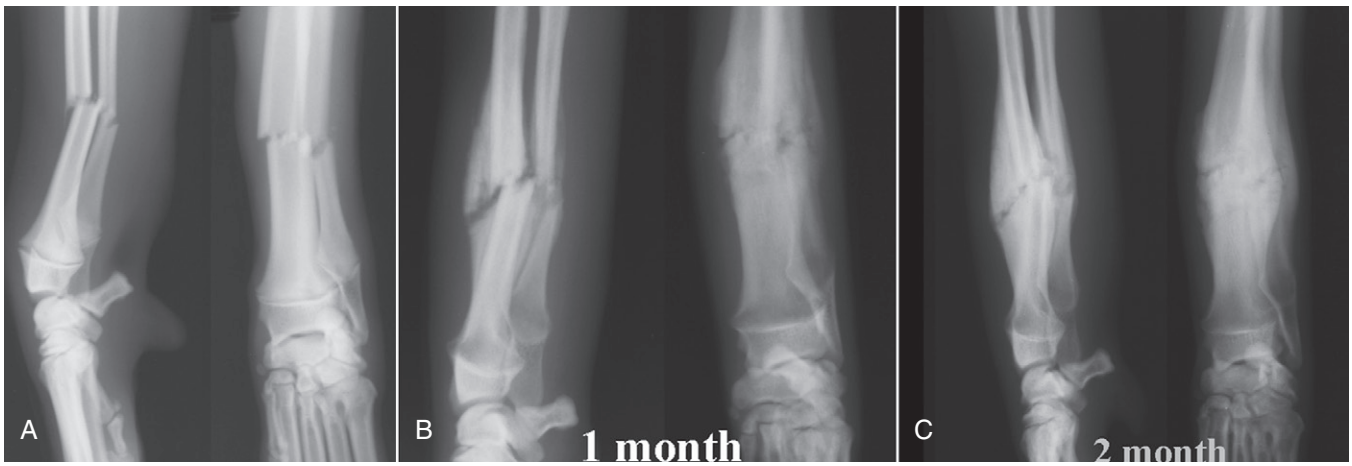


Fig. 16-2 Transverse diaphyseal fractures of the radius and ulna of an immature dog with 1- and 2-month follow-up radiographs. The lack of good fracture stabilization resulted in delayed secondary healing with exuberant callus. A radiolucent fracture line is still visible at 2 months, indicating that the fracture is not completely healed.

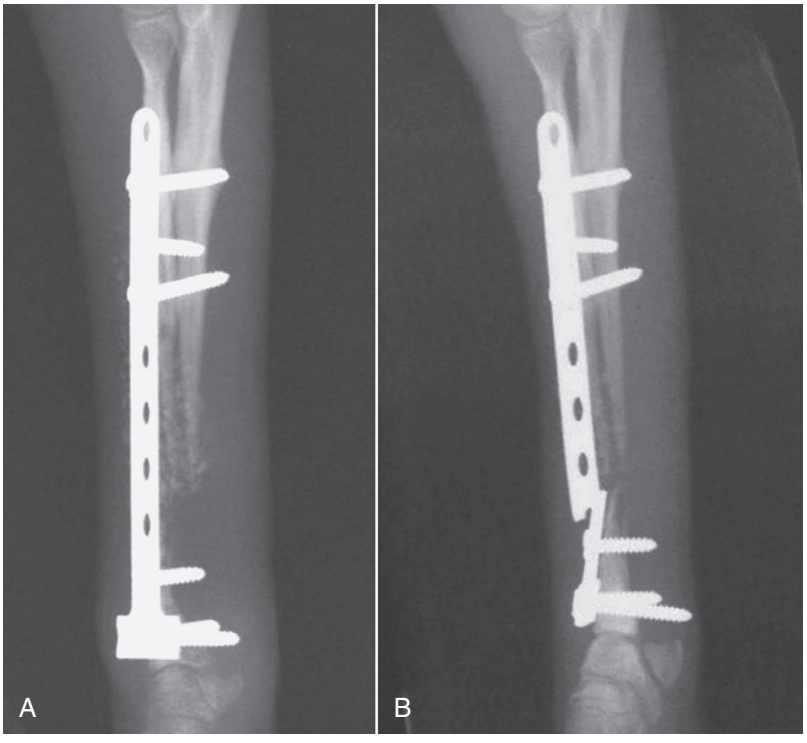


Fig. 16-3 **A,** This toy poodle has atrophic nonunion radial and ulnar fractures at 3 months after the original injury. Note the lack of callus and atrophy of the adjacent ends of the fracture fragments. The small mineral foci overlying the fragments are small islands of cancellous bone grafts placed during fixation. Poor soft tissue environment, including poor blood supply, at the fracture site prevented the formation of callus. **B,** At 4.5 months after the initial injury, bone plate failure from metal fatigue is evident.

gap directly but also indirectly by causing loosening of the fixation device, allowing the fracture to become unstable. The recognition and aggressive treatment of infection is important for successful bone healing (Fig. 16-4). More detailed information on recognition of bone infection radiographically is presented in Chapter 17.

Proper selection and application of the fixation device has a significant effect on the rate and success of fracture repair. The fixation device must provide fracture stabilization and not interfere with healing. Common problems include inadequate size and placement of intramedullary pins or insufficient number of plate-associated screws on each side of a fracture that allow fracture instability as well as excessive soft tissue disruption that delays or prevents revascularization (Fig. 16-5). Adequate knowledge, experience, and skills are necessary for the appropriate treatment of bone fractures. [2,3]

Miscellaneous factors, including species, breed, age of the patient, nutritional status, and presence or absence of metabolic disease, can affect the duration and success of fracture healing. Some species, such as horses, require longer times for clinical fracture healing because of their greater weight and slower metabolism compared with the average dog. Fractures in younger animals heal faster than those in older animals of the same species.[25] Hypothyroidism, hyperparathyroidism, diabetes mellitus, and some paraneoplastic syndromes can delay bone healing.[12]

PROMOTING FRACTURE HEALING

An estimated 5% to 10% of the 7.9 million fractures sustained annually by humans in the United States do not result in



Fig. 16-4 Advanced bacterial osteomyelitis after fixation of a distal antebrachial fracture with an external fixator. Note the active periosteal reaction that extends the entire length of the bone. Soft tissue swelling is also present and is important in differentiating septic versus nonseptic periosteal new bone. In addition, the irregular margins of the periosteal reaction are atypical for callus and suggest an aggressive process.

satisfactory union following initial treatment. The failure of bone healing results in enormous healthcare and socioeconomic costs. This represents a strong economic incentive to develop novel technologies to enhance bone healing.[26] The incidence of nonunion fracture in dogs is approximately 3.4%[27] with a range of 0% to 6%.[28] The incidence of nonunion fracture in cats is 0.85%[29] to 4.3%.[13] The following brief summary is presented to recognize the importance and diversity of innovative biologic bone healing techniques that are being developed. Many studies published in the last 6 years have added significantly to the knowledge base in the field of biologic bone healing techniques, with potential benefits for enhanced bone repair in humans and animals. Emerging biologic bone healing therapies fall into the following main categories: (1) physical stimulation therapies, including low-intensity pulsed ultrasound and electromagnetic field stimulation; (2) local biologic stimulation therapies, including platelet gel and platelet-derived growth factor, bone marrow cells, prostaglandins, cholesterol statins, bone morphogenetic proteins, and vascular endothelial growth factor; (3) systemic biologic stimulation, including parathyroid hormone, growth hormone, and modifiers of the Wnt intracellular signaling pathway.[26,30-34]

Low-intensity pulsed ultrasound and extracorporeal shockwave therapy have been in clinical use since the early 1990s; however, results of controlled and clinical studies have been mixed, and the role of these techniques in the treatment of fractures remains unclear.[35-39]

Bone grafts have been used for decades, with the use of autologous bone grafts being the gold standard. Autologous bone grafts provide osteoconductive, osteoinductive, and osteogenic characteristics without compatibility problems. However, autologous bone grafts extend surgical time and are of limited supply in smaller animals, and there are potential



Fig. 16-5 Poor postoperative alignment and fixation resulted from use of a single intramedullary pin. A large butterfly fragment is not incorporated into the fixation *(white arrowhead)*. The result is a malunion and large callus. A segment of the proximal fracture fragment lost blood supply and became devitalized, resulting in a sequestrum *(white arrows)*. A draining fistula (not observable on radiographs) was associated with the sequestrum. The sequestrum required surgical removal.

complications at the harvest site.[40,41] Bone allografts are available commercially and may be incorporated into fracture repair to provide osteoconductivity and additional support. Various types of allografts are available and differ in their intended use, with the most common use being associated with repair of large defects and in spinal fusion.[40] The development of endoprostheses may replace allograft use because of similar outcomes and easier availability.[42] Other osteoconductive biomaterials are available widely and may be grouped into ceramic-based or polymer-based bone graft substitutes. Osteoinductive bone graft substitutes stimulate osteogenic differentiation of local undifferentiated cells and are especially useful for treating nonunion or compromised fractures. Osteoinductive bone graft substitutes include demineralized bone matrix, platelet concentrates, bone morphogenetic proteins, and other growth factors. Osteogenic bone graft substitutes consist of connective tissue progenitor cells capable of differentiating into osteocytes. Bone marrow aspirates are currently the most common source of these cells that can be used alone or in combination with other fracture repair techniques to enhance bone healing.[40,41,43-48]

FRACTURE IDENTIFICATION

Physical examination is an essential first step in the evaluation of fractures and possible complicating factors. Dealing with immediate life-threatening injuries takes precedence over imaging to look for fractures. Careful systematic palpation of the entire skeleton is warranted in patients suspected of having a fracture. Obvious abnormalities must not distract from a thorough examination for less-obvious but significant fractures. Identification of open fractures, spinal fractures, and skull fractures requires careful evaluation with temporary stabilization. Appropriate treatment of open wounds associated with fractures prevents further injury and bacterial contamination that can affect the outcome negatively. Although the overall condition of the patient must be considered, unnecessary delay of treatment is undesirable because delaying fracture stabilization for more than 48 hours after injury is associated with a poorer functional outcome.[2,49]

Diagnostic imaging provides valuable information concerning the location, type, complexity, and potential complications associated with fractures. Imaging also provides a basis for planning fracture reduction and stabilization. Appropriate pain management, tranquilization, physical restraint, and anesthesia commensurate with the patient status are necessary for obtaining high-quality images for evaluation and planning. Motion is the most common cause of inferior images in animals. Motion leads to degraded images in which important smaller fractures or fissures vital for planning reduction and stabilization of the fracture may be overlooked.

Knowledge of normal anatomy and normal variations or aberrant anatomic change is critical for accurate interpretation of images. Normal and accessory ossification centers and normal or aberrant nutrient foramina can mimic fractures.[50,51] Anatomic references and skeletal models are invaluable and should be readily available.

Radiography remains the most commonly used imaging tool for fracture evaluation in veterinary medicine. Two orthogonal views of the area in question are essential for adequate evaluation of a potential fracture. A single view does not allow complete assessment of the fracture fragments and can be misleading, possibly causing disastrous results. In some patients oblique views are necessary to define or identify a subtle or complex fracture. With minimal displacement, the fracture line must be parallel to the x-ray beam for the radiolucent fracture line to be seen (Fig. 16-6).

If the clinical findings indicate a high probability of fracture and no fractures are identified on initial radiographs, oblique radiographs should be made. Small stress fractures or incomplete fractures may not have sufficient displacement immediately following the injury to allow detection. Follow-up radiographs in 7 to 10 days may be needed to detect these fractures as the fracture line becomes more conspicuous. The normal healing process begins with some resorption of the ends of the fracture fragments. Sometimes early callus formation is the only finding that allows identification of a stress fracture. In some patients, other anatomic structures may obscure a fracture on some views, and multiple views may be required to detect the fracture.[52]

For extremity fractures in small animals, the joint(s) proximal and distal to the fracture should be included on the radiograph for assessment of possible joint involvement or preconditions that may alter the treatment or outcome. The radiographic technique should be excellent for bone and

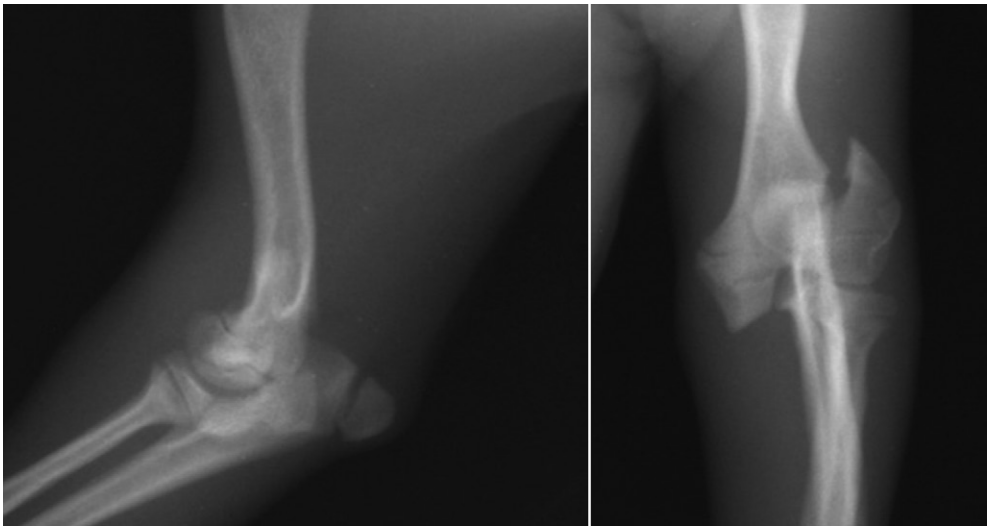


Fig. 16-6 Salter-Harris type IV intercondylar fracture of the distal humerus with the fracture line passing through the lateral metaphysis, physis, and epiphysis. The fracture is difficult to identify on the lateral view. At least two views of a suspected fracture area should be made. An oblique view is necessary for the identification of some intercondylar fractures, an oblique view is necessary for identification of the fracture.

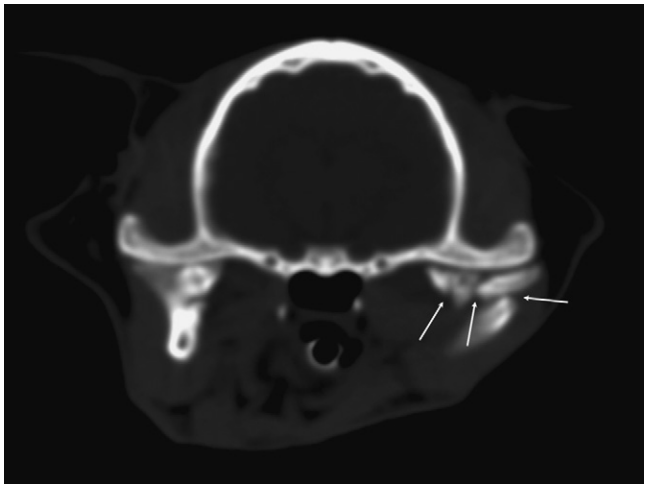


Fig. 16-7 Transverse CT image through the level of the temporomandibular joints. A comminuted articular fracture of the articular condyle of the mandible is visible *(arrows)*. The severity of the fracture was not observable on radiographs.

ideally allow evaluation of the adjacent soft tissues as well. One of the distinct advantages of digital radiography systems is the increased dynamic range that allows optimizing the same image for viewing bone and soft tissues.

Computed tomography (CT) is especially useful in characterization of fractures in regions with complex anatomy such as the nose, skull, and pelvis (Fig. 16-7). Detail of both cortical and trabecular bone is excellent, and fractures and fissures that are not observed on radiographs are readily apparent in CT images.[53,54] In addition, adjacent soft tissue injuries can be observed as well as underlying conditions contributing to a pathologic fracture.[55] Postoperative assessment of articular fractures with CT improves the detection of step deformities.[56]

Scintigraphy is a sensitive method to detect stress fractures and other occult fractures not identified on radiography. Increased uptake of a bone-seeking radiopharmaceutical is related to osteoblastic activity. Bone scintigraphy is very sensitive, being able to detect a stress fracture in an equine metacarpal bone within 24 to 72 hours of injury.[57,58] However, its specificity is low because of other diseases that can cause increased radiopharmaceutical uptake. The history, degree of uptake, degree of lameness, and information from other imaging modalities must be considered in determining a probable diagnosis of fracture.[57,59,60] Scintigraphy does require patient isolation for radiopharmaceutical clearance after the procedure. Scintigraphy in orthopedic patients is used primarily to identify possible sites of occult fracture or bone lesions not detected by other imaging means.

Magnetic resonance imaging (MRI) is the modality of choice for the diagnosis of many musculoskeletal disorders in human beings.[1] MRI provides significantly more information than radiography in evaluation of the extent of injury to an open physis and the extent of physeal closure following injury.[1] MRI is most notable for its detailed imaging of soft tissues with significantly better soft tissue contrast resolution than CT. MRI is especially useful for detecting abnormal changes in muscles, tendons, ligaments, and cartilage. MRI is sensitive to changes in bone marrow that can aid in the identification of bone lesions that would not be otherwise detected. Radiography is ineffective in the differentiation and identification of soft tissue injuries, and although CT has better soft tissue contrast resolution than radiographs, neither provides the exquisite soft tissue images possible with MRI.[55,61]

Ultrasound examination of musculoskeletal injuries is becoming more common, primarily for evaluating the soft tissue component. Evaluation of tendons and ligaments with ultrasound is common.[62,63] The integrity of bone surfaces can be evaluated with ultrasound with some success in observing occult fractures and sequestra.[64] However, sonographic skill and familiarity with the anatomy are required. Although ultrasound is useful in the evaluation of fracture healing, this is not common practice, possibly because of the high-quality equipment and advanced sonographer expertise required.[65]

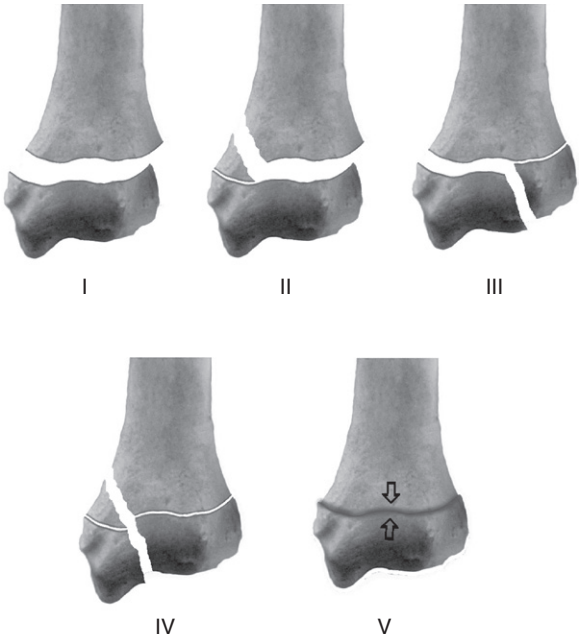


Fig. 16-8 Salter-Harris physeal fracture classification.

FRACTURE CLASSIFICATION

Fracture classifications serve to standardize language to improve communication. Some are developed to organize fractures into clinically useful groups that help guide treatment options and prognosis.[5,55] Fractures are classified commonly according to location, direction, complete or incomplete status, number of fracture lines, displacement, and open or closed status. Additional descriptive terms are used in combination with the basic classification to further describe a fracture or describe a specific type of fracture.[3,52]

Location is the first descriptor used in describing a fracture and includes the bone involved and location in the bone.

Diaphyseal fractures of long bones may be described with the diaphysis divided into thirds; *proximal*, *distal*, or *mid-diaphyseal*.

Metaphyseal fractures of long bones are described as involving the proximal or distal metaphysis.

Epiphyseal fractures involve the adjacent joint and physis commonly. If the physis is open, the Salter-Harris classification system is used to describe the fracture (discussed later).

Articular fractures consist of any fracture that enters a joint. Important aspects to describe with an articular fracture are extent and location of the articular surface involved and if there are free fragments within the joint.

Physeal fractures involving an open physis are described with the *Salter-Harris* classification system.[66] Five classes were described originally on the basis of involvement of the epiphysis, physis, and metaphysis (Fig. 16-8).

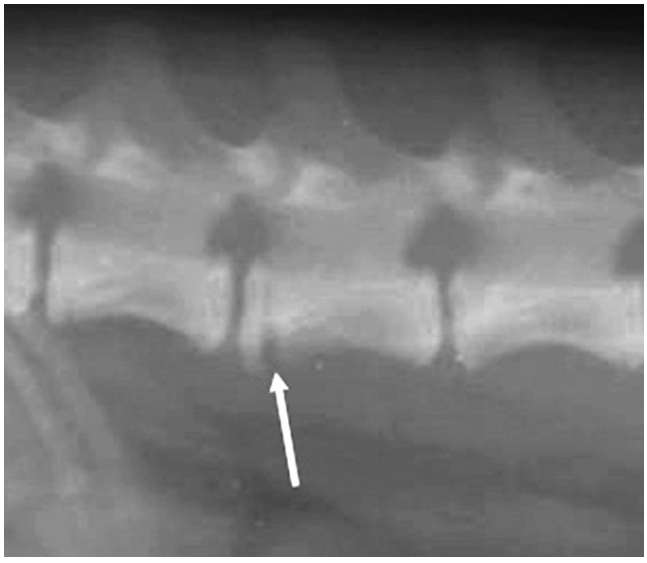


Fig. 16-9 Minimally displaced Salter-Harris type I fracture of the cranial physis of L3.



Fig. 16-10 Salter-Harris type II fracture of the proximal tibia.

Salter-Harris Type I fractures are through the physis (Fig. 16-9).
Salter-Harris Type II fractures are through the physis and a portion of the metaphysis (Fig. 16-10).
Salter-Harris Type III fractures are through the physis and epiphysis and are usually articular fractures.
Salter-Harris Type IV fractures are through the epiphysis, across the physis and through the metaphysis. These are usually articular fractures (see Fig. 16-6).
Salter-Harris Type V fractures are crushing or compression fractures that involve the physis. Increased opacity of the physis may be the only radiographic sign in the acute injury, but this opacity change is often not recognizable on initial radiographs. Comparison with the normal opposite limb may aid in identifying subtle changes. Salter-Harris type V fractures frequently cause premature closure of all or a portion of the physis, leading to growth deformities.
A Salter-Harris type VI group was added later and is a partial physeal closure resulting from damage to only a portion of the physis, leading to asymmetric closure. However, the type VI designation really described a sequel of physeal injury rather than the initial injury and is not used universally.[1]

Direction of the fracture is a description of the direction of the fracture line relative to the long axis of the bone and is typically *transverse*, *oblique*, or *spiral*.

Transverse fractures run perpendicular to the long axis of the bone (see Fig. 16-2).
Oblique fractures run at less than 90 degrees to the long axis with fractures equal to or less than 45 degrees being described as *long oblique fractures* and fractures that are greater than 45 degrees being described as *short oblique fractures* (see Fig. 16-13, p. 291).[3]
Spiral fractures are usually associated with significant torsional trauma and are an oblique fracture that wraps around the long axis of the long bone (Figs. 16-11 and 16-12).

Complete fractures extend through the entire bone and are more common than incomplete fractures. The term *complete* is not used commonly in fracture description because a fracture is assumed to be complete unless the description states that it is incomplete.

Incomplete fractures have lines that involve only a single bone cortex or small portion of a bone and do not cause separation of the bone into two or more fragments. A *greenstick* fracture usually occurs in young animals and is an incomplete fracture of one side of the bone with bending of the opposite cortex (plastic deformation) (Fig. 16-13, p. 291). *Fatigue* or *stress* fractures are another type of incomplete fracture. They are typically microfractures caused by repeated trauma over time that exceeds the load capacity of the bone slightly. Stress fractures may not be seen radiographically or may appear as faint, linear, incomplete fractures involving one portion of a bone. Scintigraphy can be used to identify stress fractures when radiographs are normal or inconclusive. Radiographic changes observed in addition to linear or curvilinear radiolucencies in a focal aspect of the cortex are increased bone opacity and early periosteal new bone production.

Number of fracture lines is generally defined as simple or comminuted.

Simple fractures are those that have only one fracture line and divide the bone into two main fragments. Generally if the fracture is not stated to be comminuted, a simple fracture is assumed and the term *simple* is not included in the description.

Comminuted fractures have more than one fracture line that communicates to a single point or plane and divide the bone into three or more fragments. Comminuted fractures with three large fragments often have a triangular fragment called a *butterfly fragment* (see Fig. 16-5). Fractures that divide the bone into five or more fragments are *severely* or *highly* comminuted (Fig. 16-14, p. 291).

Open or *closed* are descriptive terms that indicate whether the fracture is exposed to the outside environment. Open fractures can be classified according to the mechanism of puncture and severity of soft tissue injury (Fig. 16-15, p. 292).[2,3,5] Typically the term *closed* is not used in a description because a fracture is assumed to be closed unless the description states the fracture is open. The terms *type*, *grade*,



Fig. 16-11 Mildly displaced spiral fracture with good stability leading to indirect (secondary) healing by 5 weeks.

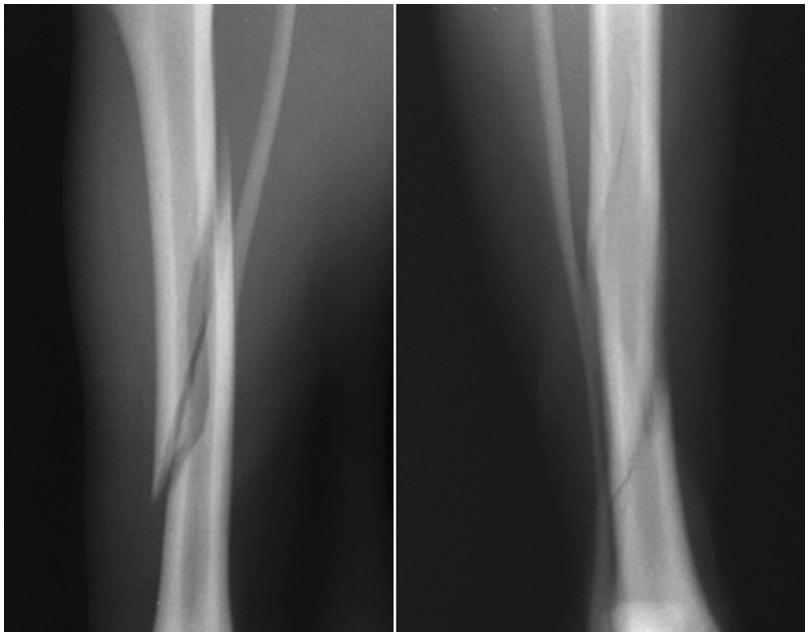


Fig. 16-12 Mid-diaphyseal spiral fracture of the tibia.

and *degree* have been used somewhat interchangeably for this classification system.

Type I: Open fracture with small puncture wound in the skin close to the fracture caused by one of the bone fragments penetrating the skin. The wound is less than 1 cm long.
Type II: Variable-sized skin wound associated with the fracture as a result of external trauma. Type II has more soft tissue damage than type I.
Type III: Severe bone fragmentation associated with extensive soft tissue injury with or without skin loss. Type III can be subdivided into:
Type IIIa: Requires no major soft tissue reconstruction such as a skin flap or graft to cover the wound.
Type IIIb: Requires soft tissue reconstruction because of insufficient viable soft tissue to cover the wound.
Type IIIc: Open fractures that have major arterial injuries that must be repaired to maintain tissue viability.
Type IV: Open fractures that involve amputation or near amputation of the limb. These fractures have severe soft tissue and neurovascular injuries.[2]

Displacement of a fracture is described in terms of the distal or caudal fracture fragment. In some fractures the fragments are moveable and change position easily. The importance of displacement is related to interference with or extent of injury to other structures. For example, medial displacement of a pelvic fracture may be associated with acute injury to the lower urinary tract or possible interference with defecation or parturition.[52] Displacement is usually defined in terms of shortening or lengthening, angular displacement, and torsional displacement. Shortening of the bone is most commonly a result of traction by surrounding musculature and may be a result of *collapse* of multiple fragments or *overriding* of the main fracture fragments. Lengthening of the bone, caused by *distraction* of the fragments resulting in widening of the fracture gap, is uncommon except with *avulsion* fractures

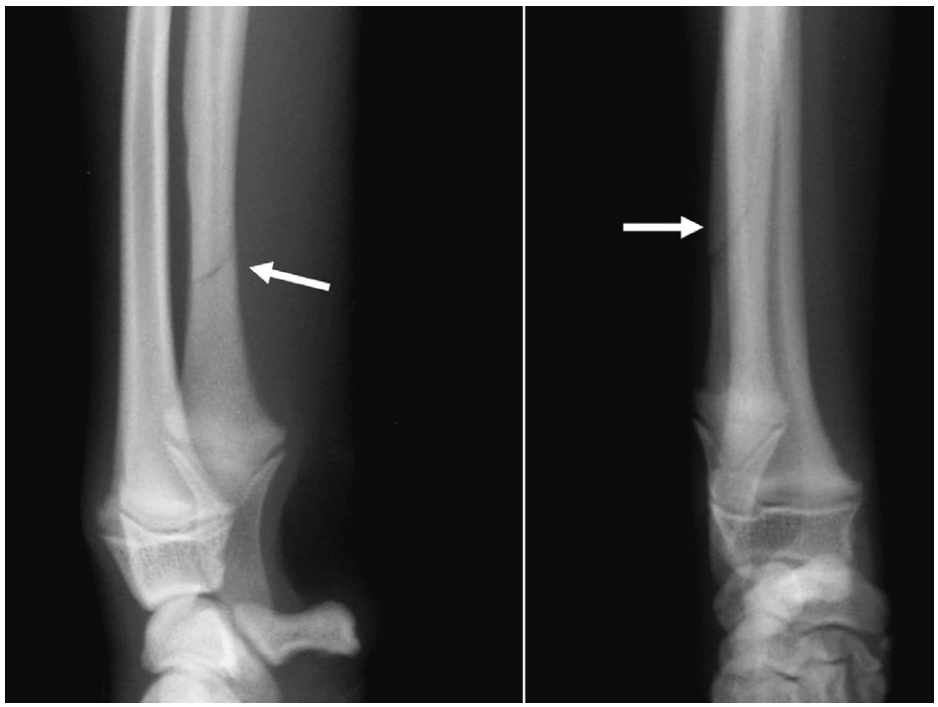


Fig. 16-13 Incomplete short oblique fracture of the distal diaphysis of the ulna *(white arrows)*.



Fig. 16-14 Severely comminuted distal diaphyseal tibial fracture caused by a ballistic injury. High-velocity projectiles cause severe soft tissue injury in addition to fracture. Projectiles made of softer materials will fragment on contact with bone, and numerous small metal fragments will be seen in association with the fracture site. There are multiple small metal fragments in this patient, indicating a high degree of fragmentation of the bullet.

(Fig. 16-16). *Angular displacement* is described as the direction taken by the distal or caudal fragment relative to the proximal or cranial fragment. *Torsional displacement* describes inward or outward rotation of the distal or caudal fragment.

Other descriptive terminology and classification can be used to describe specific fractures further.

Pathologic fractures occur without abnormal or overt trauma as a result of secondary weakening of the bone by an underlying disease. Pathologic fractures are seen commonly with neoplastic weakening of the bone (Fig. 16-17, p. 293). However, pathologic fracture can also be associated with other diseases such as hyperparathyroidism (Fig. 16-18, p. 293). Pathologic fractures are important to recognize to make an informed assessment of treatment options and prognosis.

Chip fractures are typically small fragments of bone that are broken off of a bone as a result of direct trauma. The presence of a fracture bed helps differentiate chip fractures from accessory ossification centers and dystrophic soft tissue mineralization.

Slab fractures are typically seen in cuboidal bones of the joints and are fractures that run from one joint surface of the bone to the opposite joint surface. A fracture of a cuboidal bone that involves just one joint surface would be a *chip* fracture.

Avulsion fractures occur at attachment sites of tendons, ligaments, or joint capsules and are caused by excessive forces placed on these structures that result in a piece of bone being pulled off of the parent bone. Avulsion fractures should have observable fracture beds (see Fig. 16-16).

Multiple or *segmental* fractures have more than one fracture line, but they do not communicate as in comminuted fractures.

Compression or *impacted* fractures occur from trauma that crushes the bone, thus decreasing one or more dimensions of the bone. This is most commonly seen in vertebral bodies and cuboidal bones.

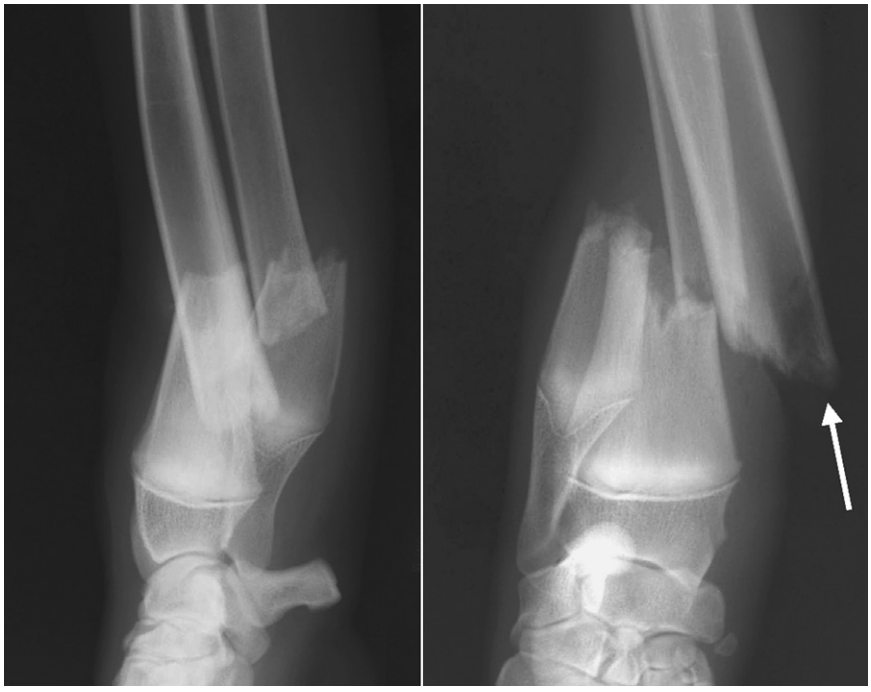


Fig. 16-15 Open transverse distal diaphyseal fractures of the radius and ulna with lateral displacement and mild overriding. The distal end of the proximal radial fracture fragment is seen outside the soft tissues on the cranial-caudal view, indicating that it is an open fracture.

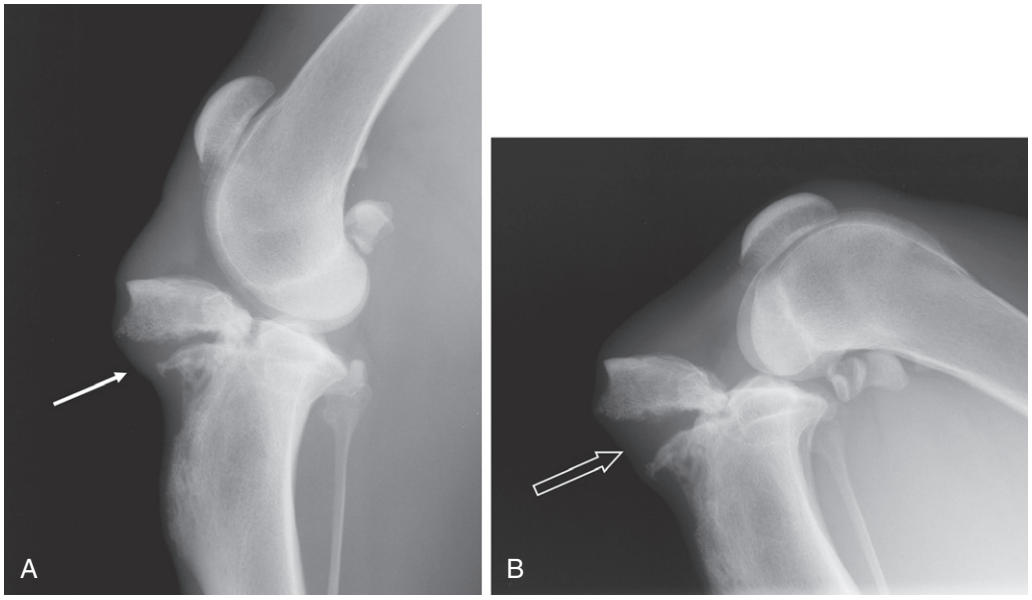


Fig. 16-16 **A,** Four-day-old avulsion fracture of tibial tuberosity *(solid arrow)*. **B,** In a flexed view, widening of the fracture gap indicates dynamic instability *(open arrow)*.

Depression fractures occur in the skull, sinuses, and nose, with fracture fragments displaced below the normal surface.

Condylar, bicondylar, and *supracondylar, T,* and *Y* fractures are terms used to describe fractures involving the metaphysis and condyles. Fractures between the condyles as well as through the epicondyles or metaphysis can be described as a T or Y fracture. Fracture of a condyle only from the parent bone is termed a *condylar* fracture.

Osteochondral fractures are defined as a disruption of articular cartilage along with a portion of subchondral bone. If the fracture fragment is loose within the joint, it is termed a *loose body* or *joint mouse*.[55]

Fissure fractures are incomplete fractures that appear as thin radiolucent lines often arising from a complete fracture (Fig. 16-19). Fissure fractures must be identified because they often develop into complete fractures during reduction and fixation and compromise the repair. Identification during initial imaging provides the information necessary for adequate planning.

Abrasion or *shearing fractures* are caused by loss of soft tissue and bone as a result of friction or glancing trauma. The most common cause is abrasion of extremities being pulled along asphalt or concrete surfaces when the animal is hit by a moving vehicle. A portion of soft tissue and bone is

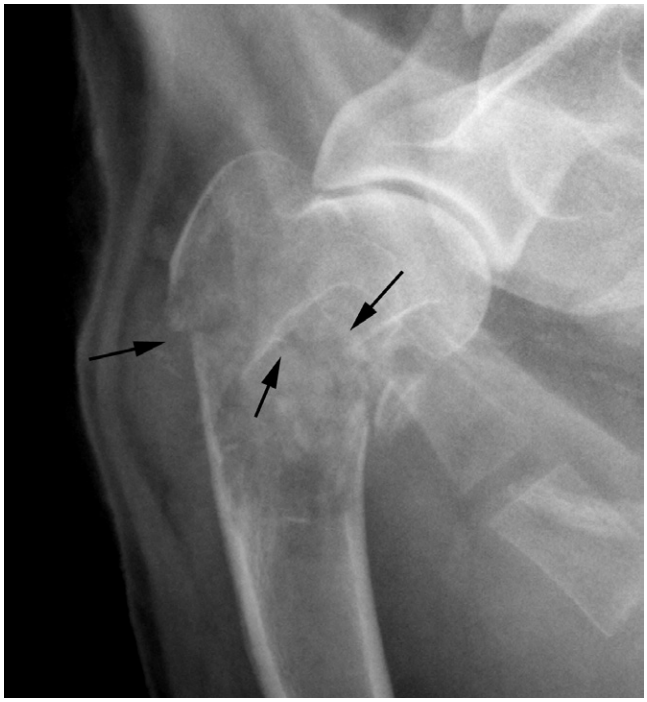


Fig. 16-17 Lateral view of the proximal humerus of a dog with a pathologic fracture *(black arrows)* secondary to an osteosarcoma.

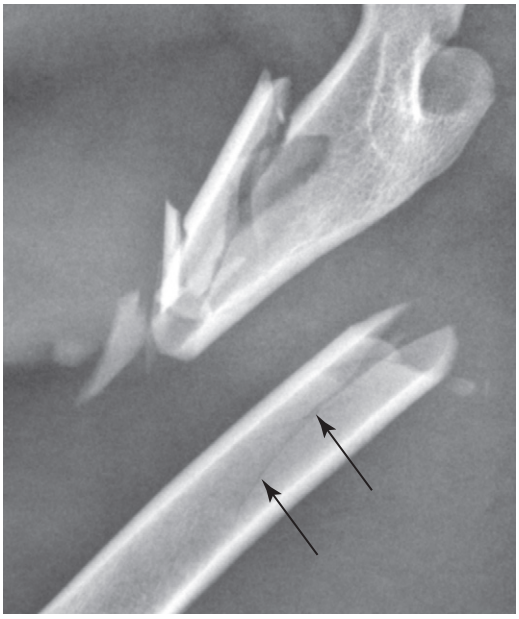


Fig. 16-19 Lateral view of the proximal aspect of the femur of a dog with a comminuted proximal diaphyseal fracture. There is a fissure fracture extending distally from the main fracture site *(black arrows)*. This fissure will affect the type of internal fixation used.



Fig. 16-18 Lateral view of the distal femur of a cat with nutritional secondary hyperparathyroidism. There is a healing malunion fracture of the distal femur. Note the thin cortices and poor contrast between the demineralized bones and adjacent soft tissue.

lost from the abrasive effect of the rough surfaces. These types of fractures are always open fractures and commonly involve joints (Fig. 16-20).

RADIOGRAPHIC EVALUATION OF BONE HEALING

Postoperative imaging is essential for evaluation of the reduction and alignment of the fracture as well as placement of orthopedic devices (Fig. 16-21). The importance of good-quality postoperative radiographs to serve as a baseline for future evaluation cannot be overemphasized. At least two orthogonal views are required to interpret the location of bony structures and orthopedic devices accurately. Radiographs should be repeated every 4 to 6 weeks or sooner if clinical signs indicate an acute change in condition.[3]

An organized paradigm is required for evaluating radiographs of orthopedic procedures. One commonly used system goes by the mnemonic ABCDS, standing for ***a***lignment, ***b***one, ***c***artilage, ***d***evice, and ***s***oft tissues.

Alignment is evaluated with reference to previous radiographs, with changes indicating possible instability of fixation. Two orthogonal views are necessary. Patient positioning for the recheck radiographs should be as close as possible to the previous radiographs. The previous radiographs should be reviewed and compared with the current images before the patient is dismissed so that views can be repeated if necessary. Minor changes in angle of view can lead to dramatic changes in the appearance of the bone fragments and orthopedic devices.

The *bone* is evaluated for evidence of healing on the basis of radiographic changes (Box 16-1). Early healing is observed as slight widening of the fracture line and callus formation. Later healing is observed as opaque, mature callus and increasing mineral opacity within the fracture line. Bone fragments that retain sharp margins and do not participate in the callus may indicate devitalization. If a fragment fails to revascularize, it may develop into a *sequestrum* (see Fig. 16-5). Excessive callus and periosteal new bone may be seen with fracture

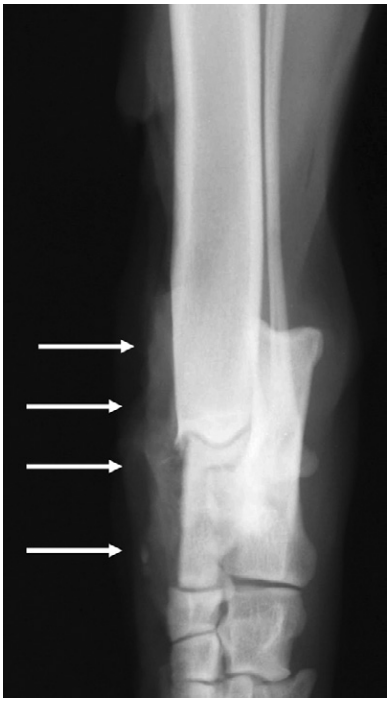


Fig. 16-20 Abrasion-type open articular fractures of the distal tibia and talus *(white arrows)*. The medial malleolus and a portion of the medial aspect of the talus are missing because of the abrasive action of the road pavement as the dog was dragged for a short distance after being hit by a car. The soft tissues on the medial aspect are irregular, indicating loss of the soft tissue as well. The tarsocrural joint is open to the environment. These fractures are typically open fractures. Blood supply and supportive ligaments in these areas can be severely compromised.



Fig. 16-21 Inadequate closed pinning of a Salter-Harris type II fracture of the distal tibia. In the lateral radiograph, the pin appears to be passing through the epiphysis and metaphysis exiting the caudal diaphyseal cortex. In the cranial-caudal radiograph, the intramedullary pin engages only a small portion of the metaphysis and extends laterally into the soft tissues of the limb. Two orthogonal views are required for accurate evaluation of the placement of the fixation devices.

instability, infection, and periosteal injury at the time of the fracture or during surgery (Fig. 16-22). History and clinical signs may help differentiate these possibilities.

The amount of callus is related to the type of fracture, degree of reduction, and fixation.[3,52] Comminuted fractures require a larger callus to achieve adequate stabilization for healing. Fractures that have large gaps either because of less-than-anatomic reduction or missing fragments will heal with a larger callus. Fractures with anatomic reduction and rigid fixation may heal with little or no visible callus. The lack of callus in some of these fractures can be differentiated from an atrophic nonunion by clinical signs, history, and serial radiographs.

Cartilage refers to evaluation of the joints directly involved in an articular fracture or joints proximal or distal to the fracture. The apposition of articular fracture fragments as indicated by alignment of the subchondral bone is an important radiographic sign. Placement or migration of orthopedic devices into a joint can also indicate a complication in fracture healing (Fig. 16-23). The presence of joint effusion with subchondral bone lysis and periosteal new bone may indicate a septic joint.

Evaluation of placement and alignment of the *orthopedic devices* is essential because these changes may signal loosening that could delay or compromise fracture healing. Migration of an orthopedic device indicates loosening and must be correlated with the clinical signs and history to determine if corrective intervention is necessary. Bending of a fixation device can also indicate instability of the orthopedic repair. Breakage of pins, screws, wires, and plates indicates significant past, current, or chronic stress on the orthopedic devices (Fig. 16-24). Evaluation for radiographic signs of healing, including bridging or nonbridging callus, and clinical signs are used to decide if corrective action is necessary or if healing is occurring

Box • **16-1**

Radiographic Signs of Secondary Bone Healing

5-10 Days After Reduction
Fracture fragments lose sharp margins
Demineralization of fracture fragment ends results in slight fracture line widening

10-20 Days After Reducton
Formation of endosteal and periosteal callus
Decreasing size of fracture gap
Variable loss in opacity of free fracture fragments

≥30 Days After Reduction
Fracture lines gradually disappear
External callus increases in opacity and remodels

≥3 Months After Reduction
Continued remodeling of external calluses
Trabecular pattern may develop within the callus
Cortical shadow becomes visible through the callus
Medullary cavity continuity gradually reestablished
Cortical remodeling along the lines of stress

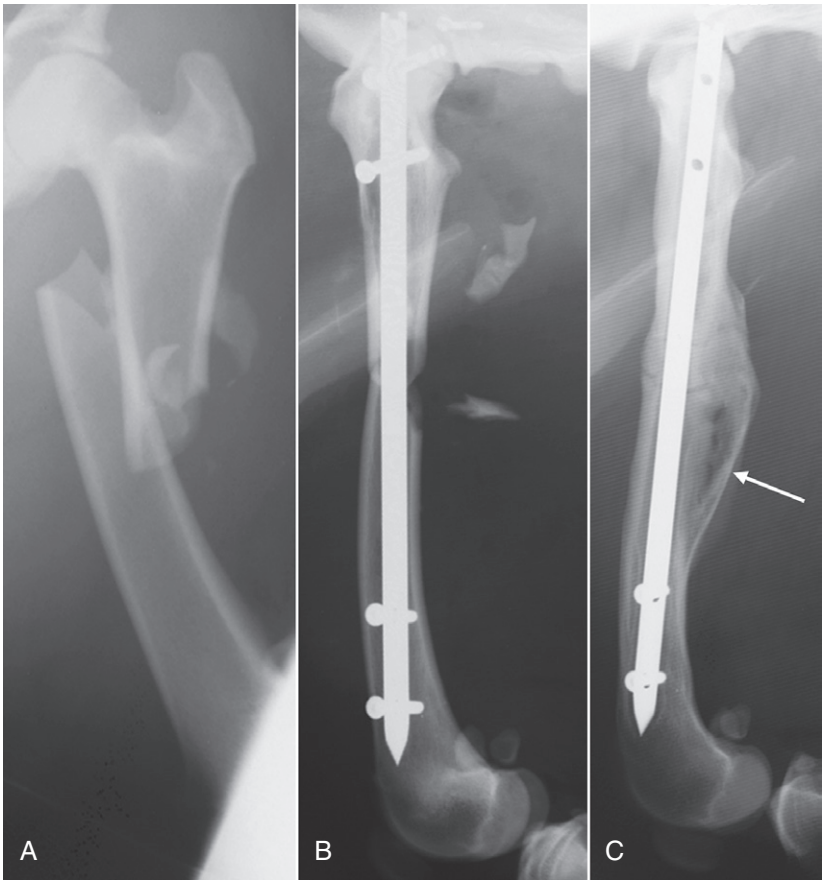


Fig. 16-22 **A,** Comminuted diaphyseal fracture of the femur. **B,** Reduction and fixation with an interlocking nail. **C,** Subsequent indirect (secondary) healing. The convex callus and new bone on the caudal aspect of the femur *(white arrow)* are caused by periosteal stripping at the time of the fracture. This appearance is common with diaphyseal femoral fractures.

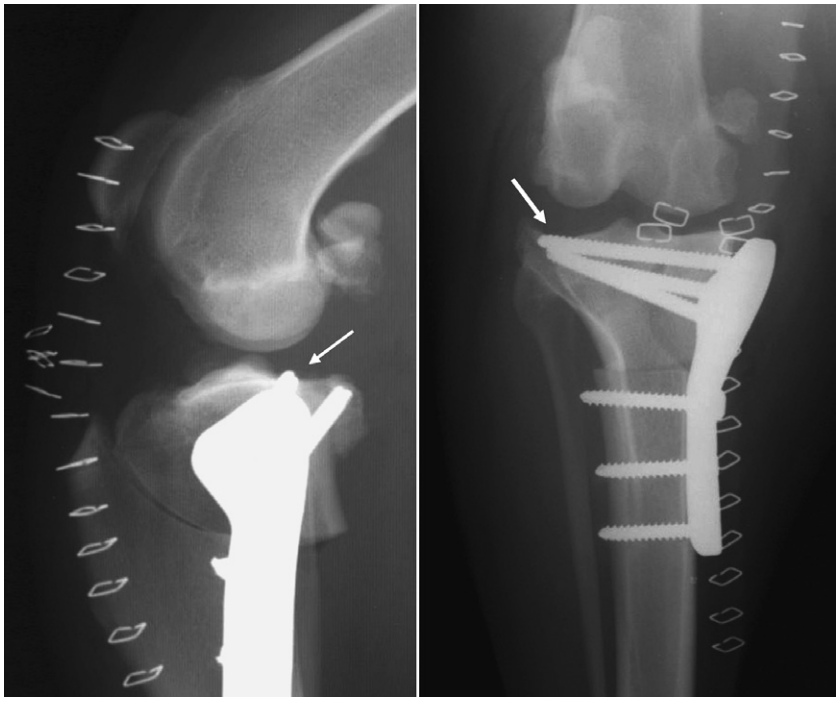


Fig. 16-23 In postoperative radiographs of a tibial plateau leveling procedure, one screw is likely within the joint *(white arrows)*. Although this screw is probably not through the articular cartilage, removal and replacement with a shorter screw or redirected screw is advisable.

in a reasonable manner. Patients with loose orthopedic devices and unstable fractures usually have signs of pain and disuse of the affected structures (Fig. 16-25).

Loosened orthopedic devices commonly have a radiolucency surrounding the device within the bone (Fig. 16-26). Other than motion, either of the implant or of the fragment, additional causes for a radiolucency around an orthopedic implant are bone necrosis caused by high-speed drills, digital radiographic artifact, or osteomyelitis (Fig. 16-27). A radiolucent zone around a metal implant that is relatively even with a visible sclerotic margin suggests a cause other than infection (Fig. 16-28). Radiolucency surrounding a metal implant that is uneven with ill-defined margins is more likely infectious.[52]

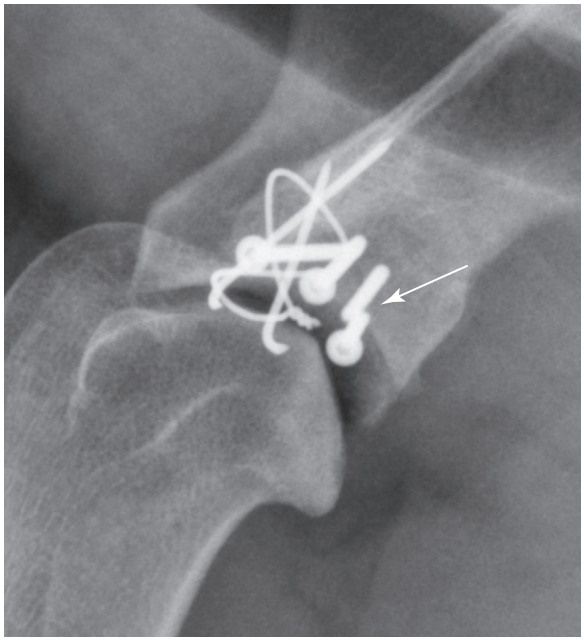


Fig. 16-24 Lateral view of the shoulder of a dog with internal fixation of a distal scapular fracture. The most caudal screw is broken *(white arrow)*.

Some computed radiographic systems produce an artifactual thin radiolucent zone immediately surrounding metallic objects such as pins and screws within bone. This artifact mimics bone lysis from motion or early infection (Fig. 16-29, p. 298) and must be recognized to avoid an incorrect assessment of loosening or infection.[67] Some new direct radiography and computed radiography systems have modified algorithms that do not produce this artifact.

The timing for removal of orthopedic devices varies with the device and with each patient. In a review of 123 human orthopedic studies, there was a lack of consensus regarding the definition of fracture healing. Fracture union was defined on the basis of a combination of clinical and radiographic criteria in 62% of the studies, on radiographic criteria only in 37%, and on clinical criteria only in 1%. Eleven different radiographic criteria were used, with the most common being callus bridging the fracture site.[68] Methods have been explored to quantify measurement of fracture healing using ultrasound, CT, or radiography. Most of these attempt to measure the stiffness of the fracture to predict the chance of failure if the fixation device is removed. Direct stiffness measurements of angulation at the fracture site with an applied load correlated more strongly with function outcome than did callus index.[69] However, these techniques are not used commonly clinically. Radiographic findings and clinical assessment remain the most regularly used method to assess union of a fracture.

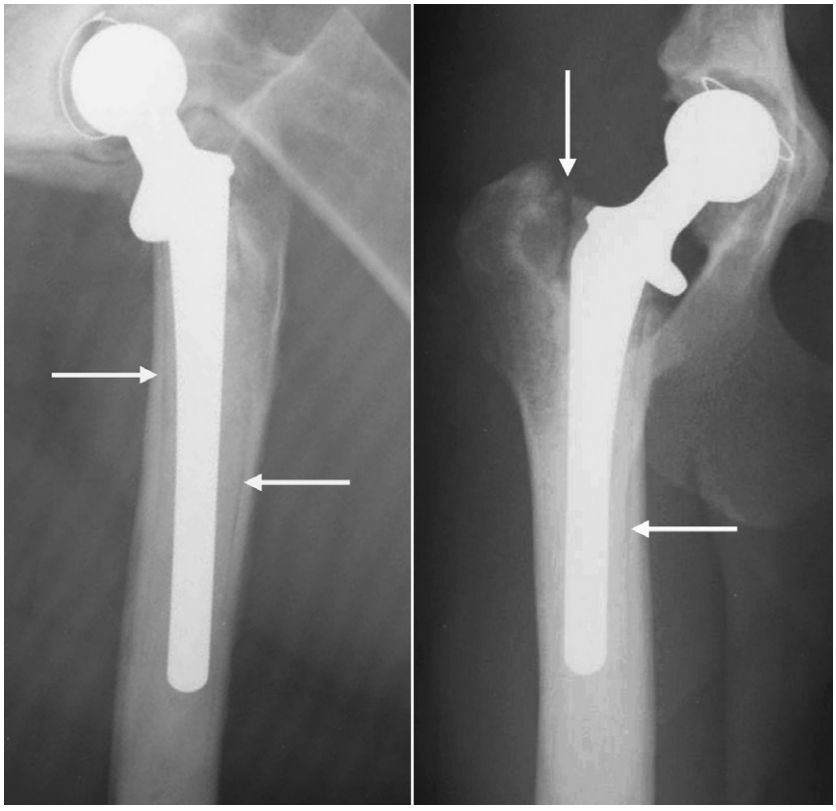


Fig. 16-25 Lameness as a result of aseptic loosening of the femoral implant observed as radiolucent lines, indicating separation of the cement mantle from the endosteal surface *(white arrows)*.

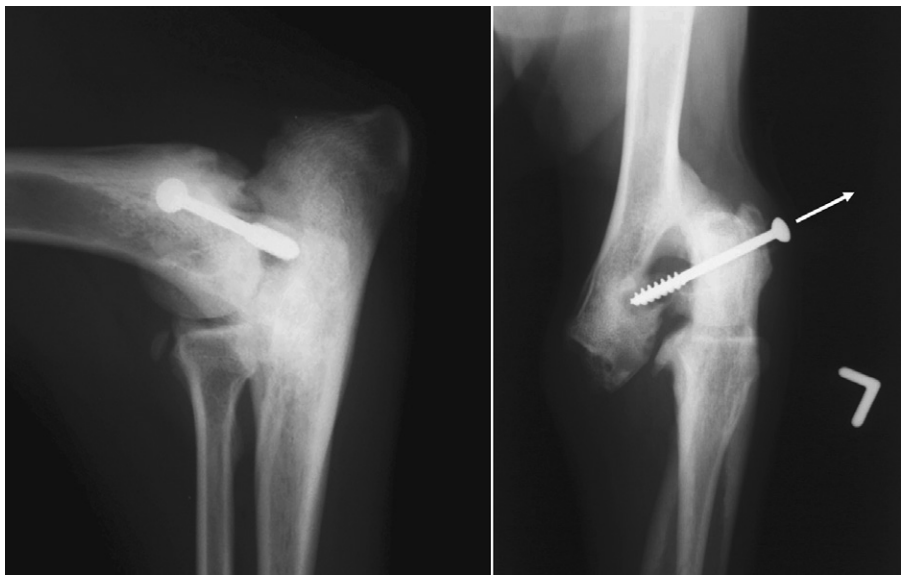


Fig. 16-26 The transcondylar lag screw has loosened and migrated laterally *(white arrow)* before bone healing. Consequently, the lateral condylar fracture has formed a malunion, and the intercondylar fracture is a nonunion with malarticulation of the medial aspect of the humeral condyle and the medial coronoid process. The radiolucent zone surrounding the screw likely indicates continued motion, most likely caused by interference with the proximal ulna. Remodeling of the medial aspect of the humeral condyle and medial coronoid process is advanced, and repair of the nonunion and malunion will not result in a normal joint.



Fig. 16-27 Radiolucencies *(white arrows)* surrounding the fixation pins in the metatarsal bones are a result of infection. Purulent discharge was found around the pins. Note the sclerotic reaction within the metatarsal bones.

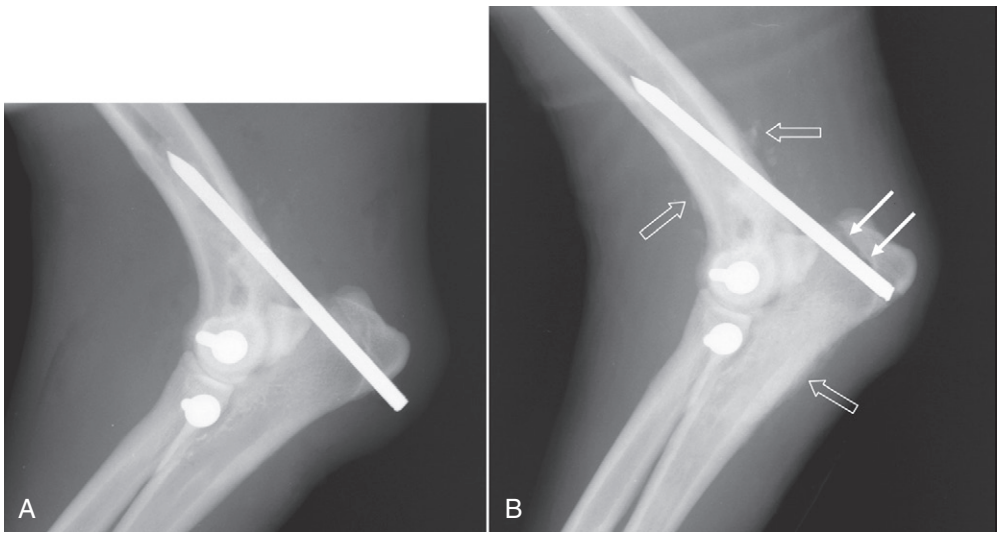


Fig. 16-28 Surgery was performed to repair an elbow luxation. **A,** Postoperative lateral radiograph. **B,** Eleven days later, a smoothly marginated radiolucency *(solid white arrows)* surrounding the pin in the proximal ulna is visible, indicating extension and flexion motion of the ulna. The periosteal new bone *(open white arrows)* is a result of trauma to the periosteum during surgery and not an indication of infection, although this periosteal appearance could occur as a result of infection.

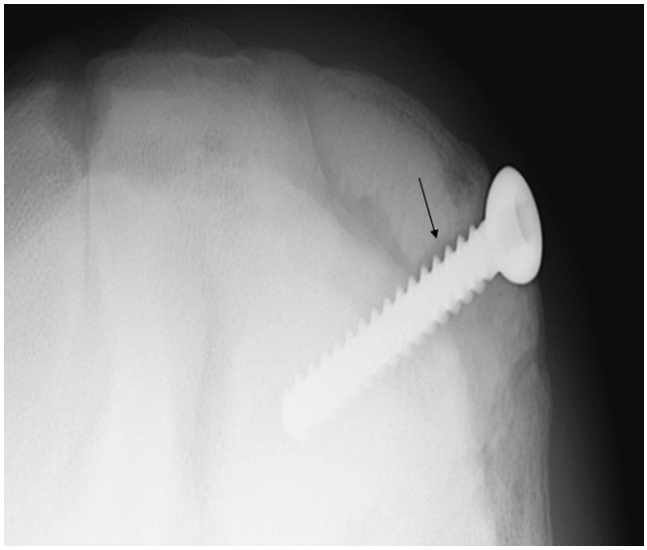


Fig. 16-29 Computed dorsoproximal-dorsodistal radiograph of an equine carpus. A screw has been inserted into the third carpal bone. A radiolucent zone surrounds the screw. This artifact, called the *Uberschwinger artifact* or *rebound effect artifact*, occurs when the opacity of adjacent objects is markedly different. It appears as a radiolucent stripe parallel to the interface between the two dissimilar objects. It is caused by the frequency-processing algorithm in CT systems in which an "unsharp" (edge enhancement) mask is applied to determine the degree of edge enhancement in the final image.

Generally, fixation devices may be removed when radiographic evidence of bridging bony callus is present. Fractures stabilized with casts generally have larger periosteal callus. Fractures stabilized with external fixators generally heal with a combination of periosteal and endosteal callus, with less periosteal callus when compared with casts. Simple fractures with excellent reduction and stable fixation with external fixators may heal with minimal periosteal and endosteal callus. Comminuted fractures will heal with mainly endosteal callus and bone bridging between fragments if the environment is good and fixation is rigid. Wires used in orthopedic bone repair are usually not removed unless they fragment and cause a problem. Bone plate and screw removal is delayed for 6 to 12 months after surgery to allow adequate time for the primary bone healing of the fracture to remodel into dense compact bone.[3]

Soft tissue evaluation completes the radiographic evaluation process. Soft tissue emphysema and swelling is seen normally immediately postoperatively but should resolve in 7 to 10 days. Air pockets that occur after the initial emphysema resolves suggest infection. Soft tissue atrophy is a common sign of disuse and signals significant lameness or disuse of the structure. Mineral opacity in the soft tissues can be seen with dystrophic mineralization caused by previous injury, mineralization of a hematoma associated with the fracture, isolated bone fragment, or cancellous graft material. Mineralization in the soft tissue can also be associated with an aggressive bone lesion such as osteomyelitis or bone tumor. Although rare, fracture- and implant-associated sarcomas can occur years after a fracture repair (Fig. 16-30).[70,71]

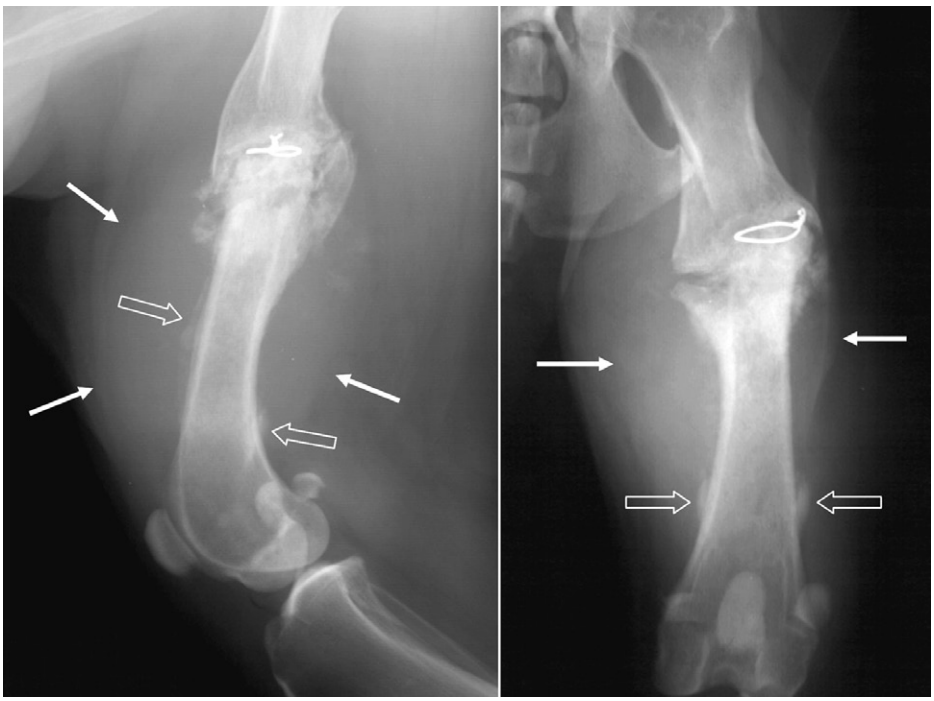


Fig. 16-30 Soft tissue mass *(solid white arrows)* and aggressive periosteal new bone *(open white arrows)* indicating an aggressive bone lesion at and distal to a malunion fracture.

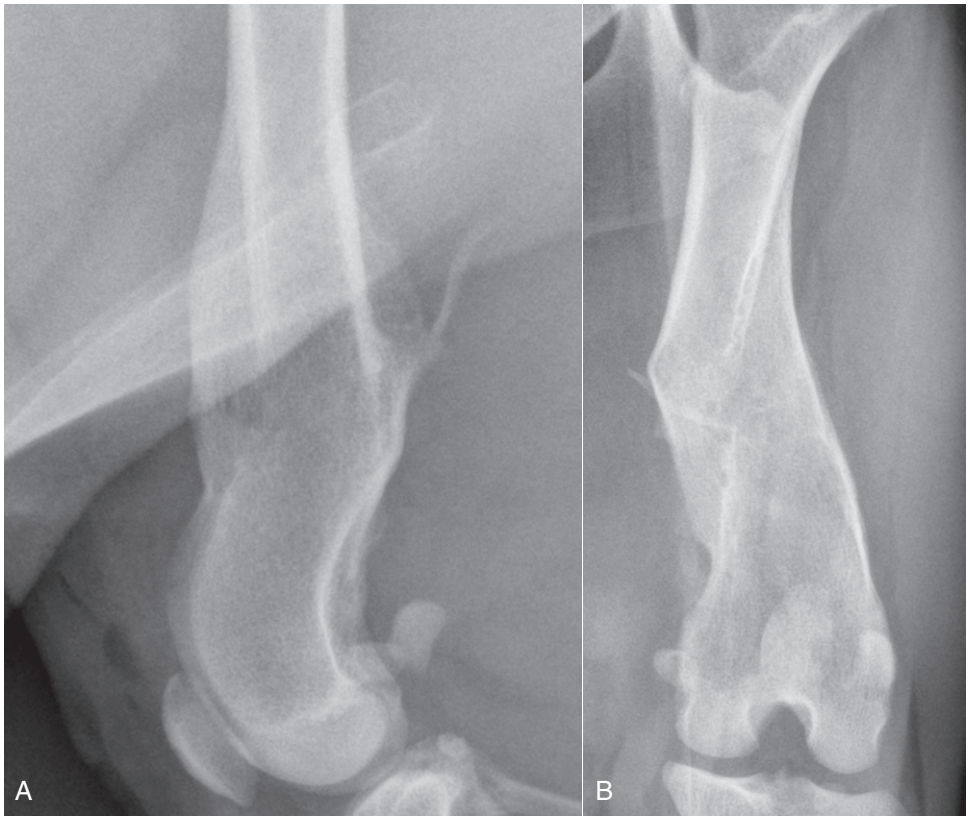


Fig. 16-31 Lateral **(A)** and craniocaudal **(B)** views of the femur of a dog with a healed malunion fracture. The distal fragment is angled cranially and displaced laterally. The appearance in the lateral view would be described as a recurvatum malunion and in the craniocaudal view as a translational malunion. Note the larger amount of cranial callus as a result of the loading pattern.

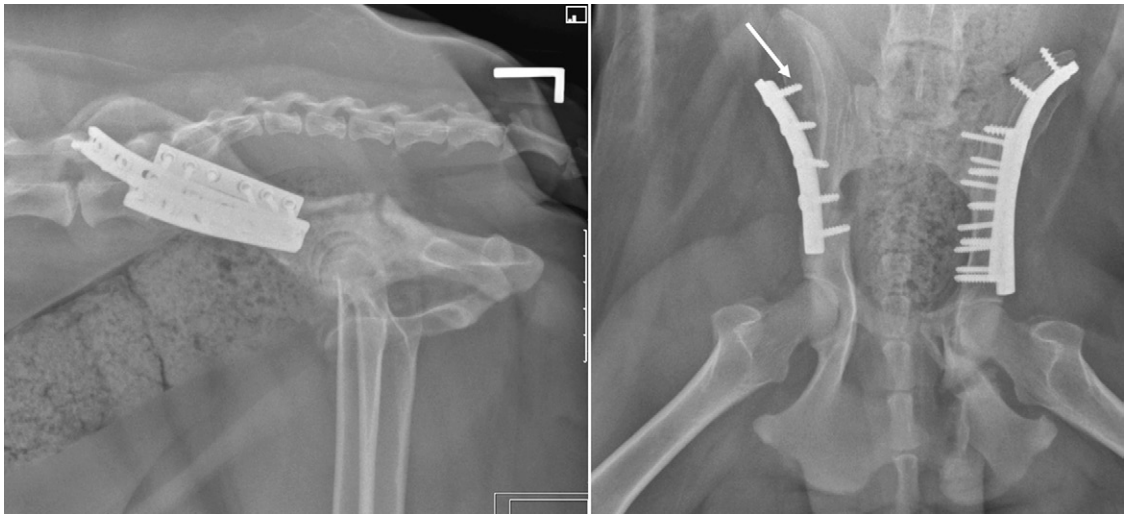


Fig. 16-32 Loosening of the bone plate and screws *(white arrow)* from the right ileum, resulting in medial displacement of the acetabulum and malunion. Callus associated with a left acetabular fracture is also present. The significant narrowing of the pelvic canal results in chronic obstipation.

COMPLICATIONS

Malunion fractures are healed but have abnormal anatomical alignment. These can occur from poor initial reduction, shifting of the fragments during the early healing phase, or premature removal of fixation devices before the fracture is stable (Fig. 16-31). Malunion fractures can have a negative effect on function if they are moderate to severe and may require correction (Fig. 16-32; see Fig. 16-26). Long bone malunion fractures can be classified as *valgus*, *varus*, *antecurvatum*, *recurvatum*, *torsional*, or *translational* (Fig. 16-33, p. 300).[3] Torsional (rotational) malunion of less than 10 degrees is difficult to detect on radiographs.[72] A patient can compensate readily for mild shortening of a single bone caused by a malunion. However, if the bone is one of a paired system (radius, ulna) or involves a joint, the resulting malalignment can lead to dysfunction (Fig. 16-34, p. 300). Descriptions of malunions can include the descriptors *functional* and *nonfunctional* to

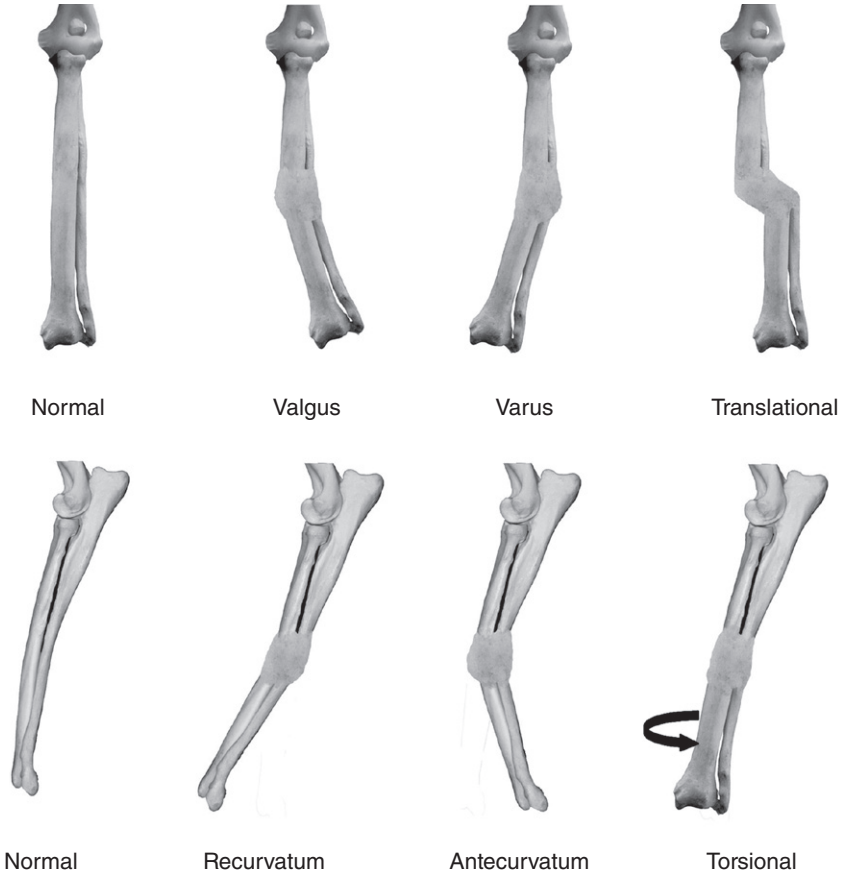


Fig. 16-33 Classification of malunion fractures.

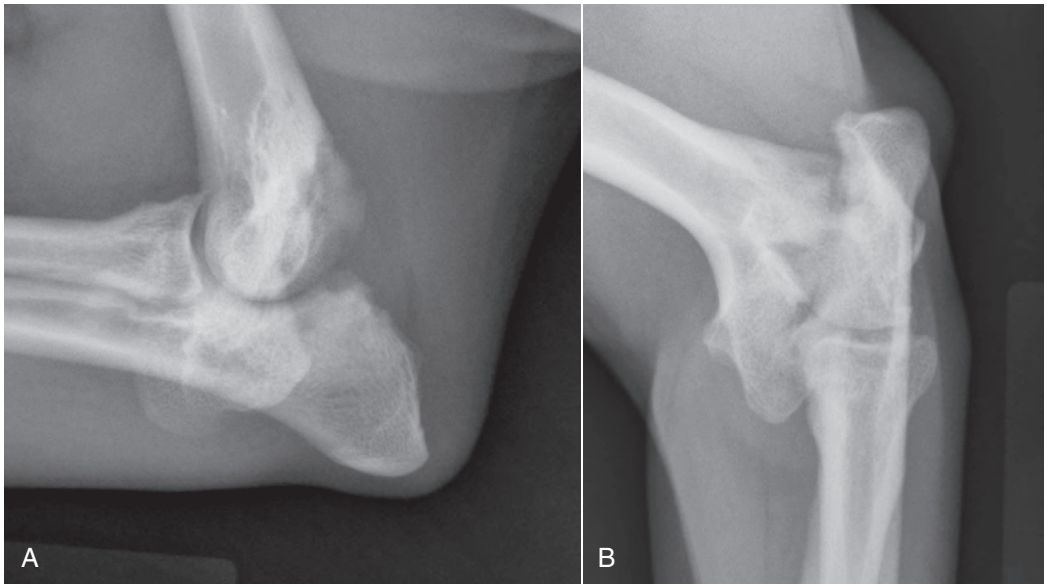


Fig. 16-34 Lateral **(A)** and craniocaudal **(B)** radiographs of a dog with a healed malunion intercondylar fracture. The incongruity has led to degenerative joint disease, seen best on the lateral view.

indicate if the malunion is causing dysfunction; however, this is often a clinical finding and not commonly used in a radiographic assessment.[2]

Delayed union is a subjective classification in which a fracture is healing but not as quickly as expected. Generally, this indicates a duration longer than typically seen with similar fractures and fixation. A definitive time required for fractures to heal is difficult to define because of the multiple factors that affect the time required for healing, including age, breed, location, type, soft tissue status, defects at the fracture site, and the type of fixation used.[73] Given enough time and no deterioration in stabilization or other complication, a delayed union fracture should eventually heal. If fixation devices are not stable or are migrating, steps may be taken to stabilize the fracture to ensure continued healing.

Nonunion is defined as a fracture that is not healed and has no evidence of progression of the healing process that would result in a bony union. All nonunion fractures first go through a delayed union phase. The key factor in distinguishing a nonunion fracture from a delayed union fracture is when it can be determined that healing has ceased and will not progress without intervention. Determination of a nonunion is subjective but relies on lack of progression of a healing callus, remodeling of the callus at the fracture ends without bridging, lack of increase in opacity of the fracture line, and duration of the healing process. Some fractures appear to be nonunion that, given enough time, may eventually heal. However, the length of time is greater than the normal healing time, and the outcome is doubtful. Intervention with improved stabilization and possible bone grafting is used commonly to increase the chance of a successful union.

Some long-term nonunion fractures may develop into a *pseudoarthrosis* as a result of chronic motion at the fracture site (Fig. 16-35). Fibrocartilage fills the fracture gap, and there is a fibrous capsule filled with serum. The patient may have good use of the limb and not have significant pain after formation of the pseudoarthrosis. Many of these are incidental findings and result from unrepaired fractures.

In other instances there is formation of dense, fibrous, and cartilaginous tissue that stabilizes a fracture forming a firm *fibrous union*.[5] In this instance a radiolucent gap or line remains at the fracture site that may or may not opacify over time. A common site for fibrous union fractures is in the equine distal phalanx.

Nonunion fractures may be divided into two major classifications, *viable* and *nonviable*, with some defined subclasses.[2]

Viable (reactive, vascular) nonunion fractures are characterized by viable active attempts to heal the fracture with reactive bone and callus formation. Viable nonunion fractures can be divided into three classes.

Hypertrophic nonunion fractures are characterized by abundant callus formation and are usually a result of excessive motion in the fracture zone, excessive activity by the patient, or premature loosening or removal of the fixation device (Fig. 16-36).



Fig. 16-35 Hypertrophic nonunion of the femoral mid-diaphysis with pseudoarthrosis. This fracture will not heal without surgical intervention. The dog had an abnormal gate but was not in pain.

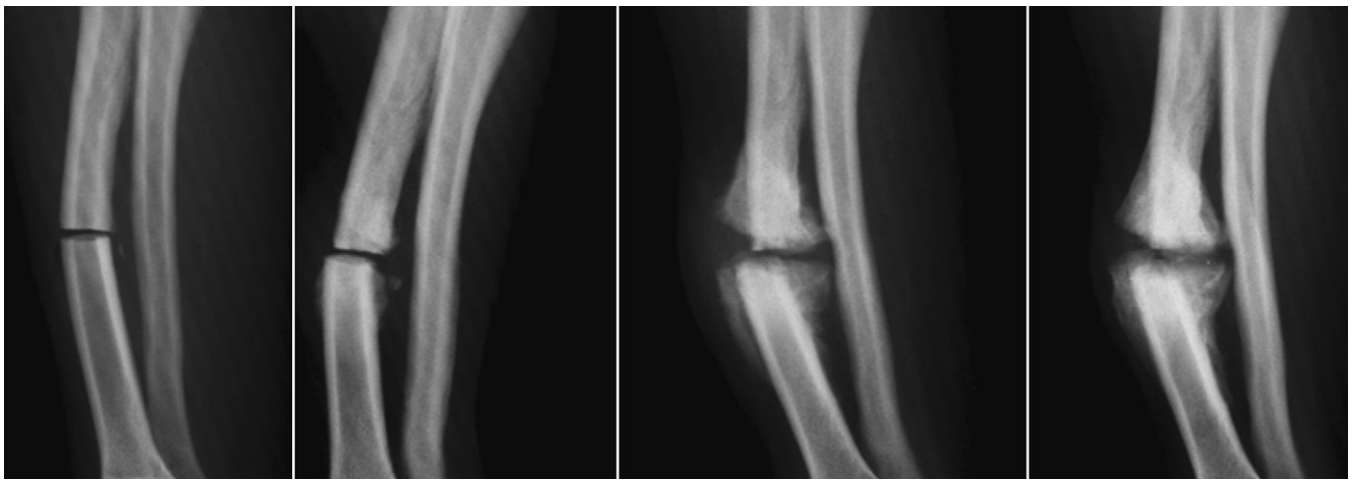


Fig. 16-36 Osteotomy of the radius with lack of fixation develops into a hypertrophic nonunion. Note the exuberant callus around the osteotomy ends with no bridging callus. This appearance is often termed an *elephant foot*.

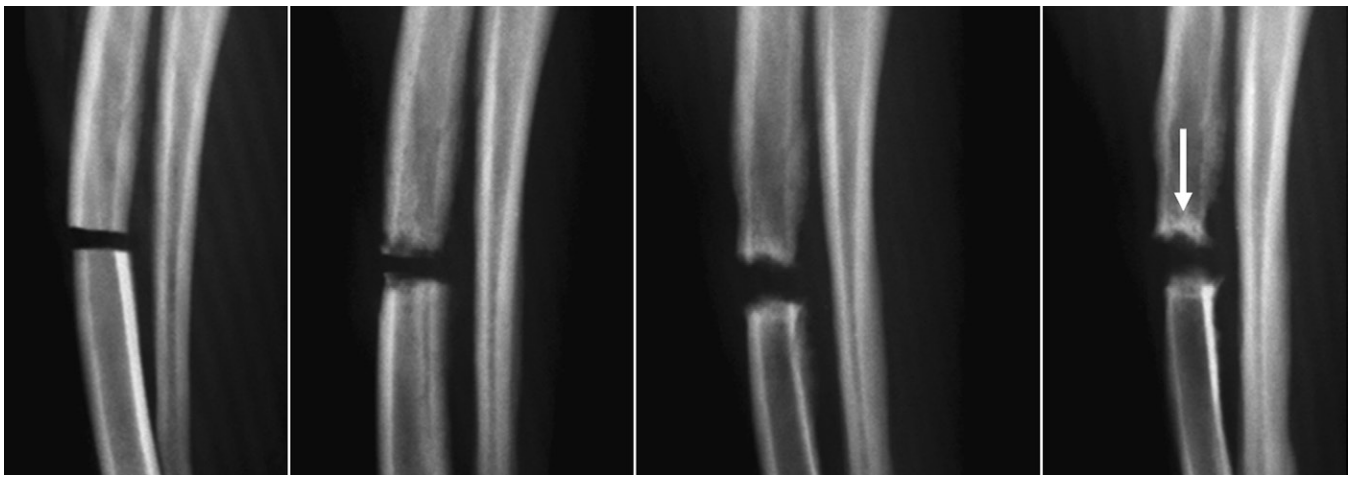


Fig. 16-37 Osteotomy with no fixation develops into an oligotrophic nonunion. Little callus is present at the osteotomy site, with filling in one of the ends of the segments seen as a sclerotic band *(white arrow)*.

Moderately hypertrophic nonunion fractures are characterized by moderate callus formation that is less than the amount observed with the hypertrophic nonunion fracture.

Oligotrophic nonunion fractures have little or no callus with bridging of the fracture fragments by fibrous tissue. These may be difficult to differentiate from a nonviable nonunion fracture because of the lack of callus and reaction at the fracture site. Scintigraphy may be used to detect blood supply to the fracture gap, indicating viable tissue. Generally, some bone reaction at the fragment ends will suggest a viable nonunion (Fig. 16-37).

Nonviable nonunion fractures are uncommon and may be mistaken for an oligotrophic nonunion, as previously stated. These nonunion fractures occur as a result of lack of adequate blood supply at the fracture site. Nonviable nonunion fractures are further classified into four subgroups.

Dystrophic nonunion fractures occur as a result of poor vascular supply to at least one side of a fragment, preventing callus from bridging with the opposite fragment. A radiolucent fracture gap will remain with no evidence of callus and rounded sclerotic bone edges.

Necrotic nonunion fractures occur because of complete loss of vascular supply to the fracture fragment that becomes necrotic and forms a sequestrum at the fracture site. Sepsis may or may not be present. Radiographically the bone fragment retains sharp edges and is sclerotic.

Defect nonunion fractures occur when a large fracture gap is present from loss or removal of a large fracture fragment. The resulting fracture gap is too large for callus to bridge. The loss may occur at the time of the original injury, during surgery, or later because of sequestra or other complications.

Atrophic nonunion fractures are usually a progression from one of the other types of nonviable nonunion fractures and are characterized by loss of vascularity, resorption, rounding of the fracture ends, and osteoporosis (see Fig. 16-3).

Osteomyelitis associated with a fracture is usually a result of contamination occurring at the time of the fracture, such as an open fracture or contamination during extended surgery. Severe soft tissue damage can also provide a suitable environment for growth of pathogens and predispose the fracture to infection. In general, callus is smoother than the periosteal reaction resulting from infection. Also, clinical signs of osteomyelitis should be recognized before radiographic signs are present. These include, pain, swelling, and heat with or without a fever. In the early stages, soft tissue swelling will be the only radiographic change observed with rare instances of soft tissue emphysema if a gas-producing organism or draining tract is present. Radiographs made 7 to 10 days after the onset of infection may have early mineralizing periosteal changes. If the infection continues, signs of an aggressive bone lesion such as bone lysis and a more extensive active periosteal reaction will be recognized. Irregular, ill-defined radiolucency surrounding pins or screws with endosteal sclerosis and periosteal reaction at the point of penetration of the device is highly suggestive of osteomyelitis around the pin or screw (Fig. 16-38; see Fig. 16-4).

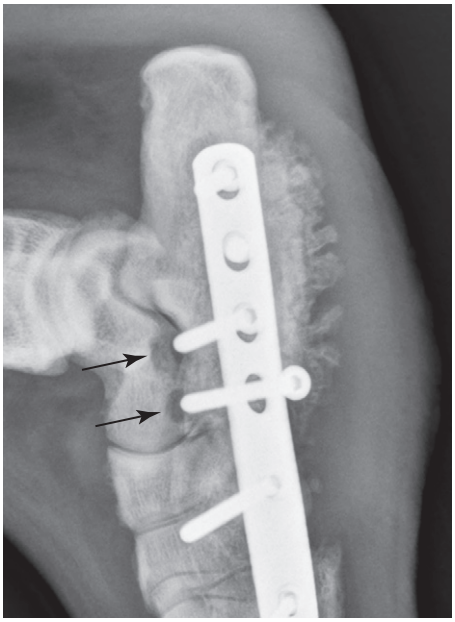


Fig. 16-38 Lateral view of the tarsus of a dog with osteomyelitis. A bone plate is present to provide stabilization of an unstable tarsal joint. There is lysis around the tip of two screws *(black arrows)*. The fourth screw from the top is backing out. There is also an irregular active columnar periosteal reaction on the plantar aspect of the calcaneus; this type of periosteal reaction, which is highly suggestive of osteomyelitis, should never be seen with normal callus. The lysis around the tips of the screws could be caused by motion, but considering the columnar periosteal reaction on the calcaneus as evidence of osteomyelitis, screw tract infection is likely.

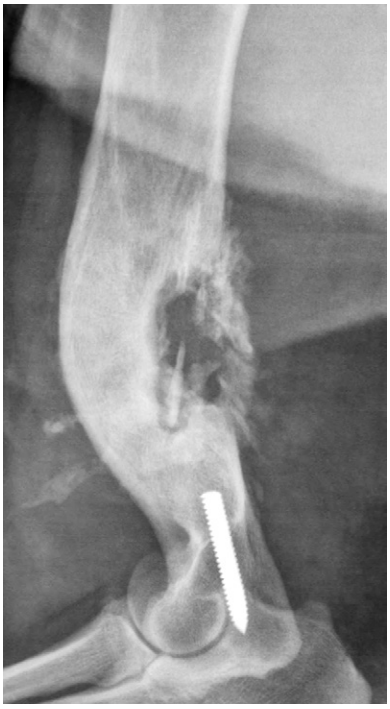


Fig. 16-39 Lateral radiograph of the distal humerus of a dog. There is a healed malunion fracture of the distal humerus with the distal fragment angled caudally (antecurvatum malunion fracture). A piece of a threaded pin is embedded in the distal humerus. There is a sharply margined opaque bone fragment surrounded by a zone of lysis and an active periosteal reaction. The adjacent medullary cavity of the humerus is sclerotic. These are classic findings of a sequestrum with secondary osteomyelitis.



Fig. 16-40 Premature distal ulnar physeal closure caused by trauma to the limb. Cessation of longitudinal growth of the ulna results in predictable changes as the radius continues to grow in length. Lateral view **(A)** shows cranial bowing of radius *(solid white arrow)* and distal subluxation of the humeroulnar joint *(open white arrow)*. Craniocaudal view **(B)** shows valgus angulation of the manus *(closed white arrows)*.

A *bone sequestrum* is a fragment of bone that has lost its blood supply and is no longer viable. The sequestrum may be parosteal, cortical, intramedullary, or a fracture fragment (Fig. 16-39; see Fig. 16-5). Bone sequestra may be *sterile* or *infectious*. A classic sequestrum is recognized as a sharply marginated sclerotic bone fragment (sequestrum) surrounded by or separated from the parent bone by a radiolucent zone that is surrounded by sclerotic bone (involucrum) (see Fig. 16-39). In some instances, a draining tract (cloaca) arises from the radiolucent necrotic area surrounding the sequestrum and extends to the skin surface. Generally, less reaction occurs surrounding a sterile sequestrum; however, determining radiographically whether the sequestrum is infected is not always possible.

Angular limb deformities develop after trauma to open physes. A Salter-Harris type fracture in an immature subject may cause premature closure of part or all of a growth plate, causing cessation of growth in that region of the bone. The most common site for this complication is premature closure of the distal ulnar physis in the dog (Fig. 16-40). This physis is especially susceptible to injury because of its conical shape, which concentrates forces into the small area of the apex of the physis. This greatly magnifies the force. The initial injury results in a Salter-Harris type V fracture that is often not observable radiographically, and the damage is noted only after cessation of growth (closure) causes complications. The radius and ulna are paired bones that must grow in a synchronous manner for normal overall growth of the antebrachium. Premature closure of the distal ulnar physis stops longitudinal growth of the ulna that interferes with the normal linear growth of the radius. As the radius grows longer, the tension caused by the ulna that is not elongating simultaneously causes cranial bowing of the radius, distal subluxation of the humeroulnar joint, distal subluxation of the ulnar carpal joint, and valgus angulation of the manus. The ulnar physis will appear closed radiographically, as indicated by a lack of the thin radiolucent line normally seen with an open physis.

Closure of the distal radial physis also occurs but is not as common as ulnar closure. Closure of the distal radial physis may be partial (Fig. 16-41) or complete compared with premature distal ulnar physis closure, which is usually complete. In premature distal radial physis closure, curvature of the limb is not as common as with premature ulnar closure. More common findings are humeroradial and humeroulnar subluxation, antebrachiocarpal subluxation, and possibly manus deflection, although not as severely valgus as with premature ulnar closure. In general, the direction and severity of the angular limb deformity will depend on factors such as paired versus nonpaired bones, partial or complete physeal closure, and at what age the closure takes place.

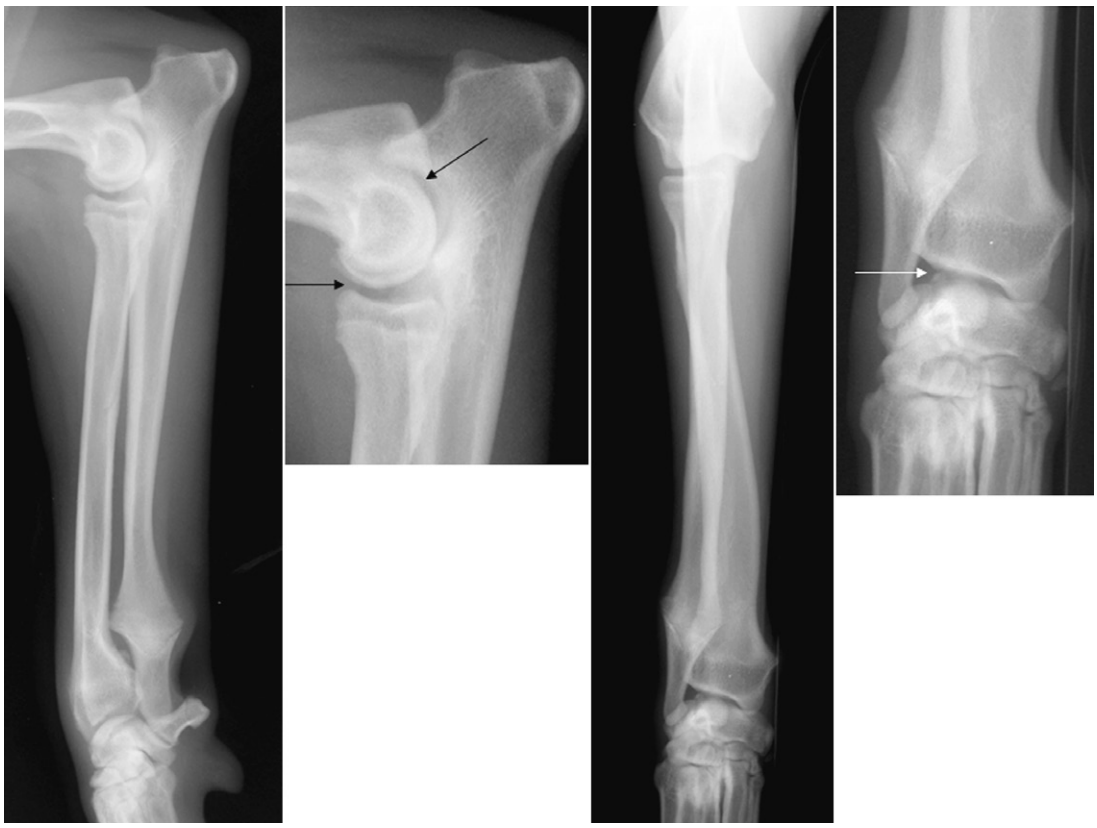


Fig. 16-41 Antebrachial radiographs of a dog with partial closure of the distal radial physis. The physis has closed laterally. The growth retardation has resulted in subluxation of the lateral aspect of the antebrachiocarpal joint *(white arrow)* and humeroradial and humeroulnar subluxation *(black arrows)*. The retarded radial growth results in distal displacement of the radius from the humerus and proximal displacement of the ulna from the humerus. The direction of humeroulnar subluxation with radial closure is opposite from what is observed in ulnar growth retardation (compare to Fig. 16-40).

REFERENCES

1. Resnick D, Kransdorf MJ: *Bone and joint imaging*, ed 3, Philadelphia, 2005, Elsevier-Saunders.
2. Slatter D: *Textbook of small animal surgery, vol 2*, ed 3, Philadelphia, 2003, Saunders.
3. Fossum TW: *Small animal surgery*, ed 3, St. Louis, 2007, Mosby.
4. Giannoudis PV, Einhorn TA, Marsh D: Fracture healing: the diamond concept, *Injury* 38(Suppl 4):S3.
5. Rockwood CA, Green DP, Heckman JD, et al: *Rockwood and Green's fractures in adults*, ed 7, Philadelphia, 2009, Lippincott, Williams & Wilkins.
6. Remedios A: Bone and bone healing, *Vet Clin North Am Small Anim Pract* 29:1029, 1999.
7. Einhorn TA: The cell and molecular biology of fracture healing, *Clin Orthop Relat Res* (355 Suppl):S7, 1998.
8. Toben D, Schroeder I, El Khassawna T, et al: Fracture healing is accelerated in the absence of the adaptive immune system, *J Bone Miner Res* 26:113, 2011.
9. Tsiridis E, Upadhyay N, Giannoudis P: Molecular aspects of fracture healing: which are the important molecules? *Injury* 38:S11, 2007
10. Welch RD, Lewis DD: Distraction osteogenesis, *Vet Clin North Am Small Anim Pract* 29:1187, 1999.
11. Barry S: Non-steroidal anti-inflammatory drugs inhibit bone healing: a review, *Vet Comp Orthop Traumatol* 23:385, 2010.
12. Follak N, Kloting I, Merk H: Influence of diabetic metabolic state on fracture healing in spontaneously diabetic rats, *Diabetes Metab Res Rev* 21:288, 2005.
13. Nolte DM, Fusco JV, Peterson ME: Incidence of and predisposing factors for nonunion of fractures involving the appendicular skeleton in cats: 18 cases (1998–2002), *J Am Vet Med Assoc* 226:77, 2005.
14. Wheeler P, Batt ME: Do non-steroidal anti-inflammatory drugs adversely affect stress fracture healing? A short review, *Br J Sports Med* 39:65, 2005.
15. Epari DR, Schell H, Bail HJ, et al: Instability prolongs the chondral phase during bone healing in sheep, *Bone* 38:864, 2006.
16. Morgan EF, Gleason RE, Hayward LNM, et al: Mechanotransduction and fracture repair, *J Bone Joint Surg Am* 90:25, 2008.
17. Wehner T, Claes L, Niemeyer F: Influence of the fixation stability on the healing time—a numerical study of a patient-specific fracture healing process, *Clin Biomech* 25:606, 2010.
18. Lienau J, Schell H, Duda GN, et al: Initial vascularization and tissue differentiation are influenced by fixation stability, *J Orthop Res* 23:639, 2005.
19. Karladani AH, Granhed H, Karrholm J, et al: The influence of fracture etiology and type on fracture healing: a review of 104 consecutive tibial shaft fractures, *Arch Orthop Trauma Surg* 121:325, 2001.

20. Hudson CC, Pozzi A, Lewis DD: Minimally invasive plate osteosynthesis: applications and techniques in dogs and cats, *Vet Comp Orthop Traumatol* 22:175, 2009.
21. Igna C, Schuslzer L: Current concepts of internal plate fixation of fractures, *Bull Univ Agric Sci Vet Med Cluj-Napoca* 67:118, 2010.
22. An Z, Zeng B, He X, et al: Plating osteosynthesis of mid-distal humeral shaft fractures: minimally invasive versus conventional open reduction technique, *Int Orthop* 34:131, 2010.
23. Saikku-Backstrom A, Raiha JE, Valimaa T, Tulamo RM: Repair of radial fractures in toy breed dogs with self-reinforced biodegradable bone plates, metal screws, and light-weight external coaptation, *Vet Surg* 34:11, 2005.
24. Welch JA, Boudrieau RJ, DeJardin LM, et al: The intraosseous blood supply of the canine radius: implications for healing of distal fractures in small dogs, *Vet Surg* 26:57, 1997.
25. Beale BS: Orthopedic problems in geriatric dogs and cats, *Vet Clin North Am Small Anim Pract* 35:655, 2005.
26. Marsell R, Einhorn TA: Emerging bone healing therapies, *J Orthop Trauma* 24:S4, 2010.
27. Atilola MAO: Nonunion fractures in dogs, *J Vet Orthop* 3:21, 1984.
28. Johnson AL, Eurell JAC, Losonsky JM: Biomechanics and biology of fracture healing with external skeletal fixation, *Comp Cont Ed Pract Vet* 20:487, 1998.
29. McCartney WT, MacDonald BJ: Incidence of non-union in long bone fractures in 233 cats, *Intern J Appl Res Vet Med* 4:209, 2006.
30. Della Rocca GJ, Crist BD, Murtha YM: Parathyroid hormone: is there a role in fracture healing? *J Orthop Trauma*, 24:S31, 2010.
31. Goto T, Fujioka M, Ishida M, et al: Noninvasive up-regulation of angiopoietin-2 and fibroblast growth factor-2 in bone marrow by pulsed electromagnetic field therapy, *J Orthop Sci* 15:661, 2010.
32. Millis DL: Bone- and non-bone-derived growth factors and effects on bone healing, *Vet Clin North Am Small Anim Pract* 29:1221, 1999.
33. Aaron RK, Ciombor DM, Simon BJ: Treatment of nonunions with electric and electromagnetic fields, *Clin Orthop Relat Res* 419:21, 2004.
34. Backstrom KC, Bertone AL, Wisner ER, et al: Response of induced bone defects in horses to collagen matrix containing the human parathyroid hormone gene, *Am J Vet Res* 65:1223, 2004.
35. Birnbaum K, Wirtz DC, Siebert CH, et al: Use of extracorporeal shock-wave therapy (ESWT) in the treatment of non-unions. A review of the literature, *Arch Orthop Trauma Surg* 122:324, 2002.
36. Pounder NM, Harrison AJ: Low intensity pulsed ultrasound for fracture healing: A review of the clinical evidence and the associated biological mechanism of action, *Ultrasonics* 48:330, 2008.
37. Watanabe Y, Matsushita T, Bhandari M, et al: Ultrasound for fracture healing: current evidence, *J Orthop Trauma* 24:S56, 2010.
38. McClure SR, Miles K, VanSickle D, et al: The effect of variable waveform low-intensity pulsed ultrasound in a fourth metacarpal osteotomy gap model in horses, *Ultrasound Med Biol* 36:1298, 2010.
39. Volpon JB, Dantas Mota FC, Beletti ME: Low-intensity ultrasound application in distal radius metaphyseal bone defects of dogs, *Ultrasound Med Biol* 36:1849, 2010.
40. Ragetly GR, Griffon DJ: The rationale behind novel bone grafting techniques in small animals, *Vet Comp Orthop Traumatol* 24:1, 2011.
41. Vertenten G, Gasthuys F, Cornelissen M, et al: Enhancing bone healing and regeneration: present and future perspectives in veterinary orthopaedics, *Vet Comp Orthop Traumatol* 23:153, 2010.
42. Liptak JM, Dernell WS, Ehrhart N, et al: Cortical allograft and endoprosthesis for limb-sparing surgery in dogs with distal radial osteosarcoma: a prospective clinical comparison of two different limb-sparing techniques, *Vet Surg* 35:518, 2006.
43. Innes JF, Myint P: Demineralised bone matrix in veterinary orthopaedics: a review, *Vet Comp Orthop Traumatol* 23:393, 2010.
44. Field JR, McGee M, Wildenauer C, et al: The utilization of a synthetic bone void filler (JAX) in the repair of a femoral segmental defect, *Vet Comp Orthop Traumatol* 22:87, 2009.
45. Guerrero TG, Makara MA, Katiofsky K, et al: Comparison of healing of the osteotomy gap after tibial tuberosity advancement with and without use of an autogenous cancellous bone graft, *Vet Surg* 40:27, 2011.
46. Long J, Li P, Du H, et al: Effects of bone morphogenetic protein 2 gene therapy on new bone formation during mandibular distraction osteogenesis at rapid rate in rabbits, *Oral Surg Oral Med Oral Pathol Oral Radiol Endod* 112(1):50, 2011. Epub December 30, 2010.
47. Griffin XL, Smith CM, Costa ML: The clinical use of platelet-rich plasma in the promotion of bone healing: a systematic review, *Injury* 40:158, 2009.
48. Moghaddam A, Elleser C, Biglari B, et al: Clinical application of BMP 7 in long bone non-unions, *Arch Orthop Traum Su* 130:71, 2010.
49. Wilson JW: Vascular supply to normal bone and healing fractures, *Semin Vet Med Surg (Small Anim)* 6:26, 1991.
50. Orsini PG, Rendano VT, Sack WO: Ectopic nutrient foramina in the third metatarsal bone of the horse, *Equine Vet J* 13:132, 1981.
51. Becht JL, Park RD, Kraft SL: Radiographic interpretation of normal skeletal variations and pseudolesions in the equine foot, *Vet Clin North Am Equine Pract* 17:1, 2001.
52. Sande R: Radiography of orthopedic trauma and fracture repair, *Vet Clin North Am Small Anim Pract* 29:1247, 1999.
53. Breederveld RS, Tuinebreijer WE: Investigation of computed tomographic scan concurrent criterion validity in doubtful scaphoid fracture of the wrist, *J Trauma* 57:851, 2004.
54. Harris JH, Coupe KJ, Lee JS, et al: Acetabular fractures revisited: a new CT-based classification, *Semin Musculoskelet Radiol* 9:150, 2005.
55. Adam A, Dixon AK, Grainger RG, et al, editors: *Grainger & Allison's diagnostic radiology: a textbook of medical imaging, vol 2*, ed 5, New York, 2008, Churchill Livingstone.
56. Borrelli J Jr, Ricci WM, Steger-May K, et al: Postoperative radiographic assessment of acetabular fractures: a comparison of plain radiographs and CT scans, *J Orthop Trauma* 19:299, 2005.
57. Hoskinson JJ: Equine nuclear scintigraphy. Indications, uses, and techniques, *Vet Clin North Am Equine Pract* 17:63, 2001.
58. Koblik PD, Hornof WJ, Seeherman HJ: Scintigraphic appearance of stress-induced trauma of the dorsal cortex of the third metacarpal bone in racing Thoroughbred horses: 121 cases (1978–1986), *J Am Vet Med Assoc* 192:390, 1988.
59. Daniel GB, Berry CR: *Textbook of veterinary nuclear medicine*, ed 2, Knoxville, Tenn, 2006, American College of Veterinary Radiology.

60. Twardock AR: Equine bone scintigraphic uptake patterns related to age, breed, and occupation, *Vet Clin North Am Equine Pract* 17:75, 2001.
61. Tucker RL, Sande RD: Computed tomography and magnetic resonance imaging of the equine musculoskeletal conditions, *Vet Clin North Am Equine Pract* 17:145, 2001.
62. Reef VB: Advances in diagnostic ultrasonography, *Vet Clin North Am Equine Pract* 7:451,1991
63. Reef VB: Superficial digital flexor tendon healing: ultrasonographic evaluation of therapies, *Vet Clin North Am Equine Pract* 17:159, 2001.
64. Davidson EJ, Martin BB Jr: Stress fracture of the scapula in two horses, *Vet Radiol Ultrasound* 45:407, 2004.
65. Craig JG, Jacobson JA, Moed BR: Ultrasound of fracture and bone healing. *Radiol Clin North Am* 37:737, 1999.
66. Salter R, Harris W: Injuries involving the epiphyseal plate, *J Bone Joint Surg* 45:587, 1963.
67. Drost WT, Reese DJ, Hornof WJ: Digital radiography artifacts, *Vet Radiol Ultrasound* 49:S48, 2008.
68. Corrales LA, Morshed S, Bhandari M, et al: Variability in the assessment of fracture-healing in orthopaedic trauma studies, *J Bone Joint Surg* 90:1862, 2008.
69. Wade R, Richardson J: Outcome in fracture healing: a review, *Injury* 32:109, 2001.
70. Stevenson S, Hohn RB, Pohler OE: Fracture-associated sarcoma in the dog, *J Am Vet Med Assoc* 180:1189, 1982.
71. Jackson LC, Pacchiana PD: Common complications of fracture repair, *Clin Tech Small Anim Pract* 19:168, 2004.
72. Newton CD, Nunamaker DM: *Textbook of small animal orthopaedics*, Philadelphia, 1985, Lippincott.
73. Piermattei DL, Flo GL, Brinker WO: *Brinker, Piermattei, and Flo's handbook of small animal orthopedics and fracture repair*, ed 4, Philadelphia, 2006, Saunders.

ELECTRONIC RESOURCES

evolve

Additional information related to the content in Chapter 16 can be found on the companion Evolve website at http://evolve.elsevier.com/Thrall/vetrad/

- Chapter Quiz

CHAPTER • 17

Radiographic Features of Bone Tumors and Bone Infection

Donald E. Thrall

Nearly all neoplastic and inflammatory bone lesions have an aggressive radiographic appearance. The radiographic signs of aggressive bone lesions were discussed in Chapter 14. A definitive distinction between neoplastic and infectious bone lesions is impossible by radiographic means. However, the radiographic features of the bone lesion—such as the number of bones involved and the location of the lesions within the bones—and the signalment, history, and physical and laboratory findings can be used to prioritize the diagnostic possibilities. Nevertheless, a biopsy with histopathologic evaluation and possibly microbiologic culture is needed for the definitive diagnosis of any aggressive bone lesion.

PRIMARY BONE TUMORS

Primary bone tumors are characterized typically by a single metaphyseal aggressive bone lesion,[1] and such a lesion should be considered a primary bone tumor until proved otherwise. Although most primary bone tumors begin in the metaphysis, they may either extend and involve the epiphysis and diaphysis or arise primarily in these other locations. The opinion that primary bone tumors do not cross joints or invade adjacent bones is incorrect because both can occur as the tumor enlarges, although these complications are relatively uncommon.

Canine Osteosarcoma

Osteosarcoma is the most common primary bone tumor in dogs; other histologic types of primary bone cancer occur but are uncommon. The age distribution of canine osteosarcoma is bimodal with a small peak in incidence at approximately 2 years of age and then a larger peak in incidence later in adult life.[2] Subclinical pulmonary metastasis of canine osteosarcoma has usually occurred by the time the primary tumor is diagnosed.

Osteosarcomas may originate anywhere in the skeleton, but occur classically in the metaphysis of long tubular bones (Table 17-1) in large- and giant-breed dogs. Common osteosarcoma sites in the forelimb are the proximal humerus and the distal radius (away from the elbow), and in the hindlimb, the distal femur and proximal tibia (toward the stifle); tumors in the distal tibia are not uncommon. Appendicular osteosarcomas may be primarily lytic (Fig. 17-1), primarily sclerotic (blastic or productive) (Fig. 17-2), or mixed, with both lytic and productive features (Fig. 17-3). The mixed pattern is the

Table • 17-1

*Common Features of Neoplastic and Infectious Bone Disease in the Appendicular Skeleton of Small Animals**

CRITERION	PRIMARY BONE TUMOR	METASTATIC BONE TUMOR	MYCOTIC OSTEOMYELITIS	BACTERIAL OSTEOMYELITIS: HEMATOGENOUS	BACTERIAL OSTEOMYELITIS: INOCULATION
Patient age	Young or Old	Old	Young	Young	Young or old
Mono- or polyostotic	Monostotic	Polyostotic†	Polyostotic[2]	Polyostotic	Monostotic or adjacent bones
Location in bone	Metaphysis‡	Metaphysis or diaphysis	Metaphysis	Metaphysis	Anywhere
Likelihood of columnar periosteal reaction	+	–	–	–	+++

*Tabular features are only guidelines, and findings in individual patients may vary. Features are also based on the experience of the author and have not been substantiated by evidence-based investigations.
†The axial skeleton may also be affected.
‡Epiphyseal and diaphyseal tumors also occur.



Fig. 17-1 Lateral view of the distal radius. There is a lytic lesion in the craniodistal aspect of the radius. The lesion is aggressive because of the marked cortex destruction and the poorly defined transition zone between the lytic lesion and normal bone.



Fig. 17-2 Lateral view of the femur. A predominantly sclerotic (blastic) lesion is present in the distal diaphysis and metaphysis. This lesion is composed mainly of smoothly marginated new bone, but the lesion is aggressive because of the lack of a sharp transition zone between normal and abnormal bone. This is a relatively uncommon appearance for a primary bone tumor.

most common. Of note, the degree of lysis versus sclerosis is not a feature that should be used in deciding whether a lesion is aggressive; this was discussed in Chapter 14.

The type of periosteal reaction produced by an osteosarcoma varies, falling typically into one of the following appearances: irregular, smooth, spiculated, or columnar (Fig 17-4; see Fig. 17-3). Some osteosarcomas result in neoplastic osteogenesis in the soft tissue component; this can appear quite bizarre (Fig. 17-5). Although bone infections may have an active periosteal reaction, extremely aggressive and amorphous types of periosteal reactions are more commonly associated with tumors.

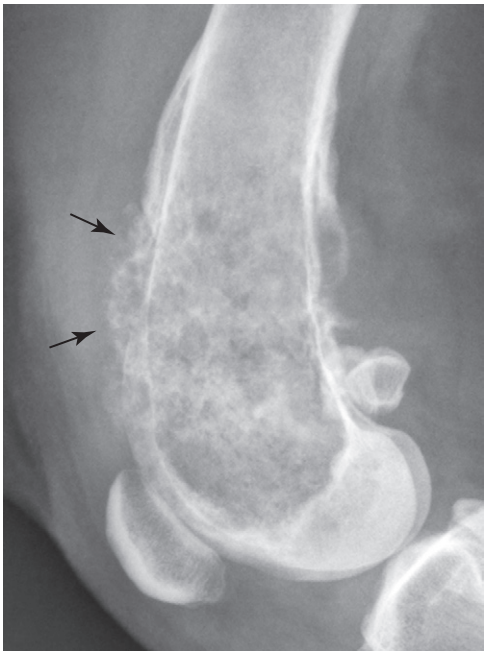


Fig. 17-3 Lateral view of the distal femur. There is a heterogeneous lesion in the distal femoral metaphysis and epiphysis characterized by a mixture of lysis and focal sclerosis, and an active, irregular, periosteal reaction *(black arrows)*. The lesion is aggressive because of the active periosteal reaction and the indistinct transition zone proximally between normal and abnormal bone. The femoral cortex is thin but not effaced completely. Mixed lytic and sclerotic primary bone tumors are common.

Codman's triangle, which is an isolated cuff (triangle) of reactive subperiosteal new bone,[3,4] is a roentgen sign sometimes considered pathognomonic for a primary bone tumor (Fig. 17-6). However, a Codman's triangle can be present at the boundary of any benign or malignant process that elevates the periosteum, including traumatic bone injury, and is not specific for any bone condition.[4]

Feline Osteosarcoma

Osteosarcoma is also the most common primary bone tumor in cats, but its prevalence is lower than in dogs.[5-9] Age distribution in cats is not bimodal; mean age at time of diagnosis is approximately 10 years.[6] As in dogs, feline osteosarcomas result in an aggressive bone lesion, but the hindlimbs are affected more often than the forelimbs. The radiographic appearance of feline osteosarcoma has been reported as primarily osteolytic,[7] but a spectrum of tumor opacities has also been reported.[5] The infrequent nature of this tumor makes accurate characterization of the radiographic spectrum impossible. Regardless, osteosarcoma should be the primary diagnosis for aggressive monostotic metaphyseal bone lesions in the cat (Fig. 17-7). Pulmonary metastasis from feline osteosarcoma is less common than with canine osteosarcoma.[9,10]

Osteosarcoma as a Secondary Event

Occasionally, osteosarcoma develops secondary to another bone abnormality. For example, dogs with bone infarction are prone to develop osteosarcoma.[11] Bone infarction, which is ischemic death of cellular elements of bone, may be

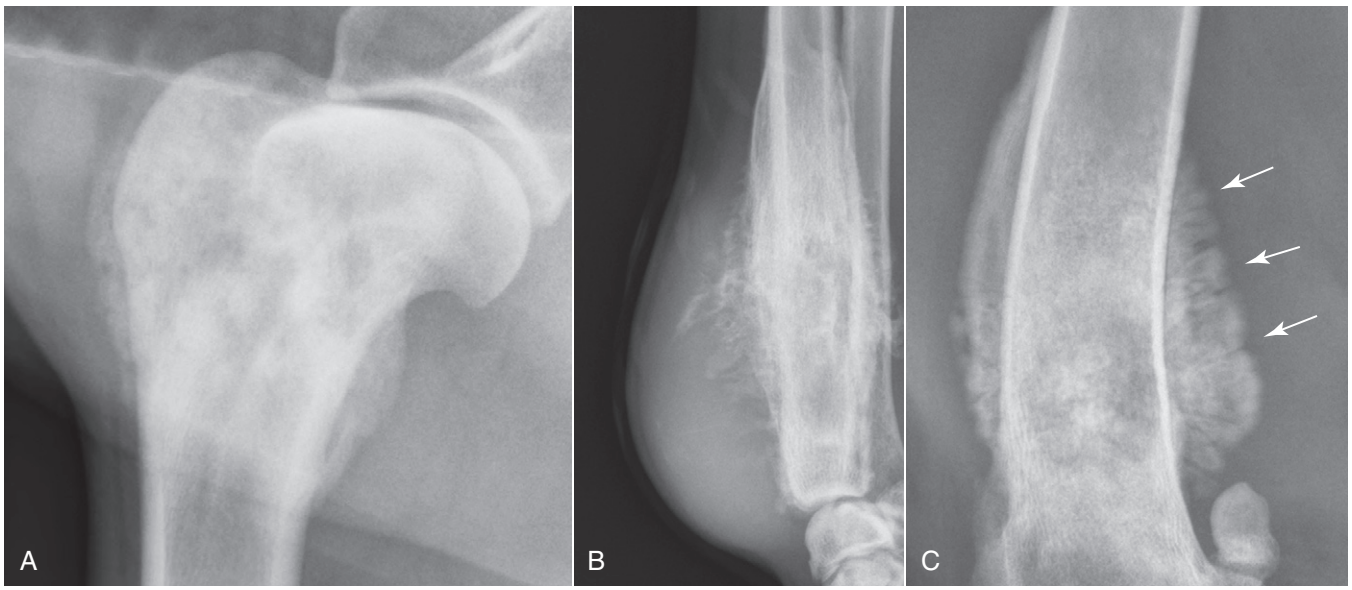


Fig. 17-4 Example of the types of periosteal reaction that can be seen with a primary bone tumor. **A,** Smooth; **B,** spiculated; **C,** columnar *(arrows)*.

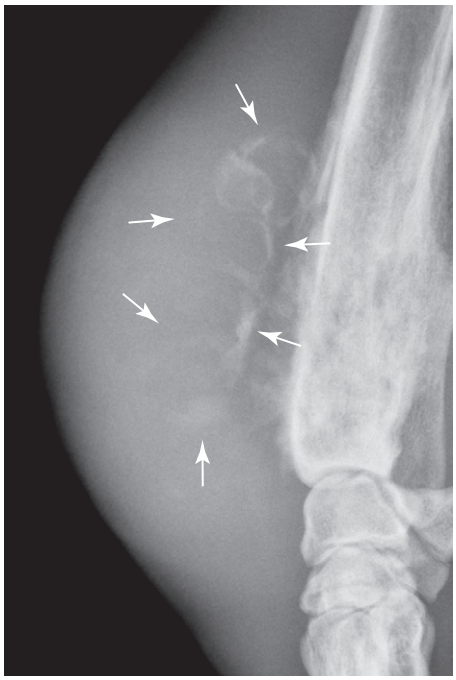


Fig. 17-5 Lateral view of a distal radial osteosarcoma. There is a large soft tissue component that contains neoplastic osteogenesis in a whirling pattern *(white arrows)* that is distinct from the periosteal reaction.

idiopathic[12] or caused by bone trauma, such as total hip arthroplasty.[13]

Idiopathic polyostotic bone infarction is rare. The medullary infarcts appear as multifocal medullary opacities in long and short tubular bones (Fig. 17-8). The specific cause-and-effect relationship between bone infarction and bone sarcoma is unknown. Dogs developing idiopathic polyostotic bone infarction and subsequent osteosarcoma are typically small-breed dogs (Shelties and terriers) in contrast to the large breeds that typically develop primary osteosarcoma. Another difference is the lytic nature of most osteosarcomas developing as a consequence of idiopathic polyostotic bone infarction compared to more common mixed appearance in large-breed dogs (Fig. 17-8, *D*)

Bone infarction also develops relatively commonly distal to the femoral component of a total hip prosthetic device[13] (Fig. 17-9), and there may be an association between stem loosening or the depth of femoral reaming and infarction.[14,15] There are isolated instances of osteosarcoma developing in the infarcted bone distal to the stem[16] (Fig. 17-10). The mechanism is likely similar to that associated with osteosarcoma developing secondary to idiopathic bone infarction, but the specifics are unknown. Bone infarcts developing distal to the femoral stem of a prosthetic hip appear different from those appearing in idiopathic polyostotic bone infarction. In idiopathic polyostotic bone infarction, the infarcts appear as polyostotic focal medullary opacities, whereas in patients with prosthetic hips, the infarcts occur only in the limb with the implant and are more wispy in appearance (compare Figs. 17-8 vs. 17-9 and 17-10).

Rarely, occurrence of a fracture or use of an internal fixation device will lead to the development of a primary bone tumor. Case history reports have been published in both dogs and cats in which the development of osteosarcoma after skeletal trauma has been documented[17,18] (see Chapter 16).

FUNGAL BONE INFECTIONS

Fungal disease with subsequent osteomyelitis in dogs typically involves large-breed young adults.[19] Fungal disease leading to osteomyelitis in cats is rare. Fungal osteomyelitis is most commonly identified in geographic areas where predisposing fungi are endemic, such as the southeast (blastomycosis) and the southwest (coccidioidomycosis) regions of the United States. However, infected dogs may relocate to nonendemic areas where the index of suspicion for fungal infections is low; this may delay the diagnosis.

Fungal osteomyelitis is generally of hematogenous origin, leading to a polyostotic distribution of the appendicular and/or axial skeleton (see Table 17-1). In the appendicular

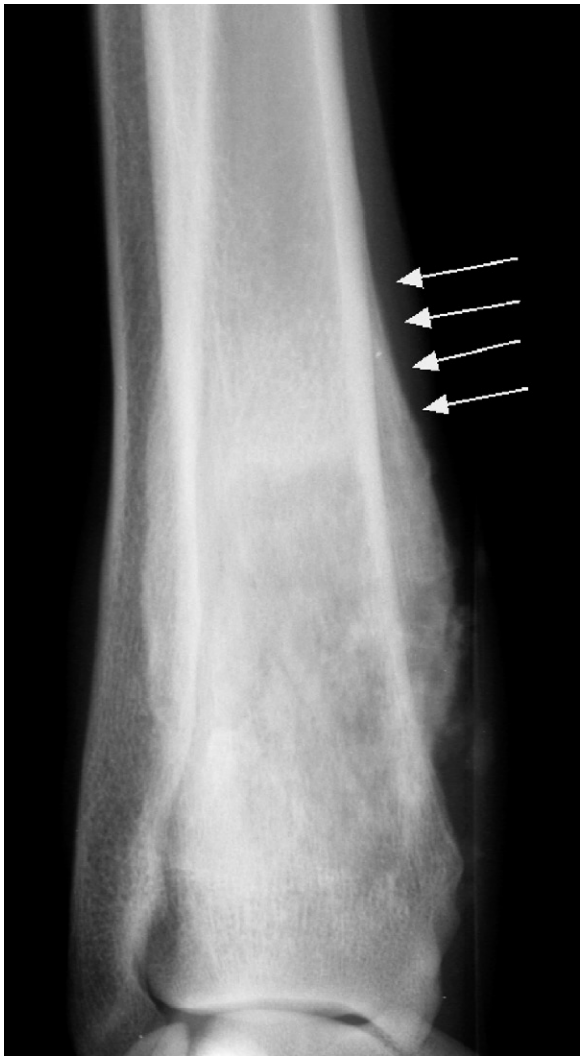


Fig. 17-6 Craniocaudal view of a distal radial osteosarcoma. The appearance of the triangular periosteal reaction at the proximomedial aspect of the lesion *(arrows)* has been termed a *Codman's triangle* and accompanies osteosarcoma so often that it has been called pathognomonic. However, this triangle results from periosteal elevation, which can occur secondary to neoplastic, infectious, and traumatic bone lesions.

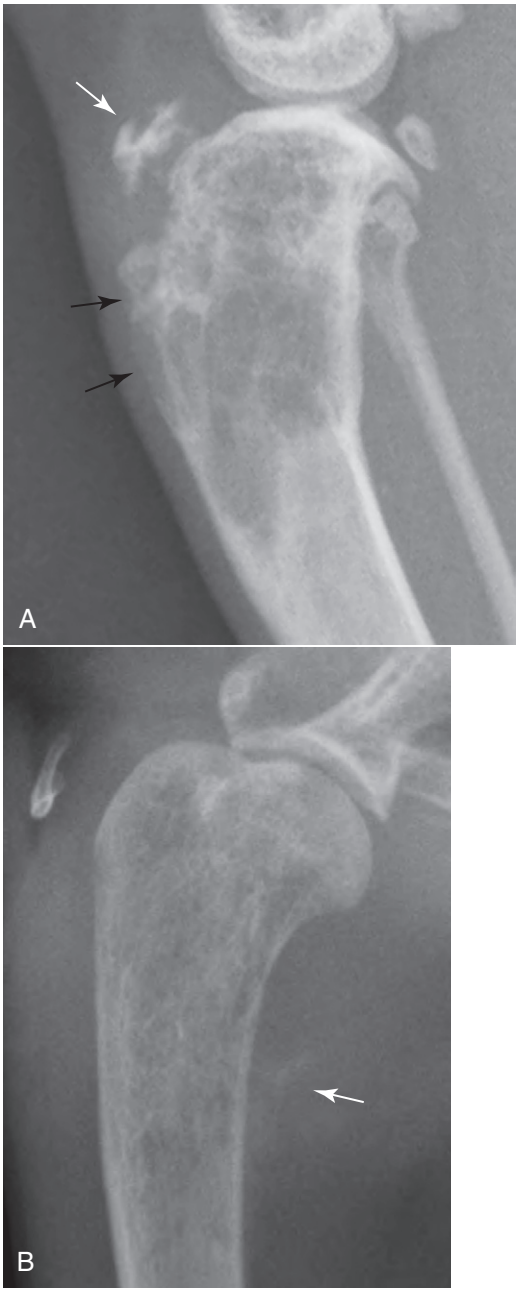


Fig. 17-7 Osteosarcoma in two cats. **A,** Lateral radiograph of the proximal tibia. There is a large aggressive lytic lesion that has effaced the proximal-cranial cortex of the tibia *(black arrows)*. The lesion is well defined distally, and there is no periosteal reaction, but it is aggressive because of the cortical destruction. The loss of bone structure has led to a pathologic avulsion fracture of the tibial crest *(white arrow)*. **B,** Lateral radiograph of the proximal humerus. There is moth-eaten to permeative lysis throughout the medullary cavity. There is a focal region of faint periosteal reaction *(white arrow)*. The lesion is aggressive because of the lack of a distinct transition zone distally and the ill-defined nature of the lysis.

skeleton, metaphyseal lesions are common because of the rich capillary network located there. This capillary network acts as a filter, and the microenvironment is rich in nutrients, providing fertile ground for colonization. Nevertheless, diaphyseal lesions also occur. Bone lesions of fungal osteomyelitis can appear very aggressive radiographically, leading them to be confused with tumors. Fungal osteomyelitis should be considered in any dog with polyostotic aggressive bone lesions (Figs. 17-11, p. 312 and 17-12, p. 313). As with all aggressive bone lesions, biopsy and possibly microbiologic testing will be necessary for final diagnosis.

Rarely, fungal osteomyelitis will be monostotic and metaphyseal-epiphyseal in location (Fig. 17-13, p. 314). These fungal lesions are impossible to distinguish radiographically from a bone tumor. Thus any monostotic metaphyseal aggressive lesion should be biopsied before a course of therapy is selected. Other radiographic evidence, such as lung lesions (Fig. 17-14, p. 314) or mediastinal lymphadenopathy, or clinical signs of systemic debilitation, may favor a diagnosis of an infectious process, but a bone biopsy is still necessary for a definitive diagnosis.

BACTERIAL BONE INFECTIONS

Most bone infections in dogs and cats are of bacterial origin[20] and are acquired by (1) direct inoculation, such as from an

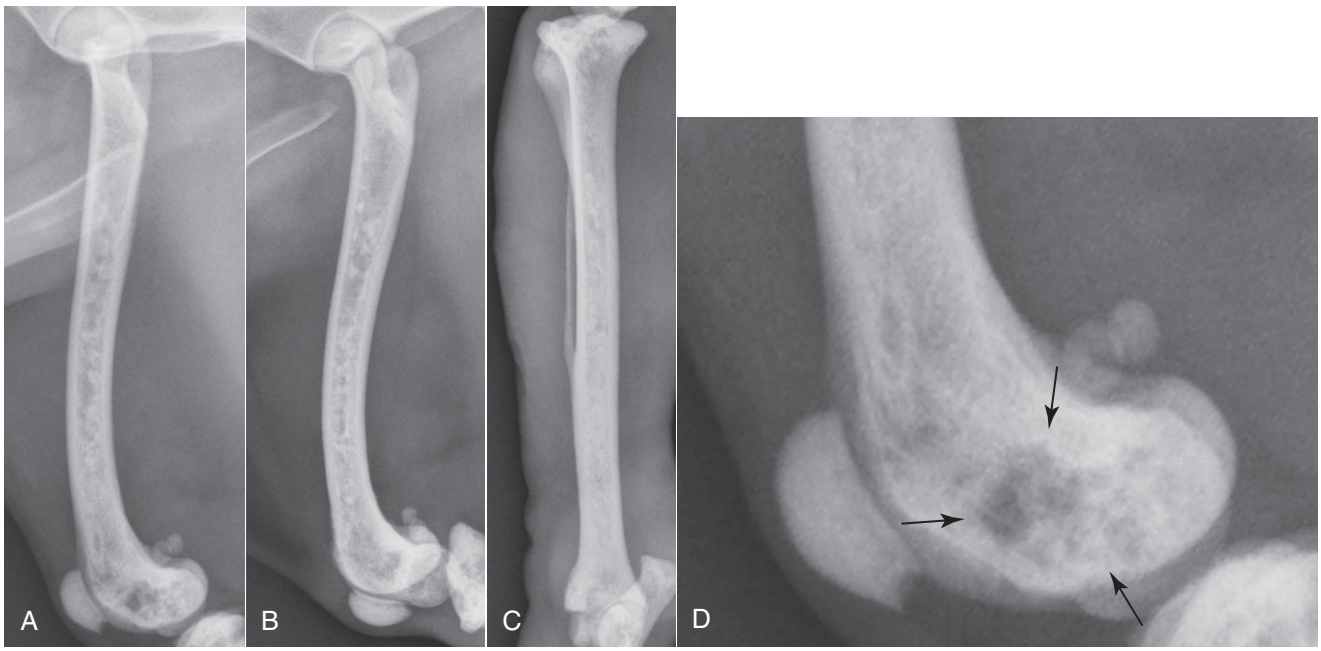


Fig. 17-8 Lateral views of the right femur **(A)**, left femur **(B)**, and left tibia **(C)** of a dog with idiopathic polyostotic bone infarction. The femurs have multifocal punctate opacities in the medullary cavity, and the tibia is characterized by more homogeneously increased medullary opacity. These findings are typical of bone infarction. There is an aggressive lytic lesion in the distal aspect of the right femur **(D)** that is consistent with an osteosarcoma. Idiopathic polyostotic bone infarction predisposes to development of primary bone tumors, which are usually lytic. The exact mechanism is not understood.

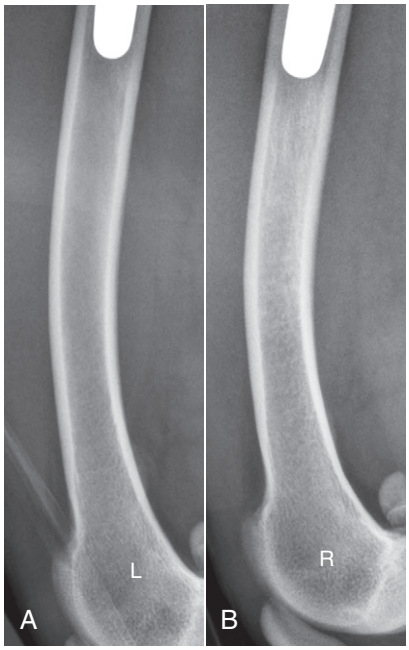


Fig. 17-9 Lateral view of the left **(A)** and right **(B)** femur of a dog with bilateral total hip prostheses. The medullary cavity of the right femur is increased in opacity and has a wispy appearance; this is typical of infarction secondary to insertion of the femoral stem. This can predispose to the development of osteosarcoma years later in some dogs.

open fracture, a bite wound, or surgery; (2) extension from soft tissue injury; or (3) hematogenous dissemination.[20] Direct inoculation and extension from soft tissue are more common than hematogenous dissemination (see Table 17-1). Neither direct inoculation nor extension from soft tissue has a predilection for skeletal localization; lesions develop at the site of injury (Figs. 17-15, p. 314 and 17-16, p. 315). Therefore bacterial osteomyelitis in dogs and cats usually involves one limb, but more than one bone may be involved. A history of previous trauma or surgery is usually present.

Although not as common as infection caused by direct inoculation, hematogenous bacterial infections do occur in dogs (see Table 17-1). They are more common in young dogs, and immunosuppression may predispose the patient to disseminated infection. Typically, hematogenous osteomyelitis results in polyostotic metaphyseal lesions, as the rich capillary network of the metaphysis provides a good environment for colonization. Either lysis or production can predominate. (Figs. 17-17 and 17-18, p. 315).

Although bacterial bone infections and bone tumors both result in aggressive bone lesions, the lesions usually have little in common (see Table 17-1). Osteomyelitic bone lesions in dogs and cats are typically not metaphyseal in location because most are associated with direct inoculation. Bacterial osteomyelitis lesions that are hematogenous are usually polyostotic and occur in young dogs and therefore are not typical for a neoplastic disease. Most bacterial osteomyelitic lesions will have a periosteal reaction that is less aggressive than with a neoplastic lesion, where spiculation is more common. Osteomyelitic periosteal reactions often have a palisading or columnar appearance to the periosteal reaction, in which vertically oriented columns of new bone are oriented perpendicular to the cortex (see Figs. 17-15 and 17-16), but a columnar periosteal reaction can sometimes be found with neoplastic bone lesions as well (Fig. 17-4, C). These generalizations can help prioritize differential diagnoses, but cytologic sampling and perhaps microbiologic testing should always be performed before initiation of any treatment.

Text continued on p. 316

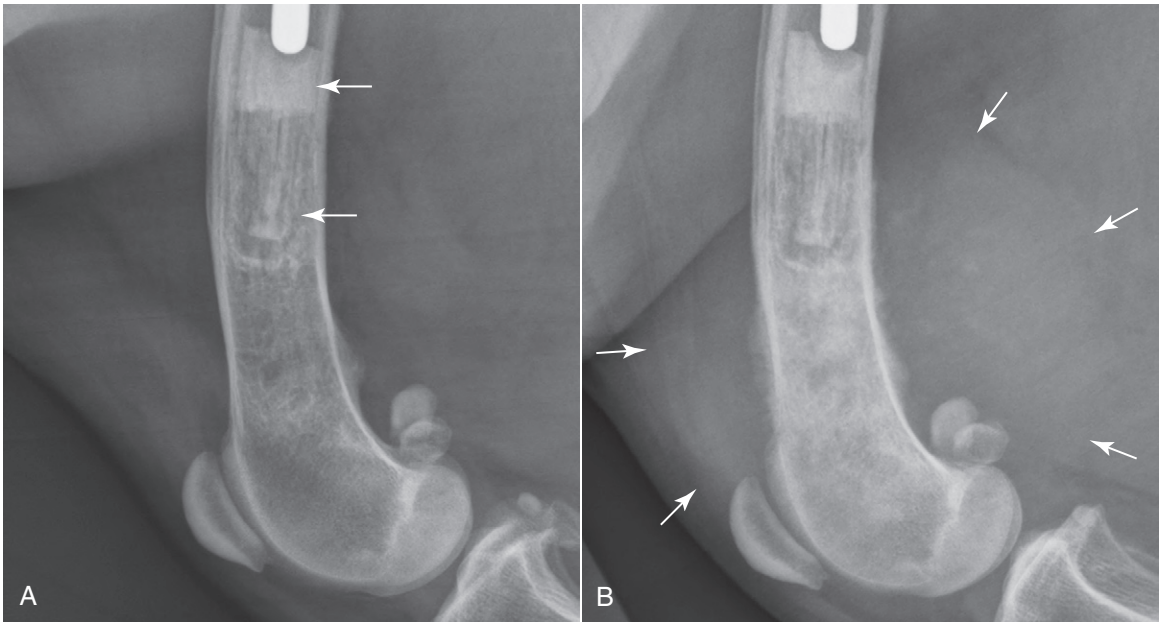


Fig 17-10 Lateral view of the distal femur of dog having received a cemented hip prosthesis 6 years previously. In **A,** the cement restrictor *(black arrows)* and distal tip of the stem can be seen. Distal to the cement restrictor, the medullary cavity is characterized by wispy regions of increased opacity that are caused by bone infarction. In **B,** made 6 months after **A,** there is progressive sclerosis of the distal femoral metaphysis because of neoplastic osteogenesis, a soft tissue mass *(white arrows)* with foci of mineralization, and a periosteal reaction. These changes are caused by malignant progression of the medullary bone infarction to osteosarcoma.

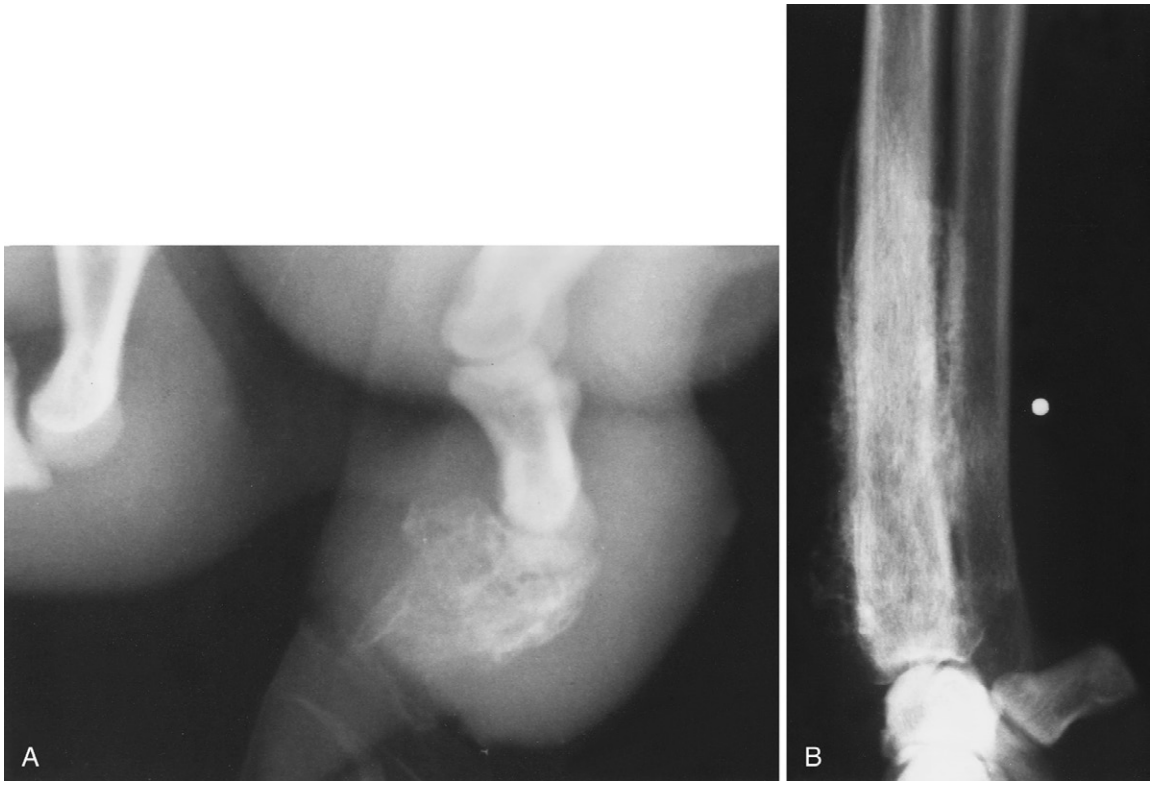


Fig. 17-11 Lateral radiographs of a rear-limb distal phalanx **(A)** and the distal antebrachium **(B)** of a 5-year-old mixed-breed dog with lameness and weight loss. The phalanx is characterized by multifocal regions of lysis, with some evidence of new bone formation. The cortex of the phalanx is destroyed. The distal radius is characterized by mottled regions of increased and decreased bone opacity. The cortex is destroyed cranially and caudally, and an active periosteal reaction is present. The transition zone between normal and abnormal bone is indistinct. The phalanx and radial lesions are both aggressive. Taken alone, each is consistent with primary neoplasia. Collectively, a more likely diagnosis is mycotic osteomyelitis or metastatic solid tumor because of the polyostotic nature of the disease. This dog is relatively young, lives in a blastomycosis-endemic area, and had no identifiable primary tumor. Blastomycosis titers were high, and *Blastomyces* species was isolated from a bone biopsy.

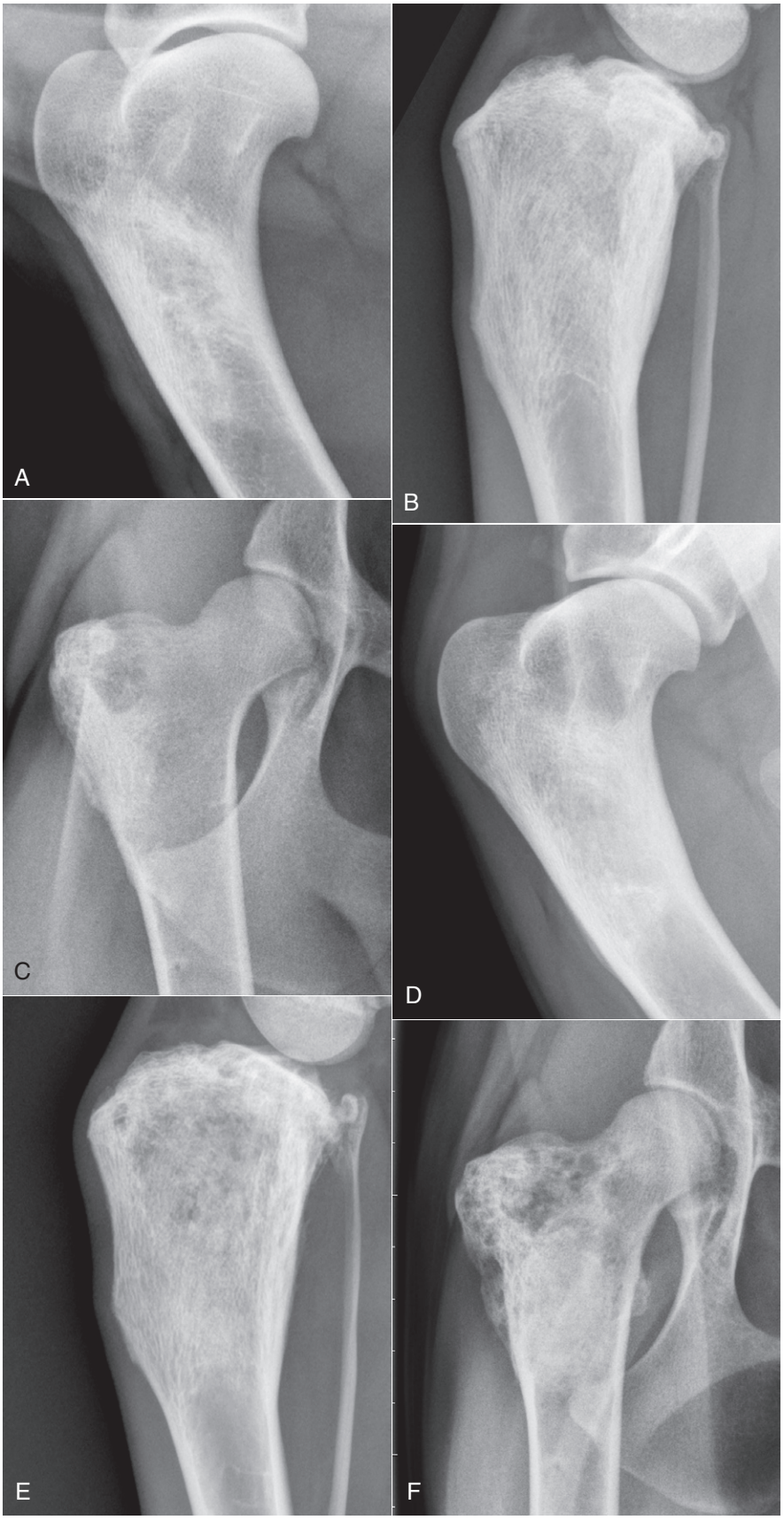


Fig. 17-12 Radiographs of the proximal humerus **(A),** proximal tibia **(B),** and proximal right femur **(C)** of a 3-year-old dog with documented coccidioidomycosis infection. There are aggressive lesions in each of the bones because of hematogenous dissemination of the organism. The lesions are mainly sclerotic, and there is minimal periosteal response. The sclerotic appearance of these lesions cannot be used to differentiate between neoplastic and infectious bone disease; metastatic tumor could have this appearance, although this dog is younger than most patients with metastatic bone cancer. Following 11 months of ineffective antifungal treatment for coccidioidomycosis, the lesions in the humerus **(D),** tibia **(E),** and femur **(F)** have progressed. The humeral lesion is larger **(D),** and the tibial **(E)** and femoral **(F)** lesions are more lytic. Following a medication change, the clinical signs resolved, and there was also significant resolution of the radiographic changes. (Images courtesy of Dr. Erik Wisner, University of California Davis.)

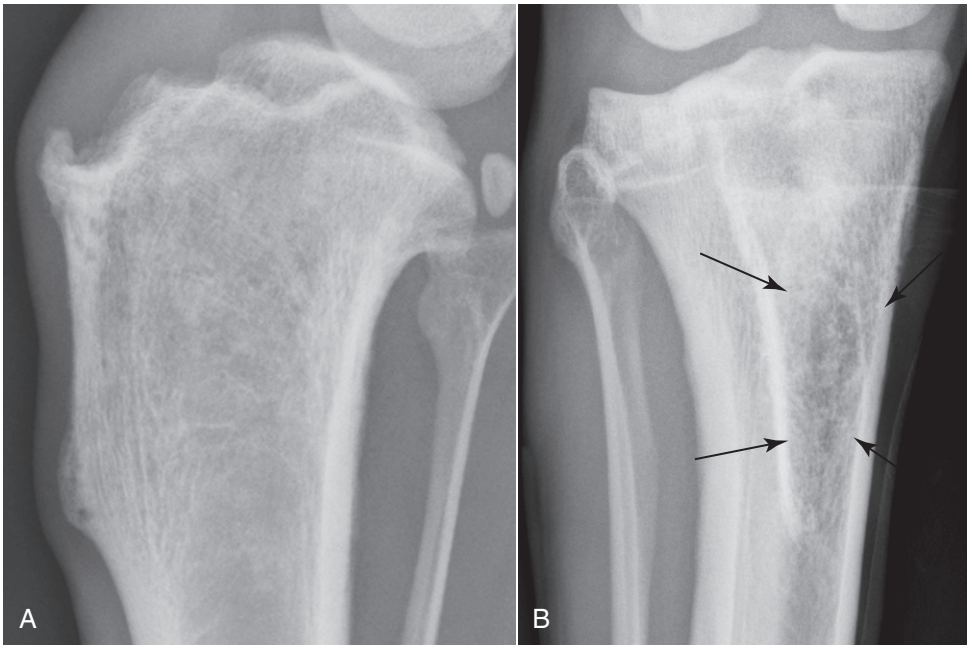


Fig. 17-13 Lateral **(A)** and craniocaudal **(B)** views of the proximal tibia of a 2-year-old Great Dane. In **A,** there is multifocal punctate lysis of the proximal tibia. In **B,** there is a more obvious region of lysis *(black arrows)* with an indistinct transition zone. This monostotic aggressive lesion is consistent with an osteosarcoma, even in a 2-year-old dog, but was caused by blastomycosis infection.

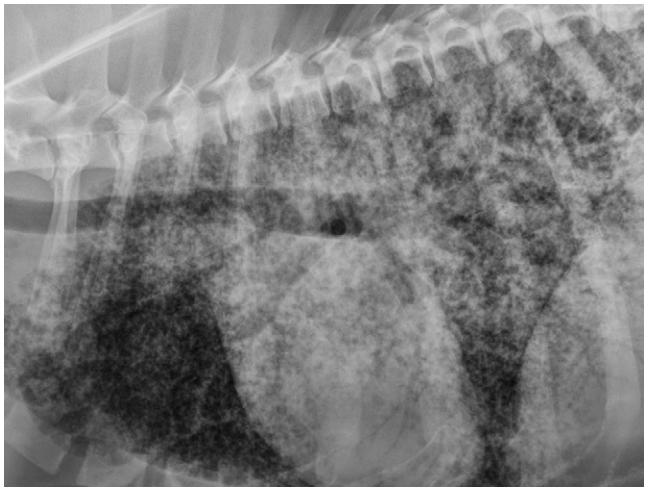


Fig. 17-14 Lateral thoracic radiograph of the same dog as in Figure 17-13. There is a diffuse unstructured interstitial pattern that is consistent with mycotic pneumonitis. This, coupled with the tibial lesion, makes fungal infection the most likely diagnosis, because this is a very unusual pulmonary pattern to be associated with metastatic osteosarcoma. Regardless, the diagnosis cannot be made radiographically, and more specific testing is needed before initiation of any treatment.

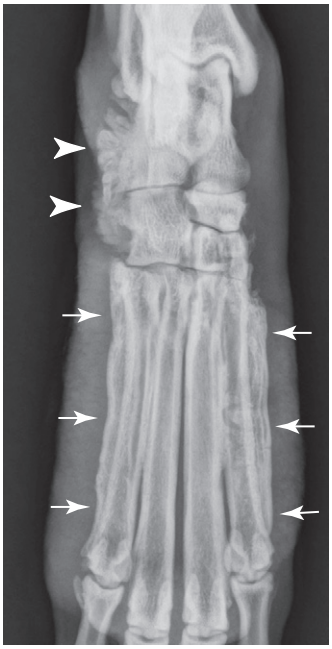


Fig. 17-15 Dorsoplantar radiograph of the pes from a dog with a chronic lick granuloma. The chronic licking has resulted in disseminated osteomyelitis. There are smooth periosteal reactions on metatarsal bones 2 and 4 *(white arrows)* because of subperiosteal exudate, and there is a columnar periosteal reaction on the lateral aspect of the calcaneus and fourth tarsal bone *(white arrowheads)*. Columnar periosteal reactions are often found with bacterial osteomyelitis, but they can also be produced by tumors (see Fig. 17-4, C).

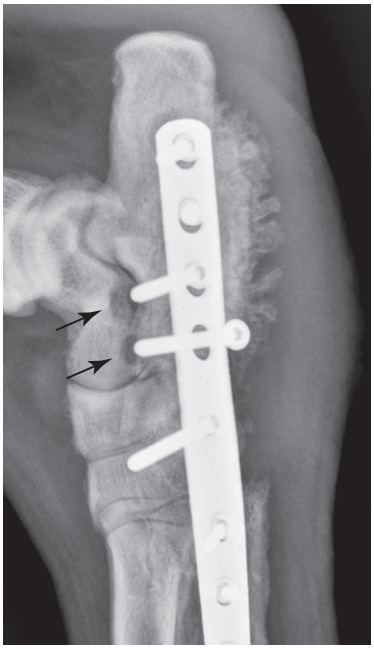


Fig. 17-16 Lateral view of the tarsus of a dog that had undergone surgical tarsal arthrodesis. There is a columnar periosteal reaction on the plantar aspect of the calcaneus and lysis around the tip of two screws *(black arrows)*. The lysis around the screws could be caused by aseptic loosening, but a columnar periosteal reaction should never be seen in a healing fracture or a healing arthrodesis. This periosteal reaction is caused by osteomyelitis.

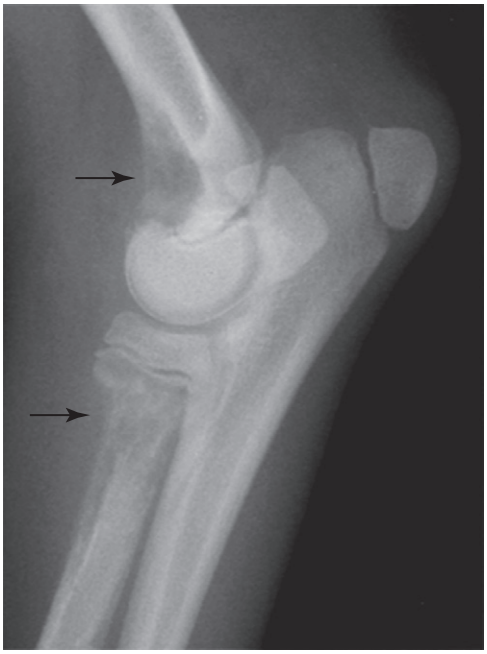


Fig. 17-18 Lateral radiograph of the elbow of a young dog with hematogenous osteomyelitis. Aggressive lytic lesions are present in the distal humerus and proximal radius *(black arrows)*. Other bones in other limbs were affected with similar lesions.

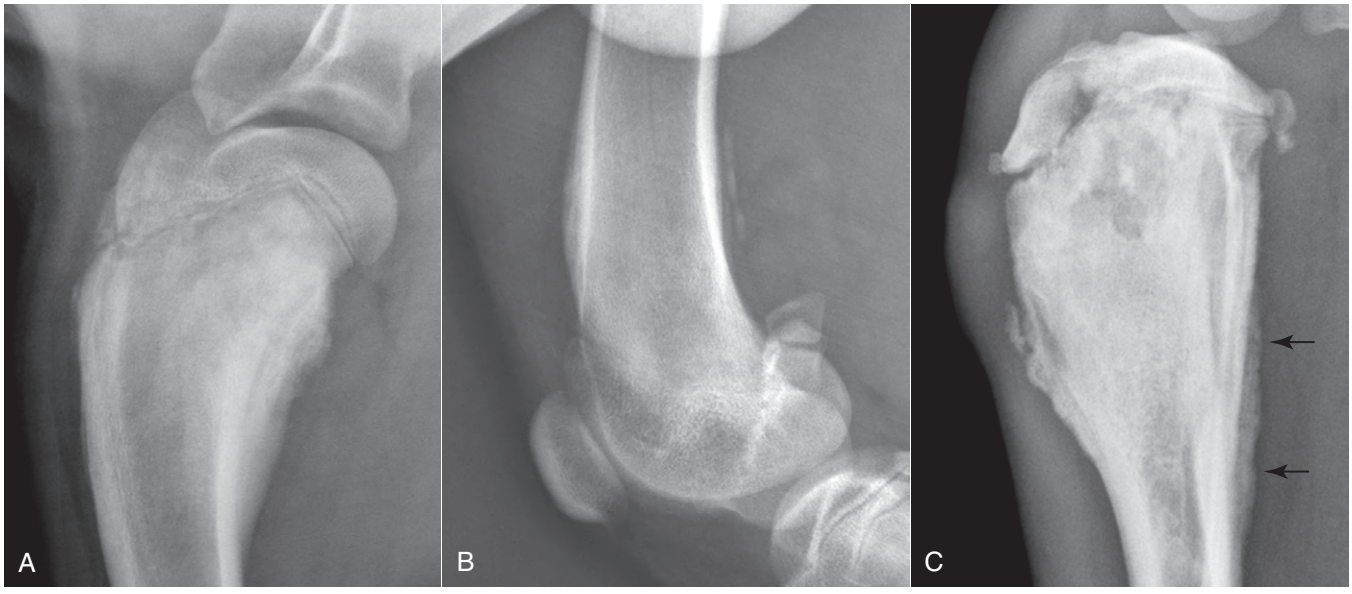


Fig. 17-17 Radiographs of a dog with hematogenous bacterial osteomyelitis. **A,** Proximal right humerus. **B,** Distal right femur. **C,** Proximal left tibia. In the right humerus, the metaphysis is thickened as a result of subperiosteal exudate. In the right femur, the only changes are localized periosteal reaction. In the tibia, there is an aggressive lytic process, medullary sclerosis, and an active periosteal reaction *(black arrows)*.

PROTOZOAN BONE INFECTIONS

Hepatozoonosis is a rare protozoan infection that may cause polyostotic aggressive lesions.[21] *Hepatozoon* infections have been diagnosed in dogs throughout the world; in the United States, most infections occur in the South.[22] The primary vector of *Hepatozoon* infections is the brown dog tick, *Rhipicephalus sanguineus*. Radiographically, findings are limited primarily to the periosteum and range from irregular periosteal proliferation to smooth laminar thickening of the periosteum.[23] Lesions have been described in the axial and the appendicular skeleton.[23] When the periosteal reaction is irregular, the appearance is consistent with a polyostotic infection or metastasis. Sometimes the extent of skeletal involvement is very great, making metastasis less likely than an infection. The smooth periosteal reaction form is misleading because one does not typically associate a smooth periosteal reaction with disseminated bone infection. Dogs with hepatozoonosis usually have clinical signs of systemic dysfunction, such as fever, weight loss, muscle atrophy, ocular discharge, and generalized pain.[21]

METASTATIC BONE CANCER

With animal cancer patients being treated more aggressively and living longer, metastatic bone tumors are being recognized more frequently. Any malignant tumor has the potential to metastasize to the skeleton, but in general bone metastasis from epithelial tumors is more common than from mesenchymal tumors.[24,25] In dogs, mammary, lung, liver, thyroid, urinary, and prostate cancers are a common source of bone metastasis.[24,26,27] Metastatic tumor sites in the skeleton arise hematogenously, leading to a polyostotic distribution (see Table 17-1). Lesions are commonly found in the axial and appendicular skeleton (Fig. 17-19). The hematogenous origin suggests that a metaphyseal distribution would be most common, but diaphyseal lesions are also common. The most common sites of metastatic bone tumors are in the axial skeleton and the proximal extent of long bones in the appendicular skeleton.[24] Metastatic bone tumors are aggressive radiographic lesions, and, as with primary bone tumors, they may be sclerotic, mixed, or predominantly osteolytic. Patients with metastatic bone tumors are generally older; they also usually have a

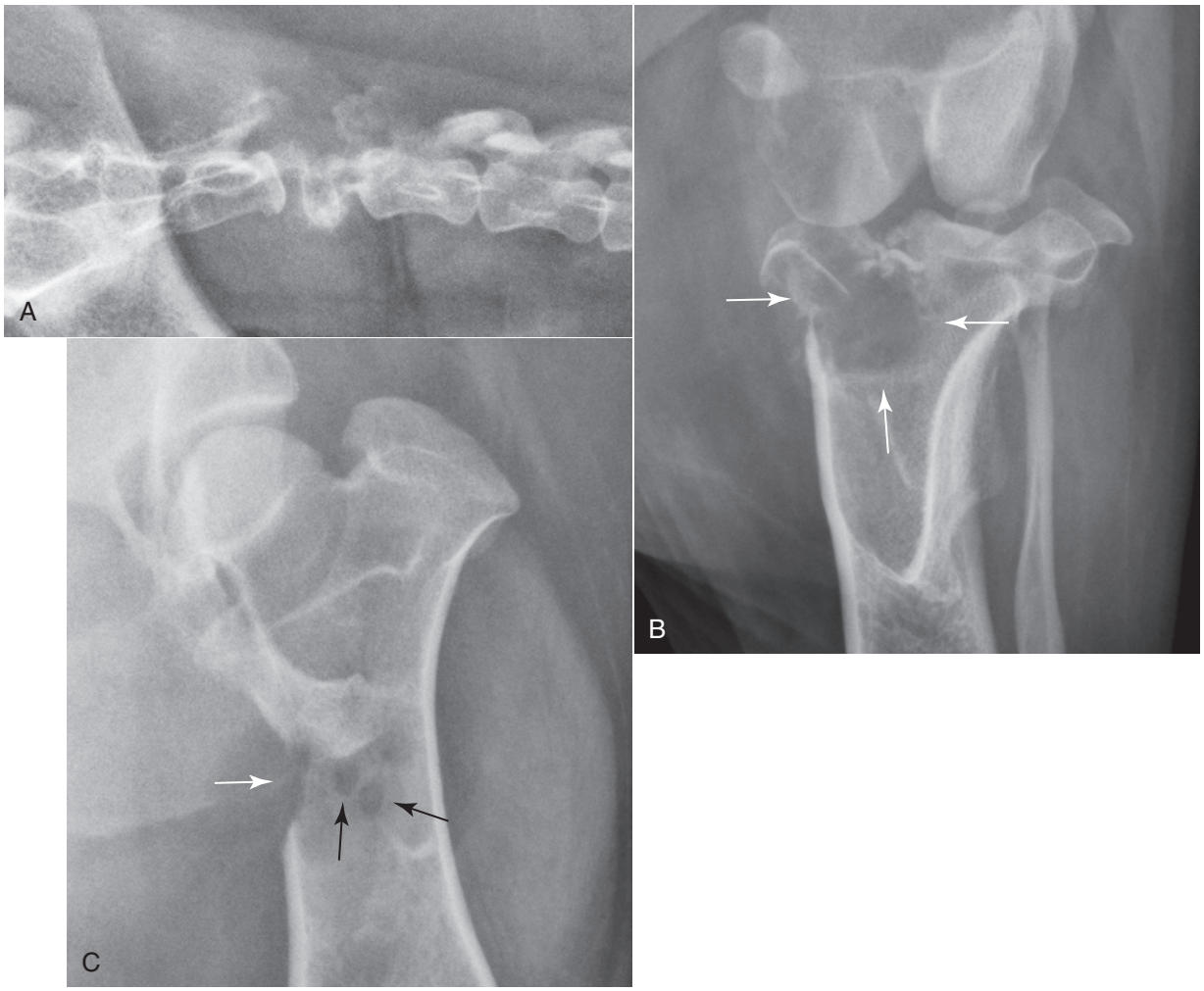


Fig. 17-19 Radiographs of a dog with metastatic round cell tumor. **A,** The first caudal vertebra is collapsed because of tumor effacement. **B,** There is lysis affecting the proximal aspect of the left femur. There is a large region of cortical lysis *(white arrow)* and multiple regions of moth-eaten lysis *(black arrows)*. **C,** There is a large region of lysis in the proximal tibia *(white arrows)* that has caused cortical effacement and collapse of the medial tibial condyle.

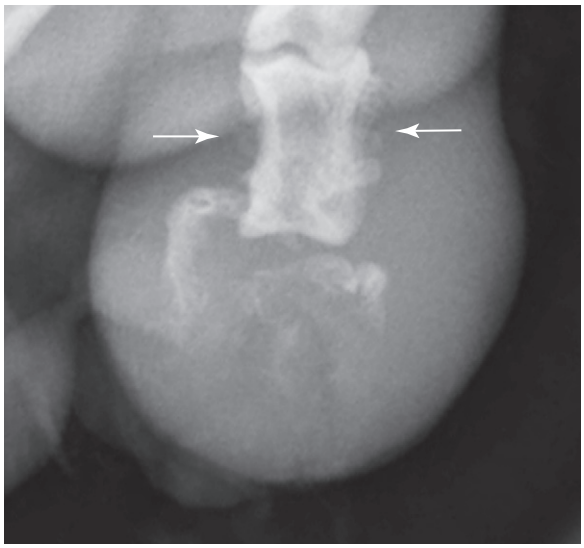


Fig. 17-20 Lateral view of the distal phalanx of the fifth digit of a dog. The digit is swollen, and there is extensive lysis of the distal phalanx. This aggressive lytic appearance is more consistent with neoplasia than with pododermatitis, but histopathologic assessment will be needed for a definitive diagnosis. The diagnosis is squamous cell carcinoma. There is active periosteal reaction on the middle phalanx of this digit *(black arrows)*. This may be because of periosteal irritation from the soft tissue mass, but tumor invasion cannot be ruled out.



Fig. 17-21 Lateral view of the swollen second digit of a dog. The most distal aspect of the distal phalanx has been effaced. These radiographic changes could result from either a tumor or inflammatory disease, but with the lack of more obvious lysis and effacement, an inflammatory lesion is more likely. A biopsy is needed for a definitive diagnosis, which was pododermatitis.



Fig. 17-22 Dorsopalmar radiograph of the manus **(A)** and dorsoplantar radiograph of the pes **(B)** of a 14-year-old cat. In the manus, there is swelling of the fourth digit with lysis of the distal phalanx. In the pes, there is lysis of the distal phalanx of the third digit and lysis of the proximal, middle, and distal phalanges of the fourth digit; some reactive bone is present on the proximal phalanx of the fourth digit. In radiographs of the thorax, multiple lung masses were present. Histologic diagnosis of the lung and digital lesions is squamous cell carcinoma. The digital tumors represent metastatic sites; that is, lung digit syndrome.

history of primary tumor, making the index of suspicion higher for tumor than for mycotic infection.

SUBUNGUAL TUMORS VERSUS SUBUNGUAL INFECTIONS

The digit is another location where radiographic differentiation between infectious and neoplastic causes is usually impossible. The most common canine subungual tumor is squamous cell carcinoma,[28] commonly occurring in large-breed dogs with black haircoats.[28,29] Melanomas are another common canine subungual tumor.[30] Inflammatory conditions of the digit also occur. When radiographic changes in dogs with pododermatitis versus digital tumors were characterized,[31] tumors and pododermatitis were distributed fairly evenly between the manus and the pes. Also, the frequency of bone involvement was similar between subungual tumors and pododermatitis: 25 of 48 (52.1%) for pododermatitis and 33 of 52 (63.5%) for digital tumors. Regarding radiographic changes, pododermatitis could not be differentiated from malignant tumors because both conditions resulted in an aggressive lesion. However, lesions characterized primarily by lysis were more likely to be neoplastic.[31] In another study of dogs with digit masses, lysis was seen with all types of masses but was more commonly associated with squamous cell carcinoma (Figs. 17-20 and 17-21).[32]

Digital tumors typically involve a single digit, but syndromes of multiple-digit tumors have been described in dogs and cats (Fig. 17-22).[28-32]

REFERENCES

1. Chun R: Common malignant musculoskeletal neoplasms of dogs and cats, *Vet Clin North Am Small Anim Pract* 35:1155, 2005.
2. Misdorp W, Hart A: Some prognostic and epidemiological factors in canine osteosarcoma, *J Natl Cancer Inst* 62, 1979.
3. Ragsdale BD, Madewell JE, Sweet DE: Radiologic and pathologic analysis of solitary bone lesions. Part II: periosteal reactions, *Radiol Clin North Am* 19:749, 1981.
4. Mirra J, Gold R, Picci P: Osseous tumors of intramedullary origin. In Mirra J, Picci P, Gold R, editors: *Bone tumors: clinical, radiologic and pathologic correlations*, Philadelphia, 1989, Lea & Febiger, p 270.
5. Kessler M, Tassani-Prell M, von Bomhard D, et al: Osteosarcoma in cats: epidemiological, clinical and radiological findings in 78 animals (1990–1995), *Tierarztl Prax* 25:275, 1997.
6. Heldmann E, Anderson M, Wagner-Mann C: Feline osteosarcoma: 145 cases (1990–1995), *J Am Anim Hosp Assoc* 36:518, 2000.
7. Turrel J, Pool R: Primary bone tumors in the cat: a retrospective study of 15 cats and a literature review, *Vet Radiol* 23:152, 1982.
8. Quigley P, Leedale A: Tumors involving bone in the domestic cat: a review of 58 cases, *Vet Pathol* 20:670, 1983.
9. Bitetto W, Patnaik A, Schrader S, et al: Osteosarcoma in cats: 22 cases (1974–1984), *J Am Vet Med Assoc* 190:91, 1987.
10. Liu S, Dorfman H, Patnaik A: Primary and secondary bone tumors in the cat, *J Small Anim Pract* 15:141, 1974.
11. Riser W, Brodey R, Biery D: Bone infarctions associated with malignant bone tumors in dogs, *J Am Vet Med Assoc* 160:414, 1972.
12. Dubielzig R, Biery D, Brodey R: Bone sarcomas associated with multifocal medullary bone infarction in dogs, *J Am Vet Med Assoc* 179:64, 1981.
13. Sebastyen P, Marcellin-Little D, DeYoung D: Femoral medullary infarction secondary to canine total hip arthroplasty, *Vet Surg*, 29:227, 2000.
14. Haney DR, Peck JN: Influence of canal preparation depth on the incidence of femoral medullary infarction with Zurich cementless canine total hip arthroplasty, *Vet Surg* 38:673, 2009.
15. Marsolais GS, Peck JN, Berry C, et al: Femoral medullary infarction prevalence with the Zurich cementless canine total hip arthroplasty, *Vet Surg* 38:677, 2009.
16. Marcellin-Little D, DeYoung D, Thrall D, et al: Osteosarcoma at the site of bone infarction associated with total hip arthroplasty in a dog, *Vet Surg* 28:54, 1999.
17. Stevenson S: Fracture-associated sarcomas, *Vet Clin North Am Small Anim Pract* 21:859, 1991.
18. Straw M: What is your diagnosis? Fracture/implant-associated osteosarcoma following TPLO procedures, *J Small Anim Pract* 46:457, 2005.
19. Kerl M: Update on canine and feline fungal diseases, *Vet Clin North Am Small Anim Pract* 33:721, 2003.
20. Johnson K: Osteomyelitis in dogs and cats, *J Am Vet Med Assoc* 205:1882, 1994.
21. Macintire D, Vincent-Johnson N, Dillon A, et al: Hepatozoonosis in dogs: 22 cases (1989–1994), *J Am Vet Med Assoc* 210:916, 1997.
22. Ewing D, Panciera R: American canine hepatozoonosis, *Clin Microbiol Rev* 16:688, 2003.
23. Drost W, Cummings C, Mathew J, et al: Determination of time of onset and location of early skeletal lesions in young dogs experimentally infected with *Hepatozoon americanum* using bone scintigraphy, *Vet Radiol Ultrasound* 44:86, 2003.
24. Cooley D, Waters D: Skeletal metastasis as the initial clinical manifestation of metastatic carcinoma in 19 dogs, *J Vet Intern Med* 12:288, 1998.
25. Russell G, Walker M: Metastatic and invasive tumors of bone in dogs and cats, *Vet Clin North Am* 13:163, 1983.
26. Brodey R, Reid C, Sauer R: Metastatic bone tumors in the dog, *J Am Vet Med Assoc* 148:29, 1966.
27. Geodegebuure S: Secondary bone tumors in the dog, *Vet Pathol* 16:520, 1979.
28. Vail D, Withrow S: Tumors of the skin and subcutaneous tissues. In Withrow S, MacEwen E, editors: *Small animal clinical oncology*, ed 2, Philadelphia, 1996, Saunders, p 167.
29. O'Brien M, Berg J, Engler S: Treatment by amputation of subungual squamous cell carcinomas in dogs: 21 cases (1987–1988), *J Am Vet Med Assoc* 201:759, 1992.
30. Aronsohn M, Carpenter J: Distal extremity melanocytic nevi and malignant melanomas in dogs, *J Am Anim Hosp Assoc* 26:605, 1990.
31. Voges A, Neuwirth L, Thompson J, et al: Radiographic changes associated with digital, metacarpal and metatarsal tumors, and pododermatitis in the dog, *Vet Radiol Ultrasound* 37:327, 1996.
32. Marino D, Matthiesen D, Stefanacci J, et al: Evaluation of dogs with digit masses: 117 cases (1981–1991), *J Am Vet Med Assoc* 207:726, 1995.

ELECTRONIC RESOURCES

evolve

Additional information related to the content in Chapter 17 can be found on the companion Evolve website at http://evolve.elsevier.com/Thrall/vetrad/

- Chapter Quiz

CHAPTER • 18

Radiographic Signs of Joint Disease in Dogs and Cats

Graeme Allan

Most radiographic signs of joint disease are nonspecific (Box 18-1, Fig. 18-1). Also, animals with progressive joint disease may have different signs when examined during different phases of the disease. Sound knowledge of joint pathophysiologic characteristics is as important in the diagnosis of joint disease as is the ability to make and interpret radiographs of joints.

RADIOGRAPHIC SIGNS OF JOINT DISEASE

Increased Synovial Volume

Any moderate increase in joint capsular or intracapsular soft tissue volume may be detected on good-quality radiographs. The joint cartilage, synovial fluid, synovial membrane, and joint capsule cannot be differentiated because they are all of soft tissue opacity and therefore silhouette with one another. In most joints, any increase in synovial mass appears as periarticular soft tissue swelling, which is identified radiographically by the increased opacity of affected soft tissues.

In the stifle, the infrapatellar fat pad sign may be used to evaluate synovial volume. The normal infrapatellar fat pad is identified readily on lateral stifle radiographs as a relatively radiolucent triangular region immediately caudal to the patellar ligament (Fig. 18-2). When stifle synovial mass increases, either from increased synovial fluid or soft tissue, a combination of inflammatory response and effusion causes the fat pad to become less visible.

Box • 18-1

Radiographic Signs of Joint Disease

Increased synovial volume
  Compressed infrapatellar fat pad
Altered thickness of the joint space
Decreased subchondral bone opacity
Increased subchondral bone opacity
Subchondral bone cyst formation
Altered perichondral bone opacity
Perichondral bony proliferation
Mineralization of joint soft tissues
Intraarticular calcified bodies
Joint displacement or incongruency
Joint malformation
Intraarticular gas

Altered Thickness of the Joint Space

The joint space is the region of soft tissue opacity between the subchondral bone of opposing weight-bearing surfaces of a joint. This space consists of two layers of articular cartilage separated by a microfilm of synovial fluid. In early joint disease, synovial effusion may cause widening of the joint space. As joint disease progresses, attrition of articular cartilage results in a thinning of the joint space (Fig. 18-3). These changes in joint space width are rarely diagnosed radiographically as a result of small animal patients not being radiographed while bearing weight and also because of inconsistency between the orientation of the primary x-ray beam and joint space.

Decreased Subchondral Bone Opacity and Bone Cyst

The subchondral bone is separated from the synovial fluid by an intact layer of articular cartilage. Any disease that changes

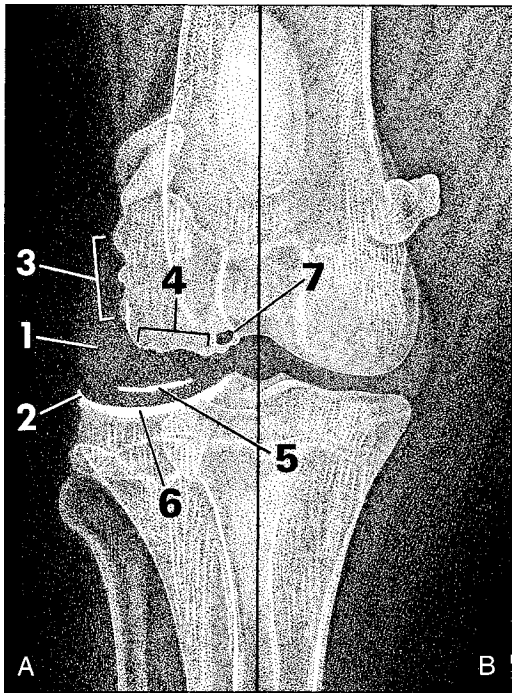


Fig. 18-1 Radiographic signs of joint disease **(A)** compared with a normal joint **(B).** Increased synovial mass *(1)*, perichondral osteophyte *(2)*, and enthesophyte formation *(3)* are common radiographic changes. Erosion of the subchondral bone surface *(4)* and joint mice *(5)* are less common, whereas increased subchondral bone opacity *(6)* and subchondral bone cyst formation *(7)* are signs of chronic joint disease.

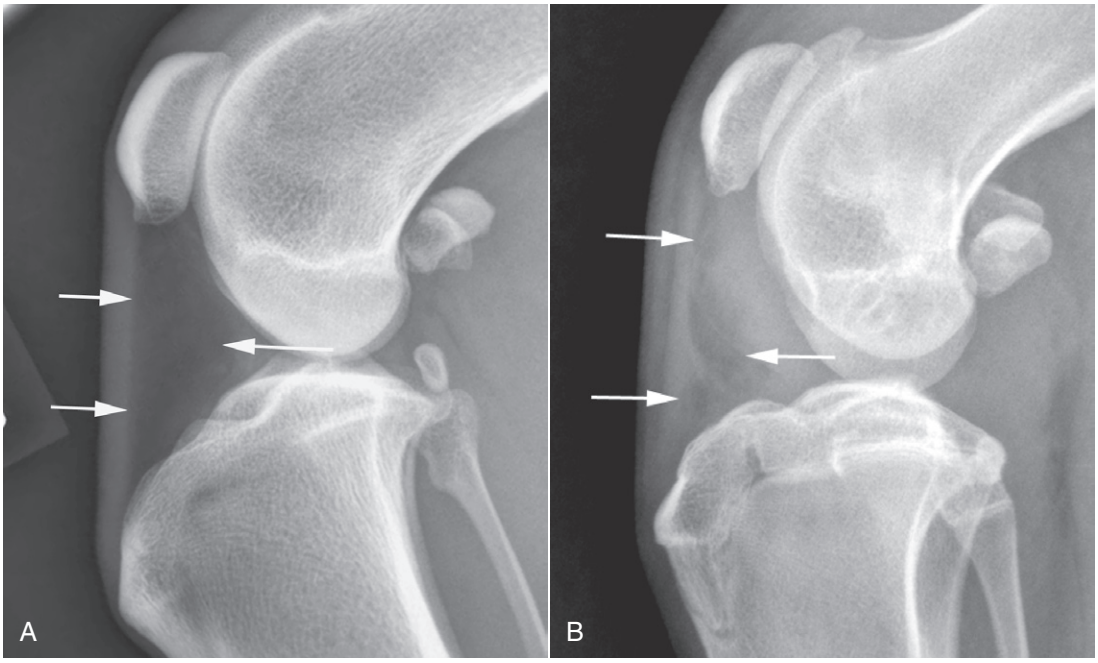


Fig. 18-2 Changes in the shape of the infrapatellar fat pad, located between the *arrows,* is a sensitive indicator of absence **(A)** or presence **(B)** of increased synovial volume in the stifle.

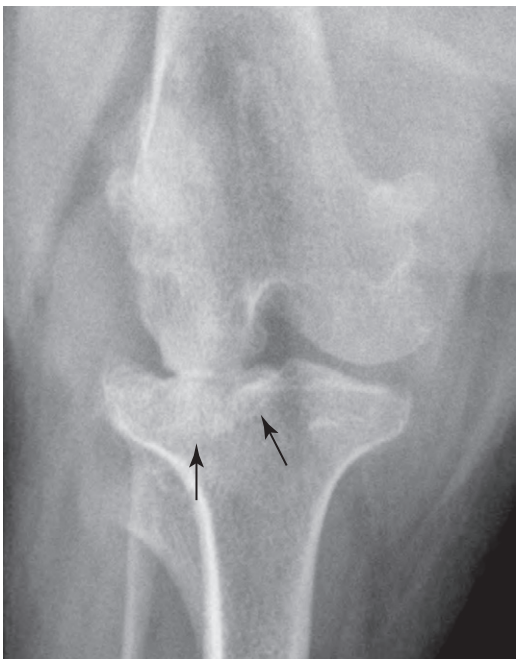


Fig. 18-3 Chronic malalignment of the stifle has resulted in narrowing of the lateral aspect of the femorotibial joint, likely because of degeneration of the lateral meniscus. The secondary altered loading of the lateral tibial condyle has resulted in secondary sclerosis *(black arrows)*.

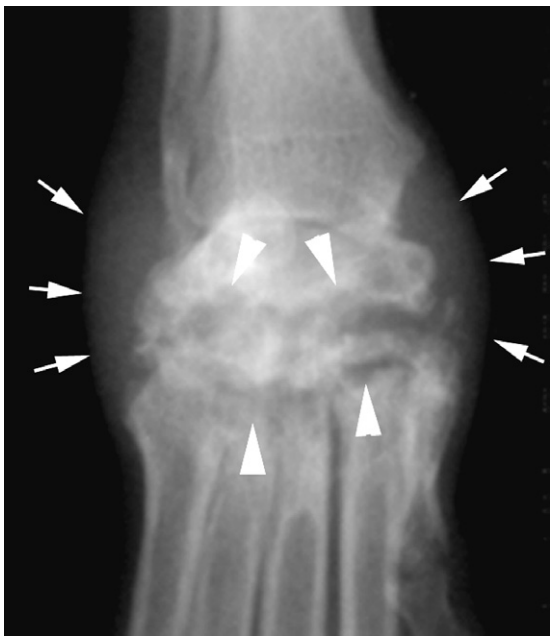


Fig. 18-4 Periarticular soft tissue swelling *(white arrows)* and subchondral bone erosion *(white arrowheads)* seen in the carpus of a dog with an erosive polyarthropathy. The small cuboidal carpal bones are misshapen as a result.

the character of synovial fluid, causing the articular cartilage to erode, potentially threatens the integrity of subchondral bone.[1,2] In inflammatory joint disease, inflammatory exudates may cause pronounced subchondral bone loss. Infectious arthritis may extend into subchondral bone. Subchondral bone loss appears initially as a ragged margin of subchondral bone, but it may extend to cause marked destruction of bone (Fig. 18-4). When bone loss affects smaller carpal and tarsal bones, these small cuboidal bones may be dramatically reduced in mass (see Fig. 18-4).

Increased Subchondral Bone Opacity

In benign joint disease, such as degenerative joint disease, subchondral bone may be more opaque than normal because of stress remodeling (see Fig. 18-3). Increased subchondral bone opacity usually appears as a subchondral zone of increased opacity 1 to 2 mm wide.

Altered Perichondral Bone Opacity

Articular cartilage merges with the synovial membrane at the chondrosynovial junction. The highly vascular membrane

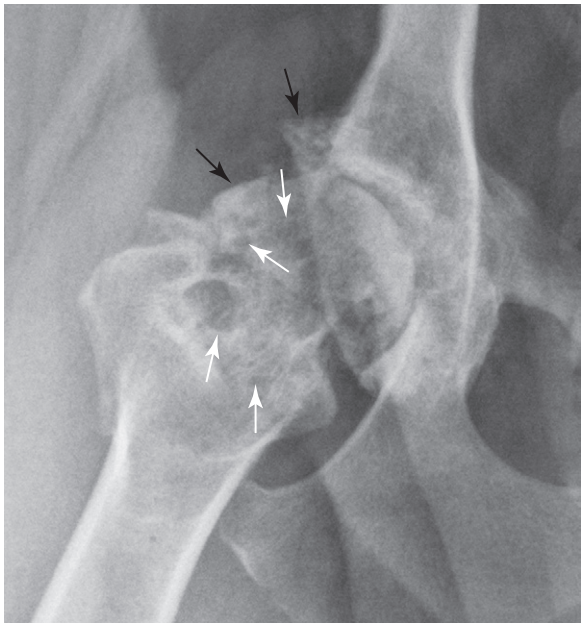


Fig. 18-5 Advanced coxofemoral degenerative joint disease. The femoral neck is thickened, the femoral head is misshapen, and there are numerous osteophytes *(black arrows)*. There are multiple small and large radiolucencies *(white arrows)* in the femoral neck because of invasion of bone by hyperplastic synovium.

is sensitive to inflammation. Synovial inflammation, or hypertrophy, may result in erosion of the bone adjacent to the synovium. Early inflammation causes the adjacent bone to appear ragged and spiculated. Longstanding or severe synovial inflammation or hypertrophy may cause pronounced bone erosion (Fig. 18-5).

Articular Soft Tissue Mineralization

Mineralization may occur within the joint capsule, the synovial membrane, or synovial fluid as a consequence of chronic joint disease. Occasionally, large accumulations of articular or periarticular calcific material may be observed. Large osteochondromas have been reported within the joints of dogs[3] and cats,[4] and intrameniscal calcification and ossification have been observed in the stifle joints of cats.[5] Pseudogout, or calcium pyrophosphate deposition disease, also causes mineralization of articular and periarticular soft tissues[6,7] and has been reported in dogs.

Intraarticular Calcified Bodies

Small, well-defined articular and periarticular calcific opacities are occasionally observed in dogs and cats. Such mineralized fragments are sometimes called *joint mice*. Not all such fragments are free within the joint, although they may appear free radiographically; fragments may become adhered to the joint capsule. Articular calcified bodies usually fall into three fairly distinct categories: avulsed fragments of articular or periarticular bone, osteochondral components of a disintegrating joint surface, or small synovial osteochondromas (Table 18-1).[8] They must be differentiated from sesamoid bones.[9]

Joint Displacement or Incongruency

When the normal spatial relation between the components of a joint is disturbed, some type of displacement has occurred. A good example is a luxated coxofemoral joint. Other less obvious incongruities, such as the cranial drawer sign in a stifle with a ruptured cranial cruciate ligament and minor elbow incongruity in dogs with elbow dysplasia, can be difficult to see radiographically.[10,11]

Table • **18-1**

Some Common Causes of Calcified Intraarticular Bodies

JOINT	ETIOLOGY
Shoulder	Osteochondritis dissecans (OCD) of the head of the humerus
	Mineralization of the bicipital tendon/sheath
	Synovial osteochondroma
	Separate centers of ossification on the glenoid rim
Elbow	Ununited anconeal process
	Fragmented coronoid process
	OCD of the humeral medial condyle
Hip	Avulsion epiphyseal fractures after femoral luxation
	Avascular necrosis of the femoral head
Stifle	OCD of the femoral condyles
	Avulsion fractures of the:
	Origin of the long digital extensor tendon
	Origin or insertion of the cruciate ligaments
	Origin of the popliteus
	Meniscal calcification
	Synovial osteochondroma
	Fragmented or fractured sesamoid bones
Tarsus	OCD of the talus

In all joints, soft tissue periarticular mineralization may occur as a result of degenerative joint disease.

Osteophytes

The proposed pathogenesis of osteophyte formation is that abnormal joint cartilage loading leads to cartilage wear, fibrillation, and loss of cartilage. The products of cartilage degradation mediate synovial hyperplasia and subsequent development of osteophytes.[12] Initially, osteophytes consist of cartilage and later become radiographically visible when they are mineralized. They are seen as bony outgrowths at the periphery of articular cartilage. They occur as a component of degenerative joint disease (see Fig. 18-5).

Entheses and Enthesophytes

An enthesis is the point of insertion of a tendon, ligament, joint capsule, or fascia to bone. During embryogenesis ligaments or tendons are attached to cartilage, but subsequent metaplasia of fibroblasts at their attachment site results in formation of fibrocartilage. This extends into the tendon or ligament, and enchondral ossification proceeds within the remaining cartilage. Enthesitis is inflammation of the site of tendon or ligament attachment to bone. An enthesophyte is a bony spondylopathy that develops at an enthesis (Fig. 18-6).[13]

Because enthesophytes, osteophytes, and ankylosing spondylopathy appear radiographically similar, confusion in terminology often occurs when referring to these structures on a radiograph. To separate osteophytes around or within joints from enthesophytes, knowing the location of the common entheses is useful information (Figs. 18-7, 18-8, and 18-9). In complex joints such as the carpus and tarsus, a large number of intraarticular ligaments are present. Every diarthrodial joint has a joint capsule, and intraarticular and periarticular ligaments and joint capsules insert onto bone at their respective entheses. New bone formations arising in or around joints

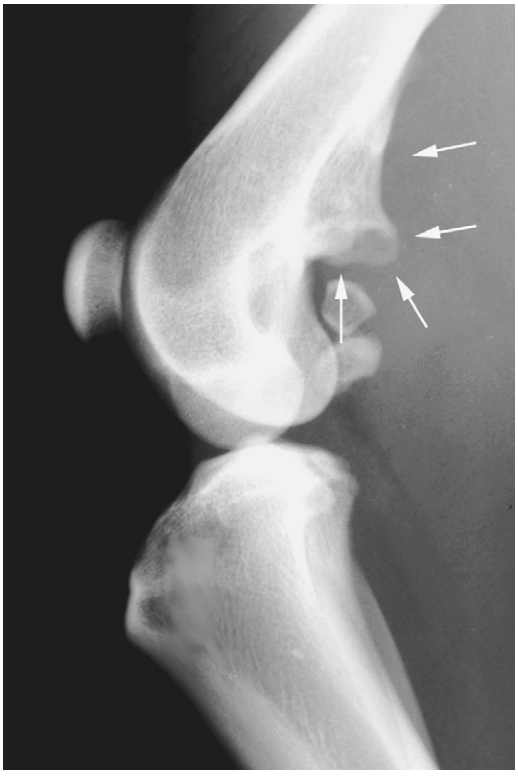


Fig. 18-6 A large enthesophyte arising from the enthesis of origin of the gastrocnemius muscle *(arrows)*.

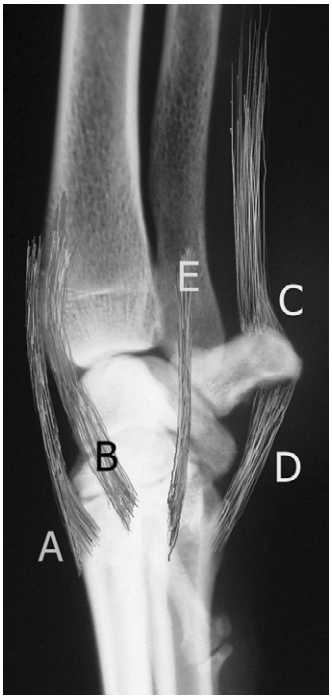


Fig. 18-8 Entheses around the carpus. In addition to the many intraarticular ligaments and the joint capsule (not depicted) are periarticular entheses of extensor carpi radialis and extensor carpi ulnaris *(A)*, abductor pollicis longus *(B)*, flexor carpi ulnaris *(C)*, the check ligaments of the accessory carpal bone *(D)*, and flexor carpi radialis *(E)*.

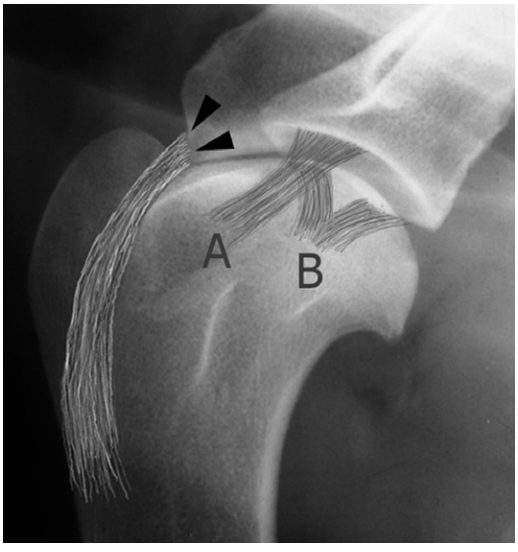


Fig. 18-7 In the scapulohumeral joint the intraarticular tendon of origin of biceps brachii muscle arises from its enthesis *(black arrowheads)* on the scapular tuberosity. Other entheses around the shoulder are related to the lateral *(A)* and medial *(B)* glenohumeral ligaments and the joint capsule and tendons of insertion of supraspinatus, infraspinatus, and subscapularis muscles (not depicted).

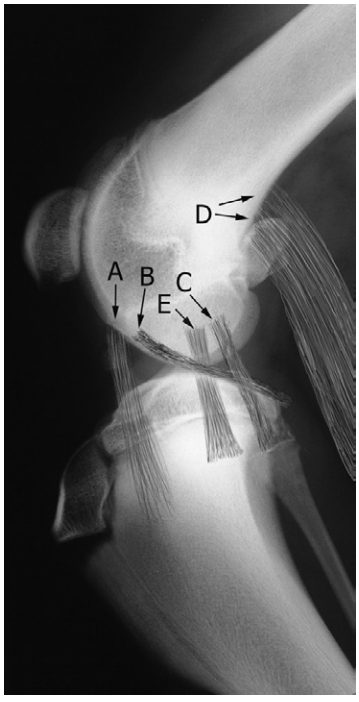


Fig. 18-9 The stifle. Entheses of origin of the long digital extensor *(A)*, popliteus *(B)*, lateral collateral ligament *(C)*, gastrocnemius *(D)*, and medial collateral ligament *(E)*. Not depicted are the cranial and caudal cruciate ligaments.

where no known entheses are present are usually referred to as *osteophytes*.

Intraarticular Gas

Spontaneous or induced gas diffusion into a joint, termed the *vacuum phenomenon*, has been reported in both horses[14] and dogs.[15-19] It has also been observed within the intervertebral disc spaces of dogs that have a prolapsed disc. The presence of intraarticular gas is identified more easily during computed tomography examinations than during radiography.[18] The theory is that noniatrogenic intraarticular gas represents diffusion of nitrogen from extracellular fluid into an adjacent

Box • 18-2

Causes of Intraarticular Gas

Iatrogenic
After arthrotomy/arthroscopy
Negative-contrast arthrography
Arthrocentesis
Tension on joints
PennHIP distraction radiography
Positioning shoulders with OCD for radiography

Trauma
Joint luxation
Penetrating injuries

Infection
Gas-producing microorganisms

Spontaneous
Intervertebral disc disease
Osteoarthritis

OCD, Osteochondritis dissecans.

joint space when negative pressure is present in the joint. This may occur naturally or be induced by applying traction to a joint. The vacuum phenomenon has many causes in dogs and cats (Box 18-2) and is observed when excessive distraction is applied to the coxofemoral joints during distraction radiography and has been reported in 20% of shoulder joint radiographs of dogs with osteochondritis dissecans (OCD) of the humeral head.[16,17] Because traction is used during positioning of the shoulder for an OCD examination, gas diffusion is theorized to be induced by traction. Interestingly, gas diffusion was not a feature of normal (non-OCD) contralateral joints of dogs in this series.[16] Positive clinical associations with intraarticular gas include degenerative disc disease, cervical vertebral instability, osteochondrosis, and degenerative joint disease (Fig. 18-10). Intraarticular gas diffuses slowly out of a joint over several hours after normal intraarticular pressure is reestablished.

SESAMOID BONES

Sesamoid bones are present commonly adjacent to the elbow, stifle, tarsus, and the metacarpophalangeal and metatarsophalangeal joints. If sesamoid bones are not visualized on a radiograph, they may be absent or have not ossified at the time of radiography. The clavicle is present in up to 96% of large dogs and in all cats, but the sesamoids in the iliopubic cartilage were identified in only 11% of one group of greyhounds.[20] In the same group of dogs, the elbow sesamoid, located in the tendon of origin of the supinator, had an incidence of 31%, the lateral plantar tarsometatarsal sesamoid 50%, and the intraarticular tarsometatarsal sesamoid 27%, whereas the popliteal sesamoid is ossified in 84% to 94% of dogs.[21,22] Sesamoid bones are identified by their size, shape, and location (Figs. 18-11 to 18-18 [pp. 324-326], Table 18-2 [p. 327]). Occasionally, displaced sesamoids are regarded as a sign of muscular or tendinous injury. Although this may be true, and has been reported in conjunction with ruptured cruciate ligaments[10] and trauma of the tendon of origin of the popliteus[23,24] and gastrocnemius,[25,26] variation in sesamoid location may also occur in the absence of a pathologic condition.[27]

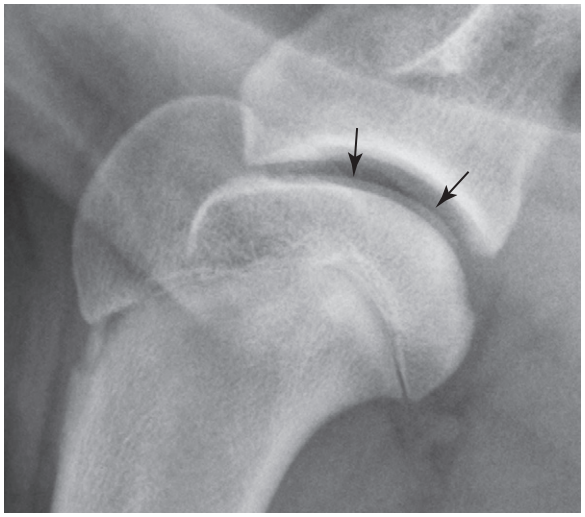


Fig. 18-10 Intraarticular gas is present in the shoulder joint of a dog with osteochondrosis. The gas itself is not very conspicuous, but its presence has reduced the opacity of the joint space leading to visualization of the articular cartilage *(black arrows)* If intraarticular gas were not present, the cartilage would not be visible.

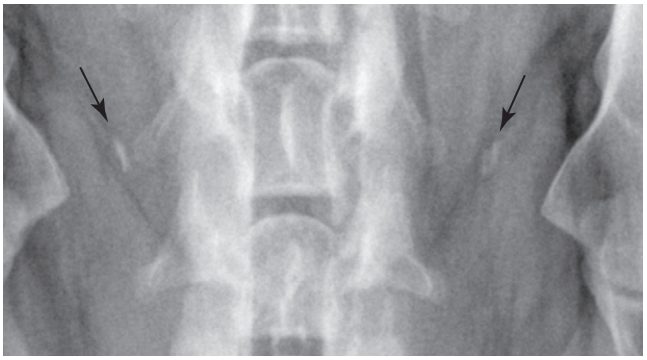


Fig. 18-11 Clavicular remnant medial to the scapulohumeral joints of a dog.

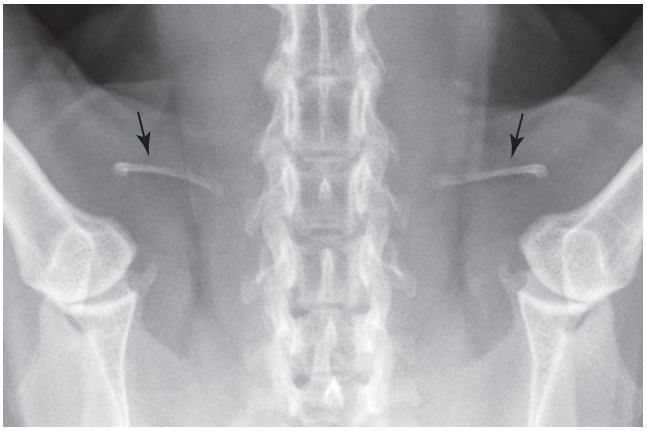


Fig. 18-12 Feline clavicle *(white arrows)*.

Meniscal Ossicles in Cats

A mineralized focus in the stifle joint is recognized commonly in domestic cats (Fig. 18-19, p. 327). Of stifle radiographs of 100 cats, 46 had meniscal mineralization detected in 1 or both stifles. Pain scores were not significantly different between

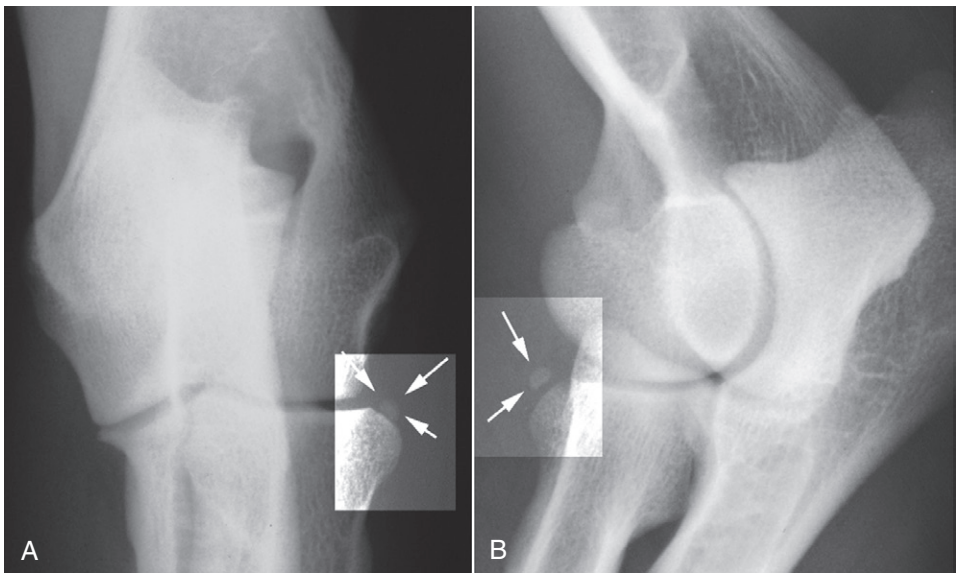


Fig. 18-13 The elbow sesamoid, in the tendon of origin of the supinator, is seen adjacent to the craniolateral surface of the head of the radius *(arrow)*.

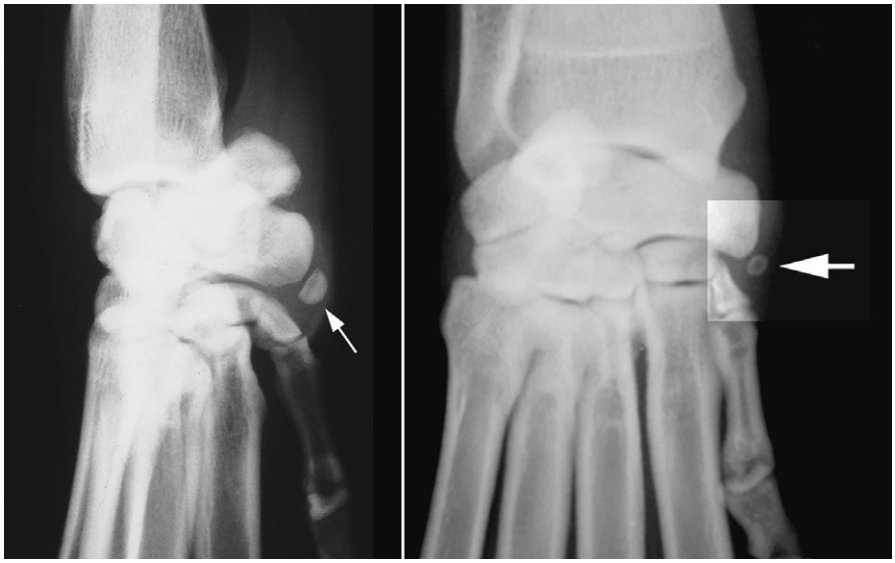


Fig. 18-14 The carpal sesamoid is located in the tendon of the abductor pollicis longus on the medial side of the carpus at the level of the intercarpal articulation *(enhanced box, large arrow)*. The tendon inserts onto the proximal end of the first digit. (Reprinted from *BSAVA manual of canine and feline musculoskeletal imaging*, Quedgeley, Gloucester, England, 2006, BSAVA Publications.)

stifles with meniscal mineralization and those without. Thirty-four of 57 cadaver stifles had meniscal mineralization, which was always located in the cranial horn of the medial meniscus. Percentage mineralization of the menisci was significantly correlated with the cartilage damage in the medial femoral and tibial condyles. Therefore, feline meniscal mineralization seems to indicate medial compartment degenerative joint disease.[28] Although this mineralization has been thought of as a sesamoid bone, that is likely incorrect.

A meniscal ossicle is also present commonly in large non-domestic cats, such as lions, where it is also located in the cranial horn of the medial meniscus.

CONTRAST RADIOGRAPHY OF JOINTS

Radiographs with added contrast medium, either air or water-soluble iodinated contrast medium, can be used to enhance visualization of intraarticular structures, such as the articular cartilage and synovium. A common use of contrast radiography was in the evaluation of the canine shoulder for evidence of osteochondrosis. Other applications include evaluation of capsular trauma, documentation of synovial hypertrophy, and identification of radiolucent-joint mice.[29-33] Arthrography has been largely replaced by computed tomography and magnetic resonance imaging (MRI).

SESAMOID DISEASE

A syndrome of metacarpophalangeal sesamoid bone fragmentation has been reported in several large breeds of dogs, but occurs most commonly in Rottweilers.[33] The underlying cause appears to be osteonecrosis[34] of selected sesamoids, although developmental, traumatic, and degenerative conditions are possible. Eight palmar/plantar sesamoids are present on the



Fig. 18-15 The metacarpophalangeal and metatarsophalangeal sesamoids are paired *(white arrowheads)* on the palmar (plantar) surface and single on the dorsal surface *(white and black arrows)*. They are numbered from medial to lateral. (Reprinted from *BSAVA manual of canine and feline musculoskeletal imaging*, Quedgeley, Gloucester, England, 2006, BSAVA Publications.)

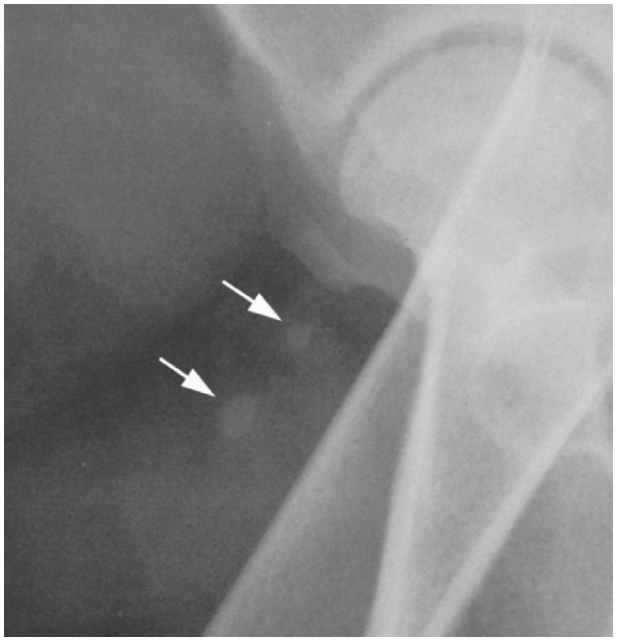


Fig. 18-16 The iliopubic sesamoids are occasionally seen cranial to the pubic eminence on lateral radiographs of the pelvis of large dogs *(white arrows)*.

four main digits of each of the manus or pes, but sesamoid fragmentation affects mainly the second and seventh palmar sesamoids (Fig. 18-20, p. 328). The incidence has been reported to be as high as 44% in one group of Rottweilers.[35] In another group of 55 Rottweilers, the radiographic incidence of sesamoid disease at 12 months of age was 73%, with an incidence of clinical signs attributable to sesamoid disease in 65% of affected dogs. Sesamoid disease was identified as the cause of forelimb lameness in 50% of young Rottweilers.[36]

Dorsopalmar radiographs usually allow identification of affected sesamoid bones, but oblique lateral projections with the digits separated by traction may provide additional information. Radiographically, fragmented sesamoid bones appear as a cluster of ossific fragments on the palmar aspect of the joint, adjacent to an unaffected paired sesamoid. The ossicles are usually multiple, with rounded margins that conform to a variety of shapes and sizes (see Fig. 18-20). In racing greyhounds, clearly defined transverse separation of sesamoid bones have been reported, leading to a belief that fracture is the cause of sesamoid fragmentation in this breed.[37]

Although less frequently than sesamoids in the manus, the fabellae are also prone to fragmentation (Fig. 18-21, p. 328).

The most common example of sesamoid displacement is medial luxation of the patella (Fig. 18-22, p. 328). Patella luxation occurs most frequently in toy dogs and also in Devon Rex cats. Some breeds have an inherited predisposition to patella luxation. Other sesamoid bones are also prone to displacement. Distal displacement of the popliteal sesamoid or the fabellae has been cited as a sign that indicates rupture or trauma to their respective tendons, although this is not always true (Fig. 18-23, p. 329).

Degenerative Joint Disease

Degenerative joint disease is a slowly progressive disease of synovial joints in which synovial effusion and cartilage degradation are key components. It is the most common joint abnormality seen in small animal practice and occurs most frequently in the weight-bearing joints of medium-sized to large dogs, although it may affect any synovial joint of both dogs and cats. The best example of canine degenerative joint disease occurs as a result of canine hip dysplasia. The incidence of hip dysplasia varies from breed to breed and in many

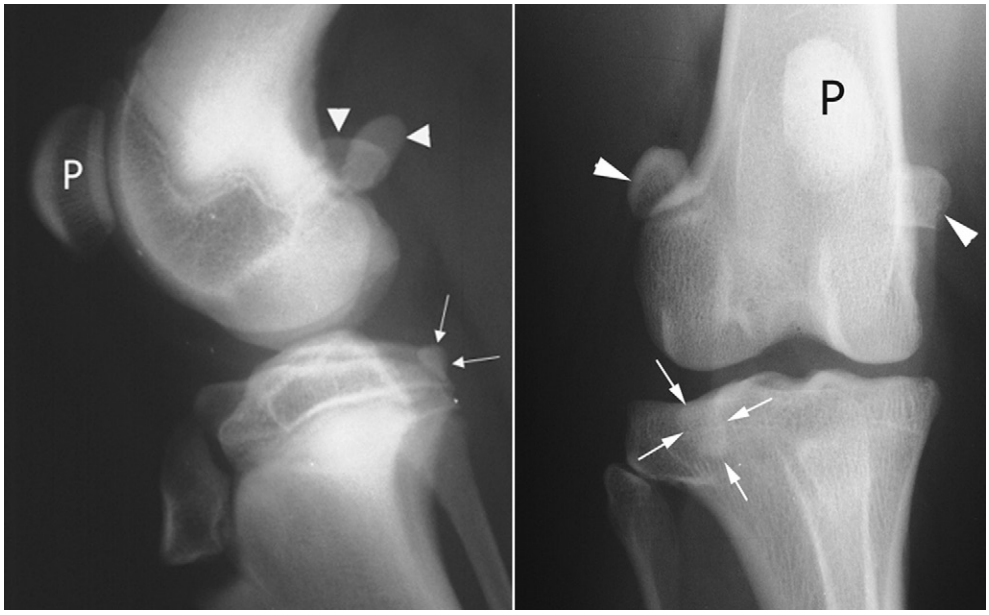


Fig. 18-17 The patella *(P)* is easily identified on the cranial aspect of the femoral condyle. The paired fabellae *(white arrowheads)* are seen on the caudal aspect of the femoral condyle, where they lie adjacent to the medial and lateral condyles near the origin of the gastrocnemius. The popliteal sesamoid *(white arrows)* is located caudolaterally, adjacent to the head of the tibia.



Fig. 18-18 The lateral tarsometatarsal sesamoid *(white arrows)* and the medially located intraarticular tarsometatarsal sesamoid *(black arrows)* are inconsistently present in dogs and can be difficult to locate. On the lateral image *(right panel)* one can be seen *(white arrowheads)*. (Reprinted from *BSAVA manual of canine and feline musculoskeletal imaging*, Quedgeley, Gloucester, England, 2006, BSAVA Publications.)

large breeds exceeds 50%. The next most frequent locations of degenerative joint disease are the canine shoulder and stifle joints. Signs of shoulder degenerative joint disease were identified in 33% to 50% of groups of dogs surveyed either at necropsy or radiographically; 20% of dogs in another survey had evidence of stifle degenerative joint disease at necropsy.[2,38,39]

Degenerative joint disease may be a primary aging change (idiopathic) or as a result of a developmental or acquired disorder. Examples of canine developmental disorders include osteochondrosis, fragmented coronoid process, ununited anconeal process, hip dysplasia, patellar luxation, achondroplasia, and conformational disorders such as valgus and varus deformities of the carpus. Acquired disorders capable of causing degenerative joint disease in dogs include trauma, joint instability, epiphyseal aseptic necrosis, recurrent hemarthrosis, and acquired postural or conformational defects such as joint malalignment after fracture repair.[40]

Radiographic Signs of Progression of Osteoarthritis in Dogs

The stifle joint is often used to study the progression of canine degenerative joint disease. The initial stages are asymptomatic, and radiographs are usually normal. The first change is mild

Table • **18-2**

Sesamoid Bones Visible on Radiographs of Joints of the Canine

APPENDICULAR SKELETON	JOINT: NAME/LOCATION
Shoulder	Clavicle (medial end of tendinous intersection in the brachiocephalicus) (see Figs. 18-11 and 18-12)
Elbow	Tendon of origin of the supinator (see Fig. 18-13)[26]
Carpus	Tendon of the abductor pollicis longus (see Fig. 18-14)
Metacarpophalangeal	Paired palmar sesamoid bones (located in the tendons of insertion of the interosseous muscles) (see Fig. 18-15)
	Single dorsal sesamoid (located in the extensor tendons)
Coxofemoral	None* (see Fig. 18-16)
Femorotibial	Patella (tendon of insertion of the quadriceps femoris) (see Fig. 18-27)
	Sesamoid bones of the gastrocnemius (fabellae) Medial head Lateral head
	Popliteal sesamoid (tendon of the popliteus)
Tarsus	Lateral plantar tarsometatarsal sesamoid bone (see Fig. 18-18)[27]
	Intraarticular tarsometatarsal sesamoid bone[27]
Metatarsophalangeal	Paired plantar sesamoid bones (see Fig. 18-15)
	Single dorsal sesamoid bone

*Sesamoid bone located in the iliopubic cartilage may be seen cranial to the iliopubic eminence.[20]

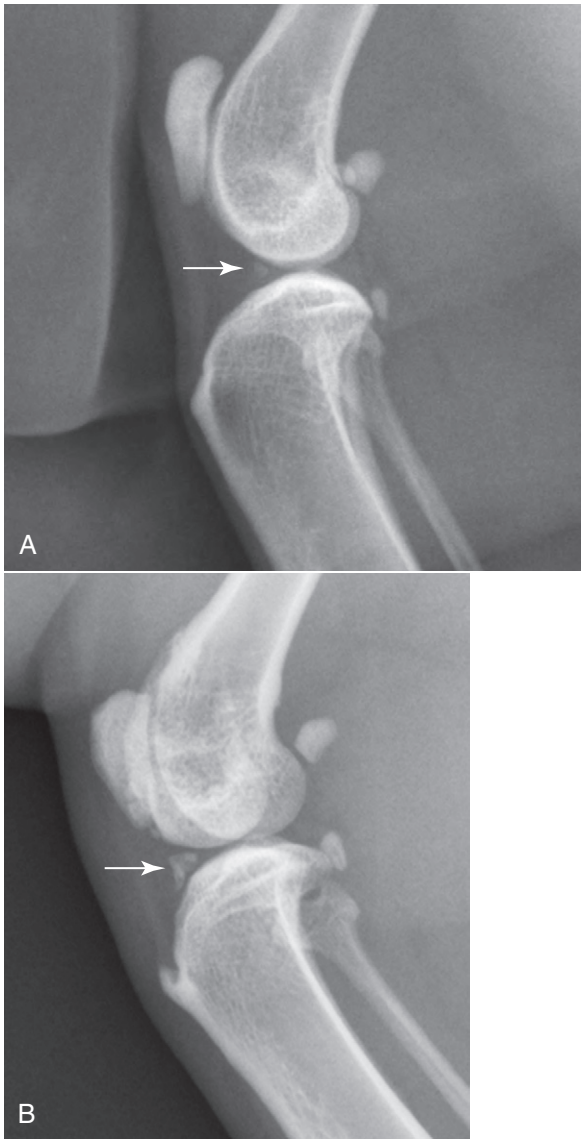


Fig. 18-19 **A,** A small meniscal ossicle in a cat *(white arrow)*. **B,** A moderately sized meniscal ossicle in another cat *(white arrow)*. There is also an enthesophyte at the patellar ligament attachment site on the proximal tibia.

nonsuppurative synovitis, accompanied by increased synovial mass. Focal articular cartilage degeneration follows. The joint space may be wider during this stage.[41] Osteophytosis is the feature that is characterized by the greatest degree of change over time in the canine stifle with naturally occurring instability. When grading stifle degenerative joint disease, evaluating the changes in the number and size of periarticular osteophytes is more reliable than evaluating subchondral sclerosis, intraarticular mineralization, or synovial effusion, but signs of synovial effusion and compression of the infrapatellar fat pad are identifiable radiographic features that often accompany stifle instability.

Osteophyte formation commences as early as 3 days after cranial cruciate ligament transection and can be seen radiographically at the margins of the femoral trochlea as early as 2 weeks after the onset of stifle instability. Initially, osteophytes consist of cartilage, and they do not become visible radiographically until they are mineralized. The proximal and distal ends of the trochlear ridges are the sites of earliest osteophyte formation in the stifle joint, but changes occur later on the lateral and medial femoral condylar surfaces and tibial condyles. Enthesophyte formation at points of origin and insertion of the cruciate and collateral ligaments occurs later than osteophytosis on the trochlear ridges.

Early identification of osteophytes on trochlear ridges is facilitated by using specific radiographic projections, such as flexed mediolateral, craniomedial-caudolateral, and caudomedial-craniolateral radiographs.[12,42-44]

In the coxofemoral joint, synovial effusion may cause subluxation. The presence of subluxation is a powerful indicator of the risk of development of coxofemoral degenerative joint disease.[45-49] There is a strong correlation between the unitless distraction index (DI), a quantifiable measure of subluxation, and subsequent development of degenerative joint disease. The likelihood of coxofemoral degenerative joint disease varies with breed and with the DI. Interestingly, the threshold DI, below which coxofemoral degenerative joint disease is unlikely to occur, is different for different breeds. The threshold DI for the German shepherd is 0.3, and it appears higher (0.4) for the Labrador retriever and Rottweiler.

Radiographic changes of degenerative joint disease vary according to the stage of the disease. The most readily

recognizable change is enthesophyte and osteophyte formation, which follows neovascularization of the chondrosynovial junction with resultant fibrocartilage formation. This fibrocartilage collar gradually ossifies with the formation of perichondral new bone (Fig. 18-24). Enthesophytes develop on non–weight-bearing surfaces and are eventually incorporated into adjacent ligamentous or capsular attachments.[37,38]

Thinning of the joint space is observed rarely (see Fig. 18-3). Pathologic alteration of subchondral bone may be detected as increased subchondral opacity of the weight-bearing surface (see Fig 18-3). Subchondral cyst formation, a feature of degenerative joint disease of the human femoral head, has also been observed in joints of small animals (see Fig. 18-5).[2,50]

Affected joints exhibit decreased range of movement, which results in increased loading of the diminished weight-bearing surface. The combination of increased load, diminished subchondral strength, and loss of shock-absorbing cartilage results in alteration in the shape of the subchondral bone table. This remodeling of subchondral bone is complemented by the addition of peripheral new bone in the form of perichondral osteophytes. Altered shape of the osseous components of affected joints is readily identified



Fig. 18-20 **A,** Fragmentation of sesamoids 2 and 7 in a Rottweiler *(white arrows)*. **B,** A similar Rottweiler *(white arrows)* has concurrent osteitis of the distal end of a metacarpal bone *(black arrowheads)*. **C,** The osteitis was identified as the active lesion using nuclear scintigraphy, and the fragmented sesamoids were not considered clinically significant. (**B** and **C** courtesy of Dr. R. M. Zuber, Gladesville Veterinary Hospital, Sydney, Australia.)

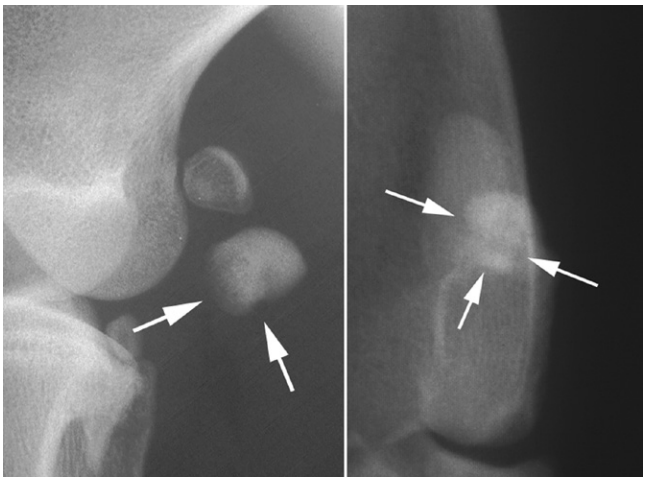


Fig. 18-21 Fragmentation of the lateral fabella *(white arrows)* of an adult Staffordshire bull terrier. (Courtesy of Sylvania Veterinary Hospital, Sydney, Australia.)

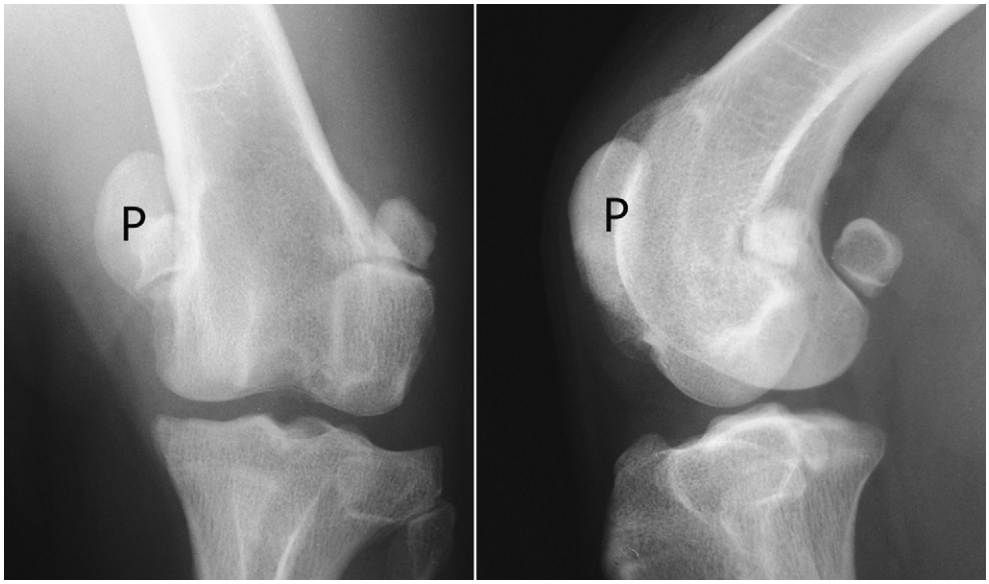


Fig. 18-22 Chronic medial luxation of the patella associated with varus angulation of the femoral condyle. On the lateral image the luxated patella is superimposed on the trochlea of the femoral condyle. (Courtesy of Animal Referral Hospital, Sydney, Australia.)

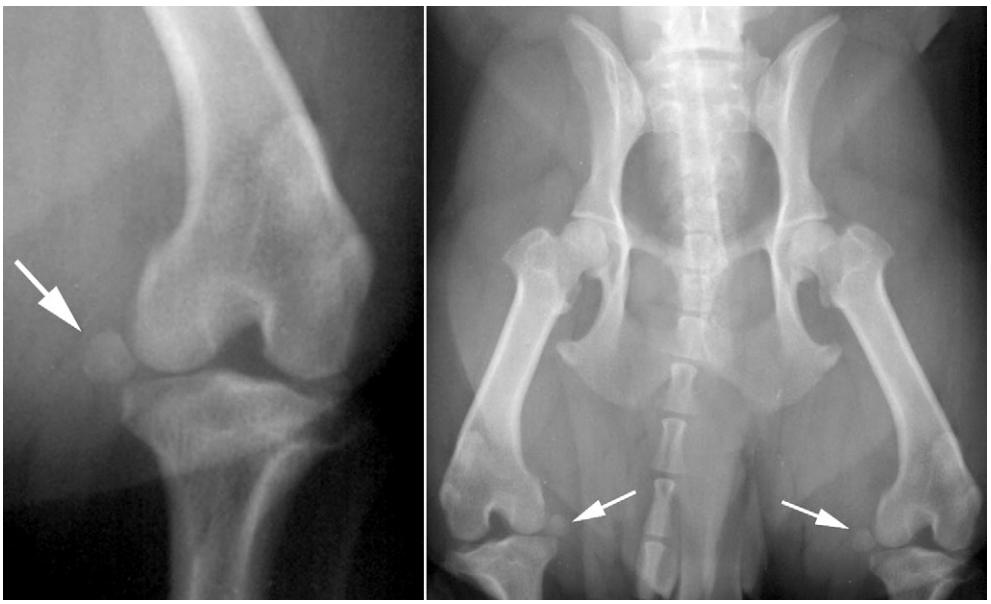


Fig. 18-23 **A,** Distal displacement of the medial fabella *(white arrow)* of the left stifle of a 2-year-old male West Highland white terrier. This may be associated with rupture of the medial head of the gastrocnemius muscle, but this abnormality was bilaterally symmetric (**B,** *white arrows)*. In this circumstance, distal displacement of the medial fabellae is unlikely to be clinically significant. (Courtesy of University Veterinary Centre, Sydney, Australia.)



Fig. 18-24 **A** and **B,** A 7-year-old German shepherd dog had chronic weight-bearing lameness of the right pelvic limb. Perichondral osteophytes and enthesophytes are visible on the distal femur and proximal tibia. Synovial effusion is also present. **C** to **E,** Osteoarthritis in the elbow of a 2-year-old German shepherd. Osteophytes on the cranial aspect of the head of the radius **(C)** and on the medial edge of the coronoid process of the ulna **(D)** and enthesophyte formation on the anconeal process **(E)** are degenerative changes often seen secondary to fragmented medial coronoid process.

Box • 18-3

Radiographic Signs of Degenerative Joint Disease

Synovial effusion
Initial widening, then thinning, of the radiolucent joint space
Perichondral enthesophyte formation of non–weight-bearing surfaces
Increased subchondral bone opacity
Remodeling of subchondral bone
Mineralization of intraarticular and periarticular soft tissues
Subchondral cyst formation



Fig. 18-25 Craniocaudal *(left)* and mediolateral *(right)* projections of a feline elbow with marked degenerative joint disease. Exuberant periarticular new bone formation is present around the elbow. On the lateral projection, an uneven radiolucent joint space indicates poor joint congruity. (Reprinted from Allan GS: Radiographic features of feline joint diseases, *Vet Clin North Am Small Anim Pract* 30:281, 2000.)

radiographically.[50] The gamut of the radiographic changes seen in degenerative joint disease is outlined in Box 18-3.

Osteoarthritis in Cats

Primary causes of articular cartilage degeneration and consequent degenerative joint disease in cats include the storage disease mucopolysaccharidosis and osteochondral dysplasia of Scottish Fold cats. Established secondary causes of feline degenerative joint disease (Fig. 18-25) include developmental and traumatic conditions that alter joint stability as well as dietary (hypervitaminosis A) causes. Many infectious and immune-based arthropathies alter the integrity of articular cartilage, leading to a cascade of articular changes, with degenerative joint disease as the end result.[51] Radiographic prevalence of signs of degenerative joint disease in cats older than 12 years of age is as high as 90%, which is far greater than the incidence of clinical signs of degenerative joint disease in older cats.

Cats with uncomplicated degenerative joint disease may be free of clinical signs of joint disease, and radiographic signs of this condition are often discovered accidentally, but most syndromes listed in Box 18-4 are characterized by recognizable clinical signs that are accompanied by appendicular skeletal pain and lameness.

The radiographic signs of degenerative joint disease in cats are similar to those reported in dogs. Periarticular new bone formation as osteophytes or enthesophytes develops around affected joints (see Fig. 18-25). Although the articular cartilage is invisible on survey radiographs, remodeling and increased opacity of subchondral bone add to the altered joint architecture.[1] Subchondral bone changes usually imply changes in joint cartilage. Signs of synovial effusion and/or thickened periarticular soft tissue are seen less commonly in cats than in dogs, whereas the incidence of intraarticular soft tissue calcification is more common in cats. Other changes that accompany feline degenerative joint disease include intraarticular and periarticular soft tissue calcification, often ascribed to synovial osteochondromatosis, and prolific periarticular osteophytosis.

Box • 18-4

Causes of Osteoarthritis in Cats

Primary
Scottish Fold osteochondrodysplasia
Mucopolysaccharidosis
Age-related cartilage degeneration

Secondary
Congenital
Hip dysplasia
Trauma
Traumatic joint instability
Physeal fractures
Infectious/inflammatory
Viral (calicivirus, coronavirus)
Bacterial (bacterial L-form, mycoplasma, bite wounds)
Fungal (cryptococcosis, histoplasmosis)
Nutritional
Hypervitaminosis A
Immune mediated
Rheumatoid arthritis
Progressive proliferative polyarthropathy
SLE
Idiopathic polyarthritides

Reprinted from Allan GS: Radiographic features of feline joint diseases, *Vet Clin North Am Small Anim Pract* 30:281, 2000.

HIP DYSPLASIA

Hip dysplasia is abnormal development of the coxofemoral joints. Hip dysplasia occurs principally in large dogs but also affects small dogs and cats. The condition is typically bilateral, but unilateral hip dysplasia has been reported in approximately 11% of dogs radiographed with the conventional extended ventrodorsal projection.

Hip dysplasia is an inherited disorder. Heritability estimates range from 0.2 to 0.6. With the use of more sensitive radiographic interpretation and newer methods of imaging the coxofemoral joints, the estimated heritability in German shepherd dogs has been raised from 0.46% to 61%.[52,53] Environmental factors influence the phenotypic expression of hip dysplasia.[54] Overnutrition is one of the principal nongenetic factors that influence the expression of canine hip dysplasia.[55] Hip dysplasia is a developmental, age-related disorder; it is not present at birth. A variable amount of time must elapse before radiographic changes manifest. Once present, these radiographic changes usually progress with age.

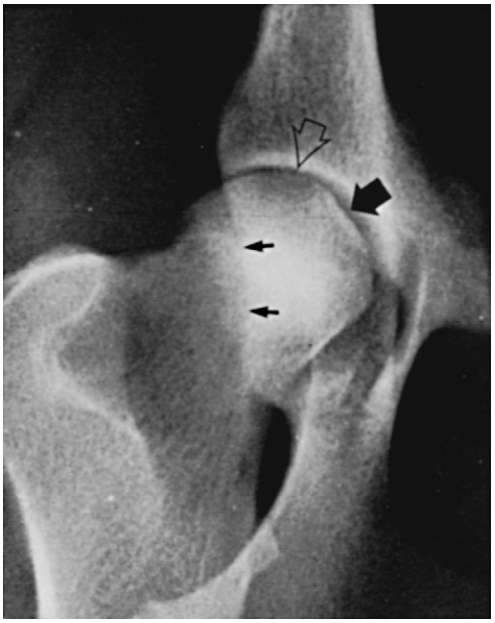


Fig. 18-26 Normal mature coxofemoral joint. Note the large amount of the femoral head that lies medial to the dorsal acetabular margin *(small white arrows)*. The cranial margin of the femoral head is separated from the adjacent acetabulum by a fine radiolucent line, which represents the joint cartilage and a microfilm of synovial fluid *(open black arrow)*. The flattened portion of the femoral head is normal and represents the fovea capitis femoris *(solid black arrow)*.

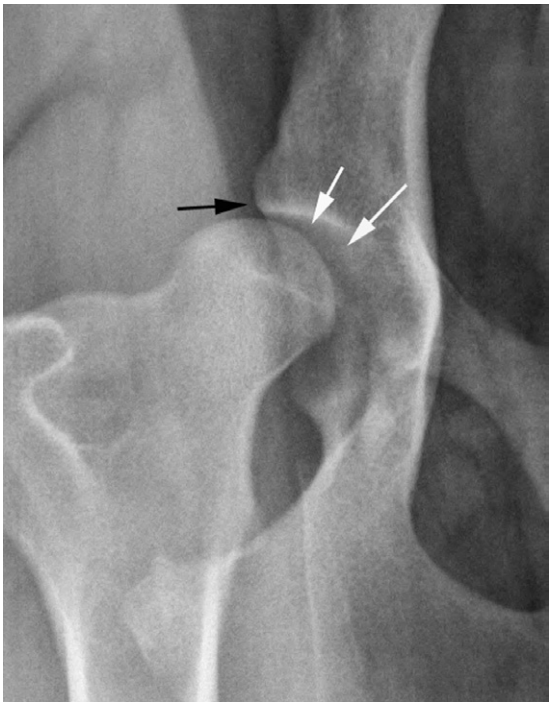


Fig. 18-27 Moderate hip dysplasia. Subluxation of the femoral head is accompanied by remodeling of the acetabulum. The cranial acetabular margin is angulated *(black arrow)*, and the acetabulum is shallow. Note the wedge-shaped joint space *(white arrows)* created by subluxation of the femoral head.

The earliest recognizable changes in the coxofemoral joints are a combination of perifoveal cartilage erosion, hypertrophy of the round ligament of the femoral head, synovial effusion, and synovitis.[56] None of these is recognizable radiographically, but the strongest clue to their presence can be obtained by testing for signs of joint laxity, which appears to be precipitated by synovial effusion. Joint laxity may be palpated and visualized radiographically (Figs. 18-26 and 18-27).[41,57,58] Subsequent radiographic changes are those of degenerative joint disease (Fig. 18-28) developing as (1) perichondral osteophyte formation, (2) remodeling of the femoral head and neck, (3) remodeling of the acetabulum, and (4) increased opacity of subchondral bone of the femoral head and acetabulum. A line of enthesophytes on the caudal aspect of the femoral neck, termed the *Morgan line*, has been described as an early sign of coxofemoral degenerative joint disease (Fig. 18-29).[59] As the degenerative disease advances, the femoral neck becomes thickened, and the surface of the neck becomes irregular as a result of the growth of a collar of perichondral osteophytes. The acetabulum loses its cuplike shape and becomes shallow. Increased bone opacity of subchondral articular surfaces represents bone sclerosis, a response to cartilage thinning. Subchondral cyst formation is an infrequent manifestation of degenerative joint disease in small animals but may be observed occasionally.

The incidence of hip dysplasia in domestic shorthaired cats, based on standard hip radiography, has been estimated at 6.6%.[60] The incidence is higher in purebred cats (12.3%), with some breeds such as the Maine Coon cat having an incidence of 18% to 21%.[60,61] When passive coxofemoral laxity is evaluated by stress radiography, the overall incidence of feline hip dysplasia may be as high as 32%.[62] The prevalence of feline hip dysplasia is lower than the prevalence in dogs.

Radiographic criteria for diagnosing feline hip dysplasia include the presence of signs of coxofemoral subluxation (Fig. 18-30), enthesophyte formation on the acetabular margins, and remodeling and degenerative changes of the femoral



Fig. 18-28 Advanced hip dysplasia. The acetabulum and the femoral head have undergone advanced remodeling. Osteophytes have formed on the femoral neck and head as well as on the cranial acetabular margin. New bone formation has filled the acetabular fossa, and the opacity of acetabular subchondral bone is increased. These are signs of degenerative joint disease.

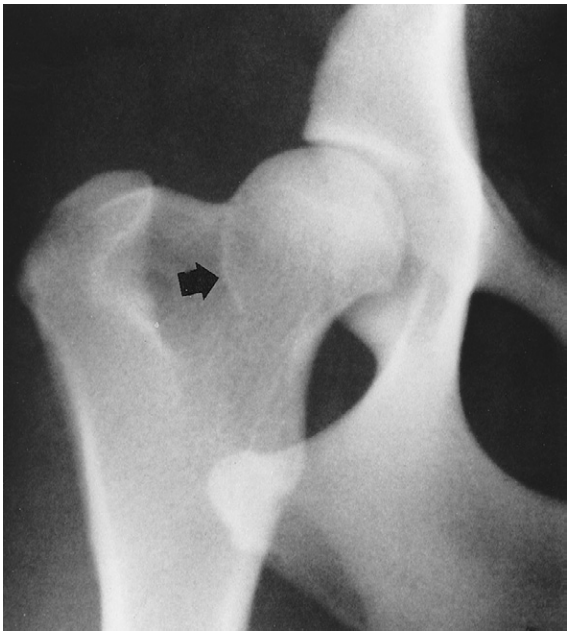


Fig. 18-29 An early sign of degenerative joint disease is the Morgan line, representing enthesophyte formation on the caudal aspect of the femoral neck, medial to the trochanteric fossa *(black arrow)*.

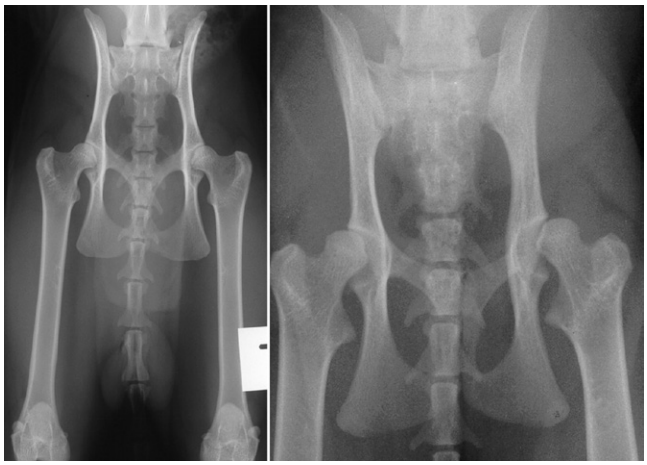


Fig. 18-30 Feline coxofemoral joints. *Left*, Normal. *Right*, Abnormal with coxofemoral subluxation. (Right panel courtesy of University Veterinary Centre, Sydney, Australia.)

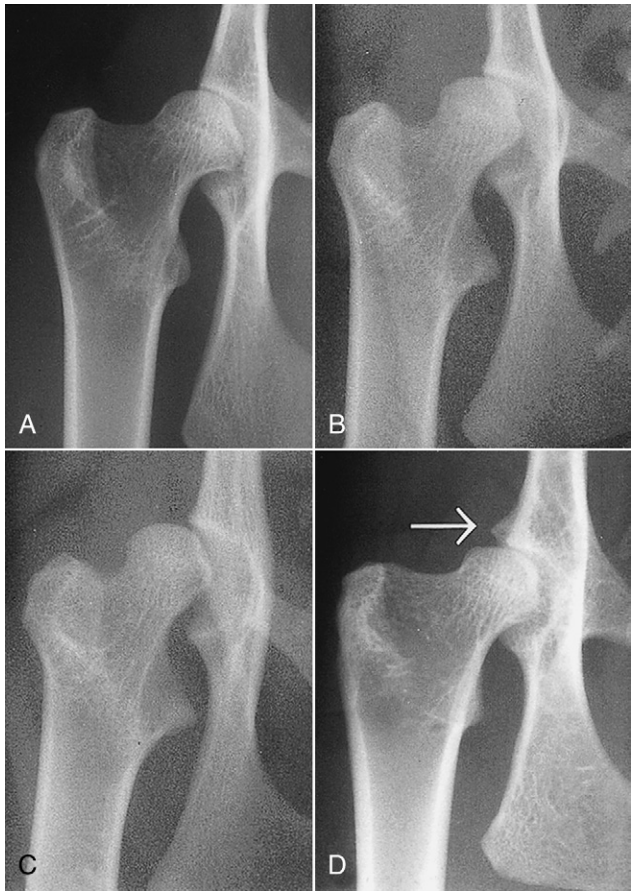


Fig. 18-31 Feline hip dysplasia. Varying degrees of coxofemoral subluxation (**B** and **C**) are compared with "normal" **(A).** Degenerative changes, with osteophyte formation on the cranial effective acetabular margin *(white arrow)*, are a typical manifestation of feline coxofemoral degenerative joint disease **(D).** (Reprinted from Allan GS: Radiographic features of feline joint diseases, *Vet Clin North Am Small Anim Pract* 30:281, 2000.)



Fig. 18-32 Extended ventrodorsal projection of the coxofemoral joints (OFA preferred view). Note bilateral symmetry of the pelvis and parallel femurs. The coxofemoral joints appear normal.

head and neck (Fig. 18-31). Unlike canine hip dysplasia, most degenerative changes in cats appear on the craniodorsal acetabular margins, with a low incidence of degenerative remodeling reported on the femoral head and neck.

Methods of evaluating the coxofemoral joints can be divided into those that identify joint laxity proactively and those that examine for radiographic evidence of degenerative joint disease. Phenotypic screening programs used internationally fall into the latter group and rely on assessment of the extended ventrodorsal radiographic projection (Fig. 18-32), although this projection is an insensitive indicator of coxofemoral joint laxity. To identify coxofemoral joint laxity reliably, a stressed ventrodorsal projection is used. With the femurs in a distracted position (Fig. 18-33), coxofemoral laxity can be quantified and the calculated laxity index (DI) used to rank individual dogs within their breed with respect to hip joint tightness or looseness.[63] The DI is also a useful indicator of the likelihood of future coxofemoral degenerative changes.

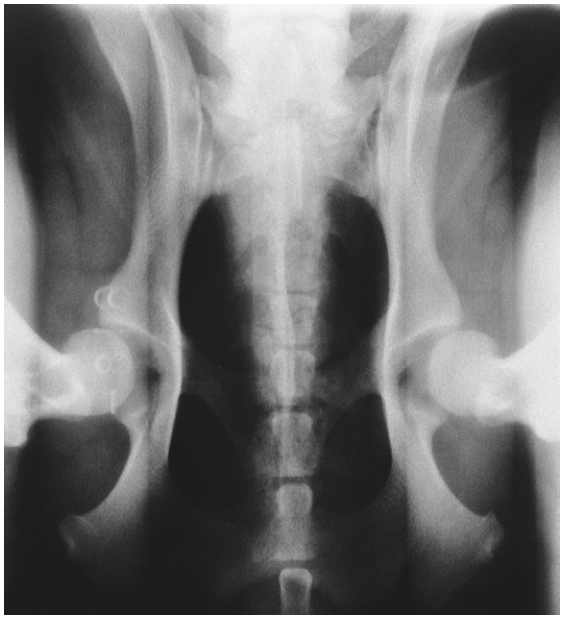


Fig. 18-33 Ventrodorsal distraction projection (PennHIP view). Bilateral coxofemoral laxity is evident.

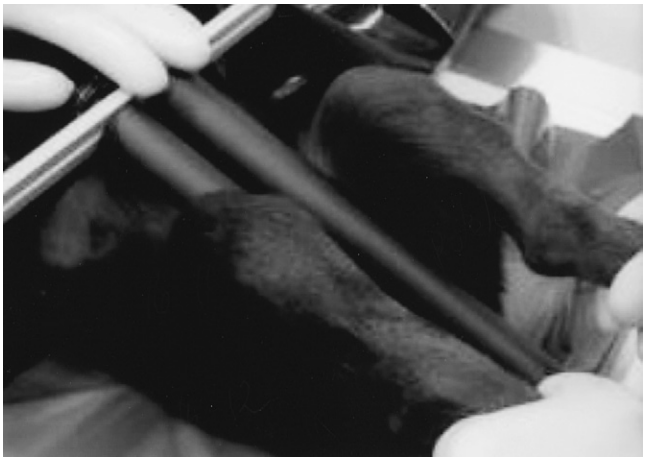


Fig. 18-34 The distracted PennHIP view is achieved by holding a rubberized distraction device between the thighs, with the femurs at 90 degrees to the pelvis. The femurs are pressed gently against the distractor during radiography.

This information can be obtained at a much earlier age by using distraction radiography than with the standard extended ventrodorsal projection. Assessing coxofemoral laxity is an important component of complete radiographic assessment of the coxofemoral joints.

Many screening programs require that the extended ventrodorsal radiograph of the coxofemoral joints be made and submitted for evaluation. The method of obtaining the extended hip projection, as required by the Orthopedic Foundation for Animals (OFA) for example, is similar to projections used by other screening programs internationally.[64] With the dog in dorsal recumbency, the hindlimbs are extended with the femurs parallel and the stifles rotated inward so that the patellae are located over the middle of the cranial surface of the distal femur. The x-ray beam should be centered over the coxofemoral joints, and the radiograph should include the entire pelvis and femurs. The pelvis must appear symmetric in the radiograph, without evidence of rotation (see Figs. 18-30, *A*, and 18-32). Although satisfactory radiographic quality may be achieved without the assistance of chemical restraint,[65] failure to anesthetize the subject may decrease radiographic sensitivity for signs of coxofemoral joint laxity.[66] Because the extended ventrodorsal projection is an insensitive method of detecting signs of coxofemoral subluxation,[63,67] care must be taken to ensure accurate subject positioning and satisfactory radiographic quality.

The PennHIP method[45,46,63] also requires the dog be in dorsal recumbency. The femurs are placed in a neutral position to duplicate standing. This neutral position avoids spiral tensioning of the joint capsule that forces the femoral head into the acetabulum and reduces subluxation, a significant disadvantage of the extended hip projection. The hindlimbs are held with the femurs positioned neutrally, and a radiograph is made while the coxofemoral joints are compressed to obtain an image of the coxofemoral joints at their most congruent position. A distraction device is then placed between the femurs for the second radiograph (Fig. 18-34). When the femurs are pressed against the bars of the distractor, which act as a fulcrum, a lateral force is translated to the proximal femur, and any laxity leads to subluxation that can be visualized radiographically. The two views of the hips are compared, and any coxofemoral laxity is quantified by a unitless measure, the DI. The extended hip projection is also made so that secondary signs of hip dysplasia, such as degenerative joint disease, can be evaluated (Fig. 18-35).

The PennHIP method has inherent advantages over the extended hip method of evaluating the coxofemoral joints (Box 18-5). First, it quantifies joint laxity, which is generally accepted as the beginning of a chain of events that culminates in coxofemoral degenerative joint disease. Second, the examination can be done on young dogs. The predictive value of the DI is constant after 6 months of age, thereby providing valuable information to breeders at an early age when selecting their stock. Third, the technique predicts a DI below which degenerative changes are unlikely to occur. Conversely, the DI and the subsequent development of degenerative joint disease appear to have a direct relation when the DI is greater than 0.3 (for German shepherd dogs) or 0.4 (for Labrador retrievers and Rottweilers).

TRAUMA INVOLVING THE OSSEOUS COMPONENTS OF JOINTS

A fracture that communicates with a joint space is an articular fracture (Fig. 18-36). Articular fractures must be diagnosed accurately to ensure appropriate reduction and stabilization Radiographic examinations should include two projections made at right angles to each other. Oblique views should be added, along with projections during flexion and stress, when needed. These additional projections are of most value when chip or avulsion fractures are suspected or when the osseous structures of interest are superimposed on other osseous structures.

Articular fractures occur frequently in immature animals because of the incidence of physeal and epiphyseal injury in these patients. Because the proximal femoral physis is intracapsular, all femoral capital physeal fractures are intraarticular fractures (Fig. 18-37). In other joints, physeal fractures that involve the joint are usually classified as Salter-Harris type III or IV fractures.[68]

SPRAINS AFFECTING JOINTS

Supporting soft tissue structures of joints appear as soft tissue opacities that silhouette each other and with adjacent soft tissues. Therefore they are not clearly visualized

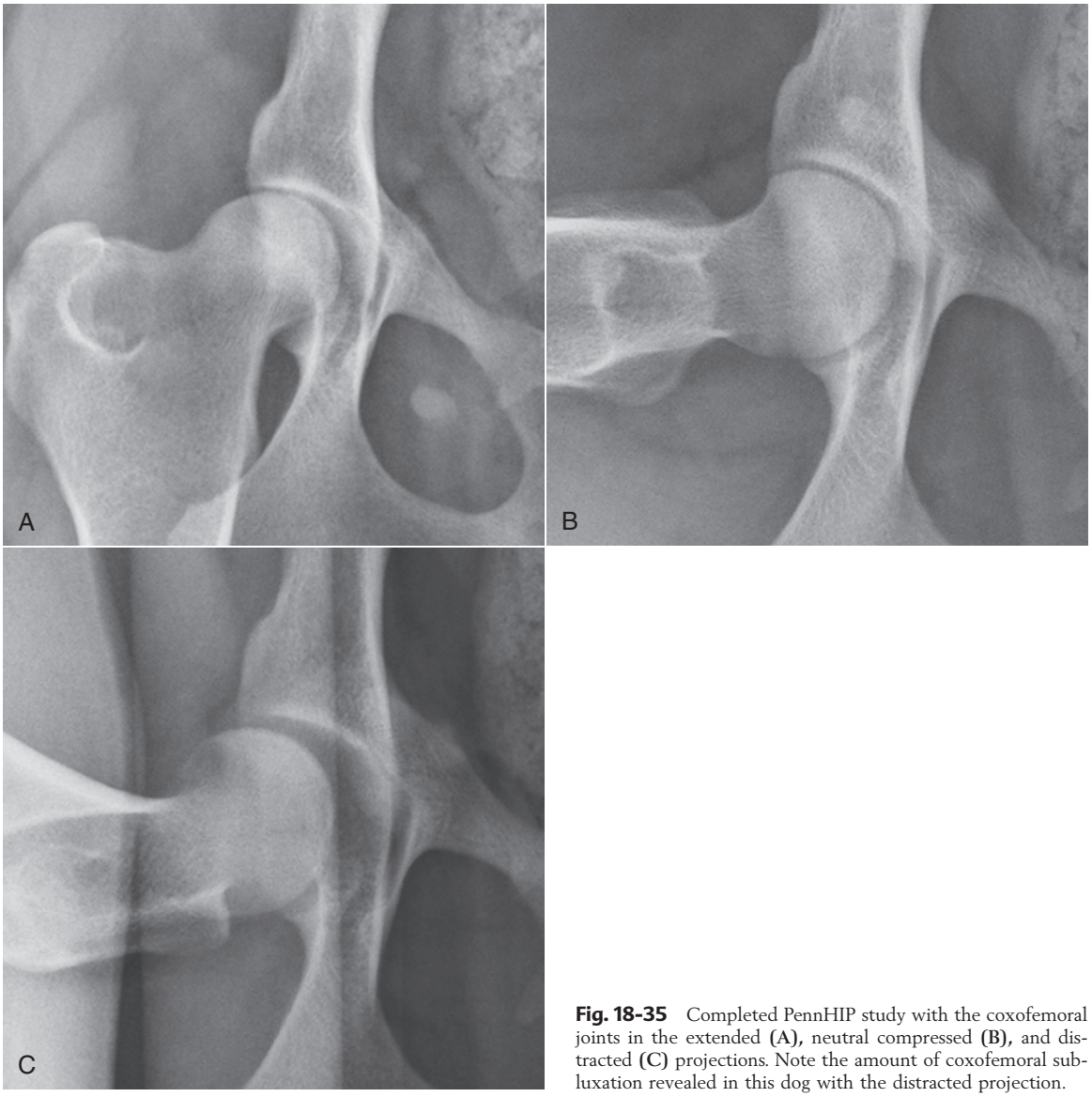


Fig. 18-35 Completed PennHIP study with the coxofemoral joints in the extended **(A),** neutral compressed **(B),** and distracted **(C)** projections. Note the amount of coxofemoral subluxation revealed in this dog with the distracted projection.

radiographically. The radiographic features of severe sprains include (1) periarticular soft tissue swelling; (2) avulsion fractures at points of attachment of ligaments, tendons, and capsules to bone (entheses); (3) joint instability or subluxation; and (4) spatial derangement of the osseous components of a joint.

Sprains must be diagnosed promptly. In many instances, appropriate medical or surgical therapy ensures return to normal joint function after moderate to severe sprain injuries. Palpation and manipulation of a sprained joint is usually the best diagnostic tool. Radiographic examination adds information that is useful for treatment planning while documenting the presence and magnitude of the sprain and identifying avulsed osseous fragments. A useful technique for radiographic assessment of a sprained joint is stress radiography (Figs. 18-38 and 18-39). Stress radiography involves application of force to the joint to demonstrate displacement. The forces applied are the same stresses to which the joint would be subjected in normal daily activity and are defined as compressive, rotational, traction, shear, and wedge forces (Fig. 18-40).[69]

An example of a compressive stress is a radiograph of a joint during weight bearing. Ligamentous trauma, as in carpal hyperextension injuries, is readily detected by this technique. The cranial drawer sign seen in cranial cruciate ligament trauma is a practical example of a shearing stress. It is stress that is used routinely in clinical examination of the stifle. The same manipulative procedure may be applied to the stifle during radiography to capture the amount of cranial drawer in the image. Traction stress involves pulling the osseous components of the joint away from one another. One application of traction stress involves capital physeal fractures of the femoral head. When traction is applied to the femur in the extended ventrodorsal position, capital physeal fractures are easy to identify.

A technique using traction stress has been described for identifying medial scapulohumeral joint instability in small dogs. With the patient in lateral recumbency, nontraction and traction radiographs are made of the shoulder joint. A significant increase in the shoulder joint space has been identified as a sign of medial shoulder joint instability.[70] Traction and wedge stresses are useful for examining joints for small avulsion fractures and intraarticular joint mice. Unilateral trauma to collateral ligaments of the elbow and stifle may be disclosed with wedge stresses. Because stress radiography requires that personnel hold the patient during x-ray exposure, care must be taken to ensure that appropriate protective clothing is worn.

Box • **18-5**

Comparison of OFA and PennHIP Methods for Hip Dysplasia Radiography

Extended Ventrodorsal Projection

Advantages

Currently the most popular screening program internationally

Does not require special training or accessory equipment

Only one radiograph required

Has amassed a large database of information about the coxofemoral phenotype

Animals can be radiographed without personnel exposure

Disadvantages

Inaccurate in young animals; accuracy increases with age; optimal time to radiograph is 24 to 36 months

An insensitive method of identifying coxofemoral joint laxity

Requires rigid application to achieve beneficial results in breeding programs

Technique of extending the femurs camouflages signs of joint laxity by spiral tensioning of the joint capsule

PennHIP Distraction Projection

Advantages

A valuable screening method for breeders before litters are placed in homes (as early as 16 weeks)

An accurate method of predicting dysplastic changes in young animals from 6 months

A sensitive method available for identifying joint laxity

Generates a unitless index (DI) that can be used to predict whether degenerative joint disease will develop

Has a greater heritability than the OFA method

Disadvantages

Requires special training to certify users

Requires special equipment

Multiple radiographic projections required

Personnel exposure during radiographic exposure is difficult to avoid



Fig. 18-36 A 3-year-old German shorthaired pointer with acute lameness of the left pelvic limb. There is a fracture through the lateral trochlear ridge of the talus *(open black arrow)*. (Courtesy of University Veterinary Centre, Sydney, Australia.)



Fig. 18-37 Because the femoral capital epiphysis is entirely intracapsular, any fracture involving the femoral head, as illustrated, is an articular fracture.

TENDONS, DESMOPATHIES

Injuries to tendons and ligaments are important causes of lameness in dogs and cats and must be distinguished from skeletal and articular causes of lameness. Many tendons and ligaments are intimately associated with joints, lying within them (cruciate ligaments), passing through them (bicipital tendon, long digital extensor tendon), or inserting adjacent to a joint (popliteus tendon). This section includes some of the common desmopathies that occur around joints.

SHOULDER

Bicipital Tendon (Biceps Brachii)

Gross changes in dogs with bicipital tenosynovitis include synovial effusion, synovial hyperplasia of the bursa, chondromalacia of the intertubercular (bicipital) groove with osteophyte formation at its edges, and metastatic calcification of the biceps tendon. The two latter changes can be seen on survey radiographs of the shoulder (Fig. 18-41) when they occur in affected dogs. Occasionally discrete mineralized opacities (joint mice) may be seen superimposed on the tendon within the bicipital groove.[71]

Ruptured Bicipital Tendon

Bicipital tendinopathy and bursitis may also be evaluated sonographically. Sonography may reveal changes in the bicipital tendon or bursa in instances of bursitis and tendonitis. The location of a rupture in the tendon may be identified sonographically (Fig. 18-42). Sonography can also be used to

identify the supraspinatus and infraspinatus tendons, the teres minor tendon, and the caudal aspect of the humeral head. Sonography assists in identification of synovial effusion and proliferation within the bicipital bursa, supraspinatus and bicipital tendonitis, dystrophic calcification, and osteochondrosis of the humeral head, but the lateral glenohumeral ligament was not seen in one study of tendons and ligaments around the shoulder joint.[72,73] MRI has the advantage of superb soft tissue contrast resolution, which is valuable for assessing edema, hemorrhage, and inflammation within tendons and ligaments around joints.

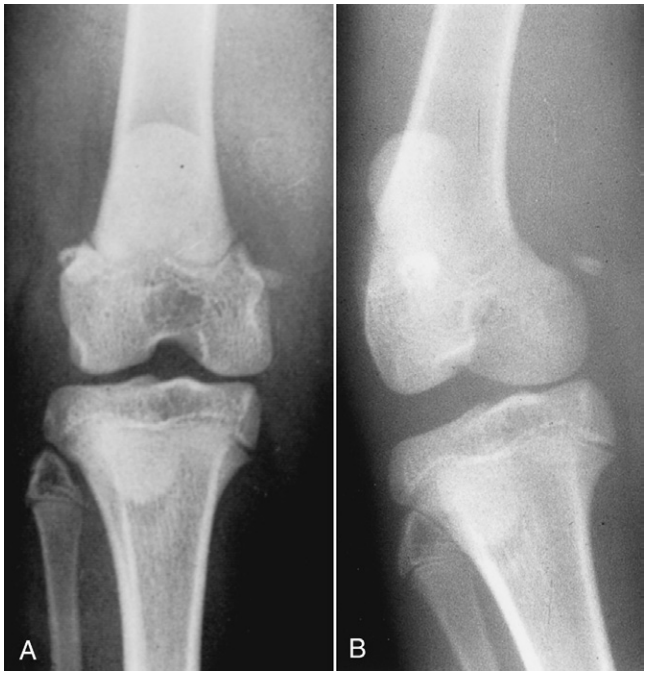


Fig. 18-38 An 8-month-old Burmese cat was lame in the left pelvic limb. A craniocaudal radiograph **(A)** was normal. In a stressed craniocaudal radiograph **(B),** widening of the lateral aspect of the joint space was apparent. The diagnosis is ruptured lateral collateral ligament.

THE CARPUS

Several important tendons pass close to the carpus or insert onto bones adjacent to it. Osteophytes arising and extending from the medial sulcus of the distal radius follow the path of the tendon of the abductor pollicis longus and are a response to synovitis where the tendon passes over the sulcus. Osteophytosis has been associated with stenosis of the synovial sheath of the tendon.[74]

The extensor carpi radialis inserts on the dorsal surface of the proximal end of metacarpals 2 and 3. An enthesopathy at the points of insertion can result in new bone formation that can be identified on lateral radiographs of the carpometacarpal region.

The flexor carpi ulnaris inserts on the proximal surface of the accessory carpal bone, and the check ligaments of the accessory carpal bone originate from the distal surface. Again, an enthesopathy can be identified on the proximal and distal surfaces of the accessory carpal bone when an enthesopathy of these tendons and ligaments is present. The tendons and ligaments around the carpus can be assessed sonographically (Fig. 18-43) as well as by MRI.

THE STIFLE

Stifle sonography is a reliable technique for identification of osteochondrosis lesions in the lateral femoral condyle. The menisci were less reliably imaged in small dogs than in large dogs, but the cranial cruciate ligament and femoral articular cartilage can be seen. The patellar ligament and the origin and



Fig. 18-39 **A,** A neutral lateral radiograph of a racing greyhound appears normal. **B,** Stress radiography was performed, which allowed identification of instability of the proximal intertarsal joint.

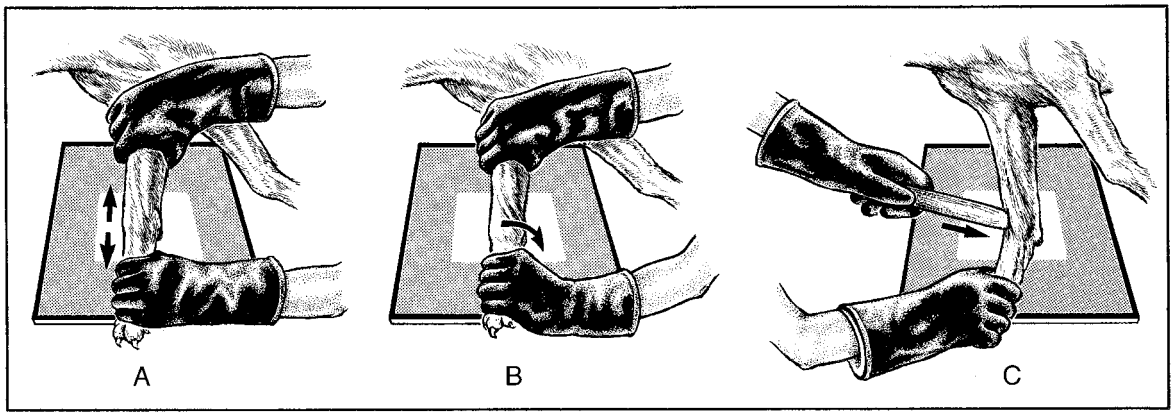


Fig. 18-40 Stress radiography of joints involves the application of traction **(A),** rotational **(B),** and wedge **(C)** forces to demonstrate subluxation that may not be evident on standard radiographic projections. (Modified from Farrow CS: Stress radiography: applications in small animal practice, *J Am Vet Med Assoc* 181:777, 1982.)

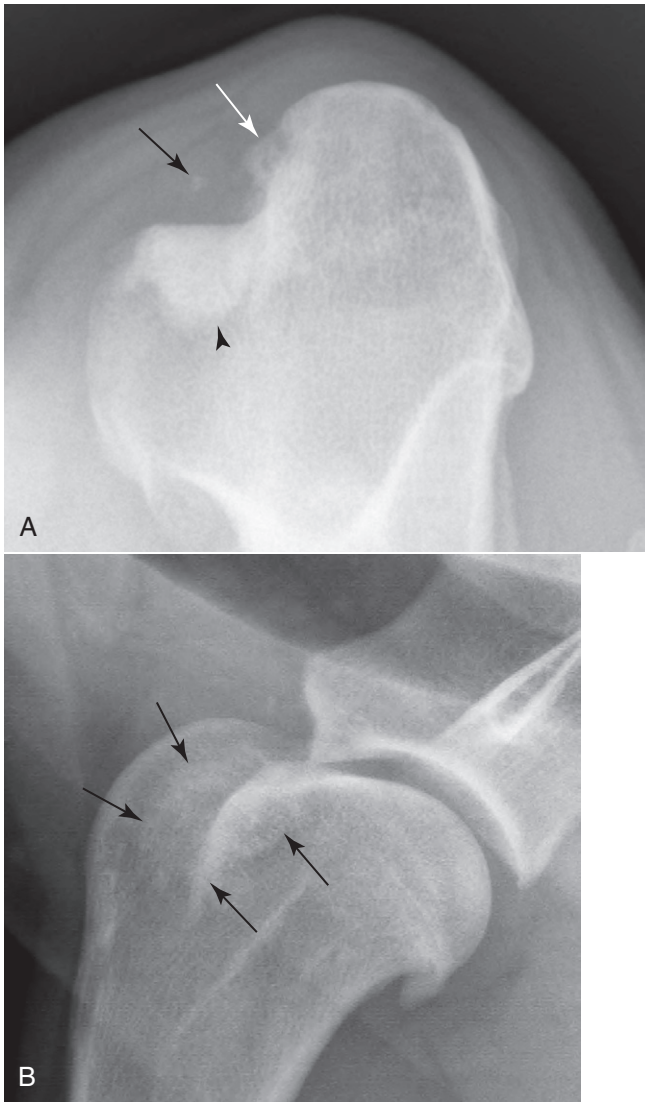


Fig. 18-41 Bicipital tendonitis. **A,** New bone proliferation superimposed on the bicipital *groove (black arrows)* and along the margin of the greater tubercle of the humerus seen in a dog with bicipital tendonitis. There is also a large osteophyte on the caudal aspect of the humeral head. **B,** A cranioproximal-craniodistal view of the proximal humerus. There are osteophytes in the bicipital groove *(white arrow)*, subchondral sclerosis of the groove *(black arrowhead)*, and a focus of mineralization in the biceps tendon *(black arrow)*.

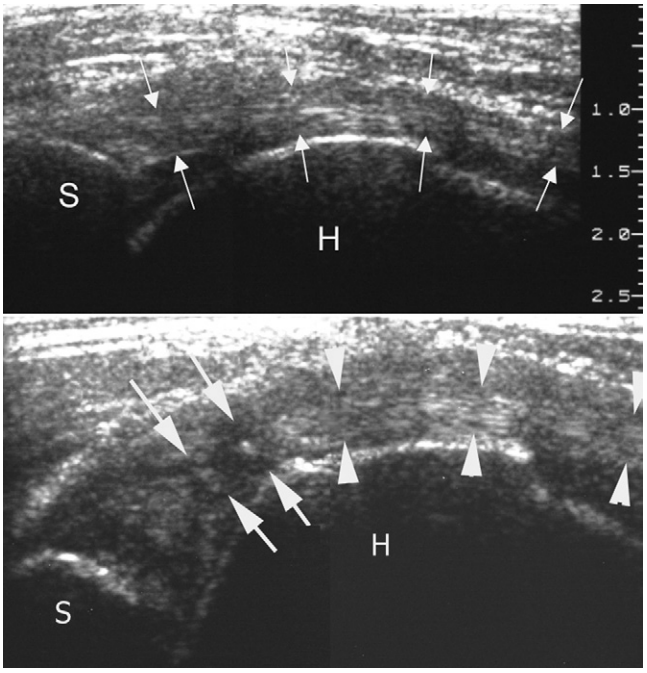


Fig. 18-42 Composite image of the right *(top)* and left *(bottom)* biceps tendon. The normal striated right tendon is *(white arrows)* in the upper image. The lower image is the ruptured left biceps tendon. The void *(white arrows)* representing the rupture contrasts with the normal striated tendon distally *(white arrowheads)*. *H*, Humerus; *S*, scapula. (Courtesy of University Veterinary Centre, Sydney, Australia.)

tendon of the long digital extensor muscle can be imaged reliably, but the collateral ligaments and joint capsule were not seen.[75,76] Sonography identified 20% of ruptured cruciate ligaments in one study of cranial cruciate ligament rupture in dogs. Although not an incisive diagnostic procedure for this condition, it does permit evaluation of soft tissue changes that occur within the stifle as a result of joint instability.[77]

TARSUS

The Achilles tendon is composed mainly of the tendons of flexor digitorum superficialis and gastrocnemius muscles, with contribution of tendons from biceps femoris, semitendinosus, and gracilis muscles. It inserts onto the calcaneal tuberosity. Chronic desmopathies of the Achilles tendon cause soft tissue

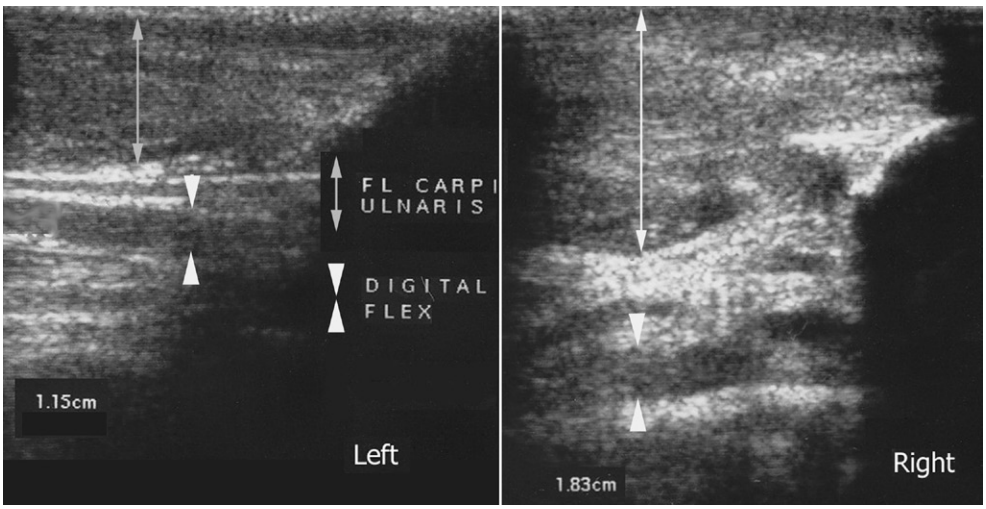


Fig. 18-43 Chronic trauma to the tendon of insertion of flexor carpi ulnaris has resulted in thickening of the affected right tendon, which is easier to identify when compared with the left tendon at the same level. (Courtesy of Dr. Soo Kuan, Northern Sydney Veterinary Specialist Centre, Sydney, Australia.)

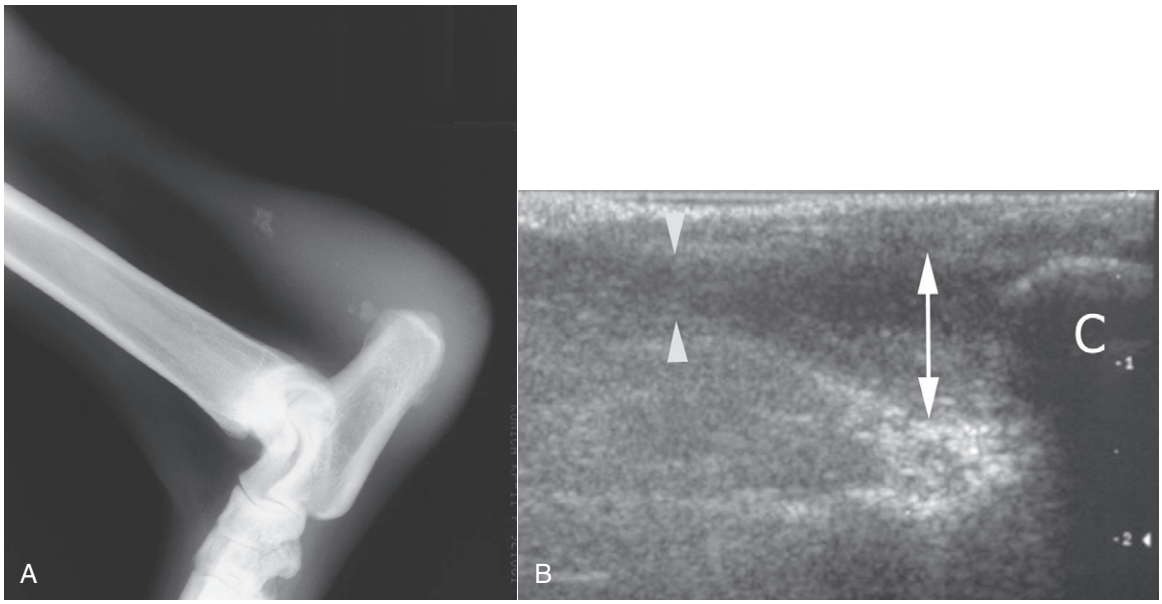


Fig. 18-44 Soft tissue swelling and dystrophic calcification along the path of the Achilles tendon in a dog **(A),** and sonographic evidence of focal swelling of the distal end *(double-headed white arrow)* of the Achilles tendon in a cat **(B)** adjacent to the calcaneus *(C)*. Compare swollen portion of tendon with normal region *(white arrowheads)*. (**A,** courtesy of Dr. M. McLachlan, Petersham Veterinary Hospital. Reproduced from *BSAVA manual of canine and feline musculoskeletal imaging,* Quedgeley, Gloucester, England, 2006, BSAVA Publications.)

swelling, occasionally containing dystrophic calcification (Fig. 18-44). Sonography enables identification of partial and total ruptures of the deep and superficial structures comprising the Achilles tendon. Tendinous trauma can be distinguished from muscle trauma.[78]

HYPERVITAMINOSIS A

Excessive dietary vitamin A produces an ankylosing arthropathy and spondylopathy. Although both dogs and cats can be affected, the disorder is more likely to affect cats. The food mostly associated with hypervitaminosis A is bovine liver, and when fed as an exclusive diet the clinical syndrome of vitamin A excess can be recognized after a few months. Affected cats become obtunded, apprehensive, reluctant to jump, hypersensitive to neck palpation, and lame. The underlying connective tissue disorder causes vertebral ankylosis and an ankylosing degenerative joint disease of the forelimbs. Recognizable radiographic manifestations of hypervitaminosis A may be seen in as little as 10 weeks after introduction of a diet rich in vitamin A. Changes include ankylosing spondylopathy of the cervical and cranial thoracic vertebral column and periarticular enthesopathy and degenerative joint disease of the shoulder and elbow joints (Figs. 18-45 and 18-46). In advanced disease the additional bone becomes incorporated seamlessly

with existing bone so that the architecture of the original bones is remodeled completely. Other regions of the vertebral column and other joints of the appendicular skeleton may become involved, but the aforementioned bones and joint appear to be the primary site of bony changes in cats. The ankylosing changes are permanent. They do not resolve once a balanced diet is substituted, but some of the clinical signs of hypervitaminosis A resolve once the dietary imbalance is corrected.

MUCOPOLYSACCHARIDOSIS

The storage diseases that comprise mucopolysaccharidosis (MPS) are characterized by tissue accumulation of glycosaminoglycans. Both dogs and cats can be affected by MPS, but the best-studied animal form is the feline form of MPS-VI. It causes polyarthropathies because of faulty cartilage formation, a result of dermatan sulfate accumulation in connective tissue because of deficiency of the lysosomal enzyme *N*-acetylgalactosamine-4-sulphatase. The morphologic appearance of affected cats ranges from normal to short-legged dwarfs with facial dysmorphism. Feline MPS-VI has two genotypes. The least affected phenotype ranges from being physically and clinically normal to having degenerative joint disease of the shoulder and stifle joints. The classic form produces phenotypic features of dwarfism and facial dysmorphia. These cats tend to have lameness and develop hindlimb paresis. Radiographic abnormalities are from epiphyseal dysplasia and range from degenerative joint disease in the shoulder and stifle to gross malformation of the appendicular and axial skeleton (Figs. 18-47 and 18-48). Severely affected animals are osteopenic. The subchondral bone of articular surfaces is distorted, and periarticular soft tissue mineralization is common. Epiphyseal dysplasia results in distortion of the epiphyses of the appendicular skeleton, which reflects high levels of lysosomal storage in chondrocytes, affecting mineralization of the matrix adversely during enchondral ossification. Vertebral malformation is a recognizable feature of feline MPS-VI. The vertebral bodies are short and square, the pedicles elongated, and articular processes malformed. Epiphyseal dysplasia causes distortion of the epiphyses of vertebral bodies. New bone formation around articular processes and ankylosing spondylopathy are common.

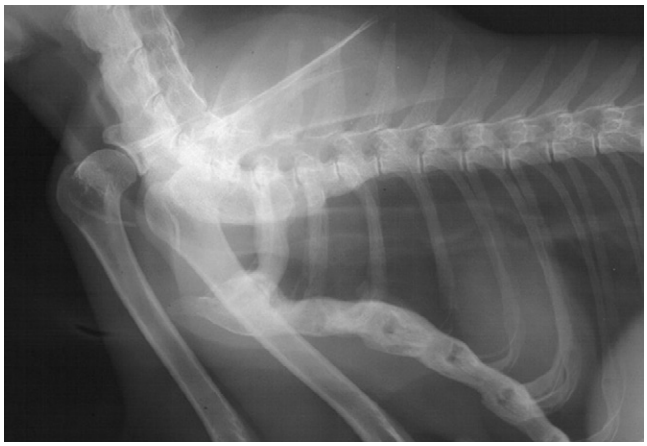


Fig. 18-45 Ankylosing spondylopathy of the cervical and cranial thoracic vertebrae and the sternum of a cat with hypervitaminosis A. (Reprinted from Allan GS: Radiographic features of feline joint diseases, *Vet Clin North Am Small Anim Pract* 30:281, 2000. Courtesy University of Queensland, Brisbane, Australia.)

SCOTTISH FOLD CHONDRO-OSSEOUS DYSPLASIA

Scottish Fold chondro-osseous dysplasia (SFCOD) is an inherited autosomal dominant trait that causes defective cartilage maturation. Although folding of the ear cartilage is a defining visible feature of SFCOD, the cascade of changes caused by faulty cartilage maturation affecting the skeleton are seen in both homozygotes and heterozygotes. In extreme forms the polyarthropathy caused by SFCOD can be crippling, and affected animals can be disinclined to ambulate and unable to jump. Defective cartilage formation manifests skeletal changes that affect joints and entheses. The joints of the distal limbs are affected most spectacularly, but some long bones such as the metacarpi, metatarsi, and the phalanges may also develop abnormally (Fig. 18-49). Large enthesophytes can form around joints at points of tendinous origin or insertion (entheses). An ankylosing arthropathy frequently results in fusion of the carpi and tarsi (Fig. 18-50) and their articulations with the metacarpi and metatarsi. Malformed bones in the manus and pes may not grow to a normal length, and these bones may appear shorter and fatter than normal. Vertebral malformation can also occur in the tail, where the caudal vertebrae may be short

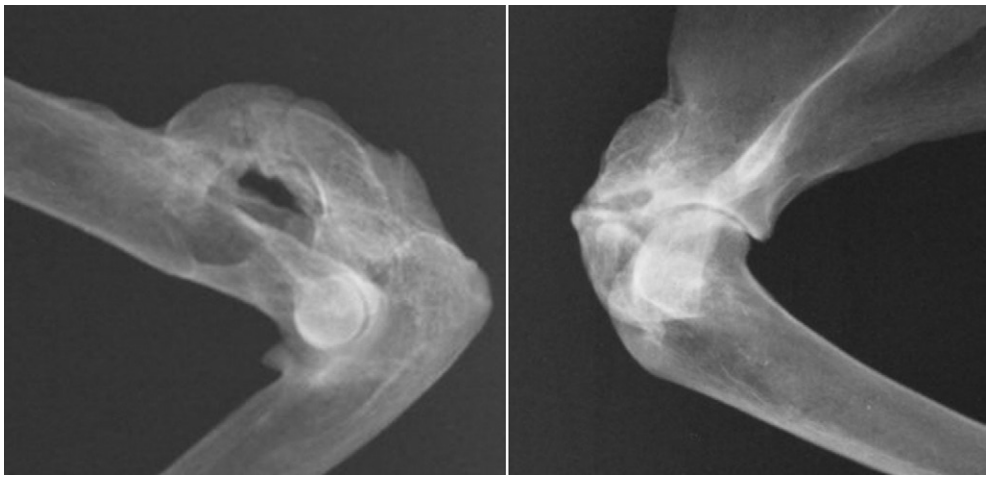


Fig. 18-46 Radiographs of the elbows and a shoulder from the skeleton of a cat that was euthanized because of ankylosing arthropathy caused by hypervitaminosis A.

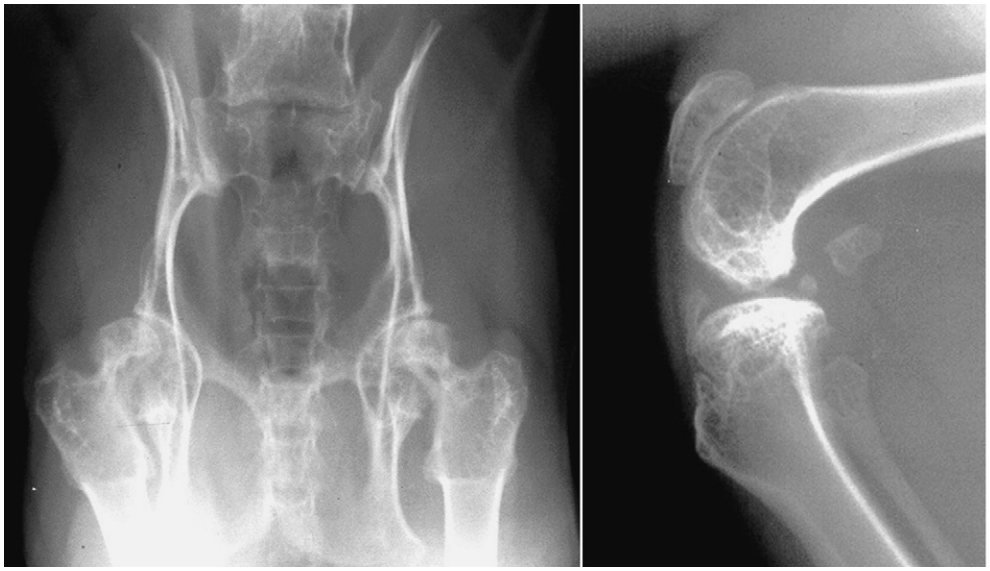


Fig. 18-47 Malformation of the coxofemoral joints, pelvis, and stifle caused by MPS-VI in a cat. (Courtesy of Dr. A. C. Crawley, Adelaide, South Australia. Reprinted from Allan GS: Radiographic features of feline joint diseases, *Vet Clin North Am Small Anim Pract* 30:281, 2000.)



Fig. 18-48 Cervical and lumbar vertebral malformation caused by MPS-VI in a cat. (Courtesy of Dr. A. C. Crawley, Adelaide, South Australia. Reprinted from Allan GS: Radiographic features of feline joint diseases, *Vet Clin North Am Small Anim Pract* 30:281, 2000.)

and wide. Spondylopathy of the caudal vertebrae may combine to produce a tail that is short and relatively inflexible.[79]

HEMARTHROSIS

Intraarticular hemorrhage may occur in dogs with coagulopathies or after joint trauma.[80] Other coagulopathies in the dog that may cause hemarthrosis include hemophilia A and B; von Willebrand's disease; deficiencies in factors VII, X, and XI; and liver disease. Isolated, infrequent episodes of intraarticular bleeding do not alter the articular cartilage significantly. Repeated hemorrhage may lead to severe damage to the cartilage as well as the subchondral bone. Affected animals have severe non–weight-bearing lameness of affected limbs, and affected joints are swollen and painful. Radiographically, in acute hemarthrosis there is soft tissue swelling of the joint, which may be extensive.[80] After chronic intraarticular hemorrhage, the joint cartilage may be eroded and thin. The subchondral bone can appear irregular. Remodeling of bones



Fig. 18-49 Carpometacarpal ankylosis and metacarpal and phalangeal malformation in a Scottish Fold cat. (Courtesy of Sylvania Veterinary Hospital, Sydney, Australia.)

adjacent to affected stifles was reported in dogs after repeated intraarticular injections of whole blood.[81] In advanced hemarthrosis, signs similar to degenerative joint disease may be present.

SEPTIC ARTHRITIS

Septic arthritis is diagnosed infrequently in small animals, with the incidence being lower than that of immune-mediated joint disease. Septic arthritis is difficult to diagnose radiographically. Initial radiographic changes are usually limited to



Fig. 18-50 Radiographic examples of tarsal and tarsometatarsal ankylosis and metatarsal malformation in a Scottish Fold cat with SFCOD.

joint effusion and periarticular swelling. Ideally, the arthritis should be diagnosed and treated successfully before radiographic changes become apparent.[82] Polyarticular septic arthritis may occur as a result of bacteremia associated with an isolated focus of infection (endocarditis, discospondylitis, or omphalophlebitis) or in conjunction with a systemic diseases (as in *Mycoplasma* arthritis, canine leishmaniasis, or feline caliciviral lameness).[83-85] Polyarticular septic arthritis must be differentiated from immune-mediated joint disease. The former is more likely to affect the larger, more proximal joints of the appendicular skeleton, whereas the latter more commonly affects the joints nearer the distal extremities (Box 18-6). Monoarticular septic arthritis most likely results from extension of focal osteomyelitis into an adjacent joint, direct joint trauma, or foreign body penetration (grass seed awns), or it may occur after joint surgery or intraarticular therapy. Hematogenous dissemination of infection to joints is more common in young animals. Septic arthritis caused by surgery, particularly cruciate ligament repair, is more common in older animals.

As already noted, the earliest radiographic changes of septic arthritis are synovial effusion and increased synovial mass, which represent an inflammatory response of the synovium. Soft tissue swelling is usually demarcated by the distended joint capsule. Joint capsule distention is identified more easily in carpal, tarsal, and stifle joints. A useful landmark in the stifle is the infrapatellar fat pad. When the fat pad is compressed cranially, it becomes smaller or unclear, indicating synovial effusion is present. In untreated septic arthritis, joint cartilage destruction follows synovial effusion and is followed by subchondral and perichondral bone destruction (Figs. 18-51 and 18-52, Box 18-7).

Box • **18-6**

Polyarthropathies Affecting the Appendicular Skeleton of Dogs and Cats

- Immune-mediated joint diseases
  - Rheumatoid arthritis
  - Systemic lupus erythematosus
  - Feline periosteal proliferative polyarthritis
  - Feline nonerosive immune-mediated polyarthropathy
- Septic arthritis
  - Hematogenous septic arthritis
  - Bacterial or fungal septic arthritis
- Inflammatory arthritides
  - Leishmaniasis
  - Rocky Mountain spotted fever
  - Rickettsia rickettsii
  - Lyme disease
  - Borrelia burgdorferi
  - Mycoplasma arthritis
  - Chinese Shar-Pei fever syndrome
  - Feline calicivirus, coronavirus
  - Greyhound polyarthritis
- Hemarthrosis
  - Chronic, recurrent, caused by blood dyscrasias
- Hypervitaminosis A
- Primary degenerative joint disease/osteoarthrosis
- Disseminated idiopathic skeletal hyperostosis syndrome
- Familial or genetic skeletal dysplasias
  - Scottish Fold osteochondrodysplasia
  - Feline mucopolysaccharidosis
  - Canine hip dysplasia
  - Canine elbow dysplasia
  - Osteochondrosis
- Drug-induced and vaccine-mediated polyarthritis
- Feline osteochondromatosis

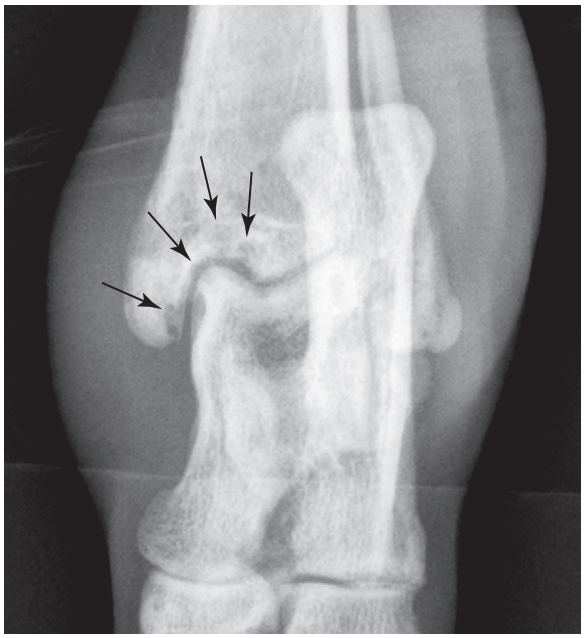


Fig. 18-51 A 1.5-year-old canine mix with lameness and tarsal swelling for 2 weeks. There are focal subchondral lucencies in the distomedial aspect of the tibia *(black arrows)*. The swelling is also obvious. Cryptococcus was isolated from synovial fluid.

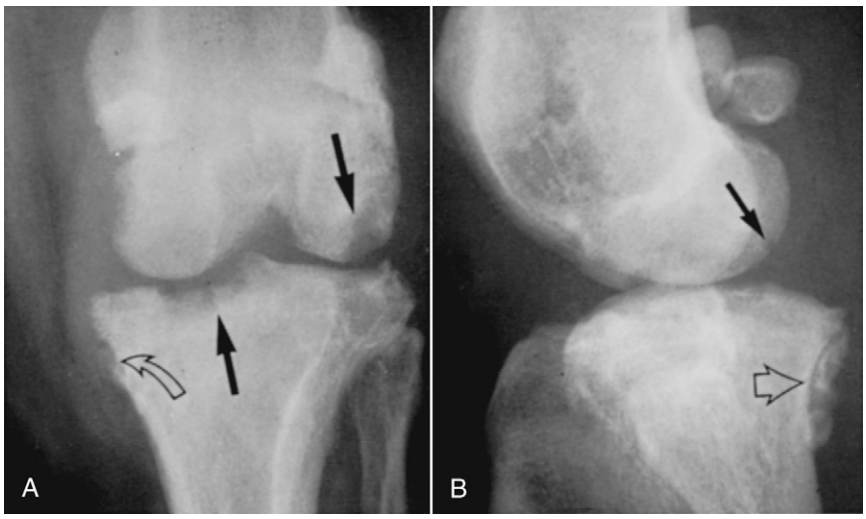


Fig. 18-52 An 8-year-old male Australian cattle dog had stifle swelling and pain that persisted after repair of a ruptured cranial cruciate ligament. **A** and **B,** Subchondral bone erosion involves the medial condyle of the tibia and the femoral condyles *(solid black arrows)*. Periarticular new bone formation is also evident *(open black arrow)*. Note the concurrent medial patellar luxation. *Staphylococcus aureus* was isolated from the synovial fluid.

Box • 18-7

Progression of Radiographic Signs of Infectious Arthritis

Increased synovial mass indicating synovial effusion and widened radiolucent joint space

Diminished radiolucent joint space indicating destruction of articular cartilage

Loss of the smooth surface of the subchondral bone plate—an early sign of infectious penetration of subchondral bone

Osteolucent signs of destruction of subchondral and perichondral bone usually highlighted by a peripheral border of increased osseous opacity

In advanced infectious arthritis, weight-bearing surfaces may collapse, causing distortion of joint architecture

Septic arthritis is being identified increasingly in joints that have chronic degenerative joint disease. Initial radiographs are characterized by degenerative joint disease, often leading to inappropriate therapy for the infection. Radiographs made 2 to 4 weeks later reveal more aggressive signs of periosteal new bone formation and intraarticular bone destruction.[85] Septic arthritis should be suspected when acute lameness and joint pain are identified in individual animals whose degenerative joint disease has been controlled previously.

The diagnosis of septic arthritis is based on cytologic assessment of synovial fluid and microbiologic examination of synovial fluid and/or synovium and joint capsule. Radiographic assessment alone has low specificity for septic arthritis, but survey radiographs are useful to rule out other conditions as well as to follow the progress of a joint infection once a diagnosis of septic arthritis is confirmed.

Septic Arthritis in Cats

In cats hematogenously disseminated septic arthritis may be caused by a variety of microorganisms, which include *Mycoplasma gateae, Mycoplasma felis,* bacterial L-form infection (*Pasteurella* spp.), calicivirus (transient arthritis in kittens), coronavirus (feline infectious peritonitis), and fungi (cryptococcosis, histoplasmosis). Hematogenously disseminated septic arthritis initially causes a nonerosive polyarthropathy characterized by lameness, synovial effusion, and synovial thickening. Affected cats may be systemically ill. Viremic polyarthropathies tend to be transient, whereas bacterial arthritis can have a protracted course. Direct injection of bacteria from bite wounds can result in mixed infections of microorganisms, which may include anaerobic bacteria.

Septic arthritis from penetrating bite wounds causes lameness that is usually restricted to one joint. Synovial effusion and periarticular soft tissue thickening precede secondary changes such as subchondral bone erosion by weeks or months. Joint infections that extend through the synovium and joint capsule into extracapsular tissue stimulate periosteal new bone formation on bone surfaces adjacent to the joint. Septic arthritis can lead to osteomyelitis in the bones on either side of an affected joint.

IMMUNE-MEDIATED ARTHROPATHIES

Rheumatoid Arthritis

Rheumatoid arthritis is a severe, progressive, erosive polyarthritis that has been reported in dogs,[86] and a similar condition has been reported in cats.[87,88] Radiographic changes usually occur in joints of the distal extremities. The stifle and elbow are affected occasionally. Synovial effusion occurs initially. Radiographs made early are characterized by nonspecific periarticular soft tissue swelling. The joint capsule may be distended. The first radiographic signs of bone involvement may be detected several weeks after the onset of clinical signs. Initial changes are mild, but the radiographic abnormalities become more obvious as the disease advances.

The progression of radiographic changes includes (1) subchondral bone destruction and cyst formation (Fig. 18-53); (2) joint space narrowing; (3) progressive decreased opacity of epiphyses adjacent to affected joints; (4) destruction of subchondral and perichondral bone; (5) mushrooming of the ends of the metacarpi and metatarsi, which occurs in advanced arthritis and represents collapse of subchondral bone; and (6) varying degrees of joint subluxation and luxation (Fig. 18-54). Other changes more characteristic of degenerative joint disease (osteophytes/enthesophytes, subchondral sclerosis, and calcified periarticular tissues) may also be present.[86]

Systemic Lupus Erythematosus

Systemic lupus erythematosus (SLE) is a multisystemic disease that affects dogs of all breeds as well as cats. It has

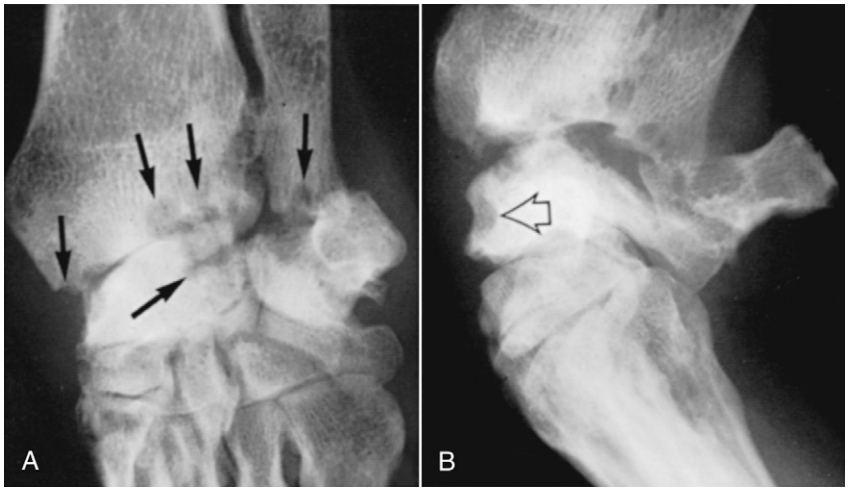


Fig. 18-53 An 8-year-old male (neutered) Corgi crossbreed with rheumatoid arthritis. **A,** Dorsolateral-palmaromedial projection. There is extensive subchondral erosion of the styloid process of the ulna and the articular surfaces of the distal radius and radial carpal bone *(black arrows)*. **B,** Lateral projection during flexion. In addition to the changes seen in **A,** note the erosion of the non–weight-bearing dorsal surface of the radial carpal bone *(open black arrow)*. (Courtesy of University Veterinary Centre, Sydney, Australia.)



Fig. 18-54 Dorsopalmar radiographs of the left **(A)** and right **(B)** manus of a dog with immune-mediated arthropathy. There is subluxation of the left antebrachiocarpal joint and the right carpometacarpal joint. There are also subluxation of distal interphalangeal joint in each manus. Numerous subchondral lytic erosive lesions are present *(white arrows)*.

a variety of clinical manifestations, including polyarthritis, anemia, nephropathy, skin disease, pericarditis, myocarditis, and lymphadenopathy.[89,90] The diagnosis of SLE is complicated and made on the basis of the concurrence of clinical manifestations and serologic evidence. The relative frequency of the different clinical manifestations in SLE varies. In one study, 121 dogs were reviewed, and joint disease was reported to be the most frequent clinical sign (69%), followed by hematologic (53%), renal (50%), cutaneous (33%), and intrathoracic (17%) manifestations.[89] The arthropathy that occurs in canine SLE is usually nonerosive and effusive. Polyarthritis is typical, but monoarticular arthritis has been reported. Affected joints may be swollen, painful, and warm. The joints most commonly affected are the carpus, tarsus, metatarsus, stifle, and elbow. Radiographic signs are usually absent or are minimal. In chronic SLE, the joint space of affected joints may be narrowed, and the joint capsule is distended. A mild periosteal response has been reported at the junction of the joint capsule and the bone.

Feline Noninfectious Polyarthritis

Feline noninfectious polyarthritis is a disease of male cats aged 1 to 5 years.[87,88,91] The polyarthritis can be erosive or nonerosive.[92] There are two types of erosive polyarthritis: the periosteal proliferative form and the erosive form. The erosive form is commonly referred to as *feline rheumatoid arthritis*. A group of nonerosive, effusive polyarthropathies thought to be immune mediated also occur in cats and are associated with a variety of conditions.

Periosteal Proliferative Form

Affected cats have fever, malaise, and stiffness, followed by periarticular soft tissue swelling and regional lymphadenopathy. Radiographic changes may be identified in affected joints after a few weeks. Commonly affected joints are the carpi and tarsi. The stifle, elbow, shoulder, and hip joints are affected to a lesser extent. During the first month, periarticular soft tissue swelling is the predominant sign. Swelling may be either intracapsular or extracapsular. One to 3 months after the onset of clinical signs, periosteal new bone production at points of joint capsule attachment may be identified. During this phase, the bone adjacent to affected joints may have decreased bone opacity and a coarse trabecular pattern. Perichondral new bone formation is pronounced 2 or 3 months after onset of the disease. Extensive enthesopathy may bridge smaller joint spaces. More severe radiographic manifestations include perichondral bone erosion and formation of subchondral cysts. Narrowing of affected joint spaces may occur late.[87] The radiographic signs of the periosteal proliferative form of feline chronic progressive polyarthritis include periarticular soft tissue swelling, periosteal new bone formation, perichondral enthesophyte production, perichondral and subchondral erosion, subchondral cysts, osteopenia of bone adjacent to affected joints, and narrowed joint spaces[93] (Fig. 18-55).

Erosive Form

A second, more erosive form of feline noninfectious polyarthritis has been described; it resembles human rheumatoid arthritis and is seen in older cats.[87,88] This form is characterized radiographically by severe subchondral bone erosion, perichondral bone erosion, and subchondral cyst formation. Perichondral enthesophyte formation, bone destruction at points of ligamentous insertion to bone, and subluxation of small



Fig. 18-55 The carpus of a young cat with feline chronic progressive polyarthritis. (Courtesy of University Veterinary Centre, Sydney, Australia. Reprinted from Allan GS: Radiographic features of feline joint diseases, *Vet Clin North Am Small Anim Pract* 30:281, 2000.)

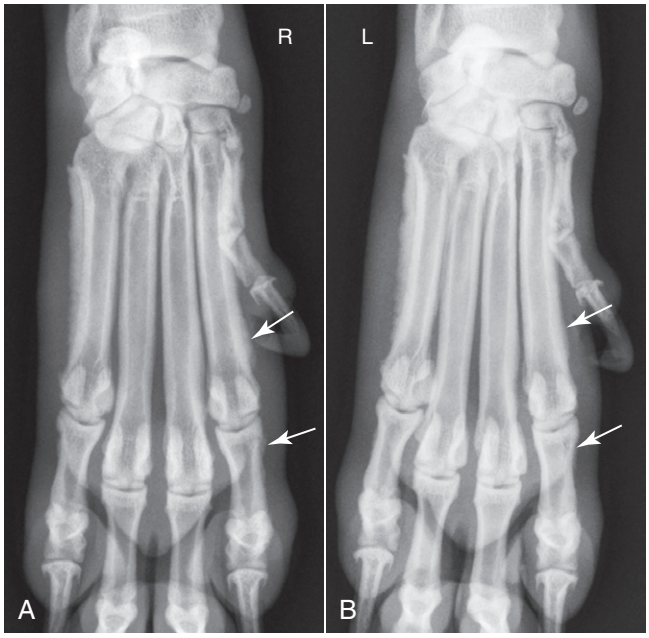


Fig. 18-56 Radiographs of the left **(A)** and right **(B)** manus of a dog with early hypertrophic osteopathy. There is irregular new periosteal reaction that is most pronounced on the lateral aspect of the fourth metacarpal bone. There is less pronounced periosteal reaction on the medial aspect of the manus *(white arrows)*. The radius also had a periosteal reaction, but that cannot be seen in this figure.

joints of the extremities also occur. A diagnosis of feline rheumatoid arthritis requires a positive rheumatoid factor test, characteristic histologic changes seen on a synovial biopsy, or both. Both test results are negative in cats with feline proliferative polyarthritis.[92]

Feline Nonerosive Polyarthritis

Two categories of nonerosive polyarthritis have been described in cats.[92] They are feline SLE and idiopathic polyarthritis. Idiopathic polyarthritis has four subtypes: (1) uncomplicated polyarthritis; (2) reactive polyarthritis, associated with a disease process elsewhere in the body; (3) enteropathic polyarthritis, associated with gastrointestinal disease; and (4) malignant-related idiopathic polyarthritis, associated with myeloproliferative disease. Radiography is used to distinguish the erosive from the nonerosive form of feline polyarthritis. The latter group is identified as having periarticular soft tissue swelling, joint capsule distention, and synovial fluid accumulation.

Hypertrophic Osteopathy

Hypertrophic osteopathy is a generalized osteoproductive disorder of the periosteum that affects the long and short tubular bones of the extremities. It is usually caused by cardiopulmonary disease or a thoracic mass. Abdominal masses, particularly those of urinary origin, have also been known to cause hypertrophic osteodystrophy. Nonneoplastic causes of hypertrophic osteopathy include inflammatory lung disease (e.g., blastomycosis), intrathoracic foreign bodies, *Dirofilaria immitis* infestation, and spirocercosis. The pathogenesis of hypertrophic osteopathy is understood incompletely. New bone formation typically commences on the distal end of both short and long tubular bones and progresses proximally. Periosteal new bone formation results in cortical thickening. The periosteal surface appears nodular or spiculated when visualized radiographically (Figs. 18-56 and 18-57).



Fig. 18-57 Lateral radiographs of the crus **(A)** and antebrachium **(B)** of a dog with hypertrophic osteopathy that is more advanced than in Figure 18-56. The abnormal periosteum has progressed to involve the more proximal aspect of the long and short tubular bones.



Fig. 18-58 A 5-year-old Burmese cat had bilateral stifle enlargement. Mineralization within the stifle joint was evident radiographically. Histologic diagnosis was synovial osteochondroma.



Fig. 18-59 A 6-year-old male (neutered) Burmese cat had progressive lameness of the right forelimb for 6 weeks. Radiographically, a large, well-defined, ossified mass was visible on the craniomedial aspect of the right elbow. Histologic diagnosis was extraarticular synovial osteochondroma.

THE SYNOVIUM

Villonodular Synovitis

Villonodular synovitis is an intracapsular joint disorder characterized by nodular synovial hyperplasia, which is thought to represent a response to trauma. Experimentally, villonodular synovitis has been reproduced in dogs by repeated intraarticular injections of whole blood. Villonodular synovitis is an established, although uncommon, disorder of human beings that has also been reported in horses and dogs.[94-97] In dogs the condition has been identified in the carpus, the coxofemoral joint, and the stifle. The radiographic signs of villonodular synovitis may be nonspecific but include articular soft tissue swelling alone or with erosion of cortical bone at the chondrosynovial junction. These cortical erosions may appear cystlike, with slightly opaque borders. In severe proximal femoral villonodular synovitis in human beings, the femoral neck has been described as looking like an apple core. The articular cartilage and subchondral bone are not involved. The differential diagnosis for perichondral erosive lesions, characteristic of villonodular synovitis, includes synovial osteochondromatosis, rheumatoid arthritis, and joint neoplasia.

Synovial Osteochondromas

Synovial osteochondromas are islands of cartilage produced by the synovial membrane. Foci of cartilage become pedunculated and may become separated to form loose bodies within the joint. Reports of synovial osteochondromatosis in cats suggest that Burmese cats are overrepresented. The radiographic appearance of mineralized synovial osteochondromas varies. These lesions are usually well-defined, rounded, often multiple intraarticular nodules of calcific opacity (Fig. 18-58). Synovial osteochondromas may also arise from extraarticular foci of synovial tissue (Fig. 18-59).

Synovial osteochondromas have been reported in the dog and the cat.[98,99] Their cause is unknown, but the theory of synovial metaplasia is generally accepted. These lesions have been reported to cause severe lameness in some dogs. Surgical removal of synovial osteochondromas relieves clinical signs of joint pain and lameness.[98] Other conditions in cats in which intraarticular and periarticular mineralization may be confused with synovial osteochondromatosis are mild forms of MPS-VI and hypervitaminosis A.[51,100]

Joint Neoplasia

Synovial sarcoma arises from primitive mesenchymal precursor cells of the synovial membrane of joints and bursae.[101] These tumors are uncommon in the dog and rare in the cat.[102] They occur most frequently in middle-aged, medium-sized to large dogs. The most commonly affected joints are the stifle and the elbow. Synovial sarcomas grow slowly and are first noticeable as a homogeneous soft tissue mass that involves or is near a joint. Portions of the tumor may be calcified, with mineral deposits appearing as hazy and punctate or as linear streaks.

Initial bone involvement usually appears as a spiculated periosteal response followed by ragged erosion of the cortical bone adjacent to the tumor. Occasionally the neoplasm initially appears relatively nonaggressive, mimicking a simple cyst, only to change later into a more extensive and destructive disease (Fig. 18-60). Destruction of cancellous bone may be extensive and most commonly occurs on both sides of the joint (Fig. 18-61). The tumor is locally invasive with a capacity to metastasize,[103] although distant metastasis, particularly to the lungs, occurs in as many as half of reported patients.[101]

Many neoplasms mimic the radiographic appearance of synovial sarcomas. In a study of joint neoplasms, synovial sarcomas were represented in only 27% of patients.[104] The other neoplasms with a radiographic appearance similar to that of synovial sarcomas included fibrosarcoma, rhabdomyosarcoma, fibromyxosarcoma, malignant fibrous histiocytoma, liposarcoma, and undifferentiated sarcoma. Histologic evaluation of the lesion is mandatory to establish its origin.



Fig. 18-60 **A,** A cystic lesion was identified in the distal end of the left ulna *(white arrows)* 6 weeks after the onset of soft tissue swelling around the antebrachiocarpal joint. The lesion progressed over the succeeding 12 months **(B),** by which time a multiloculated cystlike change was present in the distal radius, ulna, and the proximal row of carpal bones. Histologic diagnosis was synovial cell carcinoma. (Courtesy of Dr. P. Young, All Pets Veterinary Hospital, Albury, Australia.)



Fig. 18-61 Multiple radiolucent lesions are evident on both sides of this dog's stifle. Histologic diagnosis was synovial sarcoma.

REFERENCES

1. Basher AWP, Doige CE, Presnell KR: Subchondral bone cysts in a dog with osteochondrosis, *J Am Anim Hosp Assoc* 24:321, 1988.
2. Morgan JP, Pool RR, Miyabayashi T: Primary degenerative joint disease of the shoulder in a colony of beagles, *J Am Vet Med Assoc* 190:531, 1987.
3. Flo GL: Synovial chondrometaplasia in five dogs, *J Am Vet Med Assoc* 200:943, 1992.
4. Kealy JK, McAllister H: *Diagnostic radiology and ultrasonography of the dog and cat*, ed 3, Philadelphia, 2000, Saunders, p 282.
5. Whiting PG, Pool RR: Intrameniscal calcification and ossification in the stifle joints of three domestic cats, *J Am Anim Hosp Assoc* 21:579, 1985.
6. de Haan JJ, Anderson CB: Calcium crystal associated arthropathy in a dog, *J Am Vet Med Assoc* 200:943, 1992.
7. Short RP, Jardine JE: Calcium phosphate deposition disease in a fox terrier, *J Am Anim Hosp Assoc* 29:363, 1993.
8. Mahoney PN, Lamb CR: Articular, periarticular and juxtaarticular calcified bodies in the dog and cat: a radiologic review, *Vet Radiol Ultrasound* 37:3, 1996.
9. Wood AKW, McCarthy PH: A study of irregularly occurring ectopic and sesamoid bones in the dog, *Vet Radiol* 27:22, 1986.
10. DeRooster H, van Bree H: Popliteal sesamoid displacement associated with cruciate rupture in the dog, *J Small Anim Pract* 40:316, 1999.
11. Mason DR, Schultz KS, Samii VF, et al: Sensitivity of radiographic evaluation of radio-ulnar incongruence in the dog in vivo, *Vet Surg* 31:125, 2002.
12. Widmer WR, Buckwalter KA, Braunstein EM, et al: Radiographic and magnetic resonance-imaging if the stifle joint in experimental osteoarthritis in dogs, *Vet Radiol Ultrasound* 35:371, 1994.
13. McGonagle D, Benjamin M, Marzo-Ortega H, et al: Advances in the understanding of entheseal inflammation, *Curr Rheumatol Rep* 4:500, 2002.
14. Specht TE, Poulos PW, Metcalf MR, et al: Vacuum phenomenon in the metatarsophalangeal joint of a horse, *J Am Vet Med Assoc* 197:749, 1990.
15. Morgan JP: *Radiology of skeletal diseases—principles of diagnosis in dogs*, Davis, Calif, 1981, Veterinary Radiology Associates, p 22.
16. van Bree H: Vacuum phenomenon associated with osteochondrosis of the scapulohumeral joint in dogs: 100 cases (1985–1991), *J Am Vet Med Assoc* 201:1916, 1992.

17. *PennHIP Training Manual*, San Diego, CA, 1998, Synbiotics Corporation, p 22.
18. Hathcock JT: Vacuum phenomenon of the canine spine: CT findings in 3 patients, *Vet Radiol Ultrasound* 35:285, 1994.
19. Weber WJ, Berry CR, Kramer RW: Vacuum phenomenon in 12 dogs, *Vet Radiol Ultrasound* 36:493, 1995.
20. McCarthy PH, Wood AKW: Anatomical and radiological studies of the iliopubic cartilage in adult greyhounds, *Anat Histol Embryol* 15:73, 1986.
21. Pond MJ, Lasonsky JM: Avulsion of the popliteus muscle in the dog: a case report, *J Am Anim Hosp Assoc* 12:60, 1976.
22. Eaton Wells RD, Plummer GV: Avulsion of the popliteus muscle in an Afghan hound, *J Small Anim Pract* 19:743, 1978.
23. Chaffee VW, Knecht CD: Avulsion of the medial head of the gastrocnemius in the dog, *Vet Med Small Anim Clin* 70:929, 1975.
24. Robinson A: Atraumatic bilateral avulsion of the origins of the gastrocnemius muscle, *J Small Anim Pract* 40:498, 1999.
25. Rendano VT, Dueland R: Variation in location of gastrocnemius sesamoid bones (fabellae) in a dog, *J Am Vet Med Assoc* 173:200, 1978.
26. Wood AKW, McCarthy PH, Howlett CR: Anatomic and radiographic appearance of a sesamoid bone in the tendon of origin of the supinator muscle of dogs, *Am J Vet Res* 46:2043, 1985.
27. Wood AKW, McCarthy PH: Radiologic and anatomic observations of plantar sesamoid bones at the tarsometatarsal articulations of greyhounds, *Am J Vet Res* 45:2158, 1984.
28. Freire M, Brown J, Robertson ID, Pease AP, Hash J, Hunter S, Simpson W, Thomson Sumrell A, Lascelles BD: Meniscal mineralization in domestic cats, *Vet Surg* 39:545, 2010.
29. Barthez PY, Morgan JP: Bicipital tenosynovitis in the dog—evaluation with positive contrast arthrography, *Vet Radiol Ultrasound* 34:325, 1993.
30. Lowry JE, Carpenter LG, Park RD, et al: Radiographic anatomy and technique for arthrography of the cubital joint in clinically normal dogs, *J Am Vet Med Assoc* 203:72, 1993.
31. Muir P, Johnson KA: Supraspinous and biceps brachii tendinopathy in dogs, *J Am Anim Pract* 35:239, 1994.
32. Rivers B, Wallace L, Johnson GR: Biceps tenosynovitis in the dog: radiographic and sonographic findings, *Vet Comp Orthop Traumatol* 5:51, 1992.
33. Cake MA, Read RA: Canine and human sesamoid disease, *Vet Comp Orthop Traumatol* 8:70, 1995.
34. Robins GM, Read RA: Diseases of the sesamoid bones. In Bojrab MJ, editor: *Disease mechanisms in small animal surgery*, ed 2, Philadelphia, 1993, Lea & Febiger, p 1094.
35. Vaughan LC, France C: Abnormalities of the volar and plantar sesamoids in Rottweilers, *J Small Anim Pract* 27:551, 1986.
36. Read RA, Black AP, Armstrong SJ, et al: Incidence and clinical significance of sesamoid disease in Rottweilers, *Vet Rec* 130:533, 1992.
37. Davis PE, Bellenger CR, Turner DM: Fractures of the sesamoid bones in the greyhound, *Aust Vet J* 45:15, 1969.
38. Ljunggren G, Olsson S-E: Osteoarthrosis of the shoulder and elbow joints in dogs: a pathologic and radiographic study of necropsy material, *J Am Vet Radiol Soc* 16:33, 1975.
39. Tirgari M, Vaughan LL: Arthritis of the canine stifle joint, *Vet Rec* 96:394, 1975.
40. Marshall JL: Peri-articular osteophytes—initiation and formation in the knees of the dog, *Clin Orthop* 62:37, 1969.
41. Lust G, Summers BA: Early, asymptomatic stage of degenerative joint disease in canine hip joints, *Am J Vet Res* 42:1849, 1981.
42. Gilbertson E: Development of periarticular osteophytes in experimentally induced osteoarthritis in the dog. A study using microradiographic, microangiographic and fluorescent bone-labelling techniques, *Ann Rheum Dis* 34:12, 1975.
43. Marshall J: Periarticular osteophytes: initiation and formation in the knee of the dog, *Clin Orthop* 62:37, 1969.
44. Innes JF, Costello M, Barr FJ, et al: Radiographic progression of osteoarthritis of the canine stifle joint: a prospective study, *Vet Radiol Ultrasound* 45:143, 2004.
45. Smith GK, Popovitch CA, Gregor TP, et al: Evaluation of risk factors for degenerative joint disease associated with hip dysplasia in dogs, *J Am Vet Med Assoc* 206:642, 1995.
46. Smith GK, Gregor TP, Rhodes WH, et al: Coxofemoral joint laxity from distraction radiography and its contemporaneous and prospective correlation with laxity, subjective score, and evidence of degenerative joint disease from conventional hip-extended radiography in dogs, *Am J Vet Res* 54:1020, 1993.
47. Popovitch CA, Smith GK, Gregor TP, et al: Comparison of susceptibility for hip dysplasia between Rottweilers and German shepherd dogs, *J Am Vet Med Assoc* 206:648, 1995.
48. Lust G, Williams AJ, Burton-Worster N, et al: Joint laxity and its association with hip dysplasia in Labrador retrievers, *Am J Vet Res* 54:1990, 1993.
49. Marshall JL, Olsson S-E: Instability of the knee: a long-term experimental study in dogs, *J Bone Joint Surg (Am)* 53:1561, 1971.
50. Sokoloff L: The pathology of osteoarthritis and the role of ageing. In Nuki J, editor: *The aetiopathogenesis of osteoarthritis*, Tunbridge Wells, England, 1980, Pitman Medical, pp 1–15.
51. Allan GS: Radiographic features of feline joint diseases. In Watrous BJ, editor: *Veterinary clinics of North America*, Philadelphia, 2000, Saunders, pp 281–302.
52. Hedhammar A, Olsson S-E, Andersson S-A, et al: Canine hip dysplasia: study of heritability in 401 litters of German shepherd dogs, *J Am Vet Med Assoc* 174:1012, 1979.
53. Leighton EA, Smith GK, McNeil M, et al: Heritability of the distraction index in German shepherd dogs and Labrador retrievers. In *Proceedings of the American Kennel Club conference on molecular genetics and genetic health*, Florham Park, NJ, 1994.
54. Lust G, Rendano VT, Summers BA: Canine hip dysplasia: concepts and diagnosis, *J Am Vet Med Assoc* 187:638, 1985.
55. Hedhammar A, Wu F-M, Krook L, et al: Overnutrition and skeletal disease, *Cornell Vet* 64:9, 1974.
56. Todhunter RJ, Grohn YT, Bliss SP, et al: Evaluation of multiple radiographic predictors of cartilage lesions in the hip joints of eight-month old dogs, *Am J Vet Res* 64:1472, 2003.
57. Lust G, Beilman WT, Dueland R, et al: Intra-articular volume and hip joint instability in dogs with hip dysplasia, *J Bone Joint Surg (Am)* 62:576, 1980.
58. Lust G, Beilman WT, Rendano VT: A relationship between degree of laxity and synovial fluid volume in coxofemoral joints of dogs predisposed for hip dysplasia, *Am J Vet Res* 41:55, 1980.

59. Morgan JP: Canine hip dysplasia: significance of early bony spurring, *Vet Radiol* 28:2, 1987.
60. Keller GG, Reed AL, Lattimer JC, et al: Hip dysplasia: a feline population study, *Vet Radiol Ultrasound* 40:460, 1999.
61. Root CR, Sande RD, Pfleuger S, et al: A disease of Maine Coon cats resembling congenital canine hip dysplasia. In *Proceedings of the annual meeting of the American College of Veterinary Radiologists*, Chicago, 1987.
62. Langenbach A, Grigor U, Green P, et al: Relationship between degenerative joint disease and hip joint laxity by use of distraction index and Norberg angle measurements in a group of cats, *J Am Vet Med Assoc* 213:1439, 1998.
63. Smith GK, Biery DN, Gregor TP: New concepts of coxofemoral joint stability and the development of a clinical stress radiographic method for quantitating hip joint laxity in the dog, *J Am Vet Med Assoc* 196:59, 1990.
64. Rendano VT, Ryan G: Canine hip dysplasia evaluation, *Vet Radiol* 26:170, 1985.
65. Farrow CS, Back RT: Radiographic evaluation of nonanesthetized and non-sedated dogs for hip dysplasia, *J Am Vet Med Assoc* 194:524, 1989.
66. Aronson E, Kraus KH, Smith J: The effect of anesthesia on the radiographic appearance of the coxofemoral joints, *Vet Radiol* 32:2, 1991.
67. Belkoff SM, Padgett G, Soutas-Little RW: Development of a device to measure canine coxofemoral joint laxity, *Vet Comp Orthop Traumatol* 1:31, 1989.
68. Salter RB, Harris WR: Injuries involving the epiphyseal plate, *J Bone Joint Surg* 45:587, 1963.
69. Farrow CS: Stress radiography: applications in small animal practice, *J Am Vet Med Assoc* 181:777, 1982.
70. Puglisi TA, Tangner CH, Green RW, et al: Stress radiography of the canine humeral joint, *J Am Anim Hosp Assoc* 24:235, 1988.
71. Davidson EB, Griffey SM, Vasseur PB, et al: Histopathological, radiographic, and arthrographic comparison of the biceps tendon in normal dogs and dogs with biceps tenosynovitis, *J Am Anim Hosp Assoc* 36:522, 2000.
72. Long CD, Nyland TG: Ultrasonographic evaluation of the canine shoulder, *Vet Radiol Ultrasound* 40:372, 1999.
73. Mitchell RAS, Innes JF: Lateral glenohumeral ligament rupture in three dogs, *J Small Anim Pract* 41:511, 2000.
74. Grundmann S, Montavon PM: Stenosing tenosynovitis of the abductor pollicis longus muscle in dogs, *Vet Comp Orthop Traumatol* 14:95, 2001.
75. Kramer M, Stengel H, Gerwing M, et al: Sonography of the canine stifle, *Vet Radiol Ultrasound* 40:282, 1999.
76. Reed AL, Payne TJ, Constantinescu GM: Ultrasonographic anatomy of the normal canine stifle, *Vet Radiol Ultrasound* 36:315, 1995.
77. Gnudi G, Bertoni G: Echographic examination of the stifle joint affected by cranial cruciate ligament rupture in the dog, *Vet Radiol Ultrasound* 42:266, 2001.
78. Kramer M, Gerwing M, Michele U, et al: Ultrasonographic examination of injuries to the Achilles tendon in dogs and cats, *J Small Anim Pract* 42:531, 2001.
79. Malik R, Allan G S, Howlett CR, et al: Chondro-osseous dysplasia in Scottish Fold cats, *Aust Vet J* 76:85, 1998.
80. Bellah JR, Weigel JP: Hemarthrosis secondary to suspected warfarin toxicosis in a dog, *J Am Vet Med Assoc* 182:1126, 1983.
81. Hoaglund FT: Experimental haemarthrosis: the response of canine knees to injection of autogenous blood, *J Bone Joint Surg* 49:285, 1967.
82. Bennett D, Taylor DJ: Bacterial infective arthritis in the dog, *J Small Anim Pract* 29:207, 1988.
83. Moise NS, Crissman JW, Fairbrother JF, et al: *Mycoplasma gateae* arthritis and tenosynovitis in cats: case report and experimental reproduction of the disease, *Am J Vet Res* 44:10, 1983.
84. Ernst S, Cogin JM: What is your diagnosis? Mycoplasma arthritis, *J Am Vet Med Assoc* 215:19, 1999.
85. Schrader SC: Septic arthritis and osteomyelitis of the hip of six mature dogs, *J Am Vet Med Assoc* 181:894, 1982.
86. Bennett D: Immune-based erosive inflammatory joint disease of the dog: canine rheumatoid arthritis: I. Clinical, radiological and laboratory investigations, *J Small Anim Pract* 28:779, 1987.
87. Pedersen NC, Pool RR, O'Brien T: Feline chronic progressive polyarthritis, *Am J Vet Res* 41:522, 1980.
88. Carro T: Polyarthritis in cats, *Comp Cont Educ Pract Vet* 16:57, 1994.
89. Grindem CB, Johnston KH: Systemic lupus erythematosus: literature review and report of 42 new canine cases, *J Am Anim Hosp Assoc* 19:489, 1983.
90. Bennett D: Immune-based non-erosive inflammatory joint disease of the dog: I. Canine SLE, *J Small Anim Pract* 28:871, 1987.
91. Moise NS, Crissman JW: Chronic progressive polyarthritis in a cat, *J Am Anim Hosp Assoc* 18:965, 1982.
92. Bennett D, Nash AS: Feline immune-based polyarthritis: a study of thirty-one cases, *J Small Anim Pract* 29:501, 1988.
93. Cantwell HD: Radiographic diagnosis, *Vet Radiol* 27:149, 1986.
94. Kusba JK, Lipowitz AJ, Wize M, et al: Suspected villonodular synovitis in a dog, *J Am Vet Med Assoc* 182:390, 1983.
95. Somer T, Sittnikow K, Henriksson K, et al: Pigmented villonodular synovitis and plasmacytoid lymphoma in a dog, *J Am Vet Med Assoc* 197:877, 1990.
96. Marti JN: Bilateral pigmented villonodular synovitis in a dog, *J Small Anim Pract* 38:256, 1997.
97. Hanson JA: Radiographic diagnosis—carpal villonodular synovitis, *Vet Radiol Ultrasound* 39:15, 1998.
98. Flo GL, Stickle RL, Dunstan RW: Synovial chondrometaplasia in five dogs, *J Am Vet Med Assoc* 191:1417, 1987.
99. Hubler M, Johnson KA, Burling RT, et al: Lesions resembling osteochondromatosis in two cats, *J Small Anim Pract* 27:181, 1986.
100. Crawley AC, Yogalingam G, Muller VJ, et al: Two mutations within a feline mucopolysaccharidosis type VI colony cause three different phenotypes, *J Clin Invest* 101:109, 1998.
101. Vail DM, Powers BE, Getzy DM, et al: Evaluation of prognostic factors for dogs with synovial sarcoma: 36 cases (1986–1991), *J Am Vet Med Assoc* 205:1300, 1994.
102. Silva-Krott IU: Synovial sarcoma in a cat, *J Am Vet Med Assoc* 203:1430, 1993.
103. McGlennon NJ, Houlton JEF, Gorman NT: Synovial sarcoma in the dog—a review, *J Small Anim Pract* 29:139, 1988.
104. Whitelock RG, Dyce J, Houlton JEF, et al: A review of 30 tumours affecting joints, *Vet Comp Orthop Traumatol* 10:146, 1997.

ELECTRONIC RESOURCES

evolve

Additional information related to the content in Chapter 18 can be found on the companion Evolve website at http://evolve.elsevier.com/Thrall/vetrad/

- Chapter Quiz

CHAPTER • 19

The Equine Stifle and Tarsus

Valeria Busoni
Fabrice Audigié

THE STIFLE

Radiographic Examination

Stifle radiographs are acquired frequently on clinical patients, and in presale examinations and screening radiographic protocols in young horses.[1-3] Because positioning errors are the most common reason for radiographs to be nondiagnostic,[4] a good knowledge of radiographic technique is crucial to assess the thick stifle region.

The lateromedial view is the basic radiographic view of the stifle and can be obtained on the standing horse with a portable or fixed radiographic unit. With good collimation, the lateromedial view does not require the use of a grid. Centering is 5 to 7 cm proximal to the tibial plateau, between the cranial and middle third of the stifle region. The cassette should be vertical to the ground to avoid geometric distortion, and exposure must be sufficient to visualize the femoral condyles. As a result, the femoral trochlea may be overexposed, so use of a hot light, or another less-exposed radiograph, may be needed if analog radiology is used. A lateromedial view of the flexed stifle is used to examine the cranial and central intercondylar areas of the tibia.

Depending on whether a portable or fixed radiographic unit is used, and the type of disease suspected, a caudolateral-craniomedial view and/or a caudocranial view are indicated. The caudolateral-craniomedial view allows good visualization of the two most common sites of disease in the young horse: the lateral trochlear ridge (osteochondrosis site) and the medial femoral condyle (subchondral cystlike lesion site). Because the superimposed femoral condyles are often underexposed on the lateromedial view when the radiograph is made with a portable unit, the caudolateral-craniomedial view is a valuable complement. The caudolateral-craniomedial view is an important projection to evaluate the medial femorotibial joint with low exposure factors and is also helpful for documenting injuries of the articular surface of the patella. The caudocranial view is mainly aimed at the assessment of the femorotibial joints for osteoarthrosis, and it is essential for documenting axial injuries such as an avulsion fracture at the enthesis of the cranial cruciate ligament. The caudocranial view requires the use of a grid for optimal contrast and is therefore difficult to obtain with a portable x-ray unit on a large horse.

The caudomedial-craniolateral view requires similar exposure factors to the caudocranial view and is not performed routinely, although it may be useful to diagnose lateral femorotibial injuries such as subchondral cystlike lesions of the lateral femoral condyle and bone remodeling at the proximal insertion of the cranial cruciate ligament.

The cranioproximal-craniodistal view of the patella is imperative when patellar disease is being investigated. This view can be obtained easily with a portable x-ray unit because a grid is not necessary and the required exposure is relatively low.

With the advent of digital radiography and its inherently greater contrast resolution, radiographic evaluation of the soft tissues of the stifle is possible to a certain extent. Lateromedial radiographs of the stifle allow good visualization of the patellar ligaments and the cranial fat pad (Fig. 19-1). Localization of soft tissue swelling as being extraarticular or intraarticular is possible by evaluating border effacement and fat pad displacement (see Fig. 19-1).

Ultrasonography for Supplemental Stifle Imaging

Subchondral cystlike lesions and tibial or femoral osteophyte formation as a result of osteoarthrosis are the most common radiographic signs of femorotibial disease. Bony fragments, new bone formation, or radiolucent areas at ligament insertions, suggesting avulsion fractures or enthesopathy, may also be seen.[5-7] However, because of the high incidence of soft tissue lesions involving menisci and ligaments, femorotibial pain may be present with no or minor radiographic signs.[5-7] When clinical signs suggest femorotibial involvement, all abnormalities are not likely to be diagnosed radiographically because assessment of soft tissue lesions is not possible. The severity of the lameness, the midterm prognosis for a return to work, or the long-term prognosis for development of osteoarthrosis depends mainly on the severity of the soft tissue injuries, in particular meniscal damage.[8-10] A combination of ultrasonographic and radiographic examination is therefore necessary for complete assessment of the stifle.[6]

Ultrasonography of the weight-bearing stifle allows easy assessment of the femoropatellar and femorotibial synovial recesses, the femoral trochlea, the patellar ligaments, the menisci, the collateral ligaments, and the medial femorotibial joint margins (Fig. 19-2).[11-12] In the flexed stifle, ultrasonography allows visualization of the cranial horns of the menisci, the cranial meniscal ligaments, and a portion of the articular surface of the medial and lateral femoral condyles (see Fig. 19-2).[13] Ultrasonography is the technique of choice to diagnose meniscal damage, which frequently affects sport and pleasure horses.[8] Although specificity is relatively low using arthroscopy as the gold standard,[8] a good correlation between

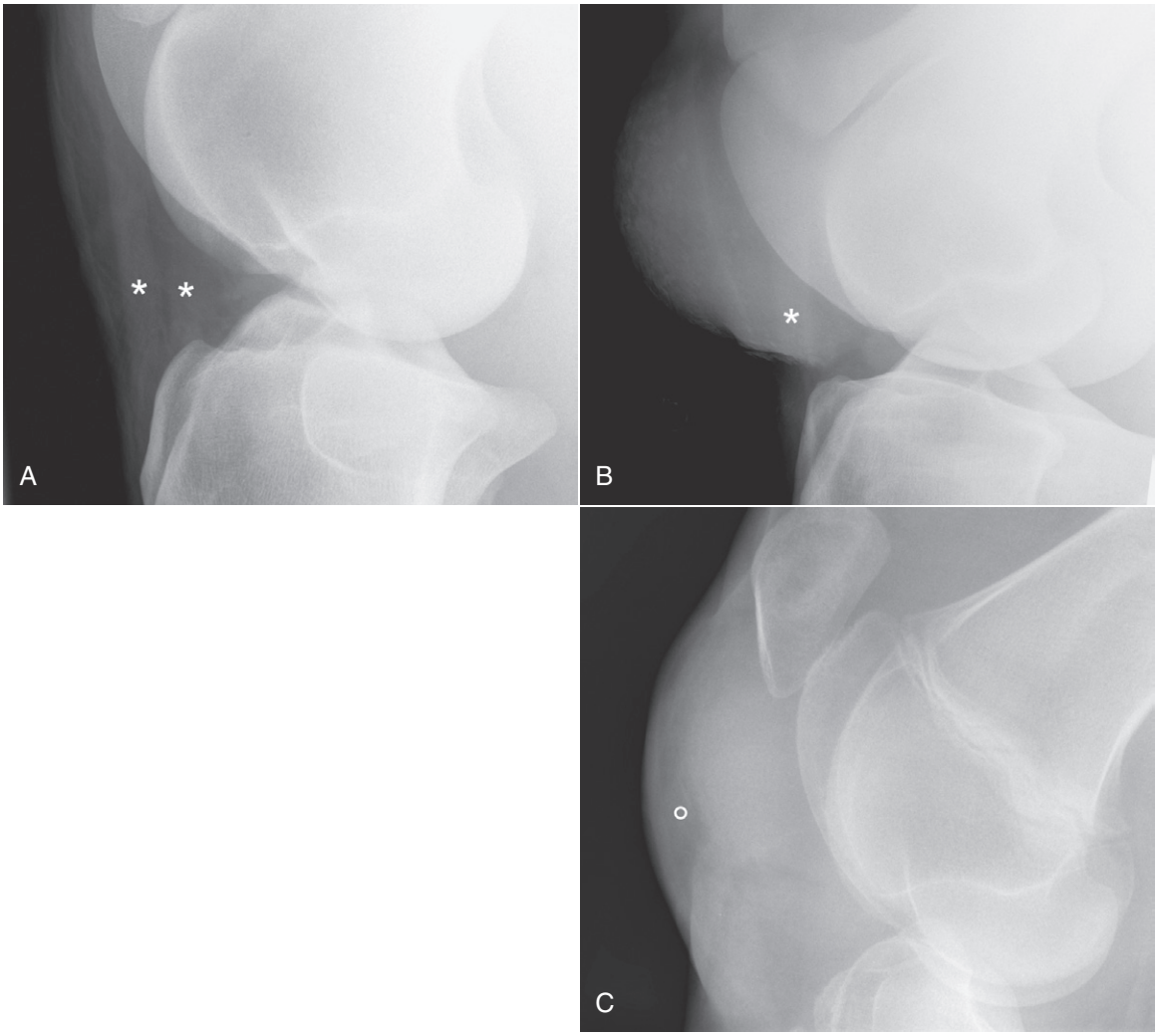


Fig. 19-1 Lateromedial radiographs of three equine stifles. **A,** Normal stifle. The patellar ligaments *(asterisks)* are delineated by the different opacity of the fat pad at the cranial aspect of the joint. **B,** A localized extraarticular soft tissue swelling is present. The middle patellar ligament is still visible *(asterisk)*. The horse had an extraarticular abscess. Note that the positioning is not correct for a lateromedial view because it is slightly oblique. **C,** Large soft tissue swelling at the cranial aspect of the stifle. The swelling is intraarticular (femoropatellar and femorotibial), and the patellar ligaments are no longer visible. The fat pad *(open circle)* is pushed cranially.

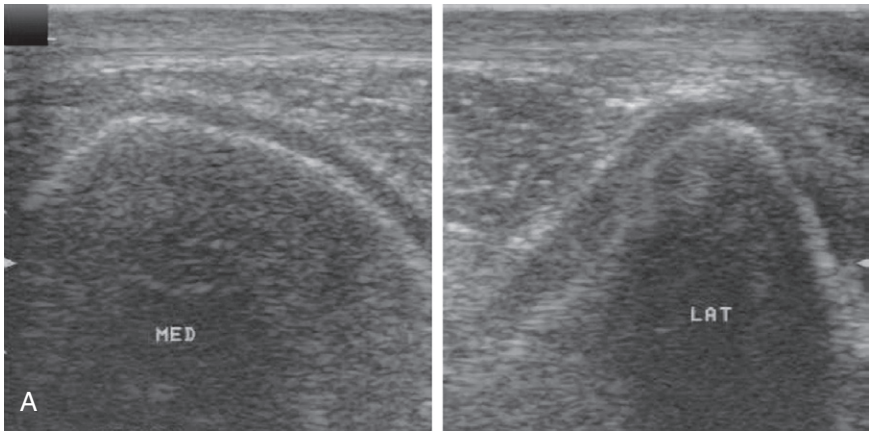


Fig. 19-2 Ultrasound images of the normal equine stifle **(A** to **D)** and meniscal tears **(E). A,** Transverse images of the medial *(MED)* and lateral *(LAT)* ridges of the femoral trochlea in a normal horse. The hyperechoic line is the subchondral bone surface. The hypoechoic band that covers the bone is the articular cartilage.

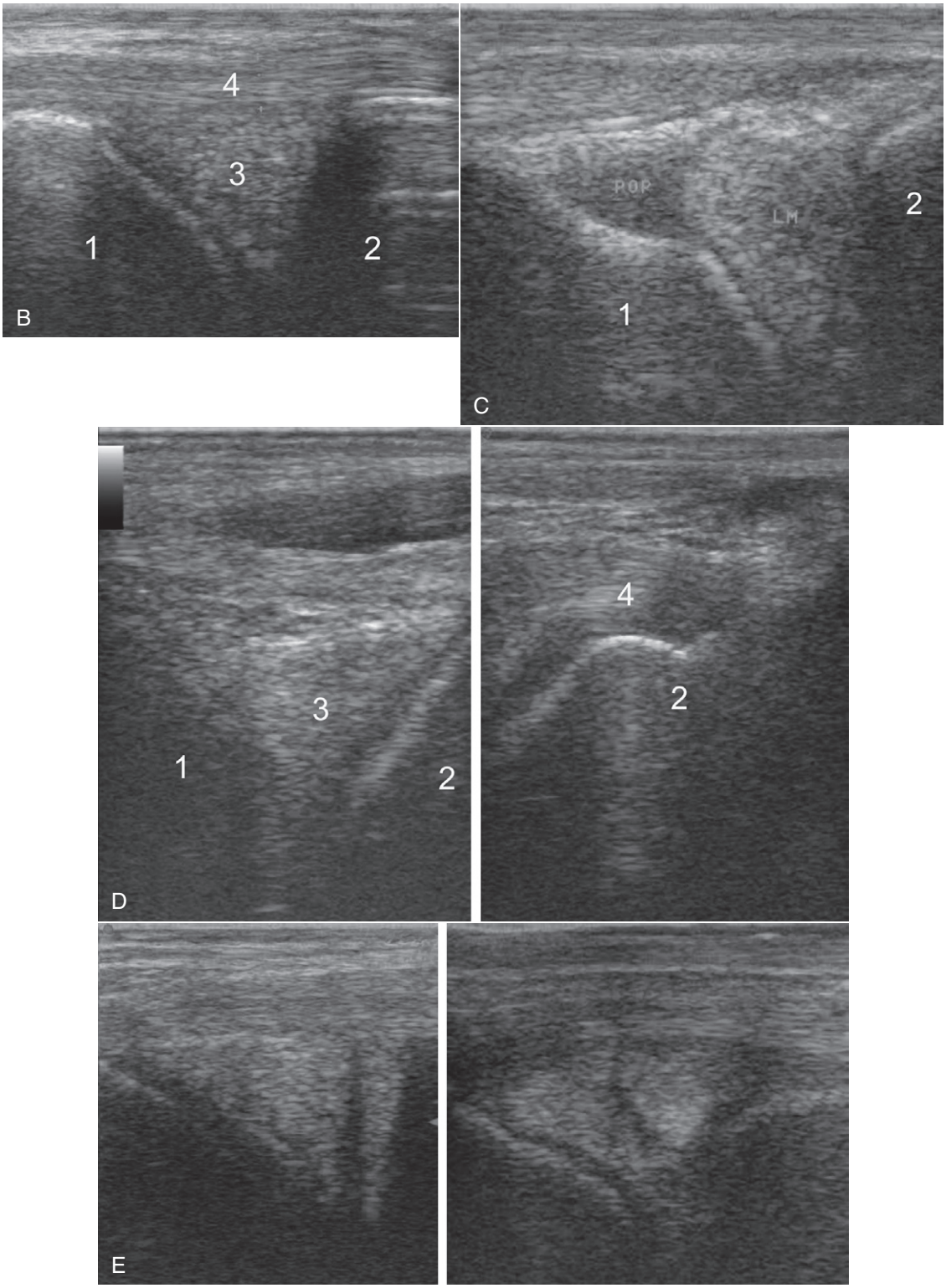


Fig. 19-2, cont'd **B,** Longitudinal image of the stifle at the medial aspect of the joint in a normal horse. *1*, Femur; *2*, tibia; *3*, medial meniscus; *4*, medial collateral ligament. **C,** Longitudinal image at the lateral aspect of the joint in a normal horse. The hypoechogenicity of the popliteus tendon *(POP)* is caused by the oblique orientation of the fibers in relation to the sound beam. *1*, Femur; *2*, tibia; *LM*, lateral meniscus. **D,** Longitudinal *(left)* and transverse *(right)* images of the flexed stifle obtained at the cranial aspect of the joint in a normal horse. *1*, Femur; *2*, tibia; *3*, cranial horn of the lateral meniscus; *4*, cranial meniscal ligament of the medial meniscus inserting on the proximal tibia. **E,** Images of meniscal tears. The linear hypoechoic regions that cross the menisci are indicative of meniscal damage. *Left*, Horizontal tear of medial meniscus. *Right*, Oblique tear of lateral meniscus.

histologic changes and ultrasonographic images has been suggested.[14]

Diseases of the Femoropatellar Joint

Osteochondrosis

Although osteochondrosis lesions develop early in life, osteochondrosis of the femoropatellar joint is a common radiographic finding in both young and older horses.[1-3,15,16] Lateromedial or caudolateral-craniomedial views are necessary to evaluate the femoral trochlea in young horses with synovial distention of the femoropatellar joint. Radiographic signs of osteochondrosis include flattening, irregular subchondral surface, heterogeneous opacity of the trochlear ridge, and presence of bony fragments attached by a radiolucent junction to the bone surface at the cranial aspect of the trochlea (Fig. 19-3). The most common site of osteochondrosis in the equine stifle is the lateral femoral trochlear ridge, especially the middle third.[1-3,15-17] This type of lesion may influence sport and racing performances of affected horses.[18] The trochlear groove may be involved occasionally,[17] with or without associated trochlear ridge involvement, but trochlear groove lesions generally have less clinical significance than ridge defects. Lesions of the medial femoral trochlear ridge are less common (see Fig. 19-3).[3,16,17,19] Patellar lesions are rare and seen mainly with severe trochlear abnormalities.[20] An osseous cystlike lesion has been reported in the proximal medial aspect of the patella in a young horse, but because it was located at the site where most patellar fractures occur, the cause was uncertain.[21]

Taking into account the age of development of osteochondral lesions of the femoral trochlea, radiographic screening of the stifle for osteochondrosis should not be performed before

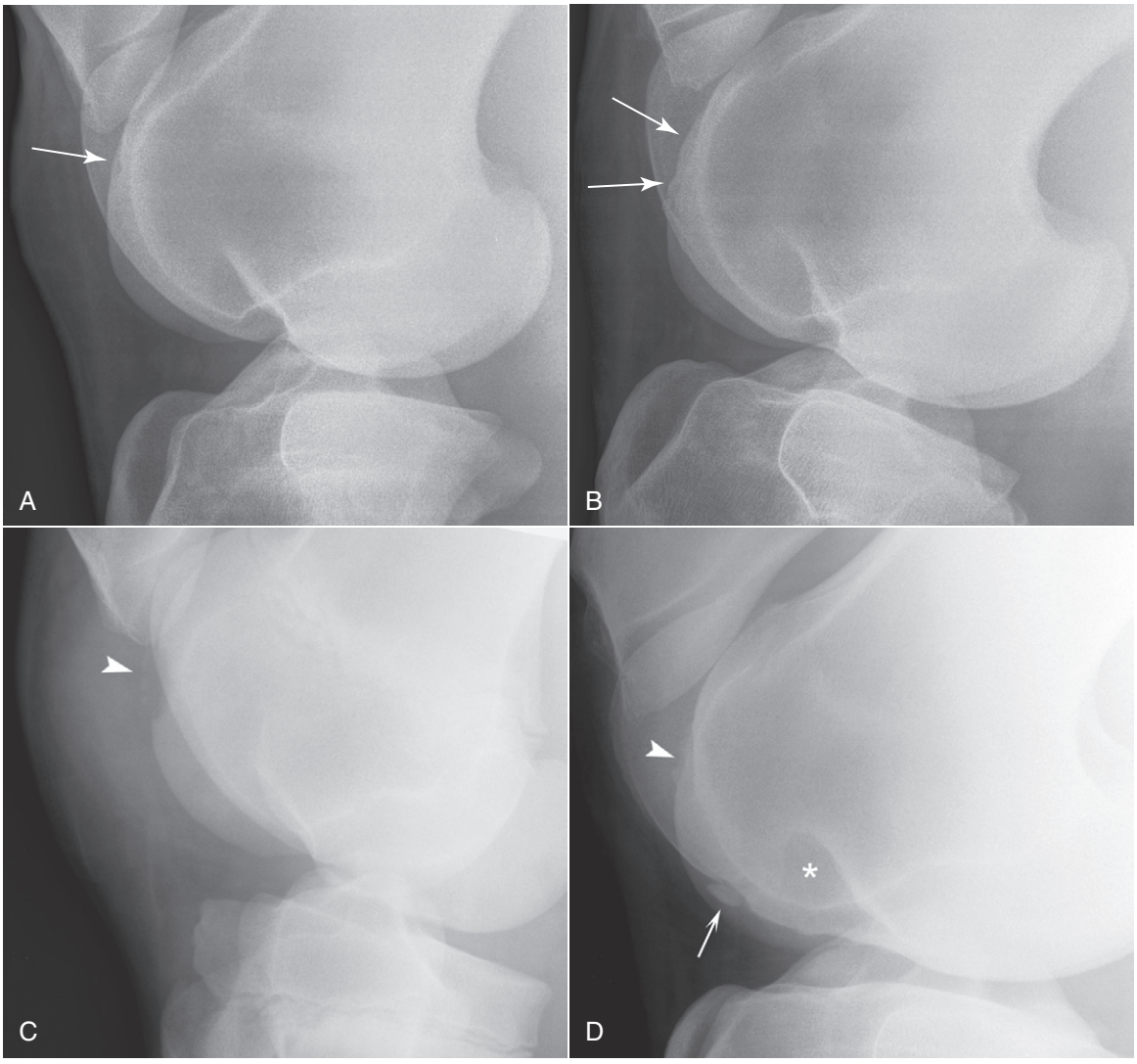


Fig. 19-3 Lateromedial **(A, B, D)** and caudolateral-craniomedial **(C)** radiographs of the stifle of four horses with osteochondrosis of the femoral trochlea. **A,** The lateral trochlear ridge is flat, and there is a small area of radiolucency in the subchondral bone in its middle third *(white arrow)*. **B,** The lateral trochlear ridge is flat, and the subchondral bone has a heterogeneous reduced opacity and an irregular surface in its middle third *(white arrows)*. Slight remodeling of the distal aspect of the patella is also present. **C,** The middle third of the lateral femoral trochlear ridge has a large radiolucent defect with small radiopaque fragments located cranial to it *(white arrowhead)*. The femoropatellar joint is distended. **D,** The lateral trochlear ridge is flat and irregular in its middle third *(white arrowhead)*. The medial trochlear ridge has a bony fragment separated by a radiolucent junction from a defect in the subchondral bone *(white arrow)*. The extensor fossa of the distal femur *(*)* is more conspicuous than normal and abnormally delineated cranially. This radiographic finding is seen in horses with chronic synovial distention and is often associated with osteochondrosis.

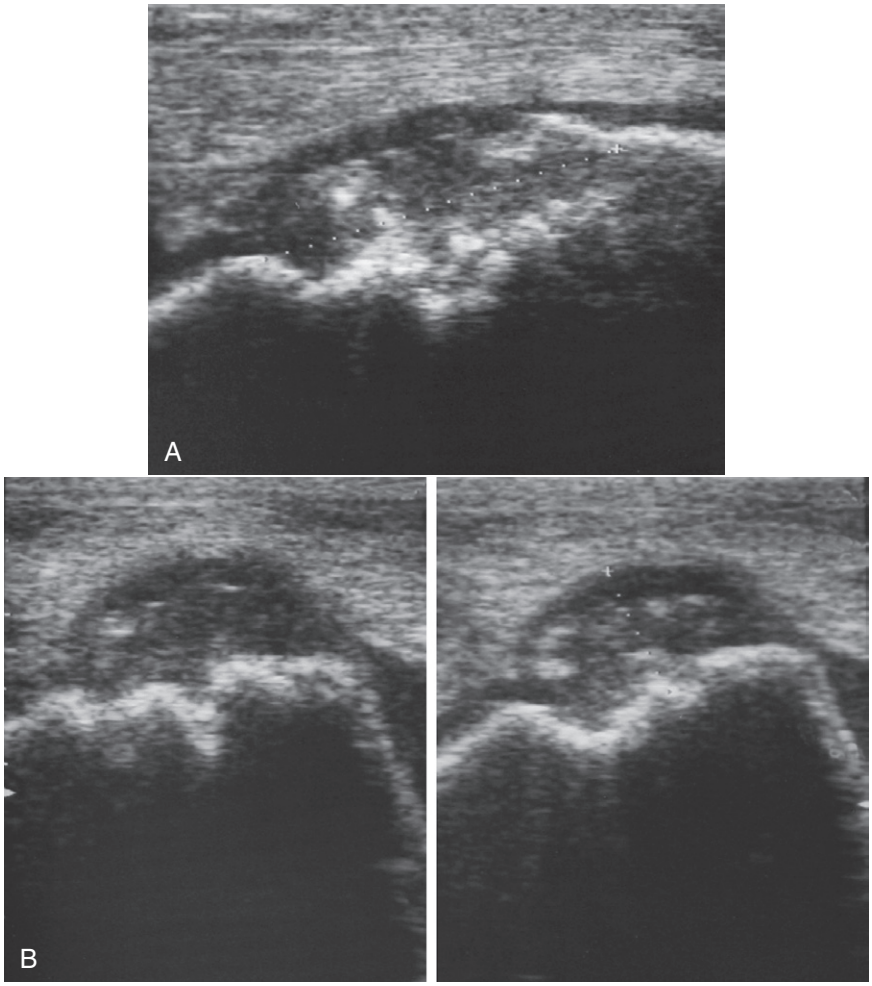


Fig. 19-4 Longitudinal **(A)** and transverse **(B)** ultrasonographic images of the lateral trochlear ridge of a horse with osteochondrosis. The cartilage thickness is uneven. The subchondral bone surface does have a smooth hyperechoic appearance at the site of the lesion because it is not ossified. The subchondral bone is hypoechoic, and the surface is irregular. Compare this figure to the normal femoral trochlea in Figure 19-2, *A*.

8 to 12 months of age.[15] Because of possible bilateral involvement, both stifles should always be examined. Because the femoral trochlea cannot be evaluated on the caudocranial view, and lateromedial and caudolateral-craniomedial views do not allow precise estimation of the mediolateral extent of the lesion, ultrasonographic examination of the cranial aspect of the stifle may be helpful before surgery to assess articular cartilage damage and to better define the long-term prognosis (Fig. 19-4). Because of its higher sensitivity compared to radiography, especially for medial trochlear ridge defects, ultrasonography is also useful in horses where radiographic signs are equivocal.[17]

Patellar Fragmentation

Patellar fragmentation affects the patellar apex and is seen primarily in horses that have undergone medial patellar desmotomy.[22-24] The fragmentation is the consequence of patellar instability after desmotomy.[22] One or multiple bone fragments may be present (Fig. 19-5). Remodeling of the tibial tuberosity at the insertion of the patellar ligaments and remodeling or enthesopathy of the patella may be present in association with fragmentation of the apex.[22-24] An increase in the angle between the proximal articular surface of the patella and the cranial surface of the femur occurs because of patellar instability following medial patellar desmotomy and may be seen in horses with patellar fragmentation.[22]

For patellar fractures, see the "Fractures Involving the Stifle" section.



Fig. 19-5 Lateromedial radiograph of the patella of a horse with patellar fragmentation *(*)* after medial patellar desmotomy.

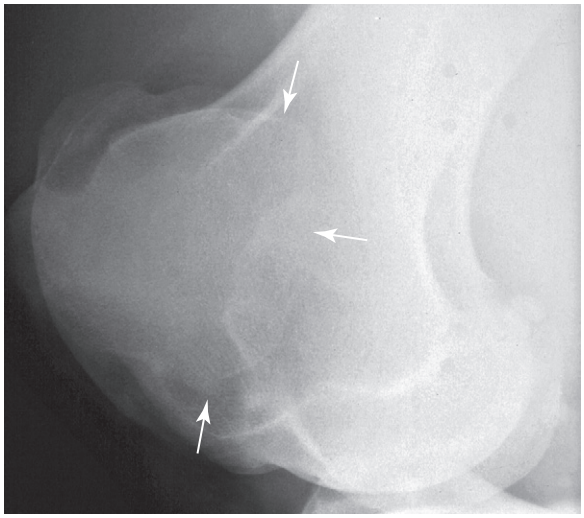


Fig. 19-6 Lateromedial radiograph of the stifle of an adult horse with permanent lateral patellar luxation. The patella *(white arrows)* is superimposed on the femoral trochlea.

Upward Patellar Fixation

No radiographic sign can be used to confirm the clinical diagnosis of recurrent upward patellar fixation. Radiographic examination of the stifle is recommended to exclude other lesions. Horses with recurrent partial upward patellar fixation may have remodeling of the patellar apex on lateromedial radiographs.[20]

Patellar Luxation and Trochlear Dysplasia

Lateral patellar luxation is an uncommon congenital condition and may be unilateral or bilateral.[25] Lateral patellar luxation is often the consequence of femoral trochlear dysplasia with trochlear ridge hypoplasia and a shallow trochlear groove. Lateral patellar luxation may be associated with incomplete ossification of the medial patellar angle.[25] Patellar luxation is recognized in horses of all ages as a cause of a nonpainful gait alteration, more commonly in miniature breeds and ponies.[20,25] Radiographically, lateral patellar luxation is seen as a malpositioning of the patella (Fig. 19-6). An increase in the craniocaudal dimension of the patella on the lateromedial view of the stifle is caused by displacement and rotation of the patella compared with the normal axis of the limb.

Osteomyelitis of the Patella

Chronic osteomyelitis of the patella may develop as a consequence of a chronic abscess at the cranial aspect of the stifle.[20] A cranioproximal-craniodistal view of the patella is essential to assess the full extent of involvement (Fig. 19-7). Radiographic signs are periosteal reaction on the cranial patellar surface and areas of reduced opacity within the patella, resulting in a patchy heterogeneous appearance of the patella (see Fig. 19-7). Ultrasonography can help assess concurrent soft tissue infection, localize the abscess, and confirm bony involvement seen as roughening of the bone surface.

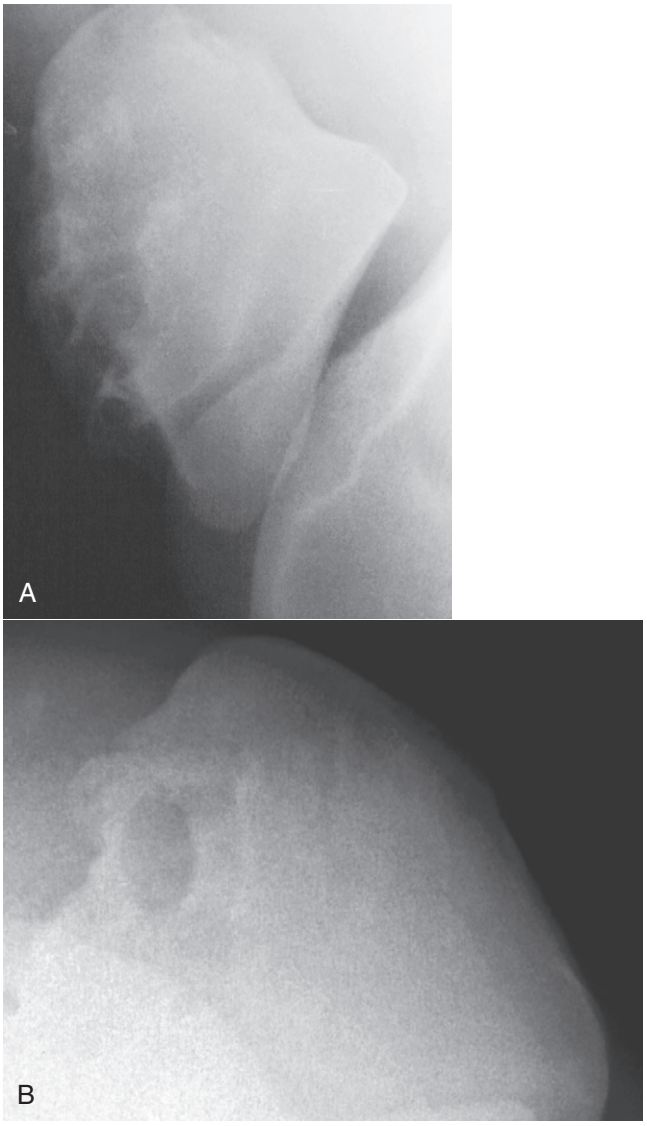


Fig. 19-7 Lateromedial **(A)** and cranioproximal-craniodistal **(B)** radiographs of the patella of a horse with an abscess at the cranial aspect of the stifle and secondary patellar osteomyelitis. The patella is heterogeneous and contains radiolucent areas. The cranial patellar surface is irregular. A large radiolucent defect is seen in the patella in the cranioproximal-craniodistal view.

Diseases of the Femorotibial Joints

Subchondral Cystlike Lesions

Subchondral cystlike lesions of the stifle are juvenile osteoarticular abnormalities but may be seen in horses of any age.[10] Their typical radiographic appearance is a round to oval radiolucent area with well-defined margins within the subchondral bone of the femoral condyles (Fig. 19-8) or, less commonly, the tibial condyles. Subchondral bone cysts may have a distal base of variable extent depending on communication and proximity with the joint space; they may also be surrounded by a sclerotic rim. The subchondral surface of the femoral condyle is flattened at the level of the cyst. Small bone cysts may be difficult to see within the thick femoral condyle, especially in large horses. Flattening or indentation of the femoral subchondral surface may be the only radiographic sign in some horses.[26] Trauma to the medial femorotibial joint may also lead to subchondral bone damage of the medial femoral condyle and induce a radiographically visible radiolucent subchondral cystlike lesion as synovial fluid is pumped into the subchondral bone.[10] Ultrasonography of the femoral condyle surface in the flexed stifle may be used to confirm radiographic suspicion[13] or to evaluate cartilage and subchondral defects better in horses with subtle radiographic changes. Radiographic signs of degenerative joint disease may be present in older horses with a cystlike lesion as a result of chronic synovitis and secondary meniscal damage (Fig. 19-8, *A* and *B*).

The most common location for subchondral cystlike lesions is the weight-bearing area of the medial femoral condyle.[20,27] In the caudocranial view, these cystlike lesions affect the

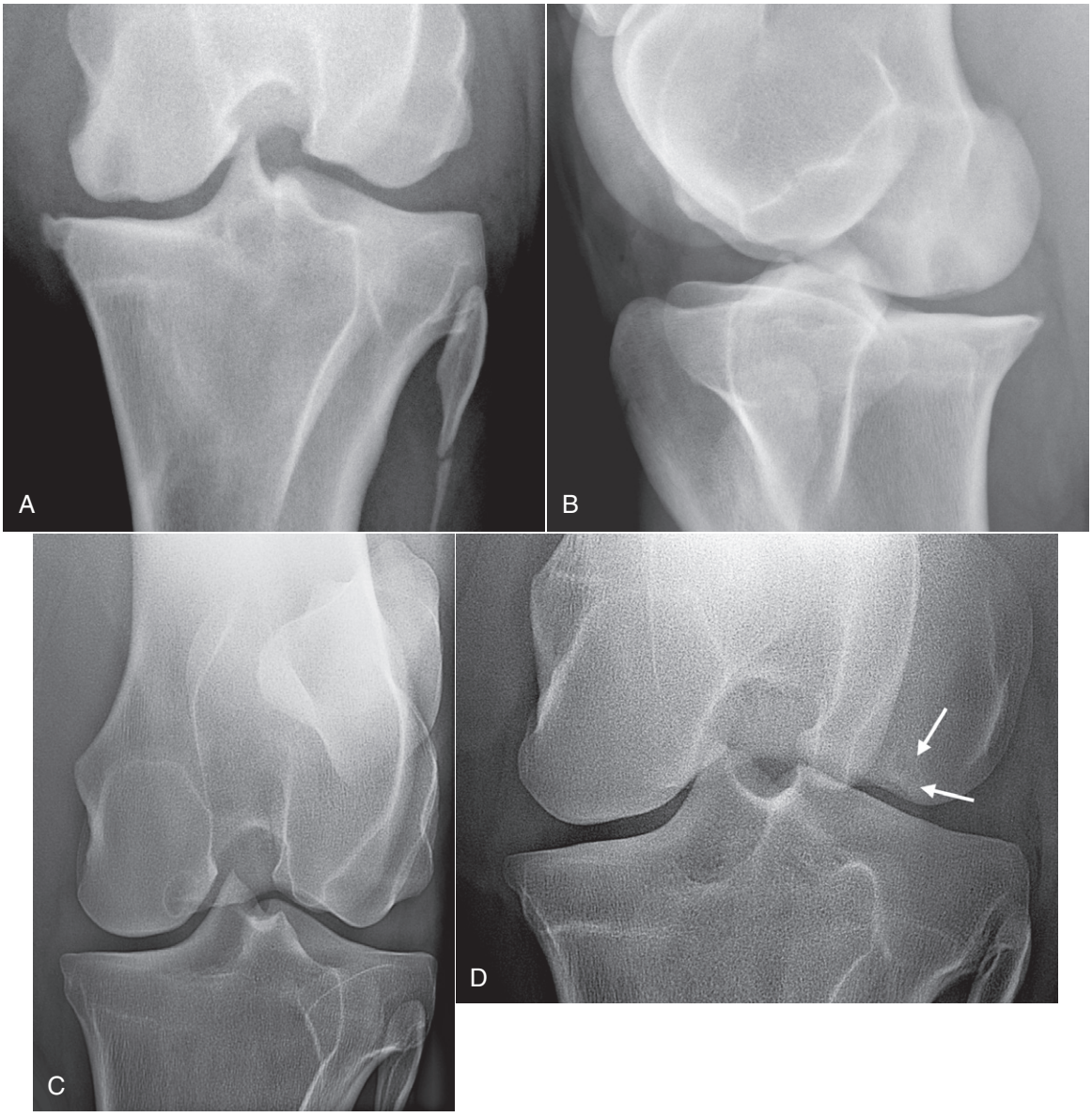


Fig. 19-8 Radiographs of the stifle of three horses with a subchondral bone cyst. Craniocaudal **(A)** and caudolateral-craniomedial **(B)** views of horse 1. There is a large, oval, subchondral radiolucent region with faint marginal sclerosis in the medial femoral condyle. Flattening of the medial femoral condyle is present. Osteophytes on the medial tibial condyle and medial intercondylar eminence indicate degenerative joint disease. Note the normally segmented fibula. Caudocranial **(C)** radiograph of horse 2. An oval, well-marginated radiolucent area surrounded by a thin sclerotic rim is visible in the axial part of the medial femoral condyle. Subchondral cystlike lesions are more commonly found in the central weight-bearing part of the medial femoral condyle, but this axial location can be observed in some horses. Caudocranial **(D)** radiograph of horse 3. Small radiolucent areas surrounded by a faint sclerosis are present in the lateral femoral condyle *(white arrows)*. Subchondral cystlike lesions of the lateral femoral condyle are in most instances more difficult to see compared with those in the medial condyle because of their smaller size.

central portion of the medial condyle most commonly, but they can also be encountered in the more axial aspect of the medial femoral condyle (Fig. 19-8, C). Osseous cystlike lesions have also been reported in the caudal aspect of either femoral condyle in foals.[28] This unusual location may be related to a septic origin. Lateral femoral condyle and proximal tibial cystlike lesions are less common (Fig. 19-8, *D*).[20,29] Subchondral cystlike lesions may be difficult to see on slightly underexposed lateromedial radiographs because of superimposition of the femoral condyles. A caudocranial view of optimal exposure and contrast and/or a caudolateral-craniomedial view are the most useful for confirming and localizing the lesion.

Degenerative Joint Disease

Degenerative joint disease of the femorotibial joint can be a sequel to any stifle injury and is seen commonly in horses with stifle lameness and meniscal damage.[5,7] Involvement of the medial femorotibial joint is more common than involvement of the lateral compartment.[5,20] The most common radiographic signs are remodeling of the tibial and femoral joint margins with production of large-based osteophytes (Fig.19-9; see Fig. 19-8, *A* and *B*). Tibial osteophytes are usually large with smooth margins and tend to form such that their proximal surface is not in the same plane as the tibial plateau. Femoral osteophytes are seen more commonly on the medial

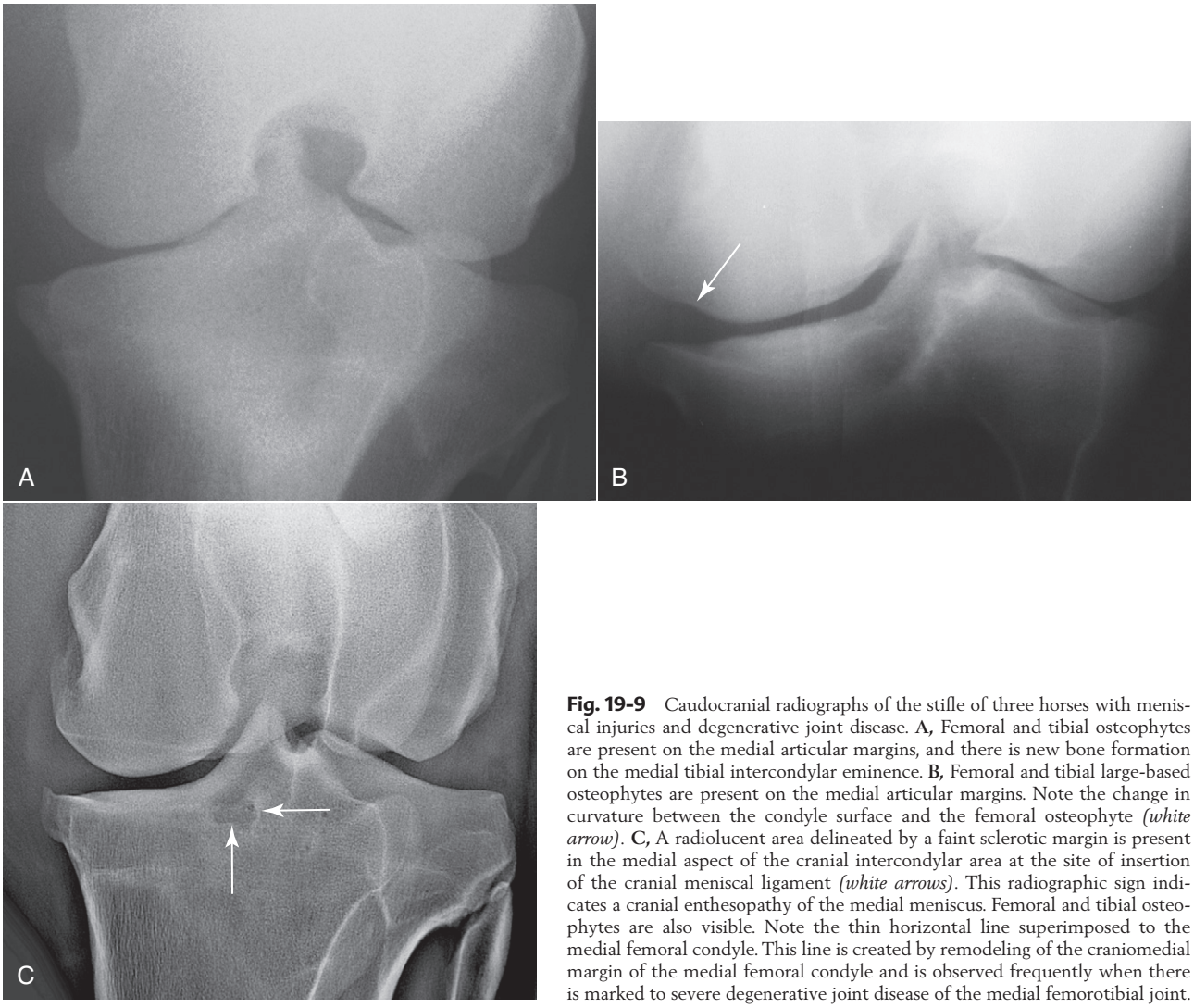


Fig. 19-9 Caudocranial radiographs of the stifle of three horses with meniscal injuries and degenerative joint disease. **A,** Femoral and tibial osteophytes are present on the medial articular margins, and there is new bone formation on the medial tibial intercondylar eminence. **B,** Femoral and tibial large-based osteophytes are present on the medial articular margins. Note the change in curvature between the condyle surface and the femoral osteophyte *(white arrow)*. **C,** A radiolucent area delineated by a faint sclerotic margin is present in the medial aspect of the cranial intercondylar area at the site of insertion of the cranial meniscal ligament *(white arrows)*. This radiographic sign indicates a cranial enthesopathy of the medial meniscus. Femoral and tibial osteophytes are also visible. Note the thin horizontal line superimposed to the medial femoral condyle. This line is created by remodeling of the craniomedial margin of the medial femoral condyle and is observed frequently when there is marked to severe degenerative joint disease of the medial femorotibial joint.

condyle margin. They are usually large-based and, as tibial osteophytes, their distal surface is not in continuity with the arc of the condylar surface (see Fig. 19-9). Narrowing of the femorotibial joint space is less common and is a sign of meniscal prolapse more than a consequence of cartilage thinning in degenerative joint disease (Fig. 19-10). Narrowing of the femorotibial joint space because of marked articular cartilage degeneration is observed only rarely; one instance is following repeated injections of long-acting steroids.[30] Areas of subchondral bone sclerosis and lucencies are mainly seen in advanced articular damage with meniscal injury and prolapse (see Fig. 19-10).

Radiographic Signs of Meniscal and Meniscal Ligament Damage

The menisci, which are of soft tissue opacity, occupy, with the articular cartilage, the space between the distal femoral condyles and the proximal tibial plateau. The menisci cannot be seen radiographically. Therefore meniscal damage can only be suspected when calcification is present in the femorotibial joint space or close to it (Fig. 19-11), or on the basis of secondary bony abnormalities, such as radiolucent areas (see Fig. 19-9, C), new bone formation, or avulsion fragments at the site of insertion of the cranial meniscal ligaments on the proximal tibia (Fig. 19-12, see page 358).[5] New bone formation cranial to the medial intercondylar eminence of the tibia has been reported as the most frequent radiographic finding in horses with meniscal damage diagnosed using arthroscopy (Fig. 19-13, see page 358).[5]

The imaging technique of choice to evaluate meniscal and meniscal ligament damage is ultrasonography (see Fig. 19-2). When the site of pain responsible for the lameness has been proved to be the stifle, or when distention of the femorotibial joint is present, a radiographically normal stifle should not be considered normal anatomically because soft tissue injuries, in particular meniscal damage, are a frequent cause of lameness.[6,7]

Radiographic Signs of Cruciate Ligament and Collateral Ligament Damage

Indirect radiographic signs of cruciate ligament damage are seen as radiolucent areas at the ligament insertion sites on the distal femur or bone remodeling at the tibial insertions (Fig. 19-14). In chronic damage, there can be mineralization of the injured ligament.[5] Avulsion of bone at the femoral and tibial cruciate ligament insertions has also been reported.[31-34] Fractures of the medial intercondylar eminence (see Fig. 19-14, p. 358) are described most commonly in association with cranial cruciate ligament damage and have been suggested to be caused by lateral pressure of the medial condyle more than avulsion.[5]

Collateral ligament damage of the stifle as a consequence of acute trauma does not result in any radiographic abnormality except joint swelling. In acute complete traumatic



Fig. 19-10 Close-up caudocranial view of the stifle of a horse with severe medial meniscal damage, calcification, and prolapse. The medial femorotibial joint space is narrowed, and the proximal tibial condyle is sclerotic because of a prolapse of the medial meniscus. Calcified meniscal material is present outside the articular space at the medial aspect of the joint. The medial femoral and tibial joint margins have large osteophytes.

collateral ligament rupture, joint instability can be assessed using a caudocranial projection with the stifle under stress.[6] Ultrasonography allows assessment of the medial and lateral collateral ligaments (see Fig. 19-2, *B*). Chronic enthesopathy may be visible on caudocranial radiographic views as a change in shape or an increased irregularity of the surface of the medial or lateral femoral epicondyles.

Fractures Involving the Stifle

Patellar Fractures

Patellar fractures involve the medial angle of the patella most commonly.[35,36] These fractures occur mainly in steeplechase and eventing horses when the flexed joint strikes a fixed fence.[35,36] Fractures of the medial angle may be incidental and not related to lameness. These fractures may be suspected on the lateromedial view because of an area of heterogeneously increased opacity in medial patellar angle (Fig. 19-15, p. 359). A cranioproximal-craniodistal view of the stifle allows confirmation of the diagnosis and a complete assessment of the extent and morphologic features of the fracture. Patellar fracture may be associated with fractures of the trochlear ridges of the femur.[20] Ultrasonographic examination adds valuable information in patellar fractures by documenting associated soft tissue injuries and defining the anatomic origin of avulsed fragments; that is, parapatellar fibrocartilages, patellar ligaments, and distal enthesis of the quadriceps femoris muscle.

Tibial and Femoral Fractures

Fractures of the tibial tuberosity are the most commonly reported fractures involving the proximal tibia in adult horses.[20,37] Fractures involving the intercondylar eminence or the caudal aspect of the proximal tibia are seen in association with cruciate ligament damage and often involve the ligament insertion sites.[31-34] The proximal aspect of the tibial diaphysis is the most common site for incomplete fracture of the tibia,

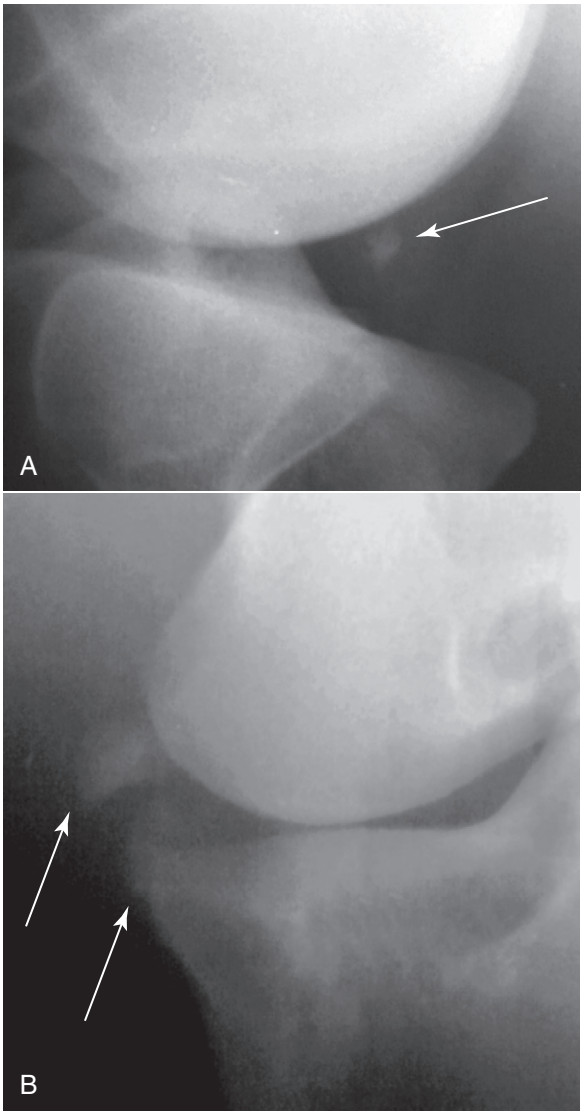


Fig. 19-11 Lateromedial **(A)** and caudocranial radiographs **(B)** of the stifle of two horses with meniscal calcification. **A,** A small radiopaque focus *(white arrow)* is present between the femoral condyle and the caudal aspect of the tibial plateau compatible with calcification in the caudal horn of the medial meniscus. **B,** Two large radiopaque bodies *(white arrows)* at the medial aspect of the medial femorotibial joint correspond to calcified portions of a prolapsed medial meniscus.

which usually begins at the lateral aspect of the bone and spirals distally (Fig. 19-16, p. 359).[20,38] Radiographic diagnosis of an incomplete fracture may be challenging even if several oblique views are made. Complete rest and repeat radiographs approximately 7 to 10 days after the onset of the acute lameness are indicated. At this stage the fracture line becomes more visible because of resorption of the fracture margins. In racehorses, tibial fatigue fractures can also be encountered (see Fig. 19-36, p. 367 in the "Fractures of the Distal Tibia and Malleolar Fractures" section). The most common radiographic signs at the site of the stress fracture are periosteal bony proliferation, thickening of the cortical bone and remodeling of the adjacent cancellous bone.

Fractures of the femur involving the distal epiphysis are uncommon in adult horses. Trochlear ridge fractures are seen as free sharp fragments and a bony defect in the trochlea or as radiolucent lines in the trochlear ridge in incomplete undisplaced fractures. These fractures result from direct external trauma and may be associated with patellar fractures.[20]

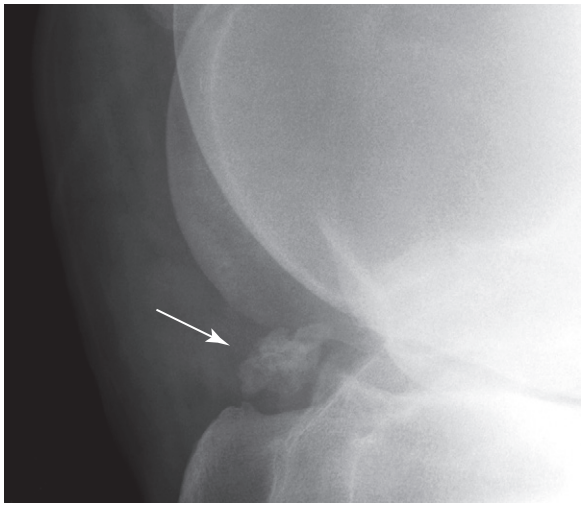


Fig. 19-12 Caudolateral-craniomedial radiograph of the stifle in a horse with severe medial meniscal damage and prolapse. A large bony fragment is visible at the cranial aspect of the femorotibial joint space *(white arrow)*, which represents an old avulsion fragment at the cranial meniscal ligament attachment.

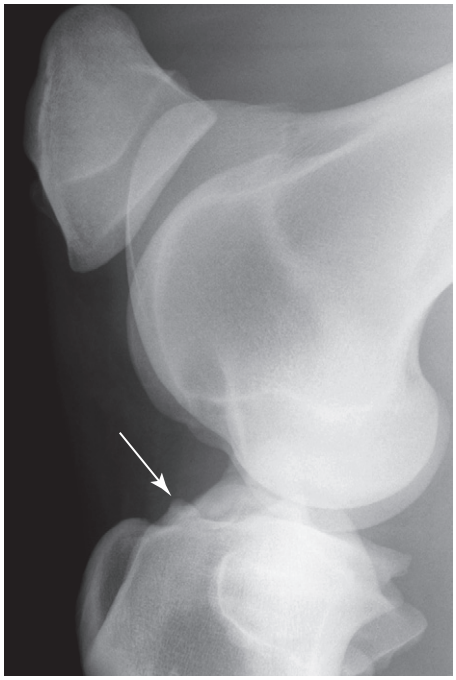


Fig. 19-13 Flexed lateromedial radiograph of an equine stifle. An osseous proliferation is present cranial to the tibial intercondylar eminence *(white arrow)*. Ultrasonographically, there was a horizontal fissure and a partial prolapse of the medial meniscus and damage to the medial cranial meniscal ligament.

Femoral avulsion fractures of the origin of the common tendon of the peroneus tertius and the extensor digitorum longus are reported in foals.[39-40]

Fibular Fractures

Fibular fractures have been reported as a cause of lameness.[20] Care should be taken not to confuse the normal radiolucent line traversing the proximal fibula as a result of incomplete ossification with a fracture line (see Fig. 19-8, *A*). Callus formation is a useful radiographic sign of the presence of a fracture.[20]

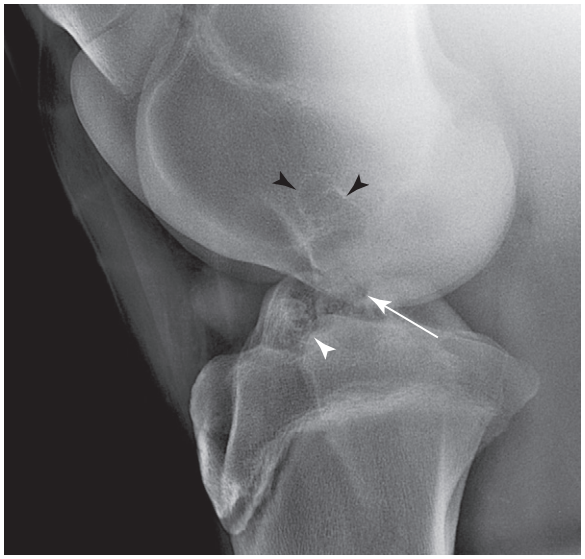


Fig. 19-14 Lateromedial radiograph of the stifle of a 1-year-old colt with a history of trauma 5 months before. The soft tissue swelling located cranial to the femorotibial joint space and without border effacement of the patellar ligaments suggests severe femorotibial joint effusion. Severe opacity changes are visible at the cranial and central tibial intercondylar areas *(white arrowhead)*. The caudal aspect of the medial intercondylar eminence is difficult to identify because of increased and heterogeneous opacity seen in the intercondylar area *(white arrow)*. In other radiographic views and based on ultrasonographic examination, there were enthesopathies of the cranial meniscal ligaments and a fracture of the medial intercondylar eminence suggesting cranial cruciate ligament damage. The large radiolucent area surrounded by a thin sclerotic rim visible in the craniproximal aspect of the femoral intercondylar fossa *(black arrowheads)* suggests an associated chronic femoral enthesopathy of the caudal cruciate ligament.

Miscellaneous Conditions Involving the Stifle

Calcinosis Circumscripta

Calcinosis circumscripta is localized deposition of calcium in small nodules in subcutaneous tissues or attached to tendons or joint capsules.[41] The lesions of calcinosis circumscripta appear grossly as hard, spherical, nonpainful, subcutaneous, or periarticular swellings. The etiology of calcinosis circumscripta is unknown but thought to be of traumatic origin.[42] In the horse, the predilection site is the lateral aspect of the stifle close to the extensor groove of the tibia.[42] The lesion is visible radiographically as a well-circumscribed, roughly oval accumulation of granular mineral opacities at the lateral aspect of the proximal tibia (Fig. 19-17). Calcinosis circumscripta may be an incidental finding because the lesion rarely causes lameness.[42] Most commonly, there is a firm, nonpainful swelling that has been increasing slowly in size. The lesions are usually bilateral, and radiographic examination of the contralateral limb is important if surgical removal is considered.

Septic Arthritis and Osteomyelitis

Septic arthritis is inflammation of a joint caused by bacterial invasion and proliferation.[43] Septic arthritis may occur in foals or adult horses. Hematogenous spread is the most common cause of septic arthritis in foals, whereas septic arthritis in adult horses is usually a consequence of penetrating wounds, injection, or surgery.[43]

Infection of the stifle joint in adult horses is rare. Periarticular infection and abscess after trauma and penetrating wounds are more common than bacterial joint invasion.[43] In foals, the femoropatellar joint and the femorotibial joints are common sites of septic arthritis, and the femur is one of the bones most commonly affected by hematogenous osteomyelitis.[44] Bone changes appear late in the condition in adult horses, whereas

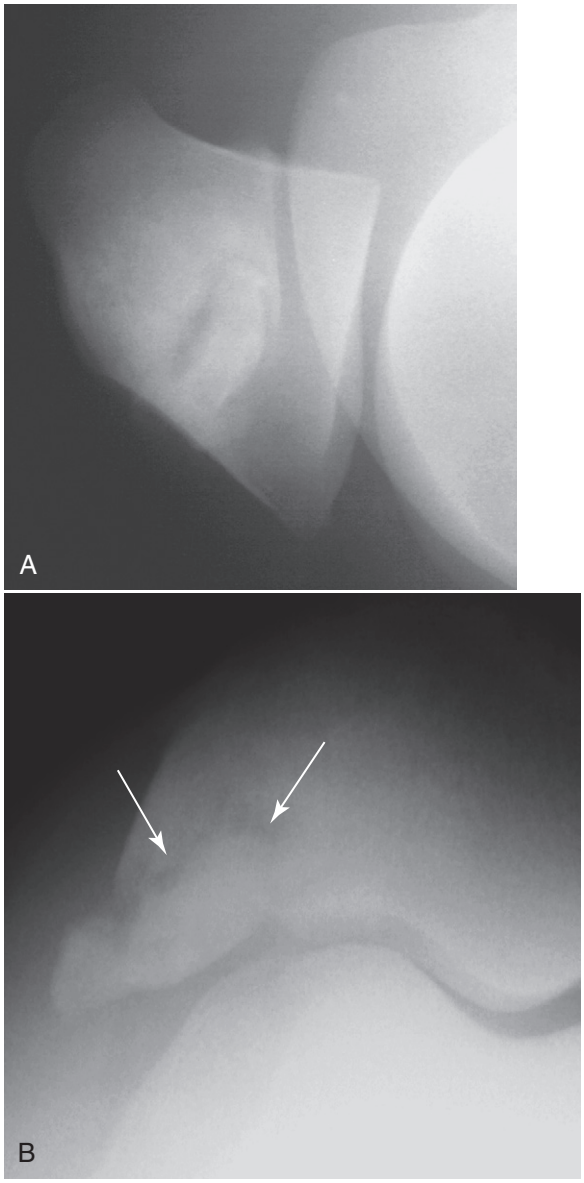


Fig. 19-15 Flexed lateromedial **(A)** and cranioproximal-craniodistal **(B)** radiographs of the stifle of a horse with a chronic nondisplaced fracture of the medial aspect of the patella. **A,** The patella has increased opacity and a radiolucent line at the level of the medial angle. The medial articular surface is irregular and interrupted by the radiolucent line. **B,** The fracture of the medial angle of the patella is seen as an ill-defined radiolucent line *(white arrows)* separating two bony fragments. The fracture involves the medial articular surface of the patella.



Fig. 19-16 Caudocranial radiograph of the tibial diaphysis of a horse with a 1-week-old incomplete fracture of the tibia. A radiolucent line begins at the lateral aspect of the proximal tibia and spirals distally through the entire tibial diaphysis *(white arrowheads)*.



Fig. 19-17 Caudolateral-craniomedial stifle radiograph of a young horse with calcinosis circumscripta. A large cluster of calcified granular material is located at the lateral aspect of the proximal tibia.

they occur earlier in foals. Concurrent septic arthritis and osteomyelitis is common in foals, and foals with osteomyelitis without septic arthritis are usually older.[44] In the same way, foals with a single bone lesion tend to be older than those with multiple bone lesions.[44] Bone changes attributable to osteomyelitis may have a physeal or epiphyseal location in foals and are located differently depending on the joint infected concomitantly. When the femoropatellar joint is affected, osteolysis is mainly seen on the patellar articular surface (Fig. 19-18). Subchondral bone abnormalities on the femoral trochlea may be more difficult to assess because the trochlear ridges normally have an irregular bone surface in young foals during ossification. Femorotibial involvement is often uniaxial (medial or lateral). Bone involvement is seen as ill-defined radiolucent areas in the subchondral bone of the tibial plateau and/or the femoral condyles, with the medial femoral condyle being affected more commonly.[28,44] Another specificity of these subchondral radiolucent areas is their potential location in the non–weight-bearing part of the femoral condyles. Physeal osteomyelitis in foals appears as widening of the radiolucent physis and ill-defined physeal margins associated with local swelling. Well-defined radiolucent areas in the subchondral bone may remain evident as a sequel of osteomyelitis when infection is eliminated.

Periarticular Soft Tissue Swelling

Localized periarticular soft tissue swelling is common in the stifle region. Main causes are seromas, hematomas, and

abscesses, mainly occurring after penetrating injuries, falls, or trauma during jumping. Radiographic examination is used to assess concurrent bone involvement. Ultrasonography is the technique of choice to localize the swelling and establish its relation to the joint cavity. The nature of the content may be confirmed by aseptic centesis of the swelling. The increased contrast resolution of computed radiography allows localization of the soft tissue swelling by using the border effacement of patellar ligaments and menisci and looking at the position relative to the patellar fat pad (see Fig. 19-1).



Fig. 19-18 Lateromedial radiograph of the patella of a foal with septic arthritis of the femoropatellar joint. The articular surface of the patella is very irregular, and there is severe lysis of subchondral bone.

THE TARSUS

Radiographic Examination

A standard radiographic series of the tarsus includes lateromedial, dorsoplantar, dorsal 35- to 45-degree lateral-plantaromedial and plantar 35- to 45-degree lateral-dorsomedial views. A flexed lateromedial view may be used to visualize the proximal articular surface of the talus. A plantaroproximal-plantarodistal view of the tarsus is useful for assessing lesions of the calcaneus, in particular of the sustentaculum tali and tuber calcanei. This view may also be used to image the proximal talar tubercle and the talocalcaneal joint. Because of the complex anatomy of the tarsus, supplementary oblique views may be necessary to project some specific locations of disease better and diagnose or fully document tarsal fractures.

Because of the paucity of soft tissues around the tarsal joint, a grid is not needed to obtain good-quality radiographs. A grid may be used when major soft tissue swelling is present around the joint, especially in draft horses.

Diseases of the Tarsocrural Joint

Osteochondrosis and Subchondral Cystlike Lesions

The tarsus is a common location for osteochondrosis lesions.[1-3,16,19] Although osteochondral lesions of the tarsocrural joint may be seen after 5 months of age, osteochondrosis is a frequent radiographic finding in horses of any age and in many breeds.[2,3,15,16,19] Radiographic abnormalities are not always associated with clinical signs.[20,45,46] Horses frequently have bilateral radiographic abnormalities, especially when fragments are present.[2] In the tarsus, osteochondrosis may affect different sites (Fig. 19-19), with the intermediate cochlear ridge of the distal tibia being affected most commonly (Fig. 19-20).[2,3,16,19] Less commonly, fragments become free in the joint and are seen in the distal aspect of the joint

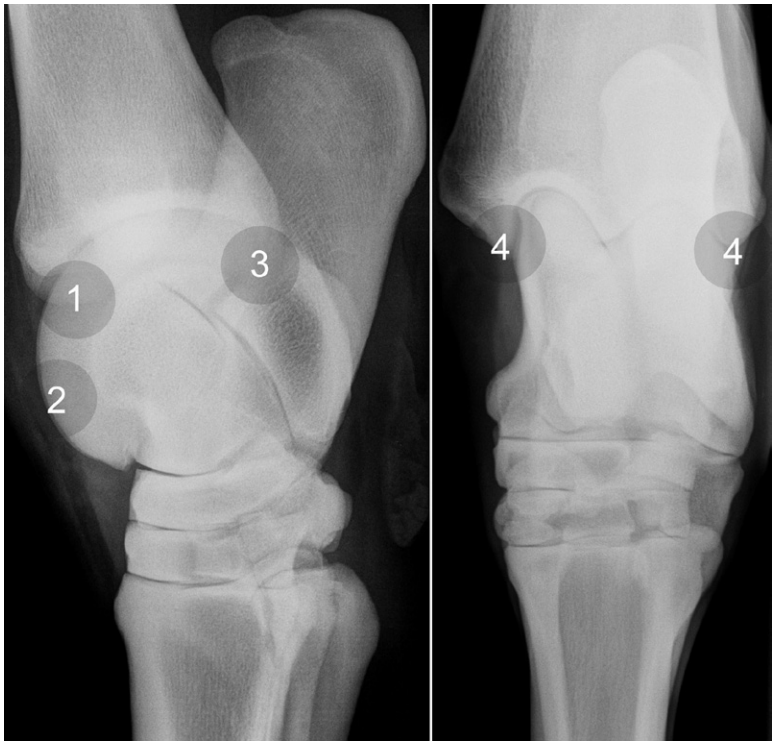


Fig. 19-19 Sites of osteochondrosis in the equine tarsus. *1*, Intermediate ridge of the tibial cochlea; *2*, ridges of the talus; *3*, proximal tubercle of the talus; *4*, tibial malleoli.

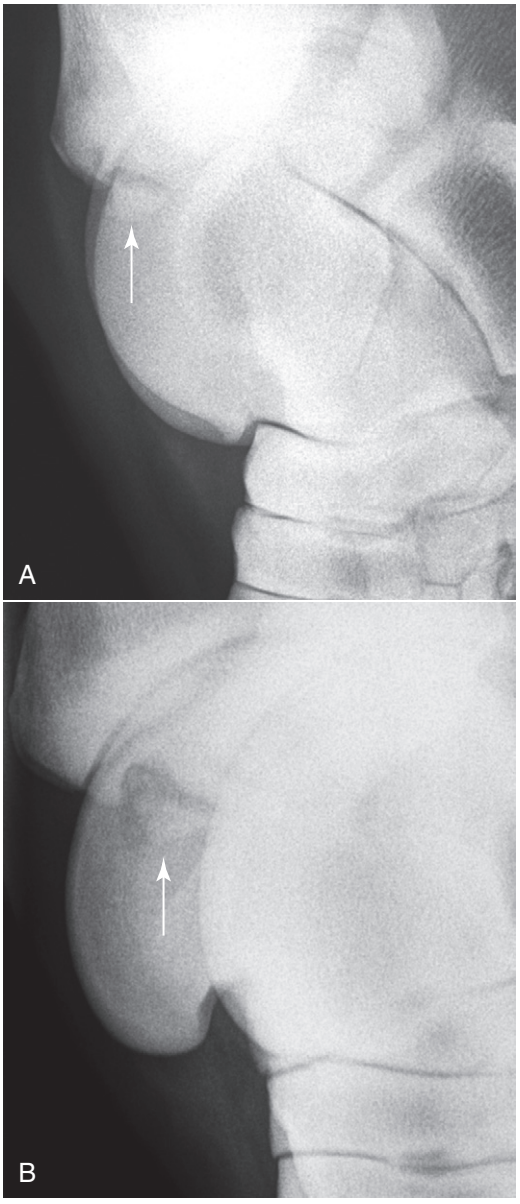


Fig. 19-20 Lateromedial **(A)** and plantarolateral-dorsomedial **(B)** radiographs of the tarsus of a horse with osteochondrosis of the intermediate ridge of the tibia. A bony fragment is visible distal to a concave defect in the intermediate ridge of the tibial cochlea *(white arrow)*. The fragment is easier to see on the plantarolateral-dorsomedial view because only the lateral trochlear ridge of the talus is superimposed on it.

pouches at the dorsal or medial aspect of the distal talus and central tarsal bone regions. In some horses with minor involvement of the distal tibia, a roughening and a radiolucent concave defect may be the only radiographic abnormality. Because shape of the dorsal intermediate cochlear ridge of the tibia changes between individuals and depending on the angle of the x-ray beam, a flat distal profile may be seen on the plantarolateral-dorsomedial view in normal horses. Larger radiolucent defects with no adjacent bony fragment are most commonly seen in radiographs of horses wherein the fragment has already been removed (Fig. 19-21).

The talar ridges are also a site of osteochondrosis (Fig. 19-22).[2,3,16,19,20] Radiographically, the affected ridges have a flattened or irregular contour and may have a heterogeneous opacity. Sometimes bony fragments are present adjacent to the regions of abnormal contour. Large fragmentations of the distal aspect are more common on the lateral ridge of heavy

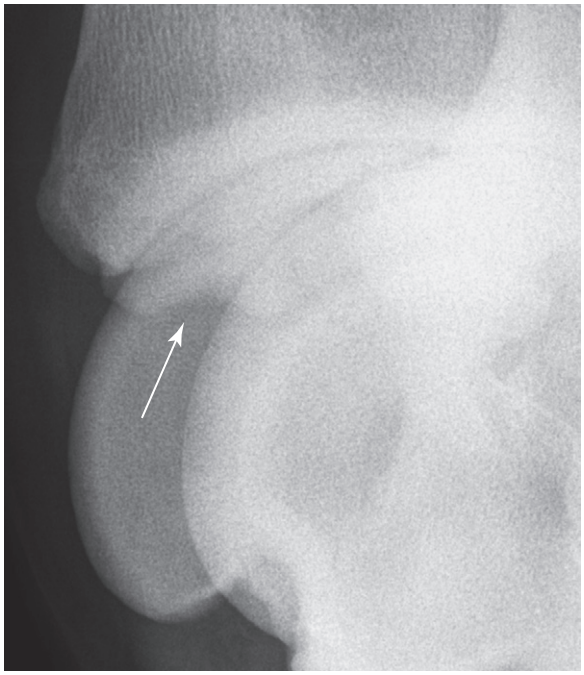


Fig. 19-21 Postoperative plantarolateral-dorsomedial radiograph of the tarsus of a horse wherein a fragment arising from the intermediate ridge of the tibia had been removed surgically. A concave radiolucent defect *(white arrow)* is present where the fragment resided.

horses and are usually clinically significant (Fig. 19-23).[45] Central smooth depressions without subchondral bone changes are seen commonly in clinically normal horses, especially in the medial talar ridge (Fig. 19-24). Semicircular subchondral defects are also relatively common, especially in the medial talar ridge, and are rarely significant clinically,[3] although this abnormality has been reported in association with severe lameness when in the weight-bearing portion.[47]

Other sites of tarsal osteochondrosis are the medial and lateral tibial malleoli and the medial proximal tubercle of the talus.[48,49] Horses affected by osteochondrosis of the tibial malleoli have subchondral defects and osteochondral fragments with smooth contours separated from the malleolus by a radiolucent gap. The fragments may be located axially or distal to the malleolus (Fig. 19-25, p. 363). Involvement of the medial malleolus is more common.[45] A dorsolateral-plantaromedial view obtained with less obliquity (15 to 30 degrees) should be added if there is clinical or radiographic suspicion because routine radiographic views have a low sensitivity for detecting malleolar osteochondrosis. Because of its higher sensitivity,[50] ultrasonography may also be considered to confirm irregular malleolar bone contour.

Osteochondrosis at the proximal tubercle of the talus appears either as a separate bony fragment or as an enlarged tubercle (Fig. 19-26, p. 363).[49] These abnormalities are better seen on the lateromedial view. A plantarolateral-dorsomedial view obtained with a degree of obliquity of approximately 20 degrees in relation to the sagittal plane will highlight the proximal tubercle of the talus tangentially. Despite marked radiographic changes seen commonly, osteochondrosis of the proximal tubercle of the talus usually has no clinical significance.[49]

Subchondral cystlike lesions are a juvenile osteoarticular abnormality but may also develop in skeletally mature horses after trauma or sepsis.[3,10,51] The occurrence of cystlike lesions in the tarsocrural joint is lower than in the stifle. In the tarsus, subchondral cystlike lesions are seen radiographically as round, usually small radiolucent areas, often surrounded by a thin

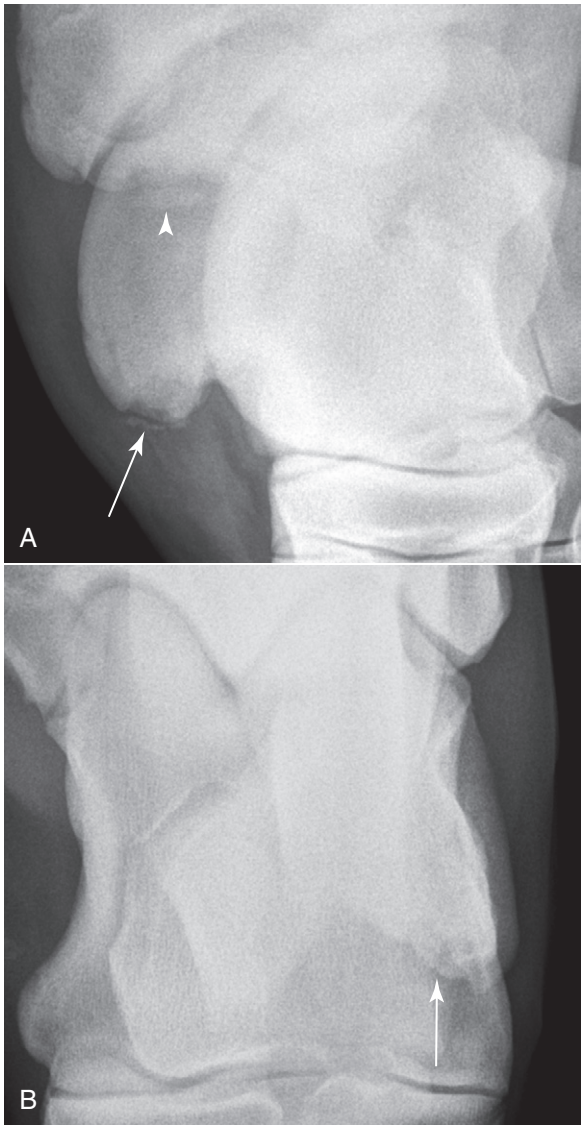


Fig. 19-22 Plantarolateral-dorsomedial **(A)** and dorsoplantar **(B)** radiographs of the tarsus of a young horse with osteochondrosis of the intermediate ridge of the tibia and the lateral talar ridge. A bony fragment is present adjacent to the intermediate ridge of the tibia on the plantarolateral-dorsomedial oblique view *(white arrowhead)*. A defect in the distal extremity of the lateral trochlear ridge is visible on both views *(white arrow)*. At this level the bone surface is irregular, and two thin bony fragments are attached by a radiolucent junction to the edge of the ridge.



Fig. 19-23 Lateromedial radiograph of the tarsus of a draft horse with osteochondrosis of the lateral talar ridge and distal intertarsal degenerative joint disease. Three large fragments are present on the lateral ridge of the talus. The fragmentation involves the dorsal aspect of the entire distal third of the trochlear ridge.

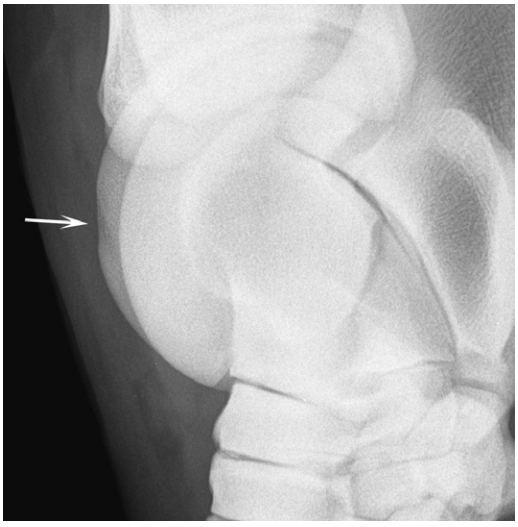


Fig. 19-24 Lateromedial radiograph of the tarsus of a clinically normal horse. A small area of flattening *(white arrow)* is present at the junction between the middle and distal third of the medial trochlear ridge of the talus. This is an incidental radiographic finding without clinical significance.

sclerotic rim in the distal tibia or talus (Fig. 19-27, p. 364). In adult horses cystlike radiolucencies may develop occasionally after subchondral trauma, mainly in the distal tibia. Occult subchondral cystlike lesions, not visible on radiographs and possibly of septic origin, are also reported in the tarsocrural joint.[52]

Collateral Ligament Injury

Injuries to the tarsocrural collateral ligaments are the consequence of a sprain of the tarsus.[6] There is usually acute lameness and severe articular swelling. Most horses have no radiographic signs at the onset of lameness except swelling of the joint. Avulsion fragments are seen occasionally at the tibial malleoli (Fig. 19-28, p. 364). The diagnosis of ligament damage is confirmed sonographically (Fig. 19-29, p. 364).[6,11,12] Ultrasonography allows detailed assessment of the long and short collateral ligaments at the medial and lateral aspect of the joint (see Fig. 19-29). Radiographic signs of enthesopathy appear in most instances as bony proliferation at the sites of attachment of the collateral ligament and may be seen in chronic sprains or 4 to 6 weeks after trauma.[20,51] Collateral ligament injuries may lead to secondary degenerative joint disease (Fig. 19-30, p. 365).

Diseases of the Distal Intertarsal and Tarsometatarsal Joints

Degenerative Joint Disease

Tarsal degenerative joint disease is common. The distal intertarsal and tarsometatarsal joints are affected most frequently, either alone or in combination.[20,53-55] Although degenerative

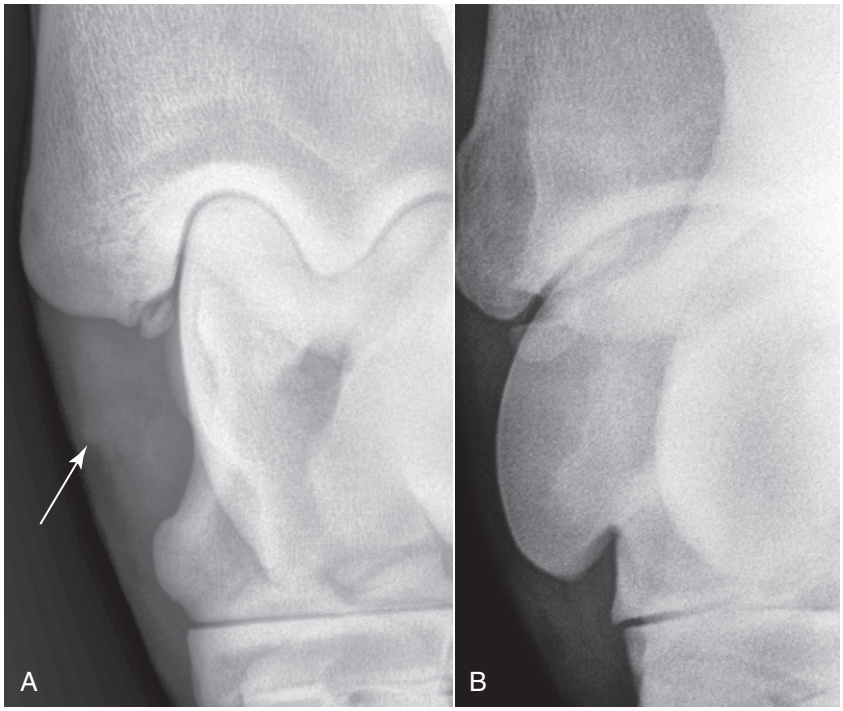


Fig. 19-25 Radiographs of two horses with osteochondrosis of the malleolus. **A,** Dorsal 25-degree lateral-plantaromedial view of the tarsus. An osteochondral fragment with smooth margins is present distal and axial to the medial malleolus. There is swelling of the tarsocrural joint characterized as increased soft tissue opacity medial to the talus *(white arrow)*. **B,** Plantarolateral-dorsomedial oblique view of the tarsus. An osseous fragment with smooth margins is present at the distal aspect of the lateral malleolus, only partially superimposed on the dorsal aspect of the lateral talar ridge. Compare the position of this fragment to the location of a fragment coming from the intermediate ridge of the tibial cochlea as in Figure 19-22, *A*.

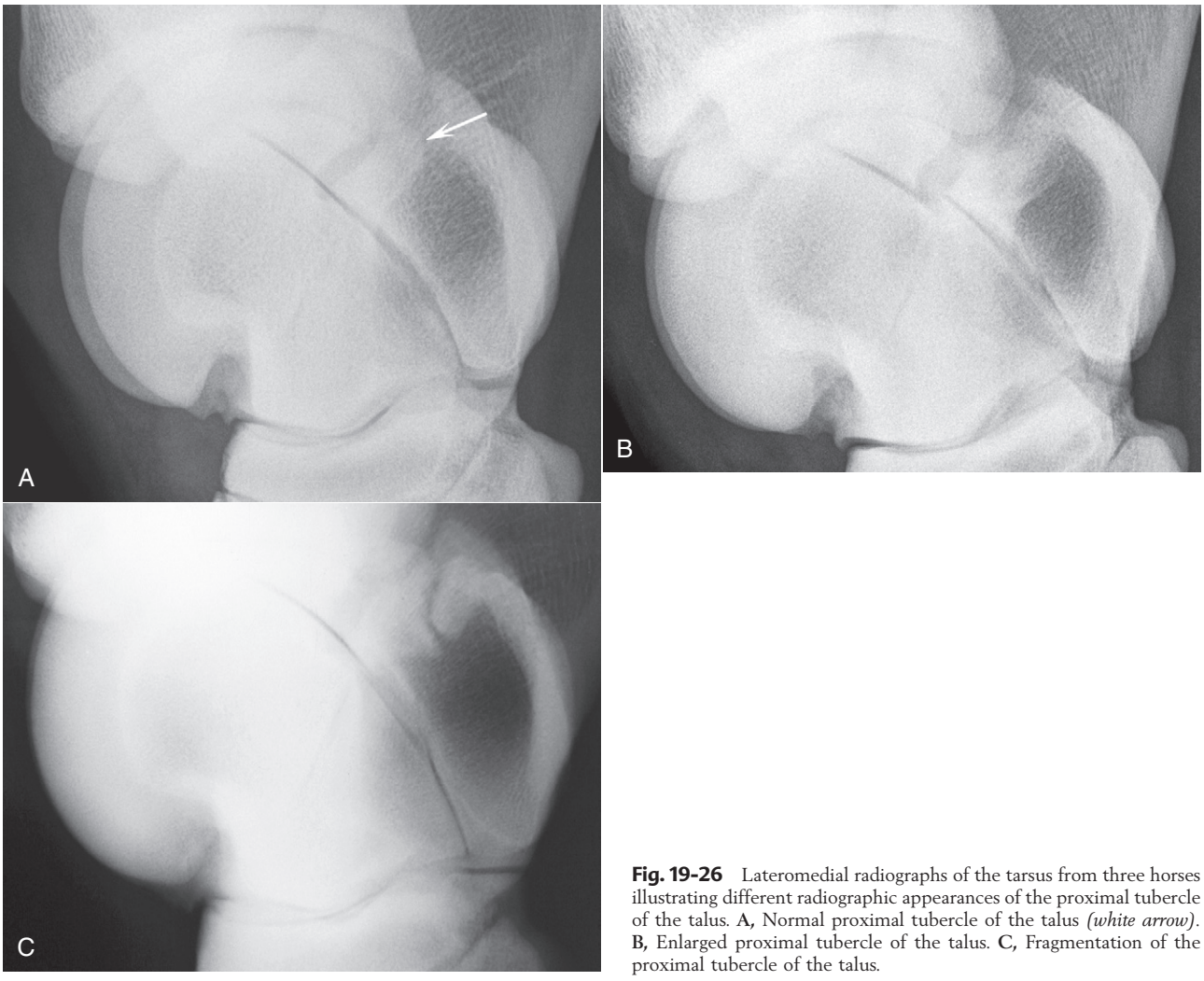


Fig. 19-26 Lateromedial radiographs of the tarsus from three horses illustrating different radiographic appearances of the proximal tubercle of the talus. **A,** Normal proximal tubercle of the talus *(white arrow)*. **B,** Enlarged proximal tubercle of the talus. **C,** Fragmentation of the proximal tubercle of the talus.

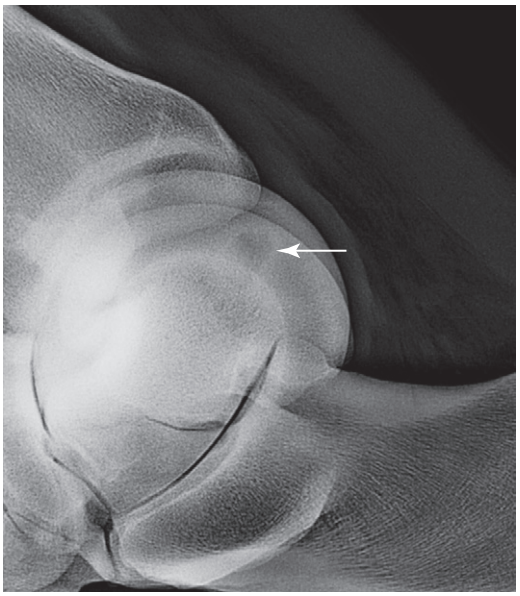


Fig. 19-27 Flexed lateromedial radiograph of the tarsus. There is a radiolucent subchondral cystlike lesion in the weight-bearing portion of the lateral talar ridge *(white arrow)*.

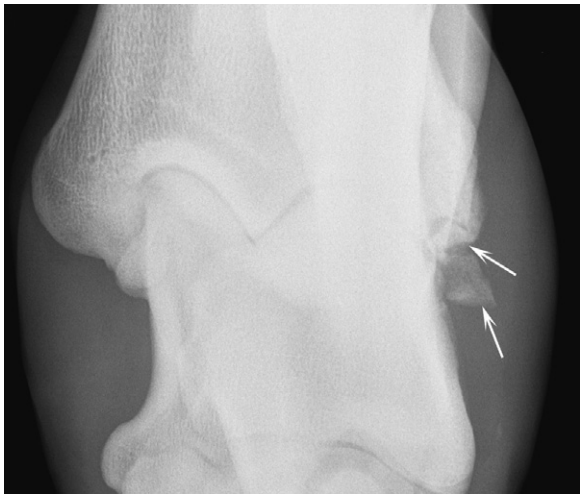


Fig. 19-28 Dorsoplantar radiograph of the tarsus of a horse with an avulsion fracture of the lateral malleolus. There are two sharp bony fragments *(white arrows)* distal to the lateral malleolus and a concave defect in the malleolus. The tarsocrural joint is distended.

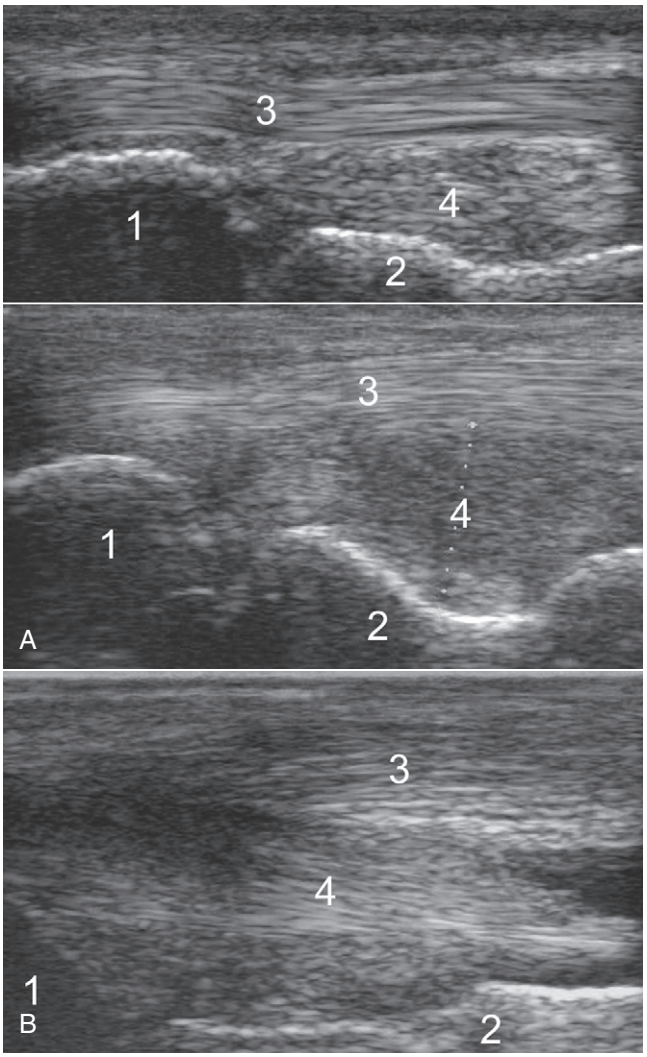


Fig. 19-29 Ultrasound images of the tarsa; collateral ligaments. **A,** Longitudinal images of the tarsus at the lateral aspect of the joint at the level of the lateral digital extensor tendon in a normal horse *(top)* and in a horse with tarsal sprain *(bottom)*. *1*, Tibial malleolus; *2*, talus; *3*, lateral extensor tendon; *4*, short bundle of the lateral collateral ligament. In the bottom image the short bundle of the collateral ligament is thickened and hypoechoic and displaces the lateral extensor tendon abaxially. **B,** Longitudinal images of the tarsus at the medial aspect of the joint at the level of the medial collateral ligament in a normal horse. *1*, Tibial malleolus; *2*, talus; *3*, long bundle of the medial collateral ligament; *4*, short bundle of the medial collateral ligament.

joint disease of these joints is considered one of the most common causes of hindlimb lameness, the clinical significance of most of the radiographic signs varies.[53,54,56] Radiographic findings are changes in shape and opacity of the joint margins, osteophyte formation, thinning of the joint space, ill-defined subchondral bone/cartilage interface, subchondral plate irregularities, subchondral lysis, and trabecular bone sclerosis (Fig. 19-31). Less frequently, opacification of the interosseous fossae can be observed because of bone remodeling associated with enthesopathies of the tarsal interosseous ligaments (Fig.19-31, *B*). Systematic evaluation of these fossae is essential in horses with distal tarsal degenerative joint disease because their involvement worsens the clinical prognosis. The association of several of the cited radiographic signs, including changes in opacity at the joint margins, is more likely to be responsible for clinical signs. Remodeling or bony spurs with smooth contours and no change in opacity at the margins of the tarsometatarsal joint are more commonly an incidental finding with no clinical significance (Fig. 19-32, p. 366). When located at the dorsal or dorsolateral aspect of the proximal metatarsus, these bony spurs are described as osteophytes or enthesophytes of the tendons of the tibialis cranialis and peroneus tertius or of the dorsal tarsometatarsal ligament.[57] This type of radiographic abnormality is common and often bilateral in distal tarsal joints and has a reported prevalence of 8% to 31% in young clinically normal horses (in tarsometatarsal and/or distal intertarsal joint).[1,3,16,19] Because subchondral bone plate irregularities are often associated with osteophyte formation at the distal intertarsal joint margins but not in the tarsometatarsal joint, this radiographic finding is likely to be more significant clinically in the distal intertarsal joint than in the tarsometatarsal joint.[55] Subchondral bone lysis, independent from location, should always be considered associated to a certain degree with joint pain. The more lytic the changes



Fig. 19-30 Dorsomedial-plantarolateral radiograph of the tarsus of a horse with a lateral collateral ligament injury diagnosed 15 months before. Two periarticular fragments are present at the level of the lateral malleolus, and there are severe remodeling and opacity changes of the tibial articular margin. The radiolucent band corresponding to the articular cartilage between the talar ridges and the grooves of the tibial cochlea is barely visible. This finding indicates severe tarsocrural degenerative joint disease and is associated with severe lameness.

in the subchondral bone, the more likely that clinical signs will be present.

Degenerative joint disease of the distal intertarsal or tarsometatarsal joints is commonly bilateral and often begins in the dorsal and dorsomedial aspects of the joints. An uneven distribution of biomechanical forces seems to be an important etiologic factor[54] and may play a role in the thickening of the medial subchondral bone plate found in horses with tarsal pain.[58] A dorsolateral location may be associated with angular limb deformity and a tarsus valgus. Mild dorsal collapse of the tarsal bones is often associated with degenerative joint disease of the distal intertarsal joint. On the lateromedial views of the tarsus of these horses, a mild to moderate bulging of the dorsal profile of the distal tarsal row can be seen, with intertarsal and tarsometatarsal joint spaces converging dorsally. In severely affected horses the entire joint is involved.

Incomplete Ossification of Tarsal Bones and Tarsal Collapse

Incomplete ossification of the tarsal bones can occur in newborn foals.[51,59,60] However, because of lack of recognition of clinical signs or lack of concern for angular deformity by some owners, foals may not be seen until later in life. This condition is more common in premature or twin foals and is thought to be a consequence of skeletal immaturity at birth.[20,51] Radiographically, incomplete ossification of the central and/or the third tarsal bone occurs, with the third tarsal bone being involved more commonly and affected more severely. Dorsal and/or lateral collapse of the affected bone is common (Fig. 19-33, p. 366). Collapse may lead to fragmentation of the tarsal bones and to angular limb deformity. Foals with incomplete ossification of the tarsal bone may develop early degenerative joint disease of the distal intertarsal and tarsometatarsal joints.[51] Prognosis for future athletic soundness is related to the degree of bone collapse, and the prognosis is guarded in foals with more than 30% collapse of a tarsal bone.[59,60]

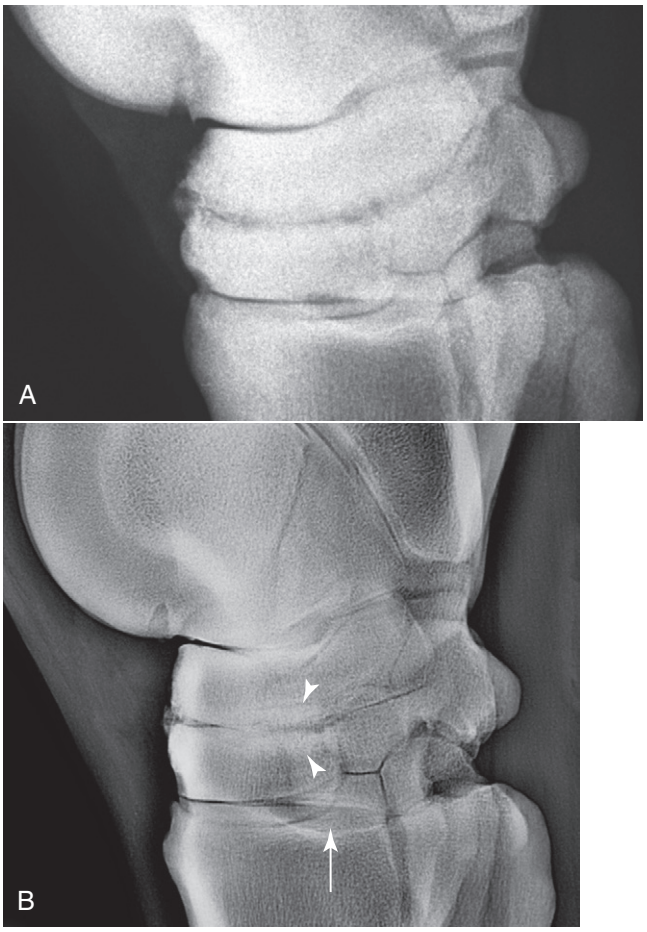


Fig. 19-31 **A,** Lateromedial tarsal radiograph of a horse with distal intertarsal degenerative joint disease. There is osteophyte formation at the dorsal aspect of the distal intertarsal joint. The joint space seems wide because of radiolucency of the lytic subchondral bone. The trabecular bone of the central and third tarsal bone is sclerotic. **B,** Lateromedial tarsal radiograph of a horse with distal intertarsal degenerative joint disease characterized by thinning of the joint space and osteophyte formation. The interosseous fossa of the joint is hardly visible. The normal radiolucent area surrounded by a thin radiopaque line (compare to the normal appearance in the tarsometatarsal joint, *white arrow*) is obscured by marked sclerosis of the osseous margins *(white arrowheads)*. This finding suggests enthesopathy of the corresponding tarsal interosseous ligament and worsens the clinical prognosis.

Subchondral Cystlike Lesions

Subchondral cystlike lesions occur occasionally in the central and third tarsal bones and in the proximal metatarsus.[3,20] Subchondral cystlike lesions are radiolucent round to oval areas, often surrounded by sclerotic trabecular bone. Because of their small size and the superimposition of the tarsal bones, their detection requires attentive radiographic scrutiny. Subchondral cystlike lesions, in particular in the third tarsal bone, have been reported in clinically normal horses[3] but are considered a predisposing factor for degenerative joint disease of the distal intertarsal joint.[20,61]

Diseases of the Talocalcaneal and Proximal Intertarsal Joints

Degenerative Joint Disease

Degenerative joint disease of the talocalcaneal and proximal intertarsal joints is uncommon.[62] However, because of the high clinical significance of the radiographic findings consistent with degenerative changes in these joints, awareness of this condition is important. It may be responsible for severe

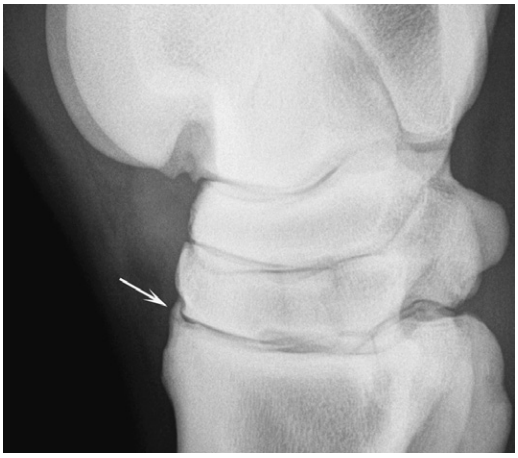


Fig. 19-32 Lateromedial radiograph of the tarsus of a clinically normal horse. A large bony spur with well-defined contour is present at the dorsoproximal margin of the third metatarsal bone *(white arrow)*. No changes in opacity are present in the articular margins or in the subchondral bone. The distal margin of the third tarsal bone is smooth and well defined.

hindlimb lameness, with guarded to poor prognosis.[51,62] Radiographic signs are subchondral lysis and sclerosis, irregular subchondral surface, and changes in joint space width (Fig. 19-34). Subchondral bone lysis is often the predominant radiographic sign.[62] In the talocalcaneal joint, osteophyte formation is difficult to assess because of the anatomy of the joint, while it can be seen in the proximal intertarsal joint. The radiographic signs in the talocalcaneal joint are more evident on the lateromedial view (Fig. 19-35).

Fractures Involving the Tarsus

Fractures of the Distal Tibia and Malleolar Fractures

Tibial stress fractures are common in racehorses and occasionally involve the distal tibia (Fig. 19-36).[38] Intraarticular involvement may follow if the stress fracture spirals distally and becomes comminuted. Severely comminuted articular fractures of the distal tibia are the result of violent traumatic events, including kicks from other horses, dramatic falls, and encounters with vehicles. Physeal Salter-Harris type II fractures are the most frequently encountered tibial fracture in foals.[20]

Sprains of the tarsus result in collateral ligament injury and severe synovial effusion.[20]Avulsion fracture of the malleolus may occur in association with collateral ligament damage.[20,51,63] One or more separated sharp bony fragments can be seen at the lateral or medial aspect of the proximal tarsal row close to the fractured malleolus, which has a bony defect (see Fig. 19-28). The lateral malleolus is involved more commonly.[20,51,63] Lateral malleolar fractures are better evaluated using a plantar 10-degree lateral-dorsomedial view.[63] The size and shape of the moderately displaced fragment, the bone defect, the shape of the fractured malleolus, and the clinical history and signs should help differentiate this condition from osteochondrosis (see Fig. 19-25).[20,51]

Central and Third Tarsal Bones and Proximal Metatarsal Fractures

Fractures of the central and third tarsal bones and the proximal metatarsus occur in racehorses, mainly Standardbreds.[64,65] Central tarsal bone fractures are usually seen best on the lateromedial view, whereas third tarsal bone fractures are seen best on the plantarolateral-dorsomedial view.[64] However, fractures of the central and third tarsal bones are difficult to detect because of the complex anatomy of the tarsus and the superimposition of tarsal bones and consequently can be missed on routine views. A marked sclerosis of the central or third tarsal bone with only minor or no degenerative joint disease of the distal tarsus is a warning sign and should be considered an indication to acquire oblique views. Often several oblique views, including a plantar 25-degree lateral-dorsomedial view for third tarsal bone fracture, are needed to identify or document the fracture line better. If the fracture line cannot be seen at the first radiographic examination, but the clinical history and signs suggest a tarsal fracture, the horse should undergo other imaging modalities, such as scintigraphy, or at least be rested and have radiographs repeated 7 to 10 days later.[20,51] Rarefaction of the fracture margins will make the fracture line more obvious in these later radiographs. Fractures of the central and third tarsal bones are usually slab fractures.[20,64] Third tarsal bone fractures are more commonly dorsal or dorsolateral.[51,64] A significant association between a

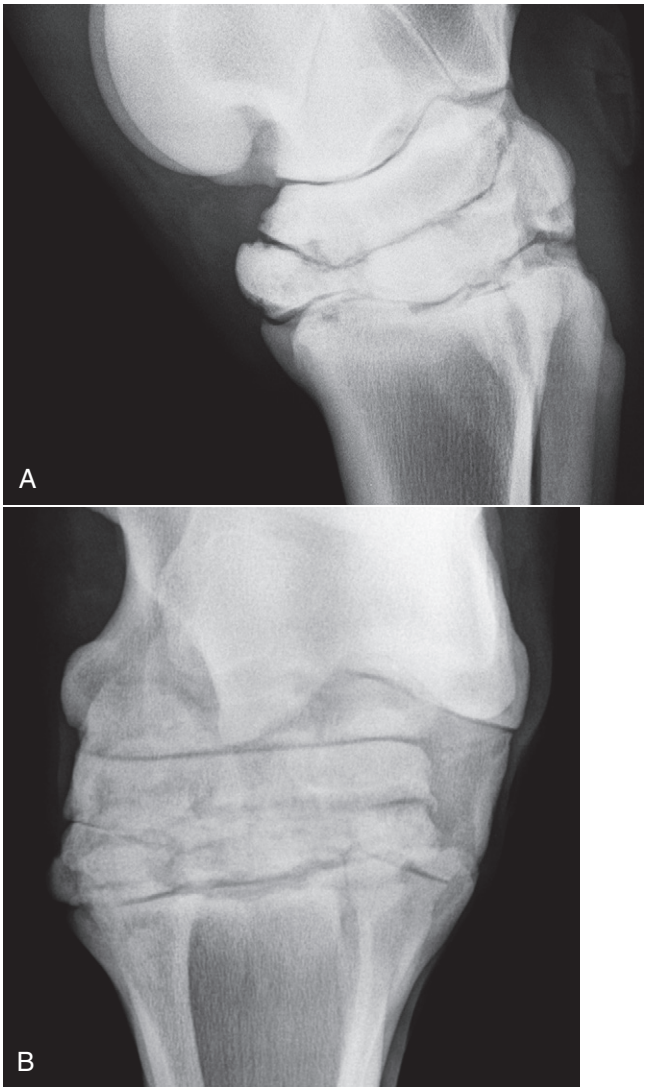


Fig. 19-33 Lateromedial **(A)** and dorsoplantar **(B)** radiographs of the tarsus of a young horse with severe tarsal bone collapse. **A,** The central and third tarsal bones are sclerotic and have an abnormal shape with a severe narrowing of the third tarsal bone in its middle third. As a consequence the distal intertarsal joint space and tarsometatarsal joint space are not parallel, and the dorsal surface of the distal tarsal row is abnormally convex. There are also areas of radiolucency in the subchondral bone of the distal intertarsal and tarsometatarsal joint, subchondral sclerosis, and a large dorsal bony spur of the proximal metatarsus. **B,** The distal intertarsal joint space and the tarsometatarsal joint space are not parallel as in a normal horse. The distal intertarsal joint space is ill defined and irregular.



Fig. 19-34 Dorsolateral-plantaromedial oblique radiograph of the tarsus in a horse with severe hindlimb lameness and moderate distention of the tarsocrural joint attributable to degenerative disease of the proximal intertarsal joint. The tarsocrural joint is swollen. Remodeling of the dorsomedial margins of the intertarsal and tarsometatarsal joints has occurred. A severe subchondral lysis and subchondral bone surface irregularity are present in the proximal intertarsal joint. The proximal intertarsal joint space appears wider because of the subchondral lysis. The distal intertarsal and tarsometatarsal joints are also thinner than normal.

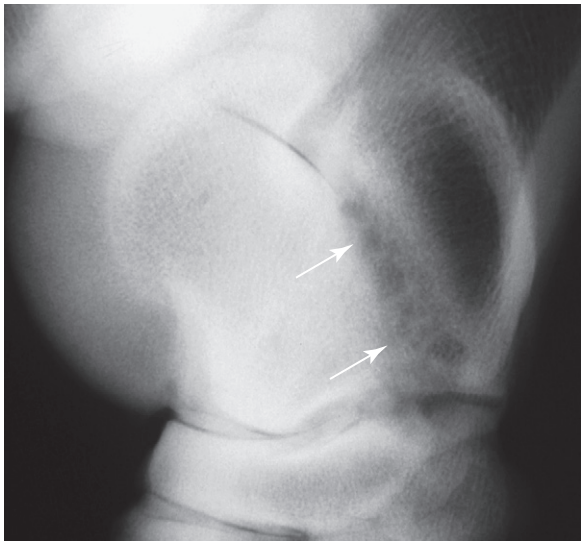


Fig. 19-35 Lateromedial radiograph of the tarsus in a horse with severe hindlimb lameness and moderate distention of the tarsocrural joint. The distal portion of the talocalcaneal joint appears widened and ill-defined *(white arrows)* because of severe subchondral bone lysis. These findings are indicative of severe talocalcaneal degenerative joint disease.

wedge-shaped conformation of the third tarsal bone and the occurrence of slab fractures of this bone has been demonstrated in racehorses.[65]Intraarticular fractures of the proximal metatarsus involving the dorsal aspect of the bone are reported in racehorses.[66,67] These fractures are more commonly incomplete.[66,67]

Miscellaneous Conditions Involving the Tarsus

Septic Arthritis

Septic arthritis may occur in foals or adult horses.[43] The tarsocrural joint is affected most commonly, especially in adult horses.[20] Septic arthritis is not a radiographic diagnosis but is

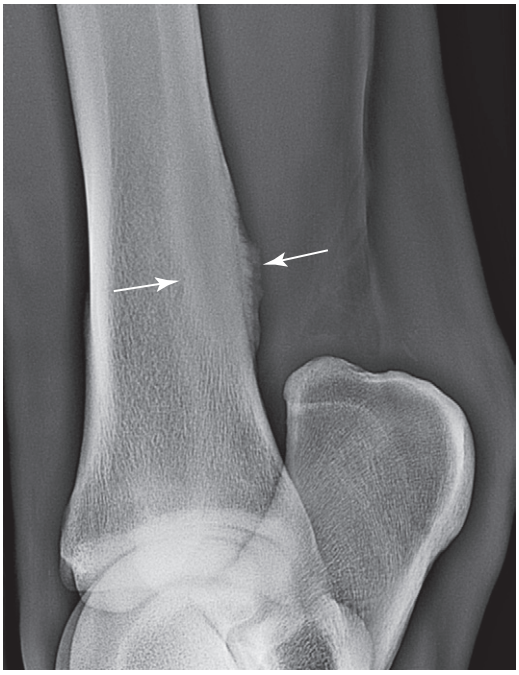


Fig. 19-36 Lateromedial radiograph of the distal tibia of a 3-year-old Thoroughbred with a fatigue fracture of the caudal cortex of the distal tibia. Thickened cortical bone, endosteal sclerosis, and periosteal proliferations are present *(white arrows)*.

based on clinical signs and analysis of synovial fluid. Radiographic examination is essential to establish bone or physeal involvement, especially in foals. Soft tissue and joint swelling in a non–weight-bearing limb may be the only radiographic signs of septic arthritis. When bone damage occurs, it is seen as ill-defined subchondral radiolucencies. Radiographic changes may be apparent within 7 to 10 days after the onset of clinical sings. In the small bones of the tarsus in foals, radiolucent changes may be delayed because infarction caused by infection may slow bone resorption.[43] In chronic infections with severe lameness, an overall increased radiolucency of the tarsus with a thinning of the cortical bone also can be seen because of disuse osteopenia.

Osteomyelitis of the Calcaneus and Enthesopathies of the Tuber Calcanei

Osteomyelitis of the calcaneus involving the tuber calcanei and/or the sustentaculum tali occurs after penetrating injuries of the point of the tarsus.[68,69] Septic calcaneal bursitis and infection of tarsal synovial sheath may be associated with osteomyelitis of the tuber calcanei and osteomyelitis of the sustentaculum tali, respectively.[68,69] Radiographic signs of calcaneal osteomyelitis are seen only after substantial bone loss has occurred, typically 10 to 15 days after injury. Repeated radiographic assessment is therefore always suggested to follow up traumatic wounds of the tarsus. Radiographic abnormalities indicative of calcaneal infection are ill-defined areas of decreased bone opacity indicating osteolysis and irregular bone contour (Fig. 19-37). In long-standing infections, surrounding diffuse sclerosis may occur. Mild to moderate bony proliferation is also more common in chronic infection.[69] Fragmentation and sequestra, seen as bony fragments surrounded by a radiolucent halo, which is then enveloped by sclerotic bone, may develop on the tuber calcanei as a result of the minimal tissue covering the region and the relatively poor blood supply.[69]

Distal enthesopathies of the gastrocnemius tendon can also result in radiolucent areas on the tuber calcanei (Fig. 19-38)



Fig. 19-37 Lateromedial radiograph of the calcaneus of a horse with calcaneal osteomyelitis that developed after a penetrating injury of the point of the tarsus. Several ill-defined radiolucent areas are present in the calcaneus, mainly at its plantar aspect. The surrounding bone is diffusely sclerotic. There is also some marginal irregularity of the dorsal and plantar contours of the calcaneus. No sharp transition zone exists between abnormal and normal bone.

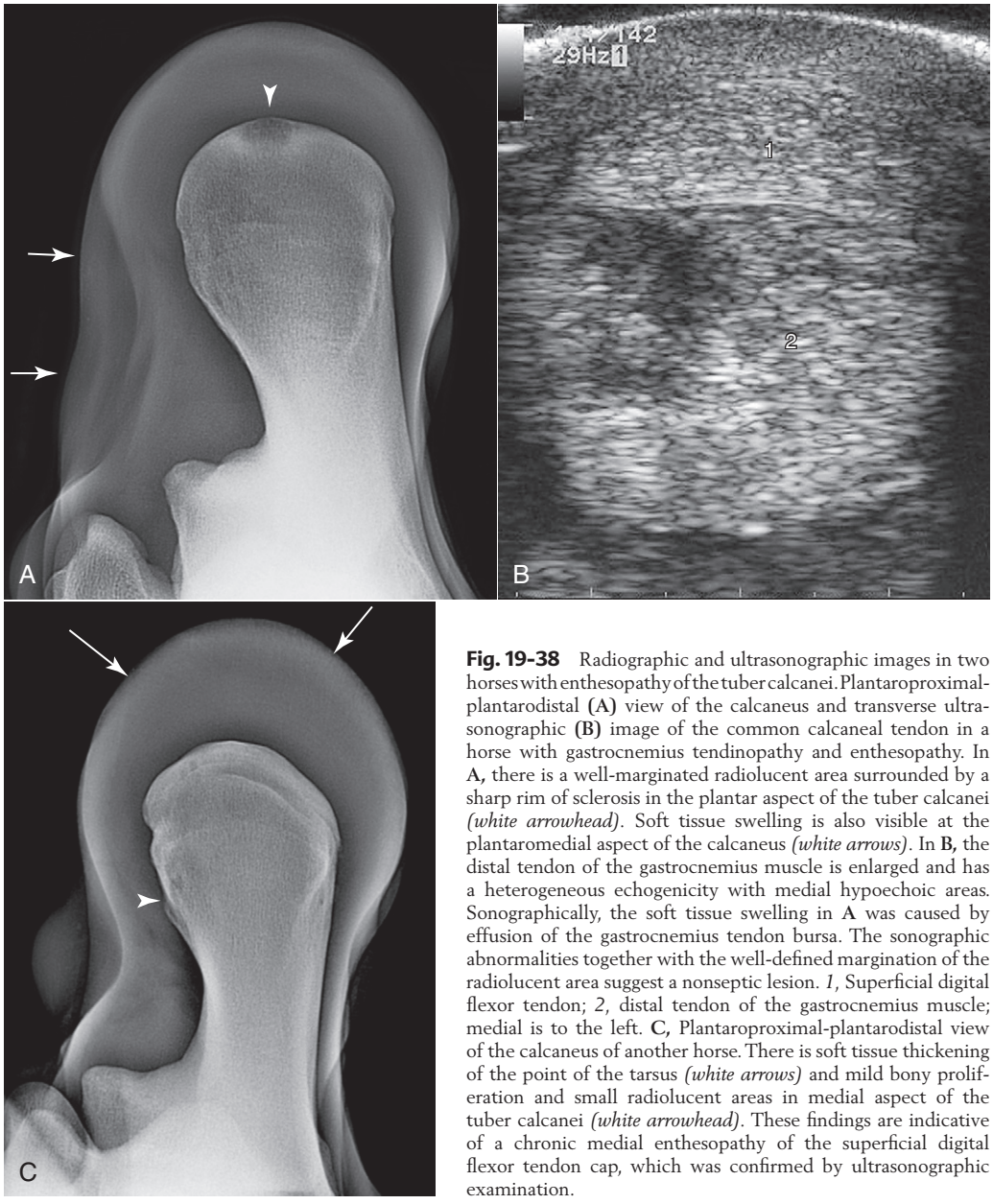


Fig. 19-38 Radiographic and ultrasonographic images in two horses with enthesopathy of the tuber calcanei. Plantaroproximal-plantarodistal **(A)** view of the calcaneus and transverse ultrasonographic **(B)** image of the common calcaneal tendon in a horse with gastrocnemius tendinopathy and enthesopathy. In **A,** there is a well-marginated radiolucent area surrounded by a sharp rim of sclerosis in the plantar aspect of the tuber calcanei *(white arrowhead)*. Soft tissue swelling is also visible at the plantaromedial aspect of the calcaneus *(white arrows)*. In **B,** the distal tendon of the gastrocnemius muscle is enlarged and has a heterogeneous echogenicity with medial hypoechoic areas. Sonographically, the soft tissue swelling in **A** was caused by effusion of the gastrocnemius tendon bursa. The sonographic abnormalities together with the well-defined margination of the radiolucent area suggest a nonseptic lesion. *1*, Superficial digital flexor tendon; *2*, distal tendon of the gastrocnemius muscle; medial is to the left. **C,** Plantaroproximal-plantarodistal view of the calcaneus of another horse. There is soft tissue thickening of the point of the tarsus *(white arrows)* and mild bony proliferation and small radiolucent areas in medial aspect of the tuber calcanei *(white arrowhead)*. These findings are indicative of a chronic medial enthesopathy of the superficial digital flexor tendon cap, which was confirmed by ultrasonographic examination.

that should not be misdiagnosed as septic lesions. Radiolucent areas caused by enthesopathy have no signs of aggressiveness compared with calcaneal osteomyelitis, being better marginated with a short transition zone. Ultrasonographic examination of the point of the tarsus may also help in distinguishing these conditions by allowing identification of associated abnormalities of the distal tendon of the gastrocnemius muscle (Fig. 19-38, *B*). Bone remodeling and localized radiolucencies on the medial and/or lateral surfaces of the tuber calcanei can also be observed in chronic enthesopathies or rupture of the insertions of the superficial digital flexor tendon cap (Fig.19-38, *C*).

Abnormalities of the Sustentaculum Tali and Tarsal Sheath Tenosynovitis

The tarsal sheath is the synovial sheath enveloping the lateral digital flexor tendon at the level of the tarsus.[70] The lateral digital flexor tendon joins the medial digital flexor tendon at the plantar aspect of the proximal metatarsus to form the deep digital flexor tendon.[70] The lateral digital flexor tendon passes over the sustentaculum tali, which serves as a gliding groove.[70] Tenosynovitis of the tarsal sheath frequently produces an obvious effusion easily detectable on radiographs as soft tissue swelling at the medial aspect of the tarsus or between the distal tibia and the calcaneus. Radiographic abnormalities of the sustentaculum tali may be seen in horses with chronic aseptic tenosynovitis or when fracture or local infection is present as a consequence of a penetrating wound (Figs. 19-39, 19-40, and 19-41).[20] There may be a heterogeneous increased opacity of the sustentaculum tali in the lateromedial view of the tarsus. Additional views, in particular plantarolateral-dorsomedial and plantaroproximal-plantarodistal views, are needed to assess the sustentaculum tali fully. Bony proliferations at the distal aspect of the sustentaculum tali may be seen in moderate to severe chronic tenosynovitis (see Fig.19-41). In chronic tenosynovitis, bony proliferations at the insertion of the flexor retinaculum on either the medial margin of the sustentaculum tali or the axial surface of the tuber calcanei are a sign of enthesopathy. Calcifications may be seen in the soft tissues (see Fig. 19-39). Fragments of the sustentaculum tali may be seen when a penetrating injury with direct trauma has occurred (see Fig. 19-40).

In horses with proven or suspected infection of the tarsal sheath, an irregular contour of the sustentaculum tali, osteolysis with or without bony proliferation, fragmentation, and sequestra are signs of concurrent bone involvement and osteomyelitis. Nevertheless, osteolysis of the flexor surface of the sustentaculum can also be observed in chronic aseptic tenosynovitis, usually associated with lateral digital flexor tendonitis. Dysplasia of the sustentaculum tali has also been reported as a cause of tarsal sheath tenosynovitis because of mechanical medial displacement of the lateral digital flexor tendon during movement.[20] Ultrasonographic evaluation of the tarsal sheath and associated structures, such as the lateral digital flexor tendon, sustentaculum tali, and adjacent part of the calcaneus, is essential to assess soft tissue injuries associated with tarsal sheath tenosynovitis fully, and particularly for diagnosing lateral digital flexor tendonitis.

Proximal Insertion Suspensory Desmopathy and Enthesopathy

Proximal insertion desmopathies of the suspensory ligament are a common cause of lameness in sport horses[71] and racehorses, particularly Standardbreds. Radiographic signs may be visible in chronic proximal enthesopathy when the point of tendon insertion onto bone is involved. Lateromedial radiographs of the tarsus and proximal metatarsus are characterized by subcortical sclerosis and thickening of the plantar cortex of the third metatarsal bone (Fig. 19-42). In the dorsoplantar view of the proximal metatarsus, there may be homogeneous or mixed opacity (Fig. 19-43, p. 371), often visible as ill-defined proximodistal opacities. Radiographic evaluation of the contralateral limb is indicated to either compare radiographic appearance with a normal bone or assess bilateral involvement because this condition is frequently bilateral in the hindlimbs. Avulsion fracture may occur at the site of the proximal insertion of the suspensory ligament on the third metatarsal bone.

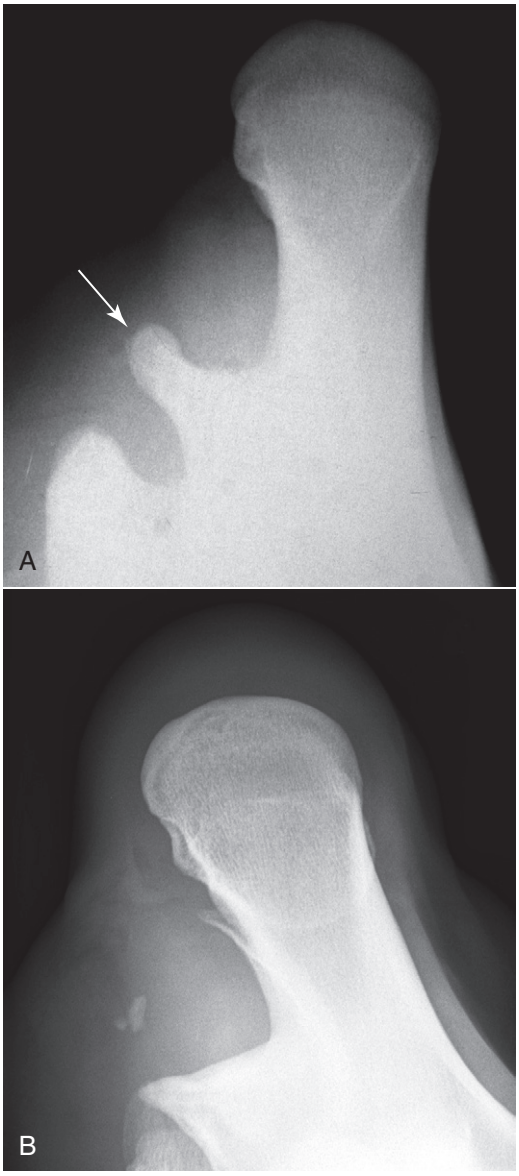


Fig. 19-39 Plantaroproximal-plantarodistal views of the sustentaculum tali of two horses with aseptic chronic tenosynovitis of the tarsal sheath. **A,** A large, smooth, bony proliferation is present on the medial margin of the sustentaculum tali *(white arrow)*. **B,** The soft tissues plantar to the sustentaculum tali are thickened, and two focal areas of mineralization with smooth margins are visible plantar to the sustentaculum tali. These likely represent dystrophic calcifications in the soft tissues. Mild remodeling of the medial margin of the sustentaculum tali and a bony proliferation on the medial surface of the tuber calcanei are also present.



Fig. 19-40 Plantarolateral-dorsomedial radiograph of the tarsus of a horse with a penetrating wound at the medial aspect of the tarsus that occurred 3 weeks prior. There is soft tissue swelling at the plantaromedial aspect of the tarsus corresponding to tarsal sheath effusion. A large defect is visible in the proximal part of the sustentaculum tali with a thin elongated fragment and several small fragments located plantar to the bony defect. Because of the large defect and the sharpness of the margins, the most likely cause is direct trauma inducing a fracture of the proximomedial aspect of the sustentaculum tali. (Radiograph courtesy of Section of Diagnostic Imaging, University Animal Hospital, Swedish University of Agricultural Sciences, Uppsala, Sweden.)

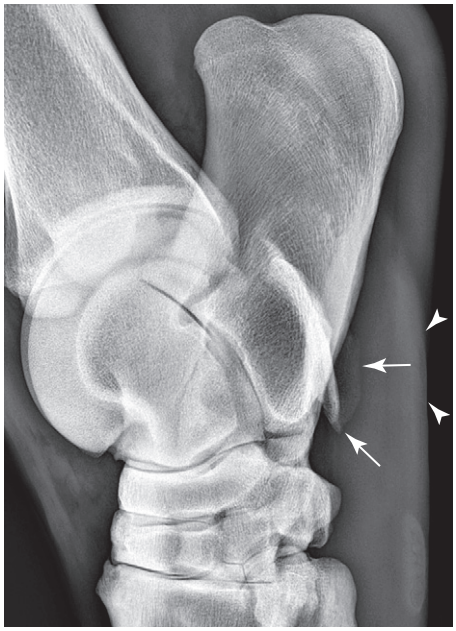


Fig. 19-41 Lateromedial radiograph of the tarsus. There is a bony proliferation at the distal aspect of the sustentaculum tali *(white arrows)*. This abnormal finding is found typically in moderate to severe chronic tarsal sheath tenosynovitis. Note also the plantar soft tissue swelling giving a convex tarsal plantar profile *(white arrowheads)*, which is caused by tarsal sheath effusion.

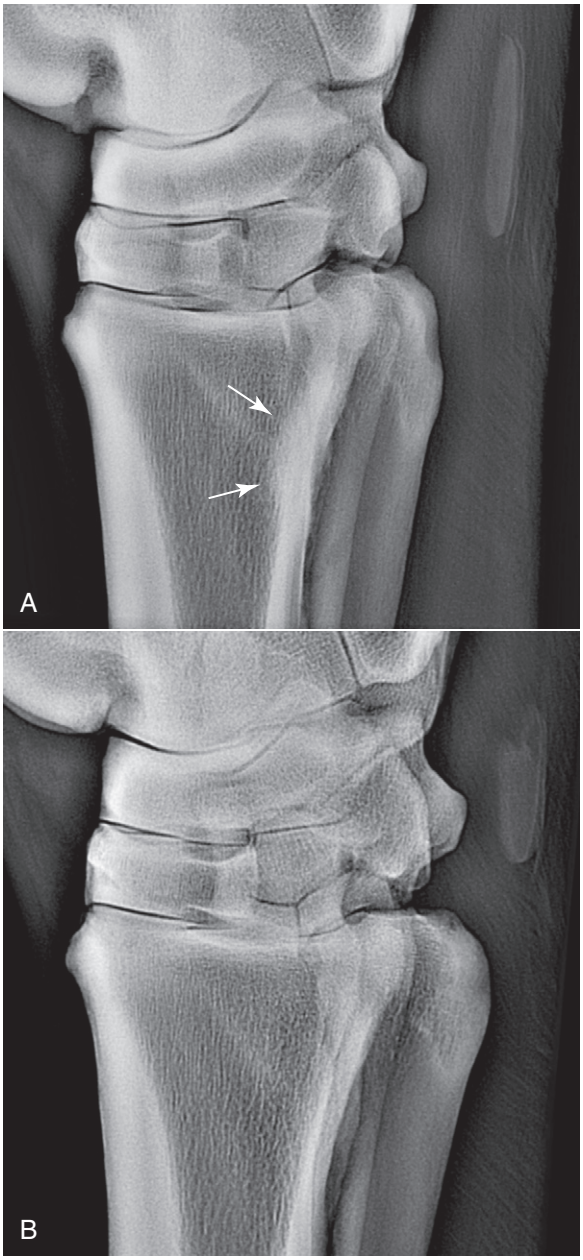


Fig. 19-42 Lateromedial radiographs of the right **(A)** and left **(B)** proximal metatarsal region of a show-jumping horse with unilateral proximal insertional desmopathy of the suspensory ligament. **A,** There is thickening of the proximal plantar cortex of the right third metatarsal bone because of endosteal sclerosis *(white arrows)*. The normal left third metatarsal bone **(B)** has a normal plantar cortex, which decreases slightly in thickness in a distoproximal direction.



Fig. 19-43 Dorsoplantar radiograph of the proximal aspect of the metatarsus of a horse with proximal insertional desmopathy of the suspensory ligament. Note the ill-defined increased opacity involving the proximolateral aspect of the third metatarsal bone.

REFERENCES

1. Preston SA, Zimmel DN, Chmielewski TL, et al: Prevalence of various presale radiographic findings and association of findings with sales price in Thoroughbred yearlings sold in Kentucky, *J Am Vet Med Assoc* 236:440, 2010.
2. Van Grevenhof EM, Ducro BJ, Van Weeren PR, et al: Prevalence of various radiographic manifestations of osteochondrosis and their correlations between and within joints in Dutch Warmblood horses, *Equine Vet J* 41:11, 2009.
3. Verwilghen D, Serteyn D, Pille F, et al: Prevalence of radiographic findings in candidate sires (2001-2008), *Vlaams Diergeneeskundig Tijdschrift* 78:419, 2009.
4. Jackson MA, Vizard AL, Anderson GA, et al: Identification and prevalence of errors affecting the quality of radiographs submitted to Australian thoroughbred yearling sale repositories, *Vet Radiol Ultrasound* 52(3):262, 2011.
5. Walmsley JP: Diagnosis and treatment of ligamentous and meniscal injuries in the equine stifle, *Vet Clin North Am Equine Pract* 21:651, 2005.
6. Denoix JM, Audigié F: Imaging of the musculoskeletal system in horses. In Hinchcliff K, Kaneps AJ, Geor RJ, Bayly W, editors: *Equine sports medicine and surgery—basic and clinical sciences of the equine athlete*, Philadelphia, 2004, Saunders, p 161.
7. De Busscher V, Verwilghen D, Bolen G, et al: Meniscal damage diagnosed by ultrasonography in horses: a retrospective study of 74 femorotibial joint ultrasonographic examinations (2000–2005), *J Equine Vet Sci* 26:453, 2006.
8. Cohen JM, Richardson DW, McKnight AL, et al: Long-term outcome in 44 horses with stifle lameness after arthroscopic exploration and debridement, *Vet Surg* 38:543, 2009.
9. Flynn KA, Whitcomb MB: Equine meniscal injuries: a retrospective study of 14 horses, *Proc Am Assoc Equine Pract* 48:249, 2002.
10. Hendrix SM, Baxter GM, McIlwraith CW, et al: Concurrent or sequential development of medial meniscal and subchondral cystic lesions within the medial femorotibial joint in horses (1996-2006). *Equine Vet J* 42:5, 2010.
11. Denoix JM: Ultrasound examination of joints and miscellaneous tendons. In Rantanen N, McKinnon A, editors: *Equine diagnostic ultrasonography*, Baltimore, 1998, Williams & Wilkins, p 475.
12. Denoix JM, Busoni V: Ultrasonography of joints and synovia. In White NA, Moore JN, editors: C*urrent techniques in equine surgery and lameness*, ed 2, Philadelphia, 1998, Saunders, p 643.
13. Jacquet S, Audigié F, Denoix JM: Ultrasonographic diagnosis of subchondral bone cysts in the medial femoral condyle in horses, *Equine Vet Educ* 19:47, 2007.
14. De Busscher V, Schreder A, Busoni V, et al: Histological study of the horse stifle menisci in relation with ultrasonographic aspect: preliminary study, *Italian J Anat Embryol* 111:132, 2006.
15. Dik KJ, Enzerink E, Van Weeren PR: Radiographic development of osteochondral abnormalities in the hock and stifle of Dutch Warmblood foals, from age 1 to 11 months, *Equine Vet J* 31(Suppl):9, 1999.
16. Oliver LJ, Baird DK, Baird AN, et al: Prevalence and distribution of radiographically evident lesions on repository films in the hock and stifle joints of yearling Thoroughbred horses in New Zealand, *N Z Vet J* 56:202, 2008.
17. Bourzac C, Alexander K, Rossier Y, et al: Comparison of radiography and ultrasonography for the diagnosis of osteochondritis dissecans in the equine femoropatellar joint, *Equine Vet J* 41:685, 2009.
18. Robert C, Valette JP, Denoix JM: Correlation between routine radiographic findings and early racing career in French trotters, *Equine Vet J* 36(Suppl):473, 2006.
19. Kane AJ, Park RD, McIlwraith CW, et al: Radiographic changes in Thoroughbred yearlings. Part 1: prevalence at the time of the yearling sales, *Equine Vet J* 35:354, 2005.
20. Butler JA, Colles CM, Dyson SJ, et al: C*linical radiology of the horse*, ed 3, London, 2008, Blackwell.
21. Trostle SS, Casinella LL, Sussman KH, et al: What is your diagnosis? Osseous cystlike lesion of the patella, *J Am Vet Med Assoc* 230:663, 2007.
22. Baccarin RY, Martins EA, Hagen SC, et al: Patellar instability following experimental medial patellar desmotomy in horses, *Vet Comp Orthop Traumatol* 22:27, 2009.
23. Labens R, Busoni V, Peters F, et al: Ultrasonographic and radiographic diagnosis of patellar fragmentation secondary to bilateral medial patellar ligament desmotomy in a Warmblood gelding, *Equine Vet Educ* 17:201, 2005.
24. McIlwraith CW: Osteochondral fragmentation of the distal aspect of the patella in horses, *Equine Vet J* 22:157, 1990.
25. Engelbert TA, Tate LP, Richardson DC, et al: Lateral patellar luxation in miniature horses, *Vet Surg* 22:293, 1993.
26. Scott GS, Crawford WH, Colahan PT, et al: Arthroscopic findings in the horses with subtle radiographic evidence of osteochondral lesions of the medial femoral condyle: 15 cases (1995–2002), *J Am Vet Med Assoc* 224:1823, 2004.
27. Howard RD, McIlwraith CW, Trotter GW: Arthroscopic surgery for subchondral cystic lesions of the medial femoral condyle in horses: 41 cases (1988–1991), *J Am Vet Med Assoc* 206:842, 1995.
28. Hance SR, Schneider RK, Embertson RM, et al: Lesions of the caudal aspect of the femoral condyles in foals: 20 cases (1980–1990), *J Am Vet Med Assoc* 202:637, 1993.

29. Textor JA, Nixon AJ, Lumsden J, et al: Subchondral cystic lesions of the proximal extremity of the tibia in horses: 12 cases (1983–2000), *J Am Vet Med Assoc* 218:408, 2001.
30. Audigié F: unpublished data, 2011.
31. Edwards RB, Nixon AJ: Avulsion of the cranial cruciate ligament insertion in a horse, *Equine Vet J* 28:334, 1996.
32. Rose PL, Graham JP, Moore I, et al: Imaging diagnosis—caudal cruciate ligament avulsion in a horse, *Vet Radiol Ultrasound* 42:414, 2001.
33. Sanders-Shamis M, Bukowiecki CF, Biller DS: Cruciate and collateral ligament failure in the equine stifle: seven cases, *J Am Vet Med Assoc* 193:573, 1988.
34. Mueller PO, Allen D, Watson E, et al: Arthroscopic removal of a fragment from an intercondylar eminence fracture of the tibia in a two-year-old horse, *J Am Vet Med Assoc* 204:1794, 1994.
35. Dyson S, Wright I, Kold S, et al: Clinical and radiographic features, treatment and outcome in 15 horses with fracture of the medial aspect of the patella, *Equine Vet J* 24:264, 1992.
36. Dyson SJ: Stifle trauma in the event horse, *Equine Vet Educ* 6:234, 1994.
37. Arnold CE, Schaer TP, Baird DL, et al: Conservative management of 17 horses with nonarticular fractures of the tibial tuberosity, *Equine Vet J* 35:202, 2003.
38. Ross MW: The crus. In Ross MW, Dyson SJ, editors: *Diagnosis and management of lameness in the horse*, ed 2, St. Louis, 2011, Elsevier-Saunders, p 526.
39. Blikslager AT: Avulsion of the origin of the peroneus tertius tendon in a foal, *J Am Vet Med Assoc* 204:1484, 1994.
40. Holcombe SJ, Bertone A: Avulsion fracture of the origin of the extensor digitorum longus muscle in a foal, *J Am Vet Med Assoc* 204:1652, 1994.
41. *Saunders comprehensive veterinary dictionary*: Calcinosis circumscripta (webpage). //medical-dictionary.thefreedictionary.com/calcinosis%20circumscripta. Accessed March 22, 2011.
42. Milner PI: Calcinosis circumscripta in the horse, *Equine Vet Educ* 21:589, 2009.
43. Bertone A: Infectious arthritis. In Ross MW, Dyson SJ, editors: *Diagnosis and management of lameness in the horse*, ed 2, St. Louis, 2011, Elsevier-Saunders, p 677.
44. Neil KM, Axon JE, Begg AP, et al: Retrospective study of 108 foals with septic osteomyelitis, *Aust Vet J* 88:4, 2010.
45. Richardson DW: Diagnosis and management of osteochondrosis and osseous cystlike lesions. In Ross MW, Dyson SJ, editors: *Diagnosis and management of lameness in the horse*, ed 2, St. Louis, 2011, Elsevier Saunders, p 631.
46. Jørgensen HS, Proschowsky H, Falk-Rønne J, et al: The significance of routine radiographic findings with respect to subsequent racing performance and longevity in Standardbred trotters, *Equine Vet J* 29:55, 1997.
47. Simpson CM, Lumsden JM: Unusual osteochondral lesions of the talus in a horse, *Aust Vet J* 79:752, 2001.
48. Torre F, Toniato M: Osteochondral fragments from the medial malleolus in horses: a comparison between radiographic and arthroscopic findings, *Proc Am Assoc Equine Pract* 45:167, 1999.
49. Verwilghen DR, Bolen G, Paindaveine P, et al: What is your diagnosis? Bone fragment in hock joint, *J Am Vet Med Assoc* 237:29, 2010.
50. Relave F, Meulyzer M, Alexander K, et al: Comparison of radiography and ultrasonography to detect osteochondrosis lesions in the tarsocrural joint: a prospective study, *Equine Vet J* 41:34, 2009.
51. Dyson SJ, Ross MW: The tarsus. In Ross MW, Dyson SJ, editors: *Diagnosis and management of lameness in the horse*, ed 2, St. Louis, 2011, Elsevier-Saunders, p 508.
52. Garcia-Lopez JM, Kirker-Head CA: Occult subchondral osseous cyst-like lesions of the equine tarsocrural joint, *Vet Surg* 33:557, 2004.
53. Björnsdóttir S, Axelsson M, Eksell P, et al: Radiographic and clinical survey of degenerative joint disease in the distal tarsal joints in Icelandic horses, *Equine Vet J* 32:268, 2000.
54. Björnsdóttir S, Ekman S, Eksell P, et al: High detail radiography and histology of the centrodistal tarsal joint of Icelandic horses 6 months to 6 years, *Equine Vet J* 36:5, 2004.
55. Laverty S, Stover SM, Bélanger D, et al: Radiographic, high detail radiographic, microangiographic and histological findings of the distal portion of the tarsus in weanlings, young and adult horses, *Equine Vet J* 23:413, 1991.
56. Byam-Cook KL, Singer ER: Is there a relationship between clinical presentation, diagnostic and radiographic findings and outcome in horses with osteoarthritis of the small tarsal joints? *Equine Vet J* 41:118, 2009.
57. Fairburn A, Dyson S, Murray R: Clinical significance of osseous spurs on the dorsoproximal aspect of the third metatarsal bone, *Equine Vet J* 42:59, 2010.
58. Branch MV, Murray RC, Dyson SJ, et al: Alteration of distal tarsal subchondral bone thickness pattern in horses with tarsal pain, *Equine Vet J* 39:101, 2007.
59. Dutton DM, Watkins JP, Walker MA, et al: Incomplete ossification of the tarsal bones in foals: 22 cases (1988-1996), *J Am Vet Med Assoc* 213:1590, 1998.
60. Dutton DM, Watkins JP, Honnas CM, et al: Treatment response and athletic outcome of foals with tarsal valgus deformities: 39 cases (1988–1997), *J Am Vet Med Assoc* 215:1482, 1999.
61. Watrous BJ, Hultgren BD, Wagner PC: Osteochondrosis and juvenile spavin in equids, *Am J Vet Res* 52:607, 1991.
62. Smith RKW, Dyson SJ, Schramme MC, et al: Osteoarthritis of the talocalcaneal joint in 18 horses, *Equine Vet J* 37:166, 2005.
63. O'Neill HD, Bladon BM: Arthroscopic removal of fractures of the lateral malleolus of the tibia in the tarsocrural joint: a retrospective study of 13 cases, *Equine Vet J* 42:558, 2010.
64. Bolt DM, Williams J, Burba DJ: Traumatic injuries of the large tarsal bones in horses, *Comp Cont Educ Pract Vet* 24:724, 2002.
65. Baird DH, Pilsworth RC: Wedge-shaped conformation of the dorsolateral aspect of the third tarsal bone in the Thoroughbred racehorse is associated with development of slab fractures in this site, *Equine Vet J* 33:617, 2001.
66. Ross MV, Sponseller ML, Gill HE, et al: Articular fracture of the dorsoproximolateral aspect of the third metatarsal bone in five Standardbred racehorses, *J Am Vet Med Assoc* 203:698, 1993.
67. Pilsworth RC: Incomplete fracture of the dorsal aspect of the proximal cortex of the third metatarsal bone as a cause of hind limb lameness in the racing Thoroughbred: a review of three cases, *Equine Vet J* 24:147, 1992.
68. Hand DR, Watkins JP, Honnas CM, et al: Osteomyelitis of the sustentaculum tali in horses: 10 cases (1992-1998), *J Am Vet Med Assoc* 219:341, 2001.
69. Post EM, Singer ER, Clegg PD, et al: Retrospective study of 24 cases of septic calcaneal bursitis in the horse, *Equine Vet J* 35:662, 2003.

70. Barone R: *Anatomie comparée des mammifères domestiques, tome 2 Arthrologie et myologie*, Paris, 1989, Vigot.
71. Dyson SJ, Genovese RL: The suspensory apparatus. In Ross MW, Dyson SJ, editors: *Diagnosis and management of lameness in the horse*, ed 2, St. Louis, 2011, Elsevier-Saunders, p 738.

ELECTRONIC RESOURCES

Evolve

Additional information related to the content in Chapter 19 can be found on the companion Evolve website at http://evolve.elsevier.com/Thrall/vetrad/

- Chapter Quiz

CHAPTER • 20

The Equine Carpus

Rachel C. Murray
Sue J. Dyson

ANATOMY

The equine carpus is composed of three main articulations: the antebrachiocarpal joint; the middle carpal joint, and the carpometacarpal joint. There are two rows of cuboidal bones interposed between the radius and metacarpus.[1] The antebrachiocarpal joint is formed by the distal aspect of the radius proximally and the proximal row of carpal bones (radial, intermediate, ulnar, and accessory carpal bones) distally. The middle carpal joint is the articulation formed between the proximal (radial, intermediate, and ulnar carpal bones) and distal (second, third, and fourth carpal bones) rows of carpal bones. The carpometacarpal joint is the articulation between the distal row of carpal bones and the second, third, and fourth metacarpal bones. Vertically oriented joints between adjacent cuboidal carpal bones within each row are referred to as intercarpal joints. The antebrachiocarpal and middle carpal joints provide flexion and extension for the carpus, whereas the carpometacarpal joint is capable of only minimal motion.

Within each row, the cuboidal carpal bones are connected by two interosseous ligaments, described as intercarpal ligaments, and two transverse dorsal ligaments.[1] Within the middle carpal joint are two palmar ligaments, which attach the proximal and distal row of carpal bones. The medial palmar intercarpal ligament joins the radial with the second and third carpal bones, and the lateral palmar intercarpal ligament joins the ulnar with the third and fourth carpal bones.

When the carpus is flexed, the radial carpal bone moves distally relative to the intermediate and ulnar carpal bones. The accessory carpal bone, situated on the palmar aspect of the carpus, articulates with the distal lateral aspect of the radius and the ulnar carpal bone.[2,3]

The complex anatomy of the carpus makes radiographic interpretation challenging. Comparison with a normal set of radiographs and with bone specimens is helpful.

NORMAL VARIATIONS

The presence of the first and fifth carpal bones is variable, as is their shape and size and proximity to adjacent bones (Figs. 20-1 and 20-2). These bones should not be confused with osteochondral fragments. The first carpal bone occurs in approximately 30% of horses but varies widely in size and may articulate with one or both of the second carpal and metacarpal bones.[3,4] The fifth carpal bone occurs rarely, reported as an incidence of 1.4%.[4] Lucent zones in the fourth carpal bone at the site of articulation of the fifth carpal bone, and in the second carpal bone and the proximal aspect of the second metacarpal bone at the site of articulation of the first carpal bone (see Fig. 20-1), are a normal feature of these articulations and should not be misinterpreted as a lytic lesion. The first and fifth carpal bones are more likely to be present bilaterally, whereas radiolucent areas in the second carpal and metacarpal bones are more commonly unilateral.[4] The accessory carpal bone may occasionally develop from more than one center of ossification. Fusion usually occurs, but radiographic separation may be identified during the first 6 months of age.[3,5]

Incidental findings in the distal aspect of the radius include medial and lateral protrusions of the cortex at the distal radial

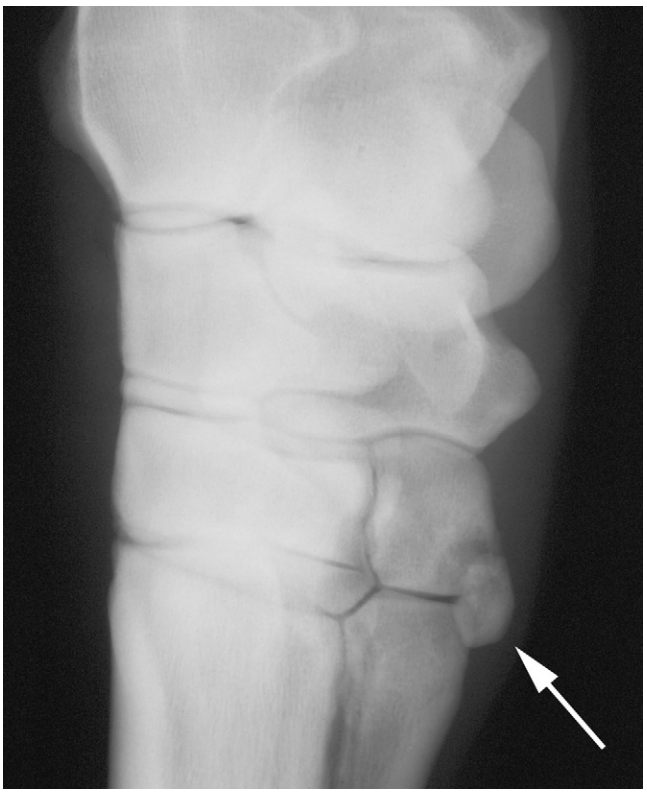


Fig. 20-1 Dorsomedial-palmarolateral radiograph of a carpus. A first carpal bone is present *(white arrow)*. Also note the radiolucent zone in the adjacent second carpal bone and second metacarpal bone. These are normal variants.

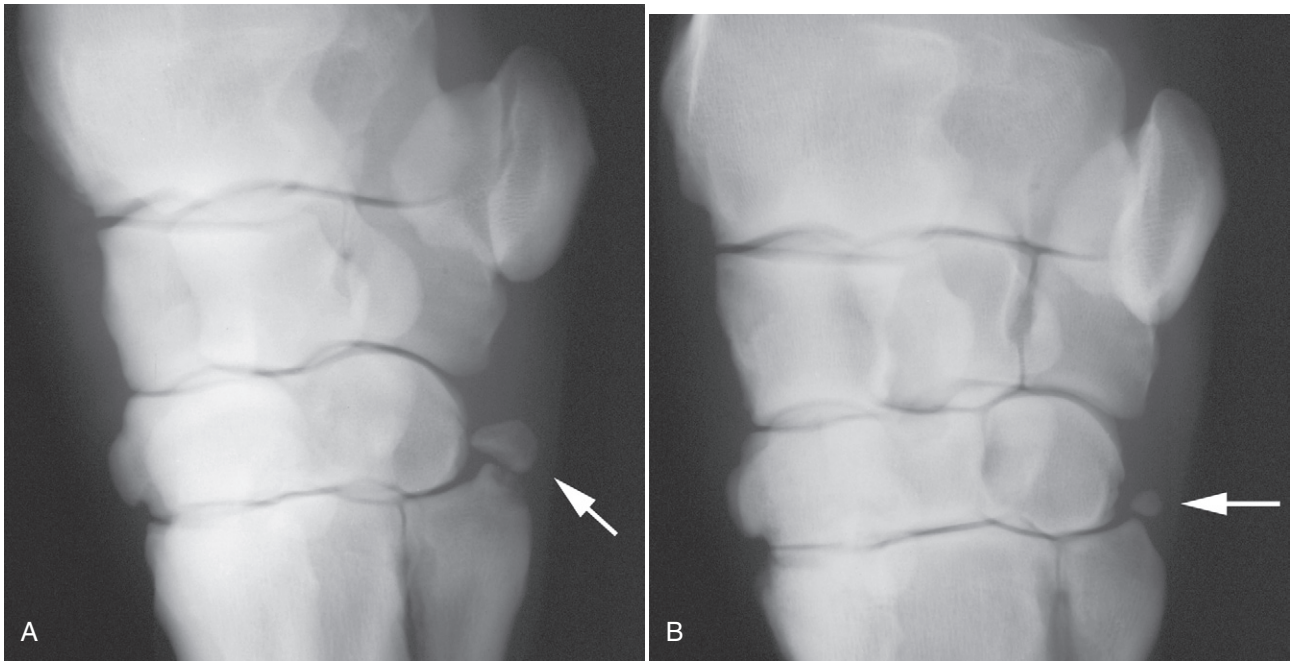


Fig. 20-2 **A,** Dorsolateral-palmaromedial oblique radiograph of a left carpus. A fifth carpal bone is present *(white arrow)*. Also note the unusual shape of the base (head) of the fourth metacarpal bone. These are normal variants. **B,** Dorsolateral-palmaromedial oblique radiograph of the right carpus of the same horse as in **A.** A fifth carpal bone is present *(white arrow)*, but it is smaller and rounder than in the left forelimb. The shape of the base of the fourth metacarpal bone is more normal.

physis in a mature horse (Fig. 20-3, *A*), noted particularly on oblique projections. The caudal aspect of the radius may be slightly irregular immediately proximal to the physis.[6] Until fusion of the distal radial and distal ulnar epiphyses occurs, a radiolucent line or rounded radiolucency may remain in the distal radial epiphysis (Fig. 20-3, *B*), possibly with a notch in the articular surface at this location. Vestigial remnants of the ulna may occur in some horses and are visible radiographically when ossification of a fibrous remnant occurs (Fig. 20-3, *C*).[3]

Small radiolucent zones may occur within any carpal bone, but especially within the ulnar and second carpal bones, the majority of which are of no clinical significance. The palmar aspect of the ulnar carpal bone can be of variable shape; the distopalmar aspect of the bone could be bilobed, rounded, pointed, or fragmented, in addition to having a simple shape (Fig. 20-4).[4] One or more osseous fragments on the palmar aspect of the ulnar carpal bone can also be seen as an incidental finding, usually in association with a lucent area in the ulnar carpal bone (see Fig. 20-4). Occasionally, separate centers of ossification are also identified on the palmaromedial or palmarolateral aspect of the proximal row of carpal bones.

The articulations between the carpal bones should not be confused with sagittal plane fractures of the third carpal bone.[7] For example, in dorsoproximal-dorsodistal (skyline) views of the distal row of carpal bones, the articulation between the third and fourth carpal bones should not be confused with a parasagittal fracture of the lateral aspect of the third carpal bone (Fig. 20-5). On the dorsomedial-palmarolateral oblique view, the articulation between the second and third carpal bones should not be confused with a parasagittal fracture of the medial aspect of the third carpal bone.

Variations in carpal bone shape and structure can depend on the training history of the horse. For example, in horses that have raced or undergone strenuous galloping training, smooth enlargement or modeling of the dorsal aspect of carpal bones is found frequently, and entheseous new bone on the dorsal surface of the carpal bones as the only radiologic abnormality may be insignificant clinically.[3]

Training also has an effect on subchondral and cancellous bone density and mineralization. Therefore horses worked on a soft surface with low training intensity are likely to have thinner subchondral bone at the carpal articular surfaces and less dense cancellous bone than horses with a history of strenuous galloping exercise.[8] This should be taken into account when evaluating radiographs and be differentiated from the severe subchondral bone sclerosis in the third carpal bone that may be associated with osteochondral and slab fractures.[9] Interpretation of the clinical significance of sclerosis of the radial facet of the third carpal in both Thoroughbred and Standardbred racehorses may require nuclear scintigraphy to distinguish between adaptational versus pathologic changes. Increased radiopacity of the third carpal bone can also be recognized in sport horses undergoing high-intensity exercise, including eventing, show-jumping, and endurance horses.

The presence of small enthesophytes or osteophytes is frequently incidental in mature sports horses but should also be considered as a potential indicator of osteoarthritic change when lameness is isolated to the carpal joints by local analgesia. The significance of these findings may depend on the athletic demands of the horse.

ABNORMALITIES

Developmental

Distal Radial Physitis/Epiphysitis

Distal radial physitis is seen most commonly in horses from 4 to 12 months of age,[10] although the distal radial physis in horses up to 2 years old that have recently entered training may also be affected.[11,12] Physitis occurs when endochondral ossification in the metaphyseal growth cartilage is disrupted.[11]

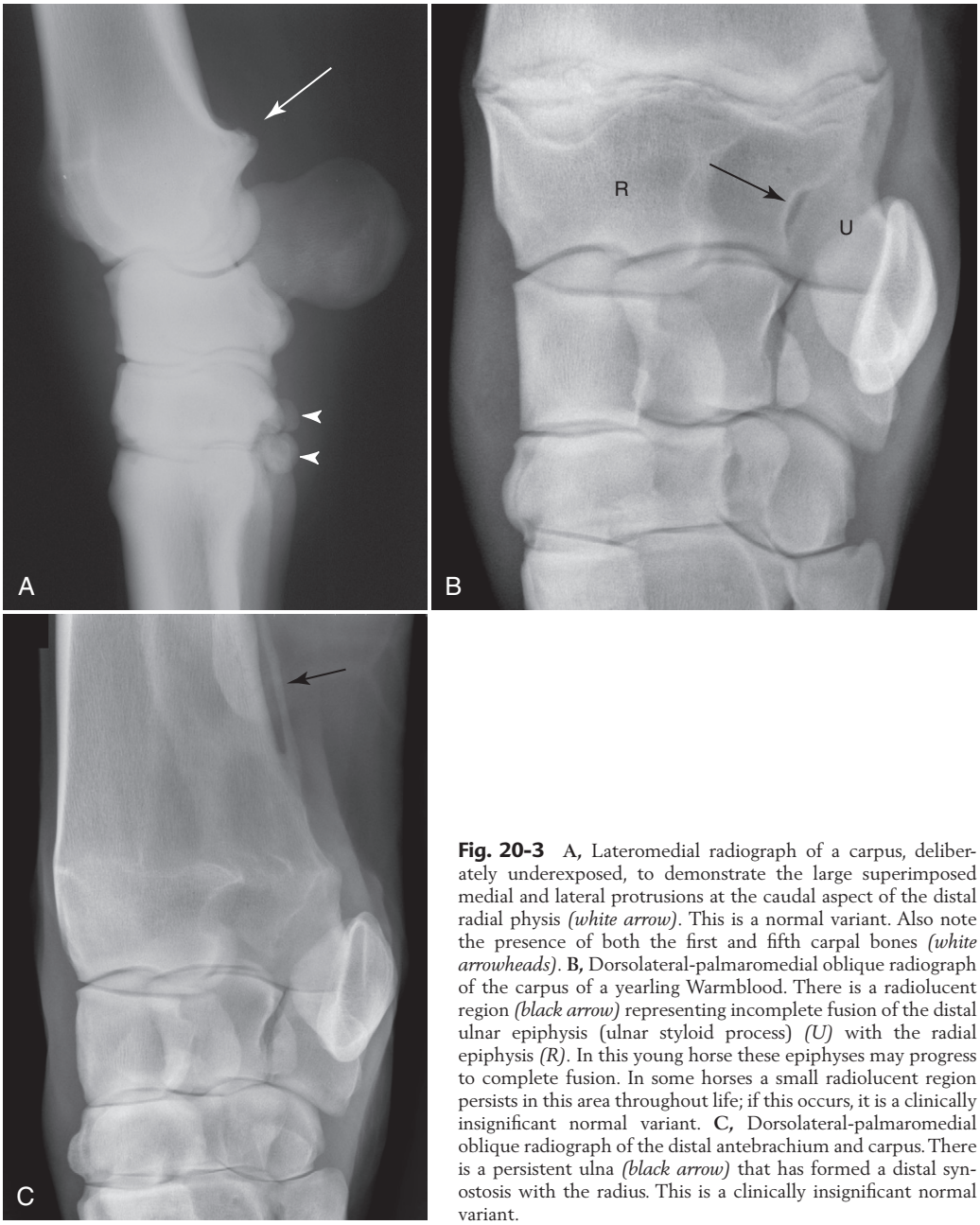


Fig. 20-3 **A,** Lateromedial radiograph of a carpus, deliberately underexposed, to demonstrate the large superimposed medial and lateral protrusions at the caudal aspect of the distal radial physis *(white arrow)*. This is a normal variant. Also note the presence of both the first and fifth carpal bones *(white arrowheads)*. **B,** Dorsolateral-palmaromedial oblique radiograph of the carpus of a yearling Warmblood. There is a radiolucent region *(black arrow)* representing incomplete fusion of the distal ulnar epiphysis (ulnar styloid process) *(U)* with the radial epiphysis *(R)*. In this young horse these epiphyses may progress to complete fusion. In some horses a small radiolucent region persists in this area throughout life; if this occurs, it is a clinically insignificant normal variant. **C,** Dorsolateral-palmaromedial oblique radiograph of the distal antebrachium and carpus. There is a persistent ulna *(black arrow)* that has formed a distal synostosis with the radius. This is a clinically insignificant normal variant.

Standard views are recommended, although the dorsopalmar may be most useful. The physis appears wider with irregular margins as a result of remodeling of the surrounding metaphysis (Fig. 20-6). The physis appears flared at the edges from periosteal new bone formation, with the edges of the physis appearing to protrude from the surface of the cortex on both proximal and distal aspects of the physis.[3,11] Associated soft tissue swelling may be present at the site.

Incomplete Ossification of Carpal Bones

Premature or dysmature foals may have incomplete ossification of the carpal bones at birth (Fig. 20-7). This may lead to secondary angular limb deformity resulting from collapse of the poorly ossified carpal bones being unable to withstand the forces of normal weight bearing.[13,14]

Although a dorsopalmar view is the most useful for assessing the degree of deformity,[13,14] obtaining a full radiographic series is recommended because carpal bone deformity exists in a variety of configurations. The carpal bones appear small and rounded, without their normal cuboidal shape (Fig. 20-8).[3,15] Relative enlargement of intercarpal joint spaces is therefore present. Angular limb deformity may be noted on radiographs, with the deformity at the level of the carpal bones and not the distal radial physis.[3,13,14] Collapse and malformation of one or more carpal bones may be observed in severe cases.

Angular Limb Deformities

Angular limb deformities can arise from congenital, developmental, or acquired conditions.[13,14,16-18] Congenital problems

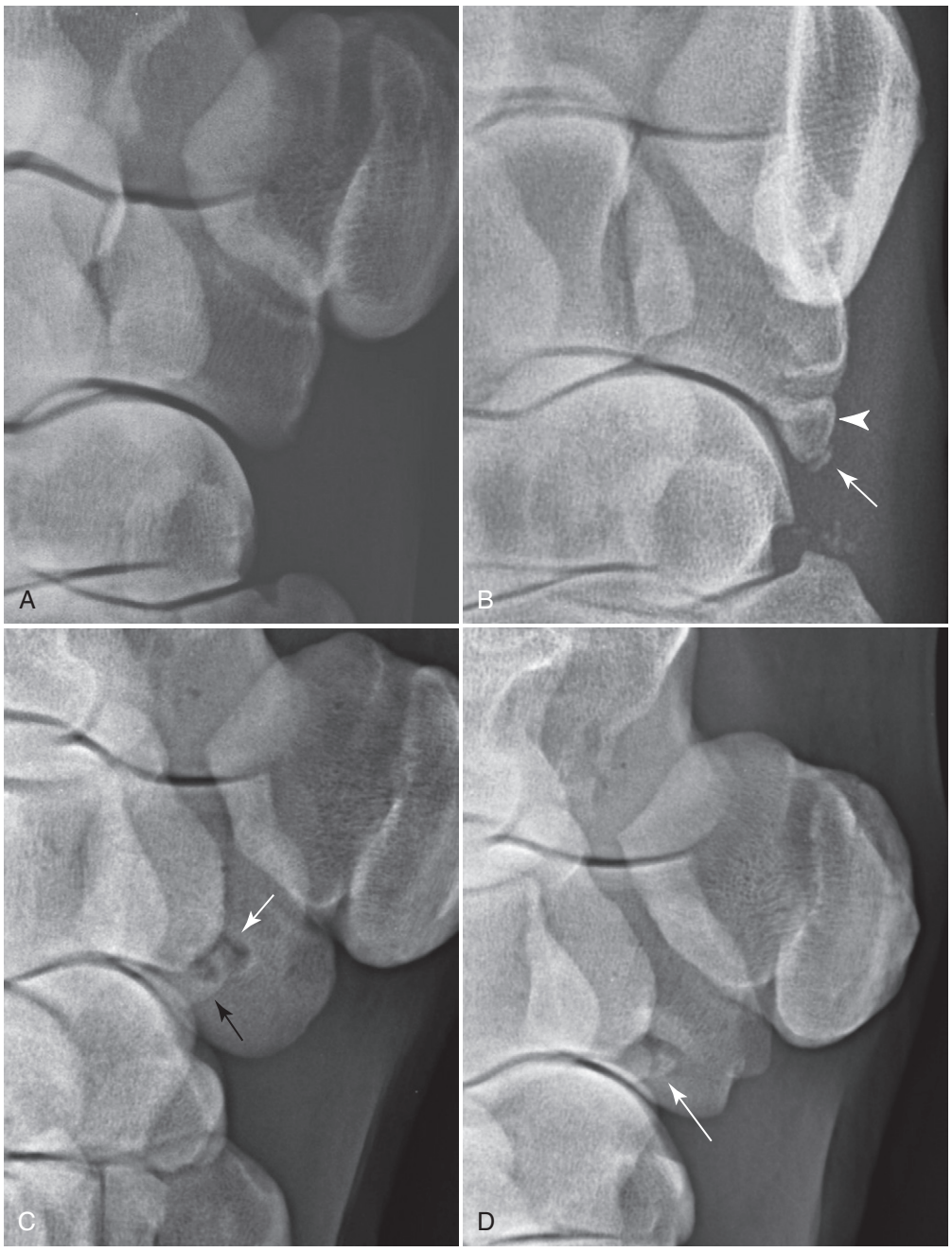


Fig. 20-4 Dorsolateral-palmaromedial oblique carpal radiographs showing the normal or normal variations in the appearance of the ulnar carpal bone. **A,** Normal homogeneous ulnar carpal bone. **B,** There is an unusual configuration of the distal palmar aspect of the ulnar carpal bone *(white arrowhead)* with a separate center of ossification immediately distal to this *(white arrow)*. Note also the poorly demarcated mineralization proximal to the base of the fourth metacarpal bone. **C,** There is an osseous cystlike lesion in the ulnar carpal bone *(white arrow)* with an osseous fragment distal to this *(black arrow)*. **D,** There are two well-defined osseous fragments overlying the ulnar carpal bone *(white arrow)* associated with a less well-demarcated radiolucent area in the ulnar carpal bone.

relate to in utero factors such as positioning, infective or chemical insult, nutrition, and skeletal maturity at birth. Developmental abnormalities have been attributed to a variety of factors associated with developmental orthopedic disease, including nutrition, exercise, and overloading, although damage to one side of the joint, epiphysis, or physis leading to asymmetric growth will be exaggerated in a developing horse. Acquired deformities may be the result of trauma, including fracture, or infection.

Extended dorsopalmar views, including as much as possible of the distal aspect of the radius and the proximal aspect of the metacarpal region, are the most useful images in the majority of horses (Fig. 20-9).[3,16] Standard radiographic views are required for assessing severe deformity, if onset is acute or swelling or lameness is present.

On dorsopalmar views, the long axis of the radius is out of line with the long axis of the third metacarpal bone. At the level of carpus, valgus deformity (lateral deviation of the distal

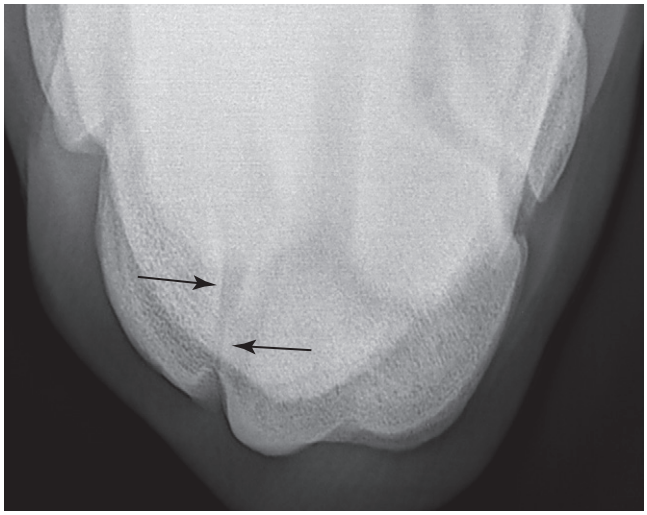


Fig. 20-5 Dorsoproximal-dorsodistal radiograph of a normal carpus. The normal articulation between the third and fourth carpal bones *(black arrows)* should not be confused with a parasagittal fracture of the third carpal bone.

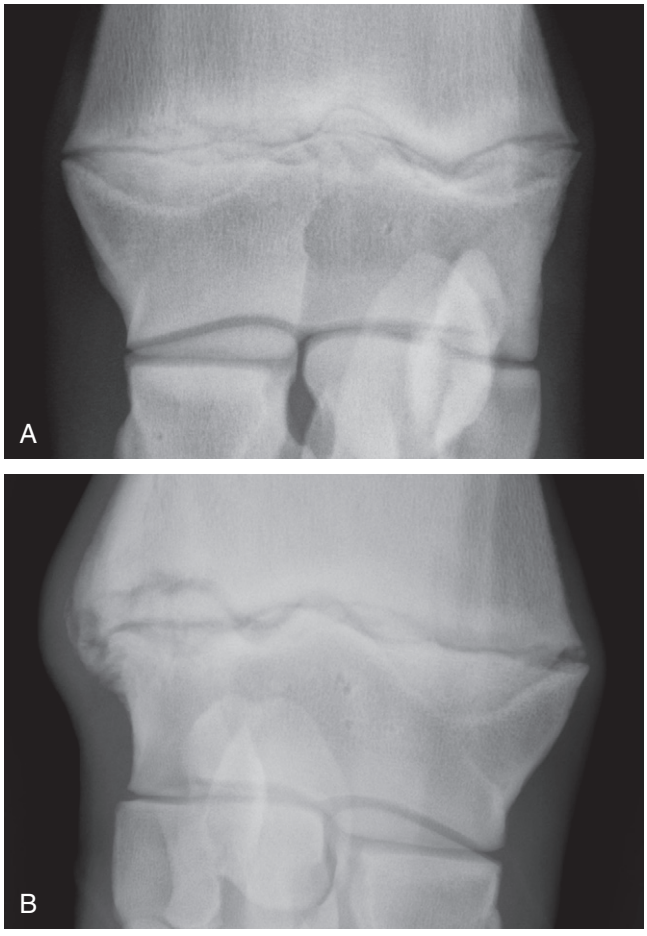


Fig. 20-6 **A,** Dorsopalmar radiograph of the distal radius of a normal 1.5-year-old Andalusian. **B,** Dorsopalmar radiograph of a 13-month-old quarter horse with distal radial physitis. Medial is to the left in both images. In **B,** there is flaring of the distal metaphyseal region of the radius, especially notable medially, and irregular new bone on the medial aspect of the distal radial epiphysis and metaphysis. The distal radial physis is irregular, there is a generalized increased radiopacity of the distal metaphyseal region of the radius, and there is irregular widening of the physis. There is also an angular deformity in **B;** this was obvious clinically and also when a greater length of the limb was included in the image.

aspect of the limb) is observed most frequently, but varus deformity (medial deviation) does occur. The location of the abnormality is usually at the level at which maximal deviation occurs. By drawing lines bisecting the long axis of radius and the long axis of the third metacarpal bone, the level of deviation can be determined (see Fig. 20-8). When an angular limb deformity is not present, the lines drawn through the long bones should be continuous. However, when a deviation is present, these lines intersect at the level of maximal deviation, giving a guide to the structures involved. This technique can also be useful for measuring the degree of deformity and monitoring response to treatment. Variation in obliquity of sequential radiographs can alter the degree of deviation assessed from the intersecting lines. Another guide to normal alignment is the positioning of the joint surfaces. When no abnormality is present, the articular surfaces of the antebrachiocarpal, middle carpal, and carpometacarpal joints should be parallel and perpendicular to the long axis of the limb. With joint-based abnormalities, a loss of articular surface alignment in the affected joint(s) may occur.[3,14,16]

Abnormalities that can be observed include the following, which can be targeted on the basis of the level of maximal deviation.[3,13,14,16-18]

Diaphyseal deformity: This occurs only rarely. The site of maximal deviation is at the level of the diaphysis, making a straight line bisecting the affected long bone impossible to draw.

Distal radial physis abnormality: On dorsopalmar radiographs, the physis may be wider on the medial or lateral aspect and narrower or fused on the opposite side. This is associated with deviation away from the wider side, because metaphyseal growth continues on that side but is restricted on the contralateral closed aspect of the physis. Location of maximal deviation is at the level of the distal radial physis.

Epiphyseal growth imbalance: The distal radial epiphysis may appear wedge-shaped on dorsopalmar radiographs. This may result from dysplasia of the distal radial epiphysis. The lateral styloid process may also be characterized by delayed development. Fusion of the distal radial and distal ulnar epiphyses should occur between 3 and 6 months of age. Altered development of the distal ulnar epiphysis can be seen as lack of growth on the lateral aspect of the distal radius. Location of maximal deviation is at the level of the epiphysis, and the distal radial physis and antebrachiocarpal articular surfaces are no longer parallel.

Incomplete ossification of carpal bones: In severe ossification defects, collapse or deformity of one or more incompletely ossified carpal bones may occur, resulting in angular limb deformity. Location of maximal deviation is at the level of the carpal bones where the collapse or deformity occurs. Lines through the joint spaces may no longer be parallel.

Flaccidity or damage to periarticular structures: Location of maximal deviation may be variable, although it is often at the distal articular surface of the radius. Widening of joint space(s) on one side may occur, although the degree of deformity can vary if medial or lateral stresses are applied.

Osseous or Subchondral Cystlike Lesions

Subchondral or osseous cystlike lesions occur in the carpal bones, the proximal aspect of the second or fourth metacarpal bones, and the distal aspect of the radius, with or without an articular component.[3,19] The most commonly reported site is the ulnar carpal bone. Osseous cystlike lesions in the proximal aspect of the second metacarpal bone seem to occur most

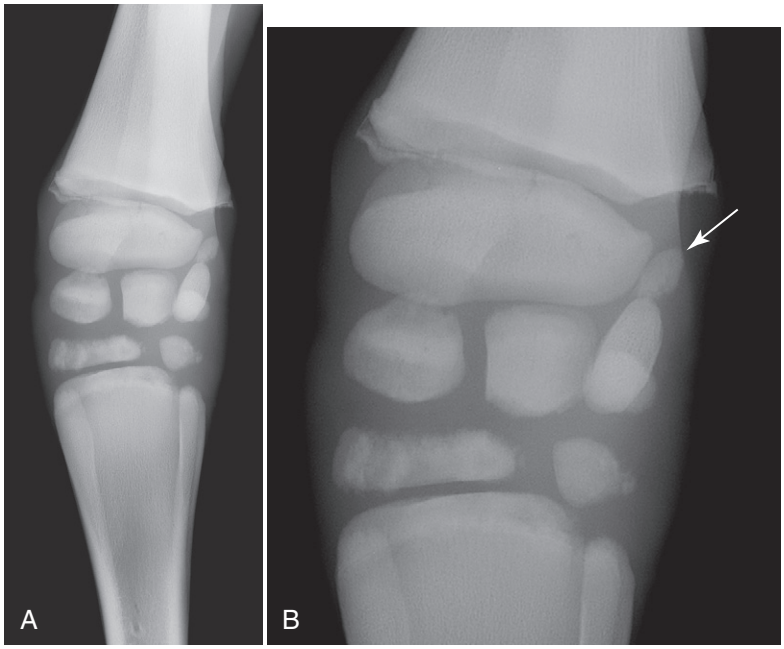


Fig. 20-7 Dorsopalmar radiograph **(A)** and close-up view **(B)** of a carpus of a premature foal. Medial is to the left. The carpal bones are small and have irregular margins as a result of incomplete ossification. An angular limb deformity is already present. In **B,** the styloid process of the ulna *(white arrow)* has not yet been incorporated into the distal radial epiphysis; this is normal in young foals.

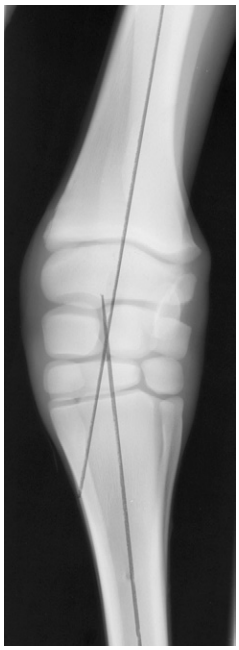


Fig. 20-8 Dorsopalmar radiograph of a carpus of a 6-week-old foal. Medial is to the left. Mild soft tissue swelling is present on the medial aspect of the carpus. The carpal bones are more rounded than normal, and the joint spaces are wider as a result of incomplete ossification. A carpal valgus deformity is associated with this incomplete ossification. Lines bisecting the long axes of the radius and third metacarpal bone intersect at the level of the proximal row of carpal bones, suggesting that the maximal deviation occurs at this level.



Fig. 20-9 Dorsopalmar image of a carpus of a 4-month-old foal. Medial is to the left. A carpal valgus angular limb deformity is present. The distal radial epiphysis is slightly wedge-shaped, being taller medially. The distal radial physis is not parallel with the antebrachiocarpal, middle carpal, or carpometacarpal joints.

frequently when a first carpal bone is present (see Fig. 20-1) and may occur in conjunction with a cystlike lesion in the first carpal bone. Osseous cystlike lesions are noted frequently as an incidental finding, but some are associated with lameness.[20] Generally, those situated deep in the bone, particularly in the first, second, and ulnar carpal bones, and proximal aspect of the second metacarpal bone, are unlikely to be associated with lameness. However, lesions associated with articular margins and subchondral cystlike lesions in the distal medial aspect of the radius are more likely to be clinically significant (Fig. 20-10).[21] Lameness can vary in severity and progression, and clinical progression may not closely relate to radiological signs. Scintigraphic imaging can give guidance about the current activity of the bone around the cystic lesion.

Osseous cystlike lesions are generally considered developmental abnormalities, but trauma to the articular cartilage and

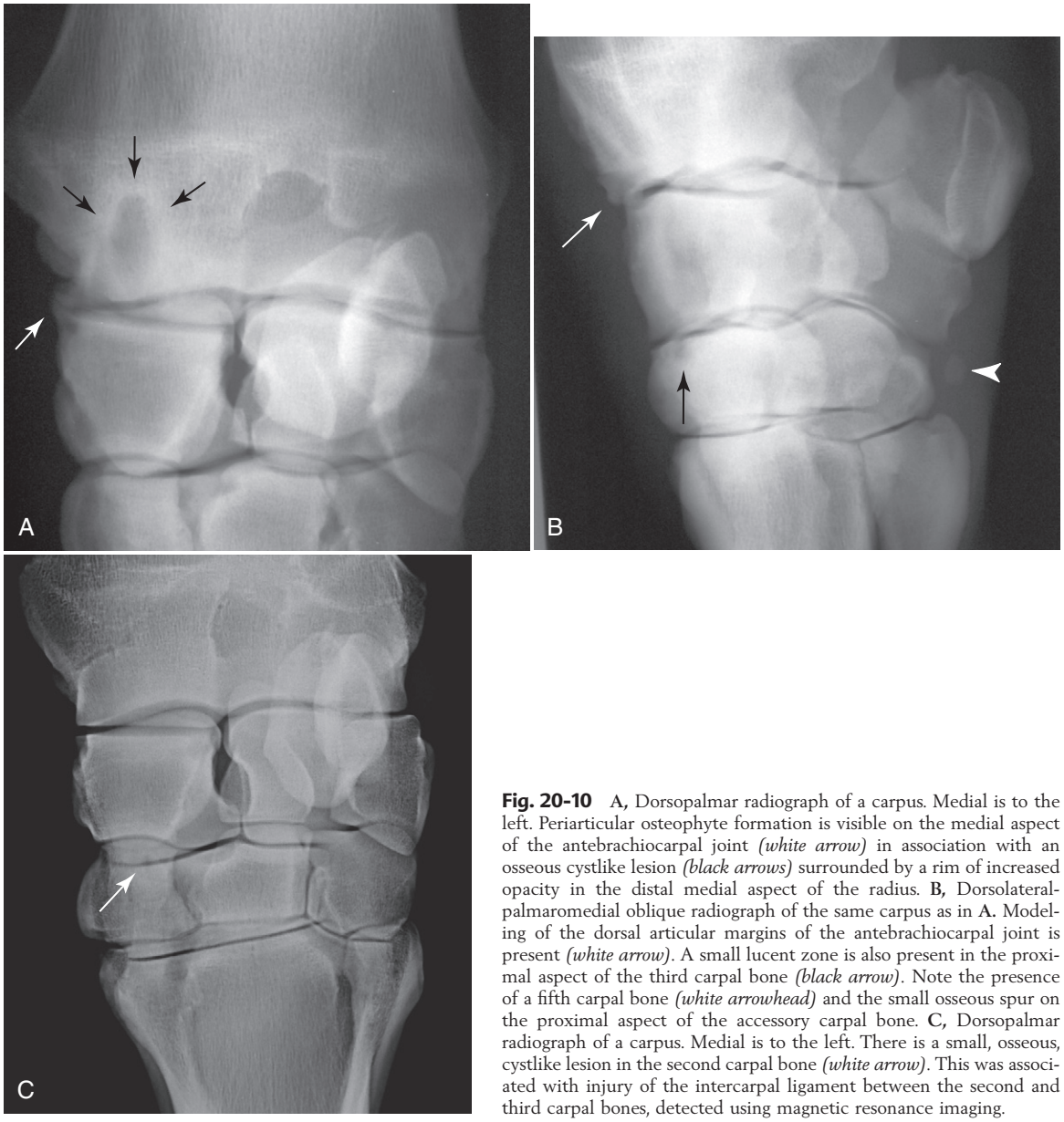


Fig. 20-10 **A,** Dorsopalmar radiograph of a carpus. Medial is to the left. Periarticular osteophyte formation is visible on the medial aspect of the antebrachiocarpal joint *(white arrow)* in association with an osseous cystlike lesion *(black arrows)* surrounded by a rim of increased opacity in the distal medial aspect of the radius. **B,** Dorsolateral-palmaromedial oblique radiograph of the same carpus as in **A.** Modeling of the dorsal articular margins of the antebrachiocarpal joint is present *(white arrow)*. A small lucent zone is also present in the proximal aspect of the third carpal bone *(black arrow)*. Note the presence of a fifth carpal bone *(white arrowhead)* and the small osseous spur on the proximal aspect of the accessory carpal bone. **C,** Dorsopalmar radiograph of a carpus. Medial is to the left. There is a small, osseous, cystlike lesion in the second carpal bone *(white arrow)*. This was associated with injury of the intercarpal ligament between the second and third carpal bones, detected using magnetic resonance imaging.

subchondral bone can potentially lead to formation of these cystlike lesions.[22] Osseous cystlike lesions in the ulnar carpal bone with or without an adjacent osseous fragment have been linked to tearing of the attachment of the lateral palmar intercarpal ligament and associated with lameness.[22] Occasionally an osseous cystlike lesion is seen in association with injury of a transverse intercarpal ligament (Fig. 20-10, *C*). If cystlike lesions are observed in a foal, then osteomyelitis should be considered and other procedures used to investigate the presence of septic foci.

Subchondral or osseous cystlike lesions are well-circumscribed circular or semicircular lucent areas within the carpal bones, the distal aspect of the radius, or in the proximal aspect of the second or fourth metacarpal bones. An area of opacity may surround the lucent zone. For articular lesions, clear communication with the articular surface may be present, although more frequently the lesions are adjacent to the articular surface and a clear communication cannot be established radiographically. Radiographic evidence of secondary osteoarthritis may be visible (Fig. 20-10, *A* and *B*).

Soft Tissue Problems

Periarticular Soft Tissues

Although alterations to periarticular soft tissues may be noted on radiographs, ultrasonographic assessment is usually more informative. For synovial structures or with penetrating wounds, contrast medium may be necessary to outline filling defects or define communication with other structures.

Periarticular soft tissue swelling may be either focal or diffuse. Cellulitis is observed most commonly as diffuse soft tissue swelling that is not localized purely to the region of the carpus and affects the limb circumferentially. However, the presence of a foreign body or wound may lead to more focal enlargement. If a foreign body is relatively radiopaque, then it may be detected radiographically, but ultrasonography is often more useful.

The following conditions are associated with swelling on the dorsal aspect of the carpal region.

Carpal Hygroma. A carpal hygroma is a subcutaneous sac or acquired bursa usually positioned over the dorsal aspect of the carpal region.[7] A hygroma usually occurs as a result of

blunt trauma at the site and is generally nonpainful, although it may have been painful at the site when the inciting event occurred. Gait alteration is not generally observed unless the hygroma is so large that carpal flexion is restricted.

Standard radiographic views and contrast-medium injection into the mass are required for diagnosis, with ultrasonography to evaluate the adjacent soft tissues. Radiographic diagnosis is based on soft tissue swelling over the dorsal aspect and the presence of a defined structure that has no communication with other structures after contrast-medium injection.

Distention/Synovitis of Extensor Carpi Radialis, Common Digital Extensor, or Long Digital Extensor Tendon Sheaths. Rupture of the extensor carpi radialis tendon should be considered in neonatal or young foals with distention of the tendon sheath of the extensor carpi radialis, particularly if flexural deformity is also present.[23,24] In horses of any age, traumatic or septic damage to an extensor tendon sheath may occur, potentially with coexisting tendon damage. Ultrasonographic examination is often more useful in assessment of these injuries than is radiographic examination, although the use of radiography with contrast-medium injection adds information about communication between synovial cavities. To determine if communication exists between the carpal joints and tendon sheath(s), double-contrast techniques may also be useful. Contrast-medium injection can also be used to identify filling defects associated with adhesion formation or synovial proliferation.

Radiographs are characterized by soft tissue swelling over the dorsal aspect of the carpus. Swelling may be more defined in the region of the tendon sheath. Chronic synovitis may be associated with periosteal new bone formation on adjacent structures. In particular, extensor carpi radialis synovitis may be associated with periosteal new bone on the cranial distal aspect of the radius (Fig. 20-11).[24]

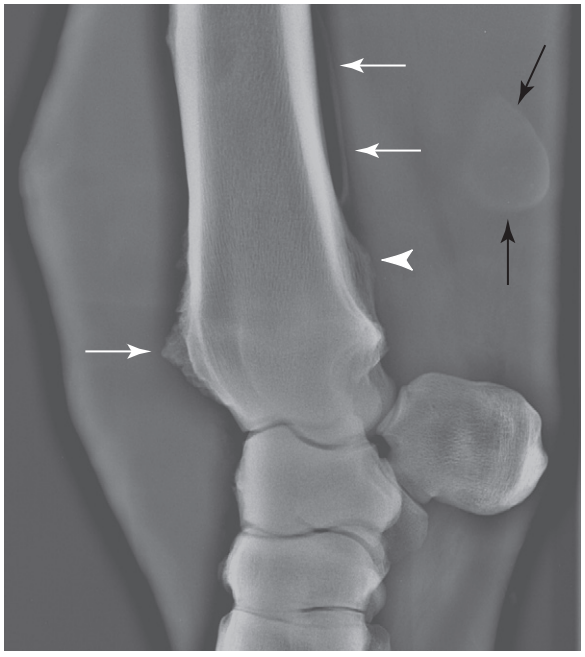


Fig. 20-11 Lateromedial radiograph of the right carpus of a 12-year-old crossbred gelding 6 weeks after a traumatic injury. There is extensive soft tissue swelling on the craniodistal aspect of the antebrachium that is centered more proximally than a sharply pointed exostosis on the distal aspect of the radius *(large white arrow)*. Ultrasonographically there was huge enlargement of the tendon of extensor carpi radialis, which had heterogeneous echogenicity and adhesions to the tendon sheath. Note also the vestigial ulna *(small white arrows)* and the normal bony protuberance on the distal caudal aspect of the radius *(white arrowhead)*. The well-demarcated opacity on the distal caudal aspect of the antebrachium *(black arrows)* is the chestnut.

Herniation of Carpal Joint Synovial Membrane. Herniation of a joint capsule can occur as a result of trauma or in association with osteoarthritis. It is likely to be nonpainful and often only noted as an incidental finding. On radiographs a focal or slightly generalized soft tissue swelling is visible, most frequently dorsolateral.[3] Contrast-medium injection reveals communication between the subcutaneous swelling and the joint of origin.

Synovitis. In most horses the antebrachiocarpal joint cavity remains separate from the other joints of the carpus, whereas the middle and carpometacarpal joints usually communicate.[2] Distention of either the antebrachiocarpal or middle carpal joint is associated with swelling on the dorsal aspect, often obscuring the normal dorsal radiolucencies associated with the fat pads (Fig. 20-12, *A*).[25] An antebrachiocarpal joint effusion is located as a swelling on the dorsal aspect in the proximal third of the carpal region at the level of the articulation between the radius and proximal row of carpal bones (Fig. 20-12, *B*), whereas middle carpal joint distention is located at the midcarpal level at the level of the articulation between the two rows of carpal bones. Carpometacarpal joint distention is difficult to see, but an effusion in the middle carpal joint may suggest synovitis in this joint. The osseous tissues should be examined carefully for abnormalities that could lead to the detected synovitis. Further examination of the soft tissues may be performed with ultrasonography.

Calcinosis Circumscripta. Periarticular or intraarticular calcified masses can occur in horses; described as calcinosis circumscripta or tumoral calcinosis. These have been reported within the equine antebrachiocarpal and middle carpal joints.[26,27] Affected horses have a firm swelling that is minimally painful on palpation and that may follow a history of previous trauma to the region. Radiographic examination usually reveals a granular, radiopaque mass with localized soft tissue swelling. Surgical excision may be indicated.

Conditions Associated with Swelling on the Palmar Aspect of the Carpal Region

Generalized swelling may occur circumferentially at the level of the carpus in conditions such as cellulitis and therefore be seen as swelling on the palmar aspect in addition to other sites. Generalized periarticular soft tissue swelling on the dorsal aspect of the carpus may be caused by fractures or severe osteoarthritis. Swelling localized to the palmar aspect may be associated with palmar wounds, foreign body penetration, or trauma.

Distention of the Carpal Sheath. Conditions affecting the carpal sheath lead to swelling on the palmar aspect, which may be detectable radiographically.[28,29] Radiographic examination is necessary in horses with carpal sheath distention to identify or rule out osseous abnormalities.[29] Ultrasonographic examination is necessary to evaluate the soft tissue structures within the carpal sheath. Primary idiopathic synovitis or hemorrhage appears unremarkable on radiographic examination, apart from the soft tissue swelling caused by the carpal sheath distention. Desmitis of the accessory ligament of the deep digital flexor tendon, superficial digital flexor tendonitis, or deep digital flexor tendonitis within the sheath may be associated with carpal sheath distention but are better evaluated by ultrasonography because no abnormalities are generally detected on radiographs.

Radiographic abnormalities are seen with acute or chronic fracture of the accessory carpal bone or palmar fractures of

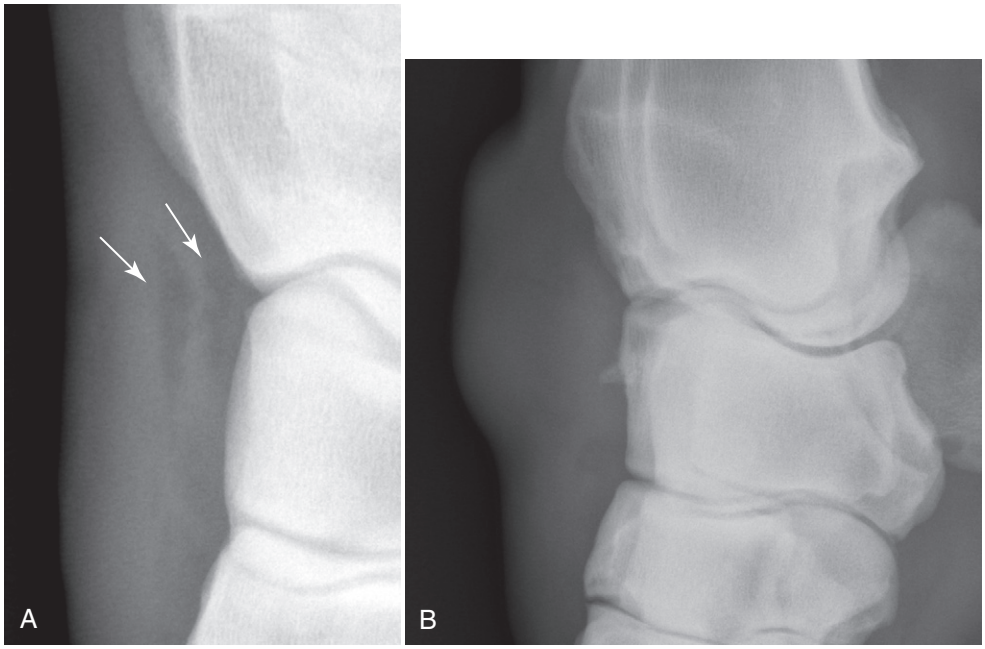


Fig. 20-12 **A,** Lateromedial radiograph of the dorsal aspect of the antebrachiocarpal region. Normal extracapsular fat collections dorsal to the proximal row of carpal bones *(white arrows)* are often misinterpreted as free tissue gas. **B,** Lateromedial radiograph of the dorsal aspect of the antebrachiocarpal region of a horse with antebrachiocarpal joint effusion. The normal dorsally located fat pads are obliterated by the swelling. There is also an osseous opacity superimposed over the dorsal aspect of the proximal row of carpal bones.

the other carpal bones, which all have the potential to cause carpal sheath distention.[30-32]

Osteochondroma of the Distal Caudal Aspect of the Radius and Radial Physeal Exostoses. Distention of the carpal sheath can be caused by the presence of an osteochondroma on the distal caudal aspect of the radius or an axial exostosis on the caudal aspect of the distal radial physis (Fig. 20-13). Both lesions may result in impingement on the deep digital flexor tendon with secondary synovitis. Horses with an osteochondroma are generally lame, with the lameness being exacerbated by flexion. However, horses with a physeal exostosis may have sporadic severe lameness that may not induce detectable synovitis of the carpal sheath. An osteochondroma, which is a cartilage-covered exostosis,[29-33] is usually located on the distal caudal aspect of the radius just proximal to the distal radial physis (Fig. 20-14). It appears as a bony outgrowth that is continuous with the cortex.

Exostoses at the level of the distal radial physis must be differentiated from the normal medial and lateral protuberances and in some horses may best be detected in oblique views (see Figure 20-13, *B*). Concurrent damage of the deep digital flexor tendon often occurs and can be detected by ultrasonographic examination. Treatment is by surgical excision of the osteochondroma or physeal exostosis.

Mineralized Opacities within the Periarticular Soft Tissues. Dystrophic mineralization may be diffuse or localized and occurs as a result of trauma (see Fig. 20-13) or local corticosteroid injection.

Osseous and Osteochondral Abnormalities

Osteochondral damage of the antebrachiocarpal and middle carpal articular surfaces occurs most frequently in Thoroughbred racehorses,[34,35] although the incidence is also high in racing quarter horses[36] and Standardbreds.[7,37] Racing on dirt tracks is associated with a higher incidence of carpal lesions than is racing on turf.[38] Carpal injures are uncommon in horses that are not subjected to race training, which may be a function of reduced stresses on the carpal joints or more advanced age at which they undergo athletic training.[38] In racehorses in the United States, an asymmetry in the incidence of middle carpal joint osteochondral lesions has been noted between the two forelimbs, with an increased incidence of fractures in the right forelimb.[36] This is attributed to the oval shape of the racetrack and anticlockwise direction of the races in the United States.[36-39]

In racehorses the middle carpal joint is affected most frequently, whereas in nonracehorses the antebrachiocarpal joint has a higher prevalence of injury. Most lesions occur on the dorsal aspect of the affected joint. In Thoroughbred and quarter horses, the most frequent site of osteochondral injuries is the dorsodistal surface of the radial carpal bone (Fig. 20-15), followed by the dorsoproximal surface of the third carpal bone (primarily medially) and then the dorsodistal surface of the intermediate carpal bone.[36,37,40] Lesions that can be observed may involve articular cartilage erosion, osteochondral chip fractures, or slab fractures (see Fig. 20-15). Chip fractures occur near the dorsal margin of a carpal bone, affecting only one articular surface. Slab fractures are observed primarily at a less-marginal location and involve both proximal and distal articular surfaces of the affected carpal bone. In the dorsal medial aspect of the third carpal bone, dorsal plane osteochondral slab fractures tend to occur most commonly, followed by very large osteochondral chip fractures, which are located less close to the dorsal margin.[41] Sagittal plane, incomplete slab fractures are observed less frequently.

Carpal Bone Sclerosis

Osteochondral injuries affecting the middle carpal joint are most likely chronic overload injuries.[38,42] Although a single massive overload can occur, repetitive trauma resulting

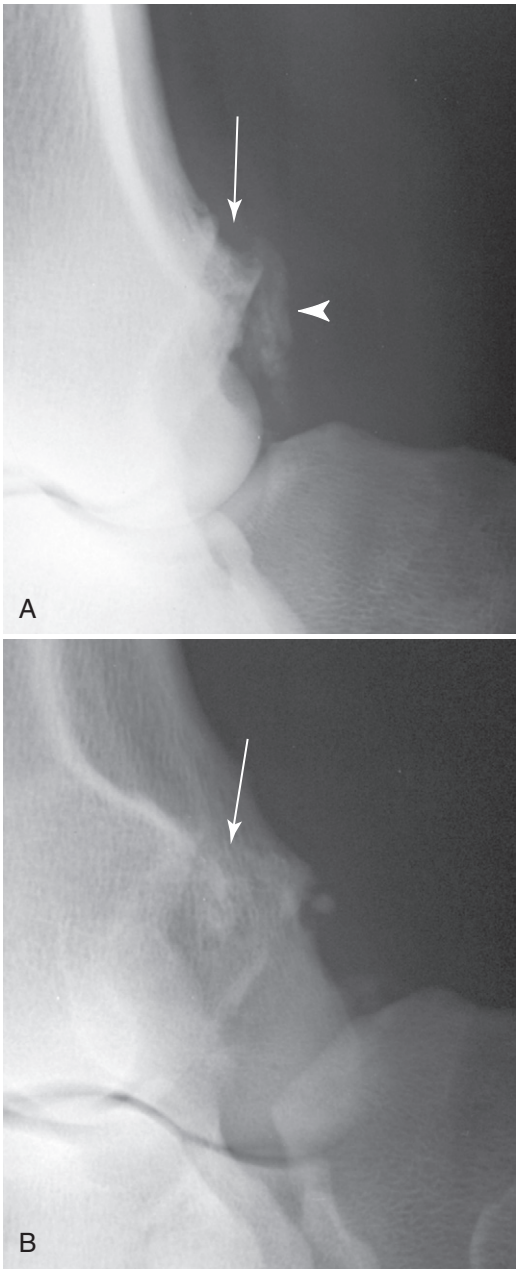


Fig. 20-13 **A,** Lateromedial radiograph of a carpus. Linear mineralization *(white arrowhead)* is present in the soft tissues on the distal caudal aspect of the radius, confirmed ultrasonographically to be within the deep digital flexor tendon. An osseous projection *(white arrow)* is present at the level of the transverse ridge of the radius, which was impinging on the deep digital flexor tendon. **B,** Dorsolateral-palmaromedial oblique image of the same carpus as in **A.** Normal bony prominences are on the caudomedial and caudolateral aspects of the radius, but the radiopacity between these *(white arrow)* represents the abnormal osseous projection that was impinging on the deep digital flexor tendon.

in microdamage, leading to ultimate overload, is a more common etiology for osteochondral injury.[8,38,43] In the radial carpal bone, osteochondral fractures may be preceded by lucency, apparent softening and collapse of the subchondral bone,[38,44] seen as a focal radiolucency on the distal aspect of the bone (Fig. 20-16). This has also been reported to occur at focal sites in the third carpal bone.[38] In the third carpal bone, cartilage erosion and fracture are often associated with bone sclerosis seen as increased radiopacity and loss of trabecular pattern.[38,45] In pathologic bones, this sclerosis is maximal in the medial facet approximately 10 to 20 mm palmar to the dorsal margin (Fig. 20-17).[45] This sclerosis has been suggested to be associated with decreased absorption of concussive forces by the trabecular bone, followed by increasing demands on the articular cartilage and subchondral bone to attenuate these forces.[8,38,43] This apparent stress concentration in the articular cartilage and subchondral bone has been suggested as the cause of articular cartilage failure and subchondral bone loss.[45]



Fig. 20-14 Lateromedial radiograph of the distal aspect of the radius of a 4-year-old Clydesdale. A small columnar exostosis arises from the distocaudal aspect of the radius *(white arrows)*. This is a common location and appearance of osteochondroma in the horse.

Subchondral lucency of the third carpal bone has been reported in Standardbred racehorses.[46] Areas of lucency are often surrounded by subchondral sclerosis.[47] These appear to be sites of bone collapse after repetitive trauma. This is seen most clearly in dorsolateral-palmaromedial oblique views.

Carpal Bone Chip Fractures

Dorsal Aspect. Osteochondral fragmentation or chip fracture formation is most likely to involve the dorsodistal articular border of the distal aspect of the radius, dorsoproximal and dorsodistal aspects of the radial and intermediate carpal bones, and the dorsoproximal aspect of the third carpal bone (Figs. 20-18 and 20-19; see Fig. 20-15).[36,37,41,48] However, the expected lesion distribution differs among breeds, with most lesions occurring on the medial aspect of the middle carpal joints in Standardbred racehorses but affecting both the antebrachiocarpal and middle carpal joints in Thoroughbred and quarter horse racehorses. Although affected horses are usually markedly lame at the time of initial damage, the degree of lameness may reduce to a mild level or progress to become severe. Although effusion and local pain may be present, only very mild signs may be observed in some horses. Arthroscopic removal of small fragments may be indicated, although with large fragments arthroscopically guided internal fixation may give an improved prognosis compared with fragment removal.[49]

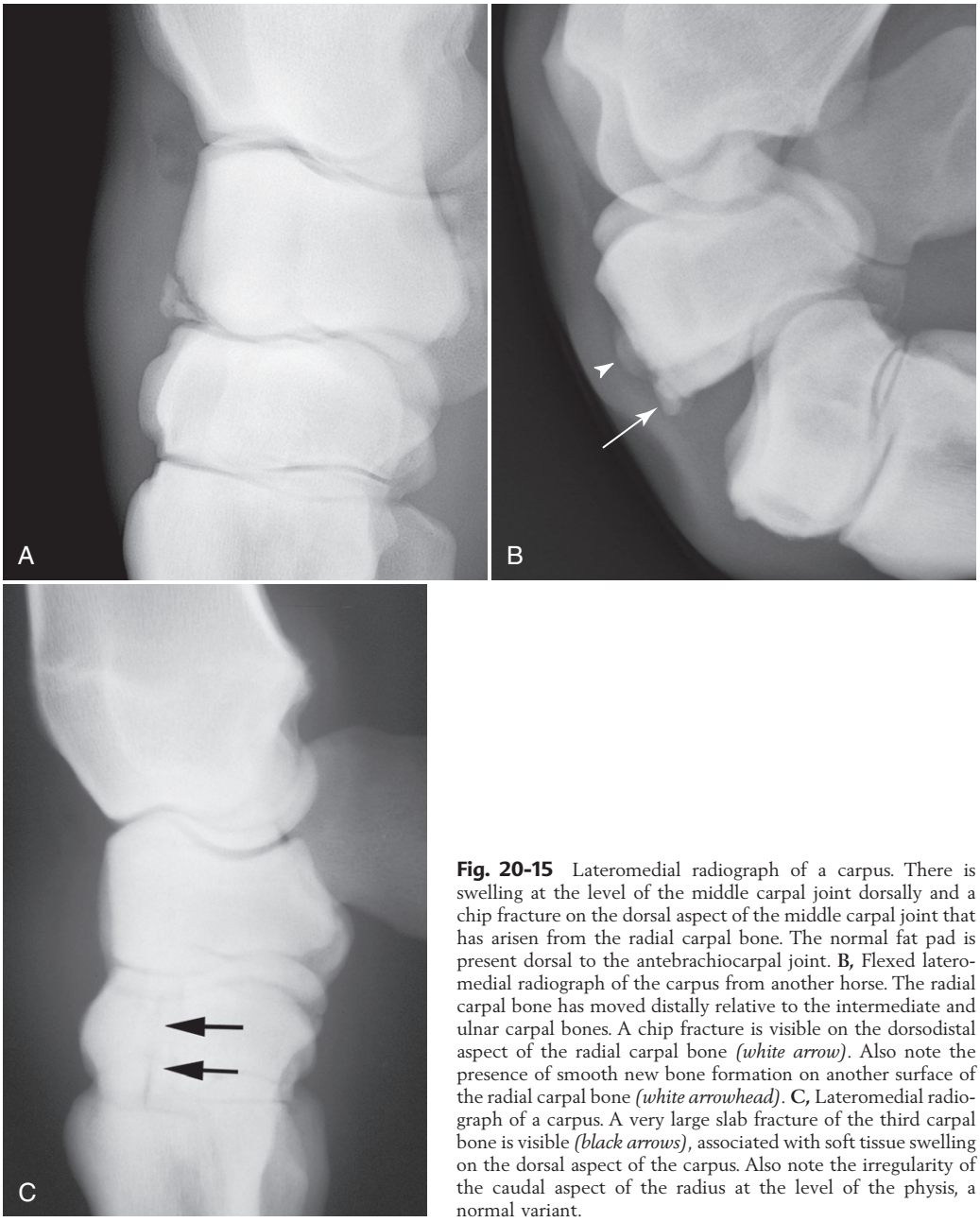


Fig. 20-15 Lateromedial radiograph of a carpus. There is swelling at the level of the middle carpal joint dorsally and a chip fracture on the dorsal aspect of the middle carpal joint that has arisen from the radial carpal bone. The normal fat pad is present dorsal to the antebrachiocarpal joint. **B,** Flexed lateromedial radiograph of the carpus from another horse. The radial carpal bone has moved distally relative to the intermediate and ulnar carpal bones. A chip fracture is visible on the dorsodistal aspect of the radial carpal bone *(white arrow)*. Also note the presence of smooth new bone formation on another surface of the radial carpal bone *(white arrowhead)*. **C,** Lateromedial radiograph of a carpus. A very large slab fracture of the third carpal bone is visible *(black arrows)*, associated with soft tissue swelling on the dorsal aspect of the carpus. Also note the irregularity of the caudal aspect of the radius at the level of the physis, a normal variant.

All radiographic views should be evaluated, including a dorsopalmar, lateromedial, at least two obliques, a flexed lateromedial, and dorsoproximal-dorsodistal views of each row of carpal bones. The contralateral limb should also be evaluated routinely because lesions are commonly found bilaterally.

When interpreting radiographs in horses with suspected osteochondral fragmentation, all potential lesion sites should be evaluated carefully. The third carpal bone should be assessed for the degree of sclerosis, and the radial carpal bone should be assessed for apparent lucency, rounding of the dorsal margins, and collapse of the subchondral bone, all changes that may precede actual fragmentation. Signs of osteoarthritis may also be present with chronic injury to the carpus, including osteophyte and enthesophyte formation (see Fig. 20-19).

Palmar Aspect. Osteochondral fractures of the palmar aspect of the carpal joints may be associated with a single traumatic incident, such as during recovery from general anesthesia, including direct impact injuries or hyperextension of the carpus.[50] Palmar osteochondral fragments may also represent migration of dorsal fragments to the palmar aspect of the joints. The presence of palmar osteochondral fragments can be used as an indicator of clinically important joint disease.[51] Horses with multiple fragments tend to have a worse prognosis for successful return to racing than horses with single fragments or dorsal fragments alone. Horses are at least moderately lame, with a marked response to flexion.

Avulsion of the lateral palmar intercarpal ligament from the medial palmar aspect of the ulnar carpal bone may be detected as an osseous fragment on a dorsolateral

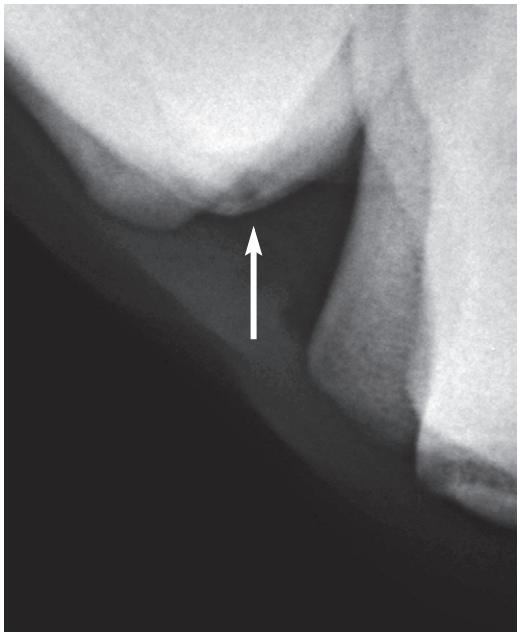


Fig. 20-16 Flexed lateromedial radiograph of a carpus. A small subchondral radiolucent area is visible in the distal dorsal aspect of the radial carpal bone *(white arrow)*. Arthroscopic examination of the middle carpal joint confirmed the presence of a focal chondro-osseous defect.

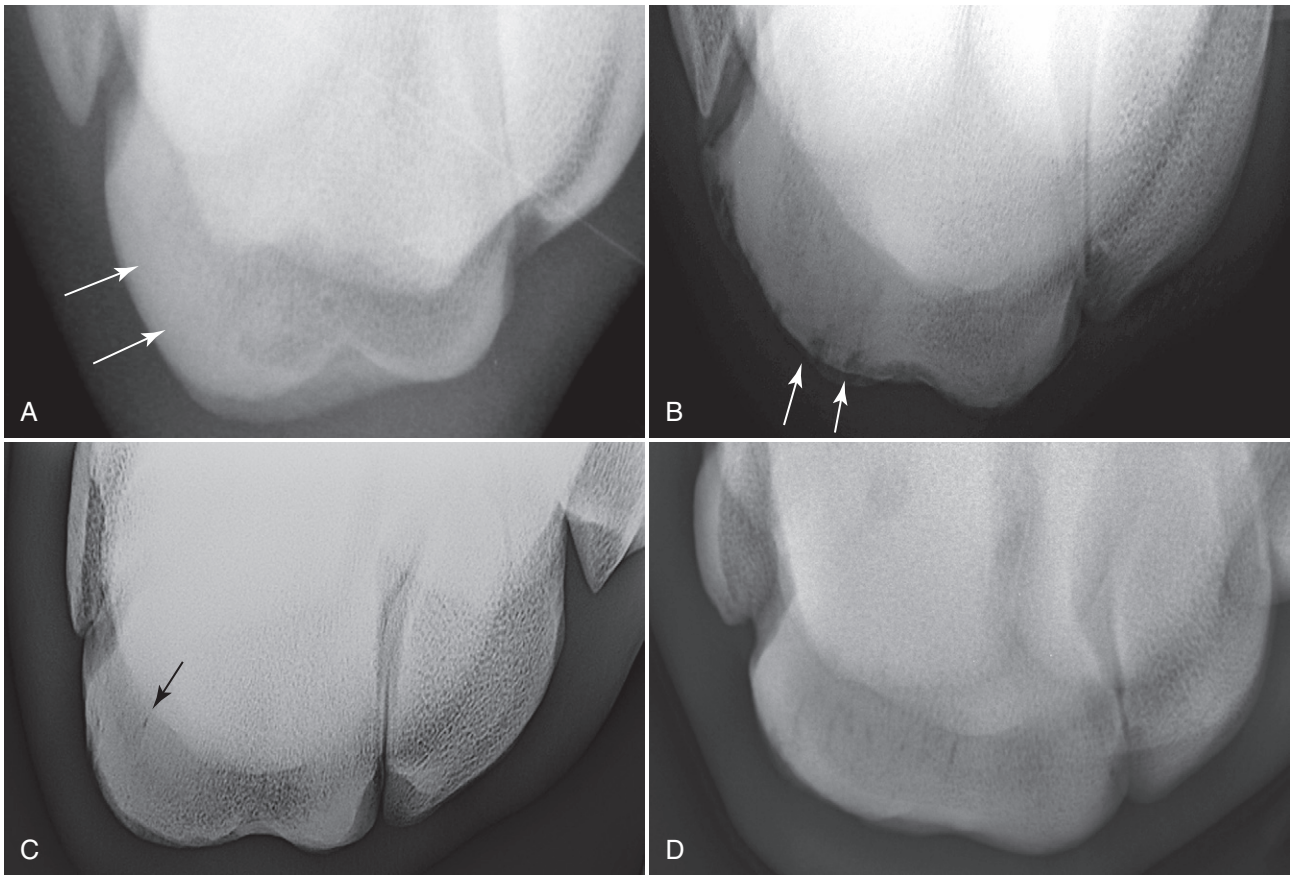


Fig. 20-17 **A,** Dorsoproximal-dorsodistal radiograph of the distal row of carpal bones. Medial is to the left. Increased radiopacity (sclerosis) of the radial facet of the third carpal bone is visible *(white arrows)*. No significant radiographic abnormality was seen in any other radiographic projection. **B,** Dorsoproximal-dorsodistal radiograph of the distal row of carpal bones of the left forelimb of an 8-year-old intermediate-level eventing horse. Medial is to the left. There is diffuse increased opacity of the third carpal bone, especially medially, with ill-defined radiolucent areas on the dorsal border of the bone *(white arrows)*. There was focal intense increased radiopharmaceutical uptake in the third carpal bone. **C,** Dorsoproximal-dorsodistal radiograph of the distal row of carpal bones of the left forelimb of a 3-year-old Thoroughbred flat racehorse. Medial is to the left. There is focal increased radiopacity of the medial aspect of the third carpal bone, with a well-defined focal radiolucent area *(black arrow)*. **D,** Dorsoproximal-dorsodistal radiograph of the distal row of carpal bones of the right forelimb of a 9-year-old upper-level show jumper. Medial is to the left. There is diffuse increased radiopacity of the third carpal bone with ill-defined radiating radiolucent lines. This was associated with focal intense increased radiopharmaceutical uptake in the third carpal bone.

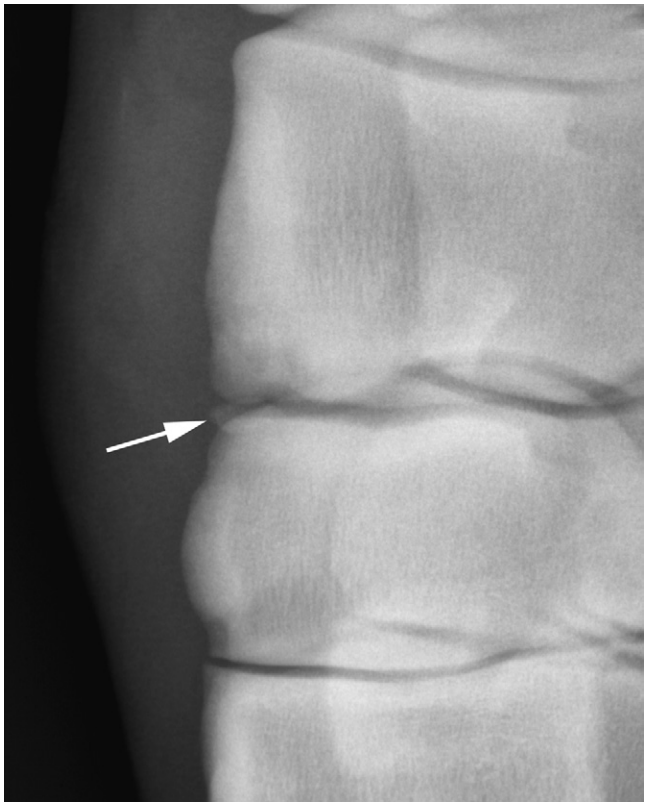


Fig. 20-18 Dorsolateral-palmaromedial oblique image of a carpus. A small chip fracture is present *(white arrow)* on the dorsomedial aspect of the middle carpal joint.

to palmaromedial projection (Fig. 20-20).[52] A dorsopalmar projection can be used to evaluate the proximity of the fragment to its fracture bed. Avulsion is generally characterized by an osseous opacity, and a concave lucent area in the ulnar carpal bone on the palmar surface of the ulnar carpal bone. However, such fragments may not represent fractures in all horses and can be incidental findings.[4]

Migration of osteochondral fragments from the dorsal aspect may result in detection of fragments in the palmar aspect of the antebrachiocarpal or middle carpal joints; therefore evaluation of the entire carpus, not solely focused on the palmar aspect, is important. The presence of palmar fragments warrants a more guarded prognosis.[51]

Carpal Bone Slab Fractures

Slab fractures extend from one articular surface to another in a proximal to distal direction. The third carpal bone is affected most frequently,[35,50,53,54] although fractures of the fourth, radial, and intermediate carpal bones have been reported.[55] Racehorses are the most likely to be affected.

Dorsal plane slab fractures are the most likely to occur, particularly affecting the medial facet of the third carpal bone.[35-38,42] They may range in depth from 8 to 25 mm and may be displaced or nondisplaced (Fig. 20-21). Lameness varies in severity from mild to severe. With complete displaced fractures, significant effusion, soft tissue swelling, and severe lameness are usually present, but horses with a nondisplaced incomplete fracture may have no localizing clinical signs. Prognosis for racing following incomplete nondisplaced fracture of the medial facet of the third carpal bone appears to be good following lag screw fixation.[56]

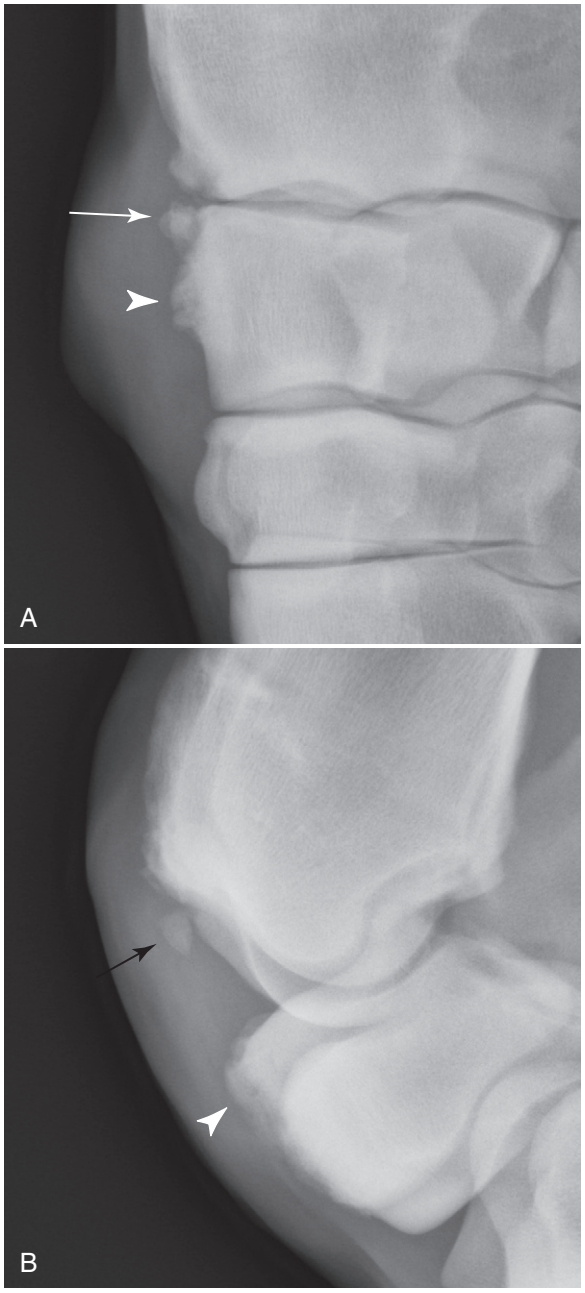


Fig. 20-19 **A,** Dorsolateral-palmaromedial radiograph of a carpus. There is a nondisplaced chip fracture of the dorsoproximomedial aspect of the radial carpal bone *(white arrow)*. Also note the entheseous nonarticular new bone on the dorsomedial aspect of the radial carpal bone *(white arrowhead)*. There is also a region of new bone at the distomedial aspect of the radius, but it is not possible to determine from this view whether this is a fracture or an osteophyte. **B,** Flexed lateromedial radiograph of the same carpus as in **A.** Modeling of the distal dorsal aspect of the intermediate carpal bone *(white arrowhead)* and a chip fracture from the dorsodistal aspect of the radius *(black arrow)* can be seen.

A complete series of radiographs should be obtained, including dorsoproximal-dorsodistal views. Fractures of the radial facet of the third carpal bone are best visualized on lateromedial, flexed lateromedial, and dorsolateral-palmaromedial oblique views and a dorsoproximal-dorsodistal view of the distal row of carpal bones.[55] In some horses a fracture can be seen only in the dorsoproximal-dorsodistal projection, especially if the fracture is nondisplaced (Fig. 20-22). Concurrent damage to the dorsal distal aspect of the radial carpal



Fig. 20-20 Dorsolateral-palmaromedial radiograph of a horse with a fragment on the palmar aspect of the ulnar carpal bone *(black arrow)*, probably in the lateral palmar intercarpal ligament. Note that this radiological feature can occur in normal horses; therefore the diagnosis of an avulsion fracture should be based on the clinical findings.

bone is a frequent occurrence, as is concurrent third carpal bone sclerosis. Complete radiographic evaluation of the contralateral limb should also be performed because lesions may occur bilaterally.

Sagittal plane fractures occur less commonly than dorsal plane fractures and may be incomplete.[57-59] They primarily affect the medial facet of the third carpal bone (see Fig. 20-22). As with other osteochondral fractures, horses are quite lame at the time of fracture, and the contralateral limb may be involved. Racehorses with sagittal slab fractures of the third carpal bone can have a favorable prognosis for return to racing, particularly if treated surgically.[60] Fracture of other carpal bones has been reported but is relatively rare.

Sagittal fractures of the third carpal bone are best seen on dorsoproximal-dorsodistal and dorsomedial-palmarolateral oblique views. The lucent fracture line is often located parallel to the articulation between the second and third carpal bones. Radiographs of the entire carpus should be assessed for concurrent osteochondral injury.

Comminuted and Multiple Fractures

Multiple or comminuted fractures are unusual but do occur, especially in racehorses.[7] They may also occur in other types of horses as a result of direct trauma or a single-event injury. Affected horses are generally in severe pain and do not bear weight on the limb. Carpal instability is a frequent finding. Prognosis is guarded to poor, although successful partial carpal arthrodesis has been reported following comminuted fourth carpal bone fracture.[61]

Full radiographic examination of the carpus is required to assess the extent and nature of osseous injury. Concurrent joint effusion and soft tissue swelling are usually present (Fig. 20-23).

Fractures of the Accessory Carpal Bone

Accessory carpal bone fractures usually occur as a result of a single incident, such as a fall, that either causes hyperextension of the carpus or results in direct trauma to the accessory carpal bone itself. Soft tissue swelling palmar to the carpus is present. Horses usually have moderate to severe pain and resent flexion of the carpus.[30-32] Fractures occur most commonly through the lateral groove of the ulnaris lateralis tendon in a dorsal plane (vertical) (Fig. 20-24). Although most fractures are simple, comminuted fractures can occur. Because the flexor muscles provide constant distraction forces and motion, a fibrocartilaginous nonunion occurs frequently at this site. The fibrous union results in a persistent fracture line on radiographs. Bony proliferative changes are also often noted radiographically during the fibrous healing period. However, the prognosis for function is usually favorable.

Less commonly, proximal dorsal chip fractures of the accessory carpal bone occur close to the articular surface. Because standard views may result in superimposition of these fragments over the other carpal bones, further oblique views may be required. A dorsal 80-degree lateral-palmaromedial oblique view has been recommended. Such fractures should be removed surgically, otherwise secondary osteoarthritis will ensue.

Periosteal New Bone on the Dorsal Aspect of the Carpal Bones, the Distal Aspect of the Radius, and the Proximal Aspect of the Metacarpal Bones

Enthesophytes not associated with the articular surface or joint margins are likely to be caused by strain on the intercarpal ligaments. Enthesophytes are often observed in association with osteoarthritis (Figs. 20-25 and 20-26; see Fig. 20-19, *B*) but may occur as a result of direct periosteal trauma.[3]

Hypertrophic Osteopathy

Hypertrophic osteopathy is often associated with intrathoracic disease. Enlargement of the proximal carpal region and mild lameness may occur from fibrous and osseous enlargement of the distal aspect of the radius resulting from hypertrophic osteopathy.[62] Pain is usually felt on palpation of the affected area. Radiographs are characterized by palisading periosteal new bone perpendicular to the cortex. This palisading bone does not usually affect the carpal joints.

Articular Problems

Luxation/Subluxation

Generally, carpal luxation and subluxation are caused by disruption of the lateral or medial collateral ligaments, with or without damage of the adjacent soft tissues. Although alterations in joint congruency may be noted on radiographs, more direct visualization of collateral ligament structure is possible with ultrasonographic evaluation. Luxation or subluxation of individual carpal joints or all the joints of the carpus may be seen depending on the extent of injury to the soft tissue structures.

In addition to standard views, stressed dorsopalmar and/or stressed lateromedial radiographs should be used to assess joint stability. The presence of asymmetric joint spaces and altered proximal-distal alignment of carpal bones on either dorsopalmar or lateromedial views indicate subluxation, although they may not always be detected without stressed views. In luxation, complete loss of alignment of the articular surface in the affected joint is observed.

Radiographs should be examined to detect avulsion fractures at the origin or insertion of collateral ligaments, seen as a discontinuity of the cortex or presence of radiopaque fragments. Enthesophytes at the origin or insertion of a collateral ligament may signify chronic damage. Severe luxations may be associated with carpal bone fractures, which may result in radiopaque intercarpal ligament avulsion fragments within the joint space. In the case of an open luxation, gas can be present within the joint and local soft tissues.

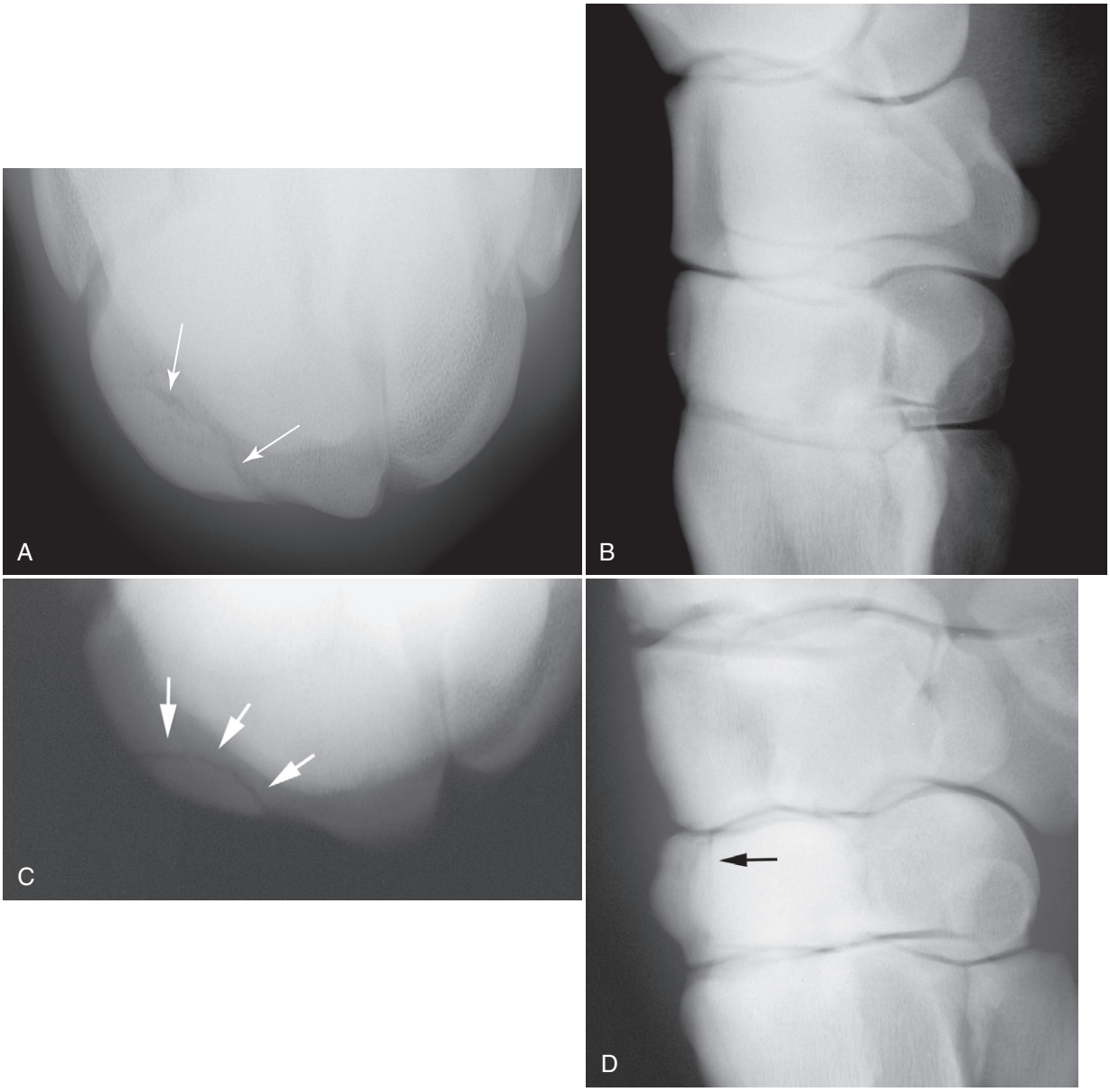


Fig. 20-21 **A,** Dorsoproximal-dorsodistal radiograph of the distal row of carpal bones. Mild increased radiopacity of the radial facet of the third carpal bone and a nondisplaced slab fracture are visible *(white arrows)*. No significant abnormality was seen in any other radiographic projection. **B,** Dorsomedial-palmarolateral oblique radiograph of a carpus. Although there are faint radiolucent lines in the dorsal aspect of the third carpal bone, a definitive diagnosis of fracture cannot be made. **C,** Dorsoproximal-dorsodistal radiograph of the distal row of carpal bones of the same limb as **B.** Medial is to the left. A nondisplaced slab fracture of the radial facet of the third carpal bone is visible *(white arrows)*. This illustrates the value of the dorsoproximal-dorsodistal oblique views to assess potential slab fractures. **D,** Dorsolateral-palmaromedial oblique radiograph of a carpus. A radiologically incomplete slab fracture of the third carpal bone is visible *(black arrow)*. Also note the mottled radiopacity of the bone dorsal to the fracture. The dorsodistal aspect of the radial carpal bone is modeled, being more rounded than normal and "cut back," moving the point of impact on the third carpal bone in a palmar direction. This change may predispose to fracture of the third carpal bone. Also note the modeling of the articular margins of the antebrachiocarpal joint and possibly a small osseous fragment on the distal dorsal aspect of the radius.

Osteoarthritis

Osteoarthritis is generally characterized by periarticular osteophyte formation, narrowing of the joint space, subchondral lucent zones, increased radiopacity of subchondral bone or thickening of the subchondral bone plate, and joint capsule distention. The degree of radiographic change does not always correlate with the degree of pain or lameness, and radiographic changes may sometimes be advanced at the time of lameness onset, so predicting onset and degree of lameness from radiographic examination is difficult.[3,7]

Antebrachiocarpal Joint. Osteoarthritis in the antebrachiocarpal joint is observed most commonly in flat-track

racehorses and is usually caused by repetitive overloading injury of the articular osteochondral structure.[38,42] Stress-related subchondral bone injury is present with overlying cartilage damage and cartilage wear lines, which are not visible radiographically. Osteochondral fragments are present frequently in these horses.[36,37] For nonracehorses, osteoarthritis is more likely to occur in older horses, with osteochondral fragments being unusual unless the horse has a prior racing history.[3,7] Although small periarticular osteophytes are sometimes observed in horses without clinically detectable



Fig. 20-22 Dorsoproximal-dorsodistal radiograph of the distal row of carpal bones. Medial is to the left. Increased radiopacity (sclerosis) of the radial facet of the third carpal bone and an incomplete parasagittal fracture are visible *(black arrows)*. The margins of the fracture line are indistinct, indicating chronicity. No significant abnormality was seen in any other radiographic projection.



Fig. 20-23 Dorsopalmar radiograph of a carpus. Lateral is to the right. Multiple displaced fractures are on the lateral aspect of the carpus, resulting in partial collapse of the carpus with abaxial displacement of part of the fourth carpal bone. Identifying all fractures, even from a complete radiographic series, will be difficult. Computed tomographic examination of such a fracture will be more precise in localizing all fractures.

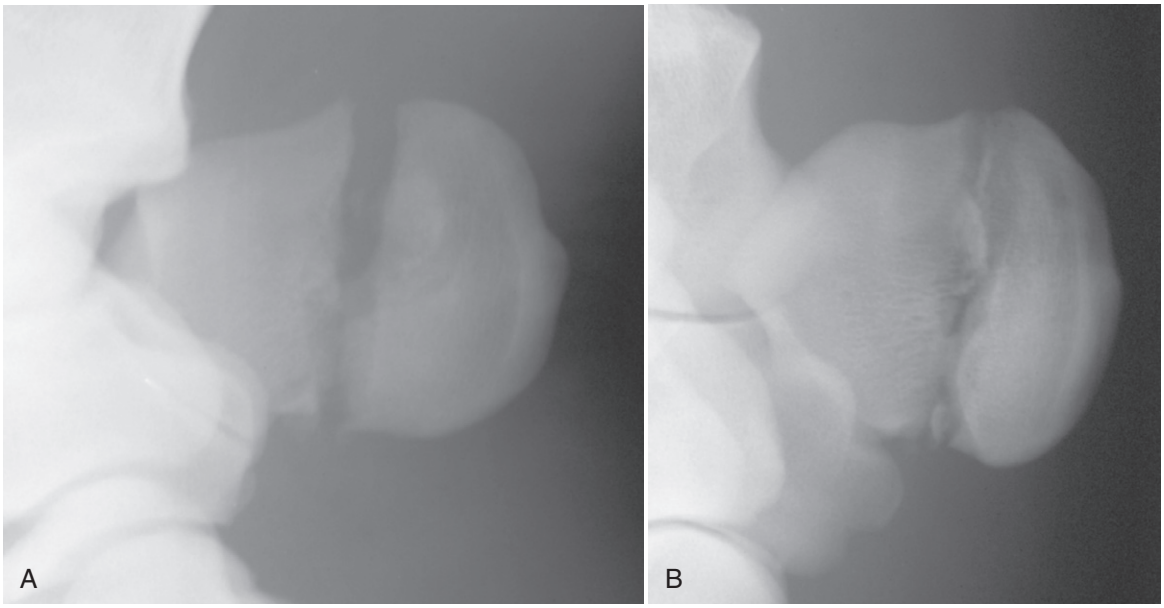


Fig. 20-24 **A,** Flexed lateromedial radiograph. A slightly displaced fracture of the accessory carpal bone is visible. **B,** Dorsolateral-palmaromedial oblique radiograph of the same carpus as in **A.** A complete fracture of the accessory carpal bone is present.

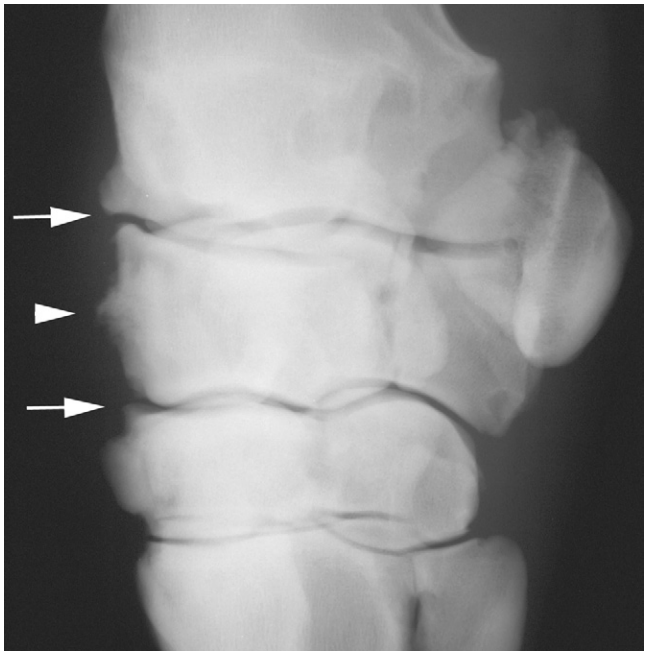


Fig. 20-25 Dorsolateral-palmaromedial oblique radiograph of a carpus. Extensive periarticular osteophyte formation involving the dorsomedial aspects of the antebrachiocarpal and middle carpal joints is visible *(white arrows)*, consistent with advanced osteoarthritis. Entheseous new bone on the dorsal aspect of the radial carpal bone is also present *(white arrowhead)*. Also note the new bone on the proximodorsal aspect of the accessory carpal bone. A small radiolucent zone in the distal palmar aspect of the ulnar carpal bone is visible but is an incidental finding.

lameness, their presence can indicate osteoarthritic change. When severe changes are present, including loss of joint space and ankylosis, they are likely to be associated with lameness no matter the horse's athletic requirements, with the horse severely resenting flexion and abducting the limb to avoid flexion during movement. However, when mild changes are present, the breed and use of the horse can influence the prognosis and potential significance of mild osteoarthritic change, suggesting a significant effect on performance in a racehorse but having little significance for a pleasure or show horse.

Periarticular osteophytes are most commonly detected on the dorsal aspect, particularly of the radial and intermediate carpal bones, but may also be observed on the palmar aspect of the joint (see Fig. 20-26).[3] Joint capsule distention is sometimes present, particularly when intercarpal ligament, chronic synovitis, or joint capsule damage is present in association with the osteochondral changes. Osteochondral fragments are observed as radiopacities within the joint space or at the joint margins.

Middle Carpal Joint. Osteoarthritis in the middle carpal joint occurs in a manner similar to the antebrachiocarpal joint (see Fig. 20-26).[8,43] Periarticular osteophytes are observed most frequently on the dorsal aspects of the radial and third carpal bones, although palmar osteophytes may be observed. Modeling of the dorsal articular margins of the radial and third carpal bones may also be seen. The dorsodistal aspect of the radial carpal bone should be well defined, with a clear subchondral margin and corner to the bone. With repetitive overloading, damage may be seen as radiolucency of the dorsodistal corner (see Fig. 20-16) and eventually either loss in the form of a clearly defined osteochondral fragment (see Fig. 20-15) or gradual rounding of the corner.[44] This results in decreased dorsal loading of the medial aspect of the third carpal bone, moving the site of maximal loading on the third carpal bone, and increasing risk of osteochondral damage to the radial facet of the third carpal bone articular surface, potentially leading to sclerosis, slab fracture, osteochondral collapse, or more generalized osteoarthritis.[38]

Carpometacarpal Joint. Osteoarthritis of the carpometacarpal joint occurs much less commonly than does osteoarthritis of the two proximal articulations and occurs largely in middle-aged to older horses.[7,63] No specific type of work history appears to predispose to the condition. Onset may be acute or insidious, progressing to severe lameness. Response to conservative treatment is poor generally,[63] although spontaneous ankylosis following conservative management can occur.[64] Treatment by surgical arthrodesis may be successful.[65]

Osteoarthritic change is generally characterized by narrowing or collapse of the joint space, frequently focal or confined to either the medial or lateral side only, involving the articulation with either the second or fourth metacarpal bones.[3] Unlike the high-motion joints of the carpus, changes are likely to include subchondral lucency as well as subchondral sclerosis and often periosteal new bone extending along the proximal metaphysis and diaphysis of the affected metacarpal bone. There may be entheseous new bone at the insertion of the ipsilateral collateral ligament of the carpus (Fig. 20-27).

Sepsis

Septic Arthritis and Osteomyelitis. Horses with septic arthritis usually become severely lame within 24 hours of infection, with heat and swelling of the carpal region. If septic arthritis is suspected, diagnosis and treatment should be instituted as an emergency because early treatment is linked to improved prognosis.[66] Once articular cartilage damage and osteomyelitis are present, prognosis for a positive outcome reduces dramatically, with the horse being unlikely to return to athletic function. Septic arthritis can occur as a result of a penetrating wound, hematogenous infection, or spread from adjacent tissues in conditions such as septic tenosynovitis or osteomyelitis.[67] Although rare, iatrogenic infection caused by intraarticular injection or arthroscopy can occur.[67,68]

Septic arthritis of the carpal joints occurs commonly in foals with failure of passive transfer of immunity, high sepsis score, or multisystemic disease.[69] These foals may be relatively less lame than older horses with septic arthritis.[67] However, the prognosis in foals is more guarded than that for adult horses, even if treatment is instigated at the onset of clinical signs.[67,68] A significant proportion of foals with septic arthritis have concurrent osteomyelitis.[69] Radiolucent changes in the bone may rapidly occur after the onset of clinical signs but can be more difficult to visualize in the carpal bones than in the distal aspect of the radius. All bones should be inspected carefully, because infection may be multifocal. Infarction can also occur and can delay recognition of bone involvement because radiolucency is less apparent.[66]

Radiographic signs include distention of the affected joint and sometimes generalized soft tissue swelling. Widening of the joint space may be present in the early stages, particularly when the limb is not bearing weight. In the more chronic phase, damage to the articular surfaces may be visible. Articular cartilage loss leads to joint space narrowing, and subchondral bone destruction is observed as irregular subchondral lucency or decreased opacity. Areas of increased opacity may also be observed. Reactive new bone on the periarticular aspects is seen as a disorganized, low-opacity irregularity on the joint margins. Increasing bridging of the antebrachiocarpal, middle carpal, or carpometacarpal joints occurs, with accompanying new bone within the intercarpal joints, progressing toward ankylosis.[3]

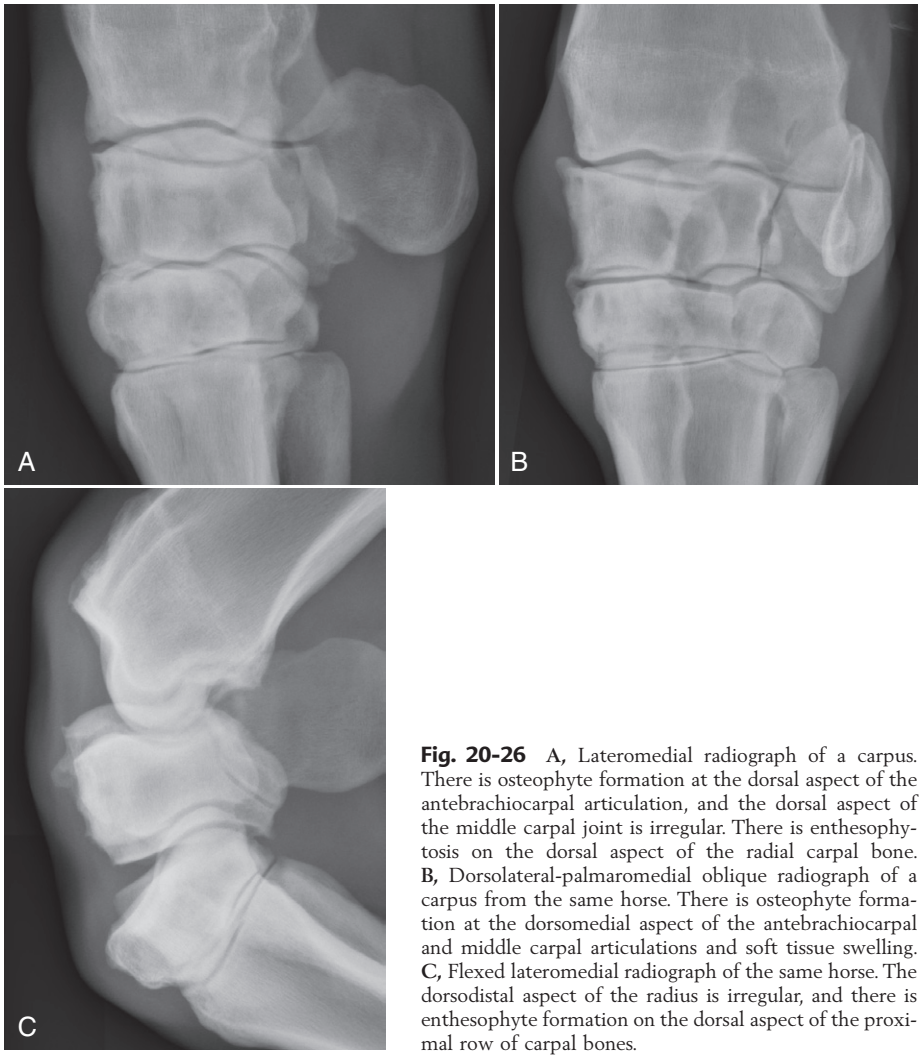


Fig. 20-26 **A,** Lateromedial radiograph of a carpus. There is osteophyte formation at the dorsal aspect of the antebrachiocarpal articulation, and the dorsal aspect of the middle carpal joint is irregular. There is enthesophytosis on the dorsal aspect of the radial carpal bone. **B,** Dorsolateral-palmaromedial oblique radiograph of a carpus from the same horse. There is osteophyte formation at the dorsomedial aspect of the antebrachiocarpal and middle carpal articulations and soft tissue swelling. **C,** Flexed lateromedial radiograph of the same horse. The dorsodistal aspect of the radius is irregular, and there is enthesophyte formation on the dorsal aspect of the proximal row of carpal bones.



Fig. 20-27 Dorsopalmar radiographic image of a 12-year-old pony with severe lameness. Medial is to the left. There is extensive new bone on the proximomedial aspect of the third metacarpal bone with soft tissue swelling extending proximally, which is associated with a severe chronic injury of the medial collateral ligament of the carpus. There is also narrowing of the medial aspect of the carpometacarpal joint, consistent with osteoarthritis.

Further diagnosis needs to be made on the basis of synoviocentesis and synovial analysis with Gram stain and culture. Hematologic examination and blood culture are also recommended in foals. Management of septic arthritis usually requires joint lavage, intraarticular and systemic antimicrobial therapy, and antiinflammatory use at a minimum. Open drainage and synovial debridement and use of antimicrobial-impregnated methylmethacrylate or regional antimicrobial infusion have all been used as additional options for management.[66]

REFERENCES

1. Sisson S: Equine syndesmology. In Getty R, editor: *The anatomy of the domestic animals*, ed 5, Philadelphia, 1975, Saunders, pp 349–375.
2. Smallwood JE, Shiveley M: Radiographic and xeroradiographic anatomy of the equine carpus, *Equine Pract* 1:22, 1979.
3. Butler JA, Colles CM, Dyson SJ, et al: *Clinical radiology of the horse*, ed 2, Oxford, 2003, Blackwell Science.
4. Simon A, Dyson SJ: Radiologic anatomic variation of the carpus in horses with carpal lameness and control horses, *Vet Radiol Ultrasound* 51:601–606, 2010.
5. Auer J, Smallwood J, Morris E, et al: The developing equine carpus from birth to 6 months. A radiographic study, *Equine Pract* 4:35, 1982.

6. Myers VS: Confusing radiological variation at the distal end of the radius of the horse, *J Am Vet Med Assoc* 147:1310, 1986.
7. Ross M: Carpus. In Ross MW, Dyson SJ, editors: *Diagnosis and management of lameness in the horse*, St. Louis, 2003, Elsevier Science, pp 376–394.
8. Murray RC, Vedi S, Birch HL, et al: Subchondral bone thickness, hardness and remodeling are influenced by short-term exercise in a site-specific manner, *J Orthop Res* 19:1035, 2001.
9. Young A, O'Brien T, Pool R: Exercise related sclerosis in the third carpal bone of the racing thoroughbred, *Proc Am Assoc Equine Pract* 34:339, 1988.
10. O'Donohue DD, Smith FH, Strickland DL: The incidence of abnormal limb development in the Irish Thoroughbred from birth to 18 months, *Equine Vet J* 24:305, 1992.
11. Watkins JP: Osteochondrosis. In Auer JA, editor: *Equine surgery*, Philadelphia, 1992, Saunders, pp 971–984.
12. Ellis DR: Physitis. In Ross MW, Dyson SJ, editors: *Diagnosis and management of lameness in the horse*, St. Louis, 2003, Elsevier Science, pp 554–556.
13. Auer JA: Angular limb deformities. In Auer JA, editor: *Equine surgery*, Philadelphia, 1992, Saunders, pp 940–956.
14. Auer JA, Marten RJ, Morris EL: Angular limb deformities in foals: congenital factors, *Compend Contin Educ Pract Vet* 4:13, 1983.
15. Adams R, Poulos P: A skeletal ossification index for neonatal foals, *Vet Radiol* 29:217, 1988.
16. Parente EJ: Angular limb deformities. In Ross MW, Dyson SJ, editors: *Diagnosis and management of lameness in the horse*, St. Louis, 2003, Elsevier Science, pp 557–561.
17. Caron JP: Angular limb deformities in foals, *Equine Vet J* 20:225, 1988.
18. Gaughan EM: Angular limb deformities in horses, *Compend Contin Educ Pract Vet* 20:944, 1998.
19. Ellis D: Some observations on bone cysts in the carpal bones of young thoroughbreds, *Equine Vet J* 17:63, 1985.
20. McIlwraith CW: Subchondral cystic lesions (osteochondrosis) in the horse, *Comp Contin Ed Pract Vet* 4:S396, 1982.
21. Specht TE, Nixon AJ, Colahan PT: Subchondral cyst-like lesions in the distal portion of the radius of four horses, *J Am Vet Med Assoc* 193:949, 1988.
22. Walmsley JP: Diagnosis and management of osteochondrosis and osseous cyst-like lesions. In Ross MW, Dyson SJ, editors: *Diagnosis and management of lameness in the horse*, St. Louis, 2003, Elsevier Science, pp 455–470.
23. Adams SB, Santschi EM: Management of flexural deformities in young horses, *Equine Pract* 21:9, 1999.
24. Platt D, Wright I: Chronic tenosynovitis of the carpal extensor tendon sheaths in 15 horses, *Equine Vet J* 29:11, 1997.
25. Dietze A, Rendano V: Fat opacities dorsal to the equine antebrachiocarpal joint, *Vet Radiol* 25:205, 1984.
26. Stone WC, Wilson DG, Dubielzig RR, et al: The pathologic mineralization of soft tissue: calcinosis circumscripta in horses, *Compend Cont Educ Pract Vet* 12:1643–1648, 1990.
27. Toth F, Schumacher J, Newman S: Calcinosis circumscripta in the antebrachiocarpal joint of a horse, *Equine Vet Ed* 21:584–588, 2009.
28. Mackey-Smith MP, Cushing LS, Leslie JA: Carpal canal syndrome in horses, *J Am Vet Med Assoc* 160:993, 1972.
29. Dyson SJ: The carpal canal and carpal synovial sheath. In Ross MW, Dyson SJ, editors: *Diagnosis and management of lameness in the horse*, St. Louis, 2003, Elsevier Science, pp 685–687.
30. Dyson S: Fractures of the accessory carpal bone, *Equine Vet Educ* 2:188, 1990.
31. Barr ARS, Sinnott MJA, Denny HR: Fractures of the accessory carpal bone in the horse, *Equine Vet J* 126:432, 1990.
32. Barr A, Sinnott M, Denny H: Fractures of the accessory carpal bone in the horse, *Vet Rec* 127:432, 1990.
33. Held JP, Patton CDS, Shores M: Solitary osteochondroma of the radius in three horses, *J Am Vet Med Assoc* 193:563, 1988.
34. Wyburn RS, Goulden BE: Fractures of the equine carpus: a report on 57 cases, *N Z Vet J* 22:133, 1974.
35. Park RD, Morgan JP, O'Brien T: Chip fractures in the carpus of the horse; a radiographic study of their incidence and location, *J Am Vet Med Assoc* 157:1305, 1970.
36. Palmer SE: Prevalence of carpal fractures in Thoroughbred and Standardbred racehorses, *J Am Vet Med Assoc* 188:1172, 1986.
37. Bramlage L, Schneider R, Gabel A: A clinical perspective on lameness originating in the carpus, *Equine Vet J* 6(Suppl):12, 1988.
38. Auer JA, Fackelman GE: Treatment of degenerative joint disease of the horse: a review of and commentary, *Vet Surg* 10:80, 1981.
39. McIlwraith CW, Yovich JV, Martin GS: Arthroscopic surgery for the treatment of osteochondral chip fractures in the equine carpus, *J Am Vet Med Assoc* 191:531, 1987.
40. Schneider RK, Bramlage LR, Gabel AA, et al: Incidence, location and classification of 371 third carpal bone fractures in 313 horses, *Equine Vet J* 6(Suppl):33, 1988.
41. Bramlage LR: Surgical diseases of the carpus, *Vet Clin North Am Large Anim Pract* 5:261, 1983.
42. Murray RC, Zhu CF, Goodship AE, et al: Exercise affects the mechanical properties and histological appearance of equine articular cartilage, *J Orthop Res* 17:725, 1999.
43. Dabareiner RM, White NA, Sullins KE: Radiographic and arthroscopic findings associated with subchondral lucency of the distal radial carpal bone in 71 horses, *Equine Vet J* 28:93, 1996.
44. Young DR, Richardson DW, Markel MD, et al: Mechanical and morphometric analysis of the third carpal bone of Thoroughbreds, *Am J Vet Res* 52:402, 1991.
45. Uhlhorn H, Carlsten J: Retrospective study of subchondral sclerosis and lucency in the third carpal bone of Standardbred trotters, *Equine Vet J* 31:500, 1999.
46. Ross MW, Richardson DW, Beroza GA: Subchondral lucency of the third carpal bone in Standardbred racehorses: 13 cases (1982–1988), *J Am Vet Med Assoc* 195:789, 1989.
47. Thrall DE, Lebel JL, O'Brien TR: A five-year survey of the incidence and location of equine carpal chip fractures, *J Am Med Assoc* 158:1366, 1971.
48. Dabareiner RM, Sulins KE, Bardley W: Removal of a fracture fragment from the palmar aspect of the intermediate carpal bone in a horse, *J Am Vet Med Assoc* 203:553, 1993.
49. Wright IM, Smith MRW: The use of small (2.7 mm) screws for arthroscopically guided repair of carpal chip fractures, *Equine Vet J* 43(3):270–279, 2010.
50. De Hann CE, O'Brien TR, Koblik PD: A radiographic investigation of third carpal injury in 42 racing Thoroughbreds, *Vet Radiol* 28:88, 1987.
51. Getman LM, Southwood LL, Richardson DW: Palmar carpal osteochondral fragments in racehorses: 31 cases (1994–2004), *J Am Vet Med Assoc* 228:1551–1558, 2006.
52. Beinlich CP, Nixon AJ: Radiographic and pathologic characterization of lateral palmar intercarpal ligament avulsion fractures in the horse, *Vet Radiol Ultrasound* 45:532, 2004.

53. Stephens PR, Richardson DW, Spencer PA: Slab fractures of the third carpal bone in Standardbreds and Thoroughbreds: 155 cases (1977–1984), *J Am Vet Med Assoc* 193:353, 1988.
54. Uhlhorn H, Ekman S, Haglund A, et al: The accuracy of the dorsoproximal-dorsodistal projection in assessing third carpal bone sclerosis in Standardbred trotters, *Vet Radiol Ultrasound* 39:412, 1988.
55. Auer JA, Watkins JP, White NA, et al: Slab fractures of the four and intermediate carpal bones in five horses, *J Am Vet Med Assoc* 188:595, 1986.
56. Rutherford DJ, Bladon B, Rogers CW: Outcome of lag-screw treatment of incomplete fractures of the frontal plane of the radial facet of the third carpal bone in horses, *N Z Vet J* 55:94–99, 2007.
57. Fischer AT, Stover SM: Sagittal fractures of the third carpal bone in horses: 12 cases (1977–1985), *J Am Vet Med Assoc* 192:106, 1987.
58. Gertsen KE, Dawson HA: Sagittal fracture of the third carpal bone in a horse, *J Am Vet Med Assoc* 169:633, 1976.
59. Palmer SE: Lag screw fixation of a sagittal fracture of the third carpal bone in a horse, *Vet Surg* 12:54, 1986.
60. Kraus BM, Ross MW, Boston RC: Surgical and nonsurgical management of sagittal slab fractures of the third carpal bone in racehorses: 32 cases (1991–2001), *J Am Vet Med Assoc* 226:945–950, 2005.
61. Waselau M, Bertone AL, Green EM: Computed topographic documentation of a comminuted fourth carpal bone fracture associated with carpal instability treated by partial carpal arthrodesis in an Arabian filly, *Vet Surg* 35:618–625, 2006.
62. Mair T, Dyson S, Fraser J, et al: Hypertrophic osteopathy (Marie's disease) in Equidae: a review of twenty-four cases, *Equine Vet J* 28:256, 1996.
63. Panizzi L, Spencer SM, Lang HM, et al: Carpometacarpal osteoarthritis in thirty-three horses, *Vet Surg* 38: 998–1005, 2009.
64. Oosterlinck M, Pille F, Gasthuys F, et al: Spontaneous bilateral ankylosis of the carpometacarpal joint in a paint horse, *Equine Vet Ed* 21:452–454, 2009.
65. Spencer SM, Panizzi L, Lang HM: Treatment of carpometacarpal osteoarthritis by arthrodesis in 12 horses, *Vet Surg* 38:1006–1011, 2009.
66. Bertone AL: Infectious arthritis. In Ross MW, Dyson SJ, editors: *Diagnosis and management of lameness in the horse*, St. Louis, 2003, Elsevier Science, pp 685–687.
67. Schneider RK, Bramlage LR, Moore RM, et al: A retrospective study of 192 horses affected with septic arthritis/tenosynovitis, *Equine Vet J* 24:436, 1992.
68. Meijer MC, van Weeren PR, Rijkenhuizen AB: Clinical experiences of treating septic arthritis in the equine by repeated joint lavage: a series of 39 cases, *J Vet Med A Physiol Pathol Clin Med* 47:351, 2000.
69. Steel CM, Hunte AR, Adams PLE, et al: Factors associated with prognosis for survival and athletic use in foals with septic arthritis: 93 cases (1987–1994), *J Am Vet Med Assoc* 215:973, 1999.

ELECTRONIC RESOURCES

evolve

Additional information related to the content in Chapter 20 can be found on the companion Evolve website at http://evolve.elsevier.com/Thrall/vetrad/

- Chapter Quiz

CHAPTER • 21

The Equine Metacarpal and Metatarsal Regions

Sue J. Dyson
Marianna Biggi

ANATOMY

The metacarpal and metatarsal regions are discussed together except where major anatomic differences occur. The osseous structures comprise the second, third, and fourth metacarpal (metatarsal) bones with interosseous ligaments joining the second and third, and fourth and third metacarpal (metatarsal) bones. There is variable ossification of these syndesmoses. In a necropsy study of 100 horses of mixed breed, age, and work discipline, the majority had some degree of ossification between the second or fourth metacarpal bone and the third metacarpal bone, which was often bilaterally symmetric and more extensive medially.[1] Five patterns of ossification were recognized, alone or in combination: (1) a small (<1 cm diameter) raised patch of bone that crossed the bone surfaces abaxially, following the line of the fibers of the interosseous ligament; (2) ossification of the interosseous ligament following the line of the fibers; (3) diffuse abaxial proliferation of bone (>1 cm diameter); (4) focal axial ossification of the interosseous ligament on the palmar surface; and (5) diffuse axial ossification on the palmar surface so that the bone margins were obscured. These variable patterns of ossification of the interosseous ligaments were age-related and may reflect a continuum, the result of repetitive trauma, but are not necessarily of clinical significance.

In forelimbs the second carpal bone and a variable portion of the third carpal bone usually articulate with the second metacarpal bone,[1] whereas the fourth carpal bone articulates with the fourth metacarpal bone. This has biomechanical implications, with forces mediated through both the second and third carpal bones being transmitted through the second metacarpal bone and the syndesmosis with the third metacarpal bone. In hindlimbs the combined first and second tarsal bone articulates with the second metatarsal bone, and the fourth tarsal bone articulates with the fourth metatarsal bone.

The interosseous muscle (known colloquially as the *suspensory ligament*) originates principally from the proximopalmar (plantar) aspect of the third metacarpal and metatarsal bones respectively, with an accessory head that originates from the palmar distal aspect of the third carpal bone in the forelimb[2,3] and from the fourth tarsal bone and calcaneus in the hindlimb.[4] There are additional fibers from the axial aspect of the fourth metacarpal and metatarsal bones.[2,3] There are two lobes of the suspensory ligament proximally that contain variable amounts of muscle and adipose tissue.[3,5,6] In hindlimbs, a dense fascial band runs between the second and fourth metatarsal bones on the plantar aspect of the suspensory ligament proximally. In the distal third of the metacarpal region, the suspensory ligament divides into lateral and medial branches that insert on the lateral and medial aspect of the proximal sesamoid bones, respectively. The suspensory ligament branches are closely related to the palmar (plantar) pouch of the metacarpophalangeal (metatarsophalangeal) joints,[7] having a subsynovial location distally. Small ligaments extend from the distal aspect of the second and fourth metacarpal bones and merge with the medial and lateral branches of the suspensory ligament, respectively. The accessory ligament of the deep digital flexor tendon originates from the palmar aspect of the third and fourth carpal bones[8] and merges with the deep digital flexor tendon in the third quarter of the metacarpal region. In the hindlimb the accessory ligament of the deep digital flexor tendon originates from the plantar aspect of the ligament between the calcaneus and the central and third tarsal bones and is much more variable in size than in the forelimb. It may be bifid or trifid but is sometimes absent.[9] In the proximal third to half of the metacarpal and metatarsal regions, the accessory ligament of the deep digital flexor tendon is within the carpal or tarsal sheath. In the proximal quarter of the metacarpal region the dense carpal retinaculum overlies the superficial digital flexor tendon. In the distal one third of the metacarpal region, the superficial and deep digital flexor tendons are contained within the digital flexor tendon sheath, which is reinforced on the palmar (plantar) aspect by the palmar (plantar) annular ligament, which attaches to the abaxial aspects of the proximal sesamoid bones. The tendonous and ligamentous structures change in their relative shapes and sizes from proximal to distal; absolute sizes vary between breeds and sizes of horses, but the relative sizes remain similar.

NORMAL RADIOGRAPHIC AND ULTRASONOGRAPHIC VARIATIONS

Superimposition of two bones often results in a radiolucent line adjacent and parallel to the margin of one bone. This is a Mach line, and such lines are particularly common in the metacarpal and metatarsal regions, especially when the second or fourth metacarpal bone is projected over the third metacarpal bone (Fig. 21-1). Nutrient vessels are present in the metacarpal and metatarsal bones at standard sites. Nutrient foramina in the proximal epiphyseal region of the third metacarpal bone are seen as small circular radiolucent areas in a dorsopalmar radiograph (Fig. 21-2). The entrance of the principal nutrient vessel is in the middle third of the third metacarpal bone and appears as a circular or oval radiolucent area

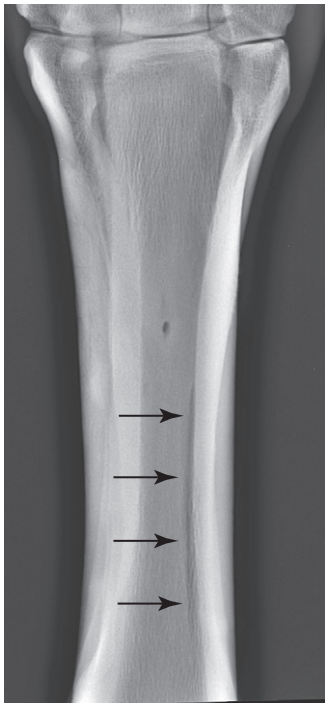


Fig. 21-1 Dorsopalmar radiograph of a metacarpus. Lateral is to the right. There is a radiolucent line *(black arrows)* on the axial aspect of the fourth metacarpal bone. This Mach line is an artifact created at the margin of two superimposed radiopacities, the third and fourth metacarpal bones.

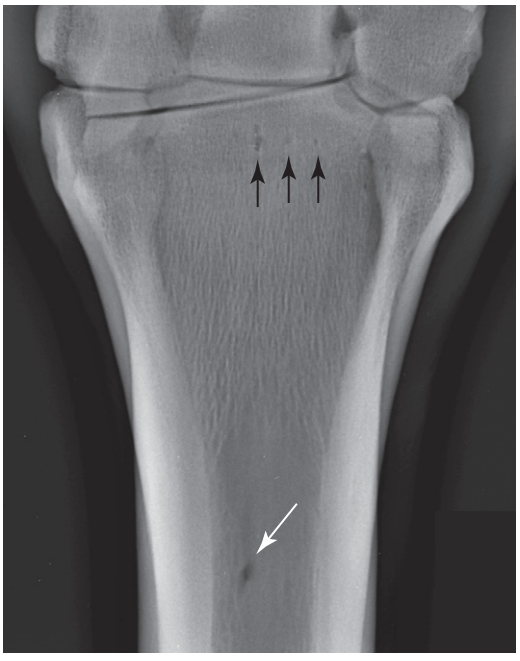


Fig. 21-2 Dorsopalmar radiographic image of a proximal metacarpal region. The radiolucent line in the middle third of the third metacarpal bone represents the principal nutrient foramen *(white arrow)*. There are additional nutrient foramina *(black arrows)* just distal to the carpometacarpal joint; these vary in number. Note the regular trabecular architecture of the proximal one third of the third metacarpal bone.

in a dorsopalmar image (see Fig. 21-2). In oblique images the nutrient canal may be seen as a broad, curved radiolucent line traversing the second or fourth metacarpal bones, which should not be confused with a fracture (Fig. 21-3). The proximal epiphyseal and metaphyseal regions of the third

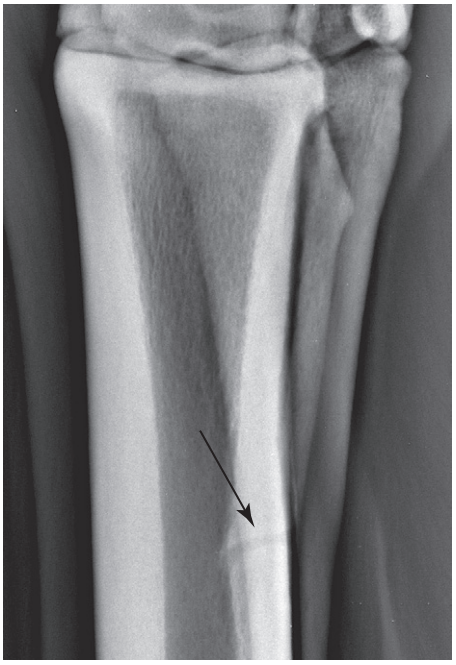


Fig. 21-3 Dorsomedial-plantarolateral radiograph of a metatarsal region. There is a broad radiolucent line, representing a nutrient vessel, crossing the plantar aspect of the cortex of the third metatarsal bone *(black arrow)*. This should not be misinterpreted as a fracture.

metacarpal bone have a conspicuous trabecular architecture and are often more radiopaque in a dorsopalmar image than the diaphyseal region of the bone (Fig. 21-4).

A radiolucent area may be present in the proximal aspect of the second metacarpal bone, especially in association with the presence of a first carpal bone[10] (Fig. 21-5). Less commonly there may be a radiolucent area in the proximal aspect of the fourth metacarpal bone, but this may not be associated with the presence of a fifth carpal bone. The base of the fourth metacarpal bone sometimes has a proximal extension[10] (Fig. 21-6, *A*). Similar modelling has been seen on the proximal aspect of the fourth metatarsal bone (Fig. 21-6, *B*). Nutrient vessels in the second and fourth metacarpal bones are seen with variable clarity. If there is no mineralization of the interosseous ligaments, the margins of the second, third, and fourth metacarpal (metatarsal) bones are smoothly marginated (Fig. 21-7).

Smooth or irregularly outlined exostoses on the second and fourth metacarpal bones are common incidental variants (Fig. 21-8, *A* and *B*), as are partial mineralization or ossification of the interosseous ligaments, especially medially (Fig. 21-8, *C*). These variably sized and shaped exostoses (splints) between or around the second and third or fourth and third metacarpal bones may be uniform in radiopacity or have heterogeneous opacity. Some exostoses are associated with long-term increased radiopharmaceutical uptake, despite generally being of no clinical significance. In hindlimbs there may be a large focal irregularly marginated exostosis on the lateral proximal aspect between the third and fourth metatarsal bones (Fig. 21-8, *D*). Such exostoses appear to occur in a characteristic location, may be unilateral or bilateral, and are always associated with focal intense increased radiopharmaceutical uptake, but generally do not appear to be of clinical significance.

In association with abnormal so-called bench knee or offset knee conformation, the metacarpal region is positioned laterally relative to the central limb axis of the antebrachium. This results in abnormal loading through the medial aspect of the

Text continued on page 398

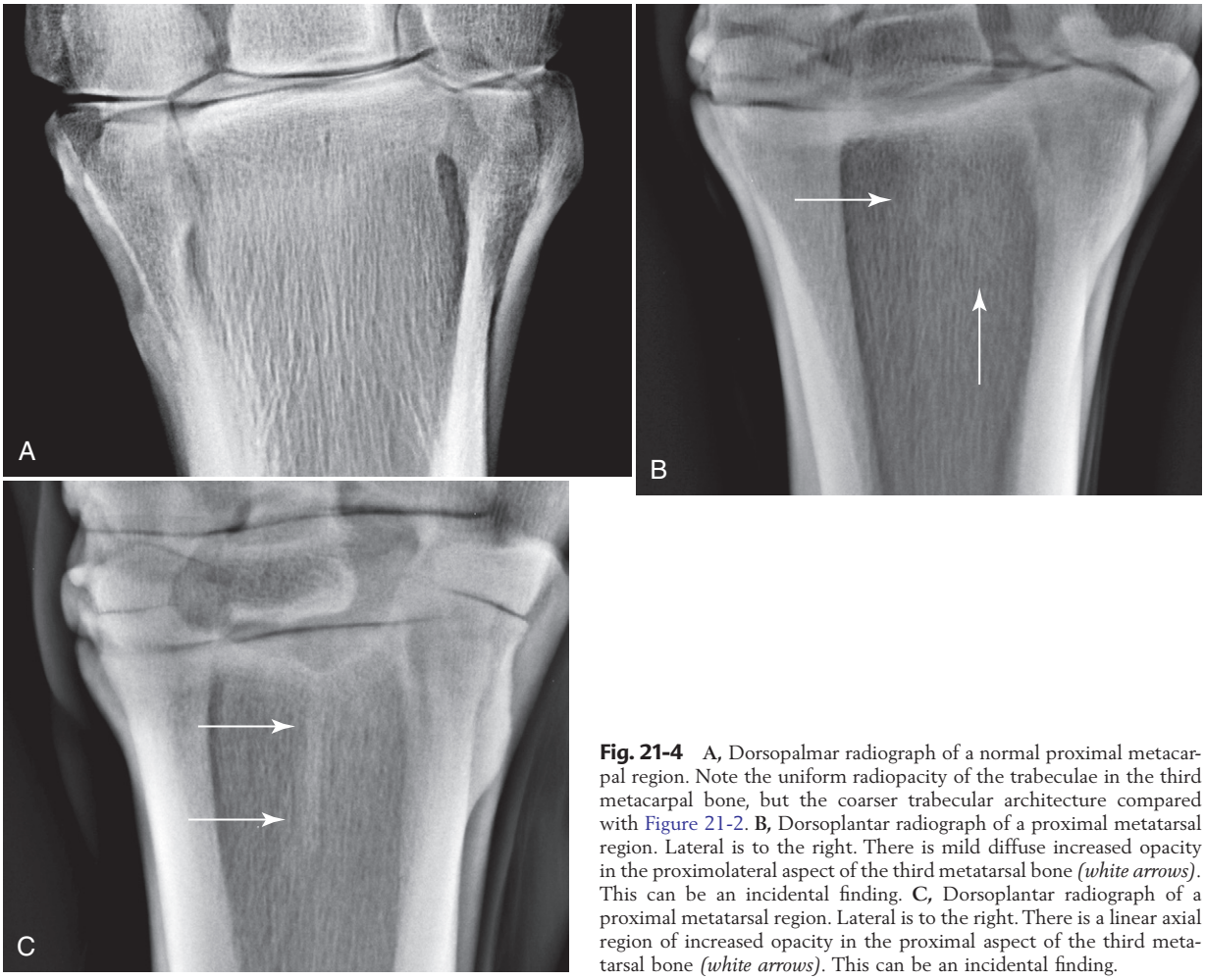


Fig. 21-4 **A,** Dorsopalmar radiograph of a normal proximal metacarpal region. Note the uniform radiopacity of the trabeculae in the third metacarpal bone, but the coarser trabecular architecture compared with Figure 21-2. **B,** Dorsoplantar radiograph of a proximal metatarsal region. Lateral is to the right. There is mild diffuse increased opacity in the proximolateral aspect of the third metatarsal bone *(white arrows)*. This can be an incidental finding. **C,** Dorsoplantar radiograph of a proximal metatarsal region. Lateral is to the right. There is a linear axial region of increased opacity in the proximal aspect of the third metatarsal bone *(white arrows)*. This can be an incidental finding.

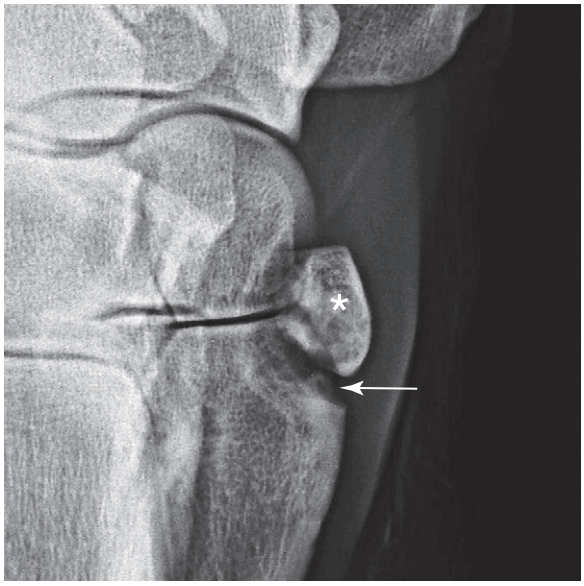


Fig. 21-5 Dorsomedial-palmarolateral oblique radiograph of a proximal metacarpal region. The palmaroproximal aspect of the second metacarpal bone is relatively radiolucent *(white arrow)* in association with the presence of a large first carpal bone *(*)*.

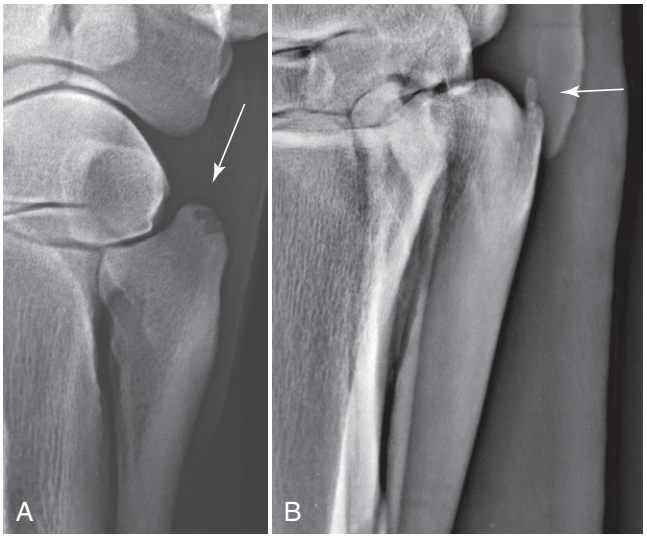


Fig. 21-6 **A,** Dorsolateral-plantaromedial oblique radiograph of a proximal metacarpal region. The base of the fourth metacarpal bone is extended proximally, and there is an ill-defined radiolucent area *(white arrow)* in the most proximal aspect. **B,** Dorsolateral-plantaromedial oblique radiograph of a proximal metatarsal region. There is a spur on the proximoplantar aspect of the fourth metatarsal bone *(white arrow)*.

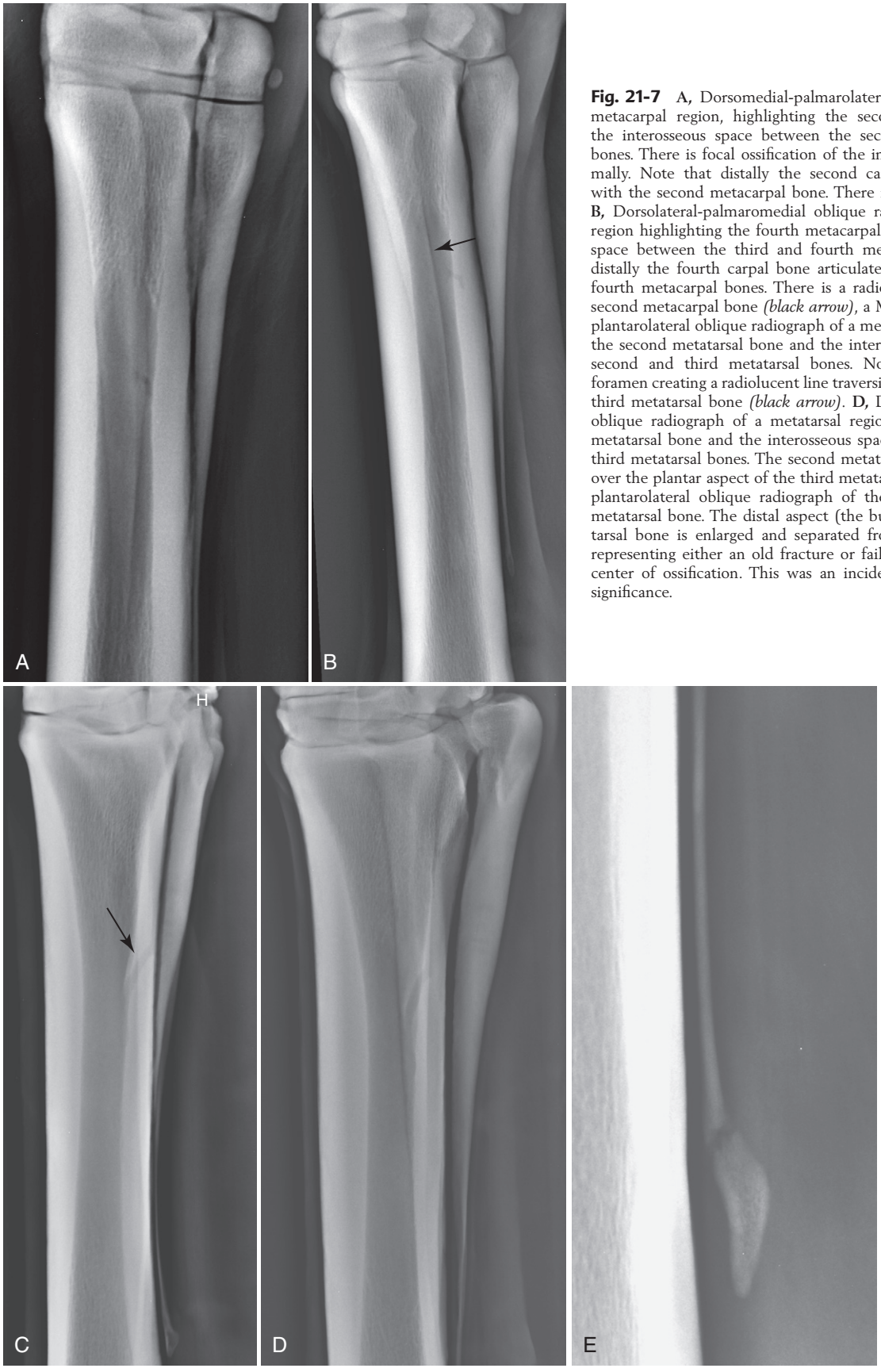
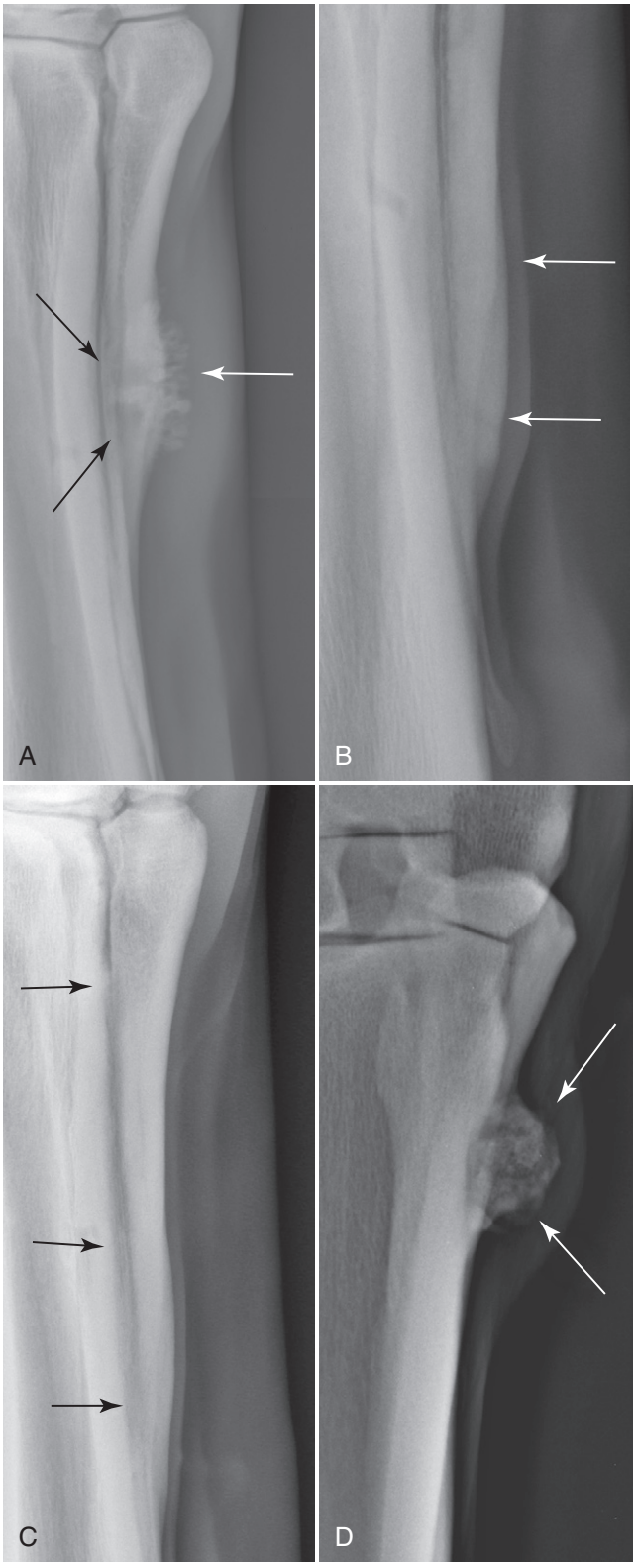


Fig. 21-7 **A,** Dorsomedial-palmarolateral oblique radiograph of a metacarpal region, highlighting the second metacarpal bone and the interosseous space between the second and third metacarpal bones. There is focal ossification of the interosseous ligament proximally. Note that distally the second carpal bone articulates only with the second metacarpal bone. There is a small first carpal bone. **B,** Dorsolateral-palmaromedial oblique radiograph of a metacarpal region highlighting the fourth metacarpal bone and the interosseous space between the third and fourth metacarpal bones. Note that distally the fourth carpal bone articulates with both the third and fourth metacarpal bones. There is a radiolucent line palmar to the second metacarpal bone *(black arrow)*, a Mach line. **C,** Dorsomedial-plantarolateral oblique radiograph of a metatarsal region, highlighting the second metatarsal bone and the interosseous space between the second and third metatarsal bones. Note the principal nutrient foramen creating a radiolucent line traversing the plantar cortex of the third metatarsal bone *(black arrow)*. **D,** Dorsolateral-plantaromedial oblique radiograph of a metatarsal region, highlighting the fourth metatarsal bone and the interosseous space between the fourth and third metatarsal bones. The second metatarsal bone is superimposed over the plantar aspect of the third metatarsal bone. **E,** Dorsomedial-plantarolateral oblique radiograph of the distal third of a second metatarsal bone. The distal aspect (the button) of the second metatarsal bone is enlarged and separated from the shaft of the bone, representing either an old fracture or failure of union of a separate center of ossification. This was an incidental finding of no clinical significance.



metacarpal region with characteristic changes in radiopacity and cortical thickness of the third metacarpal bone, often with very extensive fusion of the second and third metacarpal bones with large smoothly marginated exostoses on the proximomedial aspect of the second metacarpal bone.

There is a variably sized and shaped protuberance on the distal aspect of the second and fourth metacarpal and metatarsal bones (the button of the splint bone), which is present as a separate center of ossification in a neonatal foal. Smoothly marginated enlargement of this protuberance may reflect previous trauma. Bowing of the distal one third of the second and fourth metacarpal bones away from the cortex of the third metacarpal bone is usually the result of previous suspensory ligament branch injury. In a dorsoplantar radiograph of the proximal metatarsal region, it is common to see a linear axial region of increased radiopacity in the third metatarsal bone and/or a mild generalized increased radiopacity of the proximolateral aspect (see Fig. 21-4, *B* and C). These reactions probably reflect chronic stress at the enthesis of the suspensory ligament but are not necessarily associated with active desmopathy.

A slightly convex contour of the dorsal aspect of the diaphysis of the third metacarpal bone and, less commonly, the third metatarsal bone is often seen in Thoroughbreds that have been in race training. There is often associated increase in cortical thickness reflecting previous modelling in adaptation to loading.

In the region where the accessory ligament of the deep digital flexor tendon merges with the deep digital flexor tendon, the dorsal aspect of the combined structure often appears less echogenic, particularly in hindlimbs. This variant is usually bilaterally symmetric. In both forelimbs and hindlimbs, large muscle bundles in the proximal aspect of the suspensory ligament may be seen as well-demarcated hypoechogenic areas, which in longitudinal images are of uniform thickness and may be bordered by relatively hyperechogenic lines.

ABNORMALITIES

Soft Tissue Injuries

Proximal Suspensory Desmitis and Desmopathy

Acute and chronic injuries of the proximal third of the suspensory ligament are common causes of both forelimb[11,12] and hindlimb[13-15] lameness, and ultrasonography is the imaging modality of choice, although its sensitivity and specificity for the diagnosis of hindlimb injuries has recently been challenged.[16] However optimization of ultrasonographic technique may facilitate injury diagnosis.[17] Ultrasonographic abnormalities include enlargement, a convex palmar (plantar)

Fig. 21-8 **A,** Dorsomedial-palmarolateral oblique radiograph of the second and third metacarpal bones. The middle one third of the second metacarpal bone is smoothly enlarged, with irregularly outlined new bone on the palmar aspect of heterogeneous opacity *(white arrow)*. Within the second metacarpal bone there are ill-defined radiolucent areas *(black arrows)*. Although irregular in appearance, such lesions may not be clinically significant. **B,** Dorsomedial-palmarolateral oblique radiograph of the second and third metacarpal bones. There is a smoothly marginated exostosis *(white arrow)* on the second metacarpal bone of unlikely clinical significance. **C,** Dorsomedial-palmarolateral oblique radiograph of the second and third metacarpal bones. There is mineralization between the two bones in the interosseous space *(black arrows)*. This is of unlikely clinical significance. **D,** Dorsoplantar radiograph of a proximal metatarsal region. Lateral is to the right. There is a large exostosis of heterogeneous radiopacity on the lateral aspect of the third metatarsal bone *(white arrows)*.

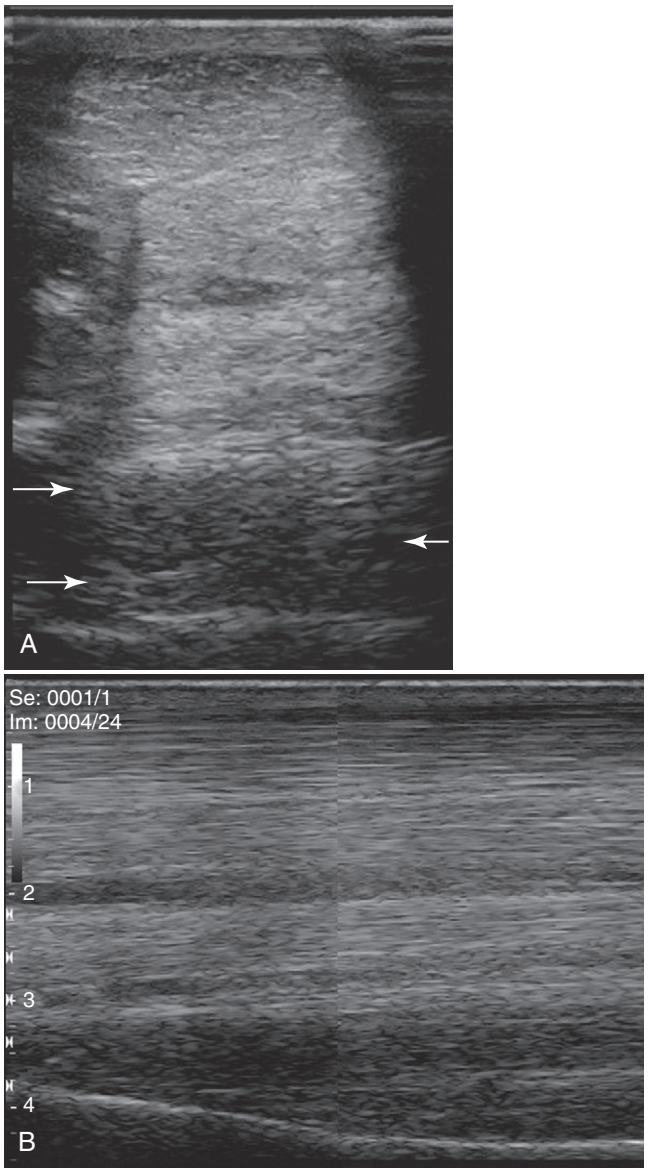


Fig. 21-9 **A,** Transverse ultrasonographic image of a palmar metacarpal region obtained 8 cm distal to the accessory carpal bone, using a 10 MHz virtual convex array transducer. Medial is to the left. The dorsal three quarters of the suspensory ligament has diffuse loss of echogenicity *(white arrows)*. The ligament is enlarged, so there is reduced space between it and the accessory ligament of the deep digital flexor tendon. **B,** Longitudinal ultrasonographic images of a palmar metacarpal region of the same limb as in **A** at approximately 7 to 14 cm distal to the accessory bone. Proximal is to the left. There is diffuse loss of echogenicity of the suspensory ligament and absence of long linear echoes, consistent with proximal suspensory desmitis.

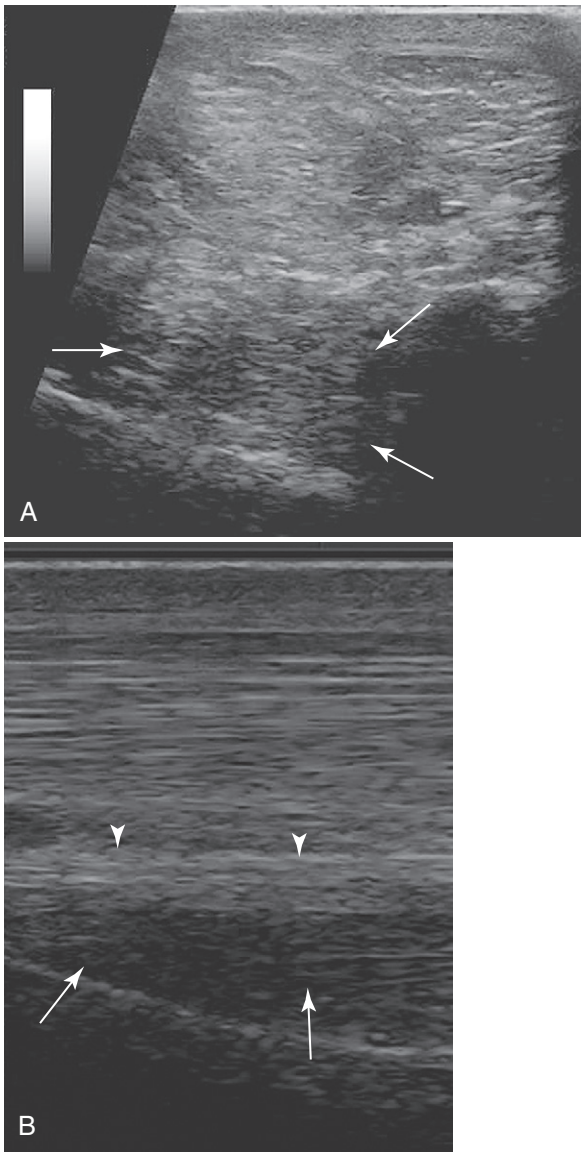
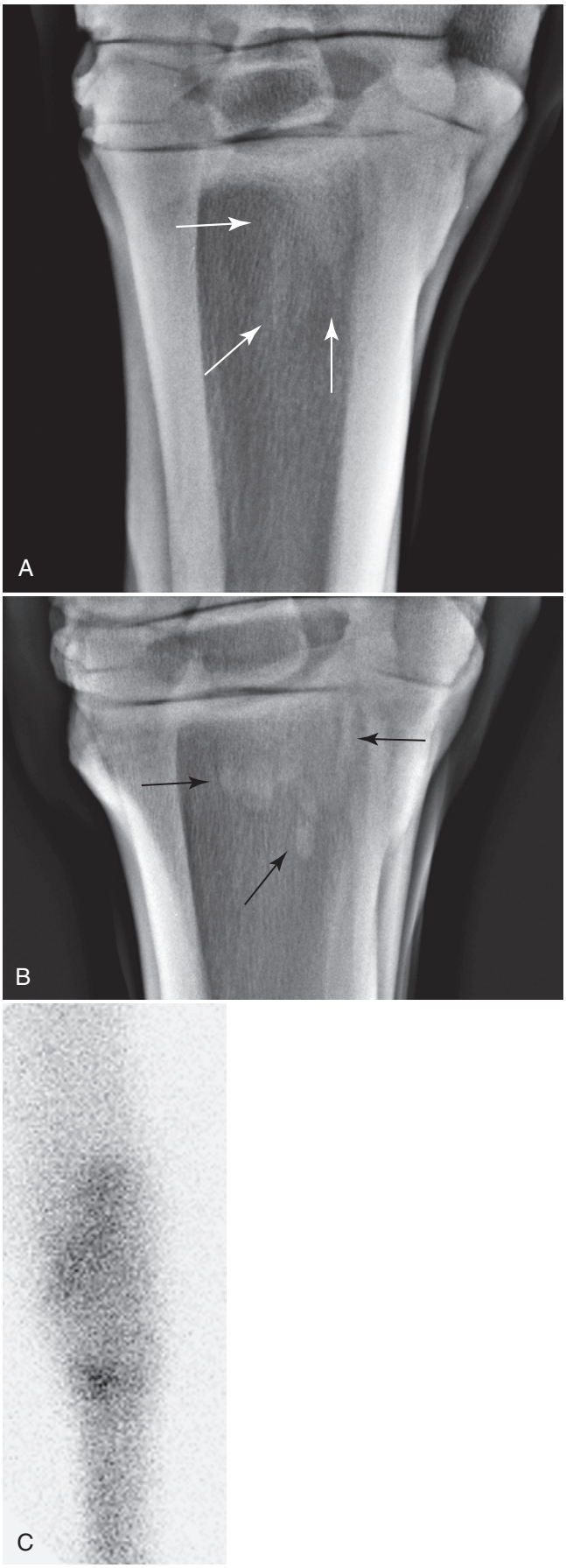


Fig. 21-10 **A,** Transverse ultrasonographic image of a proximal metatarsal region obtained at 4 cm distal to the tarsometatarsal joint. Medial is to the left. The image was obtained using a 10 MHz virtual convex array transducer. The suspensory ligament is enlarged *(white arrows)* and has a diffuse reduction in echogenicity dorsally. **B,** Longitudinal ultrasonographic image of the proximal metatarsal region of the same limb as in **A.** Proximal is to the left. There is marked loss of echogenicity and fiber pattern in the proximal aspect of the suspensory ligament *(white arrows)*. The accessory ligament of the suspensory ligament *(white arrowheads)* is of normal echogenicity.

border, focal or diffuse hypoechogenic areas, poor definition of the margins, most particularly the dorsal margin, and reduced strength of fiber pattern in longitudinal images (Figs. 21-9 and 21-10). With chronic injuries there may be areas of increased echogenicity reflecting fibrosis and chondroid metaplasia and occasionally dystrophic mineralization; periosteal irregularity may also be detected. Osseous changes may be seen radiologically in association with chronic suspensory desmopathy and include generalized or focal increased opacity reflecting stress at the enthesis and entheseous new bone (Fig. 21-11, *A*), or increased opacity of the endosteal bone of the proximal palmar (proximal plantar) aspect of the third metacarpal (metatarsal) bone. Entheseous new bone is best seen in a dorsopalmar (dorsoplantar) image (Fig. 21-11, *B*), whereas increased opacity of the endosteal bone is best seen in a lateromedial image. Nuclear scintigraphy may reveal increased radiopharmaceutical uptake in the proximopalmar (proximoplantar) aspect of the third metacarpal (metatarsal) bone in the absence of detectable radiographic abnormality in association with either acute, severe, or chronic injuries[18,19] (Fig. 21-11, C). Computed tomography[20,21] or magnetic resonance imaging[16,22-25] is sometimes necessary to identify lesions of the suspensory ligament or adjacent osseous reactions.

Suspensory Body Injuries

Desmitis of the body of the suspensory ligament is usually readily diagnosed clinically, but ultrasonography is useful to



document the severity of the injury and to monitor repair. With enlargement of the body of the suspensory ligament together with extensive periligamentous swelling, it may be difficult to palpate the second and fourth metacarpal bones accurately. Fracture at the junction of the proximal two thirds and distal one third of the second and/or fourth metacarpal bones may accompany a severe suspensory ligament body or branch injury, and radiographic assessment of these bones is warranted.

An axially projecting exostosis from the second or fourth metacarpal bones may impinge on the suspensory ligament and cause focal desmitis. Echogenic material can sometimes be seen extending between the exostosis and the suspensory ligament, but occasionally magnetic resonance imaging is required for definitive diagnosis.[26]

Suspensory Branch Injuries

Swelling in the region of a branch of the suspensory ligament may reflect enlargement of the ligament or the periligamentous tissues, or both and accurate determination can be made only by ultrasonographic evaluation from the palmaromedial and palmarolateral aspects of the limb (Fig. 21-12). Because of their superficial location, a standoff is usually required to evaluate the suspensory branches. Injuries may be biaxial; therefore both medial and lateral branches should be evaluated in their entirety, including their insertions on the proximal sesamoid bones. Entheseous new bone on a proximal sesamoid bone is readily detectable ultrasonographically (Fig. 21-12, *C*), but other osseous changes such as enlargement of vascular channels and some fractures can only be determined radiographically (Fig. 21-13, *A*). The second and fourth metacarpal bones should also be assessed radiographically; bowing of the distal one-third, fracture at the junction of the proximal two-thirds and distal one-third (Fig. 21-13, *B*), or generalized enlargement of the distal one-third (see Fig. 21-13, *A*) are common abnormalities seen in association with suspensory branch injuries. Lesions may extend proximally into the body of the suspensory ligament, which should also be evaluated ultrasonographically.

Desmitis and Desmopathy of the Accessory Ligament of the Deep Digital Flexor Tendon

Acute forelimb injuries of the accessory ligament of the deep digital flexor tendon are usually associated with a characteristically located soft tissue swelling. Ultrasonography is useful to document the severity of the injury and to monitor repair.[27-31] Examination from both the palmar and the lateral aspects of the limb is useful to examine the ligament in its entirety. Because of the broad width of the ligament, it may be useful to use a standoff to enlarge the window through which imaging can be performed or to use a convex array transducer (Fig. 21-14). Lesions may be focal or diffuse; if

Text continued on page 403

Fig. 21-11 **A,** Dorsoplantar radiograph of a proximal metatarsal region of a horse with proximal suspensory desmopathy. Lateral is to the right. There is mild diffuse increased radiopacity of the proximolateral aspect of the third metatarsal bone *(white arrows)*. **B,** Dorsoplantar radiograph of a proximal metatarsal region of an 8-year-old Warmblood dressage horse with proximal suspensory desmopathy. Lateral is to the right. There are several variably shaped radiopacities superimposed over the proximolateral aspect of the third metatarsal bone *(black arrows)* consistent with entheseous new bone. **C,** Plantar bone-phase scintigraphic image of the tarsus of a 10-year-old horse with lameness localized to the left proximal metatarsal region. A focal region of increased radiopharmaceutical uptake is visible in the proximolateral aspect of the metatarsal area associated with entheseous new bone formation secondary to proximal suspensory desmopathy.

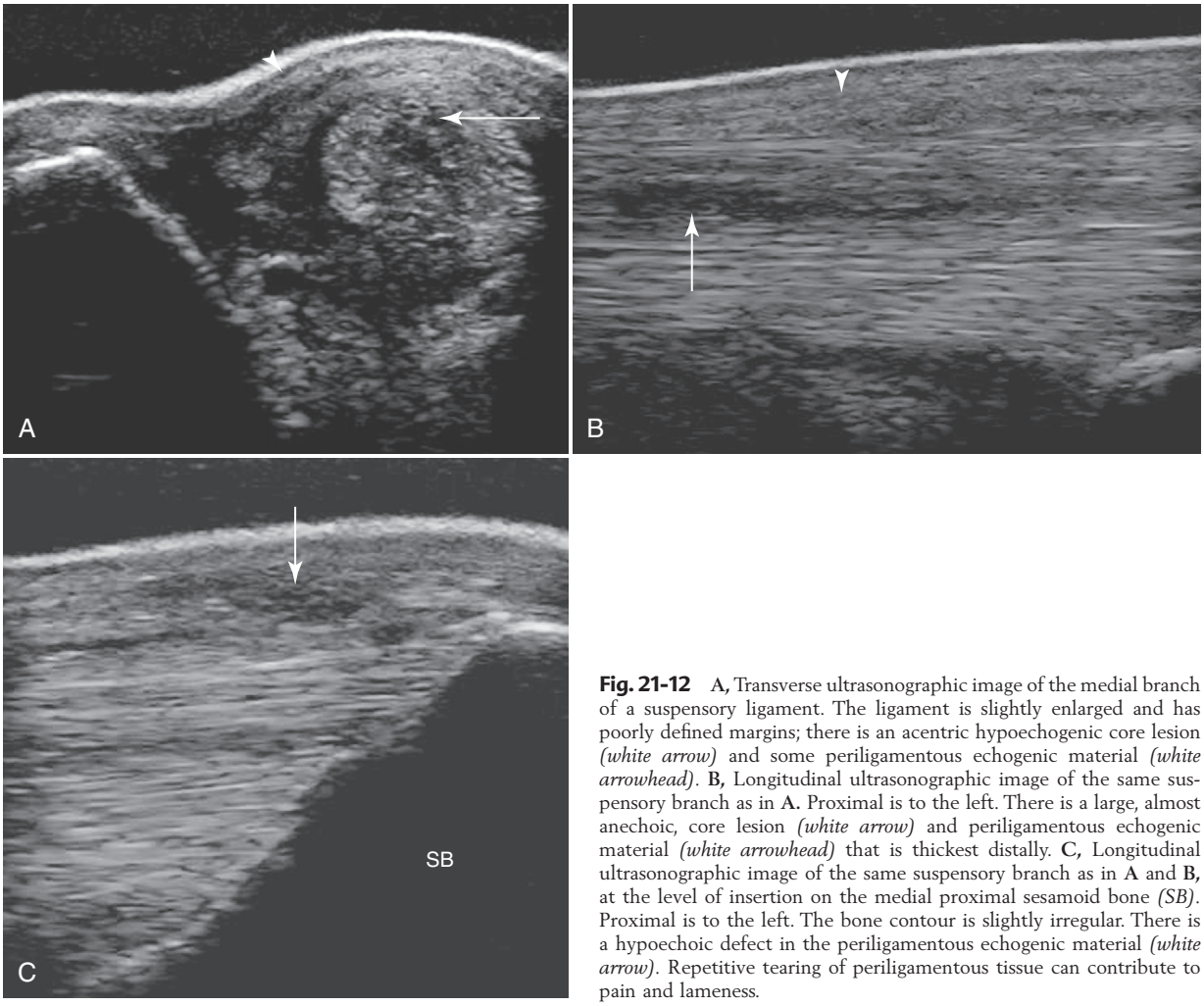


Fig. 21-12 **A,** Transverse ultrasonographic image of the medial branch of a suspensory ligament. The ligament is slightly enlarged and has poorly defined margins; there is an acentric hypoechogenic core lesion *(white arrow)* and some periligamentous echogenic material *(white arrowhead)*. **B,** Longitudinal ultrasonographic image of the same suspensory branch as in **A.** Proximal is to the left. There is a large, almost anechoic, core lesion *(white arrow)* and periligamentous echogenic material *(white arrowhead)* that is thickest distally. **C,** Longitudinal ultrasonographic image of the same suspensory branch as in **A** and **B,** at the level of insertion on the medial proximal sesamoid bone *(SB)*. Proximal is to the left. The bone contour is slightly irregular. There is a hypoechoic defect in the periligamentous echogenic material *(white arrow)*. Repetitive tearing of periligamentous tissue can contribute to pain and lameness.

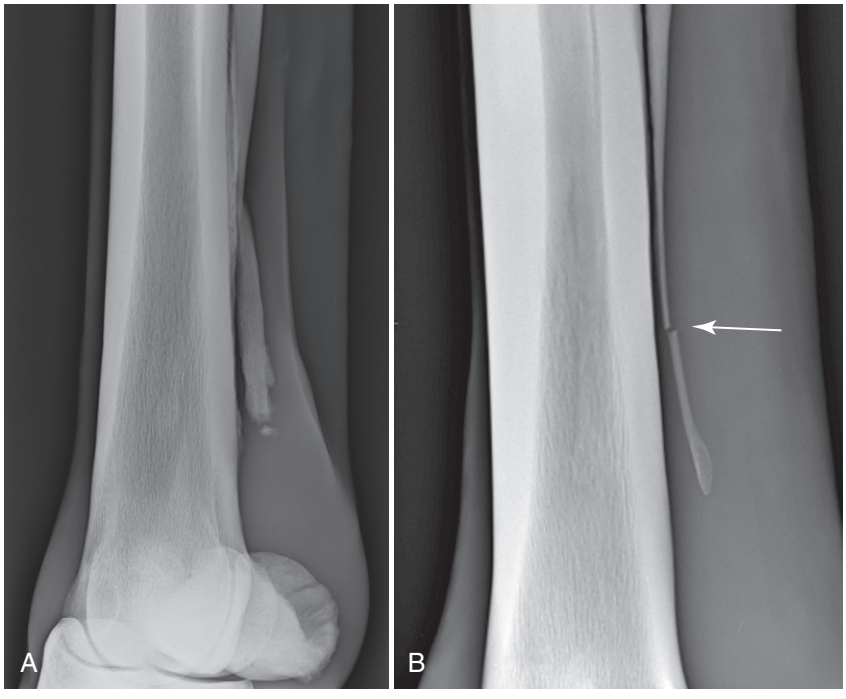


Fig. 21-13 **A,** Dorsomedial-palmarolateral oblique radiograph of a metacarpal region. There is thickening of the distal aspect of the second metacarpal bone reflecting chronic modelling, distal to which is a small mineralized opacity. There are several radiating lucent lines in the ipsilateral proximal sesamoid bone and slight new bone formation on the distal aspect. **B,** Dorsolateral–palmaromedial oblique radiograph of a metacarpal region. There is an acute slightly displaced fracture *(white arrow)* of the fourth metacarpal bone at the junction between the proximal two thirds and distal one-third. (Courtesy of Gaynor Minshall, Newmarket Equine Hospital.)

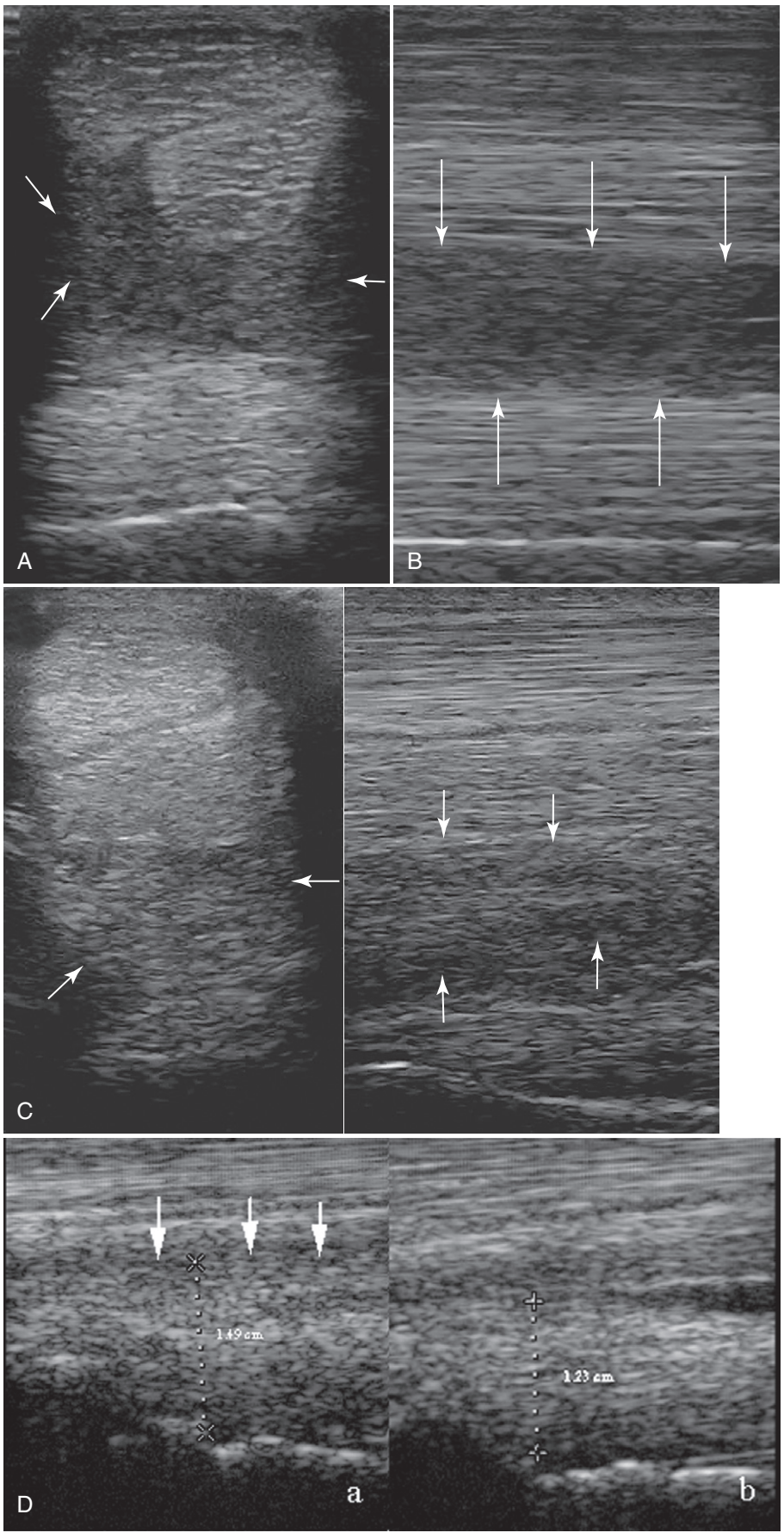


Fig. 21-14 **A,** Transverse ultrasonographic image of a metacarpal region obtained 15 cm distal to the accessory carpal bone using a 10 MHz virtual convex array transducer. Medial is to the left. The accessory ligament of the deep digital flexor tendon is markedly enlarged *(white arrows)*, wraps around the medial margin of the deep digital flexor tendon, and is contiguous with the superficial digital flexor tendon. It has a diffuse decrease in echogenicity. The lateral extremity of the ligament cannot be assessed in this image. **B,** Longitudinal ultrasonographic image of the metacarpal region of the same limb as in **A** obtained approximately 10 cm distal to the accessory carpal bone using a 10 MHz linear transducer. Proximal is to the left and palmar to the top of the image. The accessory ligament of the deep digital flexor tendon *(white arrows)* has a diffuse reduction in echogenicity and no long linear echoes. **C,** Transverse *(left)* and longitudinal (*right*, proximal is to the left) ultrasonographic images of the proximal metacarpal region of a 7-year-old intermediate event horse with lameness that was abolished by median and ulnar nerve blocks. There were no detectable palpable abnormalities. The accessory ligament of the deep digital flexor tendon is enlarged and has a diffuse reduction in echogenicity *(white arrows)*, with loss of fiber pattern in the longitudinal image. **D,** Longitudinal ultrasonographic images of the palmar aspect of the carpus of the right (*a*) and left (*b*) forelimbs of a 5-year-old event horse, showing the origin of the accessory ligament of the deep digital flexor tendon on the third carpal bone. Proximal is to the left. The origin of the accessory ligament of the deep digital flexor tendon is thickened in the right forelimb (1.49 cm) compared with the left forelimb (1.23 cm) and has some disruption of architecture. The palmar margin of the ligament is rather poorly defined *(white arrows)*. (The *dotted lines* measure the combined thickness of the origin of the accessory ligament of the deep digital flexor tendon and the palmar carpal ligament; the line in *a* is not precisely perpendicular to the margin of the accessory ligament of the deep digital flexor tendon, thus slightly exaggerating its thickness.)

the accessory ligament is enlarged considerably, it may wrap around the margins of the deep digital flexor tendon and come in to close apposition to the superficial digital flexor tendon. Focal lesions involving the lateral abaxial aspect of the ligament may be seen only in images acquired from the lateral aspect of the limb. Occasionally, lesions are identified in the distal carpal and proximal metacarpal regions without clinically detectable soft tissue swelling because of the overlying compressive palmar carpal retinaculum. However, ultrasonographic examination reveals enlargement of the ligament and diffuse decrease in echogenicity (Fig. 21-14, C and *D*).

Desmitis of the accessory ligament of the deep digital flexor tendon in hindlimbs is much less common.[32-35] Proximal lesions are missed easily unless the ligament is examined from the proximoplantar medial aspect of the metatarsal region (Fig. 21-15, *A*).[34-36] Cob-type horses and native pony breeds seem at increased risk of developing a flexure deformity of the metatarsophalangeal joint in association with desmopathy of the accessory ligament of the deep digital flexor tendon.[33] These types of horses are difficult both to palpate and examine ultrasonographically because of their thick skin and skin folds. It may be necessary to use a much lower frequency transducer (e.g., 5 to 7 MHz) than is usually used for evaluation of the metatarsal region. Lesions are usually characterized by diffuse areas of reduced echogenicity and enlargement of the ligament (Fig. 21-15, *B*).

Deep Digital Flexor Tendon Injury

Deep digital flexor tendon injuries in the metacarpal and metatarsal regions are unusual except within the digital flexor tendon sheath and are generally associated with distention of the sheath.[37-40] There may be no palpable abnormality of the tendon, and diagnosis is reliant on ultrasonography. Abnormalities include enlargement, and a focal hypoechogenic core lesion, which may or may not extend toward the periphery of the tendon (Fig. 21-16). In some horses there is multifocal fibrosis (Fig. 21-17, *A*), which may only be visible using off-incidence imaging or dystrophic mineralization resulting in acoustic shadowing. Alternatively, lesions may be restricted to the margins of the ligament, most commonly laterally but occasionally medially or dorsally, and these are typified by blunting of the normal pointed margin of the tendon with subtle loss of echogenicity or extension of ill-defined echogenic material beyond the margin of the tendon (Fig. 21-17, C and *D*). Examination of the deep digital flexor tendon from the palmaromedial and palmarolateral aspects is important to detect focal marginal lesions. Some marginal tears can only be identified using exploratory tenoscopy.

Superficial Digital Flexor Tendonitis

Superficial digital flexor tendonitis is usually associated with focal heat, pain, and swelling, and ultrasonography is used only to determine the severity of the injury and to monitor healing. However, proximally, the dense palmar retinaculum may obscure swelling, and ultrasonography is then crucial for diagnosis (Fig. 21-18). Examination should include the distal carpal region routinely in addition to the metacarpus. Although central hypoechogenic core defects are the most typical superficial digital flexor tendon injury (Fig. 21-19), core defects close to the periphery of the tendon on the dorsal, palmar, or lateral borders also occur commonly (Fig. 21-20, *A*), or a mild diffuse reduction in echogenicity of the entire cross-sectional area of the tendon. Areas of fibrosis or scarring can be detected using off-incidence scanning; the scar tissue is more echogenic than the rest of the tendon. Occasionally, in association with acute distention of the digital flexor tendon sheath, there is a

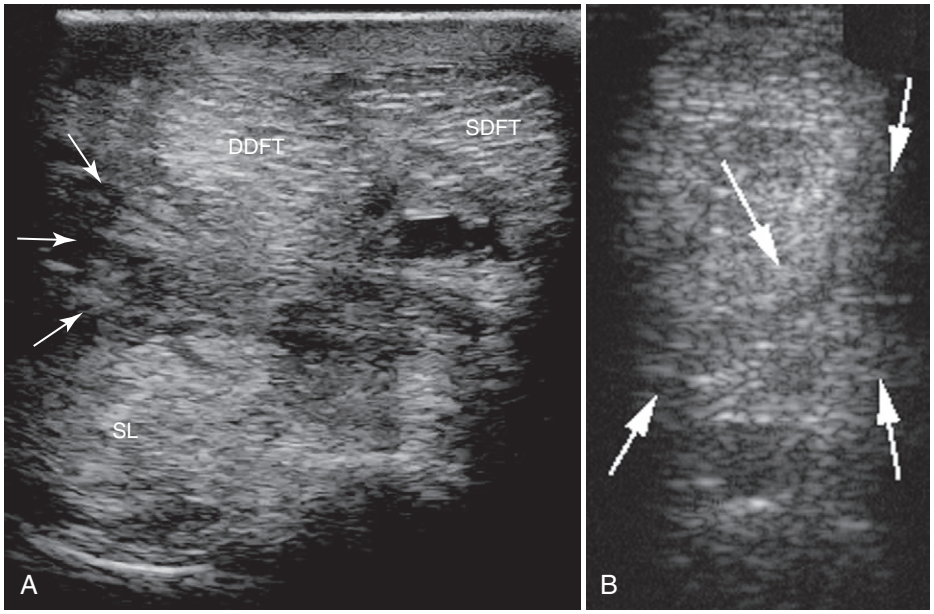


Fig. 21-15 **A,** Transverse ultrasonographic image obtained at 7 cm distal to the tarsometatarsal joint with a 10 MHz virtual convex array transducer positioned on the proximal plantaromedial aspect of the limb. Medial is to the left. The accessory ligament of the deep digital flexor tendon is enlarged *(white arrows)* and has a diffuse reduction in echogenicity especially medially. *DDFT,* Deep digital flexor tendon; SDFT, superficial digital flexor tendon; SL, suspensory ligament. This 9-year-old Warmblood dressage horse had acute onset lameness associated with subtle edematous swelling in the proximoplantar aspect of the metatarsal region. **B,** Transverse ultrasonographic image of the plantar metatarsal region obtained 14 cm distal to the tarsometatarsal joint using a 7.5 MHz transducer. Lateral is to the right. The accessory ligament of the deep digital flexor tendon is enlarged *(white arrows)* and has a generalized mild reduction in echogenicity consistent with chronic desmopathy. This 12-year-old cob gelding had lameness and a flexural deformity of the metatarsophalangeal joint. The very thick skin of the metatarsal region compromised both image quality and accurate palpation of the region.

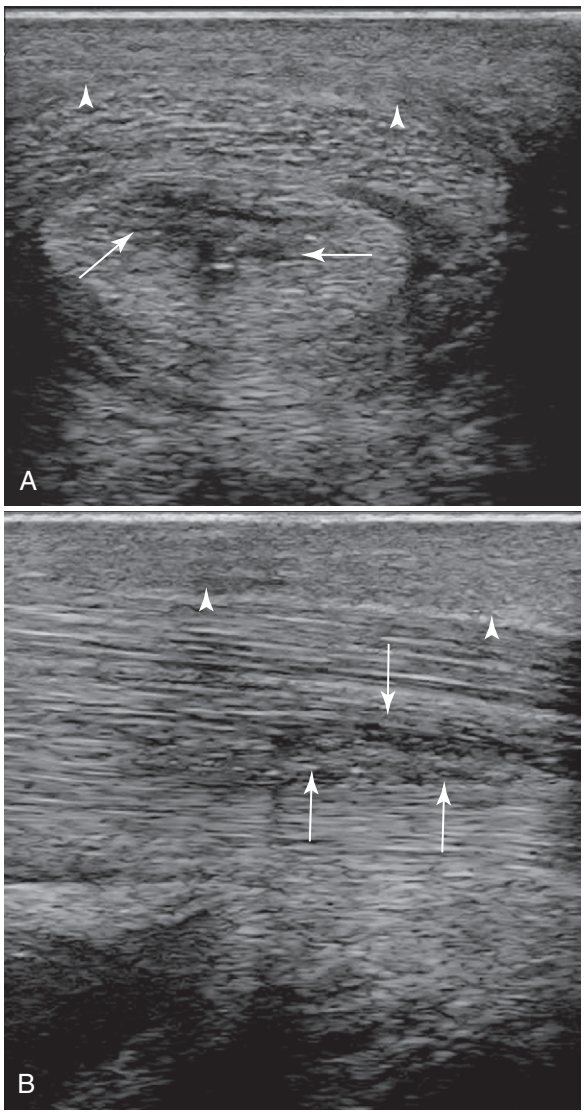


Fig. 21-16 **A,** Transverse ultrasonographic image of a distal metacarpal region, obtained using a 10 MHz linear transducer. Medial is to the left. There is a large poorly demarcated core lesion in the deep digital flexor tendon *(white arrows)*. There is also subcutaneous echogenic material *(white arrowheads)*. **B,** Longitudinal ultrasonographic image of the distal metacarpal region of the same limb as in **A.** Proximal is to the left. There is a core lesion in the deep digital flexor tendon *(white arrows)*. There is echogenic material subcutaneously *(white arrowheads)*.

defect on the lateral or medial margin of the superficial digital flexor tendon at the level of the fetlock (Fig. 21-20, *B*). Such lesions may be missed unless the limb is evaluated from the palmarolateral and palmaromedial aspects.

Infection of a Digital Flexor Tendon

Infection in the deep or superficial digital flexor tendon is an unusual cause of acute-onset severe lameness associated with diffuse soft tissue swelling.[41] Ultrasonographic examination is crucial for diagnosis. Lesions are characterized by enlargement of the tendon and rapidly progressive anechoic areas.

Osseous Injuries

Avulsion Fracture at the Origin of the Suspensory Ligament

An avulsion fracture at the origin of the suspensory ligament on the proximopalmar aspect of the third metacarpal bone is usually an injury seen in young Thoroughbred and Standardbred racehorses[42,43] and also elite endurance horses[44,45] associated with acute-onset moderate to severe lameness. The lesions are generally best seen in a dorsopalmar image but are sometimes also seen in a lateromedial image, preferably flexed. In a dorsopalmar image a fracture can usually be seen as a punched-out radiopacity partially overlying a radiolucent area or as a linear or crescent-shaped horizontally oriented radiolucent line (Fig. 21-21). In a lateromedial image a fragment is occasionally seen displaced palmarly from the palmar cortex of the third metacarpal bone. There is often focal damage of the suspensory ligament detectable ultrasonographically, as an area of reduced echogenicity dorsally in the region of the fragment. Occasionally, a fragment is identified using ultrasonography that cannot be detected radiologically.

Incomplete Longitudinal Fracture of the Proximopalmar Aspect of the Third Metacarpal Bone

An incomplete longitudinal fracture of the third metacarpal bone, otherwise known as a palmar cortical fatigue or stress fracture, usually occurs in the proximomedial aspect of the metaphyseal region but may extend from the carpometacarpal joint distally and is seen as a vertically or obliquely oriented radiolucent line (Fig. 21-22). There is frequently generalized increased opacity of the proximomedial aspect of the third metacarpal bone, and in some horses this is the only detectable radiographic abnormality. Severe fractures may extend distally to the nutrient foramen of the third metacarpal bone. Fractures may occur unilaterally or bilaterally and are best detected in dorsopalmar or slightly oblique dorsopalmar images. Occasionally, endosteal and periosteal calluses are seen on the palmar aspect of the third metacarpal bone in a lateromedial image. These fractures have most commonly been recognized in Thoroughbred and Standardbred racehorses[46-49] but also occur in sports horses.[46,48,50] With acute injuries there may be no detectable radiographic abnormalities, but there is focal intense increased radiopharmaceutical uptake in the proximomedial palmar aspect of the third metacarpal bone.[50,51] Magnetic resonance imaging may confirm the presence of a fracture,[25,52] but the pathognomonic clinical features of the lameness often make this unnecessary. If an affected horse trots in a straight line on a firm surface, the lameness usually deteriorates the further the horse trots. After the horse turns at a walk to change direction, the lameness is then improved but again deteriorates as the horse trots further.[50,51,53]

Dorsoproximal Stress Fractures of the Third Metacarpal and Third Metatarsal Bones

Dorsoproximal stress fractures of the third metacarpal[54] and third metatarsal[55, 56] bones are injuries of Standardbred and Thoroughbred racehorses. In forelimbs these dorsomedial fractures are best viewed in a dorsolateral-palmaromedial oblique radiograph, whereas in hindlimbs these dorsolateral fractures are best identified in a dorsomedial-plantarolateral oblique radiograph. In forelimbs the fracture is articular, nondisplaced, and usually incomplete. Invariably there is active periosteal new bone at the distal aspect of the fracture, close to the insertion of the extensor carpi radialis tendon, even in an acute injury. In hindlimbs the fracture is also articular and often associated with extensive modelling of the dorsolateral articular margin of the third metatarsal bone and periosteal new bone on the dorsal aspect of the fracture (Fig. 21-23).

Dorsal Cortical Stress Disease in the Diaphysis of the Third Metacarpal Bone

Cyclic loading of an immature third metacarpal bone may result in stress-adaptation mismatch and development of microfractures in the middle or distal one third of the third metacarpal bone in racing Thoroughbreds and quarter horses. This may result in periosteal and endosteal new bone. This

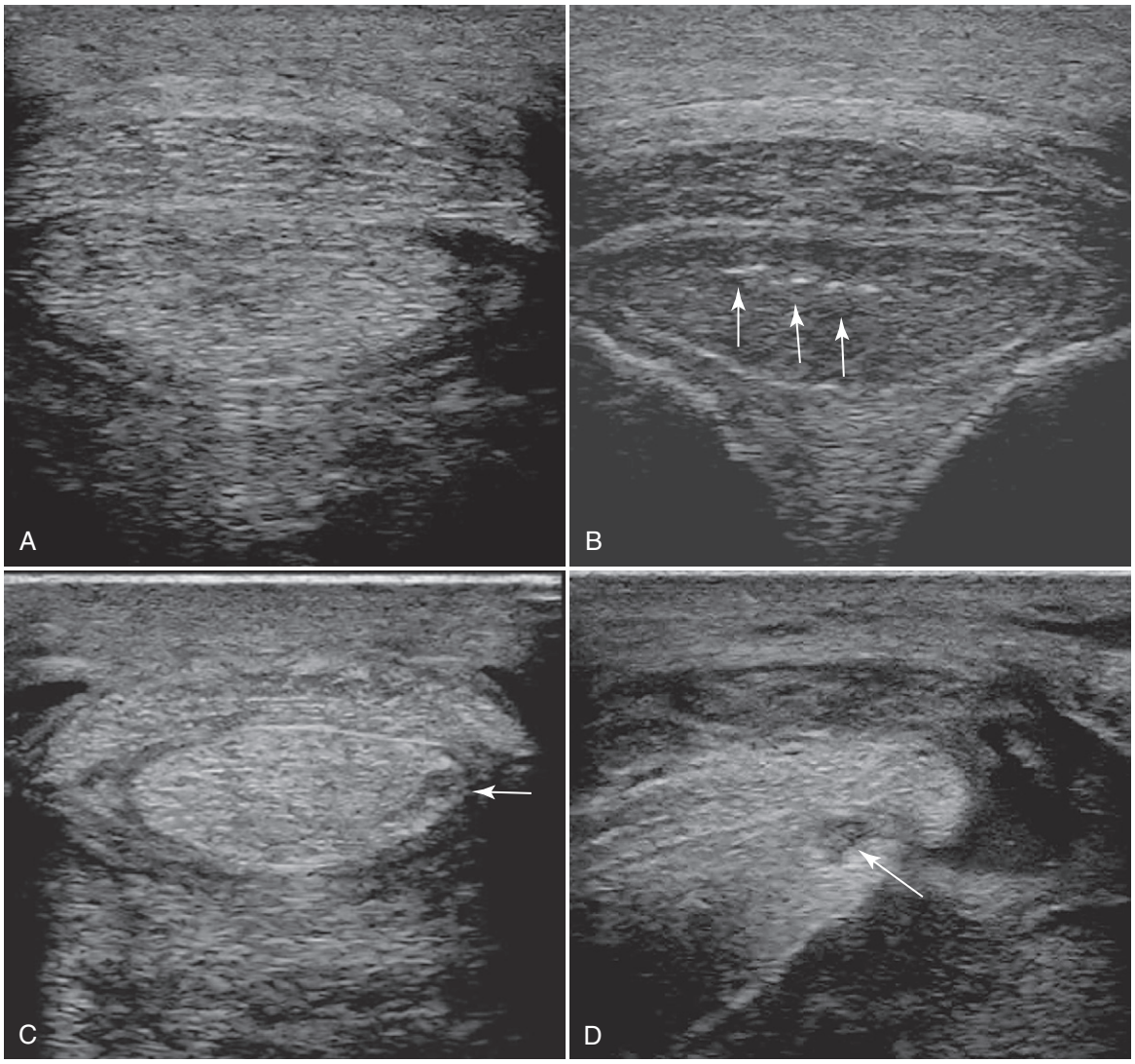


Fig. 21-17 **A,** Transverse ultrasonographic image of the plantar aspect of a metatarsophalangeal joint, obtained with the transducer perpendicular to the digital flexor tendons. The deep digital flexor tendon appears relatively uniform in echogenicity dorsally, but there are subtle areas of reduced echogenicity in the plantar aspect. There is abnormal thickening of the subcutaneous tissues. **B,** Transverse ultrasonographic image of the plantar aspect of a metatarsophalangeal joint, as in **A,** obtained with the transducer off incidence to the digital flexor tendons. The deep digital flexor tendon has focal areas of increased echogenicity *(white arrows)* reflecting fibrosis. **C,** Transverse ultrasonographic image of a distal metacarpal region, obtained using a 10 MHz linear transducer. Medial is to the left. There is a small focal defect in the lateral margin of the deep digital flexor tendon *(white arrow)*, which reflects a longitudinal tear. **D,** Transverse ultrasonographic image obtained using a 10 MHz transducer from the palmarolateral aspect of a distal metacarpal region (a different horse to **(C).** Lateral is to the right. There is a hypoechogenic lesion in the lateral margin of the deep digital flexor tendon *(white arrow)*. This lesion could not be seen when the tendon was imaged from the palmar aspect of the limb.

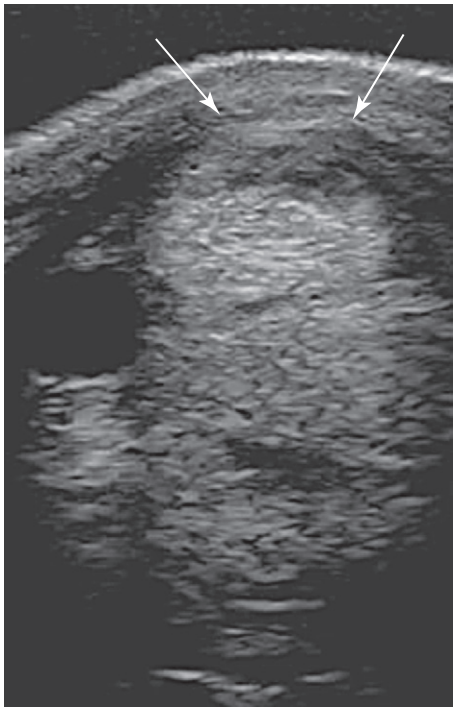


Fig. 21-18 Transverse ultrasonographic image of a palmar metacarpal region obtained 4 cm distal to the accessory carpal bone, using a 10 MHz virtual convex array transducer. The superficial digital flexor tendon is slightly enlarged and has marked loss of echogenicity of the palmar aspect *(white arrows)*.

may be difficult to detect radiographically in the acute phase, but there is generally increased radiopharmaceutical uptake.[57,58] Continued training may result in a radiographically detectable stress fracture. These stress fractures are usually oriented at an angle of approximately 30 degrees to the long axis of the bone and traverse the cortex as a slightly curved radiolucent line (Fig. 21-24). There is usually periosteal and endosteal new bone at the same level and overlying soft tissue swelling. Occasionally a complete saucer fracture develops.

Stress Fractures of the Distal Metaphyseal Region of the Third Metacarpal Bone

Transverse stress fractures of the distal metaphyseal region of the third metacarpal bone occur most commonly in Thoroughbred racehorses[59] but have also been recognized in sports horses and endurance horses.[53,60] Although usually unilateral, bilateral injuries have been seen occasionally. With acute injury there may be soft tissue swelling at the time of initial lameness recognition, but there may be no radiographically detectable osseous abnormality. However, within 7 to 10 days, a transverse radiopaque line becomes apparent across the distal metaphyseal region (Fig. 21-25, *A*). Ill-defined periosteal new bone develops proximal and distal to the radiopaque line, which may result in distortion of the distal aspect of the second or fourth metacarpal bone. In some horses a radiolucent fracture line may be identified eventually (Fig. 21-25, *B*).

In horses with more chronic injury, there may be extensive periosteal and endosteal callus on the palmaromedial or palmarolateral aspect of the third metacarpal bone extending proximal and distal to an ill-defined transverse radiolucent line, with increased opacity of the adjacent endosteal bone.

Compression Fracture of the Distal Third Metacarpal Bone Physis

A compression fracture of the distal aspect of the third metacarpal bone physis has been documented only in elite

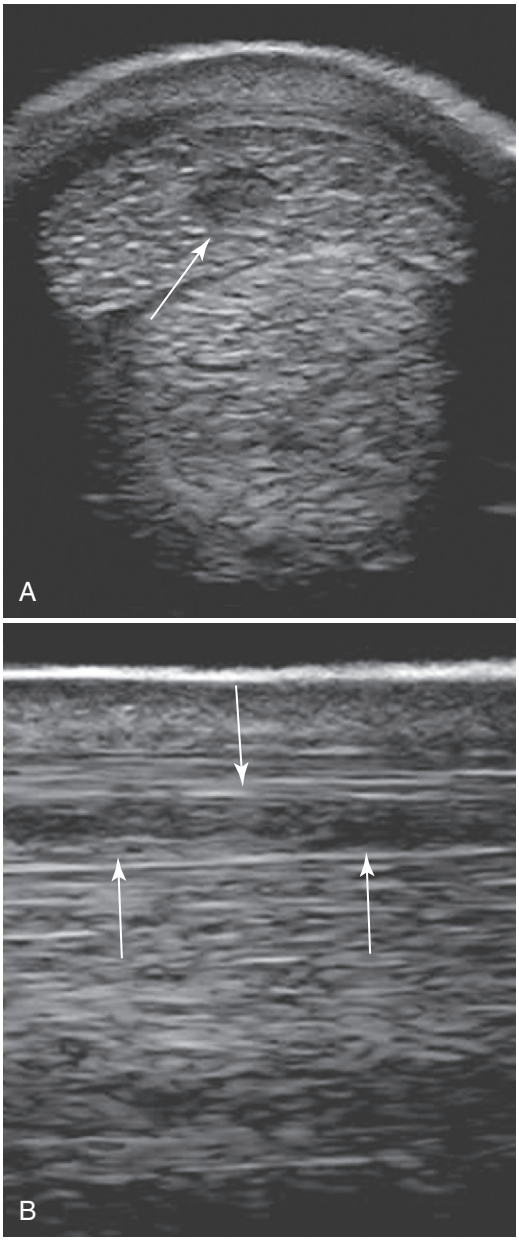


Fig. 21-19 **A,** Transverse ultrasonographic image of the palmar metacarpal region obtained 19 cm distal to the accessory carpal bone, using a 10 MHz virtual convex array transducer. Medial is to the left. There is a central core lesion in the superficial digital flexor tendon *(white arrows)*. The tendon is enlarged with rounded medial and lateral contours. **B,** Longitudinal image of the palmar metacarpal region of the same horse as in **(A)** obtained approximately 22 cm distal to the accessory carpal bone. Proximal is to the left. There is a long, almost anechoic, core lesion in the superficial digital flexor tendon *(white arrows)*.

endurance horses and may occur unilaterally or bilaterally.[44] It is characterized radiographically by increased opacity of the physis and a slight step at the lateral margin with or without periosteal callus. Dorsopalmar radiographs are most useful.

Incomplete Oblique Sagittal Fractures of the Dorsal Cortex of the Diaphysis of the Third Metacarpal Bone

Incomplete oblique sagittal fractures of the dorsal cortex of the diaphysis of the third metacarpal bone occur in racing Thoroughbreds[61] and are oriented in a proximolateral to distomedial direction, within the dorsal cortex, at an angle of 20 to 30 degrees to vertical. Fractures are best identified either on palmarodorsal radiographs, which gave better detail than

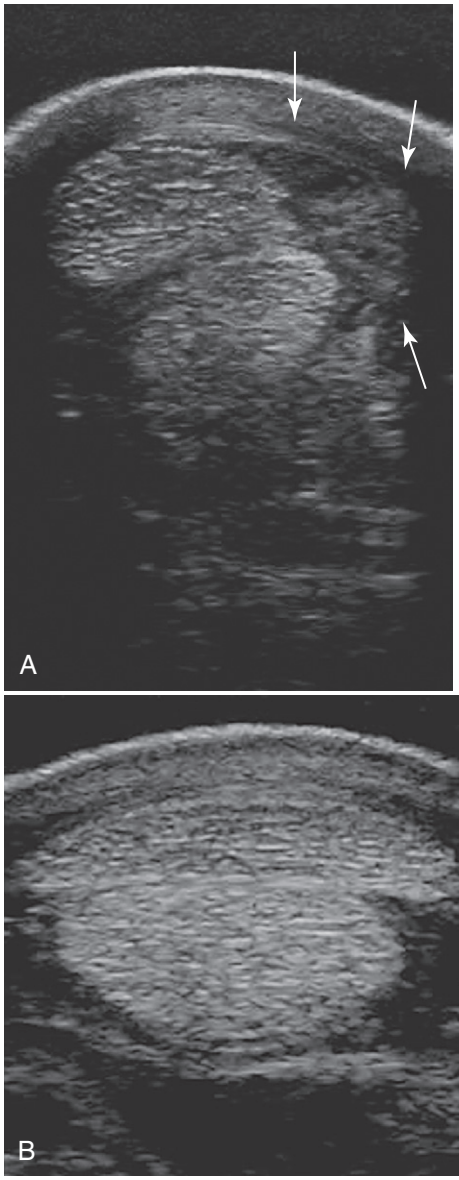


Fig. 21-20 **A,** Transverse ultrasonographic image of a palmar metacarpal region obtained 22 cm distal to the accessory carpal bone, using a 10 MHz virtual convex array transducer positioned palmarolaterally. Medial is to the left. There is a marked disruption of the architecture of the lateral aspect of the superficial digital flexor tendon *(white arrows)*. The tendon is swollen, and the medial margin is more rounded than normal. **B,** Transverse ultrasonographic image of a distal metacarpal region obtained 23 cm distal to the accessory carpal bone, using a 10 MHz linear array transducer (a different horse than in **A**). Lateral is to the right. The horse had acute onset lameness associated with distention of the digital flexor tendon sheath. There is a small defect in the lateral margin of the superficial digital flexor tendon *(white arrow)*.

dorsopalmar images, or projections slightly oblique to standard palmarodorsal projections. Similar fractures, propagating from a typical dorsal cortical stress fracture, have also been described.[62]

Other Fractures of the Third Metacarpal and Third Metatarsal Bones

Condylar fractures of the third metacarpal bone or third metatarsal bone may propagate proximally throughout most of the length of the diaphysis.[63-66] These injuries are usually confined to Thoroughbred or Standardbred racehorses but are occasionally seen in elite endurance horses.[45] The fracture may

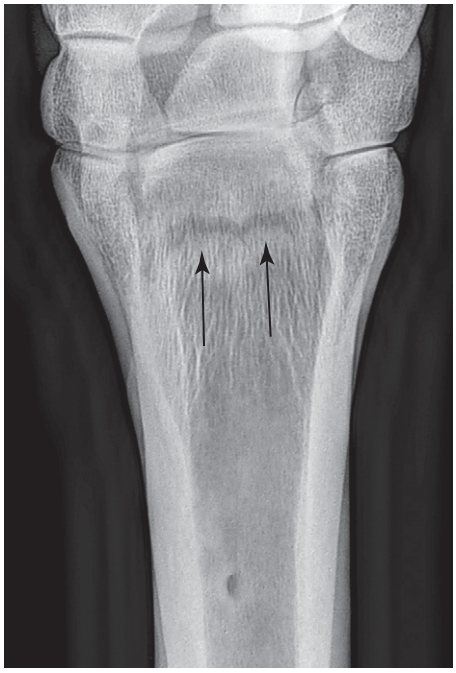


Fig. 21-21 Dorsopalmar radiograph of a proximal metacarpal region of an elite endurance horse. Lateral is to the right. There are broad curved radiolucent lines *(black arrows)* in the proximal aspect of the third metacarpal bone representing avulsion fracture of the origin of the suspensory ligament from the palmar aspect of the third metacarpal bone.

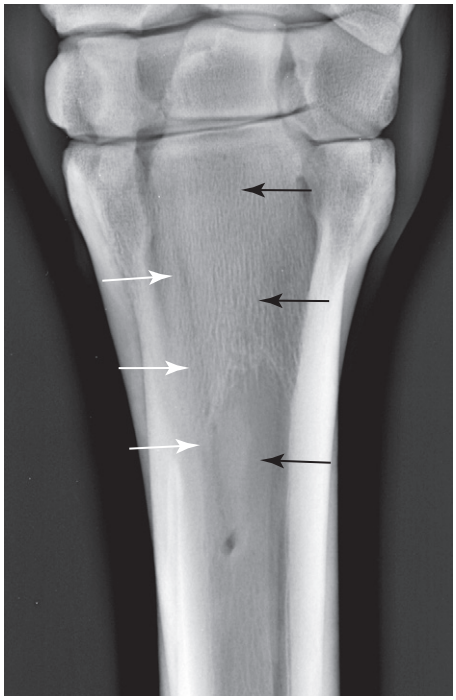


Fig. 21-22 Dorsopalmar radiograph of a proximal metacarpal region of a 6-year-old Thoroughbred event horse with lameness of 4 weeks' duration. Lateral is to the right. There is diffuse increased radiopacity of the medial aspect of the third metacarpal bone *(black arrows)* associated with an incomplete longitudinal palmar cortical stress fracture of the third metacarpal bone *(white arrows)* that extends distally to the nutrient foramen.

spiral proximally, so multiple oblique images may be required to follow the course of the fracture. The fracture is usually seen as two radiolucent lines that represent fractures of the dorsal and palmar cortices. The proximal sesamoid bones should be examined carefully because axial, linear, and vertical fractures may occur concurrently, adversely affecting prognosis.

Transverse simple or comminuted fractures of the third metacarpal or metatarsal bones or other configurations are usually the result of external trauma and may vary among horses.[67,68] Multiple radiographic images may be required to determine accurately the fracture configuration.

Enostosis-Like Lesions and Panosteitis

Enostosis-like lesions are characterized radiographically by focal or multifocal discrete areas of increased radiopacity in long bones, usually in close proximity to the nutrient foramen (Fig. 21-26, *A*).[69,70] Such lesions can be seen either incidentally unassociated with lameness or in association with pain and lameness. They may occur in one limb or several limbs and may be variably symptomatic. These lesions are often associated with focal intense increased radiopharmaceutical uptake, but clinical significance can be determined only by diagnostic analgesia. In some horses more linearly oriented areas of increased opacity are seen on the endosteal surfaces of the cortices of the third metacarpal and metatarsal bones (Fig. 21-26, *B*), closely resembling panosteitis in the dog, also associated with a similar distribution of increased radiopharmaceutical uptake.

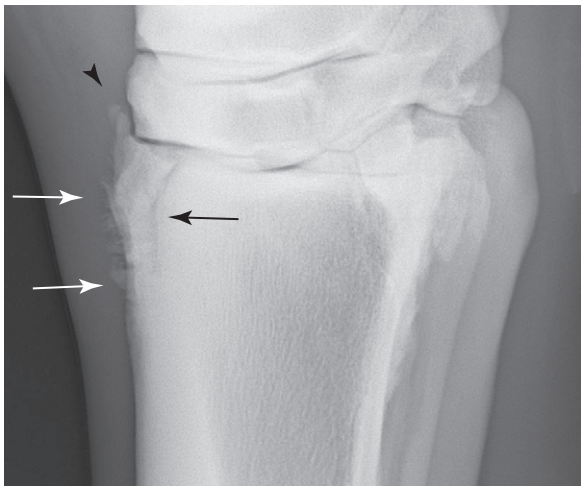


Fig. 21-23 Slightly oblique lateromedial (lateral 10-degree plantaromedial dorsal oblique) radiograph of a proximal metatarsal region of a 3-year-old Thoroughbred racehorse. There is an oblique stress fracture *(black arrow)* of the proximodorsal aspect of the third metatarsal bone, associated with diffuse periosteal new bone dorsally *(white arrows)* and a large spur *(black arrowhead)* on the proximodorsal aspect of the third metatarsal bone.

Hypertrophic Osteopathy

Hypertrophic osteopathy is an uncommon condition resulting in the development of pathognomonic palisading new bone oriented perpendicular to the long axis of long bones, involving the diaphysis and metaphyses, with overlying soft tissue swelling.[71] If the underlying lesion can be identified and treated, the lesions will slowly model, and associated pain and lameness will resolve.

Exostoses of the Second and Fourth Metacarpal and Metatarsal Bones

Exostoses, so-called splints, on the second or fourth metacarpal bones are common, but lesions also occur on the second and fourth metatarsal bones. Several oblique images obtained at slightly different angles of projection are useful to determine the extent and activity of new bone, which is much less opaque than the parent bone when first developing. Generally, new bone has a highly irregular outline (Fig. 21-27), which over time will become progressively smoother and more opaque; incorporation of fibrous tissue within the osseous reaction may result in a heterogeneous radiopacity.

Syndesmopathy Between the Third and Second and Third and Fourth Metacarpal and Metatarsal Bones

Syndesmopathy refers to injury of the syndesmosis between the second and third and third and fourth metacarpal (metatarsal) bones.[72] It is characterized by ossification between the bones and alteration in adjacent cortical or trabecular

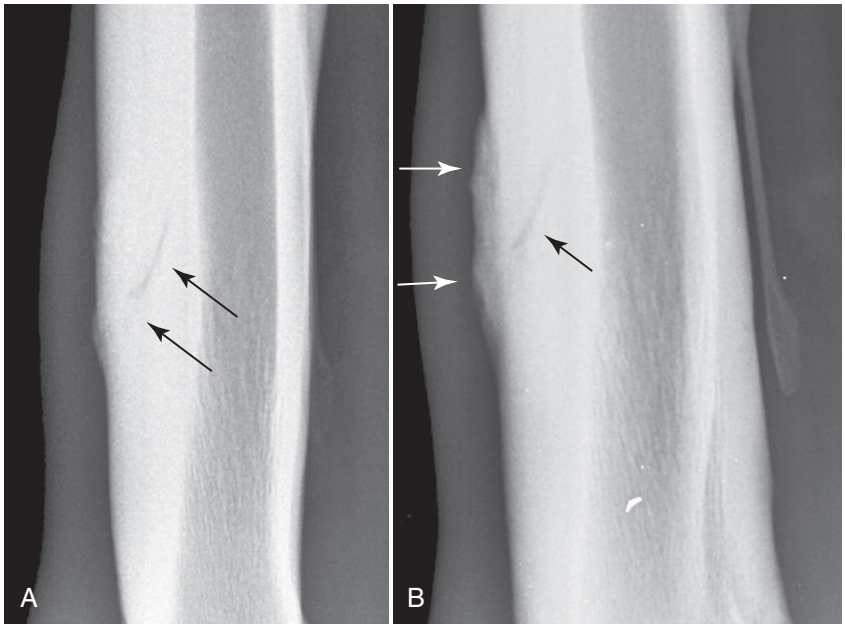


Fig. 21-24 **A,** Lateromedial radiograph of a mid metacarpal region of a 3-year-old Thoroughbred flat racehorse. Dorsal is to the left. There is a curved radiolucent line in the dorsal cortex of the third metacarpal bone *(black arrows)*, typical of an incomplete dorsal cortical stress or fatigue fracture. There is mild overlying soft tissue swelling. **B,** Dorsolateral-palmaromedial oblique radiograph of the mid-metacarpal region of the same limb as illustrated in **A.** There is an incomplete dorsal cortical stress fracture *(black arrow)*, with extensive periosteal callus *(white arrows)* and overlying soft tissue swelling. There is also a mild endosteal reaction.

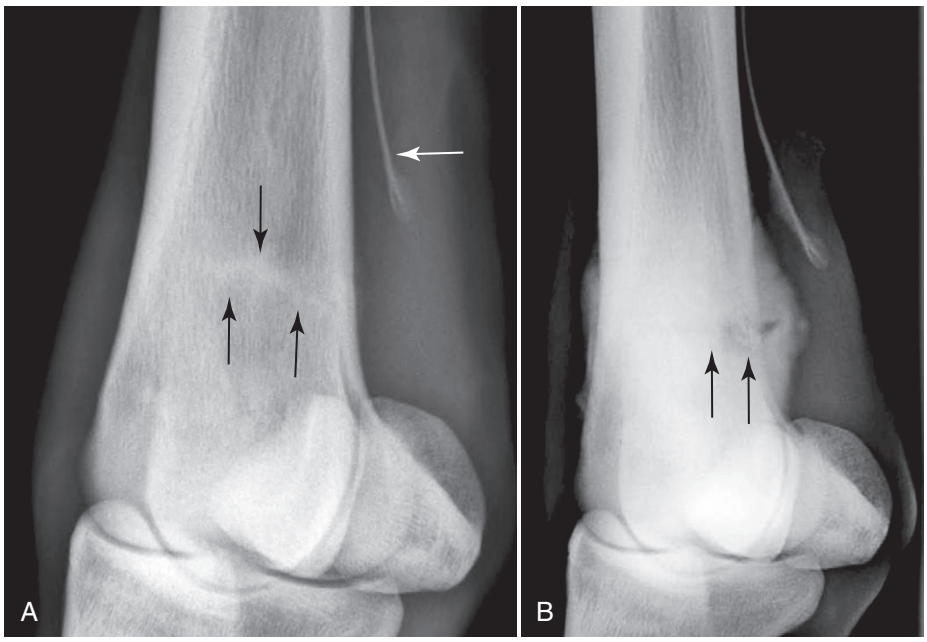


Fig. 21-25 **A,** Dorsolateral-palmaromedial oblique radiograph of a distal metacarpal region of a 3-year-old Thoroughbred flat racehorse, 3 days after the onset of acute severe lameness associated with soft tissue swelling and focal pain in the distal palmarolateral aspect of the metacarpal region. The distal aspect of the fourth metacarpal bone is distorted in shape *(white arrow)* because of the soft tissue swelling. There is an ill-defined transverse radiopaque line *(black arrows)* in the palmar aspect of the third metacarpal bone. This is a distal metaphyseal stress fracture. **B,** Dorsolateral-palmaromedial oblique radiograph of the distal metacarpal region of the same horse as in **A,** 30 days after the onset of acute severe lameness. There is increased bowing of the distal aspect of the fourth metacarpal bone because of extensive periosteal callus on the palmar aspect of the third metacarpal bone. There is also periosteal callus dorsomedially. There is diffuse increased radiopacity of the cancellous bone in the metaphyseal region of the third metacarpal bone and an ill-defined transverse radiolucent line *(black arrows)* toward the palmarolateral aspect of the third metacarpal bone.

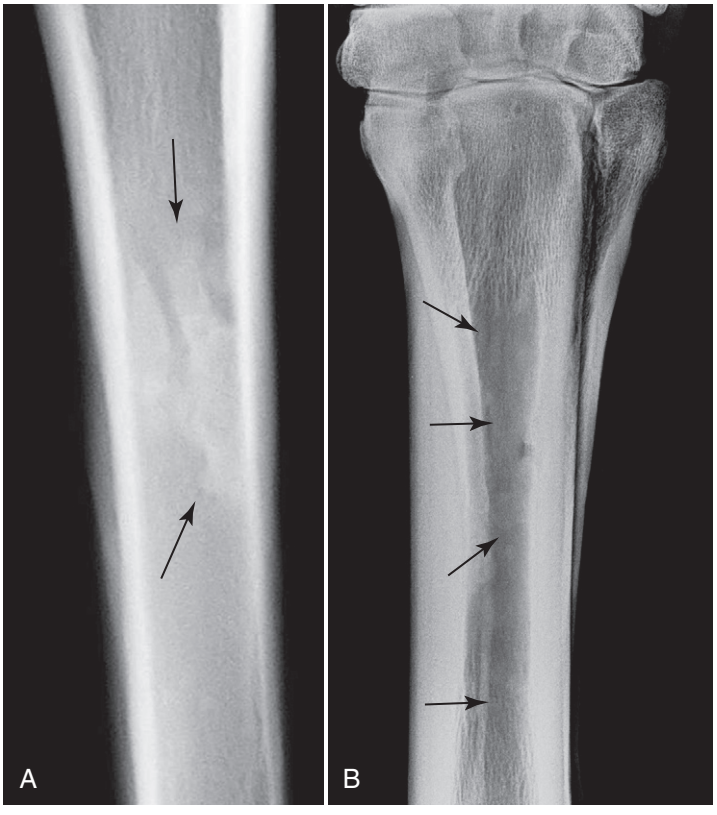


Fig. 21-26 **A,** Dorsoplantar radiograph of the left hindlimb of a 9-year-old sport horse. Lateral is to the right. There is a diffuse area of increased radiopacity *(black arrows)* in the cancellous bone close to the nutrient foramen of the third metatarsal bone. There was focal, intense, increased radiopharmaceutical uptake in the same location. This is consistent with an enostosis-like lesion. **B,** Dorsolateral-palmaromedial oblique radiograph of a metacarpal region of an 8-year-old Thoroughbred event horse. There are multiple areas of increased opacity on the axial aspect of the cortices of the third metacarpal bone. These radiopacities *(black arrows)* were associated with intense increased radiopharmaceutical uptake.

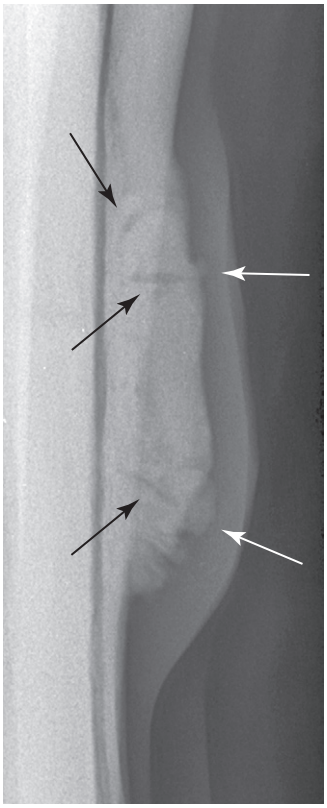


Fig. 21-27 Dorsomedial-palmarolateral oblique radiograph of the second and third metacarpal bones. There is an old exostosis with radiolucent lines *(black arrows)* traversing the bone, probably representing incorporation of fibrous tissue within the bone. There is more irregularly outlined less radiopaque periosteal new bone on the palmar aspect *(white arrows)*. Pressure applied to these areas elicited pain.

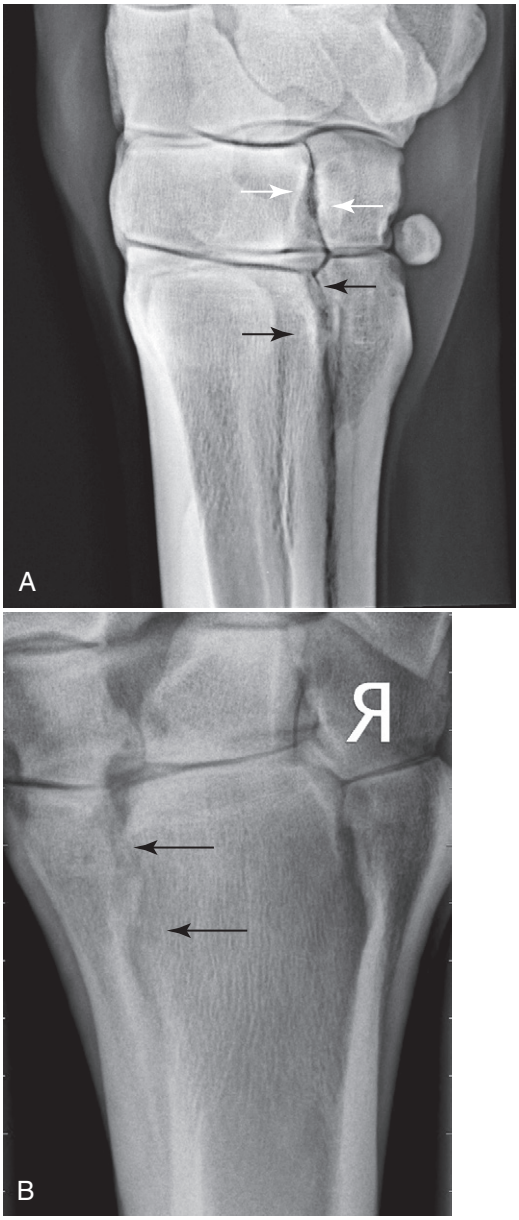


Fig. 21-28 **A,** Dorsomedial-palmarolateral oblique radiograph of a proximal metacarpal region. The margins of the second and third carpal bones are slightly irregular *(white arrows)* with subtle mineralization in the region of the transverse intercarpal ligament. There is marked narrowing of the space between the second and third metacarpal bones and some osseous bridging *(black arrows)*. **B,** Dorsopalmar radiograph of a proximal metacarpal region of a 3-year-old Thoroughbred racehorse. Lateral is to the right. There is ossification between the second and third metacarpal bones *(black arrows)* consistent with syndesmopathy. Active appearing osseous abnormalities were confirmed by magnetic resonance imaging.

architecture (Fig. 21-28), with or without osseous spurs developing on the dorsal or palmar articular margins. If seen in association with focal increased radiopharmaceutical uptake, there is reasonable evidence that the lesion is active and associated with lameness. Ultrasonography may be more sensitive than radiology for identification of osseous modelling on the palmar aspect, but magnetic resonance imaging is probably best for definitive diagnosis.[25,72]

Fractures of the Second and Fourth Metacarpal and Metatarsal Bones

The lack of overlying soft tissue protection makes the metacarpal bones extremely vulnerable to direct trauma, whether from self-inflicted interference injury, kick injuries from other horses, kicking a solid object, or as the result of a limb becoming entangled in a fence or other object.[73-79] Such injuries often result in simple or comminuted fractures of the second or fourth metacarpal and metatarsal bones. Lesion-directed oblique images are required to evaluate the fracture (Fig. 21-29). The adjacent cortex of the third metacarpal (metatarsal) bone should also be evaluated carefully because occasionally this also sustains an incomplete fracture.

Simple fractures at the junction of the proximal two thirds and distal one third of the second or fourth metacarpal bone usually occur in association with suspensory desmitis and are often also characterized by the bone bowing away from the third metacarpal bone (see Fig. 21-13, *B*).[80]

Infectious Osteitis and Osteomyelitis

The paucity of soft tissue coverage of the metacarpal and metatarsal bones makes them highly susceptible to injury as the result of direct trauma. With an open wound there is a high risk of development of infectious osteitis or osteomyelitis. However, trauma to bone may also damage the periosteum and underlying blood supply and provide a necrotic nidus in which bacteria may settle and result in infection. Infectious osteitis is characterized by the development of periosteal new bone adjacent to a linear radiolucent area in the cortex, usually extending parallel to the long axis of the bone. Ultrasonographic examination may reveal the accumulation of anechoic fluid adjacent to the cortex. Osteomyelitis is characterized by the development of a sequestrum, surrounded by a radiolucent area, often bordered by a more radiopaque rim. This

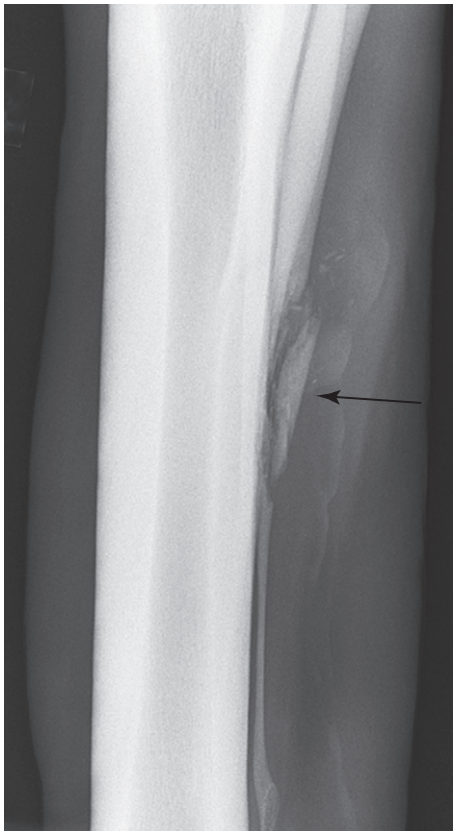


Fig. 21-29 Dorsomedial-plantarolateral oblique radiograph of the right metatarsal region of a 6-year-old event horse 2 weeks after a kick injury. There is a slightly displaced fracture of the diaphysis of the second metatarsal bone *(black arrow)*.

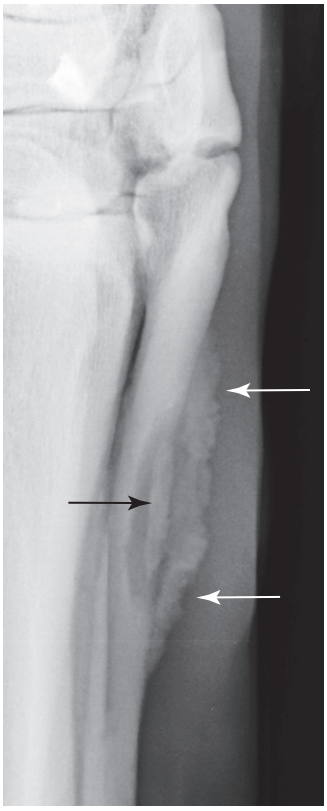


Fig. 21-30 Dorsomedial-plantarolateral oblique radiograph of a metatarsal region of a Warmblood gelding. There is a large oval-shaped sequestrum *(black arrow)* surrounded by a relatively radiolucent area axially (an involucrum) with periosteal new bone *(white arrows)* consistent with osteomyelitis. Note the variable radiopacity of the overlying soft tissues.

radiolucent area is an involucrum. There may be periosteal new bone on the abaxial aspect of the sequestrum (Fig. 21-30). Using ultrasonography it is often possible to follow an anechoic draining tract from the skin to the bone.

REFERENCES

1. Les C, Stover S, Willits N: Necropsy survey of metacarpal fusion in the horse, *Am J Vet Res* 56:1421, 1995.
2. Nagy A, Dyson S: Magnetic resonance anatomy of the proximal metacarpal region of the horse described from images acquired from low- and high-field magnets, *Vet Radiol Ultrasound* 50:595–596, 2009.
3. Nagy A, Dyson S: Magnetic resonance imaging and histological findings in the proximal aspect of the suspensory ligament of forelimbs in non-lame horses, *Equine Vet J* 44(1):43–50, 2012.
4. Schulze T, Budras K-D: Zur klinisch-funktionellen Anatomie des M. interosseus medius der Hintergliedmaße im Hinblick auf die Insertionsdesmopathie des Pferdes -Kernspin-, computertomographische—und morphologische Untersuchungen, *Pferdheilkunde* 24:343, 2008.
5. Wilson D, Baker G, Pijanowski G, et al: Composition and morphologic features of the interosseous muscle in Standardbreds and Thoroughbreds, *Am J Vet Res* 52:133, 1991.
6. Bischofberger A, Konar M, Ohlerth S, et al: Magnetic resonance imaging, ultrasonography and histology of the suspensory ligament origin: a comparative study of normal anatomy of Warmblood horses, *Equine Vet J* 38:508, 2006.
7. Minshall G, Wright I: Arthroscopic diagnosis and treatment of intra-articular insertional injuries of the suspensory ligament branches, *Equine Vet J* 38:10, 2006.
8. Nagy A, Dyson S: Anatomical, magnetic resonance imaging and histological findings in the accessory ligament of the deep digital flexor tendon in non-lame horses, *Equine Vet J* 43(3):309–316, 2011.
9. Muylle S, van den Perren K, Simoens P: Morphometric data on the accessory ligament of the deep digital flexor tendon in the hindlimb of normal horses, *Vet J* 184:298, 2010.
10. Simon V, Dyson S: Radiological anatomical variation of the carpus in horses with carpal lameness and control horses, *Vet Radiol Ultrasound* 51:601, 2010.
11. Dyson S: Proximal suspensory desmitis: clinical, ultrasonographic and radiographic features, *Equine Vet J* 27:25, 1991
12. Dyson, S: Proximal metacarpal and metatarsal pain: a diagnostic challenge, *Equine Vet Educ* 15:134, 2006.
13. Dyson S: Proximal suspensory desmitis in the hindlimb: 42 cases, *Br Vet J* 150:279, 1994.
14. Dyson S: Proximal suspensory desmitis in the hindlimb, *Equine Vet Educ* 7:275, 1995.
15. Dyson S: *Problems encountered in equine lameness diagnosis with special reference to local analgesic techniques, radiology and ultrasonography*, Newmarket, England, 1995, R & W Publications.
16. Labens R, Schramme M, Robertson I, et al: Clinical, magnetic resonance and sonographic imaging findings in horse with proximal plantar metatarsal pain, *Vet Radiol Ultrasound* 51:11, 2010.

17. Reimer J: How to maximize image quality for the sonographic evaluation of the hind proximal suspensory ligament, *Proc Am Assoc Equine Pract* 56:239, 2010.
18. Martin F, Herthel D-J, Snow V, et al: Scintigraphie osseuse et diagnostic des desmites proximales du muscle interosseux III chez le cheval: à propos de 28 cas (1990–1992), *Point Vet* 26:1061, 1995.
19. Dyson S, Weekes J, Murray R: Scintigraphic evaluation of the proximal metacarpal and metatarsal regions of horses with proximal suspensory desmitis, *Vet Radiol Ultrasound* 48:78, 2007.
20. Launois M, Vandeweerd J, Perrin R, et al: Use of computed tomography to diagnose new bone formation associated with desmitis of the proximal aspect of the suspensory ligament in third metacarpal or third metatarsal bones of three horses, *J Am Vet Med Assoc* 234:514, 2009.
21. Puchalski S: Personal communication, 2007.
22. Sampson S, Tucker R: Magnetic resonance imaging of the proximal metacarpal and metatarsal regions, C*lin Tech Equine Pract* 6:78, 2007.
23. Brokken M, Schneider R, Sampson S, et al: Magnetic resonance imaging of proximal metacarpal and metatarsal injuries in the horses, *Vet Radiol Ultrasound* 48:507, 2007.
24. Dyson S: The distal tarsal region. In Murray R, editor: *Equine magnetic resonance imaging*, Oxford, 2011, Wiley-Blackwell, p 405.
25. Nagy A, Dyson S: Magnetic resonance imaging findings in the carpus and proximal metacarpal region of 50 lame horses, *Equine Vet J* 44(2):163–168, 2012.
26. Zubrod C, Schneider R, Tucker R, et al: Use of MRI to identify suspensory desmitis and adhesions between exostoses of the second metacarpal bone and the suspensory ligament in 4 horses, *J Am Vet Med Assoc* 224:1815, 2004.
27. Dyson S: Desmitis of the accessory ligament of the deep digital flexor tendon: 27 cases, *Equine Vet J* 23:438, 1991.
28. Denoix J-M, Azevedo C: Images echographiques des lesions du tendon flechisseur profound du doigt, *Pract Vet Equine* 32:15, 1991.
29. McDiarmid A: Eighteen cases of desmitis of the accessory ligament of the deep digital flexor tendon, *Equine Vet Educ* 6:49, 1994.
30. McDiarmid A: Acquired flexural deformity of the metacarpophalangeal joint in five horses associated with tendonous damage in the palmar metacarpus, *Vet Rec* 144:475, 1999.
31. Van den Belt A, Becker C, Dik K: Desmitis of the accessory ligament of the deep digital flexor tendon in the horse: clinical and ultrasonographic features—a report of 24 cases, *Zentralbl Veterinarmed (A)* 40:492, 1993.
32. Boswell J, Schramme M: Desmitis of the accessory ligament of the deep digital flexor tendon in the hindlimb in a horse, *Equine Vet Educ* 12:129, 2000.
33. Eliashar E, Dyson S, Archer R, et al: Two clinical manifestations of desmopathy of the accessory ligament of the deep digital flexor tendon in the hindlimb of 23 horses, *Equine Vet J* 37:495, 2005.
34. Dyson S: Desmitis of the accessory ligament of the deep digital flexor tendon. In Ross M, Dyson S, editors: *Diagnosis and management of lameness in the horse*, ed 2, St. Louis, 2010, Elsevier, p 734.
35. Dyson S: Injuries of the accessory ligament of the deep digital flexor tendon in the equine hindlimb: a problem of middle age, *Vet J* 184:255, 2010.
36. Dyson S: Proximal injuries of the accessory ligament of the deep digital flexor tendon in forelimbs and hindlimbs: 12 horses (2006–2010), *Equine Vet Educ*, DOI: 10.1111/j.2042-3292.2011.00307.x
37. Barr A, Dyson SJ, Barr F, et al: Tendonitis of the deep digital flexor tendon in the distal metacarpal/metatarsal region associated with tenosynovitis of the digital sheath in the horse, *Equine Vet J* 27:348, 1995.
38. Wright I, McMahon P: Tenosynovitis associated with longitudinal tears of the digital flexor tendons in horses: report of 20 cases, *Equine Vet J* 31:12, 1999.
39. Smith M, Wright I: Noninfected tenosynovitis of the digital flexor tendon sheath: a retrospective analysis of 76 cases, *Equine Vet J* 38:134, 2006.
40. Arensburg L, Wilderjans H, Simon O, Dewulf J, Boussauw B: Nonseptic tenosynovitis of the digital flexor tendon sheath caused by longitudinal tears in the digital flexor tendons, a retrospective study of 135 tenoscopies, *Equine Vet J*, 43:660–668, 2011.
41. Kidd J, Dyson S, Barr A: Septic flexor tendon core lesions in five horses, *Equine Vet J* 34:213, 2002.
42. Bramlage L, Gabel A, Hackett R: Avulsion fractures of the origin of the suspensory ligament in the horse, *J Am Vet Med Assoc* 176:1004, 1980.
43. Launois T, Desbrosse F, Perrin R: Percutaneous osteostixis as treatment of avulsion fractures of the palmar/plantar third metacarpal/metatarsal cortex at the origin of the suspensory ligament in 29 cases, *Equine Vet Educ* 15:126, 2006.
44. Misheff M: The endurance horse. In Ross M, Dyson S, editors: *Diagnosis and management of lameness in the horse*, ed 2, St. Louis, 2010, Elsevier, p 1137.
45. Misheff M, Alexander G, Hirst G: Management of fractures in endurance horses, *Equine Vet Educ* 22:623, 2010.
46. Dyson S: Some observations on lameness associated with pain in the proximal metacarpal region, *Equine Vet J Suppl* 6:43, 1988.
47. Ross M, Ford T, Orsini P: Incomplete longitudinal fracture of the proximal palmar cortex of the third metacarpal bone in horses, *Vet Surg* 17:82, 1988.
48. Lloyd K, Kobluk P, Ragle C, et al: Incomplete palmar fracture of the proximal extremity of the third metacarpal bone in horses: ten cases (1981–1986), *J Am Vet Med Assoc* 192:798, 1988.
49. Pleasant R, Baker G, Muhlbauer M, et al: Stress reactions and stress fractures of the proximal palmar aspect of the third metacarpal bone in horses: 58 cases (1980–1990), *J Am Vet Med Assoc* 201:1918, 1992.
50. Morgan R, Dyson S: Incomplete longitudinal fractures and stress-related bone injury of the proximopalmar medial aspect of the third metacarpal bone in 55 horses, *Equine Vet J* 44(1):64–70, 2012.
51. Dyson S, Weeks J, Murray R: Scintigraphic evaluation of the proximal metacarpal and metatarsal regions of horses with proximal suspensory desmitis, *Vet Radiol Ultrasound* 48:78, 2007.
52. Powell S, Ramzan P, Head M, et al: Standing magnetic resonance imaging detection of bone marrow oedema-type signal pattern associated with subchondral bone pain in 8 racehorses: a prospective study, *Equine Vet J* 42:10, 2010.
53. Dyson S: The metacarpal region. In Ross M, Dyson S, editors: *Diagnosis and management of lameness in the horse*, ed 2, St Louis, 2010, Elsevier, p 411.
54. Ross M, Martin B: Dorsomedial articular fracture of the proximal aspect of the third metacarpal bone in Standardbred racehorses: seven cases (1978–1990), *J Am Vet Med Assoc* 201:332, 1992.
55. Ross M, Sponseller M, Gill H, et al: Articular fracture of the dorsoproximolateral aspect of the third metatarsal bone in five Standardbred racehorses, *J Am Vet Med Assoc* 203:698, 1993.

56. Pilsworth R: Incomplete fracture of the dorsal aspect of the proximal cortex of the third metatarsal bone as a cause of hind limb lameness in the racing Thoroughbred: a review of three cases, *Equine Vet J* 24:147, 1992.
57. Koblik P, Hornof W, Seeherman H: Scintigraphic appearance of stress-induced trauma of the dorsal cortex of the third metacarpal bone in racing Thoroughbred horses: 121 cases (1978–1986), *J Am Vet Med Assoc* 192:390, 1988.
58. Schallberger S, Doherr M, Ueltschi G: Scintigraphic appearance of the dorsal cortex of the third metacarpus and third metatarsus in the horse, *Vet Radiol Ultrasound* 45:352, 2004.
59. Sullivan C, Lumsden J: Distal third metacarpal bone palmar cortical stress fractures in 4 Thoroughbred racehorses, *Equine Vet Educ* 14:70, 2002.
60. Butler J, Colles C, Dyson S, Kold S, Poulos P: The metacarpal and metatarsal regions. In C*linical radiology of the horse*, ed 3, Oxford, 2008, Wiley-Blackwell, p 189.
61. Watt B, Foerner J, Haines G: Incomplete sagittal fractures of the dorsal cortex of the third metacarpal bone in six horses, *Vet Surg* 27:337, 1998.
62. Spurlock G: Propagation of a dorsal cortical fracture of the third metacarpal bone in two horses, *J Am Vet Med Assoc* 192:1587, 1988.
63. Barr A, Sridhar B, Denny H: Long incomplete longitudinal fractures of the third metacarpal and metatarsal bones in horses, *Vet Rec* 124:580, 1989.
64. Bassage L, Richardson D: Longitudinal fractures of the condyles of the third metacarpal and metatarsal bones in racehorses: 224 cases (1986–1995), *J Am Vet Med Assoc* 212:1757, 1998.
65. Smith L, Greet T, Bathe A: A lateral approach for screw repair in lag fashion of spiral third metacarpal and metatarsal condylar fractures in horses, *Vet Surg* 38:681, 2009.
66. Wright I, Smith M: A lateral approach to the repair of propagating fractures of the medial condyle of the third metacarpal bone and metatarsal bones in 18 racehorses, *Vet Surg* 38:689, 2009.
67. McClure S, Watkins J, Glickman N, et al: Complete fractures of the third metacarpal or metatarsal bone in horses: 25 cases (1980–1996), *J Am Vet Med Assoc* 213:847, 1998.
68. Lescun T, McClure S, Ward M, et al: Evaluation of transfixation casting for treatment of third metacarpal, third metatarsal, and phalangeal fractures in horses: 37 cases (1994–2004), *J Am Vet Med Assoc* 230:1340, 2007.
69. Bassage L, Ross M: Enostosis-like lesions in the long bones of 10 horses: scintigraphic and radiographic features, *Equine Vet J* 30:35, 1998.
70. Ahern B, Boston R, Ross M: Enostosis-like lesions in 79 horses, *Proc Am Assoc Equine Pract* 56:392, 2010.
71. Mair T, Dyson S, Fraser J, et al: Hypertrophic osteopathy (Marie's disease) in Equidae: a review of twenty-four cases, *Equine Vet J* 28:256, 1996.
72. Coudry V, Denoix J-M, Didierlaurent D, et al: Use of magnetic resonance imaging to diagnose the cause of proximal metacarpal pain in a standardbred trotter, *Vet Rec* 162:790, 2008.
73. Peterson P, Pascoe J, Wheat J: Surgical management of proximal splint bone fractures in the horse, *Vet Surg* 16:367, 1987.
74. Baxter G, Doran R, Allen D: Complete excision of a fractured fourth metatarsal bone in eight horses, *Vet Surg* 21:273, 1992.
75. Jenson P, Gaughan E, Lillich J, et al: Segmental ostectomy of the second and fourth metacarpal and metatarsal bones in horses: 17 cases (1993–2002), *J Am Vet Med Assoc*, 224:271, 2004.
76. Bowman K, Evans L, Herring M: Evaluation of surgical removal of fractured distal splint bones in the horse, *Vet Surg* 11:116, 1982.
77. Allen D, White N: Management of fractures and exostoses of the metacarpals and metatarsals II and IV in 25 horses, *Equine Vet J* 19:326, 1987.
78. Harrison L, May S, Edwards G: Surgical treatment of open splint bone fractures in 26 horses, *Vet Rec* 128:606, 1991.
79. Jackson, M: Splint bone fractures in the horse: a retrospective study 1992–2000, *Equine Vet Educ* 19:329, 2007.
80. Verschooten F, Gasthuys F, De Moor A: Distal splint bone fractures in the horse: an experimental and clinical study, *Equine Vet J* 16:532, 1984.

ELECTRONIC RESOURCES

evolve

Additional information related to the content in Chapter 21 can be found on the companion Evolve website at http://evolve.elsevier.com/Thrall/vetrad/

- Chapter Quiz

CHAPTER • 22

The Equine Metacarpophalangeal and Metatarsophalangeal Articulation

Lisa G. Britt
Russell L. Tucker

ANATOMY

The anatomic structures of the metacarpophalangeal (MCP) and metatarsophalangeal (MTP) articulations are so similar that differentiating the right from the left or the forelimb from the hindlimb on unlabeled radiographs cannot be done reliably. The MCP or MTP articulations are hinge joints, formed by the distal end of the metacarpal (or metatarsal) bone and the proximal end of the proximal phalanx. The articular surface of the proximal phalanx is concave and has a sagittal groove opposing the sagittal ridge at the distal end of the third metacarpal (MC III) or the third metatarsal (MT III) bone. This ridge and groove divide the weight-bearing surface into two unequal parts. The largest surface is on the medial (or axial) side, where loading is greatest. The sagittal ridge of MC III or MT III is received into a depression at the palmar* surface that is created by the proximal sesamoid bones and the intersesamoidean ligament. The joint has two radii of articulation. The dorsal radius serves the weight-bearing portion, and the palmar radius conforms to the articulation with the proximal sesamoid bones.[1] The junction of these radii of articulation often appears flat in lateral radiographs and may be confused with a lesion of the articular surface and subchondral bone.

The joint capsule attachments at the proximal end of the proximal phalanx are immediately periarticular, with no redundant capsule or recesses. The capsule attaches to the distal end of MC III or MT III at the periarticular margins. Dorsally, a large recess extends proximally and forms a pouch that allows full extension of the joint. A bursa is interposed between the extensor tendons and the dorsal joint pouch. The palmar joint capsule extends proximal to the sesamoid bones between the suspensory ligament and MC III or MT III.[1] Ligaments associated with the MCP and MTP articulations are described elsewhere.[2]

RADIOGRAPHIC EXAMINATION

The intent of the radiographic examination is to visualize the articular and periarticular skeletal structures and the adjoining soft tissues adequately. The examination should include the proximal interphalangeal joint and the distal ends of the metacarpal or metatarsal bones. Identification markers are essential in radiographic examination of the MCP or MTP articulation; right versus left and front versus hind should be designated clearly. If oblique views are obtained, the direction the x-ray beam travels designates the name of the projection from entrance to exit. Markers should be placed to the lateral surface on all views, with the exception of the lateromedial view, for which markers should be placed dorsally.[3]

Survey radiographic examination of the joint should include a lateromedial, a dorsopalmar, and two oblique projections (dorsal 45-degree lateral-palmaromedial and dorsal 45-degree medial-palmarolateral), with the limb bearing weight if possible. The survey examination should precede any special radiographic projections or contrast studies of the joint. The lateromedial projection should be made with the primary beam centered at the articulation and directed parallel to an imaginary line connecting the collateral fossae at the distal end of MC III or MT III. A true lateromedial projection is essential for proper assessment of the sagittal ridge of distal MC III or MT III.[4] The dorsopalmar projection warrants thoughtful positioning. Because the plane of the joint is at an angle to the solar surface of the hoof, the primary beam is directed from dorsoproximal to palmarodistal at approximately 30 to 40 degrees (dorsal 35-degree proximal-palmarodistal view). This should result in the projection of the proximal sesamoid bones over the distal aspect of MC III or MT III and the joint space projected with maximal width.[5,6] The dorsal 45-degree lateral-palmaromedial and dorsal 45-degree medial-palmarolateral projections should be a routine part of the survey examination. These oblique views are necessary to view the abaxial aspects of the articular surfaces, the periarticular margins, and the proximal sesamoid bones. Oblique views made in a dorsal 60-degree lateral-palmaromedial or dorsal 60-degree medial-palmarolateral direction allow the best visualization of the dorsal eminence of the proximal phalanx, which is located near midline, and the axial aspect of the proximal sesamoid bones. Some prefer using the 60-degree oblique view as the routine oblique view rather than the oblique views made at 45 degrees because axial lesions may be common (Fig. 22-1).[7]

Additional projections of the joint may be indicated according to the information gained from survey radiographs.[4] The lateromedial projection during flexion is performed while the foot is held off the ground as if the sole of the hoof were being inspected visually. Alternate positions include variations in the degree of flexion and flexed oblique views. These projections may provide better visualization of subarticular

*"Palmar(o)" is used throughout this chapter with the understanding that "plantar(o)" should be substituted if reference is being made to the hindlimb.

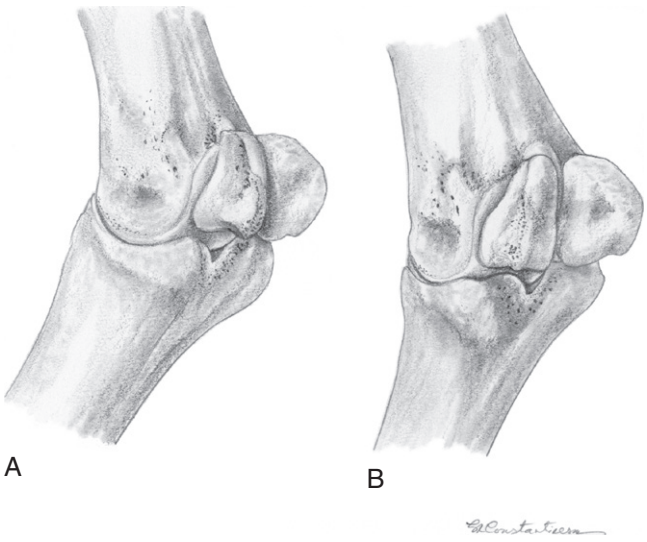


Fig. 22-1 The effect of angle of obliquity on the different aspects of the proximal sesamoid bones that can be projected. **A,** The dorsal 30-degree proximal, 45-degree medial (or lateral)-palmarodistolateral (or medial) view of the MCP joint best demonstrates the abaxial aspect of the sesamoid bones where the branches of the suspensory ligament attach. **B,** Dorsal 30-degree proximal, 60-degree medial (or lateral)-palmarodistolateral (or medial) view of the joint maximizes the evaluation of the dorsal eminence of P1. (Drawing by Gheorghe M. Constantinescu, DVM, University of Missouri, Columbia.)

surfaces at the dorsal aspect of distal MC III or MT III, the proximal part of the proximal phalanx, and the articular margins of the proximal sesamoid bones.[6]

The dorsodistal-palmaroproximal projection is made while the limb is not bearing weight. In this study, a tangential view of the articular margin of the distal aspect of MC III or MT III is created. The foot is elevated on a block, and the limb extended. The primary beam direction is approximately 125 degrees to the axis of the metacarpal or metatarsal bone.[8] The degree of flexion and the angle of the primary beam determine the tangent of the joint surface that is visualized.

The palmaroproximal-palmarodistal projection is used to visualize the palmar articular surface of MC III or MT III and the proximal sesamoid bones. Positioning of the patient requires that the x-ray tube be placed close to the horse's body. The limb should be positioned as far caudal as possible, and the foot is placed on a supporting tunnel containing a cassette.[6] Inherent magnification results from the use of this projection because of the distance between the proximal sesamoid bones and the film cassette.

The abaxial surfaces of the proximal sesamoids may be examined further by placing a cassette medial or lateral to the joint on the affected side. The x-ray beam is then directed in a dorsal 50-degree proximal, 45-degree lateral-distopalmaromedial or dorsal 50-degree proximal, 45-degree medial-distopalmarolateral direction, respectively, to create a tangential view of the proximal sesamoid bones.[9] This positioning results in the x-ray beam being directed downward at the sesamoid bones at an angle of 50 degrees from horizontal. This tangential projection is beneficial in assessing whether articular involvement is present with sesamoid lesions and thus directs the surgical approach (Fig. 22-2, *A* and C).

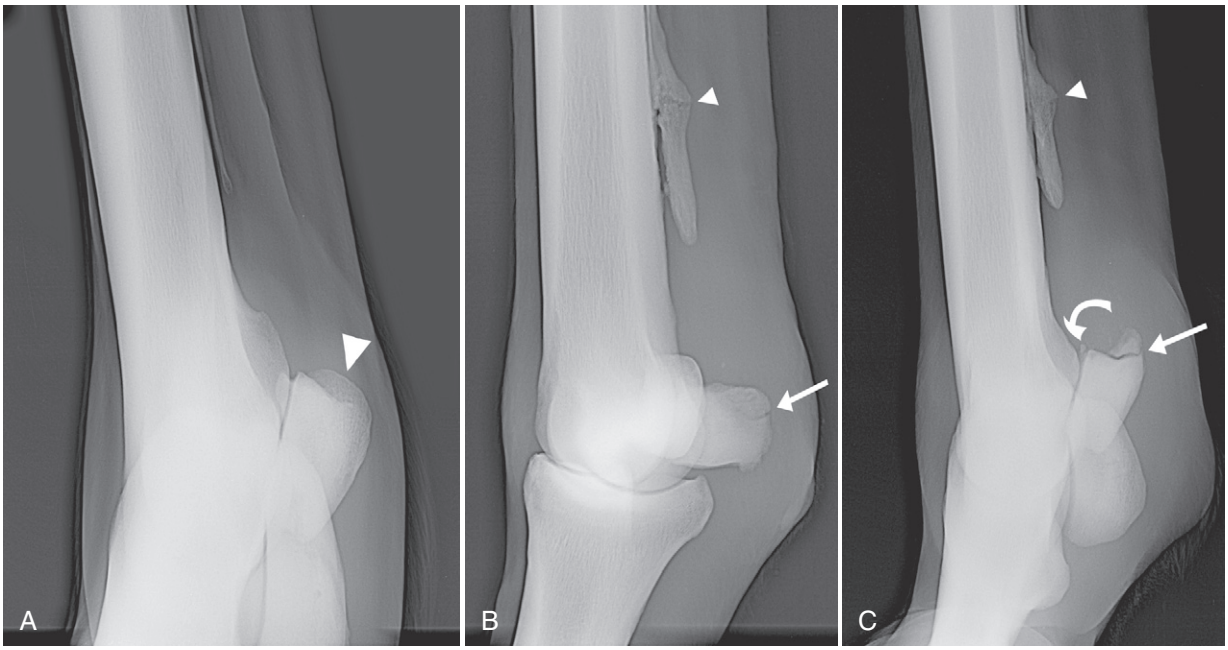


Fig. 22-2 **A,** A dorsal 50-degree proximal, 45-degree medial-distopalmarolateral view demonstrating the normal appearance of the proximal abaxial sesamoid on this tangential view *(white arrowhead)*. **B** and **C,** Oblique views of an apical sesamoid fracture. **B,** A dorsal 30-degree proximal, 60-degree lateral-palmarodistomedial oblique view. An incomplete fracture of the lateral sesamoid bone is visible *(white arrow)*. A chronic fracture of the distal MC IV is also present *(white arrowhead)*. **C,** A dorsal 50-degree proximal, 45-degree medial-distopalmarolateral view of the same horse. This view demonstrates that the sesamoid fracture is complete and articular *(straight white arrow)* with a small articular fragment *(curved white arrow)*. The chronic distal MC IV fracture is also visible *(white arrowhead)*. (Courtesy of Scott E. Palmer, VMD, Dipl. ABVP-Equine, New Jersey Equine Clinic, Clarksburg, New Jersey.)

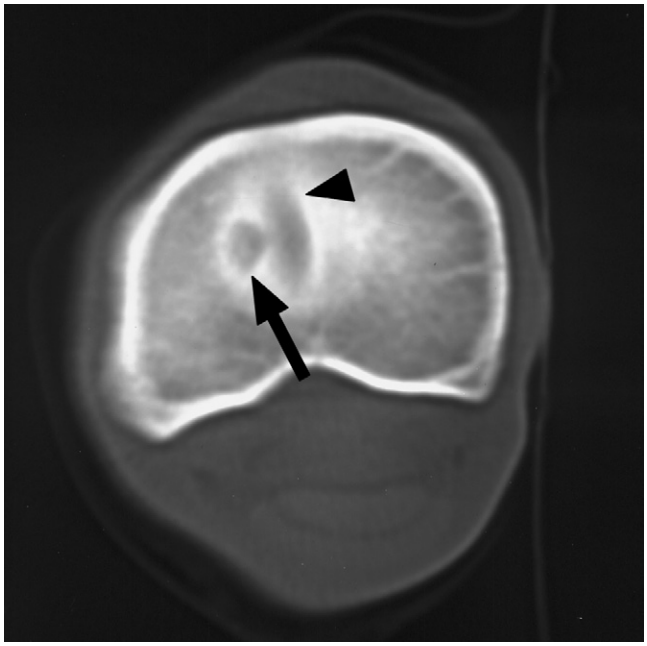


Fig. 22-3 A transverse 1.5 mm-thick CT image of the proximal aspect of the proximal phalanx. A small, oval, hypoattenuating cystic lesion *(black arrow)* is surrounded by hyperattenuating sclerotic bone just lateral to and communicating with the fossa for the median sagittal ridge *(black arrowhead)*.

Contrast arthrography of the MCP or MTP joint is sometimes useful. Five to 10 mL of water-soluble contrast medium containing 300 to 400 mg/mL of iodine is adequate. Injection of contrast medium should follow arthrocentesis and withdrawal of an equal volume of synovial fluid. Injection is made into the lateral pouch of the joint, proximal to the lateral sesamoid bones and dorsal to the suspensory ligament. The joint should be flexed, extended, and massaged vigorously before radiography to distribute the contrast medium throughout the joint.

ALTERNATIVE IMAGING MODALITIES

Ultrasound offers many advantages in evaluation of soft tissues surrounding the MCP or MTP joint and is used frequently to complement the radiographic examination. Portable ultrasound machines can be used to image the extensor and flexor tendons, the suspensory and distal sesamoidean ligaments, the synovial lining and joint recesses, collateral ligaments, and cortical margins. The normal sonographic features of the MCP and MTP joints have been described.[10]

In addition to conventional radiography, computed tomography (CT) may be useful in selected patients to image the MCP or MTP joint. CT excels in the evaluation of bones and is useful in imaging complex fractures and subchondral lesions in the MCP and MTP joints (Fig. 22-3).

More recently, magnetic resonance (MR) imaging has been used to evaluate the distal limbs in horses, including the MCP or MTP joints.[11-18] A distinct advantage of MR is the exceptional soft tissue contrast resolution (Figs. 22-4, 22-5, and

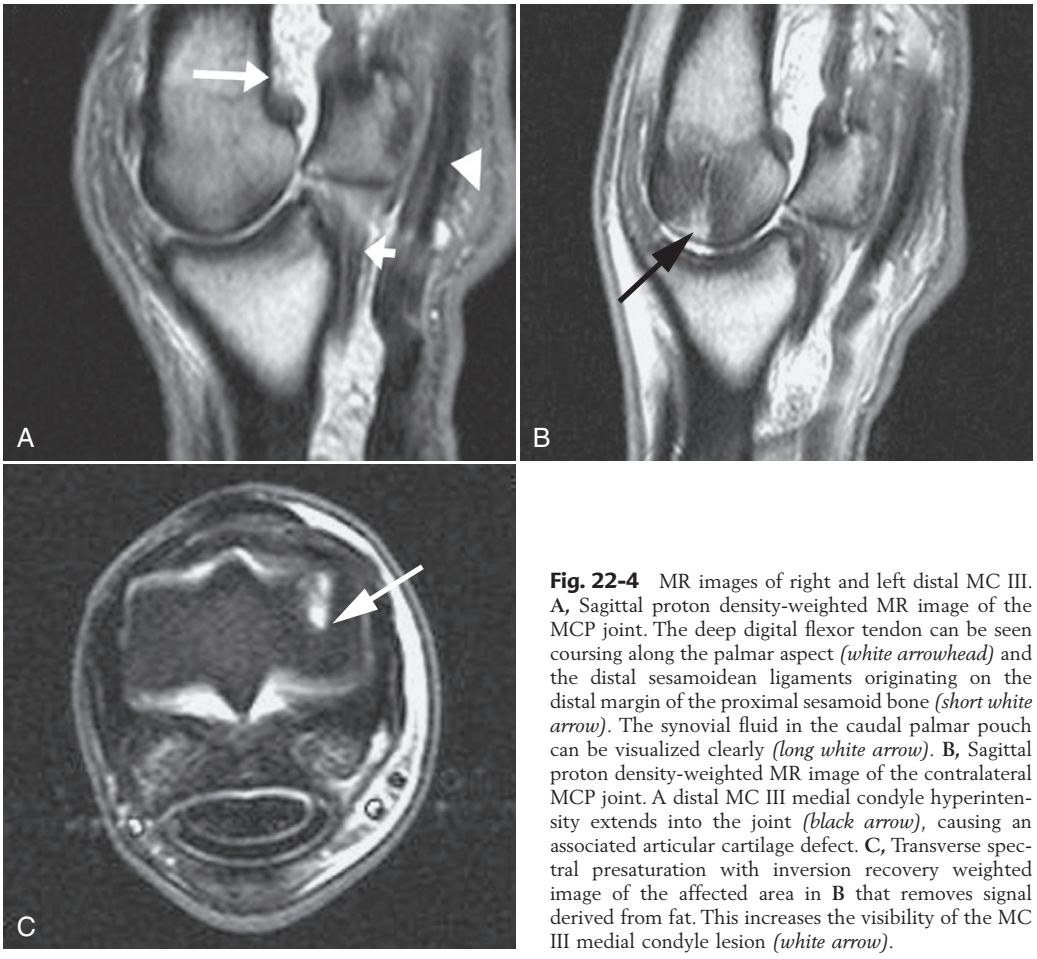


Fig. 22-4 MR images of right and left distal MC III. **A,** Sagittal proton density-weighted MR image of the MCP joint. The deep digital flexor tendon can be seen coursing along the palmar aspect *(white arrowhead)* and the distal sesamoidean ligaments originating on the distal margin of the proximal sesamoid bone *(short white arrow)*. The synovial fluid in the caudal palmar pouch can be visualized clearly *(long white arrow)*. **B,** Sagittal proton density-weighted MR image of the contralateral MCP joint. A distal MC III medial condyle hyperintensity extends into the joint *(black arrow)*, causing an associated articular cartilage defect. **C,** Transverse spectral presaturation with inversion recovery weighted image of the affected area in **B** that removes signal derived from fat. This increases the visibility of the MC III medial condyle lesion *(white arrow)*.

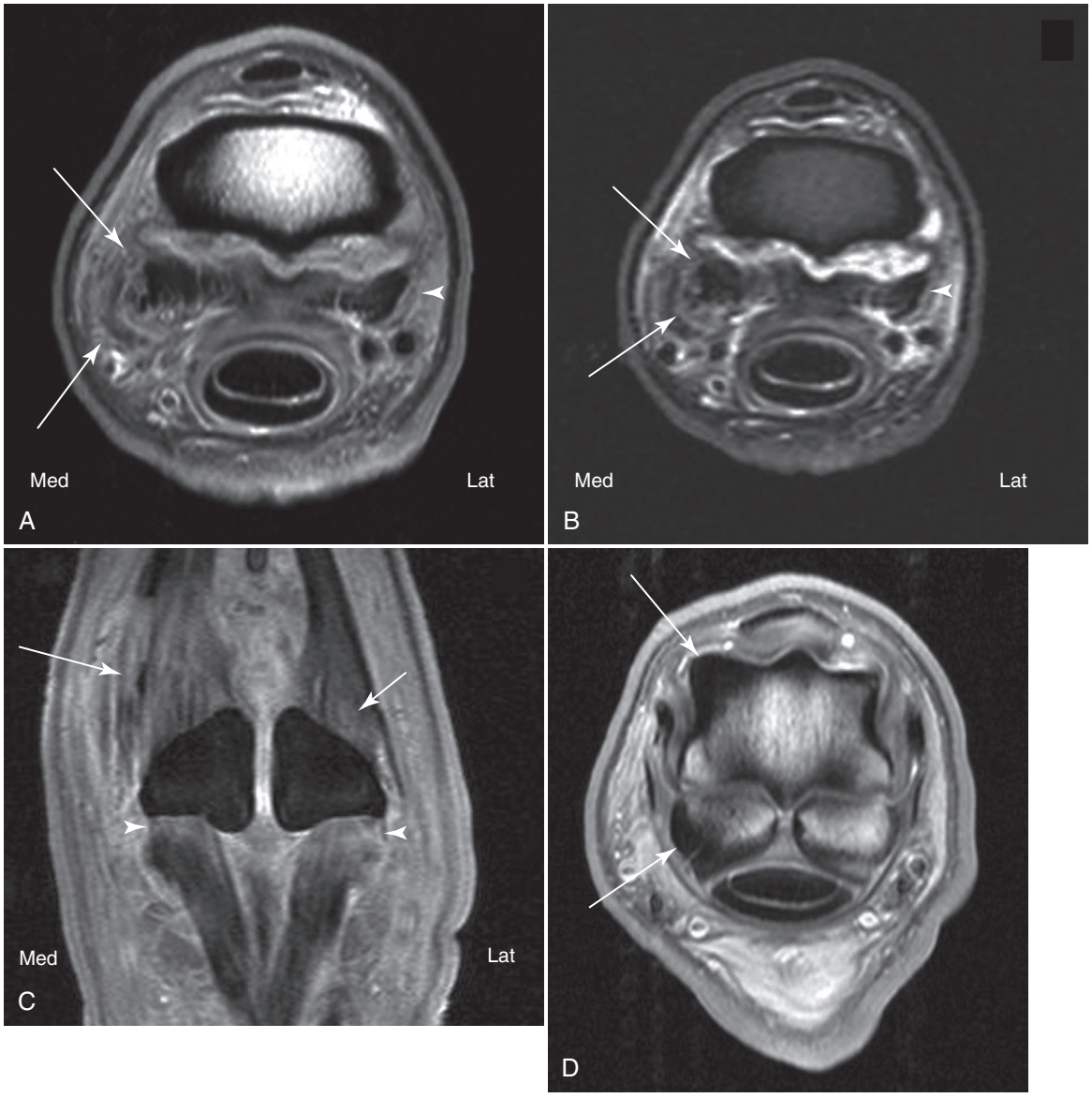


Fig. 22-5 MR images of a 12-year-old male Friesian with right MTP joint swelling and lameness. Radiographically, there was marked soft tissue swelling around the joint, especially along the medial and plantar aspects, but no bone changes were present. **A,** Transverse proton density image and **(B)** transverse short time inversion recovery image of the joint immediately proximal to the proximal sesamoid bones. There is marked enlargement and abnormal signal of the medial branch of the suspensory ligament *(white arrows)* with surrounding soft tissue swelling. The abaxial margin of the lateral branch of the suspensory ligament has an abnormal hyperintensity *(white arrowhead)*. **C,** Dorsal gradient recalled echo image of the proximal sesamoid bones. There is diffuse disruption and enlargement of the medial branch of the suspensory ligament *(large white arrow)* and focal disruption of the lateral branch of the suspensory ligament at the insertion to the sesamoid bone *(small white arrow)*. In addition, there is abnormal signal and morphology of the proximal distal sesamoidean oblique ligaments *(white arrowheads)*. **D,** Transverse proton density image at the level of the mid-body of the proximal sesamoid bones. There is sclerosis in the dorsal medial condyle of the third metatarsal bone and along the abaxial margins of the medial proximal sesamoid bone *(white arrows)*. *Lat*, Lateral; *Med*, medial.

22-6). Additionally, MR imaging is multiplanar. MR examinations are commonly performed by using several types of acquisition sequences to demonstrate different anatomic and pathologic features. MR systems usually require that horses be under general anesthesia. There are MR systems available for imaging the limbs of standing horses. However, volume averaging and motion artifact remain limitations of these, especially proximal to the distal phalanx, although motion correction techniques improve resolution.[19]

RADIOGRAPHIC INTERPRETATION OF DISEASES OF THE METACARPOPHALANGEAL/METATARSOPHALANGEAL ARTICULATION

Joint disease in many horses is often associated with repeated trauma, and the pathologic changes may be characteristic of the joint or function of the horse. A study of racetrack injuries has provided an overview of pathologic findings and pathogenesis of MCP or MTP joint disease.[20] Lameness and

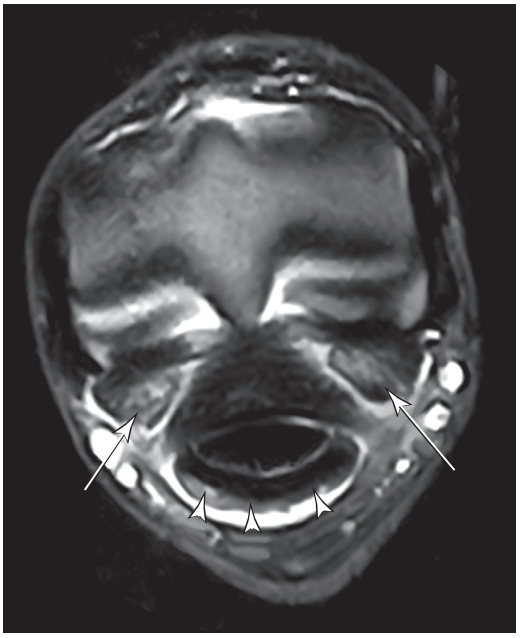


Fig. 22-6 A 9-year-old Warmblood with chronic tenosynovitis. There is digital sheath effusion and synovial proliferation at the palmar aspect of the superficial digital flexor tendon *(white arrowheads)* that do not correspond with any active lesions within the superficial or deep digital flexor tendon. The residual margin lesions appear healed. There is, however, a generalized increase in T2 signal throughout the medial and lateral oblique distal sesamoidean ligaments *(white arrows)* with disruption of the normal architecture, consistent with an active biaxial desmitis/desmopathy. (Courtesy of Alexia McKnight, DVM, DACVR and Patterson Veterinary MRI, Patterson, New York.)

distention of a joint are the initial clinical signs that typically precede the request for radiographic examination. The earliest signs of joint disease may remain obscure on radiographs because wear lines in the articular cartilage or synovial hypertrophy are usually not recognized. Radiographs of the contralateral joint may be obtained for comparison. Although pathologic change is often bilateral, it is usually in different stages of development between limbs, allowing for detection of changes.

Joint Effusion

Joint effusion is usually a result of trauma, with degenerative changes in the articular surfaces and joint capsule. Radiographic signs include soft tissue swelling and joint distention. With chronic insults, dystrophic calcification of the periarticular soft tissues may also be present.[21]

Villonodular Synovitis

Villonodular synovitis leads to a firm, nonfluctuating swelling at the dorsal aspect of the joint. The villonodular masses arise from enlargement of the synovial villi of the joint capsule and are associated with repetitive trauma. The condition is usually diagnosed by clinical signs, history, palpation, and ultrasound. With time, the radiographic signs will include mild to severe erosion of distal MC III or MT III at the region just distal to the dorsal joint capsule attachment.[22-24] Periarticular bony proliferation may be present (Fig. 22-7).With arthrography, radiolucent, space-occupying masses of the synovial villus hypertrophy can usually be identified in the dorsal recess of the joint (Fig. 22-8).

Supracondylar Lysis

In MC III or MT III, the radiographic features of supracondylar lysis are similar to those in villonodular synovitis, except

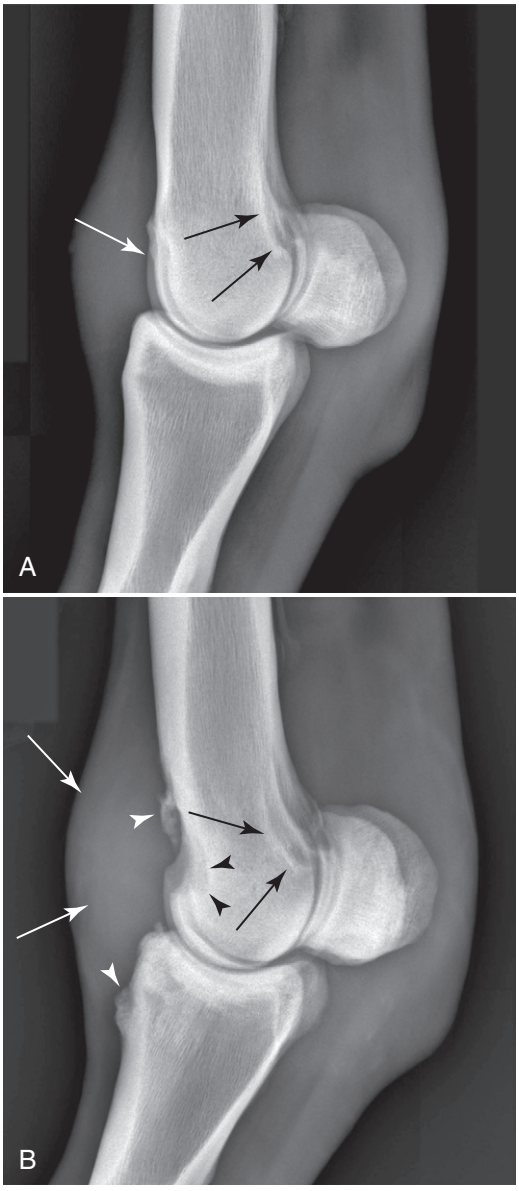


Fig. 22-7 Lateromedial radiograph of two MCP joints with changes of mild **(A)** and severe **(B)** villonodular synovitis. **A,** Swelling dorsal to the joint, erosion of bone at the dorsoproximal joint capsule attachment *(white arrow)*, and early evidence of supracondylar lysis at the palmar cortex *(black arrows)* are present. **B,** This joint has more chronic changes with severe swelling *(white arrows)*, bone erosion at the dorsoproximal joint capsule attachment *(black arrowheads)*, supracondylar lysis *(black arrows)*, and periarticular enthesophytes *(white arrowheads)*. Bone remodeling is also present at the proximodorsal aspect of the proximal phalanx as well as along the palmar border of the sesamoid bones.

that supracondylar lysis occurs at the palmar surface of the bone. Changes are caused by chronic proliferative synovitis. Radiographic signs are joint distention and lysis of bone at the distal palmar cortex of MC III or MT III, distal to the joint capsule attachment (see Fig. 22-7, *B*). Arthrography may be difficult to perform because of the presence of hypertrophied synovium and diminished synovial joint space. The erosive concavity formed in the bone is usually readily apparent (see Fig. 22-8).

Degenerative Joint Disease

Degenerative joint disease is a nonspecific term describing deterioration of articular and periarticular structures. The



Fig. 22-8 Positive-contrast arthrogram of a horse with mild villonodular synovitis. A space-occupying mass is present in the dorsoproximal aspect of the joint space *(black arrowheads)*. A space-occupying mass at the palmar surface fills the area of supracondylar lysis *(black arrows)*.

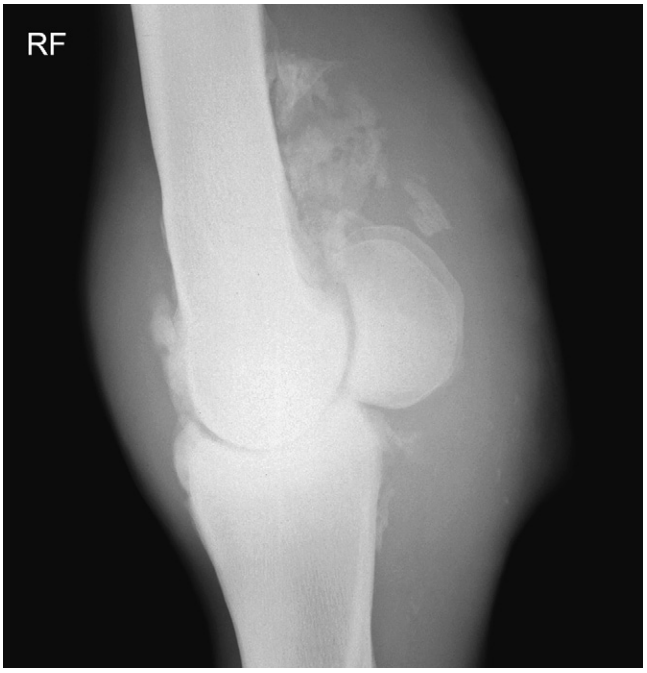


Fig. 22-9 Lateromedial radiograph of a horse with cortisone arthropathy. There is narrowing of the joint space and severe periarticular bone remodeling of the dorsal and palmar aspects of the distal metacarpal, proximal aspect of the proximal phalanx, and the apical margins of the proximal sesamoid bones. Mineralization in periarticular soft tissues is typical of cortisone arthropathy. (Courtesy of Stephanie Nykamp, DVM, DACVR, Ontario Veterinary College, Guelph, Ontario, Canada.)

pathologic events culminate in degenerative hypertrophic osteoarthritis/osteoarthrosis, regardless of the initiating causes or biochemical alterations. It is a chronic disorder characterized by progressive deterioration of articular cartilage that results in a radiographic loss in joint space and reactive changes in the joint margin and capsule.[20]

The first stages include cartilage degeneration and formation of wear lines characteristic of hinge joints. These wear lines are grooves in the articular surface that are oriented parallel to the direction of joint motion. Cartilaginous fibrillation and erosions form on the surface, and subsequent wear results in narrowing of the joint space. If reduction in the width of a joint space is confirmed on two radiographic views, cartilage thinning is likely. Progressive loss of joint width is a subjective finding and must be assessed in conjunction with clinical signs to determine its significance (Fig. 22-9).

Radiographic signs of degenerative joint disease are soft tissue swelling, narrowed joint space, and bone remodeling with lysis and proliferation. These findings may occur in any combination. Joint capsule thickening may be suspected but is rarely visualized, even on high-detail radiographs. Soft tissue swelling results from synovial effusion, as well as hypertrophy and proliferation of other periarticular tissues.

Chronic arthritis is characterized by sclerosis or eburnation of subchondral bone, with loss of trabecular architecture as a result of erosion of the overlying articular cartilage. Repetitive stress or trauma at the joint capsule attachments results in enthesophyte formation (Fig. 22-10). Similar, but not identical, are periarticular bony osteophytes that form at the joint margins in response to damage to the articular surface (Fig. 22-11). Of note, many joint disorders can progress to a

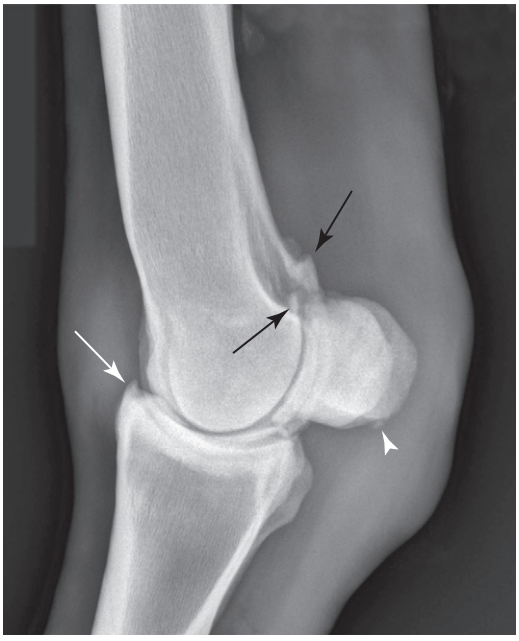


Fig. 22-10 Lateromedial radiograph of a horse with chronic degenerative joint disease, sesamoiditis, and desmitis. Generalized soft tissue swelling and joint distention are present. Chronic osteochondral fractures are present at the palmar distal metacarpus near the apexes of the proximal sesamoid bones *(black arrows)*. A periarticular osteophyte is evident on the dorsal rim of the proximal phalanx *(white arrow)*. Other changes include supracondylar lysis, remodeling of bony trabeculae in the proximal sesamoid bones, and bone proliferation at the attachments of the deep sesamoidean ligaments at the proximal palmar aspect of the proximal phalanx. In addition, there is a small smooth fragment off the base of one of the proximal sesamoid bones *(white arrowhead)*.

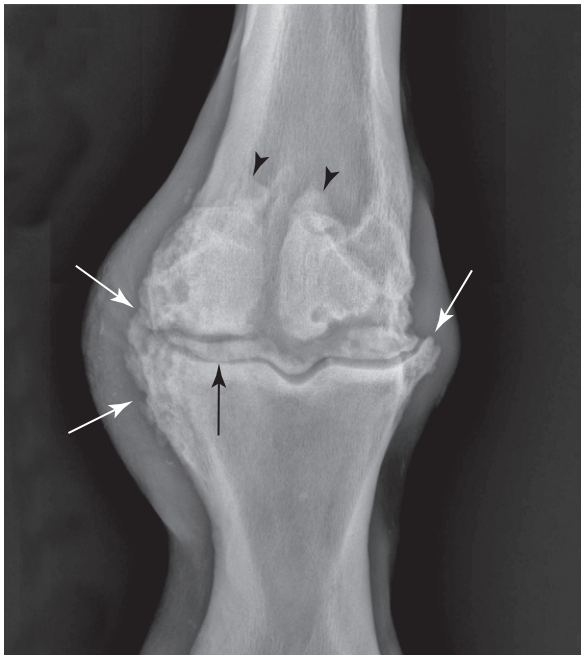


Fig. 22-11 Dorsopalmar radiograph with changes of chronic, severe degenerative joint disease. Narrowing of the joint space *(black arrow)* and formation of osteophytes at the joint margins *(white arrows)* and sesamoid bone remodeling *(black arrowheads)* are visible.

common end point having the stereotypic features of chronic degenerative joint disease.[20] The initiating factors of degenerative joint disease may be difficult or impossible to determine in the late stages of the disease.

Cortisone Arthropathy

Cortisone arthropathy may involve articular and periarticular structures and may lead to variable degrees of degeneration and proliferation. Repeated steroid injections result in localized demineralization of bone and decreased trabecular detail. Long-term changes include mineralization in the periarticular soft tissues associated with deposition of steroid within those structures. A differential diagnosis of steroid-induced arthritis should be considered in the presence of degenerative change or collapse of subchondral bone with mineralization in periarticular soft tissue (see Fig. 22-11).

Osteochondrosis

Osteochondrosis may be found in the distal aspect of MC III or MT III.[25-28] The radiographic findings are well-demarcated radiolucencies that may extend several centimeters deep to the articular margin. A lateromedial radiograph of the joint may best demonstrate the depth of the lesion in the condyle. The shape of the defect may be a shallow concavity, a deep concavity, crescentic, oval, or circular.[28] The changes are at the junction of the radii of articulation between the MCP or the MTP joint and the metacarposesamoidean or metatarsosesamoidean articular surface (Fig. 22-12). These lesions have



Fig. 22-12 Lateromedial **(A),** dorsopalmar **(B),** and dorsolateral-palmaromedial **(C)** radiographs of a horse with distal metacarpal osteochondrosis. A radiolucent subchondral cyst with surrounding radiopaque sclerosis *(black arrows)* is visible on all three images, with **B** and **C** demonstrating that the cyst involves the lateral condyle of the distal metacarpus. Proximal sesamoid bone remodeling *(white arrows)* is seen on **A,** but is best demonstrated on the oblique view **(C).** Periarticular remodeling is also seen on all three views.



Fig. 22-13 Dorsal 45-degree medial-palmarolateral radiograph of the MCP joint with a type II fragment *(black arrows)* originating from the medial palmar eminence of the proximal phalanx.

been called *traumatic osteochondrosis*—an indication of the controversy regarding their etiology.[20] Arthrographically, cavitation of the joint surface may exist, although advanced degenerative subchondral bone changes can also be found with the overlying cartilage intact at the articular surface.

Osteochondral fragments of the palmar aspect of the joint have been given three classifications.[29] Type I fragments occur at the proximal end of the proximal phalanx, just medial or lateral to the sagittal groove; type II fragments have an origin from the wing of the proximal phalanx (Figs. 22-13 and 22-14). Type III fractures originate from the basilar margin of the sesamoid bones and are discussed under the section on sesamoid basilar fractures (Fig. 22-15). Type I or II fragments have the highest incidence in Standardbreds and were originally reported as avulsion fractures.[30,31] Because of the anatomic origin, symmetry, and breed predilection, these fragments have been reported to be the result of osteochondrosis. These fragments are the subject of much controversy. Studies have focused on radiography,[32-34] etiology,[35] heritability,[36,37] the effect of patient size,[38] epidemiology,[39,40] surgical treatment,[41,42] and prognosis.[34] Subchondral bone cysts can also be seen at the proximal end of the proximal phalanx and are often difficult to see radiographically (see Fig. 22-3).

Osteochondrosis of the sagittal ridge of MC III or MT III is usually diagnosed in young horses and occurs with variable radiographic expression (Fig. 22-16). Radiographic signs may vary from small areas of flattening to large excavations of subchondral bone of the sagittal ridge. Lesions are usually best visualized on flexed lateral projections of the MCP or MTP joint. Detached osteochondral fragments may be found in close association to the bone defect or may be nestled in distant recesses of the joint.[43]

Septic Arthritis

Septic arthritis may be associated with hematogenous spread of microorganisms, such as occurs with omphalophlebitis, or by direct contamination as a result of trauma or nonsterile invasive techniques. Radiographic signs of early septic arthritis are periarticular soft tissue swelling and distention of the joint. Progression of the disease results in malalignment, subluxation, or collapse of the joint (Fig. 22-17) and bony changes of subchondral bone lysis and periosteal proliferation at the joint margins (Fig. 22-18). The cartilage space may appear increased at areas of subchondral bone lysis. Diminished joint space is evidence of the loss of articular cartilage that typically precedes subchondral bony change.

The radiographic sign of an increase in the apparent joint space must be analyzed critically. Incomplete ossification of the cartilage model is normally present in young, developing animals. The large soft tissue space at articular margins diminishes progressively with skeletal maturity. Furthermore, radiographs made in non–weight-bearing horses will cause joint spaces to be widened compared with weight-bearing projections. Whenever possible, the horse should bear normal weight on the joint at the time of radiography. Increased thickness of the articular cartilage has not been documented in animals. Excessive fluid or soft tissue in the joint space, as occurs with immune-mediated arthritis, results in a wider joint space. However, such diseases have not been documented in the horse.

Nonseptic inflammatory joint diseases have varied causes and may be difficult to classify. Radiographic signs are distention of the joint and displacement of periarticular soft tissues. If the condition is chronic, bone production at the joint margins or periarticular osteophytes may be found.

Condylar Fractures

Fractures in the distal condyle of MC III or MT III can be difficult to visualize radiographically. The radiographic signs include uneven joint surface, interruption of the metaphyseal cortex, and the presence of a radiolucent fracture line extending from the joint surface to the cortex. The dorsodistal-palmaroproximal projection, angled at 125 degrees in a non–weight-bearing position, has been useful to identify condylar fractures of the distal aspect of MC III or MT III that were not apparent on standard radiographic series.[8] These fractures usually occur at the lateral side of the joint (Fig. 22-19; see Fig. 22-4) and may be displaced, complete but nondisplaced, or incomplete.[44,45] Prognosis after surgical treatment varies.[45,46]

Fractures of the proximal phalanx often communicate with the articular surface. Fracture location and severity must be considered relative to surgical repair and prognosis.[47]

Periarticular Chip Fractures

Chip fractures are more common in racehorses and occur equally in the front and hind limbs. They commonly arise from the medial or lateral periarticular eminences at the proximal dorsal rim of the proximal phalanx.[48] Acute chip fractures may have sharp borders and angular configurations. Chronic chip fractures undergo remodeling and have smooth, rounded borders. The latter are usually attached to the joint capsule or to the joint margin as an exostosis (Fig. 22-20). Free joint bodies may displace or move about within the joint.

Osteochondral fragments arising from the plantarolateral or plantaromedial eminences of the proximal phalanx (Fig. 22-21) have been reported as fractures[20,30,31,35,49] and are considered by some to be manifestations of osteochondrosis.[29,32-41,50,51]

Fractures of the Proximal Sesamoids

Proximal sesamoid fractures are consistently of three types: apical, mid-body, or basilar.[42] Some may be found as osteochondral fragments separated from the sesamoid apex (apical

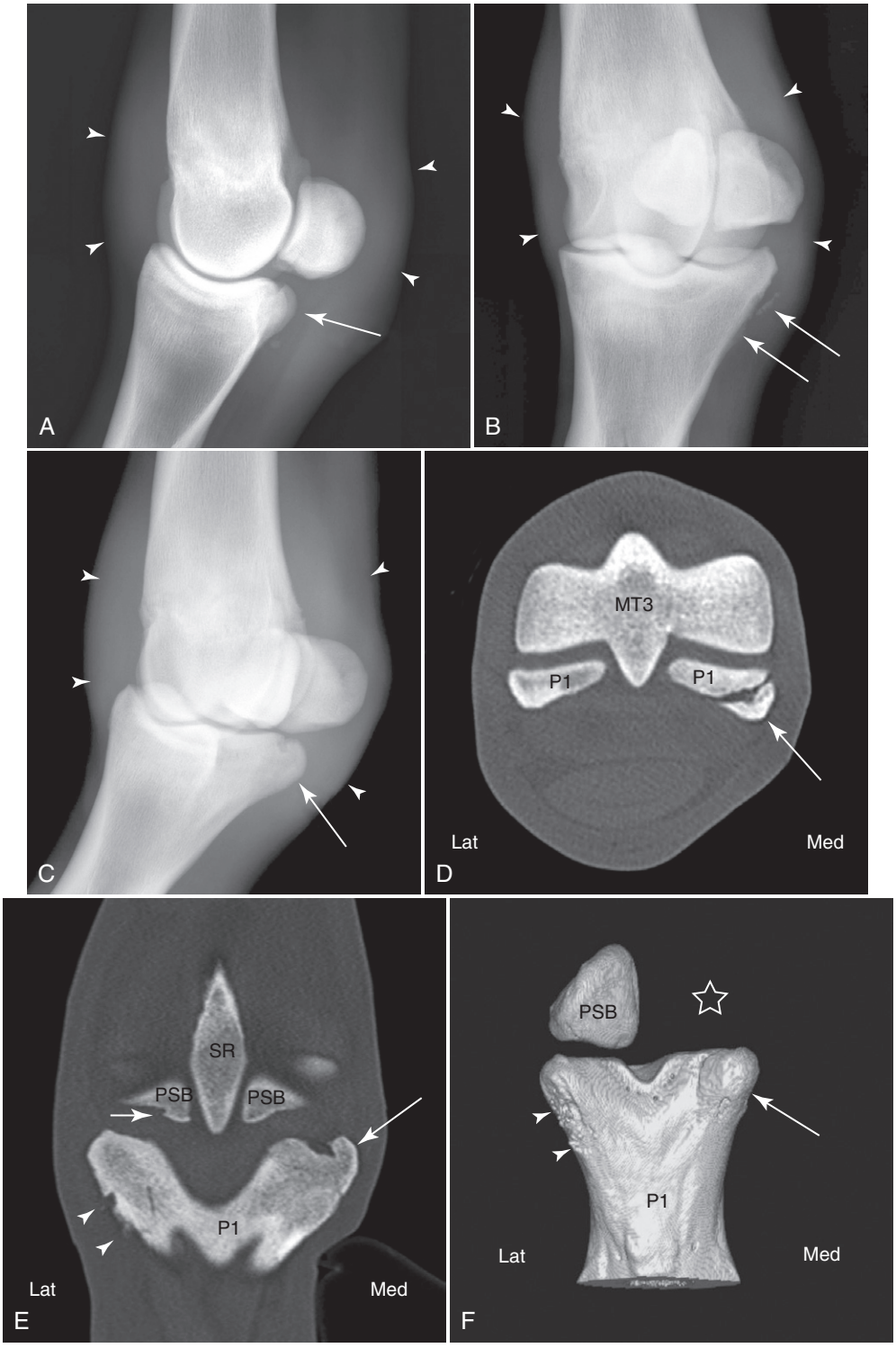


Fig. 22-14 Radiography and CT images of a 1-year-old male quarter horse. **A,** lateral radiograph of the right MTP joint. There is diffuse soft tissue swelling *(white arrowheads)* with osseous remodeling and fragments associated with the plantar process of the proximal phalanx *(large white arrow)*. **B,** Dorsolateral-plantaromedial radiograph. Note the soft tissue swelling *(white arrowheads)* and periosteal proliferation and fragmentation associated with the proximal lateral first phalanx *(white arrows)*. **C,** Dorsomedial-plantarolateral radiograph. Note the soft tissue swelling *(white arrowheads)* and slight defect of the medial plantar process of the first phalanx *(large white arrow)*. **D,** Transverse CT image at the level of MTP joint. Note the slightly displaced fragment of the medial plantar process of the proximal phalanx. **E,** Reconstructed dorsal CT image of the plantar aspect of the MCP joint. Note the large osteophyte associated with the medial plantar process *(large white arrow)*, the osseous proliferation immediately distal to the lateral plantar process *(white arrowheads)*, and a small enthesophyte off the axial aspect of the distal margin of the lateral proximal sesamoid bone *(small white arrow)*. **F,** Three-dimensional surface rendering of the plantar aspect of the MTP joint following digital elimination of the medial proximal sesamoid bone *(*)*. Note the attached osseous fragment of the medial plantar process *(long white arrow)* and periosteal proliferation along the proximal lateral cortex of the proximal phalanx *(white arrowheads)*. *MT3*, third metatarsal bone; *P1*, first phalanx; *PSB*, proximal sesamoid bones; *SR*, sagittal ridge of third metatarsal bone.

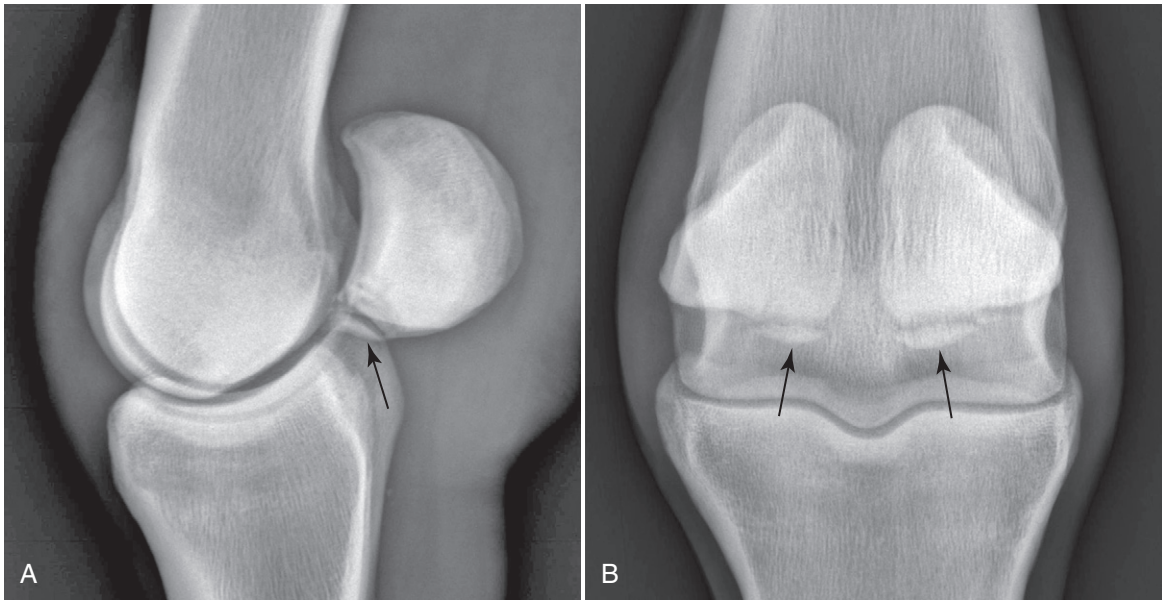


Fig. 22-15 Flexed lateromedial and dorsopalmar radiographs of an MCP joint with bilateral type III fractures originating from the basilar margin of the proximal sesamoid bones. **A,** A crescent-shaped fragment is present along the distal aspect of the proximal sesamoid bones and on **B,** it is apparent that both proximal sesamoid bones are affected *(black arrows)*.

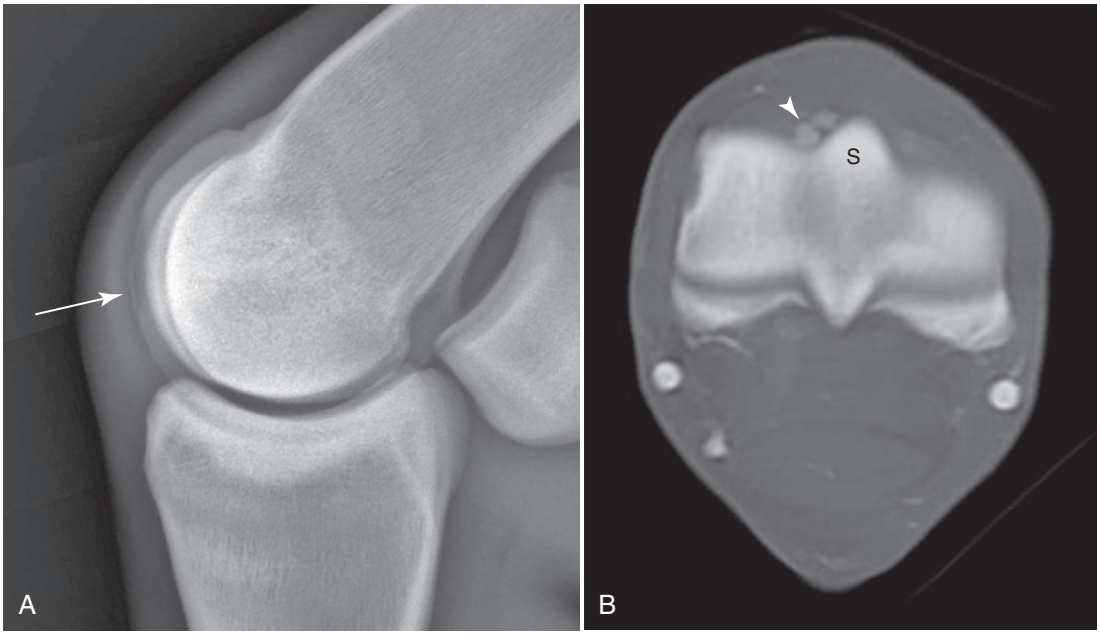


Fig. 22-16 **A,** Flexed MCP joint with osteochondrosis of the sagittal ridge of MC III. There is excavation of subchondral bone *(white arrow)*. **B,** Transverse CT image at the distal edge of the sagittal ridge of the third metacarpal bone with two adjacent osteochondral fragments *(white arrowhead)*. These fragments came from the proximal aspect of the proximal phalanx, and therefore the sagittal ridge is smooth. *S,* Sagittal ridge of third metatarsal bone. (**A,** Courtesy of John C. Janicek, DVM, MS, DACVS, Weems and Stephens Equine Hospital, Aubrey, Texas.)

fractures; see Figs. 22-2 and 22-10) or base (basilar fractures, see Fig. 22-15). Fractures through the body of a sesamoid may have a narrow cleavage line, indicating that the suspensory apparatus remains intact (Fig. 22-22, *A*). Wide separation of sesamoid fragments usually indicates bilateral sesamoid fractures and disruption of the fibers of the suspensory ligament (Fig. 22-22, *B*). Hyperextension of the MCP or MTP joint is apparent if stress is applied to the joint or if the limb is bearing weight with disruption of the suspensory ligament.

Abaxial fractures are detected by using special radiographic projections. These fractures result from avulsion of bone by a portion of the attachment of the branches of the suspensory

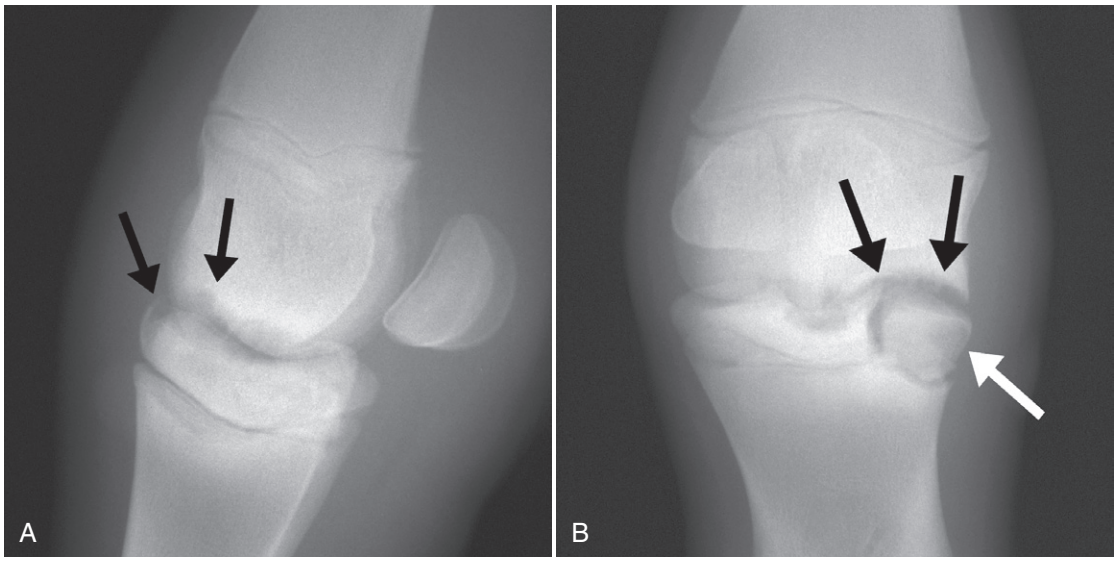


Fig. 22-17 Lateromedial and dorsopalmar views of a 1-month-old filly with soft tissue swelling, septic arthritis, and osteomyelitis. **A,** There is severe osteolysis of the subchondral bone of the distal aspect of the third metatarsal bone and the proximal epiphysis of the proximal phalanx *(black arrows)*. **B,** There is severe erosion of the subchondral bone of the distal aspect of the third metatarsal bone *(black arrows)* and a large osteolytic fragment involving the medial side of the proximal epiphysis of the proximal phalanx *(white arrow)*. These changes are consistent with advanced septic arthritis and septic epiphysitis with a pathologic Salter-Harris type III fracture of the epiphysis.

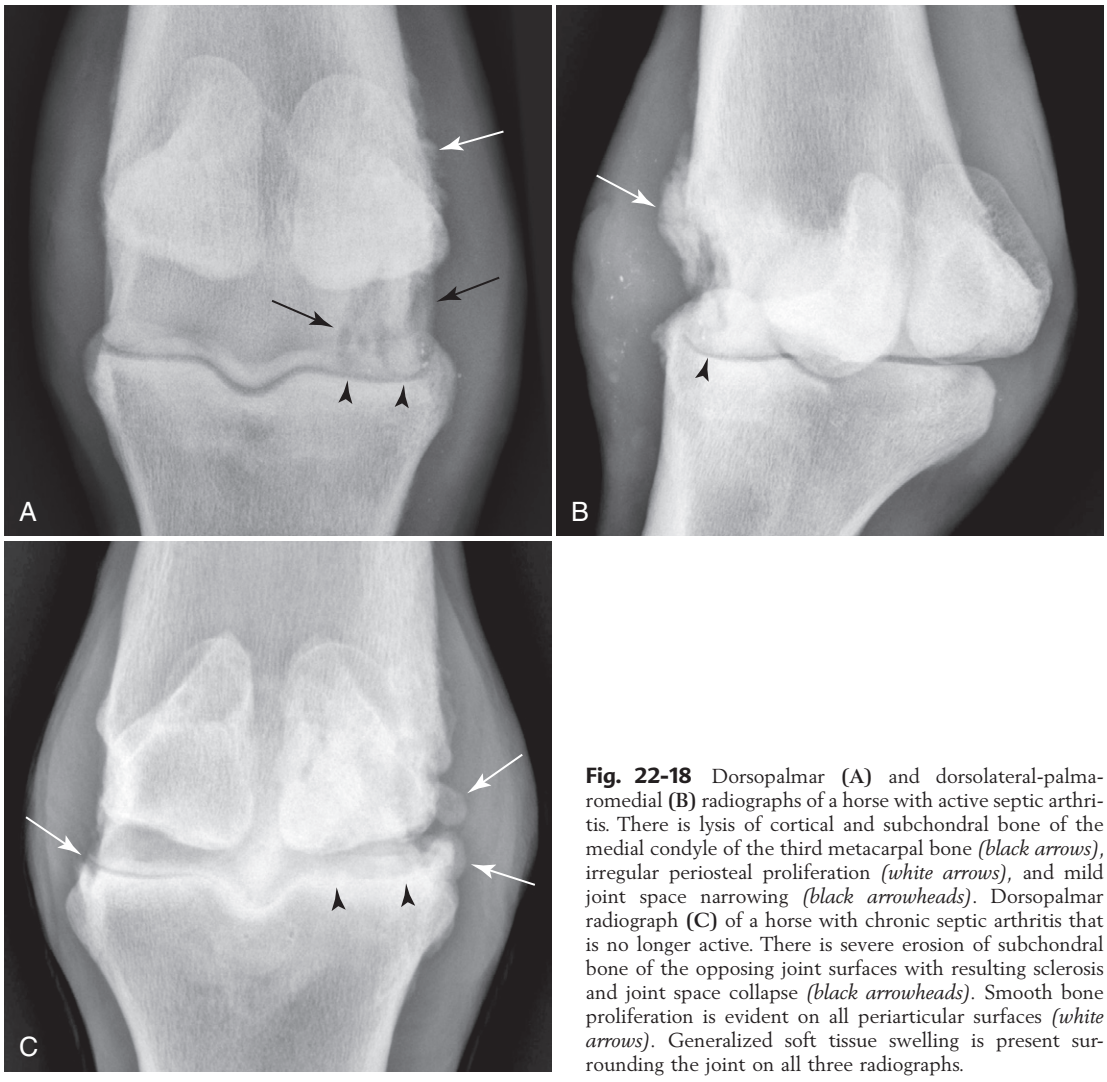


Fig. 22-18 Dorsopalmar **(A)** and dorsolateral-palmaromedial **(B)** radiographs of a horse with active septic arthritis. There is lysis of cortical and subchondral bone of the medial condyle of the third metacarpal bone *(black arrows)*, irregular periosteal proliferation *(white arrows)*, and mild joint space narrowing *(black arrowheads)*. Dorsopalmar radiograph **(C)** of a horse with chronic septic arthritis that is no longer active. There is severe erosion of subchondral bone of the opposing joint surfaces with resulting sclerosis and joint space collapse *(black arrowheads)*. Smooth bone proliferation is evident on all periarticular surfaces *(white arrows)*. Generalized soft tissue swelling is present surrounding the joint on all three radiographs.

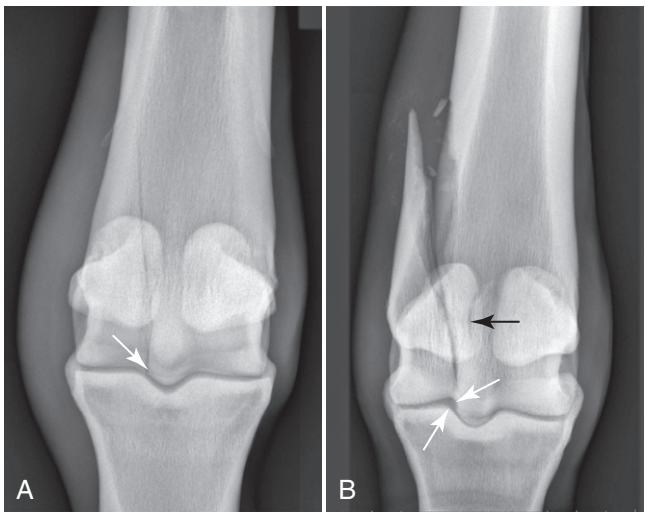


Fig. 22-19 Dorsopalmar radiographs of two horses with slab fractures of the lateral condyle of MC III. **A,** Incomplete fracture with nondisplaced articular involvement *(white arrow)*. **B,** Comminuted fracture with gross displacement and resulting articular incongruity *(white arrow)*. Some fracture lines may be difficult to visualize *(black arrow)*.

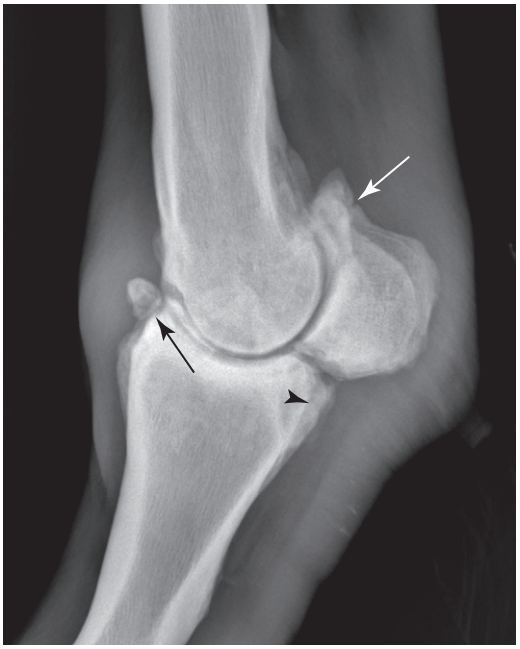


Fig. 22-20 Lateromedial radiograph of a horse with chronic degenerative joint disease. An osteochondral (chip) fracture is present at the dorsal periarticular rim of the proximal phalanx with adjacent severe fracture bed remodeling *(black arrow)*. Severe remodeling of the apexes of the proximal sesamoids is evident *(white arrow)*. Bone proliferation is present at the attachment of the deep sesamoidean ligaments at the palmaroproximal border of the proximal phalanx *(black arrowhead)*. Villonodular erosion of bone and supracondylar lysis are also apparent.

ligament on the medial or lateral abaxial aspects of the respective proximal sesamoid (Fig. 22-23; see Fig. 22-2, *A* and *C*).

The prognosis of sesamoid fractures is correlated to the type of fracture and damage to the associated structures. Reviews of the clinical aspects of apical[52] and basilar[53] sesamoid fractures are available.

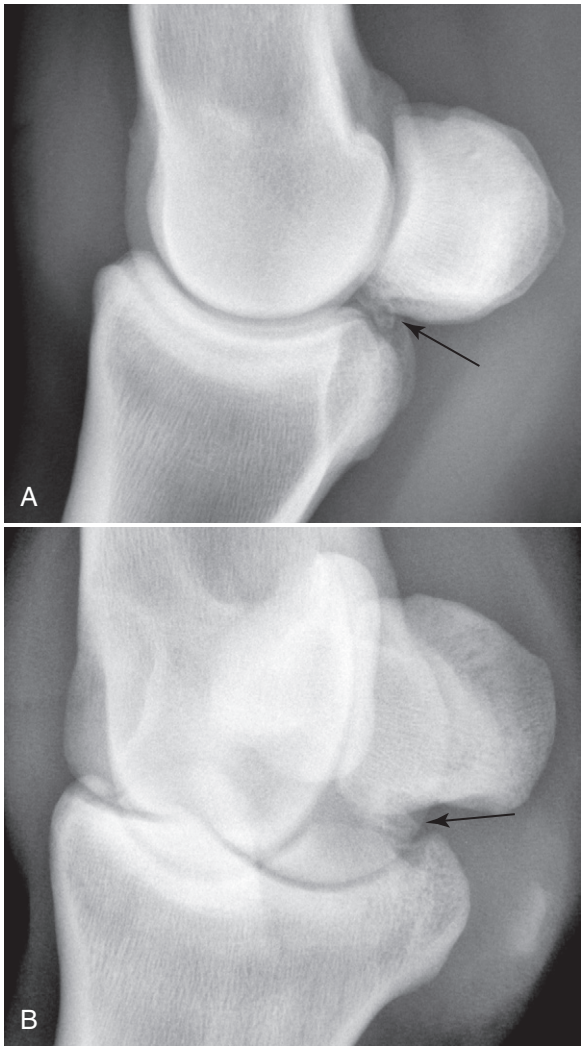


Fig. 22-21 Lateral **(A)** and dorsomedial-plantarolateral **(B)** radiographs of the MTP joint of a horse with an osteochondral fragment arising from the plantaromedial eminence of the proximal phalanx *(black arrows)*. These fragments have features of chip fractures but are still often lumped with the osteochondrosis complex of lesions.

Sesamoiditis

Sesamoiditis is characterized radiographically by bony proliferation on nonarticular surfaces of the proximal sesamoid bones.[54] Linear or cystic lysis may appear to penetrate the sesamoid from the abaxial surface (Fig. 22-24). Sesamoiditis is usually associated with degenerative change in the suspensory ligament and degenerative remodeling or fracture at the distal ends of MC II or MT IV.

Disuse Atrophy of Bone

Disuse atrophy occurs most rapidly in the proximal sesamoid bones but may also be recognized in the tubular bones as a reduction in bone opacity. Trabeculae within the bone become large and coarse. This change occurs as a result of altered stress or axial weight bearing and may not signify primary pathologic change in the joint (Fig. 22-25).

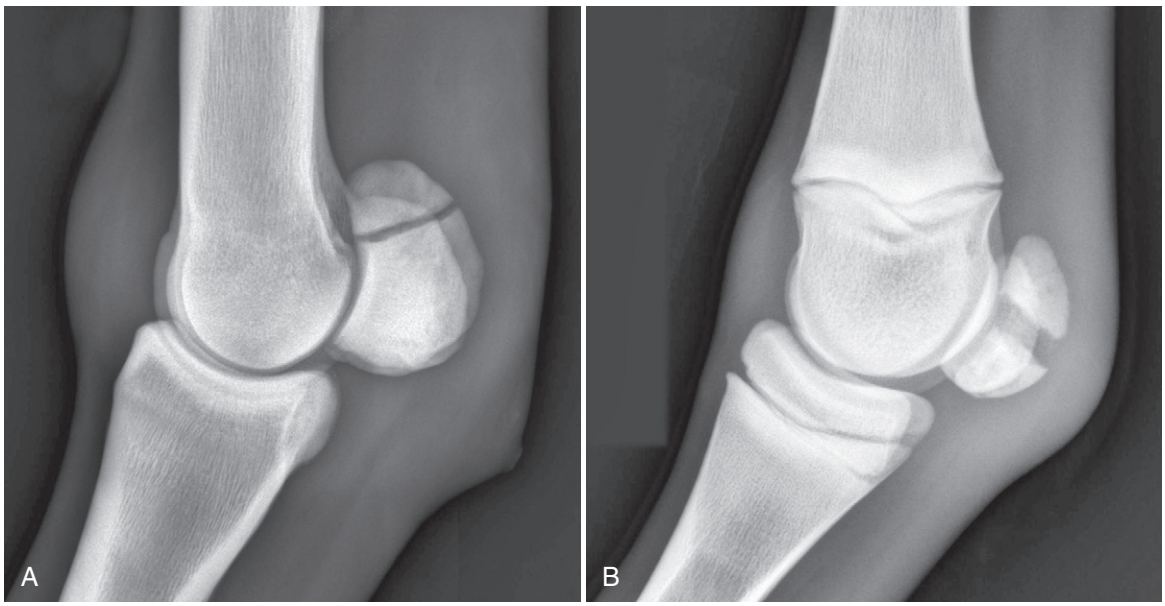


Fig. 22-22 **A,** Apical fracture of one of the proximal sesamoid bones with mild separation of fracture from sesamoid body. **B,** Mid-body fracture of a proximal sesamoid bone with separation of the sesamoid halves. (**A,** Courtesy of John C. Janicek, DVM, MS, DACVS, Weems and Stephens Equine Hospital, Aubrey, Texas.)



Fig. 22-23 Dorsal 50-degree proximal, 45-degree medial-palmarodistolateral radiograph of a horse with a periarticular fracture of the medial proximal sesamoid bone *(black arrows)*. The fracture originates at an articular surface and emerges at the abaxial surface of the sesamoid bone.

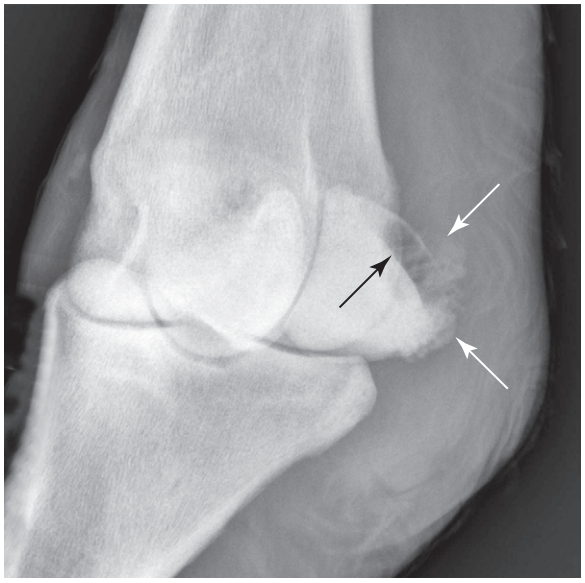


Fig. 22-24 Dorsal 45-degree medial-palmarolateral radiograph of a horse with sesamoiditis of the medial proximal sesamoid bone. Degenerative remodeling is present with increased size of vascular channels within the sesamoid bone and lysis of the cortical bone *(black arrow)* and bone remodeling of its palmar surface *(white arrows)*. Soft tissue swelling surrounds the MCP joint.

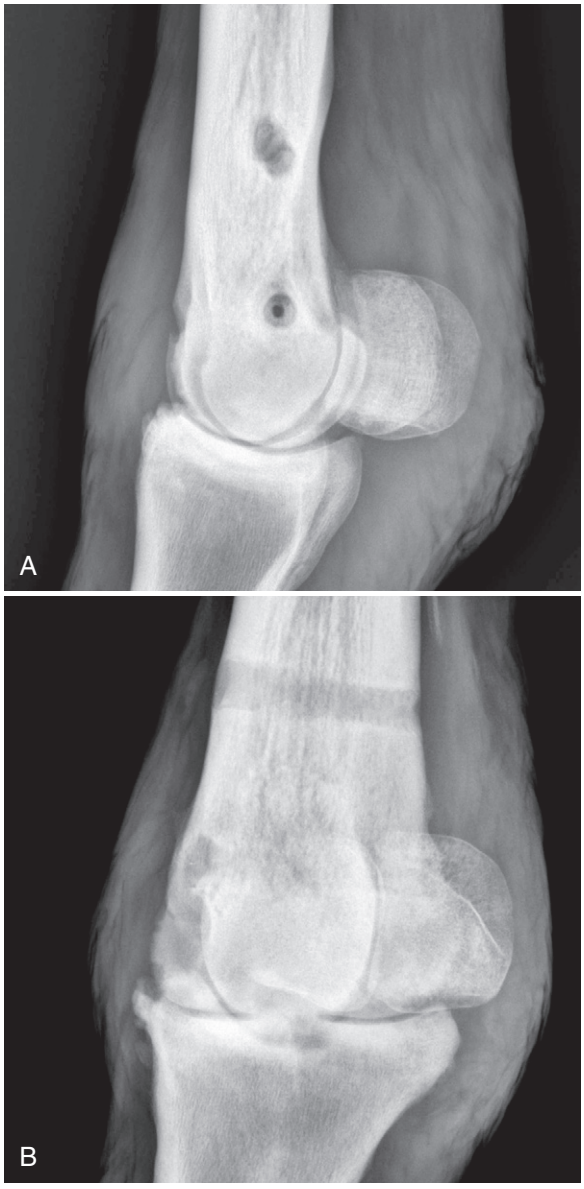


Fig. 22-25 Lateromedial **(A)** and dorsal 45-degree medial-palmarolateral radiographs **(B)** of the distal metacarpal III and the proximal phalanx of a horse recently having external support removed from the leg. Bone sclerosis is present around transverse pin tracts, but the remaining bone has advanced osteopenia. Generalized remodeling of bone has occurred, and the cortices are thin. Osseous trabeculae are coarse and irregular, with no organized pattern and linear radiolucent lines running the length of visible MC III. The sesamoid bones have a spongelike appearance. There is generalized soft tissue swelling and periarticular remodeling along the dorsal aspect of the MCP joint.

REFERENCES

1. Getty R: *Sisson and Grossman's the anatomy of the domestic animals*, ed 5, Philadelphia, 1975, Saunders, pp 357–360.
2. Weaver JC, Stover SM, O'Brien TR: Radiographic anatomy of soft tissue attachments in the equine metacarpophalangeal and proximal phalangeal region, *Equine Vet J* 24:310, 1992.
3. Rendano VT: Equine radiology: the fetlock, *Mod Vet Pract* 58:871, 1977.
4. Butler JA, Colles CM, Dyson SJ, et al: *Clinical radiology of the horse*, London, 1993, Blackwell, pp 83–99.
5. Allan GS: Radiography of the equine fetlock, *Equine Pract* 1:40, 1979.
6. Morgan JP: *Techniques of veterinary radiography*, ed 5, Ames, 1993, Iowa State University.
7. O'Brien T: *Radiography for the ambulatory equine practitioner*, Jackson, Wyo, 2005, Teton.
8. Hornof WJ, O'Brien TR: Radiographic evaluation of the palmar aspect of the equine metacarpal condyles: a new projection, *Vet Radiol* 21:161, 1980.
9. Palmer SE: Radiography of the abaxial surface of the proximal sesamoid bones of the horse, *J Am Vet Med Assoc* 181:264, 1982.
10. Denoix JM, Jacot S, Perrot P: Ultrasonographic anatomy of the dorsal and abaxial aspects of the equine fetlock, *Equine Vet J* 28:54, 1996.
11. Martinelli MJ, Baker GJ, Clarkson RB, et al: Magnetic resonance imaging of degenerative joint disease in a horse: a comparison to other diagnostic techniques, *Equine Vet J* 28:410, 1996.
12. Martinelli MJ, Kuriashkin IV, Carragher BO, et al: Magnetic resonance imaging of the equine metacarpophalangeal joint: three dimensional reconstruction and anatomic analysis, *Vet Radiol Ultrasound* 38:193, 1997.
13. Tucker RL, Sande RD: Magnetic resonance imaging and computed tomography: evaluation of equine musculoskeletal conditions, *Vet Clin North Am Equine Pract* 17:145, 2001.
14. Smith M, Dyson S: Normal anatomy: the fetlock region. In Murray R, editor: *Equine MRI*, West Sussex, UK, 2011, Wiley-Blackwell, pp 173–189.
15. Powell S: The fetlock region. In Murray R, editor: *Equine MRI*, West Sussex, UK, 2011, Wiley-Blackwell, pp 315–360.
16. Dyson S, Murray R: Magnetic resonance imaging of the equine fetlock. In Orsini J (ed), *Clinical techniques in equine practice*, Philadelphia, 2007, Elsevier-Saunders. pp 62–78.
17. Brama P, Tekoppele J, Bank R, et al: Topographical mapping of biochemical properties of articular cartilage in the equine fetlock joint, *Equine Vet J* 34:19–26, 2000.
18. Smith S, Dyson S, Murray R: Magnetic resonance imaging of distal sesamoidean ligament injury, *Vet Radiol Ultrasound* 49:516–528, 2008.
19. McKnight AL, Manduca A, Felmlee JP, et al: Motion correction techniques for standing equine MRI, *Vet Radiol Ultrasound* 45:513, 2004.
20. Pool RR, Meagher DM: Pathologic findings and pathogenesis of racetrack injuries, *Vet Clin North Am Equine Pract* 6:1, 1990.
21. Gillette EL, Thrall DE, Lebel JL: *Carlson's veterinary radiology*, ed 3, Philadelphia, 1977, Lea & Febiger, p 435.
22. Barclay WP, White KK, Williams A: Equine villonodular synovitis: a case survey, *Cornell Vet* 70:72, 1979.
23. Nickels FA, Grant BD, Lincoln SD: Villonodular synovitis of the equine metacarpophalangeal joint, *J Am Vet Med Assoc* 168:1043, 1976.
24. van Veenendaal JC, Moffat RE: Soft tissue masses in the fetlock joint of horses, *Aust Vet J* 56:533, 1980.
25. Petterson H, Reiland S: Periarticular subchondral "bone cysts" in horses, *Clin Orthop* 62:95, 1969.
26. Hornof WJ, O'Brien TR, Pool RR: Osteochondritis dissecans of the distal metacarpus in the adult racing thoroughbred horse, *Vet Radiol* 22:98, 1981.
27. Edwards GB: Interpreting radiographs. 2: The fetlock joint and pastern, *Equine Vet J* 16:4, 1984.
28. O'Brien TR, Hornof WJ, Meagher DM: Radiographic detection and characterization of palmar lesions in the equine fetlock joint, *J Am Vet Med Assoc* 178:231, 1981.

29. Foerner JJ, Barclay WP, Phillips TN, et al: Osteochondral fragments of the palmar/plantar aspect of the fetlock joint. In Milne FS: *Proceedings of the 33rd annual meeting of the American association of equine practitioners*, New Orleans, 1987, p 739.
30. Birkeland R: Chip fractures of the first phalanx in the metatarsal phalangeal joint of the horse, *Acta Radiol* 319(Suppl):73, 1972.
31. Petterson H, Ryden G: Avulsion fractures of the caudoproximal extremity of the first phalanx, *Equine Vet J* 14:333, 1982.
32. Sandgren B: Bony fragments in the tarsocrural and metacarpo- or metatarsophalangeal joints in the Standardbred horse: a radiographic survey, *Equine Vet J* 6(Suppl):66, 1988.
33. Carlsten J, Sandgren B, Dalin G: Development of osteochondrosis in the tarsocrural joint and osteochondral fragments in the fetlock joints of Standardbred trotters. I. A radiological survey, *Equine Vet J* 16(Suppl):42, 1993.
34. Grøndahl AM, Engeland A: Influence of radiographically detectable orthopedic changes on racing performance in Standardbred trotters, *J Am Vet Med Assoc* 206:1013, 1995.
35. Dalin G, Sandgren B, Carlsten J: Plantar osteochondral fragments in the fetlock joints of Standardbreds: result of osteochondrosis or trauma? *Equine Vet J* 16(Suppl):62, 1993.
36. Grøndahl AM, Dolvik NI: Heritability estimations of osteochondrosis in the tibiotarsal joint and of bony fragments in the palmar/plantar portion of the metacarpo- and metatarsophalangeal joints of horses, *J Am Vet Med Assoc* 203:101, 1993.
37. Philipsson J, Andréasson E, Sandgren B, et al: Osteochondrosis in the tarsocrural joint and osteochondral fragments in the fetlock joints in Standardbred trotters. II. Heritability, *Equine Vet J* 16(Suppl):38, 1993.
38. Sandgren B, Dalin G, Carlsten J, et al: Development of osteochondrosis in the tarsocrural joint and osteochondral fragments in the fetlock joints of Standardbred trotters. II. Body measurements and clinical findings, *Equine Vet J* 16(Suppl):48, 1993.
39. Grøndahl AM: The incidence of bony fragments and osteochondrosis in the metacarpo- and metatarsophalangeal joints of Standardbred trotters: a radiographic study, *Equine Vet Sci* 12:81, 1992.
40. Sandgren B, Dalin G, Carlsten J: Osteochondrosis in the tarsocrural joint and osteochondral fragments in the fetlock joints in Standardbred trotters. I. Epidemiology, *Equine Vet J* 16(Suppl):31, 1993.
41. Fortier LA, Foerner JJ, Nixon AJ: Arthroscopic removal of axial osteochondral fragments of the plantar/palmar proximal aspect of the proximal phalanx in horses: 119 cases (1988–1992), *J Am Vet Med Assoc* 206:71, 1995.
42. Copelan RW, Bramlage LR: Surgery of the fetlock joint, *Vet Clin North Am Large Anim Pract* 5:221, 1983.
43. Yovich JV, McIlwraith CW, Stashak TS: Osteochondritis dissecans of the sagittal ridge of the third metacarpal and metatarsal bones in horses, *J Am Vet Med Assoc* 186:1186, 1985.
44. Zekas LJ, Bramlage LR, Embertson RM, et al: Characterization of the type and location of fractures of the third metacarpal/metatarsal condyles in 135 horses in central Kentucky (1986–1994), *Equine Vet J* 31:304, 1999.
45. Rick MC, O'Brien TR, Pool RR, et al: Condylar fractures of the third metacarpal bone and third metatarsal bone in 75 horses: radiographic features, treatments, and outcome, *J Am Vet Med Assoc* 183:287, 1983.
46. Zekas LJ, Bramlage LR, Embertson RM, et al: Results of treatment of 145 fractures of the third metacarpal/metatarsal condyles in 135 horses (1986–1994), *Equine Vet J* 31:309,1999.
47. Holcombe SJ, Schneider RK, Bramlage LR, et al: Lag screw fixation of noncomminuted sagittal fractures of the proximal phalanx in racehorses: 59 cases (1973–1991), *J Am Vet Med Assoc* 206:1195, 1995.
48. Yovich JV, McIlwraith CW: Arthroscopic surgery for osteochondral fractures of the proximal phalanx of the metacarpophalangeal and metatarsophalangeal (fetlock) joints in horses, *J Am Vet Med Assoc* 188:273, 1986.
49. Nixon AJ, Pool RR: Histologic appearance of axial osteochondral fragments from the proximoplantar/proximopalmar aspect of the proximal phalanx in horses, *J Am Vet Med Assoc* 207:1076, 1995.
50. Barclay WP, Foerner JJ, Phillips TN: Lameness attributable to osteochondral fragmentation of the plantar aspect of the proximal phalanx in horses: 19 cases (1981–1985), *J Am Vet Med Assoc* 191:855, 1987.
51. Grøndhal AM: Incidence and development of ununited proximoplantar tuberosity of the proximal phalanx in Standardbred trotters, *Vet Radiol Ultrasound* 33:18, 1992.
52. Spurlock GH, Gabel AA: Apical fractures of the proximal sesamoid bones in 109 Standardbred horses, *J Am Vet Med Assoc* 183:76, 1983.
53. Parente EJ, Richardson DW, Spencer P: Basal sesamoidean fractures in horses: 57 cases (1980–1991), *J Am Vet Med Assoc* 202:1293, 1993.
54. Blevins WE, Widmer WR: Radiology in racetrack practice, *Vet Clin North Am Equine Pract* 6:31, 1990.

ELECTRONIC RESOURCES

Evolve

Additional information related to the content in Chapter 22 can be found on the companion Evolve website at http://evolve.elsevier.com/Thrall/vetrad/

- Chapter Quiz

CHAPTER • 23

The Equine Phalanges

Elizabeth A. Riedesel

TECHNICAL FACTORS

Patient Preparation

The significance of many radiographic abnormalities of the equine phalanges is difficult to ascertain unless pertinent facts obtained from the history and physical examination, including results of diagnostic nerve blocks, are correlated with the radiographic findings. Dirt, skin lesions, and iodine-containing medications can all produce opacities that complicate radiographic interpretation. All such material should be removed from the hair coat and hoof wall. Shoes and any additional pads should be removed so that optimal radiographs of the distal phalanx can be obtained. The sole and sulci of the frog should be cleaned thoroughly. The sulci may then be filled uniformly with a material of soft tissue opacity (such as Play-Doh, Hasbro, Pawtucket, RI) to the level of the solar surface (Fig. 23-1). Packing the central and collateral sulci eliminates radiolucent linear regions created when the

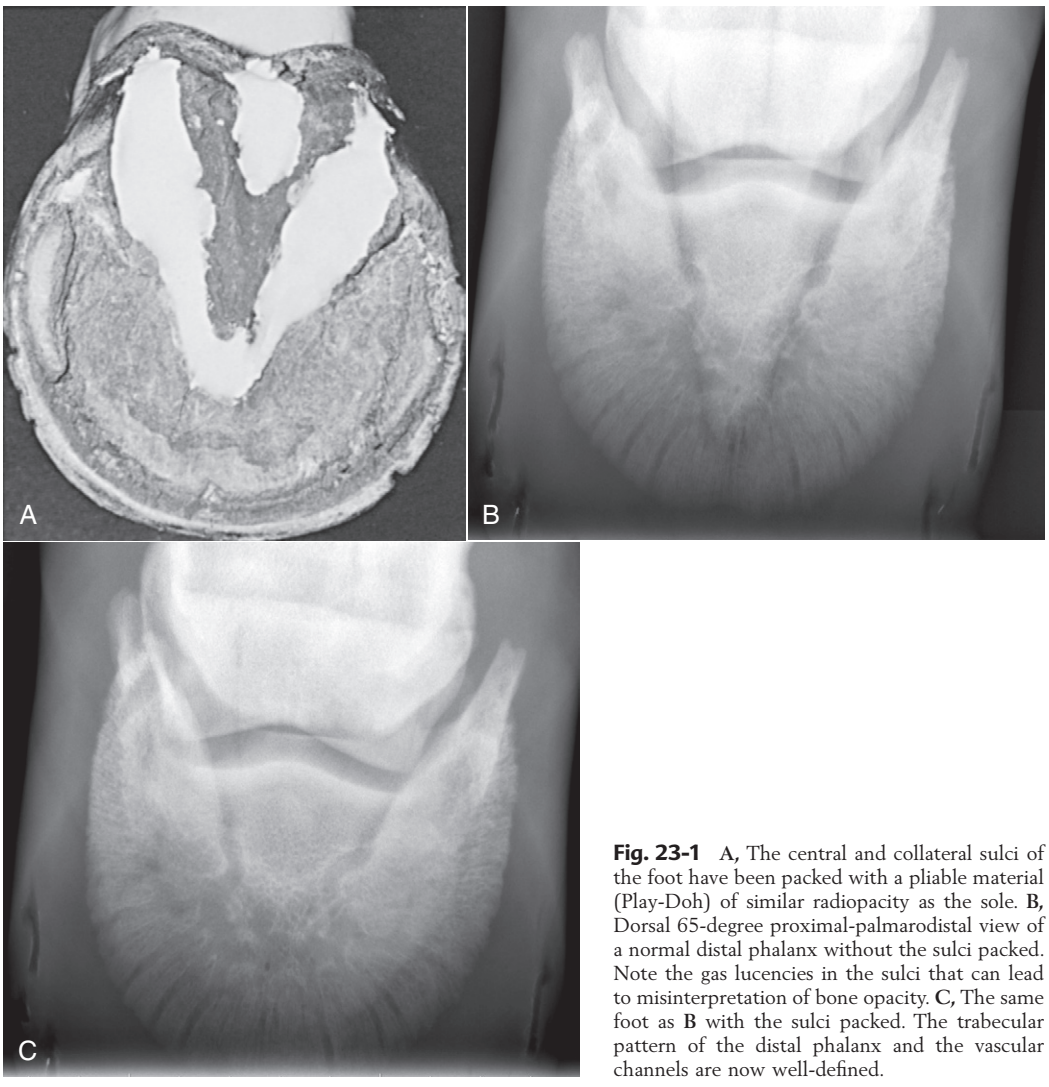


Fig. 23-1 **A,** The central and collateral sulci of the foot have been packed with a pliable material (Play-Doh) of similar radiopacity as the sole. **B,** Dorsal 65-degree proximal-palmarodistal view of a normal distal phalanx without the sulci packed. Note the gas lucencies in the sulci that can lead to misinterpretation of bone opacity. **C,** The same foot as **B** with the sulci packed. The trabecular pattern of the distal phalanx and the vascular channels are now well-defined.

Table • **23-1**

Views for Equine Phalanx Evaluation

EXAMINATION	STRUCTURES EVALUATED	VIEWS
Pastern	Proximal phalanx	Dorsal 45-degree proximal-palmarodistal
	Proximal interphalangeal joint	Lateromedial
	Middle phalanx	Dorsal 35-degree lateral-palmaromedial
		Dorsal 35-degree medial-palmarolateral
Digit	Distal phalanx	Dorsopalmar with horizontal beam (0-degree) and dorsal 45-degree proximal-palmarodistal
	Distal interphalangeal joint	Dorsal 65-degree proximal-palmarodistal with horse standing on cassette
		Lateromedial, with foot on block to include solar margin of distal phalanx and soft tissues of sole on the radiograph
		Two oblique views: dorsal 65-degree proximal, 45-degree lateral-palmarodistomedial and dorsal 65-degree proximal, 45-degree medial-palmarodistolateral (both with horse standing on cassette); are especially useful when distal phalanx fracture is suspected

air-filled sulci are superimposed on the distal phalanx in the dorsal 65-degree proximal-palmarodistal* view (see Fig. 23-1).

Recommended Views

The equine foot is structured such that certain anatomic areas can be imaged as a group (Table 23-1). Excellent descriptions of positioning are available for additional information.[1,2]

NORMAL RADIOGRAPHIC ANATOMY (INCLUDING VARIATIONS)

Osseous Structures

Normal radiographic anatomy of the digit is illustrated in Chapter 13 and other published sources.[3-5] However, several anatomic variations that are misinterpreted frequently as abnormal are worthy of mention.[6] A nutrient foramen occurs in the proximal phalanx of approximately 87% of Thoroughbreds and Standardbreds that are at least 1 year of age.[7,8] When present, these foramina are sometimes symmetric bilaterally and can be located in either the palmar or dorsal cortex. No horses were identified in those surveys to have both a dorsal and a palmar nutrient foramen, although both were present occasionally in foals. When in the dorsal cortex, the foramen is typically seen in a lateromedial view as a radiolucent line running obliquely proximal to distal through the mid-diaphyseal cortex (Fig. 23-2). In a dorsopalmar view, the nutrient foramen appears as a thin lucent line within the medullary region. When in the palmar cortex, the foramen is located in the distal third and courses in a shorter oblique-to-transverse direction. Of greatest importance is that these foramina should not be mistaken for fractures. Variability in the location of the nutrient foramen of the hindlimb proximal phalanx has not been reported. Variations have not been reported in other breeds, but they likely occur.

Variations may also occur in the appearance of trabeculae in the medullary cavity of the proximal phalanx. A conspicuous radiolucent center in the medullary cavity surrounded by a ringlike radiopacity is a normal variation and does not indicate cyst formation (Fig. 23-3).

If the lateromedial view is slightly oblique, two normal structures become more conspicuous and can be misinterpreted as abnormal. The first is the ridge for the V-shaped attachment of the oblique sesamoidean ligament along the palmar cortex of the proximal phalanx. The second is the eminence for attachment of the collateral ligaments of the distal interphalangeal joint along the dorsal aspect of the middle phalanx.

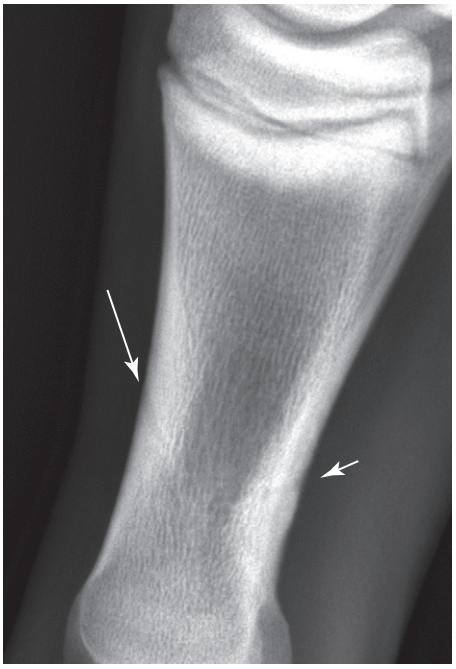


Fig. 23-2 Radiolucent lines are visible in the dorsal *(long white arrow)* and palmar (*short white arrow)* diaphyseal cortices of the proximal phalanx of this 2-month-old Paint foal. These are normal nutrient foramina and were bilaterally symmetric in the forelimbs of this foal.

The radiographic appearance of the normal distal phalanx in the dorsal 65-degree proximal-palmarodistal view varies in several respects.[2,9,10] The most obvious is the number and distribution of vascular channels (Fig. 23-4). The number of vascular channels is typically greater in the rear distal phalanx than in the front distal phalanx (ranges of 9 to 19 and 5 to 16, respectively).[9] All vascular channels radiate from the solar canal to the solar border. On their path to the periphery, some give rise to secondary branches that reach the solar

*Palmar(o) is used throughout this chapter with the understanding that plantar(o) should be substituted if reference is being made to the rear digit.

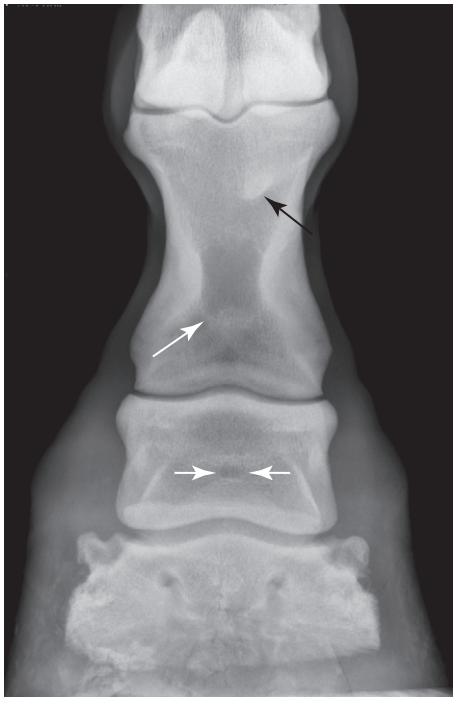


Fig. 23-3 Dorsopalmar view of normal phalanges. Note the normal thickness of the lateral and medial cortices of the proximal phalanx at the junction of the middle and distal third of the bone. The radiolucent medullary cavity is seen between the thickest parts of the cortex. A thin opaque rim *(long white arrow)* can surround the central medullary cavity, being more accentuated than in this horse. A small medullary cavity may also be visible in the middle phalanx *(between two short white arrows)*. The ergot *(black arrow)* creates a summation opacity with the proximal aspect of the proximal phalanx; the length and angle of the summation opacity vary between horses. The typical normal joint space width is shown, with the widest being the distal interphalangeal joint and the narrowest the metacarpophalangeal joint.

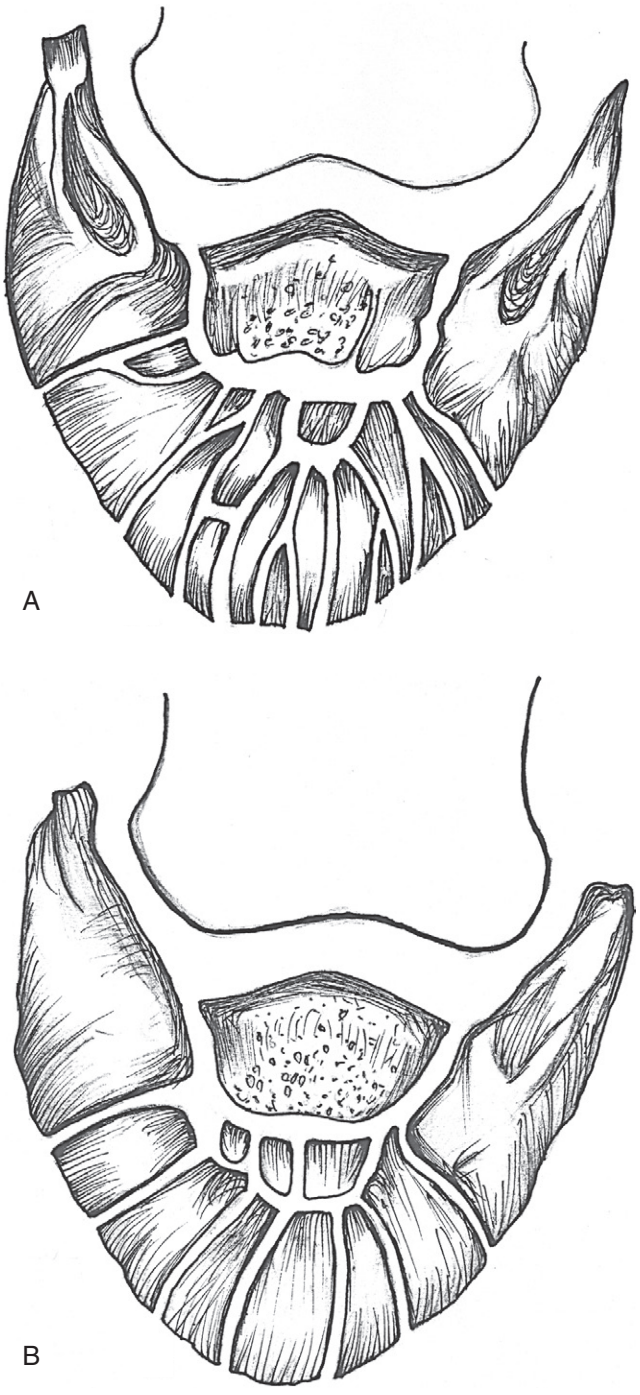


Fig. 23-4 A and B, Two variations in the normal pattern of vascular channel formation in the distal phalanx.

border. Although this branching pattern is unique to individual animals, the major channels identified at the solar margin should communicate with the solar canal.

A smoothly rounded concavity in the toe of the distal phalanx may be present in the normal horse (Fig. 23-5). This notch is referred to as the *crena margins solaris* or, more commonly, the *crena* or toe notch. In a radiographic study of the foredigit of the developing quarter horse, a crena was identified in foals between 4 and 22 weeks of age in 83% of the distal phalanges evaluated.[11] The depth of this notch usually does not exceed 1.5 cm.[2] The crena is more conspicuous in front than in hind feet.[10] Ninety percent of sound racing Thoroughbreds have bilateral symmetry in the presence of the crena in the front feet, 5% asymmetry in the front feet, and 5% in neither front foot.[10]

The shape of the extensor process of the distal phalanx may also differ among individual animals (Fig. 23-6).[9] The margin of the normal process, however, should be smooth regardless of its shape.

The palmar processes of the distal phalanx become ossified more extensively with age (Fig. 23-7). The morphologic development of the palmar process has been described in the foal (3 to 32 weeks of age).[12]

Soft Tissue

No muscle exists in the phalangeal region of the foot. Many tendons and supporting ligaments, however, are present in addition to joint capsules. Minimal amounts of fat are present in the phalangeal region. Knowledge of the attachment sites of the joint capsules, tendons, and ligaments of the foot is imperative for accurate interpretation of the osseous changes seen in radiographs. Figures 23-8 and 23-9 illustrate the attachment sites of these major structures. A clinical anatomic atlas presents these soft tissue bone relationships through side-by-side comparisons of anatomic sections, prepared in the scan planes of magnetic resonance (MR) imaging, with radiographs, ultrasound, and MR images.[5] Most of these soft tissues do not create independently distinct shadows. However, the deep digital flexor tendon can often be seen in the lateromedial view as a slightly more opaque soft tissue band as it passes between the level of the proximal aspect of the middle phalanx and the proximal margin of the navicular bone.[9] This is more evident in digital than in analog radiographs

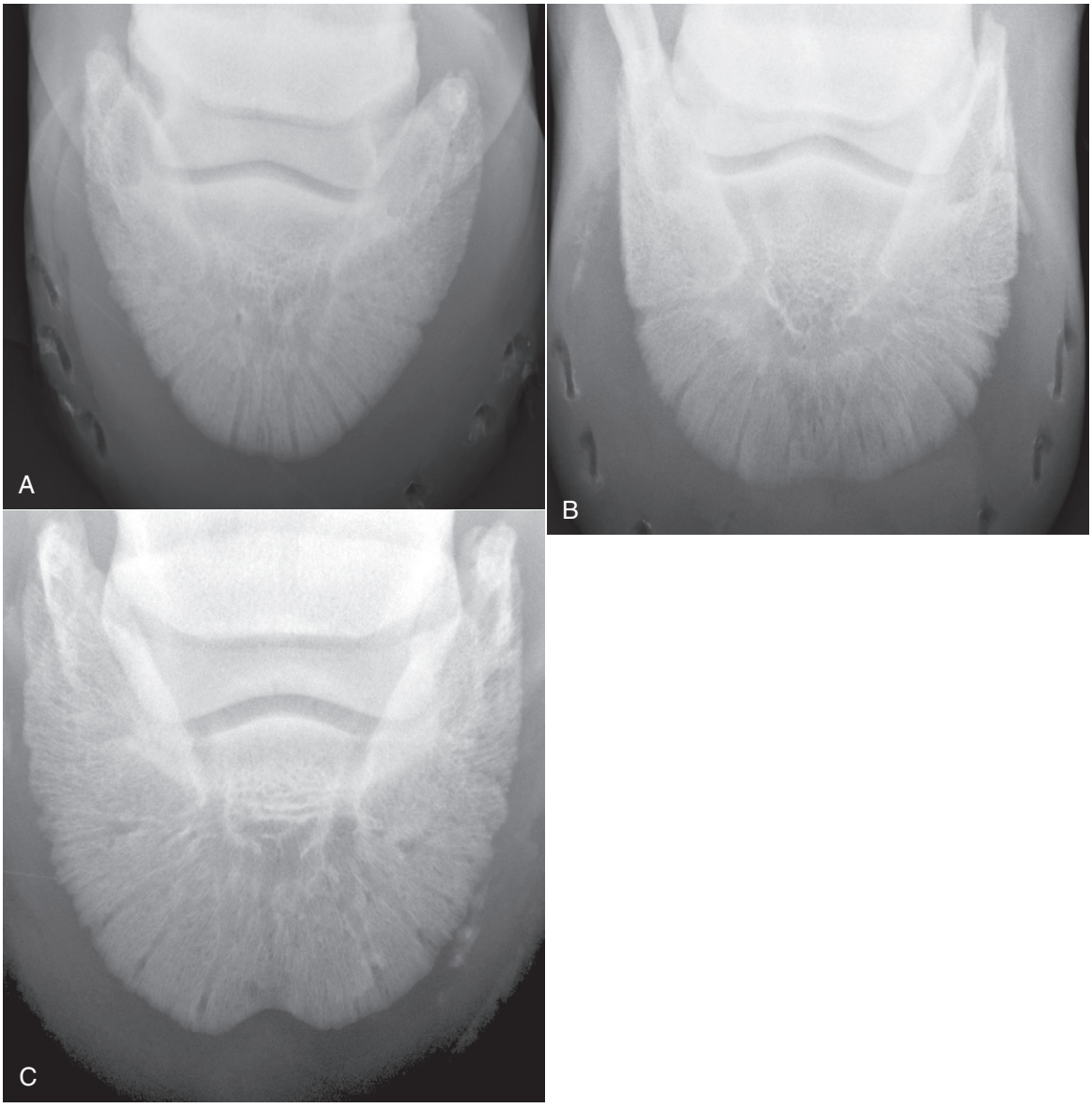


Fig. 23-5 Three horses with variation in the solar margin contour of the toe of the distal phalanx. **A,** A hind foot with a smooth convex contour; **B,** a front foot with a shallow concavity; and **C,** a front foot with a deeper concavity. The concavities in **B** and **C** are examples of the crena. These should not be misinterpreted as regions of lysis. However, current and resolved lesions can cause this same appearance and must be correlated with confirmatory evidence of foot disease. Note also the variation in the pattern of vascular channels.

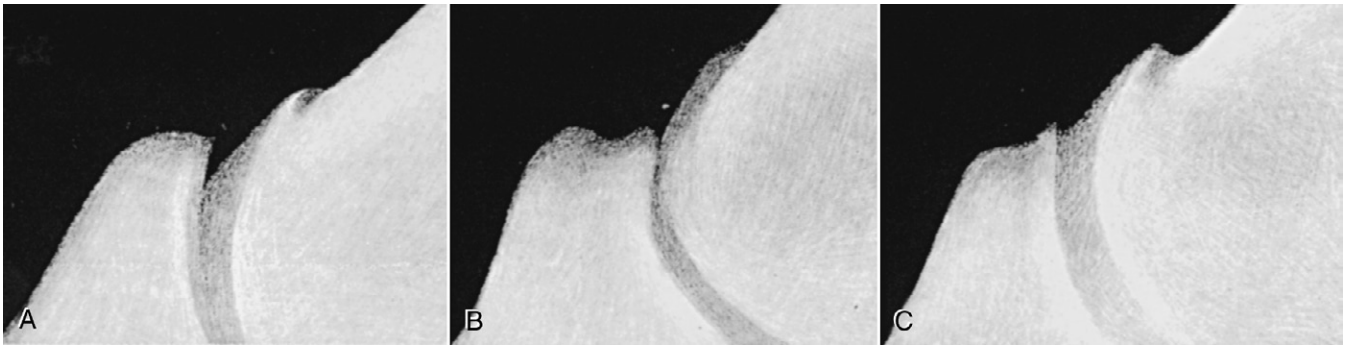


Fig. 23-6 **A** to **C,** Normal variations in the shape of the extensor process of the distal phalanx, as might be seen on the lateromedial view. (Illustration by Richard M. Shook, DVM.)

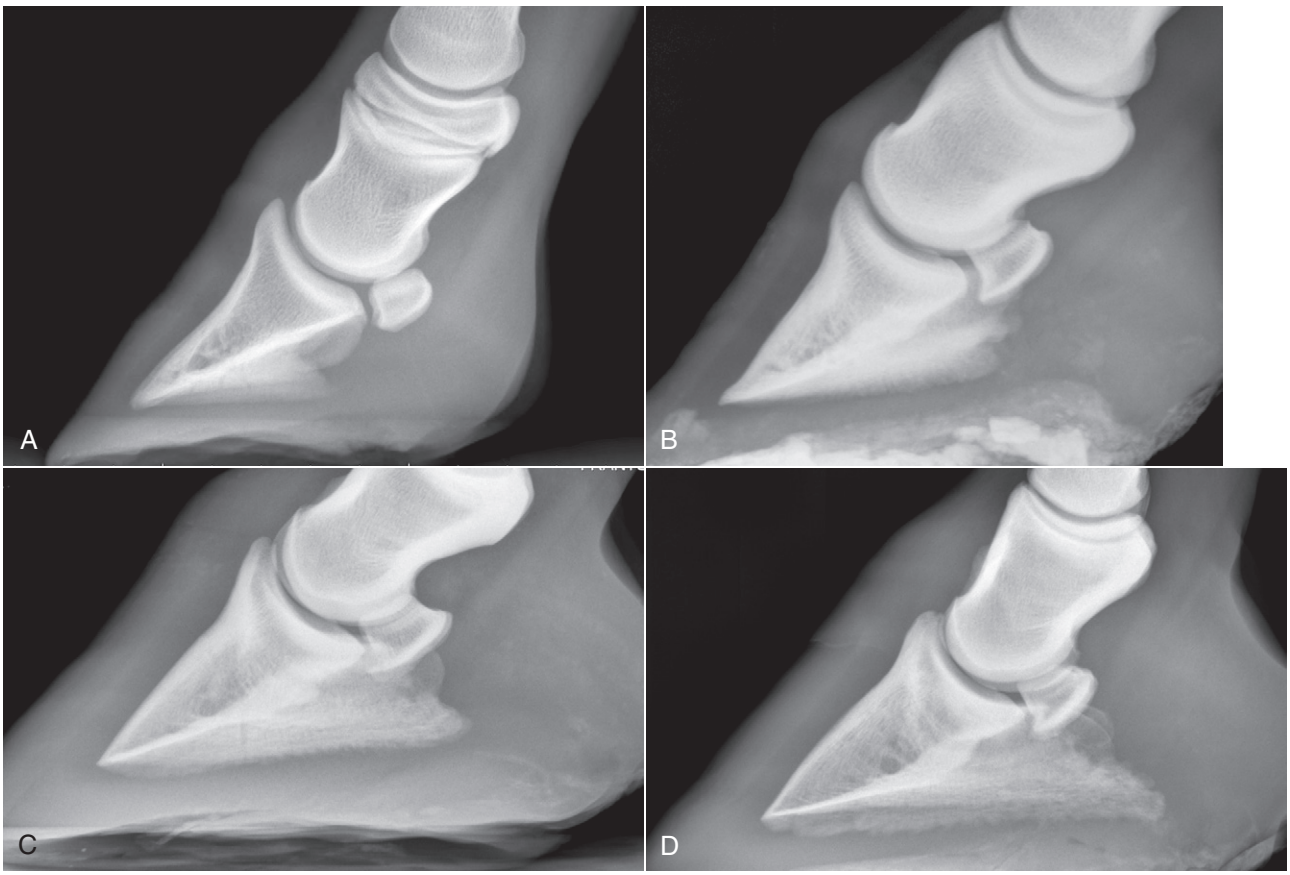


Fig. 23-7 Palmar processes of the normal distal phalanx in the horse become ossified more extensively with age. Lateromedial views of **(A)** a 3-month-old Saddlebred foal; **(B)** a 1-year-old quarter horse; and **(C)** a 6-year-old Paint; and **(D)** a 16-year-old quarter horse. In all four images the mildly more opaque soft tissue band of the deep digital flexor tendon can be seen along the palmar aspect. The distinctly less opaque corium of the hoof capsule is also visible along the dorsal border of the distal phalanx, extending around the toe and for a variable length along the solar border.

(see Fig. 23-7). The hoof capsule produces soft tissue opacity. However, the junction between the outer denser portion (stratum medium) and the inner highly vascularized portion (the stratum internum plus the corium) is well defined in digital radiographs and also visible in optimally exposed analog radiographs.[10] The inner portion is less radiopaque (see Fig. 23-7). The junction of the coronary band and the most proximal extent of the hoof wall is not always clearly distinct in lateromedial and dorsopalmar views. The ergot may create a radiopacity when superimposed on the proximal phalanx in the dorsopalmar view (see Fig. 23-3). In the lateromedial view, the ergot can be seen along the palmar surface of the skin.

Articular Cartilage and Collateral Cartilages

The properly positioned dorsal 45-degree proximal-palmarodistal view is the best for evaluation of the width of the metacarpophalangeal, proximal interphalangeal, and distal interphalangeal joints. In the normal foot, the metacarpophalangeal joint is usually the narrowest of these articulations, the proximal interphalangeal joint is slightly wider, and the distal interphalangeal joint is the widest (see Fig. 23-3). If the horse is not bearing weight evenly on the leg, the asymmetric loading forces can cause the appearance of narrowing of the loaded side and widening of the nonloaded side of the joint. This artifact can be recognized because it affects all three joints similarly. The collateral cartilages are not visible in the normal foot, and ossification of these cartilages is usually not significant clinically.

Alternate Imaging of the Foot

Ultrasound, nuclear scintigraphy, MR imaging, and computed tomography (CT) are used to enhance the anatomic and physiologic assessment of foot lameness. Standing open and conventional open and closed magnets are being used with increasing frequency to assess the soft tissues and bone of the foot. Although the contributions of these modalities cannot be discussed in detail in this chapter, specific notation will be made regarding important alternate imaging findings where applicable.

RADIOGRAPHIC CHANGES CAUSED BY DISEASES OF THE PHALANGES

General Comments

Common diseases affecting the digit are acute trauma leading to fracture; chronic repetitive trauma leading to desmitis, tendonitis, enthesopathy, and degenerative joint disease; and infection. Inflammation of the laminae of the hoof wall, laminitis, leading to a disturbance of the mechanical support of the foot, is the only common effect initiated by metabolic disease. Neoplasia of the digit is extremely rare.

Because the digit has little soft tissue, x-ray exposure technique for analog radiography is typically selected to best define the bony structures. Supplemental views altering the exposure to demonstrate the soft tissue may be needed. The postcapture image manipulation offered by digital

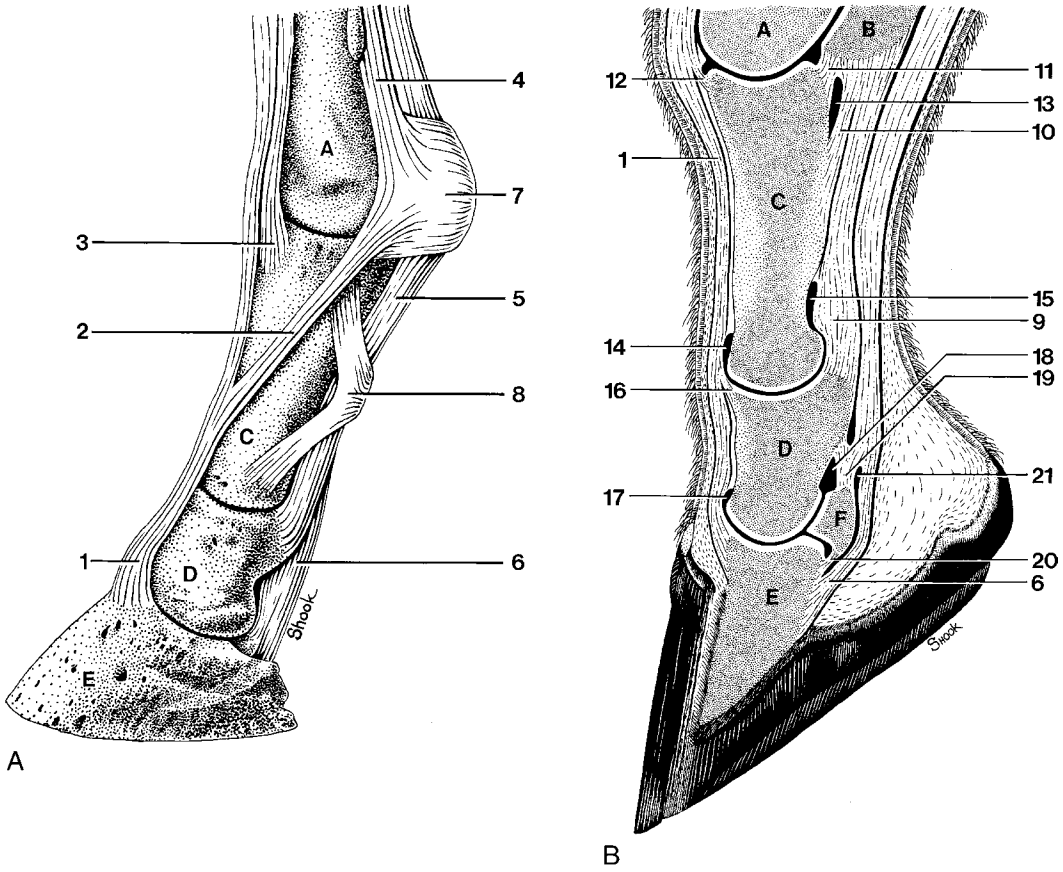


Fig. 23-8 Lateral views of the tendon and ligament attachments of the digit. **A,** Superficial tissues; **B,** Sagittal section.
(Illustration by Richard A. Shook, DVM.)
The following anatomic key is for Figures 23-8 and 23-9.

A. Third metacarpal bone
B. Proximal sesamoid bone
C. Proximal phalanx
D. Middle phalanx
E. Distal phalanx
F. Distal sesamoid (navicular) bone

1. Common digital extensor tendon
2. Extensor branch of the interosseous (suspensory) ligament
3. Lateral digital extensor tendon
4. Interosseous (suspensory) ligament
5. Superficial digital flexor tendon
6. Deep digital flexor tendon
7. Superficial transverse metacarpal ligament (palmar annular ligament)
8. Proximal digital annular ligament
9. Superficial (straight) sesamoidean ligament
10. Middle (oblique) sesamoidean ligament
11. Deep (cruciate) sesamoidean ligament
12. Metacarpophalangeal joint capsule (blended with fibers from the common digital extensor tendon)
13. Distal palmar recess of the metacarpophalangeal joint
14. Dorsal recess of the proximal interphalangeal joint capsule
15. Palmar recess of the proximal interphalangeal joint
16. Proximal interphalangeal joint capsule (blended with fibers from the common digital extensor tendon)
17. Dorsal recess of the distal interphalangeal joint
18. Palmar recess of the distal interphalangeal joint
19. Collateral sesamoidean ligament
20. Distal sesamoidean impar ligament
21. Podotrochlear bursa
22. Medial collateral ligament of the metacarpophalangeal joint
23. Lateral collateral ligament of the proximal interphalangeal joint
24. Medial collateral ligament of the distal interphalangeal joint

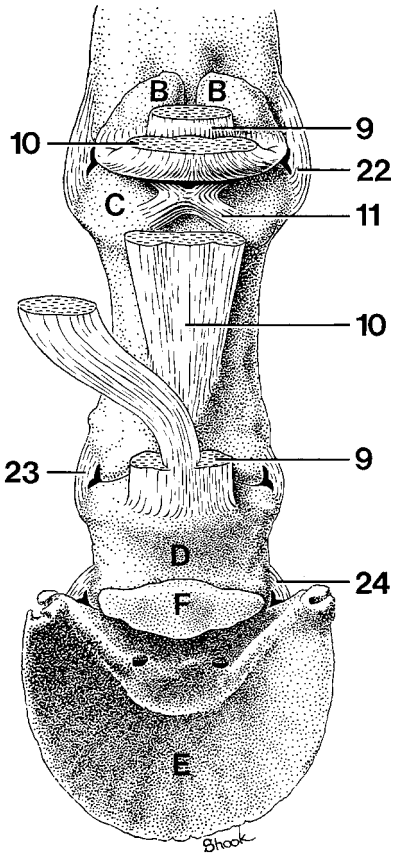


Fig. 23-9 Palmar view of the sesamoidean and collateral ligament attachments of the digit. (See Anatomic Key in legend for Fig. 23-8.) (Illustration by Richard A. Shook, DVM.)

radiography allows evaluation of osseous and soft tissue structures with one exposure per view (Fig. 23-10).

The radiographic signs of abnormal soft tissue include alteration of thickness, contour, or opacity. Increased pericapsular soft tissue thickness may be seen with intracapsular fluid accumulation, synovial tissue thickening, extracapsular inflammation (cellulitis), or fibrosis. If radiographic signs of soft tissue enlargement are confined strictly to the region of the joint, intracapsular fluid accumulation with or without synovial tissue thickening is the likely cause. If the enlargement extends proximally and distally beyond the sites of joint capsule attachment, an extracapsular process (fluid and cellular) is likely present, which obscures evaluation of intracapsular changes. Isolated enlargement, away from the joint, is most likely related to direct local trauma with or without infection. An irregular surface contour suggests acute laceration or chronic granulation tissue. Large areas of periosteal new bone may persist for a long time after resolution of the inciting cause. The soft tissue will bulge over such an area of periosteal new bone but may not be actually thickened.

Increased opacity within pericapsular soft tissue is usually caused by dystrophic mineralization. Lesions that commonly become mineralized include chronic sprain or strain of supporting ligaments and tendons (Fig. 23-11), pericapsular deposition of corticosteroids, and focal necrosis attributable to neurectomy. Ossification of the collateral cartilages of the distal phalanx should not be mistaken for dystrophic mineralization of soft tissue.

Decreased opacity within the soft tissues is caused by air or gas in the subcutis or the fascial planes of the tendons and ligaments and subsolar tissue. Soft tissue gas pockets commonly follow diagnostic nerve block and open skin wounds but rarely are caused by a gas-producing organism.



Fig. 23-10 Lateral view of horse that had a penetrating solar nail injury 2 months prior. There is soft tissue swelling in the plantar pastern region. The opaque band of the deep digital flexor tendon is no longer visible (compare with Fig. 23-7). This is suggestive of cellulitis and/or severe tenosynovitis. There is a coarse trabecular bone pattern in the distal aspect of the proximal phalanx and the proximal aspect of the middle phalanx secondary to disuse osteopenia from the chronic lameness.



Fig. 23-11 Soft tissue mineralization is evident in the superficial digital flexor tendon and straight sesamoidean ligament. There is mild smooth enthesopathy at the insertion of the oblique sesamoidean ligament on the mid-aspect of the proximal phalanx *(arrow)*. This horse also has a mild distal interphalangeal flexural deformity.

The radiographic signs of abnormal bone include alteration of contour, margination, and opacity. These signs are caused by a combination of new bone formation and bone removal. Repeated patterns of bone change tend to be associated with specific injury to the phalanges and associated joints.

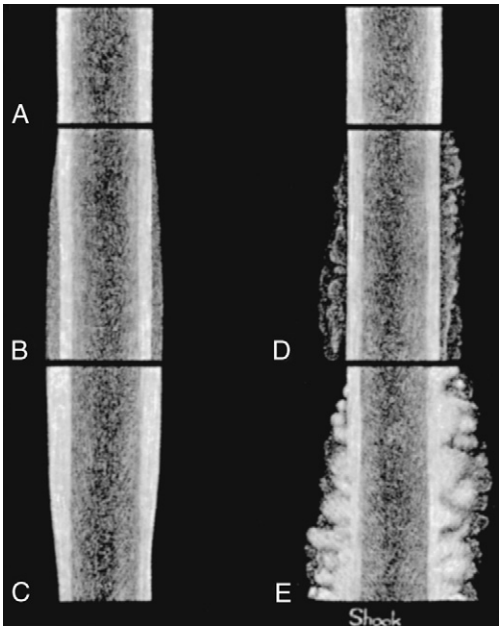


Fig. 23-12 Variable appearance of contour and opacity of periosteal bone proliferation and likely causes. *A*, Normal cortex. *B*, Smooth margin, mildly opaque; recent subperiosteal hemorrhage from direct trauma or exudate of infection. *C*, Smooth margin, opaque; inactive, remodeled trauma. *D*, Irregular margin, mildly opaque; recent or active response to direct traumatic injury including sprain/strain or infective periostitis. *E*, Irregular margin, opaque; chronic sprain/strain or infection. Note the loss of distinction between periosteal new bone and original cortex in C and *E*. (Illustration by Richard A. Shook, DVM.)

Figures 23-12 and 23-13 depict the variable appearances of the periosteal surface, joint space, and subchondral bone that occur in the more common diseases of the phalanges.

Strain and Sprain Injuries

Regions of new bone formation are commonly seen on the cortical surfaces of the phalanges, especially in the proximal and middle phalanx. Many of these are caused by strain and sprain injuries. Strain injury (tendonitis) results from damage to muscle or tendon induced by overuse or overstress. In its mildest form, strain causes only inflammation. With chronic repeated strain or more severe acute strain, disruption within the soft tissue unit or avulsion from its bone attachment occurs. Radiographically, the swelling or inflammation in the tendon may not be evident. Soft tissue changes are best imaged by ultrasound, vascular and soft tissue pool phase scintigraphy, and MR imaging. The latter has become the imaging modality of choice when lameness is persistent and the other modalities have negative or equivocal findings (Fig. 23-14).[13,14] Although uncommon, dystrophic mineralization can develop in a chronically inflamed tendon (see Fig. 23-11).

Radiography is useful for assessing the bony attachment sites of the tendons. Knowledge of the attachment sites of the flexor and extensor tendons on the phalanges is therefore needed (see Figs. 23-8 and 23-9). Avulsion fracture at the attachment site can occur and will be evident as a bone fragment displaced in the direction of traction of the tendon. Enthesophyte formation indicates a response to stress at the ligament or tendon attachment site. When seen early, it will likely be minimal in volume and have a mildly irregular surface. If the strain injury continues, the enthesopathy enlarges and continues to have a fuzzy, irregular margin. Such a change is seen occasionally at the insertion of the lateral digital extensor tendon on the dorsolateral proximal surface of the proximal phalanx. With further progression, the enthesopathy takes on a smooth, hooklike, or spurlike shape, projecting in the direction of tension or traction. Radiographically aging or determining the activity of these bone changes is difficult. Periosteal new bone formation is typically not visible until 5 to 7 days (in the foal) or 10 to 14 days (in the adult) after stimulation. When a prominent smooth enthesophyte is seen on a first radiographic evaluation of a horse, it should be taken as a signal of strain injury that occurred at least 5 to 6 weeks previously.

Sprain injury (desmitis) results from damage to the supporting ligaments of joints induced by movement of the bony components beyond their normal range. Similar to strain injury, the mild sprain injury causes inflammation that is not likely to cause visible changes radiographically. Greater degrees of injury result in loss of stability to the joint, allowing complete or partial luxation.

Stress views may be needed to detect subluxation. Laxity in a subluxated joint is often more apparent at physical examination than at radiography, especially if the horse is unwilling to bear full weight on the leg. Conversely, complete luxation is typically evident and may be accompanied by avulsion fractures at the ligament insertion sites. Non–weight-bearing flexed dorsal 45-degree lateral-palmaromedial and flexed dorsal 45-degree medial-palmarolateral views may improve the visualization of the origin and insertion sites for the collateral ligaments of the distal interphalangeal joint.[2] Larger fractures of the phalanges may also be associated with joint luxation. This is commonly seen with comminuted fractures of the middle phalanx and associated loss of congruency of the proximal interphalangeal joint (Fig. 23-15). Secondary changes expected with subluxation are enthesophyte formation at the ligament insertion sites and some degree of degenerative joint disease. The range of change will depend on the severity of the initial injury and the frequency of recurring subluxation. Although not the result of overt joint instability, a common site of enthesophyte formation associated with ligament insertion is on the palmar or plantar margin of the proximal phalanx at the insertion of the middle (oblique) sesamoidean ligament (see Fig. 23-11). Most enthesophytes do not regress after healing of the soft tissues involved in the inciting sprain or strain injury.

Collateral ligament desmitis of the distal interphalangeal joint is a significant cause of foot lameness in the absence of radiographic changes. MR imaging is the most useful imaging modality to define the changes in these ligaments (Fig. 23-16).[15,16] Most of the lesions are associated with the insertion of the ligament on the distal phalanx, and the medial collateral ligament is affected more often than the lateral ligament. The most frequent type of bone lesion is new bone formation and endosteal irregularity at the middle phalanx origin or distal phalanx insertion. Osseous cystlike lesions are found occasionally at either site. Similarly, evaluation of the straight and oblique sesamoidean ligaments by MR imaging allows identification of lesions not detected by radiography or ultrasound.[17]

FRACTURE DISEASE

Proximal Phalanx

The location of fractures of the proximal phalanx depends on the type of stress applied. The common fracture types are osteochondral edge (chip) fractures at the proximal dorsal periarticular margin and the palmar or plantar proximal tuberosity and longitudinal fractures of the diaphysis.[18,19] The most common fracture involving the proximal phalanx is the osteochondral fracture of the proximal dorsal edge, either at the medial or at the lateral eminence. This occurs as an overextension injury of the metacarpophalangeal joint in racehorses.



Fig. 23-13 Changes in joint space width, subchondral bone opacity, or both, as seen in the dorsopalmar view of the proximal interphalangeal joint, and likely causes. **A,** Normal joint space and subchondral bone. **B,** Widened joint space on the lateral or medial side, no subchondral bone changes. Artifact is caused by asymmetric weight distribution on the foot or unbalanced hoof trimming. **C,** Widened joint space, no subchondral bone changes; not weight bearing at time of radiography or increased intraarticular fluid volume. **D,** Uniformly narrowed joint space, no subchondral bone changes. Artifact caused by x-ray beam angulation or uniform degenerative wearing and loss of articular cartilage. **E,** Widened joint space, lysis of the subchondral bone; active septic arthritis. **F,** Narrowed joint space, irregular opacity, and contour of subchondral bone; chronic low-grade septic arthritis or chronic osteoarthritis caused by trauma-related instability or poor conformation. (Illustration by Richard A. Shook, DVM.)

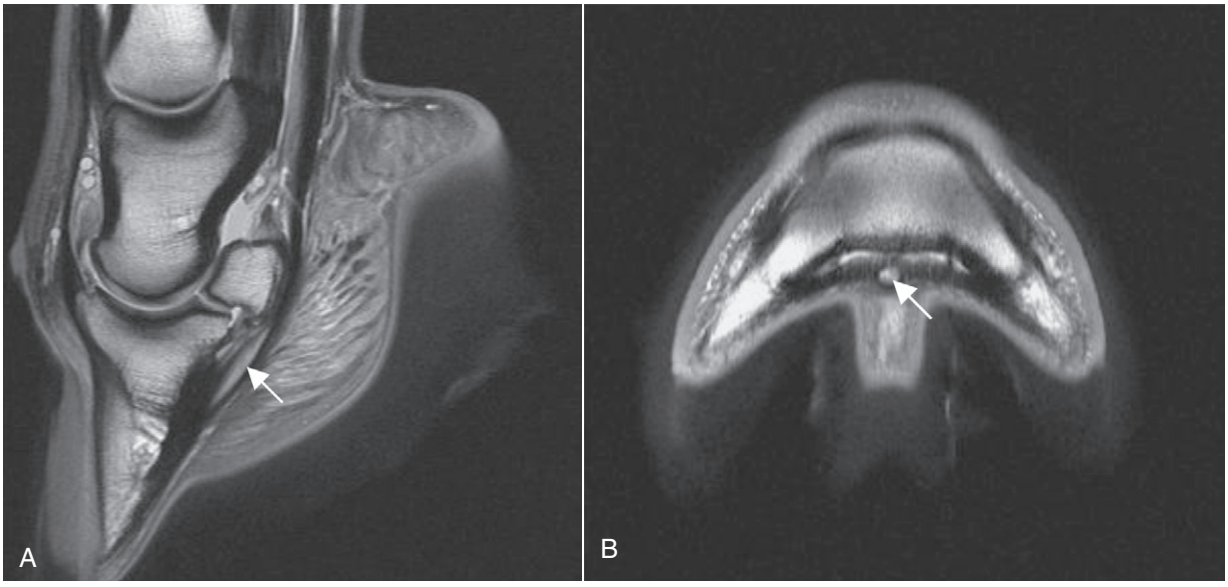


Fig. 23-14 Sagittal **(A)** and transverse **(B)** proton density-weighted MR images of an equine digit. A large hyperintense core lesion is present in the deep digital flexor tendon *(white arrows)*. This lesion would not be visible on radiographs, CT, or nuclear medicine images. The lesion might be visible by ultrasound, but examining this region of the digit with ultrasound is difficult because of the poor acoustic characteristics of the overlying tissues.

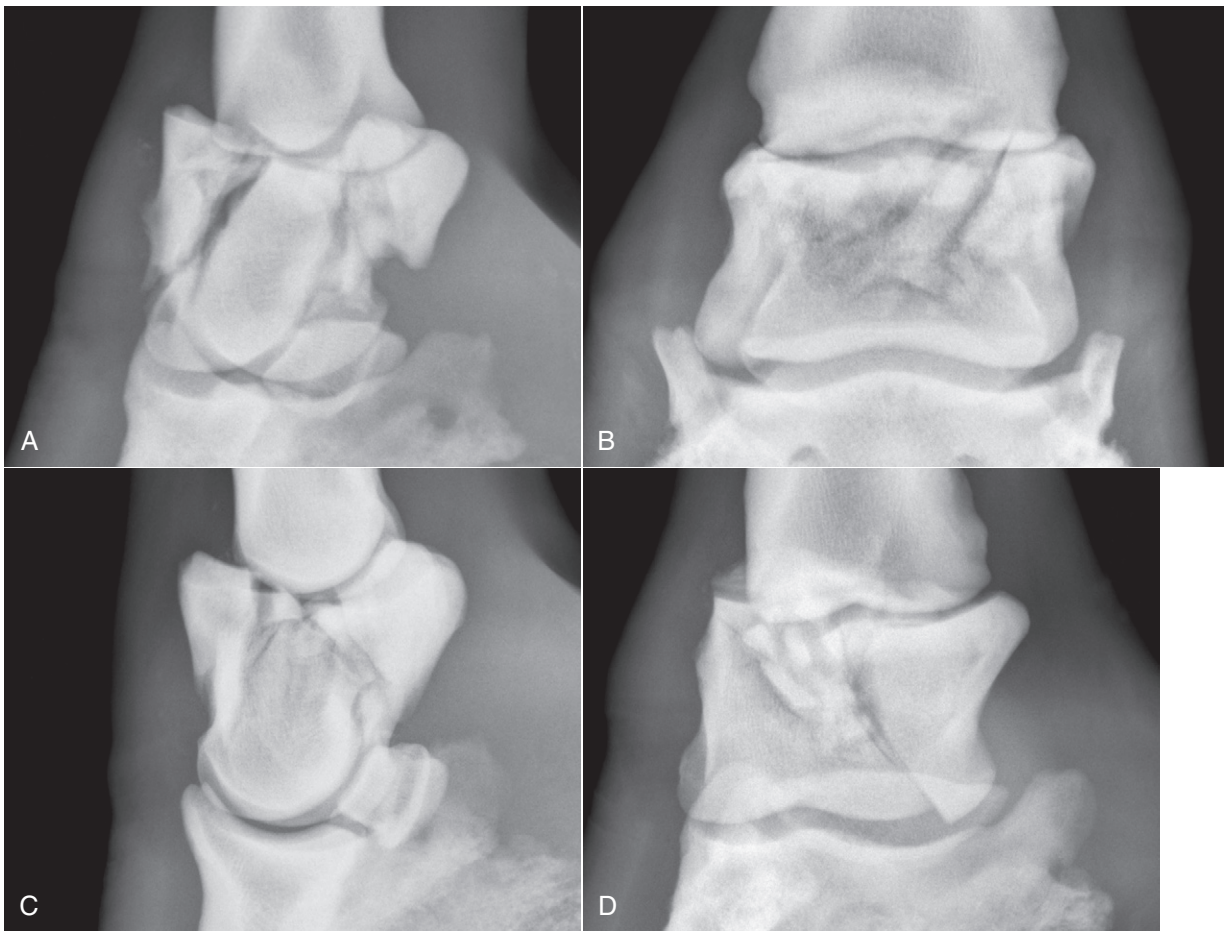


Fig. 23-15 Comminuted, multiplane, biarticular middle phalanx fracture. Despite the obvious identification of the fractures in the lateromedial and dorsopalmar projections, the oblique views confirm involvement of the proximal and distal interphalangeal joints. This horse was not bearing weight for these images. With weight-bearing load the proximal interphalangeal joint would be luxated.

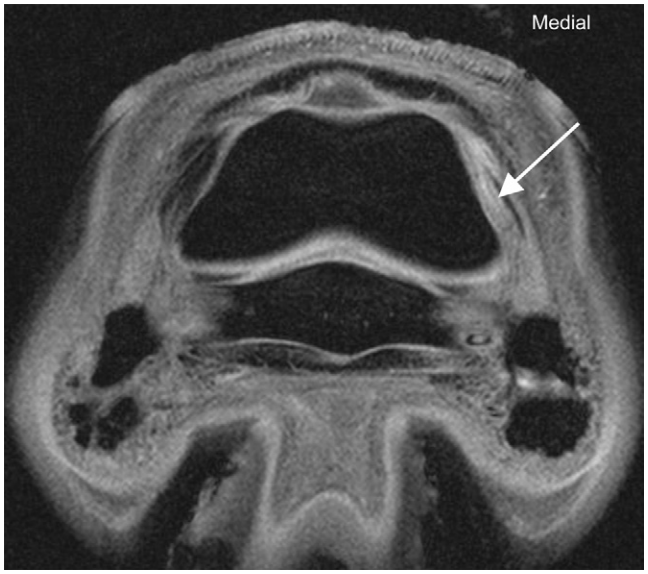


Fig. 23-16 Transverse gradient recalled echo image of a horse with interphalangeal collateral desmitis. Note the increased signal within and adjacent to the medial collateral interphalangeal ligament *(white arrow)* compared with the normal lateral side.

This fracture and those of the palmar eminence are described in Chapter 22.

Various classification schemes have been applied to all other fractures of the proximal phalanx.[20] By general classification, the fractures are noncomminuted or comminuted, incomplete or complete, monoarticular or biarticular, and in a primarily sagittal or dorsal plane to the long axis of the proximal phalanx. Figure 23-17 illustrates these fractures of the proximal phalanx. The most frequently reported fracture configuration in Thoroughbreds and Standardbreds is the noncomminuted, incomplete, monoarticular sagittal fracture (Fig. 23-17, *A*).[21,22] This fracture is common in 2- and 3-year-old horses in race training or active racing. It occurs in the front limbs and hindlimbs of these breeds. However, fractures are somewhat more common in the front limbs of Thoroughbreds and the hindlimbs of Standardbreds. This fracture typically originates at the proximal articular surface just lateral to or within the midline plane of the sagittal groove (Fig. 23-18). Few originate medial to the midline plane.

Two variations of the noncomminuted, incomplete, monoarticular sagittal fracture occur. The short (less than 30 mm extension into the diaphysis) variation is slightly more common than the long (more than 30 mm extension into the diaphysis) variation. Both fractures may course in a slightly spiral or oblique manner. This effect is depicted as two parallel or offset

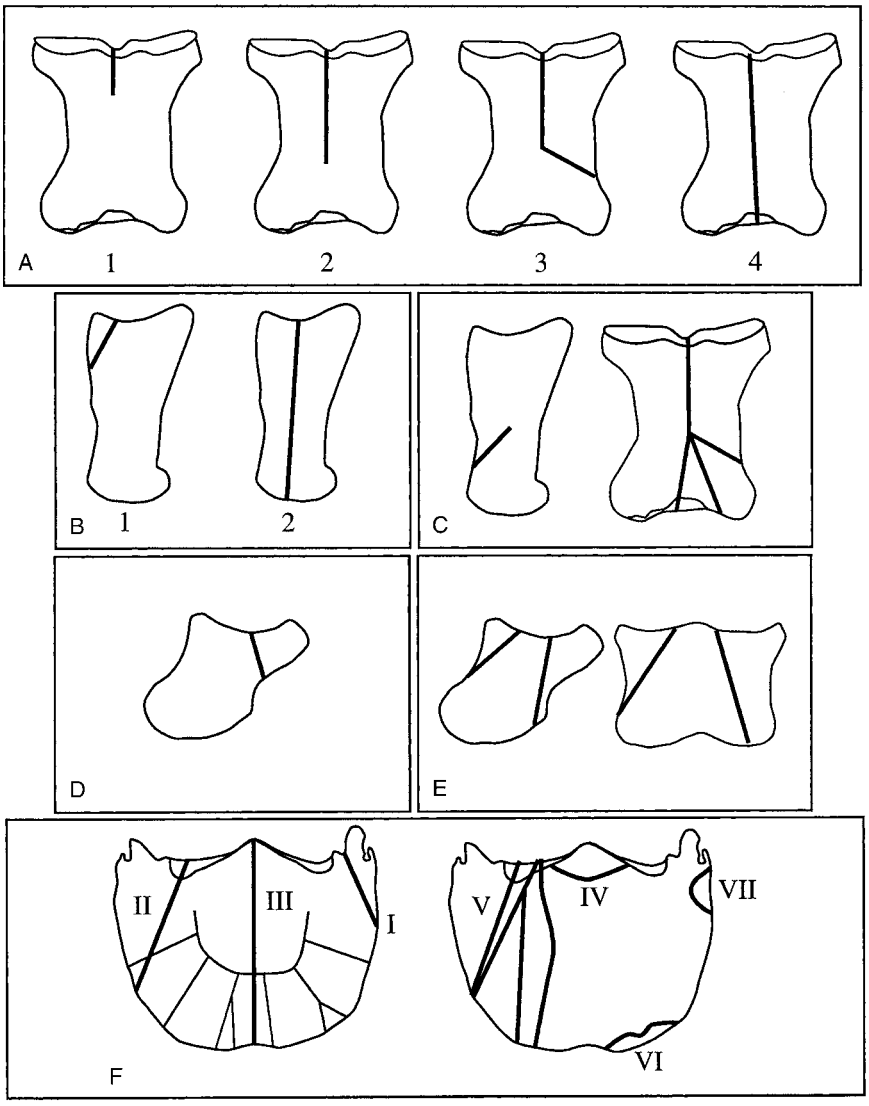


Fig. 23-17 Common fractures of the phalanges. *Proximal phalanx:* **A,** Sagittal plane fractures, noncomminuted. *1*, Incomplete, monoarticular (short, less than 30 mm variation); *2*, incomplete, monoarticular (long, more than 30 mm variation); *3*, complete, monoarticular; *4*, complete, biarticular. **B,** Dorsal plane fractures, noncomminuted. *1*, Complete, monoarticular; *2*, complete, biarticular. **C,** Comminuted, complete, biarticular, dorsal, and/or sagittal plane. *Middle phalanx:* **D,** Palmar/plantar eminence (monoarticular, complete). **E,** Comminuted, complete, biarticular. *Distal phalanx:* **F,** *I*, Nonarticular, palmar/plantar process; *II*, articular, extending from distal interphalangeal joint to solar margin; *III*, articular, midsagittal, divides into equal parts; *IV*, articular, extensor process; *V*, articular, comminuted body fracture (not of types II, III, or IV); *VI*, solar margin; *VII*, solar border of palmar/plantar process in foals.

radiolucent lines representing the fracture plane in the dorsal and palmar cortices. The short fracture may be more difficult to identify on an initial radiographic evaluation. Both variations of fracture are seen only on dorsopalmar views. Because the fracture plane typically has very little gap, the x-ray beam must pass parallel to the fracture line for the fracture gap to be detected. Repeat radiographs in 7 to 10 days should allow identification of the fracture more readily, after lysis of bone along the fracture edges has occurred during the first stages of healing. When imaging occurs several weeks after the onset of lameness, periosteal new bone will likely be present on the dorsal or palmar surface, indicating callus. At this stage, the new bone is visible on the lateromedial view, the fracture line may be less visible on the dorsopalmar view, and sclerosis in the adjoining bone should be seen. In the nonathletic horse that may have been managed conservatively for several months, an osseous cystlike lesion may also be present.[23]

This type of fracture is not mentioned in a report of diagnosis and treatment of quarter horse racehorses.[24] This fracture is generally presumed to occur subsequent to a single force incurred during exercise. Lame horses with this fracture but without radiographic lesions can have intense increased radiopharmaceutical uptake and MR imaging changes consistent with bone marrow edema and subchondral sclerosis extending a short distance from the sagittal groove. It is speculated that these changes indicate a prodromal stage of proximal phalanx fracture caused by repetitive trauma.[25]

Noncomminuted, complete sagittal fractures of the proximal phalanx occur with less frequency than do incomplete fractures in racehorses. This type of fracture is, however, reported to be more common in the Western performance horse. Two variations of this fracture occur: One is biarticular with origin at the metacarpophalangeal joint and exit at the proximal interphalangeal joint; the other is monoarticular and typically exits through the lateral distal palmar or plantar cortex (see Fig. 23-17, *A*). These fractures are most readily seen in the dorsopalmar view.

Comminuted fractures of the proximal phalanx (Fig. 23-17, C) are moderately common. Variations include comminution throughout the phalanx, only in the proximal portion, or only in the distal portion. These fractures frequently have one exit through the lateral rather than the medial cortex and are typically biarticular and more likely to be complicated by being open. The multiple fracture planes of the comminuted fracture are visible in both lateromedial and dorsopalmar views. Oblique views should also be made to obtain a more thorough depiction of the fracture configuration. Comminuted fractures have the most guarded prognosis for survival and very poor prognosis for return to athletic performance.

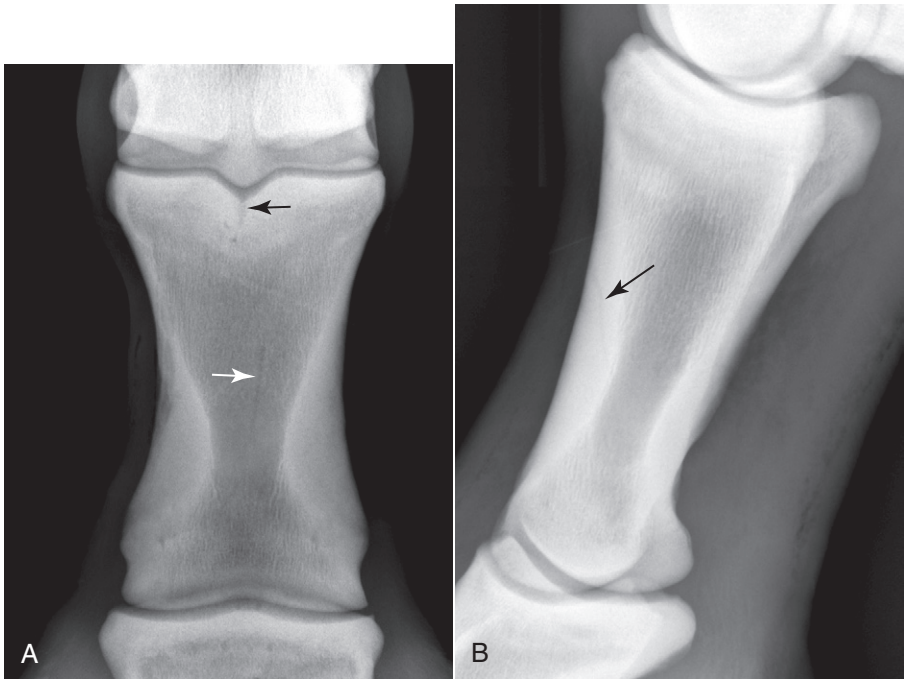


Fig. 23-18 **A,** Incomplete short sagittal fracture of the proximal phalanx originating in the sagittal groove *(black arrow)*. The x-ray beam must be parallel to the fracture plane to identify this fracture. The *white arrow* points to a long linear lucency that is the nutrient canal and should not be misinterpreted as a fracture. **B,** This vascular channel is seen in the dorsal cortex of the mildly oblique lateral view *(black arrow)*, of this horse.

Incomplete or complete dorsal plane fractures that originate at the proximal articular surface (Fig. 23-17, *B*) are much less common. These fractures may be detected only on lateromedial views. The incomplete fracture typically courses distally toward the dorsal cortex. The complete variation either breaks through the dorsal cortex or extends the entire length of the phalanx to exit in the proximal interphalangeal joint. The latter variation typically splits the proximal phalanx into roughly equal dorsal and palmar (plantar) halves. Other sporadically reported fractures of the proximal phalanx include physeal fractures (typically Salter-Harris type II) and incomplete distal articular fractures.[21,22]

Middle Phalanx

Fractures of the middle phalanx include comminuted fracture (most common) (see Fig. 23-15), fracture of the plantar or palmar proximal eminence (fracture of both medial and lateral eminences is more common than a single eminence fracture) (Fig. 23-19), and osteochondral edge fracture (rare) (Fig. 23-17, *D* and *E*). Physeal fracture can occur in the skeletally immature horse but is reported infrequently. The comminuted (complete and typically biarticular) and eminence fractures (complete monoarticular) are most common in horses whose activity subjects the middle phalanx to extreme simultaneous compression and torsion forces while the foot is fixed to the ground.[26] Thus these types of fractures are most common in working or performing Western horses, polo ponies, and jumpers. For both common fractures, the hindlimbs are involved approximately twice as frequently as the front limbs.[21,22,26] However, the front limb is more equally affected by comminuted fracture. The hindlimb is considerably more frequently reported to have a plantar eminence fracture without other comminution. Neither type of fracture is difficult to identify radiographically. When the eminence is fractured without comminution, the fragments are displaced in a plantar direction. In the most severe instances, the proximal interphalangeal joint is simultaneously luxated, allowing the distal end of the proximal phalanx to descend distally and override the middle phalanx. Comminuted fractures can involve only the proximal portion of the middle phalanx, but, more commonly, the fracture planes extend into the distal interphalangeal joint. Decision to treat and the type of treatment of the comminuted middle phalanx fracture depend on many factors; however, one of the most important is the degree of involvement of the distal interphalangeal joint. Additional oblique views at different angles compared with the standard (see Table 23-1) may be needed to identify the planes of comminution fully. CT has been used to improve assessment of the degree and configuration of comminution.[26] With CT, the number of fracture planes decreased toward the distal end of the middle phalanx. Many horses recover successfully to reach breeding or athletic soundness. Secondary degenerative joint disease in the distal interphalangeal joint may significantly complicate long-term recovery for return to athletic performance.

Distal Phalanx

A fracture classification system (types I through VII) describes the fractures of the distal phalanx.[27] This classification system is illustrated in Figure 23-17, *F*. Fractures are classified on the basis of region of the bone affected, articular or nonarticular involvement, and anatomic plane of the fracture, as follows:

I Nonarticular fracture of palmar or plantar process
II Articular fracture, extending from distal interphalangeal joint to solar margin (Fig. 23-20)
III Articular fracture, midsagittal, divides distal phalanx into equal parts (Fig. 23-21)
IV Articular fracture, extensor process (Fig. 23-22)
V Articular fracture, comminuted body fracture (not of type II, III, or IV)
VI Solar margin fracture (see Fig. 23-31, *B* and *C*)
VII Palmar process fracture in foals (Fig. 23-23)

Trauma is the most common cause of distal phalanx fractures; however, they also occur as pathologic fractures secondary to infective pedal osteitis and laminitis. Because the hoof wall restricts displacement of bone fragments, diagnosis of the

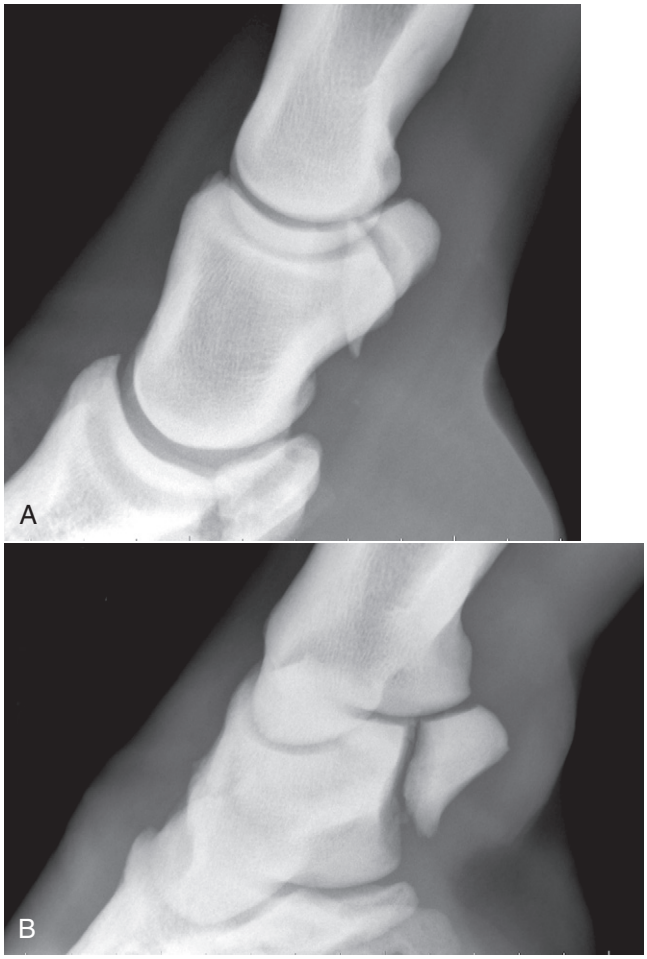


Fig. 23-19 Noncomminuted, complete, monoarticular fracture of the palmar process of the middle phalanx. Only the medial process is involved. The oblique projection aids in delineating the single obliquely directed fracture plane and the level of the subchondral bone traversed by the fracture.

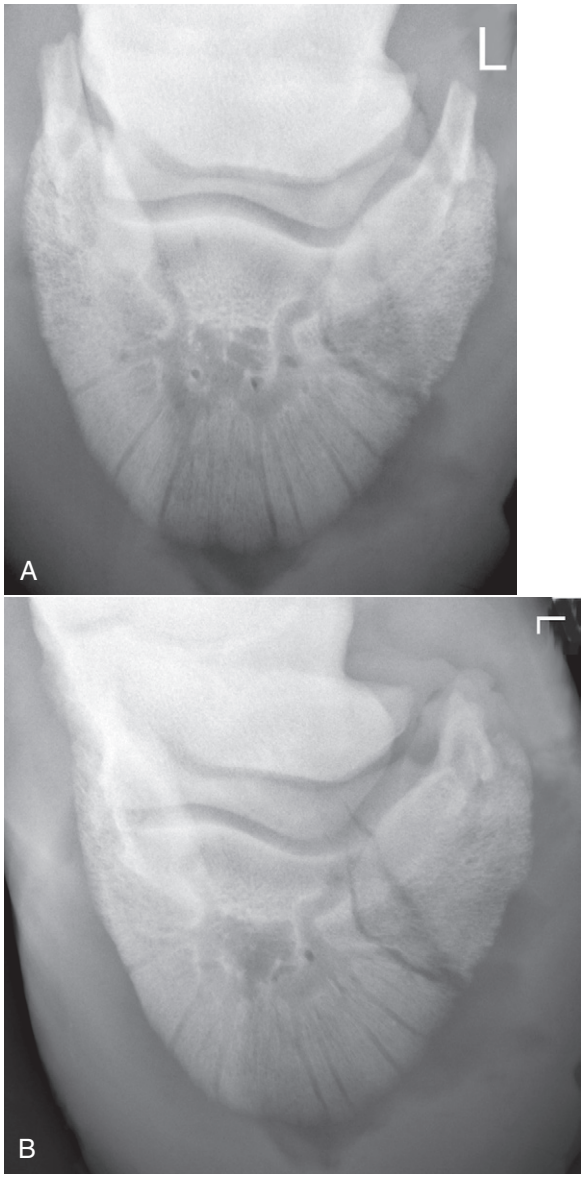


Fig. 23-20 Oblique fracture of the lateral wing of the distal phalanx. **A,** The fracture is subtle in the standard dorsal 65-degree proximal-palmarodistal view. Because there is minimal distraction, the x-ray beam must pass parallel through the fracture gap for optimal depiction. The curvature of the foot necessitates oblique projections to identify these fractures, particularly at the acute stage. **B,** This is a dorsal 65-degree proximal 45-degree lateral-palmarodistal view. The fracture is evident and approaches but does not disrupt the subchondral bone. However, the location along the joint contour makes this a type II fracture.

distal phalanx fracture depends on visualization of the fracture line. If the plane of the primary x-ray beam is not parallel to the fracture plane, the superimposed parts of the bone obscure the fracture line, and the diagnosis is missed. Therefore four views of the distal phalanx are recommended when a fracture is suspected: (1) lateromedial; (2) dorsal 65-degree proximal-palmarodistal; (3) dorsal 65-degree proximal, 45-degree lateral-palmarodistal; and (4) dorsal 65-degree proximal, 45-degree medial-palmarodistal. Views two through four are done with the horse standing on the reinforced cassette or cassette/detector tunnel. Type VI fracture requires careful assessment of the solar margin. Overexposure of the image makes this fracture difficult to see.

A wide variety of horses sustain fractures of the distal phalanx. Quarter horses were most common in a review of a large number of horses.[27] Type II fractures are often distributed to involve the lateral aspect of the left front limb or the medial aspect of the right front limb.[21,22] In racehorses the forelimb that bears the most weight in turns is at greatest risk (horses raced counterclockwise). Fractures of the extensor process (type IV) are uncommon and are seen as small or quite large fragments.[28,29] Question exists as to whether the smaller lesions are true fractures or a result of developmental defect. Larger fragments are more likely of traumatic origin. Front limbs are more often affected than hindlimbs. In 274 horses, type VI was the most frequently identified type of fracture.[27] The type VI fracture was found in association with radiographic signs of laminitis in 42 feet (32% of type VI fractures) (see Fig. 23-31, *B*).[27]

The progression of healing of a distal phalanx fracture is difficult to determine radiographically because of the minimal amount of external (periosteal) osseous callus produced by this bone. Fractures of the extensor process tend to produce the greatest amount of new bone (Fig. 23-22, *B*). The periosteum of the distal phalanx is poorly developed and does not respond with abundant proliferation to the stimulation of direct trauma. Treatment by corrective shoeing and stall rest may lead to healing in 3 to 19 months, with young horses and nonarticular fractures having the most rapid and complete progression to bone union.

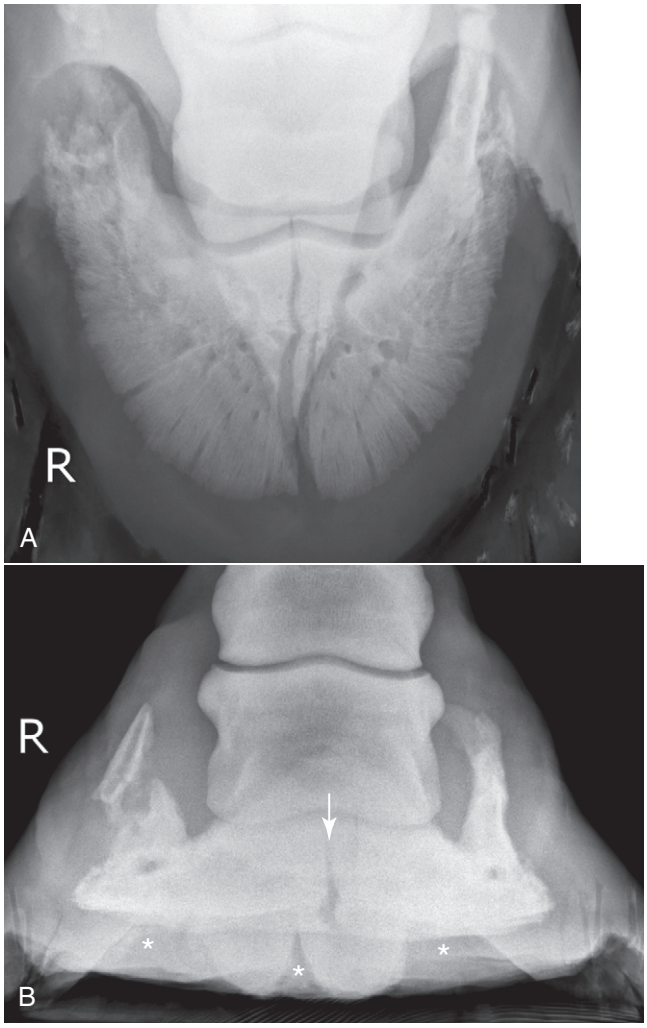


Fig. 23-21 Midsagittal, articular fracture (type III) of the distal phalanx. The fracture is seen easily in the dorsal 65-degree proximal-palmarodistal view, and a small offset is evident at the articular border. In the horizontal (0-degree) dorsopalmar view the fracture may have been mistaken for air in the heel crevice or as an extension of the air in the central sulcus of the frog. The fracture line has been marked with a *white arrow* and *asterisks* placed in the sulci of the frog. This horse also has grade 5 ossification of the collateral cartilages. The lateral ossification is separated at the base.

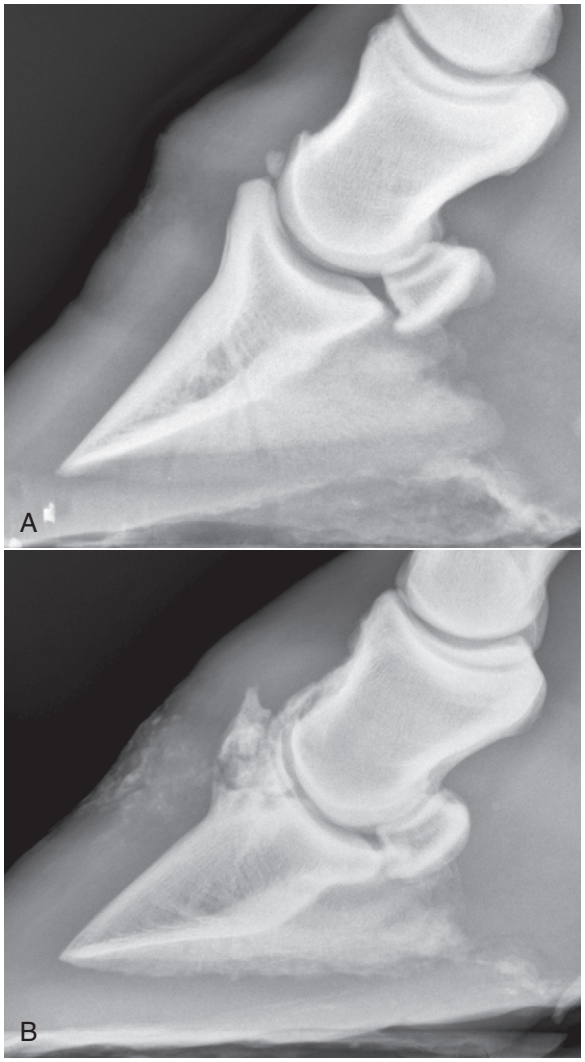


Fig. 23-22 Fractures of the extensor process in two horses. **A,** 2-year-old male Standardbred with a small rounded fragment separated from the extensor process of a front distal phalanx. There is enlargement of the soft tissue at the coronary band. There is no evident deficit in the contour of the extensor process, suggesting that this may have been of developmental origin. This horse developed fragmentation in the opposite front extensor process approximately 1 year later during race training. **B,** 20-year-old quarter horse gelding with a large extensor process fracture. Circular lucencies in the distal phalanx at the distal palmar aspect of the fracture line, rounding of the fragment edges at the articular border, and the new bone on the dorsal surface of the middle phalanx are indicative of a chronic nonunion or fibrous union.

Palmar process ossicles have been identified radiographically in the forelimb of foals aged 3 to 32 weeks.[30] Although these ossicles have been suggested to be separate centers of ossification, the microradiographic and histologic appearance in the majority of foals studied was consistent with fracture healing.[12,30] Radiographically, these are seen as a triangular fragment at the palmar aspect of the distal angle of the palmar process or as an oblong fragment separated by a radiolucent line extending from the incisure of the palmar process to the solar margin (VII—solar border of palmar/plantar process in foals in Figs. 23-17, *F,* and 23-23).[30] Fractures have been identified at either or both medial and lateral palmar borders. Radiography is an insensitive method for identifying all foals affected with these fractures. There is no relation to extensive trimming of the heels.[31] Mild, short-duration lameness can be attributed to these fractures. Healing was complete radiographically in an average of 8 weeks, and foals were sound. Foals through 12 weeks of age have a lucent line between the proximal and distal angles of the palmar process. This line is normal and should not be mistaken for a fracture (Fig. 23-24).



Fig. 23-23 A palmar process fracture in the distal phalanx of a foal (type VII in Fig. 23-17, *F*). *Black arrows* indicate a radiolucent line extending from the incisure of the palmar process to the solar margin.

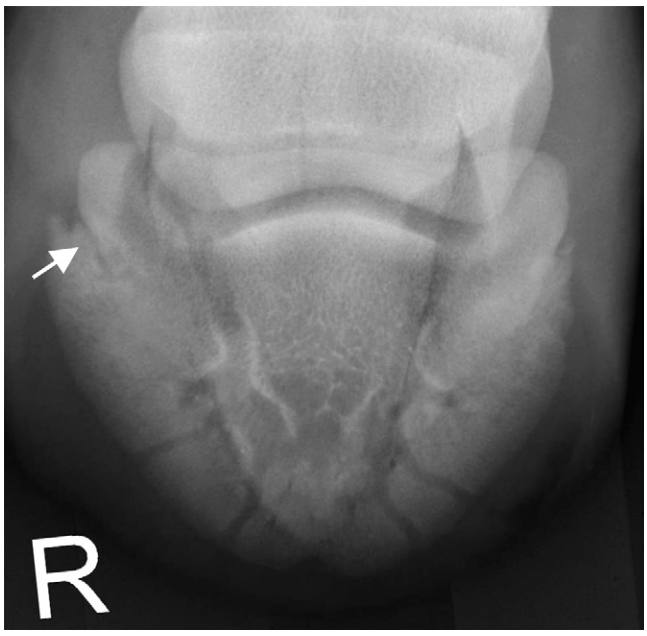


Fig. 23-24 Dorsal 65-degree proximal-palmarodistal view of the distal phalanx of a normal foal. Note the normal radiolucent line in the palmar process *(white arrow)*, which should not be confused with a fracture.

INFECTION

Osteomyelitis and Septic Osteitis

Infection of the phalanges results most commonly from trauma or as a complication of surgical treatment and less commonly as the result of hematogenous dissemination. Only one description of fungal osteomyelitis caused by *Cryptococcus gatti* has been reported.[32] The lesion was in the dorsal cortex of the proximal phalanx. Lacerations and puncture wounds by foreign objects carry a high risk of secondary infection of soft tissue and bone. Sequestrum formation associated with bacterial infection is likely associated with a currently or periodically draining soft tissue lesion. Sequestra vary widely in length and thickness. Oblique views may be necessary to profile the sequestrum. The periosteal new bone associated with a sequestrum may be smooth or mildly irregular.

Septic (infective) pedal osteitis refers to infection of the distal phalanx. The most common cause is that of penetrating foreign objects through the sole. Common radiographic changes are discrete areas of lysis, irregular margin, and decreased opacity of the distal phalanx, typical of chronic inflammation (Fig. 23-25). Gas may be present in the soft tissue adjacent to the surface of the distal phalanx. A pathologic fracture is uncommon. Separation of a piece of the distal phalanx may represent a pathologic fracture or sequestrum (see Fig. 23-25).[33] Clinically, a draining tract at the sole or coronary band may be found. Contrast sinography or images made with a metallic stylet in the tract are useful to confirm association of the tract with a bone lesion or to detect communication with the distal interphalangeal joint or navicular bursa. To avoid iatrogenic introduction of infection into the joint or bursa, an arthrogram to detect leakage out of the joint cavity should be considered in those horses with draining tracts at the coronary band. Extension of infection to these synovial cavities necessitates aggressive treatment.[34] If a metallic foreign body is evident at physical examination, radiographs should be made before removal to determine the depth of its penetration and its relation to the regional bone (Fig. 23-26).

Of 108 Thoroughbred foals with 141 sites of hematogenous osteomyelitis, there were a significant number with phalangeal involvement.[35,36] Of greatest note are the 25 distal phalanx lesions in 21 foals. These involved the extensor process (5 lesions), solar border (14 lesions, all but one at the dorsal toe region), and palmar or plantar processes (3 lesions). None of the foals with a solar margin lesion had visible evidence of sole bruising or a penetrating wound. Radiographic lysis was present in four foals with a sequestrum. The hindlimb was affected more commonly (62% of lesions). Three of four foals with extensor process lesions had concurrent septic arthritis. Although the proximal physeal and epiphyseal locations of the proximal and distal phalanges are common potential locations for hematogenous osteomyelitis, the distal phalanx has not typically been included. Eighty-six percent of the foals with distal phalanx lesions were discharged from the hospital, and 50% of those that trained for racing had official race starts.

Septic Arthritis

Infective agents are introduced into the joint by penetrating wounds, iatrogenic injections, or hematogenous introduction. The latter occurs most commonly in foals. However, neither the proximal nor the distal interphalangeal joints are typically involved in the septic polyarthritis syndrome of foals.[37] Any laceration near a joint that is associated with significant and persistent lameness warrants concern for extension to the joint and infection.

The joint pouches of the distal interphalangeal joint are large, extending proximal to the midplane of the middle phalanx.[5] During the initial stage of infection, no radiographic changes may be present. Inflammation of the synovium and effusion may create a focal enlargement or a bulge in the contour at the joint level. If the distal interphalangeal joint is infected, a bulge at or just proximal to the coronary band should be evident (Fig. 23-27). Rarely is widening of the joint space detected, especially if the horse is bearing weight.[38] Lameness caused by infected joints is usually painful, and the horse is reluctant to bear weight fully. This further complicates critical assessment of joint space width.

Positive-contrast arthrography was used in horses suspected to have joint infection but no bone changes.[38] This was successful for identification of communication of the contrast medium from the joint to the external wound. One of the earliest bone reaction signs is irregularity at the joint capsule insertion or chondro-osseous junction on the perimeter of the joint surfaces. As cartilage begins to deteriorate, thinning of the joint space is seen. As the infection invades the deeper regions of the cartilage and reaches the subchondral bone, the subchondral bone margin becomes irregular because of lysis (see Figs. 23-13, *E* and *F*). Lysis of the subchondral bone causes the joint to be widened unevenly.[38] At this stage, periosteal new bone should be evident at the joint margins (Fig. 23-28, p. 448). Septic arthritis always has a guarded prognosis.

DEGENERATIVE JOINT DISEASE

Degenerative joint disease is a chronic disorder of synovial joints characterized by progressive deterioration of articular cartilage and reactive changes in the joint margin and joint capsule.[39] Among the multiple causes of degenerative joint disease are acute trauma, infection, poor limb conformation, developmental orthopedic disease, and chronic repetitive trauma associated with intensive athletic activity. These conditions lead to what is thought of as secondary degenerative joint disease. Primary degenerative joint disease, in comparison, is an age-related disease of slow onset, resulting in gradual degradation of normal joint structure and function. The proximal and distal interphalangeal joints can be affected by any of these causes. The general changes expressed

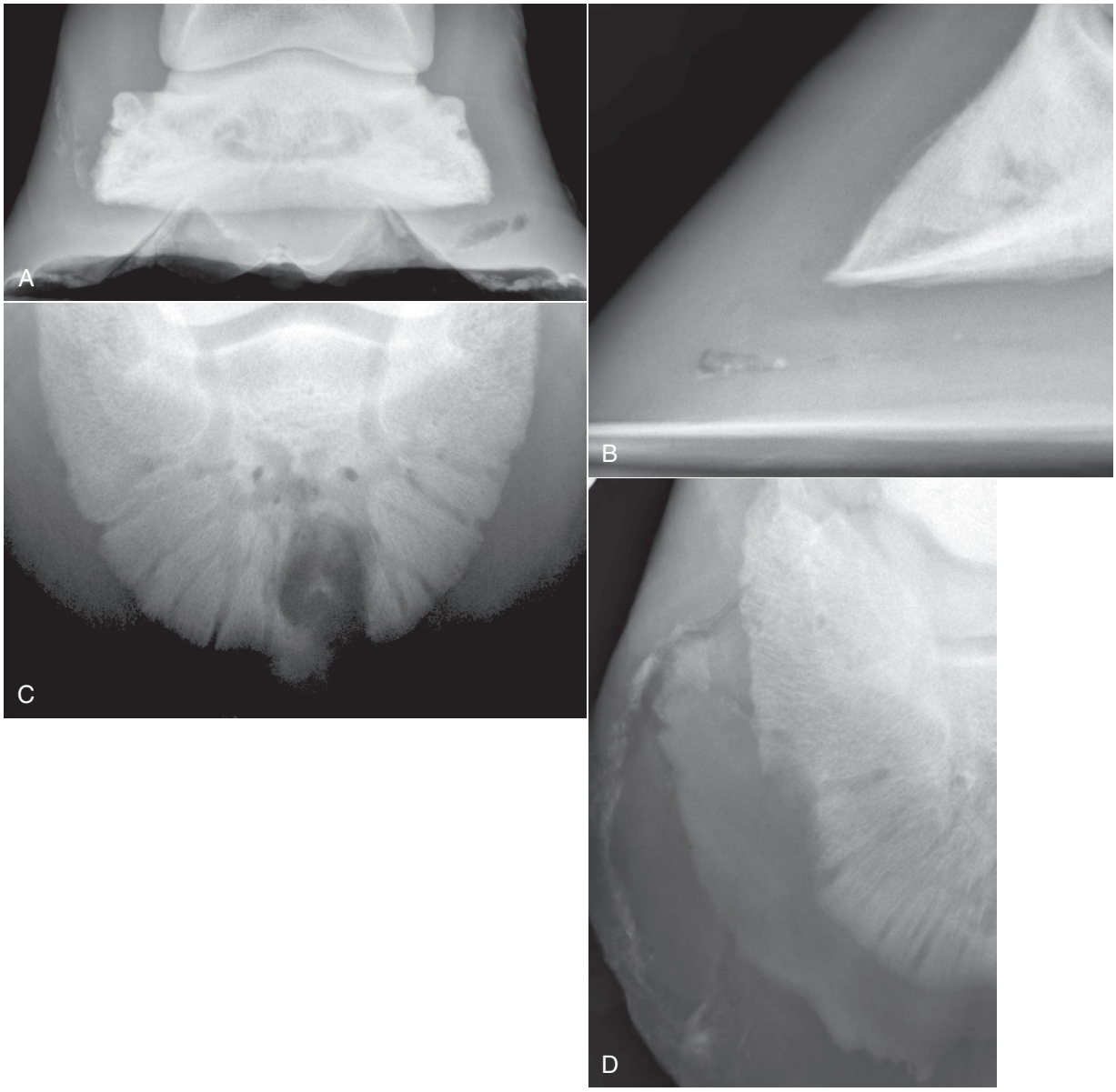


Fig. 23-25 Variations seen with infective pedal osteitis associated with foot abscesses in three horses. Horse 1 **(A)** has only gas in the subsolar soft tissues with no bone lesion. Images **B** and **C** are the second horse. In **B,** there is subsolar gas at the toe. The dorsal border of the distal phalanx from the toe to mid-body is abnormally thin and has an irregular surface. In **C,** a large circular osteolytic area is present on the midline toe. A small mineralized opacity consistent with a sequestrum is present in the lytic area. In horse 3 **(D),** there is a smoothly marginated concave defect in the solar border of the quarter region. This was associated with a resolving abscess.

radiographically are new bone formation (osteophytes) at the periarticular (chondro-osseous) margin, enthesophytes at the sites of supporting ligaments and joint capsule, sclerosis and lucency in the subchondral bone, and changes in the joint space width (Fig. 23-29, p. 448). A wide spectrum of combination and degree of the above changes is seen (see Fig. 23-13). With secondary degenerative joint disease, radiographic changes unique enough to allow the primary problem to be identified may be present, but this is unusual.

The proximal interphalangeal joint is a high-load, low-motion joint, meaning that a large range of movement does not occur during the stride motion of the limb. As a consequence, a smaller region of the joint surface sustains a more constant weight-bearing load for a longer period in the athletic horse.[39] This is the basis of an explanation for the characteristic features of progressive proximal interphalangeal degenerative joint disease seen in athletic horses, especially those active in Western-style events.[40] The movements of athletic activity are proposed to concentrate the load on the articular cartilage excessively and initiate fibrous thickening of the supporting soft tissues to restrict joint motion further. Continued compression leads to full-thickness necrosis of the cartilage. Simultaneously, modeling of the underlying bone occurs in the forms of sclerosis and resorption. The natural attempts to heal the cartilage lesions are not successful, and gaps are left in the articular cartilage surface. Osteogenic granulation tissue from the exposed subchondral bone bridges these joint gaps, initiating the process of ankylosis.

Radiographically, periarticular osteophytes and enthesophytes develop. Fibrous thickening of the joint capsule and

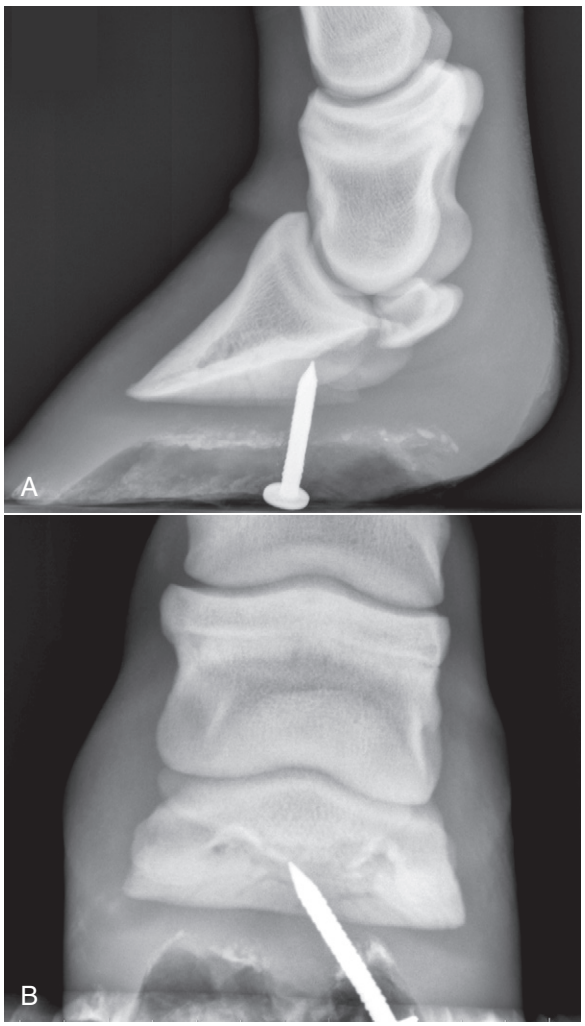


Fig. 23-26 A nail foreign body has penetrated the sole of the foot. The tip of the nail is in close proximity to the palmar surface of the distal phalanx on the midline at the level of insertion of the deep digital flexor tendon. Radiography, using orthogonal views, done with the foreign body present is more valuable in determining its relation to the bone, tendon, and ligament locations than radiographs made after the foreign body has been removed.

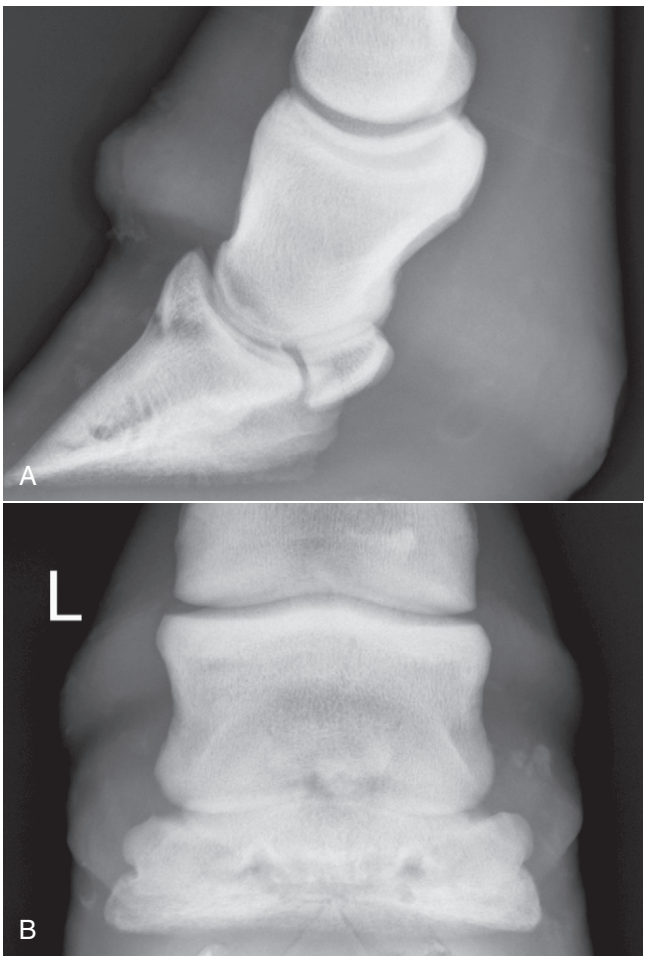


Fig. 23-27 This yearling sustained unknown trauma to the foot causing a significant lameness. The following day a draining tract developed at the dorsal coronary band. One and a half weeks later the lameness persisted, and radiographs were acquired. There is evident swelling at the coronary band, as well as thinning of the distal interphalangeal joint space (narrower than the proximal interphalangeal joint space), subchondral lucency of distal dorsal half of the middle phalanx, and a separation of a large extensor process fragment from the distal phalanx. No new bone formation is evident. These changes are indicative of septic arthritis with osteomyelitis of the middle and distal phalnges with fracture and probable sequestrum formation of the extensor process.

collateral ligaments, along with compression modeling of the articular cartilage and subchondral bone, occurs but can be subtle radiographically. Focal regions of subchondral bone resorption may be large enough to be seen as lysis (Fig. 23-30, p. 449). The osteogenic granulation tissue in the subchondral sites of bone resorption becomes visible as bone-to-bone contact.[39] This is the start of ankylosis of the joint (see Fig. 23-13, *F*).

If these initial ankylosis sites are sufficiently stable, additional ankylosis progresses to complete the union of the bone surfaces. However, if activity is continued, the initial ankylosis sites can break down and generate more periarticular new bone (see Fig. 23-29). During the ankylosis process, lameness is likely to persist. In these horses, the natural ankylosis must be replaced by surgical or chemical arthrodesis so that the lameness can be resolved.[41]

Osteoarthritis from causes other than infection or articular fracture is reported much less frequently with specific reference to the distal interphalangeal joint. It is also not as radiographically obvious. When present, the radiographic signs of osteoarthritis are small periarticular osteophytes on the dorsal edges of the proximal and distal phalanges (see Fig. 23-38, p. 454), enthesophytes on the eminences for the collateral ligaments on the middle phalanx, and narrowing of the distal interphalangeal joint. If asymmetric narrowing of the joint is noted on the dorsopalmar view (Fig. 23-13, *B*), this may be attributable to true asymmetric cartilage degeneration, asymmetric weight bearing, or unbalanced compressive forces caused by unbalanced trimming or wear of the hoof.

In 11 lame horses evaluated with MR imaging, subchondral trabecular bone damage was found that was not evident radiographically.[42] These changes consisted of subchondral fluid signals with and without cyst formation. Determining whether the subchondral changes, particularly the cysts, were initiated by trauma, prior osteochondrosis lesion, or some other insult was not possible because of insufficient histologic assessment. Characterization of the normal articular cartilage of the distal interphalangeal joint of cadaver limbs has been done with a low-field magnet.[43] Successful detection of iatrogenic full thickness cartilage defects was achieved. However, partial thickness defects simulating score lines of early cartilage damage were not detected.

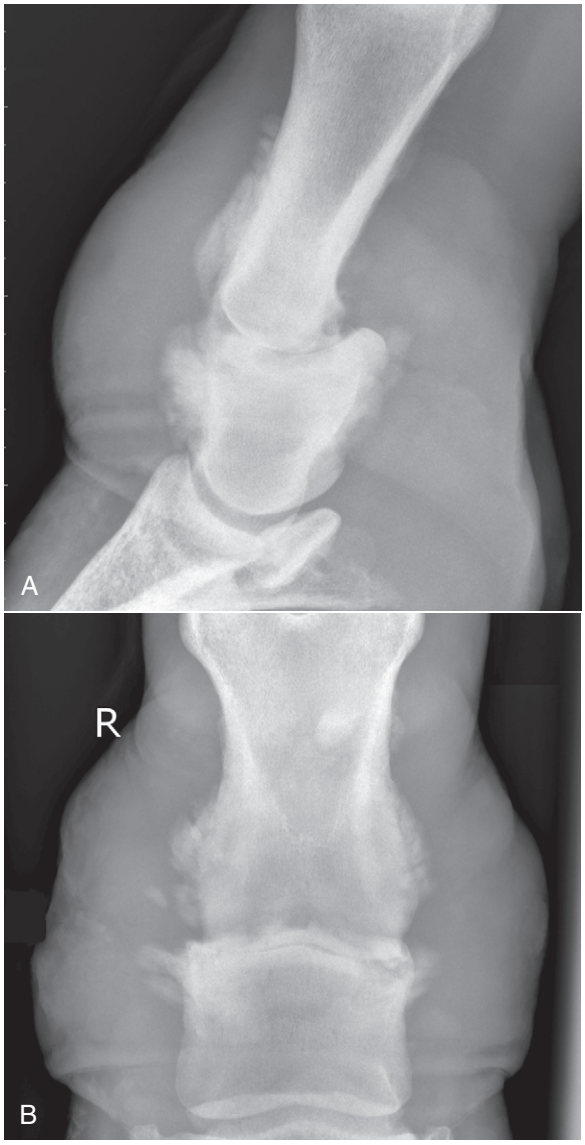


Fig. 23-28 The proximal interphalangeal joint is narrowed dramatically with mild palmar subluxation. Focal areas of subchondral lysis are evident in the proximal aspect of the middle phalanx. The periosteal new bone formation has a palisading appearance, and there is soft tissue swelling. These features are typical of chronic active infection and joint instability.

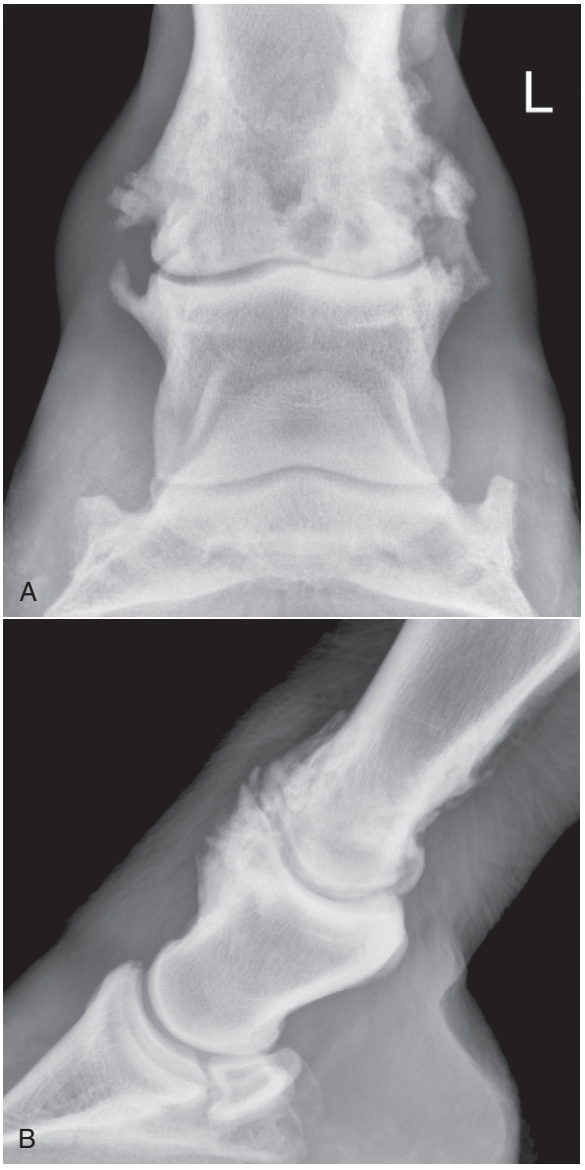


Fig. 23-29 These images depict the typical radiographic features of chronic proximal interphalangeal osteoarthritis. Osteophytes, enthesophytes, joint space narrowing (asymmetric in this example), subchondral sclerosis, and subchondral cysts are evident.

LAMINITIS

The normal orientation of the distal phalanx to the hoof is maintained by the interdigitating leaves of the laminar corium and the hornlike lamellae of the hoof wall. The laminar corium is attached to the dorsal surface of P3 by a modified periosteum, which contains a tightly meshed network of blood vessels.[44] Insult to this unique anatomic structure can result in the loss of mechanical support of the distal phalanx within the hoof capsule. *Laminitis* is the general clinical term used to refer to the complex of signs expressed by the horse and its effects on the structural relations of the hoof wall, the distal phalanx, and sole from a variety of insults. Most horses that develop clinical laminitis do so as a result of a systemic illness.[45] Concussion trauma to the feet is a less well-defined cause of laminitis. Horses with protracted, severe, unilateral limb lameness are at risk for developing laminitis in the contralateral limb.[46]

Although differences of opinion exist regarding the terminology and categorization of this complex condition, several clinical phases or stages of laminitis are recognized: developmental, acute, and chronic.[47] Developmental laminitis is defined as the period between the initial insult to the first expression of lameness. It may be as short as 24 hours or as long as 60 hours.[47] This is likely an imperceptible stage to the owner unless access to excessive grain is known to have occurred or a systemic disease or other condition is present that warrants concern for initiation of laminitis. This period is a prevention phase for mechanical failure of the foot complex.[47] Acute laminitis represents the phase from the first expression of lameness through 72 hours without evidence of mechanical collapse or at any time that signs of mechanical collapse occur.[47] Radiographs may be indicated in either the developmental or the acute phase to serve as a baseline for future comparison. Horses may recover fully from either developmental or acute laminitis with no loss of mechanical



Fig. 23-30 Oblique projection of the proximal interphalangeal joint. There is subchondral bone lysis in the opposing portions of the distal aspect of the proximal phalanx and the proximal aspect of the middle phalanx as part of the progression of osteoarthritis. Sclerosis surrounds these lytic foci. Additionally, narrowing of the joint space and moderate osteophytes and enthesophytes are evident.

support. If, however, radiographic or clinical signs of distal phalanx displacement are seen, the phase of chronic laminitis has begun.[47]

Radiographic Evaluation of Laminitis

Radiographic evaluation of any horse with a clinical impression of pain and lameness caused by laminitis is justified. The goals of radiography are to detect changes indicative of mechanical failure and observe changes that contribute to formulation of prognosis and therapy. All four feet should be evaluated initially. Although lameness may be expressed in only one leg, structural changes may be present radiographically in several feet. Front feet are affected most commonly. Optimal lateromedial, dorsopalmar, and dorsal 65-degree proximal-dorsodistal views are recommended. Placement of radiopaque markers on the foot has been advocated to help identify landmarks, particularly when measurements are to be done.[48,49] A straight marker of known length placed along the midline of the dorsal hoof wall allows for correction of magnification in measurements. If this marker is used with analog imaging, it is suggested that the marker be of sufficient length to extend approximately one half to two thirds the length of the dorsal hoof wall. This marker will assist in identification of the dorsal hoof wall surface. The postprocessing on digital radiography viewing workstations allows for easy identification of the dorsal hoof wall surface. A marker placed on the midsagittal plane at the junction of the hoof wall and the coronary band is very useful. An additional marker placed approximately 1 cm palmar to the point of the frog can be used to estimate the plane of insertion of the deep digital flexor tendon. If the horse is unshod, placement of a thin metal plate between the foot and the foot support block improves the delineation of the hoof wall to block contact interface.

The radiographic signs of distal phalanx displacement are definitive evidence of chronic laminitis. The sign seen is either palmar deviation (rotation) of the distal phalanx from the hoof wall, distal (vertical or sinking) displacement of the distal phalanx, or a combination. A spectrum of severity is found. In the normal foot, the dorsal cortex of the distal phalanx should be parallel to the dorsal margin of the hoof wall in the lateromedial view. Divergence of these surfaces, with the toe region of the distal phalanx deviating or rotating in a palmar direction, is an indication of mechanical separation of the dermal and epidermal laminae (Fig. 23-31, *A*). This is the easiest of the distal phalanx displacements to detect radiographically. When a straight edge is used to mark the comparative lines of the hoof wall and dorsal cortex (Fig. 23-32, *A*, p. 451), these lines should be parallel in the normal foot. In the horse with palmar deviation of the distal phalanx, these lines diverge at the toe region and converge proximally. The angle at the point of convergence can be measured and is referred to as the *degree of rotation* (Fig. 23-32, C).

Vertical displacement of the distal phalanx can be difficult to detect and is often overlooked. In the normal foot, the proximal edge of the extensor process of the distal phalanx is positioned roughly at the same plane or just proximal to the junction of the hoof wall and coronary band. The vertical distance between the proximal limit of the dorsal hoof wall and the proximal limit of the extensor process of the distal phalanx has been measured to generate a *founder distance* (Fig. 23-32, *B*).[49] When corrected for magnification, this distance in 25 normal horses was an average of 4 mm (range, –2 to 11 mm) in the front feet and an average of 4.6 mm (range, –2 to 9 mm) in the hind feet.[49]

An increase in the thickness of the dorsal soft tissues has been suggested to be an early sign of laminar inflammation or edema and thus a sign of acute laminitis. The thickness of the dorsal soft tissues has been measured on analog radiographs of clinically normal horses.[10,49] A statistical difference was found in thickness among normal ponies, Hanoverians, and Thoroughbreds.[49] The average thickness of the front feet for all horses, when corrected for magnification, was 16.3 mm (range, 11.1 to 20.2 mm).[49] When only Thoroughbreds were compared between two studies,[10,49] the average thickness was 16.3 mm (range, 13.9 to 19.7 mm) compared with 14.6 mm, respectively (both values corrected for magnification). The range (corrected for magnification) for the front feet of ponies was 11.1 to 16.1 mm, and for Hanoverians 17 to 19.1 mm. Ranges for the hind feet of ponies was 11.7 to 16.1 mm, for Hanoverians 15.9 to 20.4 mm, and for Thoroughbreds 14.3 to 17.9 mm.[49] A marker of known length must be in the image to correct for magnification. If this is not available, an alternative is to calculate the dorsal soft tissue thickness as a percentage of the palmar cortex length. In 41 sound Thoroughbreds, the average was 24.2%; a measurement greater than 28.1% should be considered abnormal for the Thoroughbred (Fig. 23-32, *B* and *D*).[10] When not corrected for magnification, a dorsal soft tissue thickness greater than 20 mm has been suggested to be abnormal for any breed.

Other radiographic changes that can be seen with chronic and progressive laminitis include a very thin sole. The change in the position of the toe of the distal phalanx may cause a convex bulge in the sole contour, or the toe may penetrate through the sole. Radiolucency at the laminar junction can be seen as a single linear lucency in the lateral view (Fig. 23-31, *D*) and as a series of parallel linear lucencies in the dorsal 65-degree proximal-palmarodistal oblique view. This linear radiolucency could be caused by air dissecting between the hoof wall and the laminar corium when necrosis has eroded through to the coronary band or white zone of the sole or to a vacuum phenomenon that causes nitrogen to diffuse from the blood. Larger regions of radiolucency are more likely to be associated with secondary soft tissue infection. An increase in small circular lucencies is often seen in the central region

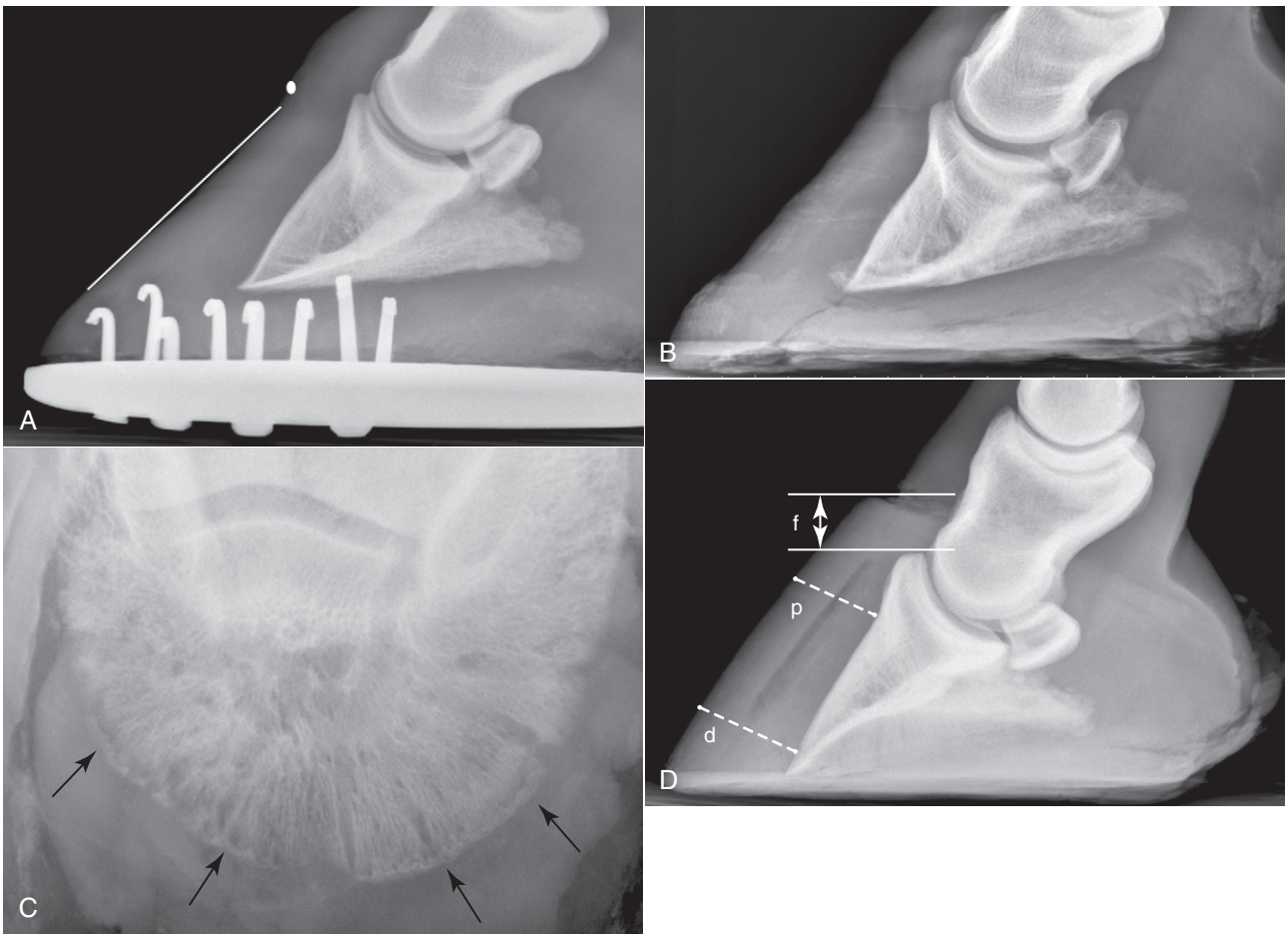


Fig. 23-31 Three variations of chronic laminitis. **A** is a horse with mild palmar rotation of the distal phalanx. The *white line* simulates the position for placement of a radiopaque marker on the dorsal hoof wall surface. The *white dot* simulates the location for placement of a marker at the coronary band. Palpation of the hoof wall and coronary band junction is important to achieve proper placement of this marker. **B** and **C** are images of a horse with more chronic laminitis. In addition to rotation of the distal phalanx, there is a linear gas shadow extending from the sole to the toe. A bone fragment is present at the toe because of pathologic distal phalanx fractures along the medial and lateral solar margins (type VI) as seen in **C** *(arrows)*. Punctate radiolucencies in the trabecular region are end-on vessels increased in number and diameter. **D** is a horse that developed plantar rotation and vertical displacement of the distal phalanx within 3 weeks of a severe injury to the contralateral limb. There is a marked indentation at the coronary band. The sole is extremely thin at the toe. Gas is also evident at the laminar junction. Measurements made on the images indicated a founder distance *(f)* of 18 mm, proximal dorsal hoof wall distance *(p)* of 28 mm, and distal dorsal hoof wall distance *(d)* of 33 mm.

of the distal phalanx in the dorsal 65-degree proximal-palmarodistal view (Fig. 23-31, C). These lucencies represent an increased number of and wider vascular channels extending from the solar canal to the dorsal cortex. This is seen typically in combination with new bone along the dorsal cortex. The new bone also creates a prominent domed shape to the dorsal surface of the distal phalanx. The toe of the distal phalanx frequently develops a lipping or ski-slope shape from either new bone, resorption of the palmar cortex, or an angular orientation of a solar margin fracture (type VI) (Fig. 23-31, *B*). Osteitis of variable severity usually develops. Additionally, disuse of the limbs can further decrease the bone opacity. Infectious osteitis can occur in the most severely affected horses. A break in the pastern angle (rotation of the distal phalanx about the distal interphalangeal joint) can occur if contraction of the deep digital flexor tendon occurs or if the more rapid growth of the hoof wall at the heel is managed improperly.

Because of the severe morbidity and protracted treatment required for chronic laminitis, indicators of prognosis for success or failure of treatment are desired. Various radiographic measurements have been assessed retrospectively to define reliable predictors of outcome for horses with chronic laminitis. Figure 23-32 illustrates several of these measurements. Even though none has been completely reliable when used as the only indicator, trends have been identified. In general, the more deviant from normal, the more guarded to worse the prognosis. Evaluating a large number of horses for prognostic indicators of poor outcome, distal displacement of the distal phalanx ("sinking") was the only radiographic variable with an increased odds of death.[50] However, the severity of the lameness using the Obel grade (I to IV) was the single best predictor of outcome. A higher grade (III and IV) was highly associated with a poor outcome. Others concur that radiographic assessment is important in establishing and monitoring bone stability within the hoof but should not be used as an isolated indicator of outcome.[51]

Some cautions regarding the use of radiographic measurements deserve mention. Measurements are most valuable when used for serial assessment of an individual horse. Strict attention to detail must be maintained in the production of images. Positioning of both the foot and x-ray beam is

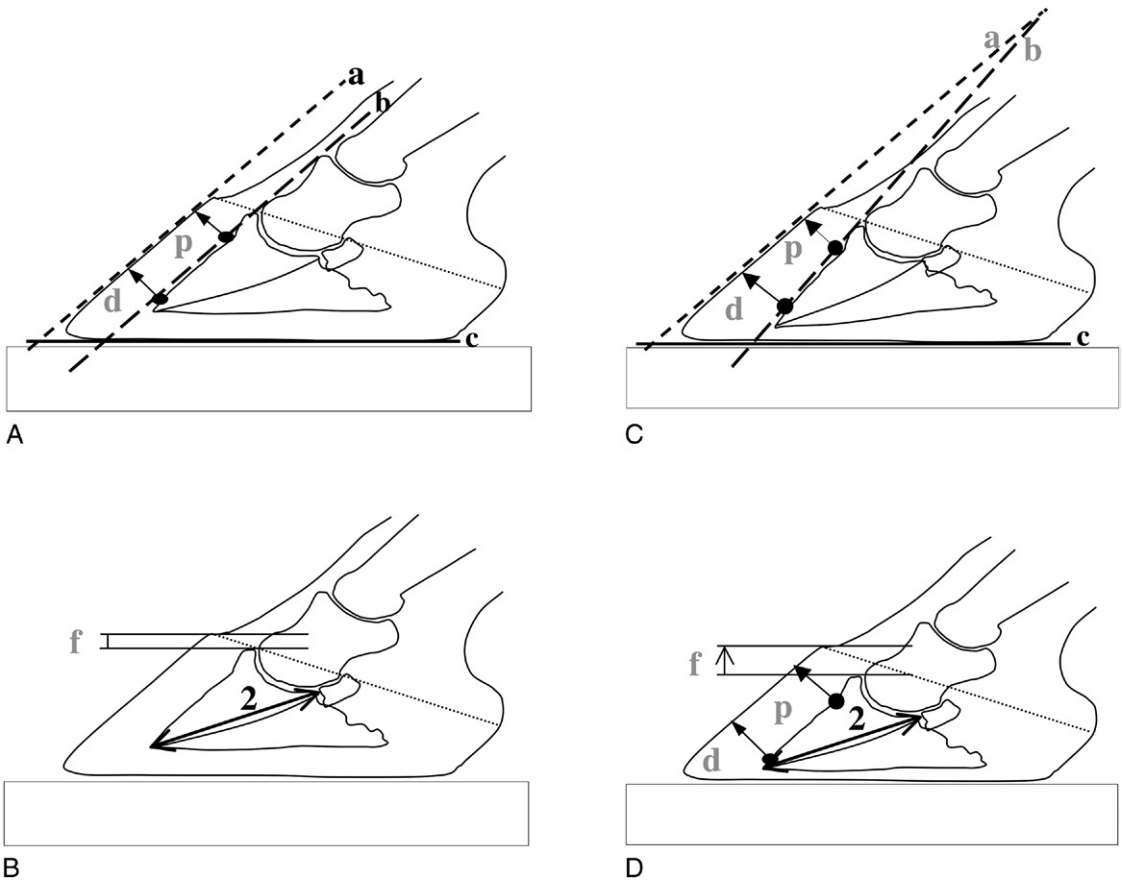


Fig. 23-32 A and B, Radiographic measurements of the normal foot. **A,** Line *a* is parallel to the hoof wall. Line *b* is parallel to the dorsal cortex of the distal phalanx. Line *c* is parallel to the weight-bearing surface of the hoof wall. Angle *ac* is the hoof axis. Angle *bc* is the foot axis. Distance *p* is the thickness of the dorsal soft tissues measured 5 mm distal to the junction of the extensor process with the dorsal cortex. Distance *d* is the thickness of the dorsal soft tissues measured 6 mm proximal to the most distal point of the dorsal cortex. **B,** Line *2* is the length of the palmar cortex measured from the solar margin at the distal toe to the palmar articular edge between the distal phalanx and the distal sesamoid bone. Distance *f* is the vertical distance or "founder" distance measured between coronary band and proximal edge of the extensor process. **C** and **D,** Radiographic measurements of the foot with chronic laminitis. **C,** Foot with chronic laminitis exhibiting displacement of the distal phalanx as rotation only. Lines *a* and *b* are no longer parallel and converge proximally, forming angle *ab* or the rotation angle. Distance *d* is greater than distance *p*. **D,** Foot with chronic laminitis exhibiting distal phalanx displacement as vertical displacement (sinking) only. Founder distance *f'* is increased. Distance *p* equals *d*, but both are greater than normal. The percentage that *d* is of line *2* will be greater than normal. (See text for normal and abnormal values.) (Reprinted from Lindford RL, O'Brien TR, Trout DR: Qualitative and morphometric radiographic findings in the distal phalanx and digital soft tissues of sound Thoroughbred racehorses, *Am J Vet Res* 54:38, 1993; and Cripps PJ, Eustace RA: Radiological measurements from the feet of normal horses with relevance to laminitis, *Equine Vet J* 31:427, 1999.)

critical. An oblique projection angle can alter measurement significantly. Likewise, placement of markers should be standardized. Failure to adhere to strict standardization renders comparative measurements unreliable.

A technique of digital venography has been developed and used to evaluate a number of foot problems including laminitis, but this will not be covered here.[52]

Studies of MR imaging for assessment of laminitis remain at the stage of feasibility and the correlation of cadaver findings with histopathology. Studies of horses with active phase and chronic state disease have been evaluated.[53,54] The study of active phase disease was done at 4.7 tesla (T), and it was possible to detect changes in laminar and corium structure and signal intensity that correlated strongly with the histologic diagnosis of acute laminitis. In another study at either 4.6 T or 7.1 T, isolated tissue blocks from the hooves of normal horses were evaluated and it was possible to visualize individual tissue layers providing a microscopic effect.[55] Thus MR imaging continues to show promise in furthering the knowledge of pathophysiology and progression of laminitis.

FLEXURAL DEFORMITY OF THE INTERPHALANGEAL JOINTS

Distal Interphalangeal Joint

The distal interphalangeal joint is the most commonly affected phalangeal joint. The clinical appearance varies with the degree of flexion from mild to an almost vertical orientation of the hoof wall to the ground (Fig. 23-33; see Fig. 23-11). Flexural deformity may be either congenital or acquired in the foal.[56] Older horses may develop a flexural deformity secondary to lesions of the accessory ligament of the deep digital flexor tendon or a chronic lesion in the tendon itself.[57] Radiography is used to assess changes in the distal phalanx and screen for unexpected bone or joint lesions. Changes in the distal phalanx range from none to varying irregularity of the



Fig. 23-33 Flexural deformity of the distal interphalangeal joint in a 4-month-old foal. The dorsal surface of the distal phalanx remains parallel to the dorsal hoof wall; however, both of these structures assume an abnormally vertical position. There is mild modeling of the toe of the distal phalanx. The straight course of the deep digital flexor tendon is visible.

solar margin centered at the toe. The irregularity is caused by widened vascular channels and bone resorption at the solar margin. If the deformity is corrected early, the bone changes can resolve to a normal appearance.

Proximal Interphalangeal Joint

Abnormal flexion alignment is uncommon at this joint and may be either congenital or acquired. Visually, a bulge in the dorsal pastern contour has been referred to as *dorsal subluxation;* this represents the position of distal aspect of the proximal phalanx relative to the normal pastern axis.[58,59] The proximal interphalangeal joint is, however, more flexed than normal. Thoroughbred racehorses have developed this malalignment after injury to the soft tissue support structures of the metacarpophalangeal joint.[58] Dorsal subluxation has also occurred after corrective desmotomy of the suspensory ligament for treatment of flexural deformities of the metacarpophalangeal joint.[58] A number of young horses with this deformity in the hindlimb have been observed. The flexion is noticeable when the horse is not bearing weight, but with full weight the alignment is reduced, often accompanied by a clicking sound.[59,60] A combination of deep digital flexor tendon contracture and concomitant superficial digital flexor tendon laxity has been postulated as the cause for this hindlimb deformity.[59] No specific bone changes other than joint alignment are expected.

Hyperextension Alignment of the Interphalangeal Joints

Hyperextension of the proximal interphalangeal joint is an unusual appearance that occurs with rupture of both the straight (superficial) sesamoidean ligament and the superficial digital flexor tendon. It may also be seen in combination with overextension of the distal interphalangeal and metacarpophalangeal joints as a congenital deformity in foals. No additional bone changes are typically present.[61]

Hyperextension of the distal interphalangeal joint may occur in newborn foals as a congenital abnormality affecting all three joints of the foot. Weakened flexor tendons may also be seen as a result of poor nutrition, slow or incomplete recovery from a systemic disease, or after prolonged periods of external support (splinting or casting) of the leg. Acquired hyperextension is also caused by rupture of the deep digital flexor tendon or avulsion of its insertion (Fig. 23-34). This lesion occurs with traumatic laceration of the tendon or extension of infection from a deep sole abscess to the palmar surface of the distal phalanx.



Fig. 23-34 Luxation of the distal interphalangeal joint as a result of severe trauma to the supporting soft tissue structures of the joint. Dorsal displacement of the distal phalanx is caused by avulsion of the deep digital flexor tendon insertion and the subsequent unreciprocated traction of the common digital extensor tendon. The distal sesamoidean impar ligament is also ruptured, allowing proximal displacement of the navicular bone.

OSSEOUS CYSTLIKE LESIONS

The phalanges are not affected by classical osteochondritis dissecans, meaning that osteochondral fragments associated with subchondral bone defects are not reported. However, single, round to conical, variably sized, radiolucent lesions surrounded by a thin or variably thick sclerotic rim occur in the phalanges. The phalanges are the second most common locations for such lesions; the stifle being the most common.[62] These have been called *subchondral cysts, osseous cysts, or subchondral cystlike osteochondrosis*, with the current preferred term *osseous cystlike lesions*. Because these lesions lack an epithelial lining and frequently communicate with the joint cavity, they are not true bone cysts. Etiology of these lesions is debated. In the young horse with no trauma history, the lesion is likely developmental. Subchondral bone ischemia and necrosis secondary to trauma, infection, and osteoarthritis has also been correlated with the presence of these cystlike lesions (see Fig. 23-29).[23]

Clinical expression of lameness is suggested to relate to the extent of articular surface involvement. Some lesions have no visible connection to the articular cartilage or joint space lucency. Others have a thin neck or a broader base of connection to the articular cartilage or joint space lucency. The lesions are most commonly found in the distal portion of either the proximal and middle phalanx. In the distal phalanx the lesion may be in the extensor process, at the weight-bearing surface, or at the insertion of the distal interphalangeal collateral ligaments or the distal sesamoidean impar ligament.[63] Some lesions have been found in clinically sound older

horses presented for prepurchase evaluation.[62] These lesions are generally evident radiographically. Those of small diameter or shallow depth can be subtle. MR (region of intermediate to high signal intensity on all sequences), scintigraphic (region of increased radionuclide uptake), and CT (low attenuating center surrounded by hyperattenuating rim) imaging can also be used to identify these lesions if radiographs are negative (Fig. 23-35).[62,64] The prognosis for return to successful performance depends on the extent of joint surface involved, presence of osteoarthritis, and treatment.

PEDAL OSTEITIS

Diffuse roughening of the solar border of the distal phalanx, creating a ragged, lacy appearance when viewed in the latero-medial or dorsal 65-degree proximal-palmarodistal projection, may be an indication of pedal osteitis (Fig. 23-36).[12] Pedal osteitis is the response of the distal phalanx to inflammation and is manifested by demineralization, either focal or more diffuse. The change is seen most commonly as a result of chronic bruising, sole abscess without extension of infection in the bone, flexural deformities, and other conditions.[65] Once the primary insult and pedal osteitis become inactive, little change in the appearance of the roughened contour of the solar margin is seen. Also, because the normal appearance of the solar surface of the distal phalanx varies considerably, a mild degree of irregularity may be normal and misinterpreted as disease. A positive response to hoof testers, an increased number and diameter of vascular channels seen concomitantly with demineralization of the bone, and thinning of the sole of the foot increase the probability of pedal osteitis being the cause of lameness. Thus clinical signs must be considered in the determination of whether a radiographically irregular



Fig. 23-35 Subchondral osseous cystlike lesion *(black arrows)* in palmarodistolateral aspect of the proximal phalanx found during evaluation of lameness that became sound with palmar digital nerve anesthesia. It is undetermined whether this is a lesion in development or resolution in this 5-year-old horse. Images are transverse **(A)**, dorsal **(B),** and sagittal **(C).**

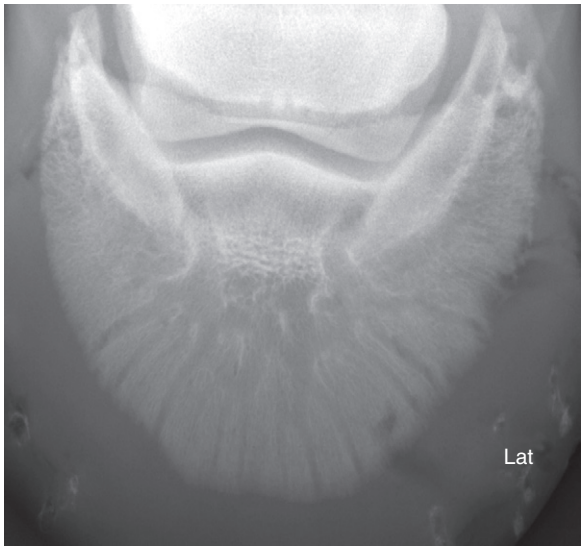


Fig. 23-36 Dorsal 65-degree proximal-palmarodistal view of the distal phalanx of a horse with pedal osteitis. The lateral solar border is irregular compared with the medial margin. The horse was sensitive to hoof testers in this region, and no lesions were found in the sole. Gas lucencies are the result of incomplete packing of the foot after the sole has been pared.

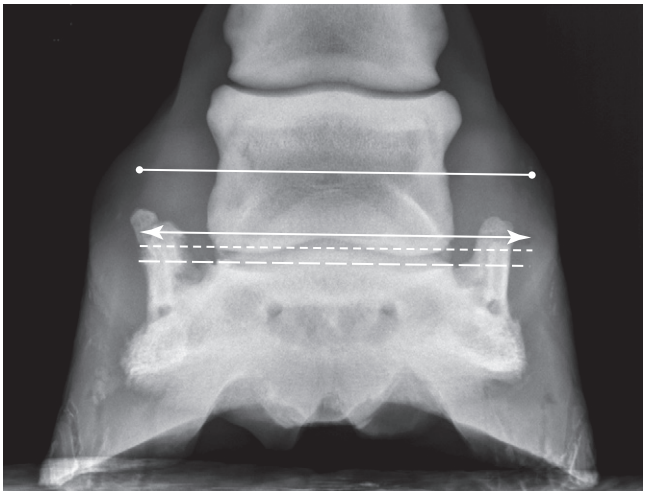


Fig. 23-37 This horse has ossification of the collateral cartilages. The *lines* demonstrate the levels used for the grading scheme to quantify ossification. Ossification to the level of the *dashed line* is grade 1; to the level of the *dotted line* is grade 2; to the level of the *line with arrows* is grade 3; to the level *between the line with arrows and line with dots* is grade 4; to the level *proximal to the line with dots* is grade 5. This horse has grade 4 ossification of both cartilages.

margin of the distal phalanx is an indicator of a current or previous pathologic condition.

COLLATERAL CARTILAGES

Ossification/Calcification (Sidebones)

This is a common finding in radiographs of the distal part of the digit, especially in draft-breed horses. Many consider this finding to be incidental or, if asymmetric within a foot, indicative of increased stress on the ossified portion.[22] A grading scheme has been used to grade the ossification as depicted in the weight-bearing horizontal dorsalpalmar view (Fig. 23-37).[66] Grade 0 is no ossification; grade 1 is minimal ossification at the base to the level of the medial/lateral joint margins of P3; grade 2 is mild ossification at the base extending to the central axial level of the distal interphalangeal joint; grade 3 is moderate ossification extending to the proximal border of the navicular bone (excluding proximal border enthesophytes); grade 4 is advanced ossification extending proximal to the navicular bone but within the distal half of the middle phalanx; grade 5 is extensive ossification extending to the level of the proximal half of the middle phalanx (see Fig. 23-21). Generally ossification begins at the base of the cartilage and advances proximally. Separate centers of ossification occur and can be located anywhere within the cartilage (Fig. 23-38). The grading scheme gives horses with a separate center of ossification a grade of 3. The radiolucent line that separates the center of ossification is smooth and should not be misinterpreted as a fracture. In a large number of Finnish and European horses, asymmetry between lateral and medial cartilage ossification was common, with lateral ossification being greater.[66,67] However, both front feet were affected typically and did not differ significantly when both cartilages were included. Grades 3 to 5 have been suggested to have an association with foot lameness. It is not clear whether there is a gender predilection for cartilage ossification. Higher grades of ossification in horses tended to occur with a low height-to-bodyweight ratio. Using MR imaging to determine the primary cause of foot lameness, a significant correlation was found in horses with possibly significant ossification and injuries of the collateral ligaments

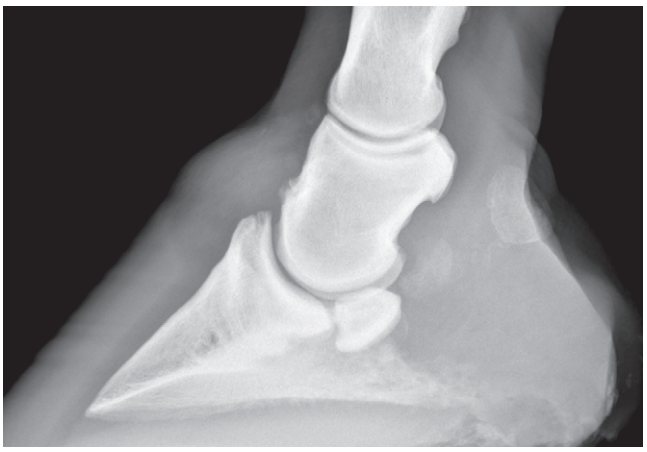


Fig. 23-38 The collateral cartilages have ossified from separate centers rather than from the base of attachment to the palmar processes. This pattern of ossification is given a grade 3. Additional abnormalities in this horse are degenerative joint disease of the distal interphalangeal joint (osteophytes on distal dorsal aspect of the middle phalanx and the extensor process of the distal phalanx) and enthesophyte formation on the proximal aspect of the middle phalanx and the distal aspect of the proximal phalanx (associated with the collateral ligament of the proximal interphalangeal joint).

of the distal interphalangeal joint and the distal phalanx.[67] The correlation was stronger with ipsilateral ossification and collateral ligament and distal phalangeal injury.

Fracture of the ossified collateral cartilage is uncommon. It is more likely to occur at the base attachment to the palmar process. Fracture borders are sharper and irregular compared to the borders of the gap between a separate center of ossification that has not fused to the base region. Scintigraphy and MR imaging are useful to establish the diagnosis.[68]

Infection (Quittor)

Penetrating wounds or lacerations in the coronary band region can introduce infection into the collateral cartilages. Necrosis associated with infection of this cartilage is called *quittor*. In

acute infections, radiography should be considered to rule out a metallic foreign body or deeper lesion in the adjacent bones. In chronic infections, a draining tract is typical. Extension to the distal interphalangeal joint is uncommon unless it occurs iatrogenically during aggressive establishment of drainage or debridement of the necrotic cartilage.

HOOF BALANCE

Unbalanced trimming and improper shoeing of the foot can result in lameness[69] and may lead to navicular syndrome and degenerative joint disease of the interphalangeal joints. Lateromedial and dorsopalmar radiographic views of the foot can be used in conjunction with direct measurements on the foot to assess foot balance.[2,70-73] When radiographic views are used in this manner, particular attention must be paid to positioning of the foot, the center of the x-ray beam, and degree of weight bearing on the limb being assessed. The measurements used to assess foot balance radiographically are shown in Figure 23-39. In the lateromedial view, the dorsal hoof wall should be parallel to the wall at the heel. The pastern axis, as seen in the lateromedial view, is a line that divides the middle phalanx into equal dorsal and palmar halves. Ideally, this line similarly bisects the proximal phalanx and is parallel to the dorsal cortex of the distal phalanx. When this line is carried through to intercept with a line on the bearing surface of the hoof wall, it should create an angle of 45 to 55 degrees (front foot) or 50 to 55 degrees (hind foot) with the bony solar margin.[70] Significant differences were induced in the angles of the interphalangeal joints when the hoof angle was altered.[70] The greatest difference in angle occurred in the distal interphalangeal joint. Clinically, such a change in the angle of the distal interphalangeal joint may have an effect on the strain on the deep digital flexor tendon.[70] The angle of intercept of a line parallel to the solar margin of the distal phalanx and the line of the weight-bearing surface of the hoof wall should be 5 to 10 degrees.[2] The length of the toe region compared with the heel region of the bearing surface of the hoof wall is judged by comparison with the distal interphalangeal joint. A line from the center of the best-fit circle of curvature of the joint space, when drawn perpendicular to the weight-bearing surface, should be at the middle of the weight-bearing surface.[2,72] The lateral and medial portions of the hoof wall should be of equal length. An elaborate set of measurements has been made on the dorsopalmar view to assess the effects of uneven mediolateral hoof wall trimming.[71,72] This method was used to assess the effects of using the corrective full rolling shoe in horses that were lame as a result of interphalangeal degenerative joint disease.[73]

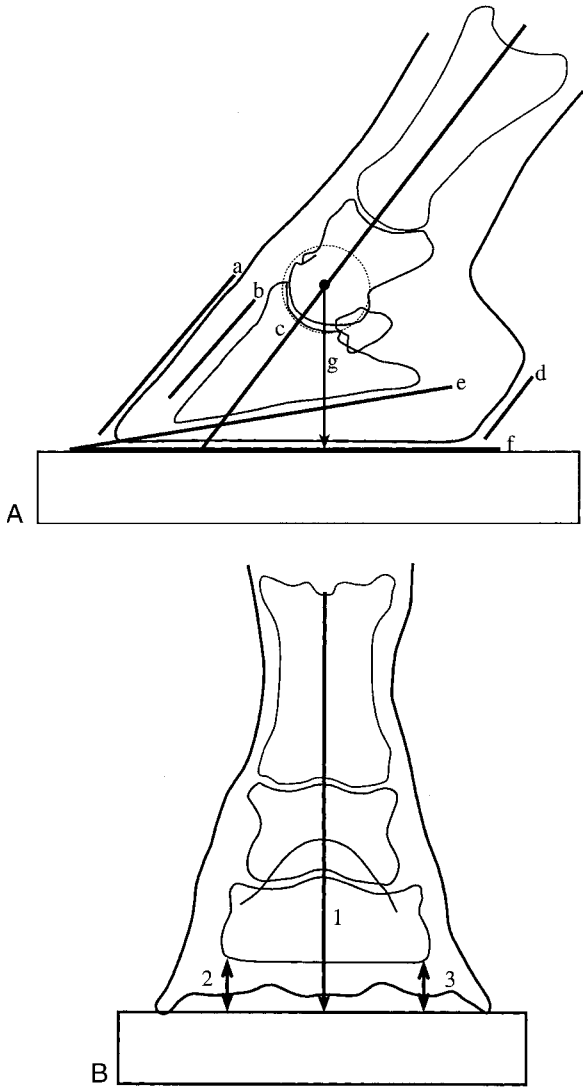


Fig. 23-39 Radiographic measurements for foot balance. **A,** Assessment from lateromedial view of normal foot. *a,* Line parallel to dorsal hoof wall; *b,* line parallel to dorsal cortex of the distal phalanx; *c,* line that bisects the middle phalanx into equal dorsal and palmar halves; *d,* line drawn parallel to the bulbs of the heel; *e,* line drawn parallel to the solar surface of the distal phalanx; *f,* line drawn parallel to the bearing surface of the hoof wall; *g,* line from center of best-fit circle for the distal interphalangeal joint drawn perpendicular to the bearing surface of the hoof wall. Line *a* should be parallel to lines *b, c,* and *d.* Line *g* should intersect at the midpoint of the bearing surface of the hoof wall. Angle *af,* 45 to 55 degrees in a front foot; 50 to 55 degrees in a hind foot; angle *ef,* 5 to 10 degrees. **B,** Assessment from dorsopalmar view of the normal foot. *1,* Line bisecting the phalanges; *2* and *3,* lines from respective lateral and medial solar margins of the distal phalanx to bearing surface of the hoof wall. These lines should be parallel to line *1.* Distance *2* = *3.*

MISCELLANEOUS DISEASES AFFECTING THE PHALANGES

Keratoma is an abnormal mass of hyperplastic squamous epithelial cells with abundant keratin and granulation tissue. These develop within the hoof wall arising from the stratum germinativum of the coronary band, from the inner dorsal wall, or in the sole and are uncommon. They are considered to be caused by traumatic or infectious insult to the hoof.[74] Lameness ranges from weeks to months and may be associated with unsuccessful resolution of presumed simple solar abscesses.

Visible deformity at the coronary band, of the hoof wall or sole is often clinically evident. The mass effect can cause localized osteolysis of an adjacent area of the distal phalanx. An oblique projection angle may be needed to demonstrate this feature. The margins of the lytic area are smooth, sometimes with a sclerotic margin, and the shape is typically round because the process of bone change is slow. Uncommonly, the mass may be partially mineralized.[75] Differential diagnoses for this type of bone lesion are septic pedal osteitis (margin should be more irregular); bone cyst (typically more centralized in the body of the distal phalanx); and squamous cell carcinoma, fibrosarcoma, or mast cell tumors of the hoof wall or sole tissues.[2,76] Histologic evaluation of soft tissue masses of the sole and hoof is needed for definitive diagnosis.

Epidermoid cyst at sites other than skin is a rare finding in the horse. Two reports in the foot region involved an intraosseous distal phalanx location in one horse and deep digital flexor tendon sheath in another.[77,78] The intraosseous lesion

was osteolytic but heterogenous radiographically and on CT images. The diagnosis was made histologically and differentiated from a keratoma by the absence of granulation tissue and associated inflammatory cells. The flexor tendon sheath cyst had no radiographic changes but was identified using MR imaging. The signal characteristics suggested a lesion containing proteinaceous material.

Hypertrophic osteopathy is rare in the horse. The lesions in the limbs are characterized by diffuse soft tissue swelling of all limbs and periosteal new bone formation in the diaphyseal regions of long bones, including the phalanges. The amount of new bone is variable. Most of the reports describe palisade or smooth new bone formation. Articular margins or surfaces are usually not altered. Of horses and donkeys with hypertrophic osteopathy, the phalanges were affected in approximately half.[79-82] The majority of animals had intrathoracic disease associated with the limb lesions. These horses presented for limb swelling or lameness and not direct clinical signs of the primary lesion. The bilateral symmetry, multilimb involvement, and pattern of the periosteal new bone are characteristic of hypertrophic osteopathy. As in the dog, the recognition of these characteristic bone lesions should prompt evaluation for thoracic disease. The etiology may be because of liberation of vascular endothelial growth factor, platelet-derived growth factor, prostaglandin E2, and growth hormone-releasing factor.[82]

Mastocytosis is a tumorous swelling of the skin that can sometimes involve the subcutis and adjacent muscle. A report summarized the findings in six horses; three had the lesion in the distal limb that created radiographic abnormalities.[83] The common radiographic lesion was localized soft tissue swelling several centimeters in size, with granular mineralization. A poorly defined periosteal new bone response was found in one horse with a pastern region lesion. However, this horse had been treated unsuccessfully, and the periosteal response may have been a consequence of treatment rather than a result of the mastocytosis. Although several lesions were close to a joint, no architectural lesions in the joint were identified. The Arab breed was overrepresented in this series.

Osteosarcoma is extremely rarely reported in the appendicular bones of the horse, with only six cases reported in the literature.[84] This diagnosis has been reported in the middle phalanx of a horse and the distal phalanx of a donkey. The radiographic appearance of the horse was similar to that in dogs with an aggressive mixed bone response. Pathologic fracture was present.

REFERENCES

1. Morgan JP, Neves J, Baker T: *Equine radiography*, Ames, 1991, Iowa State University.
2. Butler JA, Colles CM, Dyson SJ, Kold SE, Poulos PW: *Clinical radiology of the horse*, ed 3, Oxford, UK, 2008, Blackwell.
3. Schebitz H, Wilkens H: *Atlas of radiographic anatomy of the horse*, Philadelphia, 1978, Saunders.
4. Smallwood JE, Holliday SD: Xeroradiographic anatomy of the equine digit and metacarpophalangeal region, *Vet Radiol* 28:166, 1987.
5. Denoix JM: *The equine distal limb atlas of clinical anatomy and comparative imaging*, Ames, 2002, Iowa State University.
6. Becht JL, Park RD, Kraft SL, et al: Radiographic interpretation of normal skeletal variations and pseudolesions in the equine foot, *Vet Clin North Am Equine Pract* 17:1, 2001.
7. Kneller SK, Losonsky JM: Variable locations of nutrient foramina of the proximal phalanx in the forelimbs of Thoroughbreds, *J Am Vet Med Assoc* 197:736, 1990.
8. Losonsky JM, Kneller SK: Variable location of nutrient foramina of the proximal phalanx in the forelimbs of Standardbreds, *J Am Vet Med Assoc* 193:671, 1988.
9. Rendano VT, Grant B: The equine third phalanx: its radiographic appearance, *J Am Vet Radiol Soc* 19:125, 1978.
10. Linford RL, O'Brien TR, Trout DR: Qualitative and morphometric radiographic findings in the distal phalanx and digital soft tissues of sound Thoroughbred racehorses, *Am J Vet Res* 54:38, 1993.
11. Smallwood JE, Albright SM, Metcalf MR, et al: A xeroradiographic study of the developing equine foredigit and metacarpophalangeal region from birth to six months of age, *Vet Radiol* 30:98, 1989.
12. Kaneps AJ, Stover SM, O'Brien TR: Radiographic characteristics of the forelimb distal phalanx and microscopic morphology of the lateral palmar process in foals 3–32 weeks old, *Vet Radiol Ultrasound* 36:179, 1995.
13. Dyson S, Murray R, Schramme M, et al: Lameness in 46 horses associated with deep digital flexor tendonitis in the digit: diagnosis confirmed with magnetic resonance imaging, *Equine Vet J* 35:681, 2003.
14. Mair TS, Kinns J: Deep digital flexor tendonitis in the equine foot diagnosed by low-flied magnetic resonance imaging in the standing patient: 18 cases, *Vet Radiol Ultrasound* 46:458, 2005.
15. Dyson SJ, Murray P, Schramme MC: Lameness associated with foot pain: results of magnetic resonance imaging in 199 horses (January 2001–December 2003) and response to treatment, *Equine Vet J* 37:113, 2005.
16. Dakin SG, Dyson SJ, Murray RC, Tranquille C: Osseous abnormalities associated with collateral desmopathy of the distal interphalangeal joint: part 1, *Equine Vet J* 41:786, 2009.
17. Sampson SN, Schneider RK, Tucker RL, Gavin PR, Zubrod CJ, Ho CP: Magnetic resonance imaging features of oblique and straight distal sesamoidean desmitis in 27 horses, *Vet Radiol Ultrasound* 48:303, 2007.
18. McIlWraith CW, Goodman NL: Conditions of the interphalangeal joints, *Vet Clin North Am Equine Pract* 5:161,1989.
19. Kawcak CE, McIlwraith CW: Proximodorsal proximal phalanx osteochondral chip fragmentation in 336 horses, *Equine Vet J* 26:392, 1994.
20. Fackleman GE, Peutz IP, Norris JC, et al: The development of an equine fracture documentation system, *Vet Comp Orthop Trauma* 6:47, 1993.
21. Stashak TS: *Adams' lameness in horses*, ed 5, Philadelphia, 2002, Lippincott Williams & Wilkens.
22. Ross MW, Dyson SJ: *Diagnosis and management of lameness in the horse*, ed 2, St. Louis, 2011, Saunders.
23. Kuemmerle JM, Auer JA, Rademacher N, Lischer CJ, Bettschart-Wolfensberger R, Furst AE: Short incomplete sagittal fractures of the proximal phalanx in ten horses not used for racing, *Vet Surg* 37:193, 2008.
24. Goodman NL, Baker BK: Lameness diagnosis and treatment in the quarter horse racehorse, *Vet Clin North Am Equine Pract* 6:85, 1990.
25. Ramzan PHL, Powell SE: Clinical and imaging features of suspected prodromal fracture of the proximal phalanx in three Thoroughbred racehorses, *Equine Vet J* 42:164, 2010.
26. Rose PL, Seeherman H, O'Callaghan MO: Computed tomographic evaluation of comminuted middle phalangeal fractures in the horse, *Vet Radiol Ultrasound* 38:424,1997.
27. Honnas CH, O'Brien TR, Linford RL: Distal phalanx fractures in horses: a survey of 274 horses with radiographic assessment of healing in 36 horses, *Vet Radiol* 29:98, 1989.

28. Dechant JE, Trotter GW, Stashak TS, Hendrickson DA: Removal of large fragments of the extensor process of the distal phalanx via arthrotomy in horses: 14 cases (1992–1998), *J Am Vet Med Assoc* 217:1351, 2000.
29. Crowe OM, Hepburn RJ, Kold SE, Smith RK: Long-term outcome after arthroscopic debridement of distal phalanx extensor process fragmentation in 13 horses, *Vet Surg* 39:107, 2010.
30. Kaneps AJ, O'Brien TR, Redden RF, et al: Characterization of osseous bodies of the distal phalanx of foals, *Equine Vet J* 25:285, 1993.
31. Kaneps AJ, O'Brien TR, Willits NH, et al: Effect of hoof trimming on the occurrence of distal phalangeal palmar process fractures in foals, *Equine Vet J* 26(Suppl): 36, 1998.
32. Lenard ZM, Lester NV, O'Hara AJ, Hopper BJ, Lester GD: Disseminated cryptococcosis including osteomyelitis in a horse, *Aust Vet J* 85:51, 2007.
33. Baird AN, Seahorn TL, Morris EL: Equine distal phalangeal sequestration, *Vet Radiol* 31:210, 1990.
34. Cauvin ERJ, Munroe GA: Septic osteitis of the distal phalanx: findings and surgical treatment in 18 horses, *Equine Vet J* 30:512, 1998.
35. Neil KM, Axon JE, Todhunter PG, Adams PL, Caron JP, Adkins AR: Septic osteitis of the distal phalanx in foals: 22 cases (1995–2002), *J Am Vet Med Assoc* 230:1683, 2007.
36. Neil KM, Axon JE, Begg AP, Todhunter PG, Adams PL, Fine AE, Caron JP, Adkins AR: Retrospective study of 108 foals with septic osteomyelitis, *Aust Vet J* 88:4, 2010.
37. Steel CM, Hunt AR, Adams PL, et al: Factors associated with prognosis for survival and athletic use in foals with septic arthritis: 93 cases (1987–1994), *J Am Vet Med Assoc* 215:973, 1999.
38. Honnas CM, Vacek JR, Schumacher J: Diagnostic and therapeutic protocols for septic arthritis of the distal interphalangeal joint, *Vet Med* Dec:1215, 1992.
39. Pool RR, Meagher DM: Pathologic findings and pathogenesis of racetrack injuries, *Vet Clin North Am Equine Pract* 6:1, 1990.
40. Pool RR: Pathologic manifestations of joint disease in the athletic horse. In McIlwraith CW, Trotter GW, editors: *Joint disease in the horse*, Philadelphia, 1996, Saunders.
41. Caston SS: Ethyl alcohol for chemical arthrodesis of the proximal interphalangeal joint. In *Proceedings 56th annual American association of equine practitioners*, Baltimore, Md, December 2010, p 140.
42. Zubrod CH, Schneider RK, Tucker RL, et al: Use of magnetic resonance imaging for identifying subchondral bone damage in horses: 11 cases (1999–2003), *J Am Vet Med Assoc* 224:411, 2004.
43. Olive J: Distal interphalangeal articular cartilage assessment using low-field magnetic resonance imaging, *Vet Radiol Ultrasound* 51:259, 2010.
44. Pollitt CC: Microscopic anatomy and physiology of the hoof. In Floyd AE, Mansmann RA, editors: *Equine podiatry*, St. Louis, 2007, Saunders, p 90.
45. Pollitt CC: Laminitis pathophysiology. In Floyd AE, Mansmann RA, editors: *Equine podiatry*, St. Louis, 2007, Saunders, p 313.
46. Peloso JG, Cohen ND, Walker MA, et al: Case-control study of risk factors for the development of laminitis in the contralateral limb of Equidae with unilateral lameness, *J Am Vet Med Assoc* 209:1746, 1996.
47. Hood DM: Laminitis in the horse, *Vet Clin North Am Equine Pract* 15:287, 1999.
48. Floyd AE, Mansmann RA, editors: *Equine podiatry*, St. Louis, 2007, Saunders.
49. Cripps PJ, Eustace RA: Radiological measurements from the feet of normal horses with relevance to laminitis, *Equine Vet J* 31:427, 1999.
50. Orsini JA, Parsons CS, Capewell L, Smith G: Prognostic indicators of poor outcome in horses with laminitis at a tertiary care hospital, *Can Vet J* 51:623, 2010.
51. Hunt RJ, Wharton RE: Clinical presentation, diagnosis, and prognosis of chronic laminitis in North America, *Vet Clin North Am Equine Pract* 26:141, 2010.
52. Rucker A: Equine venography and its clinical application in North America, *Vet Clin North Am Equine Pract* 26:167, 2010.
53. Murray RC, Dyson SJ, Schramme MC, et al: Magnetic resonance imaging of the equine digit with chronic laminitis, *Vet Radiol Ultrasound* 44:609, 2004.
54. Arble JB, Mattoon JS, Drost WT, et al: Magnetic resonance imaging of the initial active stage of equine laminitis at 4.7T, *Vet Radiol Ultrasound* 50:3, 2009.
55. Keller MD, Galloway GJ, Pollitt CC: Magnetic resonance microscopy of the equine hoof wall: a study of resolution and potential, *Equine Vet J* 38:461, 2006.
56. Auer, JA: Diagnosis and treatment of flexural deformities in foals, *Clin Tech Equine Pract* 5:282, 2006.
57. Yiannikoruis S, Schneider RK, Samson SN, Roberts G: Desmotomy of the accessory ligament of the deep digital flexor tendon in the forelimb of 24 horses 2 years and older, *Vet Surg* 40:272, 2011.
58. Grant BD: The pastern joint. In Mansmann RA, McAllister EG, editors: *Equine medicine and surgery*, ed 3, Santa Barbara, Calif, 1982, American Veterinary Publications.
59. Shiroma JT, Engel HN, Wagner PC, et al: Dorsal subluxation of the proximal interphalangeal joint in the pelvic limb of three horses, *J Am Vet Med Assoc* 195:777, 1989.
60. Wagner PC, Watrous BJ: *Equine pediatric orthopedics: a practitioner monograph*, Santa Barbara, Calif, 1991, Veterinary Practice Publishing.
61. Wagner PC, von Matthiessen P: Treating congenital limb deformities in the foal, *Vet Med* 989, 1993.
62. Sherlock CE, Mair TS: Osseous cyst-like lesions/subchondral bone cysts of the phalanges, *Equine Vet Educ* 23:191, 2011.
63. Barrett MF, Zubrod CJ: Use of magnetic resonance imaging to detect and direct therapy of osseous cystic lesions at the solar surface of the third phalanx of a horse, *Equine Vet Educ* 20:19, 2008.
64. Mair TS, Sherlock CE: Osseous cyst-like lesions in the feet of lame horses: diagnosis by standing low-field magnetic resonance imaging, *Equine Vet Educ* 20:47, 2008.
65. Reeves MJ, Yovich JV, Turner AS: Miscellaneous conditions of the equine foot, *Vet Clin North Am Equine Pract* 5:221, 1989.
66. Down SS, Dyson SJ, Murray RC: Ossification of the cartilages of the foot, *Equine Vet Educ* 19:51, 2007.
67. Dyson S, Brown V, Collins S, Murray, R: Is there an association between ossification of the cartilages of the foot and collateral desmopathy of the distal interphalangeal joint or distal phalanx injury? *Equine Vet J* 42:504, 2010.
68. Dakin SG, Robson KE, Dyson SJ: Fractures of ossified cartilages of the foot: 10 cases, *Equine Vet Educ* 18:130, 2006.
69. Moyer W, Anderson JP: Sheared heels: diagnosis and treatment, *J Am Vet Med Assoc* 166:53, 1975.
70. Bushe T, Turner TA, Poulos P, et al: The effect of hoof angle on coffin, pastern, and fetlock joint angles, *Proc Am Assoc Equine Pract* 33:729, 1987.
71. Caudron I, Grulke S, Farnir F, et al: Radiographic assessment of equine interphalangeal joints asymmetry:

articular impact of phalangeal rotations (part I), *J Vet Med* 45:319, 1998.
72. Caudron I, Grulke S, Farnir F, et al: Radiographic assessment of equine interphalangeal joints asymmetry: articular impact of asymmetric bearings (part II), *J Vet Med* 45:327, 1998.
73. Caudron I, Miesen M, Grulke S, et al: Radiological assessment of the effects of a full rolling motion shoe during asymmetrical bearing, *Equine Vet J* 23(Suppl):20, 1997.
74. Boys Smith SJ, Clegg PD, Hughes I, Singer ER: Complete and partial hoof wall resection for keratoma removal: post operative complications and final outcome in 26 horses (1994–2004), *Equine Vet J* 38(2):127, 2006.
75. Valentine BA, Scott EA, Watrous BJ, Stonecipher CR: What is your diagnosis? Keratoma in a horse's hoof, *J Am Vet Med Assoc* 217(7):993, 2000.
76. Ritmeester AM, Denicola DB, Blevins WE, et al: Primary intraosseous mast cell tumor of the third phalanx in a quarter horse, *Equine Vet J* 29:151, 1997.
77. Sanz MG, Sampson SN, Schneider RK, Gavin PR, Baszler TV: Detection of an epidermoid cyst in the foot of a horse by use of magnetic resonance imaging, *J Am Vet Med Assoc* 228:1918, 2006.
78. Headley SA, Kummala E, Saarinen H, Tupamaki A, Tulamo RM: Diagnostic exercise: intraosseous epidermoid cysts in the third phalanx of a dressage mare, *Vet Pathol* 46:355, 2009.
79. Messer NT, Powers BE: Hypertrophic osteopathy associated with pulmonary infarction in a horse, *Comp Contin Educ Vet Pract* 5:S636, 1983.
80. Sweeney CR, Stebbins KE, Schelling CG, et al: Hypertrophic osteopathy in a pony with a pituitary adenoma, *J Am Vet Med Assoc* 195:103, 1989.
81. Mair TS, Dyson SJ, Frasser JA, et al: Hypertrophic osteopathy (Marie's disease) in Equidae: a review of twenty-four cases, *Equine Vet J* 28:256, 1996.
82. Tomlinson JE, Divers TJ, McDonough SP, Thompson MS: Hypertrophic osteopathy secondary to nodular pulmonary fibrosis in a horse, *J Vet Intern Med* 25(1):153, 2011.
83. Samii VF, O'Brien TR, Stannard AA: Radiographic features of mastocytosis in the equine limb, *Equine Vet J* 29:63, 1997.
84. Cillan-Garcia E, Kearns LJ, Hetzel U, Harrison LJ: Osteosarcoma of the middle phalanx in a horse, *Equine Vet Educ* 22:535, 2010.

ELECTRONIC RESOURCES

evolve

Additional information related to the content in Chapter 23 can be found on the companion Evolve website at http://evolve.elsevier.com/Thrall/vetrad/

- Chapter Quiz

CHAPTER • 24

The Equine Navicular Bone

Federica Morandi

ANATOMY

The normal radiographic anatomy of the navicular bone (distal sesamoid bone) is shown in Chapter 13. The navicular bone has two surfaces (flexor and articular), two borders (proximal and distal), and two extremities (medial and lateral). The navicular bone typically ossifies from a single center (Fig. 24-1).[1] The navicular bone has two separate hyaline cartilage-covered articular surfaces. The larger proximal articular surface conforms to the condyles of the middle phalanx. A smaller distal articular surface, associated with the distal navicular border, is essentially a narrow facet that articulates with the distal phalanx. The distal articular surface of the navicular bone and the articular surface of the distal phalanx are usually parallel but can be convergent.[2] The flexor surface has a prominent central ridge—termed the *central eminence*. The deep digital flexor tendon and adjacent bursa make contact with the fibrocartilage-covered flexor surface. The navicular bone is held in position by three strong ligaments. The paired suspensory navicular ligaments originate from the dorsolateral and dorsomedial aspects of the proximal phalanx and attach to the proximal navicular border and both extremities. The distal sesamoidean impar ligament originates from a projection on the distal navicular border just caudal to the articular surface and inserts on the distal phalanx deep to the deep digital flexor tendon. Blood vessels and sensory nerves traverse these ligaments and ramify into the navicular bone and synovial membrane by way of both borders.[3] No evidence exists for an anatomic communication between the distal interphalangeal joint and the navicular bursa.[4]

INDICATIONS FOR RADIOGRAPHY

Radiography is the first imaging modality employed for evaluation of the navicular bone.[5] Indications include assessment of bony changes in navicular syndrome, the identification of significant bone abnormalities during prepurchase examination, the assessment of bone or bursal involvement in foot wounds or abscesses, the evaluation of suspected trauma, and the collection of information about the morphologic progression or remission of navicular bone abnormalities.

PREPARATION FOR RADIOGRAPHIC EVALUATION

Accurate radiographic evaluation of the navicular bone depends on a radiograph that is properly positioned and exposed and on a foot that is free of distracting artifacts. Proper preparation for navicular radiography is similar to that for the distal phalanx, as discussed in Chapter 23.

Positioning aids, such as a reinforced cassette, grooved wooden blocks, and a cassette tunnel, assist in radiographic evaluation of the navicular bone (Fig. 24-2). Use of a grid for angular dorsoproximal-palmarodistal views is optional. A grid

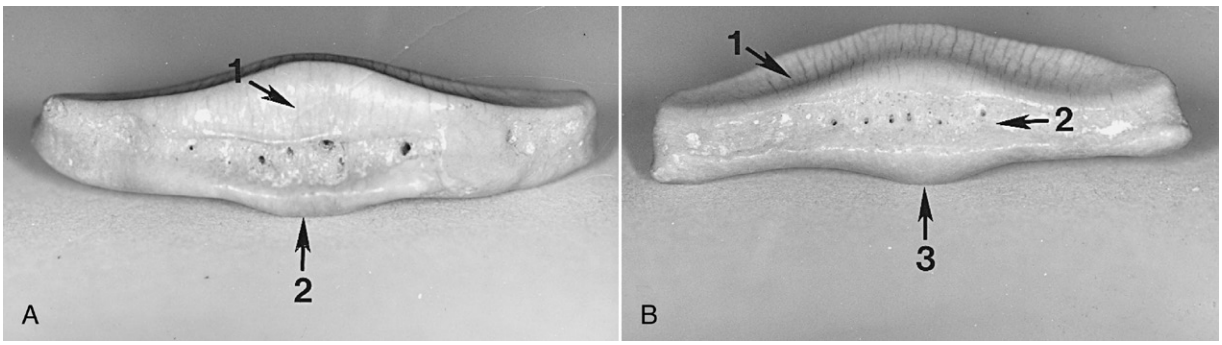


Fig. 24-1 The navicular bone. **A,** En face view of the distal border. *1*, The small articular surface with the distal phalanx; *2*, the projection off the distal border where the impar ligament attaches. **B,** En face view of the proximal border. *1*, The articular surface with the middle phalanx; *2*, the proximal border itself where the suspensory navicular ligament attaches; *3*, the central eminence. The view in **B** is analogous to that obtained in a palmaroproximal-palmarodistal radiograph.

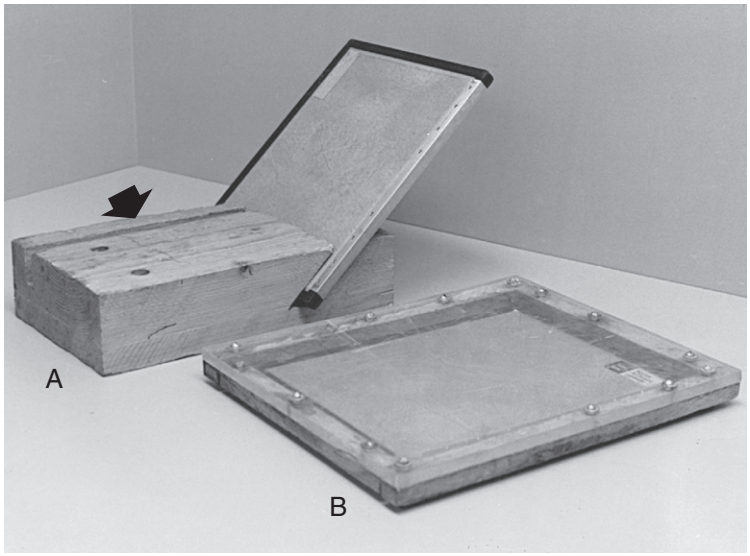


Fig. 24-2 Types of positioning aids for navicular radiography. *A*, A wooden block for angular dorsoproximal-palmarodistal views. The longitudinally oriented slot *(arrow)* is used for lateral views. The grooves are of sufficient width to allow combined insertion of a grid and cassette. *B*, A cassette tunnel covered with Plexiglas protects the cassette (and grid) during dorsoproximal-palmarodistal views.

Box • 24-1

Radiographic Views of the Navicular Bone

Dorsoproximal-Palmarodistal Views
High coronary stand-on route
- 45 degrees: Projects proximal border and extremities
- 65 degrees: Projects both borders and extremities

Upright pedal route
- 90 degrees: Projects proximal border and extremities
- 80 degrees: Projects both borders and extremities

Lateromedial View
Foreshortened projection along the axis of the bone
- Projects both borders and both surfaces in profile
- Extremities are superimposed

Palmaroproximal-Palmarodistal View ("Skyline" View)
Beam is angled tangential to the flexor surface
- Projects the flexor cortex, medulla, and central eminence
- Extremities are obscured by palmar processes of distal phalanx

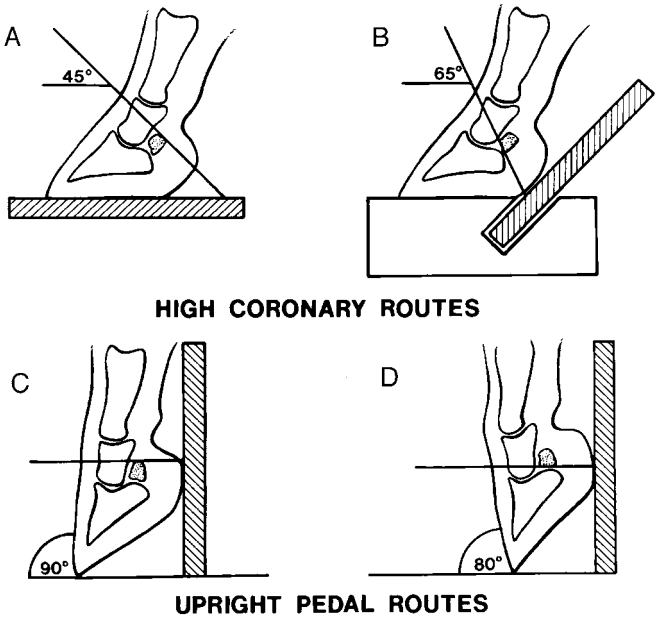


Fig. 24-3 Angular dorsoproximal-palmarodistal views. High coronary routes: **A,** Direct stand-on method. **B,** Wooden block technique. **C** and **D,** Upright pedal routes illustrated showing beam or hoof angulation relative to the horizontal plane. Only the proximal navicular border is well visualized in **A** and **C,** whereas both proximal and distal borders are clearly projected in **B** and **D.**

improves radiographic detail by reducing film fog from scatter radiation. Because the grid is fragile, its use is limited to techniques during which the foot does not bear weight directly on the grid, such as with a cassette tunnel.

RADIOGRAPHIC VIEWS

The location of the navicular bone and its complex shape require that at least three different views be made for complete evaluation. These include the angular dorsoproximal-palmarodistal views, the lateromedial view, and the palmaroproximal-palmarodistal (also called *skyline*) view (Box 24-1).[2] The horizontal beam dorsopalmar view is an additional view that is helpful for evaluating the extremities of the navicular bone. In addition, dorsoproximolateral-palmarodistomedial and dorsoproximomedial-palmarodistolateral views project the extremities of the navicular bone without superimposition on the middle phalanx.

Dorsoproximal-Palmarodistal Views

Angular dorsoproximal-palmarodistal views of the navicular bone may be made by two different hoof-positioning techniques.[6,7] These methods include (1) the high coronary stand-on route, in which the foot stands directly on a reinforced cassette, cassette tunnel, or grooved wooden block; the x-ray beam is centered just proximal to the coronary band and angled 45 or 65 degrees distally from horizontal and (2) the upright pedal route, in which the hoof rests on the toe in tiptoe fashion, with the dorsal hoof wall positioned either 80 or 90 degrees from horizontal; the x-ray beam is directed horizontally (Fig. 24-3).

By varying the x-ray beam angulation incident on the navicular bone in the high coronary route or by altering the

position of the hoof in the upright pedal route, an accurate projection of either the proximal or distal navicular border can be obtained. This is because the proximal and distal navicular borders are not parallel (they diverge in a palmar direction), and thus a true geometric projection of both borders cannot be obtained in a single dorsoproximal-palmarodistal radiograph.

An undistorted projection of the proximal navicular border is achieved by using the 45-degree high coronary stand-on route or the 90-degree upright pedal route. The distal navicular border is obscured by these routes because it is projected below the level of the distal interphalangeal joint. Because only the proximal navicular border can be evaluated accurately in these two projections, they are used as supplemental views (Fig. 24-3, *A* and *C*).

A 65-degree high coronary stand-on route or an 80-degree upright pedal route projects the distal navicular border proximal to the distal interphalangeal joint and superimposes the entire navicular bone behind the middle phalanx. The distal navicular border is well visualized, and although the proximal border is slightly distorted, it is readily identified. Either one of these two positioning methods is recommended for the angular dorsoproximal-palmarodistal projection because when they are done properly, the entire navicular bone is projected through the middle phalanx (Fig. 24-3, *B* and *D*).

Stand-on techniques are technically easier but result in slightly more magnification of the navicular bone when compared with the upright pedal route.[6] Magnification can be minimized on the high coronary stand-on route by using a grooved wooden block. A cassette and grid are placed in a precut groove behind the hoof as it rests on the block. Because of the position of the cassette, less magnification of the navicular bone occurs when compared with other stand-on techniques (see Fig. 24-3, *B*).

Lateromedial View

In the lateral view, both navicular extremities should be projected superimposed. If some degree of angulation occurs, this factor must be recognized and taken into account during interpretation or an incorrect assessment of navicular bone remodeling (sclerosis) will be made. The foot is placed on a wooden block so that the x-ray tube can be positioned low enough to center the beam on the lateral (transverse) axis of the navicular bone. A wooden block also elevates the hoof, allowing the cassette to straddle it proximally and distally. The entire hoof should be included on the radiograph.

Palmaroproximal-Palmarodistal View

The palmaroproximal-palmarodistal view, also called skyline view (Fig. 24-4), projects the flexor cortex, medulla, and central eminence. The concept is to isolate most of the bone between the palmar processes of the distal phalanx. The horse stands on a reinforced cassette or cassette tunnel. The foot is positioned as far caudal as possible while still bearing weight.[8] Local analgesia may be required to obtain ideal foot positioning. Regardless of foot location, the primary beam is positioned tangential to the estimated plane of the flexor cortex and is centered between the bulbs of the heel. Too steep of a beam angle with the foot may result in superimposition of the ergot over the navicular bone. Reduced angulation alters the apparent width of the flexor cortex and results in an indistinct interface between cortical and trabecular bone and leads to an erroneous diagnosis of medullary sclerosis.[8] Excessive superimposition of the palmar processes of the distal phalanx on the navicular bone can also occur. Oblique palmaroproximal-palmarodistal projections distort the navicular shape and superimpose it behind the palmar processes of the distal phalanx.

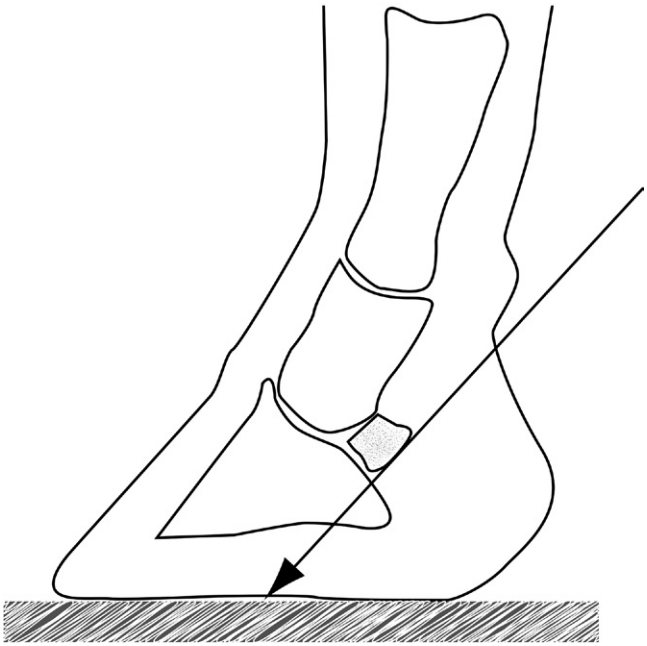


Fig. 24-4 Setup to acquire a palmaroproximal-palmarodistal view of the navicular bone. The distal interphalangeal joint is positioned in extension, with the x-ray beam angled tangentially to the flexor surface of the navicular bone.

Dorsopalmar View

In the dorsopalmar view, the x-ray beam is directed horizontally toward the hoof, which is in a normal weight-bearing position. The foot should be placed on a wooden block to allow the cassette to straddle the hoof and the navicular bone. This view is useful in evaluating the extremities of the navicular bone, particularly when subtle abnormalities are suspected.

NORMAL RADIOGRAPHIC APPEARANCE

In the angular dorsoproximal-palmarodistal views, the navicular bone is of uniform radiopacity. Its spindle shape varies somewhat from horse to horse. The extremities are fairly symmetric and are bluntly pointed. The proximal border is smoothly marginated. The shape of the proximal border has been classified variously as concave, undulating, straight, or convex.[9,10] The distal border has a variable number (usually no more than seven) of cone-shaped radiolucencies representing synovial invaginations. Their size is variable, with the height being approximately 1.5 times the width of the cone at the base. Size is related to degree of work, although their shape should remain somewhat triangular.

The lateral view offers a clear, unobstructed view of the navicular bone but presents a foreshortened image. Both extremities should be superimposed; a well-defined medullary cavity is visualized. The flexor surface is convex palmarly and is smoothly marginated. In some normal horses, a smoothly marginated dimple of variable depth is seen in the mid-portion of the central eminence. The proximal and distal borders are smooth, as are the articular surfaces. Some horses may have a mild elongation of the proximal or distal border, or both.[2] The joint space between the navicular bone and the distal phalanx is usually parallel, but a convergent joint is sometimes present.

In the palmaroproximal-palmarodistal view, a well-defined medullary cavity of uniform trabecular pattern with four or five small radiolucent invaginations may be seen. The cortex is of homogeneous opacity and is of uniform thickness

centrally, with some thinning peripherally. The width of the flexor cortex varies from 2.0 to 3.6 mm because of breed differences and geometric magnification.[2,8] The flexor surface is smoothly marginated with a central eminence, which is usually rounded and prominent, but in some horses may appear flattened normally. A small crescent-shaped radiolucency may be seen within the cortex of the central eminence, representing a normal midsagittal synovial fossa. This fossa is occasionally seen as a dimple on the flexor surface on the lateral view. In some horses, a lucent crescent is seen within the central eminence, even in bones without a dimple. This is caused by a trabecular bone island interposed between two parallel cortical bone plates of the central eminence.[11,12] The ends of both extremities are rounded, being variably superimposed over the palmar processes of the distal phalanx. The articular surface is occasionally seen in this view.

NAVICULAR DISEASE

The term *navicular disease* is used in this discussion to denote a chronic progressive syndrome involving the navicular bone, its fibrocartilaginous flexor surface, its surrounding soft tissues, including the deep digital flexor tendon, distal sesamoidean impar ligament, collateral ligaments, and navicular bursa, and the distal interphalangeal joint.[5] The precise source of pain in navicular lameness remains unclear. Variable response to local analgesia of the medial and lateral palmar digital nerves, the distal interphalangeal joint space, and the navicular bursa is noted. This variable response suggests that sensory nerves innervating the synovial membranes of the collateral sesamoidean ligament, the distal sesamoidean impar ligament, and the navicular bone itself play a separate or combined role in mediating pain in navicular disease.[4,13] In addition, pain arising from the dorsal margin of the sole has been shown to be attenuated by analgesia of the distal interphalangeal joint or palmar digital nerve block.[14] This further complicates the interpretation of nerve block results in horses suspected of having navicular origin pain.

Navicular disease is primarily a slowly developing, intermittent, bilateral forelimb lameness.[15] It is also occasionally recognized in the hindlimb. In general, navicular disease is most common between 3 and 18 years of age, with a peak incidence of 9 years of age at presentation. Males have involvement more often than do females, geldings have a greater risk than stallions, and the breed prevalence varies according to the population characteristics of the reporting institutions.[16,17] Genetic factors have been implied in the susceptibility to navicular disease: for example, horses with a more concave or undulating proximal border have higher risk of developing the disease, presumably because of altered distribution of biomechanical forces.[5]

No pathognomonic clinical test is available for navicular disease. The diagnosis is based on a characteristic gait, localization of pain to the palmar part of the foot, identification of radiographic signs of navicular degeneration, and elimination of other causes of lameness.[15,18] When navicular lameness is suspected, both feet should be radiographed because radiographic changes are often bilateral even if clinical signs are not.

The pathophysiology of navicular disease is multifactorial; although there is no consensus on the exact pathogenesis of navicular disease, current research tends to support a biomechanical etiology, rather than vascular abnormalities.[19] Classically, navicular disease has been characterized as navicular fibrocartilaginous degeneration with secondary tendon fibrillation, and later development of palmar cortex bone erosions.[15,18] Recently, the timing of onset of these abnormalities has been questioned, and there is some evidence that vascular and matrix changes within the deep digital flexor tendon may precede changes in the fibrocartilage of the navicular bone.[19,20] Other bony changes involving the distal border synovial invaginations (enlargement) have also been noted.[21] Abnormalities such as dilated vessels, vascular thrombosis, granulation tissue, and empty synovium-lined invaginations have been observed histologically to a variable degree.[3,18-24] The presence of histologic abnormalities in the distal sesamoidean impar ligament and sesamoidean collateral ligaments has also been described.[25] Whether these findings represent a continuum of events or are separate, isolated abnormalities remains unclear. Enthesopathy involving the ligaments of the proximal and distal borders can occur with or without distal border foramina changes.

Similar confusion exists regarding the significance of radiographic changes in the navicular bone in horses with lameness attributed to navicular disease. Poor correlation of pathologic and radiographic findings with clinical signs and prognosis has been demonstrated.[16,23,26] Horses without radiographic abnormalities may have clinical navicular lameness, and horses with pathologic and radiographic changes may be sound.[23,27] This paradox is explained in part by the fact that horses have different pain thresholds, are subjected to wide ranges of physical exercise, and are evaluated in variable stages of disease.[8] Additionally, some pathologic changes may represent insignificant wear lesions or may be located in tissues of soft tissue opacity and thus are not radiographically discernible.[18,28] Some authors agree that radiographic signs of navicular disease in an otherwise clinically normal horse are significant and may warrant a cautious prognosis for future soundness.[8,29] However, no universal agreement exists regarding the clinical significance of all radiographic signs seen in navicular disease.

Radiographic Signs of Navicular Degeneration

Radiographic abnormalities associated with navicular degeneration are varied. Bony abnormalities may occur separately but usually occur in combination, unilaterally or bilaterally. Their clinical relevance regarding presence, absence, or degree of lameness in a given animal is varied.[26] Additionally, no clear association exists between changes in the radiographic appearance of navicular bones and clinical outcome after treatment.[30] Thus, radiographic changes of navicular degeneration must be interpreted in context with the presenting clinical signs. This is similar for other musculoskeletal conditions.

The major radiographic signs of navicular degeneration are shown in Box 24-2. A diagram depicting various radiographic

Box • 24-2

Roentgen Signs of Navicular Degeneration

Proximal Border and Extremities
Enthesophytes (spurs) on the extremities
Remodeling

Distal Border Changes
Synovial invaginations
Small osseous fragments

Flexor Cortex Changes
Cortical erosions
Mineralization of deep digital flexor tendon

Medullary Cavity Changes
Radiolucent cysts
Sclerosis

signs of navicular degeneration is shown in Figure 24-5. Radiographic manifestations of navicular degeneration and normal variants are shown in Figures 24-6 through 24-9.

Proximal Border and Navicular Bone Extremities

The heredity aspects of the shape of the proximal navicular border and its relation to risk for navicular syndrome have been studied in Warmbloods.[9] The conclusion was that horses with a convex-shaped proximal border had the least risk for development of severe navicular disease.

Dystrophic mineralization at sites of ligamentous or tendon attachment is termed *enthesophytosis*.[24,31] Mineralization of the suspensory navicular ligament along the proximal border results in a roughened or undulating appearance of the bone

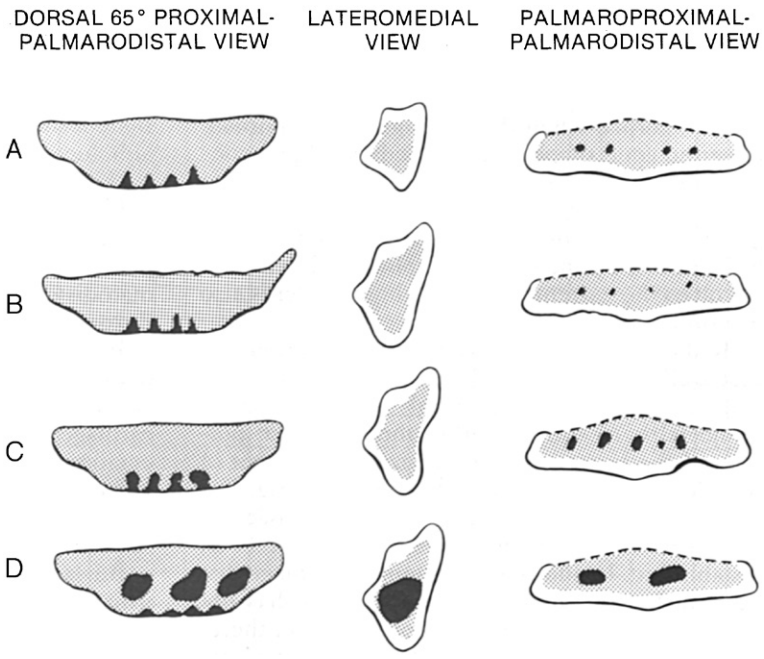


Fig. 24-5 Radiographic changes seen in navicular degeneration. Dorsal 65-degree proximal-palmarodistal view: *A*, normal; *B*, remodeling enthesophyte on extremity and irregular proximal border; C, lollipop-shaped invaginations on distal border; *D*, cystlike lesion formation. Lateromedial view: *A*, normal; *B*, elongated navicular profile from remodeling (enthesophyte formation); C, flexor cortical erosion; *D*, cystlike lesion formation. Palmaroproximal-palmarodistal view: *A*, normal; *B*, flexor cortical erosions; C, enlarged fossae and flexor cortical erosions; *D*, cystlike lesion formation. (Modified with permission from Richard Park, Fort Collins, Colo.)

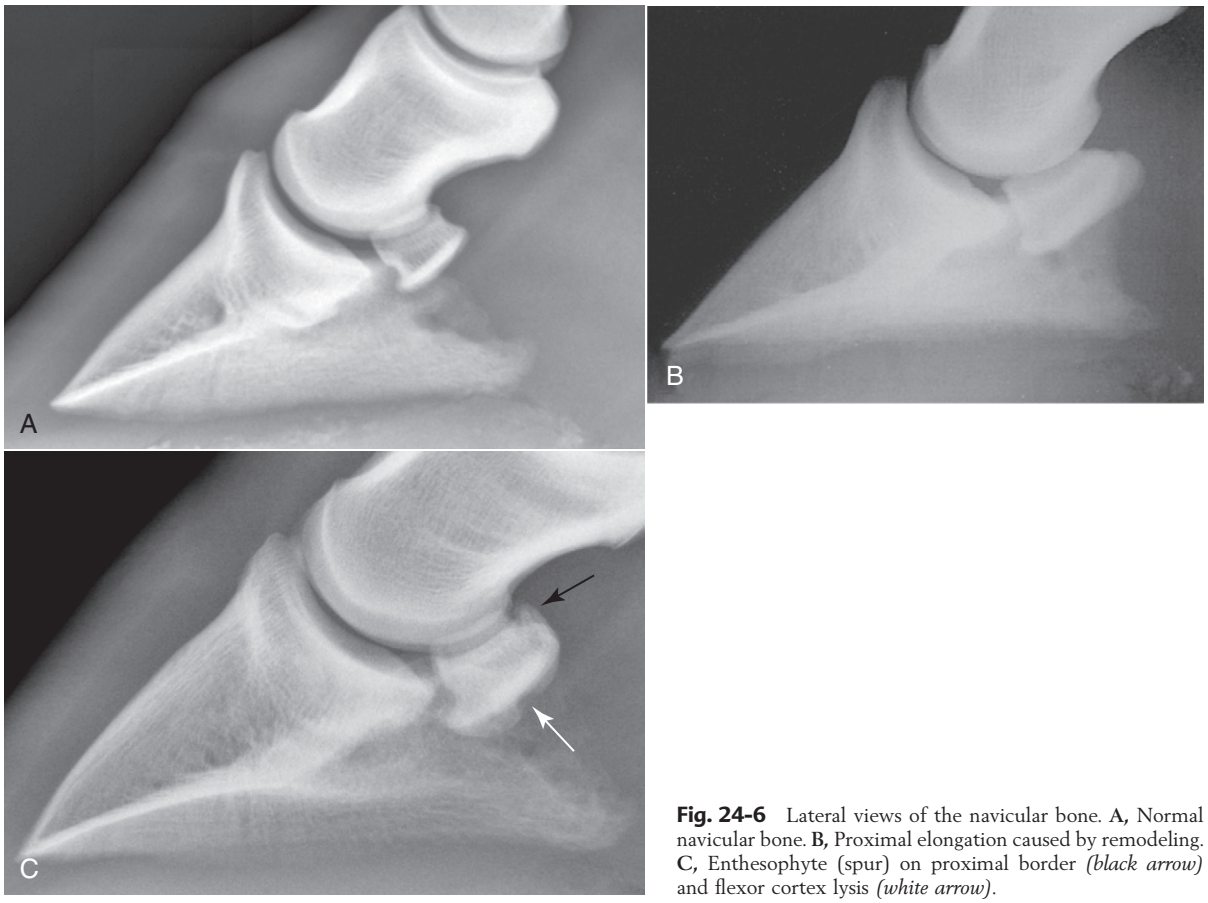


Fig. 24-6 Lateral views of the navicular bone. **A,** Normal navicular bone. **B,** Proximal elongation caused by remodeling. **C,** Enthesophyte (spur) on proximal border *(black arrow)* and flexor cortex lysis *(white arrow)*.

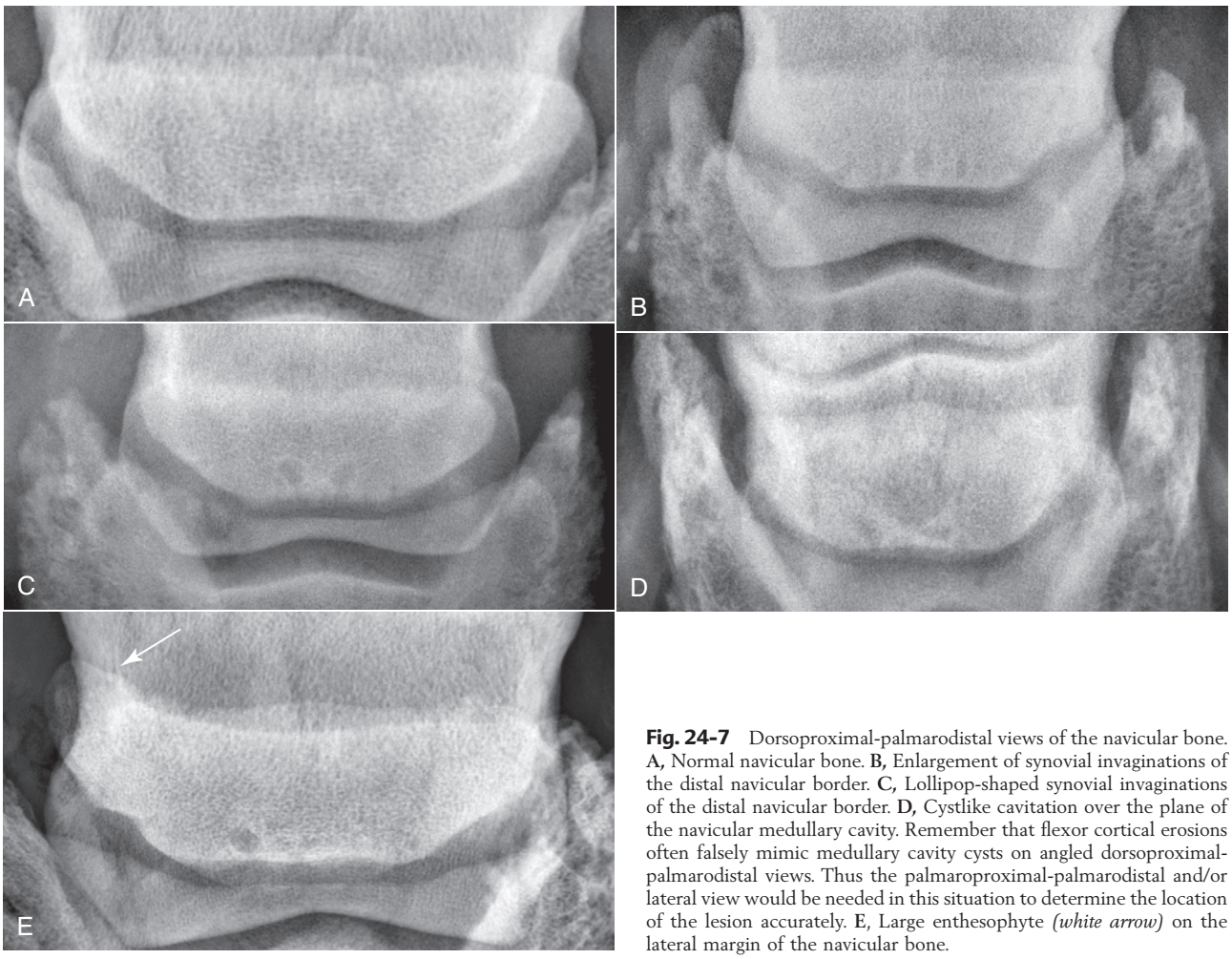


Fig. 24-7 Dorsoproximal-palmarodistal views of the navicular bone. **A,** Normal navicular bone. **B,** Enlargement of synovial invaginations of the distal navicular border. **C,** Lollipop-shaped synovial invaginations of the distal navicular border. **D,** Cystlike cavitation over the plane of the navicular medullary cavity. Remember that flexor cortical erosions often falsely mimic medullary cavity cysts on angled dorsoproximal-palmarodistal views. Thus the palmaroproximal-palmarodistal and/or lateral view would be needed in this situation to determine the location of the lesion accurately. **E**, Large enthesophyte *(white arrow)* on the lateral margin of the navicular bone.

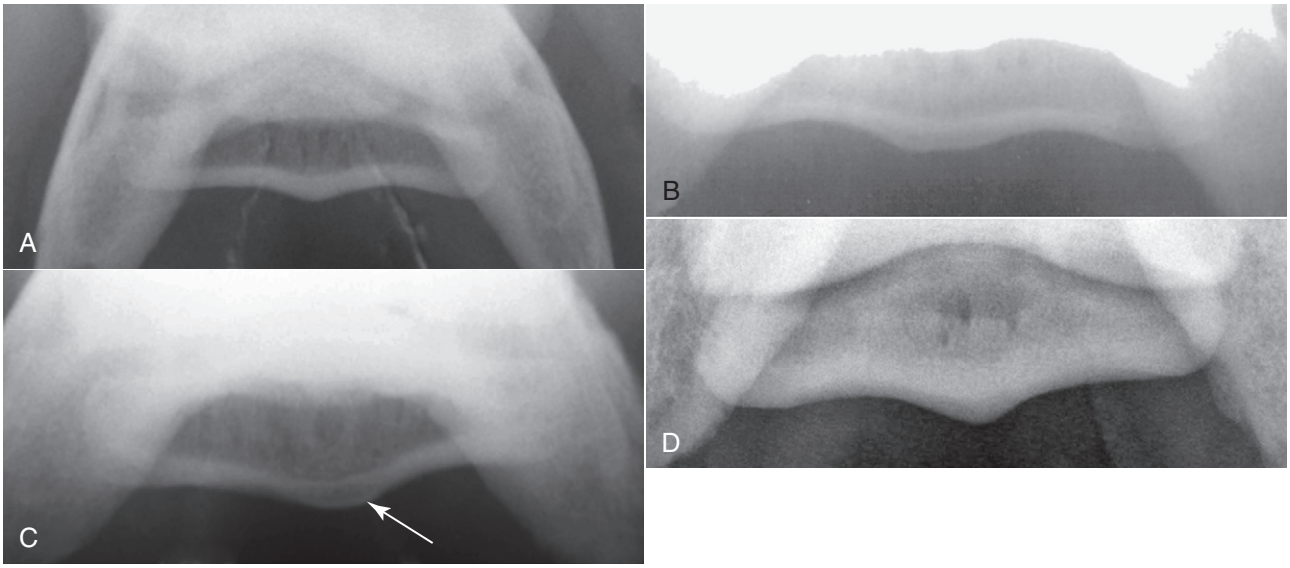


Fig. 24-8 Normal variations in the appearance of the navicular flexor cortex. The flexor cortex should be smoothly marginated and have an abrupt demarcation from the less-opaque medullary spongiosa. **A,** Prominent central eminence. **B,** Blunted central eminence. **C,** Crescent-shaped radiolucency in central eminence *(white arrow)*. **D,** Either altered beam angulation or patient motion may result in indistinct interface between the cortex and the medullary spongiosa, falsely suggesting navicular sclerosis. The lateral view in this horse was normal, and a repeat palmaroproximal-palmarodistal projection with better beam angulation showed normal corticomedullary distinction.

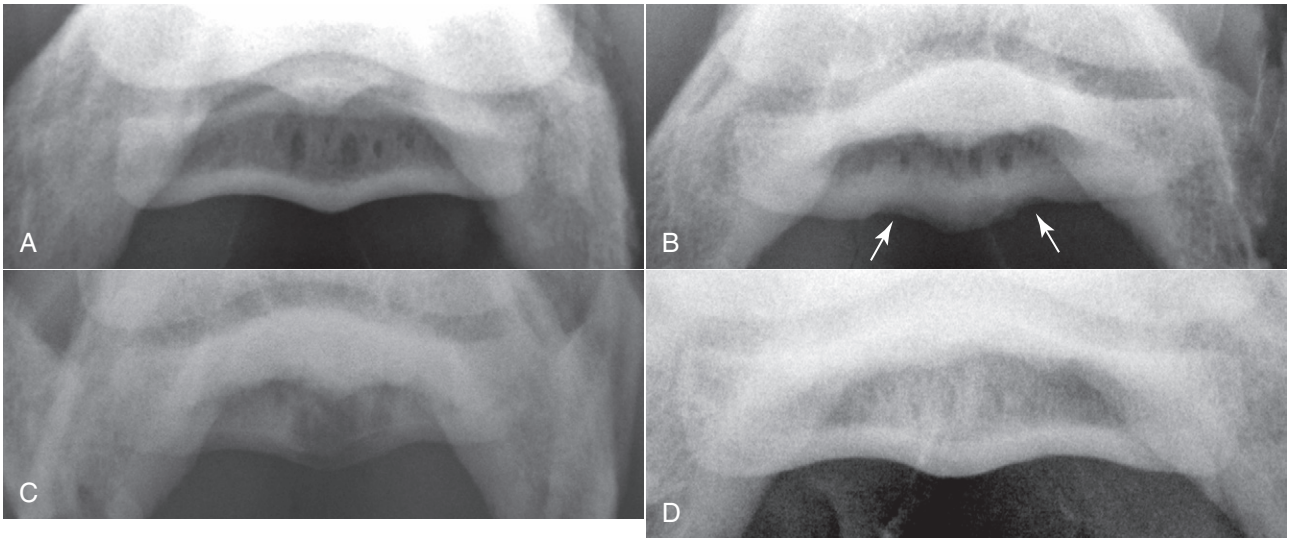


Fig. 24-9 Palmaroproximal-palmarodistal views of the navicular flexor cortex and medulla showing various abnormalities. **A,** En face view of enlarged distal border synovial invaginations. **B,** Flexor cortex erosions *(arrows)* result in a loss of the normal smooth flexor contour. **C,** Large focal cortical lysis causing disruption of the flexor cortex over the central eminence. **D,** Subchondral bone sclerosis in the central portion of the medullary cavity.

margin. Pronounced enthesophytes on the extremities of the navicular bone have been termed *spurs*. When enthesophytosis is excessive, the overall shape of the bone is altered. This is called *remodeling* (Figs. 24-6, *B* and C, and Fig. 24-7, *E*).

In general, enthesophytes are manifestations of a degenerative process.[15,31,32] They are occasionally seen in nonlame animals, particularly in older, heavily worked animals.[16] Enthesophytes in younger horses and extensive enthesophytes in others should be considered significant, particularly if accompanied by lameness.

Enthesophytes are best seen in angular dorsoproximal-palmarodistal views as new bone formation on the extremities or as bone proliferations along the proximal border (irregular border) (see Fig. 24-7, *E*). In the lateral view, excessive remodeling gives the bone an elongated appearance (see Fig. 24-6, *B* and C). Caution should be exercised because improperly positioned lateral views may artifactually distort the bone profile. Similarly, normal variants exist that resemble remodeling laterally when angular dorsoproximal-palmarodistal images are norma1.[24]

Distal Border Changes

The radiolucent invaginations along the distal border of the navicular bone are called *synovial invaginations* or *synovial fossae* (previously referred to as "vascular channels"). These are best seen in the dorsal 65-degree proximal-palmarodistal view. They are normally inverted cone to columnar in shape. Increased size and number are physiologic changes related to type and frequency of work.[2,3] A change in shape to a lollipop or mushroom is considered a signal of abnormal degenerative change (see Fig. 24-7, C).[24,33] The presence of synovial invaginations in the extremities of the navicular bone has been considered abnormal by some, but they do not correlate with lameness.[26]

Horses with clinical navicular disease have a high incidence of abnormal synovial invaginations, but their clinical specificity remains uncertain. This is because lollipop-shaped synovial invaginations have been reported in 11% of normal horses, and no correlation exists with degree of lameness in confirmed navicular lameness.[26]

Radiolucent changes of the distal border cannot be seen well in lateromedial views. The palmaroproximal-palmarodistal view, however, projects them end-on within the trabecular portion of the bone. Increases in size of visible fossae in this view are abnormal (see Fig. 24-8).[8] The range of normal shape variation of fossae for this view, however, has not been established.

Mineralization associated with the distal sesamoidean impar ligament is another possible change. The significance of this is similar to that of enthesophytes involving the proximal border. Occasionally, osseous bodies can be seen associated with the distal border. These can be seen in normal and lame horses alike. Small osseous fragments occasionally indicate chip fractures of the distal border and are discussed in the section on navicular fractures. Osseous fragments of the distal border are best seen in the angular dorsoproximal-palmarodistal views[10] but can be difficult to identify with both conventional and computed radiography. Larger fragments are more easily visible.[34]

Flexor Cortex Changes

Gross pathologic involvement of the navicular flexor fibrocartilage is varied. Lesions include yellowish discoloration, cartilage thinning, focal erosions, and cartilage ulcerations, with or without subchondral bone involvement.[19,20,35] Some of the abnormalities may be age-related phenomena, but all have been seen in navicular disease to varying degrees.

Bursa, tendon, and cartilage changes are not usually seen radiographically; only subchondral bone defects are detectable routinely. Early osseous lesions are best seen on the palmaroproximal-palmarodistal view, whereas severe defects may also be recognized in other views. A reliable radiographic sign consists of focal or diffuse subchondral bone cortical lysis (see Fig. 24-9).[8] Flexor cortex erosions are rarely seen in sound horses and have a significant correlation to the presence and degree of lameness.[2,21,26] Large, discrete flexor cortical erosions may simulate medullary cystlike lesions in the dorsopalmar view. Localization of such cystlike lesions radiographically is vital. Flexor cortical erosions are often associated with tendinous adhesions, whereas medullary cysts are not.[31,35] This added information may be important in the overall management of the animal. Navicular variants of a flat central eminence and a crescent lucency within the cortex of the central eminence exist (see Fig. 24-8). These are normal variations and should not be misdiagnosed as navicular degeneration. Well-positioned lateral radiographs depict the flexor cortex in

profile axially. Minor dimpling of the central eminence in this view may be a normal variant or may be the result of geometric distortion. Abrupt irregular cavitations are abnormal (see Fig. 24-6, C). Abnormalities of the flexor cortex observed on a lateral radiograph should be further evaluated by the palmaroproximal-palmarodistal view.

Dystrophic mineralization of the deep digital flexor tendon may be seen in conjunction with flexor erosions. This finding is reported rarely and indicates severe tendon degeneration, rendering a poor prognosis.[30,35] Faint visualization of the deep digital flexor tendon on the lateral view is a frequent normal finding. Diseased tendons that are sufficiently mineralized may be seen in both lateral and palmaroproximal-palmarodistal views.

Medullary Cavity Changes

Medullary trabecular disruption in the form of trabecular lysis or cystlike cavitations is abnormal. This is rarely seen in sound horses (see Fig. 24-7, *D*). These radiolucencies may be seen on the angular dorsoproximal-palmarodistal, palmaroproximal-palmarodistal, and occasionally lateral views. They range in size from 0.5 to 1.5 cm and are round to oval. They usually are single but may be multiple. Marginal sclerosis is variable, ranging from complete to none at all.

Lytic lesions located within the middle or distal phalanx may be superimposed over the navicular bone. By evaluating other views or repeating the dorsoproximal-palmarodistal view at a different angle, one could possibly determine whether the suspect lesion changes in position or remains associated with the navicular bone. Similarly, lucent artifacts that result from air trapped in the frog by packing material or from focal gas in the hoof wall or sole from a surface defect or abscess may be misinterpreted as radiolucent bone lesions. Air pockets usually appear as linear radiolucent shadows. When doubt exists, the frog should be repacked and radiographs repeated.

Extensive erosions of the flexor cortex can falsely mimic medullary cavity cysts on angular dorsoproximal-palmarodistal views. On a palmaroproximal-palmarodistal view, the suspect lesion can be localized regarding whether it originates from the flexor cortex or the medullary cavity (see Fig. 24-9, *B* and *C*). Localization of such lesions is also possible on a lateral projection (see Fig. 24-6, *C*).

Sclerosis of the medullary spongiosa is said to be an early finding in horses lame because of navicular disease.[2,8,26] This is seen as a fine trabecular pattern that blends with the flexor cortex, resulting in an indistinct interface between the flexor cortex and the medullary spongiosa (see Fig. 24-9, *D*).[2,8] This finding is not reliable because it can often be seen in normal horses as a result of a poorly positioned radiograph (see Fig. 24-8, *D*).[2,26,36,37] When present, it is observed on both the lateral and palmaroproximal-palmarodistal views; therefore these views should always be examined in conjunction.[38]

Normal Radiographic Findings

Many horses with clinical navicular lameness have normal radiographs.[17,28] These animals may have lesions affecting the soft tissue structures associated with the navicular bone. Before this conclusion is reached, however, an adequate number of high-quality radiographs should be obtained. The advent of magnetic resonance (MR) imaging has documented the presence of abnormal signal within the navicular bone in many radiographically normal horses: This abnormal signal may represent hemorrhage, edema, necrosis, fibrosis, or inflammation, which would not be visible radiographically. Further, the notion that navicular bursitis may represent the first stage of navicular disease has been challenged by MR imaging evaluations, because fluid distention of the navicular bursa is typically not seen as a primary entity.[28]

Technetium-99m bone scintigraphy is a valuable adjunct when radiographic findings are equivocal or when the bone is normal but disease of the navicular soft tissues is suspected. This is because nuclear scintigraphy is more sensitive than radiography in identifying early soft tissue and bone abnormalities, although a scintigram provides primarily physiologic as opposed to anatomic information. Because physiologic alterations associated with navicular degeneration are likely to precede gross anatomic changes, scintigraphy of the navicular bone should be considered when clinical signs are compatible with navicular lameness but radiographs are normal, or to elucidate the significance of equivocal radiographic findings (Fig. 24-10).[39] In addition, scintigraphic findings have been found to correlate well with abnormalities detected on MR images.[40] It is important to remember, however, that a negative scintigraphic result does not preclude the presence of significant injuries: Because scintigraphy provides a map of



Fig. 24-10 Static images of the right front foot of a horse with foot pain. The image at *left* is a soft tissue phase lateral view of the distal limb obtained within 5 minutes of the injection of approximately 120 mCi of technetium-99m hydroxyethylene diphosphonate. The images at *center* and *right* are lateral and solar views of the same foot, obtained approximately 1 hour later. Notice the increased focal uptake in the region of the navicular bone, apparent on all views. The uptake at the level of the coronary band on the soft tissue image is normal.

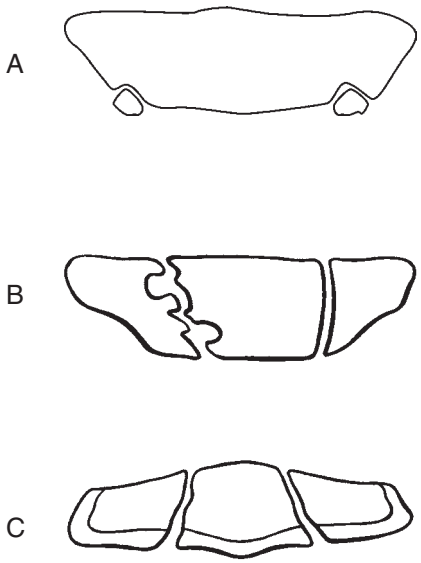


Fig. 24-11 Types of navicular fractures. **A,** Chip fractures of the distal navicular border, dorsal 65-degree proximal-palmarodistal projection. **B** and **C,** Complete navicular fractures: dorsal 65-degree proximal-palmarodistal and palmaroproximal-palmarodistal projections, respectively.

osteoblastic activity, the presence of navicular bone necrosis alone would yield a negative study.[40,41]

FRACTURES

Navicular fractures are reported infrequently; therefore data are not available from which to draw firm conclusions about their incidence and pathophysiology. Most navicular fractures are traumatic or pathologic in origin. Both chip and complete fracture types have been described. A diagram of navicular fractures is shown in Figure 24-11.

Care should be taken to avoid misinterpreting artifacts as navicular fractures. The sulci of the frog may cast overlying linear radiolucent shadows in the dorsoproximal-palmarodistal projection that simulate complete navicular fracture. This occurs when the foot is unpacked or when air is trapped in the sulcus by packing material. Sulcal lines typically extend beyond the periphery of the navicular bone. Complete fractures are confined to the bone and are seen on dorsoproximal-palmarodistal and palmaroproximal-palmarodistal views. Gravel or debris in the foot or a foot with scaly horn may simulate chip fractures. With proper hoof preparation (cleaning, paring, and packing), these artifacts can be eliminated. Lateral views or dorsoproximal-palmarodistal radiographs made at different angles help localize a suspect opacity. When in doubt about navicular fractures, the hoof should be cleaned and repacked before more radiographs are made.

Osseous Fragments of the Distal Border

Small osseous fragments associated with the distal border of the navicular bone and distal sesamoidean impar ligament are occasionally seen. They are usually identified on the dorsoproximal-palmarodistal view[10] but may also be seen superimposed over the medullary cavity of the navicular bone on the palmaroproximal-palmarodistal projection. These osseous bodies have more than one pathogenesis. They may be caused by chip fractures, damage to the impar ligament with secondary mineralization, separate centers of ossification within the impar ligament, or synovial osseous metaplasia.[10,31] When present, osseous bodies may be unilateral or bilateral, involve both the medial and lateral aspects of the bone, or involve only one side of the bone. Larger fragments are most often found on the medial side of the bone.

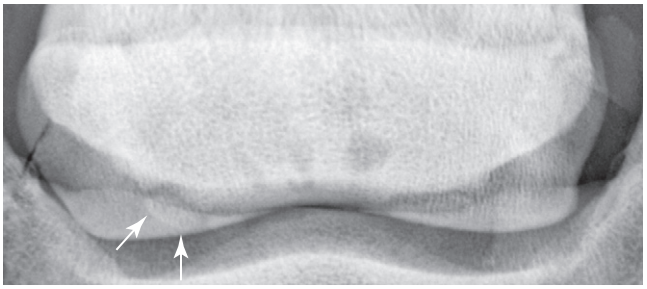


Fig. 24-12 Chip fracture at the distal navicular border. The small fragment *(white arrows)* and the underlying fracture bed can be seen. A medullary cystlike lesion is also present.

Osseous bodies that are true chip fractures may appear as small (0.2 to 1.2 cm), rectangular bone fragments separated from the distal border by a radiolucent zone. A fracture bed within the navicular bone corresponding in size and shape to the fragment is often seen.[42] Dystrophic mineralization of the impar ligament may have a similar appearance, but a fracture bed is not seen.

Although the significance of these bodies remains unclear, it does not always indicate navicular disease; an association has, however, been noted by some investigators.[21] (Fig. 24-12). There appears to be an association between the shape of the proximal articular border of the navicular bone and the presence of distal border fragments in Warmbloods: Such fragments were more prevalent in navicular bones with a concave or undulating proximal articular border compared with straight or convex shape.[10]

Complete Fractures

Complete navicular fractures may occur in normal or diseased navicular bones.[13,43-46] They are most frequently seen in the forelimb, but hindlimb fractures have been reported.[45] Initiating causes include direct navicular trauma and repeated concussive forces on a pathologic navicular bone in a neurectomized patient. Lameness associated with complete fracture is usually acute but may be chronic and is moderate to severe. In general, the long-term prognosis for competitive performance is poor.[42] Postmortem studies of limited numbers of fractured navicular bones show fibrous unions between the fragments. Variable instability is inherent because of the hingelike motion allowed by the fibrous component.

Usually, one or two vertical or oblique fracture lines may be seen within the body or at the body-extremity junction of the navicular bone. A conspicuous fracture line is usually present. Fracture fragments have irregular to smooth margins and are minimally displaced. Occasionally, fragments have mild degenerative changes of bony resorption and sclerosis adjacent to the fracture line (Fig. 24-13). Healing is thought to occur from a noncalcified fibrous union because bony union is not observed radiographically, regardless of fracture duration. Absence of periosteum and progenitor cells, constant fragment motion, and influx of regional synovial fluid are all thought to play a role in navicular fracture healing with fibrous rather than bony union.[46]

Multipartite Navicular Bone

What appear to be bilaterally symmetric fractures are occasionally seen in minimally lame animals with otherwise normal navicular bones. This finding has fostered the belief that the lines represent multiple navicular bone ossification centers that have not fused. Congenital multipartite sesamoids are occasional, incidental findings in other species. Although the navicular bone develops from a single ossification center,

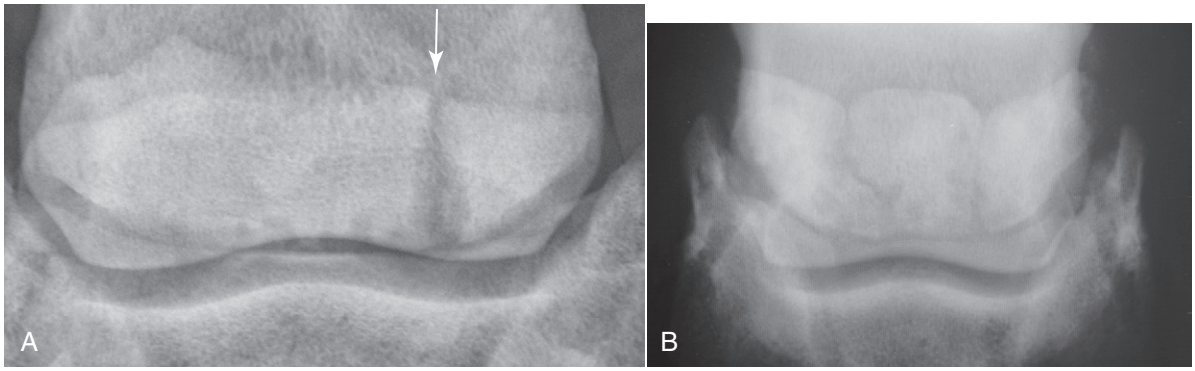


Fig. 24-13 **A,** Complete navicular bone fracture *(white arrow)*. **B,** Tripartite navicular bone; notice the smooth margins of the navicular fragments. This was a mature horse with tripartite navicular bones in both front feet and minimal lameness. (Courtesy of Dr. Robert J. Bahr, Oklahoma State University, Stillwater, Okla.)

aberrant formation is possible.[1] Radiographic differentiation between a congenitally multipartite navicular bone and a chronic fracture is impossible. Radiographically, multipartite (bipartite or tripartite) sesamoid bones are often bilateral. Individual fragments have smooth, rounded margins with wide radiolucent gaps between. In addition, multiple ossification centers initially cause no to minimal lameness. If instability is present, however, degenerative changes resulting in lameness may occur (see Fig. 24-13).

In some lame horses, a multipartite navicular bone also undergoes changes that are compatible with advanced navicular degeneration. This circumstance has two plausible explanations. One is that a pathologic fracture of a primarily diseased bone has occurred. Another is that fracture or multiple ossification centers are present initially. The resultant instability causes chronic secondary degenerative changes. Thus when a multipartite sesamoid navicular bone is seen in conjunction with severe degenerative navicular changes, determining whether the navicular bone is fractured or multipartite is difficult (see Fig. 24-13). When marked distortion of the individual fragments is present or when multiple navicular bones are involved, a multipartite development is likely. A bipartite navicular bone has also been reported in association with bipartite distal phalanx.[47]



Fig. 24-14 Fistulogram after a nail puncture wound. The tract communicates with the navicular bursa.

NAVICULAR SEPSIS

Navicular sepsis may result from penetrating puncture wounds or deep lacerations that involve the bursa or the bone itself. Radiographic signs relative to the navicular bone occurring after a puncture wound to the navicular bursa vary. The length of time between the initial injury and the first radiographic evaluation influences the findings.[48]

If a horse presents within 3 weeks of injury, and initial radiographs are negative, a fistulogram or radiograph made after insertion of a blunt probe should be considered. This examination helps establish if the puncture wound involves the navicular bursa or bone (Fig. 24-14). This is important because a puncture wound that involves the bone or bursa warrants a more cautious prognosis and more vigorous therapy because osteomyelitis may result. A negative fistulogram does not eliminate the possibility that the navicular bone or bursa was involved in the initial injury because partial tract healing in the deeper areas of the wound could prevent passage of contrast medium during fistulography, resulting in a falsely negative study.

Regardless of whether a fistulogram is performed during the initial evaluation, follow-up radiographs should be made within the subsequent 3 to 12 weeks because radiographic evidence of navicular infection may take 6 weeks or longer to become apparent. Also, an estimated 50% of horses with navicular sepsis that have initially negative radiographs subsequently develop radiographic signs of bone infection. Once present, navicular osteomyelitis may progress and result in serious complications, leading to chronic lameness that may eventually necessitate euthanasia.

Of the standard projections to evaluate the navicular bone, the lateral and palmaroproximal-palmarodistal views are more valuable than the angled dorsoproximal-palmarodistal views in detecting and staging osteomyelitis of the navicular bone.

Initial radiographic signs of navicular bone infection appear as focal areas of decreased opacity in the flexor cortical bone with disruption and irregularity of the flexor surface. These lesions are often initially located abaxial to the central eminence. The greater the duration of the injury without treatment, the more extensive the disease will be in terms of depth of the irregularity into the navicular bone and its abaxial extent.

More severe long-term findings associated with puncture wounds and navicular osteomyelitis include septic arthritis of the distal interphalangeal joint (Fig. 24-15), secondary joint disease, pathologic fracture of the navicular bone, and subluxation of the distal interphalangeal joint. Rupture of the deep

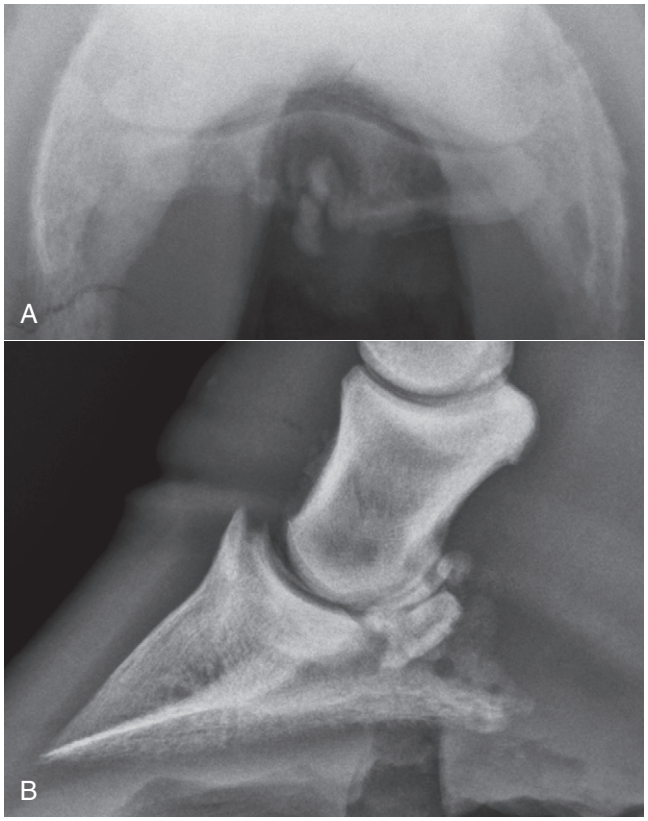


Fig. 24-15 Palmaroproximal-palmarodistal (**A**) and lateral projections (**B**) of the forefoot of a horse 5 weeks after nail puncture of the navicular bursa. Septic arthritis of the distal interphalangeal joint. There is osteolysis, fragmentation and displacement of the navicular bone, and subluxation of the distal interphalangeal joint.

digital flexor tendon or distal sesamoidean impar ligament causes subluxation of the distal interphalangeal joint, which may be observed only during weight bearing. In some horses, degenerative changes similar to those seen in navicular disease have been observed as long-term sequelae.

MISCELLANEOUS CONDITIONS

Another condition that affects the navicular bone is degenerative arthritis. The navicular bone participates in forming the distal interphalangeal joint. The articular border of the navicular bone adjacent to the middle phalanx is normally rounded. Periarticular osteophytes can be seen that result in subtle, pointed, spurlike projections. These have been seen in sound horses as well as in horses lame from navicular disease; thus their significance is uncertain. Reports of significant pathologic processes involving the articular cartilage in navicular disease are rare. However, some changes seen in navicular degeneration are believed to be a form of distal interphalangeal joint arthrosis.[24]

Congenital absence of the navicular bone (agenesis) has been reported.[49,50]

ULTRASONOGRAPHIC EVALUATION OF THE NAVICULAR BONE AND ASSOCIATED SOFT TISSUE STRUCTURES

Sonography of the navicular bone and associated soft tissue structures has been of limited use because of the inability to penetrate the hoof wall with conventional ultrasound imaging equipment. The proximal aspect of the navicular bone can be visualized by way of the palmar aspect of the middle phalanx just proximal to the bulbs of the heels, but this approach provides information limited to the paired proximal suspensory ligaments, proximal margin of the navicular bone, and proximal portion of the tendon of insertion of the deep digital flexor muscle. Approach to the podotrochlear apparatus (navicular bone, collateral and distal sesamoidean impar ligaments, distal deep digital flexor tendon, and podotrochlear bursa) through the frog (referred to as the *transcuneal approach*) has also been described. The procedure requires trimming the dry superficial layers of the frog to moist pliable tissue, producing a wide central cuneal sulcus. The foot is then soaked in warm water for 10 to 15 minutes up to 12 hours to hydrate the frog, creating an acoustic window to the navicular bone and its distal attachments. Mechanical, fixed curvilinear, linear, or phased-array transducers may be used with a frequency range of 6 to 10 MHz.[51,52] Sagittal, parasagittal, and transverse scans are performed. Structures visible on the longitudinal views include the palmar surfaces of the distal phalanx and fibrocartilage of the navicular bone, distal palmar recess of the distal interphalangeal joint, impar ligament, bursa, deep digital flexor tendon, and digital cushion. Transverse scans provide visualization of the palmar fibrocartilage of the navicular bone, navicular bursa, the fibrocartilaginous and fibrous parts of the deep digital flexor tendon, distal digital annular ligament, and digital cushion (Figs. 24-16 and 24-17).[51] A recent study evaluating 39 radiographically normal horses with positive response to palmar digital nerves analgesia identified a variety of sonographic abnormalities, the most common being deep digital flexor tendinopathy, followed by abnormalities associated with the distal interphalangeal joint and navicular bursa, with less frequent abnormalities at the level of digital flexor tendon sheath, flexor surface of the navicular bone, and navicular ligaments.[53] Thus, sonographic examination should be considered as an adjunctive imaging modality to evaluate the soft tissue of the heel, especially when MR imaging is not available.

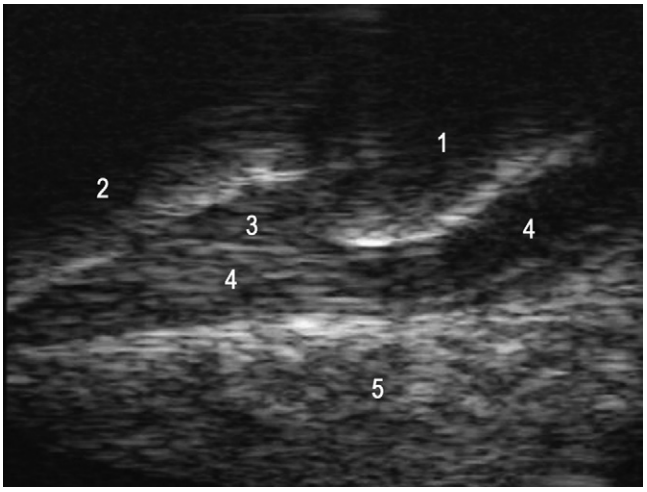


Fig. 24-16 Sagittal ultrasonographic image of the podotrochlear apparatus obtained with a linear probe by the transcuneal approach. *1*, Navicular bone; *2*, distal phalanx; *3*, distal impar sesamoidean ligament; *4*, deep digital flexor tendon; *5*, digital cushion. (Courtesy of Dr. Valeria Busoni, Université de Liège, Liège, Belgium.)

MAGNETIC RESONANCE AND COMPUTED TOMOGRAPHIC EVALUATION OF THE NAVICULAR BONE

Computed tomographic (CT) imaging and MR imaging have become more available in equine medicine. In addition, the

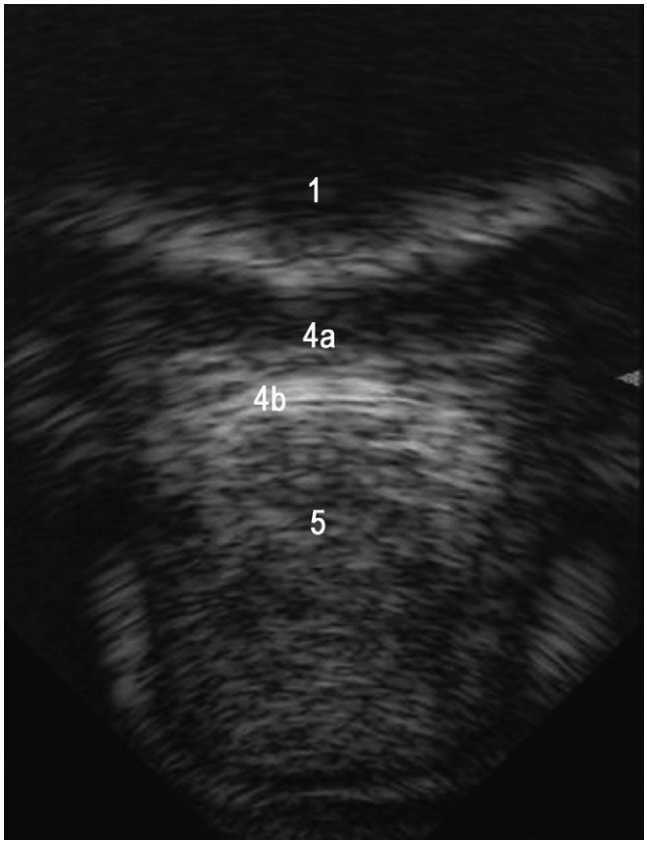


Fig. 24-17 Transverse ultrasonographic image of the podotrochlear apparatus obtained with a microconvex probe using the transcuneal approach at the level of the navicular bone. *1*, Navicular bone; *4a*, fibrocartilaginous portion of the deep digital flexor tendon; *4b*, fibrous portion of the deep digital flexor tendon; *5*, digital cushion. (Courtesy of Dr. Valeria Busoni, Université de Liège, Liège, Belgium.)

development of open magnets that allow imaging of the standing horse,[54,55] without the need for general anesthesia, has made MR imaging especially popular for the investigation of foot pain. MR and CT imaging allow visualization of the size, shape, and position of the synovial invaginations better than radiography (Fig. 24-18).[56] Osseous changes and changes in surface contour (lateral wings, articular and flexor surface) are seen better with CT,[37,56,57] and in one study CT was speculated to be more reliable than conventional radiography in assessing the flexor surface of the navicular bone.[36] However, considerable intra-observer and inter-observer variability in both radiographic and CT evaluation of navicular bones has been found, and although navicular lesions were defined better on CT compared with radiographs, the lack of agreement may be because of varying opinion as opposed to difficulty in identifying abnormalities.[58] Deep digital flexor tendon lesions associated with navicular changes have been identified with both CT and MR imaging but are best seen with MR imaging.[56] In general, MR imaging is a more powerful modality for the depiction of soft tissue lesions, including loss of signal of fibrocartilage, distention of the navicular bursa and/or of the distal interphalangeal joint (with or without chronic inflammation), distention of the digital tendon sheath, and surface and core defects of the deep digital flexor tendon and distal sesamoidean impair ligament.[25,37,56,59-62] In addition, MR imaging can allow detection of abnormal signal within the navicular bone marrow (Fig. 24-19), navicular enthesophytes, and evidence of mineralized fragments within the impar ligament.[59-62] MR imaging is able to identify the presence of soft tissue and osseous lesions in lame horses with normal radiographs.[28]

Sequences used for navicular imaging in clinical patients include three-dimensional T1-weighted spoiled-gradient recalled (SPGR) imaging, three-dimensional T2* gradient recall echo (GRE) imaging, and short time inversion recovery (STIR) or fat-saturated three-dimensional T2* GRE in the sagittal, dorsal, and transverse planes.[59,61] GRE and SPGR have the advantages of allowing three-dimensional acquisition and a sufficiently short acquisition time for practical clinical scanning compared with spin echo or fast spin echo sequences. Fat suppression techniques are used to reduce interference from

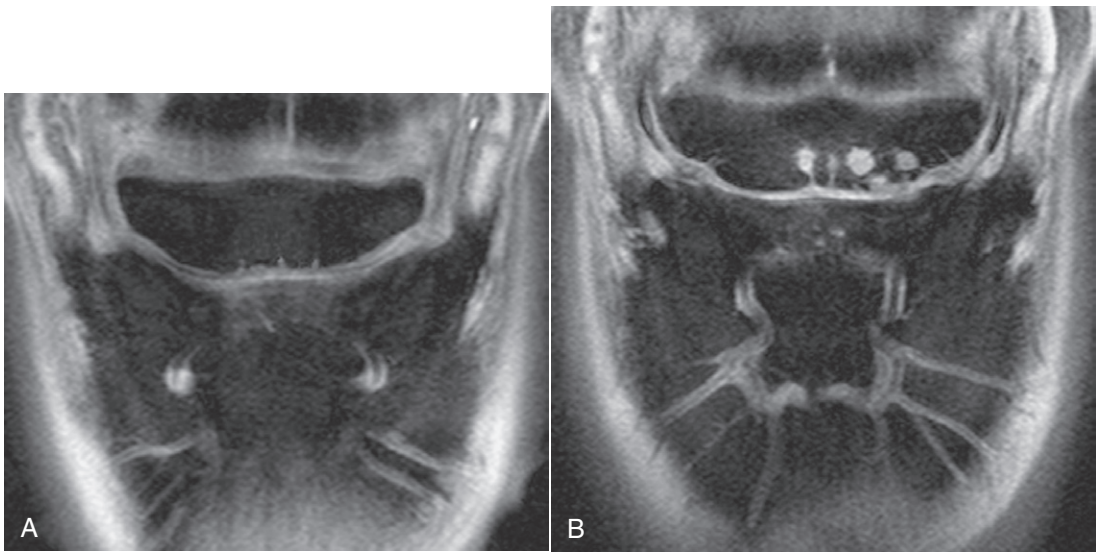


Fig. 24-18 **A,** Dorsal plane STIR image of a normal navicular bone; notice the small, conical hyperintense synovial invaginations. **B,** Dorsal plane gradient recalled echo image of the navicular bone showing enlarged lollipop-shaped synovial invaginations and irregular margination of the medial aspect of the distal border of the navicular bone. (Courtesy of Dr. Russell L. Tucker, Washington State University, Pullman, Wash.)

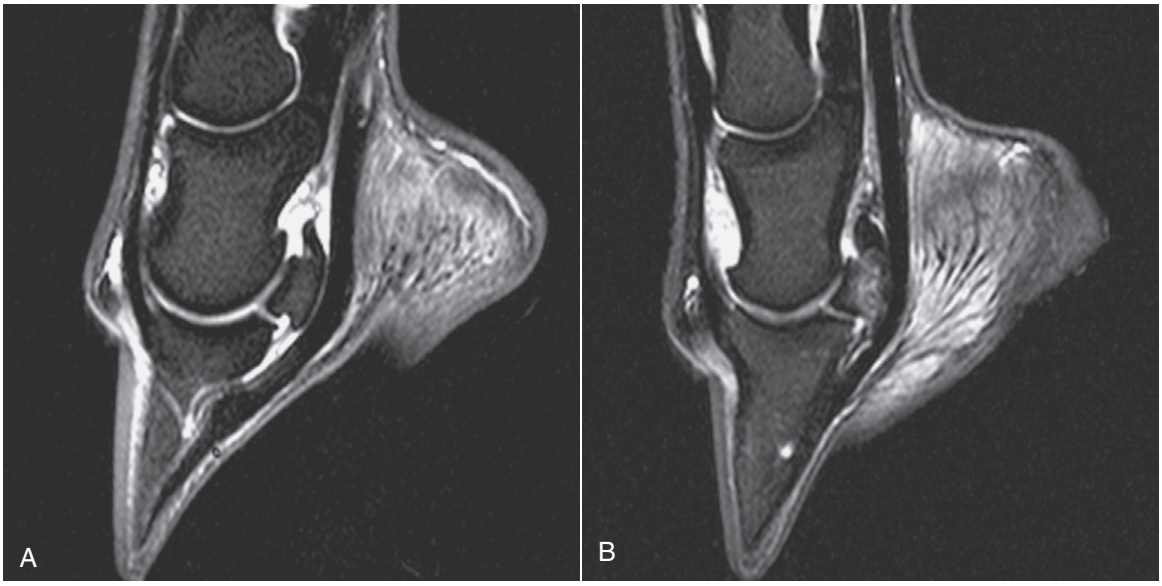


Fig. 24-19 Sagittal plane STIR images of the foot and navicular bone. **A,** Normal navicular bone. **B,** Increased fluid signal within the navicular bone, indicating marrow edema. Notice the thickening of the suspensory navicular ligament. (Courtesy of Dr. Russell L. Tucker, Washington State University, Pullman, Wash.)

fat signal and are especially useful in detecting bone medullary fluid (see Fig. 24-18, *A*; see Fig. 24-19). MR bursography with 0.9% saline can be used to improve the visibility of the palmar navicular fibrocartilage on proton dense and fat-saturated three-dimensional T1-weighted SPGR sequence and can aid in the identification of partial thickness lesions.[63] MR imaging may be performed with either high-field or low-field systems:[54,55]Although the appearance of tissues is similar between the two systems, the anatomic arrangement of structures is different because of differences in position, and the magic angle artifact can present at different sites. In general, high-field systems produce images with better resolution that may provide greater diagnostic accuracy for certain lesions (such as those involving articular cartilage).[64]

MR and CT imaging are superior to conventional radiography for navicular imaging, facilitating earlier and more accurate diagnosis.[37,56] MR imaging, in particular, is becoming the modality of choice to investigate heel pain in the horse because of its ability to provide information on both soft tissues and osseous structures. There is growing evidence that lame horses have pathology in multiple structures, rather than lesions confined to the navicular bone and bursa. In these horses and in those with normal radiographs, MR imaging is beneficial in reaching a specific diagnosis that can affect treatment choices.[28]

REFERENCES

1. Getty R: *Sisson and Grossman's the anatomy of the domestic animals*, Philadelphia, 1975, Saunders.
2. Kaser-Hotz B, Ueltschi G: Radiographic appearance of the navicular bone in sound horses, *Vet Radiol Ultrasound* 33:9, 1992.
3. Colles CM, Hickman J: The arterial supply of the navicular bone and its variations in navicular disease, *Equine Vet J* 9:150, 1977.
4. Bowker RM, Ruckershouser SJ, Kelly BV, et al: Immunocytochemical and dye distribution studies of nerves potentially desensitized by injections into the distal interphalangeal joint of the navicular bursa of horses, *J Am Vet Med Assoc* 203:1708, 1993.
5. Rijkenhuizen ABM: Navicular disease: a review of what's new, *Equine Vet J* 38:82, 2006.
6. Campbell JR, Lee R: Radiological techniques in the diagnosis of navicular disease, *Equine Vet J* 4:135, 1972.
7. Watrous BJ: *A guide to equine field radiography*, Trenton, NJ, 1995, Veterinary Learning Systems, p 13.
8. O'Brien TR, Millman TM, Pool RR, et al: Navicular disease in the Thoroughbred horse: a morphologic investigation relative to a new radiographic projection, *J Am Vet Radiol Soc* 16:39, 1975.
9. Dik K, van den Broek J: Role of navicular bone shape in the pathogenesis of navicular disease: a radiological study, *Equine Vet J* 27:390, 1995.
10. Claerhoudt S, Pille F, Vanderperren K, et al: Association between navicular bone fragmentation and shape in Belgian Warmblood horses, *Vet Comp Orthop Traumatol* 24:132, 2011.
11. Poulos P, Brown A: On navicular disease in the horse: a roentgenological and patho-anatomic study: I. Evaluation of the flexor central eminence, *Vet Radiol* 30:50, 1989.
12. Berry C, Pool R, Stover S, et al: A radiographic/morphologic investigation of a radiolucent crescent within the flexor central eminence of the navicular bone in the Thoroughbred. In *Proceedings of the American College of Veterinary Radiology annual meeting*, Chicago, 1990.
13. Dyson SJ, Kidd L: A comparison of responses to analgesia of the navicular bursa and intra-articular analgesia of the distal interphalangeal joint in 59 horses, *Equine Vet J* 25:93, 1993.
14. Schumacher J, Steiger R, Schumacher J, et al: Effects of analgesia of the distal interphalangeal joint of palmar digital nerves on lameness caused by solar pain in horses, *Vet Surg* 29:54, 2000.
15. Stashak TS, editor: *Adam's lameness in horses*, ed 4, Philadelphia, 1987, Lea & Febiger, p 499.
16. Ackerman N, Johnson JH, Dorn CR: Navicular disease in the horse: risk factors, radiographic changes, and response to therapy, *J Am Vet Med Assoc* 170:183, 1977.
17. Wright IM: A study of 118 cases of navicular disease: clinical features, *Equine Vet J* 25:488, 1993.

18. Pool RR, Meagher DM, Stover SM: Pathophysiology of navicular syndrome, *Vet Clin North Am Equine Pract* 5:109, 1989.
19. Blunden A, Dyson S, Murray R, et al: Histopathology in horses with chronic palmar foot pain and age-matched controls. Part 1: navicular bone and related structures, *Equine Vet J* 38:15, 2006.
20. Blunden A, Dyson S, Murray R, et al: Histopathology in horses with chronic palmar foot pain and age-matched controls. Part 2: the deep digital flexor tendon, *Equine Vet J* 38:23, 2006.
21. Wright IM, Kidd J, Thorp BH: Gross histological, histomorphometric features of the navicular bone and related structures in the horse, *Equine Vet J* 30:220, 1998.
22. Fricker CH, Riek W, Hugelshofer J: Occlusion of the digital arteries: a model for pathogenesis of navicular disease, *Equine Vet J* 14:203, 1982.
23. Ostblom L, Lund C, Melsen F: Histologic study of navicular bone disease, *Equine Vet J* 14:199, 1982.
24. Poulos PW, Smith MF: The nature of enlarged "vascular channels" in the navicular bone of the horse, *Vet Radiol* 2:60, 1988.
25. Dyson S, Pool R, Blunder T, et al: The distal sesamoidean impar ligament: comparison between its appearance on magnetic resonance imaging and histology of the axial third of the ligament, *Equine Vet J* 42:332, 2010.
26. Wright IM: A study of 118 cases of navicular disease: radiological features, *Equine Vet J* 25:493, 1993.
27. Turner T, Kneller S, Badertscher R, et al: Radiographic changes in the navicular bones of normal horses. In *Proceedings of the 32nd annual meeting of the American Association of Equine Practitioners,* Nashville, TN, 1986, p 309.
28. Sampson SN, Schneider RK, Gavin PR, et al: Magnetic resonance imaging in horses with recent onset navicular syndrome but without radiographic abnormalities, *Vet Radiol Ultrasound* 50:339, 2009.
29. Huskamp B, Becker M: Diagnose und prognose der röntgenologischen Veranderungen an den Strahl-beinen der Vordergliedma Ben der Pferde unter besonderer Berucksichtigung der Ankau fsuntersuchung: Ein Versuch zur Schematisierung der Befunde, *Praktische Tierarzt* 61:858, 1980.
30. Wright IM: A study of 118 cases of navicular disease: treatment by navicular suspensory desmotomy, *Equine Vet J* 25:501, 1993.
31. Poulos P, Brown A, Brown E, et al: On navicular disease in the horse: a roentgenological and patho-anatomic study: II. Osseous bodies associated with the impar ligament, *Vet Radiol* 30:54, 1989.
32. Turner TA: The anatomic, pathologic, and radiographic aspects of navicular disease, *Compend Contin Educ Pract Vet* 4:350, 1982.
33. MacGregor C: Radiographic assessment of navicular bones based on changes in the distal nutrient foramina, *Equine Vet J* 18:203, 1986.
34. Biggi M, Dyson S: Comparison between radiological and magnetic resonance imaging lesions in the distal border of the navicular bone with particular reference to distal border fragments and osseous cyst-like lesions, *Equine Vet J* 42:707, 2010.
35. Turner TA: Dystrophic calcification of the deep digital flexor tendons resulting from navicular disease, *Vet Med Small Anim Clin* 77:571, 1982.
36. Ruohoniemi M, Teruahartiala P: Computed tomographic evaluation of Finnhorse cadaver forefeet with radiographic problematic findings on the flexor aspect of the navicular bone, *Vet Radiol Ultrasound* 40:275, 1999.
37. Widmer W, Buckwalter K, Fessler J, et al: Use of radiography, computed tomography and magnetic resonance imaging for evaluation of navicular syndrome in the horse, *Vet Radiol Ultrasound* 41:108, 2000.
38. De Clercq T, Vershooten F, Ysebaert M: A comparison of the palmaroproximal-palmarodistal view of the isolated navicular bone to other views, *Vet Radiol Ultrasound* 41:525, 2000.
39. Trout DR, Hornof WJ, O'Brien TR: Soft-tissue and bone-phase scintigraphy for diagnosis of navicular disease in horses, *J Am Vet Med Assoc* 198:73, 1991.
40. Dyson S, Murray R: Use of concurrent scintigraphy and magnetic resonance imaging evaluation to improve understanding of the pathogenesis of injury to the podotrochlear apparatus, *Equine Vet J* 39:365, 2007.
41. Dyson S, Murray R: Verification of scintigraphic images for injury diagnosis in 264 horses with foot pain, *Equine Vet J* 39:350, 2007.
42. van De Watering CC, Morgan JP: Chip fractures as a radiologic finding in navicular disease of the horse, *J Am Vet Radiol Soc* 16:206, 1975.
43. Lillich JD, Ruggles AJ, Gabel AA, et al: Fracture of the distal sesamoid bone in horses: 17 cases (1982-1992), *J Am Vet Med Assoc* 207:924, 1995.
44. Smythe RH: Fracture of the navicular bone in the horse—comment, *Vet Rec* 73:1009, 1961.
45. Kaser-Hotz B, Ueltshci G, Hess N, et al: Navicular bone fractures in the pelvic limb in two horses, *Vet Radiol Ultrasound* 32:283, 1991.
46. Rick MC: Navicular bone fractures. In White NA, Moore JN, editors: C*urrent practice of equine surgery,* Philadelphia, 1990, Lippincott, pp 602–605.
47. Benninger MI, Deiss E, Ueltschi G: Bipartite distal phalanx and navicular bone in an Andalusian stallion, *Vet Radiol Ultrasound* 46:69, 2005.
48. Richardson GL, O'Brien T: Puncture wounds into the navicular bursa of the horse: role of radiographic evaluation, *Vet Radiol* 26:203, 1985.
49. Reid CF: Radiology panel-film interpretation session notes. In *Proceedings of the 22nd annual convention of the American Association of Equine Practitioners,* Dallas, TX, 1976.
50. Modransky C, Thatcher C, Welker F, et al: Unilateral phalangeal dysgenesis and navicular bone agenesis in a foal, *Equine Vet J* 19:347, 1987.
51. Busoni V, Denoix JM: Ultrasonography of the podotrochlear apparatus in the horse using a transcuneal approach: technique and reference images, *Vet Radiol Ultrasound* 42:534, 2001.
52. Grewal JS, McClure SR, Booth LC, et al: Assessment of the ultrasonographic characteristics of the podotrochlear apparatus in clinically normal horses and horses with navicular syndrome, *J Am Vet Med Assoc* 225:1881, 2004.
53. Rabba S, Bolen G, Verwilghen D, et al: Ultrasonographic findings in horse with foot pain but without radiographically detectable osseous abnormalities, *Vet Radiol Ultrasound* 52:95, 2011.
54. Sherlock CE, Kinns J, Mair TS: Evaluation of foot pain in the standing horse by magnetic resonance imaging, *Vet Record* 161:739, 2007.
55. Sherlock C, Mair T, Blunden T: Deep erosions of the palmar aspect of the navicular bone diagnosed by standing magnetic resonance imaging, *Equine Vet J* 40:684, 2008.
56. Whitton RC, Buckley C, Donovan T, et al: The diagnosis of lameness associated with distal limb pathology in a horse: a comparison of radiography, computed tomography and magnetic resonance imaging, *Vet J* 155:223, 1998.
57. Tietje S: Computed tomography of the navicular bone region in a horse: a comparison with radiographic documentation, *Pferdeheilkunde* 11:51, 1995.

58. Groth AM, May SA, Weaver MP, et al: Intra- and interobserver agreement in the interpretation of navicular bones on radiographs and computed tomography, *Equine Vet J* 41:124, 2009.
59. Dyson S, Murray R, Schramme M, et al: Magnetic resonance imaging of the equine foot: 15 horses, *Equine Vet J* 35:18, 2003.
60. Busoni V, Heirmann M, Trenteseaux J, et al: Magnetic resonance imaging findings in the equine deep digital flexor tendon and distal sesamoid bone in advanced navicular disease—an ex vivo study, *Vet Radiol Ultrasound* 46:279, 2005.
61. Dyson SJ, Murray R, Schramme MC: Lameness associated with foot pain: results of magnetic resonance imaging in 199 horses (January 2001–December 2003) and response to treatment, *Equine Vet J* 37:113, 2005.
62. Murray RC, Schramme M, Dyson S, et al: Magnetic resonance imaging characteristics of the foot in horse with palmar foot pain and control horses, *Vet Radiol Ultrasound* 47:1, 2006.
63. Schramme M, Kerekes Z, Hunter S, et al: Improved identification of the palmar fibrocartilage if the navicular bone with saline magnetic resonance bursography, *Vet Radiol Ultrasound* 50:606, 2009.
64. Murray RC, Mair TS, Sherlock CE, et al: Comparison of high-field and low-field magnetic resonance images of cadaver limbs of horses, *Vet Record* 165:281, 2009.

ELECTRONIC RESOURCES

Evolve

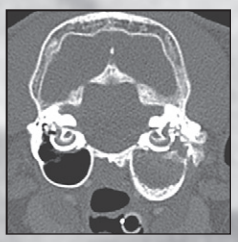
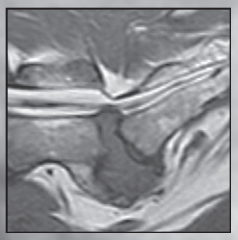
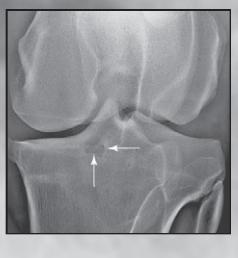
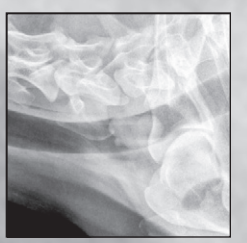
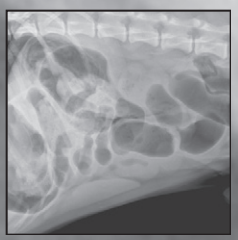
Additional information related to the content in Chapter 24 can be found on the companion Evolve website at http://evolve.elsevier.com/Thrall/vetrad/

- Chapter Quiz

This page intentionally left blank

SECTION IV

The Thoracic Cavity: Canine, Feline, and Equine

25 **Principles of Radiographic Interpretation of the Thorax**
Donald E. Thrall

26 **The Pharynx, Larynx, and Trachea**
Kate Alexander

27 **The Canine and Feline Esophagus**
Lorrie Gaschen

28 **The Thoracic Wall**
Valerie F. Samii

29 **The Diaphragm**
Elissa K. Randall
Richard D. Park

30 **The Mediastinum**
Donald E. Thrall

31 **The Pleural Space**
Donald E. Thrall

32 **The Heart and Pulmonary Vessels**
Robert Bahr

33 **The Canine and Feline Lung**
Donald E. Thrall

34 **The Equine Thorax**
Stephanie G. Nykamp

CHAPTER • 25

Principles of Radiographic Interpretation of the Thorax

Donald E. Thrall

The acquisition of thoracic radiographs is common in small animal practice but is less common in the horse. Computed tomography (CT) is very useful for characterizing intrathoracic disease in dogs and cats but is not used for thoracic imaging in horses. Magnetic resonance imaging is used rarely in veterinary medicine for assessing the thorax.

Obtaining good-quality radiographs of the thorax is relatively easy, even in the horse, as long as a few basic principles are followed. However, poor attention to detail will result quickly in degradation of image quality. Given the complexity of the thorax and the multiple structures that are visible, any degradation in image quality will lead to a disproportionate loss of diagnostic quality.

For many radiographic examinations, two orthogonal projections provide adequate information for a thorough radiographic assessment. However, for the thorax there are special circumstances that make the routine two-orthogonal-projection approach either suboptimal (dogs and cats) or impractical (horse).

NOMENCLATURE

The naming of lateral thoracic radiographs made with the patient recumbent and a vertically directed x-ray beam, as commonly done in dogs and cats, violates the point-of-entrance to point-of-exit nomenclature system described in Chapter 5. In that system, a lateral view made with the dog or cat in left recumbency would be termed a *right-left* view because the x-ray beam strikes the right aspect of the thorax and exits the left aspect of the thorax. But, for the thorax, the terminology for lateral projections has been abbreviated to describe the side of the patient lying on the x-ray table. Thus, for example, a thoracic radiograph acquired with the dog or cat lying on the left side would be termed a *left lateral* view.

In the horse, where lateral thoracic radiographs are usually made with the patient standing and a horizontally directed x-ray beam, the point-to-entrance to point-of-exit system should be used. Thus, lateral radiographs should be described as either left-right or right-left views.

In all species, ventrodorsal (VD) and dorsoventral (DV) radiographs of the thorax are named according to the point-to-entrance to point-of-exit system.

POSITIONING: DOG AND CAT

The basic thoracic radiographic examination in the dog and cat should consist of left lateral, right lateral, and either VD or DV projections. The need for obtaining left *and* right lateral views routinely is explained later. A case can be also be made for acquiring VD and DV thoracic radiographs routinely, in addition to the left and right lateral views, and a rationale supporting this is also provided later.

The effort required to complete a thoracic radiographic examination is obviously related to the number of projections. There is no reason to limit the number of projections acquired routinely, especially with a direct digital system where the image is available instantly and there are no expendable supplies. Failure to acquire both right *and* left lateral views routinely in addition to a VD or DV view will result in some diagnoses being missed. Admittedly, the increased number of exposures per patient has the potential to increase the occupational radiation dose to personnel, but as long as proper protection principles are followed, this potential increase will not be realized.

It is important that the entire thoracic cavity be included in the image. The field of view should extend from just cranial to the thoracic inlet, to a few centimeters caudal to the last rib. The dorsocaudal tips of the caudal lobes extend further caudally than often anticipated, and these regions can be omitted easily from the field-of-view, increasing the chance for missing disease in this region. Even in the largest dogs, including the entire thoracic cavity in one 14-inch by 17-inch image is usually possible. For the occasional huge dog where this is not possible, then each projection (left lateral, right lateral, VD, DV) should be divided into cranial and caudal portions. This effectively doubles the requisite number of images to evaluate the entire thoracic cavity in huge dogs.

For lateral and VD/DV views, the thoracic limbs should be pulled cranially to remove the brachial muscles from being superimposed on the cranial aspect of the thorax. Failure to do this will cause an artificial increase in radiographic opacity of the cranial aspect of the thorax and lead to errors in interpretation of the cranial mediastinum and cranial lung lobes.

Lateral Views

Atelectasis

When an animal is in lateral recumbency, as for a lateral radiographic examination, the dependent lung collapses from (1) the effects of the heart compressing the lung, (2) reduced movement of the dependent thoracic cage because of compression, and (3) cranial excursion of the dependent portion of the diaphragm. This collapse occurs in awake, sedated, and anesthetized dogs and cats relatively shortly after being placed in lateral recumbency. The magnitude of this collapse, which is related directly to the body mass of the patient, can be appreciated by making a radiograph of the thorax with the dog in lateral recumbency and using a horizontally directed

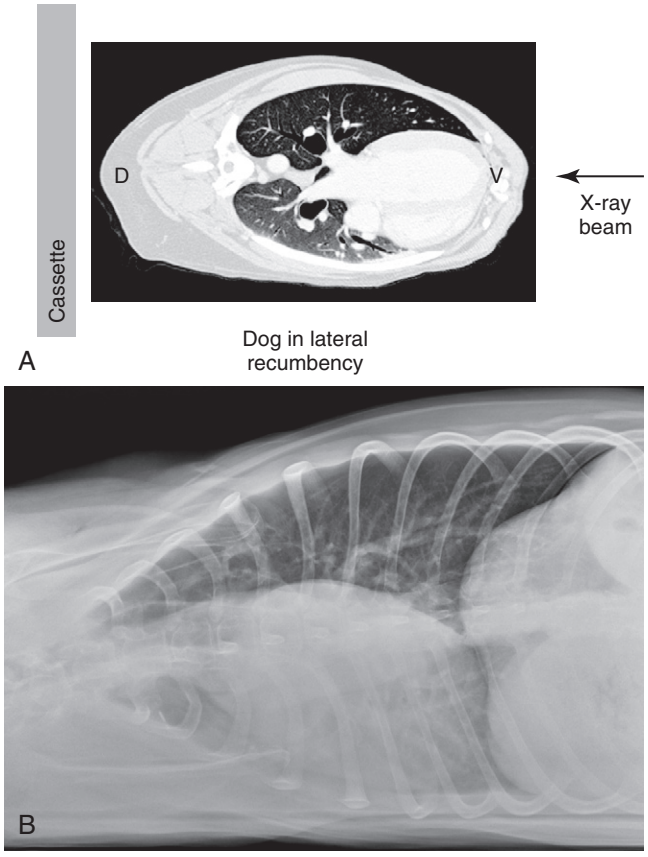


Fig. 25-1 **A,** Schematic illustration of the geometry used to acquire a horizontal-beam ventrodorsal radiograph of the thorax. For this figure, a transverse CT image of the thorax was used to represent the dog being radiographed. *D,* dorsal; *V,* ventral. **B,** Horizontal-beam ventrodorsal thoracic radiograph acquired using the geometry depicted in **A.** Note the collapse of the dependent lung. The heart is displaced into the dependent hemithorax and is compressing the lung. The dependent aspect of the diaphragm is displaced cranially, also compressing the lung. There is reduced thoracic cage movement in the dependent hemithorax caused by compression. All of these factors contribute to the dependent atelectasis.

x-ray beam. Such a projection would be termed a *right* (or *left*) *recumbent horizontal-beam VD*. The configuration for acquiring such a radiograph and an example are provided (Fig. 25-1). The amount of recumbency-associated atelectasis that occurs is striking. This atelectasis cannot be visualized directly in a conventional lateral radiograph made with a vertically directed x-ray beam because the aerated nondependent lung is superimposed on the collapsed dependent lung. Nevertheless, the increased opacity of the dependent lung contributes to an appearance of overall increased lung opacity in lateral radiographs that is misdiagnosed commonly as disease.

In addition to being misdiagnosed as lung disease, recumbent atelectasis is important because the increased radiographic opacity of the collapsed lung causes border effacement, or silhouetting, of any soft tissue lesion in the dependent lung, rendering it inconspicuous in the radiograph.[1] This phenomenon results commonly in lesions in the dependent lung not being visible radiographically in the lateral view (Fig. 25-2). The most significant aspect of this phenomenon is in the situation where the lesion is small and is not visible in the VD or DV view, such as commonly occurs with a lung nodule or small mass. If only one lateral view is made of such patients, and the lesion happens to be in the dependent lung and also in a region where it is not visible in the VD or DV radiograph, the lesion will be missed (Fig. 25-3). The collapse of the dependent lung is the main reason why both the left lateral and right lateral views should be included in every routine thoracic radiographic examination. If only one lateral view is obtained, a significant number of patients will be diagnosed incorrectly.[2]

Given the amount of dependent atelectasis that occurs in lateral recumbency, it is not surprising that the overall radiographic opacity of the lung field will be increased in lateral versus VD or DV radiographs. Overinterpreting this increased opacity as lung disease is a common mistake (Fig. 25-4). If lung disease is suspected from one or both lateral views, it is critical that this be confirmed in the VD or DV view to rule out that the suspected lung disease is caused simply by atelectasis.

The use of sedation or anesthesia for the radiographic examination will exacerbate the amount of recumbency-associated atelectasis that is present and will lead to an even greater increase in lung opacity that is misinterpreted easily as lung disease in lateral radiographs.

Other than conspicuity of lesions in the dependent versus the nondependent lung, there are some other important differences in the appearance of the lateral thoracic radiograph that can be attributed to whether the patient is in left or right lateral recumbency.

Cranial Lobe Vessels

Assessing the absolute and relative size of pulmonary vessels is an important process of thoracic radiographic interpretation.[3] The pulmonary artery and vein in the right cranial lobe are used commonly as a basis for assessing the pulmonary circulation. It is important to be able to identify these two vessels specifically and to be able to compare the size of the right cranial lobe pulmonary artery to the size of the right cranial lobe pulmonary vein without having other vessels superimposed. The pulmonary vessels in the right cranial lung lobe are more conspicuous in a left lateral than in a right lateral radiograph (Fig. 25-5). This is caused mainly by the dorsal displacement of the right cranial lobe that occurs when the patient is in right lateral recumbency resulting in the right cranial lobar vessels being superimposed on the left cranial lobar vessels.

The left cranial lobe vessels cannot usually be assessed or compared accurately in either the left or right lateral view because they are located more dorsally in the thorax and usually superimposed on other vessels or the thicker dorsal portion of the mediastinum. Occasionally, pulmonary artery-pulmonary vein pairs can be compared in DV or VD views, but assessing the right cranial lobe vessels in the left lateral view should be a standard aspect of thoracic radiographic interpretation in the dog and cat.

Diaphragm

In the left lateral view, the two dorsal crura of the diaphragm deviate from each other, whereas in the right lateral view they are more parallel (Fig. 25-6).

The diaphragmatic hiatus for the caudal vena cava is located slightly to the right of midline. In the right lateral view the dependent right crus will be cranial to the left crus because of pressure from abdominal contents, and therefore the caudal vena cava will silhouette, or merge, with the more cranial crus. In the left lateral view, the left crus will be cranial to the right crus, and the caudal vena cava will be superimposed on the left crus before silhouetting, or merging, with the more caudally located right crus (Fig. 25-7). The appearance of the junction of the caudal vena cava with the diaphragm can be used as a way to distinguish a left lateral from a right lateral radiograph if an external marking system has not been used, but this is not 100% reliable because sometimes the left crus will be cranial to the right crus in the right lateral view, and vice versa.

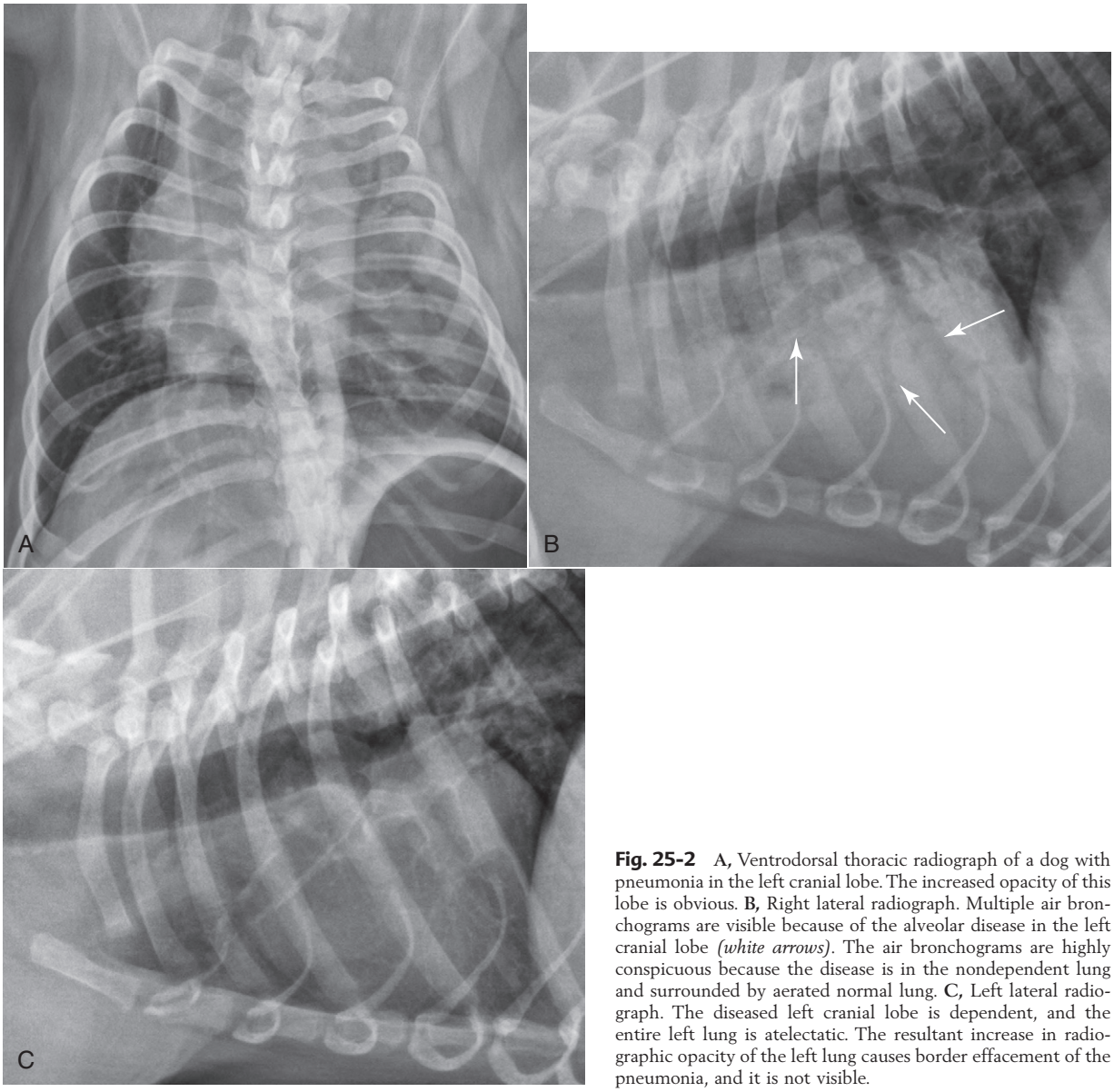


Fig. 25-2 **A,** Ventrodorsal thoracic radiograph of a dog with pneumonia in the left cranial lobe. The increased opacity of this lobe is obvious. **B,** Right lateral radiograph. Multiple air bronchograms are visible because of the alveolar disease in the left cranial lobe *(white arrows)*. The air bronchograms are highly conspicuous because the disease is in the nondependent lung and surrounded by aerated normal lung. **C,** Left lateral radiograph. The diseased left cranial lobe is dependent, and the entire left lung is atelectatic. The resultant increase in radiographic opacity of the left lung causes border effacement of the pneumonia, and it is not visible.

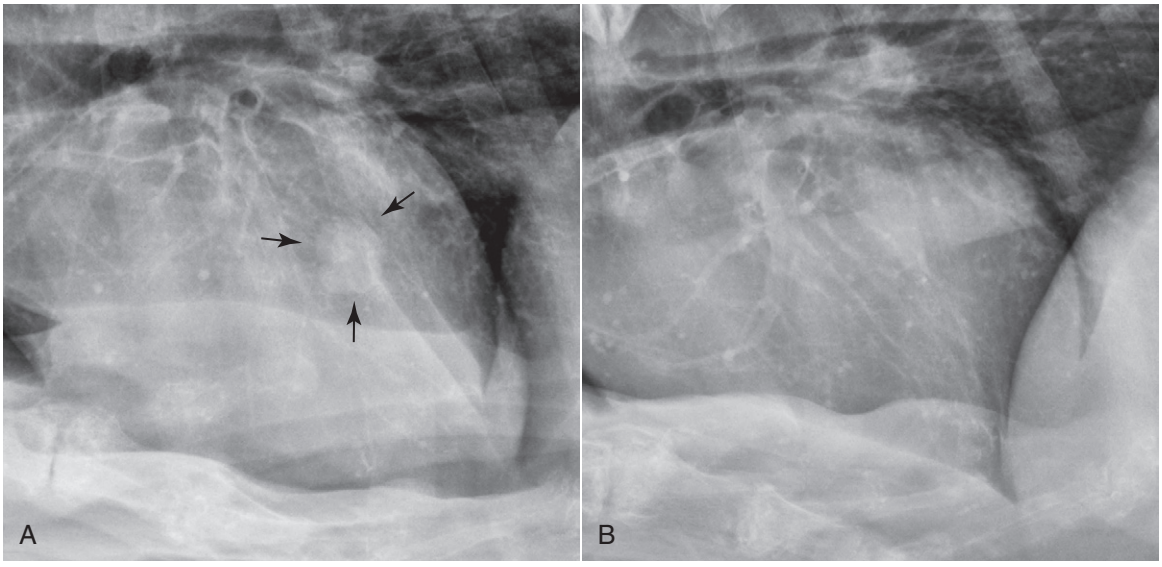


Fig. 25-3 **A,** Right lateral radiograph of a dog with a nodule in the left lung *(arrow)*. The nondependent left lung is well aerated, providing contrast for the soft tissue nodule. **B,** Left lateral radiograph of the same dog. The nodule is now in the collapsed dependent lung and is not visible because of border effacement.

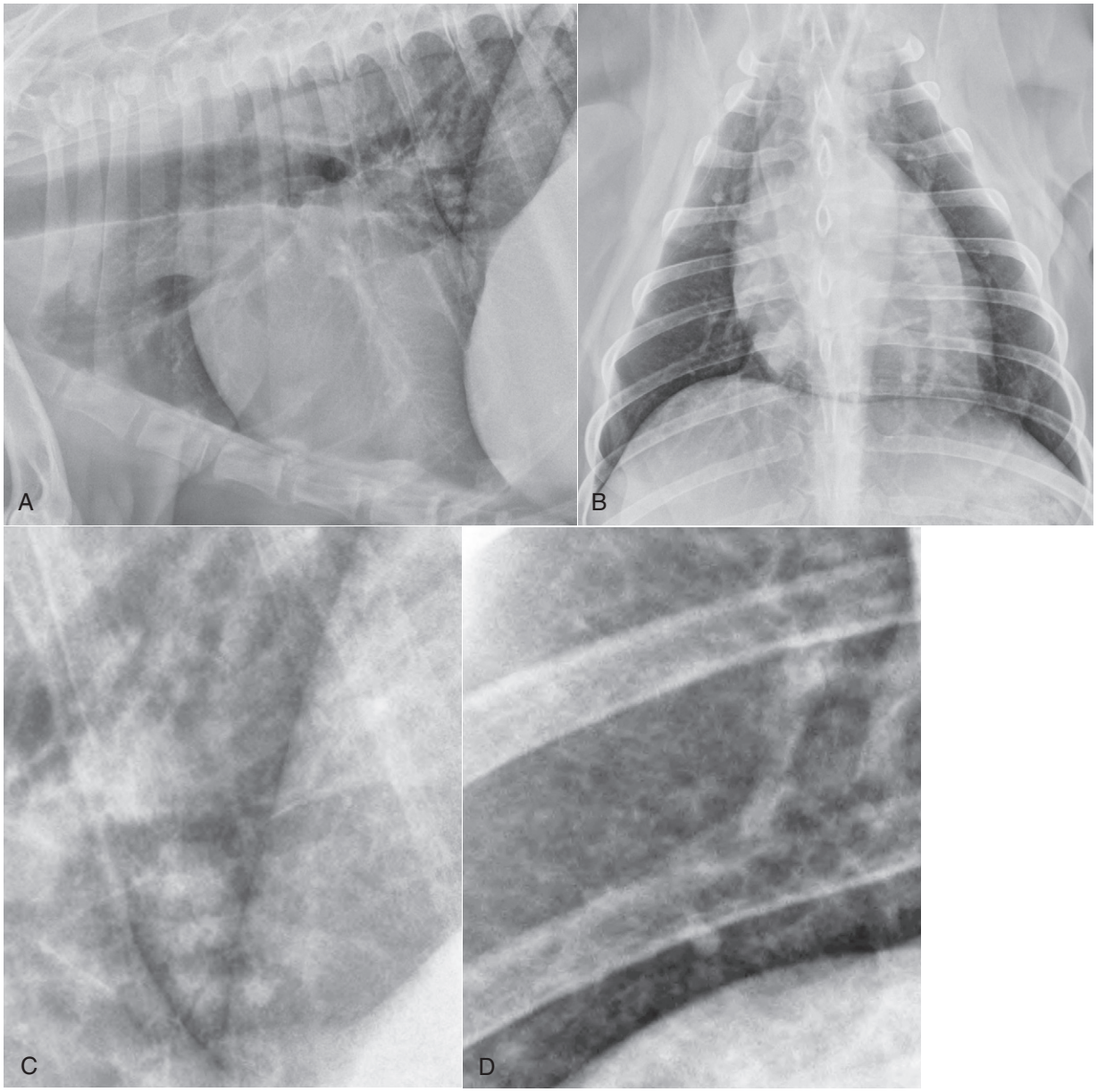


Fig. 25-4 Left lateral **(A)** and DV **(B)** thoracic radiographs of a dog, and close-up views of a region from the dorsocaudal lung field from the lateral radiograph **(C)** and the right-caudal lung field from the DV radiograph **(D).** The increased atelectasis that occurs in lateral views results in an overall increased opacity to the lungs **(A** and **C).** In the DV projection, where lungs are better aerated, they are more radiolucent **(B** and **D),** confirming that the opacity seen in the lateral view was an artifact of poor ventilation. The increased lung opacity commonly encountered in lateral views is often misinterpreted as lung disease. Any suspicious opacity seen in the lateral view must be confirmed as abnormal in either the VD or DV view.

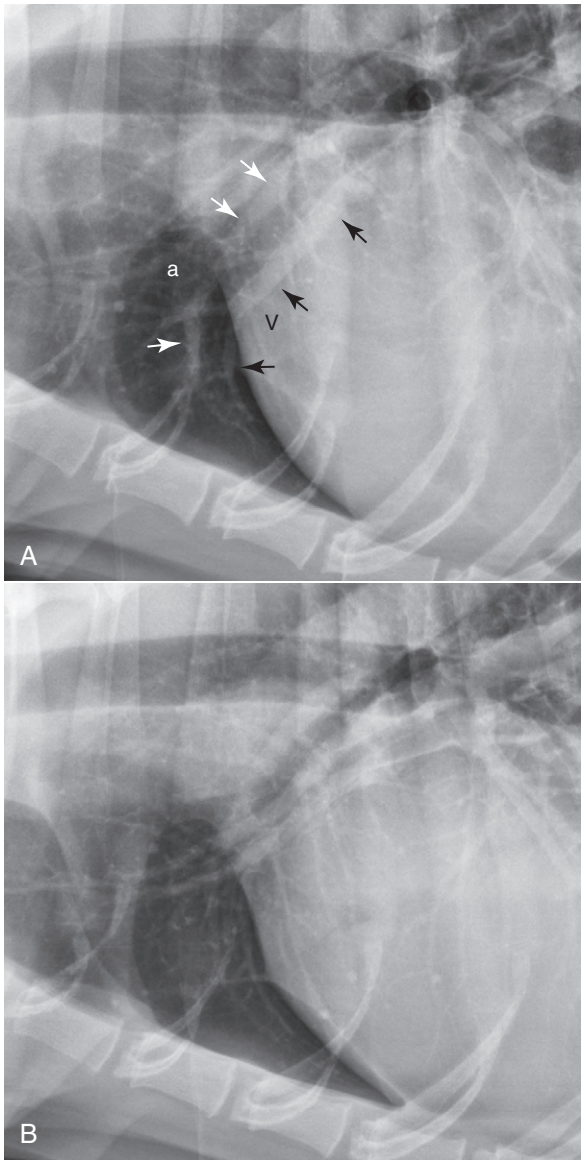


Fig. 25-5 Left lateral **(A)** and right lateral **(B)** radiographs of the cranioventral aspect of the thorax of a dog. The right cranial lobe pulmonary artery *(a, white arrows)* and right cranial lobe pulmonary vein *(v, black arrows)* can be distinguished clearly in the left lateral view. In the right lateral view, these two vessels are superimposed with each other and with the vessels from the left cranial lobe and cannot be assessed individually. In **A**, the pulmonary artery and vein in the left cranial lobe are dorsal to the right cranial lobe vessels.

Heart

In general, the heart will appear slightly more round and the apex may be slightly elevated from the sternum in the left lateral view compared with the right lateral view (Fig. 25-8).

Ventrodorsal/Dorsoventral View

The VD view is the orthogonal view made commonly to accompany the left and right lateral views. In some animals, obtaining the VD view may not be possible because of pain or respiratory distress, and the DV view may be substituted. There may also be a personal preference for the DV view over the VD view, especially when radiographic evaluation of the heart is the main reason for performing the radiographic examination.[4] However, there is no evidence that the DV view is more accurate than the VD view for radiographic examination of the heart. But, rather than debate the relative merit of VD versus DV thoracic radiographs, it is more important to understand the differences in appearance of the thorax in these two projections.[4-7]

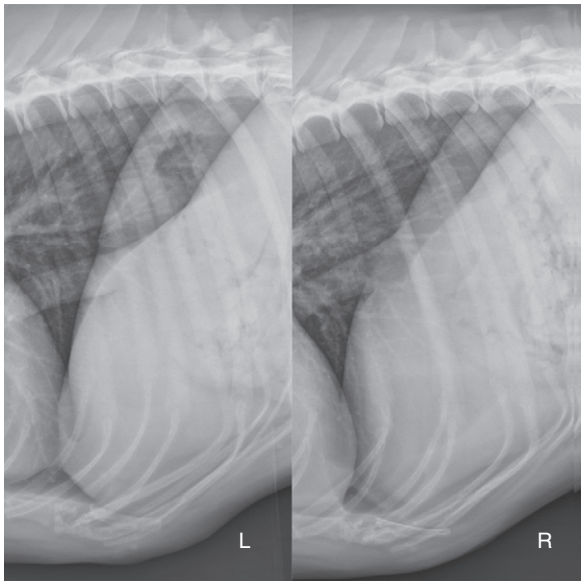


Fig. 25-6 Left *(L)* and right *(R)* lateral radiographs of the caudal thorax of a dog. In the left lateral view, the crura at the dorsal aspect of the diaphragm diverge more than in the right lateral view.

Atelectasis

Recumbency-associated atelectasis occurs in VD and DV views, but to a lesser extent than in lateral views. Of the left lateral, right lateral, VD and DV views, the least amount of recumbency-associated atelectasis occurs in the DV view. Atelectasis occurring in the dependent lung in lateral views has already been described. In the VD view, there is some collapse of the dorsocaudal aspect of the caudal lung lobes (Fig. 25-9) but not to the extent seen in lateral views (compare with Fig. 25-1, *B*). Even though there is less overall atelectasis in VD radiographs than in lateral radiographs, this atelectasis can still cause border effacement of disease located in the dorsocaudal portion of the lung (Fig. 25-10).

Caudal Lobe Vessels

Caudal lobe pulmonary vessels are more conspicuous in DV than VD radiographs for three reasons: (1) they are magnified; (2) they are oriented more perpendicular to the primary x-ray beam and therefore less distorted; and (3) there is less adjacent pulmonary atelectasis when the patient is in ventral recumbency (Figs. 25-11 and 25-12)

Cardiac Silhouette

There is a major difference in the appearance of the cardiac silhouette in VD versus DV radiographs. In ventral recumbency for the DV radiograph, the ventral aspect of the diaphragm is displaced cranially where it contacts the heart and displaces it, typically to the left. The heart is also more upright in the thoracic cavity when the patient is in ventral recumbency, making it appear more round (Fig. 25-13). The rounder appearance and displacement to the left that occur normally in DV radiographs are commonly misinterpreted as cardiomegaly. The extent of leftward cardiac displacement in DV radiographs is more pronounced in large dogs and will not be as obvious in small dogs or cats.[5,6]

Accessory Lung Lobe

The cranial excursion of the diaphragm that occurs in ventral recumbency and causes cardiac displacement also impinges on

Text continued on p. 484

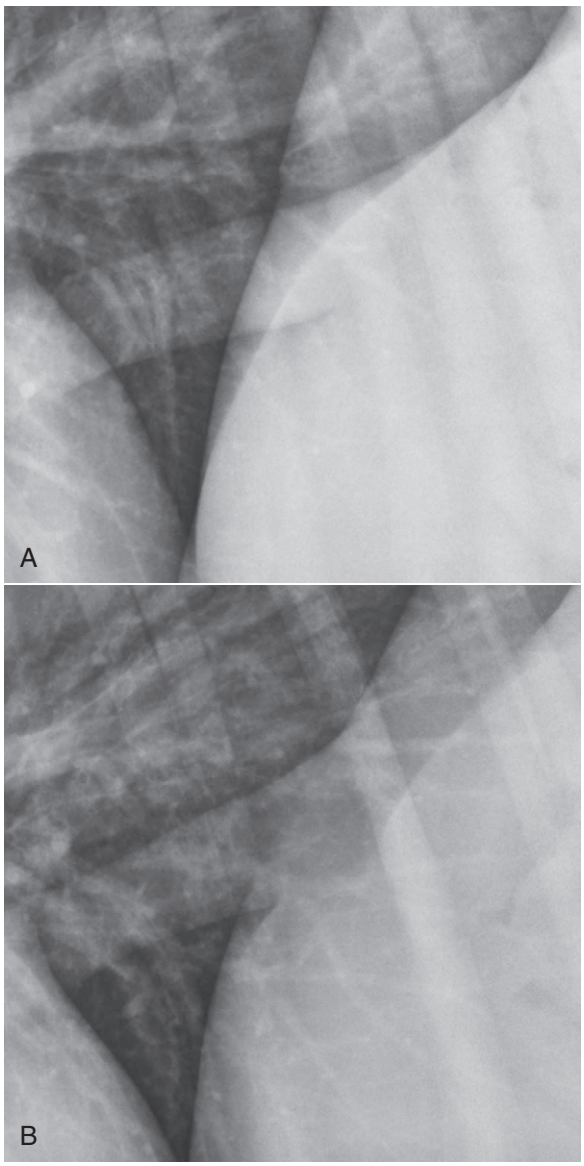


Fig. 25-7 Left **(A)** and right **(B)** lateral radiographs of the region of the junction of the caudal vena cava with the diaphragm. In the left lateral view **(A),** the left crus is more cranial, and the caudal vena cava is superimposed on it before joining the right crus. In the right lateral view **(B),** the right crus of the diaphragm is more cranial, and the caudal vena cava joins this more cranial crus.

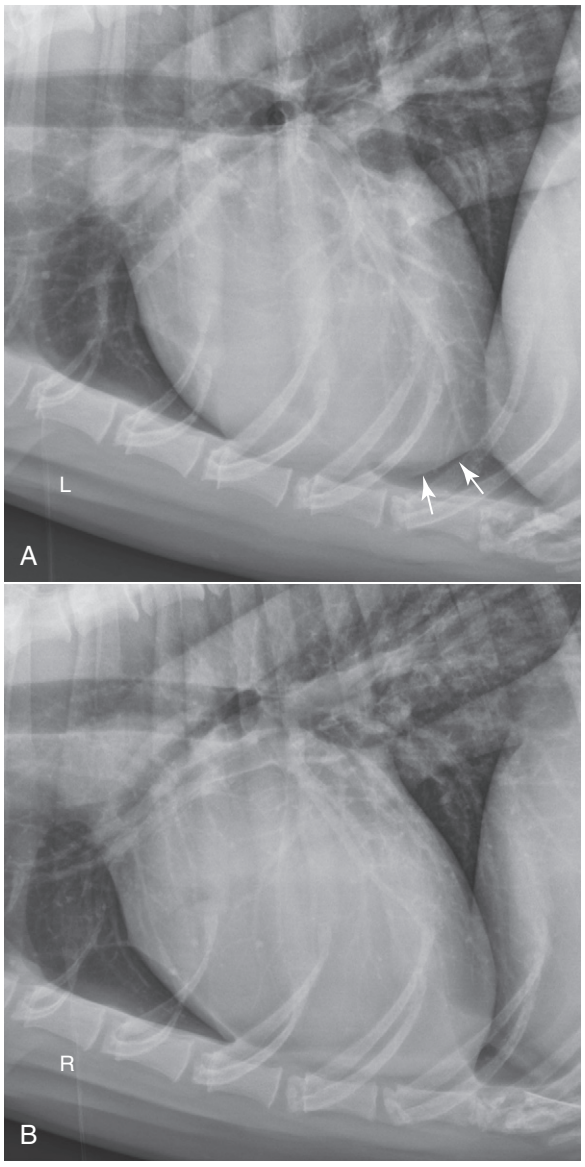


Fig. 25-8 Left lateral **(A)** and right lateral **(B)** thoracic radiographs of the cardiac region. Generally, in the left lateral view the heart will appear more round, and there will be some slight separation of the cardiac apex from the sternum (*white arrows* in **A**).

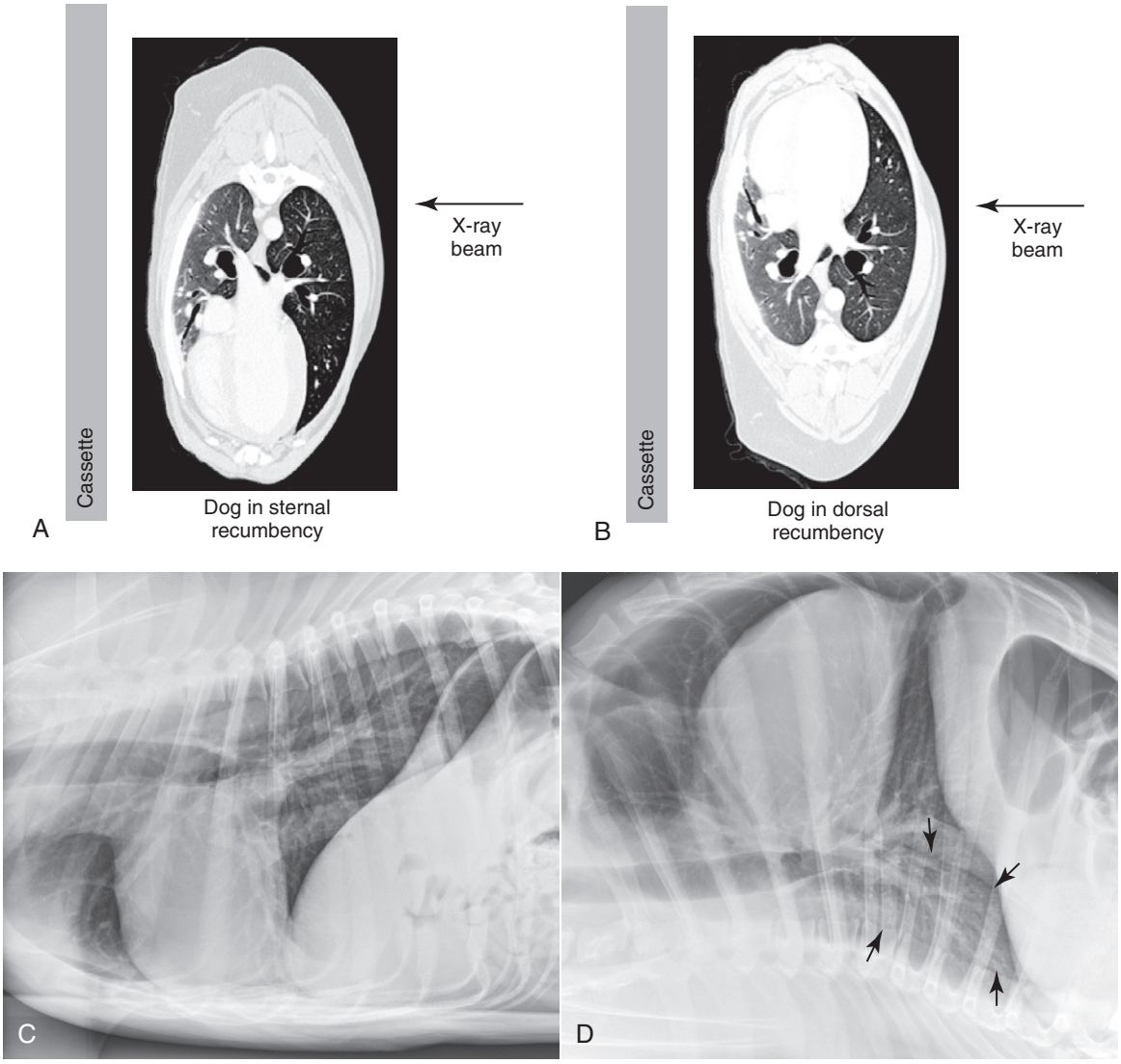


Fig. 25-9 Horizontal-beam lateral thoracic radiographs. **A,** Geometry for acquiring lateral thoracic radiograph with dog in sternal recumbency. This is the body position used for a conventional DV radiograph, but the cassette would be below the dog, and the x-ray beam striking the dog from above. **B,** Geometry for acquiring lateral thoracic radiograph with dog in dorsal recumbency. This is the body position used for a conventional VD radiograph, but the cassette would be below the dog and the x-ray beam striking the dog from above. **C,** Radiograph made with geometry illustrated in **A** with the dog in sternal recumbency. **D,** Radiograph made with geometry illustrated in **B** with the dog in dorsal recumbency. Note the absence of recumbency-associated atelectasis in the dependent ventral aspect of the lung in **C.** There is some atelectasis of the dependent dorsal aspect of the lung in **D** *(black arrows)*, but not to the extent seen in the dependent lung in a dog in lateral recumbency (compare with Fig. 25-1, *B*). In **D,** note how the caudal lobe pulmonary vessels are surrounded by the atelectasis; this will cause border effacement and render then more inconspicuous in the ventrodorsal view compared with the dorsoventral view.

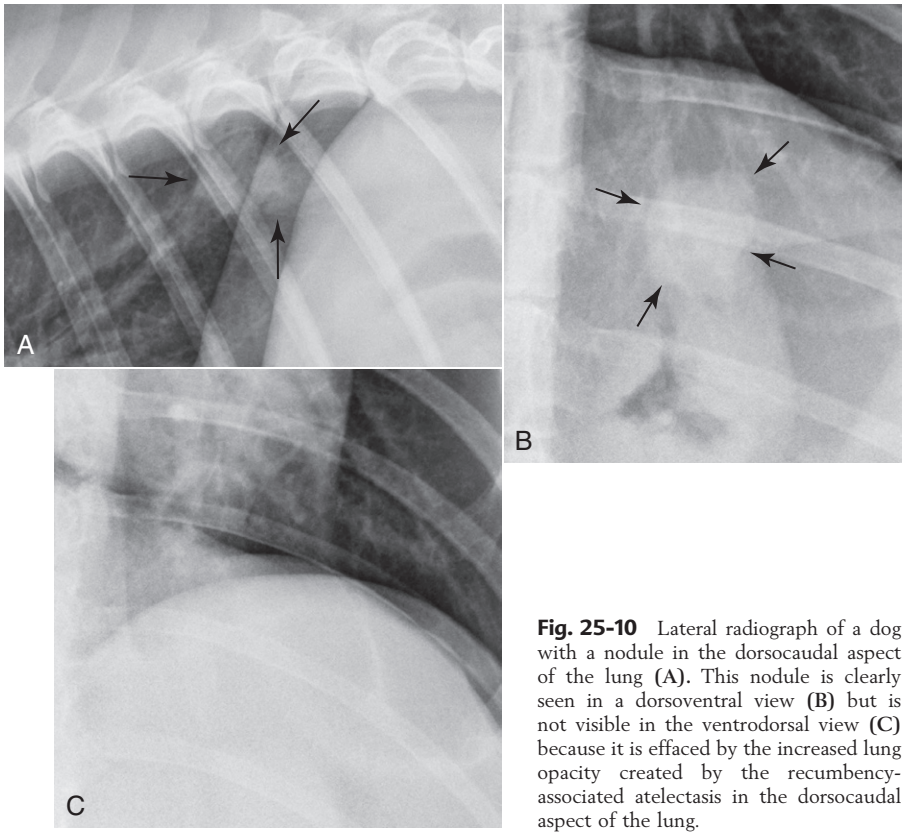


Fig. 25-10 Lateral radiograph of a dog with a nodule in the dorsocaudal aspect of the lung **(A).** This nodule is clearly seen in a dorsoventral view **(B)** but is not visible in the ventrodorsal view **(C)** because it is effaced by the increased lung opacity created by the recumbency-associated atelectasis in the dorsocaudal aspect of the lung.

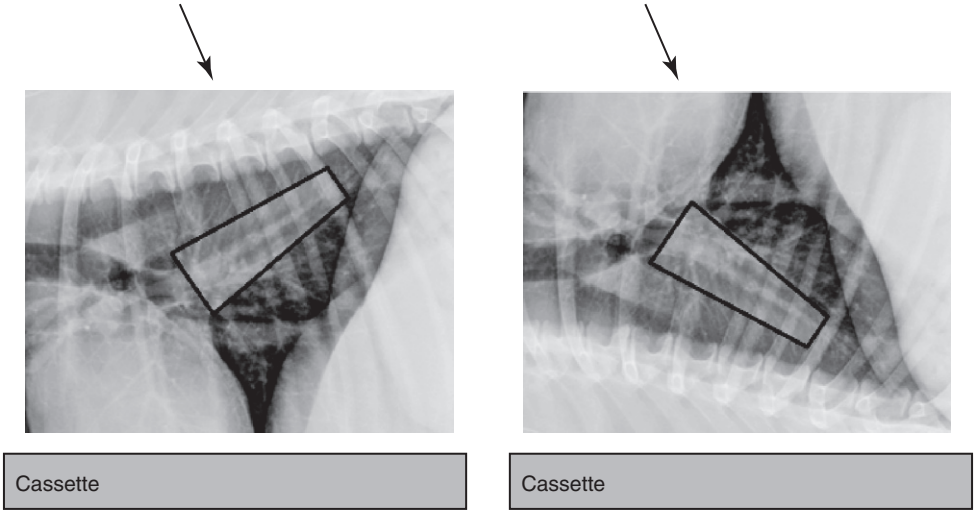


Fig. 25-11 Effect of dorsal versus ventral recumbency on the orientation of the caudal lobe pulmonary vessels with respect to the primary x-ray beam. The center of the primary x-ray beam for thoracic radiographs is approximately at the level of the cardiac silhouette. This means that in the caudal aspect of the thorax the primary beam will be diverging and be at an angle to the pulmonary vessels. In the left panel, the orientation of the caudal lobe vessels relative to the primary x-ray beam is shown for a dog in ventral recumbency—that is, for a dorsoventral radiograph. The caudal lobe vessels, shown *outlined*, are nearly perpendicular to the primary x-ray beam and will be projected without distortion. In ventral recumbency, the caudal lobe vessels are also further from the cassette and will be magnified. Although radiographic magnification does degrade detail, the amount of contrast provided by the air surrounding the caudal lobe vessels enables the caudal lobe vessels to be assessed even though magnified. In the right panel, the orientation of the caudal lobe vessels relative to the primary x-ray beam is shown for a dog in dorsal recumbency—that is, for a ventrodorsal radiograph. The caudal lobe vessels, shown *outlined*, are at an angle with respect to the primary x-ray beam, and even though they are magnified less, they will be distorted in the radiograph.

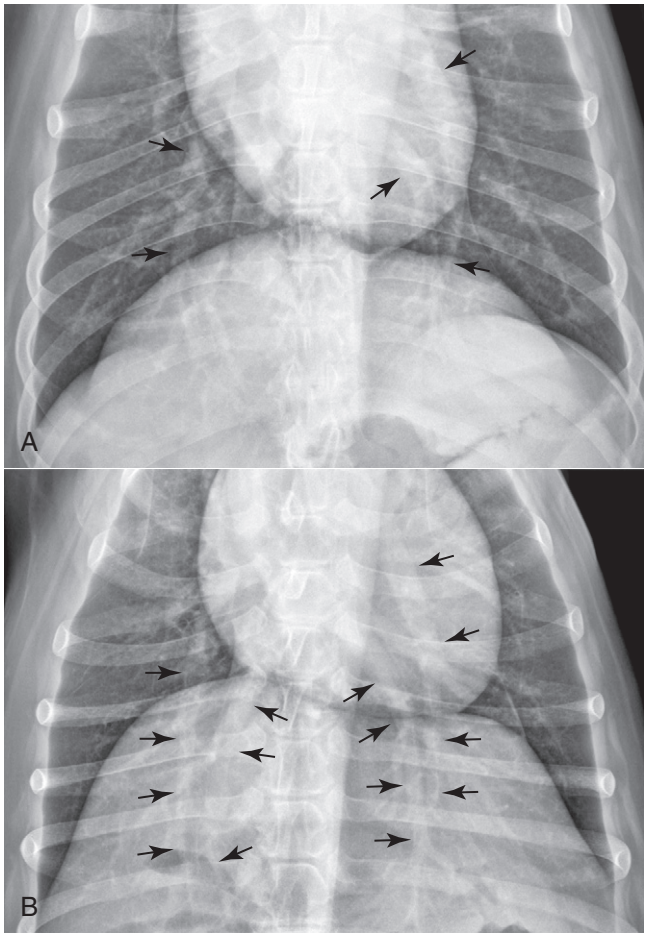


Fig. 25-12 Ventrodorsal **(A)** and dorsoventral **(B)** radiographs of the caudal aspect of the thorax of a dog. The caudal lobe pulmonary vessels *(black arrows)* are more conspicuous on the dorsoventral view than in the ventrodorsal view for the reasons mentioned in the text and illustrated in Figure 25-11.



Fig. 25-13 VD **(A)** and DV **(B)** thoracic radiographs. In the DV radiograph, the diaphragm is displaced cranially where it contacts the heart and pushes it into the left hemithorax. The cardiac silhouette is also smaller and more round as it is more upright in the thoracic cavity because of the displacement. The overall size of the thoracic cavity is reduced in the DV radiograph. The cranial excursion of the diaphragm also impinges on the accessory lung lobe region and compromises the evaluation of that region of the thorax. The appearance of the heart in the DV radiograph is often misinterpreted as cardiomegaly with an apex shift to the left.

the region of the accessory lung lobe. This interferes with evaluation of the accessory lobe and caudal mediastinum, and significant disease can be missed in DV radiographs because of this impingement (see Fig. 25-13). As with cardiac displacement, the amount of impingement on the accessory lobe and caudal mediastinal regions in DV radiographs caused by cranial excursion of the diaphragm is more noticeable in large dogs and is not as significant in small dogs or cats.

Dorsoventral, Ventrodorsal, or Both?

Based on the preceding, it is clear that there are many significant differences in the appearance of VD versus DV thoracic radiographs. As a consequence of these differences, it is justified to acquire both of these views routinely in addition to the left and right lateral views. The small increase in time and effort required to obtain four radiographic views of the thorax routinely will lead to increased diagnostic accuracy and fewer missed lesions.

POSITIONING: HORSE

In small foals or miniature horses, it may be possible to obtain lateral thoracic radiographs by restraining a compliant animal on a conventional x-ray table and use a vertically directed x-ray beam, as in dogs and cats. If this is done, then the same positioning principles as described for the dog and cat apply. Obtaining VD or DV thoracic radiographs by placing the patient on the x-ray table and using a vertically directed x-ray beam can be accomplished only in the smallest and most compliant equine patients. Because of the relatively narrow configuration of the foal thorax and the magnification of the heart in the VD view as a result of the distance of the heart from the cassette, the normal cardiac silhouette will appear relatively large in the VD view. This appearance is misinterpreted commonly as pathologic enlargement (Fig. 25-14).

Most thoracic radiographs of horses are acquired with the patient standing. Lateral views are therefore acquired with a horizontally directed x-ray beam, and DV or VD views are not obtained. When radiographing the equine thorax using a horizontally directed x-ray beam, handholding of cassettes or digital imaging plates *should not be done*. The visible light field that corresponds to the primary x-ray beam can be seen only on the x-ray tube side of the horse; that is, no part of the light field strikes the cassette. Therefore, aligning the light field with the cassette accurately when handholding the cassette is virtually impossible. This will result in the person holding the

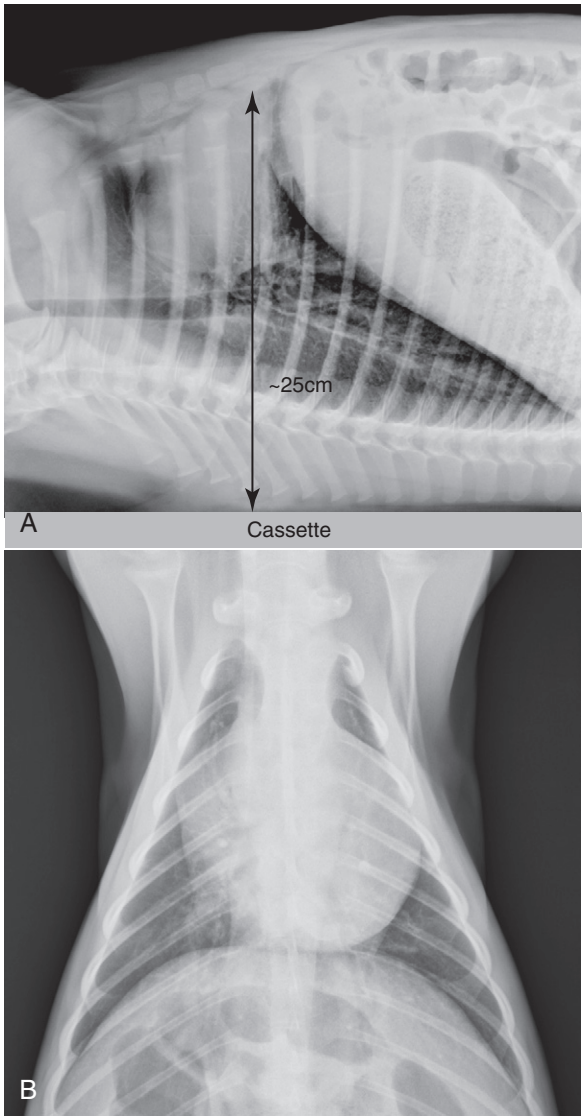


Fig. 25-14 **A,** Illustration of the geometry of a foal thorax being radiographed in dorsal recumbency for a VD view. Given the shape of the foal thorax, the cardiac apex may be on the order of 25 cm from the cassette, resulting in it being magnified and distorted in the resultant image. Other parts of the heart will also be magnified and distorted, although to a lesser extent because they are not as far from the cassette. This magnification and the relatively narrow configuration of the thorax in foals will result in the heart appearing large in the VD radiograph, and this is often misinterpreted as cardiomegaly. **B,** VD radiograph of a normal 4-week-old mule; the heart appears large for the reasons described in **A** of this illustration.

cassette being exposed frequently to the primary x-ray beam. A wall-mounted cassette holder, as described in Chapter 7, or a floor-mounted mobile cassette holder should be used for equine thoracic radiography. When using these devices, the x-ray beam can be aligned with the cassette before the horse is brought into position next to the cassette.

Given the large size of the equine thorax in all but the youngest foals or miniature horses, it is not possible to obtain a radiograph of the entire thoracic cavity in one image. For lateral radiographs of an adult horse, four radiographs are usually acquired: (1) cranioventral, (2) craniodorsal, (3) caudoventral, and (4) caudodorsal. The approximate location for each of these views is illustrated in Figure 25-15. If the long axis of the cassette or digital plate cannot be oriented horizontally for the caudodorsal radiograph because of technical

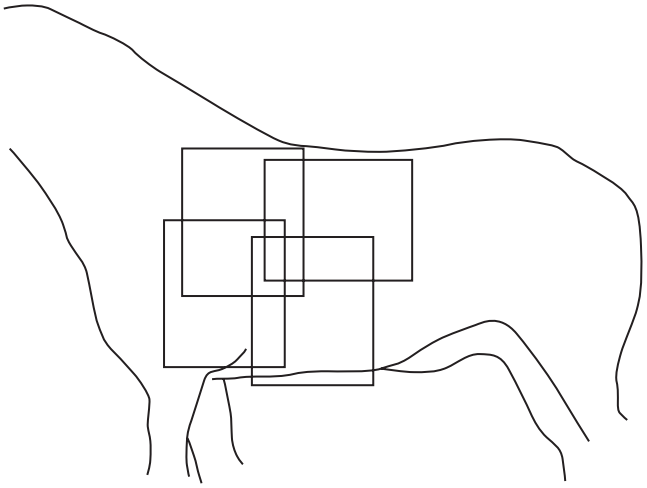


Fig. 25-15 Outline of a horse showing the approximate locations of the cassettes, or imaging plate, for a four-view radiographic examination that would include the entire thoracic cavity.

limitations, then the caudodorsal region may have to be imaged using two vertically oriented cassettes rather than one horizontally oriented cassette as shown. This would increase the number of radiographic exposures required to image the entire thoracic cavity to five rather than four. For foals that are too large to restrain on an x-ray table with a vertically directed x-ray beam but are not fully grown, it may be possible to image the entire thorax using two lateral views rather than the four that will be needed for an adult horse.

Radiographic magnification and distortion are factors that also have to be considered when acquiring and interpreting equine thoracic radiographs. This has already been discussed relative to the appearance of the heart of a foal in a VD radiograph. But, also as a result of the large diameter of the thoracic cavity of an adult horse, a lesion in the lung on the side closest to the x-ray tube could be 35 cm or more from the cassette or digital plate. If the distance from the focal spot of the x-ray tube to the cassette was 100 cm, a lesion 35 cm from the cassette would be magnified approximately 50%. This amount of magnification would lead to distortion and blurring and a reduction in the conspicuity of the lesion, especially if the lesion was small. If the possibility of a small lesion is a clinical concern, then left-right *and* right-left thoracic radiographs should be obtained. This means that eight exposures would be necessary for the complete radiographic examination of the thorax. Alternatively, the x-ray tube can be moved further from the cassette to reduce geometric magnification, but this will require an increase in the milliampere second (mAs) that is proportional to the square of the distance.[8] Whether increasing the focal spot to cassette distance to reduce magnification and distortion is feasible depends on the capabilities of the x-ray equipment.

RADIOGRAPHIC TECHNIQUE: DOG AND CAT

When radiographing the small animal thorax using a film-screen system, a high kilovoltage peak (kVp)–low mAs technique is preferable. At discussed in Chapter 1, this type of technique will lead to a long scale of contrast, with many gray shades. This is important in the thorax because of the inherently high contrast created by the large volume of air within the lung. If a low kVp–high mAs technique is used for radiographing the thorax with a film-screen system, the contrast of the image will be too high, and it will not be possible to assess the lung parenchyma adequately. If one is using a digital

system, exposure factors are less critical because of the enhanced contrast resolution of digital imaging systems and the ability to adjust the blackness and contrast of the image after it is acquired, as discussed in Chapter 2. For patients thicker than 10 cm, a grid should be used to remove scattered x-rays from the beam.

Exposure time is critical when radiographing the thorax. Motion is the biggest enemy of image detail in veterinary radiology. Respiratory motion can induce blurring, and cardiac pulsation can also lead to reduced detail, although the change in shape of the heart because of the cardiac cycle, at least in cats, is minimal.[9] To minimize the effects of motion, the shortest exposure time and highest mA setting possible should be used to produce the needed mAs.

The respiratory pattern of the patient should be observed for a few seconds before the radiographic exposure is made so that the exposure can be coordinated with peak inspiration. The increased lung volume at peak-inspiration will optimize pulmonary contrast and reduce the false impression of pulmonary disease caused by poor aeration (Fig. 25-16).

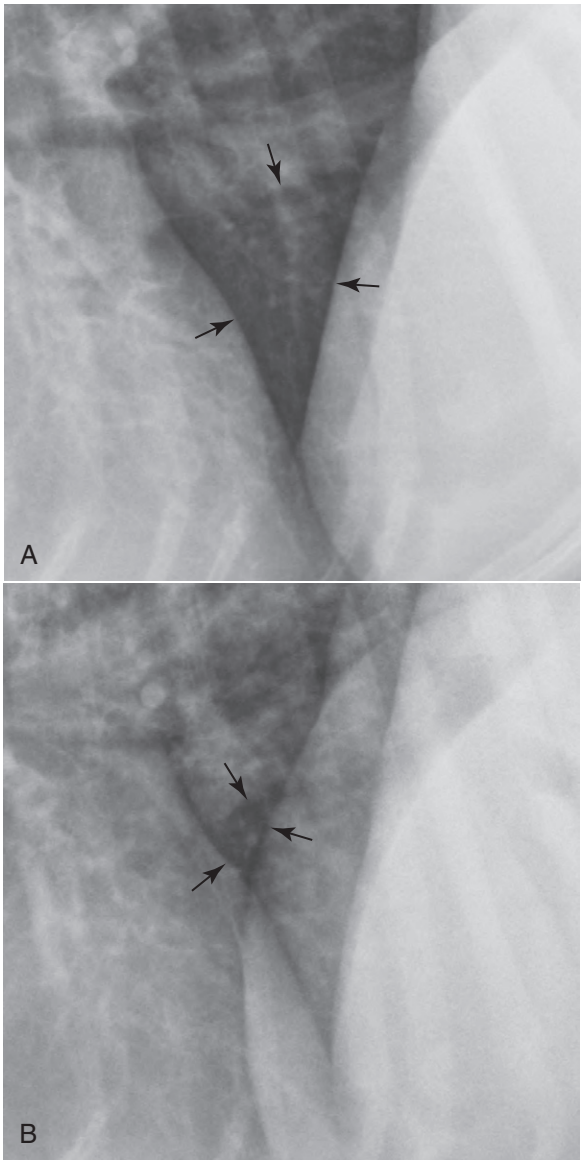


Fig. 25-16 Close-up view of the caudoventral aspect of the thorax in a dog during inspiration **(A)** and exhalation **(B).** The size of the triangular region of lung between the caudal vena cava, heart, and diaphragm *(arrows)* can be used as an indicator of the degree of lung inflation that was present when the radiograph was acquired. Note the marked reduction in size of this region of lung and the overall increased lung opacity, in **B** versus **A.** Poor ventilation is a common cause of misdiagnosis of pulmonary disease.

RADIOGRAPHIC TECHNIQUE: HORSE

The same technical principles relating to radiography of the canine and feline thorax also apply to the horse. Radiographing the equine thorax does not require the massive exposure factors that might be expected based on the sheer size of the thoracic cavity because of the large volume of air present in the equine lungs. However, obtaining radiographs of all four regions of the equine thorax when using a grid will require more output then typically available from a portable x-ray unit, such as those used commonly to radiograph equine extremities. It may be possible to obtain diagnostic-quality radiographs of the dorsocaudal portion of the thorax with a portable x-ray machine and without a grid, but this will not be possible in the other three regions because of the sheer thickness of these regions and the amount of scatter produced from intervening soft tissue.

As for small animals, high kVp–low mAs techniques are recommended for equine thoracic radiography to reduce motion and to produce an image of the lungs that has a long scale of contrast (many gray shades).

ANCILLARY FACTORS

There are few ancillary factors that affect the radiographic appearance of the equine thorax, other than body mass. However, for the dog and cat the body habitus and presence of cutaneous lesions are ancillary factors that have a significant effect on the appearance of the subsequent radiograph.

Body Habitus

The volume of extrathoracic soft tissue will influence the overall radiographic opacity of the lung (Fig. 25-17). Of course there is a vast difference in the body configuration of various canine breeds. Also, overweight patients may have reduced ventilatory capacity leading to reduced lung volume and a false impression of increased lung opacity. The overlying fat will itself also contribute to the increased opacity of the thorax, making it easy to misdiagnose lung disease or rendering the radiograph technically unacceptable. The effect of overlying fat will be especially problematic if the radiographs are acquired with film-screen technology because the contrast resolution of the film-screen system is not capable of compensating for the opacity created by the fat (Fig. 25-18).

Intrathoracic fat accumulation in obese patients can also be problematic. One common example is the accumulation of mediastinal fat that is misinterpreted as a mediastinal mass in VD or DV radiographs (Fig. 25-19). Mediastinal fat can also give the false impression of cardiac enlargement. Often, in this instance, the fat is not visible per se, and the distinction between cardiomegaly and adjacent fat may have to be made using echocardiography or with CT (Fig. 25-20).

Cutaneous Lesions

Thoracic wall structures or lesions superimposed on the thorax can be misinterpreted as a pulmonary lesion. Common examples of this include summation opacities created by nipples (Fig. 25-21), cutaneous lesions such as a pedunculated tumor or engorged tick (Fig. 25-22), and costochondral junctions (Fig. 25-23). All of these can be misinterpreted as a pulmonary nodule. The basis of cutaneous lesions creating such a conspicuous opacity was discussed in Chapter 5.

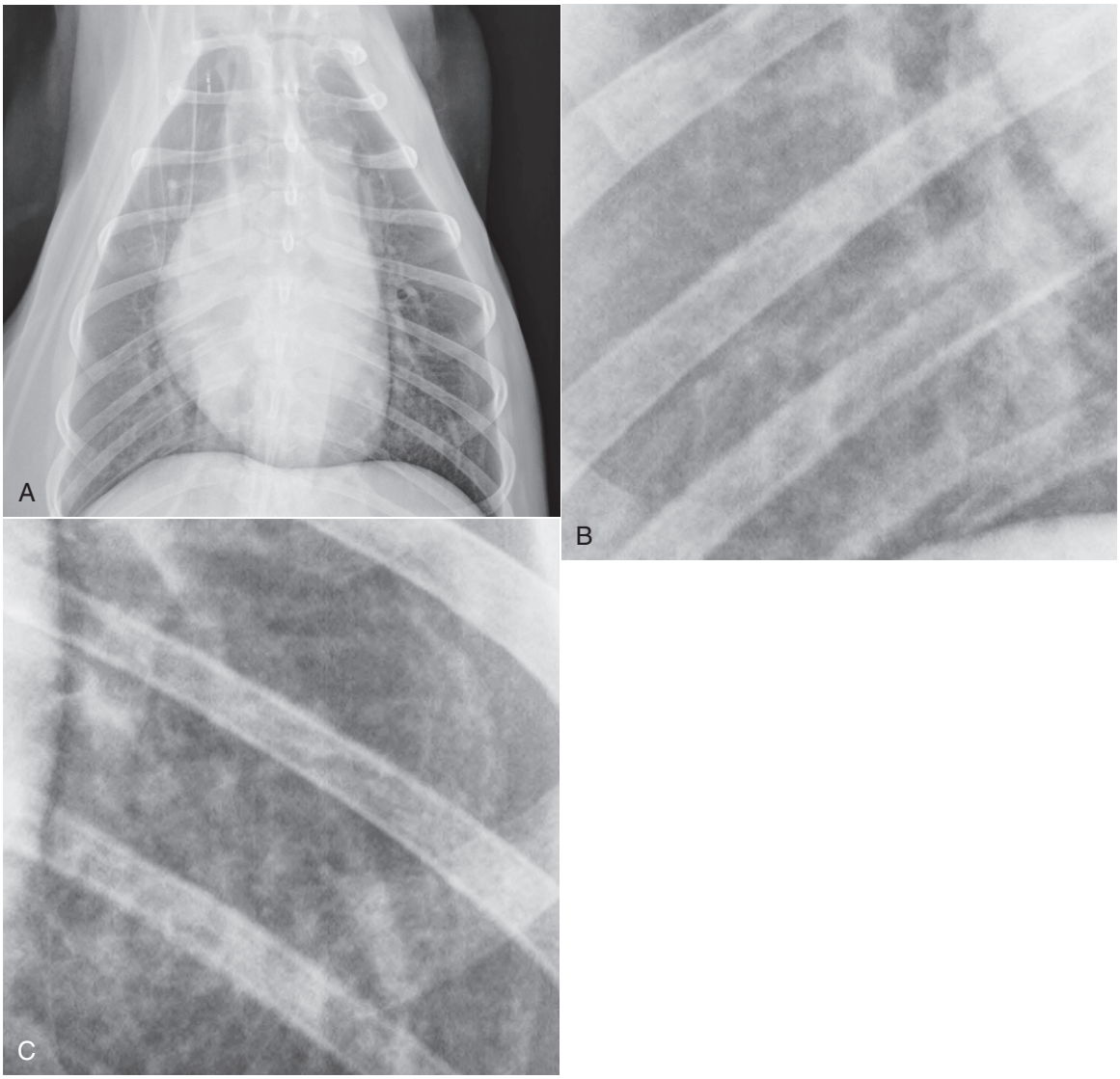


Fig. 25-17 Ventrodorsal thoracic radiograph of a dog whose left forelimb has been amputated. Note the difference in thickness of thoracic wall soft tissues on the left versus the right. The decrease on the left is a consequence of the absence of the tissue mass of the forelimb and also because of secondary disuse atrophy. Note also the increased lung opacity of the right lung compared with the left, caused by the greater thickness of thoracic wall tissue on that side. In close-up views from the right **(B)** and left **(C)** caudal lobes, the lung opacity appears increased on the right side. This illustrates how the amount of thoracic wall soft tissue can influence the radiographic opacity of the lung. The lung in **B** would be misdiagnosed as having an interstitial pattern by many observers.

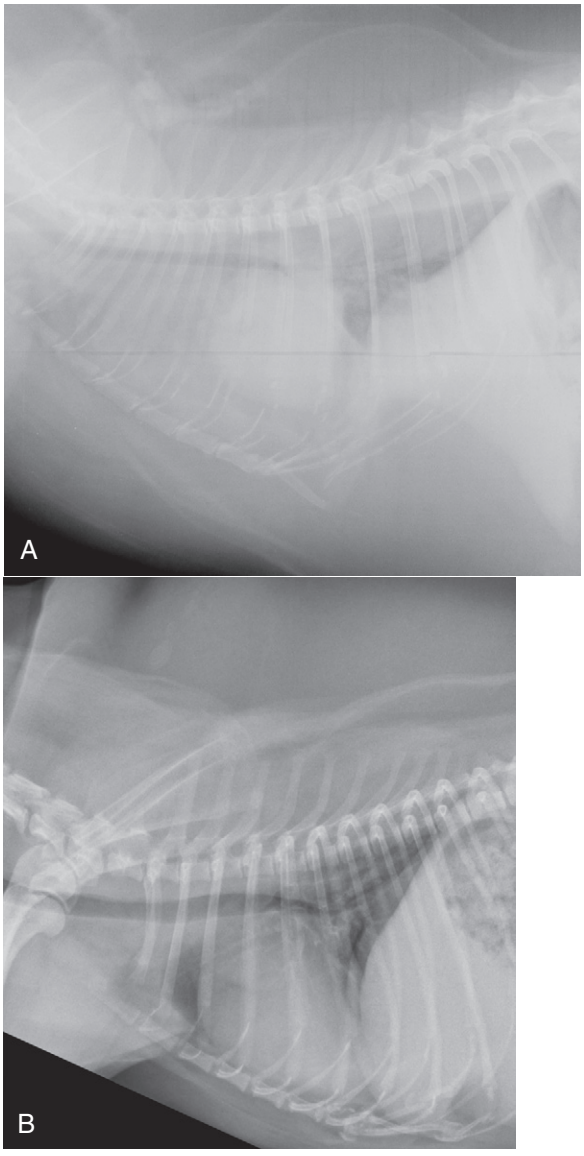


Fig. 25-18 Lateral thoracic radiographs of a morbidly obese cat made using a film-screen system **(A)** and of a morbidly obese dog made using a direct digital system **(B).** The contrast resolution of the film-screen system in **A** cannot accommodate for the huge volume of fat, and the lungs cannot be assessed. With the digital system **(B),** the lungs remain relatively radiolucent, but there will still be some background opacity created by the fat that could be misinterpreted as lung disease.

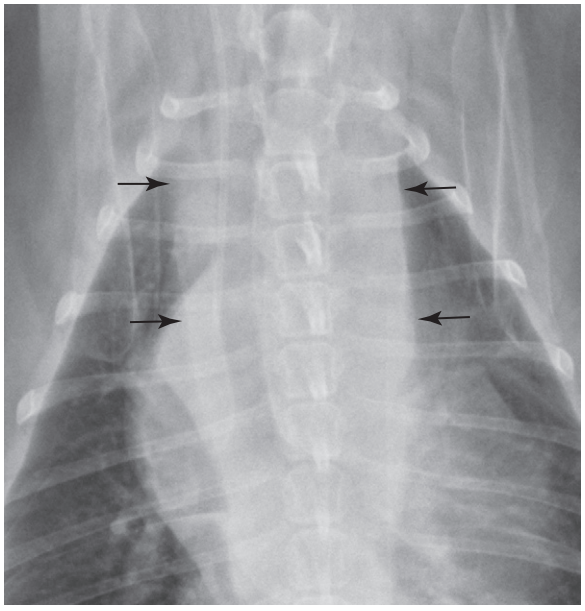


Fig. 25-19 Ventrodorsal radiograph of an obese dog. Fat has caused widening of the cranial mediastinum *(black arrows)*, which could be misinterpreted as a mass. There was no evidence of a cranial mediastinal mass in the left and right lateral projections.

INTERPRETATION PARADIGM

Radiographic interpretation is more of an art than a science. This is true for all regions of body but especially for the thorax. The many things that can influence the radiographic appearance of the thorax have been described previously, and unless one has an organized approach to interpretation, these will sooner or later be misinterpreted as an abnormality. Assessing whether there is an abnormality in the thoracic radiographs of a patient should be the *last* step in the interpretive process. The following questions should always be considered first.

- Are the radiographic views adequate, and are all of the views that are needed present? If the standard views are not present, what is likely to be missed?
- Is the positioning adequate, or are there positioning problems that will interfere with interpretation?
- Is the radiographic technique adequate, or are the images overexposed or underexposed?
- Were the images acquired using an antiscatter grid? Should an antiscatter grid have been used?
- Was the patient sedated or anesthetized for the radiographic examination, and did this affect the appearance of the images?
- What is the breed and body habitus of the patient, and how is this going to affect the appearance of the images?
- Were the images acquired with a vertically directed x-ray beam with the cassette in an x-ray table, or was a horizontally directed x-ray beam used with the cassette in a mobile or a wall-mounted cassette holder?
- Are the images analog or digital?
- Are there morphologic aspects of the patient that are going to influence the appearance of the radiographs? These include things like a missing limb or cutaneous nodules or masses that will be superimposed on the thorax.

Only after all of these things have been considered should one's attention be directed at the identification of abnormalities. Most beginning interpreters begin by looking at the lungs because a suspicion of pulmonary disease is usually the reason that thoracic radiographs are acquired. This is a mistake and will lead to other lesions being overlooked. Experienced radiologists may have a random search pattern, but it is recommended that beginning radiologists develop an organized approach to searching radiographs,[10] especially thoracic radiographs, for abnormalities. The following regions can be searched in order: (1) ribs, vertebrae, and sternebrae; (2) soft tissues of the thoracic wall; (3) pleural space; (4) mediastinum; (5) heart; (6) trachea and principal bronchi; (7) pulmonary vessels; and finally, (8) the pulmonary parenchyma. If the same procedure is followed for every patient, the order of searching will become second-nature, and as experience is gained, the search pattern will become random without a loss

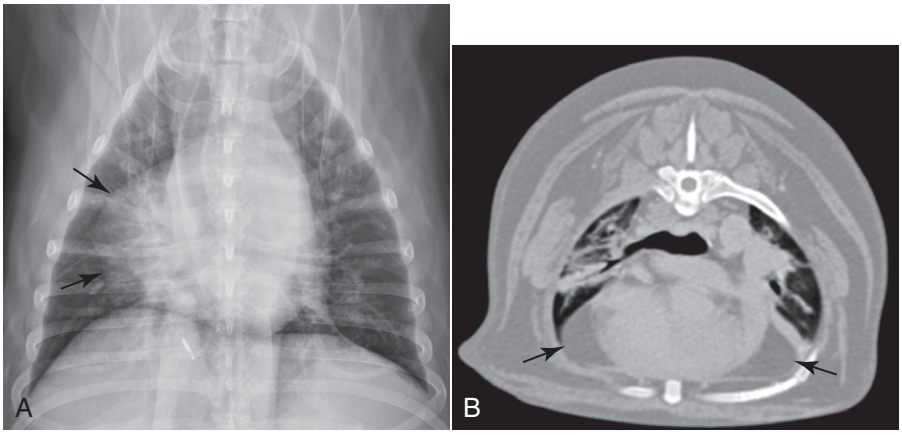


Fig. 25-20 Ventrodorsal thoracic radiograph **(A).** The cardiac silhouette appears enlarged, especially on the right side *(black arrows)*. CT image of the same patient **(B).** There is a large volume of mediastinal fat *(black arrows)* that is the cause of the apparent enlargement of the cardiac silhouette in the radiograph.

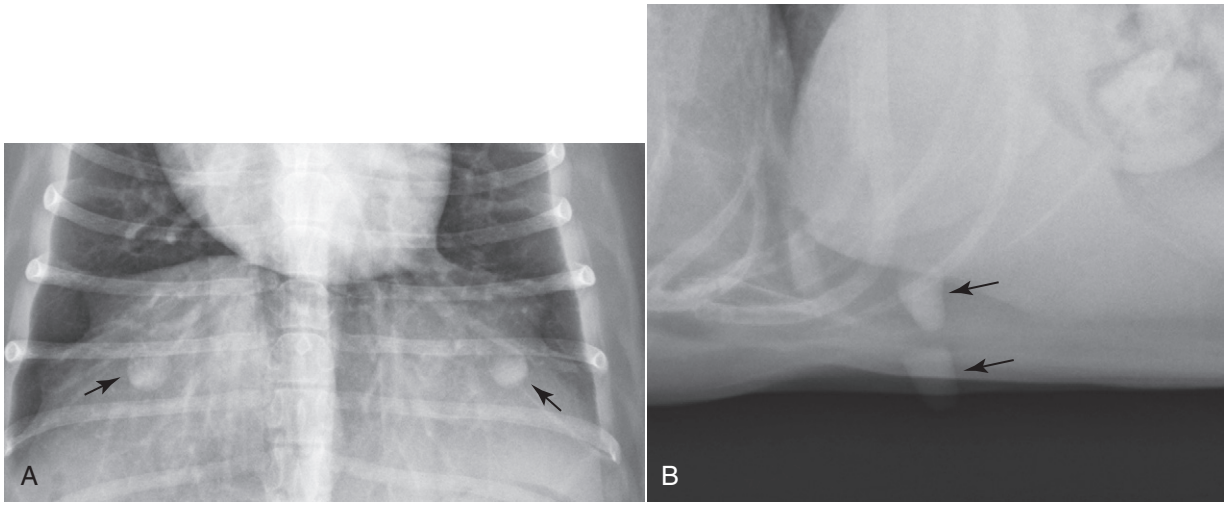


Fig. 25-21 **A,** Ventrodorsal radiograph of the caudal aspect of the thorax of a dog with two nodular opacities that are consistent with pulmonary nodules *(black arrows)*. These are caused by enlarged nipples on the cranial abdominal mammary glands. The bilaterally symmetric nature of these opacities would be unusual for pulmonary nodules, and enlarged nipples can be seen in the lateral view (*black arrows* in **B**). If the enlarged nipple is unilateral and it cannot be seen in the lateral view, the patient should be examined clinically. If necessary, a radiopaque marker can be applied to the nipples on the patient and the radiograph repeated to determine if the questionable lung opacity is caused by a nipple or by a pulmonary nodule.

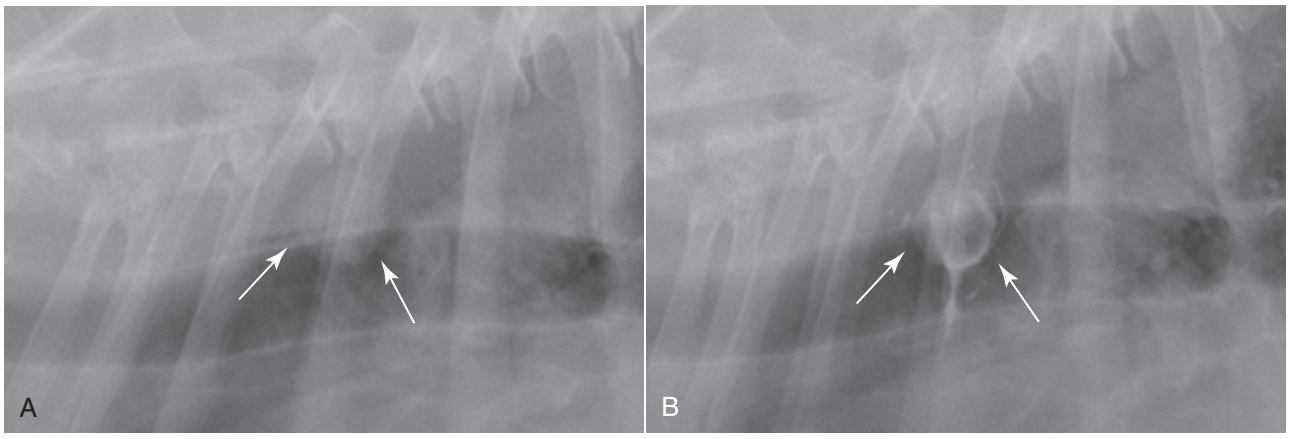


Fig. 25-22 **A,** Close-up from a right lateral thoracic radiograph of a dog where a nodular opacity is visible *(white arrows)*. The opacity has the appearance of a pulmonary nodule. A cutaneous nodule was discovered on the dog that could be the source of this opacity, and it was marked with a small amount of barium and the radiograph repeated. **B,** The barium was confined to the nodular opacity *(white arrows)*, confirming that it was not a pulmonary nodule but a summation opacity from the cutaneous nodule.

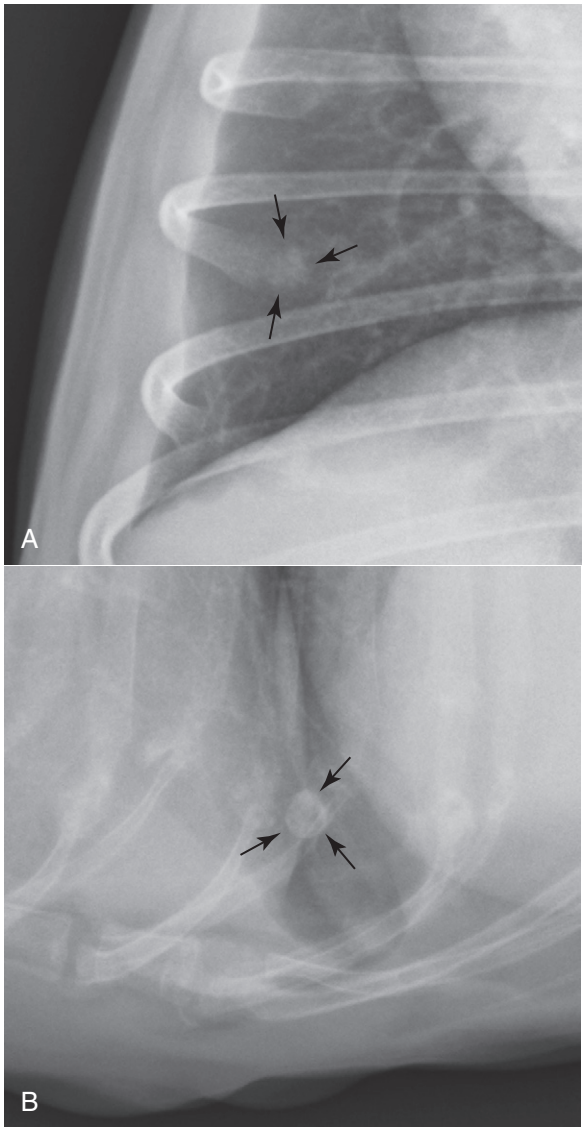


Fig. 25-23 Lateral **(A)** and ventrodorsal **(B)** radiographs of a dog with a nodular opacity *(black arrows)* that could be misinterpreted at a pulmonary nodule. In each radiograph the suspicious opacity is located at the end of a rib and is caused by remodeling of the costochondral junction with new bone formation. This is a common change, especially in older dogs.

of effectiveness. Until then, it may be beneficial for a checklist to be developed to make sure that every anatomic region of the radiograph is examined.

REFERENCES

1. Spencer C, Ackerman N, Burt J: The canine lateral thoracic radiograph, *Vet Radiol Ultrasound* 22:262, 1981.
2. Ober CP, Barber D: Comparison of two- vs. three-view thoracic radiographic studies on conspicuity of structured interstitial patterns in dogs, *Vet Radiol Ultrasound* 47:542, 2006.
3. Thrall D, Losonsky J: A method for evaluating canine pulmonary circulatory dynamics from survey radiographs, *J Am Anim Hosp Assoc* 12:457, 1976.
4. Brinkman EL, Biller D, Armbrust L: The clinical usefulness of the ventrodorsal versus dorsoventral thoracic radiograph in dogs, *J Am Anim Hosp Assoc* 42:440, 2006.
5. Carlisle C, Thrall D: A comparison of normal feline thoracic radiographs made in dorsal versus ventral recumbency, *Vet Radiol Ultrasound* 23:3, 1982.
6. Ruehl W, Thrall D: The effect of dorsal versus ventral recumbency on the radiographic appearance of the canine thorax, *Vet Radiol Ultrasound* 22:10, 1981.
7. Kirberger RM, Avner A: The effect of positioning on the appearance of selected cranial thoracic structures in the dog, *Vet Radiol Ultrasound* 47:61, 2006.
8. Feeney D, Gordon B, Johnston G, et al: A 200 centimeter focal spot-film distance (FFD) technique for equine thoracic radiography, *Vet Radiol Ultrasound* 23:13, 1982.
9. Toal R, Losonsky J, Coulter D, et al: Influence of cardiac cycle on the radiographic appearance of the feline heart, *Vet Radiol Ultrasound* 26:63, 1985.
10. Halvorsen JG, Swanson D: Interpreting office radiographs. A guide to systematic evaluation, *J Fam Pract* 31:602, 1990.

ELECTRONIC RESOURCES

evolve

Additional information related to the content in Chapter 25 can be found on the companion Evolve website at http://evolve.elsevier.com/Thrall/vetrad/

- Chapter Quiz

CHAPTER • 26

The Pharynx, Larynx, and Trachea

Kate Alexander

ANATOMIC CONSIDERATIONS: NORMAL ANATOMY AND RADIOGRAPHIC TECHNIQUE

The upper respiratory system comprises the air-filled pharynx, the larynx, and trachea. The pharynx includes the oropharynx ventrally, the nasopharynx dorsally, and larger laryngopharynx caudally. The soft palate divides the oropharynx from the nasopharynx rostrally, and the palatopharyngeal arches, which form the soft tissue line extending caudodorsally from the soft palate, divide the nasopharynx from the laryngopharynx. Finally, the epiglottis divides the oropharynx and laryngopharynx (Fig. 26-1).[1] Caudodorsally, the laryngopharynx extends to form the piriform recess. The epiglottis is often surrounded by gas and extends to just overlap dorsally or ventrally the tip of the soft palate.[2] In larger dogs, the cuneiform process, which is the rostral portion of the arytenoid cartilage, can be seen occasionally. The other laryngeal cartilages are represented by an indistinct soft tissue opacity superimposed on the laryngeal lumen. Gas-filled ventricular saccules are seen occasionally. In older dogs, and even younger large-breed dogs, laryngeal cartilages become identifiable because of mineralization, the cricoid being the most readily evident (Fig. 26-2).[3] Tracheal rings may also mineralize with age and become visible. Typically the pharynx has the widest lumen, followed by the larynx and then trachea, which is mildly smaller in diameter. A ratio between tracheal diameter and thoracic inlet height is proportionally larger in dogs with greater body weight and smaller in brachycephalic breeds.[4]

Peripheral anatomic structures of interest in the pharyngolaryngeal region are the base of the tongue and mandibular lymph nodes rostrally, the hyoid bones and mandibular and parotid salivary glands laterally, the medial retropharyngeal lymph nodes and esophagus caudodorsally, and the thyroid gland caudoventrally. Ectopic thyroid tissue can be found anywhere along the thyroglossal tract, from the base of the tongue to the base of the heart. Because the hyoid bones, except the basihyoid bone, are paired, they should be compared for abnormalities. The normal cricopharyngeus muscle representing the cranial esophageal sphincter sometimes appears as a distinct soft tissue structure. These structures are of interest for their potential secondary effects on the upper respiratory tract.

Tracheal luminal diameter is similar between the cervical and thoracic regions, but sometimes widens caudally in the cervical region in large-breed dogs. Tracheal diameter can also vary mildly between inspiration and expiration. Variable tracheal luminal narrowing in dogs can be caused by a so-called redundant trachealis dorsalis membrane, between the midcervical and midthoracic portions of the trachea (Video 26-1, Figs. 26-3 and 26-4). The narrowing caused by a redundant dorsal tracheal membrane can be dynamic, depending on phase of respiration (see Fig. 26-4). Other explanations for this appearance are displacement of the esophagus ventrally between the incomplete dorsal aspects of the tracheal rings and tracheal rotation, but a redundant drooping membrane is most common. In most dogs, a redundant dorsal tracheal

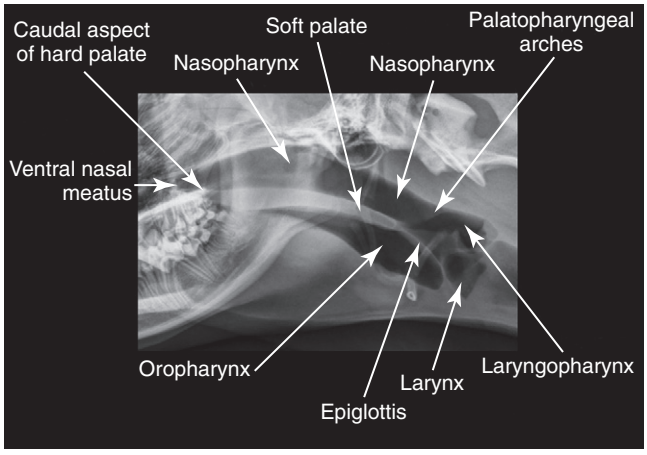


Fig. 26-1 Normal lateral canine pharyngeal/laryngeal region.

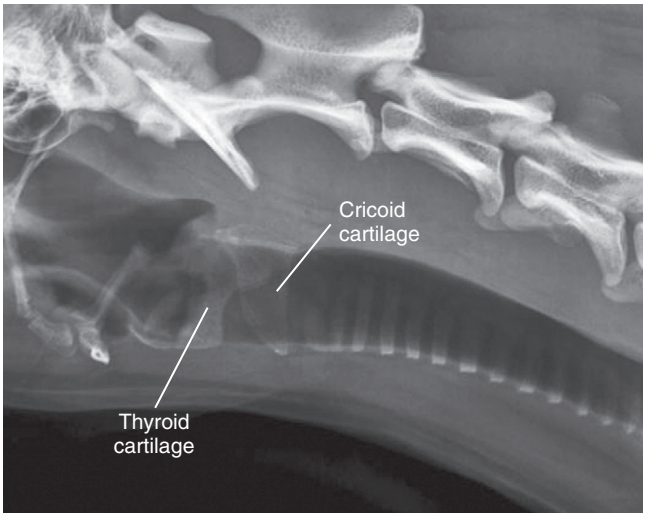


Fig. 26-2 Lateral radiograph of a 9-year-old dog. Dystrophic mineralization of the laryngeal and tracheal cartilages is seen, which aids in their differentiation. No abnormalities are present.

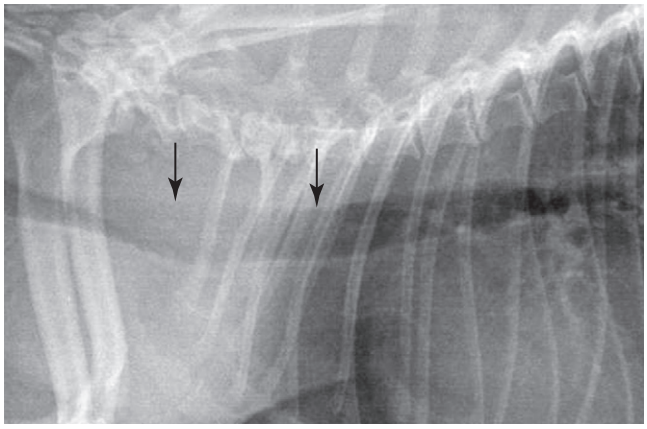


Fig. 26-3 The dorsal wall of the trachea is in its normal position *(black arrows)*, but the lumen is narrowed by a redundant dorsal tracheal membrane. There was no radiographic or fluoroscopic evidence of tracheal collapse.

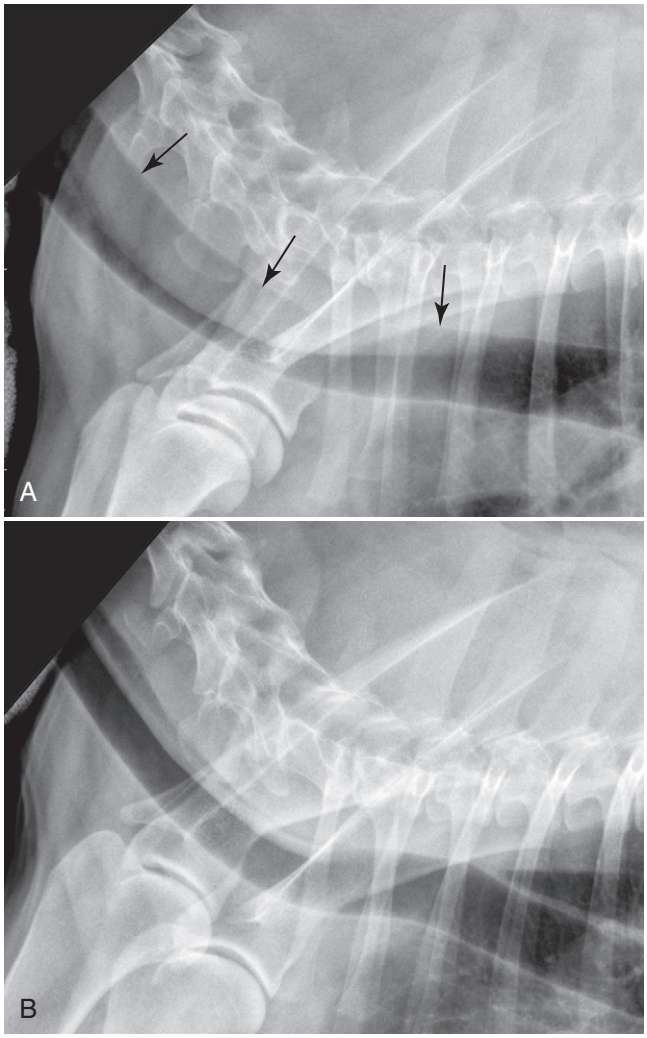


Fig. 26-4 Lateral views of the cervicothoracic region made at different phases of respiration. In **A,** the tracheal lumen is narrowed by a redundant dorsal tracheal membrane. The dorsal wall is the trachea is visible *(black arrows)*. In **B,** the lumen is wider as the membrane has relocated dorsally. In **B,** there is gas in the esophagus just dorsal to the cervical portion of the trachea.

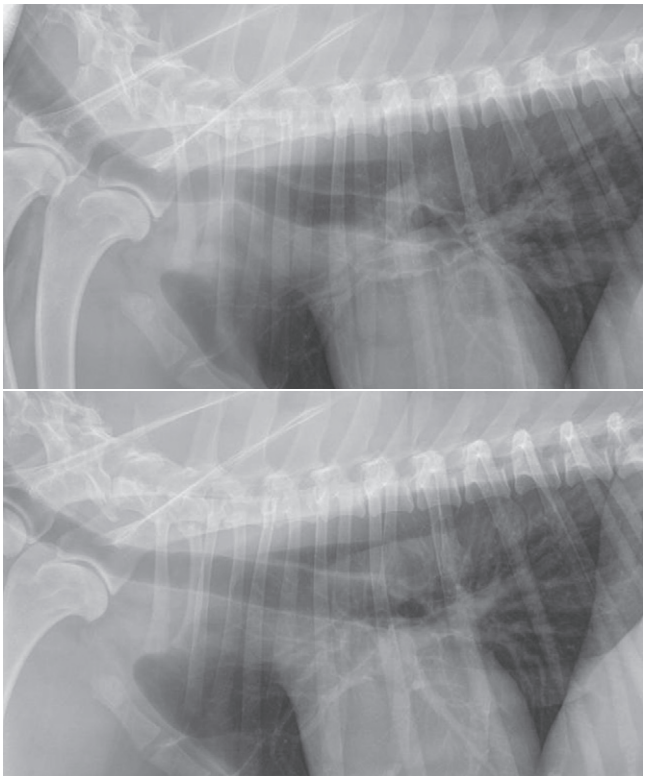


Fig. 26-5 Right lateral *(top)* and left lateral *(bottom)* thoracic radiographs where the patient positioning has affected the appearance of the trachea. In the top image, there is focal elevation of the cranial aspect of the thoracic trachea that can be misinterpreted as being caused by a mediastinal mass. In the bottom image with the forelimbs extended, the false impression of mediastinal mass displacing the trachea dorsally is eliminated. There is a focal esophageal gas collection just cranial to the carina in both radiographs.

membrane is not responsible for clinical signs, but it can be confused easily with tracheal collapse. The redundancy can be marked, with the resulting superimposed soft tissue opacity almost completely obscuring the tracheal lumen. Differentiation from tracheal collapse lies in identifying the slightly more opaque dorsal tracheal wall at its normal location when the narrowing is caused by a redundant membrane.

The importance of appropriate patient positioning cannot be overemphasized when evaluating the pharyngolaryngeal region. The lateral view with the head extended mildly is most useful, but any degree of obliquity results in underestimation of luminal diameter and overestimation of the surrounding soft tissue structures, such as soft palate and laryngeal cartilages, which can mimic a mass. Ventrodorsal and oblique views are complementary to establish lesion laterality, yet are limited by superimposition of the skull and cervical spine. Technique parameters offering high-contrast images (relatively low kilovoltage peak [kVp] and high milliampere second [mAs] if using an analog system) and measured according to the thickness of the ventral cervical soft tissues are recommended. If possible, the endotracheal tube should be withdrawn during radiography. Differentiation of the various structures is more difficult in obese patients because of narrowing of the air-filled compartments.

The position of the thoracic portion of the trachea can vary with patient positioning. Normally, it is approximately parallel with the spine, although it is slightly closer to the spine through the thoracic inlet. When the patient's head is ventroflexed, focal dorsal displacement of the trachea can mimic a cranial mediastinal mass (Fig. 26-5). Conversely, extreme extension of the neck can cause tracheal compression. On a



Fig. 26-6 Dorsoventral thoracic radiograph of an obese dog. There is rightward deviation of the thoracic trachea caused by the large amount of mediastinal fat.



Fig. 26-7 Radiograph of a dog evaluated for a cervical mass. A mass located dorsal to the pharynx, larynx and cervical portion of the trachea displaces these structures ventrally. There is effacement of the fascial planes in the cervical region. Carcinoma of salivary or sebaceous origin was diagnosed.

dorsoventral radiograph, the thoracic portion of the trachea is located on or curves mildly to the right of midline.[5] In brachycephalic breeds and obese dogs with mediastinal widening, the trachea curves more markedly to the right, and this should not be confused with displacement from a mass, such as from a heart base tumor (Fig. 26-6).

RADIOGRAPHIC SIGNS OF DISEASE

Pharyngolarynx

Indications for radiography of the pharyngolarynx are respiratory difficulty and stertor caused by a suspected upper respiratory obstruction; ptyalism, gagging, and dysphagia; dysphonia; a palpable mass, or a visible draining tract. Although ultrasound is useful for evaluating the soft tissues surrounding the upper respiratory tract, radiography is better for assessing their impact on the upper respiratory tract lumen. In addition, radiography can help screen for nonpalpable masses.[6]

Masses

As for any hollow organ, pharyngolaryngeal masses may be extramural, mural, or intraluminal. Extramural masses can originate from any of the structures surrounding the pharyngolarynx (Box 26-1) and may be neoplastic (Fig. 26-7), infectious (Fig. 26-8), traumatic, hemorrhagic, or other in nature. Radiographically, extramural masses are usually poorly defined from the surrounding soft tissues and appear as areas of soft tissue thickening, which may cause displacement and/or narrowing of the respiratory tract lumen. Their interface with the air-filled lumen is smooth, rounded, and broad-based. Their origin is determined based on their location relative to the pharyngolarynx.

In cats, the two most common forms of pharyngolaryngeal mural neoplasia are lymphoma and squamous cell carcinoma, and in the larynx the arytenoid cartilage is most often involved.[7,8] In dogs, in the pharynx, squamous cell carcinoma and melanoma are reported;[9] in the larynx, epithelial tumors and rhabdomyoma are most frequent, although mast cell tumor, various sarcomas, oncocytoma, and melanoma are also seen (Fig. 26-9).[8,10] Mural masses tend to be smaller when clinical signs appear, given that their impact on the respiratory lumen is more direct. As a result, they can be very difficult to identify radiographically, and endoscopy or direct

Box • **26-1**

Differential Diagnoses for Pharyngolaryngeal Masses

Extramural

- Lymph nodes: adenitis, neoplasia
- Salivary glands: sialocele, sialoadenitis, neoplasia
- Esophagus: neoplasia, granuloma
- Thyroid neoplasia (carcinoma) (including ectopic, base of the tongue)
- Malignant nerve sheath tumor
- Carotid body tumor
- Soft tissue trauma, penetrating wound and/or foreign body (hematoma, seroma, cellulitis, abscess)
- Coagulation disorder (hematoma)

Mural

- Neoplasia: adenocarcinoma, squamous cell carcinoma, lymphoma, plasmacytoma, rhabdomyoma, rhabdomyosarcoma, chondrosarcoma, granular cell tumor, mast cell tumor.
- Granuloma/abscess: fungal (blastomycosis, cryptococcosis, pythiosis), granulomatous laryngitis (cats), lymphoplasmacytic inflammation (cats), chronic foreign body, *Cuterebra* migration
- Polyps: nasopharyngeal (cats), laryngeal
- Chondritis, laryngitis, viral papillomatosis
- Laryngeal cyst
- Brachycephalic syndrome: elongated, edematous soft palate

Intraluminal

- Foreign body (especially if soft tissue opacity)



Fig. 26-8 Radiograph of an anesthetized cat with acute dyspnea and a submandibular mass. Ill-defined soft tissue thickening is present ventral and caudal to the mandibular and pharyngeal region, compatible with cellulitis. Complete reduction in air-filled volume of the oropharynx and incomplete reduction in volume of the nasopharynx are present.

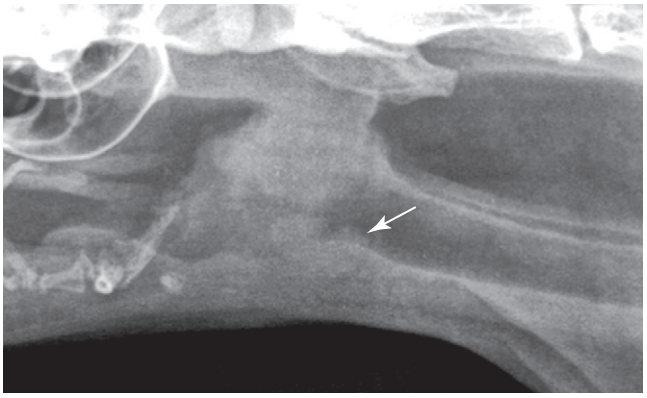


Fig. 26-10 Radiograph of a cat with inspiratory difficulty. The laryngeal margins are thickened and irregular, particularly dorsally. Caudoventrally, a well-defined, irregularly marginated oval soft tissue opacity *(white arrow)* is superimposed on the larynx and presumed to be within the tracheal lumen. Megaesophagus secondary to aerophagia is also present. Suppurative laryngitis was diagnosed and the caudoventral mass represented focal purulent debris.



Fig. 26-9 Radiograph of an adult cat presented for respiratory distress. Ill-defined soft tissue opacity fills the nasopharynx and laryngopharynx, completely obliterating the air space, except for the piriform recess, and causing border effacement of the dorsal margin of the soft palate. The airway is maintained with an endotracheal tube. A nasopharyngeal mast cell tumor was diagnosed.

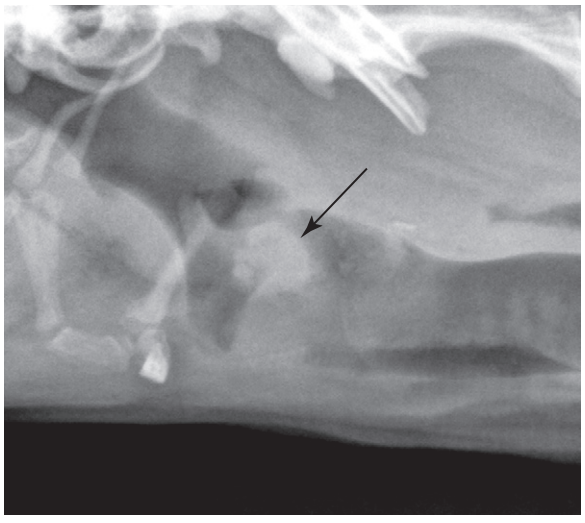


Fig. 26-11 Lateral radiograph of a dog with progressive inspiratory noise. There is a well-defined mass *(black arrow)* at the dorsal aspect of the larynx. The diagnosis was benign hyperplastic fibroepithelial polyp.

pharyngolaryngoscopic examination may be more useful. Superimposition of the normal laryngeal cartilage can make laryngeal masses difficult to detect. Masses are characterized primarily by an increase in the normal soft tissue opacity, as with diffuse thickening, decreased margination of pharyngolaryngeal structures, and/or airway stenosis (Fig. 26-10).[7] They can also appear well defined (Fig. 26-11) and/or lobulated if surrounded by air.[8] Horizontal epiglottic displacement can also occur.[11]

Trauma and Foreign Body

Pharyngolaryngeal trauma occurs most often because of a penetrating wound originating either internally from the upper respiratory tract or esophagus, such as with a stick injury, or externally, such as a bite wound or gunshot. Blunt trauma from choking is another possibility. Soft tissue thickening representing swelling and or a mass may be found with hematoma, cellulitis, myositis, and/or abscess. Gas opacities can be found in the subcutaneous tissues and between muscle and tissue planes. If linear, these represent emphysema, whereas more focal and rounded gas accumulation may indicate abscess (Fig. 26-12). Emphysema has been reported in 83% of dogs with acute oropharyngeal stick injury and can extend to pneumomediastinum, pneumothorax, mediastinitis, and pleural effusion.[12] Pharyngeal diverticulum[13] and stenosis can be complications of trauma.

In addition to other surrounding bony structures, hyoid bone fracture and laryngeal cartilage fracture are possible, particularly when the region has been crushed. These structures should be examined for symmetry and normal contour. Oblique projections may help evaluation of the hyoid apparatus. Hyoid bone fractures may be open to the upper respiratory tract and therefore contaminated.

Foreign bodies are visible when they are mineral or metallic, such as gunshot particles, needles, fishhooks, and bones. Plant material is not generally visible radiographically but, when large enough, is detected easily using computed tomography (CT). In patients with a draining tract, fistulography



Fig. 26-12 Radiograph of a cat with coughing, hemoptysis, and a history of dietary indiscretion. Multiple linear and round gas opacities are present throughout the submandibular and cervical soft tissues, and the submandibular soft tissues are thickened. There is a rectangular air-filled structure with opaque borders ventral to the epiglottis, superimposed on the oropharynx. A plastic cap was removed at surgery. There was a breach of the pharyngeal wall leading to the soft tissue emphysema.

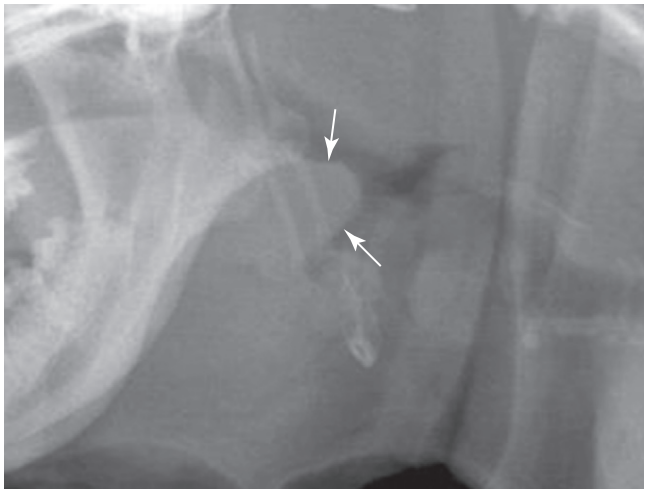


Fig. 26-13 Radiograph of a French bulldog. There is soft palate elongation and thickening *(white arrows)* and increased soft tissue opacity in the laryngeal region, which is compatible with edema and upper airway narrowing found with brachycephalic syndrome.

with iodinated contrast medium can aid in foreign body detection.

Brachycephalic Syndrome

Brachycephalic syndrome comprises a complex of upper respiratory disorders in brachycephalic breeds of dogs and cats. Diagnosis is typically made by clinical and laryngoscopic examination. Radiographically, elongated soft palate and soft palate edema appear as an extension and thickening of the soft palate beyond the tip of the epiglottis, and subsequent narrowing of the nasopharyngeal and oropharyngeal diameters (Fig. 26-13). Laryngeal collapse can also be present, but because it occurs in a laterolateral direction, it is not seen commonly on radiographs unless the collapse is severe (Fig. 26-14). Tracheal hypoplasia (see trachea section) is diagnosed radiographically.

Epiglottic Retroversion

Epiglottic retroversion is rare and caused by excessive epiglottic mobility. It appears radiographically as a more vertically positioned epiglottis that extends dorsally to the dorsal wall of the laryngopharynx.[14]

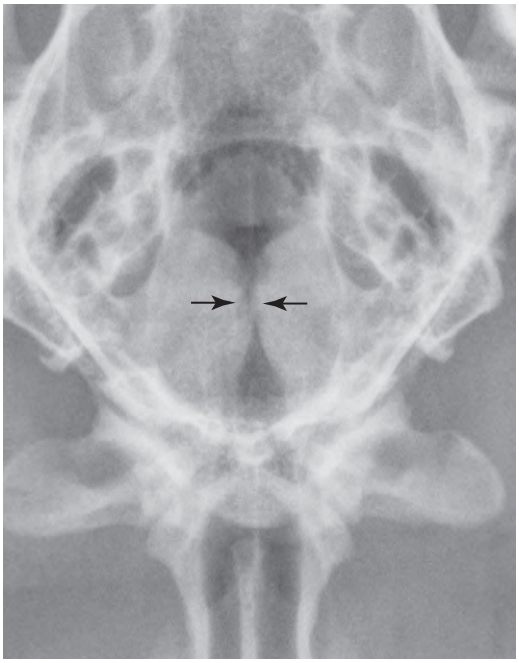


Fig. 26-14 Ventrodorsal radiograph of a dog with laryngeal collapse. The laryngeal lumen is narrow *(black arrows)*.

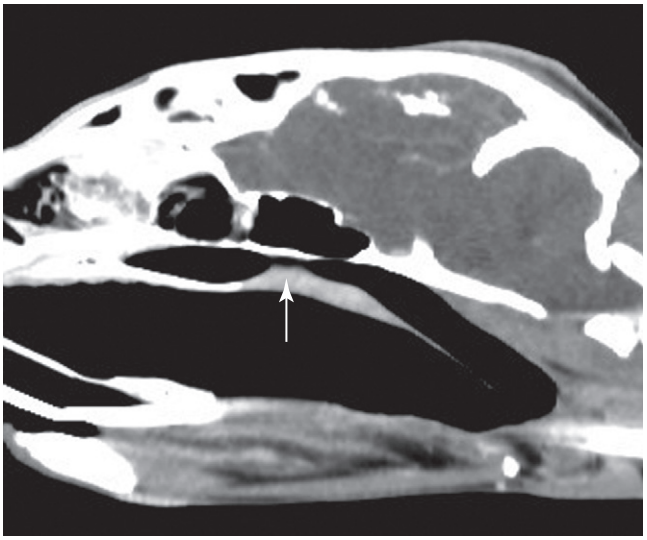


Fig. 26-15 Sagittal reformatted CT image of a cat with chronic rhinosinusitis associated with *Mycoplasma* species infection. There is approximately 75% narrowing of the airway in the rostral aspect of the nasopharynx *(white arrow)*, extending over a 7 mm length, indicating nasopharyngeal stenosis.

Nasopharyngeal Stenosis

This is an uncommon condition, usually identified in cats, and thought to be a sequel to an episode of upper respiratory inflammation or infection, such as viral rhinotracheitis, or follows upper airway surgery.[15] It appears radiographically as a narrow band of soft tissue superimposed on the nasopharyngeal lumen and slight focal dorsal deviation of the soft palate.[16] It is much more readily identified with magnetic resonance imaging (MRI) or CT including sagittal and dorsal reformatted images (Fig. 26-15). A congenital form of nasopharyngeal stenosis has been proposed in dachshunds, thought

to be caused by a primary palatopharyngeal dysgenesis causing thickening of the palatopharyngeal muscles leading to a horizontal band of soft tissue that separates or even obliterates the nasopharynx from the rest of the pharynx and larynx.[17]

Pharyngitis and Laryngitis

Generalized swelling of the upper airway can be caused by edema due to respiratory distress, as is seen in brachycephalic breeds, and/or inflammatory conditions. Other causes are upper respiratory infection, such as with infectious tracheobronchitis or viral rhinotracheitis, or oral cavity infection and ingestion of caustic or toxic substances, such as *Dieffenbachia* plant species.[18]

Trachea

Specific indications for radiography of the trachea are coughing, particularly if induced by tracheal palpation, and respiratory distress caused by a suspected upper respiratory obstruction.

Masses

Extramural cervical, cranial mediastinal, and heart-based masses can cause tracheal displacement, narrowing, and collapse. Peritracheal hemorrhage from rodenticide toxicity[19] and a peripheral nerve sheath tumor[20] are reported to cause tracheal compression in the dog. In the cat, cranial mediastinal cyst can be considered.[21] Additionally, with persistent right, fourth aortic arch, a mild-to-marked leftward displacement of the trachea is often seen on a dorsoventral radiograph.[5] Dorsal displacement of the caudal thoracic trachea and carina is seen with left-sided cardiomegaly and ventral displacement with tracheobronchial lymphadenomegaly (Table 26-1).

Mural tracheal masses are uncommon and are most often neoplastic. Benign tracheal tumors in dogs include osteochondroma, most commonly found in young dogs, followed by chondroma and leiomyoma.[8] Malignant tumors include lymphoma (cats particularly), sarcoma (fibrosarcoma, chondrosarcoma, histiocytic sarcoma), adenocarcinoma, squamous cell carcinoma, and plasmacytoma.[8,22] Other considerations are hematoma secondary to trauma or coagulation disorders, amyloidosis,[23] inflammatory polyp[24] and granuloma secondary to foreign body migration, mycobacterial infection, zygomycosis,[25] and parasitic disease. In particular, *Oslerus (Filaroides) osleri* granulomas can be seen near the carina in the dog, and aberrant tracheal *Cuterebra* migration has been reported in a cat.[26] Tracheal masses are usually solitary and distinct, protruding into the lumen, and are well seen because of the contrast provided by the adjacent air (Fig. 26-16). Masses may be mineralized when they are of cartilage origin, such as osteochondromas.[8]

Foreign Bodies

A variety of foreign bodies are possible, usually resulting from orotracheal aspiration, such as a tooth, kibble, stone, bone, or plant material (Fig. 26-17) or, uncommonly, having migrated



Fig. 26-16 Lateral radiograph of a dog with a small oval intratracheal mass at the thoracic inlet. Tracheal masses extending into the lumen will be sharply outlined by the contrast from surrounding air. This lesion was first thought to be a foreign body but was determined endoscopically to be a pedunculated mass. The diagnosis was B-cell tumor. As this radiograph is oblique slightly, one of the transverse processes of C6 is superimposed on the trachea, just cranial to the mass.

Table • **26-1**

Considerations for Radiographically Detectable Deviation of the Trachea in the Lateral Projection

LOCATION OF DEVIATION	DIRECTION OF DEVIATION	CONSIDERATIONS
Cervical	Ventral	Thyroid mass Retropharyngeal lymphomegaly Vertebral/paravertebral mass
Cranial mediastinum	Dorsal	Cranial mediastinal mass (including cranial mediastinal lymphadenomegaly, thymoma, mediastinal cyst, etc.) Neck position during radiography
Cranial mediastinum	Ventral	Neurogenic tumor Esophageal enlargement/mass
Heart base	Dorsal	Heart base mass Pulmonary artery enlargement Right atrial enlargement
Carina	Dorsal	Left atrial enlargement Tracheobronchial lymphomegaly (usually ventral but can be dorsal) Generalized cardiomegaly
Carina	Ventral	Tracheobronchial lymphomegaly

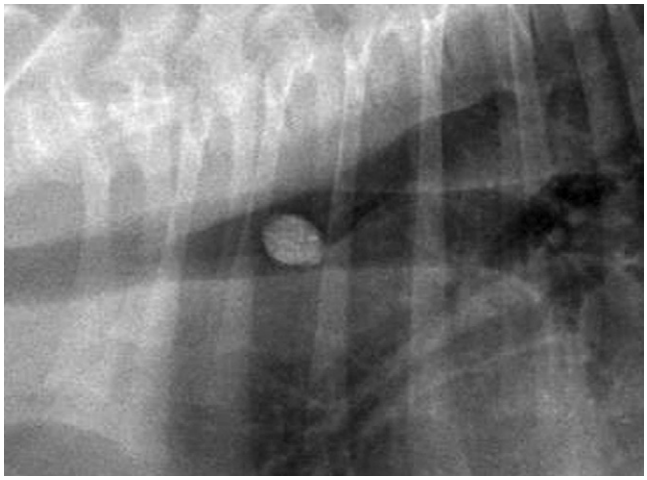


Fig. 26-17 Radiograph of a dog that developed a cough after being observed eating rocks. A well-defined granular mineral opacity structure is present in the caudal aspect of the trachea. A rock was removed endoscopically.

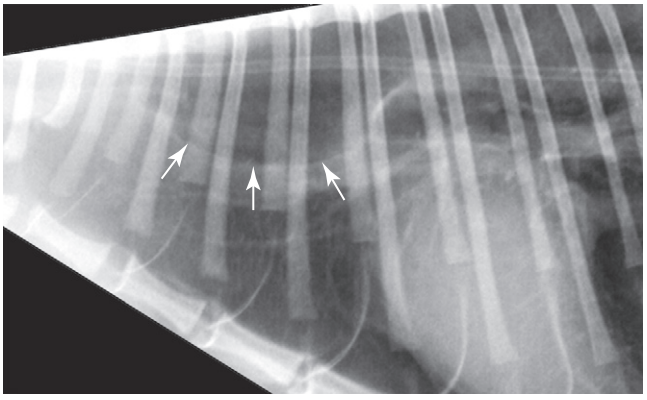


Fig. 26-19 Lateral radiograph of a cat acquired 2 weeks after being hit by a car. The trachea is visible just cranial to the carina but then becomes indistinct, and there is ventral displacement of the cranial vena cava by a gas-filled sac (*white arrows* indicate ventral margin of sac). The dorsal margin of the sac is not visible. A tube is present in the esophagus. This appearance is typical of tracheal avulsion.

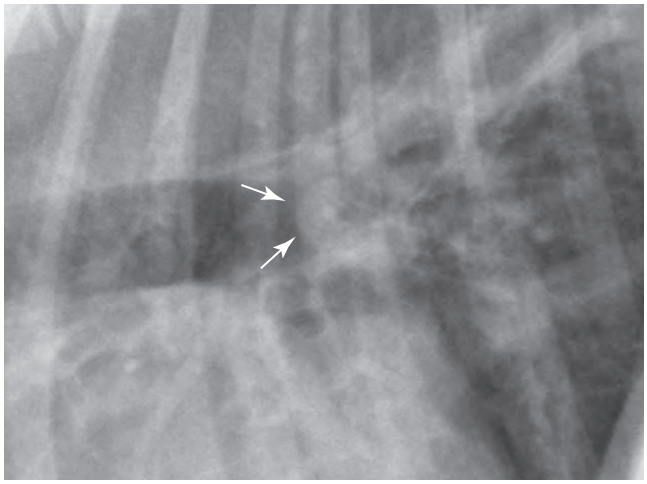


Fig. 26-18 Lateral radiograph of a dog with acute coughing and respiratory distress. There is a sharp, curving, air-tissue interface at the carina *(white arrows)*. This is not present in normal dogs. A pea was removed from the trachea endoscopically.



Fig. 26-20 Radiograph of a pug that presented for seizures and a cough. Generalized tracheal narrowing is present, measuring 8% of the height of the thoracic inlet, compatible with tracheal hypoplasia.

from the surrounding soft tissues.[27,28] Young cats and hunting dogs are reported most commonly, possibly because of the small diameter of their trachea and the nature of their activity, respectively.[28,29] The negative contrast afforded by intraluminal tracheal air helps in the detection of both mineral and soft tissue opacity foreign bodies. Aspirated foreign bodies are most often lodged at the carina, and particular attention should be paid to this area (Fig. 26-18). As an alternative to bronchoscopy, fluoroscopic guidance of forceps can be used for tracheal foreign body retrieval.[28]

Rupture/Avulsion and Stenosis

Tracheal rupture may be caused by endotracheal intubation, particularly during dental prophylaxis in cats, a penetrating wound, or a foreign body. Rupture can be caused by a tube stylet, inappropriately sized endotracheal tube, rotation of the anesthetized patient without disconnecting the tube, and/or excessive dilatation of the tube cuff.[30] Radiographic signs of secondary cervical and thoracic soft tissue emphysema and pneumomediastinum are present and more easily seen than the actual tracheal rupture, which is seen only rarely. Examples of pneumomediastinum are provided in Chapter 30.[30]

Tracheal avulsion in cats occurs following blunt trauma with severe hyperextension of the head and neck. Paradoxically, patients are often presented 1 to 3 weeks following the traumatic event, and signs of pneumomediastinum and soft tissue emphysema have resolved.[31] There is complete circumferential tracheal discontinuity 1 to 4 cm cranial to the carina, resulting in focal, well-defined, spherical dilation of the tracheal lumen outlined by a thin, soft tissue opacity margin representing either intact tracheal adventitia or surrounding mediastinal tissue and termed *pseudoairway* (Fig. 26-19).[31,32] This finding is usually associated with stenosis of the tracheal lumen at the margins of the avulsed trachea.[31]

Stenosis and tracheal diverticulum are complications of the same causes that predispose to tracheal rupture/avulsion, in addition to tracheal surgery.[33,34] A focal, static area of tracheal narrowing or widening is seen. Stenosis can also be seen with neoplasia causing annular tracheal narrowing.[8]

Hypoplasia

Tracheal hypoplasia appears as a generalized reduction in tracheal diameter (Fig. 26-20) and is caused by apposed or overlapping tracheal cartilages and a shortened or absent dorsal



Fig. 26-21 Radiograph of a dog with neck pain. No respiratory signs were reported. Approximately 75% collapse of the cervical trachea is present. The collapse was presumed to be static.

tracheal membrane. Approximately 39% of brachycephalic dogs with signs of brachycephalic airway obstruction syndrome have tracheal hypoplasia,[35] and in 10% of dogs, the diagnosis of tracheal hypoplasia is incidental.[36] Diagnosis is made more difficult by the fact that non-bulldog brachycephalic breeds, both with and without respiratory signs, have a smaller average tracheal-diameter-to-thoracic-inlet ratio (16% ± 3%) than nonbrachycephalic dogs (20% ±3%). Bulldogs have an even smaller ratio (13% ±4%).[4] The smallest ratio in asymptomatic bulldogs was 9%. The ratio between tracheal diameter and cricoid cartilage height is also smaller for brachycephalic breeds.[4]

Tracheitis

Generalized tracheal narrowing may be caused by severe tracheitis that leads to thickening of the tracheal mucosa. Tracheitis can be difficult to differentiate from tracheal hypoplasia, and the two can occur concurrently. Other causes of tracheitis are inhalation of toxic or chemical irritants, trauma, and upper respiratory infection.

Tracheal Collapse

Tracheal chondromalacia and collapse are seen commonly in middle-aged and older small- and toy-breed dogs. Affected dogs typically have chronic cough, although signs of upper respiratory obstruction can occur in severely affected patients. Collapse can be static (Fig. 26-21, Video 26-5) or dynamic; in the latter, severity depends on the phase of the respiratory cycle (Fig. 26-22, Videos 26-3 and 26-4). Collapse can occur anywhere from the midcervical region to involving the entire thoracic trachea. Particular attention should be paid to the mainstem bronchi, which are often involved, either along with tracheal collapse or as the sole abnormality. Intrathoracic collapse is usually more pronounced on expiration, whereas collapse in the cervical and thoracic inlet regions is more pronounced on inspiration.[37,38] The sudden increase in intrathoracic pressure during coughing exacerbates intrathoracic tracheal collapse.[37] The chronic cough caused by tracheal collapse contributes to a cycle of chronic inflammation, which in turn contributes to worsening chondromalacia. Cervical tracheal collapse can lead to laryngeal paresis and/or collapse and upper respiratory edema through chronic inflammation and increased inspiratory pressure.[37]

Static collapse can be seen on survey lateral radiographs of the thorax and cervical region as a persistent dorsoventral narrowing of the tracheal lumen (see Fig. 26-21). Even when collapse is not identified, an undulating appearance of the tracheal wall and mild variation in lumen diameter are suggestive of chondromalacia. If fluoroscopy is not available,

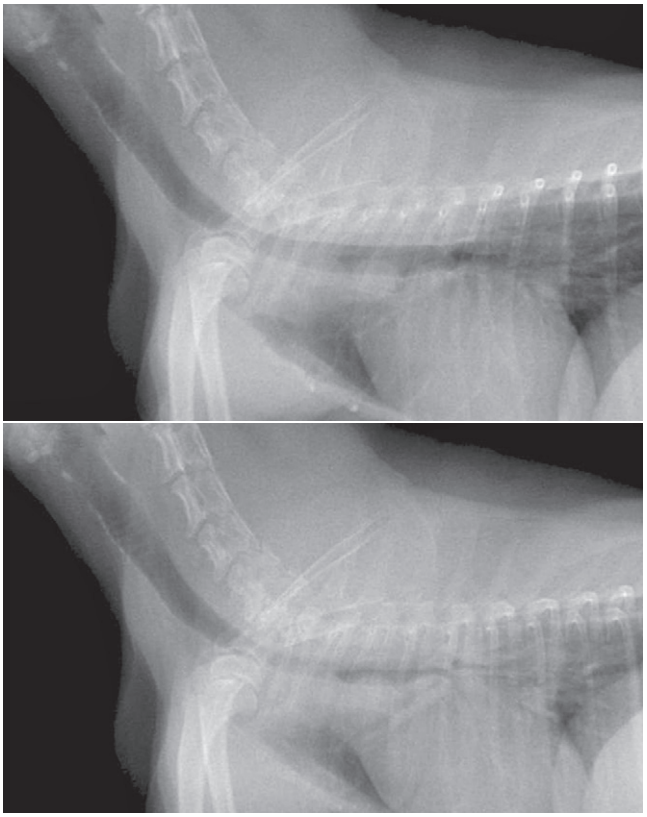


Fig. 26-22 Dynamic inspiratory *(top)* and expiratory *(bottom)* radiographic frames of a dog with chronic coughing. Approximately 50% dynamic collapse of the thoracic portion of the trachea and complete collapse of the caudal lobar mainstem bronchi occurs on expiration *(bottom)*.

lateral radiographs made on peak inspiration and expiration can help characterize dynamic tracheal collapse. A craniocaudal projection of the thoracic inlet with dorsal extension of the head and neck resulting in transverse view of the trachea at the thoracic inlet has been described to complement the diagnosis of tracheal collapse,[33] but this rarely adds useful information.

Fluoroscopy remains the best imaging method to evaluate tracheal and mainstem bronchial collapse, detecting a greater number and more severe grade of collapse than radiographs, particularly in the thoracic region.[38] A complete fluoroscopic examination includes evaluation of the tracheal diameter over several normal respiratory cycles, followed by evaluation during induced cough.* In some animals, it can be difficult to induce a cough. In this instance, intrathoracic pressure can be increased briefly by obstructing the nares and mouth during expiration. In very small patients, or to better evaluate the mainstem bronchi, additional radiographic detail can be obtained by making a rapid series of radiographic images over a respiratory cycle, while recognizing that this technique results in greater x-ray exposure. Complete radiographic evaluation of the thorax should be made in dogs suspected of tracheal collapse to evaluate for related conditions such as bronchitis, bronchiectasis, and cardiac disease.[37,39]

Location and extent of maximal collapse is often evaluated using the following scale: 25%, 50%, 75%, and 90% to 100% reduction of tracheal diameter.[38] This scale is similar to the grading system used to evaluate tracheal collapse at bronchoscopy. A reduction in tracheal diameter of 25% or less is probably within normal limits of variation of the respiratory cycle.[38]

*Videos 26-1 through 26-5 can be found on the accompanying Evolve website at http://evolve.elsevier.com/Thrall/vetrad



Fig. 26-23 Still fluoroscopic image of a dog with severe respiratory noise and distress. Complete tracheal collapse is present throughout the thoracic portion of the trachea and cranial displacement, or telescoping, of the caudal cervical trachea is also present. This is the same patient as in Video 26-2.

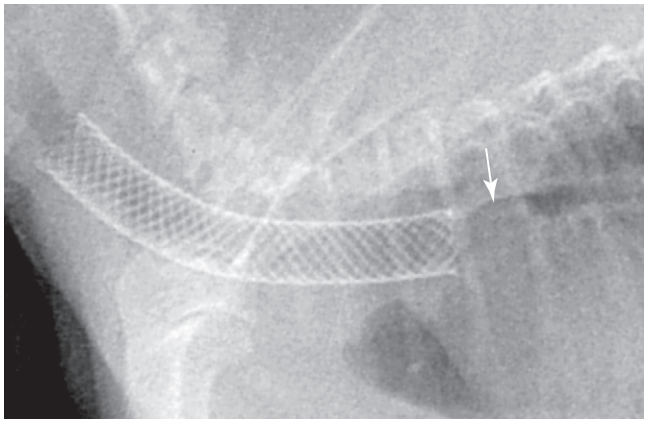


Fig. 26-24 Still fluoroscopic image of a dog made 3 weeks following tracheal stent placement. Soft tissue opacity material is present intraluminally caudal to the stent *(arrow)*, compatible with mucus or excessive granulation tissue formation.

Using CT, up to 24% change in cervical tracheal cross-sectional area and 19% variation in thoracic tracheal height is seen in healthy dogs under forced inspiration.[40] Often seen in asymptomatic dogs, the role of a redundant dorsal tracheal membrane in tracheal collapse is understood poorly, and an attempt should be made to differentiate redundant tracheal membrane from actual collapse of the dorsal aspect of the tracheal cartilages, particularly in the cervical region. Complete airway obstruction during expiration reduces the volume of the thoracic cavity while pulmonary volume is maintained and can result in a dynamic paradoxical cranial or telescoping movement of the thoracic trachea, along with herniation of the cranial lung lobes into the thoracic inlet (Fig. 26-23; see Video 26-2).

Endotracheal stenting through fluoroscopic guidance has become commonplace for the treatment of tracheal collapse. Before stenting, complete fluoroscopic evaluation should be made to characterize the extent of collapse fully and rule out mainstem bronchi involvement. Also, images made during positive-pressure maximal tracheal dilation with a radiopaque measurement device help determine appropriate stent size.[41] During follow-up radiographic evaluation, the stent should be evaluated for fracture and migration and the trachea evaluated for exuberant granulation tissue at the edges of the stent (Fig. 26-24).[41,42] Subsequent tracheal collapse can develop in the unstented portion of the trachea.

Tracheal collapse in the cat is rare. Although usually secondary to an extratracheal mass effect or intratracheal pressure changes caused by upper airway obstruction,[43,44] primary collapse has been reported.[45]

Upper Airway Obstruction

Radiographic examination of animals with signs of upper respiratory obstruction should be performed with care and minimal restraint. Radiographs should be withheld until the animal is stable enough to undergo complete examination. Several indirect radiographic findings can be seen secondary to upper airway obstruction in both dogs and cats. These findings can be useful in patients where the primary cause of obstruction is not identified readily, such as with laryngeal paralysis. These findings are often more marked in cats, possibly because of the pliability of their tissues. Changes include pulmonary hyperinflation or underinflation, upper airway dilation or collapse, caudal displacement of the larynx and pharynx, hiatal hernia,[46] and gastrointestinal signs of aerophagia.[33,47,48] In dogs an inward deviation of intercostal muscles and in cats a dorsoventral flattening of the thorax caused by increased negative intrathoracic pressure can also be seen.[48] Aspiration pneumonia and postobstruction pulmonary edema are potential complications.

ULTRASOUND

Laryngeal Paralysis

Because the upper respiratory tract is air-filled, ultrasound is of limited use for the evaluation of mural and intraluminal abnormalities. Nonetheless, ultrasound has been investigated for the evaluation of laryngeal paralysis because of the ability to evaluate arytenoid cartilage movement noninvasively in real time.[49,50] Ultrasound diagnosis is based on the ability to observe lateral motion of the cuneiform processes of the arytenoid cartilages corresponding to normal abduction.[50]

Masses and Foreign Bodies

Ultrasound is beneficial for the evaluation of the extramural soft tissues surrounding the upper respiratory tract, including determining the origin and nature of mass lesions, detecting certain foreign bodies, and guiding needle aspirates and biopsies. It has also been used for the detection of laryngeal masses in cats.[49]

COMPUTED TOMOGRAPHY AND MAGNETIC RESONANCE IMAGING

Masses

CT and MRI are both excellent for evaluating the soft tissues surrounding the upper respiratory tract. Evaluation of mural and intraluminal abnormalities can be achieved using CT, provided that endotracheal intubation does not interfere with the lesion. With faster multidetector machines, certain CT examinations can be done under sedation, thereby avoiding the need for anesthesia and intubation. Examination with the mouth opened to approximately 30 to 45 degrees improves visualization of the pharyngeal structures.[51] Intraluminal air can limit the usefulness of MRI. Lymph node involvement and osteolysis associated with aggressive pharyngolaryngeal neoplastic or infectious processes, such as extensive squamous cell carcinoma, can also be identified using CT.[52]

Trauma and Foreign Body

The layered linear appearance of oropharyngeal stick foreign bodies and their contrast-enhancing surrounding inflammatory reaction are well seen on CT.[53] Similarly, MRI readily

identifies the inflammatory reaction in addition to well-defined linear areas of low-signal intensity representing wooden foreign bodies.[54] Spatial understanding of the location of the foreign body is more intuitive on cross-sectional imaging than with ultrasound, thereby helping subsequent surgical planning.[53,54] CT sinography can also be helpful.[55]

CT is also described for hyoid bone fractures and malformation, laryngeal cartilage fracture,[56] and tracheal rupture.[57]

REFERENCES

1. Gaskell CJ: The radiographic anatomy of the pharynx and larynx of the dog, *J Small Anim Pract* 15:89, 1974.
2. Aron DN, Crowe DT: Upper airway obstruction. General principles and selected conditions in the dog and cat, *Vet Clin North Am Small Anim Pract* 15:891, 1985.
3. O'Brien J, Harvey C, Tucker J: The larynx of the dog: its normal radiographic anatomy, *Vet Radiol* 10:38, 1969.
4. Harvey C, Fink E: Tracheal diameter: Analysis of radiographic measurements in brachycephalic and nonbrachycephalic dogs, *J Am Animal Hosp Assoc* 18:570, 1982.
5. Buchanan JW: Tracheal signs and associated vascular anomalies in dogs with persistent right aortic arch, *J Vet Intern Med* 18:510, 2004.
6. Holt D, Brockman D: Diagnosis and management of laryngeal disease in the dog and cat, *Vet Clin North Am Small Anim Pract* 24:855, 1994.
7. Jakubiak MJ, Siedlecki CT, Zenger E, et al: Laryngeal, laryngotracheal, and tracheal masses in cats: 27 cases (1998–2003), *J Am Anim Hosp Assoc* 41:310, 2005.
8. Carlisle C, Bierry D, Thrall D: Tracheal and laryngeal tumors in the dog and cat: literature review and 13 additional patients, *Vet Radiol* 32:229, 1991.
9. Todoroff RJ, Brodey RS: Oral and pharyngeal neoplasia in the dog: a retrospective survey of 361 cases, *J Am Vet Med Assoc* 175:567, 1979.
10. Venker-van Haagen AJ: Diseases of the larynx, *Vet Clin North Am Small Anim Pract* 22:1155, 1992.
11. Wheeldon EB, Suter PF, Jenkins T: Neoplasia of the larynx in the dog, *J Am Vet Med Assoc* 180:642, 1982.
12. Doran IP, Wright CA, Moore AH: Acute oropharyngeal and esophageal stick injury in forty-one dogs, *Vet Surg* 37:781, 2008.
13. Ober CP, Spotswood TC, Hancock R: Fatal venous air embolism in a cat with a retropharyngeal diverticulum, *Vet Radiol Ultrasound* 47:153, 2006.
14. Flanders JA, Thompson MS: Dyspnea caused by epiglottic retroversion in two dogs, *J Am Vet Med Assoc* 235:1330, 2009.
15. Coolman BR, Marretta SM, McKiernan BC, et al: Choanal atresia and secondary nasopharyngeal stenosis in a dog, *J Am Anim Hosp Assoc* 34:497, 1998.
16. Boswood A, Lamb CR, Brockman DJ, et al: Balloon dilatation of nasopharyngeal stenosis in a cat, *Vet Radiol Ultrasound* 44:53, 2003.
17. Kirberger RM, Steenkamp G, Spotswood TC, et al: Stenotic nasopharyngeal dysgenesis in the dachshund: seven cases (2002–2004), *J Am Anim Hosp Assoc* 42:290, 2006.
18. Peterson K, Beymer J, Rudloff E, et al: Airway obstruction in a dog after *Dieffenbachia* ingestion, *J Vet Emerg Crit Care* 19:635, 2009.
19. Berry B, Gallaway A, Thrall D, et al: Thoracic radiographic features of anticoagulant rodenticide toxicity in fourteen dogs, *Vet Radiol Ultrasound* 34:391, 1993.
20. Essman SC, Hoover JP, Bahr RJ, et al: An intrathoracic malignant peripheral nerve sheath tumor in a dog, *Vet Radiol Ultrasound* 43:255, 2002.
21. Zekas LJ, Adams WM: Cranial mediastinal cysts in nine cats, *Vet Radiol Ultrasound* 43:413, 2002.
22. Stann SE, Bauer TG: Respiratory tract tumors, *Vet Clin North Am Small Anim Pract* 15:535, 1985.
23. Besancon MF, Stacy BA, Kyles AE, et al: Nodular immunocyte-derived (AL) amyloidosis in the trachea of a dog, *J Am Vet Med Assoc* 224:1302, 2004.
24. Sheaffer KA, Dillon AR: Obstructive tracheal mass due to an inflammatory polyp in a cat, *J Am Anim Hosp Assoc* 32:431, 1996.
25. Snyder KD, Spaulding K, Edwards J: Imaging diagnosis—tracheobronchial zygomycosis in a cat, *Vet Radiol Ultrasound* 51:617, 2010.
26. Fitzgerald SD, Johnson CA, Peck EJ: A fatal case of intrathoracic cuterebriasis in a cat, *J Am Anim Hosp Assoc* 32:353, 1996.
27. Volta A, Piccionello AP, Bonazzi M, et al: What is your diagnosis? Bronchial foreign body, *J Am Vet Med Assoc* 230:191, 2007.
28. Tivers MS, Moore AH: Tracheal foreign bodies in the cat and the use of fluoroscopy for removal: 12 cases, *J Small Anim Pract* 47:155, 2006.
29. Lotti U, Niebauer G: Tracheobronchial foreign bodies of plant origin in 153 hunting dogs, *Compend Cont Educ Pract Vet* 14:900, 1992.
30. Mitchell SL, McCarthy R, Rudloff E, et al: Tracheal rupture associated with intubation in cats: 20 cases (1996–1998), *J Am Vet Med Assoc* 216:1592, 2000.
31. White RN, Burton CA: Surgical management of intrathoracic tracheal avulsion in cats: long-term results in 9 consecutive cases, *Vet Surg* 29:430, 2000.
32. White RN, Milner HR: Intrathoracic tracheal avulsion in three cats, *J Small Anim Pract* 36:343, 1995.
33. Mattoon JS, Drost WT: Radiographing the trachea in small animals, *Vet Med* 72, 2004.
34. Griffiths LG, Sullivan M, Lerche P: Intrathoracic tracheal avulsion and pseudodiverticulum following pneumomediastinum in a cat, *Vet Rec* 142:693, 1998.
35. Fasanella FJ, Shivley JM, Wardlaw JL, et al: Brachycephalic airway obstructive syndrome in dogs: 90 cases (1991–2008), *J Am Vet Med Assoc* 237:1048, 2010.
36. Coyne BE, Fingland RB: Hypoplasia of the trachea in dogs: 103 cases (1974–1990), *J Am Vet Med Assoc* 201:768, 1992.
37. Johnson L: Tracheal collapse. Diagnosis and medical and surgical treatment, *Vet Clin North Am Small Anim Pract* 30:1253, 2000.
38. Macready DM, Johnson LR, Pollard RE: Fluoroscopic and radiographic evaluation of tracheal collapse in dogs: 62 cases (2001–2006), *J Am Vet Med Assoc* 230:1870, 2007.
39. Marolf A, Blaik M, Specht A: A retrospective study of the relationship between tracheal collapse and bronchiectasis in dogs, *Vet Radiol Ultrasound* 48:199, 2007.
40. Leonard CD, Johnson LR, Bonadio CM, et al: Changes in tracheal dimensions during inspiration and expiration in healthy dogs as detected via computed tomography, *Am J Vet Res* 70:986, 2009.
41. Sura PA, Krahwinkel DJ: Self-expanding nitinol stents for the treatment of tracheal collapse in dogs: 12 cases (2001–2004), *J Am Vet Med Assoc* 232:228, 2008.
42. Moritz A, Schneider M, Bauer N: Management of advanced tracheal collapse in dogs using intraluminal self-expanding biliary wallstents, *J Vet Intern Med* 18:31, 2004.
43. Fujita M, Miura H, Yasuda D, et al: Tracheal narrowing secondary to airway obstruction in two cats, *J Small Anim Pract* 45:29, 2004.
44. Hendricks JC, O'Brien JA: Tracheal collapse in two cats, *J Am Vet Med Assoc* 187:418, 1985.
45. Mims HL, Hancock RB, Leib MS, et al: Primary tracheal collapse in a cat, *J Am Anim Hosp Assoc* 44:149, 2008.

46. Arndt JW, Marks SL, Kneller SK: What is your diagnosis? Hiatal hernia due to laryngeal squamous cell carcinoma, *J Am Vet Med Assoc* 228:693, 2006.
47. Schachter S, Norris CR: Laryngeal paralysis in cats: 16 cases (1990–1999), *J Am Vet Med Assoc* 216:1100, 2000.
48. Mattoon JS, Drost WT: Pharyngeal and laryngeal radiography in small animals, *Vet Med* 50, 2004
49. Rudorf H, Barr F: Echolaryngography in cats, *Vet Radiol Ultrasound* 43:353, 2002.
50. Rudorf H, Barr FJ, Lane JG: The role of ultrasound in the assessment of laryngeal paralysis in the dog, *Vet Radiol Ultrasound* 42:338, 2001.
51. Laurenson MP, Zwingenberger AL, Cissell DD, et al: Computed tomography of the pharynx in a closed vs. open mouth position *Vet Radiol Ultrasound* 52:357, 2011.
52. Gendler A, Lewis JR, Reetz JA, et al: Computed tomographic features of oral squamous cell carcinoma in cats: 18 cases (2002–2008), *J Am Vet Med Assoc* 236:319, 2010.
53. Nicholson I, Halfacree Z, Whatmough C, et al: Computed tomography as an aid to management of chronic oropharyngeal stick injury in the dog, *J Small Anim Pract* 49:451, 2008.
54. Dobromylskyj MJ, Dennis R, Ladlow JF, et al: The use of magnetic resonance imaging in the management of pharyngeal penetration injuries in dogs, *J Small Anim Pract* 49:74, 2008.
55. Jones JC, Ober CP: Computed tomographic diagnosis of nongastrointestinal foreign bodies in dogs, *J Am Anim Hosp Assoc* 43:99, 2007.
56. Francis KA, Goggin JM, Hoskinson JJ: Imaging diagnosis-laryngeal collapse due to cricoid cartilage fracture, *Vet Radiol Ultrasound* 49:360, 2008.
57. Bhandal J, Kuzma A: Tracheal rupture in a cat: diagnosis by computed tomography, *Can Vet J* 49:595, 2008.

ELECTRONIC RESOURCES

Evolve

Additional information related to the content in Chapter 26 can be found on the companion Evolve website at http://evolve.elsevier.com/Thrall/vetrad/

- Videos
- Chapter Quiz

CHAPTER • 27

The Canine and Feline Esophagus

Lorrie Gaschen

Clinical signs related directly to esophageal disease are gagging, retching, regurgitation, painful swallowing, and inability to swallow.[1] Signs developing secondary to esophageal disease include pharyngeal and upper airway inflammation, nasal discharge, weight loss, pneumomediastinum, pneumothorax, pleural effusion, and aspiration pneumonia. Acute respiratory signs may also develop secondary to compression of the trachea by an esophageal mass. If the airway compression is severe, noncardiogenic edema can result; this is uncommon (Fig. 27-1).

RELATIVE VALUE OF RADIOGRAPHY, CONTRAST ESOPHAGRAPHY, FLUOROSCOPY, AND ALTERNATIVE IMAGING PROCEDURES

Survey radiographs of the thorax and cervical region, including the base of the tongue, are indicated in dogs and cats with clinical signs of esophageal disease. Survey radiographs and static barium esophagraphy provide structural information about the size and content of the esophagus and allow assessment of aspiration pneumonia and signs of esophageal perforation. Static contrast esophagraphy is helpful for characterizing the following conditions: esophageal mass, nonradiopaque foreign body, esophageal stricture, vascular ring anomaly, esophageal perforation, esophagitis, esophageal diverticulum, tracheo- or bronchoesophageal fistula, dysphagia, and hiatal hernia.[2] Static contrast esophagraphy is not adequate for assessing dysphagia, where dynamic contrast studies performed with fluoroscopy are required. Dynamic studies are typically performed at specialty centers.

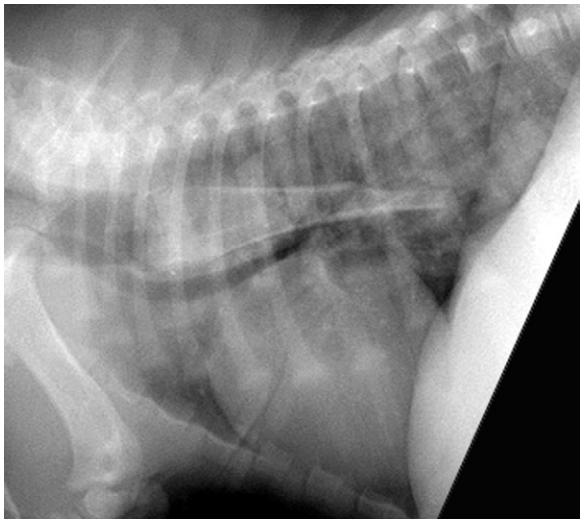


Fig. 27-1 Lateral radiograph of an 8-week-old pit bull terrier with a large bone lodged in the midthoracic esophagus. The mass of the bone displaces and compresses the trachea, leading to noncardiogenic pulmonary edema, characterized by a diffuse alveolar pattern.

Other than positive contrast radiography, other modalities are used only rarely to assess the esophagus. Scintigraphy can be used to quantify esophageal motility and transit time and diagnose gastroesophageal reflux.[3] Computed tomography (CT) is helpful for further characterization of esophageal masses and their association with adjacent tissues and vessels for both diagnostic and presurgical purposes. Radiographic or CT angiography is required for the characterization of vascular ring anomalies and esophageal varices. Conventional transcutaneous ultrasonography is limited to evaluation of the cervical esophagus and, to some extent, the caudal esophageal sphincter and gastroesophageal junction. Endoscopic ultrasonography can be used to examine the thoracic portion of the esophagus.[4] Indications include mural infiltration, fistula, diverticula, and periesophageal masses. Magnetic resonance imaging is not used for esophageal examination in animals but is used frequently to assess esophageal tumors in human beings.

ANATOMY AND PHYSIOLOGIC CONSIDERATIONS

The esophagus begins cranially at the cricopharyngeal sphincter, also called the *cranial esophageal sphincter*, and continues to the esophageal hiatus at the diaphragm. The cricopharyngeal sphincter is formed by the cricopharyngeus and thyropharyngeus muscles. In the cranial aspect of the thorax, the esophagus is related closely to the longus colli and longus capitis muscles dorsally and to the trachea ventrally and to the right.[5] In the neck, the cervical esophagus is located slightly to the left of the trachea, gradually becoming completely left-sided at the thoracic inlet (Fig. 27-2, *A*).[5] The left common carotid artery, vagosympathetic trunk, internal jugular vein, and tracheal duct course through the angle between the esophagus and the longus capitis muscle. The right common carotid artery, vagosympathetic trunk, internal jugular vein, and tracheal duct are lateral to the trachea on the right side. The thoracic portion of the esophagus is in close proximity to the trachea. The esophagus is to the left of the trachea at the thoracic inlet (Fig. 27-2, *B*), but it gradually courses dorsally over the point of bifurcation of the trachea at the level of the

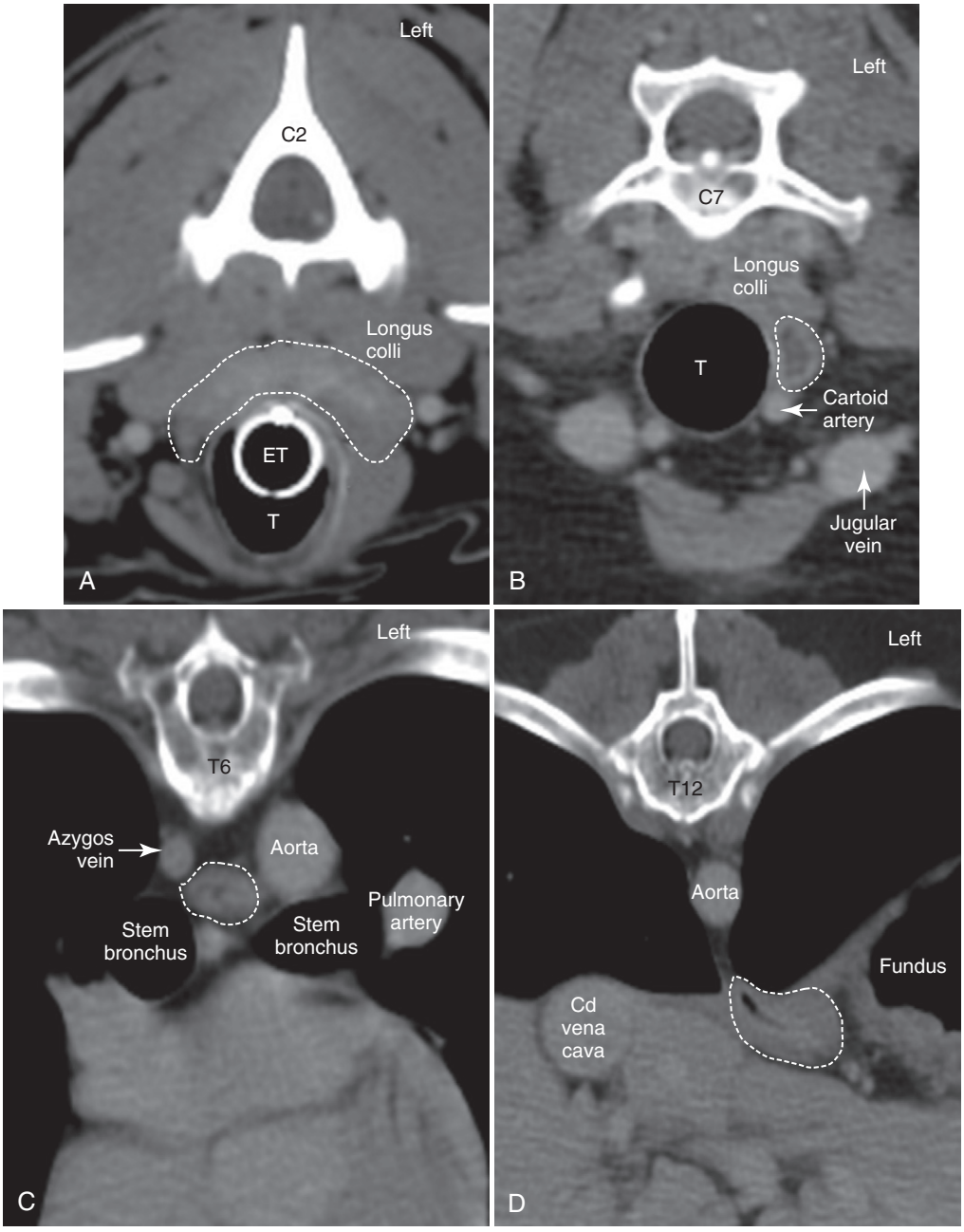


Fig. 27-2 Transverse CT images of the thorax of a dog at four different levels illustrating the relationship of the esophagus (outlined with *dotted line*) to surrounding structures: cricopharyngeal sphincter **(A),** thoracic inlet **(B),** base of the heart **(C),** and caudal esophageal sphincter **(D).** *a,* Artery; *Cd,* caudal; *ET,* endotracheal tube; *stem bronchus,* principal bronchus; *T,* trachea; *v,* vein.

fifth and sixth thoracic vertebrae (Fig. 27-2, *C*). At its dorsal location, it lies to the right of the aortic arch and is ventral to the longus colli muscles. Between the tracheal bifurcation and caudal esophageal sphincter, the esophagus lies in the median plane (Fig. 27-2, *D*). The vagal nerves run dorsocaudally across the sides of the esophagus and unite at the dorsal aspect of the esophagus a few centimeters cranial to the esophageal hiatus to form the vagal trunk, which passes through the hiatus with the esophagus.

There are numerous longitudinal folds of the esophageal mucosa (Fig. 27-3, *A*). The wall consists of four layers: fibrous, muscular, submucosa, and mucosa. The muscular layer is composed of striated muscle in dogs along its entire length, and the entire length of the mucosa is characterized by longitudinal folds. In cats, the caudal third of the muscular layer is composed of smooth muscle, which is arranged obliquely creating a striated pattern on contrast esophagrams (Fig. 27-3, *B*). The caudal esophageal sphincter is formed by the focal thickening of the esophageal smooth muscle of the muscularis, confluence of the gastric folds oriented transversely, and the muscular sling created by the right crus of the diaphragm and the deep oblique smooth muscle of the lesser curvature of the stomach.

Branches of the thyroid arteries supply the cervical portion of the esophagus, and the bronchoesophageal artery is the main source to the cranial two thirds of the thoracic portion.

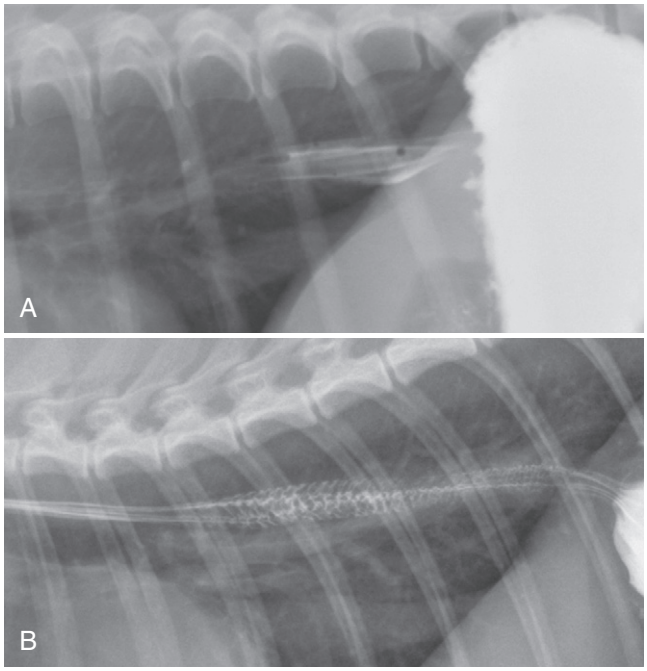


Fig. 27-3 **A,** Barium-contrast esophagram of the caudal esophagus in a normal dog. Note the linear arrangement of the mucosal folds. **B,** Barium-contrast esophagram of the caudal esophagus in a normal cat. Note the herringbone appearance to the mucosa in the caudal aspect of the esophagus that is created by the obliquely oriented smooth muscle in this region.

Esophageal branches of the aorta and/or intercostal arteries supply the remainder of the esophagus, and the terminal portion is supplied by the left gastric artery. The azygous vein and left gastric vein drain the thoracic portion. Lymphatic drainage is through the medial retropharyngeal, deep cervical, cranial mediastinal, bronchial, portal, splenic, and gastric lymph nodes.

Innervation of the esophagus is complex and involves 25 paired spinal ganglia from C2-L5. Neurologic control of swallowing is coordinated by cranial nerves V (trigeminal), VII (facial), IX (glossopharyngeal), X (vagus), and XII (hypoglossal), and their nuclei in the brain stem that, in turn, are controlled by areas of the reticular formation referred to as the *swallowing center*.[6]

NORMAL RADIOGRAPHIC APPEARANCE

The normal esophagus is usually empty and rarely evident on thoracic radiographs in cats and dogs because of its location within the mediastinum and silhouetting with adjacent muscles and mediastinal structures. On left lateral thoracic radiographs, the normal caudal thoracic esophagus sometimes contains a small amount of fluid and can be visualized as a faint tubular soft tissue opacity between the descending aorta and caudal vena cava (Fig. 27-4, *A*); this appearance is rare in right lateral radiographs. Gas can accumulate focally in the esophagus in animals that are excited, sedated, and dyspneic or under general anesthesia; this gas accumulation is usually minimal, and the most common location for this to occur is just cranial to the tracheal bifurcation (Fig. 27-4, *B*). Focal esophageal gas collections are dynamic and may appear differently or be absent in other radiographs acquired during the same study. General anesthesia or aerophagia may even lead to severe dilation of the esophagus, which can appear identical to pathologic megaesophagus (Fig. 27-4, *C*).

Box • 27-1

Survey Radiographic Signs of Esophageal Disease

- Increased radiopacity of mediastinum
  - Opaque foreign body
  - Retention of ingesta
  - Esophageal mass
  - Mediastinal fluid or mass (secondary to perforation)
- Increased radiolucency of mediastinum
  - Esophageal dilation with gas
  - Pneumomediastinum (secondary to perforation)
  - Pneumothorax (secondary to perforation)
- Ventral displacement of trachea
- Tracheal stripe sign
- Visualization of longus colli muscles
- Pleural effusion (secondary to perforation)
- Aspiration pneumonia

Anesthesia-related megaesophagus will resolve spontaneously when the patient has recovered from anesthesia.

SURVEY RADIOGRAPHIC ABNORMALITIES

Box 27-1 contains a list of radiographic signs that can be seen with esophageal disease. Gas in the esophageal lumen warrants further investigation in patients where it is thought to be pathologic and not a normal variant as described previously (see Fig. 27-4). It is important to examine the entire esophagus radiographically, meaning that radiographs of the cervical esophagus and pharynx are warranted in addition to thoracic radiographs (Fig. 27-5).

There may be a tendency to confuse esophageal gas with pneumomediastinum, although there are some basic differences in the appearance of these conditions. With pneumomediastinum, there will be increased conspicuity of the adventitial surface of the esophagus and great vessels, as described in Chapter 30. With megaesophagus, the gas collection will be more contiguous, and a tracheal stripe sign will be present. The tracheal stripe sign is a soft tissue opaque band that is formed by the summation of the ventral aspect of the esophageal wall with the dorsal aspect of the tracheal wall, each outlined by gas in their respective lumen (Fig. 27-6; see Fig. 27-4). If the gas-filled esophagus is large enough, the ventral border of the longus colli muscle and the dorsal indentation created by the overlying azygos vein will be visible (see Fig. 27-6).

When esophageal air is detected in animals with clinical signs of esophageal disease, an esophagram is indicated to rule out morphologic abnormalities such as a stricture or nonradiopaque foreign body. Normal variations such as kinks and bends in the cranial portion of the thoracic esophagus, sometimes referred to as *redundant esophagus*, can be identified in young dogs or short-necked brachycephalic breeds (Fig. 27-7). Contrast medium can accumulate temporarily in a redundant section and can appear as an outpouching as with an esophageal diverticula. Dynamic esophagraphy is needed to assess the significance of esophageal redundancy, as in some dogs the motility may be altered significantly in this region.

The absence of abnormal esophageal survey radiographic findings does not eliminate the possibility of esophageal disease. In animals with appropriate clinical signs but clinical signs of esophageal disease, contrast studies of the esophagus should be considered.

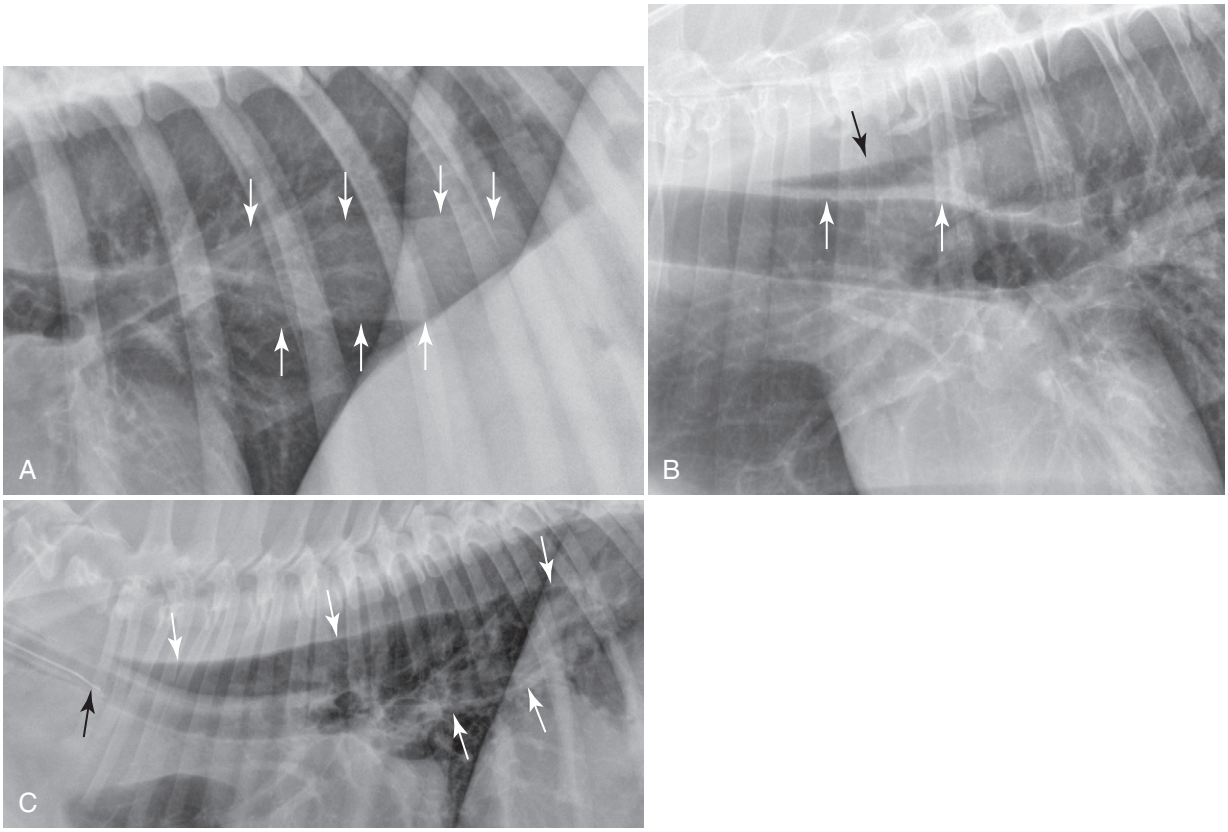


Fig. 27-4 Variations in the appearance of the normal esophagus. **A,** Left lateral radiograph of a normal adult dog. The caudal one third of the esophagus is visible as a soft tissue band between the aorta and caudal vena cava *(white arrows)*. This finding is usually not present on right lateral radiographs of normal dogs. **B,** Left lateral radiograph of a normal adult dog where there is a small amount of gas in the esophagus just cranial to the tracheal bifurcation *(black arrow)*. This will not be visible in the ventrodorsal view. The tissue band between the trachea and esophagus *(white arrows)* is termed the *tracheal stripe sign*. This is created by summation of the ventral aspect of the esophageal wall with the dorsal aspect of the tracheal wall, each outlined by gas in their respective lumen. The tracheal stripe sign is a reliable sign of esophageal gas. **C,** Left lateral radiograph of an anesthetized dog. The endotracheal tube is visible *(black arrow)*. There is generalized megaesophagus *(white arrows)* because of the anesthesia. The enlarged esophagus is causing ventral displacement of the intrathoracic trachea. Radiographically, this cannot be distinguished from pathologic megaesophagus.

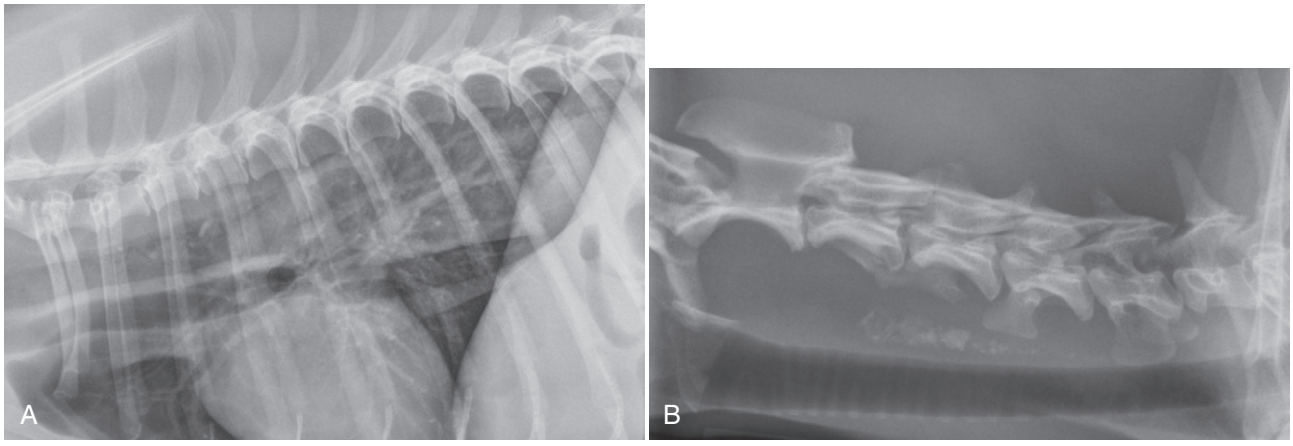


Fig. 27-5 **A,** Left lateral thoracic radiograph of a 3-year-old rat terrier. The thoracic esophagus is dilatated with gas and fluid, and there are also focal opacities that are likely in the esophagus. As the dilatation extends into the caudal cervical region, cervical radiographs are indicated. **B,** Lateral cervical radiograph of the same dog. There is amorphous mineralized material in a linear configuration dorsal to the trachea. Bone foreign material and severe esophagitis were diagnosed endoscopically.

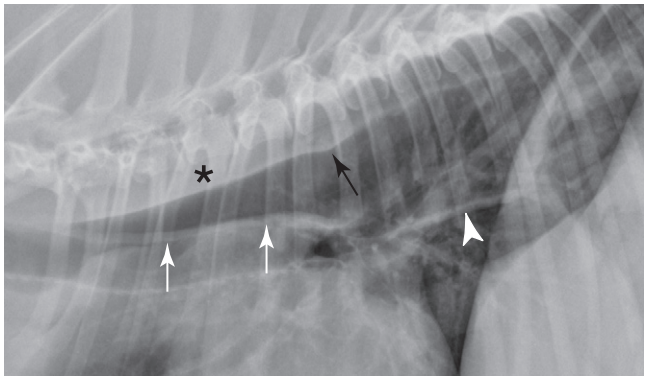


Fig. 27-6 Left lateral radiograph of a dog with a gas-dilated esophagus. The tracheal stripe sign *(white arrows)* results from summation of the tracheal and esophageal walls, each outlined by gas in their respective lumen. The gas-filled esophagus also borders the longus colli muscles *(asterisk)*. The ventral border of the caudal esophagus is visible *(white arrowhead)*, as is the indentation of the dorsal aspect of the esophageal wall because of passage of the azygos vein *(black arrow)*.

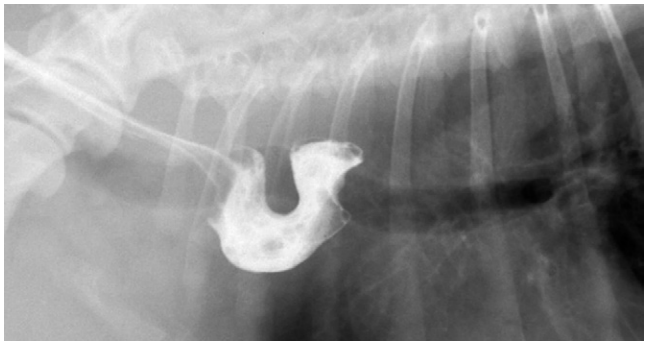


Fig. 27-7 Barium swallow in an 8-year-old Shar-Pei. There is a focal redundancy of the esophagus at the thoracic inlet. This redundancy may be insignificant, but in some dogs there is diminished contractility with retention of ingesta in this region. A dynamic esophagram is needed to assess the significance of esophageal redundancy.

CONTRAST ESOPHAGRAPHY TECHNIQUES

Survey radiographs of the thorax and cervical region must always be performed immediately before a contrast esophagram. Static contrast studies provide structural information, whereas fluoroscopy is required to assess swallowing disorders and esophageal motility. Table 27-1 lists the types of contrast media that can be used for an esophagram, along with their advantages and disadvantages. Barium aspiration is a potential complication of performing esophageal contrast studies. Barium paste is contraindicated in animals at increased risk for aspiration because aspirated paste could cause airway obstruction. Aspiration of a small amount of liquid barium is usually insignificant. Pneumonia and lung granuloma formation are rare complications of barium aspiration. Aspirated barium is cleared from the airways by ciliary action, as well as coughing (Fig. 27-8). If barium enters the alveolar space, it may remain there permanently. Lymphatic uptake of aspirated barium will also be evident as amorphous mottled opacities in the region of the mediastinal and tracheobronchial lymph nodes, which may also be a permanent finding (Fig. 27-9).

Box 27-2 contains a list of contrast study techniques used for examination of the esophagus.[7] The esophagram should be performed without sedation because most sedatives have an effect on esophageal motility and swallowing. Table 27-2 contains a description of the phases of swallowing and normal radiographic appearance of contrast studies. In general, there should be no retention of barium in the oral or pharyngeal cavity in static radiographs performed during swallowing. Some coating of the mucosa is normal. No contrast medium should be present in the pharynx, larynx, or trachea after swallowing.

Table • **27-1**

Contrast Media for the Esophagus

CONTRAST MEDIUM	ADVANTAGES/DISADVANTAGES
Barium sulfate suspension 60% weight/volume premixed	Relatively safe if aspirated
	Does not adhere well to mucosa
	May pass through a stricture or incomplete obstruction
	Contraindicated if perforation suspected
Barium sulfate paste or cream	Best adherence to esophageal mucosa
	Indicated for esophagitis, mucosal irregularities, or infiltration
	Can cause asphyxiation if inhaled
Barium sulfate suspension—soaked food, one part barium to two parts kibble or canned food	Best for detecting strictures that liquid barium or paste would pass through
	Best for assessing overall esophageal volume
	Use if animal can swallow liquid but not solids
Iodinated contrast media	Use if perforation is suspected
	Not recommended for routine esophagography
	Cause fluid influx into the gastrointestinal tract, potentially leading to hypovolemia
	Detecting extravasation may be difficult because of dilution in the pleural space
Ionic (hyperosmolar)—diatrizoate sodium or meglumine	Induce pulmonary edema if aspirated
Nonionic (low osmolar)—iohexol or iopamidol	Best choice if perforation suspected
	Most expensive

DYSPHAGIA

Dysphagia can result from morphologic or functional etiologies. Morphologic causes include trauma, foreign body, an oral or pharyngeal mass, and regional lymphadenopathy. Lateral and ventrodorsal (VD) survey radiographs of the pharyngeal and cervical region and thorax are indicated to screen for radiopaque foreign bodies such as bones, needles, and fish hooks (Fig. 27-10). Soft tissue swelling and gas pockets can be seen with perforating pharyngeal trauma, abscesses, or a nonradiopaque foreign body such as a wooden stick. Ultrasonography is useful to determine the source of

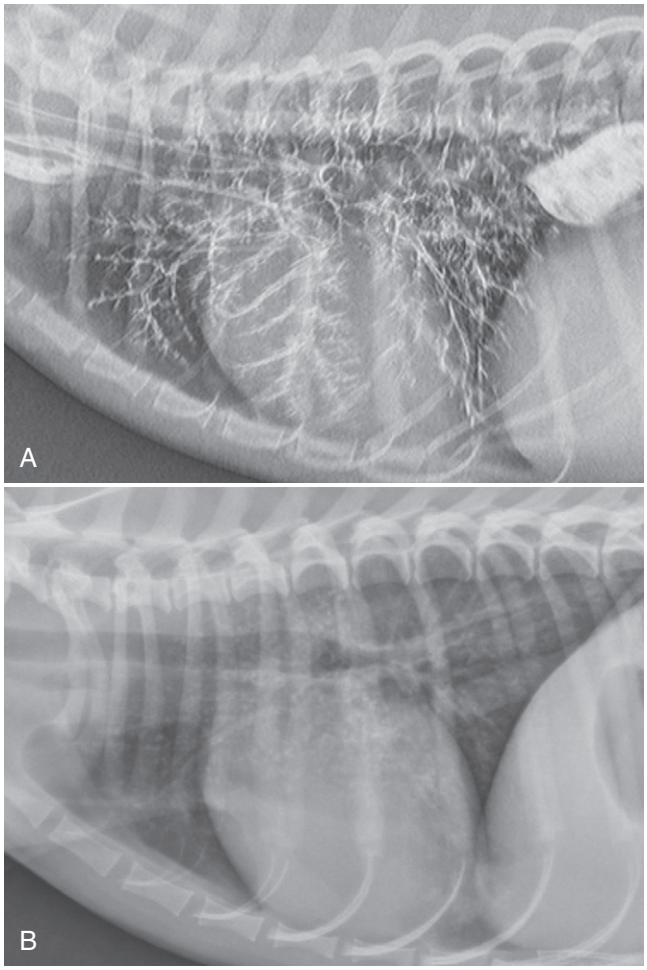


Fig. 27-8 **A,** Lateral thoracic radiograph of a 1.5-year-old Peekapoo. A barium swallow was performed, and there is diffuse barium aspiration. **B,** Lateral radiograph of the same dog 24 hours later. There has been almost complete clearing of the barium.

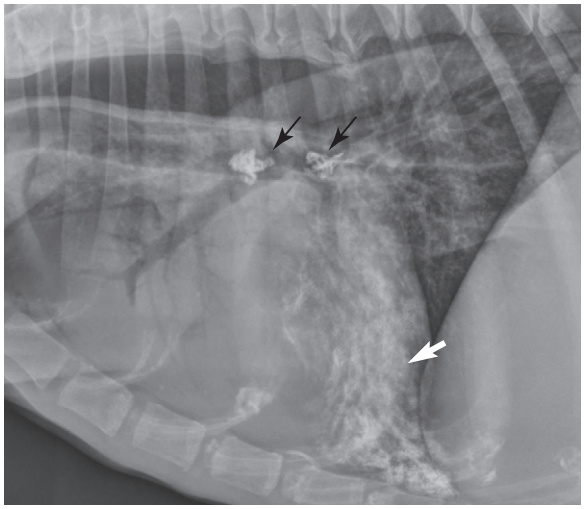


Fig. 27-9 Lateral thoracic radiograph of a 9-year-old standard poodle. Barium aspiration occurred in the right middle lung lobe 1 year prior *(white arrow)*. The regional lymph nodes have an amorphous mineral opacity *(black arrows)* because of lymphatic transport of aspirated barium. Active pneumonia, unrelated to the barium aspiration, is present in the right cranial lung lobe.

Box • **27-2**

Techniques for Esophageal Contrast Studies[7]

Static Barium Esophagram

Special Considerations

No sedation
Contraindicated for esophageal perforation
Use barium paste instead of barium suspension for evaluating mucosa
Aspiration potential

Procedure

Survey lateral and VD radiographs of the neck and thorax
Orally administer via syringe in lateral recumbency
- Small dog: 15 mL of 60% weight/volume preformulated barium sulfate suspension
- Large dog: 20—30 mL of 60% weight/volume preformulated barium sulfate suspension
- Cat: 5—7 mL of 60% weight/volume preformulated barium sulfate suspension

Lateral radiographs of the neck and thorax immediately after oral administration
VD radiographs of thorax immediately
Right and left oblique VD thoracic radiographs
Repeat entire procedure if amount of contrast medium in esophagus is insufficient

Static Barium Meal Esophagram

Special Considerations

Can identify small or incomplete obstructions that allow liquid to pass
Should be used if the esophagram with liquid barium is negative
Should be used if the patient can swallow liquids but not solid food clinically
Should not be performed if perforation is suspected

Procedure

Dogs: 1 cup dry kibble mixed with 20 mL barium sulfate suspension
Cats: 1/2 cup dry kibble or soft food mixed with 10 mL barium sulfate suspension
Perform following the swallowing study using liquid barium suspension
Provide the food mixture while in lateral recumbency or place in mouth
Perform same sequence of radiographs as for liquid barium

Static Iodinated Esophagram

Special Considerations

Can be used before endoscopy or if perforation is suspected
Do not use ionic contrast medium because it can cause pulmonary edema if aspirated

Procedure

Dog: 10—15 mL of a 50:50 mixture of nonionic iodinated contrast medium and water
Cat: 5—10 mL of a 50:50 mixture of nonionic iodinated contrast medium and water
Administer the liquid via syringe in lateral recumbency
Perform radiographic procedures as for liquid barium

Table • **27-2**

Phases of Swallowing, Control Mechanisms, and Radiographic Features in Normal Dogs

PHASE	CONTROL MECHANISMS	RADIOGRAPHIC FEATURES
Oral	Hyoid apparatus Tongue Facial nerve Vagus nerve Hypoglossal nerve	Formation of liquid or food bolus Reflex pharyngeal peristalsis starts
Pharyngeal	Pharyngeal musculature Facial nerve Vagus nerve Glossopharyngeal nerve	Craniodorsal movement of the hyoid caused by pharyngeal contraction Bolus enters laryngopharynx Tongue stops backward and forward movement Glottis closes entrance to trachea
Cricopharyngeal	Cricopharyngeal musculature Vagus and glossopharyngeal nerves	Relaxation of cricopharyngeal sphincter simultaneous with pharyngeal contraction Pharyngeal contraction propels bolus aborally
Esophageal	Mechanical stimulus of bolus Esophageal musculature Vagus nerve (sensory and motor)	Follows closure of cricopharyngeal sphincter. Longitudinal folds appear as thin lines. Primary peristalsis creates a bolus with a convex caudal border that is tapered cranially and is propelled aborally. Secondary peristalsis initiated and occurs at 2—4 seconds.
Gastroesophageal	Diaphragmatic musculature, oblique implantation of the esophagus, cardia incisura, positive intraabdominal pressure, oblique smooth muscles of the lesser curvature	Slow passage through gastroesophageal junction Small amount of reflux in normal; should induce a secondary wave

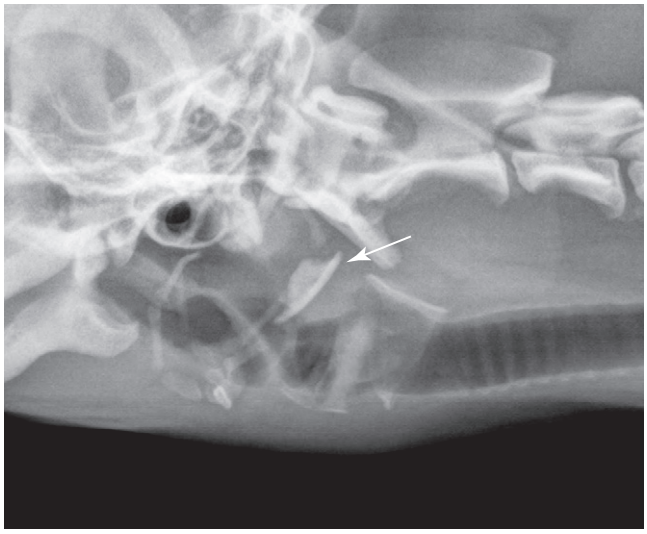


Fig. 27-10 Lateral cervical radiograph of an adult dog. An ingested bone is lodged in the pharynx *(white arrow)*.



Fig. 27-11 Ultrasound image of the cervical region of a dog with nonspecific swelling of the cranioventral aspect of the neck. There is a large subcutaneous fluid accumulation and multiple, linear, hyperechoic shadowing structures that were determined to be splinters of wood.

nonspecific pharyngeal swelling and nonradiopaque foreign bodies (Fig. 27-11).

Evaluation of functional disorders of swallowing requires contrast fluoroscopy (Table 27-3). Videofluoroscopic contrast studies allow subtle events of the oral, pharyngeal, and cricopharyngeal phases of swallowing to be recorded and observed dynamically.[a] Frame rates of 30 to 60 per second are necessary to assess the rapid events of swallowing to make an accurate frame-by-frame analysis.[6] The advantage of dynamic recordings is that subtle abnormalities associated with swallowing that would go unnoticed on static images can be detected. Cinescopy or digital fluoroscopy equipment will use slower acquisition rates of six images per second that also allow oral, pharyngeal (Fig. 27-12, *A*), cricopharyngeal (Fig. 27-12, *B*),

[a]Video 27-1 can be found on the accompanying Evolve website at http://evolve.elsevier.com/Thrall/vetrad.

Table • **27-3**

Types of Dysphagia, Causes, and Fluoroscopy Findings

TYPE	CAUSES	FLUOROSCOPIC FEATURES
Oral	Neuromuscular disease	Bolus not formed or delayed formation
	Inflammation	Bolus not propelled caudally to pharynx
	Oral foreign body	Weak plungerlike movement of tongue
	Tongue abscess	Weak pharyngeal contractions
		Subsequent stages are normal
Pharyngeal	Myositis and myopathy	Normal oral stage
	Post-cricopharyngeus myectomy	Remains synchronous with cricopharyngeal phase
	Neuromuscular disease	Retention of contrast medium in the pharynx
	Inflammation	No change in time to cricopharyngeal sphincter opening
	Trauma	Inadequate pharyngeal contraction
	Idiopathic	Pharyngeal constriction ratio prolonged (0.6)
		Misdirection of the bolus in to larynx or nasopharynx
Cricopharyngeal chalasia	Cricopharyngeus myotomy	Relaxation or incompetence of the cricopharyngeal sphincter
	Radiation therapy	Cricopharyngeal sphincter may appear air-filled
	Myasthenia gravis	Prolonged time to cricopharyngeal sphincter opening (28 seconds)
		Weak pharyngeal contractions may also be present
		Aspiration into larynx or trachea possible
Cricopharyngeal achalasia	Idiopathic	Incomplete or lack of opening of cricopharyngeal sphincter
		Vigorous attempts to pass bolus to cricopharyngeal sphincter
		Synchrony of timing of the opening of the cricopharyngeal sphincter
		Delayed time to cricopharyngeal sphincter opening
		Barium retention in pharynx
		Aspiration into larynx or trachea possible
Esophageal dysmotility	Delayed maturation	Megaesophagus may be present in young dogs
	Esophagitis	Abnormal primary wave (bolus moves <5 cm aborally)
		Abnormal secondary wave (bolus retention after >2 subsequent swallows)
		Retrograde >10 cm
		Prolonged esophageal transit time >5 seconds

and esophageal phases (Fig. 27-12, C) to be recorded, but subtle disease can go unnoticed as a result of the low frame rate.

When performing dynamic fluoroscopic swallowing studies, it is essential to protect personnel involved in the study from scattered radiation by establishing barriers of lead-impregnated rubber or other shielding between the primary beam and the attending personnel.[6] Radiolucent squeeze boxes can also be constructed out of polycarbonate sheets to allow evaluation of the patient in a standing position during the swallowing process (Fig. 27-13).[8]

The fluoroscopic contrast examination assesses the following: (1) bolus formation, (2) pharyngeal and tongue movement, (3) pharyngeal clearing of barium, and (4) cricopharyngeal sphincter function. Assessing these phases allows dysphagia to be categorized as oral, pharyngeal, or cricopharyngeal in origin.

Dogs with oral phase dysphagia have difficulty with prehension and bolus formation and transport to the pharynx. Oral dysphagia is usually characterized by the animal dropping food or liquid from its mouth and drooling.[9] The oral phase of swallowing is the only voluntary portion of the swallowing cascade. In oral dysphagia there is failure of aboral transport of liquid or food and lack of bolus formation to induce the swallowing reflex. Survey radiographs are usually normal. There may be retention of contrast medium in the oropharynx and a lack of contrast medium in the pharynx and cervical esophagus. Fluoroscopically, when performed in lateral recumbency, liquid contrast medium pools in the dependent vestibule of the mouth or flows out of the mouth. The backward and forward movement of the tongue will be normal or reduced. The bolus will not be formed and propelled aborally, or its formation will be delayed. The onset of the pharyngeal phase of swallowing may also be delayed. If a swallow is achieved, the pharyngeal and esophageal phases of swallowing are usually normal.

Pharyngeal dysphagia is more challenging to diagnose because it is often characterized by nonspecific signs such as gagging, retching, and the necessity for multiple swallowing attempts before movement of a bolus into the esophagus.[9] Pharyngeal dysphagia is diagnosed when the oral bolus is propelled inadequately across the pharynx for presentation to the cricopharyngeal sphincter. The cricopharyngeal phase should be normal. Pharyngeal dysphagia as a sole abnormality in the swallowing cascade is rare, and there is overlap in clinical signs and fluoroscopic findings with cricopharyngeal dysphagia. Survey radiographs of the pharynx are normal in most patients with pharyngeal dysphagia, but aspiration pneumonia can be present. Static contrast barium swallows may be characterized by retention of contrast medium in the pharynx with subsequent aspiration into the larynx. Videofluoroscopic abnormalities include (1) slow contraction of the pharynx, (2) incomplete enclosure of the bolus, (3) incomplete rostral and dorsal movement of the larynx, (4) absence of forceful

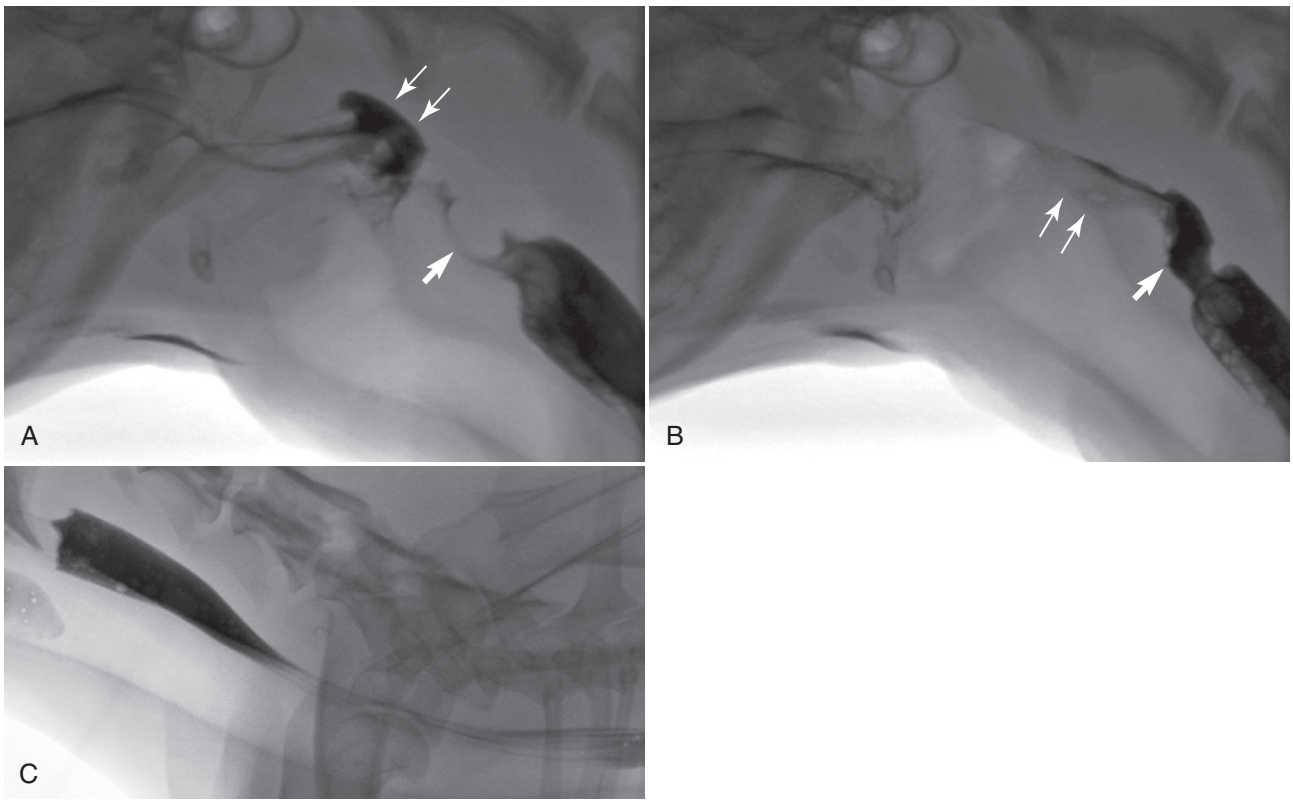


Fig. 27-12 Lateral digital fluoroscopic images. **A,** Normal pharyngeal phase of swallowing. A tight bolus *(small white arrows)* of barium is pushed dorsally as the pharynx contracts. The cricopharyngeal sphincter dorsal to the cricoid cartilage *(large white arrow)* is contracted. **B,** Normal cricopharyngeal phase of swallowing. The bolus in **A** passes through the cricopharyngeal sphincter into the cranial aspect of the esophagus *(large white arrow)*, and the cricopharyngeal sphincter *(small white arrows)* is open momentarily. **C,** Normal esophageal phase of swallowing. A tight bolus with a convex cranial border that tapers caudally is present in the cranial aspect of the esophagus. See Video 27-1.



Fig. 27-13 A radiolucent squeeze cage made of polycarbonate can be used to examine the swallowing phases in a dog in a standing position with reduced radiation exposure to personnel. (Image courtesy of the University of California, Davis.)

contraction of the pharynx to propel the bolus through the cricopharyngeal sphincter.[b] The opening of the cricopharyngeal sphincter may be small because of the weakness of the pharyngeal contraction, and this could be misinterpreted as a cricopharyngeal disorder. The pharyngeal constriction ratio was developed to identify dogs with weak pharyngeal contraction that would make them poor candidates for myotomy when cricopharyngeal dysphagia is diagnosed and to better differentiate them from those with cricopharyngeal dysphagia. The ratio is calculated by dividing the pharyngeal area at maximum contraction by the pharyngeal area at rest.[9] Dogs with decreased pharyngeal contraction have a significantly higher pharyngeal constriction ratio compared with healthy dogs, but this can also be present in dogs with cricopharyngeal dysphagia. The discerning factor between pharyngeal dysphagia and cricopharyngeal dysphagia is the time to opening of the cricopharyngeal sphincter, which is significantly shorter in pharyngeal dysphagia.[9]

Cricopharyngeal dysphagia is a functional abnormality involving failure of the cricopharyngeal sphincter to open fully (cricopharyngeal achalasia) or at the appropriate time (cricopharyngeal dyssynchrony). The clinical signs of cricopharyngeal dysphagia are similar to those of pharyngeal dysphagia (Fig. 27-14).[9] Although specific breed predilections have not been reported, cricopharyngeal achalasia is often associated with toy breeds.[10] The exact etiology has not been determined, but most affected patients develop clinical signs soon after weaning, suggesting that cricopharyngeal achalasia is a congenital disorder.[11] Gas may be present in the cervical esophagus on survey radiographs, but usually the radiographs are unremarkable. The thoracic portion of the esophagus will be normal, but aspiration pneumonia is found commonly. Static contrast esophagrams are characterized by pharyngeal stasis with barium retention, hypertrophy of the cricopharyngeus muscle, retention of contrast medium in the cervical esophagus, and normal esophageal transport of the contrast medium

[b]Video 27-2 can be found on the accompanying Evolve website at http://evolve.elsevier.com/Thrall/vetrad.

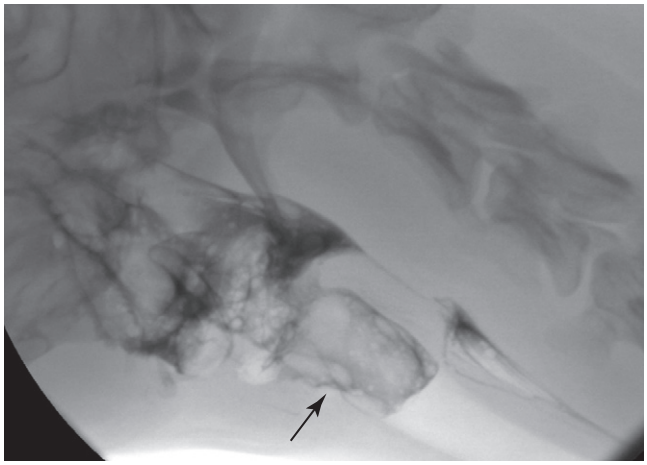


Fig. 27-14 Lateral digital fluoroscopic image of a barium swallow in a 2-year-old border collie with cricopharyngeal dysphagia. The timing of the pharyngeal and cricopharyngeal phases was abnormal, a tight bolus is not present, and barium has been aspirated into the laryngotrachea *(black arrow)*. The cricopharyngeal phase was normal, but delayed. See Video 27-4.

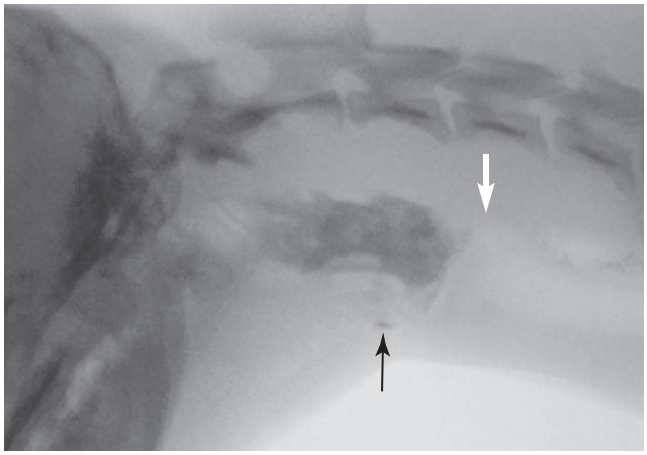


Fig. 27-15 Lateral video fluoroscopic image of a barium swallow in a 1.5-year-old Peekapoo (same dog as in Fig. 27-8) that had severe cricopharyngeal dysphagia. A large bolus *(black arrow)* is present cranial to the closed cricopharyngeal sphincter *(white arrow)*. The cricopharyngeal sphincter opened after many swallowing attempts. See Video 27-3.

in the thoracic esophagus. Liquid barium may coat the larynx, trachea, or nasopharynx because of misdirection of the bolus during failed swallowing attempts. Abnormal swallows are usually interspersed with normal ones. Critical to the diagnosis is the documentation of delayed or nonopening of the cricopharyngeal sphincter and a lack of coordination between pharyngeal contraction and opening of the sphincter, which requires fluoroscopy (Fig. 27-15).[c] Time from onset of swallowing (closure of epiglottis) to opening of the cricopharyngeal sphincter is delayed in dogs with cricopharyngeal achalasia compared with normal dogs (0.31 ± 0.14 vs. 09 ± 0.02 sec for liquids and 0.37 ± 0.06 vs. 0.10 ± 0.03 sec for kibble).[12] The same is true for sphincter closure times. No differences exist in time to maximal pharyngeal contraction and epiglottic reopening between normal dogs and those with cricopharyngeal achalasia with either liquid or kibble meals.

In cricopharyngeal chalasia, the cricopharyngeal sphincter does not maintain positive resting pressure between swallows.

[c]Videos 27-3 and 27-4 can be found on the accompanying Evolve website at http://evolve.elsevier.com/Thrall/vetrad.

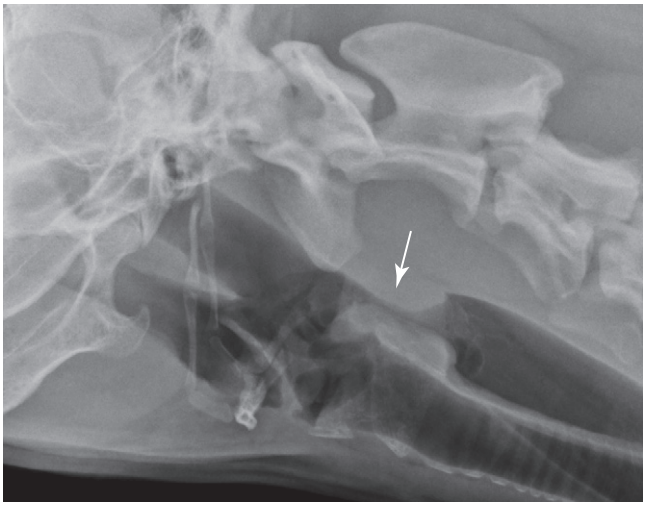


Fig. 27-16 Lateral cervical radiograph of a 5-year-old mastiff with cricopharyngeal chalasia. The cricopharyngeal sphincter is open and contains gas *(white arrow)*, as does the cervical esophagus. Cricopharyngeal and cranial esophageal gas is often seen with cricopharyngeal chalasia. The administration of barium is contraindicated in this instance because of increased risk for aspiration.

On survey radiographs air will often be present in the cricopharyngeal sphincter (Fig. 27-16). Cricopharyngeal chalasia can be found in dogs with myasthenia gravis. Barium administration is contraindicated in the presence of a statically open cricopharyngeal sphincter because of the increased risk of aspiration.

Esophageal motility disorders may result in abnormal peristalsis, transport, and motor function, and clinical signs of regurgitation are common. Survey radiographs can help detect structural abnormalities such as segmental or generalized dilation of the esophagus, abnormal esophageal content because of lack of normal peristalsis, and the presence of aspiration pneumonia. If survey radiographs are negative in animals with regurgitation, contrast studies are necessary to rule out esophageal disease. Peristaltic abnormalities, hypomotility, strictures, or radiolucent foreign bodies causing obstruction can go undetected on survey radiographs. A static barium esophagram can be used to diagnose mechanical obstruction because of foreign body or stricture, but functional studies of motility require fluoroscopy. Fluoroscopic studies can be performed in lateral recumbency or standing.[8] Following passage of a bolus through the cricopharyngeal sphincter, a primary peristaltic wave propels the bolus caudally, and secondary peristalsis propels the bolus to the caudal esophageal sphincter in normal animals.[d] Cervical esophageal transit time is significantly shorter for dogs in sternal recumbency.[8] During swallowing, pharyngeal constriction ratio, time to maximum pharyngeal contraction, time to cricopharyngeal sphincter opening, time to epiglottis reopening, and the percentage of secondary peristaltic waves do not differ between lateral and sternal recumbency.[8] The percentage of primary waves is significantly greater in liquid and kibble studies when done in sternal recumbency compared with lateral recumbency. Also, the percentage of swallows that have no associated primary peristaltic waves is higher in lateral recumbency. The percentage of secondary waves, however, does not differ between the two positions.[8]

Primary peristalsis can be disrupted by hypomotile segments, and secondary peristalsis may be absent in disease. Dogs with laryngeal paralysis may also have esophageal

[d]Videos 27-5 through 27-7 can be found on the accompanying Evolve website at http://evolve.elsevier.com/Thrall/vetrad.

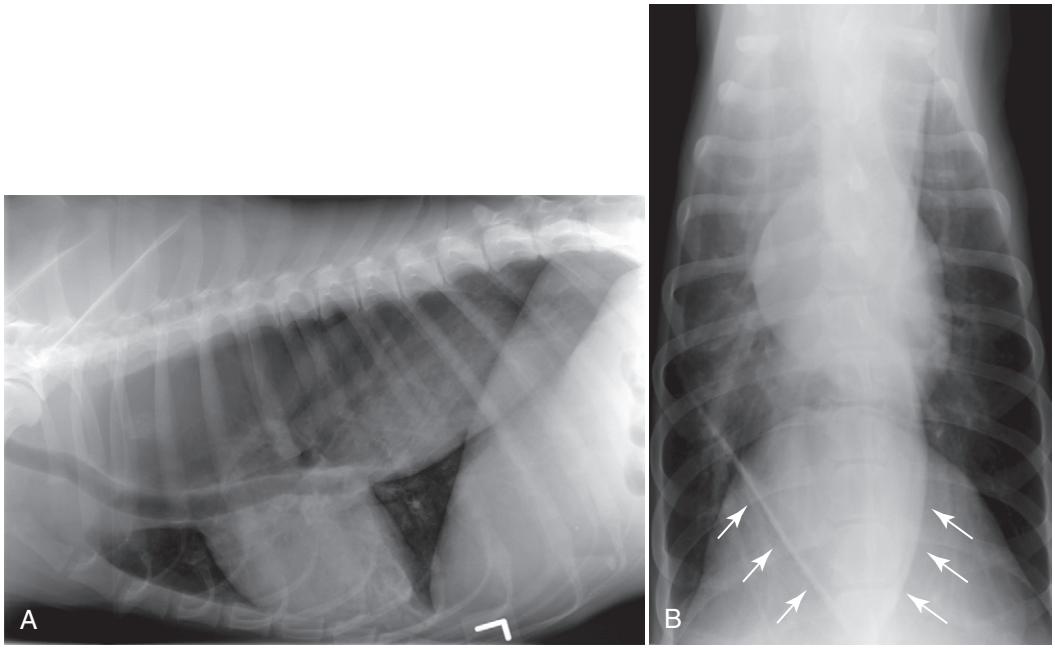


Fig. 27-17 **A,** Lateral radiograph of a 3-year-old German shepherd dog. The esophagus is severely dilated such that the trachea and heart are displaced ventrally. An alveolar pattern because of aspiration pneumonia is present in the periphery of the right middle lung lobe. **B,** VD radiograph of the same dog. The borders of the enlarged esophagus extend to the left and right side of the thorax and converge in a V shape near the caudal esophageal sphincter *(white arrows)*.

dysfunction.[13] Esophageal dysmotility in young dogs in the absence of megaesophagus is characterized by abnormal primary waves that move the bolus less than 5 cm aborally, and abnormal secondary waves that allow bolus retention in the esophagus after two subsequent swallows.[14] Retrograde flow of more than 10 cm is another finding associated with hypomotility, as is prolonged esophageal transit time (>5 sec).[14] Esophageal dysmotility can be caused by delayed maturation, and spontaneous improvement after 1 year of age can occur because of maturation of the neuromuscular system.[15] Esophagitis is another cause of abnormal esophageal motility. Gastroesophageal reflux occurs when gastric and duodenal contents enter aborally into the esophagus, and this can lead to dysmotility secondary to resultant esophagitis.[e 14]

ESOPHAGEAL DILATATION

Esophageal dilatation can be segmental or generalized depending on the cause and location of disease, and the dilatation can also be either functional or mechanical. Generalized dilatation is typically caused by functional disease, whereas segmental dilatation is usually caused by foreign body, infiltrative disease such as neoplasia or inflammation, hiatal diseases, segmental motor disease, stricture, vascular ring anomaly, or redundant esophagus. Radiographically, the dilatated esophagus can contain gas or fluid.

Megaesophagus

The term *megaesophagus* describes a dilated and hypomotile esophagus resulting from neuromuscular dysfunction; this type of esophageal dilation is often idiopathic.[16] Predominant clinical signs in esophageal neuromuscular dysfunction are effortless regurgitation of tubular-formed, undigested food. Megaesophagus is not common in cats but has been described in instances of pylorospasm. Megaesophagus is the most common cause of regurgitation in dogs and the most frequently reported motility disorder affecting the canine esophagus.[17] It is associated with reduced muscle tone and peristaltic activity and can lead to transport disorders.[15] Megaesophagus can be segmental (cervical or thoracic) or generalized and occurs secondary to diseases of the neuromuscular junction (myasthenia gravis), striated muscle (myositis), peripheral nerves (polyneuropathy), or central nervous system (inflammatory, toxic, and neoplastic).[16]

Radiographic signs of megaesophagus include dilatation of the esophagus with gas, retention of food or fluid, tracheal stripe sign, visualization of the longus colli muscle, ventral displacement of the intrathoracic trachea, ventral displacement of the heart, and aspiration pneumonia (Fig. 27-17; see Figs. 27-4, C and 27-6). When generalized megaesophagus is present, the thoracic segment of the esophagus is usually more severely dilatated than the cervical portion because of surrounding negative intrathoracic pressure. When gas-filled, the esophagus can be difficult to discern because of the lucency of the surrounding lung. On lateral thoracic radiographs, two thin soft tissue opaque, parallel bands coursing from cranial to caudal in the dorsal aspect of the thorax represent the wall of the gas-filled esophagus (see Fig. 27-6). A focal indentation of the dorsal esophageal wall is caused by the azygous vein crossing over on the right. In the VD radiograph, the wall of the gas-filled esophagus is most often identified as a thin soft tissue band to the left of the vertebral column. If the dilation is severe enough, a second band can also be seen on the right, converging with the left one at the caudal esophageal sphincter (see Fig. 27-17).

Hiatal Diseases

Esophageal hiatal diseases include sliding esophageal and paraesophageal hernias, gastroesophageal intussusception, and gastroesophageal reflux. Clinical signs may be absent, or dogs may have recurrent gastrointestinal signs such as regurgitation, retching, and possibly vomiting. Esophageal hernias can be

[e]Video 27-8 can be found on the accompanying Evolve website at http://evolve.elsevier.com/Thrall/vetrad.

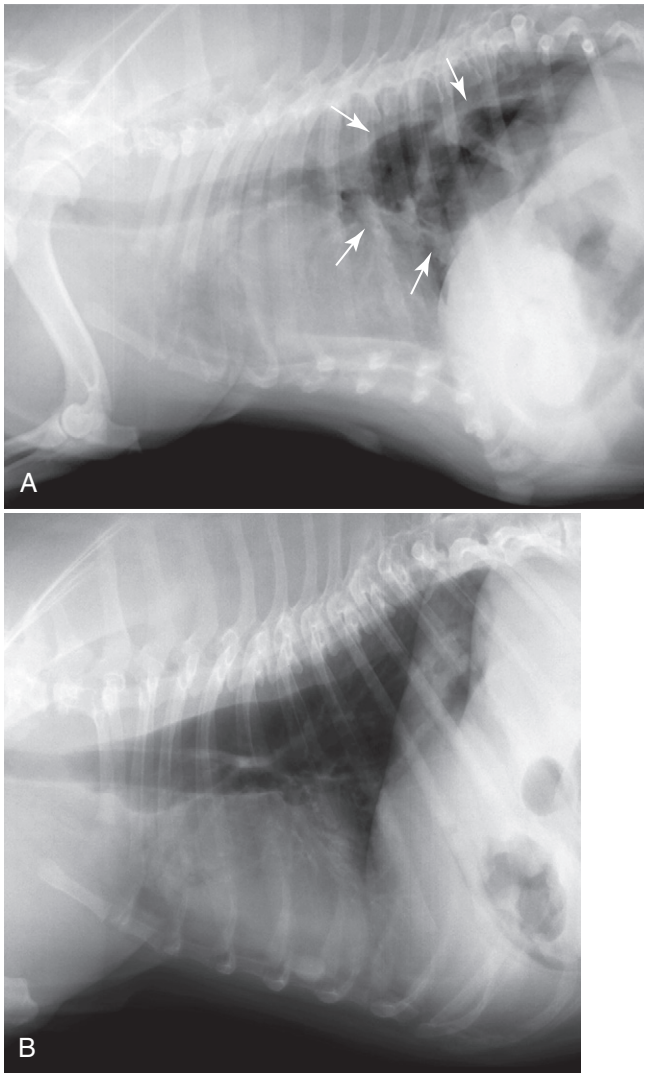


Fig. 27-18 **A,** Lateral thoracic radiograph of a 2-year-old bulldog with upper airway obstruction. There is cranial displacement of the stomach into the thorax *(white arrows)* and dorsal deviation of the sternum and ribs with a small lung volume. **B,** Same dog after endotracheal intubation and under anesthesia. The sternum resumes a normal position, the diaphragm is flatter and in a more caudal position, and the stomach is no longer displaced into the thorax. Residual gas dilatation of the esophagus could be caused by anesthesia or from previous aerophagia. The increase in intrathoracic pressure associated with alleviation of the airway obstruction allowed the stomach to reduce spontaneously into the abdomen.

congenital or acquired. The congenital form has been reported in Shar-Pei dogs.[18] In the acquired form, weakness of the diaphragm, elevated abdominal pressure, and upper airway obstruction are predisposing factors.

In sliding esophageal hernia, the caudal esophageal sphincter and part of the gastric fundus move in and out of the caudal mediastinum through a weakened esophageal hiatus of the diaphragm. Radiographically, there is a soft tissue, or mixed soft tissue and gas opacity between the aorta and caudal vena cava on lateral radiographs that silhouettes with the cranial diaphragmatic contour (Fig. 27-18). If persistent on the VD view, the opacity has a midline location and is slightly on the left of the vertebral column. Sliding esophageal hernia is confirmed with static barium esophagraphy or contrast fluoroscopy.[f] If the fundus is herniated along with the esophagus, rugal folds outlined by barium may be visible. The caudal esophageal sphincter will also be located cranial to the diaphragm, and barium can be seen to reflux from the stomach into the caudal esophagus fluoroscopically.

Paraesophageal hernias are caused by the fundus being herniated within the mediastinum alongside of the esophagus with the caudal esophageal sphincter remaining in the abdomen (Fig. 27-19, *A*). On VD radiographs, the herniated fundus is to the left of the esophagus, and the hernia contents may move in and out with respiration (Fig. 27-19, *B* and C).

Gastroesophageal intussusception occurs when part of the stomach and possibly other abdominal organs, such as the spleen, evert into the esophageal lumen. The intussusceptum may be of homogeneous soft tissue opacity or may be a mixed soft tissue and gas opacity if there is gas trapped in the herniated portion of the stomach (Fig. 27-20). A feature that distinguishes gastroesophageal intussusception from a sliding or paraesophageal hernia is the sharply marginated cranial edge of the intussusceptum contrasted against a gas-filled esophageal lumen. Gastroesophageal intussusception is often acquired and secondary to esophageal dilatation or previous surgery at the caudal esophageal sphincter resulting in chalasia. Pulmonary atelectasis may be identified if the stomach is distended because of incarceration at the hiatus, and respiratory distress may occur.

Gastroesophageal reflux occurs when gastric acid enters the esophagus; this usually results in esophagitis. Survey radiographs are usually normal, or there may be increased soft tissue opacity between the aorta and vena cava on lateral projections. With increasing severity, the caudal esophagus may become enlarged and contain either air or fluid. Contrast esophagram studies are usually negative unless severe ulceration is present that leads to adherence of the contrast medium to the mucosa. Focal dilatation of the esophagus with contrast medium can also occur if the esophagitis is severe. Inflammation can also obliterate the linear folds normally outlined with barium. If inflammation leads to scarring, a structure may develop.

Redundant Esophagus

Redundant esophagus is often an incidental finding in young brachycephalic breeds such as bulldogs and Shar-Peis (see Fig. 27-7). Survey radiographs may be normal, or focal dilatation of the esophagus with gas can be seen at the thoracic inlet. In static barium esophagrams, the esophagus has a tortuous course at the thoracic inlet that appears as a diverticulum ventral to the trachea. The accumulation of contrast medium in a redundant esophagus is usually only temporary, and the esophagus will appear normal on subsequent radiographs. With videofluoroscopy, the redundant segment typically has normal motility.[g] Occasionally, there will be a clinically significant motility disorder associated with the redundant region of the esophagus.

FOREIGN BODIES

Esophageal foreign bodies are more common in dogs than cats, and some terrier breeds appear to be predisposed.[19] Survey radiography should include the region from the base of the tongue to the diaphragm. Foreign bodies are most often located at the thoracic inlet, base of the heart, or just cranial to the diaphragm, sites where the esophagus is limited in its ability to distend. Nonobstructive foreign bodies, such as fishhooks and other sharp objects, tend to lodge in the pharyngeal region (Fig. 27-21; see Fig. 27-10). Radiopaque foreign

[f]Video 27-9 and Video 27-10 can be found on the accompanying Evolve website at http://evolve.elsevier.com/Thrall/vetrad.

[g]Video 27-11 can be found on the accompanying Evolve website at http://evolve.elsevier.com/Thrall/vetrad.

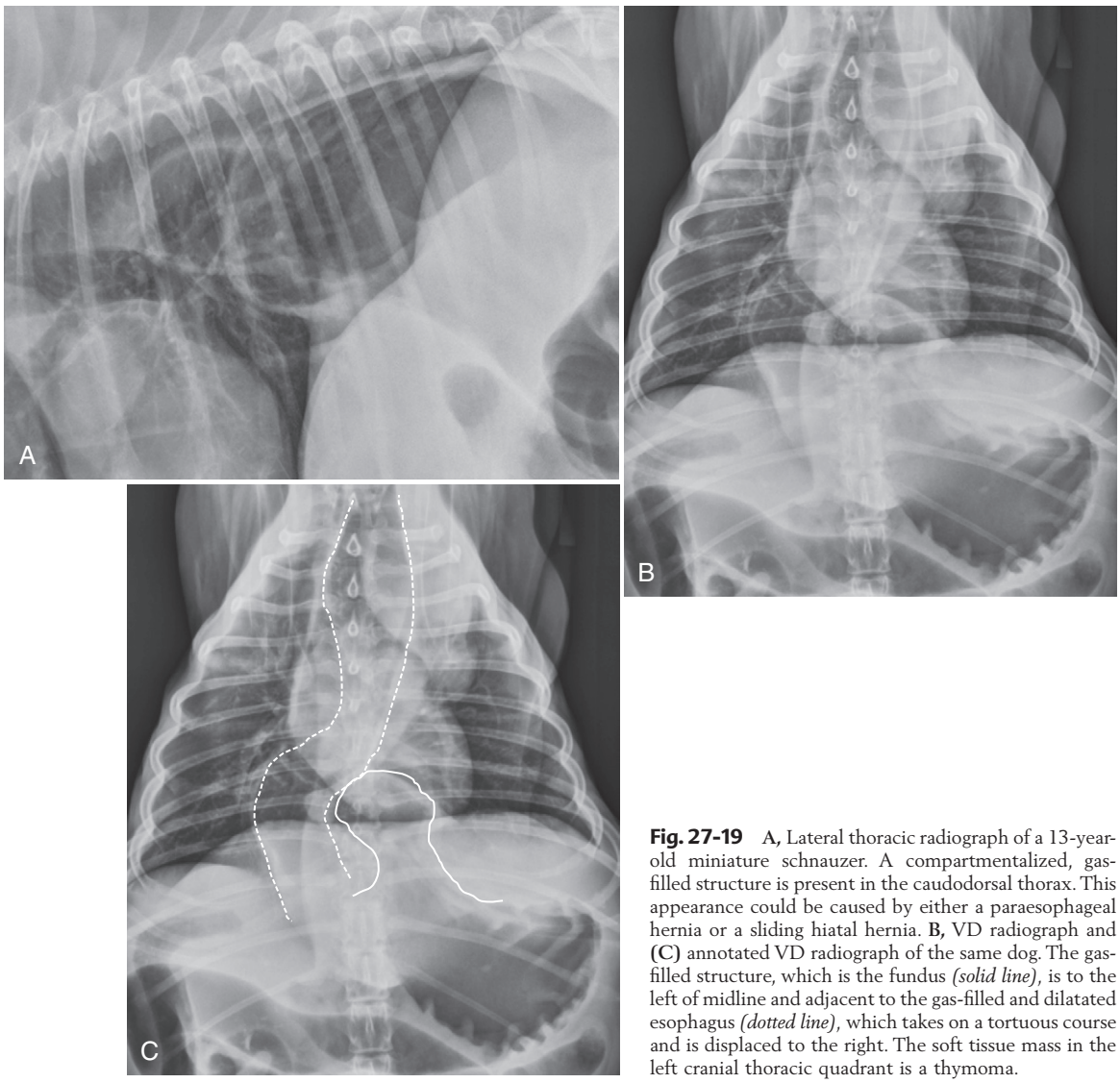


Fig. 27-19 **A,** Lateral thoracic radiograph of a 13-year-old miniature schnauzer. A compartmentalized, gas-filled structure is present in the caudodorsal thorax. This appearance could be caused by either a paraesophageal hernia or a sliding hiatal hernia. **B,** VD radiograph and **(C)** annotated VD radiograph of the same dog. The gas-filled structure, which is the fundus *(solid line)*, is to the left of midline and adjacent to the gas-filled and dilatated esophagus *(dotted line)*, which takes on a tortuous course and is displaced to the right. The soft tissue mass in the left cranial thoracic quadrant is a thymoma.

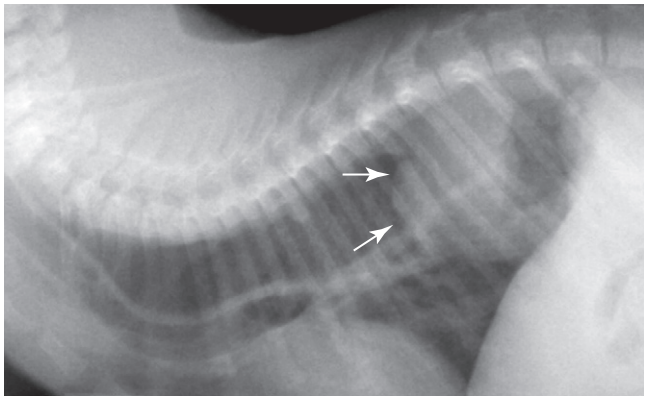


Fig. 27-20 Lateral thoracic radiograph of an 8-week-old Bengal kitten. The thoracic esophagus is gas dilatated with ventral displacement of the trachea and heart. A mixed soft tissue and gas mass with a sharply defined round cranial border *(white arrows)* is present in the dorsocaudal aspect of the thorax. This appearance of a gas-filled esophagus with a caudally located intraluminal mass having a sharply marginated cranial border is characteristic of gastroesophageal intussusception.

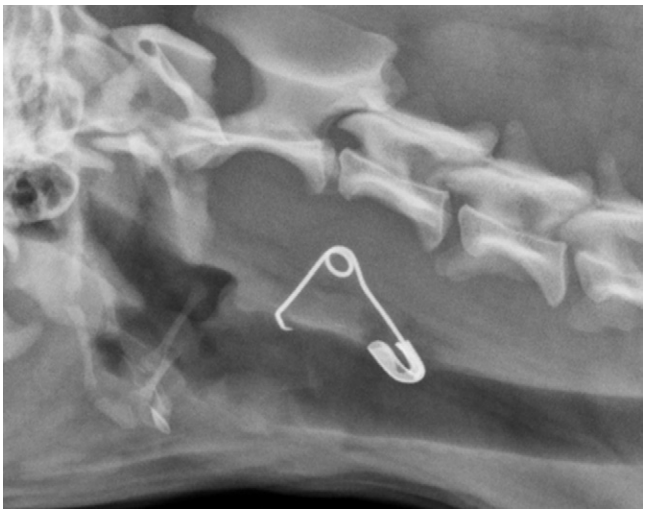


Fig. 27-21 Open safety pin obstructing the cervical esophagus caudal to the cricopharyngeal sphincter.

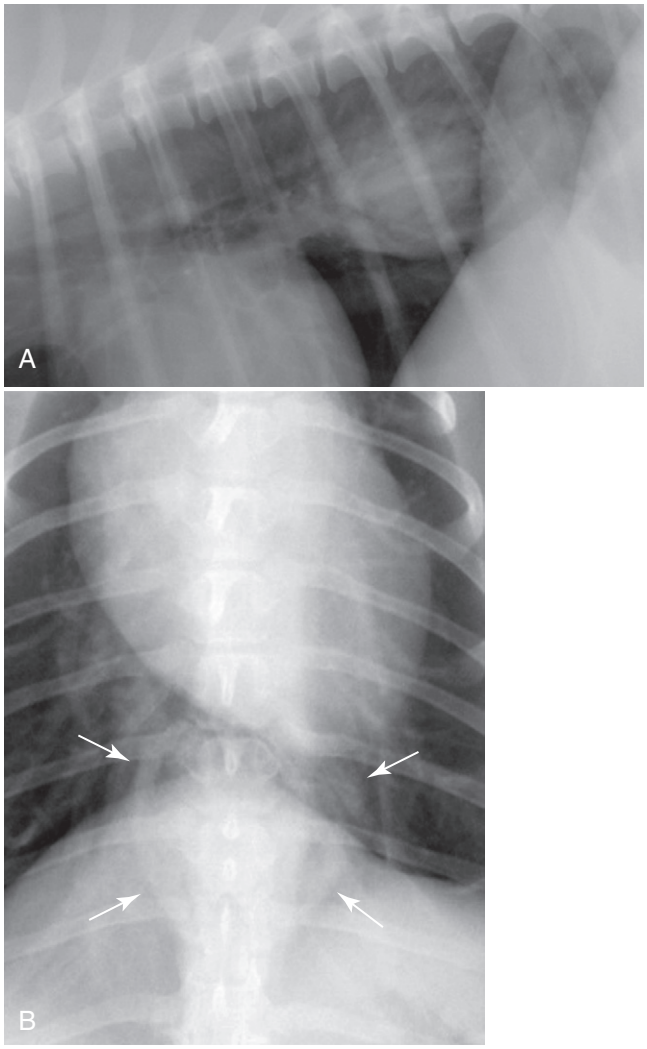


Fig. 27-22 **A,** Lateral thoracic radiograph of a 4-year-old Chihuahua. There is a soft tissue mass in the caudodorsal aspect of the thorax between the aorta and caudal vena cava with its caudal border superimposed with the diaphragm. Based on this appearance, the considerations are esophageal foreign body, esophageal mass, paraesophageal hernia, or pulmonary mass. **B,** VD radiograph of the same dog. The mass is on the midline *(white arrows)*, making a pulmonary mass unlikely. Endoscopy was performed, and a hard, cartilaginous foreign body was removed.

material, such as bones or metal, is recognized easily compared with nonradiopaque material, such as plastic and cartilage, which appears as a focal soft tissue opacity in the region of the esophagus (Fig. 27-22). A nonopaque esophageal foreign body may appear similar to an esophageal neoplasm, an esophageal abscess, mediastinal mass, paraesophageal hernia, or lung mass (see Fig. 27-22). A static contrast esophagram can help to differentiate these conditions. Contraindications for a barium swallow include survey radiographic evidence of pneumothorax, pneumomediastinum, and pleural fluid, which are signs of potential esophageal perforation (Fig. 27-23).

VASCULAR RING ANOMALIES

Under normal conditions, the aorta is derived from the left fourth aortic arch while the right fourth aortic arch typically regresses. Anomalous development of the aortic arches can lead to secondary esophageal construction. Esophageal

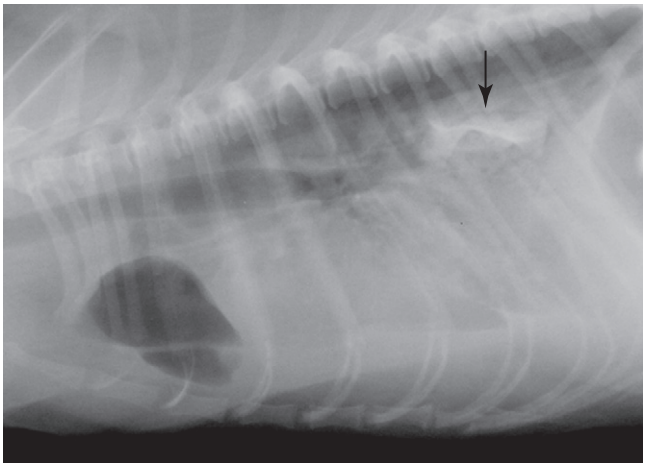


Fig. 27-23 Right lateral radiograph of a dog with a bone lodged in the caudal aspect of the esophagus *(black arrow)*. There is also pleural fluid and pneumothorax. A barium esophagram should not be done in this situation because of the high likelihood of esophageal perforation. If an esophagram is necessary, water-soluble contrast medium should be used.

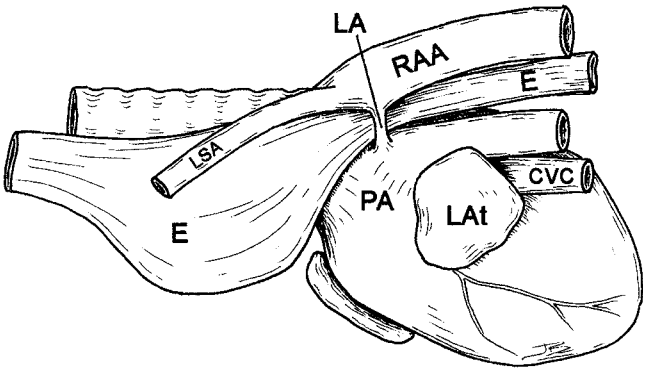


Fig. 27-24 Schematic of persistent right aortic arch. This view from the left shows the ligamentum arteriosus *(LA)* connecting the descending right aortic arch *(RAA)* to the main pulmonary artery *(PA)* causing constriction of the esophagus *(E)* between these structures and the heart base. *CVC*, Caudal vena cava; *Lat*, left atrium; *LSA*, left subclavian artery. (Figure courtesy of Dr. Barbara Watrous, DACVR.)

compression secondary to a vascular malformation is termed *vascular ring anomaly*. Of the seven types of vascular ring anomalies that are described, types I through III have a persistent right aortic arch, type IV has a double aortic arch, and types V through VII have a left aortic arch with combinations of persistent right ligamentum arteriosum and right subclavian arteries, all of which cause entrapment of the esophagus.[20-22]

Development of the aortic arch from the right fourth aortic arch with regression of the left fourth aortic arch, termed *persistent right fourth aortic arch*, is the most common vascular ring anomaly that leads to entrapment of the esophagus. In the normal situation where the aorta is derived from the left fourth arch, the aorta, main pulmonary artery, and interconnecting ligamentum arteriosum are all on the left side of the trachea and esophagus.[20] When the aorta is derived from the right fourth aortic arch rather than the left, the aorta is on the right side of the trachea and esophagus while the main pulmonary artery is on the left side. In this configuration, the ligamentum arteriosum constricts the esophagus against the trachea and base of the heart as it passes from right (aorta) to left (pulmonary artery) (Fig. 27-24). The constriction results in esophageal dilation cranial to the base of the heart. Survey radiographs may be normal if the esophagus is not dilated, but this is unusual. The dilated portion of the esophagus cranial

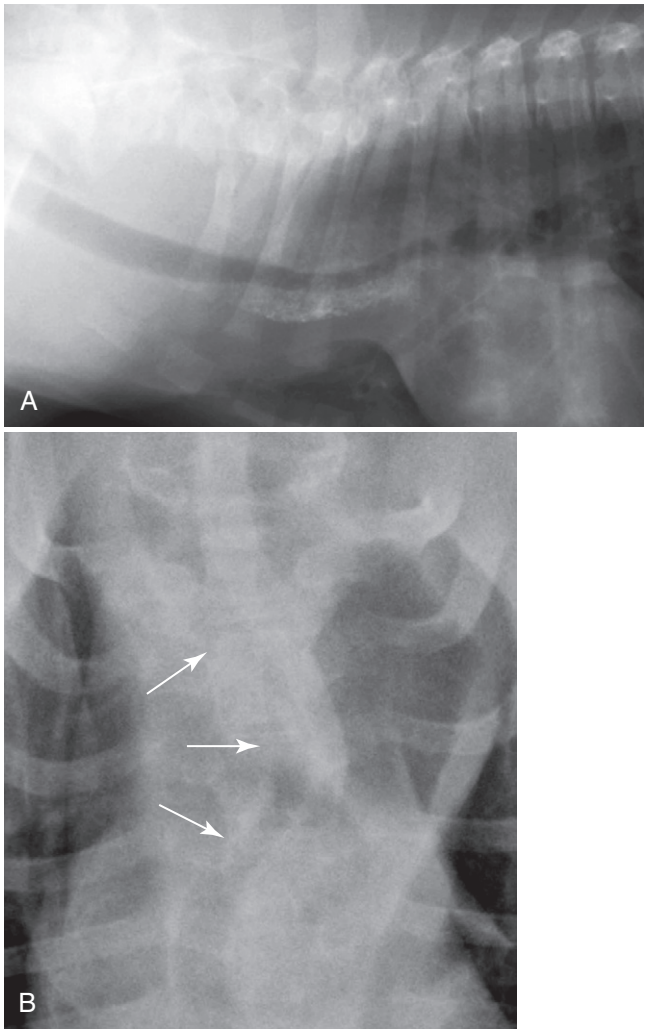


Fig. 27-25 **A,** Lateral thoracic radiograph of a 2-month-old German shepherd with a persistent right fourth aortic arch. The thoracic trachea is displaced ventrally, and there is a superimposed mottled mineral opacity because of foreign material in the enlarged esophageal segment cranial to the heart base. The caudal thoracic esophagus appeared normal. **B,** VD radiograph of the same dog. The trachea is displaced to the left *(white arrows)*.

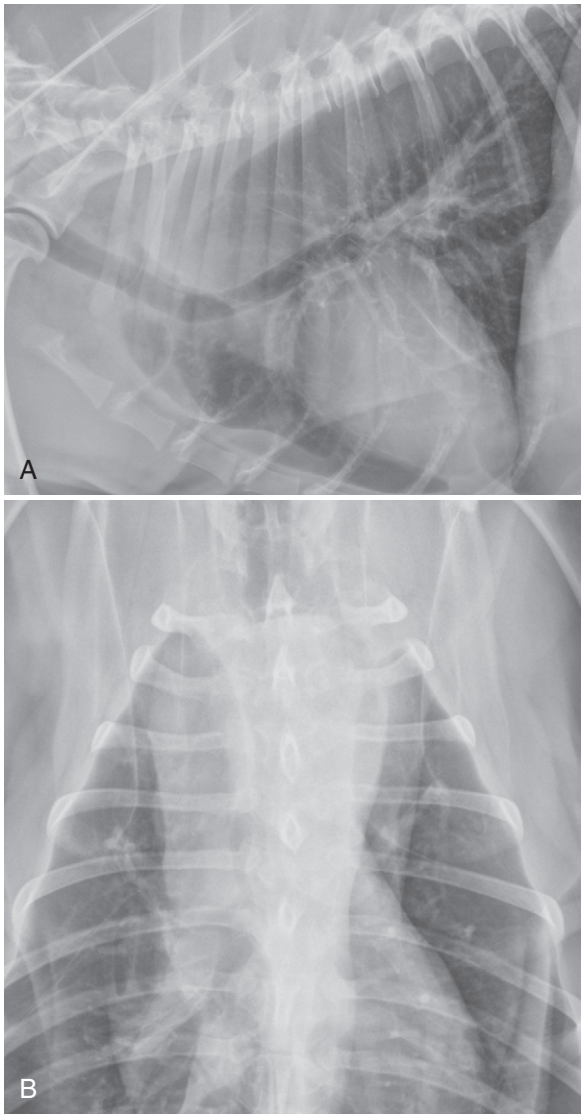


Fig. 27-26 Lateral **(A)** and DV **(B)** radiographs of a dog with a persistent right fourth aortic arch. There is dilatation of the cranial aspect of the thoracic esophagus that causes ventral displacement of the trachea. In the DV view, there is a mass effect in the cranial mediastinum. The caudal aspect of the thorax is normal.

to the heart base creates a mass effect that contains air and/or ingesta and usually displaces the trachea ventrally (Figs. 27-25 and 27-26), although occasionally the enlarged esophagus will slide laterally and become positioned ventral to the trachea (Fig. 27-27). In some dogs it will be possible to see the trachea being deviated focally toward the left on VD projections (see Fig. 27-25), and the normal left lateral margin of the aorta may not be evident. In a static barium esophagram, the stricture at the heart base can be confirmed (see Fig. 27-27). Videofluoroscopy should always be performed in patients with a persistent right fourth aortic arch because esophageal dysfunction caudal to the stricture at heart base is often present; this will influence the degree of resolution of clinical signs if the vascular ring is corrected surgically. A persistent left cranial vena cava can accompany persistent right fourth aortic arch and is important from the perspective of the abnormal left vena cava being recognized at the heart base when a left-thoracotomy is performed to correct the vascular ring constriction.[23]

An aberrant right subclavian artery can also lead to a vascular ring compression of the esophagus. Normally, the right subclavian artery branches from the brachiocephalic trunk but may instead arise directly from the aortic arch, distal to the origin of the left subclavian artery. The right subclavian artery then crosses over the dorsal aspect of the esophagus as it travels from the left side of the median plane, where the normal aortic arch resides, to supply the right forelimb (Figs. 27-28 and 27-29). The site of compression caused by an aberrant subclavian artery is usually more cranial than that caused by a persistent right fourth aortic arch (see Fig. 27-29), and the compression may not be as severe because the esophagus is not trapped against a solid organ ventrally as it is with persistent right fourth aortic arch.

INFLAMMATORY DISEASES

Esophagitis

Esophagitis can result from infection, ingestion of hot or corrosive substances, vomiting, gastroesophageal reflux, megaesophagus, and foreign body obstructions. Survey radiography is usually unremarkable in patients with esophagitis. Aspiration pneumonia can be identified, but the diagnosis of esophagitis usually requires endoscopy. The esophagus may be

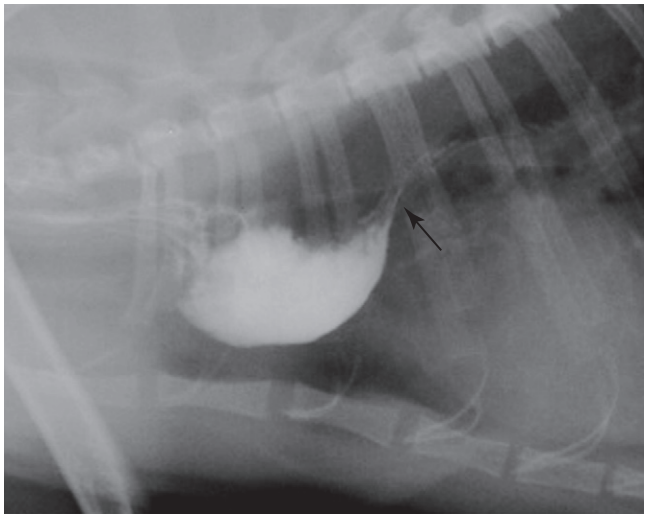


Fig. 27-27 Lateral radiograph of a barium esophagram in an 11-month-old cat with a persistent right fourth aortic arch. A focal dilatation and ventral displacement of the esophagus is present between the thoracic inlet and heart. The contrast column tapers off and narrows at the heart base *(black arrow)* because of the vascular ring constriction.

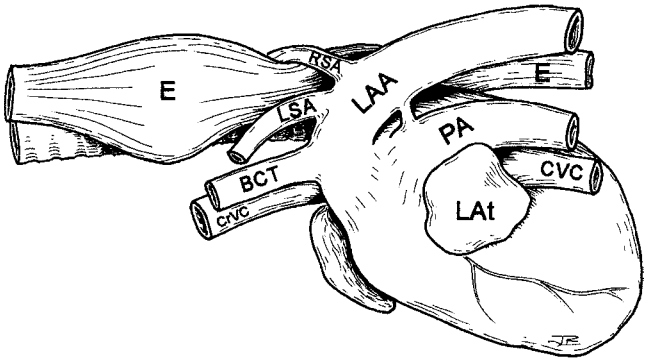


Fig. 27-28 Schematic of aberrant right subclavian artery. This view, from the left side, shows the right subclavian artery *(FSA)* arising from the left-sided aortic arch *(LAA)* and coursing over the top of the esophagus *(E)*, causing compression of the esophagus. *BCT,* Brachiocephalic trunk; *CrVC,* cranial vena cava; *LAt,* left atrium; *LSA,* left subclavian artery; *PA,* pulmonary artery. (Figure courtesy of Dr. Barbara Watrous, DACVR.)

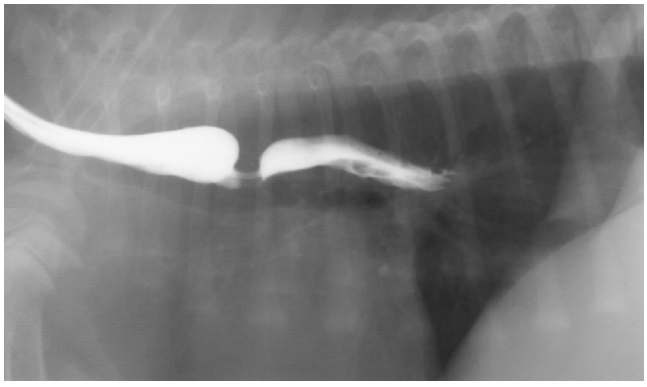
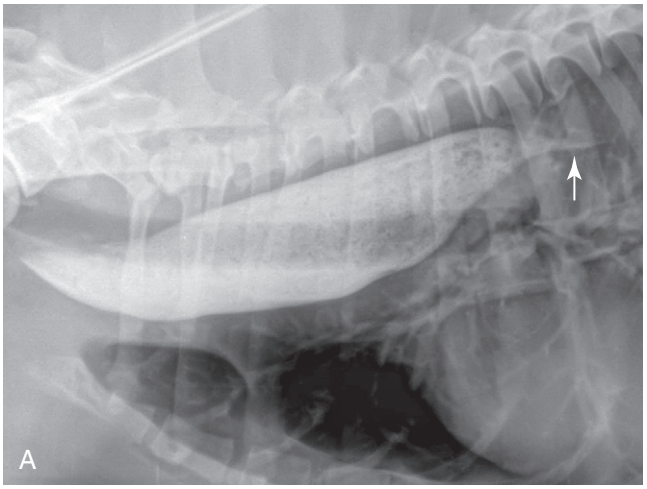


Fig. 27-29 Barium esophagram in a dog with esophageal compression caused by an aberrant right subclavian artery. The indentation in the dorsal aspect of the esophagus results from the compression created by the right subclavian artery passing dorsal to the esophagus as it courses from the left-sided aortic arch to the right forelimb.



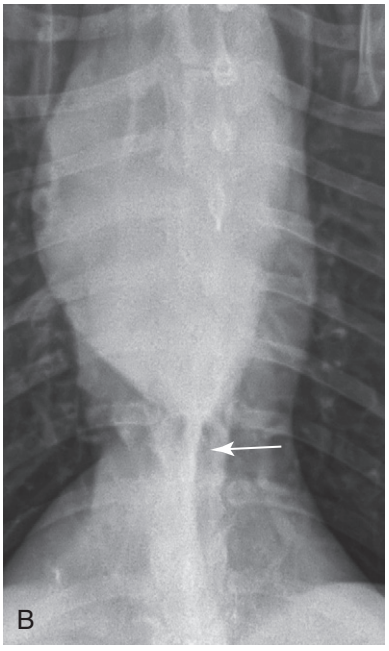


Fig. 27-30 **A,** Lateral radiograph of a barium swallow in a 3.5-year-old, Siberian husky with an esophageal stricture. There is dilatation of the esophagus cranial to the carina that tapers smoothly caudally at the site of the stricture *(white arrow)*. No contrast medium entered the caudal esophagus. **B,** VD radiograph of the same dog. The dilated, barium-filled esophagus tapers to a narrow point just caudal to the base of the heart *(white arrow)*.

dilatated with gas or fluid but this is a nonspecific finding. Ulcerations, motility disorders, or mechanical obstruction secondary to inflammation require contrast procedures to be characterized further. If severe esophagitis is present, then segmental narrowing, irregular mucosal contours, indistinct folds of the esophageal wall, and thickening of the wall may be present in static barium contrast studies. Fluoroscopic contrast studies may be characterized by segmental spasticity and minor dilation. Gastroesophageal reflux may be identified with videofluoroscopy (see Video 27-8 on the Evolve website).

Strictures

Esophageal strictures are usually secondary to a foreign body or gastroesophageal reflux. Esophageal strictures thought to be related to gastroesophageal reflux during anesthesia are usually located at the caudal portion of the thoracic esophagus, caudal to the base of the heart.[24] Strictures of the esophagus typically have a smoothly bordered, tapered appearance caudally (Fig. 27-30). Survey radiography may be

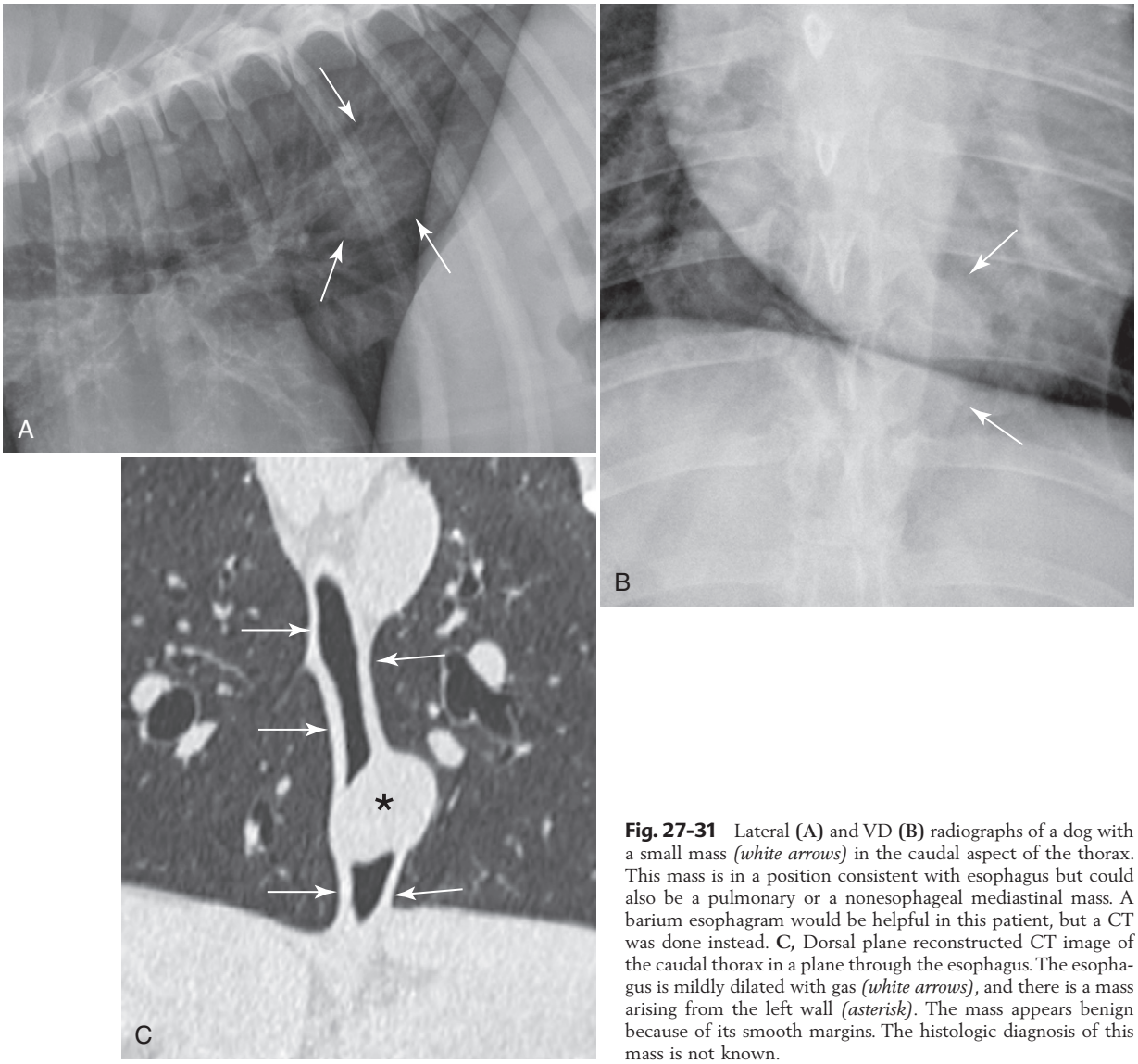


Fig. 27-31 Lateral **(A)** and VD **(B)** radiographs of a dog with a small mass *(white arrows)* in the caudal aspect of the thorax. This mass is in a position consistent with esophagus but could also be a pulmonary or a nonesophageal mediastinal mass. A barium esophagram would be helpful in this patient, but a CT was done instead. **C,** Dorsal plane reconstructed CT image of the caudal thorax in a plane through the esophagus. The esophagus is mildly dilated with gas *(white arrows)*, and there is a mass arising from the left wall *(asterisk)*. The mass appears benign because of its smooth margins. The histologic diagnosis of this mass is not known.

unremarkable, or there may be segmental or generalized dilatation of the esophagus, depending on the site and extent of the stricture. Contrast esophagraphy is used to determine the location, size, and length of the stricture for treatment planning (see Fig. 27-30). Moreover, the contrast study helps to determine if the stricture is mural, extramural, or luminal. Smoothly bordered mucosal surfaces outlined with contrast medium and having a circumferential narrowing on lateral and VD projections is the typical appearance of a mural stenosis caused by chronic inflammation or scarring. An irregularly bordered mucosal surface can be seen with neoplastic infiltration of the wall or severe ulceration because of inflammation. Extramural compressions have a smoothly bordered contrast column that is convex and tapering toward the narrowing in one projection with the narrowed portion appearing widened in the orthogonal projection. Thyroid masses, enlarged lymph nodes, and cervical abscesses can impinge on or invade the cervical esophagus causing obstruction. If liquid barium passes through the narrowed region or no abnormality is seen, then barium-soaked kibble can be used to demonstrate a larger-sized stricture that allows fluid but not solids to pass.

Esophageal neoplasms are rare in dogs and cats. Osteosarcoma and fibrosarcoma of the esophagus is reported in areas endemic for *Spirocerca lupi*.[25] Squamous cell carcinoma, adenocarcinoma, branchioma, branchial cleft cysts, papilloma, and leiomyosarcoma have also been reported but are rare.[26-29] If the neoplasm is large enough, it may be recognized on survey radiographs as a soft tissue mass associated with the esophagus (Fig. 27-31). The esophagus may be dilatated cranial to the mass, but this is not always present. Differentiation of many esophageal masses from an esophageal foreign body or a nonesophageal mass may require esophagraphy, CT, or endoscopy (see Fig. 27-31). Dystrophic mineralization of esophageal masses is rare, but its presence can be associated with neoplasia, *Spirocerca* infection, or oral administration of radiopaque medication. Esophageal dilation cranial to an esophageal mass may also be present. A static esophagram is helpful in characterizing esophageal masses further. Obstruction or stenosis at the tumor site, mucosal irregularity caused by infiltration and ulceration, and/or the location and extent of the infiltration can be evaluated. Temporary or persistent retention of barium may occur because of lack of secondary

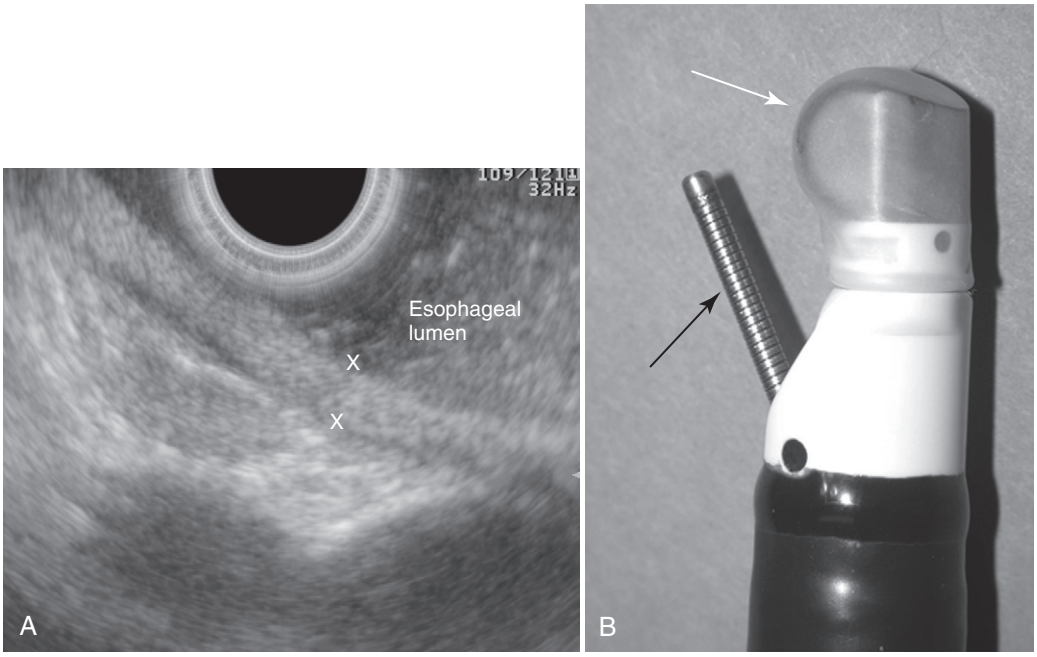


Fig. 27-32 **A,** Endoscopic esophageal ultrasound image in a normal dog. The normal esophageal wall, between the calipers, has a uniform and echogenic appearance. **B,** Ultrasound endoscope (Olympus GF-UC140-AL5, Olympus Optical, Hamburg, Germany). The scope has a linear transducer array arranged in a 180-degree arc for good near-field resolution. The working channel for interventional catheters and biopsy devices *(black arrow)* is extended. A balloon *(white arrow)* covers the transducer tip and can be filled with water to act as a standoff for better imaging of structures adjacent to the surface of the probe.

peristalsis where the wall is stiffened because of tumor infiltration. Mural thickening, asymmetry of the lumen, absence of the mucosal folds, ulceration of the mucosa with barium retention, and a locally enlarged or dilatated esophagus are suggestive of neoplasia.

Endoscopic ultrasound is an alternate imaging modality that can be used to examine the esophagus under general anesthesia and in conjunction with conventional endoscopy (Figs. 27-32 and 27-33).

Infection of dogs and other carnivores with the nematode *S. lupi* occurs in tropical and subtropical regions throughout the world.[30] The parasite infects mainly the esophagus and aorta, leading to gastrointestinal, respiratory, and circulatory signs.[31] In survey radiographs there may be a mediastinal mass in the region of the caudal thoracic esophagus because of granuloma formation (Fig. 27-34). The inflammatory esophageal mass can become neoplastic, with osteosarcoma and fibrosarcoma being reported. There may be new bone formation on the ventral aspect of thoracic vertebrae dorsal to the mass and also enlargement of the descending aorta.[4,32] *S. lupi* has also caused spinal cord chondrosarcoma.[33] Radiographic abnormalities of the aorta are rare, but dilatation of the proximal descending aorta and aortic mineralization have been reported. In spirocercosis-endemic areas, dorsoventral and right lateral projections are recommended because they also allow for better visualization of descending aortic aneurysms and prevent interpreting the potentially normally visible esophagus in left lateral images as a mass.[34] However, as noted in Chapter 25, obtaining both left and right lateral views of the thorax should be routine procedure. Contrast studies of the esophagus confirm the granuloma to be originating from the esophagus and are usually characterized by an irregular mucosal border with outpouchings and filling defects. Endoscopy provides similar information, and the parasite may be visualized directly in some dogs.[35] CT provides information in confirming nonesophageal or extraesophageal masses to be spirocercosis-related because of earlier detection of aortic mineralization and spondylitis.[35]

DIVERTICULA, PERFORATION, AND FISTULA FORMATION

Esophageal diverticula are pouches of variable size that are either acquired or congenital. The acquired form is caused by a thinning of the esophageal wall that allows it to bulge. Causes include esophagitis, strictures, ulceration from a foreign body, vascular ring anomaly, hiatal hernia, parasites, and periesophageal inflammation. Esophageal diverticula can be classified as either pulsion or traction types. Increased intraluminal pressure from a foreign body or chronic functional obstruction can cause a pulsion diverticulum. Pulsion diverticula are located most commonly between the heart and diaphragm. Traction diverticula are formed because of adhesions on the esophageal wall and are often located in the cranial and midthoracic esophagus.

With an esophageal diverticulum, survey radiographs are characterized by a circumscribed soft tissue mass or outpouching of the esophagus, impacted ingesta, or a mixed gas and soft tissue content (Fig. 27-35). Following survey radiography, further imaging may include endoscopy, CT, or contrast esophagraphy. Contrast-medium retention in the outpouching on serial radiographs helps to confirm the diagnosis. Endoscopy is indicated to fully assess the mucosal lining and the size of the opening into the diverticulum for surgical planning.

Perforation of the esophagus occurs either acutely because of a sharp foreign body or chronically because of slow pressure necrosis from a foreign body or neoplasia.[36] Perforations can communicate with the mediastinum and/or the pleural space. Bony foreign bodies, a bodyweight of less than 10 kg, and esophageal foreign body present for more than 3 days are considered significant risk factors for complications.[37]

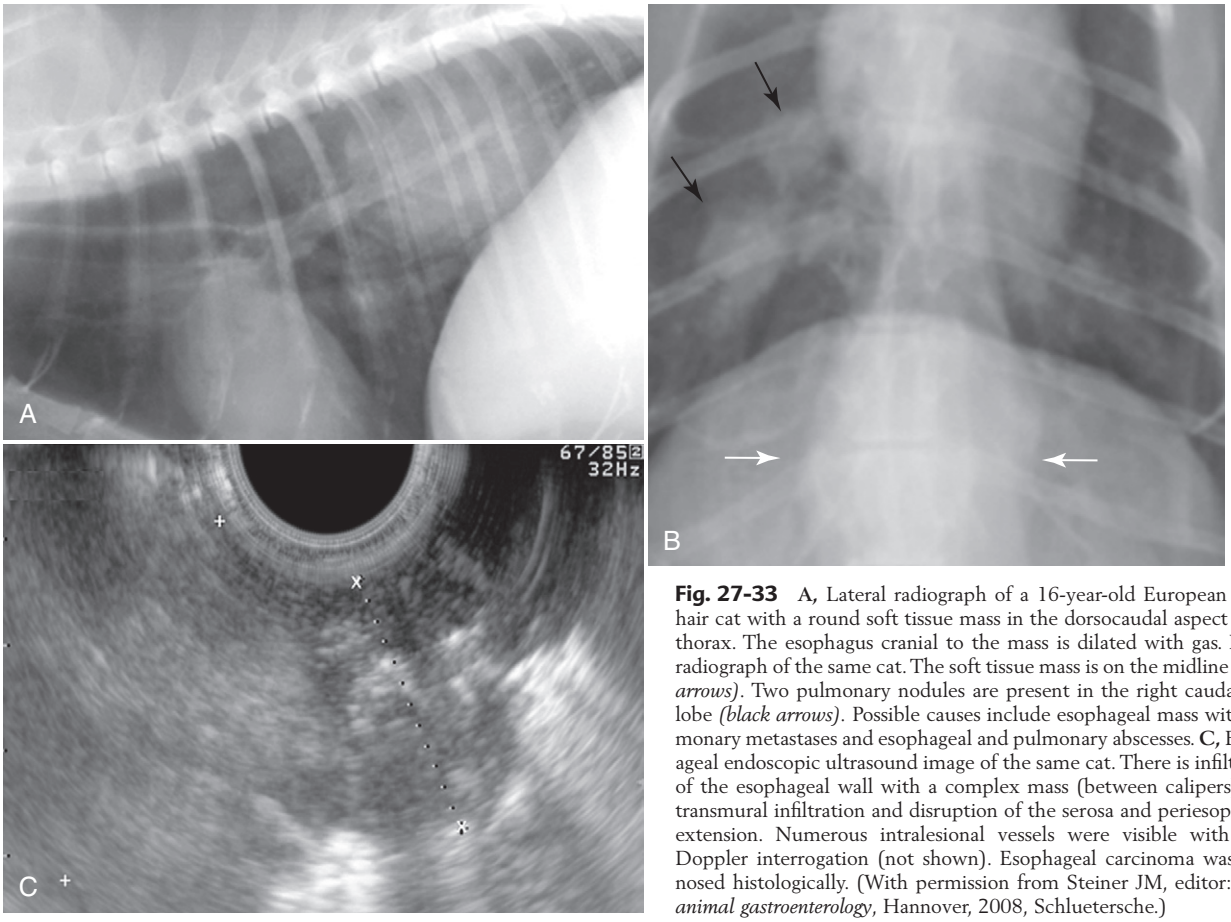


Fig. 27-33 **A,** Lateral radiograph of a 16-year-old European shorthair cat with a round soft tissue mass in the dorsocaudal aspect of the thorax. The esophagus cranial to the mass is dilated with gas. **B,** VD radiograph of the same cat. The soft tissue mass is on the midline *(white arrows)*. Two pulmonary nodules are present in the right caudal lung lobe *(black arrows)*. Possible causes include esophageal mass with pulmonary metastases and esophageal and pulmonary abscesses. **C,** Esophageal endoscopic ultrasound image of the same cat. There is infiltration of the esophageal wall with a complex mass (between calipers) with transmural infiltration and disruption of the serosa and periesophageal extension. Numerous intralesional vessels were visible with color Doppler interrogation (not shown). Esophageal carcinoma was diagnosed histologically. (With permission from Steiner JM, editor: *Small animal gastroenterology*, Hannover, 2008, Schluetersche.)

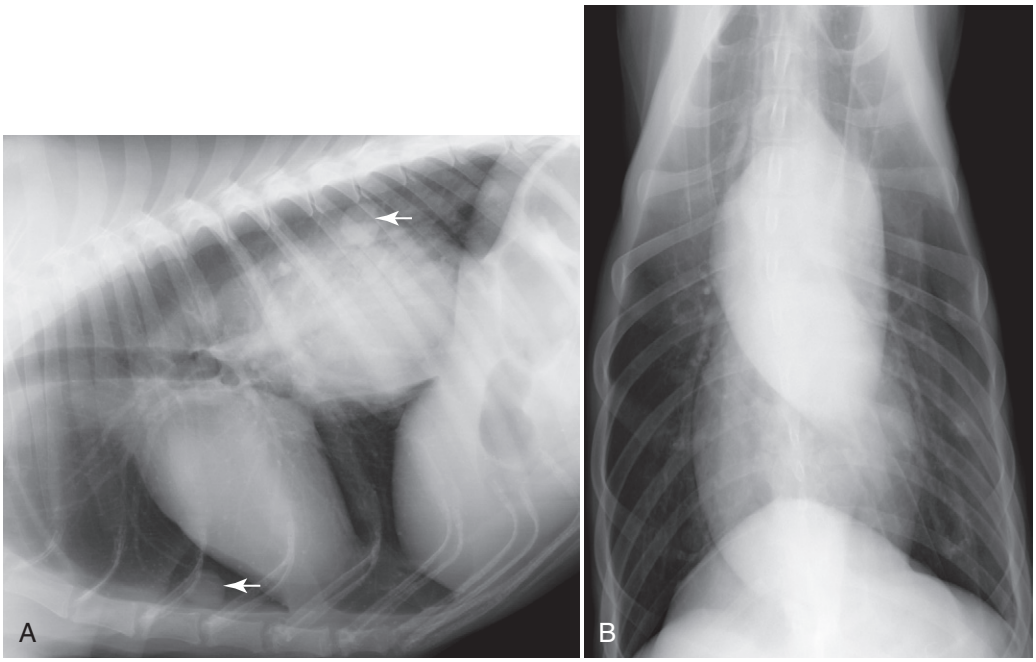


Fig. 27-34 **A,** Right lateral thoracic radiograph of a 2-year-old dog. There is a large mass caused by *Spirocerca lupi* infection in the region of the caudal esophagus. Several lung nodules are present *(white arrows)*. The lung nodules suggest malignant transformation of the esophageal mass with secondary pulmonary metastasis. **B,** VD radiograph of same dog. The mass is midline, and the aorta is not visible. (Image courtesy of the Department of Companion Animal Clinical Sciences, Faculty of Veterinary Science, University of Pretoria.)

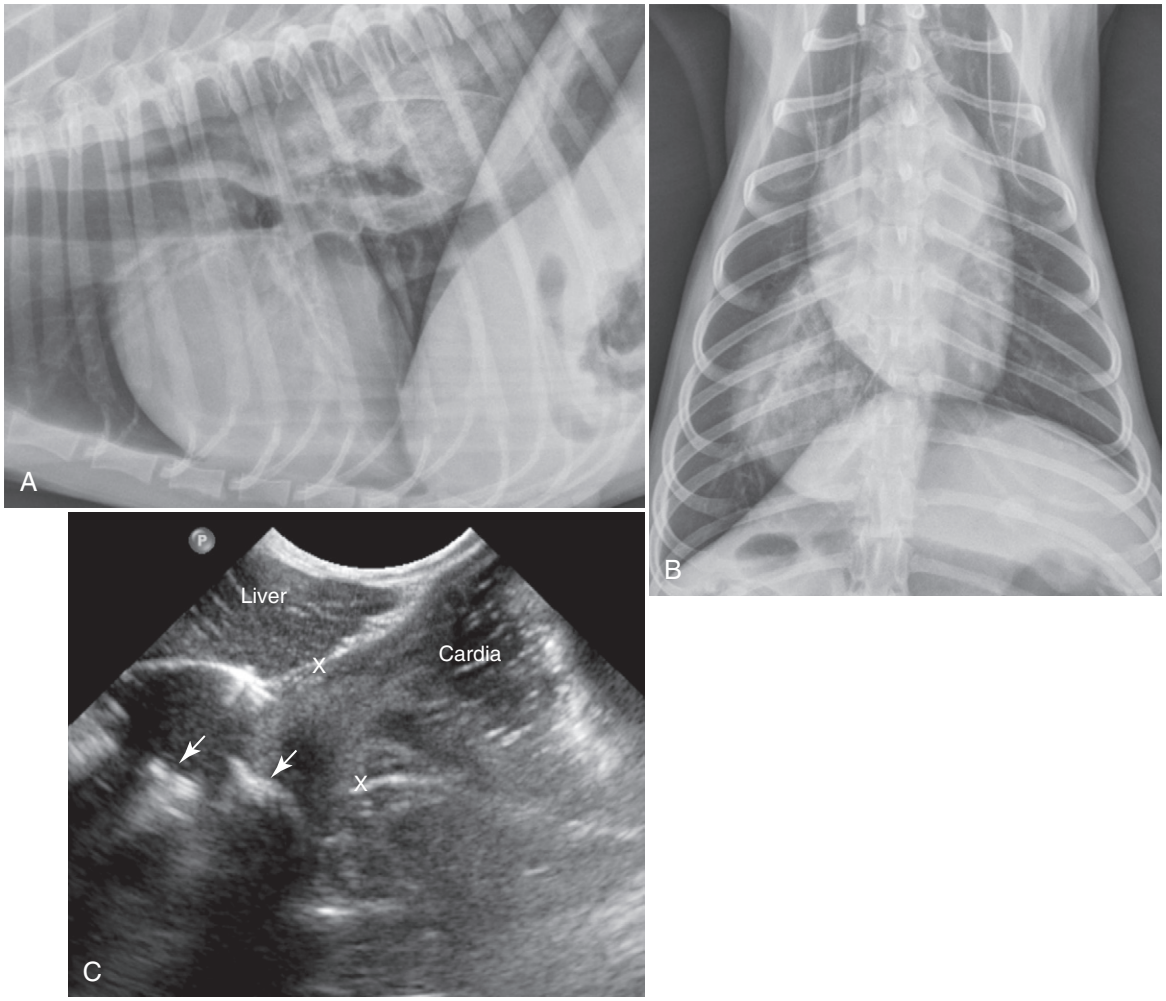


Fig. 27-35 **A,** Lateral radiograph of an 8-year-old Papillon. There is a mixed soft tissue and mineral opacity between the aorta and caudal vena cava in the caudodorsal aspect of the thorax. **B,** VD radiograph of the same dog. There is a large, right-sided mixed soft tissue and mineral opaque mass with a sharply defined right lateral border at the midline and to the right of the spine. An esophageal diverticulum containing bony foreign material was suspected. **C,** Ultrasound image of the same dog. The probe is positioned at the ventral midline pointing cranially and to the left to visualize the diaphragm and esophageal hiatus (calipers). The esophagus is dilatated at the hiatus and multiple linear, hyperechoic shadowing structures *(white arrows)* and mixed echogenic fluid can be seen filling the caudal esophagus.

Complication rates of esophageal foreign bodies are reported to be 12.7% and include perforation, stricture, diverticula, periesophageal abscess, pneumothorax, pleural effusion, and respiratory arrest.[37] Cervical perforations have a better prognosis than thoracic perforations because of the development of septic mediastinitis, pleuritis, and pyothorax. Radiographically, mediastinal widening caused by inflammation or abscess formation, pneumomediastinum, and extension of gas along the fascial planes of the neck, pneumothorax, and pleural effusion may be present (Fig. 27-36; see Fig. 27-23). Pleural fluid analysis, thoracic ultrasound, or thoracic CT may be warranted to determine the source of pleural fluid or pneumomediastinum and to best assess the mediastinal structures before administering contrast medium. An esophageal contrast study with water-soluble contrast medium can be considered to confirm the perforation. However, water-soluble contrast medium may have poor adherence to devitalized tissue, may not coat the foreign material, and may even bypass an obstruction, giving a false negative diagnosis.

Esophageal fistulas can be congenital or acquired.[38] Congenital forms are typically bronchoesophageal communications, but tracheoesophageal communications also occur.[39]



Fig. 27-36 Lateral cervical radiograph in a dog with acute ptyalism and vocalizing. Linear gas opacities are present dorsal to the cricopharyngeal sphincter and trachea. Perforating wood splinters were found on inspection of the mouth.

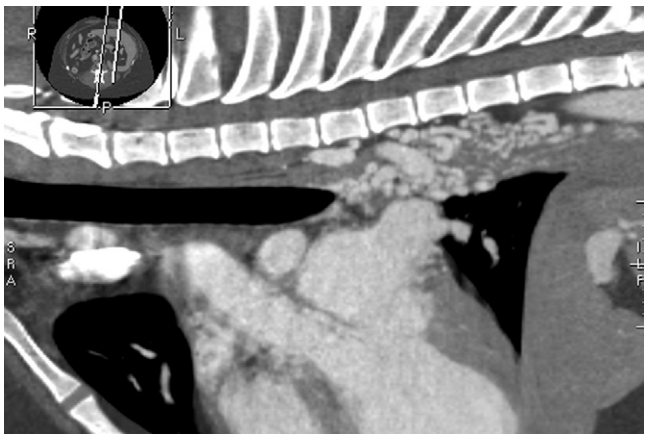


Fig. 27-37 Sagittal plane reconstruction of a CT image of a dog with esophageal varices caused by portal hypertension. (Image courtesy of Dr. Giovanna Bertolini, Clinica Veterinaria San Marco.)

Acquired forms are typically due to esophageal perforation resulting in communication with the airways of the trachea or lung.[40] Survey radiographs may be characterized by an ill-defined soft tissue or mixed pulmonary opacity. The diagnosis of an esophageal fistula relies upon demonstrating a communication between the esophagus and the airway with contrast medium. A swallow with liquid barium will usually show the communication from the esophagus into the airway via a fistula's tract. Bronchoscopy can also be used to make the diagnosis.

ESOPHAGEAL VARICES

Esophageal and paraesophageal varices may result from portal hypertension that generates reversal of portal blood flow, which diverts venous blood in a cranial direction through the left gastric vein to the venous plexus of the esophagus.[41] Obstructions of the cranial vena cava can also lead to the formation of esophageal and paraesophageal varices. The varices can drain into the azygos vein, the caudal vena cava, or into the portal system, depending on the site of the obstruction. Gallbladder and choledochal varices, omental varices, duodenal varices, phrenicoabdominal varices, colic varices, and abdominal wall varices drain into the caudal vena cava and result from portal hypertension. CT angiography is necessary for determining the origin, course, and termination of these vessels, and their underlying cause (Fig. 27-37).

REFERENCE LIST

1. Suter PF: Swallowing problems and esophageal abnormalities. In Suter PF, editor: *Thoracic radiography: thoracic diseases of the dog and cat*, ed 1, Switzerland Wettswil, 1984, Peter F. Suter, pp 295–349.
2. Rudorf H, Taeymans O, Johnson V: Basics of thoracic radiography and radiology. In Schwarz T, Johnson V, editors: *BSAVA manual of canine and feline thoracic imaging*, ed 1, Gloucester, 2008, British Small Animal Veterinary Association, pp 1–19.
3. Hoskinson JJ, Bahr A, Lora-Michiels M: Gastrointestinal nuclear medicine. In Daniel GB, Berry CR, editors: *Textbook of veterinary nuclear medicine*, ed 2, Harrisburg, Penn, 2006, American College of Veterinary Radiology, pp 290–292.
4. Gaschen L, Kircher P, Lang J: Endoscopic ultrasound instrumentation, applications in humans, and potential veterinary applications, *Vet Radiol Ultrasound* 44(6):665–680, 2003.
5. Evans HE: The digestive apparatus and abdomen. In Evans HE, editor: *Miller's anatomy of the dog*, ed 3, Philadelphia, 1993, Saunders, pp 422–425.
6. Suter PF, Watrous BJ: Oropharyngeal dysphagia in the dog: a cinefluorographic analysis of experimentally induced and spontaneously occurring swallowing disorders; I. Oral stage and pharyngeal stage dysphagias, *Vet Radiol Ultrasound* 21(1):24–39, 1980.
7. Wallack ST: Static barium esophagram. In Wallack ST, editor: *The handbook of veterinary contrast radiography*, ed 1, Solana Beach, Calif, 2003, San Diego Veterinary Imaging, pp 45–53.
8. Bonadio CM, Pollard RE, Dayton PA, et al: Effects of body positioning on swallowing and esophageal transit in healthy dogs, *J Vet Intern Med* 23(4):801–805, 2009.
9. Pollard RE, Marks SL, Leonard R, et al: Preliminary evaluation of the pharyngeal constriction ratio (PCR) for fluoroscopic determination of pharyngeal constriction in dysphagic dogs, *Vet Radiol Ultrasound* 48(3):221–226, 2007.
10. Twedt DC: Diseases of the esophagus. In Ettinger SJ, editor: *Textbook of veterinary internal medicine*, ed 4, Philadelphia, 1995, Saunders, pp 1124–1141.
11. Watrous BJ: Clinical presentation and diagnosis of dysphagia, *Vet Clin North Am Small Anim Pract* 13(3):437–459, 1983.
12. Pollard RE, Marks SL, Davidson A, et al: Quantitative videofluoroscopic evaluation of pharyngeal function in the dog, *Vet Radiol Ultrasound* 41(5):409–412, 2000.
13. Stanley BJ, Hauptman JG, Fritz MC, et al: Esophageal dysfunction in dogs with idiopathic laryngeal paralysis: a controlled cohort study, *Vet Surg* 39(2):139–149, 2010.
14. Bexfield NH, Watson PJ, Herrtage ME: Esophageal dysmotility in young dogs, *J Vet Intern Med* 20(6):1314–1318, 2006.
15. Diamant N, Szczepanski M, Mui H: Idiopathic megaesophagus in the dog: reasons for spontaneous improvement and a possible method of medical therapy, *Can Vet J* 15(3):66–71, 1974.
16. Leib MS: Megaesophagus. In Bojrab MJ, editor: *Disease mechanisms in small animal surgery*, ed 2, Philadelphia, 1993, Lea & Febiger, pp 205–209.
17. Guilford WG, Strombeck DR: Diseases of swallowing. In Guilford WG, Center SA, Strombeck DR, et al, editors: *Strombeck's small animal gastroenterology*, ed 3, Philadelphia, 1996, Saunders, pp 211–238.
18. Callan MB, Washabau RJ, Saunders HM, et al: Congenital esophageal hiatal hernia in the Chinese shar-pei dog, *J Vet Intern Med* 7(4):210–215, 1993.
19. Houlton JEF, Herrtage ME, Taylor PM, et al: Thoracic esophageal foreign bodies in the dog: a review of ninety-cases, *J Small Anim Pract* 26:521–536, 1985.
20. Helphrey M: Vascular ring anomalies. In Bojrab MJ, editor: *Disease mechanisms in small animal surgery*, ed 2, Philadelphia, 1993, Lea & Febiger, pp 350–354.
21. Holt D, Heldmann E, Michel K, et al: Esophageal obstruction caused by a left aortic arch and an anomalous right patent ductus arteriosus in two German shepherd littermates, *Vet Surg* 29(3):264–270, 2000.
22. Hurley K, Miller MW, Willard MD, et al: Left aortic arch and right ligamentum arteriosum causing esophageal obstruction in a dog, *J Am Vet Med Assoc* 203(3):410–412, 1993.
23. Larcher T, Abadie J, Roux FA, et al: Persistent left cranial vena cava causing oesophageal obstruction and consequent megaoesophagus in a dog, *J Comp Pathol* 135(2-3):150–152, 2006.

24. Adamama-Moraitou KK, Rallis TS, Prassinos NN, et al: Benign esophageal stricture in the dog and cat: a retrospective study of 20 cases, *Can J Vet Res* 66(1):55–59, 2002.
25. Dvir E, Clift SJ, Williams MC: Proposed histological progression of the *Spirocerca lupi*-induced oesophageal lesion in dogs, *Vet Parasitol* 168(1-2):71–77, 2010.
26. Gibson CJ, Parry NMA, Jakowski RM, et al: Adenomatous polyp with intestinal metaplasia of the esophagus (Barrett esophagus) in a dog, *Vet Pathol* 47(1):116–119, 2010.
27. Wray JD, Blunden AS: Progressive dysphagia in a dog caused by a scirrhous, poorly differentiated perioesophageal carcinoma, *J Small Anim Pract* 47(1):27–30, 2006.
28. Ranen E, Shamir MH, Shahar R, et al: Partial esophagectomy with single layer closure for treatment of esophageal sarcomas in 6 dogs, *Vet Surg* 33(4):428–434, 2004.
29. Gualtieri M, Monzeglio MG, Di Giancamillo M: Oesophageal squamous cell carcinoma in two cats, *J Small Anim Pract* 40(2):79–83, 1999.
30. Fisher MM, Morgan JP, Krecek RC, et al: Radiography for the diagnosis of spirocercosis in apparently healthy dogs, St. Kitts, West Indies, *Vet Parasitol* 160(3-4):337–339, 2009.
31. Harrus S, Harmelin A, Markovics A, et al: *Spirocerca lupi* infection in the dog: aberrant migration, *J Am Anim Hosp Assoc* 32(2):125–130, 1996.
32. Berry WL: *Spirocerca lupi* esophageal granulomas in 7 dogs: resolution after treatment with doramectin, *J Vet Intern Med* 14(6):609–612, 2000.
33. Lindsay N, Kirberger R, Williams M: Imaging diagnosis-spinal cord chondrosarcoma associated with spirocercosis in a dog, *Vet Radiol Ultrasound* 51(6):614–616, 2010.
34. Kirberger RM, Dvir E, van der Merwe LL: The effect of positioning on the radiographic appearance of caudodorsal mediastinal masses in the dog, *Vet Radiol Ultrasound* 50(6):630–634, 2009.
35. Dvir E, Kirberger RM, Malleczek D: Radiographic and computed tomographic changes and clinical presentation of spirocercosis in the dog, *Vet Radiol Ultrasound* 42(2):119–129, 2001.
36. Doran IP, Wright CA, Moore AH: Acute oropharyngeal and esophageal stick injury in forty-one dogs, *Vet Surg* 37(8):781–785, *ery* 2008.
37. Gianella P, Pfammatter NS, Burgener IA: Oesophageal and gastric endoscopic foreign body removal: complications and follow-up of 102 dogs, *J Small Anim Pract* 50(12):649–654, 2009.
38. Basher AW, Hogan PM, Hanna PE, et al: Surgical treatment of a congenital bronchoesophageal fistula in a dog, *J Am Vet Med Assoc* 199(4):479–482, 1991.
39. Della Ripa MA, Gaschen F, Gaschen L, et al: Canine bronchoesophageal fistulas: case report and literature review, *Compend Contin Educ Vet* 32(4):E1–E10, 2010.
40. Dodman NH, Baker GJ: Tracheo-oesophageal fistula as a complication of an oesophageal foreign body in the dog—a case report, *J Small Anim Pract* 19(5):291–296, 1978.
41. Bertolini G: Acquired portal collateral circulation in the dog and cat, *Vet Radiol Ultrasound* 51(1):25–33, 2010.

ELECTRONIC RESOURCES

Evolve

Additional information related to the content in Chapter 27 can be found on the companion Evolve website at http://evolve.elsevier.com/Thrall/vetrad/

- Videos
- Chapter Quiz

CHAPTER • 28
The Thoracic Wall

Valerie F. Samii

The thoracic wall is composed of skin, fat, subcutaneous and intercostal musculature, parietal pleura, blood vessels, nerves, and lymphatics. The spine, ribs, costal cartilages, and sternum provide rigid support for the thoracic wall soft tissues. Thoracic wall abnormalities are often overlooked on initial appraisal of thoracic radiographs. Careful inspection of the extrathoracic soft tissue and bony structures is always warranted and can provide information critical to the appropriate diagnosis and treatment.

NORMAL RADIOGRAPHIC APPEARANCE

The soft tissues of the thoracic wall are normally homogeneous in opacity. In particularly obese animals, curvilinear soft tissue opacities, representing extracostal musculature outlined by fat, may be seen paralleling the lateral curvature of the ribs on dorsoventral (DV) and ventrodorsal (VD) projections (Fig. 28-1). Thirteen pairs of ribs and eight sternebral segments are normal. On the lateral projection, the first few ribs are oriented vertically but become progressively more caudoventral in orientation, from rib head to costochondral junction, in the mid to caudal aspect of the thoracic spine (Fig. 28-2). On the DV or VD projection, the first few ribs are oriented perpendicular to the spine. In the mid to caudal thoracic spine, ribs curve in a caudolateral direction from their respective vertebrae to their most lateral extent, then continue caudomedially (Fig. 28-3).

Slight differences in thoracic wall conformation are common among various canine breeds (Fig. 28-4). Breed-associated costochondral conformation leading to a misdiagnosis of pneumothorax or pleural effusion is discussed in Chapter 31.

Mineralization of the costal cartilages may be seen in young dogs and cats and is nearly always present in older animals (Fig. 28-5). Movement at the costochondral and costosternal joints increases as the costal cartilages stiffen from mineralization. This in turn results in osseous proliferation at the costochondral and costosternal joints. The opacities resulting from enlargement of these joints may be confused with lung nodules on DV or VD radiographs. Excessive costochondral or costosternal mineralization may also be confused with aggressive processes such as infection or neoplasia.

Pedunculated soft tissue opacities on the thoracic wall, such as nipples, papillomas, or engorged ticks, may summate with the pulmonary parenchyma and be misdiagnosed as pulmonary nodules. Inspection and palpation of the thoracic wall surface usually clarify the significance of this finding. The

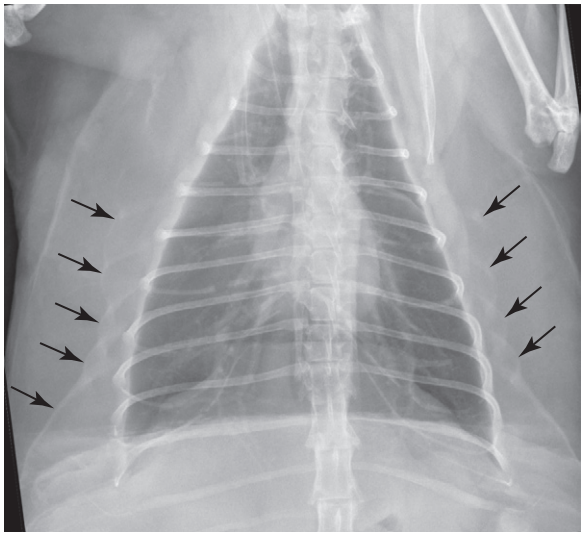


Fig. 28-1 DV thoracic radiograph of an obese cat. Note the bilateral, curvilinear, soft tissue opacities peripheral to the lateral rib margins caused by extracostal muscles interposed between fat *(black arrows)*.

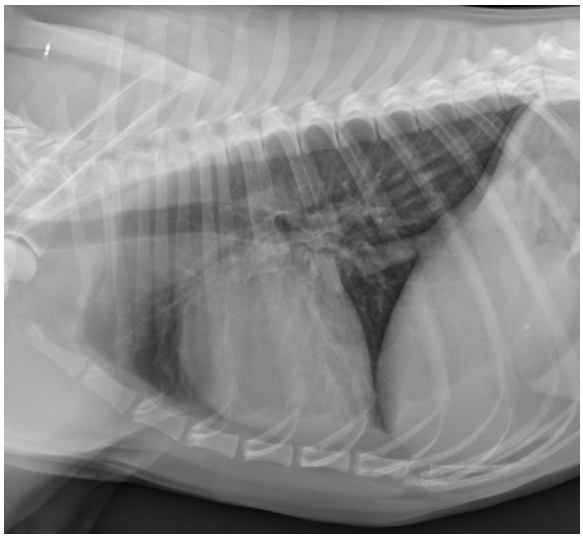


Fig. 28-2 Right lateral thoracic radiograph of a normal adult dog. The first few ribs are oriented vertically but become progressively more caudoventral in orientation, from rib head to costochondral junction, in the mid to caudal aspect of the thoracic spine.

inability to see the presumed pulmonary nodule in the lung on an orthogonal radiograph increases the likelihood of the suspicious opacity being caused by summation created by a superficial structure. Application of positive contrast medium, such as barium paste, on the thoracic wall nodule followed by repeat radiographs can be performed if localization is still in question (Fig. 28-6).



Fig. 28-3 DV thoracic radiograph of a normal adult dog. The first few ribs are oriented perpendicular to the spine. In the mid to caudal aspect of the thoracic spine, ribs curve in a caudolateral direction from their respective vertebrae to their most lateral extent, then continue caudomedially.

CONGENITAL AND DEVELOPMENTAL ABNORMALITIES

Anomalies of the ribs and sternum are fairly common. Rudimentary ribs are sometimes present on the seventh cervical vertebra (Fig. 28-7) or the thirteenth thoracic vertebra (Fig. 28-8). Ribs may be hypoplastic or absent on the thirteenth thoracic vertebral segment (Fig. 28-9). These anomalies may be unilateral or bilateral (Fig. 28-10). The clinical significance of rib asymmetry at the thoracolumbar junction with regard to their use as a surgical landmark was discussed in the "Incidental Factors" section of Chapter 7.

Congenital sternal deformities, such as reduction in number of segments, fusion of neighboring segments (Fig. 28-11), pectus carinatum (ventral displacement of the sternum), and pectus excavatum (funnel chest or dorsal displacement of the sternum) may be incidental findings, but some sternal anomalies have also been reported in animals with peritoneopericardial diaphragmatic hernia (Fig. 28-12).[1,2] Peritoneopericardial diaphragmatic hernias are discussed in Chapter 29.

Pectus excavatum (Fig. 28-13) results in dorsal to ventral narrowing of the thorax and is often associated with respiratory and cardiovascular anomalies. Although pectus excavatum may be congenital or acquired in human beings, all reports in animals describe congenital malformations.[3] The etiology is unknown; however, a hereditary component has been suggested.[4]

Most congenital thoracic wall defects are not repaired surgically unless they are associated with life-threatening complications.

THORACIC WALL TRAUMA

Thoracic wall trauma is common in small animals but may go unnoticed. Direct soft tissue injury may produce soft tissue swelling or subcutaneous emphysema (Fig. 28-14), or air can accumulate because of leakage from the airway (Fig. 28-15). Tears of the intercostal musculature can result in separation

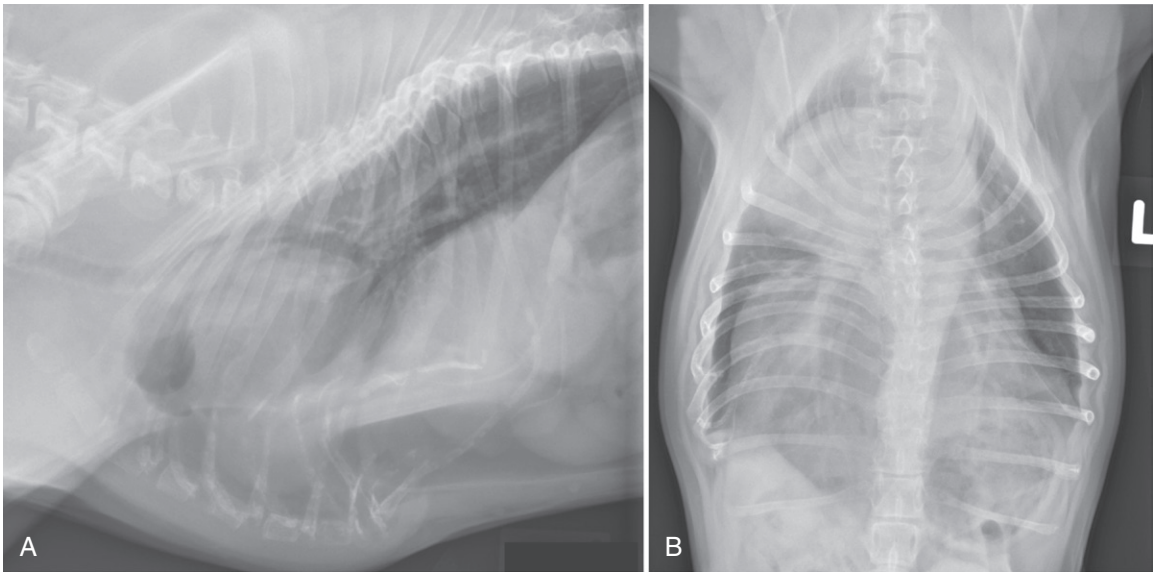


Fig. 28-4 Right lateral **(A)** and DV **(B)** thoracic radiographs of an adult Boston terrier. There are multiple wedge-shaped vertebrae and hemivertebrae in the midthoracic spine. The congenital vertebral anomalies in this dog have resulted in cranioventral angulations of the ribs on the lateral radiograph and a radiating appearance to the rib cage on the DV projection. Scoliosis of the midthoracic spine is evident. Extensive mineralization of the costal cartilages is present; this is a normal finding seen commonly in young and old dogs.



Fig. 28-5 Right lateral radiograph of a middle-aged German shepherd with extensive costal cartilage mineralization and sternebral and costochondral degeneration.

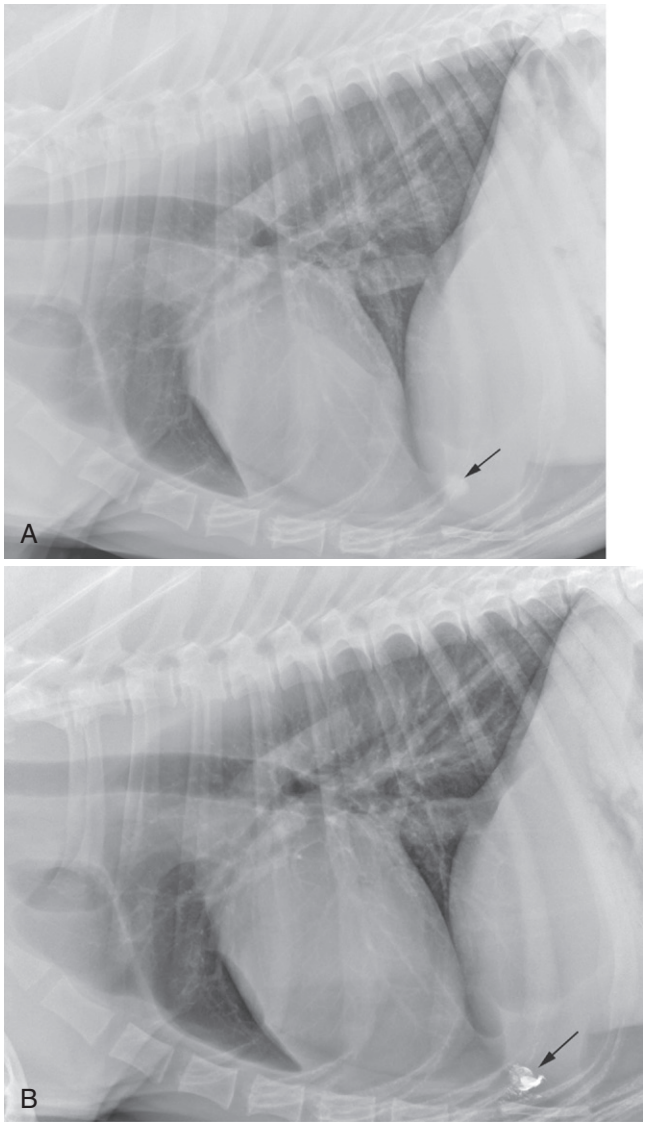


Fig. 28-6 Right lateral thoracic radiographs before **(A)** and after **(B)** application of barium paste to a nipple. In **A,** a nodular soft tissue opacity summates with the seventh costal cartilages *(black arrow)*. In **B,** barium paste was applied to a palpable nipple on the skin, confirming that the nodular opacity was created by the nipple *(black arrow)* and not a lung nodule.

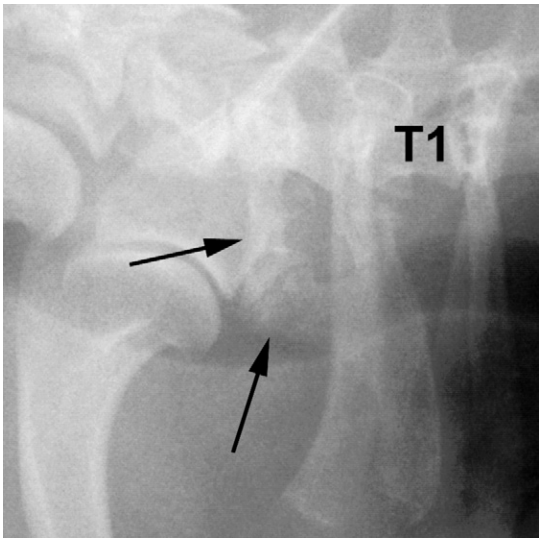


Fig. 28-7 Right lateral radiograph of a Pekingese dog with a left-sided rudimentary rib on the seventh cervical vertebra, forming a pseudoarthrosis with the first thoracic rib *(black arrows)*. *T1*, First thoracic vertebra.

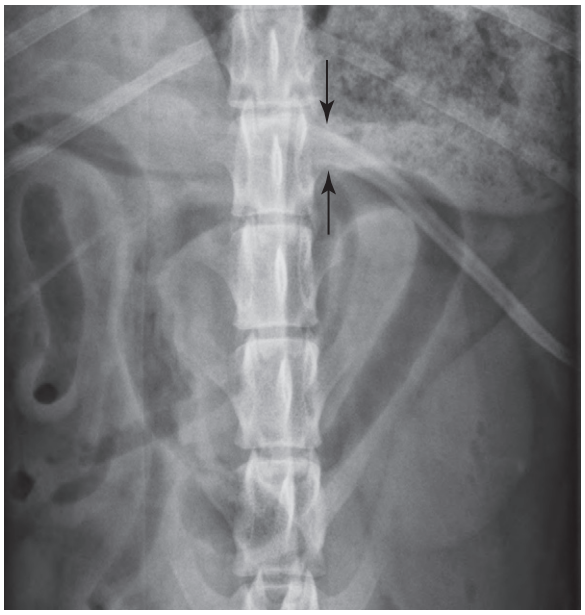


Fig. 28-8 VD radiograph of a dog with a transitional thoracolumbar vertebral segment. Note the broad-based, thick appearance to the proximal extent of the left thirteenth rib *(black arrows)* compared to the hypoplastic right. The left thirteenth rib is taking on the characteristics of a transverse vertebral process.

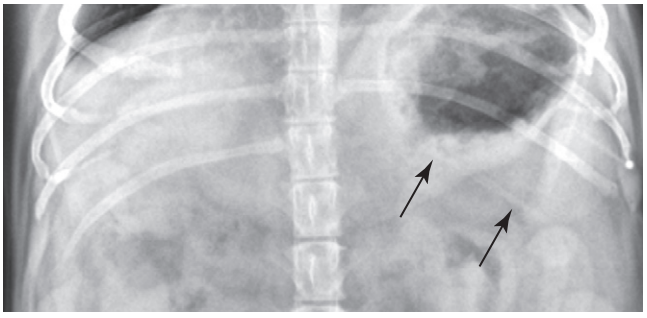


Fig. 28-9 VD radiograph of a dog with a transitional thoracolumbar vertebral segment. The left thirteenth rib is hypoplastic *(black arrows)* and only partially mineralized.

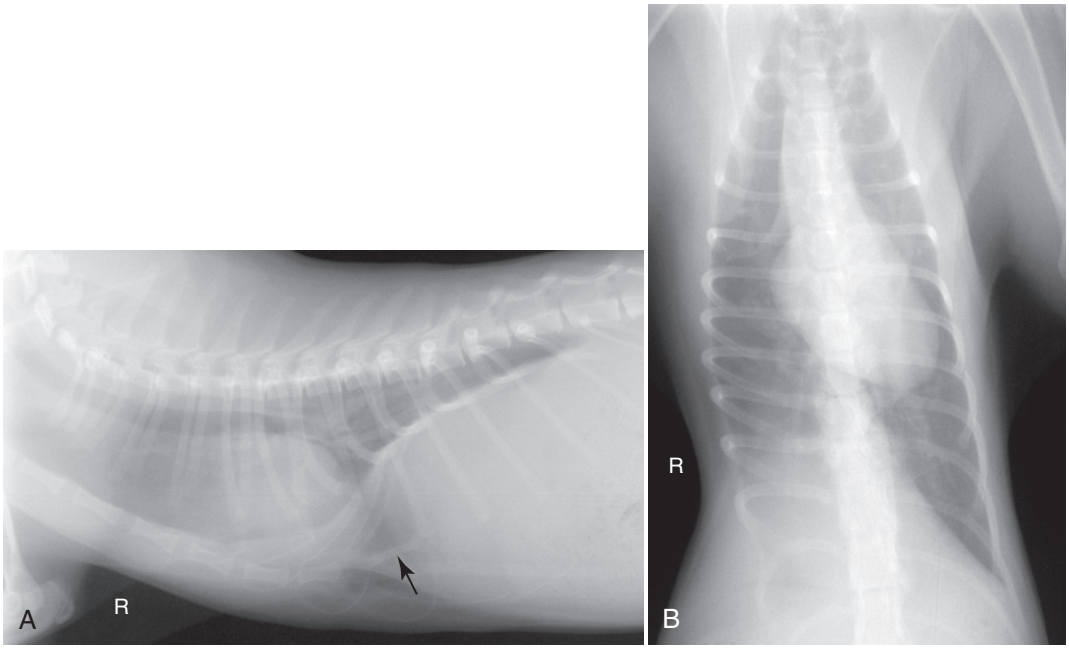


Fig. 28-10 Right lateral **(A)** and DV **(B)** thoracic radiographs of a young cat with congenital deformation of the rib cage. In **A,** the distal extent of right ribs 5 to 12 curve caudally, the severity of which is most pronounced in ribs 9 to 11. The xiphoid is displaced dorsally *(black arrow)*. In **B,** the asymmetry between the right and left thoracic wall is evident. The right caudolateral rib cage has a compressed appearance, and the right diaphragmatic crus is displaced cranially.

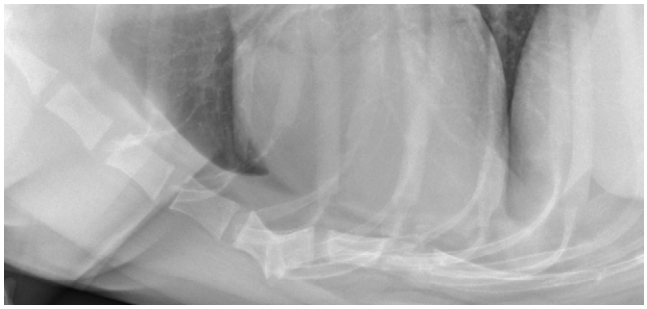


Fig. 28-11 Right lateral radiograph of a young dog. There is fusion of the fourth and fifth sternebral segments, likely because of congenital malformation. The dorsal concave margin of the fused segments is smooth, and no evidence of degenerative disease is present to suggest trauma.

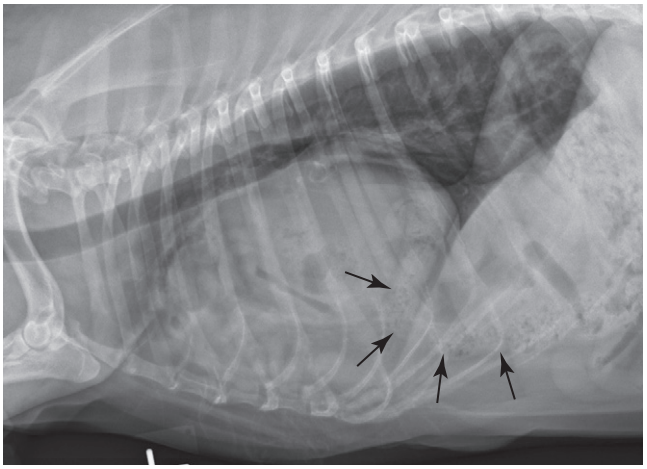


Fig. 28-12 Left lateral thoracic radiograph of a dog with a peritoneopericardial diaphragmatic hernia. Note the reduction in number of sternal segments. The cardiac silhouette is enlarged and oval in shape, causing dorsal deviation of the trachea. Multiple loops of small intestine are present within the thorax summating with the cardiac silhouette. The caudal margin of the cardiac silhouette is confluent with the cranioventral margin of the diaphragm. A segment of large intestine containing granular material is identified crossing the peritoneopericardial junction *(black arrows)*.

of ribs and are a common sequela to bite wounds, resulting in uneven spacing between ribs (Fig 28-16).[5,6]

Rib fractures following trauma are common and are identified easily if fracture fragment displacement is evident (Figs. 28-17 and 28-18). Rib and sternal fractures may be missed if fracture fragments remain in alignment. Many rib fractures are diagnosed retrospectively after callus has formed, increasing the conspicuity of the rib anomaly. Healing rib fractures may exhibit rounded fracture margins and focal periosteal reaction followed by bridging callus. Over time, the fracture margins and associated osseous callus will remodel, often creating an expansile appearance to the rib once healed (Fig. 28-19). Discrimination of the subtle differences between a healing rib fracture and an aggressive rib lesion is important. A history of trauma, overriding rib margins, or involvement of multiple adjacent ribs is supportive of prior trauma. If there is question whether a rib lesion represents a healing fracture or a more aggressive process, needle aspiration or biopsy of the rib lesion is indicated. A repeat radiographic evaluation in 2 weeks may also clarify etiology as with time progressive lysis and bone proliferation would be expected in an aggressive bone lesion.

It has been suggested that viewing ventrodorsal radiographs upside down, or rotating them 90 degrees, may improve the conspicuity of rib fractures. In a controlled study, however, changing the orientation of a thoracic radiograph by 90 degrees improved the accuracy of a novice reader, but there was no increase in accuracy of rib fracture detection for more experienced readers. Changing the orientation by 180 degrees—that is, viewing the radiograph upside down—did

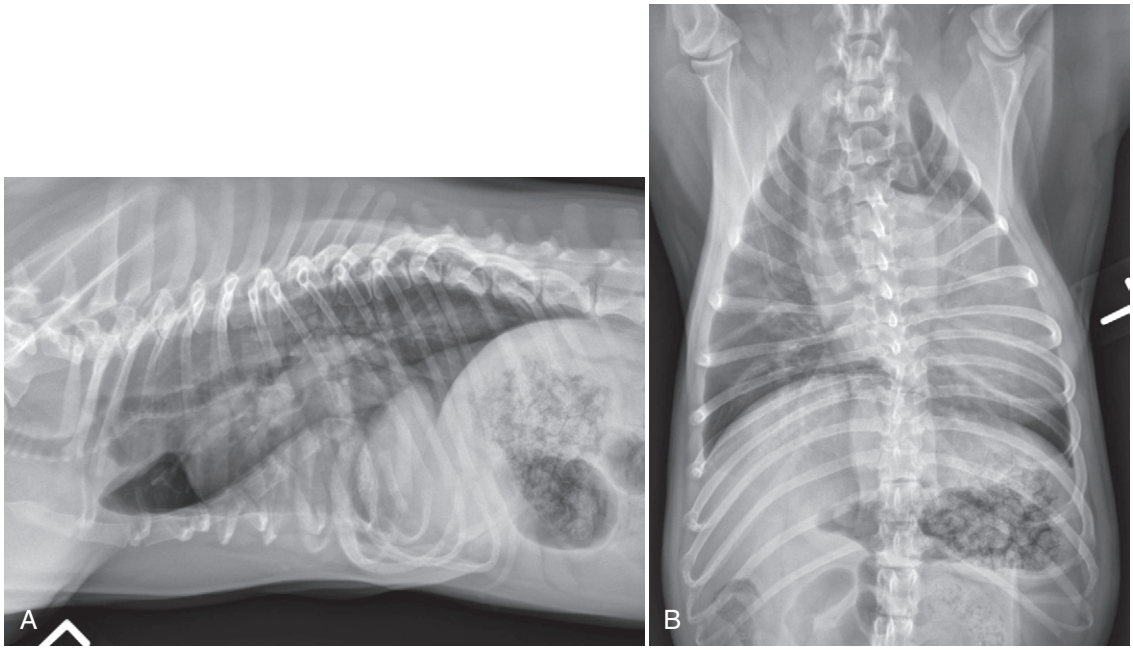


Fig. 28-13 Left lateral **(A)** and VD **(B)** thoracic radiographs of a 4-year-old pug with pectus excavatum that causes severe dorsal to ventral narrowing of the thorax. The cardiac silhouette and caudal aspect of the thoracic trachea are displaced dorsally, and the heart is also deviated into the left hemithorax. The thoracic trachea is focally, dorsally deviated in the cranial aspect of the thorax, likely an artifact of head and neck positioning. Multiple congenital vertebral anomalies are present to include shortened, wedge-shaped, and butterfly vertebral segments from T3 to T11.

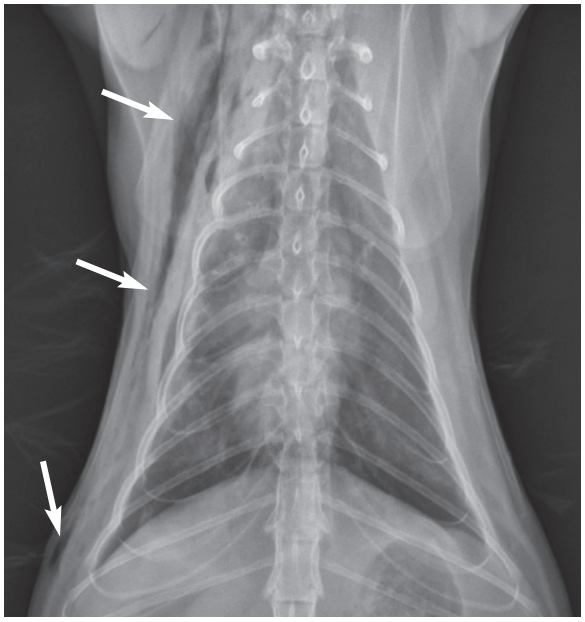


Fig. 28-14 DV thoracic radiograph of a cat with subcutaneous emphysema along the right thoracic body wall caused by bite wound trauma *(white arrows)*.



Fig. 28-15 Lateral thoracic radiograph of a cat with severe subcutaneous emphysema, pneumothorax, and pneumomediastinum that developed following general anesthesia. Tracheal laceration caused by an overinflated endotracheal tube cuff was the suspected cause.

not improve the accuracy of any reader. Therefore, altering the orientation of thoracic radiographs when looking for rib fractures is best considered a training aid rather than a technique that will benefit an experienced radiologist.[7]

Segmental rib fractures involving the dorsal and ventral aspects of at least two adjacent ribs may create thoracic wall instability, resulting in flail chest.[5,8] The flailing portion of the destabilized thoracic wall moves paradoxically to the normal thoracic wall and is characterized by inward displacement during inspiration and outward displacement during expiration (Fig. 28-20).[5,8]

As discussed in Chapter 33, cats with diseases that cause prolonged respiratory effort or coughing, metabolic diseases, or certain neoplasms are at increased risk of spontaneous nontraumatic rib fractures. Mechanical failure secondary to chronic dyspnea or coughing is a likely cause of these spontaneous rib fractures in cats with respiratory disease. Because the fractures are more common in older cats, osteopenia that weakens the structural integrity of the ribs may also play a role.[9] The most commonly affected ribs are located caudally,

involving the midportion of the ninth to thirteenth ribs. Illustration of spontaneous rib fractures is provided in Figure 33-28.

RIB TUMORS AND INFECTION

A thoracic wall mass that invades the thoracic cavity, regardless of etiology, may create an extrapleural sign.[10,11] An extrapleural sign is characterized by an intrathoracic mass with a well-circumscribed, convex margin facing the lung. The cranial and caudal edges taper along the thoracic wall, giving the mass a broad-based appearance (Fig. 28-21). The extrapleural sign is best seen when the x-ray beam strikes the intrathoracic component of the mass tangentially. Oblique radiographs may be necessary to visualize the extrapleural sign if the x-ray beam does not strike the extrapleural mass tangentially in the routine lateral, VD, and DV views.

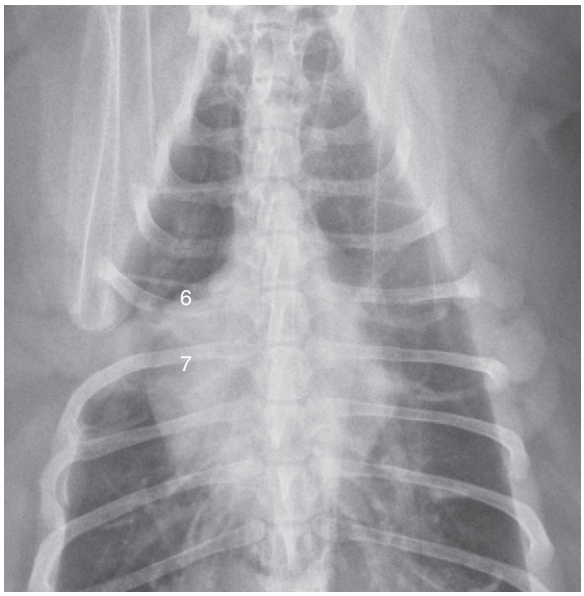


Fig. 28-16 Ventrodorsal radiograph of a cat that sustained a right thoracic wall injury resulting in tearing of intercostal muscles between ribs 6 and 7. The pull of the remaining intact intercostal muscles cranial and caudal to this site resulted in the rib splaying seen here.

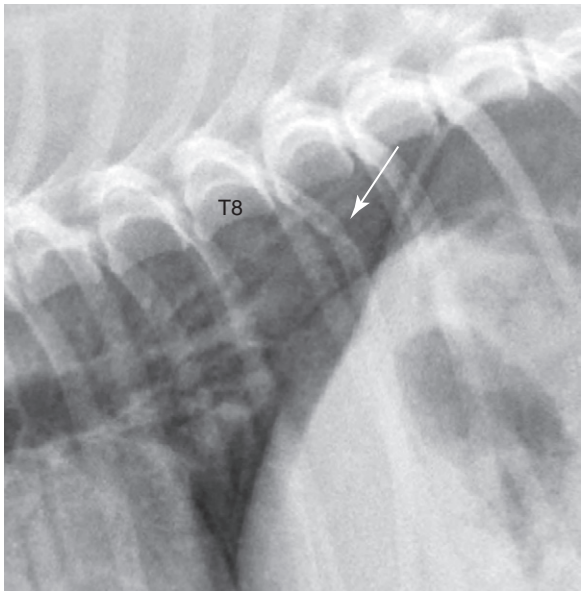


Fig. 28-17 Right lateral cranial thoracic radiograph of a dog. There is a fracture of the right eighth rib *(white arrow)*. There is no evidence of bony callus. This is consistent with acute trauma. *T8*, Eighth thoracic vertebra.

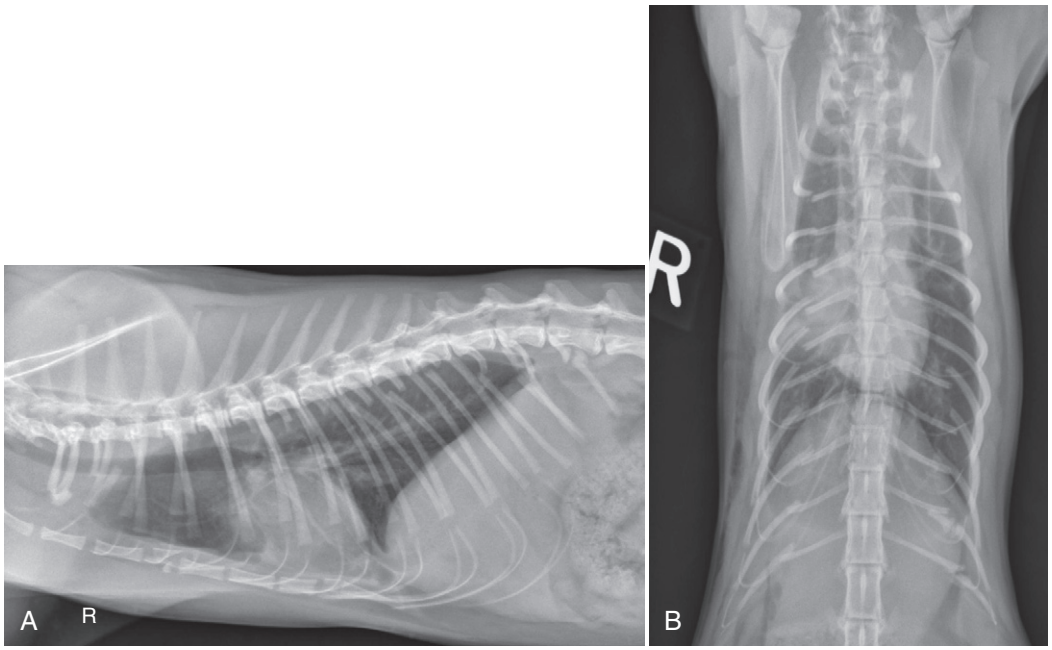


Fig. 28-18 Lateral **(A)** and VD **(B)** radiographs of a cat with acute rib fractures. Right ribs 4 through 13 and left ribs 1, 2, and 9 through 12 are fractured, the result of being hit by a car. The fracture margins are sharp and distinct. Subcutaneous emphysema is present in the right thoracic body wall. Ill-defined opacities are present in the right middle lung lobe, likely secondary to pulmonary contusions. Also present are chronic, healing fractures of left ribs 12 and 13. There is rounding of the fracture margins with bony callus formation.

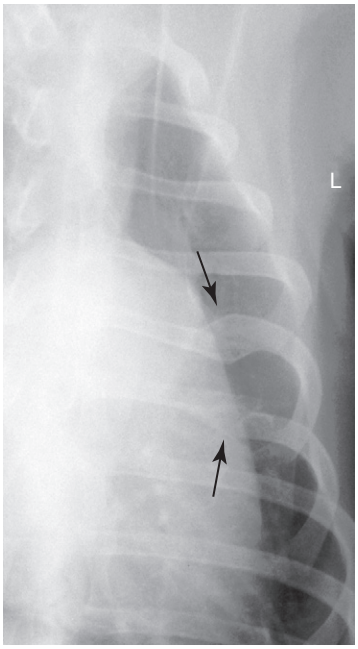


Fig. 28-19 DV thoracic radiograph of a dog with healed fractures of the left fifth, and sixth ribs *(black arrows)*. Note the smooth bony margins and expansile appearance to these malunion fractures.

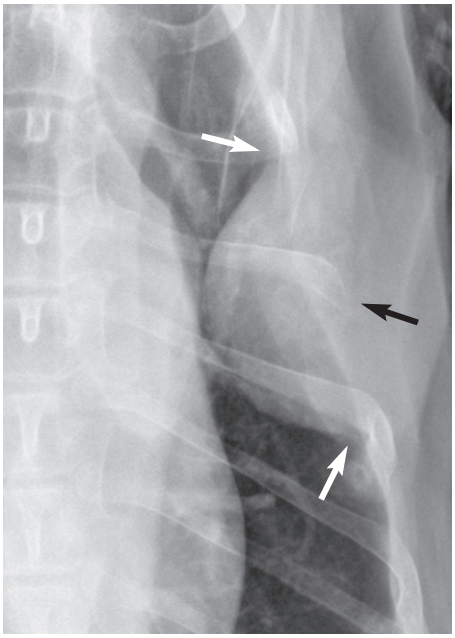


Fig. 28-21 VD thoracic radiograph of a dog. There is lysis of the distal aspect of the left fourth rib *(black arrow)* with an ill-defined extrathoracic mass and a well-defined intrathoracic mass. The intrathoracic component of the mass is broad based along the intrathoracic wall surface and has a convex margin. The cranial and caudal margins of the mass taper along the thoracic wall *(white arrows)*. These radiographic findings are characteristic of an extrapleural sign.

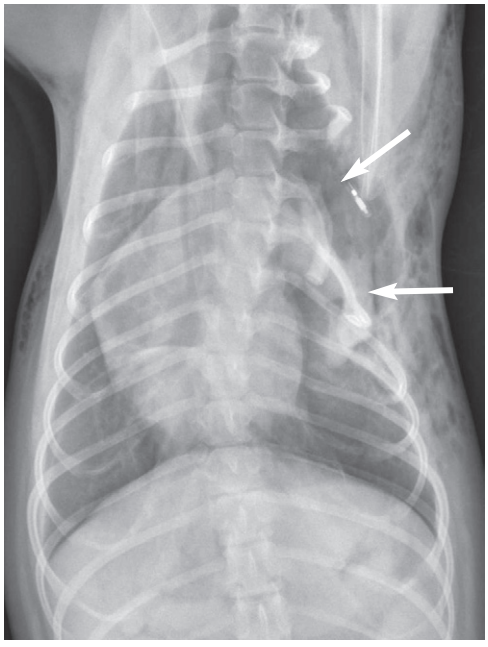


Fig. 28-20 VD thoracic radiograph of a dog that developed a flail chest after being hit by a car. Segmental fractures of the left fourth and fifth ribs lead to paradoxical collapse of the thoracic wall *(white arrows)* on this inspiratory radiograph. Partial collapse of the left cranial lung lobe and probable pulmonary contusions at the level of the flail component are present. Subcutaneous emphysema and a microchip are also present.

Extrapleural masses arise peripheral to the parietal pleura and commonly extend mainly into the thoracic cavity rather than peripherally. Extrapleural masses originate most often from ribs but may also arise from connective tissue, nerves, vessels, or muscles. If the convex margin of the extrapleural mass is not sharply delineated, invasion of the pleura overlying the lung should be considered. This occurs more commonly with neoplastic and infectious masses. Occasionally, benign extrapleural fat accumulations may be confused with extrapleural neoplastic or infectious masses.[12] The key to differentiating these conditions is noting the reduced radiographic opacity of the fat accumulation. When in doubt, a needle aspirate of the lesion may clarify its tissue type.

The characteristic imaging features of the extrapleural sign are helpful in differentiating thoracic wall masses from pulmonary masses. If a lung mass is in contact with the thoracic wall, the junction between the mass and the thoracic wall forms an angle less than 90 degrees (Fig. 28-22, *A*). If a mass originates from the thoracic wall and extends into the thoracic cavity, the junction of the mass and the wall forms an angle greater than 90 degrees (Fig. 28-22, *B* and C).

Rib infection is uncommon in the dog and cat and usually is the result of trauma caused by a penetrating wound. Occasionally, a severe pyothorax may result in rib periostitis. Mycotic rib osteomyelitis may be seen as a result of septicemia. Differentiation of rib osteomyelitis from neoplasia is not possible radiographically. Both processes may elicit mixed productive and lytic, primarily lytic, or primarily productive response. Biopsy is necessary to confirm the pathologic process involved.

Rib neoplasia is more common than infection. Primary rib tumors are typically of mesenchymal origin (e.g., chondrosarcoma, osteosarcoma).[13,14] As a result of intrathoracic extension occurring to a greater extent than peripheral extension, most primary rib tumors are diagnosed late in the course of disease (Fig. 28-23). Pleural effusion is a common result of advanced rib neoplasia. Excessive pleural fluid may summate with the rib lesion, compromising its detection radiographically. Positional radiography or removing fluid followed by repeat radiographs may be helpful to increase the conspicuity of the rib mass.

Various solid tumors can metastasize to ribs. These lesions are often lytic (Fig. 28-24) with varying degrees of periosteal/

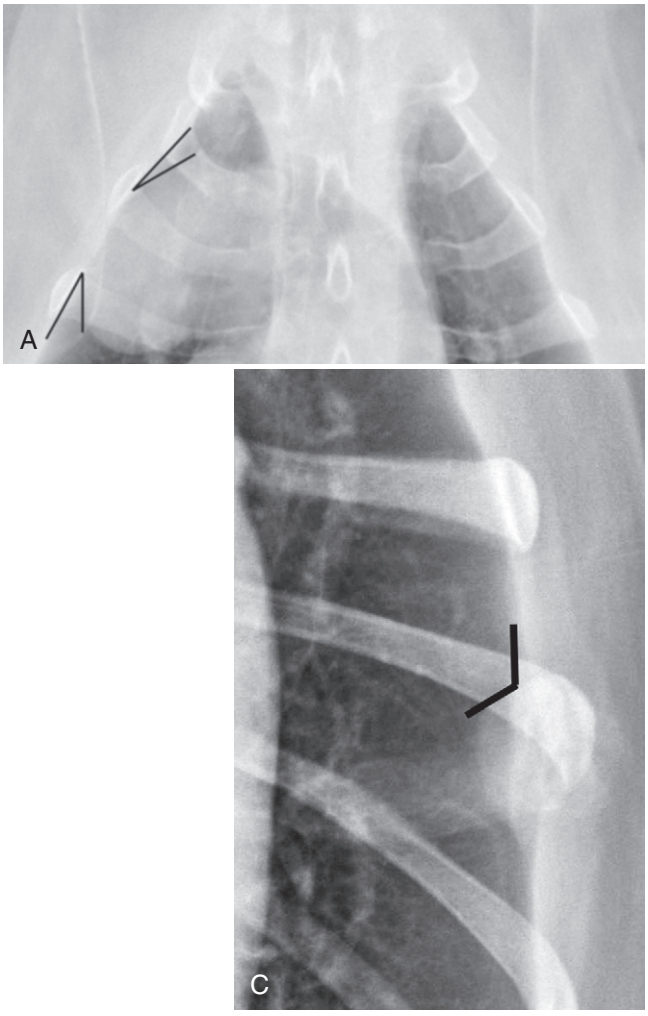


Fig. 28-22 DV cranial thoracic radiograph of a dog with a right cranial pulmonary mass **(A).** The junction of the mass and the thoracic wall forms an angle less than 90 degrees. Oblique VD midthoracic radiograph of a dog with a thoracic wall mass **(B).** An aggressive lytic lesion of the left eighth rib is present. The junction of the associated soft tissue mass and the wall forms an angle greater than 90 degrees. VD thoracic radiograph of a dog with a metastatic (osteosarcoma), osteolytic lesion of the fifth left rib **(C)**. A subtle extrapleural sign is present.

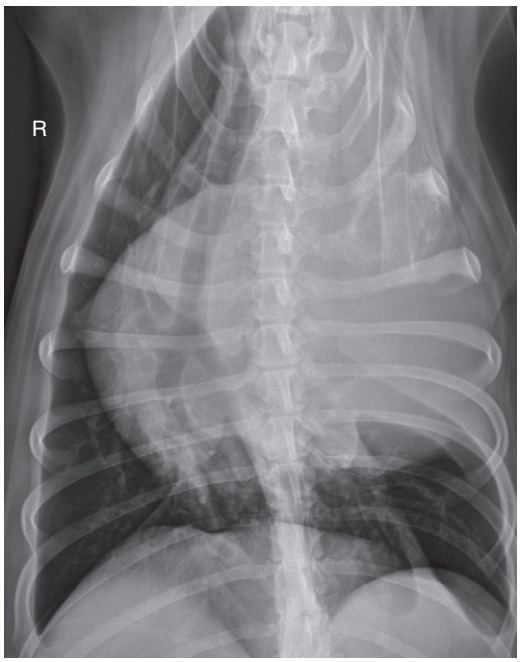


Fig. 28-23 VD thoracic radiograph of a dog with a primary tumor of the left fourth rib. There is minimal mass extrathoracically but a large mass intrathoracically that has displaced the heart to the right. This discrepancy between the size of the extrathoracic and intrathoracic components of primary rib tumors is common and leads to a delay in diagnosis.

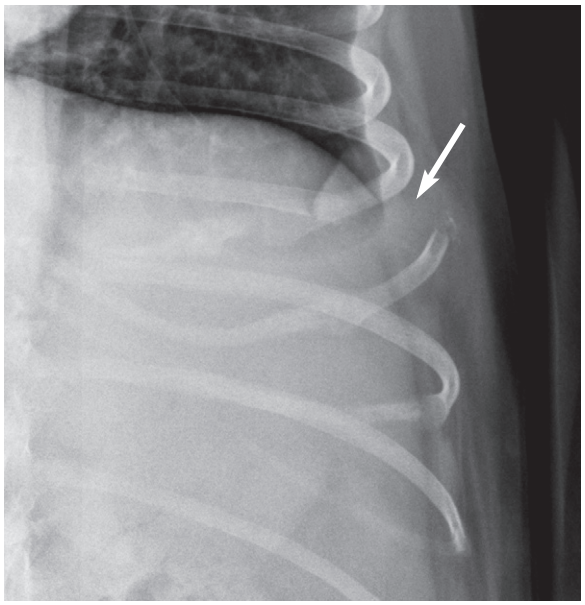


Fig. 28-24 VD radiograph of a dog with lysis of the distal aspect of the left tenth rib *(white arrow)* caused by metastatic melanoma.

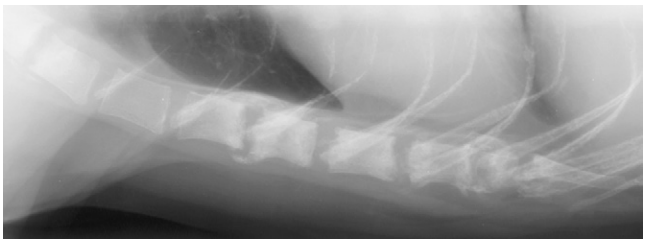


Fig. 28-25 Right lateral radiograph of the ventral aspect of the thorax of a dog. Sternebral end plate lysis and subchondral sclerosis are present from the caudal end plate of segment 4 through the cranial aspect of segment 8. The intersternebral spaces appear wide in this region. The radiographic signs are consistent with sternal osteomyelitis. *Staphylococcus aureus* was isolated from the urine and hematogenous spread to the sternum was suspected.

cortical response. Rib metastases are often overlooked on survey radiographs, especially when the radiographs were acquired for evaluation of the lung for metastasis. Most rib metastases are the result of hematogenous spread and seen in the later stages of disease.

STERNEBRAL TUMORS AND INFECTION

Primary and metastatic sternebral tumors are uncommon. As with ribs, primary sternebral tumors are typically of mesenchymal origin. Most neoplasms causing alteration of sternebral architecture are the result of local invasion by adjacent soft tissue tumors of the thoracic wall.

Sternal infections may result from external trauma, such as bite wounds. Migrating grass awns may lodge against a sternebral segment and result in local osteomyelitis with or without a draining tract. Hematogenous infection may lodge in an intersternal space, resulting in end plate lysis and subchondral, reactive osseous proliferation similar in appearance to that seen with discospondylitis (Fig. 28-25).[15]

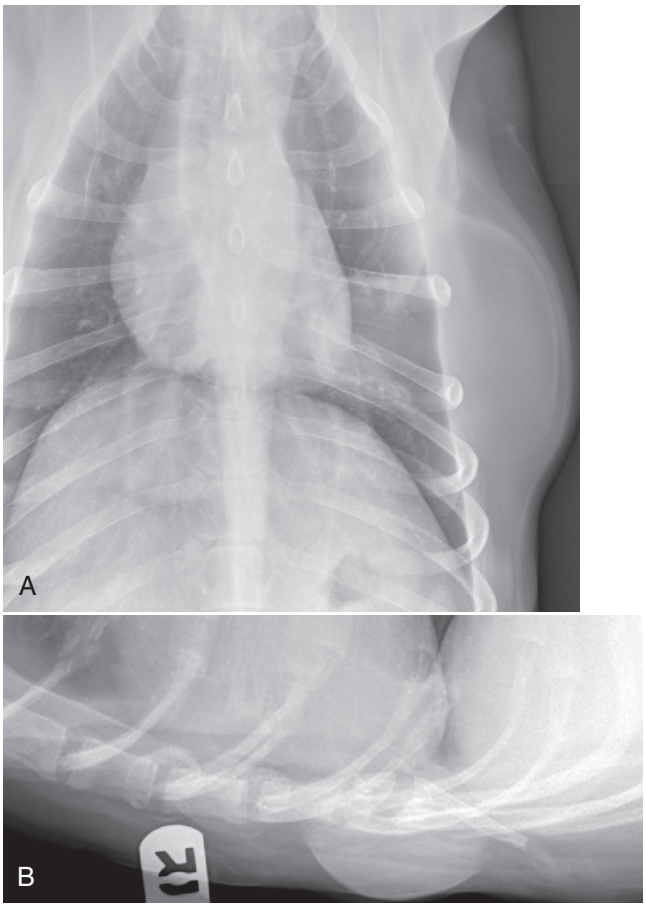


Fig. 28-26 VD thoracic radiograph **(A)** of a dog. A large, fat opacity mass (lipoma) is present along the left lateral thoracic wall. This mass is infiltrating the left fifth intercostal musculature, resulting in splaying of the left fifth and sixth ribs. Right lateral radiograph **(B)** of a dog with a thoracic wall lipoma ventral to the caudal aspect of the sternum.

SOFT TISSUE TUMORS AND INFECTION

Soft tissue tumors of the thoracic wall are fairly common. Benign lipomas are among the most recognized (Fig. 28-26). Most lipomas are subcutaneous, although some may infiltrate muscle and fibrous tissues.[16] Fibrosarcomas at sites of known vaccination, especially in the interscapular region, may be identified radiographically as a convexly margined soft tissue swelling dorsal to the cranial thoracic spinous processes. Other sarcomas (e.g., hemangiosarcoma, lymphosarcoma) or carcinomas (e.g., mammary adenocarcinoma, squamous cell carcinoma) of soft tissue origin may arise anywhere on the thoracic wall.

Trauma and migrating grass awns are the most common causes of cellulitis and infection of thoracic wall soft tissues. Calcinosis circumscripta of the thoracic wall has been reported in a German shepherd dog after surgical repair of a patent ductus arteriosus.[17] The exact cause of calcinosis circumscripta is unknown but may be seen after soft tissue injury attributable to inflammatory or neoplastic causes.[16]

ALTERNATE IMAGING OF THE THORACIC WALL

Ultrasound

Sonography can be used to characterize thoracic wall lesion texture and vascularity (Fig. 28-27).[18,19] When the presence of pleural fluid makes it impossible to distinguish radiographically between a thoracic wall and pulmonary mass, ultrasound may be beneficial because sound propagates readily through fluid. Therefore, pleural fluid provides an excellent window for visualization of pleural surfaces sonographically. If the mass in question is of pulmonary origin, it will move with the lung in conjunction with inspiration and expiration. If the mass is of thoracic wall origin, the mass will stay fixed to the thoracic wall. Cortical bone discontinuity caused by lysis and remodeling of rib or sternal lesions may also be identified sonographically (Fig. 28-28). Ultrasound-guided needle aspirate or biopsy may be performed for cytologic or histopathologic diagnosis.

Computed Tomography

Computed tomography (CT) is helpful for evaluating and defining lesion margination, particularly in large lesions that extend beyond the field of view of an ultrasound beam. Vascularity and further characterization of lesion margination can be assessed after intravenous iodinated contrast-medium administration (Fig. 28-29). CT has proved to be helpful in surgical planning of vaccine-associated fibrosarcomas in cats (Fig. 28-30).[20] Postcontrast images often depict tendrils of inflammatory or neoplastic tissue dissecting through otherwise radiographically normal-appearing soft tissues. CT is also able to differentiate simple lipomas from infiltrative lipomas.[16]

Text continued on p. 534

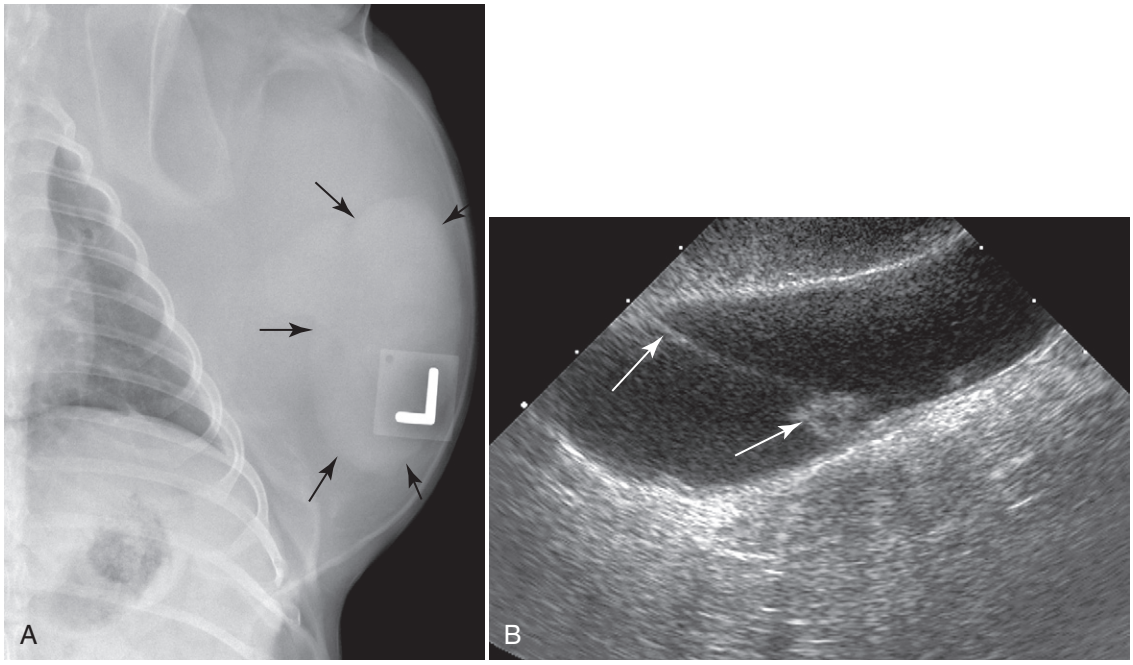


Fig. 28-27 DV thoracic radiograph **(A)** and left lateral thoracic wall ultrasound image **(B)** of a dog. In **A,** a lipoma is present along the left lateral thoracic wall. An oval, soft tissue mass *(black arrows)* is present within the larger lipoma. Sonographically **(B),** the soft tissue region corresponded to a well-margined, anechoic cystlike structure within the lipoma. Echogenic strands or septa with frondlike areas of attachment to the cyst wall were present *(white arrows)*. Ultrasound-guided needle aspirates of the fat mass and cystic structure were performed, and a brown watery fluid was obtained. Cytology was consistent with lipoma and cyst formation lined by hemosiderophages with foci of hematoidin (blood breakdown product) and granulation tissue.

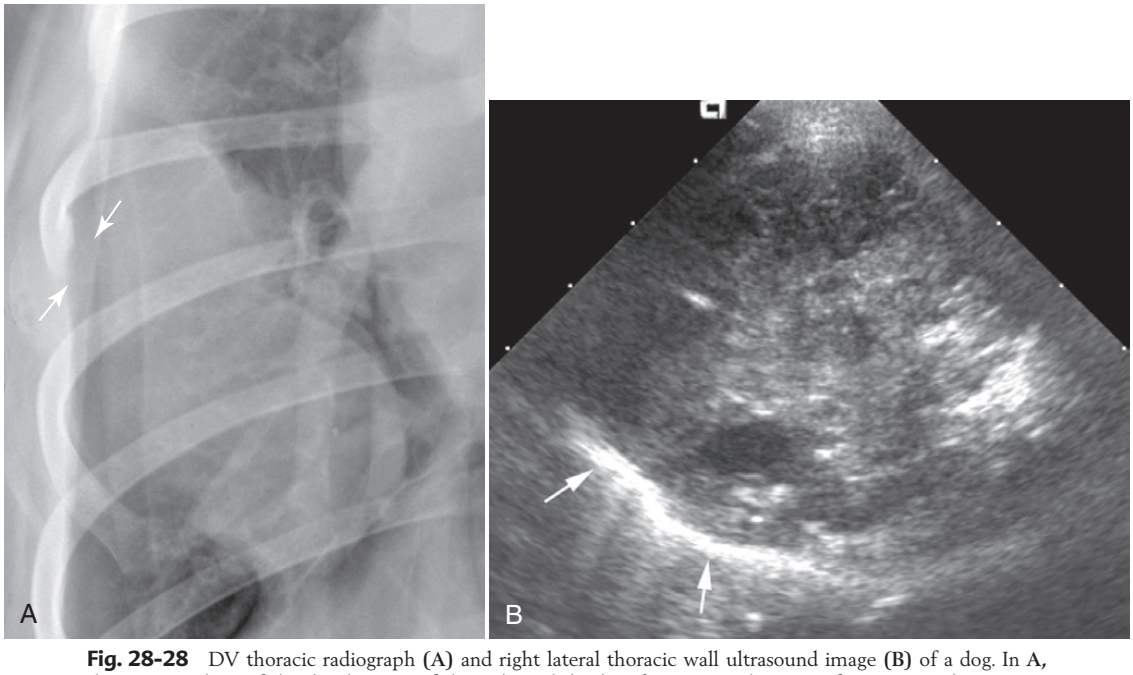


Fig. 28-28 DV thoracic radiograph **(A)** and right lateral thoracic wall ultrasound image **(B)** of a dog. In **A,** there is osteolysis of the distal aspect of the right eighth rib *(white arrows)* because of a primary rib tumor. A large, lobular soft tissue mass is also present in the caudal right thorax. This mass originates from the eighth right rib. An ultrasound examination was performed to determine the tissue characteristics of the soft tissue mass **(B)**. A heteroechoic mass interspersed with hyperechoic, shadowing foci (mineral debris) was identified within the right lateral thoracic cavity at the level of the eighth rib. The distal extent of the remaining rib was irregular and lacked a smooth cortical surface. Anechoic cavitations of varying size were also identified within the mass. These areas lacked evidence of vascularity on Doppler interrogation and likely represented areas of tissue necrosis. The lung surface is identified deep to the mass as a curvilinear hyperechoic interface impeding sound transmission deep to its surface *(white arrows)*. In real-time imaging, the lung slid cranially and caudally over the thoracic wall mass during respiration. The histopathologic diagnosis of the rib lesion was chondrosarcoma.

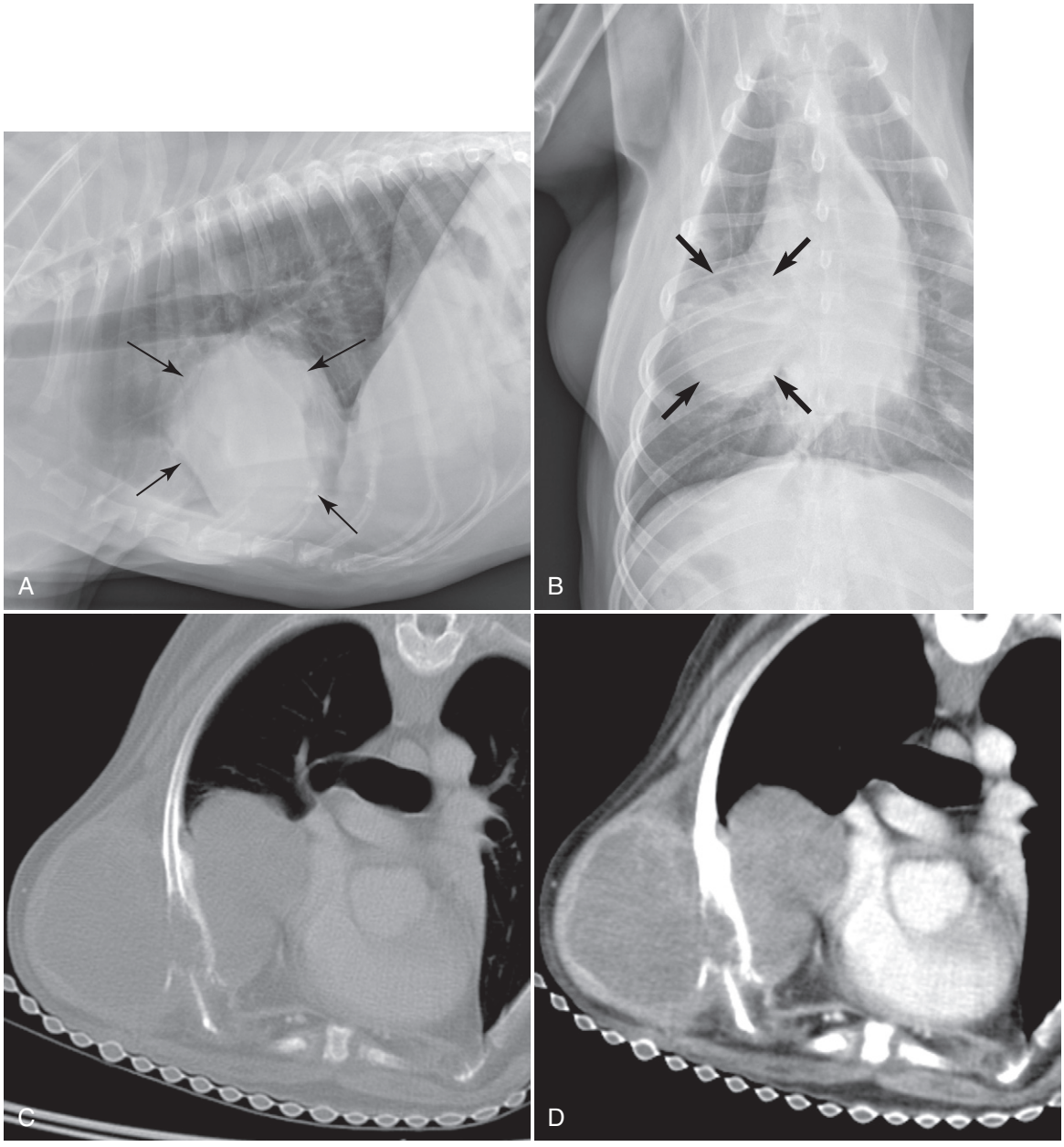


Fig. 28-29 Left lateral **(A)** and DV **(B)** thoracic radiographs of a dog. A poorly margined, soft tissue mass is present to the right of the cardiac silhouette on the DV view *(black arrows)* and summating with the cardiac silhouette on the lateral view *(black arrows)*. On the DV radiograph, the mass could be mistaken for a pulmonary lesion. Transverse CT images at the level of the fifth ribs in a bone window **(C)** and in a soft tissue window after **(D)** administration of iodinated intravenous contrast medium. The lesion originates from the distal right fifth rib. A soft tissue mass is associated with the rib lysis, and a large extrathoracic component is also present. After contrast-medium administration **(D),** slight rim enhancement of the soft tissue mass, as well as the heart, great vessels, and pulmonary vessels, is seen. The histopathologic diagnosis of the rib lesion was osteosarcoma.

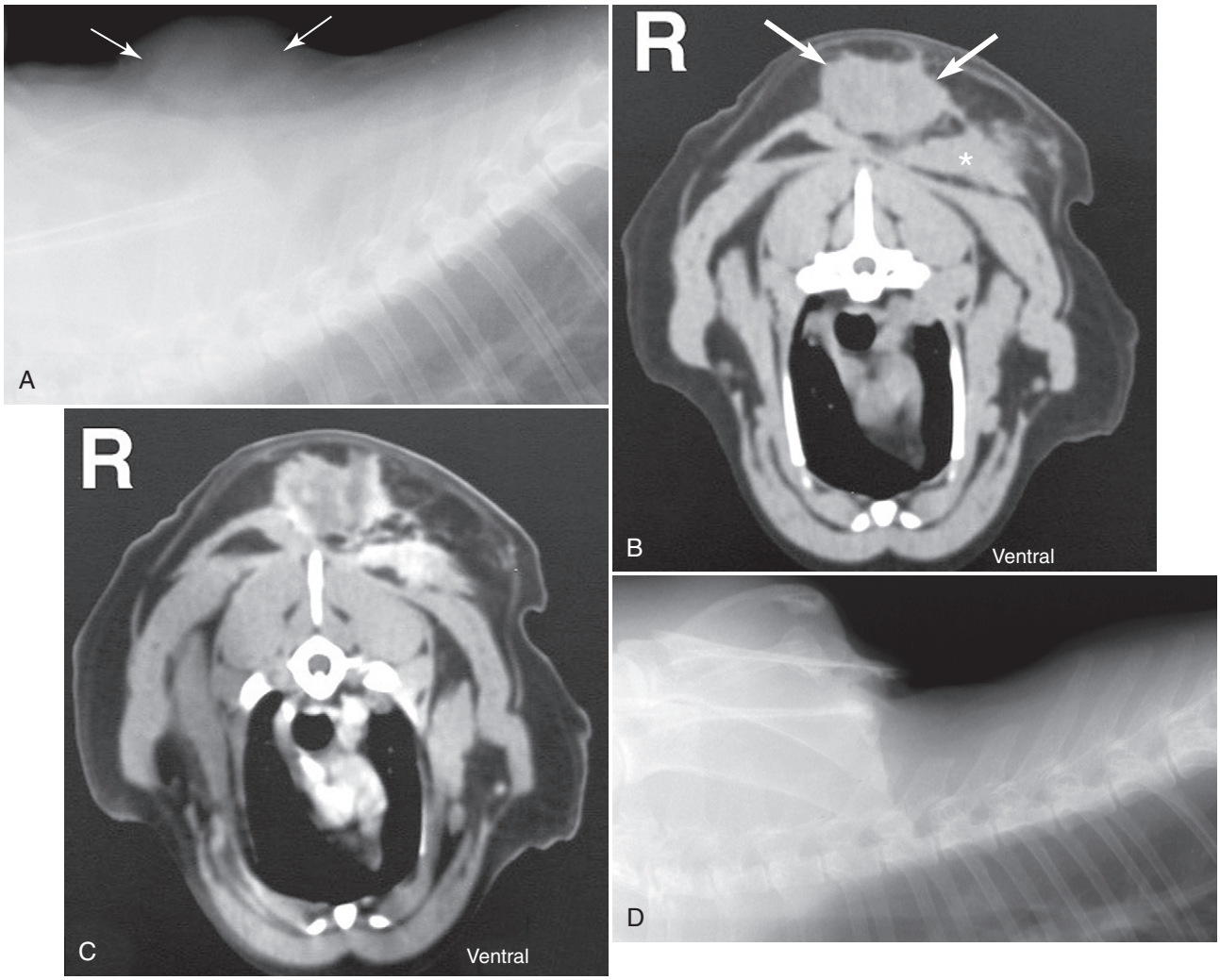


Fig. 28-30 Right lateral radiograph **(A)** and precontrast **(B)** and postcontrast **(C)** CT images of a cat with a vaccine-associated interscapular fibrosarcoma. A soft tissue mass with a dorsal convex margin is present in the subcutaneous tissues dorsal to the proximal margin of the scapulae *(white arrows)* on the thoracic radiograph **(A).** On the precontrast CT image **(B)** acquired just caudal to the scapulae, the irregularly margined mass is seen clearly in the fat just dorsal to a thoracic spinous process *(white arrows)*. In addition, soft tissue opaque stranding is identified in the fat surrounding the mass and just lateral to the left trapezius muscle *(*)*, which is also thickened and irregular in contour. After intravenous administration of iodinated contrast medium, heterogeneous enhancement of the dorsal subcutaneous mass, left trapezius muscle, and soft tissue stranding within the regional fat are present, consistent with neoplastic infiltration and associated inflammation. Contrast-medium opacification of the great vessels cranial to the heart is also seen. Although lysis and remodeling of osseous structures was not identified, soft tissue contrast opacification was observed along the peripheral surfaces of the caudal scapulae and multiple spinous processes. In the interest of obtaining a complete surgical excision, large portions of the scapulae and thoracic spinous processes 2 through 6 were removed **(D).**

REFERENCES

1. Evans SK, Biery DN: Congenital peritoneopericardial diaphragmatic hernia in the dog and cat: a literature review and 17 additional case histories, *Vet Radiol* 21:108, 1980.
2. Berry CR, Koblik PD, Ticer JW: Dorsal peritoneopericardial mesothelial remnant as an aid to the diagnosis of feline congenital peritoneopericardial diaphragmatic hernia, *Vet Radiol* 31:239, 1990.
3. Fossum TW, Boudrieau RJ, Hobson HP: Pectus excavatum in 8 dogs and 6 cats, *J Am Anim Hosp Assoc* 25:595, 1989.
4. Ellison G, Halling KB: Atypical pectus excavatum in two Welsh terrier littermates, *J Small Anim Pract* 45:311, 2004.
5. Suter PF: Injuries to thoracic wall and sternum. In Suter PF, editor: *Thoracic radiography*, Wettswil, 1984, Peter F. Suter, Zurich, Switzerland, pp 130–133.
6. Risselada M, de Rooster H, Taeymans O, et al: Penetrating injuries in dogs and cats. A study of 16 cases, *Vet Orthop Traumatol* 21:434, 2008.
7. Lamb CR, Parry AT, Baines EA, et al: Does changing the orientation of a thoracic radiograph aid diagnosis of rib fractures? *Vet Radiol* 52:75, 2011.
8. Olsen D, Renberg W, Perrett J, et al: Clinical management of flail chest in dogs and cats: a retrospective study of 24 cases (1989–1999), *J Am Anim Hosp Assoc* 38:315, 2002.
9. Adams C, Streeter EM, King R, et al: Cause and clinical characteristics of rib fractures in cats: 33 cases (2000–2009), *J Vet Emerg Crit Care (San Antonio)* 20:436, 2010.
10. Myer W: Radiography review: the extrapleural space, *J Am Vet Radiol Soc* 19:157, 1978.
11. Suter PF: The extrapleural sign. In Suter PF, editor: *Thoracic radiography*, Wettswil, Peter F. Suter, 1984, Zurich, Switzerland, pp 168–176.
12. Fisher E, Godwin JD: Extrapleural fat collections: pseudotumors and other confusing manifestations, *Am J Roentgenol* 161:47, 1993.
13. Feeney DA, Johnston GR, Grindem CB, et al: Malignant neoplasia of the canine ribs: clinical, radiographic, and pathologic findings, *J Am Vet Med Assoc* 180:928, 1982.
14. Baines SJ, Lewis S, White RA: Primary thoracic wall tumours of mesenchymal origin in dogs: a retrospective study of 46 cases, *Vet Rec* 150:335, 2002.
15. Gilding T, Guilliard MJ: What was your diagnosis? Osteomyelitis of the fourth sternebra, *J Small Anim Pract* 44:335, 2003.
16. McEntee MC, Thrall DE: Computed tomographic imaging of infiltrative lipoma in 22 dogs, *Vet Radiol Ultrasound* 42:221, 2001.
17. Davidson EB, Schulz KS, Wisner ER, et al: Calcinosis circumscripta of the thoracic wall in a German shepherd dog, *J Am Anim Hosp Assoc* 34:153, 1998.
18. Reichle JK, Wisner ER: Non-cardiac thoracic ultrasound in 75 feline and canine patients, *Vet Radiol Ultrasound* 41:154, 2000.
19. Stowater JL, Lamb CR: Ultrasonography of noncardiac thoracic diseases in small animals, *J Am Vet Med Assoc* 195:514, 1989.
20. Samii VF, McEntee MC: Utility of contrast enhanced computed tomographic imaging of soft tissue sarcomas: overview and case presentations, *Vet Cancer Soc News* 22:1, 1998.

ELECTRONIC RESOURCES

evolve

Additional information related to the content in Chapter 28 can be found on the companion Evolve website at http://evolve.elsevier.com/Thrall/vetrad/

- Chapter Quiz

CHAPTER • 29

The Diaphragm

Elissa K. Randall
Richard D. Park

The diaphragm is the musculocutaneous partition between the thoracic and abdominal cavities. Embryologically, the diaphragm is formed by the septum transversum ventrally and by the mesentery of the foregut and two pleuroperitoneal folds dorsally.

Movement of the diaphragm provides approximately 75% of the change in intrathoracic volume during quiet respiration.[1] The diaphragm also acts as a mechanical partition between the thorax and the abdomen. Lymph vessels from the abdomen penetrate the diaphragm and drain into the thoracic lymph nodes and vessels. Thus inflammatory or neoplastic abdominal disease may spread to the mediastinum and pleural space. Lymph flow is unidirectional with the final destination being the thoracic trunks.[2]

The diaphragm consists of a tendinous center and three thin peripheral muscles: the pars lumbalis, the pars costalis, and the pars sternalis. The pars lumbalis consists of the right and left crura, which attach to the cranial ventral border of L4 and the body of L3. The attachment area on these vertebrae occasionally has a concave indistinct ventral margin that may be mistaken for bone lysis (Fig. 29-1). The pars costalis attaches in an oblique direction to the thirteenth through eighth ribs, and the pars sternalis attaches to the xiphoid cartilage.[3] The diaphragm is convex and extends into the thorax from its attachments, creating the phrenicocostalis and phrenicolumbalis recesses.

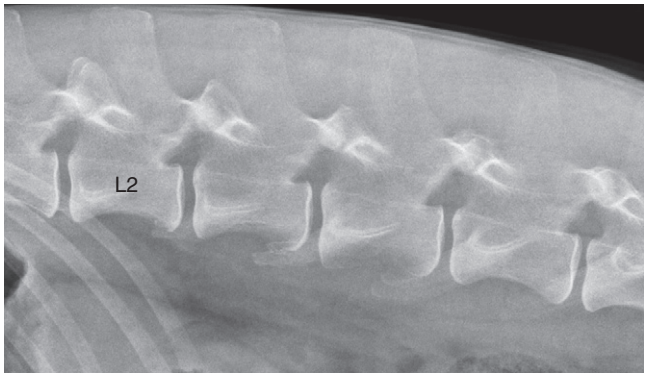


Fig. 29-1 Lateral view of the lumbar spine of a normal dog. Compared with L2 and L5, note the indistinct ventral cortex of L3 and L4 caused by the diaphragm attachment site. This can be misinterpreted as lysis if this normal appearance is not understood. *L2*, Second lumbar vertebra.

There are three openings through the diaphragm: (1) the dorsally located aortic hiatus encloses the aorta, azygos and hemiazygos veins, and the lumbar cistern of the thoracic duct; (2) the centrally located esophageal hiatus encloses the esophagus and vagus nerve trunks; and (3) the caudal vena cava foramen is located at the junction of the muscular and tendinous portions of the diaphragm.

NORMAL RADIOGRAPHIC ANATOMY

Radiographically, only a small portion of the diaphragm can be seen on any one view. Radiographic visualization of the diaphragm depends on adjacent structures being of different opacity. Most of the thoracic surface is visible because of the adjacent gas-filled lungs. Parts of the thoracic surface are not visualized where the lungs are not in contact with the diaphragm—the phrenicocostalis and phrenicolumbalis recesses. A large portion of the abdominal diaphragmatic surface is not seen because it silhouettes the adjacent liver. The ventral abdominal diaphragmatic surface is visible on the lateral view when fat is present within the falciform ligament. The dorsal aspect of the left diaphragmatic crus and the gastric wall appear as one linear structure when gas is present in the gastric cardia.

Diaphragmatic structures that may be visualized distinctly radiographically are the right and left crura, the intercrural cleft, and the cupula (body) (Figs. 29-2 to 29-5). Associated structures that may also be seen are the caudal vena cava and the caudal ventral mediastinum. On the lateral view, the right crus of the diaphragm blends with the caudal vena caval border, and the gastric fundus may be seen adjacent to the abdominal surface of the left crus. The intercrural cleft is a shorter, convex, opaque line caudal and ventral to the crura (see Figs. 29-2 and 29-3). The cupula is the most cranial convex portion of the diaphragm on both the lateral and the dorsoventral or ventrodorsal views. Also on these views, the thoracic surface of the diaphragm may be visualized as one, two, or three convex projections into the thoracic cavity (see Figs. 29-4 and 29-5).

Several normal variations of diaphragmatic position and shape may be seen radiographically. Factors that cause this variable appearance are real and apparent. Real factors consist of breed, age, obesity, respiration, and gravity. Apparent factors are x-ray beam centering and animal positioning during radiographic examination. Many combinations are possible when all permutations of these variables are considered.[4] Most of

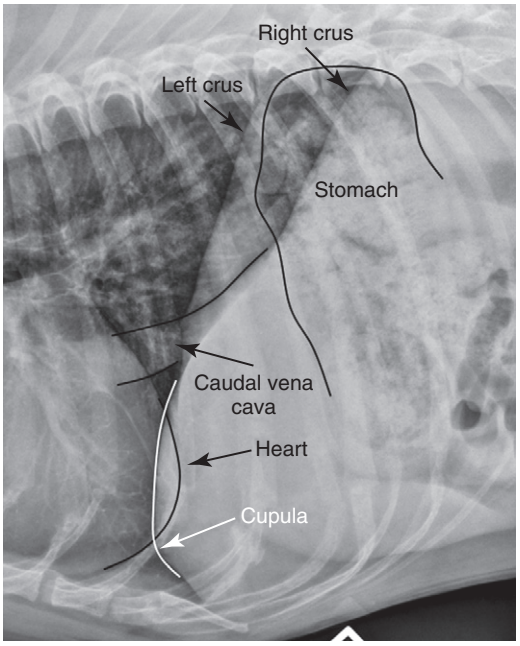


Fig. 29-2 Left lateral radiograph of the diaphragmatic region of a normal dog.

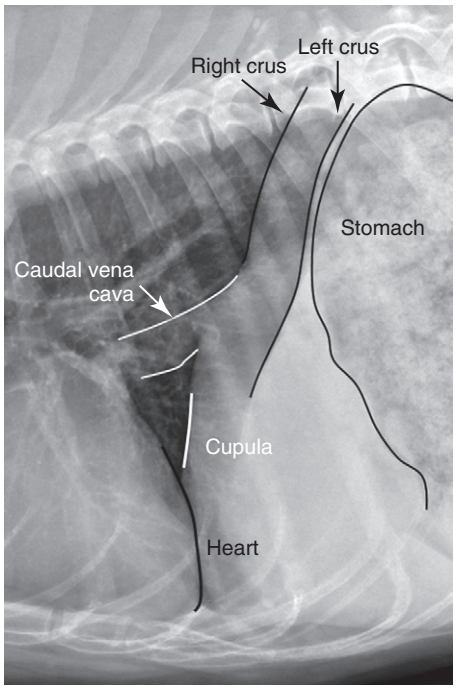


Fig. 29-3 Right lateral radiograph of the diaphragmatic region of a normal dog.

these variables are not radiographically significant; however, some must be recognized and understood. Changes most apparent radiographically are the position, shape, and visualization of the cupula and crura. The relative position of the crura depends mostly on position and size of the animal and primary x-ray beam centering.

The most dependent crus is usually displaced cranially when an animal is in lateral recumbency. In right lateral recumbency, the crura appear to be parallel (see Fig. 29-3); in left lateral recumbency, they sometimes appear to cross. The crura also appear to be more extensively separated, by up to

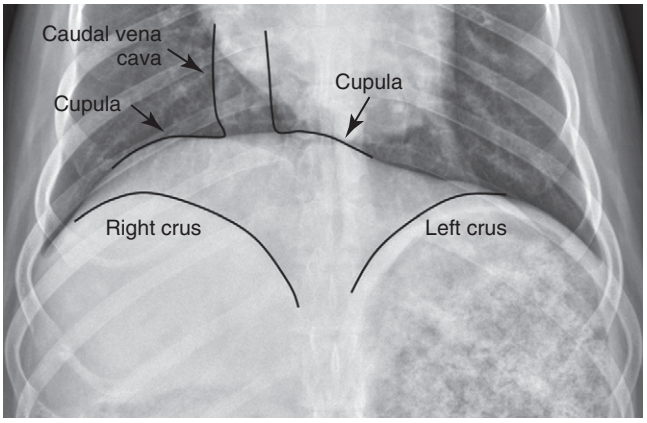


Fig. 29-4 Ventrodorsal radiograph of the diaphragmatic region of a normal dog with the cupula and both crura projecting into the thorax.

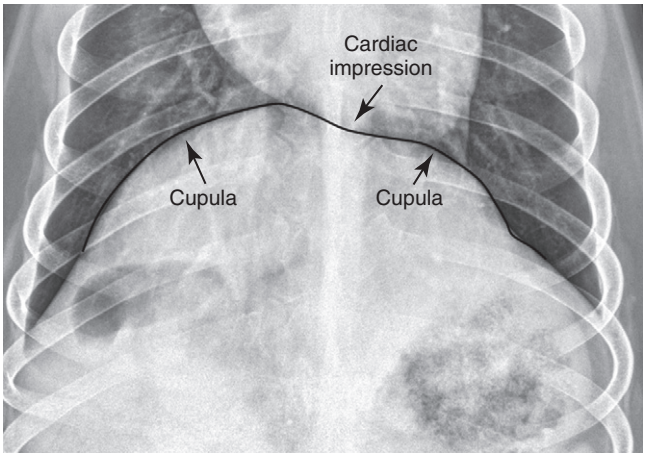


Fig. 29-5 Dorsoventral radiograph of the diaphragmatic region of a normal dog with only one convex shape projecting into the thorax.

2.5 vertebral lengths, if the animal is rotated slightly or if the x-ray beam is centered over the mid or cranial thorax.[4]

The radiographic appearance of the diaphragm in ventrodorsal or dorsoventral projections varies with x-ray beam centering. The diaphragm may appear as two or three separate domed-shaped structures (see Fig. 29-4) or as a single dome-shaped structure (see Fig. 29-5). The three structures represent the cupula and two crura. A single domed diaphragm may be seen on a ventrodorsal view when the x-ray beam is centered on the mid-abdomen or on a dorsoventral view when the x-ray beam is centered mid-thorax. Two or three separate domed structures are seen when the animal is in the ventrodorsal position and the x-ray beam is centered mid-thorax or on a dorsoventral view with the x-ray beam is centered mid-abdomen.[4]

The diaphragmatic position and shape vary with inspiration, expiration, and intraabdominal pressure. The normal intersection point of the diaphragm and spine is between T11 and T13 but may vary between T9 and L1. The diaphragm changes position with normal respiration from one half to two vertebral lengths. On extreme inspiration, the diaphragm changes position and shape. On a lateral thoracic view made in extreme inspiration, the diaphragm is oriented more vertically; the shape changes from convex to straight. The diaphragm is displaced cranially by increased intraabdominal pressure, which may be caused by obesity, ascites, gastric or intestinal distention, abdominal pain, or abdominal masses.

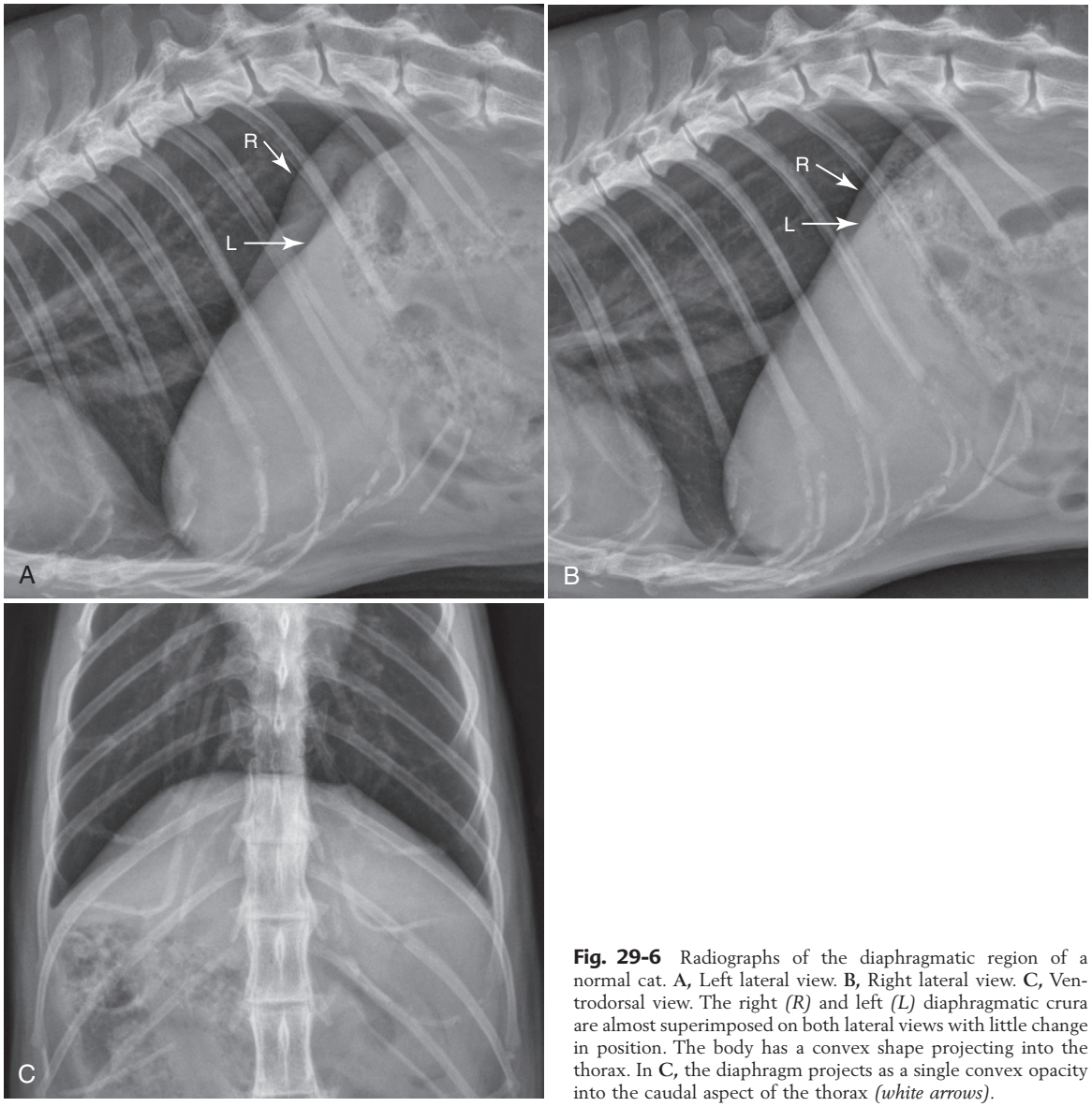


Fig. 29-6 Radiographs of the diaphragmatic region of a normal cat. **A,** Left lateral view. **B,** Right lateral view. **C,** Ventrodorsal view. The right *(R)* and left *(L)* diaphragmatic crura are almost superimposed on both lateral views with little change in position. The body has a convex shape projecting into the thorax. In **C,** the diaphragm projects as a single convex opacity into the caudal aspect of the thorax *(white arrows)*.

Separate diaphragmatic structures are not seen as distinctly in the cat, probably because of the relatively small thoracic size (Fig. 29-6). On extreme inspiration, particularly if the animal is in respiratory distress, small symmetric muscle projections are noted from the thoracic diaphragmatic surface in the ventrodorsal or dorsoventral view (Fig. 29-7). This has been referred to as *tenting* of the diaphragm and is discussed in Chapter 33 in reference to pulmonary hyperinflation.

RADIOGRAPHIC SIGNS OF DIAPHRAGMATIC DISEASE

The signs directly associated with the diaphragm are not as numerous and specific as those in many other organs. Radiographic changes observed most frequently with diaphragmatic disease include general or focal loss of the thoracic diaphragmatic surface outline and changes in diaphragmatic shape and position (Table 29-1).

The thoracic diaphragmatic surface outline will not be visualized radiographically if soft tissue or fluid contacts the surface. Changes in diaphragm shape occur most frequently

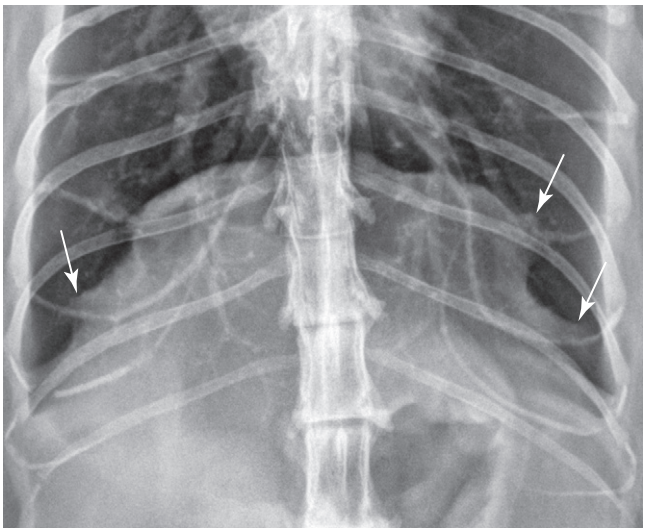


Fig. 29-7 Ventrodorsal view of the diaphragmatic region of a normal cat on deep inspiration. Small, regularly spaced projections *(white arrows)* are evident along the thoracic diaphragmatic surface. This so-called tenting reflects the pulling of the diaphragm against its costal attachments.

Table • **29-1**

Radiographic Signs of Diaphragmatic Disease

RADIOGRAPHIC SIGNS	CAUSES
General loss of diaphragmatic thoracic surface outline	Bilateral pleural fluid Generalized pulmonary disease in caudal lung lobes
Localized or partial loss of the thoracic surface outline	Thoracic masses adjacent to the diaphragm Diaphragmatic hernias Focal pulmonary disease in caudal lung lobes
Shape changes	Thoracic masses adjacent to the diaphragm Hiatal hernias Small diaphragmatic hernias Pleural reaction on the diaphragmatic surface Neoplasia arising from the diaphragm Hemiparalysis of the diaphragm Unilateral tension pneumothorax
Position Changes	
Cranial displacement	Obesity Peritoneal fluid Abdominal pain Abdominal masses or organ enlargement; liver enlargement and masses frequently cause cranial displacement Generalized diaphragmatic paralysis Cranial displacement of the cupula caused by a diaphragmatic defect with the peritoneum and pleura intact
Caudal displacement	Severe respiratory distress—ventilation or perfusion problems Tension pneumothorax Caudal displacement of the cupula caused by contact with the heart

on the cupula; they are often normal and are frequently caused by contact with the heart (Fig. 29-8) or position of the animal during radiographic examination. The shape and position may also appear altered in some large-breed dogs, with the body appearing more convex and extending to a more cranial position in the thorax. This may be the result of a flaccid tendinous membrane, or it may be associated with a peritoneopleural hernia, which often produces no clinical signs.

Thoracic masses or lung disease adjacent to the diaphragm, hiatal and small traumatic diaphragmatic hernias, masses originating from the diaphragm, and chronic pleural inflammatory reactions are the most frequent pathologic causes associated with diaphragmatic shape changes. An asymmetric diaphragmatic shape may occur with unilateral tension pneumothorax or hemiparalysis. Suspected hemiparalysis should be confirmed by observing diaphragmatic movement during fluoroscopy.

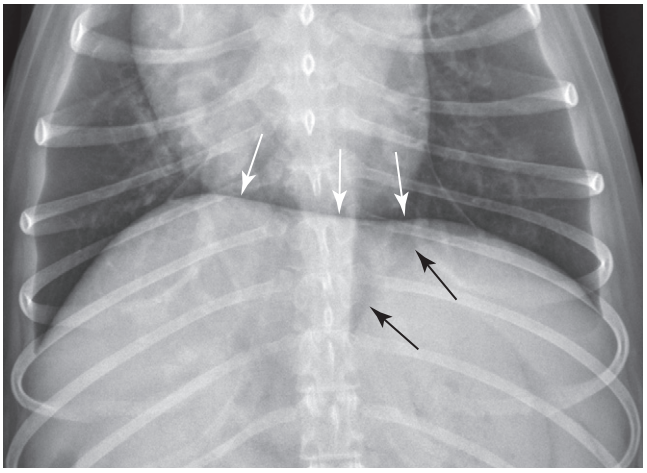


Fig. 29-8 Ventrodorsal view of the diaphragmatic region of a normal dog. A cardiac impression *(white arrows)* is present on the diaphragmatic body (cupula). The left diaphragmatic crus *(black arrows)* is visible. The right crus cannot be visualized as a separate structure.

Positional changes consist of cranial and caudal displacement. Because the position of the diaphragm changes during the respiratory cycle, minor changes are difficult to diagnose and in most instances are not clinically significant. Severe positional changes may be significant and indicative of thoracic or abdominal disease. Cranial diaphragmatic displacement is usually associated with abdominal disease (see Table 29-1) or generalized diaphragmatic paralysis, which should be confirmed by fluoroscopic observation. Caudal diaphragmatic displacement is usually associated with severe respiratory disease (Fig. 29-9). The caudally positioned diaphragm is an attempt by the animal to increase the level of systemic oxygenation, which may be low because of ventilation or perfusion deficiencies in the lungs. Bilateral tension pneumothorax may also cause a caudally displaced diaphragm from increased pleural pressure.

Although many of the radiographic signs of diaphragmatic disease are not specific, their cause should be determined. In some instances, ultrasonography or additional radiographic studies, such as positional views with a horizontally directed x-ray beam and contrast medium studies, may be indicated to determine the cause of the radiographic signs.

DIAPHRAGMATIC DISEASES

The most frequently observed diaphragmatic diseases in the dog and cat are hernias, which may be traumatic and congenitally predisposed. Motor or innervation disturbances occur less frequently.

Diaphragmatic Hernias

A diaphragmatic hernia is a protrusion of abdominal viscera through the diaphragm into the thorax. Diaphragmatic hernias that may be recognized radiographically include traumatic, peritoneopericardial, hiatal, peritoneopleural, and those secondary to congenital diaphragmatic defects.

Abdominal trauma is the most common cause of diaphragmatic hernia. A high momentary increase in abdominal pressure when the glottis is open produces a high pleuroperitoneal pressure gradient that may result in a diaphragmatic hernia. The high pleuroperitoneal gradient may produce a rent in the muscular portion of the diaphragm, or it may force abdominal viscera through congenitally weak or defective areas. Clinical

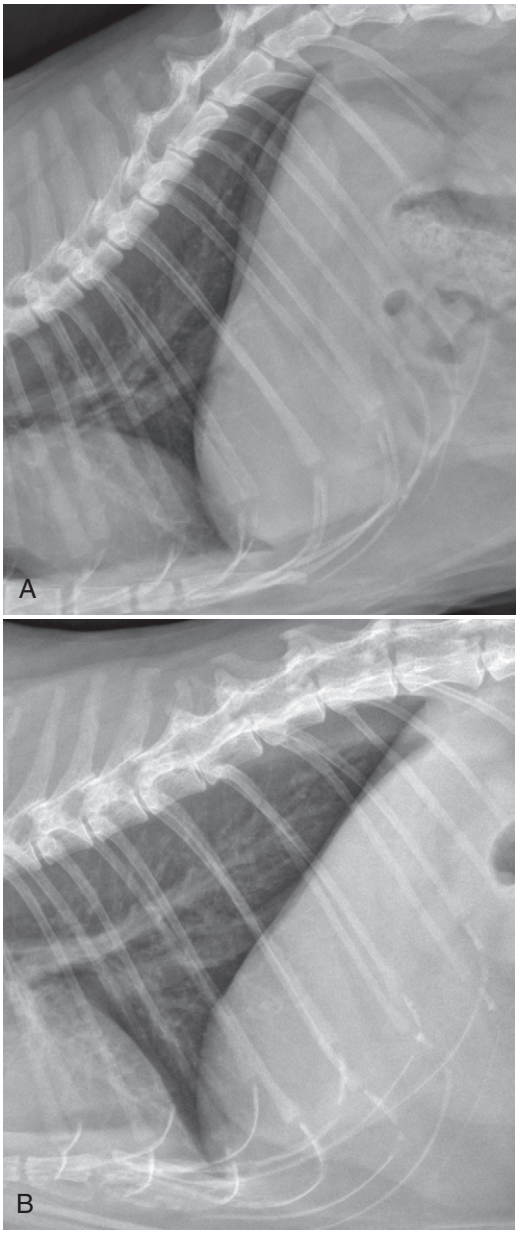


Fig. 29-9 Lateral views of the diaphragmatic region of a normal cat on expiration **(A)** and on extreme inspiration **(B).** The entire diaphragm is displaced caudally with inspiration and has a flatter contour compared with expiration.

signs that may be observed with diaphragmatic hernias include dyspnea, pain, vomiting, regurgitation, muffled heart sounds, and a weak femoral pulse.[5,6] Some diaphragmatic hernias may not cause clinical signs and are detected incidentally.

Radiography plays an important role in confirming a diagnosis of diaphragmatic hernia and may provide information about location, extent, contents, and secondary complications associated with the hernia.[7-11] If a diagnosis cannot be confirmed from survey radiographs (Box 29-1), ultrasonography and/or other imaging procedures may be performed to provide additional diagnostic information. Other radiographic procedures consist of administration of oral barium sulfate, positional radiographic views, removal of pleural fluid and repeat radiography of the thorax, and positive contrast-medium peritoneography.

Box • 29-1

Radiographic Signs Associated with Traumatic Diaphragmatic Hernia

Abdominal Viscera within the Thorax
Gas- or ingesta-filled bowel
Gas- or ingesta-filled stomach
Identifiable parenchymal organs, such as the liver and spleen

Displacement of Abdominal Structures—Cranial
Liver
Small bowel
Stomach
Spleen

Displacement of Thoracic Structures—Generally Displaced Cranially and Laterally Away from an Abnormal Opaque Area in the Thorax
Heart
Mediastinum
Lungs

Partial or Complete Loss of the Thoracic Diaphragmatic Surface Outline
Pleural fluid or mass
Lung fluid or mass

Divergence of Diaphragmatic Crura or Cranial Angulation of Diaphragm
Pleural fluid

To ascertain the position of the stomach and proximal small bowel, a small amount (20 to 40 mL) of barium sulfate (30% w/v) can be given orally and radiographs obtained after 15 to 20 minutes (Fig. 29-10). Radiographs made with a horizontal x-ray beam help differentiate solid abdominal organs in the thorax from pleural fluid (Fig. 29-11). Thoracocentesis and pleural fluid removal followed by another radiographic examination provide better radiographic visualization of structures within the thorax.

Positive-contrast peritoneography can be performed by injecting 2 mL/kg body weight of an iodinated, preferably nonionic, contrast medium into the peritoneal cavity. The animal should then be positioned such that gravity facilitates contrast medium accumulation around the liver and the diaphragm. Contrast medium within the thorax and an interrupted outline of the abdominal diaphragmatic surface are the most consistent positive-contrast peritoneographic signs of a diaphragmatic hernia (Fig. 29-12).[12,13] Any or all of these procedures may be used, but the most simple should be used first. Peritoneography should be used after other diagnostic procedures have failed to provide the needed information.

Other procedures, including positive-contrast pleurography, portography, cholecystography, angiocardiography, angiography, and nonselective cardiography are useful in diagnosing diaphragmatic hernias, but these are more difficult and are used rarely.[14]

Ultrasonographic examination of the diaphragm may add diagnostic information, particularly for patients with pleural fluid that obliterates soft tissue. The examination is best done

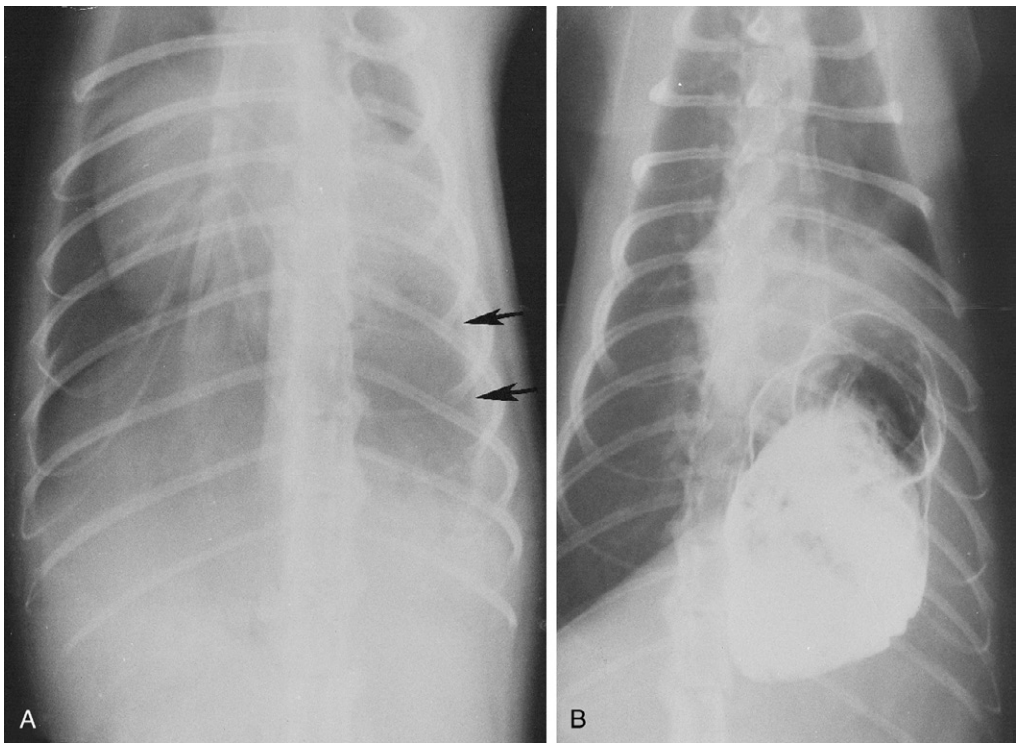


Fig. 29-10 Confirmation of a traumatic diaphragmatic hernia with a barium gastrogram. **A,** Ventrodorsal view of the thorax of a cat. An ill-defined gas opacity is present in the left caudal thorax *(black arrows)*. The identity of this opacity is not certain. The heart is displaced toward the right thoracic wall, which is likely accentuated by the slightly oblique position of the animal. **B,** After administration of barium sulfate, the stomach is identified in the left caudal thorax, thus confirming a left-sided diaphragmatic hernia.

transhepatically.[15] Ultrasonographic signs of a diaphragmatic hernia include identification of abdominal structures within the thorax, particularly the liver, and an interruption in the diaphragmatic outline.[15-17] An interruption in the diaphragmatic outline may not be seen consistently with diaphragmatic hernia.[18]

Traumatic Diaphragmatic Hernias

In one study, only half of the animals with a trauma-induced diaphragmatic hernia had a history of known trauma.[6] Traumatic diaphragmatic hernias usually involve the muscular portion of the diaphragm.[6,19] It has been suggested that right and left incidence distribution is equal,[15] but a higher incidence on the right side has been reported in the dog.[6] The organs that most frequently herniate are, in order of prevalence, the liver, small bowel, stomach, spleen, and omentum.[6,9,19-21] In patients with a chronic diaphragmatic hernia, the liver and small intestine are the most frequently herniated, followed by omentum, spleen, stomach, colon, and pancreas. Strangulation of organs may be found at surgery.[22]

The most consistent radiographic signs of traumatic diaphragmatic hernia are abdominal viscera within the thorax; displacement of abdominal or thoracic organs, or both; partial or complete loss of the thoracic diaphragmatic surface outline; asymmetry or altered slope to the diaphragm on the lateral projection[11]; and the presence of pleural fluid (Fig. 29-13).

Identification of abdominal structures in the thorax is a conclusive sign of diaphragmatic hernia. Small bowel is easily identified when it is gas filled; when fluid filled, it appears as a tubular structure. The stomach may be filled with gas, fluid, or ingested material. In addition, gastric rugal folds may provide a marker for identifying the stomach within the thorax. A herniated, gas-distended stomach may appear as a unilateral left pneumothorax, and the stomach should be decompressed and repositioned immediately by surgical intervention (Fig. 29-14).[6] Such instances are life threatening because of potential or actual cardiovascular tamponade.

Herniated solid abdominal parenchymal organs are difficult to distinguish from localized pleural fluid, pulmonary opacity, or both. Omentum is the most difficult to detect unless it is herniated in association with other abdominal organs. In such instances, it provides a fat opacity and helps outline other abdominal visceral organs.

In the absence of finding abdominal organs in the thorax, cranial abdominal organ displacement or absence of abdominal organs from their normal location is an indirect sign of diaphragmatic hernia. The liver, spleen, small bowel, and stomach must be assessed closely for displacement. Including the cranial abdomen on the thoracic radiograph when diaphragmatic hernia is suspected is helpful to evaluate abdominal organ displacement. Barium sulfate may also be administered to identify the stomach and help detect mild to moderate gastric displacement not observed on survey radiographs.

The heart, mediastinum, and lungs may also be displaced, depending on the size and position of abdominal organs within the thorax. The heart and lungs are usually displaced cranially and either medially or laterally by herniated abdominal viscera, and the mediastinum is usually shifted from its midline position. A localized diaphragmatic surface outline loss usually indicates the area through which the hernia has occurred. Abdominal viscera and/or pleural fluid adjacent to the thoracic diaphragmatic surface cause the outline loss. This occurrence must be distinguished from the many other

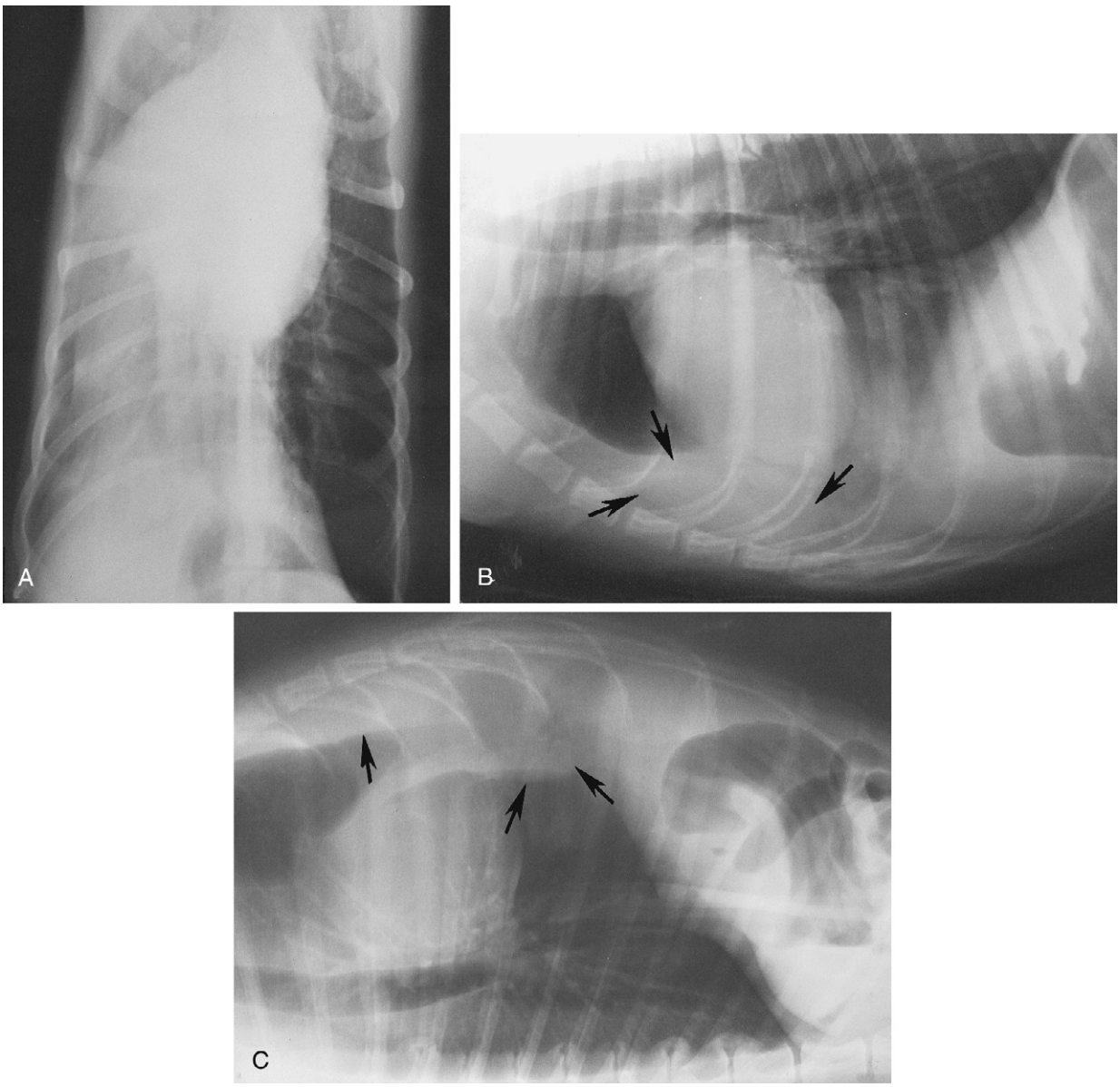


Fig. 29-11 Ventrodorsal **(A),** lateral **(B),** and dorsal recumbent, horizontal-beam lateral **(C)** views of a dog with a traumatic diaphragmatic hernia. **A,** An increased soft tissue opacity in the caudal right thorax with loss of the thoracic diaphragmatic surface outline over the cupula is apparent. **B,** The heart is displaced dorsally, and a soft tissue opacity can be seen between the heart and the sternum *(black arrows)*. The thoracic diaphragmatic outline is indistinct over the cupula. **C,** The soft tissue opacity *(black arrows)* remains in the same position, which indicates that the opacity is a solid structure and not free pleural fluid. This finding is compatible with a diaphragmatic hernia.

thoracic conditions that produce soft tissue opacity adjacent to the diaphragm. Pleural fluid is present consistently with chronic diaphragmatic hernias, or if a herniated abdominal organ, most usually the liver, is strangulated through a small diaphragmatic opening.[21] Pleural fluid is a nonspecific sign of diaphragmatic hernia and often masks other more important radiographic signs. Thoracocentesis and aspiration of the pleural fluid are often necessary before the hernia can be detected radiographically.

Congenitally Predisposed Diaphragmatic Hernias

Approximately 15% of all diaphragmatic hernias are congenitally predisposed.[9] Included in this group are peritoneopericardial diaphragmatic hernias, hiatal hernias, and peritoneopleural hernias. Herniation in association with congenital diaphragmatic defects may occur in an animal of any age after abdominal trauma or transitory increase in intraabdominal pressure. Defects in diaphragmatic development may be present and never result in a hernia.

Peritoneopericardial Diaphragmatic Hernias

A peritoneopericardial diaphragmatic hernia occurs when abdominal viscera herniates into the pericardial sac through a congenital hiatus formed between the tendinous portion of the diaphragm and the pericardial sac. This has been reported to occur in littermates,[23] and a predisposing trait may be

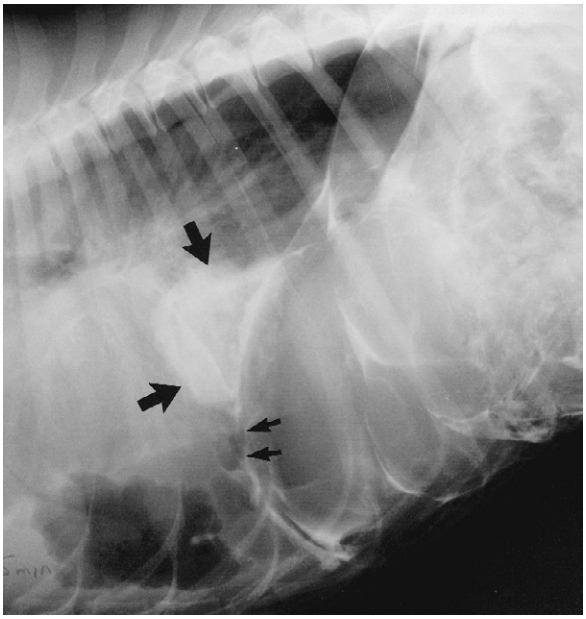


Fig. 29-12 A lateral abdominal radiograph of a positive-contrast peritoneogram. The abdominal surface of the diaphragm has an indistinct outline *(small black arrows)*, with contrast medium present within the pleural cavity *(large black arrows)*. These are reliable radiographic signs of a diaphragmatic defect and a diaphragmatic hernia.

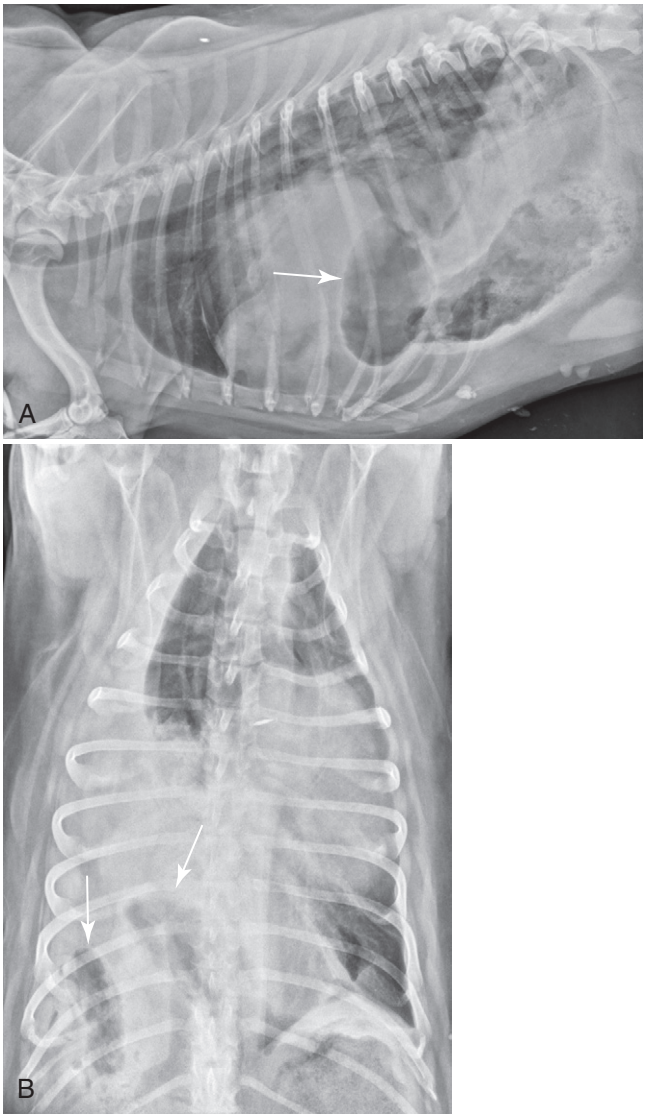


Fig. 29-13 Lateral **(A)** and ventrodorsal **(B)** views of the thorax of a dog with a traumatic diaphragmatic hernia. Radiographic signs of a diaphragmatic hernia in **A** are gas-filled stomach *(white arrow)* within the thorax, cranial displacement of abdominal structures, and a cranially displaced diaphragmatic segment. Radiographic signs in **B** are the mediastinal shift to the left, away from the herniated viscera; gas-filled stomach and bowel within the thorax *(white arrows)*; cranially displaced abdominal structures; and loss of the right diaphragmatic surface outline.

carried on a simple autosomal recessive gene in cats, with a 1:500 to 1:1500 rate of incidence.[24] Domestic longhair cats and Himalayans appear to be overrepresented.[25] The hernia may have been present from birth or acquired. Mild increases in intraabdominal pressure may cause abdominal organs to herniate through a congenital hiatus.

Peritoneopericardial hernias may produce clinical signs, or they may be an incidental radiographic finding. These hernias may be present in old or young animals.[5,25-30] The liver is herniated most frequently; the stomach, omentum, and small bowel have a less frequent occurrence of herniation.[31] Hepatic cysts have also been reported to be associated with liver herniation into the pericardial sac.[32]

Radiographic signs associated with peritoneopericardial hernias are listed in Box 29-2. Herniated abdominal organs in the pericardial sac are usually caudal, or caudal and lateral, to the heart. Gas- or ingesta-filled hollow visceral organs are not difficult to identify within the pericardial sac, but the conspicuity of the gas-containing viscus may be a function of body position during radiography (Fig. 29-15). Radiographically, gas within the bowel is in abrupt contrast to the adjacent structures of soft tissue opacity. Solid parenchymal organs, unless surrounded by omentum, are difficult to distinguish as separate structures within the pericardium. When abdominal organs are herniated into the pericardial sac, cranial and ventral organ displacement within the abdomen may be seen; but this displacement is usually not as pronounced as that noted with traumatic diaphragmatic hernias.

A large, round cardiac silhouette and a cardiac silhouette with an abnormal convex projection on the caudal border are signs consistent with peritoneopericardial diaphragmatic hernias. These two signs depend on the amount of abdominal viscera within the pericardial sac. Large amounts of viscera produce a large, round cardiac silhouette, whereas smaller amounts, such as a portion of the liver or stomach, may produce only an abnormal convex caudal cardiac border. A large, round silhouette must be differentiated from pericardial effusion, generalized heart enlargement, or both. An abnormally convex caudal cardiac border must be differentiated from neoplasia, pleural granulomas, or localized pleural fluid.

An indistinguishable outline to the ventral diaphragmatic surface and the caudal ventral cardiac silhouette is produced by the communication between the two structures. This finding must be differentiated from normal contact between the heart and diaphragm, pleural fluid, localized pleuritis, and pleural granulomas.

An apparently confluent silhouette between the heart and diaphragm may appear as a wide caudal mediastinum; depending on the size of the communication, it may or may not be seen radiographically. This confluent silhouette must also be differentiated from other pathologic conditions. On the lateral view, identification of the dorsal peritoneopericardial mesothelial remnant between the heart and diaphragm is a

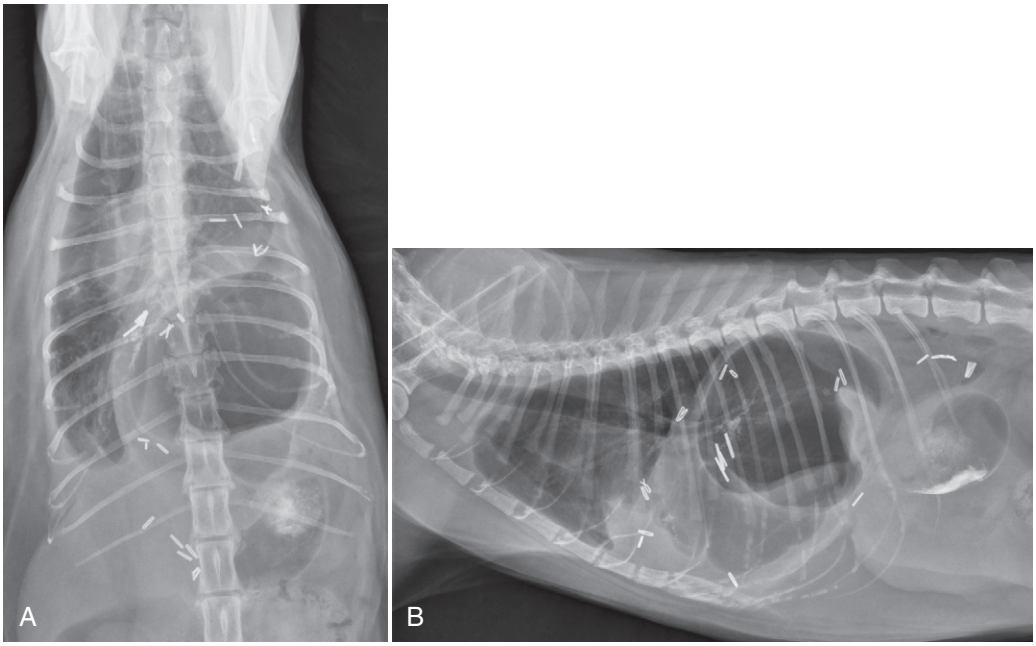


Fig. 29-14 Ventrodorsal and lateral views of the thorax of a cat with a traumatic diaphragmatic hernia of the stomach. Hemoclips are present from a previous surgery. **A,** The gas-filled stomach is herniated into the left hemithorax, displacing the heart and lungs to the right. The normal gastric and left diaphragmatic outlines are not present. **B,** The severely gas-distended stomach occupies the majority of the caudal thorax and obscures the cardiac silhouette.

Box • 29-2

Radiographic Signs Associated with Peritoneopericardial Diaphragmatic Hernias

- Abdominal organs identified in the pericardial sac; gas, ingested material, or structures of soft tissue opacity may be present
- Large, round cardiac silhouette
- Convex projection of the caudal cardiac silhouette
- Indistinguishable border of the ventral thoracic diaphragmatic surface and the caudal ventral cardiac silhouette
- Confluent silhouette between the diaphragm and the heart
- Dorsal peritoneopericardial mesothelial remnant between the heart and diaphragm on the lateral view in cats

consistent radiographic sign of peritoneopericardial hernia in cats (Fig. 29-16).[33] Additional radiographic studies that may be performed to confirm a diagnosis include oral administration of barium sulfate, nonselective angiography,[34] and peritoneography. Barium sulfate may be used to demonstrate gastrointestinal structures within the pericardial sac or cranial ventral displacement of abdominal structures (Fig. 29-17).

Ultrasonography has been successfully used to diagnose peritoneopericardial diaphragmatic hernias.[15-18] Ultrasonography is a reliable imaging modality to use for documentation of a peritoneopericardial hernia in patients where soft tissue opaque abdominal structures are in the pericardial sac and difficult to differentiate from the heart on radiographs. If available, an ultrasound examination should be considered before contrast examinations are performed to assist in the diagnosis of peritoneopericardial diaphragmatic hernia.

Hiatal Hernias

Hiatal hernias occur when a portion of stomach enters the thorax through the esophageal hiatus. These hernias occur through a congenitally or traumatically enlarged esophageal hiatus; they also may result from contraction of the longitudinal esophageal muscle.[35,36]

Two recognized types of hiatal hernias exist: sliding and paraesophageal.[37] The gastroesophageal sphincter and a portion of the stomach, usually the cardia, are herniated into the thorax with sliding hiatal hernias.[38] Sliding hiatal hernias are usually congenital and found in younger animals.[37] They are often associated with esophagitis from gastroesophageal reflux. As the name implies, the caudal esophagus and the cardia slide intermittently from the abdomen into the thorax, causing temporary cranial displacement of the thoracic esophagus. Because the hernia is dynamic, it may not be seen on any one radiograph; fluoroscopic examination is often necessary to make a diagnosis. Patients with nonsliding hiatal hernias have been reported, with the gastroesophageal sphincter and the gastric cardia displaced through the esophageal hiatus and fixed within the thorax.[38] Sliding hiatal hernias are reported intermittently in animals.[39-47] The low incidence may be a reflection of the subtle clinical signs and intermittent manifestations on survey radiographs and fluoroscopy.

A paraesophageal hiatal hernia is produced when the cardia or cardia and fundus of the stomach or other soft tissue structures herniate through, or alongside, the esophageal hiatus and become positioned adjacent to the esophagus. They are usually static and do not slide between the thorax and abdomen, and the gastroesophageal sphincter is in a normal position.[36,38,48] The herniated stomach may cause esophageal obstruction from external pressure on the caudal esophagus.

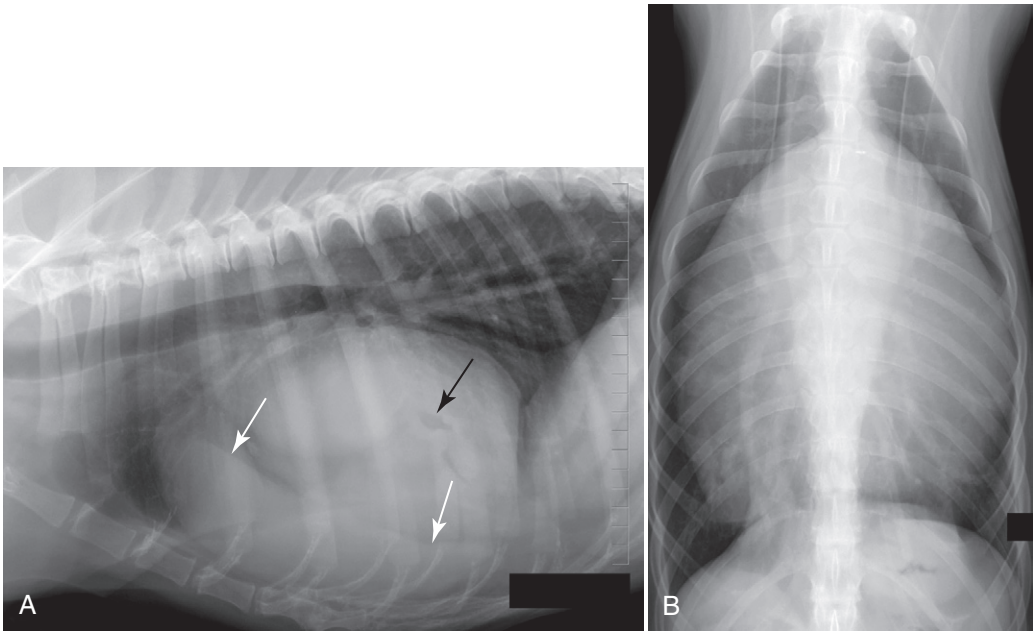


Fig. 29-15 Right lateral **(A)** and ventrodorsal **(B)** radiographs of a dog with a peritoneopericardial diaphragmatic hernia. Variable opacities are visualized in the pericardial sac, including gas, soft tissue, and fat. Gas-containing structures in the thorax are better visualized in the right lateral view *(black arrow)*. The liver is also visualized on the lateral view (*white arrows*). The amount of gas within organs in the pericardial sac will change depending on the position of the patient; no gas may be visible in some positions. (Courtesy of Dr. Amy Habing, Michigan State University, East Lansing, Mich.)

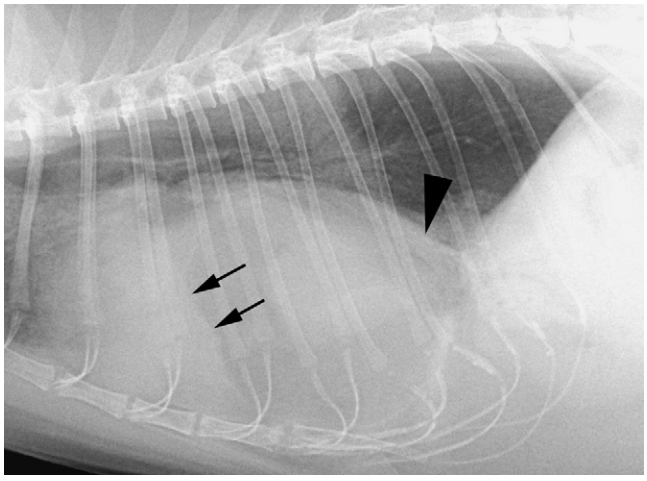


Fig. 29-16 Lateral view of a cat with a peritoneopericardial diaphragmatic hernia. The outline of a dorsal peritoneopericardial mesothelial remnant is visible cranial to the diaphragm *(black arrowhead)*. The liver, omentum, and spleen are herniated into the pericardial sac. The caudal border of the heart is visible *(black arrows)* because of fat in the adjacent omentum.

Hiatal hernias have also been classified as types I through IV. Type I represents a sliding hiatal hernia, type II represents a paraesophageal hernia, and type III represents a combination of type I and type II. Type IV has been described two ways: as a type III hernia combined with herniation of another organ rather than the stomach or as a gastroesophageal intussusception. Other complicated hernias, such as a hernia through the esophageal hiatus combined with a second, separate gastric herniation through a defect in the diaphragm have been reported.[49]

Hiatal hernias occur in both the dog and the cat.[40,42,44,47] They can be associated with other esophageal conditions in Shar-Pei dogs.[47] Clinical signs include vomiting, regurgitation, excessive salivation, dysphagia, and dyspnea.[40,46,47] Hiatal hernia may be suspected from the clinical signs and survey radiographic findings but must be confirmed by an esophagram.

Radiographic signs of a sliding hiatal hernia are listed in Box 29-3. The most consistent survey radiographic sign is stomach displacement. The cardia appears to be stretched toward the diaphragm or may extend into the thorax. This displacement produces an abnormal shape to the cardia and fundus remaining in the abdomen. The caudal esophagus may or may not be distended, and a soft tissue mass may be seen adjacent to the left diaphragmatic crus (Fig. 29-18). The size and visibility of this mass depend on the amount of stomach that has herniated into the thorax. The soft tissue mass associated with a hiatal hernia must be differentiated from pulmonary or diaphragmatic masses. Diaphragmatic tumors occur but are rare.[50]

A dilated caudal esophagus is usually best detected and evaluated with an esophagram. An esophagram is also helpful for differentiating the type of hiatal hernia. The caudal esophageal sphincter and a portion of the cardia are cranial to the diaphragm with a sliding hiatal hernia.[51] The caudal esophageal sphincter can be identified as a concentric, smooth, 1 to 2-cm narrowing in the caudal esophagus (Fig. 29-19). Displacement and narrowing of the caudal esophagus by the cardia and fundus can be seen with paraesophageal hiatal hernias. Barium outlining the caudal esophagus can also be seen superimposed over the herniated paraesophageal soft tissue (Fig. 29-20).

Gastroesophageal Intussusception

Gastroesophageal intussusception occurs when the stomach, with or without the spleen, duodenum, pancreas, and

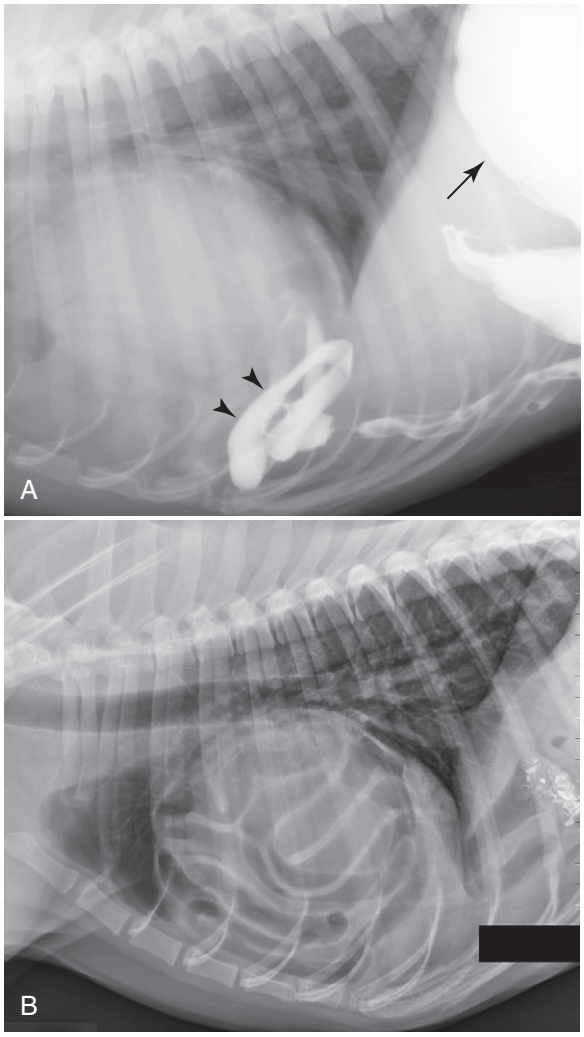


Fig. 29-17 Right lateral **(A)** and left lateral **(B)** views of the thorax of a dog with a peritoneopericardial diaphragmatic hernia. **A,** Barium is present in the normally positioned stomach *(black arrow)* as well as in small intestines *(black arrowheads)* that are herniated into the pericardial sac. **B,** Radiographs of the same patient made at a later time reveal diffuse gas filling of the small intestines, which provides negative contrast that allows easy identification of small intestines within the pericardial sac. (Courtesy of Dr. Amy Habing, Michigan State University, East Lansing, Mich.)

omentum, invaginates through the esophageal hiatus into the caudal esophagus.[36,38,52,53] They occur most frequently in male and German shepherd dogs and in animals with a preexisting dilated esophagus.[53] Gastroesophageal intussusception usually produces an esophageal obstruction, which results in rapid deterioration of the animal's condition with a high mortality rate; a timely diagnosis is therefore essential.[53]

On survey radiographs, a large soft tissue mass is seen adjacent to the diaphragm, usually accompanied by a dilated esophagus. With an esophagram, gastroesophageal intussusceptions produce a large intraluminal filling defect within the caudal esophagus, rugal folds may be outlined with barium, and barium usually does not usually enter the stomach (Box 29-4). (See Fig. 27-20 for an example of gastroesophageal intussusception.)

Peritoneopleural Hernias

Congenital diaphragmatic defects resulting in peritoneopleural hernias are rare in the dog and cat[54-58] and have been confused with pulmonary masses.[59] The defects are created when the septum transversum or the pleural peritoneal folds do not develop and fuse to form a complete diaphragm. The diaphragmatic defect allows abdominal viscera to enter the thoracic cavity, producing a pleuroperitoneal hernia.

In human beings, diaphragmatic defects have a familial incidence with a multifactorial mode of inheritance.[60] Congenital defects in dogs have been reported in the muscular diaphragm, dorsolateral in position,[61] and in the membranous diaphragm associated with umbilical hernias.[55-57]

The radiographic signs of peritoneopleural hernias associated with diaphragmatic defects are the same as for traumatic diaphragmatic hernias. With membranous defects, however, the liver (in dogs) or the falciform fat (in cats) is displaced cranially, while remaining in the caudal ventral thorax, and is often confined to the mediastinum because the peritoneal membrane and pleura are intact (Fig. 29-21).[61]

Motor Disturbances of the Diaphragm

The diaphragm is the principal muscle of respiration and is innervated by the phrenic nerve. Most motor disturbances are clinically asymptomatic and have not been well documented in animals.

Motor disturbances of the diaphragm consist of unilateral paralysis, bilateral paralysis, and diaphragmatic flutter.[1] Diaphragmatic paralysis may result from pneumonia, trauma, myopathies, and neuropathies, or the cause may be unidentified.[1] Transient posttraumatic hemidiaphragmatic paralysis has been reported in cats.[62] Diaphragmatic paralysis should be suspected when one or both diaphragmatic crura are displaced cranially (Fig. 29-22). Confirmation of paralysis is best achieved with fluoroscopy. Unequal movement between the crura is seen with unilateral paralysis. With bilateral paralysis, minimal or no diaphragmatic movement or a paradoxic cranial displacement of the flaccid diaphragm may occur during inspiration.[63] Bilateral paralysis may be more difficult to confirm with fluoroscopy because diaphragmatic movement is sometimes produced by compensatory abdominal muscle contraction during respiration.

Diaphragmatic flutter is most often associated with contractions of the diaphragm synchronous with the heartbeat. It

Box • 29-3

Radiographic Signs Associated with Sliding Hiatal Hernias

Survey Radiographs

Soft tissue mass adjacent to the left diaphragmatic crus
Loss of thoracic surface outline on the left diaphragmatic crus
Cranial displacement of the gastric cardia producing an abnormal gastric shape
Dilated esophagus
Pneumonia

Esophagram

Dilated esophagus
Hypomotile esophagus
Gastroesophageal sphincter within the thorax represented by a circumferentially narrowed area of the esophagus
Gastric cardia within the thorax
Gastroesophageal reflux

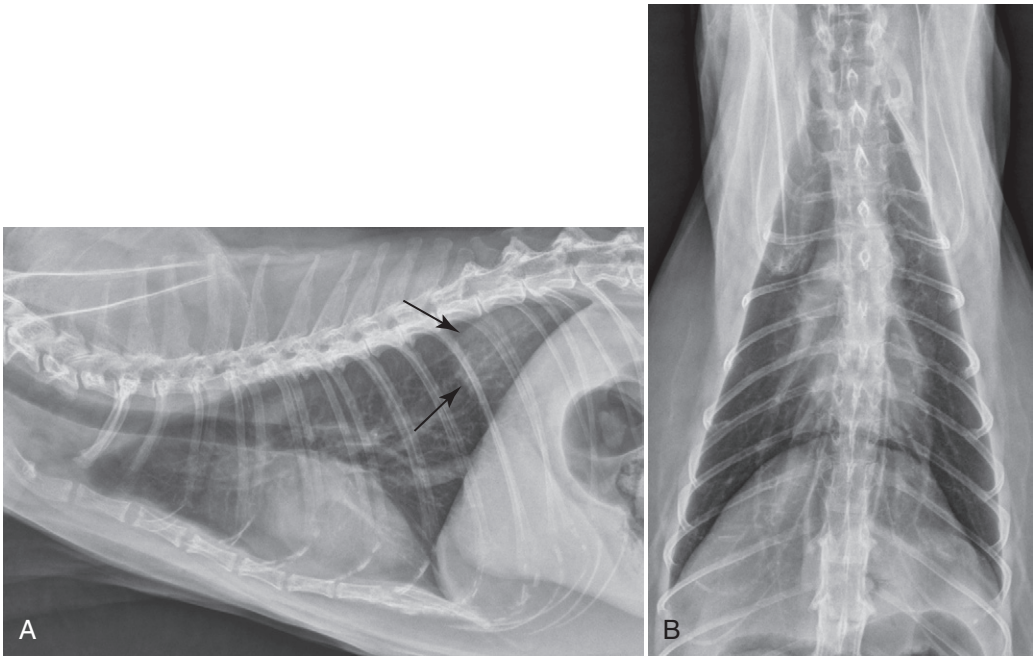


Fig. 29-18 **A,** Lateral thoracic view with a soft tissue opacity in the caudodorsal thorax *(black arrows)*. The soft tissue opacity is suspect for a hiatal hernia. **B,** Ventrodorsal view at the same time is normal, which supports the diagnosis of sliding hiatal hernia.

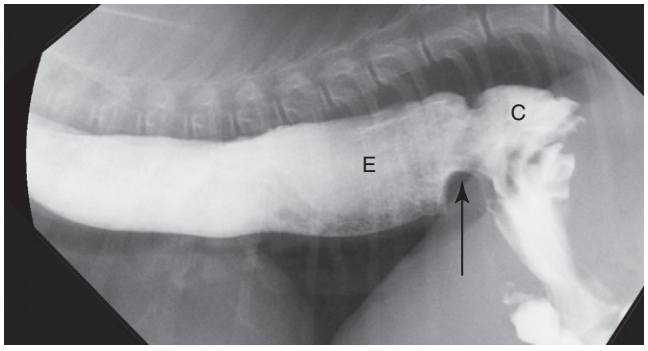


Fig. 29-19 Lateral view of barium esophagram in a patient with a sliding hiatal hernia. Contrast medium distends the caudal esophagus *(E)*, the gastroesophageal sphincter *(black arrow)*, and the cardia *(C)*. The gastroesophageal sphincter and gastric cardia are displaced cranial to the diaphragm through the esophageal hiatus.

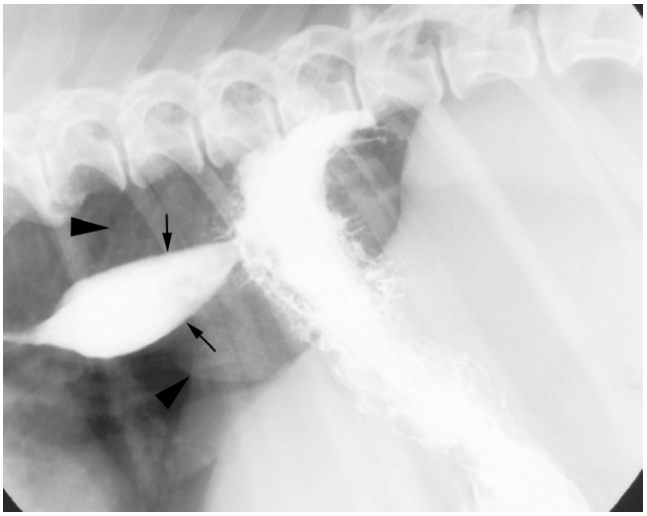


Fig. 29-20 Lateral view of the thorax. Barium is filling and outlining the caudal esophagus *(black arrows)*. The barium-filled caudal esophagus is superimposed over a soft tissue organ *(black arrowhead)* cranial to the diaphragm and adjacent to one side of the esophagus.

Box • **29-4**

Radiographic Signs Associated with Gastroesophageal Intussusception

Survey Radiographs
Soft tissue mass adjacent to the diaphragm
Cranial displacement of the stomach with or without the spleen or duodenum
Dilated esophagus

Esophagram
Intraluminal filling defect in the caudal esophagus
Barium outline of rugal folds
No barium within the stomach

is usually transient in nature and can be easily diagnosed with fluoroscopy by observing contractions of the diaphragm in synchrony with the heartbeat.[64]

Muscular Dystrophy

Muscular dystrophy caused by dystrophin deficiency occurs rarely in dogs[65] and cats.[66,67] In dogs with muscular dystrophy, radiographic abnormalities include diaphragmatic asymmetry, diaphragmatic undulation, and gastroesophageal hiatal hernia.[68] In cats an irregular, scalloped appearance of the diaphragm, particularly along the ventral margin, was a consistent finding observed on radiographs after 7 months of age.[63] The

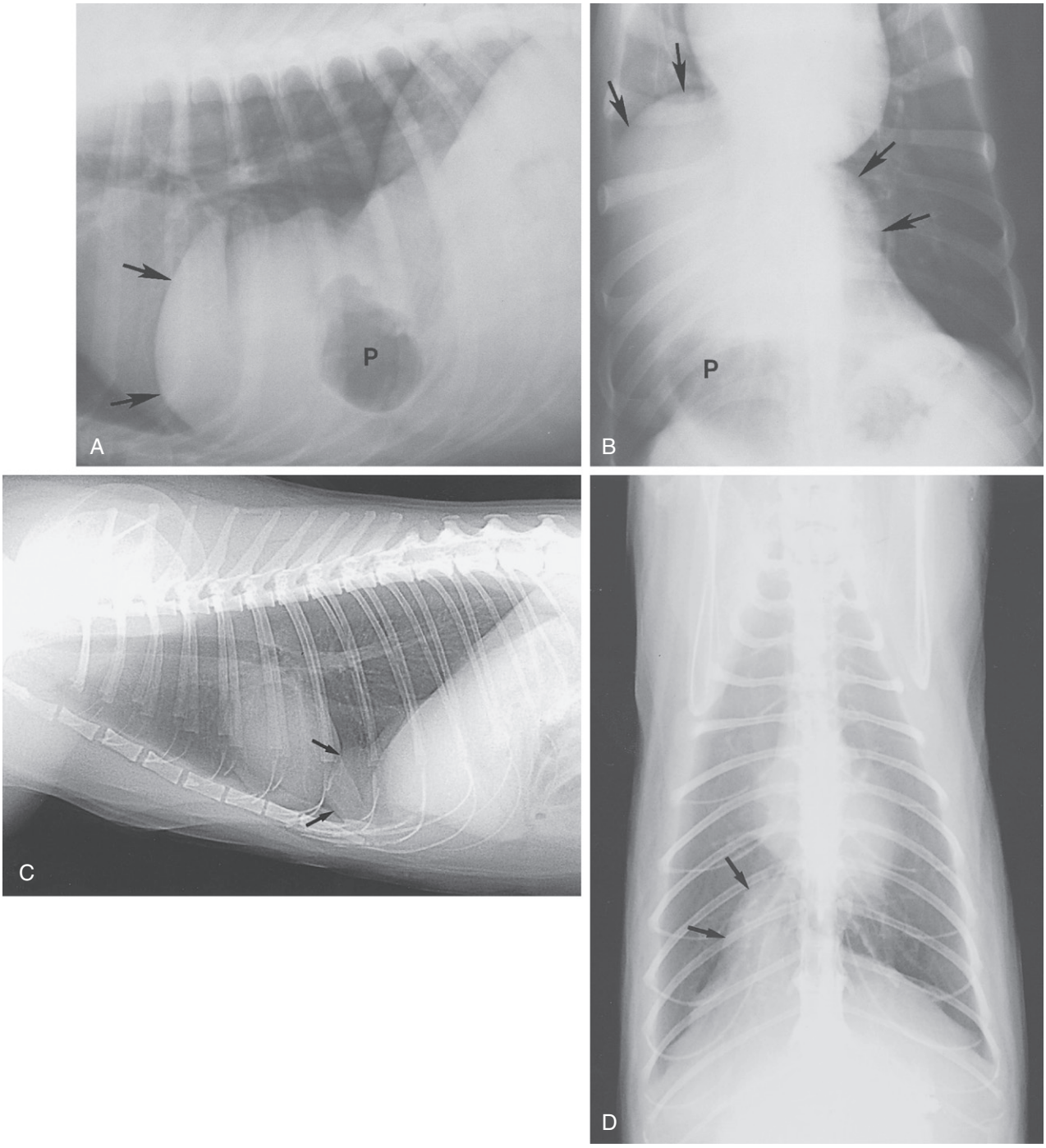


Fig. 29-21 Recumbent lateral and ventrodorsal views of a dog (**A** and **B**) and a cat (**C** and **D**) thorax. A defect in the membranous portion of the diaphragm is present in both the dog and cat. In the dog (**A** and **B**), the liver *(black arrows)* and gas-filled pyloric antrum *(P)* are within the thorax, and the stomach and liver are displaced cranially. In the cat (**C** and **D**), the falciform ligament and fat are displaced cranially to the diaphragm *(black arrows)* and surrounded with intact parietal pleura.

scalloped margin, noted best on the lateral view, should not be confused with the normal scalloping observed on the ventrodorsal view in cats on maximal inspiration (see Fig. 29-7). The scalloped appearance is caused by muscular hypertrophy, which can be confirmed by ultrasound.[66] Muscular hypertrophy produced with feline muscular dystrophy has also been reported to cause megaesophagus from extraluminal hiatal obstruction. Definitive laboratory tests, such as immunofluorescence or immunoblot tests, are necessary to establish the diagnosis of muscular dystrophy.

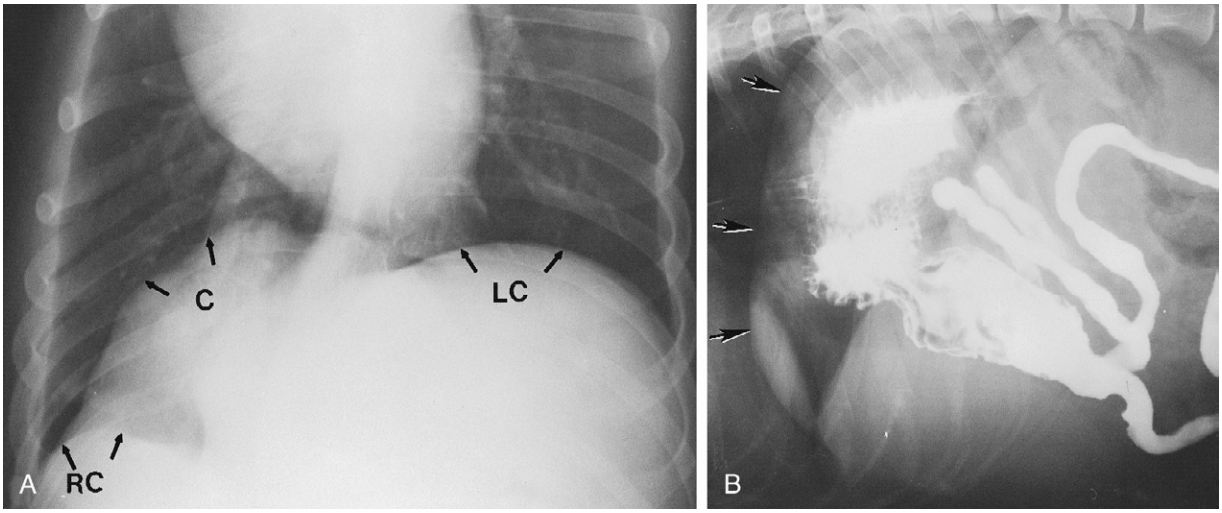


Fig. 29-22 Ventrodorsal **(A)** and lateral **(B)** radiographs of the cranial abdomen. Hemiparalysis of the left diaphragm is present. **A,** The left diaphragmatic crus *(LC)* is cranial to the right crus *(RC)*. The cupula *(C)* and right crus *(RC)* are in a normal inspiratory position. **B,** The cranial position of the left diaphragmatic crus *(black arrows)* causes the gastric cardia and fundus to be displaced cranially.

REFERENCES

1. Ganong W: *Review of medical physiology*, ed 22, New York, 2005, McGraw-Hill, p 652.
2. Rogers KS, Barton CL, Landis M: Canine and feline lymph nodes. Part I. Anatomy and function, *Compend Contin Educ Pract Vet* 15(3):397, 1993.
3. Evans HE: *Miller's anatomy of the dog*, ed 3, Philadelphia, 1993, Saunders, p 304.
4. Grandage J: The radiology of the dog's diaphragm, *J Small Anim Pract* 15:1, 1974.
5. Schulman J: Peritoneopericardial diaphragmatic hernia in a dog, *Mod Vet Pract* 60:306, 1979.
6. Garson HL, Dodman NH, Baker GJ: Diaphragmatic hernia: analysis of fifty-six cases in dogs and cats, *J Small Anim Pract* 21:469, 1980.
7. Farrow CS: Radiographic diagnosis of diaphragmatic hernia, *Mod Vet Pract* 64:979, 1983.
8. Silverman S, Ackerman N: Radiographic evaluation of abdominal hernias, *Mod Vet Pract* 58:781, 1977.
9. Wilson GP III, Hayes HM Jr: Diaphragmatic hernia in the dog and cat: a 25-year overview, *Semin Vet Med Surg* 1:318, 1986.
10. Levine SH: Diaphragmatic hernia, *Vet Clin North Am Small Anim Pract* 17:411, 1987.
11. Stokhof AA, Wolvekamp WTC, Hellebrekers LJ, et al: Traumatic diaphragmatic hernia in the dog and cat, *Tijdschr Diergeneeskd* 111(Suppl 1):62S, 1986.
12. Rendano VT: Positive contrast peritoneography: an aid in the radiographic diagnosis of diaphragmatic hernia, *J Am Vet Radiol Soc* 20:67, 1979.
13. Stickle RL: Positive-contrast celiography (peritoneography) for the diagnosis of diaphragmatic hernia in dogs and cats, *J Am Vet Med Assoc* 185:295, 1984.
14. Williams J, Leveille R, Myer CW: Imaging modalities used to confirm diaphragmatic hernia in small animals, *Compend Small Anim* 20:1199, 1998.
15. Lamb CR, Mason GD, Wallace MK: Ultrasonographic diagnosis of peritoneopericardial diaphragmatic hernia in a Persian cat, *Vet Record* 125:186, 1989.
16. Hay WH, Woodfield JA, Moon MA: Clinical, echocardiographic, and radiographic findings of peritoneopericardial diaphragmatic hernia in two dogs, *J Am Vet Med Assoc* 195:1245, 1989.
17. Hashimoto A, Kudo T, Sawashima I: Diagnostic ultrasonography of noncardiac intrathoracic disorders in small animals, *Res Bull* 55:235, 1990.
18. Hodges RD, Tucker RL, Brace JJ: Radiographic diagnosis (peritoneopericardial diaphragmatic herniation in a dog), *Vet Radiol Ultrasound* 34:249, 1993.
19. Carb A: Diaphragmatic hernia in the dog and cat, *Vet Clin North Am Small Anim Pract* 5:477, 1975.
20. Wilson GP, Newton CD, Burt JK: A review of 116 diaphragmatic hernias in dogs and cats, *J Am Vet Med Assoc* 159:1142, 1971.
21. Boudrieau RJ, Muir WW: Pathophysiology of traumatic diaphragmatic hernia in dogs, *Compend Contin Educ Pract Vet* 9:379, 1987.
22. Minihan AC, Berg J, Evans KL: Chronic diaphragmatic hernia in 34 dogs and 16 cats, *J Am Anim Hosp Assoc* 40:51, 2004.
23. Feldman DB, Bree MM, Cohen BJ: Congenital diaphragmatic hernia in neonatal dogs, *J Am Vet Med Assoc* 153:942, 1968.
24. Saperstein G, Harris S, Leipold HW: Congenital defects in domestic cats, *Feline Pract* 6:18, 1976.
25. Reimer SB, Kyles AE, Filipowisc DE, Gregory CR: Long-term outcome of cats treated conservatively or surgically for peritoneopericardial diaphragmatic hernia: 66 cases (1987–2002), *J Am Vet Med Assoc* 224:728, 2004.
26. Bjorck GR, Tigerschiold A: Peritoneopericardial diaphragmatic hernia in a dog, *J Small Anim Pract* 11:585, 1970.
27. Gourley IM, Popp JA, Park RD: Myelolipomas of the liver in a domestic cat, *J Am Vet Med Assoc* 158:2053, 1971.
28. Rendano VT, Parker RB: Polycystic kidneys and peritoneopericardial diaphragmatic hernia in the cat: a case report, *J Small Anim Pract* 17:479, 1976.
29. Weitz J, Tilley LP, Moldoff D: Pericardiodiaphragmatic hernia in a dog, *J Am Vet Med Assoc* 173:1336, 1978.
30. Evans SM, Biery DN: Congenital peritoneopericardial diaphragmatic hernia in the dog and cat, *Vet Radiol* 21:108, 1980.
31. Neiger R: Peritoneopericardial diaphragmatic hernia in cats, *Compend Contin Educ Pract Vet* 18:461, 1996.
32. Liptak JM, Bissett SA, Allan GS, et al: Hepatic cysts incarcerated in a peritoneopericardial diaphragmatic hernia, *J Feline Med Surg* 4:123, 2002.

33. Berry CR, Koblik PD, Ticer JW: Dorsal peritoneopericardial mesothelial remnant as an aid to the diagnosis of feline congenital peritoneopericardial diaphragmatic hernia, *Vet Radiol* 31:239, 1990.
34. Willard MD, Aronson E: Peritoneopericardial diaphragmatic hernia in a cat, *J Am Vet Med Assoc* 178:481, 1981.
35. Edwards MH: Selective vagotomy of the canine oesophagus: a model for the treatment of hiatal hernia, *Thorax* 31:185, 1976.
36. Teunissen GHB, Happ RP, Van Toorenburg J, et al: Esophageal hiatal hernia: case report of a dog and a cheetah, *Tijdschr Diergeneeskd* 103:742, 1978.
37. Ellison GW, Lewis DD, Phillips L, et al: Esophageal hiatal hernia in small animals: literature review, *J Am Anim Hosp Assoc* 20:783, 1984.
38. Ellis FH Jr: Controversies regarding the management of hiatus hernia, *Am J Surg* 139:782, 1980.
39. Rogers WA, Donovan EF: Peptic esophagitis in a dog, *J Am Vet Med Assoc* 163:462, 1973.
40. Prymak C, Saunders HM, Washabau RJ: Hiatal hernia repair by restoration and stabilization of normal anatomy. An evaluation in four dogs and one cat, *Vet Surg* 18:386, 1989.
41. Gaskell CJ, Gibbs C, Pearson H: Sliding hiatus hernia with reflex oesophagitis in two dogs, *J Small Anim Pract* 15:503, 1974.
42. Alexander JW, Hoffer RE, MacDonald JM, et al: Hiatal hernia in the dog: a case report and review of the literature, *J Am Anim Hosp Assoc* 11:793, 1975.
43. Iwasaki M, DeMartin BW, DeAlvarenga J, et al: Congenital hiatal hernia in a dog, *Mod Vet Pract* 58:1018, 1977.
44. Robotham GR: Congenital hiatal hernia in a cat, *Feline Pract* 9:37, 1979.
45. Peterson SL: Esophageal hiatal hernia in a cat, *J Am Vet Med Assoc* 183:325, 1983.
46. Bright RM, Sackman JE, NeNovo D, et al: Hiatal hernia in the dog and cat: a retrospective study of 16 cases, *J Small Anim Pract* 31:244, 1990.
47. Stickle R, Sparschu G, Love N, et al: Radiographic evaluation of esophageal function in Chinese Shar Pei pups, *J Am Vet Med Assoc* 201:81, 1992.
48. Miles KG, Pope ER, Jergens AE: Paraesophageal hiatal hernia and pyloric obstruction in a dog, *J Am Vet Med Assoc* 193:1437, 1988.
49. Gordon LC, Friend EJ, Hamilton MH: Hemorrhagic pleural effusion secondary to an unusual type III hiatal hernia in a 4-year-old Great Dane, *J Am Anim Hosp Assoc* 46:336, 2010.
50. Anderson GM, Miller DA, Miller SW: Peripheral nerve sheath tumor of the diaphragm with osseous differentiation in a one-year-old dog, *J Am Anim Hosp Assoc* 35:319, 1999.
51. Steiner GM: Gastro-oesophageal reflux, hiatus hernia, and the radiologist with special reference to children, *Br J Radiol* 50:164, 1977.
52. Pollock S, Rhodes WH: Gastroesophageal intussusception in an Afghan hound, *J Am Vet Radiol Soc* 11:5, 1970.
53. Leib MS, Blass CE: Gastroesophageal intussusception in the dog: a review of the literature and a case report, *J Am Anim Hosp Assoc* 20:783, 1984.
54. Bath GF: Congenital diaphragmatic hiatus in a dog: case report, *J S Afr Vet Assoc* 47:55, 1976.
55. Nicholson C: Defective diaphragm associated with umbilical hernia, *Vet Rec* 98:433, 1976.
56. Sawyer SL: Defective diaphragm associated with umbilical hernia, *Vet Rec* 98:490, 1976.
57. Swift BJ: Defective diaphragm associated with umbilical hernia, *Vet Rec* 98:511, 1976.
58. Valentine BA, Dietze CB, Noden AE: Canine congenital diaphragmatic hernia, *J Vet Intern Med* 2:109, 1988.
59. White JD, Tisdall PLC, Norris JM, Malik R: Diaphragmatic hernia in a cat mimicking a pulmonary mass, *J Feline Med Surg* 5:197, 2003.
60. Wolff G: Familial congenital diaphragmatic defect: review and conclusions, *Hum Genet* 54:1, 1980.
61. Voges AK, Hill RC, Neuwirth L, et al: True diaphragmatic hernia in a cat, *Vet Radiol Ultrasound* 38:116, 1997.
62. Vignoli AM, Toniato M, Rossi F, et al: Transient post-traumatic hemidiaphragmatic paralysis in two cats, *J Small Anim Pract* 43:312, 2002.
63. Greene CE, Basinger RR, Whitfield JB: Surgical management of bilateral diaphragmatic paralysis in a dog, *J Am Vet Med Assoc* 193:1542, 1988.
64. Mainwaring CJ: Post-traumatic contraction of the diaphragm synchronous with the heartbeat in a dog, *J Small Anim Pract* 29:299, 1988.
65. Cooper BJ, Winand NJ, Stedman H, et al: The homologue of the Duchenne locus is defective in X-linked muscular dystrophy of dogs, *Nature* 334:154, 1988.
66. Berry CR, Gaschen FP, Ackerman H: Radiographic and ultrasonographic features of hypertrophic feline muscular dystrophy in two cats, *Vet Radiol Ultrasound* 33:357, 1992.
67. Gaschen FP, Swendrowske MA: Hypertrophic feline muscular dystrophy. A unique clinical expression of dystrophin deficiency, *Feline Pract* 22:23, 1994.
68. Brumitt JW, Essman SC, Kornegay JN, et al: Radiographic features of golden retriever muscular dystrophy, *Vet Radiol Ultrasound* 47:574, 2006.

ELECTRONIC RESOURCES

evolve

Additional information related to the content in Chapter 29 can be found on the companion Evolve website at http://evolve.elsevier.com/Thrall/vetrad/

- Chapter Quiz

CHAPTER • 30

The Mediastinum

Donald E. Thrall

NORMAL ANATOMY

The mediastinum, which is the region between the right and left pleural sacs, contains many important organs and structures (Table 30-1). The mediastinum is bounded on each side by a layer of mediastinal pleura. The mediastinal pleural is just one part of each pleural sac. An understanding of pleural morphology is required to fully comprehend the morphologic aspects of mediastinal disease (Figs. 30-1 and 30-2).

Each right and left pleural sac is composed of parietal and visceral pleura. Parietal pleura is further designated as costal, diaphragmatic, or mediastinal parietal pleura, depending on the tissue or compartment that it covers. Visceral pleura covers the lung. At the hilus of the lung, the mediastinal parietal pleura is reflected onto the surface of the lung to become visceral pleura (see Fig. 30-2); thus the parietal and visceral pleural layers are continuous and form the left and right pleural sacs.

The mediastinum extends from the thoracic inlet to the diaphragm and is located mainly in the midsagittal plane of the thorax, thereby dividing the thoracic cavity into right and left halves (see Figs. 30-1 and 30-2). The mediastinum may be subdivided into a cranial portion cranial to the heart, a middle portion at the level of and containing the heart, and a caudal portion caudal to the heart. The mediastinum may also be divided into dorsal and ventral portions by a dorsal plane through the tracheal bifurcation. The mediastinum communicates cranially with the fascial planes of the neck by way of the thoracic inlet and caudally with the retroperitoneal space through the aortic hiatus. These communications provide the means for the spread of mediastinal disease to the neck and abdomen, and vice versa.

In most dogs and cats, the mediastinal pleura does not form an effective anatomic separation between the left and right sides of the thoracic cavity. Normal mediastinal pleural layers are fragile and contain fenestrations. Thus, pleural fluid or gas occurring unilaterally is not usually contained to one side by the mediastinum. For example, in a study of induced pneumothorax, 22 of 24 dogs having air injected into one pleural space quickly developed bilateral pneumothorax.[1] Pleural fluid or gas may remain unilateral if (1) the mediastinal pleura is not fenestrated, and the mediastinal pleura remains intact; (2) any existing fenestration becomes closed as a result of inflammation or plugging; or (3) the pleural fluid is too viscid to pass through an existing mediastinal fenestration.

Of all of the structures in the mediastinum (see Table 30-1), only the heart, trachea, caudal vena cava, aorta, and, in young animals, thymus are visible normally. Occasionally, a portion of the normal esophagus may be seen (see Chapter 27). The other mediastinal structures are not seen normally either because (1) they are too small or (2) insufficient fat is interposed between them to provide contrast, leading to border effacement.

The normal homogeneous appearance of the cranial mediastinum in a lateral thoracic radiograph is the result of border effacement. Cranial mediastinal structures in this region create a homogeneous opacity ventral to the trachea, but individual structures cannot be discerned (Fig. 30-3). This homogeneous opacity ventral to the trachea is caused by the collective opacity of the left subclavian artery, brachiocephalic trunk, cranial vena cava, and mediastinal lymph nodes. These structures are not seen individually because they are in contact with each other and insufficient interposed fat is present. Thus the border of these structures is effaced. The cranioventral mediastinum is more radiopaque ventral to the trachea than dorsal to the sternum on a lateral thoracic radiograph because it is thicker just ventral to the trachea (Fig. 30-4).

In ventrodorsal (VD) or dorsoventral (DV) thoracic radiographs, most of the cranial mediastinum is superimposed on the spine—that is, in the midsagittal plane of the thorax. The normal width of the cranial mediastinum in VD or DV views is usually less than approximately twice the width of the vertebral column (Fig. 30-5). In obese patients, the cranial mediastinum may become enlarged because of fat accumulation and be confused with an abnormal mediastinal mass (Fig. 30-6). Other imaging modalities, such as ultrasound or computed tomography (CT), may be necessary to distinguish fat from a mass as a cause for a widened mediastinum in obese patients.

The mediastinum deviates from midline in three normal reflections: (1) the cranioventral mediastinal reflection, (2) the caudoventral mediastinal reflection, and (3) the vena caval mediastinal reflection, or the plica vena cava. The first two are visible in thoracic radiographs of many dogs and cats, but not universally. The plica vena cava is never seen radiographically in normal dogs or cats.

The cranioventral mediastinal reflection appears in VD or DV radiographs as a curving radiopaque line, on the patient's left, extending from approximately T1 or T2 to the region of the main pulmonary artery. The concave side of the line is to the patient's right (see Figs. 30-4 and 30-5). As already noted, the cranioventral mediastinal reflection is caused by extension of the right cranial lobe across the midline, pushing the mediastinum to the left (see Fig. 30-4). The thickness of the cranioventral mediastinal reflection is affected by the amount of fat it contains (see Fig. 30-6). On the lateral view,

Table • **30-1**

Mediastinal Organs

ORGAN	CRANIAL MEDIASTINUM	MIDDLE MEDIASTINUM	CAUDAL MEDIASTINUM
Cranial vena cava	x		
Thymus	x		
Sternal lymph nodes	x		
Aortic arch	x		
Brachiocephalic artery	x		
Left subclavian artery	x		
Mediastinal lymph nodes	x		
Trachea	x	x	
Right and left vagosympathetic trunk	x	x	
Dorsal intercostal arteries and veins	x	x	x
Internal thoracic arteries and veins	x	x	x
Esophagus	x	x	x
Thoracic duct	x	x	x
Right and left sympathetic trunks	x	x	x
Right and left phrenic nerves	x	x	x
Descending aorta		x	x
Bronchoesophageal arteries and veins		x	x
Azygous vein		x	x
Heart		x	
Tracheobronchial lymph nodes		x	
Main pulmonary artery		x	
Main pulmonary veins		x	
Principal bronchi		x	
Caudal vena cava			x
Right and left vagus nerves			x

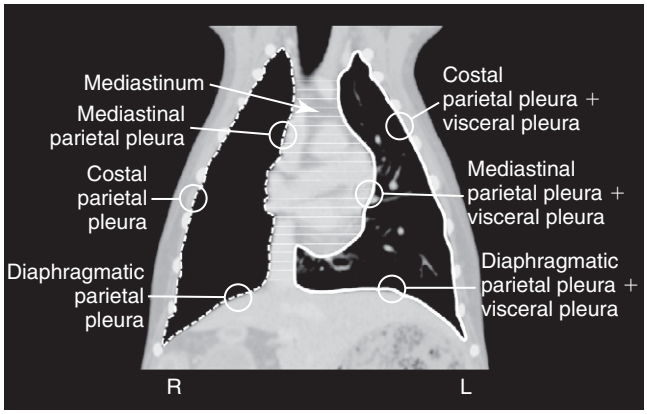


Fig. 30-1 Dorsal plane CT image of a canine thorax at the level of the base of the heart. The right lung, and thus the visceral component of the right pleural sac, has been removed from the image. The *dotted line* in the right hemithorax represents the remaining parietal portion of the right pleural sac. The designation of mediastinal versus costal versus diaphragmatic parietal pleura is based on which structure the pleura covers. Thus, mediastinal, costal, and diaphragmatic portions of the parietal pleura are contiguous sections of the right pleural sac. The left lung remains in the image. As the left lung is covered in visceral pleura, the *solid line* designates contact between the visceral and parietal pleural layers of the left pleural sac. The pleural space is the potential space between the parietal and visceral pleural layers; it is not shown as a real space in this figure because under normal circumstances, the parietal and visceral pleural layers are in contact. The mediastinum, shown here with horizontal white lines, is the space between the two pleural sacs. *L*, left; *R*, right.

the cranioventral mediastinal reflection is often identified approximately midway between the thoracic inlet and the heart (see Fig. 30-3). The thymus lies in the cranioventral mediastinal reflection, and sometimes a subinvoluted thymus can be identified in VD or DV radiographs of young animals (Fig. 30-7). An incompletely involuted thymus is not usually visible in lateral thoracic radiographs. The internal thoracic arteries and veins are also located in the cranioventral mediastinal reflection.

The caudoventral mediastinal reflection is seen only on VD or DV radiographs; it is not seen in lateral projections. It is created by extension of the accessory lobe of the right lung across the midline to the left, thereby pushing the mediastinum to the left (see Fig. 30-2). The caudoventral mediastinal reflection therefore consists of four pleural layers: (1) the visceral pleura of the accessory lobe, (2) the mediastinal parietal pleura of the right pleural sac, (3) the mediastinal parietal pleura of the left pleural sac, and (4) the visceral pleura of the left caudal lobe (see Fig. 30-2).

The caudoventral mediastinal reflection appears as a relatively straight radiopaque line in the caudal left hemithorax, extending from the region of the cardiac apex in a caudolateral direction toward the gastric fundus (Fig. 30-8). The caudoventral mediastinal reflection has been incorrectly termed the *sternopericardiac ligament* (also called the *cardiophrenic* or *phrenicopericardial ligament*), but the sternopericardiac ligament, which is a continuation of the apex of the fibrous pericardium, is not visible radiographically.[2] The thickness of the caudoventral mediastinal reflection depends on the

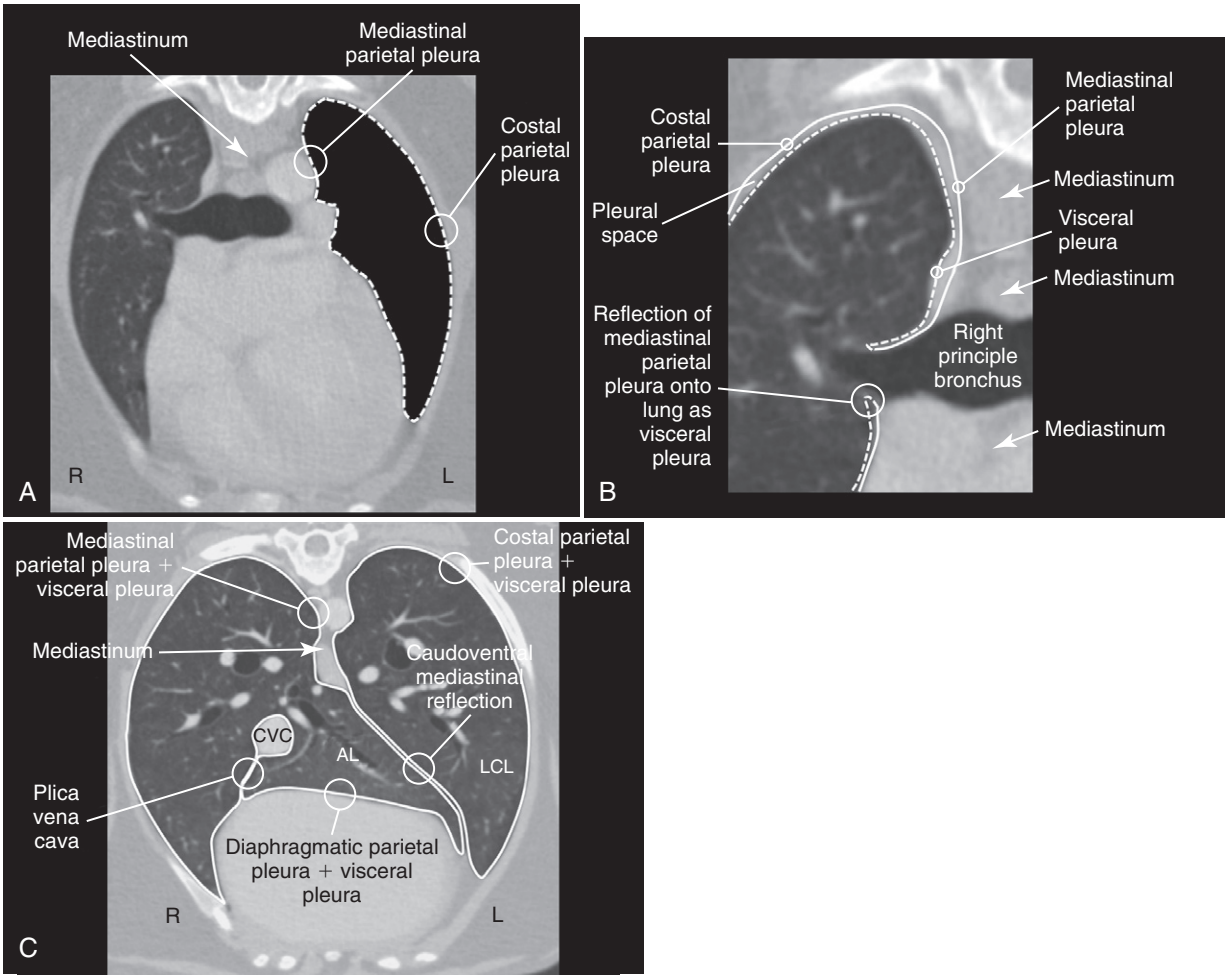


Fig. 30-2 Transverse plane CT images of a canine thorax. **A,** Just caudal to the tracheal bifurcation. The left lung has been removed from the image to show the relationship of the mediastinal and costal components of the parietal pleural sac *(dotted line)*. The diaphragmatic parietal pleura is not visible in **A** because the diaphragm is caudal to this slice. **B,** Close-up of the right hilus. At this level of the thorax, the mediastinal parietal pleura reflects onto the surface of the lung where it becomes visceral pleura. The space between the visceral and parietal pleural layers is the pleural space. The pleural space is only a potential space in normal animals; here a small space is shown, but this does not exist normally in vivo. The mediastinum is the space between the left and right pleural sacs (*white arrows* in **B**). Part **C** is a transverse slice in the caudal thorax, caudal to the tracheal bifurcation. The *solid lines* designate contact between the visceral and parietal pleural layers. The pleural space is the potential space between the parietal and visceral pleural layers. The mediastinum is the space between the two pleural sacs. A fold of pleura, the plica vena cava, encircles the caudal vena cava; the plica vena cava is not seen radiographically. The accessory lobe *(AL)* pushes the mediastinal pleura to the left, forming the caudoventral mediastinal reflection. There are then four pleural layers making up the caudoventral mediastinal reflection; from right to left these are (1) visceral pleura from accessory lobe, (2) right mediastinal parietal pleura, (3) left mediastinal parietal pleura, and (4) visceral pleura from left caudal lobe *(LCL)*. *L*, Left; *R*, right.

amount of fat it contains (Fig. 30-9); this thickness can change in individual animals as body habitus changes.

PATHOLOGIC MEDIASTINAL CONDITIONS

Mediastinal abnormalities are divided into three general classifications: mediastinal shift, mediastinal mass, and pneumomediastinum.

Mediastinal Shift

Mediastinal shift occurs as a result of a unilateral decrease in lung volume (ipsilateral mediastinal shift), a unilateral increase in lung volume (contralateral mediastinal shift), the presence of an intrathoracic mass (contralateral mediastinal shift), or unilateral increased pleural pressure (contralateral mediastinal shift). A mediastinal shift is detected in VD or DV radiographs by noting a change in position of visible mediastinal organs or the position of mediastinal reflections. Displacement of the heart to the left or right is the most reliable sign of a

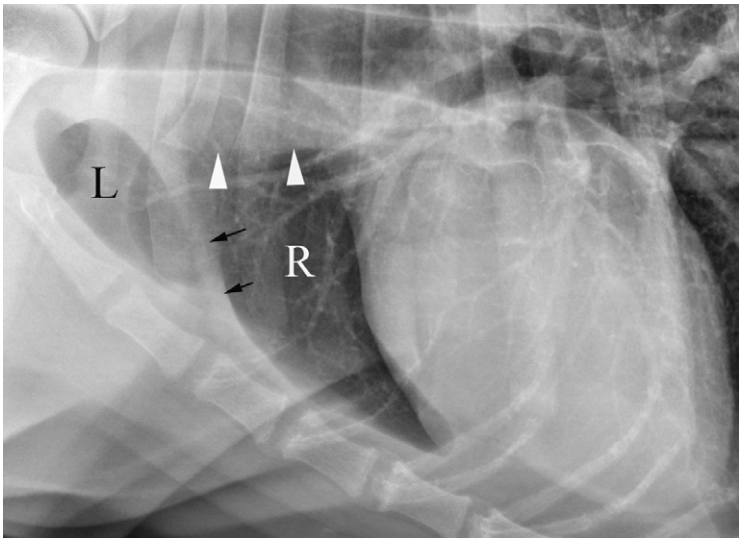


Fig. 30-3 Left lateral radiograph of the thorax of a normal dog. The opacity ventral to the trachea (*white arrowheads* indicate ventral margin of opacity) is part of the cranial mediastinum. Although several different organs are in this part of the mediastinum (e.g., left subclavian artery, brachiocephalic trunk, and cranial vena cava), they cannot be discerned because they are in contact with each other, and there is not enough intervening fat to provide contrast. The mediastinum extends from the vertebrae dorsally to the sternebrae ventrally, but the mediastinum is most radiopaque immediately ventral to the trachea because it is thickest at this location (see Fig. 30-4). Also note the cranioventral mediastinal reflection *(black arrows)* between the cranial portion of the left cranial lobe *(L)* and the right cranial lobe *(R)* (see Fig. 30-4).

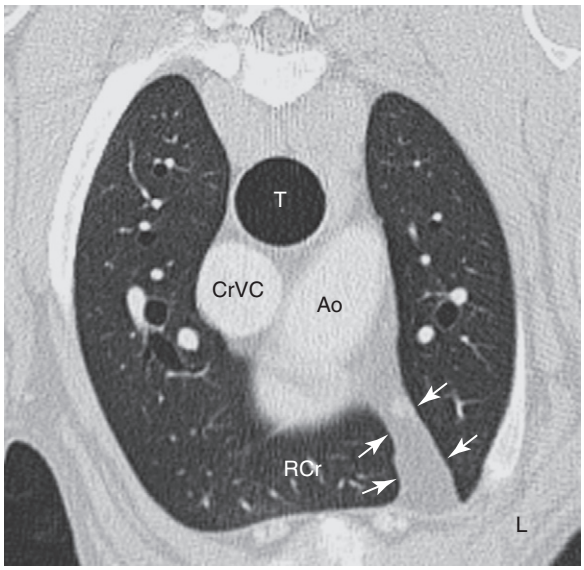


Fig. 30-4 Transverse CT image of the canine thorax just cranial to the base of the heart. Note the greater thickness of the mediastinum just dorsal and ventral to the trachea compared to its thickness just dorsal to the sternum. The greater thickness of the dorsal mediastinum accounts for the opacity seen ventral to the trachea in lateral thoracic radiographs (see Fig. 30-3). Note the cranial vena cava *(CrVC)* and aorta *(Ao)* ventral to the trachea *(T)*. Insufficient fat is present for these vessels to be seen in radiographs, but the greater inherent contrast resolution of CT images allows them to be seen when using this modality. Also note how the ventral aspect of the mediastinum is pushed to the left *(white arrows)* by the right cranial lung lobe *(RCr)*. This is the *cranioventral mediastinal reflection*, which can often be seen radiographically, as in Figures 30-3 and 30-5.

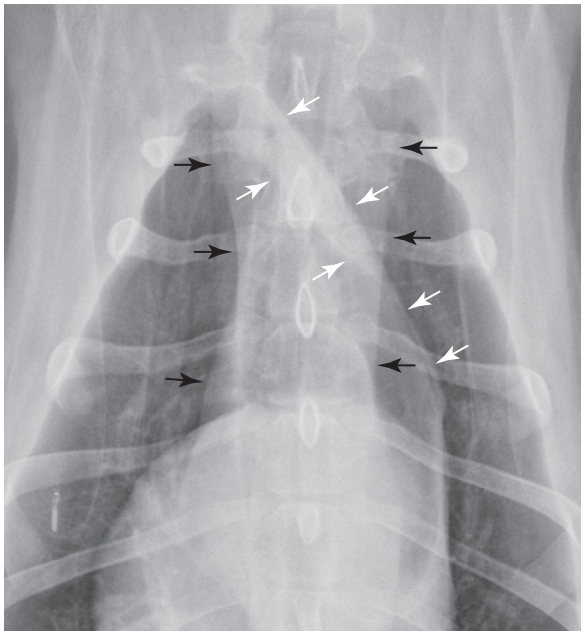


Fig. 30-5 VD radiograph of the cranial aspect of the thorax of a normal dog. The cranial mediastinum is superimposed on the cranial aspect of the thoracic spine; it is relatively indistinct, but the lateral margins of the thicker dorsal aspect of the mediastinum can be discerned *(black arrows)*. As an approximation, the width of the normal cranial mediastinum in VD or DV radiographs should not be greater than twice the diameter of the vertebrae. Note the cranioventral mediastinal reflection between the right cranial lobe and the cranial part of the left cranial lobe *(white arrows)*. See Figure 30-3 for the appearance of this reflection in the lateral view and Figure 30-4 for an illustration of the right lung pushing the mediastinum to the left to create the reflection.

mediastinal shift (Fig. 30-10). Improper patient positioning with rotation of the sternum to the right or left will create the false impression of a mediastinal shift. Detection of a mediastinal shift is often the first clue of a thoracic abnormality (Fig. 30-11).

Pulmonary atelectasis, resulting from reduced ventilation or prolonged lateral recumbency, is the most common cause of a mediastinal shift. Atelectasis will result in decreased lung volume and increased lung opacity, and the heart will be shifted toward the abnormally opaque lung. Distinguishing

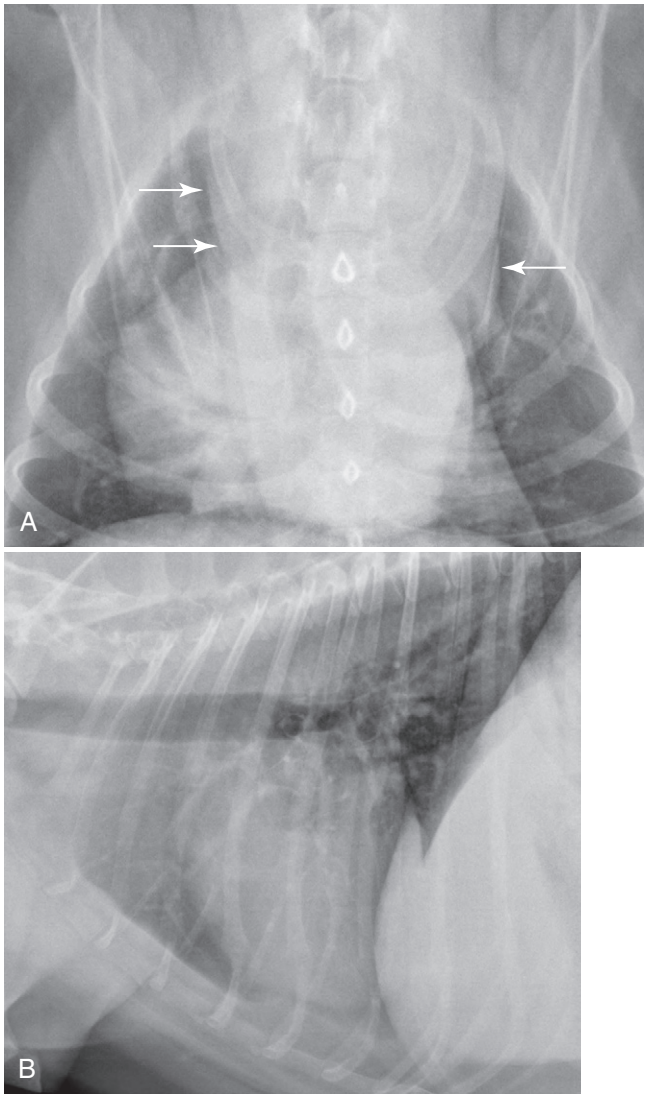


Fig. 30-6 **A,** DV radiograph of the cranial aspect of the thorax of an obese dog. The cranial mediastinum contains a large amount of fat and is much wider *(white arrows)* than twice the diameter of the vertebrae. Care should be taken to avoid misinterpreting a wide mediastinum in an obese animal as a mediastinal mass. Ultrasound or CT imaging may be necessary to make a final assessment. **B,** Lateral radiograph of the same dog as in **A.** There is no evidence of a mediastinal mass. Had there been a mass in the mediastinum as large as suggested from the VD view, there would likely have been dorsal displacement of the trachea, which is not seen here. The large amount of fat in the cranial mediastinum has, however, increased the opacity of the cranioventral aspect of the thoracic cavity nonspecifically.

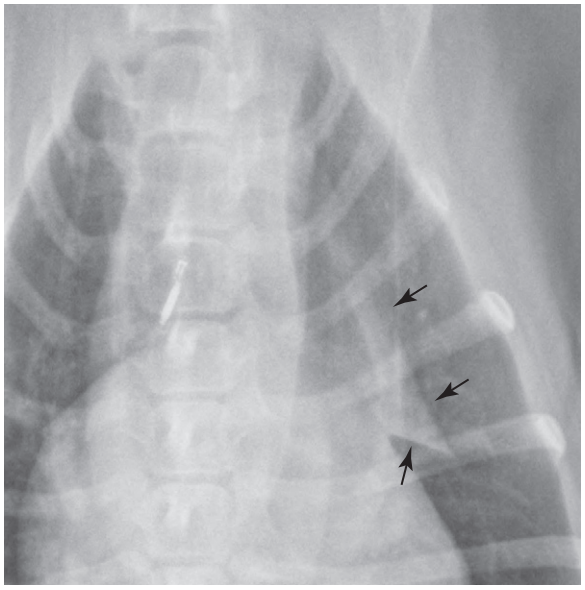


Fig. 30-7 VD radiograph of the thorax of a normal young dog. The thymus, located in the cranioventral mediastinal reflection, has not involuted completely and appears as a sail-shaped opacity cranial and to the left of the cardiac base *(black arrows)*.

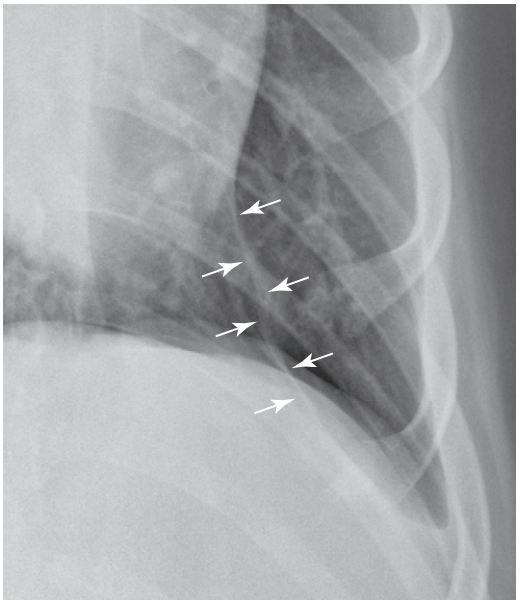


Fig. 30-8 VD radiograph of the caudal thorax of a dog with a normal habitus. The caudoventral mediastinal reflection appears as a thin opacity extending from the region of the cardiac apex caudolaterally to the left *(white arrows)*.

normal atelectatic from diseased atelectatic lung is not possible radiographically (see Fig. 30-11).

Mediastinal Masses

Mediastinal masses are common, and their etiology cannot usually be determined radiographically; an aspirate or biopsy, the application of another imaging modality, or a special radiographic procedure, such as an esophagram, is usually needed. However, the portion of the mediastinum that contains the mass can help to formulate a differential diagnosis (Table 30-2).

VD or DV projections are usually more useful than the lateral view in deciding whether a thoracic mass is located in the mediastinum versus the lung or elsewhere. Mediastinal location of a thoracic mass should be considered if (1) the mass lies on or adjacent to the midline, (2) the mass is in a position consistent with the cranioventral or caudoventral mediastinal reflection, or (3) the mass causes deviation of a mediastinal structure.

Cranioventral Mediastinal Masses

Cranioventral mediastinal masses are one of the most commonly encountered mediastinal masses, and the radiographic appearance depends on its size. Early enlargement of the sternal lymph node is perhaps the smallest detectable cranioventral mediastinal mass. This relates to the isolated location

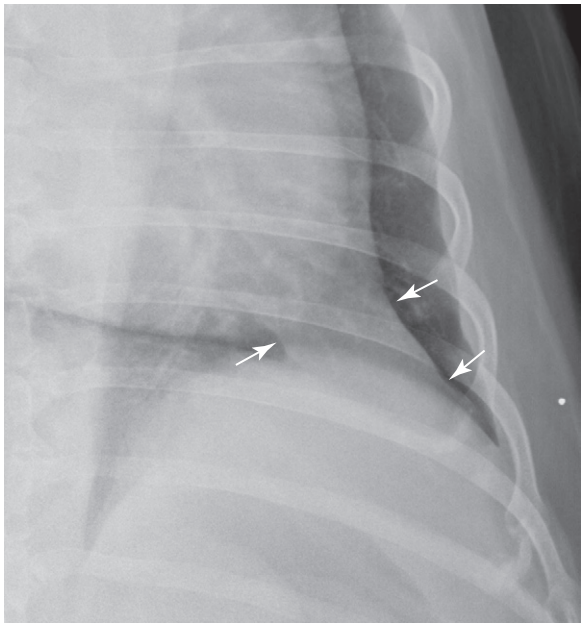


Fig. 30-9 VD radiograph of the caudal aspect of the thorax of an obese dog. The caudoventral mediastinal reflection is thick as a result of fat deposits *(white arrows)*. Compare its thickness in this radiograph with that in Figure 30-8.

of the sternal lymph node in the ventral aspect of the cranial mediastinum, dorsal to the second to third sternebra. The ventral mediastinum is thin in this region, and there are no other structures to silhouette with mild sternal lymph node enlargement.

The sternal lymph node is usually represented by a single lymph node on each side in the dog and a single lymph node in the cat. The dog occasionally has only a single median sternal lymph node. The afferent lymphatics of the sternal lymph node arise in the abdominal wall and perforate the diaphragm near the middle of the costal arch. Afferent vessels receive tributaries from the ribs, sternum, serous membranes, thymus, adjacent muscles, peritoneal cavity, and mammary glands.[3,4] A fusiform opacity up to 3 cm in length, presumably representing a normal sternal lymph node, can be seen in some normal dogs, especially in the right lateral view.[5] Care should be taken to avoid misinterpreting this as a sign of disease.

One might assume that sternal lymph node enlargement is a sign of intrathoracic disease, but enlargement of the sternal lymph node is often secondary to abdominal disease, such as peritonitis or peritoneal tumor seeding.[6] Sternal lymph node enlargement appears as an isolated small soft tissue mass dorsal to the second to third sternebra and is best seen on a lateral projection (Fig. 30-12). A mildly enlarged sternal lymph node can appear slightly different in size and shape in the left versus right lateral view, likely because of its orientation with respect to the primary x-ray beam (see Fig. 30-12).

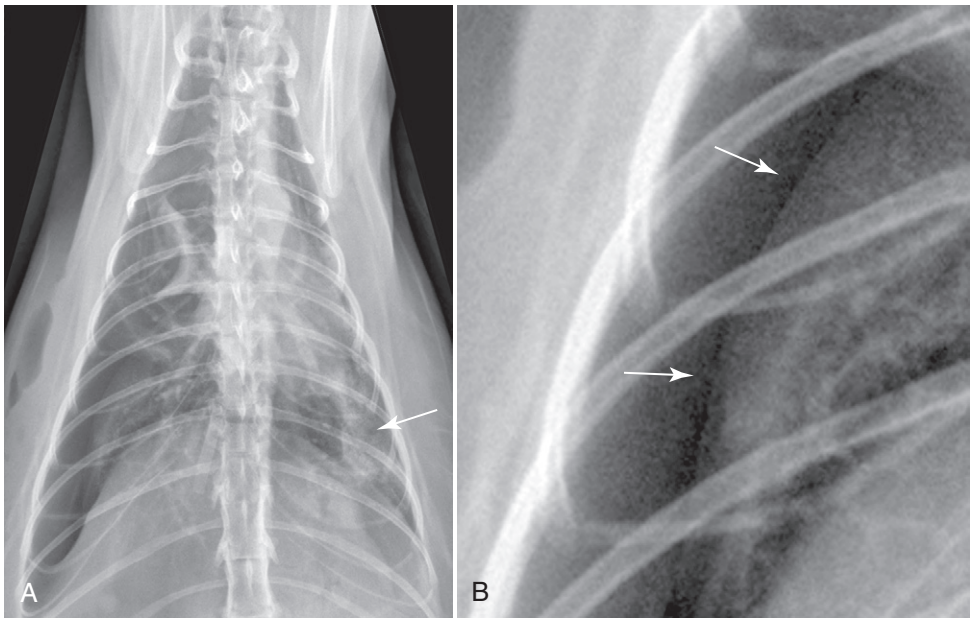


Fig. 30-10 **A.** Dorsoventral thoracic radiograph of a cat with dyspnea. The radiograph is positioned acceptably, but the heart is located in the left hemithorax. No mass is visible, but lung retraction from the thoracic wall on the right side indicates gas in the right pleural space—that is, pneumothorax. The right side of the diaphragm is also positioned more caudally than the left side. Considering the lack of a mass and the presence of pneumothorax, the leftward cardiac displacement (mediastinal shift) and caudal displacement of the diaphragm are indicative of a right-sided tension pneumothorax. This is a critical assessment because tension pneumothorax is an emergency situation. There is also alveolar disease in the left caudal lobe *(white arrow in* **A***)*; this alveolar pattern is likely because of atelectasis and is contributing to the mediastinal shift to the left. **B,** Close-up of right caudal aspect of the thorax where the displaced lung caused by pneumothorax can be seen more distinctly *(white arrows)*.

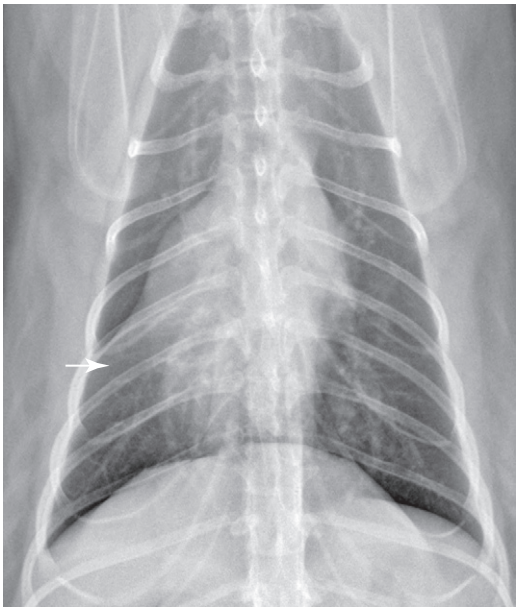


Fig. 30-11 VD radiograph of a cat with mediastinal shift, signified by malpositioning of the heart to the right. The cardiac malpositioning is the most conspicuous abnormality in the image. On close inspection, there is increased opacity of the right middle lung lobe *(white arrow)* with partial border effacement of the right aspect of the cardiac silhouette; this increased lung opacity is caused by partial collapse of the right middle lobe because of bronchial asthma, confirmed by airway sampling. Right lung atelectasis from prolonged recumbency or reduced ventilation caused by sedation would have this identical appearance. Cardiac displacement can be the most obvious radiographic sign of intrathoracic disease.

It was noted before that a presumably normal sternal lymph node can be seen in the right lateral view in some dogs; this supports a position-dependency of the appearance of the sternal lymph node. This position-dependency has not been characterized adequately. An enlarged sternal lymph node is not as conspicuous in VD or DV radiographs as in lateral radiographs.

A feline mediastinal cyst is another cause of a relatively small cranioventral mediastinal mass, especially in cats. Mediastinal cysts in cats are typically located more caudal than expected for sternal lymph nodes and more ventral than expected for mediastinal lymph nodes (Fig. 30-13). Mediastinal cysts are usually an incidental finding and not significant clinically, but occasionally they may enlarge slowly and require excision.[7] Sonography is useful in establishing the cystic nature of mediastinal cysts versus the solid nature of enlarged lymph nodes or thymoma (see Fig. 30-13).

With cranioventral mediastinal masses other than enlarged sternal lymph nodes or small mediastinal cysts, there will usually be increased opacification of the entire cranioventral mediastinum and border effacement of the cranial margin of the heart in lateral views. In VD or DV views, the cranial mediastinum will appear wide, and there will be border effacement of the cranial margin of the heart; the extent of these changes depends on the size of the mass. The trachea may or may not be displaced, again depending on the size of the mass (Fig. 30-14 and Fig. 30-15). The largest cranioventral mediastinal masses have the same features as moderately sized cranioventral masses, with the addition of more pronounced tracheal displacement and outright cardiac displacement as well (Fig. 30-16).

Table • **30-2**

Causes of Mediastinal Masses

CAUSE OF MASS	MEDIASTINAL LOCATION
Vascular ring anomaly (segmental cranial esophagomegaly)	Craniodorsal*
Neurogenic tumor	Craniodorsal or dorsal
Hematoma	Variable, but may have a craniodorsal predilection
Mediastinal lymphadenopathy	Cranioventral
Sternal lymphadenopathy	Cranioventral
Thymoma	Cranioventral
Mediastinal cyst (branchial cyst)	Cranioventral
Ectopic thyroid or parathyroid tumor	Cranioventral, perihilar
Mediastinal abscess—usually caused by esophageal perforation	Cranioventral, caudoventral, caudal, dorsal
Hilar lymphadenopathy	Middle
Heart base mass†	Middle, cranioventral to tracheal bifurcation
Mid-esophageal foreign body	Middle, dorsal to tracheal bifurcation
Paraspinal tumor	Dorsal
Generalized megaesophagus	Dorsal
Spirocerca lupi	Caudodorsal
Caudal esophageal mass or foreign body	Caudodorsal
Mediastinal diaphragmatic hernia	Caudoventral
Hiatal hernia	Caudal to caudodorsal
Diaphragmatic eventration	Caudal, caudoventral, caudodorsal

*Marked segmental esophagomegaly may lead to a cranioventral mediastinal mass as the enlarged esophagus gravitates ventral to the trachea.
†Heart base mass as used here is nonspecific and could apply to a tumor of the base of the heart, a right atrial tumor, or enlargement of the main pulmonary artery.

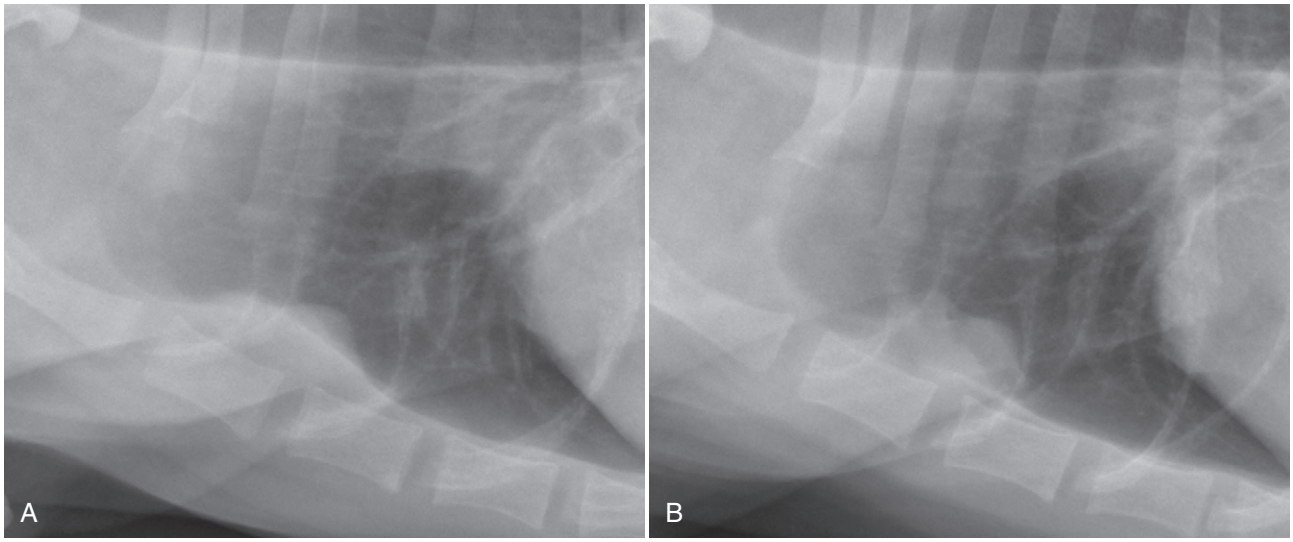


Fig. 30-12 Left **(A)** and right **(B)** lateral radiographs of a dog with mild enlargement of the sternal lymph node. The enlarged lymph node appears as a mass dorsal to the second and third sternebra. Finding a slightly different size and shape of an enlarged sternal lymph in left versus right lateral views is common. This mildly enlarged sternal lymph node was not visible in the VD view.

Because enlarged cranial mediastinal lymph nodes are a common cause of a cranioventral mediastinal mass, some understanding of their function is important. The cranial mediastinal lymph nodes vary in number and size, and most lie along the cranial vena cava and brachiocephalic, left subclavian, and costocervical arteries just ventral to the trachea. Afferent lymphatics come from the muscles of the neck, thorax and abdomen, scapula, last six cervical vertebrae, thoracic vertebrae, ribs, trachea, esophagus, thyroid, thymus, mediastinum, costal pleura, heart, and aorta. Clinically, the cranial mediastinal lymph nodes do not enlarge secondary to abdominal disorders. The cranial mediastinal lymph nodes also receive efferent lymphatics from the intercostal, sternal, middle, and caudal deep cervical, tracheobronchial, and pulmonary lymph nodes.[3] The finding of enlarged cranial mediastinal lymph nodes in dogs with lymphosarcoma is a negative prognostic factor with regard to response to chemotherapy.[8]

The thymus is another common cause of a cranioventral mediastinal mass. The thymus should have involuted and be inconspicuous in radiographs of most dogs by approximately 1 year of age. Thymomas can reach enormous proportions in the cranioventral mediastinum and then extend caudally along side of the heart, as in Figure 30-16. In general, thymomas would be expected to lie more ventral in the mediastinum than enlarged cranial mediastinal lymph nodes, which are normally located adjacent to the ventral aspect of the trachea, but this distinction cannot be used reliably to distinguish between these conditions. As noted before, the thymus can be seen radiographically in normal young dogs as a triangular opacity in the cranioventral mediastinal reflection in VD or DV views (see Fig. 30-7).

Dorsal Mediastinal Masses

Dorsal mediastinal masses are much less common than cranioventral mediastinal masses or hilar masses (see Table 30-1). Dorsal mediastinal masses, whether in the cranial, middle, or caudal aspect of the mediastinum, cause widening of the mediastinum in the VD or DV view (Figs. 30-17 and 30-18). The caudal mediastinum can be assessed more completely in a VD view compared with a DV view because of the cranial excursion of the diaphragm that occurs in the DV view that leads to compression of the caudal mediastinum.[9,10] If located in the cranial aspect of the thorax, a craniodorsal mediastinal mass will typically cause ventral and rightward displacement of the trachea (see Fig. 30-18).

The most common cause of a dorsal mediastinal mass is enlargement of the esophagus; this enlargement can be generalized or segmental. Enlargement of the cranial aspect of the thoracic esophagus, as from a vascular ring anomaly, typically causes a craniodorsal mediastinal mass with ventral displacement of the trachea in the lateral view, and widening of the cranial mediastinum in the VD or DV view. Most of the time, esophageal gas collection (see Fig. 30-17) or a heterogeneous opacity created by esophageal contents allows segmental enlargement of the cranial esophagus to be discerned from other causes of a craniodorsal mediastinal mass. If a dorsal mediastinal mass is homogeneous, it is usually impossible to determine the origin of the mass from survey radiographs alone (Fig. 30-19; see Fig. 30-18).

Clinical signs of regurgitation are not necessarily helpful in establishing the origin of a dorsal mediastinal mass as esophagus, because nonesophageal masses can compress the esophagus and also lead to regurgitation. Radiographic signs of esophageal enlargement are discussed more completely in Chapter 27. If esophagus is suspected as the origin of a dorsal mediastinal mass, an esophagram will be valuable before other invasive diagnostic techniques are employed.

Hilar-Region Mediastinal Masses

The main causes of a hilar region mediastinal mass are enlargement of the tracheobronchial lymph nodes and a mass arising from the base of the heart (see Table 30-2).

The tracheobronchial lymph nodes are subdivided into the right, left, and middle tracheobronchial lymph nodes. The right and left lymph nodes lie on the lateral side of their respective bronchus and also make contact with the trachea. The right lymph node is ventral to the azygous vein, and the left lymph node is ventral to the aorta. The middle tracheobronchial lymph node is the largest of the group. It is in the

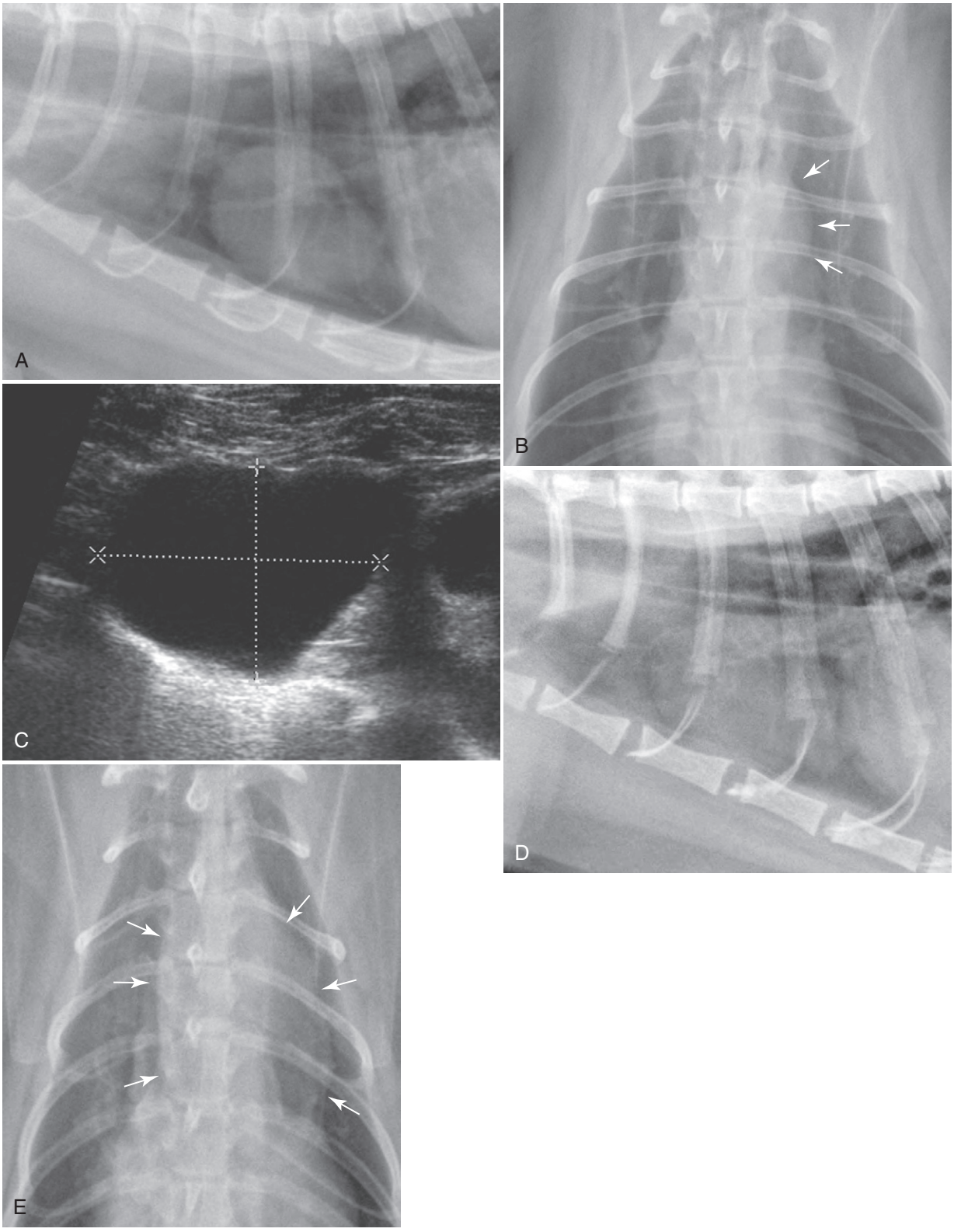


Fig. 30-13 Left lateral **(A)** and VD **(B)** thoracic radiographs of a cat. There is a well-defined mass in the cranioventral aspect of the mediastinum. The mass is very conspicuous in the lateral view and causes an ill-defined left mass effect in the VD view *(white arrows)*. This cat has mild pneumomediastinum secondary to tracheal puncture during jugular venipuncture attempt, and this may have increased the conspicuity of the mass slightly, although it would be highly conspicuous without this complication. The mass is more caudal than expected for a cranial mediastinal lymph node or a sternal lymph node mass. Sonography **(C)** allows identification of the hypoechoic cystic contents and establishes the diagnosis of mediastinal cyst. The *dotted lines* in **C** are the electronic calipers of the ultrasound machine being used to obtain measurements of the mass, which in this cat were 1.8 cm long and 2.5 cm high. The cyst in this cat was not treated, and in left lateral **(D)** and VD **(E)** radiographs made 18 months later, the cyst has enlarged *(white arrows)*. This cyst is not large enough to require excision but should be monitored subsequently to avoid complications resulting from cyst enlargement and organ compression.

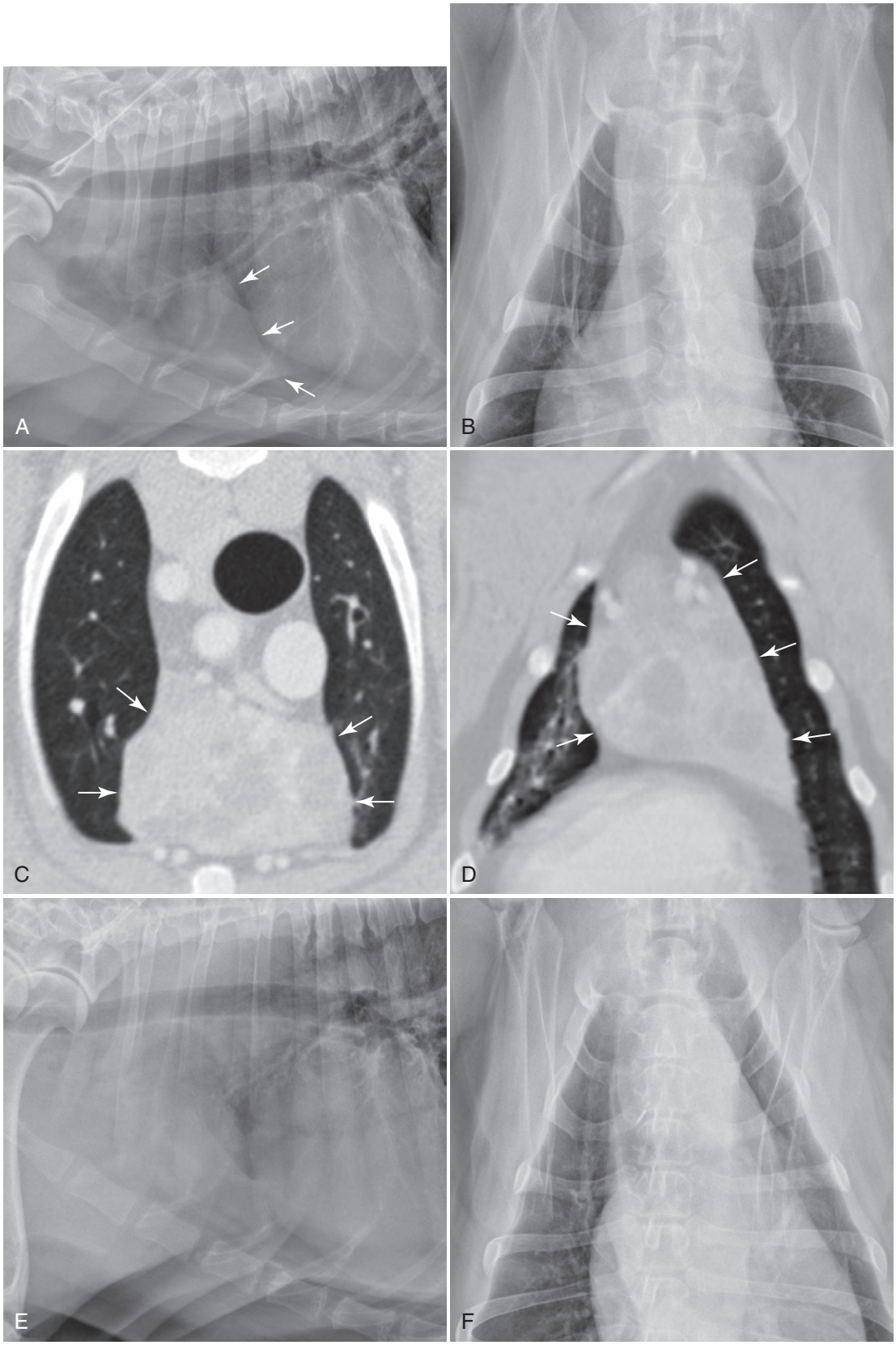


Fig. 30-14 Right lateral **(A)** and VD **(B)** radiographs of a dog with a mass in the cranioventral aspect of the mediastinum. In **A,** the cranioventral mediastinum has overall increased opacity, and the edge of a mass is visible caudoventrally *(white arrows)*, contrasted by lung. In **B,** the cranial mediastinum is wide. The trachea is not displaced in either **A** or **B.** This patient was not obese, and mediastinal fat would therefore not be a likely cause for this appearance. Transverse **(C)** and dorsal **(D)** CT images of the thorax acquired a few days after the images in **A** and **B.** The mass is clearly visible in the ventral aspect of the cranial mediastinum *(white arrows)*. Right lateral **(E)** and VD **(F)** radiographs acquired 4 months after those in **A** and **B.** The mass is larger and more obvious, displacing the trachea dorsally and to the right. The mass was removed completely by trans-sternal thoracotomy, and the histologic diagnosis was thymoma.

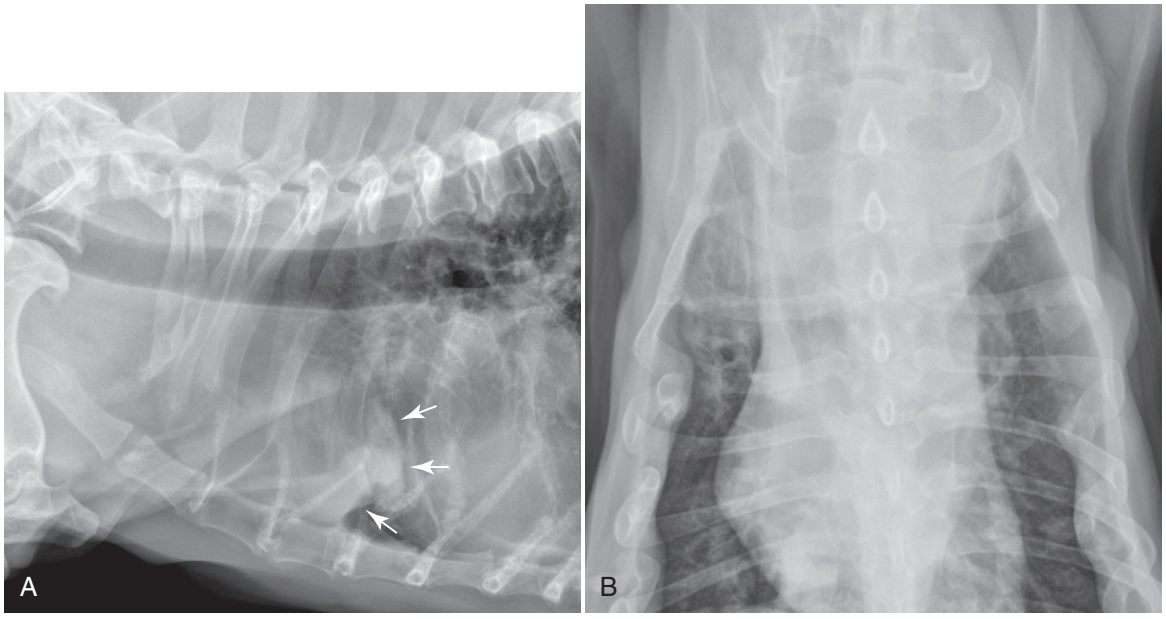


Fig. 30-15 Lateral **(A)** and VD **(B)** thoracic radiographs of a bassett hound with a moderately sized mediastinal mass. **A,** The mediastinum ventral to the trachea has increased opacity, and the edge of a mass is visible caudally *(white arrows)*, contrasted by lung. The mass has caused mild dorsal displacement of the trachea, which is now parallel to the vertebrae. The mass also causes border effacement of the cranial aspect of the cardiac silhouette. **B,** The cranial mediastinum is wide, and there is border effacement of the cranial margin of the heart. The trachea is displaced slightly to the right. This patient is not obese; thus excessive mediastinal fat is an unlikely cause of this radiographic appearance, and a cranioventral mediastinal mass is the most likely diagnosis. Considerations for the origin of this mass, which cannot be determined radiographically, are cranial mediastinal lymph node, thymus, and branchial cyst. Sonography or CT may be needed for definitive diagnosis of a mass with this radiographic appearance.

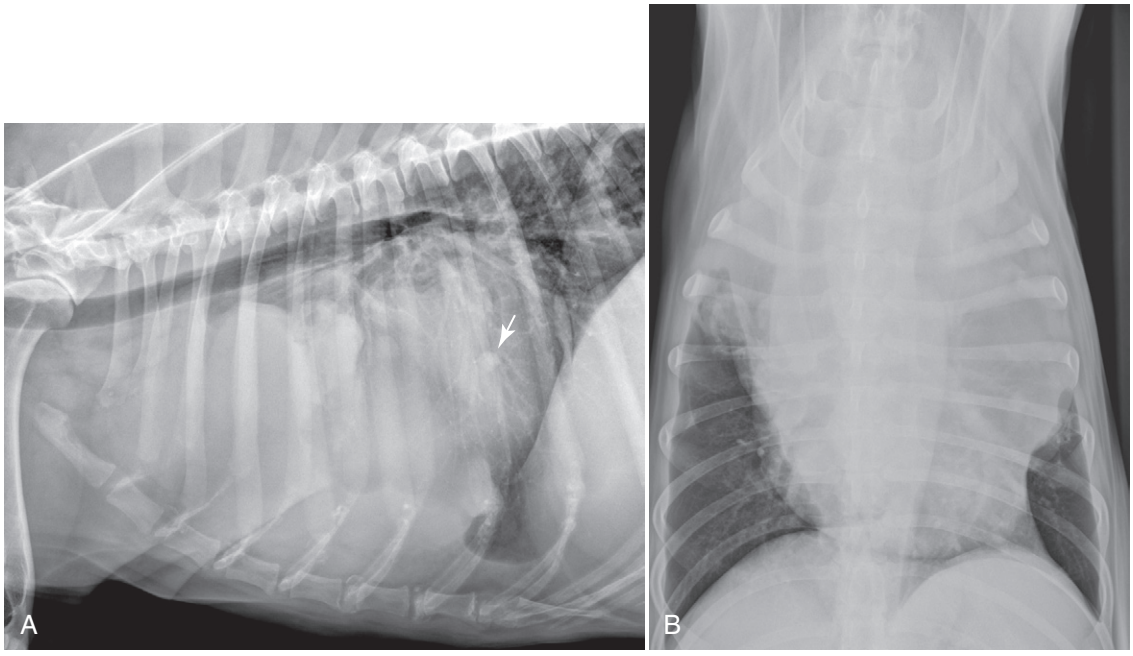


Fig. 30-16 Right lateral **(A)** and VD **(B)** radiographs of a dog with a very large lobular mass in the cranioventral aspect of the mediastinum. The trachea is displaced dorsally and to the right, and in **A** the heart is displaced caudodorsally. There is marked border effacement of the cardiac silhouette in both **A** and **B.** In **B,** the mass extends caudally along the left margin of the heart. There is a pulmonary nodule in **A,** superimposed on the cardiac silhouette *(white arrow)*. The origin of this mass cannot be determined radiographically.

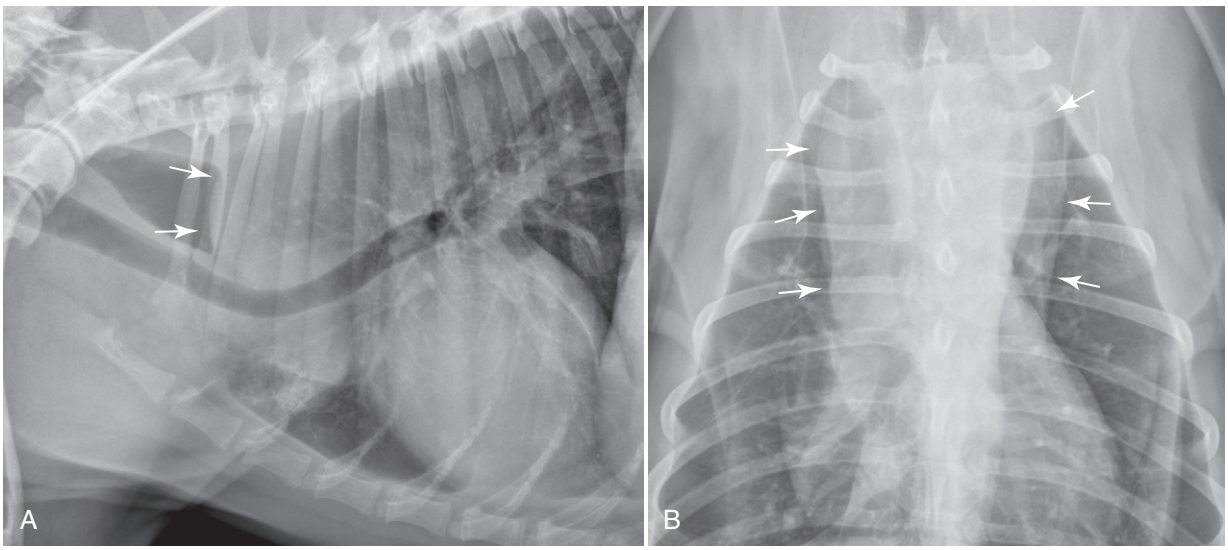


Fig. 30-17 Lateral **(A)** and DV **(B)** radiographs of a dog with a craniodorsal mediastinal mass caused by a vascular ring anomaly leading to segmental megaesophagus. The enlarged esophagus displaces the trachea ventrally. In **A,** an interface between esophageal contents and gas trapped in the cranial esophagus *(white arrows)* lends support to the mass being of esophageal origin. In **B,** the mass causes widening of the cranial mediastinum *(white arrows)* as expected. From the DV view, the mass cannot be diagnosed as esophagus or localized to the dorsal versus ventral aspects of the mediastinum.

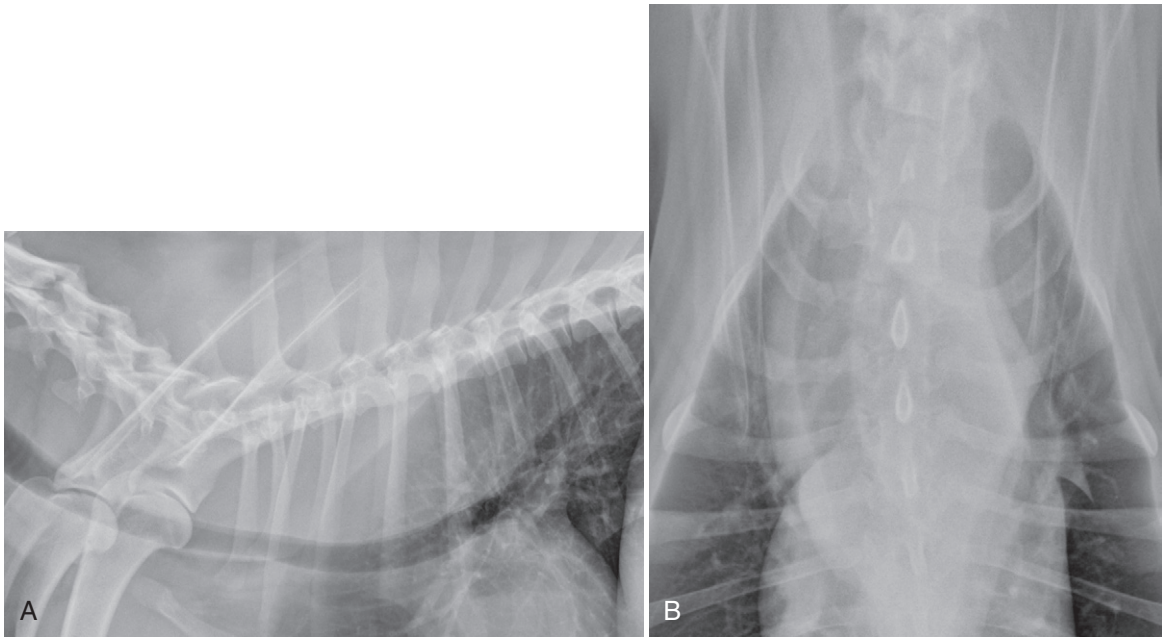


Fig. 30-18 Lateral **(A)** and VD **(B)** thoracic radiographs of a dog with a craniodorsal mediastinal abscess. In **A,** there is a homogeneously opaque mass in the craniodorsal aspect of the mediasitinum that displaces the trachea ventrally. The mass extends into the cervical region, dorsal to the trachea. In **B,** the cranial mediastinum is wider than normal and the trachea displaced to the right. The origin of this mass cannot be determined from these radiographs; esophageal origin cannot be ruled out.

form of a V with the point lying in the angle formed by the origin of the principal bronchi from the trachea. Afferent vessels to the tracheobronchial lymph nodes come from the lungs and bronchi primarily, but they also come from the thoracic parts of the aorta, esophagus, trachea, heart, mediastinum, and diaphragm. Efferent channels from the tracheobronchial lymph nodes drain into either the thoracic duct or the left tracheal trunk, or both.[3]

Enlargement of the tracheobronchial lymph nodes classically results in visualization of a soft tissue mass located

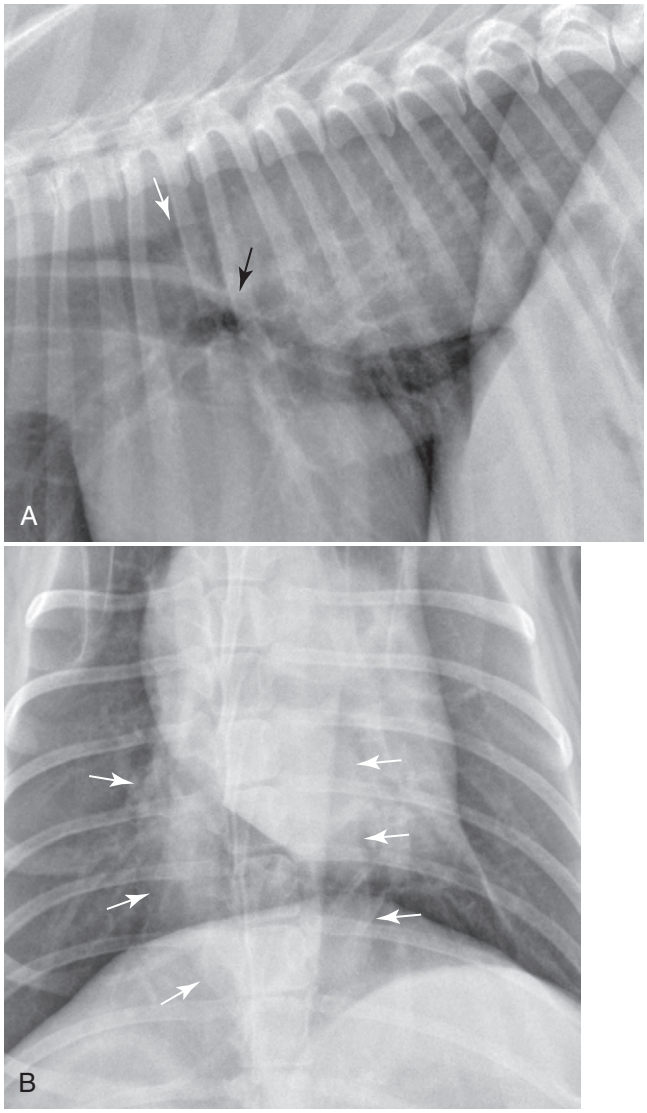


Fig. 30-19 Lateral **(A)** and VD **(B)** thoracic radiographs of a dog with a caudal esophageal foreign body. The foreign body is homogeneous and causes a caudodorsal mediastinal mass that in **A** displaces the tracheal bifurcation slightly in a cranioventral direction *(black arrow)*. There is also a focal gas collection in the esophagus cranial to the mass (*white arrow* in **A**). In **B,** the mass has caused widening of the caudal mediastinum *(white arrows)*. It is not possible to determine from these radiographs that the mass is esophageal in origin. The small esophageal gas collection could be secondary to extrinsic compression of the esophagus by a soft tissue mass of another origin.

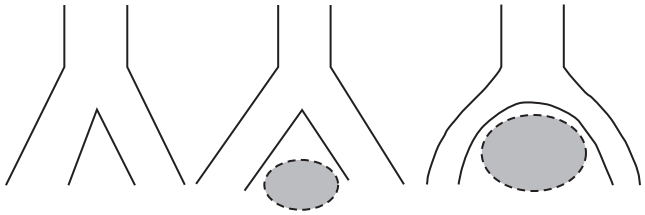


Fig. 30-20 The shape of the principal bronchi in a VD radiograph in the normal state *(left)* and when a mass is present between them (*middle* and *right*). An enlarged left atrium or tracheobronchial lymph node between the principal bronchi may result in the principal bronchi being displaced laterally *(middle)* or assuming a curved appearance *(right)*.

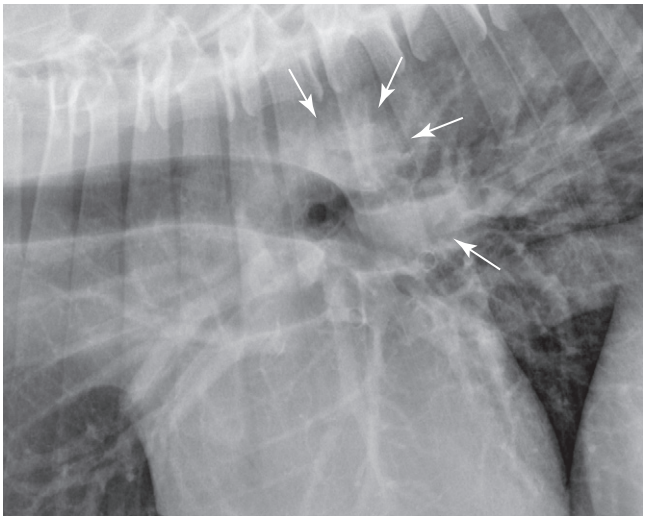


Fig. 30-21 Right lateral radiograph of a dog with mild enlargement of the tracheobronchial lymph nodes. There is a small mass effect caudodorsal to the carina *(white arrows)* that has caused cranioventral displacement of the carina. Splaying of the principal bronchi was not evident in the VD view.

dorsocaudal to the tracheal bifurcation on the lateral view. This mass usually results in cranioventral displacement of the carina. If the enlarged lymph nodes reside primarily ventral to the carina, elevation of the carina will result instead, but this is uncommon. Enlarged tracheobronchial lymph nodes causing elevation of the carina can be confused with left atrial dilation. Both tracheobronchial lymph node enlargement and left atrial dilation can cause lateral divergence or splaying of the primary bronchi on the VD or DV view (Fig. 30-20). The extent of the hilar mass effect and degree of splaying of the principal bronchi depend on the magnitude of enlargement of the tracheobronchial lymph nodes, or the extent of left atrial dilation. With mild tracheobronchial lymph node enlargement, displacement of the tracheal bifurcation in a cranioventral direction in the lateral view may be the most conspicuous abnormality (Fig. 30-21). With progressive enlargement of the tracheobronchial lymph nodes, the mass effect becomes more pronounced and splaying of primary bronchi is evident in the VD or DV view (Fig. 30-22).

Masses arising from the base of the heart tend to be relatively inconspicuous as much of the mass is usually surrounded by other soft tissue structures and not air. Therefore these masses create an ill-defined rather than a distinct mass and may become quite large before being detectable radiographically. Heart base region masses typically cause rightward displacement of the trachea just cranial to the carina, and this may be the most conspicuous finding (Fig. 30-23). As the heart base mass enlarges, the tracheal displacement becomes more pronounced, but the mass itself is still not likely to be seen (Fig. 30-24). A heart base mass may represent a heart base tumor, right atrial tumor, or an enlarged main pulmonary artery.

Caudoventral Mediastinal Masses

Masses in the caudoventral mediastinum are relatively uncommon. Many caudoventral mediastinal masses are associated with the diaphragm, either a diaphragmatic eventration, or a hernia (see Table 30-1) (Fig. 30-25). Caudoventral mediastinal masses may cause border effacement of the diaphragm and/or cardiac displacement. In VD or DV views, caudoventral mediastinal masses are often located to the left of midline

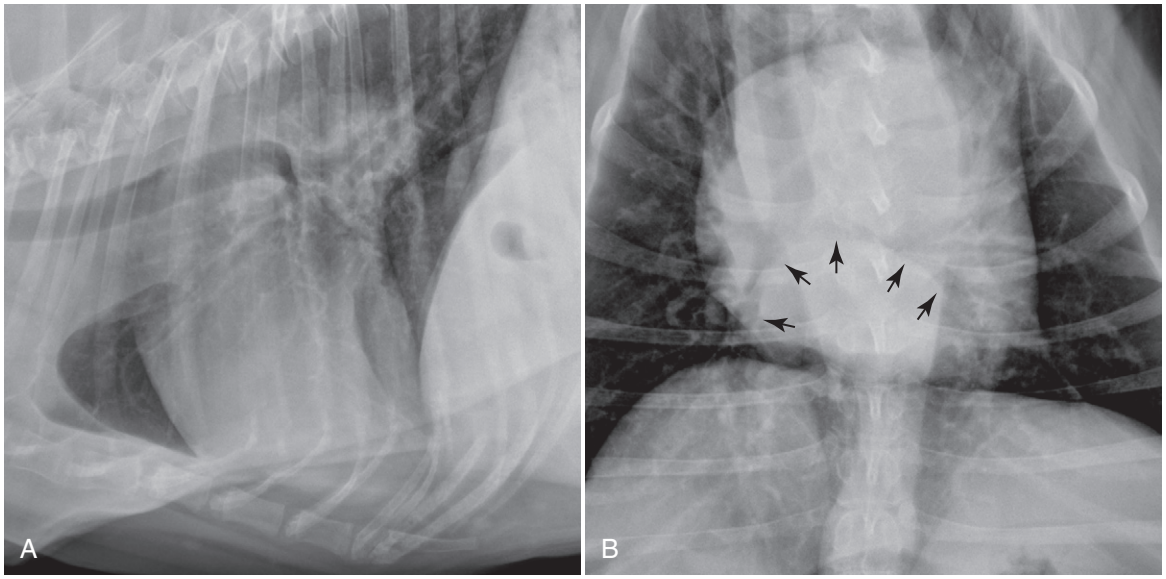


Fig. 30-22 Right lateral **(A)** and VD **(B)** radiographs of a dog with pronounced enlargement of the tracheobronchial lymph nodes. In **A,** there is a mass caudodorsal to the carina that has displaced the carina cranioventrally. In **B,** there is splaying of the primary bronchi *(black arrows)* because of the interposed enlarged tracheobronchial lymph nodes.

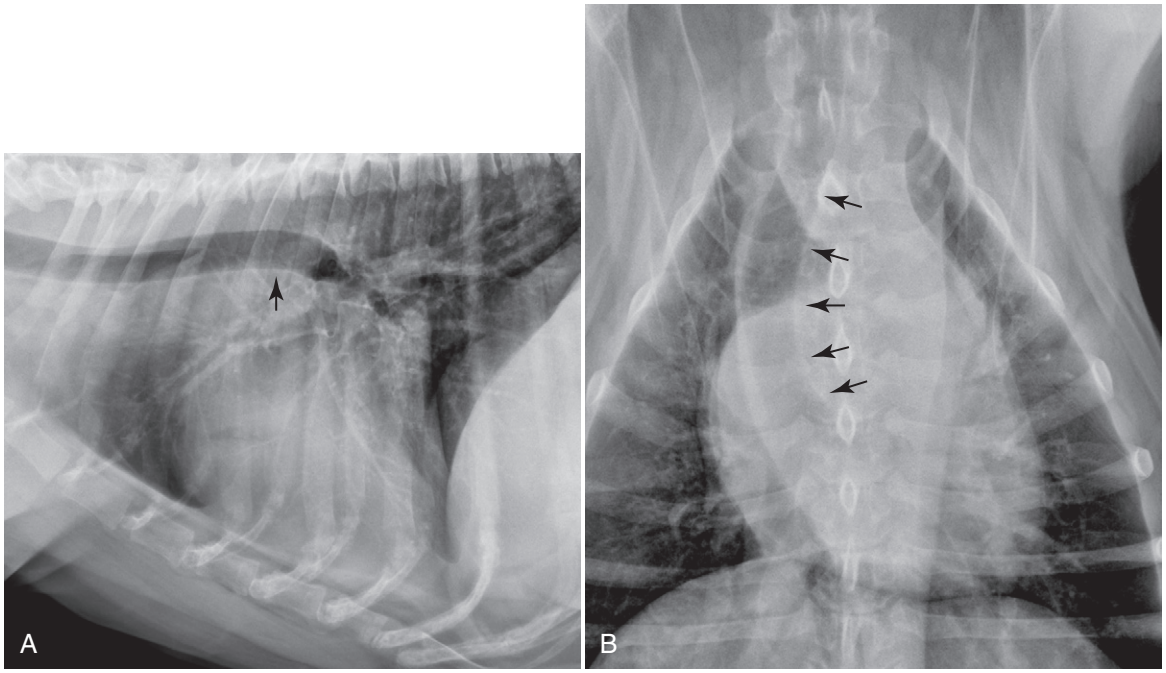


Fig. 30-23 Right lateral **(A)** and VD **(B)** radiographs of a dog with a heart base tumor (chemodectoma). In **A,** there is slight focal elevation of the trachea just cranial to the carina *(black arrow)*. Enlargement of the left and/or right tracheobronchial lymph nodes could also produce this appearance, but there is no evidence of enlargement of the middle tracheobronchial lymph node, which detracts from the tracheobronchial lymph nodes being the cause of the tracheal elevation seen here. Also, in **B** there is sharp deviation of the intrathoracic trachea to the right *(black arrows)*, which is not usually seen with tracheobronchial lymph node enlargement. The chemodectoma itself is not visible. These tracheal changes are often the only radiographic sign of the presence of this heart base mass, which is located cranioventral to the carina.

because of the normal left-sided location of the caudoventral mediastinal reflection (see Fig. 30-25).

As the accessory lung lobe is located on the midline, a mass arising from this lobe can appear identical to a caudoventral mediastinal mass[11] (Fig. 30-26). Masses arising in the accessory lung lobe will usually cause effacement of the border of the caudal vena cava as the accessory lobe surrounds this structure (see Fig. 30-26). Visualization of the caudal vena cava may be preserved with small caudoventral mediastinal masses arising from structures other than the accessory lobe (see Fig 30-25).

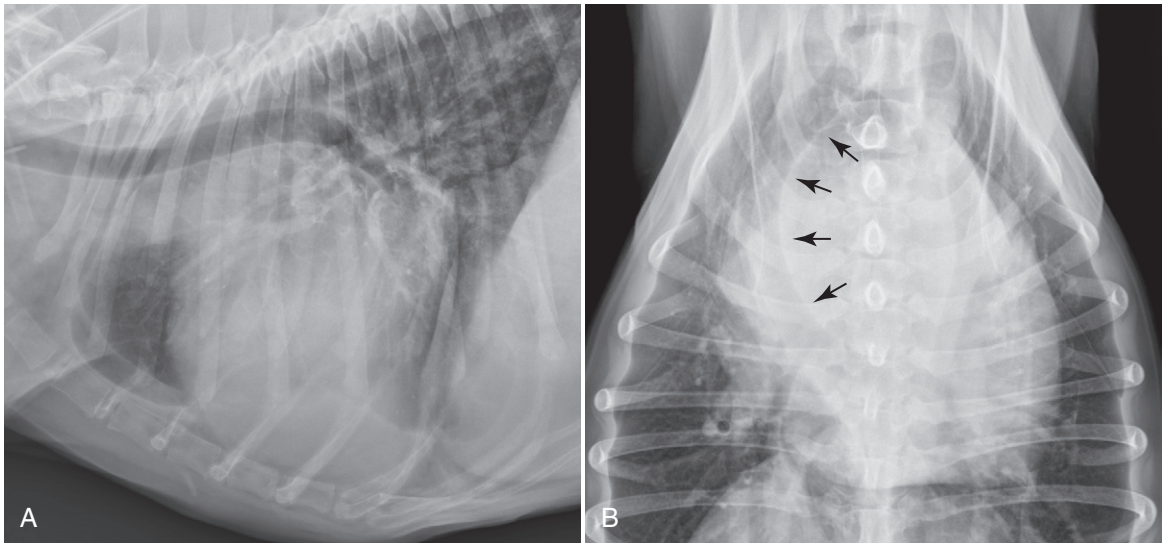


Fig. 30-24 Right lateral **(A)** and VD **(B)** radiographs of a dog with a chemodectoma that is larger than the one illustrated in Figure 30-23. In **A,** there is elevation of the trachea over the base of the heart, and in **B,** there is rightward displacement of the majority of the intrathoracic trachea *(black arrows)*. These findings are typical of a large heart base mass. In this dog, the mass itself, even though larger than the one illustrated in Figure 30-23, is still not overtly conspicuous.

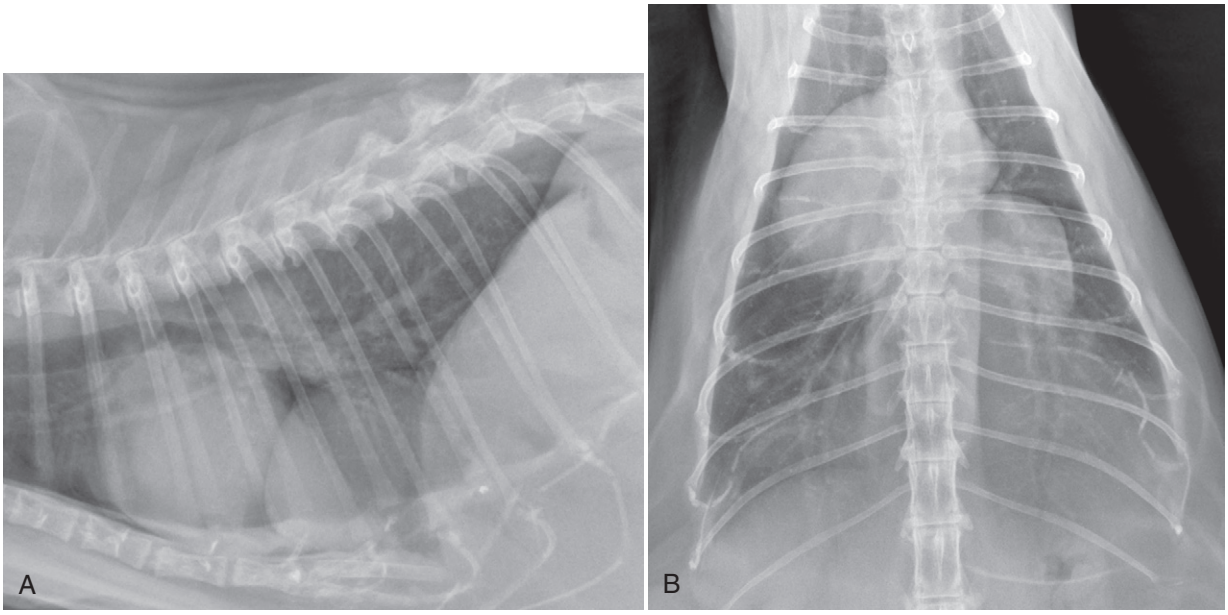


Fig. 30-25 Right lateral **(A)** and DV **(B)** radiographs of a cat with a lipoma in the caudoventral aspect of the mediastinum. In **B,** this mass causes border effacement of the diaphragm and is located to the left of midline because of the caudoventral mediastinal reflection being on the left. The heart is displaced to the right. In **A,** the opacity of the mass is slightly less than expected for soft tissue, but making the diagnosis of lipoma from these radiographs is not possible.

Caudal vena cava effacement will usually occur with any large caudoventral mediastinal mass, regardless of origin. Border effacement of the diaphragm and cardiac displacement are also likely with large accessory lung lobe masses (see Fig. 30-26).

Some Facts About Mediastinal Lymph Nodes

The drainage patterns of the lymph nodes in the mediastinum were discussed before in the section dealing with mediastinal masses. Mediastinal lymph node enlargement can be associated with a variety of diseases, but the most common causes are primary lymph node neoplasia and mycotic infection. Spread of peritoneal disease to the sternal lymph node was discussed earlier.

In the cat, lymphoma is a common cause of enlargement of the cranial mediastinal lymph nodes. The thymus may also be affected. In the dog, lymphoma results in enlargement of the sternal lymph nodes in slightly more than half of affected

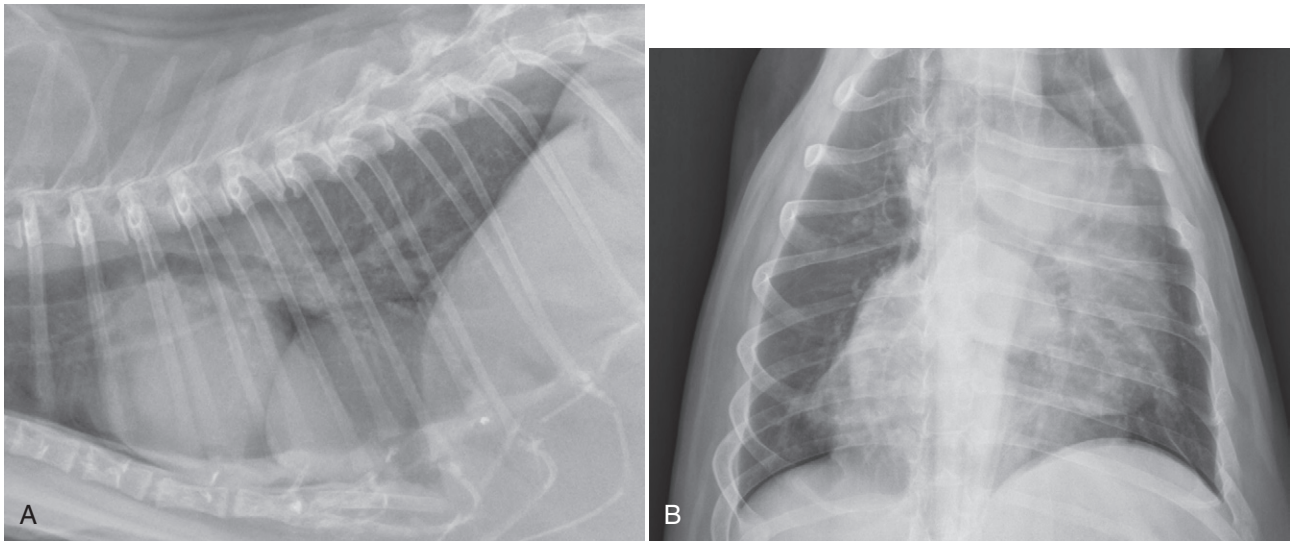


Fig. 30-26 Left lateral **(A)** and VD **(B)** radiographs of a dog with a primary tumor of the accessory lung lobe. Given the normal position of the accessory lung lobe, masses arising in the accessory lobe will be on the midline in VD or DV views and in the caudoventral aspect of the thorax in lateral view. As such, they are often confused with a mediastinal mass. Accessory lobe masses will usually cause border effacement of the caudal vena cava, as seen here. This mass is also causing border effacement of the diaphragm and displacement of the cardiac apex to the left.

Box • 30-1

Diseases Not Typically Associated with Radiographically Detectable Mediastinal Lymph Node Enlargement

Primary lung tumor
Metastatic lung tumor
Bacterial pneumonia
Pyothorax
Rib tumors

patients, but involvement of cranial mediastinal or tracheobronchial lymph nodes is uncommon.[12] Other reticuloendothelial malignancies, such as pulmonary lymphomatoid granulomatosis[13,14] and disseminated histiocytic sarcoma,[15] are also characterized by a high frequency of mediastinal lymph node enlargement, especially the tracheobronchial lymph nodes. In pulmonary lymphomatoid granulomatosis and disseminated histiocytic sarcoma, there is usually accompanying pulmonary parenchymal disease, and isolated mediastinal lymph node enlargement would be unusual. Pulmonary mycoses, especially blastomycosis and coccidiomycosis, are associated with a high prevalence of mediastinal lymph node enlargement. Interestingly, there are a variety of diseases that one might expect to lead to mediastinal lymph node enlargement but which rarely do to the extent that such is visible radiographically (Box 30-1).

Distinguishing a Mediastinal Mass from a Lung Mass

It is logical to presume that differentiating a lung mass from a mediastinal mass based on radiographic signs is easy, but this is not true in many patients. Many lung masses can be distinguished from mediastinal masses because the lung mass lies lateral to the mediastinum and is more sharply marginated because of the surrounding air-filled lung (Fig. 30-27). In some instances, however, mediastinal masses may protrude laterally (Fig. 30-28), or be in a thin portion of the mediastinum (Fig. 30-29) and, as a result, are surrounded by air where they are sharply margined and mistaken for a lung mass Therefore it is important to keep in mind that definitive localization of many intrathoracic masses is not possible based on radiographic signs. If thoracotomy is being considered, and the location of the mass is not obvious from radiographs, CT imaging of the thorax before surgery can alleviate performing a thoracotomy for an inoperable mass or may guide the surgical approach (e.g., transsternal versus intercostal thoracotomy).

Confounding Effects of Pleural Fluid

As noted before, cranial mediastinal masses often cause elevation of the trachea. Elevation of the trachea may also result from a large amount of pleural fluid that results in lung displacement from buoyancy (Fig. 30-30).[16] A small volume of pleural fluid does not result in tracheal elevation unless a mediastinal mass is also present. If pleural fluid is present, definitive radiographic identification of a concurrent mediastinal mass is usually not possible. However, if the mass is large enough to compress the trachea, the presence of a mass can be inferred because pleural fluid alone does not cause tracheal compression.

If pleural fluid obscures the mediastinum, and a mediastinal mass is being considered, various interventions can be used:

1. The fluid can be removed and the radiographs repeated.
2. The patient can be positioned upright and a horizontally directed x-ray beam used to obtain a VD thoracic radiograph; these horizontal-beam radiographs take advantage of gravity, which causes pleural fluid to migrate away from the area of the suspected mediastinal mass.

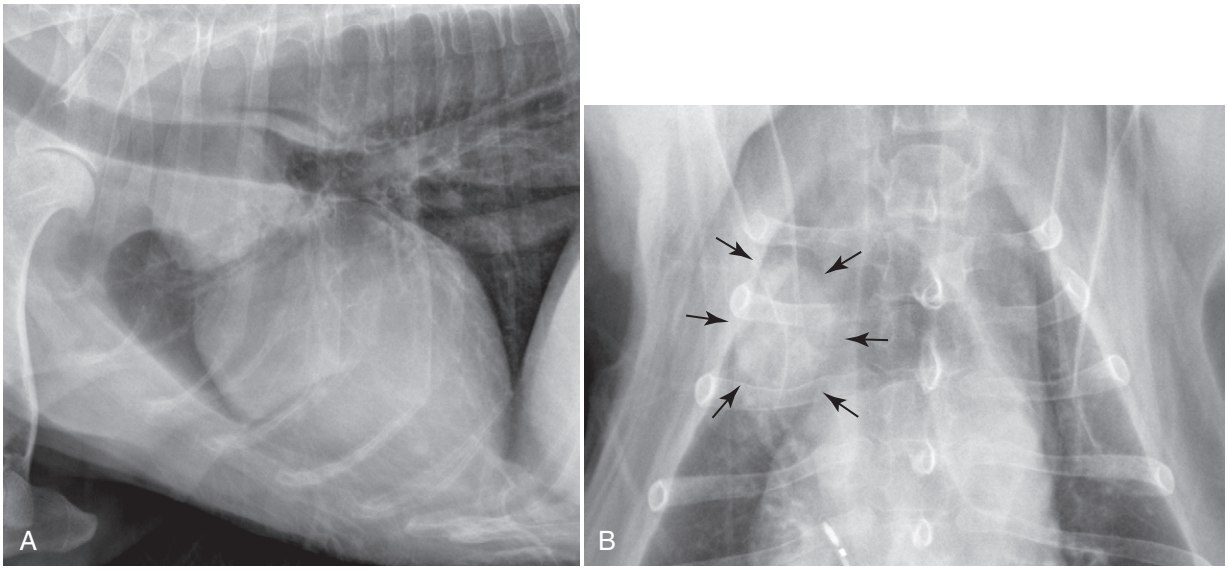


Fig. 30-27 Right lateral **(A)** and VD **(B)** radiographs of a dog. In **A,** there is a mass in the cranial aspect of the thorax, just cranial to the tracheal bifurcation. This mass is well marginated ventrally but poorly marginated dorsally. The sharp margination ventrally suggests a pulmonary location for the mass, but a mediastinal mass extending laterally where it would be surrounded by lung cannot be ruled out. In **B,** the mass is located in the right cranial aspect of the thorax *(black arrows)*. Because no part of the mediastinum is present in this region, the most likely diagnosis is pulmonary mass.

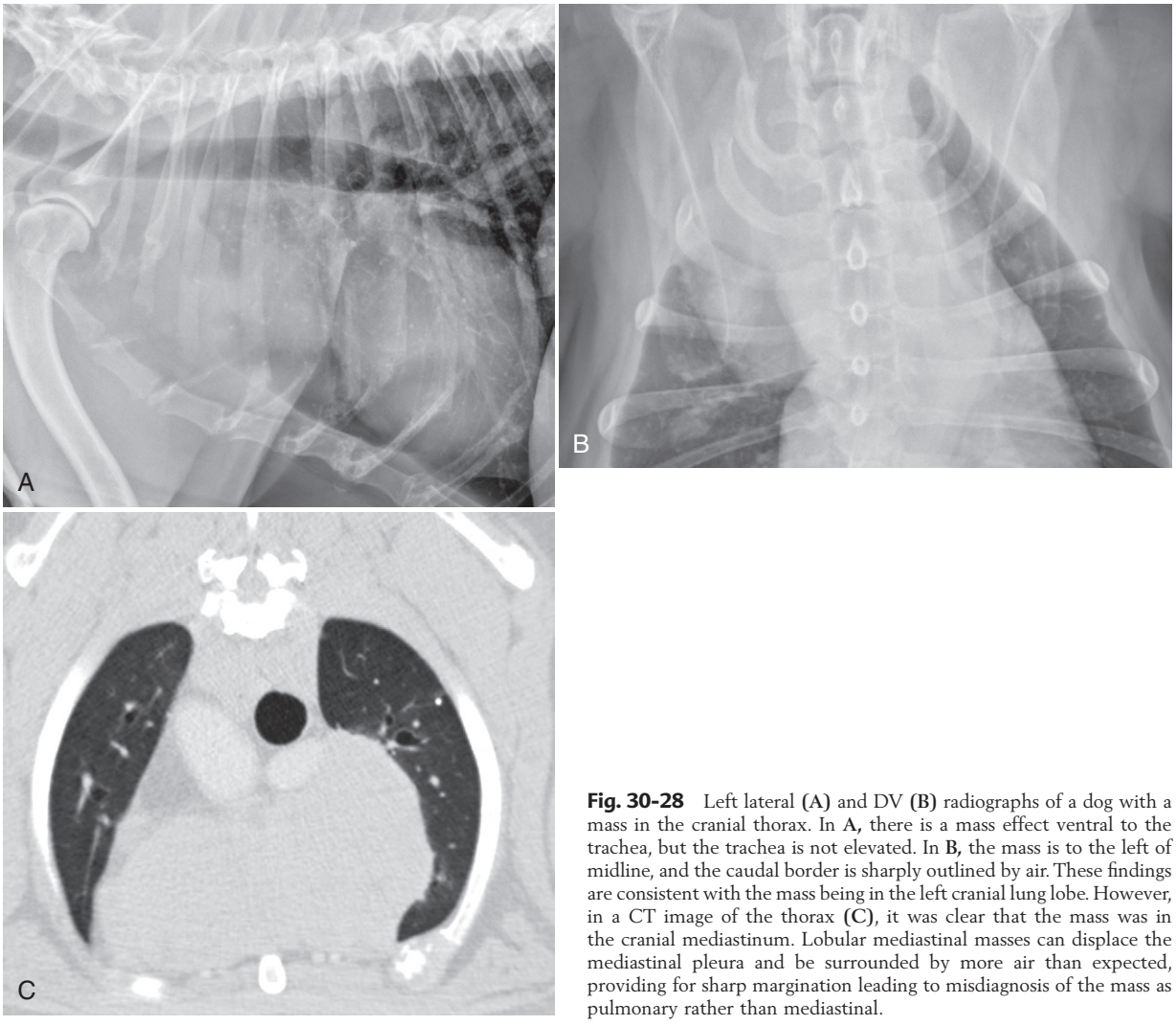


Fig. 30-28 Left lateral **(A)** and DV **(B)** radiographs of a dog with a mass in the cranial thorax. In **A,** there is a mass effect ventral to the trachea, but the trachea is not elevated. In **B,** the mass is to the left of midline, and the caudal border is sharply outlined by air. These findings are consistent with the mass being in the left cranial lung lobe. However, in a CT image of the thorax **(C)**, it was clear that the mass was in the cranial mediastinum. Lobular mediastinal masses can displace the mediastinal pleura and be surrounded by more air than expected, providing for sharp margination leading to misdiagnosis of the mass as pulmonary rather than mediastinal.

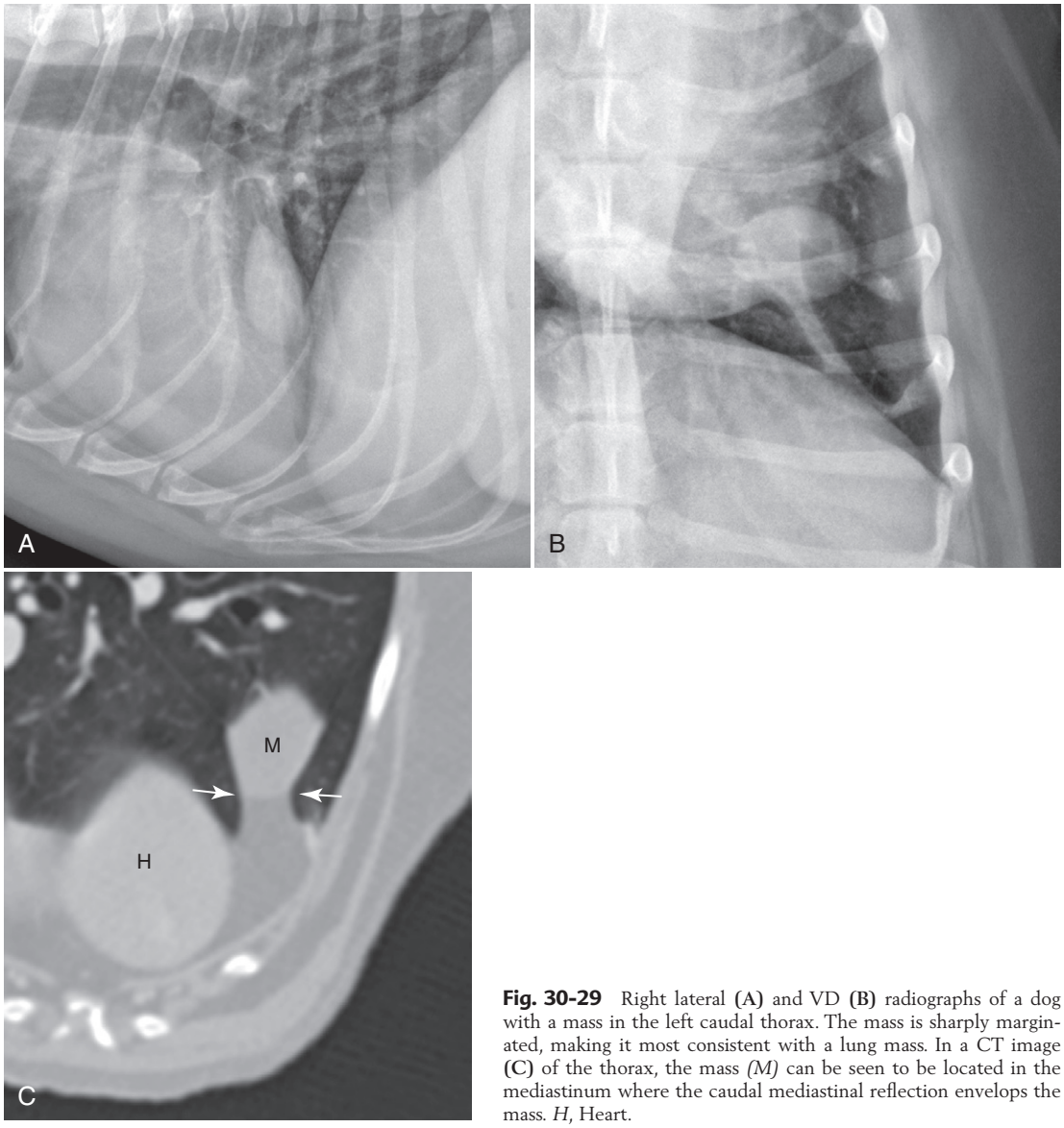


Fig. 30-29 Right lateral **(A)** and VD **(B)** radiographs of a dog with a mass in the left caudal thorax. The mass is sharply marginated, making it most consistent with a lung mass. In a CT image **(C)** of the thorax, the mass *(M)* can be seen to be located in the mediastinum where the caudal mediastinal reflection envelops the mass. *H*, Heart.

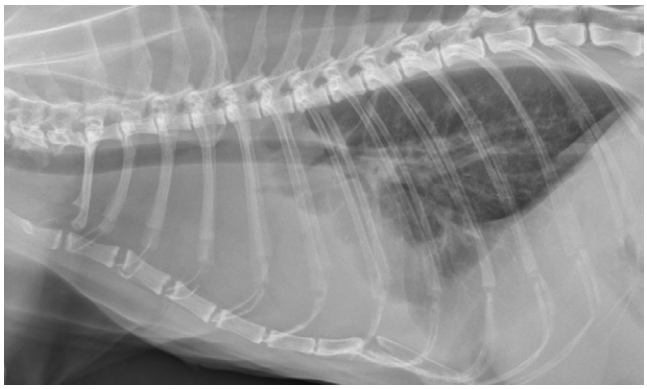


Fig. 30-30 Lateral radiograph of the thorax of a cat with pleural effusion. The trachea is displaced dorsally, but the presence of a mediastinal mass cannot be confirmed radiographically because (1) pleural fluid may be accompanied by tracheal elevation when no mediastinal mass is present because of the lungs floating in the effusion, (2) a mass cannot be seen, and (3) the trachea is not compressed. Radiography after fluid removal, positional radiography with a horizontal x-ray beam, ultrasonography, or CT would be more sensitive for determining whether a mediastinal mass was present in this cat.

3. Ultrasound or CT can be used to search for a mass in the mediastinum.[17,18]

The pleural fluid provides an excellent acoustic window for sonographic examination, and ultrasound-guided aspiration or biopsy facilitates making a definitive diagnosis. Ultrasonography of the thorax is technically challenging and is best performed by an experienced sonographer.

Pneumomediastinum

Pneumomediastinum is free gas in the mediastinum. The radiographic manifestation of free mediastinal gas depends on the volume of gas that is present and the radiographic projection. Pneumomediastinum is not readily detectable in VD or DV views because the overall size of the mediastinum is not increased, and the mediastinal gas is superimposed on the midline and thus obscured by other structures. Lateral views will be most useful. With a large volume of mediastinal gas, organs and structures not normally seen become visible because of the contrast afforded by the mediastinal gas (Fig. 30-31). With smaller amounts of mediastinal gas, the changes are less dramatic. For example, the only abnormality may be visualization of the adventitial surface of the trachea (Fig. 30-32, *A*), or a heterogeneous radiolucent appearance to

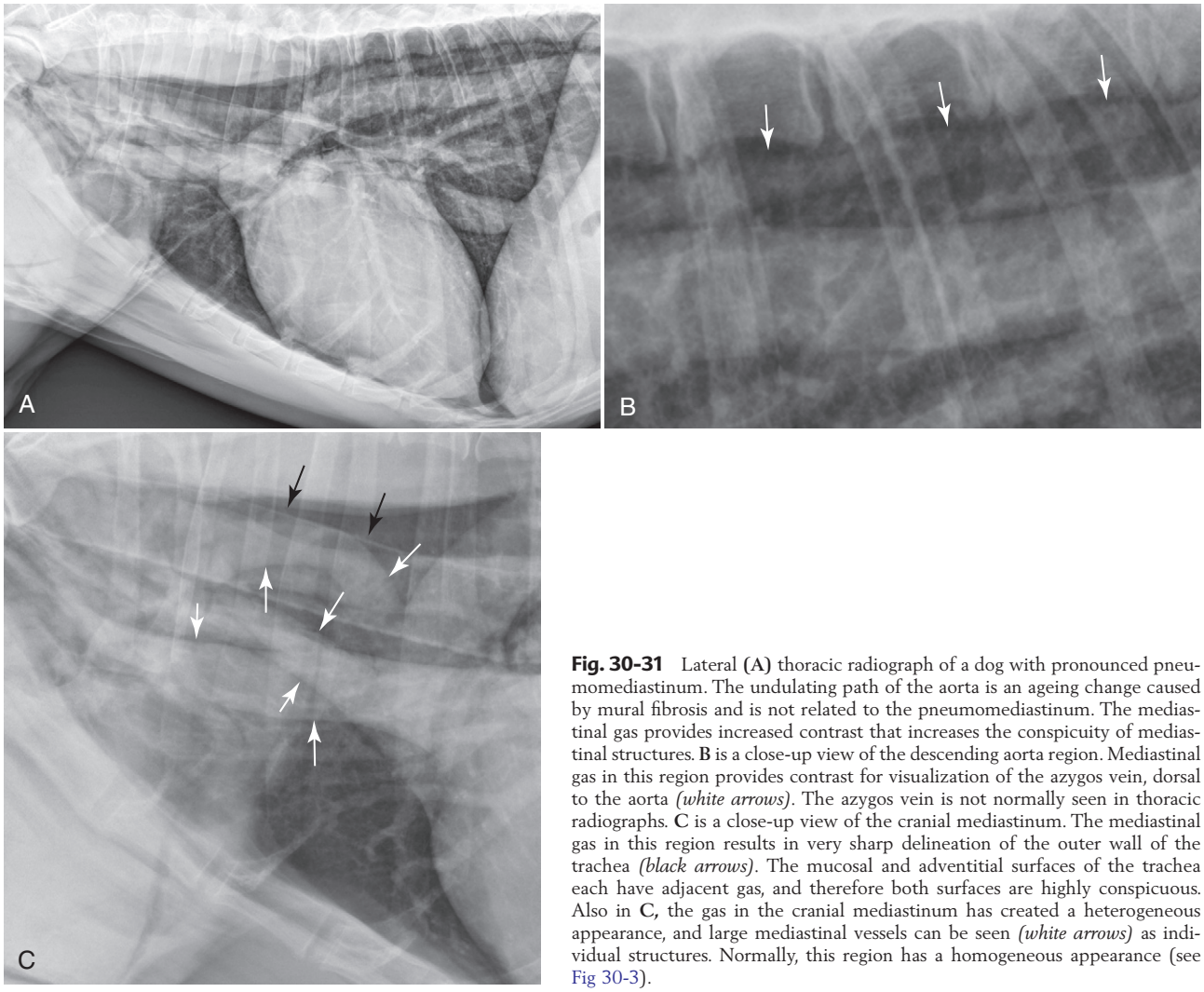


Fig. 30-31 Lateral **(A)** thoracic radiograph of a dog with pronounced pneumomediastinum. The undulating path of the aorta is an ageing change caused by mural fibrosis and is not related to the pneumomediastinum. The mediastinal gas provides increased contrast that increases the conspicuity of mediastinal structures. **B** is a close-up view of the descending aorta region. Mediastinal gas in this region provides contrast for visualization of the azygos vein, dorsal to the aorta *(white arrows)*. The azygos vein is not normally seen in thoracic radiographs. **C** is a close-up view of the cranial mediastinum. The mediastinal gas in this region results in very sharp delineation of the outer wall of the trachea *(black arrows)*. The mucosal and adventitial surfaces of the trachea each have adjacent gas, and therefore both surfaces are highly conspicuous. Also in **C,** the gas in the cranial mediastinum has created a heterogeneous appearance, and large mediastinal vessels can be seen *(white arrows)* as individual structures. Normally, this region has a homogeneous appearance (see Fig 30-3).

the cranioventral aspect of the mediastinum because of gas pocketing (Fig. 30-32, *B*). If there are large amounts of subcutaneous gas in addition to pneumomediastinum, the superimposed subcutaneous gas creates a very heterogeneous opacity in lateral views and can lead to overestimation of the volume of gas present in the mediastinum or even a misdiagnosis of pneumomediastinum (Fig. 30-33).

Pneumomediastinum may progress to pneumothorax if mediastinal pressure results in tearing of the mediastinal parietal pleura, thus establishing communication between the mediastinum and the pleural space. Pneumomediastinum can also progress to pneumothorax if gas dissects through fenestrations in the mediastinal pleura. Conversely, pneumothorax does not progress to pneumomediastinum. Dyspnea usually is not seen with pneumomediastinum unless it results in pneumothorax.

Because of the communication of the mediastinum with the neck and retroperitoneal space, pneumomediastinum may result in subcutaneous emphysema or pneumoretroperitoneum (Fig. 30-34). Alternatively, gas in the retroperitoneal space or fascial planes of the neck may diffuse into the mediastinum.

Pneumomediastinum can result from a variety of causes. It is common for air to escape into the pulmonary interstitium from sites of alveolar rupture, and this air can then diffuse in a retrograde direction in the loose connective tissue adjacent to bronchi and vessels into the mediastinum.[19,20] This phenomenon has been called the *Macklin effect* after its discoverer, and it is a relatively frequent occurrence following blunt thoracic trauma,[21,22] such as an automobile accident, and also after iatrogenic pulmonary hyperinflation during anesthesia or resuscitation.[23] Pneumothorax is not present when pneumomediastinum results from the Macklin effect unless the pulmonary pleura becomes torn or the mediastinal air accumulation extends to the pleural space.

Gas present in fascial planes of the neck can dissect caudally into the mediastinum. Gas in the neck can result from neck trauma, such as a bite wound. Pneumomediastinum can also result from a hole in the wall of the trachea; in cats it is common for the trachea to be punctured during jugular venapuncture, and this can lead to air leaks and pneumomediastinum as gas tracks down the neck. If a tracheal hole is intrathoracic, air enters the mediastinum directly. In cattle and horses, pneumomediastinum is frequently seen after transtracheal aspiration procedures.

Tracheal rupture in anesthetized cats associated with overdistention of the endotracheal tube cuff is a noteworthy cause of pneumomediastinum.[24,25] Cuff overdistention may cause

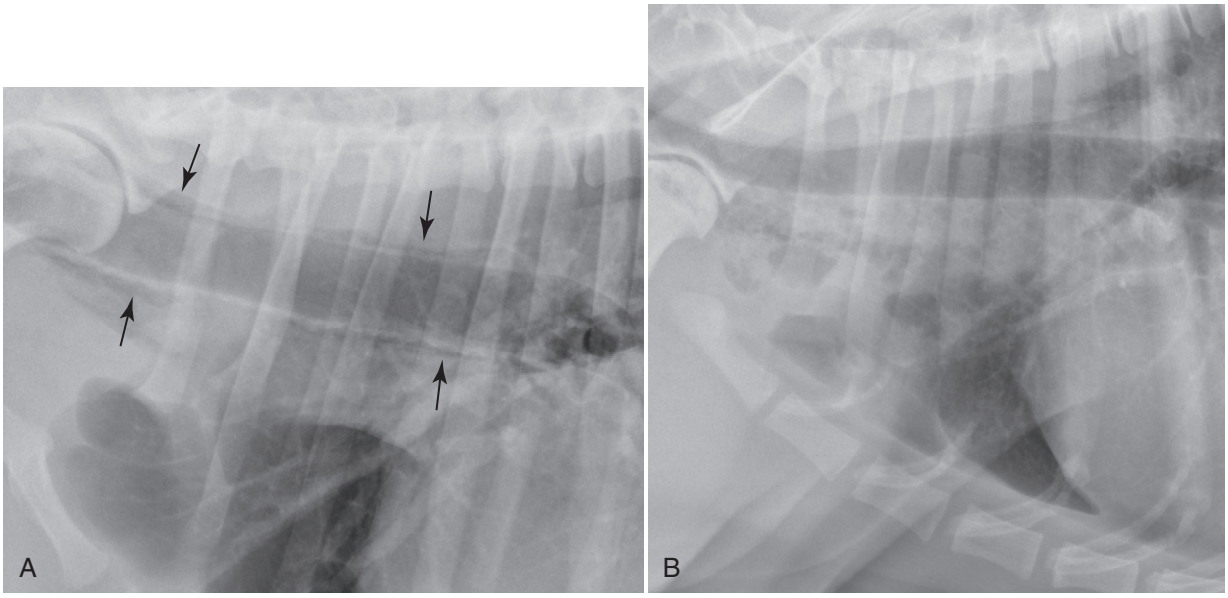


Fig. 30-32 Lateral radiographs of two dogs with a small amount of gas in the cranial mediastinum. In **A,** the gas is localized around the trachea, leading to increased conspicuity of its adventitial surface *(black arrows)*. In **B,** the gas has collected in pockets in the cranioventral aspect of the mediastinum, creating an unstructured mottled radiolucency. With regard to the appearance in **B**, the ventrodorsal view should be consulted to make sure that the mottling is not caused by superimposition of pockets of subcutaneous emphysema.

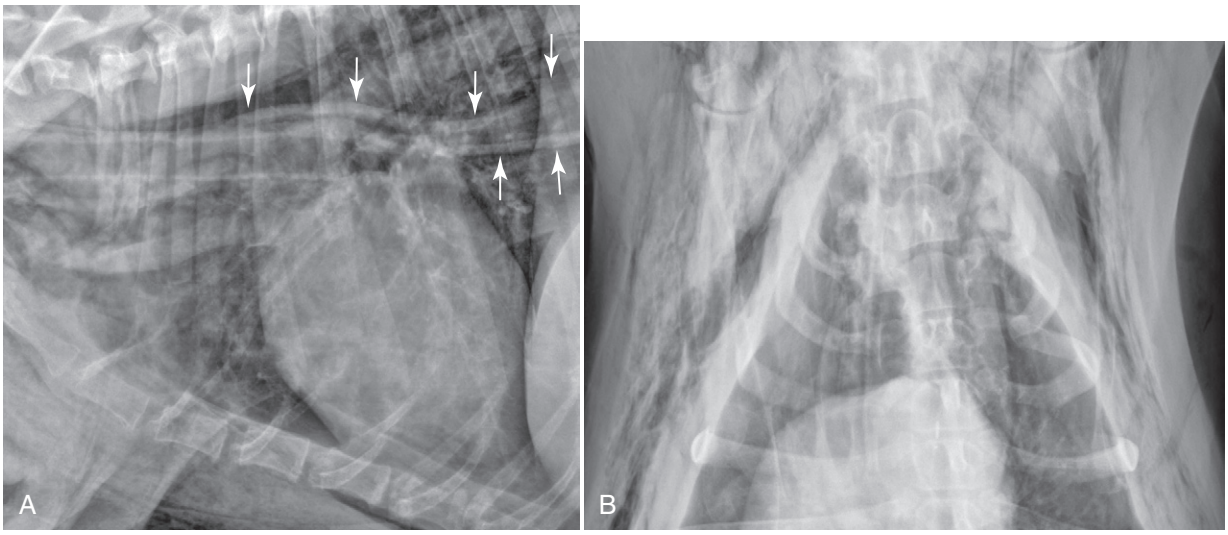


Fig. 30-33 Lateral **(A)** and ventrodorsal **(B)** radiograph of a dog with pneumomediastinum and a large amount of coexisting subcutaneous emphysema. In **A,** the adventitial margin of the trachea and cranial mediastinal vessels are seen because of the contrast afforded by the mediastinal air. The adventitial surface of the esophagus is also visible *(white arrows)*. In addition, the cranioventral mediastinum has a mottled appearance. This mottling can be caused by air pocketing in the mediastinum, but in this patient much of it is caused by superimposition of the subcutaneous emphysema, as can be seen in **B.** In **A,** the mottling extends ventral to the thorax, which is also evidence of coexisting subcutaneous emphysema.

rupture of the trachealis muscle at the point of attachment to the tracheal cartilages. Tracheal rupture may occur at a modest cuff volume and may not be immediately apparent to the anesthetist. Development of subcutaneous emphysema occurs quickly following tracheal rupture from cuff overdistention. If subcutaneous emphysema develops during a surgical procedure, the anesthetist must be aware of this potentially fatal complication.

Other rare causes of pneumomediastinum are esophageal perforation as a result of trauma, neoplasia, or inflammation; extension of retroperitoneal gas into the mediastinum; and presence of a gas-producing organism in the mediastinum.

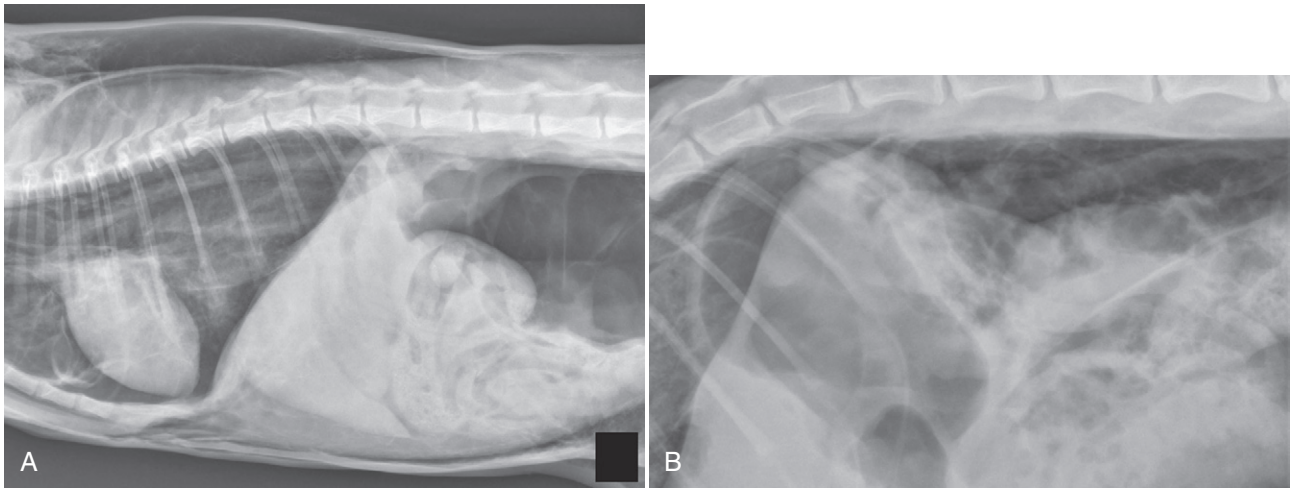


Fig. 30-34 **A,** Lateral radiograph of a cat with pneumomediastinum that has resulted in massive pneumoretroperitoneum. There is also subcutaneous emphysema. **B,** Lateral radiograph of a cat with pneumomediastinum where the extent of pneumoretroperitoneum is less.

REFERENCES

1. Kern D, Carrig C, Martin R: Radiographic evaluation of induced pneumothorax in the dog, *Vet Radiol Ultrasound* 35:411, 1994.
2. Burk R: Radiographic definition of the phrenicopericardiac ligament, *J Am Vet Radiol Soc* 17:216, 1976.
3. Bezuidenhout AJ: The lymphatic system. In Evans H, editor: *Miller's anatomy of the dog*, ed 3, Philadelphia, 1993, Saunders, p 717.
4. Tompkins M: Lymphoid system. In Hudson L, Hamilton W, editors: *Atlas of feline anatomy for veterinarians*, Philadelphia, 1993, Saunders.
5. Kirberger RM, Avner A: The effect of positioning on the appearance of selected cranial thoracic structures in the dog, *Vet Radiol Ultrasound* 47:61, 2006.
6. Hopper B, Lester N, Irwin P, et al: Imaging diagnosis: pneumothorax and focal peritonitis in a dog due to migration of an inhaled grass awn, *Vet Radiol Ultrasound*, 45:136, 2004.
7. Zekas LJ, Adams WM: Cranial mediastinal cysts in nine cats, *Vet Radiol Ultrasound* 43:413, 2002.
8. Starrak G, Berry C, Page R, et al: Correlation between thoracic radiographic changes and remission/survival duration in 270 dogs with lymphosarcoma, *Vet Radiol Ultrasound* 38:411, 1997.
9. Ruehl WW Jr, Thrall D: The effect of dorsal versus ventral recumbency on the radiographc appearance of the canine thorax, *Vet Radiol* 22:10, 1981.
10. Brinkman EL, Biller D, Armbrust L: The clinical usefulness of the ventrodorsal versus dorsoventral thoracic radiograph in dogs, *J Am Anim Hosp Assoc* 42:440, 2006.
11. Lora-Michiels M, Biller DS, Olsen D, et al: The accessory lung lobe in thoracic disease: a case series and anatomical review, *J Am Anim Hosp Assoc* 39:452, 2003.
12. Ackerman N, Madewell BR: Thoracic and abdominal radiographic abnormalities in the multicentric form of lymphosarcoma in dogs, *J Am Vet Med Assoc* 176:36, 1980.
13. Berry CR, Moore PF, Thomas WP, et al: Pulmonary lymphomatoid granulomatosis in seven dogs (1976–1987), *J Vet Intern Med* 4:157, 1990.
14. Fitzgerald SD, Wolf DC, Carlton WW: Eight cases of canine lymphomatoid granulomatosis, *Vet Pathol* 28:241, 1991.
15. Fulmer AK, Mauldin GE: Canine histiocytic neoplasia: an overview, *Can Vet J* 48:1041, 2007.
16. Snyder P, Sato T, Atkins C: The utility of thoracic radiographic measurement for the detection of cardiomegaly in cats with pleural effusion, *Vet Radiol* 31:89, 1990.
17. Reichle J, Wisner E: Non-cardiac thoracic ultrasound in 75 feline and canine patients, *Vet Radiol Ultrasound* 41:154, 2000.
18. Konde L, Spaulding K: Sonographic evaluation of the cranial mediastinum in small animals, *Vet Radiol* 32:178, 1991.
19. Macklin C: Transport of air along sheaths of pulmonic blood vessels from alveoli to mediastinum: clinical implications, *Arch Intern Med* 64:913, 1939.
20. Macklin M, Macklin C: Malignant interstitial emphysema of the lungs and mediastinum as an important occult complication in many respiratory diseases and other conditions: an interpretation of the clinical literature in the light of laboratory experiment, *Medicine* 23:281, 1944.
21. Baharudin A, Sayuti RM, Shahid H: The Macklin effect—pneumomediastinum and pneumopericardium following blunt chest trauma, *Med J Malaysia* 61:371, 2006.
22. Wintermark M, Schnyder P: The Macklin effect: a frequent etiology for pneumomediastinum in severe blunt chest trauma, *Chest* 120:543, 2001.
23. Brown D, Holt D: Subcutaneous emphysema, pneomothorax, pneumomediastinum and pneumopericardium associated with positive-pressure ventilation in a cat, *J Am Vet Med Assoc* 206:997, 1995.
24. Mitchell S, McCarthy R, Rudloff E, et al: Tracheal rupture associated with intubation in cats: 20 cases (1996–1998), *J Am Vet Med Assoc* 216:1592, 2000.
25. Hardie E, Spodnick G, Gilson S, et al: Tracheal rupture in cats: 16 cases (1983–1998), *J Am Vet Med Assoc* 214:580, 1999.

ELECTRONIC RESOURCES

evolve

Additional information related to the content in Chapter 30 can be found on the companion Evolve website at http://evolve.elsevier.com/Thrall/vetrad/

- Chapter Quiz

CHAPTER • 31

The Pleural Space

Donald E. Thrall

PLEURAL ANATOMY

As described in Chapter 30, there are two pleural sacs, one on the right and one on the left. Each pleural sac has parietal (mediastinal, diaphragmatic, costal) and visceral components. The visceral pleura covers the lung parenchyma. Of the parietal pleural layers, costal parietal pleura lines the inside of the thoracic cage, diaphragmatic parietal pleura covers the diaphragm, and mediastinal parietal pleura forms the boundaries of the mediastinal space, dividing the thorax into left and right halves.

The left and right pleural sacs are distinct entities (Fig. 31-1; see also Figs. 30-1 and 30-2). The pleural space is a potential space in normal subjects. It lies between the costal parietal pleura and visceral pleura, between the diaphragmatic parietal pleura and visceral pleura, and between the mediastinal parietal pleura and visceral pleura. The pleural space also lies between visceral pleural layers in interlobar fissures. The normal pleural space is a potential space because it contains only a small volume of fluid, which serves as a lubricant, but it can become a real space if it contains air, tissue, or an increased volume of fluid.

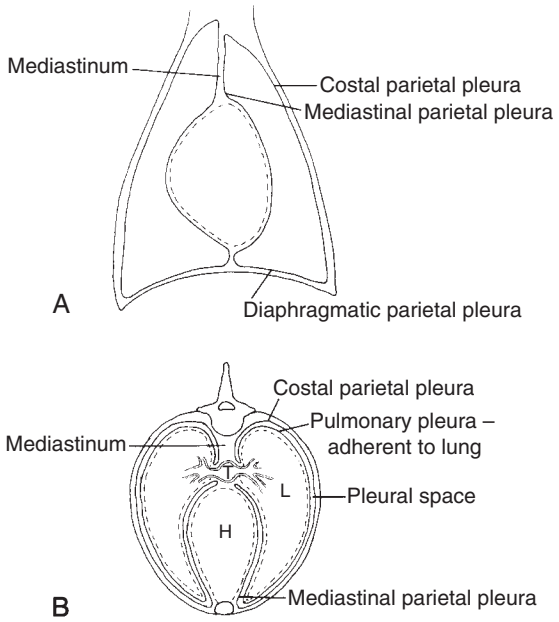


Fig. 31-1 The thorax in dorsal **(A)** and transverse **(B)** planes illustrating the relationship of the pleural layers. There are two distinct pleural sacs. **A,** Note the continuity of the costal, mediastinal, and diaphragmatic parts of each parietal sac. (Lungs have not been included in **A.**) **B,** Note how the mediastinal pleura is reflected onto the lung to become pulmonary pleura. In **B,** the lung is depicted by the *dotted line* (the heart is also designated by a *dotted line*). Also note that the pleural space is not continuous with the mediastinum. *H,* Heart; *L,* lung; *T,* trachea.

NORMAL RADIOGRAPHIC APPEARANCE OF PLEURA AND PLEURAL THICKENING

Normal pleura is usually not visible radiographically. Pleura is very thin and also silhouettes with adjacent soft tissue everywhere except in interlobar fissures, where it is in contact only with lung. Thin pleural lines between lobes are sometimes visible radiographically. These thin pleural lines may be because of the x-ray beam striking normal interlobar pleura exactly head-on, resulting in absorption of a sufficient number of x-rays for the pleura to be seen, or to slightly thickened pleura (Fig. 31-2). Radiographic determination of whether isolated, thin pleural lines are normal or are caused by mild thickening is impossible. In either instance, this finding is usually of no clinical significance. When pleural thickening is advanced, wider pleural lines between lung lobes may be seen (Fig. 31-3). With pleural fibrosis, the specific interlobar fissures seen radiographically depend on which fissures are struck tangentially by the x-ray beam. This varies with the position of the patient relative to the x-ray beam.

PLEURAL FLUID

Fluid in the pleural space can be an exudate, transudate, or modified transudate and can result from many causes (Table 31-1). The radiographic changes associated with pleural fluid depend on the volume of fluid, the position of the animal in relation to the x-ray beam, the distribution of the fluid, and whether the fluid is free or loculated. There are no radiographic criteria that allow differentiation of an exudate from a transudate. Thus, the radiographic changes associated with pleural fluid are the same, regardless of fluid type, because neither the distribution of pleural fluid nor its opacity is reliably related to the cause, although an exudate may be more asymmetrically distributed. This is discussed in more detail later.

Pleural fluid distributes itself according to gravity and the ability of the lung to expand—that is, lung compliance.[1] It is important to realize that the radiographic appearance of

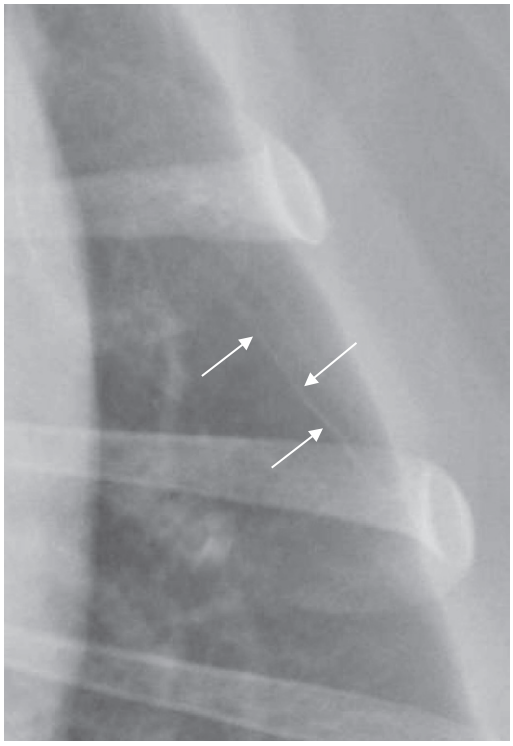


Fig. 31-2 Close-up view of a portion of the left hemithorax of a dog. A thin pleural fissure can be seen *(white arrows)*. Distinguishing radiographically whether this is caused by x-rays striking a normal fissure or by slight pleural thickening is impossible. This distinction is not significant clinically.

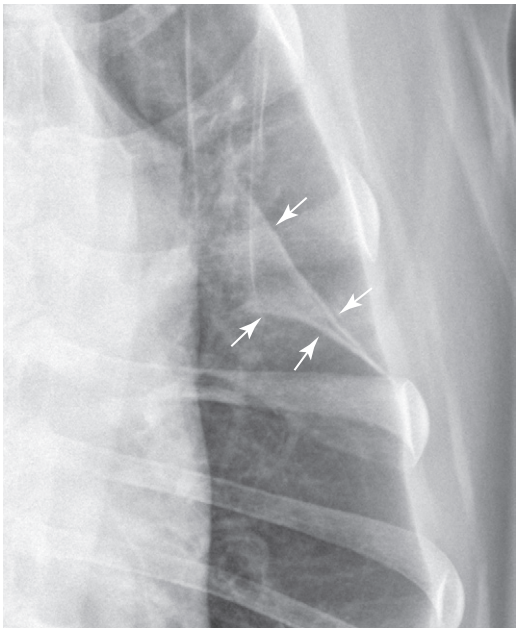


Fig. 31-3 Ventrodorsal thoracic radiograph of a dog in which mildly thickened interlobar fissures *(white arrows)* are visible. These fissures are thicker than normal (compare with Fig. 31-2) and may be caused by either pleural thickening or a small amount of pleural fluid. Sonography or a horizontal-beam radiograph would assist in distinguishing between pleural thickening and pleural fluid.

Table • **31-1**

Causes of Pleural Fluid

CAUSE	FLUID TYPE
Congestive heart failure	M
Pyothorax	E
Malignancy	M
Pneumonia	M, E
Trauma	M
Coagulation defect	M
Hypoproteinemia	T
Mediastinitis	M, E
Chylothorax	M
Diaphragmatic hernia	M

E, Exudate; *M,* modified transudate; *T,* transudate.

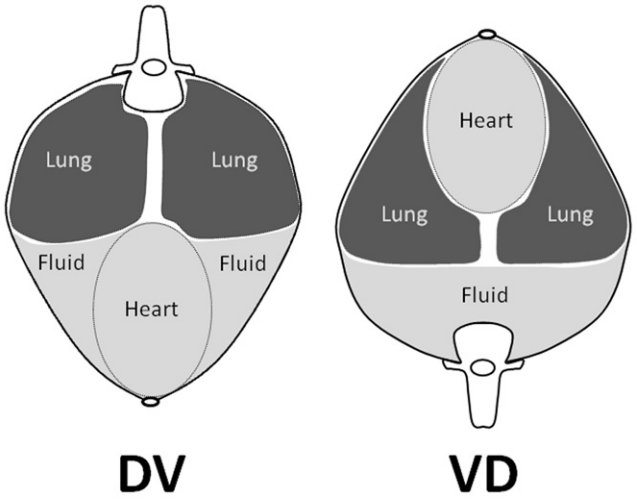


Fig. 31-4 Diagram of the effect of dorsal versus ventral recumbency on the radiographic appearance of pleural fluid. **A,** The patient is in ventral recumbency for a DV radiograph, and fluid gravitates ventrally. The fluid is in contact with the heart, thus obscuring the heart because of border effacement. When the patient is in dorsal recumbency for the VD radiograph **(B),** the fluid gravitates dorsally and is not in contact with the heart; thus the cardiac silhouette is visible because it is surrounded by air-filled lung that provides contrast. The absolute depth of the fluid is greater when the patient is in ventral recumbency **(A)** because the ventral part of the thoracic cavity is narrower, and the fluid rises to a higher level. Thus, overall thoracic radiopacity is greater in ventral recumbency in patients with pleural effusion. These effects of VD versus DV recumbency on the radiographic appearance of pleural fluid can be seen in Figure 31-6.

pleural fluid in ventrodorsal (VD) versus dorsoventral (DV) radiographs can be quite different. In DV radiographs, fluid gravitates ventrally and causes border effacement of the heart. In VD radiographs, pleural fluid usually does not obscure the heart because the fluid is in the dorsal aspect of the thorax, where it does not make contact with the heart and cause border effacement (Fig. 31-4). Also, the overall opacity of the thorax will be greater in DV radiographs in patients with pleural fluid because the fluid depth is greater (see Fig. 31-4).

Radiographic signs of free pleural fluid are listed in Box 31-1.

Box • 31-1

Roentgen Signs of Free Pleural Fluid

Widened interlobar fissures that are of soft tissue opacity.
  Usually most conspicuous in VD and lateral radiographs.
Retraction of pleural surface of lung away from pleural surface of thoracic wall, with interposed soft tissue opacity.
  Seen first in VD or DV radiographs.
Increased soft tissue opacity with scalloped margins dorsal to sternum.
  Seen in lateral radiographs.
Decreased cardiac silhouette visualization.
  Seen first in DV radiographs.
Obscured diaphragmatic outline.
  Seen in all views.
Blunting of costophrenic sulci.
  Seen rarely, only in VD radiographs.

Interlobar Fissures, Retraction of Lung Margins, and Retrosternal Opacification

The thickness and number of interlobar fissures seen with pleural fluid depend on the amount of fluid and the relative position of the patient and the x-ray beam (Fig. 31-5, p. 574). Approximately 100 mL of fluid must be present in the pleural space of a medium-sized dog before widened interlobar fissures become visible.[2] Thus, any radiographic evidence of pleural fluid signifies a relatively large fluid volume, and one that can be sampled by thoracocentesis. Visualization of fluid-containing interlobar fissures results when the x-ray beam strikes the fissure head-on. Some fluid-containing fissures may not be seen because their relation to the x-ray beam is not head-on.

With a *small amount of fluid*, interlobar fissures are more likely to be seen on VD rather than DV radiographs because when in dorsal recumbency there is a tendency for fluid to enter interlobar fissures (see Fig. 31-3). This is opposed to sternal recumbency where the fluid collects dorsal to the sternum.[2,3] A small amount of pleural fluid also usually results in visualization of interlobar fissures in lateral views as well.

With moderate or pronounced pleural fluid, the number and thickness of interlobar fissures increase, and fluid also collects between the thoracic wall and the lung, resulting in lung retraction (Figs. 31-6 and 31-7, p. 576).

The magnitude of lung retraction seen radiographically depends on the volume of fluid. Retraction of lung from the thoracic wall can be seen on lateral, DV, and VD radiographs (see Figs. 31-6 and 31-7). The pleural fluid surrounds the lung causing global retraction, but the fluid will be most apparent radiographically where the x-ray beam strikes the fluid/lung interface head-on (Fig. 31-8, p. 576). Therefore more pleural fluid is usually present than predicted based on the severity of the lung retraction.

In lateral radiographs pleural fluid often results in a region of homogeneously increased opacity dorsal to the sternum (Fig. 31-9, p. 577; also see Figs. 31-6, *C* and 31-7, *B*). This opacity results from fluid having collected in the ventral aspect of the thorax and layered against the mediastinum in the nondependent hemithorax. If the patient has unilateral pleural fluid, and the fluid is in the dependent hemithorax, this opacity will not be visible because no fluid is layered against the mediastinum. The margin of this retrosternal opacity often appears scalloped because of adjacent, partially collapsed lung that alters the configuration of the fluid.

Pleural fluid may cause blunting of the costophrenic angle in VD radiographs if fluid is present between the dorsocaudal aspect of the lung and diaphragm. Rounding of the costophrenic angles will seldom be the only radiographic sign of pleural fluid, and this finding is rarely used to diagnose pleural fluid because of the other signs described previously.

Asymmetric Distribution of Pleural Fluid

Pleural fluid is usually relatively equally distributed between the right and left pleural spaces. Some patients, however, have asymmetric fluid distribution. Causes of unilateral or asymmetric pleural fluid include a difference in compliance between lung lobes, the closing of mediastinal fenestrations from inflammation or a mass, and an anatomically complete mediastinum. When there is extensive, unilateral pleural fluid, radiographic characterization of whether the resultant opacity is caused by pleural fluid or an abnormality of the thoracic wall or lung is usually impossible. In this instance, sonographic or computed tomography may be necessary to answer the question.

Pyothorax is a common cause of unilateral or asymmetric pleural fluid because of the viscid nature of the exudate (Fig. 31-10, p. 577), but other types of fluid can also be asymmetric. Chronic pleural fluid, or an inflammatory effusion, often results in extensive pleural fibrosis. When the visceral pleura is fibrotic, the margin of the retracted lung assumes a rounder shape than normal because of altered compliance (Fig. 31-10, *B*). This appearance is typical of pleural fibrosis, which limits the ability of the lung to both expand and contract because of elastic recoil.

Horizontal-Beam Radiography

Identification of a small amount of pleural fluid may not be possible on survey radiographs if the x-ray beam fails to strike a fluid/lung interface head-on (see Fig. 31-8). To enhance fluid detection, a horizontally directed x-ray beam may be used to ensure a head-on relation between the x-ray beam and the fluid/lung interface. If free pleural fluid is present, it gravitates dependently where the x-ray beam strikes it head-on (Fig. 31-11, p. 578).

A sharply demarcated, straight fluid line is not seen in patients with pleural fluid when radiographed with a horizontal x-ray beam because the configuration of the fluid is altered by the adjacent lung, which retracts because of elastic recoil. Sharp fluid lines are seen in horizontal-beam radiographs only when there is a free fluid–free air interface, such as with coexisting pleural fluid and pneumothorax. Horizontal-beam radiographs may also be useful in distinguishing pleural fluid from an intrathoracic mass as the cause of an intrathoracic opacity, as discussed before (see Fig. 31-9).

Pitfalls in Pleural Fluid Diagnosis

Various normal structures can be misinterpreted as pleural fluid. Thickened pleura may have an appearance identical to pleural fluid (see Fig. 31-3). A distinction may be made by using a horizontally directed x-ray beam or with sonography.[4]

A mineralized costal cartilage is sometimes confused with an interlobar fissure. The position of these two structures is similar, but their shape is different. Pleural fissure lines are distinctly curving, with the concave surface on the caudal aspect of the fissure line. Costal cartilages are more linear and can usually be followed laterally and be seen to attach to the

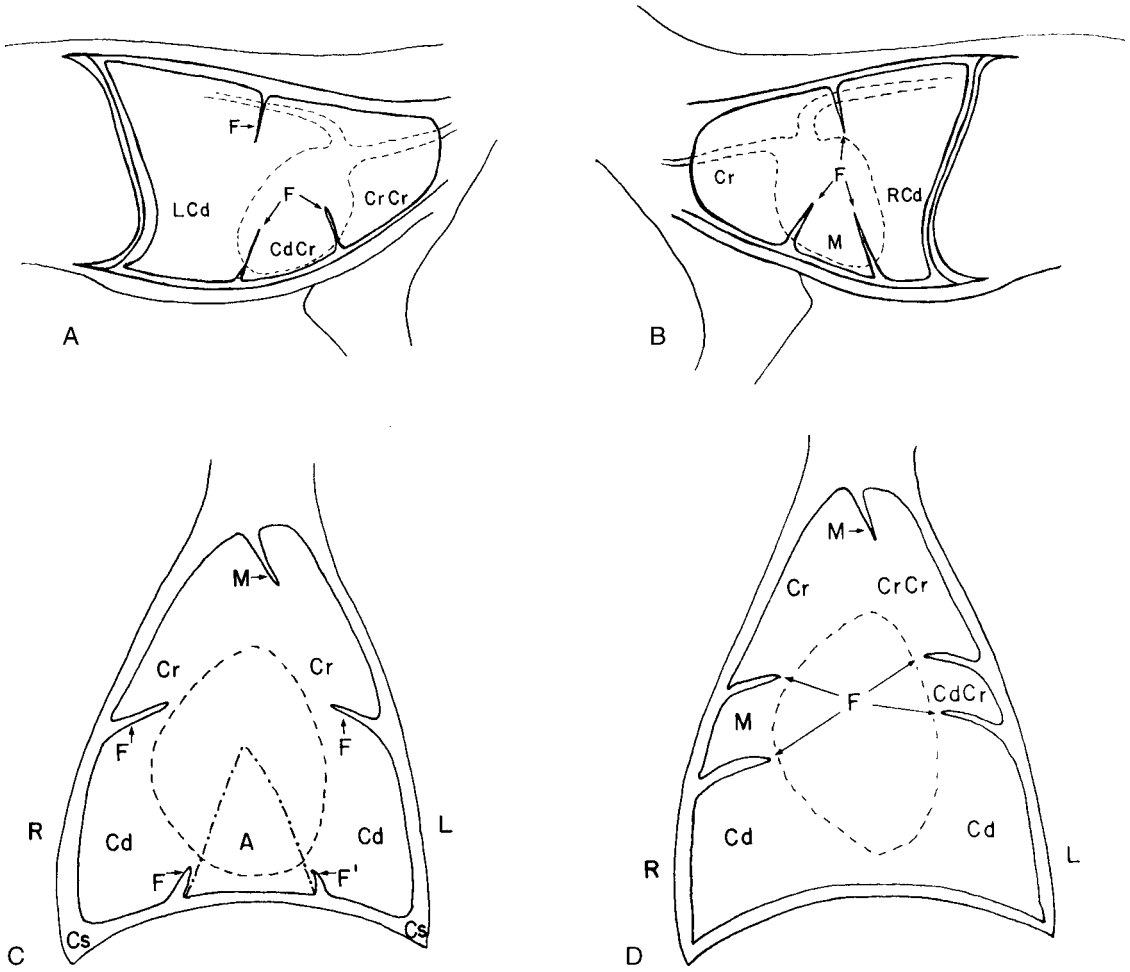


Fig. 31-5 The location of interlobar fissures in the thorax. The exact fissures visible when pleural fluid is present depends on the position of the patient, the volume of fluid, and whether the x-ray beam strikes the fissure tangentially, or head-on. Only fluid-filled fissures that are struck tangentially are seen. **A,** Fissures of the lateral aspect of the left lung (looking medial to lateral). These fissures are more likely to be seen when the patient is in left recumbency. **B,** Fissures of the lateral aspect of the right lung (looking medial to lateral). These fissures are more likely to be seen when the patient is in right recumbency. **C,** Fissures on the dorsal aspect of the lungs. These fissures are more likely to be seen when the patient is in dorsal recumbency. The costophrenic sulcus may become rounded when patients with pleural fluid are in dorsal recumbency. **D,** Fissures on the ventral aspect of the lungs. These fissures are more likely to be seen when the patient is in ventral recumbency. *A,* accessory lobe; *Cd,* caudal lobe; *CdCr,* caudal part of left cranial lobe; *Cr,* right cranial lobe; *CrCr,* cranial part of left cranial lobe; *Cs,* costophrenic sulcus; *F,* interlobar fissure; *F',* mediastinal reflection between the left caudal lobe and the accessory lobe (pleural fluid may accumulate adjacent to this reflection); *L,* left; *M,* mediastinal reflection; *Md,* right middle lobe; *R,* right.

end of a rib (Fig. 31-12, p. 578). If the costal cartilage does curve, the cranial surface is concave, not convex as with a fluid-containing fissure.

Thoracic wall deformities, such as those seen in chondrodystrophoid breeds, may result in increased radiopacity at the margin of the lung field. Without knowledge of this fact, the opacity may be misinterpreted as retraction of the lung from the thoracic wall because of pleural fluid (Fig. 31-13, p. 578).

Significance of Pleural Fluid

Pleural fluid may result from a primary pleural disorder, such as pleural neoplasm, but most often it is a sign of disease elsewhere. Determining the cause of pleural fluid from radiographs is usually impossible. When pleural fluid is present, structures are obscured, and extremely large lesions can go unidentified. Sonography will be useful for assessing the character of the fluid.[4] Sonography has also been used in an attempt to quantify pleural fluid volume. Although it was not possible to accurately predict pleural fluid volume in individual dogs or cats using sonographic findings, sonography may be useful for evaluating changes in pleural fluid volume in individual dogs.[5,6]

When pleural fluid is identified, careful scrutiny of the radiograph is necessary. Subtle radiographic findings such as a rib lesion or asymmetric distribution of the fluid can be very

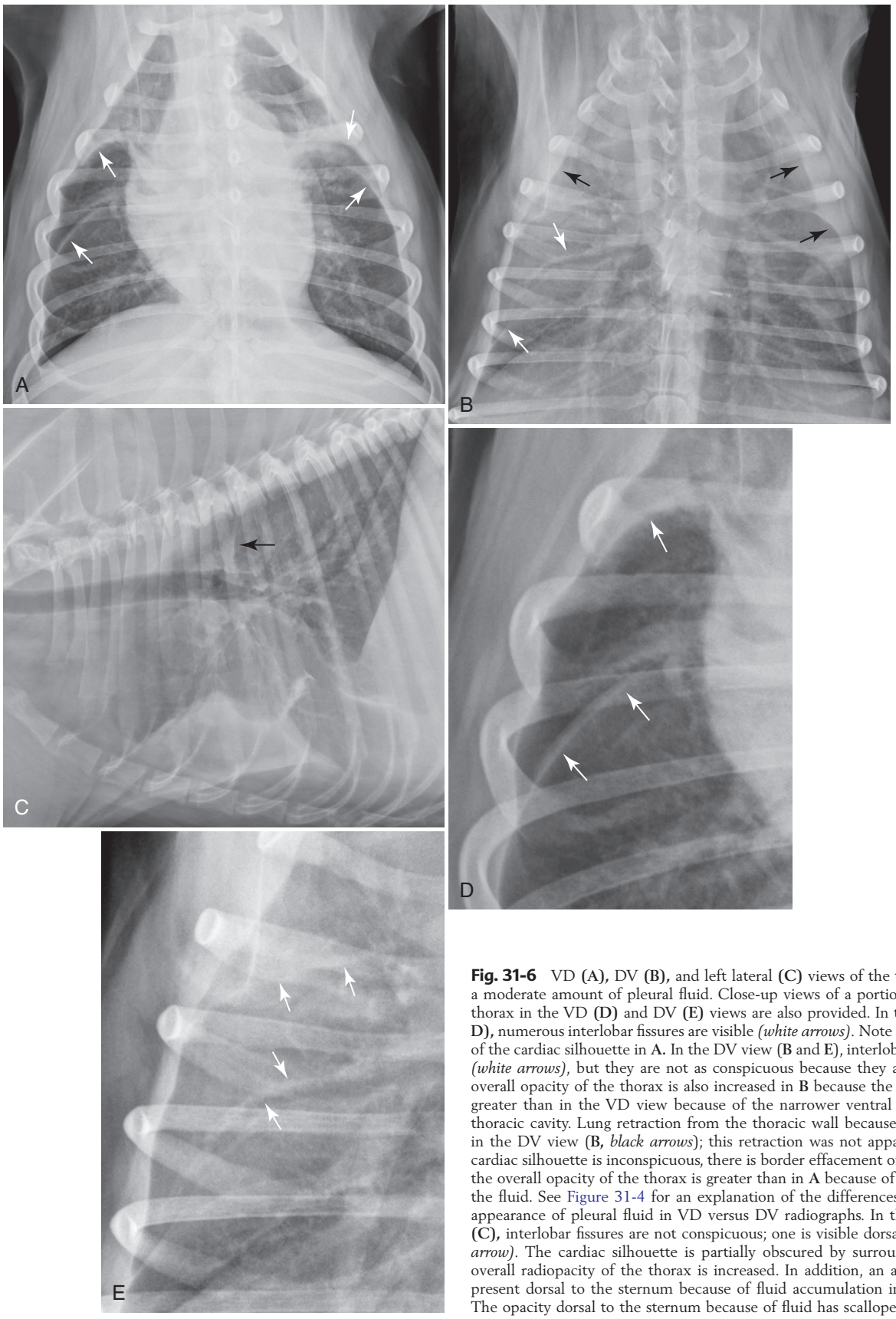


Fig. 31-6 VD **(A),** DV **(B),** and left lateral **(C)** views of the thorax of a dog with a moderate amount of pleural fluid. Close-up views of a portion of the right hemithorax in the VD **(D)** and DV **(E)** views are also provided. In the VD view **(A** and **D),** numerous interlobar fissures are visible *(white arrows)*. Note the good conspicuity of the cardiac silhouette in **A.** In the DV view (**B** and **E**), interlobar fissures are visible *(white arrows)*, but they are not as conspicuous because they are not as thick. The overall opacity of the thorax is also increased in **B** because the depth of the fluid is greater than in the VD view because of the narrower ventral configuration of the thoracic cavity. Lung retraction from the thoracic wall because of fluid is also seen in the DV view (**B,** *black arrows*); this retraction was not apparent in **A**. In **B,** the cardiac silhouette is inconspicuous, there is border effacement of the diaphragm, and the overall opacity of the thorax is greater than in **A** because of the greater depth of the fluid. See Figure 31-4 for an explanation of the differences in the radiographic appearance of pleural fluid in VD versus DV radiographs. In the right lateral view **(C),** interlobar fissures are not conspicuous; one is visible dorsal to the heart *(black arrow)*. The cardiac silhouette is partially obscured by surrounding fluid, and the overall radiopacity of the thorax is increased. In addition, an area of radiopacity is present dorsal to the sternum because of fluid accumulation in the ventral thorax. The opacity dorsal to the sternum because of fluid has scalloped margins.

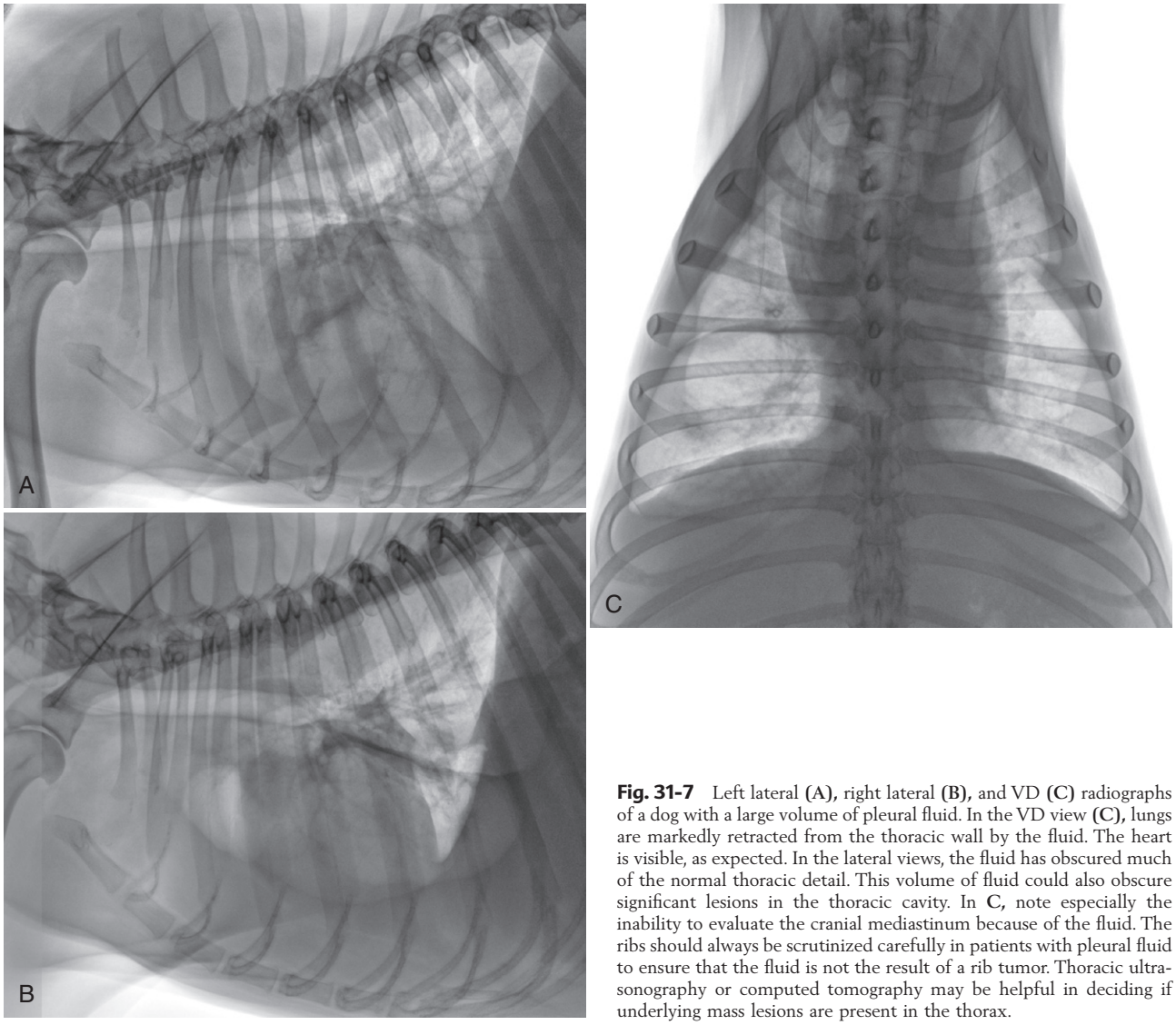


Fig. 31-7 Left lateral **(A),** right lateral **(B),** and VD **(C)** radiographs of a dog with a large volume of pleural fluid. In the VD view **(C),** lungs are markedly retracted from the thoracic wall by the fluid. The heart is visible, as expected. In the lateral views, the fluid has obscured much of the normal thoracic detail. This volume of fluid could also obscure significant lesions in the thoracic cavity. In **C,** note especially the inability to evaluate the cranial mediastinum because of the fluid. The ribs should always be scrutinized carefully in patients with pleural fluid to ensure that the fluid is not the result of a rib tumor. Thoracic ultrasonography or computed tomography may be helpful in deciding if underlying mass lesions are present in the thorax.

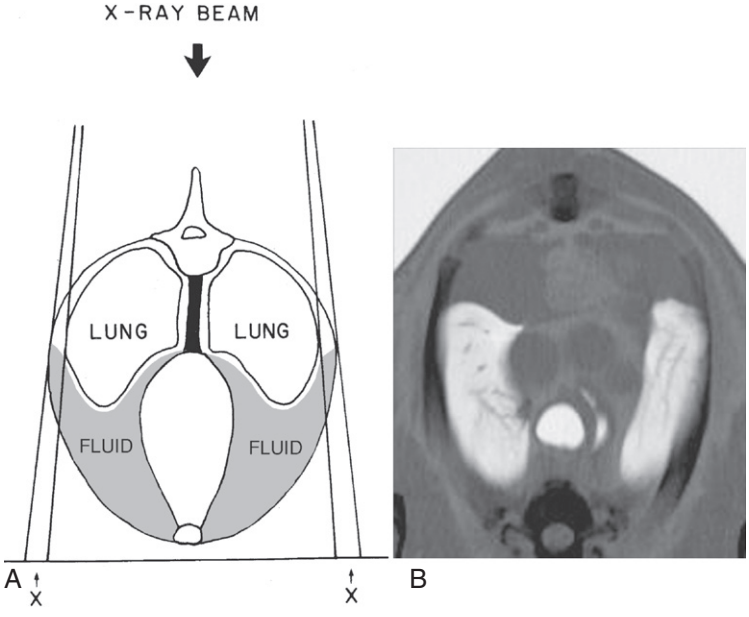


Fig. 31-8 Principle of lung retraction as a result of pleural fluid. **A,** Diagram of a patient with a large amount of pleural fluid being radiographed in ventral recumbency for a DV view. Fluid has gravitated ventrally, causing lung retraction. The full extent of the lung retraction is not apparent radiographically because the main fluid/lung interface, ventral to the lung, is not being struck head-on by the x-ray beam. The only lung retraction that will be seen is in the regions indicated by *x* because here the fluid/lung interface is struck head-on by the x-ray beam. In the central portion of the thorax, the overall radiopacity will increase, and the heart will be obscured, but the lung retraction will not be apparent. **B,** Computed tomography image of the thorax of a dog with pleural fluid. This transverse image was acquired at the level of the second thoracic vertebra. The fluid has caused lung retraction from the ventral aspect of the thoracic cavity. However, the fluid is not dissecting between the lungs and the thoracic wall; thus no part of the fluid/lung interface will be struck head-on by the oncoming x-ray beam, and there will not be evidence of lung retraction in a DV radiograph of this patient even though there is a large amount of pleural fluid.

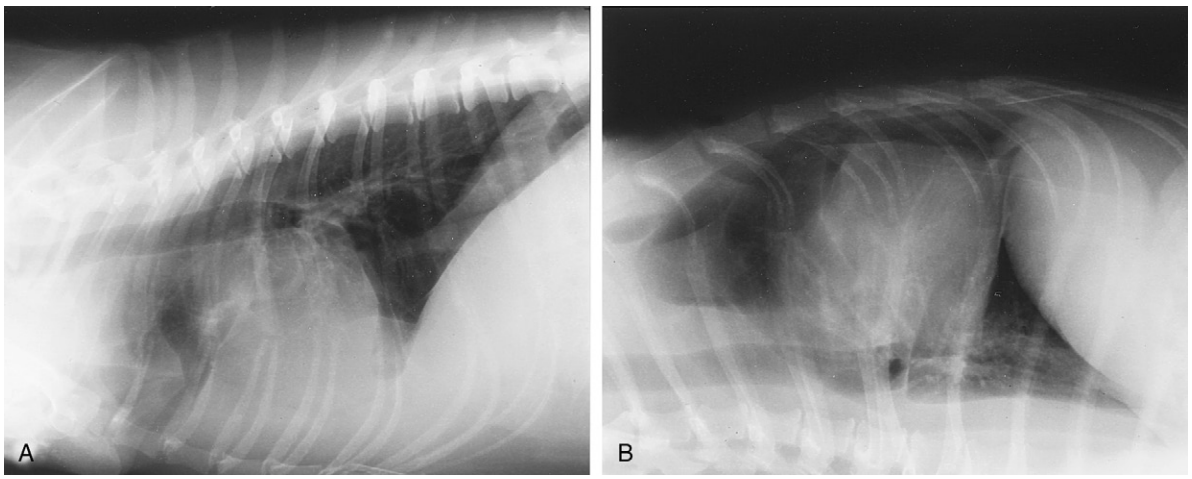


Fig. 31-9 **A,** Conventional lateral radiograph made with a vertically directed x-ray beam. **B,** Lateral radiograph made with a horizontally directed x-ray beam. For **B,** the dog is in dorsal recumbency, and the horizontal beam strikes the lateral aspect of the thorax. In the conventional right lateral radiograph **(A),** there is pleural fluid layered in the ventral aspect of the thorax creating an opacity dorsal to the sternum. It is uncertain from this radiograph whether this opacity represents a mass or pleural fluid. In the radiograph made with a horizontal-beam and the dog in dorsal recumbency **(B),** the fluid has gravitated dorsally, collecting between the spine and lung, leading to increased opacity in this region, and there is no longer an opacity adjacent to the sternum. These findings indicate that the opacity next to the sternum in **A** was caused by pleural fluid. Note that a sharp horizontal fluid line is not present in **B,** the horizontal beam radiograph. Sharp fluid lines are seen only when there is a free fluid–free air interface.

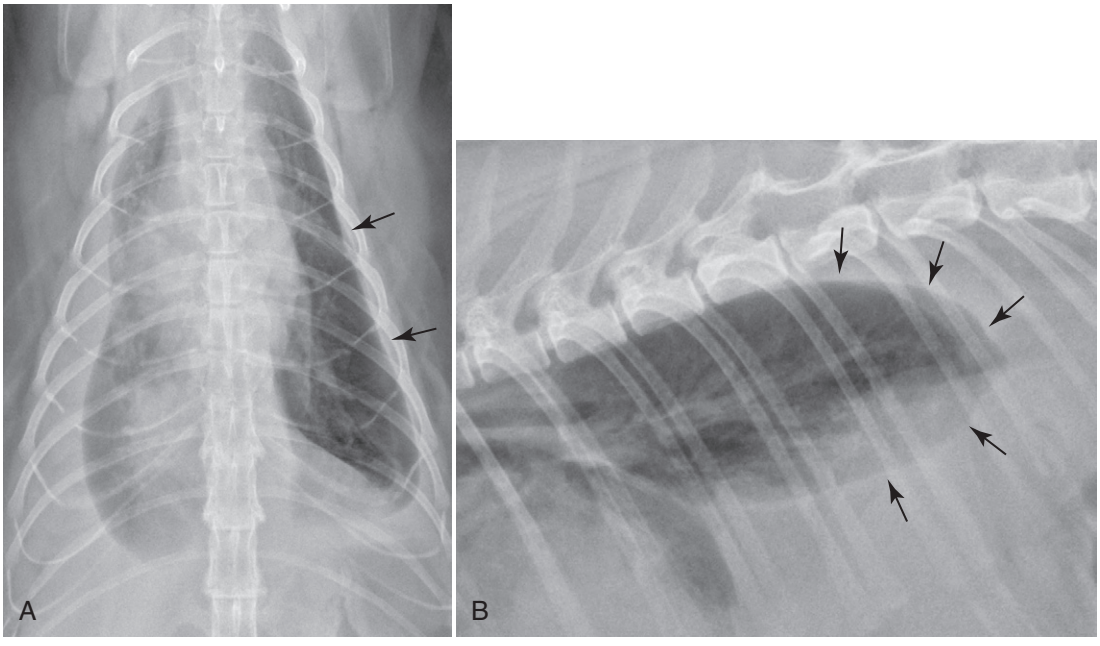


Fig. 31-10 **A,** Ventrodorsal thoracic radiograph of a cat with asymmetric pleural fluid. There is a small amount of pleural fluid on the left, evidenced by lung retraction *(black arrows)*. On the right there is extensive lung retraction. An asymmetric distribution of pleural fluid occurs commonly with an exudate, but any fluid can be asymmetric if the inciting factor is unilateral and mediastinal fenestrations are closed. Ultrasound imaging or computed tomography would be useful in further characterizing the cause of the unilateral fluid in this patient. Thoracocentesis will also be valuable. **B,** Close-up view of the dorsocaudal aspect of the thorax of the same cat. The retracted lung margin is round, indicating pleural fibrosis *(black arrows)*. Pleural fibrosis will develop with chronic pleural fluid and will limit the ability of the lung to expand on subsequent pleurocentesis.

informative. When there is a large amount of pleural fluid, the indiscriminate approach of using a horizontally directed x-ray beam with various patient positions to search for other lesions is unrewarding. However, making additional radiographs after some of the fluid has been removed may provide important information. Sonography and computed tomography of the thorax may also be helpful in elucidating the cause of pleural fluid.[4] Thoracic sonography is technically challenging, and a high skill level is needed for this imaging test to be interpreted accurately.

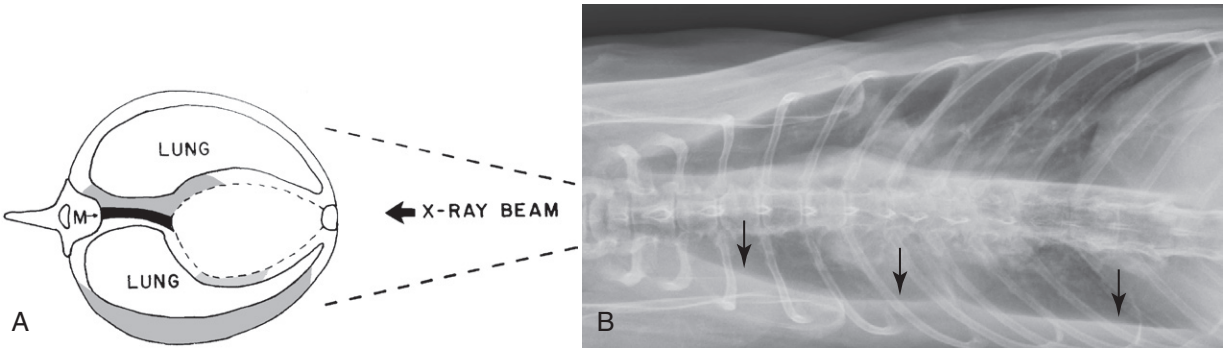


Fig. 31-11 **A,** Drawing illustrating the principle of using a horizontal-beam radiograph to detect pleural fluid. Fluid is represented by the light-gray areas. Fluid in the nondependent hemithorax layers against the mediastinum, assuming the mediastinum is complete. This nondependent fluid is not detectable radiographically. Fluid in the dependent hemithorax gravitates to the area between the lung and the thoracic wall, where the horizontally directed x-ray beam strikes it tangentially. **B,** Horizontal-beam VD thoracic radiograph of a cat with pleural fluid. The cat was placed in right lateral recumbency and a horizontally oriented x-ray beam directed onto the sternum. The fluid in the dependent hemithorax has pooled against the right thoracic wall *(black arrows)*.

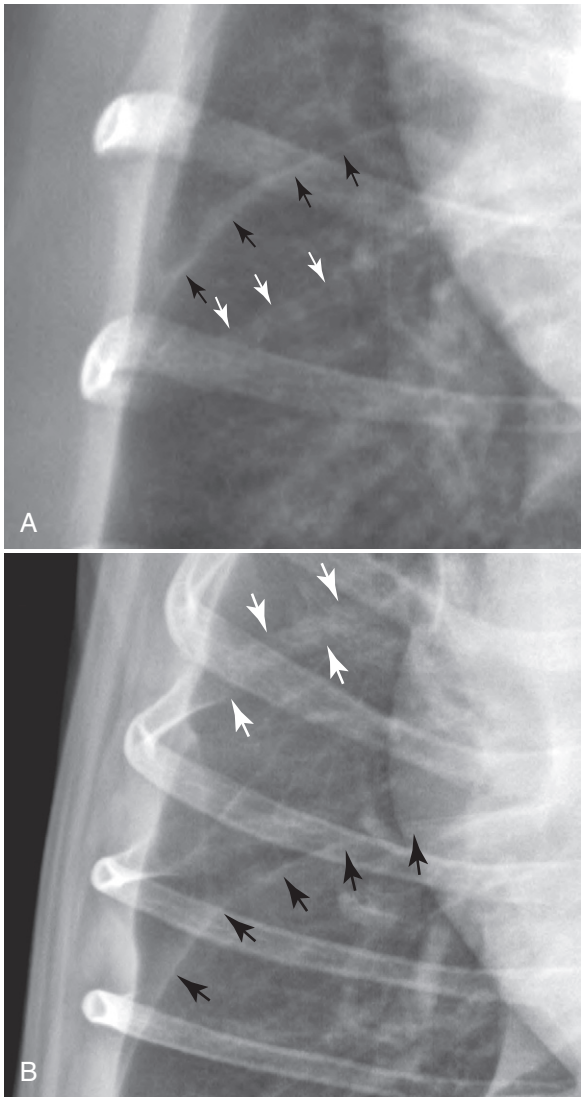


Fig. 31-12 **A** and **B,** VD radiographs of two dogs with mild pleural fluid. Interlobar fissures can be seen in each dog; the fissure lines are curving with the caudal aspect of the fissure being concave *(black arrows)*. In these dogs, the costal cartilages *(white arrows)* are larger and more linear, and they can be followed laterally to attach to a rib.



Fig. 31-13 VD view of the left caudolateral aspect of the thorax of a normal basset hound. An area of soft tissue opacity is present medial to the left thoracic wall; this is caused by the irregular thoracic wall conformation in this chondrodystrophic dog. The location and appearance of this opacity may result in it being confused with pleural fluid; however, interlobar fissures are not seen, which is a tipoff that this opacity is an artifact.

Any amount of pleural fluid is clinically significant, and attempts should be made to reach a definitive diagnosis. A small amount of fluid may not result in abnormal clinical signs, whereas larger amounts usually result in dyspnea because of secondary atelectasis. However, a small amount of pleural fluid should not be assumed to be less significant than a large amount. Thoracocentesis with appropriate fluid analysis should be considered when pleural fluid is identified.

Simultaneous Pleural and Peritoneal Fluid

The detection of simultaneous pleural and peritoneal fluid is an important finding. Thirty-two of 48 dogs with simultaneous peritoneal and pleural fluid had either neoplastic or

Box • 31-2

Causes of Pneumothorax

Tear in lung involving visceral pleura
Thoracic wall rent
Extension of pneumomediastinum
Rupture of cavitary lung mass

Box • 31-3

Radiographic Signs of Pneumothorax

Retraction of pleural surface of lung away from pleural surface of thoracic wall, with interposed radiolucency. Lung markings do not extend to thoracic wall. Seen first in lateral radiographs.
Focal air collection around cardiac apex in lateral view
Appearance of dorsal displacement of the heart. Seen in lateral view.

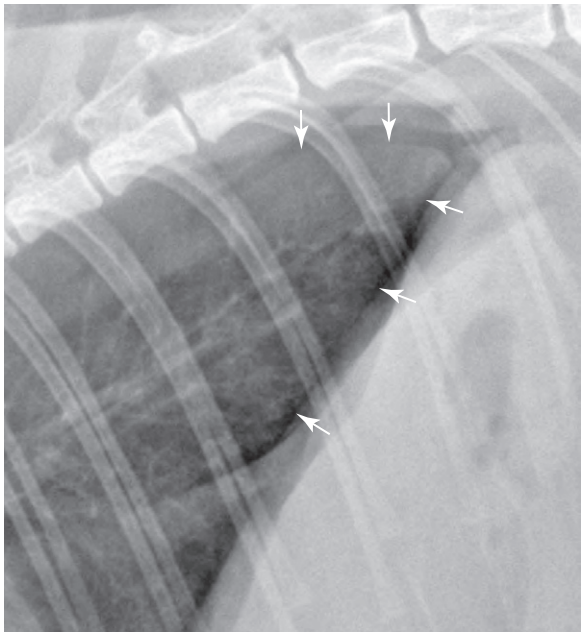


Fig. 31-14 Lateral radiograph of a cat with mild pneumothorax. The air in the nondependent hemithorax collects around the dorsocaudal aspect of the lung, causing the lung to collapse slightly *(white arrows)*.

cardiovascular disease. Simultaneous pleural and peritoneal fluid is an indicator of severe disease with poor prognosis.[7]

PNEUMOTHORAX

Air or gas in the pleural space is termed *pneumothorax*. Air can enter the pleural space from the outside or from the lung or mediastinum (Box 31-2). The character of the radiographic changes resulting from air in the pleural space depends on the volume of air and the relative position of the patient and the x-ray beam. In general, pneumothorax will be more conspicuous in lateral radiographs than in VD or DV radiographs; this is the opposite of pleural fluid. Roentgen signs of pneumothorax are listed in Box 31-3.

Lung Retraction from Pneumothorax

Retraction of the lung from the thoracic wall because of air in the pleural space can be seen in lateral, VD, and DV radiographs. With a small volume of pleural air, this separation is small and appears as a thin radiolucent line (Fig. 31-14). As in pleural fluid, air surrounds the lung but is most apparent radiographically when the air/lung interface is struck head-on by the x-ray beam. Visualization of air-containing interlobar fissures is not common with pneumothorax because air does dissect between lung lobes as fluid usually does.

A mild pneumothorax may also result in air collection against the cardiac apex. This occurs when the air is trapped against the mediastinum, most often in the nondependent hemithorax (Fig. 31-15). With increasing amounts of pleural air, these changes become more pronounced in lateral views, but the changes in the VD or DV view may remain inconspicuous or minimal (Fig. 31-16). With pronounced pneumothorax, lung collapse is visible in VD or DV radiographs as well (Fig. 31-17). The secondary lung collapse leads to the lung becoming more opaque than normal. The degree of

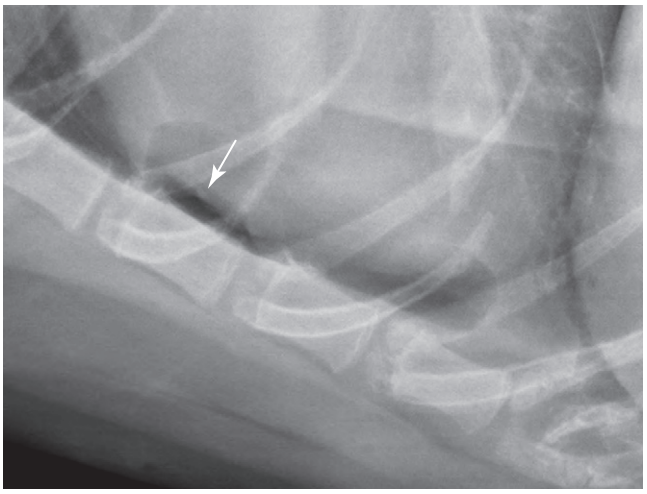


Fig. 31-15 Lateral radiograph of a dog with mild pneumothorax. In this patient, the air is trapped in the nondependent hemithorax against the cardiac apex *(white arrows)*. There were no regions of lung retraction at the periphery of the thorax in this dog, and this was the only radiographic evidence of pneumothorax.

increased lung opacity is directly related to the degree of collapse. This increased opacity resulting from atelectasis can interfere with radiographic evaluation of the lung parenchyma. The lung collapse is also responsible for the lack of visible lung markings extending to the periphery of the thoracic cavity.

If the pneumothorax is open—that is, with no valve at the site of air entrance—air may continue to enter the pleural space until pleural pressure equals atmospheric pressure. At this point, the lung is maximally collapsed, but still maintains roughly the shape of a normal lung because of its elasticity.

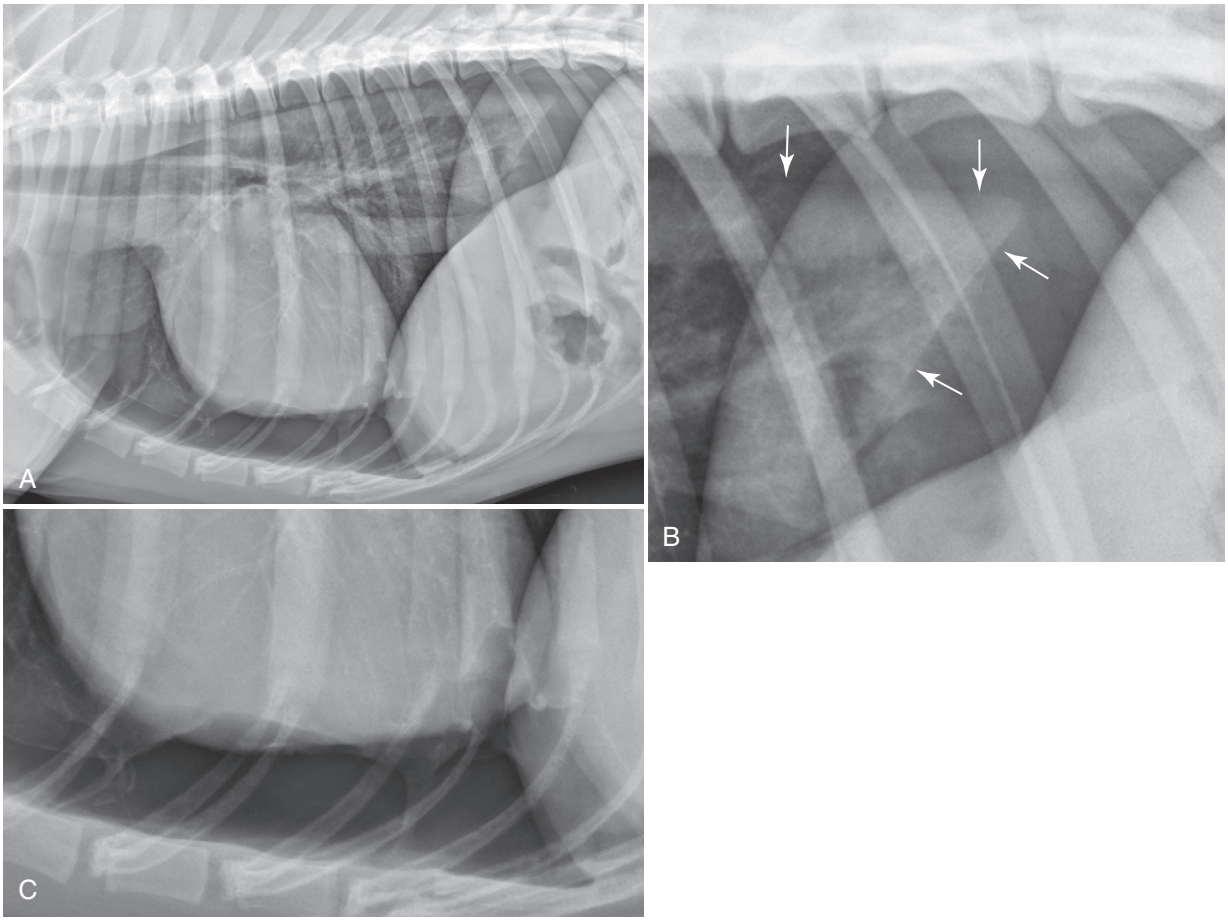


Fig. 31-16 **A,** Left lateral radiograph of a dog with moderate pneumothorax, with close-up views of the dorsocaudal **(B)** and ventral **(C)** aspects of the thorax. There was no evidence of pneumothorax in the VD view. **B,** Air in the nondependent hemithorax has risen to the dorsocaudal aspect of the thorax, causing retraction of the caudal lobe from the thoracic wall and diaphragm *(white arrows)*. **C,** Secondary atelectasis in the dependent lung allows the heart to slide into the dependent hemithorax, creating a space between the heart and sternum. The air in this region makes this space highly radiolucent.

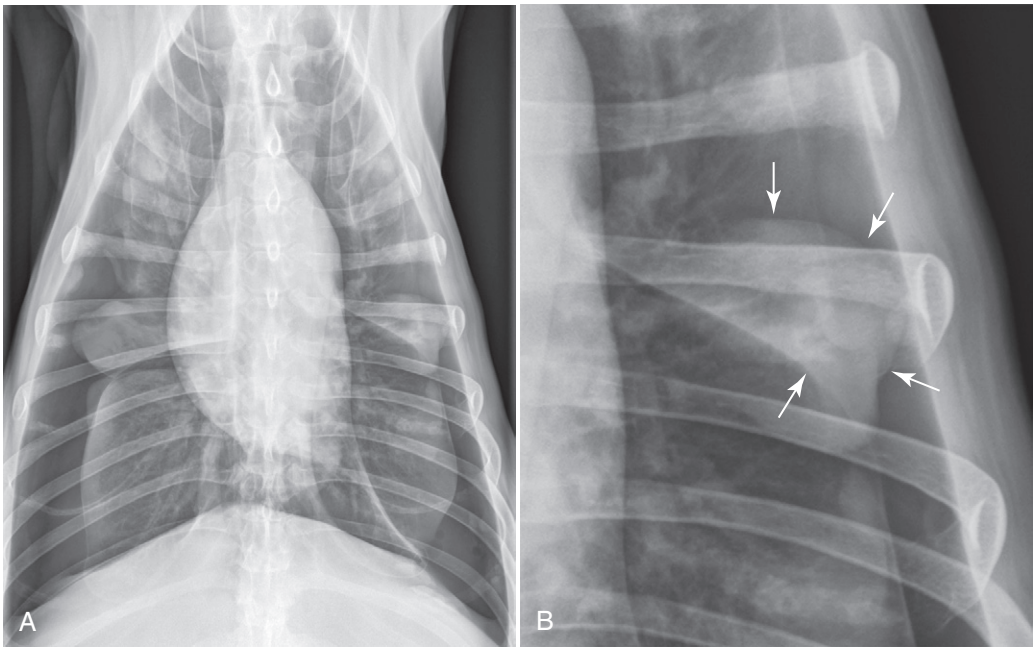


Fig. 31-17 **A,** VD thoracic radiograph of a dog with a large volume of air in the right and left pleural cavity. The lungs are partially collapsed and therefore of increased radiopacity. **B,** The caudal part of the left cranial lobe is very opaque *(white arrows)*; it cannot be determined radiographically whether this is because of atelectasis or pulmonary disease.

"Elevation" of the Heart from the Sternum

The appearance of elevation of the heart from the sternum is seen commonly in lateral radiographs of patients with pneumothorax (see Fig. 31-16). The heart is not actually elevated but displaced into the dependent hemithorax because of a lack of underlying inflated lung to support the heart in its normal midline position. As the heart falls into the dependent hemithorax, it slides dorsally, creating the appearance of elevation on a lateral radiograph (Fig. 31-18). Although pneumothorax is the most common cause of the appearance of elevation of the cardiac silhouette on the lateral view, this can also occur with decreased heart size, in normal dogs with an extremely deep thoracic cavity, and in patients with hyperinflated lungs (Fig. 31-19).

As with a small amount of pleural fluid, a small amount of pleural air may not be apparent radiographically. The likelihood of diagnosing pneumothorax is increased by using a horizontally directed x-ray beam and placing the patient in lateral recumbency and directing the x-ray beam onto the sternum. By so doing, air will collect beneath the nondependent thoracic wall where the x-ray beam strikes it head-on. Decreasing the mAs by 50% enhances visualization of the air in the horizontal-beam radiograph by rendering the lung more opaque. Justification for using horizontal-beam radiography to detect pneumothorax should be based on the suspected underlying cause. For example, pneumothorax resulting from lung disease is a potentially serious event, whereas a small pneumothorax occurring after trauma with no associated clinical signs may not be significant.

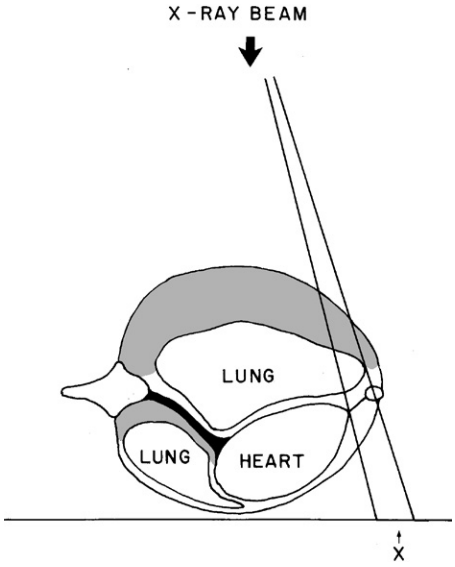


Fig. 31-18 Principle of elevation of the heart from the sternum in lateral radiographs of patients with pneumothorax. When the patient is in lateral recumbency, the lack of a fully inflated lung in the dependent hemithorax allows the heart to slide into the dependent hemithorax. As it slides, it moves dorsally because of the shape of the thoracic wall, thus creating a space between the heart and the sternum. As x-rays pass through this space, the heart appears elevated from the sternum on the lateral view by the distance *x*.

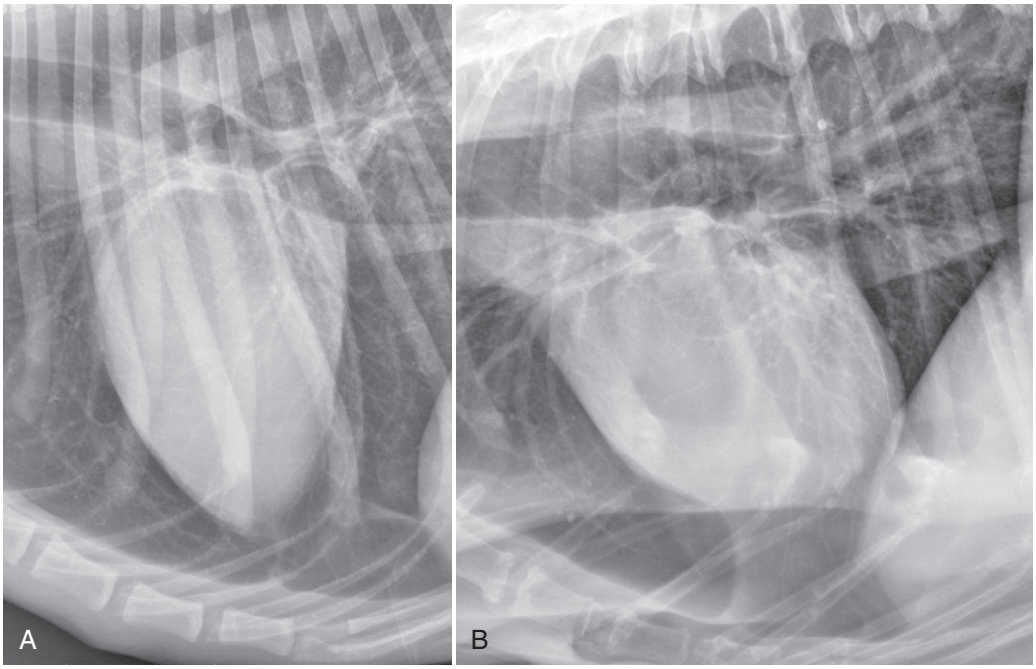


Fig. 31-19 **A,** Lateral radiograph of a dog with volume depletion secondary to Addison's disease. The heart is small and contracted from the sternum. **B,** Lateral radiograph of a dog with a very narrow ventral thoracic cavity. There is inadequate space for the heart to be located in the ventral aspect of the thorax. The position of the heart in each of these radiographs could lead to a misdiagnosis of pneumothorax. The correct assessment is based on the lack of any other signs of pneumothorax and the lack of a distinctly radiolucent region ventral to the heart.



Fig. 31-20 DV radiograph of a dog with a left-sided tension pneumothorax. Note the displacement of the heart to the right. The homogeneous mass on the left is a congenital lung cyst. This cyst is not touching the left thoracic wall and is not causing the cardiac displacement. There is a left-sided pneumothorax, and the left lung is collapsed as an amorphous opacity against the midline *(black arrows)*. The left aspect of the diaphragm is displaced caudally. Note the relative radiolucency of the caudal aspect of the left pleural cavity because of the caudal displacement of the diaphragm on that side. The degree of lung collapse, the diaphragm displacement, and the contralateral mediastinal shift (heart shift) are all signs of tension pneumothorax.

Some Facts about Pneumothorax

In general, lateral views are more sensitive for detection of pneumothorax than VD or DV views.[8] Horizontal-beam VD radiographs with the dog in lateral recumbency will also have a high sensitivity, but there is little need for this approach. Regarding the conspicuity of pneumothorax in DV versus VD radiographs, it has been suggested that pneumothorax is easier to detect in DV radiographs than in VD radiographs.[9]

In most animals pneumothorax is bilateral, and this relates either to a bilateral source of pleural air or to movement of air through the mediastinum. When unilateral pneumothorax was induced in 24 dogs, bilateral pneumothorax was observed immediately after air instillation in 22 dogs, indicating rapid movement of air through fenestrations in the mediastinum.[8] Unilateral pneumothorax, however, can occur for the same reasons as for unilateral pleural fluid.

Tension Pneumothorax

Tension pneumothorax occurs when pleural space pressure exceeds atmospheric pressure during both phases of respiration. Tension pneumothorax results from a check-valve mechanism at the origin of pleural space air. In tension pneumothorax, increased pleural pressure causes the lung to collapse to a greater degree than even its maximal collapse in an open pneumothorax. Thus it may no longer maintain the shape of a lung but may assume the appearance of an amorphous opacity compressed against the midline (Fig. 31-20). With unilateral tension pneumothorax, the increased pleural space pressure will cause a contralateral mediastinal shift (Fig. 31-21). Tension pneumothorax may also result in caudal displacement of the diaphragm to the degree that its costal attachments become visible; this has been termed *tenting* of the diaphragm (Fig. 31-22; see Fig. 31-21). In conventional pneumothorax, the heart is usually shifted toward the side of the thorax containing the most air, but in a tension pneumothorax the heart is shifted to the opposite side because of the increased pleural space pressure. Tension pneumothorax is important to recognize because it is potentially fatal and requires immediate thoracocentesis.

Pitfalls in Pneumothorax Diagnosis

On VD views, skin folds can result in an extremely radiolucent area that is superimposed over the lateral aspect of the thorax. In many patients it may not be possible to identify lung markings in the radiolucent area. In these instances a correct diagnosis of skin-fold artifact can be made by noting that the opacity of the fold extends beyond the limits of the thorax (Fig. 31-23).

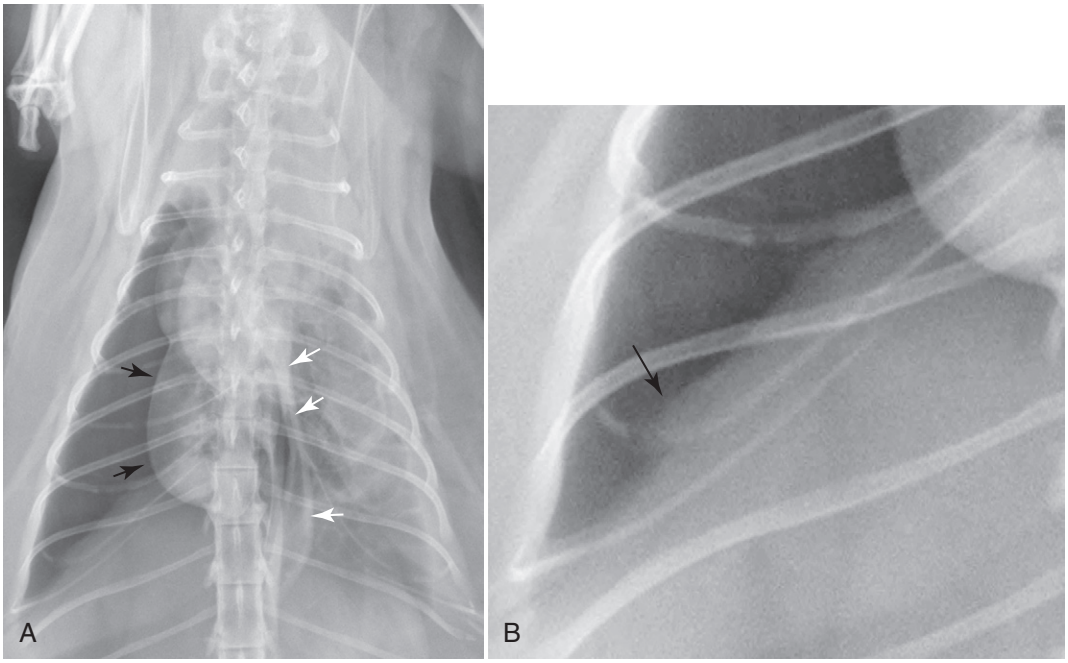


Fig. 31-21 **A,** DV radiograph of a cat with a right-sided tension pneumothorax. The right lung is collapsed, and the mediastinum *(white arrows)* is shifted to the left. The opacity in the right caudal thorax *(black arrows)* is the collapsed right caudal lung lobe. The margin is round because the pleura is fibrotic, secondary to chronic lung disease in this cat. Gas is obvious in the right pleural space. **B,** Close-up view of the caudal aspect of the right caudal hemithorax. The diaphragm is being displaced caudally by the increased pleural space pressure, resulting in tension against the costal attachment sites and creating the so-called tenting appearance *(black arrow)*. Tenting can also occur with pulmonary hyperinflation, but if seen with pneumothorax, it is a reliable sign of tension pneumothorax.

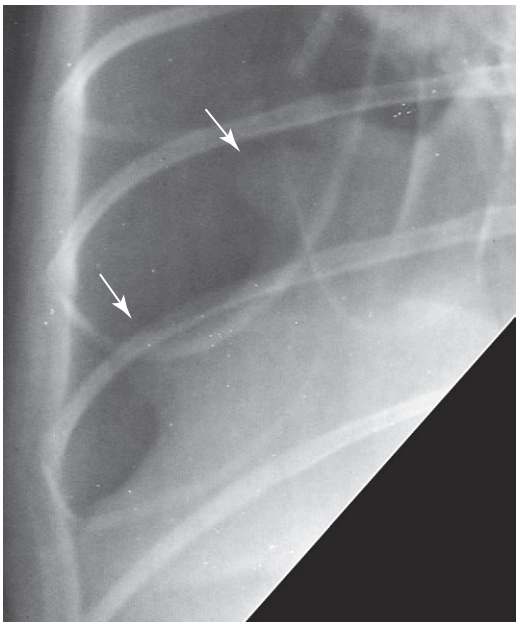


Fig. 31-22 Close-up view of the caudal aspect of the right hemithorax of a cat with tension pneumothorax. The increased pleural space pressure has displaced the right aspect of the diaphragm caudally, causing tension at the costal attachment sites and creating a tented appearance *(white arrows)*.

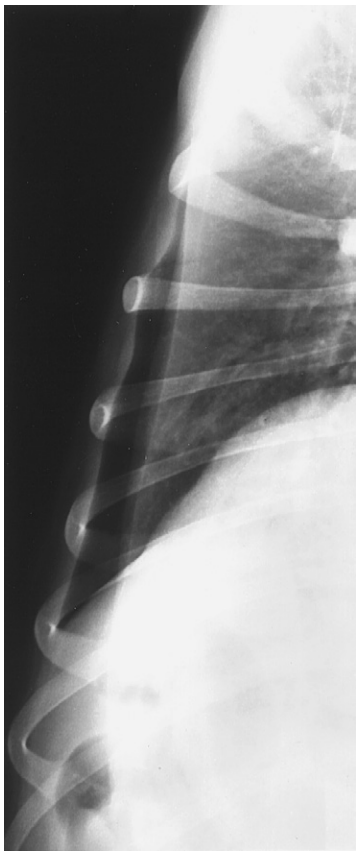


Fig. 31-23 VD view of the thorax of a dog in which a skin-fold artifact is visible. These artifacts can be confused easily with pneumothorax. The skin fold itself has the appearance of a lung margin, with adjacent radiolucency that is consistent with air in the pleural space. However, no lung markings are visible in the region lateral to the lung. The correct assessment of skin-fold artifact is made by noting that the caudal extent of the skin fold extends beyond the limits of the thoracic cavity.

REFERENCES

1. Groves T, Ticer J: Pleural fluid movement: its effect on appearance of ventrodorsal and dorsoventral radiographic projections, *Vet Radiol Ultrasound* 24:99, 1983.
2. Lord P, Suter P, Chan K, et al: Pleural, extrapleural and pulmonary lesions in small animals: a radiographic approach to diagnosis, *Vet Radiol Ultrasound* 13:4, 1972.
3. Brinkman EL, Biller D, Armbrust L: The clinical usefulness of the ventrodorsal versus dorsoventral thoracic radiograph in dogs, *J Am Anim Hosp Assoc* 42:440, 2006.
4. Larson MM: Ultrasound of the thorax (noncardiac), *Vet Clin North Am Small Anim Pract* 39:733, 2009.
5. Shimali J, Cripps PJ, Newitt AL: Sonographic pleural fluid volume estimation in cats, *J Feline Med Surg* 12:113, 2010,
6. Newitt AL, Cripps PJ, Shimali J: Sonographic estimation of pleural fluid volume in dogs, *Vet Radiol Ultrasound* 50:86, 2009.
7. Steyn PF, Wittum TE: Radiographic, epidemiologic, and clinical aspects of simultaneous pleural and peritoneal effusions in dogs and cats: 48 cases (1982–1991), *J Am Vet Med Assoc* 202:307, 1993.
8. Kern D, Carrig C, Martin R: Radiographic evaluation of induced pneumothorax in the dog, *Vet Radiol Ultrasound* 35:411, 1995.
9. Aronson E, Reed A: Radiology corner—pneumothorax: ventrodorsal or dorsoventral view, *Vet Radiol Ultrasound* 36:109, 1995.

ELECTRONIC RESOURCES

evolve

Additional information related to the content in Chapter 31 can be found on the companion Evolve website at http://evolve.elsevier.com/Thrall/vetrad/

- Chapter Quiz

CHAPTER • 32

The Heart and Pulmonary Vessels

Robert Bahr

Assessing cardiovascular function becomes important when decisions must be made regarding staging a patient with suspected cardiac disease, deciding about therapy, and monitoring response to therapy or progression of disease. Unfortunately, radiographs are not very accurate for assessing either cardiovascular function or morphology because the range of the normal cardiac appearance is very wide in dogs and the appearance of the cardiac silhouette is affected by radiographic positioning.[1-4] See Chapter 25 for a comprehensive discussion of these issues

With regard to the wide range of the normal cardiac appearance, muscular dogs or those with a barrel-shaped thorax often have a heart that looks large. Conversely, the normal heart in breeds with a laterally compressed but deep thoracic cavity, such as greyhounds and collies, can look abnormally small (Fig. 32-1). Thus the breed and body physique of the dog should always be considered when the heart is evaluated radiographically. If any suspicion of a cardiac abnormality exists, because of either radiographic appearance or clinical or historical information, then echocardiography should be performed.[5]

Radiographic positioning can have a profound effect on the appearance of the cardiac silhouette (see Chapter 25).[3] Perhaps the most important effect is the difference in cardiac silhouette appearance in ventrodorsal (VD) versus dorsoventral (DV) radiographs. In DV radiographs, the diaphragm is displaced cranially, which will physically push the heart cranially and into the left hemithorax. The magnitude of this displacement is more pronounced in medium and large dogs than in cats or small dogs (Fig. 32-2).[6] Alternately, VD views of the heart in large-breed dogs will have significant magnification when compared with DV views of the same heart.

It is important to realize that the cardiac silhouette is composed of tissues other than the heart. The pericardium, any fluid or tissue in the pericardial space, and any tissue or fluid in the mediastinum immediately adjacent to the heart will blend with the heart, thereby contributing to the overall size and shape of the cardiac silhouette. This principle is perhaps most important when attempting to assess heart size in obese patients because fat in the mediastinum silhouettes with the heart, increasing the size of the cardiac silhouette. Occasionally, this fat will be visible as a region of decreased opacity immediately adjacent to the heart (Fig. 32-3).

Despite these normal variations, a starting point for radiographic evaluation is necessary. In this chapter, the qualitative radiographic signs of enlargement are discussed for each heart chamber, the aorta, and the caudal vena cava. A quantitative method of cardiac measurement, called the *vertebral heart scale*, has been devised to take into account the inherent breed variation in cardiac size.[7] In this method, the length of the long and short axis of the heart is measured, summed, and scaled against the length of the vertebral bodies dorsal to the heart, beginning with T4, to quantify heart size. Based on 100 clinically normal dogs, the mean normal vertebral heart scale was 9.7 vertebrae, with a standard deviation of 0.5 vertebrae. By definition, 95% of any normal population lie within the mean plus or minus two standard deviations of the mean; therefore the normal vertebral heart scale ranges from 8.7 to 10.7 vertebral body lengths. The span of this range is too wide for it to be of use in an individual patient, and it has not proved superior to subjective radiographic assessment of heart size.[8,9] There is also variation between readers in the transformation of long- and short-axis dimensions into vertebral heart scale units.[10] Perhaps the best use of the vertebral heart scale is to compare cardiac size on radiographs of the same patient made on different dates to monitor disease progression or response to treatment.[11,12]

Subjective radiographic assessment of the heart will be of most value when the cardiac abnormalities are pronounced. Therefore cardiac radiography should be reserved (1) as a screening tool for assessing marked cardiac abnormalities, (2) for evaluation of the pulmonary circulation, (3) to assess whether cardiac decompensation has occurred, and (4) to evaluate response to therapy. Any suspected cardiac abnormality must be interpreted in light of signalment and physical findings. This chapter provides examples of moderate to severe chamber enlargement and describes the features of some of the more common congenital cardiac anomalies as well as the radiographic diagnosis of common acquired cardiac diseases.

For ease of recognition of various parts of cardiac anatomy as well as certain cardiac abnormalities in the DV or VD radiograph, the cardiac silhouette can be visualized in terms of a clock face. The origin of bulges on the cardiac silhouette caused by dilation of different parts of the heart or great vessels can be predicted by using this clock analogy (Fig. 32-4).

RADIOGRAPHIC SIGNS

Radiographic Signs of Specific Cardiac Chamber Enlargement

Left Atrium

Enlargement of the left atrium is perhaps the most frequently encountered cardiac enlargement. This enlargement is almost always caused by dilation. Left atrial dilation is usually a result of mitral valve disease but can occur with left-to-right pulmonary overcirculation causing volume overload of the left atrium.

In the lateral view, dilation of the left atrium causes a change in shape of the dorsocaudal aspect of the cardiac

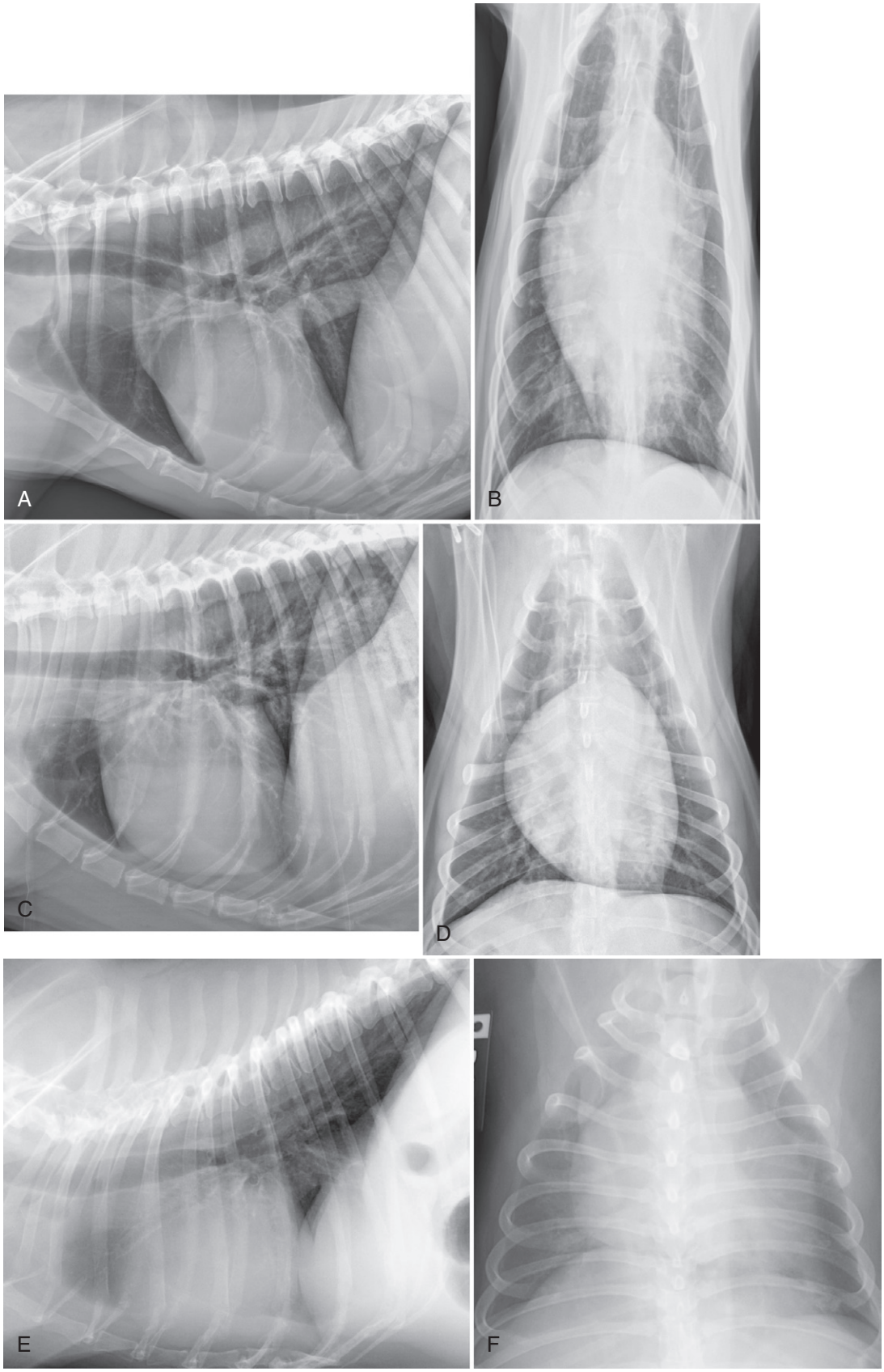


Fig. 32-1 Lateral and VD thoracic radiographs from a normal borzoi (**A** and **B**), Labrador retriever (**C** and **D**), and a pug (**E** and **F**), illustrating the effect of breed or body conformation on the appearance of the cardiac silhouette.

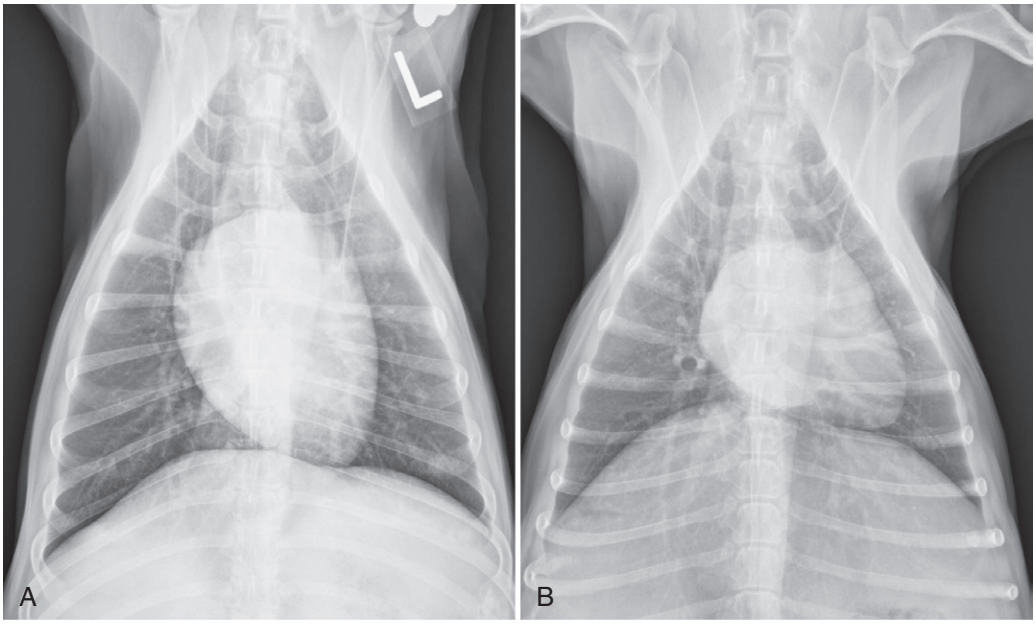


Fig. 32-2 VD **(A)** and DV **(B)** thoracic radiographs of a normal dog. In the DV radiograph, the heart appears wider and is displaced into the left hemithorax. This displacement if often misinterpreted as abnormal.

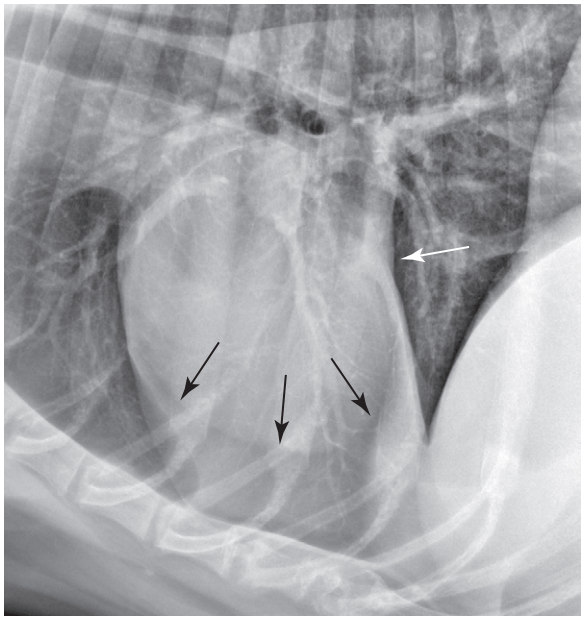


Fig. 32-3 Lateral radiograph of the thorax of a Doberman pinscher. There is fat around the heart in the mediastinum, leading to the cardiac silhouette being larger than the heart itself. The less opaque fat creates contrast for visualization of the real margin of the heart *(black arrows)*. This dog also has left atrial dilation that causes a concavity on the dorsocaudal heart border *(white arrow)*.

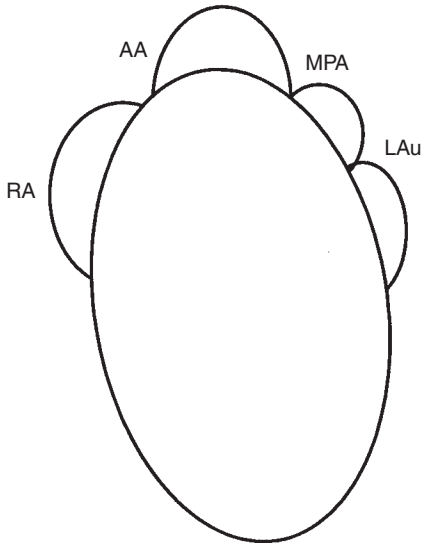


Fig. 32-4 The heart in a VD, or DV, view illustrating the clock face analogy. Locations of dilation of the left auricle *(LAu)*, main pulmonary artery *(MPA)*, aortic arch *(AA)*, and right atrium *(RA)* are shown. *LAu*, bulge at 2 to 3 o'clock; *MPA*, bulge at 1 to 2 o'clock; *AA*, bulge at 11:30 to 12:30 o'clock; *RA*, bulge at 9:30 to 11:30 o'clock.

silhouette. Rather than this region of the heart coursing in a dorsal and cranial direction toward the tracheal bifurcation, it tends to course more in a dorsal or dorsocaudal direction, with the formation of a slight concavity on the caudal margin of the heart (Fig. 32-5; see Fig. 32-3). This shape change has been referred to as loss of the caudal cardiac waist, but the normal cardiac waist is not well defined, and this term is best avoided.

Left atrial dilation also causes an increase in height of the caudodorsal heart border and elevation of the tracheal bifurcation. If left atrial dilation is severe, the left principal bronchus may become selectively elevated or even compressed between the left atrium and adjacent tissues dorsally (Fig. 32-6). Dogs with bronchial compression secondary to left atrial dilation may exhibit a cough, which may lead the clinician to think erroneously that the patient is in heart failure.

Dilation of the left atrium may also cause divergence of the principal bronchi in the VD or DV view. This appearance is similar to the bronchial displacement occurring secondary to tracheobronchial lymph node enlargement as described in Chapter 30 (see Fig. 30-20), with the normal acute angle between the principal bronchi appearing wider because of the interposed enlarged lymph nodes (Fig. 32-7).

A massively dilated left atrium may also lead to a region of increased opacity superimposed over the cardiac silhouette in the VD or DV view that creates the appearance of a double wall. This is caused by a summation effect of the enlarged left

atrium being projected superimposed on the remainder of the heart (Fig. 32-8).

Dilation of the left atrial appendage (auricle) occurs less frequently than dilation of the left atrium and, when present, appears as a focal bulge along the left cardiac border in the 2 to 3 o'clock position according to the clock face analogy (see Fig. 32-7). An extremely enlarged left atrium can also result in lateral displacement of the left auricle, resulting in its visualization without the auricle actually being dilated.

Left Ventricle

The left ventricle may enlarge as a result of hypertrophy or dilation. Concentric hypertrophy, a likely response to increased afterload such as with aortic stenosis, mainly occurs at the expense of lumen volume and may lead to no or nonspecific radiographic signs. Eccentric hypertrophy is likely a response to increased preload, as in patent ductus arteriosus or mitral insufficiency, and can cause visible left ventricular enlargement. Severe, eccentric hypertrophy that results in elongation of the left ventricle can lead to elevation of the entire intrathoracic trachea in the lateral view from the thoracic inlet to the tracheal bifurcation into the stem bronchi, thus narrowing the angle between the trachea and the thoracic vertebrae. In the VD or DV view, the apex may appear more blunted, and the left heart border may appear to be more rounded than its normally straight appearance.

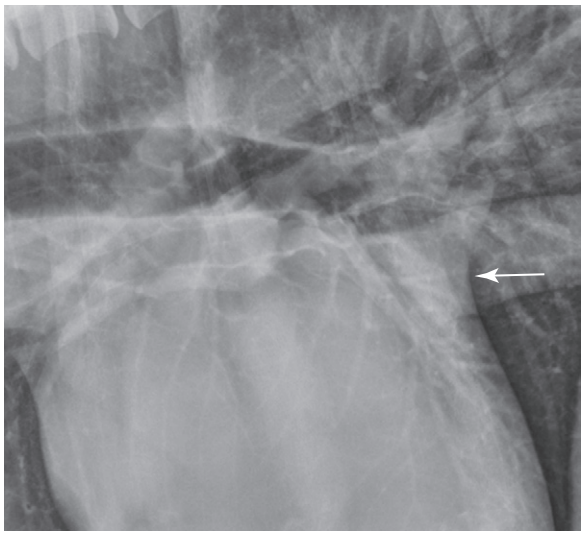


Fig. 32-5 Lateral radiograph of a dog with a dilated left atrium. The enlarged atrium has created a concave shape change on the caudal margin of the heart *(white arrow)*. This is a very common sign of left atrial dilation.

Dilation of the left ventricle is a likely response to chronically increased preload and is often associated with cardiac failure. Dilation of the left ventricle may either contribute to an overall appearance of *generalized cardiomegaly* or result in the elongation of the left ventricle, causing the tracheal elevation described before. Debate has occurred, even among experienced radiologists, about the accuracy with which left ventricular hypertrophy or dilation can be diagnosed from survey radiographs, so it is safest to describe the change as left ventricular enlargement and use echocardiography to differentiate the cause.

Right Atrium

Radiographic detection of an enlarged right atrium is uncommon. Visualization of isolated right atrial enlargement can be found in dogs with tricuspid dysplasia. As with the left atrium, enlargement of the right atrium is usually caused by dilation. When visible in the lateral view, right atrial enlargement causes a bulge or mass effect in the craniodorsal aspect of the cardiac silhouette. However, other cardiovascular enlargements, including dilation of the aortic arch and main pulmonary artery, can also cause this radiographic appearance. In the VD or DV projection, an increased bulge in the right heart border from the 9 o'clock to 11 o'clock position may be present (Fig. 32-9).

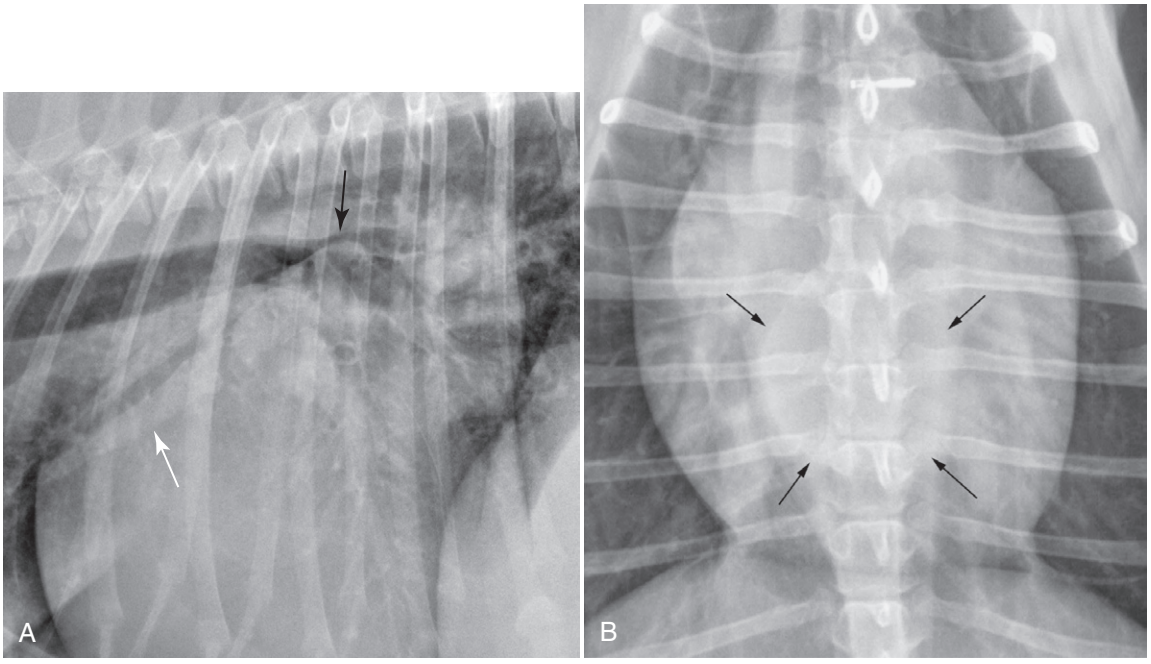


Fig. 32-6 Lateral **(A),** DV **(B),** radiographs in a dog with marked left atrial dilation. In **A,** there is elevation of the trachea and compression of the left principal bronchus as it is trapped between the left atrium and tissues dorsal to the heart *(black arrow)*. The left cranial lobe pulmonary vein is also distended *(white arrow)*, consistent with pulmonary venous hypertension. In **B,** the dilated left atrium appears as a region of increased opacity caudal to the tracheal bifurcation *(black arrows)*.

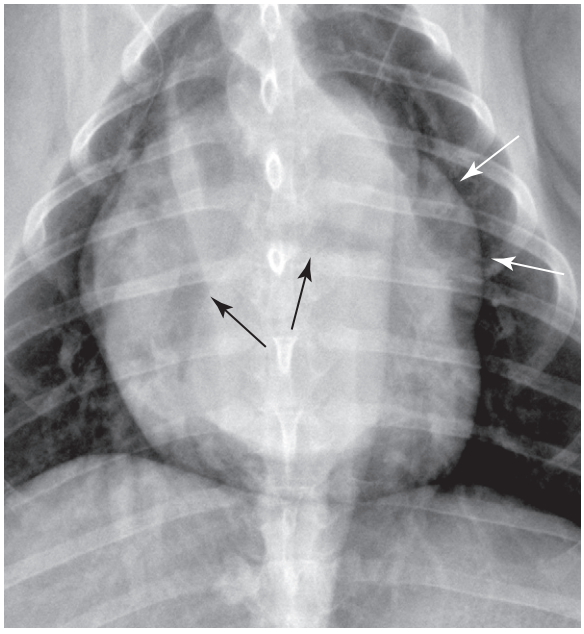


Fig. 32-7 DV radiograph of a dog with pronounced left atrial dilation. The enlarged atrium has caused abaxial displacement of the principal bronchi *(black arrows)*. There is also a bulge on the left aspect of the cardiac silhouette that is consistent with left auricular dilation or lateral displacement of the left auricle by the dilated left atrium *(white arrows)*.

Right Ventricle

As with the left ventricle, the right ventricle may enlarge as a result of hypertrophy or dilation. Common causes of hypertrophy are heartworm infection and pulmonic stenosis. Hypertrophy mainly occurs at the expense of lumen volume and may lead to no or unrecognizable radiographic signs. However, radiographs are more sensitive for detection of right ventricular hypertrophy than for left ventricular hypertrophy; this may be related to the normally thinner wall of the right ventricle, with hypertrophy then causing more obvious changes in cardiac size and shape. Because the right ventricle is normally in contact with the sternum, its enlargement, whether from dilation or hypertrophy, often causes an increased sternal contact in the lateral view (Fig. 32-10, *B*). The average dog has an amount of cardiac contact with the sternum ranging from 2.5 to 3 intercostal spaces; thus sternal contact in excess of 3 intercostal spaces suggests right ventricular enlargement. Some deep-chested breeds, such as Doberman pinschers and Irish wolfhounds, may normally have only approximately 1.5 to 2 intercostal spaces of sternal contact, so 2.5 to 3 spaces would be consistent with right ventricular enlargement for those breeds. Likewise, some barrel-chested breeds, such as the bulldog, can normally have more than 3 to 3.5 intercostal spaces of contact.

Right ventricular hypertrophy can also lead to the cardiac apex being displaced dorsally from the sternum in lateral views (Fig. 32-10, C). In VD or DV views, a hypertrophic right ventricle appears more rounded and protrudes farther into the right hemithorax than normal, giving the cardiac silhouette a reversed letter D shape (Fig. 32-10, *A*). It is important not to confuse this with the normal shape of the heart in VD and DV views, which might also be described as a reversed letter D shape.

Generalized Cardiomegaly

Generalized enlargement of the cardiac silhouette results from combinations of chamber enlargement, or all four chambers may be enlarged. Myocardial dysfunction is a common cause of generalized cardiomegaly. Subjectively, the cardiac silhouette appears larger than expected, but specific chamber enlargement may or may not be evident. Generalized cardiomegaly may also be misinterpreted because of underinflation of the lungs, making the thoracic cavity appear smaller than normal. This, in turn, makes the heart appear larger relative to the amount of aerated lung surrounding it. This was discussed in detail in Chapter 25.[7] Echocardiography should be used to confirm a cardiac abnormality when generalized cardiomegaly is suspected radiographically.

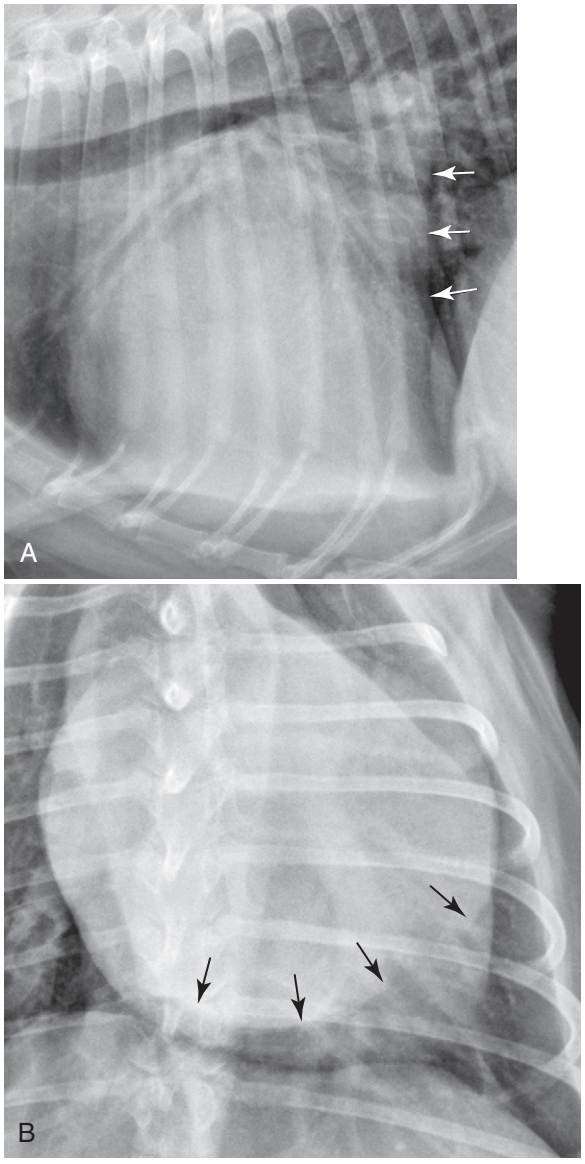


Fig. 32-8 Lateral **(A)** and DV **(B)** radiographs of a dog with extreme dilation of the left atrium. In **A,** there is a large mass effect in the dorsocaudal region of the cardiac silhouette and a concave shape change of the caudal cardiac margin *(white arrows)*. When radiographed for the DV view, the enlarged left atrium becomes superimposed on the remainder of the heart, creating a summation shadow that creates a double-wall effect. In **B,** the *black arrows* depict the margin of the enlarged left atrium.

Radiographic Signs of Major Vessel Enlargement

Caudal Vena Cava

The caudal vena cava is extremely variable in size depending on the phase of respiration and cardiac cycle. It can be judged to be enlarged only if it is consistently larger in diameter than the length of the fifth or sixth thoracic vertebral bodies of the spine as measured in the lateral view. Another measure of

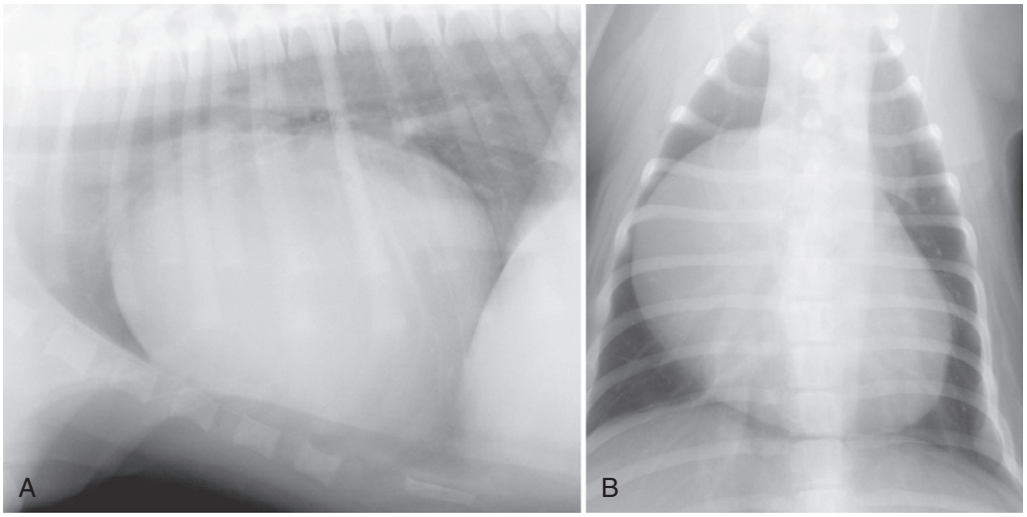


Fig. 32-9 Left lateral **(A)** and DV **(B)** radiographs of a Labrador retriever with tricuspid dysplasia. A bulge is visible in the region of the right atrium consistent with right atrial enlargement. How far ventral **(A)** and caudal **(B)** the enlarged right atrium extends on the cardiac silhouette is often surprising.

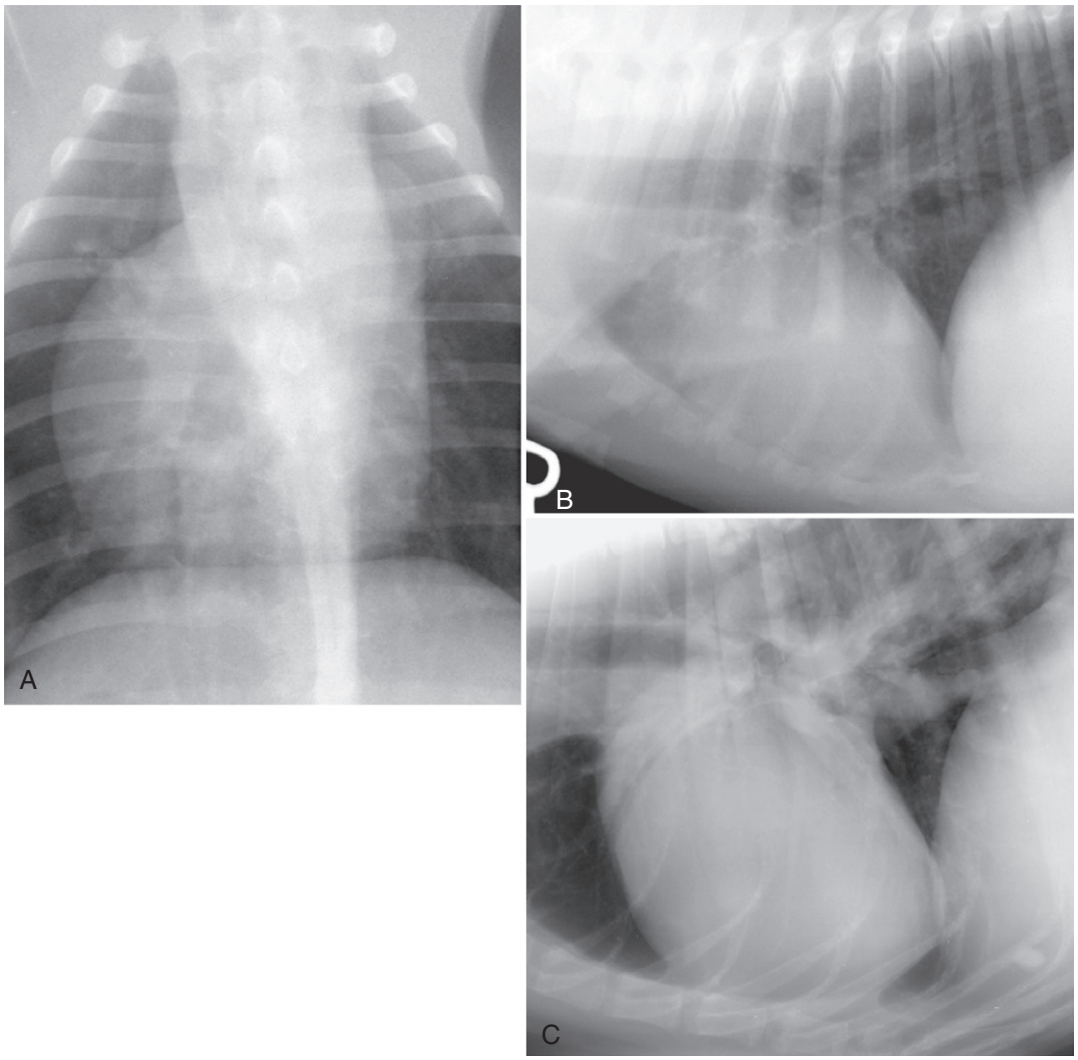


Fig. 32-10 Right ventricular hypertrophy. **A,** VD view of a dog with pulmonic stenosis. Right ventricular hypertrophy has resulted in increased cardiac mass on the right side that creates an appearance of a reverse, or backward, letter D. Enlargement of the main pulmonary artery is also visible. **B,** Right lateral radiograph of a dog with pulmonic stenosis. The increased mass of the right ventricle has resulted in increased contact of the heart with the sternum over a longer distance than normal. **C,** Right lateral radiograph of a dog with heartworm infection. The increased mass on the right side of the heart has caused elevation of the cardiac apex from the sternum. Mild elevation of the cardiac apex from the sternum may be present in normal dogs in a left lateral view, but normal apex displacement should never be this marked or appear in the right lateral view.

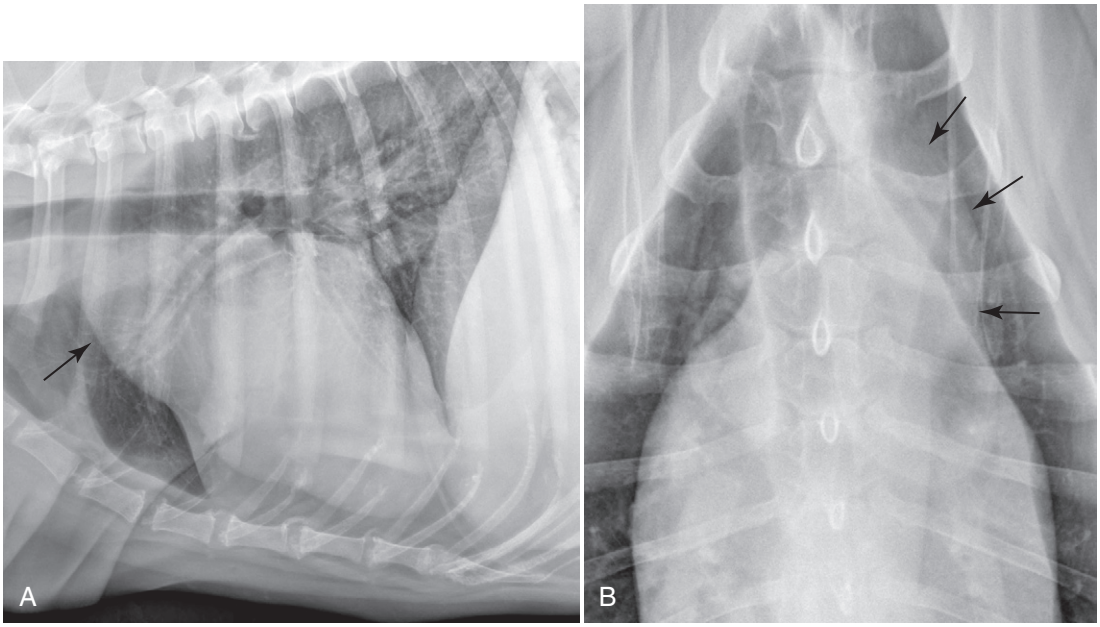


Fig. 32-11 Lateral **(A)** and DV **(B)** radiograph of a dog with aortic stenosis. In **A,** the dilated aortic arch appears as a bulge on the craniodorsal aspect of the cardiac silhouette *(black arrow)*. In **B,** the enlarged aortic arch appears as an opacity at the cranial, and slightly left, aspect of the cardiac silhouette *(black arrows)*.

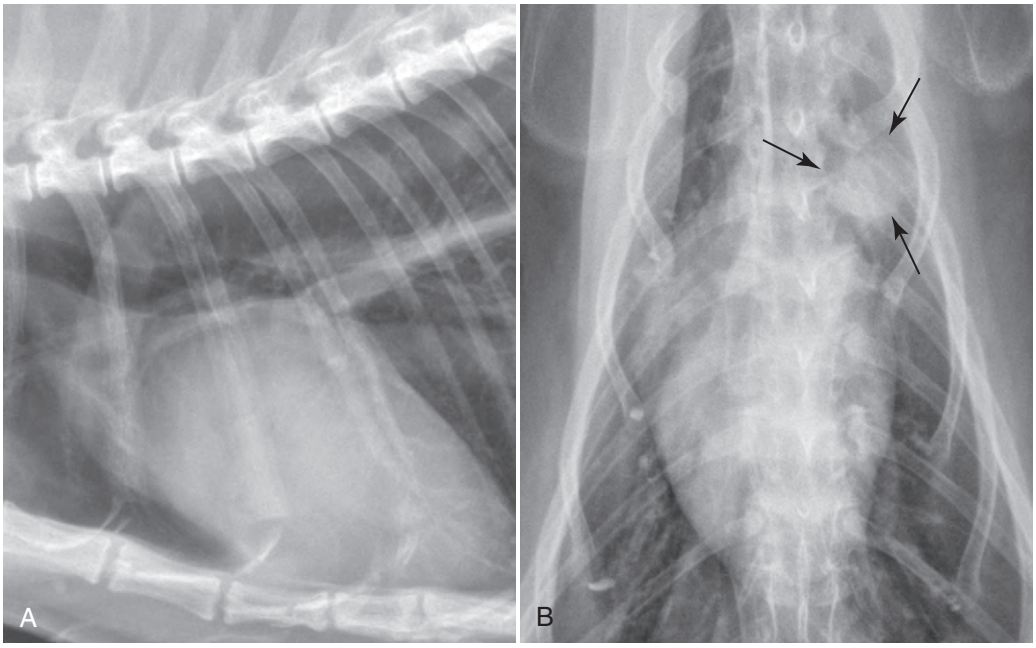


Fig. 32-12 **A,** Lateral radiograph of a cat with a tortuous aorta. In **A,** the aortic arch is more vertical than normal, and the descending aorta is tortuous. In another cat **(B)** with a tortuous aorta, the aortic arch is positioned to the left of midline *(black arrows)* and could be misinterpreted as a pulmonary mass.

caudal vena cava size is that enlargement can be inferred only if the diameter of the caudal vena cava is more than 1.5 times the diameter of the descending aorta.[13] The caudal vena cava can enlarge in response to increased central venous pressure, but the size of the vena cava is not an accurate way to attempt to assess central venous pressure. Valid inferences on cardiovascular disease cannot typically be made on the basis of the size of the caudal vena cava only.

Aorta

Widening of the precardiac mediastinum, as seen in the VD or DV views, can indicate dilation of the aortic arch. A focal bulge in the descending aorta in VD or DV views can be seen in patients with aortic stenosis and patent ductus arteriosus (Fig. 32-11). In the lateral views, an enlarged aortic arch can create increased mass at the cranial aspect of the cardiac silhouette (see Fig. 32-11).

Some older cats will have a tortuous appearing aorta in the lateral view, with a more vertical aortic arch orientation. The aortic arch then curves upward and caudally, assuming a serpentine contour as it progresses caudally toward the diaphragm (Fig. 32-12, *A*). In the DV or VD views, this aortic contour may be projected away from the mediastinum and be misinterpreted as a pulmonary nodule when projected end-on

(Fig. 32-12, *B*).[14] A tortuous aorta is clinically insignificant in aged cats.

Main Pulmonary Artery

The main pulmonary artery is not seen normally as a separate structure, but when it dilates sufficiently in dogs, it will appear as a focal bulge in the 1 o'clock position in VD or DV views (Fig. 32-13). A dilated main pulmonary artery is not recognized routinely in lateral views. Common causes of main pulmonary artery dilation include pulmonary hypertension, as from heartworm infection, and turbulence, as from pulmonic stenosis or patent ductus arteriosus.

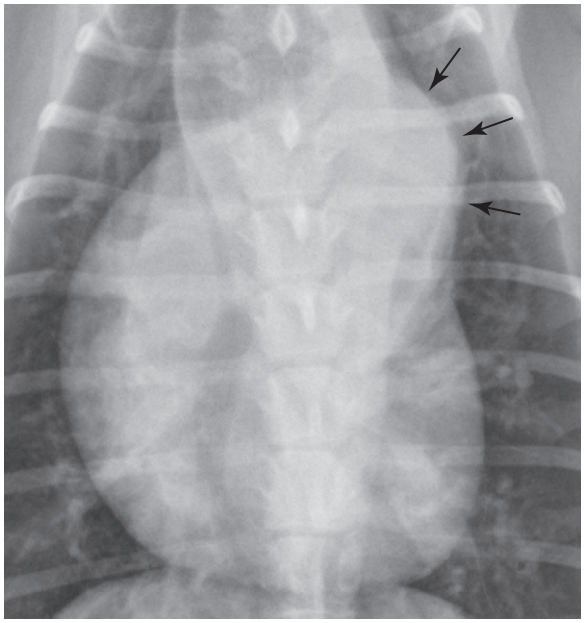


Fig. 32-13 DV radiograph of a dog with dilation of the main pulmonary artery *(black arrows)*.

Radiographic Signs of Pulmonary Vascular Changes

A radiographic assessment of cardiac size or shape is incomplete without also evaluating the main pulmonary artery as well as the peripheral pulmonary arteries and veins. Therefore knowing where to look for and how to differentiate arteries and veins in the lungs is crucial. In the lung, parenchymal vessels and airways are arranged in an artery-bronchus-vein triad, with the airway always being positioned between the pulmonary artery and pulmonary vein.

In lateral projections, when arteries can be seen as separate structures from veins, the arteries are dorsal and veins are ventral to the intervening bronchus.[15] This applies mainly to cranial lobe arteries and veins because the caudal lobar arteries and veins are superimposed in the lateral projection and caudal lobe pulmonary arteries cannot be differentiated from veins in the lateral projection. The right cranial lobar pulmonary artery and vein can serve as reference vessels because they are best seen as individual structures when the animal is placed in left lateral recumbency (Fig. 32-14).[3] This is because the right cranial lung lobe is better inflated with the animal in left recumbency, resulting in better definition of these vessels. Although the left cranial lobe will be better inflated in right recumbency, the left and right pairs of cranial lobe vessels will be more superimposed in that particular view, making their assessment more difficult (see Fig. 32-14).

In a VD or DV projection, arteries and veins are most conveniently compared in the caudal lobes where pulmonary arteries are lateral to pulmonary veins, with the bronchus interposed. The caudal lobe pulmonary vessels are better seen in the DV view than in the VD view because of the better lung inflation achieved with the dog in sternal recumbency for a DV radiograph (Fig. 32-15). In addition to the improved pulmonary inflation in sternal recumbency, the caudal lobar vessels and bronchi are more nearly perpendicular to the x-ray beam than they are with the patient in dorsal recumbency for VD radiography. Paired arteries and veins are less well seen in other lobes in either DV or VD views, although occasionally the cranial lobar vessels may be visualized.

Even though a bronchus always lies between a paired artery and vein, the entire distance between these paired

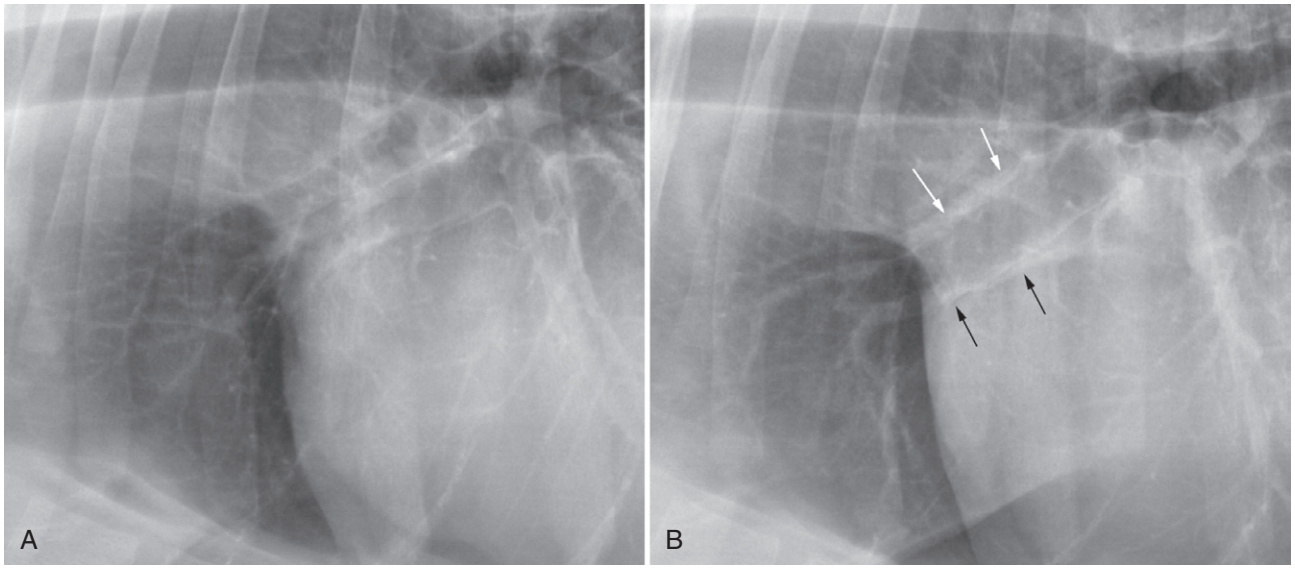


Fig. 32-14 Close-up from right **(A)** and left **(B)** lateral radiographs of a normal dog. In **A,** the cranial lobe vessels are superimposed and distinguishing the right cranial lobe artery from the right cranial lobe vein is impossible. In **B,** the artery *(white arrows)* and vein *(black arrows)* for the right cranial lobe are more clearly seen. The ability to distinguish the right cranial artery from the vein is typically easier in a left lateral radiograph. Note the similar size of the artery and vein in **B.**

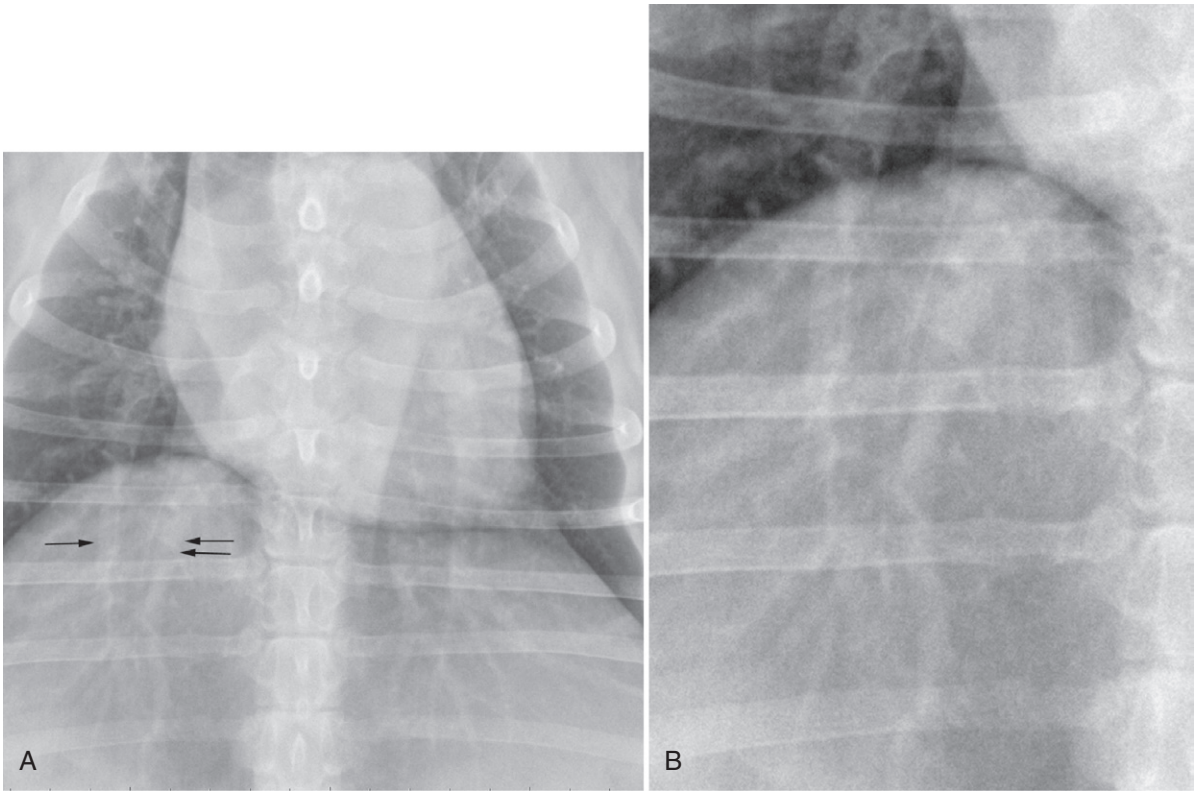


Fig. 32-15 Dorsoventral **(A)** radiograph of a normal dog. The right caudal lobe artery *(single black arrow)* is lateral to the airway, whereas the vein is medial *(double black arrows)*. Close-up view **(B)** of the right caudal lobe area giving another view of the caudal lobe vessels. On close inspection, the mineralized wall of the caudal lobe bronchus can be seen between the artery and vein. Note that the bronchus does not occupy the entire space between the artery and vein. When the bronchus is not mineralized, inferring that it occupies the entire distance between its associated artery and vein is inaccurate.

vessels is not always occupied by the bronchus. The exact position of the bronchus and its actual size can be seen in survey radiographs only if the bronchial wall either is sufficiently mineralized or appears thickened because of peribronchial diseases (Fig. 32-14, *B*).

Peripheral pulmonary arteries should be approximately the same size (matched in size) as the associated pulmonary vein.[15] Specifically, cranial lobe pulmonary arteries should be no larger than the proximal fourth of the fourth rib in a lateral view and caudal lobe arteries no larger than the thickness of the ninth rib in the VD or DV view where the artery and rib intersect.

A useful method to assess caudal lobe pulmonary artery size in VD or DV radiographs is to assess the shape of the summation shadow created by overlap of a caudal lobe pulmonary artery and the ninth rib. In normal dogs this summation shadow should have sides of equal length. If the artery is enlarged, the long axis of the summation shadow will be in a horizontal direction. If the artery is small, the long axis of the summation shadow will be oriented in a vertical direction (Fig. 32-16).

The peripheral pulmonary veins are similar to pulmonary arteries in that pulmonary veins should be no larger than the corresponding artery.

Pulmonary vessels are dynamic, and their size can change relatively quickly, being a function of intraluminal pressure and volume. Situations such as dehydration from diuretic administration or hypervolemia from overzealous intravenous fluid administration can prompt such changes, so interpretation of vessel size must be made with knowledge of any recently administered medications or therapies. More meaningful information is gathered with sequential radiographic examinations, especially if therapies have changed recently.

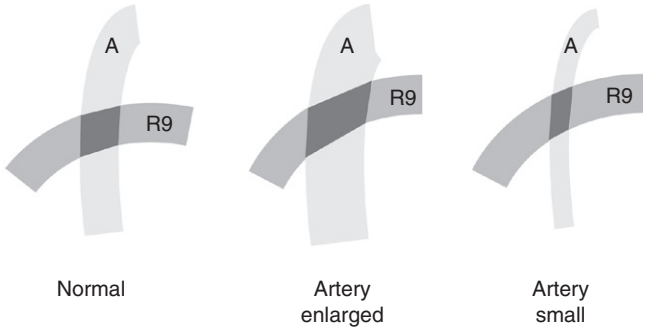


Fig. 32-16 The principle of using the summation shadow created by overlap of a caudal lobe pulmonary artery *(A)* with the right, with the ninth rib *(R9)* to assess artery size. In normal dogs, the summation shadow will have equal sides *(left panel)*. When the artery is enlarged *(center panel)*, the summation shadow will be longer in the horizontal direction than in the vertical direction. When the artery is small *(right panel)*, the summation shadow will be longer in the vertical direction than in the horizontal direction.

Normal size of pulmonary arteries and veins has been described, but certain diseases cause predictable changes in size of either pulmonary arteries alone or pulmonary veins alone, or both simultaneously.

Box 32-1 lists diseases where both pulmonary arteries and veins can be enlarged (Fig. 32-17). The degree of the

enlargement depends on the severity and duration of the cause. Differentiating these diseases depends on evaluating the history, physical examination findings, and findings from electrocardiography and echocardiography.

Pulmonary artery enlargement without venous enlargement may occur with the diseases listed in Box 32-2. The most common cause of pulmonary arterial enlargement in the dog is pulmonary hypertension secondary to heartworm infection (Fig. 32-18). In heartworm disease, arterial enlargement occurs because of pulmonary hypertension resulting from lesions in the vascular tunica intima or tunica media or because of thromboembolic disease, or both. Any or all of the pulmonary arteries may become enlarged, but the pulmonary arteries that enlarge the most frequently in spontaneous heartworm disease are the caudal lobar arteries with a predilection for enlargement of the right more than the left.[16]

In cats with heartworm disease, enlargement of the main pulmonary artery is usually not visualized on survey radiographs.[17-19] The main pulmonary artery does enlarge, but it is more medial in cats, and its border is therefore not visible on survey radiographic images. The peripheral pulmonary arteries do become visibly enlarged in cats with heartworm disease (Fig. 32-19). Enlargement of the central and peripheral portions of the caudal lobar arteries on the VD view, with normal-sized caudal pulmonary veins, has been reported to represent the earliest radiographic change seen in spontaneous feline heartworm disease. Because feline pulmonary lobar

Box • 32-1

Conditions That May Increase the Size of Pulmonary Arteries and Pulmonary Veins

- Left-to-right shunt
  - Patent ductus arteriosus
  - Ventricular septal defect
  - Atrial septal defect
- Peripheral arteriovenous fistula
- Iatrogenic intravenous fluid overload
- Fluid retention secondary to decreased cardiac output

Box • 32-2

Conditions That May Increase the Size of Pulmonary Arteries Without Associated Vein Enlargement

- Tunica intima proliferation or tunica media hypertrophy
  - Dirofilariasis
  - Angiostrongyliasis
  - Aelurostrongylus (feline)
- Thromboembolic disease or primary thromboses
  - Dirofilariasis
  - Disseminated intravascular coagulation
  - Trauma
  - Angiostrongyliasis
  - Renal disease: amyloidosis, glomerulonephritis
  - Septicemia
  - Pancreatitis
  - Hyperadrenocorticism
- Severe chronic lung disease

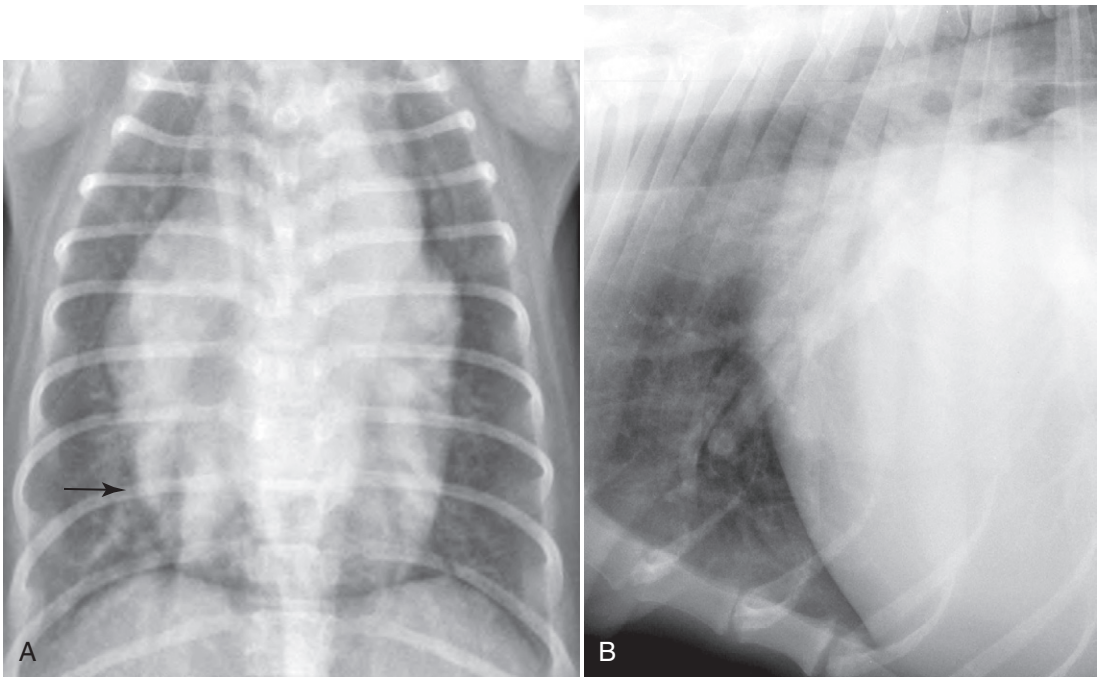


Fig. 32-17 **A,** Dorsoventral radiograph from a dog with a patent ductus arteriosus. The caudal lobe arteries and veins are both enlarged. Note the size of the vessels in the right caudal lobe where they cross the ninth rib *(black arrow)*. In a normal dog the caudal lobe vessels should be approximately the same size as the rib. **B,** Lateral thoracic radiograph of another dog with a patent ductus arteriosus where both the artery and vein of the right cranial lobe are enlarged.

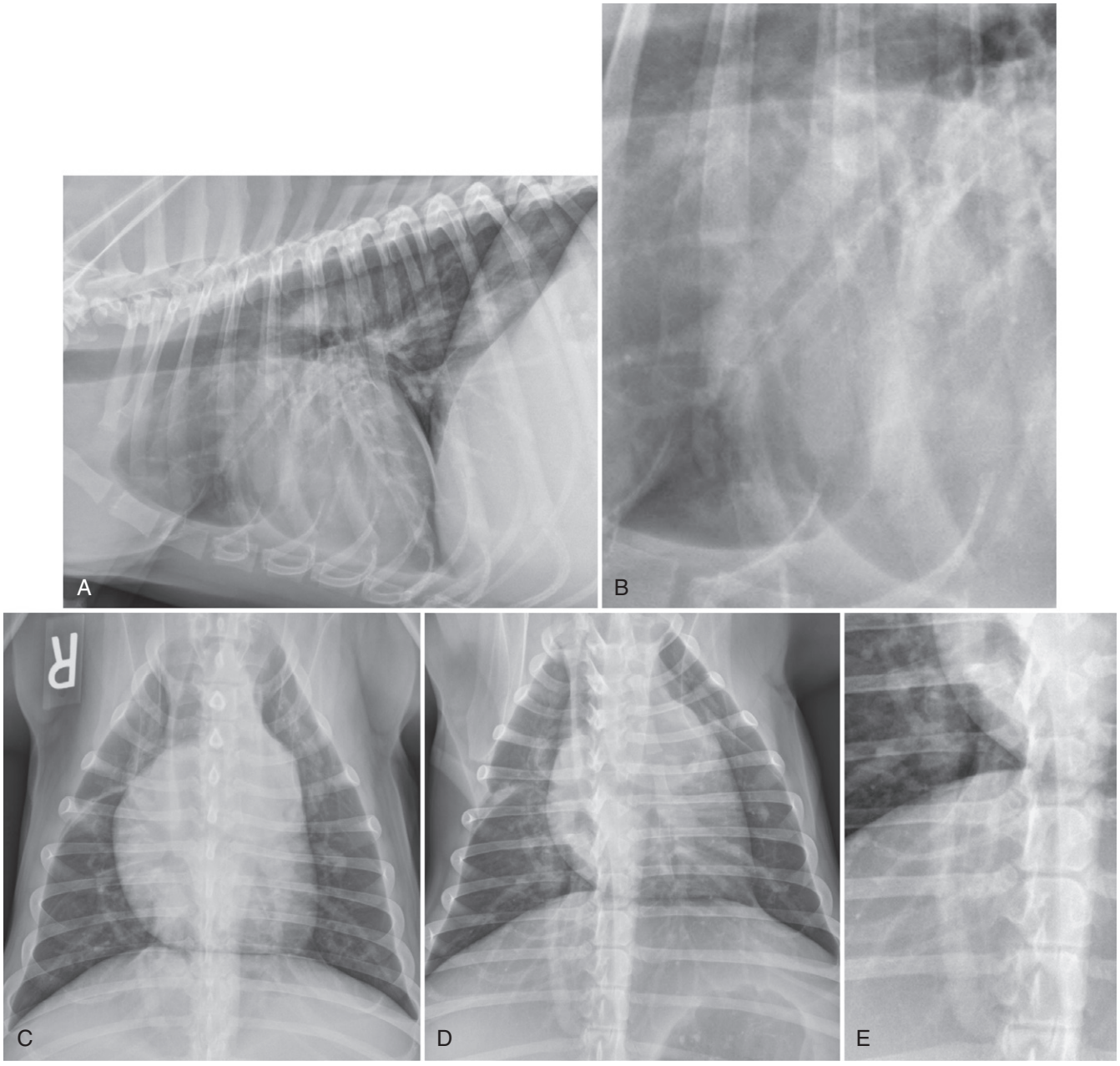


Fig. 32-18 Left lateral **(A),** close-up left lateral **(B),** VD **(C),** DV **(D),** and close-up DV **(E)** radiographs of a dog with heartworm disease. In **A** and **B,** note the enlargement of the right cranial lobe artery compared with the vein. In **C,** note the reversed D appearance of the cardiac silhouette, consistent with right ventricular hypertrophy. In **D** and **E,** note the enlargement of the right caudal lobe artery compared with the vein. These findings are typical of those found in dogs infected with heartworms.

arterial enlargement was shown to resolve and reappear over a span of 4 to 5 months in experimental heartworm infection, vascular changes cannot be relied on entirely when evaluating thoracic radiographs of cats for heartworm disease. A persistent bronchointerstitial pulmonary pattern also occurred in approximately 50% of experimentally infected cats, appearing similar to feline allergic lung disease even after the vascular changes had resolved. Thus cats with radiographic evidence of bronchointerstitial lung opacities should be considered suspects for heartworm disease even in the absence of classic vascular changes.[20] On the basis of the sometimes inconspicuous radiographic signs of feline heartworm disease, echocardiography has been proposed as an alternate screening modality.[21] Echocardiographic detection of heartworm infection may not be uniformly accurate, with better correlation related directly to worm burden.[22]

Heartworm disease is also the most common cause of pulmonary thromboembolism, caused by arterial occlusion by dying worm emboli or blood clots. This results in an increase in pulmonary opacity that at first is a mixed heterogeneous

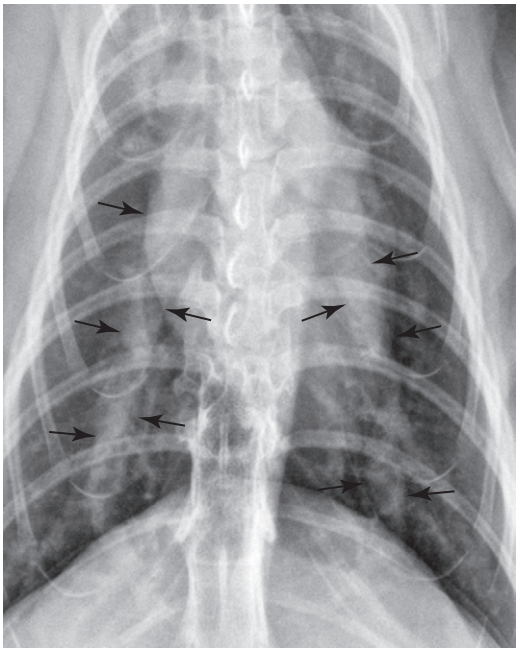


Fig. 32-19 Dorsoventral radiograph of a cat infected with heartworms. Both caudal lobe pulmonary arteries are enlarged *(black arrows)*. Looking closely, smaller (normal) caudal lobe pulmonary veins are present medial to each artery. Enlargement of the main pulmonary artery is not seen, although it is likely present. This is common in cats with heartworm disease.

pattern with a tendency to form a predominantly alveolar pattern later (Fig. 32-20). It is also possible for survey thoracic radiographs to have no evidence of pulmonary involvement in peracute thromboembolism.[23] Although overt pulmonary infarction is possible with heartworm disease, it is rare.

The differential diagnosis for pulmonary vein enlargement occurring without pulmonary arterial enlargement is listed in Box 32-3. Pulmonary vein enlargement is most commonly seen in dogs with mitral insufficiency because of pulmonary venous hypertension (Figs. 32-21 and 32-22).

Diseases associated with decreased size of both the pulmonary arteries and veins are listed in Box 32-4 (Fig. 32-23). Regardless of cause, the lung fields in these diseases appear hyperlucent because of a lesser contribution by the pulmonary arteries and veins to the overall soft tissue opacity of the lungs. Therefore few x-rays are attenuated on their passage through the aerated lung fields.

Up to this point only the size of pulmonary vessels has been considered. A change in shape of pulmonary vessels can also occur and is most commonly seen in dogs with heartworm disease where vessels become tortuous and may appear to terminate abruptly (see Fig. 32-20, *D*).

Pulmonary vascular margination should be relatively sharp. However, perivascular disease in adjacent lung results in either partial or complete loss of vascular conspicuity. This is caused by an accumulation of fluid, cells, or necrotic debris in either the interstitium or the alveoli immediately adjacent to the vessel, causing border effacement with the vessel wall and obscuring its margins (Fig. 32-24).

Congestive Heart Failure

Backward left-sided heart failure begins when increased end-diastolic filling pressure in the left ventricle leads to pulmonary venous hypertension. Pulmonary venous hypertension is recognizable when pulmonary veins are larger than the corresponding lobar artery (see Figs. 32-21 and 32-22).

Box • 32-3

Conditions That May Increase the Size of Pulmonary Veins Without Associated Artery Enlargement

- Cardiac
  - Volume overload
    - Mitral insufficiency
    - Mitral valvular endocardiosis
    - Early left-to-right shunts (thinner walls of veins dilate more easily) including patent ductus arteriosus and ventricular septal defect
  - Primary myocardial disease
    - Myocardial failure (arrhythmias, fibrosis)
    - Dilatory cardiomyopathy
    - Hypertrophic cardiomyopathy
    - Restrictive cardiomyopathy
- Noncardiac dysfunction
  - Left atrial obstruction
    - Mass (neoplastic or inflammatory) at heart base
    - Thrombosis within left atrium

This itself is not a sign of heart failure, but it may progress to transudation of fluid from the capillaries into the lung interstitium, causing a hazy, unstructured interstitial pulmonary pattern (interstitial pulmonary edema).

Cardiogenic pulmonary edema has been described as having a predilection for the perihilar area. This is an association taken from the radiographic appearance of cardiogenic pulmonary edema in human beings. In small animals the finding of a distinct perihilar distribution of cardiogenic pulmonary edema is very uncommon. The erroneous diagnosis of perihilar edema can result from the summation of the multitude of structures in the perihilar region, coupled with poor aeration from recumbent atelectasis.

Radiographic visualization of interstitial cardiogenic pulmonary edema is rare because it is short lived, and it does not create a marked increase in lung opacity. Interstitial pulmonary edema typically progresses to multifocal areas of alveolar pulmonary opacity, obscuring pulmonary vascular structures. In dogs, pulmonary edema is usually most obvious radiographically in the caudal lobes. Cardiogenic pulmonary edema could be expected to result in generalized homogeneous lung involvement, but this is not common; cardiogenic pulmonary edema is more often patchy, especially in cats (see Fig. 32-24). The symmetry of pulmonary edema distribution has been associated with the direction of the mitral regurgitant jet in dogs with mitral regurgitation. A symmetric distribution was associated predominantly with a central mitral regurgitant jet, whereas an asymmetric distribution was usually associated with an eccentric jet.[24] Some cats also have a component of pleural effusion in addition to pulmonary edema (Fig. 32-25).

Right-sided heart failure usually includes some or all of the following radiographic signs: bilateral pleural effusion with varying degrees of secondary pulmonary atelectasis, ascites, and hepatosplenomegaly. The radiographic appearance of these changes is covered elsewhere in this text.

Acquired Cardiovascular Lesions

Acquired cardiovascular lesions are much more commonly encountered in clinical practice than are congenital lesions. The most common acquired lesions are mitral insufficiency, heartworm disease, and cardiomyopathy.

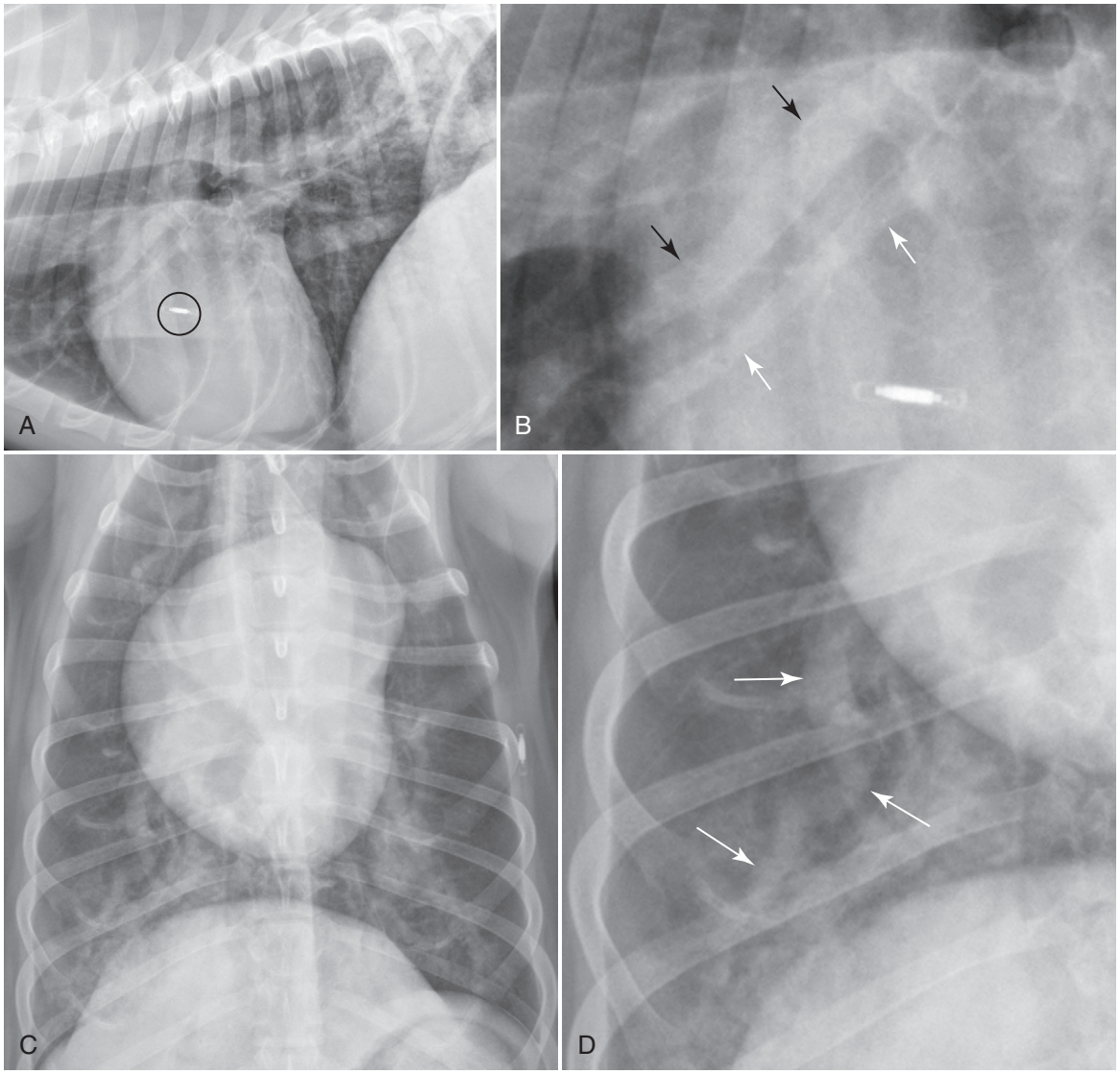


Fig. 32-20 Lateral **(A),** close-up lateral **(B),** DV **(C),** and close-up DV **(D),** radiographs of the thorax of a dog with heartworm disease. In **A,** the right cranial lobe pulmonary artery is larger than the right cranial lobe vein, and there is an intense alveolar pattern in the dorsocaudal aspect of the lung. The opacity encircled *(black circle)* is an identification microchip. In **B,** the enlarged right cranial lobe pulmonary artery *(black arrows)* compared to the right cranial lobe vein *(white arrows)* is very conspicuous. In **C,** the main pulmonary artery is dilated, the right ventricle appears enlarged, and there are patchy alveolar opacities in both caudal lung lobes, more intense on the right. In **D,** the right caudal lobe pulmonary artery is tortuous *(white arrows)*. The vein cannot be seen because of the alveolar pattern in the right caudal lobe. The alveolar pattern in this dog is likely caused by thromboembolism given its patchy intense distribution. That it is caused by an allergic reaction cannot be ruled out.

Box • **32-4**

Conditions That May Decrease the Size of Pulmonary Arteries and Veins

Right-to-left shunts
- Tetralogy of Fallot
- Ventricular septal defect with pulmonic stenosis

Severe pulmonic stenosis with decreased cardiac output
Hypovolemia
Shock
Dehydration
Adrenocortical hypofunction

Mitral Insufficiency

Mitral insufficiency is the most common cause of acquired heart disease in small animal practice, primarily occurring in small-breed dogs. Radiographic signs can include various degrees of the following (see Figs. 32-5 to 32-8 and Figs. 32-21, 32-22, 32-24):

- Left atrial enlargement, attributable to dilation caused by volume overload from mitral valve regurgitation
- Left ventricular enlargement, from dilation caused by volume overload because not as much blood is ejected from the left ventricle with each systole
- Distended pulmonary veins if venous hypertension has developed
- Pulmonary edema (left-sided heart failure)

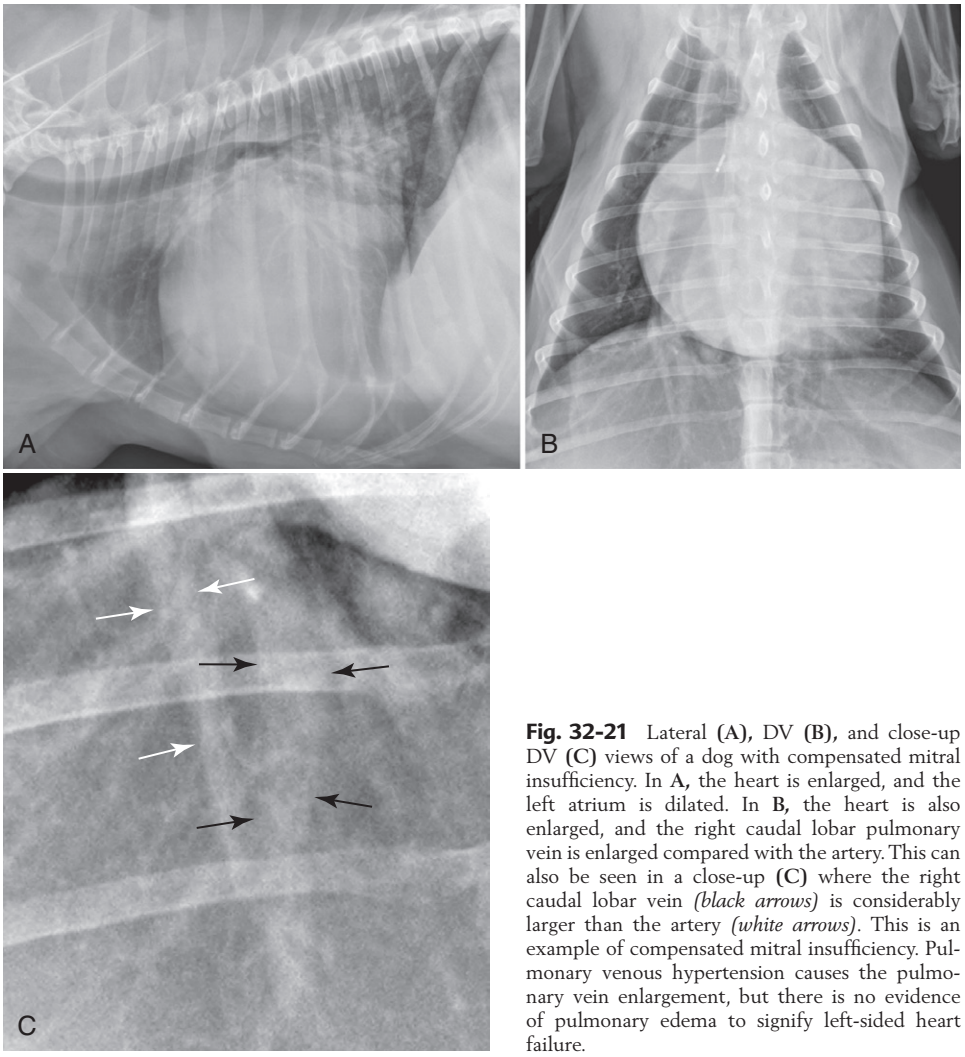


Fig. 32-21 Lateral **(A),** DV **(B),** and close-up DV **(C)** views of a dog with compensated mitral insufficiency. In **A,** the heart is enlarged, and the left atrium is dilated. In **B,** the heart is also enlarged, and the right caudal lobar pulmonary vein is enlarged compared with the artery. This can also be seen in a close-up **(C)** where the right caudal lobar vein *(black arrows)* is considerably larger than the artery *(white arrows)*. This is an example of compensated mitral insufficiency. Pulmonary venous hypertension causes the pulmonary vein enlargement, but there is no evidence of pulmonary edema to signify left-sided heart failure.

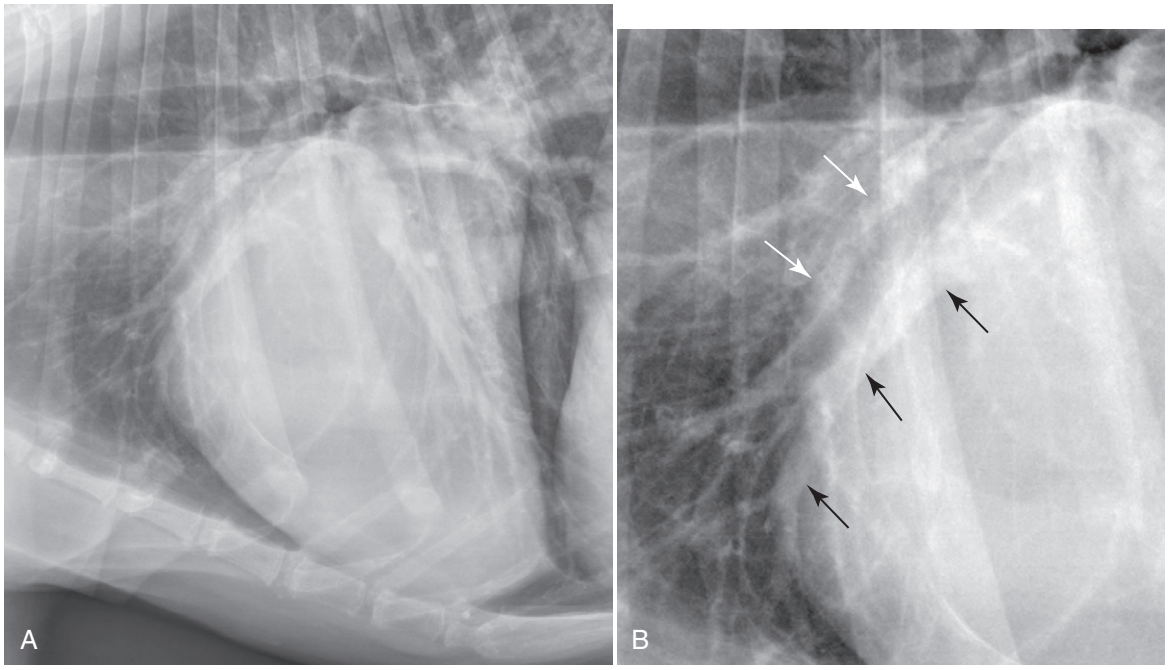


Fig. 32-22 **(A)** Lateral radiograph and **(B)** close-up lateral radiograph of a dog with compensated mitral insufficiency. The left atrium and the right cranial lobe vein are enlarged, a sign consistent with pulmonary venous hypertension. The venous enlargement *(black arrows)* compared to the artery *(white arrows)* is clearly seen in **B.**

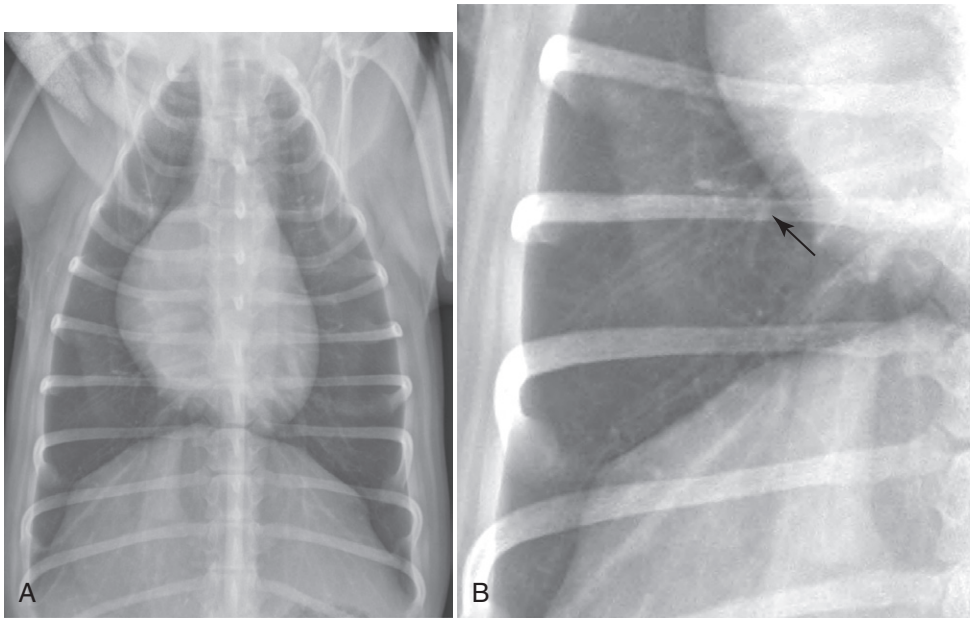


Fig. 32-23 VD **(A)** and close-up VD **(B)** thoracic radiographs of a dog with pulmonary undercirculation from multiple congenital cardiac anomalies. Note the small, inconspicuous pulmonary vessels. The appearance of hypovolemia would be similar. In **B,** note the small size of the right caudal lobe pulmonary vein where it crosses the right ninth rib *(black arrow)*.

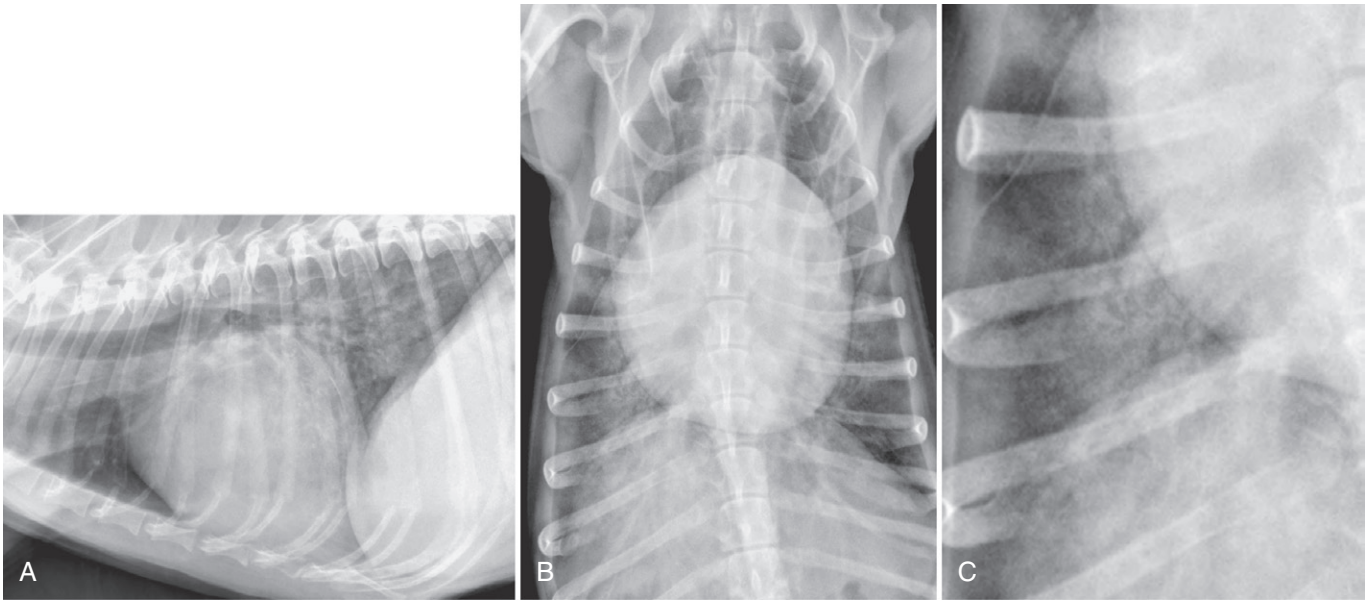


Fig. 32-24 Left lateral **(A),** DV **(B),** and close-up DV **(C)** radiographs of a dog with left-sided heart failure secondary to mitral insufficiency. In **A,** the heart and left atrium are enlarged. Pulmonary vessels are difficult to identify because of border effacement created by edema in adjacent lung. The caudal lung lobes appear abnormally opaque, but this may be caused by poor ventilation; any suspicious lung opacity identified in the lateral view must be confirmed in the DV or VD view. In **B,** there is an alveolar pattern in the right middle and caudal lobes. This can be seen in the close-up **(C).** Note the poor visualization of pulmonary vessels in these lobes because of border effacement from the pulmonary edema. This patchy alveolar pattern, even without visualization of air bronchograms, is typical of cardiogenic pulmonary edema.

Heartworm Infection

Despite the availability of highly effective preventive drugs, heartworm disease is still common in certain parts of the United States. The radiographic changes vary depending on the duration of the infection, the number of worms present, the location of the worms (right side of heart and/or pulmonary arteries), the rate and degree of cardiac compensation, and the possible die-off of adult worms naturally or in response to antihelmintic medications. Therefore radiographic changes can vary from no abnormal findings or only a mildly affected

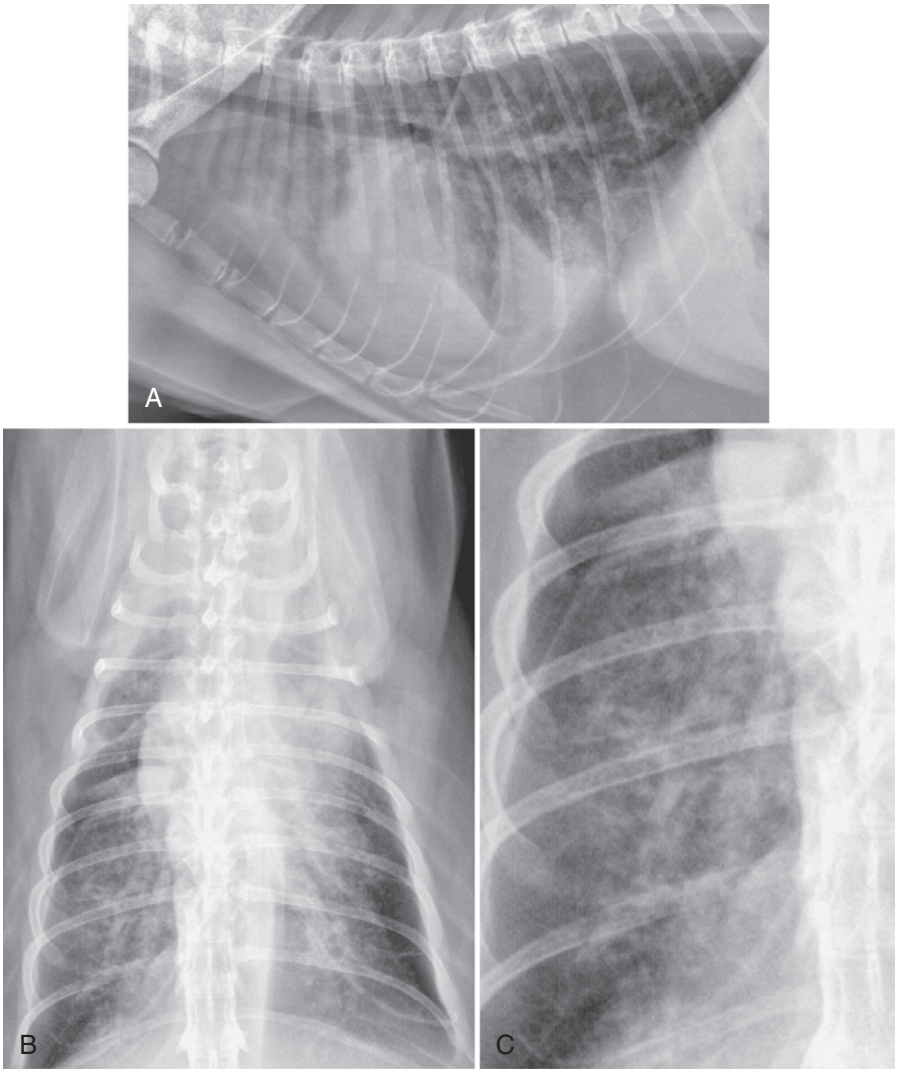


Fig. 32-25 Left lateral **(A),** VD **(B),** and close-up VD **(C)** radiographs of a cat with left-sided heart failure caused by hypertrophic cardiomyopathy. Pleural effusion is obvious in **A.** The heart cannot be seen clearly, but it may not be abnormal radiographically in cats with hypertrophic cardiomyopathy. Pleural effusion is also noted in the DV view **(B)**. Also, the caudal lobe pulmonary arteries and veins both appear enlarged. This is often seen in cats in heart failure from cardiomyopathy as a result of fluid retention. A heterogeneous, relatively unstructured pulmonary pattern is present in the caudal lobes that is consistent with pulmonary edema; see close-up in **C.** This heterogeneous pattern is typical of pulmonary edema in cats and is more common than more uniform homogenous lung opacification.

cardiovascular system to severe involvement (see Figs. 32-18 to 32-20):

- Right ventricular hypertrophy in response to pulmonary hypertension
- Dilation of the main pulmonary artery caused by turbulent blood flow and pulmonary hypertension and possibly the physical presence of heartworms
- Parenchymal pulmonary artery enlargement and/or tortuosity from pulmonary hypertension and/or loss in laminar blood flow
- Peripheral focal or multifocal alveolar pulmonary pattern from pulmonary thromboembolism caused by dead adult worm fragments or secondary allergic pneumonitis
- Hepatomegaly, ascites, and occasionally pleural effusion caused by right-sided heart failure

Cardiomyopathy

Dilated cardiomyopathy results from weakened and dysfunctional myocardial contractility. Among large dog breeds, it is most commonly encountered in Doberman pinschers and boxers. In dogs, any or all of the following radiographic signs may be seen (Figs. 32-26 and 32-27):

- The radiographs may be normal in some dogs with dilated cardiomyopathy.
- Generalized cardiomegaly is caused by volume overload or ventricular dilation.
- Left atrial dilation may be present because of volume overload or mitral dysfunction from a change in shape of the mitral annulus as a result of cardiac dilation.
- Pulmonary vein dilation from mitral valve dysfunction and regurgitation or from fluid retention is seen.

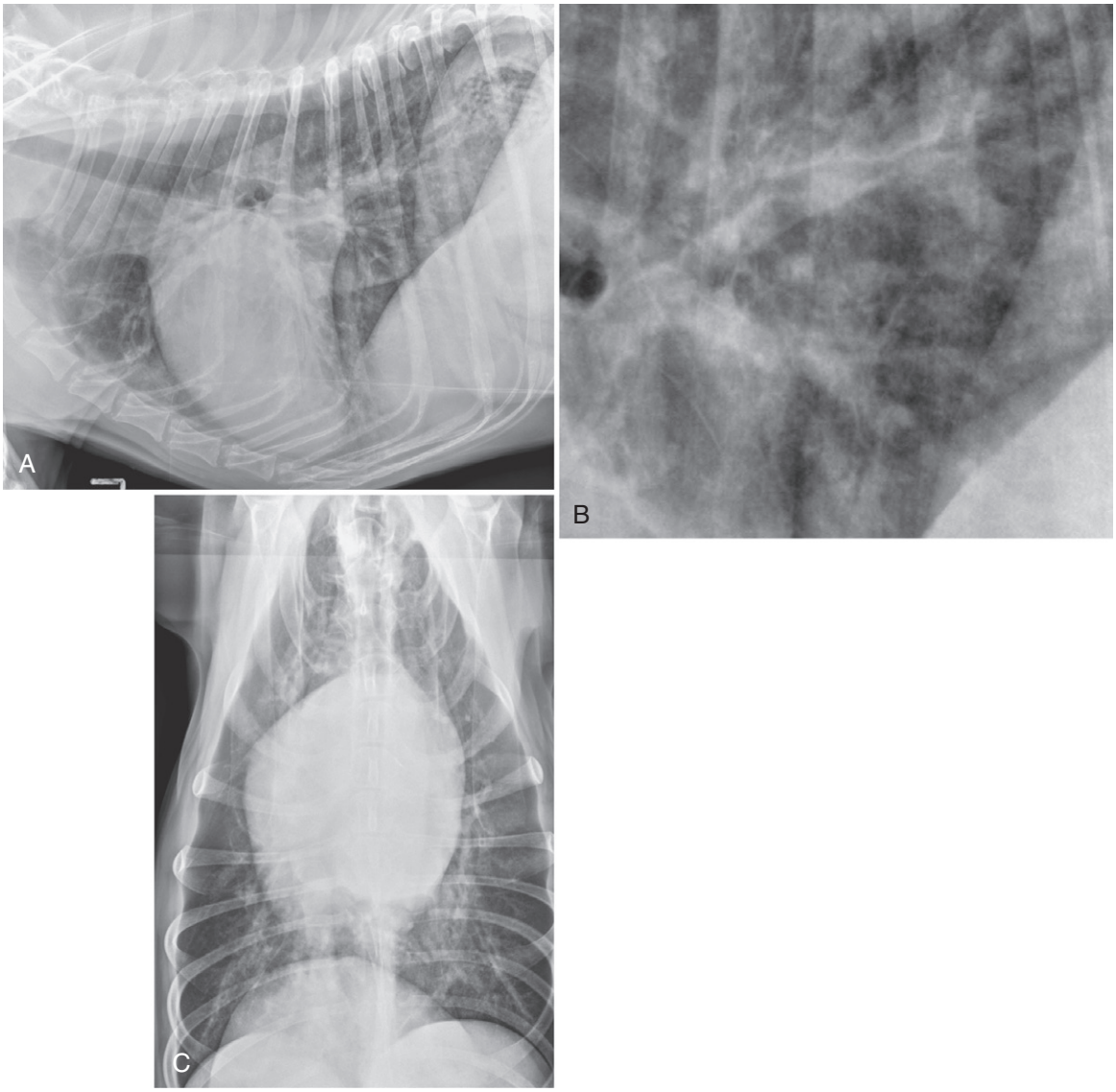


Fig. 32-26 Lateral **(A),** close-up lateral **(B),** and VD **(C)** radiographs of a dog with dilated cardiomyopathy and left-sided heart failure. The heart in patients with dilated cardiomyopathy may appear normal. In this dog there is enlargement of the left atrium and the right cranial lobe pulmonary vein **(A),** likely resulting from mitral valve dysfunction with secondary pulmonary venous hypertension. **A** and **C** have the appearance of increased lung opacity. In **B,** this opacity can be seen to have a bronchial and unstructured interstitial pattern. This lung pattern is more typical of an inflammatory etiology than cardiogenic pulmonary edema, except in dogs with dilated cardiomyopathy, where it is a typical manifestation of cardiogenic pulmonary edema.

- Parenchymal pulmonary artery dilation from fluid retention is stimulated by decreased renal perfusion, leading to activation of the renin-angiotensin system.
- Possible pleural effusion, hepatomegaly, and/or ascites from right-sided heart failure is often seen.
- Mixed interstitial and bronchial pattern caused by atypical pulmonary edema; strictly on the basis of radiographic appearance, this distribution of pulmonary edema is unusual, and the radiographic pattern is more typical of inflammatory allergic airway disease.

Hypertrophic cardiomyopathy occasionally occurs in dogs but is more common in cats. Feline hypertrophic cardiomyopathy is characterized by development of a hypertrophied, nondilated left ventricle in the absence of other cardiac diseases. The poor left ventricular diastolic filling leads to reduced cardiac output with secondary increased mitral valve pressure and left atrial dilation. Radiographic signs of feline hypertrophic cardiomyopathy include the following (Fig. 32-28; see Fig. 32-25):

- Moderate to extreme left atrial dilation. In cats, left atrial dilation with hypertrophic cardiomyopathy can become so large that it may extend to the right, giving the appearance of biatrial enlargement. Extreme left atrial dilation results in the characteristic "valentine" heart shape in the VD or DV view. Left atrial dilation may be caused by poor ventricular diastolic filling as a result of the left ventricular myocardial inward hypertrophy, systolic dysfunction, or abnormal systolic anterior motion caused by left ventricular outflow obstruction.

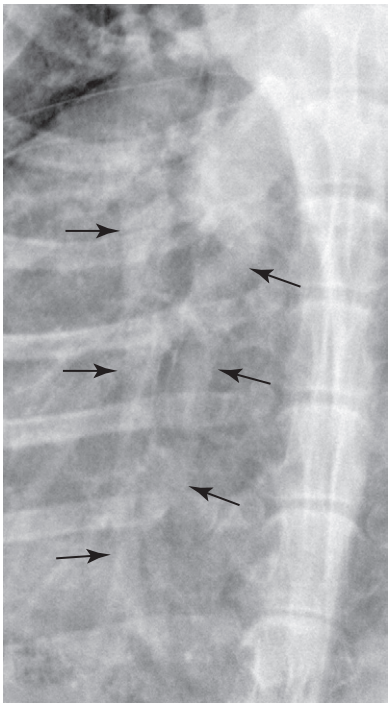


Fig. 32-27 Close-up DV thoracic radiograph of a dog with dilated cardiomyopathy and heart failure. The right caudal pulmonary artery and vein are enlarged *(black arrows)*. This is sometimes seen in dogs with heart failure and is caused by fluid retention. Decreased cardiac output results in activation of the renin-angiotensin pathway with secondary fluid retention.

- The left ventricle does not appear enlarged because the hypertrophy is constrictive (concentric), or inward, so the myocardium thickens at the expense of the left ventricular chamber size but does not increase its exterior dimensions.
- Enlarged pulmonary veins may appear in early left ventricular decompensation, but visualization of pulmonary venous enlargement is not as common in cats with mitral dysfunction as in dogs.
- Pulmonary edema will develop as left-sided heart failure progresses if not controlled by medication.
- Pleural effusion is a late development.

Pericardial Effusion

Although not a myocardial or valve problem, pericardial effusion is acquired and can alter the shape and size of the cardiac silhouette. Radiographic signs include the following (Fig. 32-29):

- There is a large round (globoid) cardiac silhouette in both lateral and VD or DV views if the effusion is severe enough.
- The margin of cardiac silhouette may appear distinct as a result of little, if any, motion caused by cardiac contractions.
- In severely affected patients, the margins of the hugely enlarged cardiac silhouette may touch the thoracic wall bilaterally.
- Signs of right heart failure (enlarged caudal vena cava, hepatomegaly, ascites, and occasionally pleural effusion) may be present if pericardial tamponade is severe enough to prevent diastolic filling of the right atrium and ventricle.
- Small to moderate volumes of pericardial effusion often do not have the previously described radiographic signs and can go undetected without echocardiography.

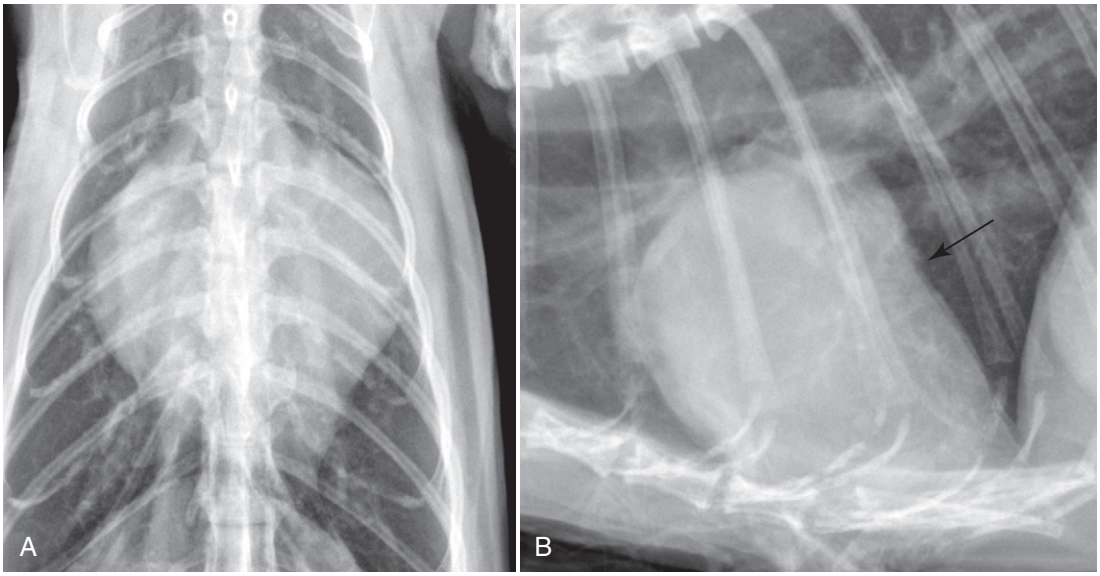


Fig. 32-28 Lateral **(A)** and VD **(B)** radiographs of a cat with hypertrophic cardiomyopathy. In **A,** the marked left atrial enlargement creates the so-called "valentine" appearance to the cardiac silhouette. This extent of left atrial enlargement is sometimes misdiagnosed radiographically as biatrial enlargement. Although one cannot be sure whether only the left atrium is dilated without echocardiography, a very large left atrium alone can create the valentine appearance. In **B,** the enlarged left atrium is not as obvious because it is superimposed on the cardiac silhouette; this is dissimilar to the dog, in which an enlarged left atrium causes a mass effect in the region of the tracheal bifurcation. The enlarged left atrium in this cat does create a focal concave defect in the shape of the cardiac silhouette (*black arrow* in **B**).

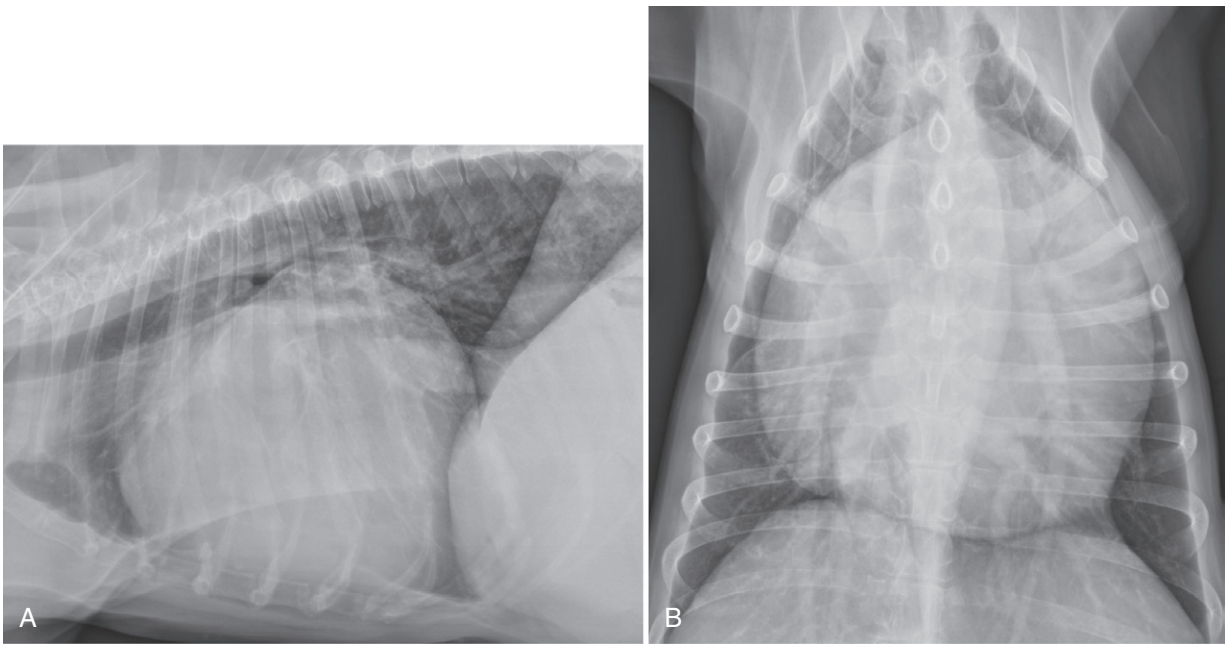


Fig. 32-29 Left lateral **(A)** and DV **(B)** radiographs of a dog with a globoid-appearing cardiac silhouette. This appearance is consistent with pericardial effusion, but based on the radiographs, a peritoneal-pericardial hernia or cardiomegaly cannot be eliminated. This dog had pericardial effusion.

Congenital Cardiovascular Lesions

Given that congenital cardiac anomalies are encountered less commonly than acquired defects, only a brief summary is presented.

Patent Ductus Arteriosus

In patent ductus arteriosus, the ductus fails to close normally after birth. This results in an abnormal communication between the descending aorta and the main pulmonary artery. Because of the marked pressure difference between these vessels, a continuous shunting of blood from the aorta into the pulmonary artery occurs during both systole and diastole. This results in pressure and volume overload of the pulmonary circulation and altered myocardial workload. Radiographic signs include the following (Figs. 32-30 through 32-32; see Fig. 32-17):

- Segmental enlargement (ductus bump)[23] of the proximal aspect of the descending aorta caused by turbulent blood flow
- Enlargement of the main pulmonary artery from increased pressure and flow
- Enlargement of the left atrium, and possibly the left auricle, from increased blood flow
- Enlarged left ventricle, initially caused by dilation followed by hypertrophy
- Enlarged pulmonary arteries *and* veins caused by volume and pressure overload

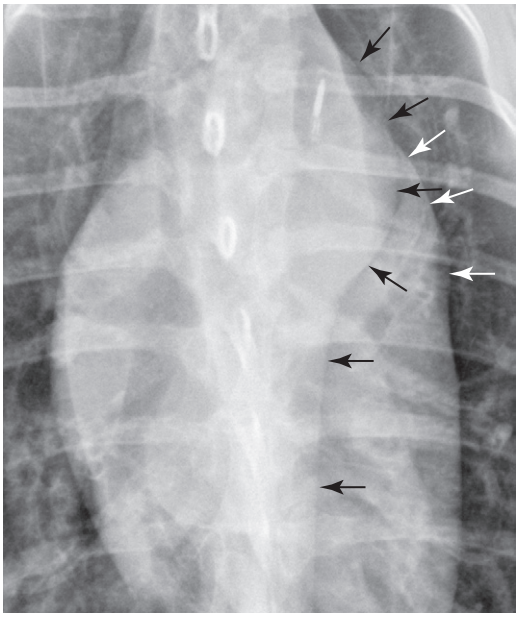


Fig. 32-30 DV radiograph from a dog with a patent ductus arteriosus. There is a diverticulum ("ductus bump") of the descending portion of the aortic arch that is contiguous with the descending aorta *(black arrows)*. There is also mild dilation of the main pulmonary artery *(white arrows)*.

Pulmonic Stenosis

Pulmonic stenosis leads to restriction of flow from the right ventricle into the pulmonary artery. It is typically caused by an abnormal pulmonic valve but can also be associated with narrowing of the pulmonary outflow tract—that is, subvalvular pulmonic stenosis. Radiographic signs include the following (Fig. 32-33):

- Dilated main pulmonary artery is caused by turbulence.
- Enlarged right ventricle is caused by hypertrophy related to increased resistance associated with ejection.
- Parenchymal pulmonary vessels are usually normal in size, but if right-sided heart failure develops, the pulmonary vessels may be small because of reduced cardiac output.

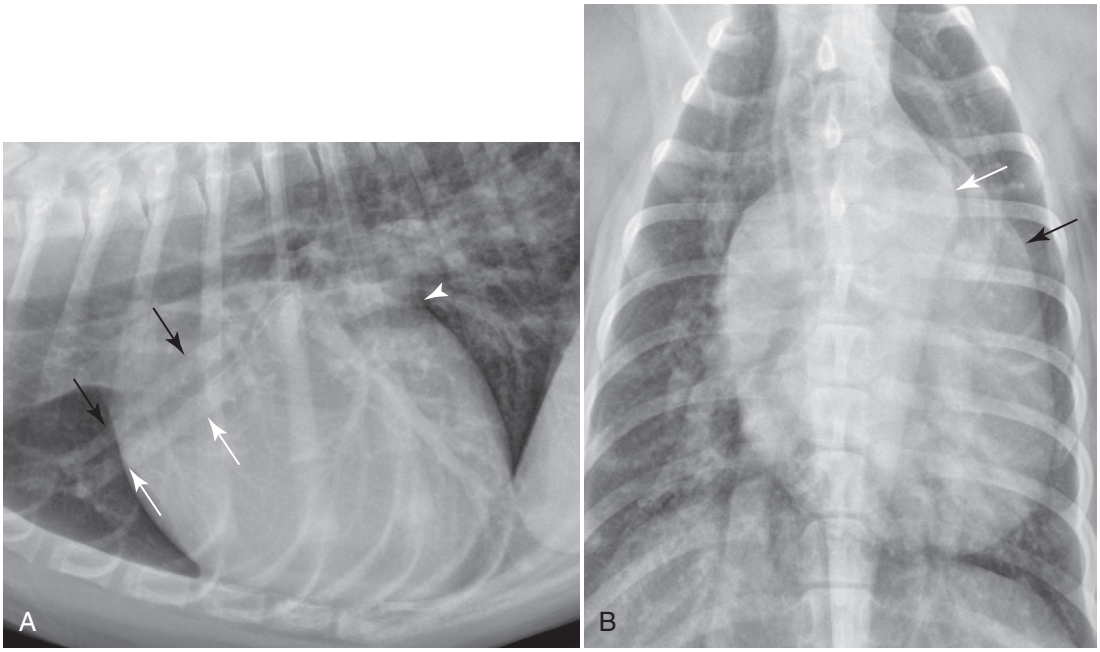


Fig. 32-31 Lateral **(A)** and DV **(B)** radiographs of a dog with a patent ductus arteriosus. The heart is enlarged in both views, mostly because of left ventricular hypertrophy, although the diagnosis of hypertrophy cannot be made from these radiographs. An aortic arch diverticulum is visible in the DV view *(white arrow)*, and the conspicuity of the left auricle *(black arrow)* is also increased slightly, either because of dilation or displacement by an enlarged left atrium. In **A,** the right cranial pulmonary lobar artery *(black arrows)* and vein *(white arrows)* are dilated. Left atrial dilation has created a concave shape change in the lateral view *(white arrowhead)*. The lungs have an unstructured increase in opacity because of overcirculation within small pulmonary vessels.

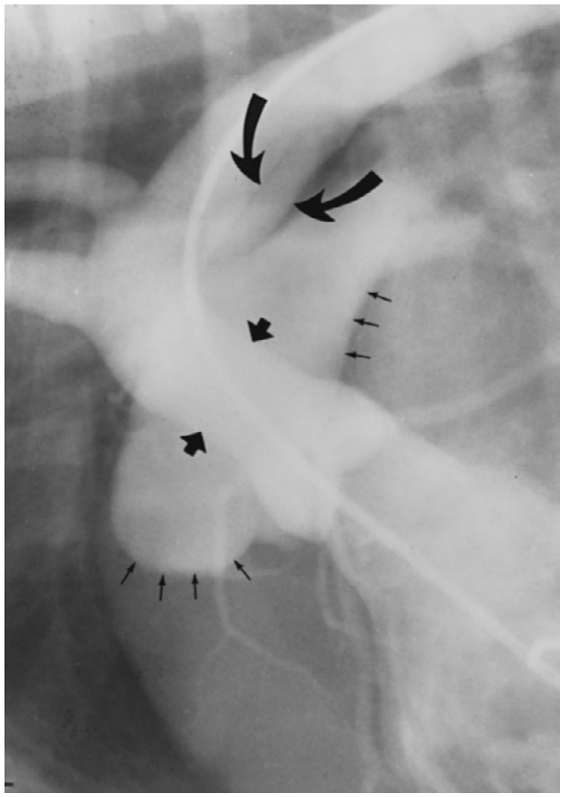


Fig. 32-32 Selective left ventricular angiocardiogram of a dog with a patent ductus arteriosus. The dilated main pulmonary artery segment *(small thin arrows)* and the ascending aorta *(solid arrowheads)* are accentuated by positive-contrast medium, and the patent ductus arteriosus *(curved arrows)* lies between the descending aorta and the main pulmonary artery segment and is opacified because of the left-to-right shunting of blood.

Aortic Stenosis

Narrowing of the subvalvular region of the left ventricle is more common than primary valvular stenosis. The narrowing results in increased resistance to left ventricular ejection. Mitral valve dysfunction and regurgitation may occur as a result of the mitral annulus becoming misshapen. Radiographic signs include the following (Fig. 32-34; see Fig. 32-11):

- Enlargement of the aortic arch from turbulent flow, appearing as widening of the precardiac mediastinum
- Elongation of the left ventricle from hypertrophy
- Left atrial dilation if secondary mitral valve dysfunction develops
- Normal pulmonary vessels unless secondary mitral valve dysfunction develops, leading to pulmonary venous hypertension
- Radiographs may be normal

Ventricular Septal Defect

Abnormal development results in a communication between the left and right ventricle, usually located dorsally in the membranous septum just below the aortic valve. Because systolic pressure is higher in the left ventricle, blood flows from the left ventricle into the right ventricle during systole. Little flow is present during diastole because of the similar diastolic pressure in the two ventricles. Because of the location of the defect, most shunted blood immediately enters the pulmonary artery and not the right ventricle. The volume of blood shunted with each contraction depends on the size of the defect, but the magnitude of shunting is typically less than with patent ductus arteriosus. The magnitude of radiographic signs depends on the amount of blood shunting through the defect and can include the following (Fig. 32-35):

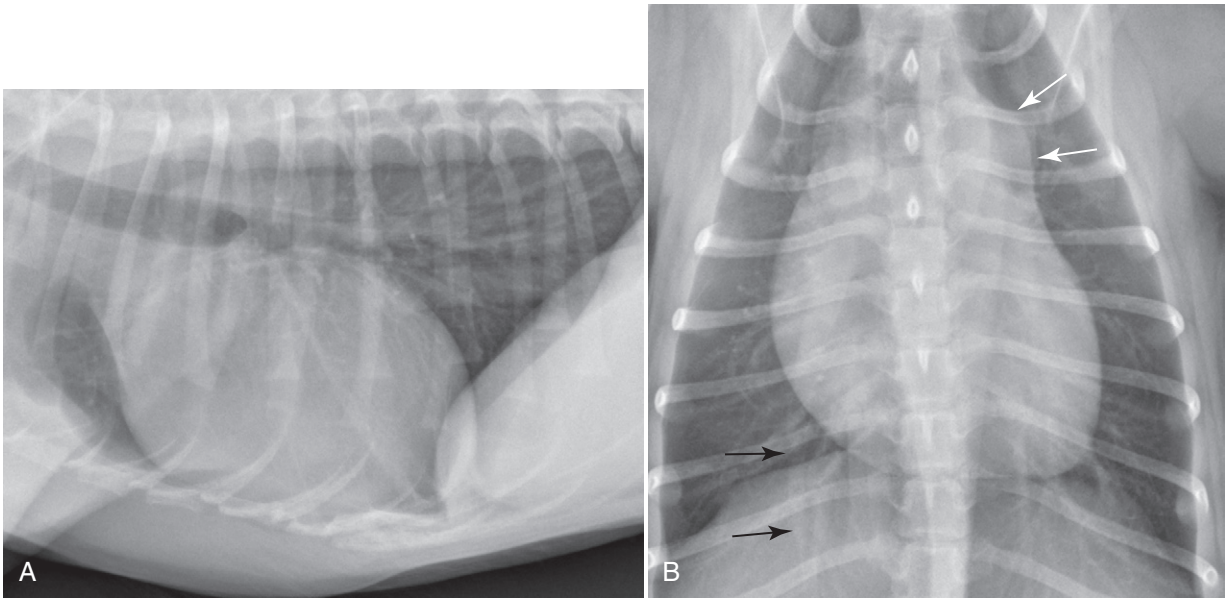


Fig. 32-33 Lateral **(A)** and DV **(B)** radiographs of a dog with pulmonic stenosis. There is excessive contact of the heart with the sternum in the lateral view indicative of right ventricular enlargement, likely hypertrophy. The main pulmonary artery is enlarged in the DV view *(white arrows)*. The parenchymal pulmonary vessels are normal in both views (*black arrows* in **B**).

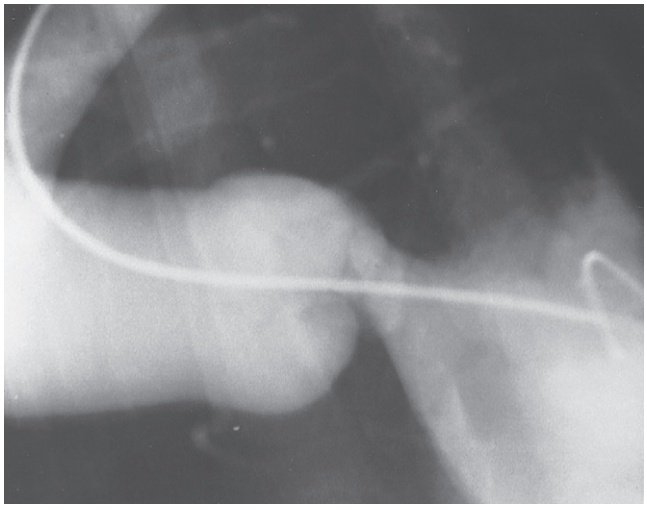


Fig. 32-34 Left ventricular angiocardiogram in a dog with subvalvular aortic stenosis. Note the narrow subvalvular region and dilation of the aorta distal to the aortic sinus. The aorta should be no wider than the sinus; enlargement of the aorta distal to the sinus is caused by turbulent flow.

- There is mild right ventricular hypertrophy from volume and pressure overload.
- Pulmonary arteries and veins can be normal or mildly dilated because of a mild to moderate increase in pulmonary blood flow; enlargement is typically less than that seen with patent ductus arteriosus.

Tricuspid Dysplasia

Tricuspid dysplasia is a congenital malformation of the tricuspid valve. Radiographic signs include the following (see Fig. 32-9):

- Right atrial enlargement from pressure and volume overload is seen.
- Pulmonary vessels are usually normal but may become small if cardiac output decreases from the right ventricle.

Reduction in Heart Size

The cardiac abnormalities discussed to this point are all associated with either a normal heart or enlargement of a portion of the heart or associated vasculature. Reduction in heart size does occur, not as a result of primary cardiac disease but because of reduction in circulating vascular volume. Acutely, this occurs secondary to blood loss and, on a more chronic basis, as a result of dehydration or metabolic hypovolemia, sometimes because of Addison's disease.[25] Radiographically, the heart appears small subjectively and may be retracted from the sternum. The lungs will usually appear overinflated, but this is an artifact caused by the reduction in cardiac size. Pulmonary vessels also appear small, leading to increased pulmonary hyperlucency (Fig. 32-36). The magnitude of these changes depends on the severity of the hypovolemia, and there will be some threshold of fluid loss that must occur before the changes are obvious.

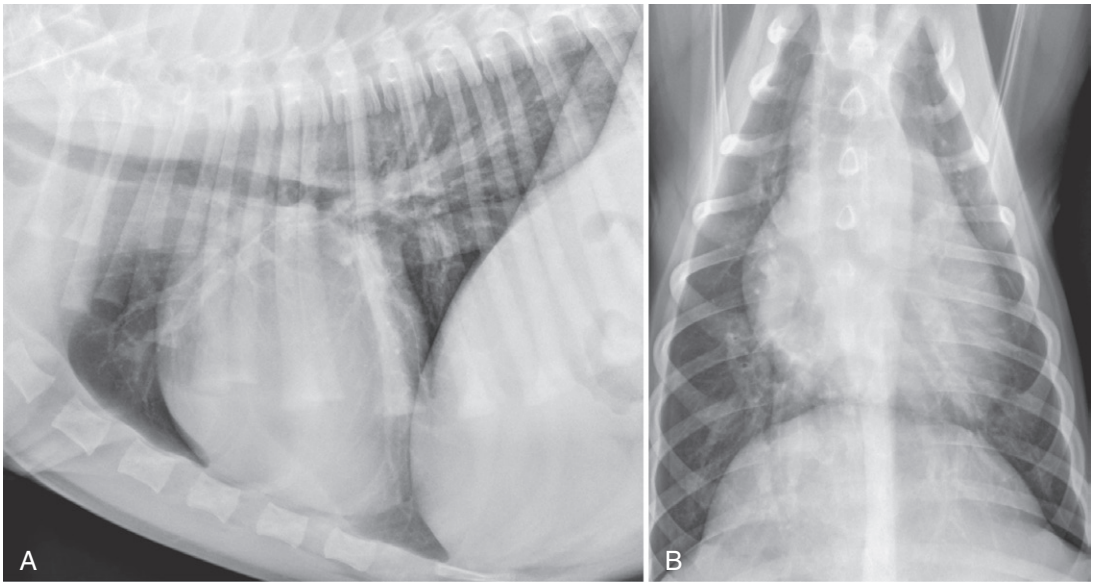


Fig. 32-35 Lateral **(A)** and DV **(B)** radiographs of a dog with a ventricular septal defect. In **A,** there is excessive elevation of the cardiac apex from the sternum consistent with right ventricular hypertrophy, mild dilation of the left atrium, and slight enlargement of the left cranial lobe pulmonary artery and vein, consistent with mild overcirculation. In **B,** the apex is displaced to the left as a result of the dog being in sternal recumbency, the appearance of excessive cardiac mass on the right is deceptive. Slight enlargement of the caudal lobe pulmonary arteries and veins is present, consistent with mild overcirculation. These findings are typical of, but not conclusive proof of, a ventricular septal defect.

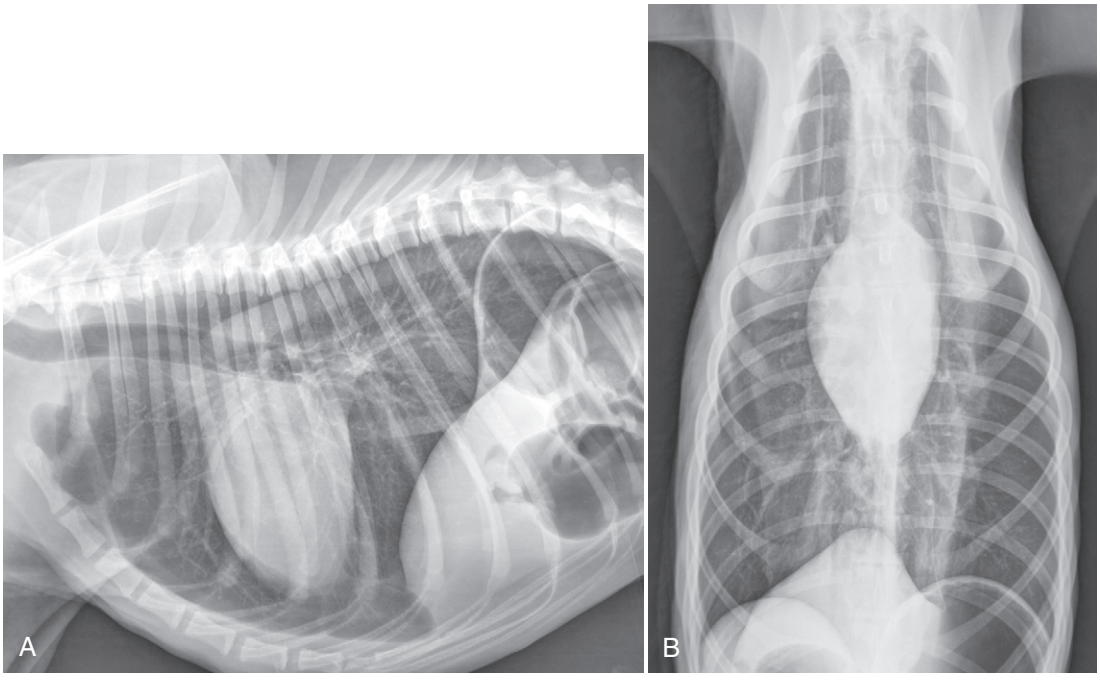


Fig. 32-36 Lateral **(A)** and VD **(B)** radiographs of a dog with hypovolemia secondary to Addison's disease. The heart is subjectively small, and the reduction in cardiac mass has resulted in the heart contracting from the sternum. The pulmonary vessels are also small. The lungs appear hyperinflated because of the relative reduction in cardiac size.

REFERENCES

1. Kittleson MD: Radiology. In Kittleson MD, Kienle RD, editors: *Small animal cardiovascular medicine*, St. Louis, 1998, Mosby, p 47.
2. Lord PF, Suter PF: Radiology. In Fox PR, Sisson D, Moise S, editors: *Textbook of feline and canine cardiology*, ed 2, Philadelphia, 1999, Saunders, p 107.
3. Ruehl WW, Thrall DE: The effect of dorsal versus ventral recumbency on the radiographic appearance of the canine thorax, *Vet Radiol* 22:10, 1981.
4. Webster N, Adams V, Dennis R: The effect of manual lung inflation vs. spontaneous inspiration on the cardiac silhouette in anesthetized dogs, *Vet Radiol Ultrasound* 50:172, 2009.

5. Lamb CR, Boswood A: Role of survey radiography in diagnosing canine cardiac disease, *Compend Contin Educ Pract Vet* 24:316, 2002.
6. Carlisle C, Thrall DE: A comparison of normal feline thoracic radiographs made in dorsal versus ventral recumbency, *Vet Radiol* 23:3, 1982.
7. Buchanan JW, Bucheler J: Vertebral scale system to measure canine heart size in radiographs, *J Am Vet Med Assoc* 206:194, 1995.
8. Lamb CR, Tyler M, Boswood A, et al: Assessment of the value of the vertebral heart scale in the radiographic diagnosis of cardiac disease in dogs, *Vet Rec* 146:687, 2000.
9. Lamb CR, Wikeley H, Boswood A, et al: Use of breed-specific ranges for vertebral heart scale in the radiographic diagnosis of cardiac disease in dogs, *Vet Rec* 148:707, 2001.
10. Hansson K, Haggstrom J, Kvart C, et al: Interobserver variability of vertebral heart size measurements in dogs with normal and enlarged hearts, *Vet Radiol Ultrasound* 46:122, 2005.
11. Lord P, Hansson K, Kvart C, et al: Rate of change of heart size before congestive heart failure in dogs with mitral regurgitation, *J Small Anim Pract* 51:210, 2010.
12. Woolley R, Smith P, Munro E, et al: Effects of treatment type on vertebral heart size in dogs with myxomatous mitral valve disease, *Int J Appl Res Vet Med* 5:43, 2007.
13. Lehmukhl L, Bonagura JD, Biller DS, et al: Radiographic evaluation of caudal vena cava size in dogs, *Vet Radiol Ultrasound* 38:94, 1997.
14. Moon ML, Keene BW, Lessard P, et al: Age related changes in the feline cardiac silhouette, *Vet Radiol Ultrasound* 34:315, 1993.
15. Thrall DE, Losonsky JM: A method for evaluating canine pulmonary circulatory dynamics from survey radiographs, *J Am Anim Hosp Assoc* 12:457, 1976.
16. Losonsky JM, Thrall DE, Lewis RE: Thoracic radiographic abnormalities in 200 dogs with spontaneous heartworm disease, *Vet Radiol* 24:120, 1983.
17. Atkins CE, DeFrancesco TC, Coats JR, et al: Heartworm infection in cats: 50 cases (1985–1997), *J Am Vet Med Assoc* 217:355, 1997.
18. Schafer M, Berry CR: Cardiac and pulmonary mensuration in feline heartworm disease, *Vet Radiol Ultrasound* 36:499, 1995.
19. Selcer BA, Newell SM, Mansour AE, et al: Radiographic and 2-D echocardiographic findings in 18 cats experimentally exposed to *D. immitis* via mosquito bites, *Vet Radiol Ultrasound* 37:37, 1997.
20. Venco L, Genchi C, Genchi M, et al: Clinical evolution and radiographic findings of feline heartworm infection in asymptomatic cats, *Vet Parasitol* 158:232, 2008.
21. DeFrancesco TC, Atkins CE, Miller MW, et al: Use of echocardiography for the diagnosis of heartworm disease in cats: 43 cases (1985–1997), *J Am Vet Med Assoc* 218:66, 2001.
22. Atkins CE, Arther RG, Ciszewski DK, et al: Echocardiographic quantification of *Dirofilaria immitis* in experimentally infected cats, *Vet Parasitol* 158:164, 2008.
23. Broaddus K, Tillson M: Patent ductus arteriosus in dogs, *Compend Contin Educ Vet* 32:E1, 2010.
24. Diana A, Guglielmini C, Pivetta M, et al: Radiographic features of cardiogenic pulmonary edema in dogs with mitral regurgitation: 61 cases (1998–2007), *J Am Vet Med Assoc* 235:1058, 2009.
25. Klein SC, Peterson ME: Canine hypoadrenocorticism: part I, *Can Vet J* 51:63, 2010.

ELECTRONIC RESOURCES

Evolve

Additional information related to the content in Chapter 32 can be found on the companion Evolve website at http://evolve.elsevier.com/Thrall/vetrad/

- Chapter Quiz

CHAPTER • 33

The Canine and Feline Lung

Donald E. Thrall

PULMONARY ANATOMY

Canine and feline lungs have identical lobation with four lobes of the right lung (the cranial, middle, caudal, and accessory lobes) and two lobes of the left lung (the cranial and caudal lobes). The left cranial lobe is characterized by two distinct segments, the cranial and caudal segments (Figs. 33-1 and 33-2). The location of the lung lobes in Figures 33-1 and 33-2 is approximate because there is considerable overlap of individual lobes in three-dimensional space, and accurate depiction of their exact location in a two-dimensional image is not possible.

The cranial and caudal segments of the left cranial lung lobe are not considered individual lobes because their bronchi are not primary branches from the left principal bronchus. Rather, the bronchi of the cranial and caudal segments are themselves branches from a common cranial lobe bronchus that arises from the left principal bronchus. This is different from the right side, where the right cranial and middle lobe bronchi each arise nearly directly from the right principal bronchus (Fig. 33-3). The segments of the left cranial lobe, although considered part of a single lobe, can behave as functionally separate compartments as conditions, such as pneumonia, neoplasia, or hemorrhage, can be localized within only one of the segments.

RADIOGRAPHIC APPEARANCE OF NORMAL LUNG

Interpreting thoracic radiographs for pulmonary disease is challenging. One reason for this is the excellent radiographic contrast that characterizes the lung; this allows numerous small pulmonary structures to be seen radiographically. The excellent radiographic contrast arises from the large volume of air in the lung.

The structure of the lung is also very heterogeneous, providing a complex background upon which changes created by disease occur. Although careful attention to technical detail is important when radiographing all body parts, the complexity of the thorax makes this even more critical. Additionally, there are a large number of patient factors that can influence the radiographic appearance of the lung. These were covered in detail in Chapter 25 and include (1) radiographic technique, encompassing exposure factors and type of acquisition hardware; (2) the effect of the position of the patient on the radiographic appearance of the thorax; (3) effects of recumbent-atelectasis and respiratory phase on radiographic appearance of the lung; and (4) the patient's habitus. These factors will not be discussed again here, but it is important that they be at the forefront of the thought process when thoracic radiographs are assessed, especially for pulmonary disease.

The structure of the lung is somewhat analogous to that of a sponge. There are numerous air spaces, the alveoli, distributed in a fine network throughout a supporting framework of interstitial connective tissue. The interstitium is the infrastructure for distribution of blood vessels, lymphatics, and bronchi throughout the lung. Vessels and bronchi situated near the hilus are relatively large compared with their size at the level of the alveoli. Thus, in a radiograph most opacity caused by normal structures will be created by x-ray absorption in medium to large vessels and bronchi, but the summed, or combined, absorption of x-rays by smaller, individually indistinguishable, vessels and bronchi also contributes to the normal background opacity of the lung. The end result of this is a heterogeneous network of opacities created by the numerous small airspaces, vessels, and bronchi within the framework of the lung (Fig. 33-4). The radiographic appearance of this normal heterogeneous lung will be affected by the factors discussed in Chapter 25, and mentioned again here, creating many opportunities for misinterpretation. Pulmonary disease will also alter this inherent opacity. Therefore, understanding the range of the normal radiographic appearance of lung, and how such is altered by the radiographic technique and patient variability, is critical to being able to detect and categorize lung disease accurately.

Understanding the range of normal cannot be learned by reading a book, although this is a good starting point. In reality, getting a grasp on normal radiographic appearances is a dynamic concept based on one's experience and the quality and frequency of feedback that is received. Therefore, enrolling one's professional associates in the radiographic interpretive process and retaining the services of a specialist to provide expertise in radiographic interpretation are important steps to improving one's own abilities.

In this chapter, only disease that results in obvious alteration in pulmonary opacity will be discussed. Radiologists themselves argue about the presence and/or significance of borderline pulmonary changes. The diagnosis of "interstitial disease consistent with the age of the patient" in old dogs is a perfect example. There is no doubt that ageing results in changes in the lungs of dogs that can be detected radiographically. A radiographic pattern consisting of pleural thickening and an increase in nonvascular linear pulmonary markings occurs regularly in older dogs without clinical evidence of pulmonary or cardiovascular disease. These dogs have foci of interstitial fibrosis, often associated with focal areas of emphysema.[1] However, sorting out real ageing changes from alterations in pulmonary opacity caused by technical factors or

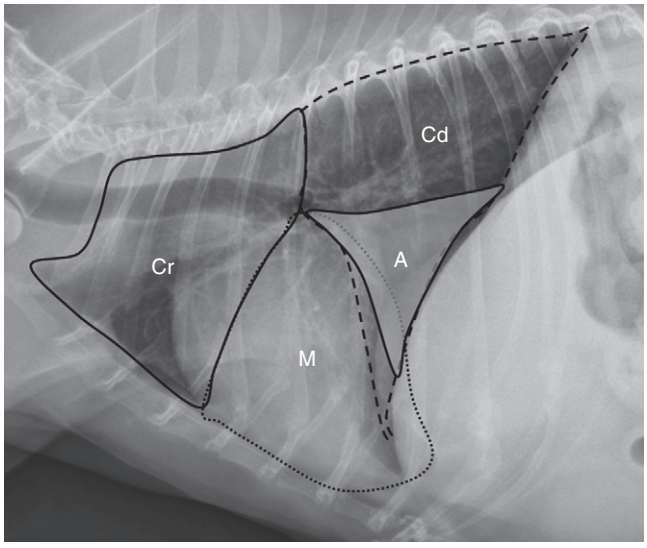


Fig. 33-1 Lateral canine thoracic radiograph where the approximate location of lung lobes is indicated. *A*, Accessory lobe; *Cd*, right and left caudal lobes; *Cr*, right cranial lobe and cranial segment of left cranial lobe; *M*, right middle lobe and caudal segment of left cranial lobe.

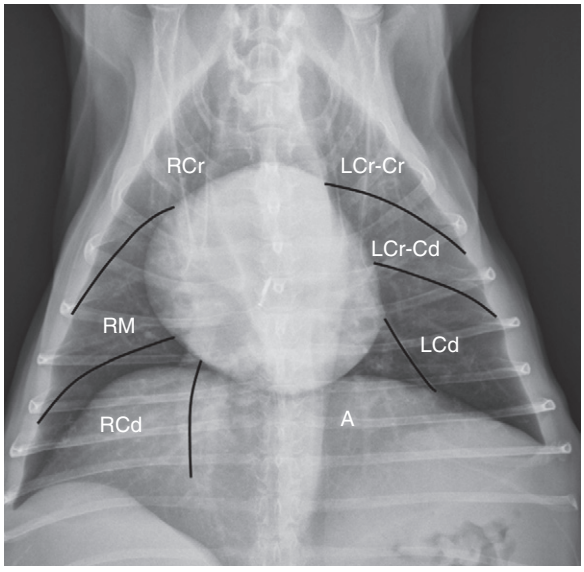


Fig. 33-2 Ventrodorsal canine thoracic radiograph where the approximate location of lung lobes is indicated. *A*, Accessory lobe; *LCd*, left caudal lobe; *LCr-Cd*, caudal segment of left cranial lobe; *LCr-Cr*, cranial segment of left cranial lobe; *RCd*, right caudal lobe; *RCr*, right cranial lobe; *RM*, right middle lobe.

patient variation is difficult, if not impossible, especially for nonspecialists. Therefore, only obvious examples of pulmonary disease are discussed herein. Fortunately, the influx of digital radiography into veterinary medicine facilitates obtaining a specialist opinion on borderline or questionable changes.

PARADIGMS FOR ASSESSING PULMONARY DISEASE

Pattern Recognition Paradigm

In the pattern recognition paradigm, the radiographic abnormalities in the lung are categorized in terms of whether they involve primarily the alveoli, the bronchi, or the interstitium.

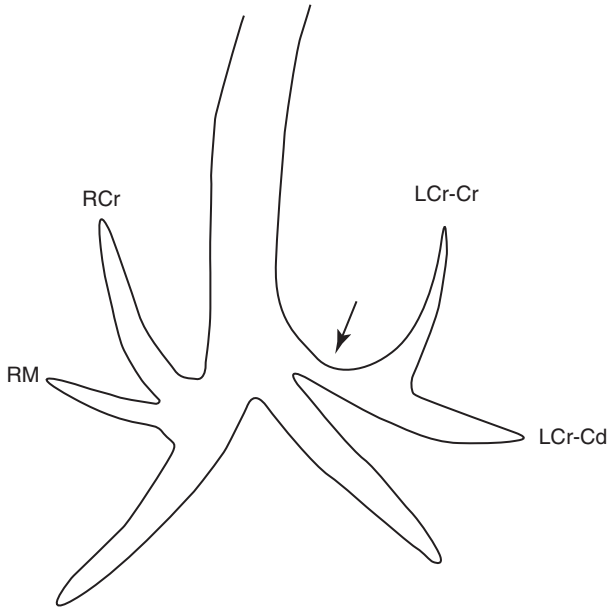


Fig. 33-3 Tracing of bronchial configuration from a series of thoracic computed tomography images. The bronchi for the right cranial *(RCr)* and right middle *(RM)* lobes arise essentially directly from the right principal bronchus, whereas the bronchi for the cranial segment of the left cranial lobe *(LCr-Cr)* and for the caudal segment of the left cranial lobe *(LCr-Cd)* arise from a short common left cranial lobar bronchus *(black arrow)*, which itself has arisen from the left principal bronchus.

A vascular pattern has also been proposed and could be included in a comprehensive discussion of pulmonary patterns, but in this book the vascular pattern is covered in Chapter 32 and not included here in the discussion of pulmonary patterns.

The pattern recognition paradigm has been in use for decades.[2-4] The intent is that focusing on the compartment of the lung that is abnormal—that is, the pattern—leads to an organized approach to image evaluation. Also, certain patterns are associated with certain diseases, and these associations streamline the formulation of differential diagnoses for a particular radiographic presentation. The association of a particular pattern or combination of patterns with a list of possibilities has been popularized under the heading of *the gamut approach*, where the gamut is the list of possibilities.[5] Of course, we all use the gamut approach regardless of whether we call it that specifically. The availability of a reference list of exclusions for a roentgen sign just increases the chance of considering all possible causes. If one has never heard of a disease, it cannot be diagnosed. In this chapter, tables of considerations are given for certain roentgen signs, but these are not intended to be comprehensive, because the emphasis is on major categories of disease seen commonly in private practice.

Some discussion of the word *infiltrate* is necessary when talking about lung patterns. *Infiltrate* is used occasionally to describe an abnormal pulmonary pattern when the specific cause is not known, which it rarely is. For example, one might conclude that there is an interstitial infiltrate in the left caudal lobe. Inherent in this usage, by some, is the implication that the disease is spreading through the organ without disturbing the normal architecture, but for others it simply means the presence of an abnormal substance in the lung. A few years ago a survey was performed where physician radiologists were asked to interpret the word *infiltrate* when used in a thoracic radiographic report and comment if the word was helpful in clinical management of patients.[6] Nearly 90% replied that

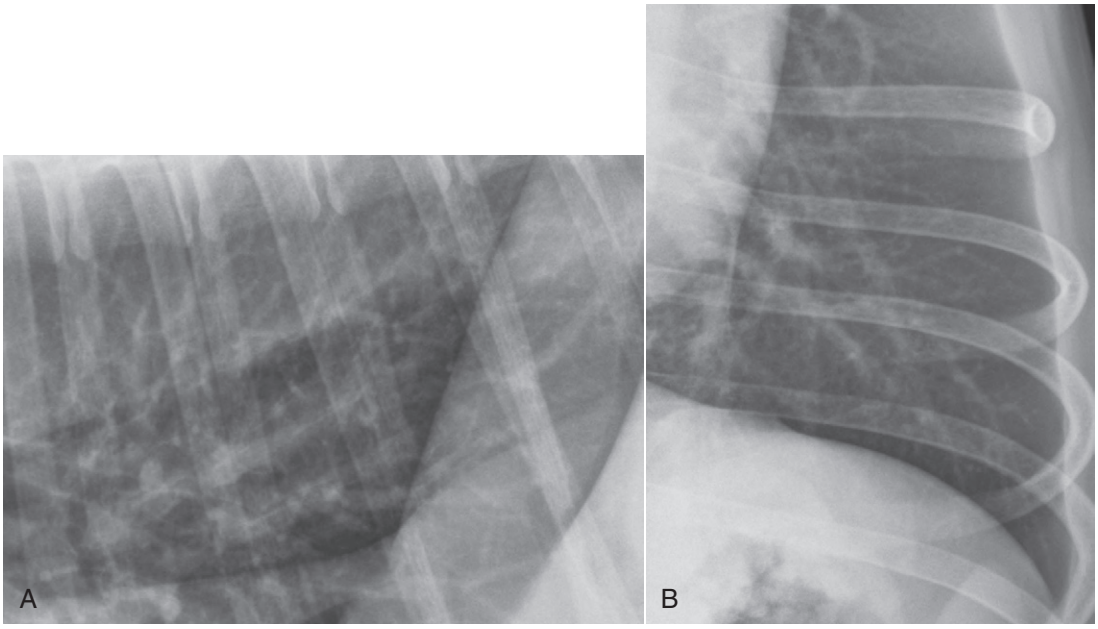


Fig. 33-4 Close-up views of the dorsocaudal **(A)** and left caudal **(B)** aspects of the lung from a normal dog illustrating the radiographic opacities created by the normal lung. Large vessels and some large airways are seen, but for the most part the pulmonary opacity is a summation of opacities created by overlapping of small vessels, small airways, and the interstitial tissue itself.

infiltrate implied more than one pathophysiologic condition, slightly more than half thought *infiltrate* could mean any of six or more different pathophysiologic conditions, and only about one third thought the term was helpful in patient care. Thus, the conclusion was that infiltrate was nonspecific and imprecise and did not usually enhance patient care. This report generated numerous responses from other radiologists, many of whom disagreed with the conclusions.[7,8] Even before the survey, the legitimacy of *infiltrate* as a radiologic descriptor had been questioned, and some had concluded that ". . . there just doesn't appear to be any better way of expressing the concept of extension or expansion without associated anatomic distortion than the word *infiltrate*."[9] So, in the discussion of lung patterns in this book, *infiltrate* is avoided whenever possible for the sake of reducing confusion. Almost always, the word *pattern* can be substituted. However, there are those certain circumstances, such as a tumor winding its way through the interstitium, where infiltrate seems to capture the process, and if *infiltrate* is used in this chapter, that concept is inherent.

Finally, the pattern recognition approach to pulmonary radiography is an oversimplification of reality. By binning pulmonary patterns into major categories, beginning interpreters usually have the opinion that only one pulmonary compartment is involved in the disease process. That is a misconception; most pulmonary diseases involve more than one anatomic compartment of the lung. The pulmonary pattern system is based on the premise that the pattern represents the pulmonary compartment that is most *conspicuously* affected, not the only compartment affected. Failure to realize that multiple pulmonary compartments are involved, regardless of the radiographic pattern, will lead to a misunderstanding of the underlying pathophysiology.

Alveolar Pattern

An alveolar pulmonary pattern is created when the air within the alveoli is replaced with a material having a higher physical density, thus increasing the radiographic opacity of lung. This does not apply to a mass growing in the interstitium that crowds or invades the adjacent lung, but to the presence of a nonsolid material in the alveoli that replaces the alveolar air. Common materials collecting in the alveoli to create an alveolar pattern are exudate, hemorrhage, and edema fluid. Much less commonly, a solid tissue, such as a neoplasm, can also replace the alveolar air and not efface the lung architecture. However, lung neoplasms usually result in mass formation rather than simply infiltrating the alveoli, and a neoplasm is a very rare cause of an alveolar pattern. Instances where a lung mass might have some features of an alveolar pattern are discussed in the section below dealing with structured interstitial patterns.

An alveolar pattern is characterized by one or more of the following radiographic features: (1) an air bronchogram, (2) a lobar sign, or (3) an area of relatively intense opacity that does not have the sharp margins that characterize a lung mass.

Air bronchograms are considered the hallmark sign of an alveolar pattern. The air bronchogram sign was named by Felson[10] but was first described in principle by Fleischner in 1948.[11] An *air bronchogram* is defined as an air-filled bronchus traversing a region of abnormal lung where alveolar air has been replaced by exudate, hemorrhage, or edema fluid. Critical requisites for air bronchogram visualization are (1) air within *bronchi* has *not* been replaced by cells or fluid, and (2) the extent of air replacement in the alveoli has been extensive enough to provide adequate background opacity—in other words, enough x-ray absorption—for the air-containing bronchi to be seen. Under these circumstances, the air-filled bronchi then appear radiolucent against the increased opacity of the abnormally opacified lung (Fig. 33-5). Typically, air bronchograms appear as a tubular radiolucent structure with occasional branching. But, if the air-filled bronchus is aligned with the primary x-ray beam such that it is struck end-on rather than side-on, it will appear as a circular radiolucency instead of being tubular (Fig. 33-6). The actual appearance of an air bronchogram in a radiograph depends on how much alveolar air has been replaced by fluid or cells; the extent of the distribution of the alveolar pattern; and, as already noted,

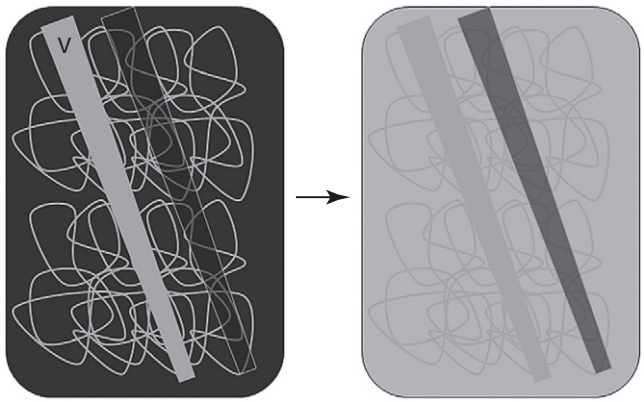


Fig. 33-5 Principle of formation of an air bronchogram. The *left panel* represents normal radiolucent lung with heterogeneous lacy background opacity. A pulmonary vessel *(V)* runs obliquely through the lung. To the right of the vessel is a bronchus. The vessel is highly conspicuous against the radiolucent lung background, whereas the bronchus is less conspicuous because its wall is thin, and its contents are the same as the content of the lung. The *right panel* represents a lung where alveolar air has been replaced with exudate, hemorrhage, or edema fluid. This increases the opacity of the lung and causes reduced conspicuity of the vessel and background lung markings because of border effacement. As long as the lumen of the bronchus remains air-filled, it will appear as a radiolucent region traversing the abnormal lung and will have increased conspicuity. The bronchial lumen is the air bronchogram.

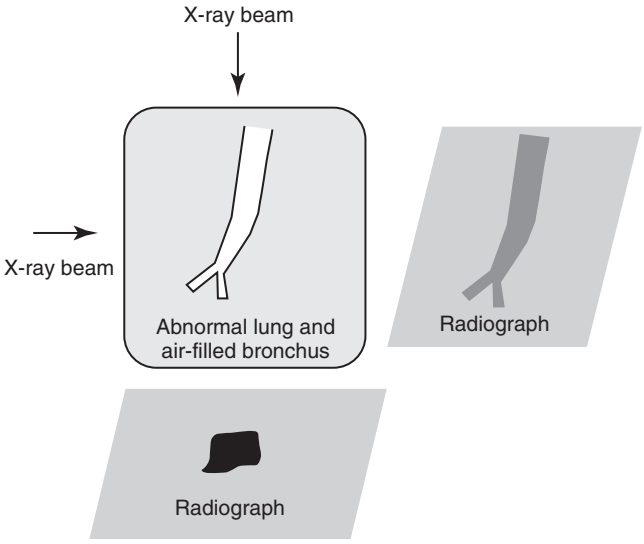


Fig. 33-6 The appearance of an air bronchogram depends on the relationship of the air-filled bronchus with the primary x-ray beam. If the x-ray beam strikes the bronchus perpendicularly, the air bronchogram will retain the basic shape of a bronchus. If the x-ray beam strikes the bronchus end-on, the bronchus will appear more as a circular radiolucency. Of course, because the bronchial tree branches in three dimensions, there will usually be a combination of side-on and end-on projections of air bronchograms in real life.

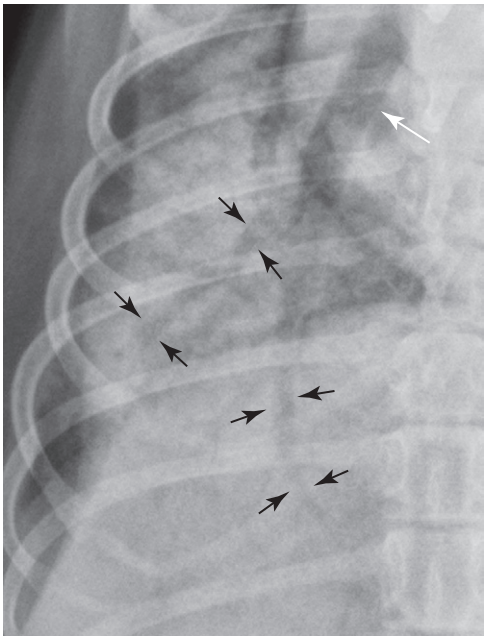


Fig. 33-7 Right caudal aspect of the thorax of a dog with an alveolar pattern. Numerous air bronchograms are visible throughout the right caudal lung lobe *(black arrows)*; not all air bronchograms have been designated with arrows. Care must be exercised in interpreting normal large bronchi as air bronchograms, especially when they are superimposed over the heart *(white arrow)*. The wall of these large bronchi is sufficiently thick that it can be conspicuous radiographically, especially when the large bronchus is contrasted against an opaque structure such as the heart.

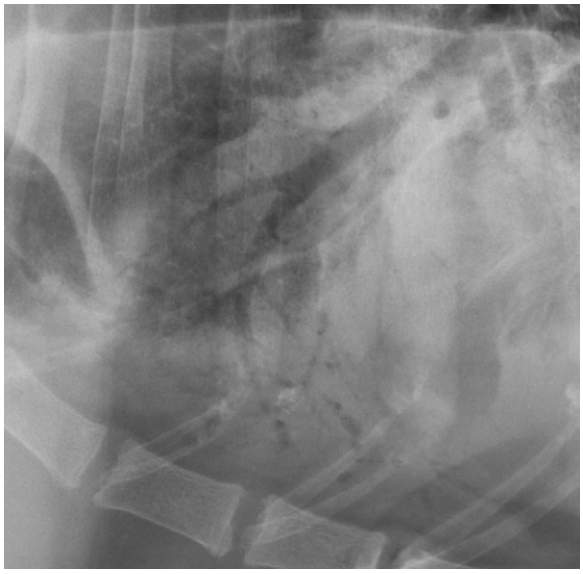


Fig. 33-8 Cranioventral aspect of the thorax of a dog with an alveolar pattern. Numerous air bronchograms are visible throughout the region of increased lung opacity.

the geometric relationship of the air-filled bronchus with the primary x-ray beam (Figs. 33-7 through 33-9). Air bronchograms are particularly valuable for diagnosing an alveolar pattern in instances where the absolute intensity of the alveolar disease is borderline, making the opacity change itself difficult to recognize if the bronchial lumen conspicuity was not increased (Fig. 33-10).

The radiographic appearance of an air bronchogram is relatively standard, and they are easy to recognize, as long as the underlying principles are understood. A common mistake is to interpret the radiolucent region between a pulmonary artery–vein pair as an air bronchogram (Fig. 33-11; see Fig. 33-10). The well-defined margin of the increased opacity next to the bronchial lumen in the instance of a bronchus being positioned between two vessels is not typical of the more diffuse nature of the increased opacity created by an alveolar pattern that surrounds a bronchus and creates an air bronchogram.

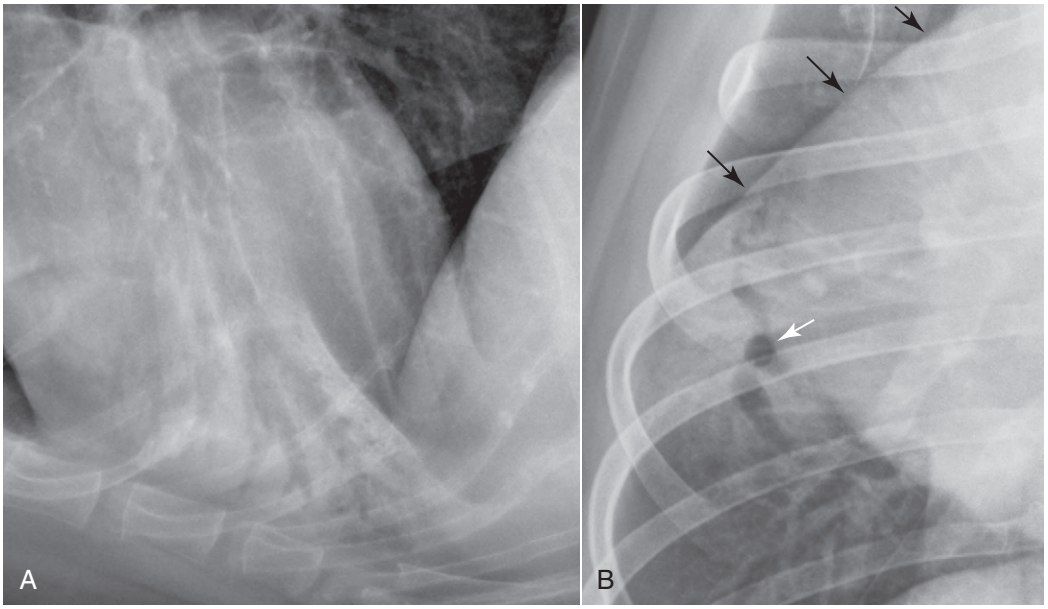


Fig. 33-9 Ventral **(A)** and right middle **(B)** regions of the thorax of a dog with an alveolar pattern. Numerous air bronchograms are seen throughout the increased lung opacity. In **A,** the branches of the air bronchogram are more crowded than normal because the lobe is partially collapsed. In **B,** note how the increased opacity of the lung has caused border effacement, or silhouetting, of the right aspect of the cardiac silhouette. Border effacement of the heart is a common finding with an intense alveolar pattern when the abnormal lung and heart are in contact. The junction between the opacified right middle lobe and the normally aerated left cranial lobe creates a distinct transition, termed a *lobar sign (black arrows)*. Also in **B,** an air bronchogram is struck end-on by the x-ray beam, creating a conspicuous circular radiolucency *(white arrow)*.

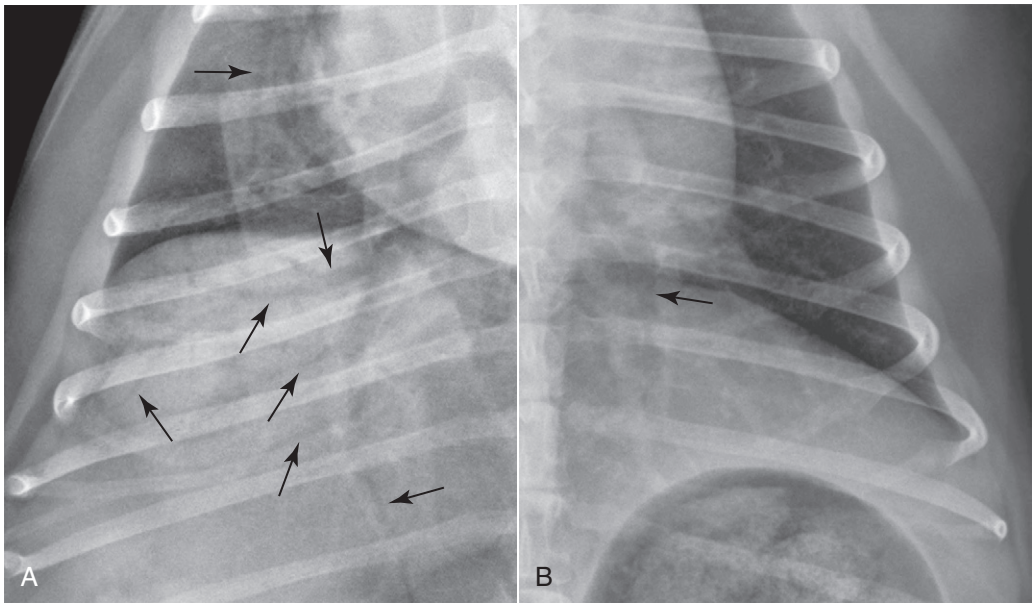


Fig. 33-10 Close-up views of the right caudal **(A)** and left caudal **(B)** aspect of the thorax of a dog with a mild alveolar pattern in the right caudal lobe. This is a minor change, and the slight increase in lung opacity might not be detected by all observers. However, numerous air bronchograms are visible in the right caudal lobe (*black arrows* in **A**), and these are the key to making the diagnosis of an alveolar pattern. Air bronchograms are not seen in **B**. The linear radiolucency in **B** *(black arrow)* is normal lung between the left caudal lobe pulmonary artery and vein. Confusing normal lung between two large vessels as an air bronchogram is a common mistake that is discussed in the text and illustrated again in Fig. 33-11.

A *lobar sign* refers to the sharp margin created when a lobe with increased opacity abuts a normally aerated lobe that has less opacity (Fig. 33-12; see Fig. 33-9, *B*). Usually, a lobar sign is observed when a lobe having increased opacity caused by alveolar air being replaced with fluid, exudate, or hemorrhage abuts a normally aerated lobe. Occasionally, a lung mass will extend to the periphery of a lobe, and this too can create a lobar sign with the adjacent normal lobe, although in this instance, the shape of the lobar sign will be altered by the mass and appear differently, more round for example,

compared with the expected shape of a normal, slightly curving, interlobar junction. To correctly identify a lobar sign, it is necessary to know normal lung lobe anatomy and where lung borders are located. If a lobar sign is seen in one view, it may not be detected in the orthogonal view because for the lobar sign to be visible the junction between the affected lobe and the adjacent normal lobe must be struck tangentially (i.e., in a parallel fashion) by the x-ray beam (Fig. 33-13). If the junction is struck at an angle, the lobar sign will not be seen. A lobar sign can be the only indicator of an alveolar pattern, especially if the extent of the disease is limited (Fig. 33-14).

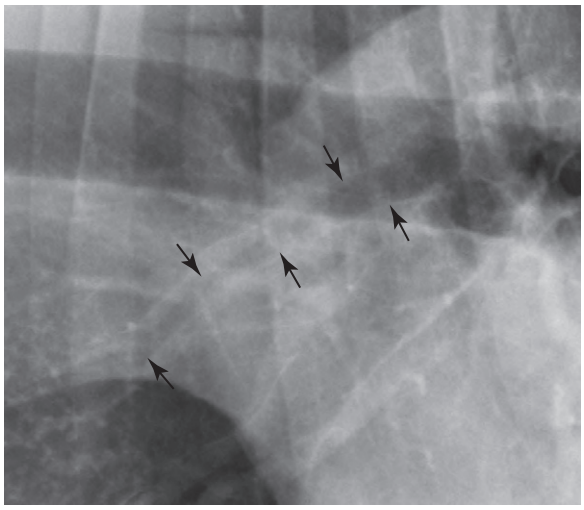


Fig. 33-11 In this portion of a lateral canine thoracic radiograph, the radiolucent region between two pulmonary vessels *(black arrows)* could be misinterpreted as an air bronchogram. However, the characteristics of this radiolucent region are not consistent with an air bronchogram because the opaque margins on each side of the radiolucent region are too well defined to represent lung disease. This radiolucent region is a bronchial lumen, but it is a normal bronchus between two pulmonary vessels, not an air bronchogram.

Although air bronchograms and lobar signs are common indications of an alveolar pattern, sometimes neither will be seen. Air bronchograms may not be seen if the alveolar disease is not concentrated adequately around a bronchus for the bronchial lumen to become visible. This might occur if sufficient contrasting alveolar material is not present or the disease has also resulted in air displacement from the bronchi. A lobar sign will not be seen if the alveolar disease does not extend to the periphery of a lobe, if adjoining lobes are both affected to the same extent, or if the lobe junction is not struck parallel by the x-ray beam. Unfortunately, these scenarios are common, and in many animals with an alveolar pattern, neither an air bronchogram nor a lobar sign will be present. In these patients, the diagnosis of an alveolar pattern is based on the finding of a region of lung opacification that is too intense per unit area to be caused by disease confined to the bronchial tree or unstructured disease confined to the interstitium. At the same time, this region of intense lung disease does not have the sharp margins expected of a lung mass. Thus, an alveolar pattern is sometimes diagnosed by exclusion (i.e., the lung disease is too intense to be caused by a bronchial or unstructured interstitial pattern), and it also does not have the margin characteristics of a lung mass (Figs. 33-15 and 33-16).

As noted before, an alveolar pattern results from the presence of cells or fluid in the alveolar spaces. Common causes of an alveolar pattern and generalizations for the distribution of the disease within the lungs are given in Table 33-1.

The association between atelectasis and an alveolar pattern deserves special mention. Up to this point the discussion of an alveolar pattern has focused on conditions where alveolar air is replaced by another substance. However, alveolar air can be diminished simply by the lung becoming collapsed, either from extrinsic compression, bronchial obstruction, or reduced

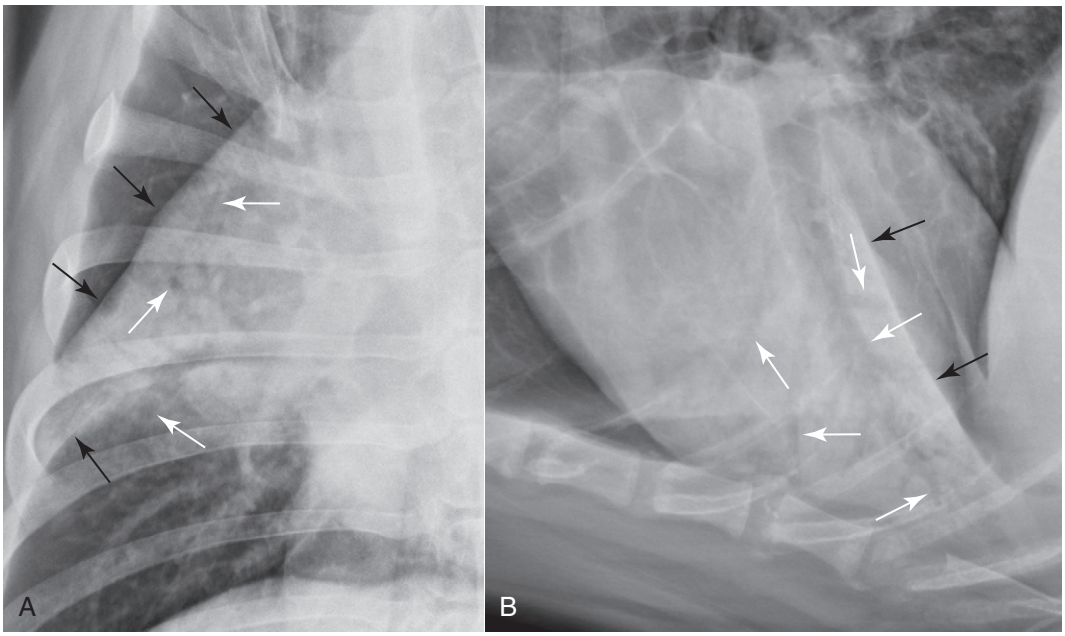


Fig. 33-12 Lateral **(A)** and VD radiographs of a dog with right middle lobe pneumonia. The intense opacification of the affected right middle lobe abutting the adjacent, aerated, unaffected lung has created a sharp opacity interface *(black arrows)*, termed the *lobar sign*. Multiple air bronchograms are visible in **A** and **B** *(white arrows)*.

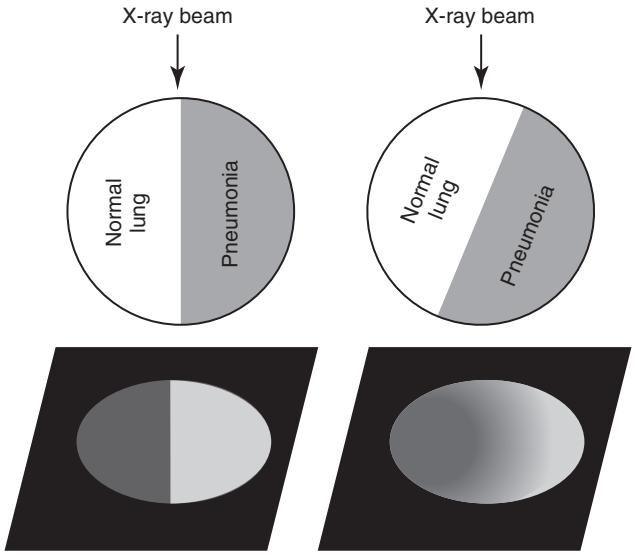


Fig. 33-13 A lobar sign will be seen only if the x-ray beam strikes the boundary between the normal and abnormal lobes in a parallel fashion, such as in the *left panel* of this figure. If the junction of the normal and abnormal lobes is struck obliquely by the primary x-ray beam, the lobar sign will not be seen, such as in the *right panel* of this figure. Note in the *right panel* that although the lobar sign is not seen, the abnormal lung will still cause a region of increased opacity in the radiograph, and air bronchograms may be seen in this region.

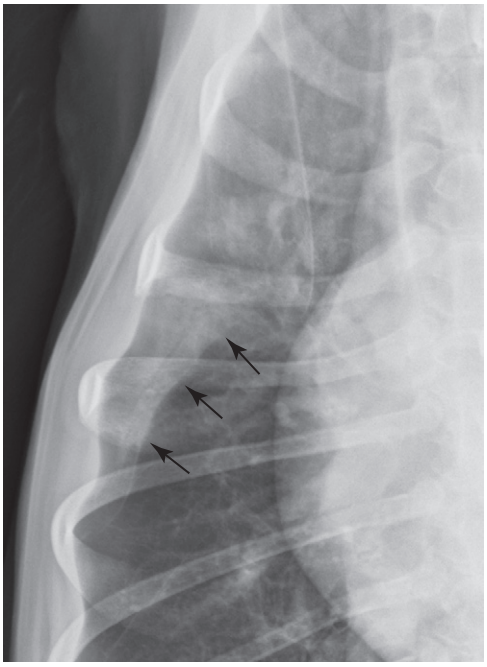


Fig. 33-14 Ventrodorsal radiograph of a dog with pneumonia in the ventral aspect of the right cranial lobe. The junction of the pneumonic right cranial lobe with the normal right middle lobe has created a lobar sign *(black arrows)*. Once the lobar sign is detected, then the subtle increase in opacity in the right cranial lobe becomes easier to see. There are no obvious air bronchograms in the right cranial lobe, and the pneumonia was barely perceptible in the lateral view and could have been overlooked easily in this dog if the lobar sign had not been present.

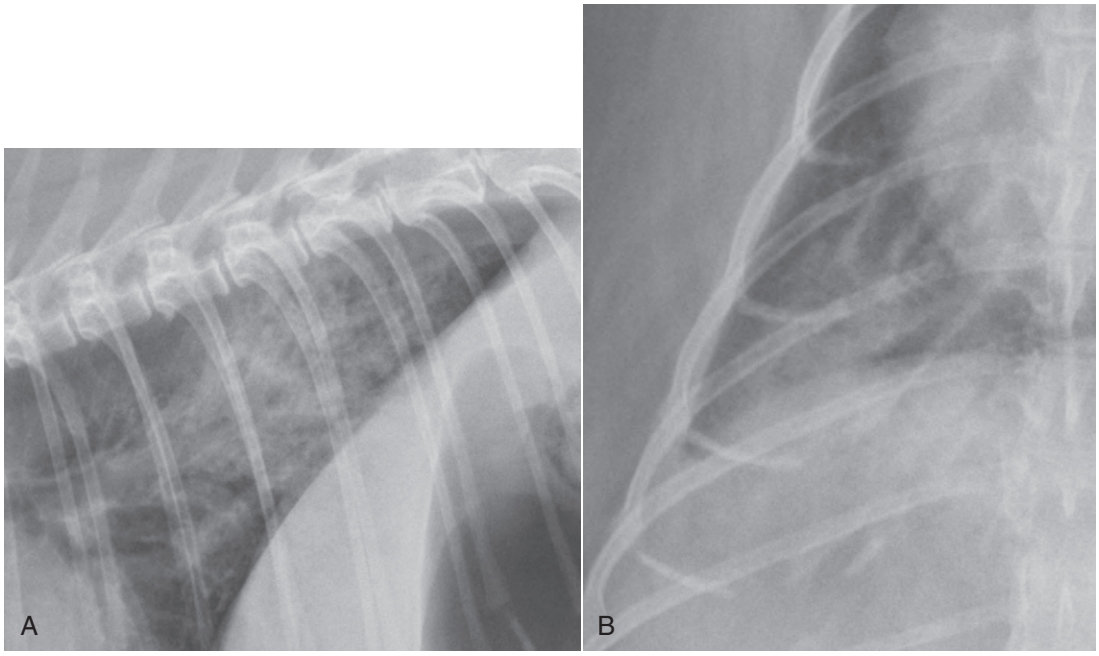


Fig. 33-15 Lateral **(A)** and VD **(B)** radiographs of a cat with pneumonia caused by *Pasteurella* species. There is intense opacification in the right caudal lung lobe. There is not a lobar sign associated with this opacity and, although it contains regions of air, conspicuous air bronchograms are not present. The intensity of this opacity on a unit area basis is too great for it to be caused by bronchial or peribronchial disease or an infiltrate into the interstitium (unstructured interstitial disease), and there are no defined margins that would be expected if this lesion were caused by a lung mass. Thus, the most reasonable conclusion is that this is an alveolar pattern.

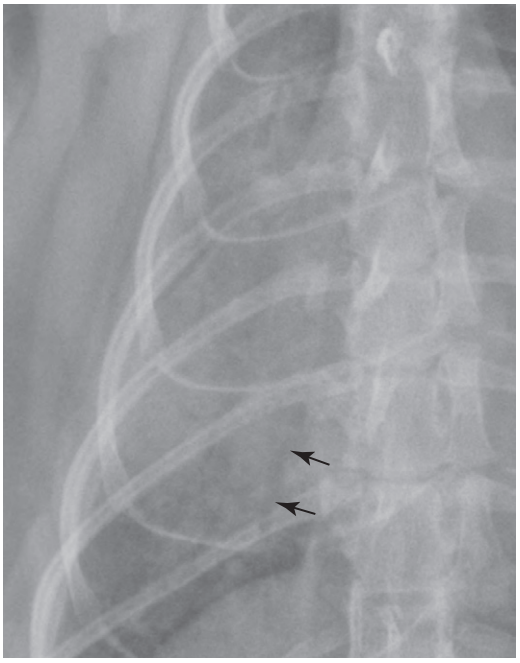


Fig. 33-16 Ventrodorsal radiograph of a cat with cardiogenic pulmonary edema. There is a region of relatively intense lung opacification in the right middle lobe. As in Figure 33-14, this is too intense to be an unstructured interstitial pattern or a bronchial pattern, and there are no sharp margins to this lesion to suggest that it is caused by a lung mass. There are some regions of air within the lesion but no obvious air bronchograms. A faint linear radiolucency *(black arrows)* is a bronchus, but this is the bronchus between the right caudal lobar artery and vein and is visible because of the contrast provided by the vessels, not necessarily because of the lung disease. The lung disease has caused border effacement of the right aspect of the cardiac silhouette. The most reasonable conclusion is that the lesion is an alveolar pattern, but this is not based in either the presence of air bronchograms or a lobar sign.

Table • **33-1**

Causes of an Alveolar Pattern

CAUSE	DISTRIBUTION*	PREVALENCE
Pneumonia	Ventral	Common
Cardiogenic pulmonary edema	Variable	Common
Noncardiogenic pulmonary edema	Dorsocaudal	Less common
Hemorrhage		
Trauma	Variable	Common
Coagulopathy	Variable	Less common
Thromboembolism	Variable	Less common
Atelectasis	Variable	Common
Allergy (eosinophilic)	Variable	Rare
Primary lung tumor	Variable	Rare

*The disease distributions noted in this table are generalizations, and the specific distribution of any disease leading to an alveolar pattern is variable.

ventilation. These situations will also result in an increase in lung opacity and, if the atelectasis is severe enough, the visualization of an alveolar pattern. A key component of atelectasis is a mediastinal shift. Therefore, finding mediastinal displacement toward the direction of an alveolar pattern is

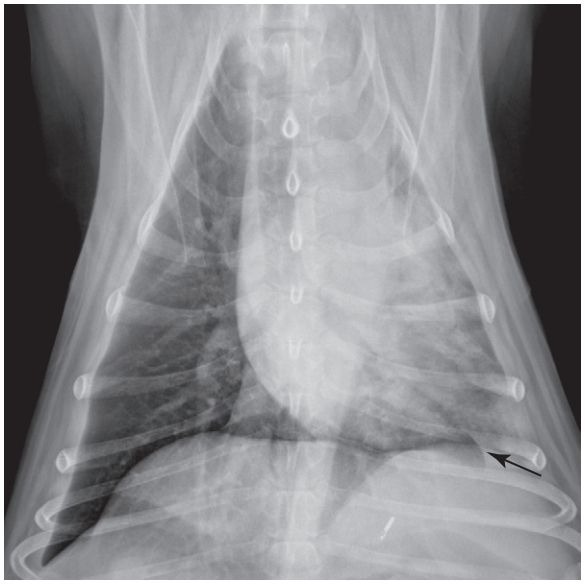


Fig. 33-17 Ventrodorsal radiograph of a dog that developed acute tetraparesis. There is intense opacification of the left lung and a mediastinal shift to the left. The intense opacification without evidence of a lung mass indicates that this is an alveolar pattern, even though neither an air bronchogram nor a lobar sign is seen. Evidence for the mediastinal shift is the leftward position of the heart and also the leftward displacement of the caudoventral mediastinal reflection *(black arrow)*. Radiographically, it is impossible to determine whether the increased lung opacity on the left is because of atelectasis alone or if there is underlying lung disease in addition to the atelectasis. However, in consideration of the history, prolonged recumbency leading to atelectasis is not an unreasonable consideration. This dog was determined subsequently to have no evidence of lung disease.

evidence that at least a portion of the alveolar pattern results from atelectasis. The determination whether all of the pulmonary opacification is caused by atelectasis alone or a combination of atelectasis and alveolar disease cannot be made from radiographs. Occasionally, the clinical history will be helpful in making this distinction, but lung sampling may be necessary to obtain the definitive answer (Figs. 33-17 and 33-18).

Bronchial Pattern

A bronchial pattern occurs when the bronchial wall thickness is increased by cellular or fluid infiltration or when air in the immediate peribronchial space has been replaced with cells or fluid. The peribronchial space is actually a component of the interstitium, but a bronchial pattern is usually interpreted to mean that airway disease is present. This is an example of how the pattern recognition system can be misleading, with there being a contradiction between the radiographic pattern and pulmonary compartment involved.

The increased radiographic opacity associated with the increased fluid content or cellularity in or around the bronchus results in increased radiographic conspicuity of the bronchial tree. Radiographically, this manifests as an increased number of *ring shadows*, created by an end-on relationship between the abnormal bronchus and the primary x-ray beam, or an increased number of parallel lines, called *tram lines* by some, created by a side-on relationship between the abnormal bronchus and the primary x-ray beam (Fig. 33-19). Important in the identification of a bronchial pattern is the understanding that the number of ring shadows and tram lines is increased over the normal allotment. A few ring shadows and tram lines can be seen in every normal radiograph because of some normal airways being projected directly end-on or side-on. In a bronchial pattern, the overall number of ring shadows and trams lines will be increased above normal, and they will

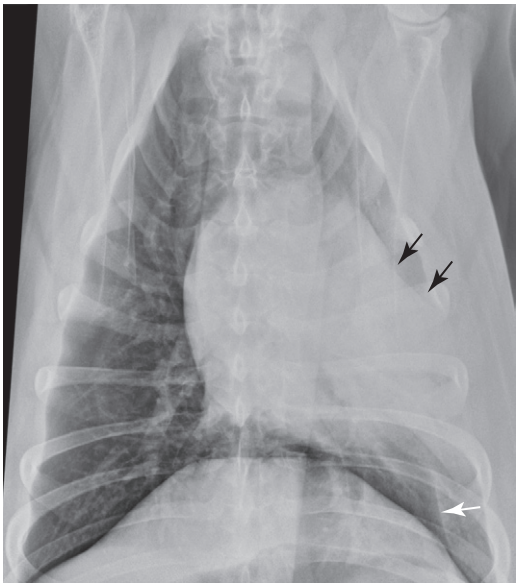


Fig. 33-18 Radiograph of a dog with sinus tachycardia and retching. There is intense opacification of the caudal segment of the left cranial lobe, mild to moderate increased opacity of the cranial segment of the left cranial lobe and the left caudal lobe, and a mediastinal shift to the left. There is a lobar sign *(black arrows)* and no mass effect; thus this is an alveolar pattern in the left lung. Evidence for the mediastinal shift is the leftward displacement of the heart and also the leftward displacement of the caudoventral mediastinal reflection *(white arrow)*. Radiographically, it is impossible to determine whether the increased lung opacity on the left is because of atelectasis alone or if there is underlying disease in addition to the atelectasis. However, in consideration of the history of retching with no obvious other reason for atelectasis to develop, pneumonia should be considered. This dog was determined subsequently to have pneumonia; thus the atelectasis was secondary to that condition, as might occur with exudative airway plugging.

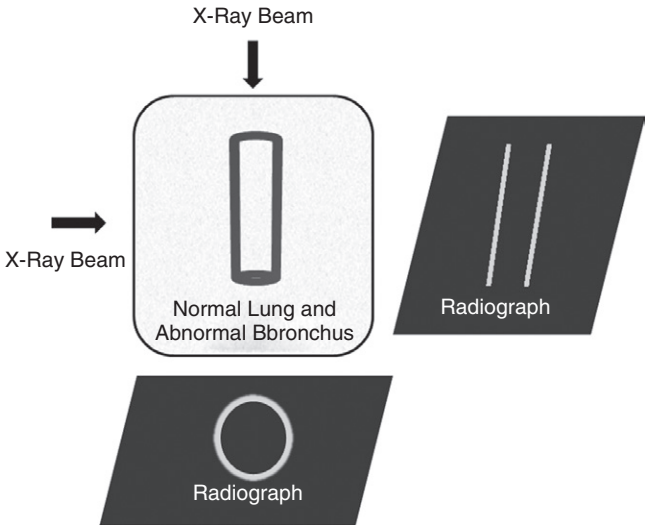


Fig. 33-19 The appearance of an abnormal bronchus in a radiograph depends on its orientation with respect to the primary x-ray beam. If the bronchus is struck end-on, the abnormal bronchial walls create a circular opacity, termed a *ring shadow*. If the bronchus is struck side-on, the abnormal bronchial walls create parallel lines, termed *tram lines*.

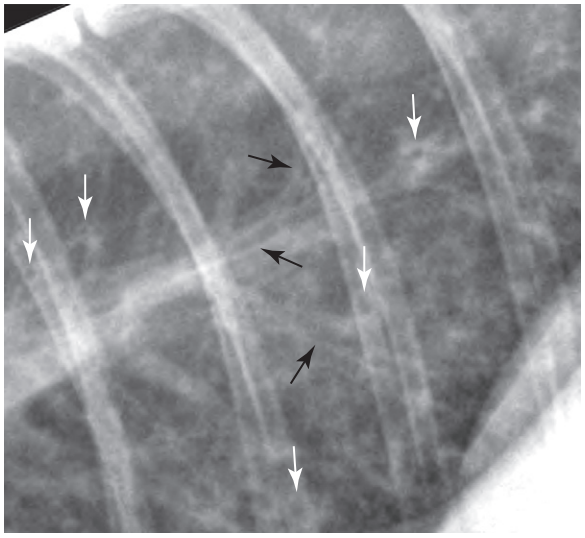


Fig. 33-20 Lateral radiograph of a cat with a mild to moderate bronchial pattern. There are numerous ring shadows *(white arrows)* and tram lines *(black arrows)*. The entire lung is abnormal, and only the most obvious ring shadows and tram lines have been pointed out.

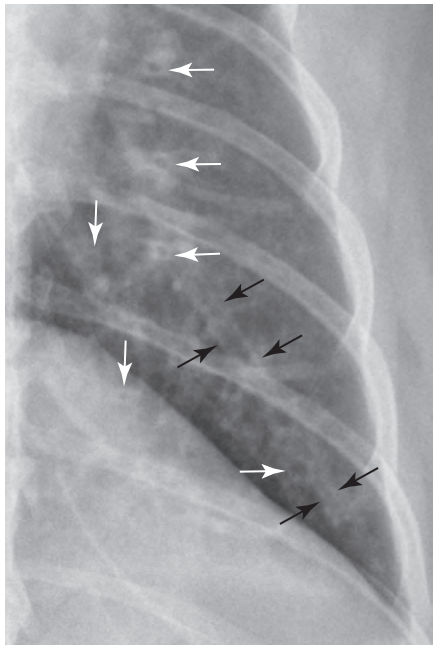


Fig. 33-21 Ventrodorsal radiograph of a cat with a moderate to pronounced bronchial pattern. There are numerous ring shadows *(white arrows)* and tram lines *(black arrows)*. The entire lung is abnormal, and only the most obvious ring shadows and tram lines have been pointed out.

usually also have a thickened wall because of the cellular or fluid infiltration (Figs. 33-20 through 33-23).

A bronchial pattern is usually related to bronchial inflammation, but peribronchial edema can also be a cause (Table 33-2). There are numerous consequences related to chronic bronchial disease that have radiographic manifestations. These include lobar collapse, bronchiectasis, spontaneous rib fractures, pulmonary hyperinflation, and bronchial mineralization.

Lobar collapse following chronic bronchial obstruction is observed most commonly in asthmatic cats, and the right middle lobe is affected most often. Chronic bronchial inflammation can lead to excess endobronchial exudate or mucus,

and if this material results in bronchial obstruction, lobar atelectasis will result from reabsorption of air trapped distal to the obstructed bronchus. Right middle lobe collapse in asthmatic cats is not common,[12] but it does occur at a high enough frequency that the salient radiographic features should be recognized to prevent misdiagnosis. The collapsed right middle lobe will appear as a homogeneous opacity, often triangular (Fig. 33-24). The collapsed lobe can be quite small and become contracted against the hilus. As expected from knowledge about the effects of positional atelectasis, collapse of the right middle lobe will be more conspicuous in the left lateral view than in the right lateral view.

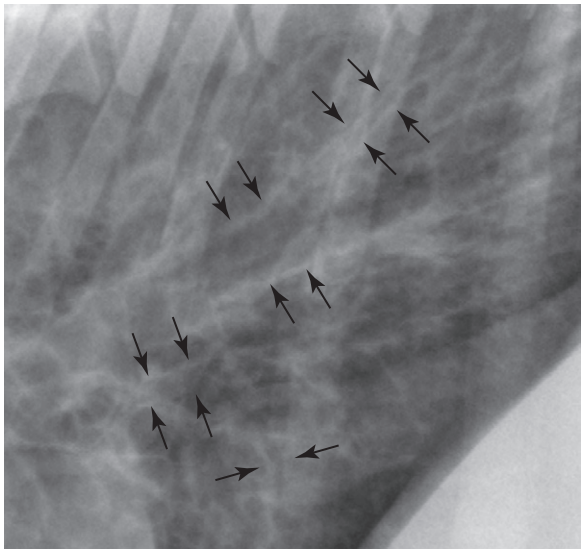


Fig. 33-22 Lateral radiograph of a dog with a mild to moderate bronchial pattern. In this dog, the most conspicuous evidence of abnormal airways relates to the large number of tram lines *(black arrows)*.

Bronchiectasis, which is abnormal permanent dilation of bronchi, has multiple risk factors that include chronic infection, mucociliary disorder, obstruction, and ageing.[13] Certain breeds appear to be predisposed, but affected dogs may survive for years.[14] In dogs, a link between tracheal collapse and bronchiectasis has been suggested, which may relate to an inherent structural cartilage disorder.[15] Radiographic features of bronchiectasis are (1) increased bronchial diameter, (2) failure of bronchi to taper, (3) nonlinear nature of bronchial wall, and (4) abnormally thickened bronchial wall if there is concurrent bronchitis (Figs. 33-25 through 33-27).

Cats with diseases that cause prolonged respiratory effort or coughing, metabolic diseases, or certain neoplasms are at increased risk of spontaneous nontraumatic rib fractures.[16] In the population of cats evaluated for spontaneous rib fracture, the majority had respiratory disease, and the remaining cats had chronic renal disease or tumors such as myeloma.[16] Mechanical failure secondary to chronic dyspnea or coughing is a likely cause of these spontaneous rib fractures in cats with respiratory disease. As the fractures are more common in older cats, osteopenia that weakens the structural integrity of the

Table • **33-2**

Causes of a Bronchial Pattern

CAUSE	PREVALENCE
Allergic airway disease	Common
Infection	
Bacterial	Less common
Parasitic	Rare
Chronic irritation	Less common
Cardiogenic pulmonary edema	Less common
Diffuse tumor	Rare

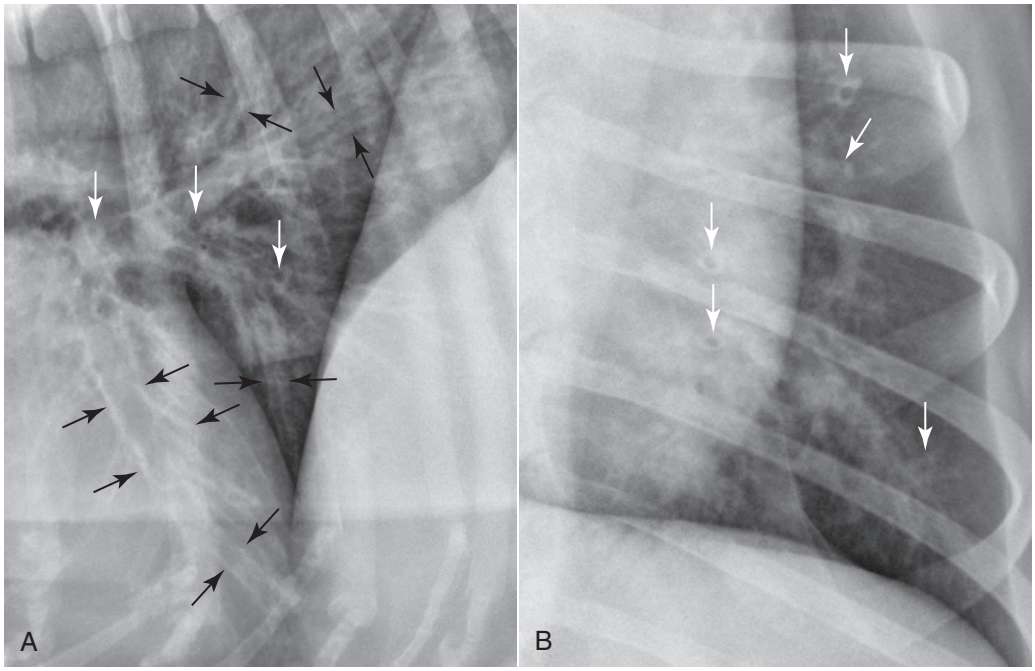


Fig. 33-23 Lateral **(A)** and VD **(B)** radiographs of a dog with a pronounced bronchial pattern. The numerous ring shadows *(white arrows)* and tram lines *(black arrows)* are evidence for the abnormal lung pattern being bronchial.

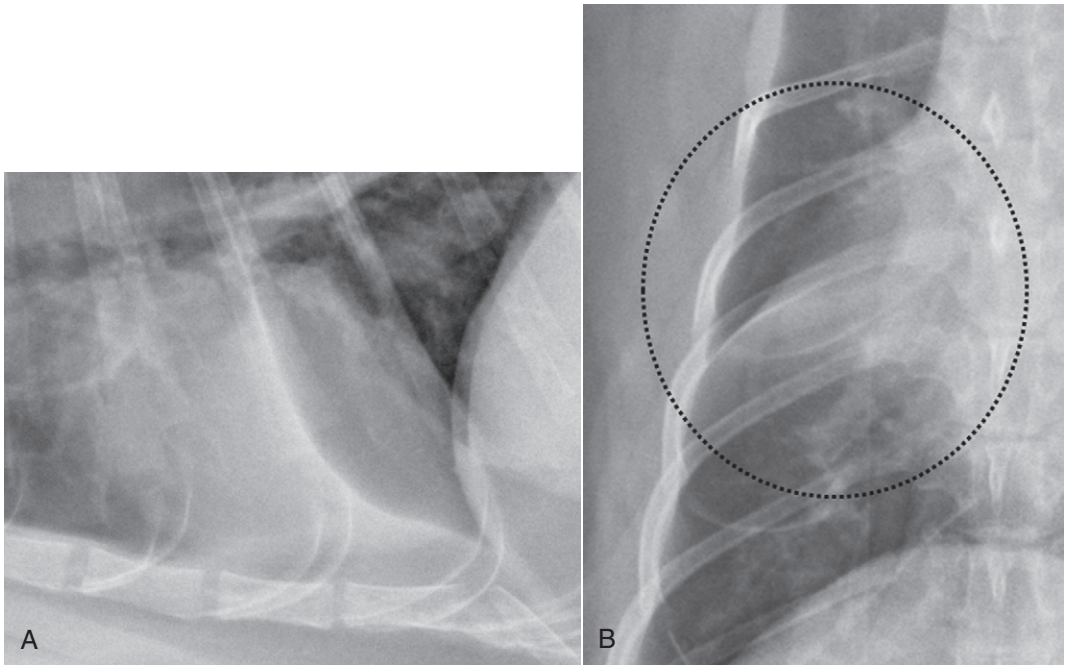


Fig. 33-24 Left lateral **(A)** and VD **(B)** radiographs of an asthmatic cat with collapse of the right middle lobe secondary to bronchial obstruction. In **A,** the collapsed lobe is not very conspicuous because it is superimposed on the heart. The radiopaque line superimposed on the heart is a lobar sign, demarcating the region of contact between the collapsed right middle lobe and the aerated right caudal lobe. The collapsed right middle lobe was not visible in the right lateral view because of the recumbent atelectasis that developed in the right lung, with resultant border effacement of the abnormal right middle lobe. In **B,** the collapsed lung appears as an ill-defined region of increased opacity lateral to the heart *(encircled)*. The collapsed lung has caused border effacement of the adjacent cardiac silhouette. Distinct lobar signs are not seen in **B** because the lobar interfaces are not perfectly parallel to the oncoming x-ray beam.

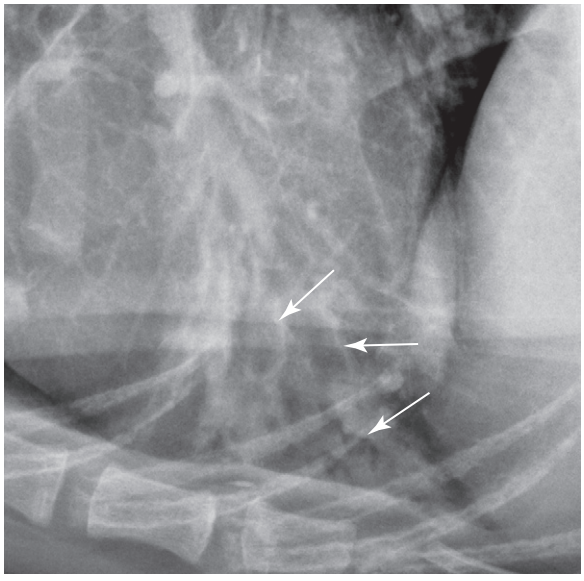


Fig. 33-25 Lateral radiograph of a dog with bronchiectasis in the ventral aspect of the right middle lobe. Bronchi in this region are larger than normal *(white arrows)*, and the bronchial walls appear saccular, especially the most distal one. These bronchi are visible because they contain air and traverse a region of pneumonic lung, that is, air bronchogram.

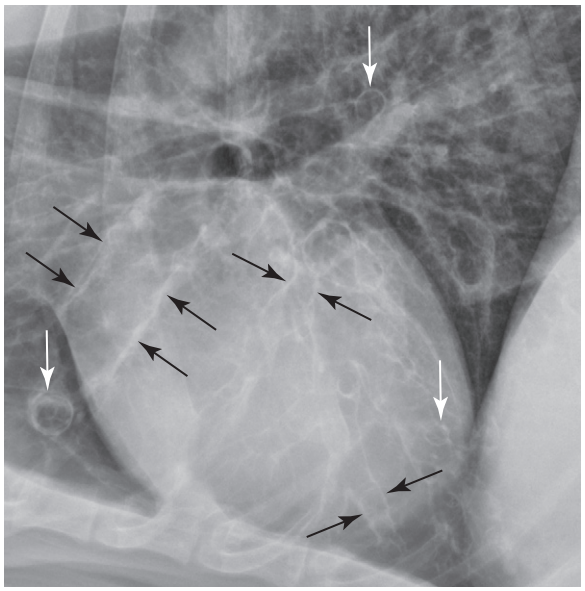


Fig. 33-26 Lateral radiograph of a dog with advanced bronchiectasis. There are numerous dilated ring shadows *(white arrows)* and wide tram lines *(black arrows)*. The bronchial walls themselves are not abnormally thickened. This suggests that if the bronchiectasis resulted from airway infection, the infection is resolved, but the bronchial wall dilation is irreversible. Alternatively, the bronchiectasis in this dog may be caused by bronchomalacia.

ribs may also play a role. The most commonly affected ribs are located caudally, involving the midportion of the ninth to thirteenth ribs.[16] The importance of recognizing this syndrome is to avoid implicating external injury as a cause of rib fracture in all cats (Fig. 33-28).

Pulmonary hyperinflation can develop secondary to chronic airway disease, especially in cats.[17] This likely results from air trapping caused by bronchial lumen narrowing from spasm, inflammation, or fibrosis. The radiographic diagnosis of pulmonary hyperinflation is subjective, and early hyperinflation may be overlooked. When more advanced, the hyperinflated lung pushes the diaphragm caudally creating a flattened appearance to the diaphragm and an increase in space between the heart and dome of the diaphragm. Tension of the caudally displaced diaphragm against its costal attachments may also create the appearance of so-called *tenting* of the diaphragm in the ventrodorsal (VD) or dorsoventral (DV) view (Fig. 33-29). The hyperinflated lung may also appear larger and more radiolucent, but these subjective changes are less accurate than evaluating the cardiac-diaphragm distance or the finding of diaphragmatic tenting.

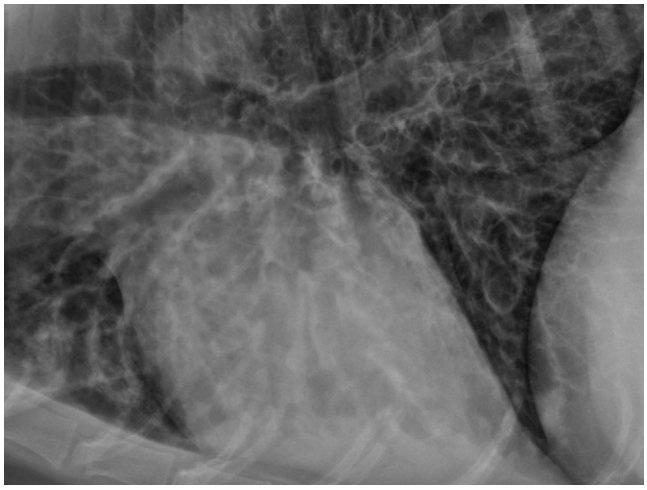


Fig. 33-27 Lateral thoracic radiograph of a dog with severe generalized bronchiectasis and ventral pneumonia. The opacity of the lung is increased in the ventral aspect of the thorax, superimposed on the heart, and there are multiple air bronchograms. The lumina of visible bronchi are dilated and somewhat saccular. In the dorsocaudal aspect of the lung there is no alveolar disease, but the lumina of multiple bronchi are markedly dilated, indicative of bronchiectasis.

Chronic bronchitis can lead to bronchial mineralization, either because of dystrophic mineralization of the bronchial wall or mineralization of endobronchial plugs.[18] If the mineralization involves the bronchial wall, a radiolucent center may be visible within the mineralized lesion, whereas if the mineralization is within an endobronchial plug, no such radiolucent center will be seen. Bronchial mineralization secondary to chronic bronchitis is most likely to be found in cats, and there will usually be coexisting signs of a typical bronchial pattern as described before (Fig. 33-30). Bronchial mineralization is not common in animals with inflammatory lung disease, but it is important to recognize it so that it is not misinterpreted as another lesion.

Another scenario where bronchial mineralization can be observed is in dogs with hyperadrenocorticism.[19] In this instance, the mineralization is more likely to be distributed uniformly throughout the lung, and the thickness of the affected bronchi will usually be normal (Fig. 33-31).

Interstitial Pattern

Understanding the interstitial lung pattern is facilitated by dividing it into *structured* and *unstructured* forms. There are interstitial pattern classification systems that are more detailed with more categories, but these more highly detailed classifications have no proven advantage.

Structured Interstitial Pattern. The *structured interstitial pattern* refers to nodular or mass lesions in the lung. The identification of nodules or masses in the lung is not difficult in many patients, but there are some situations where this assessment is not straightforward. When considering the presence of a lung nodule or mass, it is extremely important to keep in mind the (1) effect of left versus right lateral recumbency on the conspicuity of lung lesions and (2) effect of superimposed

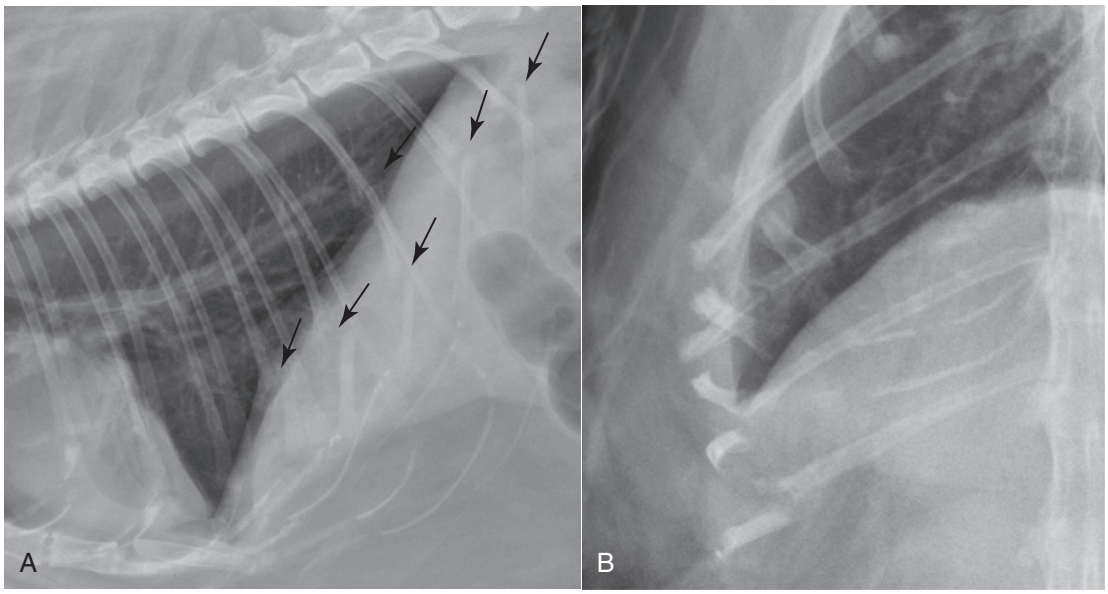


Fig. 33-28 Lateral **(A)** and VD **(B)** radiographs of a cat with chronic asthma and multiple spontaneous rib fractures involving the caudal ribs on the right side *(black arrows)*. This cat had a radiographic bronchial pattern and collapse of the right middle lobe, but these features are not conspicuous in these close-up views.

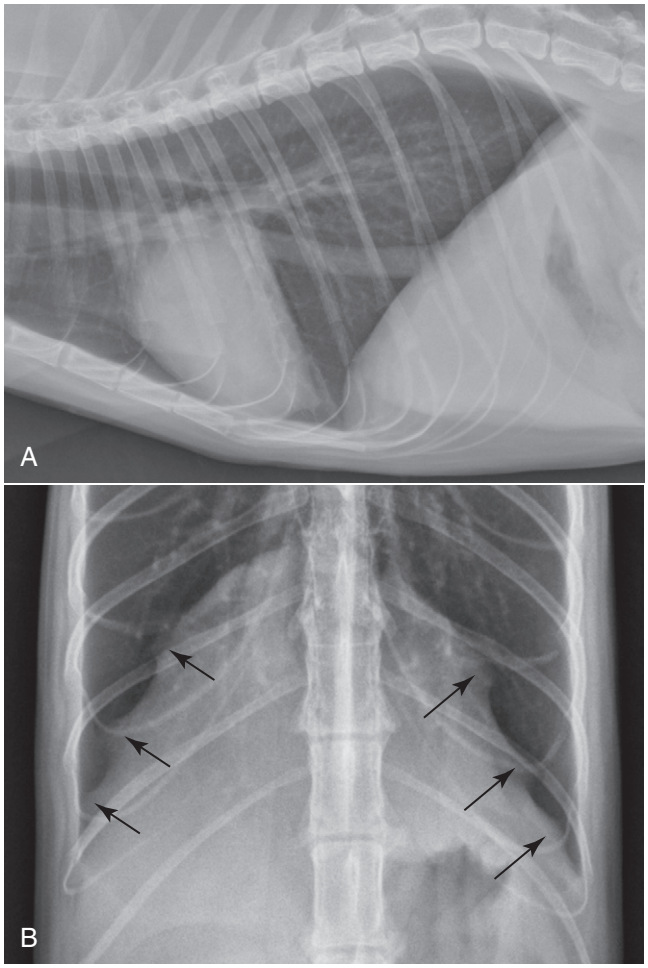


Fig. 33-29 Lateral **(A)** and VD **(B)** radiographs of a cat with pulmonary hyperinflation. In **A,** the distance between the heart and diaphragm is increased, and the diaphragm is flatter than normal. Note also the increase in size of the lung region bounded by the ventral aspect of the caudal vena cava, cranioventral aspect of the diaphragm, and the caudal margin of the heart. In **B,** there are multiple, relatively sharp protuberances from the diaphragm *(black arrows)* that represent the costal attachment sites. The attachment sites are visible because the hyperinflated lung is pushing the diaphragm caudally, leading to tension at the point where the diaphragm attaches to the ribs.

cutaneous nodules and/or structures. These were discussed in detail in Chapter 25.

When a lung nodule or mass is identified, the tendency is to consider it malignant, but it is critical to realize that inflammation can also lead to the formation of lung nodules or masses. The radiographic detection of lung nodules or masses should be interpreted in the context of the signalment and history, and a definitive diagnosis should never be made on the basis of the radiographic appearance alone (Table 33-3).

A soft tissue nodule in the lung must reach some critical diameter before it is large enough to be visible radiographically. This relates to the nodule being large enough to absorb enough x-rays and become conspicuous when superimposed on the heterogeneous background opacity of the lung. The absolute value of this critical diameter will be influenced by the location of the nodule within the lung, relating to whether it is superimposed on other structures, and also to the quality of the radiographic image.[20] It might be expected that smaller nodules could be detected with a digital imaging system than with an analog imaging system because of the inherent greater contrast resolution, but the background information of the lung is also more conspicuous in digital images.

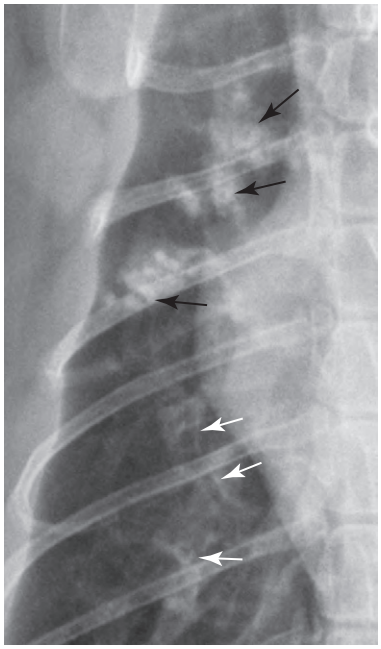


Fig. 33-30 Ventrodorsal radiograph of a cat with asthma. There is a typical bronchial pattern evidenced by ring shadows and tram lines *(white arrows)*. Other regions of the bronchial pattern are more opaque than usual because of mineralization *(black arrows)*. Some of the mineralized lesions appear as a ring with a very opaque periphery, as would be expected from end-on projection of a bronchus with a mineralized wall.

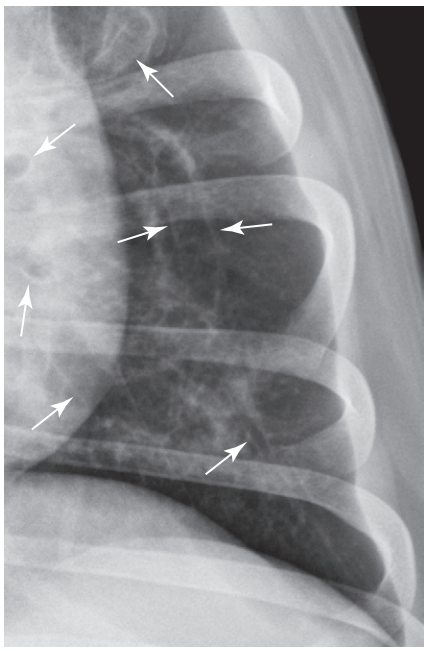


Fig. 33-31 Ventrodorsal radiograph of a dog with chronic hyperadrenocorticism. The walls of numerous bronchi are more opaque than normal because of mineralization *(white arrows)*. These airway walls are not thickened, just more than opaque than normal. This appearance was present throughout the lung field.

In human beings with confirmed lung nodules based on computed tomography (CT) images, the detection rate for lung nodules ranging in diameter from 5.4 to 8 mm was only 26% in digital radiographs.[21] The existence of a diameter threshold before pulmonary nodules become radiographically conspicuous means that failure to detect a lung nodule radiographically

Table • **33-3**

Causes of Interstitial Nodules and Masses

FINDING	CAUSE	PREVALENCE
Multiple solid nodules	Metastasis	Common
	Mycosis	Uncommon
	Septic emboli	Rare
Solitary solid mass	Primary tumor	Common
	Abscess	Rare
Multiple cavitary nodules	Metastasis	Rare
	Parasitic	Rare
	Bullae	Uncommon
Solitary cavitary mass	Primary tumor	Common
	Abscess	Rare
	Bulla	Uncommon

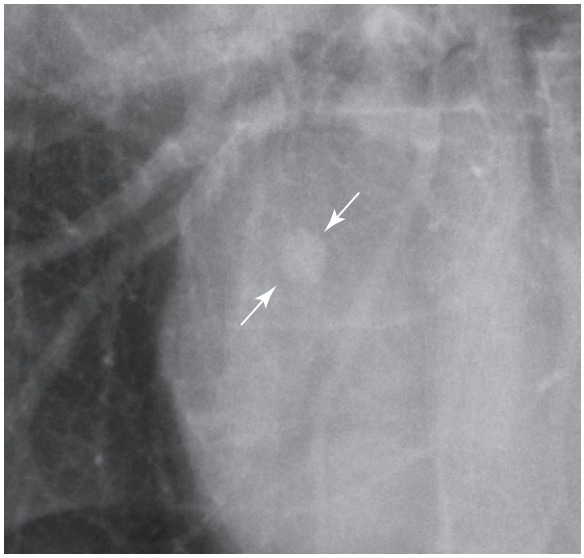


Fig. 33-32 Right lateral view of a dog with a small pulmonary nodule superimposed on the heart *(white arrows)*. This nodule was not visible in the left lateral or VD view. Individual pulmonary nodules must reach some critical diameter before they become conspicuous radiographically. The diameter of this relatively isolated nodule is 8 mm, including radiographic magnification.

is not evidence that pulmonary nodules are not present. This has been proved in dogs with pulmonary metastasis,[22,23] and a diameter threshold of 7 to 9 mm for radiographic detection has been suggested.[22] However, as noted before, it is reasonable to suspect that this critical diameter can vary, depending on both patient and technical factors. Superimposition of individual small nodules that are each below the limit of radiographic detection may create an abnormal lung pattern because of summation effects, but the resulting opacity is not likely to have the appearance of a classic nodule because summation opacities may bear no similarity to the shape of the individual objects being summed, as discussed in Chapter 5. In the case of summation of multiple small nodules, the abnormal lung pattern may assume more of an unstructured appearance, to be discussed later.

The distinction between a lung mass and a lung nodule is strictly a matter of size, and this is obviously subjective. As a general rule, a lesion with a diameter less than approximately 2.0 cm can be referred to as a nodule (Fig. 33-32), and larger lesions as a mass.

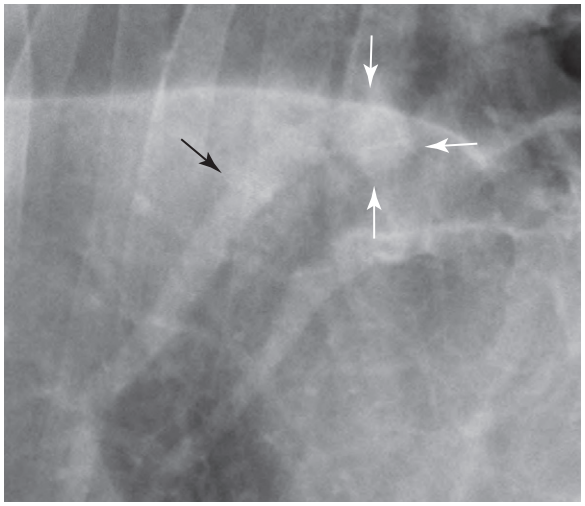


Fig. 33-33 Lateral view of a dog where there is a nodular opacity just ventral to the caudal aspect of the trachea *(white arrows)*. It would be easy to interpret this opacity as a pulmonary nodule, except there is an adjacent tubular opacity *(black arrow)* connected to the nodular opacity. Thus, the nodular opacity is a portion of a vessel projected end-on, whereas the tubular opacity represents the remainder of the vessel being projected side-on.

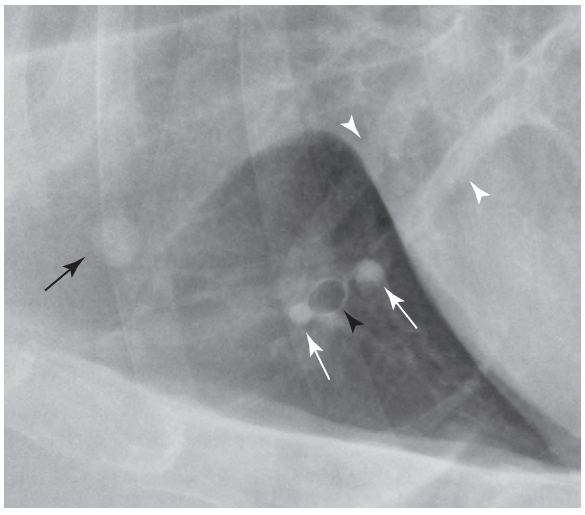


Fig. 33-34 Lateral radiograph of the cranioventral aspect of the thorax of a dog. How many pulmonary nodules are there? The most cranial opacity *(black arrow)* is a pulmonary nodule. The other smaller structures *(white arrows)* are end-on pulmonary vessels. They are easily identified as vessels because they are more opaque than expected for a nodule of this diameter, they are situated directly adjacent to a bronchus *(black arrowhead)*, and the connecting portions of the vessels are visible as they are projected side-on *(white arrowheads)*. The diameter of the end-on vessels is also less than expected for detection of a solitary pulmonary nodule, approximately 4 mm in this radiograph, including radiographic magnification.

Pulmonary vessels projected end-on will have the appearance of a solitary circular opacity, and these are often confused with a pulmonary nodule. End-on pulmonary vessels are usually found adjacent to an airway, and many times it is possible to see the connecting portion of the vessel, projected side-on, extending peripherally from the "nodule" (Figs. 33-33 and 33-34). This connecting opacity has been referred to as a *tail*. End-on pulmonary vessels are also usually more opaque than expected for a true nodule of comparable diameter because the end-on vessel has a depth—in other words,

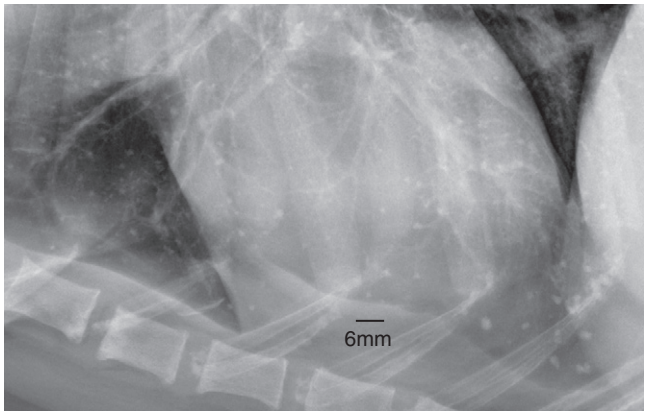


Fig. 33-35 Lateral view of the ventral aspect of the thorax of a dog with pulmonary osseous metaplasia. There are multiple, small mineralized opacities in the lung; there were only a few of these lesions dorsally. A ventral distribution is typical for pulmonary osseous metaplasia. The diameter of these lesions is smaller than that necessary for a soft tissue nodule to be apparent radiographically. The black bar has a length of 6 mm; it is questionable whether a 6 mm soft tissue nodule would be detected radiographically, but the much smaller nodules in this dog are readily detectable because of their mineralization. These mineralized nodules do not have an adjacent *tail* and are not situated adjacent to a bronchus; this is further evidence that they are mineralized pulmonary nodules and not vessels projected end-on. Given the extreme rarity of dystrophic mineralization of pulmonary metastasis, the most likely diagnosis is pulmonary osseous metaplasia.

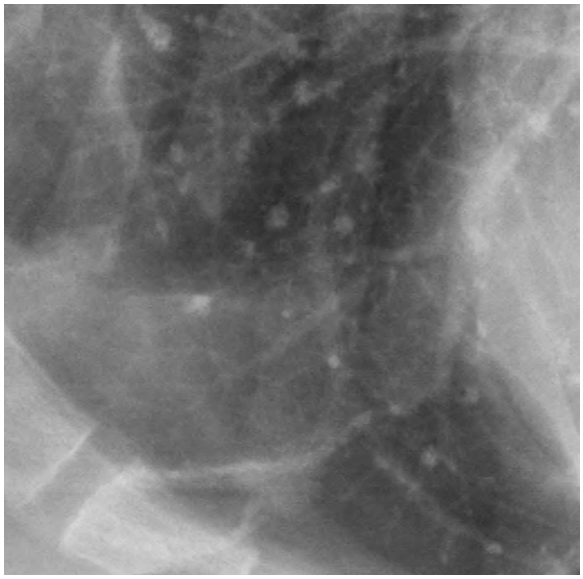


Fig. 33-36 Close-up view of the cranioventral aspect of the lung from a dog with pulmonary osseous metaplasia. Note the small size of these nodules, that they are not situated next to a bronchus, and that an adjoining *tail* is not present.



Fig. 33-37 Ventrodorsal radiograph of a dog with a 4 cm mass in the right caudal lung lobe. Centrally located intrapulmonary masses that are not associated with other intrathoracic disease are easy to detect radiographically.

cylindrical versus spherical—which leads to more x-ray absorption and greater opacity (see Fig. 33-34). Also, the diameter of an end-on vessel is often below that expected for the smallest detectable soft tissue nodule because of the increased opacity afforded by their cylindrical shape. The diameter of the vessels in Figure 33-34 is 4 mm, including radiographic magnification. This is below what might be expected to be the critical diameter for detection of a soft tissue nodule.

Mineralized nodules also become conspicuous at a very small diameter because of their higher physical density leading to enhanced x-ray absorption. Pulmonary osseous metaplasia, also called *heterotopic bone*, is a benign condition of the canine lung and is the most common cause of mineralized pulmonary nodules. Nodules caused by pulmonary osseous metaplasia can be detected at a smaller size than for a soft tissue nodule, are not situated adjacent to a bronchus, and do not have a visible connecting tail, as do end-on vessels (Figs. 33-35 and 33-36). Clearly, dystrophic mineralization of a soft tissue nodule in the lung could have the same appearance as that of pulmonary osseous metaplasia, and larger mineralized nodules or masses would also be quite conspicuous. However, radiographically detectable dystrophic mineralization of pulmonary nodules or masses is very uncommon. One might guess that osteogenic tumors, such as osteosarcoma, would have a tendency to result in metastatic lesions that are mineralized; this can occur but is highly unusual in animals. Even when metastatic nodules are calcified, the extent of calcification is typically not detectable radiographically but only with CT.[24]

Pulmonary nodules are often visible in only one radiographic projection. In this case, care must be taken to ensure that the nodule is, in fact, in the lung because superimposed nodules can appear radiographically as if they were intrapulmonary; this was discussed and illustrated in Chapter 5. Determining that a nodule is intrapulmonary is easy with fluoroscopy, based on coincident movement between the nodule and adjacent lung markings as the patient breathes. But fluoroscopy is rarely available in practice settings. CT can also be used to confirm that a suspected nodule is intrapulmonary, but access to CT may also be limited. If a nodule is seen in only one view, the patient should be examined physically for superficial structures, such as a papilloma, teat, or ectoparasite, which might have created the opacity. If no superficial structure that could be the source of the opacity is found, and neither fluoroscopy nor CT are possible, repeating the thoracic radiographs at a later date is advisable to reassess the suspected nodule.

A lung mass located in the central portion of a lung lobe that does not have an associated alveolar pattern caused by atelectasis, hemorrhage, or concurrent infection is easy to detect radiographically (Fig. 33-37). Unfortunately, many

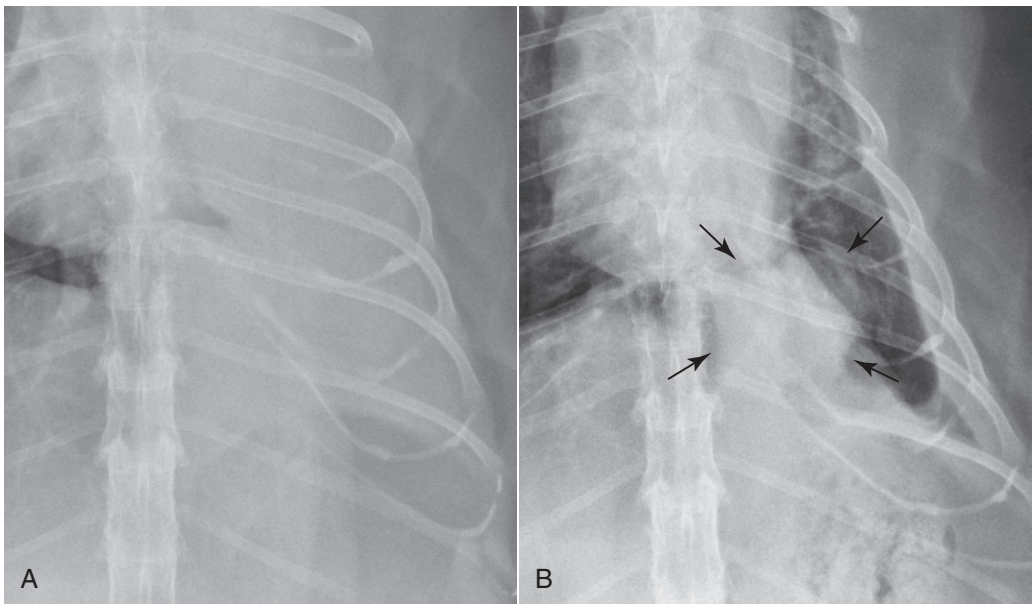


Fig. 33-38 **A,** Ventrodorsal radiograph of a cat with a large amount of fluid in the left pleural cavity. The heart is displaced to the right, and the left lung cannot be assessed. **B,** Ventrodorsal radiograph made following left pleurocentesis; a large mass is visible in the left caudal lung lobe *(black arrows)*.

pulmonary masses go undetected until they have reached a size where respiratory function is compromised. At this stage, other radiographic changes that reduce the conspicuity of the lung mass, such as pleural effusion (Fig. 33-38) or atelectasis (Fig. 33-39), are often present, and this can make radiographic diagnosis of the mass more difficult. Masses can also reside in peripheral regions of the lung where they will be conspicuous only if the radiographic study includes a projection that maximizes aeration of that portion of the lung (Fig. 33-40). This emphasizes the value of obtaining four views of the thorax routinely, as discussed in Chapter 25.

Occasionally, lung nodules or masses contain an air cavity. These are termed *cavitary* nodules or masses.[25,26] Cavitary lesions with thin walls, termed *lung bullae*, are usually benign and result from previous trauma or a congenital lung malformation; these lesions may be single or multiple (Fig. 33-41). Lung bulla formation caused by recent trauma is usually associated with other trauma-associated intrathoracic changes, such as pleural effusion, pneumothorax, or pulmonary hemorrhage. A lung bulla that results from recent trauma may have a more irregular wall than a chronic traumatic bulla or a congenital bulla (Fig. 33-42). This irregular wall may result from a hematoma in the wall of the bulla or by fluid in the bulla cavity that causes border effacement of the wall.

A cavitary lung mass with a thick wall, other than an acute traumatic lung bulla, usually results from spontaneous cavitation of a solid mass where the contents of the lesion became liquefied and drain into a connecting bronchus with the cavity then filling with gas. The development of a single cavitary mass having a thick wall is more common than is the finding of multiple small cavitary nodules (Figs. 33-43 and 33-44). Cavitary masses with a thick wall are usually more significant clinically than cavitary lesions with a thin wall, but this is only a generalization, and the significance of the lesion must be determined in context with the signalment and history. Any cavitary lesion has the potential to rupture, leading to pneumothorax.

Unstructured Interstitial Pattern. An unstructured interstitial pattern results from increased x-ray attenuation created by excess fluid, a cellular ingrowth, or infiltration into the supporting interstitial framework of the lung (Table 33-4). The abnormal fluid or tissue is not organized into a solitary lesion or multiple discrete lesions but involves the interstitium relatively uniformly. Such lesions can develop as a result of fluid transudation from interstitial capillaries, the presence of a low-grade inflammatory response, or diffuse neoplastic cell growth. *Low-grade* inflammation was specified because high-grade, or virulent, interstitial infections will usually progress quickly to produce an alveolar pattern as the disease spreads from the interstitium into adjacent alveoli.

The unstructured interstitial lung pattern is probably the most misdiagnosed of all lung patterns. The basis of this misdiagnosis lies in the number of situations where the overall pulmonary opacity is increased falsely and misinterpreted as abnormal. These include radiographic underexposure; film underdevelopment; body habitus; and atelectasis resulting from poor ventilation, sedation, or gravity. All of these were discussed in detail in Chapter 25. Thus, if a diagnosis of an unstructured interstitial pattern is considered, it is very important to go over a mental checklist of all of the things that can create this appearance erroneously so that an incorrect diagnosis will not be made.

An important feature of some diseases that result in an unstructured interstitial pattern is their dynamic nature. Left-sided heart failure, for example, will first typically lead to interstitial pulmonary edema, but this soon becomes alveolar edema, which will be more opaque and diffuse, and the resultant alveolar pattern will obscure any interstitial pattern that is present. Therefore, an unstructured interstitial pattern may be short-lived or superimposed on either a bronchial or alveolar pattern. The special situation of coexistence of multiple lung patterns is covered later.

The diagnosis of an unstructured interstitial pattern is based on the finding of an abnormal increase in the background radiographic opacity of the lung. There are a variety of radiographic appearances this can take, and some classification systems attempt to capture these variations. For example, military, reticular, reticulonodular, unstructured, and honeycombing are all subcategories of unstructured interstitial disease that have been proposed. However, this degree of

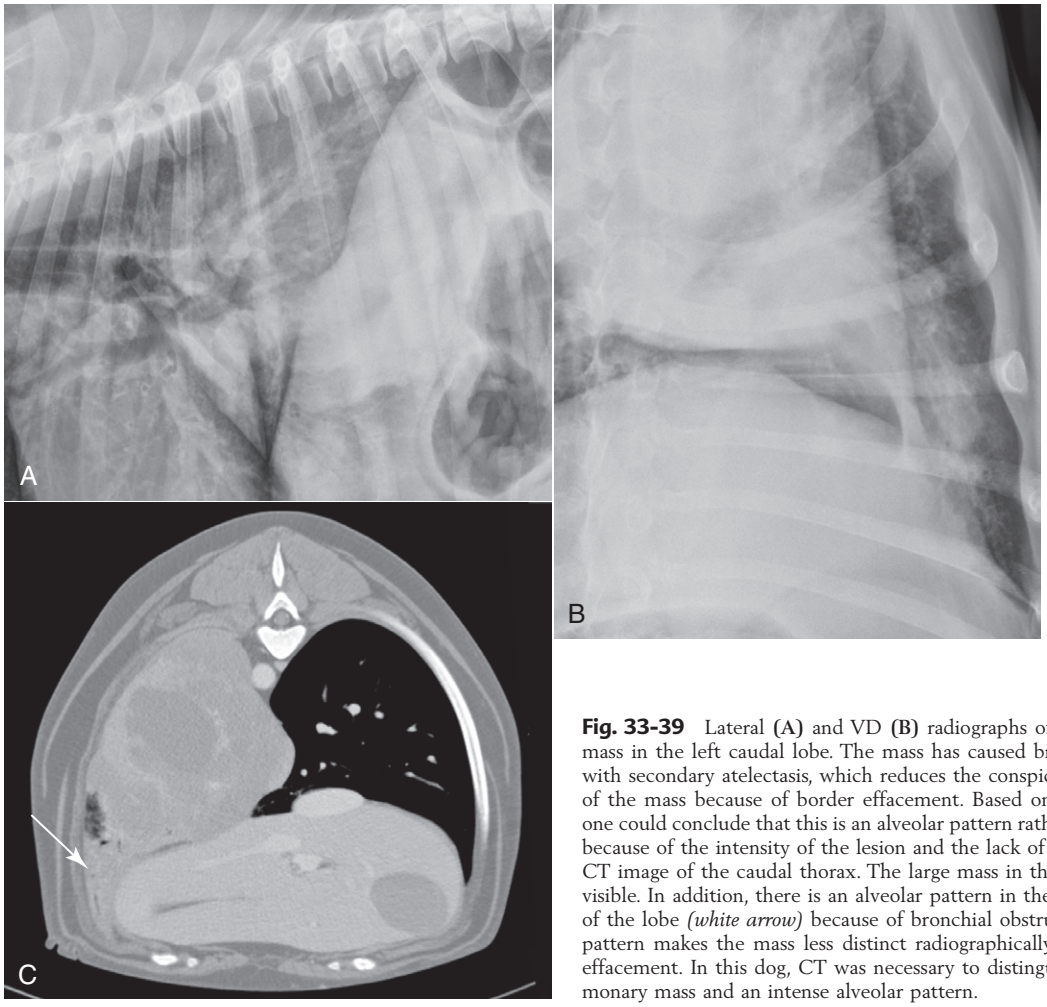


Fig. 33-39 Lateral **(A)** and VD **(B)** radiographs of a dog with a large mass in the left caudal lobe. The mass has caused bronchial obstruction with secondary atelectasis, which reduces the conspicuity of the margins of the mass because of border effacement. Based on radiographic signs, one could conclude that this is an alveolar pattern rather than a lung mass, because of the intensity of the lesion and the lack of distinct margins. **C,** CT image of the caudal thorax. The large mass in the left caudal lobe is visible. In addition, there is an alveolar pattern in the dependent portion of the lobe *(white arrow)* because of bronchial obstruction. This alveolar pattern makes the mass less distinct radiographically because of border effacement. In this dog, CT was necessary to distinguish between a pulmonary mass and an intense alveolar pattern.

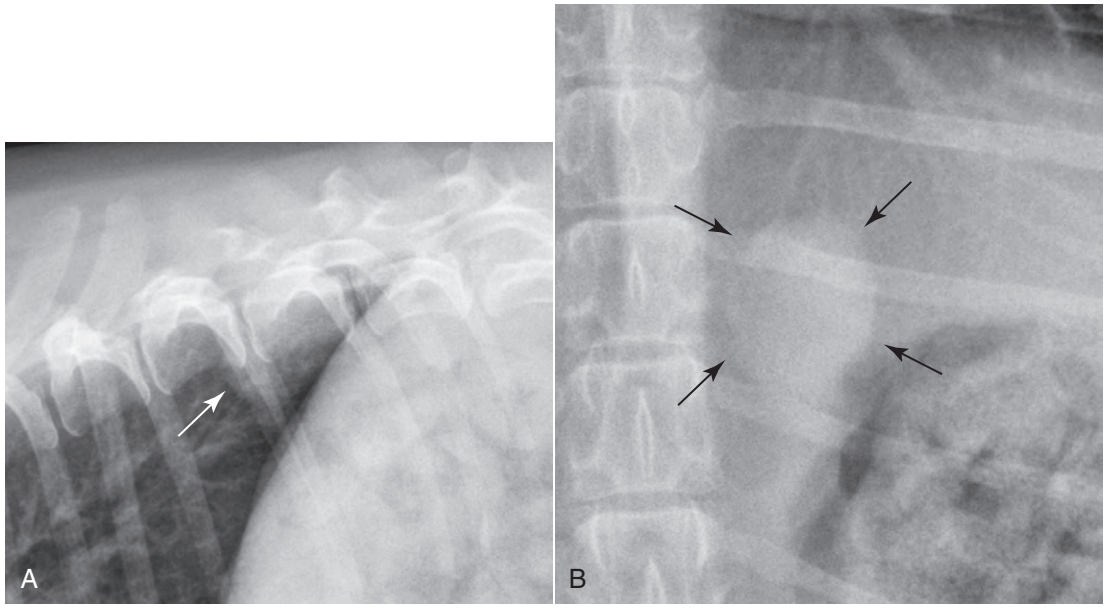


Fig. 33-40 **A,** Right lateral radiograph of a dog with a lung mass in the most dorsocaudal aspect of the left caudal lung lobe. No abnormalities were identified in the left lateral view, as expected, because of recumbent-atelectasis in the left lung causing border effacement of the mass. In the right lateral view, there is only an ill-defined region of increased opacity in the dorsocaudal aspect of the thorax *(white arrow)*; this could be overlooked easily. **B,** DV radiograph of the thorax. The lung mass in the left caudal lobe is clearly seen *(black arrows)*. The mass was also not visible in the VD view because of recumbency-associated atelectasis occurring in the dorsocaudal aspect of the lung. If a DV view had not been obtained in this patient, the lung mass may not have been detected because of its peripheral location.



Fig. 33-41 Lateral radiograph of a dog with a lung bulla in the right caudal lung lobe. The thin wall of this lesion is evidence that it is most likely benign. This lesion could be a congenital malformation or secondary to previous lung trauma.

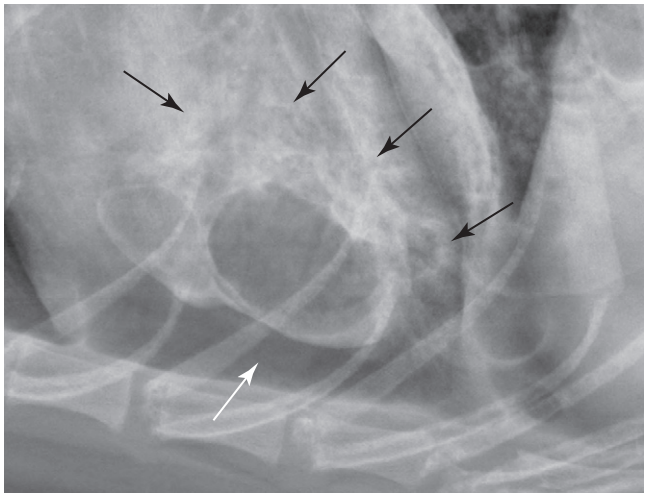


Fig. 33-42 Lateral radiograph of a dog recently hit by a car. There are multiple cavitary lesions in the periphery of the lung. These represent traumatic lung bullae. The wall of these bullae is slightly thicker and more irregular than encountered in a long-standing bulla from prior trauma, or in a congenital bulla. However, the history of recent trauma and the finding of pneumothorax *(white arrow)* and an alveolar pattern consistent with hemorrhage *(black arrows)*, support these air-filled lesions being traumatic bullae.

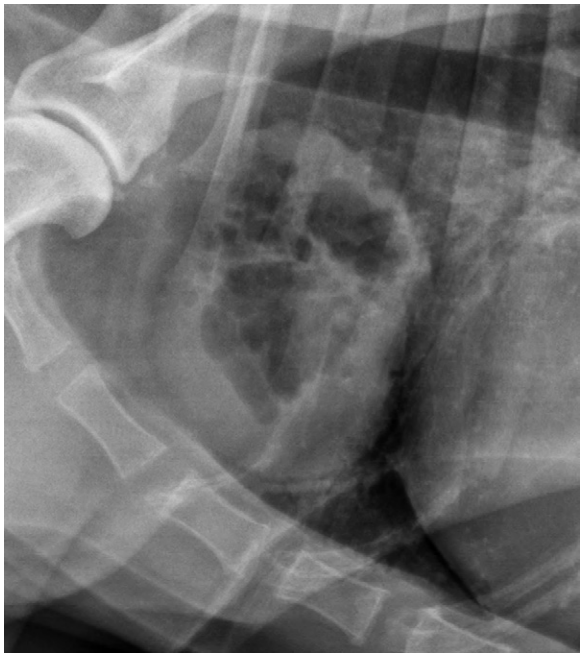


Fig. 33-43 Lateral radiograph of a dog with a large cavitary mass located in the left cranial lung lobe. There are multiple gas cavities and an irregular and thick wall. It would be highly unusual for a mass of this type to have originated from trauma, and it is more likely to be a lung tumor or lung abscess.

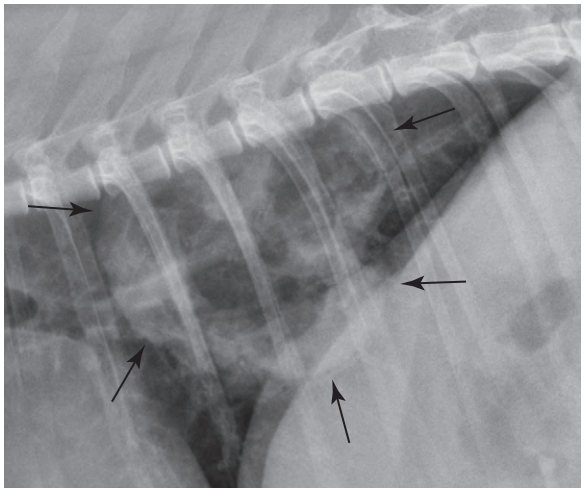


Fig. 33-44 Lateral radiograph of a cat with large cavitary mass located in the left caudal lung lobe. There are multiple gas cavities and an irregular and thick wall. It would be highly unusual for a mass of this type to have originated from trauma, and it is more likely to be a lung tumor or lung abscess.

subclassification is not necessary, especially for nonspecialists, because it introduces more confusion than clarity. Also important is the fact that diseases that result in the formation of a conspicuous unstructured interstitial pattern are relatively uncommon in comparison with diseases that result in an alveolar or bronchial lung pattern.

An important feature of unstructured interstitial lung disease is that the resulting radiographic pattern is a summation pattern created by superimposition of all of the abnormal interstitium. All radiographic lung patterns are summation patterns, but when dealing with large lesions, such as lobar alveolar disease or disease of the major airways, the effect of summation is minimized, and the radiographic abnormality is more representative of the actual disease process. With unstructured interstitial disease, however, the individual lesions are small and arranged nonuniformly and when summed in a radiograph can create an opacity that resembles a structure or pattern that is not actually present in the patient (Fig. 33-45). This summation is one reason that a detailed subcategorization of interstitial lung patterns is flawed; the end result is more of a summation opacity than a representation of the actual interstitial distribution of the disease.

The key to diagnosing an unstructured interstitial pattern is recognizing an increase in the background opacity of the lung over that which is within normal limits (Figs. 33-46 through 33-48). As the range of normal is wide, it is obvious

Table • **33-4**

Causes of an Unstructured Interstitial Pattern

CAUSE	PREVALENCE
Poor radiographic technique	Common
Poor ventilation	Common
Body habitus	Common
Lymphoma	Uncommon
Solid tumor metastasis	Uncommon
Deep mycosis	Uncommon
Cardiogenic edema	Uncommon

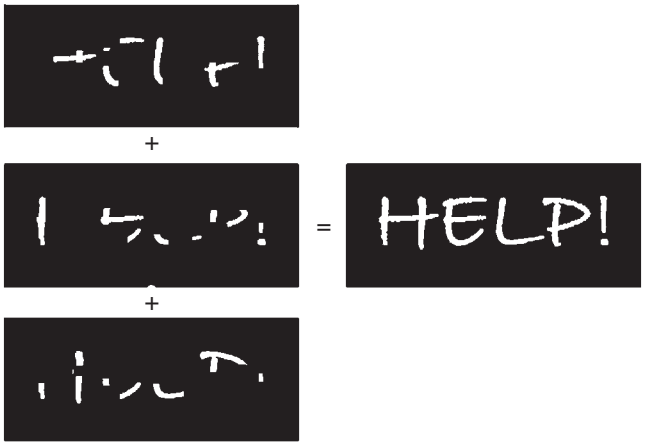


Fig. 33-45 Diagram illustrating the effect of summation on the final radiographic appearance of an unstructured interstitial pattern. The distribution of interstitial disease from three individual layers within the patient's lung is represented in the three panels. When the lesions are summed into a single two-dimensional image, the depiction of the disease creates an opacity that is not present in the patient.

that mild interstitial disease often goes undiagnosed. Or, more commonly, the normal interstitial pattern is misdiagnosed as disease. In this chapter, only obvious examples of unstructured interstitial patterns are given, because these are the only ones that can be diagnosed with certainty. Finally, it is critical that any suspicion of an unstructured interstitial pattern diagnosed in a lateral view be documented in the VD or DV views because of the tendency of lungs to have a generally increased opacity in lateral views caused by atelectasis, as discussed in Chapter 25.

Airway Versus Nonairway Paradigm

The pattern recognition system described in the previous section is a useful method for classifying lung disease radiographically, as long as the limitations are realized. The main limitation, already mentioned, is the fact that the pattern does not always correlate with the anatomic compartment of the lung that is abnormal—for example, a bronchial pattern caused by peribronchial interstitial disease. Also, there is usually involvement of more than one lung compartment, and the lung pattern just reflects the most conspicuous compartmental involvement—for example, an alveolar pattern causing border effacement and masking a coexisting bronchial and/or interstitial pattern.

In reality, there are few diseases that involve only one lung compartment, and the resulting radiographic changes reflect a summation of opacities created by the combined patterns. Similarly, disease in one compartment but distributed heterogeneously will also be summated to create a radiographic pattern that does not fall into one of the three classic patterns. In either instance, the radiographic features of the disease can lead to a mixed pattern that is highly confusing (Figs. 33-49 through 33-52). One specific combination of patterns that seems to be a particular cause for concern is whether a patient with a bronchial pattern also has interstitial involvement—that is, a bronchointerstitial pattern (Fig. 33-53). In fact, this distinction is impossible to make radiographically, and it really is inconsequential whether a bronchial pattern is combined with an unstructured interstitial pattern or not, as discussed in the following paragraph.

Mixed lung patterns need not cause great consternation if the paradigm of airway versus nonairway is considered. As already mentioned, a definitive radiographic diagnosis of a specific lung disease is rarely going to be made radiographically. The objective is to determine the best course of action to take after the radiographic findings are considered in context with the signalment and clinical signs. Determining whether the airspaces are involved provides valuable evidence regarding the potential usefulness of airway sampling, using transtracheal aspiration or bronchoalveolar lavage. The presence of an airway component is determined by looking for any of the signs that have been described for *either* an alveolar or bronchial pattern; whether one predominates is not as important because the diagnostic considerations for each pattern overlap considerably. This is also why it is not usually important whether a bronchial pattern has an interstitial component. Conversely, if the radiographic changes are more typical of either a structured or unstructured interstitial pattern, then the potential value of airway sampling is diminished because that diagnostic tool will not usually provide information pertaining to the interstitium itself. If a definitive diagnosis of an interstitial pattern is needed, this may require cytologic evaluation of the lung, either by percutaneous lung aspiration or open biopsy.

The consideration of clinical signs and signalment along with the radiographic findings when deciding whether to perform airway sampling cannot be overemphasized. Regardless of the lack of specificity of the radiographic changes, other findings can be important. For example, a mixed lung pattern with a definitive airway component in an old dog with a systolic heart murmur and radiographic evidence of left atrial dilation and pulmonary venous hypertension is most likely caused by cardiogenic pulmonary edema. Airway sampling is not indicated in this scenario unless the lung pattern fails to improve with treatment for the cardiac dysfunction. This specific example is not intended to be the only situation where airway sampling is not indicated, just as a rationale for considering the history and signalment carefully before performing these invasive procedures.

There are many diagnostic considerations for a mixed lung pattern. These include (1) primary and secondary neoplastic processes; (2) cardiogenic and noncardiogenic pulmonary edema; (3) bacterial, parasitic, and fungal lung infections; (4) allergic reaction; (5) pulmonary hemorrhage; (6) thromboembolic disease; (7) toxicosis; and (8) direct injury, as from smoke or pollutants. This large list of possibilities emphasizes the value of airway sampling to obtain the diagnosis, if clinically acceptable, based on signalment and history.

SPECIFIC PULMONARY CONDITIONS

Although one or both of the paradigms described previously relating to pulmonary pattern recognition should be used routinely in the evaluation of thoracic radiographs, there are some specific details that are important regarding some

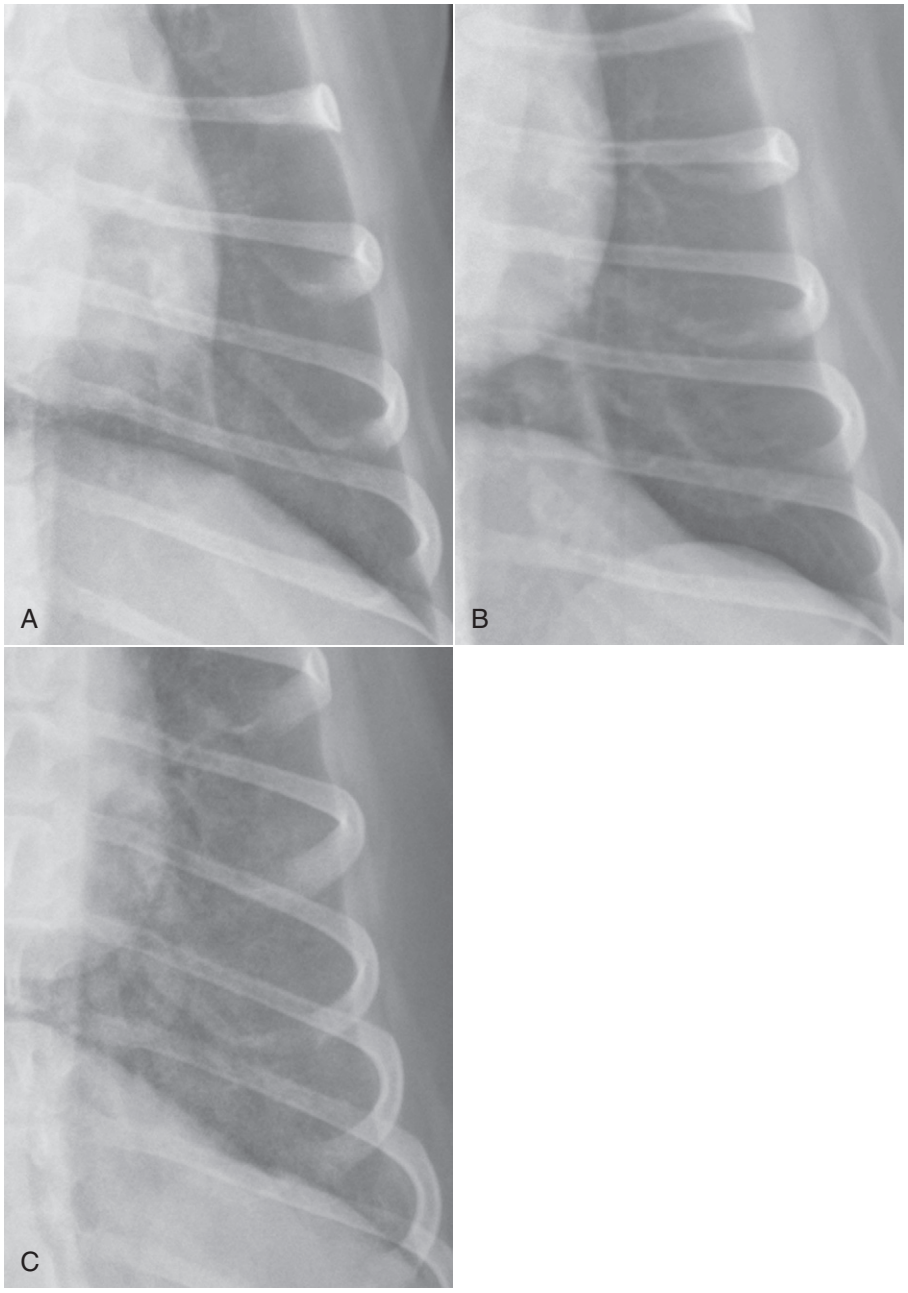


Fig. 33-46 Ventrodorsal radiograph of a dog with pulmonary lymphoma **(A).** There is a very mild increase in unstructured interstitial opacity. This is a very mild change and likely the least conspicuous unstructured pattern that can be detected radiographically. Most specialists would likely interpret this radiograph as abnormal, but beginning interpreters may conclude this appearance is normal. The dog was treated with chemotherapy, and the lung pattern underwent a complete remission **(B).** This radiograph, which depicts a normal pulmonary interstitium, provides a baseline for comparison to the radiograph in **A.** Subsequently, the lymphoma relapsed, and the unstructured interstitial pattern became more intense **(C).** The appearance in **C** would be interpreted as an unstructured interstitial pattern because the lesion is not very intense on a per-unit basis, and there are no other signs of an alveolar pattern. Similarly, there are not an abnormal number of ring shadows or tram lines in this image that would support the lung pattern being bronchial.

conditions that might not be completely amenable to these paradigms.

Cardiogenic Pulmonary Edema

The radiographic manifestation of cardiogenic pulmonary edema is described in Chapter 32, but some reiteration is important here because of the high prevalence of this abnormality. It may be expected that cardiogenic pulmonary edema will be characterized by a uniform increase in lung opacity that has an intense alveolar pattern. In reality, cardiogenic pulmonary edema is usually patchy and is often not as intense as a pneumonic process (Fig. 33-54). It has been suggested



Fig. 33-47 Ventrodorsal radiograph of a dog with an intense unstructured interstitial pattern caused by hemangiosarcoma metastasis. On initial examination one might decide there are an abnormal number of ring shadows and conclude that this is a bronchial pattern. However, common sense indicates that there are just not the numbers of bronchi per unit area to create all the ring shadows that can be seen. Therefore, the detection of numerous small ring shadows is an example of the summation of an unstructured interstitial pattern creating opacities that are not actually present in the patient. Some might also call this a miliary pattern because of the impression of multiple small nodules, as with millet seeds. However, the actual interstitial disease may not be nodular, even though this is metastatic cancer. The nodular appearance could also just be a manifestation of summation.

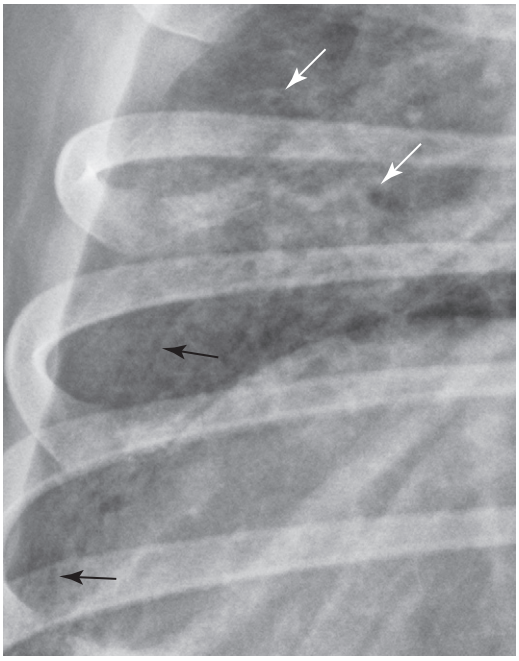


Fig. 33-49 Ventrodorsal radiograph of a dog with a mixed lung pattern. The increased pulmonary opacity is relatively intense per unit area compared with what would be expected for an unstructured interstitial pattern (compare with Figs. 33-47 and 33-48), but the opacity is not as opaque as would be expected from an alveolar pattern. There are ring shadows *(white arrows)* that represent a bronchial component. There are also radiolucent lines *(black arrows)* that are consistent with air bronchograms. The radiographic features are not specific for any one of the three classic lung patterns.



Fig. 33-48 Ventrodorsal radiograph of a dog with confirmed infection with blastomycosis. The pulmonary pattern is an unstructured interstitial pattern. Note the similarity in appearance to the lung pattern shown in Figure 33-47 that was caused by metastatic hemangiosarcoma.

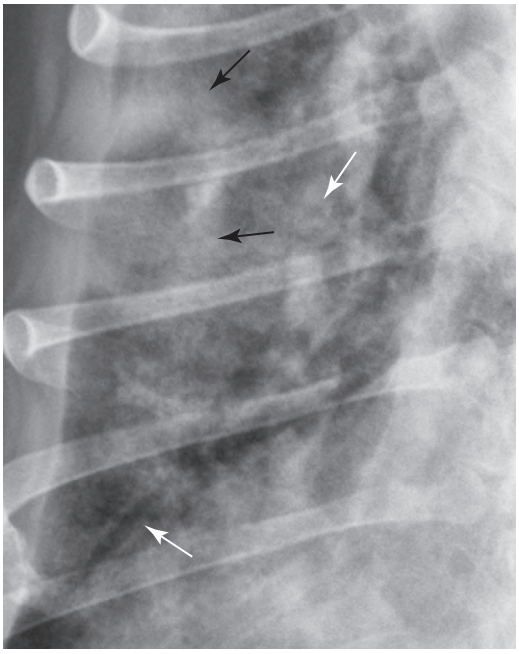


Fig. 33-50 Ventrodorsal radiograph of a dog with a mixed lung pattern. There are regions of this lung disease that are relatively intense, more than expected from an unstructured interstitial pattern *(black arrows)*. However, there are also regions where bronchi can be seen *(white arrows)*, although the adjacent lung opacity is not great enough for these bronchi to be described as air bronchograms.

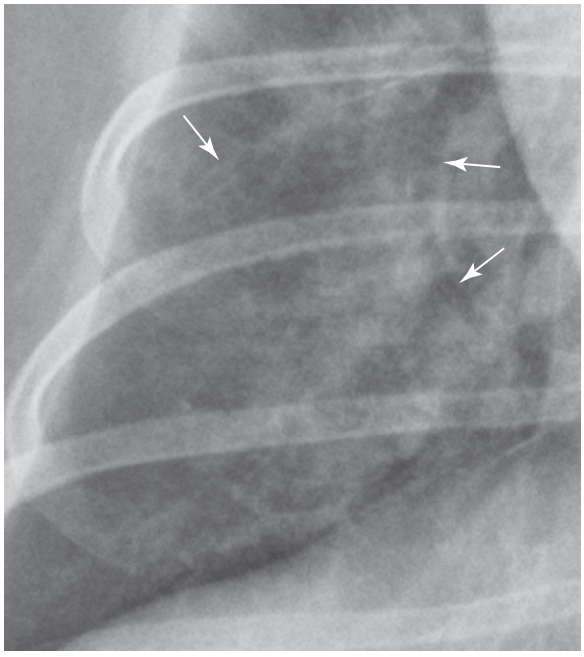


Fig. 33-51 Ventrodorsal radiograph of a dog with a mixed lung pattern. The increased opacity is relatively unstructured, but some airways are visible *(white arrows)*. The disease is not sufficiently opaque on a per-unit-volume basis to be considered an alveolar pattern, and there are not enough ring shadows or tram lines to consider this a bronchial pattern.

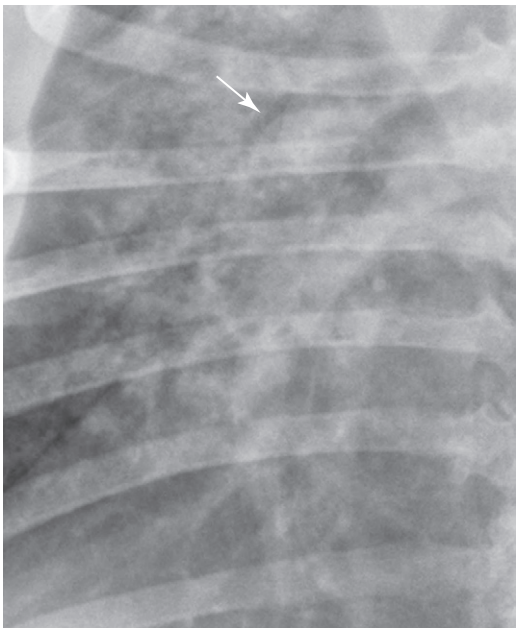


Fig. 33-52 Ventrodorsal radiograph of a dog with a mixed lung pattern. The disease is too intense to be attributed to unstructured interstitial disease and not adequately intense to be classified as an alveolar pattern, although an airway that may be an air bronchogram is present *(white arrow)*. Also, there are inadequate ring shadows or tram lines to classify the disease as a bronchial pattern.

that the asymmetry of cardiogenic pulmonary edema in dogs with mitral valve insufficiency is related to whether the dog has a central or asymmetric mitral regurgitant jet.[27]

Another misconception of cardiogenic pulmonary edema is that it always causes an alveolar pattern. This is not true, especially in cats with hypertrophic or restrictive

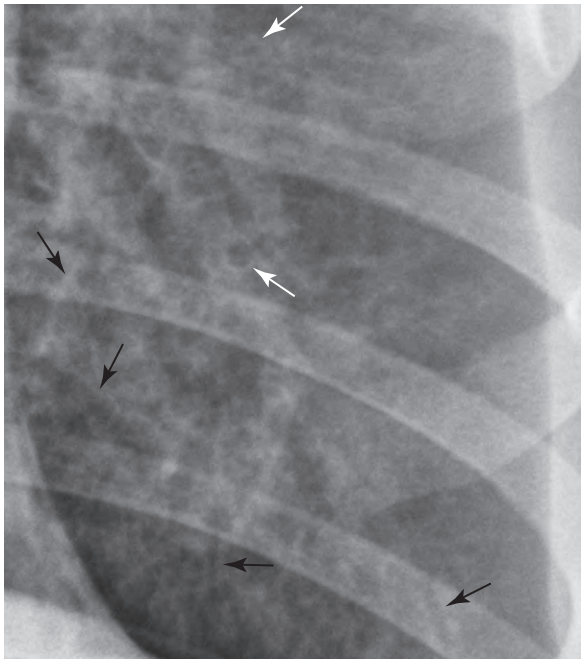


Fig. 33-53 Ventrodorsal radiograph of a dog with an obvious bronchial pattern. There are numerous ring shadows *(white arrows)* and tram lines *(black arrows)*, but the lung also has an increased unstructured pattern that is consistent with an unstructured interstitial pattern. Thus, many interpreters would get bogged down trying to decide whether this dog has a bronchial pattern or a bronchointerstitial pattern. This distinction is irrelevant. The dog has airway involvement and should have airway sampling performed, if this is judged to be a clinically acceptable test.

cardiomyopathy, and in large-breed dogs with dilated cardiomyopathy; in each of these cases the radiographic pattern resulting from cardiogenic pulmonary edema can be that of a bronchial pattern (Figs. 33-55 and 33-56).

Finally, it is typical for cardiogenic pulmonary edema in human beings to have a perihilar distribution, at least initially.[28] This association has been carried forward to the dog, without supporting evidence. Perihilar lung disease is much easier to detect in human beings because the posterior-anterior radiographic projection of the thorax provides a relatively unobstructed view of the pulmonary hila. This is not true in the dog, however, where the cardiac silhouette is superimposed on the hilar regions in the VD or DV views. And in the lateral view, the pulmonary veins and left atrium will be superimposed on the hilar region. In heart failure patients, the left atrium and pulmonary veins are often enlarged, and the resulting opacity contributes to a false impression of perihilar lung opacity. Finally, as discussed in Chapter 25, the lungs will always look more opaque in lateral views, and this too contributes to increased opacity in the hilar region. Therefore, the combination of left atrial dilation, pulmonary vein dilation, and recumbency-associated atelectasis all go together to create an artifactual increase in perihilar opacity that is commonly misdiagnosed as perihilar edema (Fig. 33-57). As mentioned in Chapter 25, any abnormal lung pattern identified in a lateral radiograph must be substantiated in the VD or DV view before considering it significant.

Lung Lobe Torsion

Lung lobe torsion is characterized by axial rotation of a lung around its bronchus leading to bronchial and pulmonary vein obstruction.[29] Arterial inflow, especially from the bronchial arterial system, is not obstructed totally, leading to congestion and consolidation as fluid moves into the interstitium, airways,



Fig. 33-54 Ventrodorsal radiograph of dog with cardiogenic pulmonary edema. The left cranial lobe is normal. The right cranial lobe has a mild increased opacity that cannot be characterized into one of the three classic lung patterns. The right caudal lobe is more opaque, and the extent of this opacity would allow it to be classified as an alveolar pattern; some faint air bronchograms are visible superimposed on the diaphragm. The left caudal lobe is the most opaque of all lung lobes and has a classic alveolar pattern with air bronchograms. This regional variation in the severity of the lung disease is typical of cardiogenic pulmonary edema.

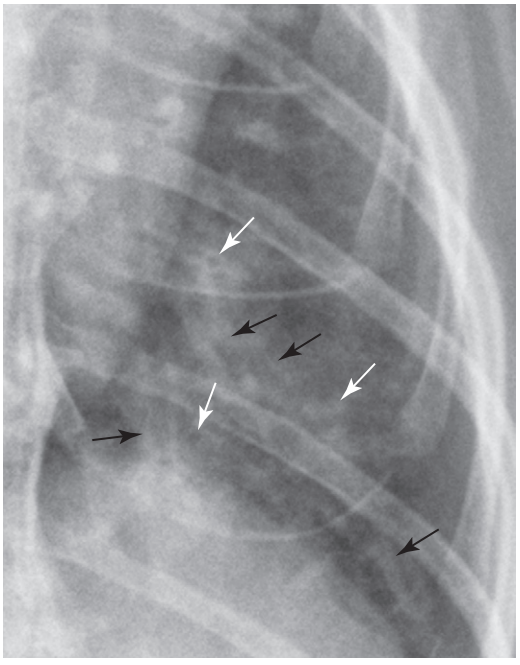


Fig. 33-55 Ventrodorsal radiograph of a cat with cardiogenic pulmonary edema secondary to hypertrophic cardiomyopathy. In this cat the pulmonary pattern resulting from the edema is primarily bronchial, with ring shadows *(white arrows)* and tram lines *(black arrows)*. The lung also has a mild unstructured interstitial pattern, but it is not critical that this be recognized, because it does not change the interpretation.

and eventually into the pleural cavity. Thus, the pattern created by lung lobe torsion will not fit into any of those described so far because of the consequential (1) enlargement of the affected lobe and (2) ultimate filling of bronchi with fluid. Torsion of the right middle lobe is more common in large dogs, whereas left cranial lobe torsion is more common in small dogs.[30] Of small-breed dogs with lung lobe torsion, pugs appear to be overrepresented.[31] Radiographic features of lung lobe torsion include (1) enlargement of the affected lobe; (2) concurrent pleural effusion; (3) an abnormal shape and/or position of the affected lobe; and (4) truncation, blunting, and/or displacement of the bronchus supplying the affected lobe (Fig. 33-58). Small dispersed air bubbles may also be seen occasionally.[30] The radiographic diagnosis of lung lobe torsion is not obvious in every patient, and CT will be needed for confirmation in some.[32]

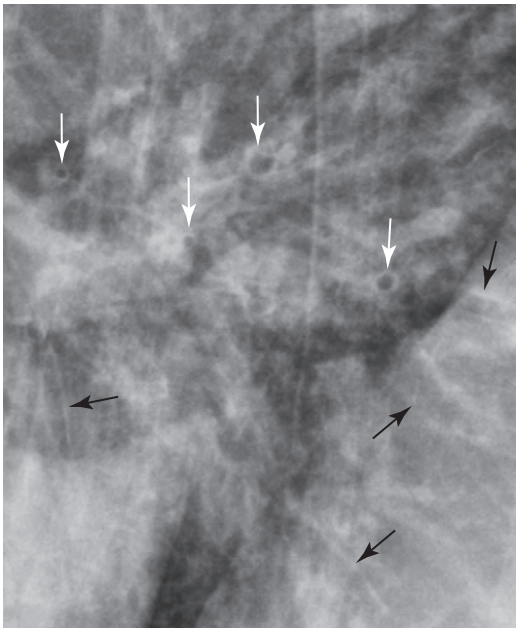


Fig. 33-56 Lateral radiograph of a dog with cardiogenic pulmonary edema secondary to dilated cardiomyopathy. The edema has created a bronchial pattern, characterized by multiple ring shadows *(white arrows)* and tram lines *(black arrows)*.

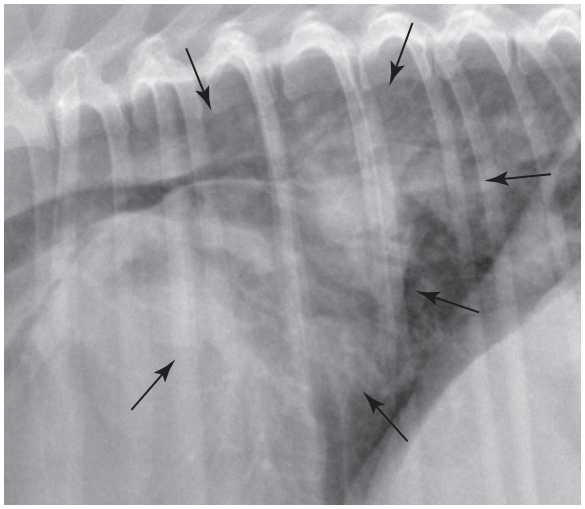


Fig. 33-57 Lateral thoracic radiograph of a dog with mitral insufficiency. There is an ill-defined increase in opacity in the perihilar region that was interpreted as cardiogenic pulmonary edema on initial inspection *(black arrows)*. However, when the DV projection was assessed, no lung abnormalities were detected. Thus, the perihilar opacity in this dog is caused by the opacity created by left atrial dilation, pulmonary vein dilation, and recumbency-associated atelectasis and is not a sign of cardiogenic pulmonary edema.

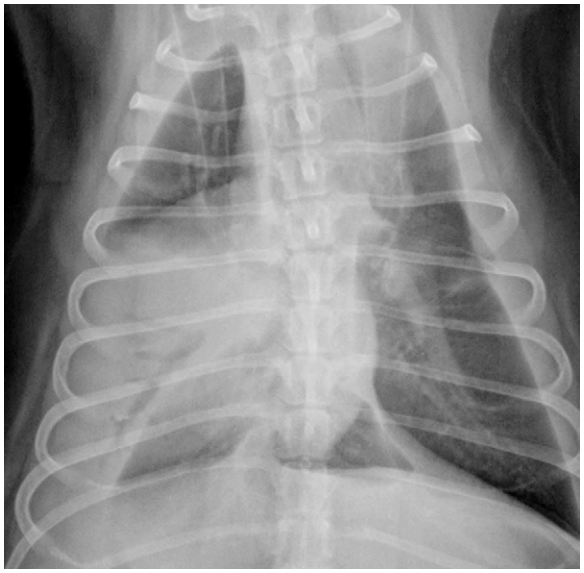


Fig. 33-58 Ventrodorsal radiograph of a dog with torsion of the right middle lobe. The right middle lobe has an alveolar pattern, and air bronchograms are visible. The shape of the right middle lobe is abnormal, being wider peripherally than at the hilus. There is bilateral pleural fluid. The radiographic findings in the lateral views were nonspecific; pleural fluid and the air bronchograms in the right middle lobe were visible, but the abnormal shape of the right middle lobe was not apparent.

REFERENCES

1. Reif J, Rhodes W: The lungs of aged dogs: a radiologic-morphologic correlation, *Vet Radiol Ultrasound* 7:5, 1966.
2. Gould D, Dalrymple G: A radiologic analysis of disseminated lung disease, *Am J Med Sci* 238:622, 1959.
3. Felson B: Disseminated interstitial diseases of the lung, *Ann Radiol* 9:325, 1966.
4. Felson B: The roentgen diagnosis of disseminated pulmonary alveolar disease, *Semin Radiol* 2, 1967.
5. Reeder M: *Reeder and Felson's gamuts in radiology—comprehensive lists of roentgen differential diagnosis*, ed 4, New York, 2003, Springer-Verlag.
6. Patterson HS, Sponaugle DN: Is infiltrate a useful term in the interpretation of chest radiographs? Physician survey results, *Radiology* 235:5, 2005.
7. Asenjo M, Ania BJ: On using the term infiltrate in radiography reports, *Radiology* 237:1123, 2005.
8. Hall FM: Infiltrate: a controversy without end, *Radiology* 237:1122; author reply 1124, 2005.
9. Tuddenham WJ: Editor's page, *Radiographics*, 4:671, 1984.
10. Felson B: Localization of intrathoracic lesions. In Felson B, editor: *Chest roentgenology*, Philadelphia, 1973, Saunders, p 22.
11. Fleischner F: The visible bronchial tree: a roentgen sign in pneumonic and other pulmonary consolidations, *Radiology* 50:184, 1946.
12. Corcoran BM, Foster DJ, Fuentes VL: Feline asthma syndrome: a retrospective study of the clinical presentation in 29 cats, *J Small Anim Pract* 36:481, 1995.
13. King PT: The pathophysiology of bronchiectasis, *Int J Chron Obstruct Pulmon Dis* 4:411, 2009.
14. Hawkins EC, Basseches J, Berry CR, et al: Demographic, clinical, and radiographic features of bronchiectasis in dogs: 316 cases (1988–2000), *J Am Vet Med Assoc* 223:1628, 2003.
15. Marolf A, Blaik M, Specht A: A retrospective study of the relationship between tracheal collapse and bronchiectasis in dogs, *Vet Radiol Ultrasound* 48:199, 2007.
16. Adams C, Streeter EM, King R, et al: Cause and clinical characteristics of rib fractures in cats: 33 cases (2000–2009), *J Vet Emerg Crit Care (San Antonio)* 20:436, 2010.
17. Gadbois J, d'Anjou MA, Dunn M, et al: Radiographic abnormalities in cats with feline bronchial disease and intra- and interobserver variability in radiographic interpretation: 40 cases (1999–2006), *J Am Vet Med Assoc* 234:367, 2009.
18. Talavera J, del Palacio MJ, Bayon A, et al: Broncholithiasis in a cat: clinical findings, long-term evolution and histopathological features, *J Feline Med Surg* 10:95, 2008.
19. Schwarz T, Stork CK, Mellor D, et al: Osteopenia and other radiographic signs in canine hyperadrenocorticism, *J Small Anim Pract* 41:491, 2000.
20. Kimme-Smith C, Hart EM, Goldin JG, et al: Detection of simulated lung nodules with computed radiography: effects of nodule size, local optical density, global object thickness, and exposure, *Acad Radiol* 3:735, 1996.
21. Wu N, Gamsu G, Czum J, et al: Detection of small pulmonary nodules using direct digital radiography and picture archiving and communication systems, *J Thorac Imaging* 21:27, 2006.
22. Nemanic S, London CA, Wisner ER: Comparison of thoracic radiographs and single breath-hold helical CT for detection of pulmonary nodules in dogs with metastatic neoplasia, *J Vet Intern Med* 20:508, 2006.
23. Eberle N, Fork M, von Babo V, et al: Comparison of examination of thoracic radiographs and thoracic computed tomography in dogs with appendicular osteosarcoma, *Vet Comp Oncol* 9:131, 2010.
24. Seo JB, Im JG, Goo JM, et al: Atypical pulmonary metastases: spectrum of radiologic findings, *Radiographics* 21:403, 2001.
25. Ryu JH, Swensen SJ: Cystic and cavitary lung diseases: focal and diffuse, *Mayo Clin Proc* 78:744,2003.
26. Lamb CR, Neiger R, Radiology corner: differential diagnosis of pulmonary cavitary lesions, *Vet Radiol Ultrasound* 41:340, 2000.
27. Diana A, Guglielmini C, Pivetta M, et al: Radiographic features of cardiogenic pulmonary edema in dogs with mitral regurgitation: 61 cases (1998–2007), *J Am Vet Med Assoc* 235:1058, 2009.
28. Gluecker T, Capasso P, Schnyder P, et al: Clinical and radiologic features of pulmonary edema, *Radiographics* 19:1507, 1999.
29. Neath PJ, Brockman DJ, King LG: Lung lobe torsion in dogs: 22 cases (1981–1999), *J Am Vet Med Assoc* 217:1041, 2000.
30. d'Anjou MA, Tidwell AS, Hecht S: Radiographic diagnosis of lung lobe torsion, *Vet Radiol Ultrasound* 46:478, 2005.
31. Murphy KA, Brisson BA: Evaluation of lung lobe torsion in pugs: 7 cases (1991–2004), *J Am Vet Med Assoc* 228:86, 2006.
32. Seiler G, Schwarz T, Vignoli M, et al: Computed tomographic features of lung lobe torsion, *Vet Radiol Ultrasound* 49:504, 2008.

ELECTRONIC RESOURCES

evolve

Additional information related to the content in Chapter 33 can be found on the companion Evolve website at http://evolve.elsevier.com/Thrall/vetrad/

- Chapter Quiz

CHAPTER • 34

The Equine Thorax

Stephanie G. Nykamp

RADIOGRAPHIC TECHNIQUE

Technical aspects of radiographing the equine thorax are covered in Chapter 25, but important principles are reiterated here. Radiographing the entire thorax of an adult horse requires a grid and large stationary x-ray tubes that are generally available only at referral centers. Portable radiographic tubes require an excessively long exposure time to penetrate the adult thorax; this usually results in motion artifact, rendering the images nondiagnostic. Four overlapping 14-inch × 17-inch views are usually required to image the entire thorax of an adult horse. They are acquired in the craniodorsal, caudodorsal, caudoventral, and cranioventral aspects of the thorax (Fig. 34-1). In addition to these standard views, radiographs centered over any identified lesions may also be useful.

Lateral radiographs of the foal thorax may be made with a single 14-inch × 17-inch cassette and some portable x-ray tubes. Dorsoventral or ventrodorsal radiographs should also be acquired on foals whenever possible.

The horse should be positioned with the thoracic limbs slightly forward to reduce the amount of muscle mass superimposed on the cranial aspect of the thorax. Radiographs should be obtained during peak inspiration. In some instances, radiographs should also be obtained during expiration because a comparison of the degree of lung inflation between inspiratory and expiratory radiographs may be helpful in the diagnosis of air trapping from chronic pulmonary disease.

When thoracic radiographs are obtained in a standing horse, the lung closest to the cassette is seen most clearly. This occurs because the large width of the equine thorax results in the lung farthest from the cassette being magnified and blurred to the extent that even large lesions can be obscured. This is opposite to the situation in lateral radiographs of dogs and cats where lesions in the nondependent lung (i.e., farthest from the cassette) are seen most clearly because of the atelectasis that occurs in the dependent lung. This was also discussed in Chapter 25. In the horse, therefore, left-right and right-left radiographs are necessary to assess both the left and right lungs adequately.[1]

Radiographic exposure and degree of inspiration play an important role in the interpretation of thoracic radiographs and must be considered both for initial and serial radiographic examinations. As the quality of the radiograph improves, the amount of perceived interstitial lung pattern decreases.[2] If a radiograph is underexposed or obtained during expiration, the lungs will appear diffusely more opaque than normal, mimicking a mild diffuse interstitial lung pattern often mistaken for disease. If the radiographs are overexposed, small or mild lung lesions may be obscured.

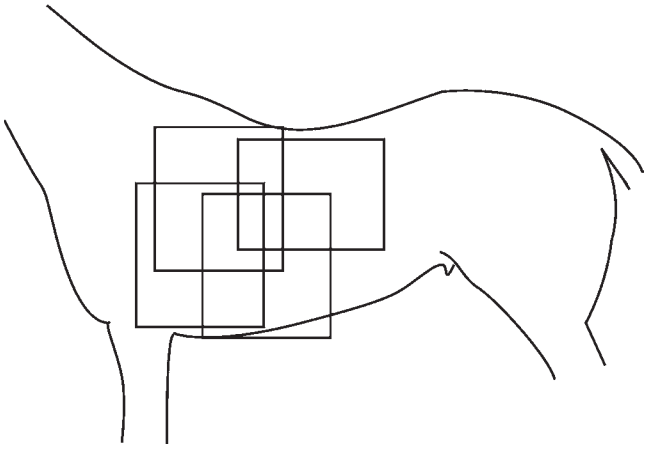


Fig. 34-1 Placement of cassettes or imaging plates for the four standard radiographic views of the equine thorax.

NORMAL ANATOMY

The right and left lungs are not clearly divided by interlobar fissures. The left lung is divided into a cranial and caudal component. The right lung is divided into a cranial and caudal component and the accessory lobe. A prominent cardiac notch is present in the left and right lungs at the level of the third to the sixth ribs.

Craniodorsal Projection

The dorsal portion of the heart, descending aorta, caudal vena cava, hilar pulmonary arteries and veins, trachea, and carina are visible (Fig. 34-2). The hilar portions of the lungs are visible but are difficult to evaluate because of the superimposition of the heart and blood vessels.

Caudodorsal Projection

This view provides the largest unobstructed view of the lungs (Fig. 34-3). The normal equine lung has a mild diffuse bronchointerstitial lung pattern when compared with canine and feline lungs. The pulmonary blood vessels should be seen clearly, tapering toward the periphery of the lung field.

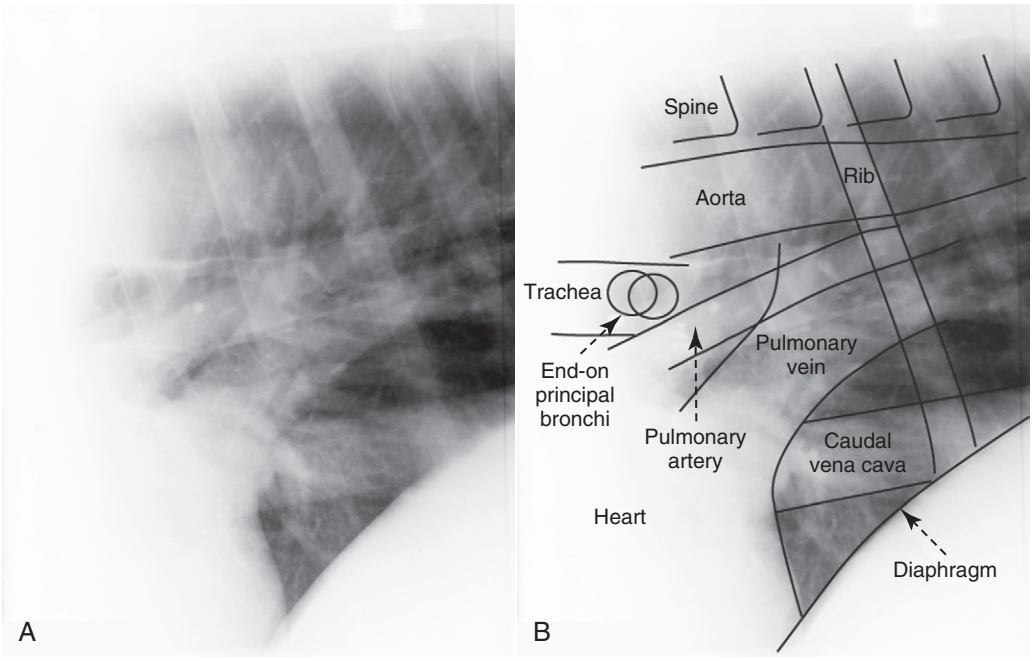


Fig. 34-2 Normal adult thoracic radiograph **(A),** craniodorsal projection, and accompanying line drawing **(B).**

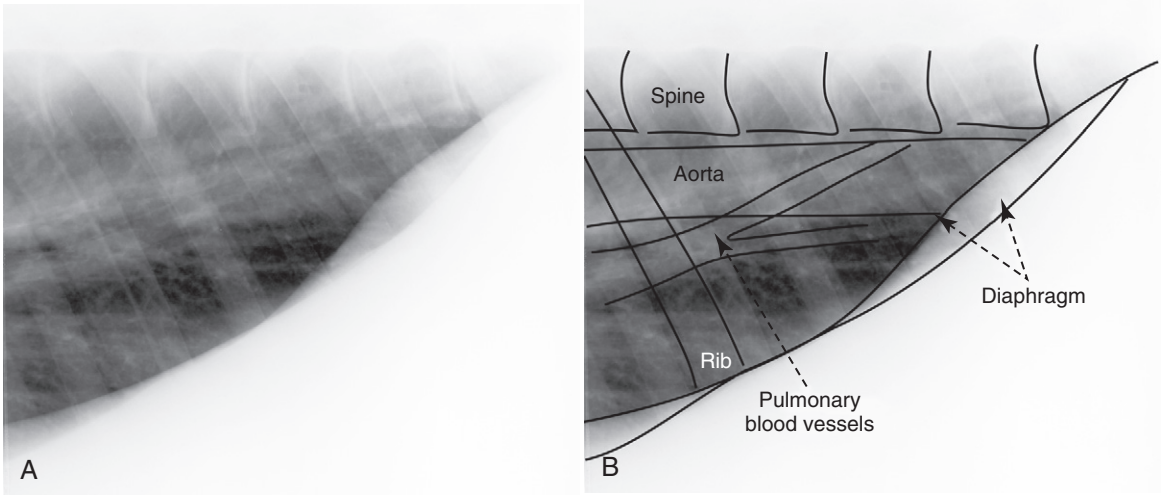


Fig. 34-3 Normal adult thoracic radiograph **(A),** caudodorsal projection, and accompanying line drawing **(B).**

Caudoventral Projection

The caudal borders of the heart, left atrium, caudal vena cava, pulmonary veins, and pulmonary arteries are evident on this view (Fig. 34-4). A small triangle of lung bounded by the caudal vena cava, caudal border of the heart, and cranioventral aspect of the diaphragm is evident. Because of the cardiac notch, no pulmonary markings are present over the central portion of the heart. The absence of pulmonary blood vessels in this region should not be mistaken for lung consolidation. The diaphragmatic reflection of the pleura follows the costochondral junctions to approximately the ninth rib and then travels dorsally, paralleling the costal arch to the middle of the last rib.[3] This means that the normal lung does not extend ventral to the costochondral junction and, in fact, usually ends approximately 4 inches above the costochondral junction in adult horses at rest. Ventral to the costochondral junction is mediastinal fat that provides contrast between the caudal border of the heart and the diaphragm. This fat opacity should not be mistaken for pleural or pulmonary disease.

Cranioventral Projection

The cranial portions of the lung, cranial mediastinum, aortic arch, and trachea are evident on this projection (Fig. 34-5). The lung is difficult to evaluate in this region because of the superimposition of the thoracic limbs. With the exception of evaluating for a mediastinal mass, this is typically the least helpful of all projections.

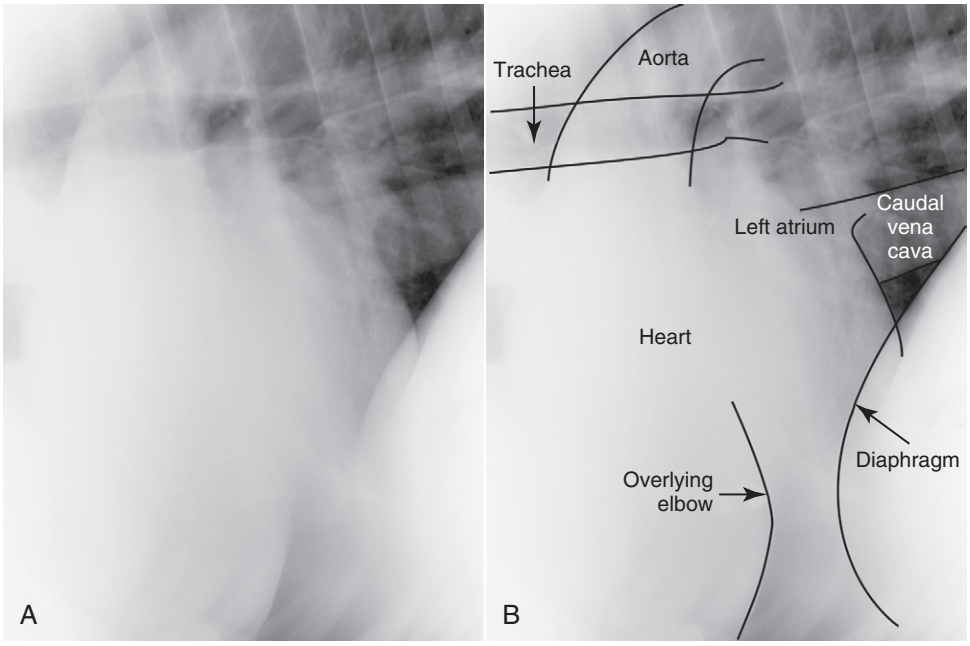


Fig. 34-4 Normal adult thoracic radiograph **(A),** caudoventral projection, and accompanying line drawing **(B).**

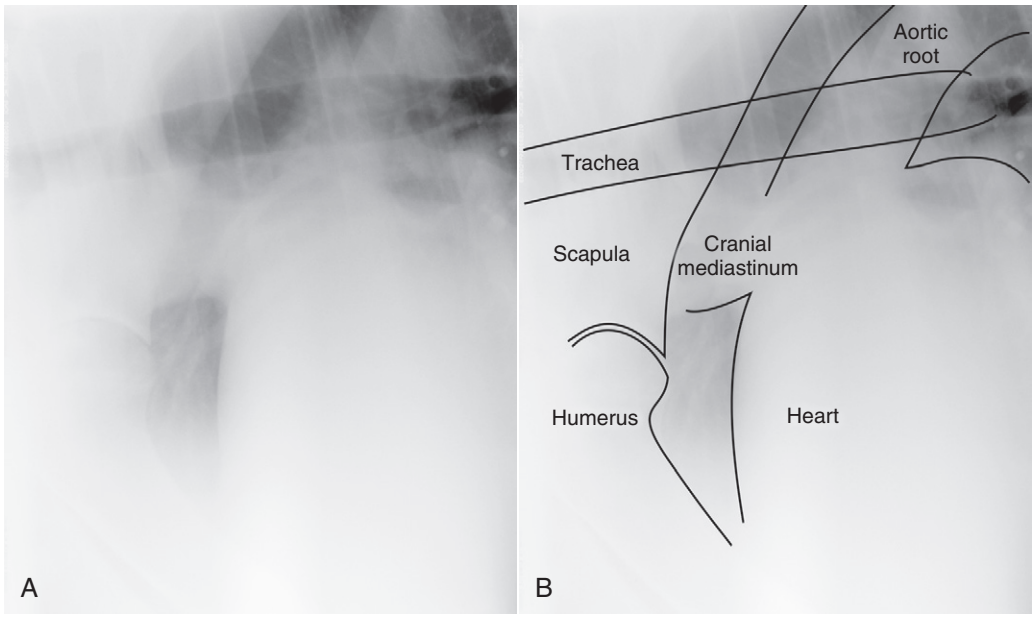


Fig. 34-5 Normal adult thoracic radiograph **(A),** cranioventral projection, and accompanying line drawing **(B).**

Foals

When radiographed immediately after parturition, foals have a mild diffuse interstitial lung pattern because of incomplete expansion of the lungs, fluid in the small airways, and the uptake of fetal alveolar fluid in the interstitium (Fig. 34-6). This opacity should resolve within 6 hours of birth.[4-6] The thymus is large in foals and can sometimes be seen as a soft tissue opacity cranial to the heart. The thymus is largest at approximately 2 months of age and should regress as the foal ages.[5] Atelectasis occurs rapidly when foals are placed in lateral recumbency. This will result in the lungs of recumbent foals appearing more opaque than those of standing foals.[5]

Adults

Age, size, and phase of respiration all affect the radiographic appearance of the lungs. Many adult horses with normal respiratory function and no clinical signs of respiratory disease have a mild, diffuse bronchointerstitial lung pattern as a normal

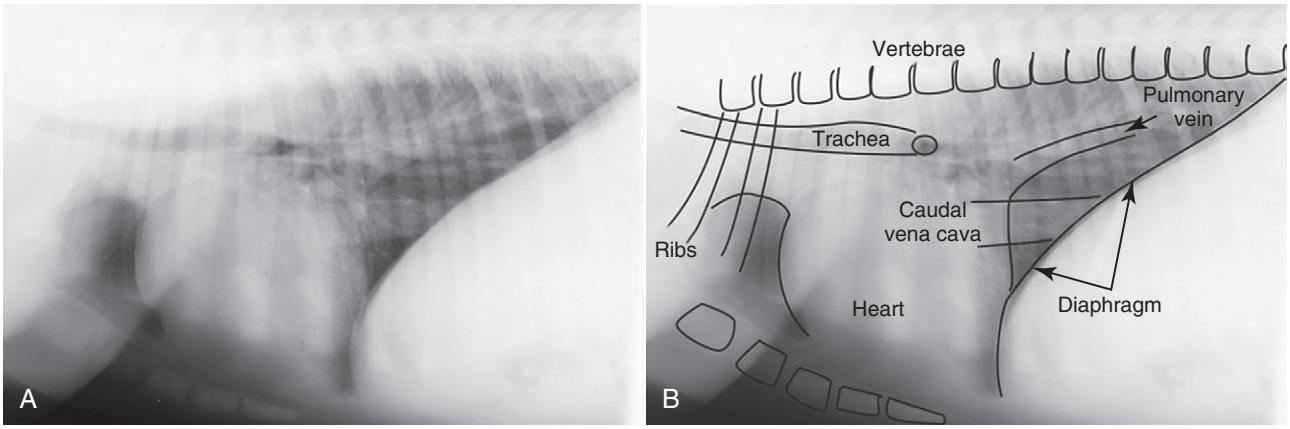


Fig. 34-6 Normal foal thoracic radiograph **(A)** and accompanying line drawing **(B).**



Fig. 34-7 Right lateral radiograph of the caudodorsal thorax in an adult horse with no clinical signs. Note the mild diffuse bronchial lung pattern seen in normal horses.

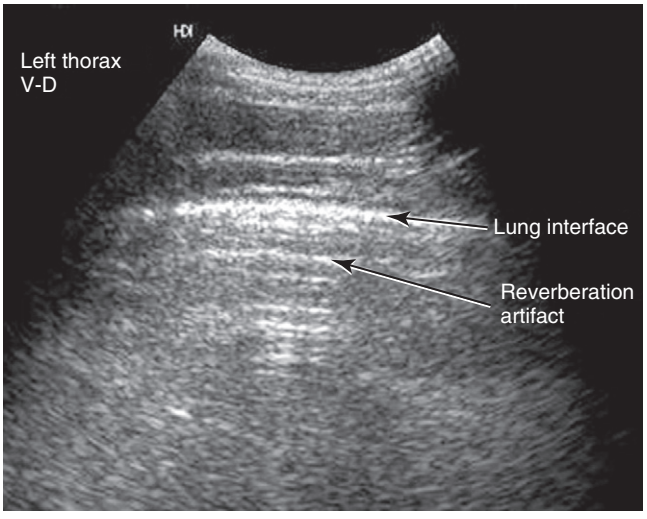


Fig. 34-8 Transverse ultrasound image of the normal left lung (ventrodorsal orientation). Note the equally spaced white lines (reverberation artifact) caused by the sound reflected at the air interface.

variation.[2,7] This opacity may be caused by the slightly more abundant lobulation and connective tissue that is present in horses or by subclinical peribronchial fibrosis.[2,3] The presence of this mild bronchointerstitial lung pattern means that many times the correlation between radiographic changes and clinical disease is poor. Therefore, mild radiographic changes should be interpreted with caution (Fig. 34-7).[2,8,9]

Heart

Objective criteria for assessing heart size have not been established in horses.[10] The caudal border of the heart should be straight and should parallel the angle of the ribs. Elevation of the trachea and increased sternal or diaphragmatic contact are indicative of cardiomegaly.[10] Assessment of cardiac size is easiest if the entire cardiac silhouette is visible in one image acquired with the x-ray beam centered over the heart. In foals, the cardiac silhouette occupies a larger volume of the thoracic cavity than it does in adults.[5] Based on objective measurements of cardiac size in foals, the height should be 6.6 to 7.8 times the length of a midthoracic vertebral body, and the width should be 5.6 to 6.3 times the width of a midthoracic vertebral body.[4] Echocardiography is superior to radiography in assessing cardiac size and function.

ALTERNATIVE IMAGING MODALITIES

Fluoroscopy, is useful to evaluate esophageal disease, tracheal collapse, and the motion of thoracic masses, but, unfortunately, fluoroscopy configured for equine evaluation is not available readily.[10,11]

The use of ultrasound has become common in equine practice. Air prevents the transmission of ultrasound waves, so the ultrasound appearance of the normal lung is a bright interface with reverberation artifact characterized by equally spaced lines that parallel the surface of the lung (Fig. 34-8).[12] In real time, the normal lung slides along the body wall during respiration. Ultrasound is more sensitive than radiographs in the detection of small pulmonary lesions as long as they extend to the pleural surface.[13] Ultrasound is the diagnostic test of choice for evaluating pleural disease in the horse

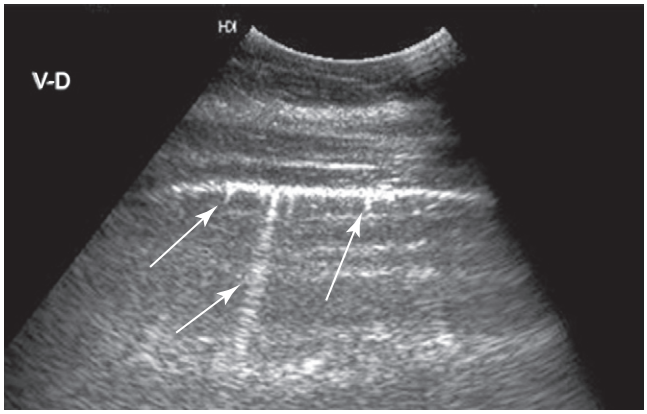


Fig. 34-9 Transverse ultrasound image of the lung. The pleural surface of the lung is rough, which results in a reverberation artifact, otherwise referred to as *comet tail artifact (arrows)*. A few comet tails can be seen in normal horses.

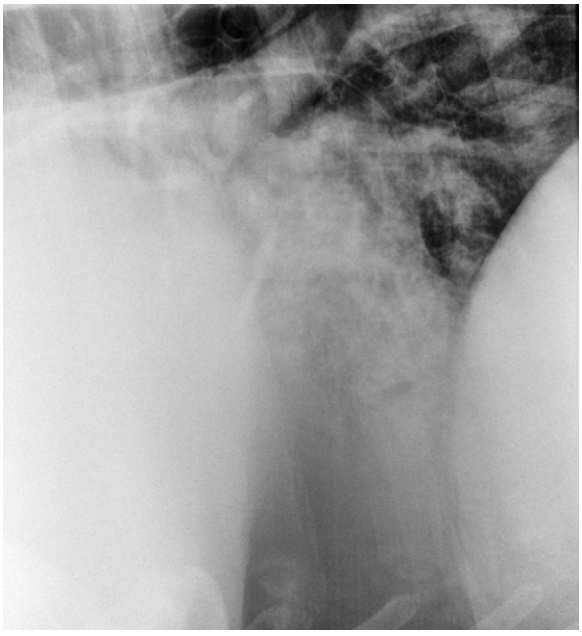


Fig. 34-10 Lateral caudoventral thoracic radiograph. A fairly intense soft tissue opacity is superimposed on the caudal aspect of the heart that partially silhouettes pulmonary blood vessels, making their margins appear indistinct. This lesion is caused by bronchopneumonia. In the pattern recognition scheme, this lesion is consistent with an interstitial pattern. The small irregular gas opacities overlying the heart are caused by small abscesses.

because it is more sensitive to the detection of small amounts of fluid and provides information on the character of the fluid.[11,14,15] Ultrasound can also be used to assess the surface of the lung. A few areas of rough pleural surfaces that create a comet tail artifact can be seen in the ventral portions of the normal lung, but more extensive lesions will be present in horses with viral pneumonia and chronic pleural fibrosis (Fig. 34-9).[16,17] Ultrasound is an inexpensive and accessible diagnostic test for serial examinations to assess for resolution or progression of disease.

Nuclear scintigraphy can provide physiologic information about perfusion and ventilation of the lungs. Ventilation studies can be useful in assessing chronic obstructive pulmonary disease and exercise-induced pulmonary hemorrhage.[18,19] The images are characterized by a patchy distribution with hot spots centrally caused by deposition of the injected isotope in the larger airways and cold spots peripherally from lack of ventilation. Additionally, radiopharmaceutical is cleared more rapidly from the lung of horses with chronic obstructive pulmonary disease than in normal horses.[20] Perfusion studies are used to evaluate for pulmonary thromboembolic disease, chronic obstructive pulmonary disease, and other diffuse diseases. In combination with ventilation studies, the patient can be evaluated for ventilation and perfusion mismatches. Because of the expensive equipment and need to isolate the patient for approximately 24 hours after the study to allow for radioactive decay, these imaging studies are usually limited to referral hospitals.

Computed tomography (CT) is an excellent imaging modality for assessment of the thorax, but because of equipment size its use is restricted to small foals.[21]

PULMONARY DISEASE

Radiographs complement a physical examination; they do not replace it. Physical examination can be unremarkable, and yet substantial radiographic abnormality can be present. Additionally, the radiographic resolution of disease often lags behind the clinical resolution. This should be considered when evaluating serial studies.[22]

The patterns of pulmonary disease have been discussed in Chapter 33. As in the dog and cat, the radiographic pulmonary pattern correlates poorly with the location of the disease histologically, diminishing the usefulness of the pattern recognition system. For example, in equine parasitic pneumonia, the most common pulmonary pattern is interstitial, but grossly, the disease is predominantly alveolar, and horses with a diffuse interstitial lung pattern have peribronchial disease on histologic examination.[2,23] But radiographic patterns can reflect the severity of the disease with bronchial and interstitial patterns suggesting less-severe disease than an alveolar pattern.[22] The distribution of the pulmonary disease may be more useful with regard to the cause of the pulmonary disease than the pattern itself.[5,24] For example, bronchopneumonia and aspiration pneumonia tend to have a cranioventral and caudoventral distribution, whereas pulmonary edema and interstitial pneumonia are more caudodorsal to diffuse in their distribution.

Pneumonia

Inhalation and aspiration pneumonia in the adult horse and foal appear similar to pneumonia in other species. In adults, bronchopneumonia is usually a result of transportation or stress, whereas in foals it is usually caused by sepsis or aspiration.[25,26] In adults and foals, bronchopneumonia can occur secondary to viral pneumonia.[26] Bacterial pneumonia usually occurs in the cranioventral and caudoventral portions of the lung.[27] Although it is present in the lung fields cranial to the heart, this region is difficult to evaluate radiographically, so the disease is most conspicuous when superimposed on the caudal border of the heart (Fig. 34-10). Bacterial pneumonia can result in an interstitial or alveolar lung pattern depending on the severity (Fig. 34-11).[23] Abscess formation is seen in 10% to 15% of horses with pneumonia (Fig. 34-12).[23]

The ultrasonographic appearance of pneumonic lung is a uniform soft tissue echogenicity that resembles the appearance of liver (Fig. 34-13). Air-filled bronchi appear as hyperechoic, linear, branching structures that have a reverberation artifact. Fluid-filled bronchi appear as anechoic branching tubes (Fig. 34-14). Fluid-filled bronchi can be differentiated from blood vessels with Doppler interrogation.

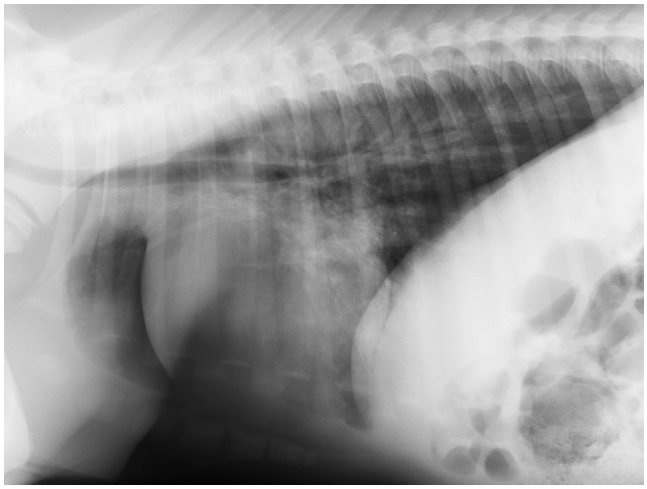


Fig. 34-11 Lateral thoracic radiograph of a foal. A soft tissue opacity that obscures the pulmonary blood vessels is superimposed on the caudal aspect of the heart. In this foal, pneumonia developed as a result of aspiration of milk. In the pattern recognition scheme, this lesion is consistent with an alveolar pattern.

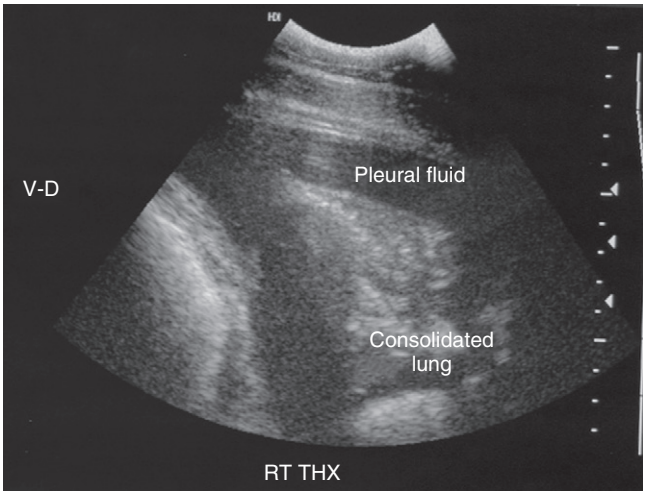


Fig. 34-13 This transverse ultrasound image is characterized by pleural fluid and consolidated lung. The lack of the normal reverberation artifact seen with aerated lung is evidence that the lung is abnormal. The lung has a relatively uniform soft tissue echogenicity similar to the appearance of normal liver and is triangular in shape. The pleural fluid is present between the lung and the body wall.

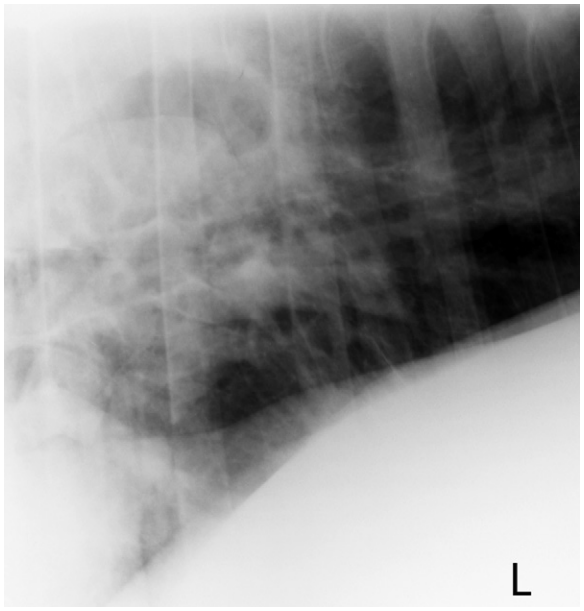


Fig. 34-12 Right-left lateral caudodorsal radiograph in an adult horse with a focal pulmonary abscess. There is a circular soft tissue rim with a central gas opacity located dorsal to the tracheal bifurcation. In the pattern recognition scheme, this is a structured interstitial pattern.

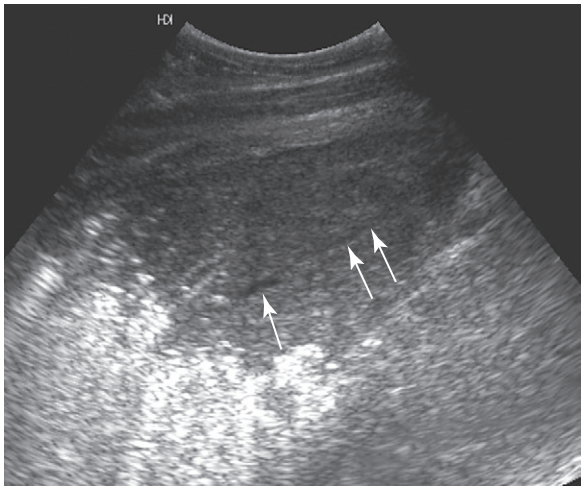


Fig. 34-14 This transverse ultrasound image shows consolidation of the lung and a fluid bronchogram *(arrows)*. The deep aerated portion of the lung is the irregular hyperechoic interface.

Interstitial pneumonia occurs in foals and adults and can be acute or chronic.[28,29] The causative agent is usually not identified but may include infectious agents, toxins, systemic inflammatory response syndrome, or allergic factors.[22,25,28-30]

Interstitial pneumonia in foals is usually acute, and affected foals are typically 6 weeks to 6 months of age.[28,31] Chronic interstitial pneumonia has a more favorable prognosis, whereas acute interstitial pneumonia has a high mortality rate.[29,32] Whether the disease is acute or chronic, the radiographic changes are the same, a diffuse interstitial lung pattern.[28,31] A mild to moderate bronchial lung pattern may also be present.[29] The disease can result in increased vascular permeability and secondary pulmonary edema.[32] The severity of the changes on the initial radiographs and progression of the changes on subsequent radiographs are negative prognostic indicators.[22]

Interstitial pneumonia is rare in adults, and because the lung has a limited range of responses to injury, it usually presents as a chronic problem with secondary fibrosis, and affected horses usually respond poorly to treatment.[26,30,32-34] The most common radiographic appearance is a patchy to diffuse alveolar lung pattern.[28] Recently, a specific form of multinodular interstitial pneumonia thought to be secondary to equine herpesvirus type 5 (EHV-5) has been reported.[33,35] Clinical signs include weight loss, fever, tachypnea, tachycardia, neutrophilic lymphocytosis and hyperfibrinogenemia, and increased respiratory effort. Imaging findings are severe multifocal nodules of 1 to 5 cm in diameter that are evident radiographically and with thoracic ultrasound.[33,36] Other causes of a diffuse interstitial to military nodular lung pattern are the eosinophilic pneumonopathy, including multisystemic

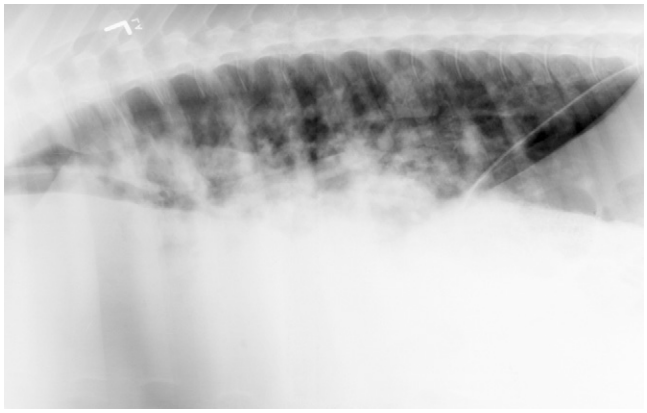


Fig. 34-15 Right-left lateral radiograph of a 3-month-old foal with pneumonia caused by *Rhodococcus equi* infection. An alveolar lung pattern is present in the ventral portion of the lung. Multiple soft tissue nodules are present dorsocaudally, the largest of which is cavitated. The nodules are caused by abscess formation.

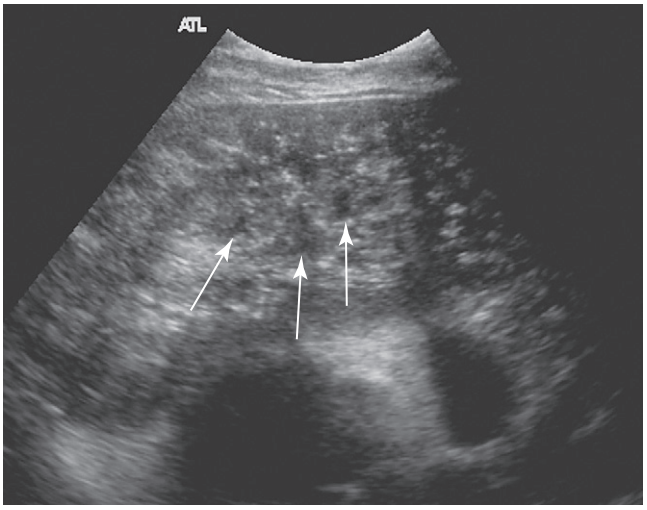


Fig. 34-16 Transverse ultrasound image of the left aspect of the thorax of a foal with *R. equi* infection. The lung is consolidated completely with a heterogenous soft tissue echogenicity. Multiple small, hypoechoic nodules are evident *(arrows)*. These are small abscesses within the consolidated lung.

eosinophilic epitheliotropic disease (systemic disease) and idiopathic chronic eosinophilic pneumonia (localized pulmonary disease) and pulmonary silicosis.[37-40]

Pneumonia caused by *Rhodococcus equi* in foals is a specific disease entity that frequently has a different radiographic appearance than bronchopneumonia or interstitial pneumonia. *Rhodococcus equi* pneumonia typically has a patchy to diffuse alveolar lung pattern and/or discrete pulmonary nodules (abscesses) (Fig. 34-15).[8,25,41,42] It can also result in consolidation of one lung lobe.[43] Radiographic changes are most apparent at approximately 3 weeks after infection.[43] The severity of the radiographic changes has been negatively associated with prognosis.[44] Foals with an extensive alveolar lung pattern or pulmonary nodules (abscesses) were more likely to die.[42] Tracheobronchial and cranial mediastinal lymphadenopathy can also be detected.[42] In most foals, the radiographic signs resolve completely within 3 months of appropriate therapy.[8,43] Ultrasonographic evidence of pneumonia has been highly associated with radiographic abnormalities and may be a useful diagnostic field test.[45] Ultrasound may also allow the detection of abscesses within consolidated lung lobes that are not evident radiographically (Fig. 34-16). Up to 74% of foals have *R. equi* infection in at least 1 additional extrapulmonary site, including gastrointestinal tract, abdominal lymphadenopathy, abdominal abscess, uveitis, synovitis, and pyogranulomatous hepatitis. A thorough physical examination and abdominal ultrasound examination are indicated in these patients to determine the extent of the disease because the prognosis is reduced significantly in foals with concurrent extrapulmonary disease.[46]

Fungal pneumonia is rare in horses. It has a wide range of radiographic appearances. Although it cannot be differentiated reliably from bacterial pneumonia on the basis of radiographic appearance, the distribution of fungal pneumonia is usually more diffuse than bacterial pneumonia and typically has an interstitial to indistinct nodular appearance.[23,47-50] Tracheobronchial lymphadenopathy and pleural effusion may also be present.[47,49]

Viral pneumonia itself does not usually result in radiographic changes, but radiographs can still be indicated to evaluate for concurrent bacterial pneumonia, which is common and results in more severe clinical disease.[16,23,51] Ultrasonographically, there may be roughening of the pleural surface with production of comet tail artifacts and consolidation of the cranioventral aspect of the lung within 5 to 10 days of infection.[16]



Fig. 34-17 Lateral radiograph of the craniodorsal thorax. A focal, cavitated pulmonary abscess is present. The dorsal portion of this abscess has a thick rim, and a distinct gas/fluid interface is seen.

Pulmonary Abscess

Pulmonary abscesses can form as a result of pleuropneumonia or develop independently and predominantly affect foals younger than 6 months of age.[52,53] They can occur anywhere in the lung, but unlike bronchopneumonia, abscesses are most commonly detected in the caudodorsal lung field.[14,54] This may be because of the excellent contrast provided by air-filled lung in this region. Abscesses are discrete, focal, soft tissue nodules or masses that may be sharply or poorly margined. If the abscess communicates with a bronchus or contains gas-forming bacteria, a discrete gas-fluid interface will be seen on horizontal-beam radiographs (Fig. 34-17). Well-margined

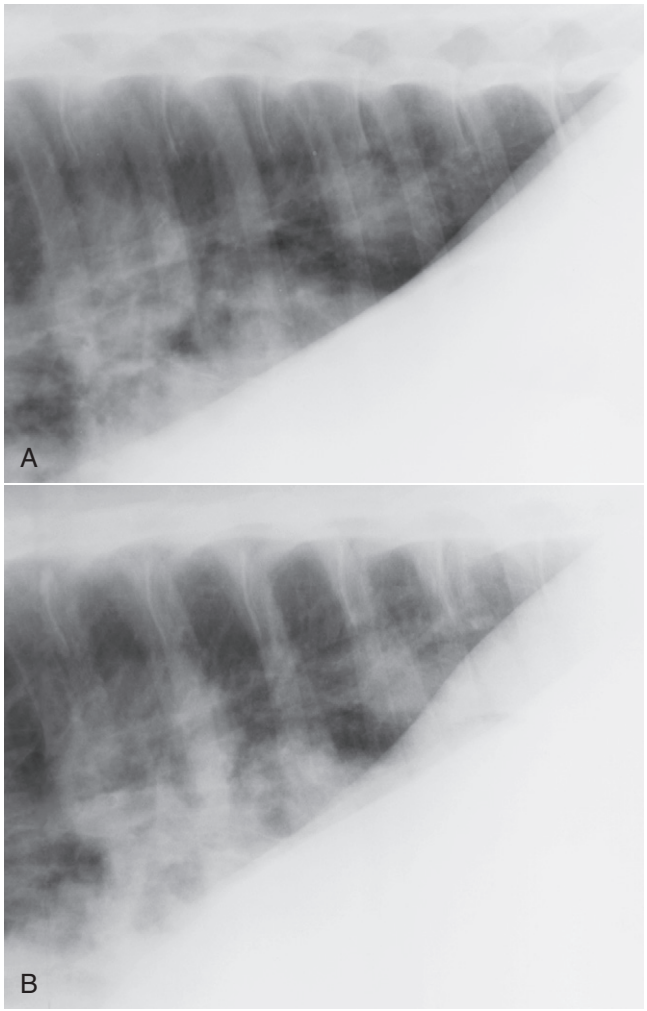


Fig. 34-18 Right-left **(A)** and left-right **(B)** radiographs of the caudal aspect of the thorax. The pulmonary nodule is smaller on the right-left radiograph, which means that it is in the left lung.

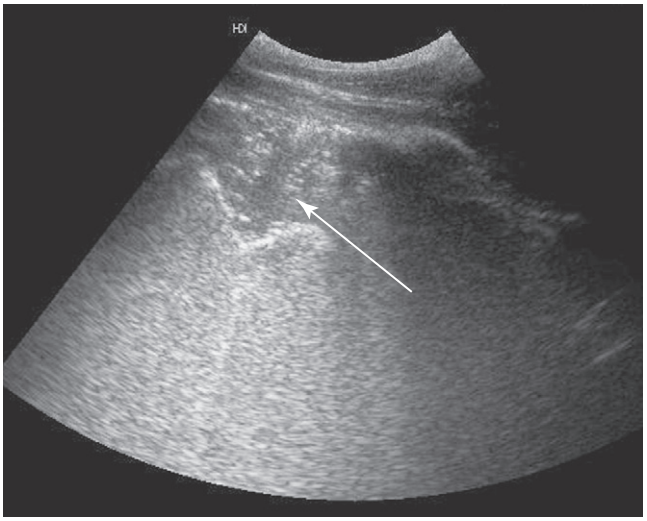


Fig. 34-19 Transverse ultrasound image of the left thorax. There is a focal hypoechoic nodule surrounded by air. This lesion was a pulmonary abscess.

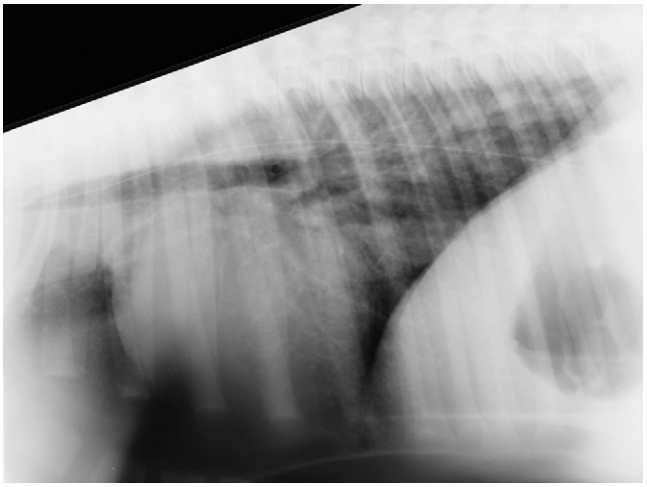


Fig. 34-20 Left-right lateral radiograph of a premature foal. A diffuse increased soft tissue opacity partially silhouettes the pulmonary blood vessels (interstitial pattern). This diffuse interstitial lung pattern was caused by prematurity and resolved with no treatment. A tube with a linear radiopaque marker is present in the esophagus.

pulmonary consolidation can mimic the appearance of a pulmonary abscess.

By obtaining left-right and right-left radiographs centered over the lesion, the abscess can be localized to one lung. When the abscess is located in the lung closest to the cassette or imaging plate, it will be smaller and more sharply marginated (Fig. 34-18). If the lesion is located close to midline, it will appear approximately the same on left-right and right-left radiographs.[55]

Ultrasound can be used to diagnose pleural-based pulmonary abscesses as well as abscesses that are within consolidated lung and that would not be evident on radiographs. Abscesses are usually hypoechoic to the surrounding pulmonary parenchyma and are defined by the absence of normal blood vessels and bronchi (Fig. 34-19).

Pulmonary Disease in Foals

A caudodorsal and caudoventral interstitial pattern is a common radiographic finding in foals.[22] This is nonspecific and can be caused by atelectasis, bacterial pneumonia, viral pneumonia, interstitial pneumonia, prematurity, dysmaturity, or failure of passive transfer, and the causes cannot be differentiated on the basis of radiographs alone (Fig. 34-20).[4,5,29,32,56] Foals with a diffuse distribution of pulmonary disease or a caudodorsal alveolar pattern have a significantly higher mortality rate.[22] Radiographs obtained immediately after parturition often have a diffuse interstitial lung pattern as a result of incomplete expansion of the lungs, fluid in the small airways, and the uptake of fetal alveolar fluid in the interstitium. This complicates the interpretation of these radiographs because it can mask pulmonary disease such as sepsis and acute respiratory distress because of a lack of surfactant. If the opacity does not resolve within 6 hours, it is more likely to be caused by underlying disease.[6]

Concurrent rib fractures may be present with severe respiratory disease in foals (Fig. 34-21).[4,5,29,32,56] Multiple ribs are usually fractured, and these can cause myocardial puncture, hemothorax, or pneumothorax.[57] Careful evaluation of the ribs is important, because rib fractures have been associated with increased morbidity and mortality.[58] Osteomyelitis of the costochondral junction is reported only rarely.[59] Ultrasound or CT is superior to radiographs for detecting rib lesions (Fig. 34-22).[60]

The syndromes *acute lung injury* and *acute respiratory distress syndrome* are characterized by bilateral pulmonary

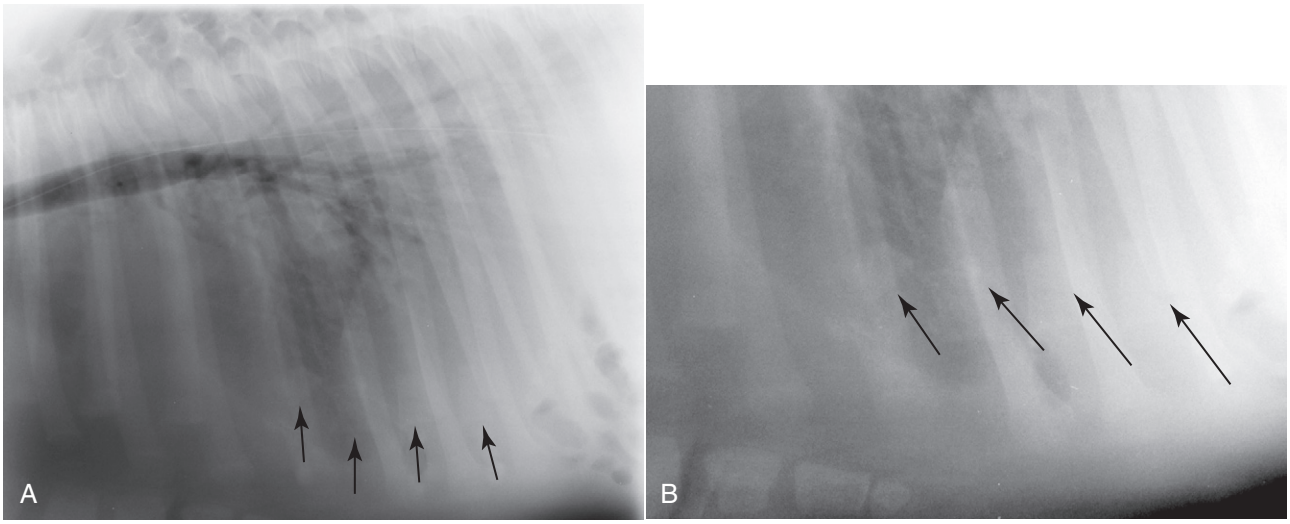


Fig. 34-21 **A,** Right-left lateral radiograph of a foal with severe respiratory distress. A diffuse alveolar pattern is throughout the lungs that silhouettes pulmonary blood vessels. Transverse fractures of the ventral portions of multiple ribs are present. **B,** Close-up of the ventral aspect of the thorax centered on the rib fractures *(arrows)*.

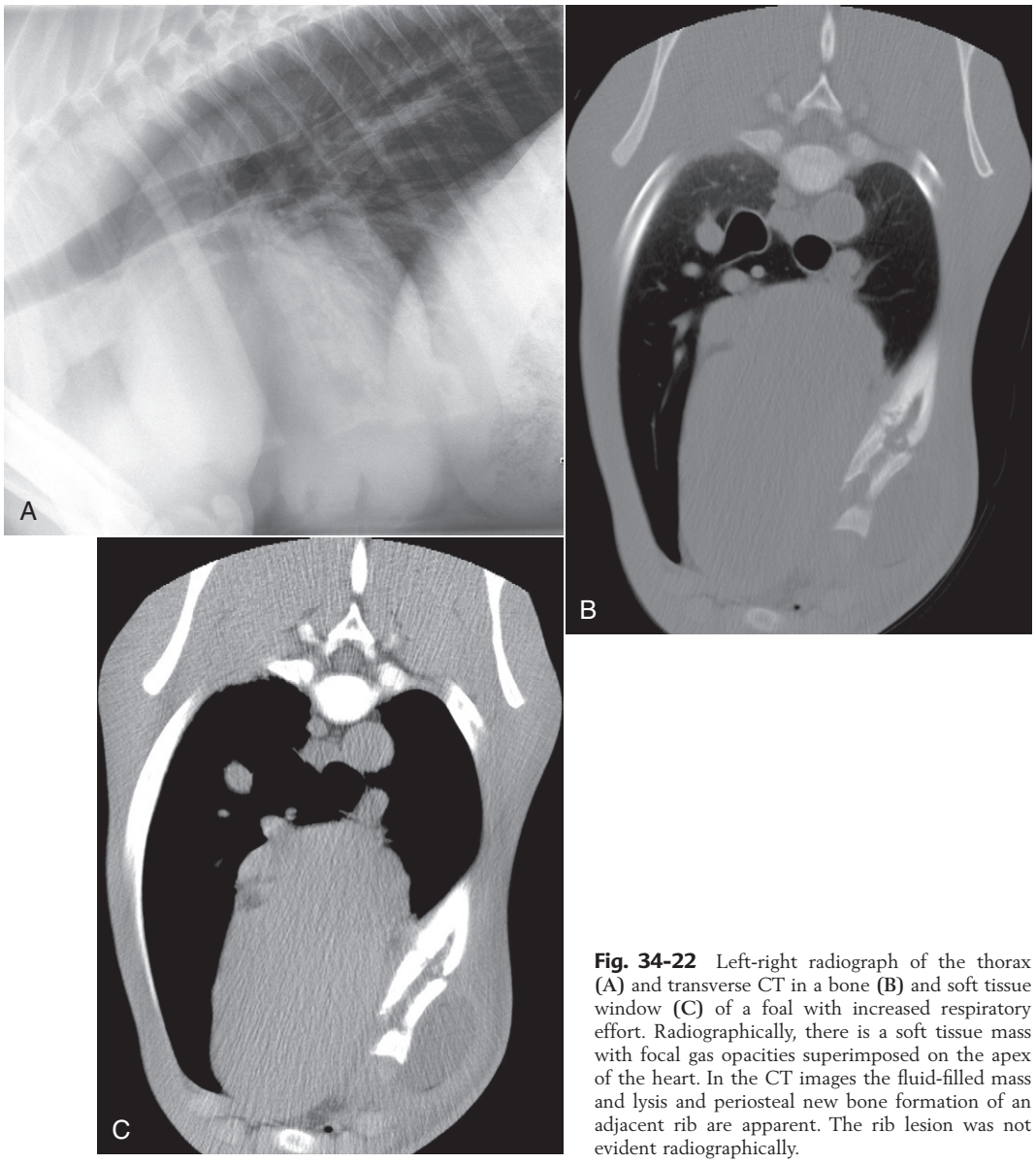


Fig. 34-22 Left-right radiograph of the thorax **(A)** and transverse CT in a bone **(B)** and soft tissue window **(C)** of a foal with increased respiratory effort. Radiographically, there is a soft tissue mass with focal gas opacities superimposed on the apex of the heart. In the CT images the fluid-filled mass and lysis and periosteal new bone formation of an adjacent rib are apparent. The rib lesion was not evident radiographically.

infiltrates on radiographs with no evidence of primary cardiac disease and an alveolar oxygen partial pressure (PAO_2) less than 200 to 300 mm Hg.[61] It is unclear whether these represent distinct clinical entities or severe manifestations of well-recognized pulmonary disease, but regardless, they represent a severe clinical syndrome that is associated with a high mortality rate.[61,62] These are syndromes and not a final diagnosis. Causes of acute lung injury and acquired respiratory distress syndrome include bacterial or viral infections as well as *Pneumocystis carinii* and coccidiomycosis.[9,31,32,48] Increased vascular permeability leads to pulmonary edema, resulting in a diffuse, interstitial to alveolar lung pattern that cannot be differentiated from other diffuse diseases.[26] Rapid resolution of the pulmonary edema has been associated with improved survival.[61]

Inflammatory Airway Disease and Recurrent Airway Obstruction

Inflammatory airway disease and recurrent airway obstruction are two distinct clinical entities that are indistinguishable radiographically. The pathogenesis of inflammatory airway disease is unclear and may be caused by environmental or infectious causes. Horses of any age can be affected, but it is most commonly seen in young performance horses.[63] The clinical signs at rest are subtle, but exercise intolerance or poor performance are often noted.[64] Recurrent airway obstruction, known previously as *chronic obstructive pulmonary disease*, is a major cause of chronic respiratory disease in mature horses and results from inhalation of aerosolized allergens and endotoxin. The lack of labored breathing and severe exercise intolerance distinguish inflammatory airway disease from recurrent airway obstruction.[64] The clinical signs are attributed to bronchitis and bronchoconstriction.[65] As such, the majority of horses with inflammatory airway disease and recurrent airway obstruction have normal thoracic radiographs.[2,66] If changes are present, they appear as a diffuse bronchointerstitial lung pattern caused by long-term remodeling of the bronchi.[66] Only the most severe forms of inflammatory airway disease and bronchiolitis result in radiographic changes.[23] Thickening of the bronchi enhances their radiographic visibility, resulting in a pronounced bronchial lung pattern with ring shadows and tram lines (Fig. 34-23). Radiographic scoring systems have been used in an attempt to improve the detection of inflammatory airway disease, but there is no correlation between the score and presence of disease.[67] In recurrent airway obstruction, pulmonary hyperinflation may be present.[68] Hyperinflation is characterized by flattening of the diaphragm and no change in lung volume between inspiratory and expiratory radiographs because of air trapping. Although radiographs are not particularly useful for diagnosing these diseases, they are useful to rule out concurrent bronchopneumonia.[66] Unlike in other species, recurrent airway obstruction generally does not result in chronic pulmonary arterial hypertension and secondary cardiomegaly. This is most likely because the disease is intermittent.[69,70] In end-stage bronchitis, tubular to saccular bronchiectasis can occur.[55]

Exercise-Induced Pulmonary Hemorrhage

Exercise-induced pulmonary hemorrhage is common in racing horses and is characterized by localized or diffuse parenchymal hemorrhage caused by mechanical failure of the walls of the pulmonary capillaries when the internal pressure rises to high levels.[71,72] Many horses with exercise-induced pulmonary hemorrhage have no radiographic abnormalities or a mild, caudodorsal bronchial or interstitial lung pattern that is not distinguishable from airway disease. Therefore radiography is a poor diagnostic tool for detecting exercise-induced pulmonary hemorrhage.[73] Repeated episodes of hemorrhage may be necessary for the lesions to become evident radiographically.[74]

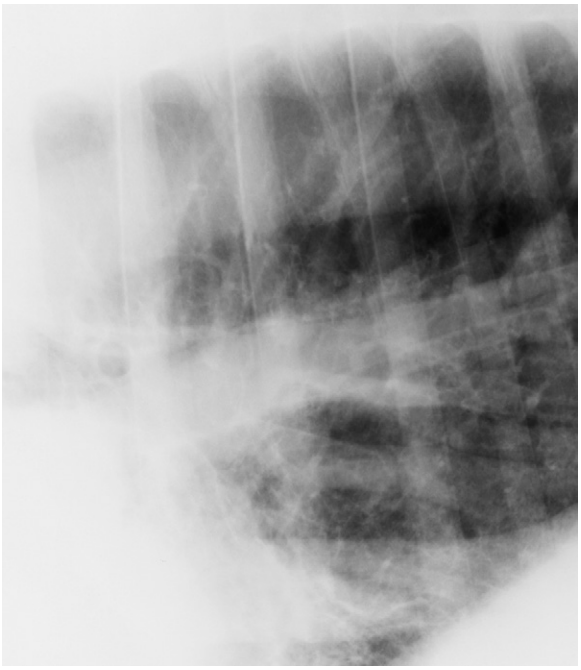


Fig. 34-23 Right lateral radiograph of an adult horse with chronic bronchitis and a bronchial pattern. Note the increased opacity that follows the airways, creating parallel lines and rings.

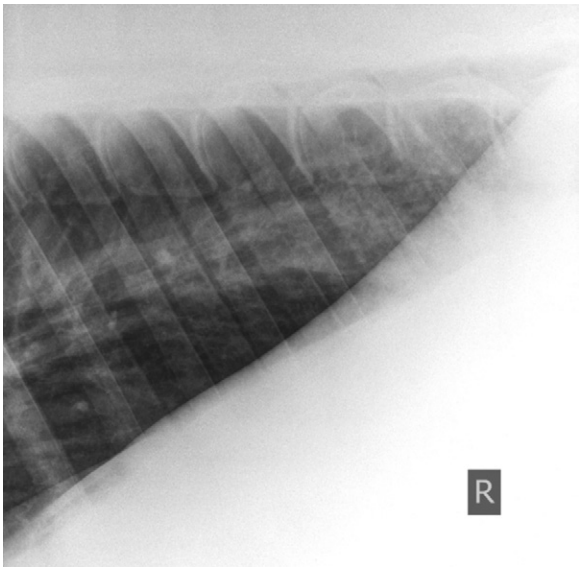


Fig. 34-24 Lateral radiograph of the caudal thorax. A patchy interstitial pattern is superimposed on the dorsal aspect of the diaphragm. This is a common location and appearance of exercise-induced pulmonary hemorrhage.

If a radiographic lesion is present, it is always located in the caudodorsal lung field, superimposed on the diaphragm, and is usually characterized as a focal area of increased opacity of variable size (Fig. 34-24).[73-76] The cranial margin of the lesion is round to oval, with indistinct margins. The radiopacity, which is usually either interstitial or alveolar in nature, can partially to completely silhouette with the pulmonary blood vessels.[75] An underlying bronchial pattern indicates a chronic lesion.[19] Resolution of the lesion is common in serial radiographs.[75] These lesions occasionally appear cavitary with a

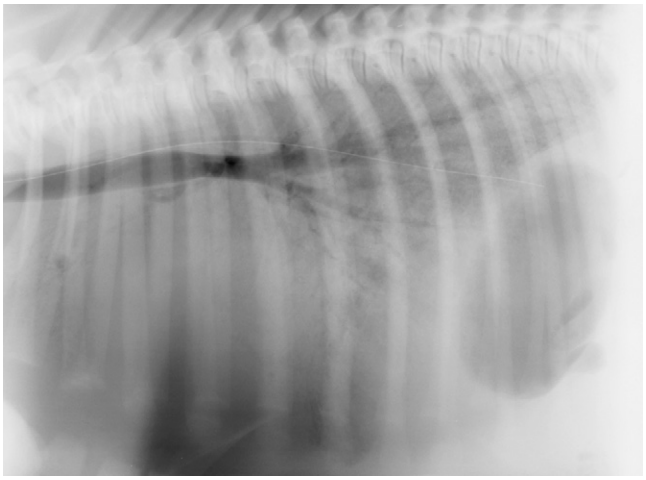


Fig. 34-25 Lateral radiograph of a premature foal with severe pulmonary edema. The lungs are diffusely increased in opacity, and multiple air bronchograms are present.

distinct gas/fluid interface, but when this is observed a concurrent infection caused by the hemorrhage is suspected.[75,77] Pleural fluid is also noted in some horses with exercise-induced pulmonary hemorrhage.[75] The presence of comet tail artifacts in the caudodorsal lung on thoracic ultrasound has a high sensitivity (85.8%) and a low specificity (25.7%) for exercise-induced pulmonary hemorrhage.[78]

Pulmonary Contusions

Pulmonary contusions can occur as a result of trauma or penetrating wounds. These lesions are seen as poorly marginated areas of increased soft tissue opacity in the lung. The distribution of these lesions corresponds to the location of the trauma.

Pulmonary Edema

Pulmonary edema can result from many causes, including vasculitis, heart failure, and upper airway obstruction.[26,79,80] The distribution is caudodorsal to diffuse, and the pattern can be interstitial or alveolar (Fig. 34-25).[81] Ultrasonographically, diffuse rough pleural surfaces with comet tail artifacts caused by focal areas of consolidation can be seen.[26]

Neoplasia

Primary and metastatic lung tumors are rare in horses.[82] Lung tumors appear as focal or multifocal soft tissue nodules in the lungs.[57,83-86] These lesions are usually discrete, with no air bronchograms. The presence of pleural fluid is also common with neoplasia.[83,87] The differential diagnoses for these radiographic signs include abscessation and fungal pneumonia. Pulmonary abscesses are the most common cause of multifocal pulmonary nodules and should be considered more likely than neoplasia. If the lesions are pleural based, they can be examined by ultrasound and ultrasound-guided needle aspiration can be performed.[87] Tracheobronchial lymphadenopathy may also be present with primary lung tumors, metastatic tumors, and lymphoma.

Alterations in Pulmonary Vasculature

Assessment of pulmonary vasculature is based on a subjective assessment of the size and number of vessels. The pulmonary veins and arteries generally cannot be distinguished from each other. Diseases that cause overcirculation of the lungs, such as right-to-left shunts, will cause an increase in the size and number of all visible pulmonary blood vessels.[10] Undercirculation of the lungs can be caused by shock or right-to-left shunts.[10]



Fig. 34-26 Lateral radiograph of the caudodorsal aspect of the thorax of a horse with moderate pleural fluid. A uniform soft tissue opacity that silhouettes the heart and diaphragm is present in the ventral aspect of the thorax. A distinct fluid line is not visible because pneumothorax is not present. Differentiation of pleural fluid from consolidated lung can be difficult radiographically and often requires ultrasound examination.

PLEURAL DISEASE

Pleural Fluid

The most common cause of pleural fluid in the horse is extension of bacterial pneumonia into the pleural space, resulting in pleuropneumonia.[51,52] Other causes of pleural fluid include neoplasia (mesothelioma, metastatic disease, and primary lung tumors), foreign bodies, and trauma (hemorrhage). Pleural fluid is uncommon in foals except as a result of uroperitoneum.[5]

Pleural fluid gravitates to the dependent portion of the thorax and results in a homogenous soft tissue opacity in the ventral aspect of the thorax (Fig. 34-26). Because horses do not have prominent interlobular fissures, pleural fissure lines are rarely seen. Approximately 1 to 2 L of pleural fluid must be present to be detected radiographically. Therefore normal thoracic radiographs do not eliminate the possibility of pleural fluid.[88] The fluid will initially silhouette the heart and diaphragm, resulting in loss of definition of these structures. As more fluid accumulates, normal lungs will be displaced dorsally. Because of surface tension, a discrete, horizontal fluid line is present only if free gas is also present in the pleural space (Fig. 34-27).

When pleural fluid is present, assessment of the lungs for concurrent disease is difficult to impossible.[23] Consolidated lung lobes are not displaced dorsally by the pleural fluid, so they are obscured. This makes the differentiation of pleural fluid from pneumonia difficult. Fibrin accumulation and inflammation can result in compartmentalization of pleural fluid with a unilateral distribution, even though the normal mediastinum is not complete. This can add to the difficulty in differentiating pulmonary disease from pleural disease. Repeating the radiographs after thoracocentesis provides more information on the presence and extent of any pulmonary disease.

Ultrasound is superior for evaluating the amount and character of pleural fluid, guiding thoracocentesis, and evaluating

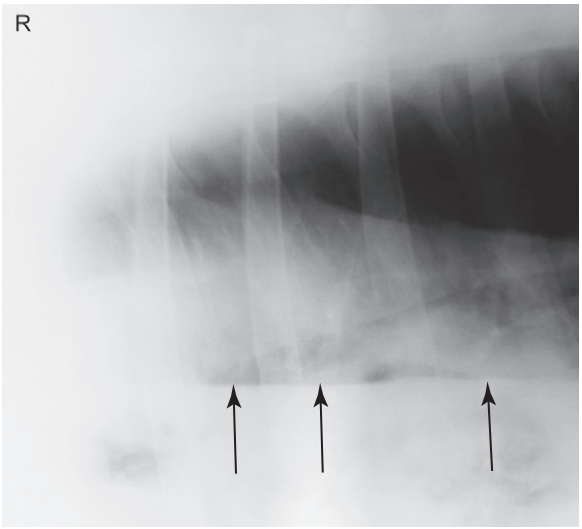


Fig. 34-27 Lateral radiograph of the thorax. A soft tissue opacity that silhouettes the diaphragm is present in the ventral thorax. This is caused by pleural fluid. A distinct, horizontal fluid line is evident *(arrows)* because of concurrent pneumothorax. A sharp pleural fluid line is seen only when concurrent pneumothorax is present.

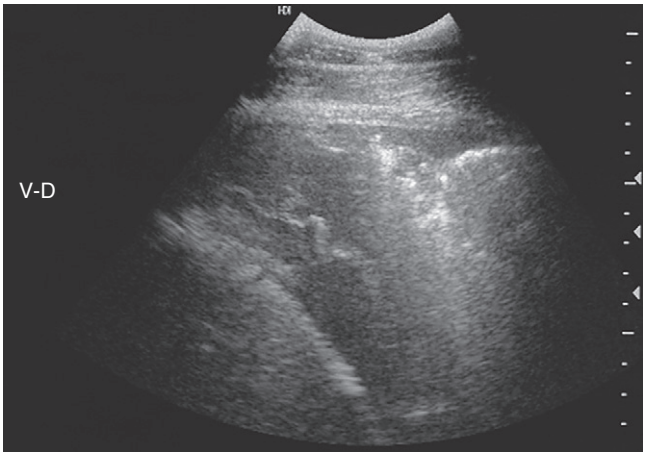


Fig. 34-29 Fibrin tags (adhesions) appear as echoic strands in the pleural effusion in this transverse ultrasound image.

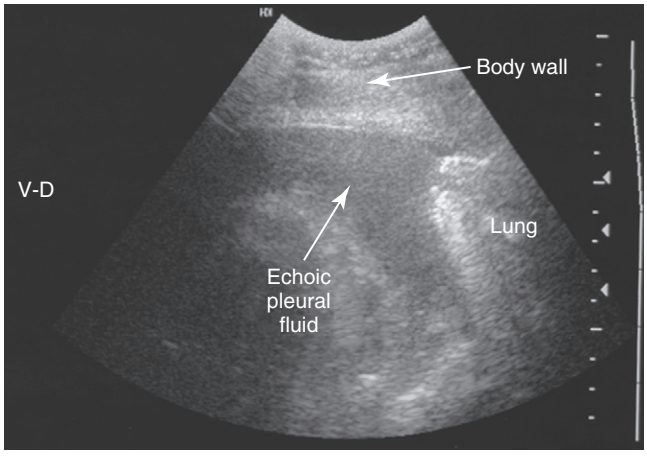


Fig. 34-28 Pleural fluid is present between the body wall and the lung; the fluid is highly echogenic. The lung is retracted away from the body wall and displaced dorsally.

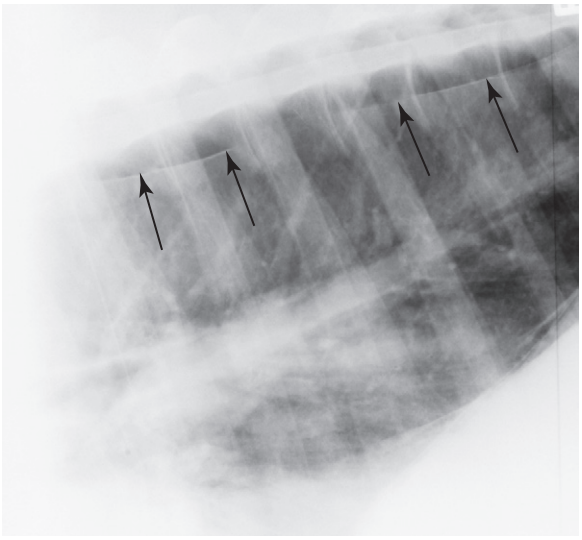


Fig. 34-30 Lateral radiograph of the caudal aspect of the thorax. Pneumothorax results in the lungs being retracted from the dorsal body wall; the edge of the lung appears as an opaque white line paralleling the vertebral column *(black arrows)*.

for resolution or progression (Fig. 34-28).[89] It also allows the identification of consolidation of the lung and other pleural-based lesions such as abscesses that may be masked radiographically by the pleural fluid.[12] The volume of pleural fluid can be estimated with ultrasound based on the level of the fluid relative to various anatomic points. If only a small amount of fluid is present in the ventral thorax, the volume is approximately 0.5 L. If the dorsal extent of the pleural fluid is at the point of the shoulder the volume is approximately 1 to 2.5 L. If the dorsal extent of the pleural fluid is 5 to 7 cm dorsal to the point of the shoulder, the volume is approximately 5 L.[14] The character of the pleural fluid can be inferred by the ultrasound appearance, with more echoic fluids being more cellular, but thoracocentesis is required to diagnose the type of fluid definitively. Ultrasound is also helpful to identify the presence of fibrinous adhesions between the pleural surface of the lung and the body wall (Fig. 34-29).[14] Neither of these changes can be identified radiographically.

Pneumothorax

Pneumothorax is rare in the horse and occurs most commonly as a result of trauma, as a sequela of pleuropneumonia, or from the tearing of pleural adhesions.[90] Iatrogenic causes of pneumothorax include complications from thoracocentesis and surgical procedures.

The presence of air in the pleural space results in retraction of the lungs from the body wall, permitting visualization of the dorsal margin of the lung because the air will rise to the dorsal aspect of the thorax. The free gas between the lung and the body wall contrasts with the edge of the lung, making it appear as an opaque line running roughly parallel to the vertebral column (Fig. 34-30). If pneumothorax is present concurrently with pleural fluid, a distinct horizontal gas/fluid interface will be present.

Radiography and ultrasound can both be used to diagnose pneumothorax, although radiography may be slightly more sensitive and is less operator dependent.[90] The

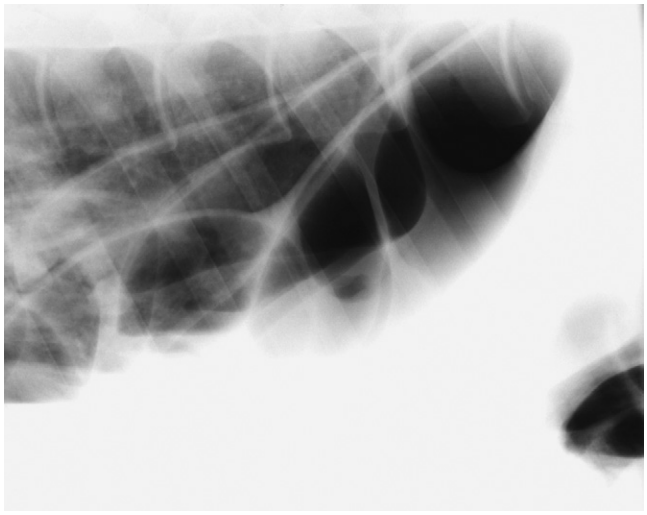


Fig. 34-31 Lateral radiograph of the caudal aspect of the thorax in an adult horse. Multiple gas-filled bowel loops are present in the thorax as a result of a diaphragmatic hernia.

ultrasonographic appearance of air (i.e., a bright interface with reverberation artifact) is the same whether it is free in the thorax or within the lung. The ultrasound diagnosis of pneumothorax requires the operator to identify that the air does not move with respiration.[14] Additionally, if the dorsal portions of the thorax are not evaluated, free air can go undetected.[90] Pneumothorax is easier to detect with ultrasound when pleural fluid is present concurrently.[90]

Diaphragmatic Hernia

Diaphragmatic hernias can occur as a result of trauma, dystocia, strenuous exercise, or laparoscopic surgery. Radiographic identification of a diaphragmatic hernia requires detection of abdominal contents in the thoracic cavity. Most often, gas-filled bowel loops are detected in the caudodorsal portion of the thorax (Fig. 34-31).[91,92] Pleural fluid may also be present.[92,93] Ultrasound can also be used to diagnose diaphragmatic hernias, particularly when pleural fluid is present. Not all of the diaphragm can be visualized with ultrasound, so the site of actual diaphragmatic disruption may not be apparent, but abdominal contents in the thoracic cavity can be seen.[94]

MEDIASTINAL DISEASE

Lymphadenopathy

The most common thoracic tumor in horses is lymphoma.[82] Lymphoma results commonly in a cranial mediastinal mass. Radiographically, this appears as a soft tissue mass cranial to the heart (Fig. 34-32).[95] With moderate cranial mediastinal lymphadenopathy, the mediastinum is wide, and the ventral border is irregular. More severe involvement causes loss of visualization of the normal aerated lung cranial to the heart as a result of atelectasis. Pleural fluid is also a common finding in lymphoma, which inhibits the radiographic detection of mediastinal masses.[95,96] Ultrasound is useful in these instances to characterize the quantity and quality of the fluid, as well as the presence of a mass, and to guide biopsy of the mass.[97] Most masses are multilobular and uniformly hypoechoic and frequently displace the heart caudally (Fig. 34-33).[95]

A poorly defined soft tissue opacity dorsal to the carina that displaces the trachea dorsally or ventrally and silhouettes the ventral border of the aorta is indicative of tracheobronchial lymphadenopathy.[21,95] Tracheobronchial lymphadenopathy may be difficult to differentiate from a pulmonary mass. Opposite lateral radiographs are helpful because the lymph nodes are a midline structure and therefore should have the same appearance on both lateral radiographs. CT can also be used in foals to differentiate tracheobronchial lymphadenopathy from a pulmonary mass.[21]

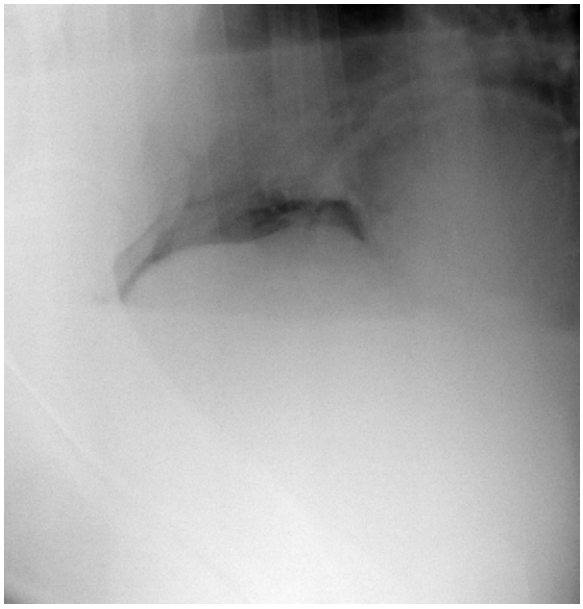


Fig. 34-32 Lateral radiograph of the cranial aspect of the thorax. A focal soft tissue mass is present cranial to the heart. The dorsal aspect of the mass is convex. Opposite lateral radiographs of the cranial aspect of the thorax had a similar appearance, indicating the structure was on the midline. This mass was confirmed to be mediastinal lymphoma.

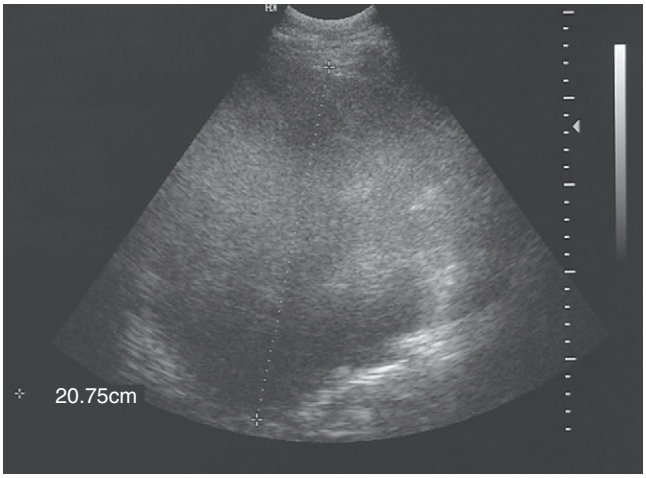


Fig. 34-33 A uniformly echoic mass can be seen in a transverse ultrasound image of the cranial aspect of the thorax of the horse in Figure 34-32.

Pneumomediastinum

Pneumomediastinum can occur as a result of punctures to the neck, rupture of the trachea, rupture of the esophagus, or a transtracheal wash. Linear gas opacities are seen tracking along the facial planes of the neck and mediastinum. This results in gas contrasting the trachea, esophagus, cranial vena cava, and aorta (Fig. 34-34). Pneumomediastinum can lead to pneumothorax.

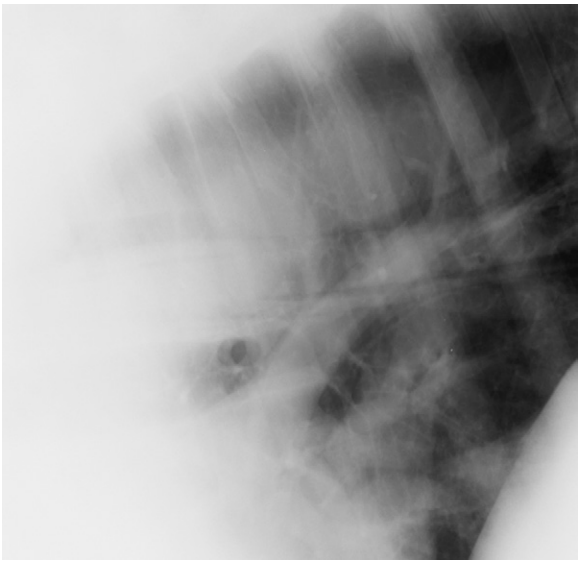


Fig. 34-34 Lateral radiograph of the craniodorsal aspect of the thorax. Gas is present in the cranial mediastinum. The gas contrasts with the esophagus, making it visible as a tubular soft tissue opacity dorsal to the trachea.

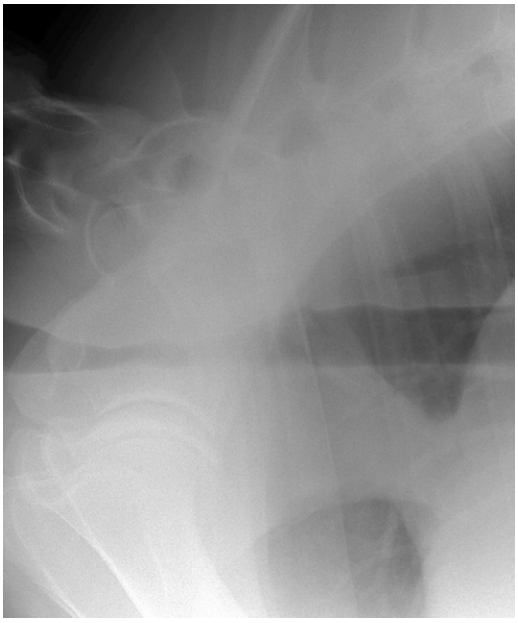


Fig. 34-35 Lateral radiograph of the cranial aspect of the thorax. The trachea is focally narrowed at the thoracic inlet, and the dorsal aspect of the lumen of the trachea has an irregular contour. This lesion was attributable to tracheal thickening from chronic tracheitis.

TRACHEAL DISEASE

Tracheal collapse has been rarely reported in horses. There may be an increased prevalence in American miniature horses, occurring in 6% of all American miniature horses referred to one hosptial.[98,99] Dorsoventral flattening of the trachea is seen on the thoracic radiographs. Comparing radiographs obtained during inspiration and expiration may demonstrate a change in tracheal diameter associated with collapse. In normal adult Thoroughbred horses, the tracheal diameter does not change with the phase of respiration.[100] Tracheal collapse can result in aspiration pneumonia, so radiographs of the entire thorax are indicated.[99]

Fluid can pool in the ventral aspect of the trachea at the thoracic inlet in horses that have aspirated. In severe tracheitis the tracheal wall may appear thick and irregular (Fig. 34-35).

ESOPHAGEAL DISEASE

The most common esophageal disease of horses is idiopathic obstruction caused by impaction of ingesta (choke).[101] Reported esophageal disease in horses includes congenital or acquired strictures, esophageal duplication cyst, esophageal atresia, vascular ring anomalies, space-occupying lesions (abscess, tumor), megaesophagus, and esophagitis.[101-105] Regardless of the cause, most esophageal disease results in impaction of food within the esophagus.[101]

The normal esophagus is not visible in survey radiographs. Contrast radiographs are useful to evaluate the esophagus. Esophagraphy can be performed with liquid or paste forms of barium as well as with barium-coated food administered orally. Barium paste coats the esophagus better, allowing the detection of mucosal abnormalities.[106] If the oropharyngeal phase of swallowing is not of interest, then the contrast medium can be administered directly into the cranial aspect of the esophagus with an esophageal tube. The use of certain sedatives and the placement of an esophageal tube, however, can result in dilation of the esophagus in normal horses.[107] The use of fluoroscopy to observe swallowing is best because it allows a dynamic assessment of the esophagus, but obtaining static radiographs after the administration of contrast medium can be diagnostic because most esophageal diseases result in delayed transit time.[107] Minimal contrast medium should be retained in the esophagus, outlining the esophageal folds after normal swallowing.[107,108]

With the exception of esophageal impactions in which focal enlargement of the esophagus with a granular radiopacity is seen, most esophageal diseases are not evident on survey radiographs.[108] In recurrent choke, esophagraphy is indicated to evaluate for underlying primary esophageal disease.[101] Focal narrowing of the esophagus is indicative of a stricture or extraluminal mass causing compression of the esophagus. Filling the esophagus with a large amount of contrast medium (up to 500 mL) through a cuffed nasoesophageal tube may be necessary to distend the esophagus adequately to detect some strictures.[106] Esophagitis results in thickening of the esophageal wall, and accumulation of contrast medium may occur as a result of hypomotility. Focal esophageal ulcerations may be noted as the contrast medium adheres to the mucosa and creates irregular filling defects. In most horses, esophagoscopy has replaced the need for contrast studies of the esophagus because of its ease and availability. However, for adequate assessment of esophageal motility and swallowing, esophagraphy is still required.

CARDIAC DISEASE

Radiographic assessment of heart size is difficult in adult horses because of a lack of objective criteria and the inability to obtain orthogonal radiographs.[10] The entire heart should be included on one 14-inch × 17-inch image, but this may be impossible in large horses. Therefore echocardiography is the most common diagnostic test for cardiac disease in horses. The radiographic signs of cardiomegaly are the same as in small animals. Straightening of the caudal aspect of the heart, increased sternal and diaphragmatic contact, and dorsal displacement of the trachea are indications of heart enlargement (Fig. 34-36).[10]



Fig. 34-36 Lateral radiograph of the thorax centered over the heart. There is loss of the caudal cardiac waist and dorsal displacement of the trachea, indicative of cardiomegaly. In the caudoventral lung field there is a mild soft tissue opacity. In the pattern recognition scheme this is an interstitial lung pattern. This change is attributed to pulmonary edema. (Courtesy of Dr. Robert Bahr, Oklahoma State University, Stillwater.)

The radiographic signs of congestive heart failure are also the same as those seen in small animals. Pulmonary edema results in a diffuse to caudodorsal interstitial to alveolar lung pattern.[10,81] Pulmonary venous enlargement may also be seen.[81] Pleural fluid may be evident if biventricular heart failure is present.[10,81] For the diagnosis of pericardial fluid and pericarditis, ultrasound is preferred.[109]

REFERENCES

1. Feeney DA, Gordon BJ, Johnston GR, et al: A 200 centimeter focal spot-film distance (FFD) technique for equine radiography, *Vet Radiol* 23:13–19, 1982.
2. Wisner ER, O'Brien TR, Lakritz J, et al: Radiographic and microscopic correlation of diffuse interstitial and bronchointerstitial pulmonary patterns in the caudodorsal lung of adult thoroughbred horses in race training, *Equine Vet J* 25:293–298, 1993.
3. Dyce KM, Sack WO, Wensing CJG: *Textbook of veterinary anatomy*, ed 3, Philadelphia, 2002, Saunders.
4. Lamb CR, O'Callaghan MW, Paradis MR: Thoracic radiography in the neonatal foal: a preliminary report, *Vet Radiol* 31:11–16, 1990.
5. Lester GD, Lester NV: Abdominal and thoracic radiography in the neonate, *Vet Clin North Am Equine Pract* 17(v):19–46, 2001.
6. Kutasi O, Horvath A, Harnos A, et al: Radiographic assessment of pulmonary fluid clearance in healthy neonatal foals, *Vet Radiol Ultrasound* 50:584–588, 2009.
7. Sanderson GN, O'Callaghan MW: Radiographic anatomy of the equine thorax as a basis for radiological interpretation, *N Z Vet J* 31:127–130, 1983.
8. Ainsworth DM, Beck KA, Boatwright CE, et al: Lack of residual lung damage in horses in which *Rhodococcus equi*–induced pneumonia had been diagnosed, *Am J Vet Res* 54:2115–2120, 1993.
9. Perron Lepage MF, Gerber V, Suter MM: A case of interstitial pneumonia associated with *Pneumocystis carinii* in a foal, *Vet Pathol* 36:621–624, 1999.
10. Koblik PD, Hornof WJ: Diagnostic radiology and nuclear cardiology. Their use in assessment of equine cardiovascular disease, *Vet Clin North Am Equine Pract* 1:289–309, 1985.
11. Hoskinson JJ, Tucker RL, Lillich J, et al: Advanced diagnostic imaging modalities available at the referral center, *Vet Clin North Am Equine Pract* 13:601–612, 1997.
12. Rantanen NW: Ultrasound appearance of normal lung borders and adjacent viscera in the horse, *Vet Radiol* 22:217–219, 1981.
13. Reef VB, Boy MG, Reid CF, et al: Comparison between diagnostic ultrasonography and radiography in the evaluation of horses and cattle with thoracic disease: 56 cases (1984–1985), *J Am Vet Med Assoc* 198:2112–2118, 1991.
14. Reef VB: *Equine diagnostic ultrasound*, Philadelphia, 1998, Saunders, 187–214.
15. Hinchcliff KW, Byrne BA: Clinical examination of the respiratory system, *Vet Clin North Am Equine Pract* 7:1–26, 1991.
16. Gross DK, Morley PS, Hinchcliff KW, et al: Pulmonary ultrasonographic abnormalities associated with naturally occurring equine influenza virus infection in standardbred racehorses, *J Vet Intern Med* 18:718–727, 2004.
17. Rantanen NW: The diagnosis of lung consolidation in horses using linear array diagnostic ultrasound, *J Equine Vet Sci* 14:79–80, 1994.
18. Rush BR, Hoskinson JJ, Davis EG, et al: Pulmonary distribution of aerosolized technetium Tc 99m pentetate after administration of a single dose of aerosolized albuterol sulfate in horses with recurrent airway obstruction, *Am J Vet Res* 60:764–769, 1999.
19. O'Callaghan MW, Hornof WJ, Fisher PE, et al: Exercise-induced pulmonary haemorrhage in the horses: results of a detailed clinical, post mortem and imaging study. VII. Ventilation/perfusion scintigraphy in horses with EIPH, *Equine Vet J* 19:423–427, 1987.
20. Votion DM, Vandenput SN, Duvivier DH, et al: Alveolar clearance in horses with chronic obstructive pulmonary disease, *Am J Vet Res* 60:495–500, 1999.
21. Wion L, Perkins G, Ainsworth DM, et al: Use of computerised tomography to diagnose a *Rhodococcus equi* mediastinal abscess causing severe respiratory distress in a foal, *Equine Vet J* 33:523–526, 2001.
22. Bedenice D, Heuwieser W, Brawer R, et al: Clinical and prognostic significance of radiographic pattern, distribution, and severity of thoracic radiographic changes in neonatal foals, *J Vet Intern Med* 17:876–886, 2003.
23. Farrow CS: Radiographic aspects of inflammatory lung disease in the horse, *Vet Radiol* 22:107–114, 1981.
24. Nykamp SG, Scrivani PV, Dykes NL: Radiographic signs of pulmonary disease: an alternative approach, *Compend Contin Edu Pract Vet* 24:25–36, 2002.
25. Wilkins PA: Lower respiratory problems of the neonate, *Vet Clin North Am Equine Pract* 19(v):19–33, 2003.
26. Wilkins PA: Lower airway diseases of the adult horse, *Vet Clin North Am Equine Pract* 19(vii):101–121, 2003.
27. Kangstrom LE: The radiological diagnosis of equine pneumonia, *Vet Radiology* 9:80–98, 1968.
28. Buergelt CD: Interstitial pneumonia in the horse: a fledgling morphological entity with mysterious causes, *Equine Vet J* 27:4–5, 1995.
29. Nout YS, Hinchcliff KW, Samii VF, et al: Chronic pulmonary disease with radiographic interstitial opacity (interstitial pneumonia) in foals, *Equine Vet J* 34:542–548, 2002.
30. Buergelt CD, Hines SA, Cantor G, et al: A retrospective study of proliferative interstitial lung disease of horses in Florida, *Vet Pathol* 23:750–756, 1986.

31. Peek SF, Landolt G, Karasin AI, et al: Acute respiratory distress syndrome and fatal interstitial pneumonia associated with equine influenza in a neonatal foal, *J Vet Intern Med* 18:132–134, 2004.
32. Lakritz J, Wilson WD, Berry CR, et al: Bronchointerstitial pneumonia and respiratory distress in young horses: clinical, clinicopathologic, radiographic, and pathological findings in 23 cases (1984–1989), *J Vet Intern Med* 7:277–288, 1993.
33. Donaldson MT, Beech J, Ennulat D, et al: Interstitial pneumonia and pulmonary fibrosis in a horse, *Equine Vet J* 30:173–175, 1998.
34. Wong DM, Belgrave RL, Williams KJ, et al: Multinodular pulmonary fibrosis in five horses, *J Am Vet Med Assoc* 232:898–905, 2008.
35. Singh K, Holbrook TC, Gilliam LL, et al: Severe pulmonary disease due to multisystemic eosinophilic epitheliotropic disease in a horse, *Vet Pathol* 43:189–193, 2006.
36. Bell SA, Drew CP, Wilson WD, et al: Idiopathic chronic eosinophilic pneumonia in 7 horses, *J Vet Intern Med* 22:648–653, 2008.
37. Arens AM, Barr B, Puchalski S, et al: Osteoporosis associated with pulmonary silicosis in an equine bone fragility syndrome, *Vet Pathol* 48(3):593–615, 2011.
38. Berry CR, O'Brien TR, Madigan JE, et al: Thoracic radiographic features of silicosis in 19 horses, *J Vet Intern Med* 5:248–256, 1991.
39. Williams KJ, Maes R, Del Piero F, et al: Equine multinodular pulmonary fibrosis: a newly recognized herpesvirus-associated fibrotic lung disease, *Vet Pathol* 44:849–862, 2007.
40. Niedermaier G, Poth T, Gehlen H: Clinical aspects of multinodular pulmonary fibrosis in two warmblood horses, *Vet Rec* 166:426–430, 2010.
41. Hillidge CJ: Review of *Corynebacterium* (*Rhodococcus*) *equi* lung abscesses in foals: pathogenesis, diagnosis and treatment, *Vet Rec* 119:261–264, 1986.
42. Falcon J, Smith BP, O'Brien TR, et al: Clinical and radiographic findings in *Corynebacterium equi* pneumonia of foals, *J Am Vet Med Assoc* 186:593–599, 1985.
43. Martens RJ, Martens JG, Fiske RA, et al: *Rhodococcus equi* foal pneumonia: protective effects of immune plasma in experimentally infected foals, *Equine Vet J* 21:249–255, 1989.
44. Ainsworth DM, Eicker SW, Yeagar AE, et al: Associations between physical examination, laboratory, and radiographic findings and outcome and subsequent racing performance of foals with *Rhodococcus equi* infection: 115 cases (1984–1992), *J Am Vet Med Assoc* 213:510–515, 1998.
45. Ramirez S, Lester GD, Roberts GR: Diagnostic contribution of thoracic ultrasonography in 17 foals with *Rhodococcus equi* pneumonia, *Vet Radiol Ultrasound* 45:172–176, 2004.
46. Reuss SM, Chaffin MK, Cohen ND: Extrapulmonary disorders associated with *Rhodococcus equi* infection in foals: 150 cases (1987–2007), *J Am Vet Med Assoc* 235:855–863, 2009.
47. Green SL, Hager DA, Calderwood MB, et al: Acute diffuse mycotic pneumonia in a 7-month-old colt, *Vet Radiol* 28:216–219, 1987.
48. Maleski K, Magdesian KG, LaFranco-Scheuch L, et al: Pulmonary coccidioidomycosis in a neonatal foal, *Vet Rec* 151:505–508, 2002.
49. Ziemer EL, Pappagianis D, Madigan JE, et al: Coccidioidomycosis in horses: 15 cases (1975–1984), *J Am Vet Med Assoc* 201:910–916, 1992.
50. Toribio RE, Kohn CW, Lawrence AE, et al: Thoracic and abdominal blastomycosis in a horse, *J Am Vet Med Assoc* 214(1335):1357–1360, 1999.
51. Mair TS, Lane JG: Pneumonia, lung abscesses and pleuritis in adult horses: a review of 51 cases, *Equine Vet J* 21:175–180, 1989.
52. Raphel CF, Beech J: Pleuritis secondary to pneumonia or lung abscessation in 90 horses, *J Am Vet Med Assoc* 181:808–810, 1982.
53. Lavoie JP, Fiset L, Laverty S: Review of 40 cases of lung abscesses in foals and adult horses, *Equine Vet J* 26:348–352, 1994.
54. Ainsworth DM, Erb HN, Eicker SW, et al: Effects of pulmonary abscesses on racing performance of horses treated at referral veterinary medical teaching hospitals: 45 cases (1985–1997), *J Am Vet Med Assoc* 216:1282–1287, 2000.
55. Lavoie JP, Dalle S, Breton L, et al: Bronchiectasis in three adult horses with heaves, *J Vet Intern Med* 18:757–760, 2004.
56. Koterba AM, Brewer BD, Tarplee FA: Clinical and clinicopathological characteristics of the septicaemic neonatal foal: review of 38 cases, *Equine Vet J* 16:376–382, 1984.
57. Jean D, Lavoie JP, Nunez L, et al: Cutaneous hemangiosarcoma with pulmonary metastasis in a horse, *J Am Vet Med Assoc* 204:776–778, 1994.
58. Schambourg MA, Laverty S, Mullim S, et al: Thoracic trauma in foals: post mortem findings, *Equine Vet J* 35:78–81, 2003.
59. Neil KM, Charman RE, Vasey JR: Rib osteomyelitis in three foals, *Aust Vet J* 88:96–100, 2010.
60. Jean D, Picandet V, Macieira S, et al: Detection of rib trauma in newborn foals in an equine critical care unit: a comparison of ultrasonography, radiography and physical examination, *Equine Vet J* 39:158–163, 2007.
61. Dunkel B, Dolente B, Boston RC: Acute lung injury/acute respiratory distress syndrome in 15 foals, *Equine Vet J* 37:435–440, 2005.
62. Jose-Cunilleras E, Sibbons PD: Acute lung injury and acute respiratory distress syndrome: fashionable names for old conditions or new clinical entities in their own right? *Equine Vet J* 37:390–392, 2005.
63. Couetil LL, Rosenthal FS, DeNicola DB, et al: Clinical signs, evaluation of bronchoalveolar lavage fluid, and assessment of pulmonary function in horses with inflammatory respiratory disease, *Am J Vet Res* 62:538–546, 2001.
64. Couetil LL, Hoffman AM, Hodgson J, et al: Inflammatory airway disease of horses, *J Vet Intern Med* 21:356–361, 2007.
65. Leguillette R: Recurrent airway obstruction—heaves, *Vet Clin North Am Equine Pract* 19(vi):63–86, 2003.
66. Farrow CS: Equine thoracic radiology, *J Am Vet Med Assoc* 179:776–781, 1981.
67. Mazan MR, Vin R, Hoffman AM: Radiographic scoring lacks predictive value in inflammatory airway disease, *Equine Vet J* 37:541–545, 2005.
68. Seahorn TL, Beadle RE: Summer pasture-associated obstructive pulmonary disease in horses: 21 cases (1983–1991), *J Am Vet Med Assoc* 202:779–782, 1993.
69. Sage AM, Valberg S, Hayden DW, et al: Echocardiography in a horse with cor pulmonale from recurrent airway obstruction, *J Vet Intern Med* 20:694–696, 2006.
70. Johansson AM, Gardner SY, Atkins CE, et al: Cardiovascular effects of acute pulmonary obstruction in horses with recurrent airway obstruction, *J Vet Intern Med* 21:302–307, 2007.

71. West JB, Mathieu-Costello O: Stress failure of pulmonary capillaries as a mechanism for exercise induced pulmonary haemorrhage in the horse, *Equine Vet J* 26:441–447, 1994.
72. Clarke AF: Review of exercise induced pulmonary haemorrhage and its possible relationship with mechanical stress, *Equine Vet J* 17:166–172, 1985.
73. Sweeney CR: Exercise-induced pulmonary hemorrhage, *Vet Clin North Am Equine Pract* 7:93–104, 1991.
74. Birks EK, Durando MM, McBride S: Exercise-induced pulmonary hemorrhage, *Vet Clin North Am Equine Pract* 19:87–100, 2003.
75. Pascoe JR, O'Brien TR, Wheat JD, et al: Radiographic aspects of exercise-induced pulmonary hemorrhage in racing horses, *Vet Radiol* 24:85–92, 1983.
76. O'Callaghan MW, Pascoe JR, O'Brien TR, et al: Exercise-induced pulmonary haemorrhage in the horse: results of a detailed clinical, post mortem and imaging study. VI. Radiological/pathological correlations, *Equine Vet J* 19:419–422, 1987.
77. Riley CB, Bolton JR, Mills JN, et al: Cryptococcosis in seven horses, *Aust Vet J* 69:135–139, 1992.
78. Ferrucci F, Stancari G, Zucca E, et al: Specificity and sensitivity of ultrasonography and endoscopy for the diagnosis of exercise-induced pulmonary haemorrhage (EIPH) in 157 race horses, *Vet Res Commun* 33(Suppl 1):185–188, 2009.
79. Kollias-Baker CA, Pipers FS, Heard D, et al: Pulmonary edema associated with transient airway obstruction in three horses, *J Am Vet Med Assoc* 202:1116–1118, 1993.
80. Kaartinen MJ, Pang DS, Cuvelliez SG: Post-anesthetic pulmonary edema in two horses, *Vet Anaesth Analg* 37:136–143, 2010.
81. Davis JL, Gardner SY, Schwabenton B, et al: Congestive heart failure in horses: 14 cases (1984–2001), *J Am Vet Med Assoc* 220:1512–1515, 2002.
82. Sweeney CR, Gillette DM: Thoracic neoplasia in equids: 35 cases (1967–1987), *J Am Vet Med Assoc* 195:374–377, 1989.
83. Jorgensen JS, Geoly FJ, Berry CR, et al: Lameness and pleural effusion associated with an aggressive fibrosarcoma in a horse, *J Am Vet Med Assoc* 210:1328–1331, 1997.
84. Cook G, Divers TJ, Rowland PH: Hypercalcaemia and erythrocytosis in a mare associated with a metastatic carcinoma, *Equine Vet J* 27:316–318, 1995.
85. Facemire PR, Chilcoat CD, Sojka JE, et al: Treatment of granular cell tumor via complete right lung resection in a horse, *J Am Vet Med Assoc* 217:1522–1525, 2000.
86. Danton CA, Peacock PJ, May SA, et al: Anaplastic sarcoma in the caudal thigh of a horse, *Vet Rec* 131:188–190, 1992.
87. Anderson JD, Leonard JM, Zeliff JA, et al: Primary pulmonary neoplasm in a horse, *J Am Vet Med Assoc* 201:1399–1401, 1992.
88. Prater PE, Patton CS, Held JP: Pleural effusion resulting from malignant hepatoblastoma in a horse, *J Am Vet Med Assoc* 194:383–385, 1989.
89. Rantanen NW, Gage L, Paradis MR: Ultrasonography as a diagnostic aid in pleural effusion of horses, *Vet Radiol* 22:211–216, 1981.
90. Boy MG, Sweeney CR: Pneumothorax in horses: 40 cases (1980–1997), *J Am Vet Med Assoc* 216:1955–1959, 2000.
91. Perdrizet JA, Dill SG, Hackett RP: Diaphragmatic hernia as a cause of dyspnoea in a draft horse, *Equine Vet J* 21:302–304, 1989.
92. Verschooten F, Ovaert W, Muylle E, et al: Diaphragmatic hernia in the horse: four case reports, *Vet Radiol* 45–49, 1977.
93. Everett KA, Chaffin MK, Brinsko SP: Diaphragmatic herniation as a cause of lethargy and exercise intolerance in a mare, *Cornell Vet* 82:217–223, 1992.
94. Hartzband LE, Kerr DV, Morris EA: Ultrasonographic diagnosis of diaphragmatic rupture in a horse, *Vet Radiol Ultrasound* 31:42–44, 1990.
95. Garber JL, Reef VB, Reimer JM: Sonographic findings in horses with mediastinal lymphosarcoma: 13 cases (1985–1992), *J Am Vet Med Assoc* 205:1432–1436, 1994.
96. Mair TS, Lane JG, Lucke VM: Clinicopathological features of lymphosarcoma involving the thoracic cavity in the horse, *Equine Vet J* 17:428–433, 1985.
97. De Clercq D, van Loon G, Lefere L, et al: Ultrasound-guided biopsy as a diagnostic aid in three horses with a cranial mediastinal lymphosarcoma, *Vet Rec* 154:722–726, 2004.
98. Carrig CB, Groenendyk S, Seawright AA: Dorsoventral flattening of the trachea in a horse and its attempted surgical correction: a case report, *Vet Radiol* 14:32–36, 1973.
99. Aleman M, Nieto JE, Benak J, et al: Tracheal collapse in American miniature horses: 13 cases (1985–2007), *J Am Vet Med Assoc* 233:1302–1306, 2008.
100. Carstens A, Kirberger RM, Grimbeek RJ, et al: Radiographic quantification of tracheal dimensions of the normal Thoroughbred horse, *Vet Radiol Ultrasound* 50:492–501, 2009.
101. Feige K, Schwarzwald C, Furst A, et al: Esophageal obstruction in horses: a retrospective study of 34 cases, *Can Vet J* 41:207–210, 2000.
102. Clabough DL, Roberts MC, Robertson I: Probable congenital esophageal stenosis in a thoroughbred foal, *J Am Vet Med Assoc* 199:483–485, 1991.
103. Orsini JA, Sepesy L, Donawick WJ, et al: Esophageal duplication cyst as a cause of choke in the horse, *J Am Vet Med Assoc* 193:474–476, 1988.
104. Murray MJ, Ball MM, Parker GA: Megaesophagus and aspiration pneumonia secondary to gastric ulceration in a foal, *J Am Vet Med Assoc* 192:381–383, 1988.
105. Baker SJ, Johnson PJ, David A, et al: Idiopathic gastroesophageal reflux disease in an adult horse, *J Am Vet Med Assoc* 224(1931):1967–1970, 2004.
106. Green EM. In Robinson NE, editor: Esophageal obstruction, vol 3, Philadelphia, 1992, Saunders, pp 175–184.
107. King JN, Davies JV, Gerring EL: Contrast radiography of the equine oesophagus: effect of spasmolytic agents and passage of a nasogastric tube, *Equine Vet J* 22:133–135, 1990.
108. Greet TR: Observations on the potential role of oesophageal radiography in the horse, *Equine Vet J* 14:73–79, 1982.
109. Worth LT, Reef VB: Pericarditis in horses: 18 cases (1986–1995), *J Am Vet Med Assoc* 212:248–253, 1998.

ELECTRONIC RESOURCES

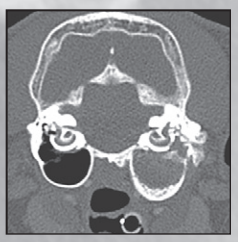
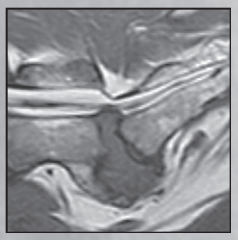
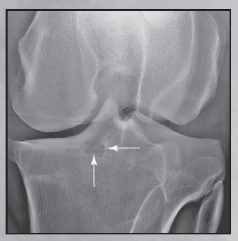
evolve

Additional information related to the content in Chapter 34 can be found on the companion Evolve website at http://evolve.elsevier.com/Thrall/vetrad/

- Chapter Quiz

SECTION V

The Abdominal Cavity: Canine and Feline



35 **Principles of Radiographic Interpretation of the Abdomen**
Donald E. Thrall

36 **The Peritoneal Space**
Paul M. Frank

37 **The Liver and Spleen**
Martha Moon Larson

38 **The Kidneys and Ureters**
Gabriela S. Seiler

39 **The Urinary Bladder**
Angela J. Marolf
Richard D. Park

40 **The Urethra**
James C. Brown, Jr.

41 **The Prostate Gland**
Jimmy C. Lattimer
Stephanie C. Essman

42 **The Uterus, Ovaries, and Testes**
Jennifer Kinns
Nathan Nelson

43 **The Stomach**
Paul M. Frank

44 **The Small Bowel**
Elizabeth A. Riedesel

45 **The Large Bowel**
Tobias Schwarz

CHAPTER • 35

Principles of Radiographic Interpretation of the Abdomen

Donald E. Thrall

As in the thorax, acquisition of abdominal radiographs is one of the more common radiographic examinations performed in small animal practice. Abdominal radiography is rarely performed in the adult horse, except for the assessment of the cranioventral and/or ventral aspects of the abdomen for sand collections or enterolith detection. The entire abdomen can be radiographed successfully in foals and miniature horses, but the conspicuity of abdominal organs is less than in dogs or cats because of the relatively reduced amount of peritoneal fat and the larger volume of the equine abdomen occupied by the gastrointestinal tract.

Abdominal sonography is also used commonly to assess the canine and feline abdomen, and it has found many applications in these species. However, in dogs and cats, sonography should not be viewed as a replacement for abdominal radiography. Sonography provides for real-time assessment of organ texture and blood vessels that cannot be obtained with radiography, but sonography does not provide for a global assessment of the abdomen, and the quality of the information obtained from an abdominal ultrasound examination is highly dependent on the abilities of the operator. With regard to equine abdominal radiography, the relatively poor quality of abdominal radiographs in adult horses has led to abdominal sonography assuming a more primary role for abdominal imaging in many equine patients.

Computed tomography (CT) imaging is also useful for evaluation of the canine and feline abdomen, and it would be expected that most, if not all, abnormalities detected using radiography and sonography would also be detected using CT. Overall, however, the use of CT use for canine and feline abdominal disease is low compared with radiography and sonography. Magnetic resonance imaging (MRI) is rarely used for abdominal imaging in dogs and cats, except for assessment of portosystemic shunts. Neither CT nor MRI is used for abdominal imaging in the horse.

NOMENCLATURE

As with the thorax, the naming of lateral abdominal radiographs made with the patient recumbent, as commonly done in dogs and cats, violates the point-of-entrance to point-of-exit nomenclature system described in Chapter 5. If that system were followed, a lateral view made with the dog or cat in left recumbency would be termed a *right-left* view because the x-ray beam strikes the right aspect of the abdomen and exits the left aspect of the abdomen. But, for the abdomen, the terminology for lateral projections has been abbreviated to describe the side of the patient lying on the x-ray table. Thus, for example, an abdominal radiograph acquired with a dog or cat lying on the left side would be termed a *left lateral*.

In the horse, where lateral abdominal radiographs are usually made with the patient standing and a horizontally directed x-ray beam, the point-to-entrance to point-of-exit system should be used. Thus, lateral radiographs should be described as either left-right or right-left views.

In all species, ventrodorsal (VD) and dorsoventral (DV) radiographs of the abdomen are named according to the point-to-entrance to point-of-exit system.

PREPARATION

In the dog and cat, unless one is (1) looking specifically for small abdominal masses, small mineralizations such as urethral calculi, or abnormalities of the peritoneum; or (2) preparing the patient for an abdominal contrast study, such as a barium upper-gastrointestinal examination or an excretory urogram, no special preparation such as fasting or enema administration is needed before abdominal radiography. If a bowel obstruction is being considered, enema administration is contraindicated because it will alter the native pattern of bowel gas and fluid. The native appearance of bowel gas and fluid is critical to the radiographic diagnosis of bowel obstruction and should not be altered by enema administration.

There are no specific circumstances in the horse where abdominal fasting or enema administration is recommended before abdominal radiography.

POSITIONING—DOG AND CAT

A lateral and a VD radiograph will be adequate for assessing the abdomen completely in many canine and feline patients. However, the abdomen contains a valuable inherent contrast medium—gas. Thus, by routinely acquiring left *and* right lateral radiographs in addition to the VD view, redistribution of bowel gas between the two lateral views can provide valuable additional information that can make the difference between obtaining the diagnosis or not (Fig. 35-1). Dorsoventral radiographs of the abdomen are rarely made and should not form the basis of the orthogonal view to complement the lateral projections. A DV view may have to suffice when a patient cannot be positioned in dorsal recumbency for a VD view, but the abdomen will be more crowded, organ conspicuity will be reduced, and portions of the pelvic limbs are often superimposed on the abdomen (see Fig. 35-9 for an example).

As in the thorax, the effort required to complete an abdominal radiographic examination is obviously related to the number of projections. There is no reason to limit the number of projections acquired routinely, especially with a

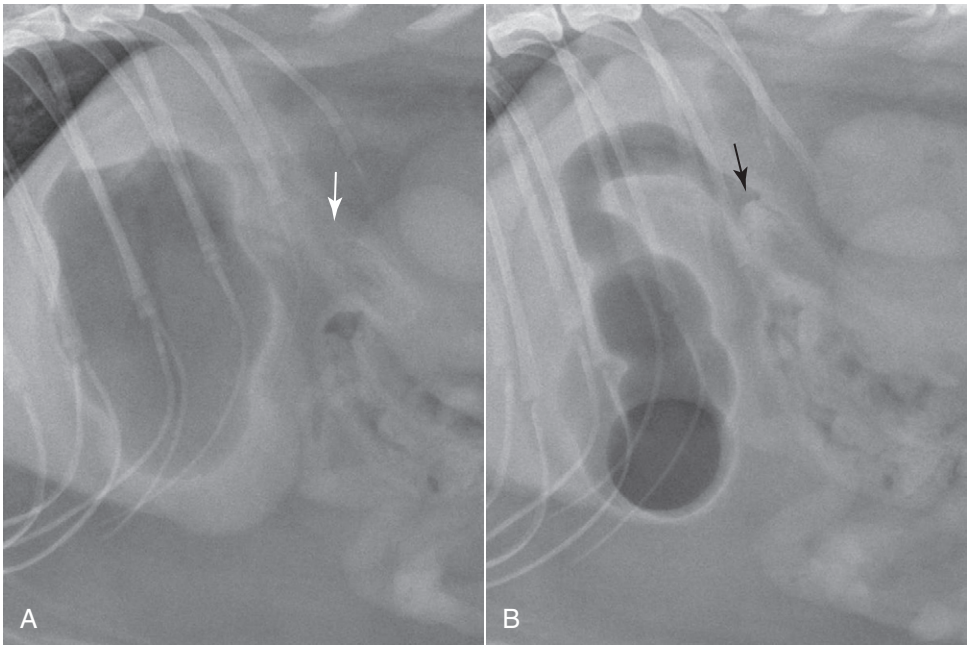


Fig. 35-1 Right **(A)** and left **(B)** lateral radiographs of the cranial aspect of the abdomen of a cat with acute vomiting. In the right lateral view **(A),** the stomach contains gas and there is heterogeneous material in the duodenum *(white arrow)*, but there is no diagnosis. In the left lateral view **(B),** gas from the stomach fills the proximal aspect of the duodenum outlining a foreign object *(black arrow)*, supporting a diagnosis of bowel obstruction.

direct digital system where the image is available instantly and there are no expendable supplies. Not acquiring both right *and* left lateral views routinely in addition to the VD view will result in some diagnoses being missed. Admittedly, the increased number of exposures per patient has the potential to increase the occupational radiation dose to personnel, but as long as proper protection principles are followed, this potential increase will not be realized.

It is important that the entire abdominal cavity be included in the image. The field of view should extend from just cranial to the diaphragm to a few centimeters caudal to the coxofemoral joints. For lateral views, the pelvic limbs should not be pulled caudally but should be kept perpendicular to the spine. This relaxes the caudoventral aspect of the abdominal wall and reduces crowding. Likewise, in the VD view, the pelvic limbs should be flexed into a so-called frog-leg position rather than being pulled caudally. If the pelvic limbs are pulled caudally for the VD view, crowding will be increased, and skin folds will be created in the lateral thigh and/or caudal abdomen region. These skin folds create noticeable superimposed opacities that will interfere with assessment of the caudal aspect of the abdomen (Fig. 35-2).

It is usually possible to include the entire abdominal cavity in one 14-inch × 17-inch image, even in the largest dogs. For the occasional huge dog where this is not possible, then each projection (left lateral, right lateral, VD) should be divided into cranial and caudal portions. This effectively doubles the requisite number of images to evaluate the entire abdominal cavity.

Right and left lateral and VD views of the abdomen will suffice for almost all canine and feline patients. If the status of the urethra in male dogs is of concern, as for assessment of urethral calculi, the right and left lateral views should be supplemented with a third lateral view made with the pelvic limbs pulled cranially. This provides an unobstructed view of the ischial arch and os penis, allowing for assessment of urethral calculi without superimposition of the pelvic limbs (Fig. 35-3).

A compression radiograph can be used to clarify a suspicious finding that cannot be confirmed because of superimposition.[1] The theory is to apply mild compression to displace superimposed organs from the field of view, leaving an unobstructed view of the region of interest. This technique can be applied to assess structures such as the uterine body (lateral view) or the caudal aspect of the retroperitoneal space (VD view). Specialized inflatable compression paddles are available, but a wooden spatula or wooden spoon can also be used. If using a film-screen system, the kVp should be decreased by approximately 15% because the compressed part will be reduced in thickness. Of course, care should be taken not to place compression on organs that are obviously diseased, and the amount of pressure placed should always be gentle (Fig. 35-4). The increased use of ultrasound for abdominal assessment has reduced the need for compression radiographs, but they remain a convenient method to increase the accuracy of radiographic interpretation in some patients where ultrasonography is not possible.

Lateral View

One major difference between left and right lateral abdominal radiographs in dogs and cats is the appearance of the stomach. This relates to the difference in the anatomic position of the gastric fundus versus the gastric pylorus.[2,3] When looking at a cross-section of the abdomen from the caudal aspect of a dog or cat, the fundus is located dorsally and on the left versus the pylorus, which is located ventrally and on the right (Fig. 35-5). Therefore, when the dog is in left as opposed to right recumbency, different portions of the stomach will contain gas rather than fluid, simply as a result of gravity. When the patient is in right recumbency, the pylorus will usually contain fluid or ingesta, and if there is gas in the stomach, the gas will rise and collect in the body and fundus of the stomach (Fig. 35-6, *top*). Alternatively, when the patient is in left recumbency, the fluid will usually gravitate to the fundus, and gas will rise and fill the pylorus (Fig. 35-6, *bottom*). This results in the pylorus being of soft tissue opacity in the right lateral view and

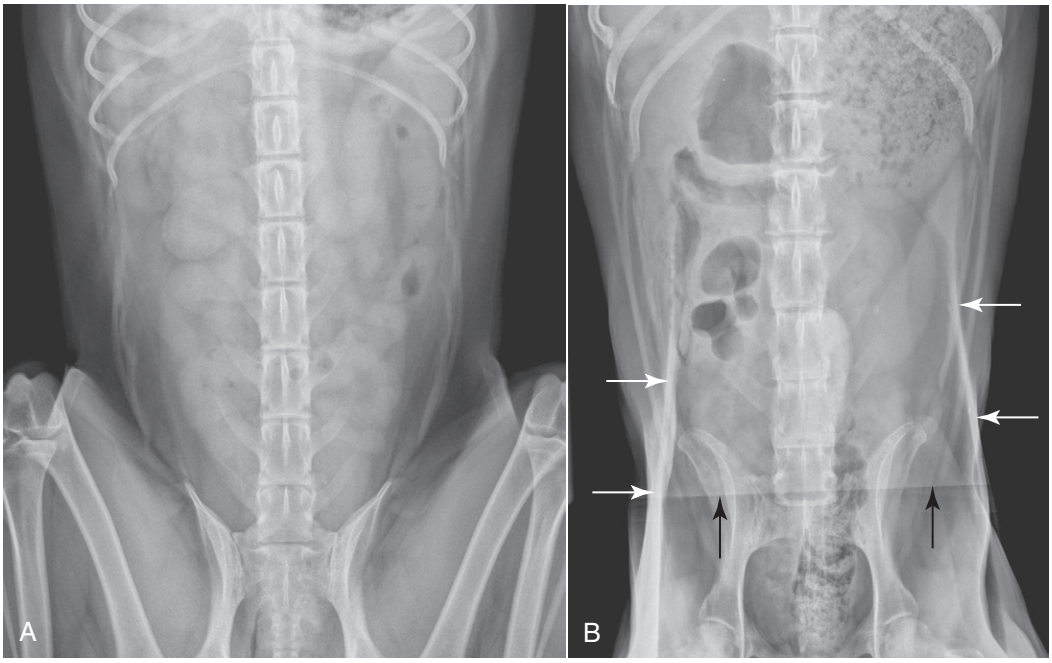


Fig. 35-2 Ventrodorsal abdominal radiographs from two dogs. In **A,** the pelvic limbs are flexed, allowing relaxation of the caudal abdominal muscles and greater expansion of the caudal aspect of the abdomen. In **B,** the pelvic limbs are pulled caudally, creating skin folds *(white arrows)* that can interfere with interpretation, and the caudal aspect of the abdominal cavity is narrower and more crowded. Also in **B,** the edge of the positioning trough has created a linear opacity *(black arrows)* that can also interfere with interpretation. (Reprinted from Thrall DE, Robertson IR: *Atlas of radiographic anatomy and normal anatomic variants in the dog and cat*, St. Louis, 2011, Elsevier-Saunders., p 170.)

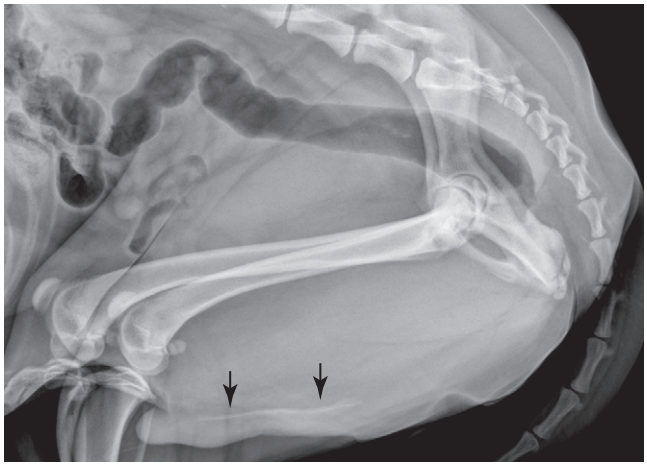


Fig. 35-3 Lateral radiograph of the caudal aspect of the abdomen with the pelvic limbs pulled cranially. This provides an unobstructed view of the urethral region and of the os penis *(black arrows)*. This view is useful for assessing for the presence of urethral calculi or lesions of the os penis.

containing gas in the left lateral view (Fig. 35-7). Of course, the difference in appearance of the stomach in left versus right lateral radiographs depends on the contents themselves, and the relative amount of liquid versus solids. If there is mostly gas or mostly fluid or ingesta in the stomach, the difference in appearance of the stomach in left as opposed to right recumbency will be minimized. The maximal difference in appearance of the stomach in left rather than right lateral views occurs when the stomach is moderately distended and contains both gas and fluid. Of particular importance is the knowledge that in right lateral views, especially in dogs, the pylorus can take on the appearance of a mass or foreign object because of the dependent fluid collection (Fig. 35-8).

The difference in appearance of the diaphragm in left versus right recumbency has been covered in Chapters 25 and 29.

Ventrodorsal and Dorsoventral Views

As noted above, DV views of the abdomen are made rarely. Occasionally, a DV abdominal radiograph will be useful when a VD view cannot be made (Fig. 35-9). The gravitational dependence of gas is one aspect of DV radiographs that may be useful, as illustrated in Figure 35-9, but other specific differences in VD rather than DV radiographs are not discussed because of the infrequent need to evaluate DV abdominal radiographs.

POSITIONING—HORSE

In foals and miniature horses it may be possible to obtain abdominal radiographs by restraining a compliant animal on a conventional x-ray table and using a vertically directed x-ray beam, as in dogs and cats, but this is rarely done. As noted before, the overall conspicuity of abdominal organs in the horse is less than in the dog or cat because of the increased volume of the gastrointestinal tract and relatively reduced amount of peritoneal fat. Therefore, VD radiographs are rarely useful, or even possible to obtain, and most questions being addressed radiographically can be answered from lateral views. These questions usually pertain to the presence of gastrointestinal foreign material, such as an enterolith or sand, or the presence of mechanical bowel obstruction, which will often be accompanied by increased bowel diameter and increased intraluminal fluid and gas. Increased bowel gas can often be detected, in spite of the inability to recognize other

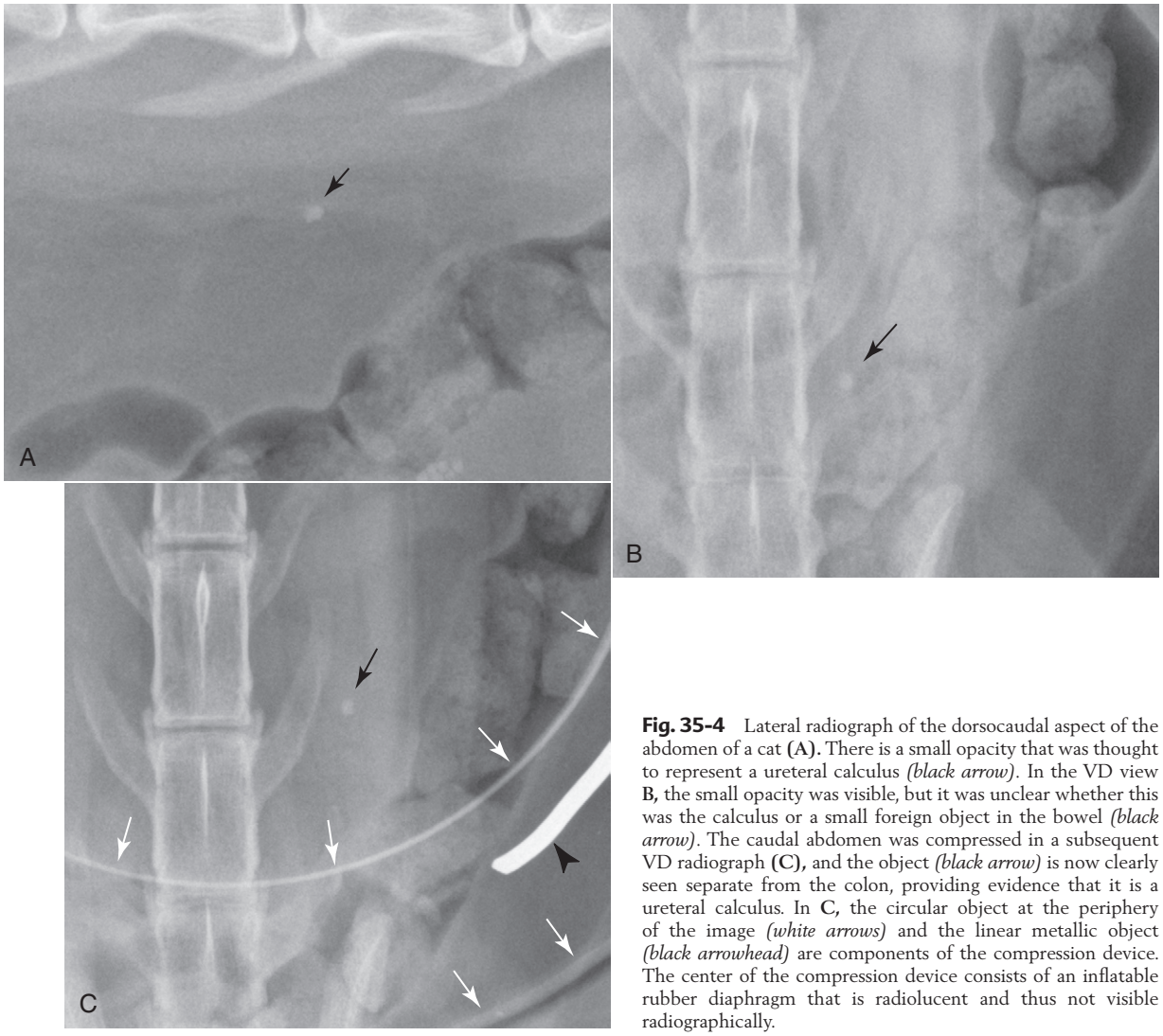


Fig. 35-4 Lateral radiograph of the dorsocaudal aspect of the abdomen of a cat **(A).** There is a small opacity that was thought to represent a ureteral calculus *(black arrow)*. In the VD view **B,** the small opacity was visible, but it was unclear whether this was the calculus or a small foreign object in the bowel *(black arrow)*. The caudal abdomen was compressed in a subsequent VD radiograph **(C),** and the object *(black arrow)* is now clearly seen separate from the colon, providing evidence that it is a ureteral calculus. In **C,** the circular object at the periphery of the image *(white arrows)* and the linear metallic object *(black arrowhead)* are components of the compression device. The center of the compression device consists of an inflatable rubber diaphragm that is radiolucent and thus not visible radiographically.

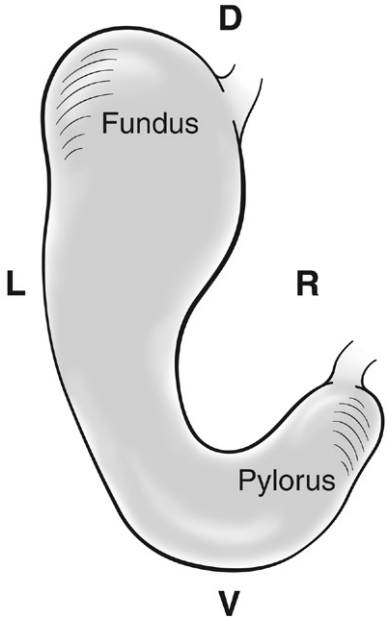


Fig. 35-5 Transverse diagram of the stomach from a caudal perspective. The fundus is located dorsally and on the left, and the pylorus is located ventrally and on the right. *D,* Dorsal; *L,* left; *R,* right; *V,* ventral.

abdominal organs or the bowel wall itself, because of the radiolucency it creates. The radiographic detail in the abdomen will be better in foals or miniature horses than in adult standard horses (Fig. 35-10), but meaningful information about bowel contents can sometimes be obtained even in adult horses (Fig. 35-11).

Handholding of cassettes or digital imaging plates for equine abdominal radiography *should not be done*. The visible light field that corresponds to the primary x-ray beam can be seen only on the x-ray tube side of the horse; that is, no part of the light field strikes the cassette. Therefore, aligning the light field with the cassette accurately when handholding the cassette is virtually impossible. This will result in the person holding the cassette being exposed frequently to the primary x-ray beam. A wall-mounted cassette holder, as described in Chapter 7, or a floor-mounted mobile cassette holder should be used for equine abdominal radiography. When using these devices, the x-ray beam can be aligned with the cassette before the horse is brought into position.

Radiographic magnification and distortion are factors that also have to be considered when acquiring and interpreting equine abdominal radiographs. This has already been discussed relative to equine thoracic radiography. Similarly, a result of the large diameter of the abdominal cavity of an adult horse, a lesion in the abdomen on the side closest to the x-ray tube could be 35 cm or more from the cassette or digital plate.

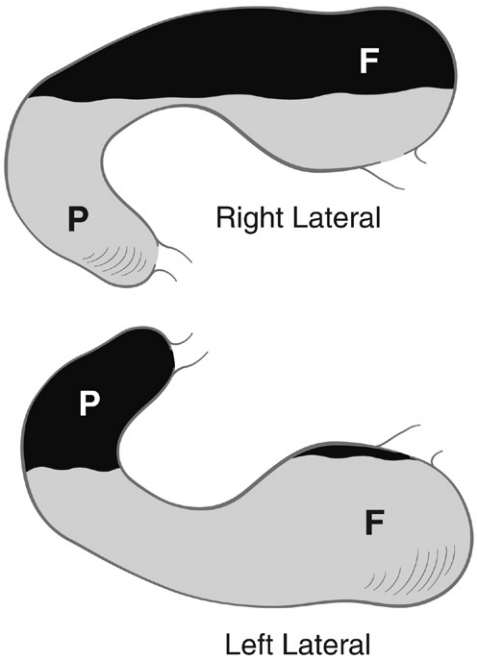


Fig. 35-6 Drawing illustrating the effect of gravity on the relative distribution of gas and fluid in the stomach in left versus right lateral recumbency. In right recumbency *(top)*, gas rises to the fundus, and body of the stomach and fluid gravitates to the pylorus. In left recumbency *(bottom)*, gas rises to the pylorus, and fluid gravitates to the body. Even in left recumbency, there may be some gas trapped in the fundus, as shown in the bottom panel. *F,* Fundus; *P,* pylorus.

If the distance from the focal spot of the x-ray tube to the cassette was 100 cm, a lesion 35 cm from the cassette would be magnified approximately 50%. This amount of magnification would lead to distortion and blurring and a reduction in the conspicuity of the lesion. If a lateralized lesion is possible, then left-right *and* right-left abdominal radiographs should be obtained.

RADIOGRAPHIC TECHNIQUE—DOG AND CAT

When radiographing the canine or feline abdomen using a film-screen system, a low kVp–high mAs technique is preferable. At discussed in Chapter 1, this kVp–mAs relationship will lead to a short scale of contrast, with few gray shades and more blacks and whites. This is important in the abdomen because of the inherently low patient contrast. Bowel gas provides contrast for assessing the lumen of the bowel, but bowel gas is not helpful for comparing parenchymal organs or for assessing the peritoneum; it is the peritoneal fat located in the mesentery and omentum that provides contrast between organs. As the absorption characteristics between fat and water (soft tissue) are minimal, the differential absorption between water and fat must be accentuated in film-screen radiography with a low kVp–high mAs technique, as discussed in Chapter 1. If a high kVp–low mAs technique is used for radiographing the abdomen with a film-screen system, the contrast of the image will be too low, and the abdomen will not be able to be assessed adequately. If one is using a digital system, exposure factors are less critical because of the enhanced contrast resolution of digital imaging systems as discussed in Chapter 2. For patients thicker than 10 cm, a grid should be used to remove scattered x-rays from the beam.

Exposure time is not as critical when radiographing the abdomen as when radiographing the thorax. This is fortunate because it allows a longer exposure time to be used to achieve the higher mAs values to use in the preferable low kVp–high mAs techniques.

The respiratory pattern of the patient should be observed for a few seconds before the radiographic exposure is made so that the exposure can be coordinated with peak exhalation. At exhalation the diaphragm is further cranial and there is less crowding of the abdomen. Timing of the radiographic exposure to phase of respiration is not as important as in the thorax, but timing the exposure to peak exhalation is a small adjustment that can be made that will add to the quality of the radiograph.

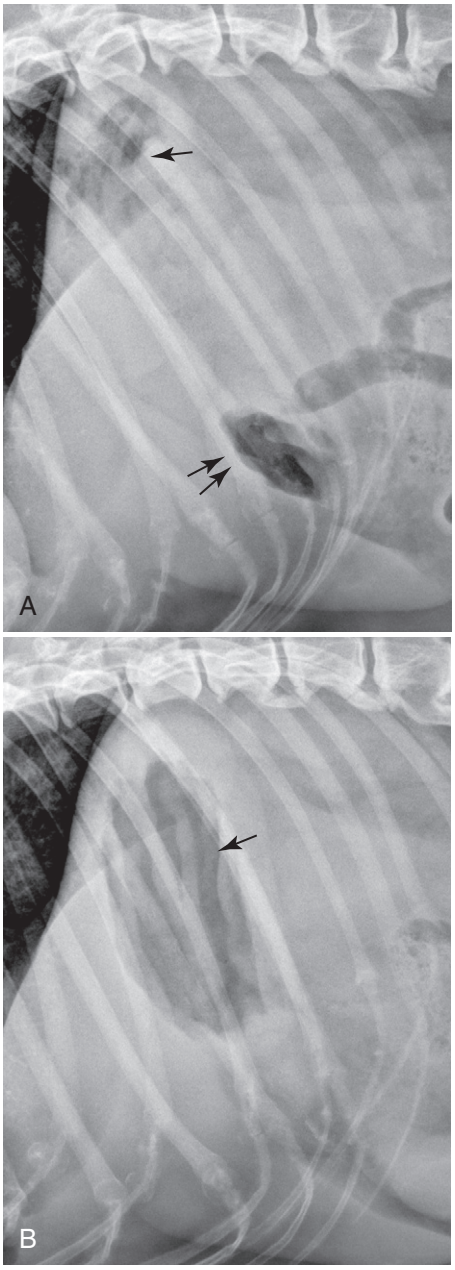


Fig. 35-7 Left **(A)** and right **(B)** lateral radiographs of the cranial aspect of the abdomen of a dog. In the left lateral view **(A),** there is a collection of gas in the fundus *(single black arrow)* and also in the pylorus *(double black arrow)*. In right lateral recumbency, there is now much more gas in the fundus *(black arrow)*, but the pylorus is filled with fluid, and it is not readily distinguishable.

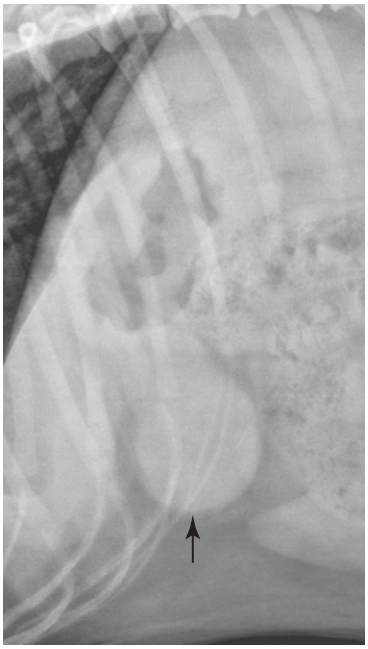


Fig. 35-8 Right lateral radiograph of a dog where fluid has collected in the pylorus *(black arrow)*. The fluid-filled pylorus takes on a masslike appearance, which can be confused with a gastric mass or a gastric foreign body. (Reprinted from Thrall DE, Robertson IR: *Atlas of radiographic anatomy and normal anatomic variants in the dog and cat*, St. Louis, 2011, Elsevier-Saunders, p 191.)

RADIOGRAPHIC TECHNIQUE—HORSE

Radiographing the abdomen of all but the smallest equine subjects requires massive exposure factors because of the sheer mass of the part. Considering the need for such high exposures, high kVp–low mAs techniques can be used, even though they might not lead to optimization of radiographic contrast. Abdominal contrast in adult horses is so poor inherently, as already noted, that it cannot be improved on through selection of radiographic technical factors. Use of low kVp–high mAs techniques in the adult horse will put excessive stress on the x-ray tube, and these have no advantage over high kVp–low mAs techniques, which will result in less x-ray tube heating.

Lower overall exposure factors can be used in young foals and miniature horses, but as noted earlier, the abdominal radiographic detail in these small subjects is less than in dogs and cats and, again, there is no advantage in using low kVp–high mAs techniques.

In adult horses, is will be difficult to assess anything but the position of large gas-containing structures or to identify large collections of radiopaque material or objects such as ingested sand[4] or a large enterolith. A portable x-ray unit, such as those used commonly to radiograph equine extremities, will not be adequate for equine abdominal radiography.

In principle, an antiscatter grid will be necessary for all equine abdominal radiographs. However, this becomes impractical because of the increased exposure factors needed to compensate for the grid, unless a high-output x-ray machine is available.

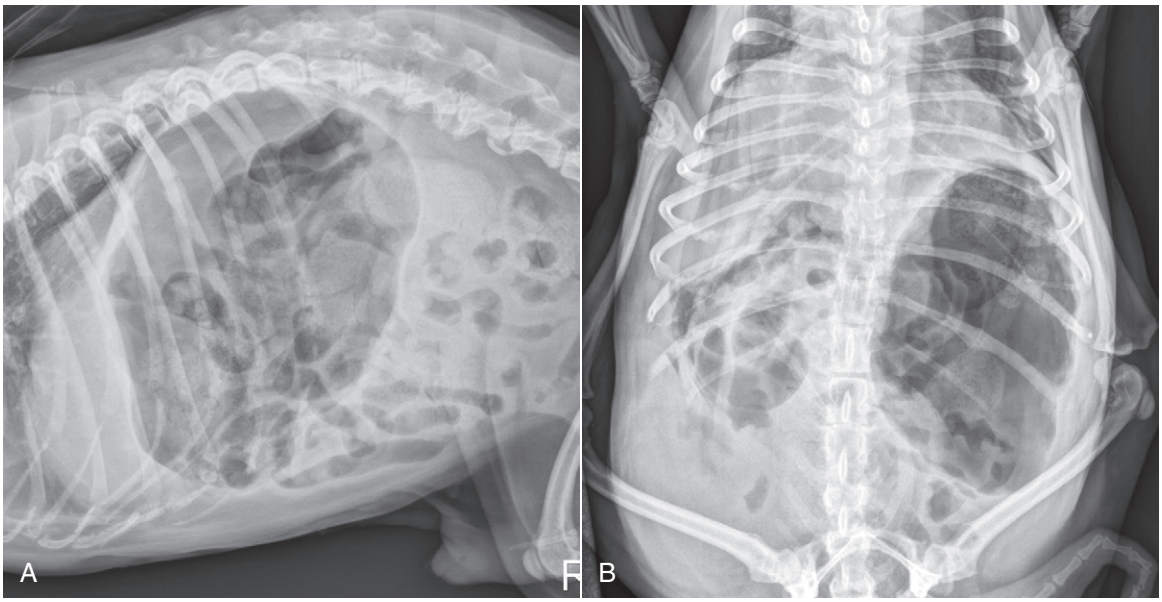


Fig. 35-9 Lateral **(A)** and DV **(B)** radiographs of the abdomen of a 15-year-old pug with acute abdominal distention and thoracic pain from rib fractures. In the lateral view **(A),** there was concern whether the dilated stomach was in a normal or abnormal position. The thoracic pain precluded obtaining a VD abdominal radiograph, so a DV was obtained instead. In the DV view **(B),** gas has risen to the fundus because this part of the stomach is the most nondependent. There is no evidence of gastric malpositioning or gastric compartmentalization, which are common features of gastric volvulus. This illustrates one of the few indications for obtaining a DV view of the abdomen versus a VD view. Note the increased crowding of the abdomen and the superimposition of the pelvic limbs on a portion of the abdomen, which are common problems with DV compared with VD abdominal radiographs.

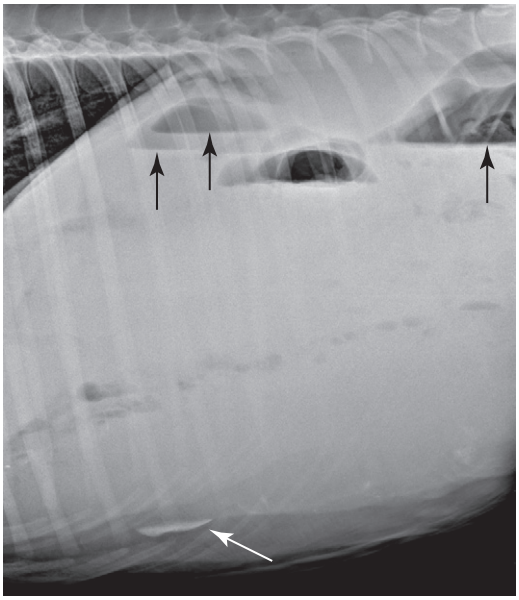


Fig. 35-10 Lateral radiograph of the cranial aspect of the abdomen of a 7-year-old American miniature horse. The small size of this horse allows for reasonable radiographic quality, but the conspicuity of organs is less than in a dog or cat because of the relatively reduced amount of peritoneal fat and the larger volume of the abdomen occupied by the gastrointestinal tract. There is a small amount of sand in the ventral aspect of the large bowel *(white arrow)*. Horizontal gas/fluid interfaces *(black arrows)* in the bowel are seen because the radiograph was made with a horizontally directed x-ray beam. Visualization of gas/fluid interfaces to this extent is normal in the horse.

ANCILLARY FACTORS

There are few ancillary factors that affect the radiographic appearance of the equine abdomen other than body mass. However, for the dog and cat, the body habitus and presence of cutaneous lesions are ancillary factors that have a significant effect on the appearance of the subsequent radiograph

Body Habitus

The volume of abdominal fat contained in the mesentery and omentum is directly related to the conspicuity of parenchymal organs and serosal margins in the abdomen. As discussed before, fat is more radiolucent than soft tissue and provides contrast between organs; it is absolutely critical for some fat to be present if organs are going to be distinguished from one another (Fig. 35-12). In emaciated (Fig. 35-13) or young (Fig. 35-14) animals, there is reduced fat that results in loss of conspicuity of the serosal margins.

Cats often have a particularly large collection of fat in the falciform ligament (see Fig. 35-12). This is often misinterpreted by beginning students as peritoneal fluid. Using the basic principles of radiographic opacities and the silhouette sign discussed in Chapter 5, this cannot be fluid, or the absolute opacity of the region would be greater, and there would also be border effacement of the adjacent liver and jejunum.

In addition to a large amount of falciform fat, cats also often accumulate large amounts of fat in the omentum and mesentery. This will cause crowding of the jejunum in the midabdomen (Fig. 35-15). Jejunal crowding has been listed as one radiographic sign of linear foreign body.[5] With a linear foreign body, the crowding is caused by plication, and there

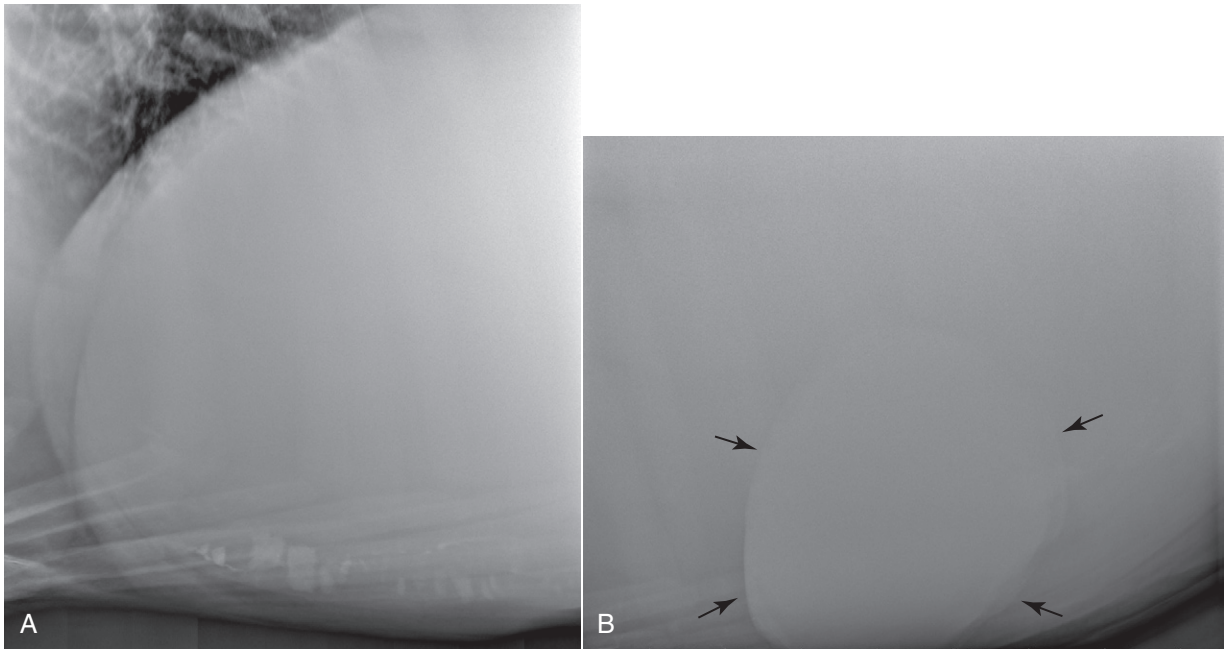


Fig. 35-11 Lateral radiographs of the cranioventral **(A)** and midventral **(B)** aspects of the abdomen of a 10-year-old Standardbred horse. The massive size of the abdomen of adult horses, the large volume of the peritoneal cavity that is taken up by the gastrointestinal tract, and the relative lack of fat prevent visualization of abdominal detail to the same extent as in dogs or cats, or even foals. However, some abnormalities can be detected. In this horse, the cranioventral aspect of the abdomen in **A** is devoid of any detail because of the extreme thickness of this region and the relatively homogeneous contents of the bowel; this is a normal appearance. However, this is a common location for sand to accumulate, and clinically insignificant segmental accumulations are seen here. In **B,** there is a large circular radiopaque structure in the ventral aspect of the abdomen that represents an enterolith *(black arrows)*.

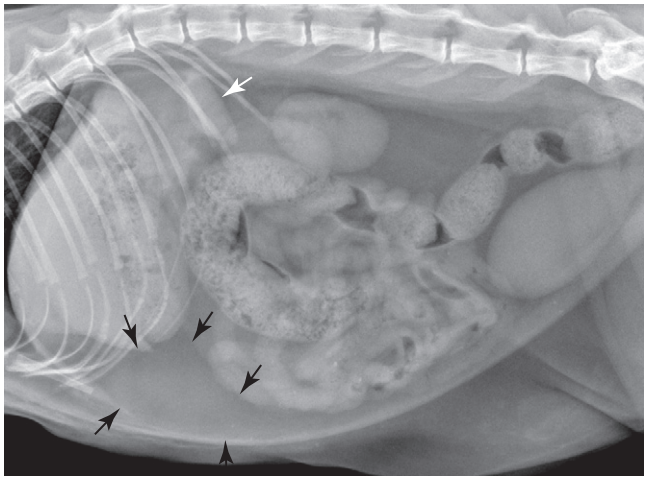


Fig. 35-12 Lateral radiograph of a cat with abundant fat in the peritoneal cavity and retroperitoneal space. The fat provides contrast, and there is excellent discrimination between parenchymal organs. The kidneys, proximal aspect of the spleen *(white arrow)*, jejunal segments, and the urinary bladder are all highly conspicuous because of the peritoneal fat. Note the large collection of fat in the falciform ligament *(black arrows)*.

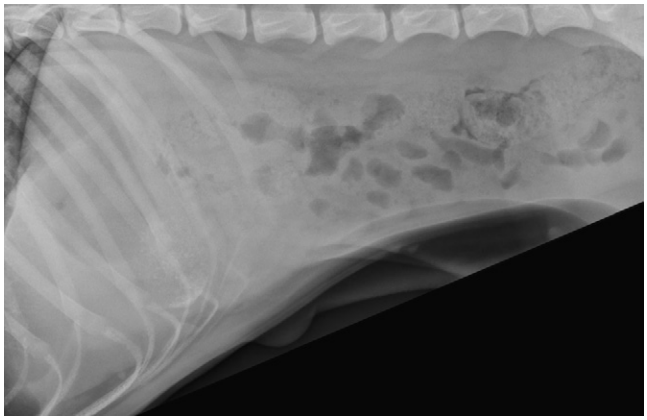


Fig. 35-13 Lateral radiograph of the abdomen of an emaciated dog. The conspicuity of the margin of abdominal organs is poor because of the lack of intraperitoneal and retroperitoneal fat to provide contrast. With this appearance, radiographic assessment of the abdomen is compromised.

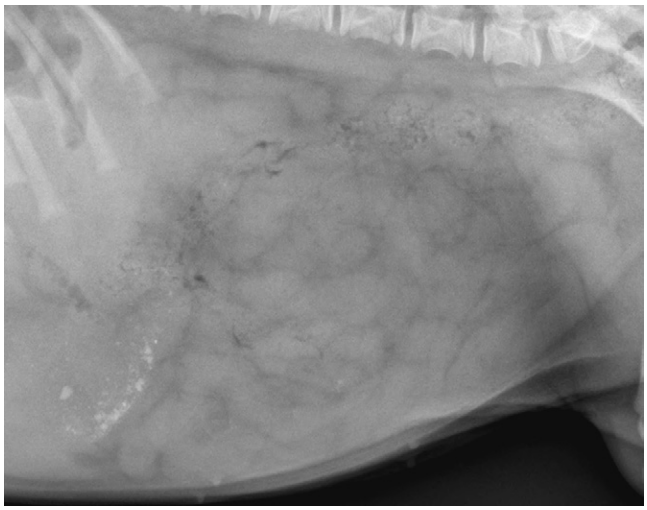


Fig. 35-14 Lateral radiograph of an 11-week-old dog. Conspicuity of serosal margin detail is diminished because of the relative lack of abdominal fat; this is a common finding in young animals. Margin visualization is, however, better than in patients who are undernourished and emaciated (compare with Fig. 35-13).

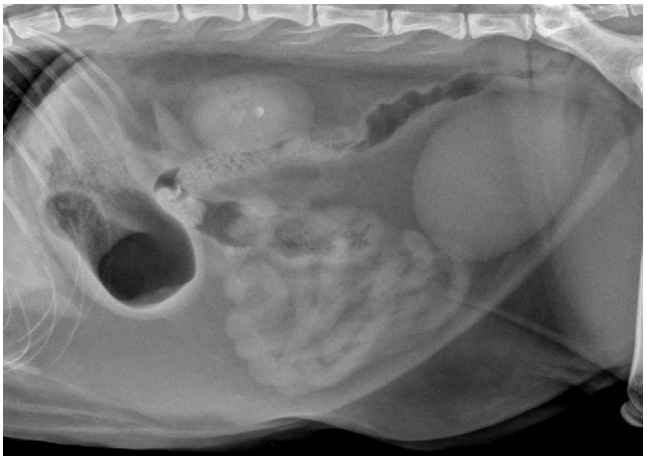


Fig. 35-15 Lateral radiograph of a cat with jejunal crowding in the central abdomen because of excessive omental and mesenteric fat. There are no other signs of a linear foreign body to justify attributing this appearance to anything but crowding caused by excessive fat. Small nephroliths are also present.

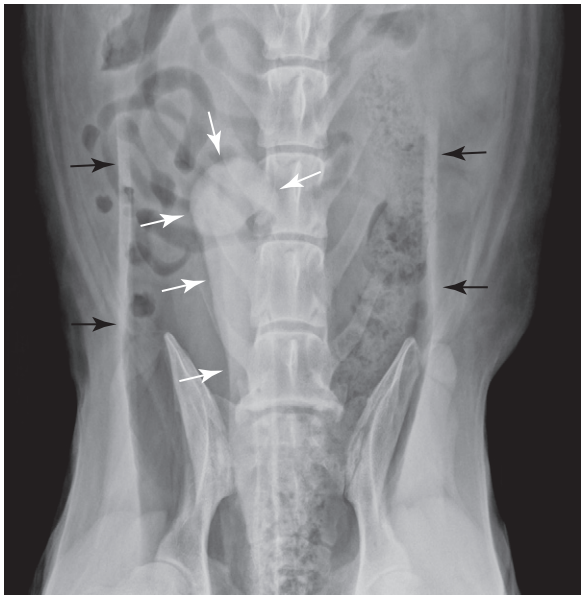


Fig. 35-16 Ventrodorsal view of the caudal aspect of the abdomen in a male dog. The summation opacity created by the prepuce *(white arrows)* can be misinterpreted as a mass. Note also the skin folds created by pulling the pelvic limbs caudally *(black arrows)* rather than having them flexed during radiography.

will almost always be other signs of linear foreign body obstruction such as eccentric gas bubbles or bowel distention. Jejunal centralization as the only sign of linear foreign body is unreliable, but nevertheless the centralization from crowding caused by omental fat is sometimes misinterpreted as a sign of a linear foreign object.

Cutaneous Lesions and Structures

Cutaneous lesions or normal superficial structures superimposed on the abdomen are not misinterpreted as a lesion as often as they are in thoracic radiographs. One specific example of a superficial structure that is often misinterpreted as an abnormality in abdominal radiographs is superimposition of the prepuce and os penis on the caudal aspect of the abdomen in VD radiographs of male dogs (Fig. 35-16). The reason that cutaneous lesions create such a conspicuous opacity was discussed in Chapter 5.

INTERPRETATION PARADIGM

The things that can influence the radiographic appearance of the abdomen have been described here, and unless one has an organized approach to interpretation, these will sooner or later be misinterpreted as an abnormality. Assessing whether there is an abnormality in the abdominal radiographs of a patient should be the *last* step in the interpretive process. The following questions should always be considered first.

- Are the radiographic views adequate, and are all of the views needed present? If all of the standard views are not present, what is likely to be missed?
- Is the positioning adequate, or are there positioning problems that will interfere with interpretation?
- Is the radiographic technique adequate, or are the images overexposed or underexposed?
- Were the images acquired with an antiscatter grid?
- What is the body habitus of the patient, and how is this going to affect the appearance of the images?
- Were the images acquired with a vertically directed x-ray beam with the cassette in an x-ray table, or was a horizontally directed x-ray beam used with the cassette in a mobile or a wall-mounted cassette holder?
- Are the images analog or digital?
- Are there morphologic aspects of the patient that are going to influence the appearance of the radiographs? These include things such as cutaneous nodules or masses.

Only after all of these things have been considered should one's attention be directed at the identification of abnormalities. Assessing the small bowel for an obstruction is one area where many beginning interpreters struggle. Guidelines for determining normal small bowel from abnormal small bowel are covered in Chapter 44, but it should be clear that a definitive assessment of normal versus abnormal small bowel cannot be made in some patients.

Organs not typically seen in normal abdominal radiographs of dogs and cats are the gallbladder, adrenal glands, ureters, uterus, mesenteric lymph nodes, retroperitoneal lymph nodes, and the prostate gland. The normal pancreas is never seen radiographically in the dog, but occasionally the left limb of the normal pancreas can be seen in VD abdominal radiographs of cats as a soft tissue structure between the gastric fundus and the proximal extremity of the spleen.

Experienced radiologists may have a random search pattern, but it is recommended that beginning radiologists develop an organized approach to searching radiographs[6] for abnormalities. The following regions can be searched in order: (1) ribs, vertebrae, and the visible portions of the pelvis and pelvic limbs; (2) soft tissues of the abdominal wall; (3) serosal detail and character of retroperitoneal space; (4) serosal detail and character of peritoneal space; (5) parenchymal organs (liver, spleen, kidneys); (6) urinary bladder; (7) organs not typically seen; (8) stomach; (9) duodenum and jejunum; and finally (10) the cecum and colon. If the same procedure is followed for every patient, the order of searching will become second nature, and as experience is gained, the search pattern will become random without a loss of effectiveness. Until then, it may be beneficial for a checklist to be developed to make sure that every anatomic region of the radiograph is examined.

REFERENCES

1. Carrig C: The use of compression in abdominal radiography of the dog and cat, *J Am Vet Radiol Society* 17:178, 1976.
2. Grandage J: The radiological appearance of stomach gas in the dog, *Aust Vet J* 50:529, 1974.
3. Love N: The appearance of the canine pyloric region in right versus left lateral recumbent radiographs, *Vet Radiol Ultrasound* 34:169, 1993.
4. Kendall A, Ley C, Egenvall A, et al: Radiographic parameters for diagnosing sand colic in horses, *Acta Vet Scand* 50:17, 2008.
5. Root C, Lord P: Linear radiolucent gastrointestinal foreign bodies in cats and dogs: their radiographic appearance, *Vet Radiol Ultrasound* 12:45, 1971.
6. Halvorsen JG, Swanson D: Interpreting office radiographs. A guide to systematic evaluation, *J Fam Pract* 31:602, 1990.

ELECTRONIC RESOURCES

evolve

Additional information related to the content in Chapter 35 can be found on the companion Evolve website at http://evolve.elsevier.com/Thrall/vetrad/

- Chapter Quiz

CHAPTER • 36

The Peritoneal Space

Paul M. Frank

The peritoneum, a thin, serous membrane, is divided into parietal, visceral, and connecting layers, which are all continuous.[1] The parietal peritoneum covers the inner surface of the abdominal cavity and is closely adhered to abdominal musculature; it separates extraperitoneal and intraperitoneal spaces. The visceral peritoneum covers the organs of the abdominal cavity either in whole or in part. The connecting peritoneum includes mesenteries, omenta, and intraabdominal ligaments. The peritoneal space, between the parietal and visceral peritoneal layers, normally contains only a small amount of fluid for lubrication.

The space between the dorsal margin of the parietal peritoneum and the abdominal wall is the retroperitoneal space. The retroperitoneal space is outside the peritoneal cavity and contains adrenal glands, kidneys, ureters, major blood vessels, and lymph nodes. The retroperitoneal space communicates cranially with the mediastinum through the aortic hiatus and caudally with the pelvic canal.[2]

Fat is typically present throughout the abdomen, primarily in the falciform ligament, the greater omentum, the mesentery, and the retroperitoneal space. The presence of intraabdominal fat is important for visceral organ visualization in radiographs because fat provides an interposed opacity between viscera (Fig. 36-1).

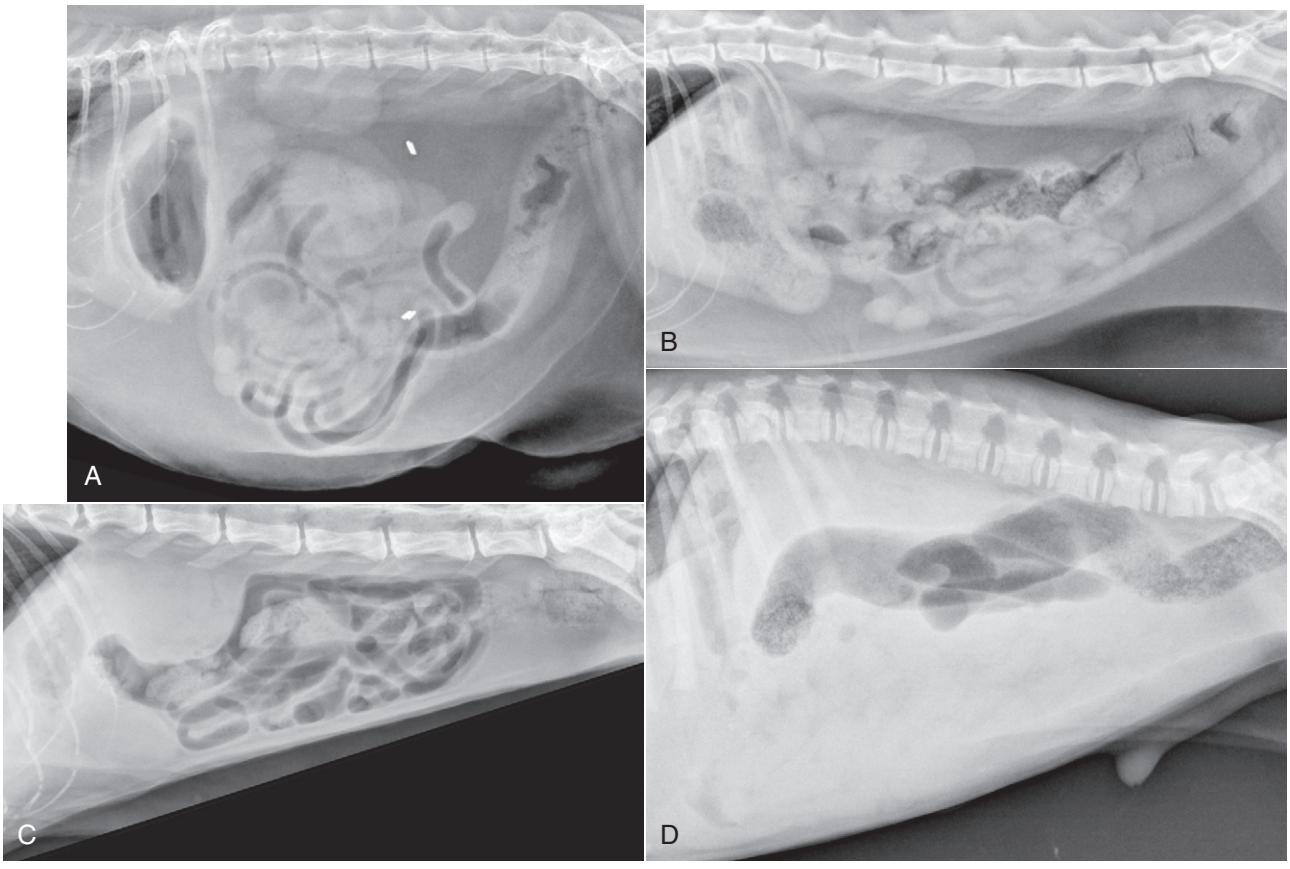


Fig. 36-1 Lateral views of the abdomen illustrating the effect of different amounts of abdominal fat. **A,** Obese cat. Extensive fat deposition in the falciform, omental, mesenteric, and retroperitoneal areas provides contrast between viscera. Metallic objects represent vascular clips from a previous ovariohysterectomy. **B,** Normal cat. Fat deposition is less than that in **A,** but it is adequate to allow visualization of viscera. **C,** Emaciated cat. Without interposed fat, border effacement of viscera is present, producing a uniform, homogeneous abdomen devoid of contrast except for gas in the bowel loops. **D,** Normal 2-month-old golden retriever. Poor contrast is caused by a relative lack of fat in this young subject; this is a normal finding.

Box • **36-1**

Phrases Used to Describe Loss of Contrast in the Abdomen

Decreased serosal surface visualization
Decreased serosal margin visualization
Decreased visualization of serosal surfaces
Increased intraabdominal soft tissue opacity
Increased intraabdominal fluid opacity
Decreased peritoneal detail

PERITONEAL SPACE

Loss of Contrast Caused by Increased Fluid Opacity

Increased fluid within the peritoneal cavity causes a loss of the differential opacity interface between soft tissue and fat and therefore a loss of contrast between organs. Phrases commonly used to describe this loss of contrast are listed in Box 36-1. Causes for loss of intraabdominal contrast include lack of fat, peritoneal effusion, peritonitis, and peritoneal neoplasia. A wet hair coat, or hair coated with ultrasound gel, may create the appearance of altered peritoneal space opacity.

The amount and character of intraabdominal fat depends on the age of the animal and the body habitus. In emaciated patients, the abdomen is often tucked up, which can be visualized on radiographs (Fig. 36-1, *C*); however, the possibility of coexisting peritoneal fluid or peritonitis cannot be excluded. Normal dogs and cats younger than a few months of age lack sufficient fat to provide intraabdominal contrast; thus the abdomen appears to be of relatively uniform soft tissue opacity (Fig. 36-1, *D*). Another factor is that young patients have a relatively higher proportion of brown (multilocular) fat than adults. Brown fat has an opacity closer to that of soft tissue because of its higher water content. As young animals mature, the water content of the brown fat decreases.[3] As brown fat is replaced by white fat, the contrast between intraabdominal soft tissues increases.

Fluid between abdominal viscera, causes border effacement of viscera and a loss of intraabdominal contrast and also provides added overall opacity. Classification of abdominal effusion is broad and includes transudates, exudates, blood, urine, bile, and chyle.[4] In practice, all abdominal fluids are of soft tissue opacity, comparable to the visceral organs. In many instances, the fluid is limited to the peritoneal space, and contrast between the kidneys and adjacent retroperitoneal fat is preserved.

The idea that any accumulation of fluid results in complete obliteration of serosal margins is incorrect. The degree to which serosal margin detail is obscured by fluid is determined by the relative amounts of fat versus fluid. The more fat that is present, the more fluid is needed to cause complete obliteration of serosal margins. Thus organ margins may still be visible when free intraperitoneal fluid is present.

A large volume of abdominal fluid appears as a homogeneous soft tissue opacity uniformly distributed throughout the abdominal cavity (Fig. 36-2). The homogeneous appearance is caused by border effacement of the soft tissue structures in the abdomen by the fluid. A large volume of fluid will also cause abdominal distention with outward protrusion of the contour of the abdominal wall. The abdomen may also be somewhat pendulous in normal immature patients. A large volume of fluid may also displace the diaphragm cranially. If relatively mobile segments of bowel contain gas, they often float to the highest or uppermost area within the abdominal cavity. These segments will be located in the central portion of the abdomen on a lateral radiograph made with a vertical x-ray beam. Gas-filled bowel loops in a noncentral location in patients with a large amount of intraperitoneal fluid suggest the presence of an abdominal mass or adhesions that prevent free movement of intestinal segments. This finding should be interpreted with caution, however, because the presence of a large amount of peritoneal fat may also cause asymmetric bowel location, especially in cats. The presence or absence of coexistent peritonitis cannot be ascertained radiographically in patients with a large amount of intraperitoneal fluid.

Smaller amounts of abdominal fluid or peritonitis may produce a mottled, hazy, or irregular loss of contrast on survey radiographs (Fig. 36-3). Individual viscera may be visualized, but the margins of soft tissue structures are indistinct or blurred. With small amounts of fluid, this appearance may be the result of interdigitation of fluid with folds in the greater omentum and small bowel but without total border

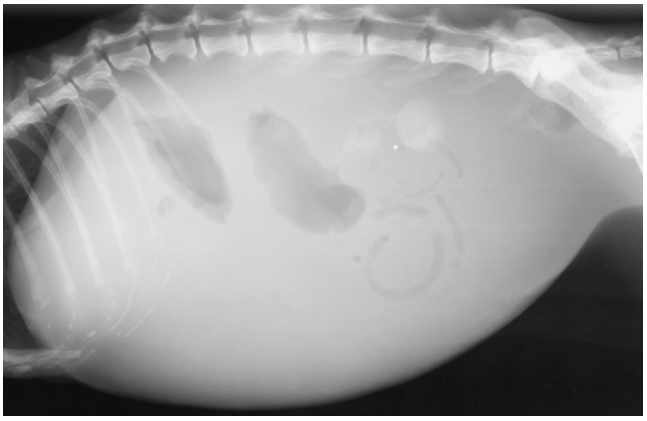


Fig. 36-2 Lateral view of the abdomen of a cat with a large volume of intraperitoneal fluid. Homogeneous soft tissue opacity is distributed uniformly throughout the distended abdomen. No fluid is in the retroperitoneal space, but fascial planes and organs in the retroperitoneal space are not visible because of superimposition of the peritoneal fluid.



Fig. 36-3 Lateral radiograph of the midabdomen of a dog with peritoneal fluid. There is a mottled, hazy, irregular fluid opacity within the abdomen leading to blurring of the margins of soft tissue structures. This radiographic appearance could be caused by the presence of an exudate or hemorrhage, but in this dog it was caused by hypoproteinemia.



Fig. 36-4 Lateral view of the abdomen of a cat with peritoneal fluid. Serosal detail in the intraperitoneal space is obliterated, but there is good visualization of fascial planes and fat in the retroperitoneal space. The falciform fat in the cranioventral aspect of the abdomen, which is extraperitoneal, is also normal. Comparison of the appearance of the fat in the intraperitoneal versus retroperitoneal spaces can assist in the radiographic detection of either retroperitoneal or intraperitoneal disease. There is also renal mineralization and a large calcified peritoneal body.

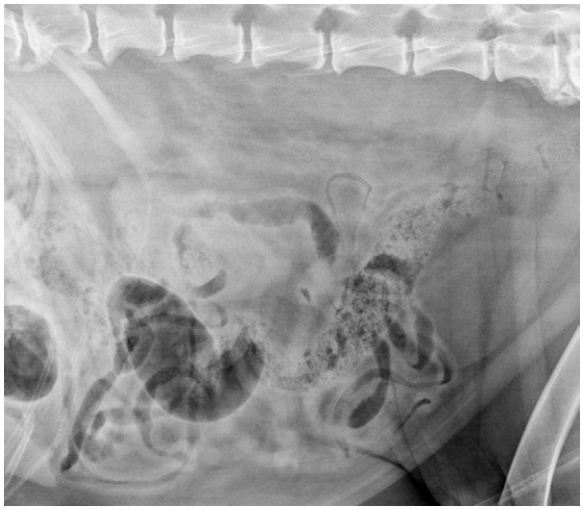


Fig. 36-5 Lateral view of the abdomen of a dog with rodenticide toxicity. There is fluid opacity in the retroperitoneal space with blurring of the margin of the lumbar musculature and a streaky appearance to the retroperitoneal fat. Note the normal sharp serosal margin detail and contrast within the intraperitoneal space.

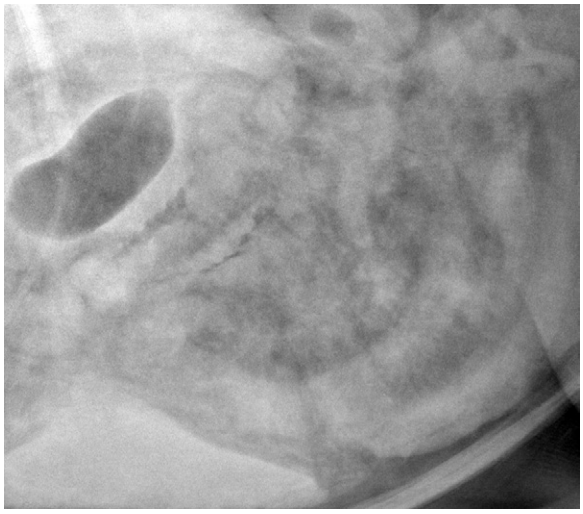


Fig. 36-6 Close-up of the cranioventral aspect of the abdomen of a dog with a ruptured splenic hemangiosarcoma leading to peritoneal carcinomatosis. The mottled appearance of the mesenteric fat is typical of carcinomatosis.

effacement.[5] Peritonitis may produce a similar effect. Smaller amounts of effusion may be caused by early fluid accumulation of a generalized process or by more localized disease. Localized disease may lead to abnormal serosal margin detail in the area of the disease with normal serosal margins visible elsewhere in the peritoneal space.

Manipulation of viscera during laparotomy produces changes that may appear similar to peritonitis, and these changes may be modified by the amount of tissue trauma.[5] Solutions containing water, electrolytes, and relatively low molecular weight components are absorbed by the peritoneal membrane within 24 hours.[6] Proteinaceous fluids such as serum, blood, and lymph are absorbed more slowly and may be present for 1 to 2 weeks. These changes can be visualized after laparotomy, and they should not be mistaken for more significant complications. Static or increasing fluid accumulation during this period is abnormal. If complications are suspected, cytologic evaluation of the fluid will be necessary to differentiate between normal postsurgical fluid and fluid caused by septic peritonitis or other conditions.

One method of assessing the intraperitoneal space for fluid accumulation or peritonitis is to compare the contrast of the intraperitoneal space with that of the retroperitoneal space. Normally, detail and contrast in the intraperitoneal and retroperitoneal spaces should be identical. However, because many diseases resulting in intraperitoneal fluid accumulation do not affect the retroperitoneal space, retroperitoneal detail is often preserved when intraperitoneal fluid has altered the serosal margin of bowel and other intraperitoneal organs (Fig. 36-4). It is important to remember, however, that a large volume of intraperitoneal fluid can obscure the retroperitoneal space because of superimposition. Loss of contrast and detail can also occur specifically in the retroperitoneal space, and is an indication of fluid accumulation or, less commonly, inflammation (Fig. 36-5). Fluid in the retroperitoneal space can lead to alternating fat and soft tissue opacities, or streaking, as the fluid dissects between fascial planes. The most common causes of isolated retroperitoneal fluid are hemorrhage, as with rodenticide toxicity and trauma, and urine leakage. Retroperitoneal inflammation with increased fluid can also result from a migrating grass awn, a penetrating wound, ligatures from ovariohysterectomy, and perforation of the urethra during catheterization.[7,8]

An ill-defined nodular or granular pattern to the abdomen (Fig. 36-6) may be caused by seeding of the peritoneum with multiple, metastatic neoplastic foci, or it may result from proteolytic enzymes escaping from an inflamed pancreas, causing saponification of omental and mesenteric fat. Examples of tumors associated with such spread include hemangiosarcoma of the spleen and carcinoma of various abdominal organs. The term *carcinomatosis* may be used to describe any cancer disseminated throughout the abdomen; it may be limited to carcinomas with this distribution, or it can be used as a general term to describe loss of serosal detail with nodularity, as with fat saponification secondary to pancreatitis.[9]

See Box 36-2 for causes of decreased serosal surface visualization.

Box • 36-2

Differential Diagnoses for Decreased Serosal Surface Visualization

- Lack of intraabdominal fat
- Young patient (brown fat)
- Peritoneal effusion (transudate, exudate, blood, urine, bile, chyle)
- Peritonitis
- Peritoneal neoplasia (primary or metastatic)
- Mass effect caused by crowding
- Superimposed external material (wet hair, ultrasound gel, etc.)
- Underexposure

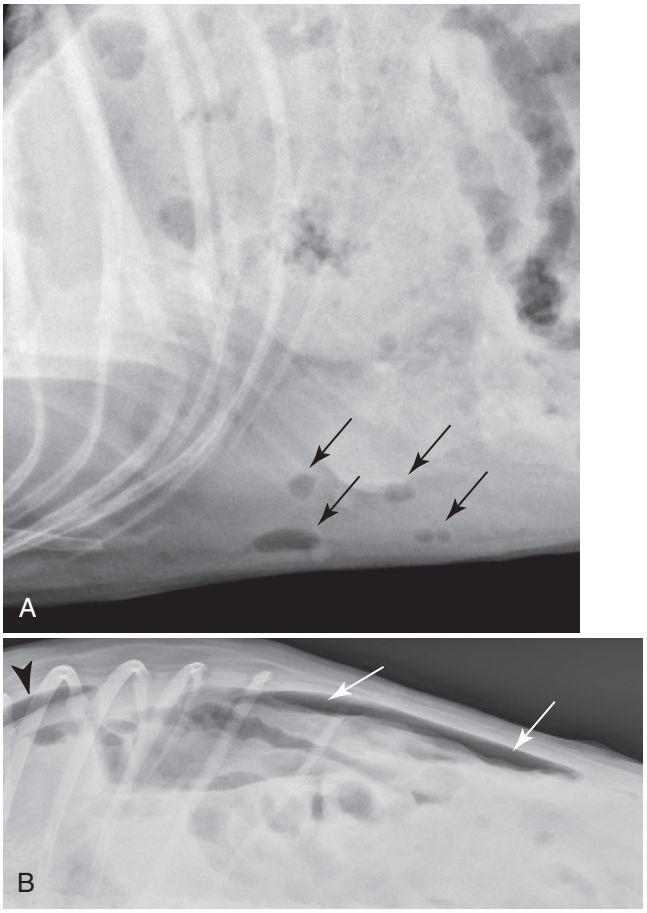


Fig. 36-7 **A,** Lateral radiograph of the cranioventral aspect of the abdomen of a dog with a ruptured bowel that has led to pneumoperitoneum. Extraluminal gas in this patient appears as small gas bubbles in a location not expected for bowel *(black arrows)*. The location of this gas is a good indicator that it is extraluminal. Had these gas collections been located in the midaspect of the abdomen, they might not have been recognized as abnormal. **B,** Horizontal-beam abdominal radiograph of the same dog as in **A.** The dog was placed in left recumbency and a horizontally directed x-ray beam was used to make the radiograph. The free peritoneal gas has collected beneath the right abdominal wall *(white arrows)*. The more cranially located gas is in the lung *(black arrowhead)*. There is more free intraperitoneal gas than would be estimated from the conventional lateral projection in part **A.**

Increased Contrast Caused by Increased Gas Opacity

The two most common causes of free intraperitoneal gas are penetration of the abdominal wall, either by surgery or by penetrating wounds, and perforation of the bowel. However, not all bowel perforations lead to free abdominal gas.[10] Laparotomy is the most common cause of free abdominal gas, and the history is usually known in this instance. After laparotomy, a moderate amount of gas may persist for days to weeks.[11] Penetrating abdominal wounds are usually diagnosed by physical findings. In patients with a penetrating wound, differentiating whether free abdominal gas is caused solely by penetration of the abdomen or is the result of concurrent organ rupture is impossible to tell from radiographs. If subcutaneous emphysema is superimposed over the abdominal cavity, such as caused by trauma, it may be difficult to discern whether or not there is concurrent intraperitoneal gas.

A small volume of free abdominal gas can be difficult to recognize on conventional radiographs made with a vertically directed x-ray beam because the gas bubbles are small and irregular in shape and may be misinterpreted as bowel gas unless they reside in a region where bowel is not found normally (Fig. 36-7).[5] Larger gas volumes may coalesce into a larger bubble. This larger bubble may still be difficult to recognize on a radiograph made with a vertical x-ray beam because it is superimposed over other viscera. In addition, this larger bubble may simulate a gas-containing organ, such as the stomach. Free abdominal gas usually floats to the highest point within the abdomen. In lateral recumbency, this is usually under the caudal aspect of the ribs or in the midabdomen. The concurrent presence of abdominal effusion may make recognition of the gas bubble easier because the fluid provides a more uniform, homogeneous soft tissue background opacity (Fig. 36-8, *A*). Occasionally, the amount of gas will be large enough to outline serosal surfaces of viscera, such as bowel loops, the stomach, and the diaphragm (Fig. 36-8, *B*).

Because free gas rises to the highest point within the abdomen, it may be isolated visually from superimposed structures by a horizontally directed x-ray beam. With a small volume of gas, putting the patient in position for 10 minutes before radiographic exposure may be helpful to allow most of the gas to migrate and coalesce at the uppermost portion of the abdomen. The most sensitive projection for detecting a small volume of peritoneal gas is a lateral view, made with a horizontally directed x-ray beam with the patient in dorsal recumbency and with the cranial portion of the abdomen elevated slightly so small amounts of gas accumulate between the liver, diaphragm, and ventral aspect of the abdominal wall (Fig. 36-9).[12] Another projection used for documenting free gas is a ventrodorsal view obtained with the patient in left recumbency with the use of a horizontally directed x-ray beam. Gas will usually collect under the highest portion of the right abdominal wall (Fig. 36-7, *B*), which is usually under the caudal aspect of the ribs. Raising or lowering either end of the animal shifts the point of gas accumulation. Exposure factors should be lowered to underexpose the abdomen, making the gas more conspicuous. A horizontal-beam view with the animal in right recumbency is not recommended because the gas bubble rises to the left side and gas within the fundus of the stomach may be misinterpreted as free gas.

Horizontal-beam radiography is a useful tool for diagnosing free peritoneal gas quickly, cheaply, and with confidence; however, making radiographs with a horizontally directed x-ray beam is technically challenging with many newer digital radiography systems because the imaging plate is large, fragile, and not intended to be moved. However, with patience and care, most imaging plates can be positioned carefully and used for horizontal-beam radiography. Caution should be exercised

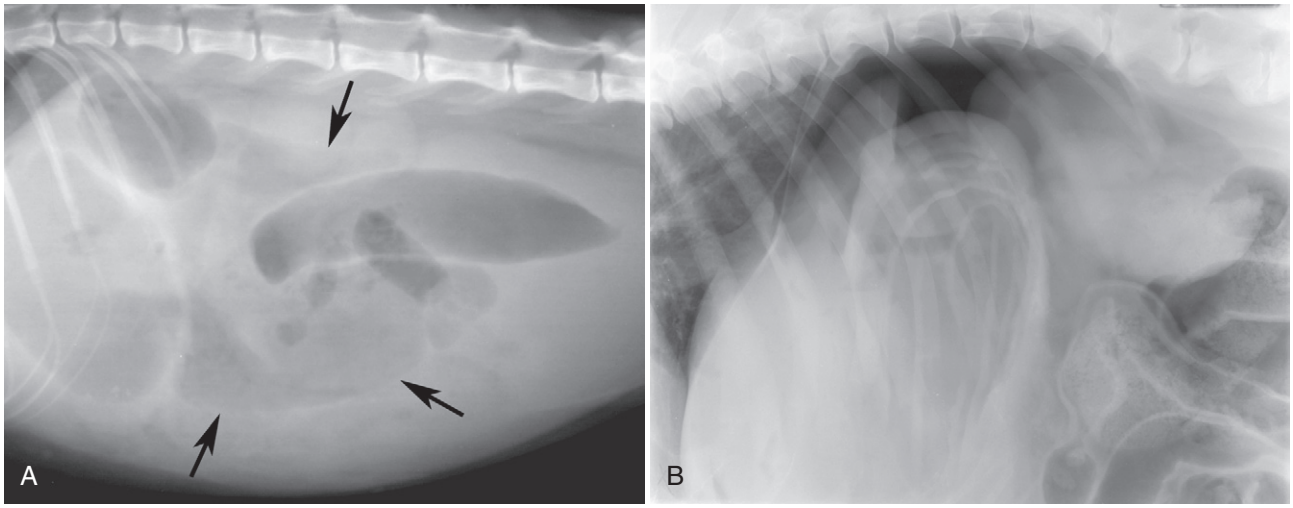


Fig. 36-8 **A,** Lateral survey radiograph of a cat with abdominal effusion and a large amount of free intraabdominal gas with margins of the gas pocket indicated by *black arrows*. **B,** Lateral survey radiograph of the abdomen of a dog immediately after laparotomy. A large volume of free abdominal gas outlines the caudal surface of the right crus of the diaphragm, the cranial pole of the right kidney, the caudal surface of part of the liver, and the serosal surfaces of some bowel loops.

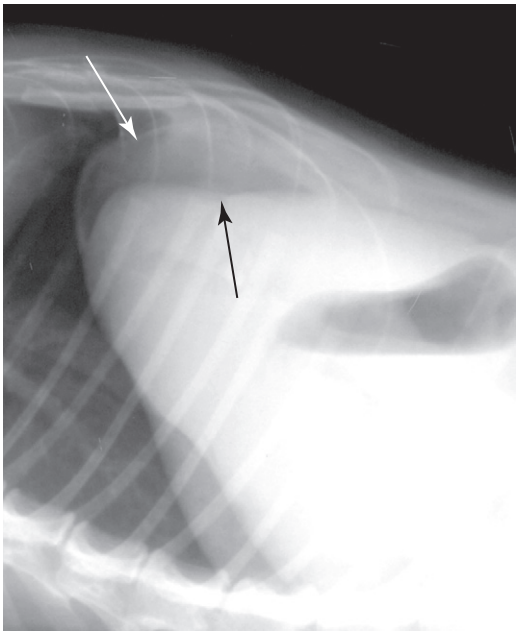


Fig. 36-9 Lateral view of the abdomen made with the patient in dorsal recumbency with the cranial abdomen slightly elevated, and the use of a horizontally directed x-ray beam. Free abdominal gas has accumulated between the diaphragm *(white arrow)*, the liver *(black arrow)*, and the ventral abdominal wall. The diagnosis was ruptured stomach.

when moving the imaging plate because it is often the most expensive part of the entire system. One advantage of computed radiography systems compared to direct digital radiography systems is the increased ease of producing radiographs with a horizontal beam. The ease of performing horizontal-beam radiography should be one factor considered when purchasing a new digital radiography system. See Chapter 2 for more information on digital radiography systems.

Gas may also accumulate in the retroperitoneal space.[8] Retroperitoneal gas is most often the result of extension of pneumomediastinum (see Chapter 30). Retroperitoneal gas is confined to the retroperitoneal space in the dorsal abdomen and is best seen on a lateral radiograph (Fig. 36-10).

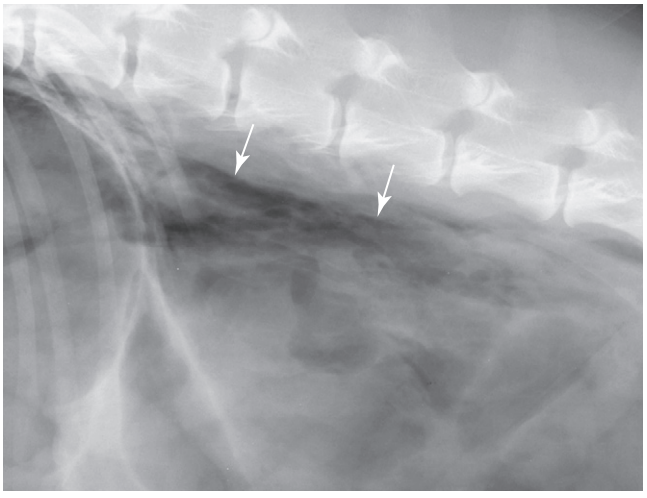


Fig. 36-10 Lateral view of a dog with pneumomediastinum. The pneumomediastinum is not visible in this image. Some of the mediastinal gas dissected along the fascial planes through the aortic hiatus into the retroperitoneal space *(white arrows)*.

Intraabdominal Mineral Opacity

Increased mineral opacity not associated with the gastrointestinal tract is relatively uncommon. Focal calcified bodies, usually with a more opaque periphery, may be found in the peritoneal space (Fig. 36-11; see Fig. 36-4). These are thought to be the result of dystrophic calcification of necrotic mesenteric fat and are not considered clinically significant.[13,14] Although not common, they are seen more often in cats than dogs. These have been referred to as *Bates bodies*.[14] Metastatic calcification of the abdominal vasculature is rare (Fig. 36-12) and is associated with abnormal calcium metabolism, primarily in animals with chronic uremia,[13,15] or hypothyroidism. A mineralized fetus may be seen in the peritoneal space with ectopic pregnancy. Clinical signs may be caused by necrosis or mechanical interference, or the condition may be an incidental finding.[16]



Fig. 36-11 Lateral radiograph of a cat with a focal calcified body in the peritoneal space. The calcified body was an incidental finding and thought to be a result of dystrophic calcification of necrotic fat.

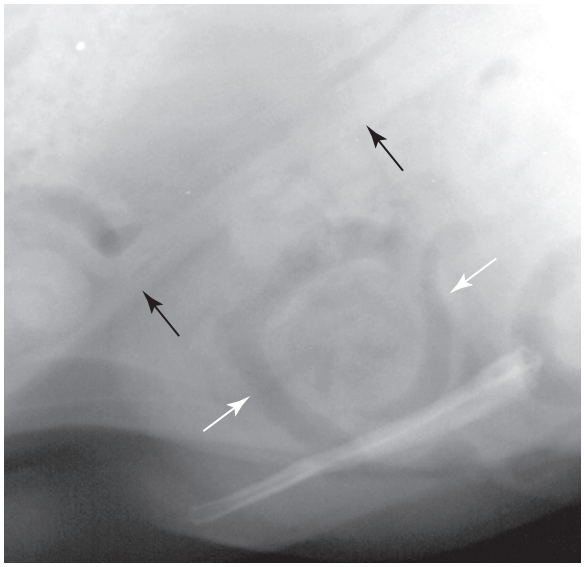


Fig. 36-13 Lateral view of the abdomen of a dog with tubular gas opacities *(white arrows)* ventral to the abdominal wall from an inguinal hernia with entrapped small intestine within the hernia. The level of the abdominal wall is indicated by the *black arrows*.

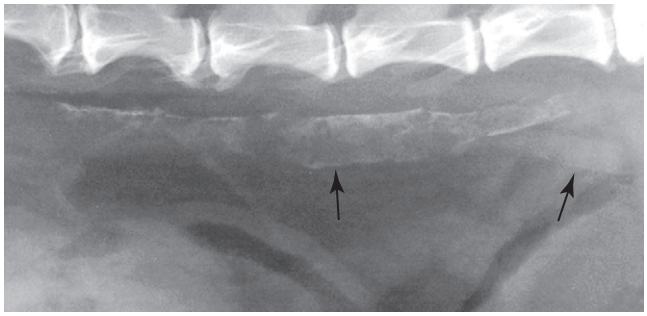


Fig. 36-12 Lateral view of the caudal abdomen of a 13-year-old Shetland sheepdog in chronic renal failure. The aorta and external iliac arteries *(black arrows)* are visible because of metastatic calcification.

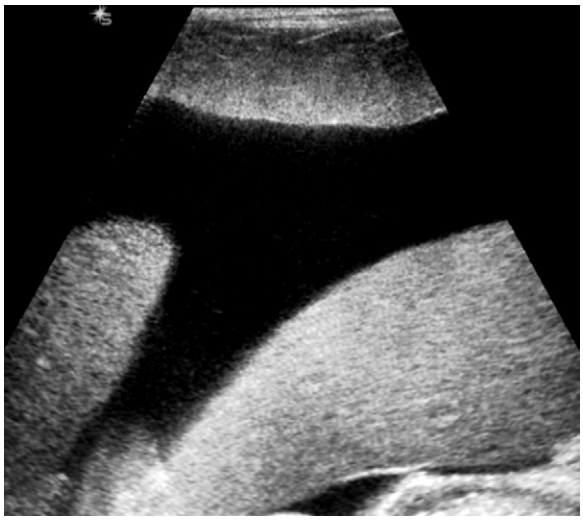


Fig. 36-14 Sagittal sonogram of a dog with ascites. Anechoic fluid is present between and surrounding liver lobes. The lack of echoes in the fluid is consistent with the fluid being of low cellular content.

Abdominal Wall Abnormalities

Mineralization may be visualized occasionally in the soft tissues surrounding the abdomen. For example, calcinosis cutis associated with Cushing's syndrome may produce nodular or linear calcification of soft tissues, most often dorsally and in the ventral abdominal wall.[17] Gas from a variety of causes may be seen in the soft tissues surrounding the abdomen. Abrasions with lacerations often produce a mottled, irregular gas pattern. Tubular or round gas pockets may be contained within herniated bowel loops (Fig. 36-13).

Sonography of the Peritoneal Space

Ultrasound is extremely useful for evaluating the peritoneal space, especially when increased fluid is suspected. Small fluid volumes can be detected readily and ultrasound guidance can be used to collect samples. Fluid can also be characterized by its echogenicity. Fluid with low cellular content, such as urine or a transudate, is anechoic (Fig. 36-14); fluid with moderate to high cellular content, such as exudate, blood, or chyle, is more echoic (Fig. 36-15).

Peritoneal masses can be solid or cavitary, and samples can be obtained for cytologic evaluation. Differentials are similar to those for any mass (e.g., cyst, hematoma, abscess, neoplasia, granuloma). Although uncommon, peritoneal metastases can be detected and appear as fingerlike projections of hypoechoic material scattered throughout the mesentery (Fig. 36-16). In the northwestern portion of the United States and Canada, as well as portions of Europe, peritoneal infection by *Mesocestoides* species tapeworms may manifest as varying-sized, cavitary, septated structures with echogenic particles within the fluid.[18,19]

Small volumes of free peritoneal gas can appear as focal artifacts adjacent to the nondependent portion of the peritoneum (Fig. 36-17); they may not interfere with sonographic evaluation, but large volumes of gas hinder complete evaluation of the peritoneal space. Free peritoneal gas can be found sonographically in patients in which it is not diagnosed radiographically, and the specific location and cause of the

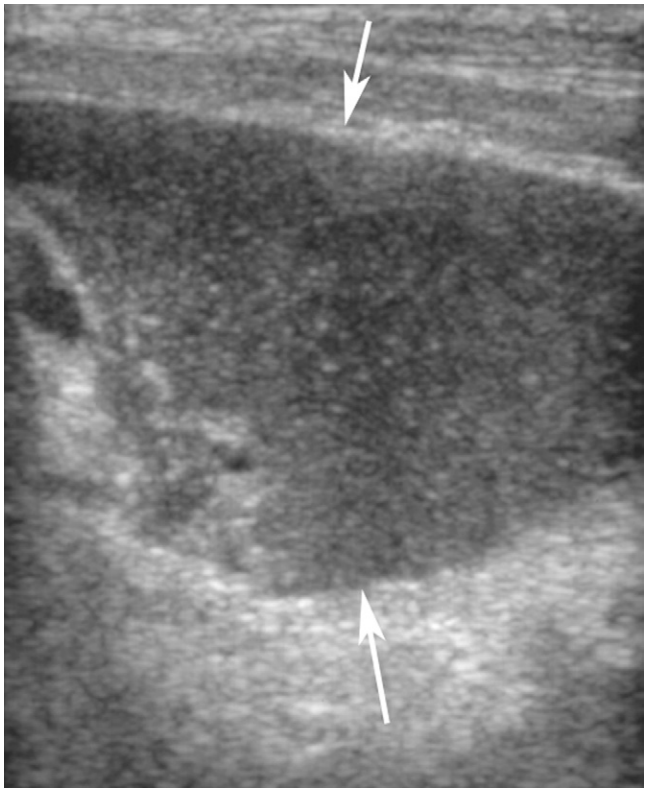


Fig. 36-15 Sagittal sonogram of a 6-year-old dog with an abdominal mass and peritoneal effusion. Free peritoneal fluid *(white arrows)* with low-level echoes is compatible with highly cellular fluid.

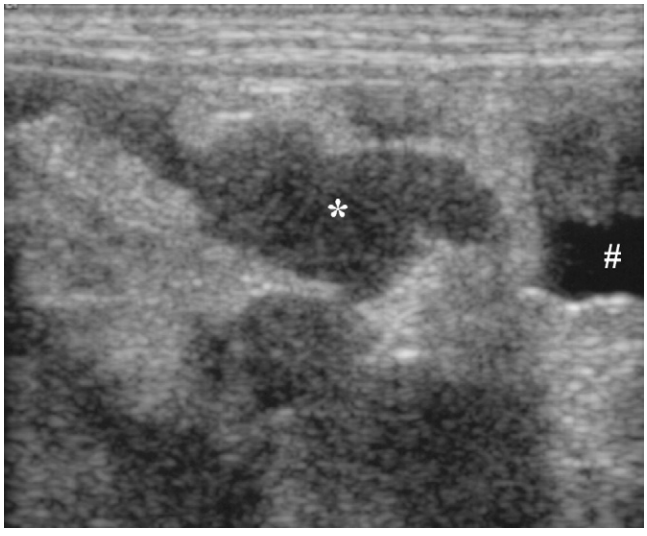


Fig. 36-16 Sagittal sonogram of a 9-year-old dog with peritoneal metastasis, which is seen as hypoechoic, irregularly shaped material *(*)* interspersed through the more echogenic mesenteric fat. A small amount of anechoic peritoneal fluid is present on the right edge of the image *(#)*.

pneumoperitoneum can be identified more frequently sonographically than in radiographs. The findings of hyperechoic fat, free peritoneal fluid, and a dilated fluid-filled stomach or intestine were considered indirect evidence of gastrointestinal perforation.[20] As would be expected, pneumoperitoneum in conjunction with gastric dilatation or volvulus is predictive for gastric necrosis. Prior percutaneous trocharization can confound the situation by leading to pneumoperitoneum and/or pneumatosis mimicking gastric necrosis.[21]

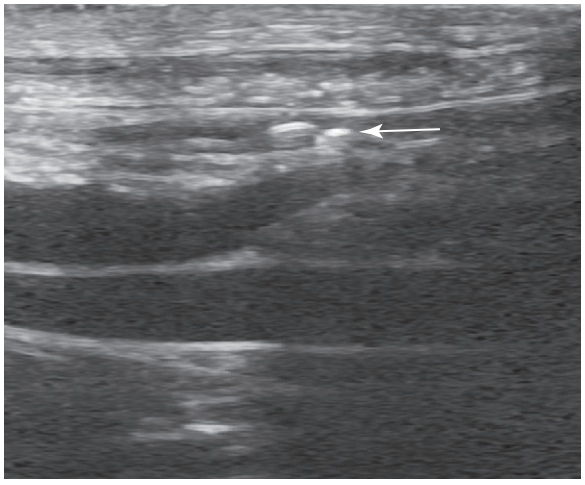


Fig. 36-17 Abdominal sonogram of a dog with a small amount of peritoneal gas. Even small gas collections create strong reflective artifacts *(white arrow)*.

Abdominal Lymph Nodes

Abdominal lymph nodes are divided into two groups: parietal and visceral. Parietal lymph nodes lie in the retroperitoneal space and receive afferent lymphatics from the spine, adrenal glands, kidneys, caudodorsal abdomen, pelvis, and pelvic limbs. Efferent vessels from the parietal lymph nodes drain into the lumbar trunk, which in turn empties into the cisterna chyli. The more cranially located of the parietal lymph nodes may bypass the lumbar trunk and drain directly into the cisterna chyli. Many of the parietal lymph nodes are developed inconsistently and may be absent. However, the medial iliac lymph nodes, the largest lymph nodes of the sublumbar group, are constant. The medial iliac lymph nodes, previously known as the *external iliac lymph nodes*,[1] are located ventral to the vertebra and between the deep circumflex iliac and external iliac arteries. Although medial iliac lymph nodes are reported to lie ventral to L5 and L6,[1] these lymph nodes often are located ventral to L6 and L7.[5] One lymph node is usually present on each side, but occasionally two lymph nodes are on one or both sides. The medial iliac lymph nodes receive afferent lymphatics from the urogenital tract as well as from other structures in the caudal abdomen, pelvis, and pelvic limbs.

The visceral group of abdominal lymph nodes drains the liver, spleen, pancreas, stomach, and intestine. The largest of the visceral lymph nodes are the cranial mesenteric lymph nodes, which receive afferent lymphatics from the jejunum, ileum, and pancreas. The efferent vessels of the visceral lymph nodes drain into the intestinal trunk, which then empties into the cisterna chyli.

Abnormalities of Lymph Nodes

Abdominal lymph nodes are seen radiographically only if they are enlarged or mineralized. Abundant retroperitoneal fat helps provide contrast between enlarged lymph nodes and surrounding soft tissue structures. Of the parietal lymph nodes, the medial iliac nodes are usually the only lymph nodes that enlarge to the degree that they are seen radiographically. Care should be taken not to confuse the deep circumflex arteries and veins that are projected end-on in lateral radiographs as enlarged medial iliac lymph nodes (Fig. 36-18). Enlarged medial iliac lymph nodes appear as a soft tissue mass in the retroperitoneal space ventral to L6 and L7 (Fig. 36-19). If node enlargement is severe, the lymph nodes are more conspicuous and extend more cranially (Fig. 36-20). Enlarged lymph nodes frequently displace the descending colon and



Fig. 36-18 Lateral view of the abdomen of a normal dog. Note the fat opacity within the retroperitoneal space. Ill-defined nodular soft tissue opacities in the caudal retroperitoneal space seen ventral to L6 *(black arrows)* represent end-on projections of the deep circumflex iliac arteries and veins, not lymph nodes.

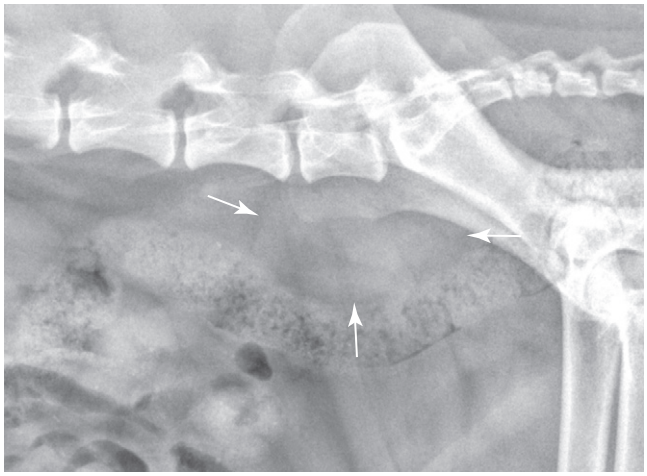


Fig. 36-19 Lateral view of the abdomen of a dog with anal gland adenocarcinoma. The medial iliac lymph nodes are mildly enlarged and appear as an ill-defined soft tissue mass *(white arrows)* in the retroperitoneal space ventral to L7. The colon is displaced ventrally.

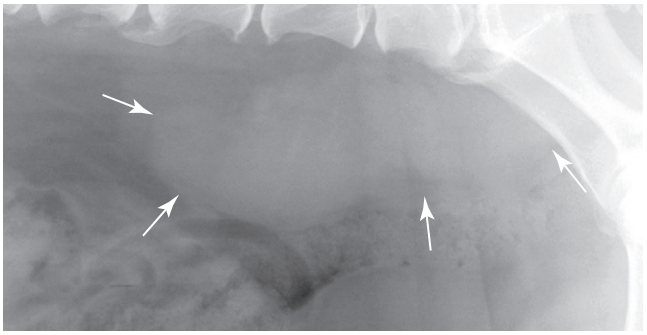


Fig. 36-20 Lateral view of the abdomen of a dog with lymphosarcoma. Medial iliac lymph node enlargement is severe and appears as a soft tissue mass in the retroperitoneal space extending caudally from L4-L5 into the pelvic canal *(white arrows)*.



Fig. 36-21 Lateral view of the abdomen of a dog with metastatic mast cell tumor. A large soft tissue mass caused by enlargement of the medial iliac lymph nodes extends from L3-L4 into the pelvic canal, displacing the colon and rectum ventrally.

rectum ventrally (Fig. 36-21). However, a ventral course of the colon is not an indication of medial iliac lymph node enlargement unless a soft tissue mass is present in the expected location of the lymph nodes because the colon may be positioned more ventral than usual without being displaced by a mass. The most common cause of medial iliac lymphadenopathy is neoplasia. Neoplastic lymph node involvement may be primary (e.g., lymphosarcoma) or metastatic (e.g., from caudal abdominal or pelvic neoplasms).[22] Inflammatory disease may also cause enlargement of the medial iliac lymph nodes, but this is unusual.

Visceral abdominal lymph nodes rarely enlarge enough to be seen radiographically, tending to silhouette with surrounding organs. Cranial mesenteric lymph nodes may occasionally enlarge sufficiently so as to be seen as an ill-defined central abdominal mass displacing the intestine peripherally.

Sonography of Parietal and Visceral Lymph Nodes

Ultrasound is more sensitive than radiography for imaging lymph nodes. Because the medial iliac and jejunal lymph nodes are the largest and most consistent in the abdominal cavity, they can be found more often than other lymph nodes when normal.[23] Normal lymph nodes have an echogenicity similar to surrounding mesentery and adjacent musculature,[23] but knowledge of their location and careful identification of elongated structures of uniform echotexture and thin echogenic capsules can permit detection (Fig. 36-22). High-frequency transducers are necessary to obtain resolution adequate for imaging normal lymph nodes. Lymph nodes are generally identified more easily in young or thin animals.[23] When abnormal, lymph nodes tend to enlarge and become more round and hypoechoic (Fig. 36-23, see page 668).[23-25] Neoplastic lymph nodes tend to have a short-to-long axis ratio of more than 1:2, narrow or absent hilus, hypoechogenicity, sharp borders, a resistive index (RI) greater than 0.65, a pulsatility index (PI) greater than 1.45, and often distal acoustic enhancement. These findings tend to not be present in reactive lymph nodes.[25] Neoplasia should be suspected if the RI is greater than 0.675, or the PI is greater than 1.025 for medial iliac lymph nodes; and if the RI is greater than 0.76, or the PI is greater than 1.23 for mesenteric lymph nodes.[26] Heterogeneity of enlarged lymph nodes is associated with malignancy in the dog, but lymph node heterogeneity is not predictive of malignancy in the cat.[27] Aspirates obtained with ultrasound guidance are helpful for determining the cause of lymph node enlargement.

The medial iliac lymph nodes are found by scanning the caudal abdominal region and searching the area around the

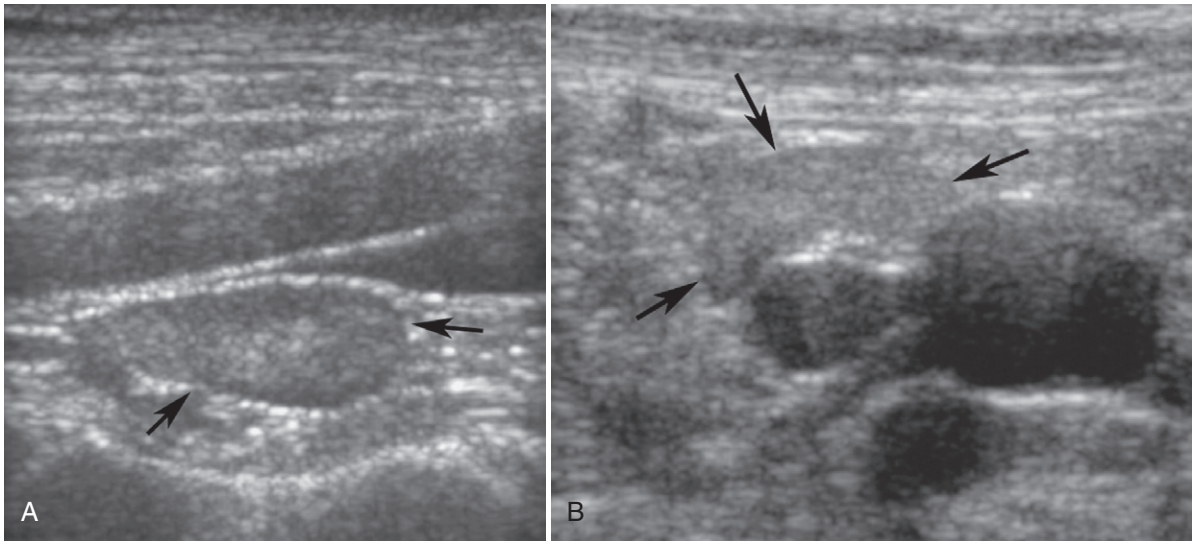


Fig. 36-22 Sagittal **(A)** and transverse **(B)** sonograms of a normal medial iliac lymph node. On the sagittal view, the lymph node *(black arrows)* is elongated and just ventral to the aorta near the aortic bifurcation. The lymph node is nearly isoechoic to surrounding structures and has a thin echogenic capsule. On the transverse image, the lymph node *(black arrows)* is a curved structure just ventrolateral to the aorta. Ventral is to the *top* (**A** and **B**), and cranial is to the left **(A).**

terminal portion of the aorta and caudal vena cava carefully. In some instances, finding the lymph nodes by scanning in a transverse plane and looking for subtle round structures with thin echogenic borders on either side of the aorta is easier (Fig. 36-22, *B*). Alternatively, the medial iliac lymph nodes may be easier to find in the dorsal plane.[28] In the sagittal plane, the lymph nodes appear fusiform (Fig. 36-22, *A*). The visceral lymph nodes are seen more often when abnormal and are encountered as hypoechoic nodules detected during routine scanning. They are identified as lymph nodes on the basis of their location.[23]

PANCREAS

The body of the pancreas lies between the pylorus and the proximal descending duodenum. The right limb of the pancreas extends caudally from the body and lies adjacent to the descending duodenum. The left limb of the pancreas lies between the stomach and transverse colon, extending from the body toward the left kidney. The normal pancreas is not visualized on abdominal radiographs of dogs because of silhouetting with the adjacent tissues. Occasionally, the left limb of the pancreas can be seen on ventrodorsal views in obese cats as an area of soft tissue opacity between the fundus of the stomach, the spleen, and the left kidney (Fig. 36-24).

Abnormalities of the Pancreas

Acute pancreatitis is a common cause of localized peritonitis. The frequency and appearance of radiographic changes caused by acute pancreatitis are variable.[29-31] Changes are usually localized to the right cranial abdomen, where the right lobe of the pancreas is closely associated with the proximal duodenum and pyloric antrum, or to the midline just caudal to the stomach, where the left lobe of the pancreas is located. The major radiographic abnormality is usually an increased, irregular soft tissue opacity in the right mid- to cranial abdomen, indicating localized peritonitis (Fig. 36-25, *A*). On the ventrodorsal view, the cranial right abdomen is normally more opaque than the left side, and care should be taken not to misdiagnose this normal opacity as pancreatitis.[5]

The proximal descending duodenum may be displaced ventrally or toward the right to produce a broad curvature, and the pylorus of the stomach may be displaced toward the left. Less frequently, the transverse colon may be displaced caudally. Bowel loops adjacent to the pancreas, such as the proximal descending duodenum, may contain gas; they may also have loss of tone and be dilated. This gas dilation of the duodenum has been referred to as the *sentinel loop sign*,[32] but this finding is not definitive evidence for pancreatitis. Spasticity of the duodenum has also been described. Foci of mineralization may occur in areas of fat necrosis.[32] Abscesses, inflammatory masses, and pseudocysts may be sequelae to pancreatitis (Box 36-3).[33-35]

Sonography of the Pancreas

Sonographic evaluation of the pancreas is standard practice for evaluating patients suspected of having pancreatitis or pancreatic masses because the pancreas is better evaluated sonographically than radiographically. The normal pancreas is difficult to identify sonographically because of its small size, echogenicity similar to that of surrounding fat, and lack of a well-defined capsule.[36,37] In addition, gas in adjacent bowel often obscures the pancreatic region. Therefore identifiable landmarks are used to scan the pancreatic area. Patients can be scanned in dorsal[38-41] or lateral recumbency[37] with the highest frequency transducer that will provide sufficient depth penetration. The body and right limb of the pancreas is found by scanning the stomach in a sagittal (longitudinal) plane and sliding the transducer to the right until the duodenum is identified. The right limb lies just dorsal and medial to the duodenum, medial to the right kidney, and lateral to the portal vein. Another approach is to scan the cranial pole of the right kidney in a sagittal plane and move the transducer medially or laterally until the descending duodenum is found. The left limb of the pancreas lies between the greater curvature of the stomach and the transverse colon and extends to the level of the spleen. The pancreatic area should be examined in both sagittal and transverse planes. Occasionally, it is useful to use an intercostal approach to image the pancreas fully.[42]

When visible, the pancreas has indistinct margins (Fig. 36-26), and it is somewhat hypoechoic, being less echogenic

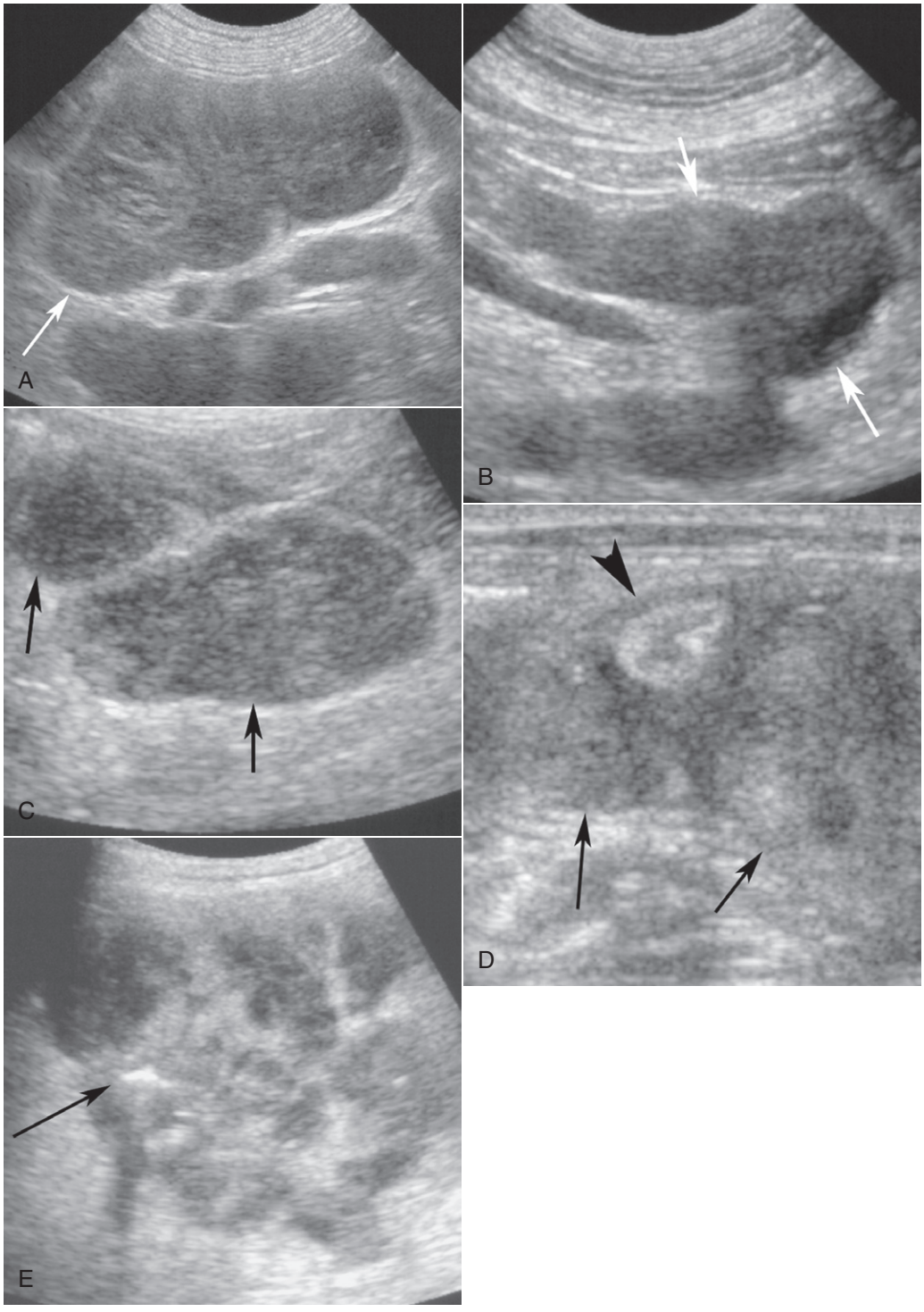


Fig. 36-23 Sonographic appearance of abnormal lymph nodes. **A,** Enlarged, hypoechoic medial iliac lymph node *(white arrow)* surrounding the aorta in a dog with lymphosarcoma. **B,** Enlarged jejunal lymph node *(white arrows)* in a dog with lymphosarcoma. This lymph node is hypoechoic to surrounding tissues and is irregular in shape. **C,** Enlarged jejunal lymph nodes *(black arrows)* in a dog with inflammatory bowel disease. Lymphoid hyperplasia was found on evaluation of lymph node aspirates. Both lymph nodes are hypoechoic and appear similar to those seen in the dog with lymphosarcoma (**B**). **D,** Enlarged ileocolic lymph nodes in a cat with lymphosarcoma. The ileum *(black arrowhead)* is seen in cross section surrounded by enlarged hypoechoic lymph nodes *(black arrows)*. **E,** A large mixed echogenic mass in the midabdomen of a dog. The mass incorporated intestinal segments. Gas *(black arrow)* within one bowel segment is seen as an echogenic focus producing acoustic shadowing. The hypoechoic to nearly anechoic areas were presumed to be enlarged mesenteric lymph nodes because lymphosarcoma was diagnosed from aspirates of these structures.

than the spleen[37] but more echogenic than the liver.[37,38] Occasionally, the pancreaticoduodenal vein, which lies within the pancreas and runs parallel to the duodenum, can be identified (see Fig. 36-26).[37-41,43] The pancreas is more likely to be identified in puppies, thin dogs, and dogs with peritoneal fluid.[37] In people, fatty infiltration of the pancreas is associated with obesity, and increased pancreatic echogenicity is associated with age, making the pancreas similar in echogenicity to surrounding fat and therefore difficult to identify.[44] In cats, the normal pancreas is isoechoic to the liver and hypoechoic to the surrounding mesentery, findings that do not appear to change with age, gender, body weight, or body condition.[45,46] The normal width (ventral to dorsal dimension) of left limb and body of the pancreas are approximately 0.25 to 1.0 cm, and the right limb is slightly smaller at between approximately 0.3 and 0.6 cm.[42,43,47] The feline pancreatic duct width should normally be less than approximately 0.25 cm.[42,47]

Combined with history and clinical findings, ultrasound has become a useful diagnostic aid for patients with pancreatitis.[37,43,48-51] In patients with mild pancreatitis, the pancreas may be uniformly hypoechoic surrounded by more echogenic fat (Fig. 36-27).[37,49] Dilation of the pancreatic duct may be more sensitive as an initial sign of pancreatitis in cats,[52] similar to children.[53] However, the feline pancreatic duct does tend to increase in width with increasing age; thus, dilation of the pancreatic duct should not be used as the only marker of pancreatitis in older cats.[42,47] In more severe inflammation, the

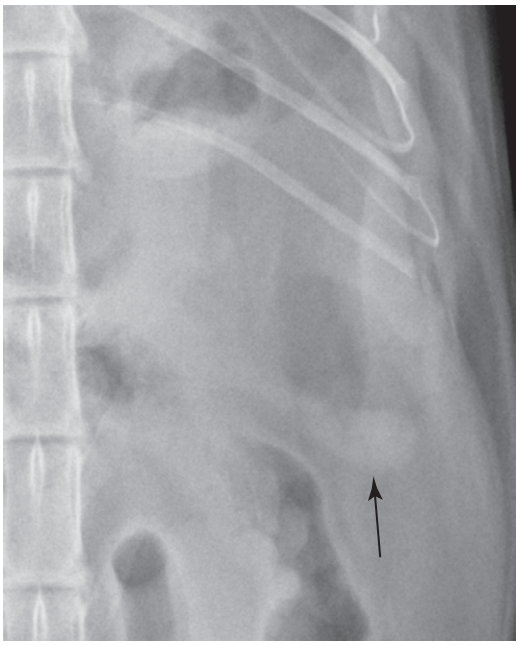


Fig. 36-24 Ventrodorsal radiograph of a normal cat. The left limb of the pancreas is visible *(black arrow)*.

Box • 36-3

Radiographic Signs of Pancreatitis

Increased soft tissue opacity, cranial right abdomen
Soft tissue mass effect caudal to stomach
Focal decrease in serosal detail, cranial right abdomen
Gas-distended descending duodenum (sentinel loop sign)
Displacement of adjacent intestinal structures
Radiographs may be normal

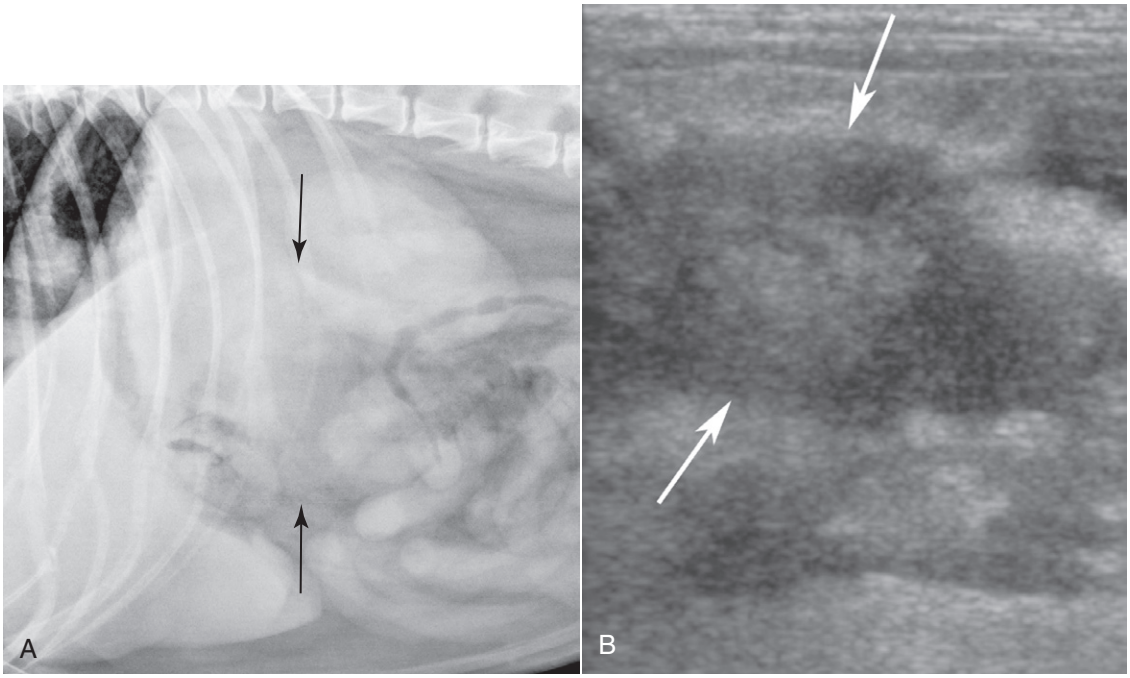


Fig. 36-25 **A,** Lateral survey radiograph of a dog with increased irregular soft tissue opacity in the midcranial to cranial abdomen as a result of localized peritonitis *(between black arrows)*. This is a difficult assessment to make; recognizing this change requires high-contrast radiographs and a patient with adequate abdominal fat. **B,** Transverse ultrasonographic view of the right limb of the pancreas in the same dog. Note the pancreas *(white arrows)* is enlarged, hypoechoic, and irregular in shape, and the surrounding mesentery is hyperechoic. The diagnosis was pancreatitis.

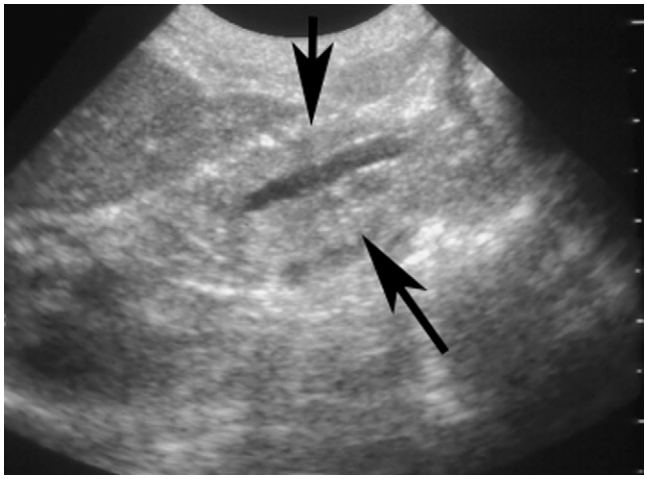


Fig. 36-26 Sagittal sonogram of the pancreatic region of a normal dog. The pancreas *(black arrows)* is the poorly defined structure adjacent to the liver, having approximately the same echogenicity as the mesentery. The hypoechoic structure in the middle of the pancreas is the pancreaticoduodenal vein.

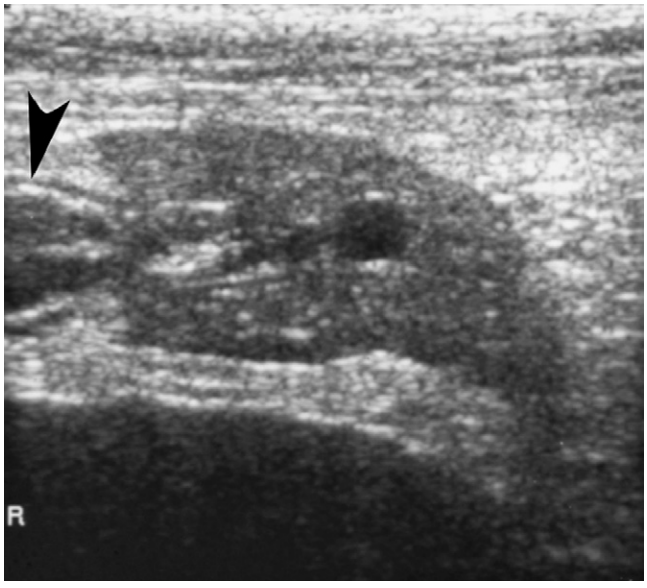


Fig. 36-27 Transverse sonogram of the right lobe of the pancreas of a dog with mild pancreatitis. The pancreas is less echogenic than normal, is hypoechoic to surrounding fat, and lies just ventral to the liver and medial to the duodenum *(black arrowhead)*. The pancreaticoduodenal vein is the round anechoic structure within the pancreas.

pancreas may be enlarged and contain irregularly shaped hypoechoic and hyperechoic areas (Fig. 36-28).[33,38,40] Other findings may include cavitary lesions, thickened duodenum, biliary obstruction, localized peritoneal fluid, and dilation of the pancreatic duct.[37,48-51,54] Hypoechoic areas within the pancreas are likely caused by inflammation, hemorrhage, necrosis, and edema.[38,50,55] Hyperechoic areas may be from fibrosis.[55] The surrounding tissue may be increased in echogenicity as a result of acoustic enhancement through hypoechoic areas or saponification of mesenteric fat.[33,37,50] In spite of these criteria, pancreatitis remains difficult to diagnose, especially in cats.[56] Differentiation of acute versus chronic pancreatitis also remains elusive,[57] and chronic pancreatitis may be more common in dogs than previously thought.[58] However, ultrasound appears to be more sensitive than helical computed tomography in detecting pancreatitis in cats (Box 36-4).[59]



Fig. 36-28 Sagittal sonogram of the right lobe of the pancreas in a dog with pancreatitis. The pancreas is enlarged and hypoechoic, and the surrounding mesentery is hyperechoic. This is a common appearance in dogs with moderate to severe pancreatitis.

Box • 36-4

Ultrasonographic Signs of Pancreatitis

Enlarged pancreas
Hypoechoic pancreas
Hyperechogenicity of the surrounding mesentery
Possible cavitary lesions
Possible dilation of biliary or pancreatic ducts
May be normal

Ultrasound of the pancreas using intravenous microbubble contrast media shows some promise in cats in differentiating a diseased versus normal pancreas.[60]

Pancreatic pseudocysts and abscesses may occur as a result of pancreatitis;[4,6,37,61-65] they appear as large, mostly anechoic masses in the pancreatic area with distal acoustic enhancement and low-level internal echoes (Fig. 36-29, *A*). They may be difficult to differentiate ultrasonographically from a pseudocyst; ultrasound-guided aspirates are helpful.[6] If a pancreatic mass lies near the opening of the common bile duct, biliary obstruction may result.[65] True pancreatic cysts are rare but have been reported in at least two cats. Clinical signs (vomiting) resolved after surgical removal of the cyst in one patient,[66] and multiple recurring cysts were identified in another patient associated with pancreatic inflammation, atrophy, and diabetes mellitus.[67] Another rare finding is a calculus within the pancreatic duct.[68]

Pancreatic tumors are uncommon but may be detected sonographically. Exocrine pancreatic carcinomas tend to invade the duodenum and often metastasize to regional lymph nodes, liver, and the peritoneum.[69] Functional islet cell tumors may be benign or malignant and should be suspected in dogs with persistent hypoglycemia. Both types of tumors may appear as discrete hypoechoic nodules or masses in the pancreatic region.[38,37,48,70] A potential source of error is misinterpretation of enlarged hypoechoic lymph nodes as a pancreatic

mass.[70] Islet cell tumors can be small and difficult to detect sonographically; therefore a negative examination does not rule out neoplasia.[37] Only approximately 30% of insulinomas can be detected with ultrasound.[71] Computed tomography shows promise in evaluation of pancreatic masses, including insulinomas,[72-74] but surgical evaluation remains the gold standard. Both pancreatitis and pancreatic neoplasms may cause biliary dilation, lymphadenopathy, and peritoneal fluid. Hyperechoic or heterogeneous masses are more often found in pancreatitis, and discrete hypoechoic nodules are more characteristic of neoplasia. Some suggest that the main sonographic features that may help distinguish between inflammation and neoplasia are a diffusely hypoechoic pancreas in dogs with pancreatitis and hypoechoic nodules in dogs with neoplasms.[48] Others suggest that abnormalities of the liver and pancreas, combined with a lack of pain, are suggestive of neoplasia (Fig. 36-29, *B*).[75] In cats, there was overlap in the radiographic and sonographic appearance of neoplasia and nodular hyperplasia; however, if a solitary pancreatic nodule 2 cm in diameter or larger is present, neoplasia is more likely.[76]

Correlation with history, clinical signs, and other diagnostic findings may negate the need for tissue sampling. However, if a definitive diagnosis is needed, tissue sampling is necessary.[75] Needle aspiration and surgical biopsy has been associated with increased serum trypsin-like immunoreactivity and mild pancreatic inflammation and/or necrosis, but not an increase in canine-specific pancreatic lipase.[77] A single biopsy may not be sufficient because pancreatic diseases tend to be focal and randomly distributed.[78] Again, a normal sonographic examination of the pancreas does not rule out pancreatic disease, especially infiltrative or inflammatory disease. This is particularly true for cats.

The fear of complications may decrease the enthusiasm for tissue sampling of the pancreas. Severe pancreatitis can be induced by sampling procedures, but delaying pursuit of definitive therapy because of the lack of a definitive diagnosis carries its own risks and costs. In the author's experience, clinically significant complications secondary to tissue sampling, especially needle aspiration, of the pancreas are rare.

ADRENAL GLANDS

The adrenal glands are located in the retroperitoneal space. The left adrenal gland is located more cranially with respect to its corresponding kidney than the right adrenal gland, which is located near the hilus of the right kidney. The right adrenal gland is bordered dorsally by the psoas minor muscle and the crus of the diaphragm, medially by the caudal vena cava, ventrolaterally by the right kidney, and cranioventrally by the right lateral liver lobe. The left adrenal gland is bordered dorsally by the psoas minor muscle, ventrally by the spleen, laterally by the left kidney, and medially by the aorta.[1] Because of their small size and soft tissue opacity, normal adrenal glands are not seen radiographically.

Abnormalities of the Adrenal Glands

Adrenal glands are seen radiographically only when enlarged or mineralized. Radiographically detectable adrenal gland enlargement may be caused by pheochromocytoma,[79] cortical carcinoma, or adenoma.[80,81] An adrenal mass should be suspected when a soft tissue or partially mineralized mass is present craniomedial to a kidney. The kidney may be displaced caudolaterally by the mass. Large left adrenal masses may displace the fundus of the stomach cranially, the transverse colon caudoventrally, and the left kidney caudally. Masses of the right adrenal gland may be more difficult to detect than those of the left because the right adrenal gland is in close

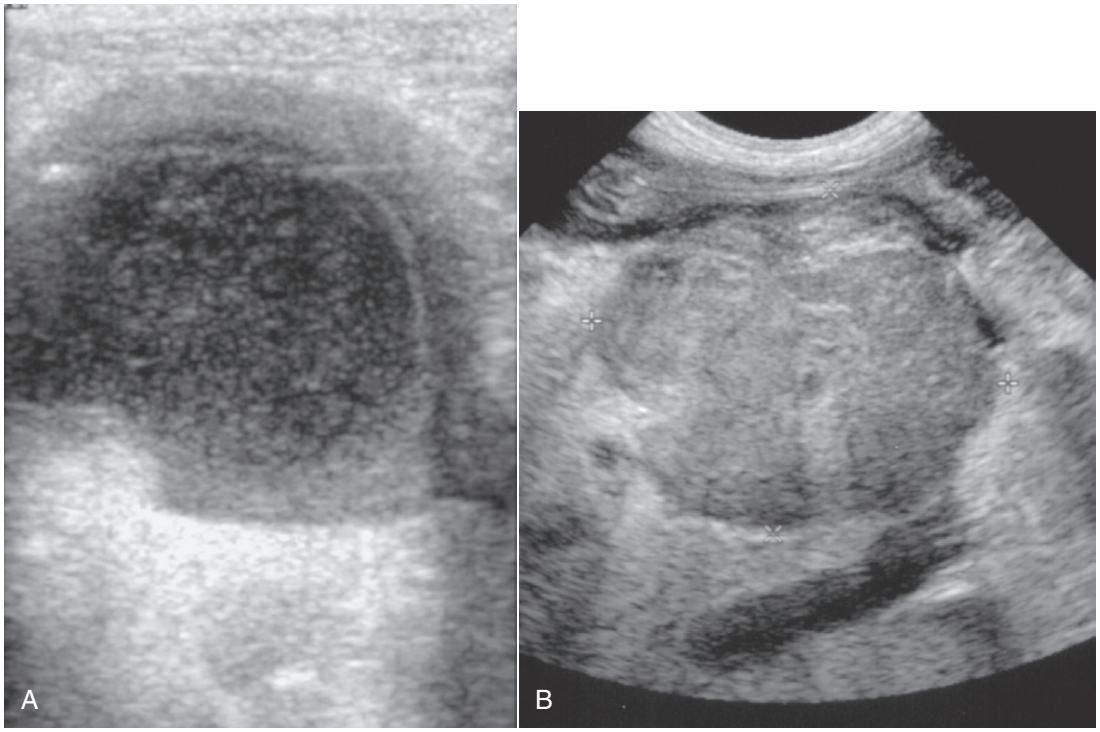


Fig. 36-29 **A,** Sagittal sonogram of the right limb of the pancreas in a dog. A large pancreatic abscess is present with a thick hyperechoic capsule and less echogenic internal contents. **B,** Sagittal sonogram of the right limb of the pancreas in a dog. A solid, midlevel echogenic pancreatic tumor is present adjacent to the duodenum *(top right)*.

proximity to the liver. Functional adrenal carcinomas and adenomas occur with equal frequency in the right and left adrenal glands; adrenal tumors occasionally occur bilaterally.[81,82] Functional adrenocortical carcinomas or adenomas are found in 10% to 20% of dogs with Cushing's syndrome.[83,84]

Dystrophic mineralization of adrenal tumors may occur (Fig. 36-30).[80,81,85-87] Radiographically visible adrenal calcification in dogs with Cushing's syndrome is highly suggestive of neoplasia. In dogs with functional adrenal tumors, 92% and 54% of radiographically visible carcinomas and adenomas, respectively, were calcified.[81] In another study, adrenal calcification was found in 54% and 60% of carcinomas and adenomas, respectively.[80] Carcinomas may invade local tissues, including the caudal vena cava, and metastasize to the liver, lymph nodes, lungs, and kidneys.[81,88-90] When adrenal carcinomas are advanced, it may not be possible to determine the origin of the primary mass lesion radiographically. In such an instance, the metastases may be the major radiographic finding, although an ill-defined soft tissue mass may be present in the craniodorsal abdomen.

Mineralization may occur in nonneoplastic adrenal glands (Fig. 36-31), especially in cats.[86,87] Histologic detection of adrenal calcification was reported in 3.5% of dogs, 30% of cats, and 50% of monkeys in one study,[91] and in 25% of cats[92] and 1% of dogs[93] in two other studies. Calcification occurred in the zona reticularis of the adrenal cortex in the dogs, monkeys,

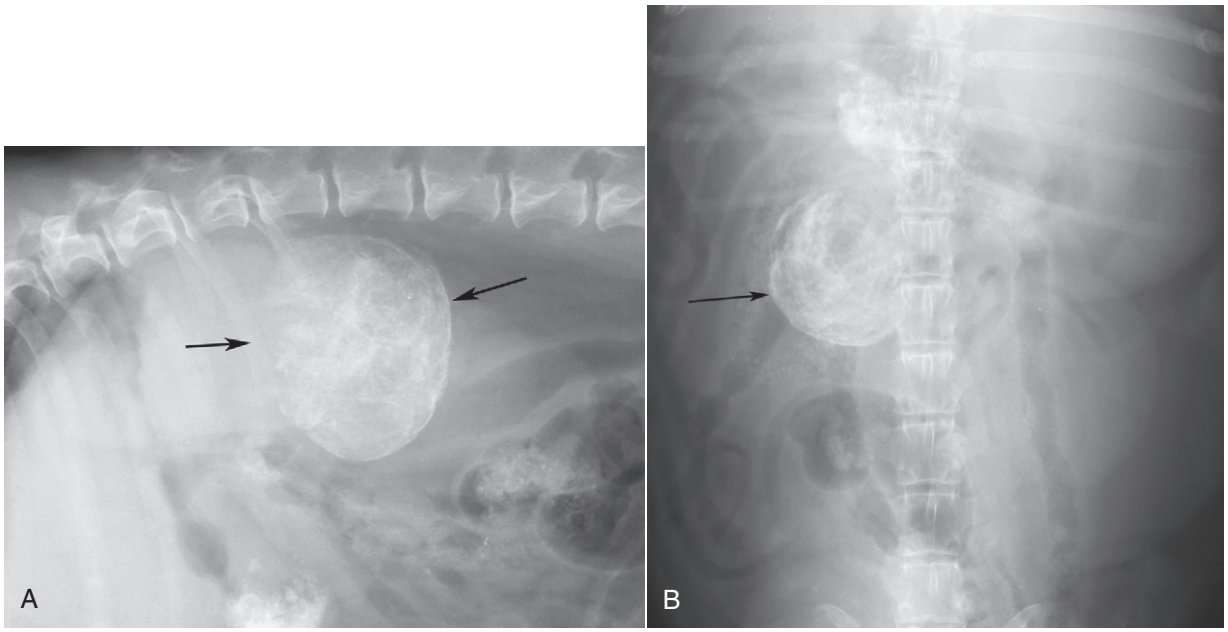


Fig. 36-30 Lateral **(A)** and ventrodorsal **(B)** radiographs of a 14-year-old dog. A large mineralized mass is present caudal to the stomach and just to the right of midline *(black arrows)*. The mass is a malignant functional adrenocortical tumor causing hyperadrenocorticism. A small amount of mineralized ingesta is present within the pyloric region of the stomach.

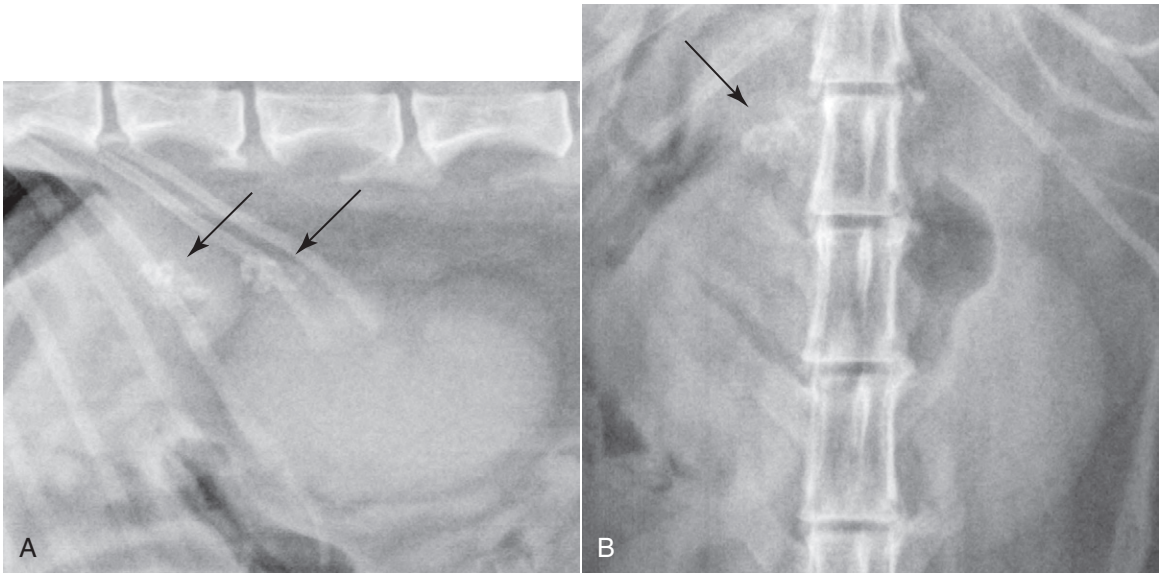


Fig. 36-31 Lateral **(A)** and ventrodorsal **(B)** radiographs of an 8-year-old domestic cat. The adrenal glands are mineralized *(black arrows)*. The left adrenal gland is not visible in the ventrodorsal image because it is superimposed on the spine. This finding is clinically insignificant.

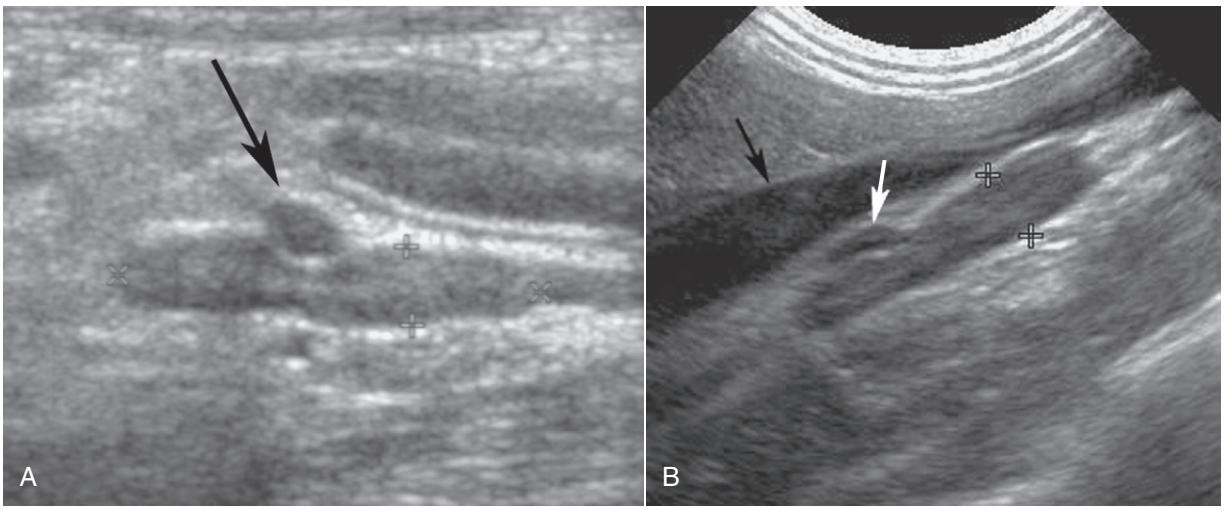


Fig. 36-32 Sagittal sonograms of a left **(A)** and right **(B)** normal canine adrenal gland. **A,** The left adrenal gland has a dumbbell shape and lies just ventral to the phrenicoabdominal vein *(black arrow)*. It is less echogenic than surrounding fat. **B,** The right adrenal gland is seen as an elongated hypoechoic structure just dorsal to the caudal vena cava *(black arrow)*. The right adrenal gland in this dog is surrounded by a hyperechoic capsule. The phrenicoabdominal vein *(white arrow)* is less often visualized on the right side. The head is to the left and ventral to the top.

and cats; however, in some cats, calcification affected the entire adrenal cortex and extended into the medulla.[94] Adrenal calcification was not associated with clinical findings. The cause and pathogenesis of adrenal calcification are unknown. In human beings, adrenal calcification has been associated with intraadrenal hemorrhage, tuberculosis, Addison's disease, tumors (benign and malignant), cysts, Niemann-Pick disease,[94] and Wolman's disease.[95]

Adrenal gland dysfunction usually causes radiographically detectable changes. In patients with Cushing's syndrome, this includes hepatomegaly, bronchopulmonary mineralization, dystrophic mineralization of the skin and other soft tissues, and adrenal gland enlargement with mineralization when functional tumors are present.[80,86,87] Pulmonary arterial thrombosis also occurs in dogs with Cushing's syndrome, but this is difficult to detect radiographically.[96] Decreased size of the heart,[97-99] peripheral pulmonary arteries, caudal vena cava, and liver[99] has been associated with Addison's disease. Although esophageal dilation has also been associated with Addison's disease,[86] it is rare because esophageal dilation was not found in a review of 22 affected dogs.[99]

Sonography of Adrenal Glands

Ultrasound has been used to evaluate normal canine adrenal glands,[100-104] normal feline adrenal glands,[105,106] and dogs with hyperadrenocorticism,[81,100,102,103] hypoadrenocorticism,[107] and adrenal masses.[108,109] However, the ability to image the adrenal glands accurately depends on the quality of the equipment, operator experience, and size of the patient. The highest frequency transducer that produces adequate penetration is recommended. If possible, 7.5 MHz or higher transducers should be used, but lower frequency transducers may be necessary to obtain adequate penetration in larger dogs. The adrenal glands are more easily imaged in smaller patients where higher resolution probes can be used to obtain quality images with adequate penetration. Overlying bowel gas often obscures the adrenal glands.

Most patients are scanned in dorsal recumbency. To find the left adrenal gland, the cranial pole of the left kidney is scanned in a sagittal plane, then the transducer is slid medially to the aorta. The left adrenal gland lies just ventrolateral to the aorta between the cranial mesenteric and renal arteries. Occasionally, the left adrenal gland may be located slightly cranial to the celiac and cranial mesenteric arteries. To obtain a full longitudinal view of the left adrenal gland, the probe may need to be rotated so the aorta is imaged obliquely. The normal canine left adrenal gland is usually shaped like a peanut shell[110] or dumbbell (Fig. 36-32, *A*).[111]

Care should be taken not to confuse the adrenal gland with a lymph node. Both adrenal glands of dogs and cats are hypoechoic to the surrounding fat and hypoechoic or isoechoic when compared with the renal cortex. Occasionally, the adrenal gland has a layered appearance, with the medulla being more echogenic than the cortex. This layered appearance has been ascribed to both normal[106,112] and hyperplastic glands.[113] A hyperechoic capsule can often be identified (Fig. 36-32, *B*).[106,114] In cats, both adrenal glands are oblong and oval to bean shaped.[105,106]

The right adrenal gland is more difficult to image than the left, especially in larger dogs.[115] After the cranial pole of the right kidney is scanned in a sagittal plane, the transducer is moved medially to find the caudal vena cava. The right adrenal gland lies dorsolateral to the caudal vena cava and cranial to the renal vein. The phrenicoabdominal veins cross the ventral surfaces of both adrenal glands and can occasionally be identified with high-resolution transducers. The shape of the right adrenal gland of the dog is different from that of the left. The right has been described as having a comma-shaped[49] or bent-arrow conformation.[111] Many large-breed dogs have adrenal glands with an elongated, thin shape. This is suspected to be a normal variant.

Overlying bowel gas obscuring the adrenal glands is a major problem, especially on the right side. If this happens, the patient or transducer can be repositioned in an attempt to move the overlying bowel. Sedation may be helpful in some patients who resist abdominal compression by the transducer. Imaging the adrenal glands in the dorsal plane is an alternative method of avoiding the overlying bowel gas problem and is preferred by some sonographers.[114] An intercostal approach may be necessary to image the right adrenal gland. Both adrenal glands can be imaged in a dorsal plane with the patient in lateral recumbency. Imaging the dependent adrenal gland is often made easier by placing the transducer under the patient and directing the sound beam upwards.

Ultrasonographic determination of adrenal gland size has been used as an aid for evaluating dogs suspected of having

hyperadrenocorticism and hypoadrenocorticism. Adrenal gland size depends on the age of the dog,[102] with middle-aged and older dogs having larger glands. Adrenal gland length is proportional to body weight, but the diameter (thickness or width) is not.[100,101] Therefore cross-sectional measurements are more valuable than length in the assessment of adrenal gland size. Adrenal gland thickness greater than 0.6 cm in small-breed and 0.7 cm in middle-aged to older large-breed dogs has been used as the criterion for maximum normal adrenal gland size.[102] However, adrenal gland measurements should not be used alone to diagnose abnormalities because there is considerable overlap of adrenal size between normal versus abnormal dogs. The shape of the adrenal glands, the response of the patient to pituitary-adrenal axis testing, and the clinical signs must be correlated with the size of the adrenal glands when making a diagnosis.

The use of ultrasound is not recommended as a screening test for hyperadrenocorticism,[116] although ultrasound is useful in differentiating pituitary-dependent hyperadrenocorticism (PDH) and functional adrenocortical neoplasia.[100,101,117] In dogs with PDH, the adrenal glands have a plump appearance; they are bilaterally enlarged, uniformly hypoechoic, and normally shaped (Fig. 36-33).[100,102,103,117] Normal adrenal gland size does not rule out PDH.[102] Adrenal gland tumors cause gland enlargement with loss of normal shape and a change in echotexture (Figs. 36-34 through 36-36).

Adrenal tumors are most often unilateral but may occur bilaterally.[108,109] In dogs with functional adrenocortical tumors, there is some disagreement regarding atrophy of the contralateral gland, with some studies suggesting that atrophy occurs,[45,118] whereas others suggest that the contralateral adrenal gland is often of normal size.[108,109,117] One study in dogs suggests that in instances of asymmetric adrenal gland size, if the thickness of the smaller gland is less than 0.5 cm, it is most likely caused by adrenal dependent hyperadrenocorticism (vs. PDH) with atrophy of the contralateral gland.[118]

Ultrasound is not useful in differentiating benign and malignant lesions.[108] Mineralization may be seen in both benign and malignant neoplasms as well as in adrenocortical hyperplasia.[102,108] In one report, pheochromocytomas and adenocarcinomas tended to be round masses, whereas adenomas, hyperplasia, and adrenal metastasis tended to appear as nodules.[108] Because PDH-induced nodular cortical



Fig. 36-33 Sagittal sonogram of the left adrenal gland *(cursors)* of a dachshund with pituitary-dependent hyperadrenocorticism. The adrenal gland has a plump appearance but is normally shaped. The gland is enlarged, measuring 2.6 cm in length and 1.0 cm in thickness. The hypoechoic cortex can be differentiated from the more echogenic medulla. This layered appearance has been described in normal dogs and in dogs with hyperadrenocorticism. The *white arrow* points to the aorta.

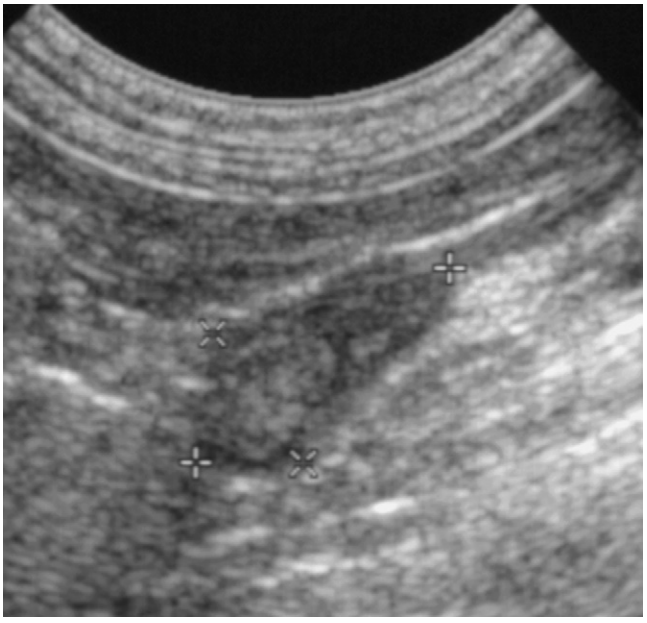


Fig. 36-34 Sagittal sonogram of the left adrenal gland of a 12-year-old mixed-breed dog. A hyperechoic nodule is present in the cranial pole of the adrenal gland. The ultrasonographic appearance of this nodule is not specific and could be caused by neoplasia (varying types), granuloma, or nodular hyperplasia.

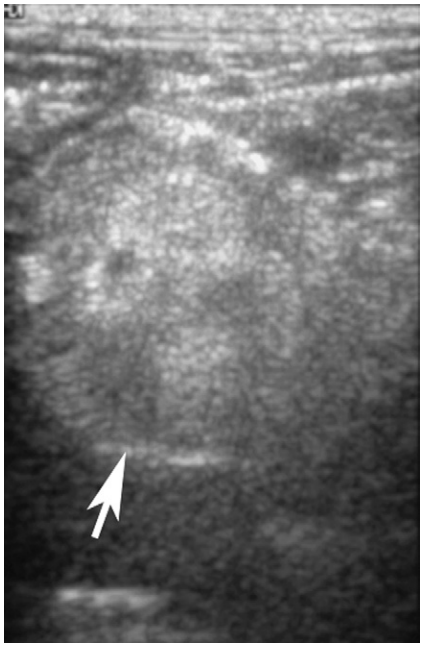


Fig. 36-35 Transverse sonogram of the right adrenal gland *(white arrow)* of a 13-year-old Shih Tzu with hyperadrenocorticism. The adrenal gland is enlarged, round, and of mixed echogenicity, containing hyperechoic nodules. Histopathologically, the adrenal gland contained myelolipomas and adenomas.

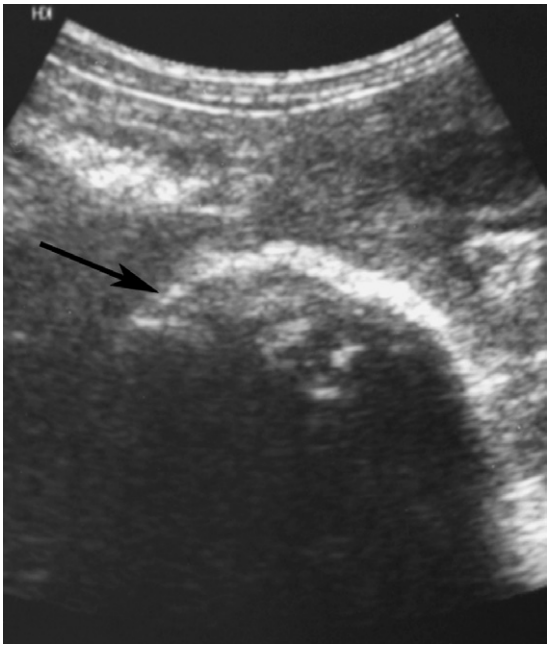


Fig. 36-36 Sagittal sonogram of the left adrenal gland of the same dog as in Figure 36-30. The adrenal gland is seen as a large, curvilinear hyperechoic line *(black arrow)* with distal acoustic shadowing, consistent with the appearance of mineral. The diagnosis was adrenocortical tumor.

hyperplasia may appear similar to small functional adrenocortical tumors, ultrasound is not useful in differentiating the two.[102] Screening for hyperadrenocorticism by imaging of the adrenal glands with computed tomography or magnetic resonance imaging is also not recommended, although these modalities are useful for imaging the pituitary gland.[116]

Ultrasound is helpful in evaluating extension of tumors into surrounding tissues, especially the caudal vena cava. An adrenal mass invading the caudal vena cava may extend to the right atrium.[119] Adrenal gland lymphoma has been described to appear as hypoechoic adrenal glands in one cat and as a mass involving the adrenal glands and midline structures in another.[120] Another cat with a hypoechoic adrenal mass had primary hyperaldosteronism.[121] Ultrasound-guided biopsy and fine-needle aspiration of the adrenal gland are not commonly performed in veterinary medicine, but they have been reported without complication in a small number of patients.[108,121-123] Many clinicians are wary of aspiration of adrenal masses, because if the mass is a pheochromocytoma, the possibility exists of stimulating a hypertensive crisis from a massive release of catecholamines. Adrenal gland tumors have also been reported to hemorrhage spontaneously, leading to retroperitoneal hemorrhage[124] or complex masses of the adrenal glands (Box 36-5).[108]

Treatment of patients with hyperadrenocorticism with mitotane or trilostane is common. Trilostane causes an increase in adrenal gland size,[125,126] with the maximum size seen at 6 weeks after initiation of therapy.[125] The differentiation of the layers within the adrenal glands is increased with the outer hypoechoic zone being increased in echogenicity and the inner hyperechoic zone being decreased in echogenicity. After 6 months to 1 year of treatment, the size of the adrenal glands is unchanged, but the shape may become irregular and the parenchyma inhomogeneous with an inability to discern the layers of the glands.[125,126] These changes may be caused by coagulative necrosis.[127] Mitotane causes adrenal gland heterogeneity, presumably from necrosis.[112] Mitotane may also cause the adrenal glands to become smaller, in contrast to the effects of trilostane.[128]

Box • 36-5

Differential Diagnosis for Adrenal Masses

Adenoma
Nodular hyperplasia
Adrenocortical carcinoma
May be:
- Metabolically inactive
- Cortisol secreting
- Aldosterone secreting

Granuloma
Metastatic neoplasia
Pheochromocytoma

Both adrenocorticotropic hormone and ultrasound have a sensitivity of 100% and a specificity of 95% in differentiating PDH from adrenal dependent hyperadrenocorticism in dogs.[117] Although uncommonly reported, enlarged adrenal glands can be found in patients with oversecretion of sex hormones.[129]

In six dogs with hypoadrenocorticism, the adrenal glands were measurably smaller than the adrenal glands of normal dogs.[107] It has also been suggested that an adrenal width of less than 0.32 cm is highly suggestive of hypoadrenocorticism.[130] Cats with interstitial cystitis have been suggested to have primary adrenal insufficiency because these animals have small adrenal glands at necropsy. Antemortem imaging findings in these animals were not reported.[131]

REFERENCES

1. Evans HE, Christensen GC: *Miller's anatomy of the dog*, ed 3, Philadelphia, 1993, Saunders.
2. Johnson DE, Christie BA: The retroperitoneum in dogs: anatomy and clinical significance, *Comp Contin Educ Prac Vet* 12:1027, 1990.
3. Johnson PR, Greenwood MRC: The adipose tissue. In Weiss L, editor: *Cell and tissue biology: a textbook of histology*, ed 6, Baltimore, 1988, Urban and Schwarzenberg.
4. Ettinger SJ, Barrett KA: Ascites, peritonitis, and other causes of abdominal distention. In Ettinger SJ, Feldman EC, editors: *Textbook of veterinary internal medicine*, ed 4, Philadelphia, 1995, Saunders.
5. O'Brien TR: *The radiographic diagnosis of abdominal disorders of the dog and cat*, Philadelphia, 1978, Saunders.
6. Boen ST: *Peritoneal dialysis in clinical practice*, Springfield, Ill, 1964, Charles C. Thomas.
7. Johnston DE, Christie BA: The retroperitoneum in dogs: retroperitoneal infections, *Comp Contin Educ Prac Vet* 12:1035, 1990.
8. Roush JK, Bjorling DE, Lord P: Diseases of the retroperitoneal space in the dog and cat, *J Am Anim Hosp Assoc* 26:47, 1990.
9. Root CR, Lord PF: Peritoneal carcinomatosis in the dog and cat: its radiographic appearance, *J Am Vet Radiol Soc* 12:54, 1971.
10. Suter PF, Olsson SE: The diagnosis of injuries to the intestines, gall bladder and bile ducts in the dog, *J Small Anim Pract* 11:575, 1970.
11. Probst CW, Stickle RL, Bartlett PC: Duration of pneumoperitoneum in the dog, *Am J Vet Res* 47:176, 1986.
12. Guffy M: *A radiological study of hydroperitoneum and pneumoperitoneum in the dog [thesis]*, Fort Collins, 1966, Colorado State University.

13. Lamb CR, Kleine LJ, McMillan MC: Diagnosis of calcification on abdominal radiographs, *Vet Radiol* 32:211, 1991.
14. Schwarz T, Morandi F, Gnudi G, et al: Nodular fat necrosis in the feline and canine abdomen, *Vet Radiol Ultrasound* 41:335, 2000.
15. Yaphe W, Forrester SD: Renal secondary hyperparathyroidism, pathophysiology, diagnosis, and treatment, *Comp Contin Educ Prac Vet* 16:73, 1994.
16. Johnson CA: Disorders of pregnancy, *Vet Clin North Am Small Anim Pract* 18:477, 1986.
17. Huntley K, Fraser J, Gibbs C, et al: The radiological features of canine Cushing's syndrome: a review of forty-eight small cases, *J Small Anim Pract* 23:369, 1982.
18. Crosbie PR, Boyce WM, Platzer ED, et al: Diagnostic procedures and treatment of eleven dogs with peritoneal infections caused by *Mesocestoides* spp, *J Am Vet Med Assoc* 213:1578, 1998.
19. Caruso KJ, James MP, Fisher D, et al: Cytologic diagnosis of peritoneal cestodiasis in dogs caused by *Mesocestoides* sp, *Vet Clin Pathol* 32:50, 2003.
20. Boysen SR, Tidwell AS, Pennick DG: Ultrasonographic findings in dogs and cats with gastrointestinal perforation, *Vet Radiol Ultrasound* 44:556, 2003.
21. Fischetti AJ, Saunders HM, Drobatz KJ: Pneumatosis in canine gastric dilatation-volvulus syndrome, *Vet Radiol Ultrasound* 45:279, 2004.
22. Leav I, Ling GV: Adenocarcinoma of the canine prostate, *Cancer* 22:1329, 1968.
23. Pugh CR: Ultrasonographic examination of abdominal lymph nodes in the dog, *Vet Radiol Ultrasound* 35:110, 1994.
24. Homco LD: Lymph nodes. In Green RW, editor: *Small animal ultrasound*, Philadelphia, 1996, Lippincott-Raven.
25. Nyman HT, Kristensen AT, Flagstad A, et al: A review of the sonographic assessment of tumor metastasis in liver and superficial lymph nodes, *Vet Radiol Ultrasound* 45:438, 2004.
26. Prieto S, Gomez-Ochoa P, De Blas I, et al: Pathologic correlation of resistive and pulsatility indices in canine abdominal lymph nodes, *Vet Radiol Ultrasound* 50:525–529, 2009
27. Kinns J, Mai W: Association between malignancy and sonographic heterogeneity in canine and feline abdominal lymph nodes, *Vet Radiol Ultrasound* 48:565–569, 2007.
28. Llabres-Diaz FJ: Ultrasonography of the medial iliac lymph nodes in the dog, *Vet Radiol Ultrasound* 45:156, 2004.
29. Gibbs C, Denny HR, Minter HM, et al: Radiological features of inflammatory conditions of the canine pancreas, *J Small Anim Pract* 13:531, 1972.
30. Kleine LJ, Hornbuckle WE: Acute pancreatitis: the radiographic findings in 182 dogs, *J Am Vet Radiol Soc* 19:102, 1978.
31. Suter PF, Lowe R: Acute pancreatitis in the dog: a clinical study with emphasis on radiographic diagnosis, *Acta Radiol (Stockh)* 319(Suppl):195, 1970.
32. Davis S, Parbhoo SP, Gibson MJ: The plain abdominal radiograph in acute pancreatitis, *Clin Radiol* 31:87, 1980.
33. Edwards DF, Bauer MS, Walker MA, et al: Pancreatic masses in seven dogs following acute pancreatitis, *J Am Anim Hosp Assoc* 26:189, 1990.
34. Salisbury SK, Lantz GC, Nelson RW, et al: Pancreatic abscesses in dogs: six cases (1978–1986), *J Am Vet Med Assoc* 193:1004, 1988.
35. Wolfsheimer KJ, Hedlund CS, Pechman RD: Pancreatic pseudocyst in a dog with chronic pancreatitis, *Canine Pract* 16:6, 1991.
36. Lamb CR: Abdominal ultrasonography in small animals: examination of the liver, spleen, and pancreas, *J Small Anim Pract* 31:6, 1990.
37. Saunders HM: Ultrasonography of the pancreas, *Probl Vet Med* 3:583, 1991.
38. Nyland TG, Mulvany MH, Strombeck DR: Ultrasonic features of experimentally induced, acute pancreatitis in the dog, *Vet Radiol* 24:260, 1983.
39. Nyland TG, Mattoon JS, Herrgesell EJ, et al: Pancreas. In Nyland TG, Mattoon JS, editors: *Small animal diagnostic ultrasound*, Philadelphia, 2002, Saunders.
40. Murtaugh RJ, Herring DS, Jacobs RM, et al: Pancreatic ultrasonography in dogs with experimentally induced acute pancreatitis, *Vet Radiol* 26:27, 1985.
41. Mahaffey MB: The pancreas. In Cartee RE, editor: *Practical veterinary ultrasound*, Philadelphia, 1995, Williams & Wilkins, p 52.
42. Brinkman-Ferguson EL, Biller DS: Ultrasound of the right lateral intercostal space, *Vet Clin North Am Small Anim Pract* 39:761–781, 2009.
43. Lamb CR: Recent developments in diagnostic imaging of the gastrointestinal tract of the dog and cat, *Vet Clin North Am Small Anim Pract* 29:307, 1999.
44. Worthen NJ, Beabeau D: Normal pancreatic echogenicity: relation to age and body fat, *Am J Radiol* 139:1095, 1982.
45. Larson MM, Panciera DL, Ward DL, et al: Age-related changes in the ultrasound appearance of the normal feline pancreas, *Vet Radiol Ultrasound* 46:238, 2005.
46. Etue SM, Penninck DG, Labato MA, et al: Ultrasonography of the normal feline pancreas and associated anatomic landmarks: a prospective study of 20 cats, *Vet Radiol Ultrasound* 42:330, 2001.
47. Hecht S, Penninck DG, Mahony OM, et al: Relationship of pancreatic duct dilation to age and clinical findings in cats, *Vet Radiol Ultrasound* 47:287–294, 2006.
48. Lamb CR, McEvoy FJ: Comparison of ultrasonographic findings in canine pancreatitis and pancreatic neoplasia [abstract], *Vet Radiol Ultrasound* 36:434, 1995.
49. Saunders HM, Pugh CR, Rhodes WH: Expanding applications of abdominal ultrasonography, *J Am Anim Hosp Assoc* 28:369, 1992.
50. Homco LD: Pancreas. In Green RW, editor: *Small animal ultrasound*, Philadelphia, 1996, Lippincott-Raven, p 177.
51. Simpson KW, Shiroma JT, Biller DS, et al: Antemortem diagnosis of pancreatitis in four cats, *J Small Anim Pract* 35:93, 1994.
52. Wall M, Biller DS, Schoning P, et al. Pancreatitis in a cat demonstrating pancreatic duct dilatation ultrasonographically, *J Am Anim Hosp Assoc* 37:49, 2001.
53. Siegel MJ, Martin KW, Worthington JL: Normal and abnormal pancreas in children: US studies, *Radiology* 165:15, 1987.
54. Lamb CR: Dilation of the pancreatic duct: an ultrasonographic finding in acute pancreatitis, *J Small Anim Pract* 30:410, 1989.
55. Saunders HM: Ultrasonographic detection and characterization of pancreatitis in dogs. In *Proceedings of the American College of Veterinary Radiology Annual Meeting*, Chicago, 1990, p 66.
56. Saunders HM, VanWinkle TJ, Drobatz K, et al: Ultrasonographic findings in cats with clinical, gross pathologic, and histologic evidence of acute pancreatic necrosis: 20 cases (1994–2001), *J Am Vet Med Assoc* 221:1724, 2002.
57. Ferreri JA, Hardam E, Kimmel SE, et al: Clinical differentiation of acute necrotizing from chronic

nonsuppurative pancreatitis in cats: 63 cases (1996–2001), *J Am Vet Med Assoc* 223:469, 2003.
58. Watson PJ, Roulois AJ, Scase T, et al: Prevalence and breed distribution of chronic pancreatitis at post-mortem examination in first-opinion dogs, *J Small Anim Pract* 48:609–618, 2007.
59. Forman MA, Marks SL, DeCock HEV, et al: Evaluation of serum feline pancreatic lipase immunoreactivity and helical computed tomography versus conventional testing for the diagnosis of feline pancreatitis, *J Vet Intern Med* 18:807, 2004.
60. Rademacher N, Ohlerth S, Scharf G, et al: Contrast-enhanced power and color Doppler ultrasonography of the pancreas in healthy and diseased cats, *J Vet Intern Med* 22:1310–1316, 2008.
61. VanEnkevort BA, O'Brien RT, Young KM: Pancreatic pseudocysts in 4 dogs and 2 cats: ultrasonographic and clinicopathologic findings, *J Vet Intern Med* 13:309, 1999.
62. Rutgers C, Herring DS, Orton C: Pancreatic pseudocyst associated with acute pancreatitis in a dog: ultrasonographic diagnosis, *J Am Anim Hosp Assoc* 21:411, 1985.
63. Hines BL, Salisbury SK, Jakovljevic S, et al: Pancreatic pseudocyst associated with chronic-active necrotizing pancreatitis in a cat, *J Am Anim Hosp Assoc* 32:147, 1996.
64. Barnhart MD, Smeak D: Pericolonic mass containing chyle as a presumed sequela to chronic pancreatitis in a dog, *J Am Vet Med Assoc* 212:70, 1998.
65. Marchevsky AM, Yovich JC, Wyatt KM: Pancreatic pseudocyst causing extrahepatic biliary obstruction in a dog, *Aust Vet J* 78:99, 2000.
66. Coleman MG, Robson MC, Harvey C: Pancreatic cyst in a cat, *N Z Vet J* 53:157, 2005.
67. Branter EM, Viviano KR: Multiple recurrent pancreatic cysts with associated pancreatic inflammation and atrophy in a cat, *J Feline Med Surg* 12:822–827, 2010.
68. Bailiff NL, Norris CR, Seguin B, et al: Pancreatolithiasis and pancreatic pseudobladder associated with pancreatitis in a cat, *J Am Anim Hosp Assoc* 40:69, 2004.
69. Jubb KVF, Kennedy PC, Palmer N: The pancreas. In Jubb KVF, Kennedy PC, Palmer N, editors: *Pathology of domestic animals, vol 2*, ed 3, Orlando, Fla, 1985, Academic Press.
70. Lamb CR, Simpson KW, Boswood A, et al: Ultrasonography of pancreatic neoplasia in the dog: a retrospective review of 16 cases, *Vet Rec* 137:65, 1995.
71. Feldman EC, Nelson RW: *Canine and feline endocrinology and reproduction*, Philadelphia, 2004, Saunders.
72. Head LL, Daniel GB, Becker TJ, et al: Use of computed tomography and radiolabeled leukocytes in a cat with pancreatitis, *Vet Radiol Ultrasound* 46:263–266, 2005.
73. Iseri T, Yamada K, Chijiwa K, et al: Dynamic computed tomography of the pancreas in normal dogs and in a dog with pancreatic insulinoma, *Vet Radiol Ultrasound* 48:328–331, 2007.
74. Robben JH, Pollak YW, Kirpensteijn J, et al: Comparison of ultrasonography, computed tomography, and single-photon emission computed tomography for the detection and localization of canine insulinoma, *J Vet Intern Med* 19:15–22, 2005.
75. Bennett PF, Hahn KA, Toal RL, et al: Ultrasonographic and cytopathological diagnosis of exocrine pancreatic carcinoma in the dog and cat, *J Am Anim Hosp Assoc* 37:466, 2001.
76. Hecht S, Penninck DG, Keating JH: Imaging findings in pancreatic neoplasia and nodular hyperplasia in 19 cats, *Vet Radiol Ultrasound* 48:45–50, 2007.
77. Cordner AP, Armstrong PJ, Newman SJ, et al: Effect of pancreatic tissue sampling on serum pancreatic enzyme levels in clinically healthy dogs, *J Vet Diagn Invest* 22:702–707, 2010.
78. Newman S, Steiner J, Woosley K, et al: Localization of pancreatic inflammation and necrosis in dogs, *J Vet Intern Med* 18:488, 2004.
79. Schaer M: Pheochromocytoma in a dog: a case report, *J Am Anim Hosp Assoc* 16:583, 1980.
80. Pennick DG, Feldman EC, Nyland TG: Radiographic features of canine hyper-adrenocorticism caused by autonomously functioning adrenocortical tumors: 23 cases (1978–1986), *J Am Vet Med Assoc* 192:1604, 1988.
81. Reusch CE, Feldman EC: Canine hyperadrenocorticism due to adrenocortical neoplasia, *J Vet Intern Med* 5:3, 1991.
82. Ford SL, Feldman EC, Nelson RW: Hyperadrenocorticism caused by bilateral adrenocortical neoplasia in dogs: four cases (1983–1988), *J Am Vet Med Assoc* 202:789, 1993.
83. Meijer JC: Canine hyperadrenocorticism. In Kirk RW, editor: *Current veterinary therapy*, Philadelphia, 1980, Saunders.
84. Owens JM, Drucker WD: Hyperadrenocorticism in the dog: canine Cushing's syndrome, *Vet Clin North Am Small Anim Pract* 7:583, 1977.
85. Huntley K, Frazer J, Gibbs C, et al: The radiological features of canine Cushing's syndrome: a review of forty-eight cases, *J Small Anim Pract* 23:369, 1982.
86. Ticer JW: Roentgen signs of endocrine disease, *Vet Clin North Am* 7:465, 1977.
87. Widmer WR, Guptill L: Imaging techniques for facilitating diagnosis of hyper-adrenocorticism in dogs and cats, *J Am Vet Med Assoc* 206:1857, 1995.
88. Jubb KVF, Kennedy PC: *Pathology of domestic animals*, ed 2, New York, 1970, Academic Press, p 427.
89. Kelly DF, Darke PGG: Cushing's syndrome in the dog, *Vet Rec* 98:28, 1976.
90. Siegel ET: *Endocrine disorders of the dog*, Philadelphia, 1977, Lea & Febiger, p 166.
91. Ross MA, Gainer JH, Innes JRM: Dystrophic calcification in the adrenal glands of monkeys, cats, and dogs, *Arch Pathol Lab Med* 60:655, 1955.
92. Marine D: Calcification of the suprarenal glands of cats, *J Exp Med* 43:495, 1926.
93. Rajan A, Mohiyuddeen S: Pathology of the adrenal gland in canines *(Canis familiaris)*, *Indian J Anim Sci* 44:123, 1974.
94. Bergman SM, Scouras GC: Incidental bilateral adrenal calcification, *Urology* 22:665, 1983.
95. Raafat F, Hashemian MP, Abrishami MA: Wolman's disease: report of two new cases with a review of the literature, *Am J Clin Pathol* 59:490, 1973.
96. Burns MG, Kelly AB, Hornof WJ, et al: Pulmonary artery thrombosis in three dogs with hyperadrenocorticism, *J Am Vet Med Assoc* 178:388, 1981.
97. Rendano VT, Alexander JE: Heart size changes in experimentally induced adrenal insufficiency in the dog: a radiographic study, *J Am Vet Radiol Soc* 17:57, 1976.
98. Scott DW: Hyperadrenocorticism (hyperadrenocorticoidism, hyperadrenocorticalism, Cushing's disease, Cushing's syndrome), *Vet Clin North Am* 9:3, 1979.
99. Melian C, Stefanacci J, Peterson ME, et al: Radiographic findings in dogs with naturally occurring primary hypoadrenocorticism, *J Am Anim Hosp Assoc* 35:208, 1999.
100. Barthez PY, Nyland TG, Feldman EC: Ultrasonographic evaluation of the adrenal glands in dogs, *J Am Vet Med Assoc* 207:1180, 1995.

101. Grooters AM, Biller DS, Miyabayashi T, et al: Evaluation of routine abdominal ultrasonography as a technique for imaging the canine adrenal glands, *J Am Anim Hosp Assoc* 30:457, 1994.
102. Grooters AM, Biller DS, Theisen SK, et al: Ultrasonographic characteristics of the adrenal glands in dogs with pituitary-dependent hyperadrenocorticism: comparison with normal dogs, *J Vet Intern Med* 10:110, 1996.
103. Hoerauf A, Reusch C: Ultrasonographic evaluation of the adrenal glands in healthy dogs, dogs with no evidence of endocrine disease, and dogs with Cushing's disease [abstract], *Vet Radiol Ultrasound* 36:434, 1995.
104. Douglass JP, Berry CR, James S: Ultrasonographic adrenal gland measurements in dogs without evidence of adrenal disease, *Vet Radiol Ultrasound* 38:124, 1997.
105. Cartee RE, Finn-Bodner ST, Gray BW: Ultrasound examination of the feline adrenal gland, *J Diagn Med Sonog* 9:327, 1993.
106. Zimmer C, Hoerauf A, Reusch C: Ultrasonographic examination of the adrenal gland and evaluation of the hypophyseal-adrenal axis in 20 cats, *J Small Anim Pract* 41:156, 2000.
107. Hoerauf A, Reusch C: Ultrasonographic evaluation of adrenal glands in six dogs with hypoadrenocorticism, *J Am Anim Hosp Assoc* 35:214, 1999.
108. Besso JG, Penninck DG, Gliatto JM: Retrospective ultrasonographic evaluation of adrenal lesions in 26 dogs, *Vet Radiol Ultrasound* 38:448, 1997.
109. Hoerauf A, Reusch C: Ultrasonographic characteristics of both adrenal glands in 15 dogs with functional adrenocortical tumors, *J Am Anim Hosp Assoc* 35:193, 1999.
110. Tidwell AS, Penninck DG, Besso JG: Imaging of adrenal gland disorders, *Vet Clin North Am Small Anim Pract* 27:237, 1997.
111. Schelling CG: Ultrasonography of the adrenal glands, *Probl Vet Med Ultrasound* 3:604, 1991.
112. Nyland TG, Mattoon JS, Herrgesell EJ, et al: Adrenal glands. In Nyland TG, Mattoon JS, editors: *Small animal diagnostic ultrasound*, Philadelphia, 2002, Saunders.
113. Homco LD: Adrenal glands. In Green RW, editor: *Small animal ultrasound*, Philadelphia, 1996, Lippincott-Raven.
114. Barthez PY, Nyland TG, Feldman EC: Ultrasonography of the adrenal glands in the dog, cat, and ferret, *Vet Clin North Am Small Anim Pract* 28:869, 1998.
115. Grooters AM, Biller DS, Merryman J: Ultrasonographic parameters of normal canine adrenal glands: comparison to necropsy findings, *Vet Radiol Ultrasound* 36:126, 1995.
116. Behrend EN, Kemppainen RJ: Diagnosis of canine hyperadrenocorticism, *Vet Clin N Am Small Anim Pract* 31:985, 2001.
117. Gould SM, Baines EA, Mannion PA, et al: Use of endogenous ACTH concentration and adrenal ultrasonography to distinguish the cause of canine hyperadrenocorticism, *J Small Anim Prac* 42:113, 2001.
118. Benchekroun G, de Fornel-Thibaud P, Rodríguez Piñeiro MI, et al: Ultrasonography criteria for differentiating ACTH dependency from ACTH independency in 47 dogs with hyperadrenocorticism and equivocal adrenal asymmetry, *J Vet Intern Med* 24:1077–1185, 2010.
119. Pradelli D, Quintavalla C, Domenech O, et al: Tumor thrombus: direct endoluminal "caudal vena cava-right atrium" extension in a dog affected by adrenal neoplasia, *Vet Res Comm* 27:787, 2003.
120. Parnell NK, Powell LL, Hohenhaus AE, et al: Hypoadrenocorticism as the primary manifestation of lymphoma in two cats, *J Am Vet Med Assoc* 214:1208, 1999.
121. Moore LE, Biller DS, Smith TA: Use of abdominal ultrasonography in the diagnosis of primary hyperaldosteronism in a cat, *J Am Vet Med Assoc* 217:213, 2000.
122. Chun R, Jakovljevic S, Morrison WB, et al: Apocrine gland adenocarcinoma and pheochromocytoma in a cat, *J Am Anim Hosp Assoc* 33:33, 1997.
123. Rosenstein DS: Diagnostic imaging in canine pheochromocytoma, *Vet Radiol Ultrasound* 41:499, 2000.
124. Whittemore JC, Preston CA, Kyles AE, et al: Nontraumatic rupture of an adrenal gland tumor causing intraabdominal or retroperitoneal hemorrhage in four dogs, *J Am Vet Med Assoc* 219:329, 2001.
125. Ruckstuhl NS, Nett CS, Reusch CE: Results of clinical examinations, laboratory tests, and ultrasonography in dogs with pituitary-dependent hyperadrenocorticism treated with trilostane, *Am J Vet Radiol* 63:506, 2002.
126. Mantis P, Lamb CR, Witt AL, et al: Changes in ultrasonographic appearance of adrenal glands in dogs with pituitary-dependent hyperadrenocorticism treated with trilostane, *Vet Radiol Ultrasound* 44:682, 2003.
127. Chapman PS, Kelly DF, Archer J, et al: Adrenal necrosis in a dog receiving trilostane for the treatment of hyperadrenocorticism, *J Small Anim Prac* 45:307, 2004.
128. Horauf A, Reusch C: Effects of mitotane therapy in dogs with pituitary dependent Cushing's syndrome on the adrenal gland size—an ultrasonographic study, *Schweiz Arch Tierheilkd* 141:239, 1999.
129. Boag AK, Neiger R, Church DB: Trilostane treatment of bilateral adrenal enlargement and excessive sex steroid hormone production in a cat, *J Small Anim Prac* 45:263, 2004.
130. Wenger M, Mueller C, Kook PH, Reusch CE. Ultrasonographic evaluation of adrenal glands in dogs with primary hypoadrenocorticism or mimicking diseases, *Vet Rec* 167:207–210, 2010.
131. Westropp JL, Welk KA, Buffington CA: Small adrenal glands in cats with feline interstitial cystitis, *J Urol* 170:2494, 2003.

ELECTRONIC RESOURCES

evolve

Additional information related to the content in Chapter 36 can be found on the companion Evolve website at http://evolve.elsevier.com/Thrall/vetrad/

- Chapter Quiz

CHAPTER • 37

The Liver and Spleen

Martha Moon Larson

RADIOLOGY OF THE LIVER

The liver is the largest solid organ in the abdomen. Changes in hepatic size, shape, location, and opacity are used to assess the liver for possible abnormality.[1-7]

The liver is located in the cranial aspect of the abdomen between the diaphragm, which delineates its cranial border, and the stomach, right kidney, and cranial portion of the duodenum, which define the caudal extent. The liver is nearly entirely within the costal arch, with the caudal ventral border, composed of the left lateral liver lobe in the dog, extending just slightly beyond the costal arch (Fig. 37-1). In dogs with a deep thoracic cavity, the liver lies more completely within the costal arch, whereas greater caudal hepatic extension is present in dogs with shallow, wide thoracic conformation. Abundant falciform fat, especially in cats, can result in dorsal displacement of the ventral aspect of the liver on lateral views. On ventrodorsal views, the liver is distributed fairly symmetrically in dogs, but a larger portion is often right sided in cats (Fig. 37-2).

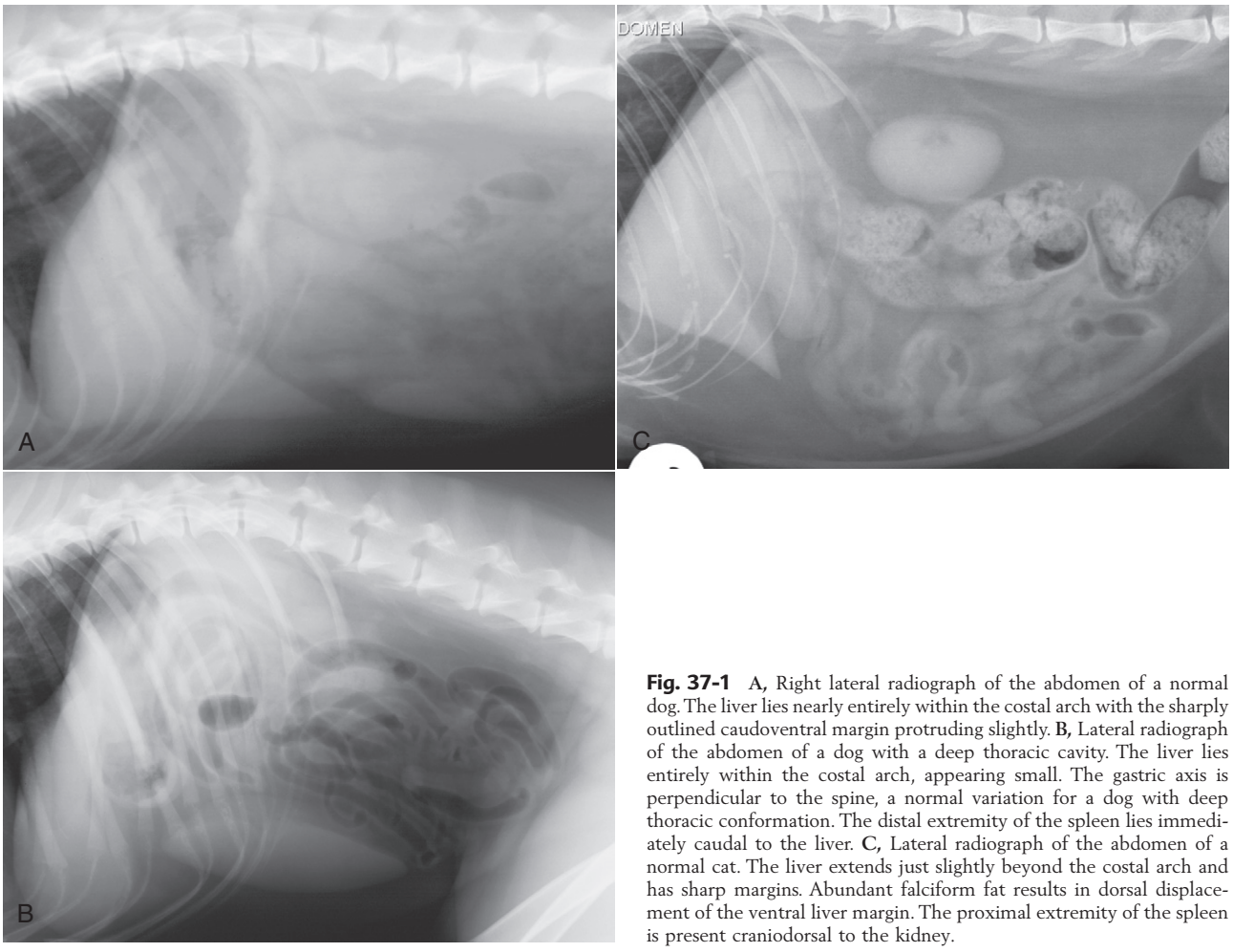


Fig. 37-1 **A,** Right lateral radiograph of the abdomen of a normal dog. The liver lies nearly entirely within the costal arch with the sharply outlined caudoventral margin protruding slightly. **B,** Lateral radiograph of the abdomen of a dog with a deep thoracic cavity. The liver lies entirely within the costal arch, appearing small. The gastric axis is perpendicular to the spine, a normal variation for a dog with deep thoracic conformation. The distal extremity of the spleen lies immediately caudal to the liver. **C,** Lateral radiograph of the abdomen of a normal cat. The liver extends just slightly beyond the costal arch and has sharp margins. Abundant falciform fat results in dorsal displacement of the ventral liver margin. The proximal extremity of the spleen is present craniodorsal to the kidney.

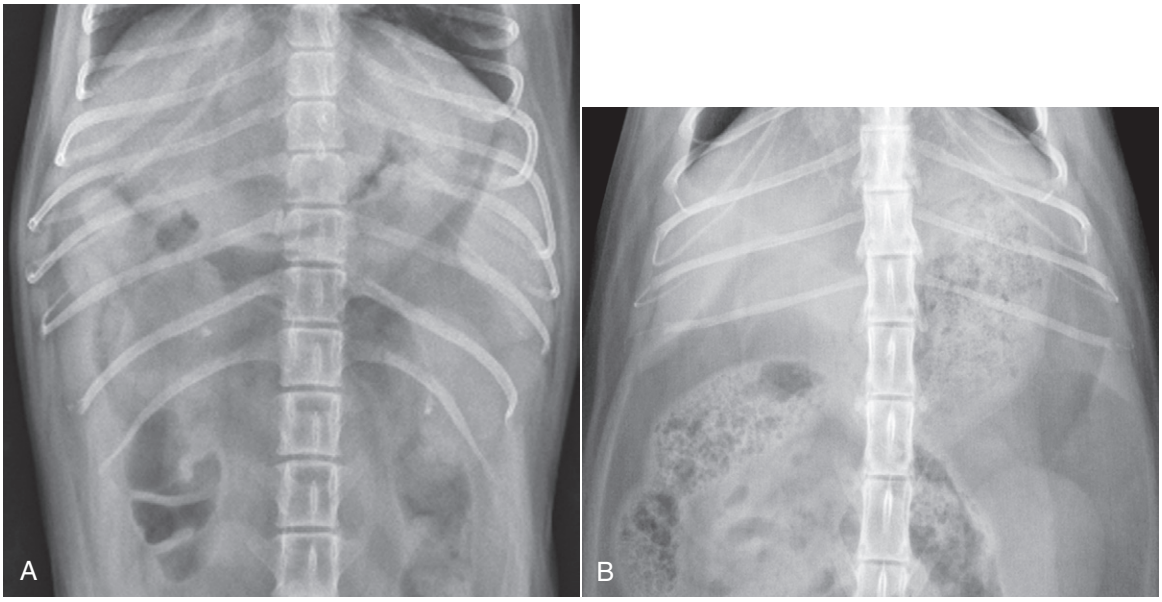


Fig. 37-2 **A,** Ventrodorsal radiograph of the cranial aspect of the abdomen of a normal dog. The liver lies cranial to and silhouettes the gastric shadow. Bilateral renal pelvic calculi are present. **B,** Ventrodorsal radiograph of the abdomen of a normal cat. The liver is more to the right side than in a dog and is better visualized in this cat because of surrounding abundant fat.

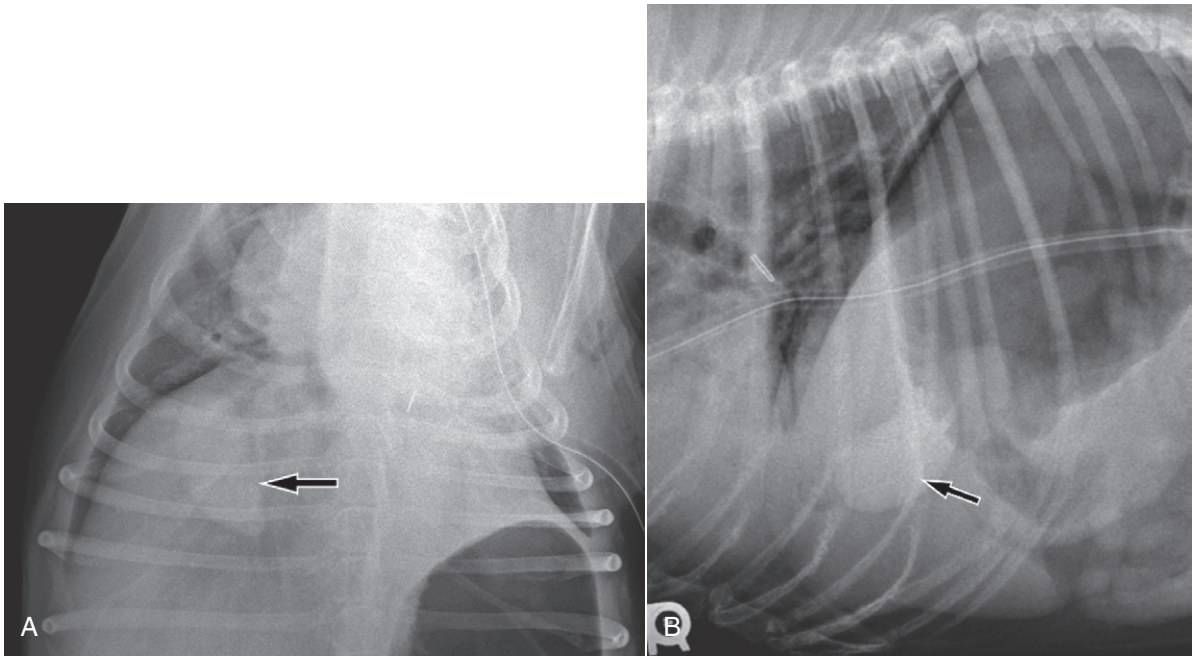


Fig. 37-3 Lateral and dorsoventral radiograph of the cranial abdomen in a dog made several hours after intravenous contrast-medium administration for an excretory urogram. The gallbladder contains contrast medium because biliary excretion of iodinated contrast medium is a secondary route of excretion. The gallbladder is therefore conspicuous in the right cranial portion of the liver *(black arrows)*. A chest tube extends across the cranial abdomen.

Hepatic shape may not be visualized without abundant surrounding omental and falciform fat. The caudoventral hepatic margin protruding slightly from the costal arch should be relatively sharply marginated and triangular in shape. It may protrude farther caudally in right lateral recumbent views, where it may merge with the spleen, blurring exact definition. If lateral views are slightly oblique, the liver can appear to have round margins, which should not be confused with hepatic enlargement.

The gallbladder is located just to the right of midline, in the cranioventral portion of the liver, but is not visible normally because of silhouetting with the soft tissue of the liver (Fig. 37-3). In some cats, however, the gallbladder can be seen on lateral abdominal radiographs

as a curved structure protruding from the ventral liver margin.[8]

Hepatomegaly

Hepatic enlargement can be detected radiographically, although mild size changes cannot be assessed accurately. The classic radiographic signs of generalized hepatomegaly are rounding or blunting of the caudoventral liver margins, along with extension beyond the costal arch, and caudal, and perhaps medial, displacement of the gastric axis (Figs. 37-4 to 37-6).[9-11]

Several nonpathologic conditions can result in extension of hepatic margins beyond the costal arch, including overexpansion of the thorax or deep inspiration (Fig. 37-7). Older dogs and cats can have stretching or elongation of the triangular ligaments attaching the liver to the diaphragm, resulting in sagging and caudal extension of the liver. The same phenomenon can occur in obese dogs with a pendulous abdomen. In the obese dog, the liver does not extend as far dorsally. Some brachycephalic and chondrodystrophic dogs have caudal extension of the liver as a result of it being aligned more horizontally compared with deep-chested breeds. In addition, neonatal and young dogs and cats have a larger liver size compared with body size, creating the appearance of hepatomegaly without a true hepatic abnormality (Fig. 37-8).[1,12] Because of the numerous normal variations that can cause hepatic lobe extension beyond the costal arch, rounding or blunting of these lobes should also be present before hepatomegaly is concluded.

With generalized hepatomegaly, caudal displacement of the stomach, right kidney, transverse colon, and cranial duodenal flexure may occur, along with dorsal elevation of the

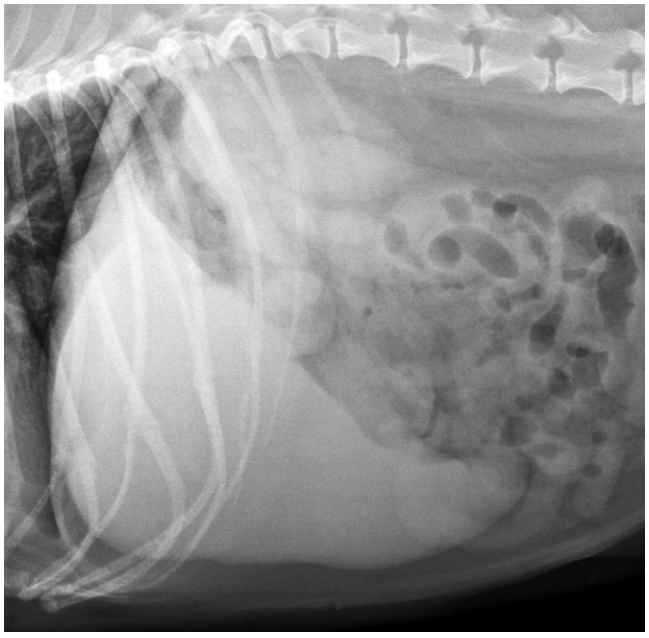


Fig. 37-4 Lateral radiograph of a dog with steroid hepatopathy and hepatomegaly. The liver has rounded, blunt margins and extends well beyond the costal arch.

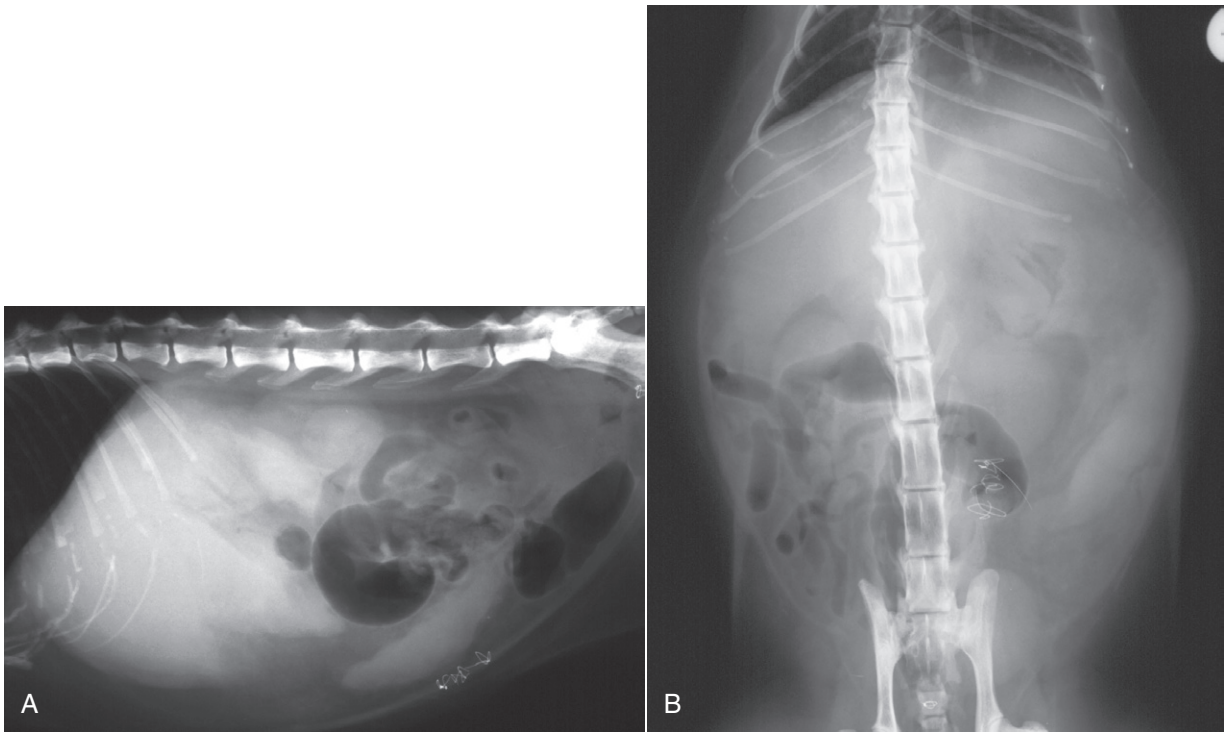


Fig. 37-5 Lateral **(A)** and ventrodorsal **(B)** radiographs of the abdomen of a cat with lymphosarcoma involving the liver and spleen. There is caudal, dorsal, and leftward displacement of the stomach as well as caudal extension of the liver margins. The spleen, which is also enlarged and has an irregular margin, extends along the ventral abdominal wall in **A,** just dorsal to the metallic sutures.

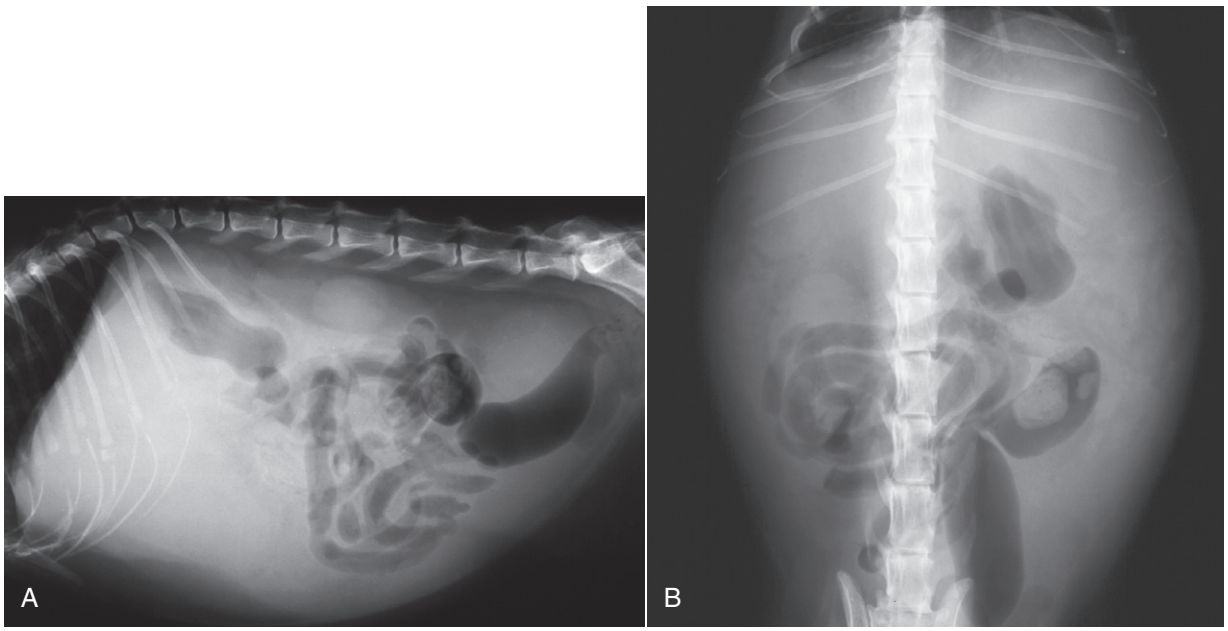


Fig. 37-6 Lateral **(A)** and ventrodorsal **(B)** radiographs of the abdomen of a cat with lymphosarcoma. Although peritoneal fluid obscures abdominal detail, the marked caudal, dorsal, and left-sided gastric displacement is consistent with severe hepatomegaly.

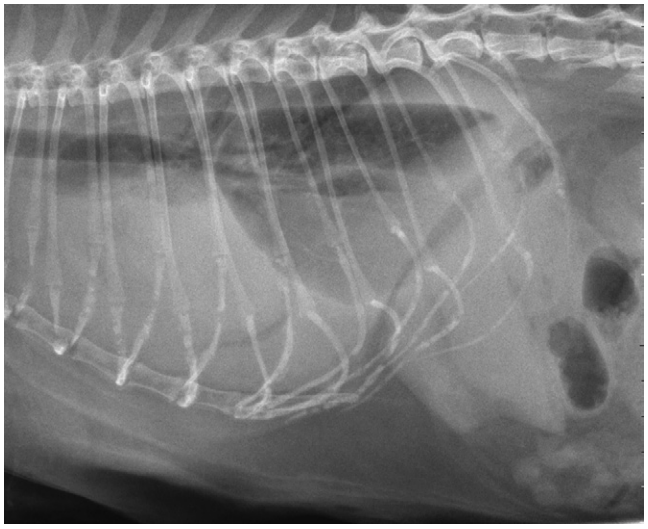


Fig. 37-7 Lateral radiograph of the thorax of a cat with pleural effusion. The overexpanded thorax results in caudal displacement of the diaphragm and liver margins with subsequent apparent hepatomegaly. The liver margins remain relatively sharp.

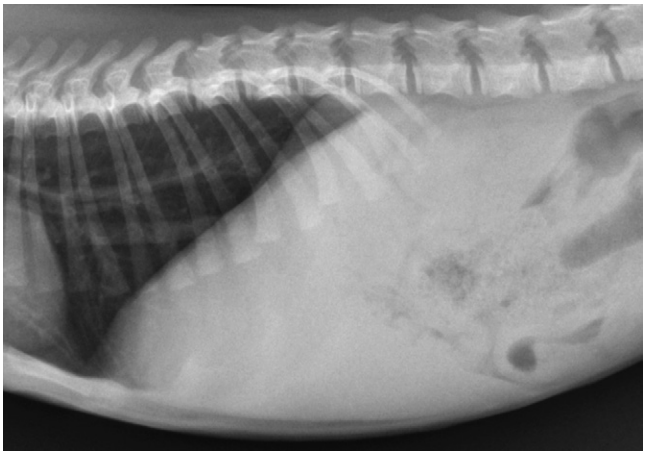


Fig. 37-8 Lateral radiograph of the abdomen of a normal puppy. The liver is large compared with overall abdominal size, a normal finding in young dogs and cats.

pylorus. On ventrodorsal views, an increased opacity may be present in the right cranial abdominal quadrant along with displacement of the body and pyloric portion of the stomach caudally, and to the left. Both lateral and ventrodorsal abdominal views should be examined to evaluate liver size because hepatomegaly is sometimes obvious only on one view. The position of the stomach is important in determining hepatomegaly, but the stomach may be poorly visualized if empty of gas or food. Administration of a small amount of barium (1 mL/kg) to define the gastric position can help evaluate hepatic size.[7]

Causes of generalized hepatomegaly are numerous, and radiographs alone are insufficient in most instances to narrow the list. Hepatic congestion, steroid hepatopathy, hepatic lipidosis, inflammatory and infiltrative disease, and primary and metastatic neoplasia are all possibilities. Metastatic disease is common because the liver contains the first capillary bed encountered by venous return from the gastrointestinal tract, pancreas, and spleen. Hepatic ultrasound can be used to determine internal architecture and is better suited than radiography for narrowing the list of considerations for hepatomegaly.

Visualization of focal hepatomegaly depends on the degree of enlargement and the lobe affected. Focal hepatic masses

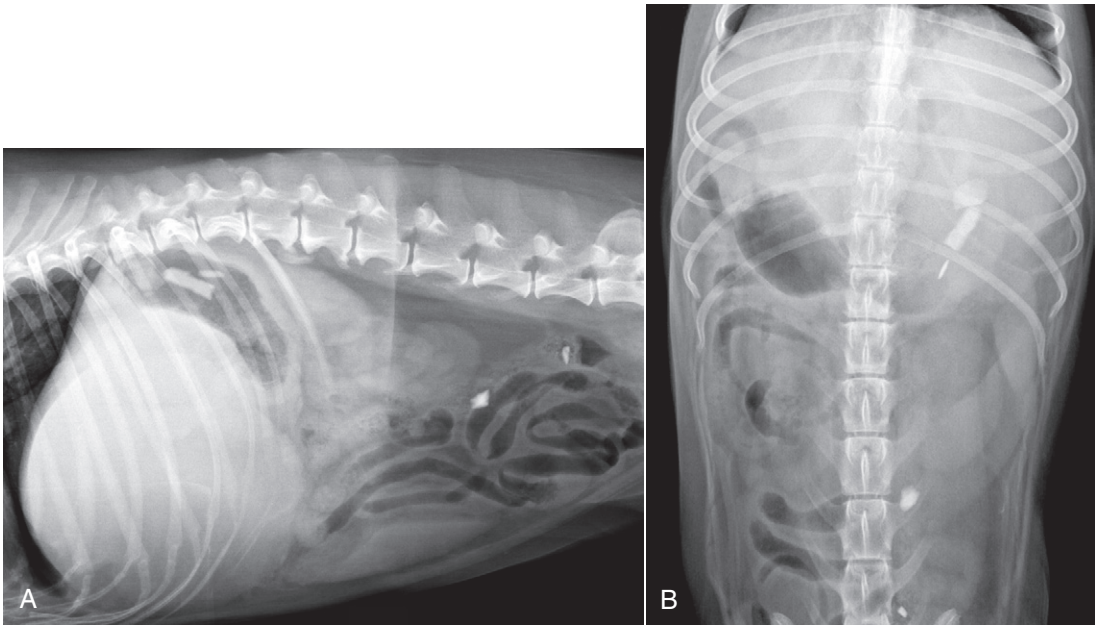


Fig. 37-9 Lateral **(A)** and ventrodorsal **(B)** radiographs of the abdomen of a dog with hepatic carcinoma. The central and right portions of the liver are enlarged, resulting in caudal and dorsal displacement of the stomach.

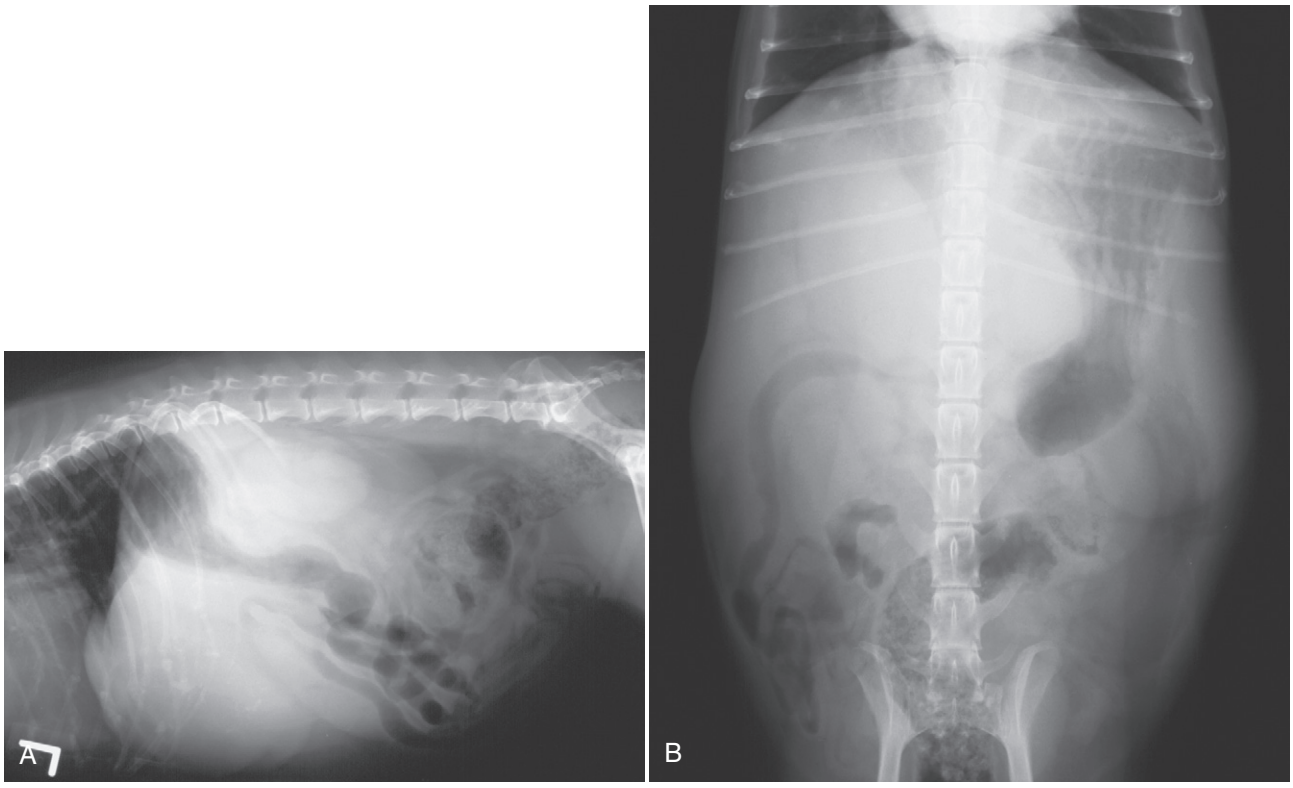


Fig. 37-10 Lateral **(A)** and ventrodorsal **(B)** radiographs of the abdomen of a dog with hepatic carcinoma. The right side of the liver is enlarged, resulting in caudal, dorsal, and left-sided displacement of the stomach. The small bowel is displaced caudally. Faint mineralization is present in the ventral portion of the liver on the lateral view.

usually result in distortion of the hepatic outline and are continuous with the liver in at least one projection.[9-11] Right-sided hepatic masses displace the stomach and duodenum to the left and dorsally and the small bowel caudally (Figs. 37-9 and Fig. 37-10). The right kidney and distal extremity of the spleen may also be displaced caudally by a right-sided hepatic mass.

Left hepatic masses result in displacement of the stomach and spleen dorsally and to the right. With few exceptions, masses located cranial to the ventral aspect of the stomach are

hepatic in origin.[9] Although hepatic masses classically result in caudal displacement of the stomach, a focal mass can extend caudal to the stomach (Fig. 37-11).[10,11] Differentiation of a caudally located hepatic mass from a splenic mass based on radiographs alone is difficult in these instances. Differentials for focal hepatic masses include primary and metastatic neoplasia, abscess, granuloma, and hepatic cyst.

As with subtle hepatomegaly, slight decreases in hepatic size are not identified accurately radiographically. Marked microhepatia results in cranial displacement of the stomach and decreased distance between the diaphragm and gastric lumen (Fig. 37-12). Congenital portosystemic shunts and hepatic cirrhosis are the two most common causes of microhepatia. Diaphragmatic hernia with displacement of the liver cranial to the diaphragm can give the appearance of a small liver, but there will be intrathoracic abnormalities in this instance.

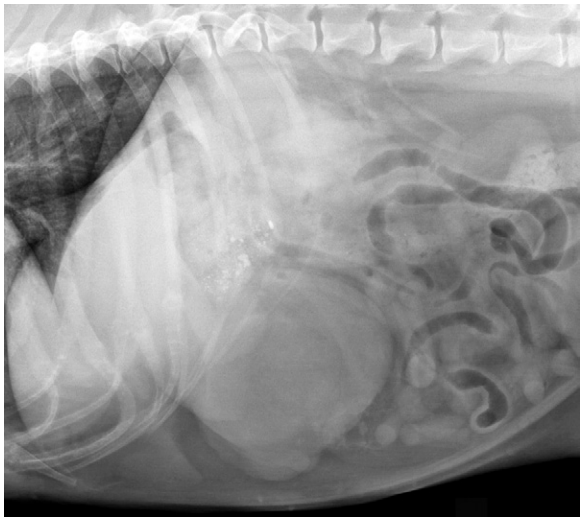


Fig. 37-11 Lateral radiograph of the abdomen of a dog with hepatic carcinoma. The hepatic mass extends caudal to the stomach, mimicking a splenic mass.

Hepatic Opacity

The normal liver is of soft tissue opacity. Mineral opacities can occur in the hepatic parenchyma or biliary system.[13] Choleliths should be considered when focal mineral opacities are visible in the area of the gallbladder (Fig. 37-13). Linear trails of mineralized opacities extending peripherally are indicative of choledocholiths.[14] Biliary calculi are uncommon in dogs and cats but are visible radiographically if they contain sufficient calcium (Fig. 37-14).[15-22] These are usually incidental findings, but choledocholiths can cause biliary obstruction. Mineralization of the gallbladder wall has been associated with gallbladder carcinoma as well as cholecystitis or cystic mucinous hyperplasia.[13,23]

Hepatic parenchymal mineralization may be localized or diffuse and have a variety of patterns.[13] Dystrophic calcification of hepatic granulomas, abscesses, hematomas, neoplastic masses, or areas of hepatic necrosis have been documented (see Fig. 37-10). Mineralization of the biliary tree is seen occasionally in dogs with bile duct carcinoma.[24] Echinococcosis infection can result in large hepatic soft tissue masses with mineralization of varying patterns and should be considered in endemic areas.[25]

Radiolucent areas within the liver are indicative of intrahepatic gas, either in the biliary system, portal venous system, or hepatic parenchyma. Gas within portal vessels may occur as a result of severe necrotizing gastritis or enteritis, often associated with gastric dilation and volvulus complex. Gastrointestinal ulceration, distention, trauma, or interventional procedures may allow gas to ascend into the portovenous circulation.[1,26,27] A linear, branching radiolucent appearance, similar to air bronchograms, may be visible.

Gas in or around the gallbladder occurs with emphysematous cholecystitis and occurs in both diabetic and nondiabetic

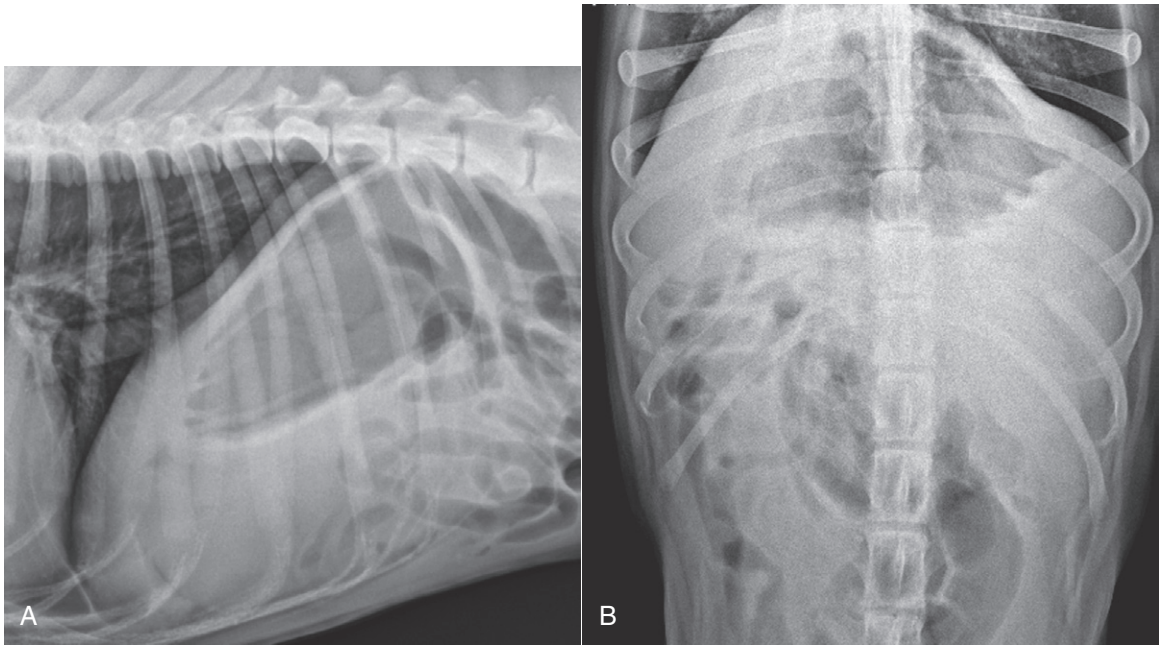


Fig. 37-12 Lateral **(A)** and ventrodorsal **(B)** radiograph of the abdomen of a dog with chronic hepatitis that led to microhepatia. There is marked cranial displacement of the stomach.

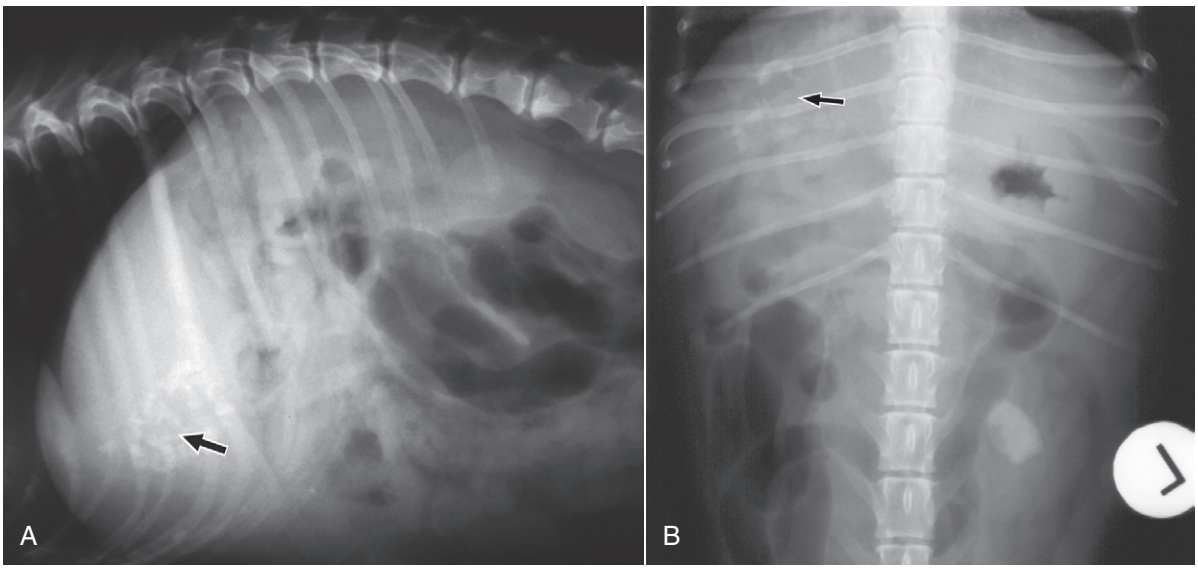


Fig. 37-13 Lateral **(A)** and ventrodorsal **(B)** radiographs of a dog with radiopaque choleliths in the right cranial portion of the liver *(black arrows)*. A left renal pelvic calculus is present.



Fig. 37-14 Lateral radiograph of the abdomen of a dog with trails of mineralized choledocholiths in the ventral aspect of the liver.

dogs.[28,29] Gas is seen initially in the gallbladder wall, followed by more complete filling of the lumen. The gas eventually extends to the pericholecystic tissues. Gas bubbles conforming to the shape of the distended gallbladder can be seen within 24 to 48 hours of onset of disease. Obstruction of the cystic duct may be a common predisposing factor for emphysematous cholecystitis. Gas lucencies within the biliary system can also be seen after surgery of the duodenum or biliary system.[1] Incidental reflux of gas into the bile duct from the duodenum is occasionally seen in cats. This may be because of incompetence of the sphincter of Oddi.[4]

Hepatic abscesses caused by gas-forming organisms may result in gas opacities within the hepatic parenchyma.[30-33] These abscesses appear as irregularly stippled or mottled gas patterns, usually in a localized area (Fig. 37-15). Hepatomegaly or hepatic mass is typically present with hepatic abscess with or without gas formation.

Special Radiographic Procedures of the Liver

Portosystemic shunts are congenital or acquired anomalies of the portal vasculature in which blood bypasses the liver and enters the systemic circulation directly.[34] Various imaging techniques have been used to identify and characterize the anomalous vessels, including cranial mesenteric portography, percutaneous splenoportography, and operative mesenteric portography.[34-37] Portography, where the portal system is opacified with iodinated contrast medium, provides visualization of the anomalous vessel, any acquired collateral vessels, the direction of portal blood flow, and patency of the portal vein and its branches. Intraoperative mesenteric portography involves intraoperative catheterization of a jejunal vein, or sometimes a splenic vein, to outline the portal system (Figs. 37-16 and 37-17). Ultrasound-guided percutaneous splenic vein catheterization can also be used but this may be challenging, especially in smaller patients.[38] Patient position during contrast-medium injection may have an effect on the visualization of the opacified vessels as a result of gravity-dependent alterations in the distribution of portal blood flow. Contrast-medium injection should be performed with the patient in left lateral and dorsal recumbency, followed by a repeat injection in right lateral recumbency if the results of the first two injections are negative or inconclusive.[39]

The use of postshunt ligation intraoperative mesenteric portography provides confirmation that the shunt has been identified correctly and ligated as well as information on the extent of hepatic portal vasculature.[40]

With increased availability of high-quality computed tomography scanners, abdominal computed tomography angiography is replacing most invasive portography procedures for assessment of the portal venous system. This technique provides portogram-like images of the normal and abnormal vasculature.[41,42]

Hepatic Ultrasound

Ultrasound examination of the liver allows detailed evaluation of hepatic internal architecture, including the hepatic vasculature and biliary system. Ultrasound is also useful in guiding aspirates and biopsies for nonsurgical, less invasive diagnoses.

The liver can be imaged through a combination of subcostal, subxiphoid, and right and left intercostal windows.

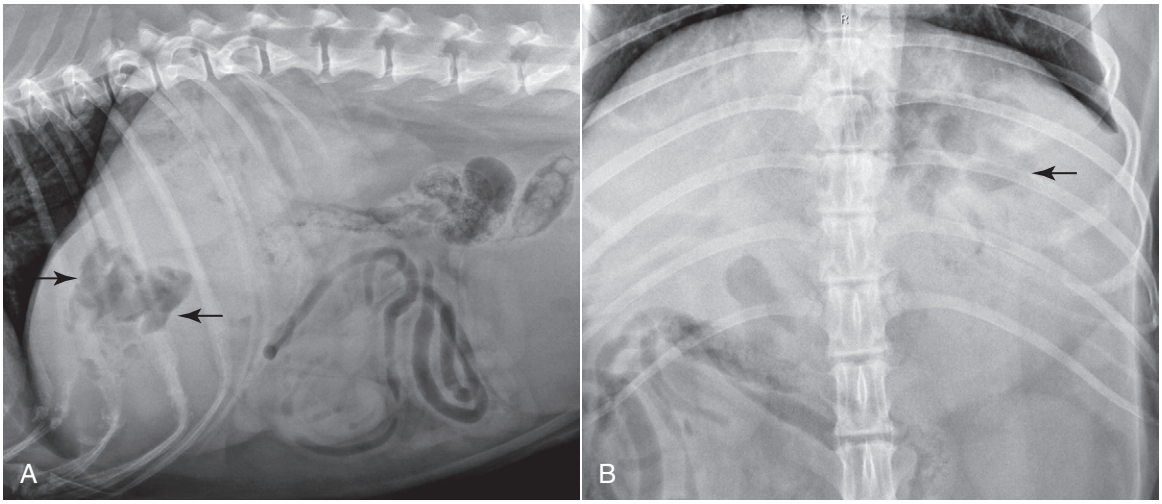


Fig. 37-15 Lateral **(A)** and ventrodorsal **(B)** radiographs of the abdomen of a dog with hepatic abscessation secondary to hepatic carcinoma. An irregular, focal radiolucency is in the midportion of the liver, just to the left of midline *(black arrows)*.



Fig. 37-16 Lateral intraoperative mesenteric portogram of a normal dog outlining the portal vasculature.

Intercostal windows may be the best way to evaluate the liver in a deep-chested dog or in patients with microhepatia. The right dorsal intercostal window allows excellent visualization of the porta hepatis, the caudate liver lobe, and the right kidney. Biliary obstruction, and intra- and extrahepatic portosystemic shunts can also be visualized with this window. The selection of transducer and frequency for hepatic evaluation depends on patient size, and size of the liver. Transducer frequencies ranging from 5 to 10 MHz can be used. Transducers with smaller footprints are best for intercostal windows.

The hepatic parenchyma has medium-level echogenicity with a homogeneous and uniform texture that is somewhat coarser than in the spleen.[43-47] The normal echogenicity of the liver is isoechoic to either slightly hyperechoic or slightly hypoechoic to the renal cortex and hypoechoic to the spleen (Fig. 37-18). The cranial pole of the right kidney provides a good reference point for assessing liver echogenicity in the immediately adjacent caudate liver lobe. Hepatic echogenicity is a subjective assessment, and mild changes should be interpreted with caution. The liver margins should be smooth and sharp but are better visualized if adjacent peritoneal fluid is present (Fig. 37-19). The liver is bordered cranially and dorsally by an echogenic line representing the interface between the diaphragm and lung/pleura. A mirror-image artifact is frequently noted deep to the diaphragmatic interface, giving the false impression of liver on both sides of the diaphragm (see Chapter 3 for a detailed explanation of this artifact).

The ultrasound assessment of liver size is subjective and based on operator experience.[48] A small liver is difficult to evaluate sonographically because of cranial displacement of the stomach, limiting the imaging window (Fig. 37-20). Liver size may appear decreased in dogs with a deep thoracic cavity wherein liver location is more completely within the costal arch. Intercostal ultrasound windows may be needed in these patients. The enlarged liver can be examined relatively easily with ultrasound because it extends well beyond the xiphoid cartilage and covers the right kidney more completely (Fig. 37-21). Liver margins may appear rounded and may extend beyond the left lateral margin of the stomach.

Hepatic and portal veins are visualized routinely within hepatic parenchyma. Portal veins are smoothly tapering vessels characterized by bright, echogenic borders.[43-46,49] The larger left and smaller right branch originate from the main portal vein near the porta hepatis, although they branch in different imaging planes.[49] Hepatic veins are anechoic linear structures extending through the parenchyma. Hepatic vein borders are not echogenic with the exception of their confluence with the caudal vena cava, immediately adjacent to the diaphragm. The right lateral dorsal intercostal window provides an excellent window to the aorta, caudal vena cava, and main portal vein (Fig. 37-22). Normal hepatic arteries are not visualized easily without color Doppler examination. The caudal vena cava can be visualized coursing through the liver in the right lateral abdominal quadrant.

The gallbladder is well visualized as an oval, anechoic structure in the right cranioventral portion of the liver. Gallbladder size varies widely, and distention is normal in fasting or anorexic patients. Intraluminal contents are typically anechoic, although gallbladder sludge, which is dependent echogenic material without acoustic shadowing, is seen frequently and is usually an incidental finding (Fig. 37-23).[50]

The normal gallbladder wall is thin and poorly visualized. In the cat, gallbladder wall thickness should be less than 1 mm or not visualized at all.[51] The normal canine gallbladder wall

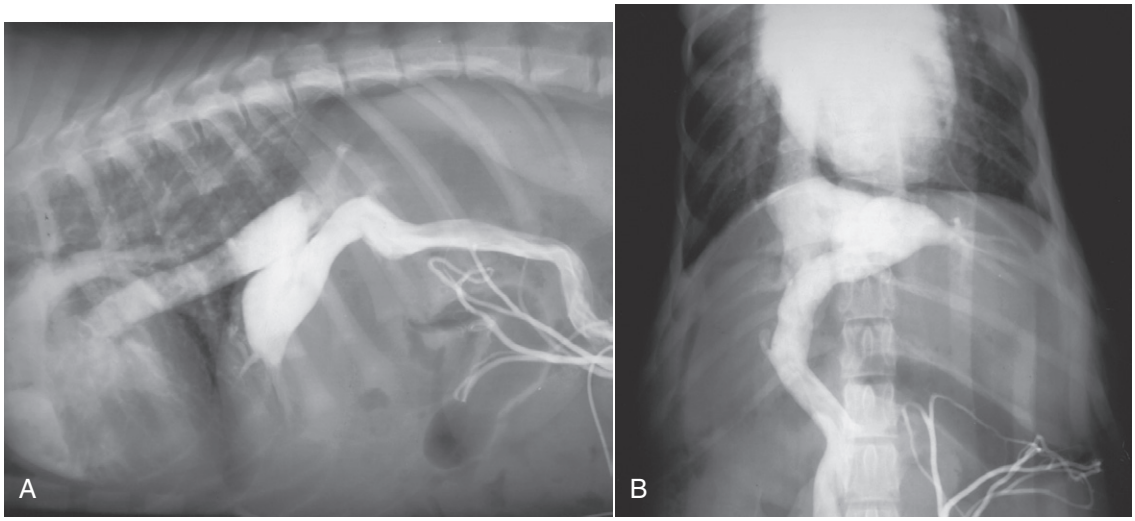


Fig. 37-17 Intraoperative mesenteric portogram (lateral **[A]** and ventrodorsal **[B]** views) outlining an intrahepatic portocaval shunt.

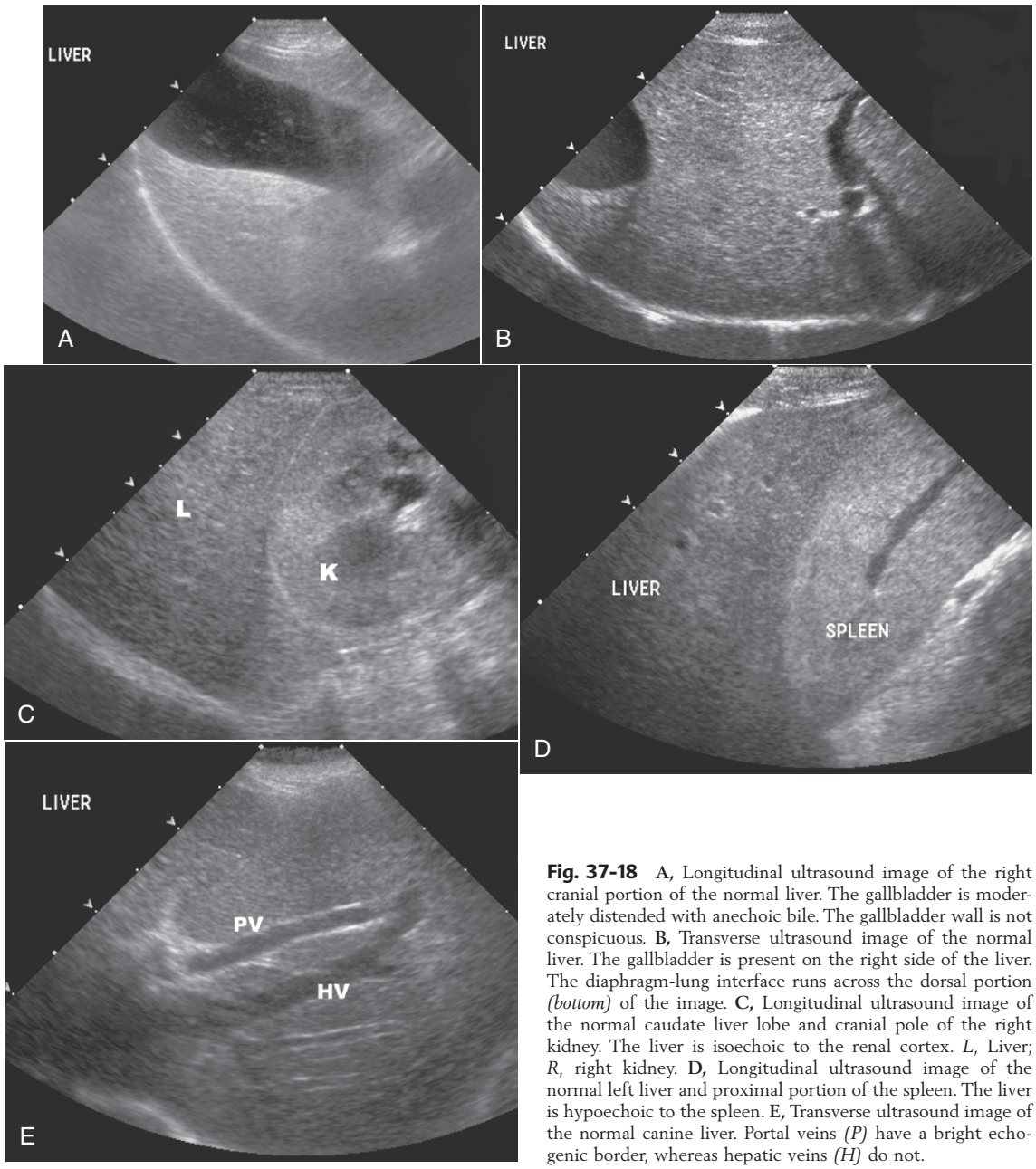


Fig. 37-18 **A,** Longitudinal ultrasound image of the right cranial portion of the normal liver. The gallbladder is moderately distended with anechoic bile. The gallbladder wall is not conspicuous. **B,** Transverse ultrasound image of the normal liver. The gallbladder is present on the right side of the liver. The diaphragm-lung interface runs across the dorsal portion *(bottom)* of the image. **C,** Longitudinal ultrasound image of the normal caudate liver lobe and cranial pole of the right kidney. The liver is isoechoic to the renal cortex. *L*, Liver; *R*, right kidney. **D,** Longitudinal ultrasound image of the normal left liver and proximal portion of the spleen. The liver is hypoechoic to the spleen. **E,** Transverse ultrasound image of the normal canine liver. Portal veins *(P)* have a bright echogenic border, whereas hepatic veins *(H)* do not.

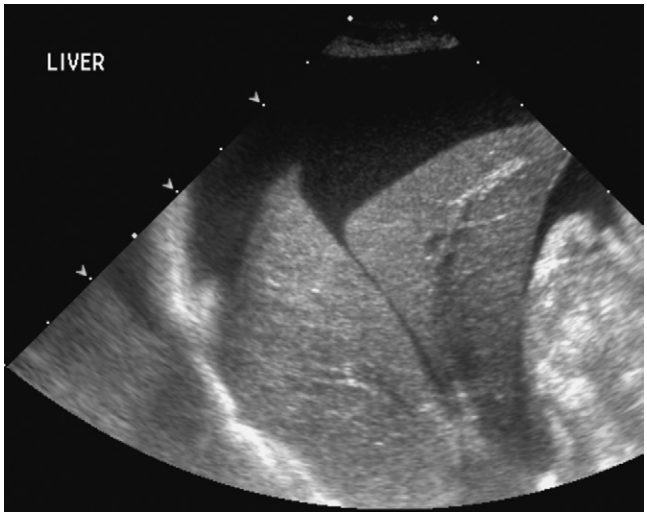


Fig. 37-19 Longitudinal ultrasound image of a dog with ascites. The normal liver lobes have a well-defined sharp, linear margin.

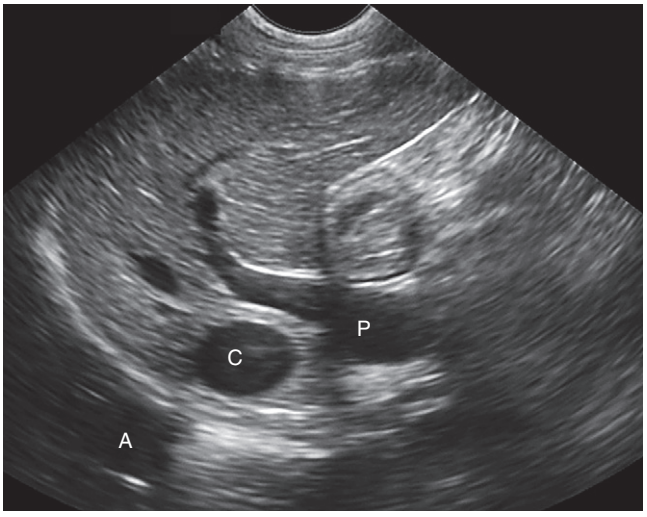


Fig. 37-22 Right lateral intercostal ultrasound image of a normal dog. Dorsal is at left and ventral is at right of the image. The top of the image represents the right abdominal wall with the left abdominal wall being at the bottom of the image. *A*, Aorta; *C*, caudal vena cava; *P*, portal vein.

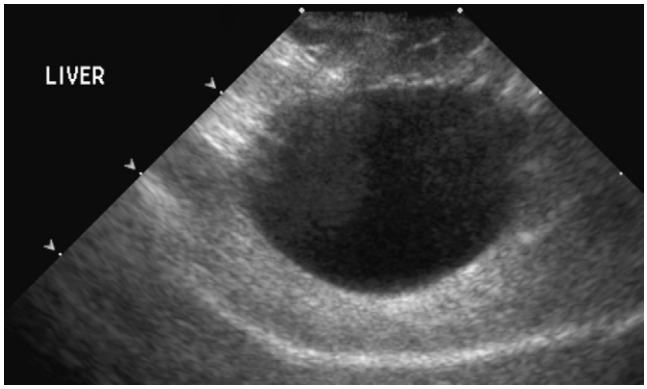


Fig. 37-20 Transverse ultrasound image of the liver in a dog with a small liver secondary to a portosystemic shunt. The liver is subjectively small with the gallbladder occupying a large portion.

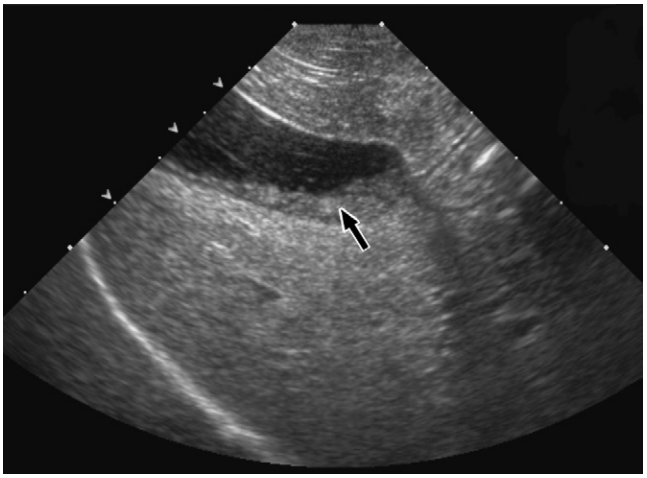


Fig. 37-23 Longitudinal ultrasound image of the liver and gallbladder of a normal dog. Echogenic biliary sludge *(black arrows)* is present in the dependent portion of the gallbladder.

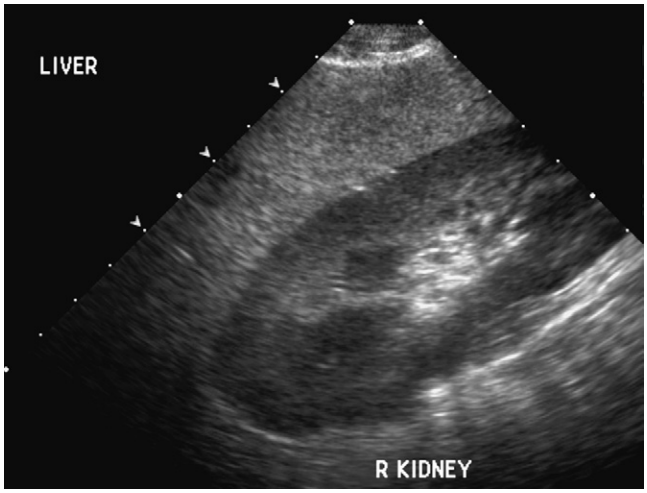


Fig. 37-21 Longitudinal ultrasound image of the caudate liver lobe and right kidney of a dog with hepatic lipidosis. The caudate lobe surrounds the right kidney completely, consistent with hepatomegaly. The liver is markedly hyperechoic to the renal cortex.

typically measures 2 to 3 mm, but normal ranges have not been established.[52,53] A duplicate or septated gallbladder is seen occasionally as a normal variation in cats and is caused by abnormal embryonic development.[54] The common bile duct is immediately ventral to the portal vein but is visible more consistently in the cat, where it can usually be followed to the duodenal papilla (Fig. 37-24). Normal common bile duct diameter in the cat is 4 mm or less.[55] If visible, the canine bile duct should be 3 mm or less.[56] Intrahepatic bile ducts are not visible unless dilated pathologically.

Abnormal Sonographic Appearance of the Liver

Ultrasound is helpful in differentiating between diffuse and focal hepatic disease. Diffuse hepatic disease can result in changes in shape, size, and echogenicity.[43-46,57-61] A *hyperechoic* liver is identified by comparison with the echogenicity of an adjacent organ, such as liver being hyperechoic to renal cortex, or isoechoic or hyperechoic to spleen. Also, there will be loss of visualization of the conspicuous periportal echoes and increased attenuation of sound as it passes through the

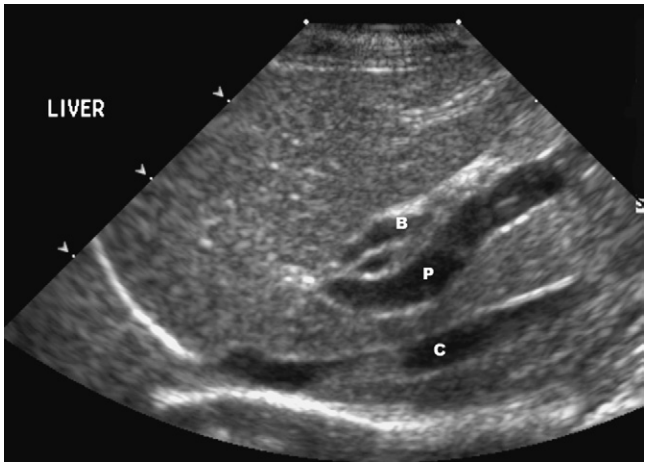


Fig. 37-24 Longitudinal ultrasound image of the liver in a normal cat. *C,* Caudal vena cava; *B,* bile duct; *P,* portal vein.

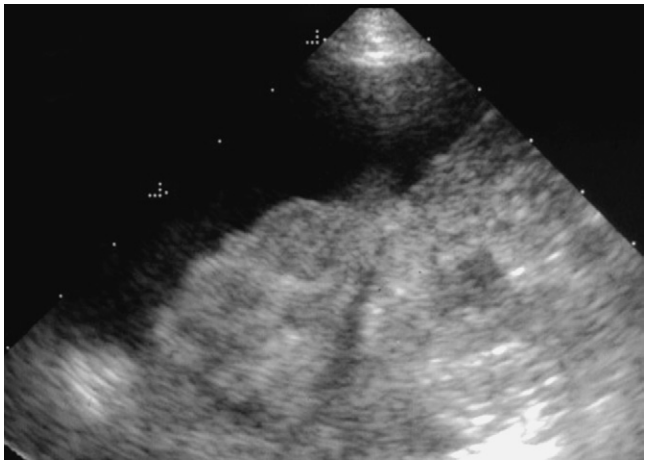


Fig. 37-25 Longitudinal ultrasound image of the liver in a dog with cirrhosis and ascites. The liver margins are irregular and rounded, and hypoechoic nodules are present within the parenchyma.

hyperechoic liver. Vacuolar hepatopathies, including lipidosis and steroid hepatopathy, result commonly in an enlarged, hyperechoic liver (see Fig. 37-21). In cats, liver parenchyma that is hyperechoic to adjacent falciform fat is suggestive of hepatic lipidosis, but this may be normal in some obese cats.[59,62] Chronic hepatitis with parenchymal fibrosis can also cause increased echogenicity, although liver size is variable and may be normal, increased, or decreased. Hepatic cirrhosis typically results in a small, irregular, hyperechoic liver (Fig. 37-25). Ascites often accompanies cirrhosis, enhancing visualization of irregular liver margins. Other hepatic diseases that may result in increased parenchymal echogenicity include lymphosarcoma, amyloidosis, and cholangiohepatitis. Mast cell infiltration in the liver results in a variable appearance, from normal to increased echogenicity and size. Hypoechoic nodules are occasionally noted as well.[63] A diffuse mottled hepatic parenchyma, characterized by a hyperechoic background with poorly defined hypoechoic nodules, is seen commonly with various combinations of vacuolar hepatopathy, nodular hyperplasia, and chronic inflammation (Fig. 37-26).

A decrease in hepatic echogenicity results in increased periportal echoes and abnormal comparison to the renal cortex because the liver becomes hypoechoic to the cortex. Decreased hepatic echogenicity occurs with hepatic congestion, lymphosarcoma, and cholangiohepatitis; a dilated caudal

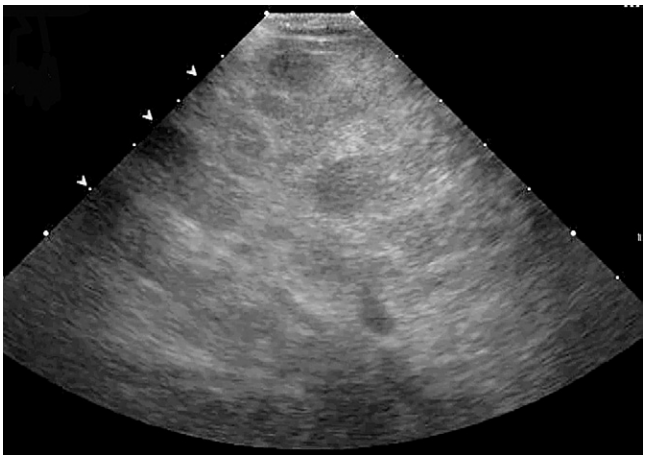


Fig. 37-26 Longitudinal ultrasound image of the liver in a dog with vacuolar hepatopathy. The liver is mottled with a hyperechoic background and poorly defined hypoechoic nodules.

vena cava and hepatic veins will accompany hepatic congestion. Acute suppurative hepatitis can cause hypoechogenicity from inflammation and edema. However, this may be uncommon, even with severe disease.[64]

Of note, a normal hepatic ultrasound examination does not rule out diffuse hepatic disease because structural changes need to be severe before ultrasound changes are visible. Ultrasound appears to be relatively insensitive in detecting parenchymal changes of hepatic lymphosarcoma.[65,66] Subtle changes in hepatic echogenicity should be compared with clinical signs and laboratory data, and a biopsy is necessary for definitive diagnosis.[67,68] Prebiopsy coagulation screening is a useful precaution when liver disease is suspected.

Focal hepatic disease appears as a nodule or mass that differs in texture and echogenicity from surrounding normal liver parenchyma. They may interrupt the hepatic margin, resulting in change of shape or contour. Relatively small nodules can be detected, especially when using high-frequency transducers. However, although ultrasound is sensitive in detecting hepatic nodules, it is not specific and numerous considerations are possible for focal disease. Cysts, abscesses, primary or metastatic neoplasia, hematomas, granulomas, nodular hyperplasia, and extramedullary hematopoiesis can all produce focal hepatic disease and may be difficult to differentiate on the basis of ultrasound appearance alone.[43-46,59] However, ultrasound is extremely useful in differentiating cystic versus solid masses; focal, multifocal, or diffuse distribution of masses; the relation of the mass to adjacent structures, such as large blood vessels or the gallbladder; and assessment of tumor vascular patterns with Doppler imaging techniques.[11]

Hepatic neoplasia has a variable appearance.[43-46,69] Primary hepatic carcinoma may appear hypoechoic, hyperechoic, or of mixed echogenicity (Fig. 37-27). Primary neoplasia may be a solitary large mass confined to a single liver lobe; multifocal, involving several lobes; or multifocal or coalescing nodules in all liver lobes.[11,70] Hepatic lymphosarcoma, although sometimes seen as a change in size and echogenicity, can also result in focal nodules, usually hypoechoic.[65,66] Tumor type cannot be determined from the ultrasound appearance alone because varying amounts of hemorrhage, necrosis, and fatty infiltration within the tumor create an inconsistent appearance that varies even from lobe to lobe.[58,59] Likewise, metastatic hepatic disease is variable in appearance but more often has a multifocal nodular or masslike appearance.

Primary and metastatic neoplasia cannot be differentiated solely on ultrasound appearance. Target lesions, which are

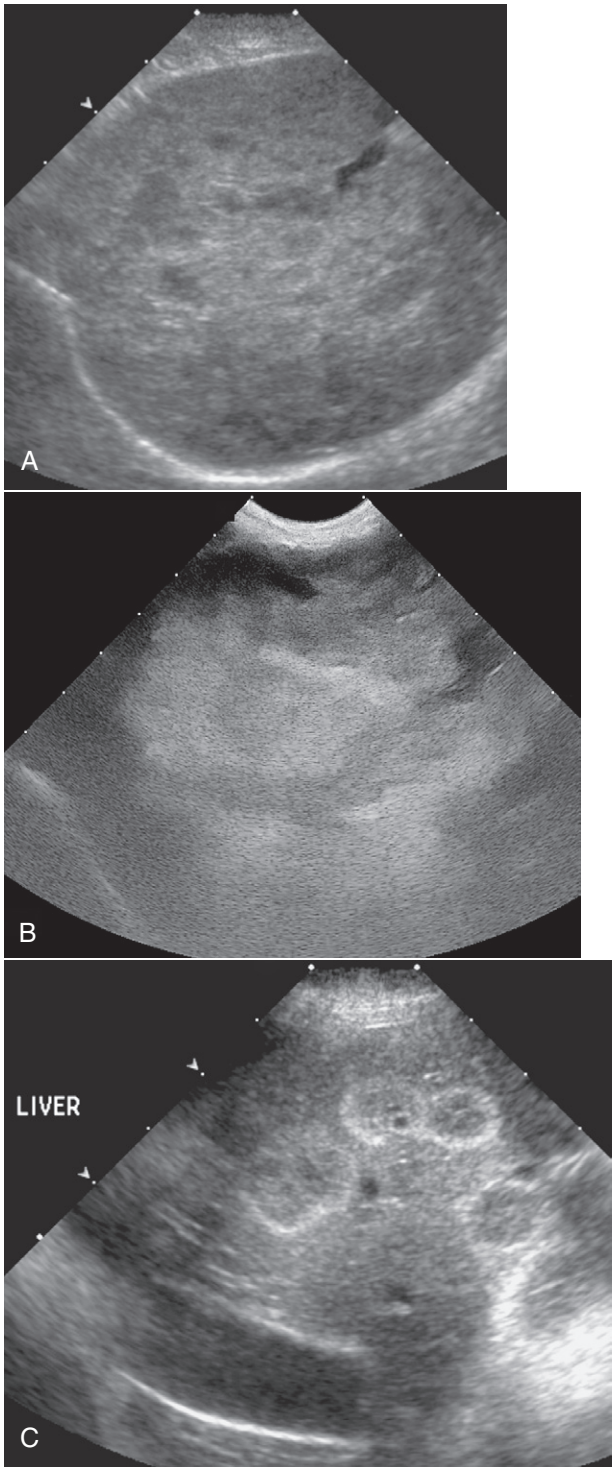


Fig. 37-27 **A,** Longitudinal ultrasound image of the liver from the cat in Figure 37-5. Multiple hypoechoic nodules are present in the enlarged liver (lymphosarcoma). **B,** Longitudinal ultrasound image of the liver from the dog in Figure 37-9. A large, irregular hyperechoic mass fills most of this portion of the liver. **C,** Longitudinal ultrasound image of a liver from a dog with primary hepatic hemangiosarcoma. Multiple lesions (hyperechoic rim, hypoechoic center) are present.

focal masses with a hyperechoic center and hypoechoic periphery, have been reported with both neoplastic and benign disease processes.[46,71] Hepatic nodular hyperplasia, a common benign lesion in older dogs, is usually silent clinically but may result in elevations in serum alkaline phosphatase.[72] It has a variety of appearances and cannot be differentiated from

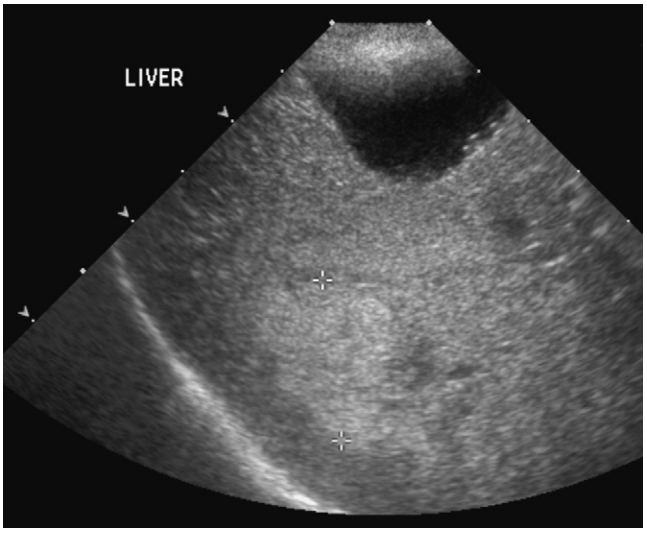


Fig. 37-28 Longitudinal ultrasound image of the liver from a dog with a hyperechoic nodule dorsal to the gallbladder (between calipers). Nodular hyperplasia was diagnosed histopathologically.

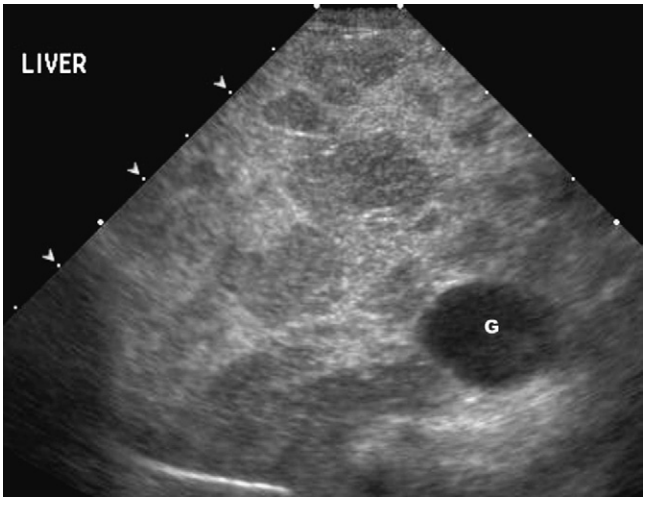


Fig. 37-29 Transverse ultrasound image of the liver from a dog with chronic hepatitis. Multiple hypoechoic nodules are present within a hyperechoic liver parenchyma. G, Gallbladder.

neoplasia without biopsy (Fig. 37-28). Hyperechoic, hypoechoic, isoechoic, and mixed echogenicity nodules, some with cavitation, are all possible.[73]

Contrast-enhanced ultrasonography is being used with some success in improving visualization of hepatic nodules and differentiating benign and malignant hepatic nodular disease.[74-76] After injection of an ultrasound contrast agent, benign regenerative nodules were isoechoic to surrounding normal liver during peak normal liver perfusion while malignant nodules were hypoechoic to surrounding liver at peak normal liver perfusion. Identification of tumor type was not possible.

Chronic hepatitis may also result in a diffuse nodular appearance (Fig. 37-29). Hyperechoic hepatic parenchyma surrounds multifocal hypoechoic nodules (nodular hyperplasia).[43,46,59] Liver size may be normal or decreased. Hepatocutaneous syndrome (superficial necrolytic dermatitis) results in a similar appearance. Hepatocutaneous syndrome should be suspected when the liver parenchyma has a honeycomb appearance with hyperechoic hepatic parenchyma surrounding hypoechoic focal nodular areas (Fig. 37-30).[77-80] These

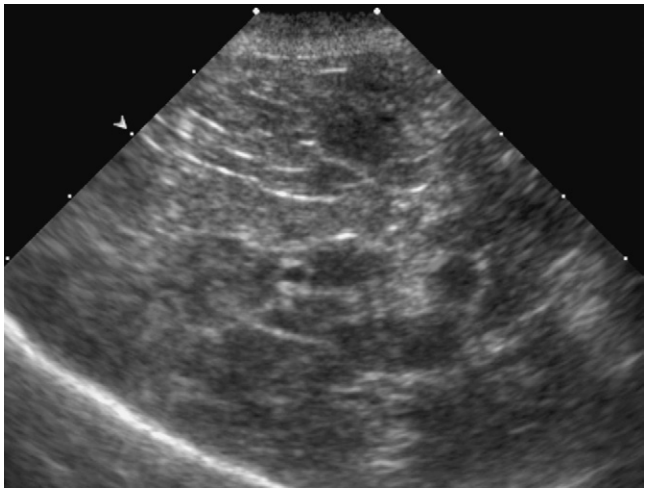


Fig. 37-30 Longitudinal ultrasound image of the liver from a dog with hepatocutaneous syndrome. Multiple hypoechoic nodules within the liver result in a honeycomb appearance.

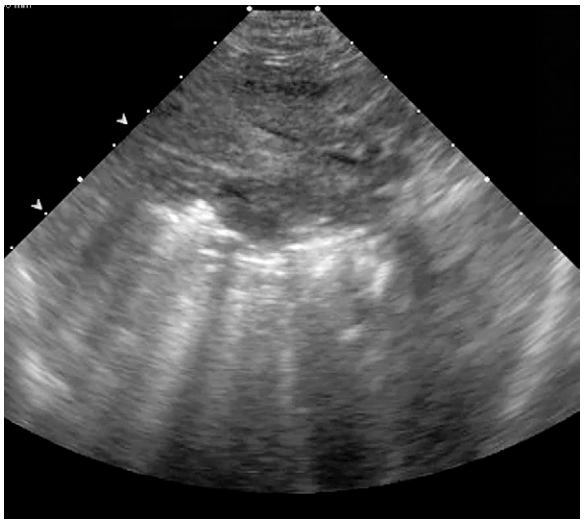


Fig. 37-31 Longitudinal ultrasound image of the liver from the dog in Figure 37-15. Echogenic shadows and reverberation artifacts are noted deep to gas pockets within the liver. This dog had hepatic abscessation secondary to hepatic carcinoma.

patients have concurrent dermal lesions in the footpads and mucocutaneous junctions. An aspirate or biopsy is critical in making the diagnosis.

Hepatic abscesses and hematomas have a variable appearance depending on duration. Abscesses often have an echogenic rim with a central anechoic or hypoechoic area.[31,33,81,82] They may contain gas, resulting in an echogenic interface with deep acoustic shadowing (Fig. 37-31). Hepatic abscesses appear commonly as a simple hypoechoic mass resembling nodular hyperplasia or neoplasia. Hematomas may be hyperechoic initially because of gas or red blood cell aggregates and then progress to hypoechoic or anechoic and finally back to hyperechoic because of reorganization or possible mineralization.[43,83,84] Hepatic cysts have a more consistent appearance, as a fluid-filled, anechoic structure with a well-defined, thin wall and acoustic enhancement. Usually an incidental finding, hepatic cysts have the potential to produce clinical signs if large enough or numerous enough to replace liver parenchyma. They can be associated with polycystic kidney disease, so the kidneys should be evaluated carefully for cystic structures if hepatic cysts are noted. Biliary cystadenomas are



Fig. 37-32 Longitudinal ultrasound image of the liver from a cat with cystadenoma. A mass with anechoic cystic components, some with acoustic enhancement, is present.

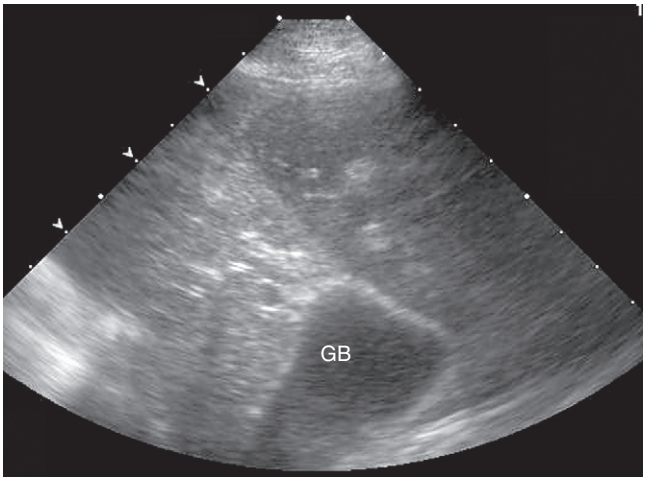


Fig. 37-33 Transverse image of the liver from a dog with torsion of the right medial liver lobe. The left portion of the liver is hypoechoic and is sharply demarcated from the normal right side of liver. Doppler signal was not present in the abnormal liver lobe.

benign cystic hepatic tumors seen mainly in older cats and may be focal or multifocal.[85] Although variable in appearance, the presence of a cystic component somewhere in the mass is a consistent finding (Fig. 37-32). Biliary cystadenomas may appear multilocular, containing thin-walled cysts, or as hyperechoic masses with a cystic component. Most cystic portions of these masses will be characterized by acoustic enhancement.

Liver lobe torsion is variable in appearance.[86,87] The abnormally positioned lobe may be hypoechoic or mixed in echogenicity. Doppler evidence of blood flow is reduced or absent (Fig. 37-33).

Disease of the Biliary System

Ultrasound is advantageous in the diagnosis of gallbladder and bile duct disease. Thickening of the gallbladder wall is a

nonspecific sign reported with inflammatory conditions such as cholecystitis, cholangiohepatitis, and both acute and chronic hepatitis.[43-45] A double-layered, or onion skin, appearance is seen frequently (Fig. 37-34). Wall edema results in a thickened hypoechoic wall with echogenic inner and outer rims, creating a layered appearance. Gallbladder wall thickening is also seen with right-sided congestive heart failure, hypoalbuminemia, sepsis, and neoplasia.[43-45,53,83] Peritoneal fluid surrounding the gallbladder can result in a false impression of wall thickening. Percutaneous cholecentesis for culture and cytology of the intraluminal bile should be performed with care.[53] Gallbladder thickening may be permanent as a result of inflammation and fibrosis despite resolution of the underlying disease process.[43]

Choleliths are echogenic focal structures, usually with acoustic shadowing, within the gallbladder lumen.[17,22,43] They may be single or multiple and are typically mobile, falling to the dependent portion of the gallbladder (Fig. 37-35). Although choleliths are usually incidental, they have the potential to obstruct the bile duct.

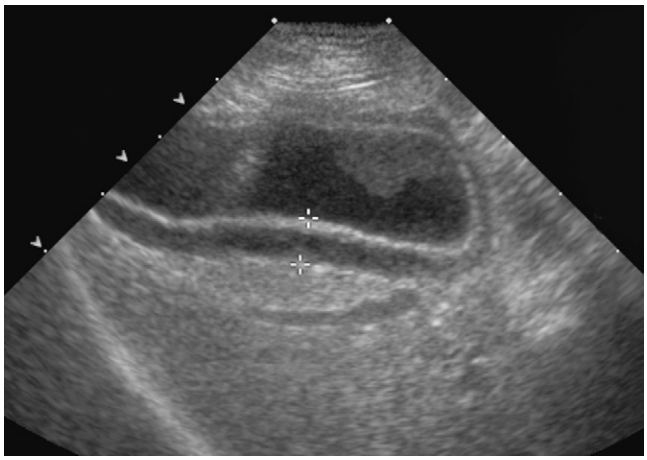


Fig. 37-34 Longitudinal ultrasound image of the liver and gallbladder from a dog with right-sided congestive heart failure. The gallbladder wall (between calipers) is thickened and has a layered appearance.

Intraluminal dependent biliary sludge is usually of no clinical significance. However, a biliary mucocele is a more organized form of centralized nondependent sludge, a semisolid mass of mucus, that creates either a stellate or striated appearance within the gallbladder lumen. The presence of a gallbladder mucocele may indicate gallbladder infection and necrosis (Fig. 37-36).[88-92] There is hyperplasia of mucus-secreting glands within the mucosa and abnormal accumulation of mucus within the lumen with subsequent biliary obstruction by mucinous plugs within the cystic and bile duct. Distention of the intrahepatic and/or extrahepatic biliary system may be present. Ischemic necrosis of the gallbladder wall can lead to rupture. Gallbladder mucoceles have been associated with a 50% incidence of loss of gallbladder wall integrity and/or acute rupture.[88] The presence of discontinuity of gallbladder wall, pericholecystic hyperechoic fat, and/or pericholecystic fluid was strongly suggestive of gallbladder rupture in patients with biliary mucocele.[88,89,92] Cholecystocentesis is discouraged in these patients because gallbladder wall rupture may be imminent. A biliary mucocele is found occasionally as an incidental finding in patients without clinical signs or changes in serum biochemical analysis.

Extrahepatic biliary obstruction results in a retrograde dilation of the biliary system.[93] With complete obstruction, the gallbladder and cystic duct distend within 24 hours of obstruction with progressive dilation of the common bile duct within 48 hours (Fig. 37-37). Gallbladder distention may be minimal in the face of chronic inflammation and fibrosis. Progressive dilation of the common bile duct and hepatic ducts occur during the next 3 to 4 days with dilation of lobar and interlobar ducts seen by 7 days. This results in multiple tortuous, irregularly branching anechoic linear tracks within the liver. Although calculi in the bile duct can result in obstruction, more common causes include pancreatitis and neoplasia in the adjacent pancreas, duodenum, or liver.[94]

Sludge accumulation within the bile duct associated with cholangiohepatitis can also result in extrahepatic biliary obstruction. Incomplete or early obstruction may not cause visible biliary dilation. Bile duct dilation may be prolonged, persisting after resolution of the obstruction.[43]

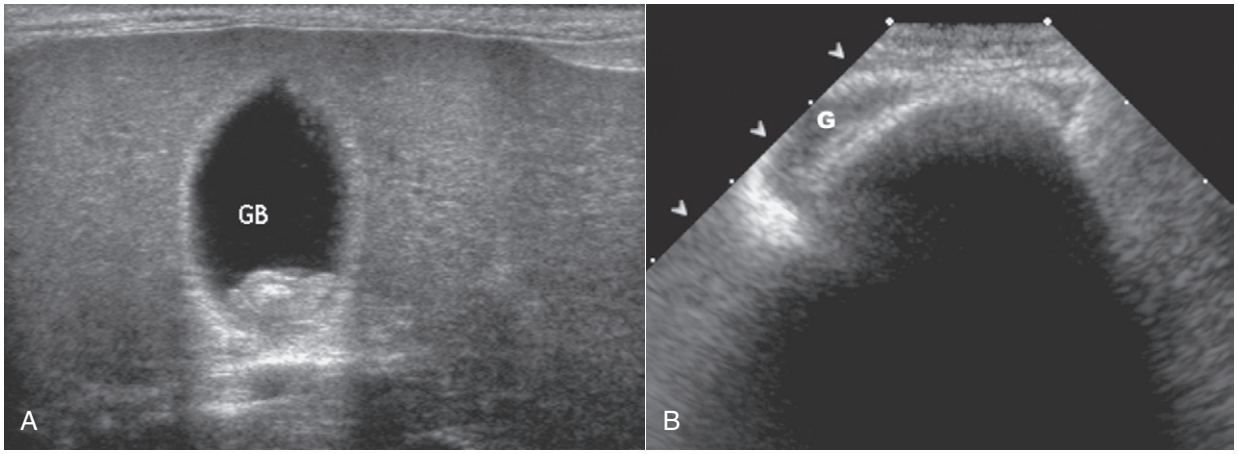


Fig. 37-35 Transverse ultrasound images of the gallbladder from two dogs. **A,** A small, dependent cholelith is present in the gallbladder lumen. Minimal shadowing is present. **B,** A large, mineralized cholelith fills most of the lumen of the gallbladder *(G)*. Only the echogenic rim of the cholelith and large acoustic shadow deep to the cholelith are visible. *GB,* Gallbladder.

Vascular Disease

Venous congestion occurs with right-sided congestive heart failure or obstructive lesions in the posthepatic caudal vena cava. The hepatic caudal vena cava and hepatic veins both dilate in response to the elevated pressure (Fig. 37-38). The liver may also enlarge and become hypoechoic, although echogenicity changes may not be consistent. Dilated caudal vena cava and hepatic veins, along with ascites, suggests the possibility of disease cranial to the diaphragm.

Ultrasonography can be used to identify most portosystemic shunts reliably, although detection of these vascular anomalies requires a high skill level.[95] An abnormal shunting vessel is the most reliable indication of portosystemic shunt, but other changes, including a small liver, decreased or absent intrahepatic portal vasculature, increased vena cava size, enlarged kidneys, and renal and/or cystic calculi (urate calculi), are often present (Fig. 37-39).[43,95,96]



Fig. 37-36 Longitudinal ultrasound image of a gallbladder mucocele. Echogenic biliary sludge fills the gallbladder lumen, creating a striated appearance along the periphery.

With extrahepatic shunts, which affect cats and small-breed dogs primarily, the most common finding is a single shunt vessel connecting the portal vein, or a major tributary of the portal vein, to the left lateral aspect of the caudal vena cava between the right renal vein and hepatic veins.[96-99] Extrahepatic shunt vessels are more difficult to visualize because of poor acoustic windows associated with the small liver, or the presence of bowel gas. A right dorsal intercostal window, in addition to routine views, is helpful in detecting the anomalous shunt vessel. In this window, the portal vein and caudal vena cava are visible as they enter the porta hepatis, and abnormal shunting vessels may be visualized more easily. Pulsed-wave or color Doppler interrogation of the caudal vena cava is helpful in assessing for abnormal flow turbulence where a shunting vessel enters the vena cava.[95] Portoazygos shunts are a less-common type of extrahepatic shunt. The presence of a large vessel in the craniodorsal abdomen coursing along the aorta with flow directed cranially is indicative of an abnormally enlarged azygos vein or the shunt vessel itself and is considered diagnostic for a portoazygos shunt.[95] Acquired extrahepatic shunt vessels attributable to hepatic disease and portal hypertension may appear as a grouping of multiple small, tortuous vessels, often medial to the spleen and left kidney. In some patients, these abnormal vessels are not visualized easily without color flow Doppler imaging.[96]

Intrahepatic shunts, affecting primarily large-breed dogs, are usually easier to identify. A right lateral dorsal and left ventral intercostal window, in addition to the standard ventral abdominal approach, is helpful in visualizing intrahepatic anomalous vessels. Intrahepatic shunt vessels are typically large with aberrant, tortuous courses connecting the intrahepatic portal vein and caudal vena cava and hepatic vein.[100] Measurement of portal flow velocity and the use of portal vein to aortic and portal vein to caudal vena cava ratios may also

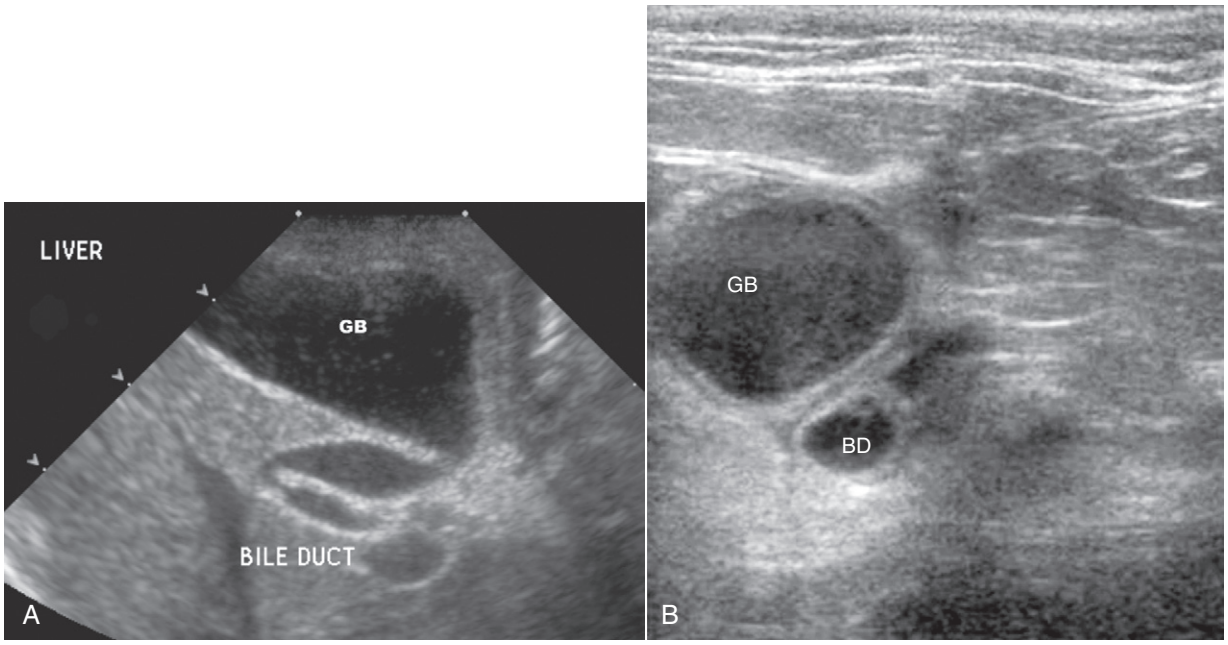


Fig. 37-37 Extrahepatic biliary obstruction. **A,** Longitudinal ultrasound image of a dog with extrahepatic biliary obstruction as a result of pancreatitis. The gallbladder *(GB)* and bile duct are moderately distended. **B,** Longitudinal ultrasound image of a cat with extrahepatic biliary obstruction secondary to cholangitis. A cross section of one segment of the bile duct (*BD*) is thickened and dilated. The gall bladder (*GB*) wall is thickened.

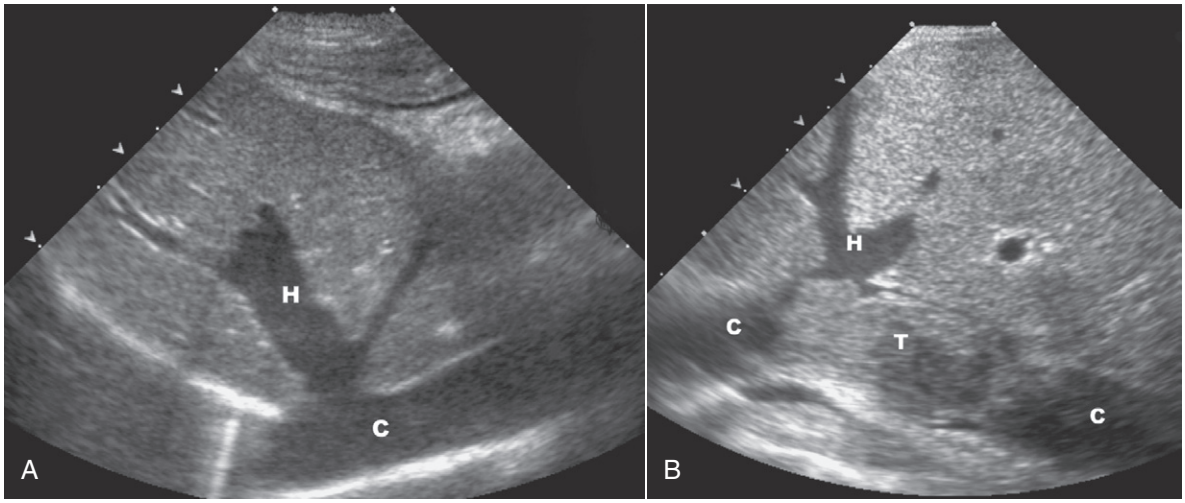


Fig. 37-38 Venous congestion. **A,** Right lateral oblique ultrasound image of the liver. The caudal vena cava and hepatic veins are distended as a result of right-sided congestive heart failure. **B,** Longitudinal ultrasound image of the liver in a dog with ascites. The lumen of the caudal vena cava *(C)* is filled with an echogenic thrombus *(T)*. The hepatic veins *(H)* are dilated as a result of the obstruction. *C,* Caudal vena cava; *H,* hepatic vein.

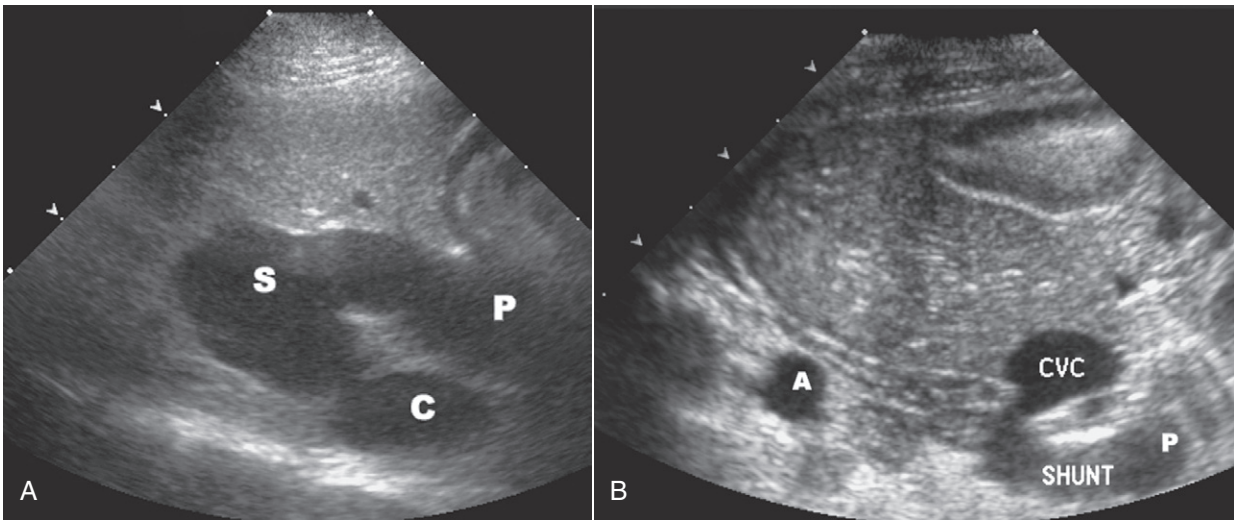


Fig. 37-39 Portosystemic shunts. **A,** Right lateral intercostal ultrasound image of a young dog with an intrahepatic portosystemic shunt. *C,* Caudal vena cava; *P,* portal vein; *S,* shunt. Dorsal is to the *left* of the image and right is at the *top* of the image. **B,** Right lateral intercostal ultrasound image of a young dog with an extrahepatic portosystemic shunt. *A,* Aorta; *CVC,* caudal vena cava; *P,* portal vein. Dorsal is to the *left* of the image, and right is at the *top* of the image.

be valuable in the search for portosystemic shunts.[95] Contrast harmonic sonography has been used to detect increased hepatic arterial flow as an indicator of portosystemic shunting and may be useful as an additional diagnostic test.[101]

RADIOLOGY OF THE SPLEEN

The spleen is a dynamic organ whose normal size and location vary widely, especially in the dog. There are numerous variations on the radiographic appearance of the normal spleen.[1-5] The spleen is divided typically into a proximal extremity, termed the *head* of the spleen; a body; and a distal extremity, termed the *tail* of the spleen. The proximal extremity is relatively fixed in the left craniodorsal aspect of the abdomen because of the gastrosplenic ligament. The distal extremity is not fixed, and its position can vary considerably. On ventrodorsal views of the canine abdomen, the proximal extremity of the spleen is seen typically as a triangular soft tissue opacity caudolateral to the gastric fundus and craniolateral to the left kidney (Fig. 37-40). The remainder of the spleen may extend caudally, adjacent to the left lateral abdominal wall, or more medially across the midline. When the spleen extends medially, the full length of the spleen is not visualized completely in the ventrodorsal view.

On lateral views, the triangular soft tissue opacity of the proximal extremity of the spleen is located dorsally, caudal to the stomach. The distal extremity is visualized typically as a triangular soft tissue opacity immediately caudal and slightly ventral to the pylorus or liver (Fig. 37-41). The distal extremity

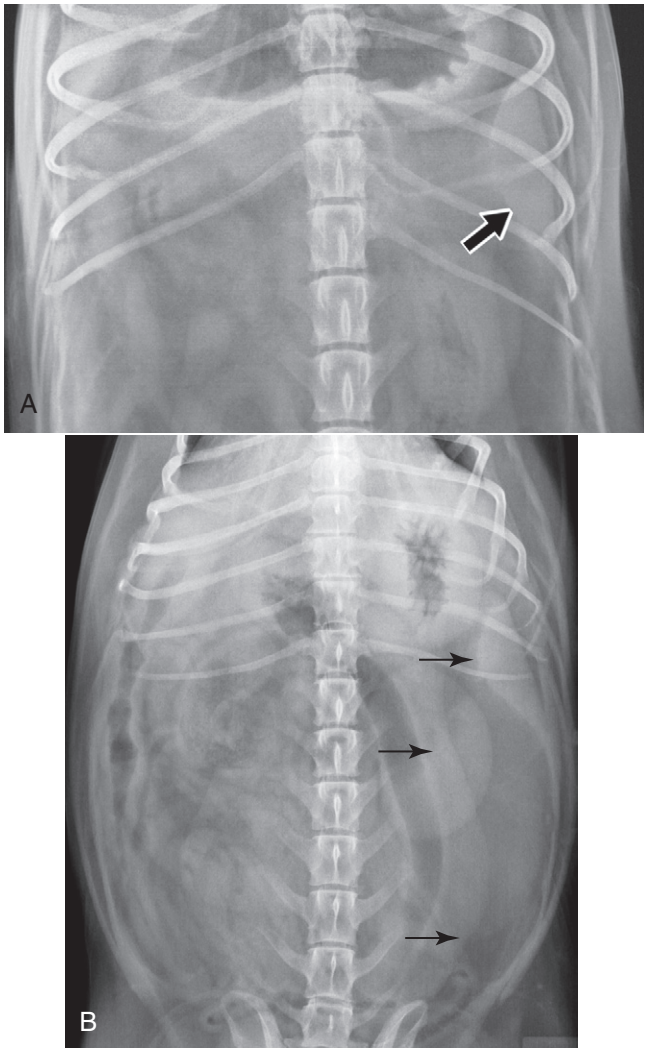


Fig. 37-40 Normal spleen. **A,** Ventrodorsal radiograph of the abdomen of a normal dog. The proximal portion of the spleen is visible in the left cranial abdomen, caudolateral to the gastric fundus and craniolateral to the left kidney *(black arrow)*. **B,** Ventrodorsal radiograph of the abdomen of a normal dog. The entire spleen can be visualized extending caudally along the left lateral abdomen *(black arrows)*.

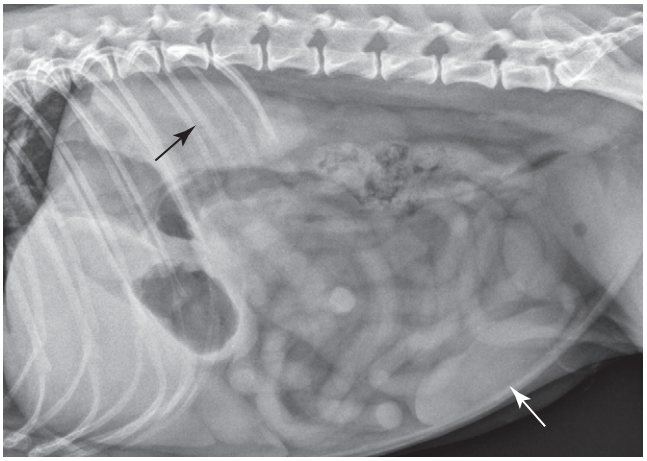


Fig. 37-41 Left lateral radiograph of the abdomen of a normal dog. The distal extremity of the spleen is visualized along the caudoventral abdomen *(white arrow)*. The proximal extremity is visualized in the craniodorsal abdomen, caudal to the gastric fundus *(black arrow)*.

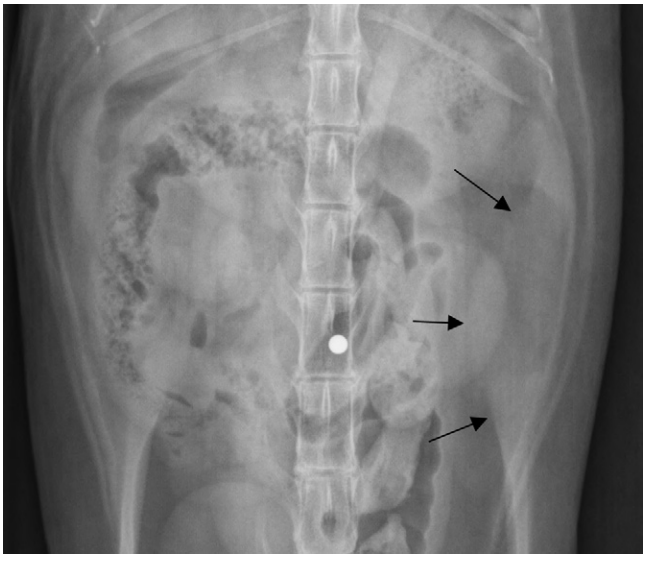


Fig. 37-42 Ventrodorsal radiograph of the abdomen of a normal cat. The entire spleen is visualized along the left lateral abdominal wall *(black arrows)*.

of the spleen is often more conspicuous on right lateral views of the abdomen but may silhouette the caudal margin of the liver and be poorly visualized as a separate structure.

The feline spleen is thinner and smaller compared with the canine spleen and less variable in size and position (Fig 37-42; also see Fig. 37-1, C). Similar to the dog, the proximal extremity of the spleen can be visualized on ventrodorsal views in the left cranial abdomen, caudolateral to the stomach and craniolateral to the left kidney. On ventrodorsal views the distal extremity usually extends caudally along the left lateral abdominal wall, allowing visualization of the entire spleen.

On lateral abdominal views in the cat, the proximal extremity may be visualized caudal and dorsal to the gastric fundus. The distal extremity may occasionally be visible caudal to the stomach but is usually not seen on lateral views in the normal cat.

Splenic Size

Radiographic assessment of splenic size is very subjective because its normal size varies widely. Generalized splenomegaly results in thickened, rounded, blunted margins, and dorsal and caudal displacement of the jejunum on lateral views (Fig. 37-43). Organ displacement on the ventrodorsal view as a result of the enlarged spleen depends on the portion of the spleen that is enlarged and the degree of enlargement. The jejunum may be displaced to the right or left, whereas an enlarged proximal extremity results in cranial displacement of the stomach.

Considerations for diffuse splenomegaly are numerous and include inflammation (splenitis caused by infection with toxoplasmosis, fungal organisms, *Mycoplasma haemofelis*, ehrlichiosis), hyperplasia (hemolytic disorders, systemic lupus erythematosus, chronic bacteremic disorders), congestion (impaired venous drainage, portal hypertension, splenic torsion/infarction, tranquilization and barbiturate administration), and infiltrative disease (neoplasia, both primary and metastatic; extramedullary hematopoiesis).[102] Lymphosarcoma, leukemia, systemic mastocytosis, multiple myeloma, and malignant histiocytosis can all result in diffuse neoplastic

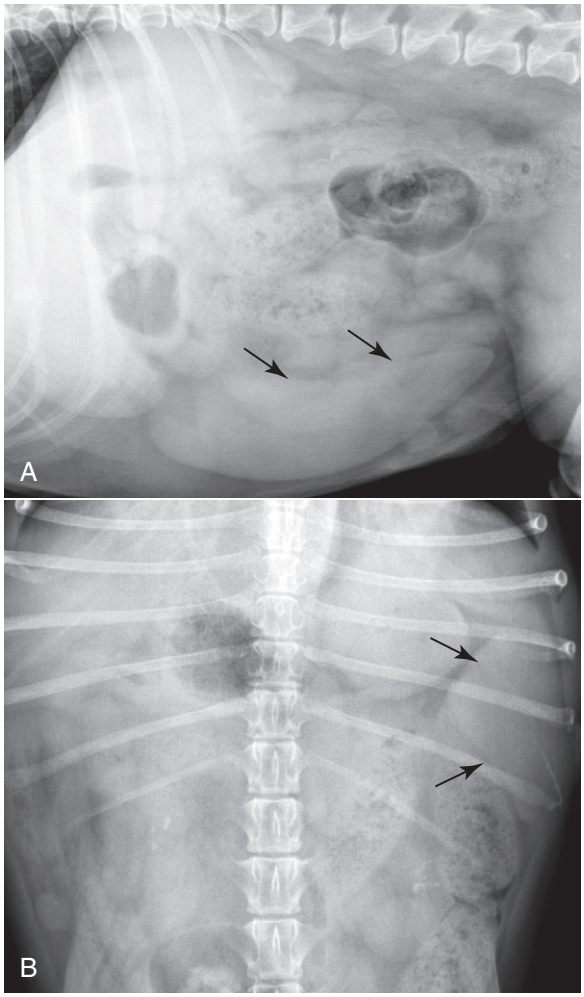


Fig. 37-43 Lateral (**A**) and ventrodorsal (**B**) radiographs of the abdomen of a dog with lymphosarcoma. The enlarged spleen is elongated with rounded margins on both views *(black arrows)*.

splenic enlargement. Compared with the dog, generalized splenomegaly in the cat is most commonly caused by neoplastic infiltration, primarily lymphosarcoma and mast cell tumor (see Fig. 37-5).[103,104]

Splenic torsion occurs when the spleen rotates around its mesenteric axis, resulting in complete occlusion of venous drainage and eventual arterial occlusion. This results in marked splenomegaly as well as atypical splenic location.[105] The spleen may undergo torsion on its own or in association with gastric volvulus; it may acquire a reverse C-shape on the lateral view or may simply appear as a mass in the ventral abdomen (Fig. 37-44). The proximal extremity of the spleen may not be visualized in the normal left craniodorsal location because of the malposition or accompanying peritoneal fluid. If gas-producing bacteria proliferate within the ischemic parenchyma, emphysematous changes may occur and result in a mottled or foamy radiographic appearance (Fig. 37-44, *B*).[26,106] Computed tomography has been used in the diagnosis of splenic torsion; findings include splenomegaly, a corkscrew-like soft tissue mass representing the rotated splenic pedicle, and lack of contrast enhancement.[107]

A splenic mass results in local displacement of adjacent viscera according to the location of the mass in the spleen (Figs. 37-45 and 37-46). Although often sharply marginated, the splenic mass may be obscured partially or completely by secondary peritoneal hemorrhage. A mass in the body or distal extremity of the spleen is a very common cause of a ventral abdominal mass, and on the lateral view results in dorsal and caudal displacement of the jejunum. On ventrodorsal views, distal splenic masses may be midline or to the right or left of midline.

Masses of the proximal extremity of the spleen are less common than distal masses and may displace the stomach cranially with caudal, medial, and ventral displacement of the jejunum and descending colon. The left kidney may be displaced caudally as well.

Differentials for a splenic mass include benign and neoplastic conditions. Primary and metastatic neoplasia, hematoma, nodular hyperplasia, extramedullary hematopoiesis, and abscess are all considerations.[104,108-110] Hemangiosarcoma is the

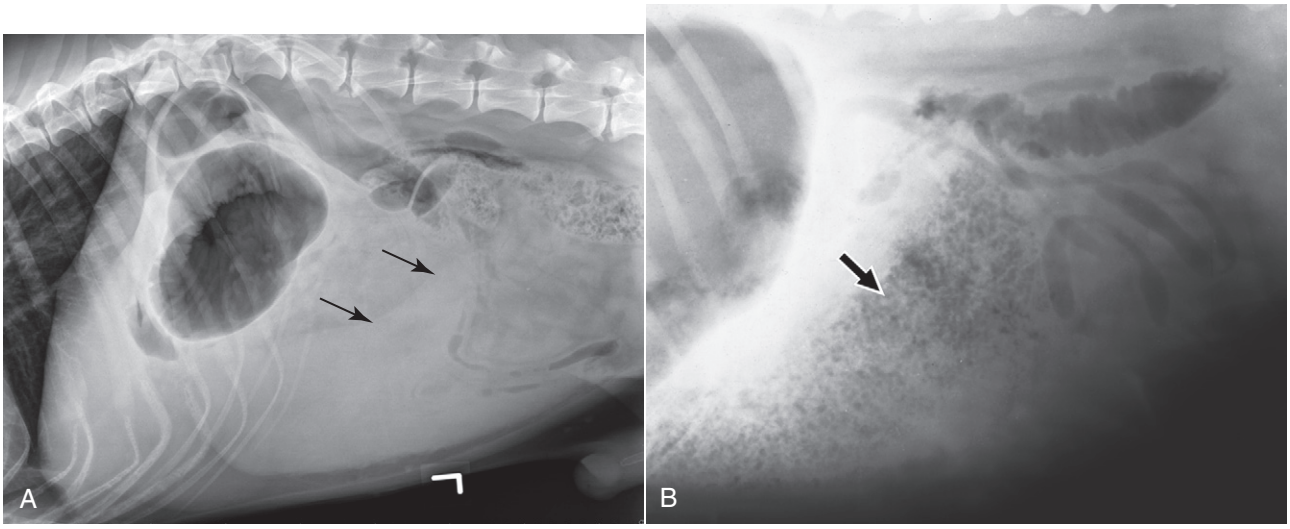


Fig. 37-44 Splenic torsion. **A,** Lateral radiograph of the abdomen of a dog with splenic torsion. The spleen is enlarged and displaced caudally and dorsally *(black arrows)*. **B,** Lateral radiograph of the abdomen of a dog with emphysematous splenic torsion. A mottled gas pattern is present within the enlarged and caudally displaced spleen *(black arrow)*. Abdominal effusion obscures the splenic outline.

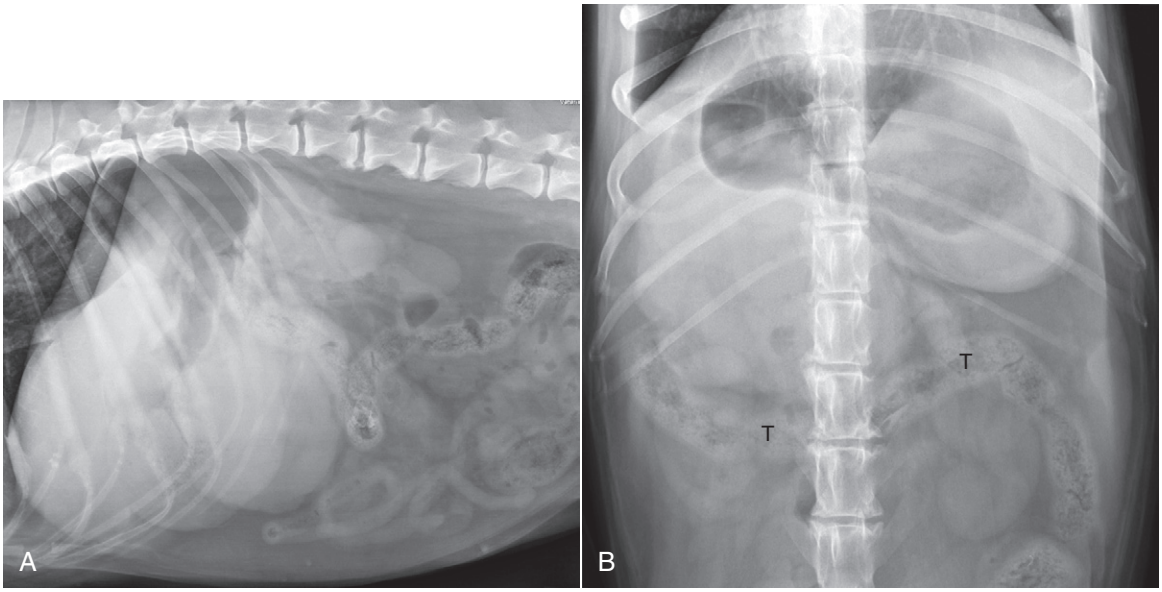


Fig. 37-45 Lateral **(A)** and ventrodorsal **(B)** radiographs of the abdomen of a dog with splenic hemangiosarcoma in the distal extremity of the spleen, seen along the ventral abdomen on the lateral view, and to the right of midline on the ventrodorsal view. The stomach is displaced cranially and to the left with caudal displacement of the transverse colon *(T)*.

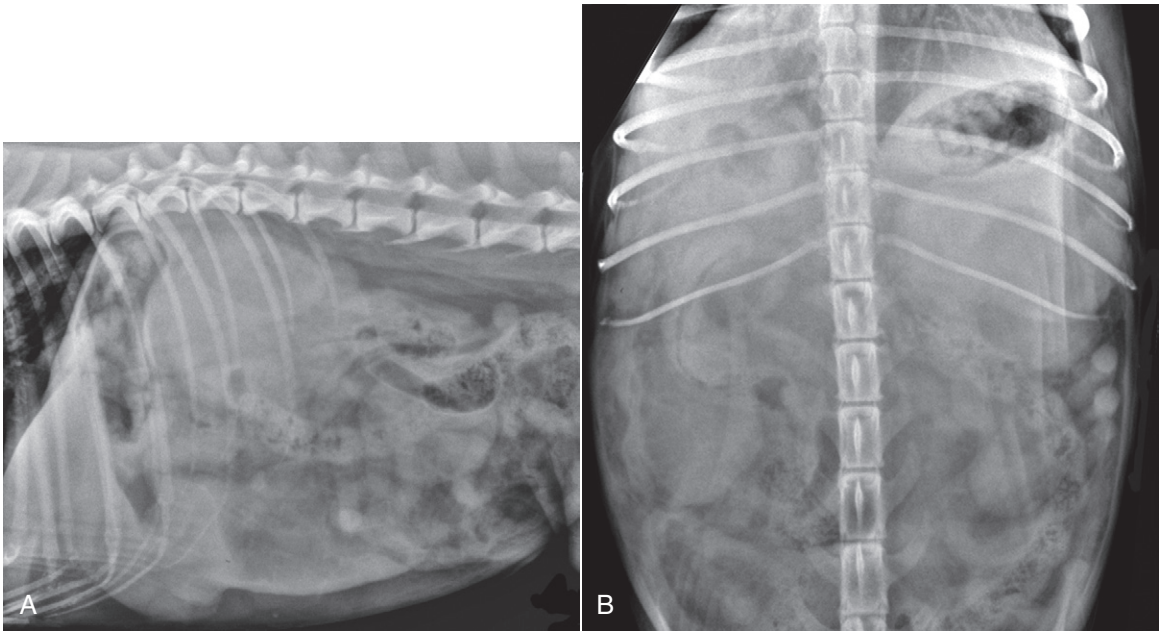


Fig. 37-46 Lateral **(A)** and ventrodorsal **(B)** radiographs of the abdomen of a dog with a splenic hemangiosarcoma in the proximal extremity of the spleen, seen dorsally, just caudal to the gastric fundus, on the lateral view, and in the left cranial abdomen on the ventrodorsal view. There is also a smaller mass on the distal extremity of the spleen, seen in the midabdomen on the lateral view and along the right lateral abdomen on the ventrodorsal view. Abdominal effusion results in a partial loss of contrast and detail in the cranioventral abdomen.

most common neoplasm of the canine spleen, but splenic hematoma and hyperplastic nodules are the most common cause of splenic lesions.[110] Peritoneal effusion may accompany both benign and neoplastic diseases.

Normal splenic opacity is that of soft tissue. Mineralization of the spleen may be the result of dystrophic calcification of abscesses, hematomas, fungal granulomas, or neoplastic masses.[13] Gas within the spleen may result from splenic torsion (Fig. 37-45, *B*). However, as in the liver, gas may ascend into the portovenous circulation and affect the spleen.[1,26,27]

Ultrasound of the Spleen

The canine spleen is well suited to ultrasound examination because it is superficial, and there are no intervening

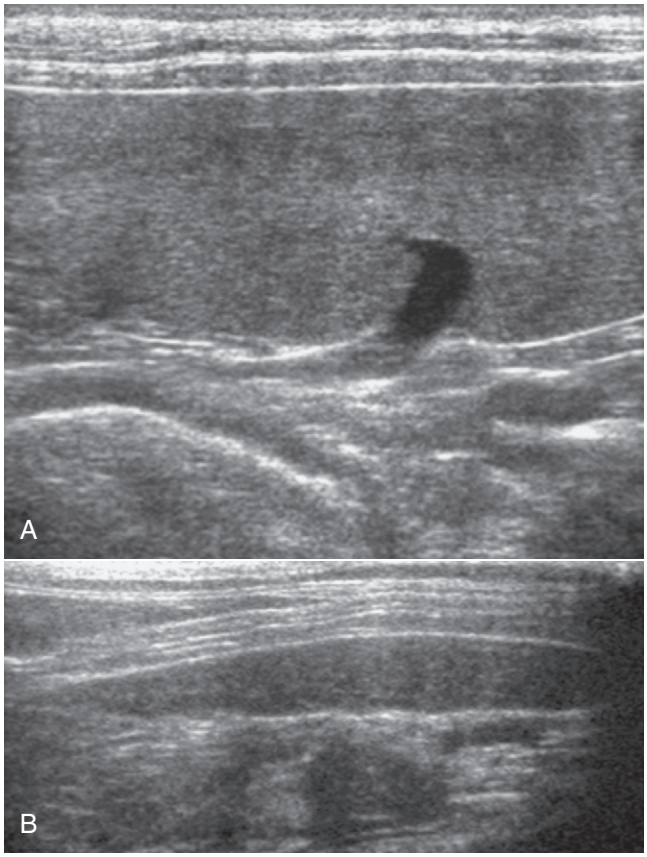


Fig. 37-47 Normal ultrasound appearance of the spleen. **A,** Longitudinal ultrasound image of the normal canine spleen. A splenic vein is visible leaving the splenic hilus. **B,** Longitudinal ultrasound image of the normal feline spleen. The feline spleen is typically a linear, thin structure, and smaller than in the dog.

gas-containing structures. The feline spleen may be difficult to image sonographically in some cats because of its smaller size.

Splenic location varies. The proximal extremity of the spleen is in the left craniolateral abdominal quadrant and may be beneath the costal arch. Intercostal windows may be necessary, especially in deep-chested dogs. The canine splenic body and distal extremity may extend caudally along the left lateral abdomen or move medially across the ventral midline. It often appears folded on itself. The feline spleen is more consistent in location, along the left lateral abdominal wall, and rarely folds on itself unless enlarged.

The splenic parenchyma has a uniform echotexture with a fine, dense pattern.[111,112] Echogenicity is slightly greater than the liver and renal cortex (Fig. 37-47). Splenic arteries are not usually seen without Doppler interrogation, but splenic veins are visualized as a Y-shaped confluence at the hilus. Tissue surrounding splenic veins at the hilus may be highly echogenic normally because of capsular invagination and fat.[111] Splenic size is subjective and based on sonographer experience.

When enlarged, the spleen may extend caudally or more completely cover the ventral abdomen. Splenic borders become rounded or blunted, or appear to bulge from the capsule, compared with the normal sharp, linear appearance. The spleen has no absolute size limits in the dog or cat (Fig. 37-48). Splenic thickness greater than 1 cm in the cat is suggestive of splenomegaly. Splenic size change suspected from sonography should be confirmed by palpation or radiographically.



Fig. 37-48 Longitudinal ultrasound image of an enlarged feline spleen caused by mast cell tumor. The spleen is rounded and thickened with folding of the cranial extremity (compare with Fig. 47, *B*). Mast cell tumor was diagnosed on fine-needle aspiration.

Abnormal Splenic Sonographic Findings

Diffuse Disease

As in the liver, diffuse splenic disease potentially causes an increase in size or a change in echogenicity. However, these changes may be difficult to identify or characterize, especially with mild or early disease. Splenomegaly with either normal or decreased echogenicity has numerous causes, including congestion, neoplasia, infarction, inflammation, immune-mediated disease, chronic hemolytic anemia, parasitic infection, extramedullary hematopoiesis, and bacterial or fungal infection.[63,103,105,111-120]

Splenic congestion as a result of a phenothiazine and pentobarbital drug group results in splenomegaly with no associated change in echogenicity.[113] Congestion from portal hypertension appears similar, but dilated splenic veins may also be present. Splenic torsion, a form of splenic congestion, has a variety of appearances.[105,114] Splenomegaly may be the only finding. However, splenomegaly with a diffuse hypoechoic parenchyma, separated by linear echogenicities that represent dilated hyperechoic vessels, is highly suggestive of torsion (Fig. 37-49). Splenic veins may be dilated with visible intravascular echogenicities representing formed thrombi or static echogenic blood. Complete absence of flow at the splenic hilus is also common, as is accompanying peritoneal fluid. A hyperechoic triangular area surrounding the splenic veins has been associated with splenic torsion.[115] Gas within the parenchyma may indicate the presence of necrosis and gas-forming organisms. Diffuse splenic infarction as a result of other disease processes can have an identical appearance.[116,117]

Diffuse neoplastic infiltration of the spleen has a variety of appearances, and tumor type cannot be determined from the ultrasound appearance.[63,65,103,111,112,118-120]

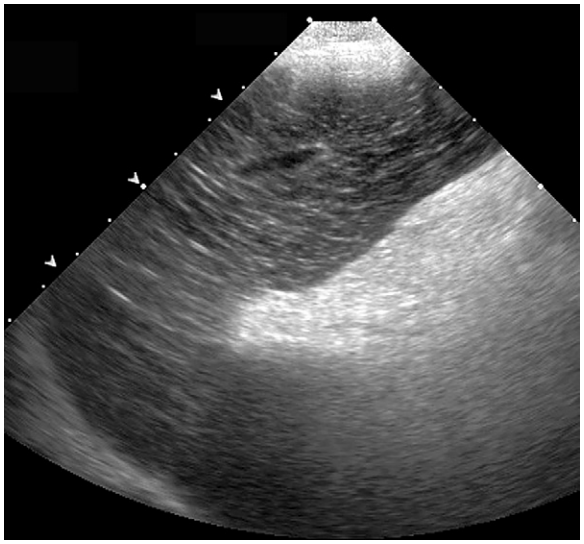


Fig. 37-49 Longitudinal ultrasound image of the spleen in a dog with splenic torsion (dog from Fig. 37-44, *A*). The spleen is enlarged and hypoechoic with linear echogenicities representing dilated vessels.

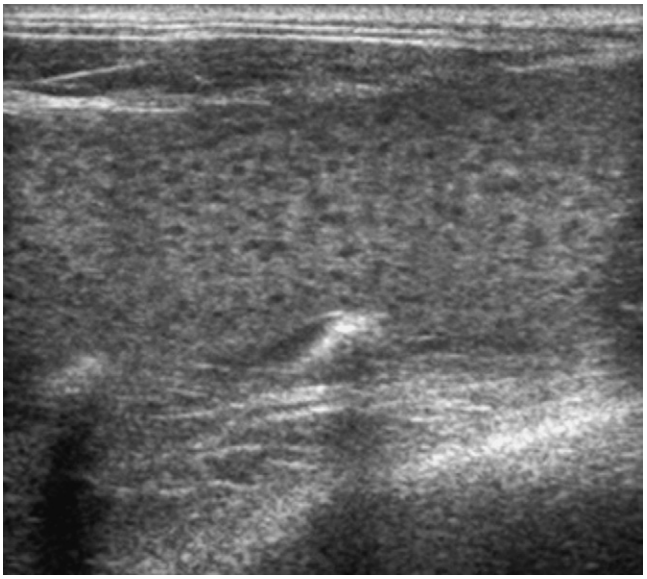


Fig. 37-51 Longitudinal ultrasound image of the spleen in a cat with lymphosarcoma. The spleen is enlarged with rounded margins and multiple small hypoechoic nodules are present diffusely throughout the parenchyma.



Fig. 37-50 Longitudinal ultrasound image of the spleen in a dog. A focal hypoechoic nodule caused by histiocytic sarcoma is present in the proximal extremity.

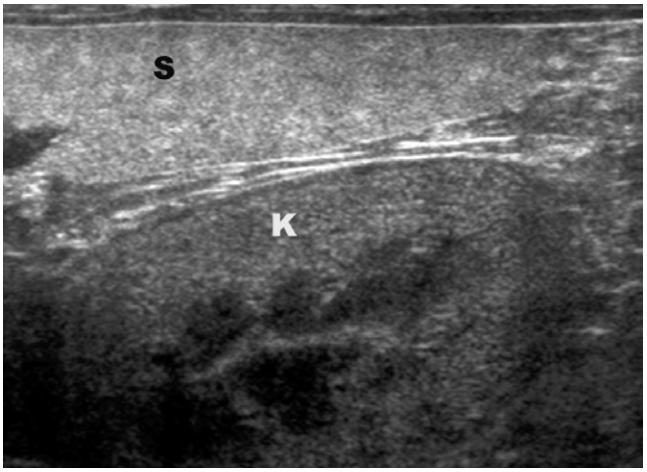


Fig. 37-52 Longitudinal ultrasound image of the spleen and left kidney in a dog. The spleen is markedly hyperechoic to the renal cortex with poorly defined hyperechoic nodules caused by extramedullary hematopoiesis. *K*, Kidney; *S*, spleen.

Lymphosarcoma, mast cell tumor, malignant histiocytosis, leukemic infiltration, and multiple myeloma can all result in splenomegaly with normal or decreased echogenicity. The parenchyma may appear uneven or coarse. Focal or multifocal nodules of varying sizes that are usually hypoechoic may also be present (Fig. 37-50). A miliary nodular pattern of small hypoechoic nodules, termed a *moth-eaten* or *Swiss cheese* appearance, is suggestive of lymphosarcoma, but other tumors, such as malignant histiocytosis, must also be considered (Fig. 37-51).[120]

Diffusely increased splenic echogenicity is less common but may be seen with chronic vascular compromise, peritonitis, infection, or diffuse nonneoplastic infiltrative disease such as extramedullary hematopoiesis (Fig. 37-52).[111,112]

As in the liver, numerous considerations exist for focal disease, including primary and secondary neoplasia, nodular hyperplasia, hematoma, extramedullary hematopoiesis, abscess, and infarction (Fig. 37-53). Lymphosarcoma, one of the most common splenic tumors, has a variety of appearances. In addition to the diffuse changes described previously, lymphosarcoma may also produce focal hypoechoic or anechoic nodules or a single complex or cavitated mass.[65,103,120] Splenic masses attributable to hemangiosarcoma are typically complex with hypoechoic, hyperechoic, and anechoic areas caused by hemorrhage, necrosis, and fibrotic or calcified tissue (Fig. 37-54).[111,112] Peritoneal fluid often accompanies hemangiosarcoma, and the liver should be evaluated carefully for metastasis. Splenic hematomas are similar in appearance to those described in the liver and may be associated with acute or previous trauma or develop from neoplastic disease (Fig. 37-55).[108,111,112,121] Splenic hematomas are indistinguishable sonographically from splenic hemangiosarcoma, and both may enlarge over time.[122]

Splenic abscesses are uncommon, but they can have a complex appearance similar to hemangiosarcoma or hematoma.[111,112,123] Splenic abscesses can vary from a simple hypoechoic, poorly defined area to a complex, cavitated mass.

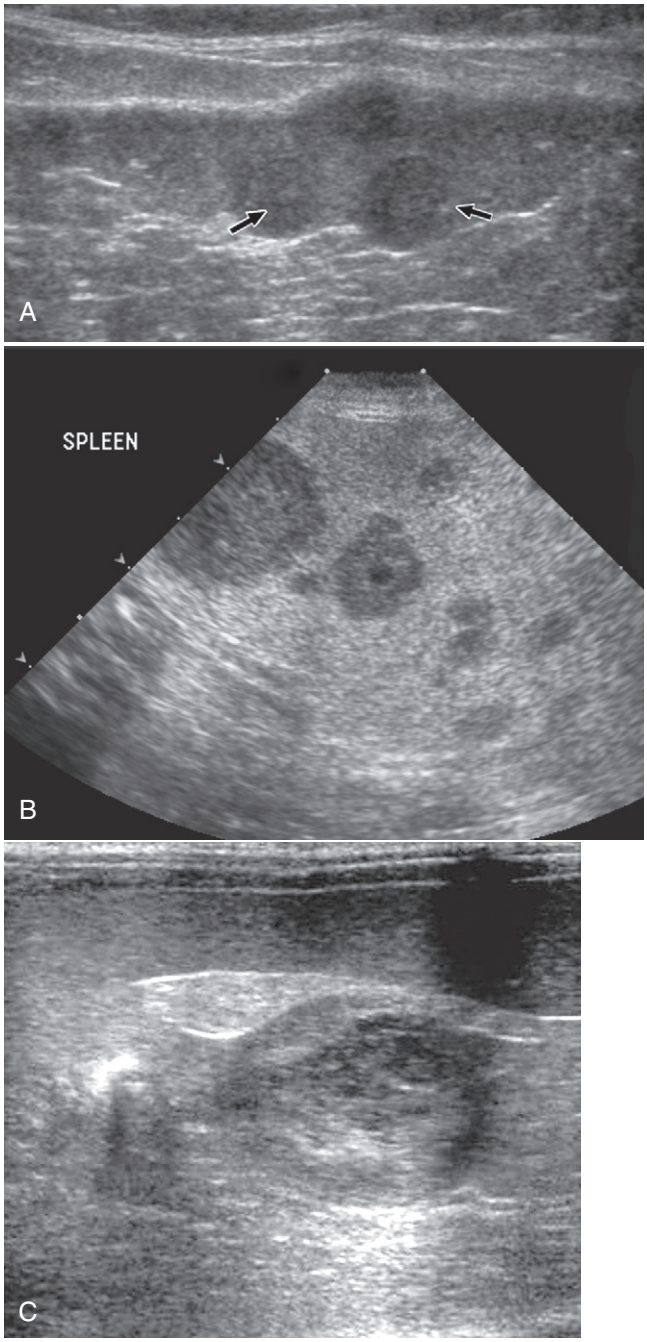


Fig. 37-53 Splenic nodules. **A,** Longitudinal ultrasound image of the spleen in a cat. Multiple hypoechoic nodules caused by lymphosarcoma are present, causing focal bulging of the splenic margin *(black arrows)*. **B,** Longitudinal ultrasound image of the spleen in a dog. Multiple irregular hypoechoic nodules caused by metastatic carcinoma are present in the hyperechoic splenic parenchyma. **C,** Longitudinal image of the spleen in a dog with a focal mass on the distal extremity caused by extramedullary hematopoiesis.

Echogenic areas with shadowing within the mass may indicate gas formation. Myelolipomas are fatty, hyperechoic nodules occasionally seen in the normal spleen, especially along the peripheral margin or adjacent to vessels (Fig. 37-56).[124,125] Splenic myelolipomas are benign incidental findings, but mast cell tumors have been reported to cause hyperechoic nodules in the spleen and should also be considered when hyperechoic foci are seen.[96]

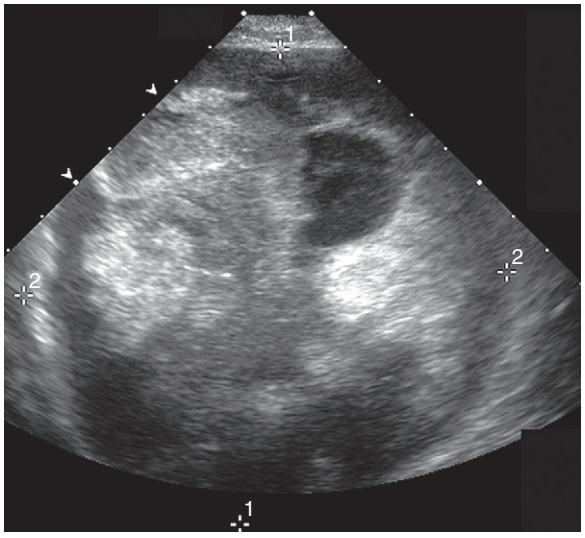


Fig. 37-54 Longitudinal ultrasound image of a splenic hemangiosarcoma in a dog. Areas of hyperechogenicity, hypoechogenicity, and anechogenicity likely represent hemorrhage and necrosis.

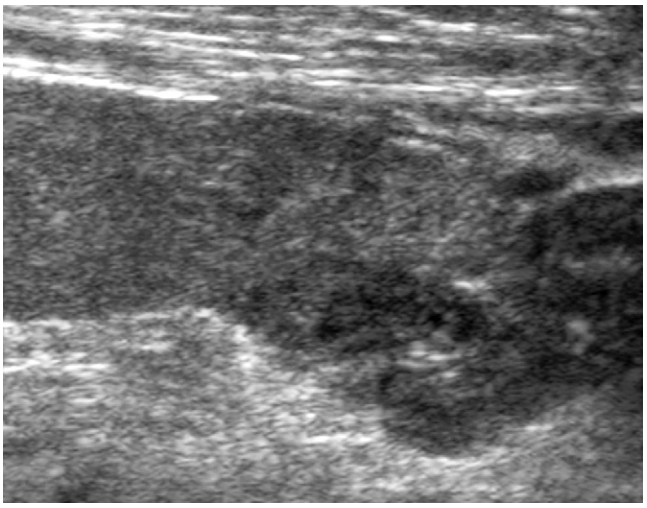


Fig. 37-55 Longitudinal ultrasound image of the distal extremity of the spleen in a dog with a splenic hematoma after being hit by car. Multiple poorly defined, coalescing hypoechoic nodules are present as a result of hematoma formation.

The echogenicity of focal splenic infarction changes over time. Initially infarcts are hypoechoic and may appear as a well-demarcated round or bulging mass or simple focal enlargement of the spleen (Fig. 37-57).[106,107] With age, infarcts become increasingly echogenic and often are demarcated sharply from the normal splenic parenchyma. With color Doppler interrogation, there is a lack of blood flow in the infarcted area. Extramedullary hematopoiesis can appear as hypoechoic, hyperechoic, or mixed echogenicity nodules and/or masses.

Nodular hyperplasia in the spleen has a similar appearance to that in the liver.[43] The splenic border may simply be smoothly irregular, or isoechoic, hypoechoic, or hyperechoic nodules may be present. Metastatic carcinoma can result in variably sized hypoechoic nodules (Fig. 37-52,*B*)

As in the liver, splenic ultrasound is sensitive but not specific. Tissue samples are necessary for a more definitive diagnosis. Although diagnosis of diffuse splenic disease such as lymphosarcoma or extramedullary hematopoiesis may be

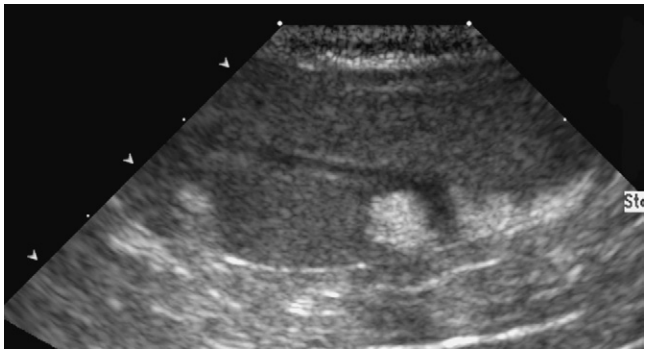


Fig. 37-56 Longitudinal ultrasound image of the spleen in a dog. Myelolipomas, seen as focal hyperechoic nodules, some with acoustic shadowing, are present along the dorsal border.

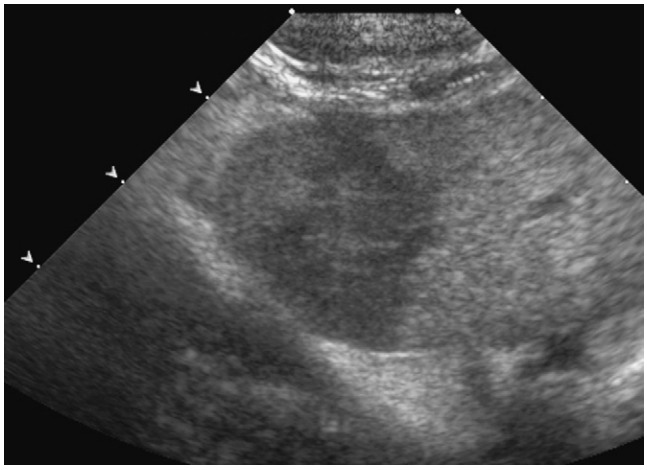


Fig. 37-57 Longitudinal ultrasound image of the spleen in a dog. The cranial extremity of the spleen is hypoechoic with well-demarcated margins. No perfusion was present in the hypoechoic portion, consistent with an acute infarct.

achieved with needle aspiration, cavitated mass lesions, such as hemangiosarcoma or hematoma, may be diagnosed more accurately by splenectomy and histopathologic evaluation.

REFERENCES

1. O'Brien T: The liver and spleen. In O'Brien T, editor: *Radiographic diagnosis of abdominal disorders in the dog and cat: radiographic interpretation, clinical signs, pathophysiology*, Philadelphia, 1979, Saunders, pp 396–458.
2. Burk RL, Ackerman N: The abdomen. In Burt RL, Ackerman N, editors: *Small animal radiology and ultrasonography. A diagnostic atlas and text*, ed 2, Philadelphia, 1996, Saunders.
3. Farrow CF: The abdomen. In Farrow CF, editor: *Radiology of the cat*, St. Louis, 1996, Mosby–Year Book, pp 139–218.
4. Schwarz T: The liver and gall bladder. In O'Brien R, Barr F, editors: *BSAVA manual of canine and feline abdominal imaging*, Gloucester, 2009, British Small Animal Veterinary Association, pp 144–156.
5. Kealy JK: The Abdomen. In Kealy JK, McCallister H, editors: *Diagnostic radiology & ultrasonography of the dog and cat*, ed 4, St. Louis, 2005, Elsevier-Saunders, pp 35-48.
6. Suter PF: Radiographic diagnosis of liver disease in dogs and cats, *Vet Clin North Am* 12:153, 1982.
7. Biller DS, Partington BP: Hepatic imaging with radiology and ultrasound, *Vet Clin North Am Small Anim Pract* 25:305, 1995.
8. Carlisle CH: Radiographic anatomy of the cat gallbladder, *Vet Radiol* 18:170, 1977.
9. Root CR: Abdominal masses: the radiographic differential diagnosis, *Vet Radiol* 15:26, 1974.
10. Evans SM: The radiographic appearance of primary liver neoplasia in dogs, *Vet Radiol* 28:192, 1987.
11. Liptak JM, Cernell WS, Withrow SJ: Liver tumors in cats and dogs, *Compend Cont Educ Small Anim Pract* 50–57, 2004.
12. Nickel R, Schummer A, Seiferle E, et al: *The viscera of the domestic mammals*, Berlin, 1973, Verlag Paul Parey.
13. Lamb CR, Kleine LJ, McMillan MC: Diagnosis of calcification on abdominal radiographs, *Vet Radiol* 32:211, 1991.
14. Cantwell HD, Blevins WE, Hanika-Rebar C, et al: Radiopaque hepatic and lobar duct choleliths in a dog, *Am Anim Hosp Assoc* 19:373, 1983.
15. Heidner GL, Campbell KL: Cholelithiasis in a cat, *J Am Vet Med Assoc* 186:176, 1985.
16. Jorgensen LS, Pentlarge VW, Flanders JA, et al: Recurrent choleliths in a cat, *Compend Cont Educ Pract Vet* 9:265, 1987.
17. Kirpenstein J, Fingland RB, Ulrich T, et al: Cholelithiasis in dogs: 29 cases (1980–1990), *J Am Vet Med Assoc* 202:1137, 1993.
18. Brömel C, Léveillé R, Scrivani PV, et al: Gallbladder perforation associated with cholelithiasis and cholecystitis in a dog, *J Small Anim Pract* 39:541, 1998.
19. Smith SA, Biller DS, Kraft SL, et al: Diagnostic imaging of biliary obstruction, *Compend Cont Educ Pract Vet* 20:1225, 1998.
20. Rosenstein DS, Reif U, Stickle RL, et al: Radiographic diagnosis: pericardioperitoneal diaphragm hernia and cholelithiasis in a dog, *Vet Radiol Ultrasound* 42:308–310, 2001.
21. Johnson SE: Cholelithiasis and cholangitis. In Kirk RW, editor: *Current veterinary therapy X: small animal practice*, Philadelphia, 1989 Saunders, pp 884–889.
22. Eich CS, Ludwig LL: The surgical treatment of cholelithiasis in cats: a study of nine cases, *J Am Anim Hosp Assoc* 38:290, 2002.
23. Brömel C, Smeak DD, Léveillé R: Porcelain gallbladder associated with primary biliary adenocarcinoma in a dog, *J Am Vet Med Assoc* 213:1137, 1998.
24. Thamm DH: Hepatobiliary tumors. In Withrow SJ, MacEwen EG, editors: *Small animal clinical oncology*, Philadelphia, 2001, Saunders, pp 327–334.
25. Scharf G, Deplazes P, Kaser-Hotz B, et al: Radiographic, ultrasonographic, and computed tomographic appearance of alveolar echinococcosis in dogs, *Vet Radiol Ultrasound* 45:411, 2004.
26. Gaschen L, Kircher P, Venzin C, et al: Imaging diagnosis: the abdominal air-vasculogram in a dog with splenic torsion and clostridial infection, *Vet Radiol Ultrasound* 44:553, 2003.
27. Sebastiá C, Quiroga S, Espin E, et al: Portomesenteric vein gas: pathologic mechanisms, CT findings, and prognosis, *Radiographics* 20:1213, 2000.
28. Burk RL, Johnson GR: Emphysematous cholecystitis in the nondiabetic dog: three case histories, *Vet Radiol* 21:242, 1980.
29. Avgeris S, Hoskinson JJ: Emphysematous cholecystitis in a dog: a radiographic diagnosis, *J Am Anim Hosp Assoc* 28:344, 1992.

30. Lord PF, Carb A, Halliwell WH, et al: Emphysematous hepatic abscess associated with trauma, necrotic hepatic nodular hyperplasia and adenoma in a dog: a case history report, *Vet Radiol* 23:46, 1982.
31. Grooters AM, Sherding RG, Biller DS, et al: Hepatic abscess associated with diabetes mellitus in two dogs, *J Vet Intern Med* 8:203, 1994.
32. Grooters AM, Sherding RG, Johnson SE: Hepatic abscesses in dogs, *Compend Cont Educ* 17:833, 1995.
33. Farrar ET, Washabau RJ, Saunders HM: Hepatic abscesses in dogs: 14 cases (1982–1994), *J Am Vet Med Assoc* 208:243, 1996.
34. Suter P: Portal vein anomalies in the dog: their angiographic diagnosis, *J Am Vet Radiol Soc* 16:84, 1975.
35. Schmidt S, Suter PF: Angiography of the hepatic and portal venous system in the dog and cat: an investigative method, *Vet Radiol* 21:57, 1980.
36. Moon ML: Diagnostic imaging of portosystemic shunts, *Semin Vet Med Surg (SA)* 5:120, 1990.
37. Lamb CR, Daniel GB: Diagnostic imaging of dogs with suspected portosystemic shunting, *Compend Cont Educ Small Anim Exotics* 24:626, 2002.
38. Hergessell EJ, Hornoff WJ, Koblik PD: Percutaneous ultrasound-guided trans-splenic catheterization of the portal vein in the dog, *Vet Radiol Ultrasound* 40:509, 1999.
39. Scrivani PV, Yeager AE, Dykes NL, et al: Influence of patient positioning on sensitivity of mesenteric portography for detecting an anomalous portosystemic blood vessel in dogs: 34 cases (1997–2000), *J Am Vet Med Assoc* 219:1251, 2001.
40. White RN, Macdonald NJ, Burton CA: Use of intraoperative mesenteric portovenography in congenital portosystemic shunt surgery, *Vet Radiol Ultrasound* 44:514, 2003.
41. Thompson MS, Graham JP, Mariani CL: Diagnosis of a porto-azygous shunt using helical computed tomography angiography, *Vet Radiol Ultrasound* 44:287, 2003.
42. Frank P, Mahaffey M, Egger C, et al: Helical computed tomographic portography in ten normal dogs and ten dogs with a portosystemic shunt, *Vet Radiol Ultrasound* 44:392, 2003.
43. Nyland TG, Mattoon JS, Herrgesell EJ, et al: Liver. In Nyland TG, Mattoon JS, editors: *Small animal diagnostic ultrasound*, ed 2, Philadelphia, 2002, Saunders, pp 93–127.
44. Lamb CR: Ultrasonography of the liver and biliary tract, *Probl Vet Med* 3:555, 1991.
45. d'Anjou MA: Liver. In Penninck D, d'Anjou MA, editors: *Atlas of small animal ultrasonography*, Ames, Ia., 2008, Blackwell.
46. Nyland TG, Park RD: Hepatic ultrasonography in the dog, *Vet Radiol* 24:74, 1983.
47. Ivancic M, Mai W: Qualitative and quantitative comparison of renal vs. hepatic ultrasonographic intensity in healthy dogs, *Vet Radiol Ultrasound* 49:368, 2008.
48. Godshalk CP, Badertscher RR, Rippy MK, et al: Quantitative ultrasonic assessment of live size in the dog, *Vet Radiol* 29:162, 1988.
49. Wu JX, Carlisle CH: Ultrasonographic examination of the canine liver based on recognition of hepatic and portal veins, *Vet Radiol Ultrasound* 36:234, 1995.
50. Brömel C, Barthez PY, Léveillé R, et al: Prevalence of gallbladder sludge in dogs as assessed by ultrasonography, *Vet Radiol Ultrasound* 39:206, 1998.
51. Hittmair KM, Vielgrader HD, Loupal G: Ultrasonographic evaluation of gallbladder wall thickness in cats, *Vet Radiol Ultrasound* 42:149, 2001.
52. Spaulding KA: Ultrasound corner: gallbladder wall thickness, *Vet Radiol Ultrasound* 34:270, 1993.
53. Rivers BJ, Walther PA, Johnston GR, et al: Acalculous cholecystitis in four canine cases: ultrasonographic findings and use of ultrasonographic-guided, percutaneous cholecystocentesis in diagnosis, *J Am Anim Hosp Assoc* 33:207, 1997.
54. Moentk J, Biller DS: Bilobed gallbladder in a cat: ultrasonographic appearance, *Vet Radiol Ultrasound* 34:354, 1993.
55. Léveillé R, Biller DS, Shiroma JJ: Sonographic evaluation of the common bile duct in cats, *J Vet Intern Med* 10:296, 1996.
56. Zeman RK, Taylor KJW, Rosenfield AT, et al: Acute experimental biliary obstruction in the dog. Sonographic findings and clinical implications, *Am J Roentgenol* 136:965, 1981.
57. Biller DS, Kantrowitz B, Miyabayashi T: Ultrasonography of diffuse liver disease: a review, *J Vet Intern Med* 6:71, 1992.
58. Newell SM, Selcer BA, Girard E, et al: Correlation between ultrasonographic findings and specific hepatic diseases in cats: 72 cases (1985–1997), *J Am Vet Med Assoc* 213:94, 1998.
59. Vörös K, Vrabély T, Papp L, et al: Correlation of ultrasonographic and patho-morphological findings in canine hepatic diseases, *J Small Anim Pract* 32:627, 1991.
60 Drost WT, Henry GA, Meinkoth JH, et al: Quantification of hepatic and renal cortical echogenicity in clinically normal cats, *Am J Vet Res* 61:1016, 2000.
61. Yeager AE, Mohammed H: Accuracy of ultrasonography in the detection of severe hepatic lipidosis in cats, *Am J Vet Res* 53:597, 1992.
62. Nicoll RG, O'Brien RT, Jackson MW: Qualitative ultrasonography of the liver in obese cats, *Vet Radiol Ultrasound* 39:47–50, 1998.
63. Sato AF, Solano M: Ultrasonographic findings in abdominal mast cell disease: a retrospective study of 19 patients, *Vet Radiol Ultrasound* 45:51–57, 2004.
64. Tchelepi H, Ralls PW, Radin R, et al: Sonography of diffuse liver disease, *J Ultrasound Med* 21:1023, 2002.
65. Lamb CR, Hartzband LE, Tidwell AS, et al: Ultrasonographic findings in hepatic and splenic lymphosarcoma in dogs and cats, *Vet Radiol* 32:117, 1991.
66. Nyland TG: Ultrasonic patterns of canine hepatic lymphosarcoma, *Vet Radiol* 25:167, 1984.
67. Léveillé R, Partington BP, Biller DS, et al: Complications after ultrasound–guided biopsy of abdominal structures in dogs and cats: 246 cases (1984–1991), *J Am Vet Med Assoc* 203:413–415, 1993.
68. De Rycke LM, Van Bree HJ, Simoens PJM: Ultrasound-guided soft tissue core biopsy of liver, spleen, and kidney in normal dogs, *Vet Radiol Ultrasound* 40:294, 1999.
69. Whiteley MB, Feeney DA, Whiteley LO, et al: Ultrasonographic appearance of primary and metastatic canine hepatic tumors, *J Ultrasound Med* 8:621, 1989.
70. Liptak JM, Dernell WS, Monnet E, et al: Massive hepatocellular carcinoma in dogs: 48 cases (1992–2002), *J Am Vet Med Assoc* 225:1225, 2004.
71. Cuccouillo A, Lamb C: Cellular features of sonographic target lesions of the liver and spleen in 21 dogs and a cat, *Vet Radiol Ultrasound* 43:275, 2002.
72. Prause LC, Twedt DC: Hepatic nodular hyperplasia. In Bonagura JD, editor: *Current veterinary therapy XIII: small animal practice*, Philadelphia, 2000, Saunders, pp 675–676.
73. Stowater JL, Lamb CR, Schelling SH: Ultrasonographic features of canine hepatic nodular hyperplasia, *Vet Radiol Ultrasound* 31:268, 1990.

74. Ziegler LE, O'Brien RT, Waller KR, et al: Quantitative contrast harmonic ultrasound imaging of the normal canine liver, *Vet Radiol Ultrasound* 44:451, 2003.
75. O'Brien RT, Iani M, Matheson J, et al: Contrast harmonic ultrasound of spontaneous liver nodules in 32 dogs, *Vet Radiol Ultrasound* 45:547, 2004.
76. Ohlerth S, O'Brien RT: Contrast ultrasound: General principles and veterinary clinical applications, *Vet J* 174:501, 2007.
77. Jacobson LS, Kirberger RM, Nesbit JW: Hepatic ultrasonography and pathological findings in dogs with hepatocutaneous syndrome: new concepts, *J Vet Intern Med* 9:399, 1995.
78. Nyland TG, Barthez PY, Ortega TM, et al: Hepatic ultrasonography and pathologic findings in dogs with canine superficial necrolytic dermatitis, *Vet Radiol Ultrasound* 37:200, 1996.
79. Kimmel SE, Christiansen W, Byrne KP: Clinicopathological, ultrasonographic, and histopathological findings of superficial necrolytic dermatitis with hepatopathy in a cat, *J Am Anim Hosp Assoc* 39:23, 2003.
80. March PA, Hiller A, Weisbrode SE, et al: Superficial necrolytic dermatitis in 11 dogs with a history of phenobarbital administration (1995–2002), *J Vet Intern Med* 18:65, 2004.
81. Schwarz LA, Penninck DG, Léveillé-Webster C: Hepatic abscesses in 13 dogs: a review of the ultrasonographic findings, clinical data and therapeutic options, *Vet Radiol Ultrasound* 39:357, 1998.
82. Zatelli A, Bonfanti U, Zini E, et al: Percutaneous drainage and alcoholization of hepatic abscesses in five dogs and a cat, *J Am Anim Hosp Assoc* 41:34, 2005.
83. Nyland TG, Hager DA: Sonography of the liver, gallbladder, and spleen, *Vet Clin North Am Small Anim Pract* 15:1123, 1985.
84. Nyland TG, Hager DA, Herring DS: Sonography of the liver, gallbladder, and spleen, *Semin Vet Med Surg (Small Anim)* 4:13, 1989.
85. Nyland TG, Koblick PD, Tellyer SE: Ultrasonographic evaluation of biliary cystadenomas in cats, *Vet Radiol Ultrasound* 40:300, 1999.
86. Sonnenfield JM, Armbrust LJ, Radlinsky MA, et al: Radiographic and ultrasonographic findings of liver lobe torsion in a dog, *Vet Radiol Ultrasound* 42:344, 2001.
87. Hinkle Schwartz SG, Mitchell SL, Keating JH, et al: Liver lobe torsion in dogs: 13 cases (1995–2004), *J Am Vet Med Assoc* 228:242, 2006.
88. Besso JG, Wrigley RH, Gliatto JM, et al: Ultrasonographic appearance and clinical findings in 14 dogs with gallbladder mucocele, *Vet Radiol Ultrasound* 41:261, 2000.
89. Pike FS, Berg J, King NW, et al: Gallbladder mucocele in dogs: 30 cases (2000–2003), *J Am Vet Med Assoc* 224:1615, 2004.
90. Worley DR, Hottinger HA, Lawrence HJ: Surgical management of gallbladder mucoceles in dogs: 22 cases (1999–2003), *J Am Vet Med Assoc* 225:1418, 2004.
91. Walter R, Dunn ME, d'Anjou MA, et al: Nonsurgical resolution of gallbladder mucocele in two dogs. *J Am Vet Med Assoc* 232:1688, 2008.
92. Crews LJ, Feeney DA, Jessen CR, et al: Clinical, ultrasonographic, and laboratory findings associated with gall bladder disease and rupture in dogs: 45 cases (1997–2007), *J Am Vet Med Assoc* 234:359, 2009.
93. Nyland TG, Gillett NA: Sonographic evaluation of experimental bile duct ligation in the dog, *Vet Radiol* 23:252, 1982.
94. Fahie MA, Martin RA: Extrahepatic biliary tract obstruction: a retrospective study of 45 cases (1983–1993), *J Am Anim Hosp Assoc* 31:478, 1995.
95. D'Anjou MA, Penninck D, Cornejo L, et al: Ultrasonographic diagnosis of portosystemic shunting in dogs and cats, *Vet Radiol Ultrasound* 45:424, 2004.
96. Lamb CR: Ultrasonography of portosystemic shunts in dogs and cats, *Vet Clin North Am Small Anim Pract* 28:725, 1998.
97. Martin RA, Payne JT: Angiographic results of intrahepatic portocaval shunt attenuation in three dogs, *Semin Vet Med Surg (Small Animal Pract)* 5:134, 1990.
98. Lamb CR: Ultrasonographic diagnosis of congenital portosystemic shunts in dogs: results of a prospective study, *Vet Radiol Ultrasound* 37:281, 1996.
99. Lamb CR, White RN: Morphology of congenital intrahepatic portocaval shunts in dogs and cats, *Vet Rec* 142:55, 1998.
100. Holt DE, Schelling C, Saunders HM, et al: Correlation of ultrasonographic findings with surgical, portographic, and necropsy findings in dogs and cats with portosystemic shunts: 63 cases (1987–1993), *J Am Vet Med Assoc* 207:1190, 1995.
101. Salwei RM, O'Brien RT, Mathieson JS: Use of contrast harmonic ultrasound for the diagnosis of congenital portosystemic shunts in three dogs, *Vet Radiol Ultrasound* 44:301, 2003.
102. Neer TM: Clinical approach to splenomegaly in dogs and cats, *Compend Contin Educ Pract Vet Small Anim* 18:35, 1996.
103. Hanson JA, Papageorges M, Girard E, et al: Ultrasonographic appearance of splenic disease in 101 cats, *Vet Radiol Ultrasound* 42:441, 2001.
104. Spangler WL, Culbertson MR: Prevalence and type of splenic disease in cats: 455 cases (1985–1991), *J Am Vet Med Assoc* 201:773, 1992.
105. Konde LJ, Wrigley RH, Lebel JL, et al: Sonographic and radiographic changes associated with splenic torsion in the dog, *Vet Radiol* 30:41, 1989.
106. Stickle RL: Radiographic signs of isolated splenic torsion in dogs: eight cases (1980–1987), *J Am Vet Med Assoc* 194:103, 1989.
107. Patsikas MN, Rallis T, Kladakis SE, et al: Computed tomography diagnosis of isolated splenic torsion in a dog, *Vet Radiol Ultrasound* 42:235, 2001.
108. Wrigley RH, Konde LJ, Park RD, et al: Clinical features and diagnosis of splenic hematomas in dogs: 10 cases (1980–1987), *J Am Anim Hosp Assoc* 25:371, 1989.
109. Weinstein MJ, Carpenter JL, Mehlaff Schunk CJ: Nonangiogenic and nonlymphomatous sarcomas of the canine spleen: 57 cases (1975–1987), *J Am Vet Med Assoc* 195:784, 1989.
110. Spangler WL, Culbertson MR: Prevalence, type, and importance of splenic diseases in dogs: 1,480 cases (1985–1989), *J Am Vet Med Assoc* 200:829, 1992.
111. Nyland TG, Mattoon JS, Herrgesell ER, et al: The spleen. In Nyland TG, Mattoon JS, editors: *Small animal diagnostic ultrasound*, Philadelphia, 2002, Saunders, pp 128–143.
112. Hecht S: Spleen. In Penninck D, d'Anjou MA, editors: *Atlas of small animal ultrasonography*, Ames, Ia., 2008, Blackwell, pp 263–280.
113. O'Brien RT, Waller KR, Osgood TL: Sonographic features of drug-induced splenic congestion, *Vet Radiol Ultrasound* 45:225, 2004.
114. Saunders HM, Neath PJ, Brockman DJ: B-mode and Doppler ultrasound imaging of the spleen with canine splenic torsion: a retrospective evaluation, *Vet Radiol Ultrasound* 39:349, 1998.

115. Mai W: The hilar perivenous hyperechoic triangle as a sign of acute splenic torsion in dogs, *Vet Radiol Ultrasound* 47:487, 2006.
116. Hardie EM, Vaden SL, Spaulding K, et al: Splenic infarction in 16 dogs: a retrospective study, *J Vet Intern Med* 9:141, 1995.
117. Schelling CG, Wortman JA, Saunders MH: Ultrasonic detection of splenic necrosis in the dog. Three case reports of splenic necrosis secondary to infarction, *Vet Radiol* 29:227, 1988.
118. Cruz-Arámbulo R, Wrigley R, Powers B: Sonographic features of histiocytic neoplasms in the canine abdomen, *Vet Radiol Ultrasound* 45:554, 2004.
119. Ramirez S, Douglass JP, Robertson ID: Ultrasonographic features of canine abdominal malignant histiocytosis, *Vet Radiol Ultrasound* 43:167, 2002.
120. Wrigley RH, Konde LJ, Park RD, et al: Ultrasonographic features of splenic lymphosarcoma in dogs: 12 cases (1980–1986), *J Am Vet Med Assoc* 193:1565, 1988.
121. Hanson JA, Penninck DG: Ultrasonographic evaluation of a traumatic splenic hematoma and literature review, *Vet Radiol Ultrasound* 35:463, 1994.
122. Wrigley RH, Park RD, Konde LJ, et al: Ultrasonographic features of splenic hemangiosarcoma in dogs: 18 cases (1980–1986), *J Am Vet Med Assoc* 192:1113, 1988.
123. Konde LJ, Lebel JL, Park RD, et al: Sonographic application in the diagnosis of intraabdominal abscess in the dog, *Vet Radiol* 27:151, 1986.
124. Walzer C, Hittmair K, Walzer-Wagner C: Ultrasonographic identification and characterization of splenic nodular lipomatosis or myelolipomas in cheetahs (*Acinonyx jubatus*), *Vet Radiol Ultrasound* 37:289, 1996.
125. Schwarz LA, Penninck D, Gliatto J: Ultrasound corner: canine splenic myelolipomas, *Vet Radiol Ultrasound* 42:347, 2001.

ELECTRONIC RESOURCES

Evolve

Additional information related to the content in Chapter 37 can be found on the companion Evolve website at http://evolve.elsevier.com/Thrall/vetrad/

- Chapter Quiz

CHAPTER • 38
The Kidneys and Ureters

Gabriela S. Seiler

Renal diseases are common in dogs and cats, and imaging is an integral part of the diagnostic workup of these patients. Multiple imaging modalities are available to evaluate the kidneys and ureters, and it is important to select the modality according to the clinical question. In this chapter, the indications, technique, and normal imaging findings, as well as the imaging appearance of diseases of the upper urinary tract, are reviewed.

NORMAL ANATOMY AND IMAGING PROCEDURES

Radiography

Indications

Radiographs are useful to identify changes in size, shape, and opacity of the kidneys and to identify associated retroperitoneal disease. Radiopaque nephroliths and ureteral calculi are identified readily. Radiographs should always be obtained if urinary tract obstruction is suspected because ureteral calculi can be difficult to detect ultrasonographically.[1] Also, survey radiographs should always be obtained if there is a history of trauma to the abdomen or pelvis with suspected involvement of the urinary tract or if a dorsal abdominal mass is suspected. Survey radiographs are an essential part of any abdominal radiographic procedure involving contrast medium.

Technique

Orthogonal radiographic projections are needed for a thorough evaluation of the abdomen. This was discussed in detail in Chapter 35. Right lateral radiographs provide more longitudinal separation between the right and left kidney.[2] Suspected ureteral calculi can be separated from gastrointestinal content by use of oblique projections or compression techniques. Feces may have to be eliminated, by means of fasting or an enema, before a radiographic study to evaluate the distal ureters fully.

Normal Imaging Findings

The kidneys are located in the retroperitoneal space and outlined by surrounding fat.

Canine kidneys are oval (Fig. 38-1). The cranial pole of the right kidney is often poorly visible because it abuts the caudate lobe of the liver. The right kidney is usually located at the level of the thirteenth rib. The left kidney is located more caudally, at the level of L1-L3, and is visible more consistently. The left kidney is also more mobile than the right, and it can be positioned relatively ventrally in animals with a large amount of retroperitoneal fat. On the ventrodorsal projection, the right kidney is often obscured by liver and other superimposed abdominal organs, whereas the left kidney is normally visible caudal to the gastric fundus and caudomedial to the proximal extremity of the spleen.

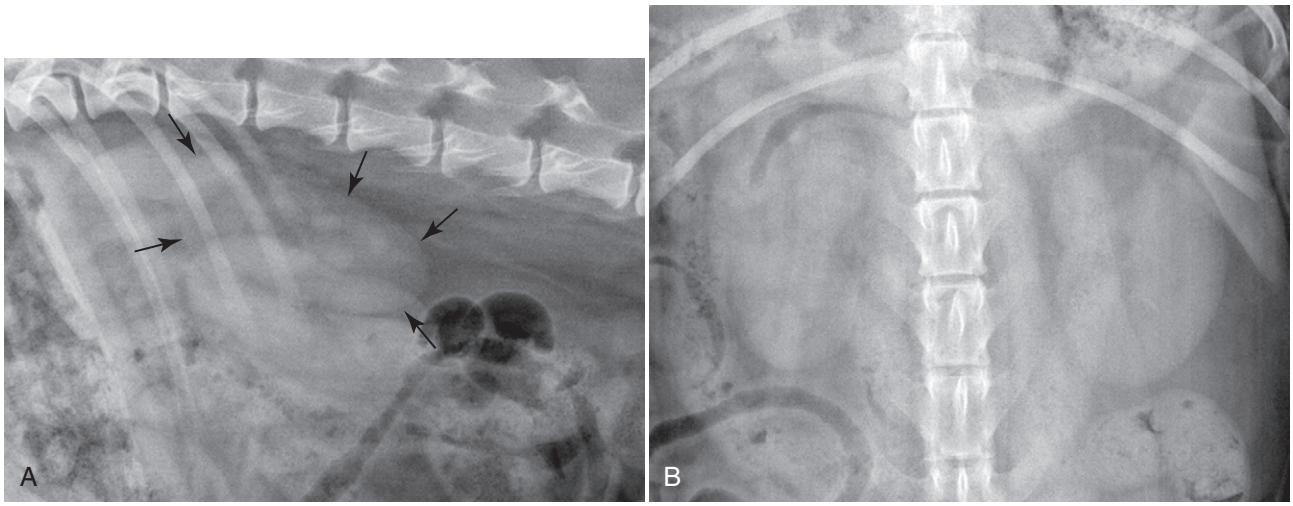


Fig. 38-1 Lateral **(A)** and ventrodorsal **(B)** radiographs of the abdomen of a normal dog. The kidneys are oval and outlined by retroperitoneal fat. The right kidney *(black arrows)* is more cranial and, in this dog, slightly more dorsal to the left kidney.

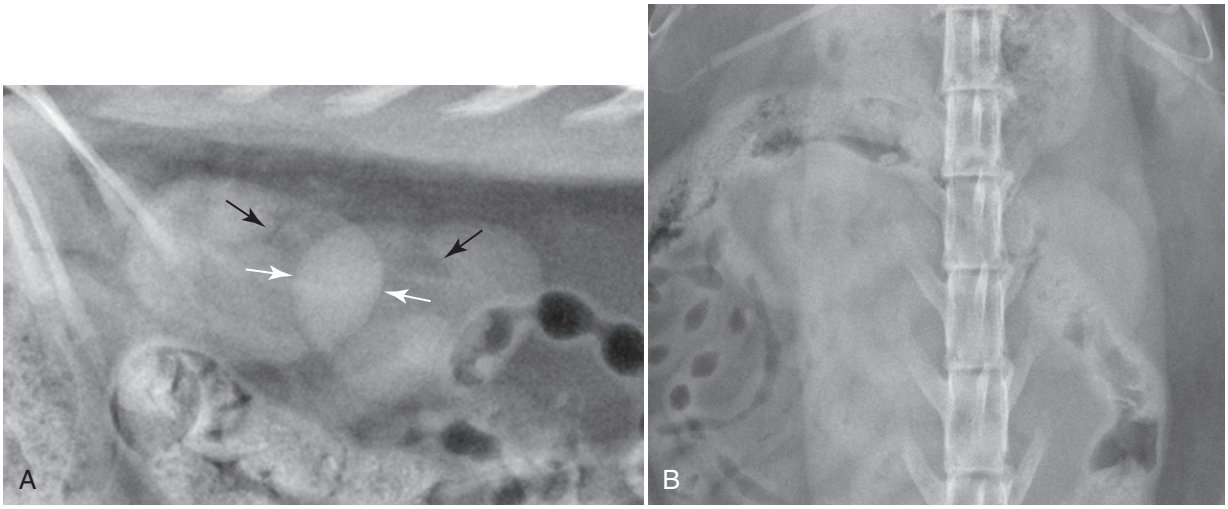


Fig. 38-2 Lateral **(A)** and ventrodorsal **(B)** radiographs of the abdomen of a normal cat. Both kidneys are round with a smooth surface. Fat opacity is visible at the renal hilus in the lateral view *(black arrows);* this is a normal finding in many cats. Note the summation opacity in the lateral view *(white arrows)* where the kidneys overlap. The right kidney is not readily perceptible in the ventrodorsal view because of superimposed bowel.

Feline kidneys are round or oval and are located typically between L1 and L4, either at the same level or with the right kidney in a more cranial position (Fig. 38-2). On lateral radiographs, the caudal pole of the right kidney may overlap the cranial pole of the left kidney and the summation of the two poles can give the false impression of a small rounded kidney or a retroperitoneal mass (Fig. 38-2, *A*). Normal feline kidneys often have a fat opacity at the renal hilus (see Fig. 38-2, *A*).

Ectopic kidneys in a very caudal location are reported sporadically.[3] Normal ureters are not visible radiographically.

Detecting a change in kidney size is helpful for classification of renal diseases into acute or chronic. In general, assessment of renal length is more reliable on ventrodorsal projections because there is no overlap of the kidneys, and magnification of both kidneys is equal. Normal renal length has been described in relationship to the length of the second lumbar vertebra. Renal length in normal dogs ranges between 2.5 and 3.5 times the length of L2.[4] In cats, the normal renal length has been measured to be 2.4 to 3.0 times the length of L2.[5] Older cats without signs of renal disease can have smaller kidneys (1.9 to 2.6 times the length of L2); however, it is difficult to know whether subclinical renal disease may have been present in these cats.[5-6] Hormonal influence depending on reproductive status alters renal length in cats, both in males and females. Intact cats tend to have larger kidneys (range 2.1 to 3.2 times the length of L2) than neutered cats (1.9 to 2.6 times the length of L2).[7] It is important to realize that these normal relationships were determined from a relatively small number of cats and are intended only to be guidelines.

Normal kidneys are of homogeneous soft tissue opacity, although fat deposition in the renal pelvis in cats can lead to focal central radiolucency (see Fig. 38-2, *A*). Mineralizations associated with the kidneys or ureters are always abnormal, although they may not necessarily be associated with clinical signs.

Excretory Urography

Indications

The use of excretory urography has decreased because of widespread availability of ultrasound. Suspected trauma to the kidney or ureters, however, is still an excellent indication for excretory urography. Other indications include hematuria, suspected ectopic ureters, or locating a kidney in the presence of a retroperitoneal mass.

Adverse reactions to intravenous administration of iodinated contrast medium, such as nausea, vomiting, hives, hypotension, and contrast-medium–induced renal failure are uncommon but do occur occasionally. Use of nonionic contrast medium leads to fewer complications because of the lower osmolarity.[8-9] Risk factors for contrast-medium–induced nephropathy include renal insufficiency and poor hydration status.[10-11] Contraindications for excretory urography, therefore, include anuric renal failure, dehydration, or hypotension and known hypersensitivity to iodinated contrast media.

Technique

Patient preparation is a key to obtaining a diagnostic excretory urogram. Food, but not water, should be withheld for at least 12 to 24 hours before the study. A cleansing enema can be used to evacuate the colon, preferably several hours before the study to allow fecal material and gas to pass. The patient should be hydrated and have adequate renal function. Because iodinated contrast medium leads to increased urine-specific gravity and may also inhibit bacterial growth for at least 24 hours, urinalysis should be performed before excretory urography.[12] Survey radiographs are always obtained before an excretory urogram to ensure correct radiographic technique and assess colon contents, but most important, small radiopaque calculi may be obscured by the contrast medium. Sedation or general anesthesia is recommended, and an intravenous catheter should be in place throughout the study to provide venous access if complications arise. Iodinated contrast medium is administered intravenously as a bolus injection at a dose of 600 to 700 mg iodine (I) per kg body weight.[13-14] Ventrodorsal and right lateral radiographs are acquired immediately after injection and are repeated typically after 5, 20, and 40 minutes or until a diagnosis is reached. Oblique projections for better visualization of the ureters can be added at 5 minutes and later time points. To evaluate the renal arteries, a ventrodorsal radiograph should be acquired 5 to 7 seconds after bolus injection of contrast medium.

Normal Imaging Findings

The renal arteries become opacified approximately 5 to 7 seconds after injection of a bolus of contrast medium. The

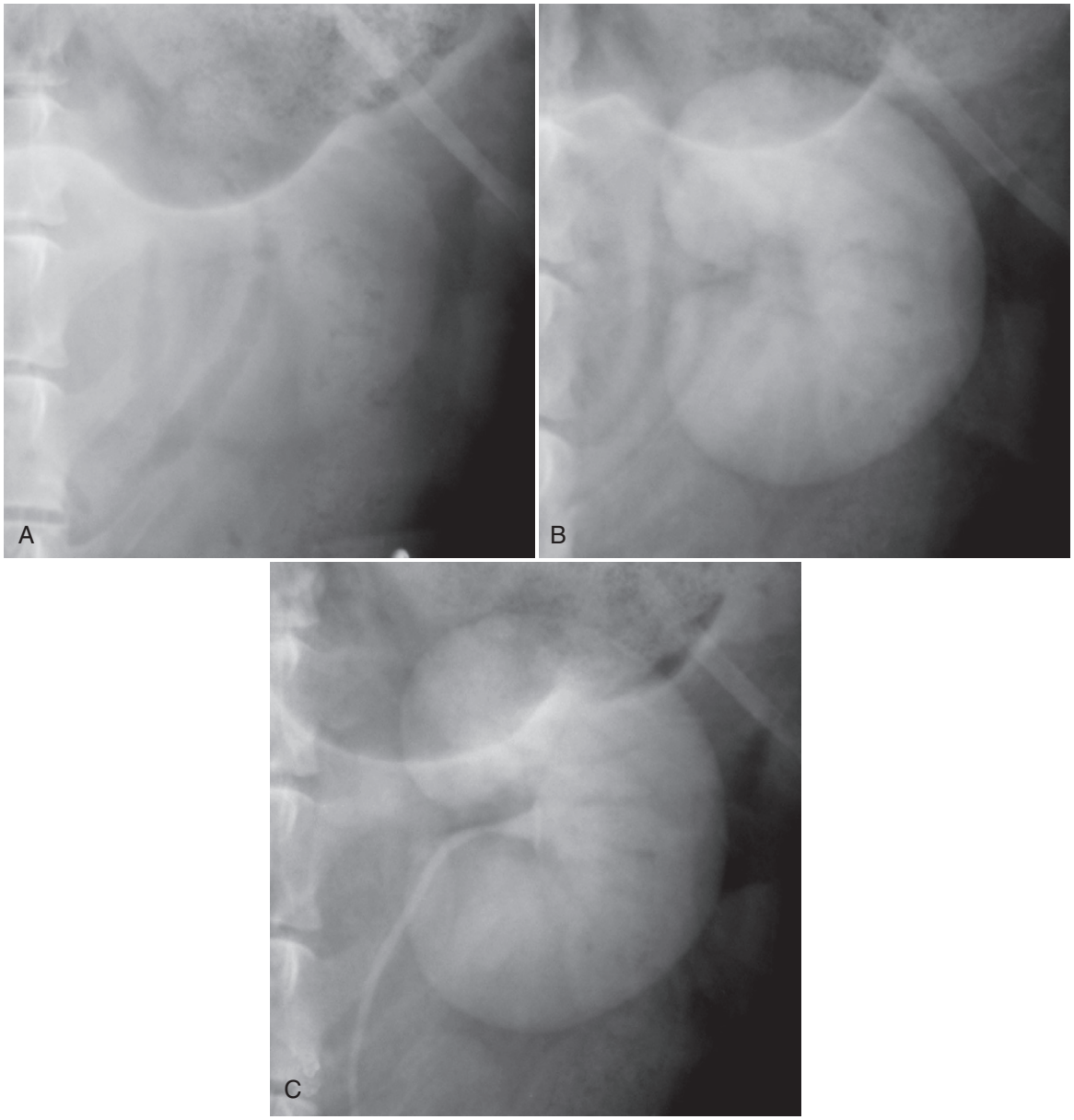


Fig. 38-3 Normal canine excretory urogram. The left kidney is shown before **(A),** 1 minute **(B),** and 5 minutes **(C)** after intravenous administration of iodinated contrast medium at a dose of 800 mg I/kg. In image **B,** the renal parenchyma is enhanced (nephrogram phase); in image **C,** contrast medium has reached the renal pelvis and proximal ureter (pyelogram phase).

excretory urogram can be divided into two phases: the nephrogram phase and pyelogram phase. In the nephrogram phase, contrast-medium arrival in the glomerular vessels and filtration into the nephron leads to uniform opacification of the renal parenchyma (Fig. 38-3, *B*). Initially, the cortex can be more opaque than the medulla. The nephrogram begins after approximately 10 seconds and lasts up to 2 minutes until the pyelogram phase starts and the nephrogram begins to fade. Nephrogram opacity should continue to decrease progressively; only approximately 25% of normal dogs still have a detectable nephrogram 2 hours after contrast medium injection.[15] In the pyelogram phase, contrast medium is concentrated in renal tubules as a result of reabsorption of water and excreted into the renal pelvis with its diverticula, and the ureters (Fig. 38-3, C). If renal function is normal, the collecting system is consistently more opaque than the renal parenchyma. The normal renal pelvis is curvilinear and less than 2 mm in width. The pelvic diverticula may be seen in some dogs and most cats and appear as thin (1 mm) spikes radiating from the pelvis toward the periphery. Neither the renal pelvis nor diverticula should have blunted, rounded edges. The ureters tend not to be filled with contrast medium uniformly throughout their length because of ureteral peristalsis. Radiographs, therefore, may have to be repeated to assess the entire length of the ureters. Normal ureters are not more than 2 to 3 mm in width. They terminate at the dorsal aspect of the bladder neck, where they curve cranially for a short distance before entering the wall. Duration and intensity of the opacification of the kidney during an excretory urogram depends on the dose of contrast medium administered; renal perfusion; glomerular filtration; tubular reabsorption of water; the patient's hydration status, which is important to maintain

adequate renal perfusion; and patency of the renal outflow tract.[14] Duration and degree of kidney opacification during an excretory urogram is an indication, although not very precise, of renal function and has to be monitored closely throughout the study, as described later under *renal function*.

Antegrade Ultrasound-Guided Pyelography

Indications

Ultrasound-guided injection of contrast medium into the renal pelvis leads to excellent opacification of the collecting system because the contrast medium is not diluted, and its presence in the collecting system is not dependent on renal function. This procedure can be performed in azotemic patients without loss of image quality. In addition, each renal pelvis and ureter can be assessed individually. Other advantages include the lack of systemic contrast-medium reactions, and collection of urine directly from the renal pelvis for urinalysis and microbiologic testing. The main indication for this procedure is suspected ureteral obstruction. Some degree of renal pelvis distention (at least 3-5mm) has to be present to perform the procedure. Contraindications include clotting disorders, as some hemorrhage may occur. Contrast medium may also leak into the retroperitoneal space.[16] Although this leakage is usually insignificant clinically, radiographic interpretation may be compromised. Loss of renal function secondary to the procedure is minimal but should be a consideration in patients with already severely compromised renal function.

Technique

Sedation or general anesthesia is necessary. The skin is prepared aseptically, and a 25-gauge needle connected with an extension set and three-way stopcock is introduced into the renal pelvis under ultrasound or fluoroscopic guidance. Depending on the size of the renal pelvis, 1 to 2 mL of urine is removed for laboratory testing. Ionic or nonionic iodinated contrast medium equivalent to half of the volume of urine removed is then introduced slowly, and the size of the renal pelvis is monitored with ultrasound or fluoroscopy.[16] Occasionally, replacement of the entire volume of urine removed is needed. Overdistention of the renal pelvis should be avoided because rupture may occur. Immediately after contrast-medium injection, ventrodorsal, oblique, and lateral abdominal radiographs are acquired. If bilateral abnormalities are suspected, the procedure can be repeated on the contralateral side.

Normal Imaging Findings

The renal pelvis becomes distended with mild blunting of the pelvic diverticula, as contrast medium is introduced under mild pressure. If the ureter is patent, contrast medium should appear in the urinary bladder almost immediately (Fig. 38-4). Narrowing of the ureter may be observed because of peristalsis.

Ultrasonography

Indications

Ultrasound is the method of choice to evaluate renal architecture and vascularity. Ultrasonographic evaluation of the renal parenchyma is indicated at the first sign of renal dysfunction. Although ultrasound findings are usually not disease-specific, it allows differentiating acute and chronic renal changes, mass lesions, cysts, mineralizations, and alterations of the collecting system and ureters. Needle aspirates or biopsies can be obtained under ultrasound guidance.[17-19] Renal ultrasound can be used as a screening tool for congenital renal disease such as aplasia, hypoplasia or dysplasia, and polycystic

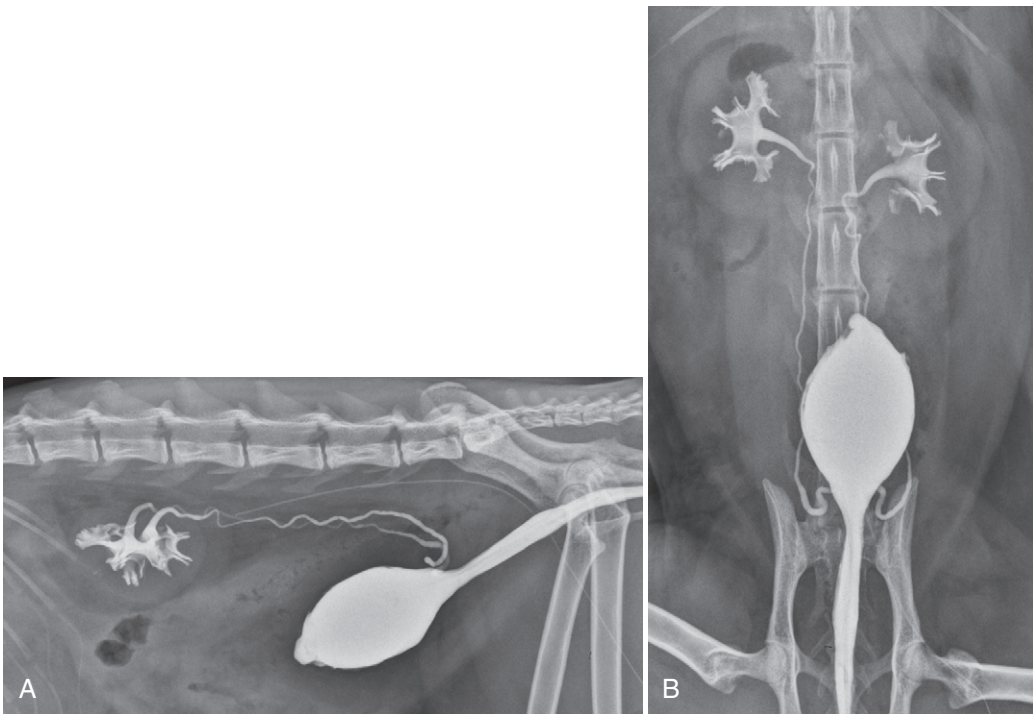


Fig. 38-4 Lateral **(A)** and ventrodorsal **(B)** radiographs of a cat after an ultrasound-guided antegrade pyelogram was performed in both kidneys. The renal pelvis is mildly dilated in both kidneys because of injection pressure. Both ureters are filled with contrast medium and terminate in the dorsal aspect of the bladder neck. Ureteral obstruction is not present. Note the curved appearance of the normal distal ureter. The apex of the urinary bladder is irregular because of polypoid cystitis. A central venous catheter is present in the caudal vena cava.

kidney disease.[3,20-22] Abnormal renal perfusion caused by infarction, transplant rejection, or mass lesions can be investigated using Doppler ultrasound.[23] Contrast-enhanced ultrasound of the canine and feline kidney has potential for delineation of renal parenchymal lesions such as masses or infarcts.[24-26]

Technique

The highest frequency transducer that manages to penetrate adequately should be chosen to image the kidneys. In smaller dogs and cats, 7.5 to 15 MHz is appropriate; 5 MHz or lower frequency transducers should be used only in large dogs. Subcostal or intercostal windows with the patient in sternal or dorsal recumbency allow access to the kidneys, depending on patient size and thoracic conformation. Standard image planes include dorsal (Fig. 38-5, *A*), sagittal (Fig. 38-5, *B*), and transverse (Fig. 38-5, C) views, always followed by fanning the transducer through the entire kidney. The renal pelvis is visible best in dorsal and transverse image planes. The ureters can be followed caudally from the renal pelvis if dilated. To verify patency and normal location of the ureterovesical junction, the bladder should be evaluated for presence of two urine jets from the dorsolateral bladder wall. If not seen with conventional grayscale imaging, Doppler ultrasound can be used to better delineate the jet. In some animals, administration of a diuretic is necessary to increase urine production and alter the specific gravity of the urine produced compared with the urine already present in the bladder; this will increase the frequency and visibility of a ureteral jet.

Normal Imaging Findings

Normal canine and feline kidneys are outlined smoothly by a thin hyperechoic capsule and have a clear distinction between cortex and medulla (see Fig. 38-5). The renal cortex in most patients is hypo- to isoechoic to the liver and spleen, although dogs and cats without evidence of renal disease may have a renal cortex that is hyperechoic to liver.[27] In cats, cortical hyperechogenicity can be seen in association with fat deposition.[28]

The normal medulla is very hypoechoic, creating a well-defined transition to the cortex. The interlobar vessels and pelvic diverticula give the renal medulla a lobulated appearance. The arcuate vessels are seen at the corticomedullary junction as short, hyperechoic parallel lines that may produce a distal shadow, not to be confused with renal mineralization. The renal pelvis is collapsed normally, but a smoothly margined, thin rim of fluid of up to 2 mm in diameter can be seen in normal animals, especially when using high-resolution

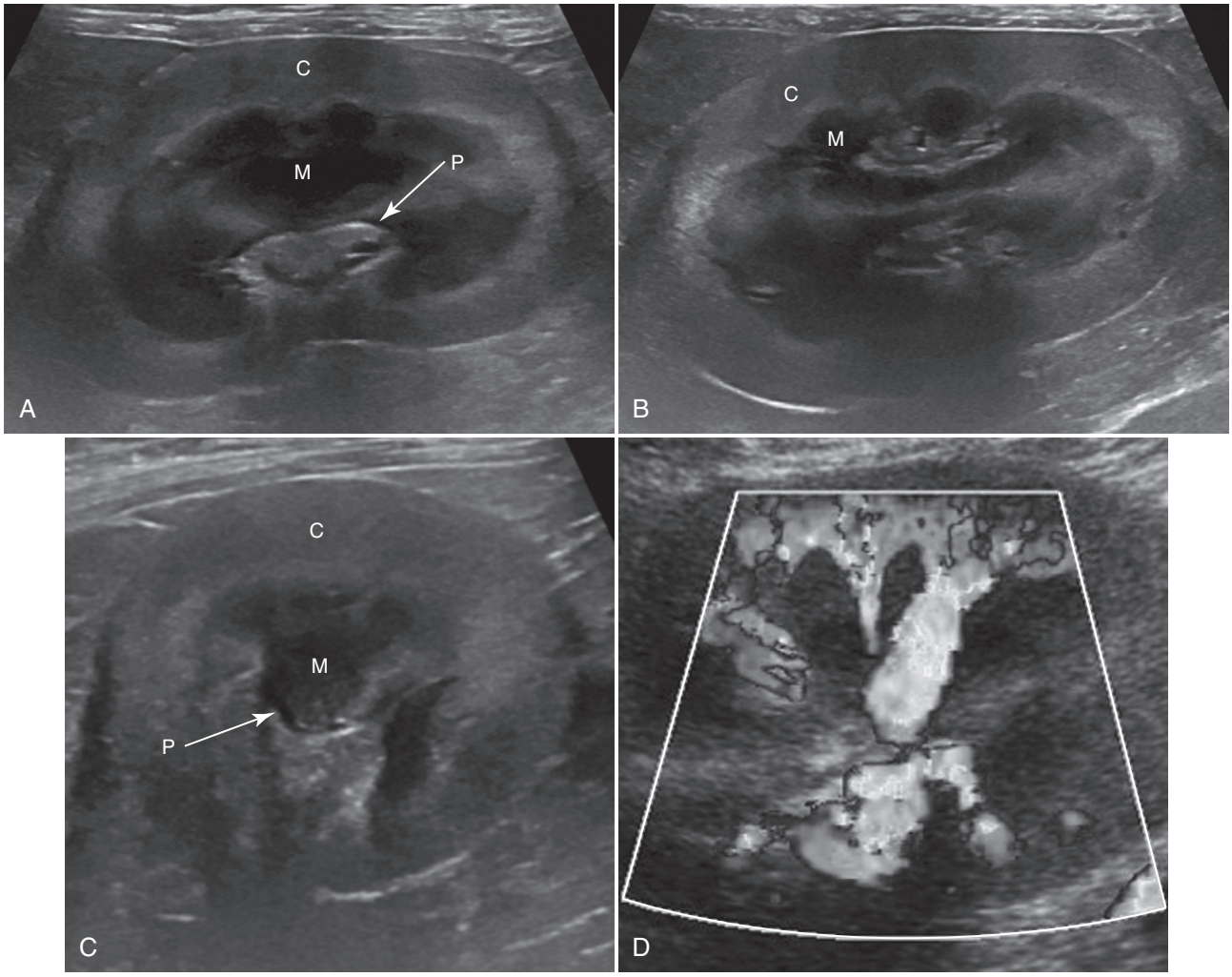


Fig. 38-5 Ultrasound images of a normal canine kidney in dorsal **(A),** sagittal **(B),** and transverse **(C)** planes. The renal vasculature is shown with color Doppler **(D).** The medulla *(M)* is hypoechoic relative to the cortex *(C)* and is divided by the hyperechoic interlobar vessels and pelvic diverticula. The renal pelvis *(P)* is mildly distended, best seen in transverse and dorsal planes *(white arrows)*.

transducers.[29] Increased diuresis, caused by exogenous fluid administration or polyuria/polydipsia, results in mild pyelectasia.[29] The pelvic diverticula are not visible normally. The renal pelvis is surrounded by the hyperechoic sinus, which contains dense fibrous tissue and fat, particularly in overweight cats.

Normal kidney size in cats ranges between 3.0 and 4.3 cm.[30-31] In dogs, size is much more variable depending on body weight and conformation. As a rule of thumb, 10 mm per 10 pounds can be added within the normal range of 3 to 10 cm.[32] A ratio of 5.5 to 9.1 of the maximal renal length to the luminal diameter of the aorta at the level of the kidney is proposed to take patient size into account.[33] Even using this method, the large range of normal values makes detection of subtle size changes challenging. Renal length, therefore, is not very helpful as an isolated criterion, unless markedly abnormal and all other ultrasonographic findings have to be taken into account to determine if a kidney is normal or not.

With Doppler ultrasound, the renal artery and vein, interlobar, arcuate, and interlobular vessels can be identified (Fig. 38-5, *D*). The resistive index should be less than 0.72 in dogs and 0.70 in cats, and the pulsatility index less than 1.52 in dogs and 1.29 in cats.[34] Normal ureters are visible only with high-resolution imaging systems, and ideal patient-related conditions. Ureters are best followed from a transverse view of the renal pelvis, as they turn medially and can be tortuous until they extend caudally, lateral to the aorta and caudal vena cava. Thin hyperechoic walls and occasional waves of peristalsis with a small bolus of fluid passing through can be seen in a normal ureter.

Computed Tomography

Indications

Computed tomography (CT) is being used with more frequency for renal imaging. Indications are essentially the same as for an excretory urogram, but CT has the advantage that the entire urinary tract can be imaged without superimposition of any other structure. A reduced dose of contrast medium (400 mg I/kg body weight) results in adequate image quality, which could be advantageous in patients with compromised renal function.[35-36] Multiplanar and 3D reconstructions add valuable information. Additionally, it is possible to calculate glomerular filtration rate using contrast-enhanced CT imaging.[37] As with excretory urography, limitations include the need for anesthesia or sedation and the need for intravenous contrast-medium administration.

Technique

Imaging protocols always include a precontrast image series to identify presence of mineralization in the renal parenchyma or collecting system because mineralization cannot be differentiated from the hyperattenuating contrast medium. In most patients, intravenous contrast medium has to be administered (400 to 800 mg I/kg body weight) to outline renal parenchymal lesions and filling defects in the collecting system. The renal parenchyma is enhanced immediately after contrast-medium administration. Optimal ureteral opacification occurs 3 minutes post injection[35]; however, image series may have to repeated several times to visualize the entire course of both ureters because of ureteral peristalsis. Ureteral opacification persists for about 1 hour.[35] Patient positioning in sternal recumbency with the pelvis elevated is helpful in outlining the ureterovesical junctions because the contrast medium will accumulate in the bladder apex away from the neck, facilitating the distinction between the contrast-medium–filled ureters and the bladder neck (Fig. 38-6). Filling the bladder with carbon dioxide increases the contrast between the bladder and ureters further; however, the balloon of the Foley catheter may distort anatomy and impair visibility of the ureteral openings. Dual-phase renal angiography can be performed to assess

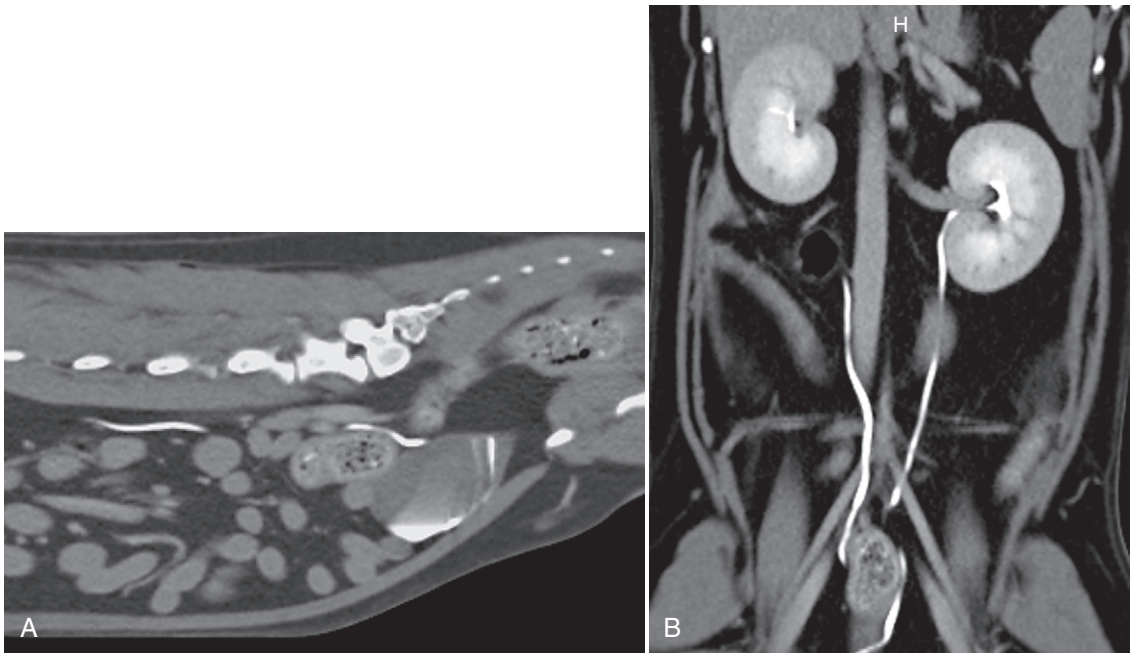


Fig. 38-6 Sagittal **(A)** and dorsal **(B)** CT images of a dog with a normal urinary tract. Intravenous contrast medium was administered, and the abdomen imaged after a 3-minute delay. Contrast medium is concentrated in the renal pelvis and ureters, and, in the sagittal view, streaks of contrast medium are seen in the bladder neck, extending from the two ureteral papillae along the bladder wall to the cranioventral pool of contrast medium. The pelvis of the dog is elevated to facilitate accumulation of contrast medium away from the bladder neck.

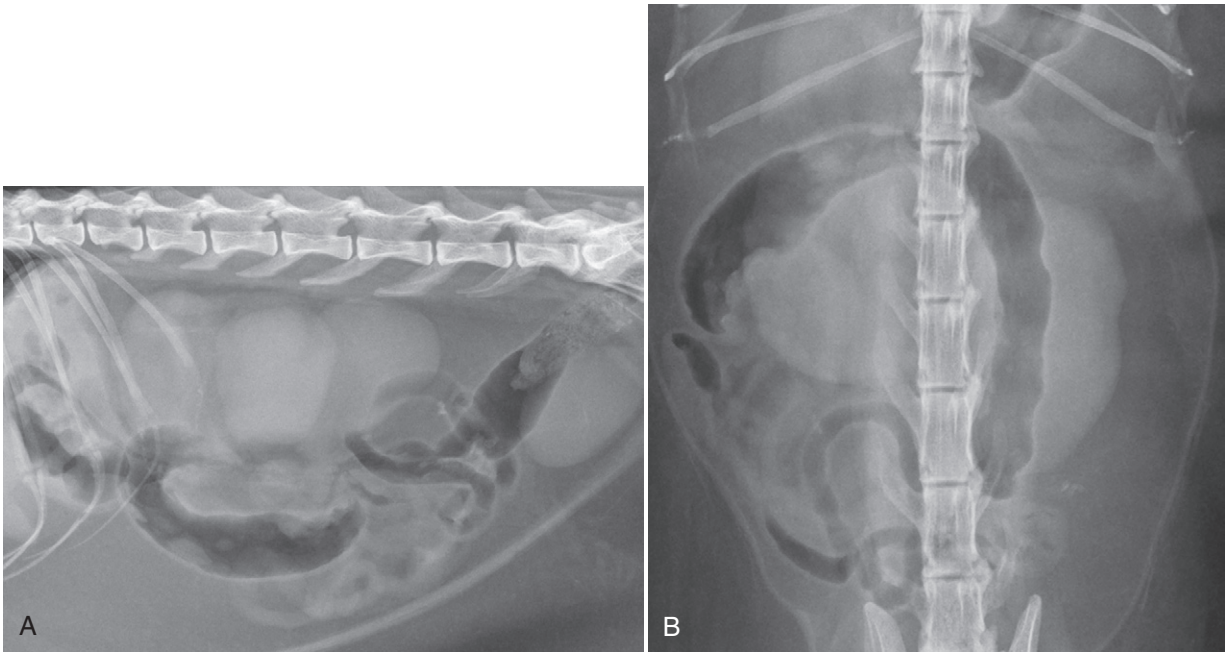


Fig. 38-7 Left lateral **(A)** and ventrodorsal **(B)** radiographs of the abdomen of a cat with bilateral renomegaly caused by renal lymphoma. Both kidneys are large and have undulating margins. The gastrointestinal tract is displaced ventrally.

the arterial and venous blood supply of the kidneys separately. This is used mainly for presurgical assessment of feline kidney donors.[38-39]

Normal Imaging Findings

Normal kidneys are soft tissue attenuating, except for a small amount of fat surrounding the renal pelvis. Uniform contrast enhancement is expected, followed by concentration of the contrast medium in the renal pelvis and diverticula, ureters, and urinary bladder (see Fig. 38-6).

Magnetic Resonance Imaging

Magnetic resonance imaging is used in people to assess renal diseases, perfusion, and function, but little work has been performed in small animals. Advantages and indications are similar to those described for CT, but use has so far been limited by cost, availability, and duration of the imaging studies. Protocols for magnetic resonance angiography of the renal vasculature in renal transplant donors are available.[40]

Scintigraphy

Compared with other renal function testing, renal scintigraphy using technetium-99m diethylenetriamine pentaacetic acid has the advantage of being able to determine the relative contribution of each kidney to total renal function. This is especially important in patients with impaired renal function before planned nephrectomy. To describe the technique of renal scintigraphy in detail is beyond the scope of this chapter, and readers are referred to the literature.[41]

RENAL DISEASES

Abnormal Renal Size

It is important to keep in mind that renal size and shape may be normal in the presence of renal disease. Especially acute toxic, inflammatory, or infectious nephropathies, as well as amyloidosis, do not always lead to alteration of renal size or shape.[42]

Large Kidneys

Renomegaly leads to a mass effect in the retroperitoneal space, evidenced by ventral displacement of the gastrointestinal tract and other organs (Fig. 38-7). Left renal enlargement leads to ventral or lateral displacement of the descending colon and small intestines (Fig. 38-8), whereas right renomegaly is associated with ventral displacement of the ascending colon and duodenum (Fig. 38-9). Differential diagnoses for renomegaly are subdivided based on presence of unilateral versus bilateral enlargement and alterations in margination and are listed in Table 38-1.[43] Contrast procedures (excretory urography or CT), as well as ultrasound, have to be used to determine if the renal enlargement is caused by parenchymal disease or by dilation of the collecting system or renal capsule. Ultrasound is currently the method of choice to evaluate an enlarged kidney; detailed findings are described later.

Small Kidneys

Smoothly margined small kidneys may be seen with congenital renal hypoplasia or dysplasia, amyloidosis, and occasionally with chronic renal disease.[20] Typically, cortical infarctions are present in chronic renal disease, leading to an irregular cortical margin (Fig. 38-10).

Abnormal Renal Structure

Diffuse Parenchymal Abnormalities

Renal structure is evaluated best with ultrasound. As stated above, normal renal size and structure do not rule out the presence of renal disease. In fact, it is common for patients with acute kidney injury and glomerulonephritis to have normal appearing kidneys on ultrasound.[44-45] Because of the large variability in normal renal size, architecture, and echogenicity, subtle changes in renal structure are not always detected. Increased renal echogenicity is the most common

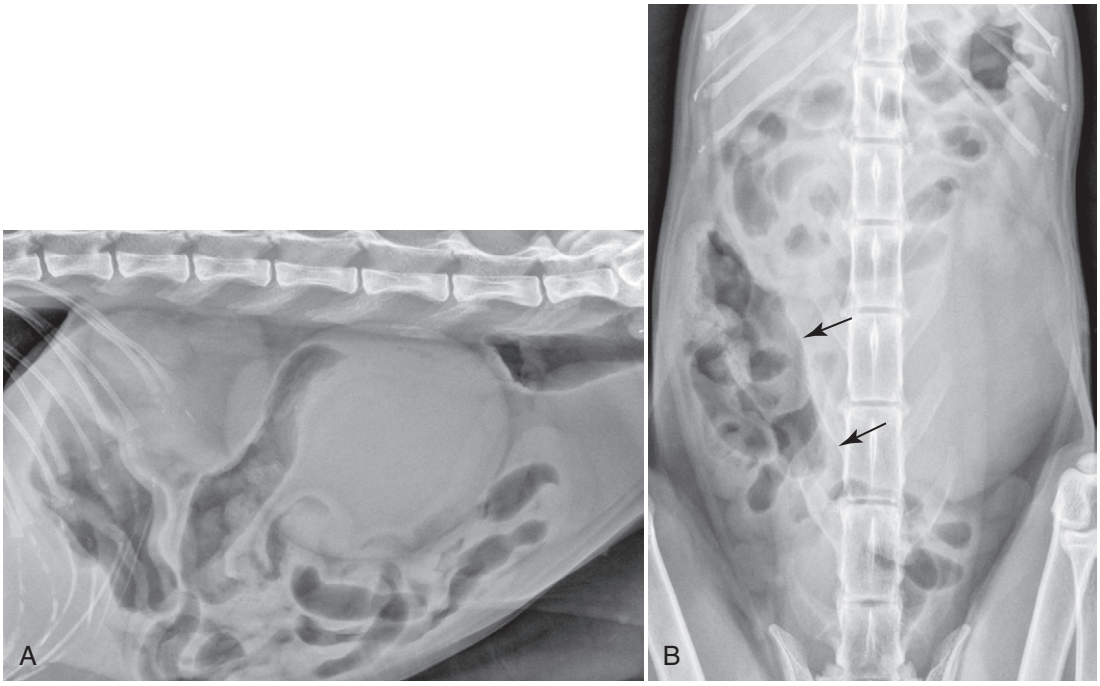


Fig. 38-8 Lateral **(A)** and ventrodorsal **(B)** abdominal radiographs of a cat with left renal enlargement. The enlarged kidney displaces the small intestines ventrally and the descending colon *(black arrows)* to the right **(B).**

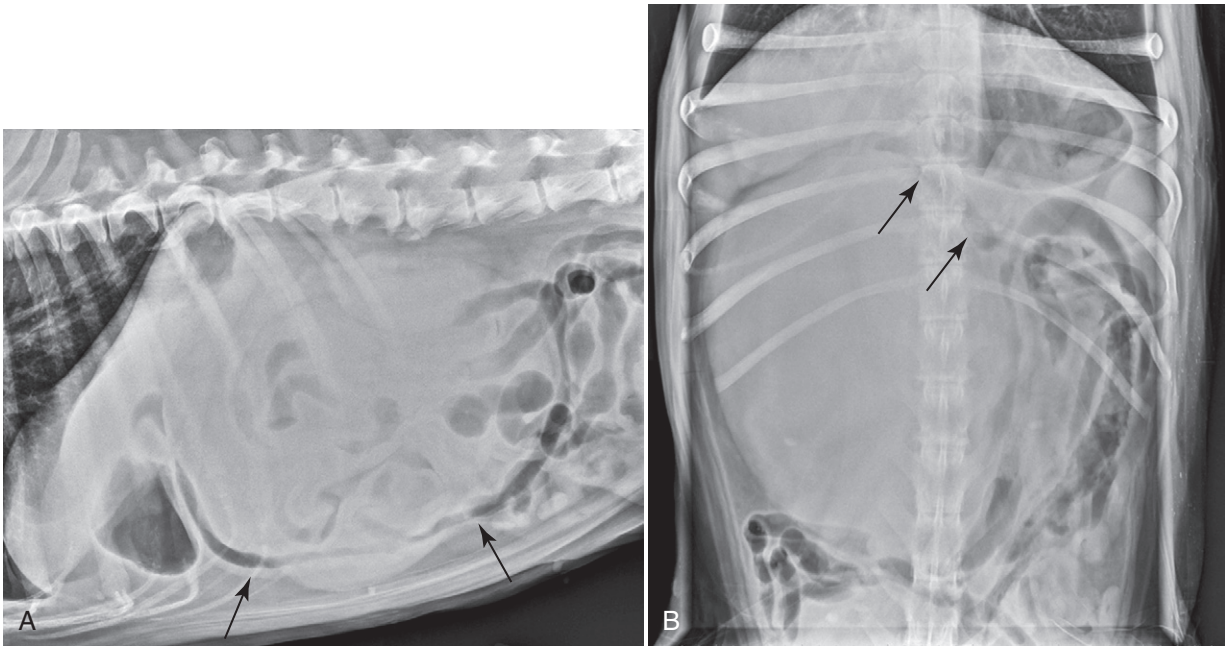


Fig. 38-9 Lateral **(A)** and ventrodorsal **(B)** abdominal radiographs of a dog with right renal carcinoma. The right kidney is severely enlarged, and displaces the duodenum *(black arrows)* ventrally **(A)** and to the left **(B).**

ultrasonographic abnormality and is observed with both acute and chronic nephropathy. Ultrasonographic findings associated with acute kidney injury leading to acute tubular nephrosis or necrosis, interstitial nephritis or glomerulonephritis include renal enlargement, subcapsular or perirenal effusion, and cortical hyperechogenicity. In severe or advanced disease the medullary echogenicity increases as well, leading to reduced corticomedullary distinction. Acute kidney injury in dogs and cats has many causes, including toxins (ethylene glycol, lily in cats, and grapes in dogs), bacterial, protozoal, and rickettsial infections (leptospirosis, babesiosis, Lyme disease, pyelonephritis) drugs, hypercalcemia, sepsis, ischemia, multiple organ dysfunction syndrome, pancreatitis, and hyperviscosity.[46] It is usually not possible to determine the cause of acute kidney injury by ultrasound, and biopsy may be needed. The Doppler examination of renal vasculature with calculation of the resistive index may add some information. For example, elevation of the renal resistive index is seen with

Table • **38-1**

Differential Diagnoses for Changes in Renal Size and Shape

BILATERAL	UNILATERAL
MILDLY ENLARGED KIDNEY, SMOOTH OUTLINE	
• Acute kidney injury • Acute pyelonephritis • Congenital portosystemic shunts • Amyloidosis • Acromegaly	• Compensatory hypertrophy • Renal neoplasia (except lymphoma) • Subcapsular abscess or hemorrhage
MARKEDLY ENLARGED KIDNEY, SMOOTH OUTLINE	
• Hydronephrosis • Renal lymphoma • Feline infectious peritonitis • Feline perinephric pseudocysts	• Hydronephrosis • Renal tumor • Subcapsular hematoma or abscess • Cats: perinephric pseudocyst
ENLARGED KIDNEY, IRREGULAR OUTLINE	
• Metastatic neoplasia • Polycystic kidney disease • Feline infectious peritonitis	• Primary renal tumor • Metastatic neoplasia • Renal abscess • Renal hematoma • Renal granuloma • Renal cysts
SMALL KIDNEY, SMOOTH OR IRREGULAR IN OUTLINE	
• Chronic renal disease • Developmental hypoplasia or dysplasia	• Chronic renal disease • Atrophy secondary to obstruction

active tubulointerstitial or vascular disease; however, it remains a nonspecific parameter.[47] Ethylene glycol toxicity leads to the most dramatic increase in cortical and medullary echogenicity with a hypoechoic rim at the corticomedullary junction and hypoechoic central medullary regions (Fig. 38-11). The increased echogenicity is attributed to deposition of calcium oxalate crystals in the kidneys.[48-49]

Renal lymphoma tends to occur bilaterally and causes enlarged, irregularly shaped kidneys with a hyperechoic cortex. Focal or multifocal nodules and masses have also been reported.[50-51] A subcapsular, hypoechoic rim is associated with renal lymphoma in cats, with a positive predictive value of 80.9% and a negative predictive value or 66.7%.[52] The subcapsular thickening is thought to represent regional subcapsular infiltrate with lymphoma rather than fluid (Fig. 38-12).[52]

A hyperechoic medullary rim parallel to the corticomedullary junction is observed commonly. It can be seen with mineralization, necrosis, and hemorrhage associated with many different disease processes, including acute tubular necrosis, leptospirosis, pyogranulomatous vasculitis in cats with feline infectious peritonitis, and in hypercalcemic nephropathy (Fig. 38-13).[53-57] Hypercalcemic nephropathy is characterized by variable degrees of calcification and necrosis of renal tubules and collecting ducts. The corticomedullary rim corresponds to increased calcium deposits at this site.[54] However, a corticomedullary rim is a nonspecific finding that is also seen commonly in clinically normal dogs and cats.[55]

Poor corticomedullary definition caused by cortical and medullary hyperechogenicity is one of the changes associated with chronic renal disease, together with small renal size, cortical infarcts and cysts, and parenchymal mineralizations (Fig. 38-14). Parenchymal atrophy, infarction and fibrosis can result in distortion of the shape of the renal pelvis. Infarcts appear as wedge-shaped, hyperechoic areas in the cortex with an associated cortical defect and reduced blood flow on Doppler investigation. The type of underlying renal disease cannot usually be determined at this stage. Renal dysplasia is usually diagnosed late in the disease process when chronic interstitial fibrosis is present; at this point the changes in the kidneys resemble those from any other chronic renal disease.[58] Ultrasound findings in Cairn terriers with preclinical renal dysplasia include poor corticomedullary definition, medullary hyperechogenicity, and punctuate medullary hyperechogenicities.[20]

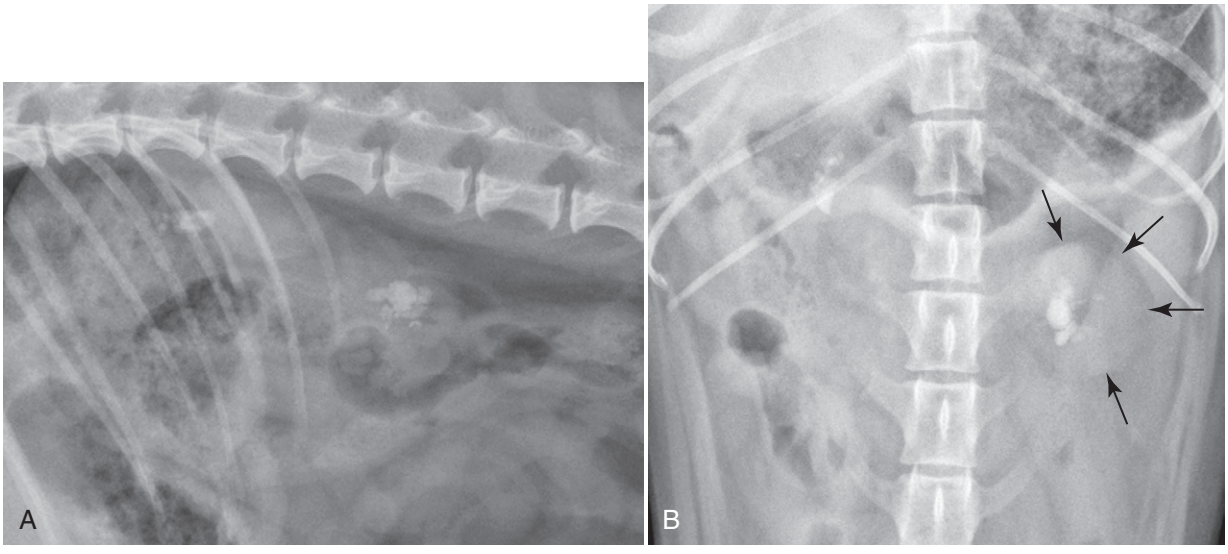


Fig. 38-10 Left lateral **(A)** and ventrodorsal **(B)** radiographs of a dog with chronic renal disease. Both kidneys are very small, rounded, and irregular and contain multiple nephroliths. *Black arrows,* left kidney.



Fig. 38-11 Ultrasound image of the right kidney of a dog that ingested ethylene glycol the night before. The renal cortex and medulla are extremely hyperechoic; a thin hypoechoic rim delineates the corticomedullary junction.

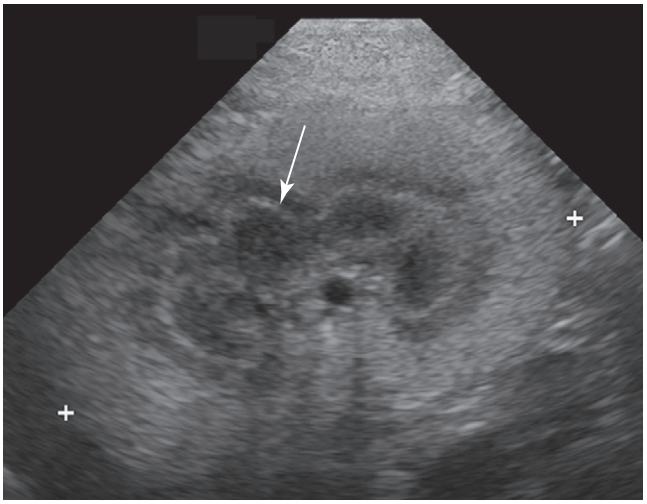


Fig. 38-13 Ultrasound image of a dog with leptospirosis. The kidney is enlarged, and the renal cortex is hyperechoic. A thin hyperechoic band is present parallel to the corticomedullary junction *(white arrow)*.

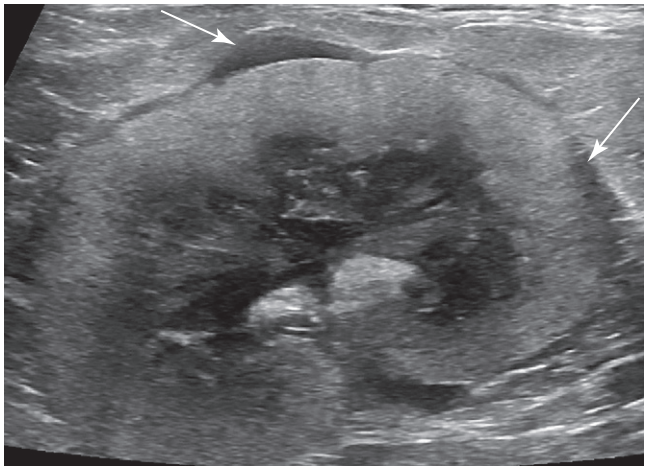


Fig. 38-12 Long-axis ultrasound image of the kidney of a cat with renal lymphoma. The kidney is enlarged, irregular in shape, and has a hyperechoic cortex. A hypoechoic subcapsular thickening is seen surrounding the kidney *(white arrows)*.

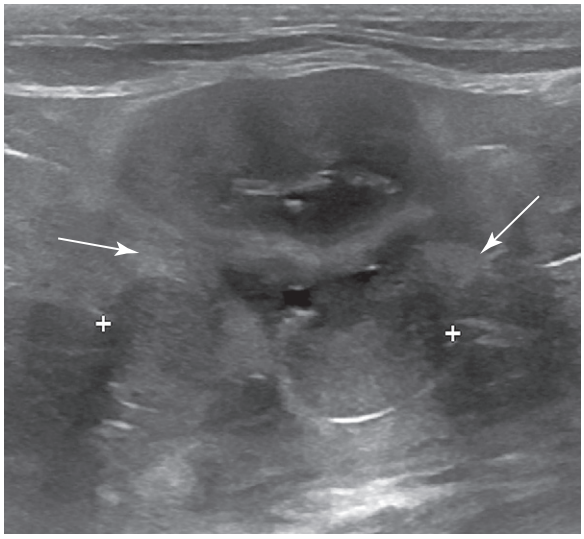


Fig. 38-14 Ultrasound image of chronic renal disease in a cat. The kidney is small (2.5-cm length), rounded, and irregular with multiple wedge-shaped hyperechoic cortical indentations consistent with chronic infarction *(white arrows)* and mild pyelectasia. The cortex and medulla cannot be distinguished from each other.

Focal or Multifocal Abnormalities

Renal Mineralization. Renal mineralization, because of nephrolithiasis or dystrophic mineralization, is common, especially in older patients. All types of nephroliths are detectable ultrasonographically and are characterized by a very echogenic surface and a distal acoustic shadow. Calculi in the renal pelvis may lead to obstruction either directly in the renal pelvis or if they move into the ureter. Dystrophic mineralization in the renal parenchyma by itself is of questionable clinical significance but is often accompanied by other chronic renal changes. Nephrocalcinosis tends to occur along the pelvic diverticula to form linear hyperechoic striations with a distal acoustic shadow (Fig. 38-15). It is not always possible to differentiate dystrophic mineralization from small nephroliths in the pelvic diverticula. Diffuse cortical or medullary foci of mineralizations are often not detected radiographically but appear as punctate hyperechogenicities on ultrasound.

Renal Cysts. Radiographic changes are seen only if cysts lead to kidney enlargement or distortion of the renal capsule. Round filling defects may be seen in the nephrogram phase of an excretory urogram or CT, although nodules or masses could have the same appearance. Ultrasonographically, renal cysts are identified readily as anechoic round structures with distal acoustic enhancement and a thin-edge artifact (Fig. 38-16).[21] The anechoic cystic content is more easily distinguished from the hypoechoic renal medulla or solid renal nodules when temporarily increasing the gain settings. Internal echoes caused by hemorrhage or cellular debris may be observed. Inherited polycystic kidney disease is seen in long-haired cats (autosomal dominant) and Cairn terriers (recessive mode of inheritance) and can be identified at a young age.[21,59] In severe instances where the renal parenchyma is replaced almost completely by the cysts, renal function may be impaired (Fig. 38-17). Cysts are usually located at the corticomedullary junction.[21] Solitary cysts occur in any feline and canine breed

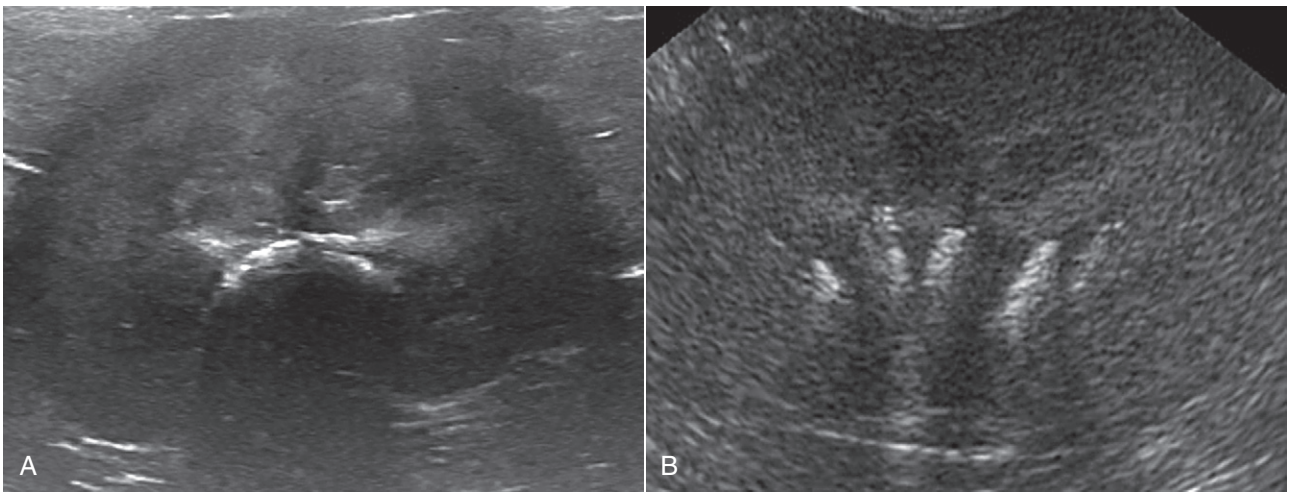


Fig. 38-15 Long-axis ultrasound images of two canine kidneys with mineralization. In image **A,** a curvilinear nephrolith is present in the renal pelvis, creating a distal shadow. In image **B,** the mineralization is dystrophic in nature and extends along the pelvic diverticula, creating a striated appearance.

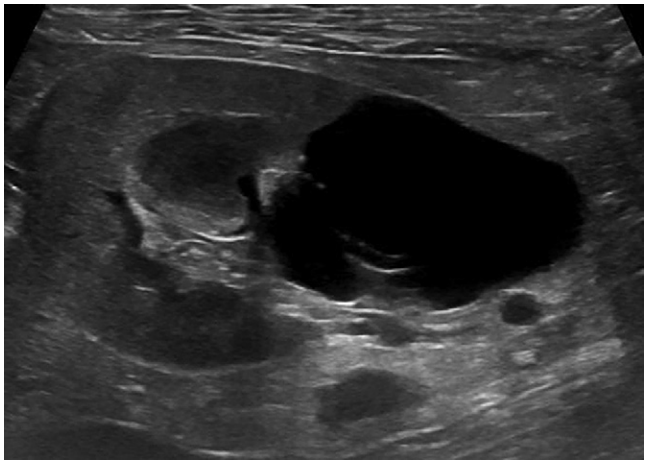


Fig. 38-16 Ultrasound image of a canine kidney with a very large cyst deforming the caudal cortex. The cyst is anechoic and leads to distal enhancement. There were no clinical signs associated with the cyst.

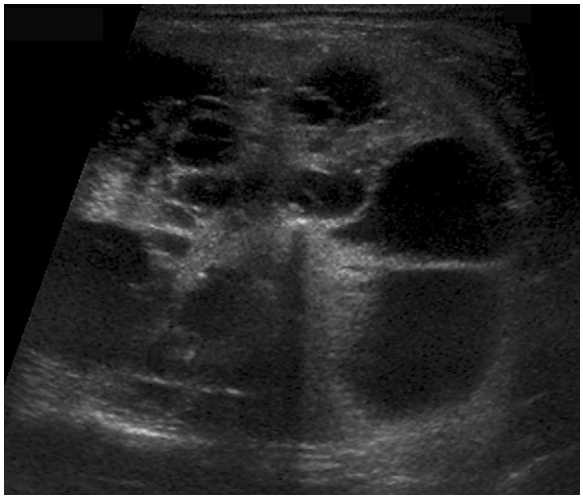


Fig. 38-17 Ultrasound image of the left kidney of a cat with polycystic kidney disease. The renal parenchyma is replaced by small and large anechoic cysts. A small focus of mineralization is present in the center of the kidney.

and are not clinically significant if the renal architecture is otherwise normal. Small cortical cysts are observed commonly in conjunction with chronic degenerative renal disease. Nodular dermatofibrosis in German shepherd dogs is associated with renal cystadenocarcinoma. Although predominantly cystic, these lesions have a masslike tissue component that infiltrates the renal parenchyma and may protrude into the cysts.[60] Other differential diagnoses for cystic lesions with a thick wall or a solid component include renal abscess or a cavitated, necrotic tumor.

Perirenal Fluid. Perirenal or subcapsular fluid may be the result of acute renal failure, urine leakage, ureteral obstruction, hemorrhage, abscessation, perirenal pseudocysts, and neoplasia. If the fluid is subcapsular, renomegaly is seen on radiographs. Excretory urography, ultrasound, or contrast-enhanced CT will be necessary to determine if enlargement is caused by perirenal rather than renal disease. Fluid buildup outside the renal capsule leads to an increased opacity of the retroperitoneal space with a mottled or streaked appearance and loss of the outline of the kidneys and enlargement of the retroperitoneal space (see Chapter 36). Extracapsular fluid is characterized sonographically by triangular fluid accumulations adjacent to the kidney, predominantly on the dorsal aspect. Even in absence of urinary tract rupture, large amounts of perirenal fluid can accumulate with acute renal failure.[61] Proposed mechanisms for the fluid accumulation include tubular back-leak of an ultrafiltrate into the renal interstitial space in excess of what the lymphatics can drain, either because of increased tubular permeability or obstructive disease.[61] Focal inflammation of the retroperitoneal fat resulting in an increased echogenicity may be seen with renal abscessation and pyelonephritis (Fig. 38-18). A large amount of uni- or bilateral subcapsular fluid is a characteristic of perinephric pseudocyst, primarily seen in older cats.[62-63] Pseudocyst formation is caused by a transudate and has been associated with underlying renal parenchymal disease

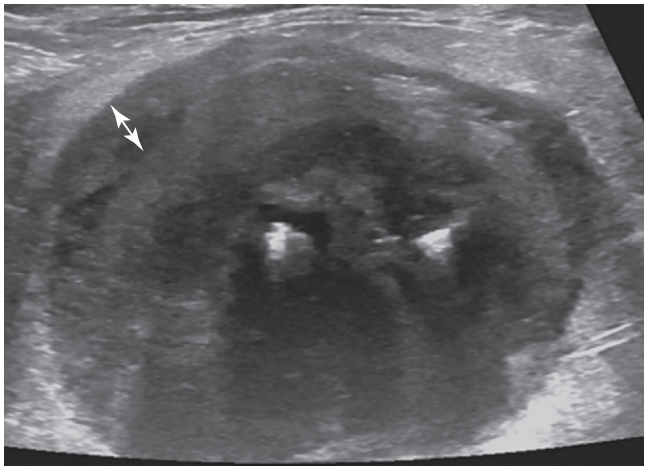


Fig. 38-18 Ultrasound image of the right kidney of a cat with severe pyelonephritis, abscess formation, and subsequent rupture of the renal pelvis. A thick rim of echogenic fluid surrounds the kidney *(white double arrow)*; the adjacent retroperitoneal fat is hyperechoic. Two mineralizations are present in the diverticula of the renal pelvis.



Fig. 38-20 Postcontrast sagittal CT image of the right kidney of a dog with a nephroblastoma. The cranial pole of the kidney becomes opacified with contrast medium and still resembles the original kidney, but the caudal portion is replaced by a large, heterogeneously contrast-enhancing mass.

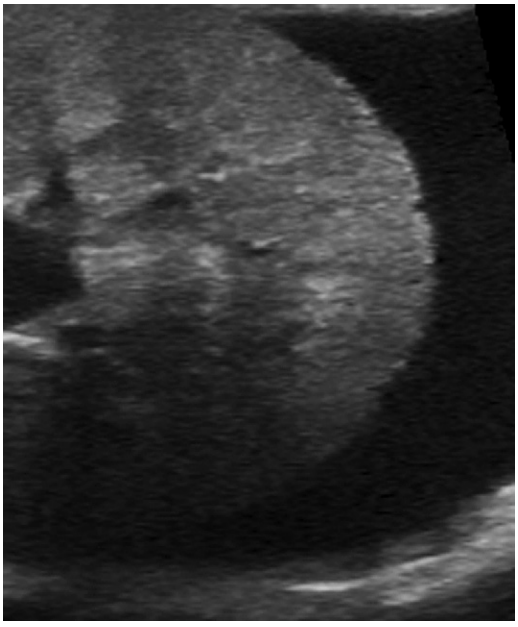


Fig. 38-19 Ultrasound image of the caudal pole of the left kidney of a cat with a perinephric pseudocyst. The structure of the kidney is abnormal with poor corticomedullary distinction, and there is a large amount of encapsulated anechoic perirenal fluid.

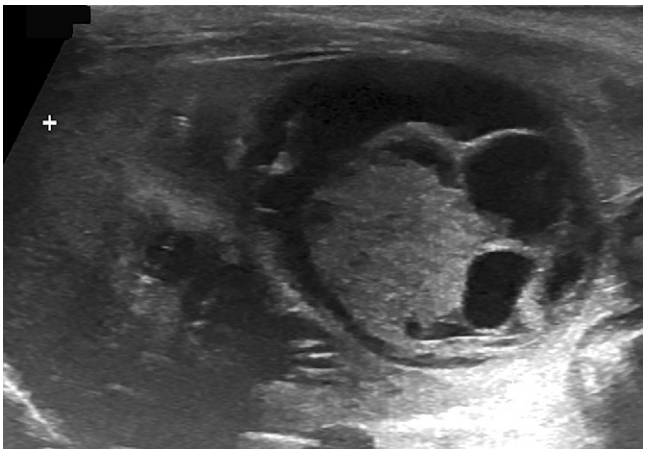


Fig. 38-21 Long-axis ultrasound image of the nephroblastoma in the dog in Figure 38-20. A complex, partially cavitated mass occupies the caudal pole of the kidney distorting the normal architecture. A small portion of residual renal tissue remains in the cranial pole (the cursor marks the cranial aspect of the cranial pole).

such as interstitial nephritis. The affected kidneys are often reduced in size and have signs of chronic renal disease (Fig. 38-19).[62]

Renal Mass Lesions. Renal mass lesions can be caused by hematoma, abscess, neoplasia, and granuloma. Primary renal tumors include renal adenocarcinoma, squamous cell carcinoma, papillary carcinoma, and nephroblastoma.[64] Other tumors that may affect the kidneys are histiocytic sarcoma, plasma cell tumor, metastatic carcinoma, hemangiosarcoma, and lymphosarcoma.[65] Larger masses can be identified radiographically as asymmetric renal enlargement. After contrast-medium administration (excretory urogram or CT), renal masses remain less opaque than the surrounding or contralateral renal parenchyma, because of lack of filtration and concentration of the contrast medium. Heterogeneous contrast enhancement within the mass may be seen if the mass is necrotic or cavitated (Fig. 38-20). There is a wide variability in the ultrasound appearance of renal tumors. Most primary renal tumors appear as complex, well-perfused masses obliterating the normal renal architecture (Fig. 38-21). Cavitated masses are seen typically with renal hemangiosarcoma. Round cell tumors, such as histiocytic sarcoma and lymphosarcoma, tend to be very hypoechoic.[66] Lymphosarcoma differs from the other types of tumor in that it is typically bilateral and especially in cats is often associated with hypoechoic subcapsular thickening (see Fig. 38-12).[52] However, focal or multifocal nodules have been described in dogs and cats with lymphosarcoma. An abscess typically has a liquid content surrounded by a thick capsule; occasionally, hyperechoic comet-tail speckles may be seen if gas is produced within the abscess.

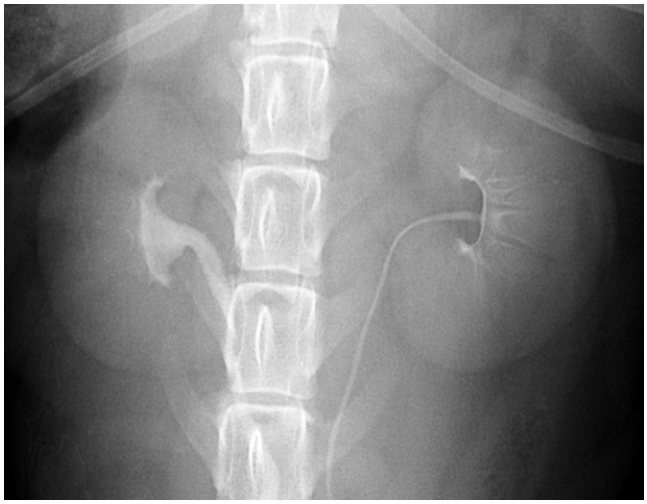


Fig. 38-22 Ventrodorsal image obtained 20 minutes after intravenous administration of iodinated contrast medium in a dog with pyelonephritis of the right kidney. The renal pelvis and proximal ureter are dilated on the right. The renal pelvis is distorted, and the pelvic diverticula are short and blunt compared with the contralateral normal left kidney.

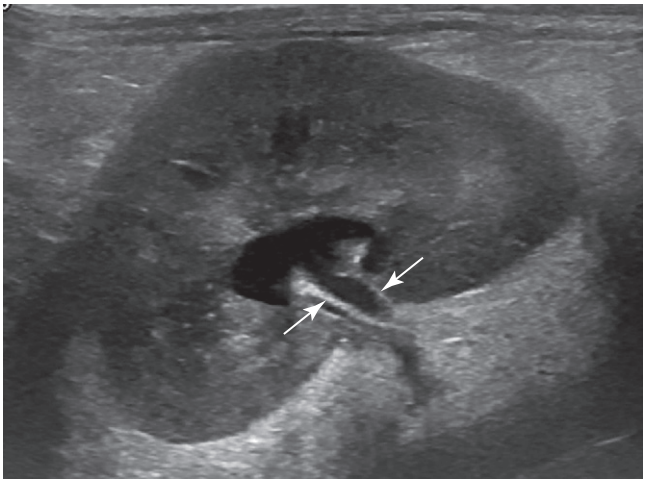


Fig. 38-23 Long-axis ultrasound image of the left kidney of a dog with acute pyelonephritis. The renal pelvis is dilated and distorted, and the pelvic diverticula are blunted. Note the hyperechoic lining of the proximal ureter *(white arrows)*, consistent with fibrotic change. The renal medulla is hyperechoic, resulting in poor corticomedullary definition. The retroperitoneal fat surrounding the kidney is very hyperechoic and inflamed.

The fluid is often very echogenic, and the cellular component tends to settle in the dependent portion.[67] Hematomas secondary to trauma or renal biopsy lead to disruption of the normal kidney structure with hypo- or hyperechoic areas within the parenchyma and/or subcapsular fluid accumulation. However, many inflammatory lesions such as solid abscesses, fungal granulomas, or pyogranulomas associated with feline infectious peritonitis can look very similar to neoplastic masses. Needle aspirates or biopsy is required for a definitive diagnosis.

Diseases of the Collecting System

Distention of the renal pelvis can be observed in dogs and cats with increased urine production caused by diuretic therapy or renal insufficiency, or it can be associated with congenital malformations of the ureters, such as ectopic ureter or ureterocele, infection, or lower urinary tract obstruction.[29]

Pyelonephritis

Acute pyelonephritis can lead to mild renal enlargement, whereas renal size is reduced in chronic pyelonephritis. Typically, there is mild to moderate pyelectasia.[68] The mean diameter of the renal pelvis with pyelonephritis was 3.6 mm in dogs and 4.0 mm in cats.[29] However, this range is quite wide, with overlap with other nonobstructive or obstructive renal diseases, and even with normal animals.[29] More important, the shape of the renal pelvis is usually distorted with infection, resulting in blunted and asymmetric pelvic diverticula, seen both on excretory urography and ultrasound (Figs. 38-22 and 38-23). Additionally, on ultrasound imaging, echogenic debris may be observed in the renal pelvis and proximal ureter rather than anechoic urine, and the renal pelvis may be surrounded by an echogenic rim caused by fibrotic change.[68-70] The echogenicity of the renal cortex may be uniformly or heterogeneously increased. In severe acute pyelonephritis, regional inflammation of the perirenal fat results in a hyperechoic rim around the kidney and proximal ureter (see Fig. 38-23), often with a small amount of retroperitoneal effusion. Thickening of the proximal ureteral wall and mild ureteral dilation without evidence of intraluminal obstruction are observed commonly. Chronic pyelonephritis is difficult to distinguish from other chronic renal diseases because it is characterized by small, irregularly shaped kidneys with mild pyelectasia.[68]

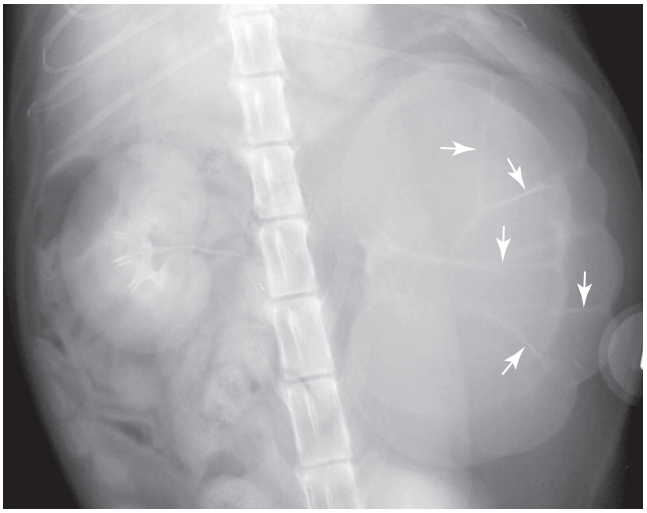


Fig. 38-24 Excretory urogram of a cat with severe left hydronephrosis. Contrast enhancement is seen only in the left kidney along the elongated renal vasculature *(white arrows)* and has not accumulated in the renal pelvis.

Hydronephrosis

Hydronephrosis is distention of the renal pelvis caused by urinary tract obstruction.[71] In severe hydronephrosis, the renal parenchyma is obliterated almost completely, and only a thin rim of cortex remains. As renal vessels must still reach the cortex, elongated thin interlobar vessels may be seen forming radial streaks in the fluid-filled cavity in the nephrogram phase of an excretory urogram (Fig. 38-24). If the remaining renal parenchyma is functional, contrast medium will outline the dilated renal pelvis in the pyelogram phase. Anechoic fluid distention of the renal pelvis and diverticula is seen on ultrasound, until the kidney essentially becomes one cystic structure with a thin cortical rim (Fig. 38-25). Pyonephrosis is

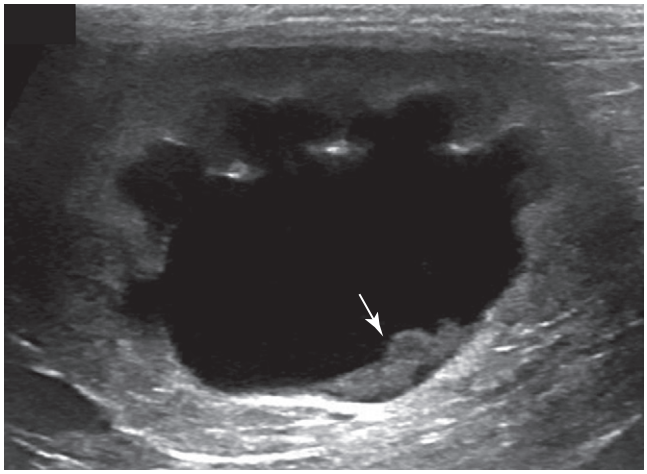


Fig. 38-25 Ultrasound image of a dog with severe hydronephrosis because of ureteral obstruction by a urinary bladder mass. The renal pelvis and pelvic diverticula are distended, and the renal cortex is thin. A small amount of cellular debris is accumulated in the dependent portion of the renal pelvis *(white arrow)*.

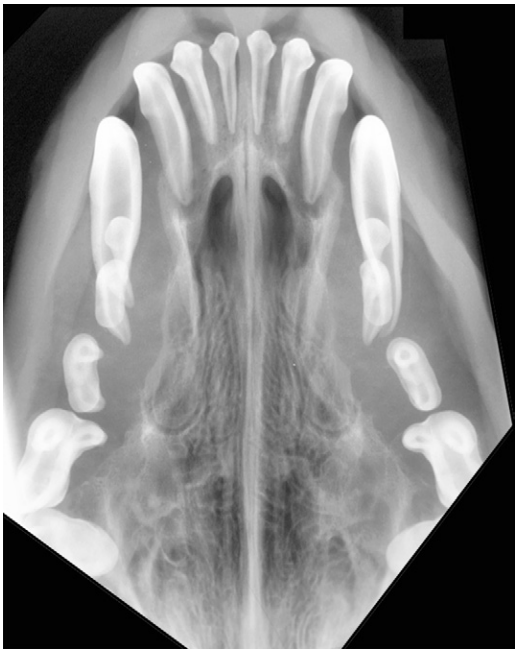


Fig. 38-26 Dorsoventral radiograph of the maxilla of a dog with renal failure and secondary hyperparathyroidism. The lamina dura and adjacent maxillary bone surrounding the teeth have been resorbed and replaced by fibrous tissue, resulting in markedly reduced opacity around the teeth.

characterized by echogenic fluid in the renal pelvis with sediment settling to the dependent portion (see Fig. 38-25).[69] Ureteral obstruction or aberrant termination of the ureters is a primary concern if hydronephrosis is present, and a detailed investigation of the ureters should be performed (discussed later).

Abnormal Renal Function

Abnormal renal function cannot be determined radiographically or ultrasonographically. However, secondary signs of renal failure may be apparent. Acute renal failure is often associated with perirenal effusion, best seen with ultrasound imaging. Renal hyperparathyroidism leads to generalized osteopenia evidenced by cortical thinning with a double cortical line. The skull is usually affected first. Bone resorption of the maxilla and mandible with fibrous replacement results in thickening with reduced radiopacity. The normally opaque lamina dura disappears, resulting in dramatically increased contrast to the teeth (Fig. 38-26).[72-73] Metastatic mineralization of stomach wall, blood vessels, and parenchymal organs such as liver and spleen may be observed with chronic renal failure if the calcium-to-phosphate ratio is increased.[74] Mild hyperplasia of the parathyroid glands can be detected ultrasonographically in animals with chronic, but not with acute, renal failure.[75]

Renal function can only be estimated crudely using excretory urography or contrast-enhanced CT. However, there are instances where a crude estimation of renal function, such as determining whether there is any function in a kidney, may be adequate for surgical planning. The degree and change of renal opacification over time after contrast-medium injection, as well as the relationship between nephrogram and pyelogram phase, can be used to determine problems with renal function (Fig. 38-27).[72] The findings and their possible interpretation are listed in Box 38-1. Observation of abnormal opacification patterns after intravenous contrast-medium administration is essential to recognize and treat contrast-medium–associated renal dysfunction. If more precise measurement of renal function is needed, renal scintigraphy using technetium-99m diethylenetriamine pentaacetic acid can be used to calculate individual and global renal function.[41] A protocol for glomerular filtration rate measurement using CT is also available.[37]

Box • 38-1

Functional Aspects of the Excretory Urogram

Good initial nephrogram followed by gradual decrease over 1—3 minutes, simultaneous with the appearance of the pyelogram
- Normal

Poor initial nephrogram that fades quickly
- Insufficient dose of contrast medium
- Primary polyuric renal failure

Poor initial nephrogram followed by persistent opacification
- Severe generalized renal disease (primary glomerular dysfunction or severe generalized acute or chronic renal disease)

Poor initial nephrogram followed by progressive increase in opacification
- Acute extrarenal obstruction
- Systemic hypotension before contrast-medium administration
- Poor renal blood flow

Good initial nephrogram followed by persistent or increasing opacity
- Systemic hypotension (may be contrast-medium—induced)
- Contrast-medium—induced renal failure
- Acute tubular necrosis
- Acute tubular obstruction

Poor opacification of the pyelogram phase
- Renal failure—decreased concentrating ability

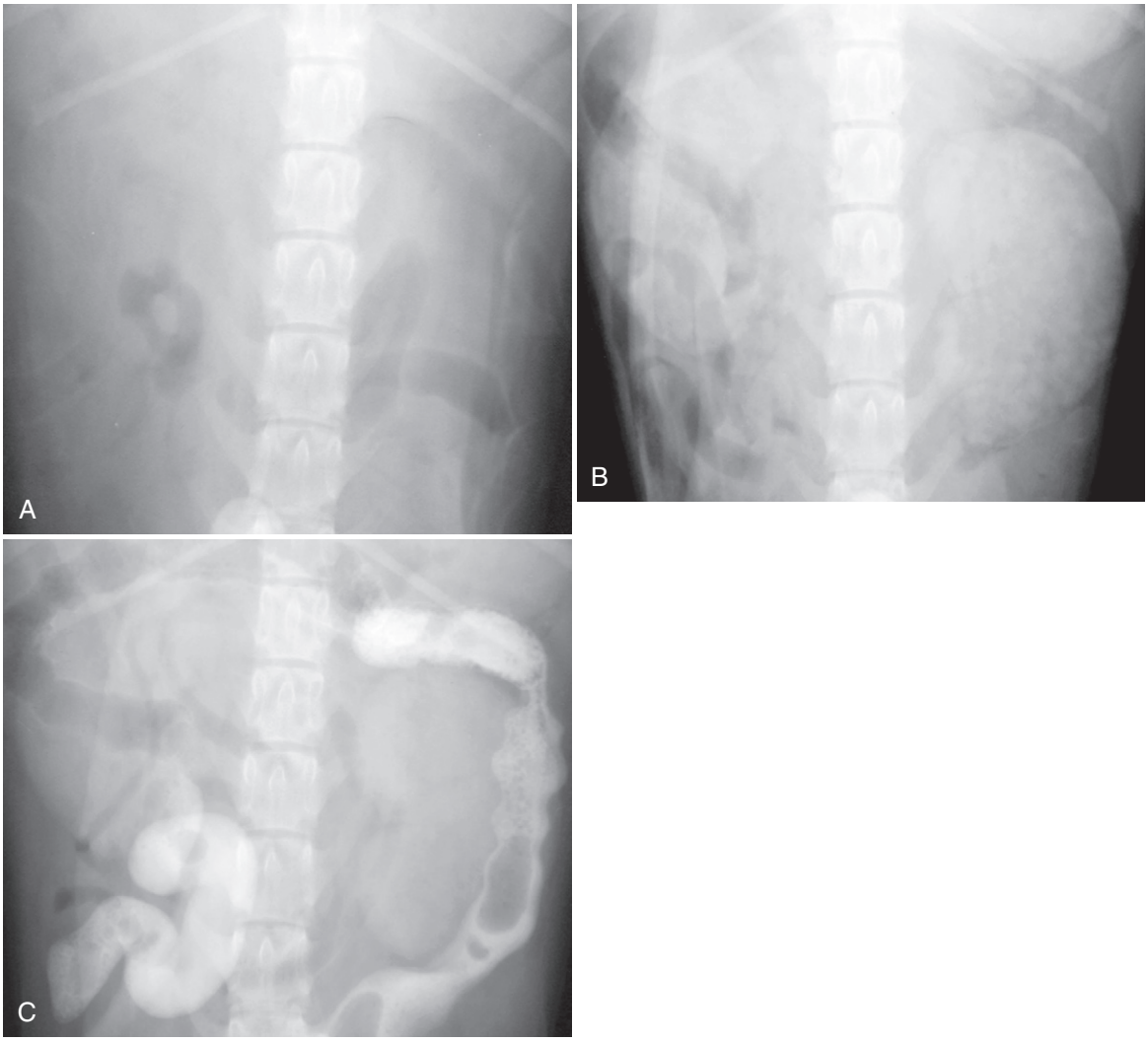


Fig. 38-27 Ventrodorsal radiographs of the kidneys of a dog with congenital polycystic kidney disease, before **(A)** 5 minutes **(B),** and 18 hours **(C)** after intravenous injection of iodinated contrast medium. There is opacification of the kidneys during the nephrogram phase **(B)** with multiple small filling defects corresponding to the cystic lesions. The pyelogram phase, however, is delayed, and the nephrogram persists over a long period of time **(C).** Contrast medium has been excreted through the biliary system and had accumulated in the colon **(C).** Contrast medium–induced renal failure was suspected.

DISEASES OF THE URETERS

Most ureteral diseases result in dilatation of some or all of the ureter. Differential diagnoses for ureteral dilatation include obstruction (calculi, clots, strictures, masses), ectopic ureter, inflammation (ureteritis, pyelonephritis), atony, and ureteral tears. Differentiation of these conditions is essential for determination of the best treatment.

Ureteral Obstruction

Ureteral calculi and masses associated with the urinary bladder neck are the most common causes of ureteral obstruction. Ureteral dilation and varying degrees of hydronephrosis are consequences of ureteral obstruction that are apparent with most imaging modalities. A severely dilated ureter may even be seen on survey radiographs as a tubular, tortuous structure in the retroperitoneal space extending from the kidneys to the dorsal aspect of the urinary bladder trigone (Fig. 38-28). Presence, location, and degree of obstruction have to be verified

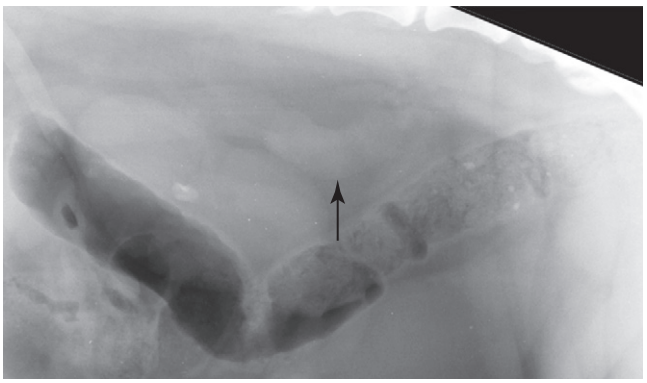


Fig. 38-28 Lateral radiograph of the retroperitoneal space of a dog with ureteral obstruction and dilation. A tortuous dilated ureter *(black arrow)* extends from the right kidney caudally toward the bladder neck. There is a nephrolith in the left kidney.

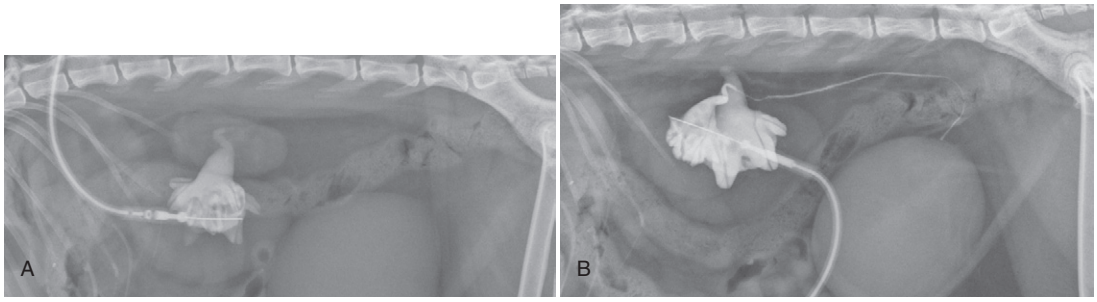


Fig. 38-29 Antegrade pyelogram in a cat with suspected bilateral ureteral obstruction. A needle was placed into the renal pelvis **(A)** under ultrasound guidance, followed by injection of iodinated contrast medium. The procedure was then repeated for the left kidney **(B)**. The right renal pelvis and proximal ureter are dilated, but contrast medium does not extend to the bladder. The left kidney is small and deformed. After contrast medium injection, the entire left ureter is filled and contrast medium reaches the bladder, confirming patency of the left ureter. A right ureteral calculus was removed surgically.

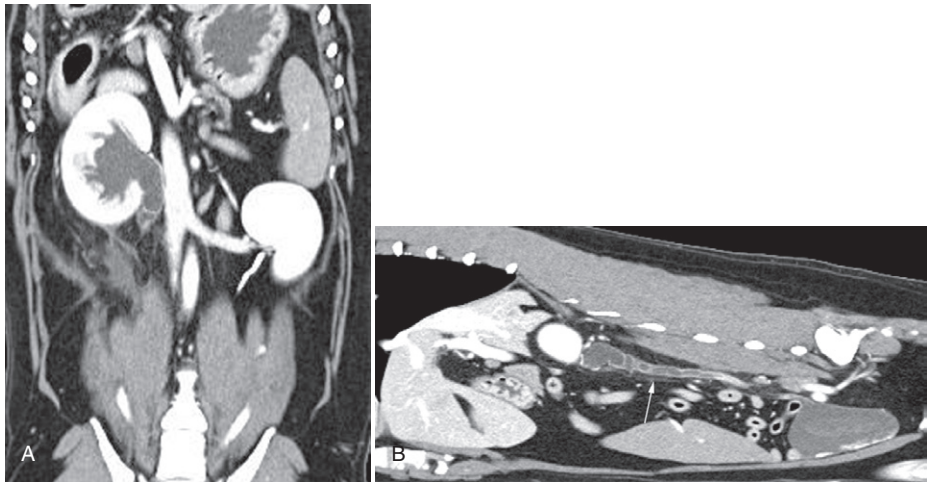


Fig. 38-30 Dorsal **(A)** and sagittal **(B)** reformatted post contrast CT images of the right kidney and ureter of a dog with suspected ureteral obstruction. Ultrasonographically, the ureter was dilated and filled with anechoic material, presumed to be fluid. On the dorsal image **(A),** the renal pelvis is distended but not filled with contrast medium; instead there is a large filling defect. This filling defect extends into a dilated, tortuous proximal ureter, obstructing it. The kidney and ureter were removed surgically after unsuccessful attempts to flush out the obstructive ureteral material. Histopathologically, severe pyelonephritis and ureteritis with hemorrhage and fibrin deposition were diagnosed.

using additional imaging modalities such as ultrasound, antegrade pyelography, excretory urography, or CT. On an excretory urogram or CT study with contrast medium, a filling defect and lack of contrast medium distal to the filling defect confirm ureteral obstruction. Ultrasonographically, a dilated ureter can usually be followed from the renal pelvis to an intraluminal obstruction such as a calculus. However, it should be noted that in some patients the ureter is not dilated all the way to the obstruction, and in those instances, a small calculus or ureteral stricture may be missed.[1] Obstructions caused by soft tissue structures, such as hypoechoic mucous plugs and hematomas, as well as strictures, can be difficult to identify ultrasonographically because they are often not distinct from the retroperitoneal fat and ureteral wall. If in doubt, the ultrasound examination can be repeated the next day to assess progression of ureteral or renal pelvic dilation, which would warrant decompression surgically or by stent placement. The resistive index is expected to increase in an obstructed kidney after administration of a diuretic.[76] Or, contrast procedures such as antegrade pyelography or CT could be considered (Figs. 38-29 and 38-30). Excretory urography is the least valuable method for detecting the site of ureteral obstruction because ureteral opacification is often poor owing to increased interstitial pressure in the kidney and decreased renal function. In addition, it is more difficult to clearly identify and follow each ureter with this technique.

Ureteroliths

Ureteral calculi are often radiopaque and therefore visible on survey abdominal radiographs, best seen on lateral radiographic views (Fig. 38-31). In cats, calcium oxalate calculi are diagnosed increasingly, whereas in dogs both struvite and calcium oxalates are common.[77-79] Radiographic identification of ureteral calculi can be hindered by superimposition of mineralized particles in the gastrointestinal tract, especially the colon (Fig. 38-32). The round opacity created by the

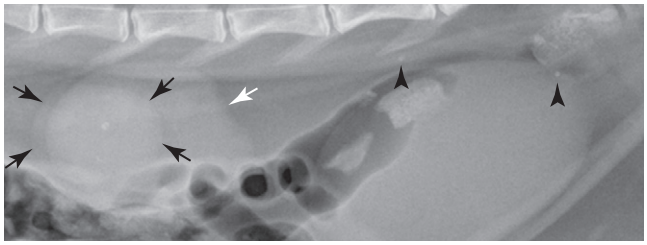


Fig. 38-31 Lateral radiograph of a cat with ureteral calculi leading to obstruction of the left ureter. The right kidney *(black arrows)* is small and round, consistent with chronic disease, and there is a small urolith in the right renal pelvis. The left kidney is larger but has a cortical defect *(white arrow)* in the caudal pole indicating infarction. Two small round calculi *(black arrowheads)* are present along the path of the ureter. These were confirmed to be calculi with ultrasound.

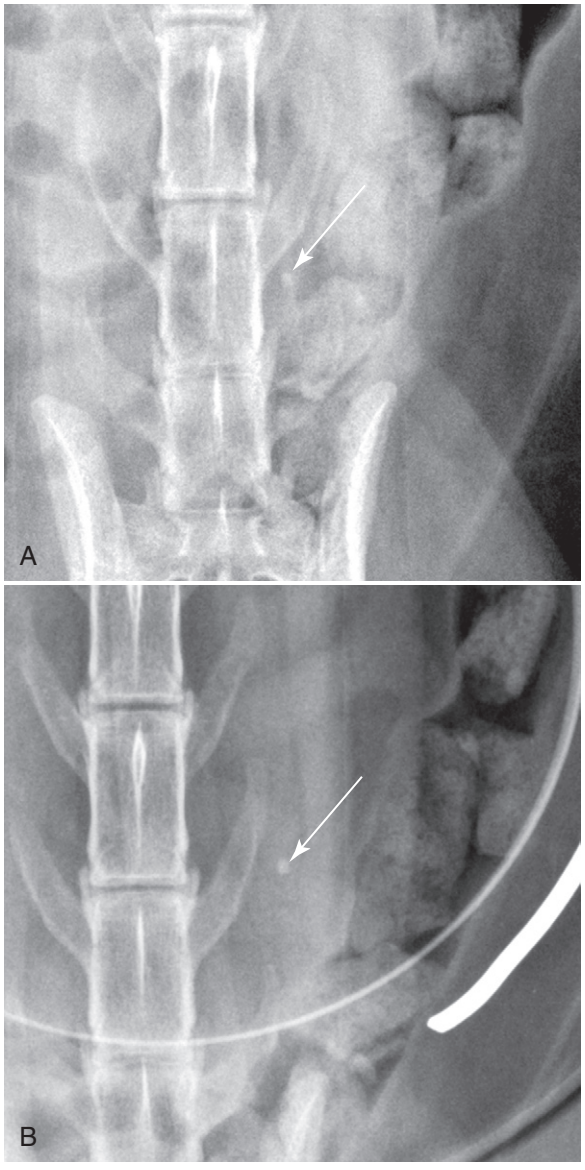


Fig. 38-32 Ventrodorsal radiographs of a cat with ureteral obstruction acquired without **(A)** and with abdominal compression **(B).** A suspected ureteral calculus was seen on lateral radiographs, but the side could not be determined. On **A,** a focal mineral opacity *(white arrow)* to the left of the spine is superimposed partially on the colon and could be fecal material. Using compression with a radiolucent paddle, the colon was displaced and a calculus *(white arrow)* in the left ureter was confirmed.

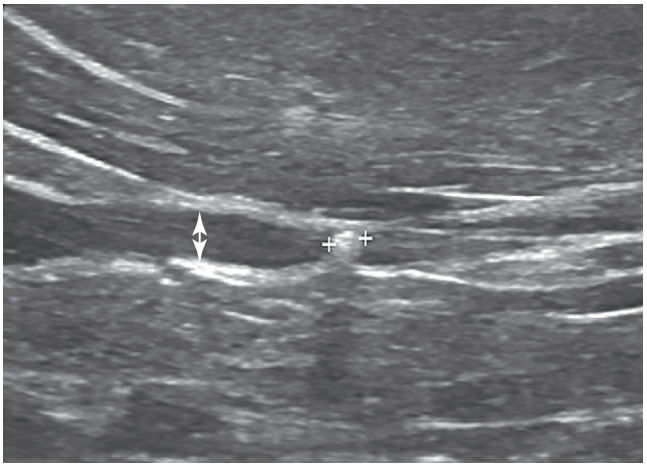


Fig. 38-33 Ultrasound image of a cat with a round hyperechoic calculus with a distal shadow in the ureteral lumen. The ureter is dilated proximal to the obstruction *(white arrow)*; distal to the calculus the ureter tapers to a normal size.

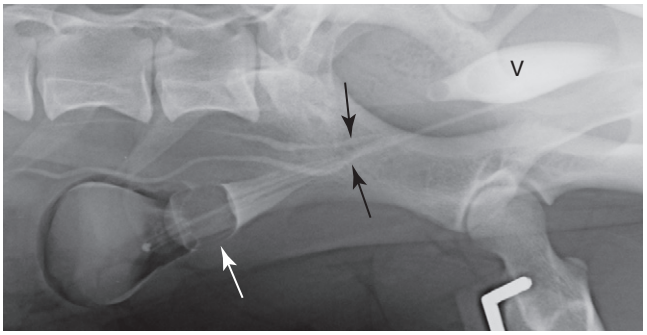


Fig. 38-34 Ventrodorsal oblique radiograph from an excretory urogram of a dog with bilateral ectopic ureter. A catheter was inserted into the urinary bladder, which was instilled with gas to provide negative contrast for the ureterovesical junctions. The bulb of the catheter *(white arrow)* is in the bladder neck. The ureters *(black arrows)* extend beyond the bladder neck and enter the proximal urethra. Contrast medium is also present in the vagina *(V)*.

end-on view of the deep circumflex iliac vessels seen on lateral radiographs should not be confused with ureteral calculi (see Fig. 35-4 in Chapter 35). A sensitivity of 90% to detect ureteroliths in cats has been reported when combining radiographs and ultrasound.[1] Ultrasonographically, ureteral calculi appear as round to slightly irregular, hyperechoic structures with a strong distal acoustic shadow (Fig. 38-33). A twinkling artifact may be seen when using color Doppler ultrasound.[80]

Ectopic Ureters

Ectopic ureters are congenital abnormalities of the ureteral junction with the bladder. One or both ureters may be affected. Ectopic ureters may terminate in the bladder neck, urethra (Fig. 38-34), and in rare instances in the vagina. The distal portion of the abnormal ureter may tunnel in the wall of the bladder neck and proximal urethra before opening into the urethral lumen. In these instances, the ureter appears to terminate normally at the bladder neck but continues

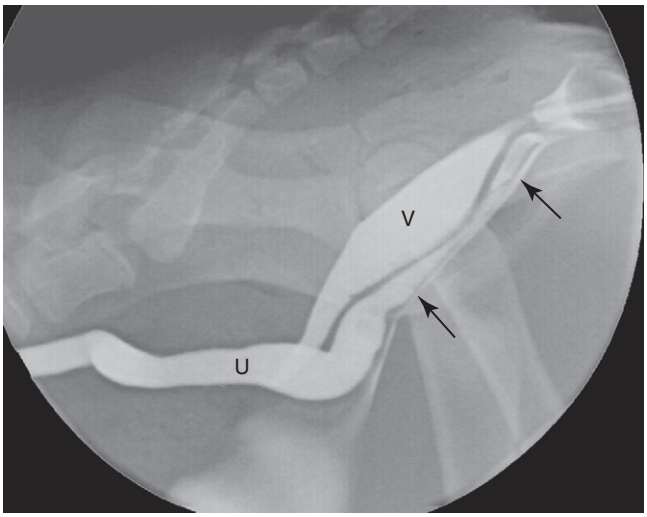


Fig. 38-35 Vaginourethrogram of a female dog with a single ectopic ureter. Contrast medium was injected into the vestibule of the vagina. The ureter *(U)* is dilated and tortuous. It extends caudally between the vagina *(V)* and urethra *(black arrow)* and enters the distal urethra.

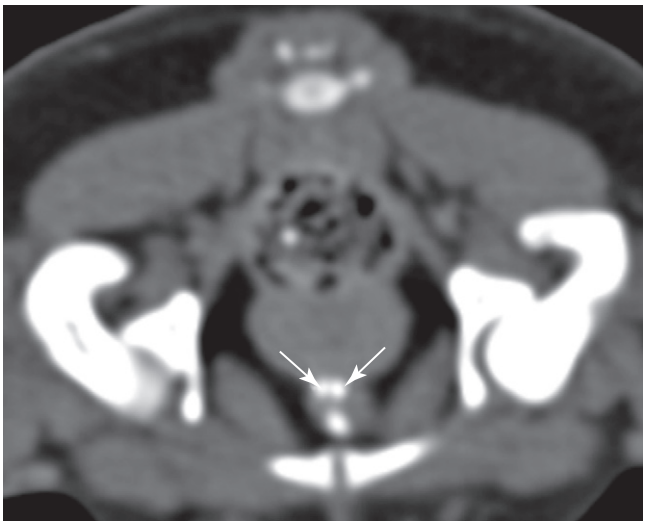


Fig. 38-36 Transverse CT image of the urethra and distal ureters in a dog with bilateral ectopic ureters. The two ureters *(white arrows)* course dorsal to the urethra. They inserted into the urethra just caudal to this image plane.

to tunnel caudally below the mucosa.[81] Ectopic ureters can be normal in size but are often dilated and tortuous with associated hydronephrosis. The intrapelvic location of the terminal ureter in these patients creates difficulties for evaluation with both excretory urography and ultrasonography. Careful patient preparation (sedation, empty colon, and rectum) are important. Urethrography and vaginography may have to be added to an excretory urogram if it is inconclusive (Fig. 38-35). Fluoroscopy may also be helpful to identify the ureteral opening. Administration of a diuretic is very helpful to enhance the ureteral jets during ultrasound evaluation.[82] CT is increasingly used for diagnosis of ectopic ureter.[81, 83-84] Lack of superimposition of skeletal and gastrointestinal structures is a major advantage of the method (Fig. 38-36).

Ureteroceles

Ureteroceles are cystic dilations of the submucosal portion of the distal ureter and are often associated with an ectopic ureter.[85] Ureteroceles appear as round contrast-medium–filled structures in the bladder lumen on excretory urography or CT. On ultrasound, they appear as a round, anechoic cystic structure at the ureterovesical junction, usually within the bladder lumen.[86-87]

Ureteral Tumors

Ureteral tumors are rare. Reported types include leiomyoma, leiomyosarcoma, and transitional cell carcinoma. Extension of a transitional cell carcinoma of the urinary bladder neck into the distal ureter is common. Fibroepithelial polyps in the proximal aspect of the ureter have been described in dogs.[88] The etiology is unclear; they may be inflammatory in origin, similar to polypoid cystitis, or hamartomatous or neoplastic, but have a good prognosis when removed.

Trauma to the Ureters and Kidney

Abdominal or pelvic canal trauma may affect the kidneys and/or ureters. Renal hemorrhage, renal rupture, renal artery or vein avulsion, or ureteral or renal pelvis tears are possible consequences. Survey radiographs are always indicated if retroperitoneal trauma is suspected. Either urine or hemorrhage in the retroperitoneal space appears as widening of the retroperitoneal space with secondary ventral displacement of large and small bowel. Additionally, retroperitoneal detail is decreased as the normal fat opacity surrounding the kidneys and large vessels is replaced by heterogeneous soft tissue opacity with a streaked appearance caused by fluid traveling along fascial planes. Renal displacement is associated with vascular avulsion, and body wall or diaphragmatic hernias. Renal enlargement can be the result of subcapsular hemorrhage or encapsulated urine accumulation (urinoma). Urinoma formation can also be associated with ureteral injury and urine leakage.[89] All these radiographic findings need to be evaluated further with additional imaging methods. CT provides the most complete evaluation of suspected renal trauma.[90] CT allows simultaneous assessment of trauma to soft tissue and bones, as well as blood supply of injured organs (Fig. 38-37). If urinary tract rupture is suspected, a contrast study using either excretory urography or CT is indicated. The site of urinary tract rupture is apparent as leakage of contrast medium (Fig. 38-38).

In clinical practice, ultrasound is often the first advanced imaging method used when urinary tract trauma is suspected because it is noninvasive and can be performed in the awake patient. However, information gained is often limited, except in patients with complete disruption of the renal architecture or blood supply. More subtle urinary tract tears are difficult to detect with certainty, and the use of ultrasound is limited to guide sampling of retroperitoneal fluid pockets. Complete ureteral tears of some duration can be suspected if focal dilatation of the proximal ureter is seen, in addition to retroperitoneal effusion because the site of rupture often contracts and adhesions form, essentially leading to ureteral obstruction. Doppler ultrasound can be used to verify both arterial supply and venous drainage of the kidney.

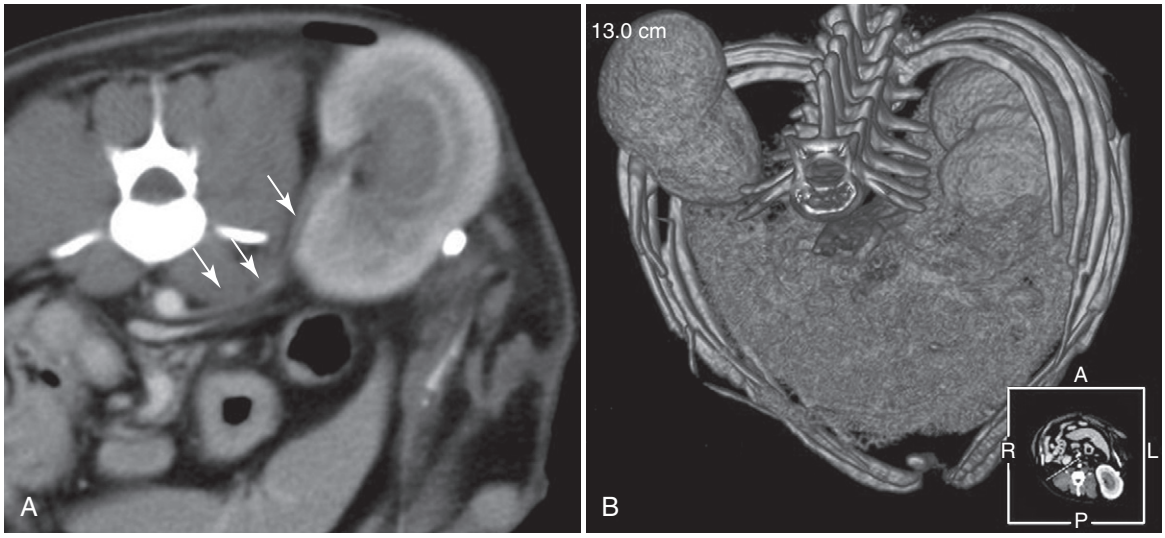


Fig. 38-37 **A,** Transverse CT image acquired after intravenous contrast-medium administration in a dog with a body wall hernia. The left kidney is displaced dorsally into paraspinal soft tissues. The kidney enhances normally, and the renal vessels are intact *(white arrows)*. **B,** Volume-rendered image of the same patient. (Images courtesy of Dr. Federica Rossi, Clinica Veterinaria Dell'Orologio, Sasso Marconi, Italy.)

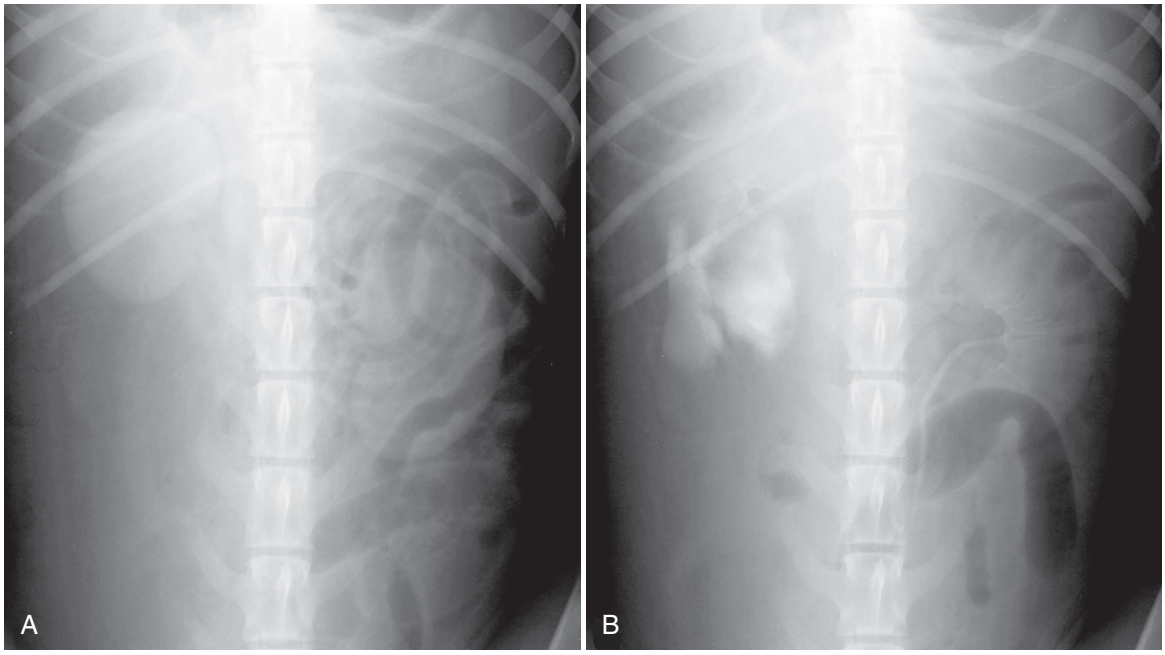


Fig. 38-38 Nephrogram **(A)** and pyelogram **(B)** phase of an excretory urogram in a traumatized dog with retroperitoneal effusion. The nephrogram phase is normal, but the retroperitoneal detail caudal to the right kidney is decreased. In the pyelogram phase, contrast medium has leaked into the retroperitoneal space, consistent with rupture of the right ureter.

REFERENCES

1. Kyles AE, Hardie EM, Wooden BG, et al: Clinical, clinicopathologic, radiographic, and ultrasonographic abnormalities in cats with ureteral calculi: 163 cases (1984–2002), *J Am Vet Med Assoc* 226:932, 2005.
2. Allan G: Radiology in the diagnosis of kidney disease, *Aust Vet Pract*, 12:97, 1982.
3. Greco DS: Congenital and inherited renal disease of small animals, *Vet Clin North Am Small Anim Pract* 31:393, 2001.
4. Finco DR, Stiles NS, Kneller SK, et al: Radiologic estimation of kidney size of the dog, *J Am Vet Med Assoc* 159:995, 1971.
5. Barrett RB, Kneller SK: Feline kidney mensuration, *Acta Radiol Suppl* 319:279, 1972.
6. Bartels JE: Feline intravenous urography, *J Am Anim Hosp Assoc* 9:349, 1973.
7. Shiroma JT, Gabriel JK, Carter RL, et al: Effect of reproductive status on feline renal size, *Vet Radiol Ultrasound* 40:242, 1999.

8. Pollard RE, Puchalski SM, Pascoe PJ: Hemodynamic and serum biochemical alterations associated with intravenous administration of three types of contrast media in anesthetized cats, *Am J Vet Res* 69:1274, 2008.
9. Pollard RE, Puchalski SM, Pascoe PJ: Hemodynamic and serum biochemical alterations associated with intravenous administration of three types of contrast media in anesthetized dogs, *Am J Vet Res* 69:1268, 2008.
10. Thomsen HS: European Society of Urogenital Radiology (ESUR) guidelines on the safe use of iodinated contrast media, *Eur J Radiol* 60:307, 2006.
11. Rao QA, Newhouse JH: Risk of nephropathy after intravenous administration of contrast material: a critical literature analysis, *Radiology* 239:392, 2006.
12. Feeney DA, Osborne CA, Jessen CR: Effect of multiple excretory urograms on glomerular filtration of normal dogs: a preliminary report, *Am J Vet Res* 41:960, 1980.
13. Feeney DA, Thrall DE, Barber DL, et al: Normal canine excretory urogram: effects of dose, time, and individual dog variation, *Am J Vet Res* 40:1596, 1979.
14. Feeney DA, Barber DL, Johnston GR: The excretory urogram: techniques, normal radiographic appearance, and misinterpretation, *Compend Contin Educ Pract Vet* 4:233, 1982.
15. Feeney DA, Barber DL, Culver DH, et al: Canine excretory urogram: correlation with base-line measurements, *Am J Vet Res* 41:279, 1980.
16. Adin CA, Herrgesell EJ, Nyland TG, et al: Antegrade pyelography for suspected ureteral obstruction in cats: 11 cases (1995–2001), *J Am Vet Med Assoc* 222:1576, 2003.
17. Gaschen L, Kunkler A, Menninger K, et al: Safety of percutaneous ultrasound-guided biopsy of renal allografts in the cynomolgus monkey: results of 348 consecutive biopsies, *Vet Radiol Ultrasound* 42:259, 2001.
18. Vaden SL: Renal biopsy of dogs and cats, *Clin Tech Small Anim Pract* 20:11, 2005.
19. Vaden SL, Levine JF, Lees GE, et al: Renal biopsy: a retrospective study of methods and complications in 283 dogs and 65 cats, *J Vet Intern Med* 19:794, 2005.
20. Seiler GS, Rhodes J, Cianciolo R, et al: Ultrasonographic findings in Cairn terriers with preclinical renal dysplasia, *Vet Radiol Ultrasound* 51:453, 2010.
21. Reichle JK, DiBartola SP, Leveille R: Renal ultrasonographic and computed tomographic appearance, volume, and function of cats with autosomal dominant polycystic kidney disease, *Vet Radiol Ultrasound* 43:368, 2002.
22. Lees GE: Congenital renal diseases, *Vet Clin North Am Small Anim Pract* 26:1379, 1996.
23. Schmiedt CW, Delaney FA, McAnulty JF: Ultrasonographic determination of resistive index and graft size for evaluating clinical feline renal allografts, *Vet Radiol Ultrasound* 49:73, 2008.
24. Kinns J, Aronson L, Hauptman J, et al: Contrast-enhanced ultrasound of the feline kidney, *Vet Radiol Ultrasound* 51:168, 2010.
25. Haers H, Vignoli M, Paes G, et al: Contrast harmonic ultrasonographic appearance of focal space-occupying renal lesions, *Vet Radiol Ultrasound* 51:516, 2010.
26. Waller KR, O'Brien RT, Zagzebski JA: Quantitative contrast ultrasound analysis of renal perfusion in normal dogs, *Vet Radiol Ultrasound* 48:373, 2007.
27. Ivancic M, Mai W: Qualitative and quantitative comparison of renal vs. hepatic ultrasonographic intensity in healthy dogs, *Vet Radiol Ultrasound* 49:368, 2008.
28. Yeager AE, Anderson WI: Study of association between histologic features and echogenicity of architecturally normal cat kidneys, *Am J Vet Res* 50:860, 1989.
29. D'Anjou MA, Bedard A, Dunn ME: Clinical significance of renal pelvic dilatation on ultrasound in dogs and cats, *Vet Radiol Ultrasound* 52:88, 2011.
30. Walter PA, Feeney DA, Johnston GR, et al: Feline renal ultrasonography: quantitative analyses of imaged anatomy, *Am J Vet Res* 48:596, 1987.
31. Walter PA, Johnston GR, Feeney DA, et al: Renal ultrasonography in healthy cats, *Am J Vet Res* 48:600, 1987.
32. Barr FJ, Holt PE, Gibbs C: Ultrasonographic measurement of normal renal parameters, *J Small Anim Pract* 31:180, 1990.
33. Mareschal A, d'Anjou MA, Moreau M, et al: Ultrasonographic measurement of kidney-to-aorta ratio as a method of estimating renal size in dogs, *Vet Radiol Ultrasound* 48:434, 2007.
34. Novellas R, Espada Y, Ruiz de Gopegui R: Doppler ultrasonographic estimation of renal and ocular resistive and pulsatility indices in normal dogs and cats, *Vet Radiol Ultrasound* 48:69, 2007.
35. Barthez PY, Begon D, Delisle F: Effect of contrast medium dose and image acquisition timing on ureteral opacification in the normal dog as assessed by computed tomography, *Vet Radiol Ultrasound* 39:524, 1998.
36. Rozear L, Tidwell AS: Evaluation of the ureter and ureterovesicular junction using helical computed tomographic excretory urography in healthy dogs, *Vet Radiol Ultrasound* 44:155, 2003.
37. O'Dell-Anderson KJ, Twardock R, Grimm JB, et al: Determination of glomerular filtration rate in dogs using contrast-enhanced computed tomography, *Vet Radiol Ultrasound* 47:127, 2006.
38. Bouma JL, Aronson LR, Keith DG, et al: Use of computed tomography renal angiography for screening feline renal transplant donors, *Vet Radiol Ultrasound* 44:636, 2003.
39. Caceres AV, Zwingenberger AL, Aronson LR, et al: Characterization of normal feline renal vascular anatomy with dual-phase CT angiography, *Vet Radiol Ultrasound* 49:350, 2008.
40. Cavrenne R, Mai W: Time-resolved renal contrast-enhanced MRA in normal dogs, *Vet Radiol Ultrasound* 50:58, 2009.
41. Daniel GB, Mitchell SK, Mawby D, et al: Renal nuclear medicine: a review, *Vet Radiol Ultrasound*, 40:572, 1999.
42. Stokes JE, Forrester SD: New and unusual causes of acute renal failure in dogs and cats, *Vet Clin North Am Small Anim Pract* 34:909, 2004.
43. Cuypers MD, Grooters AM, Williams J: Renomegaly in dogs and cats: part I. Differential diagnosis, *Compend Contin Educ Pract Vet* 19:1019, 1997.
44. Feeney DA, Johnston GR, Walter PA: Ultrasonography of the kidney and prostate gland. Has gray-scale ultrasonography replaced contrast radiography? *Probl Vet Med* 3:619, 1991.
45. Rivers BJ, Johnston GR: Diagnostic imaging strategies in small animal nephrology, *Vet Clin North Am Small Anim Pract* 26:1505, 1996.
46. Ross L: Acute kidney injury in dogs and cats, *Vet Clin North Am Small Anim Pract* 41:1, 2011.
47. Morrow KL, Salman MD, Lappin MR, et al: Comparison of the resistive index to clinical parameters in dogs with renal disease, *Vet Radiol Ultrasound*, 37:193, 1996.
48. Adams WH, Toal RL, Breider MA: Ultrasonographic findings in dogs and cats with oxalate nephrosis attributed to ethylene glycol intoxication: 15 cases (1984–1988), *J Am Vet Med Assoc* 199:492, 1991.
49. Adams WH, Toal RL, Walker MA, et al: Early renal ultrasonographic findings in dogs with experimentally induced ethylene glycol nephrosis, *Am J Vet Res* 50:1370, 1989.

50. Walter PA, Feeney DA, Johnston GR, et al: Ultrasonographic evaluation of renal parenchymal diseases in dogs: 32 cases (1981–1986), *J Am Vet Med Assoc* 191:9, 1987.
51. Walter PA, Johnston GR, Feeney DA, et al: Applications of ultrasonography in the diagnosis of parenchymal kidney disease in cats: 24 cases (1981–1986), *J Am Vet Med Assoc* 192:7, 1988.
52. Valdes-Martinez A, Cianciolo R, Mai W: Association between renal hypoechoic subcapsular thickening and lymphosarcoma in cats, *Vet Radiol Ultrasound* 48:357, 2007.
53. Forrest LJ, O'Brien RT, Tremelling MS, et al: Sonographic renal findings in 20 dogs with leptospirosis, *Vet Radiol Ultrasound* 39:337, 1998.
54. Barr FJ, Patteson MW, Lucke VM, et al: Hypercalcemic nephropathy in three dogs: sonographic appearance, *Vet Radiol Ultrasound* 30:169, 1989.
55. Mantis P, Lamb CR: Most dogs with medullary rim sign on ultrasonography have no demonstrable renal dysfunction, *Vet Radiol Ultrasound* 41:164, 2000.
56. Lewis KM, O'Brien RT: Abdominal ultrasonographic findings associated with feline infectious peritonitis: a retrospective review of 16 cases, *J Am Anim Hosp Assoc* 46:152, 2010.
57. Biller DS, Bradley GA, Partington BP: Renal medullary rim sign: ultrasonographic evidence of renal disease, *Vet Radiol Ultrasound* 33:286, 1992.
58. Felkai C, Voros K, Vrabely T, et al: Ultrasonographic findings of renal dysplasia in cocker spaniels: eight cases, *Acta Vet Hung* 45:397, 1997.
59. McKenna SC, Carpenter JL: Polycystic disease of the kidney and liver in the Cairn terrier, *Vet Pathol* 17:436, 1980.
60. Moe L, Lium B: Computed tomography of hereditary multifocal renal cystadenocarcinomas in German shepherd dogs, *Vet Radiol Ultrasound* 38:335, 1997.
61. Holloway A, O'Brien R: Perirenal effusion in dogs and cats with acute renal failure, *Vet Radiol Ultrasound* 48:574, 2007.
62. Beck JA, Bellenger CR, Lamb WA, et al: Perirenal pseudocysts in 26 cats, *Aust Vet J* 78:166, 2000.
63. Ochoa VB, DiBartola SP, Chew DJ, et al: Perinephric pseudocysts in the cat: a retrospective study and review of the literature, *J Vet Intern Med* 13:47, 1999.
64. Bryan JN, Henry CJ, Turnquist SE, et al: Primary renal neoplasia of dogs, *J Vet Intern Med* 20:1155, 2006.
65. Borjesson DL: Renal cytology, *Vet Clin North Am Small Anim Pract* 33:119, 2003.
66. Cruz-Arambulo R, Wrigley R, Powers B: Sonographic features of histiocytic neoplasms in the canine abdomen, *Vet Radiol Ultrasound* 45:554, 2004.
67. Hylands R: Veterinary diagnostic imaging. Retroperitoneal abscess and regional cellulitis secondary to a pyelonephritis within the left kidney, *Can Vet J* 47:1033, 2006.
68. Neuwirth L, Mahaffey M, Crowell W, et al: Comparison of excretory urography and ultrasonography for detection of experimentally induced pyelonephritis in dogs, *Am J Vet Res* 54:660, 1993.
69. Choi J, Jang J, Choi H, et al: Ultrasonographic features of pyonephrosis in dogs, *Vet Radiol Ultrasound* 51:548, 2010.
70. Vourganti S, Agarwal PK, Bodner DR, et al: Ultrasonographic evaluation of renal infections, *Radiol Clin North Am* 44:763, 2006.
71. Pugh CR, Schelling CG, Moreau RE, et al: Iatrogenic renal pyelectasia in the dog, *Vet Radiol Ultrasound* 35:50, 1994.
72. Feeney DA, Barber DL, Osborne CA: Functional aspects of the nephrogram in excretory urography: a review, *Vet Radiol* 23:42, 1982.
73. Sarkiala EM, Dambach D, Harvey CE: Jaw lesions resulting from renal hyperparathyroidism in a young dog—a case report, *J Vet Dent* 11:121, 1994.
74. Grooters AM, Miyabyashi T, Biller DS, et al: Sonographic appearance of uremic gastropathy in four dogs, *Vet Radiol Ultrasound* 35:35, 1994.
75. Reusch CE, Tomsa K, Zimmer C, et al: Ultrasonography of the parathyroid glands as an aid in differentiation of acute and chronic renal failure in dogs, *J Am Vet Med Assoc* 217:1849, 2000.
76. Choi H, Won S, Chung W, et al: Effect of intravenous mannitol upon the resistive index in complete unilateral renal obstruction in dogs, *J Vet Intern Med* 17:158, 2003.
77. Cannon AB, Westropp JL, Ruby AL, et al: Evaluation of trends in urolith composition in cats: 5,230 cases (1985–2004), *J Am Vet Med Assoc* 231:570, 2007.
78. Snyder DM, Steffey MA, Mehler SJ, et al: Diagnosis and surgical management of ureteral calculi in dogs: 16 cases (1990–2003), *N Z Vet J* 53:19, 2005.
79. Ling GV, Ruby AL, Johnson DL, et al: Renal calculi in dogs and cats: prevalence, mineral type, breed, age, and gender interrelationships (1981–1993), *J Vet Intern Med* 12:11, 1998.
80. Shabana W, Bude RO, Rubin JM: Comparison between color Doppler twinkling artifact and acoustic shadowing for renal calculus detection: an in vitro study, *Ultrasound Med Biol* 35:339, 2009.
81. Berent AC, Mayhew PD, Porat-Mosenco Y: Use of cystoscopic-guided laser ablation for treatment of intramural ureteral ectopia in male dogs: four cases (2006–2007), *J Am Vet Med Assoc* 232:1026, 2008.
82. Lamb CR, Gregory SP: Ultrasonographic findings in 14 dogs with ectopic ureter, *Vet Radiol Ultrasound* 39:218, 1998.
83. Samii VF, McLoughlin MA, Mattoon JS, et al: Digital fluoroscopic excretory urography, digital fluoroscopic urethrography, helical computed tomography, and cystoscopy in 24 dogs with suspected ureteral ectopia, *J Vet Intern Med* 18:271, 2004.
84. Yoon HY, Mann FA, Punke JP, et al: Bilateral ureteral ectopia with renal dysplasia and urolithiasis in a dog, *J Am Anim Hosp Assoc* 46:209, 2010.
85. Stiffler KS, Stevenson MA, Mahaffey MB, et al: Intravesical ureterocele with concurrent renal dysfunction in a dog: a case report and proposed classification system, *J Am Anim Hosp Assoc* 38:33, 2002.
86. Lautzenhiser SJ, Bjorling DE: Urinary incontinence in a dog with an ectopic ureterocele, *J Am Anim Hosp Assoc* 38:29, 2002.
87. Eisele JG, Jackson J, Hager D: Ectopic ureterocele in a cat, *J Am Anim Hosp Assoc* 41:332, 2005.
88. Reichle JK, Peterson RA 2nd, Mahaffey MB, et al: Ureteral fibroepithelial polyps in four dogs, *Vet Radiol Ultrasound* 44:433, 2003.
89. Tidwell AS, Ullman SL, Schelling SH: Urinoma (paraureteral pseudocyst) in a dog, *Vet Radiol Ultrasound* 31:203, 2005.
90. Kawashima A, Sandler CM, Corl FM, et al: Imaging of renal trauma: a comprehensive review, *Radiographics* 21:557, 2001.

ELECTRONIC RESOURCES

evolve

Additional information related to the content in Chapter 38 can be found on the companion Evolve website at http://evolve.elsevier.com/Thrall/vetrad/

- Chapter Quiz

CHAPTER • 39
The Urinary Bladder

Angela J. Marolf
Richard D. Park

NORMAL ANATOMY

The urinary bladder is divided grossly into three parts: the apex or vertex (apex vesicae) cranially, the body (corpus vesicae) in the middle, and the neck (cervix vesicae) caudally (Fig. 39-1).[1,2] Three ligaments formed from peritoneal reflections hold the bladder loosely in position.[2] The middle bladder ligament (ligamentum vesicae medianum) extends along the ventral bladder surface, and two lateral ligaments (ligamenta vesicae lateralia) extend along the lateral bladder surfaces. These ligaments often contain large fat deposits, facilitating radiographic visualization of the bladder neck and body. The cranial and dorsal surfaces of the bladder are visible radiographically because of adjacent fat within the omentum and mesentery (Fig. 39-2).

The musculomembranous urinary bladder wall consists of mucosal, submucosal, and muscular layers. The peritoneum is adherent to the serosal surface, providing a separate fourth layer. The thickness of the bladder wall or mucosa cannot be identified on survey radiographs because of border effacement by urine in the lumen.

Radiographic visualization of the urinary bladder is reduced by insufficient abdominal fat, inadequate distention, and superimposition opacities. Emaciated or young animals may not have sufficient abdominal fat to provide good tissue contrast. Ingested material in the small bowel, fecal material in the large bowel, pelvic limb muscle, and bone from the spine and pelvis may cause superimposition opacities that obscure all or part of the urinary bladder. Focal superimposition opacities may be created by fluid-filled small bowel, nipples, the prepuce, and cutaneous masses. Some of these superimposition opacities can be eliminated or minimized by withholding food for 24 hours preceding the study or giving cleansing enemas, though these interventions are usually not necessary.

Bladder size varies with the amount of urine. The bladder is small after voiding and may not be visible radiographically. With extreme distention, the apex/vertex may extend to the umbilicus. Severe distention may occur normally if the animal has not voided owing to lack of opportunity or because of a strange or unfamiliar environment. The urinary bladder in the dog is usually oval, but with distention it becomes more ellipsoid. The feline urinary bladder is almost always ellipsoid (Fig. 39-3).

The bladder is cranial to the pubis, dorsal to the rectus abdominis muscle, caudal to the small bowel and omentum,

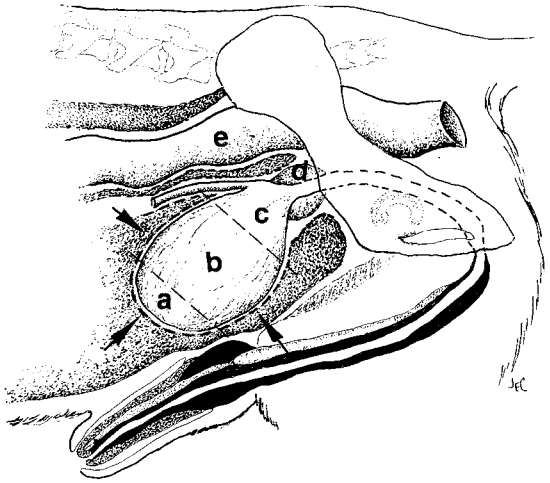


Fig. 39-1 Lateral view of the abdomen in a normal male dog. *a*, Apex or vertex; *b*, body of the bladder; *c*, neck of the urinary bladder; *d*, prostate; *e*, descending colon. The *broken line* around the urinary bladder *(black arrows)* represents the peritoneal reflection around and adherent to the serosal surface of the bladder.

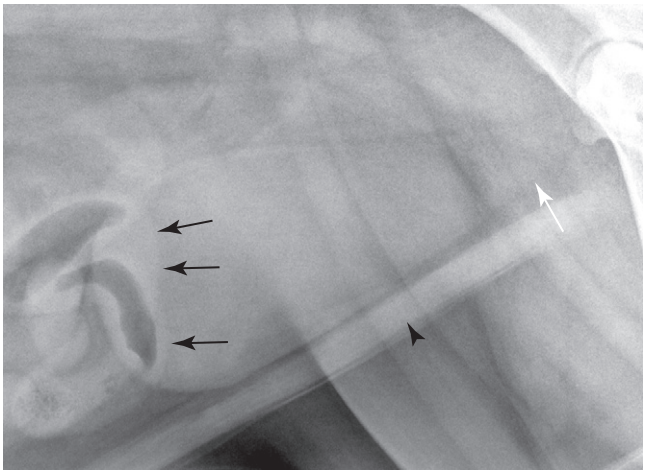


Fig. 39-2 Lateral radiograph of the caudal abdomen in a normal dog. The bladder neck *(white arrow)* is well visualized because of fat within the bladder ligaments. The rectus abdominis muscle *(black arrowhead)* is ventral to the bladder. Bowel *(black arrows)* is superimposed over the vertex of the bladder.

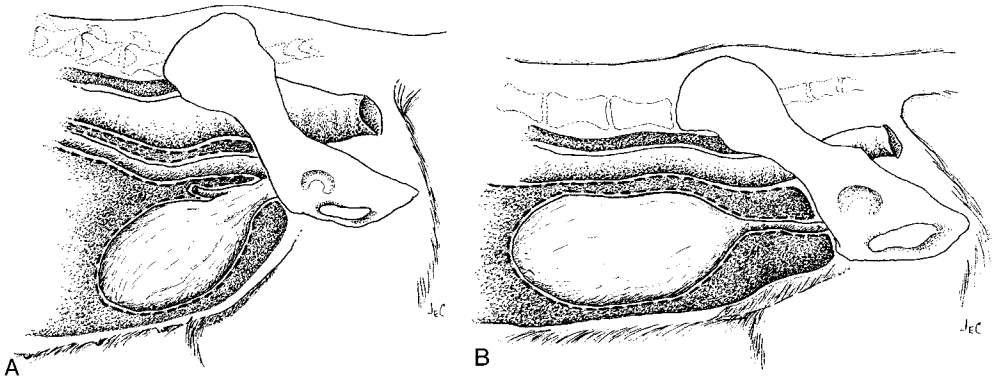


Fig. 39-3 **A,** Bladder in a normal female dog. The bladder is adjacent to the pubis and is oval. **B,** Bladder in a normal cat. The bladder is ellipsoid and has a long neck, which makes the bladder appear displaced cranially from the pubis. The *broken line* around the bladder in **A** and **B** denotes the peritoneal reflection. (From Park RD: Radiology of the urinary bladder and urethra. In O'Brien TR, editor: *Radiographic diagnosis of abdominal disorders in the dog and cat*, Davis, Calif, 1981, Covell Park Veterinary.)



Fig. 39-4 Lateral radiograph of the caudal abdomen in a normal cat. The feline urinary bladder is ellipsoid and is located more cranially than in the dog because of a longer bladder neck. Descending colon is superimposed over the dorsal aspect of the bladder.

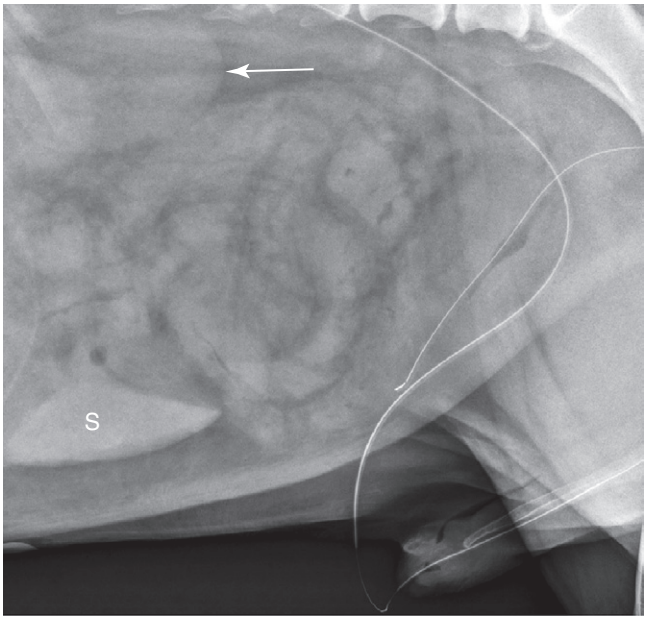


Fig. 39-5 Lateral radiograph of the abdomen of a dog. The left kidney *(white arrow)* is visible because of surrounding retroperitoneal fat. The serosal surfaces of the bowel and urinary bladder in the caudal aspect of the abdomen are indistinct because of free peritoneal fluid. The spleen *(S)* can be seen because of the focal nature of the free fluid in the caudal abdomen. A catheter is in the urinary bladder and looping over the caudal part of the abdomen.

and ventral to the large bowel. In females, the caudal aspect of the uterus lies between the bladder and colon/rectum. The caudal portion of the normal urinary bladder may be cranial to the pubis or within the pelvic canal.[3,4] When distended, the caudal part of the urinary bladder is usually cranial to the pubis.[3,4] The normal urinary bladder in the cat is always intraabdominal, being located 2 to 3 cm cranial to the pubis because of the long bladder neck in this species (Fig. 39-4).[5]

The normal urinary bladder has a soft tissue radiographic opacity. Any opacity greater or less than soft tissue within the bladder on survey radiographs is abnormal.

RADIOGRAPHIC SIGNS OF URINARY BLADDER DISEASE

Survey radiographic signs of urinary bladder disease are limited. In many instances, abnormalities indicate disease in adjacent structures. Signs that indicate disease of the urinary bladder or adjacent structures are poor or nonexistent bladder visualization and abnormal bladder position, shape, size, and opacity (Table 39-1).

Poor radiographic visualization of the urinary bladder may occur regardless of whether serosal detail in the caudal abdomen is good or decreased. If serosal detail is good and the bladder is not seen, the bladder is empty or has been displaced caudally or ventrally. If serosal detail is decreased and the bladder surface is not seen distinctly, free peritoneal fluid or inadequate peritoneal fat may be the cause (Fig. 39-5).

The bladder may be displaced abnormally in various directions.[6] The cause of bladder displacement may sometimes be determined by observation of surrounding structures (Fig. 39-6). With severe bladder displacement, as with a hernia, the bladder may not even be visible radiographically but can be identified using cystography or ultrasonography. Bladder retroflexion was found in 12 (20%) of 61 dogs with a perineal hernia.[7] A urinary bladder partially within the pelvic canal (Fig. 39-7) may be associated with congenital urinary tract anomalies.[8] A minimally distended bladder may be pelvic in position normally and move more cranially when distended; a pelvic bladder has been reported as a normal variation.[4,9]

Table • **39-1**

Urinary Bladder: Survey Radiographic Signs

RADIOGRAPHIC SIGN	GAMUT OF CONDITION(S) OR DISEASE(S)
Visualization	
Bladder not seen; abdominal serosal outlines are clear	Postvoiding Displaced bladder Perineal hernia Inguinal hernia Pelvic bladder Normal Short urethra Ectopic ureter(s) Congenital urethrorectal fistula
Bladder not seen; abdominal serosal outlines are not clearly seen	Peritoneal fluid Urine secondary to bladder tear/rupture Transudate Exudate Hemorrhage Lack of peritoneal fat Emaciation Young animal (<4 months of age)
Abnormal Position	
Ventral displacement	Abdominal wall hernia
Cranial displacement	Prostatic disease Neoplasia Prostatitis Prostatic cyst Benign hypertrophy Large intrapelvic mass
Cranioventral displacement	Enlarged uterus Pyometra Pregnancy Sublumbar mass Large bowel distention Uterine stump granuloma or abscess Persistent patent urachus or urachal ligament Inguinal hernia
Caudal displacement	Perineal hernia Large abdominal mass
Dorsal displacement	Abdominal mass
Abnormal Shape	Adjacent abdominal mass Neoplasia Abscesses/granulomas Persistent urachal ligament
Abnormal Size	
Increased	Urethral obstruction Bladder neck obstruction Neurologic deficiencies
Decreased	Congenital anomalies Ectopic ureters Fistulas Cystitis Neoplasia
Mineral opacity	Calculi Bladder wall mineralization
Lucent areas	Gas Iatrogenic Emphysematous cystitis

Incontinent female dogs with a pelvic bladder usually have a shorter urethra than continent dogs.[10,11] Because a pelvic bladder does not always indicate a clinical problem, a pelvic bladder should be correlated with clinical signs to determine its clinical significance.

A change in shape of the urinary bladder is not detected commonly. Abdominal masses adjacent to the serosal surface of the bladder may distort the bladder shape. Tumors originating from the bladder wall occasionally protrude from the serosal surface and produce a discernible bladder shape change (Fig. 39-8).[12] A pointed apex with an elongated bladder may occur with a persistent urachal ligament.[13] An abnormally small or large urinary bladder is difficult to diagnose radiographically because of the wide variation in normal bladder size. In most instances, a consistently small or large bladder with associated clinical signs is an indication that a contrast study or ultrasound examination should be performed to determine the cause of the suspected size change.

Any change in radiographic opacity in the urinary bladder is abnormal and usually easy to detect. Gas in the bladder may be introduced iatrogenically from catheterization or cystocentesis. Small luminal gas bubbles are usually seen in the center of the bladder on a recumbent lateral view (Fig. 39-9). Gas in the bladder lumen, bladder wall, and occasionally the bladder ligaments occurs with emphysematous cystitis (Fig. 39-10). Emphysematous cystitis is produced by glucose-fermenting organisms and may be seen in association with diabetes mellitus.[14] Occurrence of emphysematous cystitis without diabetes mellitus also has been reported.[15,16]

Most radiopacities associated with the bladder are calculi (Fig. 39-6, *B*; Fig. 39-11). Opacities cannot be confirmed to be in the bladder based on one radiograph; confirmation requires examination of orthogonal radiographs. If doubt exists regarding the location or presence of cystic calculi after examining orthogonal radiographs, sonography would be the most expeditious way to obtain further information. If cystic calculi are identified, the remainder of the urinary tract from the kidneys to the terminus of the urethra should be examined for additional calculi. Not all calculi are radiopaque; thus the absence of radiopacities within the bladder does not rule out the presence of cystic calculi (Table 39-2). In cats with suspected feline idiopathic cystitis, survey radiographs and cystography can be used to evaluate the bladder. Often, mild bladder wall thickening may be observed with cystography.[17] Additionally, a horizontal-beam radiograph can be made to diagnose sandlike material that will collect within the dependent portion of the bladder. This additional view may be helpful in cats with feline idiopathic cystitis (feline urologic

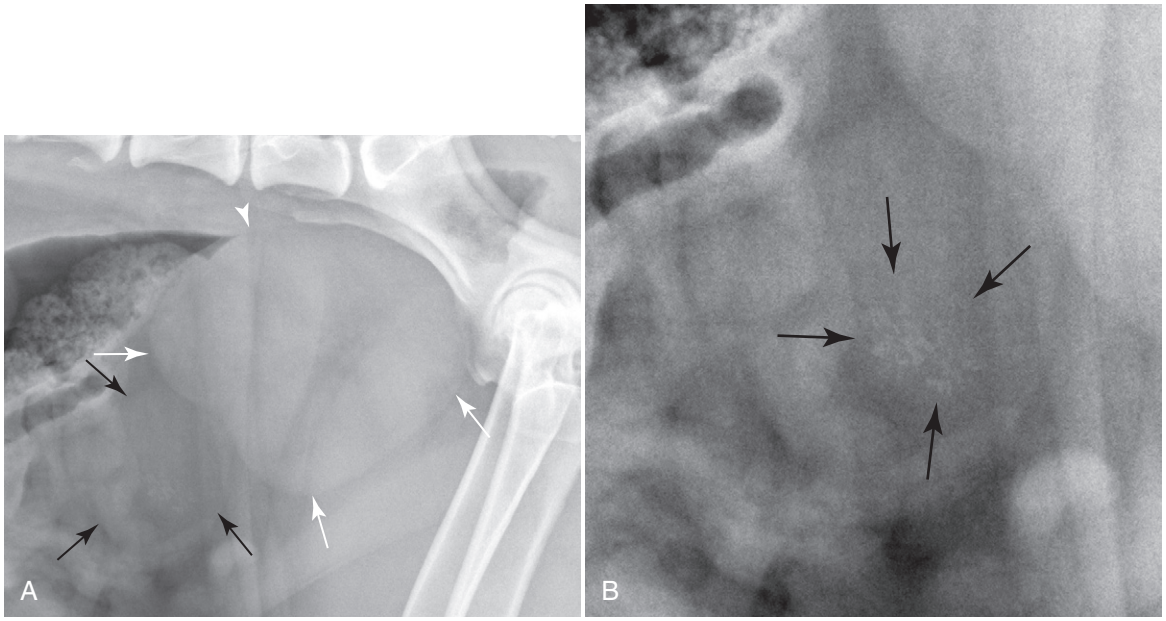


Fig. 39-6 **A,** Lateral radiograph of a dog with a large prostatic carcinoma *(white arrows)*. The enlarged prostate gland displaces the bladder *(black arrows)* cranially and compresses the terminal portion of the descending colon *(white arrowhead)*. The mass is more opaque than the bladder because of its increased thickness and could be misinterpreted as bladder, except for the atypical shape. If there is a question whether a caudal abdominal mass is of bladder origin, a positive-contrast cystogram or sonography would provide more information. **B,** Close-up of the urinary bladder from the same dog. There are numerous small radiopaque calculi in the bladder *(black arrows)*.

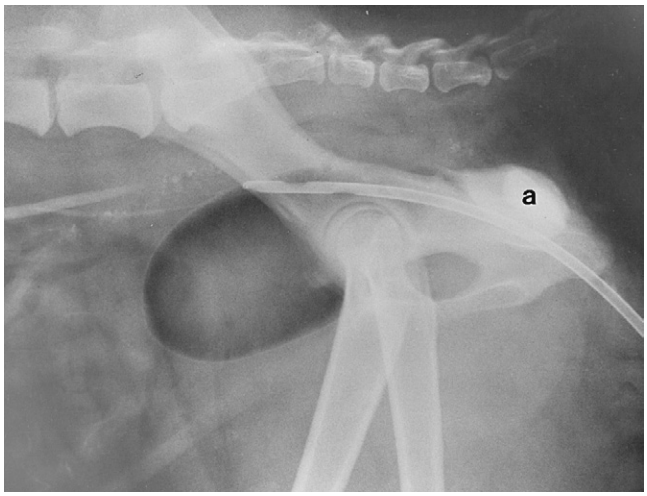


Fig. 39-7 Lateral radiograph of the caudal abdomen and pelvis after intravenous urography and double-contrast cystography. A radiopaque catheter is present in the bladder, and the caudal aspect of the bladder is within the pelvic canal. Contrast medium has accumulated in the vagina *(a)* because of an ectopic ureter.

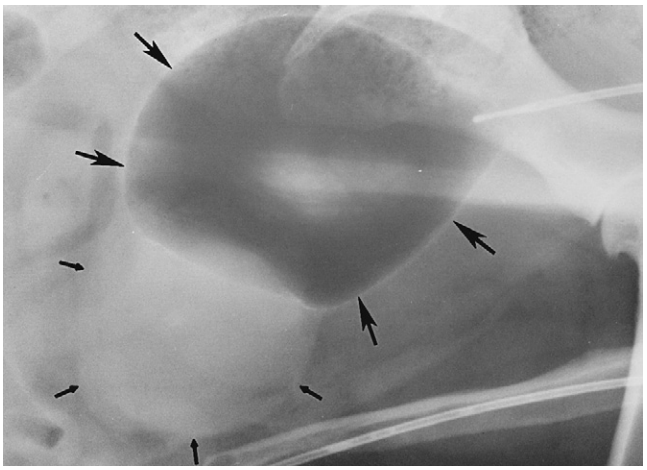


Fig. 39-8 Oblique view of the abdomen after double-contrast cystography. A mass *(small black arrows)* is present on the cranioventral aspect of the gas-filled bladder *(large black arrows)*. The mass is a leiomyosarcoma originating from the bladder; it gave the bladder a bilobed appearance on the survey radiograph.

syndrome).[18] Radiopacities in the urinary bladder can also be produced by mineralization of the bladder wall associated with neoplasia or chronic cystitis, but this is unusual.[19]

CONTRAST CYSTOGRAPHY

Retrograde contrast cystography is a fast, simple, and inexpensive technique that may provide valuable diagnostic and prognostic information about bladder disease. Clinical indications for cystography include dysuria, pollakiuria, and intermittent or persistent chronic hematuria. Radiographic signs that suggest a need for cystography include identification of increased or decreased opacity in the urinary bladder, evaluation of caudal abdominal masses that may be associated with the urinary bladder, nonvisualization of the bladder after abdominal trauma, and evaluation of the urinary bladder with an abnormal shape or location.

Voiding cystography is not discussed in this chapter. The reader is referred to other publications for more information on this technique.[20-23] Voiding cystography coupled with cystometry and urethral pressure profiles is the technique of choice for investigating dynamic bladder disease such as urinary incontinence and urethral incompetence.[24]

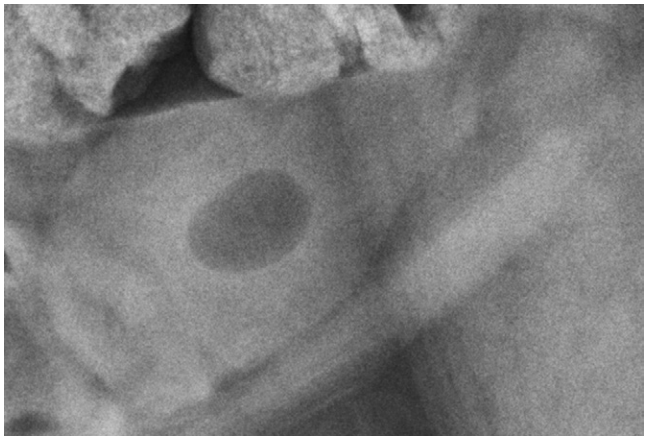


Fig. 39-9 Lateral view of the caudal abdomen of a cat. A central oblong air bubble introduced during cystocentesis is present. This radiolucency should not be misinterpreted as a calculus because positive-contrast medium has not been administered. So-called radiolucent calculi are really of soft tissue opacity and are not visible on survey radiographs. However, nonopaque calculi will appear relatively radiolucent, creating a filling defect, when surrounded by positive-contrast medium is in the bladder.

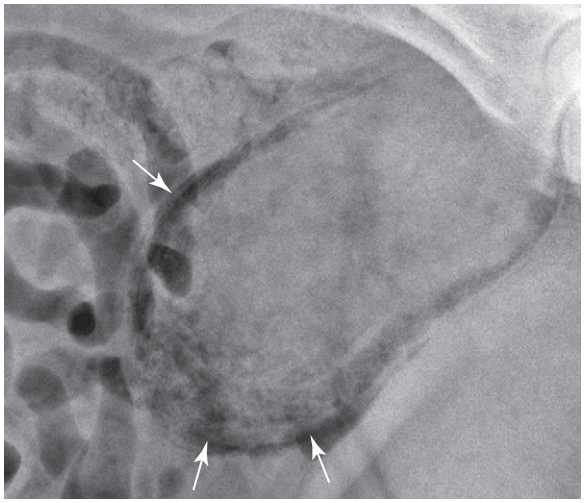


Fig. 39-10 Lateral view of the abdomen of a dog with gas *(white arrows)* within the bladder wall and lumen. This appearance is typical of emphysematous cystitis, which in this dog was secondary to diabetes mellitus.

Cystography Technique

If possible, food should be withheld for 24 hours and an enema given preceding cystography because fecal material superimposed over the urinary bladder may mask important radiographic information.

All catheters and equipment should be sterilized, and the genitalia should be cleaned before the bladder is catheterized. The equipment necessary for bladder catheterization is illustrated in Figure 39-12. To reduce bladder pain and spasm during cystography, 2 to 5 mL of 2% lidocaine (Xylocaine) without epinephrine may be injected into the bladder before cystography is performed.

Complications resulting from catheterization and cystographic procedures occur infrequently and are usually not detrimental to the animal. Iatrogenic trauma, bacterial contamination,[25] or kinked[26] and knotted urethral catheters may occur from improper catheterization techniques. Intramural and subserosal accumulation of contrast medium has been reported after maximal bladder distention with a Foley catheter (Fig. 39-13).[27-30] This complication occurs more

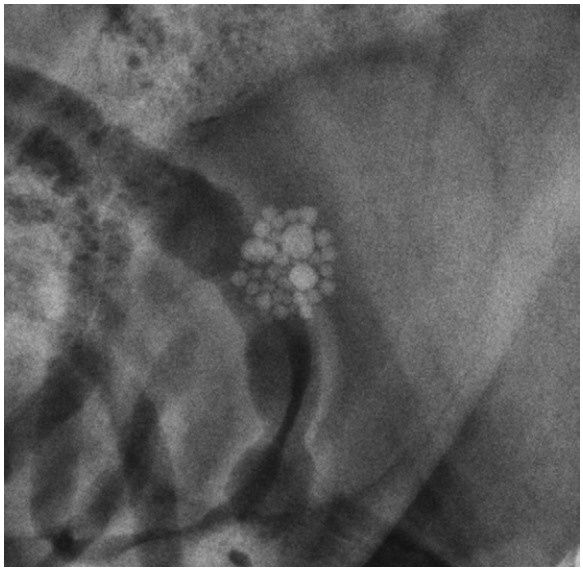


Fig. 39-11 Lateral radiograph of a dog with multiple, variably sized cystic calculi. Gas-filled bowl loops are superimposed over the vertex of the bladder.

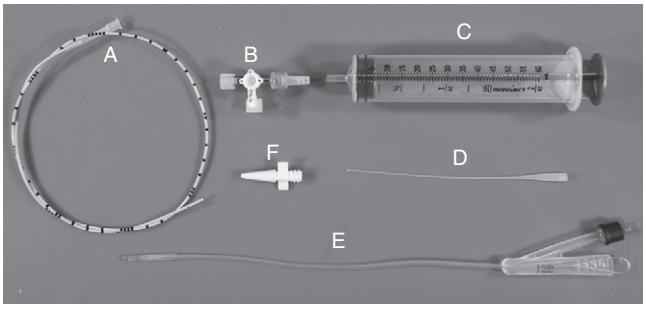


Fig. 39-12 Equipment for bladder catheterization and cystography. *A*, Male urethral catheter; *B*, three-way valve; *C*, large syringe; *D*, Tomcat catheter; *E*, Foley (balloon-type) catheter; *F*, catheter connector for use with the male urethral catheter.

Table • **39-2**

Radiopacity of Cystic Calculi on Survey Abdominal Radiographs

CALCULUS COMPOSITION	OPACITY	SURFACE CHARACTERISTICS
Calcium oxalate	Moderately to markedly radiopaque	Sharp projections or smooth
Calcium phosphate	Moderately to markedly radiopaque	Smooth
Struvite (ammonium phosphate)	Moderately to markedly radiopaque	Usually smooth; can be spiculated
Silica	Moderately radiopaque	Jackstone appearance
Urate	Nonradiopaque to faintly radiopaque	Smooth
Cystine	Nonradiopaque to faintly radiopaque	Smooth

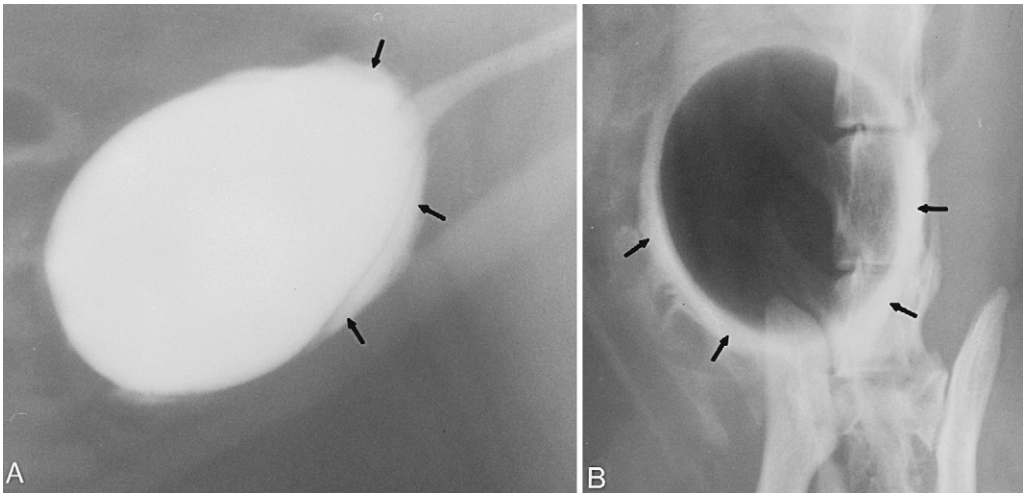


Fig. 39-13 Positive- **(A)** and double-contrast **(B)** cystogram in which subserosal accumulation of contrast medium has occurred *(black arrows)*. This usually produces no severe or long-lasting complications. It is produced by a high intraluminal bladder pressure and is predisposed by bladder disease, particularly cystitis.

frequently in cats, often with a nondistended bladder and minimal intravesicular pressure. It usually does not result in a clinical problem. Mucosal ulceration, inflammation, and granulomatous reactions may occur, but the changes are usually transitory and produce no serious clinical problems.[9] The most serious complication from negative-contrast cystography is gas embolization into the circulatory system, which may result in death.[31-33] Fortunately, such complications occur rarely. Death from gas embolism may be prevented by using more soluble nitrous oxide or carbon dioxide instead of room air.

Both negative- and positive-contrast media are used for cystography. Negative-contrast media include room air, carbon dioxide, and nitrous oxide. Positive-contrast media are water-soluble organic iodides that should be used in an approximate 20% iodine solution. Barium should never be used for cystography.[27,34] The volume of positive-contrast medium used for cystography varies with body weight, the species, and the pathologic process present in the bladder. An approximation of 10 mL, or a range of 3.5 to 13.1 mL of contrast medium per kilogram body weight, may be used.[34] The injection should be terminated before the estimated volume has been administered if the bladder feels adequately distended by external palpation, if reflux occurs around the catheter, or if back pressure is felt on the syringe plunger. Moderate bladder distention is recommended because maximal distention may obliterate subtle mucosal and bladder wall changes.[35] Four radiographic views of the caudal abdomen (lateral, ventrodorsal, ventral left–dorsal right, ventral right–dorsal left) should be made to examine the contrast-medium–filled bladder adequately.

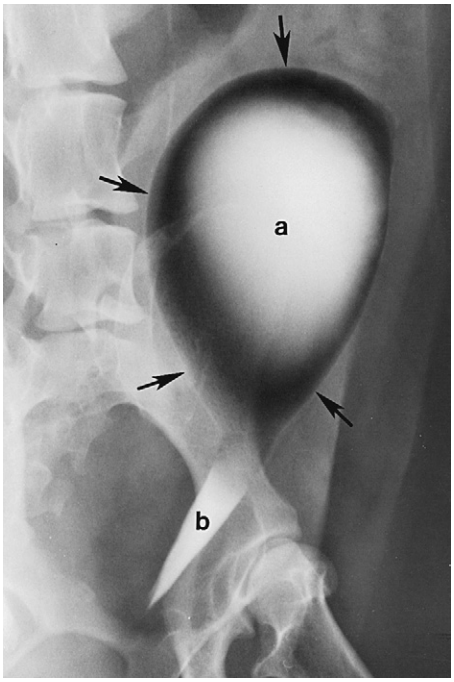


Fig. 39-14 Ventral left–dorsal right radiograph of a normal double-contrast cystogram. The urinary bladder wall *(black arrows)* is seen clearly. The contrast puddle in the dependent portion of the bladder *(a)* and the contrast-medium–filled urethra *(b)* are easily identified.

Cystographic Procedures

Retrograde positive- and double-contrast procedures are often more useful to evaluate the bladder than is negative-contrast cystography. Positive-contrast cystography is performed by injecting a 20% solution of an organic iodide compound into an evacuated bladder by a urethral catheter. This procedure is the method of choice for identifying bladder location, tears, ruptures, hernias, and abnormal communication with adjacent structures.

A double-contrast cystogram is performed by injecting a small volume of undiluted positive-contrast medium into an empty bladder. The recommended dose of positive-contrast medium is 0.5 to 1 mL for a cat, 1 to 3 mL for a dog weighing less than 25 lb, and 3 to 6 mL for animals weighing more than 25 lb. Positive–contrast-medium injection is followed by bladder distention with negative-contrast medium (Fig. 39-14). Double-contrast cystography is better than positive-contrast cystography for assessing bladder wall lesions and intraluminal filling defects. The selection of positive- or double-contrast cystography is based on clinical history, clinical signs, radiographic signs, and the character of aspirate obtained with bladder catheterization (Table 39-3).

Radiographic Signs with Contrast Cystography

Radiographic signs observed with urinary bladder disease include an irregular mucosal border, intramural thickening, filling defects, and extravasation patterns (Table 39-4).[36] These radiographic changes must be differentiated from artifacts such as air bubbles and inadequate bladder distention.

Table • **39-3**

Indications for Type of Cystographic Procedure

CONTRAST STUDY	INDICATIONS
Double-contrast cystogram	Suspect bladder wall lesion(s), filling defects (calculi, blood clots, masses)
Positive-contrast cystogram	Suspect ruptured or abnormal bladder location
Negative-contrast cystogram	Not preferred; can determine bladder location

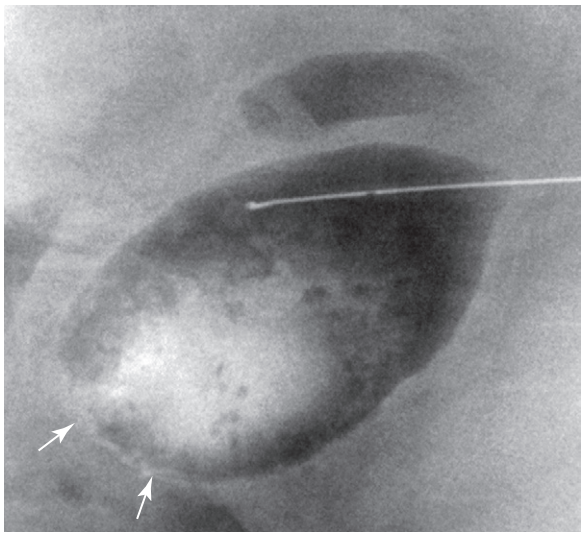


Fig. 39-15 Lateral radiograph of the bladder during double-contrast cystography. Mild mucosal irregularity is present along the vertex of the bladder *(white arrows)* as a result of mild chronic cystitis.

Mucosal Changes

The urinary bladder has a transitional epithelium, which appears smooth on a normal cystogram. The bladder epithelium is capable of metaplastic, neoplastic, and nonneoplastic proliferation.[37] Mucosal proliferation appears as an irregular outline along the inside bladder surface and may be accentuated with inadequate bladder distention. The irregular mucosa is usually focally distributed but may be diffuse; it may vary in severity from a slightly irregular brush-type surface to a severe cobblestone appearance (Fig. 39-15). Mild mucosal irregularity may be obliterated on a cystogram if the bladder is distended completely.[35] Ulcers may be present with mucosal proliferation and can be identified where contrast medium adheres to the mucosal surface.

Intramural Changes (Bladder Wall Thickening)

The normal bladder wall is approximately 1 mm thick regardless of the degree of distention.[9] Intramural changes are demonstrated best with double-contrast cystography and include focal or diffuse increased bladder wall thickness (Fig. 39-16). Mild bladder wall thickening may be missed if the bladder is distended completely.[35] Bladder wall thickening may be caused by fibrous tissue proliferation or cellular infiltration from inflammation, hemorrhage, or neoplasia. Intramural bladder thickening causes decreased bladder distensibility, which may be symmetric with diffuse intramural bladder disease or asymmetric with focal intramural bladder disease.

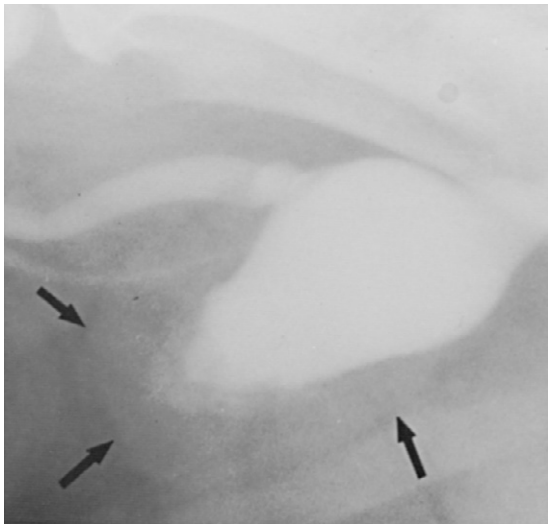


Fig. 39-16 Lateral radiograph of the urinary bladder filled with positive-contrast medium during intravenous urography. Diffuse bladder wall thickening is present as the result of cytoxan-induced cystitis. The serosal surface *(black arrows)* is outlined by fat. Bladder distensibility is decreased by the severe intramural changes. One ureter is distended as a result of obstruction at the ureterovesicular junction.

Filling Defects

A bladder filling defect is anything occupying space within the bladder lumen that alters normal filling with contrast medium. All filling defects appear radiolucent when surrounded with positive-contrast medium even though the opacity of the defect may not be inherently radiolucent. The size, shape, number, border contour, position within the bladder, and attachment to the bladder wall helps determine the nature of the filling defect (Table 39-5).

Filling defects may be *free* or *attached*. Common causes of free luminal filling defects are air bubbles, calculi, and blood clots[36] (Fig. 39-17). Abnormalities causing a free luminal filling defect are best demonstrated with double-contrast cystography and are located in the center of the bladder on a recumbent lateral view. The concentration of the contrast medium and depth of the contrast puddle have an effect on visualization of cystic calculi.[38,39] Combining patient signalment and double-contrast cystographic findings can improve prediction of type of mineral calculus noninvasively.[40] Attached filling defects may be caused by neoplasia (Fig. 39-18), inflammatory polyps, blood clots, adherent calculi, and ureteroceles (Fig. 39-19).[41-43] Ureteroceles may communicate partially with the bladder and fill with positive-contrast medium and create what is known as the *cobra-head sign*, or they may not communicate and be a negative filling defect (see Figure 39-19).[44] With double-contrast cystography, mural masses may be seen only when the x-ray beam is parallel to the interface between the mass and contrast medium.[45] Mucosal irregularity and ulceration is frequently present on the surface of large attached filling defects. Bladder wall infiltration may be diagnosed as a thickened bladder wall adjacent to the filling defect.[46] Often, a specific diagnosis of an attached filling defect cannot be made and cytologic evaluation is needed.

Contrast Leakage Patterns from the Urinary Bladder

Retrograde positive-contrast cystography is the best technique to assess leakage of urine from the bladder. Urine leakage may occur into the urinary tract, adjacent visceral soft tissue structures, or the peritoneal cavity.

Urine reflux or retention occurs with vesicoureteral reflux, urachal anomalies (Fig. 39-20), and traumatic bladder diverticula (Fig. 39-21). Urachal anomalies include congenital or

Table • **39-4**

Radiographic Signs of Pathologic Processes of the Bladder

	MUCOSAL CHANGES		INTRAMURAL THICKENING		FILLING DEFECT		CONTRAST MEDIUM LEAKAGE	
DISEASE	**FOCAL**	**DIFFUSE**	**FOCAL**	**DIFFUSE**	**ATTACHED**	**FREE**	**SMOOTH**	**IRREGULAR**
Chronic cystitis	Cranioventral	Occasional	Cranioventral	Occasional (Cytoxan-induced cystitis)	Blood clots	Blood clots, calculi	—	—
Polypoid cystitis	Cranioventral	—	Cranioventral	—	Cranioventral (Pedunculated or plaquelike)	Blood clots	—	—
Acute cystitis	—	—	—	—	—	Occasional blood clots	—	—
Cystic calculi	Cranioventral from cystitis	—	Cranioventral from cystitis	—	—	Calculi and occasional blood clots	—	—
Neoplasia	Any location within bladder	Occasional	Any location within bladder	Occasional	Sessile, occasionally pedunculated	Blood clots	—	—
Bladder contusion	Any location	Large areas of bladder often involved	Any location	Large areas of bladder often involved	Bladder wall hematoma	Blood clots	—	—
Bladder rupture or perforation	—	—	—	—	—	Blood clots	—	Most leakage is into peritoneal cavity
Traumatic diverticula	—	—	—	—	—	Blood clots	Any location	—
Urachal diverticula	Cranioventral associated with cystitis	—	Cranioventral associated with cystitis	—	—	—	Cranioventral	—

Table • **39-5**

Bladder Filling Defects

LESION	SHAPE	ATTACHMENT	BORDER/CONTOUR	BLADDER WALL INFILTRATION (THICKENING)
Calculi	Round to slightly irregular	Free in lumen; center of contrast puddle	Indistinct	Variable; usually cranioventral if associated with cystitis
Sebaceous or mucous plug	Round or irregular	Free in lumen; center of contrast puddle	Smooth or irregular, distinct or indistinct	Variable; associated with cystitis
Polyp	Pedunculated or convex	Stalk or sessile	Smooth or irregular, often with ulceration	Variable; bladder wall may be thick at attachment site
Epithelial neoplasia	Irregular or convex	Sessile	Irregular, often with ulceration	Bladder wall often thick or infiltrated at base of attachment
Mesenchymal neoplasia	Convex	Sessile	Usually smooth	Originates within the bladder wall
Blood clots	Irregular	Variable; may be free luminal	Irregular and indistinct	Thickened bladder wall from primary disease process
Bladder wall hematoma	Convex	Sessile	Smooth to slightly irregular	Originates within bladder wall
Ureterocele	Convex to round	Sessile	Smooth	Originates within trigone region of the bladder wall

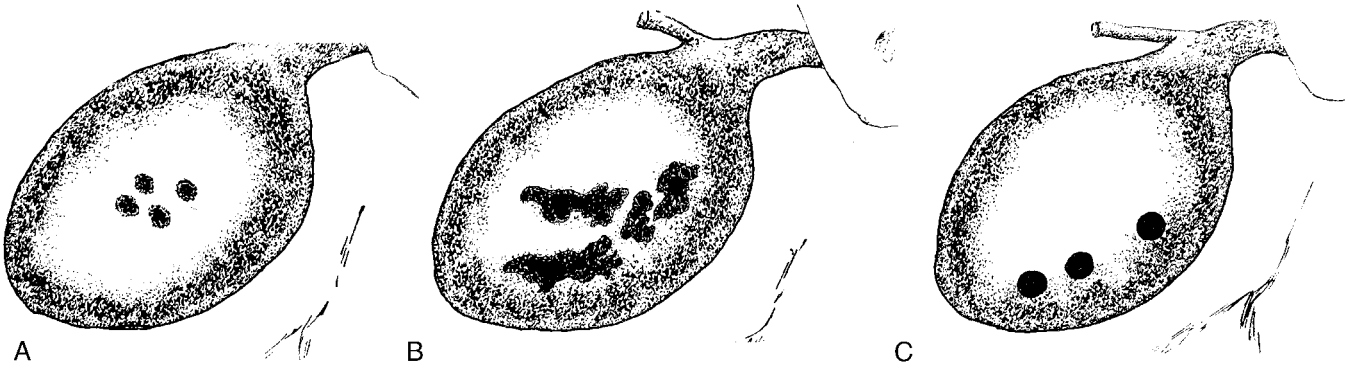


Fig. 39-17 Free luminal filling defects demonstrated by double-contrast cystography. **A,** Cystic calculi, in the center of the contrast puddle, are round with an indistinct border. **B,** Blood clots are irregularly shaped with irregular, indistinct borders; they may be located anywhere in the bladder. **C,** Air bubbles are round with smooth, distinct borders; they are shown here at the periphery of the contrast puddle but are more often seen centrally. (From Park RD: Radiology of the urinary bladder and urethra. In O'Brien TR, editor: *Radiographic diagnosis of abdominal disorders in the dog and cat*, Davis, Calif, 1981, Covell Park Veterinary.)

acquired diverticula, cysts, and persistent patent urachus or urachal ligament.[47-51] A urachal diverticulum can lead to retention of urine, which predisposes to urinary tract infection. Congenital urachal anomalies are characterized by smooth contrast-medium margins; they may be identified as an extension from the urinary bladder.

Contrast medium leakage from the urinary bladder to adjacent visceral structures may be seen with a congenital or acquired fistula. The organs most commonly involved are the rectum and the vagina. Such fistulas can usually be diagnosed dynamically with fluoroscopy or statically from a positive-contrast cystogram by noting contrast medium in the rectum or vagina simultaneously with or shortly after contrast medium is injected into the bladder.[52]

Contrast medium leakage into the peritoneal cavity and surrounding soft tissues has an irregular outline and usually occurs simultaneously with injection of contrast medium into the bladder (Fig. 39-22). With small bladder neck tears, leakage of contrast medium may be slow with only a small volume appearing outside the bladder.[5,50] In these instances, a second radiograph may be required 5 to 10 minutes after injection to identify delayed leakage from the bladder into the peritoneal cavity.

Pitfalls with Cystographic Interpretation

Interpretation pitfalls seen commonly with contrast cystography are air bubble artifacts and pseudofilling defects. Three types of air bubble artifacts have been recognized: small



Fig. 39-18 Positive-contrast cystogram. A large transitional cell carcinoma is present on the right side of the bladder *(arrows)*. The neoplasm causes a large filling defect with an irregular surface.

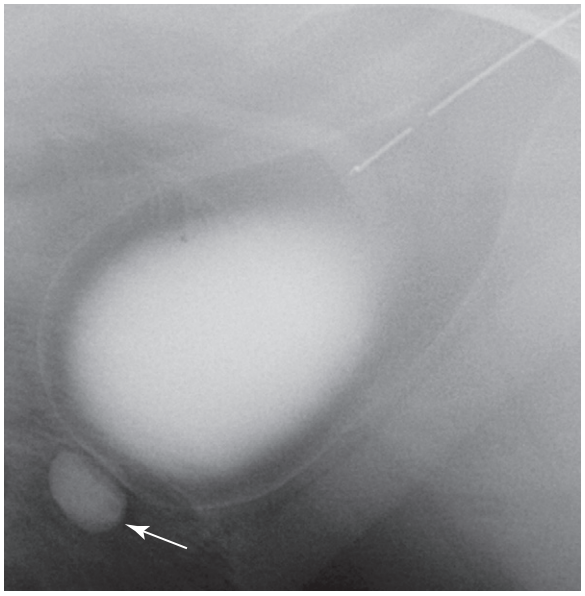


Fig. 39-20 Appearance of the cranioventral aspect of the bladder during double-contrast cystography in a dog. A small oblong urachal diverticulum fills with contrast medium *(white arrow)*. Contrast medium persisted in the diverticulum, evidence of urine retention that may predispose to a urinary tract infection.

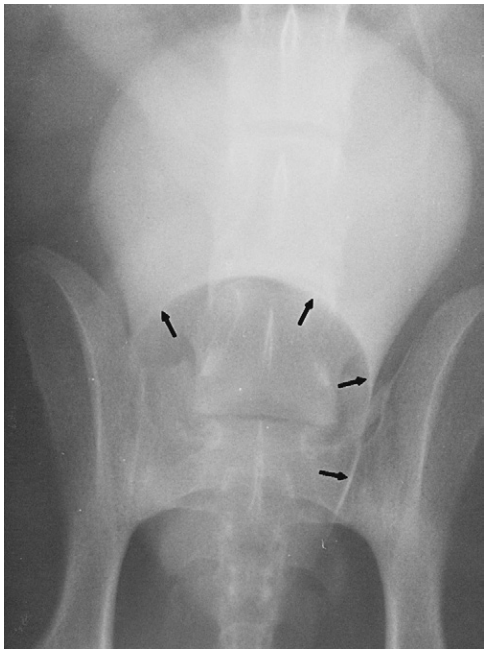


Fig. 39-19 Ventrodorsal radiograph of the bladder filled with contrast medium during intravenous urography. The smooth luminal filling defect *(black arrows)* that projects into the bladder neck is an ureterocele.

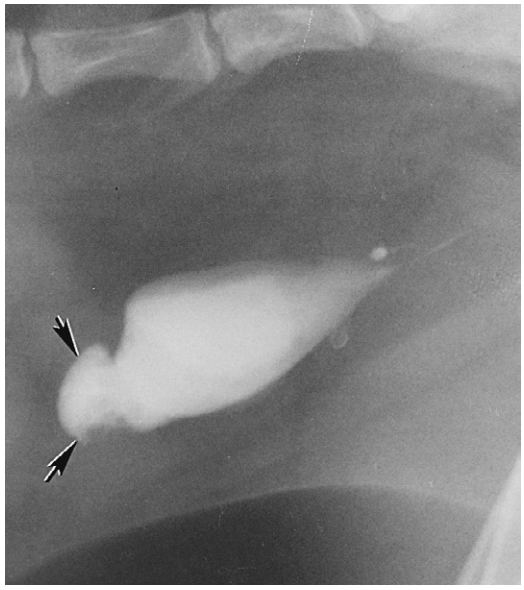


Fig. 39-21 A traumatic bladder diverticulum is present *(black arrows)*. Immediately after trauma, traumatic diverticula must be differentiated from a bladder contusion. Contusions usually heal within 48 hours, and the bladder then distends symmetrically.

air bubbles simulating calculi or other small luminal filling defects, a large air bubble simulating bladder wall thickening, and multiple air bubbles creating a honeycomb appearance (Fig. 39-23). Air bubbles are radiolucent and have smooth, distinct borders.

Pseudofilling defects may be mistaken for bladder neoplasia or other attached filling defects. These defects are created by inadequate bladder distention combined with external pressure from adjacent abdominal structures. Pseudofilling defects have a smooth surface and taper on both borders; they can be obliterated with further bladder distention (Fig. 39-24).

SONOGRAPHY

The fluid-filled urinary bladder is easily evaluated sonographically. The superficial location of the bladder enables high-resolution imaging, and urine provides high sonographic

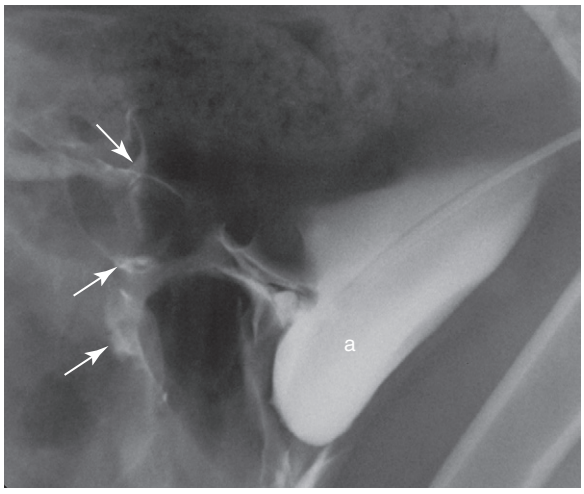


Fig. 39-22 Positive-contrast cystogram in a dog. Contrast medium fills the urinary bladder *(a)* but has also leaked into the peritoneal cavity *(white arrows)* from a dorsal bladder wall tear.

contrast, which results in clear visualization of the bladder wall and intraluminal abnormalities. Urolithiasis, neoplasia, cystitis, urachal, and vesicoureteral junction abnormalities can be identified by using sonography.[53-55]

High-resolution transducers (7 to 10 MHz) are best for examination of the bladder. A 5 MHz transducer may be necessary to penetrate to the far wall of a distended bladder in large dogs. Linear and curved wide-aperture format transducers are particularly useful. Image contrast settings should be set to high-contrast display; acoustic power and near gain should be decreased to suppress reverberation echoes generated between the transducer, the skin, and abdominal wall structures.

The sonographic examination is best performed when the bladder is moderately full. An empty or nearly empty bladder is difficult to locate because the wall is thicker, and image contrast is reduced. If a nearly empty bladder is encountered, it should be reexamined when it is moderately distended after some hours of inside confinement, after administration of a diuretic, or after catheterization and saline injection. The wall of a flaccid bladder can be deviated inward by a distended

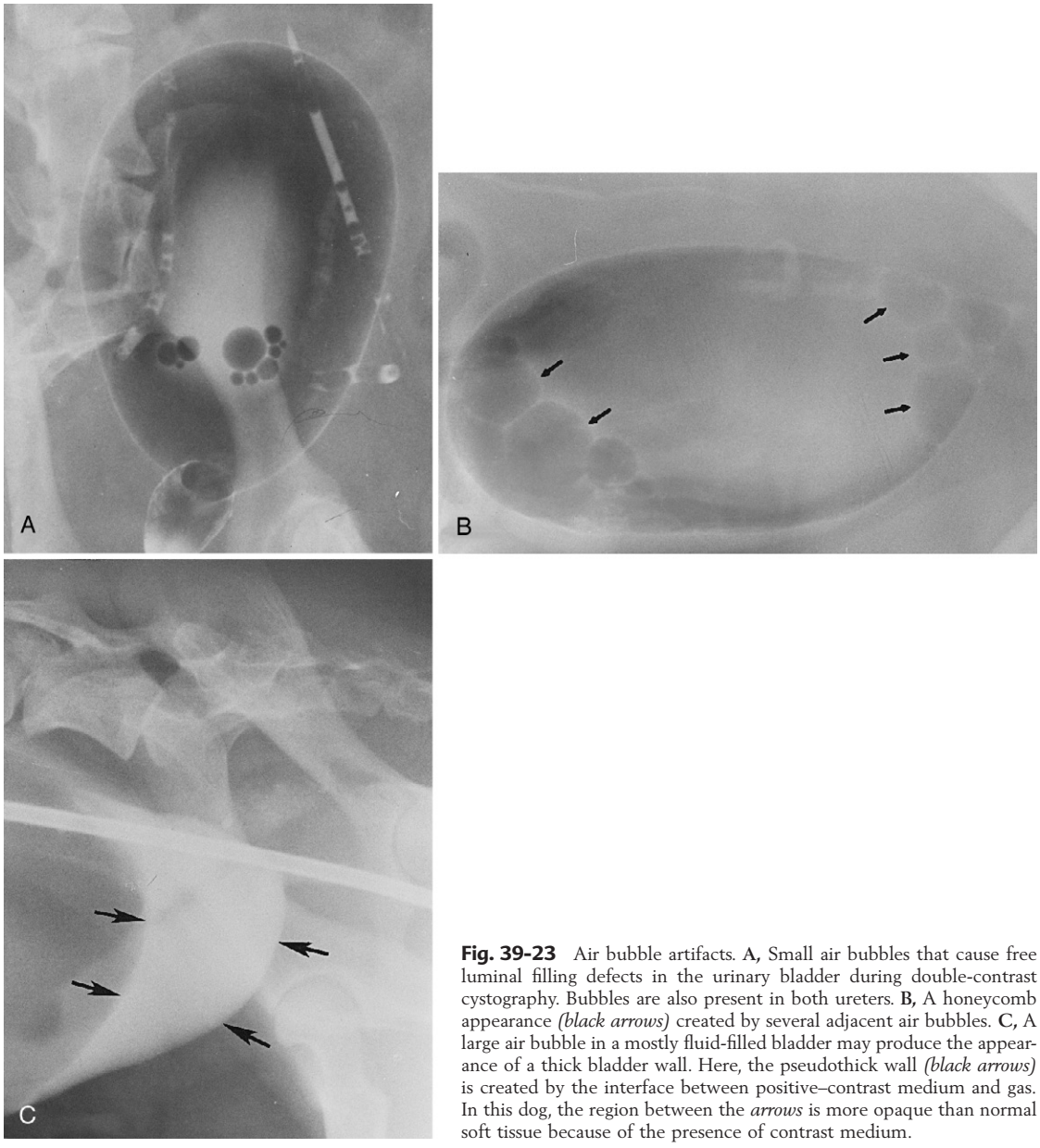


Fig. 39-23 Air bubble artifacts. **A,** Small air bubbles that cause free luminal filling defects in the urinary bladder during double-contrast cystography. Bubbles are also present in both ureters. **B,** A honeycomb appearance *(black arrows)* created by several adjacent air bubbles. **C,** A large air bubble in a mostly fluid-filled bladder may produce the appearance of a thick bladder wall. Here, the pseudothick wall *(black arrows)* is created by the interface between positive–contrast medium and gas. In this dog, the region between the *arrows* is more opaque than normal soft tissue because of the presence of contrast medium.

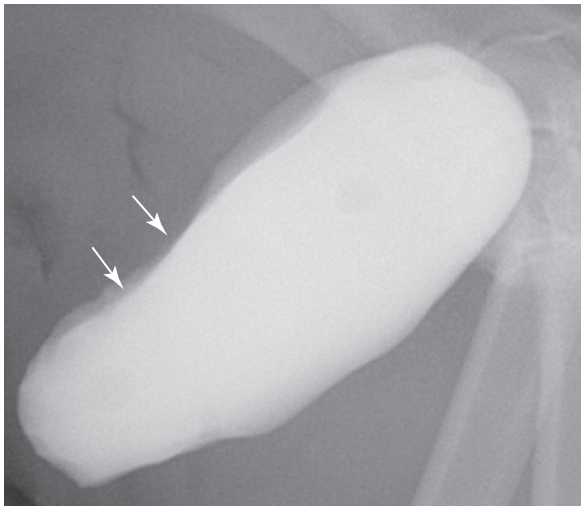


Fig. 39-24 Lateral radiograph of a positive-contrast cystogram. Pseudofilling defects *(white arrows)* are created by pressure from adjacent abdominal structures on a partially distended bladder.

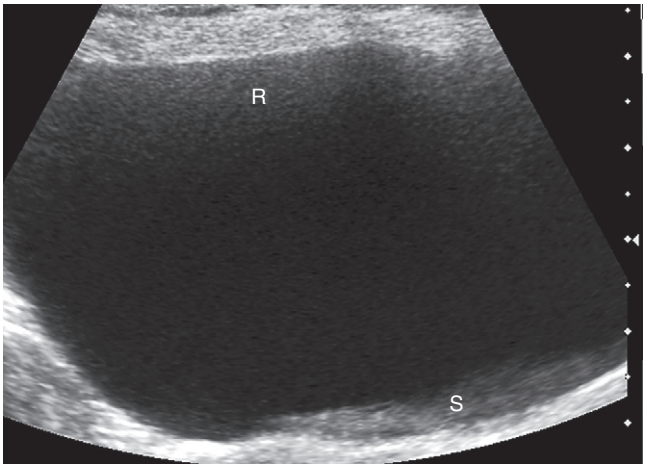


Fig. 39-25 Sonographic artifacts. Spurious echoes *(R)* are present in the ventral aspect of the lumen of the bladder from reverberation artifact. Slice thickness and/or side (grating) lobe artifact *(S)* is present in the dorsal aspect of the bladder, creating pseudoechogenic debris in the urine.

colon, and the acoustic shadow artifacts generated by colonic contents can appear like the shadows generated by calculi.[56] In medium to large dogs, a fully distended bladder is also less desirable because a lower frequency transducer that has lower resolution will be needed. Also, the thinner wall of a more distended bladder is more difficult to visualize and measure. Normal bladder wall thickness varies depending on the degree of bladder distention and body weight, being 2.3 mm thick with minimal distention and 1.4 mm thick with moderate distention.[57] In normal adult cats, the mean bladder wall thickness should not exceed 1.7 mm ± 0.6 mm.[58]

Bladder sonography can be performed with the patient in either dorsal or lateral recumbency. The bladder should be evaluated in a transverse plane and orthogonally in either a sagittal or dorsal plane. Accurate assessment of bladder wall thickness requires a perpendicular orientation of the ultrasound beam with the bladder wall. Assessment of the cranial aspect of the bladder wall is challenging because of the suboptimal beam alignment and the adjacent gas-filled bowel.[59] Side and grating lobe artifacts generated by the adjacent colon can give rise to an erroneous display of echogenic material in the bladder lumen, and the curved bladder wall can create additional echoes adjacent to the dorsal bladder wall (Fig. 39-25).[60] Transducer rotation of 90 degrees over such suspicious areas is often helpful to enable recognition of the proximity of the colon and determination of the nature of the artifact. Free intraluminal abnormalities such as calculi, sediment, and blood clots gravitate to the most dependent aspect of the bladder. In lateral recumbency, careful examination of the most dependent area of the bladder is required so that small calculi are not overlooked. Ballottement is useful for initiating sediment swirling across the real-time display. Additional imaging after the animal has been positioned in the opposite lateral recumbent or standing position allows detection of gravitation of free intraluminal objects to a dependent position within the bladder.

The normal bladder is ovoid in shape with a slight elongation caudally at the neck. The ureters and urethra are not visualized unless they become distended with urine. With high-resolution transducers, three distinct wall layers can be seen. The mucosa is a thin hyperechoic surface outlined against the urine, the middle muscle layer is hypoechoic, and the outer serosal layer is hyperechoic.[58] The cranioventral aspect of the wall is slightly thinner than in other regions. Normal urine is anechoic. The turbulence created by discharge of urine through the ureteral openings may generate transient echo jets in the bladder lumen adjacent to the trigone.[61]

Intraluminal Changes

Urinary calculi, cellular and crystalline debris, gas, hemorrhage, and blood clots are detected readily by sonography (Fig. 39-26, *A*). Consideration of the gravitational alignment is especially helpful in differentiating calculi and blood clots that gravitate dependently from gas bubbles that rise. The location of cellular and crystalline debris and fresh hemorrhage is more variable. Severe acute hemorrhage can fill the bladder and give rise to a lacy hyperechoic pattern, which may change little with ballottement or animal repositioning (Fig. 39-26, *B*). A similar appearance can be observed with severe proteinuria and fat droplets.[62] Sedimentation can occur, and vigorous ballottement will generate swirling echo patterns on real-time display.

Calculi

The urine/calculus interface is intensely hyperechoic and usually appears convex. Multiple calculi often aggregate together and give rise to an irregular, somewhat continuous surface, which makes distinguishing and measuring individual calculi difficult. Distinct acoustic shadows may be observed deep to calculi (Fig. 39-27). Shadowing is related to size (height) of the calculus and transducer frequency, with increasing height of the calculus and increasing transducer frequency more likely to produce acoustic shadows.[63] The application of color Doppler to distinguish calculi based on the twinkling artifact occurring deep to the calculus can be used to discriminate mineralized from nonmineralized structures.[64] Smaller calculi may not generate the characteristic shadows; however, optimizing the focal zone of the beam at the depth of the calculi may generate shadows. Echogenicity and acoustic shadow generation are independent of chemical composition, so radiopaque and nonradiopaque calculi can be detected by sonography.[61] Ballottement usually does not cause calculi to move, but placing the animal in a standing position allows detection of the relocated calculi into the cranioventral aspect of the bladder. This action helps differentiate calculi from an adjacent colonic acoustic shadow and dystrophic mineralization in the bladder wall.

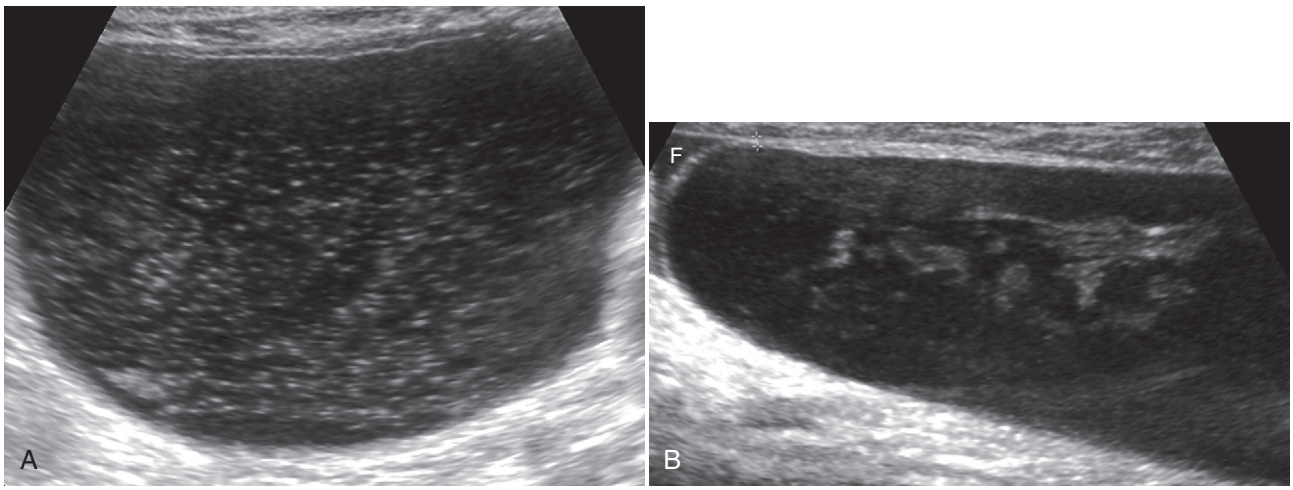


Fig. 39-26 **A,** Sagittal sonogram of the urinary bladder. Intraluminal, hyperechoic foci representing crystals (crystalluria) are present in the dependent portion of urinary bladder. **B,** Sagittal sonogram of the urinary bladder. Intraluminal, hyperechoic, lacy material is acute hemorrhage located in the mid and ventral aspects of the urinary bladder. A small amount of echogenic fluid representing free abdominal hemorrhage *(F)* is present adjacent to the cranioventral aspect of the urinary bladder.

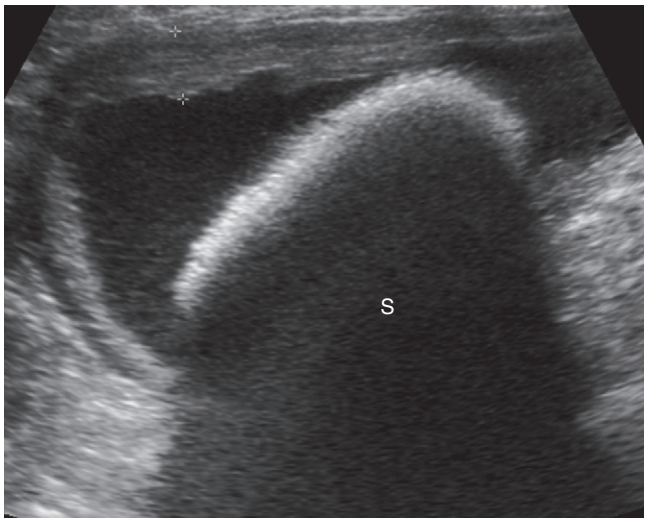


Fig. 39-27 Sagittal sonogram of the urinary bladder. A solitary, large calculus creates characteristic acoustic shadows *(S)* and irregular thickening of the cranioventral bladder wall (calipers in image) secondary to cystitis.

Gas bubbles introduced accidentally by bladder catheterization or cystocentesis appear echogenic and can generate acoustic shadows or reverberation artifacts. Differentiation from calculi is easy because the bubble floats on top of the urine.

Crystalline and cellular sediments generate a variably echogenic pattern in more dependent urine. In cats, the crystalline deposits may become thick enough to form a hyperechoic layer confluent with the bladder wall that creates acoustic shadowing. Ballottement or changing patient position can differentiate the swirling sediment from calculi.

Blood Clots

Blood clots tend to be associated with the clinical observation of severe hematuria. Relative to normal urine, a blood clot commonly appears as a hyperechoic, nonshadowing, mobile mass.[65,66] Sometimes the clot may be attached to the wall, covering, or adjacent to a traumatic injury or a neoplastic mass.

Foreign Bodies

Urinary bladder foreign bodies, such as grass awns, have been reported and appear as linear to V-shaped hyperechoic structures with or without distal acoustic shadows.[67]

Mural Changes

Sonography is especially useful for detecting changes from chronic cystitis and neoplasia. Contrast radiographic techniques are superior to sonography in diagnosing congenital abnormalities of the urachus and ureters as well as bladder rupture. However, infusion of microbubbled saline into the urinary bladder has been effective for diagnosing urine leakage in some patients.[68]

Cystitis

Chronic cystitis results in focal or diffuse thickening of the bladder wall and is readily detected by sonography. The bladder wall becomes abnormally hypoechoic, and the normal layering becomes less parallel. Measurements reveal abnormal wall thickness (see Fig. 39-27), and hyperechoic cellular debris frequently accumulates in the bladder lumen.[69] A normal sonographic appearance of the bladder does not rule out the presence of mild or acute cystitis or idiopathic lower urinary tract disease in cats. Small polypoid mucosal masses are also occasionally observed with chronic cystitis. Polypoid cystitis is uncommon in dogs and can vary in sonographic appearance ranging from pedunculated, ovoid, or nodular bladder wall changes (Fig. 39-28).[70] Polypoid cystitis is often located in the cranioventral and craniodorsal portions of the bladder, which may aid in differentiation from neoplasia, such as transitional cell carcinoma, which is usually located near the bladder neck.[70,71] Follow-up sonographic evaluations should be made after treatment of polypoid cystitis to reevaluate the masses. Biopsy is needed for definitive diagnosis. Muscular hypertrophy resulting from chronic partial lower urinary tract obstruction can also cause bladder wall thickening and may simulate the sonographic appearance of cystitis.

Emphysematous cystitis creates a confusing sonographic appearance because the gas artifacts may obscure bladder

anatomy (Fig. 39-29). Sonographic changes including linear hyperechogenicities with or without reverberation artifact, trapped in the bladder wall and free in the bladder lumen, can be seen.[16]

Mural Hemorrhage

Mural hemorrhage can occur in patients with trauma or a bleeding disorder. This is associated with diffuse thickening of the urinary bladder wall that can resolve quickly after treatment is initiated.[72]

Neoplasia

Several kinds of bladder tumors have been documented, with transitional cell carcinoma being the most common.[54] Transitional cell carcinoma of the bladder is characterized most frequently by an irregularly shaped, broad-based, complex to hypoechoic mass protruding into the bladder lumen.[54] Single or multiple masses may be present (Fig. 39-30). The echo pattern can vary if fibrosis, mineralization, and necrosis have developed. Adjacent blood clots can occur and can contribute falsely to the size and echogenic texture of the mass. An abrupt transition is often observed between the neoplastic mass and the adjacent bladder wall.[54] Smooth muscle neoplasia, such as leiomyoma or leiomyosarcoma, can appear as a single, round, well-defined intraluminal mass.[73] Urinary bladder fibrosarcomas and rhabdomyosarcomas are often located in the neck of the bladder and are typically found in young dogs.[74,75] Lymphoma has a similar sonographic appearance to other urinary bladder tumors but will usually be accompanied by lesions in other abdominal organs and lymph nodes.[76] Some highly aggressive carcinomas and mesenchymal tumors can spread through the bladder wall. If a small intraluminal mass occurs, the bladder can take on the appearance of severe cystitis. Unfortunately, the sonographic appearance of polypoid cystitis, adherent blood clots, and mural hematomas is similar to that of bladder neoplasia. The observation of ureter dilation adjacent to the bladder wall mass (see Fig. 39-30) and focal medial iliac lymphadenopathy tends to support the diagnosis of neoplasia. An aspirate, biopsy, or both are necessary to confirm the presence of bladder neoplasia. The information gained from percutaneous aspiration of a bladder mass must be weighed against the possibility of seeding the needle tract with tumor cells.[77]

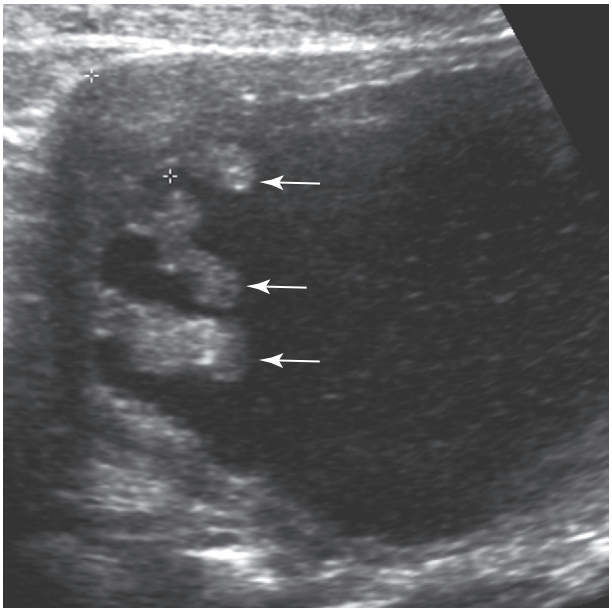


Fig. 39-28 Sagittal sonogram of the urinary bladder. There is focal bladder wall thickening (calipers in image) with associated pedunculated, hyperechoic polyps *(white arrows)* secondary to polypoid cystitis. Echogenic intraluminal debris is present within the urine.

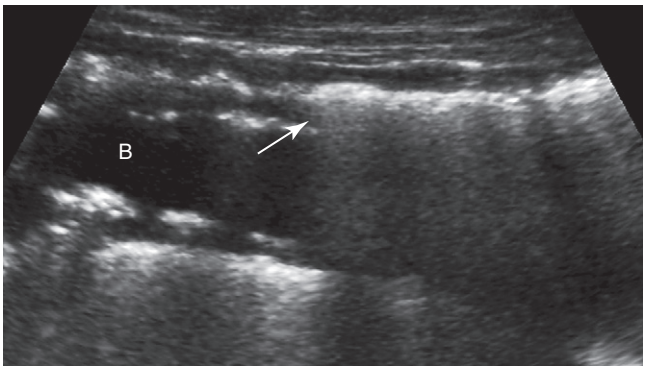


Fig. 39-29 Sagittal sonogram of the urinary bladder. Note the linear hyperechogenicities with and without reverberation *(white arrow)* artifact, trapped within the bladder wall secondary to emphysematous cystitis. Anechoic urine is within the bladder *(B)*.

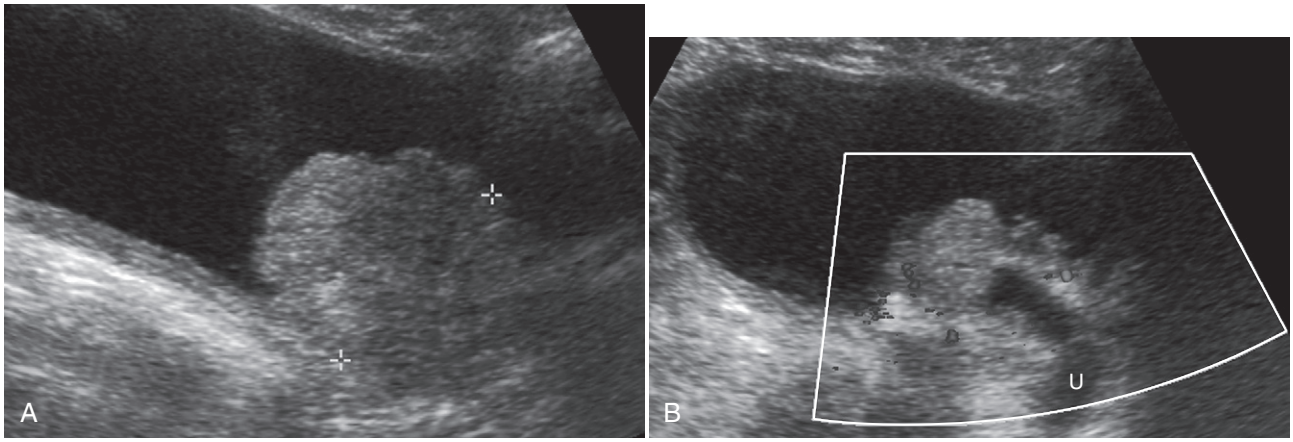


Fig. 39-30 **A,** Sagittal sonogram of the urinary bladder. There is a hyperechoic, broad-based mass in the bladder neck from transitional cell carcinoma. **B,** This mass obstructed the adjacent ureter, causing hydroureter *(U)*. Note the color Doppler box over the mass and ureter confirming no blood flow within the ureter.

Ureterovesicular Junction

The ureterovesicular junction can be visualized in normal dogs as small convex structures on the dorsal part of the bladder.[78] However, they may not be identified if the bladder is caudally located. Identifying a ureteral jet in the bladder confirms a normal ureterovesicular junction.[78] Ureteral ectopia can be diagnosed with ultrasound by identifying dilated ureters coursing past the bladder neck (Fig. 39-31).[79] Concurrent renal pyelectasia and hydroureter may be present. Orthotopic and ectopic ureteroceles can be identified with ultrasound.[42,44] Sonographically, ureteroceles are smooth, thin-walled cystic structures within the bladder lumen, bladder wall, or proximal urethra.[44] Ureteroceles have been described sonographically as a cyst within a cyst (Fig. 39-32).[80]

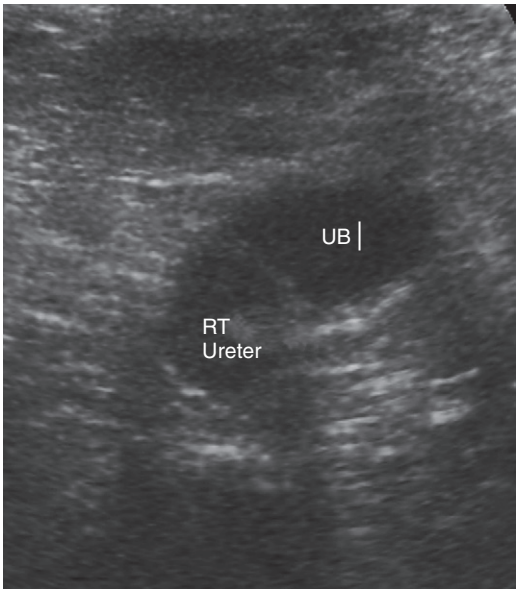


Fig. 39-31 Transverse sonogram at the level of the bladder neck. Note the dilated, anechoic right ureter adjacent to the bladder neck *(UB)*. The dilated ureter coursed past the ureterovesicular junction and continued past the bladder, indicating ureteral ectopia.

COMPUTED TOMOGRAPHY AND MAGNETIC RESONANCE IMAGING OF THE URINARY BLADDER

Computed tomography (CT) imaging is useful to diagnose abnormalities of the urinary bladder wall and ureterovesicular junction. CT-excretory urography can be used to diagnose ureteral ectopia by following the course of the ureters as they enter or continue past the ureterovesicular junction (Fig. 39-33).[81,82] Transitional cell carcinoma of the bladder can be evaluated with CT to determine extent of tumor size for pretreatment staging (Fig. 39-34).[83]

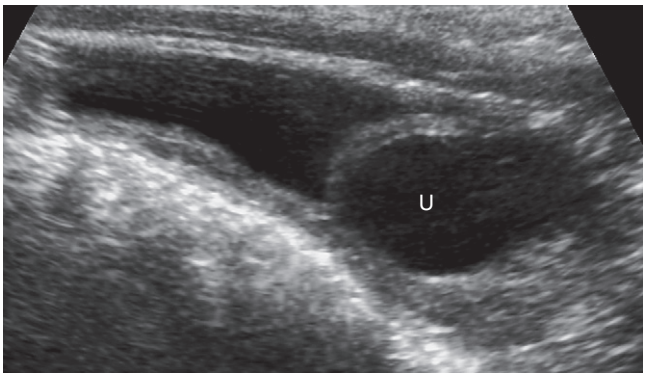


Fig. 39-32 Sagittal sonogram of the urinary bladder. Note the "cyst-within-a-cyst" appearance to the ureterocele *(U)* with the urinary bladder neck.

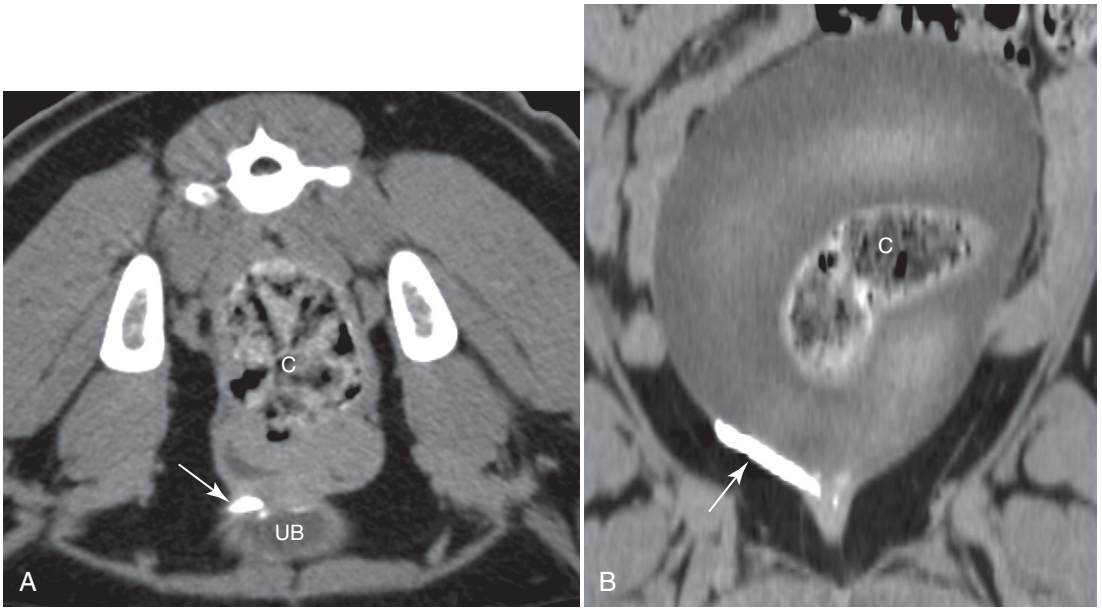


Fig. 39-33 **A,** CT excretory urogram at the level of the bladder neck. The dilated, contrast-medium–filled right ureter *(white arrow)* is located dorsal to the urinary bladder *(UB)*. The ureter coursed into the urethra, confirming ureteral ectopia. The colon is filled with gas and fecal material*(C)*. **B,** Reformatted dorsal plane image of the distal right ureter. Note the dilated, contrast-medium–filled right ureter *(white arrow)* at the level of the bladder neck beyond the ureterovesicular junction. A portion of descending colon *(C)* appears to be within the urinary bladder because of slice thickness artifact.

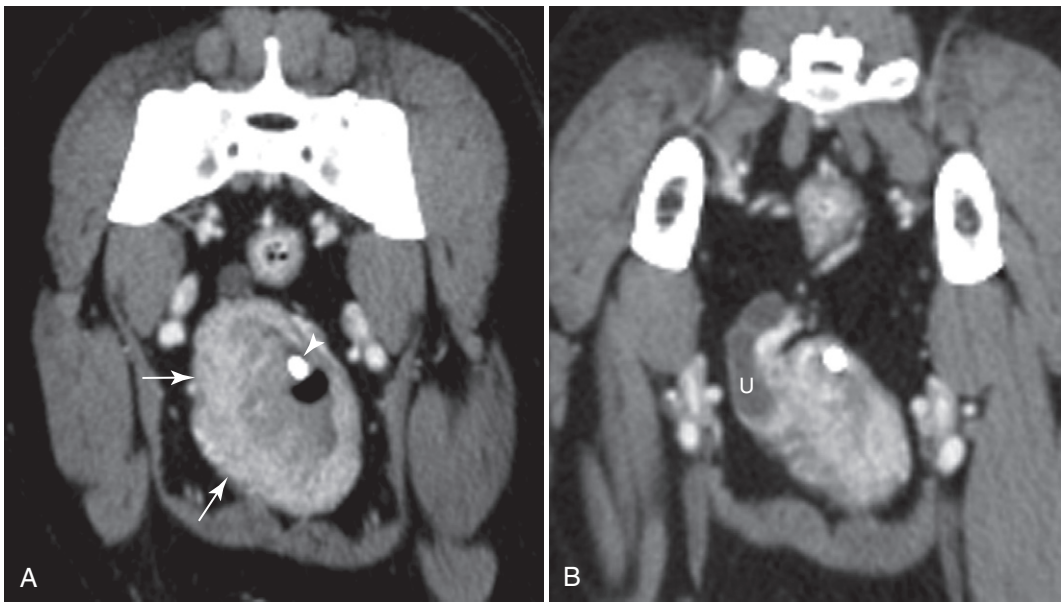


Fig. 39-34 **A,** CT excretory urogram of the urinary bladder. Note the irregularly contrast-enhancing thickened bladder wall from infiltrative tumor *(white arrows)*. The gas and oval hyperattenuating structure within the bladder lumen is the inflated Foley bulb catheter *(white arrowhead)*. **B,** Same study at level of ureterovesicular junction. Note the hydroureter *(U)* secondary to obstruction from the plaquelike mass.

Magnetic resonance imaging is used in people to evaluate inflammatory and malignant conditions of the urinary bladder and may be used in veterinary medicine in the future.[84]

REFERENCES

1. International Committee on Veterinary Gross Anatomical Nomenclature (ICVGAN): *Nomina anatomica veterinaria*, ed 5, Hannover, Columbia, 2005, Editorial Committee.
2. Evans, HE: *Miller's anatomy of the dog*, ed 3, Philadelphia, 1993, Saunders.
3. Mahaffey MB, et al: Pelvic bladder in dogs without urinary incontinence, *J Am Vet Med Assoc* 184(12):1477–1479, 1984.
4. Johnston GR, et al: Effects of urinary bladder distention on location of the urinary bladder and urethra of healthy dogs and cats, *Am J Vet Res* 47(2):404–415, 1986.
5. Nickel R, Schummer A, Seiferle E, Sack WO: *The viscera of the domestic mammals*, vol 184, ed 2, Berlin, 1973, Paul Parey/Springer-Verlag.
6. Park R: Radiology of the urinary bladder and urethra. In O'Brien T, editor: *Radiographic diagnosis of abdominal disorders in the dog and cat*, Davis, Calif, 1981, Covell Park Veterinary, p 543.
7. White R, Herrtage M: Bladder retroflexion in the dog, *J Small Anim Pract* 27:735–746, 1986.
8. Adams WM, DiBartola SP: Radiographic and clinical features of pelvic bladder in the dog, *J Am Vet Med Assoc* 182(11):1212–1217, 1983.
9. Mahaffey M, Barber D, Basanti J: Simultaneous double-contrast cystography and cystometry in dogs, *Vet Radiol* 25, 254–259, 1984.
10. Massat BJ, et al: Cystourethropexy to correct refractory urinary incontinence due to urethral sphincter mechanism incompetence. Preliminary results in ten bitches, *Vet Surg* 22(4):260–268, 1993.
11. Holt P: Urinary incontinence in the bitch due to sphincter mechanism incompetence: prevalence in referred dogs and retrospective analysis of 60 cases, *J Small Anim Pract* 26, 181–190, 1985.
12. Patnaik AK, Greene RW: Intravenous leiomyoma of the bladder in a cat, *J Am Vet Med Assoc* 175(4):381–383, 1979.
13. Hansen JS: Persistent urachal ligament in the cat (report of two cases), *Vet Med Small Anim Clin* 67(10):1090, 1972.
14. Root CR, Scott RC: Emphysematous cystitis and other radiographic manifestations of diabetes mellitus in dogs and cats, *J Am Vet Med Assoc* 158(6):721–728, 1971.
15. Lobetti RG, Goldin JP: Emphysematous cystitis and bladder trigone diverticulum in a dog, *J Small Anim Pract* 39(3):144–147, 1998.
16. Petite A, et al: Radiographic and ultrasonographic findings of emphysematous cystitis in four nondiabetic female dogs, *Vet Radiol Ultrasound* 47(1):90–93, 2006.
17. Buffington CA, et al: Clinical evaluation of cats with nonobstructive urinary tract diseases, *J Am Vet Med Assoc* 210(1):46–50, 1997.
18. Steyn P, Lowry J: Positional radiographic as an aid to diagnose sand-like uroliths in the urinary bladder of feline urologic syndrome in cats, *Feline Pract* 19, 21–23, 1991.
19. Zotti A, et al: Chronic cystitis with ossification of the bladder wall in a 6-month-old German shepherd dog, *Can Vet J* 48(9):935–938, 2007.
20. Moreau PM, Lees GE, Gross DR: Simultaneous cystometry and uroflowmetry (micturition study) for evaluation of the caudal part of the urinary tract in dogs: studies of the technique, *Am J Vet Res* 44(9):1769–1773, 1983.
21. Moreau, PM, Lees GE, Gross DR: Simultaneous cystometry and uroflowmetry (micturition study) for evaluation of the caudal part of the urinary tract in dogs: reference values for healthy animals sedated with xylazine, *Am J Vet Res* 44(9):1774–1781, 1983.
22. Rosin AE, Barsanti JA: Diagnosis of urinary incontinence in dogs: role of the urethral pressure profile, *J Am Vet Med Assoc* 178(8):814–822, 1981.

23. Oliver JE Jr, Young WO: Air cystometry in dogs under xylazine-induced restraint, *Am J Vet Res* 34(11):1433–1435, 1973.
24. Lane IF, Lappin MR, Seim HB 3rd: Evaluation of results of preoperative urodynamic measurements in nine dogs with ectopic ureters, *J Am Vet Med Assoc* 206(9):1348–1357, 1995.
25. Mooney JK Jr, Cox CE, Hinman F: Vesical contamination from insertion of everting cot or catheter in inoculated canine urethra, *Invest Urol* 11(3):248–257, 1973.
26. Buchanan J: Kinked catheter: complication of pneumocystography, *J Am Vet Radiol* 8, 54–56, 1967.
27. Feeney DA, et al: Effects of sterilized micropulverized barium sulfate suspension and meglumine iothalamate solution on the genitourinary tract of healthy male dogs after retrograde urethrocystography, *Am J Vet Res* 45(4):730–738, 1984.
28. Johnston GR, et al: Complications of retrograde contrast urethrography in dogs and cats, *Am J Vet Res* 44(7):1248–1256, 1983.
29. Barsanti JA, et al: Complications of bladder distension during retrograde urethrography, *Am J Vet Res* 42(5):819–821, 1981.
30. Farrow CS: Exercise in diagnostic radiology, *Can Vet J* 22(11):359–360, 1981.
31. Ackerman N, Wingfield WE, Corley EA: Fatal air embolism associated with pneumourethrography and pneumocystography in a dog, *J Am Vet Med Assoc* 160(12): 1616–1618, 1972.
32. Zontine W, Andrews L: Fatal air embolization as a complication of pneumocystography in two cats, *J Am Vet Med Assoc* 19:8–11, 1978.
33. Thayer GW, Carrig CB, Evans AT: Fatal venous air embolism associated with pneumocystography in a cat, *J Am Vet Med Assoc* 176(7):643–645, 1980.
34. Brodeur AE, Goyer RA, Melick W: A potential hazard of barium cystography, *Radiology* 85(6):1080–1084, 1965.
35. Mahaffey M, Barsanti J, Browell W: Cystography: effect of technique on diagnosis of cystitis in dogs, *Vet Radiol* 30(261), 1989.
36. Johnston G, Feeney D: Radiographic evaluation of the urinary tract in dogs and cats: contemporary issues in small animal practice, *Nephrol Urol* 4:203, 1989.
37. Mostofi FK: Potentialities of bladder epithelium, *J Urol* 71(6):705–714, 1954.
38. Weichselbaum RC, et al: Urocystolith detection: comparison of survey, contrast radiographic and ultrasonographic techniques in an in vitro bladder phantom, *Vet Radiol Ultrasound* 40(4):386–400, 1999.
39. Weichselbaum RC, et al: In vitro evaluation of contrast medium concentration and depth effects on the radiographic appearance of specific canine urolith mineral types, *Vet Radiol Ultrasound* 39(5):396–411, 1998.
40. Weichselbaum RC, et al: An integrated epidemiologic and radiographic algorithm for canine urocystolith mineral type prediction, *Vet Radiol Ultrasound* 42(4):311–319, 2001.
41. Johnston GR, Walter PA, Feeney DA: Radiographic and ultrasonographic features of uroliths and other urinary tract filling defects, *Vet Clin North Am Small Anim Pract* 16(2):261–293, 1986.
42. Stiffler KS, et al: Intravesical ureterocele with concurrent renal dysfunction in a dog: a case report and proposed classification system, *J Am Anim Hosp Assoc* 38(1):33–39, 2002.
43. Colopy SA, et al: What is your diagnosis? Ectopic ureterocele, *J Am Vet Med Assoc* 238(3):293–294, 2011.
44. Sutherland-Smith J, et al: Ectopic ureters and ureteroceles in dogs: presentation, cause, and diagnosis, *Compend Contin Educ Pract Vet* 303–316, 2004.
45. Scrivani PV, Leveille R, Collins RL: The effect of patient positioning on mural filling defects during double contrast cystography, *Vet Radiol Ultrasound* 38(5):355–359, 1997.
46. Archibald J: Urinary system. In Archibald J, editor: *Canine surgery*, Wheaton, Ill, 1965, American Veterinary Publications, p 553.
47. Remedios AM, et al: Diverticula of the urinary bladder in a juvenile dog, *Can Vet J* 35(10):648–650, 1994.
48. Scheepens ET, L'Eplattenier H: Acquired urinary bladder diverticulum in a dog, *J Small Anim Pract* 46(12):578–581, 2005.
49. Rahal SC, Mamprim MJ, Torelli SR: What is your diagnosis? Patent urachus, *J Am Vet Med Assoc* 225(7):1041–1042, 2004.
50. Osborne CA, et al: Etiopathogenesis and biological behavior of feline vesicourachal diverticula. Don't just do something—stand there, *Vet Clin North Am Small Anim Pract* 17(3):697–733, 1987.
51. Park R: Radiographic contrast studies of the lower urinary tract, *Vet Clin North Am* 4(4):863–887, 1974.
52. Osuna D, Stone E, Metcalf M: A urethrorectal fistula with concurrent urolithiasis in a dog, *J Am Anim Hosp Assoc* 25:35–39, 1989.
53. Biller D, Kantrowitz B, Partinton R: Diagnostic ultrasound of the urinary bladder, *J Am Anim Hosp Assoc* 26:397–402, 1990.
54. Leveille R, Biller D, Partington B: Sonographic investigation of transitional carcinoma of the urinary bladder in small animals, *Vet Radiol* 33:103–107, 1992.
55. Leveille R: Ultrasonography of urinary bladder disorders, *Vet Clin North Am Small Anim Pract* 28(4):799–821, 1998.
56. Berry C: Differentiating cystic calculi from colon, *Vet Radiol* 33:283–285, 1992.
57. Geisse AL, et al: Sonographic evaluation of urinary bladder wall thickness in normal dogs, *Vet Radiol Ultrasound* 38(2):132–137, 1997.
58. Finn-Bodner S, Carter R, Gray B: Sonographic architecture and morphometric evaluation of the normal feline urinary bladder wall, *Am Coll Vet Radiol*, 1992.
59. Douglass J, Kremkan F: Ultrasound corner: the urinary bladder wall hypoechoic pseudolesion, *Vet Radiol Ultrasound* 34, 45–46, 1993.
60. Barthez PY, Leveille R, Scrivani PV: Side lobes and grating lobes artifacts in ultrasound imaging, *Vet Radiol Ultrasound* 38(5):387–393, 1997.
61. Spaulding K, Stone EA: Color Doppler evaluation of ureteral flow dynamics in the dog as influenced by relative specific gravity, *Am Coll Vet Radiol*, 1993.
62. Finn-Bodem ST: The urinary bladder. In Cartee RE, editor: *P.V. Practical veterinary ultrasound*, Philadelphia, 1995, Lea & Febiger, p 219.
63. Weichselbaum RC, et al: Relevance of sonographic artifacts observed during in vitro characterization of urocystolith mineral composition, *Vet Radiol Ultrasound* 41(5):438–446, 2000.
64. Louvet A: Twinkling artifact in small animal color-Doppler sonography, *Vet Radiol Ultrasound* 47(4):384–390, 2006.
65. Feeney D, Walter P: *Ultrasonography of the kidneys, adrenal glands and urinary bladder*, 1989, in Proceedings of the American Institute of Ultrasound in Medicine.
66. Ackerman N: *Radiology and ultrasound of urogenital disease in dogs and cats*, Ames, 1991, Iowa State University, p 1.

67. Cherbinsky O, et al: Ultrasonographic features of grass awns in the urinary bladder, *Vet Radiol Ultrasound* 51(4), 462–465, 2010.
68. Cote E, et al: Diagnosis of urinary bladder rupture using ultrasound contrast cystography: in vitro model and two case-history reports, *Vet Radiol Ultrasound* 43(3):281–286, 2002.
69. Finn-Bodner S, Hudson J, Brewer WG: Transabdominal sonographic evaluation of experimentally induced cystitis of the feline urinary bladder, In Scientific Proceedings of the ACVR, 1993.
70. Takiguchi M, Inaba M: Diagnostic ultrasound of polypoid cystitis in dogs, *J Vet Med Sci* 67(1):57–61, 2005.
71. Martinez I, et al: Polypoid cystitis in 17 dogs (1978–2001), *J Vet Intern Med* 17(4):499–509, 2003.
72. O'Brien RT, Wood EF: Urinary bladder mural hemorrhage associated with systemic bleeding disorders in three dogs, *Vet Radiol Ultrasound* 39(4):354–356, 1998.
73. Heng HG, et al: Smooth muscle neoplasia of the urinary bladder wall in three dogs, *Vet Radiol Ultrasound* 47(1):83–86, 2006.
74. Takiguchi M, et al: Rhabdomyosarcoma (botryoid sarcoma) of the urinary bladder in a Maltese, *J Small Anim Pract* 43(6):269–271, 2002.
75. Olausson A, et al: A urinary bladder fibrosarcoma in a young dog, *Vet Radiol Ultrasound* 46(2):135–138, 2005.
76. Benigni L, et al: Lymphoma affecting the urinary bladder in three dogs and a cat, *Vet Radiol Ultrasound* 47(6):592–596, 2006.
77. Nyland TG, Wallack ST, Wisner ER: Needle-tract implantation following US-guided fine-needle aspiration biopsy of transitional cell carcinoma of the bladder, urethra, and prostate, *Vet Radiol Ultrasound* 43(1):50–53, 2002.
78. Lamb CR: Ultrasonography of the ureters, *Vet Clin North Am Small Anim Pract* 28(4):823–848, 1998.
79. Lamb CR, Gregory SP: Ultrasonographic findings in 14 dogs with ectopic ureter, *Vet Radiol Ultrasound* 39(3):218–223, 1998.
80. Takiguchi M, et al: Ultrasonographic appearance of orthotopic ureterocele in a dog, *Vet Radiol Ultrasound* 38(5):398–399, 1997.
81. Samii VF, et al: Digital fluoroscopic excretory urography, digital fluoroscopic urethrography, helical computed tomography, and cystoscopy in 24 dogs with suspected ureteral ectopia, *J Vet Intern Med* 18(3):271–281, 2004.
82. Barthez PY, Begon D, Delisle F: Effect of contrast medium dose and image acquisition timing on ureteral opacification in the normal dog as assessed by computed tomography, *Vet Radiol Ultrasound* 39(6):524–527, 1998.
83. Murphy S, et al: Laparoscopically implanted tissue expander radiotherapy in canine transitional cell carcinoma, *Vet Radiol Ultrasound* 49(4):400–405, 2008.
84. Silverman SG, Leyendecker JR, Amis ES: What is the current role of CT urography and MR urography in the evaluation of the urinary tract? *Radiology* 250(2):309, 2009.

ELECTRONIC RESOURCES

Evolve

Additional information related to the content in Chapter 39 can be found on the companion Evolve website at http://evolve.elsevier.com/Thrall/vetrad/

- Chapter Quiz

CHAPTER • 40

The Urethra

James C. Brown, Jr.

ANATOMY

The urethra is a tubular organ that serves as an outlet for urine from the urinary bladder and, in the male, semen and reproductive secretions. Anatomically, the male urethra comprises three major areas: the prostatic urethra, membranous urethra, and penile urethra (Fig. 40-1).[1] Together, the prostatic and membranous portions make up the pelvic part of the urethra.[2] The prostatic urethra is surrounded completely by the prostate gland in the dog, although only dorsolaterally in the cat.[3] The membranous urethra is enveloped by cavernous tissue and the urethralis muscle.[3] The penile urethra extends from the ischial arch to the tip of the penis. This part of the urethra is also known as the cavernous urethra because the majority of it is encased by erectile tissues of the penis.[2] The most distal part of the penile urethra is received and protected by the ventral urethral groove of the os penis. The arrangement of urethral muscle and surrounding spongy tissues confers a diffuse sphincter mechanism to the urethra in male dogs.

The female urethra is comparatively shorter and wider than in males and entirely pelvic in position. The external urethral orifice lies caudal to the vestibulovaginal junction, where a muscular urethral sphincter is present.[2]

In the cat, the urinary bladder is typically intraabdominal in position, and a relatively long prepelvic part of the urethra extends between the neck of the urinary bladder and the pelvic urethra.[3]

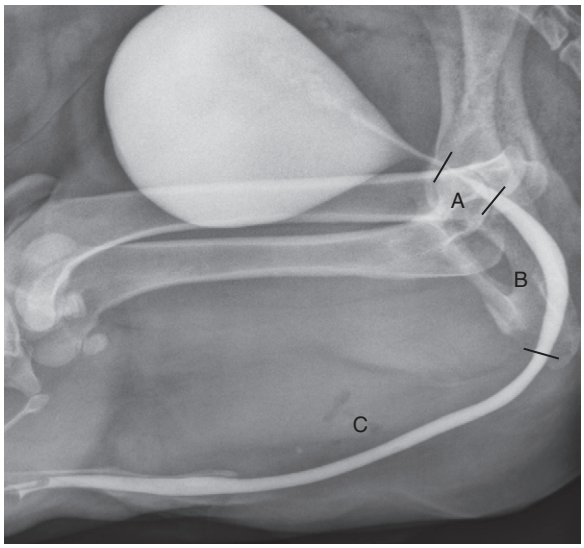


Fig. 40-1 Retrograde urethrography in a normal male dog. A Foley catheter is present in the distal penile urethra, and iodinated contrast medium was injected. The urethra comprises **(A)** the prostatic urethra, **(B)** the membranous urethra, and **(C)** the penile urethra. The normal urethra is smooth and distinctly margined with normal variation in diameter seen in the prostatic and membranous urethra.

RADIOGRAPHY AND URETHROGRAPHY

Radiography of the urethra must include caudal abdominal and/or pelvic images to ensure that the urethra is evaluated fully. In male dogs, lateral pelvic radiographs with the pelvic limbs both hip-extended and hip-flexed are also recommended to avoid missing lesions of the penile urethra caused by superimposition of the pelvic limbs. In a normal dog, the urethra is not visible on radiographs. Because of the more cranial position of the urinary bladder in cats, the prepelvic urethra may be seen, provided there is adequate surrounding fat.

Retrograde urethrography is a technique to examine the urethra using positive-contrast medium. Only water-soluble, iodinated contrast medium should be used. The contrast medium can be diluted with sterile saline to a final concentration of 15% (150 mg iodine [I]/mL).[1,4] Patients generally require sedation, and evacuation of the colon and rectum through defecation or cleansing enemas is recommended. A fully distended urinary bladder provides counterpressure to contrast-medium injection to allow maximal distention of the urethra.[5] Often cystography is performed initially, and distention of the bladder with contrast medium should be maintained for urethrography. If necessary, sterile saline can be infused into an inadequately distended bladder. In addition to the aforementioned radiographic projections, right ventral-left dorsal and left ventral-right dorsal views should be included because the standard ventrodorsal projection may be less informative owing to superimposition of the pelvic and penile urethra.

In male dogs and cats, the procedure is performed by inserting a catheter into the distal penile urethra. A balloon-tipped (Foley) catheter is preferred in dogs, although a red rubber catheter may also be used.[4,6] The bulb of the Foley catheter is gently inflated and left inflated no more than 15 minutes, because excessive and prolonged pressure can damage the urethra.[7] In male cats, a red rubber or Tomcat catheter may be used (Fig. 40-2). Depending on patient size, a 5 to 20 mL injection of contrast medium is given and radiographs acquired during the delivery of the final 1 to 2 mL of the injection.[4] The normal urethra should be smoothly margined along its entire length. The prostatic urethra is wider than the

membranous urethra, although each can be variable in diameter depending on the degree of distention.[8] The penile urethra has a generally uniform diameter in dogs; in cats, it is relatively narrow.[9] Luminal narrowing with tapered margins may be seen normally at the ischial arch in dogs.[4]

Retrograde urethrography is challenging in female dogs and cats because of the relatively shorter urethra. A Foley catheter is inserted into the distal urethra and inflated gently. A 5 to 10 mL injection of contrast medium is used to distend the urethra and radiographs made at the end of injection (Fig. 40-3).[4] Vaginocystourethrography is an alternate technique for evaluation of the female urethra and may be performed in dogs and cats (Fig. 40-4). Video 40-1 can be found on the accompanying Evolve website. General anesthesia is required when performing vaginocystourethrography. A Foley catheter is inserted into the vestibule and inflated. The tip of the catheter is removed from the bulb to avoid the tip entering the vagina and causing rupture on injection.[10] Tissue forceps may be used to clamp the vulva to prevent expulsion of the catheter and leakage of contrast medium. Contrast medium at a volume of 1 mL/kg is injected slowly, avoiding high pressure. Contrast medium fills the vagina, and with increased pressure during injection, there is retrograde filling of the urethra. The normal urethra should be smoothly margined, and longitudinal striations attributable to mucosal folding may be seen depending on the degree of distention.[4]

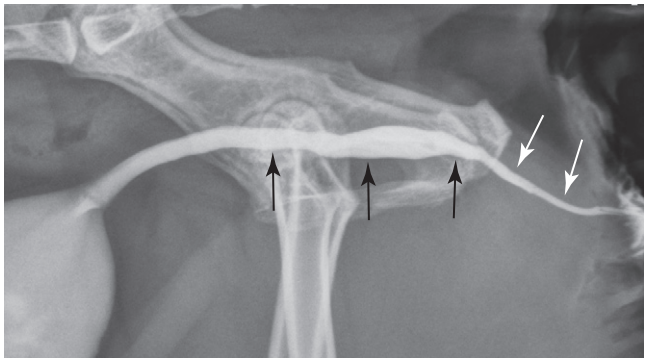


Fig. 40-2 Retrograde urethrography in a normal male cat. A Tomcat catheter is present in the distal penile urethra, and iodinated contrast medium is injected. The pelvic urethra *(black arrows)* is wide and smoothly margined. The penile urethra *(white arrows)* has a smaller diameter and does not distend as much.

The most significant potential complications of urethrography are iatrogenic rupture and urinary tract infection. These and other complications are uncommon when the procedure is performed correctly.[7]

ULTRASOUND OF THE URETHRA

Ultrasound examination of the urethra is generally limited to the most cranial portion of the pelvic urethra as seen from a ventral abdominal window.[11] Full distention of the urinary bladder promotes a more cranial position within the abdomen to allow examination of a greater length of pelvic urethra, but the urethra cannot typically be seen beyond the pubic bone. In some patients, limited evaluation of the caudal aspect of the pelvic urethra can be performed using a sagittal perineal window. In males, the penile urethra can be traced along the penis best by using a high-frequency, linear array transducer with or without a standoff pad. Ultrasound is a complement to urethrography with the advantage of not requiring patient sedation.

The normal urethra is a smoothly margined, thin-walled, tubular structure of uniform diameter traced from the neck

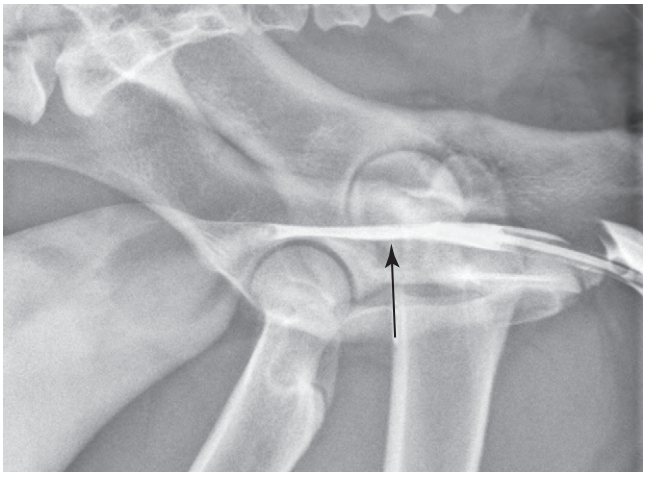


Fig. 40-3 Retrograde urethrography in a normal female dog. A Foley catheter is inserted 1 cm cranial to the external urethral sphincter and iodinated contrast medium is injected. The urethra *(black arrow)* has a smooth and distinct mucosal margin.

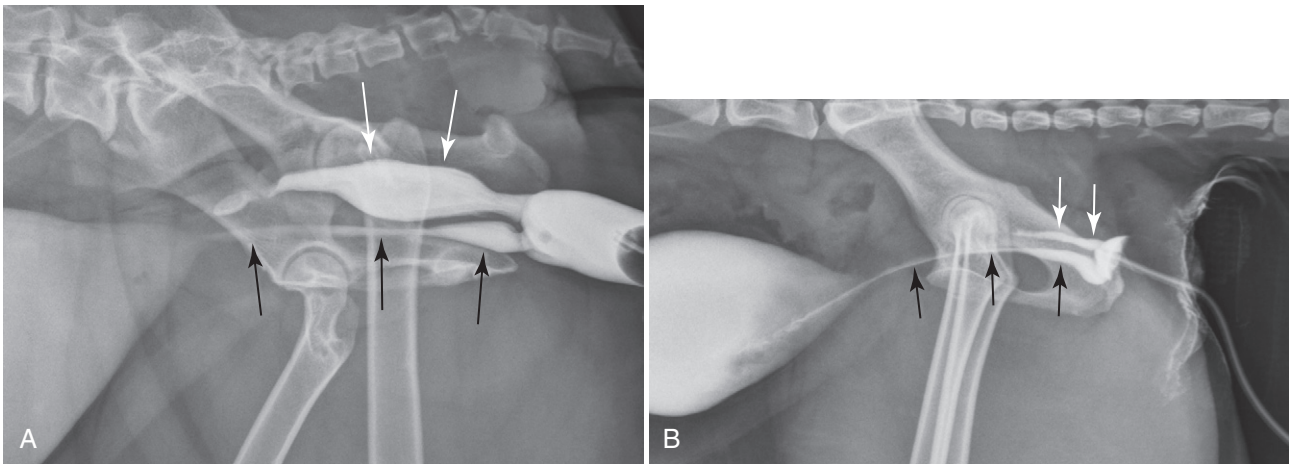


Fig. 40-4 Vaginocystourethrography in **(A)** a normal female dog and **(B)** a normal female cat. A Foley catheter is in the vestibule and insufflated. As contrast medium is injected, the more cranial vagina *(white arrows)* fills, followed by filling of the urethra *(black arrows)*. Smooth, distinct mucosal margins of the urethra are seen.

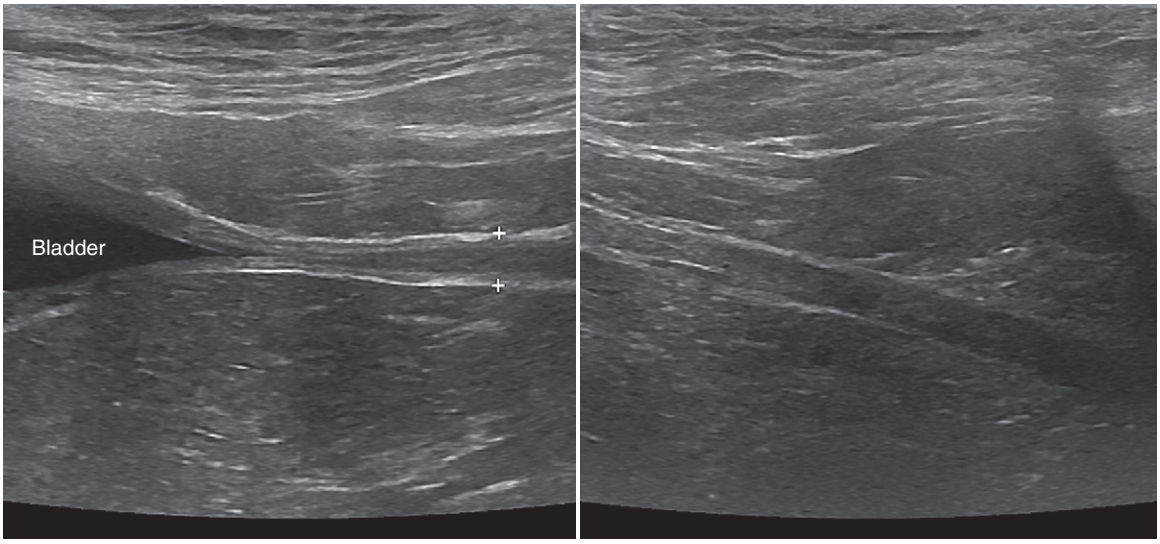


Fig. 40-5 Sonogram of the urethra in a normal female dog, sagittal views. The urethra is traced from the urinary bladder neck caudally in the image on the left *(white calipers)*. The more caudal aspect of the urethra is seen in the right image and is a uniform tubular structure. Visualization of the urethra becomes more difficult caudally because of the pubic bone.

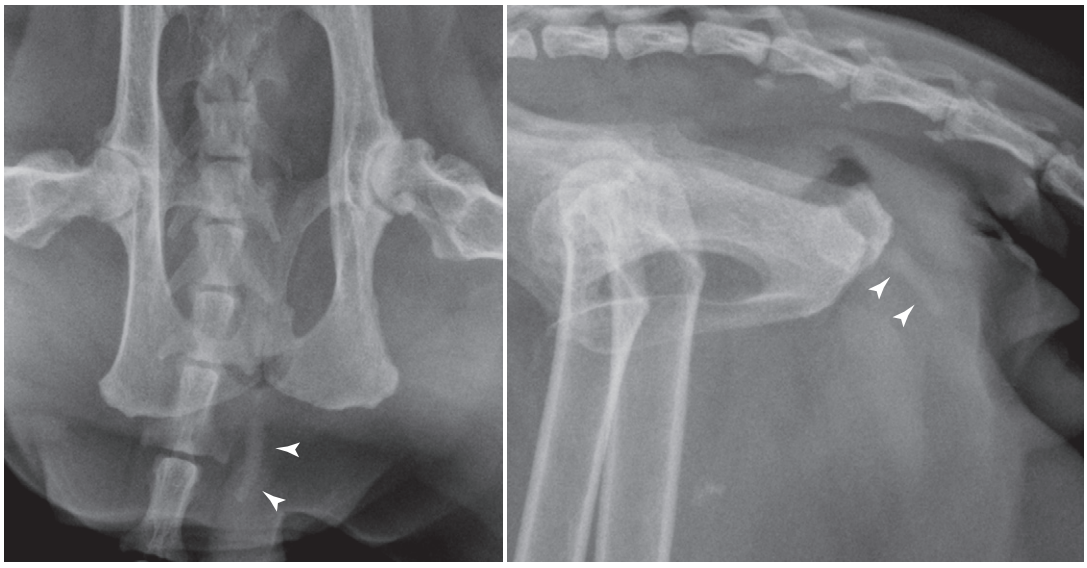


Fig. 40-6 Survey radiographs of a male cat with urinary obstruction. A faint, cone-shaped mineral opacity is seen in the region of the penile urethra *(white arrowheads)*, consistent with urethral obstruction by sandy mineral calculi. (Courtesy of Wm. Tod Drost, DVM, Ohio State University, Columbus, Oh.)

of the urinary bladder. The layers of the urethra usually cannot be resolved, and the lumen is not distended (Fig. 40-5).

DISEASES OF THE URETHRA

Urethral Calculi

Calculi within the urethra may be seen on survey radiographs if they are mineral opacity. In male dogs, calculi commonly occur at regions of luminal narrowing or restriction: the ischial arch and base of the os penis. In male cats with urethral obstruction secondary to sandy mineral calculi, a mineral plug may be seen in the penile urethra (Fig. 40-6). Because the urethra is not visible on survey radiographs, urethrography is required to confirm urethral calculi. Calculi appear as persistent, large focal or multifocal filling defects that distend the lumen of the urethra (Fig. 40-7). They are typically irregularly shaped and indistinctly margined. Air bubbles introduced into the urethra during contrast-medium injection can generally be distinguished from calculi by their smoothly rounded shape, which does not distend the urethra, and inconsistent presence with subsequent injections of contrast medium (Fig. 40-8). Blood clots may be similar in appearance to calculi but may also be present inconsistently.[6,12]

On ultrasound, urethral calculi appear as focal or multifocal hyperechoic and intensely distally shadowing foci within the lumen, which may be distended proximal to the obstruction. Video 40-2 can be found on the accompanying Evolve website. The associated urethral wall may be increased in thickness.[11,13]

Urethral Neoplasia and Inflammation

Urethral mass lesions caused by neoplasia or inflammation are generally indistinguishable. Neoplasia is more common and



Fig. 40-7 Retrograde urethrogram in a male dog with hematuria. An irregularly margined focal filling defect distends the lumen of the membranous urethra proximal to the ischial arch, consistent with a urethrolith.



Fig. 40-9 Retrograde urethrogram in a male dog with straining and pollakiuria. The mucosal margin of the prostatic urethra is markedly irregular and filled incompletely, and there is attenuation of the lumen diameter of the proximal membranous urethra. This patient had a prostatic carcinoma that had invaded the urethra.

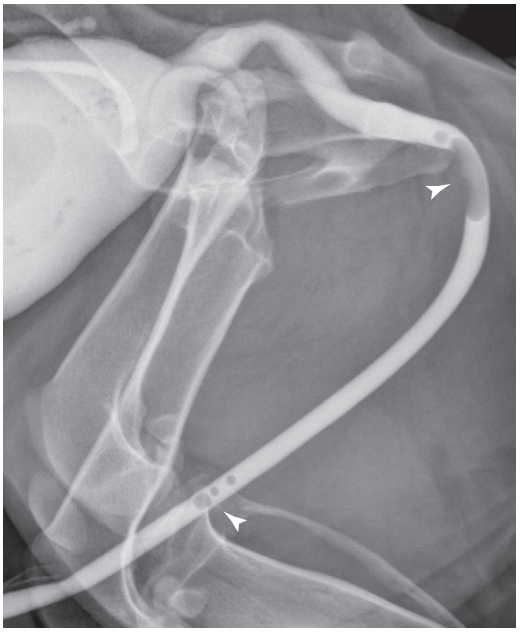


Fig. 40-8 Retrograde urethrogram in a male dog. Several gas bubbles are present in the penile urethra *(white arrowheads)*. They are smoothly rounded, distinctly margined, and do not distend the urethral lumen. These artifacts were not present on subsequent images following repeat injection of contrast medium.

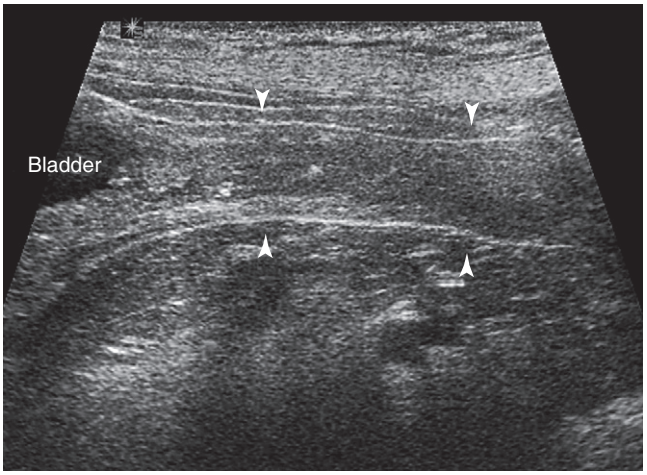


Fig. 40-10 Sonography of the urethra in a female dog with chronic hematuria and straining. The urethra *(white arrowheads)* is markedly thickened and heteroechoic with extension of disease into the neck of the urinary bladder. Transitional cell carcinoma was diagnosed with biopsy. Granulomatous urethritis may have a similar appearance.

may originate from the urethra or extend into the urethra from the urinary bladder or prostate gland, as with transitional cell carcinoma and prostatic carcinoma.[11,14,15] Granulomatous urethritis is a less common infiltrative inflammatory disease reported in female dogs.[15] With urethrography, the mucosal margin of the urethra is markedly irregular, and filling defects may be seen in the lumen (Fig. 40-9).[16] Narrowing of the lumen with intramural disease is expected, but widening may be seen with mass extension into the lumen. Extravasation of contrast medium may also be seen with neoplasia, indicating urethral erosion.

Sonographic features of these lesions are variable but most often appear as a hypoechoic increase in thickness of the urethral wall, which may be uniform and circumferential or asymmetric (Fig. 40-10).[11,14] Video 40-3 can be found on the accompanying Evolve website.

Urethral Rupture

Rupture of the urethra is most commonly the result of pelvic trauma and is diagnosed with urethrography with extraluminal extension of contrast medium (Fig. 40-11). Depending on the level of compromise, extravasation of contrast medium may extend into the peritoneal space, cavernous tissues of the penis, or soft tissues adjacent to the urethra.[4,6]

Other Diseases

Urethral stricture may occur secondary to urethral trauma or obstruction and is seen as an abrupt, focal luminal narrowing on urethrography. To differentiate a stricture from inadequate urethral distention or urethral spasm, the lesion should be persistent on multiple images made during injection of contrast medium into the urethra. They may be accompanied by irregular margination and luminal dilation proximal to the lesion.[4] Fluoroscopy can provide real-time evaluation of the urethra during contrast medium injection to help confirm

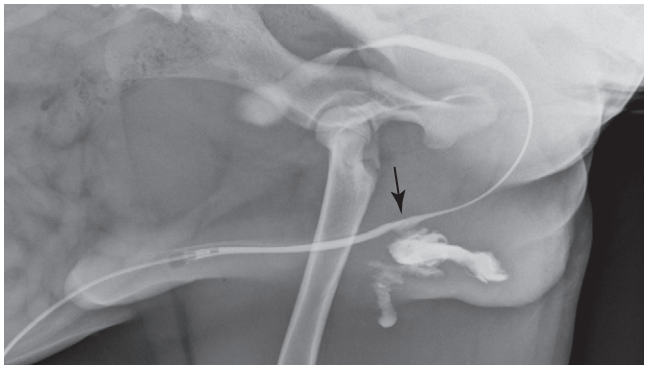


Fig. 40-11 Retrograde urethrogram in a male dog with a history of bite wounds in the region of the penile urethra. A large region of contrast medium extravasation is seen proximal to the os penis *(black arrow)* and extends through a cutaneous wound cranially, consistent with rupture of the penile urethra following puncture.

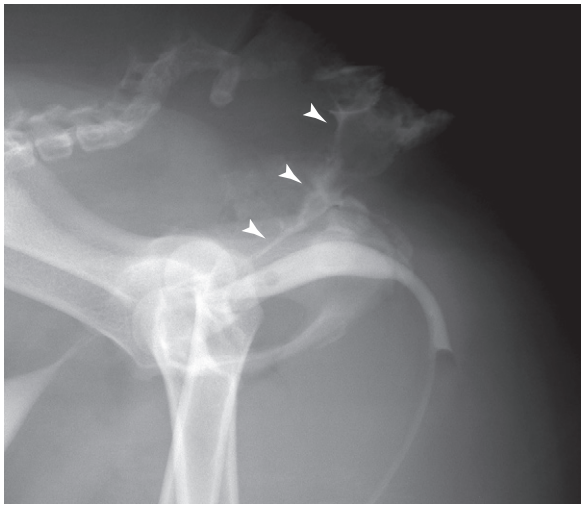


Fig. 40-12 Retrograde urethrogram in a young male English bulldog with a history of chronic urinary tract infections and urine leakage from the anus. Contrast medium extends dorsally from the membranous urethra *(white arrowheads)* to outline fecal material in the rectum. This urethrorectal fistula is likely congenital.

the diagnosis of stricture. Video 40-4 can be found on the accompanying Evolve website.

Extraluminal masses arising from tissues adjacent to the urethra may cause broadly tapering narrowing of the lumen and displacement of the urethra.[6]

Urethral fistulas can be demonstrated as extraluminal extension of contrast medium to another hollow organ (e.g., the colon or vagina) (Fig. 40-12). In young patients, they are most often congenital anomalies but may also be acquired as a sequel to urethral rupture, for example.[1,17]

REFERENCES

1. Park RD: Radiology of the urinary bladder and urethra. In O'Brien TR, editor: *Radiographic diagnosis of abdominal disorders in the dog and cat: radiographic interpretation, clinical signs, pathophysiology*, Philadelphia, 1978, Saunders, pp 605–609.
2. Evans HE, Chistensen GE: The urogenital system. In Evans HE, Miller ME, editors: *Miller's anatomy of the dog*, ed 3, Philadelphia, 1993, Saunders, pp 529–546.
3. Dyce KM, Sack WO, Wensing CJG: The pelvis and reproductive organs of the carnivores. In *Textbook of veterinary anatomy*, ed 2, Philadelphia, 1996, Saunders, pp 438–446.
4. Ticer JW, Spencer CP, Ackerman N: Positive contrast retrograde urethrography—a useful procedure for evaluating urethral disorders in the dog, *Vet Radiol* 21:2, 1980.
5. Johnston GR, Jessen CR, Osborne CA: Effects of bladder distension on canine and feline retrograde urethrography, *Vet Radiol* 24:271, 1983.
6. Pugh CR, Rhodes WH, Biery DN: Contrast studies of the urogenital system, *Vet Clin North Am Small Anim Pract* 23:281, 1993.
7. Johnston GR, Stevens JB, Jessen CR, et al: Complications of retrograde contrast urethrography in dogs and cats, *Am J Vet Res* 44:1248, 1983.
8. Feeney DA, Johnston GR, Osborne CA, et al: Dimensions of the prostatic and membranous urethra in normal-male dogs during maximum distension retrograde urethrocystography, *Vet Radiol* 25:249, 1984.
9. Johnston GR, Feeney DA, Osborne CA: Urethrography and cystography in cats. 1. Techniques, normal radiographic anatomy, and artifacts, *Compend Contin Educ Pract Vet* 4:823, 1982.
10. Leveille R, Atilola MAO: Retrograde vaginocystography—a contrast study for evaluation of bitches with urinary-incontinence, *Compend Contin Educ Pract Vet* 13:934, 1991.
11. Nyland TG, Mattoon JS, Herrgesell EJ, Wisner ER: Urinary tract. In Nyland TG, Mattoon JS, editors: *Small animal diagnostic ultrasound*, ed 2, Philadelphia, 2002, Saunders, pp 181–191.
12. Johnston GR, Feeney DA: Comparative organ imaging—lower urinary-tract, *Vet Radiol* 25:146, 1984.
13. Sutherland-Smith J: Bladder and urethra. In Penninck D, d'Anjou M-A, editors: *Atlas of small animal ultrasonography*, ed 1, Ames, Ia, 2008, Blackwell, pp 365–381.
14. Hanson JA, Tidwell AS: Ultrasonographic appearance of urethral transitional cell carcinoma in ten dogs, *Vet Radiol Ultrasound* 37:293, 1996.
15. Moroff SD, Brown BA, Matthiesen DT, et al: Infiltrative urethral disease in female dogs—41 cases (1980–1987), *J Am Vet Med Assoc* 199:247, 1991.
16. Ticer JW, Spencer CP, Ackerman N: Transitional cell-carcinoma of the urethra in 4 female dogs—its urethrographic appearance, *Vet Radiol* 21:12, 1980.
17. Chandler JC, MacPhail CM: Congenital urethrorectal fistulas, *Compend Contin Educ Pract Vet* 23:995, 2001.

ELECTRONIC RESOURCES

evolve

Additional information related to the content in Chapter 40 can be found on the companion Evolve website at http://evolve.elsevier.com/Thrall/vetrad/

- Videos
- Chapter Quiz

CHAPTER • 41

The Prostate Gland

Jimmy C. Lattimer
Stephanie C. Essman

NORMAL ANATOMY AND RADIOGRAPHIC APPEARANCE

The normal prostate gland surrounds the most proximal aspect of the urethra and lies ventral to the rectum and caudal to the urinary bladder, typically within the pelvic canal. In most dogs, especially neutered dogs, the normal prostate gland is not visible radiographically. With slight enlargement, whether normal or abnormal, the prostate gland is recognized radiographically by its round shape and soft tissue opacity and by the relation of the gland to the organs around it. Inability to see the normal prostate gland is influenced by the fact that it is usually in direct contact with the rectum, resulting in the dorsal border of the gland being effaced, especially if the rectum contains feces. A full rectum may also obscure the prostate gland on the ventrodorsal view. Also, if the shape or position of the prostate gland is altered, the gland may not be recognizable other than as a nondescript opacity between the bladder, rectum, and pelvis.[1]

The normal prostate gland is not visible in the cat.

DISEASES OF THE PROSTATE GLAND

Intrinsic disease of the prostate gland usually results in enlargement. Enlargement may also occur in response to extraprostatic influences, such as an androgen-producing testicular tumor and orchitis.[2] Because of the close functional association of the prostate gland and testes, any animal with prostatic disease should also be examined, preferably ultrasonographically, for testicular disease.

The most common prostatic abnormality is benign prostatic hypertrophy, in which the prostate gland enlarges as a result of increased volume in the intercellular and ductal spaces rather than from increased intracellular volume or cell number. Thus once hypertrophy reaches a certain point, development of dilated cystic spaces and ducts is inevitable. Solid and cystic hypertrophy are therefore different stages of the same disease, with the latter being the advanced form.[2,3] The size of the cystic spaces varies from microscopic to large; these spaces may become so large that they distort the shape of the entire gland. A cystic prostate gland may have cysts of many different sizes. Large cystic spaces predispose the gland to infection.

Another common cause of prostatic enlargement is prostatitis, which is usually bacterial.[4] The infection may arise within the prostate gland, or it may extend from other sources, such as the bladder or testicles.[5] Because many antibiotics do not penetrate the prostate gland readily, the gland may also be a reservoir for reinfection or extension to other organs.[6,7] A normal prostate gland is more resistant to infection than is a hypertrophied gland with many secretion-filled cystic spaces. The inflammation may vary from a mild transient process that causes minimal or no clinical signs to a fulminating hemorrhagic process that destroys the entire gland rapidly.[8] The latter may result in rupture of the capsule with secondary peritonitis.[7]

Chronic, recurrent prostatitis may result in a scarred, fibrotic gland that is smaller than normal. Chronic scarring may result in stricture of the urethra.[9] Such a stricture is difficult to recognize radiographically unless a urethrogram is performed.

A prostatic abscess may form as a result of prostatitis or primary cystic disease. As with cyst formation, abscesses may be small or large. Large abscesses distort the shape of the prostate gland and may eventually rupture, causing peritonitis. As previously stated, cysts form in advanced benign hypertrophy and are usually contained within the gland. However, cysts occasionally become so large that the shape of the gland is distorted and the predominant opacity seen on the radiograph is caused by the large cyst. Such large cysts are also referred to as *paraprostatic cysts* because they are no longer confined within the gland. These cysts are usually sterile but may become infected.[10]

Cysts occasionally result from neoplasia.[11] Formation of functional neoplastic secretory cells without an accompanying ductal system results in a cystic structure lined with neoplastic epithelium. Osteocollagenous retention cysts are rare and of unknown origin, but they do not appear to be the direct result of cystic hypertrophy.[12] A rare form of cyst, which is truly paraprostatic, is cystic enlargement of the müllerian ducts, called *uterus masculinus*.[13] Enlargement of the müllerian ducts results in a bilateral tubular mass that resembles uterine enlargement. The prostate gland itself may or may not be enlarged and usually is not distinguishable as a separate opacity.[9]

Prostatic adenocarcinoma is relatively uncommon; however, the incidence in intact and neutered males is similar.[14,15] Prostatic adenocarcinoma is often advanced at presentation with metastasis to regional lymph nodes, the pelvis, and distant sites such as the liver and lungs.[16-18] The gland is massively enlarged by the tumor in some dogs, and in others the degree of enlargement is minimal. Small in situ prostatic carcinomas are unusual but do occur; they are usually discovered as a result of metastasis rather than from their local effects. Prostatic neoplasms are often secondarily infected or necrotic, and

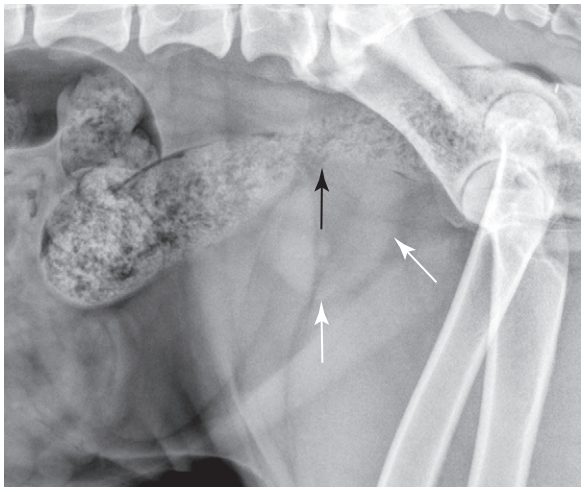


Fig. 41-1 Prostatic enlargement. The prostate gland *(white arrows)* is enlarged and the bladder is displaced cranially. The enlarged prostate gland is displacing the colon dorsally and indenting it *(black arrow)*. The enlargement seen here is relatively symmetric with relation to the neck of the bladder.

affected dogs may therefore have clinical signs of prostatitis. These tumors are difficult to diagnose, unless signs of metastasis are present, because of the tendency of infection to overshadow neoplasia.[19-21]

Clinical Signs

The clinical signs of prostate gland disease are usually referable to either urinary or rectal problems. Stranguria, hematuria, and pyuria are seen commonly.[5,8,10,13] Complete urethral obstruction is possible but unusual.[3,22] Another common symptom with prostatic disease is dyschezia with small or ribbonlike stools.[8,22] As the enlarging prostate gland displaces the colon and/or rectum dorsally (Fig. 41-1), the bowel can be compressed against the sacrum and pelvis, resulting in narrowing. Severe rectal compression by the prostate gland may cause clinical and radiographic signs of constipation or obstipation.

A less common sign of prostate gland disease is a pelvic limb gait abnormality. The animal may refuse to climb stairs and jump. Owners often believe the animal has developed osteoarthritis, but such animals may have severe, active septic prostatitis.[5,8] The pain caused by the prostatic infection is exacerbated by walking, climbing, and jumping. Both pelvic limbs are usually affected. These animals are also usually sensitive to palpation of the caudal abdomen. Gait abnormalities are seen rarely in uncomplicated benign prostatic hypertrophy.

Radiographic Changes

All common prostate gland diseases cause enlargement. The enlargement may be symmetric (diffuse in origin), asymmetric (focal in origin), or a combination of the two. Prostatic symmetry is usually judged by the shape of the prostate gland and the relative mass of the prostate gland with respect to the neck of the bladder. Hypertrophy and prostatitis are examples that usually cause symmetric enlargement (see Fig. 41-1), whereas neoplasia and cysts are examples that usually cause asymmetric enlargement (Fig. 41-2). Radiographic identification of the prostate gland depends on the presence of surrounding fat; the gland may not be seen in very thin animals or those with fluid in the area of the neck of the bladder. A reliable sign of prostatomegaly is a triangular region of fat between the bladder, prostate gland, and ventral abdominal wall (Fig. 41-3).

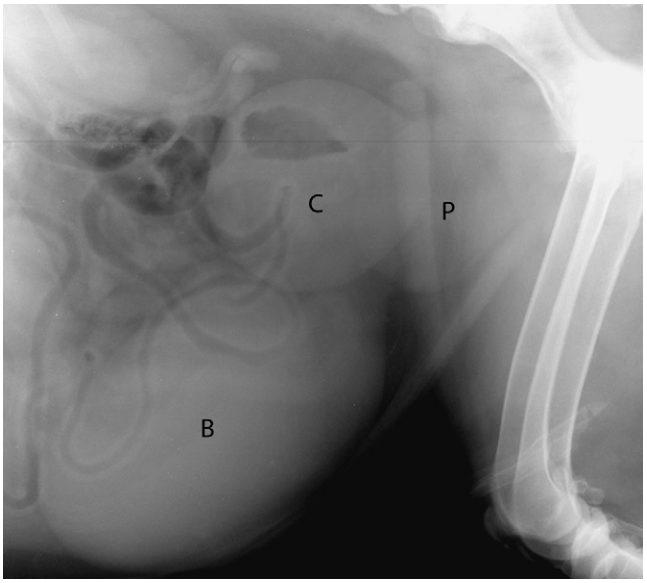


Fig. 41-2 A large, dorsally located paraprostatic cyst *(C)* arising from a prostate gland enlarged because of benign hypertrophy *(P)*. Note the cranial displacement of the urinary bladder *(B)* by the enlarged prostate gland and the asymmetric enlargement created by the cyst.

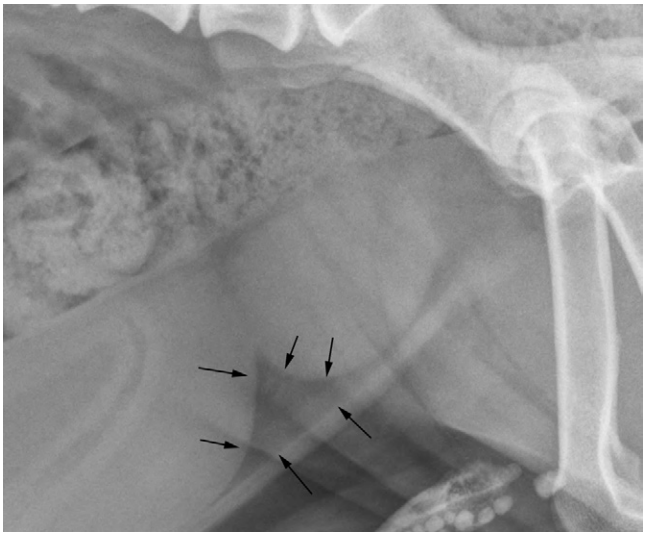


Fig. 41-3 Abdominal radiograph of a dog with prostatic hypertrophy. Note the cranial displacement of the bladder and the triangular region of fat between the caudoventral aspect of the bladder, the cranioventral aspect of the prostate gland, and the ventral abdominal wall *(black arrows)*. This sign is a reliable indicator of a prostate-associated mass. There are also multiple calculi in the penile urethra.

Identification of prostatomegaly hinges on identification of a soft tissue mass in the caudal aspect of the abdomen and on the relation of that mass to surrounding structures, principally the bladder and colon. Prostatomegaly typically displaces the bladder cranially (see Fig. 41-1). If prostatomegaly is uniform, bladder displacement is cranial along the floor of the abdomen. If prostatomegaly is eccentric, as often occurs with large cysts and abscesses and occasionally with tumors, the direction of bladder displacement may be different. A cyst or abscess occasionally may extend dorsal to the bladder (see Fig. 41-2). Alternatively, with ventral prostatomegaly the bladder neck may be elevated (Fig. 41-4). Benign prostatic hyperplasia rarely results in asymmetric prostate gland enlargement.

The more severe the enlargement of the prostate gland, the farther cranially the bladder will be displaced (Fig. 41-5).

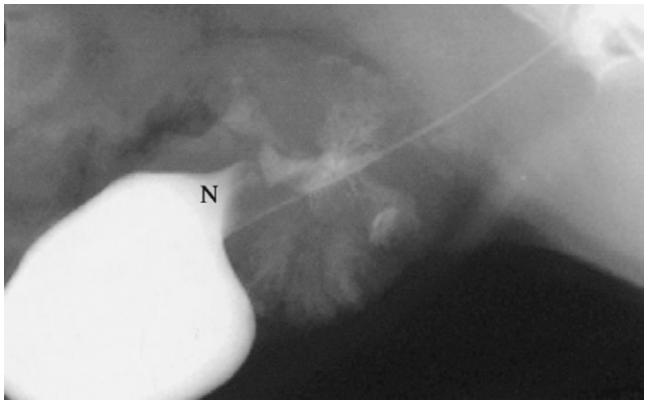


Fig. 41-4 Marked prostatic enlargement with dorsal elevation of the neck of the bladder *(N)*. Note the reflux of contrast medium into the prostate gland. A catheter is present in the urethra.

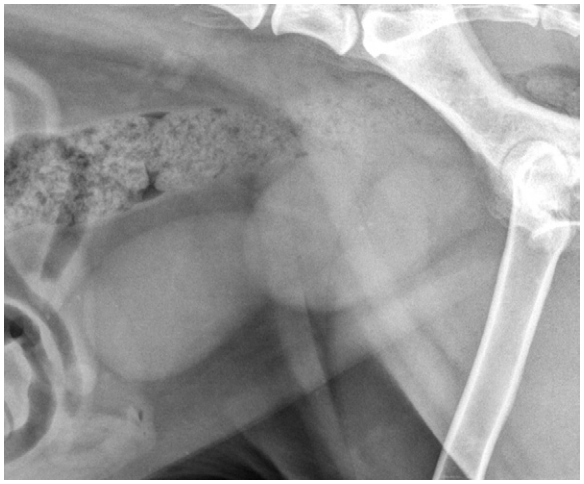


Fig. 41-5 A large prostate gland that is displacing the urinary bladder cranially and lifting the neck off the ventral abdominal wall.

Extreme enlargement may also results in obliteration of the normal triangle of fat formed by the caudal ventral bladder and the prostate gland.

The other major radiographic sign of prostatomegaly is dorsal displacement of the colon (see Fig. 41-1). Prostatic enlargement may also cause narrowing of the lumen of the colon or rectum. This compression may be visible radiographically, or the colon may simply become confluent with the prostate mass at the pelvic inlet.

A tremendously enlarged prostate gland displaces other abdominal organs cranially. Huge prostatic lesions usually lie on the floor of the abdomen, so some dorsal displacement of the remainder of the abdominal contents occurs. Prostatic and paraprostatic cysts may become so large that they reach almost to the costal arch.[13] Masses of this magnitude cause organ displacement so severe that the actual source of the mass may be difficult to determine without using special radiographic procedures or sonography. Prostatic disease that results in urethral stricture may result in severe urinary bladder distention, which is then secondarily responsible for the displacement of the abdominal structures cranial and dorsal to it.

Prostatic size that exceeds 90% of the distance from the pubis to the sacral promontory is suggestive of a mass lesion (cyst, abscess, or neoplasm).[23] The actual degree of prostatic enlargement varies tremendously, however. For example, prostatic size may vary from slight enlargement to 10 times normal size for benign prostatic hypertrophy, and the gland may actually decrease in size in chronic prostatitis. Therefore if prostatic cysts or abscesses are present, the prostatic silhouette may be as great as 20 or more times normal size, or the degree of enlargement may be minimal. Acute prostatitis and neoplasia do not usually cause severe enlargement, as is seen with hypertrophy and cyst formation. Some small in situ prostatic tumors are not recognized until the animal is examined for another problem, such as cough or lameness caused by metastasis, or they may be discovered as an incidental finding at postmortem.

Paraprostatic cysts and abscesses usually have well-defined margins that are easily seen (see Fig. 41-2). An occasional abscess is poorly marginated, although this is the exception. A cyst or abscess may occasionally form in the pelvic canal; such lesions may not be readily visible on survey radiographs or produce the usual displacement of the bladder.[24] These lesions do, however, produce marked displacement and compression of the rectum and are therefore recognized as an intrapelvic mass. Distinguishing a cyst from an abscess on the basis of radiographic examination alone is impossible.

Margination of the prostate gland is important. The presence of adequate abdominal fat is essential to see the margin of the gland. In the presence of emaciation, normally thin animals, pelvic trauma, or abdominal effusion, the prostatic margin and even the entire prostate gland itself may be inconspicuous. If the prostate gland has a smooth margin that is easily seen, the disease involving the gland is likely to be benign or is slowly progressing (see Fig. 41-1), such as benign hypertrophy and low-grade or chronic prostatitis. A rough or indistinct margin in the presence of adequate abdominal fat is more likely to be caused by an acute or aggressive process such as neoplasia or prostatitis.[20,25,26] When the margin is indistinct or not discernible, the impression is that of a localized peritonitis in the caudal abdomen. Most patients with aggressive prostatic disease have some evidence of secondary inflammation affecting the surrounding tissues.

A change in the opacity of the prostate gland from its normal soft tissue opacity indicates severe or chronic disease. Areas of calcification within the gland are a sign either of longstanding prostatitis or of neoplasia.[13,21,23] Wispy or indistinct calcification has a strong positive predictive value for neoplasia, particularly in dogs neutered at an early age. Therefore, although unusual, calcification in the prostate gland is a serious finding that warrants biopsy.[24] Prostate gland calcification is seen more commonly with sonography or computed tomography (CT) because of their better soft tissue contrast resolution.

The prostate gland does not normally communicate with any air-containing organ, so it should not contain gas. Intraprostatic gas is evidence of gas-forming bacterial prostatitis. Coliform or clostridial prostatitis results in severe hemorrhagic necrosis of the gland, potentially causing a generalized peritonitis and septic shock. Because of the rapidly fatal course of these infections, identification of noniatrogenic gas within the prostate gland is an unfavorable prognostic sign. Even if the patient survives, severe, permanent scarring of the prostate gland is likely. Sterility and urinary retention or incontinence may become long-term sequelae to such scarring. Rarely, the prostate gland may contain air because of reflux from the bladder during a negative- or double-contrast cystogram. Simple filling of the ducts with air does not necessarily indicate prostatic disease, but the finding of air in pockets within the prostate gland is abnormal and most often associated with cyst formation as a result of benign hypertrophy.

Periosteal proliferation is sometimes seen on the ventral aspect of the caudal lumbar vertebrae (Fig 41-6) and pelvis because of regional metastasis from prostatic neoplasia.[20-23,27,28] Hyperostosis in this region from metastasis can also be caused by other urinary tumors or hematogenously metastasizing tumors of the pelvic canal or perineum.

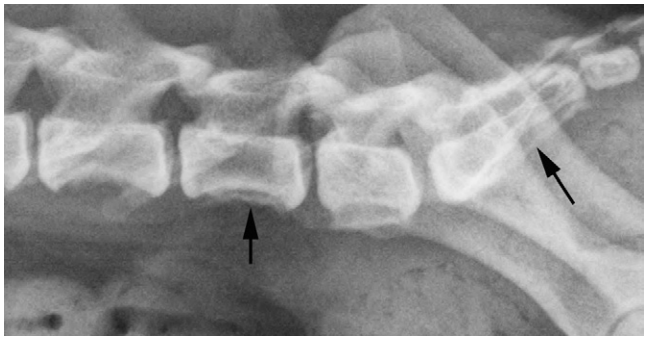


Fig. 41-6 Later lumbar radiograph of a dog with metastatic prostate adenocarcinoma to the ventral aspect of L6 and the sacrum *(black arrows)*. L7 is likely affected, as well, but the overlying ilium makes its evaluation impossible. The prostate gland was not abnormal radiographically because of the small size of the tumor.

SPECIAL RADIOGRAPHIC PROCEDURES FOR EVALUATING THE PROSTATE GLAND

Although ultrasonography has enhanced the imaging of the prostatic parenchyma, retrograde urethrography is still an important and useful imaging procedure that should be considered in patients with suspected prostatic disease.

The only special radiographic procedure that has been found to be uniformly useful in evaluation of the prostate gland is the positive-contrast urethrogram. This procedure allows evaluation of the urethra itself and the position of the urethra in relation to suspected prostatic disease. Asymmetric positioning of the urethra indicates the enlargement is either extrinsic to the prostate gland or is occurring asymmetrically within the prostate gland (see Fig. 41-4), with the latter being more common.[23] Invasion or stricture of the urethra in association with a prostatic mass is a poor prognostic finding because of the danger that a urinary obstruction could occur and because it is a sign that aggressive disease is present.[23] Evidence of either asymmetric prostatic enlargement or urethral abnormalities is an indication for prostatic biopsy.

Urethrography can be performed easily in the male dog, and several methods may be used (see Chapter 40).[29,30] Urethrography provides indirect evidence of prostatic disease. If the urethra is deviated around a large mass or does not pass directly through the center of the prostate gland, the disease within the prostate gland is asymmetric, such as a cyst. If the urethra passes directly through the middle of an enlarged prostate gland, the disease is more likely to be diffuse, such as hypertrophy or prostatitis.

In addition, a urethrogram identifies the true location of the urinary bladder. In some instances, abdominal masses, such as an omental tumor, a paraprostatic cyst, or an enlarged retained testicle, lie cranial to the bladder and the mass can be misinterpreted as the urinary bladder (see Fig. 41-4). Knowing the identity of each mass is important, and urethrography is useful for this, especially if ultrasound is not available.

Direct signs of urethral disease of prostatic origin are urethral stricture, ulceration of the mucosa, and filling defects within the urethra. Ulceration or stricture of the prostatic urethra should be regarded as highly suggestive of neoplasia.[6,23]

Extravasation of contrast medium into the prostate gland should not be interpreted as abnormal as long as only the prostatic ducts fill with contrast medium (Fig. 41-7). This appearance is often seen in animals with a normal prostate gland.[31] Definite pooling of the contrast medium within the prostate gland is abnormal, however. Large, irregularly shaped cavities with rough walls that communicate with the urethra or cavitary smooth-walled lesions containing intraluminal masses are suggestive of neoplasia; biopsy is indicated in these instances.[15,26] Conversely, if extravasation does not occur, the prostate gland is not necessarily normal or solid. Many times, large cavitary lesions, such as cysts and abscesses, attain their size because they do not communicate with the urethra.[10,13,22] If these lesions do fill with contrast medium, they are usually ovoid with smooth walls.

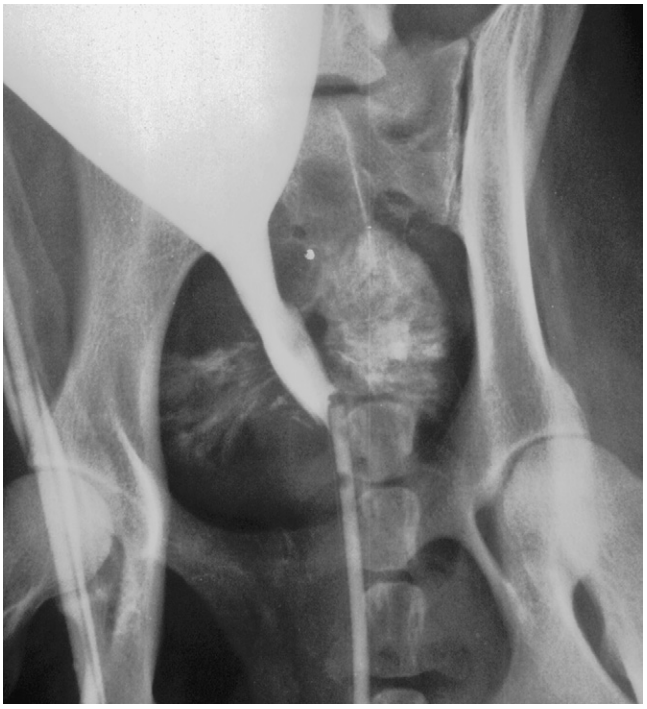


Fig. 41-7 Filling of the prostatic ducts with contrast medium. No cavities are present. Although the prostate gland in this dog is mildly enlarged, the filling of the prostatic ducts with contrast medium has no clinical significance.

The normal prostatic urethra as seen on the urethrogram has a smooth mucosal border. The urethra is usually slightly greater in diameter near the center of the prostate gland and tapers slightly at the cranial and caudal borders. The degree of the central dilation depends somewhat on the size of the prostate gland, the disease present, the degree of bladder distention, and the amount of pressure applied during injection.[32] A small, smooth filling defect in the dorsal wall of the urethra near the center of the prostate gland represents the colliculus seminalis and is a normal finding (Fig. 41-8). Some dogs may also have a normal groove in the colliculus.

The point at which the prostatic urethra joins the neck of the bladder should be evaluated carefully. Small filling defects or mucosal ulcers that may be early lesions of transitional cell carcinoma may be detected. These small lesions may not be detected on a cystogram because they are obscured by the internal urethral sphincter, which is actually encircled by the prostate gland.[27]

SONOGRAPHY FOR EVALUATING THE PROSTATE GLAND

Diagnostic ultrasonography has largely supplanted radiography for the diagnosis of prostatic disease. Ultrasonography is easy, safe, and inexpensive to perform, and the examination can often be performed in less time than a contrast urethrogram. The major advantage of ultrasonography is its ability to

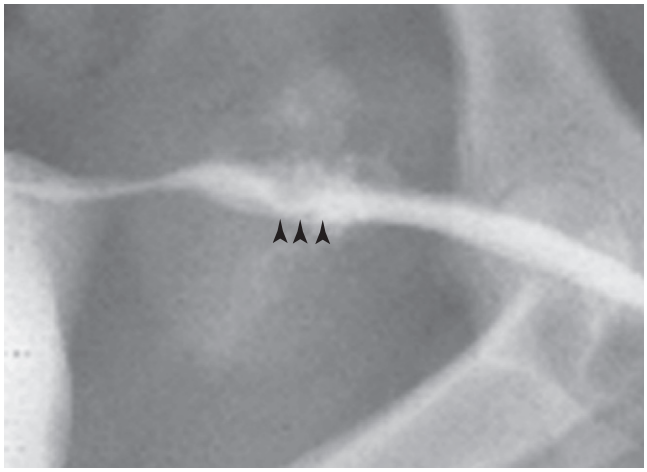


Fig. 41-8 The small filling defect (*black arrowheads* at the ventral aspect) in the dorsal wall of the prostatic urethra is a normal structure, the colliculus seminalis. It should not be mistaken for a lesion caused by prostatic or urethral disease.

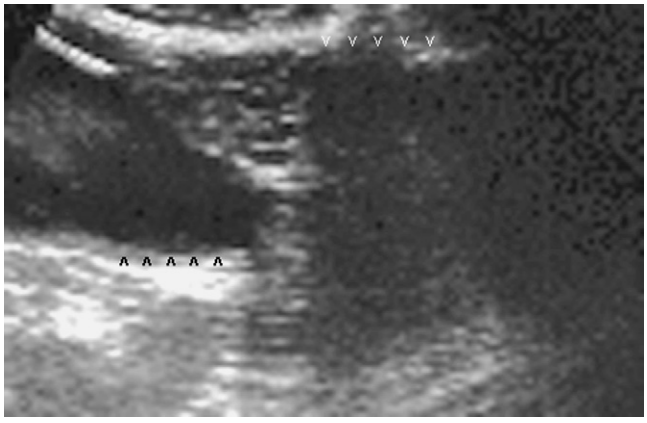


Fig. 41-9 This moderately enlarged prostate gland is difficult to assess sonographically because of its intrapelvic location. The cranial aspect of the prostate gland is present between the bladder *(black arrowheads)* and the pubic brim shadow *(white arrowheads)*; the remainder of the gland cannot be seen. If the proper probe is available, this prostate gland could be imaged more completely with a transrectal approach.

image the structure of the tissues within the prostate gland. This is important for delineating differences between mass lesions such as cysts and tumors.

Sonographic examination of the prostate gland should also include the bladder and testicles. These associated structures may be affected secondarily in prostatic disease, or they may be the site of the primary disorder when the prostate gland is the secondary site of involvement. The ultrasonographic examination should be performed from the prepubic position. The prostate gland in most dogs can be examined effectively from this approach. A very small normal gland, such as seen in a neutered dog, may not be seen occasionally, but an abnormal prostate gland is usually visible cranial to the pubis (Fig. 41-9). The examination should consist of images of the prostate gland in the transverse, sagittal, and parasagittal planes. The prostate gland is imaged most easily from the right side of the os penis with the dog is in dorsal recumbency. In some dogs, angling the probe caudally is necessary to see the caudal pole of the prostate gland where it lies just dorsal to the pubic brim. Sonographic measurement of the prostate gland and its lesions is performed easily with ultrasonography and has been found to be accurate.[33]

The normal prostate gland is uniformly echogenic with an echogenicity similar to that of surrounding fat. However, the



Fig. 41-10 Longitudinal sonographic image of normal prostate gland. The organ margins are distinct, and the echogenicity is close to that of the surrounding fat. The urethra is a small echolucency in the center of the prostate gland *(white arrowheads)*.

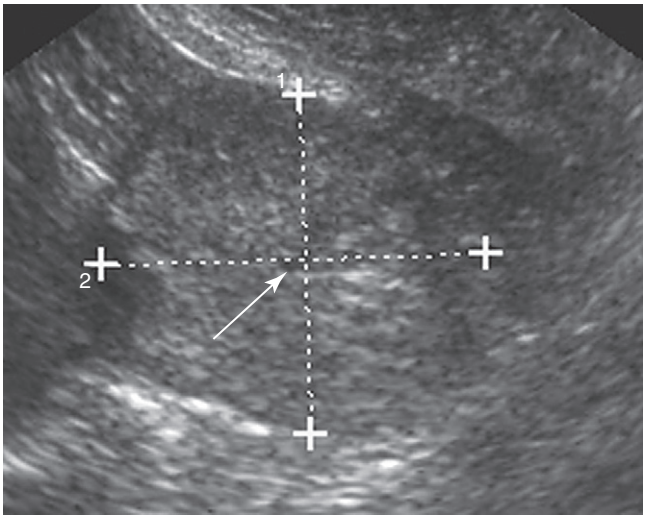


Fig. 41-11 Benign prostatic hypertrophy. The prostate gland is relatively symmetric but is increased in echogenicity compared with the surrounding fat. As the prostate gland enlarges, it will lose its symmetry. The position of the urethra is indicated by *white arrow.*

echotexture of the prostate gland is different than that of fat because the prostate gland has a homogenous, medium to fine texture, whereas fat is more coarsely echotextured. The urethra is usually seen as a small echolucency in the center of the gland surrounded by a narrow band of slightly hyperechoic tissue (Fig. 41-10). Although the position of the urethra can usually be ascertained sonographically, involvement of the urethra must be confirmed by urethrography.

Benign prostatic hypertrophy usually appears sonographically as a uniformly enlarged gland that is mildly hyperechoic (bright) and has a smooth margin. The dorsal portion of the gland may be enlarged to a greater degree than the ventral portion, or vice versa, but the changes are symmetric from right to left (Fig. 41-11). This symmetry may be lost as the hypertrophy increases in severity and cysts develop. As cysts form, some invariably become larger than others and distort the shape of the prostate gland. Differentiating the solid versus cystic forms of hypertrophy was generally not possible before application of ultrasound. A presumptive diagnosis of benign prostatic hypertrophy based on sonographic imaging characteristics should still be confirmed by biopsy.

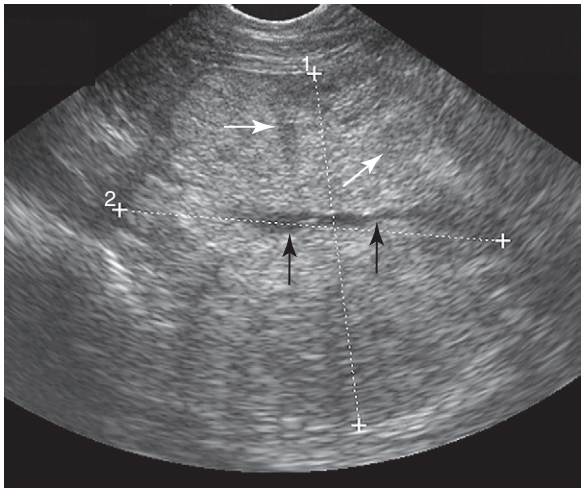


Fig. 41-12 Prostatitis. The prostate gland is enlarged slightly asymmetrically dorsally, and slightly hypoechoic regions are suggestive of focal necrosis *(white arrows)*. Such a mottled appearance is typical of prostatitis but can also be seen with neoplasia. *Black arrows* indicate the urethra.

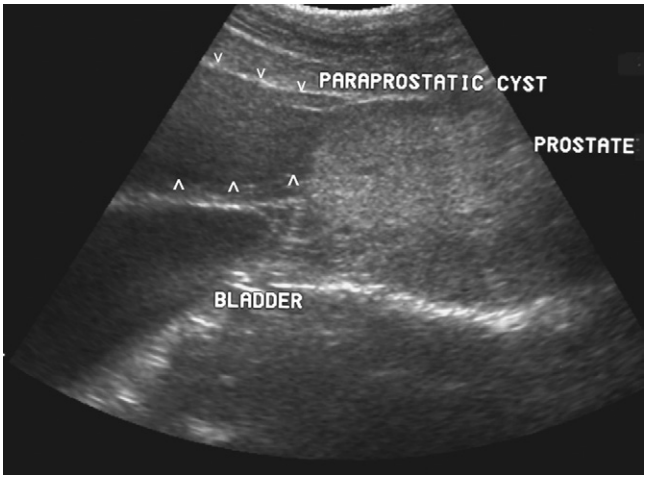


Fig. 41-13 A large paraprostatic cyst *(white arrowheads)* is present ventral and cranial to the prostate gland and ventral to the bladder. Notice the minimal evidence of cyst formation within the prostate gland itself, which is only mildly enlarged. The fluid in the cyst is more echogenic fluid than in the bladder.

The sonographic changes seen in prostatitis vary from mild hyperechogenicity and enlargement of the prostate gland to severe enlargement with a mottled hyperechoic to hypoechoic pattern (Fig. 41-12). The shape of the prostate gland is usually normal, but in severe prostatitis it may be distorted. This is especially true if abscess formation is present in the gland. Some dogs may have a hypoechoic band of edema in the joint capsule outlining the prostate gland. Other dogs, in which the inflammation has extended into the surrounding fat, may have hyperechoic fat surrounding the gland. In severe necrotizing prostatitis, delineation of the gland from the surrounding fat may be lost, and the prostate gland may appear as a dark structure with an irregular and indistinct margin with the surrounding hyperechoic fat.

Cysts and abscesses within and attached to the prostate gland appear as thin-walled structures with echolucent centers. They vary widely in size from a couple of millimeters to several centimeters. Their contents may be anechoic, or they may have varying amounts of cellular debris within the lumen.[34] As a general rule, the presence of septation or large amounts of debris within the lumen is more indicative of abscess, whereas anechoic contents are suggestive of a cyst; however, this is not a universally accurate distinction. The presence of through transmission deep to a highly echogenic structure is usually indicative of a fluid-filled rather than a solid cellular mass. Both cysts and abscesses occasionally occur in conjunction with neoplasia. As with urethrography, cavitary lesions with irregular internal margins or solid tissue masses within them are highly suggestive of neoplasia, whereas smooth margins are more indicative of cysts (Fig. 41-13).

Calcification within the prostate gland, indicated sonographically by bright echoes that cast shadows, is generally considered a sign of malignancy, particularly if it is linear and irregular (Fig. 41-14). However, in some instances chronic inflammation can cause slight calcification of the prostate gland, which is detectable with ultrasonography. Thus a diagnosis of malignancy should not be made on the basis of ultrasonographic evidence of calcification alone, but calcification is strong justification for prostatic aspirate or biopsy.

Malignant tumors of the prostate gland in the dog are usually advanced at the time of detection. These are highly aggressive diseases that destroy the architecture of the gland, resulting in a mixed echogenic pattern that causes asymmetric enlargement (Figs. 41-15 and 41-16).

Contrast ultrasonography is another means of evaluating the prostatic parenchyma. With microbubble contrast studies



Fig. 41-14 Sonographic image of the prostate gland of a dog with a prostatic adenocarcinoma. The scattered focal hyperechoic regions that create shadowing represent mineralizations within the gland. These mineralizations, which are highly suggestive of prostatic neoplasia, were not visible radiographically.

in normal dogs, there is diffuse and uniform enhancement of the prostate gland.[35] Peak enhancement of the normal prostate gland occurred approximately 30 seconds after intravenous injection of the contrast agent. Benign diseases such as prostatitis and benign prostatic hypertrophy exhibited no statistical difference in either time to enhancement or degree of enhancement whereas prostatic carcinoma exhibited a significantly shorter time to enhancement and a greater level of enhancement than either normal dogs or dogs with benign disease.[36]

A definitive diagnosis of the type of prostatic disease cannot be made on the basis of sonographic findings alone.[37] An ultrasonographically guided biopsy should be performed to support the sonographic diagnosis. In dogs with suspected



Fig. 41-15 The cavities within the prostate gland are detected easily sonographically. Such cavities may represent small cysts or abscesses, but they are also seen with neoplasia. Such a finding warrants an ultrasound-guided biopsy or aspiration of the gland.

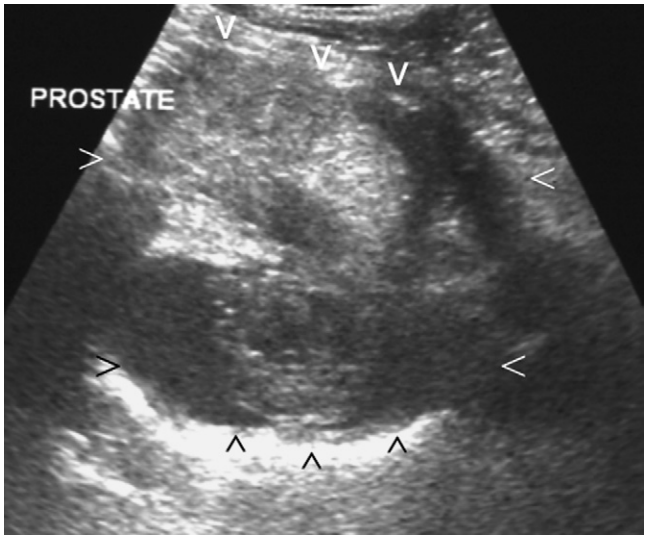


Fig. 41-16 Transverse sonographic image of the prostate gland. The margins of the gland *(black and white arrowheads)* are difficult to define. The prostate gland has a markedly mottled appearance. Some areas are quite hyperechoic and others almost sonolucent. Such a pattern is characteristic of neoplasia but may be seen in severe prostatitis.

neoplasia, biopsies should be taken of the primary lesion of interest as well as the other quadrants of the gland.

COMPUTED TOMOGRAPHY AND MAGNETIC RESONANCE IMAGING

Few reports exist of CT or magnetic resonance (MR) imaging being used for the evaluation of prostatic disease in dogs despite widespread use for this purpose in human beings. Both CT and MR imaging may be used to evaluate the prostate gland and surrounding tissues. These imaging systems are not degraded by superimposition. Lesion conspicuity is less in CT images than in MR images but still much better than in radiographs. CT is more sensitive to changes in shape and opacity of the prostate gland than is standard radiography. For example, even without contrast-medium administration, differentiation

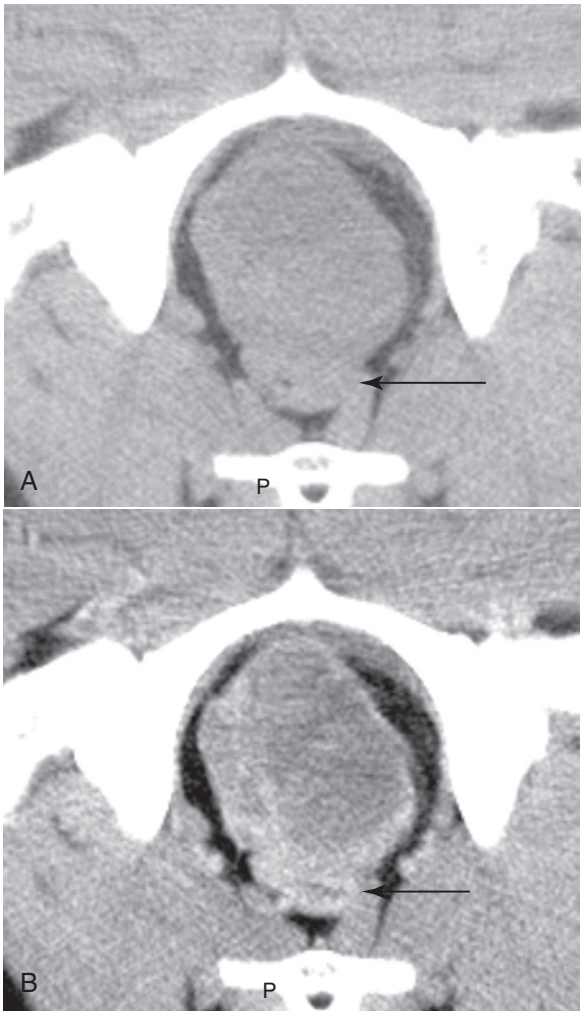


Fig. 41-17 CT images of the prostate gland *(P)*. **A,** There is asymmetric enlargement of the prostate gland. **B,** This image was acquired after intravenous administration of contrast medium and is at the same location as image **A.** Irregular contrast enhancement of the prostate gland is present. The heterogeneity reflects the presence of nonperfused regions because of cyst formation or necrosis. The urethra cannot be seen. Note the dorsal displacement and compression of the rectum *(black arrow)*. The diagnosis of prostatic carcinoma was confirmed by ultrasound-guided biopsy.

of cystic and solid cellular regions is often possible. Contrast medium can improve the diagnostic usefulness of CT markedly. Contrast medium is conspicuous in the wall of cystic structures and the vascular lakes of most neoplastic lesions (Fig. 41-17). Hypertrophy of the gland and prostatitis are characterized by a uniform enlargement and change in attenuation after contrast-medium administration. Minor changes in size and shape of the draining lymph nodes are also detected more easily with CT than with ultrasound. CT may also be used to guide biopsies of small intraglandular sites with minimal special equipment needed.

MR imaging may also be used to assess the prostate gland; greater contrast generally exists between the prostate gland and the surrounding tissues and between normal and diseased gland. In addition, cystic lesions can be detected easily without the use of contrast media, but small neoplastic lesions may not be. The greatest advantage of MR imaging is the excellent tissue contrast, which allows better lesion characterization and localization.

Both CT and MR imaging are being used increasingly to characterize prostatic lesions and assess response to treatment.

REFERENCES

1. Finco DR: Diseases of the prostate gland of the dog. In Morrow DA, editor: *Current therapy in theriogenology*, Philadelphia, 1980, Saunders, pp 654–661.
2. O'Shea JD: Studies on the canine prostate gland: 1. Factors influencing its size and weight, *J Compend Pathol* 73:321, 1962.
3. Metten S: *A morphologic study of benign prostatic hypertrophy in the dog [dissertation]*, Fort Collins, 1978, Colorado State University.
4. Barsanti JA, Shotts EB Jr, Prasse K, et al: Evaluation of diagnostic techniques for canine prostate disease, *J Am Vet Med Assoc* 177:160, 1980.
5. Greiner TP, Johnson RG: Diseases of the prostate gland. In Ettinger SI, editor: *Textbook of veterinary internal medicine: diseases of the dog and cat*, ed 2, Philadelphia, 1983, Saunders, pp 1462–1464.
6. Rogers KS, Wanrschek L, Lees GE: Diagnostic evaluation of the canine prostate, *Compend Small Anim* 8:799, 1986.
7. Zolton GM, Gricner TP: Prostatic abscess: surgical approach, *J Am Anim Hosp Assoc* 14:698, 1978.
8. Barsanti JA, Finco DR: Canine bacterial prostatitis, *Vet Clin North Am* 9:679, 1979.
9. Kornegay J: Canine prostatic disease, *SW Vet* 26:257, 1973.
10. Zolton GM: Surgical techniques for the prostate, *Vet Clin North Am Small Anim Pract* 91:349, 1979.
11. Price D: Comparative aspects of development and structure in the prostate, *Natl Cancer Inst* 12:1, 1962.
12. Rife J, Thornburg LP: Osteocollagenous prostatic retention cyst in the canine, *Canine Pract* 7:44, 1980.
13. Weaver AD: Discrete prostatic (paraprostatic) cysts in the dog, *Vet Rec* 102:435, 1978.
14. O'Shea JD: Studies on the canine prostate gland: 11. Prostatic neoplasms, *J Comp Pathol* 73:244, 1963.
15. Weaver AD: Fifteen cases of prostatic carcinoma in the dog, *Vet Rec* 109:71, 1991.
16. Gill CW: Prostatic adenocarcinoma with concurrent Sertoli tumor in a dog, *Can Vet J* 22:230, 1981.
17. Grant CA: Carcinoma of the canine prostate, *Acta Pathol Scand* 40:197, 1957.
18. Rabaut SM, Kelch WJ: Undifferentiated carcinoma in the canine prostate, *Mod Vet Pract* 60:401, 1979.
19. Jameson RM: Prostatic abscess and carcinoma of the prostate, *Br J Urol* 40:288, 1968.
20. Leav E, Ling GV: Adenocarcinoma of the canine prostate, *Cancer* 22:1329, 1968.
21. Rendano VT Jr, Slauson DO: Hypertrophic osteopathy in a dog with prostate adenocarcinoma and without thoracic metastasis, *J Am Anim Hosp Assoc* 18:905, 1982.
22. Bortwiek R, Mackenzie CP: The signs and results of treatment of prostatic disease in dogs, *Vet Rec* 89:374, 1971.
23. Feeney DA, Johnston GR, Klausner JS, et al: Canine prostatic disease—comparison of radiographic appearance with morphologic and microbiologic findings: 30 cases (1981–1985), *J Am Vet Med Assoc* 190:1018, 1987.
24. McClain DL: Surgical treatment of perineal prostatic abscesses, *J Am Anim Hosp Assoc* 18:794, 1982.
25. Zontine WJ: Radiographic interpretation: the prostate gland, *Mod Vet Pract* 56:341, 1975.
26. O'Brien T: Abdominal masses. In O'Brien T, Biery DN, editors: *Radiographic diagnosis of abdominal disorders in the dog and cat: radiographic interpretation, clinical signs, pathophysiology*, Philadelphia, 1978, Saunders, p 85.
27. Christensen GC: The urogenital apparatus. In Evans HE, Christensen GC, Miller ME, editors: *Miller's anatomy of the dog*, ed 2, Philadelphia, 1979, Saunders, p 565.
28. Franks LM: The spread of prostatic carcinoma to the bones, *J Pathol* 66:91, 1953.
29. Root CA: Urethrography. In Ticer JW, editor: *Radiographic techniques in veterinary practice*, ed 2, Philadelphia, 1984, Saunders, p 387.
30. Johnston GR, Feeney DA, Osborne CA, et al: Effects of intravesical hydrostatic pressure and volume on the distensibility of the canine prostatic portion of the urethra, *Am J Vet Res* 46:509, 1985.
31. Ackerman N: Prostatic reflux during positive contrast retrograde urethrography in the dog, *Vet Radiol* 24:251, 1983.
32. O'Brien T: Normal radiographic anatomy of the abdomen. In O'Brien T, Biery DN, editors: *Radiographic diagnosis of abdominal disorders in the dog and cat: radiographic interpretation, clinical signs, pathophysiology*, Philadelphia, 1978, Saunders, p 9.
33. Cartee RE, Rowles T: Transabdominal sonographic evaluation of the canine prostate, *Vet Radiol* 24:156, 1983.
34. Stowater JL, Lamb CR: Ultrasonographic features of paraprostatic cysts in 9 dogs, *Vet Radiol* 30:232, 1989.
35. Russo M, Vignoli M, Catone G, et al: Prostatic perfusion in the dog using contrast-enhanced Doppler ultrasound, *Reprod Domest Anim* 44:(Suppl 2):334, 2009.
36. Vignoli M, Russo M, Catone G, et al: Assessment of vascular perfusion kinetics using contrast-enhanced ultrasound for the diagnosis of prostatic disease in dogs, *Reprod Domest Anim* 46:209, 2011.
37. Hager DA, Nyland TG, Fisher P: Ultrasound-guided biopsy of the canine liver, kidney and prostate, *Vet Radiol* 26:82, 1985.

ELECTRONIC RESOURCES

evolve

Additional information related to the content in Chapter 41 can be found on the companion Evolve website at http://evolve.elsevier.com/Thrall/vetrad/

- Chapter Quiz

CHAPTER • 42

The Uterus, Ovaries, and Testes

Jennifer Kinns
Nathan Nelson

UTERUS

Imaging Procedures and Normal Imaging Findings

Survey Radiographs

Survey radiographs are used to evaluate the uterus in a limited number of clinical situations. The normal uterus is not seen radiographically in the bitch or queen, and evaluation is therefore limited to pregnancy and pathologic conditions resulting in uterine enlargement. Radiographs can be used to confirm uterine enlargement in diseases such as pyometra. In pregnancy, radiography is used to confirm the pregnant state, provide an estimate of fetal number and to a limited extent can be used to evaluate fetal viability and dystocia.

Radiographic visualization of the uterus is limited by image contrast as well as uterine size. Radiographic technique, as for all abdominal imaging, should maximize radiographic contrast. Compression radiography can increase visualization of a mildly enlarged uterus by increasing separation of the uterus from the bladder, colon, and overlying small intestine and by reducing thickness, which will decrease scatter radiation.[1] Use of a radiolucent paddle is the most commonly employed technique. The effectiveness of compression radiography is reduced by conformation and obesity in addition to gastrointestinal contents and bladder distention. Where there is indication for elective radiography of the uterus, patient preparation is recommended to increase visualization; a 24-hour fast and enema administration will reduce gastrointestinal superimposition.

Ultrasound

Two-dimensional B-mode ultrasonography can provide more information than radiographs with regard to the diseased and gravid uterus and also allows evaluation of the normal uterus. A transabdominal approach is used in both the bitch and queen. The use of higher sound frequencies, within depth limitations, and harmonic and compounding techniques can improve resolution of relatively small structures such as the uterine wall. Doppler evaluation can be used in pregnancy to confirm fetal viability.

The uterine body can be located most easily by scanning between the bladder and caudal aspect of the descending colon with the patient in dorsal or lateral recumbency. It appears as a tubular echogenic structure, similar in size to a loop of intestine. It is differentiated from intestine by location and absence of distinct wall layering. A distended urinary bladder acts as an acoustic window to improve imaging of the uterus. The uterine body is smaller in diameter than the cervix, which is visualized caudally as a hyperechoic linear structure.[2] The endometrium of the uterine body and horns should be uniform in echogenicity and smoothly marginated (Fig. 42-1). Wall thickness depends on the stage of the estrus cycle. The uterine lumen is not seen typically. If present, intraluminal mucus appears as a hyperechoic central area. In anestrus, the uterine wall is thinnest with no fluid present. A small amount of hypoechoic to anechoic fluid can be present during proestrus and estrus when the endometrium is thickened mildly. During diestrus the endometrium is thickened further because of progesterone-driven glandular hyperplasia. The uterine horns can be traced forward from the bifurcation on each side and they terminate a short distance from the ovary. A normal uterine stump can be visualized occasionally in neutered females, dependent on the length of uterine body removed. Interrogation of this most caudal region of the uterus is important in evaluating for stump pyometra.

Cross Sectional Imaging

Advanced imaging modalities are rarely indicated in initial evaluation of the uterus, and computed tomography (CT) in the gravid uterus is contraindicated because of the magnitude of the radiation dose. An understanding of the normal appearance of the uterus in CT and magnetic resonance (MR) images may be important as the use of advanced imaging becomes more common in evaluation of the canine and feline abdomen. Cross-sectional imaging can also be of advantage in evaluating more complex anatomic abnormalities of the uterus and in

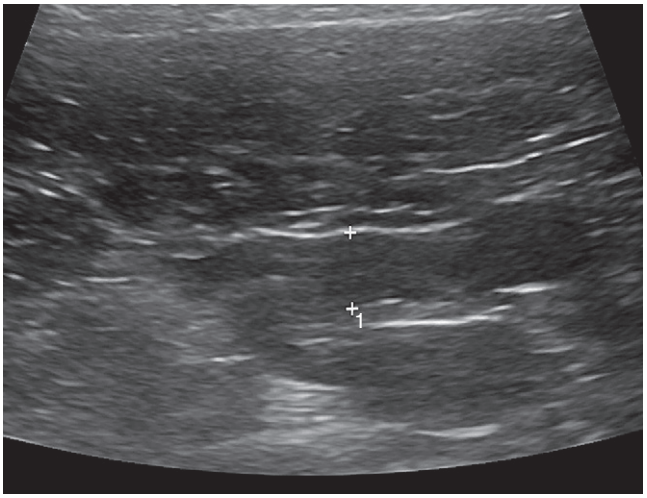


Fig. 42-1 Sonographic image of the horn of a normal canine uterus *(between calipers)*.

evaluation of mass lesions that are not definitively confirmed as uterine by other imaging modalities. The normal appearance of the nongravid uterus on CT is of a small linear structure between the bladder and colon that is isoattenuating to jejunum. The endometrium is not seen readily, and the lumen is occasionally filled with a small amount of hypoattenuating fluid during estrus. The bifurcation and uterine horns can be recognized, particularly if spatial resolution is improved by thin-slice acquisition. However, CT is not the modality of choice for more detailed evaluation of the uterus, for which ultrasound would be recommended.

Pregnancy

Normal Imaging Findings in Pregnancy

Palpation likely remains the most common method of pregnancy detection in the bitch, being fairly accurate around 24 to 35 days.[3] Ultrasound improves accuracy, allows earlier pregnancy detection, and can be used to evaluate litter size. Definitive sonographic diagnosis of pregnancy can be made in the queen at 15 to 17 days gestation when the chorionic vesicle becomes visible.[2] In the bitch, this occurs at 18 to 20 days.[4] However, definitive conformation is easier when cardiac motion can be detected after 23 days. Prediction of the timing of parturition is one of the primary reasons for imaging the gravid uterus. The normal gestation length in both dogs and cats is approximately 63 to 66 days. Ultrasonographically, chorionic vesicle diameter, crown rump length, head diameter (biparietal diameter), and body diameter measurements can be used to predict the age of the fetus. Using established growth curves,[5] inner chorionic cavity diameter in early gestation, from 18 to 40 days, and biparietal diameter in late gestation are equally accurate predictors of age with approximately 85% of litters likely to be whelped within 2 days of the predicted parturition date using these methods.[6] The timing of organ development is also a reliable indicator of fetal age.[7] Cardiac motion can be detected consistently from 23 to 25 days, and limb buds and an echogenic fetal skeleton can be identified by day 35 in the dog.[4,8] Fetal movement can also be detected from this time.[4,9] Radiographic diagnosis of pregnancy is possible after fetal mineralization, which occurs from 43 days in the dog[10] and 38 days (25 to 29 days before parturition) in the cat.[11]

Radiographs obtained late in pregnancy may also be used to predict impending parturition. In cats, fetal mineralization occurs first at 25 to 29 days before parturition[11] and in dogs at 20 to 22 days before parturition.[10] Table 42-1 shows the radiographic mineralization of fetal structures that can be used to predict parturition.

Imaging is also used to predict litter size, for which radiography is more accurate than ultrasonography. Best sonographic estimates of litter size are achieved in early to midgestation,[7] whereas radiographic evaluation can be made after fetal mineralization. Radiographic estimates of litter size are best made by counting the number of skulls and spines (Fig. 42-2). Superimposition of fetuses will make accurate radiographic determination of fetal number challenging with large litters, and orthogonal views are always indicated. Radiographic estimations of litter size are more easily achieved at later stages of mineralization. Sonographically, the number of vesicles in early pregnancy or fetal heads in later gestation may be counted. Fetal resorption is relatively common, and evaluation in early pregnancy may therefore provide an overestimate of litter size. Prediction of litter size with an associated error of plus or minus one fetus may be possible sonographically in up to 89.5% of dogs.[7]

Abnormal Imaging Findings in Pregnancy

Fetal Demise. Sonographic evaluation of fetal heartbeat is the most reliable method of fetal viability. Fetal demise is characterized by loss of the heartbeat. With increasing time after death, fetal structures become progressively less recognizable. Early embryonic resorption can also be documented sonographically with a characteristic appearance of echogenic particles within the yolk sac, progressive loss of fluid volume, and hypoechogenicity of the adjacent uterus in addition to eventual loss of the fetal heartbeat and blurring of the fetal margins.[8] Delayed embryonic development is a good predictor for embryonic resorption.[8] Radiographic signs of fetal demise occur later, at least 24 hours after death, and are less reliable than sonographic indicators. The presence of gas within or around the fetus, overlapping of the bones of the cranium, a tightly curled fetus, and collapse of the fetal skeleton may be evident (Fig. 42-3). The presence of delayed development of a fetus relative to litter mates is also an indication of demise.

Table • **42-1**

Approximate Timing of Mineralization of Fetal Structures in Dogs and Cats

	TIMING IN DAYS BEFORE PARTURITION*	
FETAL STRUCTURE	**FELINE[11]**	**CANINE[10]**
Uterus first seen		33—41
Spine	22—27	20—22
Skull	21—27	20—22
Ribs	20—25	20—22
Femur	19—23	15—18
Humerus	20—24	15—18
Radius	15—22	9—13
Tibia	15—21	9—13
Pelvis	8—20	9—13
Metacarpals/metatarsals	3—14	2—9
Phalanges	0—11	2—9
Calcaneus	0—10	2—9
Teeth	1—6	3—8

*The timings are given as the number of days before parturition.

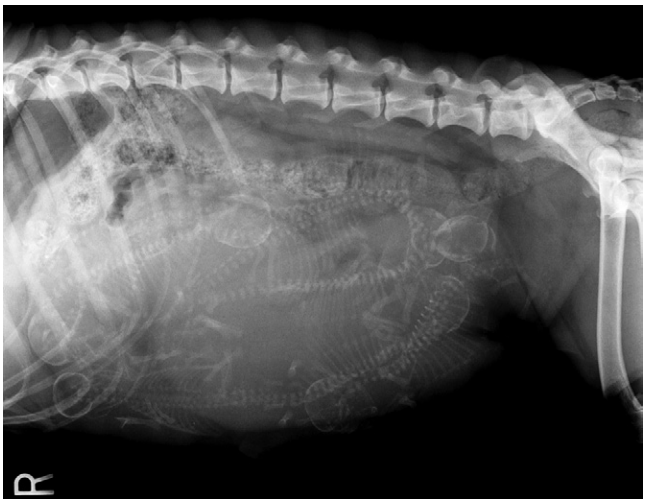


Fig. 42-2 Radiograph of a dog with a normal gravid uterus. Note the direction of displacement of other organs resulting from the enlarged uterus.

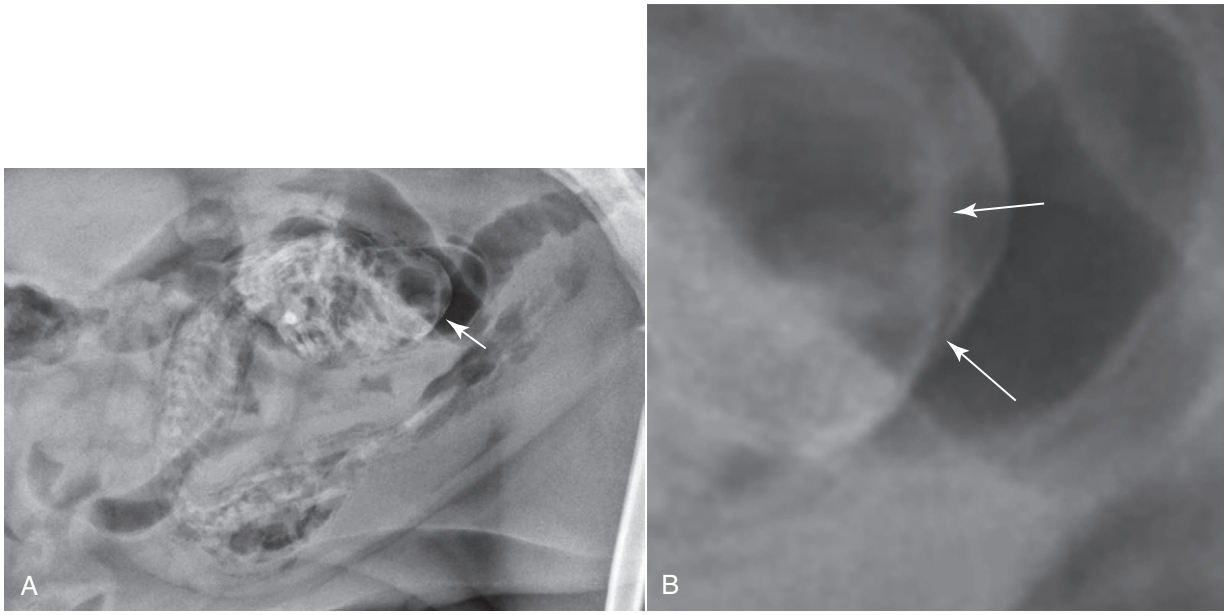


Fig. 42-3 Fetal demise in a cat. **A,** There is gas around the fetus and overlap of the skull bones *(white arrow)*. **B,** Close-up of the skull and area of bone overlap *(white arrows)*.

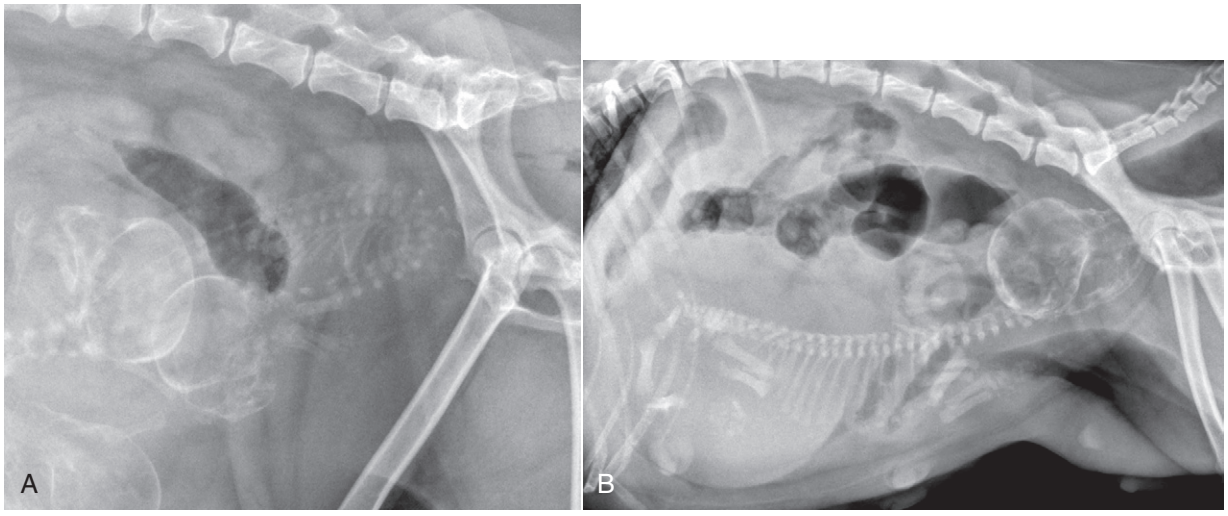


Fig. 42-4 Lateral radiograph of dogs with dystocia. In **A,** the fetus is presenting transversely. In **B,** there is a single fetus that has grown to a size that cannot pass through the pelvic canal.

Dystocia. Dystocia can occur through maternal or fetal causes. Several of these, such as uterine inertia, are undetectable radiographically. However, dystocia caused by fetal malposition, fetomaternal disproportion, or anatomic abnormality of the pelvic canal can be detected radiographically. Lateral and ventrodorsal views are recommended in dystocia patients where any of these are suspected. Fetal malposition is rarely a major problem in species that have large litter sizes. However, caudal, breech, lateral, or downward deviation of the head and transverse presentation (Fig. 42-4, *A*) can lead to obstruction within the pelvic canal. Occasionally, two fetuses will present simultaneously from each horn, which can also lead to dystocia. Fetomaternal disproportion is difficult to determine accurately. It generally occurs if the bitch has been bred by a much larger breed, if there is a single large fetus (Fig. 42-4, *B*), or in brachycephalic breeds where the head is large and the maternal pelvis flattened. If the skull or shoulders are wider on the ventrodorsal view than the pelvic canal, disproportion is the likely cause of dystocia. Abnormalities of the pelvic canal are most often traumatic in origin. Healed fractures can lead to pelvic canal narrowing in both canine and feline patients, preventing normal delivery. In breeding animals with a known history of trauma, prebreeding radiographs may be indicated to determine the likelihood of complication. Radiographs can also be used after whelping if there is clinical concern that a retained fetus may be present.

Abnormal Imaging Findings in Uterine Disease

Uterine Anomalies

Anomalous lesions of the uterus are rare, occurring in less than 0.1% of canine and feline patients undergoing ovariohysterectomy.[12] Uterus unicornis, uterine horn aplasia, and uterine horn hypoplasia are reported. Segmental aplasia, with absence of a uterine body resulting in dilated fluid-filled uterine horns, has also been described.[13] Renal agenesis is common in association with uterine anomalies,[12] and in some patients, this will be the only abnormality recognized radiographically. Fluid accumulation occurs commonly in the affected horn proximal

to the occlusion and may be visible sonographically or, in some instances, radiographically. Clinically, the majority of uterine anomalies will be incidental unless they are the cause of unsuccessful attempts to breed or if pyometra develops.

Cystic Endometrial Hyperplasia and Pyometra

Cystic endometrial hyperplasia-pyometra complex is the most common uterine disorder in bitches. Cystic endometrial hyperplasia occurs as a result of an abnormal response of the endometrium to progesterone during the luteal phase of the cycle. Fluid accumulates in the endometrial glands and lumen of the uterus, and pyometra results if bacteria are present. Mucometra or hydrometra occur if the uterus becomes distended with mucus but remains sterile; these patients are often asymptomatic. The uterine enlargement associated with chronic endometrial hyperplasia is not recognized radiographically. Pyometra and mucometra or hydrometra result in generalized uterine distention, the degree of which will depend on patency of the cervix. Radiographically, the typical appearance of uterine enlargement is of a soft tissue tubular structure within the caudal and ventral aspects of the abdomen (Figs. 42-5, *A* and *B*, and 42-6, *A* and *B*). On lateral views, enlargement of the uterine body is seen characteristically as a soft tissue structure between the bladder and colon. However, this

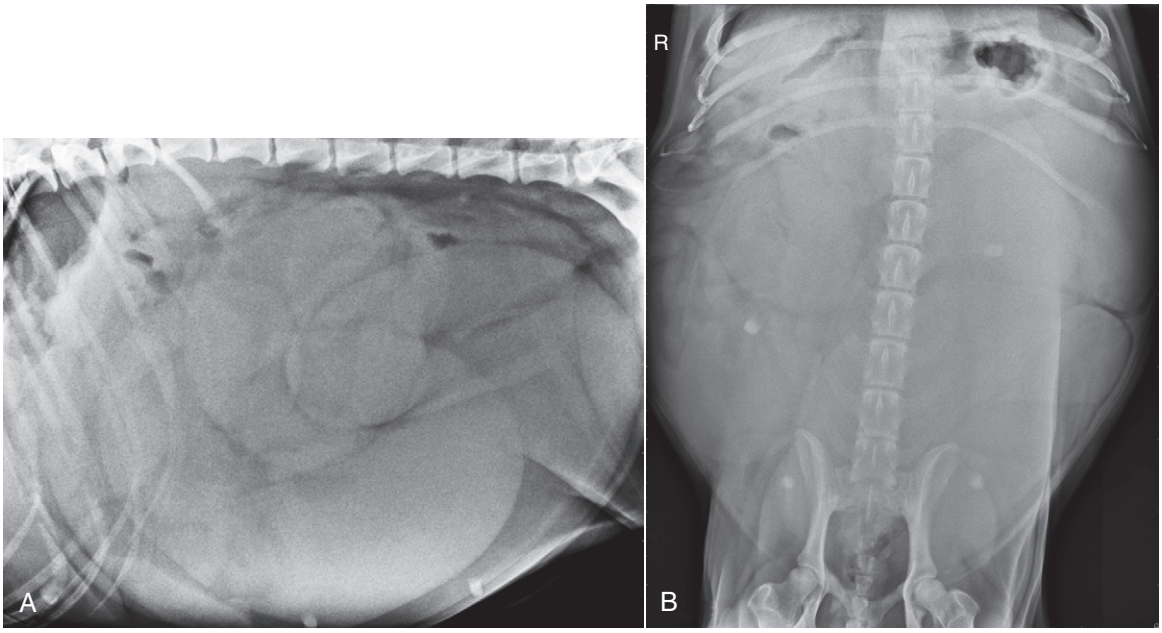


Fig. 42-5 **A** and **B,** Massive uterine distention associated with pyometra in a dog. There is a very large distended tubular soft tissue structure within the caudal and ventral aspects of the abdomen causing a marked associated mass effect.

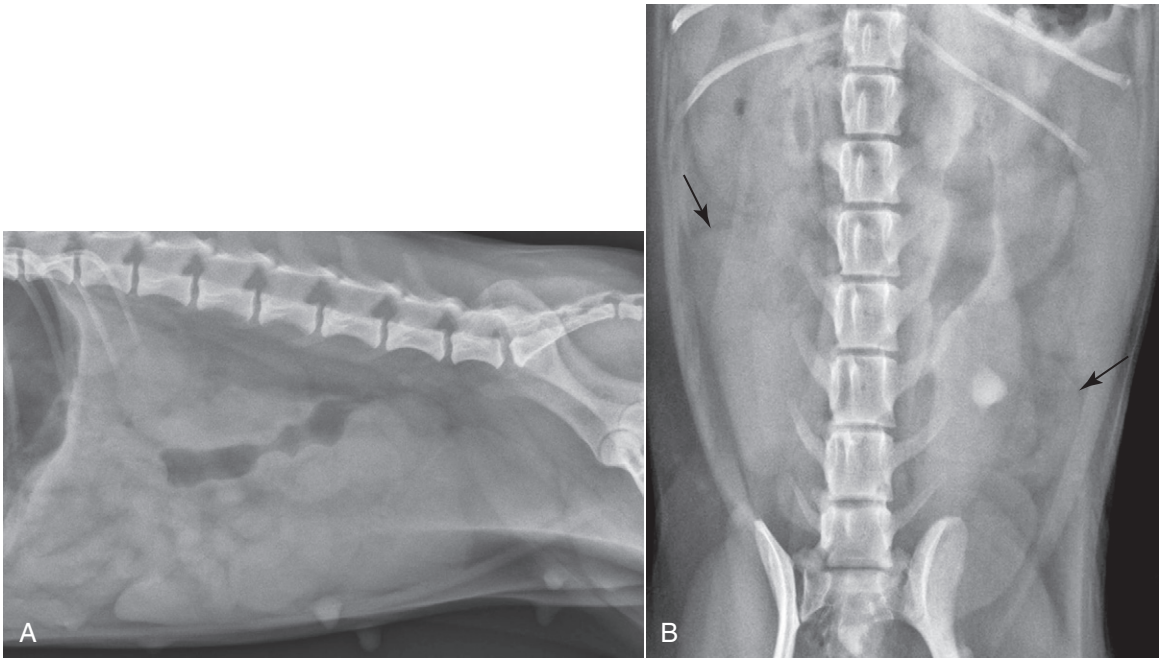


Fig. 42-6 **A and B,** Moderate diffuse uterine enlargement associated with pyometra. Note the evidence of uterine enlargement bilaterally *(black arrows)* on the ventrodorsal view.

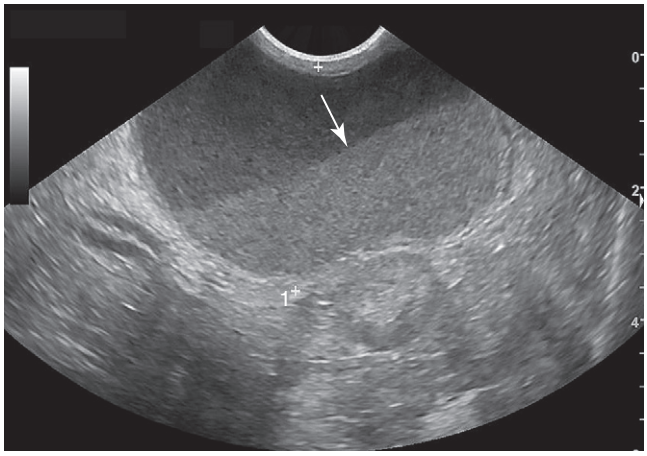


Fig. 42-7 The sonographic appearance of pyometra. The uterine horn is distended with echogenic fluid, and there is a large dependent accumulation of particulate material creating a visible boundary *(white arrow)*.

is not always easy to identify; a lateral compression radiograph may facilitate identification of enlargement of the uterine body. Enlargement of the uterine horns leads to tubular structures of homogeneous opacity in the caudal and ventral aspects of the abdomen. In early enlargement, it may not be possible to differentiate the enlarged uterine horns from jejunum. On the ventrodorsal view, the enlarged uterus will appear as a soft tissue tubular structure lateral to the descending colon on the left and along the peripheral abdominal wall on the right. Ultrasonographically, cystic endometrial hyperplasia results in endometrial thickening with multifocal anechoic dilated cystic glands and glandular ducts. Fluid accumulation within the uterine lumen is not definitive for pyometra, because both mucometra and hydrometra can have this appearance, although they can progress to pyometra. Increasing cellularity from infection results in more echogenic fluid (Fig. 42-7). Increased serum progesterone levels, indicating diestrus, can be used to support a diagnosis of pyometra. Rarely, infection of the uterus can occur for etiologies other than progesterone-related disease. Infection postwhelping or after caesarian section are possible (Fig. 42-8).

Uterine Stump Disease

Following ovariohysterectomy, the uterine stump and cervix is accessible sonographically by imaging lateral to the caudal aspect of the urinary bladder. The uterine stump will rarely be visualized sonographically when normal. Progesterone-related stump pyometra can occur only if the ovaries have been left in situ, permitting ongoing estrus cycling (Fig. 42-9, *A* and *B*). However, stump granuloma and abscessation can occur secondary to local inflammation and infection independent of the presence of progesterone and can occur as a reaction to nonabsorbable suture material. The sonographic appearance of granuloma is of a focal echogenic mass, typically mildly heterogeneous, adjacent to the bladder neck. A stump hematoma occurs most often as a consequence of surgery and may be associated with underlying coagulopathy. The early sonographic appearance is of an echogenic fluid-filled structure that becomes progressively solid in appearance and will eventually decrease in size.

Uterine Neoplasia

Neoplasia originating from the uterus or uterine stump is rare in dogs and cats. In dogs, the majority of uterine neoplasms are leiomyomas, with leiomyosarcoma being much less common. Leiomyomas are benign and slow growing and are most often an incidental finding. By contrast, aggressive

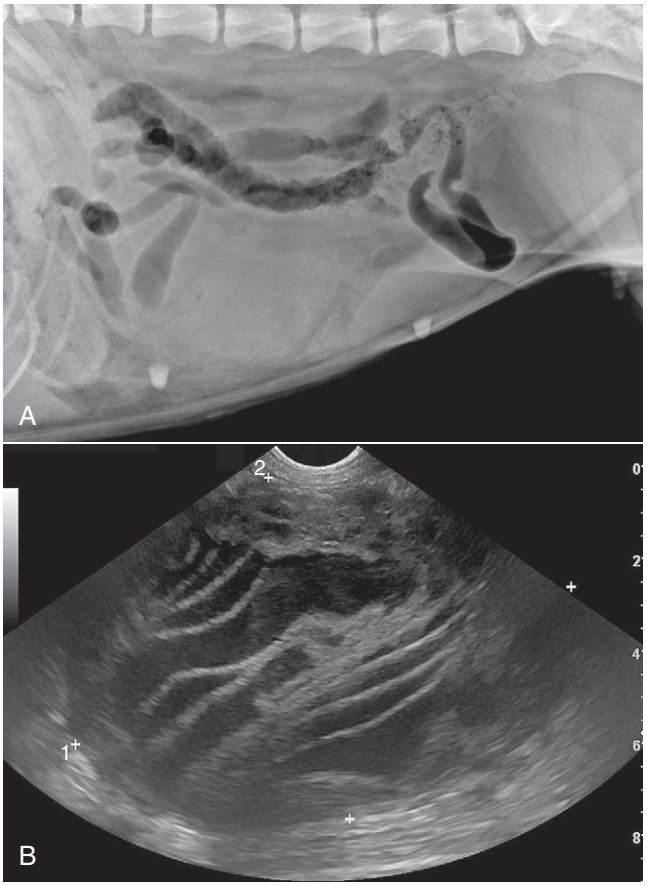


Fig. 42-8 **A,** Uterine abscess associated with a retained surgical sponge after cesarean section. The radiographic appearance is of a midabdominal mass with loss of serosal margin contrast, and it is not possible to confirm the mass as uterine. **B,** Sonographic appearance of the uterine abscess. Ultrasound evaluation confirmed a uterine origin, although the diagnosis of foreign body–associated abscess was made surgically.

adenocarcinoma is most common in cats and has a high metastatic potential.[14] Uterine neoplasia typically results in a sonographically heterogeneous mass that variably distorts the lumen (Fig. 42-10). Uterine neoplasia typically results in focal rather than generalized uterine enlargement radiographically, and depending on size, the tumor may not be apparent radiographically. Although unilateral uterine distention makes pyometra less likely than neoplasia, pyometra can be unilateral.

Uterine Torsion

Uterine torsion is a rare complication of pregnancy in the bitch and also occurs rarely in association with pyometra and hematometra. It is associated with a high mortality rate because of peritonitis and endotoxemia.[15,16] The radiographic and sonographic appearance is not specific, and in all instances, the uterus will already be enlarged in association with pregnancy or pyometra. Correlation with clinical signs is important. In pregnancy, uterine torsion has been associated with dystocia. In most instances, the diagnosis will be made surgically.

VAGINA/VESTIBULE

Imaging Procedures

Retrograde vaginography is a useful adjunct test to digital palpation and endoscopy for investigation of abnormalities of the vagina and vestibule. An enema should be performed

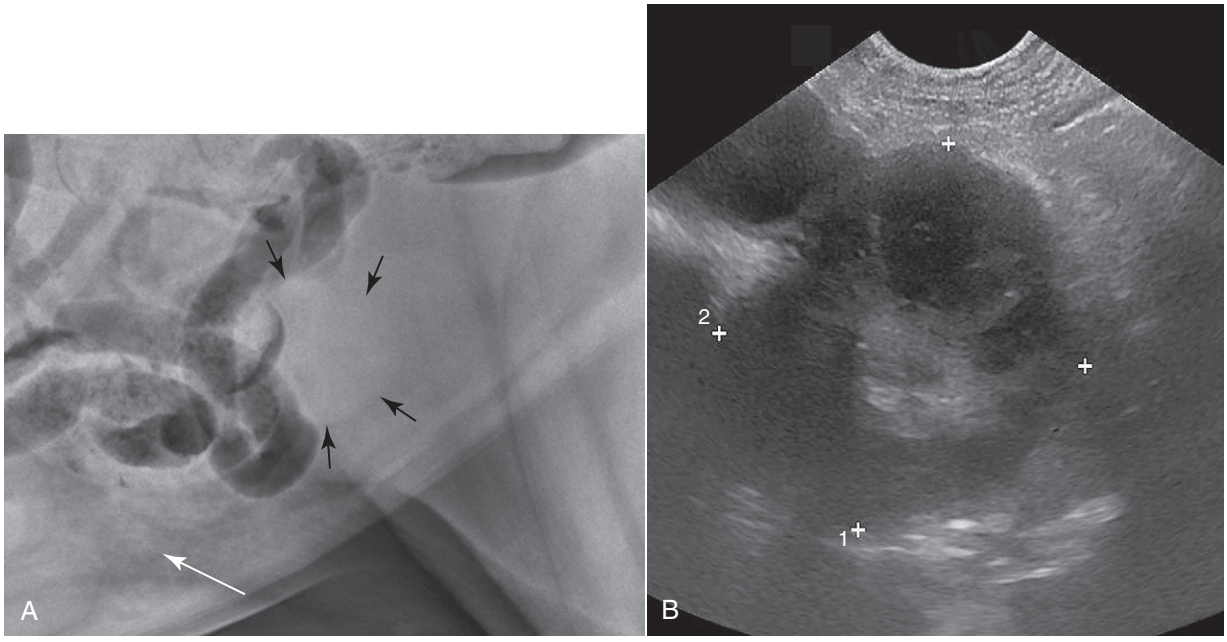


Fig. 42-9 **A,** Stump pyometra in a dog. There is a soft tissue mass in the caudal abdomen *(black arrows)*, superimposed on the cranial margin of the urinary bladder. A focal loss of serosal detail is present adjacent to the cranial margin of the lesion *(white arrow)*. This dog had the ovaries in situ, and also had a granulosa cell tumor. There was severe inflammation of the omental fat. **B,** Sonographic image of uterine stump pyometra.

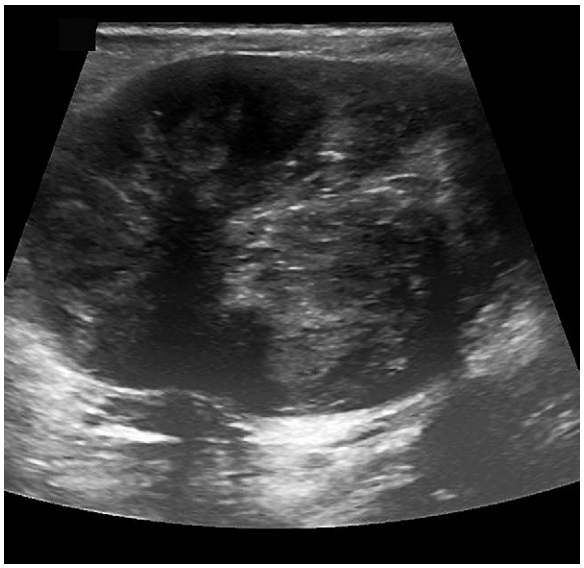


Fig. 42-10 Sonographic image of a uterine leiomyoma in a dog. The mass was an incidental finding during evaluation for an unrelated problem.

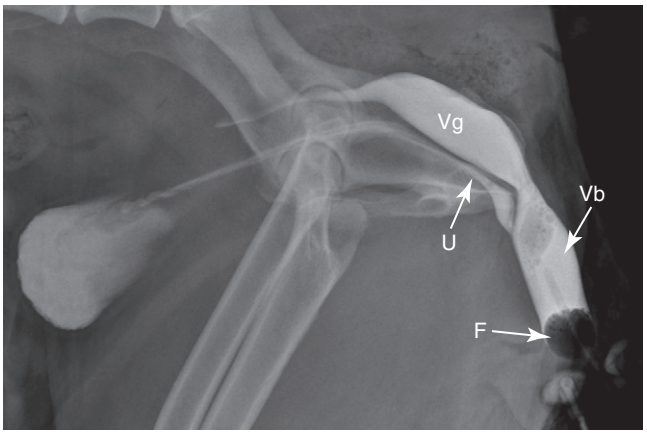


Fig. 42-11 Lateral view of a normal vaginogram. The balloon of the Foley catheter *(F)* is visible in the caudal aspect of the vestibule *(Vb)*. To avoid overdistention or rupture of the vagina *(Vg)*, it is important to make sure the tip of the catheter is within the vestibule, and not the vagina, when contrast medium is injected. As an added margin of safety, the tip of the Foley catheter can be removed before insertion. When the vestibule and vagina are distended maximally, further contrast-medium injection usually results in filling of the urethra *(U)*.

before the procedure because superimposed fecal material can complicate interpretation, particularly on ventrodorsal or oblique projections. Sedation or anesthesia is necessary. Iodinated contrast medium (150 to 200 mg iodine/mL concentration) is infused into the vestibule through a balloon catheter. It is important that the tip of the catheter remain in the vestibule and not be located in the vagina because vaginal rupture can occur if the balloon occludes the orifice between the vagina and vestibule. The vulva is sealed with the use of atraumatic forceps to prevent retrograde leakage of contrast medium. The amount of contrast medium necessary to distend the vagina and vestibule maximally varies between dogs, but a typical dose is approximately 1 mL/kg. Contrast medium will usually enter the urethra near the end of the injection, when the vagina and vestibule are nearly distended maximally. Fluoroscopic guidance during injection helps guide the decision as to when maximal distention is present.[17] Lateral views are usually acquired first as the dog is in lateral recumbency for the procedure. Ventrodorsal and oblique projections may be of value in the diagnosis of some abnormalities; however, additional contrast medium may need to be injected if leakage occurs during repositioning.

Normal Findings

The vagina, cranially to the level of the cervix, the vestibule, and the urethra become opacified with injection of an appropriate volume of contrast medium (Fig. 42-11). If the procedure is performed during estrus, contrast medium may pass

through the cervix into the uterus.[17] The vestibulovaginal junction, also termed the *cingulum*, is a normal slight narrowing between the vestibule and vagina.

Abnormal Imaging Findings

Vaginal/Vestibular Mass Lesions

Vaginal or vestibular masses appear as filling defects within the contrast medium and may distort the adjacent anatomy. There are many differential diagnoses for vaginal/vestibular mass lesions. Vaginal neoplasms are usually seen in older bitches.[18] Benign smooth muscle tumors, such as leiomyoma and fibromas, comprise the majority of vaginal tumors. If large enough, urethral neoplasms may extend into the vagina and vestibule and mimic a primary vaginal mass. Urethral neoplasia is usually malignant and is epithelial or mesenchymal in origin. Vaginal polyps are common in older dogs but are usually small and occur in the late part of the estrous cycle.[18]

True vaginal prolapse is rare in the bitch and involves the entire vaginal wall and sometimes other organs such as the urinary bladder or uterus.[19] This usually occurs near or after parturition but may also be associated with tumors or trauma. The vaginal wall may become focally edematous and thickened with prolapse of this tissue into the vaginal vault or, in severe instances, through the vulva.[18] Vaginal prolapse is seen mostly in young, intact, large-breed dogs in proestrus or estrus. A mass lesion may be identified with these conditions on vaginography. Prioritization of differential diagnoses is based on the site of origin of the mass, involvement of other organs, patient history, and knowledge of patient reproductive status. Vaginal/vestibular masses in young bitches (<2 years) are usually vaginal edema/prolapse, with neoplasia most common in older dogs.[18] Neoplasia of the vagina/vestibule occurs in both intact and neutered dogs.

Other Conditions

Vestibulovaginal stenosis is a developmental defect resulting from incomplete perforation of the hymen or hypoplasia of the genital canal and manifests as a narrowing at the vestibulovaginal junction.[20] Patients may be asymptomatic or experience chronic urinary tract infections, vaginitis, or incontinence.[21] Diagnosis on vaginography is made by a severe narrowing at the vestibulovaginal junction with or without a decrease in size of the vagina. Differentiating this condition from the normal narrowing at the vestibulovaginal junction may be difficult. Traditionally, diagnosis was made with a vestibulovaginal junction less than a third the height of the vagina or a vaginal height less than a third the height of the vestibule, but it has become apparent that clinically normal dogs may have vestibulovaginal junction or vaginal height ratios lower than this range. Moreover, vaginal and vestibular dimensions, including diameter of the vestibulovaginal junction, are larger in intact than neutered female dogs likely because of the trophic effects of estrogen.[22] When making the diagnosis of vestibulovaginal stenosis, the clinical history and reproductive status of the patient should be taken into account.[22]

Ectopic ureters terminate infrequently in the vagina rather than the urethra in young female dogs. In these cases, retrograde vaginography may result in retrograde filling of the ureter. This is discussed in Chapter 38.

OVARIES

Imaging Procedures

Normal or mildly enlarged ovaries are not visible radiographically, limiting the usefulness of this test in evaluating ovarian disease. The primary indication for survey radiography is in the evaluation of potential ovarian masses. Survey radiography provides little information regarding ovarian mass architecture except in the rare instance that the mass is mineralized. Ultrasonography is more sensitive at detecting ovarian disease and allows better characterization of ovarian abnormalities. Ovaries are mobile structures, and they can be displaced by pressure applied by the transducer. They are also located more ventrally in the standing animal.[23] Some ovaries may contact the kidneys, whereas others will be several centimeters caudal, caudodorsal, or caudoventral to the kidney. To best identify the ovaries, a large area caudal to the kidneys is imaged in the sagittal plane sweeping from medial to lateral.[23] Clipping of hair assists in ovary identification by allowing a large area of the abdomen to be scanned. In cats and dogs weighing less than 40 pounds, high-frequency transducers (8 to 12 MHz) may be employed. Lower frequency transducers may be required in larger or obese dogs, but they may not have sufficient resolution to differentiate normal ovaries from adjacent abdominal tissues.

CT and MR imaging are used rarely in veterinary medicine to evaluate the ovaries. More often, ovaries are seen on CT or MR imaging examinations of the spine or when imaging the abdomen for other reasons. The normal appearance of the ovaries with these modalities has not been characterized.

Normal Findings

Normal ovaries are not visible radiographically. Focal areas of mineralization may be seen caudal to one or both kidneys in neutered female dogs and cats, representing dystrophic mineralization of the ovarian pedicles.

The normal sonographic appearance of the ovary varies with the estrus cycle. During diestrus, normal ovaries are homogenous, ovoid structures with an echogenicity similar or slightly greater than the renal cortex (Fig. 42-12). They are small, typically 1 to 2 cm in length, and may be difficult to differentiate from adjacent tissues. Ovaries are identified more easily during proestrus and estrus, when they enlarge and become more rounded.[23,24] Follicles form in proestrus. They are initially small but enlarge until the time of ovulation and are often seen first 1 to 3 days before ovulation.[23] Follicles appear as anechoic, spherical structures that are typically 4 to 6 mm in diameter, with a wall less than 1 mm thick, and may cause the outer ovarian margin to be irregular. After ovulation, fewer follicles will be seen and may be replaced by moderately hypoechoic tissue, likely a result of hemorrhage combining with follicular fluid in the follicular cavity. Corpora lutea are cavitary and anechoic centrally and increase in size for up to 6 days after ovulation with a gradual thickening of the wall, with some becoming solid. Unfortunately, the similar appearance of the ovary before and after ovulation restricts



Fig. 42-12 Long-axis ultrasound image of a normal anestrus ovary. The ovary is hypoechoic and homogenous without visible follicles.

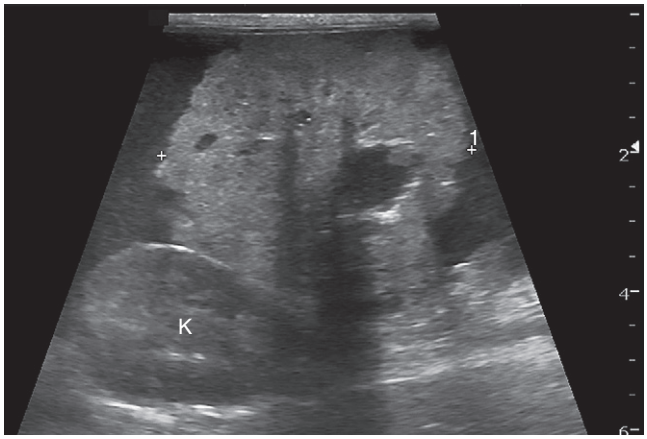


Fig. 42-13 Transverse ultrasound image of a left ovarian carcinoma. The mass contains several hypoechoic fluid-filled regions and is surrounded by hypoechoic peritoneal fluid. The mass contacts the ventral surface of the left kidney *(K)*.

the usefulness of ultrasound alone to predict when ovulation has occured.[24]

Abnormal Findings in Ovarian Disease

Neoplasia

Multiple tumor types may occur in the ovary. Adenomas and adenocarcinomas, cystadenomas, and undifferentiated carcinomas develop from surface epithelium, with papillary adenomas and adenocarcinomas accounting for 40% to 50% of ovarian tumors.[25] Sex cord-gonadal stromal tumors are the granulosa cell tumor, thecoma, and luteoma, with granulosa cell tumors representing the other most common tumor type. Dysgerminoma and teratoma arise from the ovarian germ cells and are less common than the other two classes of tumors.[25] Any of these tumor types may develop without clinical signs, and granulosa cell tumors and cystadenomas may secrete sex hormones.

The ovaries are located within the peritoneum and are suspended by the ovarian ligaments. When the ovary enlarges, these ligaments elongate, allowing the enlarged ovary to displace ventrally along the adjacent body wall. This results in a ventrally located mass resulting in medial but not ventral displacement of adjacent organs on radiographs. Right ovarian masses displace the descending duodenum and ascending colon medially, and left ovarian masses displace the descending colon medially. They may also result in ventral deviation of the caudal pole of the ipsilateral kidney.

Most ovarian masses that are large enough to be seen radiographically are neoplastic. Ovarian neoplasia may be unilateral or bilateral, with epithelial tumors the most likely type to occur bilaterally.[25] Most ovarian tumors appear similar radiographically, but mineralization is a common finding in teratomas and may be seen occasionally in teratocarcinomas.

Ultrasonography provides detailed images of tumor architecture (Fig. 42-13). Tumors may be small or large and may be solid, contain small cysts, or be primarily cystic in appearance. Determination of a mass as ovarian in origin is based on its appropriate location, being caudal to the kidneys, and association with an adjacent uterine horn. Because the ovaries are small, even very small tumors may obliterate normal ovarian tissue.[25] Mineralization within teratomas and teratocarcinomas appears as hyperechoic shadowing areas within the tumor and is helpful in distinguishing these tumors.[25] As with radiography, the sonographic appearance of ovarian tumors overlap, so cytologic or histologic diagnosis is required for definitive diagnosis.

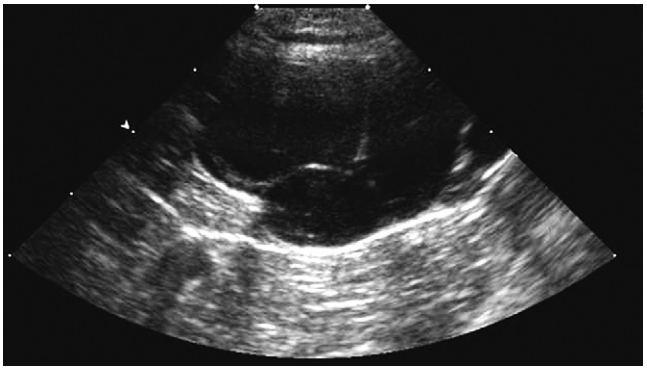


Fig. 42-14 Transverse image of a left ovary with multiple ovarian follicular cysts. Note the thin-walled appearance to the cysts and the anechoic cyst contents.

Other radiographic or sonographic abnormalities may be present with ovarian neoplasms. Peritoneal fluid is common in animals with ovarian tumors and is often seen with carcinomatosis or compression of lymphatics by the mass itself. Pyometra or cystic endometrial hyperplasia may be concurrent and are related to hormonal disturbances.[25]

Cystic Ovarian Disease

Follicular and luteinizing cystic disease can occur. Most cats and dogs with ovarian cysts have no clinical signs or reproductive abnormalities. Follicular cysts may serve as endogenous sources of estrogens, resulting in signs of estrus or proestrus, and are most common in younger animals. Luteinizing cysts may secrete progesterone and result in prolonged anestrus and cystic endometrial hyperplasia.[23] If cysts become large enough, several centimeters or greater, they may be visible radiographically and should be considered as a differential diagnosis for an ovarian mass. More commonly, cystic ovarian disease is diagnosed on ultrasound by the presence of one or more anechoic structures within the ovary (Fig. 42-14). The cysts typically appear as single or multiple, spherical thin-walled structures that may deform the outer margin of the ovary and be unilateral or bilateral.

Cystic ovarian disease should be differentiated from normal follicular development during estrus. Pathologic ovarian cysts may be larger than those that develop during estrus, which typically do not exceed 1 cm and persist over time.[23] Additionally, cystic ovarian disease should be suspected in a patient with prolonged estrus or prolonged interestrus.[23] Ovarian neoplasms may develop cystic areas, but the walls of the cystic areas will usually be thick and irregular, and the contents of the cyst may be echogenic or irregular. Peritoneal fluid is not usually present with cystic ovaries. Overlap between cystic ovarian disease and neoplasia occurs in some patients, so histopathology may be necessary for definitive diagnosis.

TESTICLES

Imaging Procedures

Radiographs are rarely employed in the evaluation of intrascrotal testicular disorders. Enlarged testicles or testicular masses may cause an enlarged scrotal silhouette, but this cannot be differentiated from intrascrotal fluid or thickening of the scrotal soft tissues. An intraabdominal retained testicle can be visualized on abdominal radiographs if neoplastic transformation has occurred.

Ultrasound examination is a sensitive test for testicular parenchymal disease and differentiates testicular from extratesticular causes of scrotal enlargement.[26] Given their superficial location, testicular ultrasound examination is readily

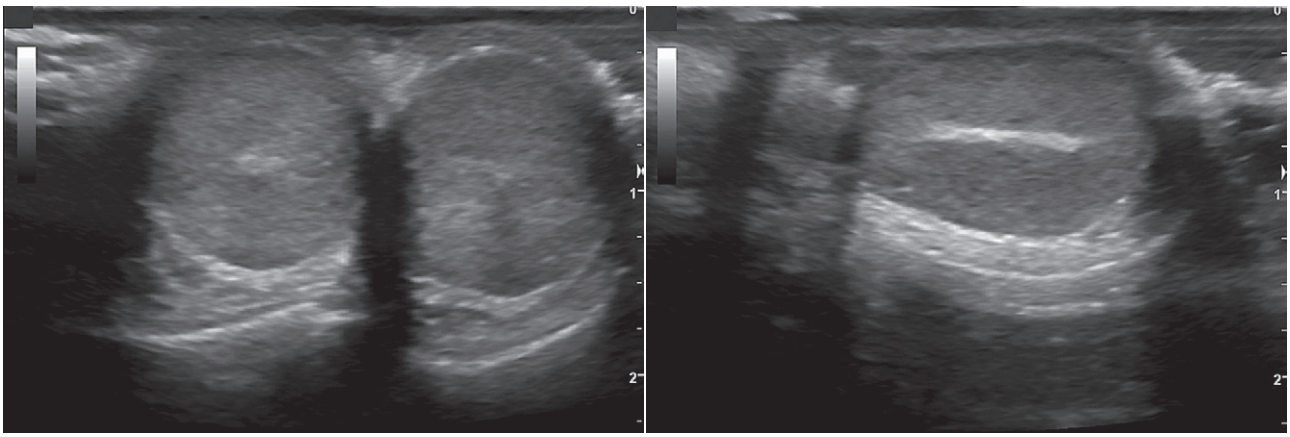


Fig. 42-15 Transverse and longitudinal images of normal feline testicles. Both testicles are included on the transverse imaging plane. The mediastinum testes are seen as hyperechoic foci on transverse images and a hyperechoic line on longitudinal images.

performed. High-frequency (7.5 to 12 MHz) linear transducers are the best choice for sonographic assessment of the scrotum and testicles. Stabilization of the testicles by an assistant or by the sonographer's free hand is usually necessary. Hair on the scrotum should not be clipped because skin irritation may occur. However, as scrotal skin is free from hair, clipping is not necessary.[27] Transverse and long-axis images of each testicle should be acquired. Doppler evaluation can be used for the testicle and adjacent soft tissues and should be optimized for low velocity flow. Ultrasound examination of the testicles gives more accurate measurements of testicular volume than using external caliper measurements or an orchidometer and may be of benefit in assessing pubertal development or response to therapies.[28,29]

Normal Findings

The normal testicle is ovoid on ultrasound examination. A thin hyperechoic line surrounds the testicle peripherally, representing the tunica albuginea and parietal and visceral tunics (Fig. 42-15). The parenchyma should have a generally homogenous, moderately echogenic appearance, although small hyperechoic flecks may be seen internally, representing radiating connective tissues.[26] The most cranial and caudal aspects of the testicle may be difficult to image because of prominent edge refraction artifacts. The mediastinum testes, a fibrous extension of the tunica albuginea that extends along the long axis of the testis, is present in the center of the normal testicle. It is a linear hyperechoic structure on a midsagittal plane and a central echogenicity on a midtransverse plane.[26] Both testicles can often be imaged on one transverse scan plane, allowing easy comparison.

The epididymis is a hypoechoic, poorly defined structure immediately adjacent and mediodorsal to the testicle.[26] The epididymis has a head, body, and tail. The head and tail of the epididymis are along the cranial and caudal testicular margins, respectively, and have a triangular shape. The body of the epididymis is thinner than the head or tail. On ultrasound examination, the epididymis is hypoechoic to the testicle and may even be anechoic. The tail is seen more consistently and is the largest epididymal structure, with the thinner body more difficult to see routinely.[26] The scrotal soft tissues are thin and rarely seen sonographically. Feline testicles have a similar appearance to those of the dog but are associated more closely with the perineal region, just dorsal to the penis. With color Doppler examination, flow can be seen in arterial and venous structures of the spermatic cord in most dogs.[30] The testicular artery is a discrete structure immediately adjacent to the testicle. Intratesticular blood flow is difficult to discern but may be seen with power Doppler.[30]

Abnormal Findings in Testicular Disease

Neoplasia

Testicular neoplasms arise from one of three cell types: the interstitial cells of Leydig, resulting in interstitial cell tumors; the sustentacular Sertoli cells, resulting in Sertoli cell tumors; and the spermatic germinal epithelium, resulting in seminomas. Each of these three tumor types occur with similar frequency in intrascrotal testicles and are most common in older dogs but very rare in cats.[31] Other testicular tumors, such as teratomas, hemangiomas, and lymphomas, may occur but are uncommon. Approximately 40% of dogs with testicular cancer have more than one tumor type.[26] Most intrascrotal tumors have benign biologic behavior, but metastasis occurs and is more likely from cryptorchid neoplastic testicles.[32-34] Sertoli cell tumors are associated commonly with hyperestrogenism, although seminomas and interstitial tumors may also result in hormone imbalances.

Radiographs can be used in the assessment of neoplastically transformed cryptorchid testicles (Fig. 42-16). When intra-abdominal, these tumors must be at least several centimeters in diameter to allow differentiation from adjacent structures such as small intestine, urinary bladder, kidneys, or spleen. Most enlarged intraabdominal testicles will be neoplastic. They are typically of soft tissue opacity and located between the kidney and the inguinal canal. Many larger testicular tumors will be located within the ventral abdomen and cause similar organ displacement as ovarian tumors. Occasionally, a neoplastic testicle will be identified caudoventral to the abdomen in the superficial inguinal soft tissues.

Cystic hyperplasia/squamous metaplasia of the prostate commonly accompanies functional Sertoli cell tumors. Therefore, there may be three distinct masses in the caudal abdomen in a patient with a functional Sertoli cell tumor in a retained testicle: the urinary bladder, the neoplastic testicle, and the enlarged prostate gland. It is often impossible to distinguish these masses from one another radiographically because of their similar radiographic opacity, and a positive-contrast cystogram or sonography may be necessary.

Ultrasound is a sensitive test to detect the presence of testicular nodules, even if they are not palpable.[26] Neoplasia may appear as a nodule or mass, which may or may not malform the testicular margin, displace the mediastinum testes, or make identification of the epididymis difficult (Fig. 42-17).[35] Masses often result in palpable testicular

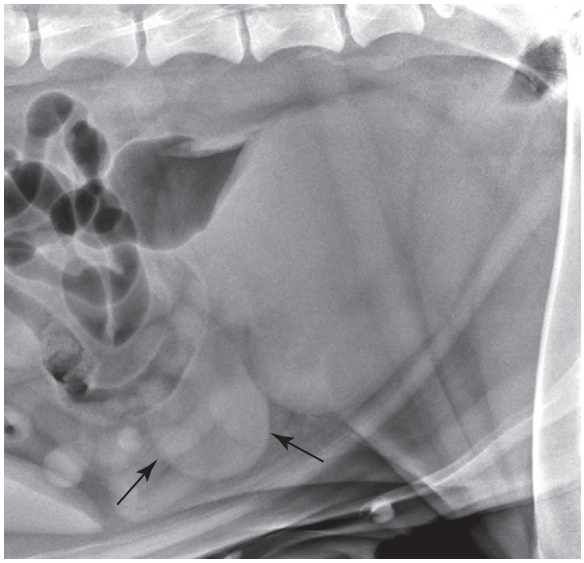


Fig. 42-16 Lateral radiograph of a dog with a retained testicular Sertoli cell tumor *(black arrows)*. There are also two oval masses in the caudal abdomen, representing two lobes of a severely enlarged cystic prostate gland, which often accompanies Sertoli cell tumors. The urinary bladder is empty and not visible.



Fig. 42-17 Longitudinal ultrasound image of a testicular seminoma. The seminoma is hypoechoic to adjacent testicular tissue. A mediastinum testes is not present.

enlargement and compression of internal and adjacent structures. Nodules and masses may be hyperechoic or hypoechoic and either solitary or multiple. Multiple tumor types may occur within the same testicle. Neoplasms may have a heterogeneous interior, representing areas of internal ischemia, necrosis, or hemorrhage.[35] Larger masses are more likely to be heterogeneous, regardless of tumor type.[35] Seminomas are often larger, solitary, and unilateral. With functional tumors, the contralateral testicle may be reduced in size because of negative feedback, and squamous metaplasia of the prostate gland may be seen.[36] Ultrasound alone cannot replace cytologic evaluation because testicular tumors have overlapping sonographic features. The appearance of intra-abdominal testicular tumors is variable, but many become large and may not have sonographically recognizable testicular architecture.[35]

Abnormal Location

Cryptorchidism is a common development defect in dogs and cats, with an incidence reported between 1% and 15%. Some breeds, such as the German shepherd dog and boxer, are at increased risk.[37,38] Cryptorchidism also occurs in cats but at a lower incidence.[37] Cryptorchidism is usually unilateral, with the right testis approximately twice as affected.[38] Cryptorchidism predisposes to neoplasia, spermatic cord torsion, and inguinal herniation of the retained testicle.

Testicles in an abnormal location may be located anywhere from caudal to the kidneys to the superficial inguinal soft tissues. If retained testicles are normal in size or small, they cannot usually be identified radiographically. Retained testicles may be identified radiographically if neoplastic. The intraabdominal location of retained testicles allows greater movement of the testicle than when in the scrotum, and testicular masses may have a slightly different location depending on body position. It is unusual for abdominal masses arising from other viscera to be this mobile. The retained testicle may displace the ipsilateral kidney caudally through retained soft tissue connections.

Locating the cryptorchid testicle on sonography may be difficult because the retained testicle is frequently reduced in size compared with the scrotal testicle, and the mediastinum testes may be inconspicuous. A thorough sonographic search requires investigation of the area from the inguinal ring to the kidneys. Failure to locate a retained testicle on ultrasound may be a result of either monorchidism or technical failure in finding a small, retained testicle in a large scan area. Inability to locate a testicle sonographically in a suspected cryptorchid patient may require CT or MR imaging to confirm the diagnosis. In cryptorchid patients, the other testicle should be normal sonographically if descended fully.[38]

Torsion

Testicular torsion is uncommon in dogs and usually a sequel to neoplastic transformation of a retained testicle because the increased mass and greater mobility predisposes to rotation along the pedicle.[39,40] Torsed, descended testicles are usually non-neoplastic.[39]

Ultrasonographically, the affected testicle is larger than the contralateral testicle with a diffusely hypoechoic parenchyma.[40,41] The scrotum, epididymis, and spermatic cord are thickened, and Doppler signal will be absent. With chronic testicular torsion, the testicle will become smaller and may become more heterogenous.[41] Differentiation of testicular torsion from testicular neoplasia as a cause of testicular enlargement is based on preservation of testicular architecture and loss of Doppler signal, although definitive diagnosis based on imaging alone may be difficult.

Inflammation

Orchitis is uncommon in dogs and cats. Bacteria ascending from the prostate or urethra through the ductus deferens is the usual cause of orchitis. Trauma may also result in testicular inflammation. Viral orchitis has been described in the cat as an early component of noneffusive feline infectious peritonitis.[42] Rickettsial or fungal disease rarely results in orchitis.[43] Testicular and/or scrotal enlargement is the only radiographic finding with orchitis. Ultrasound reveals an enlarged, hypoechoic, and possibly heterogenous testicle. The appearance may be irregular or masslike and mimic neoplasia; however, orchitis typically results in more fluid and epididymal involvement than neoplasia. Testicular torsion is an important differential diagnosis for orchitis on ultrasound examination, but differentiation can usually be made with Doppler ultrasound examination.[43]

Inflammation of the epididymis may occur with or without orchitis (Fig. 42-18). Abscesses may occur within the testicle or epididymis secondary to infection. On ultrasound examination, the contents will usually be hypoechoic and the adjacent surrounding tissue hyperechoic. Chronic epididymitis may

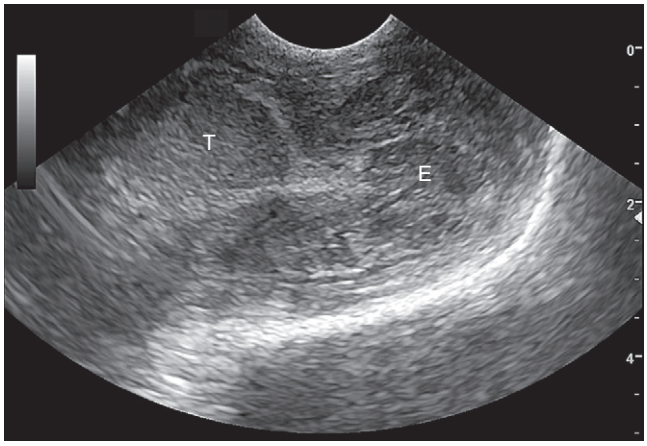


Fig. 42-18 Transverse ultrasound image of a severely enlarged epididymis secondary to ascending bacterial epididymitis. The epididymis *(E)* is hypoechoic and larger than the adjacent testicle *(T)*.

cause a reduction in testicular size and a more irregular appearance to the surrounding soft tissues.

Extratesticular Findings

On ultrasound examination, fluid may be present surrounding the testicle. Extratesticular fluid accumulation may be serous (hydrocele), blood (hematocele), pus (pyocele), or urine.[26] Animals with peritoneal fluid may also have fluid within the scrotum, between the parietal and vaginal tunics, presumably from extension through the inguinal canal. Hydrocele is the most common extratesticular fluid accumulation and can be from trauma, neoplasia, torsion, infarction, or herniation or be idiopathic.[26] Accumulation of blood around the testicle is usually a result of trauma or neoplasia. Pyoceles are usually related to testicular infection and/or abscess formation. Herniation of jejunum through the inguinal ring into the scrotum may be identified. Ultrasound allows differentiation of scrotal enlargement from testicular disease and is helpful in patients with scrotal trauma or inflammation.[26]

INTERSEX CONDITIONS

Intersex conditions are rare but can have an impact on the imaging appearance of the genital tract, and imaging may be used in diagnosis and specific anatomic description. Disorders of sexual development can be categorized as chromosomal, gonadal, and phenotypic. Chromosomal disorders may not result in any anatomic abnormalities of the genital tract, although these animals are typically infertile. Gonadal disorders of sexual development include XX hermaphrodites that have both ovaries and testes and XX males that have bilateral testes. They usually appear female phenotypically with an abnormal vulva or as males with bilateral cryptorchidism and an abnormal prepuce and penis.[44] Radiographically, there may be absence or underdevelopment of the os penis. Sonographically, an intraabdominal testicle may be identified. In phenotypic disorders of sexual development, the chromosomal and gonadal sex are the same, but the internal or external genitalia are inconsistent with the gonadal sex.[44] A female pseudohermaphrodite has ovaries present sonographically but masculinized internal or external genitalia. A male pseudohermaphrodite has testes, but a uteruslike structure may be visible sonographically, and there is typically feminization of the external genitalia. Persistent müllerian duct syndrome is a form of male pseudohermaphroditism recognized in the miniature schnauzer.[44] The testes and external male genitalia are present, but the müllerian ducts develop into oviducts, uterus, cervix, and cranial vagina that may be visible sonographically or during contrast studies.

REFERENCES

1. Armbrust LJ, Biller DS, Hoskinson JJ: Compression radiography: an old technique revisited, *J Am Anim Hosp Assoc* 36:537–541, 2000.
2. Davidson AP, Baker TW: Reproductive ultrasound of the bitch and queen, *Top Companion Anim Med* 24:55–63, 2009.
3. Allen WE, Meredith MJ: Detection of pregnancy in the bitch: a study of abdominal palpation, A-mode ultrasound and Doppler ultrasound techniques, *J Small Anim Pract* 22:609–622, 1981.
4. Yeager AE, Mohammed HO, Meyers-Wallen V, et al: Ultrasonographic appearance of the uterus, placenta, fetus, and fetal membranes throughout accurately timed pregnancy in beagles, *Am J Vet Res* 53:342–351, 1992.
5. Luvoni GC, Grioni A: Determination of gestational age in medium and small size bitches using ultrasonographic fetal measurements, *J Small Anim Pract* 41:292–294, 2000.
6. Beccaglia M, Luvoni GC: Comparison of the accuracy of two ultrasonographic measurements in predicting the parturition date in the bitch, *J Small Anim Pract* 47:670–673, 2006.
7. Lenard ZM, Hopper BJ, Lester NV, et al: Accuracy of prediction of canine litter size and gestational age with ultrasound, *Aust Vet J* 85:222–225, 2007.
8. England GC, Russo M: Ultrasonographic characteristics of early pregnancy failure in bitches, *Theriogenology* 66:1694–1698, 2006.
9. Kim BS, Son CH: Time of initial detection of fetal and extra-fetal structures by ultrasonographic examination in miniature schnauzer bitches, *J Vet Sci* 8:289–293, 2007.
10. Rendano VT, Lein MSDH, Concannon PW: Radiographic evaluation of prenatal development in the beagle, *Vet Radiol* 25:132–141, 1984.
11. Haney DR, Levy JK, Newell SM, et al: Use of fetal skeletal mineralization for prediction of parturition date in cats, *J Am Vet Med Assoc* 223:1614–1616, 2003.
12. McIntyre RL, Levy JK, Roberts JF, et al: Developmental uterine anomalies in cats and dogs undergoing elective ovariohysterectomy, *J Am Vet Med Assoc* 237:542–546, 2010.
13. Oh KS, Son CH, Kim BS, et al: Segmental aplasia of uterine body in an adult mixed breed dog, *J Vet Diagn Invest* 17:490–492, 2005.
14. Chun R, Garret L: Urogenital and mammary gland tumors. In Ettinger SJ, Feldman EC, editors: *Textbook of veterinary internal medicine*, St. Louis, 2005, Elsevier, pp 784–789.
15. Barrand KR: Unilateral uterine torsion associated with haematometra and cystic endometrial hyperplasia in a bitch, *Vet Rec* 164:19–20, 2009.
16. Misumi K, Fujiki M, Miura N, et al: Uterine horn torsion in two non-gravid bitches, *J Small Anim Pract* 41:468–471, 2000.
17. Rivers B, Johnston GR: Diagnostic imaging of the reproductive organs of the bitch. Methods and limitations, *Vet Clin North Am Small Anim Pract* 21:437–466, 1991.
18. Manothaiudom K, Johnston SD: Clinical approach to vaginal/vestibular masses in the bitch, *Vet Clin North Am Small Anim Pract* 21:509–521, 1991.
19. Gouletsou PG, Galatos AD, Apostolidis K, et al: Vaginal fold prolapse during the last third of pregnancy, followed by normal parturition, in a bitch, *Anim Reprod Sci* 112:371–376, 2009.

20. Kyles AE, Vaden S, Hardie EM, et al: Vestibulovaginal stenosis in dogs: 18 cases (1987–1995), *J Am Vet Med Assoc* 209:1889–1893, 1996.
21. Wang KY, Samii VF, Chew DJ, et al: Vestibular, vaginal, and urethral relations in spayed dogs with and without lower urinary tract signs, *J Vet Intern Med* 20:1065–1073, 2006.
22. Wang KY, Samii VF, Chew DJ, et al: Vestibular, vaginal and urethral relationships in spayed and intact normal dogs, *Theriogenology* 66:726–735, 2006.
23. Wallace SS, Mahaffey MB, Miller DM, et al: Ultrasonographic appearance of the ovaries of dogs during the follicular and luteal phases of the estrous cycle, *Am J Vet Res* 53:209–215, 1992.
24. England GC, Yeager AE: Ultrasonographic appearance of the ovary and uterus of the bitch during oestrus, ovulation and early pregnancy, *J Reprod Fertil Suppl* 47:107–117, 1993.
25. Diez-Bru N, Garcia-Real I, Martinez EM, et al: Ultrasonographic appearance of ovarian tumors in 10 dogs, *Vet Radiol Ultrasound* 39:226–233, 1998.
26. Pugh CR, Konde LJ: Sonographic evaluation of canine testicular and scrotal abnormalities: a review of 26 case histories, *Vet Radiol Ultrasound* 32:243–250, 1991.
27. Pugh CR, Konde LJ, Park RD: Testicular ultrasound in the normal dog, *Vet Radiol* 31:195–199, 1990.
28. Paltiel HJ, Diamond DA, Di Canzio J, et al: Testicular volume: comparison of orchidometer and US measurements in dogs, *Radiology* 222:114–119, 2002.
29. Gouletsou PG, Galatos AD, Leontides LS: Comparison between ultrasonographic and caliper measurements of testicular volume in the dog, *Anim Reprod Sci* 108:1–12, 2008.
30. Gumbsch P, Gabler C, Holzmann A: Colour-coded duplex sonography of the testes of dogs, *Vet Rec* 151:140–144, 2002.
31. Doxsee AL, Yager JA, Best SJ, et al: Extratesticular interstitial and Sertoli cell tumors in previously neutered dogs and cats: a report of 17 cases, *Can Vet J* 47:763–766, 2006.
32. Takiguchi M, Iida T, Kudo T, et al: Malignant seminoma with systemic metastases in a dog, *J Small Anim Pract* 42:360–362, 2001.
33. Miller MA, Hartnett SE, Ramos-Vara JA: Interstitial cell tumor and Sertoli cell tumor in the testis of a cat, *Vet Pathol* 44:394–397, 2007.
34. Silva JF: Malignant Sertoli cell tumor in an ectopic testis of a cat (*Felis catus*), *Rev Port Ciênc Vet* 97:87–92, 2002.
35. Johnston GR, Feeney DA, Johnston SD, et al: Ultrasonographic features of testicular neoplasia in dogs: 16 cases (1980–1988), *J Am Vet Med Assoc* 198:1779–1784, 1991.
36. England GC: Ultrasonographic diagnosis of non-palpable Sertoli cell tumours in infertile dogs, *J Small Anim Pract* 36:476–480, 1995.
37. Yates D, Hayes G, Heffernan M, et al: Incidence of cryptorchidism in dogs and cats, *Vet Rec* 152:502–504, 2003.
38. Veronesi MC, Riccardi E, Rota A, et al: Characteristics of cryptic/ectopic and contralateral scrotal testes in dogs between 1 and 2 years of age, *Theriogenology* 72:969–977, 2009.
39. Pearson H, Kelly DF: Testicular torsion in the dog: a review of 13 cases, *Vet Rec* 97:200–204, 1975.
40. Hecht S, King R, Tidwell AS, et al: Ultrasound diagnosis: intra-abdominal torsion of a non-neoplastic testicle in a cryptorchid dog, *Vet Radiol Ultrasound* 45:58–61, 2004.
41. Hricak H, Lue T, Filly RA, et al: Experimental study of the sonographic diagnosis of testicular torsion, *J Ultrasound Med* 2:349–356, 1983.
42. Sigurdardottir OG, Kolbjornsen O, Lutz H: Orchitis in a cat associated with coronavirus infection, *J Comp Pathol* 124:219–222, 2001.
43. Ober CP, Spaulding K, Breitschwerdt EB, et al: Orchitis in two dogs with Rocky Mountain spotted fever, *Vet Radiol Ultrasound* 45:458–465, 2004.
44. Lyle SK: Disorders of sexual development in the dog and cat, *Theriogenology* 68: 338–343, 2007.

ELECTRONIC RESOURCES

evolve

Additional information related to the content in Chapter 42 can be found on the companion Evolve website at http://evolve.elsevier.com/Thrall/vetrad/

- Chapter Quiz

CHAPTER • 43
The Stomach

Paul M. Frank

ANATOMY

In the normal dog and cat, the empty stomach usually lies cranial to the last pair of ribs,[1,2] but it may extend slightly caudal to the costal arch. The stomach lies in a transverse plane immediately caudal to the liver, primarily to the left of the median plane.

The stomach is subdivided into the cardia, fundus, body, and pylorus (Fig. 43-1).[1] The cardia is a small area at the esophagogastric junction. The fundus is the dome or outpouching from the left dorsal aspect of the stomach. The body is the middle portion from the fundus to the pyloric portion and is the largest portion of the stomach. The distal third of the stomach is the pyloric portion, which is further subdivided into the pyloric antrum and the pyloric canal. The pyloric antrum is the proximal two thirds of the pyloric portion and is relatively thin walled and slightly expanded. The pyloric canal, the distal third of the pyloric portion, is more muscular and contains a double sphincter.

Additional landmarks of the stomach include the greater and lesser curvatures and the angular incisure (notch).[1] The greater curvature is the convex surface of the stomach that originates at the cardia and extends caudoventrally around to the pylorus. The lesser curvature is the concave surface that originates to the right of the cardia and extends cranioventrally to the pylorus. It is the shortest distance between the cardia and the pylorus. The angular notch is the point of acute angulation of the lesser curvature, located approximately at the junction of the body and the pyloric antrum. The mucosal surface of the stomach is characterized by numerous folds or ridges called *rugal folds* or *rugae*.

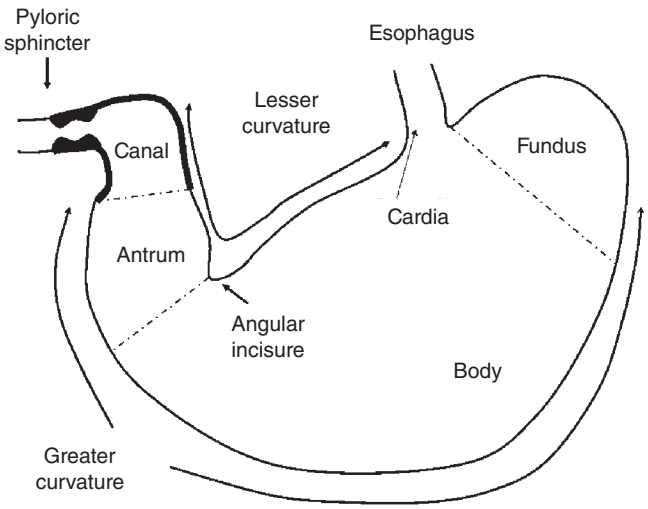


Fig. 43-1 The divisions of the stomach.

RADIOGRAPHIC EXAMINATION

Preparation

Ingesta within the stomach may obscure some lesions or simulate other lesions and thus create false-negative or false-positive results. Ideally, radiographic examination of the stomach should be performed on an animal that has fasted for 12 to 24 hours,[3-5] but this is usually not practical, and in some patients fasting is contraindicated. A cleansing enema may be useful if a subsequent contrast study is contemplated. Fasting and enemas should be avoided in patients with acute abdominal disorders for which time delays are medically contraindicated or when fluid and gas patterns in the bowel may be of diagnostic importance. Also, many drugs used for treatment of gastrointestinal disorders or for sedation to facilitate radiographic positioning reduce gastric motility and may cause gas distention of the stomach. These preparations should be avoided or discontinued for an appropriate interval before any contrast study is undertaken.[6-10]

Radiographic Technique

Survey radiographs may be sufficient for diagnosing some gastric abnormalities. If contrast studies are necessary, survey radiography should always precede them. Various special procedures to assess the stomach are available and include conventional barium sulfate gastrography, low-volume gastrography, double-contrast gastrography, pneumogastrography, gastrography with iodinated contrast media, and gastric-emptying studies with barium/food or radiopaque marker/food mixtures.[2,3,6,11-23] See Box 43-1 for one method of performing a positive-contrast gastrogram.

Four radiographic projections are needed for complete evaluation of the stomach: ventrodorsal, dorsoventral, right lateral, and left lateral. Oblique views may occasionally be of value to isolate or project certain areas of the stomach, such as the pylorus.

NORMAL RADIOGRAPHIC FINDINGS

The stomach is easy to recognize by its location and shape and the content of gas, ingesta, or both. The entire stomach may not be discernible on survey radiographs if it is empty or if the gastric fluid content silhouettes with the liver or other

Box • **43-1**

Positive-Contrast Gastrogram with Barium Sulfate

- Fast for 12 to 24 hours with or without cleansing enemas.
  - Food in the stomach will interfere with interpretation of gastric emptying time.
  - Ingesta may also obscure foreign bodies or small gastric lesions.
  - Gastrograms performed with food in the stomach are difficult to interpret.
- If possible, perform radiography without the use of sedatives.
  - Motility-altering drugs such as antiemetics may interfere with interpretation.
  - If sedatives are required because of the fractious nature of the patient, use the lowest dose possible, and interpret gastric emptying times with caution.
- Perform survey radiographs to assess patient preparation, establish radiographic technique, and possibly identify the problem without gastrography.
- Administer barium sulfate suspension by an orogastric tube with the patient on the x-ray table ready for radiography (cassette in position, technique set, etc.).
  - Barium USP powder mixed with water is not recommended.
- The dosage is 2.3 to 3.6 mL barium/kg body weight (5 to 8 mL/lb).
  - Feeding barium orally (i.e., without an orogastric tube) results in suboptimal distention of the stomach from emptying of the initial portions of barium before administration of the last portion.
  - Not administering enough barium is a common mistake. Small dogs typically need the high end of the dosage range, and large dogs may need only the low end. This means a 100-lb dog gets at least 500 mL of barium.
  - Use caution to ensure that the orogastric tube is located in the esophagus, not the trachea.
    - Verify tube position by using fluoroscopy, survey radiograph, or palpation.
  - Before removing the tube, instill a small volume of air to clear the tube, then kink the tube before removal to prevent leakage of barium into the trachea.
- After removing the tube, immediately make radiographs centered over the stomach. All four views are recommended (right lateral, left lateral, dorsoventral, and ventrodorsal) and should be made as rapidly as possible.
- Additional radiographs (with or without obliques) should be made pending the results of the initial radiographs. If available, fluoroscopy is extremely helpful in the evaluation of gastrograms.
- Continue making radiographs (usually right lateral and ventrodorsal) until the majority of the barium is no longer seen within the stomach.
  - A small amount of residual barium coating the mucosa diffusely for several hours may be normal. Focal barium retention is suggestive of ulceration.
- The gastrogram may be combined with contrast evaluation of the small intestine.

abdominal structures. As a general guide, on the lateral view the axis of the stomach from the fundus through the body and pylorus is either perpendicular to the spine, parallel to the ribs, or somewhere between these angles (Fig. 43-2, *A*). On the lateral view, the pylorus may be superimposed over the body or located slightly cranial to the body. On the ventrodorsal view of the dog, the cardia, fundus, and body of the stomach are located to the left of midline, and the pyloric portions are located to the right of midline. The pyloric sphincter usually is located in the right cranial abdominal quadrant at approximately the level of the tenth or eleventh ribs and is usually cranial to the pyloric canal.[2] In immature dogs the pylorus may be located closer to midline than in adults.[11]

In ventrodorsal radiographs, the long axis of the stomach is generally perpendicular to the spine with the stomach running transversely across the abdomen, making the angular notch difficult to identify (Fig. 43-2, *B*). The stomach may also have a U-shaped appearance with a more obvious angular notch and still be within its normal location. On the ventrodorsal view of the cat, the stomach is more acutely angled with the pylorus located at or near the midline (Fig. 43-2, *C*). Variations in the appearance of the stomach in the dog based on the shape of the thorax and cranial abdomen (i.e., breed conformation) have been described.[2] The shape of the stomach also varies with the degree of gastric distention.

One of the most important factors in the appearance of the stomach is the position of the patient during radiography.[24] This is an important concept that must be understood for accurate interpretation of radiographs and for demonstration of some gastric lesions. Variation in appearance of the stomach with different patient positions is caused by shifts in fluid and gas distribution within the stomach. The stomach usually contains both fluid and gas, with the fluid being either of soft tissue or mineral opacity. This fluid and gas distribution varies with the position of the patient because fluid settles dependently because of gravity, and gas rises to the highest part of the lumen. Gas and positive-contrast medium are relatively easy to visualize on radiographs, whereas fluid within the stomach may be more difficult to see because it may cause border effacement with other structures of similar opacity. To optimize the amount of information provided by fluid and gas shifts, obtaining right *and* left lateral radiographic projections routinely, along with a ventrodorsal radiograph, is recommended.[25] This was discussed in Chapter 35.

To understand the radiographic appearance of the stomach, it should be visualized as lying in a transverse plane with the fundus located dorsally and on the left and the pylorus ventrally and on the right (Fig. 43-3). Thus, for example, with a patient in dorsal recumbency for a ventrodorsal view, fluid within the lumen settles dependently to the fundus and body of the stomach. Gas rises to the uppermost portion, which with the patient in dorsal recumbency is in the pyloric antrum and the body near midline. Figure 43-3, *B* is a transverse computed tomographic image of the cranial abdomen at the level of the stomach acquired with the dog in dorsal recumbency. Note the fluid opacity filling most of the stomach with the gas bubble floating near midline. With this image as a

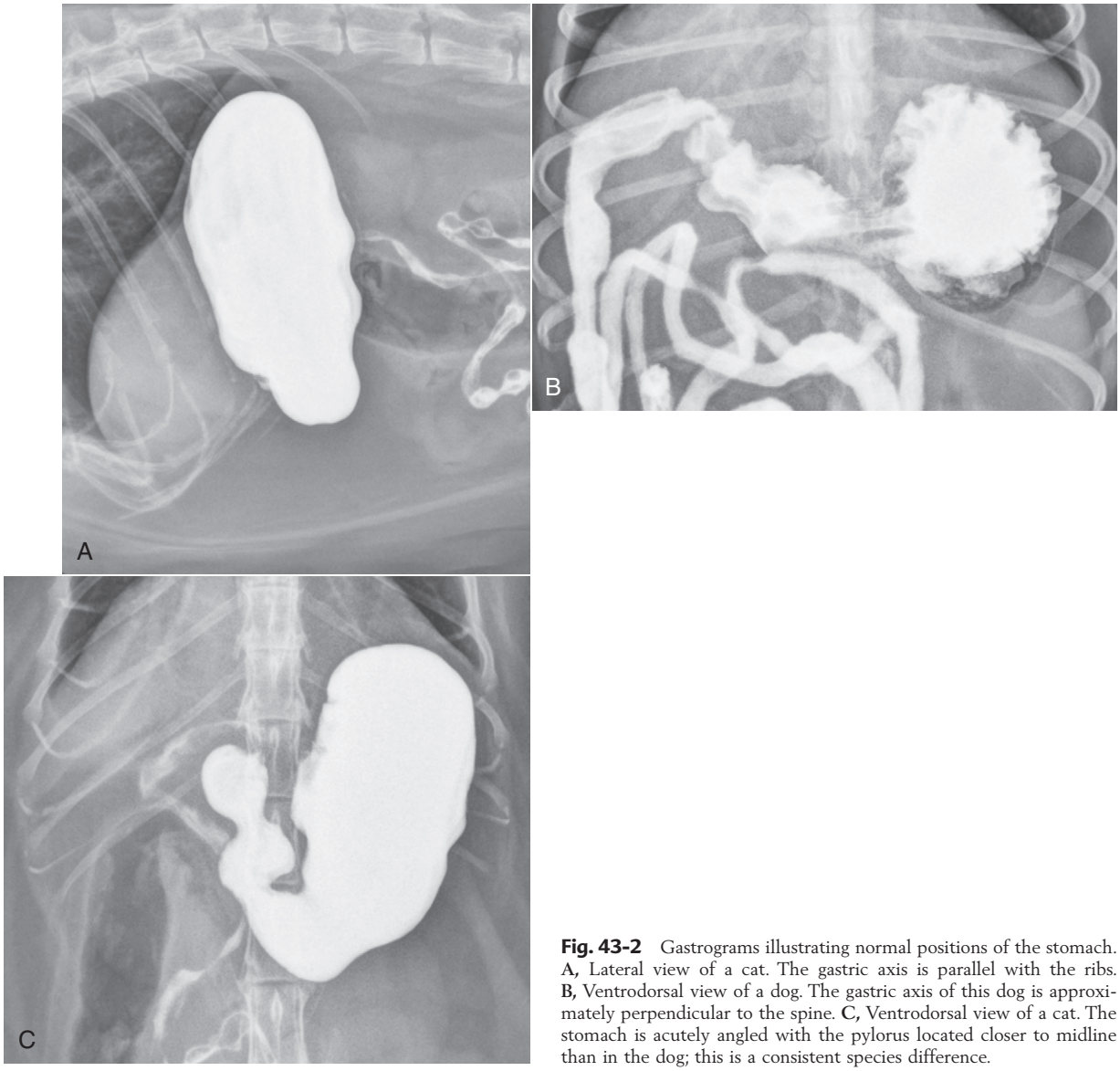


Fig. 43-2 Gastrograms illustrating normal positions of the stomach. **A,** Lateral view of a cat. The gastric axis is parallel with the ribs. **B,** Ventrodorsal view of a dog. The gastric axis of this dog is approximately perpendicular to the spine. **C,** Ventrodorsal view of a cat. The stomach is acutely angled with the pylorus located closer to midline than in the dog; this is a consistent species difference.

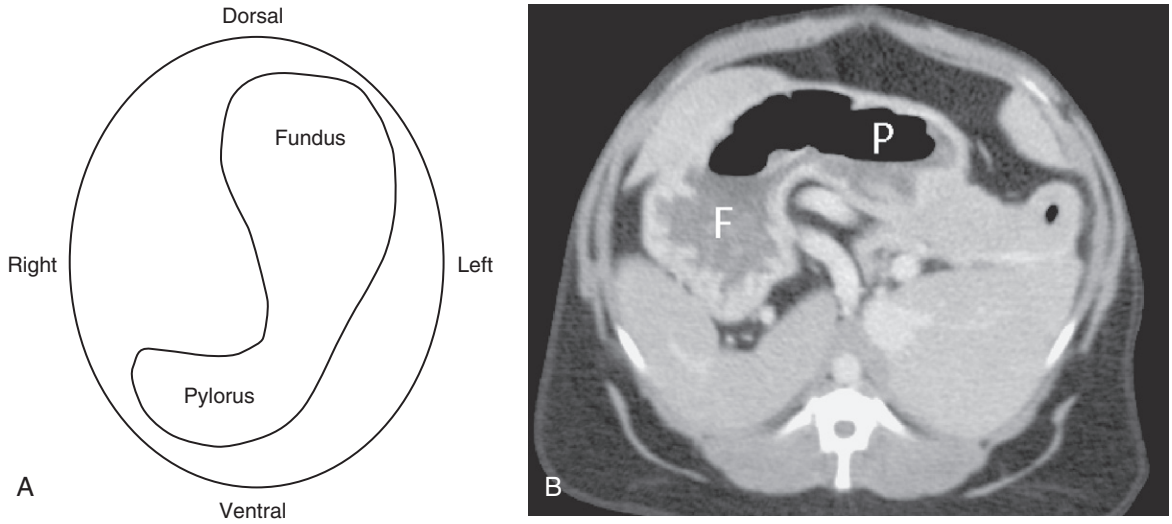


Fig. 43-3 **A,** Illustration of the anatomy of the stomach when viewed from the caudal aspect. The fundus is located dorsally and on the left, whereas the pylorus is located ventrally and on the right. **B,** Computed tomographic image of a normal dog in dorsal recumbency at the level of the stomach. Fluid fills most of the fundus *(F)* and part of the pylorus *(P)*, and the gas bubble floats near the midline.

starting point, it is possible to predict how the fluid and gas would be distributed if the animal were rotated in 90-degree increments for a left recumbent lateral view, a dorsoventral view in sternal recumbency, a right recumbent lateral view, and back to a ventrodorsal view in dorsal recumbency. These variations in appearance of the stomach are altered further by the volume and ratio of fluid to gas within the stomach. Examples of the appearance of the stomach with various views are illustrated in Figures 43-4 and 43-5; these views were made with a vertically directed x-ray beam. In Figure 43-4, barium is present to facilitate understanding how the fluid shifts as a function of gravity.

On the ventrodorsal view (Fig. 43-4, *A*), gas is located in the pylorus and the body near midline. Fluid gravitates to the fundus; some fluid may be trapped in the pyloric antrum in a ventrodorsal view, but this is usually minimal. On a dorsoventral view (Fig. 43-4, *B*), gas rises to the fundus, and fluid settles dependently to fill the pyloric portions and part of the body. On the left recumbent lateral view (Figs. 43-4, *C*, and 43-5, *A*), gas rises to the pyloric portion of the stomach, and fluid settles dependently to the fundus and body. A gas pocket may be trapped occasionally in the fundus in a left lateral view. The fundus and/or body may be difficult to see in a left lateral view because of the intraluminal fluid silhouetting with adjacent structures. (see Fig. 43-5, *A*). On the right lateral view (Figs. 43-4, *D*, and 43-5, *B*), gas rises to the fundus and body, and fluid settles dependently to fill the pyloric portions and part of the body of the stomach. In a right lateral view, the pyloric portion is well visualized with positive-contrast medium. The pyloric antrum and distal part of the body may appear occasionally as a soft tissue mass in the right lateral view (see Fig. 43-5, *B*). If a mass or foreign body is suspected on a right lateral view in the pylorus, a left lateral view should be made to better visualize this area as gas will fill the pylorus.

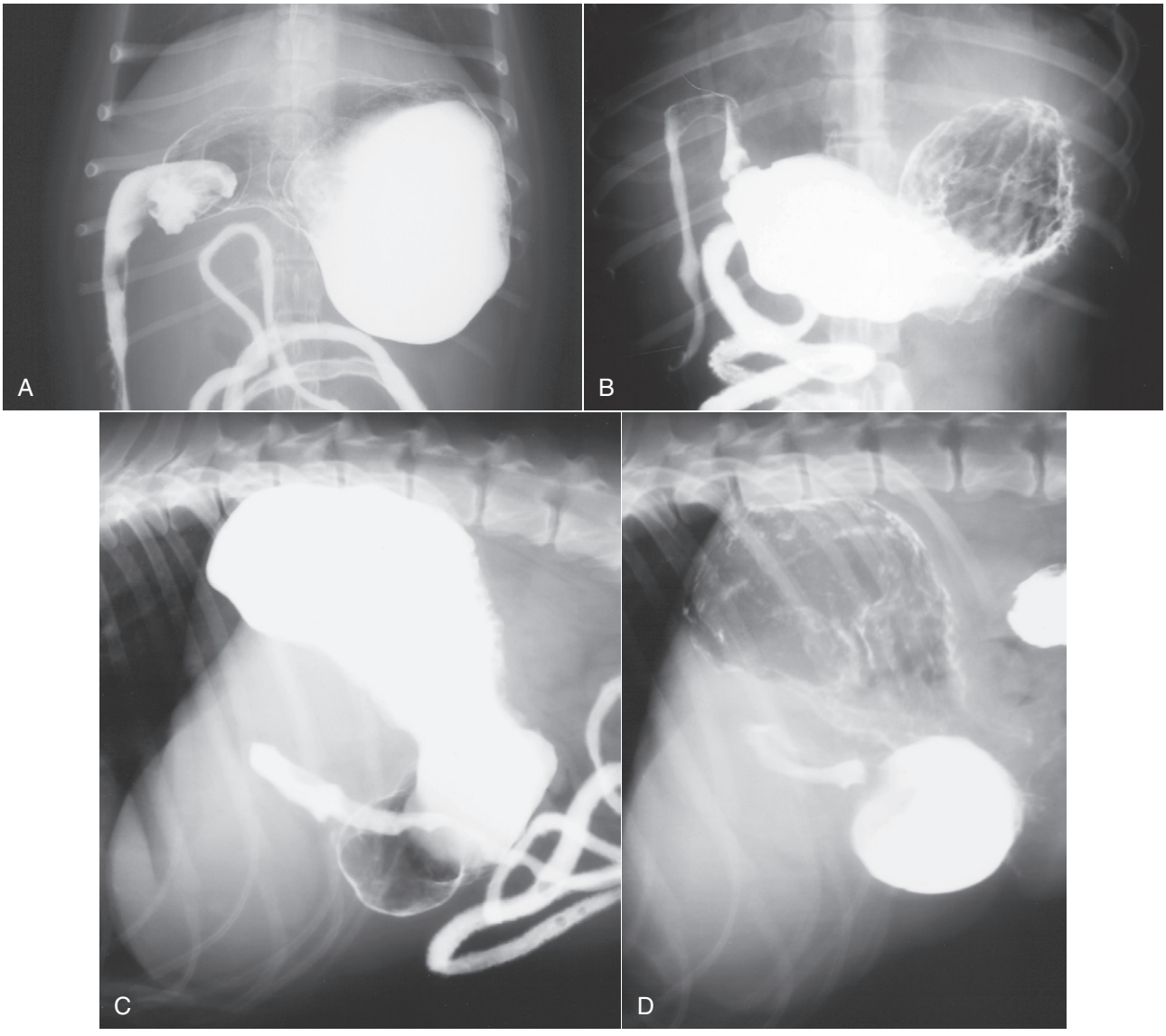


Fig. 43-4 Normal variations in fluid (barium) and gas distribution in the stomach with different patient positions. **A,** Ventrodorsal view, in dorsal recumbency. Gas is located in the body and pyloric antrum. Fluid settles dependently to fill the fundus and body. In this dog, there is a small amount of barium trapped in the pyloric antrum. **B,** Dorsoventral view, in ventral recumbency. Gas rises to the fundus and fluid settles dependently to fill pyloric portions and part of the body. **C,** Left lateral view. Gas rises to the pyloric portion, and fluid settles dependently to fill the fundus and body. **D,** Right lateral view. Gas rises to the fundus and body, when there is some barium adherent to the mucosa. Fluid settles dependently to fill the pyloric portion.

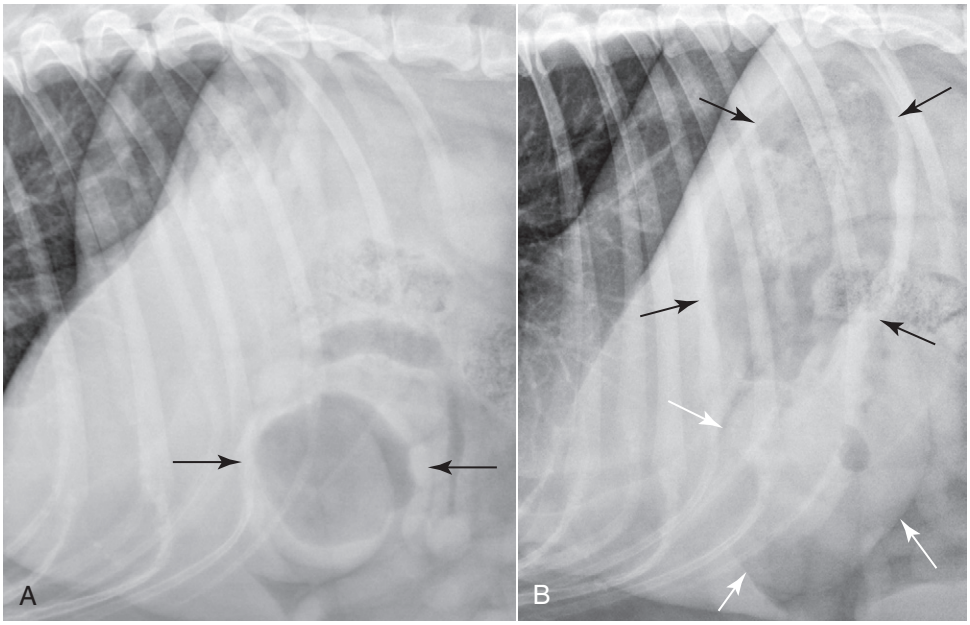


Fig. 43-5 Normal variation in fluid and gas distribution in the stomach as function of left versus right recumbency. **A,** Left lateral view. Gas rises to the pyloric portion *(black arrows)*. In this dog, there is also some gas trapped in the fundus. Fluid settles dependently to the body, which is difficult to see. **B,** Right lateral view. Gas rises to fill the fundus and body *(black arrows)*. Fluid settles dependently to the pyloric portion, which appears as a soft tissue mass (*white arrows*).

Table • **43-1**

Distribution of Stomach Gas and Fluid as a Function of Radiographic Projection Using a Vertical X-Ray Beam

RADIOGRAPHIC VIEW	LOCATION OF GAS	LOCATION OF FLUID
Dorsoventral	Fundus	Body/pylorus
Ventrodorsal	Body (± pylorus)	Fundus
Left recumbent lateral	Pylorus (± body)	Fundus
Right recumbent lateral	Fundus	Pylorus

Recognizing that variations from factors, such as the position of the patient and the volume and ratio of fluid to gas within the stomach, exist in the appearance of the normal stomach is important. The ability to take advantage of fluid and gas shifts within the stomach to visualize certain portions of the stomach more clearly is also important. Table 43-1 is a simplified summary of the expected changes in gas and fluid within the stomach on change in patient position.

Rugal folds are seen inconsistently on survey radiographs. With positive-contrast gastrography, rugal folds are best seen at the peripheral portions of the stomach, where they may be visualized end-on as regular small filling defects at the mucosal surface. If projected en face, rugal folds are not visible with positive-contrast gastrography unless the barium is well penetrated by the x-ray beam, or there is only a small amount of barium in the stomach. Rugal folds then appear as relatively radiolucent, linear filling defects separated by barium in the interrugal spaces (Fig. 43-6). Radiographic assessment of rugal folds is subjective because they vary in size and number,[5,26] and their appearance depends on the degree of gastric distention. Rugal folds are more tortuous in the nondistended stomach and become more uniform and parallel to the gastric curvature with increasing distention.[5,12] Rugal folds are smaller and more spiral in the pyloric antrum.[27] Rugal folds may not be visible if the stomach is overdistended.[13] Rugal folds are smaller and fewer in number in cats than in dogs.[2] A reference range for normal rugal-fold thickness in dogs weighing 2 to 50 kg has been reported to be 1 to 8 mm.[26]

Gastric peristalsis and gastric emptying may be observed directly during fluoroscopy with the use of positive-contrast medium. Ultrasound can also be used to assess gastric motility. Although a peristaltic contraction may be seen on a conventional radiograph during gastrography, this is a chance event depending on when the radiograph was made. A peristaltic contraction appears as an indentation of the wall of the stomach with slight dilation of the lumen immediately preceding the contraction. Peristaltic contractions are stronger and most obvious in the pyloric portion of the stomach.

After administration of barium, gastric emptying should start within 15 minutes in most normal patients.[2,28,29] During gastrography with barium sulfate, the stomach generally empties within 1 to 4 hours in dogs.[6,28] Rapid emptying of the stomach has no clinical significance, whereas delayed emptying is potentially of much greater significance.

The rate of gastric emptying is a complex phenomenon that is altered by the volume of contents, chemical and physical properties of chyme entering the duodenum, various reflex mechanisms, certain medications, and the type of contrast medium used. Thus a standard approach must be used to evaluate the rate of gastric emptying radiographically. Because the stomach starts to empty faster with an increased intraluminal volume,[14] the dosage of contrast medium for a barium study must be standardized. Low dosages may result in delayed gastric emptying, which leads to a false impression of pyloric obstruction. If a standard technique has been used, and no medications that affect gastric emptying were administered, then delays in gastric emptying are likely related to psychological influences or disease at the pylorus. Emotional

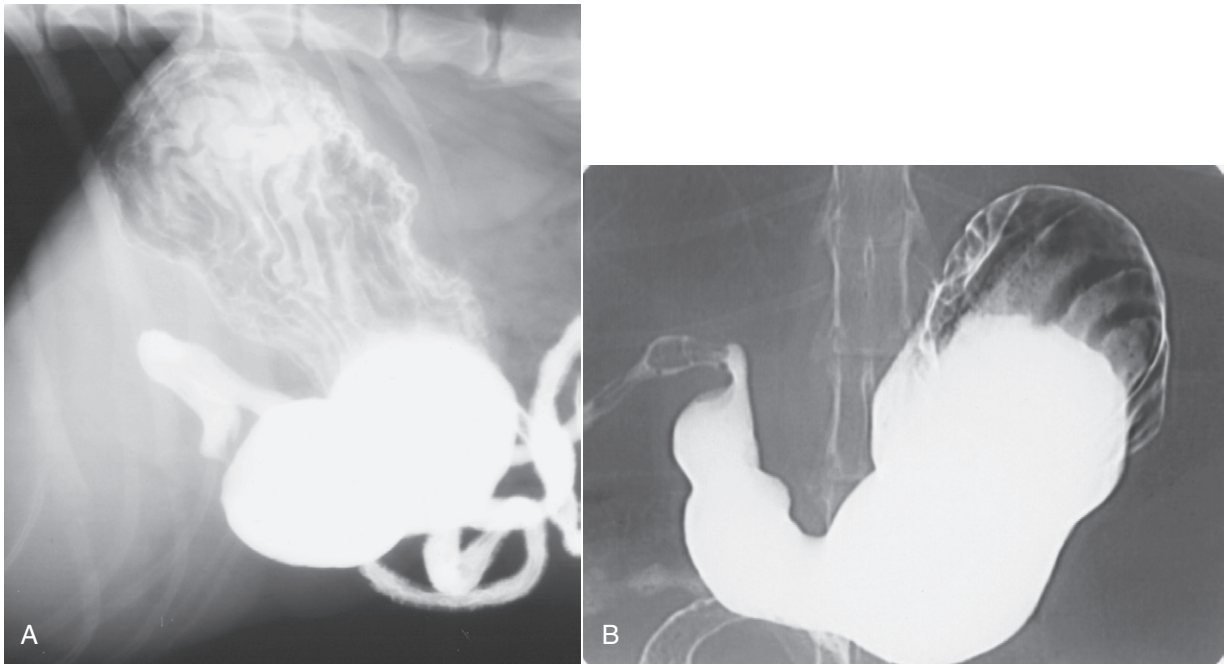


Fig. 43-6 **A,** Right lateral gastrogram. Note the multiple curvilinear filling defects in the fundic region of the stomach. These filling defects are the rugae. **B,** Dorsoventral gastrogram. Radiolucent linear filling defects are from rugal folds projected en face.

stress and noise may inhibit gastric movement.[30] Anxiety, fear, rage, or pain induced by physical manipulation of the patient, gastric intubation, and physical restraint may contribute to temporary delayed gastric emptying. Thus patients with delayed gastric emptying must be allowed to calm down in a quiet environment before diagnostic significance is placed on this finding. For these reasons, minimal significance is usually placed on slight or minor delays in gastric emptying if the stomach proceeds to empty in a normal manner after an initial delay.

Studies that use barium-food mixtures have been performed to evaluate gastric function further.[15,16] Emptying times for individual dogs were repeatable; however, the range of normal gastric emptying was so wide (7 to 15 hours) that this procedure is not useful for evaluation of gastric emptying unless gross abnormalities are present.[15] Gastric emptying times for dogs and cats can vary from 4 hours for high-moisture food to 16 hours for dry food.[5] An alternative technique for evaluating gastric emptying of solids in dogs and cats has been developed by using radiopaque barium-impregnated polyethylene spheres (BIPS, Chemstock Animal Health Ltd., Christchurch, New Zealand) mixed with food.[20-23] The number and size of radiopaque spheres, type and amount of food, and fasting period must be standardized. An advantage of the BIPS technique is that it can be performed in most veterinary practices; however, study times may be long (up to 10 hours). Some controversy exists about the usefulness of BIPS for gastric emptying analysis, and these studies should be interpreted by a specialist.

Scintigraphic evaluation of gastric emptying of food may be considered the gold standard technique. Scintigraphy can be completed in 4 to 5 hours, but availability is limited.[9,31,32] Gastric emptying time is significantly different in cats versus dogs as measured by BIPS compared with scintigraphy. Emptying times measured by BIPS were significantly longer relative to scintigraphy.[33,34]

A radiolucent line occasionally can be seen within the stomach wall of the cat because of submucosal fat.[35]

ULTRASONOGRAPHIC EXAMINATION

Ultrasound is a useful addition to radiography for evaluation of the gastrointestinal tract. It may eliminate the need for barium studies because gastric motility; wall thickness and architecture; and, to a lesser extent, luminal contents may be evaluated sonographically. In addition, ultrasound examination is quicker than an upper gastrointestinal series and may be equally sensitive and specific for detection of gastric disease.[36] Gas and ingesta within the stomach may obscure the far wall, but the lumen and far wall can be evaluated in those patients in which the stomach contains fluid and little gas (Fig. 43-7, *A*). Ideally, sonography should be performed after a 12-hour fast and before barium is administered. If needed, intraluminal gas can be removed by an orogastric tube and the stomach distended with fluid to act as an acoustic window.[37,38] The stomach should be scanned in longitudinal and transverse planes. For evaluating stomach wall layers, 7.5 MHz (or higher) transducers are preferred, but 5 MHz transducers may be needed to evaluate deeper portions of the stomach. Ultrasound has been used to help diagnose gastric neoplasms,[39-46] inflammation or infection,[47] ulcers,[48] foreign bodies,[45,49] pyloric hypertrophy,[50] gastric mineralization,[51] and gastroduodenal and gastrogastric intussusceptions,[52,53] and to evaluate gastropexy sites.[54,55]

NORMAL ULTRASONOGRAPHIC FINDINGS

The appearance of the stomach varies with the amount of distention and the extent of luminal contents. When empty, the stomach may have a wagon-wheel appearance because of infolding of rugal folds (Fig. 43-7, *B*). This is especially noticeable in the cat, and the empty stomach is sometimes mistaken for an abnormal kidney by inexperienced sonographers. With increasing distention, rugal folds become less conspicuous. Stomach wall thickness in dogs is 3 to 5 mm depending on the location and size of the dog, with larger dogs having a

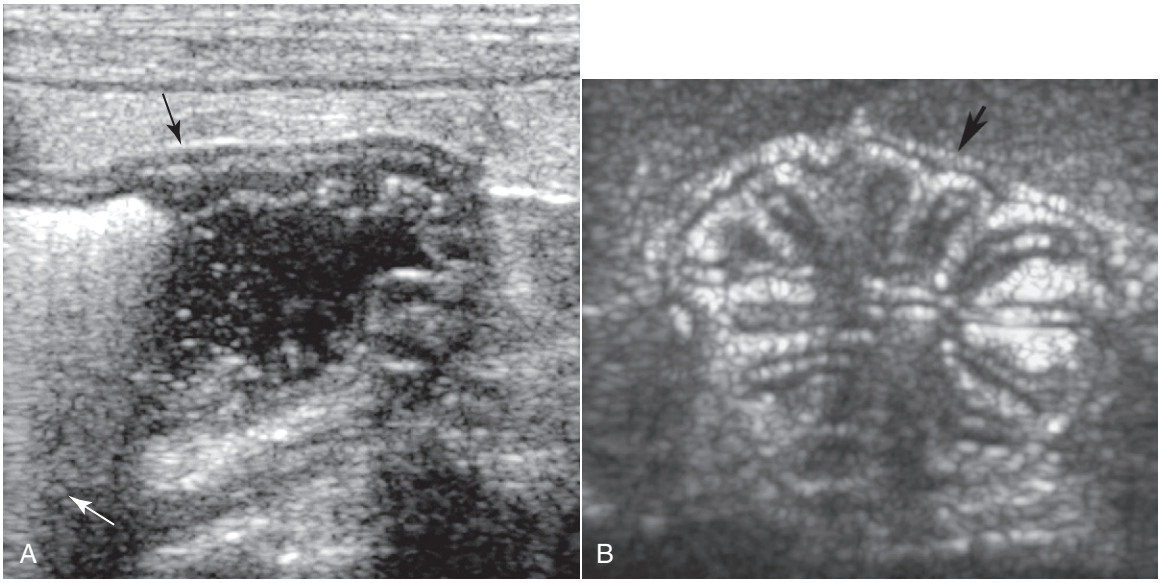


Fig. 43-7 Longitudinal ultrasonogram of the stomach in a normal dog **(A)** and a normal cat **(B). A,** The stomach is distended partially with gas and fluid. Gas within the lumen appears as a bright echo against the mucosal surface, producing reverberation artifact that prevents visualization of a portion of the far wall (region of *white arrow*). Fluid within the caudal half of the stomach provides a window for identification of the far wall. The five normal layers of the stomach wall can be identified as well as several rugal folds. The *black arrow* identifies the bright serosal layer. **B,** The stomach is empty and contracted, giving it a wagon-wheel appearance. The normal layered appearance of the stomach can be seen. The *black arrow* identifies the bright serosal surface. Caudal is to the *right*, and ventral is to the *top*.

thicker stomach wall.[37,56] In cats, the rugal-fold thickness has been reported as 4.4 mm,[57] 2.6 mm,[57] or 2.0 mm[58] for the interrugal area and 2.1 mm for the pylorus.[58] Five wall layers corresponding to the mucosal surface, mucosa, submucosa, muscularis propria, and subserosa/serosa can be identified.[37] These layers have alternating hyperechoic and hypoechoic appearances, with mucosal surface, submucosa, and subserosa/serosa being hyperechoic and the mucosa and muscularis layers being hypoechoic (see Fig. 43-7). The mean number of peristaltic contractions observed ultrasonographically in dogs has been reported to be 4 to 5 contractions per minute.[37]

ABNORMAL RADIOGRAPHIC AND ULTRASONOGRAPHIC FINDINGS

Displacement

The position of the stomach is a useful indicator for localization of some extragastric abnormalities in the cranial abdomen. Some diseases of the liver, spleen, pancreas, and diaphragm may affect the stomach. The relation between the stomach and a particular extragastric abnormality may help define the primary organ involved or the nature of the primary lesion.

Because the stomach is in close apposition with the liver, changes in size or position of the liver may cause a change in position of the stomach. Generalized hepatomegaly often produces caudal and dorsal displacement of the stomach.[59] This displacement may be asymmetric if caused by a mass.[2] However, because the cardia is relatively fixed, even generalized hepatomegaly produces a nonuniform displacement of the stomach. Thus on the lateral view, generalized hepatomegaly often produces caudal and dorsal displacement of the pylorus and body of the stomach. This displacement changes the axis of the stomach so that the axis is no longer parallel with the ribs (Fig. 43-8, *A*). On the ventrodorsal or dorsoventral view, generalized hepatomegaly often causes displacement of the body and pylorus of the stomach caudally and toward the left (Fig. 43-8, *B*). This displacement changes the axis of the stomach so that it is no longer transverse. The assessment of gastric displacement as an indicator of liver size becomes especially valuable when the liver is not visible because of emaciation or abdominal effusion. In such patients, air in the stomach can often be used to define the axis of the stomach. A small volume of room air or barium may also be given to clarify the gastric axis if it cannot be assessed from the survey radiographs.

If the diaphragm is intact, cranial displacement of the stomach relative to the diaphragm can occur only with a decrease in the size of the liver (Fig. 43-9). Axial patient rotation can create the artifactual impression of microhepatia; use care to ensure that the patient is in a true lateral position before assessing the gastric axis. Cranial displacement of the stomach may also occur with rupture of the diaphragm and herniation of the liver, part of the liver, or the stomach (Fig. 43-10). Even if the stomach may not pass through a diaphragmatic hernia, the position of the stomach is an important consideration in patients suspected of having a diaphragmatic hernia. A cranial shift of the axis of the stomach may help define whether the liver has herniated cranially through the diaphragm.

Abdominal masses that originate caudal to the stomach do not displace the stomach cranially because of the presence of the liver. Instead, such masses may distort the shape of the stomach as they press against and indent the stomach, or they may displace the stomach to the right or left. The relation of an abdominal mass to the stomach is often of value in helping define whether the mass originates in the liver, spleen, or pancreas (Fig. 43-11).

Gastric Foreign Bodies

Radiopaque material within the stomach is visualized easily and is present commonly on survey radiographs. These opacities are most often the result of ingested food or bone fragments and usually have no clinical significance. More clinically significant foreign bodies, such as fishhooks and needles, are also readily visualized and present no diagnostic dilemma. The

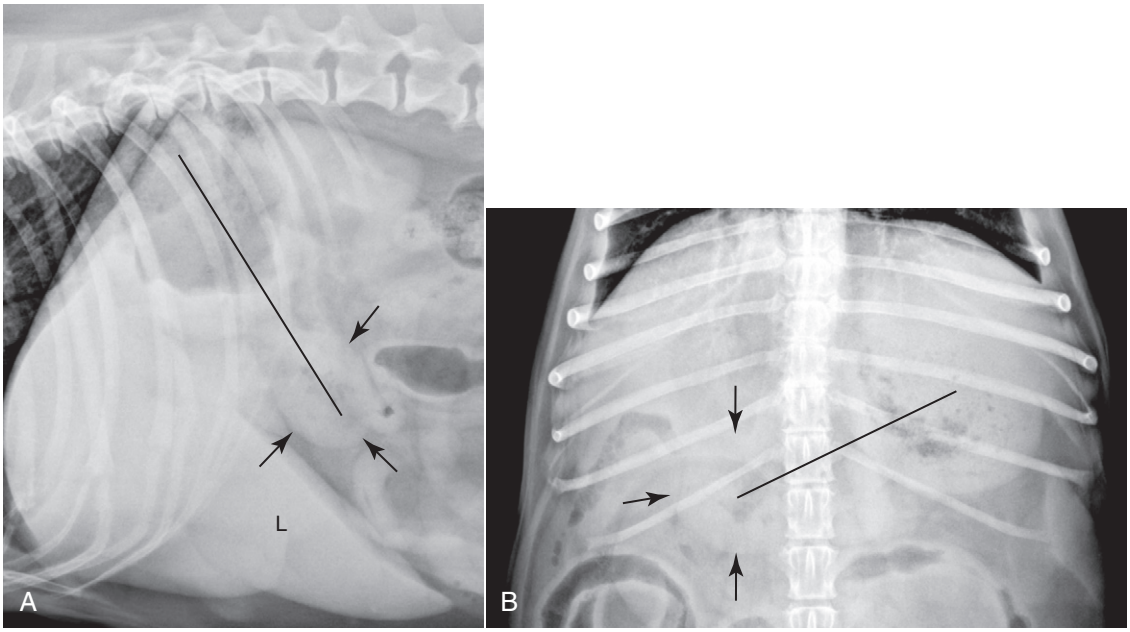


Fig. 43-8 Gastric displacement caused by hepatomegaly. **A,** Lateral view. The pylorus *(black arrows)* is displaced caudally by an enlarged liver *(L)*, and the fundus-pylorus axis *(black line)* is no longer parallel with the ribs. **B,** Ventrodorsal view. The pylorus *(black arrows)* is displaced caudally and to the left, and the fundus-pylorus axis *(black line)* is no longer transverse.

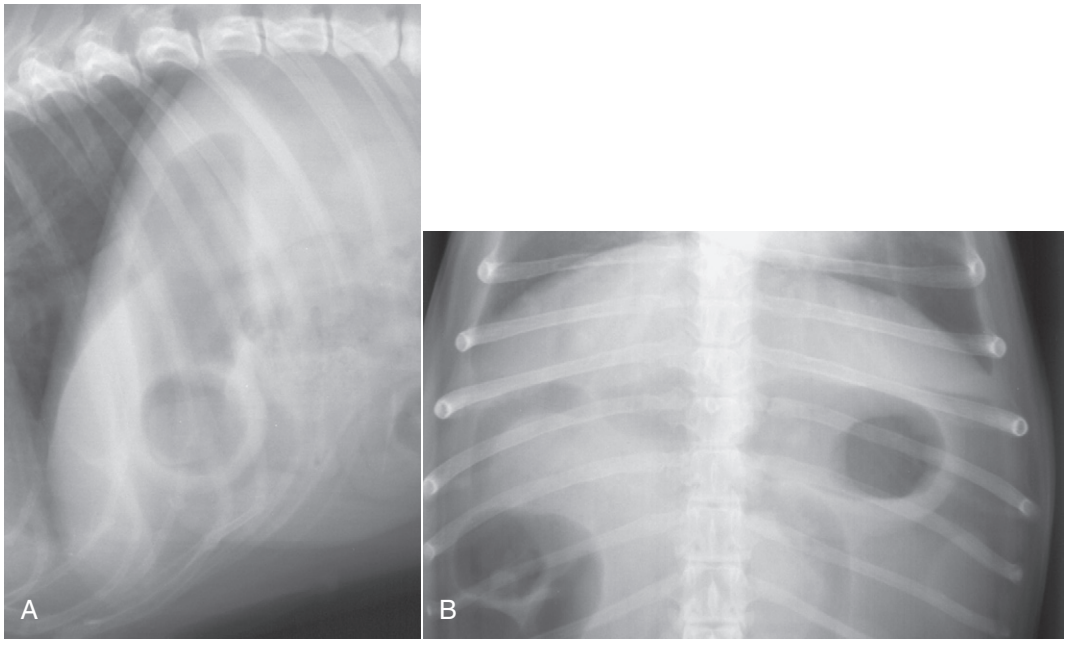


Fig. 43-9 Cranial gastric displacement from a small liver secondary to a portosystemic shunt. The pylorus and body are displaced cranially on lateral **(A)** and ventrodorsal **(B)** views. In **B,** the fundus-pylorus angle is abnormal, with the pylorus being located more cranially than normal.

finding of discoid metallic foreign bodies are significant because certain zinc-containing coins (U.S. pennies minted after 1982 and Euro cents) can induce intravascular hemolysis.[60,61] Radiographs of the abdomen are indicated in the evaluation of patients with intravascular hemolysis for this reason. Other types of metallic objects may also contain zinc. Determining the denomination of suspected coins may be possible radiographically. If projected en face, the diameter can be measured and corrected for magnification and compared to the known diameter of coins. Occasionally, the image of the coin will contain adequate details that allow its identification (Fig. 43-12).

The stomach may occasionally contain nondescript radiopaque material of questionable significance (Fig. 43-13). The persistence of the abnormality is important. If the patient is stable and endoscopy is not used, repeat radiographs made 24 hours later may provide valuable information about the digestibility or potential transit of the suspicious material.

A greater problem exists with radiographic diagnosis of nonopaque gastric foreign bodies. Such objects are usually



Fig. 43-10 Ventrodorsal radiograph of a dog with a left-sided diaphragmatic hernia that has allowed the fundus to shift cranially. Although there are no gas-containing bowel segments in the pleural space, the cranial position of the stomach is diagnostic for a hernia.

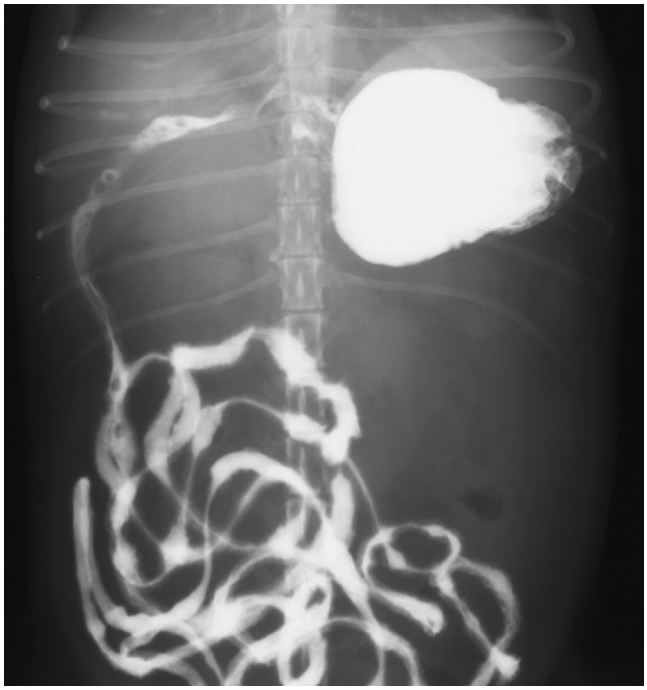


Fig. 43-11 Ventrodorsal radiograph of a dog with a large pancreatic abscess. Barium has been administered. The pylorus is displaced to the left and cranially. The cranial duodenal flexure and proximal part of the descending duodenum have a broad arc around the cranial surface of the mass, which itself is not visible.

difficult to see on survey radiographs. Endoscopy is valuable and should be performed if possible. Contrast studies may be necessary for diagnosis. Several approaches exist to help in the radiographic identification of nonopaque gastric foreign bodies. The simplest is to use different patient positions. If the foreign body does not shift dependently with gastric fluid, then a different view may help outline the foreign body with gas. Giving a small amount of barium or gas (Fig. 43-14) may make such foreign bodies easier to visualize than with a standard gastrogram using a large volume of barium because the large volume may obscure the foreign body. Pneumogastrography is simple, easy to perform, cheap, and quick and requires no special equipment.[62]

The appearance of a foreign body on a gastrogram varies depending on the type of foreign body present. An object such as a solid ball creates a round, discrete filling defect within the barium. If the object has a nonabsorbent surface, it may not be visible after the stomach has emptied. Conversely, a rag or sock may not create an initial filling defect because the contrast medium may permeate the object. Because of absorption and retention of contrast medium, however, the foreign body may be better visualized after the stomach has emptied.

Gastric foreign bodies may be identified ultrasonographically.[43,49] The ability to detect these objects depends on the presence of other gastric contents (e.g., gas, fluid, and food), the position of the object relative to the sound beam, and the object composition. Strong acoustic shadows with or without an echogenic acoustic interface are strongly suggestive of a foreign body. A semicircular border is suggestive of a ball. Intraluminal fluid surrounding a foreign object facilitates its detection and the ability to distinguish rounded reflective foreign body surfaces from intraluminal gas; therefore adding water to the stomach may be beneficial in some patients. Objects that transmit sound may be visualized more completely than those producing strong acoustic shadows.

Acute Gastric Dilation and Volvulus

Acute gastric dilation and gastric volvulus produce gaseous distention of the stomach. Although both fluid and gas are present in the stomach, gaseous distention is the predominant abnormality in these conditions. Gastric dilation and volvulus have been reported in a dog as young as 5 weeks old.[63] Although rare, a similar condition has been reported in the cat.[64] Diaphragmatic hernia may be a predisposing factor in the cat.[65]

Acute gaseous distention of the stomach may be attributable to a variety of causes. Gaseous distention of the stomach may also be caused by aerophagia as a result of severe dyspnea or pain. In such instances, the gastric distention is usually less severe, and other correlative findings may be present to help in the differential diagnosis. With acute gastric dilation, the stomach is enlarged and is filled primarily with gas but retains its normal position and anatomic relations (Fig. 43-15). Thus the pylorus is still located on the right and the fundus on the left. The normal position of the stomach usually can be determined on survey radiographs by using and comparing the right and left lateral views or the ventrodorsal and dorsoventral views. Recognition of the pylorus of a distended stomach is usually easier on lateral views than on the ventrodorsal or dorsoventral view. Contrast gastrography may help in this localization but is usually not necessary.

Gastric dilation/volvulus is differentiated from acute gaseous dilation by the presence of gastric malpositioning. The radiographic appearance of the stomach varies depending on the type and degree of rotation and the amount of distention.[66,67] As the stomach dilates, the fundus and greater curvature rotate clockwise, when viewed from caudal to cranial, to lie along the ventral abdominal wall. The pylorus therefore shifts dorsally, cranially, and to the left, and the body of the stomach shifts toward the right.[27] Because of the gastrosplenic ligament, the spleen follows the greater curvature toward the right.

The major radiographic feature of gastric volvulus is gas and fluid distention of the stomach (more gas than fluid). Additionally, the pylorus is usually displaced dorsally and to the left. Thus radiographic determination of the location of the pylorus is the key differentiating feature between gastric dilation and gastric volvulus. Radiographic localization of the pylorus is best accomplished by making left and right lateral views or ventrodorsal and dorsoventral views. Lateral views are usually of most value. When filled with gas, the pyloric portion of the stomach appears more tubular and narrower

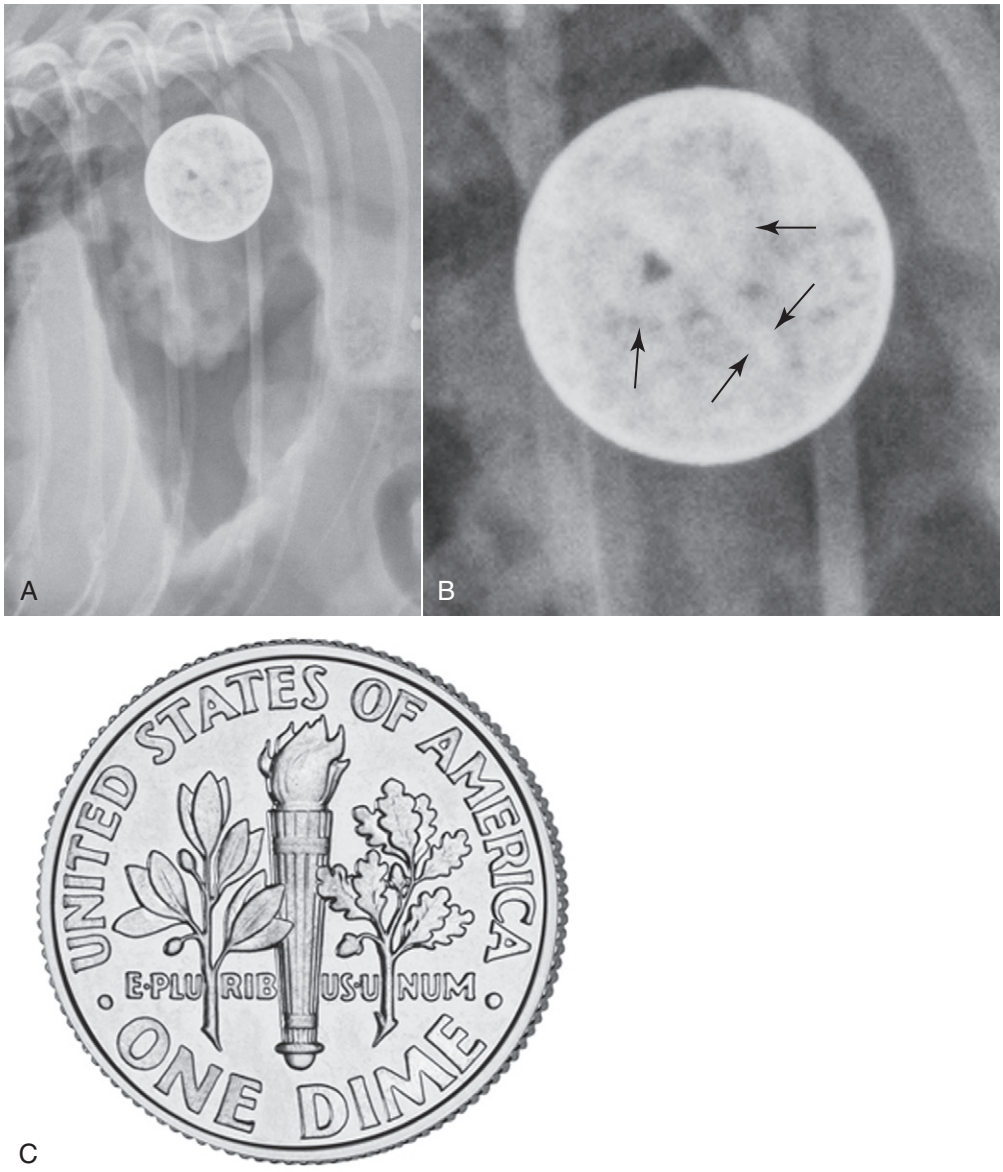


Fig. 43-12 Lateral radiograph **(A)** of a dog with a discoid metallic gastric foreign body. Determining the type of coin is important based on the association of zinc toxicity with some coin types. This object is likely a U.S. dime, based on the markings **(B)** that resemble the engraving present on that particular coin **(C).** The magnification-corrected diameter of the coin was also identical to that expected for a U.S. dime.

than the rest of the stomach. Although the stomach is filled primarily with gas, it usually contains enough fluid so that the pyloric portion may fill with fluid in one lateral view and thus not be seen. Both lateral views may be needed to ensure that the pylorus fills with gas and can be recognized. In the unstable, acutely ill patient in which gastric dilatation and volvulus are suspected, a right lateral radiograph should be made first. In many instances, the diagnosis may be obvious on this one radiograph, and the unstable patient will not have to undergo manipulation to perform other positional radiographs. Also, overall mortality is decreased if time between presentation and surgical intervention is decreased;[68] thus, minimizing time spent acquiring radiographs is of benefit. If the diagnosis is not obvious on this first radiograph, other radiographic views are necessary.

With the pylorus shifted to the left and with the patient in left recumbency, fluid in the stomach fills the pylorus and gas fills the rest of the stomach. With the patient in right recumbency, gas fills the pyloric portion and fluid shifts to the fundus or body of the stomach. This gas distribution is opposite to what is normally expected. Thus the radiographic finding that the pyloric portion fills with fluid on the left lateral view and fills with gas on the right lateral view indicates that the pylorus is on the left side and that the stomach has rotated (Fig. 43-16). Recognition of this shift is more difficult on the ventrodorsal and dorsoventral views because specific recognition of the pyloric portion is more difficult. Positive-contrast gastrography may be performed to confirm the position of the stomach but usually is not needed. An additional variation is a volvulus of 360 degrees in which the pylorus and fundus are in their normal positions (Fig. 43-17), and diagnosis depends on findings at physical examination or surgery.

Gastric volvulus may also be present without severe gastric distention. This situation may often exist for days or weeks after previous gastric decompression[69] or may be present

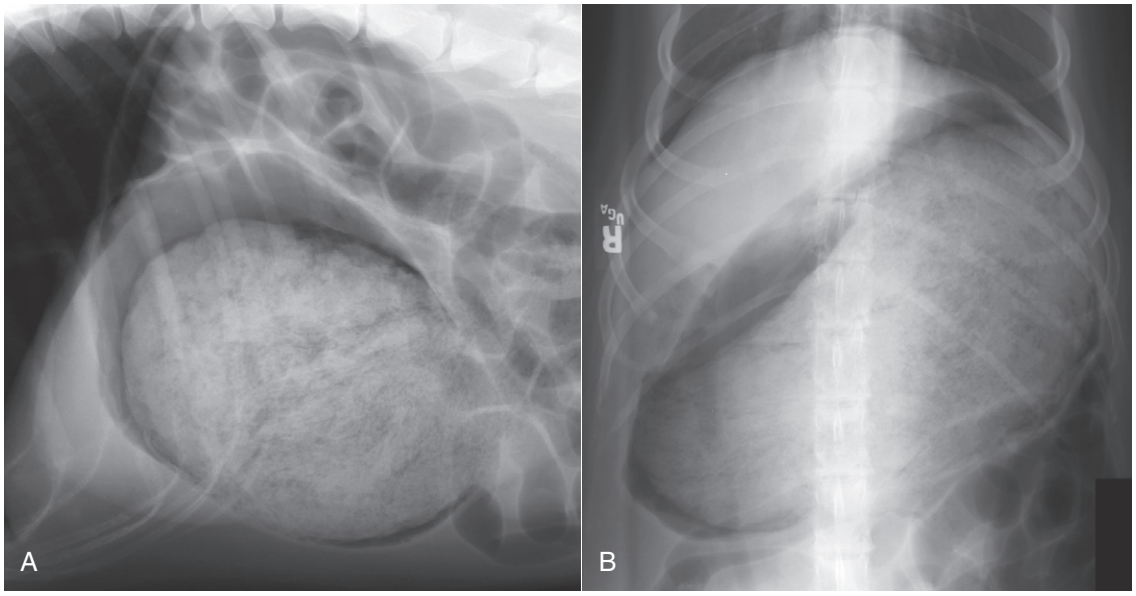


Fig. 43-13 Lateral **(A)** and ventrodorsal **(B)** radiographs of a dog with a large gastric foreign body. This radiopaque material is easy to visualize because of the large amount of gas surrounding the foreign body, which was aggregated leaves and plant material. Expansion of ingested polyurethane glue can also lead to this particular appearance.

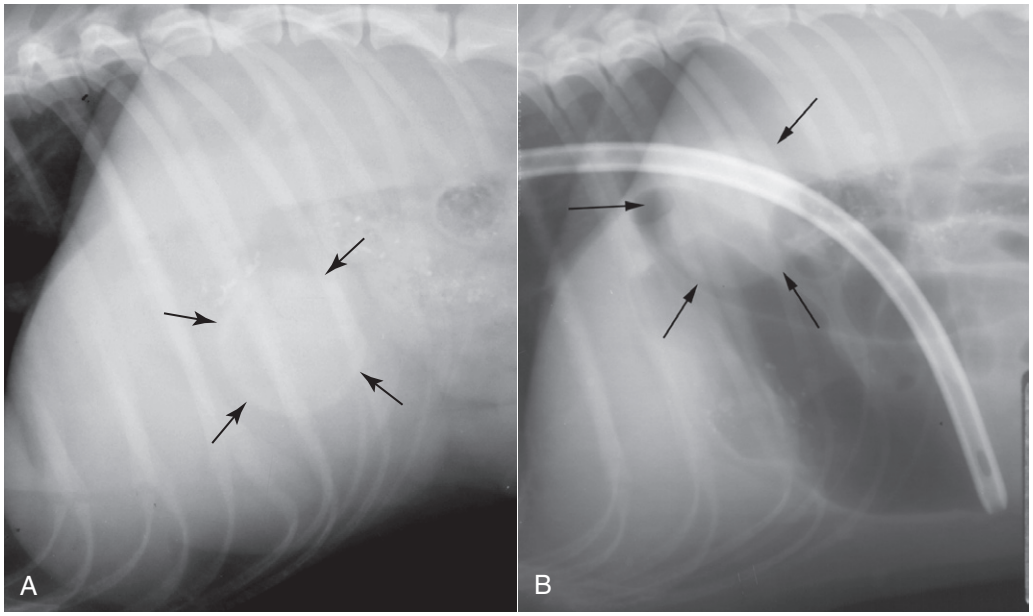


Fig. 43-14 A ball in the pyloric portion of the stomach *(black arrows)* is difficult to see on the right lateral view **(A)** because of fluid in the pylorus. In **B,** gas has been administered by a gastric tube, making the ball *(black arrows)* easier to see. Note the ball has moved to the fundus.

at the time of initial presentation.[28] The aforementioned radiographic principles still apply as a means to recognize rotation of the stomach, except that the stomach will not be markedly dilated.

Compartmentalization is a term that refers to the radiographic appearance of soft tissue bands that project into or across the gas-filled lumen of the rotated stomach. These soft tissue bands result from folding of the stomach on itself as the folded wall projects into the lumen and is outlined by gas within the lumen.[2] These bands may become more obvious with greater degrees of distention (see Fig. 43-16). With progressive distention of the stomach, the stomach wall becomes thinner. Gas within the gastric wall, termed *pneumatosis*, has also been described but is infrequent (Fig. 43-18).[2] Gastric pneumatosis or pneumoperitoneum should alert the clinician to the possibility of gastric necrosis. Prior trocharization of the stomach will complicate assessing the significance of pneumatosis or pneumoperitoneum, and the lack of pneumatosis does not rule out the possibility of gastric necrosis.[70]

As the stomach enlarges, other mobile structures within the abdomen are displaced caudally and the resultant crowding may make visualization of other abdominal organs difficult. The spleen is also usually involved in gastric volvulus, because of impaired circulation, and may shift with the stomach (see Fig. 43-16). Outright torsion of the spleen may also occur; this further compromises the patient. The greater

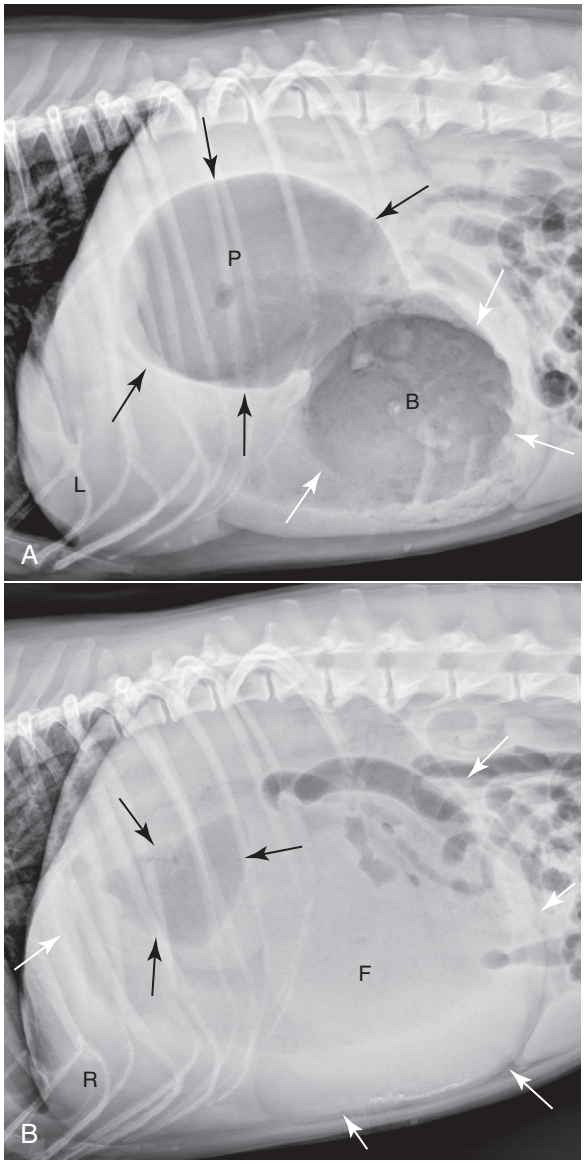


Fig. 43-15 Gastric dilation without volvulus. **A,** Left lateral view. Gas is present in the pyloric antrum *(P, black arrows)* and body *(B, white arrows)* of the stomach as expected. The narrowing between the body and pyloric antrum is a peristaltic contraction. **B,** Right lateral view. The fundus *(F, white arrows)* is extremely distended. There is a small amount of gas trapped in the pyloric antrum *(black arrows)*. The distribution of gas as a function of left versus right recumbency is as expected in a normal subject, indicating that the stomach is not rotated, unless the rotation is 360 degrees, which is unusual.

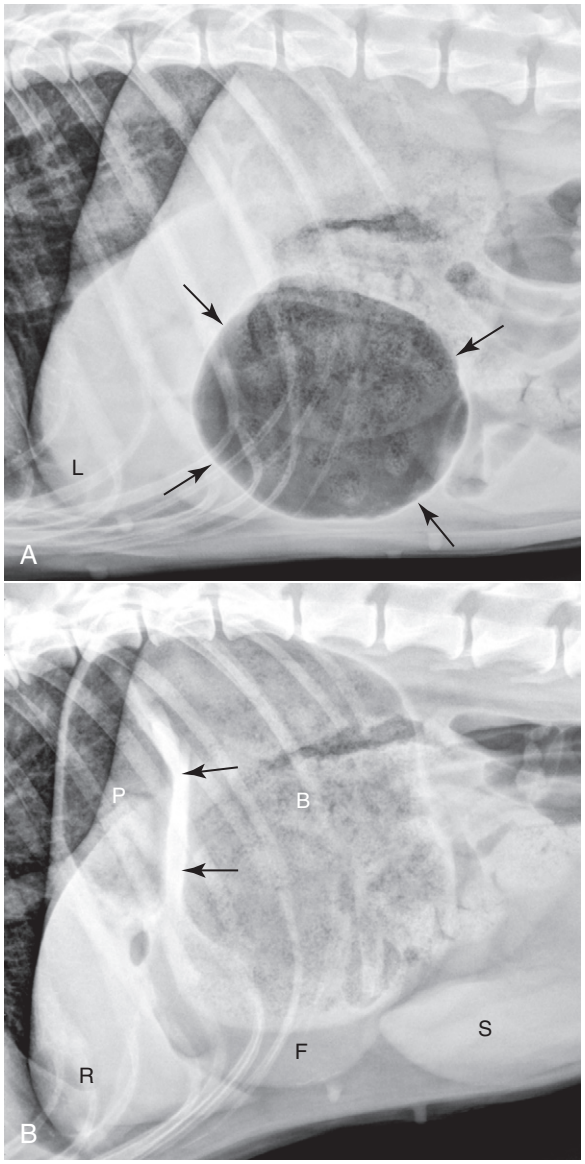


Fig. 43-16 Gastric volvulus. **A,** Left lateral view. The stomach is moderately distended with gas in the fundus *(black arrows)*. This is easily misinterpreted as gas in the pylorus, as expected in the left lateral view. **B,** Right lateral view. The fluid shifts into the fundus *(F)*, and gas outlines the pyloric portion *(P)* as well as the body *(B)*. The compartmentalization *(black arrows)* between the pylorus and body, and the characteristic appearance of the pylorus in the dorsocranial aspect of the abdomen indicate that the pylorus is on the left and the fundus is on the right and that there is a gastric volvulus. Note the malpositioned and slightly enlarged spleen *(S)*. The spleen will follow the fundus because of the connection afforded by the short gastrosplenic ligament.

the gastric distention, the less likely the spleen is to be visualized radiographically because of crowding. Thus splenomegaly and splenic displacement may be visualized more easily with less-severe gastric volvulus. Other changes that may be seen with gastric volvulus include reflex paralytic ileus of the small intestine, esophageal dilation, and microcardia and pulmonary hypovolemia (small vessels) associated with shock.

Chronic Pyloric Obstruction

Pyloric outflow obstruction may be acute or chronic. Causes of acute obstruction include gastric volvulus and foreign bodies. Chronic pyloric obstruction is usually the result of narrowing of the pyloric orifice caused by diseases affecting the wall or blocking the orifice, such as hypertrophic pyloric stenosis, pylorospasm, inflammation or fibrosis, neoplasia, and mucosal antral hypertrophy. These conditions usually cause a chronic partial obstruction at the pylorus, leading to chronic retention of gastric content.

Chronic partial pyloric obstruction often manifests on survey radiographs as fluid-filled gastric distention as opposed to the acute gaseous distention of gastric volvulus (Fig. 43-19). The stomach may be quite large with chronic partial pyloric obstruction. However, the enlarged stomach may be more difficult to identify on survey radiographs when it is filled with fluid. Even when distended with fluid, the stomach usually still contains some gas. In these instances, however, the gas does not totally outline or fill the entire stomach. Instead, the smaller amount of gas floats as a bubble on top of the fluid

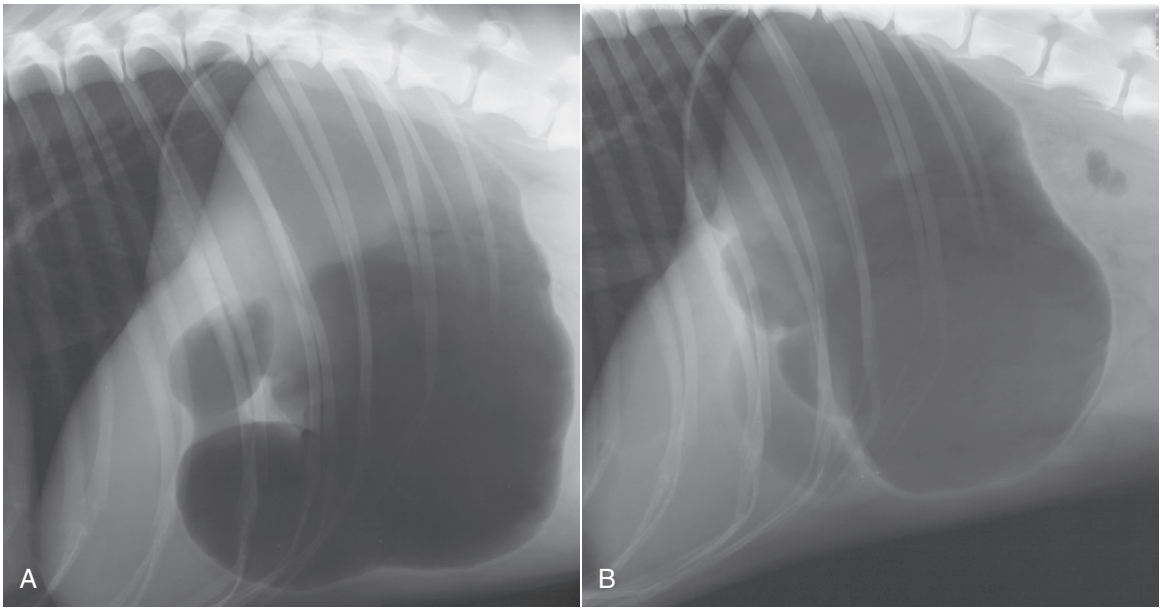


Fig. 43-17 Left **(A)** and right **(B)** lateral views of a dog with acute gastric dilatation. On the basis of these radiographic findings, the pylorus and the fundus are positioned normally. A gastric tube could not be passed into the stomach. Final diagnosis was 360-degree gastric volvulus.

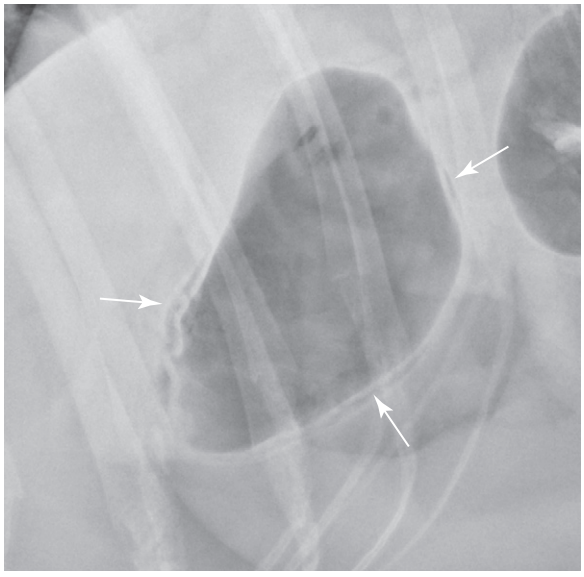


Fig. 43-18 Lateral radiograph of a dog with gas in the wall of the pyloric antrum *(white arrows)*. This dog did not have gastric malpositioning.

and should not be mistaken as the limits of the stomach or wall thickening.

The major effect of pyloric obstructive diseases is to restrict gastric emptying. Survey radiographic findings may vary from normal gastric size to enlargement depending on the severity and duration of the obstruction. With contrast studies, the major radiographic abnormality is delayed gastric emptying. However, an initial delay in gastric emptying may be of no clinical significance because of the influence of various psychologic factors discussed previously. This point is especially important if the stomach starts to empty normally after an initial delay or after the animal is allowed to calm down. Of more significance is a pronounced delay in gastric emptying when only a small amount of contrast medium passes from the stomach in a few hours. Because the normal stomach should be empty 1 to 4 hours after administration of contrast medium, retention of most of the barium within the stomach 3 or 4 hours after administration usually indicates pyloric obstructive disease (Fig. 43-20).

Differentiation of the pyloric obstructive diseases is difficult radiographically, especially without fluoroscopy. The stomach is a dynamic organ that changes appearance rapidly because of peristaltic waves, and a radiograph is simply a snapshot of the morphologic features of the stomach. Although some diseases may produce characteristic radiographic abnormalities, such abnormalities may be visible only during certain moments within the gastric cycle and thus may not be seen on a randomly exposed radiograph. The advantage of fluoroscopy is that sequential changes of the shape of the stomach can be visualized. Even with fluoroscopy, however, differentiating some pyloric obstructive diseases is not possible. For example, hypertrophic pyloric stenosis, neoplasia, and mural scarring all may produce an annular type of stricture of the pylorus that prevents the pylorus from opening adequately. Thus dividing obstructive pyloric diseases into those that encircle the pylorus, and are thus restrictive, and those that obstruct the pylorus by blocking its orifice may be a more practical choice.

Restrictive diseases of the pylorus include hypertrophic pyloric stenosis, pylorospasm, inflammation or scarring, and neoplasia. If characteristic abnormalities are present on radiographs, they are usually those of an annular type of stricture narrowing the pyloric sphincter. If barium fills only the entrance of the lumen at the pyloric sphincter, the resultant radiographic appearance is referred to as the *beak sign*.[71] If barium fills the length of the narrowed lumen through the pyloric sphincter, the resultant radiographic appearance is referred to as the *string sign*.[71] A tit sign has been described as a relatively sharp, pointed outpouching of the pyloric antrum along the lesser curvature as a peristaltic wave pushes contrast medium in a peristaltic pouch up against the mass-type lesion around the pylorus.[71] Variations in severity, symmetry, and radiographic projection all contribute to create variations in the radiographic appearance of pyloric restrictive lesions

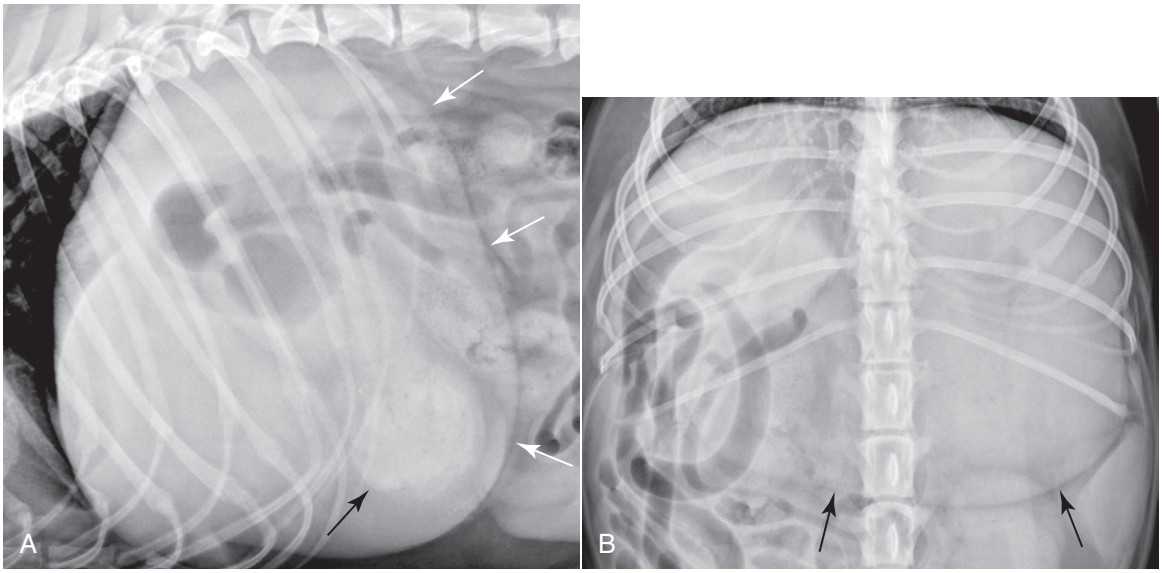


Fig. 43-19 Lateral **(A)** and dorsoventral **(B)** radiographs of a dog with fluid-filled gastric distention caused by chronic pyloric obstruction. The stomach is more difficult to identify when filled with fluid instead of gas. The caudal margin of the stomach is indicated in **A** by the *white arrows* and in **B** by the *black arrows.* In **A,** some opaque gastric contents have settled into the dependent pyloric region of the stomach *(black arrow)*.

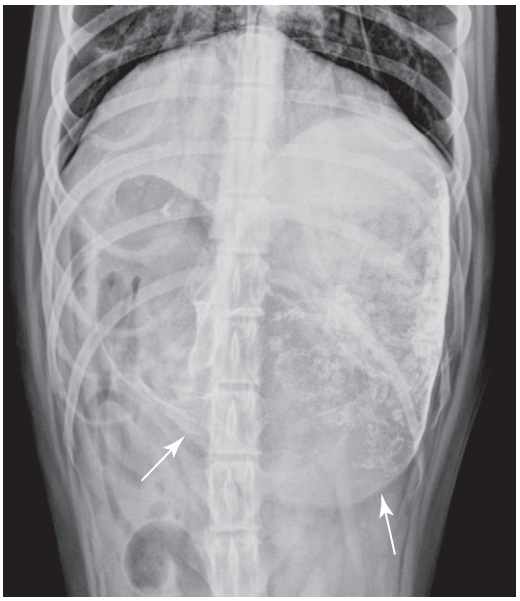


Fig. 43-20 Ventrodorsal radiograph 10 hours after barium was given. The stomach is distended *(white arrows)* with intraluminal gas and fluid and some of the barium. There should be no residual barium after 10 hours and this, along with the distention, is indicative of gastric outflow obstruction.

(Fig. 43-21). In dogs with chronic pyloric hypertrophy, the hypertrophic muscularis may be detected ultrasonographically as a thick hypoechoic layer. The thickness of the muscularis is greater than 3 mm in mild to moderate hypertrophy and greater than 8 mm in severely affected dogs. Vigorous, but ineffective, peristaltic contractions that fail to propel contents into the duodenum are seen in some patients.[50]

The second group of pyloric obstructive diseases includes gastric foreign bodies, mucosal inflammation or hypertrophy, and some mural lesions of the pyloric antrum. These types of lesions are more likely to produce filling defects within the lumen that occlude the orifice of the pyloric sphincter (Fig. 43-22). Again, radiographic recognition of such a lesion is usually adequate diagnostically, and differentiation of the underlying cause may not be possible on radiographs.

Gastric Ulcers

Gastric ulcers are difficult to identify on conventional radiographs. Ulcers are more conspicuous in barium studies, in which they produce craters in the wall of the stomach that appear as outpouchings from the lumen (Fig. 43-23). The radiographic appearance of a gastric ulcer may vary depending on whether the ulcer is projected in profile, en face, or obliquely.[72] The appearance of the ulcer may be altered further by gastric peristalsis. Manipulation of the patient during fluoroscopy allows a more complete and continuous evaluation of the margin and contour of the stomach. Double-contrast gastrography may also be of value because ulcers that are projected en face may be visualized with double-contrast studies but are obscured with positive-contrast gastrography.

Gastric ulcers may be benign or malignant. Benign gastric ulcers result from a variety of causes.[27,73,74] Use of nonsteroidal antiinflammatory drugs is a common cause of benign gastric ulcers.[75-77] Dachshunds with disc prolapse have a high prevalence of gastroduodenal ulceration.[78] This is thought to be from ulcerogenic drug administration as well as autonomic disturbances, stress, hypovolemia, and other factors.[78]

Malignant gastric ulcers occur in association with gastric neoplasia and may be caused by tumor necrosis.[74] Criteria have been established for the radiographic differentiation of benign and malignant gastric ulcers in human beings.[72,79,80] Thus, although radiography may provide an excellent method for the recognition of gastric ulcers, infrequent use of single- and double-contrast gastrography, lack of fluoroscopy, and insufficient views all combine to limit the recognition of gastric ulcers in dogs and cats. In addition, experience is limited in differentiating benign and malignant gastric ulcers radiographically in dogs and cats. Ulceration is often associated with gastric carcinoma,[81,82] and gastric ulcers in dogs that are recognized on radiographs are often the result of neoplasia.[83] Thus the radiographic recognition of a gastric ulcer should lead to strong consideration of neoplasia and further

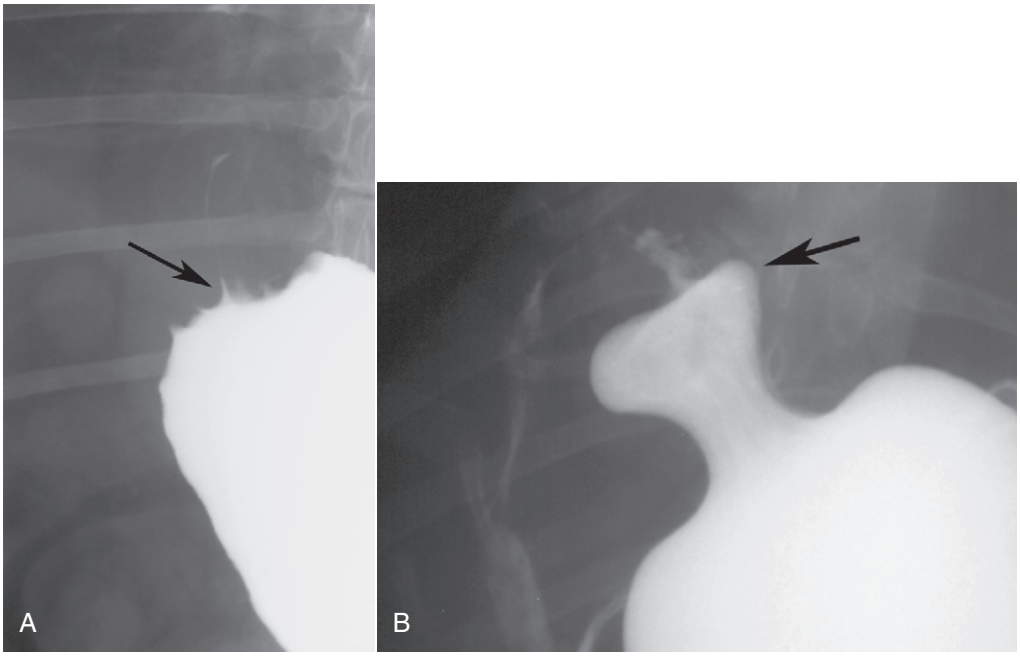


Fig. 43-21 **A,** Ventrodorsal radiograph of the pyloric region of a dog with restrictive disease of the pylorus. The string sign *(black arrow)* is caused by barium that fills the length of the lumen of the narrowed pyloric sphincter because of an annular type of stricture. **B,** Ventrodorsal radiograph of the pyloric region of another dog with restrictive disease of the pylorus. The peristaltic pouch *(black arrow)* is the outpouching of the pyloric antrum along the lesser curvature as a peristaltic wave pushes contrast medium up against the mass-type lesion encircling the pylorus. A pronounced delay in gastric emptying was also present.

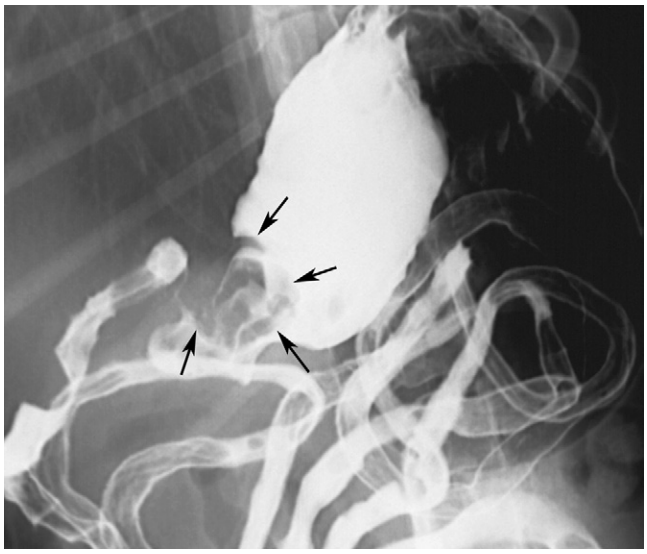


Fig. 43-22 Ventrodorsal oblique radiograph of the pylorus of a dog with obstructive disease of the pylorus. A hemispheric filling defect is at the pylorus that projects into the lumen *(black arrows)*. Pronounced delay in gastric emptying was present.

evaluation of the stomach with endoscopy and biopsy or by surgical exploration.

Some gastric ulcers may be detected sonographically (see Fig. 43-23, *B*) but are not always found.[48,84] Features include the presence of a wall defect (crater) usually within the center of a locally thickened area of stomach wall. The thickened area may have loss of the normal layered appearance. Gastric fluid accumulation and decreased motility may also be noted. Ulcers from nonneoplastic causes do not appear distinctly different from those seen with neoplasms.

Gastric Neoplasia

Several types of gastric neoplasms occur, and any region of the stomach may be involved. Polyps may be silent clinically and most are found incidentally.[85] Adenocarcinoma is the most common malignant gastric tumor in dogs.[82,86] This tumor may occur in any region of the stomach but is found most often in the pyloric portion.[86,87] Gastric neoplasia occurs less frequently in the cat than in the dog,[88] and lymphosarcoma is the most common type of feline gastric neoplasm.[89]

The radiographic appearance of gastric neoplasia varies and primarily depends on the size, shape, and location of the tumor. The major radiographic feature is that of a mass lesion that projects into the gastric lumen, creating a filling defect within the contrast medium. The more nodular and pedunculated the lesion, the easier to recognize it as a distinct mass (Fig. 43-24). Smaller mass lesions may be obscured completely by a relatively large volume of barium. Oblique projections, conformation of the stomach, and peristaltic contractions may all contribute to obscure some mass lesions of the stomach.

Tumors that are diffuse and less discrete are more difficult to identify. Diffuse infiltrative lesions of the stomach wall may not produce distinct filling defects. Instead, they may alter the shape of the stomach and produce decreased motility of the involved area. If such diffuse lesions encircle a portion of the stomach, the radiographic appearance may be that of an annular narrowing or one in which the stomach has decreased distensibility in the affected area (Fig. 43-24, *B*). Because of variations in appearance of the stomach created by peristalsis, persistence of a suspected abnormality on sequential radiographs is important. The recognition of a gastric ulcer should also suggest the possibility of gastric neoplasia.

Gastric masses can be found on ultrasound examination of the stomach, thus eliminating the need for radiographic contrast studies. Common features include thickening of the stomach wall, distortion of the normal layered appearance of

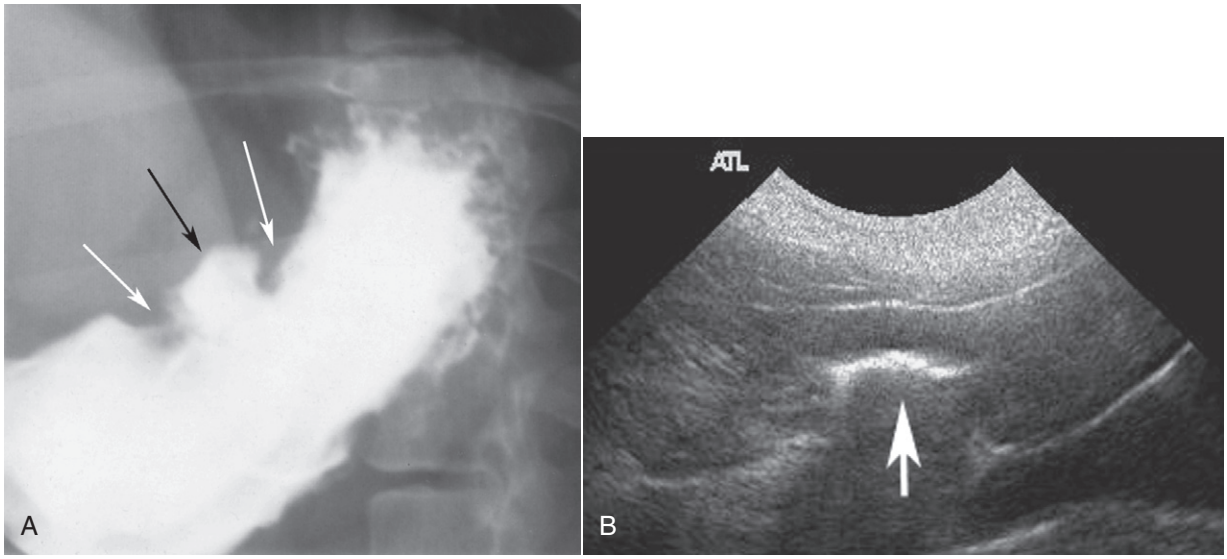


Fig. 43-23 **A,** Ventrodorsal oblique radiograph of the stomach of a dog with a gastric ulcer *(black arrow)*. The filling defects protruding into the stomach *(white arrows)* represent the collar of the ulcer. **B,** Sagittal sonograph of the stomach of another dog. The pyloric region of the stomach is thickened, and layers are not identifiable. The *white arrow* indicates a portion of the stomach wall that is focally thinner than the remainder. The mucosal surface of this area is hyperechoic. A large ulcer was found in this area at necropsy; the diagnosis was adenocarcinoma.

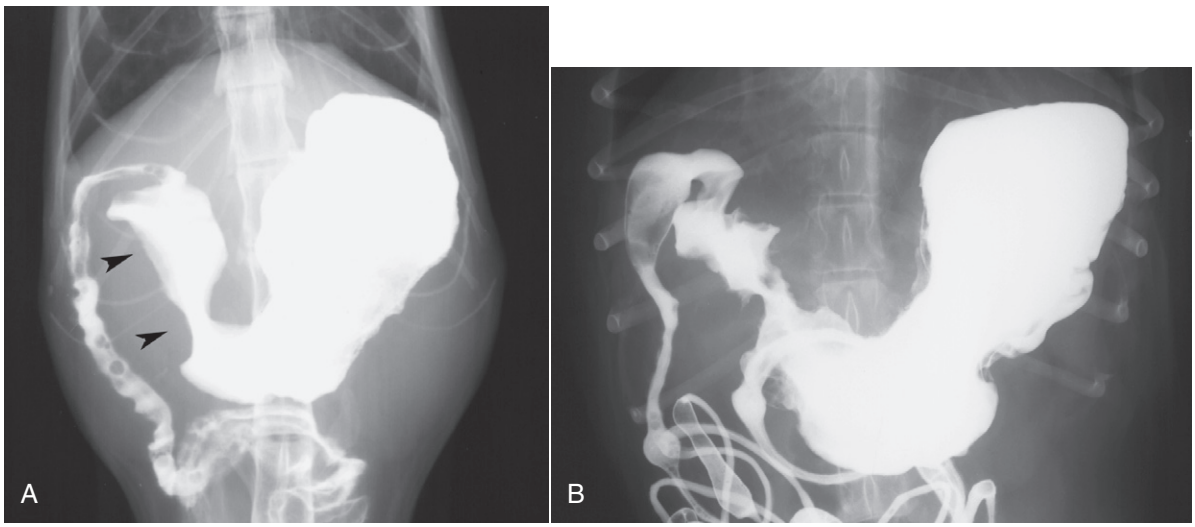


Fig. 43-24 **A,** Ventrodorsal gastrogram of a cat. A smooth filling defect is present from a mass lesion along the greater curvature *(black arrowheads)*. **B,** Ventrodorsal gastrogram of a dog. An annular mass encircles the pyloric portion and part of the body. This area failed to distend, and the abnormality persisted throughout the study. Final diagnosis was gastric adenocarcinoma.

the wall, and decreased echogenicity and motility in the affected area (Fig. 43-25).[39-46] Although such lesions are most often associated with gastric neoplasia, similar changes have been reported in dogs with pythiosis[47] and zygomycosis.[90] Extension of the lesion through the serosal surface of the stomach has been reported in dogs with gastric carcinoma.[46] Another reported sonographic feature of gastric carcinoma is *pseudolayering* of the stomach wall, which is thought to be associated with uneven distribution of tumor in the layers of the stomach wall.[39,41] Instead of the five layers seen normally, a central, moderately echogenic zone between two lesser echogenic lines is seen. Loss of wall layering in the intestines has also been associated with neoplasia, as opposed to inflammatory disease. Dogs with loss of layers were 51 times more likely to have neoplasia than inflammatory bowel disease.[91] Although the stomach was not included in this study, the same trend may exist for the stomach, with loss of layers being suggestive of neoplasia.

Concurrent regional lymph node enlargement and ulceration of the affected area have been reported in both gastric carcinoma and lymphosarcoma.[46] Reports of maximal gastric wall thickness range from 10 to 27 mm in dogs[41,42,46] and 8 to 25 mm in cats[40,43] with gastric neoplasia, measurements clearly greater than the reported normal gastric wall thickness of 3 to 5 mm (dogs) and 2 mm (cats). Gastric wall measurements greater than 6 to 7 mm have been proposed as abnormal.[37] Although gastric wall thickening is an important abnormal finding, caution must be exercised when assessing wall thickness in a contracted, empty stomach because a false-positive diagnosis of gastric mass can be made.[92] Distending

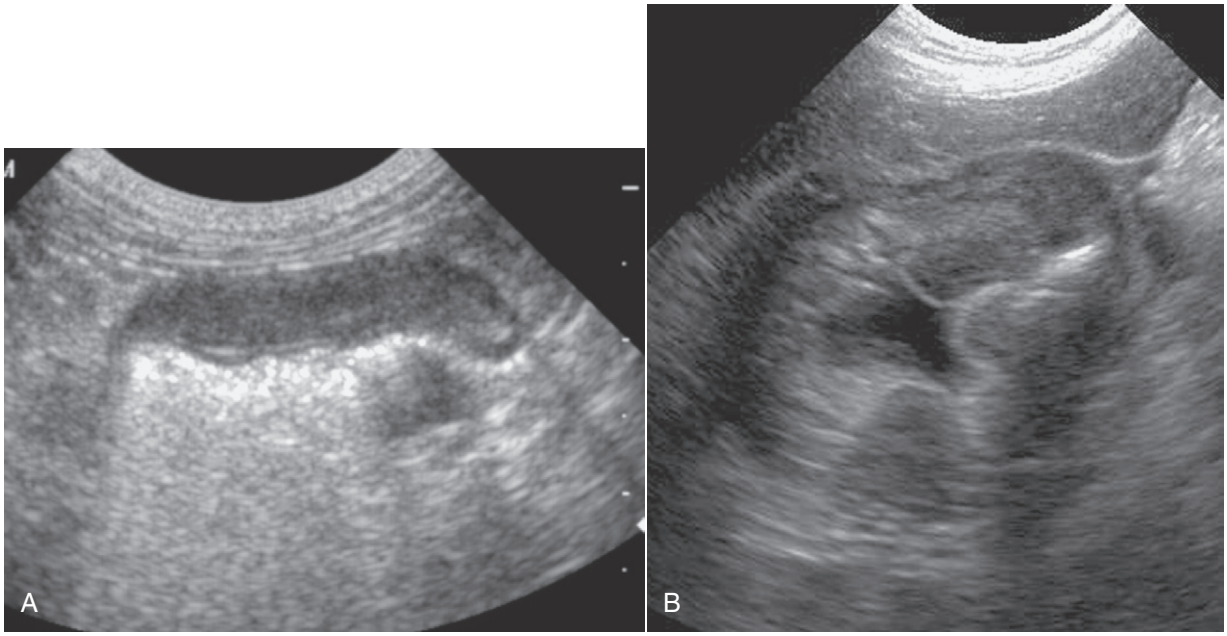


Fig. 43-25 Longitudinal ultrasonograms of gastric neoplasia. **A,** Lymphosarcoma in the stomach wall of a cat. The stomach wall is thickened and hypoechoic and has lost the normal layered appearance. **B,** Suspected adenocarcinoma in the stomach wall of a dog. The wall is thickened uniformly and decreased in echogenicity. The normal layered appearance is disrupted. Caudal is to the *right*, and ventral is to the *top*.

the stomach with water may help distinguish true- and false-positive lesions, but real-time observation of gastric motility may be an easier way to distinguish the two because a lack of motility usually is seen in an abnormal wall segment. Cytologic or histopathologic evaluation is necessary for a definitive diagnosis. Specimens can be obtained by ultrasound-guided fine-needle aspiration or tissue-core biopsy.[93,94]

Diffuse Diseases of the Stomach

The stomach may be involved diffusely in a variety of diseases that produce inflammation, hypertrophy, atrophy, or mineralization. Acute gastritis may result from a variety of causes and is rarely associated with radiographic abnormalities. Chronic gastritis is diagnosed infrequently clinically and may also result from a variety of causes. Examples include chronic atrophic gastritis, chronic hypertrophic gastritis, eosinophilic gastritis, and pythiosis and zygomycosis.[95,96] Paucity of rugal folds, large rugal folds, nodules, or a thickened gastric wall may be seen with these diseases (Fig. 43-26).[95] Care must be taken when evaluating stomach wall thickness on survey radiographs. Fluid within the stomach may cause border effacement with the stomach wall, creating the illusion of increased thickness.

Ultrasonographic findings of gastric pythiosis and zygomycosis are similar to those reported for gastric neoplasms.[47,95] Nonfungal inflammation may cause diffuse stomach wall thickening with maintenance of wall layers.[43,97] Although loss of the normal layered appearance of the intestines is generally associated with neoplasia,[91] some patients with inflammatory bowel disease or infectious gastritis (pythiosis) also have loss of the normal layered appearance.[47,98] Wall layering is usually preserved in gastric polyps but may have the appearance of a large sessile mass with the loss of wall layering.[99] As with most mass lesions discovered with ultrasound, biopsy is usually necessary for a definitive diagnosis.

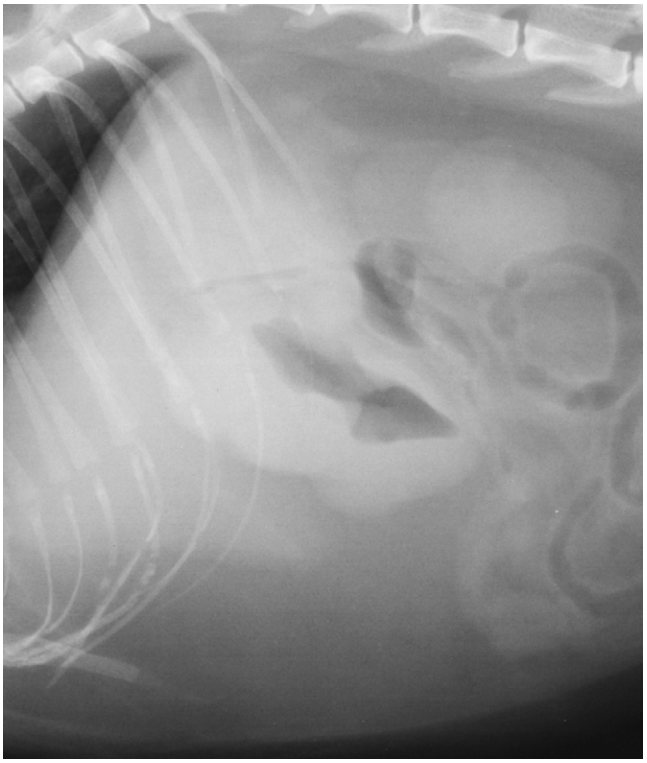


Fig. 43-26 Lateral survey radiograph of the abdomen of a cat with a thick gastric wall. The thickened wall is best visualized in the ventral midabdomen and is associated with a narrow, tubular, gas-filled lumen. Care should be taken when evaluating the stomach wall on survey radiographs because fluid in the lumen can silhouette with the wall, creating a false impression of wall thickening.



Fig. 43-27 Close-up ventrodorsal radiographs of a dog with gastric mineralization secondary to chronic renal failure. Thin, curvilinear, mineralized opacities that parallel the rugal folds of the stomach are caused by gastric calcification.

Soft tissue calcification may occur in association with chronic renal failure.[51,100,101] In such patients, mineralization of the gastric wall may be visible radiographically as thin, linear, mineralized opacities (Fig. 43-27).[100] Rugal mineralization is often more easily visualized when the stomach is empty, and the mineralized mucosal fold pattern is more tightly grouped. Ultrasonographic findings of dogs with uremic gastropathy include thickened gastric wall and rugal folds and a hyperechoic zone at the mucosal/luminal interface caused by mucosal mineralization.[51,97] Ultrasound is likely more sensitive than radiography for detection of gastric lesions associated with uremia.

Although in many patients endoscopy is the gold standard for the diagnosis of gastric diseases, in some patients the mucosal surface of the stomach may be normal, leading to false-negative results by endoscopy. Ultrasound demonstrates the morphologic features of the entire gastric wall unless the wall is hidden by gas or echogenic ingesta. In some patients, ultrasound may be more informative than endoscopy.[102]

REFERENCES

1. Evans HE: *Miller's anatomy of the dog*, ed 3, Philadelphia, 1993, Saunders.
2. O'Brien TR: *Radiographic diagnosis of abdominal disorders in the dog and cat*, Philadelphia, 1978, Saunders.
3. Brawner WR, Bartels JE: Contrast radiography of the digestive tract: indications, techniques, and complications, *Vet Clin North Am* 13:599, 1983.
4. Root CR: Interpretation of abdominal survey radiographs, *Vet Clin North Am* 4:763, 1974.
5. Arnbjerg J: Gastric emptying time in the dog and cat, *J Am Anim Hosp Assoc* 28:77, 1992.
6. Gomez JA: The gastrointestinal contrast study: methods and interpretation, *Vet Clin North Am* 4:805, 1974.
7. Bargai U: The effect of xylazine hydrochloride on the radiographic appearance of the stomach and intestine in the dog, *Vet Radiol* 23:60, 1982.
8. Hogan PM, Aronson E: Effect of sedation on transit time of feline gastrointestinal contrast studies, *Vet Radiol* 29:85, 1994.
9. Steyn PF, Twedt D, Toombs W: The effect of intravenous diazepam on solid phase gastric emptying in normal cats, *Vet Radiol Ultrasound* 38:469, 1997.
10. Scrivani PV, Bednarski RM, Meyer CW: Effects of acepromazine and butorphanol on positive-contrast upper gastrointestinal tract examination in dogs, *Am J Vet Res* 59:1227, 1998.
11. Miyabayashi T, Morgan JP: Upper gastrointestinal examinations: a radiographic study of clinically normal beagle puppies, *J Small Anim Pract* 32:83, 1991.
12. Evans SM, Lauffer I: Double-contrast gastrography in the normal dog, *Vet Radiol* 22:2, 1981.
13. Evans SM, Biery DN: Double-contrast gastrography in the cat: technique and normal radiographic appearance, *Vet Radiol* 24:3, 1983.
14. Root CR, Morgan JP: Contrast radiography of the upper gastrointestinal tract in the dog, *J Small Anim Pract* 10:279, 1969.
15. Burns J, Fox SM: The use of a barium meal to evaluate total gastric emptying time in the dog, *Vet Radiol* 27:169, 1986.
16. Miybayashi T, Morgan JP: Gastric emptying in the normal dog: a contrast radiograph technique, *Vet Radiol* 25:187, 1984.
17. Allan GS, Rendano VT, Quick CB, et al: Gastrografin as a gastrointestinal contrast medium in the cat, *Vet Radiol* 20:110, 1979.
18. Agut A, Sanchezvalverde MA, Torrecillas FE, et al: Iohexol as a gastrointestinal contrast medium in the cat, *Vet Radiol Ultrasound* 35:164, 1994.
19. Williams J, Biller DS, Miyabayashi T, et al: Evaluation of iohexol as a gastrointestinal contrast medium in normal cats, *Vet Radiol Ultrasound* 34:310, 1993.
20. Allan FJ, Guilford WG, Robertson ID, et al: Gastric emptying of solid radiopaque markers in healthy dogs, *Vet Radiol Ultrasound* 37:336, 1996.
21. Guilford GW, Lawoko CRO, Allan FJ: Accuracy of localizing radiopaque markers by abdominal radiography and correlation between their gastric emptying rate and that of a canned food in dogs, *Am J Vet Res* 58:1359, 1997.
22. Chandler ML, Guilford G, Lawoko CRO: Radiopaque markers to evaluate gastric emptying and small intestinal transit time in healthy cats, *J Vet Intern Med* 11:361, 1997.
23. Hall JA, Willer RL, Seim HB, et al: Gastric emptying of nondigestible radiopaque markers after circumcostal gastropexy in clinically normal dogs and dogs with gastric dilatation-volvulus, *Am J Vet Res* 53:1961, 1992.
24. Grandage J: The radiologic appearance of stomach gas in the dog, *Aust Vet J* 50:529, 1974.
25. Armbrust LJ, Biller DS, Hoskinson JJ: Case examples demonstrating the clinical utility of obtaining both right and left lateral abdominal radiographs in small animals, *J Am Anim Hosp Assoc* 36:531, 2000.
26. Jakovljevic S, Gibbs C: Radiographic assessment of gastric mucosal fold thickness in dogs. *Am J Vet Res* 54:1827, 1993.
27. Twedt DC, Wingfield WE: Diseases of the stomach. In Ettinger SJ, editor: *Textbook of veterinary internal medicine, vol 2*, ed 2, Philadelphia, 1983, Saunders, p 1233.
28. Funkquist B, Garmer L: Pathogenetic and therapeutic aspects of torsion of the canine stomach, *J Small Anim Pract* 8:523, 1967.
29. Gibbs C, Pearson H: The radiological diagnosis of gastrointestinal obstruction in the dog, *J Small Anim Pract* 14:61, 1973.

30. Gue M, Fioramonti J, Frexinos J, et al: Influence of acoustic stress by noise on gastrointestinal motility in dogs, *Dig Dis Sci* 32:1411, 1987.
31. Hornof WJ, Koblik PD, Strombeck DR, et al: Scintigraphic evaluation of solid-phase gastric emptying in the dog, *Vet Radiol* 30:242,1989.
32. Kunze CP, Hoskinson JJ, Butine MD, et al: Evaluation of solid phase radiolabels of dog food for gastric emptying, *Vet Radiol Ultrasound* 40:169, 1999.
33. Lester NV, Roberts GD, Newell SM, et al: Assessment of barium impregnated polyethylene spheres (BIPS) as a measure of solid-phase gastric emptying in normal dogs: comparison to scintigraphy, *Vet Radiol Ultrasound* 40:465, 1999.
34. Goggin JM, Hoskinson JJ, Kirk CA, et al: Comparison of gastric emptying times in healthy cats simultaneously evaluated with radiopaque markers and nuclear scintigraphy, *Vet Radiol Ultrasound* 40:89, 1999.
35. Heng HG, Wrigley RH, Kraft SL, et al: Fat is responsible for an intramural radiolucent band in the feline stomach wall, *Vet Radiol Ultrasound* 46:54, 2005.
36. Keith DG, Wortman JA, Saunders HM, et al: A comparison of the sensitivity and specificity of barium gastrography and ultrasonography for gastric and duodenal disease [abstract], *Vet Radiol Ultrasound* 40:657, 1999.
37. Penninck DG, Nyland TG, Fisher PE, et al: Ultrasonography of the normal canine gastrointestinal tract, *Vet Radiol* 30:272, 1989.
38. Lamb CR: Abdominal ultrasonography in small animals: intestinal tract and mesentery, kidneys, adrenal glands, uterus, and prostate, *J Small Anim Pract* 31:295, 1990.
39. Penninck DG: Characteristics of gastrointestinal tumors, *Vet Clin North Am Small Anim Pract* 28:777, 1998.
40. Penninck DG, Moore AS, Tidwell AS, et al: Ultrasonography of alimentary lymphosarcoma in the cat, *Vet Radiol Ultrasound* 35:299, 1994.
41. Penninck DG, Moore AS, Gliatto J: Ultrasonography of canine gastric epithelial neoplasia, *Vet Radiol Ultrasound* 39:342, 1998.
42. Kaser-Hotz B, Hauser B, Arnold P: Ultrasonographic findings in canine gastric neoplasia in 13 patients, *Vet Radiol Ultrasound* 37:51, 1996.
43. Grooters AM, Biller DS, Ward H, et al: Ultrasonographic appearance of feline alimentary lymphoma, *Vet Radiol Ultrasound* 35:468, 1994.
44. Rivers BJ, Walter PA, Johnston GR, et al: Canine gastric neoplasia: utility of ultrasonography in diagnosis, *J Am Anim Hosp Assoc* 33:144, 1997.
45. Penninck DG, Nyland TG, Kerr LY, et al: Ultrasonographic evaluation of gastrointestinal diseases in small animals, *Vet Radiol Ultrasound* 31:134, 1990.
46. Lamb CR, Grierson J: Ultrasonographic appearance of primary gastric neoplasia in 21 dogs, *J Small Anim Pract* 40:211, 1999.
47. Graham JP, Newell SM, Roberts GD, et al: Ultrasonographic features of canine gastrointestinal pythiosis, *Vet Radiol Ultrasound* 41:273, 2000.
48. Penninck DG, Matz M, Tidwell AS: Ultrasonography of gastric ulceration in the dog, *Vet Radiol Ultrasound* 38:308, 1997.
49. Tidwell AS, Penninck DG: Ultrasonography of gastrointestinal foreign bodies, *Vet Radiol Ultrasound* 33:160, 1992.
50. Biller DS, Partington BP, Miyabayashi T, et al: Ultrasonographic appearance of chronic hypertrophic pyloric gastropathy in the dog, *Vet Radiol Ultrasound* 35:30, 1994.
51. Grooters AM, Miyabayashi T, Biller DS, et al: Sonographic appearance of uremic gastropathy in four dogs, *Vet Radiol Ultrasound* 35:35, 1994.
52. Huml RA, Konde LJ, Sellon RK, et al: Gastrogastric intussusception in a dog, *Vet Radiol Ultrasound* 33:150, 1992.
53. Watson PJ: Gastroduodenal intussusception in a young dog, *J Small Anim Pract* 38:163, 1997.
54. Tanno F, Weber U, Wacker CH, et al: Ultrasonographic comparison of adhesions induced by two different methods of gastropexy in the dog, *J Small Anim Pract* 39:432, 1998.
55. Wacker CA, Weber UT, Tanno F, et al: Ultrasonographic evaluation of adhesions induced by incisional gastropexy in 16 dogs, *J Small Anim Pract* 39:379, 1998.
56. Agut A, Wood AKW, Martin ICA: Sonographic observations of the gastroduodenal junction of dogs, *Am J Vet Res* 57:1266, 1996.
57. Newell SM, Graham JP, Roberts GD, et al: Sonography of the normal feline gastrointestinal tract, *Vet Radiol Ultrasound* 40:40, 1999.
58. Goggin JM, Biller DS, Debey BM, et al: Ultrasonographic measurement of gastrointestinal wall thickness and the ultrasonographic appearance of the ileocolic region in healthy cats, *J Am Anim Hosp Assoc* 36:224, 2000.
59. Suter PF: Radiographic diagnosis of liver disease in dogs and cats, *Vet Clin North Am Small Anim Pract* 12:153, 1982.
60. Meurs KM, Breitschwerdt EB, Baty CJ, et al: Postsurgical mortality secondary to zinc toxicity in dogs, *Vet Hum Toxicol.* 33:579–583, 1991.
61. Weingart C, Kohn B: [Zinc intoxication in a Yorkshire terrier due to Euro cent ingestion], *Schweiz Arch Tierheilkd* 151:75–81, 2009.
62. Bowlus RA, Biller DS, Armbrust LJ, et al: Clinical utility of pneumogastrography in dogs, *J Am Anim Hosp Assoc* 41:171–178, 2005.
63. Mazin RM, Christman A, Pasek A: What is your diagnosis? GDV in a 5-week-old puppy, *J Am Vet Med Assoc* 221:489, 2002.
64. Bredal WP, Eggertsdottir AV, Austefjord O: Acute gastric dilatation in cats: a case series, *Acta Vet Scand* 37:445, 1996.
65. Formaggini L, Schmidt K, De Lorenzi D: Gastric dilatation-volvulus associated with diaphragmatic hernia in three cats: clinical presentation, surgical treatment and presumptive aetiology, *J Feline Med Surg.* 10:198–201, 2008.
66. Funkquist B: Gastric torsion in the dog: I. Radiological picture during nonsurgical treatment related to the pathological anatomy and to the future clinical course, *J Small Anim Pract* 20:73, 1979.
67. Kneller SK: Radiographic interpretation of the gastric dilatation-volvulus complex in the dog, *J Am Anim Hosp Assoc* 12:154, 1976.
68. Mackenzie G, Barnhart M, Kennedy S, et al: A retrospective study of factors influencing survival following surgery for gastric dilatation-volvulus syndrome in 306 dogs, *J Am Anim Hosp Assoc* 46(2):97–102, 2010.
69. Frendin J, Funquist B, Stavenborn M, et al: Gastric displacement in dogs without clinical signs of acute dilatation, *J Small Anim Pract* 29:775, 1988.
70. Fischetti AJ, Saunders HM, Drobatz KJ: Pneumatosis in canine gastric dilatation-volvulus syndrome, *Vet Radiol Ultrasound* 45:279, 2004.
71. Rhodes WH, Brodey RS: The differential diagnosis of pyloric obstructions in the dog, *J Am Vet Radiol Soc* 6:65, 1965.
72. Zboralske FF: Gastric ulcer. In Margulis AR, Burhenne HJ, editors: *Alimentary tract roentgenology*, St Louis, 1967, CV Mosby.

73. Howard EB, Sawa TR, Nielson SW, et al: Mastocytoma and gastroduodenal ulceration, *Vet Pathol* 6:146, 1969.
74. Robbins SL: *Pathologic basis of disease*, Philadelphia, 1974, Saunders.
75. Jones RD, Baynes RE, Nimitz CT: Nonsteroidal anti-inflammatory drug toxicosis in dogs and cats: 240 cases (1989–1990), *J Am Vet Med Assoc* 201:475, 1992.
76. Stanton ME, Bright RM: Gastroduodenal ulceration in dogs, *J Vet Intern Med* 3:238, 1989.
77. Wallace MS, Zawie DA, Garvey MS, et al: Gastric ulceration in the dog secondary to the use on nonsteroidal anti-inflammatory drugs, *J Am Anim Hosp Assoc* 26:467, 1990.
78. Dowdle SM, Joubert KE, Lambrechts NE, et al: The prevalence of subclinical gastroduodenal ulceration in Dachshunds with intervertebral disc prolapse, *J S Afr Vet Assoc* 74:77, 2003.
79. Nelson SW: The discovery of gastric ulcers and the differential diagnosis between benignancy and malignancy, *Radiol Clin North Am* 7:5, 1969.
80. Porcher P, Buffard P: Malignancy of the stomach. In Margulis AR, Burhenne HJ, editors: *Alimentary tract roentgenology*, St Louis, 1967, CV Mosby.
81. Hayden DW, Nelson SW: Canine alimentary neoplasia, *Zentralbl Veterinarmed [A]* 20:1, 1973.
82. Sautter JH, Hanlon GF: Gastric neoplasms in the dog: a report of 20 cases, *J Am Vet Med Assoc* 166:691, 1975.
83. Barber DL: Radiographic aspects of gastric ulcers in dogs: a comparative review and report of 5 case histories, *Vet Radiol* 23:109, 1982.
84. Liptak JM, Hunt GB, Barrs VRD, et al: Gastroduodenal ulceration in cats: eight cases and a review of the literature, *J Feline Med Surg* 4:27, 2002.
85. Willard MD: Diseases of the stomach. In Ettinger SJ, Feldman EC, editors: *Textbook of veterinary internal medicine, vol 2*, ed 4, Philadelphia, 1995, Saunders, p 1143.
86. Murray M, Robinson PB, McKeating FJ, et al: Primary gastric neoplasia in the dog: a clinico-pathological study, *Vet Rec* 91:474, 1972.
87. Patnaik AK, Hurvitz AI, Johnson GE: Canine gastric adenocarcinoma, *Vet Pathol* 15:600, 1978.
88. Brodey RS: Alimentary tract neoplasms in the cat: a clinicopathologic survey of 46 cases, *Am J Vet Res* 27:74, 1966.
89. Tyler DE: Gastric neoplasia in the dog and cat [abstract], *Arch Am Coll Vet Surg* 6:47, 1977.
90. Burke RL, Ackerman N: The abdomen. In Burk RL, Ackerman N, editors: *Small animal radiology and ultrasonography: a diagnostic atlas and text*, ed 2, Philadelphia, 1996, Saunders.
91. Penninck D, Smyers B, Webster CR, et al: Diagnostic value of ultrasonography in differentiating enteritis from intestinal neoplasia in dogs, *Vet Radiol Ultrasound* 44: 570, 2003.
92. Lamb CR, Forster-van Hijfte M: Beware of the gastric pseudomass, *Vet Radiol Ultrasound* 35:398, 1994.
93. Penninck DG, Crystal MA, Matz ME, et al: The technique of percutaneous ultrasound guided fine-needle aspiration biopsy and automated microcore biopsy in small animal gastrointestinal diseases, *Vet Radiol Ultrasound* 34:433, 1993.
94. Crystal MA, Penninck DG, Matz ME, et al: Use of ultrasound-guided fine-needle aspiration biopsy and automated core biopsy for the diagnosis of gastrointestinal diseases in small animals, *Vet Radiol Ultrasound* 34:438, 1993.
95. Twedt DC, Magne ML: Diseases of the stomach. In Ettinger SJ, editor: *Textbook of veterinary internal medicine, vol 2*, ed 3, Philadelphia, 1989, Saunders, p 1289.
96. Miller RI: Gastrointestinal phycomycosis in 63 dogs, *J Am Vet Med Assoc* 165:473, 1985.
97. Homco LD: Gastrointestinal tract. In Green RW, editor: *Small animal ultrasound*, Philadelphia, 1996, Lippincott-Raven, p 149.
98. Baez JL, Hendrick MJ, Walker LM, et al: Radiographic, ultrasonographic, and endoscopic findings in cats with inflammatory bowel disease of the stomach and small intestine: 33 cases (1990–1997), *J Am Vet Med Assoc* 215:349, 1999.
99. Diana A, Penninck DG, Keating JH: Ultrasonographic appearance of canine gastric polyps, *Vet Radiol Ultrasound* 50(2):201–204, 2009.
100. Barber DL, Rowland GN: Radiographically detectable soft tissue calcification in chronic renal failure, *Vet Radiol* 20:117, 1979.
101. Parfitt AM: Soft tissue calcification in uremia, *Arch Intern Med* 124:544, 1969.
102. Beck C, Slocombe RF, O'Neill T, et al: The use of ultrasound in the investigation of gastric carcinoma in a dog, *Aust Vet J* 79:332, 2001.

ELECTRONIC RESOURCES

evolve

Additional information related to the content in Chapter 43 can be found on the companion Evolve website at http://evolve.elsevier.com/Thrall/vetrad/

- Chapter Quiz

CHAPTER • 44

The Small Bowel

Elizabeth A. Riedesel

Abdominal imaging can help in making a definitive diagnosis or in deciding between medical or surgical treatment. However, imaging should not take precedence over a complete history, a thorough physical examination, and pertinent laboratory tests. Survey radiographs, ultrasonography, and intestinal contrast examinations may be useful in the diagnosis of acute and chronic intestinal disorders. The patient that does not respond to symptomatic therapy for vomiting or diarrhea should be given a more extensive evaluation, including radiographic and sonographic studies. Although radiographic and sonographic abnormalities are not present in every intestinal disorder, one or more of the roentgen signs and sonographic patterns discussed in this chapter characterize many lesions.

THE NORMAL SMALL BOWEL

Radiography

The standard views used to evaluate the small bowel are the recumbent left-to-right lateral and ventrodorsal (VD) views. As discussed in Chapter 35, there is rationale for obtaining left-right and right-left lateral views, in addition to the VD view, as standard in every patient.[1] Briefly, obtaining both lateral views takes advantage of repositioning of intraluminal gas to change the conspicuity of various bowel segments, leading to a more complete examination. Other views, such as compressions radiographs, may also be useful.[2]

Withholding food for 24 hours and administering a cleansing enema 2 to 4 hours before radiography will optimize radiographic interpretation, but daily routine usually prohibits this extent of preparation. For the patient with acute abdominal pain; acute persistent vomiting; or palpable, enlarged fluid- or gas-filled bowel, no preparation is needed, and in fact, the native pattern of gas and fluid can be helpful diagnostically, and this valuable information may be altered by an enema. The roentgen sign assessment for the small intestine is summarized in Box 44-1. Abnormal margination, size, position, shape, and radiopacity can be assessed by survey radiographs, but mucosal irregularities and abnormal peristalsis or transit time must be determined from ultrasound or contrast studies.

A moderate amount of intraperitoneal fat provides good contrast for definition of the intestinal serosal surfaces (Fig. 44-1). Animals younger than 6 months or emaciated animals have poor serosal definition because of a lack of intraabdominal fat for contrast.[3] Serosal surfaces should be smooth and are seen most easily in regions where superimposition of bowel is minimal. A false interpretation of decreased serosal definition often results when the small bowel loops are overlapping in the central abdomen, when loops are crowded together by an abdominal mass, or when little or no gas is present in the bowel lumen (Fig. 44-2, *A*). These effects should not be misinterpreted as abdominal effusion. If gas is present in the stomach, a left lateral view may redistribute the gas into the bowel and confirm that the effect was simply lack of bowel lumen contrast (Fig. 44-2, *B*).

Because of the variation in canine body size and the magnification effects of radiography, no accurate, specific measurement for normal diameter of the small bowel exists. Table 44-1 summarizes the schemes for relative bowel diameter that use nearby bones as reference structures. The maximal normal diameter (serosa to serosa) for the dog has been reported to be less than twice the width of a rib,[4] or less than 1.6 times the height of the L5 vertebral body at its narrowest point.[5] Because most cats tend to have a similar body size, a more specific definition of normal bowel diameter has been stated as not exceeding a 12 mm diameter when gas filled,[6] or twice the height of the central portion of the L4 vertebral body.[7] Cats without intestinal disease had a maximum small intestinal diameter to L2 vertebral endplate height ratio of 2.0 or less when compared with cats with gastrointestinal disease.[8] For measurements and calculated ratios to be most accurate, optimally positioned radiographs and positive identification that it is the small bowel being measured needs to be ensured. Although the duodenum may be slightly wider, the jejunum and ileum should have approximately the same diameter.[9] In reality, as a clinician gains experience in evaluating abdominal radiographs, qualitative assessment of bowel size will become just as accurate as measurement techniques.

Attempts to judge the thickness of the intestinal wall on survey radiographs are unreliable. An empty bowel loop with a small volume of intraluminal air should not be mistaken for a pathologically thickened segment. However, there will be patients in which the bowel wall is unquestionably too thick (Fig. 44-3). In most instances, true thickening of the intestinal wall is better judged by ultrasound, contrast study, or palpation than by radiography.

The small bowel has fixed and moveable segments. In the dog, the cranial duodenal flexure is fixed along the caudal surface of the right side of the liver by the hepatoduodenal ligament. The descending duodenum lies along the right abdominal wall. The caudal duodenal flexure is located at a transverse plane through the tuber coxae with the ascending duodenum continuing cranially from this point on the left side of the root of the mesentery. The jejunoileum should be distributed uniformly throughout the peritoneal cavity, occupying space not taken up by distensible organs (stomach or urinary bladder), solid organs (liver, spleen, or kidneys), or fat. The ileum crosses from the left to the right midabdomen to terminate at the ileocolic junction.

Box • 44-1

Roentgen Signs in the Small Intestine

Margination: serosal surface definition
Size: diameter of lumen and/or serosa-to-serosa
Position: location within abdominal cavity
Shape: contour of bowel loops
Radiopacity: lumen contents and bowel wall
Architecture: mucosa/bowel wall smoothness
Motility: intermittent narrowing of contractions

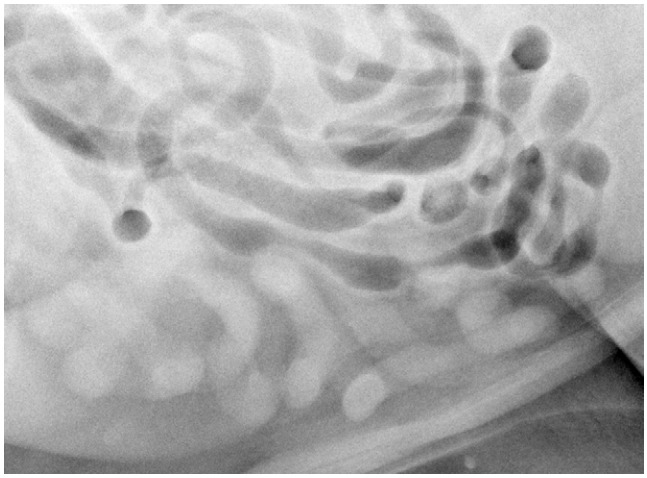


Fig. 44-1 Serosal edges of small intestine are seen easily in this dog with ample intraperitoneal fat. Bowel segments projected end-on appear as rings if the lumen contains air or as round nodules if the lumen is empty or contains fluid. Longitudinal sections are straight or curved with intermittent narrowing caused by contractions.

The cat differs from the dog in the position of the cranial duodenal flexure. In the cat, the cranial flexure usually creates a sharper angle with the pylorus and is located closer to the midline. The descending duodenum courses in a gently curved loop, positioning the caudal duodenal flexure at approximately midabdomen. The position of the remainder of the small bowel is the same as the dog.

Common positional variations of small bowel seen in normal dogs and cats include (1) a full stomach displacing the bowel caudally; (2) a distended urinary bladder displacing the bowel cranially; (3) intraperitoneal fat in obese cats causing the small bowel to be located centrally and/or on the right side; (4) in very obese cats, fat displacing the bowel into the central region of the abdominal cavity; and (5) in obese dogs, the bowel occupying the ventral portion of the pendulous abdominal cavity. Positional changes in the small intestine may also be indicative of disease in adjacent organs.

The normal small bowel is recognized in survey radiographs as smooth, continuously curving tubes or as solid circles or rings (see Fig. 44-1). These shapes are produced by the contractile activity of the smooth muscle. Segmental contractions give rise to spherical shapes, whereas peristaltic contractions cause long tubular shapes.

The radiopacity of the normal small intestine is variable because of differing opacities of material within the lumen. In a nonfasted animal, any of the following may be seen in the lumen: air; grainy-appearing mottled ingesta, which may include mineral or metal; or fluid of homogeneous soft tissue opacity. The nondiscretionary eating habits of some dogs and cats may result in mineral or metallic opacities of small size being present in the small bowel. Clay-based cat litter and small gravel from dog runs are common examples. Gastrointestinal medications that contain calcium, magnesium, aluminum, bismuth, or silicate can impart significant radiopacity to the intestinal content.[10] Some pet vitamin and mineral supplements contain sufficient mineral to be visible radiographically. In general, tablets or capsules containing minerals, either as active ingredients or in the coating, are more likely to be visible than liquids containing these minerals.[10] In a fasted

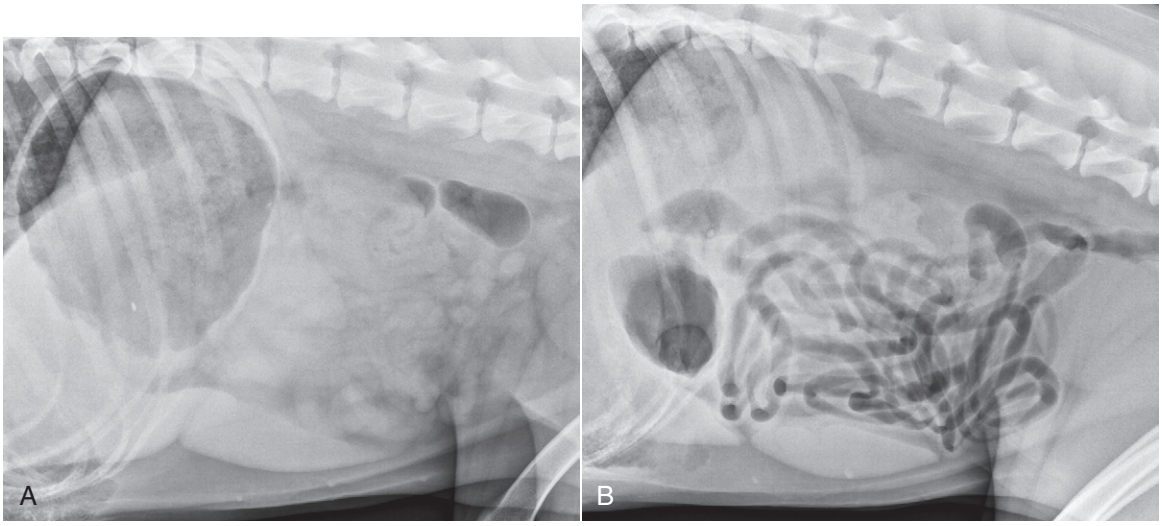


Fig. 44-2 Lack of gas within the bowel can lead to the perception of poor serosal margin detail. In the right lateral view **(A),** there is moderate distention of the stomach and the urinary bladder, crowding the bowel into the center of the abdomen and simulating a loss of serosal detail. There is very little to no gas in many of the small bowel segments. However, the serosal borders of the liver, spleen, and urinary bladder are clearly defined. The left lateral view **(B)** redistributes the gastric gas throughout the small bowel, and serosal margin detail appears to be restored because of the addition of the gas contrast to the bowel lumen.

Table • **44-1**

Small Bowel Normal Measurements

	DOG	CAT
Radiographic*	≤2 times width of rib Ratio of maximal small bowel diameter to narrowest height of L5 body <1.6	≤12 mm† ≤2 times the central height of L2 Ratio of maximum small bowel diameter to end plate height of L2 < 2.0
Ultrasound wall thickness‡ Duodenum	Up to 20 kg, ≤5.1 mm 20—29.9 kg, ≤5.3 mm >30 kg, ≤6.0 mm Puppies§: 3.8 ± 0.5 mm (3.2—4.8 mm)	2.0—2.4 mm
Ultrasound wall thickness‡ Jejunum	Up to 20 kg, ≤4.1 mm 20—29.9 kg, ≤4.4 mm >30 kg, ≤4.7 mm Puppies§: 2.5 ± 0.5 mm (1.2—3.4 mm)	2.1—2.5 mm
Ultrasound wall thickness‡ Ileum	Not specifically defined	2.5—3.2 mm

*Serosa to serosa.
†Mucosa to mucosa based on gas or barium filled.
‡Mucosa to serosa.
§Beagles 7–12 weeks of age with weight range 2.3–5 kg.

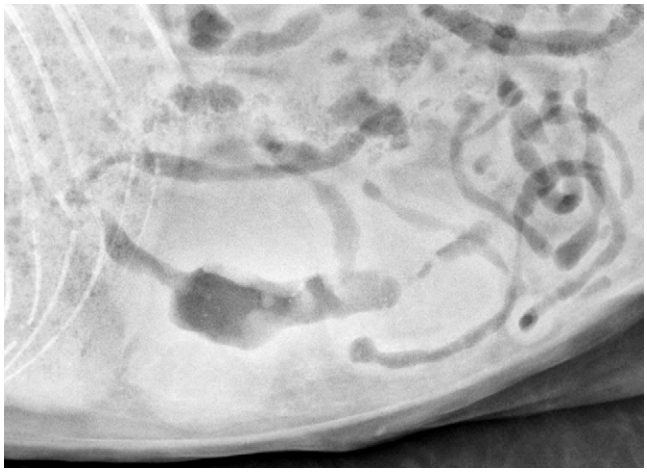


Fig. 44-3 Despite the overall lack of accuracy in radiographic measurement of small bowel wall thickness, there is no question that the wall of this bowel loop is abnormally thickened. The lumen is not uniformly distended. There is mottled soft tissue and fluid opacity between the thickened segment and the ventral abdominal wall consistent with focal fluid or deposition of cells on the serosa or mesentery and omentum. Ultrasound assessment is warranted to further characterize the bowel wall changes, to direct aspirate or core biopsy, and to obtain a peritoneal fluid sample for analysis. See Figure 44-31 for the ultrasound findings.

animal, the lumen may contain a small amount of ingested air, or it may be of homogeneous fluid or soft tissue opacity.

The amount of bowel that contains gas in the normal cat and dog is variable. In nonfasted cats with no gastrointestinal disease, 65% had gas in greater than 25% of the small bowel.[8] Cats without gastrointestinal disease that are not fasted before radiography may have gas throughout the bowel.[8] In the fasted cat, gas is rarely present in the small intestine, but in fasted dogs, 30% to 60% of the small bowel content may be gas.[6,11] Animals stressed by handling or dyspneic animals frequently are aerophagic, resulting in more air-containing small bowel. The gas pattern is variable; however, most cats and dogs have a linear pattern with gas in a continuous column except where interrupted by contraction. The bowel wall should be of uniform soft tissue opacity. This uniformity is most easily assessed in loops that contain air. As noted before, bowel wall thickness cannot usually be determined accurately in survey radiographs.

Ultrasound or contrast radiography is indicated when the following are present:

- Acute, persistent vomiting with negative findings on survey radiographs
- Recurrent vomiting, especially in animals refractory to symptomatic therapy and without other organ disease to explain the vomiting
- Palpable abdominal mass without obstructive bowel signs on survey radiographs
- Acute abdominal pain with an unusual or unexplained abnormality seen in the survey radiographs
- Weight loss with intermittent or recurrent diarrhea
- Melena
- Hematemesis

Ultrasound

Observations that can be made from intestinal sonography include assessment of wall thickness, wall layer pattern, and motility. Transducer frequencies of 7.5 MHz and higher enable the best identification of individual layers of the intestinal wall. Ultrasound imaging also allows assessment of structures adjacent to the intestine. The character of the mesentery and regional lymph nodes and evaluation for peritoneal fluid should be assessed. Evaluation of the solid organs, particularly the pancreas and liver, should be included to eliminate or include them as a primary cause for vomiting, anorexia, or weight loss that has not responded to symptomatic therapy. Ultrasound-guided fine-needle aspiration sampling for cytology and culture evaluation can be done in many patients.

The major obstacle for optimal ultrasound imaging is the presence of gas in the bowel. When gas is present, the far wall cannot be assessed (Fig. 44-4). Repositioning the patient, using gravity-based transducer placement, administering fluid by orogastric intubation, or repeating the examination at a later time may overcome the artifacts induced by gas.

The normal small intestinal wall pattern consists of alternating hyperechoic and hypoechoic layers. When no fluid or gas is present, a thin, hyperechoic line represents the lumen. From the lumen to the serosa, the layers and echogenicities are as follows: mucosa and hypoechoic, submucosa and hyperechoic, muscularis and hypoechoic, and serosa and hyperechoic (Fig. 44-5). The hypoechoic mucosal layer is the thickest of the individual layers and thus is dominant visually.[12] When fluid is in the lumen, the mucosal surface is normally hyperechoic (see Fig. 44-4). If gas is present within the lumen, a prominent reverberation artifact occurs in a relatively long length of bowel and a *comet tail* reverberation artifact is present during peristaltic contraction. Both of these artifacts inhibit the assessment of the deeper wall. However, the presence of gas helps to identify the lumen in some abnormal segments. Acoustic shadowing artifact occurs frequently, either with focal luminal gas or with dense particles of ingesta in transit. A short linear or focal hyperechogenicity occurs frequently at the equatorial tangents of transverse sections of empty bowel. This occurs as a result of widening of the intervillous space when the bowel folds.[13]



Fig. 44-4 Three small bowel loops with different content. The oval section is empty and collapsed; the longitudinal section contains a small amount of mucoid fluid; and the section in the far right of the image contains gas. The ring-down or comet-tail artifact of the gas obscures evaluation of the deep wall of this segment completely.

Wall thickness variations for the dog and cat are summarized in Table 44-1. Higher frequency transducers and measures of wall thickness in a longitudinal axis segment provide a correlation between the thickness of the duodenum and jejunum relative to the weight of dogs.[14] When a 10 MHz linear transducer is used in the normal cat, a subtle difference in thickness is found from the duodenum through the ileum.[15] In normal 7- to 12-week-old beagle puppies ranging in weight from 2.3 to 5 kg, the bowel wall thickness was less than in adult dogs of similar weight.[16]

The normal duodenum can be identified distinctly by its superficial right-side location and can be traced cranially into the stomach and caudally to the descending loop, which courses to the left. With high-resolution transducers, the duodenal papilla can be seen in many cats and dogs (Fig. 44-6). The feline duodenal papilla ranges from 2.9 to 5.5 mm wide and averages 4.0 mm in height when imaged in the transverse plane.[17] The major duodenal papilla is intimately adjacent to the right limb of the pancreas. Pseudoulcers can be seen occasionally in the canine duodenum, and the strong segmental contractions described as the *string-of-pearls* in a barium series can be seen in the feline duodenum.

The jejunum and most of the ileum appear as nondescript loops. The terminal 1 to 2 cm of the ileum, or the ileocolic junction, in the cat has the appearance of a wagon wheel because of projection of the mucosa into the lumen.[15] Peristaltic contractions can be seen and vary from less than 1 to 3 per minute in the small intestine depending on the fasted state or amount of time after being fed.[18]

Regional lymph node assessment should be included in any assessment of the small bowel. The duodenum is drained by hepatic and pancreaticoduodenal nodes. These nodes are not seen consistently in normal patients. The jejunum and ileum are drained by the jejunal and colic nodes, respectively, in the dog. In the cat, an ileocecal node is also present. Normal mesenteric lymph nodes can be difficult to identify with 5 MHz transducers; however, when 7.5 MHz or greater frequencies are used, these lymph nodes can be found in the majority of patients.[15] Normal lymph nodes are typically

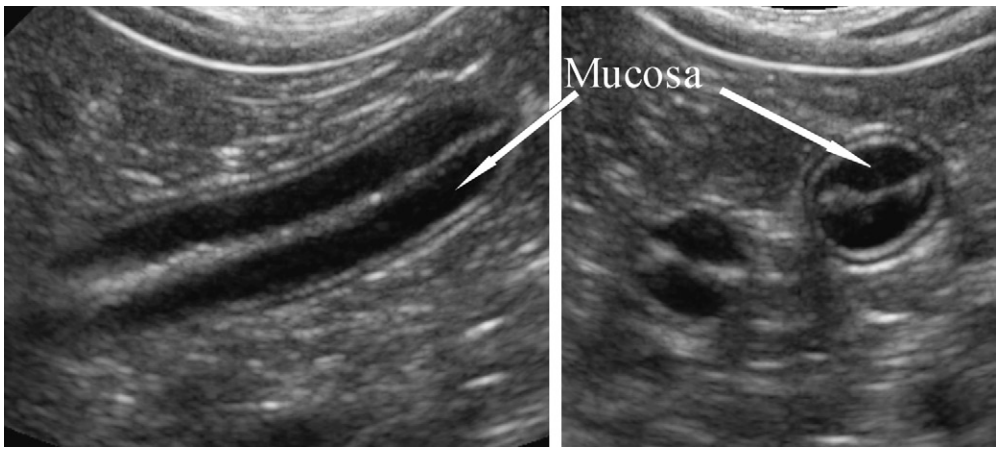


Fig. 44-5 Ultrasound images of a normal canine jejunum. The long axis is depicted on the *left* and transverse on the *right*. A five-layer alternating echogenicity pattern can be identified. The mucosal layer is indicated by *arrows*. The central hyperechoic *line* represents the empty lumen.

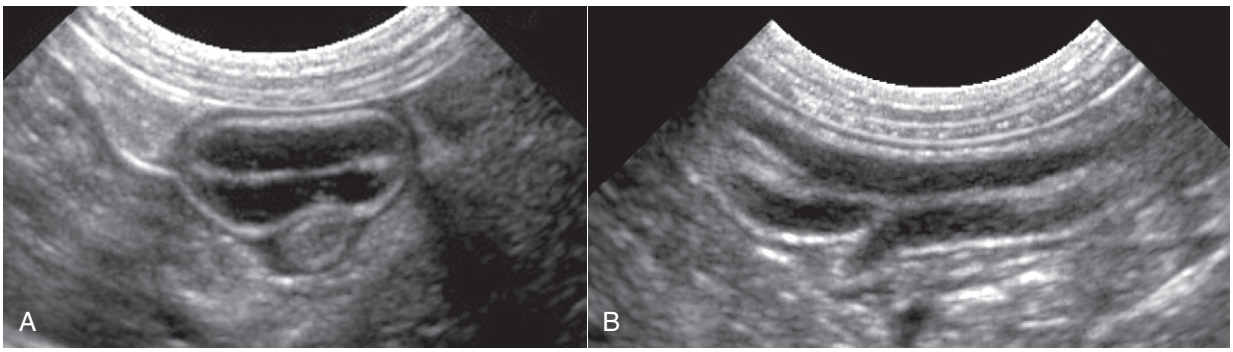


Fig. 44-6 Transverse and oblique long axis views of the major duodenal papilla. With dynamic imaging, the common bile duct can be followed into the lumen.

isoechoic to adjacent fat and may not be differentiated readily. In the adult dog, the normal length of the jejunal nodes ranges from 5 to 200 mm.[19] In normal beagle puppies, the jejunal lymph nodes were easily found and hypoechoic. Mean thickness ranged from 1.5 to 12.5 mm (mean 7.5 mm).[16] In cats, the normal lymph node size guidelines in millimeters are pancreaticoduodenal length (L) 8.4 (6.6 to 13), diameter (D) 4.6 (3.6 to 6.2); jejunal L 20.1 (11.4 to 39.0), D 5.0 (2.8 to 7.2); and ileocecal L 11.8 (6.7 to 23.2), D 4.1 (2.7 to 4.8).[20]

Contrast Examinations

Indications

Contrast studies of the small bowel can be used to identify the location of the bowel (e.g., displacement through hernias), to determine patency of the lumen, to identify perforation, and to identify irregularities in the contrast medium/mucosal interface. The concept of gastrointestinal contrast studies has been limited typically to the use of positive-contrast agents. However, the inherent gas contrast in the stomach and bowel should be used to full advantage as a contrast medium when present. The simple addition of the opposite lateral view and less frequently the dorsoventral view may shift the gas sufficiently to confirm an initial suspicion (Fig. 44-7) or discover new findings (Fig. 44-8).[1]

Ultrasound imaging affords greater contrast differentiation between soft tissue and fluid and between different soft tissue components such as the bowel wall layers. Because of this ability, ultrasound studies have replaced most radiographic positive-contrast studies of the bowel. If ultrasound imaging or the needed ultrasound interpretation expertise is not available, the positive-contrast small bowel study still has value. Probably its greatest usefulness for the general practice situation is the identification of abnormal bowel location and complete bowel obstruction. A few comments regarding positive-contrast small bowel studies follow; however, the reader is referred to the previous editions of this text for more thorough information.[21]

Positive-contrast evaluation is not indicated in the patient with clearly defined survey radiographic evidence of bowel obstruction.[22] Minimal additional information will be gained because of the slowed passage through atonic bowel proximal to the obstruction, especially in a weakened or debilitated animal. If the clinical and survey radiographic findings are strongly suggestive of mechanical obstruction, surgery is indicated. Further attempts to define the specific site and type of obstructing lesion with contrast medium only delay and possibly complicate surgery and cause additional patient stress.

Patients with survey radiographic evidence of free peritoneal gas that is not residual from recent celiotomy, penetrating trauma, or abdominocentesis are also not appropriate patients for intestinal contrast studies. In these patients, the peritoneal

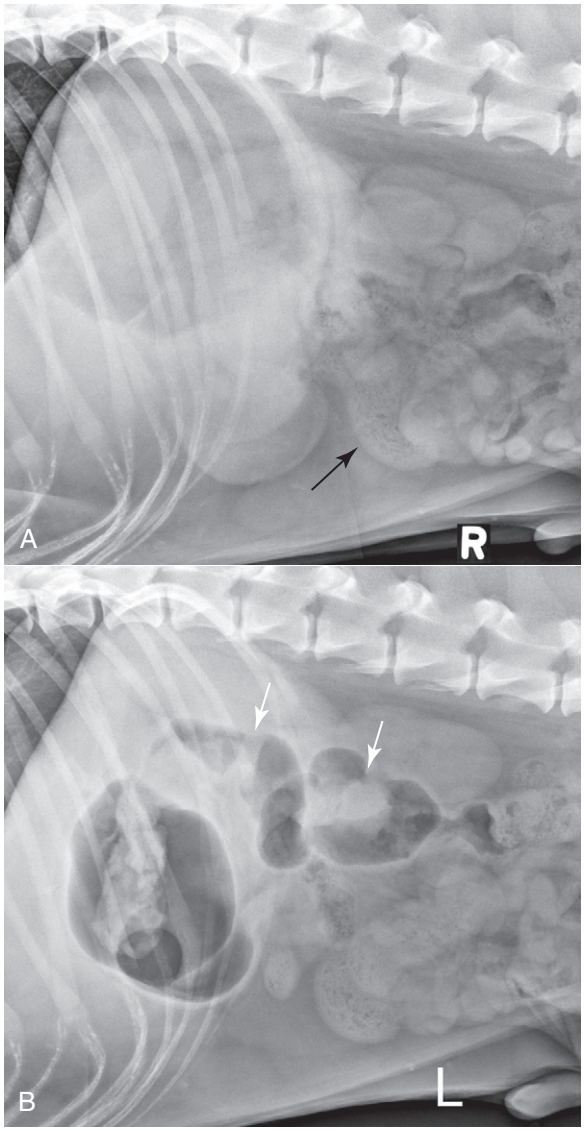


Fig. 44-7 The images show the use of the inherent gas contrast to confirm a gastrointestinal foreign body. In the right lateral view *(R)*, there is mottled gas and soft tissue opacity in a moderately focally dilated loop *(black arrow)* in the cranial ventral region. Moderate gas and fluid distention of the stomach is also evident. In the left lateral view *(L)*, the redistribution of gastric gas provides contrast for identification of a soft tissue foreign body in the pylorus and mild plication of the course of the proximal duodenum *(white arrows)*. These findings confirm a fabric-type foreign body involving the stomach with a linear component extending into the duodenum and proximal jejunum.

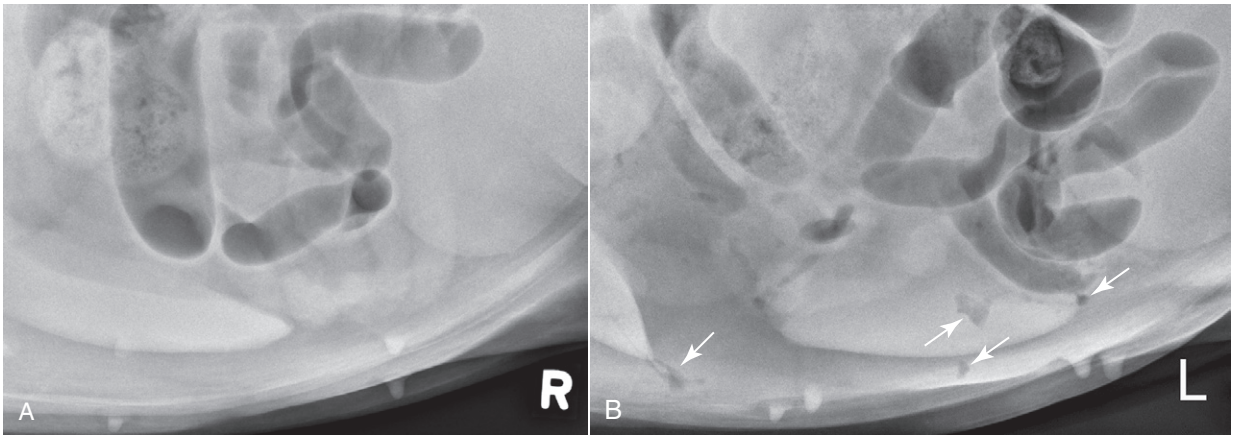


Fig. 44-8 In a close-up right lateral view *(R)*, there is normal serosal contrast and detail of the bowel. Loops immediately cranial to the urinary bladder are of normal diameter and empty; however, one of the gas-filled loops is dilated (2.5× the height of L5 as measured on the original image). In the left lateral view *(L)*, there are four gas lucencies *(white arrows)* not within a bowel lumen. These are indicative of free peritoneal gas, most likely secondary to bowel perforation. A perforation in the distal duodenum caused by a linear foreign body was found at surgery.

gas is most likely from gastrointestinal perforation.[23] The combination of barium and ingesta within the peritoneal cavity causes more severe peritonitis, foreign body granulomas, or serosal adhesions.[22,24,25] However, if treated promptly and aggressively, patient outcome can be good.[26] Attempting to identify the location of the perforation is not as important as providing aggressive medical and surgical intervention. Ultrasound can also be used to detect free peritoneal gas associated with gastrointestinal perforation and prevents the additional contamination associated with barium leakage. Water-soluble organic iodine contrast media are either ionic or nonionic.[27] Most ionic contrast media are hypertonic and cause an influx of fluid into the gastrointestinal tract. Ionic iodinated contrast media are not recommended for oral administration in young and debilitated patients and especially dehydrated patients, because the resultant fluid shift can worsen any hypovolemic state.[28]

Technique and General Interpretation

A brief presentation of the techniques and interpretation of intestinal contrast studies follows. More detailed descriptions of techniques and normal interpretation can be found elsewhere.[21] Contrast studies can be divided into two categories based on the radiographic opacity imparted by the contrast medium. Positive-contrast studies increase the opacity of the bowel lumen and are done with barium sulfate suspensions, iodinated products, and barium-impregnated polyethylene spheres (BIPS, Chemstock Animal Health Ltd., Christchurch, New Zealand). These contrast media are given orally or by orogastric intubation. Because the stomach is also opacified by these agents, except for the special case of BIPS, the phrase *upper gastrointestinal contrast study* is used.

The volume of contrast medium in the intestinal lumen is a critical factor in interpretation. The intestine should be distended to its reasonable physiologic maximum. Failure to administer an adequate volume of contrast medium is one of the most frequent causes for a nondiagnostic barium study. Some recommended dosages for contrast medium are given in Table 44-2. A summary of the portions of the gastrointestinal tract seen at specific intervals after positive-contrast medium administration is presented in Table 44-3.

Normal anatomic features of the duodenum made visible by positive-contrast medium should not be misinterpreted as lesions. Dogs often have multiple square-shaped outpocketings on the antimesenteric side of the descending duodenum. One or several may be present. These are termed *pseudoulcers* and are normal and caused by mucosal depressions over submucosal lymphoid accumulations (Fig. 44-9). Pseudoulcers are not found in the cat. Approximately 30% of normal cats have strong segmental contractions throughout the length of the duodenum that produce a *string-of-pearls* effect during the contrast study (see Fig. 44-9).[6] Pseudoulcers and the string-of-pearls appearance are seen mainly in positive-contrast studies and only rarely in survey radiographs. Throughout the remainder of the small bowel, concentric narrowing of short lengths of bowel should be seen and are caused by peristalsis

Table • **44-2**

Recommended Dose Rate for Contrast Medium

CONTRAST MEDIUM	DOG	CAT
Barium sulfate suspension*	6—12 mL/kg 20% (w/w)[14] or 6—10 mL/kg 60% (w/w)	12—16 mL/kg[6]
Organic iodine preparation (full strength)	2—3 mL/kg[8,14,15]	2 mL/kg[15]
Organic iodine, nonionic (240—300 mg iodine/mL)	10 mL/kg (1:2 dilution)[28]	10 mL/kg (1:2 dilution)[28,31]
Radiopaque markers (BIPS)†	10 5-mm and 30 1.5-mm spheres	10 5-mm and 30 1.5-mm spheres

*A large volume of relatively dilute contrast medium is preferred by some to distend the intestinal lumen but not to obscure radiolucent luminal filling defects. The author prefers a full-strength barium suspension for its superior mucosal pattern definition.
†Follow manufacturer's specific directions for administration with or without food.

Table • **44-3**

Upper Gastrointestinal Tract Film Sequence

	BARIUM	IONIC AND NONIONIC ORGANIC IODINE	STRUCTURES USUALLY OPACIFIED IN NORMAL ANIMALS*
Dog	Immediate	Immediate	Stomach
	15 minutes	15 minutes	Stomach, duodenum
	30 minutes	30 minutes	Stomach, duodenum, jejunum
	1 hour	1 hour	
	2 hours		Stomach, duodenum, jejunum
	4 hours		
			Stomach, all parts of small bowel
			Small bowel, colon
Cat	Immediate	Immediate	Stomach
	5 minutes	5 minutes	Stomach, duodenum
	30 minutes	30 minutes	All parts of small bowel
	1 hour	1 hour	Small bowel, colon

*Because of the extreme variability of individual transit times, this list is only an approximation of the parts of the gastrointestinal tract seen at these times.



Fig. 44-10 Variations of normal that can be seen during the progression of small bowel transit. Several loops contain gas and barium providing a double-contrast effect. One loop has several adjacent contractions.

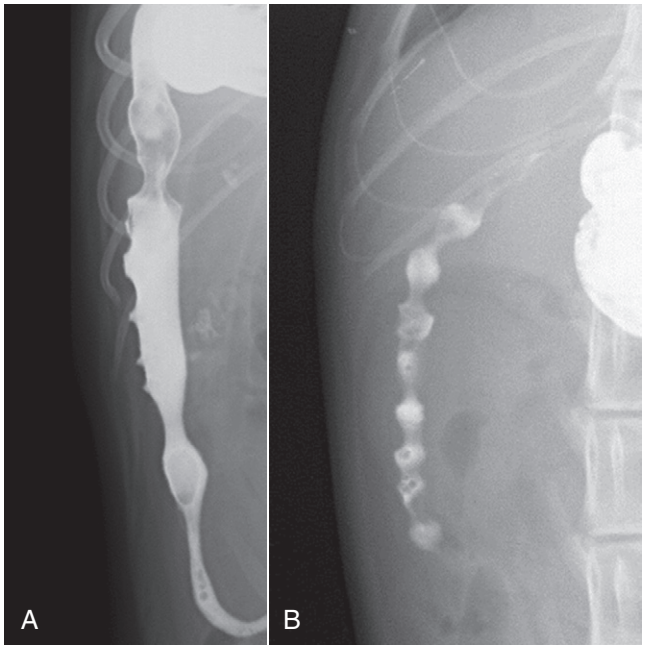


Fig. 44-9 Normal duodenal barium contrast images wherein the pseudoulcers of the dog **(A)** and normal *string-of-pearls* effect of the cat **(B)** can be seen. The pseudoulcers in the antimesenteric wall are caused by depression in the mucosa at sites of lymphoid follicles. One or more may be present. The *string-of-pearls* effect is caused by circular muscle contractions that almost completely obliterate the lumen. Neither of these features is seen in noncontrast images and is rarely seen in ultrasound studies.

(Fig. 44-10). The location of such narrowing should vary during the time of study in the normal animal.

In a normal upper gastrointestinal study, barium and gas may be present simultaneously in loops (see Fig. 44-10). A double-contrast effect is present when the distention by gas is greater than that caused by the barium. The barium/mucosa interface appears typically in such loops as a thin opaque line. In other loops, gas may be present only as small bubbles. Findings on the barium contrast images that most strongly correlate with abnormalities are changes in the diameter of the bowel, extensive changes in the barium/mucosa interface, and changes in the rate of passage of barium. The intestinal tract is normally characterized by dynamic changes; thus documenting a suspicious finding on multiple radiographs over time increases the significance of the finding.

BIPS are used mainly for evaluation of gastric dysmotility and intestinal transit time in the dog and cat. The spheres are made in two diameter sizes: 1.5 mm and 5 mm. The larger spheres are designed to become trapped at the oral aspect of an obstructing lesion, making them suitable for evaluation of partial and complete obstruction (Fig. 44-11).[29] BIPS are administered typically with a meal. The type of meal influences the rate of gastric emptying; thus strict adherence to the manufacturer's recommendations must be maintained when the product is used for calculation of gastric emptying time and assessment of orocolic transit.

ABNORMAL SMALL BOWEL

Disease Resulting in Bowel Dilation

Numerous diseases result in dilation of the small intestine. Failure of intestinal contents to pass through the tract is called *ileus*. Ileus can be mechanical, caused by physical obstruction of the bowel, or functional (paralysis), in which peristaltic contractions of the bowel cease as a result of vascular or neuromuscular abnormalities within the bowel wall. In functional ileus, the bowel remains patent.

In general, the appearance of mechanically obstructed bowel differs from functionally obstructed bowel by the following parameters: (1) mechanically obstructed bowel is usually of larger diameter than functionally obstructed bowel; (2) both gas and fluid typically are in the lumen of mechanically obstructed bowel, whereas functionally obstructed bowel tends to contain more gas or may be completely gas filled; (3) patients with mechanical obstruction usually have some

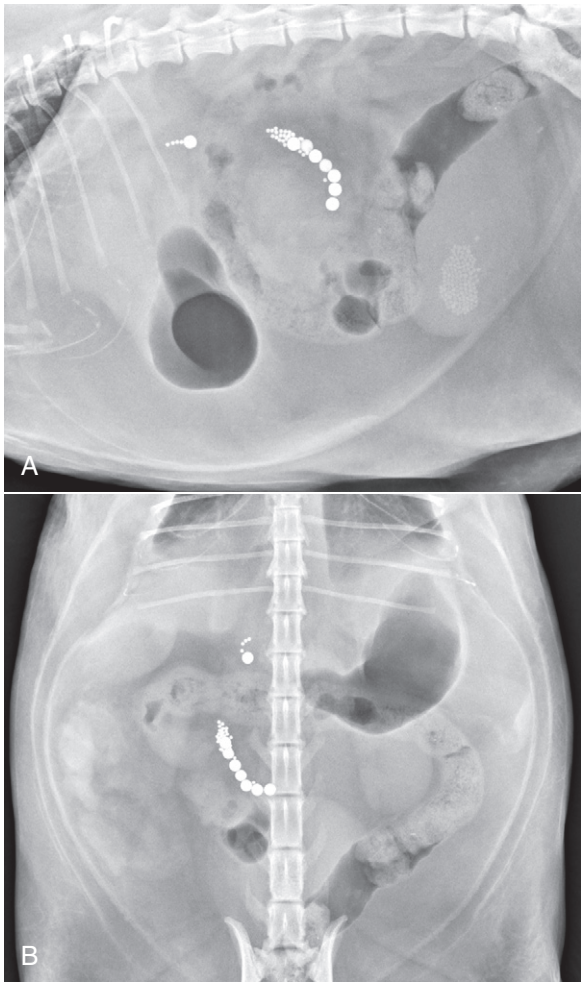


Fig. 44-11 Left lateral and VD views of a cat given BIPS 12 hours before these radiographs were made. There is retention and clustering of the spheres in the duodenum. This is highly indicative of an obstruction. There is reduced serosal detail in the mid-right abdomen. Ultrasonographically, there was plication of the jejunum. At surgical exploration, several perforations had been caused by fishing line foreign material. A large number of opaque cystoliths are evident.

bowel segments of normal size, whereas patients with functional obstruction may have generalized involvement of the bowel. These parameters, however, are only guidelines and some overlap exists between mechanical and functional ileus, making the radiographic distinction impossible in some patients.

Table 44-4 lists diagnostic considerations for the more common patterns of bowel dilation. Patterns of dilation include (1) focal/mild: one to three loops are involved, and luminal distentions are 1.5 to 2 times normal; (2) focal/severe: one to three loops are involved, and luminal distention is greater than twice normal (Fig. 44-12); (3) generalized/mild: all loops are involved, and luminal distention is 1.5 to 2 times

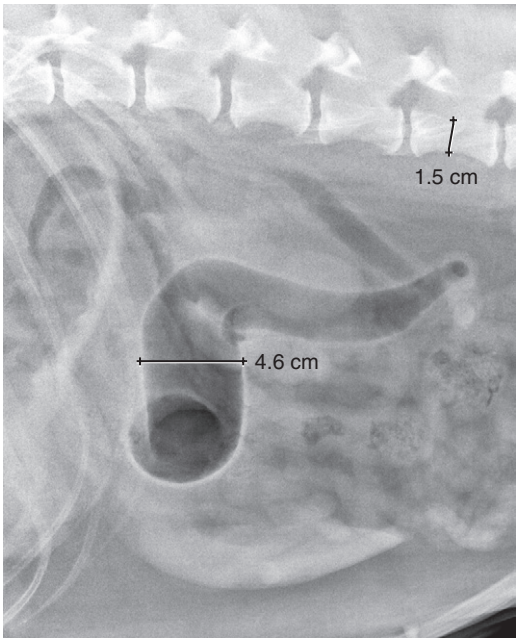


Fig. 44-12 A single severely dilated small bowel loop is present in this dog. The diameter is three times the central height of the L5 vertebral body. Several small bowel loops are seen caudal to the spleen and ventral to the fecal material in the colon. A segment of corncob, not visible, in the proximal jejunum was the cause of obstruction.

Table • **44-4**

Pathologic Conditions by Length and Relative Distention of Affected Bowel

FOCAL/MILD	FOCAL/SEVERE	GENERALIZED/MILD	GENERALIZED/SEVERE
Regional enteritis	Mechanical ileus	Functional ileus	Mechanical ileus
Regional peritonitis	Foreign object	Enteritis	Complete obstruction, distal bowel
Mechanical ileus, partial obstruction	Intussusception	Anticholinergic drugs	Intussusception
Early functional ileus	Bowel wall neoplasia	Electrolyte imbalance	Foreign object
Vascular compromise	Granulomatous wall infiltrate	Malabsorption	Bowel wall neoplasia
	Bowel stricture	Abdominal pain	Functional ileus
	Stenosis/atresia	Mechanical	Recent abdominal surgery
	Postsurgical adhesion	Partial obstructions at ileocolic junction (usually cats)	Spinal trauma (neurologic injury)
	Herniation		Intestinal volvulus (rare)
	Functional ileus		
	Parvovirus enteritis		
	Dysautonomia		

normal (Fig. 44-13); and (4) generalized/severe: all loops are involved, and luminal distention is greater than twice normal.

Mechanical Obstruction

The small intestinal lumen can be occluded by foreign objects, intussusception, mural mass, or extrinsic lesions. The radiographic features of the obstruction depend on its completeness, the location in the gastrointestinal tract, and the duration. The most consistent radiographic sign of mechanical obstruction is a variable degree of dilation of bowel loops orad to the site of obstruction (Fig. 44-14). Prediction of the presence of obstruction in the dog can be made by determining the ratio of the small intestinal diameter relative to the L5 vertebral body height.[5] Values greater than 1.6 are suggestive of obstruction. In the cat, a ratio of the maximum small intestinal diameter to vertebral end plate height of L2 greater than 4 provides a very high likelihood of intestinal obstruction.[8] Alternatively, qualitative assessment of bowel size may be as accurate once a clinician has gained experience. A more distal or more complete obstruction leads to a greater number of distended loops. Obstructed bowel typically contains both fluid and gas unless the obstruction is quite proximal, allowing gas and fluid to reflux into the stomach. More complete and longer duration obstruction results in greater bowel distention. As bowel becomes progressively more distended, the segments become crowded into a relatively smaller space, often assuming a *stacked* appearance (Fig. 44-15).

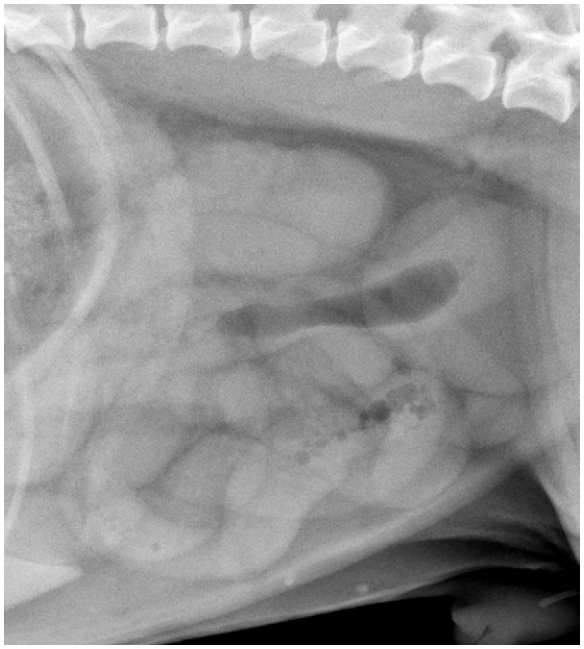


Fig. 44-13 This dog has mild generalized dilation of the small bowel. The majority of loops are fluid filled based on their uniform soft tissue/fluid opacity interface. One loop has small fragmented gas bubbles. This bubble effect is a nonspecific finding of enteritis. This dog was suspected to have viral enteritis. The radiographic changes were complicated by the pharmacologic effects of aggressive phenobarbital and diazepam treatment for acute severe seizures.

Acute duodenal obstruction is difficult to detect in survey radiographs because the stomach acts as a reservoir for gas and fluid that might collect. Also, if vomiting is frequent, the accumulated fluid and gas are removed from the stomach and duodenum. With chronic duodenal obstruction, however, gastric distention becomes apparent (Fig. 44-16). A moderate to large volume of fluid and gas in the stomach in a vomiting patient should raise suspicion of duodenal obstruction as well as pyloric outflow obstruction.

Partial obstructions may be difficult to detect. This is particularly true when the partial obstruction is of short duration and in the proximal duodenum. Dilation of such a relatively short length of duodenum may be easily overlooked. Longstanding partial obstructions that are distal in the bowel result in accumulation of opaque granular material proximal to the site of obstruction. This is caused by desiccation of ingesta that becomes trapped proximal to the obstruction. The desiccated material often has the appearance of feces, and the identification of this fecal-like material in the small rather than large bowel is a reliable sign of partial distal small bowel obstruction. This appearance has been referred to as the *gravel sign*. One scenario in which chronic partial obstruction occurs is elderly cats that develop an ileal adenocarcinoma causing partial bowel obstruction (Fig. 44-17). If a bowel obstruction

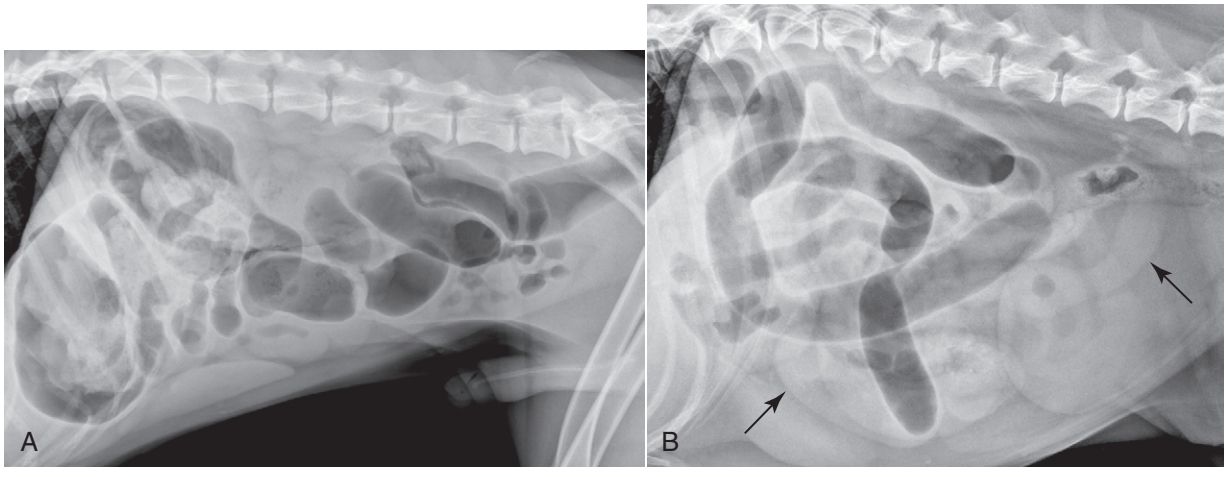


Fig. 44-14 **A,** Lateral radiograph of a dog with mechanical jejunal obstruction caused by a cloth foreign body. There are multiple small intestinal segments that are abnormally dilated. The configuration of the dilated loops indicates that they cannot all be colon. There are two populations of bowel: large segments and normal segments. Having multiple populations of bowel size is common in dogs with mechanical obstruction. This dog has less intraluminal fluid than most dogs with mechanical obstruction. **B,** Lateral radiograph of a dog with mechanical obstruction caused by a peach pit. There are a few gas-distended loops of jejunum, and some distended segments also contain fluid *(black arrows)*.

is complete, the small intestine distal to the obstruction is likely to be empty.

Foreign objects are a common cause of obstruction. Foreign bodies composed of mineral or metal are easily recognized. Disk-shaped metallic foreign objects consistent with a penny should be closely checked for erosion. Pennies minted since 1983 have a major zinc composition and can cause anemia from acute zinc toxicity.[30] Conversely, a patient with malaise and Heinz body anemia should be radiographed to assess for ingested zinc-containing coins or other objects (e.g., nuts or bolts).

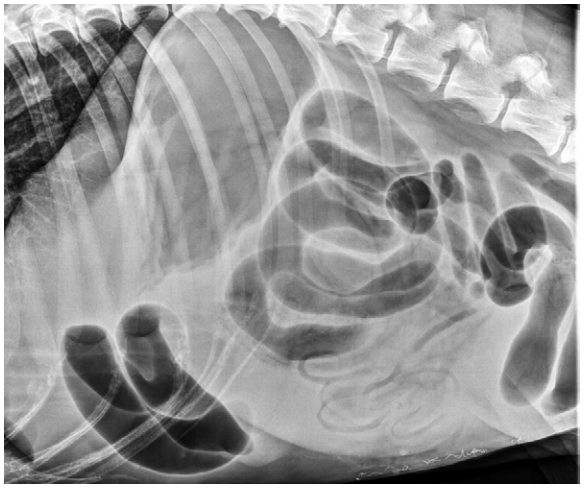


Fig. 44-15 Lateral view of a dog with a distal small bowel obstruction. The bowel is not severely dilated, and there are several loops of normal diameter. However, those loops that are gas dilated are aligned vertically and horizontally in a *stacked* pattern. Metallic abdominal wall sutures are present from a surgery 7 years prior for removal of a foreign body.

Small-sized rocks, clay litter, hard-shelled seeds, or other dirt debris from the ground are ingested frequently by dogs and cats. These are usually incidental and pass without causing obstruction. However, small particles of radiopaque ingesta and debris can also accumulate proximal to a chronic partial obstruction (see Fig. 44-17). Nonmineralized, nonmetallic foreign objects are much more difficult to identify. Fruit pits, corncobs, and other nonopaque objects may be recognized by their geometrically shaped radiolucencies on survey radiographs (Fig. 44-18).[31] The nonopaque foreign object with irregular surfaces, especially with grooves or pockets, can entrap small, mineralized ingested debris and gas and may become more visible. Careful application of abdominal compression may enhance the conspicuity of these foreign objects (Fig. 44-19).

A pneumocolon can be used to differentiate the source of dilated bowel as small intestine versus colon and define the location of mottled mineralized material to be in the small versus large bowel (Fig. 44-20). The use of 24-hour serial survey radiographs, ultrasound evaluation, or a contrast study may be necessary to confirm the diagnosis of partial obstruction suggested by abnormal luminal contents. Persistence of small opaque foreign objects in the same intestinal location in serial radiographs over a 24- to 48-hour period should increase the suspicion of partial obstruction.

The ultrasonographic appearance of ingested foreign material varies according to the composition of the material (Fig. 44-21).[32] The acoustic pattern caused by the rigid foreign object may have a shape that can be recognized specifically. Objects that transmit the beam, such as some types of rubber balls, are more readily identified. Those that create a strong reflection with marked acoustic shadowing may be more difficult to define initially. When these objects cause incomplete obstruction, they are frequently associated with increased intestinal motility resulting from irritation. With more complete obstruction, the foreign object may be associated with accumulation of fluid in the bowel cranial to the obstruction.

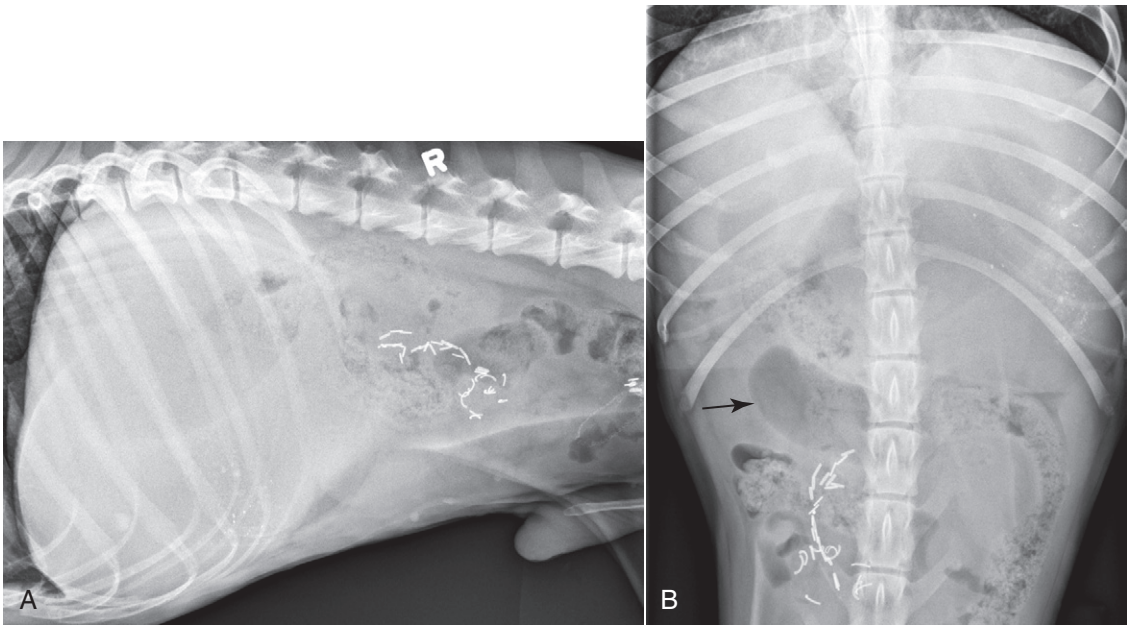


Fig. 44-16 Right lateral and VD views of a dog with a moderately dilated gas and fluid-filled stomach. There is mineral opacity dispersed in the pyloric region in the lateral view. This dog had been vomiting three to four times per day. This degree of gastric distention should raise the suspicion for pyloric or duodenal obstruction. In the VD view, a dilated small bowel segment is seen in the right cranial region adjacent to the plane of L2 *(black arrow)*. The metallic hemostatic clips are from previous surgery.

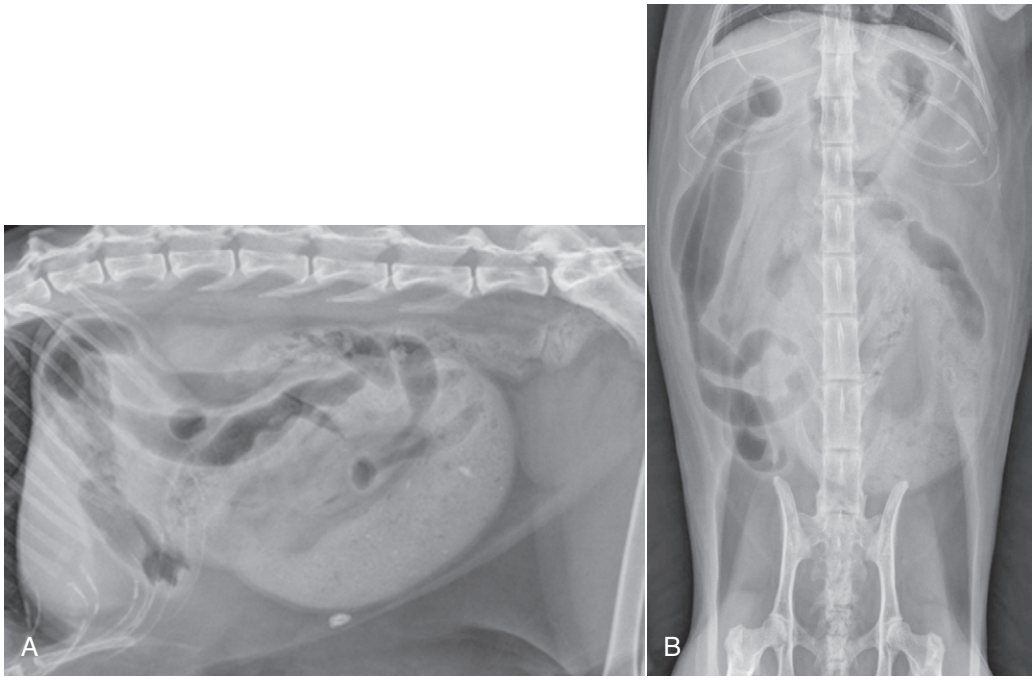


Fig. 44-17 Lateral **(A)** and VD **(B)** radiographs of a cat with chronic partial ileal obstruction from an adenocarcinoma. The ileum is markedly distended with fecal-like material. This loop is differentiated from large bowel by its position ventral to the colon in **A** and its caudal flexure in **B**; the colon does not have a caudal flexure as seen in **B.** The opacity of the material in the bowel is caused by continued desiccation because of its inability to pass the obstruction. More proximal bowel segments may continue to remain normal.

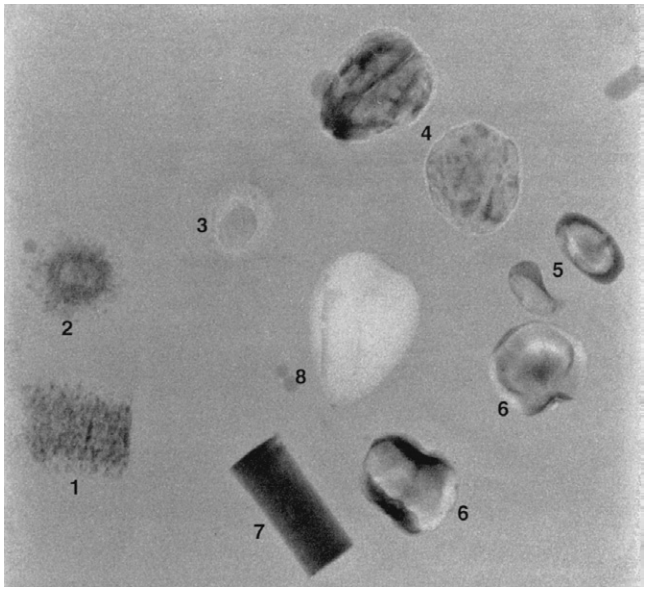


Fig. 44-18 Various nonopaque foreign bodies radiographed in a water bath. *1*, Section of corncob viewed side on; *2*, section of corncob viewed end-on; *3*, peach pit; *4*, walnuts; *5*, acorns; *6*, chestnuts; *7*, wine cork; *8*, avocado pit. (From Lamb CR, Hanson K: Radiological identification of nonopaque intestinal foreign bodies, *Vet Radiol Ultrasound* 35:87, 1994.)

In vomiting dogs, ultrasound findings of jejunal serosa-to-serosa greater than 1.5 cm in diameter, normal wall layering, and fluid- or gas-filled lumen should prompt careful searching of the bowel for an obstructive lesion.[33] Reduced or lack of intestinal motility is used in the definition of mechanical versus functional ileus, the latter being characterized by decreased motility. A wide range of hypo- and hypermotility was observed in dogs with mechanical obstruction and was not found to be a useful discriminatory feature relative to nonobstructive causes of vomiting.[33]

Linear foreign material (e.g., string, nylon hosiery) acts differently than short or solid foreign objects. Linear foreign material that becomes trapped in the intestine usually causes both an abnormal shape and contour of the loops and an abnormal gas pattern (see Fig. 44-7).[8] Some portion of the linear material typically becomes fixed at an orad location, most commonly in the stomach in dogs and under the tongue in cats.[34,35] The remainder of the length passes into the small intestine. The peristaltic action of the bowel causes it to climb the linear foreign body, which results in a pleated, or plicated, appearance of the affected loops. These loops may not become markedly distended, but gas commonly becomes trapped in pockets formed by the pleats. The result is an abnormal pattern of round, tapered, short-tubular, and sometimes crescent- or comma-shaped gas shapes (Fig. 44-22). The abnormal contour and plication pattern is particularly well depicted in a barium-contrast study (Fig. 44-23). If the linear material is absorptive in nature, such as fabric, it can absorb fluid incompletely and have a mottled to linear, streaked gas pattern. In the cat, the plication of the bowel can cause a *clumped* or *bunched* positioning of the bowel. The displacement of the small bowel into the middle or right side of the abdomen in the obese cat should not be misinterpreted as plication caused by a linear foreign body (Fig. 44-24).

The ultrasound appearance of linear material depends on the amount of gas and fluid accumulated around the foreign material. Plication of the bowel around an echogenic line has been described most frequently (Fig. 44-25).[32] This differs from the smooth, straight mucosa normally seen on either side of the bright linear stripe of an empty normal bowel lumen. If the linear foreign material is in duodenum, it may

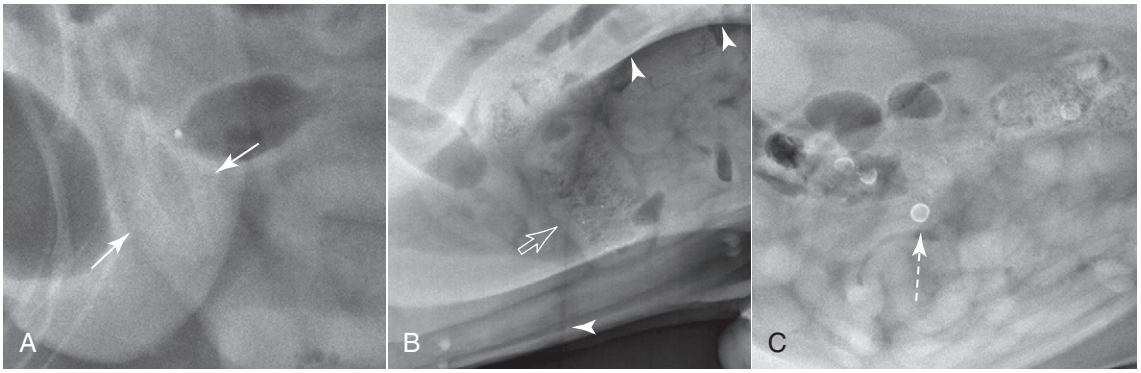


Fig. 44-19 Radiolucent and opaque foreign bodies. **A** is an obstructive peach pit *(between the white arrows)*. Its subtle shape is defined best by the radiolucent oval center. A small focus of opaque debris is trapped in one of the crevasses of the outer surface. **B** is an obstructing corncob *(open arrow)*. A compression paddle *(border indicated by white arrowheads)* was used to displace bowel, making the corncob more easily seen. Note the gas as well as mineral debris trapped in the kernel pockets. **C** is a dog with ingested Hackberry tree seeds *(dashed arrow)*. Based on their size, they would not be expected to cause obstruction, and several are present in the colon.

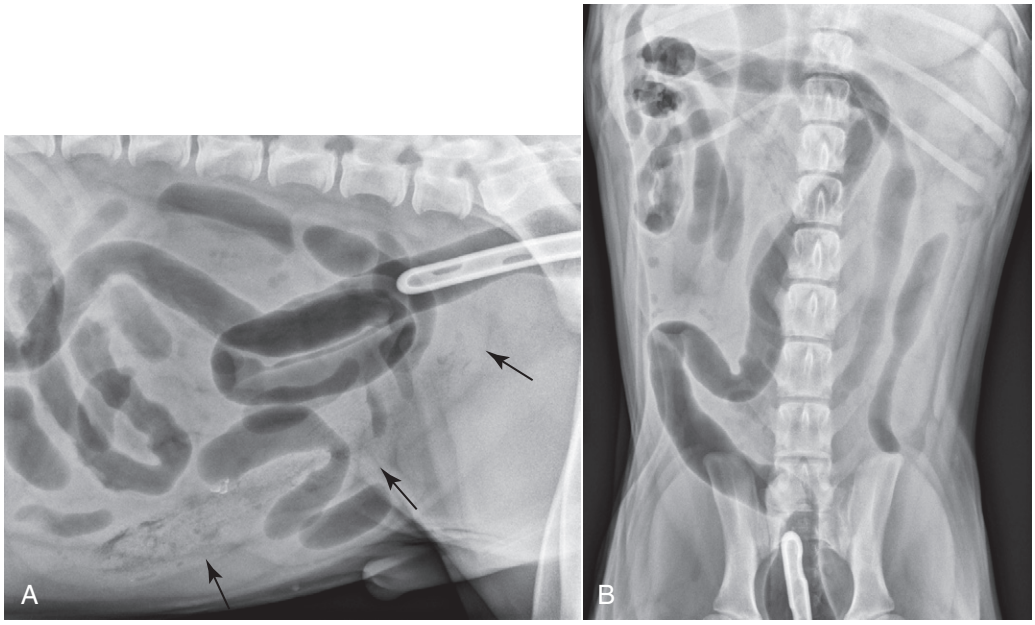


Fig. 44-20 Left lateral and VD views following introduction of air into the colon (tubing evident in the distal descending colon). The pneumocolon defines that the soft tissue gas-streaked material is not fecal material in the colon. This heterogeneous material in the lateral view extends cranially from the plane of caudal L7 *(black arrows)* and was suspected to be fecal material. This linear gas streaking within soft tissue opacity is typical of gas being trapped within the folds of cloth. A small mineralized foreign body is present within this material. A sock was removed from the midjejunum.

be traceable into the stomach.[36] Thickening of the wall or obliteration of the wall layer pattern has not been described with a linear foreign body.

A serious complication of a chronic linear foreign body is laceration of the intestinal wall. If the laceration is small, serosal adhesion to an adjacent loop can occur, resulting in a fixed position of two or more loops. If the laceration is large, septic peritonitis and potential gas leakage occur.

There are differences between dogs and cats with linear foreign objects: (1) affected dogs are older and have less irregularity in the gas pattern; (2) one-quarter of dogs had concurrent intussusception; (3) on both radiographic and surgical assessment, dogs had greater evidence of bowel trauma or bowel laceration and peritonitis; and (4) the probability of death as a result of linear foreign body in dogs was nearly double that in cats.[34,35] Intestinal perforation caused by linear foreign material or other diseases should be suspected when a combination of focal hyperechoic mesenteric fat, echogenic peritoneal effusion, and fluid in the bowel is identified sonographically.

Intussusception, the invagination of one portion (intussusceptum) of the gastrointestinal tract into the lumen (intussuscipiens) of an adjacent segment, can be initiated by many events, including motility disorders, inflammatory wall lesions,

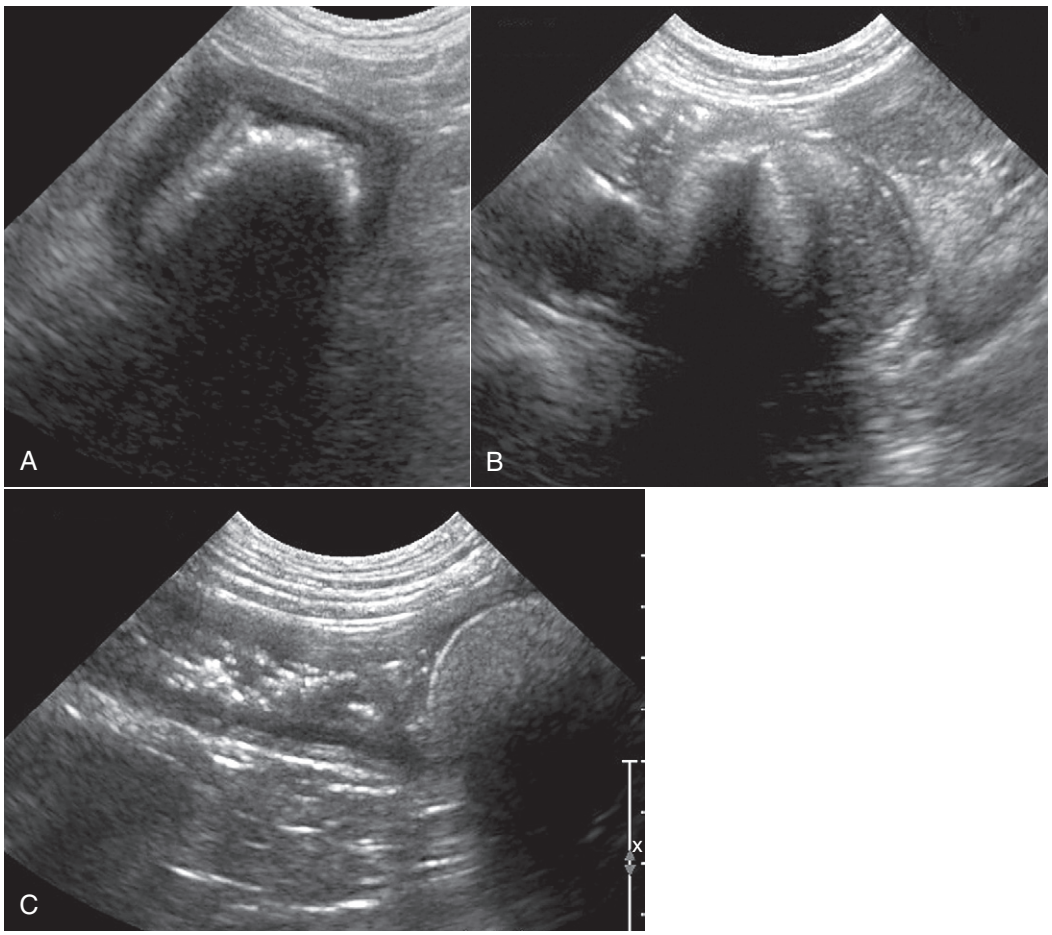


Fig. 44-21 Three ultrasound images of intestinal foreign bodies show differences in shape. All show strong acoustic shadowing. The object in **A** was undetermined; **B** was part of several pieces of hoof material; and **C** was a portion of a rubber ball. **C** shows a longitudinal section of the bowel orad to the foreign body that is filled with mucoid fluid.



Fig. 44-22 Lateral view of a cat with a linear foreign body obstruction. The jejunum is bunched in the ventral abdomen, and gas has become trapped in the plications, creating small irregularly shaped bubbles *(black arrows)* that are not seen typically in normal bowel.

neoplasia, or idiopathic causes.[37,38] Although an intussusception can occur anywhere along the digestive tract, the majority occur in the small intestinal tract and at the ileocolic or cecocolic junction. The radiographic appearance of intussusception is influenced considerably by the completeness of the obstruction.[9] Many distal intussusceptions result in generalized severe dilation of the small bowel, creating the typical appearance of mechanical obstruction. The intussusceptum can be seen occasionally in the colon if sufficient colon gas is present to provide contrast (Fig. 44-26). In most patients, however, differentiating intussusception from other causes of mechanical obstruction solely on the basis of survey radiographs is not possible. Upper or lower contrast studies can be used to differentiate intussusception from other causes of bowel obstruction. However, ultrasound evaluation is preferred to positive-contrast studies.

Intussusceptions have a characteristic ultrasound pattern (Fig. 44-27). The telescoping effect results in a concentric ring appearance when viewed in the transverse plane and a multilinear pattern when viewed in the longitudinal plane.[39-41] A hyperechoic region is typically noted mildly eccentrically positioned within the concentric or linear pattern. The shape of this hyperechoic material may be round or semilunar and is caused by mesenteric fat pulled into the intussuscipiens. If an anechoic feature is evident centrally, it most likely represents a small volume of fluid within the lumen of the inner loop; if evident eccentrically, it likely represents fluid between the inner and outer loops. When viewed in the long axis, fluid distention is often seen in the bowel proximal to the lesion. Multiplane imaging of the suspected intussusception is important to confirm its features. Bowel loops situated immediately adjacent to each other may be misinterpreted as an intussusception.[42] Doppler evaluation of blood flow to the

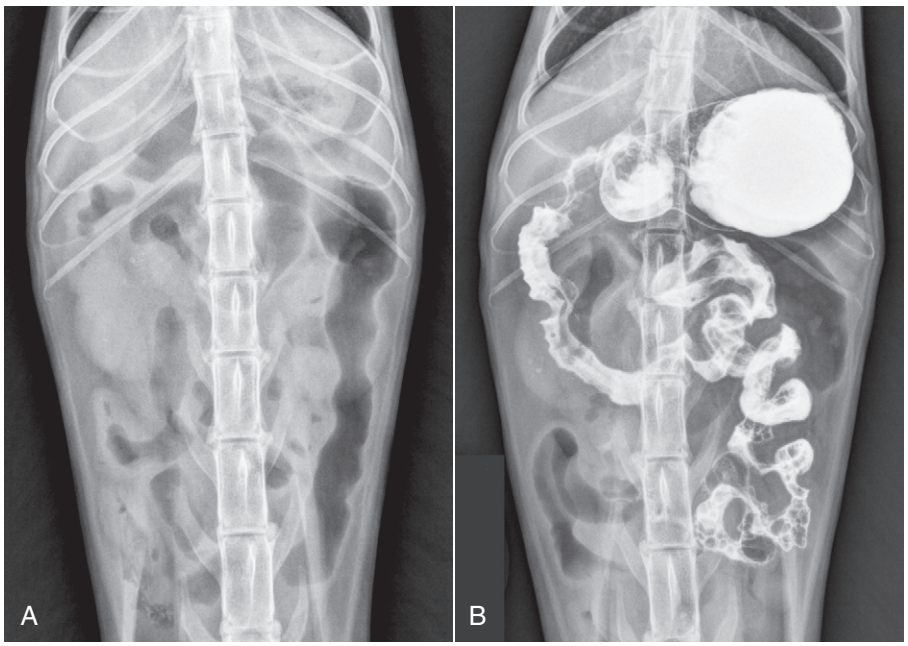


Fig. 44-23 Survey VD and barium-contrast study of linear foreign body in a cat. In the survey image, there is an abnormally shaped gas accumulation in the right twelfth intercostal space. The classic plication pattern of the bowel is visible in the barium image.

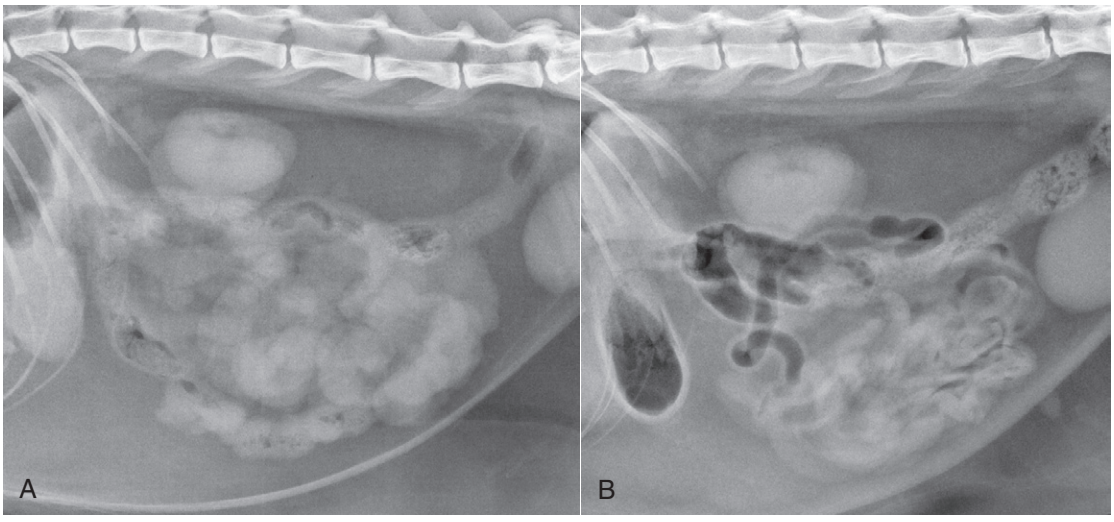


Fig. 44-24 Image **A** is an obese cat with an extensive jejunal linear foreign body. Image **B** is an obese cat without linear foreign body. Both have a relative *clumping* of the small intestine in the central abdomen. The effect of the intraabdominal fat on the positioning of the small intestine makes differentiation of true plication difficult in the obese cat, particularly where there is trivial gas in the bowel to increase the conspicuity of abnormal lumen shapes. There is more pronounced serosal border undulation in cat **A** compared with **B** to increase suspicion of plication. Ultrasound or barium contrast can be used in such patients to confirm the linear foreign body.

intussusceptum has been evaluated in the dog with the intent of predicting the reducibility of the intussusception.[43] Dogs with color flow in the mesentery of the intussuscepted bowel were more likely to have successful reduction compared with those with no color flow.

Proliferating tissue masses originating within the intestinal wall include tumors, polyps, and granulomatous infiltrates. The development of an obstructive bowel pattern from these lesions depends on the size of the lesion and whether growth of the lesion is directed toward or away from the lumen. Over time, most could progress from no effect to partial obstruction to complete obstruction. Most present clinically during the phase of partial obstruction with focal mild to severe distention. Additional features of these masses are discussed later.

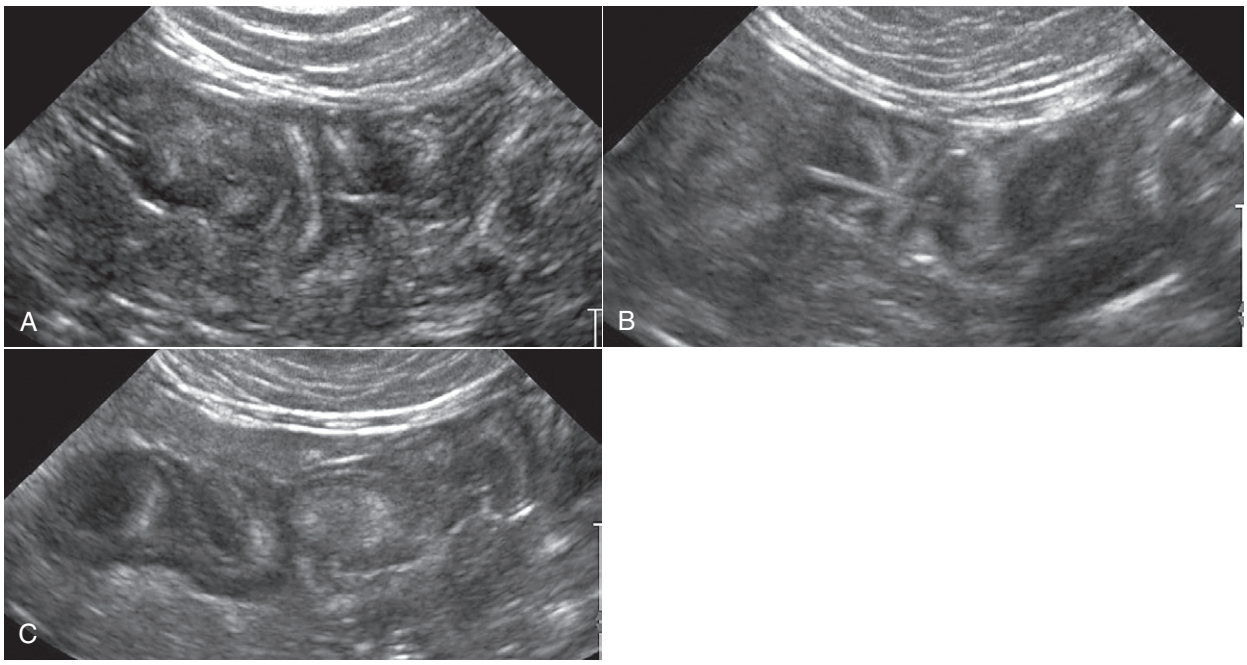


Fig. 44-25 Three ultrasound frames from a cat with a linear foreign body. The plication of the bowel is evident by the tightly undulating contour of the bowel wall and little distention of the lumen. The linear hyperechoic streak in the central image represents the foreign material.

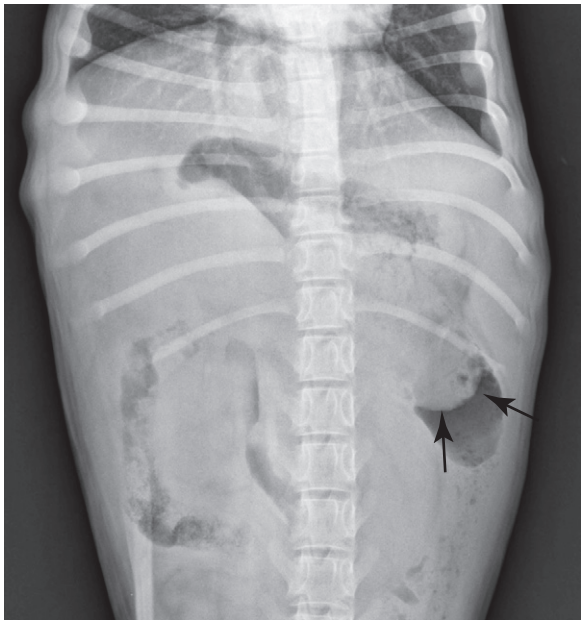


Fig. 44-26 Ventrodorsal radiograph of a dog with an ileocolic intussusception. This intussusception has not yet caused jejunal dilation, but the leading edge of the intussusceptum *(black arrows)* appears as a round mass contrasted by colon gas. This appearance could be caused by a colonic foreign body but is more typical of an intussusception, and ultrasound should be performed for confirmation.

Lesions originating outside the intestinal wall can cause compression on a loop and result in partial or complete obstruction. Lesions in this category include adhesions from prior surgery, abdominal boundary hernias (congenital or traumatic), and occasionally masses originating from other abdominal organs (Fig. 44-28).

Functional Ileus

When peristaltic contractions of bowel cease because of vascular or neuromuscular abnormalities within the bowel wall, the lumen dilates and the bowel lumen remains patent. Many patients have no specific survey radiographic changes to differentiate the bowel dilation caused by functional ileus from that of mechanical ileus. As previously noted, the length of bowel affected may provide some differentiation, with localized dilation more likely from a mechanical cause and diffuse dilation more likely from functional ileus. However, obvious overlap between these two occurs. Furthermore, chronic moderate to severe mechanical obstruction can eventually lead to functional ileus. The degree of dilation is not a specific differentiating feature.

There are no specific ultrasound or positive-contrast study features to differentiate chronic complete mechanical obstruction from functional ileus. The finding of peristalsis suggests exclusion of functional ileus. A thorough search of the bowel should be done to look for obvious obstructive causes. Dilation of the bowel with gas adds difficulty in examining the entire dilated bowel by ultrasound. The finding of echogenic peritoneal effusion supports a diagnosis of peritonitis that can be confirmed by fluid sampling and analysis. The more common diseases that cause functional ileus include viral enteritis (canine parvovirus type 2 in particular), chronic mechanical obstruction, and peritonitis.[44] Other less common diseases with a primary radiographic change of dilated intestinal loops include strangulation of the intestine through a hernia (vascular compromise), mesenteric volvulus (vascular compromise), spinal trauma (neurologic injury), segmental jejunal arterial thrombosis (vascular compromise), dysautonomia (autonomic nervous system disease), and intestinal pseudoobstruction (tunica muscularis atrophy). Small intestinal loops can slip through traumatic tears or developmental hernias of the peritoneal cavity boundaries. The identification of such loops in an extraabdominal location is usually easy because of gas within their lumen. Bowel dilation occurs if

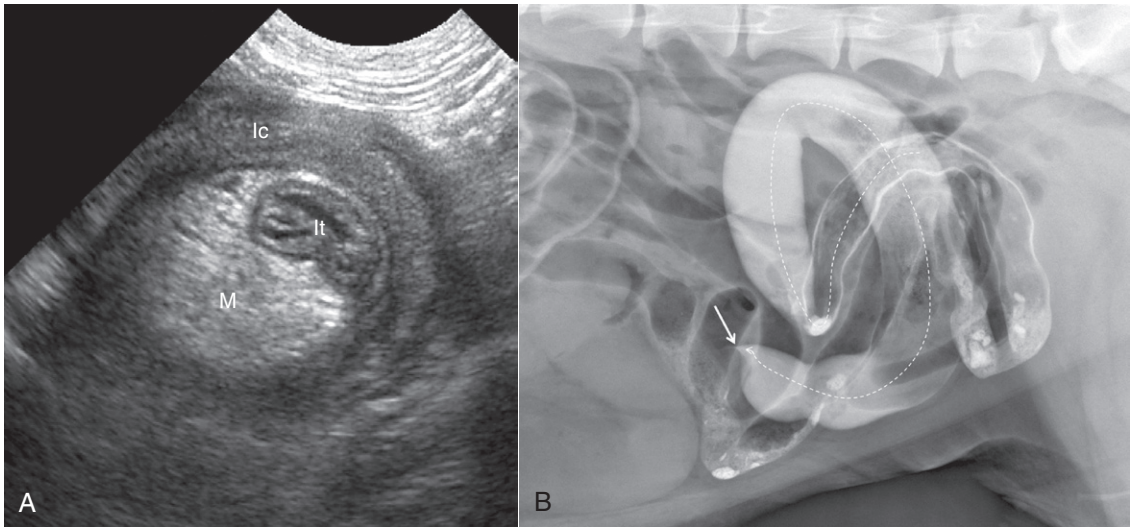


Fig. 44-27 A transverse ultrasound image of an intussusception. The wall layer pattern of the intussuscepiens in this patient is not clearly defined because of mucosal edema and dilation of mucosal lymphatics. In the radiograph, the narrowed lumen *(white arrow)* of the orad aspect of the intussusceptum is visible. The edema in the wall of the intussuscepiens in this patient has resulted in a stricture of the lumen, with resulting proximal dilation of small bowel. The *dashed white line* follows the course of the dilated bowel as it approaches the orad end of the intussusceptum. The increased opacity of the lumen of the dilated bowel was thought to be caused by medications that increased the opacity of the fluid. *It*, intussusceptum; *Ic*, intussuscepiens; *M*, hyperechoic mesenteric fat pulled in with the intussusceptum.

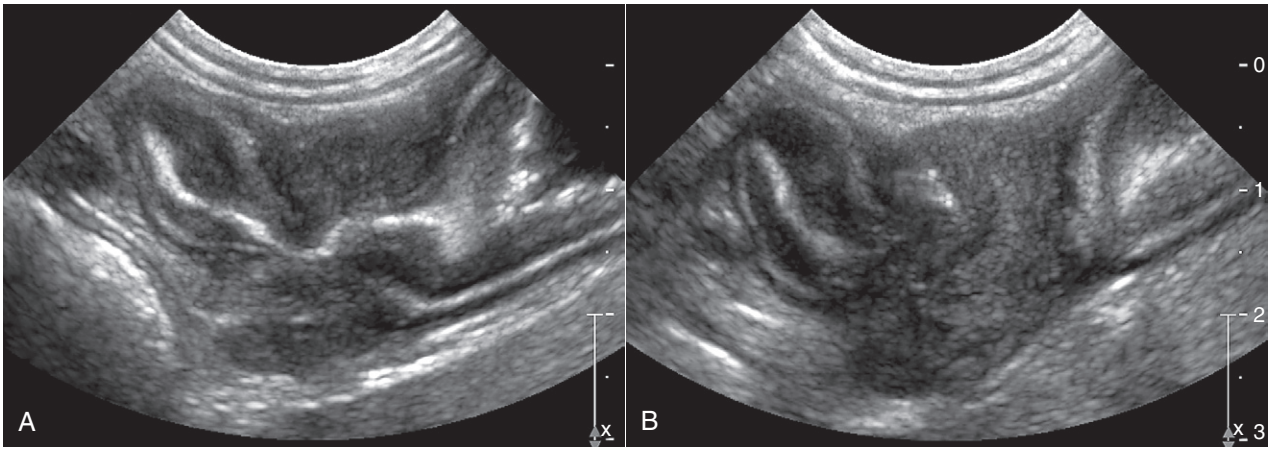


Fig. 44-28 Partial bowel obstruction from an extrinsic granuloma caused by *Cryptococcus neoformans* infection. The constricting tissue does not originate from the bowel wall but can be seen to focally encircle this loop. There is dilation of the orad segment on the right side of each image and normal empty lumen in the aborad side on the left side of each image.

the rent becomes constrictive or if the loop twists, effectively occluding its outflow.

Mesenteric volvulus results in occlusion of the cranial mesenteric artery. The reduced blood supply leads to ischemic necrosis, gastrointestinal toxin release, and shock.[45,46] The initiating event for volvulus typically is not known. The majority of dogs reported have been of larger breed size. Many dogs have no distant or immediate prior history of gastrointestinal signs and are presented for peracute or acute abdominal distention, abdominal pain, and shock. However, mesenteric volvulus has occurred subsequent to prior treatment for acute gastric dilatation with volvulus and for intussusception. A series of dogs with mesenteric volvulus had a previous clinical diagnosis of pancreatic insufficiency and clinical signs of vomiting.[47] The radiographic signs are moderate to severe dilation of the small intestine with fluid and gas (Fig. 44-29). Peritoneal effusion may be concurrent. A cat with jejunal thrombosis resulting in segmental bowel infarction had radiographic evidence of segmental bowel dilation and delayed gastric emptying and intestinal transit times. Sonographically, over the course of 72 hours, this bowel segment underwent progressive wall thickening, conversion to loss of wall layers, and finally a generalized hypoechoic wall. Perienteric hyperechoic mesenteric fat also developed.[48]

A syndrome of chronic intestinal pseudo-obstruction, defined as chronic dilation and dysmotility in the absence of mechanical obstruction, has been reported in nine dogs and one cat.[49-54] Diagnosis was based on full-thickness intestinal biopsy with histopathologic changes restricted to the tunica muscularis but apparently not involving the myenteric plexuses. In the majority, the tunica muscularis exhibited fibrosis and atrophy. Some dogs had cellular infiltrate in the



Fig. 44-29 Lateral radiograph of a dog with a jejunal volvulus. The extensive dilation of nearly all bowel segments is typical of jejunal volvulus. The metallic foreign body was incidental in this dog. A distal small bowel obstruction could cause this appearance, but more intraluminal fluid would be expected with a foreign body.



Fig. 44-30 There are bulges deforming the contour of a focal segment of small bowel. The loops entering and exiting the abnormal segment are easily seen. Differentials are neoplasia, granuloma, and abscess. Ultrasound imaging can further characterize the lesion and guide fine-needle aspirates and core biopsy.

muscle. One dog was suspected to have an immune-mediated etiology based on immunohistochemical staining features.[55] All dogs had progressive deterioration caused by emaciation from malabsorption; the cat had a successful outcome following resection of the visibly most affected segment and prokinetic medical therapy.

Dysautonomia is an autonomic nervous system disease that among other clinical signs can include vomiting, diarrhea, and inappetence. Radiographs of the abdomen are often characterized by focal or diffuse gastrointestinal dilation. Barium transit is delayed markedly. The most unique feature of these patients is their geographic origin, the first being reported from the United Kingdom. Additional patients have been reported in Europe and predominantly in Missouri and Kansas in the United States.[56-58]

The vaccination history (parvovirus), geographic region of origin (Missouri, Kansas, United Kingdom, and Europe) of a patient with concomitant signs of other autonomic nervous system dysfunction (dysautonomia), history of thromboembolic disease, and a thorough current history and physical examination are the most useful factors in ranking these causes of functional ileus as having a higher likelihood than the causes of mechanical obstruction.

Ultrasound features of proven parvovirus enteritis have been assessed in a cohort of puppies younger than 6 months of age.[59] A combination of nonspecific small bowel features suggest parvovirus as a diagnosis in puppies presented with suspicious clinical signs. Fifty percent or greater of the puppies exhibited fluid-filled small bowel; absent peristalsis; decreased duodenal and jejunal mucosal layer thickness despite normal total wall thickness; indistinct jejunal wall layers; hyperechoic jejunal mucosa; and jejunal lymph nodes within normal limits for age. Duodenal wall corrugation, hyperechoic duodenal mucosal layer, and irregular duodenal mucosal border were found less frequently. The bowel diameter in these puppies was not measured; however, puppies with intussusception were excluded, thus attributing the fluid distention and atony to nonobstructive ileus.

Infiltrative Bowel Disease

Infiltrative bowel disease broadly indicates generalized or segmental infiltration of the bowel wall as a result of nonseptic inflammation, infection, or neoplasia. The desired results of diagnostic images are to identify the presence of infiltrative disease and differentiate the underlying cause. With cellular infiltration into the wall layers, the anticipated effects are a change in wall thickness and alterations in the tissue character of individual layers. Secondarily, bowel motility may be altered, resulting in a change in bowel diameter. Bowel wall thickness cannot be determined reliably from survey radiographs but can be evaluated in ultrasound and barium studies, the former providing the most sensitive detection of thickening. Ultrasound is the only readily available imaging modality that can differentiate bowel wall layers. The utility of survey radiography is to exclude the presence of bowel masses that would be more suggestive of neoplasia or focal infection and to exclude obvious nonenteric organ changes that would direct further diagnostic tests away from the bowel.

Common neoplasms of the small intestine include adenocarcinoma, lymphosarcoma, mastocytoma, and leiomyosarcoma. Atypical tumors are osteosarcoma, fibrosarcoma, carcinoid, neurilemmoma, and hemangiosarcoma.[60-72] Benign adenomatous polyps of the duodenum have also been reported in cats, with an increased frequency noted among Asian breeds.[73] There are no unique survey radiographic findings for any of these tumors. They may create no changes, be seen as a soft tissue mass of variable size, or cause partial to complete obstruction resulting in bowel dilation signs. Accumulation of radiopaque foreign material may be seen as a consequence of partial obstruction. Identification of these bowel tumors is improved with either ultrasound or positive-contrast evaluation.

Masses associated with intestinal wall tumors typically cause smoothly rounded protrusions toward the lumen but may be evident as a mass deforming the serosal contour (Fig. 44-30). If the mural mass surrounds the lumen, the lumen often becomes enlarged and irregularly shaped (see Fig. 44-3). Distinguishing radiographically between a large emphysematous mural tumor and a bowel-associated abscess is not possible in most patients

Sonographically, intestinal neoplasia usually results in more extensive obliteration of the intestinal wall layering and greater wall thickness and is more likely to be focal than are inflammatory infiltrates.[11,74-81] In 150 dogs, loss of wall layer pattern was the most predictive feature for differentiating

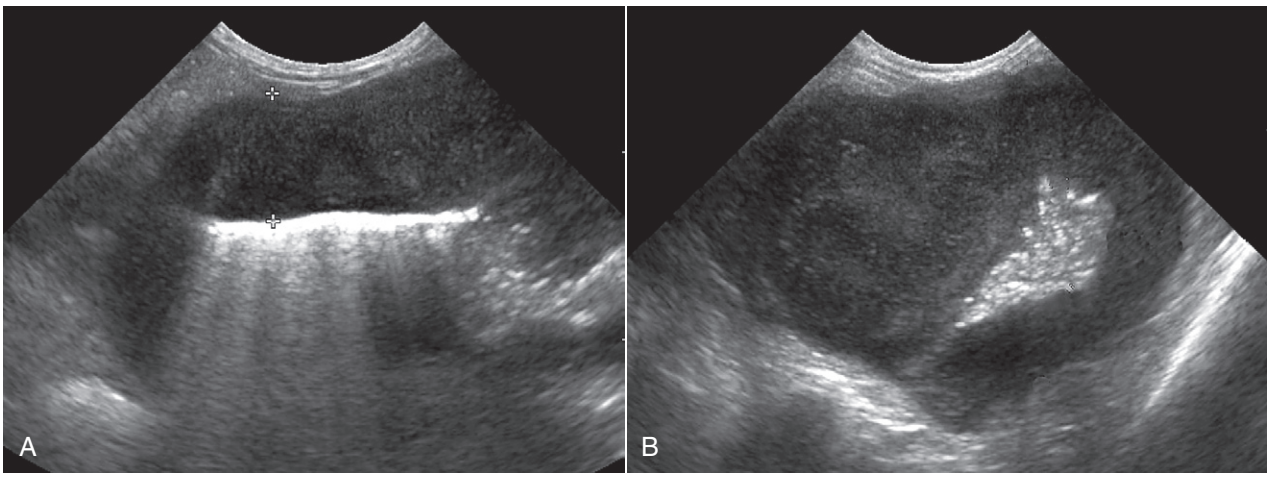


Fig. 44-31 Same cat as Figure 44-3. The abnormal bowel wall has transmural thickening and a loss of layer pattern. The lesion is circumferential but asymmetric, and the patent lumen is evident by gas and mucoid fluid. Although not pathognomonic, this is very characteristic of the mass form of feline alimentary lymphoma.

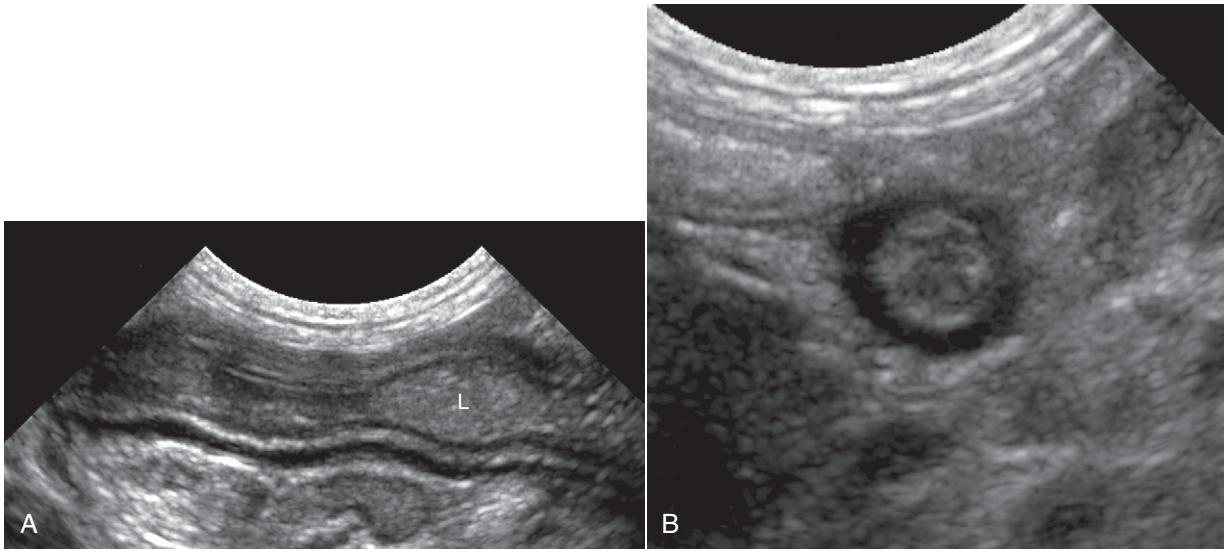


Fig. 44-32 Longitudinal section of the duodenum and transverse section of the ileum in a cat with muscular layer thickening associated with lymphoma. In the duodenum, the thickness of the muscular layer is best detected through the region where there is content in the lumen *(L)*. At necropsy, there was extension of neoplastic cells into the submucosa and muscularis and occasionally outside of the serosa into the adjacent mesentery.

between enteritis and neoplasia.[82] No ultrasonographic pattern is entirely specific for differentiating the type of small intestinal neoplasia.

Feline alimentary lymphoma is characterized by one of two patterns of intestinal change; a segmental mass or more diffuse thickening of the muscular layer. The mass form, found in 75% of cats with alimentary lymphosarcoma, is expressed as transmural circumferential thickening in the transverse plane (4 to 22 mm) with the wall layers replaced by hypoechoic or mixed echogenicity tissue (Fig. 44-31). Half of these cats have associated enlargement of the mesenteric lymph nodes.[83,84] Recognized more recently is the variation of feline lymphoma that has preserved wall layers but thickening of the muscular layer (Fig. 44-32). Thickening of the muscular layer is present when it is of equal or greater thickness than the mucosal layer. Thickening of the muscular layer in the cat has been attributed to compensatory hypertrophy in response to a distal obstruction and idiopathic hypertrophy in the absence of obstruction.[85,86] In an earlier report the idiopathic form was associated with chronic enteritis. Of 142 cats grouped as being normal or with full-thickness biopsy diagnosis of inflammatory bowel disease (IBD) or lymphoma, there was a significant correlation between a thickened muscular layer and lymphoma.[87] Only 1 of 24 cats with IBD had muscular layer thickening compared with 30 of 62 cats with lymphoma. However, 7 of 56 normal cats also had muscular layer thickening. Regional lymphadenopathy supported lymphoma but did not further discriminate between IBD and lymphoma. Cats with lymphoma were significantly older. This suggests that although not pathognomonic, the odds are greater for a diagnosis of intestinal lymphoma in older (>9 years) cats with muscular layer thickening.

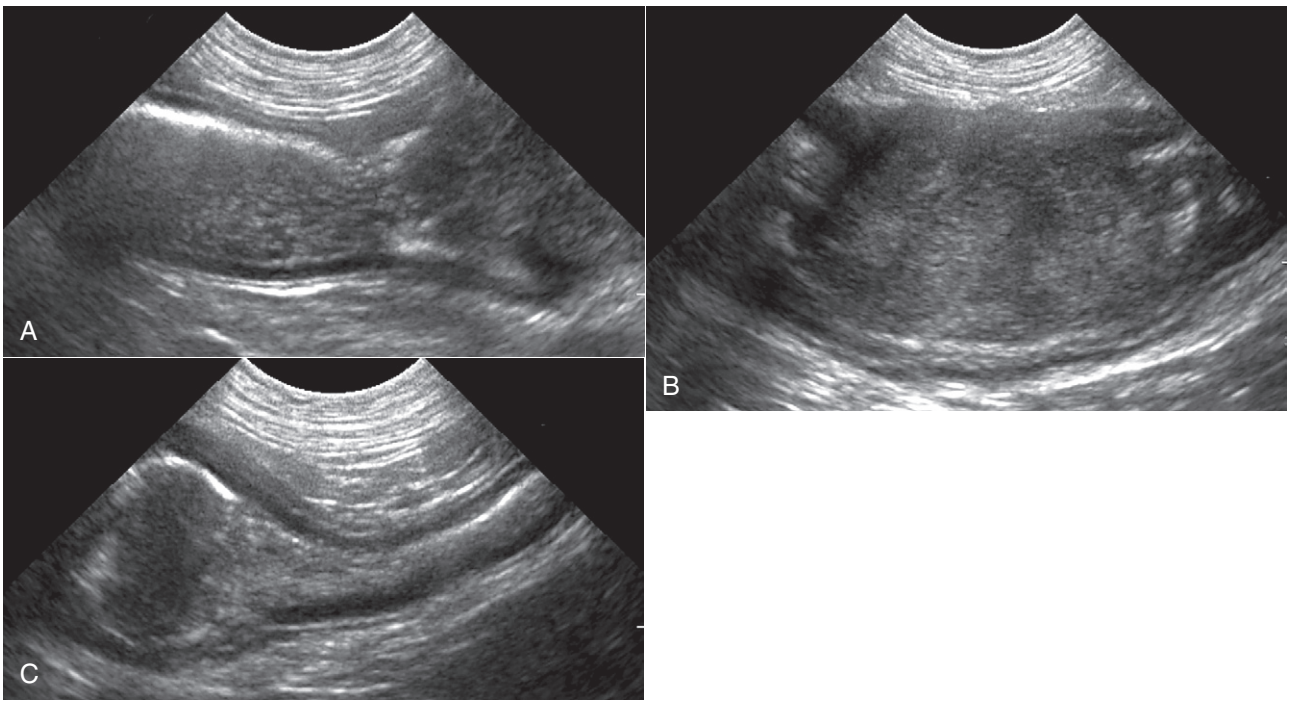


Fig. 44-33 Same dog as Figure 44-30. These images are in sequence through the length of affected bowel. **A** is orad to the mass, and there is mild dilation of the lumen filled with mucoid fluid. The mass is just evident to the right of the frame. **B** is at the level of the mass. The deep wall retains some evidence of wall layer pattern and the mass bulges into the lumen. **C** is aborad, and the bowel returns to normal. Histopathologic diagnosis was hemangiosarcoma.

Fewer sonographic characteristics have been described for specific intestinal neoplasms in the dog with the exception of leiomyosarcoma and leiomyoma.[79] Leiomyosarcoma tends to be a large (2 to 8 cm thick), eccentrically positioned mass with mixed echogenicity. The larger the mass, the more likely that areas of necrosis will appear as hypoechoic foci. The large size of many leiomyosarcomas can cause difficulty in determining whether they are of bowel origin. Other tumors of the canine small intestine are reported insufficiently to enable any conclusions about trends in their sonographic appearance (Fig. 44-33).[80] Ultrasound evaluation of the intestine combined with ultrasound-guided fine-needle aspiration and microcore biopsy is an accurate method of minimally invasive diagnosis (Fig. 44-34).[81]

Infectious enteritides may be caused by viruses or bacterial, rickettsial, or fungal organisms (Fig. 44-35). Parvovirus (canine parvovirus type 2)-induced radiographic changes have been discussed in a previous section with reference to a differential diagnosis for abnormal bowel dilation. When there is reasonable suspicion of parvoviral enteritis, it should be tested for before ultrasound or barium is used. Other viral diseases that infect the small intestinal tract do not cause any specific radiographic or sonographic changes and thus are not discussed here. Bacterial overgrowth in the small intestine has also not been related to specific radiographic or sonographic changes.

When neoplasia, infection, and food-responsive disease are excluded from the broad category of infiltrative bowel disease, the general term *idiopathic IBD* is used. In both the canine and the feline patient, *IBD* refers to a group of disorders of undetermined etiology that cause chronic (>3 weeks) vomiting and/or diarrhea and have various populations of inflammatory cells in the bowel wall layers.[88-91] The most common of these is a lymphocytic-plasmacytic enteritis. Some breed-associated forms of IBD have been described—immunoproliferative enteropathy of basenjis, familial protein-losing enteropathy and protein-losing nephropathy in soft-coated wheaten terriers, and gluten-sensitive enteropathy in Irish setters.[88] None of these breed-specific disorders has unique radiographic or ultrasonographic diagnostic findings. Survey radiographs are usually within normal limits. Because infiltrative bowel disease can be a diagnosis made by exclusion, the negative survey radiographic findings help exclude other diseases.

Inflammatory infiltrates are expected to increase bowel wall thickness or alter the character of the tissue. Bowel wall thickness has been insensitive to differentiating normal from affected dogs, although some dogs have mild thickening.[88-92] The finding of normal wall thickness may lead to a significant rate of false-negative diagnoses. Distinction of protein-losing enteropathy (PLE) from IBD and food-responsive disease is based on finding increased mucosal layer echogenicity in dogs with protein-losing enteropathy, because of varying severity of hyperechoic vertical striations in the duodenum and jejunum (Fig. 44-36). Histologically, the vertical striations are associated with lymphangiectasia.[89,93,94] Dogs with IBD and food-responsive disease can also have increased echogenicity in the mucosal layer described as hyperechoic speckles, being oriented in a horizontal or focal dot pattern compared to the striation pattern. Total bowel wall thickening is inconsistent in PLE and, when present, is mild. Secondary findings in dogs with PLE included peritoneal effusion, edema of the pancreas, and distended bowel segments; however, these findings can also be present in dogs with IBD. Dogs with food-responsive disease do not typically have these secondary findings. Intestinal biopsy remains the definitive diagnostic test for infiltrative bowel disease.

Bowel-Associated Masses

Bacterial abscesses can occur as focal lesions associated with the intestinal wall. A bowel-associated abscess can be a

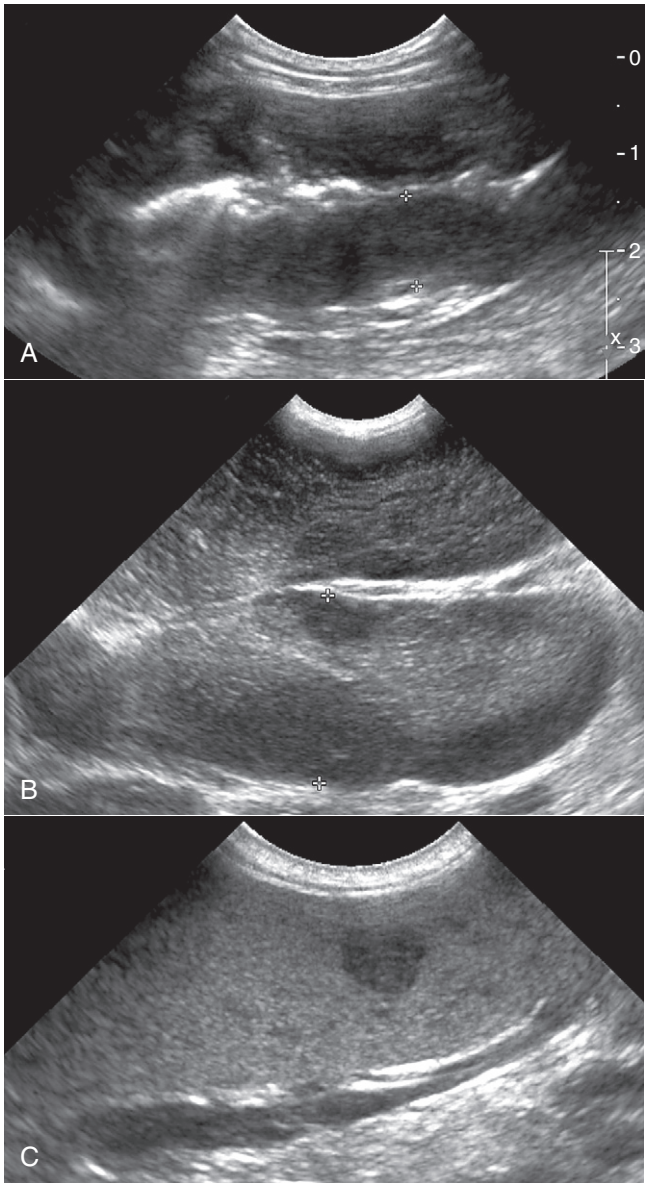


Fig. 44-34 Images of the small bowel **(A)**, mesenteric lymph node **(B)**, and spleen **(C)** in a dog with stage V lymphoma. Bowel wall layering is absent, and there is transmural thickening. The lymph node is markedly enlarged and predominantly hypoechoic. Other abdominal lymph nodes were also abnormal. The spleen exhibits multifocal hypoechoic foci.

consequence of partial or complete intestinal perforation by foreign material with subsequent adhesions and abscess formation. The mass may result in regional loss of serosal detail, or may displace adjacent bowel (Fig. 44-37). A mottled appearance may be seen in bowel-associated abscesses when exudate from the abscess drains into the lumen and is replaced by gas (see Fig. 44-37). Abscesses associated with the small intestine may originate from a source extrinsic to the wall. This may occur as a result of retained surgical sponges (gossypiboma) or be caused by a pancreatic abscess. For example, inflammation of the proximal duodenum as a result of pancreatitis can cause the duodenum to take on a fixed or rigid appearance demonstrated radiographically by mild gas dilation.[95] A left lateral view may help show this mild dilation. Sonographically, a corrugated mucosal and submucosal contour pattern has been observed to be associated with pancreatitis.[96] This corrugation may also be apparent in a barium

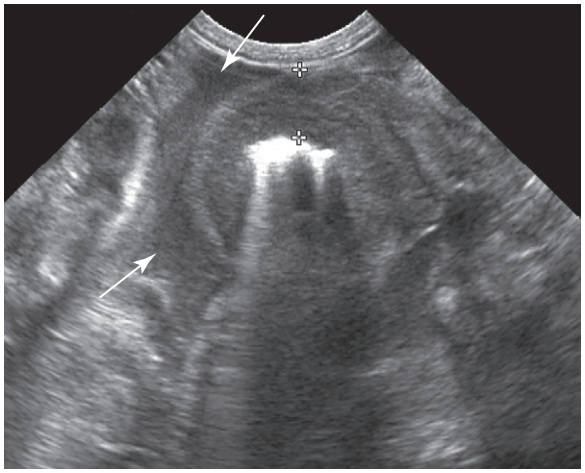


Fig. 44-35 Same dog as Figure 44-28 at the time of initial presentation. There is echogenic peritoneal fluid *(white arrows)*. A segment of jejunum was abnormal, characterized by transmural thickening (0.89 cm) with relative hyperechogenicity and no layering. Lymph nodes were enlarged. A diagnosis of *Cryptococcus neoformans* was made from mesenteric lymph node aspirates and confirmed when this segment of the jejunum was removed. Histopathologically, there were inflammatory cells and multiple granulomas with numerous yeasts in all layers.

study. However, this corrugated pattern is not specific to pancreatitis and can be seen with other causes of peritonitis as well as enteritis, neoplasia, and bowel wall ischemia.[27,96]

Although uncommon, mycotic infections of the intestinal tract include histoplasmosis, cryptococcosis,[97] and pythiosis. Pythiosis, an opportunistic water-borne fungus, has been diagnosed in dogs in Oklahoma (including the northern region) in addition to its more common endemic locale in the states along the Gulf Coast.[98,99] Pathologic changes are often advanced by the time of clinical presentation. Pyogranulomatous lesions cause localized thickening of the intestinal wall that frequently extends through the serosa, along the mesentery, and into the mesenteric lymph nodes. This combination results in a palpable abdominal mass. Ultrasound features in dogs with pythiosis include thickening of the intestinal wall associated with loss of the layer pattern.[100] The sonographic features are similar to those of intestinal neoplasia. Histologic examination of tissue is required for diagnosis.

Miscellaneous Small Intestinal Diseases

Opacity changes in the intestinal wall are rare. Diffuse mineralization of the wall can occur by metastatic calcification as a result of hypercalcemia. Dogs and cats poisoned by cholecalciferol-based rodenticides and having ingested human antipsoriasis ointment containing calcitriol analogues can develop vomiting, which may prompt radiography and/or ultrasonography of the abdomen.[101-104] Diffuse calcification of the gastrointestinal tract may be found in these patients. Radiographically, the degree of calcification typically creates a thin line of opacity, imparting an enhanced contrast effect. Differential diagnosis for this type of diffuse mineralization should include other causes of hypercalcemia, including severe primary renal disease.

Pneumatosis intestinalis and pneumatosis coli both refer to the presence of air in the intestinal wall.[105] Numerous underlying causes can lead to this gas accumulation, including necrotizing enterocolitis, ischemic necrosis caused by volvulus, trauma, and bacterial origin in immunocompromised patients. Pneumatosis intestinalis has not been reported in small animals; however, two instances of pneumatosis coli have been reported.[106,107]

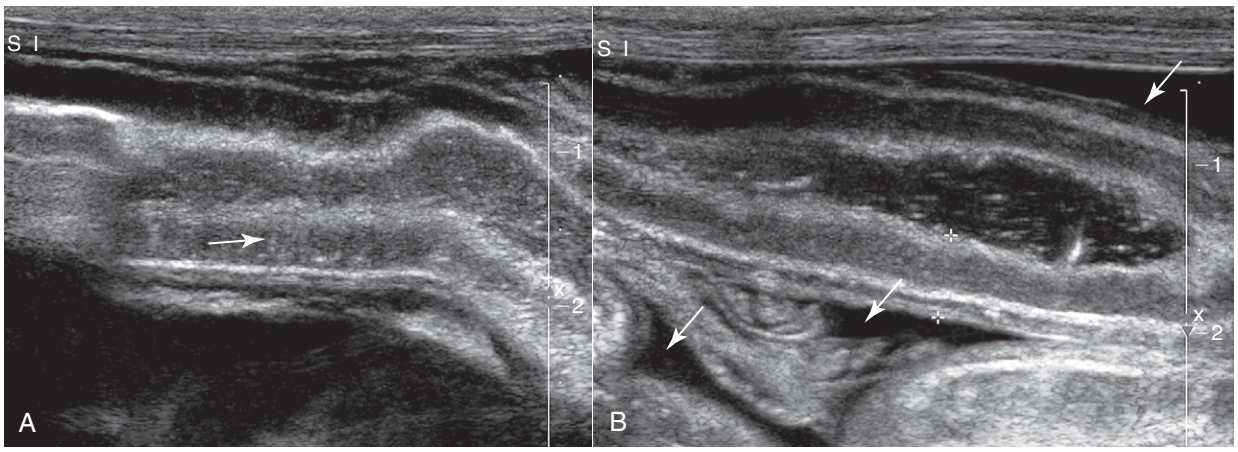


Fig. 44-36 Increased echogenicity of the mucosal layer and vertically oriented hyperechoic *(white arrow)* streaks are consistent with dilated lacteals in a patient with protein-losing enteropathy. In the right image, another patient with anechoic peritoneal fluid *(white arrows)* has a hyperechoic mucosal layer but with less evident streaking pattern. Biopsy would be needed for confirmation and identification of additional histologic abnormalities.

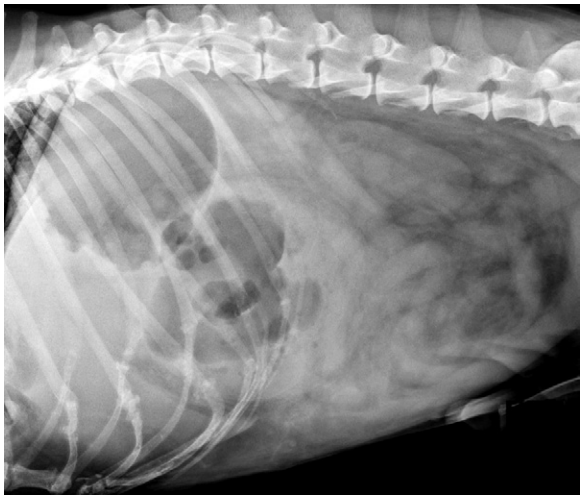


Fig. 44-37 Lateral radiograph of a dog with a large emphysematous mass caused by a jejunal abscess. The intraluminal gas arises when liquid contents of the mass drain into the bowel and the resulting cavity is filled with bowel gas. There is also a loss of serosal detail around the mass. A jejunal tumor could have this appearance also.

REFERENCES

1. Armbrust LJ, Biller DS, Hoskinson JJ: Case examples demonstrating the clinical utility of obtaining both right and left lateral abdominal radiographs in small animals, *J Am Anim Hosp Assoc* 36:531, 2000.
2. Armbrust LJ, Biller DS, Hoskinson JJ: Compression radiography: an old technique revisited, *J Am Anim Hosp Assoc* 36:537, 2000.
3. Root CR: Interpretation of abdominal survey radiographs, *Vet Clin North Am* 4:763, 1974.
4. Owens JM, Biery DN: *Radiographic interpretation for the small animal clinician*, ed 2, Baltimore, 1999, Williams & Wilkins.
5. Graham JP, Lord PF, Harrison JM: Quantitative estimation of intestinal dilation as a predictor of obstruction in the dog, *J Small Anim Pract* 39:521, 1998.
6. Morgan JP: The upper gastrointestinal examination in the cat: normal radiographic appearance using positive-contrast medium, *Vet Radiol* 22:159, 1981.
7. Riedesel EA: Unpublished data, 1996.
8. Adams WM, Sisterman LA, et al: Association of intestinal disorders in cats with findings of abdominal radiography, *J Am Vet Med Assoc* 236:880, 2010.
9. O'Brien TR: Small intestine. In O'Brien TR, editor: *Radiographic diagnosis of abdominal disorders in the dog and cat*, Philadelphia, 1978, Saunders, pp 279–352.
10. Hall JA, Watrous BA: Effect of pharmaceuticals on radiographic appearance of selected examinations of the abdomen and thorax, *Vet Clin North Am Small Anim Pract* 30:349, 2000.
11. Weichselbaum RC, Feeney DA, Hayden DW: Comparison of upper gastrointestinal radiographic findings to histopathologic observations: a retrospective study of 41 dogs and cats with suspected small bowel infiltrative disease, *Vet Radiol Ultrasound* 35:418, 1994.
12. Lamb CR: Recent developments in diagnostic imaging of the gastrointestinal tract of the dog and cat, *Vet Clin North Am Small Anim Pract* 29:307, 1999.
13. Rault DN, Besso JG, Boulouha L, et al: Significance of a common extended mucosal interface observed in transverse small intestine sonograms, *Vet Radiol Ultrasound* 45:177, 2004.
14. Delaney F, O'Brien RT, Waller K: Ultrasound evaluation of small bowel thickness compared to weight in normal dogs, *Vet Radiol Ultrasound* 44:577, 2003.
15. Goggin JM, Biller DS, Debey BM, et al: Ultrasonographic measurement of gastrointestinal wall thickness and the ultrasonographic appearance of the ileocolic region in healthy cats, *J Am Anim Hosp Assoc* 36:224, 2000.
16. Stander N, Wagner WM: Normal canine pediatric gastrointestinal ultrasonography, *Vet Radiol Ultrasound* 51:75, 2010.
17. Etue SM, Pennick DG, Labatto MA, et al: Ultrasonography of the normal feline pancreas and associated anatomic landmarks: a prospective study of 20 cats, *Vet Radiol Ultrasound* 42:330, 2001.
18. An Y, Lee H, Chang D, et al: Application of pulsed Doppler ultrasound for the evaluation of small intestinal motility in dogs, *J Vet Sci* 1:71, 2001.
19. Pugh CR: Ultrasonographic examination of the abdominal lymph nodes in the dog, *Vet Radiol Ultrasound* 35:110, 1994.
20. Schreurs E, Vermote K, et al: Ultrasonographic anatomy of the abdominal lymph nodes in the normal cat, *Vet Radiol Ultrasound* 49:68, 2008.

21. Riedesel EA: Small bowel. In Thrall DE, editor: *Textbook of veterinary diagnostic radiology*, ed 5, St. Louis, 2007, Elsevier-Saunders.
22. Gomez JA: The gastrointestinal contrast study, *Vet Clin North Am* 4:805, 1974.
23. Smelstoys JA, Davis GJ, Learn AE, et al: Outcome of and prognostic indicators for dogs and cats with pneumoperitoneum and no history of penetration trauma: 54 cases (1988–2002), *J Am Vet Med Assoc* 225:251, 2004.
24. Foley MJ, Ghahremani GG, Rogers LF: Reappraisal of contrast media used to detect upper gastrointestinal perforations, *Radiology* 144:231, 1982.
25. Seltzer SE, Jones B, McLaughlin GC: Proper choice of contrast agents in emergency gastrointestinal radiology, *Crit Rev Diagn Imaging* 12:79, 1979.
26. Renschler J, Tarigo J: What is your diagnosis? Particulate material in peritoneal fluid from a dog, *Vet Clin Pathol* 37:129, 2008.
27. Boysen SF, Tidwell AS, Pennick DG: Ultrasonographic findings in dogs and cats with gastrointestinal perforation, *Vet Radiol Ultrasound* 44:556, 2003.
28. Allan GS, Rendano VT, Quick CB, et al: Gastrografin as a gastrointestinal contrast medium in the cat, *Vet Radiol* 20:3, 1979.
29. Robertson ID, Burbridge HM: Pros and cons of barium-impregnated polyethylene spheres in gastrointestinal disease, *Vet Clin North Am Small Anim Pract* 30:449, 2000.
30. Luttgen PJ, Whitney MS, Wolf AM, et al: Heinz body hemolytic anemia associated with high plasma zinc concentration in a dog, *J Am Vet Med Assoc* 197:1347, 1990.
31. Lamb DR, Hansson K: Radiological identification on nonopaque intestinal foreign bodies, *Vet Radiol Ultrasound* 35:87, 1994.
32. Tidwell AS, Penninck DG: Ultrasonography of gastrointestinal foreign bodies, *Vet Radiol Ultrasound* 33:160, 1992.
33. Sharma A, Thompson MS, et al: Comparison of radiography and ultrasonography for diagnosing small-intestinal mechanical obstruction in vomiting dogs, *Vet Radiol Ultrasound* 52:248, 2011.
34. Evans KL, Smeak DD, Biller DS: Gastrointestinal linear foreign bodies in 32 dogs: a retrospective evaluation and feline comparison, *J Am Anim Hosp Assoc* 30:445, 1994.
35. Felts JF, Fox PR, Burk RL: Thread and sewing needles as gastrointestinal foreign bodies in the cat: a review of 64 cases, *J Am Vet Med Assoc* 184:56, 1984.
36. Hoffmann, KL: Sonographic signs of gastroduodenal linear foreign body in 3 dogs, *Vet Radiol Ultrasound* 44:466, 2003.
37. Lewis DD, Ellison GW: Intussusception in dogs and cats, *Compend Contin Educ Pract Vet* 9:523, 1987.
38. Burkitt JM, Drobatz KJ, et al: Signalment, history, and outcome of cats with gastrointestinal tract intussusception: 20 cases (1986–2000), *J Am Vet Med Assoc* 234:771, 2009.
39. Penninck DG, Nyland TG, Kerr LY, et al: Ultrasonographic evaluation of gastrointestinal diseases in small animals, *Vet Radiol* 31:134, 1990.
40. Lamb CR, Mantis P: Ultrasonographic features of intestinal intussusception in 10 dogs, *J Small Anim Pract* 39:437, 1998.
41. Patsikas MN, Jakovljevic S, Moustardas, et al: Ultrasonographic signs of intestinal intussusception associated with acute enteritis or gastroenteritis in 19 young dogs, *J Am Anim Hosp Assoc* 39:57, 2003.
42. Patsikas MN, Papazoglou LG, et al: Normal and abnormal ultrasonographic findings that mimic small intestinal intussusception in the dog, *J Am Anim Hosp Assoc* 40:147, 2004.
43. Patsikas MN, Papazoglou LG, et al: Color Doppler ultrasonography in prediction of the reducibility of intussuscepted bowel in 15 young dogs. *Vet Radiol Ultrasound* 46:313, 2005.
44. Farrow CS: Radiographic appearance of canine parvovirus enteritis, *J Am Vet Med Assoc* 180:43, 1982.
45. Nemzek JA, Walshaw R, Hauptman JG: Mesenteric volvulus in the dog: a retrospective study, *J Am Anim Hosp Assoc* 29:357, 1993.
46. Junius G, Appeldoorn AM, Schrauwen E: Mesenteric volvulus in the dog: a retrospective study of 12 cases, *J Small Anim Pract* 45:104, 2004.
47. Westermarck E, Rinaila-Parnanen E: Mesenteric torsion in dogs with chronic pancreatic insufficiency: 21 cases (1978–1987), *J Am Vet Med Assoc* 195:1404, 1989.
48. Wallack ST, Hornof WJ, Herrgesell EJ: Ultrasonographic diagnosis-small bowel infarction in a cat, *Vet Radiol Ultrasound* 44:81, 2003.
49. Arrick RH, Kleine LJ: Intestinal pseudoobstruction in a dog, *J Am Vet Med Assoc* 172:1201, 1978.
50. Moore R, Carpenter J: Intestinal sclerosis with pseudoobstruction in three dogs, *J Am Vet Med Assoc* 184:830, 1984.
51. Lamb WA, France MP: Chronic intestinal pseudoobstruction in a dog, *Aust Vet J* 71:84, 1994.
52. Harvey AM, Hall EJ, et al: Chronic intestinal pseudoobstruction in a cat caused by visceral myopathy, *J Vet Intern Med* 19:111, 2005.
53. Couraud L, Jermyn K, et al: Intestinal pseudo-obstruction, lymphocytic leiomyositis and atrophy of the muscularis externa in a dog, *Vet Rec* 159:86, 2006.
54. Johnson CS, Fales-Williams AJ, et al: Fibrosing gastrointestinal leiomyositis as a cause of chronic intestinal pseudo-obstruction in an 8-month old dog, *Vet Pathol* 44:106, 2007.
55. Eastwood JM, McInnes EF, White RN, et al: Cecal impaction and chronic intestinal pseudo-obstruction in dog, *J Vet Med Ser A* 52:43, 2005.
56. Longshore RC, O'Brien DP, Johnson GC, et al: Dysautonomia in dogs: a retrospective study, *J Vet Intern Med* 10:103, 1996.
57. Detweiler DA, Biller DS, Hoskinson JJ, et al: Radiographic findings of canine dysautonomia in twenty-four dogs, *Vet Radiol Ultrasound* 42:108, 2001.
58. O'Brien DP, Johnson GC: Dysautonomia and autonomic neuropathies, *Vet Clin North Am Small Anim Pract* 32:251, 2002.
59. Stander N, Wagner WM, et al: Ultrasonographic appearance of canine parvoviral enteritis in puppies, *Vet Radiol Ultrasound* 51:69, 2010.
60. Brodey RS: Alimentary tract neoplasms in the cat: a clinicopathologic survey of 46 cases, *Am J Vet Res* 27:74, 1966.
61. Patniak AK, Liu S-K, Jonhson GF: Feline intestinal adenocarcinoma, *Vet Pathol* 13:1, 1976.
62. Patniak AK, Hurvitz AI, Johnson GF: Canine gastrointestinal neoplasms, *Vet Pathol* 14:547, 1977.
63. Patniak AK, Hurvitz AI, Johnson GF: Canine intestinal adenocarcinoma and carcinoid, *Vet Pathol* 17:149, 1980.
64. Feeney DA, Klausner JS, Johnston GR: Chronic bowel obstruction caused by primary intestinal neoplasia: a report of five cases, *J Am Anim Hosp Assoc* 18:67, 1982.
65. Gibbs C, Pearson H: Localized tumors of the canine small intestine: a report of twenty cases, *J Small Anim Pract* 27:506, 1986.

66. Bruecker KA, Withrow SJ: Intestinal leiomyosarcomas in six dogs, *J Am Anim Hosp Assoc* 24:281, 1988.
67. Kosovsky JE, Matthiesen DT, Patnaik AK: Small intestinal adenocarcinoma in cats: 32 cases (1978–1985), *J Am Vet Med Assoc* 192:233, 1988.
68. Couto CG, Rutgers HC, Sherding RG, et al: Gastrointestinal lymphoma in 20 dogs, *J Vet Intern Med* 3:73, 1989.
69. Pardo AD, Adams WH, McCracken MD, et al: Primary jejunal osteosarcoma associated with a surgical sponge in a dog, *J Am Vet Med Assoc* 196:935, 1990.
70. Bortnowski HB, Rosenthal RC: Gastrointestinal mast cell tumors and eosinophilia in two cats, *J Am Anim Hosp Assoc* 28:271, 1992.
71. Crawshaw J, Berg J, Sardinas JC, et al: Prognosis for dogs with nonlymphomatous, small intestinal tumors treated by surgical excision, *J Am Anim Hosp Assoc* 34:451, 1998.
72. Takahashi T, Kadosawa T, Nagase M, et al: Visceral mast cell tumors in dogs: 10 cases (1982–1997), *J Am Vet Med Assoc* 216:222, 2000.
73. MacDonald JM, Mullen HS, Moroff SD: Adenomatous polyps of the duodenum in cats: 18 cases (1985–1990), *J Am Vet Med Assoc* 202:647, 1993.
74. Hayden DW, Van Kruiningen HJ: Lymphocytic-plasmacytic enteritis in German shepherd dogs, *J Am Anim Hosp Assoc* 18:89, 1982.
75. Vest B, Margulis AR: Experimental infarction of small bowel in dogs, *AJR Am J Roentgenol* 92:1080, 1964.
76. Hendirk M: A spectrum of hypereosinophilic syndromes exemplified by six cats with eosinophilic enteritis, *Vet Pathol* 18:1888, 1981.
77. Tams TR: Chronic feline inflammatory bowel disorders: II. Feline eosinophilic enteritis and lymphosarcoma, *Compend Contin Educ Vet Pract* 8:464, 1986.
78. Rivers BJ, Walter PA, Feeney DA, et al: Ultrasonographic features of intestinal adenocarcinoma in five cats, *Vet Radiol Ultrasound* 38:300, 1997.
79. Myers NC, Penninck DG: Ultrasonographic diagnosis of gastrointestinal smooth muscle tumors in the dog, *Vet Radiol Ultrasound* 35:391, 1994.
80. Paoloni MC, Pennick DG, Moore AS: Ultrasonographic and clinicopathologic findings in 21 dogs with intestinal adenocarcinoma, *Vet Radiol Ultrasound* 43:562, 2002.
81. Crystal MA, Penninck DG, Matz ME, et al: Use of ultrasound-guided fine-needle aspiration biopsy and automated core biopsy for the diagnosis for gastrointestinal disease in small animals, *Vet Radiol Ultrasound* 34:438, 1993.
82. Penninck D, Smyers B, Webster CRL, et al: Diagnostic value of ultrasonography in differentiating enteritis from intestinal neoplasia in dogs, *Vet Radiol Ultrasound* 44:570, 2003.
83. Grooters AM, Biller DS, Ward H, et al: Ultrasonographic appearance of feline alimentary lymphoma, *Vet Radiol Ultrasound* 35:468, 1994.
84. Penninck DG, Moore AS, Tidwell AS, et al: Ultrasonography of alimentary lymphosarcoma in the cat, *Vet Radiol Ultrasound* 35:299, 1994.
85. Bettini G, Maracchini M, et al: Hypertrophy of intestinal smooth muscle in cats, *Res Vet Sci* 75:43, 2003.
86. Diana A, Pietra M, Guglielmini C, et al: Ultrasonographic and pathologic features of intestinal smooth muscle hypertrophy in four cats, *Vet Radiol Ultrasound* 44:566, 2003.
87. Zwingenberger AL, Marks SL, et al: Ultrasonographic evaluation of the muscularis propria in cats with diffuse small intestinal lymphoma or inflammatory bowel disease, *J Vet Intern Med* 24:289, 2010.
88. German AJ, Hall EJ, Day MJ: Chronic intestinal inflammation and intestinal disease in dogs, *J Vet Intern Med* 17:8, 2003.
89. Gaschen L, Kircher P, et al: Comparison of ultrasonographic findings with clinical activity index (CIBDAI) and diagnosis in dogs with chronic enteropathies, *Vet Radiol Ultrasound* 49:56, 2008.
90. Trepanier L: Idiopathic inflammatory bowel disease in cats—rational treatment selection, *J Fel Med Surg* 11:32, 2009.
91. Washabau RJ: 2005 *Report from WSAVA gastrointestinal standardization group*. Available from http://www.wsava.org/GIStandards1.htm.
92. Rudorf H, van Schaik G, O'Brien RT, et al: Ultrasonographic evaluation of the thickness of the small intestinal wall in dogs with inflammatory bowel disease, *J Small Anim Pract* 46:322, 2005.
93. Kull PA, Hess RS, Craig LE, et al: Clinical, clinicopathologic, radiographic and ultrasonographic characteristics of intestinal lymphangiectasia in dogs: 17 cases (1996–1998), *J Am Vet Med Assoc* 219:197, 2001.
94. Sutherland-Smith J, Penninck DG, et al: Ultrasonographic intestinal hyperechoic mucosal striations in dogs and associated lacteal dilation, *Vet Radiol Ultrasound* 48:51, 2007.
95. O'Brien TR: Liver, spleen and pancreas. In O'Brien TR, editor: *Radiographic diagnosis of abdominal disorders in the dog and cat*, Philadelphia, 1978, Saunders, pp 460–480.
96. Moon ML, Billar DS, Armbrust LJ: Ultrasonographic appearance and etiology of corrugated small intestine, *Vet Radiol Ultrasound* 44:199, 2003.
97. Malik R, Hunt GB, Bellenger CR, et al: Intra-abdominal cryptococcosis in two dogs, *J Small Anim Pract* 40:387, 1999.
98. Helman RG, Oliver J III: Pythiosis of the digestive tract in dogs from Oklahoma, *J Am Anim Hosp Assoc* 35:111, 1999.
99. Miller RI: Gastrointestinal phycomycosis, *J Am Vet Med Assoc* 186:473, 1985.
100. Graham JP, Newell SM, Roberts GD, et al: Ultrasonographic features of canine gastrointestinal pythiosis, *Vet Radiol Ultrasound* 41:273, 2000.
101. Gunther R, Felice LJ, Nelson RK, et al: Toxicity of a vitamin D_3 rodenticide to dogs, *J Am Vet Med Assoc* 193:211, 1988.
102. Morita T, Awakura T, Shimada A, et al: Vitamin D toxicosis in cats: natural outbreak and experimental study, *J Vet Med Sci* 57:831, 1995.
103. Fan TM, Simpson KW, Trasti S, et al: Calcipotriol toxicity in a dog, *J Small Anim Pract* 39:581, 1998.
104. Hare WR, Dobbs CE, Slaymen SA, et al: Calcipotriene poisoning in dogs, *Vet Med* 95:770, 2000.
105. Pear BL: Pneumatosis intestinalis: a review, *Radiology* 207:13, 1998.
106. Anderson GR, Geary JC: Pneumatosis coli (interstitial emphysema of colon): a case report, *J Am Anim Hosp Assoc* 9:352, 1973.
107. Morris EL: Pneumatosis coli in a dog, *Vet Radiol Ultrasound* 33:154, 1992.

ELECTRONIC RESOURCES

evolve

Additional information related to the content in Chapter 44 can be found on the companion Evolve website at http://evolve.elsevier.com/Thrall/vetrad/

- Chapter Quiz

CHAPTER • 45
The Large Bowel

Tobias Schwarz

IMAGING OPTIONS FOR LARGE BOWEL DISEASE

Both survey and contrast radiographic procedures can be used to assess the colon.[1-3] Now, however, endoscopy has largely replaced radiographic contrast studies of the colon with the additional advantage of obtaining aspirates and biopsies if needed.[4]

Ultrasound is a sensitive and practical modality that is less time consuming than most radiographic contrast studies of the colon. It also provides information complementary to endoscopic and survey radiographic findings.[5] Although air and feces in the bowel limit the usefulness of colon sonography, near-field bowel wall thickness and symmetry, mural and extramural bowel masses, regional lymph nodes, and intussusceptions can be assessed. Transabdominal cytologic sampling of colon masses can also be obtained with ultrasound-guided techniques.[6,7]

Less commonly used techniques for examining the colon include rectocolonic lymphangiography, mesenteric angiography, and colonic transit scintigraphy. These techniques enable assessment of anatomic or functional abnormalities but require specialized equipment and expertise.[8-10] Computed tomography (CT) is an excellent modality to assess the pericolonic and perirectal areas, particularly for the pelvic canal.[11]

NORMAL RADIOGRAPHIC ANATOMY

The large bowel of the dog and cat is composed of the cecum, colon, rectum, and anal canal (Fig. 45-1). The cecum, a diverticulum of the proximal colon, has different anatomic and radiographic appearances in the dog and the cat (Fig. 45-2).[1] The canine cecum appears semicircular and compartmentalized and normally contains some intraluminal gas. The cecum joins the colon through a cecocolic junction. The intraluminal gas and characteristic shape enable recognition of the cecum in the right midabdomen on most survey radiographs. The feline cecum is usually not visible on survey radiographs. It is a short, conelike diverticulum of the colon with no distinct

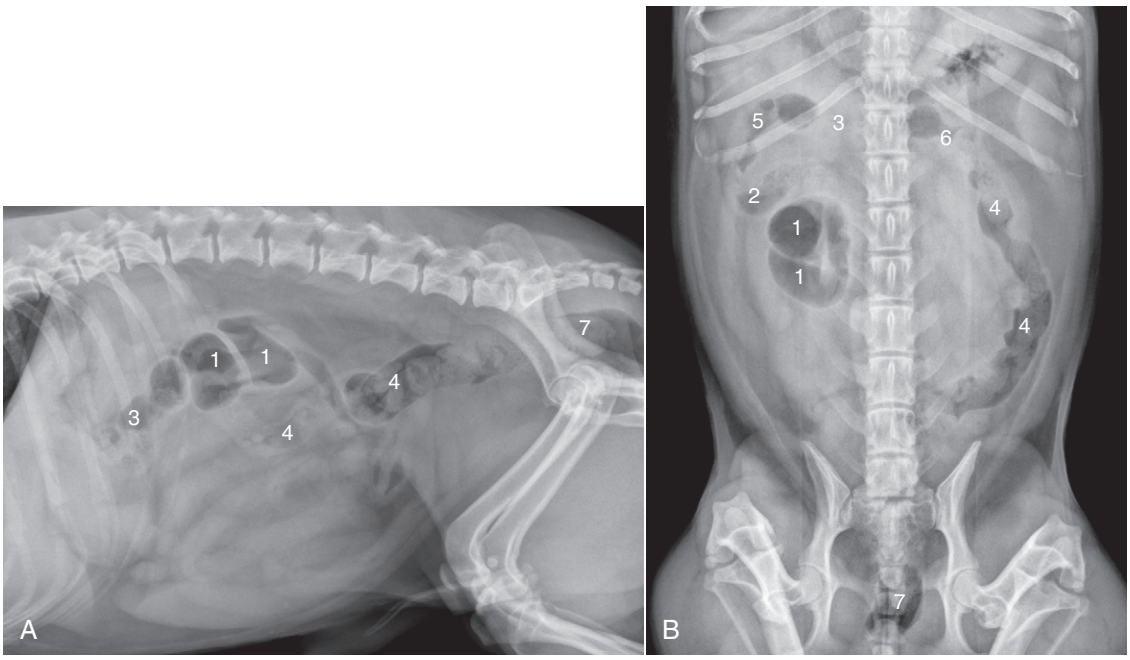


Fig. 45-1 Survey lateral **(A)** and ventrodorsal **(B)** radiographs of a normal canine abdomen. The large bowel is divided into the cecum *(1)*, ascending colon *(2)*, transverse colon *(3)*, descending colon *(4)*, right colic flexure *(5)*, left colic flexure *(6)*, rectum *(7)*, and anal canal. Note the admixture of gas and feces in the cecum, colon, and rectum.

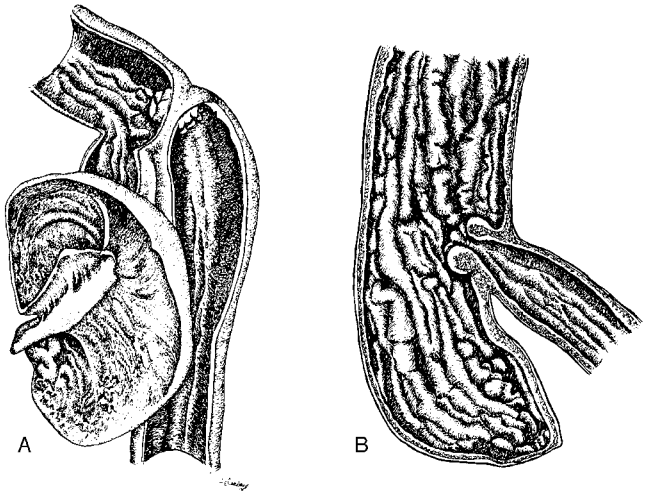


Fig. 45-2 The cecum of the dog **(A)** and cat **(B)** are anatomically and radiographically different. The canine cecum is semicircular and compartmentalized and normally contains some gas. The feline cecum is a short, conelike structure with no compartmentalization, and it rarely contains adequate gas or feces to be visualized radiographically. (Reprinted from O'Brien TR: *Radiographic diagnosis of abdominal disorders in the dog and cat*, Davis, Calif, 1981, Covell Park Veterinary.)

cecocolic junction and no compartmentalization. The feline cecum rarely contains gas or feces.

The colon of the dog and the cat is a thin-walled distensible tube that is divided into ascending, transverse, and descending parts. These divisions are recognized easily on survey radiographs based on shape, size, and location. The distal ileum enters the ascending colon from a medial direction by way of the ileocolic sphincter. This circular sphincter is not visible on survey radiographs, but it can be identified as a filling defect when barium is present in the colon adjacent to the sphincter.

The shape of the colon is similar to that of a question mark or a shepherd's crook (see Fig. 45-1). The junction between the ascending and transverse colon is the right colic flexure, and the junction between the transverse and descending colon is the left colic flexure. The ascending colon and right colic flexure are to the right of midline. The transverse colon passes from right to left cranial to the root of the mesentery. The left colic flexure and proximal descending colon are to the left of midline. The distal descending colon courses to the midline and enters the pelvic canal to become the rectum. The rectum is the terminal portion of the colon, beginning at the pelvic inlet and ending at the anal canal.

An understanding of the anatomic relation of the large bowel to other viscera is important for the radiographic recognition of diseases of the large bowel and adjacent organs (Fig. 45-3).

- The ascending colon lies adjacent to the descending duodenum, right lobe of the pancreas, right kidney, mesentery, and small bowel.
- The transverse colon lies adjacent to the greater curvature of the stomach, left lobe of the pancreas, liver, small intestine, and root of the mesentery.
- The proximal descending colon lies in close proximity to the left kidney and ureter, spleen, and small bowel. The right ureter travels directly adjacent to the colon wall in the mesocolon toward the bladder neck.

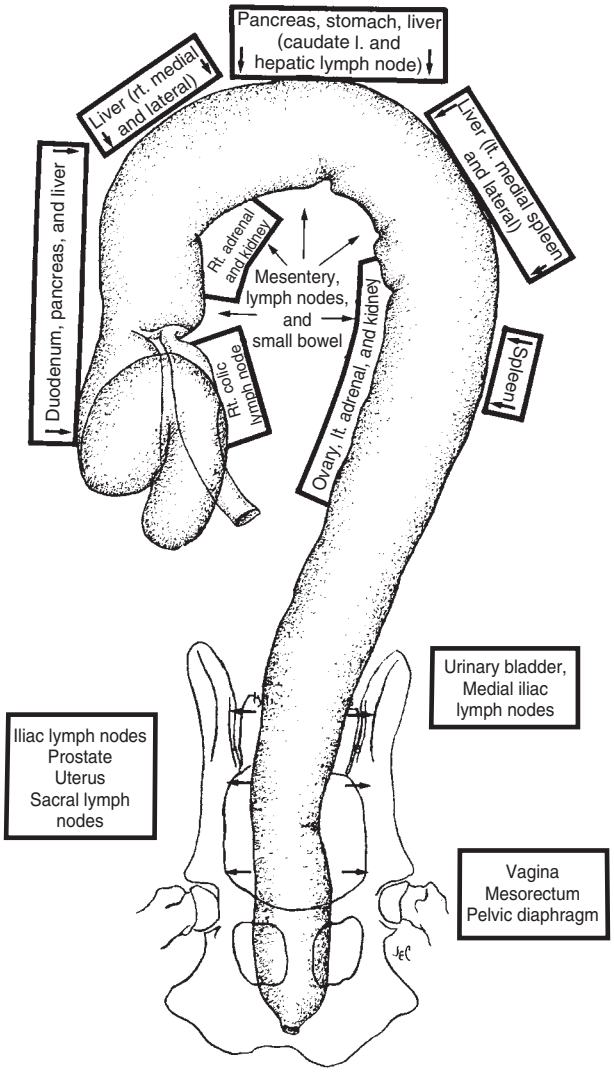


Fig. 45-3 Viscera adjacent to the large bowel may cause a change in position of a portion of the colon. This change in position may be indicative of disease or a variant of normal, depending on the cause of the deviation (e.g., enlarged bladder versus enlarged medial iliac lymph nodes). *Arrows*, Usual direction of large bowel position displacement when an organ enlarges (also see Fig. 45-10). (Reprinted from O'Brien TR: *Radiographic diagnosis of abdominal disorders in the dog and cat*, Davis, CA, 1981, Covell Park Veterinary.)

- The midportion of the descending colon lies adjacent to the small bowel, urinary bladder, and uterus. Because it is less fixed, the midportion of the descending colon has a variety of normal positions in the caudal left abdomen. In some dogs, the descending colon is positioned along or slightly right to the median axis of the body. Such normal variations are caused by various amounts of ingesta within the bowel, intraabdominal fat, and urinary bladder distention (Fig. 45-4). Some dogs appear to have an excess of length of colon. This finding, called *redundant colon*, is a variant of normal and is not clinically significant.[1,3,12]
- The distal portions of the descending colon and rectum are also closely associated with the urethra, the medial iliac, hypogastric and sacral lymph nodes, the prostate or uterus and vagina, and the pelvic diaphragm.

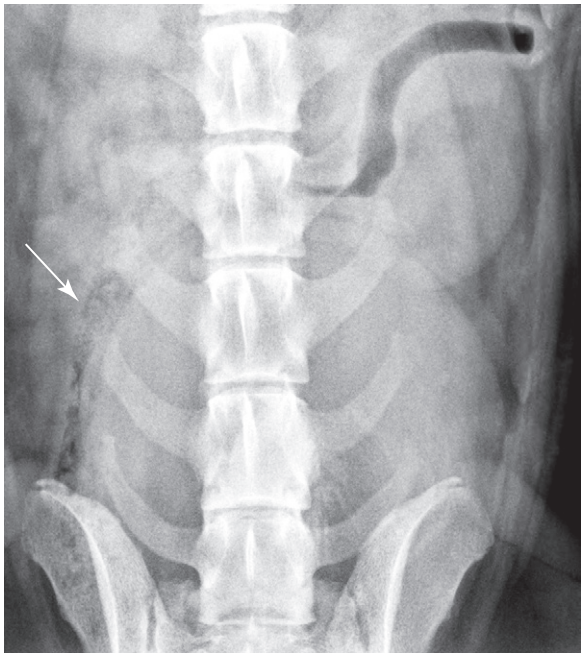


Fig. 45-4 Ventrodorsal radiograph of a dog with a distended urinary bladder that resulted in displacement of the descending colon to the right *(white arrow)*. This is a common malpositioning and is not clinically significant.

RADIOGRAPHIC TECHNIQUES OF LARGE BOWEL EVALUATION

Survey Radiography

Because feces and gas produce contrasting radiographic opacities and are usually present in the large bowel, some or all of the large bowel is identifiable on survey radiographs of the abdomen. Normal large bowel content usually has a characteristic pattern of fine and evenly distributed gas bubbles, which is helpful in differentiating the colon from small intestinal loops and abnormal conditions of the large bowel. When present, mineral- or metal-opaque foreign bodies are recognized easily. Neither the wall thickness nor the mucosal pattern of the large bowel can be evaluated from survey radiographs.

When the large bowel is evaluated radiographically, the entire abdomen and pelvic area must be included on orthogonal radiographic views. Rectal examination, vigorous abdominal palpation, aerophagia from restraint and struggling, and enema administration before survey radiography may increase the amount of gas or fluid present within the colon and in other parts of the gastrointestinal tract. Although an abnormality in position, size, or shape of the large bowel may be seen on survey radiographs, it may not be a significant finding.

Compression Radiography

Compression radiography of the abdomen is a simple technique that may help clarify the presence of a lesion. When the abdomen is compressed with a wooden or plastic spoon or paddle, bowel or masses adjacent to the large intestine are displaced or compressed, which enhances radiographic conspicuity (Fig. 45-5). More definitive radiographic evaluation of the large bowel usually requires a contrast study with barium sulfate suspension (barium enema), air (pneumocolon), or a combination of barium sulfate suspension and air (double-contrast study). There is a risk of rupturing masses or hollow viscera with this technique, and it should be used with caution.

Barium Enema

Barium enema findings in large bowel disease include (1) irregularity of the barium/mucosa interface, (2) spasm of the bowel lumen, (3) partial or complete occlusion of the bowel lumen, (4) outpouching of the bowel wall from a hernia or diverticulum, (5) displacement of bowel, and (6) perforation with peritonitis. Unfortunately, the barium enema findings are usually nonspecific. Although spasm and mucosal irregularity are commonly associated with severe local inflammation, other causes include toxicity, reflex mechanism, and idiopathic factors. Bowel inflammation may occur with generalized or regional areas of bowel wall thickening from edema and small ulcerations. There are frequently no abnormal findings in the acute stage of bowel inflammation.

A barium enema is indicated when (1) narrowing of the lumen prevents passage of an endoscope; (2) limitations of the endoscope prevent examination of all the colon and cecum; and (3) a mural or extramural lesion is suspected, but the mucosa is normal endoscopically.[4] Survey radiographs should always be made before the contrast study. For a high-quality barium enema, the colon should be cleansed thoroughly. This is best done by withholding food for 24 hours followed by a warm-water enema. The colon should be free of fecal material with a clear effluent visible on the enema performed immediately before the study. Generally, the radiographic technique should be increased by 6 to 8 kVp over the survey technique when barium is used. Although the techniques can vary, barium is administered at room temperature through an inflatable cuffed catheter in the distal rectum.[1,12-14] General anesthesia is almost always necessary. Micropulverized barium suspension is the contrast medium of choice for obtaining a smooth coating of the mucosal surface. The colon should be filled slowly by gravity, preferably with fluoroscopic observation. Because fluoroscopic equipment may not be available, and the volume of barium needed to fill the colon is variable, the contrast medium should be given in small increments until the desired effect is seen radiographically. The approximate barium dosage is 7 to 15 mL per kilogram of body weight. Multiple radiographic views, left lateral, ventrodorsal, right ventral–left dorsal oblique, and left ventral–right dorsal oblique, should be made when the colon is distended with barium and again after evacuation of the barium from the colon. The detection of subtle mucosal lesions may be enhanced by a double-contrast study. In most instances, this is done by removing as much of the barium as possible and then inflating the colon with room air through the catheter.

When distended with barium, the normal colon has a smooth contrast medium/mucosa interface and a uniform diameter. After evacuation of the barium, longitudinal mucosal folds are visible. If air is then infused, a double-contrast study is obtained, which provides the most detailed visualization of the mucosal surface.

A variety of radiographic appearances result from adherence of barium to mucus, clumping and flocculation of barium, and filling defects of feces that are either within the lumen or attached to the wall. The colon of the dog and the cecum and colon of the cat have lymph follicles in the mucosa, which can appear as spicules on a barium enema study or as pinpoint radiopacities when visualized en face with a double-contrast study. These normal follicles must be differentiated from small ulcers.

The large bowel cannot be evaluated properly after oral administration of contrast medium because large bowel luminal distention is inadequate and there will be intraluminal filling defects from ingesta carried aborally with the barium.



Fig. 45-5 **A,** Lateral radiograph of a cat with a uterine stump pyometra *(black open arrows)* interposed between the descending colon and urinary bladder. **B,** Survey lateral radiograph of the abdomen during lateral compression of the caudal abdomen with a compression paddle. The mass appears fixed and separate from the descending colon and urinary bladder. **C,** Survey lateral radiograph of the abdomen after a pneumocolon performed by retrograde introduction of gas. The soft tissue mass is visualized as an extramural mass. Feces were not removed before the contrast study was conducted.

Barium enemas are time consuming and must be done meticulously to assess the mucosa, wall, lumen, and adjacent viscera and to avoid artifacts, complications, and technical failures. Partial large bowel contrast studies, which are less thorough, quicker, and easier, may be performed with the introduction of small amounts of air or barium into the rectum using a dose syringe. These studies do not allow visualization of the entire large bowel or of small lesions, such as mucosal irregularities; however, they may enable visualization of large intraluminal lesions and differentiation of the colon from adjacent organs and masses (Fig. 45-5, C).

Complications Associated with Contrast Studies

The most serious complication is perforation and subsequent peritonitis, but this can usually be avoided by the use of common sense. Rupture can occur from a cleansing enema, improper selection or use of a barium enema catheter, and overdistention of weakened or diseased bowel, or after a biopsy.[15-17] If colonic perforation is suspected before the study is performed, a 15% to 20% concentration of nonionic aqueous iodine contrast medium can be substituted for the barium, but mucosal detail will be diminished significantly.[13]

A common inconsequential complication is retrograde filling of the distal small bowel, which may obscure visualization of the colon. This can occur in up to one third of dogs and may occur without overdistention of the colon.[12] Spasm, which is usually transient, may also occur when the contrast medium is cold, when narcotic premedications are used, or when the wall is irritated by the catheter (Fig. 45-6).

RADIOGRAPHIC FINDINGS IN LARGE BOWEL DISEASE

Disease affecting the large bowel may produce alterations in size, shape, location, and radiopacity of the colon.[1-4] Although function cannot be evaluated radiographically, the quantity or location of feces may suggest impaired motility. A colon filled with homogeneous fluid without the finely dispersed gas pattern typical for formed feces is suggestive of diarrhea. A soft tissue mass or an intussusception also appears as a homogeneous soft tissue radiopacity. A curved gas/soft tissue interface of a homogeneous luminal soft tissue opacity in the large bowel can sometimes be seen at the edge of an

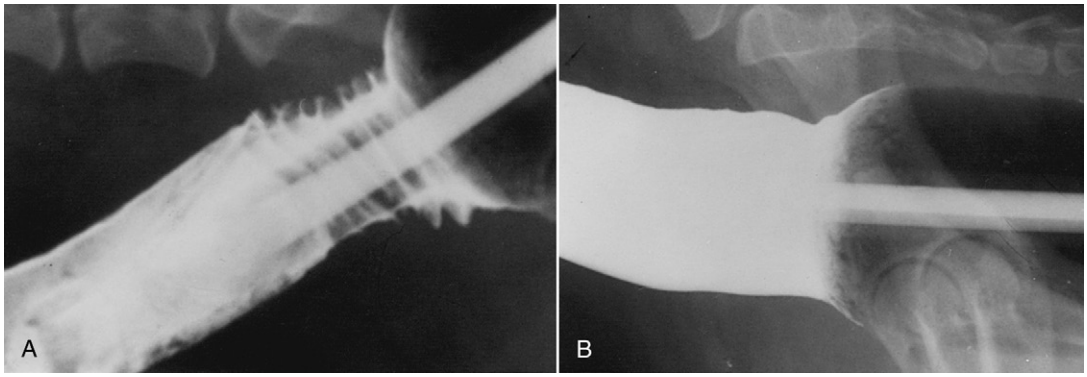


Fig. 45-6 Narrowing and irregularity of the descending colon are present immediately cranial to the air-inflated catheter cuff. This was a spasm **(A)** and was transient based on a subsequent radiograph **(B)** made several minutes later.

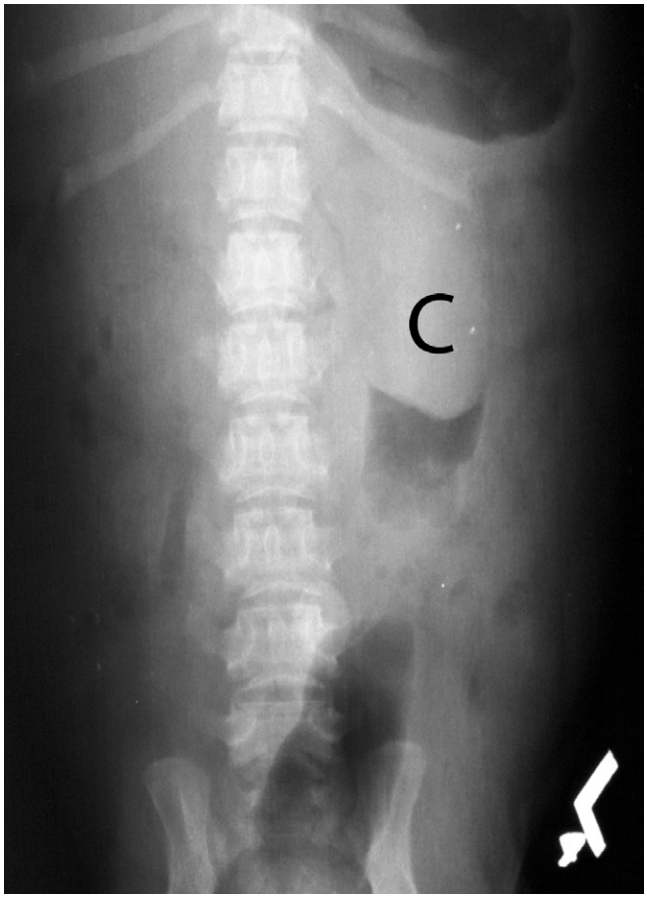


Fig. 45-7 Survey ventrodorsal abdominal radiograph of a young dog with a cecocolic intussusception. The proximal descending colon *(C)* is distended by a homogeneous soft tissue mass with a curved gas interface caudally. This mass is the leading edge of the intussusceptum, and this sign, sometimes called the *meniscus sign*, is highly suggestive of intussusception.

intussusception and is sometimes referred to as a *meniscus sign* (Fig. 45-7).[18]

Most radiographic findings in large bowel disease are not pathognomonic. Many different diseases have similar radiographic findings, and any particular disease may have a spectrum of different appearances. In addition, parasitic, dietary, and other inflammatory causes of large bowel disease commonly have no detectable radiographic abnormality.

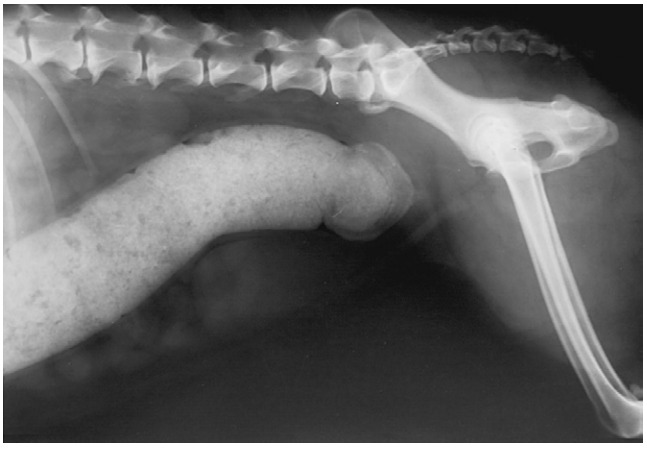


Fig. 45-8 Survey lateral radiograph of a dog with a pelvic fibroleiomyoma that caused partial colonic obstruction and secondary megacolon.

The diameter of the normal colon varies with the amount of feces and individual defecation habits. As a rule of thumb, the diameter of the normal canine colon should be less than the length of the body of L7.[1] In cats without gastrointestinal disease, the radiographically measured maximal colonic diameter should be approximately 2.2 times the small intestinal diameter and approximately 2.8 times the length of the cranial end plate of the second lumbar vertebra.[19] In another study in cats, it was determined that a colon diameter/L5 length ratio of less than 1.28 indicates a normal or constipated colon, whereas a value of more than 1.48 is indicative of megacolon.

Colonic impaction is characterized by accumulation of feces that are more radiopaque than normal as a consequence of continued water absorption from colon contents. Chronic impaction can also result in generalized enlargement of the colon.

Localized dilatation of the colon is usually related to impaction or localized diseases such as mechanical obstruction, narrowed pelvic canal, mural disease, or extramural tumor (Fig. 45-8).

Generalized enlargement of the colon is commonly referred to as *megacolon*. Megacolon can be caused by mechanical or functional obstruction and is characterized by diffuse colonic dilatation with ineffective motility. Megacolon may be idiopathic or associated with underlying causes such as (1) chronic constipation and obstipation from nutritional, metabolic, or

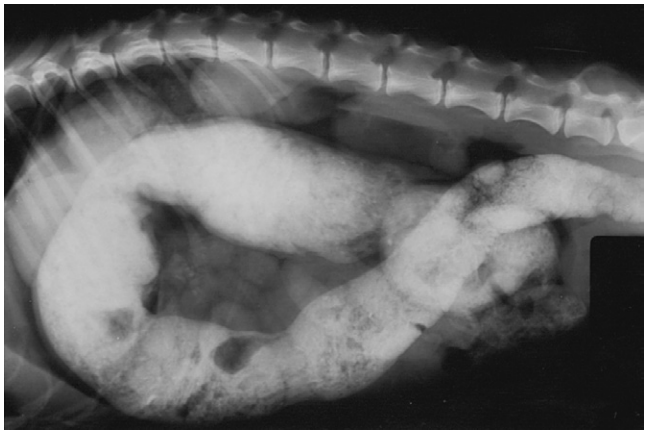


Fig. 45-9 Generalized megacolon in a young dog because of Hirschsprung's disease. Note the increased opacity of the fecal material caused by inspissation.

mechanical causes; (2) spinal anomalies such as cauda equina syndrome or sacrococcygeal agenesis in Manx cats; (3) neuromuscular disorders such as dysautonomia, aganglionosis, or Hirschsprung's disease (Fig. 45-9); (4) metabolic disorders such as hypokalemia or hypothyroidism; (5) ureterocolic diversion; and (6) congenital anorectal anomalies.[1,3,20-23] Mechanical causes of colon obstruction include narrowing of the pelvic canal from pelvic malunion fractures, prostatomegaly, lymphadenopathy, colonic masses, and foreign bodies.

Congenital anomalies of the large bowel are rare in the dog and the cat. Anomalies reported include imperforate anus; atresia recti; atresia coli; fistulation; diverticula; duplication of the large bowel and rectum; and a short, straight colon with the cecum in the left hemiabdomen.[1,3,24-31]

Abnormal location is a common radiographic alteration seen with large bowel disease in the dog and cat. Although the normal location of the large bowel can vary, mass lesions, particularly those of organs adjacent to the colon, cause displacement of the cecum, colon, or rectum (Figs. 45-10 and 45-11; see also Fig. 45-3).

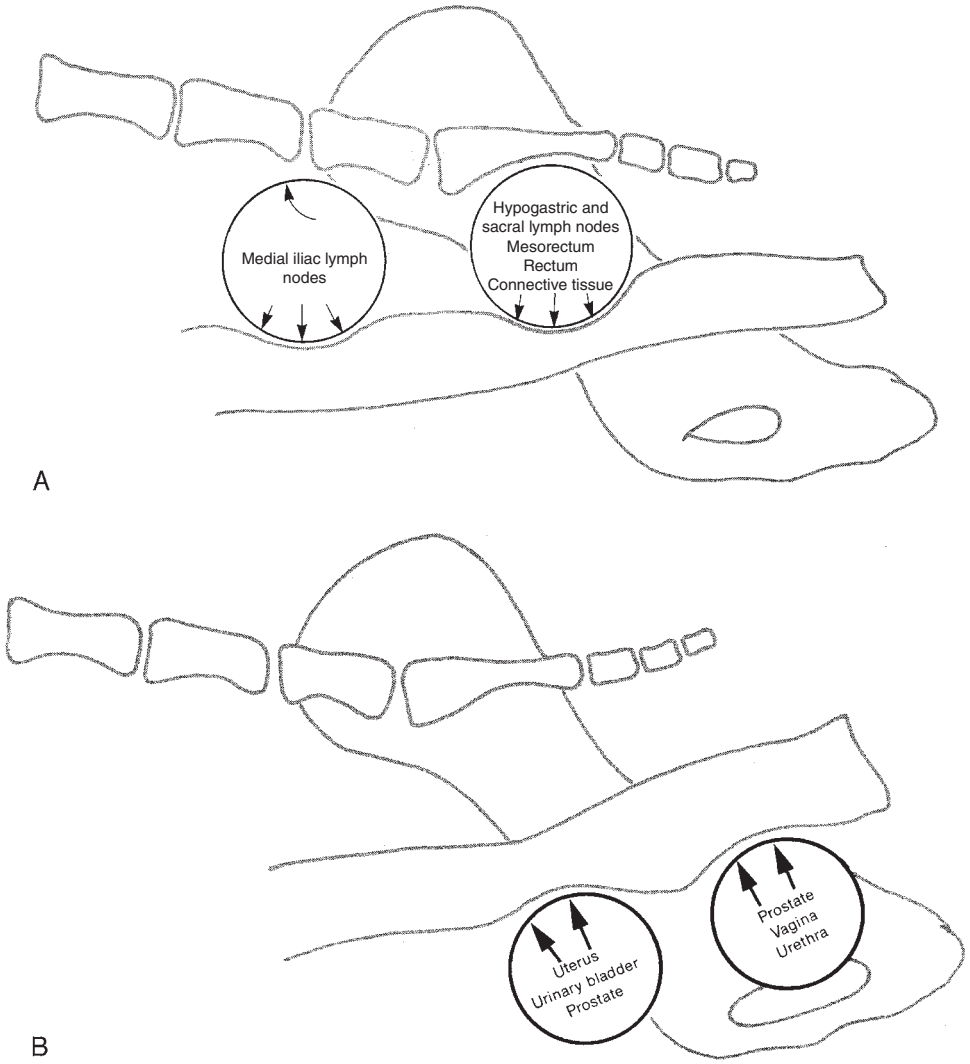


Fig. 45-10 Terminal colon and rectal displacement by adjacent organ enlargement. **A,** Ventral displacement of the terminal colon and rectum commonly results from medial iliac and sacral lymph node enlargement. Although less common, a hematoma, abscess, or tumor may produce similar displacement alterations. **B,** Dorsal displacement of the rectum commonly results from enlargement of the prostate, the uterus, the vagina, or the intrapelvic urinary bladder. (Reprinted from O'Brien TR: *Radiographic diagnosis of abdominal disorders in the dog and cat*, Davis, Calif, 1981, Covell Park Veterinary.)

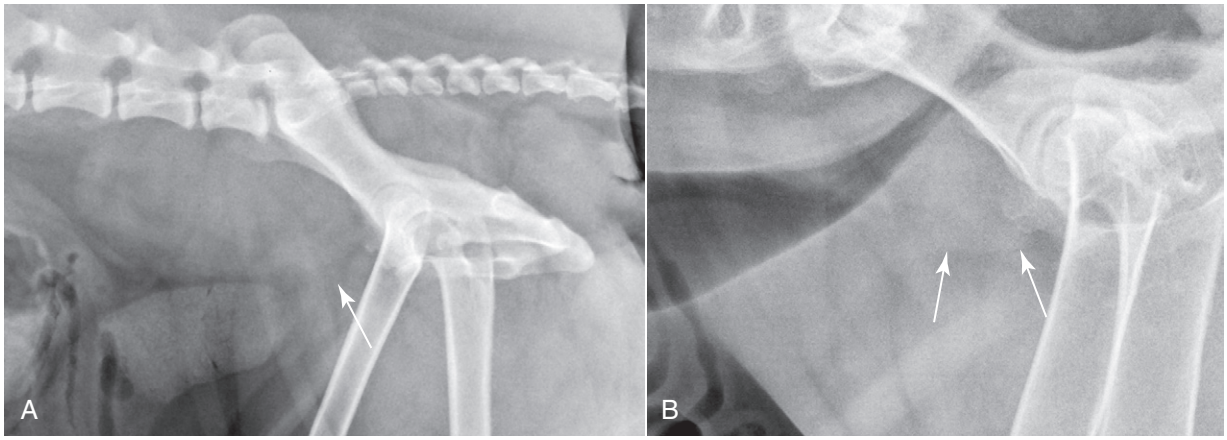


Fig. 45-11 **A,** Lateral radiograph of a dog with metastatic anal sac carcinoma to the medial iliac lymph nodes. The enlarged lymph nodes displace the colon ventrally, and there is obstruction *(white arrow)* at the pelvic inlet. **B,** Lateral radiograph of a dog with narrowing of the large bowel at the junction of the descending colon and rectum from an enlarged prostate gland *(white arrows)*.



Fig. 45-12 Lateral radiograph of a barium enema of a cat with a colocolic intussusception. The intussusceptum creates a filling defect in the barium that has a coiled-spring appearance.

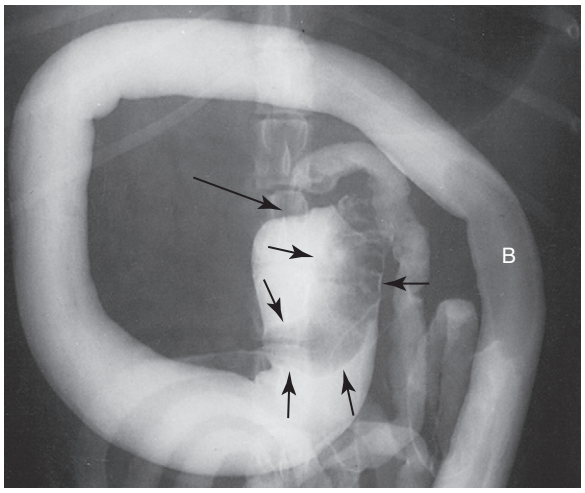


Fig. 45-13 Ventrodorsal radiograph of a barium enema of a young dog with a cecocolic intussusception. The intussusceptum appears as a radiolucent filling defect *(short black arrows)* in the proximal aspect of the ascending colon. Note that the ileocolic junction *(long black arrow)* and distal ileum are normal, ruling out ileocolic intussusception. The radiolucent region in the descending colon *(B)* is a gas bubble.

Many large bowel diseases exhibit radiographic changes in the colon similar to those in other parts of the gastrointestinal tract. These include (1) foreign body; (2) obstruction, including ileocolic intussusception (Fig. 45-12), cecocolic intussusception (Fig. 45-13), volvulus (Fig. 45-14), and strangulation; (3) inflammation (Fig. 45-15); (4) stricture (Fig. 45-16); (5) neoplasia (Fig. 45-17); and (6) diverticula or hernia.[32-44]

Differences in the appearance of intraluminal, intramural, and extramural lesions of the large bowel in a contrast study are important to recognize. For example, a lesion that is plaquelike is intramural and arises from the mucosal or submucosal tissues. An extramural mass usually causes extrinsic narrowing of the lumen, displacement of the bowel and adjacent viscera, or both. In most diseases of the large bowel, particularly those that are not extramural, a contrast study is required for detection and for decision making regarding the most probable diagnosis (Fig. 45-18).

Narrowing of the large bowel lumen results from extraluminal compression (see Fig. 45-11) or from spasm or constriction caused by neoplasia or scar tissue. Unlike constriction, spasm is transient and frequently is caused by the barium enema technique (see Fig. 45-6). When evaluating a constriction with a barium enema examination, the base and length of the defect, the mucosal surface, and the mural involvement should be assessed (see Fig. 45-16). Most constrictions of the large bowel are produced by neoplasms (usually carcinoma and lymphosarcoma), but benign disease such as adenoma, scar tissue, eosinophilic colitis, and ulcerative colitis may mimic the radiographic findings of a malignant lesion.

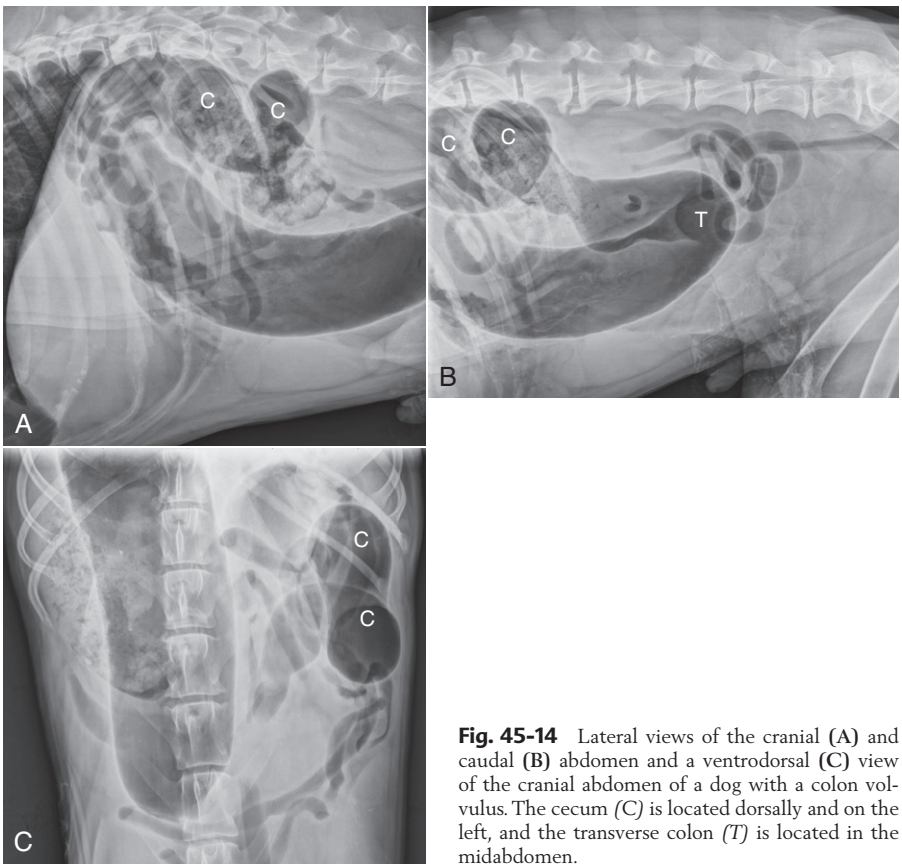


Fig. 45-14 Lateral views of the cranial **(A)** and caudal **(B)** abdomen and a ventrodorsal **(C)** view of the cranial abdomen of a dog with a colon volvulus. The cecum *(C)* is located dorsally and on the left, and the transverse colon *(T)* is located in the midabdomen.

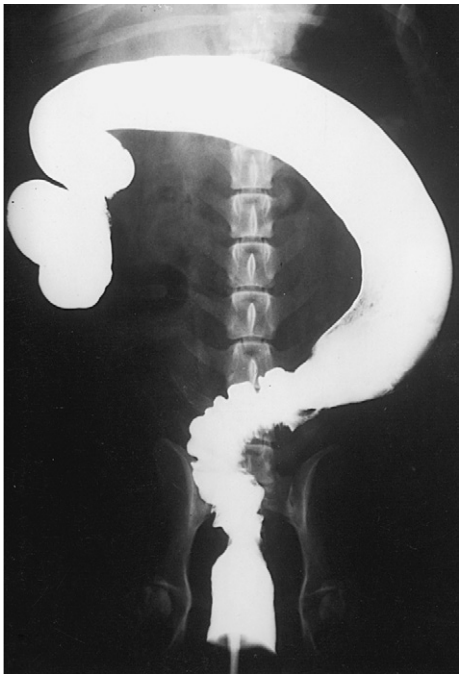


Fig. 45-15 Barium enema examination in a dog with localized colitis, characterized by nondistensibility and mucosal irregularity of the distal portion of the descending colon just cranial to the rectum.

ULTRASONOGRAPHIC EVALUATION OF THE LARGE BOWEL

Ultrasonographic evaluation of the colon and cecum follows the same principles that apply to the small intestine but is somewhat limited because of the reflective nature of feces and gas and the thinner wall of the large intestine. The parts of the intestinal wall that are distant to reflective content cannot be assessed. Despite these limitations, assessing the colon should be part of a standard abdominal ultrasonographic examination. The colon can be identified in a short axis plane in the region of the urinary bladder neck as the only multilayered tubular structure and by the curved shadowing hyperechoic rim emanating from gas or feces (Fig. 45-19). In females, care should be taken to differentiate colon from the uterine body, or stump in neutered animals, which is smaller, lacks wall layering, bifurcates in intact females, and normally does not contain reflective material. The colon can then be followed cranially, although not always along its entire course. The cecum and ascending colon are best located by first identifying the terminal ileum, which has a conspicuous muscularis layer and ileocolic junction in the right midabdomen, in proximity to the right kidney and caudal duodenal flexure (Fig. 45-20). Cats have a small cecum that is visible ultrasonographically. The cecum should not be confused with abnormally distended small bowel loops or other tubular structures. Under optimal conditions five wall layers can be distinguished in the large intestinal wall, similar to the small bowel (see

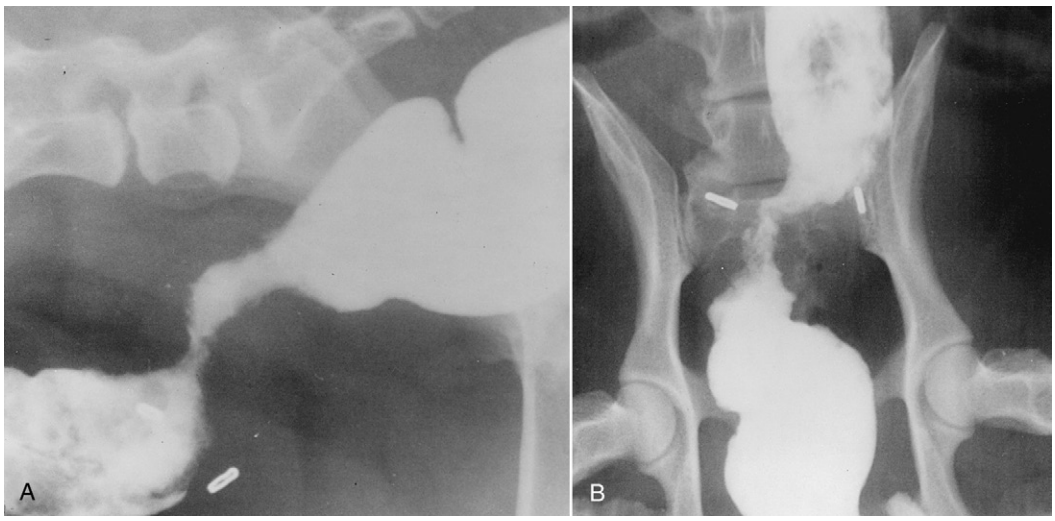


Fig. 45-16 Lateral **(A)** and ventrodorsal **(B)** views of a barium enemation in a dog with a benign colon stricture of unknown etiology. The surgical clips are from a previous ovariohysterectomy.

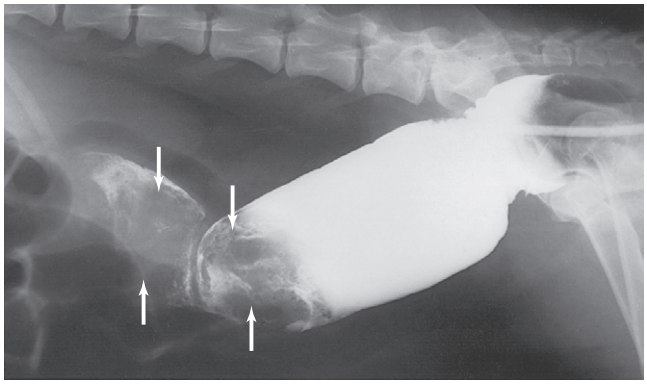


Fig. 45-17 A barium enema in a dog with a mass *(white arrows)* creating a polypoid filling defect in the mid-portion of the descending colon. The mass was lymphoma.



Fig. 45-18 Postevacuation ventrodorsal radiograph of a barium enema. There are both normal longitudinal mucosal folds *(curved arrow)* and an abnormal mucosal pattern *(straight arrow)*. The abnormal area was localized colitis and was not visible with the colon distended with barium.

Fig. 45-19). However, the large intestine has a very thin wall (2 to 3 mm in dogs; 1.7 mm in cats), and layers are not always distinguishable.[44,45] The colon is accompanied by right, middle, and left colic lymphocenters in the adjacent mesocolon.[46,47] The right colic lymph node is in the vicinity of the ileocolic junction and is visible normally as a small ovoid structure with a homogenous echogenicity similar to other abdominal lymph nodes (Fig. 45-21). The middle and left colic lymph nodes, which are adjacent to the transverse and descending colon, respectively, are usually only visible if abnormal. Abnormal lymph nodes, whether neoplastic or reactive, are enlarged, often abnormally shaped, and hypoechoic (see Fig. 45-21).[48]

A distinction between extramural and intramural masses usually can be made. Most ultrasonographic large bowel abnormalities are not specific and should be interpreted along with other imaging findings, lesion extent, and, if possible, guided aspirates or biopsy. Intussusception, however, has a pathognomonic ultrasonographic appearance. Juxtaposition of the combined wall layers of the intussuscipiens and intussusceptum creates a concentric ring sign in short-axis images and multiple parallel lines with alternating echogenicity in longitudinal views (Fig. 45-22).[19] The mesentery entrapped between the two intestinal segments appears as a hyperechoic region within the lesion. Reducibility of intestinal intussusception depends on tissue viability and intact blood supply and can be predicted with color Doppler studies.[49] Intestinal masses can be involved in intussusception and interrupt the layered appearance. Ulcerations and perforations of the large intestine are difficult to diagnose ultrasonographically because colonic reflective material (gas, feces) prohibits evaluation of the large bowel wall distant to the reflection. Ultrasonographic assessment of the rectum is best performed intrarectally, which requires an obstetric probe, general anesthesia, and previous bowel evacuation. However, an assessment of the anal and perianal region can be made with a standard small footprint probe with a perianal approach. This allows



Fig. 45-19 Short-axis ultrasonogram of a normal descending colon of a dog. Despite the fact that the wall is thinner (2.5 mm) than in the small bowel, five wall layers with alternating echogenicity can still be distinguished. The colonic content appears as a heterogeneously hyperechoic curved rim with dirty distal shadowing that prohibits assessment of the colon wall in the far field.

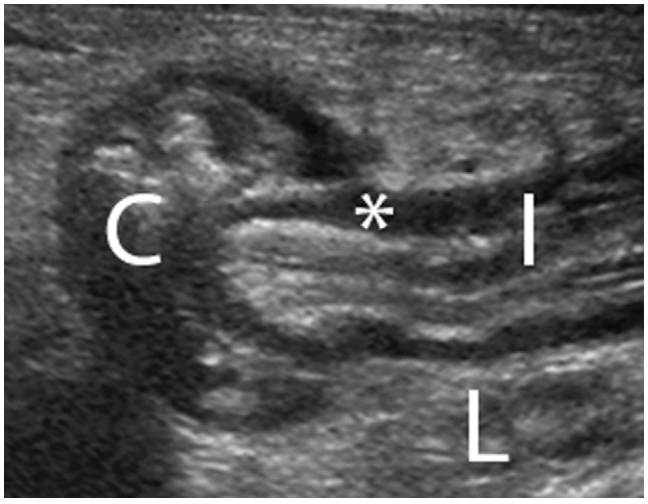


Fig. 45-20 Ultrasonogram of the normal ileocolic junction in a cat with the ileum *(I)* and right colic lymph node *(L)* in a longitudinal plane and the ascending colon *(C)* in a short-axis plane. Note the conspicuous hypoechoic ileal muscularis layer *(asterisk)* commonly seen in cats.

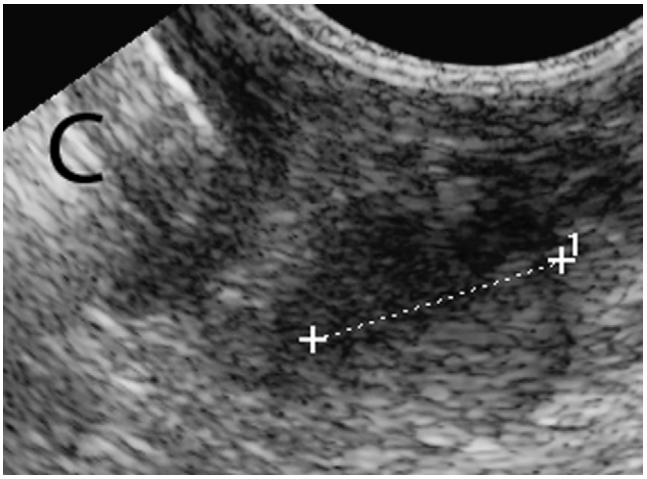


Fig. 45-21 Ultrasonogram of the ascending colon *(C)* in short axis and an adjacent, moderately enlarged (1 cm thick) normoechoic right colic lymph node *(between calipers)* of a cat with feline infectious peritonitis.

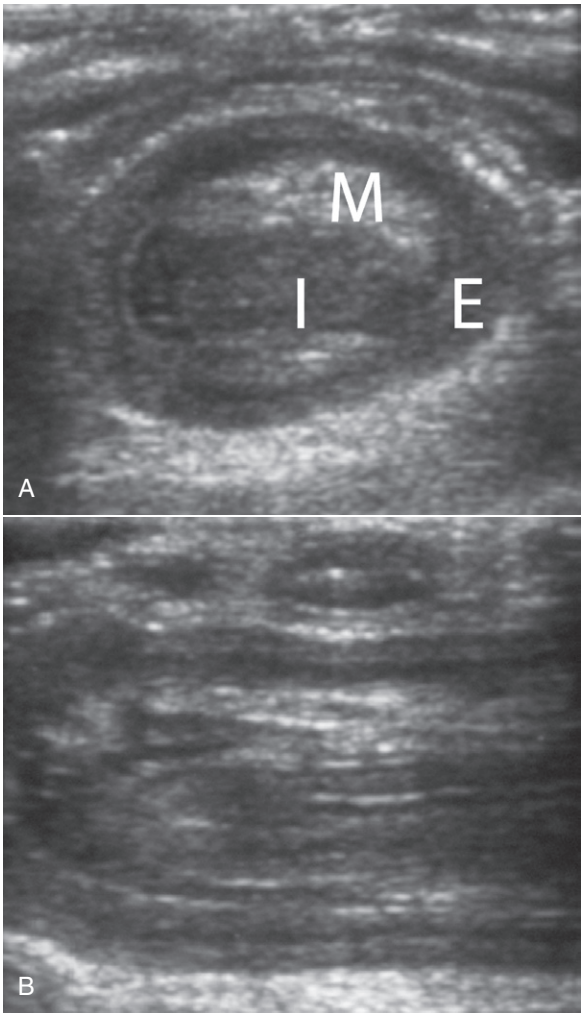


Fig. 45-22 Short axis **(A)** and longitudinal **(B)** sonograms of the descending colon of a dog with a cecocolic intussusception (same dog as in Fig. 45-7). In **A,** note the ringlike juxtaposed wall layers with alternating echogenicity of the external intussuscipiens *(E)* and internal intussusceptum *(I)* (concentric ring sign) as well as the entrapped hyperechoic mesentery between the segments *(M)*. In **B,** the same wall layers have a parallel orientation.

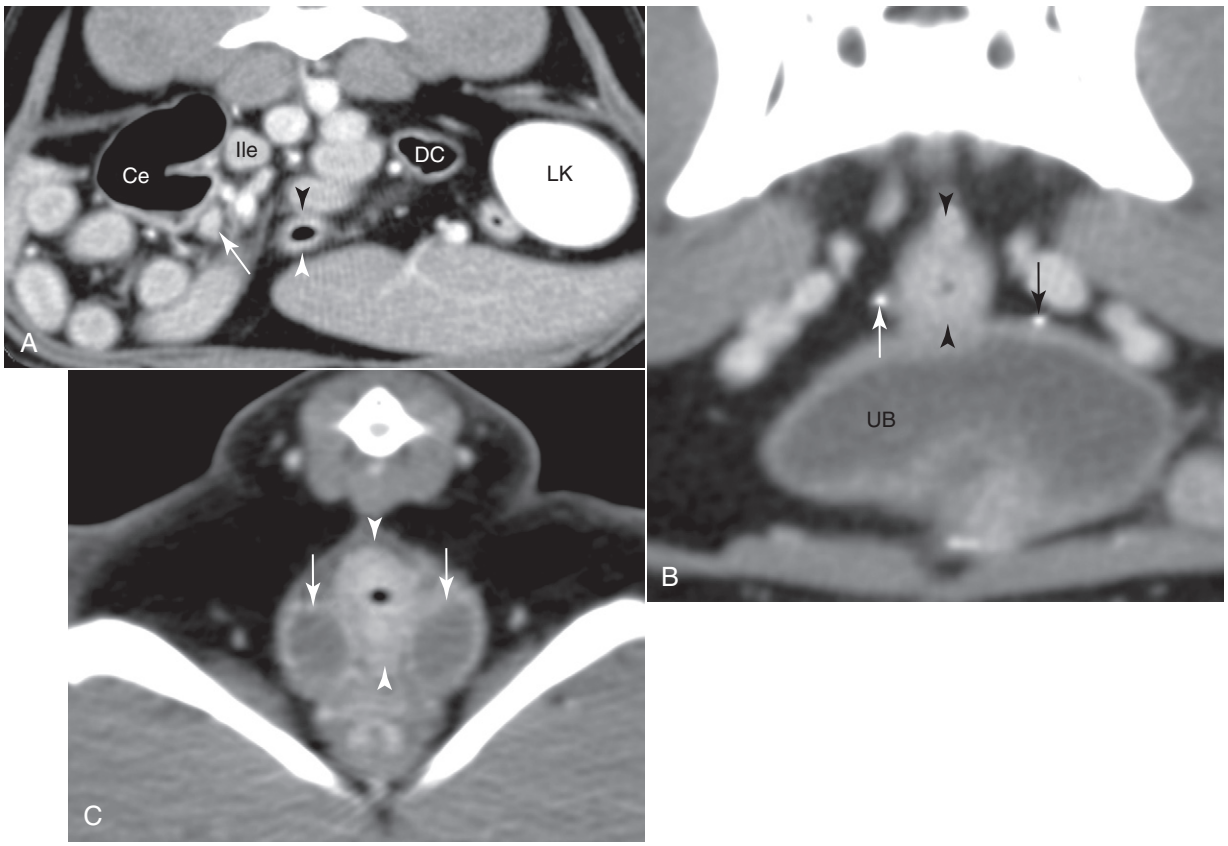


Fig. 45-23 Transverse, contrast-enhanced computed tomography images of the large intestine and adjacent organs in a normal dog. **A,** Cranial abdomen with a gas-filled cecum *(Ce)*, terminal ileum *(Ile)*, right colic lymph node *(white arrow)*, transverse colon *(between white and black arrowheads)* and descending colon *(DC)*; *LK*, Left kidney. **B,** Pelvic inlet with the descending colon *(between black arrowheads)*, ureters *(white and black arrows)*, and urinary bladder *(UB)*. The right ureter *(white arrow)* is traveling toward the bladder neck in the right mesocolon directly adjacent to the colon wall. **C,** Caudal pelvis with rectum *(between black arrowheads)* and adjacent anal gland sacs *(white arrows)*.

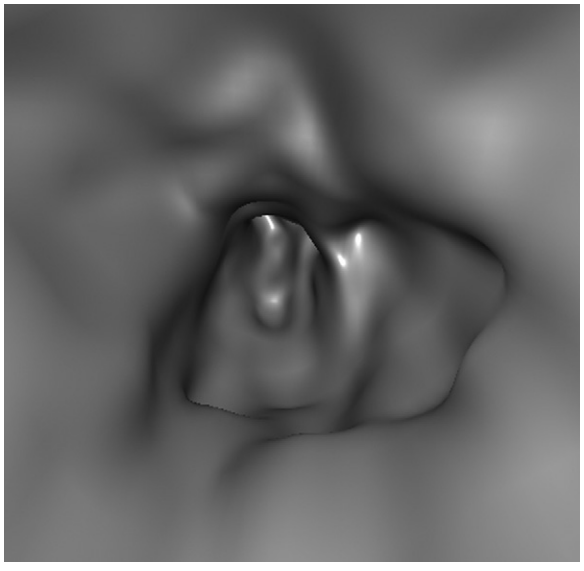


Fig. 45-24 Virtual colonoscopy image displaying the partially compressed lumen of a gas-filled descending colon in a dog.

visualization of the anal gland sacs and evaluation of their possible involvement in perianal masses and fistulae.

COMPUTED TOMOGRAPHIC EVALUATION OF THE LARGE BOWEL

Abdominal CT for large bowel assessment should be performed in a helical acquisition with induced apnea, caudal scan direction, thin slice width (2 to 3 mm), low pitch, and a medium frequency image reconstruction algorithm. The entire large intestine can be assessed, and in particular, its association with neighboring organs, such as the ileum and ileocolic junction, colic and sublumbar lymph nodes, duodenum, pancreas, liver, kidneys, mesenteric root, ureters, urethra, vagina, uterus, prostate, and the anal glands (Fig. 45-23). Wall layers are not distinguishable on survey CT images, but after intravenous administration of iodinated contrast medium, the mucosa enhances strongly. It is possible to generate virtual colonoscopy images from CT series with a gas- or fluid-filled colon, but the validity of this technique for lesion detection has not yet been established for dogs and cats (Fig. 45-24). Currently, CT is most commonly used to assess colonic

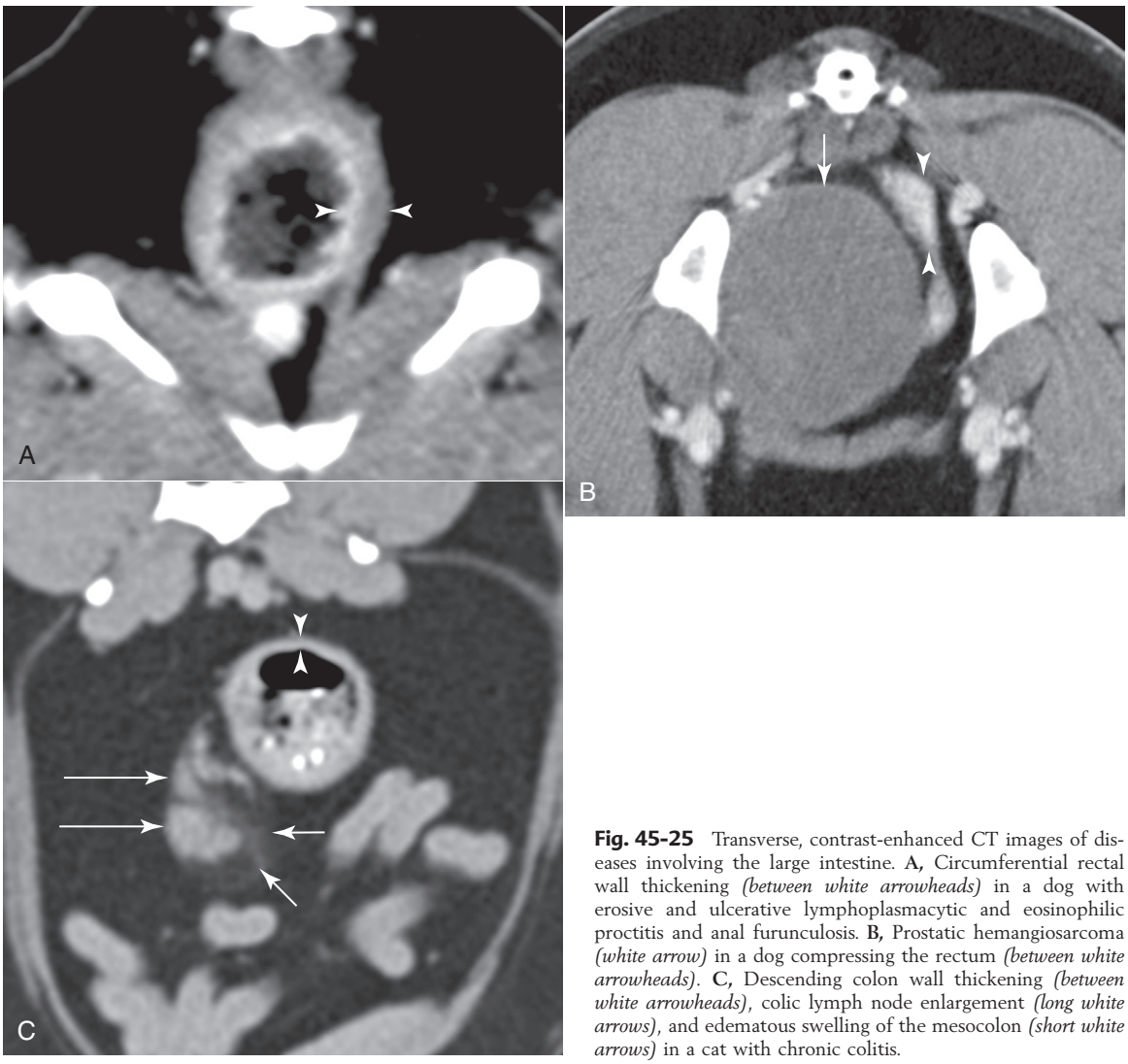


Fig. 45-25 Transverse, contrast-enhanced CT images of diseases involving the large intestine. **A,** Circumferential rectal wall thickening *(between white arrowheads)* in a dog with erosive and ulcerative lymphoplasmacytic and eosinophilic proctitis and anal furunculosis. **B,** Prostatic hemangiosarcoma *(white arrow)* in a dog compressing the rectum *(between white arrowheads)*. **C,** Descending colon wall thickening *(between white arrowheads)*, colic lymph node enlargement *(long white arrows)*, and edematous swelling of the mesocolon *(short white arrows)* in a cat with chronic colitis.

involvement or compression by lesions in the pelvic canal, such as anal gland tumors, prostatomegaly, and lymphadenopathy (Fig. 45-25).[11,50]

REFERENCES

1. O'Brien TR: *Radiographic diagnosis of abdominal disorders in the dog and cat*, Davis, Calif, 1981, Covell Park Veterinary.
2. Farrow CS, Green R, Shiveley M: *Radiology of the cat*, St. Louis, 1995, Mosby.
3. Kealy KJ, McAllister H: *Diagnostic radiology and ultrasonography of the dog and cat*, ed 3, Philadelphia, 2000, Saunders.
4. Jergens AE, Willard MD: Diseases of the large intestine. In Ettinger SJ, Feldman EC, editors: *Text book of veterinary internal medicine*, ed 5, Philadelphia, 2000, Saunders, p 1238.
5. Lamb CR: Recent developments in diagnostic imaging of the gastrointestinal tract of the dog and cat, *Vet Clin North Am Small Anim Pract* 29:307, 1999.
6. Homco LD: Gastrointestinal tract. In Green R, editor: *Small animal ultrasound*, Philadelphia, 1996, Lippincott Raven.
7. Penninck DG: Ultrasonography of the gastrointestinal tract. In Nyland T, Mattoon J, editors: *Veterinary diagnostic ultrasound*, ed 2, Philadelphia, 2002, Saunders. pp 207–230.
8. Becker M, Adler L, Parish JF: Rectal lymphangiography in dogs, *Radiology* 91:1037, 1968.
9. Gomez JA, Korobkin M, Lawson TL, et al: Selective abdominal angiography in the dog, *J Am Vet Radiol Soc* 14:72, 1973.
10. Krevsky B, Somers MB, Mauere AH, et al: Quantitative measurement of feline colonic transit, *Am J Physiol* 255:G529, 1988.
11. Spector DL, Fischetti AJ, Kovak-McClaran JR: Computed tomographic characteristics of intrapelvic masses in dogs, *Vet Radiol Ultrasound* 52:71, 2011.
12. Ticer JW: *Radiographic technique in veterinary practice*, ed 2, Philadelphia, 1984, Saunders.
13. Kleine LJ, Lamb CR: Comparative organ imaging: the gastrointestinal tract, *Vet Radiol* 30:133, 1989.
14. Brawner WB, Bartels JE: Contrast radiography of the digestive tract: indications, techniques, and complications, *Vet Clin North Am* 13:599, 1983.
15. Seaman WB, Walls J: Complications of the barium enema, *Gastroenterology* 48:728, 1965.

16. Toombs JP, Caywood DD, Lipowitz AJ, et al: Colonic perforation following neurosurgical procedures and corticosteroid therapy in four dogs, *J Am Vet Med Assoc* 177:68, 1980.
17. Toombs JP, Collins LG, Graves GM, et al: Colonic perforation in corticosteroid-treated dog, *J Am Vet Med Assoc* 188:145, 1986.
18. Lamb CR, Mantis P: Ultrasonographic features of intestinal intussusception in 10 dogs, *J Small Anim Pract* 39:437, 1998.
19. Adams WM, Sisterman LA, Klauer JM, et al: Association of intestinal disorders in cats with findings of abdominal radiography, *J Am Vet Med Assoc* 236:880, 2010.
20. Washabau RJ, Hasler AH: Constipation, obstipation and megacolon. In August JR, editor: *Consultations in feline internal medicine*, ed 3, Philadelphia, 1997, Saunders.
21. Matthiesen DT, Scale TD, Whitney WO: Megacolon secondary to pelvic fractures, *Vet Surg* 20:113, 1991.
22. Sharp NJH, Nash AS, Griffiths IR: Feline dysautonomia (Key-Gaskell syndrome): a clinical and pathologic study of forty cases, *J Small Anim Pract* 25:599, 1984.
23. DeForest ME, Gasrur PK: Malformations and the Manx syndrome in cats, *Can Vet J* 2:304, 1979.
24. Jones BR, Gruffydd-Jones TJ, Sparkes AK: Preliminary studies on congenital hypothyroidism in a family of Abyssinian cats, *Vet Rec* 131:145, 1992.
25. Rawlings CA, Capps WF: Rectovaginal fistula and imperforate anus in a dog, *J Am Vet Med Assoc* 159:320, 1971.
26. Fluke MH, Hawkins EC, Elliott GS, et al: Short colon in two cats and a dog, *J Am Vet Med Assoc* 195:87, 1989.
27. Jakowski RM: Duplication of colon in a Labrador retriever with abnormal spinal column, *Vet Pathol* 14:256, 1977.
28. Bredal WP, Thoressen SI, Kvellestad A: Atresia coli in a nine week old kitten, *J Small Anim Pract* 35:643, 1994.
29. Longhofer SL, Jackson RK, Cooley AJ: Hindgut and bladder duplication in a dog, *J Am Anim Hosp Assoc* 27:97, 1991.
30. Schlesinger DP, Philbert D, Breur GJ: Agenesis of the cecum and the ascending and transverse colon in a twelve year old cat, *Can Vet J* 33:544, 1992.
31. Shinozaki JK, Sellon RK, Tobias KM, et al: Tubular colonic duplication in a dog, *J Am Anim Hosp Assoc* 36:209, 2000.
32. Guffy MM, Wallace L, Anderson NV: Inversion of the cecum into the colon of a dog, *J Am Vet Med Assoc* 156:183, 1970.
33. Kolata RJ, Wright JH: Inflammation and inversion of the cecum in a cat, *J Am Vet Med Assoc* 162:958, 1976.
34. Lansdown ABG, Fox EA: Colorectal intussusception in a young cat, *Vet Record* 19:429, 1991.
35. Carberry CA, Flanders JA: Cecal-colic volvulus in two dogs, *Vet Surg* 22:225, 1993.
36. Drobatz KJ, Hughes D, Hill C, et al: Volvulus of the colon in a cat, *J Vet Emerg Crit Care* 6:99, 1996.
37. Hassinger KA: Intestinal entrapment and strangulation caused by rupture of the duodenocolic ligament in four dogs, *Vet Surg* 26:275, 1997.
38. Morris EL: Pneumatosis coli in a dog, *Vet Radiol Ultrasound* 33:154, 1992.
39. Bolton GR, Brown TT: Mycotic colitis in a cat, *Vet Med Small Anim Clin* 67:978, 1972.
40. Birchard SJ, Couto CG, Johnson S: Nonlymphoid intestinal neoplasia in 32 dogs and 14 cats, *J Am Anim Hosp Assoc* 22:533, 1986.
41. Slawienski MJ, Mauldin GE, Mauldin GN, et al: Malignant colonic neoplasia in cats, *J Am Vet Med Assoc* 211:878, 1997.
42. Sealer RJ: Colorectal polyps of the dog: a clinicopathologic study of 17 cases, *J Am Vet Med Assoc* 174:72, 1979.
43. Welches CD, Scavelli TD, Aronsohn MG, et al: Perineal hernia in the cat: a retrospective study of 40 cases, *J Am Anim Hosp Assoc* 28:431, 1992.
44. Penninck DG, Nyland TG, Fisher PE, et al: Ultrasonography of the normal canine gastrointestinal tract, *Vet Radiol* 30:272, 1989.
45. Newell SM, Graham JP, Roberts GD, et al: Sonography of the normal feline gastrointestinal tract, *Vet Radiol Ultrasound* 40:40, 1999.
46. Bezuidenhout AJ: The lymphatic system. In Evans HE, editor: *Miller's anatomy of the dog*, ed 3, Philadelphia, 1993, Saunders, pp 717–757.
47. Pugh CR: Ultrasonographic examination of abdominal lymph nodes in the dog, *Vet Radiol Ultrasound* 35:110, 1994.
48. Graham JP, Newell SM, Roberts GD, et al: Ultrasonographic features of canine gastrointestinal pythiosis, *Vet Radiol Ultrasound* 41:273, 2000.
49. Patsikas MN, Papazoglou LG, Jakovljevic S, et al: Color Doppler ultrasonography in prediction of the reducibility of intussuscepted bowel in 15 young dogs, *Vet Radiol Ultrasound* 46:313, 2005.
50. Saunders J, Vignoli M: Chapter 31—gastrointestinal tract. In Schwarz T, Saunders J, editors: *Veterinary computed tomography*, Oxford, 2011, Wiley-Blackwell, pp 325–330.

ELECTRONIC RESOURCES

evolve

Additional information related to the content in Chapter 45 can be found on the companion Evolve website at http://evolve.elsevier.com/Thrall/vetrad/

- Chapter Quiz

Index

Page numbers followed by “f” indicate figures, “t” indicate tables, and “b” indicate boxes.

A

Abaxial fracture, 423–425
ABCDS (alignment, bone, cartilage, device, and soft tissues), 293
Abdominal fat, 659f
Abdominal lateral radiography, 657f, 682f, 705f–706f, 727f
  of chronic hepatitis, 684f
  of hepatic abscessation, 686f
  of hepatic carcinoma, 683f
  of left renal enlargement, 712f
  of lymphosarcoma, 681f–682f, 696f
  of mineralized choledocholith, 685f
  of splenic hemangiosarcoma, 697f
  of tubular gas opacity, 664f
Abdominal lymph node, 665–666
Abdominal radiography, 650–658. *See also* specific types of
  ancillary factors for, 656–657
  distortion in, 653–654
  of equine, 650
  of gallbladder, 680–681
  interpretation paradigm for, 658
  of nomenclature, 650
  organs not typically seen in, 658
  of pancreas, 667
  positioning for, 650–654
  preparation for, 650
  techniques for, 654–655
Abdominal right thoracic lateral radiography, 651f, 654f, 679f
Abdominal ventrodorsal radiography, 695f, 705f–706f
  with bilateral renomegaly, 711f
  with chronic hepatitis, 684f
  cranial aspect of, 680f
  with hepatic abscessation, 686f
  with hepatic carcinoma, 683f–684f
  with left renal enlargement, 712f
  with lymphosarcoma, 681f–682f, 696f
  with splenic hemangiosarcoma, 697f
Abdominal wall, 726f
  abnormalities of, 664
  anal gland adenocarcinoma in, 666f
  of canine, 666f
  caudal aspect of, 652f
  compression of, 673, 721f
  cranial aspect of, 656f
  distention of, 655f
  dorsal recumbency in, 663f
  dorsocaudal aspect of, 653f
  effusion of, 660, 662, 663f, 696f–697f
  fat in, 659f
  gas in, 730f
  granular pattern in, 661
  ill-defined nodular in, 661
  interpretation paradigm for, 658
  intraperitoneal fluid in, 660f
  left thoracic lateral radiography of, 695f
  lymphosarcoma in, 666f
  metastatic mast cell tumor in, 666f
Abdominal wall *(Continued)*
  midventral aspects of, 656f
  peritoneal fluid in, 661f
  rodenticide toxicity in, 661f
  ruptured splenic hemangiosarcoma in, 661f
  sonography of, 735–740
Aberrant subclavian artery, 514, 515f
Abrasion fracture, 292–293, 294f
Abscess, 444f, 697. *See also* specific types of
Absorbed dose, 3–4, 5f, 13
Absorption, 3. *See also* specific types of
Acanthomatous ameloblastoma, 120
Acanthomatous epulis, 120
Accessory carpal bone fracture, 387
Accessory ligament, 381, 400–403
Accessory lung lobe, 565f
Acetabulum, 299f
Achilles tendon, 337–338, 338f
Acinetobacter, 185
Acoustic enhancement, 41, 43, 44f
Acoustic impedance, 38–40, 39f, 39t, 45–46
Acoustic shadow/shadowing. *See also* specific types of
  to calculi, 737, 738f
  to cholelith, 692f
  defined, 43
  dystrophic mineralization caused by, 403
  gallbladder, caused by, 43, 686, 692
  gas causing, 668f, 691, 738
Acquired cardiovascular lesion, 596–602
Acquisition hardware, 23–27
Actinomyces, 215
Acute coughing, 495f
Acute discospondylitis, 186f
Acute gastric dilation, 777–780
Acute injury to lung, 639–641
Acute intervertebral disc herniation, 199f
Acute lameness, 335f
Acute noncompressive intervertebral disc extrusion, 203–204
Acute ptyalism, 519f
Acute respiratory distress syndrome, 639–641
Acute rib fracture, 527f
Acute suppurative hepatitis, 689
Acute tubular necrosis, 713
Adamantinoma, 156
Addison’s disease, 581f, 606f
Adenocarcinoma, 117, 161, 494, 674–675. *See also* specific types of
Adenoma, 116–117, 671–672
Adrenal calcification, 672–673
Adrenal dependent hyperadrenocorticism, 674–675
Adrenal gland, 671–675, 672f–675f
  abnormalities of, 671–673
  dysfunction of, 673
  lateral radiograph of, 672f
Adrenal gland *(Continued)*
  sonography of, 673–675, 673f–675f
  ventrodorsal radiography of, 672f
Adrenal mass, 675b
Adrenal tumor, 672–674
Adrenocorticotropic hormone, 675
Advanced coxofemoral degenerative joint disease, 321f
Advanced hip dysplasia, 331f
Aerophagia, 492f, 497, 502, 511f
Agenesis, 271, 273f. *See also* specific types of
Aggressive bone disease, 258–259
Aggressive bone lesion, 258, 261–264
  from bacterial bone infection, 311
  biopsy of, 310
  from bone tumor, 311
  nonaggressive *vs.*, 259–261
  radiography of, 182–183, 307
Air. *See also* specific types of
  in pleural space, 579, 582
  radiation exposure in, 4
  radiopacity of, 75, 75f, 324
Air bronchogram, 610–611, 613, 684
  alveolar pattern in, 610–611, 613
  defined, 610–611
  formation of, 611f
  in neoplasia, 642
  radiography of, 611, 611f–615f, 618f, 628f–631f
Air bubble, 629–630, 734f
  during cystocentesis, 730f
  from luminal filling defect, 732
  tetrahedron of, 44
  in urethra, 746
Air bubble artifact, 731, 734–735, 736f
Air opacity, 74–75, 76f
Airway obstruction, 495–497, 504, 641. *See also* Upper airway obstruction
Airway paradigm, 626
ALARA (as low as reasonably achievable) principle, 6
Aliasing, 47f–48f, 49
Aliasing artifact, 48–49, 71–72
Alignment, 293
Alternate imaging of foot, 433
Alternating current, 9–11
Alternative imaging procedure, 500
Alveolar air, 573, 610, 611f, 612–615
Alveolar bone recession, 129
Alveolar crest, 114, 129, 129f
Alveolar pattern, 500f, 610–615, 611f–612f, 639. *See also* Thorax
  in air bronchogram, 610–611, 613
  in alveolar space, 613
  in alveoli, 610
  atelectasis and, association between, 613–615, 622–623
  border effacement, cause of, 626
  causes of, 613, 615t
  cranioventral aspect of, 611f
  left caudal aspect of, 612f

Alveolar pattern *(Continued)*
lobar sign as indication for, 612–613
radiography of, 510f, 555f, 597f, 599f, 611f–612f, 614f–616f, 624f–625f, 627f–631f, 637f
right caudal aspect of, 612f
right middle region of, 612f
ventral region of, 612f
Alveolar space, 613
Alveoli, 610
Ameloblastic odontoma, 161
Amorphous, 118f, 123f, 278, 308, 503f, 504, 505f, 582, 582f
Amorphous selenium, 26, 26f
Amorphous silicone, 26f
Amputated forelimb, 183f
Anal gland, 666f
Analog film image, 35–36
Analog-to-digital converter (ADC), 61f, 70f
Analog *vs*. digital radiography, 29–37, 33f, 74
contrast optimization, 29–35
darkroom, elimination of, 29
exposure latitude, 29–35
image storage consolidation, 35
inherent spatial resolution in, 30b
portability, enhanced, 35–36
postprocessing, 35
professionalism, enhanced, 36–37
of skull, 32f
supply cost, reduced expendable, 29
thoracic radiographs made with, 32f
wide contrast resolution of, 31f
Anatomic directional terms, 83f
Anatomic reduction, 284, 294
Ancillary radiography, 103t
Ancillary view, 101, 104, 252
Anconeal process, 268, 271f
Andalusian, 378f
Anechoic structure, 670f, 686, 691
Anesthesia, 107, 118
Aneurismal bone cyst, 156, 156f
Angiocardiogram, 605f
Angiography, 60, 60f, 67, 71, 500, 520, 539, 685, 711. *See also* specific types of
computed tomography and, 60, 60f, 500, 520, 685
history of, 2
Angiostrongylus, 215
Angle of incidence, 38–39, 39f
Angle of obliquity, 415f
Angular displacement, 290–291
Angular limb deformity, 278, 303, 376–378, 379f
asynchronous growth, 276
cartilage retention, 278
radial osteotomy for correcting, 284f
radiography of, 278, 376
Ankylosing arthropathy, 339f
Ankylosing spondylopathy, 321–322, 338–339, 339f
Annular array, 40, 55
Annulus, 196
Annulus fibrosus, 174, 182, 186, 194–196, 198, 205, 208
Anode, 9, 9f, 12, 12f
Antebrachial fracture, 286f
Antebrachial radiography, 304f
Antebrachiocarpal joint, 304f, 343f, 346f, 374, 380f, 381–382, 382f, 384f, 388–390, 388f
Antebrachiocarpal region, 382f
Antebrachium, 228f, 262f, 265f, 344f
craniocaudal radiography of, 228f, 262f
lateral radiography of, 262f, 265f, 344f
Antebrachium *(Continued)*
mediolateral radiography of, 228f
with nonaggressive lesion, 262f
Antecurvatum, 299–301, 303f
Antegrade pyelogram, 708f, 720f
Antegrade ultrasound-guided pyelography, 708
Anticlinal vertebrae, 107
Antiscatter grid, 30–31
Anus, 748f
Aorta, 47f–48f, 591–592, 605f
Aortic arch, 591f, 603f–604f. *See also* specific types of
Aortic arch diverticulum, 603f–604f
Aortic stenosis, 588, 591, 591f, 604, 605f
Apical fracture, 426f
Appendicular skeleton. *See also* individual topics on
disorders of, 268b
equine carpus, 374–393
fracture healing, 283–306
metacarpal and metatarsal bones, 394–413
metacarpophalangeal and metatarsophalangeal articulation, 414–428
navicular bone, 457–471, 457f
neoplastic and infectious bone disease in, 307t
orthopedic disease, 267–282
phalanges, 429–456
polyarthropathies affecting, 341b
radiography of, 224–266, 307–348
stifle, 349–360
tarsus, 360–369
Apron, 6–8, 14, 102–103, 252–253
Arachnoid cyst, 135
Arachnoid diverticula, 207
Archiving image, 28–29, 29f
Array, 40. *See also* specific types of
Array transducer, 40, 40f, 44f
Arteries. *See* specific types of
Arthritis, 319–320, 342, 342b. *See also* specific types of
Arthropathy, 339f, 419f, 420
Articular cartilage, 326–327, 330, 336–337, 355–356, 433
Articular fracture, 288, 333, 335f, 440, 442f
Articular process
cyst of, 181f, 207–208, 209f
degenerative joint disease of, 181f, 187, 187f
hypertrophy of, 187, 205, 208
of lamina, 172
malformation of, 179, 181f
osteophytosis in, 202–203
subluxation of, 202–203
Articular process joint, 172–174, 194–195, 197f, 204
Articular soft tissue, 321
Artifacts, 583f. *See also* specific types of
on digital radiography, 37
magnetic resonance imaging of, 71–72
on ultrasound imaging, 43–46
Artifactual color Doppler signal, 49
Aryepiglottic fold entrapment, 168
Arytenoiditis, 168
Ascending colon, 711
Ascite, 536, 596, 600, 664f, 688–689, 688f–689f, 693
Aseptic necrosis, 269–271, 273f
As low as reasonably achievable (ALARA) principle, 6
Aspergillosis, 121–122, 123f
Aspergillus, 121–122
Aspiration, 504
Aspiration pneumonia, 497, 500, 507–510, 510f, 514–515, 636, 645
Asynchronous growth, 276
Atelectasis, 478, 613–615, 622–623
Atlantoaxial instability, 109–110
Atlantoaxial subluxation, 109, 175, 177–178, 178f
Atrophic nonunion fracture, 285f, 302
Attached filling defect, 732, 735
Attenuation
in sonography, 43, 44f
of sound wave, 39–40, 42, 688–689
in tissue, 57, 58f
in x-ray, 22, 24–25, 30f, 50, 57, 136, 623
Autologous bone graft, 286–287
Automatic film processor, 21
Avulsion fracture, 290–291, 292f
Axial resolution, 40–41, 41f
Axial skeleton. *See also* individual topics on
brain disease, 135–152
cranial and nasal cavity, 114–134
equine head, 153–171
radiography of, 88–113
spinal cord disease, 194–221
vertebrae, 172–193

B

Bacterial bone infection, 311
Bacterial infection, 122, 311, 443, 494
Bacterial osteomyelitis, 286f
Balance of foot, 453f
Ballottement, 737–738
Barium-contrast esophagram, 502f
Barium enema, 814–815
Barium esophagram, 515f, 546f
Barium esophagram hernia, 546f
Barium gastrogram, 540f
Barium paste, 524f
Barium sulfate, 539–540, 540f, 542–543, 770b
Barium swallow, 504f–505f, 509f, 515f
Bates body, 663
Beam divergence, 15f
Behavioral change, 144f
Benign bone lesion, 262f
Benign joint disease, 320
Biarticular middle phalanx fracture, 438f
Bias, 86
Biaxial desmitis, 418f
Bicep, 337f
Bicep tendon, 337f
Bicipital groove, 253f
Bicipital tendonitis, 335–336, 337f
Bicipital tenosynovitis, 335
Bicondylar fracture, 292
Bilateral coxofemoral laxity, 333f
Bilateral ectopic ureter, 707f, 721f–722f
Bilateral paralysis, 545
Bilateral stifle enlargement, 345f
Bilateral total hip prostheses, 311f
Bilateral ureteral obstruction, 720f
Biliary calculi, 684
Biliary cystadenoma, 691
Biliary dilation, 670–671, 692
Biliary sludge, 688f, 692, 693f
Biliary system disease, 691–692
Binding energy, 9
Biologic injury, 2–3
Bit depth, 23, 23f–24f
Blackness, 8, 14–16, 74
Bladder, 726–743, 741f
of canine, 727f
catheterization of, 661, 728, 730–731, 730f, 738

Bladder *(Continued)*
contusion of, 735f
cranioventral aspect of, 735f
cystography of, 730f
distention of, 744
filling defect in, 734t
lateral radiography of, 732f
pathologic process of, 733t
sonography of, 737
ventrodorsal radiography of, 735f
Bladder neck, 740f
Blastomyces, 215
Blastomycosis, 121–122, 309, 312f, 314f, 344, 564–565
Block vertebrae, 175, 176f
Blood clot, 738
Body habitus, 484, 656–657
Body wall hernia, 723f
Bone, 283, 500f. *See also* specific types of
agenesis of, 271
destruction of, 258–259
disease of, 258–259
disuse atrophy of, 425, 485f
graft/grafting of, 286–287, 301
healing of (*See* Bone healing)
infarction of, 309
loss of, 259
opacity of, 276
Bone cyst, 453. *See also* specific types of
Bone disorder. *See also* specific types of
congenital hypothyroidism, 274
mucopolysaccharidosis, 274–275
nutritional secondary hyperparathyroidism, 273–274
osteogenesis imperfecta, 275
osteopetrosis, 275–276
Bone-filtering, 58f
Bone formation, 283
Bone healing, 283–285, 293–298, 294b
Bone infarction, 309
Bone infection, 258–259, 309–311, 316
Bone lesion, 258t, 262f. *See also* Aggressive bone lesion
Bone lysis, 259–261
Bone phase scintigram, 153f
Bone recession, 129
Bone scintigraphy, 288, 464–465
Bone-seeking radiopharmaceutical, 153
Bone sequestrum, 303
Bone tissue, 283
Bone tumor, 311
Border effacement, 79–80, 82f, 626
Borzoi, 586f
Bowel-associated mass, 807–808
Bowel dilation, 795–797
Bowel gas, 43, 650, 652–654, 662, 673, 693
Brachycephalic airway obstruction syndrome, 495–496
Brachycephalic breed, 114
Brachycephalic syndrome, 493, 493f
Brain, 218f. *See also* Cranium
abscess in, 165
compression of, 138, 138f, 146f
computed tomography of, 115f, 166f
developmental conditions of, 138
inflammatory conditions of, 139–141
magnetic resonance imaging of, 135–138
Brain disease, 135–152
brain neoplasia, 141–143
intracranial conditions of, 138–141
invasive extracranial tumor, 145–147
magnetic resonance imaging of, 135–152
vascular disruption in, 147–150
Brain metastases, 146–147
Brain neoplasia, 141–143
Brain tumor, 165
Braking model of x-ray, 10f–11f
Braking process, 9
Braking radiation, 9
Breaking model of x-ray production, 10f
Bremsstrahlung radiation, 9
Bremsstrahlung x-ray, 9
Bridging callus, 284, 296–298, 301f, 525
Bright light, 84f
Brightness mode (B-mode) imaging, 42, 47–48
Broad bandwidth technology, 41
Bronchi, 610–611, 617, 618f
Bronchial compression, 587, 588f
Bronchial mineralization, 616, 619
Bronchial obstruction, 616–617, 618f
Bronchial pattern, 601, 615–619, 615f–617f, 617t, 619f–620f, 626–629, 629f–630f, 641–642, 641f
Bronchiectasis, 496, 616–617, 618f–619f
Bronchitis, 496, 641. *See also* specific types of
Bronchopneumonia, 636, 636f, 638–639, 641
Bronchus, 616f
Brown fat, 660
Brownian motion, 69–71, 147–149
Bucky, 17–18
Butterfly fragment, 286f, 289
Butterfly vertebrae, 217

C

Calcaneal osteomyelitis, 367–369, 368f
Calcaneus, 367–369, 368f
Calcification, 452. *See also* Ossification; specific types of
Calcified intraarticular body, 321t
Calcinosis circumscripta, 358, 359f, 381
Calcitonin, 283
Calcium tungstate ($CaWO_4$), 17
Calculated laxity index (DI), 332–333
Calculi/calculus, 670, 737, 738f. *See also* specific types of
Callus, 294–296. *See also* specific types of
formation of, 274f, 283–284, 285f, 287, 293–294, 301–302
fracture associated with, 262f
remodeling of, 284, 301
Callus index, 296–298
Calvaria, 114
Calvarial hyperostosis, 129
Calvarium, 283
Cancellous bone, 194–195, 285f, 345, 357, 375, 409f
Canine and feline. *See also* specific topics regarding
cranial and nasal cavity of, 114–134
esophagus of, 500–521
joint disease of, 319–348
orthopedic disease of, 267–282
spinal cord disease of, 194–221
vertebrae of, 172–193
Capillary network of physis, 309–311
Capital epiphysis, 335f
Capture hardware options for image, 27f
Carcinoma. *See* specific types of
Carcinomatosis, 661
Cardia, 535, 543–544, 546f, 548f
Cardiac chamber enlargement, 585–589
Cardiac disease, 585, 605, 639–641, 645
Cardiac region, 479f
Cardiac silhouette, 478, 532f, 542, 585, 589, 603f
dorsoventral thoracic radiography of, 532f
ventrodorsal thoracic radiography of, 186f
Cardiogenic pulmonary edema, 596, 615f, 626–629, 630f
Cardiomegaly, 85, 478, 482f–483f, 484, 494, 588–589, 600, 603f, 635, 641, 645, 646f
Cardiomyopathy, 600–602, 600f–602f
Cardiophrenic ligament, 551–552
Cardiovascular lesion, 596–605
Carpal bone. *See also* specific types of
distal row of, 242f, 385f, 388f–389f
dorsal row of, 387
incomplete ossification of, 376, 378
sclerosis of, 382–383
Carpal bone fracture, 383–387
Carpal dorsolateral palmaromedial oblique radiography, 377f, 397f, 408f
Carpal hygroma, 380–381
Carpal sesamoid, 324f
Carpal sheath, 381–382
Carpometacarpal ankylosis, 340f
Carpometacarpal joint, 374, 381, 390, 395f, 404
Carpus
see also specific types of radiography of
antebrachiocarpal joint of, 374
cellulitis in, 380–381, 380f, 435, 492, 492f
dorsomedial-palmarolateral view of, 258
entheses around, 322f
of equine, 374–393
joint disease of, 336
left, 240f–241f
polyarthritis of, 344f
Cartilage, 294, 336–337, 419, 433, 445, 452–453. *See also* specific types of
Cartilage core, 278, 279f
Cartilage degeneration, 326–327, 330, 355–356, 419, 445
Cartilage flap, 267–268
Cartilage retention, 278
Cassette, 17f, 101–102, 252–253
Cassette holder device, 106, 111, 112f, 253
Cat. *See* Feline
Catheterization, 661, 728, 730–731, 730f, 738
Cathode, 9, 9f
Cathode-ray tube (CRT), 28
Cauda equina syndrome, 188, 194, 202–203
Caudal abdomen, 664f, 726f–727f, 729f–730f
Caudal aspect, 79f–80f, 108f, 111f, 482f, 643f–644f, 652f
of abdomen, 652f
of cervical spine, 108f
of esophagus, 513f
of lumbar spine, 79f
of thoracic spine, 108f, 111f
of thorax, 643f–644f
Caudal brain, 218f
Caudal cervical spine, 100f, 206f
Caudal cervical spondylomyelopathy, 205f
Caudal equina syndrome, 187–188
Caudal esophageal foreign body, 562f
Caudal esophagus, 502f, 518f, 544, 562f
Caudal fragment, 182f
Caudal frontal sinus, 115f
Caudal lobe, 624f

Caudal lobe artery, 593f
Caudal lobe pulmonary artery, 593f
Caudal lung lobe, 624f–625f
Caudal maxillary arcade, 127f
Caudal mediastinum, 478–482, 511, 542–543, 557, 562f
Caudal nasal neoplasia, 145
Caudal region of head, 97f
Caudal thorax, 478f, 567f, 641f
Caudal veins, 48f
Caudal vena cava (CVC), 48f, 479f, 589–591
Caudal vertebrae, 107, 172, 276–277, 339–340
Caudocranial radiography
  of elbow, 262f
  of elbow joint, 226f
  of humerus, 225f, 260f
  of shoulder joint, 224f
  of stifle, 356f–358f
  of stifle joint, 248f
  of tibial diaphysis, 359f
Caudodorsal alveolar pattern, 639
Caudodorsal aspect, 519f, 637f, 642f
Caudodorsal projection, 633f
Caudodorsal thorax, 512f, 635f
Caudolateral-craniomedial radiography, 249f, 352f, 359f
Caudoventral mediastinal mass, 562–564
Caudoventral mediastinal reflection, 550–552
Caudoventral projection, 634f
Caudoventral thoracic vertebrae, 636f
Caval mediastinal reflection, 550
Cavitary lung mass, 623
Cavitary mass, 623
Cavitary nodule, 623
Cavitation, 218, 420–421, 462f, 464, 531f
Cecum, 658
Cellulitis, 380–381, 380f, 435, 492, 492f, 530
Cemented hip prosthesis, 312f
Centering points, 110f–111f
Centimeter-gram-second (CGS) system of measures, 3
Central eminence, 457
Central sulic of foot, 429f
Centrum, 172
Cerebellar abscess, 140f
Cerebellum, 140f
Cerebral infarction, 147–149
Cerebrospinal fluid (CSF), 67, 116, 137–139, 141, 143, 195, 200, 218
Cervical disc degeneration, 182
Cervical esophagus caudal, 512f
Cervical intervertebral disc disease, 200
Cervical intervertebral disc space, 198f
Cervical lateral radiography
  of acute ptyalism, 519f
  of block vertebra, 176f
  of cervical spondylomyelopathy, 180f–181f
  of cricopharyngeal chalasia, 509f
  of ingested bone, 506f
  of multiple myeloma, 190f
  of vocalizing, 519f
Cervical mass, 491f, 494
Cervical radiography, 109f
Cervical spine, 108f, 178f, 216f, 218f
Cervical spondylolisthesis, 204
Cervical spondylomyelopathy, 178–179, 180f–181f, 204–207, 206f–207f
  computed tomography of, 205, 206f
  lateral cervical radiography of, 180f–181f
Cervical spondylomyelopathy *(Continued)*
  magnetic resonance imaging of, 205–207
  sagittal reformatted, 205f
  T1-weighted images of, 207f
  T2-weighted images of, 180f–181f, 206f–207f
  in vertebral column, 178–179
Cervical spondylo-myelopathy, 179t
Cervical spondylopathy, 204
Cervical vertebrae, 91f, 99f, 108f, 167, 557
  instability of, 204
  left-right lateral radiography of, 91f, 99f
  malarticulation of, 204
  malformation of, 204, 340f
  ventrodorsal radiography of, 92f
Cervicothoracic region, 112f, 490f
Characteristic x-ray, 9, 10f–11f, 13
Charge-coupled device (CCD) radiography, 23–24, 26–27, 26f
Chemical fat saturation (FS), 69, 69f
Chemodectoma, 564f
Chihuahua, 513f
Chip fracture, 291, 421
  of carpal bone, 383–386
  of navicular bone, 465f
Choledocholiths, 684, 685f
Cholelith, 684, 685f, 692, 692f
Cholesterol granuloma, 165, 166f
Chondrocyte, 276, 278, 339
Chondrodysplasia, 276–277, 276f
Chondroid, 167, 167f, 182, 398–399
Chondrosarcoma, 117, 188–190, 208, 494, 517, 528, 531f
Choroid plexus tumor, 143, 143f
Chronic asthma, 619f
Chronic bronchial obstruction, 616–617
Chronic bronchitis, 619, 641f
Chronic coughing, 496f
Chronic degenerative joint disease, 425f
Chronic desmopathy, 337–338
Chronic hepatitis, 684f
Chronic laminitis, 448f
Chronic lick granuloma, 314f
Chronic lumbosacral pain, 188f
Chronic medial luxation, 328f
Chronic nasal discharge, 123f
Chronic pyloric obstruction, 780–782
Chronic renal disease, 713f
Chronic renal failure, 117f, 664f
Chronic rhinosinusitis, 493f
Chronic tenosynovitis, 418f
Chronic urinary tract infection, 748f
Chronic weight-bearing lameness, 329f
Cirrhosis, 684, 688–689, 689f
Clavicle, 323f
Clavicular remnant medial, 323f
Cloaca, 303
Closed fracture, 289–290, 294f
Cobra-head sign, 732
Coccidioides, 215
Coccidioidomycosis, 309, 313f
Codman's triangle, 308, 310f
Coherent scattering, 12–13
Collapse of multiple fragment, 290–291
Collateral cartilage, 433, 452–453, 452f
Collateral ligament, 356–357, 362, 364f, 435f, 436
Collateral sulic of foot, 429f
Collecting system diseases, 717–718
Collimation, 56f, 126, 349
Collimator, 6–8, 14, 14f
Collisional interaction, 9
Collisional model of x-ray production, 10f
Collisional process, 9
Colon, 653f, 658, 665–666, 666f, 721f. *See also* specific parts of
Color Doppler image, 48f
Color Doppler signal, 47–49, 48f, 686, 693, 700, 709f, 720–721, 737, 739f
Color LCD monitor, 28
Columnar periosteal reaction, 263f, 302f, 311, 314f–315f
Comet tail artifact, 43–44, 45f, 635–636, 636f, 638, 641–642
Comminuted fracture, 110f, 289, 291, 294, 387, 408, 410, 425f, 436, 438f, 439–440. *See also* specific types of
Comminuted proximal diaphyseal fracture, 293f
Common bile duct, 670, 686–688, 692
Compensated mitral insufficiency, 598f
Complete agenesis, 271
Complete airway obstruction, 496–497
Completed PennHIP study, 334f
Complete fracture, 289, 292, 378–379, 441f, 465
Complete navicular bone fracture, 465, 466f
Compression. *See* specific types of
Compression fracture, 189f, 291, 406
Compression radiography, 651, 653f, 814
Compressive stress, 334
Compton absorption, 13–14, 14f
Compton electron, 13–14
Compton scattering, 12–14, 17
Computed dorsoproximal-dorsodistal radiography, 298f
Computed radiography (CR), 23–26, 29, 30f, 37, 104f, 296, 359–360, 463
Computed tomography (CT), 53–60, 154–155, 288. *See also* specific types of
  angiography using, 60, 60f, 500, 520, 685
  of brain, 115f, 166f
  of calcification, 622
  of cervical spondylomyelopathy, 205, 206f
  characteristics of, 51f
  components of, 56f
  contrast-enhanced ultrasonography using, 59–60
  contrast resolution using, 52f, 60f
  of equine head, 51f
  excretory urogram using, 740f–741f
  geometry of, 55
  hoist for, 155f
  image display of, 57
  image formation of, 50–53, 57
  of intervertebral disc disease, 198–200
  of kidneys and ureters, 710–711
  of left mandibular squamous cell carcinoma, 120f
  of left tympanic bulla cholesteatoma, 127f
  multiplanar reformatting with, 54f
  for myelogram, 205f–206f, 209f
  of nasal cavity, 123f
  of navicular bone, 467–469
  numbers in, 57
  of pharynx, larynx, and trachea, 497–498
  for portosystemic shunt, 60f
  range of Hounsfield unit for composing, 59f
  spatial resolution using, 52f
  of spinal cord disease, 194–221
  of temporal multilobular osteochondrosarcoma, 121f
  tissue attenuation measured by, 58f

Computed tomography (CT) *(Continued)*
of tympanic bulla region, 127f
in veterinary practice, 50
without intrathecal contrast medium, 199f
Conchofrontal sinus, 158
Concurrent bronchitis, 617–619
Concurrent disc degeneration, 186
Concurrent rib fracture, 639
Condylar fracture, 278–280, 287f, 292, 297f, 300f, 407–408, 421
Congenital anomalies, 114–116
hydrocephalus, 114–115
incidental factors for, 264
mucopolysaccharidosis, 116
occipital bone malformation and syringomyelia, 116
occipital dysplasia, 115–116
radiography of, 112–113
of spinal cord, 217
temporomandibular joint dysplasia, 116
Congenital cardiovascular lesion, 603–605
Congenital hydrocephalus, 114–115, 138, 138f
Congenital hypothyroidism, 274, 275f
Congenitally predisposed diaphragmatic hernia, 541
Congenital sternal deformity, 523
Congenital thoracic wall defect, 523
Congestive heart failure, 596, 646, 691–693, 692f, 694f
Conspicuous superimposition opacity, 80f
Constant velocity, 38
Consultation, 35–36
Continuous-wave Doppler image, 47
Contrast, 57
enhancing, 67
factors affecting, 19–20
in fluoroscopy, 506–507
of image, 30–31
long scale of, 19–20
optimization of, 31–32
of peritoneal space, 660–663
in small bowel examination, 793–795
in T1-weighted image, 70f
Contrast cystography, 729–735
interpretation of, 734–735
pitfalls with, 734–735
procedures for, 731
radiography of, 731–734
techniques for, 730–731
Contrast-enhanced angiography, 71, 711
Contrast-enhanced ultrasonography, 59–60, 71, 690, 711
Contrast esophagraphy, 500, 504
Contrast fluoroscopy, 506–507
Contrast leakage pattern, 732–734
Contrast media, 67, 504t
Contrast medium, 60f, 144f, 199f, 734, 747
Contrast optimization, 29–35
Contrast radiography, 324, 500
Contrast resolution (CR), 31–32, 50, 52f, 60f, 69f, 74–75
Control mechanism, 506t
Contusion, 179, 198, 203f, 204, 735f
Conus medullaris, 194
Conventional lateral radiography, 577f
Conventional x-ray machine, 22
Convex array, 40
Core lesion, 401f, 403, 404f, 406f, 437f
Coronoid process, 266. *See also* specific types of
Cortical bone, 194–195
Cortisone arthropathy, 419f, 420
Costal cartilage, 524f, 573–574
Costal parietal pleura, 571
Costochondral degeneration, 524f
Costochondral junction, 277, 488f, 522, 522f, 633
Costophrenic angle, 573
Costosternal mineralization, 522
Coughing, 493f, 495f–496f
Coxofemoral joint, 331–333, 331f–332f, 334f, 340f
Cranial abdomin, 548f, 680f
Cranial and nasal cavity, 114–134. *See also* Nasal cavity
anatomy of, 114
congenital anomalies of, 114–116
disease of, 127–129
infectious disorder of, 121–126
metabolic anomalies of, 116–117
neoplastic abnormalities of, 117–121
traumatic injury of, 127
Cranial aspect, 178f, 326f, 554f, 644f–645f, 656f
Cranial callus, 299f
Cranial cervical region, 168f
Cranial cervical vertebrae, 99f
Cranial dorsoventral thoracic radiography, 529f
Cranial lobe artery, 592f
Cranial lung lobe, 625f
Cranial mediastinal mass, 494
Cranial mediastinum, 474, 486f, 514f, 550, 553f–554f, 554–557, 559f–561f, 566f, 568f–569f, 645f
Cranial nerve-sheath tumor, 145–146
Cranial thoracic vertebrae, 527f
Cranial thorax, 566f
Cranial tumor, 121
Craniocaudal radiography
of antebrachium, 24f, 228f, 262f
of crus, 235f
of elbow joint, 226f, 239f
of femur, 233f, 259f
of malunion intercondylar fracture, 300f
of stifle joint, 234f
Craniocaudal view, 252, 299f, 310f, 314f
Craniodorsal mediastinal abscess, 561f
Craniodorsal mediastinal mass, 561f
Craniodorsal projection, 633f
Craniodorsal thorax, 638f, 645f
Craniolateral-caudomedial oblique radiography, 227f
Craniomandibular osteopathy (CMO), 127–129, 129f, 273
Craniomedial-caudolateral oblique radiography, 227f
Cranioproximal-craniodistal view, 252, 253f, 349, 354f, 359f
Craniaventral aspect, 611f, 621f, 656f, 661f–662f
Cranioventral mediastinal mass, 554–557
Cranioventral mediastinal reflection, 550–551, 553f–554f, 557, 560f
Cranioventral projection, 634f
Cranium. *See also* Brain
cruciate ligament of, 342f
drawer sign in, 321, 334
esophageal sphincter in, 500–501
fat pad in, 349
mediastinal lymph node of, 557, 564–565
mediastinal mass in, 494
Crena margins solaris, 431
Cribriform plate, 114, 117–118, 118f
Cricopharyngeal achalasia, 507–509
Cricopharyngeal chalasia, 508–509, 509f
Cricopharyngeal dysphagia, 507–509, 509f
Cricopharyngeal phase, 508f
Cricopharyngeal sphincter, 500–501, 501f, 507–509, 508f–509f, 512f, 519f
Cross-sectional imaging, 114
Cruciate ligament, 68f–69f, 265, 327, 336–337, 340–341, 342f
cranial, 68f–69f, 336–337, 342f, 349, 356, 358f
radiography of, 356–357
Crus, 235f, 344f
Cryptococcus neoformans, 121–122, 122f, 215, 443
Cuboidal bone, 277f, 291
Cuboidal carpal bone, 374
Cumulative exposure, 6
Cupula, 535–538, 536f, 538f, 541f, 548f
Curved array transducer, 40f, 44f
Cutaneous lesion, 484, 657
Cyst, 162. *See also* specific types of
Cystadenoma, 691, 691f
Cystic calculi, 730f, 730t
Cystic duct, 684–685, 692
Cystic endometrial hyperplasia, 760–761
Cystic lesion, 346f
Cystic ovarian disease, 764
Cystitis, 728, 730f, 738–739, 739f
Cystocentesis, 730f
Cystography. *See also* specific types of
of bladder, 730f
equipment for, 730f
interpretation of, 734–735
procedures using, 731, 732t
techniques for, 730–731
voiding, 729

D

Decision making, 179, 190
Decreased bone cyst, 319–320
Deep digital flexor tendon injury, 403
Defect nonunion fracture, 302
Degeneration. *See* specific types of
Degenerative, anomalous, metabolic, neoplastic, infectious, traumatic, and vascular (DAMNITV), 86
Degenerative intervertebral disc disease, 196–197
Degenerative joint disease, 325–330, 365–366, 418–420. *See also* specific types of
of articular process, 181f, 187, 187f
of distal intertarsal joint, 362–365
dorsolateral-plantaromedial oblique radiography of, 367f
dorsopalmar radiography of, 420f
of elbow, 330f
of equine, 367f
of femorotibial joint, 355–356
lateromedial radiography of, 419f, 425f
of metacarpophalangeal and metatarsophalangeal articulation, 418–420
in Morgan line, 332f
osteoarthritis and, 330
of phalanges, 443–445
radiography of, 326–330, 330b
of stifle, 356f
of talocalcaneal and proximal intertarsal joints, 365–366
Degenerative lumbosacral stenosis, 202–203
Degree of fracture, 289–290
Delayed union, 301
Demarcated histologic zone, 283
Density, 74, 75f

Dental anatomy, 159–160
Dental disease, 126, 129f, 153–154, 160
Dental formula, 115b
Dental laminar epithelium, 120–121
Dental nomenclature, 159
Dental x-ray machine, 126
Dentigerous cyst, 160–161, 161f
Depression fracture, 160f, 292
Depth perception, 75, 77
Dermoid cyst, 208
Descending colon, 696, 711, 712f, 726f–727f, 729f, 740f
Desmitis, 400–403, 419f, 436. *See also* specific types of
Desmopathy, 335, 337–338, 369, 398–403
Destructive rhinitis, 122
Details, 16f
Detector system, 55
Deterministic effect, 4–5
Developmental laminitis, 446–447
Developmental lesion, 267
Developmental skeletal disease, 267
Diagnostic images/imaging, 6, 287
Diagnostic medical imaging, 22
Diagnostic radiology, 3
  concept of, 8, 14–16
  contrast of, 19–20
  distortion of, 18
  film processing during, 20–21
  image detail during, 16–18
  physics of, 2–21
  radiation protection during, 2–21
  raditation with matter interaction in, 12–14
  x-ray in, 2–3, 9–12
Diagnostic ultrasound machine, 40
Diaphragm, 479f, 535–549
  diaphragmatic disease of, 538–547
  gastroesophageal intussusception in, 544–545
  hernia of, 538–540, 543–545
  motor disturbance in, 545–546
  muscular dystrophy in, 546–547
  radiography of, 535–538
Diaphragmatic disease, 538–547, 538t
Diaphragmatic flutter, 545–546
Diaphragmatic hernia, 538–540
Diaphragmatic paralysis, 545
Diaphragmatic region, 536f–537f, 539f
Diaphyseal comminuted fracture, 295f
Diaphyseal deformity, 378
Diaphyseal fracture, 288
Diaphyseal tibial fracture, 291f
Diaphysis, 288, 291f, 378, 390, 404–407. *See also* specific types of
Diarthrodial joint, 172, 194–195
Dieffenbachia, 494
Differential absorption, 13–14, 20, 74, 75f, 654
Differential diagnosis, 160, 168, 265, 344, 420, 554, 596, 675b
Diffuse alveolar pattern, 500f
Diffuse disease, 785–786
Diffusely increased splenic echogenicity, 699
Diffuse neoplastic infiltration, 698
Diffusion-weighted imaging (DWI), 69–71, 70f
Digital flexor tendon, 403–404, 407f
Digital image file, 22
Digital imaging, 27f
Digital Imaging and Communications in Medicine (DICOM), 22, 27–29, 28f, 35–36, 57, 84, 85f
Digital radiographic imaging artifact, 37
Digital radiography, 22–37. *See also* Analog *vs.* digital radiography
  acquisition hardware for, 23–27
  artifact on, 37
  charged-coupled device for, 26–27
  components of, 23
  description of, 22
  digital image file in, 22
  of distal humerus, 35f
  flat-panel detectors for, 25–26
  image processing/viewing in, 27–28
  of lumbar spine, 34f
  in medical practice, 28–29
  of tarsus, 34f
Digital tendon sheath distention, 467–468
Digital tumor, 317, 317f
Dilated aortic arch, 591f
Dilated cardiomyopathy, 600–601, 601f–602f, 630f
Dilated caudal esophagus, 544
Dilation. *See also* specific types of
  of aorta, 605f
  of bronchi, 617, 618f
  of common bile duct, 692
  of pancreatic duct, 669–670
  of pulmonary artery, 592f, 600, 603f
  of pulmonary vein, 629
  of upper airway, 497
Direct bone healing, 283–284
Direct digital radiography (DDR), 23–26, 29, 30f, 37
Direct flat-panel detector, 25–26
Directional terms, 81, 83f
Direction of fracture, 289
Dirofilaria immitis, 215, 344
Discal cyst, 208
Discal mineralization, 183–185
Disc degeneration, 175–177, 176f, 179, 182–187, 184f, 196–197, 202–203
Disc explosion, 198
Discospondylitis, 183–185, 186f, 188, 215, 216f, 530
Disease. *See* specific types of
Disk-space width, 109f
Disorder. *See* specific types of
Dispersed air bubbles, 629–630
Displacement, 290–291. *See also* specific types of
Disseminated idiopathic skeletal hyperostosis (DISH), 190
Distal acoustic shadow/shadowing, 43f, 675f, 714, 720–721
Distal antebrachial fracture, 286f
Distal antebrachium, 24f, 262f, 265f, 312f, 376f
Distal aorta, 48f
Distal aspect, 84f, 383f
Distal border change, 463
Distal diaphyseal tibial fracture, 291f
Distal diaphysis, 288, 291f
Distal displacement, 329f
Distal epiphysis, 357–358
Distal femur, 261f, 264f, 293f, 308f, 312f
Distal humeral epiphysis, 277f
Distal humerus, 35f, 263f, 287f, 303f
Distal interphalangeal joint, 343f, 430, 431f, 433, 436, 438f, 440, 443, 445, 445f, 449–450, 450f
Distal intertarsal degenerative joint disease, 365f
Distal intertarsal joint, 362–365, 362f, 365f–367f
  degenerative joint disease of, 362–365
  subchondral cystlike lesion of, 365
  tarsal bones of, 365
  tarsometatarsal joint of, 365
Distal metacarpal bones, 406, 409f, 427f
Distal metacarpus, 260f
Distal metaphyseal region, 406
Distal phalanx, 317f, 429–431, 429f, 431f–433f, 439f, 440–442, 442f
  articular fracture of, 442f
  of equine, 443f
  extensor process of, 432f
  fracture of, 442f
  lateral radiography of, 312f
  lateral view of, 317f
  oblique fracture of, 441f
  palmar process of, 433f
  of pedal osteitis, 452f
  of phalanges, 440–442
  solar margin contour of, 432f
  vascular channel formation in, 431f
  without sulci, 429f
Distal radial epiphysis, 374–375, 378, 379f
Distal radial osteosarcoma, 262f, 309f–310f
Distal radial physis, 303, 304f, 374–376, 376f, 378, 378f–379f
Distal radius, 308f, 378f
Distal row of carpal bone, 242f, 385f, 388f–389f
Distal tibia, 366, 367f
Distal ulnar epiphysis, 376f
Distal ulnar physis, 276, 303
Distended colon, 736–737
Distended pulmonary veins, 597
Distention
  of bladder, 744
  of carpal sheath, 381–382
  of digital tendon sheath, 403–404, 407f, 467–468
  of endotracheal tube cuff, 568–569
  of femorotibial joint, 356
  of navicular bursa, 464, 467–468
  radiography of, 421
  of renal pelvis, 717–718
  of spinal cord, 218
Distinct transition zone, 310f, 612f
Distortion, 18, 72f, 76–77
  in abdominal radiography, 653–654
  causes of, 19f
  in diagnostic radiography, 18
  geometry of, 78f
  magnification and, 75–77
Distracted PennHIP view, 333f
Distraction of fragment, 290–291
Distraction osteogenesis, 283–284
Disuse atrophy of bone, 425, 485f
Diverticula/diverticulum, 207, 208f. *See also* specific types of
Dog. *See* Canine and feline
Dolichocephalic breed, 114
Doppler angle, 46
Doppler artifact, 49
Doppler image, 47, 48f
Doppler mode, 47–49
Doppler shift, 46–47, 49
Doppler signal, 47–48
Doppler technique, 38
Dorsal acetabular rim, 252
Dorsal arachnoid, 208f
Dorsal articular process, 173f, 176f, 184f, 186f, 194–195
Dorsal aspect, 108f, 382f
Dorsal calvarial multilobular osteochondrosarcoma, 121f
Dorsal computed tomography, 211f, 551f, 710f, 720f
Dorsal cortex of diaphysis, 406–407
Dorsal cortical stress disease, 404–406

Dorsal fat-saturated postcontrast T1-weighted image, 212f
Dorsal longitudinal ligament, 174, 194, 198–199
Dorsal mediastinal mass, 557
Dorsal plane fracture, 385f, 387, 440
Dorsal postcontrast T1-weighted images, 140f–142f, 212f
Dorsal recumbency, 481f, 572f
Dorsal recumbent lateral view, 541f
Dorsal row of carpal bone, 387
Dorsal subluxation, 450
Dorsal subvolume maximum intensity projection, 205f
Dorsocaudal aspect, 81f, 610f, 653f
Dorsocaudal lung field, 477f
Dorsolateral palmaromedial oblique (DLPaMO) radiography, 81. *See also* specific types of
  of calcaneus, 264f
  of carpus, 241f, 253–258, 256f, 375f, 386f, 390f
  of manus, 230f
  of metacarpal osteochondrosis, 420f
  of metacarpal region, 409f
  of metacarpophalangeal joint, 245f
  of metacarpus, 261f
  of MTP joint, 422f
  of septic arthritis, 424f
  of tarsus, 237f, 250f
  of ulnar carpal bone, 387f
Dorsolateral-palmaromedial view, 253–258, 367f, 396f–397f
Dorsomedial-palmarolateral radiography, 242f, 257f, 258, 374f
Dorsomedial-palmarolateral view, 258
Dorsomedial-plantarolateral radiography, 365f, 395f, 425f
Dorsomedial-plantaromedial radiography, 422f
Dorsopalmar radiography
  of carpus, 229f, 240f, 253, 254f, 379f–380f, 389f
  of degenerative joint disease, 420f
  of distal metacarpus, 260f
  of distal radius, 378f
  of foredigit, 246f
  of immune-mediated arthropathy, 343f
  of interphalangeal joint, 437f
  of lameness, 391f
  of manus, 230f, 317f
  of metacarpal osteochondrosis, 420f
  of metacarpal region, 395f–396f, 407f, 410f
  of metacarpus, 395f
  of osteomyelitis, 424f
  of phalanges, 431f
  of septic arthritis, 424f
  of slab fracture, 425f
Dorsopalmar view, 253
Dorsoplantar radiography, 236f–237f, 249f, 314f, 317f, 362f, 364f, 366f, 371f, 398f, 400f, 409f
Dorsoproximal-dorsodistal radiography, 298f, 378f, 385f, 388f–389f, 458f. *See also* specific types of
Dorsoproximal-palmarodistal radiography, 244f, 462f
Dorsoproximal stress fracture, 404
Dorsoproximolateral-palmarodistomedial oblique radiography, 247f
Dorsoventral radiography, 157
  of abdominal distention, 655f
  of aortic stenosis, 591f
  of caudal lobe artery, 593f
  of caudal region, 97f
Dorsoventral radiography *(Continued)*
  of cranial abdomin, 680f
  of cranial thorax, 566f
  of craniodorsal mediastinal mass, 561f
  of diaphragmatic region, 536f
  of globoid-appearing cardiac silhouette, 603f
  of heart, 587f, 599f
  of heartworm disease, 595f–596f
  of left atrial dilation, 589f
  of left atrium, 589f
  of maxilla, 718f
  of mediastinum, 564f
  of middle region, 95f
  of obesity, 522f
  of otitis media, 124f
  of patent ductus arteriosus, 594f, 603f–604f
  of pneumothorax, 582f–583f
  of pulmonary artery, 592f
  of pulmonic stenosis, 605f
  of rib cage, 525f
  of temporomandibular osteopathy, 165f
  of thorax, 482f, 554f, 597f, 624f
  of tricuspid dysplasia, 590f
  of ventricular septal defect, 606f
Dorsoventral thoracic radiography, 482f, 523f
  of canine, 523f
  of cardiac silhouette, 532f
  of dyspnea, 555f
  of heart failure, 602f
  of left hemithorax, 587f
  of left lateral thoracic wall ultrasound image, 531f
  of lipoma, 531f
  of obesity, 491f
  of rib, 528f, 531f
  of subcutaneous emphysema, 526f
Dorsoventral view, 101–102, 102f, 105f, 477f, 575f, 598f
Dose equivalent, 4
Double aortic arch, 513
Double-contrast cystography/cystogram, 729f, 731, 731f–732f, 734f–735f
Dual-phase renal angiography, 710–711
Duodenum, 544–545, 651f, 658, 667–671, 670f–671f, 684–685, 712f
Duplex Doppler image, 47–48, 47f
Dural tail sign, 142f
Dynamic inspiratory radiography, 496f
Dynamic range, 31–32
Dysphagia, 491, 500, 504–510, 509f
  causes of, 507t
  of esophagus, 504–510
  fluoroscopy findings for, 507t
  types of, 507t
Dysplasia. *See* specific types of
Dyspnea, 492f
Dystocia, 644, 759
Dystrohphic calcification, 335–338, 338f, 369f
  of abscess, 697
  of hepatic granulomas, 684
  of necrotic fat, 663, 664f
  of periarticular soft tissue, 418
Dystrohphic nonunion fracture, 302
Dystrophic calcification, 418, 664f
Dystrophic mineralization, 403, 672–673

E

Ear, 125f
Ear canal tumor, 126
Ear tooth, 160–161
Eccentric hypertrophy, 588
Echinococcosis infection, 684
Echo detection, 65
Echo display, 42
Echo formation, 38
Echogenicity, 42–43, 43b, 44f, 689
Ectopic kidney, 706
Ectopic ureter, 706, 717, 719, 721–722, 721f–722f
Edema. *See* specific types of
Edge enhancement, 27, 298f
Edges, 253, 258–259
Edge-shadowing artifact, 46, 46f
Effusion. *See* specific types of
Ehrlichia, 215
Elbow, 226f, 262f, 315f, 330f
Elbow dysplasia, 268
Elbow joint, 226f–227f, 239f
Elbow luxation, 297f
Elbow sesamoid, 324f
Electric current, 9–11
Electromagnetic radiation, 2–3, 3f, 3t
Electron, 13–14
Electronic transducer, 40
Electron volt (eV), 2
Elephant foot, 301f
"Elevation" of heart from sternum, 581
Emaciated abdomenal lateral radiography, 657f
Embolism, 204, 213, 214f, 730–731
Emphysema, 492, 608–609. *See also* specific types of
Emphysematous cholecystitis, 684–685
Emphysematous cystitis, 728, 730f, 738–739, 739f
Encephalitis, 67f, 137f, 139, 147–149
Enchondrodystrophy, 276
Endochondral ossification, 267, 278, 283–284
Endoscopic esophageal ultrasonography, 517f
Endoscopic ultrasonography, 500, 517
Endosteal callus, 296–298, 406
Endotracheal stenting, 497
Endotracheal tube cuff, 568–569
End-stage bronchitis, 641
Enema for cleansing colon, 706
Enhanced portability for consultation, 35–36
Enhanced professionalism, 36–37
Enhancing contrast, 67
Enlarged aortic arch, 591, 591f
Enostosis-like lesion, 408
Enteritis, 684
Enterococci, 185
Entheses, 321–322, 322f
Enthesitis, 321
Enthesopathy, 186, 367–369, 368f
Enthesophytes, 321–322, 322f, 463
Enthesophytosis, 461–463
Ependymoma, 143, 208, 213
Epidermoid cyst, 156, 208, 453–454
Epidural hemorrhage, 200
Epidurography, 109–110, 188, 188f
Epiglottic retroversion, 493
Epiglottis, 168, 169f, 493f
Epiphyseal dysplasia, 274–280, 277f. *See also* Chondrodysplasia; Metaphysical and epiphyseal dysplasia
  of humeral condyle, 278–280
  of multiple cartilaginous exostosis, 278
  osteochondral dysplasia and, 276
  retained cartilage core in, 278
  ununited medial epicondyle in, 280
Epiphyseal fracture, 288
Epiphyseal growth imbalance, 378
Epiphyseal malformation, 275

Epiphysis, 265–266, 287f, 357–358, 424f. *See also* specific types of
Epiphysitis, 375–376
Epithelium, 120–121
Epulide of periodontal origin, 120
Equine. *See also* specific topics regarding
  carpus of, 374–393
  head of, 153–171
  thorax of, 632–648
Equine-extremity radiography, 252–253
Equine herpesvirus Type 5 (EHV-5), 637–638
Equipment, 730f
Ergot, 431–433, 431f, 459
Erosion, 463–464, 463f
Erosive polyarthropathy, 320f
Esophageal air, 502
Esophageal compression, 513–514, 515f, 562f, 645
Esophageal contrast study, 505b
Esophageal dilation, 502, 510–511, 673
Esophageal disease, 500, 502b
Esophageal diverticula/diverticulum, 517
Esophageal fistulas, 519–520
Esophageal foreign body, 511–513, 513f
Esophageal hiatal disease, 510–511
Esophageal motility disorder, 509
Esophageal neoplasm, 516–517
Esophageal perforation, 569
Esophageal phase, 508f
Esophageal sphincter, 500–501
Esophageal stricture, 500, 515–516, 515f
Esophageal varices, 520
Esophagitis, 500, 503f, 509–511, 514–515
Esophagram, 502f, 515f
Esophagus, 500–521. *See also* specific types of
  alternative imaging procedure for, 500
  anatomy of, 500–502
  contrast esophagraphy of, 500, 504
  contrast media for, 504t
  diverticula of, 517–520
  dysphagia of, 504–510
  esophageal dilation of, 510–511
  esophageal varices of, 520
  fluoroscopy of, 500
  foreign body in, 511–513
  inflammatory disease of, 514–517
  lateral radiography of, 510f
  perforation of, 517–519, 569
  physiologic considerations with, 500–502
  radiography of, 500, 502, 503f
  survey radiographic abnormalities of, 502
  vascular ring anomalies of, 513–514
Ethmoid hematoma, 158, 160–161, 162f
Ethmoid labyrinth region, 162f
Excitation, 61–63, 63f
Excretory urogram/urography, 706–708
  of bilateral ectopic ureter, 707f, 721f
  of bladder neck, 740f
  functional aspects of, 718b
  indications for, 706
  of left hydronephrosis, 717f
  nephrogram phase of, 723f
  normal image findings in, 706–708
  pyelogram phase of, 723f
  techniques for, 706
  of urinary bladder, 741f
Exercise-induced pulmonary hemorrhage, 641–642
Expiratory radiography, 496f
Exposure, 4, 5f
Exposure dose, 3, 5f
Exposure index (EI), 33
Exposure latitude, 29–35, 33f
Exposure standards, 6
Extended ventrodorsal projection, 332f
Extensive bridging ventral spondylosis, 190f
Extensive costal cartilage mineralization, 524f
Extensor carpi radialis, 322f, 336, 381, 381f
Extensor process, 432f, 442f
External marking system, 105f
Extraaxial tumor, 141
Extracorporeal shockwave therapy, 286
Extradural sciatic nerve tumor, 212f
Extradural tumor, 201f, 208–210
Extrahepatic biliary obstruction, 692, 693f
Extrahepatic shunt, 693
Extraluminal masses, 748
Extramural cervical masses, 494
Extramural compression, 515–516
Extrapleural mass, 528
Extrapleural sign, 527–528, 528f–529f
Extravasation of contrast medium, 747
Extrusion of intervertebral disc, 198, 203–204, 203f–204f
Exuberant callus, 285f, 301f

F

Fabella, 80f, 328f–329f
Fan-beam geometry, 57
Faraday's law of induction, 61f
Far field, 42
Fast spin-echo sequence, 65, 150
Fast spin-echo T2-weighted magnetic resonance imaging, 118f
Fat. *See* Obesity; specific types of
Fatigue fracture, 289
Fat opacity mass, 530f
Fat pad, 319, 320f, 349
Federal exposure standards, 6
Feline. *See* Canine and feline
Femoral articular cartilage, 336–337
Femoral capital epiphysis, 335f
Femoral condyle, 270f
Femoral epiphysis, 269, 271, 275, 335f
Femoral fracture, 295f, 357–358
Femoral mid-diaphysis, 301f
Femoral osteosarcoma, 263f
Femoropatellar joint, 352, 352f, 358–359, 360f
  disease of, 352–354
  osteochondrosis of, 352–353
  osteomyelitis of, 354
  patellar fragmentation of, 353
  patellar luxation of, 354
  trochlear dysplasia of, 354
  upward patellar fixation of, 354
Femorotibial joint, 320f, 349–352, 354, 356f–357f
  degenerative joint disease of, 355–356
  disease of, 354–357
  distention of, 356
  narrowing of, 355–356
Femur, 308f, 311f
  bilateral total hip prostheses of, 311f
  comminuted diaphyseal fracture of, 293f, 295f
  craniocaudal radiography of, 233f, 259f
  craniocaudal view of, 299f
  with femoral osteosarcoma, 263f
  lateral radiography of, 259f, 263f
  lateral view of, 80f, 299f, 308f, 311f
  malunion fracture of, 299f
Femur *(Continued)*
  mediolateral radiography of, 233f
  with metastatic carcinoma, 259f
  mid-diaphysis of, 263f
  radiography of, 313f
Fetal demise, 758
Fibrin tag, 643f
Fibroameloblastoma, 120–121
Fibrocartilage, 196
Fibrocartilaginous embolism, 204, 213, 214f
Fibrocartilaginous navicular degeneration, 460
Fibroid degeneration, 182, 197
Fibromatous epulis, 120
Fibrosarcoma, 118–120, 161, 210f, 533f
Fibrous osteodystrophy, 117
Fibrous union, 301
Fibular fracture, 358
Field of view (FOV), 71–73
50-degree proximal radiography, 426f
Filament, 9, 12
Filling defect, 732. *See also* specific types of
Filly. *See* Equine
Film blackness, 14–16
Film image
  analog, 35–36
  blackness of, 8, 14–16
  contrast of (*See* Contrast)
  fog/fogging of, 20
  opacity of, 8, 14–16
  processing of, 20–21
  underdevelopment of, 623
Film processor, 21
Film-screen system, 104–106, 111, 184f
  cassette for, 25–26
  radiography using, 654
  technology for, 484
Filtered backprojection, 57
Filum terminale, 194
First maxillary molar, 154f
Fissure fracture, 292, 293f
Fistulogram, 466, 466f
Fixation device, 285, 294f
Flaccidity of periarticular structure, 378
Flail chest, 526
FLAIR. *See* Fluid-attenuated inversion recovery (FLAIR) sequence
Flat-panel detector, 26f
Flat-panel direct digital radiography, 26
Flexed dorsoplantar view of tarsus, 252
Flexed lateromedial radiography
  of carpus, 241f, 385f, 389f
  of metacarpophalangeal joint, 244f
  of MTP joint, 423f
  of stifle, 358f–359f
  of tarsus, 364f
Flexor carpi ulnaris, 336, 338f
Flexor cortex change, 463–464
Flexor cortex erosion, 463–464, 463f
Flexural deformity, 381, 403f, 435f, 449–450, 450f
Flip angle, 61–62
Fluid-attenuated inversion recovery (FLAIR) sequence, 67, 135, 139
Fluoroscopy, 496, 538, 543, 545–546, 622, 635, 708, 721–722, 747–748
  contrast examination using, 506–507
  of dysphagia, 507t
  relative value of, 500
  swallowing study using, 506–507
Foal. *See* Equine
Focal areas of emphysema, 608–609
Focal articular cartilage, 326–327
Focal disease, 699

Focal encephalitis, 147–149
Focal hepatic disease, 689
Focal hepatomegaly, 682–683
Focal intracranial conditions/disease, 138
Focal pulmonary abscess, 637f
Focal splenic infarction, 700
Focal spot, 12, 12f
Focal spot-film distance (FFD), 15–16, 18
Focal spot size, 16, 16f
Focused grid, 18
Fog/fogging of film image, 17, 20
Foley catheter, 744–745
Foot, 301f
  abscess of, 444f
  alternate imaging of, 433
  balance of, 453f
  lameness from, 445f
  measurement of, 449f
  radiography of, 449f
  sagittal plane STIR image of, 469f
  static image of, 464f
  sulic of, 429f
  unknown trauma in, 445f
Footprint, 40
Foramen magnum, 114–116, 138, 138f
Foredigit, 245f–246f, 431
Foreign body, 497. *See also* specific types of
45-degree medial-palmarolateral radiography, 421f, 426f–427f
45-degree medial-palmarodistolateral radiography, 426f
Fourth metacarpal and metatarsal bones, 408–410
Four-view radiography, 483f, 632f
Fracture, 465–466. *See also* specific types of
  callus associated with, 262f
  degree of, 289–290
  direction of, 289
  fragment of, 290–291
  grade of, 289–290
  location of, 288
  repair of, 283
Fracture classification system, 440
Fracture healing, 283–306
  bone healing, 283–284
  bone tissue, 283
  classification of, 288–293
  complication with, 299–303
  identification of, 287–288
  promoting, 285–287
Fragment, 290–291
Fragmented medial coronoid process, 266, 268–269, 272f, 280, 297f, 326, 329f
Free filling defect, 732
Free fluid-free air, 573, 577f
Free intraperitoneal gas, 662, 662f
Free luminal filling defect, 732, 734f
Frequency, 38
Frequency-encoding gradient (G_{FE}), 65
Frontal bone, 160f
Frontal sinus, 89f, 102f, 114, 115f, 158
Frontal sinus neoplasia, 145
Full-wave rectification, 11f
Functional ileus, 803–805
Functional malunion fracture, 299–301
Fundus, 511, 512f
Fungal disease, 122
Fungal granuloma, 697, 716–717
Fungal infection, 121–122, 309, 314f, 698
Fungal osteomyelitis, 309–310
Fungal pneumonia, 638
Funnel chest, 523

G

Gain, 42
Gallbladder, 45f, 686–688
  abdominal radiology of, 680–681
  acoustic shadow/shadowing, caused by, 43, 686, 692
  lateral abdominal radiography of, 680–681
  mirror image artifact of, 45f
  ultrasonography of, 688f, 690f, 692f
Gallbladder mucoele, 693f
Gamma ray, 2–3, 3b
Gamut, 86, 609
Gantry, 55
Gas. *See also* specific types of
  acoustic shadow/shadowing, cause of, 668f, 691, 738
  in cranial mediastinum, 569f
  embolism caused by, 730–731
  in head, 153
  opacity of, 662–663, 664f
  in stomach, 654f
Gas-dilated esophagus, 504f
Gastric compartmentalization, 85, 655f
Gastric dilation, 684
Gastric foreign body, 655f, 775–777
Gastric neoplasia, 783–785
Gastric ulcer, 782–783
Gastric volvulus, 86, 655f, 696
Gastrocnemius muscle, 322f
Gastroesophageal intussusception, 510–511, 512f, 543–545, 546b
Gastroesophageal reflux, 500, 509–511, 514–516, 543
Gastrointestinal tract, 638, 650, 652–653, 656f, 711, 711f
General anesthesia, 107, 118
Generalized cardiomegaly, 588–589
Generalized hepatomegaly, 682
Generalized megaesophagus, 503f, 510
Generalized osteosclerosis, 276
Geographic bone lysis, 259–261
Geographic pattern, 259
Geometry, 55, 57, 77f–78f, 106f. *See also* Radiographic geometry
Glioma, 143, 147–149, 148f
Globoid-appearing cardiac silhouette, 603f
Glomerulonephritis, 711–713
Gloves, 8
Golf tee sign, 211, 214f
Grade of fracture, 289–290
Gradient pulse, 63
Gradient recalled echo (GRE) sequence, 63, 67, 68f, 71–72, 72f, 136, 147f, 150, 468–469, 468f
Grafts/grafting of bone, 286–287, 301
Granular pattern in abdomen, 661
Granulation tissue, 269, 284, 435, 444, 497f, 531f
Granuloma, 494. *See also* specific types of
Granuloma cholesterol, 165, 166f
Granuloma hepatitis, 638
Granulomatous meningoencephalitis (GME), 139
Grating lobe artifact, 44–45, 45f, 737f
Gray (Gy), 4
Grayscale display, 28
Gray shades, 23
Greenstick fracture, 289
Grid, 17–18, 30–31, 106
  composition of, 17f
  efficacy of, 18t
  misalignment of, 18f
  proper orientation of, 19f
  scatter removal by, 30f
Grid artifact, 30–31
Grid ratio, 18, 18f
Guttural pouch, 98f, 101–102, 107, 153, 164f, 166–168, 167f–168f
Gyromagnetic ratio, 61

H

Half-wave rectification, 11f
Handholding of cassette, 252–253
Hansen Type II intervertebral disc disease, 197
Hansen Type I intervertebral disc disease, 196–197
Harmonic imaging, 41
Head, 106f, 153. *See also* Equine
  left 45-degree dorsal-right ventral oblique radiography of, 159f
  left-right lateral radiography of, 88f
  left-right radiography of, 164f, 167f
  left rostrodorsal-right caudoventral oblique radiography of, 164f
  middle region of, 95f–96f
  radiography of, 106f
Head of spleen, 694
Head tilt, 140f
Healing. *See* specific types of
Heart, 587f
  cardiac chamber enlargement in, 585–589
  pulmonary vascular change in, 592–596
  pulmonary vessel in, 585–607
  radiography of, 585–605
  size of, reduction in, 605
  vessel enlargement in, 589–592
Heart-based mass, 494
Heart base tumor, 563f
Heart failure, 599f–601f. *See also* specific types of
Heartworm disease, 594–596, 595f–597f, 599–600
Heartworm infection, 599–600
Helical computed tomography, 56f
Helical scanning, 55
Hemangiosarcoma, 146–147, 147f, 161, 628f, 661f, 697f, 700f
Hemarthrosis, 326, 340
Hematogenous bacterial infection, 311
Hematogenous bacterial osteomyelitis, 315f
Hematogenous osteomyelitis, 311, 315f, 358–359, 443
Hematoma, 150t, 158, 160–161, 162f, 700f
  hepatic abscess and, 691
  in human central nervous system tissue, 150t
Hematuria, 747f
Hemilaminectomy, 183–185
Hemithorax, 572f, 583f, 587f
Hemivertebrae, 175, 177f, 523f
Hemoptysis, 493f
Hemorrhage. *See* specific types of
Hemothorax, 527f, 639
Hepatic abscess, 685, 686f, 691, 691f
Hepatic abscessation, 686f
Hepatic carcinoma, 210f, 683f–684f, 686f, 689, 691f
Hepatic cirrhosis, 684, 688–689
Hepatic cyst, 542, 683–684, 691
Hepatic disease, 689
Hepatic echogenicity, 689
Hepatic granuloma, 684
Hepatic lipidosis, 682, 688–689, 688f
Hepatic mass, 683–684
Hepatic neoplasia, 689
Hepatic opacity, 684–685

Hepatic parenchyma, 686
Hepatic parenchymal mineralization, 684
Hepatic ultrasound, 682, 685–688
Hepatic vein, 686
Hepatitis, 638, 684f, 688–692, 690f
Hepatocutaneous syndrome, 690–691, 691f
Hepatomegaly, 600–601, 673, 681–684, 681f. *See also* specific types of
Hepatozoon infection, 316
Hepatozoonosis, 316
Hernia. *See* specific types of
Hertz (Hz), 38, 46
Heterotopic bone, 622
Hiatal disease, 510–511
Hiatal hernia, 543–544
High-contrast radiography, 19–20, 21f, 669f
High-frequency generator, 11f, 12
Highly comminuted fracture, 289
High-pass filtering, 58f
High-velocity-low-volume disc disease, 198
Hilar-region mediastinal mass, 557–562
Hindlimb of equine, 409f
Hip dysplasia, 330–333, 331f–332f, 335b
Hip joint, 247f
Hip prosthesis, 261f, 312f
Histiocytic sarcoma, 146
Histoplasma, 215
Hoist, 155f
Hoof. *See* Foot
Hoof balance, 453
Horizontal-beam abdominal radiography, 662f
Horizontal-beam lateral thoracic radiography, 480f
Horizontal-beam lateral view, 541f
Horizontal-beam radiography, 573, 578f
Horizontal-beam ventrodorsal radiography, 474–475, 475f–476f
Horn, 162
Horse. *See* Equine
Hot light, 83–84, 84f
Hounsfield unit (HU), 57, 67, 198–199
Human central nervous system tissue, 150t
Humeral condyle, 270f, 278–280, 279f
Humeral epiphysis, 277f
Humerus. *See also* specific types of
  caudocranial radiography of, 225f, 260f
  mediolateral radiography of, 225f
  osteosarcoma of, 260f
  ununited medial epicondyle of, 280f
Hydrocephalus, 114–115, 115f, 138, 138f
Hydrogen proton, 61, 62f
Hydronephrosis, 717–718, 717f–718f
Hyoid bone, 489, 492
Hyperadrenocorticism, 165–166, 166f, 674–675
Hyperechoic calculi/calculus, 721f
Hyperechoic medullary rim, 713
Hyperechoic nodule, 43f
Hyperechoic structure, 720–721, 738
Hyperintense core lesion, 437f
Hyperintensity, 147–149
Hyperostosis, 141
Hyperparathyroidism, 116–117, 156, 191, 191f, 273–275, 274f, 718, 718f
Hyperplasia, 674–675, 700
Hypertension, 600
Hyperthyroidism, 117f
Hypertrophic cardiomyopathy, 600f, 601–602, 602f
Hypertrophic nonunion fracture, 301–302, 301f
Hypertrophic osteodystrophy, 271–273, 274f
Hypertrophic osteopathy, 344, 344f, 387, 408, 454
Hypertrophy, 187, 205, 208, 320–321, 588
Hypervitaminosis A, 338–339
Hypoadrenocorticism, 675
Hypoechogenic core lesion, 401f, 403
Hypoplasia, 271, 495–496
Hypothyroidism, 274, 275f
Hypovolemia, 606f

I

Identification microchip, 72f
Idiopathic polyarthritis, 344
Idiopathic polyostotic bone infarction, 309, 311f
Iliac lymph node, 666–667, 667f
Iliopubic sesamoid, 325f
Illdefined nodular, 661
Ill-defined T2-signal hyperintensity, 147–149
Image detail
  factors affecting, 16–18
  focal spot size, 16
  grid, 17–18
  intensifying screen, 16–17
  motion, 16
Image display, 57
Image formation, 42, 50–53, 57, 74
Image matrix, 53f
Images/imaging. *See also* specific types of
  alternative procedure for, 500
  archiving, 28–29, 29f
  blackness in, 74
  capture hardware options for, 27f
  contrast of, 30–31
  diagnostic, 6, 287
  modalities with, 30t
  noise in, 33–34, 34f
  postprocessing of, 35
  processing of, 27–28
  quality of, 71
  reconstruction algorithm of, 58f
  reformatted, 50–53, 55f
  storage consolidation of, 35
  viewing of, 27–28
Imaging time, 71
Immature appendicular skeleton disorder, 268b
Immune-mediated arthropathy, 342–344
  dorsopalmar radiography of, 343f
  feline noninfectious polyarthritis, 343–344
  hypertrophic osteopathy, 344
  rheumatoid arthritis, 342
  systemic lupus erythematosus, 342–343
Impacted fracture, 291
Incidental factors, 112, 264
Incisive bone, 156f
Incomplete fracture, 289
Incomplete ossification
  of carpal bones, 376, 378
  of humeral condyle, 278–280, 279f
  of tarsal bones, 365
  tarsal collapse caused by, 365
Incomplete short oblique fracture, 291f
Increased contrast resolution, 50
Increased T2-signal intensity, 135
Indirect bone healing, 283–284
Indirect flat-panel detector, 25–26, 26f
Induction, 61f
Inductive fibroameloblastoma, 120–121
Infarction, 147–149, 309. *See also* specific types of
Infection, 452–453. *See also* specific types of
Infectious arthritis, 319–320, 342b
Infectious bone sequestrum, 303
Infectious disorder, 121–126
Infectious osteitis, 410–411
Infectious peritonitis, 141, 141f
Infiltration, 609–610
Infiltrative bowel disease, 805–807
Infiltrative lipoma, 210
Inflammatory/infectious conditions, 185, 190t, 215–217, 317, 494, 514–517, 691–692, 766–767
  of brain, 139–141
  discospondylitis, 185, 215
  esophagitis, 514–515
  meningomyelitis, 215–217
  radiography of, 190t
  spinal epidural empyema, 215
  spondylitis, 185
  stricture, 515–517
  vertebral osteomyelitis, 185
  vertebral physitis, 185
Infrapatellar fat pad, 319, 320f
Ingested bone, 506f
Inguinal hernia, 664f
Inherent spatial resolution, 30b, 30t
Injury. *See* specific types of
Inspiratory difficulties, 492f
Inspiratory dyspnea, 125f
Inspiratory noise, 492f
Instability, 109–110, 204
Intensifying screen, 16–17, 16f
Interarcuate ligament, 194
Intercapital ligament, 194
Intercondylar malunion fracture, 300f
Intercrural cleft, 535
Interfaces of ultrasound wave, 39t
Interlobar fissures, 571, 572f, 573
Internal fixation of distal scapular fracture, 296f
International Commission on Radiological Protection (ICRP), 5–6
International System of Units (SI units), 3–4
Interosseous muscle, 394
Interphalangeal collateral desmitis, 438f, 450–451
Interphalangeal osteoarthritis, 446f
Interpretation paradigm, 112–113, 658
Interscapular fibrosarcoma, 533f
Intersex conditions, 767
Interstitial cardiogenic pulmonary edema, 596
Interstitial mass, 621t
Interstitial nodule, 621t
Interstitial pattern, 485f, 601f, 610, 613, 615f, 619–626, 626f, 626t, 628f
Interstitial pneumonia, 637–638
Interstitium, 623, 625–626, 627f
Intervertebral articular process joint, 187
Intervertebral articular process joint space, 183–185
Intervertebral disc
  anatomy of, 175f, 195f
  degeneration of, 175–177, 176f, 179, 183–187, 184f, 196–197, 202–203
  extrusion of, 198, 203–204, 203f–204f
  herniation of, 199f
  normal, 196
Intervertebral disc disease (IVDD), 196–204. *See also* specific types of
  classification of, 196–198
  computed tomography of, 198–200

Intervertebral disc disease (IVDD) *(Continued)*
intervertebral disc extrusion, 203–204
magnetic resonance imaging of, 200–204
regional characteristics of, 200–203
survey radiography of, 184f
of vertebrae, 182–185
Intervertebral disc herniation, 199f
Intervertebral disc space, 196f–198f
Intervertebral foramen, 183–185, 184f
Intraabdominal fat, 659–660
Intraabdominal mineral opacity, 663
Intraarticular calcified body, 321, 321t
Intraarticular gas, 322–323, 323b, 323f
Intraarticular hemorrhage, 340
Intraarticular tarsometatarsal sesamoid, 326f
Intraaxial tumor, 143
Intracranial conditions/disease, 135, 138–141
Intracranial feline infectious peritonitis, 141
Intracranial lymphoma, 146–147
Intradural-extramedullary tumor, 210–213
Intrahepatic shunt, 693–694
Intraluminal changes, 737–738
Intraluminal dependent biliary sludge, 692
Intraluminal tracheal air, 494–495, 497
Intramedullary pin, 263f, 285, 286f
Intramedullary tumor, 213
Intramembranous bone formation, 283
Intramembranous ossification, 283
Intramural changes, 732
Intranasal foreign body, 123
Intraoperative mesenteric portography, 685, 686f–687f
Intraoral dorsoventral radiography, 89f, 104f, 120f, 122f, 156f
Intraperitoneal fluid, 660, 660f
Intraperitoneal gas, 662, 662f
Intrathecal contrast medium, 199f
Intravenous injection, 60f
Intravenous urography, 60, 729f
Invasive extracranial tumor, 145–147
Invasive paravertebral fibrosarcoma, 210f
Inverse square law, 15–16
Inversion recovery, 65–67, 66f
Involucrum, 303, 410–411, 411f
Iodinated contrast medium, 60f
Ionization, 2, 3f
Ionization density, 4, 5f
Ionizing radiation, 6f
Irregular periosteal margin, 261–263
Irregular soft tissue opacity, 669f
Ischemic myelopathy, 213–214
Ischemic stroke, 70f
Islet cell tumor, 670–671

J

Jejunal crowding, 657f
Jejunum, 656–658
Joint, 321, 324, 327t. *See also* specific types of
Joint capsule attachment, 414
Joint disease, 320, 367f. *See also* Degenerative joint disease
of articular soft tissue, 321
bone cyst, 319–320
of carpus, 336
of entheses, 321–322
of enthesophytes, 321–322
of hemarthrosis, 340
of hip dysplasia, 330–333
of hypervitaminosis A, 338–339
immune-mediated arthropathy, 342–344
Joint disease *(Continued)*
intraarticular calcified body, 321
of intraarticular gas, 322–323
of joint displacement, 321
of joint incongruency, 321
of joint space, 319
of mucopolysaccharidosis, 339
of osseous, 333
osteophyte, 321
of perichondral bone opacity, 320–321
radiography of, 319–348, 319b, 319f
of Scottish Fold chondro-osseous dysplasia, 339–340
of septic arthritis, 340–342
of sesamoid bone, 323–324
of sesamoid disease, 324–330
in shoulder, 335–336
sprain, 333–334
of stifle, 336–337
of subchondral bone opacity, 319–320
of synovial volume, 319
of synovium, 345
of tarsus, 337–338
of tendon, 335
Joint disorder, 267–271
aseptic necrosis, 269–271
elbow dysplasia, 268
fragmented medial coronoid process, 268–269
osteochondritis dissecan, 267–268
osteochondrosis, 267–268
ununited anconeal process, 268
Joint displacement, 321
Joint effusion, 68f, 267, 294, 340–341, 358f, 418
Joint incongruency, 321
Joint mouse/mice, 292, 321
Joint neoplasia, 345
Joint space, 186f, 319, 437f
JPEG file, 22, 35–36

K

Keratoma, 453
Kidneys and ureters, 40f, 705–725, 716f. *See also* Ureters
anatomy of, 705–711
antegrade ultrasound-guided pyelography of, 708
computed tomography of, 710–711, 720f
excretroy urography of, 706–708
imaging procedurest for, 705–711
lateral radiography of, 708f
magnetic resonance imaging of, 711
with nephroblastoma, 716f
radiography of, 705–706
renal disease of, 711–718
scintigraphy of, 711
trauma to, 722
ultrasonography of, 708–710
with ureteral obstruction, 720f
Kiloelectron volt (keV), 9–11
Kilovoltage peak (kVp) value, 9–11, 14, 17, 19–20, 20f, 31–32, 104–106, 111
Kissing lesion, 267

L

Lamellae, 446
Lameness, 296f, 329f, 335f–336f, 345f, 378–379, 400f
in foot, 445f
magnetic resonance imaging of, 417f
osteochondrosis, as cause of, 267
of pelvic limb, 329f
tarsal bones and, 341f
tarsus with, 367f
Lamina, 172
Laminar epithelium, 120–121
Laminitis, 446–449, 448f
Large bowel, 812–824
barium enema for, 814–815
compression radiography of, 814
computed tomography of, 822–823
contrast study of, 815
large bowel disease of, 812, 815–818
radiography of, 812–815
survey radiography of, 814
ultrasonography of, 819–822
Large bowel disease, 812, 815–818
Larmor frequency, 61–62, 65
Laryngeal paralysis, 497
Laryngeal region, 167f, 169f
Laryngitis, 494
Laryngoscopy, 168
Larynx. *See* Pharynx, larynx, and trachea
Lateral coronoid process, 269
Lateral decentering, 18, 19f
Lateral digital fluoroscopic image, 508f–509f
Lateral fabella, 328f
Lateral intraoperative mesenteric portogram, 686f
Lateral meniscus, 320f
Lateral myelogram, 187f
Lateral projection, 467f
Lateral radiography, 183f, 189f, 577f, 639f. *See also* specific types of
of adrenal gland, 672f
of antebrachium, 262f, 265f, 344f
of aortic arch, 514f
of aortic stenosis, 591f
of asthma, 619f
of barium esophagram, 515f
of barium swallow, 515f
of bladder, 732f
of block vertebra, 176f
of bronchial pattern, 616f–617f
of bronchiectasis, 618f
of cardiogenic pulmonary edema, 630f
of carpus, 376f
of caudal abdomen, 664f, 726f–727f, 729f
of caudal aspect, 79f, 108f, 111f, 643f–644f, 652f
of caudal fragment, 182f
of caudal lobe, 624f
of caudodorsal aspect, 519f, 637f, 642f
of caudoventral thoracic vertebrae, 636f
of cervical spine, 216f
of cervicothoracic region, 112f
of compensated mitral insufficiency, 598f
of compression fracture, 189f
of coughing, 495f
of cranial abdomin, 548f, 680f
of cranial aspect, 178f, 644f–645f, 656f
of cranial mediastinum, 569f
of cranioventral aspect, 621f, 656f, 662f
of crus, 344f
of cystic calculi, 730f
of degenerative joint disease, 187f
of dilated cardiomyopathy, 601f
of dilated left atrium, 588f–589f
of discospondylitis, 186f
of distal antebrachium, 262f
of dorsal aspect, 108f
of dorsal calvarial multilobular osteochondrosarcoma, 121f
of dorsocaudal aspect, 653f
of elbow, 315f
of esophagus, 510f

Lateral radiography *(Continued)*
of extensive bridging ventral spondylosis, 190f
of feline after being hit by car, 495f
of femur, 259f, 261f, 263f–264f
of heart failure, 601f
of humerus, 260f, 263f, 303f
of hydrocephalus, 115f
of hypertrophic cardiomyopathy, 602f
of hypertrophic osteopathy, 344f
of hypovolemia, 606f
of inspiratory dyspnea, 125f
of inspiratory noise, 492f
of jejunal crowding, 657f
of kidneys, 708f
of lumbar spine, 187f
of lumbosacrum, 188f
of lung bulla, 625f
of lung lobe, 625f
of lung recently hit by car, 625f
of malunion intercondylar fracture, 300f
of mandible, 115f, 156f
of mediastinal mass, 561f
of metacarpus, 260f
of midabdomen, 660f
of mid-diaphysis, 263f
of midthoracic esophagus, 500f
of midventral aspect, 656f
of mineralized mass in stomach, 672f
of MTP joint, 422f
of mucopolysaccharidosis, 191f
of nail, 76f
of nodule, 187f, 481f
of nutritional secondary hyperparathyroidism, 191f
of opossum, 117f
of patent ductus arteriosus, 604f
of peritoneal cavity, 657f
of peritoneal space, 664f
of pharynx, 489f
of pneumomediastinum, 569f–570f
of pneumonia, 613f–614f
of pneumothorax, 579f, 581f
of positive-contrast cystogram, 737f
of pronounced bronchial pattern, 617f
of prostatic carcinoma, 729f
of pulmonary edema, 642f
of pulmonary hyperinflation, 620f
of pulmonic stenosis, 605f
of radiopaque choleliths, 685f
of rear-limb distal phalanx, 312f
of respiratory distress, 495f
of retroperitoneal space, 657f, 719f
of rib fractures, 527f, 619f, 655f
of Salter-Harris type II fracture, 294f
of skull, 105f, 165f
of spine, 110f
of steroid hepatopathy, 681f
of thoracic inlet, 494f
of thoracic vertebrae, 32f, 527f
of thoracolumbar region, 110f
of thorax, 516f, 518f, 567f, 587f, 597f, 638f, 641f, 643f, 645f–646f, 682f
of tooth root abscess, 157f
of tortuous aorta, 591f
of tumor, 189f
of ureteral calculi, 721f
of urinary bladder, 732f
of ventricular septal defect, 606f
of volume depletion, 581f
Lateral resolution, 41
Lateral skull radiography, 102f, 115f, 117f
Lateral spinal radiography, 84f, 109f
Lateral survey radiography, 663f, 669f
Lateral tarsometatarsal sesamoid, 326f
Lateral thoracic radiography. *See also* specific types of
of barium swallow, 505f
of borzoi, 586f
of bronchiectasis, 619f
of emphysema, 526f
of film-screen system, 184f
of foreign body, 513f, 562f
of lung lobes, 609f
of mediastinal abscess, 561f
of mediastinal mass, 560f
of mitral insufficiency, 630f
of multiple hemivertebra, 176f
of mycotic pneumonitis, 314f
of persistent aortic arch, 514f
of pneumomediastinum, 526f, 568f
of pneumonia, 619f
of pneumothorax, 526f
of pulmonary blood vessels, 637f
of radiolucent region, 613f
of thoracic esophagus, 512f
of thorax, 512f
of upper airway obstruction, 511f
Lateral trochlea, 267
Lateral trochlear ridge, 353f
Lateral video fluoroscopic image, 509f
Lateral view, 101–102, 252, 474–478. *See also* specific types of
of abdominal wall, 659f–661f, 663f, 666f, 726f, 730f
of atelectasis, 474–475
of barium esophagram, 546f
of caudal abdomen, 730f
of caudal aspect, 80f
of cervicothoracic region, 490f
of cranial lobe vessels, 475
of diaphragmatic region, 475, 539f
of distal radial osteosarcoma, 309f
of femur, 293f, 299f, 308f, 311f–312f
of heart, 478
of idiopathic polyostotic bone infarction, 311f
of ligament attachments, 434f
of lumbar spine, 535f
of midlumbar spine, 108f
of mitral insufficiency, 598f
of navicular bone, 461f
of penetrating solar nail injury, 435f
of peritoneopericardial diaphragmatic hernia, 544f
of phalanx, 317f
of pneumomediastinum, 663f
of proximal aspect, 293f
of radius, 308f
of sagittal section, 434f
of shoulder, 296f
of skull, 32f
of superficial tissues, 434f
of tarsus, 302f, 315f
of tendon, 434f
of thorax, 542f–543f, 546f, 622f
of tibia, 84f, 311f, 314f
of trachea, 621f
of traumatic diaphragmatic hernia, 541f
Lateromedial radiography. *See also* Flexed lateromedial radiography
of calcaneus, 368f
of carpus, 240f–241f, 253, 255f, 381f, 383f–385f, 389f, 391f
of cortisone arthropathy, 419f
of degenerative joint disease, 419f, 425f
of desmitis, 419f
of distal aspect, 383f
of dorsal aspect, 382f
of foredigit, 245f
of lateral patellar luxation, 354f
Lateromedial radiography *(Continued)*
of metacarpal bones, 408f, 427f
of metacarpal osteochondrosis, 420f
of metacarpophalangeal joint, 243f, 418f
of metatarsal region, 370f
of MTP joint, 425f
of osteomyelitis, 424f
of patella, 353f–354f, 360f
of phalanx, 427f
of septic arthritis, 424f
of sesamoiditis, 419f
of stifle, 350f, 352f, 357f–358f
of stifle joint, 248f
of tarsal bone, 365f
of tarsus, 250f, 361f–363f, 366f–367f, 370f
of tibia, 367f
Lateromedial view, 253
Lattice, 62–63
Lead apron, 8
Leakage of contrast medium, 734
Left abdominal wall, 688f, 694–695, 695f, 698
Left aortic arch, 513
Left atrial dilation, 589f, 604, 604f, 626, 629, 630f
Left atrial enlargement, 597
Left atrium, 585–588, 588f–589f
Left carpus, 240f–241f
Left caudal aspect, 610f, 612f
Left caudoventral-right rostrodorsal oblique radiography, 167f
Left dorsal-right ventral oblique radiography, 125f
Left femur, 311f
Left foredigit, 246f
Left 45-degree dorsal-right ventral oblique (LDRVO) radiography, 106f, 156, 159, 159f
Left heart failure, 599f
Left hemithorax, 572f, 587f
Left hepatic mass, 683–684
Left hydronephrosis, 717f
Left lateral abdominal radiography, 650–652
Left lateral thoracic radiography
of cardiac silhouette, 532f
of mediastinum, 558f
of pectus excavatum, 526f
of peritoneopericardial diaphragmatic hernia, 525f
of thoracic esophagus, 503f
of trachea, 490f
Left lateral thoracic wall ultrasonography, 531f
Left lateral view, 474, 545f, 575f–576f, 650
Left mandibular squamous cell carcinoma, 120f
Left maxillary gingival mass, 120f
Left metacarpophalangeal joint, 245f
Left pelvic limb, 336f
Left renal enlargement, 712f
Left renal pelvic calculi/calculus, 685f
Left-right lateral (Le-RtL) radiography, 639f
of caudal cervical, 100f
of cervical vertebrae, 91f, 99f
of guttural pouch, 98f
of head, 88f
of laryngeal area, 98f
of lumbar vertebrae, 93f
of occipital region, 98f
of thoracic vertebrae, 93f
of withers region, 100f

Left-right lateral (Le-RtL) radiography *(Continued)*
Left-right radiography, 164f, 167f, 169f, 639f–640f
Left rostrodorsal-right caudoventral oblique radiography, 164f
Left-sided (LAA) aortic arch, 513, 515f
Left-sided rudimentary rib, 524f
Left-sided tension pneumothorax, 582f
Left tarsus, 249f–250f
Left temporal muscle atrophy, 146f
Left temporal region, 161f
Left 10-degree dorsal-right ventral radiography, 159f
Left thoracic lateral radiography
of abdomenal wall, 651f, 654f, 695f, 711f
of accessory lung lobe, 565f
of bronchial obstruction, 618f
of cardiac region, 479f
of caudal vena cava, 479f
of cranial lobe artery, 592f
of diaphragmatic region, 536f
of dorsocaudal lung field, 477f
of gas-dilated esophagus, 504f
of globoid-appearing cardiac silhouette, 603f
of heart failure, 599f–600f
of heartworm disease, 595f
of pneumothorax, 580f
of renal disease, 713f
of sternal lymph node, 557f
of thorax, 478f, 553f, 566f
of tricuspid dysplasia, 590f
Left tibia, 311f
Left 20-degree rostral-right caudal radiography, 104f
Left 20-degree ventral-right dorsal radiography, 124f
Left tympanic bulla cholesteatoma, 127f
Left ventral-right dorsal oblique (LeV-RtDO) radiography, 90f, 96f, 159
Left ventricle, 588
Left ventricular angiocardiogram, 605f
Left ventricular enlargement, 597
Lesion, 259. *See also* specific types of
Level (L), 57
Lick granuloma, 314f
Ligament. *See also* specific types of
Ligament attachment, 434f
Ligamentous trauma, 334
Ligamentum flavum, 174, 194
Light diffusion, 17f, 26
Linear array, 40
Linear array transducer, 45f
Linear attenuation coefficient, 57
Linear calcification, 664
Linear foreign body, 656–657, 657f
Linear transducer, 43f
Lipoma, 210, 531f
Liquid crystal display (LCD), 28
Liver, 40f
biliary system disease of, 691–692
cirrhosis of, 689f
with echogenic shadow, 691f
hepatic opacity of, 684–685
hepatic ultrasound of, 685–688
hepatomegaly of, 681–684
mineralized choledocholith in, 685f
radiography of, 679–694
special procedures for, 685
ultrasonography of, 688–691
vascular disease of, 693–694
Liver lobe torsion, 691
Lobar collapse, 616–617
Lobar sign, 612–613, 612f, 614f
Localized lesion, 267
Localizer-image, 67
Location of fracture, 288
Long-axis ultrasonography, 714f–715f, 717f
Longitudinal image of spleen, 43f
Longitudinal ligament, 194
Longitudinal magnification, 62–63
Longitudinal sonography, 155f
Longitudinal ultrasonography, 353f
of ascite, 688f
of carpus, 402f
of caudate liver lobe, 688f
of gallbladder, 688f
of gallbladder mucoele, 693f
of liver, 687f–692f
of metacarpal region, 402f
of spleen, 698f–701f
of splenic hemangiosarcoma, 700f
Long scale of contrast, 19–20
Loose body, 292
Lower respiratory infection, 123f
Low-grade inflammation, 623
Low-intensity pulsed ultrasound, 286
Lumbar intervertebral disc space, 196f
Lumbar spine, 34f, 79f, 187f, 535f
Lumbar vertebrae, 93f, 173f, 175f, 195f, 340f
Lumbosacral disease, 203f
Lumbosacral herniation, 200
Lumbosacral instability, 109–110
Lumbosacral stenosis, 202–203
Lumbosacrum, 188f
Luminal air bubbles, 732
Luminal filling defect, 732, 734f
Lung, 608–631
acute injury to, 639–641
dorsocaudal aspect of, 610f
left caudal aspect of, 610f
nodule in, 481f
pulmonary anatomy of, 608
pulmonary conditions/disease of, 609–630
radiography of, 608–609
recently hit by car, 625f
Lung bulla, 623, 625f
Lung granuloma, 504
Lung lobe, 609f
Lung lobe torsion, 629–630
Lung mass, 565, 623
Lung nodule, 623
Lung pattern, 626
Lung retraction, 573, 576f, 579
Luxation, 297f, 325, 431f. *See also* specific types of
Lymph node, 665. *See* specific types of
Lymphoma, 146–147, 564–565, 713
Lymphoplasmacytic rhinitis, 122
Lymphosarcoma, 161, 681f–682f, 696f, 699

M

Mach line, 394–395
Macklin effect, 568
Macroadenoma, 165
Magnetic field, 61, 72–73, 72f
Magnetic resonance imaging (MRI), 61–73, 288. *See also* specific types of
angiography using, 71, 711
of artifact, 71–72
of brain disease, 135–152
of cervical spondylomyelopathy, 205–207
componenets of, 61f
of contrast media, 67
Magnetic resonance imaging (MRI) *(Continued)*
contrast resolution in, 69f
excitation during, 61–63
of gradient recalled sequence, 67
of hematoma, 150t
hoist for, 155f
hydrogen proton used for, 62f
image quality of, 71
imaging time of, 71
instrumentation for, 61
of intervertebral disc disease, 200–204
of kidneys, 711
of lameness, 417f
magnetic field strength of, 61, 72–73
of MC III, 416f
of MTP joint, 417f
of navicular bone, 467–469
of pharynx, larynx, and trachea, 497–498
of plane, 54f
radiofrequency energy of, 61
relaxation during, 61–63
signal localization in, 65
signal-to-noise ratio in, 71f
of spinal cord disease, 194–221
spin during, 61–63
spin echo sequence used in, 63–67, 68f
of tissue contrast, 64–65
T1-weighted postcontrast, 116f
T2-weighted, 163f
of ureters, 711
veterinary use of, 50
Magnification, 62–63, 75–77, 77f
Main pulmonary artery, 592
Major vessel enlargement, 589–592
Malarticulation of cervical vertebrae, 204
Malformation
of articular process, 179, 181f
of cervical vertebrae, 204, 340f
Chiari-like, 116, 218, 218f
of coxofemoral joint, 340f
epiphyseal, 275
of lumbar vertebra, 340f
of metacarpal and metatarsal bones, 340f
of phalanges, 340f
of stifle, 340f
of tarsal bones, 341f
Malignant bone tumor, 258–259
Malignant nasal tumor, 119f
Malignant nerve sheath tumor, 145
Malignant tumor, 494
Malleolus, 363f
Malunion fracture, 298f–300f, 299–301
Mammary adenocarcinoma, 530
Mandible, 115f, 119–120, 129f, 156–157, 156f, 158f
Mandibular squamous cell carcinoma, 120f
Mandibular tumor, 119–121
Mandibular wolf teeth, 160f
Manus, 230f–231f, 317f
Margination, 85–86
Mass, 491–492, 497, 623. *See* specific types of
Mastocytosis, 454
Matrix metalloproteinase activity, 258–259
Matter, 12–14
Maxilla, 104f, 120f, 718f
Maxillary dental arcade, 104f
Maxillary sinus cyst, 161
Maxillary tumor, 119–121

Maxillary wolf teeth, 160f
Maximum permissible dose (MPD), 5
Mechanical obstruction of small bowel, 797–803
Medial coronoid process, 266, 268–269, 272f, 280, 297f, 326, 329f
Medial displacement, 299f
Medial epicondyle, 280, 280f
Medial fabella, 329f
Medial femorotibial joint, 349–352, 354, 356f–357f
Medial iliac lymph node, 666–667, 667f
Medial trochlea, 270f
Mediastinal abscess, 561f
Mediastinal air, 568, 569f
Mediastinal fat, 186f
Mediastinal lymph node, 557, 564–565, 565b
Mediastinal mass, 494, 554–567, 556t, 560f
Mediastinal organ, 551t
Mediastinal reflection, 550
Mediastinal shift, 552–554
Mediastinum, 550–570, 558f–560f, 564f. *See also* specific types of
Medical digital image, 23
Medical-grade monochrome LCD monitor, 28
Medical imaging, 22
Medical practice digital radiography, 28–29
Mediolateral radiography
  of antebrachium, 228f
  of carpus, 229f
  of crus, 235f
  of elbow, 226f
  of elbow joint, 239f
  of femur, 233f
  of humerus, 225f
  of manus, 231f
  of pes, 238f
  of shoulder joint, 224f, 238f
  of stifle joint, 234f
  of tarsus, 236f
Medulla, 463f
Medullary cavity change, 464
Megaesophagus, 503f, 510
Megahertz (MHz), 38, 41, 46, 736
Meningeal layers, 196f
Meninges, 194
Meningioma, 141
Meningitis, 215
Meniscal calcification, 357f
Meniscal ossicle, 323–324, 327f
Mesaticephalic breed, 114
Mesocestoides, 664
Metabolic anomalies, 116–117
Metacarpal and metatarsal bones, 394–413, 396f–397f, 401f, 409f–410f, 420f
  abnormalities of, 398–411
  anatomy of, 394
  diaphysis of, 404–407
  fourth, 408–410
  malformation of, 340f
  oblique dorsomedial-palmarolateral radiography of, 398f, 410f
  osseous injury of, 404–411
  radiography of, 394–398
  second, 408–410
  soft tissue injury to, 398–404
  third, 404–410
  ultrasonography of, 394–398
Metacarpal bone physis, 406
Metacarpal osteochondrosis, 420f
Metacarpophalangeal and metatarsophalangeal articulation, 414–428
  alternative imaging modalities of, 416–417
  anatomy of, 414
  degenerative joint disease of, 418–420
  disease of, 417–425
  radiography of, 414–416
Metacarpophalangeal joint, 243f–245f, 394, 414, 418f, 421f
Metacarpophalangeal sesamoid, 325f
Metacarpus, 260f–261f, 395f
Metallic foreign body, 443, 452–453
Metaphyseal fracture, 288
Metaphysical and epiphyseal dysplasia, 276–280. *See also* Chondrodysplasia
  of humeral condyle, 278–280
  multiple, 277–278
  of multiple cartilaginous exostosis, 278
  of osteochondral dysplasia, 276
  of retained cartilage core, 278
  of ununited medial epicondyle, 280
Metastases, 146–147
Metastatic bone cancer, 316–317
Metastatic calcification, 663, 664f
Metastatic carcinoma, 210f, 259f
Metastatic hemangiosarcoma, 147f, 628f
Metastatic lesion, 146–147
Metastatic neoplasia, 689–690
Metastatic round cell tumor, 316f
Metatarsal bones, 341f, 395f, 397f, 411f. *See also* Metacarpal and metatarsal bones
Metatarsophalangeal (MTP) joint, 414, 417f, 422f, 425f
Metatarsophalangeal articulation. *See* Metacarpophalangeal and metatarsophalangeal articulation
Metatarsophalangeal sesamoid, 325f
Metatstatic prostate adenocarcinoma, 752f
Midabdomen, 660f
Mid-diaphyseal diaphysis, 288
Mid-diaphyseal spiral fracture, 290f
Mid-diaphysis, 263f, 301f
Middle carpal joint, 374
Middle cervical vertebrae, 99f
Middle phalanx, 439f, 440, 441f
Middle region of head, 95f–96f
Midlumbar spinal cord, 108f
Mid metacarpal region, 408f
Midthoracic esophagus, 500f
Midventral aspect, 656f
Milliampere second (mAs) value, 9, 12, 16, 19–20, 30–32, 104–106, 111
  range of, 20f
  time combination and, 12t
  on x-ray machine control panel, 12
Mineral calculi/calculus, 732
Mineral ions in serum, 283
Mineralization, 321, 672–673. *See also* specific types of
Mineralized choledocholith, 685f
Mineralized mass in stomach, 672f
Mineralized nodule, 622
Miniature schnauzer, 512f
Mirror-image artifact, 44, 45f
Miscellaneous factors, 285
Missile disc, 198
Missile disc lesion, 182
Mitotane, 675
Mitral insufficiency, 597, 599f, 630f
Mitral valve, 42f
Mixed lung pattern, 626
Mobile CT unit, 154–155
Modality worklist, 28–29
Moderate hip dysplasia, 331f
Moderately hypertrophic nonunion fracture, 302
Monitor quality, 28
Monoarticular fracture, 441f
Monoarticular septic arthritis, 340–341
Monochrome monitor, 28
Morgan line, 331, 332f
Moth-eaten bone lysis, 259–261
Moth-eaten pattern, 259, 699
Motion, 16
Motion mode (M-mode), 42, 42f
Motor disturbances in diaphragm, 545–546
MR signal, 64–65
Mucinous gland adenocarcinoma, 126
Mucopolysaccharidosis (MPS), 116, 190, 191f, 275, 339
Mucopolysaccharidosis VI (MPS-VI), 116
Mucosal change, 732
Multilobular osteochondrosarcoma (MLO), 121
Multipartite navicular bone, 465–466
Multiplanar reformatting, 50–53, 54f
Multiplane fracture, 438f
Multiple air bronchogram, 476f, 613f, 619f, 642f
Multiple cartilaginous exostosis, 278, 278f
Multiple epiphyseal dysplasia, 277–278
Multiple fractures, 291
Multiple hemivertebra, 176f
Multiple myeloma, 190f
Multi-row computed tomography, 57f
Mural change, 738–739
Mural tracheal mass, 494
Muscular dystrophy, 546–547
Mycoplasma gateae, 342
Mycoplasma haemofelis, 340–342, 695–696
Mycotic pneumonitis, 314f
Myelitis, 215
Myelogram/myelography, 195, 205f–206f, 209f
Myelographic effect, 195
Myelomalacia, 213
Myxoma, 161

N

Nail, 76f, 445f
Nail puncture, 467f
Nasal adenocarcinoma, 165
Nasal aspergillosis, 121–122, 123f
Nasal cavity, 118f–119f, 123f, 161f. *See also* Cranial and nasal cavity
Nasal discharge, 122f–123f
Nasal neoplasia, 145
Nasal passage, 114
Nasal rhinitis, 122–123
Nasal tumor, 117–119
Nasofrontal suture separation, 162
Nasopharyngeal polyp, 125f–126f
Nasopharyngeal stenosis, 493–494
Naturally occuring acoustic shadow/shadowing, 43
Navicular bone, 457–471, 457f, 461f
  anatomy of, 457
  chip fracture of, 465f
  computed tomography image of, 467–469
  dorsoproximal-dorsodistal radiography of, 458f
  gradient recall echo image of, 468f
  magnetic resonance imaging of, 467–469
  navicular sepsis, 466–467

Navicular bone *(Continued)*
palmaroproximal-palmarodistal radiography of, 459f
positioning aids for, 458f
radiography of, 457–460, 458b
STIR image of, 468f–469f
ultrasonography of, 467
Navicular bone agenesis, 467
Navicular bone extremities, 461–463
Navicular bone fracture, 465–466, 465f. *See also* specific types of
Navicular bursa, 464, 466f–467f, 467–468
Navicular conditions/diseases, 460–465, 467
distal border change, 463
flexor cortex change, 463–464
medullary cavity change, 464
navicular bone extremities, 461–463
proximal border extremities, 461–463
radiography of, 460–461, 464–465
Navicular degeneration, 460–461, 460b, 461f, 463–467
Navicular flexor cortex, 462f–463f
Navicular sepsis, 466–467
Near field, 42
Neck pain, 496f
Necrotic fat, 663, 664f
Necrotic nonunion fracture, 302
Necrotizing encephalitis, 139
Negative summation, 79
Neoplasia, 161, 188–190, 642, 764–766. *See also* specific types of
Neoplasm, 162, 345, 516–517
Neoplastic abnormalities, 117–121
Neoplastic bone lesion, 311
Neospora caninum, 215
Nephroblastoma, 716f
Nephrogram phase, 723f
Nerve root compression, 112, 175–177, 186
Nerve-sheath tumor, 145–146, 212f
Net magnetization, 61
Neural compression, 109–110
Neutral lateral radiography, 336f
Nocardia, 215
Nodular cortical hyperplasia, 674–675
Nodular hyperplasia, 700
Nodular opacity, 187f, 621f
Nodule. *See* specific types of
Noise in image, 33–34, 34f
Nomenclature, 159
Nonaggressive bone cyst, 258, 260f
Nonaggressive bone lesion, 258t, 259–261
Nonaggressive lesion, 262f
Nonairway paradigm, 626
Nonarticular fracture, 440
Noncomminuted fracture, 441f
Noncompressive intervertebral disc extrusion, 203–204
Noncompressive nucleus pulposus extrusion, 198
Noncontrast CT, 205, 212, 215
Nonfunctional malunion fracture, 299–301
Nonopaque esophageal foreign body, 511–513
Nonradiopaque foreign body, 502
Nonradiopaque pad, 109f
Nonselective angiography, 542–543
Nonunion fracture, 301. *See also* specific types o
Nonviable nonunion fracture, 301–302
Nuchal ligament, 174
Nucleus, 196
Number change, 85–86
Nutritional secondary hyperparathyroidism, 191f, 274f
Nutritional secondary hyperthyroidism, 117f

O

Obesity, 491f, 522f
Oblique caudolateral-craniomedial radiography, 249f, 352f
Oblique dorsolateral palmaromedial oblique radiography, 367f
Oblique dorsomedial-palmarolateral radiography, 242f, 251f, 257f, 396f–398f, 401f, 410f–411f
Oblique dorsoproximal-dorsodistal radiography, 242f
Oblique dorsoproximal-palmarodistal radiography, 244f
Oblique fracture, 289, 291f, 441f
Oblique palmaroproximal-palmarodistal radiography, 247f
Oblique projection, 253–258
Oblique radiography, 105f, 127f, 129f, 156, 159, 161f, 163f, 258t
Oblique 65-degree proximal-palmarodistal radiography, 246f
Oblique view, 104, 106f, 729f
Occipital bone malformation, 116, 218, 218f
Occipital dysplasia, 115–116
Occipital region, 98f
Occipitosphenoid suture separation, 162
Occlusive infarction, 149
Occupational radiation exposure, 6, 252–253
Ocular chondrodysplasia, 277
Odontoma, 51f, 120–121, 161
Oligotrophic nonunion fracture, 302, 302f
Opacities. *See also* specific types of
air, 74–75, 76f
change in, 85–86
of film image, 8, 14–16
of gas, 662–663, 664f
radiography of, 76f–77f, 76t
of soft tissue, 162f, 546f
of subchondral bone, 319–320, 437f
of trachea, 621f
Opaque callus, 275
Open fracture, 289–290
Open-leg lateral view, 80f
Open-mouth, ventrodorsal radiography, 118f, 122f
Open-mouth jaw locking, 116
Open-mouth-left 20-degree ventral-right dorsal projection, 104f
Open-mouth rostrocaudal view, 102f
Open transverse distal diaphyseal fracture, 292f
Opossum, 117f
Optimization of contrast, 31–32
Oral phase dysphagia, 507
Oral squamous cell carcinoma, 119–120
Organized search pattern, 266
Orthogonal projection, 77
Orthopedic device, 294–296
Orthopedic disease, 266t, 267–282
Oslerus (Filaroides) osleri granuloma, 494
Osseous callus, 441, 525
Osseous cyst, 450
Osseous cyst-like lesion, 259–261, 379–380, 450–451
Osseous fragment, 465
Osseous injury, 404–411. *See also* Metacarpal and metatarsal bones
distal metacarpal bone physis, 406
enostosis-like lesion, 408
Osseous injury *(Continued)*
hypertrophic osteopathy, 408
infectious osteitis, 410–411
osteomyelitis, 410–411
panosteitis, 408
suspensory ligament, 404
Osseous metaplasia, 622f
Osseous structure, 430–431
Ossification, 394, 452, 452f. *See also* Calcification; Incomplete ossification
Osteoarthritis, 187, 326–330, 330b, 388–390
Osteoarthropathy, 157
Osteoblast, 283
Osteochondral dysplasia, 276
Osteochondral fracture, 292
Osteochondritis dissecan (OCD), 267, 322–323
Osteochondrosis, 267, 353f, 360–362, 360f, 362f, 420–421
of femoral condyle, 270f
of humeral condyle, 270f
lameness, as cause of, 267
of lateral trochlea, 267
of malleolus, 363f
of MC III, 423f
of medial trochlea, 270f
of metacarpals, 420f
radiography of, 267
of shoulder, 269f
of tarsus, 360f
Osteoclast, 258–259, 283
Osteocyte, 283
Osteodystrophy, 117, 273, 274f
Osteogenesis, 283–284
Osteogenic bone graft, 286–287
Osteoma, 121, 161
Osteomyelitic bone lesion, 311
Osteomyelitis, 302, 302f, 358–359, 410–411, 424f, 443. *See also* specific types of
Osteopathy, 127, 129f, 273. *See also* Hypertrophic osteopathy
Osteopenia, 191
Osteopetrosis, 275f
Osteophyte, 321–322
Osteophytosis, 202–203
Osteosarcoma, 121, 161, 260f, 262f–264f, 310f, 454
Osteosclerosis, 276
Osteotomy, 284f
Otitis, 123–126
Otitis externa, 123, 140f
Otitis media, 123–124, 124f
Ovaries, 763–764
Overexposure, 33–35

P

Pair production, 12
Palmaromedial-dorsolateral oblique radiography, 231f
Palmaroproximal-palmarodistal radiography, 247f, 459f, 463f, 467f
Palmar process, 433f
Palmar process fracture, 440
Palmar view, 435f
Pancreas, 667–671, 670f–671f
Pancreatic abscess, 670, 671f
Pancreatic duct, 669–670
Pancreatic pseudocyst, 670
Pancreatic region, 670f
Pancreatic tumor, 670–671
Pancreatitis, 669b–670b, 670f
Panosteitis, 271, 273f, 408
Paraesophageal hernia, 511
Paraesophageal hiatal hernia, 543

Paralysis, 545
Paranasal sinuses, 114, 159
Paraplegia, 200–202
Paraprostatic cyst, 749, 754f
Parathyroid adenoma, 116–117
Parathyroid hormone, 283
Paravertebral soft tissue tumor, 210
Parenchyma, 686, 698
Parenchymal mineralization, 684
Parenchymal pulmonary artery enlargement, 600
Parenchymal T2-signal intensity, 139
Parietal abdominal lymph node, 665
Partial agenesis, 271
Pasteurella, 215, 342, 614f
Patella, 325, 326f, 328f, 349, 353f–354f, 360f
Patellar fracture, 357
Patellar fragmentation, 353f
Patent ductus arteriosus, 594f, 603f–604f
Pathologic acoustic shadow/shadowing, 43
Pathologic fracture, 275, 291, 293f
Pathologic mediastinal conditions, 552–569
Patient hit by car, 183f, 189f
Pattern recognition paradigm, 609–626
Pectus excavatum, 523, 526f
Pedal osteitis, 451–452, 452f
Pelvis, 252, 340f, 729f
Penetrating solar nail injury, 435f
Penicillium, 121–122
Penile urethra, 747f–748f
Peracute thromboembolism, 595–596
Perception, 80–86
Perception artifact, 82f
Perforation of esophagus, 517–519, 569
Perfusion-weighted imaging, 69–71
Periapical (tooth root) abscess, 126
Periarticular chip fracture, 421
Periarticular connective tissue, 208
Periarticular fracture, 426f
Periarticular soft tissue, 320f, 359–360, 418
Periarticular structure, 378
Pericardial effusion, 602
Perichondral bone opacity, 320–321
Periodontal disease, 129
Periosteal bone proliferation, 436f
Periosteal callus, 296–298, 404, 406, 408f–409f
Periosteal margin, 261–263
Periosteal reaction, 309f
Peripheral focal pulmonary pattern, 600
Peristalsis, 509–510
Peritoneal cavity, 657f
Peritoneal effusion, 665f
Peritoneal fluid, 578–579, 660f
Peritoneal metastasis, 665f
Peritoneal space, 659–678, 664f
  abdominal wall abnormalities in, 664
  adrenal gland in, 671–675
  contrast of, 660–663
  intraabdominal mineral opacity of, 663
  lymph node in, 665–667
  pancreas in, 667–671
  sonography of, 664–665
Peritoneopericardial diaphragmatic hernia, 525f, 541–543, 543b, 544f–545f
Peritoneopleural hernia, 545
Peritonitis, 141f
Peritracheal hemorrhage, 494
Permanent lateral patellar luxation, 354f
Permeative lysis, 259–261
Permeative pattern, 259
Persistent aortic arch, 513–514, 513f–515f
Personal shielding, 6–8
Personnel monitoring of radiation, 8
Pes, 20f, 237f–238f, 314f, 317f
Petrous temporal bone, 162
Phalange fracture, 436–442, 439f
Phalanges, 429–456
  collateral cartilage in, 452–453
  degenerative joint disease of, 443–445
  disease affecting, 453–454
  distal phalanx, 440–442
  dorsopalmar radiography of, 431f
  hoof balance and, 453
  infection of, 443
  interphalangeal joint in, 449–450
  laminitis in, 446–449
  malformation of, 340f
  osseous cystlike lesion in, 450–451
  pedal osteitis in, 451–452
  radiography of, 430–436
  technical factors for, 429–430
Phalanx, 430t, 442f. *See also* specific types of
Pharyngeal dysphagia, 507–508
Pharyngeal phase, 508f
Pharyngitis, 494
Pharyngolaryngeal mass, 491b
Pharyngolarynx, 491–494
  brachycephalic syndrome of, 493
  epiglottic retroversion of, 493
  laryngitis of, 494
  mass of, 491–492
  nasopharyngeal stenosis of, 493–494
  pharyngitis of, 494
  trauma to, 492–493
Pharynx, larynx, and trachea, 489–499
  anatomy of, 489–491
  compartments of, 489f
  computed tomography image of, 497–498
  lateral radiography of, 489f
  magnetic resonance imaging of, 497–498
  pharyngolarynx, 491–494
  radiography of, 491–497
  trachea, 494–497
  ultrasound of, 497
  upper airway obstruction of, 497
Phase-encoding gradient (G_{pe}), 65
Photodisintegration, 12
Photoelectric absorption, 13–14, 20
Photoelectric effect, 12–13, 13f
Photoelectron, 13
Photographic film, 14
Photon, 2, 12, 17
Photostimulable phosphor (PSP), 24–25, 25f
Phrenicopericardial ligament, 551–552
Physeal fracture, 288–289
Physical examination, 287
Physis capillary network, 309–311
Picture Archiving and Communication System (PACS), 29, 35–36
Picture elements, 50
Pituitary-dependent hyperadrenocorticism (PDH), 143, 674–675
Pituitary gland, 165–166, 166f
Pituitary tumor, 143, 144f
Pixel, 23, 50
Pixel-to-voxel translation, 52f
Planck's constant, 2
Plane, 50–53, 54f
Plantar bone-phase scintigraphic image, 400f
Plantarolateral-dorsomedial radiography, 361f–362f, 370f
Plantaroproximal-plantarodistal view, 369f
Pleural effusion, 567f, 600, 682f
Pleural fluid, 571–579
  cause of, 572t
  compartmentalization of, 642
  confounding effects of, 565–567
  diagnosis of, 573–574
  distribution of, 573
  dorsal *versus* ventral recumbency of, 572f
  horizontal-beam radiography of, 573, 578f
  interlobar fissure, 573
  lung retraction resulting from, 573, 576f
  presence of, 643f
  retrosternal opacification, 573
  roentgen sign of free, 573b
  significance of, 574–578
  simultaneous, 578–579
Pleural granuloma, 542
Pleural space, 571–584
  air in, 579, 582
  anatomy of, 571
  pleural fluid in, 571–579
  pneumothorax in, 579–582
  radiography of, 571
Pleural thickening, 571
Pneumocystis carinii, 639–641
Pneumomediastinum, 526f, 567–569, 568f–570f, 663f
Pneumonia, 614f. *See also* specific types of
Pneumoretroperitoneum, 570f
Pneumothorax, 526f, 579–582, 579f–581f
  causes of, 579b
  diagnosis of, 582
  "elevation" of heart from sternum, 581
  facts about, 582
  left-sided tension, 582f
  lung retraction from, 579
  radiography of, 579b
Point-of-entrance, 81
Point-of-exit, 81
Polyarthritis, 344, 344f
Polyarthropathy, 320f
Polyarticular septic arthritis, 340–341
Polyostotic aggressive bone lesion, 309–310
Portal hypertension, 520f
Portal vein, 686
Portosystemic shunt (PSS), 60f, 685, 694f
Positioning aids, 458f
Position of appendicular skeleton, 252–253
Positive-contrast arthrogram, 419f
Positive-contrast cystogram, 731f, 735f–737f
Positive-contrast gastrogram, 770b, 771f
Positive-contrast peritoneogram, 542f
Positive summation, 79
Postcontrast computed tomography, 533f, 716f
Postcontrast T1-weighted image, 146f, 207f, 212f, 216f
  of acute seizure, 150f–151f
  of disc herniation, 201f
  of lumbosacral discospondylitis, 216f
  of lymphoma, 147f
  in meningioma, 213f
  of metastatic hemangiosarcoma, 147f
Postcontrast transverse T1-weighted image, 141f, 144f, 202f, 217f
Postoperative imaging, 293

Postoperative plantarolateral-dorsomedial radiography, 361f
Postoperative radiography, 295f
Postprocessing, 27, 35
Power control, 42
Power Doppler information, 47–48
Precession, 61
Precessional frequency, 69
Precontrast computed tomography, 533f
Precontrast T1-weighted image, 150f, 201f, 216f
Precontrast transverse T1-weighted image, 202f, 217f
Pregnant women, 6
Premature distal physeal closure, 303f
Preprocessing, 27
PRF, 49
Primary bone tumor, 307–309
Primary cardiac disease, 605, 639–641
Primary hyperparathyroidism, 116–117
Primary intracranial tumor, 146–147
Primary neoplasia, 689–690
Primary peristalsis, 509–510
Processing of image, 20–21, 27–28
Progressive degenerative joint disease, 275
Progressive ethmoid hematoma, 161
Progressive inspiratory noise, 492f
Progressive lameness, 345f
Pronounced bronchial pattern, 617f
Pronounced left atrial dilation, 589f
Pronounced pneumomediastinum, 568f
Prostate gland, 749–756
  anatomy of, 749, 753f
  computed tomography of, 755, 755f
  disease of, 749–751
  enlargement of, 750f–751f
  magnetic renosance imaging of, 755
  radiology of, 749, 752
  sonography of, 752–755, 755f
Prostatic adenocarcinoma, 754f
Prostatic carcinoma, 729f
Prostatic duct, 752f
Prostatic hypertrophy, 750f, 753f
Prostatitis, 754f
Prosthesis, 261f, 312f
Proton-density (PD) weighting, 64–65, 136, 437f
Prototheca wickerhamii, 215
Prototheca zopfii, 215
Protrusion, 182
Proximal aspect, 260f, 293f, 371f
Proximal border extremities, 461–463
Proximal diaphysis, 288
Proximal epiphysis, 424f
Proximal fibular epiphysis, 273f
Proximal humerus, 252, 253f, 260f, 293f, 313f
Proximal insertion desmopathy, 369
Proximal insertion suspensory desmopathy, 369
Proximal interphalangeal joint, 414, 437f, 446f–447f
Proximal intertarsal joint, 365–366
Proximal metacarpal region, 395f–396f, 407f, 410f
Proximal metatarsal region, 370f, 398f, 400f
Proximal phalanx, 416f, 427f, 436–440, 439f–440f, 451f
Proximal right femur, 313f
Proximal sesamoid, 421–425
Proximal suspensory desmitis, 398–399, 399f
Proximal tibia, 313f–314f
Proximopalmar aspect, 404
Pseudoachondroplasia, 277
Pseudoairway, 495
Pseudoarthrosis, 301, 301f
Pseudofilling defect, 735
Pulmonary abscess, 637f, 638–639
Pulmonary arteries, 592, 592f, 594b, 597b, 600, 603f
Pulmonary atelectasis, 553–554
Pulmonary blood vessel, 637f
Pulmonary conditions/diseases, 609–630
Pulmonary edema, 596–597, 615f, 626–629, 630f, 642, 642f
Pulmonary hemorrhage, 641–642
Pulmonary hyperinflation, 619, 620f
Pulmonary hypertension, 600
Pulmonary lymphomated granuloma, 564–565
Pulmonary nodule, 622
Pulmonary osseous metaplasia, 622f
Pulmonary thromboembolism, 595–596, 600
Pulmonary vascular change, 592–605
Pulmonary vascular margination, 596
Pulmonary veins, 594b, 596–597, 596b–597b, 629
Pulmonary vessels, 585–607
Pulmonic stenosis, 605f
Pulse, 65
Pulsed-wave Doppler interrogation, 47–49, 47f
Pulse echo principle, 42
Pyelogram phase, 723f
Pylorus, 655f
Pyometra, 760–761
Pyothorax, 573

Q

Quality, 55f, 71
Quality factor, 3
Quittor, 452–453

R

Rad, 4
Radial carpal bone, 374
Radial osteosarcoma, 262f, 310f
Radial osteotomy, 284f
Radiation. *See also* specific types of
  absorption of, 3–4
  equivalent in man, 4
  exposure to, 5f
  matter and, 12–14
  pregnant women, regulations for, 6
  radiation weighting factor for, 4t
  units of, 5t
Radiation exposure, 3–6
Radiation-induced cancer, 4–5
Radiation-induced cataract, 4–5
Radiation protection, 2–21
Radiation safety, 4–6, 7f, 8, 102–103
Radiation supervisor, 8
Radiation therapy, 6
Radiation units, 3–4
Radiation weighting factor, 4t
Radiative interaction, 9
Radiative x-ray, 10f
Radioactive labeling of white blood cells, 154
Radiofrequency energy, 61
Radiographic film processing, 20–21
Radiographic geometry, 75–80
Radiographic opacity, 74–75, 76f–77f, 76t
Radiography, 74–86, 185f, 287. *See also* specific types of
  of angular limb deformity, 278, 376
  of brachycephalic syndrome, 493f
  of bronchus, 616f
Radiography *(Continued)*
  careless approach to, 4f
  of cervical mass, 491f
  of coccidioidomycosis infection, 313f
  of coughing, 493f, 495f
  of diaphragmatic region, 537f
  of dyspnea, 492f
  of foot, 449f, 453f
  of head, 106f
  of hematogenous bacterial osteomyelitis, 315f
  of hypertrophic osteopathy, 344f
  image formation in, 74
  of inspiratory difficulty, 492f
  of interphalangeal osteoarthritis, 446f
  of joints, 327t
  of malleolus, 363f
  of metastatic round cell tumor, 316f
  of navicular degeneration, 460–461
  of neck pain, 496f
  opacity of, 74–75
  perception in, 80–86
  of pes, 20f
  of proximal humerus, 313f
  of proximal right femur, 313f
  of proximal tibia, 313f
  radiographic geometry and, 75–80
  recognizability of objects on, 78f
  of respiratory distress, 492f
  of seizure, 495f
  of shoulder, 21f
  of sinus tachycardia, 616f
  of stifle, 355f
  of submandibular mass, 492f
  of Swiss cheese, 81f
  techniques for, 19–20
  three-dimensional thinking and, 75–80
Radiolucency, 297f
Radiolucent lesion, 346f
Radiolucent line, 430f
Radiolucent region, 613f
Radiolucent squeeze cage, 508f
Radiopacity, 75, 75f, 324, 730t
Radiopaque cholelith, 685f
Radio wave, 38
Radius, 378f
Radon's mathematic principle, 55
Rami of mandible, 156
Random search pattern, 265–266
Range ambiguity, 49
Rare-earth phosphor, 17
Ray, 57
Rear-limb distal phalanx, 312f
Receiver, 74
Receiving coil, 63
Recoil electron, 13–14
Reconstruction algorithm of image, 55, 58f
Reconstruction filter, 57
Rectification, 11f
Recumbent lateral view, 547f
Recurrent airway obstruction, 641
Recurrent hemarthrosis, 326
Recurvatum fracture, 299–301
Redundant array of independent disk (RAID), 35
Redundant esophagus, 511
Reformatted image, 50–53, 55f
Refraction, 45–46. *See also* specific types of
Regurgitation, 557
Reject function, 42
Relative inherent radiopacity, 75
Relaxation, 61–63
Remodeling, 461–463
Renal abscess, 714–715

Renal adenocarcinoma, 714–717
Renal angiography, 710–711
Renal carcinoma, 712f
Renal disease, 711–718
Renal enlargement, 712f
Renal failure, 718f
Renal function, 718
Renal lymphoma, 713
Renal pelvic calculi/calculus, 685f
Renal pelvis, 717–718
Renal region, 81f, 713t
Renal size, 711
Renal structure, 711–717
Resolution, 40
Resonance, 61–62
Respiratory distress, 492f, 495f, 497f
Respiratory noise, 497f
Retained cartilage core, 278, 279f
Retching, 616f
Retrograde positive-contrast cystogram, 731
Retrograde urethrography, 744–745, 744f–745f
  of hematuria, 747f
  of penile urethra, 747f–748f
  of pollakiuria, 747f
  of straining, 747f
  of urinary tract infection, 748f
  of urine leakage, 748f
Retroperitoneal gas, 569
Retroperitoneal space, 657f, 719f
Retrosternal opacification, 573
Reverberation artifact, 43, 44f, 691f
RF pulse, 61–65
Rheumatoid arthritis, 342, 343f
Rhinitis, 122
Rhipicephalus sanguineus, 316
Rhodococcus equi, 638
Rib cage, 525f
Rib fracture, 525, 527f, 619f, 639, 655f
Rib infection, 527–530
Rib neoplasia, 528
Rib tumor, 527–530
Rickettsia rickettsii, 215
Right (RAA) aortic arch, 513–514, 513f
Right abdominal wall, 662, 688f
Right aortic arch, 425, 513–514, 513f–515f
Right atrium, 588
Right caudal aspect, 611f–612f
Right cranial pulmonary mass, 529f
Right distal antebrachium, 265f
Right dorsal-left ventral oblique radiography, 125f, 128f
Right femur, 311f
Right 45-degree dorsal-left ventral oblique (RDLVO) radiography, 156, 157f–158f
Right hemithorax, 583f
Right ischial region, 80f
Right lateral abdominal radiography, 651–652
Right lateral skull radiography, 160f
Right lateral thoracic radiography, 187f, 490f, 518f, 522f–525f
Right lateral view, 545f, 576f, 621f
Right-left caudoventral oblique radiography, 164f
Right-left lateral radiography, 95f, 232f, 638f, 640f
Right-left radiography, 160f, 162f, 167f–169f, 639f
Right-left standing radiography, 160f
Right-left view, 474, 650
Right middle lobe collapse, 616–617
Right middle lobe pneumonia, 613f
Right middle region, 612f
Right-sided heart failure, 596, 600
Right temporomandibular joint, 104f
Right thoracic lateral radiography. *See also* specific types of
  of bronchial pattern, 641f
  of cardiac region, 479f
  of caudal lung lobe, 624f
  of caudal thorax, 478f, 567f
  of caudodorsal thorax, 635f
  of chemodectoma, 564f
  of costochondral degeneration, 524f
  of cranial lobe artery, 592f
  of diaphragm, 479f, 536f
  of esophagus, 513f
  of extensive costal cartilage mineralization, 524f
  of heart base tumor, 563f
  of left-sided rudimentary rib, 524f
  of mediastinum, 559f–560f, 564f
  of nodule in left lung, 476f
  of peritoneopericardial diaphragmatic hernia, 544f
  of pylorus, 655f
  of sternal lymph node, 557f
  of sternebral segment, 524f–525f
  of thorax, 478f, 530f, 566f
  of tracheobronchial lymph node, 562f–563f
  of vaccine-associated interscapular fibrosarcoma, 533f
Right 20-degree ventral-left dorsal radiography, 124f
Right tympanic bulla, 104f
Right ventricle, 589
Right ventricular hypertrophy, 590f, 600
Ring-down artifact, 43–44
Ring shadow, 615–616
Ripple factor, 11f
Roentgen, Wilhelm Conrad, 2
Roentigen sign, 85–86, 88, 258, 460b, 573b, 648b
Room air, 730–731
Rostral aspect, 156f–157f
Rostral mandible, 119–120, 129f
Rostral premolar area of Oldenburg, 159f
Rostral 10-degree ventral-caudodorsal radiography, 125f
Rostral 10-degree ventral-caudodorsal view, 105f
Rostrocaudal-frontal sinus radiography, 118f, 122f
Rostrocaudal frontal sinus view, 102f
Rostrocaudal open mouth radiography, 124f
Rostrodorsal-caudodorsal oblique (RD-CdVO) radiography, 89f, 97f
Rotational stress, 334
Rudimentary PACS system, 29f
Rudimentary rib, 523
Ruptured bowel, 662f

S

Sacrococcygeal disc herniation, 202
Sacrum, 172
Safety pin obstruction, 512f
Sagittal computed tomography, 126f, 178f, 218f, 493f, 520f, 710f, 720f
Sagittal plane fracture, 387
Sagittal plane STIR image, 469f
Sagittal postcontrast fat-saturated T1-weighted image, 210f
Sagittal reformatted cervical spondylomyelopathy, 205f
Sagittal reformatted image, 203f
Sagittal section, 434f
Sagittal sonogram, 664f–665f, 667f, 670f–671f, 673f–675f, 738f–740f
Sagittal spin echo, 116f
Sagittal T1-weighted image, 203f, 214f
Sagittal T1-weighted postcontrast image, 144f
Sagittal T2-weighted image
  of caudal brain, 218f
  of cervical spine, 197f
  of cervical spondylomyelopathy, 180f–181f, 206f
  in discal cyst, 209f
  of disc herniation, 200f, 202f
  of dorsal arachnoid diverticulum, 208f
  with fluid-attenuated inverson recovery, 214f
  of Hansen Type 1 disc herniation, 198f
  in lumbar spine, 214f
  of meningitits, 207f
  of meningomyelitis, 217f
  of noncompressive intervertebral disc extrusion, 203f–204f
  of occipital-cervical junction, 138f
  of pituitary gland, 166f
  presumed fibrocartilaginous embolism, 214f
Sagittal T2-weighted postcontrast image, 142f
Sagittal ultrasonography, 467f
Salient imaging sign, 179t
Salient radiography, 190t
Salter-Harris classification system, 288–289
Salter-Harris Type I fracture, 289, 289f
Salter-Harris Type II fracture, 289, 289f, 294f
Salter-Harris Type III fracture, 289
Salter-Harris Type IV fracture, 287f, 289
Salter-Harris Type V fracture, 289
Sarcoma, 146
Satisfaction of search, 86
Scapulohumeral joint, 322f–323f
Scatter correction software algorithm, 30f
Scattered photon, 30–31
Scattered radiation, 20
Scattering, 12–14, 17, 40
Scatter removal by grid, 30f
Sciatic nerve tumor, 212f
Scintigraphic image, 168f
Scintigraphy, 153–154, 288, 500, 711
Sclerosis, 382–383
Scottish Fold chondro-osseous dysplasia (SFCOD), 277f, 339–340
Screen capture image, 28f, 85f
Secondary angular limb deformity, 376
Secondary bone healing, 294b
Secondary degenerative joint disease, 267
Secondary hyperparathyroidism, 116–117, 117f, 275, 293f, 718f
Secondary intracranial neoplasia, 146–147
Second metacarpal and metatarsal bones, 408–410
Sedation, 101, 107
Segmental fracture, 291
Segmental rib fracture, 526
Seizure, 144f, 148f, 495f
Selective left ventricular angiocardiogram, 604f
Septic arthritis, 340–342, 358–359, 360f, 367, 421, 424f, 443. *See also* specific types of
Septic osteitis, 443
Sequence, 63. *See* specific types of
Sequential mode, 55
Sequestrum, 293–294

Serosal suface visualization, 662b
Sesamoid bone, 323–324, 435f
  of carpal bone, 324f
  of elbow, 324f
  fracture of, 415f
  fragmentation of, 328f
  intraarticular tarsometatarsal, 326f
  meniscal ossicle, 323–324
  metacarpophalangeal, 325f
  metatarsophalangeal, 325f
  proximal, 415f, 426f
Sesamoid disease, 324–330
Sesamoiditis, 419f, 425
Severely comminuted fracture, 289
Shadow, 38–39
Sharpey fiber, 186f
Shearing fracture, 292–293
Shear stress, 334
Short interarcuate ligament, 174
Short interspinous ligament, 174
Short scale of contrast, 19–20
Short TI recovery (STIR) sequence, 65–67, 66f, 69, 468f–469f
Shoulder, 335–336
  bicipital tendon in, 335
  joint disease in, 335–336
  lateral view of, 296f
  osteochondrosis of, 269f
  radiography of, 21f, 335–336
  ruptured bicipital tendon in, 335–336
Shoulder joint, 224f, 238f, 323f
Shunt, 60f, 685, 693–694, 694f
Siberian husky, 515f
Side lobe, 44–45
Signal averaging, 53f
Signal localization, 65
Signalment, 83
Signal reception, 64f
Signal-to-noise ratio (SNR), 71–73, 71f
Signal void, 72f
Silhouette sign, 79–80, 82f
Simple fracture, 289
Simultaneous pleural fluid, 578–579
Sine wave, 2, 39f
Single-shot fast spin echo (SSFSE), 195, 200, 200f
Sinuses. *See* specific types of
Sinusitis, 160
Sinus tachycardia, 616f
65-degree proximal-palmarodistal radiography, 246f, 429f, 443f, 452f
Skeletal disease, 267
Skull, 32f, 101–107, 105f, 165f
  ancillary factors for, 106
  interpretation paradigm for, 106–107
  positioning of, 101–104
  radiography of, 102f, 104–106, 105f, 129f
  with temporomandibular osteopathy, 165f
Skyline, 458
Slab fracture, 291, 386–387
Slice-by-slice mode, 55
Slice reconstruction interval, 57
Slice selection gradient (G_{ss}), 65
Slice thickness artifact, 45, 46f
Slice thickness on quality, 55f
Sliding esophageal hernia, 511
Sliding hiatal hernia, 543–544, 546f
Slightly oblique lateromedial radiography, 408f
Slip-ring electromechanical device, 55
Sludge, biliary, 688f, 692, 693f
Small bowel, 789–811
  abnormal, 795–808
  bowel-associated mass in, 807–808
Small bowel *(Continued)*
  contrast examination of, 793–795
  functional ileus of, 803–805
  infiltrative bowel disease of, 805–807
  measurements of, 790b
  mechanical obstruction of, 797–803
  radiography of, 789–791
  small intestinal disease of, 808
  ultrasonography of, 791–793
Small intestinal disease, 808
Soft tissue, 162f, 298, 431–433, 546f
Soft tissue emphysema, 298, 302, 493f, 495
Soft tissue infection, 530
Soft tissue injury, 398–404
Soft tissue tumor, 530
Solar margin contour, 432f
Solar margin fracture, 440
Solar nail injury, 435f
Solid state computed tomography, 57f
Sonographic artifact, 737f
Sonography
  of abdominal wall, 735–740
  of abnormal lymph node, 668f
  of adrenal gland, 673–675, 673f–675f
  attenuation in, 43, 44f
  of bladder, 737
  longitudinal, 155f
  of urethra, 746f–747f
Sound beam reflection, 40
Sound frequency, 46
Sound wave, 38–40, 42, 46, 688–689
Sound wave fraction, 46f
Soundwave penetration, 41
Spatial compounding, 41
Spatial pulse length (SPL), 40–41, 41f
Spatial resolution (SR), 23, 29–31, 50, 52f–53f, 71
Sphenopalatine sinus, 158
Sphincter, 500–501. *See also* specific types of
Spin, 61–63
Spina bifida, 177
Spinal arachnoid diverticula, 207–208
Spinal cord, 107–113, 110f, 194
  anatomic relation of, 196f
  compression of, 109, 175, 176f, 177–179, 178f, 180f–181f, 185, 194, 198f–199f, 205
  congenital anomalies of, 217
  contusion of, 179, 198, 203f, 204
  cyst of, 207–208
  distention of, 218
  incidental factors for, 112
  interpretation paradigm for, 112–113
  meningeal layers of, 196f
  midlumbar, 108f
  normal appearance, 194–195
  positioning of, 107–111
  radiography of, 109, 111
  subarachnoid space of, 196f
Spinal cord disease, 194–221
  cervical spondylomyelopathy, 204–207
  cystic changes, 207–208
  inflammatory/infectious conditions, 215–217
  intervertebral disc disease, 196–204
  ischemic myelopathy, 213–214
  myelomalacia, 213
  spinal trauma, 214–215
  spinal tumor, 208–213
  syringomyelia, 218
  vertebral anomalies, 217
Spinal cord thromboembolism, 213
Spinal fracture, 290f
Spinal nerve root, 194
Spinal trauma, 214–215
Spinal tumor, 208–213
Spin-echo pulse sequence, 63–67, 64f, 68f, 116f, 136, 150
Spin-echo T2-weighted sequence, 135
Spin precession, 62f
Spiral fracture, 289
Spirocerca lupi, 185, 516–517
Spleen, 698f
  diffuse neoplastic infiltration of, 698
  focal disease of, 699
  head of, 694
  longitudinal image of, 43f
  normal, 695f
  radiography of, 694–701
  size of, 695–697
  splenic sonography of, 698–701
  ultrasonography of, 697–698
Splenic abscess, 699–700
Splenic congestion, 698
Splenic echogenicity, 699
Splenic hemangiosarcoma, 661f, 697f, 700f
Splenic hematoma, 700f
Splenic infarction, 700
Splenic mass, 696–697, 699
Splenic nodule, 700f
Splenic opacity, 697
Splenic parenchyma, 698
Splenic torsion, 696, 696f
Splenic ultrasound, 700–701
Split spinous process, 177f
Spoiled gradient recalled (SPGR) echo sequence, 67, 468–469
Spondylitis, 185, 185f
Spondylosis, 185
Spondylosis deforman, 185–186
Spontaneous nontraumatic rib fracture, 526–527, 617–619
Spotlight, 84f
Sprain, 333–334, 436
Spurs, 461–463
Squamous cell carcinoma, 119–120, 120f
Stability, 284
Standing CT unit, 154–155
Staphylococcus, 215
Static collapse, 496
Static image, 464f
Stenosis, 495
Stenting, 497
Sterile bone sequestrum, 303
Sternal deformity, 523
Sternal fracture, 525
Sternal lymph node, 555–556, 557f
Sternebral degeneration, 524f
Sternebral infection, 530
Sternebral segment, 525f
Sternebral tumor, 530
Steroid hepatomegaly, 681f
Steroid hepatopathy, 681f
Stifle, 322f, 349–360
  bilateral enlargement of, 345f
  caudocranial radiography of, 356f–358f
  caudolateral-craniomedial radiography of, 359f
  caudomedial-craniolateral view of, 349
  conditions/diseases involving, 358–360
  degenerative joint disease of, 356f
  femoropatellar joint disease of, 352–354
  femorotibial joint disease of, 354–357
  fracture involving, 357–358
  joint disease in, 336–337
  lateral radiography of, 85f
  lateromedial radiography of, 350f, 352f, 357f–358f

Stifle *(Continued)*
lateromedial view of, 349
malalignment of, 320f
malformation of, 340f
medial fabella of, 329f
radiography of, 349, 355f
radiolucent lesion of, 346f
supplemental stifle imaging of, 349–352
Stifle joint, 234f, 248f
Stifle sonography, 336–337
Still fluoroscopic image, 497f
Stochastic effect, 4–5
Stomach, 653f–654f, 672f, 769–788
acute gastric dilation of, 777–780
anatomy of, 769, 771f
chronic pyloric obstruction of, 780–782
diffuse disease of, 785–786
displacement of, 775
gastric foreign body in, 775–777
gastric neoplasia of, 783–785
gastric ulcer of, 782–783
radiography of, 769–774
ultrasonography of, 774–786
Storage consolidation of image, 35
Straight sesamoidean ligament, 435f
Strain, 436
Straining, 747f
Stress fracture, 289, 334
Stress radiography, 337f
Stricture, 515–517
Structural shielding, 6
Structured interstitial pattern, 619–623
Stylohyoid bone, 162
Subarachnoid space, 196f
Subchondral bone, 319–320, 319f–320f, 342f, 354, 355f, 421, 437f
Subchondral cyst, 450
Subchondral cyst-like osteochondrosis, 380, 450, 451f
Subcutaneous emphysema, 523–525, 526f–528f, 568–569, 569f–570f, 662
Subluxation, 109, 157, 175, 177–178, 178f, 202–203, 450
Submandibular mass, 492f
Substantial capital outlay, 22
Subtle hepatomegaly, 684
Subungual infection, 317
Subungual tumor, 317
Subvalvular aortic stenosis, 605f
Sulci, 429f
Summation shadow effect, 79, 81f, 593f, 626f
Summation sign, 78
Superficial digital flexor tendon, 435f
Superficial digital flexor tendonitis, 403–404
Superficial mass, 80f
Superficial tissue, 434f
Superimposition, 77–79
Superior teeth, 90f
Supplemental stifle imaging, 349–352
Supracondylar fracture, 292
Supracondylar lysis, 418
Supraorbital process, 163f
Surgical tarsal arthrodesis, 315f
Survey abdominal radiography, 705, 730t
Survey radiographic sign, 184f
Survey radiography, 502, 746f
Susceptibility artifact, 72f
Suspected cardiac disease, 585
Suspensory body injury, 399–400
Suspensory branch injury, 400
Suspensory desmitis, 410
Suspensory ligament, 404
Sustentaculum tali, 369, 369f
Swallowing
cricopharyngeal phase of, 508f
esophageal phase of, 508f
fluoroscopy, study using, 506–507
pharyngeal phase of, 508f
radiography of, 506t
radiolucent squeeze cage for examining phase of, 508f
Swiss cheese pattern, 79, 81f, 699
Synovial cyst, 181f, 207
Synovial fossae, 463
Synovial inflammation, 320–321
Synovial invagination, 463
Synovial joint, 172
Synovial osteochondroma, 345
Synovial sarcoma, 345
Synovial volume, 319
Synovium, 345
Syringomyelia, 116, 218
Systemic lupus erythematosus (SLE), 342–343

T

Tail of spleen, 694
Talar ridge, 361
Talocalcaneal intertarsal joint, 365–366
Tangential view, 415f
Tarsal bones, 341f, 365, 366f
Tarsal lateromedial radiography, 365f
Tarsocrural joint disease, 360–362
Tarsometatarsal ankylosis, 341f
Tarsometatarsal sesamoid, 326f
Tarsus, 360–369
diseases/conditions involving, 367–369
distal intertarsal joint, 362–365
dorsolateral palmaromedial oblique radiography of, 237f
dorsoplantar radiography of, 236f
fracture involving, 366–367
joint disease in, 337–338
lateral view of, 302f, 315f
lateromedial radiography of, 250f, 361f–363f, 366f–367f, 370f
mediolateral radiography of, 236f
oblique dorsomedial-palmarolateral radiography of, 251f
osteochondrosis of, 360f
proximal intertarsal joint, 365–366
radiography of, 360
talocalcaneal intertarsal joint, 365–366
tarsocrural joint, 360–362
tarsometatarsal joint, 362–365
Teeth, 114
Temporal multilobular osteochondrosarcoma, 121f
Temporal teratoma, 160–161
Temporohyoid osteoarthropathy, 162–165
Temporomandibular joint (TMJ), 97f, 104f, 114, 156, 167f, 288f
dysplasia of, 116
luxation of, 127, 128f
osteoarthropathy of, 162
osteopathy of, 165f
Tendon, 335, 337f, 434f. *See also* specific types of
Tendonitis, 335–336, 337f
Tenosynovitis, 335, 418f
Tension pneumothorax, 582, 583f
Tenting, 537
Testicles, 764–767
Tetrahedron of air bubbles, 44
T fracture, 292
Thickened interlobar fissure, 572f
Thickness of fluorescent layer, 17f
Third metacarpal (MC III), 416f, 423f
distal metaphyseal region of, 406
dorsal cortex of diaphysis of, 406–407
dorsal cortical stress disease in diaphysis of, 404–406
dorsoproximal stress fracture of, 404
fracture of, 407–408
proximopalmar aspect of, 404
second and, 408–410
Thoracic cage, 474–475
Thoracic computed tomography, 609f
Thoracic esophagus, 503f, 512f
Thoracic hemivertebrae, 177f
Thoracic inlet, 494f
Thoracic pain, 655f
Thoracic radiography, 84f, 477f, 633f–634f
Thoracic spine, 108f, 111f, 209f
Thoracic spinous process, 108f
Thoracic vertebrae, 32f, 93f, 514f, 546f
Thoracic wall, 522–534
alternate imaging of, 530
congenital defect in, 523
developmental abnormalities in, 523
radiography of, 522–523
rib tumor/infection in, 527–530
soft tissue tumor/infection in, 530
sternebral tumor/infection in, 530
trauma to, 523–527
Thoracolumbar disc extrusion, 200–202
Thoracolumbar herniation, 200
Thoracolumbar intervertebral disc disease, 200–202
Thoracolumbar region, 110f
Thorax, 516f, 518f, 551f, 624f, 643f. *See also* specific types of
alveolar pattern in, 612f
artifact of, 583f
caudal aspect of, 482f, 643f–644f
caudoventral aspect of, 182f
centered over heart, 646f
computed tomography of, 551f
cranial aspect of, 644f–645f
in dorsal plane, 571f
dorsocaudal aspect of, 81f
four-view radiography of, 632f
with heartworm disease, 597f
horizontal-beam ventrodorsal radiography of, 475f
interlobar fissure in, 574f
lateral radiography of, 516f, 518f, 567f, 587f, 597f, 643f, 646f, 682f
lateral view of, 542f–543f, 546f, 622f
left thoracic lateral radiography of, 478f, 553f
with peritoneopericardial diaphragmatic hernia, 545f
with pleural effusion, 567f, 682f
with pleural fluid, 575f–576f
radiography of, 474–488
right thoracic lateral radiography of, 478f, 530f, 566f
transverse computed tomography of, 109f, 501f, 552f–553f
in transverse plane, 571f
Three-dimensional radiography, 75
Three-dimensional reconstruction, 128f, 154f
Three-dimensional surface rendering, 173f–174f, 422f
Three-dimensional thinking, 75–80
Three-dimensional T2* gradient recall echo imaging, 468–469
Three-dimensional volume rendering, 215f
Thromboembolism, 213, 595–596, 597f, 600

Thymus, 557
Tibia, 311f. *See also* specific types of
Tibial agenesis, 273f
Tibial diaphysis, 359f
Tibial fracture, 357–358
Tibial plateau leveling procedure, 295f
TIFF file, 22
Time combination, 12t
Time of echo (TE), 64–65, 64f, 67
Time of inversion (TI), 65–67
Time of repetition (TR), 64–65, 64f
Tissue attenuation, 57, 58f
Tissue contrast, 64–65, 64f
Tissue magnetization, 65
Tomographic imaging, 52f
T1 hypointensity, 136–137, 147–149
T1 relaxation, 62f
T1-weighted dorsal image, 145f
T1-weighted image, 70f, 136–137, 144f, 195, 207f. *See also* specific types of
T1-weighted postcontrast magnetic resonance imaging, 116f
T1-weighted postcontrast transverse image, 140f
T1-weighted pulse sequence, 67
T1-weighted sagittal image, 145f
T1-weighted spin-echo sequence, 135–136
T1-weighted spoiled-gradient recalled imaging, 468–469
T1-weighting, 64–65
Tongue depressor, 45f
Tooth root abscess, 154f, 157f, 160
Torsion, 766
Torsional displacement, 290–291
Torsional fracture, 299–301
Tortuous aorta, 591f
Toxoplasma gondii, 215
Trachea, 494–497. *See also* Pharynx, larynx, and trachea
  avulsion of, 495
  collapse of, 496–497
  compression of, 490–491, 494, 500, 565
  dilation of, 495, 497
  diverticula/diverticulum of, 495
  dorsal wall of, 490f
  foreign body in, 494–495
  hypoplasia of, 495–496
  in lateral projection, 494t
  left lateral thoracic radiography of, 490f
  mass in, 494
  opacity of, 621f
  right lateral thoracic radiography of, 490f
  rupture of, 495, 568–569
  stenosis of, 495
  stent placement in, 497f
  tracheitis in, 496
Tracheal air, 494–495, 497
Tracheal avulsion, 495
Tracheobronchial lymph node, 557–562, 562f–563f
Traction stress, 334
Tram lines, 615–616
Transcondylar lag screw, 297f
Transcuneal approach, 467
Transitional vertebrae, 175–177
Transition zone, 258, 261–264, 310f, 612f
Translational fracture, 299–301
Transverse colon, 667, 671–672, 681–682, 697f
Transverse computed tomography, 211f
  of bilateral ectopic ureter, 722f
  of body wall hernia, 723f
  of brain, 115f, 166f
Transverse computed tomography *(Continued)*
  of caudal frontal sinus, 115f
  of ear, 125f
  of ethmoid labyrinth region, 162f
  of first maxillary molar, 154f
  of lumbar intervertebral disc space, 196f
  of lumbar vertebra, 173f
  of malignant nasal tumor, 119f
  of MTP joint, 422f
  of nasal cavity, 119f, 161f
  of nasopharyngeal polyp, 126f
  of patient hit by car, 189f
  of pituitary gland, 166f
  of temporomandibular joint, 288f
  of thorax, 109f, 501f, 552f–553f
  of vertebra, 199f
Transverse diagram of stomach, 653f
Transverse diaphyseal fracture, 285f
Transverse fat-saturated postcontrast T1-weighted image, 212f
Transverse fracture, 289
Transverse gradient recall echo image, 438f
Transverse magnetization, 62–63
Transverse postcontrast T1-weighted image, 142f
Transverse sonogram, 667f, 670f, 674f, 740f
Transverse spine echo, 116f
Transverse T1-weighted image, 140f, 146f, 148f, 197f, 209f, 211f. *See also* specific types of
  of head tilt, 140f
Transverse T2-weighted fluid-attenuated inversion recovery (T2-FLAIR) sequence, 138f–139f, 147f
Transverse T2-weighted image
  of cervical intervertebral disc space, 198f
  of cervical spondylomyelopathy, 180f–181f, 206f
  of congenital hydrocephalus, 138f
  of fibrocartilaginous embolism, 214f
  of foraminal disc herniation, 202f
  of Hansen type 1 disc herniation, 198f
  of intervertebral disc space, 197f
  of left-sided left articular process cyst, 209f
  in meningioma, 213f
  in nerve sheath tumor, 212f
  of noncompressive intervertebral disc extrusion, 204f
  of rostral aspect of cerebellum, 148f
  of seizures, 148f
Transverse ultrasonography, 353f
  of distal metacarpal region, 404f
  of fluid bronchogram, 637f
  of gallbladder, 692f
  of liver, 688f
  of lung, 636f
  of metacarpal region, 402f
  of metatarsophalangeal joint, 405f
  ov left thorax, 639f
  of palmar metacarpal region, 399f, 406f–407f
  of plantar metatarsal region, 403f
  of pleural fluid, 637f
  of podotrochlear apparatus, 468f
  of proximal metatarsal region, 399f
  of suspensory ligament, 401f
  of tarsometatarsal joint, 403f
  of thorax, 638f
  uniformly echoic mass in, 644f
Trauma associated with foreign body, 492–493, 497–498
Traumatic bladder diverticulum, 732–734, 735f
Traumatic diaphragmatic hernia, 539b, 540–541, 540f–543f
Traumatic disc herniation, 198
Traumatic disc lesion, 182
Traumatic disc prolapse, 198
Traumatic injury, 127
Traumatic intervertebral disc extrusion, 198
Traumatic osteochondrosis, 420–421
Triadan numbering system, 159f
Tricuspid dysplasia, 590f, 605
Trigeminal nerve, 145–146
Trilostane, 675
Tripartite navicular bone fracture, 466f
Trochlear dysplasia, 354
T2-fluid-attenuated inversion recovery (FLAIR) sequence, 136
T2* gradient echo sequence, 68f
T2-hyperintense intramedullary lesion, 213
T2-hyperintense lesion, 135
T2 hyperintensity, 136–139, 147–149, 200–202
T2 relaxation, 63f, 69f, 196
T2-weighted fluid-attenuated inversion recovery (T2-FLAIR) sequence, 67f, 137–138, 139f. *See also* specific types of
T2-weighted GRE sequence, 136, 149f
T2-weighted image, 135, 137f, 195–196, 200. *See also* specific types of
  of cervical spondylomyelopathy, 180f–181f, 206f–207f
  in dorsal plane, 136f
  of intervertebral disc space, 197f
  in sagittal plane, 136f
  in transverse plane, 136f
  transverse spin echo, 201f
T2-weighted magnetic resonance imaging (MRI), 163f
T2-weighted sagittal image, 145f
Tt2-weighted sequence, 67, 200
Tt2-weighted spin echo, 136, 137f, 150
Tt2-weighted transverse image, 140f, 144f, 149f, 200–202
Tt2-weighting (T2w), 64–65, 69f
Tubular gas opacity, 664f
Tubular necrosis, 713
Tumor, 189f, 674. *See also* specific types of
Tungsten, 11
Turbo spin echo sequence, 65
T-weighted postcontrast image, 142f
Twinkling artifact, 49
Two-dimensional radiography, 75
Tympanic bullae, 89f, 102f, 104f–105f, 114, 127f
Tympanic bullae cholesteatoma, 127f
Tympanic bulla radiography, 124f
Type I cervical intervertebral disc disease, 200
Type I fracture, 290
Type II fracture, 290
Type II herniation, 197
Type IIIa fracture, 290
Type IIIb fracture, 290
Type IIIc fracture, 290
Type III fracture, 290
Type I intervertebral disc disease, 196–197
Type IV fracture, 290

U

Ulna, 262f
Ulnar carpal bone, 377f
Ulnar physis, 276, 303
Ultrasonography, 155, 288. *See also* specific types of
  artifact on, 43–46
  of carpus, 402f
  of cervical region, 506f
  of chronic renal disease, 714f
  of collateral ligament, 364f
  contrast-enhanced, 690
  display on, 42
  doppler artifact on, 49
  doppler mode on, 47–49
  doppler techniques for, 46
  of gallbladder, 688f, 690f, 692f
  hepatic, 682, 685–688
  interpretation of, 42–43
  of kidneys and ureters, 46f, 708–710, 709f, 714f–716f
  of laryngeal region, 170f
  of left lateral thoracic wall, 531f
  of leptospirosis, 714f
  of navicular bone, 467
  of perinephric pseudocyst, 716f
  physics of, 38–49
  of right lateral intercostal, 688f
  of right lateral thoracic wall, 531f
  scanner control on, 42
  shape of, 40
  splenic, 700–701
  of stifle, 350f–351f
  of tarsa, 364f
  transducer for, 40–41
  of tuber calcanei, 368f
  ultrasound wave on, 38–40
  of ureteral lumen, 721f
  of urinary bladder, 46f, 718f
Ultrasound beam, 39, 41f, 698f
Ultrasound endoscope, 517f
Ultrasound transducer, 40, 41f
Ultrasound wave, 39f, 39t, 41f
Underdevelopment of film image, 623
Underexposure, 33–34
Unequal magnification, 76–77
Unfamiliar image, 77
Unilateral paralysis, 545
Units of radiation, 5t
Unknown trauma in foot, 445f
Unstructured interstitial pattern, 619, 623–626, 626f, 626t, 628f
Ununited anconeal process, 268, 271f
Ununited medial epicondyle, 280, 280f
Upper airway dilation, 497
Upper airway obstruction, 497, 510–511, 511f, 642
Upper gastrointestinal tract film sequence, 795t
Urachal anomalies, 732–734
Urachal diverticula/diverticulum, 732–734
Ureteral calculi, 721f
Ureteral calculi/calculus, 80f, 653f, 719–720, 720f–721f
Ureteral dilation, 717, 719–720, 719f
Ureteral obstruction, 719–721, 719f–720f
Ureteral tumor, 722
Ureteroliths, 720–721
Ureterovesicular junction, 740
Ureters, 706, 707f, 711, 717, 719–722, 721f–722f. *See also* Kidneys and ureters
Urethra, 744–748
  air bubbles in, 746
  anatomy of, 744
  disease of, 746–748
  radiography of, 744–745
Urethra *(Continued)*
  sonography of, 746f–747f
  ultrasonography of, 745–746
Urethral calculi, 746
Urethral fistula, 748
Urethral inflammation, 746–747
Urethral neoplasia, 746–747
Urethral rupture, 747
Urethral stricture, 747–748
Urinary bladder, 726–743, 729f, 732f, 738f–740f
  anatomy of, 726–727
  computed tomography of, 740–741
  contrast cystography of, 729–735
  contrast leakage pattern from, 732–734
  disease of, 727–729
  excretory urogram/urography of, 741f
  lateral radiography of, 732f
  magnetic resonance imaging of, 740–741
  radiography of, 727–729, 728t
  sonography of, 735–740, 738f–740f
  ultrasonography of, 46f, 718f
Urinary tract, 710f
Urine, 732–734, 748f
Urography, 60
Uterine neoplasia, 761
Uterine stump disease, 761
Uterine torsion, 761
Uterus, 757–761
  cross sectional imaging of, 757–758
  imaging procedure for, 757–758
  pregnancy and, 758–759
  survey radiography of, 757
  ultrasonography of, 757
  uterine disease of, 759–761
Uterus masulinus, 749

V

Vaccine-associated interscapular fibrosarcoma, 533f
Vacuum phenomenon, 267, 322–323
Vaginal lesions, 763
Vagina/vestibule, 761–763
Vaginocystourethrography, 745, 745f
Vaginourethrogram, 722f
Valgus fracture, 299–301
Variable signal intensity, 65f
Varus fracture, 299–301
Vascular channel, 431f, 463
Vascular disease, 693–694
Vascular disruption, 147–150
Vascular ring anomalies, 513–514
Velocity, 38, 39t, 42
Velocity scale, 49
Venous congestion, 693, 694f
Ventral abdominal wall, 662, 663f, 664, 681f
Ventral life-dorsal right radiography, 731f
Ventral longitudinal ligament, 174, 194
Ventral pneumonia, 619f
Ventral recumbency, 481f
Ventral region, 612f
Ventricular compression, 141, 144f, 147f
Ventricular hypertrophy, 590f, 600
Ventricular septal defect, 606f
Ventrodorsal distraction projection (PennHIP view), 333, 333f–334f, 335b
Ventrodorsal intraoral radiography, 156f
Ventrodorsal oblique radiography, 721f
Ventrodorsal radiography, 109. *See also* specific types of
  of accessory lung lobe, 565f
  of adrenal gland, 672f
  of asthma, 620f
  of bladder, 735f
  of blastomycosis, 628f
Ventrodorsal radiography *(Continued)*
  of bronchial pattern, 616f–617f, 629f
  of cardiogenic pulmonary edema, 615f, 630f
  of caudal fragment, 182f
  of caudal lobe, 624f
  of caudal lung lobe, 622f
  of caudal thorax, 554f–555f, 567f
  of cervical vertebrae, 92f
  of chemodectoma, 564f
  of chronic hyperadrenocorticism, 620f
  of chronic renal disease, 713f
  of cranial abdomen, 548f
  of cranial lobe, 614f
  of diaphragmatic region, 536f
  of esophagus, 510f
  of heart, 587f
  of heart base tumor, 563f
  of heartworm disease, 595f
  of hemangiosarcoma metastasis, 628f
  of hypertrophic cardiomyopathy, 600f, 602f
  of hypovolemia seconard, 606f
  of kidneys, 708f, 717f, 719f
  of laryngeal collapse, 493f
  of left heart failure, 601f
  of left temporomandibular luxation, 128f
  of lumbar spine, 79f
  of lumbar vertebrae, 94f
  of lumbosacral region, 112f
  of mediastinal shift, 556f
  of mediastinum, 559f–560f
  of metal nail, 75f
  of mineralized mass in stomach, 672f
  of mixed lung pattern, 628f–629f
  of nodular opacity, 187f
  of normal feline pancreas, 669f
  of obesity, 185f
  o pulmonary lymphoma, 627f
  of patient hit by car, 183f, 189f
  of pelvic region, 79f
  of pelvis, 232f
  of peritoneopericardial diaphragmatic hernia, 544f
  of pleural cavity, 623f
  of pleural fluid, 578f
  of pleurocentesis, 623f
  of pneumomediastinum, 569f
  of pneumonia, 614f
  of principal bronchi, 562f
  of pulmonary hyperinflation, 620f
  of radiopaque choleliths, 685f
  of rib fractures, 527f, 619f
  of right middle lobe, 618f, 631f
  of right middle-lobe pneumonia, 82f, 613f
  of spine, 110f
  of subcutaneous emphysema, 569f
  of tetraparesis, 615f
  of thoracic hemivertebrae, 177f
  of thoracic spine, 176f
  of thoracic vertebrae, 94f
  of thoracic wall injury, 527f
  of thoracolumbar junction of canine with transitional anomaly, 112f
  of thorax, 180f, 186f, 482f, 516f, 553f–554f, 566f, 576f
  of tracheobronchial lymph node, 563f
  of transitional thoracolumbar vertebral segment, 524f
  of ureteral obstruction, 721f
Ventrodorsal spinal radiography, 177f
Ventrodorsal thoracic radiography, 79f, 482f
  of amputated forelimb, 183f

Ventrodorsal thoracic radiography *(Continued)*
of borzoi, 586f
of cardiac silhouette, 186f
of caudal esophageal foreign body, 562f
of craniodorsal mediastinal abscess, 561f
of distal aspect of rib, 528f
of fat opacity mass, 530f
of flail chest, 528f
of left hemithorax, 587f
of lung lobes, 609f
of mediastinal fat, 186f
of mediastinal mass, 560f
of mediastinum, 558f
of pectus excavatum, 526f
of pleural cavity, 580f
of pleural fluid, 577f
of primary tumor of rib, 529f
of pulmonary undercirculation, 599f
of split spinous process, 177f
of thickened interlobar fissures, 572f
Ventrodorsal view, 101, 109, 478–482
of abdomen, 657f
of accessory lung lobe, 478–482
of atelectasis, 478
of cardiac silhouette, 478
of caudal lobe vessel, 478
of caudodorsal thorax, 546f
combination of, 482
of diaphragmatic region, 537f–538f
of thorax, 542f–543f, 547f, 575f, 578f, 583f
of traumatic diaphragmatic hernia, 541f
Ventromedial-dorsolateral oblique radiography, 247f
Vertebrae, 172–193. *See also* specific types of
anatomy of, 172–174
anomalies of, 217
degenerative conditions of, 186–188
fractures of, 179–182
inflammatory conditions of, 185
intervertebral disc disease of, 182–185
luxation of, 179–182
metabolic conditions of, 190–191
Vertebrae *(Continued)*
neoplasia of, 188–190
transverse computed tomography of, 199f
vertebral column, anomalies of, 175–179
Vertebral arch, 172
Vertebral canal, 194
Vertebral column, 174b, 178–179, 190t
anomalies of, 175–179
atlantoaxial subluxation of, 177–178
block vertebrae of, 175
cervical spondylomyelopathy of, 178–179
hemivertebrae of, 175
spina bifida of, 177
transitional vertebrae of, 175–177
Vertebral osteochondroma, 209f
Vertebral osteomyelitis, 185
Vertebral physitis, 185
Vertebral tumor, 209–210
Vertical aortic arch, 591–592
Vertical displacement of gastrointestinal tract, 711, 711f
Vertically directed x-ray beam, 577f
Vesicoureteral reflux, 732–734
Vestibular mass lesion, 763
Vestibule. *See* Vagina/vestibule
Veterinarian, 50
Veterinary practice, 6, 50
Viability of the surrounding soft tissue, 284
Viable nonunion fracture, 301
Videofluoroscopic contrast study, 506–507
Viewing of image, 27–28
Villonodular synovitis, 345, 418, 418f–419f
Viral pneumonia, 638
Visceral abdominal lymph node, 665–666
Vitamin D, 283
Vocalizing, 519f
Voiding cystography, 729
Volume depletion, 581f
Volume element, 50
Volvulus, 86, 655f, 696, 777–780
Voxel, 50
Voxel-to-pixel translation, 50

W

Wallerian degeneration, 205–206
Wall-mounted cassette holder, 106, 111, 112f
Warmblood, 418f
Wavelength, 3t, 38
Wedge force stress, 334
Weight-bearing stifle, 349–352
Weighting factor, 3
West Highland white terrier, 329f
White blood cells, 154
Wide contrast resolution, 31f
Window width (W), 57
Withers region, 100f
Wobbler disease, 204
Word pattern, 609–610

X

X-ray, 2, 74. *See also* specific types of
absorption of, 4, 5f, 13–14, 17f, 19, 26, 31, 32f, 55, 74–75, 75f, 81f, 608, 610–611, 621–622
attenuation of, 22, 24–25, 30f, 50, 57, 136, 623
basic properties of, 2–3
biologic injury produced by, 2–3
characteristic, 9, 10f–11f, 13
discovery of, 2
gamma rays *vs.*, 2
production of, 9–12
properties of, 3b
substances absorbed in, 75f
X-ray beam, 78f
divergence of, 18f, 109f
energy of, 19
intensity of, 15f
orientation of, 259f
primary, 481f
radiographic projections by, 83f
X-ray energy, 11f, 16
X-ray film, 14
X-ray generator, 12
X-ray intensifying screen, 25–26
X-ray machine, 9f, 12, 14, 22, 126
X-ray production, 10f, 15f
X-ray tube, 9, 9f, 12, 12f, 14f

Y

Y fracture, 292

This page intentionally left blank

evolve learning system

ELSEVIER

YOU'VE JUST PURCHASED MORE THAN A TEXTBOOK



ACTIVATE THE COMPLETE LEARNING EXPERIENCE THAT COMES WITH YOUR BOOK BY REGISTERING AT

http://evolve.elsevier.com/Thrall/vetrad/

Once you register, you will have access to your

FREE STUDY TOOLS:

- **Video/Audio Clips**
  22 video clips and audio files assist in the understanding of complex physical principles
- **Image Collection**
  All images from the book can be accessed in one convenient location
- **Chapter Quizzes**
  An online test bank that contains multiple choice and true/false self-assessment exercises for every chapter
- **Bonus Chapters**
  4 bonus chapters provide still-current and practical information from the previous five editions
- **An Atlas of Normal Radiographic Anatomy of the Dog and Horse**
  Compiles all normal radiographic anatomy chapters from the fifth and sixth editions into a single atlas in digital image format

REGISTER TODAY!

This page intentionally left blank

This page intentionally left blank

This page intentionally left blank

This page intentionally left blank